Earth Observation:
Data, Processing and Applications

Volume 3: Applications

This publication is available in PDF format at *eopublications.au*.
We welcome your comments regarding the readability and usefulness of this report.
To provide feedback, please email *feedback@eopublications.au*.

Publisher:
Australia and New Zealand CRC for Spatial Information

ISBN [ONLINE]:
Volume 3A 978-0-6482278-5-4
Volume 3B 978-0-6482278-3-0

Copyright:
All material in this publication is licensed under a Creative Commons Attribution 4.0 Australia Licence, save for content supplied by third parties, and logos. Creative Commons Attribution 4.0 Australia Licence is a standard form licence agreement that allows you to copy, distribute, transmit and adapt this publication provided you attribute the work. The full licence terms are available from *https://creativecommons.org/licenses/by/4.0/legalcode*. A summary of the licence terms is available from *https://creativecommons.org/licenses/by/4.0/*.

Disclaimer:
While every effort has been made to ensure its accuracy, the CRCSI does not offer any express or implied warranties or representations as to the accuracy or completeness of the information contained herein. The CRCSI and its employees and agents accept no liability in negligence for the information (or the use of such information) provided in this report.

Recommended Citation:
CRCSI (2021). *Earth Observation: Data, Processing and Applications. Volume 3: Applications*. (Eds: Harrison, B.A., Anstee, J.M., Dekker, A.G., Gibson, R., Bastin, G., Thackway, R., King, E.A., Huete, A., Donald, G., Lyons, M., Sparks, T., Byrne, G., Lewis, M.M., and Xie, Q.). CRCSI, Melbourne.

Latest Revision:
October 2025

Background image on previous page: Sentinel-2A imagery acquired on 8 June 2020 over the eastern portion of the Wide Bay Burnett region in southeast Queensland. This region includes the cities of Bundaberg in the northeast and Maryborough, west of Fraser Island. In addition to tourism and fishing, this district supports a variety of agricultural production, principally beef, citrus, sugarcane, and forestry.
Source: Norman Mueller, Geoscience Australia

About this Series

This text, *Earth Observation: Data, Processing and Applications*, is an Australian Earth Observation (EO) community undertaking, which has been jointly sponsored by the Cooperative Research Centre for Spatial Information (CRCSI), the Commonwealth Scientific and Industrial Research Organisation (CSIRO), Geoscience Australia (GA) and the Bushfire and Natural Hazards Cooperative Research Centre (BNHCRC). This publication describes EO data, processing and applications in an Australian context, and includes a wide range of local case studies. It aims to:

- Consolidate EO teaching resources in Australia;
- Encourage a greater number of tertiary courses involving EO in Australia; and
- Promulgate Australia's growing dependence on EO data.

This new text substantially revises and updates two previous books published by CSIRO, namely *Introduction to Remotely Sensed Data* and *Introduction to Image Processing*, which were written to support users of the microBRIAN Image Processing system and used as tertiary texts throughout Australasia for over a decade. The new series comprises multiple volumes, with the option to expand into the future. Unlike the previous publications, the new text is envisaged as an ongoing, community resource, involving a broader range of professionals from academia, government and industry, with relevance to a wider audience. Each volume has been prepared by an editorial panel of local experts, supported by contributing authors who have written and/or reviewed application chapters and case studies. Planning and production of the series has been overseen by advisors from the sponsor organisations.

This series currently comprises three volumes:

Volume 1: Data

This volume outlines the basics of EO in terms of energy sources, data acquisition, sampling characteristics, and image availability. Discussion focuses on the scientific foundations of EO. This volume also considers the interactions of electromagnetic radiation with various targets and media, as relevant to understanding optical, thermal, passive microwave and radar imagery. Volume 1 comprises three sub-volumes:

- 1A—Basics and Acquisition
- 1B—Image Interpretation
- 1X—Appendices

Volume 2: Processing

Volume 2 describes the various options involved with image representation, analysis, transformation, integration and modelling, including details of relevant algorithms, with emphasis on their underlying mathematical and statistical principles. It comprises six sub-volumes:

- 2A—Basic Image Operations
- 2B—Image Rectification
- 2C—Image Transformations
- 2D—Image Integration
- 2E—Image Classification
- 2X—Appendices

Volume 3: Applications

This final volume introduces the Australian terrestrial and aquatic environment, and covers a broad range of application areas reliant on EO data. Specific case studies are included to demonstrate individual applications as appropriate. Volume 3 currently comprises two sub-volumes:

- 3A—Terrestrial Vegetation
- 3B—Surface Waters

This comprehensive series of publications also enables consistent nomenclature to be established within the Australian EO sector. The inclusion of updated methods, applications, and case studies into the future will continue to enhance its value to a wide range of readers.

About this Volume

Volume 3 in this series builds on the information provided in the first two volumes to describe applications of EO in an Australian context. It currently comprises two sub-volumes:

Volume 3A — Terrestrial Vegetation

Volume 3A details how EO data and processing methods can be used to understand and monitor vegetation growing on land. This volume is structured into seven parts:

- Introduction: describes background topics that are relevant to maximising the value of EO for studies of terrestrial vegetation, namely the Australian vegetated environment in terms of topography, climate, ecoregions, land use, and vegetation dynamics, and some of the methods that have been developed to map and monitor it;
- Measurable properties of terrestrial vegetation: discusses particular attributes of foliage, plants, communities, and ecosystems that are relevant to categorising vegetation using EO datasets;
- EO methods: reviews EO-based methods that can be used to map, monitor, and model terrestrial vegetation;
- Observing agriculture: considers the use of satellite, airborne, and proximal EO datasets to observe vegetation in the Australian landscape for the agricultural applications of crops, irrigated horticulture, pastures, rangelands and forestry;
- Observing carbon dynamics: considers the use of EO to map and monitor the Australian landscape in terms of carbon cycling and fire;
- Observing ecosystems: considers ecological integrity in terms of biodiversity and sustainability; and
- Observing our future: concludes this volume with a global perspective of how EO technologies can help to improve the management of terrestrial vegetation.

Volume 3B — Surface Waters

Volume 3B details how EO data and methods are used to map, monitor, and model various characteristics of Australia's inland, coastal, and marine waters. In this context, surface waters include sea ice, ice sheets and shelves, and icebergs in Antarctica and the Southern Ocean. This volume is also structured into seven parts:

- Introduction: describes background topics that are relevant to understanding EO studies of surface waters, namely their distribution, circulation, and other characteristics, both globally and within Australia's jurisdiction, and aquatic ecosystems in the Australian environment;
- Measurable properties of surface waters: introduce variations that can occur in, and the measurement methods used for, waterbodies in terms of the water surface, water column, substratum, and the whole water mass;
- EO data and models: focuses on those properties of water that can be measured and modelled using EO sensors in the context of Australian surface waters, namely optical, microwave, and acoustic;
- Observing surface water dimensions: details EO-based analyses that can be used to map and monitor the surface water extent, level, and bathymetry;
- Observing surface water energy: details EO-based analyses that can be used to map and monitor temperature, ice, wind and waves, and circulation of surface waters;
- Observing the waterscape: details EO-based analyses that can be used to map and monitor the surface water colour, quality, and ecology; and
- Looking ahead: concludes this volume with a global perspective of how EO technologies can help to improve our management of surface waters.

Preface

It has been suggested that business schools do three things for students[1]:

- provide them with a vocabulary that enables them to talk with authority about subjects they do not understand;
- transmit to them a set of principles that have demonstrated an ability to withstand any amount of disconfirming evidence; and
- provide a ticket of admission to a job where they can learn something about these subjects.

Some would say that these characteristics apply to current approaches to education in many other disciplines, including Earth Observation.

It is the aspiration of the authors of this text that students will learn more than the vocabulary of Earth Observation from these pages; hopefully they will acquire the knowledge to develop robust analytical and synthetic skills that will enable this field to advance and expand with insight and integrity.

A range of additional resources to assist readers is compiled in various Appendices. In particular, numerous online tutorials are now available from a range of sources to complement the material presented in this series.

1 Comments by Russell L. Ackoff in an interview with Robert J. Allio as reported in: Allio, R.J., and Ackoff, R.L. (2003). Iconoclastic management authority, advocates a 'systematic' approach to innovation. Strategy and Leadership 31 (3), 19–26.

Earth Observation:
Data, Processing and Applications

Volume 3A: Applications—Terrestrial Vegetation

This publication is available in PDF format at *eopublications.au*.
We welcome your comments regarding the readability and usefulness of this report.
To provide feedback, please email *feedback@eopublications.au*.

Publisher:
Australia and New Zealand CRC for Spatial Information

ISBN [ONLINE]:
978-0-6482278-5-4

Copyright:
All material in this publication is licensed under a Creative Commons Attribution 4.0 Australia Licence, save for content supplied by third parties, and logos. Creative Commons Attribution 4.0 Australia Licence is a standard form licence agreement that allows you to copy, distribute, transmit, and adapt this publication provided you attribute the work. The full licence terms are available from *https://creativecommons.org/licenses/by/4.0/legalcode*. A summary of the licence terms is available from *https://creativecommons.org/licenses/by/4.0/*.

Disclaimer:
While every effort has been made to ensure its accuracy, the CRCSI does not offer any express or implied warranties or representations as to the accuracy or completeness of the information contained herein. The CRCSI and its employees and agents accept no liability in negligence for the information (or the use of such information) provided in this report.

Recommended Citation for Volume 3A:
CRCSI (2021). *Earth Observation: Data, Processing and Applications. Volume 3A: Applications—Terrestrial Vegetation*. (Eds: Harrison, B.A., Gibson, R., Bastin, G., Thackway, R., Huete, A., Donald, G., Lyons, M., Sparks, T., Byrne, G., Lewis, M.M., and Xie, Q.). CRCSI, Melbourne.

The recommended citation for each contributed chapter is given on the first page of the chapter.

Latest Revision:
October 2025

Background image on previous page: Sentinel-2A imagery acquired on 8 June 2020 over the eastern portion of the Wide Bay Burnett region in southeast Queensland. This region includes the cities of Bundaberg in the northeast and Maryborough, west of Fraser Island. In addition to tourism and fishing, this district supports a variety of agricultural production, principally beef, citrus, sugarcane, and forestry.
Source: Norman Mueller, Geoscience Australia

Acknowledgements

Production of this series of texts would not have been possible without the financial support of CSIRO, CRCSI, GA and BNHCRC, input from members of the editorial panels, and direction from members of the various advisory panels. Administrative support from FrontierSI is also gratefully acknowledged.

Volumes 1 and 2 of this series are based on text originally published in Harrison and Jupp (1989, 1990, 1992, and 1993)[1]. Many illustrations and some text from these publications have been reproduced with permission from CSIRO.

The following authors are thanked for their contributed chapters:

- 12. **Crops**: Barbara Harrison (ex CSIRO) and Graham Donald (ex CSIRO)
- 13. **Irrigated Horticulture**: Des Whitfield, Andrew McAllister, Mohammad Abuzar, and Mark O'Connell (Agriculture Victoria)
- 14. **Pastures:** Graham Donald (ex CSIRO)
- 15. **Rangelands**: Gary Bastin (ex CSIRO)
- 16. **Forestry**: Nicholas Coops (University of British Columbia) and Barbara Harrison (ex CSIRO)
- 17. **Carbon Cycling**: Alfredo Huete (University of Techology, Sydney)
- 18. **Fire**: Rebecca Gibson (Environment NSW), Marta Yebra (Australian National University), Barbara Harrison (ex CSIRO), and Ross Bradstock (University of Wollongong)

Other contributors are gratefully acknowledged:

- excursus authors: Nicholas Coops and Glenn Newnham (Excursus 5.1), Qiaoyun Xie (Excursus 9.1), John Carter (Excursus 10.1), Graham Donald (Excursus 14.1), Peter Scarth (Excursus 14.2), Alfredo Huete (Excursus 17.1, Excursus 17.2)
- reviewers: Albert van Dijk (full draft), Laurie Chisholm (early draft), Michael Hill (Sections 1 to 4), Richard Lucas (Sections 3.2 and 20.5), David Jupp (Excursus 5.1), Peter Scarth (Excursus 6.1 and Section 14.5), James Cleverly, Jason Beringer, Peter Isaac, and Caitlin Moore (Excursus 7.2), Bob Denholm (Excursus 8.2), Juan Pablo Guerschman (Sections 8, 11, 12, 14, and 15), Franz Waldner (Sections 11 and 12), Jorge L. Peña-Arancibia (Section 13), Terry Beutel (Excursus 15.1), Glenn Newnham and Stuart Davey (Section 16), Norman Mueller (Section 18), Angela Robb (Excursus 19.2), Alison Cowood and Terry Hills (Section 20.5), David Hudson (Section 21), Brian Walker (Excursus 21.1)
- illustrations: Norman Mueller, Tony Sparks, Richard Thackway, Gary Bastin, John Ludwig, Laurie Chisholm, Mitchell Lyons, Jenny Lovell, Glenn Newnham, Randall Donohue, Qiaoyun Xie, Mark Grant, Franz Waldner, Fred Hughes, Graham Donald, Mark O'Connell, Des Whitfield, Mohammad Abuzar, Peter Scarth, Barney Foran, John Carter, Terry Beutel, Ivan Kotzur, Robert Norman, Sue Ogilvy, Kirsty Yeates, Matthew Bolton, Carl Davies (CMDphotographics), Peter Harrison.

We thank those owners of copyrighted illustrative material for permission to reproduce their work. Credits for individual illustrations are provided below the relevant graphic.

All volumes in this series are covered by the copyright provisions of CC BY 4.0 AU.

1 Harrison, B.A., and Jupp, D.L.B. (1989) Introduction to Remotely Sensed Data: Part ONE of the microBRIAN Resource Manual. CSIRO, Melbourne. 156 p.
Harrison, B.A., and Jupp, D.L.B. (1990) Introduction to Image Processing: Part TWO of the microBRIAN Resource Manual. CSIRO, Melbourne. 256 p.
Harrison, B.A., and Jupp, D.L.B. (1992) Image Rectification and Registration: Part FOUR of the microBRIAN Resource Manual. MPA, Melbourne.
Harrison, B.A., and Jupp, D.L.B. (1993) Image Classification and Analysis: Part THREE of the microBRIAN Resource Manual. MPA, Melbourne.

Table of Contents

Volume 3A: Applications—Terrestrial Vegetation a

Acknowledgements i

Introduction 1

1 The Vegetated Landscape 3

1.1 Environmental Factors and Gradients 3

1.1.1 Biotic factors 5

1.1.2 Abiotic factors 6

1.1.3 Environmental gradients 9

1.2 Ecological Units 10

1.2.1 Individuals and populations 10

1.2.2 Communities 11

1.2.3 Ecosystems 11

1.3 Terrestrial Ecosystems 13

1.3.1 Biogeography and biodiversity 13

1.3.2 Major habitat zones 13

1.3.3 A dynamic tapestry 15

1.4 Further Information 18

1.5 References 18

2 The Australian Environment 21

2.1 Topography and Hydrology 24

2.2 Climate 27

2.2.1 Weather patterns 27

2.2.2 Climatic drivers 31

2.2.3 Climate classifications 31

2.3 Biota 35

2.3.1 Classifying vegetation 35

2.3.2 Weeds 39

2.3.3 Indigenous and feral animals 39

2.4 Ecoregions and Fire Patterns 40

2.4.1 Deserts and xeric shrublands 42

2.4.2 Mediterranean forests, woodlands and scrub 42

2.4.3 Montane grasslands and shrublands 43

2.4.4 Temperate broadleaf and mixed forest 43

2.4.5 Temperate grasslands, savannas and shrublands 43

2.4.6 Tropical and subtropical grasslands, savannas and shrublands 44

2.4.7 Tropical and subtropical moist broadleaf forests 44

2.5 Land Use 45

2.5.1 Indigenous patterns 46

2.5.2 European settlement patterns 47
2.5.3 Current land use 47
2.6 Further Information 49
2.7 References 50

3 Mapping Vegetated Landscapes 57
3.1 Key Concepts in Landscape Mapping 57
3.1.1 Vegetation type versus vegetation condition 57
3.1.2 Land cover versus land use 58
3.2 How Do We Map Land Cover? 59
3.2.1 Classification schemes 59
3.2.2 Mapping methods and accuracy assessment 63
3.3 Mapping Approaches 66
3.3.1 Land evaluation based on mapping units 66
3.3.2 Actual distribution of current vegetation 68
3.3.3 Probable distribution of natural vegetation 68
3.3.4 Actual distribution of current land use 69
3.4 Monitoring Landscape Change 73
3.4.1 Changes in land condition 74
3.4.2 Changes in land use 78
3.5 Further Information 81
3.6 References 82

Measurable Properties of Terrestrial Vegetation 87

4 Attributes of Foliage 89
4.1 Structure and Shape 89
4.1.1 Anatomy 89
4.1.2 Morphology 90
4.1.3 Texture 92
4.1.4 Strength 92
4.2 Chemical Composition 93
4.2.1 Water 93
4.2.2 Inorganic components 95
4.2.3 Organic components 96
4.3 Spectral Properties 99
4.4 Boundary layer 101
4.5 Further Information 103
4.6 References 103

5 Attributes of Individual Plants 107
5.1 Structure 107
5.1.1 Growth form 107
5.1.2 Biomass 111
5.2 Physiological Processes 111
5.2.1 Photosynthesis 111
5.2.2 Respiration 113

5.2.3 Transpiration 114
5.2.4 Thermal stability 114
5.3 Growth 116
5.3.1 Life cycle 116
5.3.2 Phenology 116
5.3.3 Abscission 117
5.3.4 Photomorphogenesis 118
5.3.5 Nutrient use efficiency 118
5.4 Further Information 119
5.5 References 119

6 Attributes of Plant Communities **125**
6.1 Formations 126
6.2 Horizontal Spacing and Pattern 130
6.3 Density and Cover 130
6.3.1 Foliage cover 130
6.3.2 Cover-abundance 131
6.3.3 Leaf area index (LAI) 131
6.3.4 Fraction of absorbed photosynthetically active radiation (fAPAR) 132
6.3.5 Basal area (BA) 133
6.3.6 Fractional cover 133
6.4 Canopy Colour and Texture 133
6.5 Growth Stages 135
6.6 Succession 135
6.7 Further Information 137
6.8 References 137

7 Attributes of Ecosystems **141**
7.1 Biodiversity 142
7.2 Stability and Equilibrium 143
7.3 Function and Condition 147
7.4 Productivity 150
7.5 Energy Balance 152
7.6 Water Balance 155
7.7 Further Information 156
7.8 References 156

EO Methods 163

8 Mapping **165**
8.1 Spectral Indices 166
8.1.1 Greenness 166
8.1.2 Hyperspectral indices 170
8.1.3 Vegetation cover and condition 171
8.1.4 Plant productivity 172
8.1.5 Water content 173
8.1.6 Landscape 'leakiness' 174

8.2 Spectral Classification 174
8.2.1 Vegetation 175
8.2.2 Geology and soils 176
8.2.3 Water 178
8.2.4 Urban features 178
8.3 Sub-pixel Analyses 179
8.4 Further Information 183
8.5 References 183

9 Monitoring **191**
9.1 Vegetation types 193
9.2 Change Indices 194
9.2.1 Fire footprints 194
9.2.2 Ecosystem disturbance 195
9.3 Phenology 195
9.4 Evapotranspiration 200
9.5 Plant Water Stress 203
9.6 Plant Vigour 204
9.7 Further Information 205
9.8 References 206

10 Modelling **213**
10.1 Modelling Considerations 214
10.1.1 Underlying EO model 214
10.1.2 Interpolation and extrapolation 215
10.1.3 Scaling 216
10.1.4 Spatial patterns 217
10.2 EO-based Models for Terrestrial Vegetation 218
10.2.1 Leaf models 218
10.2.2 Plant productivity models 219
10.2.3 Global and regional models 220
10.3 Further Information 224
10.4 References 224

Observing Agriculture 229

11 Agriculture Overview **231**
11.1 Agriculture in Australia 232
11.2 Essential Agricultural Variables 233
11.3 Monitoring Managed Landscapes 235
11.4 Land Degradation 237
11.5 Food Security 241
11.6 Further Information 243
11.7 References 243

12 Crops **249**
Barbara Harrison and Graham Donald
12.1 Crops in Australia 249

12.2 EO Sensors for Crops 250
12.3 Crop Type and Agricultural Land Use 251
12.4 Crop Extent, Condition and Production Forecasts 252
12.5 Global Crop Monitoring Systems 255
12.6 Precision Agriculture 256
12.7 Further Information 258
12.8 References 258

13 Irrigated Horticulture **263**
Des Whitfield, Andrew McAllister, Mohammad Abuzar, and Mark O'Connell
13.1 Irrigated Horticulture in Southeast Australia 263
13.2 EO Sensors for Irrigated Horticulture 264
13.3 Fundamentals of Irrigation Management 265
13.4 Irrigation Requirements of Horticultural Crops 266
13.4.1 Weather-based estimates of soil water status in orchards 266
13.4.2 Reference crop evapotranspiration 266
13.4.3 Crop characteristics 267
13.4.4 Why two reference crops? 267
13.5 Satellite-based Estimates of ET 268
13.5.1 K_c-VI relationships 268
13.5.2 T_s-VI relationships 268
13.5.3 Surface energy balance models 269
13.6 METRIC Model: Summer Crops 269
13.7 METRIC Model: Irrigated Horticulture 270
13.7.1 Introduction 270
13.7.2 Model implementation 271
13.7.3 ET_rF /NDVI relationships 273
13.8 Application to Irrigated Horticultural Crops in Southeast Australia 278
13.9 Further Information 279
13.10 References 279

14 Pastures **281**
Graham Donald
14.1 Pastures in Australia 282
14.2 EO Sensors for Pastures 283
14.3 Phenology and Production 284
14.4 Pasture Growth Rate 286
14.5 Biomass Monitoring 290
14.6 Precision Grazing 294
14.7 Wool Production 294
14.8 Further Information 295
14.9 References 295

15 Rangelands **299**
Gary Bastin
15.1 Rangelands in Australia 300
15.1.1 Vegetation 302
15.1.2 Water 303

15.1.3 Fire 304
15.1.4 Grazing 304
15.1.5 Socio-economic factors 306
15.2 EO Sensors for Rangelands 307
15.3 Rangeland Condition 308
15.3.1 Vegetation resilience 310
15.3.2 Landscape condition and leakiness 311
15.3.3 Persistence of ground cover 312
15.4 Operational Systems for Monitoring Rangelands 313
15.5 Conserving Biodiversity 315
15.6 Further Information 318
15.7 References 318

16 Forestry **323**
Nicholas Coops and Barbara Harrison
16.1 Forestry in Australia 324
16.2 EO Sensors for Forestry 327
16.3 Forest Type 329
16.4 Forest Hydrology 329
16.5 Forest Structure 330
16.5.1 Stand height and cover 330
16.5.2 Individual trees 331
16.5.3 Geometric-optical models 332
16.5.4 Biomass and fuel load 333
16.6 Forest Functionality 334
16.6.1 Plant nutrition 334
16.6.2 Plant stress 334
16.7 Forest Diversity 335
16.7.1 Floral diversity 335
16.7.2 Faunal monitoring 338
16.8 Forest Disturbance 338
16.8.1 Insect damage 338
16.8.2 Fire monitoring 338
16.8.3 Environmental monitoring 339
16.9 Further Information 340
16.10 References 340

Observing Carbon Dynamics 351

17 Carbon Cycling **353**
Alfredo Huete
17.1 Carbon Cycling in Australia 359
17.2 EO Sensors for Carbon Cycling 360
17.3 Biosphere productivity 361
17.3.1 Relationships between EO and flux tower GPP estimates 362
17.3.2 Solar-induced chlorophyll fluorescence (SIF) as proxy for GPP 363
17.4 Net Primary Productivity 363

17.4.1 VIs as proxies for ANPP 363
17.4.2 Ecosystem respiration 364
17.4.3 Net ecosystem productivity and net biome productivity 364
17.4.4 Growing season phenology 364
17.4.5 Photochemical Reflectance Index 365
17.5 Carbon Models 365
17.5.1 EO-based LUE models 366
17.5.2 Greenness and radiation (G-R) models 366
17.5.3 Temperature-Greenness (T-G) model 367
17.5.4 Carbon modelling 368
17.5.5 Vegetation Photosynthesis Model (VPM) 370
17.6 Anthropogenic carbon emissions 371
17.6.1 CO_2 emissions 372
17.6.2 Examples of satellite studies of CO_2 emissions and flux inversions 373
17.6.3 Land use and land cover modification 373
17.6.4 Effects of Carbon Cycle Changes 374
17.7 Carbon stocks 376
17.7.1 Biomass carbon stock 376
17.7.2 Soil organic carbon 376
17.7.3 Microwave EO 377
17.7.4 Lidar and above ground biomass 378
17.8 The Future 378
17.9 Further Information 379
17.10 References 379

18 Fire **389**
Rebecca Gibson, Marta Yebra, Barbara Harrison, and Ross Bradstock
18.1 Fire in Australia 390
18.2 EO Sensors for Fire 392
18.3 Predictive Fire Analyses 395
18.3.1 Fuels 395
18.3.2 Weather conditions and topography 398
18.3.3 Ignitions 399
18.3.4 Risk analysis 399
18.4 Active Fire Analyses 400
18.4.1 Satellite imagery 400
18.4.2 Airborne imagery 401
18.5 Retrospective Fire Analyses 403
18.5.1 Fire extent and severity 404
18.5.2 Fire recovery 407
18.5.3 Fire history and behaviour 408
18.6 Operational Systems for Fire Management 409
18.6.1 Flammability models 409
18.6.2 Hotspot imagery 410
18.6.3 Fire extent and severity 410
18.7 Further Information 412
18.8 References 413

Observing Ecosystems 427

19 Biodiversity **429**

19.1 Biodiversity in Australia 432
19.2 EO Sensors for Biodiversity 434
19.3 Global Biodiversity Indicators 435
19.4 Risk Assessment 437
19.5 Australian Biodiversity Monitoring 442
19.6 Further Information 445
19.7 References 446

20 Sustainability **451**

20.1 Sustainability in Australia 453
20.2 EO Sensors for Sustainability 454
20.3 Ecosystem Services 455
20.4 Sustainable Development 460
20.5 Environmental-Economic Accounting 464
20.6 Further Information 471
20.7 References 472

Observing Our Future 477

21 The Road Ahead **479**

21.1 The Smart Environment 479
21.2 An Objective Worldview 482
21.3 Societal Benefit Areas 483
21.4 Stewards of Tomorrow 486
21.5 Further Information 488
21.6 References 488

Glossary 490

List of Figures

Figure 1.1 Holdridge life zone classification scheme 13

Figure 1.2 Whittaker's biome classification 14

Figure 1.3 Processes and interactions within Earth System Science 16

Figure 1.4 Terrestrial carbon cycle 17

Figure 2.1 Australia 22

Figure 2.2 Major landform categories 25

Figure 2.3 Australian Soil Resource Information System (ASRIS) 25

Figure 2.4 Major drainage basins 26

Figure 2.5 Great Artesian Basin 27

Figure 2.6 Climate zones derived from humidity and temperature 28

Figure 2.7 Average annual rainfall 28

Figure 2.8 Seasonal temperature variations in Australia 29

Figure 2.9 Evaporation and evapotranspiration over Australia 30

Figure 2.10 Modified Köppen climate classification 32

Figure 2.11 Agroclimatic classifications 33

Figure 2.12 Major Vegetation Groups derived from NVIS Version 3 38

Figure 2.13 Interim Biogeographic Regionalisation of Australia (IBRA) Version 7 41

Figure 2.14 Terrestrial Ecoregions in Australia 41

Figure 2.15 Australia's towns by population size groupings, 2016 45

Figure 2.16 Aboriginal grain harvest map 46

Figure 2.17 Land use in Australia for 2010–11 48

Figure 3.1 Multi-level EO 64

Figure 3.2 Idealised spectral signatures 65

Figure 3.3 National VAST-2 dataset 76

Figure 3.4 Landscape change summary 78

Figure 3.5 Likelihood of ALUM land use change 80

Figure 4.1 Typical leaf cell structure 90

Figure 4.2 Absorption spectra of leaf pigments 97

Figure 4.3 Reflectance of green foliage 100

Figure 4.4 Leaf reflectance changes with stress 101

Figure 4.5 Impact of vegetation density on wind flow 102

Figure 5.1 Vegetation cover classes 108

Figure 5.2 Foliage profile 108
Figure 5.3 Lidar operation 109
Figure 5.4 TLS-based three-dimensional complexity of forest 110
Figure 5.5 Reflectance characteristics of typical green leaf structure 112
Figure 6.1 Height strata 126
Figure 6.2 Processing overview 128
Figure 6.3 Vegetation height and structure 129
Figure 6.4 Population distribution patterns 130
Figure 6.5 Fraction of Absorbed Photosynthetically Active Radiation (fAPAR) 132
Figure 6.6 Vegetation cover triangle 134
Figure 6.7 Simulated reflectance for increasing grass cover 134
Figure 6.8 Forest succession 136
Figure 7.1 Biodiversity factors 142
Figure 7.2 The grazing system 144
Figure 7.3 Ecosystem processes and feedback loops 147
Figure 7.4 Landscape function examples 148
Figure 7.5 Landscape function versus landscape condition 149
Figure 7.6 GPP over Australia 150
Figure 7.7 Flux tower distribution and site data 154
Figure 8.1 Normalisation effect in 'Normalised Difference Vegetation Index' (NDVI) 167
Figure 8.2 Within field crop variability 171
Figure 8.3 Leakiness index 174
Figure 8.4 Fractional cover index image 181
Figure 8.5 Fractional cover endmembers 182
Figure 9.1 Seasonal vegetation trends derived from AVHRR NDVI data 1981–2006 194
Figure 9.2 Greenness changes in annual plants 197
Figure 9.3 NDVI time series of pine plantation 198
Figure 9.4 Australian Phenology Product 199
Figure 9.5 Seasonally-integrated EVI from Australian Phenology Product 199
Figure 9.6 Budyko's framework and curve 201
Figure 10.1 Modelling error 213
Figure 10.2 Measurement and analysis of image features 214
Figure 10.3 Basic framework for extrapolation in ecology 215
Figure 10.4 Scaling procedure 216
Figure 10.5 Hypothetical landscape patterns 217

Figure 10.6 Modular structure of Dynamic Global Vegetation Models 221
Figure 11.1 Agricultural land uses in Australia 232
Figure 11.2 Driving force–pressure–state–impact–response (DPSIR) framework 233
Figure 11.3 Essential Variables in the context of UN Sustainable Development Goals 234
Figure 11.4 Seasonal quality matrix 235
Figure 11.5 Dust storm 239
Figure 12.1 Crop response to fertiliser application 257
Figure 13.1 Variation of surface-air temperature differences with vegetation cover 268
Figure 13.2 Crop coefficient variations 270
Figure 13.3 Typical crop coefficient curve 271
Figure 13.4 Irrigation districts 272
Figure 13.5 Quartile representations 274
Figure 13.6 Relationships for selected crops 275
Figure 13.7 Representative ET_rF/NDVI relationships for selected crops 276
Figure 13.8 Endmember regression estimates of ET_rF_{min} and ET_rF_{max} 277
Figure 14.1 Area of agricultural land 282
Figure 14.2 Basic metrics 284
Figure 14.3 Examples of Pasture Growth Rate imagery 288
Figure 14.4 Biomass calibration/validation sites 292
Figure 14.5 Sample national biomass map, September 2020 293
Figure 15.1 Framework for ACRIS reporting 300
Figure 15.2 Land uses in Australian rangelands 301
Figure 15.3 Vegetation Recovery 303
Figure 15.4 Density of waterpoints 304
Figure 15.5 Impact of artificial waterpoints on native species 305
Figure 15.6 Remote populations in Australia 306
Figure 15.7 Monitoring approaches 309
Figure 15.8 Stylised grazing gradient based on remotely sensed ground cover 310
Figure 15.9 Landscape function 311
Figure 15.10 Leakiness index example 312
Figure 15.11 VegMachine comparisons 314
Figure 16.1 Australian forests 326
Figure 16.2 Native forest categories 327
Figure 16.3 Penetration of radar wavelengths into vegetation layer 328
Figure 16.4 TLS-derived tree structure 332

Figure 16.5 Spectranomics Database elements 337
Figure 17.1 The carbon cycle between land, atmosphere, and oceans 354
Figure 17.2 Terrestrial photosynthetic carbon cycle 355
Figure 17.3 Seasonal variations in photosynthesis (GPP) between hemispheres 357
Figure 17.4 EO of terrestrial carbon cycle studies 359
Figure 17.5 Australian territorial carbon budget 1990–2011 360
Figure 17.6 NDVI-APAR relationship 362
Figure 17.7 Combined temperature-greenness model 368
Figure 17.8 MODIS NPP product based on BIOME-BGC model 369
Figure 17.9 Primarily Satellite-based Vegetation Photosynthesis and Respiration Model (VPRM) 370
Figure 17.10 Global Carbon Budget 2009–2018 371
Figure 17.11 Changes in carbon dioxide concentration 372
Figure 17.12 Change in global leaf area across 1982–2015 374
Figure 17.13 Australian interannual variations in carbon-related indicators 375
Figure 18.1 Fire seasonality in Australia 390
Figure 18.2 Fuel Moisture Content estimates 394
Figure 18.3 Aerial imagery of active fire 403
Figure 19.1 Human population growth 430
Figure 19.2 Response-pressure-state-benefit (RPSB) framework 435
Figure 19.3 Biodiversity change in terms of loss and alterations 437
Figure 19.4 EO framework for ecosystem risk assessment 438
Figure 19.5 RLE categories and criteria and categories 440
Figure 19.6 Application of RLE 441
Figure 20.1 Global GDP versus global material extraction 1900 to 2005 452
Figure 20.2 System of Environmental Economic Accounting 454
Figure 20.3 Ecosystem services in extensive agriculture 457
Figure 20.4 EO in ecosystem service assessment 459
Figure 20.5 Three pillars of sustainability 460
Figure 20.6 Ecological Footprint and Biocapacity for Australia 463
Figure 20.7 Overview of SEEA Central Framework 467
Figure 20.8 Environmental accounts versus environmental-economic accounts 468
Figure 21.1 The Internet of Things technology roadmap 480

List of Tables

Table 1.1 The plant kingdom 4

Table 1.2 Interactions between biotic components 5

Table 1.3 Ecosystem processes 12

Table 1.4 Terrestrial biomes 15

Table 2.1 Geography and settlement of Australia 23

Table 2.2 Australian DEM 24

Table 2.3 Australian climate types 31

Table 2.4 Agroclimatic class descriptions for Figure 2.11 34

Table 2.5 Common definitions for Australian vegetation 36

Table 2.6 Structural classification of Australian vegetation 37

Table 2.7 NVIS information hierarchy 37

Table 2.8 Native vegetation classification systems 38

Table 2.9 Land uses in Australia 2010–11 47

Table 3.1 Structure of FAO Land Cover Classification System 60

Table 3.2 Dichotomous phase classifiers and land cover types 61

Table 3.3 LCCS classification of primarily vegetated areas 62

Table 3.4 LCCS classification of primarily non-vegetated areas 63

Table 3.5 Australian landscape mapping approaches 67

Table 3.6 ALUM classification 70

Table 3.7 National Landcare Program 73

Table 3.8 VAST-2 diagnostic components, criteria and indicators 75

Table 3.9 Selected site attributes 77

Table 3.10 Drivers of land use change 79

Table 4.1 Photosynthetic pigments 98

Table 5.1 Photosynthetic pathways 113

Table 5.2 Plant growth factors 116

Table 6.1 Vegetation formations 127

Table 6.2 Height strata 127

Table 6.3 Height classes 127

Table 6.4 Summary of structural classes 128

Table 6.5 Effect of sensor quantisation on radiometric sensitivity 134

Table 7.1 Equilibrium versus nonequilibrium systems 145

Table 7.2 Rangeland management models 145
Table 7.3 State-and-Transition model terms 146
Table 7.4 Grazing land condition classes 146
Table 7.5 Examples of land condition indicators 149
Table 8.1 Sampling dimensions in EO imagery 166
Table 8.2 SVTM workflow 177
Table 9.1 Potential reference site measurements 192
Table 9.2 Ecohydrological characteristics of perennial and annual vegetation 193
Table 9.3 Significant phenological metrics 196
Table 9.4 Phenological stages of rice crop 197
Table 10.1 Leaf models 219
Table 11.1 RaPP spatial datasets 236
Table 11.2 Eight extended droughts in Australia 239
Table 11.3 Total economic value of ecosystem services 240
Table 12.1 EO sensors relevant to crops 250
Table 12.2 Crop-SI model 253
Table 12.3 Scales of crop forecasting 254
Table 12.4 Global and regional agricultural monitoring systems 256
Table 13.1 EO sensors relevant to irrigated horticulture 264
Table 13.2 Definition of major water use terms 266
Table 13.3 Values of C_n and C_d coefficients 266
Table 13.4 Landsat-5 images used in analysis 272
Table 13.5 Automatic weather station sites 273
Table 14.1 EO sensors relevant to pastures 283
Table 14.2 Description of NDVI metrics 285
Table 14.3 Supplementary metrics 285
Table 15.1 Potential responses of vegetation to grazing exclusion 305
Table 15.2 EO sensors relevant to rangelands 307
Table 15.3 Rangelands in Australia 313
Table 15.4 BioCondition indicators 316
Table 16.1 Forest area in Australia 325
Table 16.2 Native forest classes 325
Table 16.3 EO sensors relevant to forestry 328
Table 17.1 EO sensors relevant to carbon cycling 361
Table 18.1 Major bushfires in Australia 391

Table 18.2 EO sensors relevant to fire-related studies 393
Table 18.3 Current and potential uses of the Australian Flammability Monitoring System 410
Table 19.1 Land management practices with ongoing impact on biodiversity in Australia 432
Table 19.2 Biodiversity in Australia's terrestrial vegetation 433
Table 19.3 EO sensors relevant to biodiversity 434
Table 19.4 RPSB indicators 436
Table 19.5 EBV classes and candidates 436
Table 19.6 Policy tools 442
Table 19.7 Australian Biodiversity Conservation Strategy 2010–2030 Targets 443
Table 19.8 NSW Biodiversity Indicator Program 443
Table 19.9 VQA scoring 444
Table 20.1 Comparison of natural resource management models 452
Table 20.2 EO sensors relevant to sustainability 454
Table 20.3 Ecosystem services—challenges and opportunities 457
Table 20.4 EO capabilities relevant to ecosystem services 458
Table 20.5 Definitions of sustainabililty pillars 461
Table 20.6 Examples of ecosystem accounting measures 465
Table 20.7 Australian environmental economic accounts based on SEEA 469
Table 21.1 GEO projects 485
Table 21.2 Recommended reading 487

List of Excurses

Excursus 1.1—Classifying Vegetation 4

Excursus 1.2—Earth System Science 16

Excursus 3.1—FAO Land Cover Classification System 61

Excursus 3.2—Vegetation Assets, States and Transitions (VAST) 76

Excursus 4.1—Plant Pigments 97

Excursus 5.1—Lidar 109

Excursus 6.1—Vegetation Height and Structure Map 127

Excursus 7.1—Modelling Grazed Landscapes 144

Excursus 7.2—Flux Towers 153

Excursus 8.1—Composite Image Products 170

Excursus 8.2—NSW State Vegetation Type Map (SVTM) 177

Excursus 8.3—Fractional Cover 181

Excursus 9.1—Australian Phenology Product 198

Excursus 9.2—Budyko Framework 200

Excursus 10.1—AussieGRASS 222

Excursus 10.2—Water Resources Assessment 223

Excursus 11.1—GEOGLAM RaPP 236

Excursus 11.2—Learning from History 238

Excursus 12.1—Graincast 254

Excursus 14.1—EO-based Pasture Products 287

Excursus 14.2—Integrated Biomass Estimation 291

Excursus 15.1—VegMachine 314

Excursus 15.2—Rangelands Biodiversity Monitoring Framework 317

Excursus 16.1—Carnegie Spectranomics Project 336

Excursus 17.1—The Carbon Cycle 354

Excursus 17.2—Measuring Biosphere Productivity 358

Excursus 18.1—Fire Detection Products 402

Excursus 19.1—IUCN Red Lists of Threatened Species and Ecosystems 439

Excursus 19.2—Vegetation Quality Assessment 444

Excursus 20.1—Millennium Ecosystem Assessment 456

Excursus 20.2—Global Sustainable Development Agreements 462

Excursus 20.3—Global Footprint Network 463

Excursus 20.4—System of Environmental Economic Accounting 466

Excursus 21.1—Social-ecological Resilience 484

Introduction

This series of publications, *Earth Observation: Data, Processing and Applications*, comprises three volumes. Volume 1 in this series, *Data,* is presented as three sub-volumes, which together outline the basics of Earth Observation (EO) in terms of energy sources, data acquisition, sampling characteristics, image availability, data interpretation, and usage. Volume 2, *Processing*, (six sub-volumes) describes the various options involved with image representation, analysis, transformation, integration, and modelling, including details of relevant algorithms, with emphasis on their underlying mathematical and statistical principles. These volumes provide valuable background information for understanding specific applications of EO. They also define terminology used in Volume 3, *Applications*, which currently comprises two sub-volumes: 3A, Terrestrial Vegetation, and 3B, Surface Waters.

Volume 3A details how EO methods can be used to understand and monitor vegetation growing on land. The introductory sections in this sub-volume describe background topics that are relevant to maximising the value of EO for studies of terrestrial vegetation. Sections 1 to 3 below introduce the Australian vegetated environment in terms of topography, climate, ecoregions, land use, and vegetation dynamics, and some of the methods that have been developed to map and monitor it. Sections 4 to 7 respectively summarise attributes of foliage, plants, communities, and ecosystems that are relevant to EO-based studies. Sections 8 to 10 review EO-based methods that are relevant to vegetation mapping, monitoring, and modelling, while Sections 11 to 20 introduce specific application areas where EO datasets are being used in Australia. Section 21 concludes this sub-volume by looking ahead.

Contents

1 The Vegetated Landscape 3

2 The Australian Environment 21

3 Mapping Vegetated Landscapes 57

Background image on previous page: This view of the Australian continent (shown as Mercator projection) was created by merging colour-coded topography with relief shading using data acquired by the Shuttle Radar Topography Mission (SRTM; see Volume 1) in February 2002. Northeast slopes appear bright and southeast slopes appear dark, with green indicating low elevations, rising through yellow and tan to white for highest elevations
Source: NASA. (Retrieved from *https://earthobservatory.nasa.gov/images/5100/australia-shaded-relief-and-colored-height*)

1 The Vegetated Landscape

Vegetation plays a crucial role in regulating environmental conditions, including weather and climate. The amount of water and carbon dioxide in the air and the albedo of our planet are all influenced by vegetation, which in turn influences all life on Earth. Soil properties are also strongly influenced by vegetation, through biogeochemical cycles and feedback loops (see Volume 1A—Section 4). Vegetated landscapes on Earth provide habitat and energy for a rich diversity of animal species, including humans. Vegetation is also a major component of the world economy, through the global production of food, fibre, fuel, medicine, and other plant-based resources for human consumption.

In this section, we introduce vegetation in the context of:

- environmental factors and gradients (see Section 1.1);
- ecological units (see Section 1.2); and
- terrestrial ecosystems (see Section 1.3).

Life did not take over the globe by combat,
but by networking.
(Margulis and Sagan, from 'Microcosmos')

1.1 Environmental Factors and Gradients

All living organisms interact with the environment in which they live. The environment largely determines where organisms can survive and reproduce and, conversely, organisms modify their environment over time to enhance their survival and prosperity.

Any element of the environment that influences living organisms is termed an environmental factor. While these factors are interrelated, they are generally discussed individually to discern the many and complex relationships that exist within the environment as a whole. These factors are generally subdivided into two categories:

- biotic—plants (see Excursus 1.1), animals (including humans), and microorganisms (see Section 1.1.1); and
- abiotic—climate, substrate, and disturbances (see Section 1.1.2).

Environmental factors can have a wide and diverse range of potential influences on vegetation establishment and development. Different species have varying tolerances to various environmental factors, their impact being most critical at the stages of reproduction and establishment. While a balance is important in any environment, all factors can interact and compensate for changes in other factors. For example, nutrient requirements for certain plants are altered when growing in shade rather than in full sun (see Section 4).

Some environmental factors, such as parent material, can change abruptly, but most change gradually with boundary conditions being defined along a gradient (see Section 1.1.3). Both abrupt and gradual environmental changes are generally evidenced by corresponding changes in the distributions and assemblages of species, although gene flow and genetic drift may explain cases where the range of species ends abruptly along smooth environmental gradients (Polechova and Barton, 2015).

Background image: New England National Park, NSW, photographed on 31 December 2008. **Source:** Cgoodwin, Wikimedia Commons. (Retrieved from *https://commons.wikimedia.org/wiki/File:NewEnglandNP.jpg*)

Excursus 1.1—Classifying Vegetation

Classification of life forms was introduced in Volume 1A—Section 3.4. The Plant Kingdom has been further sub-divided on the basis of morphology and reproductive characteristics. Many classifications have been developed for this purpose based on the basis of different distinguishing traits. The terms referenced in this text are summarised in Table 1.1.

Vascular plants are those with vascular tissues (xylem and phloem) to distribute water and nutrients, such as ferns, grasses, shrubs, trees, and other flowering plants. Please note that some photosynthesising forms of algae, such as blue-green algae, are now regarded as bacteria, not plants (see Volume 3B).

Table 1.1 The plant kingdom

Internal transport mechanism	Reproductive mechanism	Group	Sub-group
Non-vascular	Non-flowering and non-seeding plants; reproduce via spores	Algae and fungi	Mostly aquatic algae (see Volume 3B)
		Bryophytes	Liverworts
			Hornworts
			Mosses
Vascular	Non-flowering and non-seeding plants; reproduce via spores	Pteidophytes	Psilophytes (two small genera of fern-like plants)
			Lycophytes (club mosses; five genera with > 1000 species)
			Sphenophytes (horsetails; one genus)
			Pterophytes (ferns; ~9,000 species)
	seeding plants with roots, stems, and leaves	Gymnosperms (non-flowering; seed not enclosed in fruit)	Cycads (one genus: *Cycadaceae*; < 200 species)
			Ginkgo (one genus and species: *Ginkgo biloba*)
			Conifers (two orders: Pinales and Taxale; ~200 species)
			Gnetophytes (three genera; ~ 100 species)
		Angiosperms (flowering plants with enclosed seeds)	Monocotyledons (one seed leaf; ~60,000 species)
			Dicotyledons (two seed leaves; ~200,000 species)

Adapted from: Campbell *et al.* (2006) Table 29.1

A number of categorisation schemes have been proposed to differentiate plants on the basis of defined traits and/or their function within an ecosystem, such as:

- life form—based on perennating bud height (Raunkiær, 1904):
  - phanerophytes (> 50 cm above ground);
  - chamaephytes (< 50 cm above ground);
  - hemicryptophytes (at soil surface);
  - crytophtyes (below ground or under water);
  - therophytes (annuals from seed); or
  - epiphytes (in the air, on other plants);
- growth form—based on general appearance or habit:
  - woody (trees and shrubs); or
  - herbaceous (grasses), see Section 5.1);
- habitat—based on growing conditions:
  - terrestrial;
  - aquatic;
  - aerial; or
  - lithophytes;
- water content—based on moisture requirements:
  - hydrophytes (aquatic);
  - helophytes (marsh);
  - hygrophytes (moist); or
  - xerophyte (dry);
- leaf loss—based on foliage longevity:
  - evergreen;
  - semi-deciduous; or
  - deciduous; and
- longevity—based on plant life span:
  - annual;
  - biennial; or
  - perennial.

1.1.1 Biotic factors

Biotic environmental factors include all living and dead organisms. These components can be broadly divided into three categories on the basis of their environmental function:

- producers (autotrophs)—plants that convert solar energy into food via photosynthesis;
- consumers (heterotrophs)—animals and fungi that rely on producers (or other consumers) for food; and
- decomposers (detritivores)—microorganisms that decompose producers and consumers to recycle their components.

For an environment to be stable, it is important that the size of these groups be balanced with respect to the available resources. Producers extract basic nutrients from the abiotic environment and thereby increase their availability to consumers and decomposers. While plant growth assists soil formation, plant decomposition enriches the humic content of soil. Decomposers play an essential role by recycling nutrients within the environment. In excess, however, they may threaten the livelihood of both consumers and producers. Likewise, an excess of consumers would devour all producers and threaten their own existence.

Both within and between these sub-categories, various types of interactions can exist between a given pair of organisms. As summarised in Table 1.2, some interactions benefit one or both organisms, while others are detrimental to one organism. The dynamics of these interactions, however, continuously change with the number of organisms, limitations in resources, and variations in abiotic factors.

By virtue of their consumption, heterotrophs use the productivity of autotrophs to survive. Animals, for example, eat plants (or other animals). These dependencies create a unidirectional flow of energy within the local environment in the form of food. Most environments involve a series of dependent organisms that can be represented as a food chain. These may be interlinked to form a food web in large ecosystems, with simple food webs tending to occur in less stable ecosystems (see Section 1.2.3).

Consumers assist producers by spreading reproductive material (called propagules: seeds, spores or cuttings). Propagules can be either carried by animals or eaten then excreted. These processes allow species to be introduced into new areas, which may offer more appropriate conditions and/or less competition. Plant species can also migrate to new regions when propagules are dispersed by wind or water.

Migration enables organisms to escape an unfavourable environment and, over time, can lead to large scale environmental changes. Dispersion and emigration may occur to avoid a variety of undesirable outcomes, such as competition for mates or resources, inbreeding, or aggression resulting from overcrowding.

Various interactions can also occur between producers, which can help or hinder other species. Canopy vegetation in a tropical rainforest, for example, creates microclimates that allow more delicate species to survive. In other environments, such as pine forests, dominant species expand to use all available resources (space, light, water, and nutrients) to the exclusion of less vigorous plants.

Table 1.2 Interactions between biotic components

Interaction	Impact	Description	Example
Mutualism	Favourable	Mutual interdependence between species for growth and survival	Bees pollinating flowers while collecting nectar; Legumes growing with soil bacteria to fix nitrogen
Commensalism	Neutral	One species depends on another without cost to the host	Epiphytes growing on host plants; Exocarpus deriving nutrients from eucalypt roots
Co-operation	Neutral	Both species can live separately but choose to help each other	Predator alarm systems between species
Exploitation	Unfavourable	Host species is harmed by dependent species	Parasites and predators
Competition	Unfavourable	One species is suppressed by the presence of another	Often related to restricted resources such as light or food
Amensalism	Unfavourable	One species is inhibited by another without benefit to either	Animal traffic on vegetation

Vegetative cover also modifies the impact of specific abiotic factors. For example, vegetation tends to reduce throughfall, that is, the amount of atmospheric water reaching the ground. Different forest types allow different degrees of throughfall: 50–80% in broadleaf evergreen forests compared with 90% in eucalypt forests. A reduction in throughfall reduces the risk of soil erosion and enables vegetation to absorb more moisture. Similarly, vegetative cover insulates the soil from solar radiation and reduces soil temperature and evaporation. It also offers protection from wind and water erosion (see Section 11.5).

Many plants growing in harsh environments have adapted to those conditions and developed mechanisms to withstand climatic extremes and capitalise on favourable conditions. The continued survival of all biotic components depends on adaptation to changes in abiotic factors.

Some plant and animal species are opportunistic—they can exploit the conditions created by disturbance and rapidly colonise the modified environment. Opportunistic plants are often labelled 'weeds' and can present significant challenges to land managers (see Sections 2.3.2 and 15).

Indicators serve four basic functions: simplification, quantification, standardisation and communication. They summarise complex and often disparate sets of data and thereby simplify information. They should be based on comparable scientific observations and statistical measures. They also need to provide a clear message that can be communicated to, and used by, decision makers, stakeholders and the general public. (UNEP, 2003)

1.1.2 Abiotic factors

Abiotic factors will be discussed in terms of three groups:

- climate—precipitation, rainfall, light, and wind (see Section 1.1.2.1);
- edaphic factors—parent material, soil, and topography (see Section 1.1.2.2); and
- disturbances—fire, storms, and tectonic activity (see Section 1.1.2.3).

1.1.2.1 Climatic factors

Climate is the net result of a delicate balance of physical factors, being expressed as the pattern in weather over a period of time (see Volume 1A—Section 4). It is primarily concerned with parameters such as light, temperature, precipitation, humidity, evaporation, and wind. While these factors largely shape global vegetation distribution, their impact on the local environment is moderated by vegetative cover. Conversely, vegetation has been recognised as one of the primary indicators of land condition (see Section 7.3) and can affect regional climate and weather patterns due to the release of water vapour during photosynthesis (Green *et al*., 2017).

Although the 'macroclimate', or major climate forces, is easily discernible, its manifestation can vary considerably within short distances and with changes in edaphic factors (see Section 1.1.2.2) and the blanketing effect of vegetation cover. The principal climatic factors impacting terrestrial vegetation are:

- Precipitation—while the frequency, abundance, and form of precipitation collectively shape biome distribution, vegetation cover also influences the volume of water that can penetrate the soil to recharge the water table (see Volume 3B). Furthermore, precipitation responds to vegetation changes through land-atmosphere feedbacks (Sheil and Murdiyarso, 2009; Li *et al*., 2018). Precipitation is viewed as the major limiting factor in terrestrial ecosystems and has been correlated with Gross Primary Productivity (GPP; see Section 7.4).
- Humidity—the proportion of atmospheric moisture, directly impacts—and is impacted by—biota. Relative humidity within dense vegetation, for example, is higher than in the air above bare ground due to plant transpiration (see Section 5.2.3). Such variations create microclimates for a range of organisms.

- Temperature—both affects and is affected by vegetation cover. Vegetation distribution is directly related to air and soil temperature. Evapotranspiration, the release of water vapour into the atmosphere from evaporation and transpiration, increases with air temperature (see Sections 5.2.3 and 7.5). Thermal profiles, showing changes in temperature with height above ground, reveal that the greatest variations in the diurnal temperature range occurs near the soil due to absorption of solar energy (see Section 7.5). Shading by vegetation can also modify thermal profiles (Pianka, 2011). For example, forest vegetation can reduce heat loss by 1–3° over the annual cycle. A suitable temperature range for a species generally coincides with a particular geographic range but pockets of atypical temperature can result from topographic variations, or microclimates created by other plants, allowing species to exist outside their usual range.
- Light levels—also help to determine species distribution. Many plant species are light dependent, with seedlings relying on canopy gaps to become established beneath overstorey plants. Those species occupying the upper stratum of vegetation, whose foliage is more exposed to solar radiation, generally contain the largest portion of total biomass. Diurnal and seasonal cycles determine photoperiodism, the length of day or night, which is also important for germination and flowering.
- Wind—aspect and topography determine the degree of exposure, and hence the effect of wind, at a given location. Vegetation growing along ridgelines is generally smaller and less densely spaced as a result of exposure to wind, although ridgelines are also generally more eroded, which results in shallower and drier soils to support growth. Diurnal cycles in wind are also common, with greatest velocities being observed shortly after solar noon. The interaction of wind and vegetation (fuels) is also a key driver in the rate of spread for fire (see Section 18). Forest vegetation can reduce wind run by 50–75%, and thus mollifies the impact of harsh environments on more sensitive plants. A similarly protective microclimate can be observed in aquatic vegetation, where the presence of periphyton (such as algal films) reduces water turbulence (see Volume 3B).

Disturbance by fire, defoliation, or other agents is an intrinsic and necessary part of the function of most terrestrial ecosystems—a mechanism for reversing declining rates of nutrient cycling or relieving stand stagnation.
(Aber and Melillo, 1991)

1.1.2.2 Edaphic factors

Edaphic factors include the physical landform, geological substratum (or parent material) and soil. Although modified by altitude and aspect, the trends in vegetation across elevation gradients are quite marked, with interacting factors including soil depth, temperature, and effective rainfall having the greatest influence.

The effect of soils on vegetation distribution is secondary to that of climate. Within a given climate, however, much of the variation in soil and vegetation is caused by the substratum. Soils characteristics impact water availability, nutrient status, and soil depth. Topographic factors, such as slope and aspect, can create microclimates that suit particular species. The major edaphic factors influencing the distribution of terrestrial vegetation are:

- Parent material—whereas climatic boundaries are generally gradational, parent material boundaries are often sharp, causing a very marked change in species. The substratum can also have pronounced effects on vegetation in extreme climates, such as the very dry or very cold, where soil development tends to be slow. Similarly, there is a marked effect on vegetation where the parent material contains an excess of particular mineral compounds, such as dolomite. In this way, highly distinctive parent material can underlie similar soils and vegetation even in areas with different climates.

- Soil—results from the interaction of climate and vegetation on the substratum, but it is often very difficult to separate soil from the substratum. Being developed over a period of time, certain characteristics of soil will be indicative of past and present local environments. Nutrient status tends to be reflected in the age of a soil with the older, degraded soils generally only supporting poor quality vegetation. Nonetheless, there are many examples of plant adaptations to relatively poor soils. Soils have a very complex physical/biological system, being the action site for the decomposers in nutrient cycling. Physical properties, such as pore size, will affect the infiltration rate of light rain. Such soil factors can also potentially limit root penetration and thus moisture availability to plants.
- Topography—changes in altitude are accompanied by evident changes in vegetation. Increasing altitude generally parallels decreasing temperature and, often, reduced soil depth. In many ways, the climatic changes involved with increased altitude are similar to those involved with increasing latitude. Aspect can enhance or diminish altitudinal changes in vegetation. For example, in the Southern Hemisphere, the more sheltered eastern and southern facing aspects experience a smaller diurnal temperature range than the more exposed western and northern faces so are generally cooler and moister. Soil depth and moisture tend to increase with decreasing slope. Lower, shallower, and less exposed slopes generally have deeper, alluvial deposits with improved fertility and moisture, and support a greater variety of larger, more productive plants. Topography also determines drainage, the ease with which water in the landscape flows or percolates into the ground.

The richness and diversity of ecosystems are in large measure the result of the pattern of their disturbances: the storms, fires, droughts, frosts and the animals, following occasional major events. .... Because the disturbances occur unexpectedly, systems need to be able to cope with them when they do occur. Coping capacity is another term for being resilient and it is maintained and enhanced by continuous exposure to all the different kinds of disturbances across all locations at different timescales under which the systems developed. .... Novel disturbances due to humans often exceed the evolved resilience of ecosystems, frequently reaching tipping points into new, mostly unwanted states. (Walker, 2019)

1.1.2.3 Disturbances

Disturbances are responsible for the largest environmental changes in the shortest time. They often result in 'ecological drift', a major change in the composition and/or structure of an ecosystem (Jackson, 1968; Bowman and Wood, 2009; Bowman and Haberle, 2010). The primary disturbances shaping terrestrial vegetation distribution are:

- Fire is a significant ecological factor in many locations and its effects can be long lasting. The impact of fire on an environment varies with its frequency, intensity, and environmental history. Various indigenous plant species in Australia have developed mechanisms, such as epicormic shoots and lignotubers, that accelerate recovery from fire. Many species also have hard seed coatings that require fire to germinate. Serotiny describes the adaptation by some plants in which seed release occurs in response to an external trigger factor, such as fire (pyriscence), even when the parent plant is killed by fire. Fire changes the light and moisture environments and acts as a nutrient recycling process, which may promote germination. This is particularly important in dry conditions where decomposition rates are slow. The ash bed bequeathed by fire also provides a fertile environment for establishment of seedlings. Not surprisingly, fire-adapted plant traits tend to dominate in areas that experience high fire incidence. Given its frequency in some landscapes such as Australia, however, Jurkis (2015) questions the classification of fire as a disturbance.

- Storms or wild weather is a form of environmental disturbance that involves excessive rain and wind. Apart from lightning strikes, the primary impacts of storms on vegetation are flooding and windthrow. While most plants benefit from additional moisture, a massive excess of moisture can overwhelm the requirements of many species. Combined with loosened soil and strong winds, saturated substrates often result in uprooted vegetation and consequent damage to other organisms. In sloping ground, saturation also accelerates erosion and invites landslides. The environmental damage resulting from extreme weather is often substantial and widespread. While never welcomed, such changes allow environments to re-establish, often on a more stable underlying landscape.
- Tectonic activity, such as earthquakes and volcanoes, are expressions of movement within or between tectonic plates (see Volume 1A—Section 3). Earthquakes release energy from strained fault planes along tectonic plate boundaries. This energy creates major upheaval on the Earth's crust and generates tsunami when the fault lies beneath the ocean. Volcanoes introduce new mineral matter into the atmosphere and lithosphere from the Earth's interior. When viewed from a sufficiently long timeframe, both types of tectonic activity refresh the environment on the surface of Earth. When measured in terms of human life however, recovery from such massive damage is extremely slow.
- Anthropogenic disturbances that drive vegetation and ecosystem change include land clearing for agriculture and urban development, invasive species, altered disturbance regimes and altered hydrological and biogeochemical cycles. Human-induced changes in ecosystems have reached all corners of the globe and the rates of impact are increasing exponentially as human population density increases (see Sections 19 and 20).

The precise impact of these factors on any environment will depend on the prevailing climatic and edaphic conditions. Human activity causes significant disturbance to ecosystem function and declines in biodiversity, both locally and globally. While some plant species are opportunistic, exploiting the conditions created by disturbance to rapidly colonise the modified environment, others are susceptible to local extinction. EO-based time series analyses are particularly suited to assessing the impact of disturbances on terrestrial landscapes (see Section 9 and Volume 2D).

Resilient systems are learning systems. …Trying to prevent one disturbance completely, in the name of keeping a system safe, actually reduces its resilience. (Walker, 2020)

1.1.3 Environmental gradients

Environmental factors, both biotic and abiotic, change with space and time. In many landscapes, the natural distribution of botanical species is closely related to the environmental gradients of elevation, latitude, soils, and fire (Kessell, 1979, Billings, 1970). While it is convenient to draw clear boundaries on maps showing vegetation distribution, welldefined transitions rarely occur in nature. Changes in species composition are often very gradual and can result in a variety of mixtures along the way (see Section 1.3).

A population of organisms with a particular genetic form resulting from genetic sorting is called an ecotype. This can be considered as a subspecies with particular environmental adaptations or preferences for survival. Ecotypes of the same species can interbreed without detrimental consequences.

A gradual change in ecotypes is called an ecocline and is often related to changes in climate (since parent material changes tend to occur more abruptly; see Section 1.1.2.2). Examples of ecoclines include:

- thermocline—a temperature gradient;
- halocline—a salinity gradient; and
- chemocline—a chemistry gradient (see Volume 3B).

Ecoclines and ecotypes allow a given species to increase its geographic range by extending the interactions that can occur with its environment. In time, a greater geographic range is likely to provide a greater chance of survival for that species.

Hybrid zones, where the ranges of species or evolutionarily significant units overlap and result in genetic hybridisation, are considered a sensitive marker of environmental change (Taylor *et al.*, 2015). Changes in hybrid zone extent may shift, expand, or originate in new locations in response to changing environmental conditions.

Despite all of our accomplishments we owe our existence to a six-inch layer of topsoil and the fact that it rains. (Farm equipment association of Minnesota and South Dakota)[2]

1.2 Ecological Units

Dynamic vegetated landscapes cover around 80% of the terrestrial surfaces of our planet. Vegetation can be considered in terms of three broad spatial scales:

- single plants (or individuals) and groups of similar individuals (or populations; see Section 1.2.1);
- gatherings of populations—communities (see Section 1.2.2); and
- tapestries of communities—ecosystems (see Section 1.2.3).

A key concept in ecology is that of habitat, namely that region where an organism likes to live. Organism habitats are generally defined by both biotic and abiotic factors. Biotic factors are important in the structure and pattern of vegetation communities (see Sections 1.1.1). The term habitat can also be used to refer to the locality of a community, in which case it is defined by abiotic environmental factors (see Sections 1.1.2). A related concept is the ecological niche, which describes the habitat characteristics as well as the role of the organism in its environment, including ecological functions, services, and interactions (see Section 1.2.3). For organisms to coexist they either become tolerant of each other, and sympatric, or they compete until one species is eliminated. Successive generations may also hybridise.

The combined impact of vegetative scale on the landscape is to create a mosaic of colour and texture. This mosaic not only informs about vegetation type and condition but also highlights the underlying landscape characteristics. With an understanding of the dominant environmental factors that shape this mosaic, landscapes can be better managed to improve productivity and sustainability.

1.2.1 Individuals and populations

Populations comprise collective groups of individuals from the same species—that is, genetically related plants that can interbreed. Sexual reproduction results in more genetically diverse offspring than asexual means and generally delivers the benefits of greater capacity for seed dispersal, more offspring, and higher success rates for germination and establishment. While individuals are characterised by those traits that are common to their species, namely germination, growth habit, and reproduction (see Section 5), populations are characterised by the way they group, persist, disperse, and survive (see Section 6). Thus, measures of size, density, age composition, and growth rate are used to compare populations and derive management concepts such as carrying capacity.

Populations change with the survival rates of individuals and the immigration or emigration of species. A stable population of plants achieves a balance between the initial life cycle phases of seed dispersal, germination, and establishment, and the final stages of senescence and death. The success or failure of a plant largely depends on the impact of the environment on the rates of its vital processes.

Disturbance of one kind or another plays a crucial role in all ecosystems. (Walker, 2020)

2 Sourced from NSW Soil Knowledge Network: *http://www.nswskn.com/soil-quotes-2/*

1.2.2 Communities

At any locality, the assemblage of plant species into a community results from the cumulative, extended impact of all environmental factors on the ambient flora (Billings, 1970). Vegetation communities can indicate past environmental conditions or events (such as forest fires or past climatic cycles), soil conditions (physical structure, salts, or available nutrients) and the presence of predatory animals. A community is characterised by a sense of order in that it has an identity over and above the individual and population, and functions as a unit via combined metabolic processes (Odum, 1971).

The distribution of organisms in their environment, and their interaction with that environment, creates a structure that ecologist call 'pattern' (Hutchinson, 1953). Within a vegetation community, pattern principally occurs in terms of vertical layering or stratification, horizontal segregation or zonation, and periodicity of organism life cycles (see Section 6). Stratification is obvious in many natural communities, for example, as different species and individuals adapt to different levels of light and moisture. For example, some species, such as acacias, typically play a transitory role in Australian forests, with both high light requirements and lack of dominance, while others are destined to exert dominance but may require specific conditions for establishment. Certain pathogens can also influence species distribution in favourable locations.

The transition between two communities is called an ecotone, that is, the region where they can integrate and develop hybrid species. Such transitions may be sharp or gradual, as evidenced by changes in vegetation colour or height, or represent a change in species prevalence. Species diversity may increase within ecotones as members of both communities co-exist.

Wherever the reign of nature is not disturbed by human interference, the different plant species join together in communities, each of which has a characteristic form, and constitutes a feature in the landscape of which it is a part. These communities are distributed and grouped together in a great variety of ways, and, like the lines on a man's face, they give a particular impress to the land where they grow. The species of which a community is composed may belong to the most widely different natural groups of plants. The reason for their living together does not lie in their being of common origin, but in the nature of the habitat. They are forced into companionship not by any affinity to one another but by the fact that their vital necessities are the same. ....

A knowledge of the communities which exist within the realm of plants is of great importance in many ways. It throws a strong light, not only on the mutual relations of the different species which are associated by common or similar needs, but also on the connection of plant-life with local and climatic conditions and with the nature of the soil. It may fairly be said that in the various zones and regions of our earth no kind of phenomenon so thoroughly gives expression to the climate and the constitution of the soil as the presence of particular plant-communities which prevail, and, accordingly, the determination and description of such communities constitutes an important part of geography.

(Anton Kerner Von Marilaun, 1895)

1.2.3 Ecosystems

The total biotic and abiotic factors of an environment present in a particular area is called an ecosystem. It represents the net result of all interactions of biotic and abiotic factors (see Sections 1.1.1 and 1.1.2). Ecosystems are self-regulatory and self-sustaining systems. Other definitions include:

- a symbol of structure and function of nature (Tansley, 1935); and
- the smallest structural and functional unit of nature or environment (Odum, 1969).

The concept of an ecosystem has also been referred to as biocoenosis (Möbius, 1877) or biogeocoenosis (Sukachev, 1944; Puzachenko, 2008), or a biome. More recently the term biome has been used to describe a group of terrestrial ecosystems (Whittaker, 1962; see Section 1.3.2).

Ecosystem boundaries are often indistinct and overlapping. They can be large or small, short term or long term, natural or artificial. A stable ecosystem achieves and maintains balance between living organisms, water, atmosphere, and earth (Patten, 1991). The process of balancing food webs and chains to maintain a stable ecosystem is called homeostasis.

Table 1.3 Ecosystem processes

Ecosystem Process	Function		Balanced Ecosystem	Unbalanced Ecosystem
	Landscape/ Community	Organisms		
Water Cycle	Maintain healthy aquifers, surface water flows and soil moisture	Maintain adequate moisture for all metabolic processes	Precipitation replenishes soil moisture to support plant growth and decomposition, recharges stores in aquifers, collects in reservoirs for consumers to drink, and/ or flows into rivers and oceans to support aquatic life	Precipitation insufficient for plant growth, and runs off ground surface removing soil and propagules Moisture insufficient for healthy nutrient levels
Energy Flow	Conserve energy levels and maintain stores	Maintain adequate energy for all metabolic processes	Producers capture sufficient solar energy for the needs of consumers and decomposers	Insufficient solar energy captured by producers to feed consumers and decomposers
Mineral Cycle	Maintain nutrient availability and replenish stores; avoid excessive availability	Maintain adequate nutrients for all metabolic processes	Nutrients from plant and animal wastes are recycled by decomposers to enrich the soil	Plant and animal wastes are not decomposed but washed away or burnt Excessive nutrients encourage dominance
Community Dynamics	Balance population growth with available resources	Maintain adequate diversity in communities	High diversity of producers, consumers, and decomposers Size of populations suited to constraints of resources	Low diversity of producers, consumers, and decomposers Excessive competition for resources

Ecosystem services describe ecosystem changes in terms of their impact on human populations, that is the the services they deliver (see Section 20.3). Ecosystems can also be viewed in terms of their structure or function, and how these change over space and time. Some basic biological, physical and chemical processes sustain ecosystems. Four key ecosystem processes include:

- the water cycle—how and why water interacts with the ecosystem (see Section 7.6 and Volume 3B);
- the energy cycle—how energy flows drive ecosystems (see Section 7.5, including food chains/webs: see Section 1.1.1; productivity: see Section 7.4; and the carbon cycle: see Section 17 and Excursus 1.2);
- the mineral cycle—how biogeochemical nutrients are recycled by the ecosystem, including the nitrogen cycle (see Volume 1A—Section 4.2); and
- community dynamics—how communities develop and change within an ecosystem, including diversity patterns, succession, and cybernetics (see Sections 1.3.3, 6 and 19).

Balanced and unbalanced ecosystems are compared in terms of these processes in Table 1.3.

Analysis of energy cycling underlies many modelling applications of EO for terrestrial vegetation (see Section 10.2). Solar energy is absorbed by vegetation during the process of photosynthesis and this stored energy can be likened to a battery (see Section 5.2.1). Estimates of the proportion of photosynthetically active radiation (PAR) that is absorbed by vegetation are used to quantify both carbon dioxide usage and water loss due to evapotranspiration. Such estimates are further discussed in Section 7. Monitoring of vegetation productivity is particularly important as an indicator of the sustainability of environments, land management practices and lifestyles (see Sections 7.4 and 19).

It is hard for us to accept that the way natural ecosystems work is exemplary: plants synthesise nutrients which feed herbivores; these in turn become food for carnivores, which produce significant quantities of organic waste which give rise to new generations of plants. But our industrial system, at the end of its cycle of production and consumption, has not developed the capacity to absorb and re-use waste and by-products. We have not yet managed to adopt a circular model of production capable of preserving resources for present and future generations, while limiting as much as possible the use of non-renewal resources, moderating their consumption, maximising their efficient use, re-using and recycling them.
(Pope Francis, 2015)

1.3 Terrestrial Ecosystems

1.3.1 Biogeography and biodiversity

Biogeography addresses the question of why plants grow where they do. This discipline combines aspects of biology and geography to determine how organisms are distributed in space and time. An understanding of the patterns of biogeography enables biodiversity to be protected.

The term 'biodiversity' describes the collective variety within all forms of life on Earth. The highest levels of biodiversity generally occur in warm, moist environments. On a global scale, the highest levels of biodiversity, in terms of both marine and terrestrial plants and animals, occur at the equator, then biodiversity declines with latitude. Across the landscape, biodiversity is highest near coastlines and declines towards the interior of most land masses.

Biodiversity indicates both the stability and productivity of an ecosystem. Stable environments, such as large tropical islands, maintain high levels of biodiversity, and high species richness enhances the efficient use of resources and therefore productivity (Fjeldsa and Lovett, 1997). However, the conservation of biodiversity may not necessarily be maximised by prioritising management efforts in stable environments. Ecosystems exposed to more variable environmental conditions may contain species with greater tolerance of extremes and higher resilience to a rapidly changing climate (see Section 1.1.2.3).

1.3.2 Major habitat zones

Biomes are contiguous areas with similar climate and geography and as such they represent major habitat types. A variety of schemes have been developed to describe ecosystem zones on the basis of climatic and topographic factors such as latitude and humidity, and sometimes altitude. The categories defined by Holdridge (1947) are illustrated in Figure 1.1. Temperature gradients are strongly related to changes in latitude and altitude, so temperature and precipitation alone are often used to map the distribution of vegetation as in Whittaker's classification (Whittaker, 1962; see Figure 1.2).

All are but parts of one stupendous whole,
Whose body Nature is, and God the soul.
(Alexander Pope, from 'An Essay on Man', 1733)

Figure 1.1 Holdridge life zone classification scheme

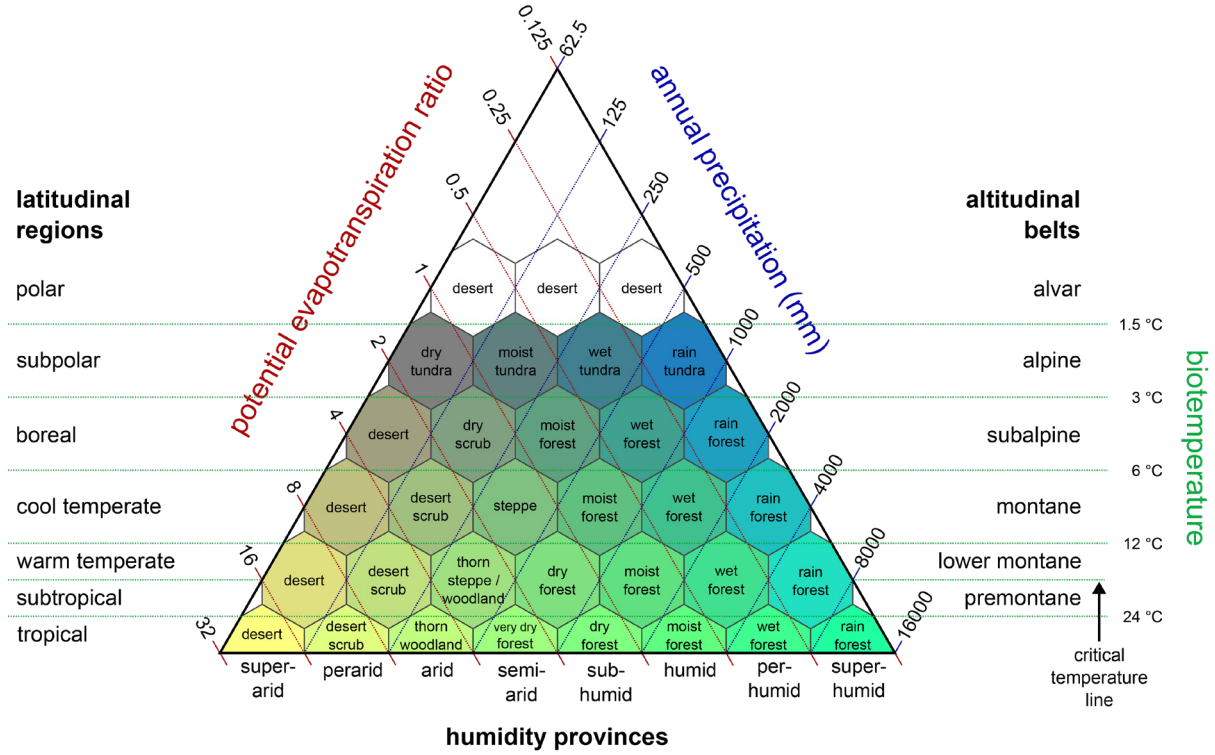

Source: Peter Halasz, Wikimedia Commons. (Retrieved from *https://commons.wikimedia.org/wiki/File:*Lifezones_Pengo.svg)

Figure 1.2 Whittaker's biome classification

Average annual temperature and precipitation needed for different categories of common terrestrial biomes

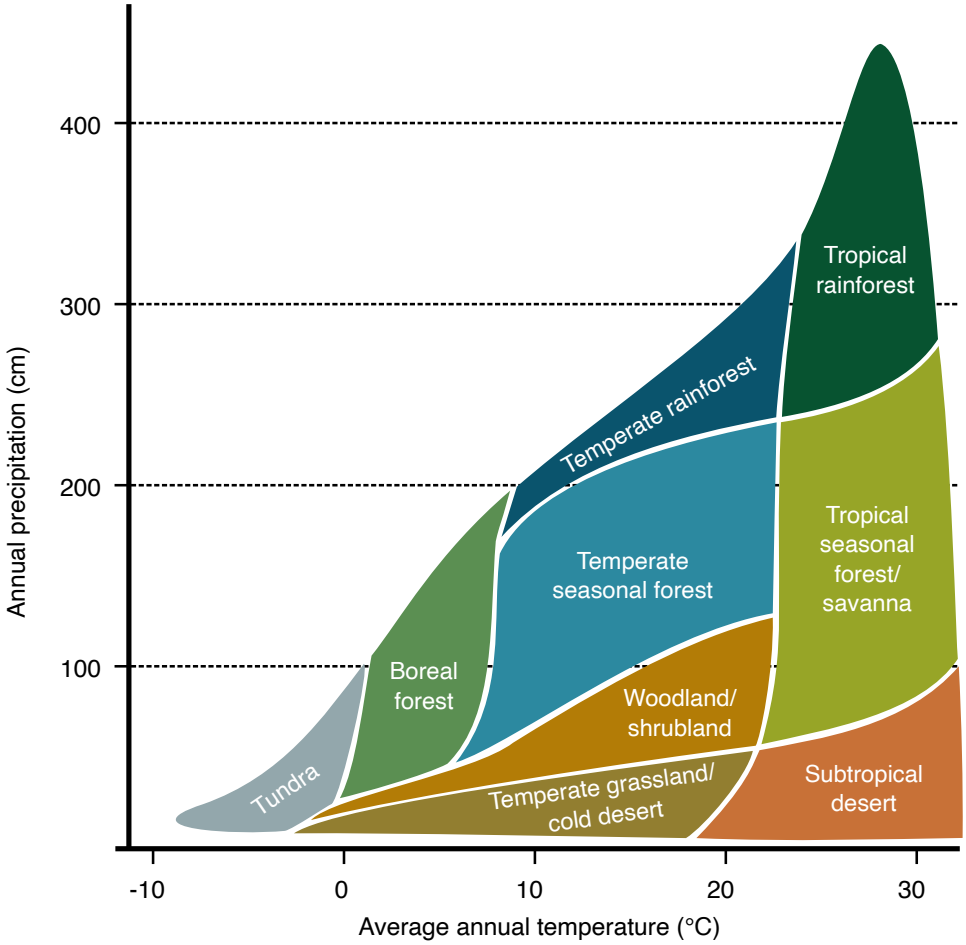

Source: Navarras, Wikimedia Commons. (Retrieved from *https://commons.wikimedia.org/wiki/File:Climate_influence_on_terrestrial_biome.svg*)

The Terrestrial Ecoregions of the World (TEOW) project offered a biogeographic regionalisation of terrestrial biodiversity on Earth (Olson *et al.*, 2001). This World Wildlife Fund (WWF) product defines 14 major habitat types, or biomes, which were further sub-divided into 867 terrestrial ecoregions. The major habitat types are listed in Table 1.4. These ecoregion categories form the basis of the Interim Biogeographical Regionalisation of Australia (IBRA) as illustrated in Figure 2.13. Eight of these major habitat types exist in Australia.

A biome-based, global land cover map derived from MODIS imagery was released by the International Geosphere-Biosphere Program (IGBP, 1990; Friedl *et al.*, 2010a, 2010b; Channan *et al.*, 2014—see Section 1.4). This series of global mosaics use the MODIS land cover product (MCD12Q1) in the IGBP Land Cover Type classification of 17 terrestrial vegetation categories. The Global Environmental Stratification (GEnS), a high resolution bioclimate stratification based on multivariate statistical clustering (Metzger *et al.*, 2013; Metzger, 2018), has been proposed as an appropriate framework for global monitoring networks (Jongman *et al.*, 2017; see Section 19.3). More recently, a global stratification of World Ecosystems, derived from the integration of temperature, moisture, landform, and vegetation/land use datasets, was developed by Sayre *et al.* (2020) and used to assess the representation of ecosystems in global protected areas (see Section 19).

Table 1.4 Terrestrial biomes

Biome		Description	
Number	Name	Latitude	Humidity
1	Tropical and subtropical moist broadleaf forest	Tropical, Subtropical	Humid
2	Tropical and subtropical dry broadleaf forest	Tropical, Subtropical	Semi-humid
3	Tropical and subtropical coniferous forest	Tropical, Subtropical	Semi-humid
4	Temperate and broadleaf and mixed forest	Temperate	Humid
5	Temperate coniferous forest (Northern Hemisphere only)	Temperate	Humid to semi-humid
6	Boreal	Sub-arctic	Humid
7	Tropical and subtropical grasslands, savannas and shrublands	Tropical, Subtropical	Semi-arid
8	Temperate grasslands, savannas and shrublands	Temperate	Semi-arid
9	Flooded grasslands and shrublands	Temperate to Tropical	Fresh or brackish water inundated
10	Montane grasslands and shrublands	Temperate to Tropical	Alpine to Montane
11	Tundra	Polar	Arid
12	Mediterranean forests, woodlands and scrub or sclerophyll forests	Temperate Warm	Semi-humid to semi-arid with winter rainfall
13	Deserts and xeric shrublands	Temperate to Tropical	Arid
14	Mangrove	Subtropical, Tropical	Saltwater inundated

1.3.3 A dynamic tapestry

Perhaps the most significant characteristic of our planet is that it is constantly changing. The ceaseless processes of growth and decay, erosion and deposition, precipitation and evaporation are driven by diurnal, lunar, seasonal, and annual cycles, irregularly punctuated by disturbances. Everything changes with time; some changes just take more time than others.

To cope with the inevitable changes in abiotic components of the environment, individual species need to adapt to the changes or become vulnerable to more competitive species. Mechanisms for adaptation for a given species include reordering its existing genetic resources to create new gene combinations that would be better suited to the changed environment or developing new genes via mutations in a process known as genetic drift.

A community or ecosystem can be thought of as developing via the gradual, and somewhat theoretical, process of ecological succession. As detailed in Section 6.6, this process involves a variable series of stages:

- a pioneer community colonises a new area; then
- one or more seral communities replace the previous community; until
- a climax community reaches a form of homeostasis which persists for a relatively long time period.
- The number of seral communities, the lifespan of each stage, and the degree of homeostasis varies with individual ecosystems. Ecologists also distinguish between primary succession (very long term development on new landscapes) and secondary succession (shorter term development on disturbed landscapes).

One part of analysing vegetation dynamics involves reconstructing former distributions. Palynology analyses pollen and spores found in fossils and sediments to track the composition and diversity of past landscapes.

The dynamic nature of the Earth somewhat complicates the task of natural resource mapping and necessitates regular revision of maps to quantify the type and extent of change. Knowledge of where and how changes are occurring can contribute to an understanding of why they occur and, possibly, how the extent of change can be managed. One approach that has emerged in recent decades for exploring the dynamic nature of Earth is Earth System Science (ESS; see Excursus 1.2). This integrated view of our planet is particularly valuable when observing large scale processes and relates readily to the perspective of Earth Observation (EO).

The only constant in life is change.

Excursus 1.2—Earth System Science

Further Information: Xiao *et al.* (2019)

Earth System Science (ESS) is a multidisciplinary approach to understanding the structure and function of Earth as an integrated system (Steffen *et al.*, 2020). Large scale monitoring of our planet is closely related to the concept of Earth being an essentially closed system, and comprising four integrated spheres:

- atmosphere—gaseous protective envelope;
- hydrosphere—surface water, groundwater and atmospheric water;
- geosphere—solid components of Earth (land and under water); and
- biosphere—all forms of life (see Volume 1A—Section 4.1).

These spheres exchange energy and matter via the ongoing cycling of energy, water, and minerals (see Volume 1A—Section 4.2). One conceptual framework that links major Earth components with the processes that impact them is shown in Figure 1.3 (NRC, 1986). Since all processes on Earth are interrelated and impacted by human activities, updated representations show human activity (anthroposphere) as a fully integrated and interacting sphere (Steffen *et al.*, 2020).

Of particular relevance to terrestrial vegetation is the terrestrial carbon cycle which describes the continual exchange of carbon between the biosphere, the geosphere, and the atmosphere (see Volume 1A—Section 4). As detailed in Section 17 below, the typical components of this process are usefully described in terms of carbon fluxes (flows) and stocks (volume of reserves; see Figure 1.4). EO-based analyses can be used to estimate the carbon fluxes of gross primary production (GPP), ecosystem respiration (ER), net primary production (NPP), net ecosystem production (NEP), and net biome production (NBP), and the carbon stocks of aboveground biomass (AGB) and soil organic carbon (SOC; Xiao *et al.*, 2019). The use of EO to quantify and monitor the terrestrial carbon cycle is detailed in Sections 7.4, 10.2.2, and 17 below.

Figure 1.3 Processes and interactions within Earth System Science

This conceptual framework was proposed by Francis Bretheton and is commonly referenced as the NASA Bretherton diagram.

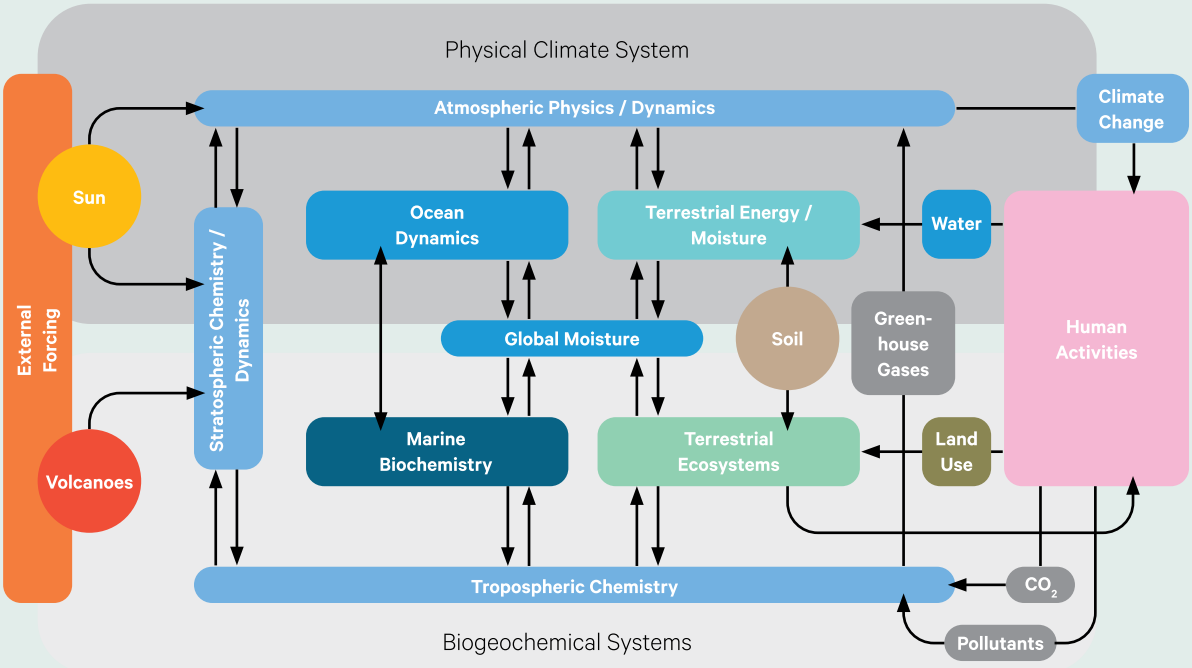

Adapted from: NASA at *http://education.gsfc.nasa.gov/experimental/all98invproject.site/pages/trl/inv4-3.abstract.html*

Figure 1.4 Terrestrial carbon cycle

a. Carbon fluxes and stocks

Fluxes: GPP: Gross Primary Productivity; AR: Autotrophic Respiration; NPP: Net Primary Productivity; HR: Heterotrophic Respiration; NEP: Net Ecosystem Productivity; NBP: Net Biome Productivity;

Stocks: AGB: Above Ground Biomass; SOC: Soil Organic Carbon;

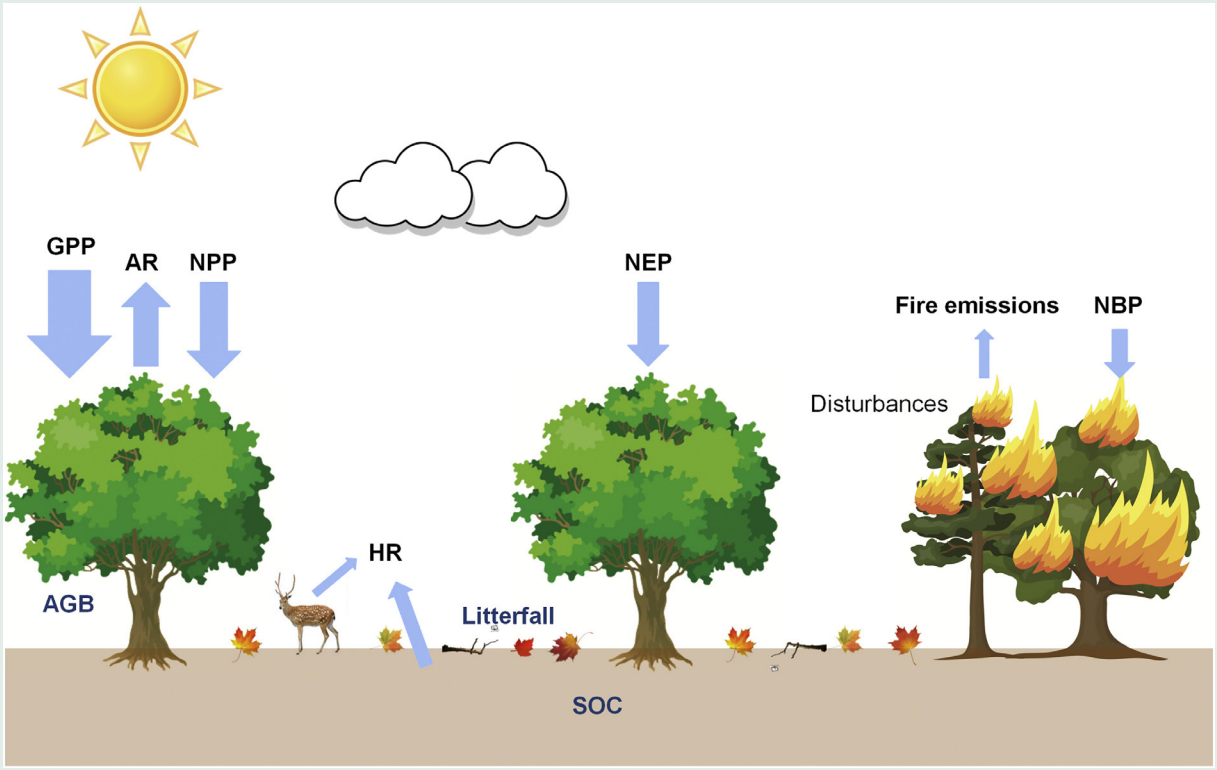

b. Computation of fluxes

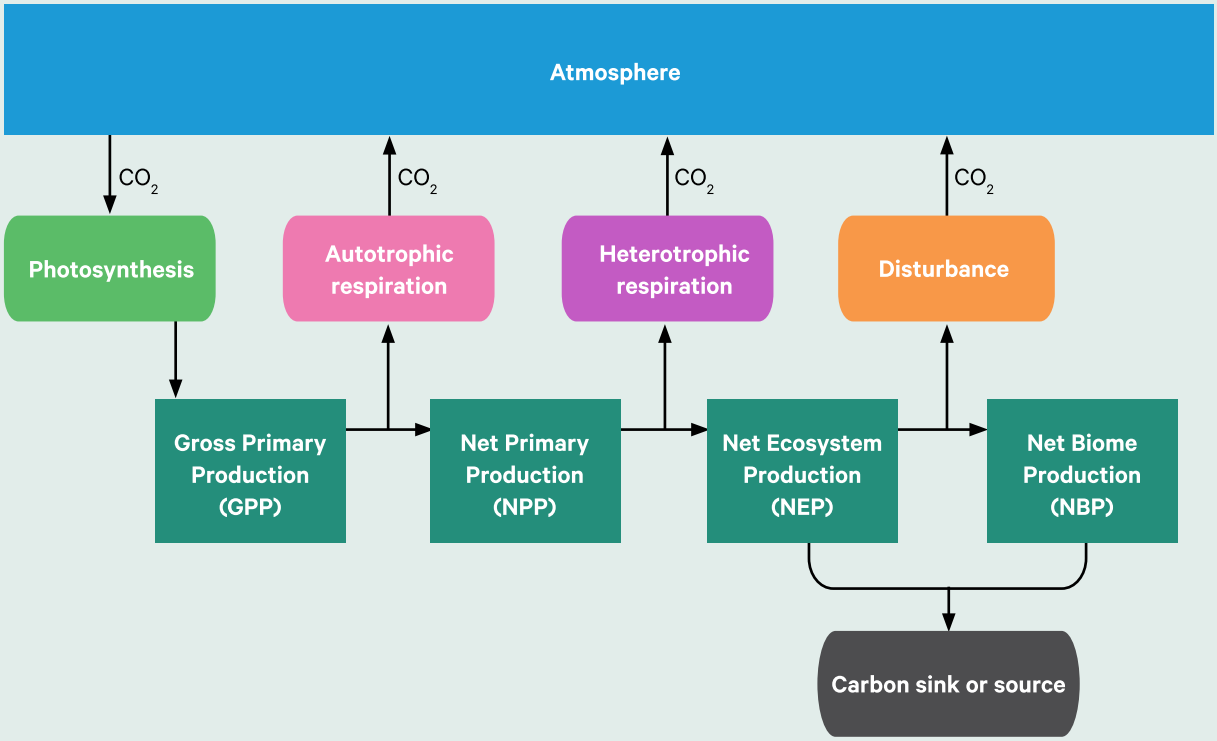

Source: a. Xiao *et al.* (2019) Figure 1

1.4 Further Information

Global Climate Map

Global Environmental Stratification: *https://datashare.is.ed.ac.uk/handle/10283/3089*

Global Terrestrial Ecosystem Maps

IGBP: IGBP (1990)
Friedl *et al.* (2010)
Global Land Cover Facility: *http://glcf.umd.edu/data/lc/*

WWF: Olson *et al.* (2001)
Terrestrial ecoregion definitions: *https://www.worldwildlife.org/biome-categories/terrestrial-ecoregions*
Map: *https://c402277.ssl.cf1.rackcdn.com/publications/347/files/original/Ecoregions_Map.pdf?1345734390*

Global ecological zones: *http://www.fao.org/geonetwork/srv/en/main.home?uuid1⁄42fb209d0-fd34-4e5e-a3d8-a13c241eb61b*

1.5 References

Aber, J.D., and Melillo, J.M. (1991). *Terrestrial Ecosystems*. Saunders College Publ., Holt, Rinehard and Winston Inc, Orlando, Florida.

Billings, W.D. (1970). *Plants, Man and the Ecosystem*. 2nd Edn. Wadsworth Publ. Co., Belmont. 160pp. ISBN 0-333-14633-6.

Bowman, D., and Wood, S.W. (2009). Fire-driven land cover change in Australia and W.D. Jackson's theory of fire ecology of southwest Tasmania. Chapter 8 in *Tropical Fire Ecology: Climate change, land use, and ecosystem dynamics* (Ed: Cochrane, M.). pp 87–106. Springer, New York. doi:*10.1007/978-3-540-77381-8_4*

Bowman, D.M.J.S, and Haberle, S.G. (2010). Paradise burnt: how colonizing humans transform landscapes with fire. *PNAS*, 107(50), 21234–21235. doi:*10.1073/pnas.1016393108*

Campbell, N.A., Reece, J.B., and Meyers, N. (2006). *Biology*. 7th edn. Pearson Education Australia. ISBN 1 74103 386 1.

Channan, S., Collins, K., and Emanuel, W.R. (2014). *Global mosaics of the standard MODIS land cover type data*. University of Maryland and the Pacific Northwest National Laboratory, College Park, Maryland, USA.

Fjeldsa, J., and Lovett, J.C. (1997). Biodiversity and environmental stability. *Biodiversity and Conservation*, 6(3), 315–323.

Friedl, M.A., Sulla-Menashe, D., Tan, B., Schneider, A., Ramankutty, N., Sibley, A., and Huang, X. (2010a). MODIS Collection 5 global land cover: Algorithm refinements and characterization of new datasets. *Remote sensing of Environment*, 114(1), 168–182.

Friedl, M.A., Strahler, A.H., Hodges, J., Hall, F.G., Collatz, G.J., Meeson, B.W., Los, S.O., Brown De Colstoun, E., and Landis, D.R. (2010b). *ISLSCP II MODIS (Collection 4) IGBP Land Cover, 2000-2001*. ORNL DAAC, Oak Ridge, Tennessee, USA. *https://doi.org/10.3334/ORNLDAAC/968*

Green, J.K., Konings, A.G., Alemohammad, S.H., Berry, J. Entekhabi, D., Kolassa, J., Lee, J.E., Gentine, P. (2017). Regionally strong feedbacks between the atmosphere and terrestrial biosphere. *Nature Geoscience*, 10(6), 410–414. doi:*10.1038/NGEO2957*

Holdridge, L.R. (1947). Determination of world plant formations from simple climatic data. *Science*, 105(2727), 367–368. doi:*10.1126/science.105.2727.367*. PMID 17800882.

Hutchinson, G.E. (1953). The Concept of Pattern in Ecology. *Proceedings of the Academy of Natural Sciences of Philadelphia*, 1–12.

IGBP (1990). *The International Geosphere–Biosphere Programme: A study of global change—The initial core projects, IGBP Global Change Report no. 12*. International Geosphere–Biosphere Programme. Stockholm, Sweden.

Jackson, W.D. (1968). Fire, air, water and earth—an elemental ecology of Tasmania. *Proceeding of Ecological Society of Australia*, 3, 9–16.

Jongman, R.H.G., Skidmore, A.K., (Sander) Mücher, C.A., Bunce, R.G., Metzger, M.J. (2017). Global Terrestrial Ecosystem Observations: Why, Where, What and How?. In: *The GEO Handbook on Biodiversity Observation Networks* (Eds: Walters M., and Scholes R.). Springer, Cham.

Jurskis, V. (2015). *Firestick Ecology*. Connor Court Publishing, Ballarat.

Li, Y., Piao, S., Li, L.Z.X., Chen, A., Wang, X., Ciais, P., Huang, L., Lian, X., Peng, S. Zeng, Z. Wang, K., and Zhou, L. (2018). Divergent hydrological responses to large-scale afforestation and vegetation greening in China. *Sciences Advances*, 4(5), eaar4182. doi:*10.1126/sciadv.aar4182*

Kerner von Mariluan, A. (1895). *The natural history of plants: Their forms, Growth, Reproduction, and Distribution*. Translated by Oliver, F.W. (1902) and published by Blackie and Son, Ltd, Glasgow and Dublin. *https://doi.org/10.5962/bhl.title.18169*

Kessell, S.R. (1979). *Gradient Modelling: Resource and Fire Management*. Springer-Verlag, New York.

Laseron, C.F. (1953). *The Face of Australia*. Angus and Robertson. 244 p.

Metzger, M.J. (2018). *The Global Environmental Stratification: A high-resolution bioclimate map of the world* [dataset]. The University of Edinburgh. *https://doi.org/10.7488/ds/2354*.

Metzger, M. J., Brus, D. J., Bunce, R. G. H., Carey, P. D., Gonçalves, J., Honrado, J. P., Jongman, R.H.G., Trabucco, A., and Zomer, R. (2013). Environmental stratifications as the basis for national, European and global ecological monitoring. *Ecological Indicators*, 33, 26–35.

Möbius, K. (1877). *Die Auster und die Austernwirtschaft*. Hemple and Parey, Berlin.

NRC (1986). *Earth System Science. Overview: A Program for Global Change*. National Research Council. National Academies Press.

Odum, E.P. (1969). The Strategy of Ecosystem Development. *Science*, 164(3877), 262–270.

Odum, E.P. (1971). *Fundamentals of Ecology*. 3rd edn. W.B. Saunder Co., Philadelphia.

Olson, D.M., Dinerstein, E., Wikramanayake, E.D., Burgess, N.D., Powell, G.V.N., Underwood, E.C., D'Amico, J.A., Itoua, I., Strand, H.E., Morrison, J.C., Loucks, C.J., Allnutt, T.F., Ricketts, T.H., Kura, Y., Lamoreux, J.F., Wettengel, W.W., Hedao, P., and Kassem, K.R. (2001). Terrestrial ecoregions of the world: a new map of life on Earth. *Bioscience*, 51(11), 933–938.

Patten, B.C. (1991). Network ecology: indirect determination of the life–environment relationship in ecosystems. In *Theoretical Ecosystem Ecology: The Network Perspective* (Eds: Higashi, M., and Burns, T.P.), London, Cambridge University Press. pp. 288–351.

Pianka, E.R. (2011). *Evolutionary Ecology*. 7th edn. Eric R. Pianka.

Polechova, J., and Barton, N.H. (2015). Limits to adaptation along environmental gradients, *Proceedings of the National Academy of Sciences*, 112(20), 6401–6406.

Pope Francis (2015). *Laudato Si': On Care for Our Common Home*. Catholic Truth Society, London.

Puzachenko, J. (2008). Biogeocoenosis as an Elementary Unit of Biogeochemical Work in the Biosphere. In Global Ecology, Volume 1 of *Encyclopedia of Ecology* (Eds: S.E. Jørgensen and B.D. Fath). Elsevier, Oxford. pp. 396–402

Raunkiær, C. (1904). Om biologiske Typer, med Hensyn til Planternes Tilpasninger til at overleve ugunstige Aarstider. *Botanisk Tidsskrift*. 26 p. XIV.

Sayre, R., Karagulle, D., Frye, C., Boucher, T., Wolff, N.H., Breyer, S., Wright, D., Martin, M., Butler, K., Van Graafeiland, K., Touval, J., Sotomayor, L., McGowan, J., Game, E.T., and Possingham, H. (2020). An assessment of the representation of ecosystems in global protected areas using new maps of World Climate Regions and World Ecosystems. *Global Ecology and Conservation*, 21, e00860. *https://doi.org/10.1016/j.gecco.2019.e00860*

Sheil, D., and Murdiyarso, D. (2009). How forests attract rain: an examination of a new hypothesis. *BioScience*, 59(4), 341–347. *https://doi.org/10.1525/bio.2009.59.4.12*

Steffen, W., Richardson, K., Rockström, J., Schellnhuber, H.J., Dube, O.P., Dutreuil, S., Lenton, T.M., and Lubchenco, J. (2020). The emergence and evolution of Earth System Science. *Nature Reviews Earth and Environment*, 1, 54–63. *https://doi.org/10.1038/s43017-019-0005-6*

Sukachev, V.N. (1944). Principles of genetic classification in biogeocoenology. *Zhurnal Obshchei Biologii*, 5(4), 213–227, Moscow.

Tansley, A.G. (1935).The use and abuse of vegetational terms and concepts. *Ecology*, 16(3), 284–307. doi:*10.2307/1930070*

Taylor, S.A., Larson, E.L., and Harrison, R.G. (2015). Hybrid zones: windows on climate change. *Trends in Ecology and Evolution*, 30(7), 398–406.

UNEP (2003). *Monitoring and indicators: designing national-level monitoring programmes and indicators*. Note by the Executive Secretary. Subsidiary Body on Scientific, Technical and Technological Advice, Convention on Biological Diversity, UNEP/CBD/SBSSTA/9/10.

Walker, B. (2019). *Finding Resilience*. CSIRO, Melbourne.

Walker, B. (2020). Resilience: what it is and is not. *Ecology and Society*, 25(2), 11. *https://doi.org/10.5751/ES-11647-250211*

Whittaker, R.H (1962) Classification of Natural Communities. *Botanical Review*, 28(1), 1–239. Reprinted (1977) New York, Arno Press.

Xiao, J., Chevallier, F., Gomez, C., Guanter, L., Hicke, J.A., Huete, A.R., Ichii, K., Ni, W., Pang, Y., Rahman, A.F., Sun, G., Yuan, W., Zhang, L., Zhang, X. (2019). Remote sensing of the terrestrial carbon cycle: A review of advances over 50 years. *Remote Sensing of Environment*, 233, 111383. *https://doi.org/10.1016/j.rse.2019.111383*.

2 The Australian Environment

The Australian mainland is both the largest island and the smallest continent in the world, as well as the lowest and flattest land mass (see Section 2.1). In terms of land area, Australia is the sixth largest country after Russia, Canada, China, the USA and Brazil, and the only one of these to be encircled by water (GA, 2020a). Some basic information about Australia's location, dimensions, features and population is summarised in Table 2.1 (see also Figure 2.1).

Australia spans 31° of latitude, centred on 27.5° S (just below the Tropic of Capricorn, 23.43657° S—see Volume 2B—Figure 1.14), so experiences a wide range of climates, which can vary significantly from one year to the next (BoM, 2020a). Drought, floods, and cyclones are a natural part of Australia's climatic variation (see Section 2.2).

The Commonwealth of Australia is governed as a federation of six states (see Figure 2.1b; Western Australian: WA, South Australia: SA, Tasmania: TAS, Victoria: VIC, New South Wales: NSW, and Queensland: QLD), each of which is responsible for local land management and many public services. Territories that are not directly administered by specific states are either under federal control or granted the right to self-government (as occurs in the Northern Territory: NT, and the Australian Capital Territory: ACT; AG, 2020). The Commonwealth also governs some 12,000 smaller islands within its marine jurisdiction (see Volume 3B). Land in Australia is either:

- owned by the 'crown' or government—crown land covers almost a quarter of the total land mass and is regulated by relevant State government legislation;
- leased by the crown to specified users for a defined purpose, such as mining or pastoral activities—leasehold land comprises around half the land area; or
- privately owned, including indigenous land tenure—freehold tenure accounts for nearly 30% of the land in Australia (Austrade, 2020).

In the sub-sections below, we introduce aspects of Australia's topography (see Section 2.1), climate (see Section 2.2), biota (see Section 2.3), ecoregions and fire patterns (see Section 2.4), and land use (see Section 2.5).

... Flood, fire, and cyclone in successive motion
Complete the work the pioneers began
Of shifting all the soil into the ocean.
(James McCauley, from 'The True Discovery of Australia')

Background image: Drone image of TERN Calperum Mallee Supersite, SA. **Source**: TERN Australia

Figure 2.1 Australia

a. Next generation Blue Marble Image with topography and bathymetry, August 2004

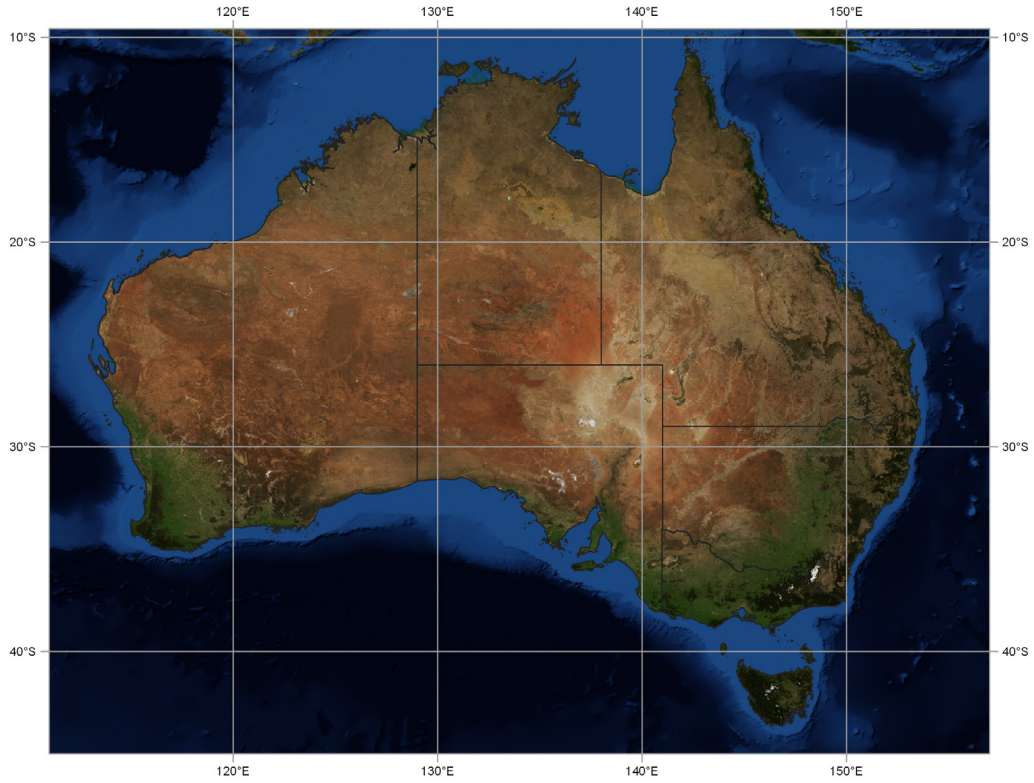

b. Locational map (see also Volume 2B—Figure 1.14)
WA: Western Australian; SA: South Australia; TAS: Tasmania; VIC: Victoria; NSW: New South Wales; QLD: Queensland; NT: Northern Territory; ACT: Australian Capital Territory (not labelled but surrounds Canberra)

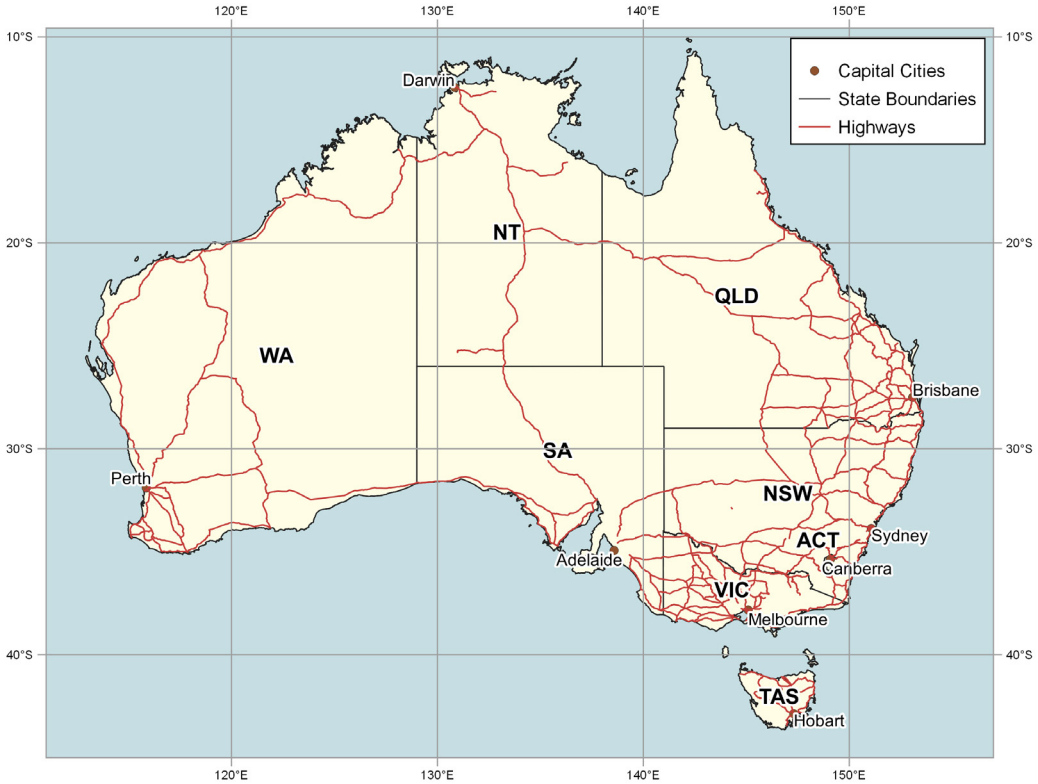

Source: Tony Sparks, Icon Water, using NASA Visible Earth imagery for figure a, and GA (2002) data for roads in figure b

Table 2.1 Geography and settlement of Australia

Characteristic		Details	Value
Area (sq. km; GA, 2020a)	Total, including islands	6th largest in world	7,688,287
	States and Territories, including islands	Western Australia (WA)	2,527,013
		Queensland	1,729,742
		Northern Territory (NT)	1,347,791
		South Australia (SA)	984,321
		New South Wales (NSW)	801,150
		Victoria	227,444
		Tasmania	68,401
		Australian Capital Territory (ACT) (including Jervis Bay)	2,452
Location	Northern Extremity	Cape York (Queensland)	10° 41' 21" S, 142° 31' 50" E
	Eastern Extremity	Cape Byron (NSW)	28° 38' 15" S, 153° 38' 14" E
	Southern Extremity	South East Cape (Tasmania)	43° 38' 40" S, 146° 49' 30" E
	Western Extremity	Steep Point (WA)	26° 09' 05" S, 113° 09' 18" E
Altitude	Highest	Mount Kosciuszko (NSW)	2,228 m
	Lowest	Lake Eyre (SA)	15 m below mean sea level
Climate	Annual Rainfall	Average	165 mm
	Temperature Extremes	Maximum recorded range	-23°C to 50.7°C
Water Features	Longest River	River Murray	2508 km
	Largest Lake	Lake Eyre (salt)	9690 sq. km
Land Cover	Arid and Semi-arid land	< 500 mm annual rainfall	~70%
	Arable land	Agricultural production	~6%
	Native Vegetation Cover	Including sparse arid vegetation	~90%
	Dominant land cover	Hummock Grasslands	23%
Population at 30/9/2019 (ABS, 2020)	Total	Australian Bureau of Statistics (ABS)	25,464,100
	States and Territories	New South Wales (NSW)	8,118,000
		Victoria (VIC)	6,629,000
		Queensland (QLD)	5,115,500
		Western Australia (WA)	2,630,600
		South Australia (SA)	1,756,500
		Tasmania (TAS)	535,500
		Australian Capital Territory (ACT)	428,100
		Northern Territory (NT)	245,600

2.1 Topography and Hydrology

A well-known Australian poetess, Dorothea Mackellar, aptly describes Australia as a 'wide brown land' (see Section 15.1). With an average elevation of less than 300 m, barely 6% of the continent exceeds 600 m. The current topography of Australia has been formed from ongoing erosion and sedimentation by wind and water over hundreds of millennia, resulting in large areas of flat, infertile land (see image on page before Section 1). The topography of mainland Australia can be described in terms of four major landform regions (see Figure 2.2):

- coastal plains—narrow, sandy fringes along the east coast. These plains are relatively fertile and well-irrigated.
- eastern highlands—adjacent to the coastal plains, these run continuously for nearly 4,000 km from northern Queensland through NSW and into Victoria, and ultimately reappear in Tasmania. On the Australian mainland, these highlands are known as the Great Dividing Range, which directs rain onto the coastal plains and separates east-flowing from west-flowing rivers.
- central lowlands—stretch from the Gulf of Carpentaria in the north to the Great Australian Bight in the south, and include large parts of western Queensland and NSW, northwest Victoria and most of SA. These constitute 25% of the mainland, comprise flat, sedimentary material and contain large areas of desert.
- western plateau—or peneplain, covering one third of the continent and large parts of SA, NT, and WA, and composed of igneous and metamorphic rocks.

The distribution of soils in the Australian landscape has been mapped in terms of major soil types using the Australian Soil Resource Information System (ASRIS; McKenzie *et al*., 2012; CSIRO, 2014; see Figure 2.3 and Section 3.3.1), or as soil attributes in the Soil and Landscape Grid of Australia (TERN, 2020). The Australian Soil Classification defines a national standard for classifying soils (Isbell and NCST, 2021).

National DEM available for Australia are listed in Table 2.2. The Australian Hydrological Geospatial Fabric (more commonly referred to as 'the Geofabric'; BoM, 2020b; see Section 2.6 and Volume 2D—Excursus 13.2) defines important hydrological features including rivers, waterbodies, catchments, and aquifers. By accurately defining the spatial locations and dimensions of these features and their interconnections, water storage, movement, and use through the landscape can be monitored and modelled. In particular, by enforcing drainage conditions based on an accurate, national Digital Elevation Model (DEM) within a hierarchy of drainage areas, the boundaries of topographic drainage divisions and river regions are reliably mapped at a range of scales (see Figure 2.4). Two major drainage basins are:

- Lake Eyre Basin—Australia's largest endorheic (closed) drainage basin, covering around 1.2 million km^2 in SA, NT, Queensland and NSW (DAWE, 2019); and the
- Murray-Darling Basin—the largest and most permanent river system in southeastern Australia, within SA, Queensland, NSW and Victoria (MDBA, 2013).

Table 2.2 Australian DEM

Name	Spatial resolution (m)	Based on
GEODATA 9-second DEM and D8 Flow Direction Grid 2008 (DEM-9S) v3	250	Elevation data at 1:100,000 and 1:250,000 cartographic scales
SRTM 3-second DEM v1.0	90	Shuttle Radar Topographic Mission, 2000
SRTM, 1-second DEM v10	30	Shuttle Radar Topographic Mission, 2000
Lidar 25 m grid	25	236 Lidar surveys between 2001 and 2015
Lidar 5 m grid	5	236 Lidar surveys between 2001 and 2015

Source: GA (2019)

Figure 2.2 Major landform categories

Note that the blue waterbodies in central Australia are ephemeral salt lakes.

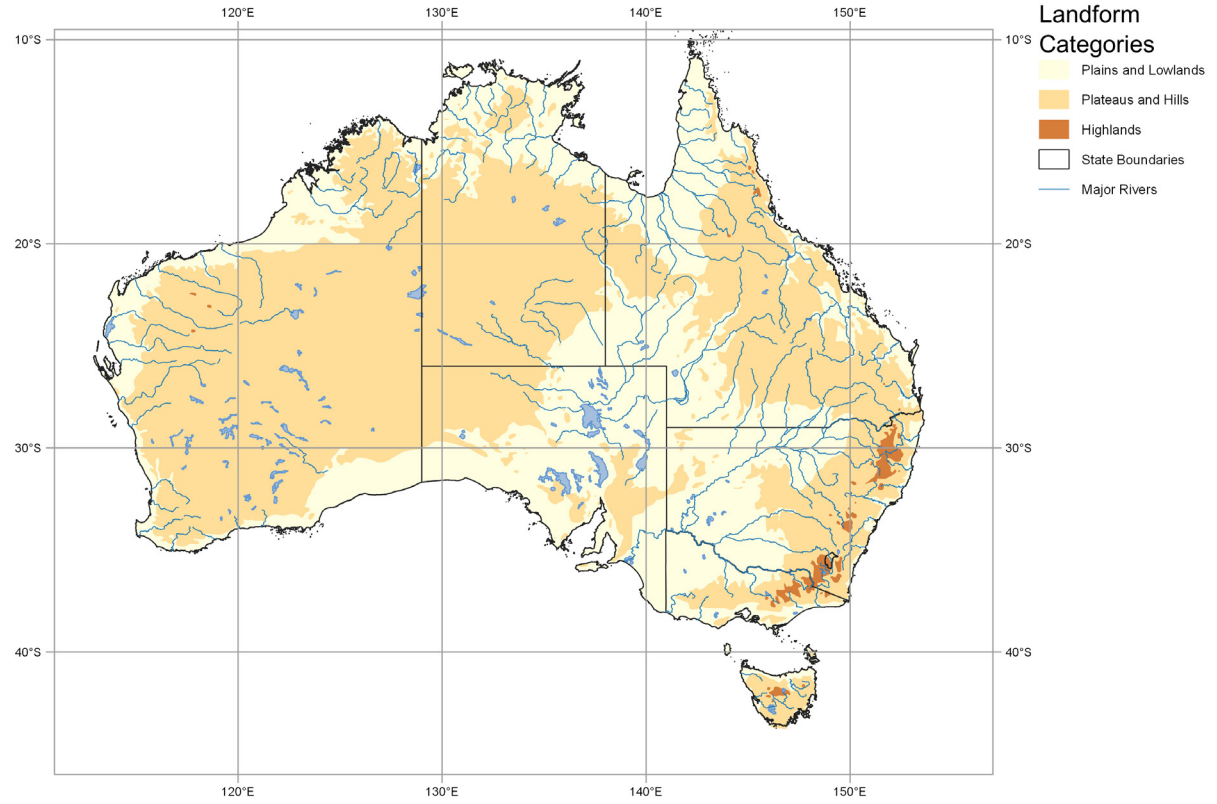

Source: Tony Sparks, Icon Water, using data from GA (2002) for waterbodies

Figure 2.3 Australian Soil Resource Information System (ASRIS)

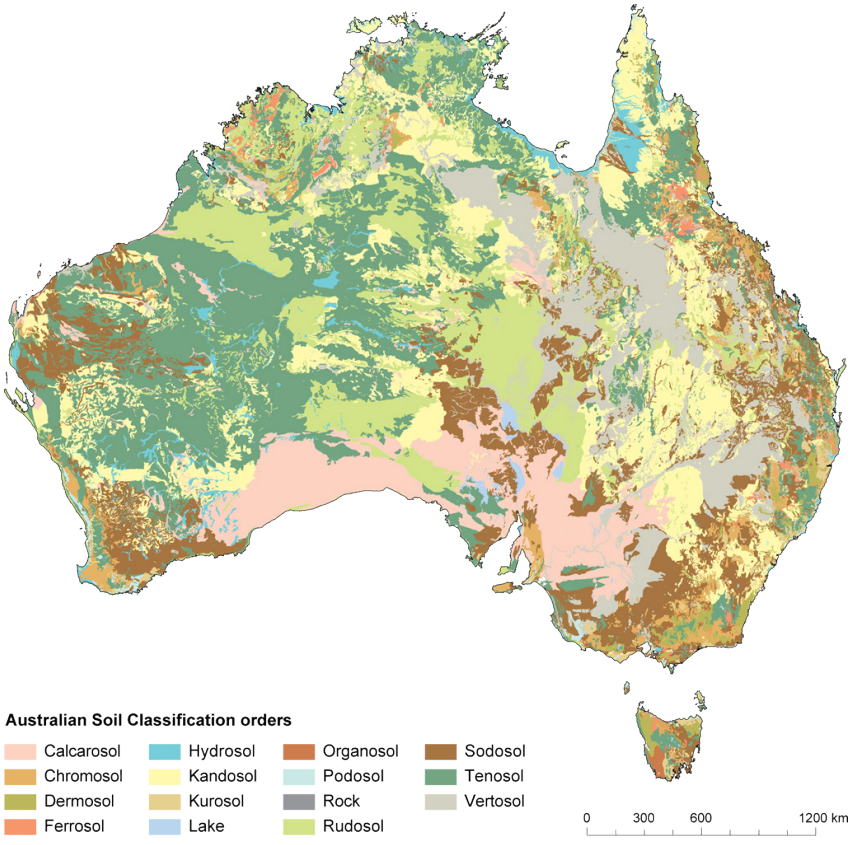

Figure 2.4 Major drainage basins

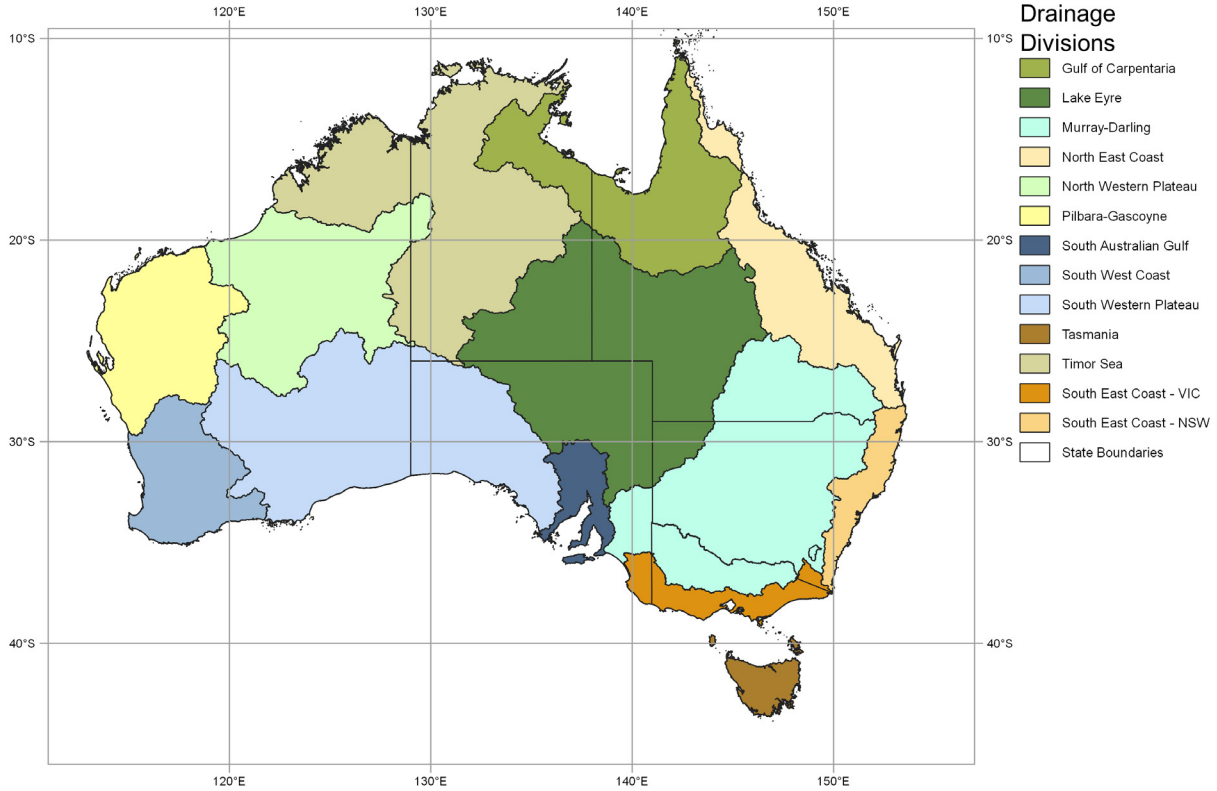

Source: Tony Sparks, Icon Water, using data derived from the Geofabric Hydrology Reporting Catchments product (BoM, 2020c)

Most of Australia's rivers do not carry a permanent supply of water and around half drain inland, often terminating in ephemeral salt lakes (see Volume 1A—Excursus 5.1). The major river system, formed by the Murray, Darling, and Murrumbidgee Rivers, is in southeast Australia and forms part of the boundary between NSW and Victoria (see Figure 2.2). The catchment for this river system, the Murray-Darling Basin (MDB; see Figure 2.4), serves as Australia's major food production region (see Section 12.1 and 13). The MDB covers around one-seventh of the Australian landmass, including the whole ACT, most of NSW, half of Victoria, and smaller portions of Queensland and SA.

... the eastern coastlands exhibit marked juvenile topography, while the rest of Australia is more or less senile throughout (Taylor, 1927)

The Great Artesian Basin (GAB) is the largest groundwater aquifer in Australia, underlying nearly one quarter of Australia in SA, NT, Queensland, and NSW (Booth and Tubman, 2011; see Figure 2.5). It spans 1.7 million km^2, contains an estimated 64,900 million Ml of water, and provides a permanent water supply for much of the arid interior (GA, 2020b; see Section 15.1.2). Water in the GAB is up to 2 million years old. To ensure long term sustainable use of this important resource across Australia's arid interior, careful land management is needed to balance extraction and replenishment (see Section 15.1.2). Accordingly, the Great Artesian Basin Sustainability Initiative (GABSI) was funded by federal and state government agencies from 1999 to 2017 to improve spring pressure and manage water more sustainably within the GAB. During its activity, GABSI upgraded > 750 bores, decommissioned > 21,000 km of bore drains, installed > 31,000 km of new, efficient pipe drains and saved > 250Gl of water per year (DAWE, 2020a).

Figure 2.5 Great Artesian Basin

Lambert conformal conic projection with standard latitudes 18°S and 36°S, centred on 136°E and 24°S, and based on revised Great Artesian Basin Jurassic-Cretaceous sequence boundary from Ransley and Smerdon (2012)

Source: Wikimedia: *https://upload.wikimedia.org/wikipedia/commons/8/8d/Great_Artesian_Basin.png*

2.2 Climate

2.2.1 Weather patterns

The Australian mainland is the driest inhabited continent on Earth, with Antarctica being the only continent with a lower rainfall (BoM, 2020a). The combined impact of temperature and humidity creates climate zones that are largely stratified by latitude (see Figure 2.6). 70% of the Australian land mass receives less than 500 mm of rain annually (GA, 2020c), with half of that area being defined as arid (< 250 mm annual rain; see Figure 2.7). Temperatures can also vary significantly, both diurnally and seasonally, especially in the arid central region (see Figure 2.8).

The dry central regions have high levels of evaporation (see Figure 2.9a). The combined impact of rainfall and temperature on land cover is summarised by evapotranspiration (ET), the release of water vapour from vegetated and non-vegetated land into the atmosphere (see Figure 2.9b). In most of Australia, the potential ET is greater than precipitation, with only an estimated 10% of actual ET contributing to groundwater recharge and surface flows (Glenn *et al.*, 2011).

Of all countries the primitive areas of Australia are the safest for mankind. Natural hazards are at a minimum. Possible hunger and thirst and the fear of getting lost are the greatest.
(Charles F. Laseron, 1953)

Figure 2.6 Climate zones derived from humidity and temperature

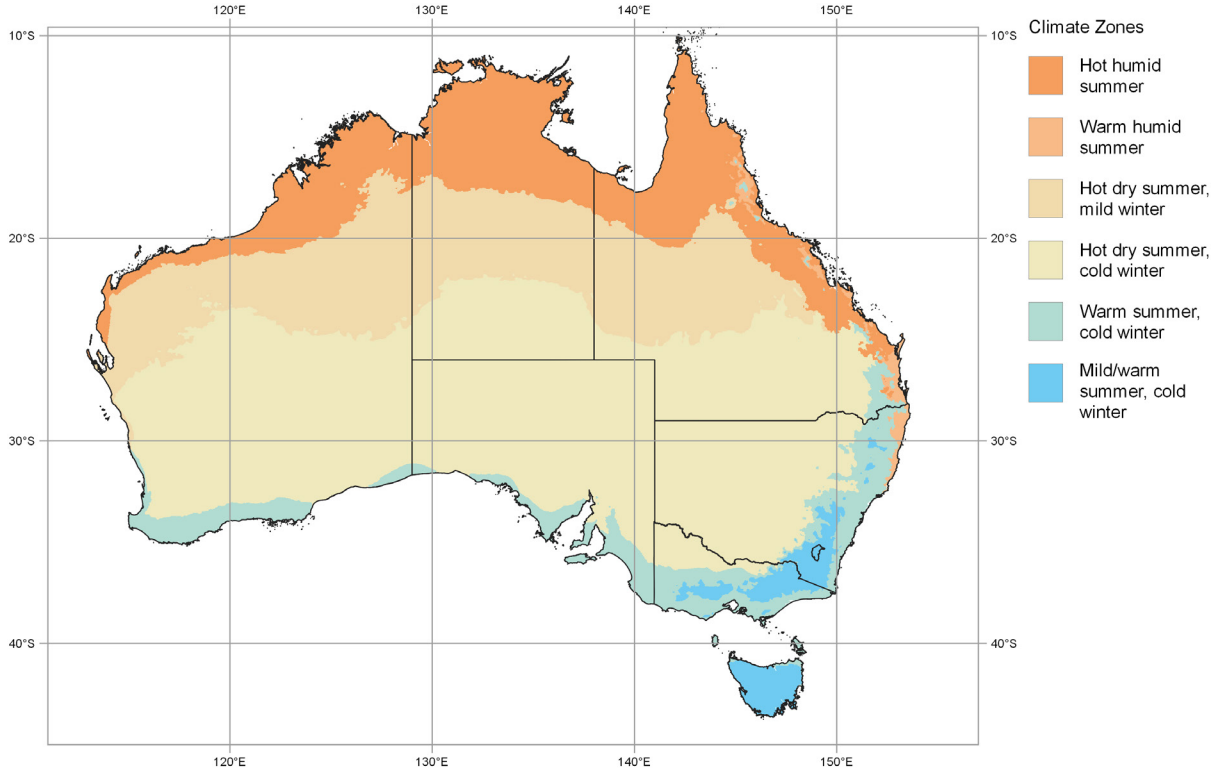

Source: Tony Sparks, Icon Water, using gridded data from BoM (2020a) based on a standard 30-year climatology (1961–1990)

Figure 2.7 Average annual rainfall

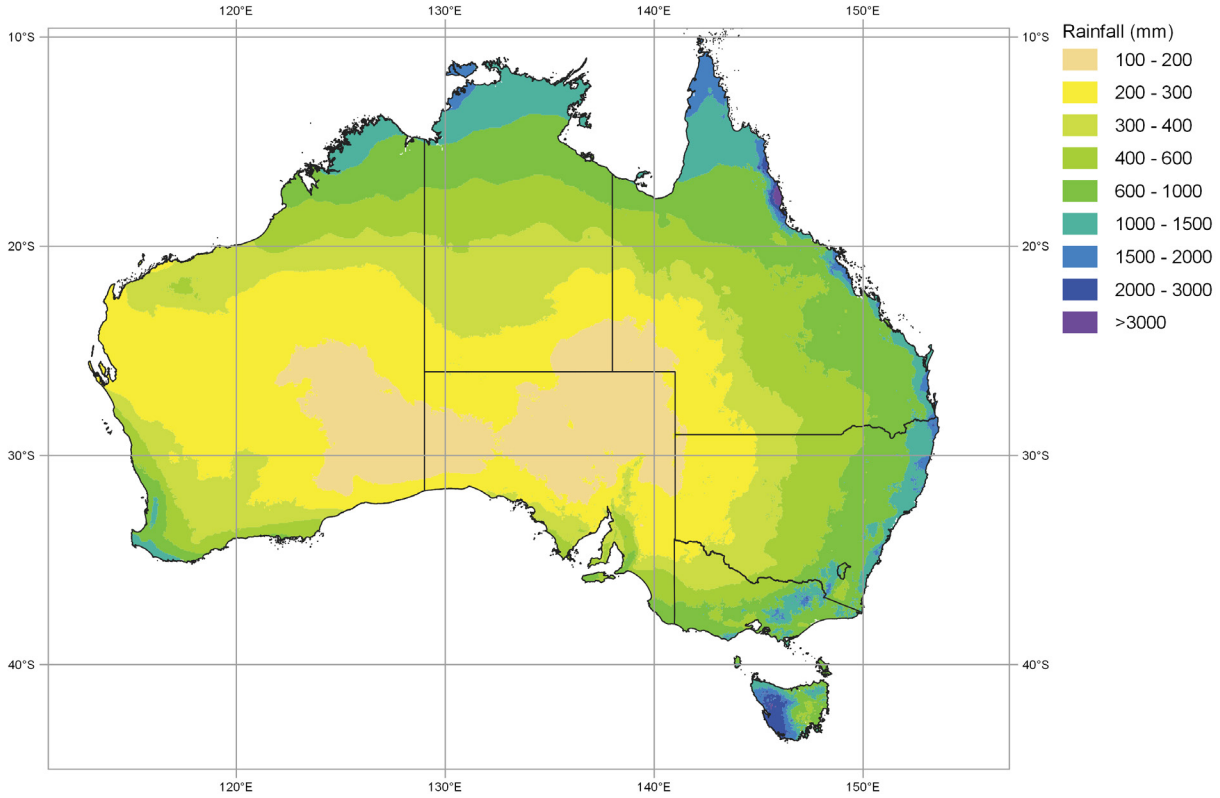

Source: Tony Sparks, Icon Water, using gridded data from BoM (2020a) based on a standard 30-year climatology (1961–1990)

Figure 2.8 Seasonal temperature variations in Australia

a. Summer average daily maximum temperature

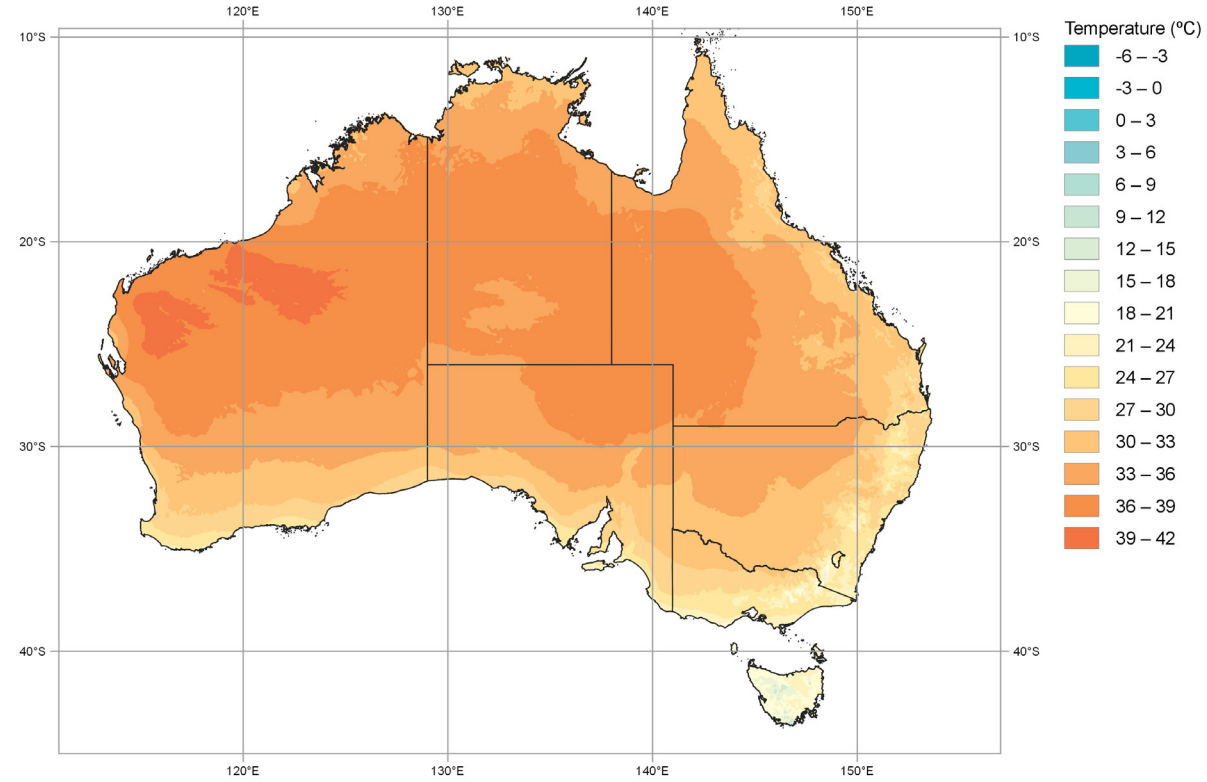

b. Winter average daily minimum temperature

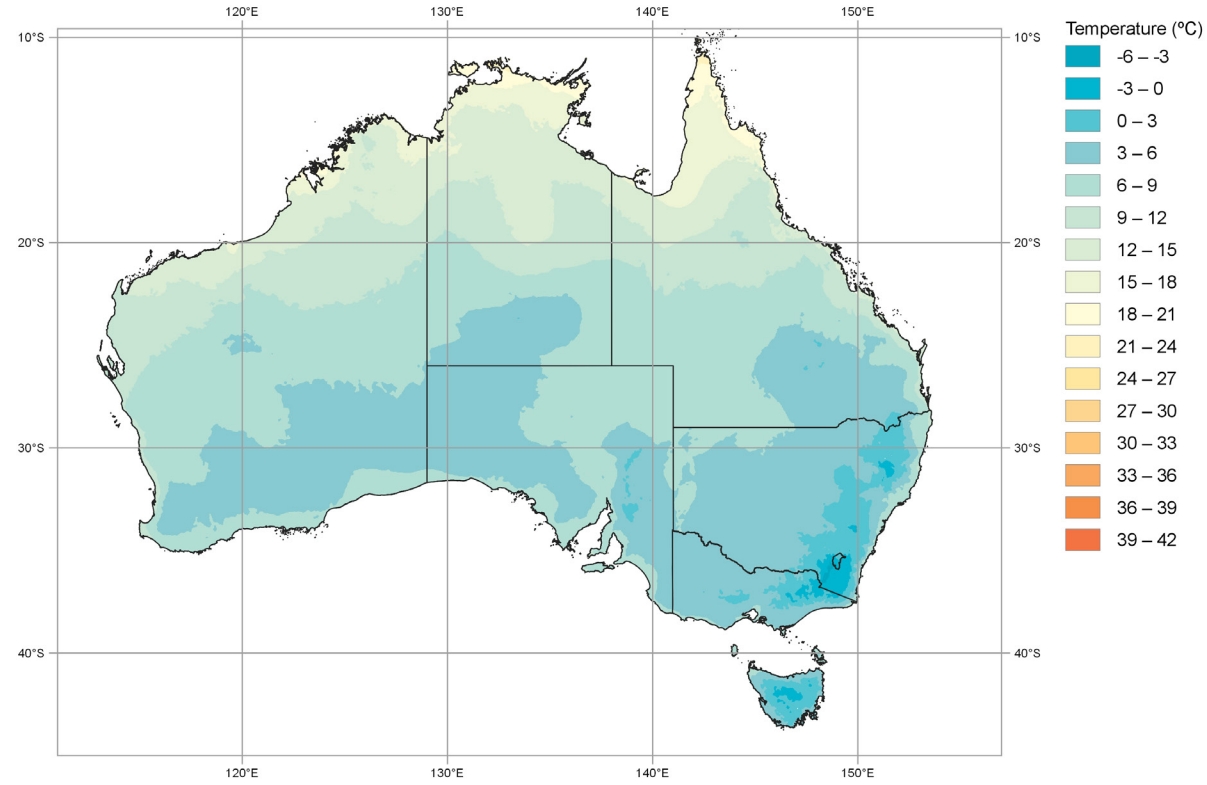

Source: Tony Sparks, Icon Water, using gridded data from BoM (2020a) based on a standard 30-year climatology (1961–1990)

Figure 2.9 Evaporation and evapotranspiration over Australia

a. Average pan evaporation based on at least 10 years of records (1975–2005)

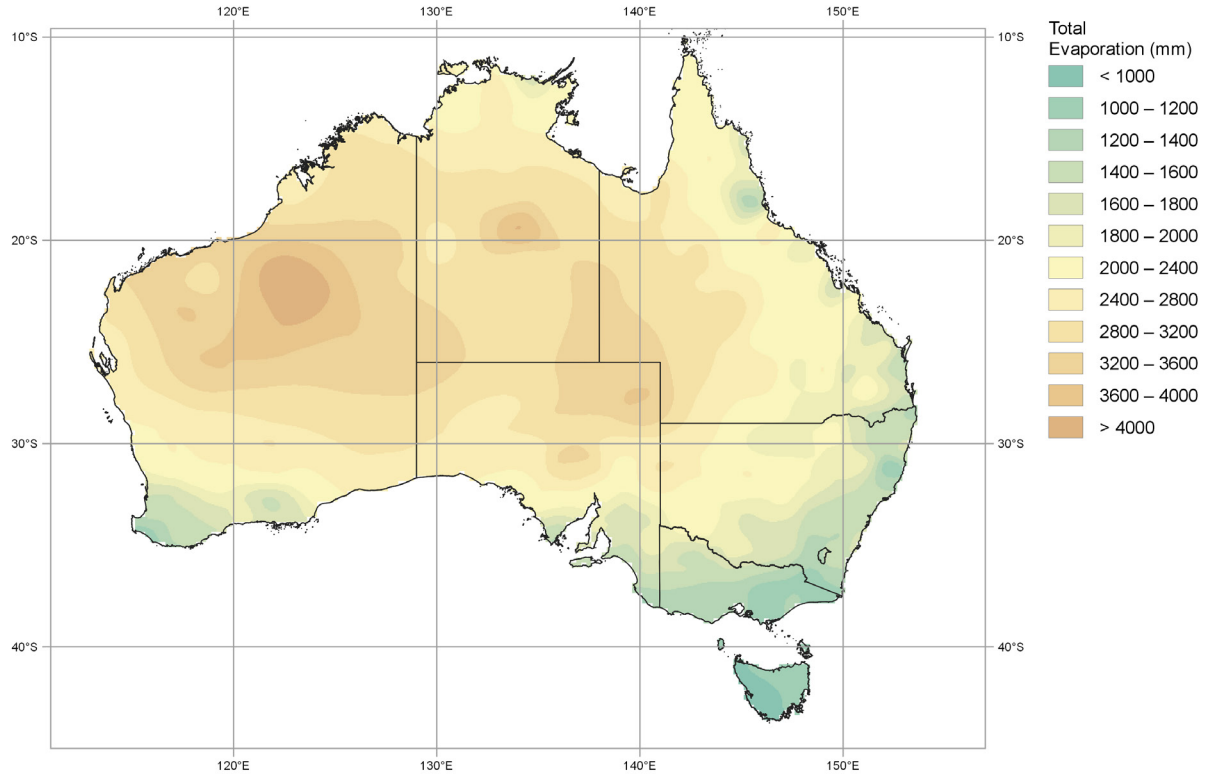

b. Average areal actual evapotranspiration based on a standard 30-year climatology (1961–1990)

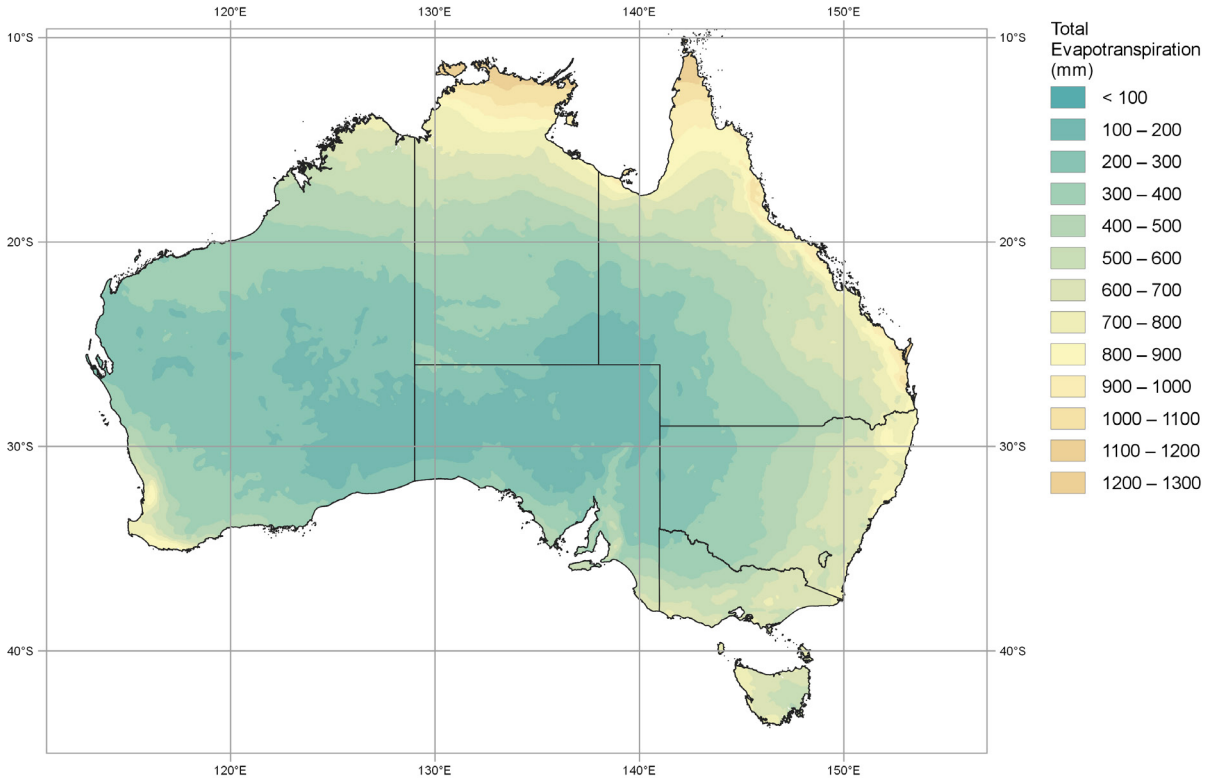

Source: Tony Sparks, Icon Water, using gridded data from BoM (2020a)

2.2.2 Climatic drivers

Australian climatic conditions are driven by the major air and water circulation patterns in the Southern Hemisphere. There are two main atmospheric circulation patterns that influence our climate:

- warm, moist equatorial air is drawn towards Northern Australia as the continent heats up in the warmer months, resulting in monsoonal rains in the tropics and a ridge of warm dry air in the sub-tropics. Movement of this sub-tropical ridge induces Australia's seasonal rainfall pattern: summer rainfall in the north and winter rainfall in the south; and
- warm air in the Pacific Ocean is moved into eastern Australia via southeast trade winds which carry moisture during the La Niña phase and drier air during the El Niño phase. This is part of the Walker circulation, which describes the large scale, atmospheric circulation over the Pacific Ocean driven by movement of deep, equatorial waters in the cooler eastern Pacific towards the warmer western Pacific Ocean (Lau and Yang, 2002).

As detailed in Volume 3B, three ocean currents significantly impact the Australian climate:

- a cold current from the southern Indian Ocean moves northward along the WA coast during summer;
- the warm Leeuwin Current moves towards the South Pole along the west and south coasts of Australia with significant effects on marine ecosystems (Feng *et al*., 2009); and
- a warm Eastern Australian Current moves down the east coast (FAO, 2009).

2.2.3 Climate classifications

The Thornthwaite classification system for climate was proposed in 1931 and revised in 1948 (Thornthwaite, 1931, 1948). The final system was based on the interplay between local moisture and temperature, with the view that temperature was a driver for potential evapotranspiration (see Section 7.6). This system derived indices for humidity and aridity from water balance indicators:

$$\text{humidity} = \frac{\text{water surplus}}{\text{water need}}$$

$$\text{aridity} = \frac{\text{water deficit}}{\text{water need}}$$

where for annual estimates:

water surplus = precipitation – actual evapotranspiration;

water deficit = potential evapotranspiration – actual evaporation; and

water need = potential evapotranspiration.

Geographic regions are classified on the basis of their Thornthwaite Moisture Index (M):

$$M = \text{humidity} - 0.61 \times \text{aridity}$$

or

$$M = \frac{100 \times \text{water surplus} - 60 \times \text{water deficit}}{\text{water need}}$$

In Australia, the Thornthwaite Moisture Index has been used to define six types of climate that are commonly referenced for infrastructure planning (Austroads, 2004; Philp and Taylor, 2012; see Table 2.3).

Table 2.3 Australian climate types

Climate Types		Thornthwaite Moisture Index
i	Alpine/coastal	> 40
ii	Wet temperate	10 to 40
iii	Temperate	-5 to 10
iv	Dry temperate	-25 to -5
v	Semi-arid	-40 to -25
vi	Arid	< -40

Source: Philp and Taylor (2012)

Figure 2.10 Modified Köppen climate classification

This classification of Australian climatic regions was derived from 0.025°´0.025° resolution mean rainfall, mean maximum temperature, and mean minimum temperature gridded data. All means are based on a standard 30-year climatology (1961–1990).

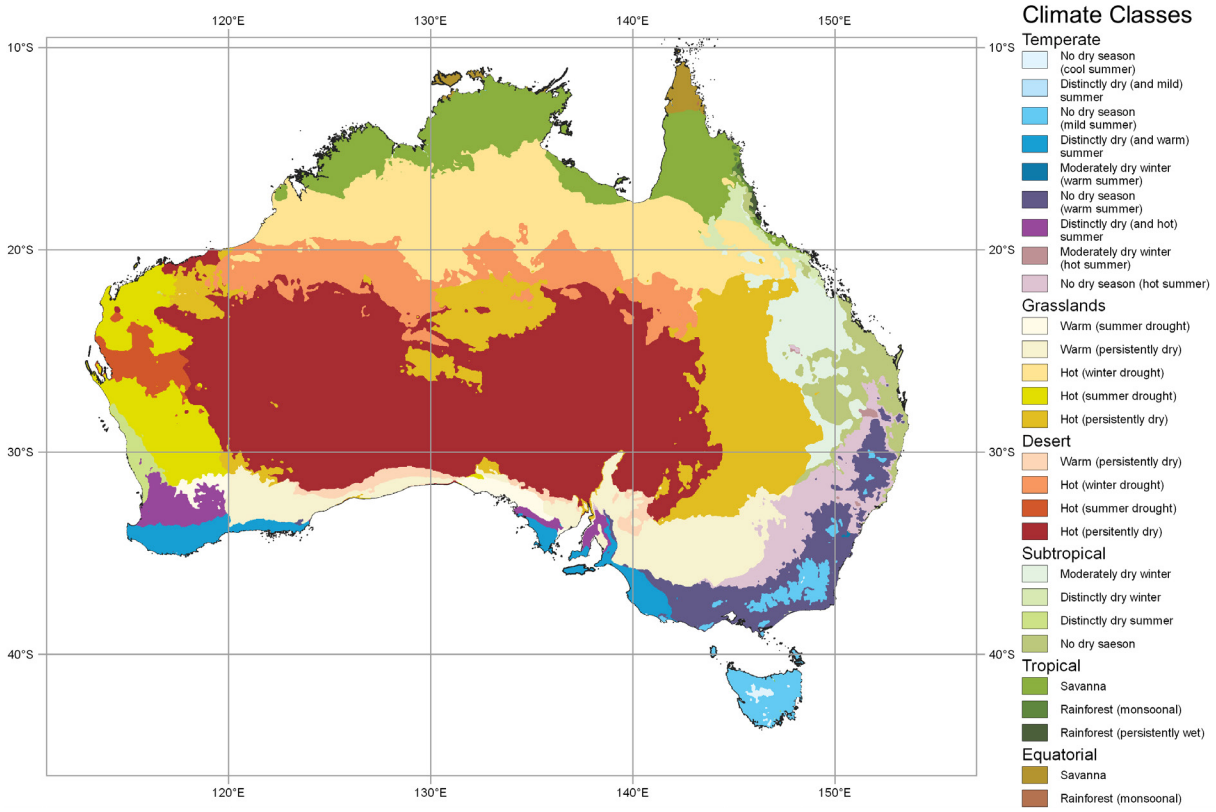

Source: Tony Sparks, Icon Water, using gridded data from BoM (2020a)

Temperature and rainfall data have been used to classify Australia into six broad climatic classes and 27 sub-divisions (see Figure 2.10). These zones are based on a modified Köppen classification (Köppen, 1931; Stern *et al*., 1999) and are strongly correlated with topography, land cover, and land use.

An alternate agroclimatic classification, derived from climate and topography, and aligned with bioregion data, was developed by Hutchinson *et al*. (2005). These 18 classes are illustrated in Figure 2.11a and described in Table 2.4. This classification was subsequently modified by Hobbs and McIntyre (2005) to 10 classes. More recently, Thackway and Freudenberger (2016; see Figure 2.11b) adjusted selected bioregion boundaries and merged them with the agroecological regions defined by Williams *et al*. (2002) to better reflect recent changes in climatic patterns, especially in tropical savanna regions.

Figure 2.11 Agroclimatic classifications

a. 18 classes

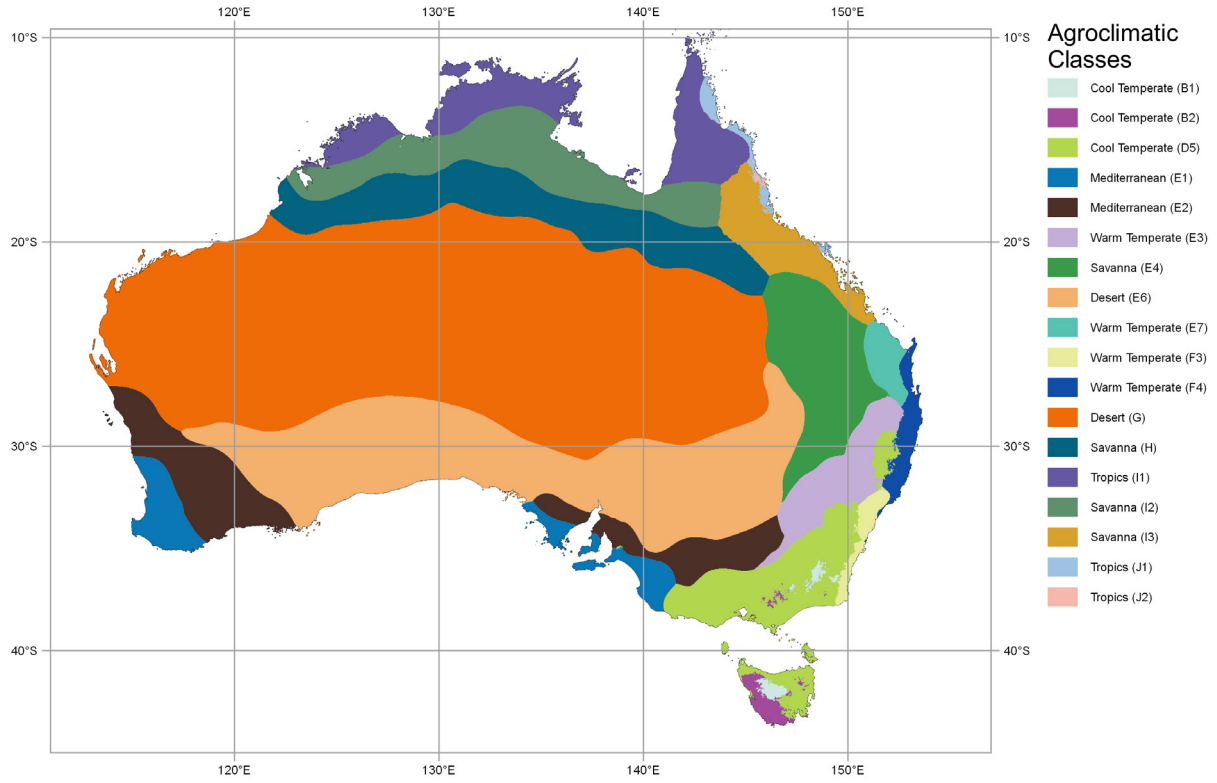

b. 10 classes

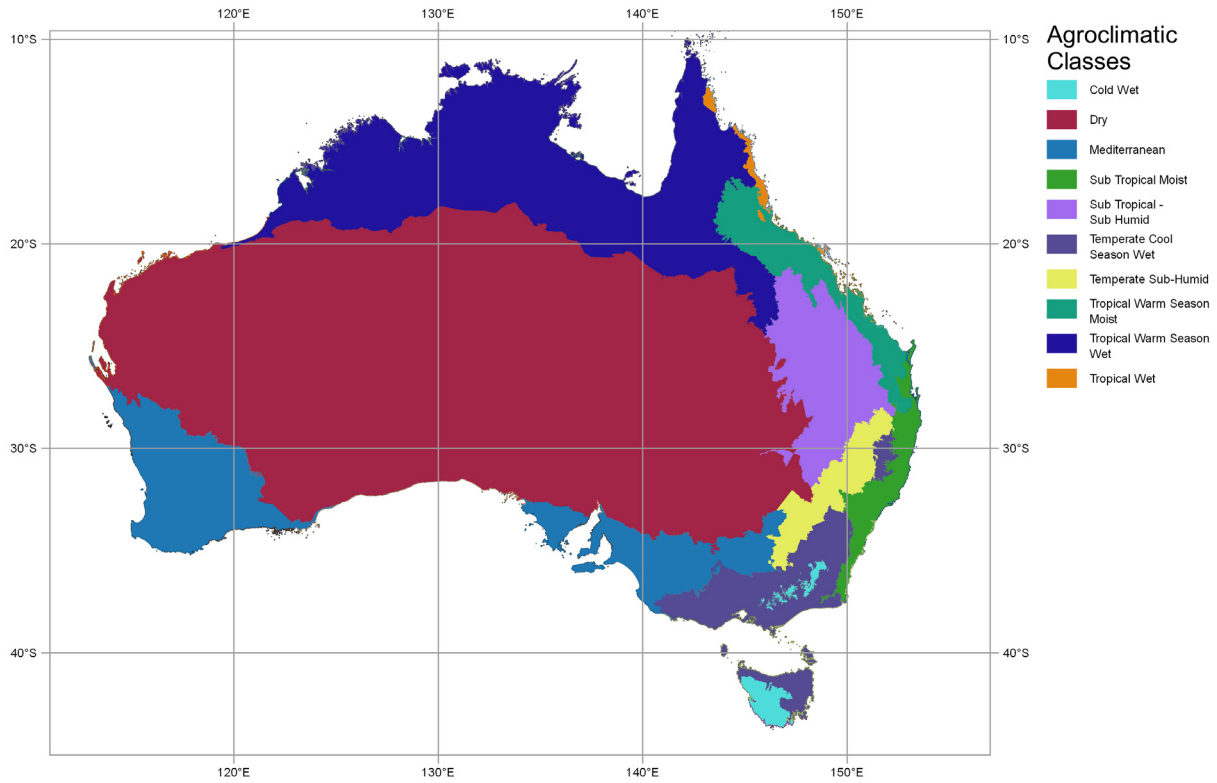

Source: a. Tony Sparks, Icon Water, using data from Hutchinson *et al.* (2005) Figure 3, b. Tony Sparks, Icon Water, using data from Thackway and Freudenberger (2016) Figure 1a and Table S2

Table 2.4 Agroclimatic class descriptions for Figure 2.11

18 class code	Agroclimate	Location	Land use	10 class label
B1	Very cold winters with summers too short for crop growth	Alpine areas of NSW, Victoria and Tasmania.	Water harvesting, hydroelectricity, tourism and nature conservation	Cold wet
B2	Less severe winters and longer moist summers suitable for some crops	Tasmanian highlands.		
D5	Moisture availability high in winter-spring, moderate in summer, most plant growth in spring	Tasmanian lowlands, southern Victoria, southern and northern Tablelands of NSW.	Forestry, cropping, horticulture, improved and native pastures	Temperate cool season wet
E1	Classic "Mediterranean" climate with peaks of growth in winter and spring and moderate growth in winter	Southwest WA and southern SA.	Forestry, horticulture, winter cropping, improved pastures	Mediterranean
E2	"Mediterranean" climate, but with drier cooler winters and less growth than E1	Inland of E1 in southwest WA, southern SA, northwest Victoria and southern NSW.	Horticulture, winter cropping, improved pastures	
E3	Most plant growth in summer, although summers are moisture limiting.; temperature limits growth in winter	Western slopes of NSW and part of the North Western Plains.	Winter cereals and summer crops, grazing	Temperate sub-humid
E4	Growth is limited by moisture rather than temperature and the winters are mild; growth is relatively even through the year	Unique in the world to sub-tropical continental eastern Australia and associated with the brigalow belt of QLD and NSW.	Winter cereals (after summer fallowing), summer crops (including cotton) and sown pastures	Sub-tropical to sub-humid
E6	Semi-arid climate that is too dry to support field crops; soil moisture tends to be greatest in winter	Southern edge of the arid interior in WA, SA, NSW and QLD.	Rangeland	Dry
E7	Moisture is the main limit on crop growth; growth index lowest in spring	Maritime sub-tropical areas in southern QLD.	Sugar, crops and cattle grazing	Tropical warm season moist
F3	Cooler end of the warm, wet sub-tropical climates	The Sydney Basin and the NSW south coast.	Cooler temperatures slightly favour temperate crops and sown pastures	Sub-tropical moist
F4	Warmer and wetter than F3	NSW north coast, extending to southern QLD and the Great Sandy province.	Horticulture, sown pasture and tourism. Potential for wheat, cotton and maize	
G	Desert, supporting very little plant growth due to water limitation	Central Australia.	Cropping possible only with irrigation. Rangeland, wildland	Dry
H	Semi-arid, with some growth in the warm season, but too dry for cropping	Transition between the wet/dry tropics and the arid interior in WA, NT and QLD.	Rangeland	Tropical warm season wet
I1	Strongly developed wet and dry seasons with plant growth determined by moisture availability	NT, northern WA and Cape York Peninsula.	Predominately rangeland. Potential for tropical field crops	
I2	Temperature and moisture are more seasonal than for I1 and the growing season is shorter	Occurs inland of I1	Some crop potential, but predominantly rangeland	
I3	This has cooler winters than I1 and I2 with a growing season lasting at least six months	Occurs in the coastal and hinterland areas of northeast QLD, south of Cape York Peninsula.	Sugar, cropping and rangelands	Tropical warm season moist
J1	Moisture and temperature regime supports growth for 8–9 months of the year, with a 3–4 month dry season	Limited areas in the central Mackay coast and the Wet Tropics.	Sugar cane and horticulture	Tropical wet
J2	As for J1 but with a shorter dry season	Limited areas on the east coast of Cape York Peninsula		

Source: Hutchinson ***et al.*** (2005) Table 1; Thackway and Freudenberger (2016)

2.3 Biota

Australia supports a diverse and unique range of indigenous plants and animals. Being an isolated continent, Australia's terrestrial biota largely evolved independently from the rest of the world with over 80% of its angiosperms, mammals, reptiles, and frogs, and over half of its birds, being unique. The remainder migrated during prehistoric times, before land bridges with then adjacent continents were submerged by rising sea levels. Fossil evidence suggests that marsupial (but not placental) mammals arrived via Antarctica, and placental rats and bats came from Asia (Cox, 2000).

In addition to these naturally-occurring species, thousands of plants and hundreds of animals have been introduced to the Australian landscape in recent centuries, some of which now produce most of our agricultural income. A significant number of species, however, have become invasive and present serious threats to natural ecosystems and agricultural activities. In 2012, feral animals and invasive weeds were identified as the two major threats to sustainable natural resource management (NRM) in all NRM regions in Australia (NRM, 2019). Changes in land management practices since European settlement, which started with the arrival of the First Fleet in 1788, have also modified the populations and distributions of some indigenous biota, resulting in some species becoming endangered or extinct and others having a greater impact on the environment (Burrows, 2018).

The following sub-sections introduce aspects of Australia's biota that have direct relevance to EO-based studies of terrestrial vegetation:

- vegetation classification systems (see Section 2.3.1);
- weeds (see Section 2.3.2); and
- indigenous and feral animals (see Section 2.3.3).

2.3.1 Classifying vegetation

The intricate composition of natural vegetation and the gradual transitions that occur between different types of vegetation complicate the task of defining discrete vegetation classes. While many different approaches have been used to classify vegetation, three basic attributes of vegetation underpin most classification systems, namely growth form, foliage cover, and floristic composition. Plants can also be grouped into functional groups or plant functional types (PFT) on the basis of their function in an ecosystem and their resource usage (Smith *et al.*, 1997; see Sections 4.1.2, 4.2.1, and 7.4).

Current vegetation classification systems define labels on the basis of specific, measurable attributes rather than descriptive criteria. The standard methods and terminology for field survey of land and soil attributes, including vegetation, in Australia are detailed in NCST (2009). While this approach cannot solve the problems associated with attempts to classify the complexities of natural vegetation, it does reduce ambiguity in class nomenclature.

The first systematic floristic classification for Australia's vegetation, including origins, development, and composition, was published by Beadle (1981). Since 1973, the Australian Biological Resources Study (ABRS, 2012) has been compiling the definitive reference on taxonomy for Australian flora based on the Cronquist system (Cronquist, 1968, 1981). Keith (2017) reviews the development of nomenclature to map and classify Australian vegetation, describes significant ecological processes, and provides details of each major vegetation type.

Criteria useful in the description of vegetation include: life form; size; density of individual plants; shape, size and texture of leaves; and whether evergreen or deciduous. Each of these criteria includes several classes which differ in kind (e.g. life form and leaf attributes) or in degree (e.g. size and density), and the possible number of combinations of all these classes is so large as to lead to an unworkable system so far as classification is concerned, although any particular plant community can be defined with accuracy by such a system. A workable system necessarily must select among possible criteria and make arbitrary divisions among characteristics which are continous in magnitude; in so far as it does this it cannot define the many combinations met with in nature. (Specht, 1970).

Table 2.5 Common definitions for Australian vegetation

Specht Land Cover Label	Equivalent Label	Rainfall (mm)	Species Composition	Height (m)	Foliage Projective Cover (%)
Closed Forest	Rainforest	> 900	Wide range of rainforest trees and understorey plants	15–40	70–100
Tall Open Forest	Wet Sclerophyll	> 900	Mostly *Eucalyptus* plus ferns, and shrubs/small trees with soft foliage	> 30	30–70
Low Open Forest	Dry Sclerophyll	> 900	Mostly *Eucalyptus* plus grasses/shrubs with hard leaves	5–30	30–70
Woodland	Savanna	< 900	Mostly *Eucalyptus* plus *Callitrus*, *Casuarina* and *Acacia* species	5–25	10–30
Open Woodland	Open savanna	400–500	*Eucalyptus* and *Corymbia*, plus *Callitrus*, *Casuarina* and *Acacia* species	< 10	0–10
Shrublands	Heath	< 400	Mostly *Acacia* species, e.g. Mulga	2–8	30–100
Shrub Steppe	Low Shrubland	< 200	Mostly mallee eucalypts	< 2	10–30
Closed Grassland	Alpine Meadows, Herbland	< 400	*Poa*	< 1	30–100
Tussock Grassland	Mitchell Grasslands, Bluegrass Grasslands	400–700	Perennial grasses, rushes, sedges, *Lomandra* species	< 1	< 70
Hummock Grassland	Spinifex Grasslands	200–300	*Triodia*	< 2	10–30
Desert	Bare, Exposed	< 250	*Acacia aneura*, *Eremophila glabra*, *Atriplex vesicaria*, *Swainsona formosa*	< 2	0–10

Source: Specht (1970); Florence (1985); DEWR (2007)

The descriptive labels commonly used in Australia for vegetation were originally defined on the basis of rainfall, species composition and biomass density (measured as Foliage Projective Cover, FPC), which is defined as the "vertically projected percentage cover of photosynthetic foliage of all strata of the forest stand" (Specht, 1983), that is, the percentage of ground area occupied by the vertical projection of woody vegetation foliage. As summarised in Table 2.5, this approach tended to embrace alternative, and sometimes ambiguous, labels and imprecise boundary conditions (Gillison and Anderson, 1981). For example, one of the earliest national vegetation maps for Australia, compiled by Williams (1959) and derived from aerial photography and expert knowledge, used category labels based on structure and cover.

A widely used classification system for Australian vegetation, attributed to Specht (1970), is based on two structural features that are characteristic of most natural Australian flora—namely that the largest proportion of total biomass is contained in the upper stratum of vegetation and that biomass can be reasonably estimated from FPC plus height or growth form (see Section 3.2.1 and 5.1.1)—to define the 28 categories indicated in Table 2.6. This system for classifying vegetation is compatible with the ISO standards for terrestrial vegetation and has been adopted by several Australian land cover mapping projects.

In more recent decades, however, Australian vegetation classification systems explicitly derive vegetation class names from the structural formation of the vegetation (for example, see Excursus 6.1), in addition to the floristic association of the dominant species, rather than using labels that imply these characteristics (Walker and Hopkins, 1990; Thackway *et al*., 2008; Hnatiuk *et al*., 2009). In this context, a formation is defined as a "synthetic structural unit to which are referred all climax communities exhibiting the same structural form, irrespective of floristic composition" (Beadle and Costin, 1952), such as a tropical forest. A sub-unit of a formation, with two or more dominant species, is called an association (see Section 6.1). The Australian Vegetation Attribute Manual (NVIS Technical Working Group, 2017) includes the new attribute standard for compiling non-native and non-vegetated cover types. This new standard enables monitoring and reporting of the whole landscape and will complement monitoring land cover changes using the FAO Land Cover Classification (see Section 3).

Table 2.6 Structural classification of Australian vegetation

Growth form of tallest stratum	Foliage cover of tallest stratum			
	> 70%	30–70%	10–30%	< 10%
Tall trees (> 30 m)	Tall closed forest (T4)	Tall open forest (T3)	Tall Woodland (T2)	–
Medium trees (10–30 m)	Closed forest (M4)	Open forest (M3)	Woodland (M2)	Open woodland (M1)
Low trees (< 10 m)	Low closed forest (L4)	Low open forest (L3)	Low woodland (L2)	Low open woodland (L1)
Tall shrubs (> 2 m)	Closed scrub (S4)	Open scrub (S3)	Tall shrubland (S2)	Tall open shrubland (S1)
Low Shrubs (< 2 m)	Closed heath (Z4)	Open heath (Z3)	Low shrubland (Z2)	Low open shrubland (Z1)
Hummock grasses	–	–	Hummock grassland (H2)	–
Tussocky or Tufted grasses or Graminoids	Closed tussock grassland or closed sedgeland (G4)	Tussock grassland or sedgeland (G3)	Open tussock grassland (G2)	Sparse open tussock grassland (G1)
Other herbaceous plants	Dense sown pasture (F4)	Sown pasture (F3)	Open herbfield (F2)	Sparse open herbfield (F1)

The National Vegetation Information System (NVIS; NVIS Technical Working Group, 2017; DAWE, 2020b) is an ongoing collaborative initiative between the Australian federal, state, and territory governments to manage national vegetation data and has become the standard system for all Australian federal, state and territory government land management agencies. NVIS was developed to improve vegetation planning and management within Australia, and assist in managing a range of ecosystem services and practices (see Section 20.3), such as conserving biodiversity, controlling salinity, improving water quality, and managing vegetative fuel loads.

NVIS classifies Australian vegetation types at the sub-formation, association and sub-association levels using structural and floristic criteria (see Table 2.7 and Volume 2D—Excursus 12.1 for details). The NVIS Version 5.1 map product defines 33 Major Vegetation Groups (MVG; see Figure 2.12) and 85 sub-groups, which comprehensively describe the extent and distribution of vegetation in Australia, for both estimated pre-1750 and extant vegetation. A complementary national database, the National Forest Inventory (NFI), focuses on the productivity and sustainability of Australia's forests (see Section 16.1).

NVIS has enabled a nationally consistent vegetation dataset to be compiled from data collected by various state and territory jurisdictions. The recommended data collection level is Level 5 or better, with Levels 1–4 generated algorithmically for consistency (see Table 2.7). All NVIS data—both spatial data and the underlying vegetation attribute information—is open source. The classification systems used by relevant Australian federal state and territory authorities for mapping native vegetation are summarised in Table 2.8. Further information on some of these systems is provided in Sections 2.6 and 3.3.

Table 2.7 NVIS information hierarchy

Level 5 (association) is recommended as the minimum level of input for input data to NVIS. Hnatiuk *et al.* (2009) refer to Level 1 as Formation.

Level	Category	Description
1	Class	Dominant growth form for the structurally dominant stratum
2	Structural formation	Dominant growth form, cover and height for the structurally dominant stratum
3	Broad floristic formation	Dominant genus (or genera) plus growth form, cover and height for the structurally dominant stratum
4	Sub-formation	Dominant genus (or genera) plus growth form, cover and height for each of the three main strata. (Upper, Mid, and Ground)
5	Assocation	Dominant growth form, height, cover and species (to a maximum of 3 species) for each of the three main strata. (Upper, Mid, and Ground)
6	Sub-association	Dominant growth form, height, cover, and species (to a maximum of 5 species) for each of the substrata

Source: NVIS Technical Working Group (2017)

Figure 2.12 Major Vegetation Groups derived from NVIS Version 3

EPSG:3577 Australian Albers projection with 30 m spatial resolution

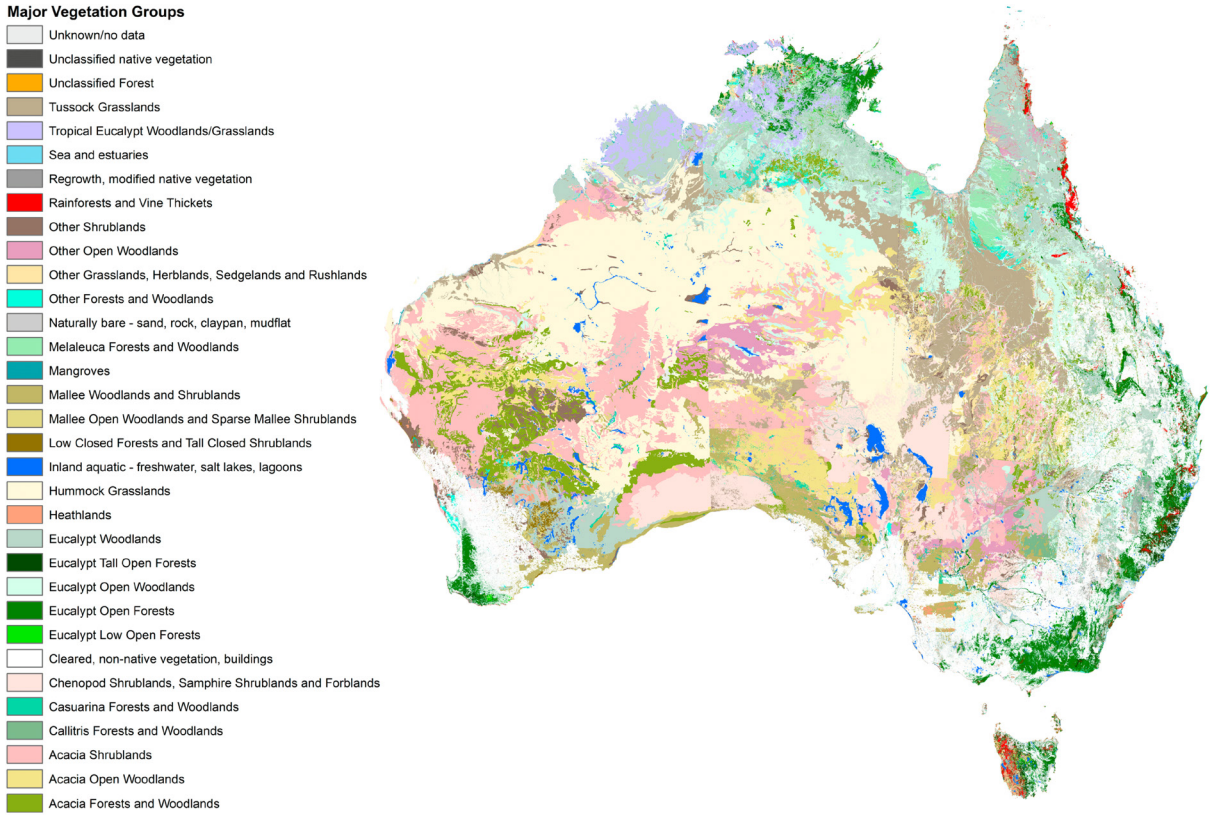

Source: Scarth *et al.* (2019) Figure 2 (from DEWR, 2007)

Table 2.8 Native vegetation classification systems

Jurisdiction	Categories
Federal	33 Major Vegetation Groups (MVG; DAWE, 2020b) 85 Major Vegetation Subgroups (MVS; DAWE, 2020b)
ACT	Ecological Communities (ACT EPSDD, 2020)
NSW	16 Vegetation Formations (Keith, 2004) 99 Vegetation Classes (Keith, 2004) ~1500 NSW Plant Community Types (PCT) in BioNet Vegetation Classification (NSW DPIE, 2020) State Vegetation Type Mapping (SVTM; see Excursus 8.2)
NT	Vegetation Associations (NT EPA, 2013; Brocklehurst *et al.*, 2007) 174 Vegetation Types (Lewis *et al.*, 2008; NTNVIS, 2020)
Queensland	16 Broad Vegetation Groups (BVG) (Queensland Government, 2020a; Neldner *et al.*, 2019) 1384 Regional Ecosystems (RE) (Queensland Government, 2020b)
SA	NVIS Framework (SA DEWNR, 2019)
Tasmania	~ 158 TASVEG Vegetation Communities (Harris and Kitchener, 2005)
Victoria	28 Bioregions (DELWP, 2020) 897 Ecological Vegetation Classes (EVC)
WA	819 Vegetation Associations (Shepherd *et al.*, 2002)

Source: Richard Thackway, Australian National University

2.3.2 Weeds

Weeds or invasive plants are defined as "any plant that requires some form of action to reduce its effect on the economy, the environment, human health and amenity" (DEE, 2019a). Many weeds in Australia were introduced by European settlers, but natives species can also become weeds, either when their native habitat changes favourably, or when they wander into 'new' ecosystems with suitable conditions. The introduction of any exotic vegetation has the potential to become a weed problem. Ecosystems can be permanently changed by the invasion of exotic weeds, which can transform faunal habitats, food sources, and fire regimes. Further, native vegetation may not be equipped to compete with invasive weeds, which can form dense, smothering thickets.

Weeds reproduce readily, usually through an abundance of seeds, and rapidly colonise disturbed sites. They impact urban, rural, and natural environments, including surface waters, deserts, and alpine regions. Despite active control measures being enforced by legislation in all levels of government, weeds are still spreading in Australia (DEE, 2019b). As such, they are considered to be a serious threat to both Australian agriculture and conservation areas (DEE, 2019a).

3,480 of the 28,000 plant species introduced into Australia since European settlement are now classified as weeds (Lesslie *et al.*, 2011). Of these weeds, 32 have been identified as 'Weeds of National Significance' on the basis of their "invasiveness, potential for spread and environmental, social and economic impacts" (DEE, 2019c). Specific lists of noxious weeds—those posing the greatest threat to native species and agricultural productivity—are also ranked and administered by each state and territory government for areas within its jurisdiction.

The average cost of weed impact and control was estimated as $4,989.2 million for Australian agricultural industries in 2018 (McLeod, 2018). In order to prevent land degradation in the longer term, weed control is viewed by farmers as one of their highest priorities (Lesslie *et al.*, 2011). While weed management is a significant problem throughout Australia, it is most challenging in the arid areas (Scott *et al.*, 2018), where both population density and productivity are low (see Section 15).

Weeds contaminate crops, displace pasture plants and compete with crop and pasture plants for water and nutrients. Weeds also harbour diseases and insect pests, reduce livestock carrying capacity and condition and can be toxic to livestock.
(Lesslie et al., 2011)

2.3.3 Indigenous and feral animals

While Australia's unique fauna adapted to its environment in isolation from the rest of the world, human management of the Australian landscape has modified the composition and distribution of fauna for millennia (Gammage, 2012; Pascoe, 2018). At the time of European settlement, the only widespread and large carnivorous animal on the Australian mainland was the dingo, which may have been introduced from Papua New Guinea some 5,000 years ago (Ardalan *et al.*, 2012). All other indigenous mammals were non-ungulate (non-hoofed) herbivores, and their distributions were managed by the culture and activities of their indigenous custodians (see Section 2.5.1).

As with indigenous flora, Australia's native fauna has competed with a wide variety of introduced faunal species in recent centuries (see Section 2.3.2). While these exotic species were initially introduced for the purposes of grazing, hunting, fishing, and transport, several quickly adapted to their new environment and continue to successfully compete with native animals for food, shelter and territory. Some introduced species also prey on native fauna (Clarke, 2001; Denny and Dickman, 2010), destroy their habitats (McKenzie *et al.*, 2006), and/or spread diseases (Henderson, 2009). Additionally, ungulate (hoofed) species, such as horses, sheep, goats, deer, and cattle, introduced significant soil compaction and 'erosion' problems (Lunt *et al.*, 2007), and extensively damage riparian zones. This is due, in part, to total grazing pressure, that is, competition for limited resources between domestic stock and native herbivores.

Feral animals have permanently transformed Australia.
(Norris et al., 2005)

Environmentalists cannot be animal liberationists. Animal liberationists cannot be environmentalists. The environmentalist would sacrifice the lives of individual creatures to preserve the authenticity, integrity and complexity of ecological systems. The liberationist—if the reduction of animal misery is taken seriously as a goal—must be willing, in principle, to sacrifice the authenticity, integrity and complexity of ecosystems to protect the rights, or guard the lives, of individual animals.
(Mark Sagoff, 1984)

Exotic species typically have a number of competitive advantages in new territory and can severely impact native biodiversity. In Australia, these advantages included few natural predators, few fatal diseases and conditions favorable to high rates of reproduction. Accordingly their populations increased quickly (DEE, 2019d) and wild populations of over 80 species of exotic vertebrate animals have now become established in Australia (Lesslie *et al*., 2011). Of these, more than 30 are considered pests to agriculture and/or the environment. In the 2013–14 financial year, the annual economic impact of pest animals in Australia was estimated as approaching $600 million (McLeod, 2016).

The term 'feral' is used for wild animals that have descended from domestic animals. The most significant impacts of feral animals in Australia include:

- rabbits, goats, buffalo, donkeys, horses, camels, deer, and cattle—grazing and land degradation;
- dogs, foxes, pigs, and cats—livestock and native fauna predation; and
- mice and birds—damage to grain and horticultural crops.

Land management practices also changed rapidly after European settlement, which both positively and negatively impacted the populations of native fauna. As the number of grazing animals (both pastoral species and native herbivores) increased, so did predation of dingoes, foxes, and feral dogs on stock, resulting in a 5,400 km dingo-proof fence being erected nearly continuously from the west coast of SA to the east coast of northern NSW (PIRSA, 2019). As pastures were improved and extended and watering points were installed, the numbers of kangaroos, wallabies, and feral herbivores also increased, especially in southeast Australia where the dingo had been fenced out (Eldridge *et al*., 2016).

The impact of feral animals in the rangelands of Australia is significant in terms of biodiversity and productivity, and the geographic range of eight feral species is expanding (Norris *et al*., 2005). As well as devouring crops and livestock, feral animals have degraded large areas of habitat, resulting in the loss of native mammals, irreversible erosion, and invasion by weeds, which further threatens rare biota (Burrows, 2018). While accurate estimates of feral animal distribution and abundance is lacking in this sparsely-populated region, potential solutions are further confounded by lack of rigorous knowledge about regional biodiversity and the impacts of feral animals on rangeland ecosystems (Norris *et al*., 2005). These concerns are further considered in Section 15.

2.4 Ecoregions and Fire Patterns

Fire in the Australian landscape is frequent and recurrent, especially following drought conditions. Fire extent and intensity can vary dramatically with differences in vegetation composition and age, and ambient weather conditions (see Section 18). Recovery from fire also varies with fire intensity and vegetation type, with younger vegetation often being more susceptible. Severe and extensive fires can thus change the age distribution of vegetation and potentially increase future fire risk.

Ecological regions, or ecoregions, are biogeographic units that attempt to categorise the natural distribution of biodiversity (Olson *et al*., 2001). Each ecoregion is a geographically distinct assemblage of fauna, flora, and ecosystems, with similar geology, lithology, landform, and climate. Ecoregions are separated by distinct geographic features, such as oceans or mountain ranges. Associated with their vegetation patterns, ecoregions have characteristic fire patterns, in terms of both frequency and severity, which significantly impact vegetation structure and extent.

Figure 2.13 Interim Biogeographic Regionalisation of Australia (IBRA) Version 7

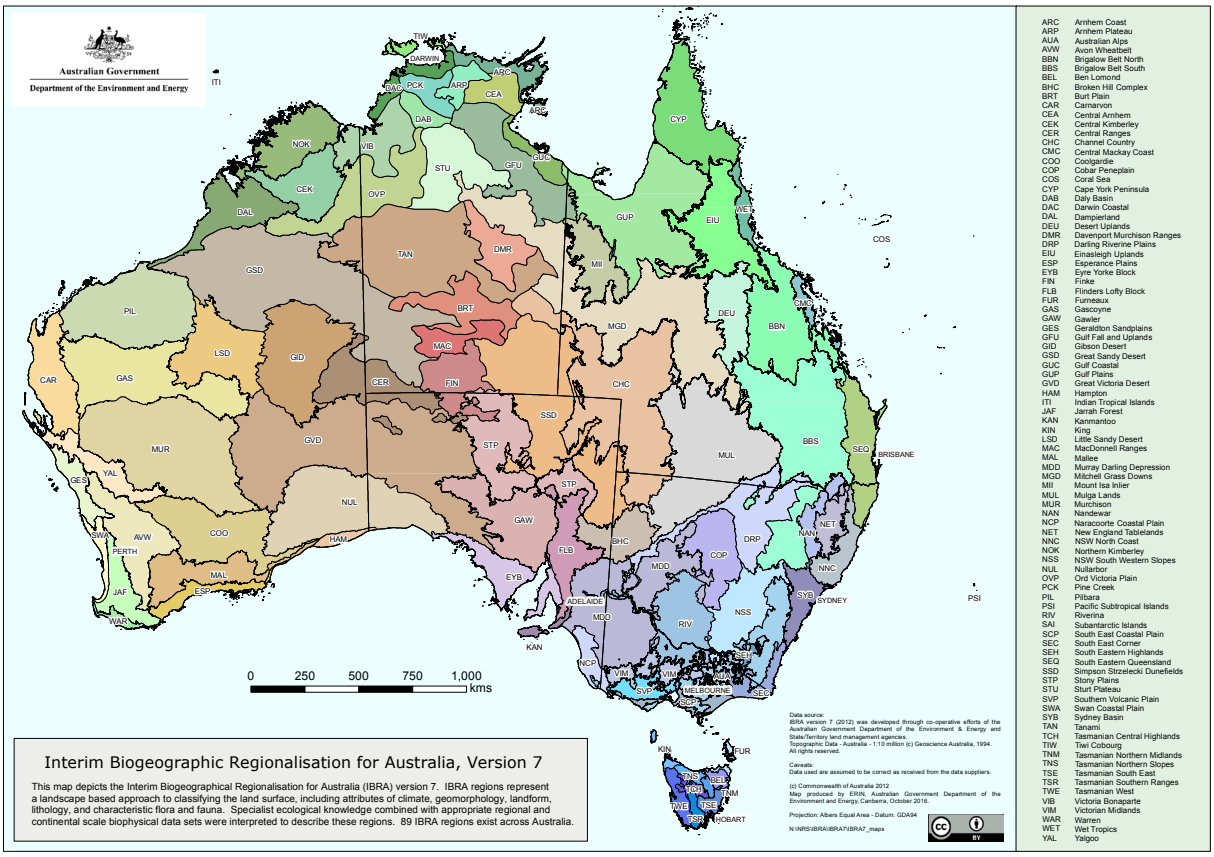

Source: DAWE (2020c)

Figure 2.14 Terrestrial Ecoregions in Australia

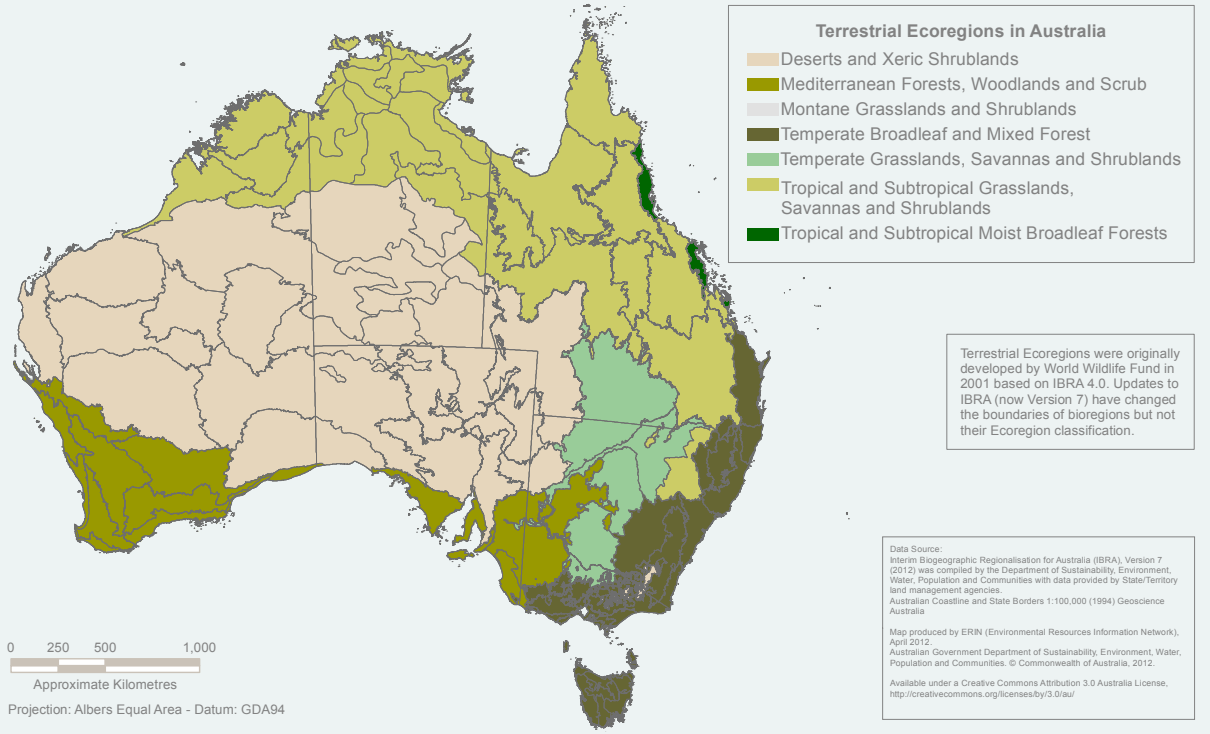

Source: ERIN (2012)

In the whole country I scarcely saw a place without the marks of a fire; whether these had been more or less recent—whether the stumps were more or less black, was the greatest change which varied the uniformity, so wearisome to the traveller's eye. (Charles Darwin's description of NSW, from 'The Voyage of the Beagle', 1845)

Similarly, the Interim Biogeographic Regionalisation for Australia (IBRA; Thackway and Cresswell, 1995; see Figure 2.13) classifies landscapes in Australia "into 89 large geographically distinct bioregions based on common climate, geology, landform, native vegetation and species information" (DAWE, 2020c). This forms part of a global, hierarchical classification of 14 terrestrial habitats or biomes (Olson *et al*., 2001), eight of which occur in Australia (DAWE, 2020d). IBRA has been simplified into seven broad habitats by the Terrestrial Ecoregions classification (see Figure 2.14; note that the eighth habitat, Tundra, only occurs in Subantarctic islands).

IBRA acts as the planning framework for the National Reserve System (NRS), and ecoregion descriptions in the following sub-sections have been derived from the NRS to provide an overview of the Australian landscape and its response to fire (Harrison and Bradstock, 2010 and Section 18). The following descriptions are based on the estimated pre-European extents of these ecoregions and do not discuss their modification or fragmentation.

2.4.1 Deserts and xeric shrublands

Arid and semi-arid landscapes cover 70% of the Australian continent, including over half of WA, SA and NT, and smaller portions of western Queensland and NSW. This ecoregion varies greatly in the amount of annual rainfall received, with evaporation generally exceeding rainfall. Temperature extremes characterise most deserts, resulting in hot days and cold nights. These harsh, but diverse, climatic conditions support a rich array of habitats, many of which are ephemeral (DAWE, 2020d). Vegetation types include hummock grasslands, tussock grasslands, chenopod shrublands, and *Acacia* woodlands.

In arid Australia, rainfall is not only low, but irregular, and vegetation has adapted to these conditions. Significant, sporadic rainfall events trigger rapid growth, resulting in dramatic changes in vegetation extent and greenness. The fire distribution trends have been observed to follow latitude-based rainfall gradients, with most wildfires occurring in spring (late dry season), due to higher fuel loads and temperatures, coupled with reduced fuel moisture (Allan *et al*., 2003). The fire return interval varies regionally between three and 30 or more years and is considered to be directly related to fuel accumulation following antecedent rainfall (Allan and Southgate, 2002; Russell-Smith *et al*., 2003). Patchiness of fires is related to the heterogeneity of fire 'ages' in a region (Allan and Southgate, 2002), so prescribed burning using patchy, early dry season fires is encouraged to avoid later conflagrations. In this landscape, fire footprints are clearly visible on satellite EO imagery and persist for a long time, which can result in overlapping fire scars over several years.

2.4.2 Mediterranean forests, woodlands and scrub

Mediterranean ecoregions feature hot, dry summers, cool, moist winters, and regular periods of drought, and generally occur in areas of low topography. These conditions only occur in five regions globally and, together, they support over 10% of the known species of flora. The Fynbos (in South Africa) and shrublands in southwest Australia have greater biodiversity than the other Mediterranean ecoregions. In southwest WA, southeast SA, and western Victoria, Mediterranean vegetation has been heavily fragmented by land clearing. Some large, intact areas of Mediterranean woodlands and scrub still exist in sparsely populated areas, such as the Great Western woodlands in WA. Vegetation in the Mediterranean ecoregion includes heath, mallee, and forest.

Most plants endemic to this ecoregion are adapted to, and dependent on, fire. Heath vegetation, which also occurs in tropical and temperate climates, is particularly fire prone. Fires are seasonal, predominantly occurring in summer with lightning being the primary cause, and often follow drought. Fire frequency estimates vary from five to 30 years, with large fires occurring every 20–30 years (Bradstock and Cohn, 2002). Since rainfall, and hence fuel moisture content, is generally low during summer in this climate, fire risk is primarily related to fuel load. High severity burns in this ecoregion can be accurately delineated in EO imagery.

Bushfires have a fundamental and irreplaceable role in sustaining many of Australia's natural ecosystems and ecological processes and are a valuable tool for achieving land management objectives. However, if they are too frequent or too infrequent, too severe or too mild, or mistimed, they can erode ecosystem health and biodiversity and compromise other land management goals.
(Ellis et al., 2004)

2.4.3 Montane grasslands and shrublands

This ecoregion includes high elevation (montane and alpine) grasslands and shrublands. In Australia, montane grassland and shrublands are restricted to the mountainous regions of southeastern Australia above 1300 m, in which trees do not grow. This region occupies less than 3% of the Australian landmass and straddles the borders of the ACT, Victoria, and NSW on the Australian mainland, with a significant element occurring in Tasmania (DAWE, 2020d).

Fires are rare in montane grasslands and usually follow extreme drought. Fire is limited by fuel load and moisture content, with montane shrubland species being more flammable than grassland species. These areas are believed to burn naturally only once or twice a century (Ross Bradstock, *pers. comm.*). While rare, however, fires in this region of Australia can be massive and uncontrollable, as occurred in 1938/39, 2002/03 and 2019/20.

2.4.4 Temperate broadleaf and mixed forest

Temperature and precipitation vary widely in temperate forests. These forests generally comprise four layers of vegetation (upper and lower canopies plus shrub and ground layers), with biodiversity being highest near the forest floor. *Eucalyptus* and *Acacia* species typify the composition of the temperate broadleaf and mixed forests in Australia. This ecoregion also includes areas of temperate rainforest. In Australia, these forests stretch along the Great Dividing Range and coastal regions from southeast Queensland, through NSW and the ACT into Victoria. The moderate climate and high rainfall of this region support unique *Eucalyptus* forests and open woodlands. The temperate rainforests and mixed forests of Tasmania are also extraordinarily complex (DAWE, 2020d).

These forests generally occur in mountainous landscapes where topography affects vegetation density and composition and, in turn, fuel volume and exposure. In this ecoregion, topography and fuel load have been identified as the most important factors influencing fire propagation and severity (Bradstock *et al.*, 2010). Fires in temperate forests are linked to irregular drought conditions, with megafires following periods of extreme drought (Bartlett *et al.*, 2007).

The predominant fuel in these forests is leaf litter so most fires occur in hotter, drier seasons. In wetter areas, the natural fire frequency is estimated to be 50–100 years, while drier areas may experience fire every 10–20 years. In recent years, there has been an increased frequency of large fires in these regions with several major fire seasons resulting in 4 million ha being burned between 2000 and 2010 (Ross Bradstock, *pers. comm.*) and more in 2019/20 (see Section 18.1). Most major towns and cities in southeast Australia are situated near temperate forests so their populations are directly and indirectly affected by wildfires occurring in these regions.

While the relatively dense canopies in these forests obscure understorey vegetation in imagery from passive EO sensors, crown fires can be clearly discerned in these datasets.

2.4.5 Temperate grasslands, savannas and shrublands

This ecoregion has cooler and more varied annual temperatures than tropical grasslands. Trees tend to only occur along streams and rivers. Located between temperate forests and the arid interior of Australia, the southeast Australian temperate savannas span a broad north-south swath on the drier side of the Great Dividing Range through Queensland, NSW and Victoria, and into Tasmania. Since European settlement, most of this ecoregion has been converted to sheep and wheat farms so that only small fragments of the original vegetation remains (DAWE, 2020d).

Distinct fire seasons occur in this ecoregion, which are related to grassland curing. Southern areas with winter rainfall experience summer fires and northern areas of summer rainfall are most likely to burn in late winter and spring. In these relatively flat regions with scattered tree cover, fires are clearly delineated in EO imagery.

2.4.6 Tropical and subtropical grasslands, savannas and shrublands

The tropical and subtropical grasslands, savannas, and shrublands are characterised by rainfall levels between 900–1500 mm per year, following a predictable, seasonal pattern of wet summers and extended, warm, dry winters. The abrupt onset of the dry season, evidenced by a sudden decline in atmospheric and surface moisture, signals the start of fire weather.

Tropical savannas occupy 25% of Australia, covering about 200 million ha in northern WA, the top half of NT, and inland of the Great Dividing Range in Queensland. These biologically diverse regions do not receive sufficient rainfall to support extensive tree cover. Patches of dry rainforest also occur throughout this ecoregion.

Fire is extensive and frequent, with both extent and frequency varying regionally, and is predominantly initiated by human activity. Conversely, population and infrastructure are sparse. New fire footprints are clearly discernible in EO data in this landscape. Given its dynamic nature, the timing of EO data acquisition is particularly important for mapping fire effects in this ecoregion. The relatively simple and open structure of savanna vegetation with predominately grassy understoreys, which quickly recover from fire, means that the focus for fire mapping is on burned area rather than severity. The rate of regrowth of grasslands can also result in overlap of fire scars within a fire season.

2.4.7 Tropical and subtropical moist broadleaf forests

These forests are generally found in large, discontinuous patches in tropical latitudes. They are characterised by low variability in annual temperature and high annual rainfall (> 2000 mm). Forest structure comprises five layers (three canopy layers plus shrub and ground layers) with greatest biodiversity generally occurring in the canopy. Species composition in these forests is dominated by semi-evergreen and evergreen deciduous trees.

In Australia, small and scattered areas of this type of forest only occur in Queensland. These forests are noted for their southern location and their highly endemic fauna and flora. Subtropical moist forests with high levels of plant and bird endemism also occur on Lord Howe Island and Norfolk Island (DAWE, 2020d).

Fire risk is low in rainforest areas due to the high fuel moisture content. Some research has noted expansion of rainforest vegetation in recent decades, possibly due to the absence of fire (Jurskis, 2015).

Eucalyptus was excellent at extracting and hoarding precious nutrients, but so were most of the Australian flora. What made it special was its extraordinary opportunism, a relationship reinforced by fire. Eucalypts accepted wretched soils and tolerated drought, but they thrived amid fire. (Pyne, 1992).

2.5 Land Use

Today, the vast majority of Australians live in, and derive their livelihood from, the coastal fringe. The highest population densities occur in southeast Australia, spanning from Brisbane to Adelaide, and in the southwest of WA around Perth (see Table 2.1 and Figure 2.15). 71% of Australians live in major cities, and another ~10% live in small towns (ABS, 2020).

However, this has not always been the case. Below we consider traditional indigenous land use patterns (see Section 2.5.1), the changes that followed European settlement (see Section 2.5.2), and the methods that are currently used to map and monitor land use in Australia (see Section 2.5.3).

Land use in Australia today is a legacy of patterns of land occupation since European settlement—from early pastoralism, agriculture and prospecting through to today's major agricultural, forest and mining industries, reserve landscapes and urban communities. For most of the past 200 years, land use change has been driven by relatively unrestricted access to land, technological change and growth in productivity and population.
(Lesslie et al., 2011)

Figure 2.15 Australia's towns by population size groupings, 2016

In this classification, major cities > 100,000 residents, large towns 50,000–100,000 residents, medium towns 10,000–50,000 residents and small towns < 10,000 (and generally > 200) residents.

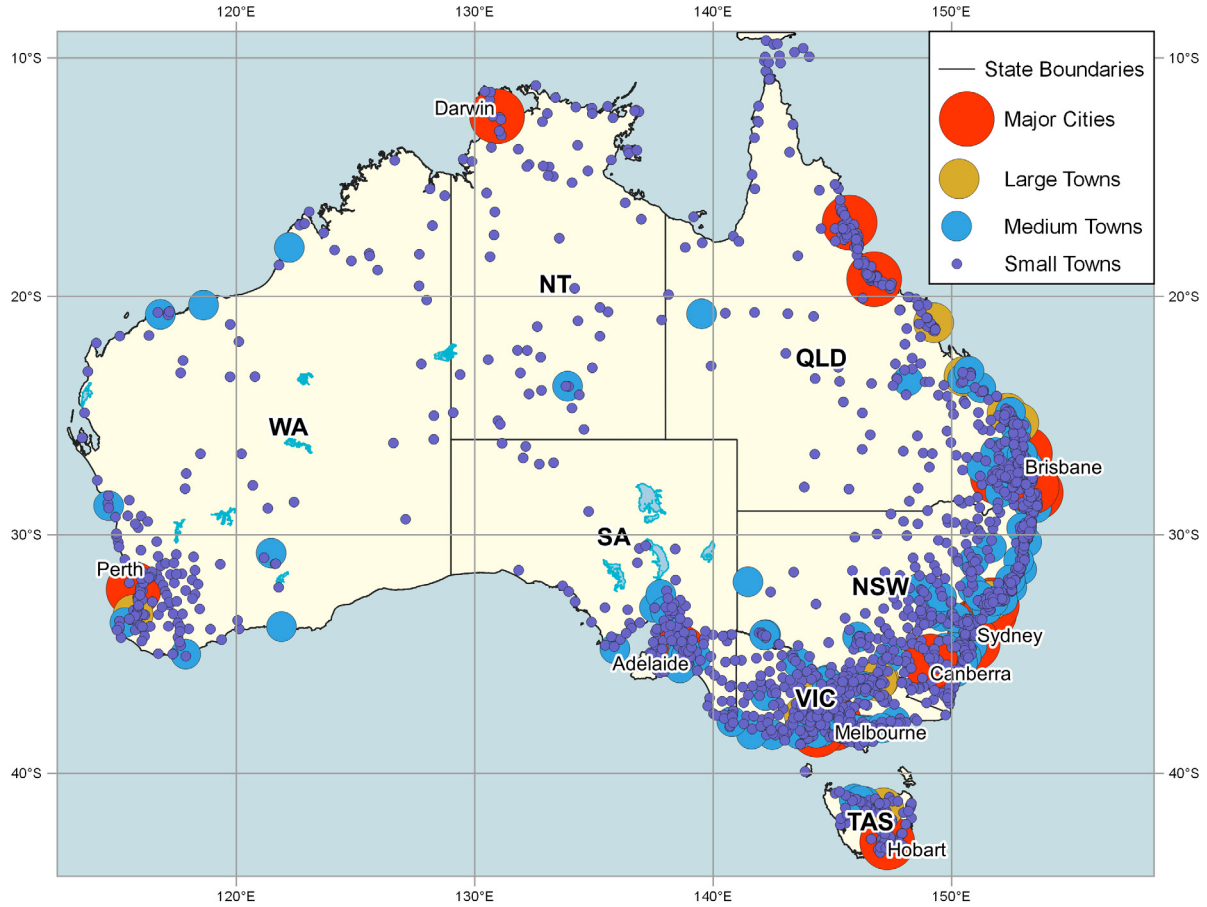

Source: Tony Sparks, Icon Water, using gridded data from ABS (2016)

2.5.1 Indigenous patterns

For scores of millennia, the Australian landscape supported an indigenous population that may have numbered more than one million people (ABS, 2008). For most of the last two centuries, these people of Australia's first nations were believed to have followed a semi-nomadic lifestyle based on hunting and gathering. More recently, analysis of reports by early settlers and explorers has cast a different light on the lifestyles of these indigenous communities (Tindale, 1974; Gerritsen, 2008). Gammage (2012) summarises the Aboriginal land management 'law' in terms of three rules:

- ensure that all life flourishes;
- make plants and animals abundant, convenient and predictable; and
- think universal, act local.

Early reports of Australian coastal vegetation, such as "the whole country or at least a great part of it might be cultivated without being obliged to cut down a single tree"[3] or "the country looked very pleasant and fertile; and the trees, quite free from underwood, appeared like plantations in a gentleman's park",[4] describe a rather different landscape from the one that exists today. Numerous other descriptions—both narratives and artworks—by early settlers and explorers support the view that portions of Australia's landscape (particularly higher rainfall areas of open woodlands and woodlands, and some drier open forests) have changed significantly since European settlement, partly by overgrazing and partly by underburning (Gammage, 2012).

Traditional land management practices included the use of fire to reduce vegetative fuel loads, which helped to shape the distribution of native vegetation until the time of European settlement: "For more than 40,000 years, Aborigines lit mostly mild fires that consumed dead wood and dry herbage, killed seedlings, reduced some saplings back to ground level and scorched the leaves of some small trees and large shrubs. These fires allowed annual herbs to germinate and perennials to flush with new growth. They recycled nutrients from dead and dry into new growth. They maintained a diverse, open, safe and productive environment. After European settlers disrupted Aboriginal burning, dead wood, litter, and dry herbage accumulated. Too many seedlings and saplings grew into trees or bushes. Delicate herbage was smothered and nutrient cyclings was disrupted. Megafires, chronic decline of eucalypts, scrub invasion, pestilence, loss of biodiversity and socio-economic distress have been the result." (Jurskis, 2015)

Figure 2.16 Aboriginal grain harvest map

Grassland areas managed by aborigines as important sources of grain food, with names of some tribes overlaid.

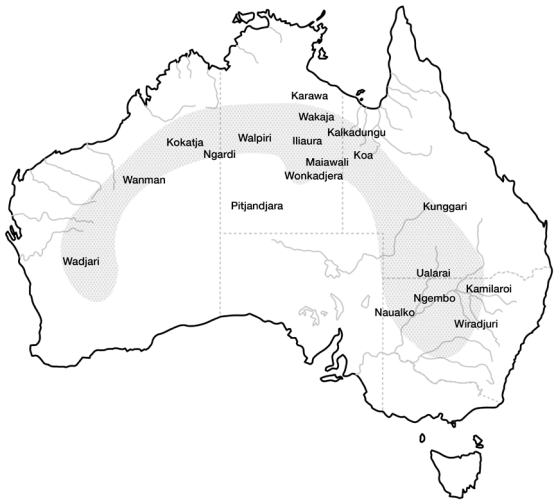

Adapted from: Tindale (1974) Figure 31

Tindale (1974) compiled evidence suggesting that, prior to European settlement, most of the continent was managed to harvest grains, tubers, and fruits, including complex systems of aquaculture. For example, grassland regions from which Aboriginal tribes harvested grains are shown in Figure 2.16. It is interesting to compare this area with the extent and distribution of the current grain production zones shown in Figure 2.17 and Figure 11.1. Except in southwest and southeast Australia, the locations of grains harvested by indigenous peoples do not coincide with current grain production zones.

... it may perhaps be doubted whether any section of the human race has exercised a greater influence on the physical condition of any large portion of the globe than the wandering savages of Australia.
(Edward Curr, 1883)

3 James Cook (1770) quoted by Gammage (2012) page 5

4 Sydney Parkinson (1770) quoted by Gammage (2012) page 5

They live in a tranquillity which is not disturbed by the inequality of condition;
the earth and sea of their own accord furnishes them with all things necessary for life;
... they live in a warm and fine climate and enjoy a very wholesome air ...
in my opinion ... they think themselves provided with all the necessities of life
and that they have no superfluities
(James Cook, 1770, from Endeavour Journal)

2.5.2 European settlement patterns

European settlement patterns in Australia have been driven, and continue to be limited, by the availability of water and pastoral lands. The vast majority of the current population, estimated at more than 25 million (see Table 2.1), live in capital cities within the high rainfall zone (see Section 2.2). The advent of European culture introduced clearing and thinning of vegetation for agriculture, mining, and urban development, and modification of waterways for townships and irrigation. Since the First Fleet arrived in 1788, around one third of the traditionally vegetated land has been cleared or thinned for various land use purposes (AUSLIG, 1990), predominantly cropping and intensive pasture production (see Figure 2.12).

The agricultural regions, in which different forms of agricultural activity are considered to be viable, are closely related to topography and climate (see Sections 2.1 and 2.2 respectively) and broadly follow the coastal plains (see Sections 2.5.3 and 11.1). Within these regions, soil type tends to determine the most appropriate agricultural approach (FAO, 2009; see Figure 2.3).

In higher rainfall zones in the south and east of the continent, land management practices have both decreased the extent and density of natural vegetation and accelerated soil erosion, land degradation, and salinity (McKenzie *et al.*, 2006). In recent decades, regulations governing stocking rates, land clearing and cultivation practices, with controls on feral animals and chemical usage, have reduced the rate of soil degradation (see Sections 3.4 and 11.4).

2.5.3 Current land use

Current land use is mapped and monitored nationally by the Australian Land Use and Management (ALUM) classification system (DAWE, 2020e; see Section 3.3.4), based on a scheme proposed by Baxter and Russell (1994). This dataset compiles relevant federal, state, and territory data to indicate the dominant land use in each 50 m by 50 m grid cell. The relative proportions of area occupied by the major categories of land use in 2010–11 are listed in Table 2.9. A simplified map of these classes is shown in Figure 2.17. The latest datasets are available from DAWE (2020f). Land use mapping and monitoring, and details of the ALUM categories, are further discussed in Sections 3.3.4 and 3.4.2.

Table 2.9 Land uses in Australia 2010–11

Land use	Area (sq.km)	Percent (%)
Nature conservation	604,671	7.87%
Other protected areas including Indigenous uses	1,163,676	15.14%
Minimal use	1,172,679	15.26%
Grazing natural vegetation	3,448,896	44.87%
Production forestry	103,494	1.35%
Plantation forestry	25,752	0.34%
Grazing modified pastures	710,265	9.24%
Dryland cropping	275,928	3.59%
Dryland horticulture	743	0.01%
Irrigated pastures	6,048	0.08%
Irrigated cropping	9,765	0.13%
Irrigated horticulture	4,552	0.06%
Intensive animal and plant production	1,414	0.02%
Intensive uses (mainly urban)	13,806	0.18%
Rural residential	17,632	0.23%
Waste and mining	1,860	0.02%
Water	125,542	1.63%
No data	401	0.005%
Total	7,687,124	100.00%

Source: ABARES (2020)

Figure 2.17 Land use in Australia for 2010–11

17 class summary of land use derived using a modelling approach based on agricultural statistics, satellite imagery, and other land use information.

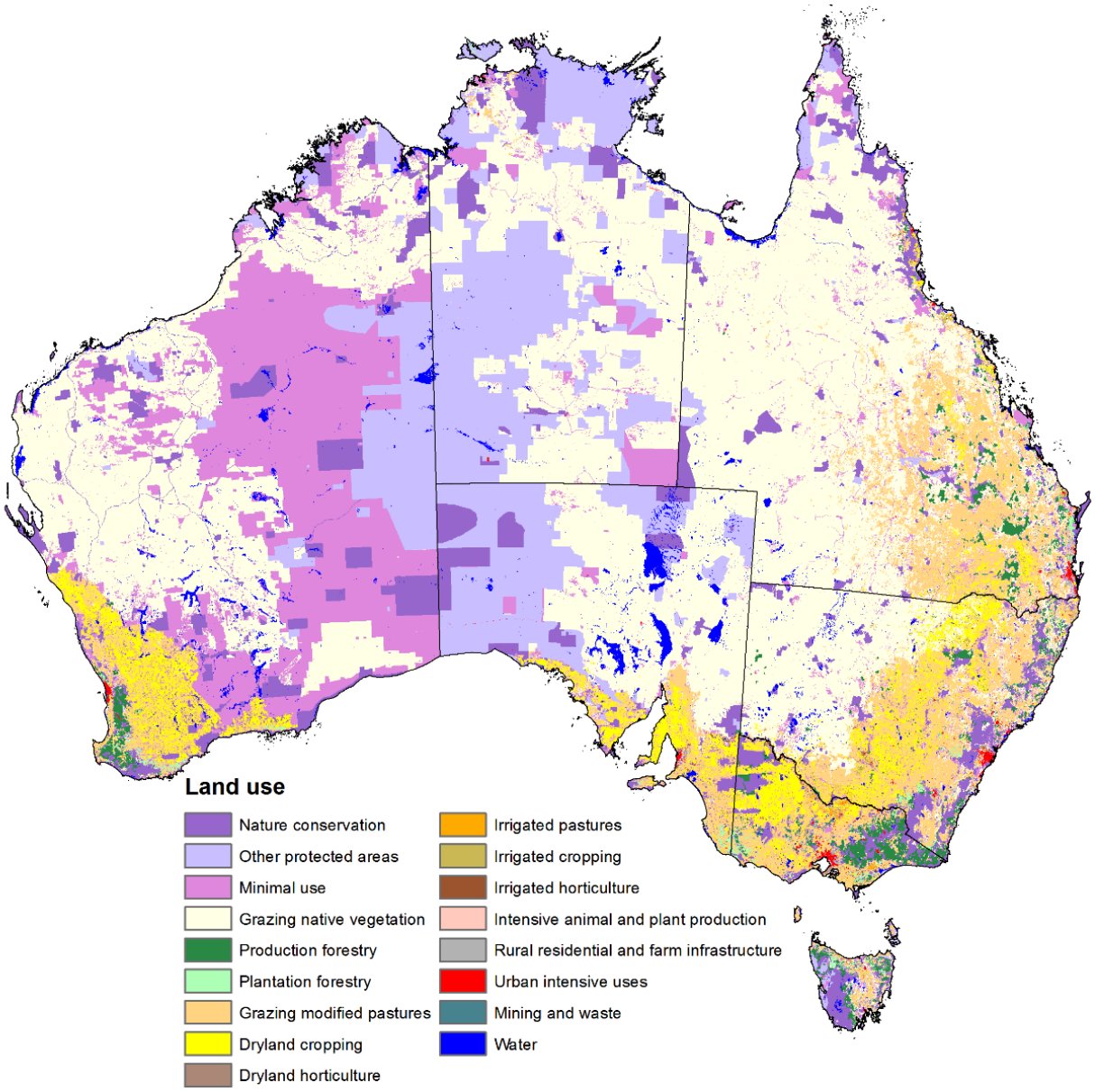

Source: ABARES (2020)

The Australian is fortunate that close to the main cities there still lie areas of virgin bush where it is possible to find direct contact with nature. There are few who have not boiled a billy under the gum-trees.
(Charles F. Laseron, 1953)

2.6 Further Information

About Australia

Overview: *https://www.australia.gov.au/about-australia/our-country*

Natural Environment: *https://www.australia.gov.au/about-australia/our-country/our-natural-environment*

National Location Information: *https://www.ga.gov.au/scientific-topics/national-location-information*

ANUDEM: *https://fennerschool.anu.edu.au/research/products/anudem*

Geofabric V3.2 products, documentation and tutorials: *http://www.bom.gov.au/water/geofabric/*

Australian Ecosystem and Climate Datasets

TERN Data Discovery Portal: *https://portal.tern.org.au/#/e8fbc61b*

Australian Soil Datasets

Australian Soil Resource Information System (ASRIS): *https://www.asris.csiro.au/*

Soil and Landscape Grid of Australia: TERN (2020)

ALUM Datasets

Land use data download: *http://www.agriculture.gov.au/abares/aclump/land-use/data-download*

Indigenous Land Use

Tindale (1974)

Gerritsen (2008)

Gammage (2012)

Invasive Species

Invasive Species CRC: *https://invasives.com.au/our-publications*

Vegetation Resources

Australia:

Keith (2017)

NVIS: *http://www.environment.gov.au/land/native-vegetation/national-vegetation-information-system*

New South Wales:

NSW State Vegetation Type Mapping (SVTM): see Excursus 8.2; *https://www.environment.nsw.gov.au/vegetation/state-vegetation-type-map.htm*

BioNET vegetation (biodiversity data repository): *http://www.bionet.nsw.gov.au*

Native Vegetation publications: *https://www.environment.nsw.gov.au/vegetation/OtherPublications.htm*

Queensland:

Dept. Science and Environment: *https://environment.des.qld.gov.au/maps-imagery-data/online/*

Queensland Herbarium: *https://www.qld.gov.au/environment/plants-animals/plants/herbarium/mapping-ecosystems*

Tasmania:

Barker (2001)

Kitchener and Harris (2013)

TASVEG: *https://dpipwe.tas.gov.au/conservation/development-planning-conservation-assessment/planning-tools/monitoring-and-mapping-tasmanias-vegetation-(tasveg)/tasveg-the-digital-vegetation-map-of-tasmania*

Victoria:

Newell *et al.* (2006)

Sinclair *et al.* (2012)

Habitat hectares: *https://www.ari.vic.gov.au/research/modelling/mapping-vegetation-extent-and-condition*

Western Australia:

Shepherd *et al.* (2002)

Native Vegetation Extent: *https://catalogue.data.wa.gov.au/dataset/native-vegetation-exten*

2.7 References

ABARES (2020). *Land Use in Australia—At a Glance* brochure, Australian Bureau of Agricultural and Resource Economics and Sciences website: *https://www.agriculture.gov.au/sites/default/files/abares/aclump/documents/Land%20use%20in%20Australia%20at%20a%20glance%202016.pdf*

ABRS (2012). *Flora of Australia Online*. Australian Biological Resources Study, Canberra. *http://www.environment.gov.au/biodiversity/abrs/online-resources/flora/main/index.html*

ABS (2008). Aboriginal and Torres Strait Islander Population. *Year Book Australia, 2008*. Australian Bureau of Statistics. *https://www.abs.gov.au/ausstats/abs@.nsf/0/68AE74ED632E17A6CA2573D200110075?opendocument*

ABS (2010). *Year Book Australia, 2009-10*. Australian Bureau of Statistics. *https://www.abs.gov.au/AUSSTATS/abs@.Nsf/7d12b0f6763c78caca257061001cc588/bb322d1ad0d30a7fca25773700169c19!OpenDocument*

ABS (2016). *Census of Population and Housing* webpage, Australian Bureau of Statistics website: *https://www.abs.gov.au/ausstats/abs@.nsf/Lookup/by%20Subject/2071.0~2016~Main%20Features~Small%20Towns~113*

ABS (2020). *Australian Demographic Statistics, Sep 2019* webpage, Australian Bureau of Statistics website: *https://www.abs.gov.au/AUSSTATS/abs@.nsf/Latestproducts/3101.0Main%20Features1Sep%202019?opendocument&tabname=Summary&prodno=3101.0&issue=Sep%202019&num=&view=*

ACT EPSDD (2020). *Conservation and Ecological Communities* webpage, Environment, Planning and Sustainable Development Directorate, ACT government website: *https://www.environment.act.gov.au/cpr/conservation_and_ecological_communities*

AG (2020). *How Government Works* webpage, Australian Government website: *https://info.australia.gov.au/about-government/how-government-works*

Allan, G., and Southgate, R. (2002). Fire regimes in the spinifex landscapes of Australia. In: *Flammable Australia: the Fire Regimes and Biodiversity of a Continent* (Eds: R. Bradstock, J. Williams and A. Gill) pp. 145–176. Cambridge University Press, Cambridge.

Allan, G., Johnson, A., Cridland, S., and Fitzgerald, N. (2003). Application of NDVI for predicting fuel curing at landscape scales in northern Australia: Can remotely sensed data help schedule fire management operations? *International Journal of Wildland Fire*, 12(4), 299–308. doi:*10.1071/WF03016*

Ardalan, A., Oskarsson, M., Natanaelsson, C., Wilton, A.N., Ahmadian, A., and Savolainen, P. (2012). Narrow genetic basis for the Australian dingo confirmed through analysis of paternal ancestry. *Genetica*, 140 (1–3), 65–73. doi:*10.1007/s10709-012-9658-5*

Austrade (2020). *Land Tenure* webpage, Australian Trade and Investment Commission website: *https://www.austrade.gov.au/land-tenure/Land-tenure/about-land-tenure*

AUSLIG (1990). *Atlas of Australian Resources (Third Series) Volume 6: Vegetation*. Australian Land and Surveying Information Group, AUSMAP, Department of Administrative Services, Canberra. 64 p.

Austroads (2004). *Impact of Climate Change on Road Infrastructure*. Austroads Inc, Sydney. ISBN 0 85588 692 7 *http://www.bitre.gov.au/publications/2004/files/cr_001_climate_change.pdf*

Barker, P. (2001). *A Technical Manual for Vegetation Monitoring*. Department of Primary Industries, Water and Environment, Hobart.

Bartlett, T. Leonard, M., and Morgan, G. (2007). The mega-fire phenomenon: some Australian perspectives. In: *The 2007 Institute of Foresters of Australia and New Zealand Institute of Forestry Conference: Programme, Abstracts and Papers*. Institute of Foresters of Australia, Canberra.

Baxter, J.T., and Russell, L.D. (1994). *Land use mapping requirements for natural resource management in the Murray-Darling Basin, Project M305: Task 6*. Victorian Department of Conservation and Natural Resources, Melbourne.

Beadle, N.C.W. (1981). *The Vegetation of Australia*. Cambridge University Press, Cambridge. 690p.

Beadle, N.C., and Costin, A.B. (1952). Ecological Classification and Nomenclature. *Proceedings of Linnaeus Society NSW*, 77(1–2), 61–82.

BoM (2020a). *Long-range weather and climate* webpage. Bureau of Meteorology website: *http://www.bom.gov.au/climate/averages/maps.shtml*

BoM (2020b). *About the Geofabric* webpage. Bureau of Meteorology website: *http://www.bom.gov.au/water/geofabric/about.shtml*

BoM (2020c). *Topographic Drainage Basins and River Regions* webpage. Bureau of Meteorology website: *http://www.bom.gov.au/water/about/riverBasinAuxNav.shtml*

Booth, C., and Tubman, W. (2011). *Water Down Under: Understanding and Managing Australia's Great Artesian Basin*. Department of Sustainability, Environment, Water, Populations and Communities., Canberra. ISBN: 978-1-921733-19-2.

Bradstock, R.A., and Cohn, J (2002). Fire regimes and biodiversity in semi-arid mallee ecosystems. In *Flammable Australia: The Fire Regimes and Biodiversity of a Continent*. (Eds: R.A. Bradstock, J.E. Williams, and M.A. Gill) Cambridge University Press, Cambridge.

Bradstock, R.A., Hammill, K.A., Collins, L., and Price, O. (2010). Effects of weather, fuel and terrain on fire severity in topographically diverse landscapes of south-eastern Australia. *Landscape Ecology*, 25(4), 607–619. doi:*10.1007/s10980-009-9443-8*

Brocklehurst, P., Lewis, D., Napier, D., and Lynch, D. (2007). *Northern Territory Guidelines and Field Methodology for Vegetation Survey and Mapping*. Technical Report No. 02/2007D. Department of Natural Resources, Environment and the Arts, Palmerston, Northern Territory.

Burrows, N.L. (2018). Feral Animals in the Semi-arid and Arid Regions of Australia: Origins, Impacts and Control. In *On the Ecology of Australia's Arid Zone*. (Ed: H. Lambers). Springer, Cham. *https://doi.org/10.1007/978-3-319-93943-8*

Clarke, G.M. (2001). *Environmental pest species in Australia*. Australian Government, Environment Australia, Canberra.

Cox, C.B. (2000). Plate Tectonics, Seaways and Climate in the Historical Biogeography of Mammals. *Memórias do Instituto Oswaldo Cruz*, 95(4), 509–516. *https://doi.org/10.1590/S0074-02762000000400012*

Cronquist, A. (1968). *The Evolution and Classification of Flowering Plants*. Houghton Mifflin, Boston.

Cronquist, A. (1981). *An Integrated System of Classification of Flowering Plants*. Columbia University Press, New York. 1262pp.

CSIRO (2014). *Australian Soil Resource Information System*. *www.asris.csiro.au*

Curr, E.M. (1883). *Recollections of Squatting in Victoria Then called the Port Phillip District (From 1841 to 1851)*. George Robertson, Melbourne. *http://classic.austlii.edu.au/au/journals/AUColLawMon/1883/1.pdf*

DAWE (2019). *About Kati Thanda—Lake Eyre Basin* webpage, Department of Agriculture, Water and the Environment website: *https://www.agriculture.gov.au/water/national/lake-eyre-basin/about*

DAWE (2020a). *Great Artesian Basin Sustainability Initiative* webpage. Department of Agriculture, Water and the Enviroment website: *https://www.agriculture.gov.au/water/national/great-artesian-basin/great-artesian-basin-sustainability-initiative*

DAWE (2020b). *NVIS Data Products* webpage, Department of Agriculture, Water and the Environment website: *http://www.environment.gov.au/land/native-vegetation/national-vegetation-information-system/data-products#nvis31*

DAWE (2020c). *Australia's bioregions (IBRA)* webpage, Department of Agriculture, Water and the Environment website: *https://www.environment.gov.au/land/nrs/science/ibra*

DAWE (2020d). *Australia's ecoregions* webpage, Department of Agriculture, Water and the Environment website: *https://www.environment.gov.au/land/nrs/science/ibra/australias-ecoregions*

DAWE (2020e). *Australian Land Use and Management Classification Version 8 (October 2016)* webpage, Department of Agriculture, Water and the Environment website: *https://www.agriculture.gov.au/abares/aclump/land-use/alum-classification*

DAWE (2020f). *Land Use and Management Information for Australia* webpage, Department of Agriculture, Water and the Environment website: *https://www.agriculture.gov.au/abares/aclump*

DELWP (2020). *Bioregions and EVC benchmarks* webpage, Victorian Department of Environment, Land, Water and Planning website: *https://www.environment.vic.gov.au/biodiversity/bioregions-and-evc-benchmarks*

DEE (2019a). *Weeds in Australia* webpage, Department of Environment and Energy website: *https://www.environment.gov.au/biodiversity/invasive/weeds/*

DEE (2019b). *Weeds in Australia/Grants and Government/Roles and Responsibilities* webpage, Department of Environment and Energy website: *https://www.environment.gov.au/biodiversity/invasive/weeds/government/roles/index.html*

DEE (2019c). *Weeds in Australia/About weeds/National weeds list* webpage, Department of Environment and Energy website: *https://www.environment.gov.au/biodiversity/invasive/weeds/weeds/lists/index.html*

DEE (2019d). *Feral Animals in Australia* webpage, Department of Environment and Energy website: *https://www.environment.gov.au/biodiversity/invasive-species/feral-animals-australia*

Denny, E.A., and Dickman, C.R. (2010). *Review of cat ecology and management strategies in Australia*. Invasive Animals Cooperative Research Centre, Canberra. ISBN: 978-0-9806716-6-7

DEWR (2007). *Australia's Native Vegetation: A summary of Australia's Major Vegetation Groups*, 2007. Department of the Environment and Water Resources, Canberra, ACT.

Eldridge, D.J., Poore, A.G., Ruiz-Colmenero, M., Letnic, M., and Soliveres, S. (2016). Ecosystem structure, function, and composition in rangelands are negatively affected by livestock grazing. *Ecological Applications*, 26(4), 1273–1283.

Ellis, S., Kanowski, P., and Whelan, R. (2004), *National Inquiry on Bushfire Mitigation and Management*. Commonwealth of Australia, Canberra.

ERIN (2012). *Terrestrial Ecoregions in Australia* (map based on IBRA7). Environmental Resources Information Network, Department of Sustainability, Environment, Water, Population and Communities. *https://www.environment.gov.au/system/files/pages/1716eb1c-939c-49a0-9c0e-8f412f04e410/files/ecoregions_1.pdf*

FAO (2009). Country Pasture/Forage Resource Profiles: Australia. Prepared by Edwin Wolfe. Food and Agriculture Organisation of the United Nations. *http://www.fao.org/ag/agp/AGPC/doc/Counprof/Australia/australia.htm*

Feng, M., Weller, E., Hill, K. (2009). The Leeuwin Current. In *A Marine Climate Change Impacts and Adaptation Report Card for Australia*. (Eds. E.S. Poloczanska, A.J. Hobday and A.J. Richardson), NCCARF Publication 05/09. ISBN 978-1-921609-03-9.

Florence, R.G. (1985). Eucalypt Forests and Woodlands. In *Think Trees, Grow Trees*, AGPS, Canberra.

GA (2002). *GEODATA TOPO 10M 2002* webpage, Geoscience Australia website: *https://ecat.ga.gov.au/geonetwork/srv/eng/catalog.search#/metadata/60803*

GA (2019). Geoscience Australia website, *Digital Elevation Data* webpage: *http://www.ga.gov.au/scientific-topics/national-location-information/digital-elevation-data*

GA (2020a). *Area of Australia—States and Territories* webpage, Geoscience Australia website: *https://www.ga.gov.au/scientific-topics/national-location-information/dimensions/area-of-australia-states-and-territories*

GA (2020b). *Great Artesian Basin* webpage, Geoscience Australia website: *http://www.ga.gov.au/scientific-topics/water/groundwater/gab*

GA (2020c). *Deserts* webpage, Geoscience Australia website: *https://www.ga.gov.au/scientific-topics/national-location-information/landforms/deserts#:~:text=Apart%20from%20Antarctica%2C%20Australia%20is,arid%2C%20or%20semi%2Darid*.

Gammage, B. (2012). *The Biggest Estate on Earth*. Allen and Unwin, Sydney.

Gerritsen, R. (2008). *Australia and the Origins of Agriculture*. British Archaeological Reports International Series 1874, Oxford.

Gillison, A.N., and Anderson, D.J. (1981). *Vegetation Classification in Australia*. CSIRO, Canberra. *https://openresearch-repository.anu.edu.au/bitstream/1885/114747/2/b12586894.pdf*

Glenn, E., Doody, T.M., Guerschman, J.P., Huete, A.R., King, E.A., McVicar, T.R., van Dijk, A.I.J.M., van Niel, T.G., Yebra, M., and Zhang, Y. (2011). Actual evapotranspiration estimation by ground and remote sensing methods: the Australian experience. *Hydrological Processes*, 25(26), 4103–4116. doi:*10.1002/hyp.8391*

Harris. S., and Kitchener, A. (2005). *From Forest to Fjaeldmark: Descriptions of Tasmania's Vegetation* (edition 1). Department of Primary Industries, Parks, Water and Environment. Printing Authority of Tasmania, Hobart.

Harrison, B.A., and Bradstock, R.A. (2010). *Current Use of Remote Sensing to Map and Monitor Fire in Australia*. Report by CERMB, University of Wollongong for NSW Rural Fire Service.

Henderson, W.R. (2009). *Pathogens in invasive animals of Australia*. Invasive Animals Cooperative Research Centre, Canberra. ISBN: 978-0-9806716-4-3.

Hnatiuk R.J., Thackway R., and Walker J. (2009). *Vegetation. In: Australian Soil and Land Survey: Field Handbook* (3rd Edn). (Ed: National Committee on Soil and Terrain) pp. 73–125. CSIRO Publishing, Melbourne.

Hobbs, R.J., and McIntyre, S. (2005). Categorizing Australian landscapes as an aid to assessing the generality of landscape management guidelines. *Global Ecology and Biogeography*, 14, 1–15.

Hutchinson, M.F., McIntyre, S., Hobbs, R.J., Stein, J.L., Garnett, S., and Kinloch, J. (2005). Integrating a global agro-climatic classification with bioregional boundaries in Australia. *Global Ecology and Biogeography* 14, 197-212.

Isbell, R.F., and NCST (2021). *The Australian Soil Classification*, 3rd edn. Volume 4 of Australian Soil and Land Survey Handbooks Series, National Committee on Soil and Terrain. CSIRO Publishing, Melbourne.

Jurskis, V. (2015). *Firestick Ecology*. Connor Court Publishing, Ballarat.

Keith, D.A. (2004). *From ocean shores to desert dunes: the vegetation of New South Wales and the ACT*. Department of Environment and Conservation, Hurstville.

Keith, D.A. (2017). *Australian Vegetation*. 3rd edn. Cambridge University Press, Cambridge. ISBN 978-1-107-11843-0

Kitchener, A., and Harris, S. (2013). *From Forest to Fjaeldmark: Descriptions of Tasmania's Vegetation*. 2nd Edn. Department of Primary Industries, Parks, Water and Environment, Tasmania.

Köppen, W. (1931). *Klimakarte der Erde. Grundriss der Klimakunde*, 2nd Ed., Berlin and Leipzig.

Laseron, C.F. (1953). *The Face of Australia*. Angus and Robertson. 244 p.

Lau, K.-M., and Yang, S. (2002). *Walker Circulation*. NASA, USA. *http://meteo.fisica.edu.uy/Materias/climatologia/teorico_climatologia_2013/LauWalkercirculation.pdf*

Lesslie, R., Mewett, J., and Walcott, J. (2011). *Landscapes in transition: Tracking land use change in Australia. Science and Economic Insights, 2.2*. Australian Bureau of Agricultural and Resource Economics and Sciences, Canberra, ACT.

Lewis, D.L., Brocklehurst, P.B., Thackway, R., and Hill, J.V. (2008). Adopting national vegetation guidelines and the National Vegetation Information System (NVIS) framework in the Northern Territory. *Cunninghamia*, 10(4), 557–567.

Lunt, I., Eldridge, D.J., Morgan, J.W., and Witt, G.B. (2007). Turner Review No. 13: A framework to predict the effects of livestock grazing and grazing exclusion on conservation values in natural ecosystems in Australia. *Australian Journal of Botany*, 55, 401–415. doi:*10.1071/BT06178*

McKenzie, N.L., Burbidge, A.A., Baynes, A., Brereton, R.N., Dickman, C.R., Gordon, G., Gibson, L.A., Menkhorst, P.W., Robinson, A.C., Williams, M.R., and Woinarski, J.C.Z. (2006). Analysis of factors in the recent decline of Australia's mammal fauna. *Journal of Biogeography*, 34, 597–611. *https://doi.org/10.1111/j.1365-2699.2006.01639.x*

McKenzie, N.J., Jacquier, D.W., Maschmedt, D.J., Griffin, E.A., and Brough, D.M. (2012). *The Australian Soil Resource Information System (ASRIS) Technical Specifications* Revised Version 1.6, June 2012. The Australian Collaborative Land Evaluation Program. *http://www.asris.csiro.au/downloads/ASRIS%20Tech%20Specs%201.6.pdf*

McLeod, R. (2016). *Cost of Pest Animals in NSW and Australia, 2013–14*. eSYS Development Pty Ltd, Sydney. ISBN 978-0-6480750-3-5 (online) *https://invasives.com.au/wp-content/uploads/2019/01/Cost-of-weeds-report.pdf*

McLeod, R. (2018). *Annual Costs of Weeds in Australia*. eSYS Development Pty Ltd, Sydney. *https://invasives.com.au/wp-content/uploads/2019/01/Cost-of-weeds-report.pdf*

MDBA (2013). *Murray Darling Basin Authority* website: *http://www.mdba.gov.au/about-basin*

NCST (2009). *Australian Soil and Land Survey Field Handbook*. 3rd edn. National Committee on Soil and Terrain, CSIRO, Canberra. 264p.

Neldner, V.J., Niehus, R.E., Wilson, B.A., McDonald, W.J.F., Ford, A.J., and Accad, A. (2019). *The Vegetation of Queensland. Descriptions of Broad Vegetation Groups*. Version 4.0. Queensland Herbarium, Department of Environment and Science.

Newell, G., White, M., Griffioen, P., and Conroy, M. (2006). Vegetation condition mapping at a landscape-scale across Victoria. *Ecological Management and Restoration*, 7, S65–S68.

Norris, A., Low, T., Gordon, I., Saunders, G., Lapidge, S., Lapidge, K., Peacock, T., and Pech, G. (2005). *Review of the management of feral animals and their impact on biodiversity in the Rangelands. A resource to aid NRM planning*. Pest Animal Control CRC Report 2005, Pest Animal Control CRC, Canberra.

NRM (2019). *Biosecurity* webpage, NRM Regions Australia website: *http://nrmregionsaustralia.com.au/biosecurity/*

NSW DPIE (2020). *BioNet Vegetation Classification* webpage, NSW Department of Planning, Industry and Environment: *https://www.environment.nsw.gov.au/research/Visclassification.htm*

NT EPA (2013). *Guidelines for Assessment of Impacts on Terrestrial Biodiversity*. Version 2.0. Northern Territory Environment Protection Authority. *https://ntepa.nt.gov.au/__data/assets/pdf_file/0004/287428/guideline_assessment_terrestrial_biodiversity.pdf*

NTNVIS (2020). *NVIS Version 3.1, National Vegetation Information System, NT Data Compilation*: *http://www.ntlis.nt.gov.au/metadata/export_data?metadata_id=2DBCB771207006B6E040CD9B0F274EFE&type=html*

NVIS Technical Working Group (2017). *Australian Vegetation Attribute Manual: National Vegetation Information System, Version 7.0*. (Eds: Bolton, M.P., deLacey, C., and Bossard, K.B.). Department of the Environment and Energy, Canberra.

Olson, D.M., Dinerstein, E., Wikramanayake, E.D., Burgess, N.D., Powell, G.V.N., Underwood, E.C., D'Amico, J.A., Itoua, I., Strand, H.E., Morrison, J.C., Loucks, C.J., Allnutt, T.F., Ricketts, T.H., Kura, Y., Lamoreux, J.F., Wettengel, W.W., Hedao, P., and Kassem, K.R. (2001) Terrestrial ecoregions of the world: a new map of life on Earth. *Bioscience*, 51(11), 933–938.

Philp, M., and Taylor, M. (2012). *Beyond Agriculture: Exploring the application of the Thornthwaite Moisture Index to infrastructure and possibilities for climate change adaptation*. ACCARNSI Discussion Paper X, National Climate Change Adaptation Research Facility.

PIRSA (2019). *The Dog Fence in South Australia* webpage, Primary Industry and Regions, South Australia: *https://www.pir.sa.gov.au/biosecurity/weeds_and_pest_animals/animal_pests_in_south_australia/established_pest_animals/wild_dogs/dog_fence?SQ_VARIATION_299639=0*

Pyne, S.J. (1992). *The Burning Bush: A Fire History of Australia*. Allen and Unwin, Sydney. 520pp. ISBN: 1863731946

Queensland Government (2020a). *Broad vegetation groups* webpage: *https://www.qld.gov.au/environment/plants-animals/plants/ecosystems/broad-vegetation*

Queensland Government (2020b). *Regional ecosystems* webpage: *https://www.qld.gov.au/environment/plants-animals/plants/ecosystems*

Ransley, T.R., and Smerdon, B.D. (Eds) (2012). *Hydrostratigraphy, hydrogeology and system conceptualisation of the Great Artesian Basin*. A technical report to the Australian Government from the CSIRO Great Artesian Basin Water Resource Assessment. CSIRO Water for a Healthy Country Flagship, Australia.

Russell-Smith, J., Yates, C., Edwards, A., Allan, G.E., Cook, G.D., Cooke, P., Craig, R., Heath, B., and Smith, R. (2003) Contemporary fire regimes of northern Australia, 1997-2001: change since Aboriginal occupancy, challenges for sustainable management. *International Journal of Wildland Fire*, 12, 283–297.

SA DEWNR (2019). *Native Vegetation Floristic Areas (NVIS)* webpage, SA Department of Environment, Water and Natural Resources: *http://location.sa.gov.au/lms/Reports/ReportMetadata.aspx?p_no=898+&pa=dewnr*

Sagoff, M. (1984). Animal liberation and environmental ethics: bad marriage, quick divorce. *Osgoode Hall Law Journal*, 22, 297–307.

Scarth, P., Armston, J., Lucas, R., and Bunting, P. (2019). A Structural Classification of Australian Vegetation Using ICESat/GLAS, ALOS PALSAR, and Landsat Sensor Data. *Remote Sensing*, 11(2), 147. *https://doi.org/10.3390/rs11020147*

Scott, J.K., Friedel, M.H., Grice, A.C., and Webber, B.L. (2018). Weeds in Australian Arid Regions. In *On the Ecology of Australia's Arid Zone*. (Ed: H. Lambers). Springer, Cham. *https://doi.org/10.1007/978-3-319-93943-8*

Shepherd, D.P, Beeston, G.R, and Hopkins, A.J. (2002). *Native vegetation in Western Australia : extent, type and status*. Department of Agriculture and Food, Western Australia, Perth. Report 249.

Sinclair, S.J., White, M.D., Medley, J., Smith, E., and Newell, G.R. (2012). Mapping the past: constructing a digital land-use history map for Victoria, Australia. *Proceedings of the Royal Society of Victoria,* 124(3), 193–206.

Smith, T.M., Woodward, I.A., Shugart, H.H. (Eds) (1997). *Plant Functional Types: Their Relevance to Ecosystem Properties and Global Change*. Cambridge University Press. England.

Specht, R.L. (1970). Vegetation. In *The Australian Environment*. 4th Edn. (Ed: Leeper, G.W.) CSIRO, Melbourne.

Specht, R.L. (1983). Foliage projective covers of overstorey and understorey strata of mature vegetation in Australia. *Austral Ecology*, 8, 433–439. doi:*10.1111/j.1442-9993.1983.tb01340.x*

Stern, H., de Hoedt, G., and Ernst, J. (1999). *Objective classification of Australian climates*. 8th Conference on Aviation, Range and Aerospace Meteorology, Amer. Meteor. Soc., Dallas, Texas, 10-15 Jan., 1999. *http://www.bom.gov.au/climate/environ/other/koppen_explain.shtml*

Taylor, G. (1927). The Topography of Australia. Feature Article in *Year Book Australia, 1927*. *https://www.abs.gov.au/AUSSTATS/abs@.nsf/Previousproducts/1301.0Feature%20Article20601927?opendocument&tabname=Summary&prodno=1301.0&issue=1927&num=&view=*

TERN (2020). Soil and Landscape Grid option on *TERN Data Discovery Portal*: *https://portal.tern.org.au/#/e8fbc61b*

Thackway, R., and Cresswell, I.D. (1995). *An Interim Biogeographic Regionalisation for Australia: a Framework for Establishing the National System of Reserves, Version 4.0*. Australian Nature Conservation Agency, Canberra.

Thackway, R., and Freudenberger, D. (2016). Accounting for the Drivers that Degrade and Restore Landscape Functions in Australia. *Land*, 5, 40. doi:*10.3390/land5040040*

Thackway, R., Neldner, J., and Bolton, M. (2008). Vegetation. In: *Australian Soil and Land Survey Handbook Guidelines for Conducting Surveys* (2nd Edition). (Eds: N.J. McKenzie, M.J. Grundy, R. Webster, and A.J. Ringrose-Voase). CSIRO Publishing, Melbourne.

Thornthwaite, C.W. (1931). The climates of North America according to a new classification. *Geographical Review*, 21, 633–655.

Thornthwaite, C.W. (1948). An approach toward a rational classification of climate. *Geographical Review*, 38, 55–94

Tindale, N.B. (1974). *Aboriginal Tribes of Australia: Their Terrain, Environmental Controls, Distribution, Limits, and Proper Names*. ANU Press, Canberra. ISBN: 0-7081-0741-9

Walker, J., and Hopkins, M.S. (1990). *Vegetation. Australian Soil and Land Survey Handbook: Guidelines for Conducting Surveys*. (Eds: R.H. Gunn, J.A. Beattie, R.E. Reid and R.H.M. v.d. Graaff). Inkata Press, Melbourne. pp 58–86.

Williams, R.J. (1959). Vegetation map of Australia in *The Australian Environment*. 3rd Edition. CSIRO, Melbourne. Reproduced with changed legend in *The Australian Environment*. 4th Edition (Ed: G.W. Leeper, 1970) CSIRO, Melbourne.

Williams, J., Hook, R.A., and Hamblin, A. (2002). *Agro-Ecological Regions of Australia, Methodologies for Their Derivation and Key Issues in Resource Management*. CSIRO Land and Water, Canberra, Australia.

3 Mapping Vegetated Landscapes

In this section we differentiate between mapping the extent, type, condition, and use of vegetated landscapes. Initially we will consider some key concepts that underpin landscape mapping (see Section 3.1) and methods used to map land cover (see Section 3.2), before discussing specific approaches used to map (see Section 3.3) and monitor (see Section 3.4) terrestrial vegetation in the Australian landscape.

3.1 Key Concepts in Landscape Mapping

The terms 'vegetation type', 'vegetation condition', 'land cover', and 'land use' are frequently encountered in landscape mapping applications. In the following two sub-sections we distinguish between these terms in the context of mapping the Australian terrestrial landscape.

3.1.1 Vegetation type versus vegetation condition

Traditional vegetation maps show the type, or variety, of vegetation in a particular location. While this information is a useful summary of the diversity of terrestrial vegetation in a landscape, it does not indicate the condition or 'quality' of that vegetation against some defined 'benchmark' or reference state. Information about the extent and condition of each vegetation type is critical for monitoring rates of loss and gain in different types of vegetation and across defined regions (such as IBRA regions or different jurisdictions). More recently, several federal, state, and territory mapping projects in Australia have considered approaches to benchmarking vegetation condition as well as defined the vegetation type. As a benchmark for assessing the condition of current vegetation, these projects infer the likely condition of each vegetation type in the year 1750—that is, before European settlement (see Figure 2.12 and Excursus 8.2). This benchmark is derived from:

- observations of recent changes in vegetation patterns; and
- models that consider those changes in conjunction with coincident changes in relevant environmental variables.

The value of such a benchmark is twofold as it provides:

- a picture of vegetation distribution and condition before European settlement; and
- a consistent baseline for measuring future vegetation changes.

Vegetation condition mapping has particular relevance in the context of monitoring compliance of land owners to environmental legislation governing land clearing in Australia (see Volume 2D—Excursus 14.3 and Excursus 19.2 below). Specific examples of mapping and monitoring vegetation type and condition in Australia are given in Sections 3.3 and 3.4 respectively. We note here that spatial mapping of changes and trends is not the same as site-based monitoring of changes and trends, although there is close relationship between directly-measured attributes and indicators and mapping these as classes of vegetation condition.

Land cover is a convenient label for that part of the biosphere that is critical for the continued existence of all terrestrial life.
(Graetz et al., 1992)

Background image: Astronaut photograph of Kangaroo Island, SA, taken from the International Space Station on 21 November 2002. **Source**: NASA Gateway to Astronaut Photography of Earth

3.1.2 Land cover versus land use

A wide variety of land cover inventories have been conducted by human civilisations over several millennia. This information has allowed societies to understand their environment, and plan and monitor their opportunities for development and sustainability.

Land cover is an excellent indicator of the resilience—or fragility—of the Earth's biophysical resources, including soils, nutrients, water, plants, and wildlife (ANRA, 2009). Mapping and monitoring of existing land cover enable the impact of specific land uses and management practices to be observed and quantified. Land cover assessment may also indicate the suitability of potential land uses (such as nature conservation, urban development, agriculture, or mining) in a particular area. Additionally, long term monitoring of land cover is invaluable for understanding the impacts of climate variability and relating these to patterns of severe climate events including wildfire, droughts, floods, and cyclones.

Natural vegetation patterns are largely determined by climate (especially rainfall), elevation (plus slope and aspect), and soil type, such that, in a pristine environment, natural land covers can often be modelled from these environmental attributes (Nix, 1982; see Section 2). Once these natural patterns have been modified by human activities, however, land cover cannot necessarily be inferred from such models but needs to be surveyed, measured, and/or inferred in some way.

Although the terms 'land cover' and 'land use' are sometimes used interchangeably, they do refer to different characteristics of land. Land cover is defined as the "observed (bio)physical cover on the Earth's surface" (Di Gregorio, 2005). Strictly speaking, while this definition only includes vegetation and man-made features, the term is generally accepted to embrace water surfaces, bare rock, and exposed soil as well. Examples of common land covers include grass, shrubs, trees, water, bare ground, artificial surfaces, and buildings.

The simplest definition of resilience is the ability to cope with shocks and to keep functioning in much the same kind of way. It is a measure of how much an ecosystem, a business, a society can change before it crosses a tipping point into some other kind of state that it then tends to stay in.
(Walker, 2020)

By contrast, land use has been described as the "arrangements, activities and inputs people undertake in a certain land cover type to produce, change or maintain it" (Di Gregorio, 2005). Thus, land use describes the impact of human occupation on an environment rather than simply its biophysical components (Fisher *et al.*, 2005). A single land use can involve multiple land cover features, and multiple land uses can contain the same single land cover. For example, the term 'rangelands' describes land used to graze livestock, but may comprise different land covers, such as trees, shrubs, and grasses (see Section 15). Conversely, the land cover type 'trees' may be used for timber production or nature conservation. Accordingly, land use is not readily discriminated by EO of specific land cover features but can often be inferred by combining land cover information with data from other sources.

The importance of land use and land cover (LULC) datasets has been recognised by several major international research programs (Cihlar, 2000; DeFries and Belward, 2000), including the International Geosphere–Biosphere Program (IGBP; (IGBP, 1990); Lambin and Geist, 2006). Similarly, the Group on Earth Observations (GEO) determined land cover to be the fifth most important parameter derived from satellite datasets (GEO, 2012).

Land use refers to the purpose to which the land cover is committed, including the production of goods (such as crops, timber and manufactures) and services (such as defence, recreation, biodiversity and natural resources protection). Some uses, such as cropping, have a distinctive land cover pattern, and are regular inclusions in land cover classifications. Others, such as nature conservation, are not readily identified from a characteristic land cover pattern. For example, where the land cover is forest, land use may be timber production or nature conservation. A single land cover class may support multiple uses and a single land use may involve several land cover conditions.
(ABARES, 2010)

3.2 How Do We Map Land Cover?

A land cover map represents the spatial distribution of a selected set of land covers. Creating a land cover map involves two fundamental considerations, namely, how do we define the:

- categories of land cover to map—or the classification scheme (see Section 3.2.1); and the
- boundaries for these land cover categories—or the mapping method (see Section 3.2.2).

However, these considerations raise several difficulties, the first being the inevitable diversity and complexity of any natural resource, and the unavoidable outcome that no classification can truly represent the vast array of 'classes' that exist in nature. Another difficulty in classifying and mapping land cover is that most natural land covers, especially vegetation, transition gradually from one type to another rather than at readily defined boundaries (Kessell, 1979). For example, the transition from woodland to open forest is often gradual, such that it can be difficult to precisely locate where one land cover becomes another. Inevitably, when classifying natural resources, the final decisions on class boundaries are somewhat arbitrary. The process of defining the transition point does, however, provide a valuable reference datum for consistent use of each class label.

Natural vegetation types do not generally change from one type to another at a given location over time. What does change are some attributes associated with the type such as cover/density, age class, height, strata, and to some extent composition (see Section 2.3.1). These changes are driven by changes in climate patterns, episodic severe climate events, and recurring land management regimes.

Another significant difficulty with land cover classification is the method used to name classes, that is, its nomenclature. In many traditional systems for mapping land cover, labels were not defined precisely and could easily be assumed to have a different meaning in a different context or community. For example, early settlers in Australia used the term 'scrub' to describe rainforest in eastern Australia, drier Mallee vegetation in southern Australia and the more open Mulga vegetation in arid Australia (Specht, 1970). Where labels were defined, they were not necessarily used consistently in different classification systems. As a result, a single land cover label could have multiple interpretations and a single land cover could have multiple labels—precisely the opposite outcome desired of such classifications, namely that a single land cover would have a single, unambiguous label.

3.2.1 Classification schemes

Although by its nature land cover can be described in many different ways, the essential goal of any classification of land cover is that the categories are unique, so that a single land cover will always be represented by a single category. All classification methods attempt to identify similar features and represent them as a particular group or class (see Volume 2E). The number of classes in a classification needs to be sufficient to allow discrimination of the significant differences between features, but no greater than is necessary to enable efficient analysis of variations between classes. Efficiency is particularly important when dealing with very large datasets, as are required for continental or global coverage (see Volume 2D).

Many classification systems have been developed to categorise land cover. These systems group the major similarities and differences in natural land cover types by selected attributes, such as:

- Vegetation: colour, type, density, structure, and condition/health;
- Water: depth, colour, quality, and temperature; and
- Bare rock and soil: colour, mineralogy, and texture.

Similarly, man-made land cover types can be grouped by characteristics such as:

- Artificial surfaces: colour and texture; and
- Constructions: colour, density, and height.

A wide variety of methods and data sources have been used to describe and group land cover features. In many cases these have focused on individual land cover attributes, such as floral characteristics, vegetation density, or indicators of land degradation. Some approaches to classifying land cover focus on specific attributes that directly relate to a particular end use. The datasets resulting from such activities are not readily comparable with other land cover classifications and may not be useful for other purposes. Other classification approaches attempt to define a comprehensive set of criteria that could be used to define all possible land covers. The latter approach allows land cover data collected at different times and locations, by different methods, to conform to a common set of underlying definitions of land cover attributes. As such, the results of these surveys can be easily applied to a range of analyses and readily compared with other datasets.

Table 3.1 Structure of FAO Land Cover Classification System

First Level	Second Level	Third Level	Example Land Cover
Primarily vegetated	Terrestrial	Managed/Cultivated	Cropping, Forestry
		Natural/Semi-natural	Native vegetation
	Aquatic or regularly flooded	Managed/Cultivated	Aquaculture
		Natural/Semi-natural	Native aquatic vegetation
Primarily non-vegetated	Terrestrial	Managed/Cultivated	Artificial surfaces
		Natural/Semi-natural	Bare land
	Aquatic or regularly flooded	Managed/Cultivated	Artificial waterbodies, snow and ice
		Natural/Semi-natural	Natural waterbodies, snow and ice

The Food and Agriculture Organisation of the United Nations (FAO) developed a Land Cover Classification System (LCCS; Di Gregorio, 2005) to standardise global land cover mapping. It allows scale-independent classes to be defined using discrete diagnostic criteria, which are arranged hierarchically in two phases:

- primary—defines three classification levels leading to eight basic land cover classes as shown in Table 3.1; and
- secondary—uses criteria, or 'classifiers', specific to each of the eight basic classes to further differentiate land cover types (see Excursus 3.1 for details)

While the biophysical environment cannot be fully or accurately represented by any classification system, the consistency and stability resulting from a standardised system improves communication between users and increases the utility of the classified data (Yang *et al*., 2017). Accordingly, a standardised land cover system allows classified data from different sources to be compared and integrated with confidence, especially for national and international datasets (see Volume 2D).

A number of EO-based systems have implemented the LCCS taxonomy for land cover classification, including the Earth Observation Data for Ecosystem Monitoring (EODESM; EcoPotential, 2021; see Section 20.5). In Australia, the LCCS has been applied nationally to describe land cover categories in the Dynamic Land Cover Dataset (DLCD; Lymburner *et al*., 2011). The capacity and conceptual framework of EODESM has also been demonstrated within Digital Earth Australia (DEA; see Volume 2D—Section 11.2) for two time periods across four test sites (Lucas *et al*., 2019).

Nature is a tireless sculptor, forever fashioning new masterpieces, yet, as if unsatisfied, commencing their destruction from the very moment of their completion. Something of the old always remains to be built into the new. The shape of a hill, the contour of a waterfall, the rocky ledges on the sides of a gully, the meanderings of a river, the alluvium of a plain are all links with the past, and within them lies the story of what has gone before.
(Charles F. Laseron, 1953)

Excursus 3.1—FAO Land Cover Classification System

Further Information: Di Gregario (2005, 2016); Di Gregario and Jansen (2000)

The land cover classification system (LCCS) developed by the UN Food and Agriculture Organisation (FAO) is a hierarchical system that classifies land covers in two phases (Di Gregorio, 2005):

- a primary, dichotomous phase which uses three classifiers to define eight major land cover types as summarised in Table 3.2; and
- a secondary, modular-hierarchical phase which refines the eight major land cover types into specific land cover classes using pre-defined classifiers tailored to each major type. In addition, environmental attributes (such as climate, landform, or soil type) or specific technical attributes (such as floristic characteristics) can also be used to define detailed classes in this phase. The pre-defined classifiers and attributes for each major land cover type are summarised in Table 3.3 and Table 3.4.

In order to define an international standard for land cover classification systems, FAO submitted the LCCS to the ISO Technical Committee 211 on Geographic Information in 2003. Although ISO had previously only defined standards for more abstract standards with established rules, a general classification system (ISO 19144-1 Classification Systems) and a land cover classification system (ISO 19144-2 Land Cover Meta Language: LCML) were approved in 2012 as official international ISO standards. The LCML characterises geographic features using an open, object-oriented system. Fundamentally, LCML uses a predefined set of biotic and abiotic elements (see Section 1.1) arranged in different 'patterns' to describe a wide range of land cover 'situations'. This "allows not only an unambiguous description of real world features more consistent with the logic and structure of modern databases but also enlarges the capability of the system to describe phenomena related to inputs and activities peoples undertake on a certain land cover feature typical of agriculture" (Di Gregario, 2016).

Table 3.2 Dichotomous phase classifiers and land cover types

Classifier	Presence of Vegetation	Edaphic Condition	Artificiality of Cover
Decision	Is vegetative cover > 4% for woody and/or herbaceous vegetation, or > 25% for lichen/mosses, during at least two months each year?	Is the environment significantly influenced by the presence of water for extensive periods of time?	Is the land cover significantly modified by human activity?
Land Cover Types	A: Primarily Vegetated Areas (see Table 3.3)	A1: Terrestrial Primarily Vegetated Areas	A11: Cultivated and Managed Terrestrial Areas
			A12: Natural and Semi-Natural Vegetation
		A2: Aquatic or Regularly Flooded Primarily Vegetated Areas	A23: Cultivated Aquatic or Regularly Flooded Areas
			A24: Natural and Semi-Natural Aquatic or Regularly Flooded Vegetation
	B: Primarily NonVegetated Areas (see Table 3.4)	B1: Terrestrial Primarily Non-Vegetated Areas	B15: Artificial Surfaces and Associated Areas
			B16: Bare Areas
		B2: Aquatic or Regularly Flooded Primarily Non-Vegetated Areas	B27: Artificial Waterbodies, Snow and Ice
			B28: Natural Waterbodies, Snow and Ice

Source: Di Gregario and Jansen (2000)

Table 3.3 LCCS classification of primarily vegetated areas

LCCS land cover type	Type of classifier	Classification level	Characteristics used to refine classes
A11: Cultivated and Managed Terrestrial Areas Natural vegetation has been removed or modified and replaced by other vegetation by human activity. Such vegetation requires long term maintenance and is planted with a view to harvesting. Example land covers include crops (with seasonal variation in cover), orchards, and plantations	'Pure' land cover classifiers	I	Life Form + Spatial Aspects
		II	Crop Combination
		III	Cover-related Cultural Practice
	Environmental attributes	IV	Landform + Lithology/Soils + Climate
		V	Altitude + Erosion + Cover/Density
	Specific technical attributes	VI	Crop Type
A12:Natural and Semi-natural Vegetation Natural vegetated areas are defined as areas where the vegetative cover is in balance with the abiotic and biotic forces of its biotope. Semi-natural vegetation is defined as vegetation not planted by humans but influenced by human actions. Example land covers include grazing, selective logging, and abandoned or shifting cultivation	'Pure' land cover classifiers	I	Life Form and Cover + Height + Macro Pattern
		II	Leaf Type and Leaf Phenology
		III	Stratification
	Environmental attributes	IV	Landform + Lithology/Soils
		V	Climate + Altitude + Erosion
	Specific technical attributes	VI	Floristic Aspect
A23: Cultivated Aquatic or Regularly Flooded Areas This category includes areas where an aquatic crop is purposely planted, cultivated and harvested, and which is standing in water over extensive periods during its cultivation period (such as paddy rice, tidal rice, and deepwater rice, but not irrigated cultivation).	'Pure' land cover classifiers	I	Life Form + Spatial Aspects
		II	Water Seasonality
		III	Cover-related Cultural Practice
		IV	Crop Combination
	Environmental attributes	V	Landform + Lithology/Soils + Climate
		VI	Altitude + Erosion + Cover/Density
	Specific technical attributes	VII	Crop Type
A24: Natural and Semi-natural Aquatic or Regularly Flooded Areas Transitional areas between pure terrestrial and aquatic systems and where the water table is usually at or near the surface, or the land is covered by shallow water, are included in this class. Examples include mangroves, marshes, swamps, and aquatic beds.	'Pure' land cover classifiers	I	Life Form and Cover + Height
		II	Water Seasonality
		III	Leaf Type + Leaf Phenology
		IV	Stratification
	Environmental attributes	V	Landform + Lithology/Soils + Climate
		VI	Altitude + Erosion + Cover/Density
	Specific technical attributes	VII	Floristic Aspect

Source: Di Gregario and Jansen (2000)

LCML acts as a method to bring the LC community together to create a common understanding of LC nomenclatures with the aim to produce global, regional and national data sets able to be reconciled at different scales, level of detail and geographic location. The LCML provides a general framework of rules from which more exclusive conditions can be derived to create specific legends. It is a language based on physiognomy and stratification of both biotic and abiotic materials. The system may be used to specify any LC feature anywhere in the world, using a set of independent diagnostic criteria that allow correlation with existing classifications and legends.
(Di Gregario, 2016)

Table 3.4 LCCS classification of primarily non-vegetated areas

LCCS land cover type	Type of classifier	Classification level	Characteristics used to refine classes
B15: Artificial Surfaces and Associated Areas Areas that have an artificial cover as a result of human activities such as construction (cities, towns, transportation), extraction (open mines and quarries) or waste disposal	'Pure' land cover classifiers	I	Surface Aspect
	Environmental attributes	II	Landform + Climate + Altitude
	Specific technical attributes	III	Built-Up Object
B16: Bare Areas Areas that do not have an artificial cover as a result of human activities (such as bare rock areas, sands, and deserts), including areas with less than 4% vegetative cover.	'Pure' land cover classifiers	I	Surface Aspect
		II	Macro-pattern
	Environmental attributes	III	Landform + Climate
		IV	Altitude + Erosion + Water Quality
	Specific technical attributes	V	Soil Type/Lithology
B27: Artificial Waterbodies, Snow and Ice Areas that are covered by water only as a result of the construction of artefacts such as reservoirs, canals, or artificial lakes	'Pure' land cover classifiers	I	Physical Status + Persistence
		II	Depth + Sedimentation
	Environmental attributes	III	Climate + Altitude + Vegetation
	Specific technical attributes	IV	Salinity
B28: Natural Waterbodies, Snow and Ice Areas naturally covered by water (such as lakes, rivers, snow, or ice)	'Pure' land cover classifiers	I	Physical Status + Persistence
		II	Depth + Sedimentation
	Environmental attributes	III	Climate + Altitude + Vegetation
	Specific technical attributes	IV	Salinity

Source: Di Gregario and Jansen (2000)

3.2.2 Mapping methods and accuracy assessment

All methods for mapping land cover utilise data from at least one of three primary sources:

- ground-based survey;
- aerial photography; and/or
- satellite imagery, or Earth Observation from Space (EOS).

Ground-based surveys require trained teams to visit field sites and record the land cover types encountered at precise locations (see Volume 2D—Section 12.1). Surveys generally involve measurements of pre-defined attributes for a range of land covers (Avery, 1975; TERN Australia, 2018). These measurements can involve the use of instrumentation and/or rely on the experience and judgement of the survey team. Different forms of ground-based survey have been used to map various types of land cover for thousands of years, and these have become increasingly standardised in recent decades. For example, the standard Australian methods and terminology for surveying land and soil attributes in the field are detailed in NCST (2009). In recent decades, however, given the labour-intensive and time-consuming nature of field data collection, this is generally limited to checking the accuracy of more synoptic data sources that can be acquired remotely (see Figure 3.1).

Figure 3.1 Multi-level EO

Analysis of low and medium resolution imagery can be more easily related to ground data through high resolution imagery. Low resolution imagery tends to be acquired more quickly and cover a larger extent, so is most appropriate for large area surveys. Selected locations within the surveyed area would typically be checked using data with higher spatial resolution, such as aerial photography. Some of these locations would then be visited in the field to verify the image analysis. This scaled approach enables the results of expensive and time-consuming field work to be extended to a larger area.

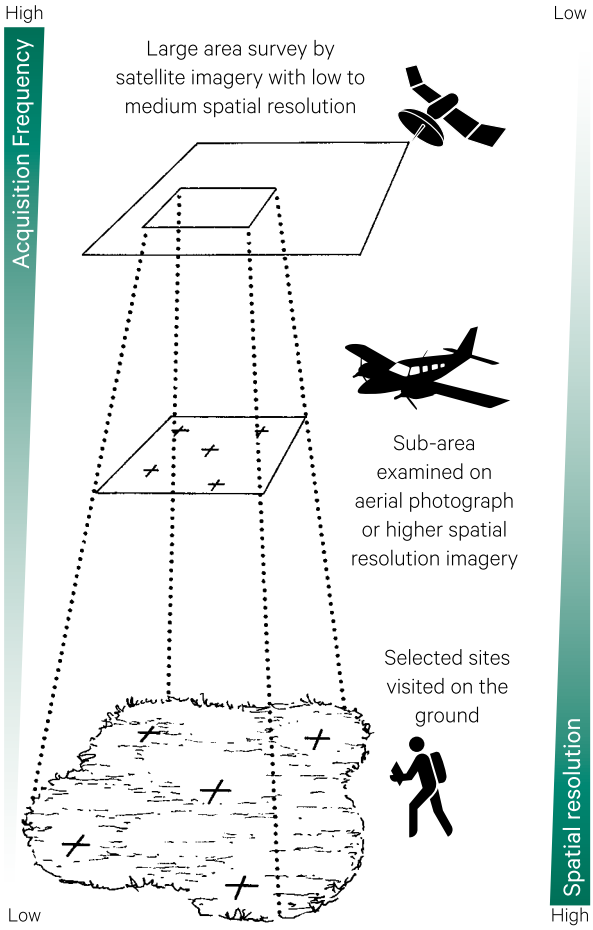

Adapted from: Harrison and Jupp (1989) Figure 39

It seems inevitable that, with increasing auto-scanning and data handling, as our knowledge of land increases, and as the demands of the land user become more specialised, that parametric analysis will become general practice (Mabbutt, 1968)

Aerial photography interpretation (API) has been used internationally to map different types of land cover for well over a century (see Volume 1A—Section 11). The Australian archive of aerial photography dates from 1928 and has supported various detailed inventories of natural resources with panchromatic, colour, and infrared photography. While still used to survey land cover in Australia for some applications, aerial imagery is now more frequently used to validate broader area analyses from space-based data (see Figure 3.1).

As detailed in Volume 1, EO datasets offer a range of approaches to observe and measure Earth surface properties. Space-based data have been available internationally for over five decades and offer a unique source of Earth surface data by recording:

- accurate geo-locations for contiguous target areas;
- objective, consistent measurements of physical properties of the land surface that can be interpreted to define its features and condition; and
- repeated coverage to enable detection of changes in features and/or their condition.

As introduced in Volume 1, different land and water cover features have varying, and often characteristic, reflectance in different wavelengths of the EM spectrum (see Figure 3.2). For any land cover to be discernible in EO, both the resolution and extent of the remote measurements need to be appropriate for the measurable properties of that land cover (see Volume 1B—Section 1). To separate one land cover from others, these measurements must also be able to discriminate between the differences in radiation from those land covers (Townshend, 1992).

A wide variety of statistics have been developed to exploit the similarities and differences between reflectance characteristics of different land covers, most of which highlight the high near infrared (NIR) reflectance and low red reflectance of healthy vegetation. Some of the standard image processing options used with EO data are described in Volumes 2A and 2C and reviewed in Section 8.1. The expanding archive of EO imagery now enables sophisticated time series analyses, which are being used to further quantify landscape dynamics, highlight the environmental drivers in natural processes, monitor compliance with resource usage regulations, and address issues related to climatic variations (Wulder *et al.*, 2018; see Volume 2D and Section 9).

Figure 3.2 Idealised spectral signatures

Reflectance from different Earth surface features varies for different wavelengths. Characteristic spectral reflectance curves can be created for different features to indicate a 'typical' shape over a particular range of wavelengths. This information can be used to differentiate between different surface features on the basis of their observed reflectance characteristics.

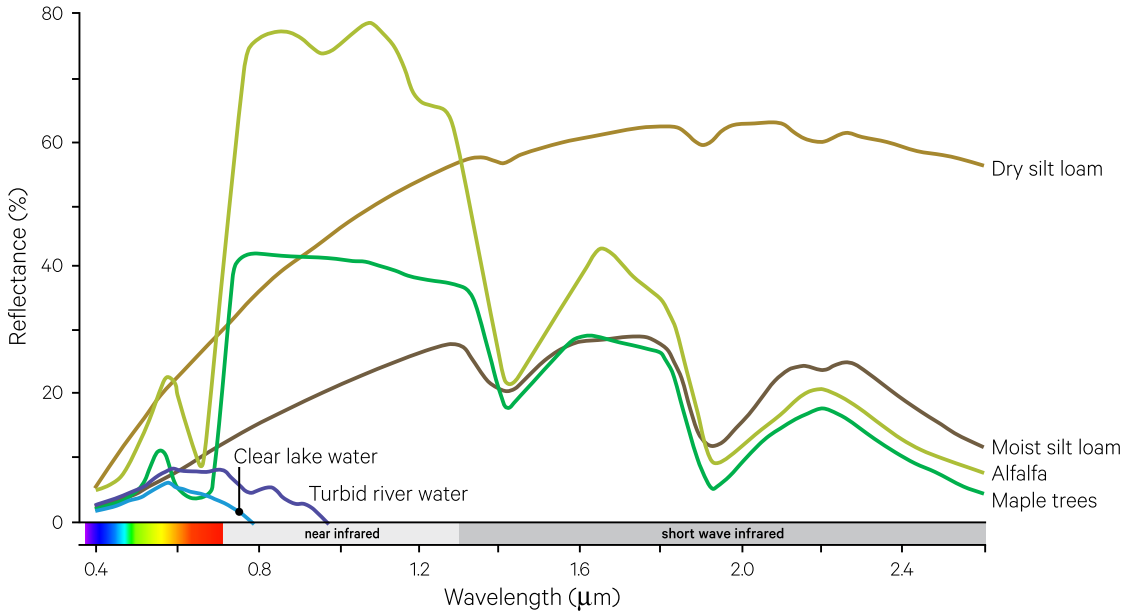

Adapted from: Harrison and Jupp (1989) Figure 6

A complete EO exercise usually involves the integration of imagery at several different 'levels' of resolution with data from other sources, such as maps or aerial photography. Within a large region represented in a satellite image, certain areas are usually selected for comparison with aerial photography, some of which would be visited in the field, or compared with field data. The concept of a multi-level approach is illustrated in Figure 3.1. This approach was implemented in the BigFoot Project, in which EO and field datasets with a variety of scales were analysed to characterise relationships between leaf area Index, net primary productivity, and carbon allocation within and between biomes, and validate relevant, landscape scale, EO-based products (NASA, 1999; see Section 7.4).

Accuracy assessments tend to assume that one dataset represents 'truth' and, thus, can be used to measure the 'value' of the other. In any landscape scale mapping exercise, few datasets can be viewed this way, so discrepancies in cross-comparison may show deficiencies in either dataset, or a lack of commonality in their intrinsic 'world views'.

Thus, when relating EO radiance to a reference dataset, correlation will depend on how accurately each dataset represents surface features. A lack of correlation does not necessarily imply that EO imagery cannot be used to map relevant landscape attributes but suggests that it may not differentiate them in the same way as the reference dataset. Any analysis of results must retain an awareness of this situation (see Volume 2E). Procedures for validation of EO analyses are detailed in TERN Australia (2018) and Malthus *et al.* (2013).

For example, since API largely relies on pattern interpretation by trained operators, it tends to generate maps that cleanly delineate regions characterised by internal heterogeneity. This approach contrasts with the pixel-based, spectral classification methods used with EO datasets (see Volume 2E). However, neither the results of API nor EO image analysis actually represent the whole 'truth'. When discrepancies between these two representations are being compared, the differences in their provenances should be considered.

In recent decades, a number of global and regional datasets have been derived from EO imagery to monitor land cover. For example, 21 global products and 43 regional products are reviewed by Grekousis *et al.* (2015). These freely available products cover different spatial and temporal scales, depending on the imagery used to generate them. Some examples include[5]:

- GlobCover (ESA with JRC, EEA, FAO, UNEP, GOFC-GOLD and IGBP)—annual global land cover maps derived from various satellite image sources at 300 m from 1992 to 2015 (ENVISAT; *http://cci.esa.int/content/land-cover-annual-global-land-cover-maps-v207-dataset-release*); Bontemps *et al.* (2011);
- Global Land Survey (NASA/USGS Land Cover Institute)—based on 30 m Landsat imagery, from 2009 to 2011 (*https://www.usgs.gov/land-resources/nli/landsat/global-land-survey-gls?qt-science_support_page_related_con=0#qt-science_support_page_related_con*);
- MODIS Land Cover (University of Maryland)—IGBP Land Cover Type classification (16 vegetation classes plus water) from 2001 to 2012 reprojected to geographic coordinates in WGS 1984 (EPSG: 4326) in two resolutions: 0.5° and 5' square pixels (*http://glcf.umd.edu/data/lc/*); and
- GLC2000 (EC coordinated consortium of researchers)—global and regional classifications of land cover derived from SPOT VEGETATION imagery (SPOT-4) for the year 2000 (*http://forobs.jrc.ec.europa.eu/products/glc2000/data_access.php*; Bartholomé and Belward, 2007).

3.3 Mapping Approaches

Classifying landscapes in terms of their biophysical characteristics allows geographers, land managers, and decision makers to focus on the similarities and differences between different regions. This information provides insight into the processes that determine these characteristics and allows the impact of land management practices to be evaluated objectively. Such data and classifications are used for a range of activities, including conservation planning, resource assessment, and agricultural management.

The interrelationship between land cover and environmental factors, such as climate, topography, and soil substrate, is well-established for the Australian environment (Graetz *et al.*, 1992). As outlined in Section 2, the distribution of natural vegetation in Australia is strongly dependent on rainfall, aspect, and soil type. Since World War II, numerous classifications of landscape biodiversity have been developed for both research and operational use in Australia. These have involved varying methods, scales, products, and coverage. Some of these systems are summarised in Table 3.5. While these efforts have substantially contributed to the current knowledge of Australia's biophysical resources and have each delivered iterative improvements in terms of reliability and accessibility, none currently offers consistent land cover information over the Australian landmass that can be updated readily.

Below, we will consider the existing landscape classifications in terms of four categories:

- land evaluation based on mapping units (see Section 3.3.1);
- actual distribution of current vegetation (see Section 3.3.2);
- probable distribution of natural vegetation (see Section 3.3.3); and
- actual distribution of current land use (see Section 3.3.4).

3.3.1 Land evaluation based on mapping units

The CSIRO Land Systems project (Christian and Stewart, 1953, 1968) developed the first landscape classification system to be based on 'mapping units'. Reconnaissance surveys were conducted in northern and central Australia and Papua New Guinea from 1946 to 1977, to identify and map land resources and the potential for regional development. To integrate the various types of landscape data, a new system of land evaluation was required. Each area or group of areas characterised by a recurring pattern of topography, soils, and vegetation was identified as a discrete mapping unit or 'land system'. Initial mapping of land systems was generally based on patterns identified from aerial photography, in conjunction with supporting information available from topographic and thematic maps, reports and other documents, and expert knowledge. Successive surveys used more advanced classifications of soils, vegetation, and terrain as these became available. The results of these surveys are still used as a reference data source in other mapping exercises.

5 ESA: European Space Agency; JRC: Joint Research Centre (EC); EEA: European Economic Area; FAO: UN Food and Agriculture Organisation; UNEP: UN Environment Program; GOFC-GOLD: Global Observations of Forest Cover and Land Dynamics; IGBP: International Geosphere-Biosphere Programme

A similar approach to land evaluation was used to develop the Interim Biogeographic Regionalisation for Australia (IBRA; DAWE, 2020a; see Figure 2.13), part of a nested series of bioregionalisations used to define global terrestrial habitats and world ecoregions by the World Wildlife Fund (WWF; Olson *et al.*, 2001; see Section 1.3.2). This classification was developed for conservation planning and represents Australia's landscapes as geographically distinct bioregions on the basis of climate, geology, landform, and native flora (see Section 2.4). Each bioregion has been subdivided into more homogeneous geomorphological units or subregions. In IBRA7, 89 bioregions and 419 subregions collectively describe the Australian landmass and selected marine areas.

A hierarchy of mapping units was also used to compile the Australian Soil Resource Information System (ASRIS; CSIRO, 2014; see Figure 2.3). This provides online access to consistent soil and land resource information across Australia in a seven-tiered hierarchy. Different attributes are used to map each level in the hierarchy, as deemed appropriate to each mapping scale, based on the most recent publicly available data. This system can be used to summarise the soil and landscape properties for other classifications, such as IBRA.

Land, then, is not merely soil; it is a fountain of energy flowing through a circuit of soils, plants, and animals. (Aldo Leopold)

Table 3.5 Australian landscape mapping approaches

Name	Description	Coverage	Further Information
CSIRO Land Systems	First systematic approach to land evaluation in Australia, conducted from 1946–1977, based on evolving classifications of soils, vegetation and terrain	Primarily northern and central Australia, approximately 50% of continental Australia	Christian and Stewart (1953, 1968); *www.publish.csiro.au/nid/289.htm*
Vegetation Map of Australia	Probable distribution of major natural vegetation groups	16 categories across the Australian landmass	Williams (1959)
Major Vegetation Types in Australia	Probable distribution of major vegetation groups prior to European settlement based on Specht structural types and Beard and Webb (1974) notation	1977—1:12,000,000 1988—1:5,000,000	Carnahan (1976, 1988)
Present Vegetation (Atlas of Australian Resources, 3rd Edition)	First continental map of actual vegetation based on Landsat MSS satellite imagery with input from existing maps, reports, and expert knowledge.	24 broad structural categories with supplementary codes Australian landmass; 1:5,000,000	AUSLIG (1990)
Interim Biogeographic Regionalisation of Australia (IBRA)	Divides Australia into geographically distinct areas with common characteristics (such as geology, landform patterns, climate, and ecology) as a broad framework for conservation planning	Digital data for 89 bioregions and 419 sub-regions across Australian land mass and selected marine areas	Thackway and Cresswell (1995); *https://www.environment.gov.au/land/nrs/science/ibra*
Australian Soil Resource Information System (ASRIS)	Online access to best available soil and land resources information using a seven-tiered hierarchy of mapping units	Digital data for Australian landmass	McKenzie ***et al.*** (2012); *www.asris.csiro.au*
National Vegetation Information System (NVIS)	National collaboration of state and federal datasets that combines floristic and structural parameters to describe all layers of native vegetation, both current and pre-1750.	National hierarchical framework for inventory and monitoring of vegetation type and extent. Dataset covers the Australian landmass and contains over 9,000 distinct vegetation types	*https://www.environment.gov.au/land/native-vegetation/national-vegetation-information-system*
Major Vegetation Groups (MVG)	Aggregations of NVIS 4.1 vegetation types to estimate major groups of vegetation in Australia, both current and pre-1750.	33 Major Vegetation Groups and 85 sub-groups over Australian landmass	DE (2012) *https://data.gov.au/data/dataset/57c8ee5c-43e5-4e9c-9e41-fd5012536374*
Australian Land Use and Management Classification (ALUM)	National scale land use classification using modelling approach to integrate agricultural commodity data, satellite data, and other land use data	1:2,500,000	*http://www.agriculture.gov.au/abares/aclump/land-use/alum-classification*
Catchment Scale Land Use of Australia (CLUM)	A seamless raster dataset that combines land use data for all state and territory jurisdictions, at a resolution of 50 m, by combining state cadastre, public land databases, fine scale satellite data, other land cover and use data, and information collected in the field	1:5,000 to 1:25,000 for irrigated and peri-urban; 1:100,000 for broadacre cropping; 1:250,000 for semi-arid and arid pastoral zone.	*http://data.daff.gov.au/anrdl/metadata_files/pb_luausg9abll20171114_11a.xml*

3.3.2 Actual distribution of current vegetation

The first national scale map of actual vegetation in Australia based on satellite imagery was produced by Carnahan (1988) for the Australian Surveying and Land Information Group (AUSLIG) publication series Atlas of Australian Resources (AUSLIG, 1990). This two-part dataset mapped both natural (pre-European settlement; see Section 3.3.3) and present (current) vegetation at 1:1 million scale. The 'present vegetation' map, which showed both native and exotic vegetation, was based on visual interpretation of Landsat MSS satellite imagery with reference to existing maps, reports and expert knowledge (especially for crop and pasture classes). Land cover labels were based on eight growth forms and four categories of foliage cover for the tallest stratum, resulting in 22 broad categories for terrestrial vegetation with two additional classes for wetland vegetation and bare areas. Supplementary mapping detail describing floristic type and vegetation in the lower stratum was added using alphanumeric codes and shading patterns. Each major vegetation type was also detailed and mapped in AUSLIG (1990).

The National Land and Water Resources Audit (NLWRA) was founded in 1997 to collate information relating to Australia's natural resources and finished operation in 2008 (Land and Water Australia, 2009). One of its collaborative projects with state agencies was the Australian Native Vegetation Assessment 2001 (NLWRA, 2001), the first Australia-wide, regional level, assessment of type, extent, and change in Australia's native vegetation cover since European settlement. Included in this project was the development of a consistent national classification framework, based on Walker and Hopkins (1990) Figure 8, which became known as the National Vegetation Information System (NVIS; see Section 2.3.1 and Volume 2D—Excursus 12.1). Over 10,000 distinct vegetation types are contained in the NVIS database (NVIS Technical Working Group, 2017). In NVIS Version 5.1, these detailed data records are aggregated into 33 Major Vegetation Groups (MVG) and 85 Major Vegetation Subgroups (MVS) for Australia on the basis of similarity in structure and floristic composition in the dominant stratum (see Section 2.3.1). These datasets have been used to map both current (extant) and pre-1750 vegetation in Australia (see Figure 2.12 and Section 3.3.3).

3.3.3 Probable distribution of natural vegetation

Since the spatial distribution of natural vegetation is largely determined by climate (principally precipitation and temperature) and moderated by factors relating to soils and topography (especially aspect and slope) (Graetz *et al.*, 1992), the probable distribution of vegetation prior to European settlement in Australia has been modelled on the basis of these variables (Nix, 1982). Current vegetation, however, has been modified by anthropogenic influences and can only be determined using surveying and modelling methods. Several maps showing the likely distribution of Australian vegetation before European settlement have been produced using expert knowledge (from field surveys, existing maps, and reports). Natural vegetation maps showing the probable state of Australia's vegetation around 1788 (Carnahan, 1976, 1988) were produced for AUSLIG (1990). The earliest of these maps was based on API and other data sources, while the latter map was compiled from visual interpretation of Landsat MSS imagery and all relevant information (see Table 3.5). Such maps have allowed the impact of land cover change since European settlement to be identified and quantified.

It should be noted that, at the state level, numerous maps of potential natural vegetation have been also produced, including for WA, SA, Tasmania, NSW, and Queensland. These maps are generally produced at a coarser scale than maps of present or actual native vegetation.

Using assumptions about undisturbed land condition and the environmental drivers for landscape change, the probable distribution of natural vegetation can also be inferred from the distribution of current vegetation. This type of mapping has been applied to NVIS (NVIS Technical Working Group, 2017; see Figure 2.12) and several state-based vegetation maps (see Section 19.5). For such approaches to operate reliably, however, it is essential that the back-engineering models (which simulate vegetation type and condition in the pre-European landscape from those existing in the present landscape) be based on accurate benchmarks for all ecosystems within the study area, for each jurisdiction.

3.3.4 Actual distribution of current land use

The distinction between 'land cover' and 'land use' was discussed in Section 3.1.2 above. Identification of land use is critical for planning and managing land resources, both for productive industries and environmental protection.

Australian Land Use and Management (ALUM; see Section 2.5.3) is a land use classification system that comprises a three-tiered hierarchy of classes, broadly structured by their potential for disturbance. The primary level in this hierarchy includes six classes, with classes 1 to 5 being ordered by increasing modification to the natural landscape:

1. Conservation and natural environments—land that has a relatively low level of human intervention. The land may be formally reserved by government for conservation purposes, or conserved through other legal or administrative arrangements. Areas may have multiple uses, but nature conservation is the prime use. Some land may be unused as a result of a deliberate decision of government or landowner, or due to circumstance.
2. Production from relatively natural environments—land that is subject to relatively low levels of intervention. The land may not be used more intensively because of its limited capability. The structure of the native vegetation generally remains intact despite deliberate use, although the floristics of the vegetation may have changed markedly. Where the native vegetation structure is, for example, open woodland or grassland, the land may be grazed.
3. Production from dryland agriculture and plantations—land that is used principally for primary production, based on dryland farming systems. Native vegetation has largely been replaced by introduced species through clearing, the sowing of new species, the application of fertilisers or the dominance of volunteer species. The range of activities in this category includes plantation forests, pasture production for stock, cropping and fodder production, and a wide range of horticultural production.
4. Production from irrigated agriculture and plantations—agricultural land uses where water is applied to promote additional growth over normally dry periods, depending on the season, water availability and commodity prices.
5. Intensive uses—land uses that involve high levels of interference with natural processes, generally in association with closer residential settlement, commercial or industrial uses.
6. Water—water features are regarded as an essential aspect of the ALUM classification, primarily as a cover type (ABARES, 2016).

The three levels in this hierarchical classification system are summarised in Table 3.6. The range of secondary and tertiary classes indicates the diversity of land uses in Australia. In this system, agricultural activities are further differentiated by their dependence on irrigation, extent of land disturbance, and current status of activity. Two scales of land use map are generated from ALUM:

- national scale (1:2,500,000)—integrates agricultural commodity data, satellite imagery, and other land use information using a modelling approach; and
- catchment scale (1:5,000–1:25,000 for irrigated and peri-urban, 1:100,000 for broadacre cropping and 1:250,000 for semi-arid and arid pastoral zone)—combines state cadastre, public land databases, high spatial resolution satellite data, other land cover and use data, and field data (Figure 2.17). Overall attribute accuracy of catchment scale maps is assessed as greater than 80% (ABARES, 2011).

While national scale land use maps (1:2,500,000) have been available biennially since 1992/93, continental coverage at catchment scale was first completed in 2008. The ALUM dataset is updated periodically to reflect changes in land use and serves as a valuable national and regional monitoring tool (see Section 3.4.2). The current national map, updated in December 2018 from CLUM data, features 18 broad land use classes and 33 ALUM secondary classes (DAWE, 2020b), with interactive viewing of recent maps being available via the National Map tool (see Volume 2D—Excursus 13.1).

ALUM is managed by the Australian Collaborative Land Use and Management Program (ACLUMP), which is overseen by the National Committee for Land Use and Management Information (NCLUMI—a consortium of federal, state and territory government partners seeking to develop nationally consistent land use and land management information for Australia; DAWE, 2020c). In addition to compiling land use maps, ACLUMP produces guidelines for land use mapping and handbooks for field measurement (see Section 3.5).

The way in which land is used has a profound effect on Australia's unique climate, soil, water, vegetation and biodiversity resources (Thackway and Freudenberger, 2016). There is a strong link between spatial and temporal patterns of land use and prevailing environmental, economic and social conditions. Therefore, information on land use and management is fundamental to the development and implementation of land use policy and planning. (Thackway, 2018)

Table 3.6 ALUM classification

Notes: Classes 1.1.1–1.1.6 are based on the Collaborative Australian Protected Areas Database (CAPAD) classification (Cresswell and Thomas, 1997) and can be translated to IUCN (2008) categories I to V. Class 1.1.7 covers additional forms of nature conservation protection, including heritage agreements, voluntary conservation arrangements, registered property agreements, and recreation areas with primarily native cover. Classes 1.2.1–1.2.4 are based on the CAPAD classification (IUCN, 2008 Category VI).

Primary class	Secondary class	Tertiary class	Area (%) 2010–11	Area (%) 2010–11
1. Conservation and natural environments	1.1 Nature conservation	1.1.1 Strict nature reserve 1.1.2 Wilderness area 1.1.3 National park 1.1.4 Natural feature protection 1.1.5 Habitat/species management area 1.1.6 Protected landscapes 1.1.7 Other conserved area	7.86	38.26
	1.2 Managed resource protection	1.2.1 Biodiversity 1.2.2 Surface water supply 1.2.3 Groundwater 1.2.4 Landscape 1.2.5 Traditional indigenous land uses	15.14	
	1.3 Other minimal use	1.3.1 Defence land—natural areas 1.3.2 Stock route 1.3.3 Residual native cover 1.3.4 Rehabilitation	15.26	
2. Production from relatively natural environments	2.1 Grazing native vegetation		44.87	46.22
	2.2 Production native forests	2.2.1 Wood production forestry 2.2.2 Other forest production	1.35	
3. Production from dryland agriculture and plantations	3.1 Plantation forests	3.1.1 Hardwood plantation forestry 3.1.2 Softwood plantation forestry 3.1.3 Other forest plantation 3.1.4 Environmental forest plantation	0.34	13.18
	3.2 Grazing modified pastures	3.2.1 Native/exotic pasture mosaic 3.2.2 Woody fodder plants 3.2.3 Pasture legumes 3.2.4 Pasture legume/grass mixtures 3.2.5 Sown grasses	9.24	
	3.3 Cropping	3.3.1 Cereals 3.3.2 Beverage and spice crops 3.3.3 Hay and silage 3.3.4 Oilseeds 3.3.5 Sugar 3.3.6 Cotton 3.3.7 Alkaloid poppies 3.3.8 Pulses	3.59	
	3.4 Perennial Horticulture	3.4.1 Tree fruits 3.4.2 Olives 3.4.3 Tree nuts 3.4.4 Vine fruits 3.4.5 Shrub berries and fruits 3.4.6 Perennial flowers and bulbs 3.4.7 Perennial vegetables and herbs 3.4.8 Citrus 3.4.9 Grapes	0.01	
	3.5 Seasonal horticulture	3.5.1 Seasonal fruit 3.5.2 Seasonal flowers and bulbs 3.5.3 Seasonal vegetables and herbs		
	3.6 Land in transition	3.6.1 Degraded land 3.6.2 Abandoned land 3.6.3 Land under rehabilitation 3.6.4 No defined use 3.6.5 Abandoned perennial horticulture	0.00	13.18

Primary class	Secondary class	Tertiary class	Area (%) 2010–11	Area (%) 2010–11
4. Production from irrigated agriculture and plantations	4.1 Irrigated plantation forests	4.1.1 Irrigated hardwood plantation forestry 4.1.2 Irrigated softwood plantation forestry 4.1.3 Irrigated other forest plantation 4.1.4 Irrigated environmental forest plantation	0.00	0.27
	4.2 Grazing irrigated modified pastures	4.2.1 Irrigated woody fodder plants 4.2.2 Irrigated pasture legumes 4.2.3 Irrigated legume/grass mixtures 4.2.4 Irrigated sown grasses	0.08	
	4.3 Irrigated cropping	4.3.1 Irrigated cereals 4.3.2 Irrigated beverage and spice crops 4.3.3 Irrigated hay and silage 4.3.4 Irrigated oilseeds 4.3.5 Irrigated sugar 4.3.6 Irrigated cotton 4.3.7 Irrigated alkaloid poppies 4.3.8 Irrigated pulses 4.3.9 Irrigated rice	0.12	
	4.4 Irrigated perennial horticulture	4.4.1 Irrigated tree fruits 4.4.2 Irrigated olives 4.4.3 Irrigated tree nuts 4.4.4 Irrigated vine fruits 4.4.5 Irrigated shrub berries and fruits 4.4.6 Irrigated perennial flowers and bulbs 4.4 7 Irrigated perennial vegetables and herbs 4.4.8 Irrigated citrus 4.4.9 Irrigated grapes	0.03	
	4.5 Irrigated seasonal horticulture	4.5.1 Irrigated seasonal fruits 4.5.2 Irrigated seasonal flowers and bulbs 4.5.2 Irrigated seasonal vegetables and herbs 4.5.4 Irrigated turf farming	0.02	
	4.6 Irrigated land in transition	4.6.1 Degraded irrigated land 4.6.2 Abandoned irrigated land 4.6.3 Irrigated land under rehabilitation 4.6.4 No defined use—irrigation 4.6.5 Abandoned irrigated perennial horticulture	0.00	
5. Intensive uses	5.1 Intensive horticulture	5.1.1 Production nurseries 5.1.2 Shadehouses 5.1.3 Glasshouses 5.1.4 Glasshouses—hydroponic 5.1.5 Abandoned intensive horticulture	0.00	0.41
	5.2 Intensive animal production	5.2.1 Dairy sheds and yards 5.2.2 Feedlots 5.2.3 Poultry farms 5.2.4 Piggeries 5.2.5 Aquaculture 5.2.6 Horse studs 5.2.7 Saleyards/stockyards 5.2.8 Abandoned intensive animal production	0.01	
	5.3 Manufacturing and industrial	5.3.1 General purpose factory 5.3.2 Food processing factory 5.3.3 Major industrial complex 5.3.4 Bulk grain storage 5.3.5 Abattoirs 5.3.6 Oil refinery 5.3.7 Sawmill 5.3.8 Abandoned manufacturing and industrial	0.01	
	5.4 Residential and farm infrastructure	5.4.1 Urban residential 5.4.2 Rural residential with agriculture 5.4.3 Rural residential without agriculture 5.4.4 Remote communities 5.4.5 Farm buildings/infrastructure	0.33	
	5.5 Services	5.5.1 Commercial services 5.5.2 Public services 5.5.3 Recreation and culture 5.5.4 Defence facilities—urban 5.5.5 Research facilities	0.04	

Primary class	Secondary class	Tertiary class	Area (%) 2010–11	Area (%) 2010–11
5. Intensive uses (cont.)	5.6 Utilities	5.6.1 Fuel powered electricity generation 5.6.2 Hydro electricity generation 5.6.3 Wind electricity generation 5.6.4 Solar electricity generation 5.6.5 Electricity substations and transmission 5.6.6 Gas treatment, storage and transmission 5.6.7 Water extraction and transmission	0.00	0.41
	5.7 Transport and communication	5.7.1 Airports/aerodromes 5.7.2 Roads 5.7.3 Railways 5.7.4 Ports and water transport 5.7.5 Navigation and communication	0.00	
	5.8 Mining	5.8.1 Mines 5.8.2 Quarries 5.8.3 Tailings 5.8.4 Extractive industry not in use	0.02	
	5.9 Waste treament and disposal	5.9.1 Effluent pond 5.9.2 Landfill 5.9.3 Solid garbage 5.9.4 Incinerators 5.9.5 Sewage/sewerage	0.00	
6. Water	6.1 Lake	6.1.1 Lake–conservation 6.1.2 Lake–production 6.1.3 Lake–intensive use 6.1.4 Lake–saline	1.13	1.63
	6.2 Reservoir/dam	6.2.1 Reservoir 6.2.2 Water storage—intensive use/farm dams 6.2.3 Evaporation basin	0.07	
	6.3 River	6.3.1 River-conservation 6.3.2 River-production 6.3.3 River-intensive use	0.06	
	6.4 Channel/aqueduct	6.4.1 Supply channel/aqueduct 6.4.2 Drainage channel/aqueduct 6.4.3 Stormwater	0.00	
	6.5 Marsh/wetland	6.5.1 Marsh/wetland–conservation 6.5.2 Marsh/wetland–production 6.5.3 Marsh/wetland–intensive use 6.5.4 Marsh/wetland–saline	0.12	1.63
	6.6 Estuary/coastal waters	6.6.1 Estuary/coastal waters–conservation 6.6.2 Estuary/coastal waters–production 6.6.3 Estuary/coatal waters–intensive use	0.25	

Source: ABARES (2016)

Landscapes have been transformed by harvesting native food and fibre, removing vegetation and regolith to extract minerals, removing vegetation to provide housing and urban infrastructure, draining floodplains to create productive agricultural soils, [and] irrigating previously dryland native vegetated areas. Landscapes have also been transformed inadvertently through the combined effects of feral animals, weeds and changed fire regimes. (Thackway et al., 2015)

3.4 Monitoring Landscape Change

Any landscape mapping exercise needs to consider the fact that landscapes change. Variations in landscape features may occur as part of natural cycles or may result from disturbances in the natural balance. In this section we will consider those factors in a landscape that can change land cover condition (see Section 3.4.1) and/or land use (see Section 3.4.2).

Biotic and abiotic factors in the environment are introduced in Section 1.1. Changes in these factors can modify the vegetated landscape of any environment. In the Australian context, critical factors include fire (see Sections 2.4 and 18), weeds (see Section 2.3.2), and feral animals (see Section 2.3.3). Changes in climate patterns (see Section 2.2) also impact vegetation directly by varying temperatures, wind exposure, and rainfall as well as indirectly by altering the distribution of predators. Land use activities can accelerate natural erosion patterns, reduce runoff, and alter drainage systems (see Sections 2.1 and 11.4). Finally tectonic activity can have a dramatic effect on topography and any vegetation it supports (see Volume 1A—Section 3.2).

In the last two centuries, the condition of native vegetation in the Australian landscape has changed significantly (Gammage, 2012), creating fragmentation of ecosystems in many regions. In Central Australia, where population pressure is much lower than along the coastal fringe, changes in grazing and fire management practices have also transformed native vegetation (Thackway *et al.*, 2015).

Now that various forms of environmental legislation govern land clearing in Australia, it is important that changes in land cover can be assessed accurately and consistently. Understanding change patterns in the landscape helps to predict future distribution and condition of plants and animals, and also enables modelling of the likely distribution of biodiversity in the past.

The National Landcare Program (and its numerous predecessors) has federally funded natural resource management in Australia for several decades to protect and rehabilitate our environment (NLP, 2017), with the specific goal of improving soil, water, and biodiversity (see Table 3.7). This program involves collaboration between landowners, researchers, local communities, and the 56 regional natural resource management (NRM) groups (NRM, 2019a, 2019b) to ensure that Australia satisfies both national and international obligations that are relevant to the environment (NLP, 2019). As part of this program, a number of online tools, based on EO and other spatial datasets, have been developed to assist landowners towards sustainable land management (see Sections 3.5 and 19).

Table 3.7 National Landcare Program

Phase One (2014/15–2017/18) of the National Landcare Program defines the four strategic objectives listed below.

Objective	Outcome	Contribution to obligations
Communities are managing landscapes to sustain long term economic and social benefits from their environment.	Maintain and improve ecosystem services through sustainable management of local and regional landscapes	Protection and restoration of ecosystem function, resilience and biodiversity Appropriate management of invasive species which threaten ecosystems, habitats or native species
Farmers and fishers are increasing their long term returns through better management of the natural resource base.	Increase in the number of farmers and fishers adopting practices that improve the quality of the natural resource base, and the area of land over which those practices are applied	Sustainable management of agriculture and aquaculture to conserve and protect biological diversity and reduce greenhouse gas emissions and increase carbon stored in soil
Communities are involved in caring for their environment.	Increase engagement and participation of the community, including landcare, farmers, and Indigenous people, in sustainable natural resource management	Build community awareness of biodiversity values, skills, participation and knowledge, including Indigenous knowledge and participation, to promote conservation and sustainable use of biological diversity
Communities are protecting species and natural assets.	Increase restoration and rehabilitation of the natural environment, including protecting and conserving nationally and internationally significant species, ecosystems, ecological communities, places, and values	Reduce the loss of natural habitats, degradation and fragmentation Protect or conserve 'Matters of National Environmental Significance' including management of World Heritage Areas, Ramsar wetlands, national heritage, etc Reduce the number of nationally threatened species and improve their conservation status

Source: NLP (2017) Table 1

3.4.1 Changes in land condition

While the type of vegetation in an area may essentially stay the same over time, the condition of that vegetation may change (see Section 3.1.1). Methods to objectively and consistently assess vegetation condition—as well as vegetation type—have been developed for Australia in recent years. For example, Thackway *et al.* (2015) propose a seven step process based on Sbrocchi (2013) to account for the condition of native vegetation as an example of an environmental 'asset':

1. Document the environmental assets;
2. Select environmental indicators;
3. Determine reference benchmarks;
4. Collect data;
5. Calculate indicator condition scores;
6. Calculate environmental condition index; then
7. Submit for accreditation.

To streamline the accounting process for native vegetation at the property and regional levels, this seven step process was refined by Butler *et al.* (2020) to four steps:

1. Defining the accounting area;
2. Compile existing published standardised data for native vegetation types;
3. Stratifying accounting area into assessment units; and
4. Measure indicators.

The environmental condition index (*Econd*™; see Section 20.5) is derived to allow comparison of the relative condition of different assets. This index ranges from pre-industrial condition (100) to absent (0). Indicators of change need to efficiently reflect ecological productivity and resilience, and involve measures of both the quality (condition) and quantity (extent) of native vegetation, as well as its composition (the functional and structural integrity and landscape complexity).

One system that has been developed to monitor changes in the condition of vegetated landscapes is the Vegetation Assets, States and Transitions (VAST; see Excursus 3.2). The VAST system offers "a structured way to record observed, measured responses of native plant communities against historic and contemporary land use and land management practices relative to a reference state" (Thackway *et al.*, 2015). The key indicators and key functional, structural, and composition criteria that are identified by VAST Version 2 (VAST-2) are summarised in Table 3.8.

The national VAST-2 dataset is shown in Figure 3.3, which emphasises characteristic patterns of vegetation condition in different jurisdictions:

- very large areas of residual and modified vegetation in the rangelands of central and northern Australia;
- large areas of residual and modified vegetation in temperate regions that are less suited to agriculture;
- replaced vegetation occurs in fertile, moist regions, principally being used for cropping and improved pasture;
- extensive modified and transformed vegetation in arid and semi-arid rangelands due to grazing; and
- small areas of removed vegetation in coastal margins due to human settlement (Lessie *et al.*, 2010).

This approach to mapping the condition of vegetated landscapes offers "a simple communication and reporting metric that can assist in describing, valuing, and evaluating anthropogenic modification of native vegetation" (Lessie *et al.*, 2010). Such datasets can closely track the way vegetation responds to land management practices, quantify changes in vegetation type and extent, and monitor progress towards defined vegetation targets.

Table 3.8 VAST-2 diagnostic components, criteria and indicators

Diagnostic components	Key criteria	Key indicators
Regenerative capacity	1. Fire regime	1. Area/size of fire footprints
		2. Interval between fire starts
	2. Soil hydrology	3. Plant available water holding capacity
		4. Groundwater dynamics
	3. Soil physical state	5. Effective rooting depth of soil profile
		6. Bulk density of soil through changes to soil structure or soil removal
	4. Soil nutrient state	7. Nutrient stress—rundown (deficiency) relative to reference soil fertility
		8. Nutrient stress—excess (toxicity) relative to reference soil fertility
	5. Soil biological state	9. Organisms responsible for maintaining soil porosity and nutrient recycling
		10. Surface organic matter, soil crusts
	6. Reproductive potential	11. Reproductive potential of overstorey structuring species
		12. Reproductive potential of understorey structuring species
Vegetation structure	7. Overstorey structure	13. Overstorey top height (mean) of plant community
		14. Overstorey Foliage Projective Cover (mean) of the plant community
		15. Overstorey structural diversity (i.e. a diversity of age classes) of the stand
	8. Understorey structure	16. Understorey top height (mean) of plant community
		17. Understorey ground cover (mean) of the plant community
		18. Understorey structural diversity (i.e. a diversity of age classes) of the stand
Species composition	9. Overstorey composition	19. Densities of overstorey species functional groups
		20. Richness—number of indigenous overstorey species relative to the number of exotic species
	10. Understorey composition	21. Densities of understory species functional groups
		22. Richness—number of indigenous understorey species relative to the number of exotic species

Source: Thackway (2014)

Condition information is needed to inform regional priorities, to establish policies, and to design and evaluate natural resource management programs for maintaining, restoring and rehabilitating native vegetation assets to improve the health of rivers, wetlands and estuaries, protect degraded landscapes against soil erosion, mitigate against dryland salinity, and improve habitat for Australia's unique native plants and animals.
(Thackway et al., 2015)

Figure 3.3 National VAST-2 dataset

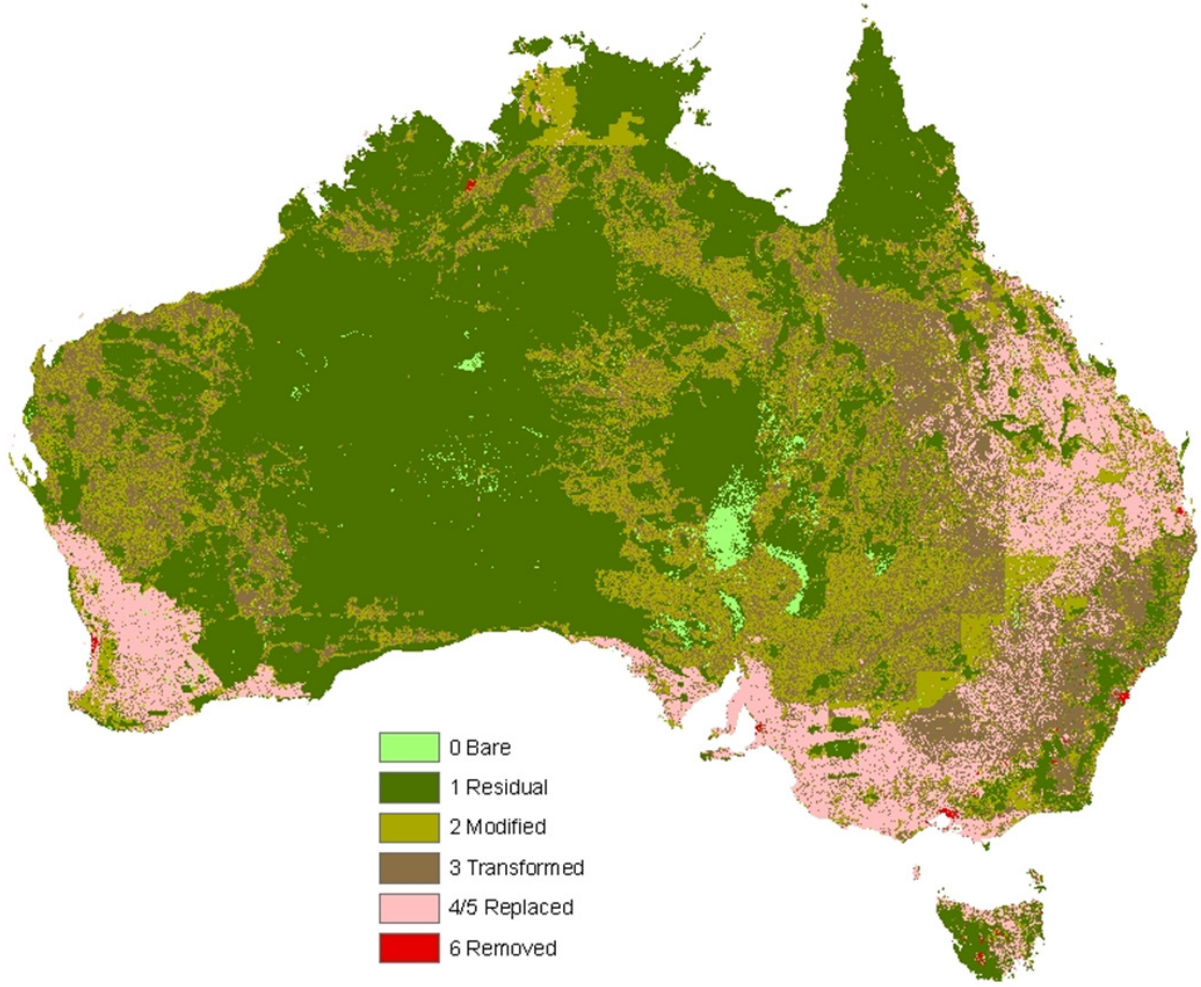

Source: ABARES (2008)

Excursus 3.2—Vegetation Assets, States and Transitions (VAST)

Source: Lesslie *et al.* (2010); Thackway and Lesslie (2006, 2008); Thackway (2014); Thackway and Freudenberger (2016)

VAST classifies vegetation condition by assessing the degree of anthropogenic modification from a benchmark reference state (I) through five states of increasing human modification, where states I, II, and III represent native vegetation cover and states IV, V, and VI represent non-native vegetation cover. The VAST framework includes reporting the condition of native vegetation at regional and national scales, accounting for changes in the status and condition of vegetation, and describing the consequences of land management on vegetation condition (Thackway and Lesslie, 2006). VAST-2 (VAST Version 2) vegetation condition classes were developed from national spatial datasets (1995 to 2006) on a 1 km by 1 km grid, in conjunction with an expert model comparing land management effects relative to a benchmark of pristine vegetation condition (assumed pre-1750; Lesslie *et al.*, 2010). Primary datasets used were:

- biophysical naturalness disturbance information forming part of the Australian Land Disturbance Database (ALDD; previously known as the National Wilderness Inventory, NWI; Lesslie and Maslen, 1995); updated in temperate forested environments in the Comprehensive Regional Assessment and Regional Forest Agreement (CRA–RFA) process (JANIS, 1997) ;
- land use datasets developed by the Australian Collaborative Land Use Mapping Program (BRS, 2006; Lesslie *et al.*, 2006);

- bare ground cover derived from MODIS satellite imagery (2004); and
- native vegetation extent baseline (2004) compiled from datasets collected by the states and territories (Thackway *et al.*, 2010).

For example, a study by Thackway and Freudenberger (2016) selected ten sites that are representative of Australia's agroclimatic regions (see Section 2.2.3), to systematically examine the response of plant communties to land management regimes over the past 250 years. The VAST framework was used to track changes in regenerative capacity, vegetation structure, species composition, and overall vegetation status. To demonstrate the information that can be derived from such analyses, Table 3.9 summarises relevant information for three of these sites. The impact of fragmentation and the extent of site modification for all ten sites are summarised in Figure 3.4.

All sites observed in this study occurred in intact landscapes during the early stages of rural development. While site 1 currently represents an intact landscape (> 90% vegetation retained and mostly unmodified), site 7 occurs in a variegated landscape (60–90% native vegetation retained, but mostly modified), and site 3 occurs in a relictual landscape (< 10% native vegetation retained). These condition assessments can be translated to estimates of the resilience of each site, from highest for site 1, to medium for site 7, to lowest for site 3. This type of landscape model is valuable for monitoring and reporting vegetation changes with a view to better understanding ecosystem resilience. Such understanding will allow appropriate management interventions to be prioritised for sites with low resilience and thus avoid further degradation into the future.

Table 3.9 Selected site attributes

Vegetation condition dynamics indicate status score of change relative to reference state.

Attribute	Site Reference Number		
	1. Rocky Valley, Bogong High Plains	2. Wirilda, Harrogate	3. Conkerberry Paddock, Victoria River Research Station
Agroclimatic region	Cold-wet	Mediterranean	Tropical warm season wet
Bioregion	Victorian Alps (Victoria)	Kanmantoo (SA)	Ord Victoria Plain (NT)
Plant community	*Poa* tussock grassland	*Callitris*, eucalypt low mallee woodland	Eucalypt open woodland
Vegetation condition dynamics	10% loss due to livestock grazing then recovery to near reference conditions	70% loss due to clearing, then significant recovery by active restoration	50% loss due to livestock and feral herbivore grazing with modest recovery due to improved grazing management and increasing woody cover due to climate change
Government policies	State government reduction, then prohibition of livestock grazing, then creation of a national park	Various regulations that required clearing, then fertiliser subsidies to increase intensification More recently, agri-environmental schemes support farmers to restore native vegetation	Government-managed livestock reserve, and subsidies for artificial watering points and fencing, then research into improved range management
Markets	Rapid development of national and international markets for meat and wool	Domestic and international demand for grains, meat and wool	Domestic and particularly international demand, including live cattle exports
Technological changes	Domestic livestock	Broadscale cropping and exotic pasture systems, domestic livestock, fencing, and feral rabbits No till cropping into dormant native pasture with cell-based sheep grazing	Artificial watering points (bores), then fencing to improve grazing management, improved roads and transport, introduction of *Bos indicus* breeds of cattle
Climate variation	Periods of drought that increased livestock grazing pressure on alpine grassland	Drought and wildfire were a stimulus for land management change coupled with localised rising groundwater that was saline.	Large seasonal fluctuations in rainfall affecting livestock and feral herbivore numbers, but overall increasing rainfall over a longer season
Cultural	Total indigenous displacement by Western European values and land management practices	Total indigenous displacement by Western European values and land management practices	Total indigenous displacement by Western European values and land management practices; a conditional land claim was granted in 1990, enabling continued use of the area as a research station

Source: Thackway and Freudenberger (2016) Tables 3 and S1

Figure 3.4 Landscape change summary

Both the landscape alteration levels and VAST classes are shown for ten sites.

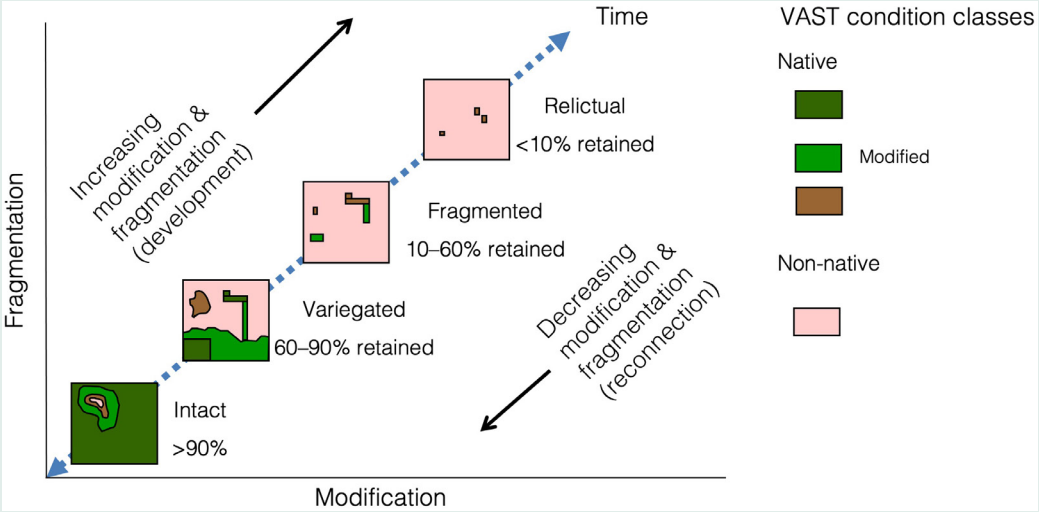

Source: Thackway and Freudenberger (2016) Figure 12

3.4.2 Changes in land use

The diversity of land use activities being undertaken in Australia is introduced in Sections 2.5.3 and 3.3.4. Information about land use change is needed to determine trends in agricultural activities and assess the management of natural resources, both in terms of regional and national changes (Lesslie and Mewett, 2013). Land use changes can have long term impacts on agricultural sustainability, food security, water availability, air quality, and biodiversity, all of which need to be monitored in terms of their social, economic and environmental consequences (Lesslie *et al.*, 2011). Thoughtful reviews of various aspects of land use practices and policies in Australia are presented in Thackway (2018).

Some of the drivers for changing land uses have been summarised as:

- resource scarcity leading to an increase in the pressure of production on resources;
- changing opportunities created by markets (such as production, infrastructure and transport costs);
- outside policy intervention (such as subsidies, taxes, property rights, infrastructure, governance);
- loss of adaptive capacity and increased vulnerability (such as exposure to natural hazards); and
- change in social organisation, attitudes, and access to resources (Lambin *et al.*, 2003).

Specific examples of events and conditions in each of these driver categories are listed in Table 3.10.

Land use and land use change are central to our understanding of human impacts on the environment (Clancy et al., 2018)

Table 3.10 Drivers of land use change

Driver	Example events and conditions determining rate of change	
	Slow	Fast
Resource scarity	Natural population growth Inappropriate land uses reduce land productivity Degraded environmental resources	Forced population displacement (e.g. refugees) Allocation of previously productive land to other land uses
Market changes	Increased commercialisation and agro-industrialisation Improved access to land (e.g. new roads) Changes in prices of inputs/outputs Alternative employment opportunites	Capital investment in new land use(s) Price changes due to macro economics or trade conditions New technologies for intensification of resource use New commodities and land use activities
Government intervention	Economic development programs Inappropriate subsidies, taxes, price distortions, incentives Poor governance and corruption Insecurity of land tenure	Rapid policy changes (e.g. devaluation) Government instability War
Increased vulnerability	Impoverishment; Increased dependence on welfare Social discrimination	Internal conflicts Epidemics Natural hazards
Social changes	Institutional changes in resource management Increased urbanisation Extended family breakdown Increased materialism Reduced public awareness of environmental degradation	Expropriation of communal resources and/or private property Ecological marginalisation of the poor

Adapted from: Lambin *et al.* (2003) Table 4 and Thackway (2018)

Specific approaches to land use monitoring will vary with the intended end use and the spatial and temporal resolutions of available data. Most land use change reporting by ABARES, for example, relies on the ALUM time series (see Sections 2.5.3 and 3.3.4) and agricultural statistics from the Australian Bureau of Statistics (ABS; Mewett *et al.*, 2013). While ACLUMP aims for 80% accuracy in overall spatial and thematic attributes when a land use map is released (ABARES, 2015), this accuracy will inevitably reduce with time as land uses change.

Approaches that may be used to maintain the accuracy of land use maps include:

- update all areas at appropriate intervals (such as every five years for intensive agriculture regions and every ten years for pastoral and rangelands areas);
- use authoritative ancillary datasets to update specific land uses and/or regions as needed; or
- prioritise areas to update based on assessed likelihood of land use changes (see Figure 3.5; ABARES, 2015).

EO datasets are being used by some Australian state land use mapping agencies (e.g. QLUMP, 2017; Lawrence *et al.*, 2018) to identify areas of change in land use and land cover annually. Only those areas identified as changed are then updated in the relevant land use maps (ABARES, 2015; Hicks, 2018).

Land use planning has never been widely popular in democracies, as it is seen to impinge on the rights of the individual. However, a shift from rights to responsibilities is long overdue.
(Henry Nix, 2018)

Figure 3.5 Likelihood of ALUM land use change

These likelihoods are based on a national assessment, and will vary by region.

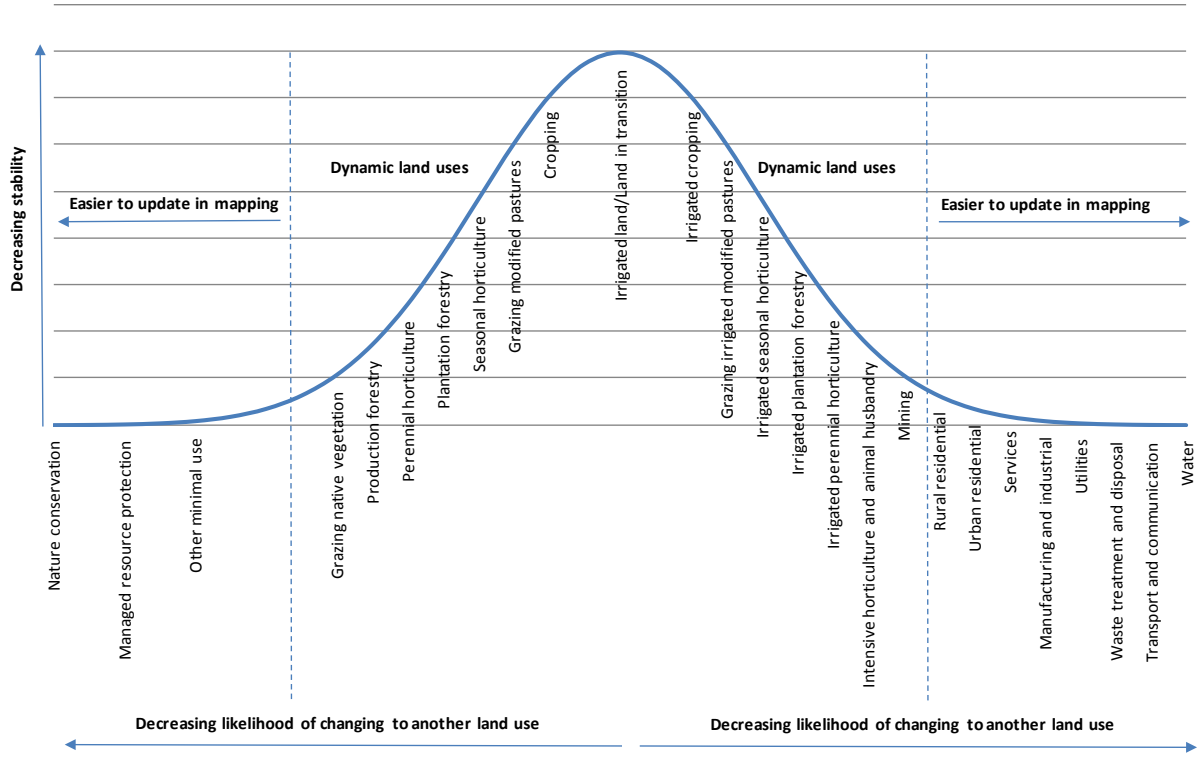

Source: ABARES (2015) Figure 4

The patterns of land use change can be variously described in terms of:

- area—spatial extent;
- productivity—efficiency associated with converting inputs to outputs;
- intensification—increased consumption of inputs (such as nutrients, water, and energy); and
- innovation—improvements aimed at 'better' outcomes such as greater productivity, more efficient use of inputs, or reduced degradation of landscape (Lesslie *et al.*, 2011).

For example, the intensification of agricultural land use, expressed in terms of the cost of production per unit area during the two decades from 1985/86 to 2005/06, was mapped by Leslie *et al.* (2011; see map 4).

Monitoring of land use change is closely coupled to monitoring of land cover (see Section 3.1.2) and increasingly relies on the use of EO datasets in combination with cadastre and ancillary spatial datasets. For example, ABARES coordinated a national Ground Cover Monitoring project that developed the Fractional Cover Product (see Excursus 8.3) to monitor soil erosion, and ultimately management practices, in cropped areas of Australia.

In combination with historical land use patterns, and datasets tracking climatic variables, such products may eventually enable the development of methods for forecasting land use changes, and thereby improve our understanding of resource utilisation across Australia. Spatial Decision Support Systems (DSS), such as the Multi-Criteria Analysis Shell for Spatial Decision Support (MCAS-S, 2018; Lesslie, 2013; Lesslie *et al.*, 2008), will assist this process by manipulating vast quantities of spatial data and highlighting the relevance of their patterns and interactions. To maximise the capabilities of available resources and best serve the interests of relevant stakeholders in Australia, an organising framework has been proposed to integrate land use and land resources information within a virtual centre (Clancy and Lesslie, 2013; Clancy *et al.*, 2018). Such an integrated framework would greatly simplify the process of monitoring land use changes in Australia.

3.5 Further Information

Australian Land Use

Land use data downloads: *https://www.agriculture.gov.au/abares/aclump/land-use/data-download*

ALUM (Australian Land Use and Management Classification system): *http://www.agriculture.gov.au/abares/aclump/land-use/alum-classification*

CLUM (Catchment scale Land Use for Australia): *https://www.agriculture.gov.au/abares/aclump/land-use/catchment-scale-land-use-of-australia-update-december-2018*

Australian Vegetation

NVIS: *https://www.environment.gov.au/land/native-vegetation/national-vegetation-information-system*

Major Vegetation Groups (based on NVIS): *https://data.gov.au/data/dataset/57c8ee5c-43e5-4e9c-9e41-fd5012536374*

New South Wales Vegetation/Land Cover

Bionet: *http://www.bionet.nsw.gov.au/*

SEED (NSW): *https://www.seed.nsw.gov.au*

SVTM: *https://www.environment.nsw.gov.au/vegetation/state-vegetation-type-map.htm*

Victoria Vegetation/Land Cover

Habitat Hectares: Parkes *et al.* (2003); McCarthy *et al.* (2004);

https://www.environment.vic.gov.au/native-vegetation/native-vegetation/biodiversity-information-and-site-assessment

https://www.ari.vic.gov.au/research/modelling/mapping-vegetation-extent-and-condition

EO-based Study of Land Cover Change

Graetz, D., Fisher, R., and Wilson, M. (1992). *Looking Back: The Changing Face of The Australian Continent, 1972–1992.* CSIRO Division of Wildlife and Ecology, Canberra.

Interactive Maps for Australian Resources

National Map: *https://nationalmap.gov.au/*

NEII (National Environmental Information Infrastructure): *http://neii.gov.au/data-viewer*

AURIN (Australian Urban Research Infrastructure Network): *https://map.aurin.org.au*

AREMI (Australian Renewable Energy Agency): *https://nationalmap.gov.au/renewables/*

Investor Map (locates opportunities for mining, tourism and agriculture): *https://nationalmap.gov.au/investormap/*

State of Environment maps: *https://soe.terria.io*

NRM Tools

FarmMap4D Spatial Hub (formerly NRM Spatial Hub; see Volume 1B—Excursus 10.4): *https://www.farmmap4d.com.au/*

VegMachine: *https://vegmachine.net/* (see Excursus 15.1 below)

Earth Observation Data for EcoSystem Monitoring (EODESM)

EODESM classifies land cover and change by combining essential environmental descriptors using the FAO LCCS taxonomy: *https://www.ecopotential-project.eu/products/eodesm.html*

Global Land Cover and Ecosystem Products

NASA Land Cover/Land Use Change Program (LCLUC): *https://lcluc.umd.edu/*

GLC2000: Global Land Cover 2000 database. European Commission, Joint Research Centre, 2003. *http://forobs.jrc.ec.europa.eu/products/glc2000/data_access.php*

GlobCover: *http://due.esrin.esa.int/page_globcover.php*

MODIS Land Cover: *http://glcf.umd.edu/data/lc/*

Sayre *et al.* (2020)

IUCN Red List of Ecosystems (RLE) Global Ecosystems Typology: *https://iucnrle.org/about-rle/ongoing-initiatives/global-ecosystem-typology/*

3.6 References

ABARES (2008). *National Scale Vegetation Assets, States and Transitions (VAST Version 2)—2008*. Australian Bureau of Agricultural and Resource Economics and Sciences, Department of Agriculture and Water Resources. *http://data.daff.gov.au/anrdl/metadata_files/pa_vast_g9abll0032008_11a.xml*

ABARES (2010). *Land Use and Land Management Information for Australia. Workplan of the Australian Collaborative Land Use and Management Program*. Australian Bureau of Agricultural and Resource Economics and Sciences, Canberra.

ABARES (2011). *Guidelines for land use mapping in Australia: principles, procedures and definitions*. 4th edn. Australian Bureau of Agricultural and Resource Economics and Sciences, Canberra.

ABARES (2015). *Addendum to the guidelines for land use mapping in Australia: Principles, procedures and definitions* 4th edn. Australian Bureau of Agricultural and Resource Economics and Sciences, Canberra, ACT. *http://data.daff.gov.au/data/warehouse/pe_abares99001806/AddendumGuidelinesLandUseMapping2015_v1.0.0.pdf*

ABARES (2016). *The Australian Land Use and Management Classification Version 8*. Australian Bureau of Agricultural and Resource Economics and Sciences, Canberra.

ANRA (2009). *Australian Natural Resources Atlas*. *www.anra.gov.au*

AUSLIG (1990). *Atlas of Australian Resources (Third Series) Volume 6*: Vegetation. Australian Land and Surveying Information Group, AUSMAP, Department of Administrative Services, Canberra. 64 p.

Avery, T.E. (1975). *Natural Resources Measurements* 2nd edn. McGraw-Hill, New York.

Bartholomé, E., and Belward, A.S. (2007). GLC2000: a new approach to global land cover mapping from Earth Observation data. *International Journal of Remote Sensing*, 9, 1959–1977. *doi.org/10.1080/01431160412331291297*

Beard, J.S., and Webb, M.J. (1974). *Vegetation Survey of Western Australia: Great Sandy Desert—Part I. Aims, Objectives and Methods*. University of Western Australia Press, Nedlands, WA.

Bontemps, S., Defourny, P., Van Bogaert, E., Arino, O., Kalogirou, V., and Perez, J.R. (2011). *Globcover 2009. Products Description and Validation Report*. ESA/UCL. *http://due.esrin.esa.int/files/GLOBCOVER2009_Validation_Report_2.2.pdf*

BRS (2006). *Guidelines for Land Use Mapping in Australia: Principles, Procedures and Definitions*. 3rd edn. Bureau of Rural Sciences, Canberra.

Butler, D., Thackway, R., and Cosier, P. (2020). *Technical Protocol for Constructing Native Vegetation Condition Accounts Version 1.0 - May 2020*. Accounting for Nature Limited, Sydney, Australia. *https://static1.squarespace.com/static/5dc38cde1d028031235ca3cf/t/5fa246b73c71c92e01513cc7/1604470479988/AfN+Native+Vegetation+Technical+Protocol+ACCREDITED.pdf*

Carnahan, J.A. (1976). Natural Vegetation map with commentary. *Atlas of Australian Resources, Second Series*. Department of Natural Resources, Canberra.

Carnahan, J.A. (1988). Present Vegetation map. In *Atlas of Australian Resources, Second Series*. Department of Natural Resources, Canberra.

Christian, C.S., and Stewart, G.A. (1953). *General report on survey of Katherine-Darwin region, 1946*. CSIRO, Melbourne.

Christian, C.S., and Stewart, G.A. (1968). Methodology of integrated surveys. In *Aerial surveys and integrated studies. Proceedings of Toulouse Conference of 1964*. UNESCO, Paris.

Cihlar, J. (2000). Land cover mapping of large areas from satellites: Status and research priorities, *International Journal of Remote Sensing*, 21, 1093–1114.

Clancy, T.F., and Lesslie, R.G. (2013). *A needs assessment for a national research centre addressing land use and food security issues*. ABARES Report to client prepared for the International Agricultural Cooperation Program, Trade and Market Access Division of the Department of Agriculture, Canberra.

Clancy, T., Bryan, B.A., and Guru, S.M. (2018). The Future for Land Use Mapping: National E-Infrastructure, Modelling Analytics, Synthesis and Securing Institutional Capacity. Ch. 10 in *Land Use in Australia: Past, Present and Future*. (Ed: Thackway, R.). ANU eVIEW, Canberra. ISBN: 9781921934421

Cresswell, I., and Thomas, G. (1997). *Terrestrial and Marine Protected Areas in Australia (1997)*. Environment Australia, Biodiversity Group, Canberra.

CSIRO (2014). *Australian Soil Resource Information System*. *www.asris.csiro.au*

DAWE (2020a). *Australia's bioregions (IBRA)* webpage, Department of Agriculture, Water and the Environment website: *https://www.environment.gov.au/land/nrs/science/ibra*

DAWE (2020b). *Catchment scale land use for Australia—Update December 2018* webpage, Department of Agriculture, Water and the Environment website: *https://www.agriculture.gov.au/abares/aclump/land-use/catchment-scale-land-use-of-australia-update-december-2018*

DAWE (2020c). *Australian Land Use and Management Classification Version 8 (October 2016)* webpage, Department of Agriculture, Water and the Environment website: *https://www.agriculture.gov.au/abares/aclump/land-use/alum-classification*

DE (2012). *Australia—Present Major Vegetation Groups: NVIS Version 4.1 (Albers 100m analysis product)*. Bioregional Assessment Source Dataset, Department of the Environment. *http://data.bioregionalassessments.gov.au/dataset/57c8ee5c-43e5-4e9c-9e41-fd5012536374*.

DeFries, R.S., and Belward, A.S. (2000). Global and regional land cover characterization from satellite data: An introduction to the special issue. *International Journal of Remote Sensing*, 21, 1083–1092.

Di Gregorio, A. (2005). *Land Cover Classification System: Classification Concepts and User Manual. Software version 2*. FAO Environment and Natural Resources Service Series, No. 8. FAO, Rome. 208 p.

Di Gregorio, A. (2016). *Land Cover Classification System Software version 3*. FAO, Rome. ISBN 978-92-5-109017-6 *http://www.fao.org/3/a-i5232e.pdf*

Di Gregorio, A., and Jansen, L.J.M. (2000). *Land Cover Classfication System (LCCS): Classification Concepts and User Manual*. FAO. ISBN 92-5-104216-0 *http://www.fao.org/3/x0596e/X0596e00.htm#P-1_0*

EcoPotential (2021). *EODESM: Earth Observation Data for Ecosystem Monitoring* webpage, EcoPotential website: *http://www.ecopotential-project.eu/products/eodesm.html*

Fisher, P., Comber, A.J., and Wadsworth, R. (2005). Land Use and Land Cover: Contradiction or Complement. In *Representing GIS*. (Eds: R. Fisher and D. Unwin). John Wiley and Sons Ltd.

Gammage, B. (2012). *The Biggest Estate on Earth*. Allen and Unwin, Sydney.

GEO (2012). *Task US-09-01a: Critical Earth Observation Priorities*. Final Report (2nd edition). Group on Earth Observations. *https://www.wmo.int/pages/prog/sat/meetings/documents/ARCH-3_Inf_02_GEO-US-09-01a-final-report.pdf*

Graetz, D., Fisher, R., and Wilson, M. (1992). *Looking Back. The changing face of the Australian continent, 1972–1992*. CSIRO, Canberra.

Grekousis, G., Mountrakis, G., Kavouras, M. (2015). An overview of 21 global and 43 regional land-cover mapping products. *International Journal of Remote Sensing*, 36(21), 5309–5335. *doi.org/10.1080/01431161.2015.1093195*

Harrison, B.A., and Jupp, D.L.B. (1989) *Introduction to Remotely Sensed Data: Part ONE of the microBRIAN Resource Manual*. CSIRO, Melbourne. 156 p.

Hicks, R. (2018). Responding to Land Use Pressures: A State and Territory Perspective. Ch. 6 in *Land Use in Australia: Past, Present and Future*. (Ed: Thackway, R.). ANU eVIEW, Canberra. ISBN: 9781921934421

IGBP (1990). *The International Geosphere–Biosphere Programme: A study of global change—The initial core projects. IGBP Global Change Report no. 12*. International Geosphere–Biosphere Programme, Stockholm, Sweden.

IUCN (2008). *Guidelines for applying protected area management categories*. International Union for Conservation of Nature, Switzerland. *http://www.iucn.org/sites/dev/files/import/downloads/iucn_assignment_1.pdf*.

JANIS (1997). *Nationally Agreed Criteria for the Establishment of a Comprehensive, Adequate and Representative Reserve System for Forests in Australia*. A report by the Joint ANZECC–MCFFA, National Forest Policy Statement Implementation Sub-committee. Commonwealth of Australia, Canberra. 20 p.

Kessell, S.R. (1979). *Gradient Modelling: Resource and Fire Management*. Springer-Verlag, New York.

Lambin, E.F., Geist, H.J., and Lepers, E. (2003). Dynamics of land-use and land-cover change in tropical and subtropical regions. *Annual Review of Environmental Resources*, 28, 205–241.

Lambin, E.F., and Geist, H.J. (Eds) (2006). *Land-Use and Land-Cover Change: Local Processes and Global Impacts*. The IGBP Series. Springer-Verlag, Berlin.

Land and Water Australia (2009). *National Land and Water Audit*. *http://lwa.gov.au/programs/national-land-and-water-resources-audit*

Lawrence, P., Shephard, C., Norman, P., Jones, C., and Witte, C. (2018). Monitoring and Reporting Land Use Change and Its Effects on the Queensland Environment. Ch. 13 in *Land Use in Australia: Past, Present and Future*. (Ed: Thackway, R.). ANU eVIEW, Canberra. ISBN: 9781921934421

Lesslie, R. (2013). Mapping our priorities—innovation in spatial decision support. In *Innovation for 21st century conservation* (Eds: P. Figgis, J. Fitzsimons and J. Irving). Australian Committee for the International Union of Conservation of Nature, Sydney, NSW. pp. 156–163.

Lesslie, R.G, and Maslen, M.A. (1995). *National wilderness inventory Australia : handbook of procedures, content, and usage*. AGPS, Canberra.

Lesslie, R., and Mewett, J. (2013). *Land use and management: The Australian context*. Australian Bureau of Agricultural and Resource Economics and Sciences Research Report 13.1. Canberra, ACT.

Lesslie, R., Barson, M., and Smith, J. (2006). Land use information for integrated natural resources management—a coordinated national mapping program for Australia. *Journal of Land Use Science*, 1(1), 45–62.

Lesslie, R.G., Hill, M.J., Hill, P., Cresswell, H.P., and Dawson, S. (2008). The application of a simple spatial multi-criteria analysis shell for natural resource management decision making. In *Landscape analysis and visualisation: Spatial models for natural resource management and planning*. (Eds: C. Pettit, W. Cartwright, I. Bishop, K. Lowell, D. Pullar and D. Duncan). Springer, Berlin. pp. 73–96. *doi.org/10.1007/978-3-540-69168-6_5*

Lesslie, R., Thackway, R., and Smith, J. (2010). *A national-level Vegetation Assets, States and Transitions (VAST) dataset for Australia (version 2.0)*. Bureau of Rural Sciences, Canberra. ISBN 978-1-921192-48-7

Lesslie, R., Mewett, J., and Walcott, J. (2011). *Landscapes in transition: Tracking land use change in Australia. Science and Economic Insights, 2.2*. Australian Bureau of Agricultural and Resource Economics and Sciences, Canberra, ACT.

Lucas, R., Mueller, N., Siggins, A., Owers, C., Clewley, D., Bunting, P., Kooymans, C., Tissott, B., Lewis, B., Lymburner, L., and Metternicht, G. (2019). Land Cover Mapping using Digital Earth Australia. *Data*, 4, 143. doi:*10.3390/data4040143*

Lymburner, L., Tan, P., Mueller, N., Thackway, R., Thankappan, M., Islam, A., Lewis, A., Randall, L., and Senarath, U. (2011). *The National Dynamic Land Cover Dataset - Technical report*. Record 2011/031. Geoscience Australia, Canberra. ISBN 978-1-921954-30-6 *http://cmi.ga.gov.au/dlcd_25_1.0.0*

Mabbutt, J.A. (1968). Review of concepts of land classification. In *Land Evaluation* (Ed: A.G. Stewart) Macmillan, Melbourne. pp 11–28.

McCarthy, M.A., Parris, K.M., van der Ree, R., McDonnell, M.J., Burgman, M.A., Williams, N.S.G., McLean, N., Harper, M.J., Meyer, R., Hahs, A., and Coates, T. (2004). The habitat hectares approach to vegetation assessment: An evaluation and suggestions for improvement. *Ecological Management and Restoration*, 5(1), 24–27.

Malthus, T.J., Barry, S., Randall, L.A., McVicar, T., Bordas, V.M., Stewart, J.B., Guerschman, J.-P., and Penrose, L. (2013). *Ground cover monitoring for Australia: Sampling strategy and selection of ground control sites*. CSIRO, Australia.

MCAS-S (2018). *Multi-criteria analysis (MCAS-S)* webpage: *http://www.agriculture.gov.au/abares/aclump/multi-criteria-analysis*

McKenzie, N.J., Jacquier, D.W., Maschmedt, D.J., Griffin, E.A., and Brough, D.M. (2012). *The Australian Soil Resource Information System (ASRIS) Technical Specifications Revised Version 1.6*, June 2012. The Australian Collaborative Land Evaluation Program. *http://www.asris.csiro.au/downloads/ASRIS%20Tech%20Specs%201.6.pdf*

Mewett, J., Paplinska, J., Kelley, G., Lesslie, R., Pritchard, P., and Atyeo, C. (2013). *Towards national reporting on agricultural land use change in Australia*. ABARES technical report, Canberra.

NASA (1999). *BigFoot. Characterizing Land Cover, LAI, and NPP at the Landscape Scale for EOS/MODIS Validation. Field Manual Version 2.1*. National Aeronautics and Space Administration, ORNL/TM-1999/216.

NCST (2009). *Australian Soil and Land Survey Field Handbook*. 3rd edn. National Committee on Soil and Terrain, CSIRO, Canberra. 26 pp.

Nix, H. (1982). Environment determinants of biogeography and evolution in Terra Australis. In *Evolution of the Flora and Fauna of Arid Australia*. (Eds: W.R. Barker and P.J.M. Greenslade). Peacock Publications, Frewville. pp. 47–66.

Nix, H. (2018). Foreward in *Land Use in Australia: Past, Present and Future*. (Ed: Thackway, R.). ANU eVIEW, Canberra. ISBN: 9781921934421

NLP (2017). *The Report on the Review of the National Landcare Program*. Commonwealth of Australia.

NLP (2019). *National Landcare Program Phase One* webpage: *http://www.nrm.gov.au/national-landcare-programme/phase-one*

NLWRA (2001). *Australian Native Vegetation Assessment 2001*. National Land and Water Resources Audit, Land and Water Australia, Canberra. ISBN: 0 642 37128 8

NRM (2019a). *What is NRM?* webpage, NRM Regions Australia website: *http://nrmregionsaustralia.com.au/what-is-nrm/*

NRM (2019b). *NRM regional model* webpage, NRM Regions Australia website: *http://nrmregionsaustralia.com.au/nrm_regional_model/*

NVIS Technical Working Group (2017). *Australian Vegetation Attribute Manual: National Vegetation Information System, Version 7.0*. (Eds: Bolton, M.P., deLacey, C., and Bossard, K.B.). Department of the Environment and Energy, Canberra.

Olson, D.M., Dinerstein, E., Wikramanayake, E.D., Burgess, N.D., Powell, G.V.N., Underwood, E.C., D'Amico, J.A., Itoua, I., Strand, H.E., Morrison, J.C., Loucks, C.J., Allnutt, T.F., Ricketts, T.H., Kura, Y., Lamoreux, J.F., Wettengel, W.W., Hedao, P., and Kassem, K.R. (2001). Terrestrial ecoregions of the world: a new map of life on Earth. *Bioscience*, 51(11), 933–938.

Parkes, D., Newell, G., and Cheal, D. (2003). Assessing the quality of native vegetation: The 'habitat hectares' approach. *Ecological Management and Restoration*, 4, S29–S38.

QLUMP. (2017). *Queensland land use mapping program (QLUMP)*. Queensland Government. *https://www.qld.gov.au/environment/land/management/mapping/statewide-monitoring/qlump*

Sayre, R., Karagulle, D., Frye, C., Boucher, T., Wolff, N.H., Breyer, S., Wright, D., Martin, M., Butler, K., Van Graafeiland, K., Touval, J., Sotomayor, L., McGowan, J., Game, E.T., and Possingham, H. (2020). An assessment of the representation of ecosystems in global protected areas using new maps of World Climate Regions and World Ecosystems. *Global Ecology and Conservation*, 21, e00860. *https://doi.org/10.1016/j.gecco.2019.e00860*

Sbrocchi, C. (2013). *Guidelines for Constructing Regional Environmental (Asset Condition) Accounts: Quick Guide*. Wentworth Group of Concerned Scientists, Sydney.

Specht, R.L. (1970). Vegetation in *The Australian Environment*. 4th edn. (Ed: Leeper, G.W.). CSIRO, Melbourne.

TERN Australia (2018). *Effective Field Calibration and Validation Practices: A practical handbook for calibration and validation satellite and model-derived terrestrial environmental variables for research and management*. A TERN Landscape Assessment Initiative, NCRIS. ISBN 978-0-646-94137-0. *https://www.tern.org.au/NEW-CalVal-handbook-for-remote-sensing-bgp4370.html*

Thackway, R. (Ed.) (2018). *Land Use in Australia: Past, Present and Future*. ANU eVIEW, Canberra. ISBN: 9781921934421

Thackway, R., and Cresswell, I.D. (1995). *An Interim Biogeographic Regionalisation for Australia: a Framework for Establishing the National System of Reserves*, Version 4.0. Australian Nature Conservation Agency, Canberra.

Thackway, R., and Lesslie, R. (2006). Reporting vegetation condition using the Vegetation Assets, States, and Transitions (VAST) framework. *Ecological Management and Restoration*, 7(1), 53–62.

Thackway, R., and Lesslie, R. (2008). Describing and mapping human-induced vegetation change in the Australian landscape. *Environmental Management*, 42, 572–590.

Thackway, R., Wilson, P., Hnatiuk, R., Bordas, V., and Dawson, S. (2010). *Establishing a national baseline (2004) to assess change in native vegetation extent*. Bureau of Rural Sciences, Canberra.

Thackway, R. (2014). VAST-2 Tracking the Transformation of Vegetated Landscapes, *Handbook for Recording Site-based Effects of Land Use and Land Management Practices on the Condition of Native Plant Communities*, version 3.0. The University of Queensland, Brisbane. 35 p.

Thackway, R., Cosier, P., McIntosh, E., Saunders, D., Possingham, H., and Sbrocchi, C.D. (2015). *Draft Protocol for Constructing a Native Vegetation Condition Account*. Australian Regional Environmental Accounts Working Paper Series (1/5). Wentworth Group of Concerned Scientists, Sydney.

Thackway, R., and Freudenberger, D. (2016). Accounting for the drivers that degrade and restore landscape functions in Australia. *Land*, 5(4), 40. *doi.org/10.3390/land5040040*

Townshend, J.R. (1992). Land Cover. *International Journal of Remote Sensing*, 13(6–7), 1319–1328.

Walker, B. (2020). Resilience: what it is and is not. *Ecology and Society*, 25(2), 11. *https://doi.org/10.5751/ES-11647-250211*

Walker, J., and Hopkins, M.S. (1990). *Vegetation. Australian Soil and Land Survey Handbook: Guidelines for Conducting Surveys*. (Eds: R.H. Gunn, J.A. Beattie, R.E. Reid and R.H.M. v.d. Graaff). Inkata Press, Melbourne. pp 58–86.

Williams, R.J. (1959). Vegetation map of Australia in *The Australian Environment*. 3rd edn. CSIRO, Melbourne. Reproduced with changed legend in *The Australian Environment*. 4th edn (Ed: G.W. Leeper, 1970). CSIRO, Melbourne.

Wulder, M.A., Coops, N.C., Roy, D.P., White, J.C., and Hermosilla, T. (2018). Land cover 2.0. *International Journal of Remote Sensing*, 39(12), 4254–4284. doi:*10.1080/01431161.2018.1452075*

Yang, H., Li, S., Chen, J., Zhang, X., Xu, S.(2017). The standardization and harmonization of land cover classification systems towards harmonized datasets: a review. *International Journal of Geo-Information,* 6, 154–170.

Measurable Properties of Terrestrial Vegetation

Most of the terrestrial surfaces on Earth are covered by vegetation of some description. Given that waterbodies cover over 70% of the Earth's surface (see Volume 3B), vegetation has been estimated to cover some 20% of the total surface of our planet.

An enormous diversity of vegetation exists on Earth, exhibiting major differences in appearance, life cycle, and growth requirements (see Section 1.3.2). Different plants are best suited to particular climates and landscapes and most tend to flourish in association with 'friends' and 'healthy competition', forming unique communities of species that are mutually supportive (see Section 1.2). This synergy contributes to recovery from external changes and enriches the environment for other organisms.

Our planet is dynamic at a variety of scales (see Section 1.3.3). The characteristics of vegetation cover on Earth vary not only over space but also with the passage of time. Change can occur in cycles, resulting from natural rhythms related to the movement of the Earth and the Moon relative to the Sun, or as a consequence of 'irregular' events such as natural disasters or anthropogenic activities. Natural changes are fundamental to the Earth's stability and resilience, and enable natural resources to be recycled and sustained. Anthropogenic changes, however, can outstrip the intrinsic timeframes of landscape recovery, so require prudent monitoring and management.

Botany is concerned with classifying and understanding plants (see Excursus 1.1). The characteristics of vegetation that botanists use to identify plants, however, are not necessarily directly related to EO image interpretation. The following sections discuss particular characteristics of individual plants and groups of plants that are relevant to categorising vegetation using EO datasets:

- attributes of foliage (Section 4);
- attributes of individual plants (Section 5);
- attributes of communities (Section 6); and
- attributes of ecosystems (Section 7).

Contents

4 Attributes of Foliage 89

5 Attributes of Individual Plants 107

6 Attributes of Plant Communities 125

7 Attributes of Ecosystems 141

Background image on previous page: Sentinel 2A image over Liverpool Plains, NSW, covering Mt Kaputar. This image was acquired on 15 November 2020 and is displayed using SWIR, NIR and green bands as red, green and blue respectively.
Source: Norman Mueller, Geoscience Australia

4 Attributes of Foliage

Plant leaves are collectively called foliage. Leaves are the primary site for photosynthesis, and occur in a wide variety of colours, sizes, shapes, and textures. Foliage is one of the principal characteristics of vegetation that is used to identify individual species. Several aspects of foliage that are relevant to analysing EO images are discussed in the following sub-sections:

- structure and shape (see Section 4.1);
- chemical composition (see Section 4.2);
- spectral reflectance properties (see Section 4.3); and
- aerodynamic forces (see Section 4.4).

4.1 Structure and Shape

Leaf structure and shape are discussed below in terms of:

- anatomy—internal structure (see Section 4.1.1);
- morphology—external shape and orientation (Section 4.1.2);
- texture—external surfaces (Section 4.1.3); and
- strength—vulnerability to external forces (Section 4.1.4).

4.1.1 Anatomy

A 'typical' plant leaf comprises multiple layers with characteristic functions. As illustrated in Figure 4.1, when traversed from the top surface to the bottom surface, specialised cell types can be distinguished:

- upper epidermis (and often cuticle)—top outer layer with waxy, waterproof coating;
- mesophyll—containing chloroplast and comprising:
  - palisade parenchyma—elongated cells adjacent to epidermis; and
  - spongy mesophyll parenchyma—looser irregular cells bordered by palisade parenchyma; and
- lower epidermis (and often cuticle)—bottom surface with guard cells that open and close stomata (pores) to control transpiration and carbon dioxide (CO_2) exchange (Esau, 1965).

In many plants, the epidermis secretes a waxy coating called the cuticle, which protects the leaf from pests and predators, such as insects and bacteria, and water loss (Yeats and Rose, 2013). The cuticle surface diffuses light and has low reflectivity. Most of the sunlight reaching the cuticle is transmitted through the epidermis to the palisade cells, with shaded leaves having thinner cuticles and shorter palisade cells than leaves in direct sunlight (see Section 4.1.2). The epidermis can contain trichomes (hair cells), which offer further protection against predators and reduce the intensity of sunlight on the leaf (Esau, 1965; see Section 4.1.3).

The palisade mesophyll cells have a high concentration of chloroplasts and act as 'pipes' that direct light towards their pigment molecules for photosynthesis (Croft and Chen, 2017). These cells are generally arranged in rows, with plants growing in full sun having more layers than those growing in shade. In some plants whose leaves hang vertically, such as adult eucalypts, palisade cells are adjacent to both the upper and lower epidermis and thus form a sandwich around the spongy mesophyll cell layer (Evans and Vogelmann, 2006).

Background image: Tropical rainforest foliage. **Source:** © Shutterstock image ID 24807769

Figure 4.1 Typical leaf cell structure

The fine scale structure of an angiosperm leaf featuring the major tissues: the upper and lower epithelia (and associated cuticles); the palisade and spongy mesophyll; and the guard cells of the stoma. Vascular tissue (veins) is not shown. Key plant cell organelles (the cell wall, nucleus, chloroplasts, vacuole, and cytoplasm) are also shown.

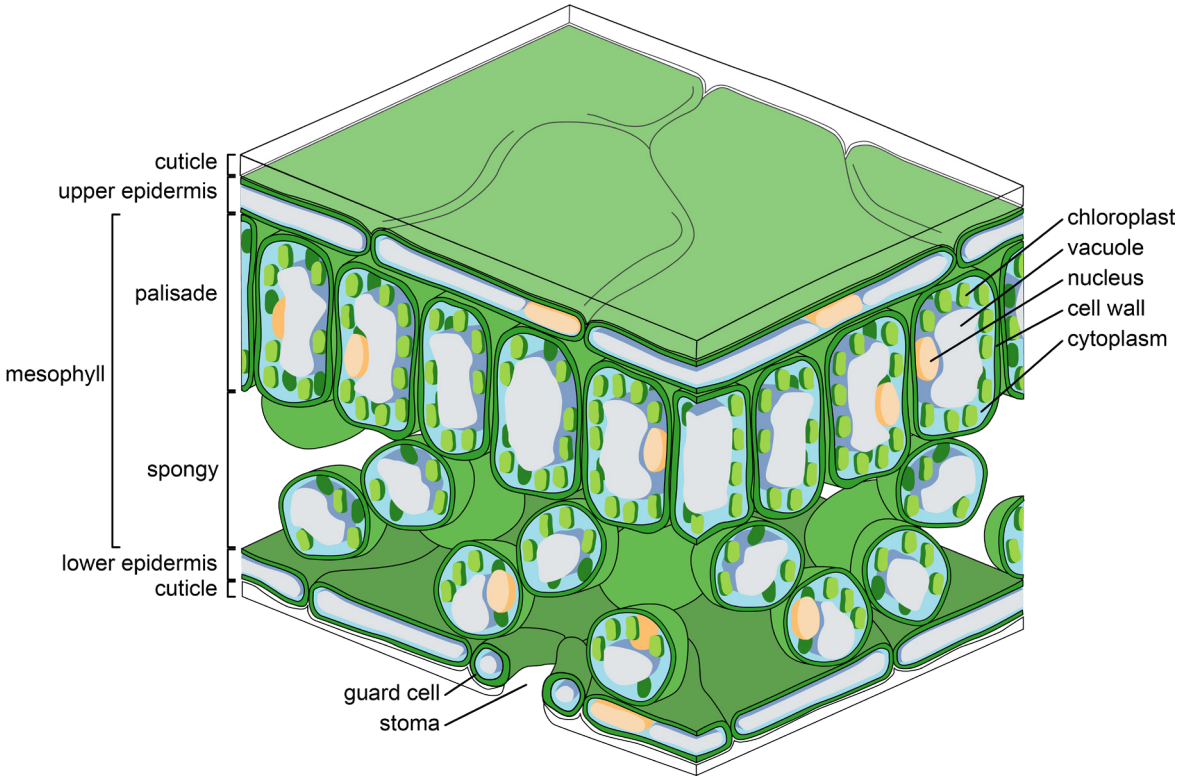

Source: Richard Wheeler, Zephyris, Wikimedia Commons. (Retrieved from *https://en.wikipedia.org/wiki/Leaf#/media/File:Leaf_Tissue_Structure.svg*)

Air spaces between the smaller spongy mesophyll cells allow gas exchange of water vapour, CO_2, and oxygen with the atmosphere via stomata. The guard cells control stomatal opening to conserve water and heat within the leaf. In most plants, stomata are often more numerous on the lower than the upper leaf surface and also in plants from cooler climes (Harrison *et al.*, 2020).

A network of veins throughout the leaf transport food, water, and minerals to and from the rest of the plant. The vein pattern, or venation, of a leaf is characteristic of its species. Veins comprise vascular tissue located within the spongy mesophyll layer. A vein includes two types of conducting cells: xylem, which transports water and minerals from the roots to the leaf; and phloem, which moves photosynthetic products from the leaf to the rest of the plant. These conducting structures are surrounded by a sheath of lignin, which increases leaf rigidity.

The three mechanisms for photosynthesis, namely C_3, C_4, and CAM are introduced in Section 5.2.1. Most plants use C_3 carbon fixation for photosynthesis. Those that use the C_4 or CAM metabolic pathways have slightly different leaf anatomy (Edwards, 2019).

4.1.2 Morphology

Most leaves are flat, but some are folding or bulbous; most are photosynthetic, but in some plants this function has been adopted by other structures, such as cladodes in *Casuarina* species. Leaf allometry considers the impact of the size characteristics of leaves on their anatomy and physiology (Niklas, 1994; John *et al.*, 2013). Some of the major foliage differences that occur between and within plant species include the size of the leaf blade, the overall leaf shape, the extent of dissection into leaflets, the shape on leaf/leaflets margins, the pattern of veins (venation), the size of the leaf stem (petiole), the arrangement and orientation of leaves along a branching stem, and/or the arrangement of leaves on the petiole. The composite impact of leaf shape, size, arrangement, and orientation is particularly relevant to water and light availability (see Section 4.2.2).

A number of plant classification systems rely on plant functional traits (PFT)—"morphological, biochemical, physiological, structural, phenological, or behavioural characteristics that are expressed in phenotypes of individual organisms" (Violle *et al.*, 2007)—rather than their taxonomic characteristics (see

Section 1.1). These traits define the ecological role of species—their interaction with the environment and other species. An understanding of the costs and benefits of these traits also provides insight into vegetation changes along physical geography gradients (Westoby and Wright, 2006). Several PFT have been nominated for this purpose, with simplicity of measurement being an advantage. Below we will consider leaf size, area, shape, and orientation.

Leaf size, measured as the one-sided projected surface area of a fresh leaf (as mm^2), impacts leaf energy production, carbon assimilation, and water balance. Variations in leaf size between species have been related to climatic variation, geology, altitude, and latitude, with environments involving the stresses of heat, cold, drought, and fire showing a preference towards smaller leaves. Plants with larger leaves tend to live in warmer, sunnier, and moister climates, with small leaves offering more control over the loss of heat and water. For a given species, however, shaded leaves tend to become both larger and thinner than their sunlit counterparts, presumably endeavouring to capture more sunlight with a larger surface area (Larcher, 1980). Compound leaves may enable better air exchange over the leaf surface and thus improve the efficiency of heat transfer within a plant (Xu *et al*., 2009). Larger and thicker leaf types are more 'expensive' for the plant to make and maintain, that is they require a greater investment in non-productive infrastructure, so they need to be more durable to justify their production (Milla *et al*., 2008). Similarly, leaf temperature and evaporative demand both increase with leaf size (Gates, 1980; Givnish, 1979).

Specific Leaf Area (SLA) is computed as the ratio of the leaf size to its oven-dry mass (leaf dry matter content) in m^2/kg. It indicates the leaf area available for photosynthesis per unit of biomass and appears to be indicative of the potential relative growth rate of a plant. It is also used to estimate stomatal density. SLA can be expressed as a function of leaf dry matter content (LDMC; see Section 4.2.1) and leaf thickness (Perez-Harguindeguy *et al*., 2013). Lower values of SLA tend to correspond to plants with structural leaf defence mechanisms and high leaf longevity, although SLA is typically lower in evergreen than in deciduous species (Reich *et al*., 1997; Ackerly *et al*., 2002) and in sun leaves compared with shade leaves (Lichtenthaler, 2009). Higher SLA values occur in permanently or temporarily resource-rich environments and also in selected shade-tolerant understorey species. Larger leaves, with a smaller proportion of photosynthetically active material per unit mass, generally have lower SLA than smaller leaves, although variations in this relationship can occur when leaf thickness changes are unrelated to leaf cell density (Milla *et al*., 2008). SLA is considered to be more indicative of resource usage by plants than LDMC in sand dune environments (Li *et al*., 2005) and may be indicative of climate response, CO_2 response, nutrient response, competitive strength, plant defence, and biogeochemical cycles, and related to flammability (Cornelissen *et al*., 2003; Perez-Harguindeguy *et al*., 2013). When CO_2 levels increase, SLA and stomatal density decrease (Juneau and Tarasoff, 2012).

Leaf shape can be considered in terms of the degree of dissection (number of leaflets per leaf) and lobation (number of lobes or segments). One measure of leaf shape and complexity is the Dissection Index (DI), which is standardised to a value of one for a circle (McLellan and Endler, 1998):

$$DI = \frac{\text{perimeter}}{\sqrt{\text{area}}}$$

Leaf shape characteristics have been related to hydraulic resistance in plants (Sisó *et al*., 2001), photosynthetic rates and optimal temperature range (Nicotra *et al*., 2008), and also climatic distribution (Royer *et al*., 2005). Lobation effectively reduces the active leaf area and offers plants particular advantages in terms of controlling water and temperature balance (Williams *et al*., 2004). For example, lobed leaves demonstrate greater efficiency in thermal control in calm weather (Vogel, 1970).

Leaf orientation also differs between species and can vary with plant age. For example, eucalypt seedlings start life with juvenile leaves, which can intercept maximum sunlight for rapid growth. Such leaves are often round and grow horizontally from the plant structure. As the tree matures (at around seven years old) the leaves of most species change form and orientation, becoming long, thin, and pendulous (Jacobs, 1955). With this shape and orientation, adult leaves intercept less solar radiation but conserve moisture, which is essential for survival in many regions of Australia (James and Bell, 2000). Orientation, size, and density of leaves determine their shading value to understorey species and, hence, the extent of cast shadows for a given Sun position. The degree of shading projected by leaves (and stems) can be used to indicate leaf volume as detailed in Section 5.1.2.

4.1.3 Texture

Leaf texture can significantly impact the way light interacts with foliage, and hence its appearance. The surface of a leaf can include a range of textural features, including hairs, spikes, coatings, patterns, and bumps, which modify light reflection properties (Esau, 1965). The flatness of a leaf also affects the way light will reflect and refract from its surface. The texture of the uppermost (adaxial) leaf surface often differs from that of the underside (abaxial). All these factors contribute to the intensity and wavelengths of light reflected by a leaf and also influence the radiation that is allowed to reach underlying vegetation (see Section 4.3).

The texture of a leaf also affects its function in terms of heat transfer, ultraviolet (UV) protection, photosynthetic efficiency, moisture loss, and susceptibility to both biotic and abiotic factors (see Section 1.1). Frost damage can be reduced by leaf coatings and hairs, while some predators can be discouraged by rough and prickly textures. While the propensity of a species towards a particular leaf texture is related to genetic traits, its manifestation in individual plants can be significantly varied by environmental factors (Roy *et al.*, 1999).

The cuticle layer on the epidermis protects the leaf from gaining or losing too much water and from invasion by a range of potential pathogens, such as fungi. This microcrystalline structure mostly comprises waterproof waxes (lipids), but also contains a much smaller proportion of polysaccharide compounds, such as cellulose and pectin, that attract water (hydrophilic). Microfibrils into the leaf selectively transport water and mineral salts between the leaf surface and internal tissues (Popp *et al.*, 2005), thus avoiding excessive leaching of plant metabolites in damp environments. This structure also allows the leaf to release volatile solutions to deter pests or attract insects. Natural leaf coatings can vary in thickness and appear shiny, glaucous, rough, or smooth. Various leaf coatings for crop protection are based on disguising or enhancing the natural leaf surface (Walters, 2006).

Hairs on plant leaves can vary in terms of number, density, width, length, colour, and orientation. Plants with leaf hairs are termed pubescent; those without are called glabrous. The presence of leaf hairs varies with plant species, location, and function. Pubescent leaves are generally less palatable to predators and less susceptible to frost damage. Most leaf hairs allow solar radiation to be transmitted through the cuticle layer to the photosynthetic cells. A dense covering of hairs, however, protects underlying cells from intense solar radiation, and thus effectively insulates the leaf from burning (Karabourniotis *et al.*, 1995). By reducing leaf absorptance (the effectiveness with which it absorbs radiant energy), pubescence tends to lower both the leaf temperature (relative to ambient air temperature) and transpiration, which is advantageous in windy locations. Not surprisingly, pubescence is particularly common among leaves of desert and drought-tolerant plants (Ehleringer, 1984; Grammatikopoulous and Manetas, 1994). A negative correlation has been observed between leaf size and leaf hair density, with smaller leaves having a higher density of hair (Roy *et al.*, 1999). This relationship may result from cumulative stresses, such that both smaller leaf size and increased pubescence offer greater protection to the plant. The cost of this protection, however, is reduced absorption of light for photosynthesis (Ehleringer and Mooney, 1978).

Other potential leaf protuberances include spinose structures, such as thorns (modified stems), spines (modified leaves and stipules), and prickles (modified hairs). Spinosity deters herbivores and other predators. A range of leaf bumps or irregular thickenings can also result from interactions with pathogens. These features change the air flow around (see Section 4.4) and reflectance properties (see Section 4.3) of foliage and, in some instances, shade the leaf.

Another leaf variant that can impact texture is the scale and symmetry of internal patterns, largely resulting from venation (see Section 4.1.1). Variations in size, density, and topology of veins influence plant performance, ultimately favouring certain plants in particular environments (Sack and Scoffoni, 2013). Leaves with more complex outlines tend to have more primary veins and experience less shrinkage when dried, whereas simpler leaves tend to show more secondary veins and greater shrinkage potential (Holbrook and Zwieniecki, 2005). Venation also determines leaf flatness, which directly affects leaf reflectance and scattering properties.

4.1.4 Strength

Leaves endure various forms of mechanical stress, including gravity, rubbing, wind, rain, and predators (Niklas, 1992). Stronger leaves are more resistant to such stresses, which may reduce leaf loss and increase the leaf lifespan (Reich *et al.*, 1991). Leaves growing in shaded positions are typically less dense to allow better light transmission and absorption (see Section 4.1.1). Plants with an ample supply of nutrients generally grow larger, more nitrogen-rich leaves with a shorter lifespan, and more photosynthetic proteins (Evans, 1989).

The mechanical resistance of a leaf affects not only its lifespan but also its rate of decomposition, and its interactions with both the abiotic environment and potential consumers. Leaf fracture properties can be measured by shearing, punching, or tearing tests and expressed in terms of leaf lamina strength (the maximum force per unit area required to fracture the leaf), toughness (the work required to fracture the leaf), and stiffness (the resistance against deformation; Onoda, 2017). All leaf strength properties have been observed to increase with the availability of light, such that leaves in full sun were more resistant to fracture than those growing in shaded positions. Sun leaves demonstrated greater Leaf Mass per Area (LMA), while shade leaves showed greater punch strength per leaf mass. Since cell walls provide most of the mechanical strength in leaves, containing 60% of the total leaf carbon, this characteristic of shade leaves is attributed to the more reinforced structure of their cell walls (Onoda *et al*., 2008).

4.2 Chemical Composition

The chemical composition of foliage is determined by both environmental factors, such as soil fertility, and plant genetic traits. The foliar concentration of various biochemicals is directly related to essential biochemical processes in plants, including photosynthesis, respiration, evapotranspiration, and decomposition (Curran, 1989; Curran *et al*., 2001; see Section 5.2). Foliar chemistry is particularly relevant to herbivore survival, with variations in forage quality directly impacting the distribution, diversity, and abundance of animal species. Plant chemical composition can thus be indicative of soil nutrient availability, habitat quality, and ecosystem processes (Youngentob *et al*., 2012).

Analytical techniques such as atomic absorption spectrophotometry or chromatography can be used to identify and quantify the chemical components in foliage. While the specific chemical composition of plants varies between species and locations, the major constituent by weight in green leaves is water (Weisz and Fuller, 1962). Below we further discuss the chemical composition of leaves in terms of their most significant components:

- water—the heaviest component in green foliage (see Section 4.2.1);
- inorganic components—minerals (see Section 4.2.2); and
- organic components (see Section 4.2.3):
  - carbohydrates—energy storage and structural elements ;
  - lipids—waterproofing and structure;
  - proteins and nucleoproteins—structure and genetic codes; and
  - pigments—colour.

4.2.1 Water

Water is the major constituent of plant tissue, comprising over 75% of most green foliage and governing most plant processes (Weisz and Fuller, 1962). The internal moisture content of leaves varies enormously both between and within species with variations in ambient climatic and edaphic factors, especially water availability, and significant variations in leaf moisture content can occur during diurnal, seasonal, and phenological cycles. Water also acts as a solvent to transfer gases, minerals, and other solutes between plant cells and organs, as a reactant in photosynthesis, and as a substrate in hydrolytic processes. It maintains the turgor of living plants, controls cell growth and stomatal opening, and directly supports the form of herbaceous plants. As water content decreases, leaves wilt—they reduce photosynthesis rates, close stomata, and stop cell enlargement—until a critical threshold is reached when cells begin to die (Kramer and Boyer, 1995).

Leaf moisture content is indicative of plant stress, productivity, and evapotranspiration, as well as the availability of moisture in the soil and atmosphere. As such, leaf water content has been used as an indicator for scheduling irrigation and assessing the risk of drought and fire (Peñuelas *et al*., 1993, 1996; see Sections 13 and 18). Plants adapt to water stress by either using water more efficiently or reducing water loss (Dudley, 1996). Both these adaptations can be achieved by reducing leaf size, as smaller leaves typically have fewer stomata and higher hair density (see Section 4.1.3). Water stress is increased in saline environments since the presence of salt reduces water potential in the plant root zone, resulting in loss of turgidity in plant tissue (Pasternak, 1987).

…. many biochemical processes, such as photosynthesis, respiration, evapotranspiration and decomposition are related to the foliar concentration of biochemicals such as chlorophyll, water, nitrogen, lignin and cellulose. (Curran, 2001).

Water does not occur in its pure form in plants, but as a solution, which modifies some of its basic properties (Salisbury and Ross, 1969). It moves within plants primarily via osmosis, that is, diffusion through a permeable membrane (such as a cell wall) from a less concentrated (hypotonic) to a more concentrated (hypertonic) solution. Since this movement represents a form of energy, solutions can be viewed in terms of their osmotic potential. It is a characteristic of water that it moves to achieve equilibrium across a permeable membrane such that the water potentials on both sides are equivalent (isotonic). By contrast, osmotic pressure is the pressure required on a solution to stop water diffusing across a semi-permeable membrane, that is, to act against osmosis (Kramer and Boyer, 1995).

The concentration of fluids determines their chemical potential—the force they can exert. In plants, the cell water potential derives from the cumulative potentials of solutes, porous solids, pressure, and gravity. As a cell dehydrates, its contents become more concentrated and its water volume decreases, so its cell water potential decreases—it is less likely to force water out of the cell. The extent of cell shrinkage during dehydration, however, is also determined by the cell wall elasticity, with greater changes in cell water potential being observed in cells with more rigid walls. Leaf water potential is correlated with its net CO_2 assimilation rate and stomatal conductance to water vapour. Plant and soil water potentials are expected to be in equilibrium before dawn for non-transpiring plants, enabling plant water potential at that time to be used as a surrogate for soil water availability (Ehlers and Goss, 2003).

A leaf begins to lose moisture when it is removed from a plant, resulting in reduced turgidity in cells and generalised shrinking. Leaves with high initial water content are more likely to shrink in storage than those with low water content. Complex leaves generally have more structural support against shrinkage than simple leaves. Leaf cell structure determines the impact of water loss on leaf appearance, with those plants containing elastic cell walls withstanding up to 40% of water loss before contracting, while those with inelastic cell walls wilting after losing only 1–3% (Weatherley, 1965). Most crop species wilt when leaf water content is around 60–70%. This is an important consideration for leaf sample collection and measurement during field work (Juneau and Tarasoff, 2012; TERN Australia, 2018).

The water status of a plant can be described in terms of physical characteristics, such as its chemical potential within the plant cells, or in terms of its water content, that is, the proportion of water relative to plant tissue. Both approaches require destructive sampling of individual leaves. Since chemical potential and pressure are related, a thermocouple psychrometer, which detects vapour pressure, can be used to measure cell water potential in leaves. Other methods for measuring water potential involve using a pressure chamber (which determines the tension on water in the xylem) and a pressure probe (which quantifies the turgor pressure of single cells; Boyer, 1995). Water potential is directly related to the energy status of plant water but does not account for osmotic adjustment, which conserves cell moisture in drought conditions. Accordingly measures of water content are considered more appropriate in this context.

Water content is expressed either as a mass or a volume. Both are determined by drying a leaf sample and comparing the dried and fresh quantities. This approach underlies a number of EO-based indices, including Water Content (WC), Live Foliar Moisture Content (LFMC), Relative Water Content (RWC), and Equivalent Water Thickness (EWT; see Sections 8.1.5 and 9.5). WC (also called Gravimetric Water Content, GWC) actually determines the ratio of leaf water to leaf dry weight, where leaf water is computed as the difference between fresh and dry weights:

$$WC = \frac{FW - DW}{DW}$$

where

FW is fresh leaf weight (g); and
DW is oven dried leaf weight (g).

Live Foliar Moisture Content (LFMC) computes the same ratio as a percentage. A similar measure is succulence, which compares the water mass with leaf area:

$$Succulence = \frac{FW - DW}{area}$$

A related metric is the Leaf Dry Matter Content (LDMC, in mg/g):

$$LDMC = \frac{DW}{FW}$$

LDMC is currently in favour as a PFT to differentiate plants on the basis of their ecological behaviour. LDMC and SLA (specific leaf area, see Section 4.1.2) together represent the balance achieved by plants between rapid biomass production and efficient nutrient management (Garnier *et al*., 2001).

RWC or 'relative turgidity' (Barr and Weatherley, 1962) compares the difference between the water mass of a sample leaf with its fully hydrated water content:

$$RWC = \frac{FW - DW}{TW - DW}$$

RWC is a preferred measure of leaf water content as it is invariant within a leaf and changes in proportion to leaf turgor. EWT represents the volume of water per unit area of leaf (g/cm^2). This measure has been most closely approximated by analysis of spectral properties of leaves in the short wave infrared (SWIR) and near infrared (NIR) wavelengths (see Section 4.3).

Various studies have observed differences in both the leaf water content and leaf dry matter content (LDMC) of species that are enabled with strategies to regenerate after fire (Trabaud, 1987, 1991; Keeley, 1995). Common fire survival strategies include the capacity to resprout from adventitious shoots (resprouters) and/or produce abundant fire-hardy seed (seeders). Resprouting species were found to have consistently higher measurements of LDMC throughout the year compared with seeders, while seeders were observed to be more drought tolerant (Saura-Mas and Lloret, 2007).

Leaf wetness is a measure of meteorological precipitation (water from clouds) and dew (water from condensation near the ground) on the leaf surface. It is difficult to quantify directly, but a number of sensors rely on measuring the dielectric constant of the adaxial surface (Magarey *et al.*, 2005). Leaf wetness is also estimated by artificial leaf surface sensors, which electronically log the moisture that accumulates on a prepared surface. In conjunction with air temperature, leaf wetness duration (LWD) is important for control of fungal diseases in agriculture (Yarwood, 1978; Huber and Gillespie, 1992; Rowlandson *et al.*, 2015).

The water status of foliage is not only indicative of the physiological status and productivity of a plant, but at a landscape scale it is also informative for assessing drought conditions, scheduling irrigation, and rating fire risk. Net Primary Productivity (NPP; above ground) correlates directly with actual evapotranspiration (AET) for a range of biomes (see Section 7.6), with both estimates being indicative of the availability of water and solar energy (Rosenzweig, 1968).

While it is possible to scale up from leaf porometer measurements to canopy estimates of water content, most studies have found this approach to be problematic (Jarvis, 1985; Rollin and Milton, 1998). Leaf optical properties contribute to canopy reflectance, but so too do structural characteristics, background strata and viewing configuration factors (Jacquemoud and Ustin, 2003). EO-based techniques for mapping and monitoring water content of vegetation are further discussed in Sections 8 and 9.

4.2.2 Inorganic components

Mineral solids generally comprise 1–2% of living foliage (Weisz and Fuller, 1962). Most plant minerals exist in solution, but some can also occur as crystals. Minerals can occur freely or as part of organic compounds. For an individual species, low foliar nutrient content generally indicates low site mineral availability.

Terrestrial vegetation requires a range of inorganic minerals, which are absorbed from the growing medium. At least 14 minerals are considered essential for plant nutrition: six macronutrients (nitrogen, phosphorus, potassium, calcium, magnesium, and sulphur), which are required in large amounts, and eight micronutrients (chlorine, boron, iron, manganese, copper, zinc, nickel, and molybdenum). These and other minerals, when present in high concentrations in the growing medium, can be toxic to plant growth, including sodium, chlorine, boron, iron, manganese, and aluminium (White and Brown, 2010).

The most limiting nutrient for growing crops in many agricultural areas is nitrogen. This mineral is important for herbivores but exists in relatively low concentrations in some genera such as *Eucalyptus*. Nitrogen Use Efficiency (NUE) indicates the efficiency of nitrogen usage by plants for food production (see Section 5.3.5).

All mineral nutrients and trace elements—both essential and non-essential—detected in an organism define its 'ionome' (Salt *et al.*, 2008). Since the leaf ionome indicates the interactions between the plant and its environment, especially soil composition, ionomic characteristics are being analysed to understand phenotypic variation within species (Stein *et al.*, 2017).

4.2.3 Organic components

With the exception of compounds from mineral origins, such as CO_2 and carbonic acid, compounds containing carbon are collectively considered as organic. Some organic components support plant structure while others are dissolved or suspended in water in plant cells. The actual proportions of different organic compounds vary between species and locations. The major categories of organic compounds that occur in foliage with relevance to EO studies are carbohydrates, proteins, fats, and pigments:

- Carbohydrates account for around 20% of the mass of living plants (Weisz and Fuller, 1962) or 50–80% of the total dry weight of most plants (Salisbury and Ross, 1969). These compounds occur as sugars, polysaccharides, and the more complex configurations of the elements carbon, hydrogen, and oxygen. A simple sugar molecule is based on a 6-carbon structure resulting from photosynthesis. Two of these sugars can combine into a double sugar (12-carbon or disaccharide), and multiple sugars can combine to form a polysaccharide, such as cellulose, glycogen, or starch. The carbohydrates primarily function as energy reserves but also contribute to the structure of organelles. Structural carbohydrate derivatives include pectin, lignin, hemicellulose, and chitin. Cellulose and lignin, the most abundant renewable carbon resources on Earth, work together to strengthen cell walls and water transportation networks in vascular plants, thereby providing mechanical support for stems and leaves.
- Proteins are formed from long chains of amino acids. They occur in greater variety than any other organic components (with every type of living organism developing a different, and characteristic, type of protein) but only comprise a small proportion of living plant matter by weight (< 2%; Weisz and Fuller, 1962). Protein chains can be broken (denatured) by heat, pressure, electricity, and radiation. They provide the main structural material in plants, supply enzymes in cells, and help to form other organic compounds such as nucleoproteins that are built from nucleic acid and proteins. The two major nucleic acids are ribose nucleic acid (RNA) and deoxyribose nucleic acid (DNA). RNA exists throughout cells while DNA only occurs within the cell nucleus as a structural component of genes.
- Lipids include fats, fatty acids, glycerine, waxes, and sterols that do not dissolve in water. These compounds are formed from varying combinations and configurations of the elements of carbon, hydrogen, and oxygen and are generally insoluble in water. They form the framework for cell membranes and release energy when decomposed. Fat derivatives, such as cutin, act as a waterproofing agent in the leaf cuticle and are believed to reduce transpiration (see Section 4.1). Lipids occur in small quantities (< 2% of dry weight) in plant leaves, stems and roots (Salisbury and Ross, 1969).
- Pigments are molecules that absorb light, and the colour of a leaf is determined by its pigment composition. These compounds selectively absorb some wavelengths of electromagnetic radiation (EMR) and reflect others, such that those wavelengths that are reflected determine the apparent colour of a pigment (see Volume 1B—Section 6). While chlorophyll a is the primary photosynthetic pigment in all photosynthetic plants, most organisms contain multiple pigments to absorb energy across a wider range of wavelengths (see Excursus 4.1). This is particularly important to vegetation that does not have direct access to sunlight, such as understorey or submersed plants. The precise pigment composition within an individual leaf results from its generic heritage, its age, and its vigour, as well as its location with respect to intercepting direct sunlight. The latter will be impacted by latitude and aspect for all plants, and either horizontal layering for terrestrial plants or depth below water surface for aquatic plants.

Excursus 4.1—Plant Pigments

Further information: Salisbury and Ross (1969), Croft and Chen (2017)

The EMR wavelengths that are absorbed by some major leaf pigments are illustrated in Figure 4.2. The precise absorption characteristics of pigments can be determined by various biochemical and photochemical analyses (Lichtenthaler, 1987; Lichtenthaler and Buschmann, 2001; Croft and Chen, 2017). Leaf absorption characteristics can also be approximated by field instruments, such as spectrophotometers, and by hyperspectral remote sensing (Curran, 1989; Blackburn, 2007). Relevant characteristics of photosynthetic pigments are listed in Table 4.1. These pigments are contained in plastids, the major organelles in plants and algae. In addition, non-photosynthetic plant pigments occur in the cell vacuole (see Figure 4.1), or sap.

Chlorophyll pigments are produced by chloroplasts (green plastids; see Figure 4.1) and are responsible for photosynthesis. They absorb blue and red light and reflect green wavelengths, so appear green. Chlorophyll molecules are large, stable, nutrient-rich, and repel water. All forms of chlorophyll have the same basic molecular structure based on a chlorin (tetrapyrrole) ring with a central magnesium ion (Croft and Chen, 2017). Being the primary pigment for photosynthesis, chlorophyll a is the most abundant, with 2.5 to 4.0 times more chlorophyll a than chlorophyll b in photosynthetic plants. The other forms of chlorophyll are accessory pigments which collaborate with chlorophyll a by capturing a wider range of wavelengths. Chlorophyll c, chlorophyll d, and chlorophyll e only occur in aquatic algae and chlorophyll d primarily exists in organisms living in deeper waters. Photosynthetic bacteria contain a modified form of chlorophyll known as bacteriochlorophylls, which exists as a range of compounds (see Volume 3B).

Phycobilins are attached to water-soluble proteins (phycobiliproteins) and absorb a wider range of wavelengths than chlorophyll. This is particularly useful for organisms growing in water. These molecules comprise a chain of pyrrole rings. Phycoerythrin is the main phycobilin in red algae which can photosynthesise using dim blue-green light, and the proportion of this phycobilin relative to chlorophyll increases with water depth. Blue-green algae that grows in surface waters, and some terrestrial algae, contain a greater proportion of Phycocyanin.

Figure 4.2 Absorption spectra of leaf pigments

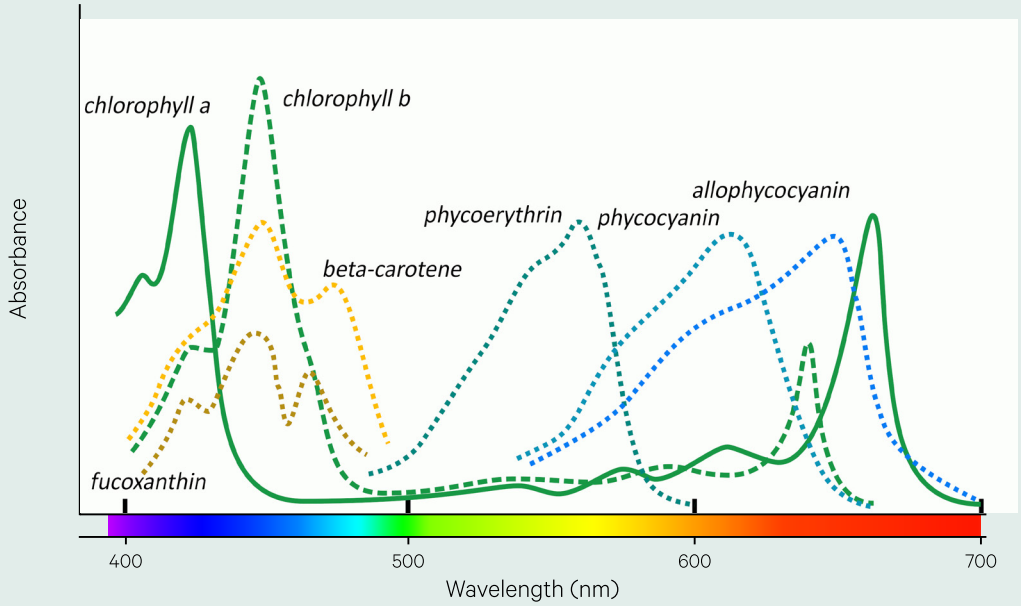

Adapted from: Goodwin and Mercer (1990) by Qiaoyun Xie, University of Technology Sydney. (Original retrieved from *http://biologywiki.apps01.yorku.ca/index.php?title=File:Pigment_spectra.png*)

Carotenoids are long molecules created in chromoplasts (pigmented plastids). They mostly absorb blue wavelengths, so generally appear as yellow-orange colours in petals, fruits, and leaves. These carbon-based compounds do not dissolve in water. While carotenoids help to capture a greater range of solar wavelengths than chlorophyll, they are considered to be accessory pigments for photosynthesis since this energy needs to be transferred to chlorophyll for photosynthesis to occur. Carotenes are hydrocarbons, with the three common forms being stereoisomers of the same molecular formula. Xanthophylls (or carotenols) also contain oxygen as a hydroxyl, carbonyl, or carboxyl group.

Anthocyanins are a type of water-soluble flavonoid that vary in colour from red to purple and blue depending on pH. They absorb blue-green wavelengths and are predominantly found in petals and fruit, where they attract pollinators, but are also responsible for red juvenile and autumn leaves. Red anthocyanins are believed to offer pharmacological benefit as antioxidants. The production of anthocyanins uses carbohydrate reserves in a plant. They are produced in the leaf as it dies, possibly as a defence against pests which would be attracted to the declining chlorophyll levels, or to enable efficient resorption of foliar nutrients (see Section 5.3.3). This group of pigments also act as a natural sunscreen for plants by trapping excessive solar radiation, with production increasing in response to ultraviolet (UV) light, and provide photostability during leaf expansion (Close and Beadle, 2003; Liakopoulos *et al*., 2006). Another group of vacuole pigments (see Figure 4.1) includes tannins, which occur in leaf, bud, seed, root, and stem tissues. Tannins are water soluble and coloured brown. When leached from nearby vegetation (such as eucalypts), they contribute to the dark water colour of many inland waterbodies in Australia. Tannins are astringent to taste and play a defensive role against plant predators.

Higher concentrations of chlorophyll a generally mask the presence of other pigments in leaves. As light levels fall with the approach of winter, the volume of chlorophyll a decreases in deciduous plants, allowing other pigments to become more visible. A similar process occurs as plants senesce. The precise colours of autumn leaves depend on the pigment composition in the leaves of different plant species.

Table 4.1 Photosynthetic pigments

Absorption peaks (in nm) are approximate values only.

Pigment Group	Pigment	Colour/ spectral region	Characteristic Absorption Peaks	Occurrence
Chlorophyll	Chlorophyll a	Blue-green	435, 675	All photosynthetic organisms except bacteria
	Chlorophyll b	Yellow-green	480, 650	All green plants, green algae and some prokaryotes
	Chlorophyll c	Golden-brown	~645	Chromista, dinoflagellates, brown algae
	Chlorophyll d	Far red	~740	Red algae, blue-green algae
	Chlorophyll e	Golden-yellow	415, 654	Golden-yellow algae
Bacterioviridin	Chlorobium chlorophyll	Far red	750/770	Green bacteria
Bacteriochlorophyll	Bacteriochlorophyll a	Far red, NIR	800, 850, 890	Purple and green bacteria
	Bacteriochlorophyll b	NIR	1,017	*Rhodopseudomonas* (purple bacteria)
Phycobilin	Allophycocyanin	Blue-red	654	Red algae, blue-green algae,
	Phycoerythrin	Red	490, 546, 576	
	Phycocyanin	Blue-green	618	
	Phycourobilin	Orange	~495	
Carotene	α-carotene	Yellow-orange	420, 440, 470	Green leaves and some bacteria and fungi
	β-carotene	Yellow-orange	425, 450, 480	Main carotene in most plants
	γ-carotene	Brown	440, 460, 495	Green sulphur bacteria; some amounts in other plants
Xanthophyll	Luteol	Pale yellow	425, 445, 475	Green leaves, green algae and red algae
	Violaxanthol	Brown	425, 450, 475	Main carotenol in green leaves, green algae and red algae
	Fucoxanthol	Brown	425, 450, 475	Brown algae, diatoms
	Spirilloxanthol		464, 490, 524	Purple bacteria

Sources: Rabinowitch and Govindjee (1969) and Lichtenthaler and Buschmann (2001)

4.3 Spectral Properties

Electromagnetic radiation (EMR), originating from the Sun or an artificial light source, is either absorbed, reflected, or transmitted by foliage, where

incident energy = reflected energy
+ transmitted energy + absorbed energy

For convenience, names are assigned to the various regions of the electromagnetic spectrum, but there are no precise divisions between these regions—they are generally defined by the sensing method by which they are detected (see Volume 1A—Section 5). Commonly accepted ranges for the EMR spectral regions that are most relevant to EO are:

- visible: 0.38–0.7 μm (380–700 nm);
- infrared (IR): 0.7–1,000 μm;
- microwave: > 1 mm–1 m.

Infrared wavelengths are often sub-divided into the regions:

- near infrared (NIR): 0.7–1.3 μm;
- short wave infrared (SWIR): 1.3–3 μm;
- middle infrared (MIR) or mid-wavelength (or medium wave) infrared (MWIR): 3–8 μm;
- thermal infrared (TIR) or long wavelength infrared (LWIR): 8–15 μm; and
- far infrared (FIR): 15–1,000 μm.

Reflectance of an object is defined as the proportion of incident energy it reflects:

$$\text{reflectance} = \frac{\text{reflected energy}}{\text{incident energy}}$$

with similar definitions for transmittance and absorptance, so that:

reflectance + transmittance + absorptance = 1

A typical reflectance curve for green vegetation is shown in Figure 4.3a. Absorption of visible and NIR wavelengths of EMR results from energy transfer to molecules, atoms, or electrons whereas SWIR and TIR wavelengths produce molecular vibrations in leaves, largely due to the presence of water (see Volume 1). However, the precise interaction for an individual leaf with a radiation source will depend on the wavelength(s) of radiation and the physical structure (morphology) and chemical composition of the leaf, as well as its orientation and surface features. Accordingly, reflectance spectra can vary for different species in a genus (see Figure 4.3b) and different leaves on the one plant.

UV to visible wavelengths excite electrons and determine the apparent colour of foliage, that is, those wavelengths that it reflects rather than absorbs. Chlorophyll molecules, for example, absorb blue and red wavelengths and reflect green, resulting in the characteristic colour of vegetation, while other photosynthetic pigments absorb different wavelengths. In terrestrial vegetation, the range of wavelengths that can be absorbed for photosynthesis approximately spans from 400–700 nm and is called Photosynthetically Active Radiation (PAR). The major groups of pigments associated with photosynthesis can be grouped in terms of their chemical structure:

- Tetrapyrrols:
  - Chlorophylls—enable photosynthesis in plants and algae;
  - Bacteriochlorophylls—enable photosynthesis in bacteria;
  - Phycobilins—accessory pigment for photosynthesis in aquatic algae; and
- Carotenoids—carotenes and xanthophylls—accessory pigment for photosynthesis in plants, algae, and bacteria (see Excursus 4.1).

While leaf optical properties have been researched for well over a century, there are still a number of unknowns. We know that reflectance and transmittance characteristics result from both the concentration of compounds that absorb light and the internal scattering of the light that is not absorbed. A healthy leaf absorbs:

- violet and blue wavelengths—due to the presence of chlorophyll, carotenoid, and xanthophyll pigments;
- red wavelengths—due to the presence of chlorophyll pigment(s); and
- SWIR—due to the presence of water with characteristic absorption peaks near 1450 nm and 1900 nm (see Figure 4.3).

These characteristics produce reflectance peaks for those wavelengths that are not absorbed, namely green and NIR, with two 'bumps' in SWIR wavelengths that are not absorbed by water, and reflectance troughs for those wavelengths that are absorbed (namely blue, red, and SWIR wavelengths). The NIR reflectance plateau (700–1100 nm) results from structural biochemicals and multiple scattering from structures and air spaces within the leaf (see Figure 4.1). Water absorption in the SWIR region produces primary reflectance dips at 1450 nm, 1940 nm, and 2500 nm, and secondary dips at 980 nm and 1240 nm (Carter, 1991). In addition, various aspects of the physical morphology of leaves will impact reflectance properties (see Section 4.1.2). In particular, the leaf surface shape, size, orientation, and texture all affect the way it intercepts and reflects light.

Figure 4.3 Reflectance of green foliage

a. Reflectance properties of green vegetation primarily derive from leaf pigments in visible wavelengths, cell structure in NIR wavelengths and water content in SWIR wavelengths. Characteristic absorption features occur in visible wavelengths (due to chlorophyll) and SWIR wavelengths (due to water content).

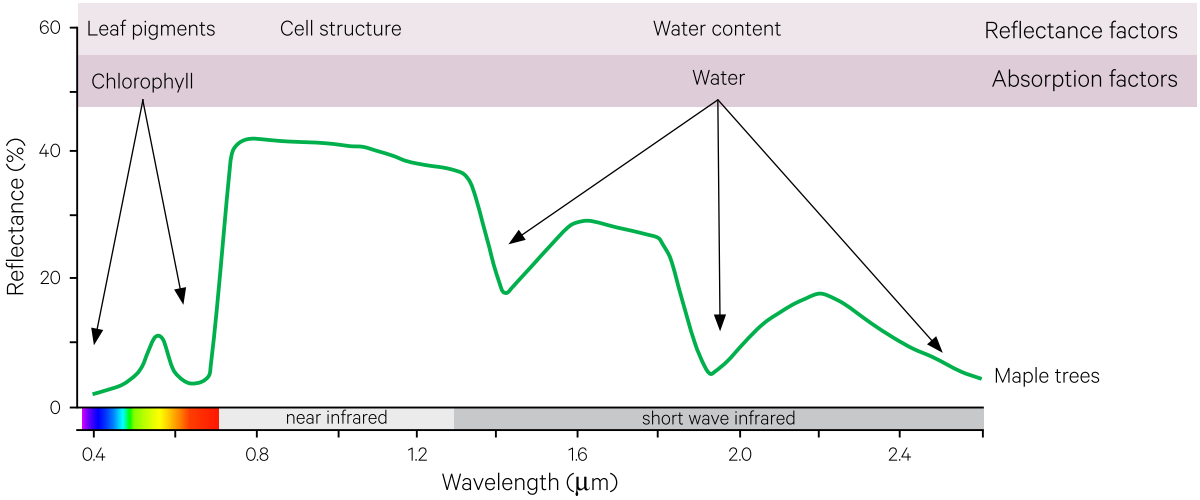

b. Reflectance spectra varies for different species. Below is shown the mean reflectance spectra for four species of *Eucalyptus* and one species of *Angophora*.

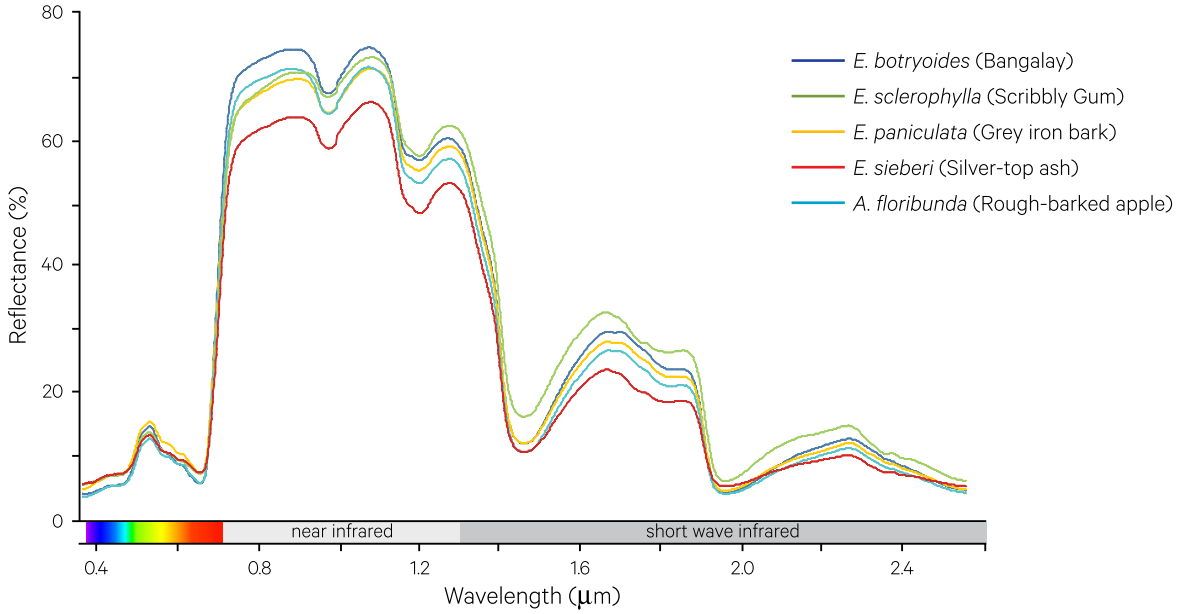

Source: a. Based on Harrison and Jupp (1989) Figure 30; b. Laurie Chisholm, University of Wollongong

Spectral properties of leaves are also known to vary with various forms of plant stress, including dehydration, flooding, freezing, herbicides, competition, disease, predators, and deficiencies. As foliage dries, the spectral absorption features in SWIR and TIR wavelengths are less dominated by water and those resulting from its biochemical components become more evident. Stressed plants have increased transmittance and decreased absorptance of wavelengths near 700 nm, resulting from changes in leaf chlorophyll concentration (Carter and Knapp, 2001). As the chlorophyll concentration reduces in a leaf, either from abscission or stress, the leaf colour also changes (Jacquemoud and Ustin, 2014; see Section 5.3.3).

Figure 4.4 Leaf reflectance changes with stress

a. In the initial stages of disease, NIR reflectance is reduced. As disease progresses, NIR reflectance continues to decrease and the colour of foliage changes markedly.

b. Increasing plant stress shifts the 'red edge' towards shorter wavelengths

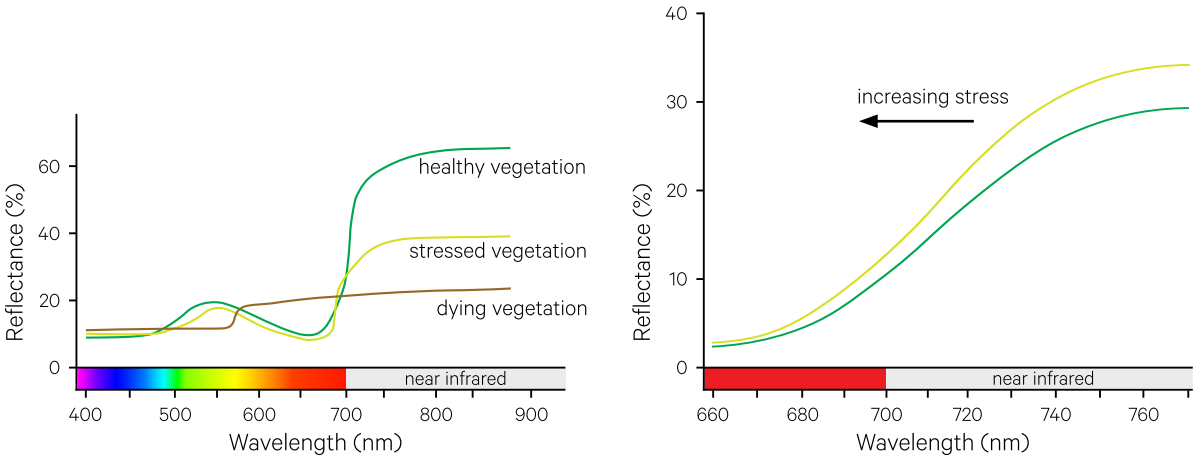

Adapted from: a. Barrett and Curtis (1976) Figure 15.1b; b. Cho *et al.* (2012)

The onset of stress, senescence, or disease in plants reduces reflectance in both green and NIR wavelengths and shifts the transition between red absorption and NIR reflectance (see Figure 4.4a). In green leaves, the transition from low red reflectance to high NIR reflectance corresponding to the spectral range 680–780 nm is referred to as the 'red edge'. Changes in vegetation vigour affect the precise position and slope of the red edge (see Figure 4.4b).

Many spectral indices developed for EO datasets focus on changes in these spectral regions (see Section 8.1) and are used to determine the chlorophyll content of foliage (Croft and Chen, 2017). Physical and mathematical models that simulate the spectral consequences of variations in leaf biochemical and physical composition are introduced in Sections 9 and 10.

4.4 Boundary layer

A boundary layer results from aerodynamic forces between a fluid and an object. This can occur when either an object moves through a fluid or a fluid moves past an object. The speed and shape of the object together with the mass, viscosity, and compressibility of the fluid determine the magnitude of the aerodynamic forces. The net effect of these forces is a layer at the boundary of the fluid that is most strongly affected by its viscosity, that is the resistance of the fluid to its flow. Boundary layers occur on the surfaces of many moving vehicles and in the transition zone between fluid layers. Some commonplace examples of boundary layers include the air zone around aerofoils, such as aircraft wings, the water zone around aerofoils, such as ship hulls, and the interface between the Earth and its atmosphere. They also surround leaf surfaces and can impact essential physiological processes.

Within the boundary layer, the velocity of the fluid is reduced as some of the fluid attaches to the surface of the object, creating shearing stresses within the fluid. Movement within the boundary layer can be either laminar (flowing in layers), or turbulent (mixing across layers), or a transition between the two. Mixing across layers involves non-laminar currents called eddies. These typically create swirling movement within fluids, and often result from diversion around some obstacle. Eddies occur at various scales between and within fluid layers in the ocean and in the atmosphere (see Volume 3B).

Between a fluid and an object's surface, turbulence can result from surface roughness, uneven fluid flow, and/or increased distance from the object's leading edge. In fluid dynamics, the degree of turbulence is quantified by the dimensionless Reynolds Number (RN):

$$RN = \frac{\text{density} \times \text{velocity} \times \text{diameter}}{\text{viscosity}}$$

where

RN < 100,000 indicates laminar flow;
RN > 1,000,000 indicate turbulent flow; and
100,000 < RN < 1,000,000 indicates a transition between laminar and turbulent flow.

Figure 4.5 Impact of vegetation density on wind flow

This aerial photograph of the dingo-proof fence in the Strzelecki Desert, Australia, shows increased woody shrub density where dingoes have been removed. The diagram below demonstrates predicted wind flow regimes—'isolated roughness' and 'wake interference' at low to medium shrub density; 'skimming flow' at high shrub density—and increased root structure and canopy shade at high shrub density.

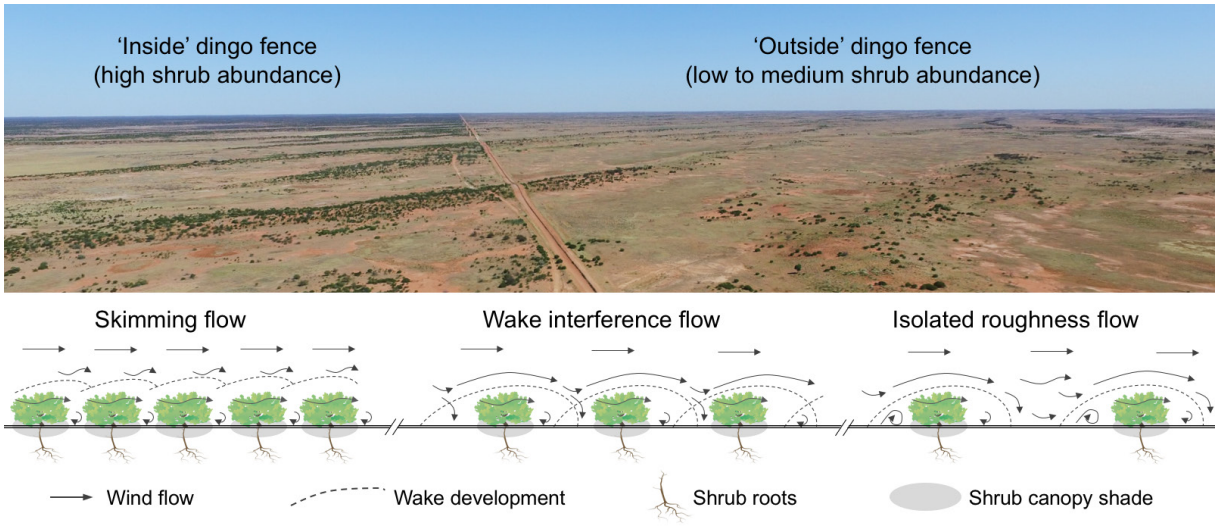

Source: Lyons *et al.* (2018)

A boundary layer surrounds any leaf surface, providing a thin interface of relatively stationary air between the leaf and the atmosphere. Within the boundary layer, turbulence is effectively reduced by friction and the thickness of this layer is modified by a number of factors, including:

- leaf texture—dense hairs effectively create a windbreak, which increases the thickness of the boundary layer and reduces transpiration rates, while sparse hairs may increase turbulence (Jones, 1992);
- stomatal structure—recessed stomata increase the boundary layer thickness;
- leaf size—the boundary layer increases with leaf size and distance from the leading edge of the leaf (Grace and Wilson, 1976) and with variations in leaf shape that effectively reduce leaf size (for example leaf lobes and serration also reduce the thickness of the boundary layer; Schuepp, 1993); and
- atmospheric turbulence—wind will reduce the thickness of the boundary layer.

The boundary layer between leaves and the atmosphere directly impacts the rate of plant water loss via transpiration (see Section 5.2.3) and the transfer of heat into the atmosphere (see Section 5.2.4). The density of foliage and plants also impacts wind flow regimes (see Figure 4.5). This effect is particularly relevant in dryland regions with patchy vegetation, where higher plant densities reduce wind erosion and sediment transport (Mayaud *et al.*, 2016) and encourage more stable dune formations (Lyons *et al.*, 2018).

4.5 Further Information

Physiology

Taiz *et al*. (2015): *www.plantphys.net*

Pigments

Light and photosynthetic pigments: *https://www.khanacademy.org/science/biology/photosynthesis-in-plants/the-light-dependent-reactions-of-photosynthesis/a/light-and-photosynthetic-pigments*

4.6 References

Ackerly, D.D., Knight, C.A., Weiss, S.B., Barton, K., and Starmer, K.P. (2002). Leaf size, specific leaf area and microhabitat distribution of chaparral woody plants: contrasting patterns in species level and community level analyses. *Oecologia*, 130(3), 449–457.

Barr, H.D., and Weatherley, P.E. (1962). A re-examination of the relative turgidity technique for estimating water deficit in leaves. *Australian Journal of Biological Science*, 15, 413–428.

Barrett, E.C., and Curtis, L.F. (1976). *Introduction to Environmental Remote Sensing*. Chapman and Hall, London.

Blackburn, G.A. (2007). Hyperspectral remote sensing of plant pigments. *Journal of Experimental Botany*, 58(4), 855–867.

Boyer, J.S. (1995). *Measuring the Water Status of Plants and Soils*. Academic Press, San Diego. *http://udspace.udel.edu/handle/19716/2828*

Carter, G.A.(1991). Primary and secondary effects of water content on the spectral reflectance of leaves. *American Journal of Botany*, 78(7), 916–924.

Carter, G.A., and Knapp, A.K. (2001). Leaf optical properties in higher plants: linking spectral characteristics to stress and chlorophyll concentration. *American Journal of Botany*, 88(4), 677–684.

Cho, M.A., Debba, P., Mutanga, O., Dudeni-Tlhone, N., Magadla, T., and Khuluse, S.A. (2012). Potential utility of the spectral red-edge region of SumbandilaSat imagery for assessing indigenous forest structure and health. *International Journal of Applied Earth Observation and Geoinformation*, 16, 85–93. doi:http://dx.doi.org/10.1016/j. jag.2011.12.005

Close, D.C., and Beadle. C.L. (2003). The ecophysiology of foliar anthocyanin. *The Botanical Review*. 69, 149–161.

Cornelissen, J.H.C., Lavorel, S., Garnier, E., Díaz, S., Buchmann, N., Gurvich, D.E., Reich, P.B., ter Steege, H., Morgan, H.D., van der Heijden, M.G.A., Pausas, J.G., and Poorter, H. (2003). A handbook of protocols for standardised and easy measurement of plant functional traits worldwide. *Australian Journal of Botany*, 51, 335–380.

Croft, H., and Chen, J.M. (2017). Leaf Pigment Content. In *Comprehensive Remote Sensing Volume 3*, Reference Module in Earth Systems and Environmental Sciences (Ed: Liang, S.). Elsevier. pp 117–142. *https://doi.org/10.1016/B978-0-12-409548-9.10547-0*

Curran, P.J. (1989). Remote sensing of foliar chemistry. *Remote Sensing of Environment*, 29, 271–278.

Curran, P. (2001). Imaging spectroscopy for ecological applications. *International Journal of Applied Earth Observation and Geoinformation*, 3(4), 305–312.

Curran, P.J., Dungan, J.L., and Peterson, D.L. (2001). Estimating the bio-chemical concentration of leaves with reflectance spectrometry: testing the Kokaly and Clark methodologies. *Remote Sensing of Environment*, 76, 349–359.

Dudley, S.A. (1996). Differing selection on plant physiological traits in response to environmental water availability: a test of adaptive hypotheses. *Evolution*, 50, 92–102.

Edwards, E.J. (2019). Evolutionary trajectories, accessibility and other metaphors: the case of C4 and CAM photosynthesis. *New Phytologist*, 223(4), 1742–1755. *https://doi.org/10.1111/nph.15851*

Ehleringer, J. (1984). Ecology and ecophysiology of leaf pubescence in North American desert plants. In: *Biology and Chemistry of Plant Trichomes* (Eds: E. Rodrigues, P.L. Healey and I. Mehta) pp 113–132. Plenum, New York.

Ehleringer, J.R., and Mooney, H.A. (1978). Leaf Hairs: Effects on Physiological Activity and Adaptive Value to a Desert Shrub. *Oecologia*, 37, 183–200.

Ehlers, W., and Goss, M.J. (2003). *Water Dynamics in Plant Production*. CABI Publishing, Oxon. ISBN 0-85199-694-9

Esau, K. (1965). *Plant Anatomy*. 2nd edn. John Wiley and Sons, New York.

Evans, J.R. (1989). Photosynthesis and nitrogen relationships in leaves of C_3 plants. *Oecologia*, 78, 9–19.

Evans, J.R., and Vogelmann, T.C. (2006). Photosynthesis within isobilateral *Eucalyptus pauciflora* leaves. *New Phytology*, 171(4), 771–782. doi:*10.1111/j.1469-8137.2006.01789.x*

Garnier, E., Shipley, B., Roumet, C., and Laurent, G. (2001). A standardized protocol for the determination of specific leaf area and leaf dry matter content. *Functional Ecology*, 15, 688–695.

Gates, D.M. (1980). *Biophysical Ecology*. Springer-Verlag, New York.

Givnish, T.J. (1979). On the adaptive significance of leaf form. In: *Topics in Plant Population Biology* (Eds: O.T. Solbrig, S. Jain, G.B Johnson, and P.H. Raven) pp. 375–407. Columbia University Press, New York.

Goodwin, T.W., and Mercer, E.I. (1990). *Introduction to Plant Biochemistry*. Pergamon Press.

Grace, J., and Wilson, J. (1976). The boundary layer over a Populus leaf. *Journal of Experimental Botany*, 27, 231–241.

Grammatikopoulous, G., and Manetas, Y. (1994). Direct absorption of water by hairy leaves of Phlomis fruticosa and its contribution to drought avoidance. *Canadian Journal of Botany*, 72, 1805–1811.

Harrison, B.A., and Jupp, D.L.B. (1989) *Introduction to Remotely Sensed Data: Part ONE of the microBRIAN Resource Manual*. CSIRO, Melbourne. 156pp.

Harrison, E.L., Arce Cubas, L., Gray, J.E., and Hepworth, C. (2020). The influence of stomatal morphology and distribution on photosynthetic gas exchange. *The Plant journal : for cell and molecular biology*, 101(4), 768–779. *https://doi.org/10.1111/tpj.14560*

Holbrook, N.M., and Zwieniecki, M.A. (2005). *Vascular transport in plants*. Elsevier Academic Press, Burlington MA. 564 p.

Huber, L., and Gillespie.,T.J. (1992). Modeling Leaf Wetness in Relation to Plant Disease Epidemiology. *Annual Review of Phytopathology*, 30(1), 553–577.

Jacobs, M. (1955). *Growth Habit of the Eucalypts*. CSIRO, Canberra. (Reprinted in 1986 by IFA).

Jacquemoud, S., and Ustin, S.L. (2003). Application of radiative transfer models to moisture content estimation and burned land mapping. *Proceedings of 4th International Workshop on Remote Sensing and GIS Applications to Forest Fire Management*. pp 3–12. (Eds: E. Chuvieco, P. Martin and C Justice). Ghent (Belgium), 5–7 June, 2003.

Jacquemoud, S., and Ustin, S.L. (2014). Modeling Leaf Optical Properties. In *Photobiological Sciences Online* (Ed: S.C. Smith). American Society of Photobiology. *http://www.photobiology.info/*

James, S.A., and Bell, D.T. (2000). Leaf orientation, light interception and stomatal conductance of *Eucalyptus globulus ssp. globulus* leaves. *Tree Physiology*, 20, 815–823.

Jarvis, P.G. (1985). Transpiration and assimilation of tree and agricultural crops: the 'omega factor'. In *Attributes of Trees as Crop Plants* (Eds: M.G.R. Cannell and J.E. Jackson). Institute of Terrestrial Ecology. pp 460–480.

John, G.P., Scoffoni, C., and Sack, L. (2013). Allometry of cells and tissues within leaves. *American Journal of Botany*, 100(10), 1936–1948. doi:*10.3732/ajb.1200608*

Jones, H.G. (1992). *Plants and Microclimate*. Cambridge, Cambridge University Press.

Juneau, K.J., and Tarasoff, C.S. (2012). Leaf area and water content changes after permanent and temporary storage. *PloS ONE*, 7(8), e42604. *https://doi.org/10.1371/journal.pone.0042604*

Karabourniotis, G., Kotsabassidis, D., and Manetas, Y. (1995). Trichome density and its protective potential against ultra-violet-B radiation damage during leaf development. *Canadian Journal of Botany*, 73, 376–383.

Keeley, J.E. (1995) Seed-germination patterns in fire-prone Mediterranean climate regions. In: *Ecology and biogeography of Mediterranean eco- systems in Chile, California, and Australia*. (Eds: Arroyo, M.T.K., Zedler, P.H., Fox, M.D.) New York, Springer-Verlag. pp. 239–73.

Kramer, P.J., and Boyer, J.S. (1995). *Water relations of plants and soils*. Academic Press, San Diego. *http://udspace.udel.edu/handle/19716/2830*

Larcher, W. (1980). *Plant Physiological Ecology*. Springer-Verlag, Berlin.

Li, Y., Johnson, D.A., Su, Y., Cui, J., and Zhang, T. (2005). Specific leaf area and leaf dry matter content of plants growing in sand dunes. *Botanical Bulletin of Academia Sinica*, 46, 127–134

Liakopoulos, G., Nikolopoulos, D., Klouvatou, A., Vekkos, K.A., Manetas, Y., and Karabourniotis, G. (2006). The photoprotective role of epidermal anthocyanins and surface pubescence in young leaves of grapevine (*Vitis vinifera*). *Annals of Botany*, 98, 257–265.

Lichtenthaler, H.K. (1987). Chlorophylls and carotenoids: Pigments of photosynthetic biomembranes. Ch 34 in *Methods in Enzymology*. Volume 148 in *Plant Cell Membranes* (Eds: Packer, L., and Douce, R.). Academic Press. pp. 350–382. *https://doi.org/10.1016/0076-6879(87)48036-1*

Lichtenthaler, H.K. (2009). Biosynthesis and Accumulation of Isoprenoid Carotenoids and Chlorophylls and Emission of Isoprene by Leaf Chloroplasts. *Bulletin of the Georgian National Academy of Sciences*, 3(3), 81–94.

Lichtenthaler, H.K., and Buschmann, C. (2001). Chlorophylls and Carotenoids: Measurement and Characterization by UV-VIS Spectroscopy. *Current Protocols in Food Analytical Chemistry*, F4.3.1-F4.3.8.

Lyons, M.B., Mills, C.H., Gordon, C.E., and Letnic, M. (2018). Linking trophic cascades to changes in desert dune geomorphology using high-resolution drone data. *Journal of the Royal Society Interface*, 15(144), 20180327.

Magarey, R.D., Seem, R.C., Weiss, A., Gillespie, T., and Huber, L. (2005). Estimating Surface Wetness on Plants. Ch 10 in *Micrometeorology in Agricultural Systems*, Agronomy Monograph 47, American Society of Agronomy. *https://digitalcommons.unl.edu/cgi/viewcontent.cgi?article=1696&context=agronomyfacpub*

Mayaud, J.R., Wiggs, G.F.S., and Bailey, R.M. (2016). Dynamics of skimming flow in the wake of a vegetation patch. *Aeolian Research*, 22, 141–151. doi:*10.1016/j.aeolia.2016.08.001*

McLellan, T., and Endler, J.A. (1998). The relative success of some methods for measuring and describing the shape of complex objects. *Systematic Biology*, 47, 264–281.

Milla, R., Reich, P.B., Niinemets, U., and Castro-Díez, P. (2008). Environmental and developmental controls on specific leaf area are little modified by leaf allometry. *Functional Ecology*, 22(4), 565–576. doi:*10.1111/j.1365-2435.2008.01406*

Nicotra, A., Cosgrove, M., Cowling, A., Schlichting, C., and Jones, C. (2008). Leaf shape linked to photosynthetic rates and temperature optima in South African *Pelargonium* species. *Oecologia*, 154, 625–635.

Niklas, K.J. (1992). *Plant biomechanics: an engineering approach to plant form and function*. University of Chicago Press. 607 p. *https://hdl.handle.net/1813/28577*

Niklas, K.J. (1994). *Plant allometry*. University of Chicago Press, Chicago, Illinois, USA.

Onoda, Y. (2017). Fracture Toughness. *Prometheus Wiki*, CSIRO Publishing. *http://prometheuswiki.org/tiki-index.php?page=Fracture+toughness*

Onoda, Y., Schieving, F., and Anten, N.P.R. (2008). Effects of light and nutrient availability on leaf mechanical properties of *Plantago major*: A conceptual approach. *Annals of Botany*, 101, 727–736.

Pasternak, D. (1987). Salt tolerance and crop production—a comprehensive approach. *Annual Review of Phytopathology*, 25, 271–291.

Peñuelas, J., Gamon, J.A., Griffin, K.L., and Field, C.B. (1993). Assessing type, biomass, pigment composition and photosynthetic efficiency of aquatic vegetation from spectral reflectance. *Remote Sensing of Environment*, 46, 110–118.

Peñuelas, J., Filella, I., Serrano, L., and Save, R. (1996). Cell wall elasticity and water index (r970nm/r900nm) in wheat under different nitrogen availabilities. *International Journal of Remote Sensing*, 17, 373–382.

Pérez-Harguindeguy, N., Díaz, S., Garnier, E., Lavorel, S., Poorter, H., Jaureguiberry, P., Bret-Harte, M.S., Cornwell, W.K., Craine, J.M., Gurvich, D.E., Urcelay, C., Veneklaas, E.J., Reich, P.B., Poorter, J.L., Wright, I.J., Ray, P., Enrico, L., Pausas, J.G., de Vos, A.C., Buchmann, N., Funes, G., Quétier, F., Hodgson, J.G., Thompson, K., Morgan, H.D., ter Steege, H., van der Heijden, M.G., Sack, A.L., Blonder, B., Poschlod, P., Vaieretti, M.V., Conti, G., Staver, A.C., Aquino, S., and Cornelissen, J.H.C. (2013). New handbook for standardised measurement of plant functional traits worldwide. *Australian Journal of Botany*, 61, 167–234.

Popp, C., Burghardt, M., Friedmann, A., and Riederer, M. (2005). Characterization of hydrophilic and lipophilic pathways of *Hedera helix L*. cuticular membranes: permeation of water and uncharged organic compounds. *Journal of Experimental Botany*, 56(421), 2797–2806.

Rabinowitch, E., and Govindjee, R. (1969). *Photosynthesis*. Wiley, New York.

Reich, P.B., Uhl, C., Walters, M.B., and Ellsworth, D.S. (1991). Leaf lifespan as a determinant of leaf structure and function among 23 amazonian tree species. *Oecologia*, 86, 16–24. *https://doi.org/10.1007/BF00317383*

Reich, P.B., Walters, M.B., and Ellsworth, D.S. (1997). From tropics to tundra: global convergence in plant functioning. *PNAS*, 94, 13730–13734.

Rollin, E.M., and Milton, E.J. (1998). Processing of high spectral resolution reflectance data for the retrieval of canopy water content information. *Remote Sensing of Environment*, 65, 86–92.

Rosenzweig, M. (1968). Net Primary Productivity of Terrestrial Communities: Prediction from Climatological Data. *The American Naturalist*, 102(923), 67–74.

Rowlandson, T., Gleason, M., Sentelhas, P., Gillespie, T., Thomas, C., and Hornbuckle, B. (2015). Reconsidering leaf wetness duration determination for plant disease management. *Plant Disease*, 99(3), 310–310.

Roy, B.A., Stanton, M.L., and Eppley, S.M. (1999) Effects of environmental stress on leaf hair density and consequences for selection. *Journal of Evolutionary Biology*, 12, 1089–1103.

Royer, D.L., Wilf, P., Janesko, D.A., Kowalski, E.A., and Dilcher, D.L. (2005). Correlations of climate and plant ecology to leaf size and shape: potential proxies for the fossil record. *American Journal of Botany*, 9, 1141–1151.

Sack, L., and Scoffoni, C. (2013). Leaf venation: structure, function, development, evolution, ecology and applications in the past, present and future. *New Phytologist*, 198, 983–1000.

Salisbury, F.B., and Ross, C. (1969). *Plant Physiology*. Wadsworth Publishing Company, Belmont.

Salt, D.E., Baxter, I., and Lahner, B. (2008). Ionomics and the Study of the Plant Ionome. *Annual Review of Plant Biology*, 59, 709–733.

Saura-Mas, S., and Lloret, F. (2007). Leaf and Shoot Water Content and Leaf Dry Matter Content of Mediterranean Woody Species with Different Post-fire Regenerative Strategies. *Annals of Botany*, 99, 545–554.

Schuepp, P.H. (1993). Tansley Review No. 59. Leaf boundary layers. *New Phytologist*, 125, 477–507.

Sisó, S., Camarero, J., and Gil-Pelegrín, E. (2001). Relationship between hydraulic resistance and leaf morphology in broadleaf Quercus species: a new interpretation of leaf lobation. *Trees—Structure and Function*, 15, 341–345.

Stein, R.J., Höreth, S., de Melo, J.R.F., Syllwasschy, L., Lee, G., Garbin, M.L., Clemens, S., and Krämer, U. (2017). Relationships between soil and leaf mineral composition are element-specific, environment-dependent and geographically structured in the emerging model *Arabidopsis halleri*. *New Phytologist*, 213, 1274–1286. doi:*10.1111/nph.14219*

Taiz, L., Zeiger, E., Moller, I.M., and Murphy, A. (2015). *Plant Physiology and Development*. 6th edn online. Sinauer Associates. *www.plantphys.net*

TERN Australia (2018). *Effective Field Calibration and Validation Practices: A practical handbook for calibration and validation satellite and model-derived terrestrial environmental variables for research and management*. A TERN Landscape Assessment Initiative, NCRIS. ISBN 978-0-646-94137-0. *https://www.tern.org.au/NEW-CalVal-handbook-for-remote-sensing-bgp4370.html*

Trabaud, L. (1987). Fire and survival traits of plants. In *The role of fire in ecological systems*. (Ed: Trabaud, L.) The Hague, SPB Academic Publishing. pp. 65–89.

Trabaud, L. (1991). Fire regimes and phytomass growth dynamics in a *Quercus coccifera* garrigue. *Journal of Vegetation Science*, 2, 307–14.

Violle, C., Navas, M.L., Vile, D., Kazakou, E., Fortunel, C., Hummel, I., and Garnier, E. (2007). Let the concept of trait be functional! *Oikos*, 116, 882–892.

Vogel, S. (1970). Convective cooling at low airspeeds and the shapes of broad leaves. *Journal of Experimental Botany*, 21, 91–101.

Walters, D.R. (2006). Disguising the leaf surface: the use of leaf coatings for plant disease control. *European Journal of Plant Pathology*, 114, 255–260.

Weatherley P (1965). The state and movement of water in the leaf. *Symposia of the Society for Experimental Biology*, 19, 157–184.

Weisz, P.B., and Fuller, M.S. (1962). *The Science of Botany*. McGraw-Hill, New York.

Westoby, M., and Wright, I.J. (2006). Land-plant ecology on the basis of functional traits. *Trends in Ecology and Evolution*, 21(5), 261–268.

White, P.J., and Brown, P.H. (2010). Plant nutrition for sustainable development and global health. *Annals of Botany*, 105(7), 1073–1080.

Williams, M., Woodward, F.I., Baldocchi, D.D., and Ellsworth, D. (2004). CO_2 capture from the leaf to the landscape, In: *Photosynthetic Adaptation: Chloroplast to Landscape* (Eds: W.K. Smith, T.C. Vogelmann and C. Critchley). Ecological Studies 178, Springer.

Xu, F., Guo, W., Xu, W., Wei, Y., and Wang, R. (2009). Leaf morphology correlates with water and light availability: What consequences for simple and compound leaves? *Progress in Natural Science*, 19, 1789–1798.

Yarwood, C.E. (1978). Water and the infection process. In *Water deficits and plant growth. Volume V. Water and plant disease*. (Ed: T.T. Kozlowski). Academic Press, New York. pp. 141–173.

Yeats, T.H., and Rose, J.K. (2013). The formation and function of plant cuticles. *Plant physiology*, 163(1), 5–20. *https://doi.org/10.1104/pp.113.222737*

Youngentob, K.N., Renzullo, L.J., Held, A.A., Jia, X., Lindenmayer, D.B., and Foley, W.J. (2012). Using imaging spectroscopy to estimate integrated measures of foliage nutritional quality. *Methods in Ecology and Evolution* 3, 416–426. doi:*10.1111/j.2041-210X.2011.00149.x*

5 Attributes of Individual Plants

Plants supply food, oxygen, medicines, clothing, shelter, and fuel for human populations. They also modulate local atmospheric conditions, recharge groundwater, and stabilise and enrich soils. The following sub-sections describe specific attributes of plants that are relevant to the interpretation of EO datasets:

- structure (see Section 5.1)—shape, size and volume;
- physiological processes (see Section 5.2)—photosynthesis, respiration, transpiration, and thermal stability; and
- growth (see Section 5.3)—life cycle, phenology, abscision, photomorphogenesis, and nutrient use efficiency.

5.1 Structure

Within any organism, groups of similar cells form tissue, which become specialised for particular functions. For example, xylem tissues transport fluids within a plant. Likewise, groups of tissues with a common function form organs, such as roots, stems, leaves, or flowers. The plant organs determine its internal and external structure. The stems or trunks of plants not only provide their structural scaffolding, but also enclose the vascular pipeline, which distributes water and nutrients from the roots to plant leaves, flowers, and fruit, and circulates energy resources from leaves to other parts of the plant. Below we consider two structural attributes of plants that are relevant to EO: growth form (see Section 5.1.1) and biomass (see Section 5.1.2).

5.1.1 Growth form

Growth form, or habit, describes the overall dimensions and branching, or structural characteristics, of plants, and results from both hereditary and environmental factors. Some plant classification systems refer to growth form as life form (see Section 1.1), while others use that term to differentiate between woody and non-woody vegetation (Hnatiuk *et al*., 2009). The broadest categories for growth form are:

- trees—large, woody plants supported on a main stem or trunk with secondary branches;
- shrub (or bush)—smaller woody plant with multiple stems;
- vine—woody or herbaceous plant with climbing or twining stem; and
- ground covers:
  - forbs—herbaceous, broad-leaved plant, often with conspicous flowers; and
  - grass—herbaceous plant with slender leaves (blades) and inconspicous flowers.

These categories are often further sub-divided into height classes and/or described in terms of their vertical position in the canopy relative to their neighbouring plants, that is, overstorey, midstorey, or understorey (see Figure 5.1).

Background image: Aerial view of a mangrove canopy. **Source:** © Shutterstock image ID 440199721

Figure 5.1 Vegetation cover classes

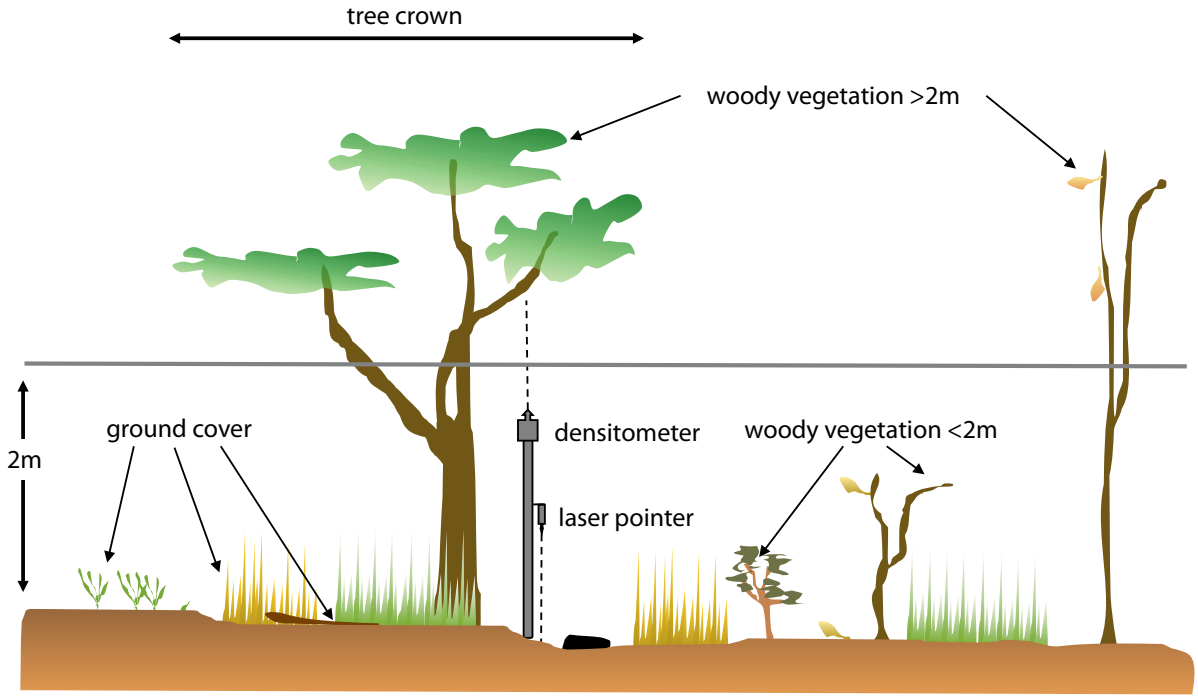

Source: Muir *et al.* (2011) Figure 10

Taller and heavier plants generally require the support of a woody structure, either as part of its own habit or provided by a host plant. Woody plants are characterised by thickened xylem tissue, such as occurs in trees, shrubs, palms, and some cycads, ferns, and vines. The standard Australian system for describing growth forms in vegetation is detailed in Hnatiuk *et al.* (2009). This system has been used extensively for national classifications of vegetation, such as NVIS (see Section 2.3.1).

Plant height can be measured in absolute or relative terms (see Section 5.1.2). Actual plant height can be estimated from trigonometry using a clinometer or sensed remotely using lidar equipment (see Excursus 5.1 and Section 16.5). The vertical distribution of vegetation can also be represented as foliage profile diagrams for either individual plants or groups of plants (see Figure 5.2). This provides more information than just the maximum height as it shows where most foliage will intercept incoming radiation and has been related to various aspects of plant ecology (Yokozawa and Hara, 1995). Vegetation profiles can vary with species and development stages and are indicative of wildlife habitat.

Figure 5.2 Foliage profile

Foliage profile for a multi-layer canopy

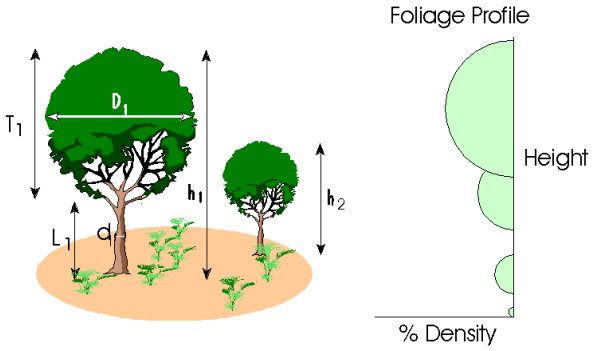

Source: Jupp and Lovell (2007) Figure 2.4

Excursus 5.1—Lidar

Source: Nicholas Coops, University of British Colombia, and Glenn Newnham, CSIRO

Lidar (Light Detection and Ranging) imaging systems can operate on a range of EO platforms (see Volume 1A—Section 15.1). These active remote sensing systems emit pulses of light to determine the distance (or range) to a target. Transmission of each emitted pulse is precisely timed, as is the time when its return (or echo) from the target is detected. Using the speed of light and the elapsed time between transmission and return of the pulse, the distance between the sensor and the target can be calculated. Based on the known trajectory of the laser beam, a three-dimensional point cloud can also be computed (Lim *et al.*, 2003; see Volume 1A—Excursus 15.1).

Figure 5.3 Lidar operation

A continuous waveform sensor would record the continuous height profile shown on the left of tree in the diagram below. Multiple discrete return sensors record the heights of discrete targets intercepted by the laser pulse. A first-return sensor would only record the height of the first target encountered, which in this example is the height of the first intercepted branch. A last-return sensor would only record the distance to the last object encountered by the laser beam, so is useful for terrain mapping.

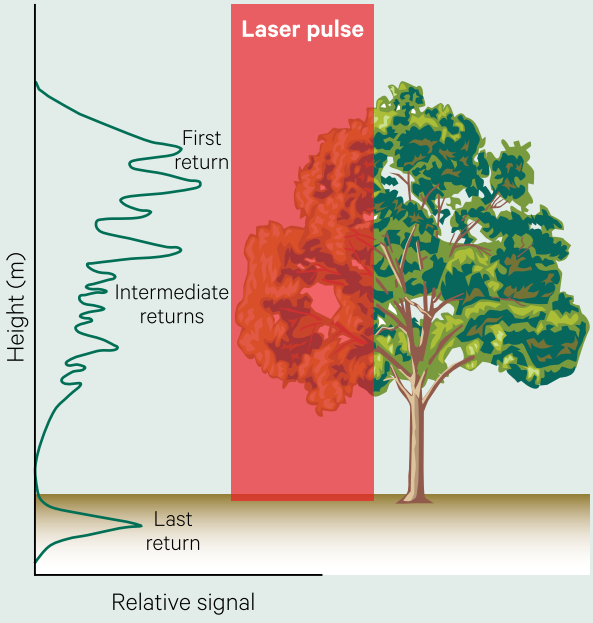

A lidar system comprises three major components: a laser device, an inertial navigational measurement unit (IMU), and a Global Positioning System (GPS) unit. Lidar systems can be classified as either small footprint or large footprint systems, and sample with either:

- discrete return—recording up to five returns per laser footprint (Lim *et al.*, 2003) and optimised to derive terrain surface heights with sub-metre accuracy (Blair *et al.*, 1999, Schenk *et al.*, 2001); or
- full waveform—acquiring a fully digitised, returned pulse for continuous, sub-metre, vertical profiles (see Figure 5.3).

Small footprint lidar systems for both discrete return and full waveform sampling are widely available and, as the number of returns recorded per emitted pulse increases with new sensor developments, these systems provide increasingly detailed structural information. For a given species, small footprint lidar measurement error has been demonstrated to be:

- < 1.0 m for individual tree heights (Persson *et al.*, 2002);
- < 0.5 m for plot-based estimates of maximum and mean canopy height with full canopy closure (Magnussen and Boudewyn, 1998; Magnussen *et al.*, 1999; Næsset, 2002); and
- more precise than manual, field-based measurements (Næsset and Økland, 2002).

Large footprint, full waveform systems are less common but systems such as the Scanning Lidar Imager of Canopies by Echo Recovery (SLICER) and Laser Vegetation Imaging Sensor (LVIS) instruments (Harding *et al.*, 2001; Blair *et al.*, 1999) have been proven for mapping forest structure (Lefsky *et al.*, 2005).

Airborne

Airborne platforms used for Earth Observation (EO) include manned and unmanned aeroplanes and helicopters (see Volume 1A—Section 11 for details). Airborne Laser Scanning (ALS) systems can be carried on any of these platforms. Unmanned Aerial Vehicles (UAV) potentially offer greater flexibility, increased spatial resolution, and more rapid assessment of vegetated landscapes than manned aircraft (although current systems are restricted both by weight and flying time and, to some extent, aviation restrictions). For example, Wallace *et al.* (2012a, 2012b) describe the development of a low-cost UAV lidar system that includes a discrete return lidar and high definition video camera. This system was capable of acquiring extremely dense lidar point clouds (62 points per m^2), from which detailed measurements of tree locations, heights and crown dimensions could be derived. Point cloud density also varies with flying height and speed, so for a given lidar system, there is a trade-off between data density and extent of coverage. An increasing range of portable lidar scanning units are becoming available, often including smart interfaces to avoid potential collisions and providing localisation, navigation, and flight control when GPS is not available.

Satellite

Satellite laser sensors such as the Geoscience Laser Altimeter System (GLAS), which was onboard the Ice, Cloud and land Elevation Satellite (ICESat), acquired global waveform data over forests from 2003 to 2009 with a large footprint spanning over 90 m (see Excursus 6.1). Two additional spaceborne lidar systems have been launched and are acquiring lidar data in 2020. Specifically, both the full waveform Global Ecosystem Dynamics Investigation (GEDI) on the International Space Station (ISS) and single photon lidar system on ICESAT2 are beginning to provide valuable space-based data for vegetation assessments (Hancock *et al.* 2019; Markus *et al.*, 2017).

Terrestrial

While ALS systems are relatively cost-effective for large areas (Næsset and Nelson, 2007; Wulder *et al.*, 2008), the structure of understorey components is often obscured by taller vegetation from an overhead perspective (Lovell *et al.*, 2003), and information about tree trunks is not directly visible to the scanner. Accordingly, to complement airborne lidar data, a number of studies have used ground-based lidar (or Terrestrial Laser Scanning, TLS) systems, which observe the canopy structure from below (Henning and Radtke, 2006; Hilker *et al.*, 2010; Jupp *et al.*, 2009). These systems can be mounted on tripods or moving vehicles to acquire data for all or selected portions of the hemispherical field of view (Hyyppa *et al.*, 2012). TLS instruments mounted on a tripod can scan forest stands out to radial distances of hundreds of metres (Calders *et al.*, 2020) depending on vegetation density, and have been installed on a permanent basis at selected locations to monitor growth following disturbances.

TLS allows extremely dense point clouds to be acquired (see Figure 5.4) which can be used to generated very detailed, three-dimensional models of vegetation structure for individual trees (see Section 16.5.2). Established methods exist to derive tree height, diameter at breast height (DBH), and above ground biomass (AGB) from TLS (Calders *et al.*, 2015a, 2015b; see Section 16.5). Thus, TLS already delivers information on forest structure that cannot be derived from plot-based forest surveys (Newnham *et al.*, 2015) and promises to enable full, three-dimensional mapping of ecosystem structure (Calders *et al.*, 2020).

Figure 5.4 TLS-based three-dimensional complexity of forest

Grey shades in image below indicate distance from RIEGL VZ-400 TLS instrument to vegetation elements in a simple notophyll vine forest at Robson Creek, Queensland. The graph shows derived plant area volume density as a function of canopy height using method outlined by Calders *et al.* (2015b).

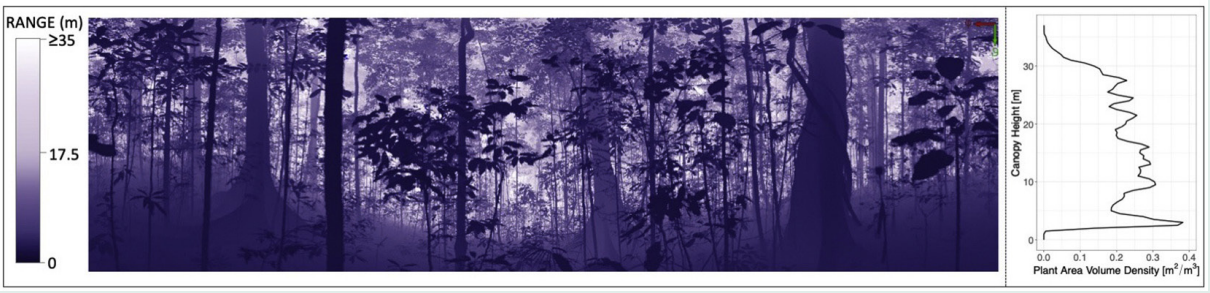

Source: Calders *et al.* (2020) Figure 1

5.1.2 Biomass

Any biological matter from organisms that are alive or decomposing is called biomass (see Section 7.4 for related productivity terms). Biomass predominantly comprises carbon, hydrogen, and oxygen, with lesser amounts of nitrogen and other elements. It represents the solar energy stored in organic matter and, as such, can be used for fuel. In ecological terms, biomass estimates express the mass of biological organisms per unit area and can be referenced for individual species or communities (see Section 7.4).

Depending on the location and state of decomposition of biomass, it can be differentiated into four categories:

- above ground biomass—all living plant matter above the soil surface, including foliage, stems, branches, bark, flowers, and seeds;
- below ground biomass—all living roots below the soil surface, including:
  - fine roots (< 2 mm diameter);
  - small roots (2–10 mm diameter); and
  - large roots (> 10 mm diameter);
- litter—all dead plant material on the soil surface that is less than some specified diameter[6], usually decomposing; and
- dead mass—all other dead woody biomass both above and below the soil surface.

Plant biomass is an indicator of plant vigour (see Section 9.6), site productivity (see Sections 7.4 and 10.2.2), carbon stocks (see Section 17), and fire risk (see Section 18). It is traditionally measured by destructive sampling of selected plants and expressed in terms of fresh and/or dry weight. Biomass measurements are reported in terms of Fresh Biomass (FBM), Oven-dried Biomass (DBM), or Dry Matter Content (DMC). Litter traps are commonly used to non-destructively measure falling plant parts, such as fruit, leaves, flowers, and petioles. Other non-destructive methods for measuring biomass include visual obstruction sampling, vertical and horizontal image analysis, radiation reflectance measurement, allometric relationships, scaled digital image of plant silhouettes, aerial and terrestrial laser scanning (see Excursus 5.1), and analysis of EO imagery (Tanaka *et al.*, 1998; Montes *et al.*, 2000; Holzgang, 2001; Tomasel *et al.*, 2001; Vermeire and Gillen, 2001; Thursby *et al.*, 2002; Tackenberg, 2007; Zehm *et al.*, 2003). Detailed reviews of biomass sampling methods are provided by Catchpole and Wheeler (1992) and Schaefer (2018).

Biomass monitoring is used to derive estimates of net primary production (NPP; see Section 7.4) and analyse plant growth (Cornelissen *et al.*, 2003; Perez-Harguindeguy *et al.*, 2013). The vertical biomass distribution can be derived from sampling at defined cutting heights (Tackenberg, 2007). While this profile is indicative of the competitive vigour of particular species (Schwinning and Weiner, 1998), it is not commonly measured (Tackenberg, 2007).

EO measures of biomass offer an efficient mechanism to generate landscape scale estimates of biomass. Optical reflectance data have been reliably related to foliage biomass (see Section 8) and SAR data has been used to infer woody biomass for forest carbon tracking (Mitchell *et al.*, 2010, 2012; Lehmann *et al.*, 2012) and pasture biomass (Schmidt *et al.*, 2016; see Sections 13 and 15). Lidar instruments, by effectively constructing a three-dimensional model of a target (see Excursus 5.1), furnish valuable information on vegetation structure, and both terrestrial laser scanning (TLS) and airborne laser scanning (ALS) are gaining popularity for estimating woody biomass in forestry and environmental surveys (Jupp and Lovell, 2007; Schaefer, 2018; see Section 16).

5.2 Physiological Processes

Plants function via a number of physiological processes. The following processes have direct relevance to EO-based studies: photosynthesis (see Section 5.2.1); respiration (see Section 5.2.2); transpiration (see Section 5.2.3); and thermal stability (see Section 5.2.4).

5.2.1 Photosynthesis

Photosynthesis is the primary energy capture mechanism in the biosphere. This process transforms light energy into chemical energy. Photosynthetic organelles, principally chloroplasts in leaves (see Figure 4.1), convert light and carbon dioxide (CO_2) and water into glucose and oxygen:

light energy + carbon dioxide + water
= glucose + oxygen

6 For example 10 cm—specified by individual countries (Schaefer, 2018)

Figure 5.5 Reflectance characteristics of typical green leaf structure

Chloroplasts reflect green wavelengths but absorb blue and red wavelengths for use in photosynthesis. Spongy mesophyll cells strongly reflect infrared wavelengths.

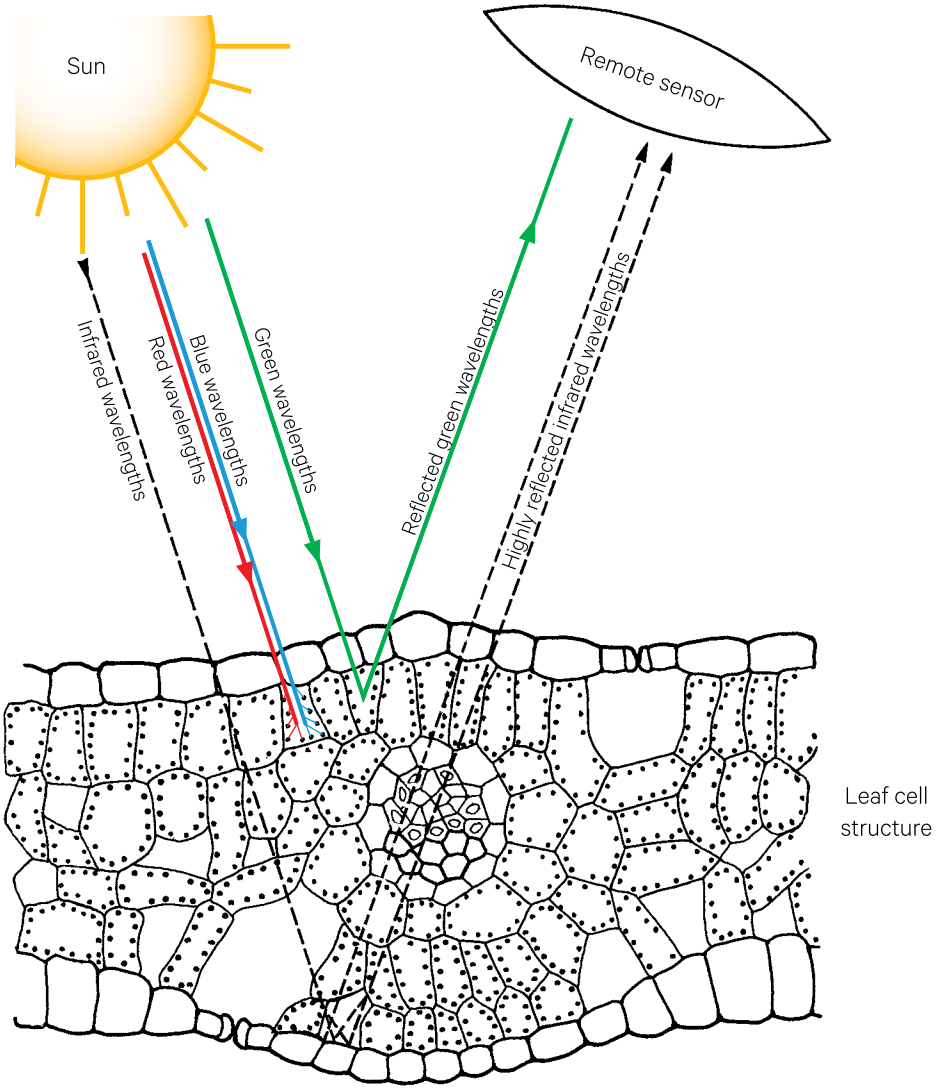

Source: Harrison and Jupp (1989) Figure 5

Principally blue and red wavelengths from the Sun's energy are absorbed by plant pigments during this process (see Section 4.3), with green and NIR wavelengths being reflected (hence the green colour of most living vegetation; see Figure 4.3 and Figure 5.5). As introduced in Section 4.1.1 above, gaseous exchange of water and CO_2 between the leaf surface and the atmosphere occurs via the stomata, whose opening and closing are controlled by guard cells. The plant sugars resulting from photosynthesis form an energy store, which is either consumed by the plant (to fuel internal metabolic processes and growth) or by external heterotrophs.

In simplistic terms, the rate of photosynthesis determines plant growth and vigour and, below species-specific thresholds, increased levels of CO_2, sunlight and heat can increase photosynthetic activity. As the name implies, photosynthesis is a photochemical reaction, that is, one that is initiated by the absorption of light energy (Rabinowitch and Govindjee, 1965). The speed of this process is limited by the:

- intensity of light—low intensities reduce the speed of photosynthesis;
- concentration of CO_2—low concentrations limit photosynthetic activity; and
- ambient temperature—extreme conditions, too hot or too cold, limit photosynthesis.

Table 5.1 Photosynthetic pathways

Characteristic	Photosynthetic Pathway		
	C_3	C_4	CAM
Name	First stable product from CO_2 is a 3-carbon compound	First stable product from CO_2 is a 4-carbon compound	Process discovered in Crassulaceae family CO_2 initially stored as 4-carbon acid
Carbon Fixation	In single chloroplast using RuBiCO enzyme	In chloroplast of thin-walled mesophyll cell using phosphoenol pyruvate (PEP) enzyme	In chloroplast at night using PEP enzyme then stored in cell vacuole as malate
Calvin Cycle	In same chloroplast	In chloroplast of thick-walled bundle sheath cell	In same chloroplast during daytime
Stomata	Open during day and generally close at night	Open during day and generally close at night	Open during the night and generally closed during the day
Advantages	Better performance with ample water and sunshine	Better performance when CO_2 levels are low Highest growth rates, comprising 25% of terrestrial photosynthesis Withstand higher light levels plus salinity and dryness No photorespiration Stomata open for shorter periods for CO_2 intake so less transpiration	Use less water than C_3 or C_4 plants Better recovery from drought stress Can assimilate CO_2 during day with abundant moisture
Disadvantage	Photorespiration	Energy used to move intermediate products to different cell locations	Low rates of photosynthesis; slow growth and low yield
Location	Throughout leaf (and some stems)	Inner leaf cells with Kranz anatomy	Thick, fleshy leaves and stems
Occurrence	~85% plants; Mostly in cooler temperate regions	> 19 families including sugar cane, saltbush, corn, summer annuals, and many grasses Mostly in tropical and subtropical grasslands and savannas	~10% plants: cacti, agaves, some orchids, ferns, and bromeliads Mostly in arid environments

Photosynthesis involves two fundamental biochemical processes:

- carbon fixation—CO_2 is converted into a stable intermediate product; then the
- Calvin Cycle—sugar is produced from the intermediate product.

Three metabolic pathways for photosynthesis have been identified: C_3, C_4, and CAM (Crassulacean Acid Metabolism). While most plants use the C_3 process, both the C_4 and CAM processes offer efficiency advantages to plants growing in arid environments. C_4 plants compartmentalise the intermediate processing steps to photosynthesise at a faster rate than C_3 plants and thus avoid photorespiration (see Section 5.2.2 below), while CAM plants can delay the Calvin Cycle to conserve energy. C_4 plants are very productive, comprising only 3% of vascular plants but conducting 25% of terrestrial photosynthesis (Sage, 2004), and have been observed to be more dominant geographically as temperature increases and rainfall decreases (Hattersley, 1983). Since photosynthesis in C_4 plants requires less nitrogen, these plants can also thrive in less fertile soils. Relevant characteristics of these three photosynthetic pathways are summarised in Table 5.1.

5.2.2 Respiration

The opposite process to photosynthesis is respiration, that is, the energy stored in the sugar product is released in the presence of oxygen, to produce CO_2 and water:

Glucose + oxygen =
energy + carbon dioxide + water

By consuming oxygen, this can be viewed as an oxidation reaction. Unlike photosynthesis, respiration occurs in most plant cells and is not dependent on light.

Respiration fuels plant metabolic processes and permits growth. In most plants, the rates of both photosynthesis and respiration increase with temperature up to a species-dependent threshold, at which point respiration occurs more rapidly than photosynthesis. In bright, hot conditions, stomata close and the ambient CO_2 levels in a plant can drop. If photosynthesis continues when the concentration of CO_2 levels drop below 50 ppm, oxygen is fixed instead of CO_2. This process is called photorespiration and is less efficient in terms of energy production for the plant.

5.2.3 Transpiration

Transpiration releases water from plants via stomata, the leaf pores that permit water vapour from the leaf to transfer into the atmosphere and CO_2 from the atmosphere to enter the leaf. Guard cells surround each stomate to control its opening and closing, and hence are an important factor in determining the rate of transpiration (see Section 4.1.1). In hot and dry conditions plants generally close their stomata to avoid excessive moisture loss. Most water loss from plants results from transpiration, but there is also a small volume of water lost via evaporation from leaf surfaces. Water stress restricts transpiration, reduces photosynthetic efficiency, and limits plant productivity (Salisbury and Ross, 1969).

The transpiration process achieves three essential functions in plants:

- water provides both the solvent and the vehicle to transport:
  - minerals from the roots to plant stems and leaves via xylem cells; and
  - sugars from the leaves to the rest of the plant via phloem cells;
- turgor pressure in plant cells is maintained by water, providing both structural support and controlling the operation of guard cells (see Section 4.2.1); and
- evaporative cooling from transpiration delivers most of the cooling provided by a shade tree (with an increase in vegetative cover of 10% in urban areas reducing the land surface temperature by 1.2°C; Coutts *et al.*, 2016).

The rate of transpiration is determined by the balance between two primary forces:

- water potential differential between the soil and atmosphere around the plant—dry air will encourage more water to leave the plant and hence increase transpiration; and
- resistance of leaf cuticle, stomata, and the leaf boundary layer to water movement—leaves slow down water loss from transpiration by closing stomata and increasing cuticle thickness. The boundary layer comprises a thin, stationary layer of air surrounding the leaf surface through which leaf water must diffuse to enter moving air (see Section 4.4).

Thus, transpiration rates increase in response to several environmental conditions:

- light—stomata open in bright light to allow CO_2 into the leaf for photosynthesis;
- temperature—due to evaporation and diffusion of water at higher temperatures;
- wind—windy conditions quickly remove water vapour and speed up diffusion;
- soil moisture—plants with access to adequate soil moisture will transpire more than those in dry soil;

and decreases with

- humidity—humid conditions slow diffusion of water vapour from the leaf.

The rate of transpiration (in mols of water/cm^2/sec) can be expressed as the equation:

$$TR = \frac{\text{LW potential} - \text{ambient AW potential}}{\text{resistance}}$$

where TR is transpiration rate, LW is leaf water, and AW is atmospheric water.

Leaf transpiration is either measured directly using a leaf porometer or indirectly via leaf temperature (Leinonen *et al.*, 2006). Models of transpiration rates at the level of individual leaves have been developed from detailed measurements of conductance characteristics, including CO_2 capture (involving a porometer or infrared gas analyser; Jones, 1992) and boundary layer properties (Brenner and Jarvis, 1995). Whole plant transpiration can also be measured via thermal sensors that monitor xylem sap fluxes from the root system to the canopy (Granier, 1987; Bush *et al.*, 2010). The Bowen ratio (ratio of sensible to latent heat flux; see Section 5.2.4) is used to estimate whole ecosystem evapotranspiration (see Sections4.4 and 7.6). Optical spectroscopy has also been used in conjunction with chemometric methods to determine leaf water content (Zhang *et al.*, 2012).

5.2.4 Thermal stability

The temperature of a material is indicative of its energy content. Thermal energy is exchanged between plants and their environment by:

- conduction and convection;
- absorption and emission; and
- evaporation of moisture.

Only a small proportion (3–6%) of the solar energy intercepted for photosynthesis is actually converted into chemical energy (FAO, 1997). The harvested energy that is not converted into biomass is dissipated as heat or chlorophyll fluorescence.

Within any biological system, the net (or stored) energy is the difference between the energy input and energy output. At equilibrium, the energy balance sums to zero, that is, energy input equals energy output, so that no energy is stored. The energy produced and/or consumed in metabolic processes within a leaf is relatively insignificant in comparison with other heat exchange processes in leaves. While convective heat transfer is encouraged by windy conditions or when the air temperature is higher than the leaf temperature, little heat is lost by conduction. Evaporation provides a generous mechanism for heat dissipation, especially in hot, dry conditions.

The boundary layer surrounding a leaf resists heat transfer from the leaf to the surrounding air (see Section 4.4), so impacts leaf temperature. If the adjacent air is cooler than the leaf surface, air circulates around the leaf and removes some heat by convection, but high boundary layer conductances resist this transfer of heat and water vapour (Martin *et al*., 1999). Leaf temperature depends on the leaf energy balance and can be expressed as a function of the temperature, humidity, density, water vapour pressure, and specific heat capacity of the ambient air, and the isothermal radiation absorption, boundary layer resistance, and stomatal resistance of the leaf (Jones, 1992).

The metabolic processes that enable plants to survive only operate within a restricted range of temperatures, with different plants being suited to different temperature ranges. Leaf temperatures generally track within 2°C of the diurnal cycle of air temperatures but may be much higher in full sunlight with little air movement, especially when water stressed (Nelson and Bugbee, 2015). Both within a single plant, and between plants of the same species in different locations, however, individual leaves are exposed to differing amounts of sunlight and wind. To enable all leaves within a plant to maintain comparable temperatures, sunlit foliage in the upper canopy of trees and shrubs intercepts light less efficiently than shaded foliage. Variations can occur in leaf shape and orientation, as well as transpiration rates, with the result that more exposed leaves are generally smaller and have a greater perimeter than less exposed ones (see Section 4.1.2). Nonetheless, being composed largely of water, leaves exposed to full sunlight carry a high heat load. Much of this load is dissipated by:

- sensible (meaning perceptible) heat loss as thermal EMR (or emitted energy: E_R); and
- evaporative (or latent energy: E_L) heat loss, or evaporation.

The ratio of sensible and evaporative heat losses is called the Bowen Ratio (BR; Lewis, 1995):

$$BR = \frac{\text{sensible heat loss}}{\text{latent heat loss}}$$

This ratio is high when the supply of water is limited (low evaporation) and low for well-watered plants. Accordingly, BR is typically higher for dry ecosystems such as deserts and lower for tropical vegetation. Some plants, such as cactii, have adapted to dry climates by minimising transpiration and enduring high leaf temperatures. Such adaptations are usually associated with slow growth rates. When air and leaf temperatures are very similar, as occur for irrigated grass in calm conditions, BR values are close to zero. Canopy measurements of evapotranspiration can be derived from BR, net incident radiation, soil heat loss, and gradients in temperature and water vapour above the canopy (Taiz *et al*., 2015; see Section 7.6).

Leaf temperature is important as an indicator of transpiration rate and is frequently monitored for irrigation scheduling (see Sections 9.4 and 9.5). Studies employing suites of proximal sensors to quantify plant water status have demonstrated that leaf temperature is strongly correlated with stem water potential, air temperature, relative humidity, photosynthetically active radiation, and wind speed, especially for shaded leaves (Udompetaikul *et al*., 2011).

The temperature of a leaf can be measured using a thermocouple (generally attached to shaded side; Tarnopolsky and Seginer, 1999), infrared thermometer (Blad and Rosenberg, 1976), or thermal imaging (Hartz *et al*., 2006; Leuzinger *et al*., 2010). For example, WaterWise is a smart irrigation tool that uses proximal infrared thermometers to detect when a plant is approaching stress (CSIRO, 2019). Such monitoring is being integrated with weather forecasts, soil moisture status, and other crop data to optimise the water use efficiency and yield of high-value crops (see also Section 9.5). Thermal imagery (8–14 μm; Volume 1B—Section 7) can also be used to monitor evapotranspiration and water deficit stress (see Section 9.4).

Certain metabolic processes associated with heat dissipation in plants, including xanthophyll pigment interconversion, have been related to variations in leaf absorption characteristics near wavelength 531 nm (Demmig-Adams, 1990). EO-based spectral indices such as the Photochemical Reflectance Index (PRI) have been proposed to assess the efficiency of photosynthetically active radiation usage when plants are water stressed (Peñuelas *et al*., 1997; see Section 8.1.4).

5.3 Growth

Most fundamental characteristics of plant species are determined by their genetic inheritance, but environmental factors such as the availability of nutrients, sunlight, moisture, and CO_2 can accelerate and enhance plant growth. Likewise, the presence of predators and adverse environmental conditions (excess moisture, wind, heat, or cold) can impede growth. Table 5.2 summarises the principal factors that are responsible for the quantity and quality of plant growth. These primary factors are related by the sequence (Kramer and Boyer, 1995):

Hereditary Potential + Environmental Factors —>
Plant Processes and Conditions —>
Quantity and Quality of Growth

The following sub-sections consider plant growth in the context of plant life cycle (see Section 5.3.1), phenology (see Section 5.3.2), abscision (see Section 5.3.3), photomorphogenetic (light-dependent) processes (see Section 5.3.4), and nutrient use efficiency (see Section 5.3.5).

Table 5.2 Plant growth factors

Primary Factor	Components
Hereditary Potential	Root system—depth, extent
	Leaves—size, shape, area, thickness
	Stomata—number, location, behaviour
Environmental Factors	Soil—texture, structure, depth, chemical composition, pH, aeration, temperature, water holding capacity, water conductivity
	Atmospheric—precipitation (amount and seasonal distribution), evaporation, CO_2 concentration, radiant energy, temperature, wind, vapour pressure
	Biotic—competing plants, pathogens, predators
Plant Processes and Conditions	Water absorption, distribution, transpiration
	Internal water balance—water potential, turgidity, stomatal opening, cell enlargement
	Chemical composition—pigments, growth regulators, nutrients
	Metabolic processes—photosynthesis, respiration, nutrient cycling
Quantity and Quality of Growth	Size of cells, organs, plant
	Dry weight, succulence, chemical composition
	Root to shoot ratio
	Vegetative versus reproductive growth

Adapted from: Kramer and Boyer (1995) Figure 1.1

5.3.1 Life cycle

The life cycle of all plants spans from germination to death, with a wide range of variations between species in terms of modes of reproduction and stages of maturation. Annual plants complete their life cycle within a single year and generally expend more energy on seed production than establishment. Biennial plants grow and die within two years, using the first growing season for growth and the second for reproduction. Perennial plants live for more than two years and generally become stronger and larger plants that produce seed over many years.

Different plants use different mechanisms to create their next generation. Reproduction can occur asexually, creating genetically identical offspring, via cuttings, runners, stolons, or suckers, or division of rhizomes, bulbs, and corms. Alternatively, sexual reproduction combines genes from both male and female parent plants to produce genetically different offspring. This mechanism is used by most seed and spore producing plants and enables greater biological diversity.

The life cycle of a typical angiosperm, for example, can be summarised in terms of several consecutive stages. For a tree, a seed germinates, grows through the seedling stage into a sapling or young tree, develops into a mature tree, then produces seed-bearing fruit of some form. During these stages of growth, the size, shape, and structure of the tree changes. At senescence the tree dies, shedding limbs and leaves to create compost for future generations. Growth stages of groups of plants is further discussed in Section 6.5.

5.3.2 Phenology

Phenology studies the relationships between life cycle stages in biota (plants and animals) and weather and climate (Schwartz, 2013). Plant phenology considers plant life cycles and their interactions with seasonal, climatic, and other rhythms. Seasons are largely driven by variations in the amount of solar radiation that reaches the Earth's surface at different locations (see Volume 1A—Section 3). Recurring events within plant life cycles are triggered by periodic environmental changes, particularly those related to seasonal changes in ambient temperature and light levels. In order to better understand and manage plant growth, phenology attempts to identify these trigger factors and relies heavily on chronology, that is, the analysis of historical records relating to the dates of key events. Indeed, indigenous communities have traditionally used phenological indicators as a climatic almanac.

For annual plants, the stages of growth are clearly delineated within an annual cycle by the extent of green plant cover (see Sections 5.1.2 and 9.1). Four key event dates can be identified in the growth of annual plants:

- greening—green leaves become visible as photosynthesis begins;
- maturity—growing leaves attain maximum green leaf area;
- senescence—brown leaves appear as photosynthesis rapidly decreases; and
- dormancy—end of cycle when photosynthesis ceases.

Broad scale phenological changes are most obvious during leaf emergence and senescence. Plants respond to both diurnal variations in light levels, temperature and precipitation, and seasonal changes in day length, or photoperiodism. The latter often operates in conjunction with a chilling threshold for many temperate species. Similarly, the developmental responses of some plants are affected by the ratio of red to far red light in different seasons, whereas the growing cycles of crops are more closely related to changes in temperature and precipitation.

While the dates of key phenological events can vary from season to season and from year to year, they provide valuable insight into longer term vegetation responses to climatic variations. Inter-seasonal and interannual variations in phenology affect different parts of the biosphere in different ways, so an understanding of phenological trigger factors is fundamental to understanding the spatiotemporal dynamics of carbon, water, and thermal cycles of Earth (Schwartz, 2013). Thus, phenology is relevant to studies of vegetation distribution (Chuine, 2010), agricultural management (Chmielewski, 2003; Keatinge *et al*., 1998), food web interactions (Straile, 2002), ecosystem productivity dynamics (Myneni *et al*., 1997, 2007), land surface modelling (Richardson *et al*., 2012), biosphere-atmosphere interactions (Flanagan, 2009), and epidemiology (Luvall *et al*., 2011; Malone *et al*., 2019).

5.3.3 Abscission

For efficiency reasons, plants shed, or abscise, any part of their structure that is no longer required. Deciduous plants produce leaves that only last one seasonal cycle, whereas evergreen leaves are designed to function for many years. These two types of leaves offer distinct advantages and disadvantages in particular environments. The key factors that appear to determine whether deciduous or evergreen species dominate or intermix in a geographic region are photosynthetic capacity, nutrient availability, and winter desiccation (Smith, 1993).

To replace their photosynthetic system each year, deciduous plants expend more nutrient resources than evergreen plants, whose leaves are replaced gradually. Deciduous plants typically have greater capacity for both photosynthesis and transpiration. They accumulate food reserves in warm weather, which are stored in roots and stems to enable survival through winter. The productivity of such plants is driven by seasonal or climatic changes. In cold environments, it is easier for plants to abscise their leaves than to protect them from the drying impact of freezing in winter. Abscision usually involves significant resorption of soluble nutrients, such as phosphorus, nitrogen, and potassium, from senescing tissue. Routine abscision also discourages parasites, pathogens, and predators.

Rather than shed their leaves, evergreen species have developed various mechanisms to protect their leaves from winter temperatures, such as converting free water in cells into a gel which will not freeze. However, evergreen plants lose more water during winter and are more susceptible to predators.

In temperate regions, deciduous plants abscise leaves in response to seasonal temperature changes, so are dormant during winter. In subtropical areas, leaf drop is triggered by non-seasonal rainfall patterns with foliage being shed to reduce water loss. The longevity of leaves in woody plants has obvious relevance to measuring foliage attributes in different seasons and localities. Plants that maintain green leaves throughout the year are categorised as Persistent Green Vegetation (see Section 9.1), that is, evergreen perennials such as vascular plants with deep roots and slow rates of biomass growth and decay (Donohue *et al*., 2009).

5.3.4 Photomorphogenesis

In addition to pigments, plants contain a number of photoreceptors that are sensitive to particular wavelengths of EMR, such as phytochrome (red and far red), cryptochrome (blue and UVa), and phototropin (blue; Casal, 2000; Briggs and Olney, 2001). While the concentrations of these photoreceptors are much lower than those of the major plant pigments (see Section 4.3), they have distinct absorption spectra and impact the reflectance spectra of leaves (Blackburn, 2007).

Apart from photosynthesis, many processes involved with plant growth and development are dependent on the presence or absence of light (Sullivan and Deng, 2003). Photomorphogenetic processes include:

- germination of seeds in response to red light;
- leaf development in dicotyledon seedlings in red light;
- photoperiodism in older plants triggers seasonal changes, such as flowering after extended periods of long nights;
- phototropism—bending plant organs towards (blue) light source due to rapid cell growth on shaded side of plant; and
- nyctinastic movements (diurnal changes controlled by circadian rhythms and light reception) in higher plants in low, 'far red' (700–750 nm) light levels (such as folding leaves or flower petals at night).

5.3.5 Nutrient use efficiency

One measure of the efficiency of nutrient usage in plants is the proportion of organic matter produced per unit of absorbed nutrient. For short-lived plants, this has been observed to be inversely correlated with the nutrient concentration in plant tissue, with plants growing on less fertile soils having higher nutrient concentrations than the same plants grown on more fertile sites (Chapin, 1980). Long-lived perennials, however, are more likely to recycle nutrients as leaves senesce, so for these plants nutrient use efficiency is inversely related to the concentration of nutrients in above ground litterfall, root turnover, and live organic matter (Vitousek, 1982).

The minerals nitrogen, phosphorus, and calcium are more likely to be removed from forest trees in the fine litter fraction (comprising leaves, twigs, small branches, flowers, fruit, and seeds), while potassium tends to be leached by rain as throughfall. Nitrogen Use Efficiency (NUE), the ratio of nitrogen output to nitrogen input, is used as an indicator of the efficiency of nutrient usage in food production (EU Nitrogen Expert Panel, 2015). NUE varies between different types of plants, with plants growing on less fertile soils typically using nitrogen more efficiently in active leaves and/or resorbing more nitrogen from senescing leaves, and as stem wood transitions to heartwood. The rate of nitrogen release from decomposing plant matter is highly correlated with its C:N ratio, such that slower rates of litter decomposition are observed when N levels are low (Vitousek, 1982).

5.4 Further Information

Photosynthesis

Rabinowitch and Govindjee (1965, 1969)

Bowen Ratio

Lewis (1995): *ftp://195.37.229.5/pub/outgoing/jwinder/BowenRatioLiterature/Lewis_BullAmeriMeteoSoc_1995.pdf*

Plant Physiology Protocols

Prometheus Wiki, CSIRO: *http://prometheuswiki.publish.csiro.au/tiki-custom_home.php*

5.5 References

Blackburn, G.A. (2007). Hyperspectral remote sensing of plant pigments. *Journal of Experimental Botany*, 58(4), 855–867.

Blad, B.L., and Rosenberg, N.J. (1976). Measurement of crop temperature by leaf thermocouple, infrared thermometry and remotely sensed thermal imagery. *Agronomy Journal*, 68, 635–641.

Blair, J.B., Rabine, D.L., and Hofton, M.A. (1999). The Laser Vegetation Imaging Sensor (LVIS): A medium-altitude, digitization-only, airborne laser altimeter for mapping vegetation and topography. *ISPRS Journal of Photogrammetry and Remote Sensing*, 54, 115–122.

Brenner, A.J., and Jarvis, P.G. (1995). A heated leaf replica technique for determination of leaf boundary layer conductance in the field. *Agricultural and Forest Meteorology*, 72, 261–275.

Briggs, W.R., and Olney, M.A. (2001). Photoreceptors in Plant Photomorphogenesis to Date. Five Phytochromes, Two Cryptochromes, One Phototropin, and One Superchrome. P*lant Physiology*, 125(1), 85–88. *https://doi.org/10.1104/pp.125.1.85*

Bush, S.E., Hultine, K.R.J.S., Sperry, J.S., and Ehleringer, J.R. (2010). Calibration of thermal dissipation sap flow probes for ring- and diffuse-porous trees. *Tree Physiology*, 30, 1545–1554.

Calders, K., Newnham, G., Burt, A., Murphy, S., Raumonen, P., Herold, M., Culvenor, D., Avitabile, V., Disney, M., Armston, J., and Kaasalainen, M. (2015a). Nondestructive estimates of above-ground biomass using terrestrial laser scanning. *Methods in Ecology and Evolution*, 6, 198–208. doi:*10.1111/2041-210X.12301*

Calders, K., Schenkels, T., Bartholomeus, H., Armston, J., Verbesselt, J., and Herold, M. (2015b). Monitoring spring phenology with high temporal resolution terrestrial LiDAR measurements. *Agricultural and Forest Meteorology*, 203, 158–168. *https://doi.org/10.1016/j.agrformet.2015.01.009*

Calders, K., Adams, J., Armston, J., Bartholomeus, H., Bauwens, S., Patrick Bentley, L., Chave, J., Danson, F.M., Demol, M., Disney, M., Gaulton, R., Krishna Moorthy, S.M., Levick, S.R., Saarinen, N., Schaaf, C., Stovall, A., Terryn, L., Wilkes, P., Verbeecka, H. (2020). Terrestrial laser scanning in forest ecology: Expanding the horizon. *Remote Sensing of Environment*, 251, 112102. *https://doi.org/10.1016/j.rse.2020.112102*

Casal, J.J. (2000). Phytochromes, Cryptochromes, Phototropin: Photoreceptor Interactions in Plants. *Photochemistry and Photobiology*, 71(1), 1–11. *https://onlinelibrary.wiley.com/doi/pdf/10.1562/0031-8655(2000)0710001PCPPII2.0.CO2*

Catchpole, W.R., and Wheeler, C.J. (1992). Estimating plant biomass: A review of techniques. Australian *Journal of Ecology*, 17, 121–31.

Chapin, S.F. (1980). The Mineral Nutrition of Wild Plants. *Annual Review of Ecology and Systematics*, 11, 233–60.

Chmielewski, F.-M. (2003). Phenology and Agriculture, In: *Phenology: An Integrative Environmental Science, Tasks for Vegetation Science*. (Ed: M.D. Schwartz) Springer, Netherlands. pp. 505–522.

Chuine, I. (2010). Why does phenology drive species distribution? *Philosophical Transactions of the Royal Society B Biological Sciences*, 365, 3149–3160. doi:*10.1098/rstb.2010.0142*

Cornelissen, J.H.C., Lavorel, S., Garnier, E., Díaz, S., Buchmann, N., Gurvich, D.E., Reich, P.B., ter Steege, H., Morgan, H.D., van der Heijden, M.G.A., Pausas, J.G., and Poorter, H. (2003). A handbook of protocols for standardised and easy measurement of plant functional traits worldwide. *Australian Journal of Botany*, 51, 335–80.

Coutts, A.M., Harris, R.J., Phan, T., Livesley, S.J., Williams, N.S.G., and Tapper, N.J. (2016). Thermal infrared remote sensing of urban heat: Hotspots, vegetation, and an assessment of techniques for use in urban planning. *Remote Sensing of Environment*, 186, 637–651.

CSIRO (2019). *WaterWise* webpage, Digiscape Future Science Platform website: *https://research.csiro.au/digiscape/digiscapes-projects/waterwise/*

Demmig-Adams, B. (1990). Carotenoids and photoprotection: a role for the xanthophyll zeaxanthin. *Biochimica et Biophysica Acta*, 1020, 1–24.

Donohue, R.J., McVicar, T.R., and Roderick, M.L. (2009). Climate-related trends in Australian vegetation cover as inferred from satellite observations. 1981–2006. *Global Change Biology*, 15(4), 1025–39.

EU Nitrogen Expert Panel (2015). *Nitrogen Use Efficiency (NUE)—an indicator for the utilization of nitrogen in agriculture and food systems*. Wageningen University, Alterra, PO Box 47, NL-6700 Wageningen, Netherlands. *http://www.eunep.com/wp-content/uploads/2017/03/Report-NUE-Indicator-Nitrogen-Expert-Panel-18-12-2015.pdf*

FAO (1997). Renewable biological systems for alternative sustainable energy production. *FAO Agricultural Services Bulletin*. *http://www.fao.org/docrep/w7241e/w7241e05.htm#1.2.1*

Flanagan, L.B. (2009). Phenology of Plant Production in the Northwestern Great Plains: Relationships with Carbon Isotope Discrimination, Net Ecosystem Productivity and Ecosystem Respiration. In: *Phenology of Ecosystem Processes: Applications in Global Change Research*. Springer, New York, USA, pp. 169–185. doi:*10.1007/978-1-4419-0026-5_7*

Granier, A. (1987). Evaluation of transpiration in a Douglas-Fir stand by means of sap flow measurements. *Tree Physiology*, 3, 309–319.

Hancock, S., Armston, J., Hofton, M., Sun, X., Tang, H., Duncanson, L.I., Kellner, J.R., and Dubayah, R. (2019). The GEDI simulator: a large-footprint waveform Lidar simulator for calibration and validation of spaceborne missions. *Earth and Space Science*, 6(2), 294–310.

Harding, D.J., Lefsky, M.A., Parker, G.G., and Blair, J.B. (2001). Laser altimeter canopy height profiles. Methods and validation for closed-canopy, broadleaf forests. *Remote Sensing of Environment*, 76, 283–297.

Harrison, B.A., and Jupp, D.L.B. (1989). *Introduction to Remotely Sensed Data: Part ONE of the microBRIAN Resource Manual*. CSIRO, Melbourne. 156pp.

Hartz, D.A., Prashad, L., Hedquist, B.C., Golden, J., and Brazel, A.J. (2006). Linking satellite images and hand-held infrared thermography to observed neighborhood climate conditions. *Remote Sensing of Environment*, 10, 190–200.

Hattersley, P.W. (1983). The distribution of C3 and C4 grasses in Australia in relation to climate. *Oecologia*, 57, 113–128.

Holzgang. O. (2001). Assessing above-ground phytomass in an alpine region using a hand-held radiometer. *Botanica Helvetica*, 111, 73–85.

Hnatiuk R.J., Thackway R., and Walker J. (2009). Vegetation. In: *Australian Soil and Land Survey: Field Handbook* (3rd Edn). (Ed: National Committee on Soil and Terrain) pp. 73–125. CSIRO Publishing, Melbourne.

Jones, H.G. (1992). *Plants and Microclimate*. Cambridge, Cambridge University Press.

Jupp, D.L.B., and Lovell, J.L. (2007). *Airborne and ground-based lidar systems for forest measurement: background and principles*. CSIRO Marine and Atmospheric Research, Canberra. 151 p. *https://doi.org/10.4225/08/58615c112f355*

Keatinge, J.D.H., Qi, A., Wheeler, T.R., Ellis, R.H., and Summerfield, R.J. (1998). Effects of temperature and photoperiod on phenology as a guide to the selection of annual legume cover and green manure crops for hillside farming systems. *Field Crops Research*, 57 (2), 139–152.

Kramer, P.J., and Boyer, J.S. (1995). *Water relations of plants and soils*. Academic Press, San Diego. *http://dspace.udel.edu:8080/dspace/handle/19716/2830*

Lefsky, M.A., Harding, D.J., Keller, M., Cohen, W.B., Caraba-jal, C.C., Del Bom Espirito-Santo, F., Hunter, M.O., and de Oliveira Jr., R. (2005). Estimates of forest canopy height and aboveground biomass using ICESat. *Geophysical Research Letters*, 32, L22S02. doi:*10.1029/2005GL023971*.

Lehmann, E.A., Caccetta, P.A., Zhou, Z-S., McNeill, S.J., Wu, X., and Mitchell, A.L. (2012). Joint processing of Landsat and ALOS PALSAR data for forest mapping and monitoring. *IEEE Transactions on Geoscience and Remote Sensing*, 50, (1), 55–67.

Leinonen, I., Grant, O.M., Tagliavia, C.P.P., Chaves, M.M., and Jones, H.G. (2006). Estimating stomatal conductance with thermal imagery. *Plant Cell and Environment*, 29, 1508–1518.

Leuzinger, S., Vogt, R., and Korner, C. (2010). Tree surface temperature in an urban environment. *Agricultural and Forest Meteorology*, 150, 56–62.

Lewis, J.M. (1995). The Story behind the Bowen Ratio. *Bulletin of the American Meteorological Society*, 76(12), 2433–2443. *ftp://195.37.229.5/pub/outgoing/jwinder/BowenRatioLiterature/Lewis_BullAmeriMeteoSoc_1995.pdf*

Lim, K., Treitz, P., Wulder, M., St-Onge, B., and Flood, M. (2003). LiDAR remote sensing of forest structure. *Progress in Physical Geography*, 27, 88–106.

Luvall, J.C., Sprigg, W.A., Levetin, E., Huete, A., Nickovic, S., Pejanovic, G.A., Vukovic, A., Van deWater, P.K., Myers, O.B., Budge, A.M., Zelicoff, A.P., Bunderson, L., Crimmins, T.M. (2011). Use of MODIS satellite images and an atmospheric dust transport model to evaluate Juniperus spp. Pollen phenology and dispersal. Proceedings of *WG VIII/2: Advances in Geospatial Technologies for Health, ISPRS 34*, Santa Fe, New Mexico, USA.

Magnussen, S., and Boudewyn, P. (1998). Derivations of stand heights from airborne laser scanner data with canopy-based quantile estimators. *Canadian Journal of Forest Research*, 28, 1016–1031.

Magnussen, S., Eggermont, P., and LaRiccia, V. (1999). Recovering tree heights from airborne laser scanner data. *Forest Science*, 45, 407–422.

Malone, J.B., Bergquist, R., Martins, M., and Luvall, J.C. (2019). Use of Geospatial Surveillance and Response Systems for Vector-Borne Diseases in the Elimination Phase. *Tropical medicine and infectious disease*, 4(1), 15. *https://doi.org/10.3390/tropicalmed4010015*

Martin, T.A., Hinckley, T.M., Meinzer, F.C., and Sprugel, D.G. (1999). Boundary layer conductance, leaf temperature and transpiration of Abies amabilis branches. *Tree Physiology*, 15, 435–443.

Mitchell, A.L., Milne, A.K., Tapley, I., Lowell, K., Caccetta, P., Lehmann, E., and Zhou, Z-S. (2010). Wall-to-wall mapping of forest extent and change in Tasmania using ALOS PALSAR data. *Proceedings of IGARSS*, July, 2010, Hawaii.

Mitchell, A.L., Tapley, I., Milne, A.K., Williams, M., and Lowell, K. (2012). *Radar processing methodologies for the generation of wall-to-wall mosaics*. CRC Spatial Information. *http://www.crcsi.com.au/assets/Uploads/Files/1-IFCIRA-SARproc.pdf*

Montes, N., Gauquelin, T., Badri, W., Bertaudiere, V., and Zaoui, E.H. (2000). A non-destructive method for estimating above-ground forest biomass in threatened woodlands. *Forest Ecology and Management*, 130, 37–46.

Muir, J., Schmidt, M., Tindall, D., Trevithick, R., Scarth, P., and Stewart, J., (2011). *Guidelines for Field measurement of fractional ground cover: a technical handbook supporting the Australian collaborative land use and management program*. Tech. rep., Queensland Department of Environment and Resource Management for the Australian Bureau of Agricultural and Resource Economics and Sciences, Canberra. *http://data.daff.gov.au/data/warehouse/pe_hbgcm9abll07701/HndbkGrndCovMontring2011_1.0.0_HR.pdf*

Myneni, R.B., Keeling, C.D., Tucker, C.J., Asrar, G., and Nemani, R.R. (1997). Increased plant growth in the northern high latitudes from 1981 to 1991. *Nature*, 386(6626), 698. doi:*10.1038/386698a0*

Myneni, R.B., Yang, W., Nemani, R.R., Huete, A.R., Dickinson, R.E., Knyazikhin, Y., Didan, K., Fu, R., Negrón Juárez, R.I., Saatchi, S.S., Hashimoto, H., Ichii, K., Shabanov, N.V., Tan, B., Ratana, P., Privette, J.L., Morisette, J.T., Vermote, E.F., Roy, D.P., Wolfe, R.E., Friedl, M.A., Running, S.W., Votava, P., El-Saleous, N., Devadiga, S., Su, Y., Salomonson, V.V. (2007). Large seasonal swings in leaf area of Amazon rainforests. *Proceedings of the National Academy of Science*, 104, 4820–4823.

Næsset, E. (2002). Predicting forest stand characteristics with airborne scanning laser using a practical two-stage procedure and field data. *Remote Sensing of Environment*, 80(1), 88–99.

Næsset, E., and Økland, T. (2002). Estimating tree height and tree crown properties using airborne scanning laser in a boreal nature reserve. *Remote Sensing of Environment*, 79, 105–115.

Næsset, E., and Nelson, R. (2007). Using airborne laser scanning to monitor tree migration in the boreal-alpine transition zone. *Remote Sensing of Environment*, 110, 357–369.

Nelson, J.A., and Bugbee, B. (2015). Analysis of Environmental Effects on Leaf Temperature under Sunlight, High Pressure Sodium and Light Emitting Diodes. *PloS one*, 10(10), e0138930. *https://doi.org/10.1371/journal.pone.0138930*

Newnham, G.J., Armston, J.D., Calders, K., Disney, M.I., Lovell, J.L., Schaaf, C.B., Strahler, A.H., and Danson, F.M. (2015). Terrestrial Laser Scanning for Plot-Scale Forest Measurement. *Current Forestry Reports*, 1, 239–251. doi:*10.1007/s40725-015-0025-5*

Penuelas, J., LLusia, J., Pinol, J., and Filella, I. (1997). Photochemical reflectance index and leaf photosynthetic radiation-use-efficiency assessment in Mediterranean trees. *International Journal of Remote Sensing*, 18(13), 2863–2868.

Pérez-Harguindeguy, N., Díaz, S., Garnier, E., Lavorel, S., Poorter, H., Jaureguiberry, P., Bret-Harte, M.S., Cornwell, W.K., Craine, J.M., Gurvich, D.E., Urcelay, C., Veneklaas, E.J., Reich, P.B., PoorterJ, L., Wright, I.J., Ray, P., Enrico, L., Pausas, J.G., de Vos, A.C., Buchmann, N., Funes, G., Quétier, F., Hodgson, J.G., Thompson, K., Morgan, H.D., ter Steege, H., van der Heijden, M.G., Sack, A.L., Blonder, B., Poschlod, P., Vaieretti, M.V., Conti, G., Staver, A.C., Aquino, S., and Cornelissen, J.H.C. (2013). New handbook for standardised measurement of plant functional traits worldwide. *Australian Journal of Botany*, 61, 167–234.

Persson, A., Holmgren, H., and Söderman, U. (2002). Detecting and measuring individual trees using an airborne Laser scanner. *Photogrammetric Engineering and Remote Sensing*, 68, 925–932.

Rabinowitch, E.I., and Govindjee, R. (1965). The role of chlorophyll in photosynthesis. *Scientific American*, 213(1), 74–83. doi:*10.1038/scientificamerican0765-74*

Rabinowitch, E., and Govindjee, R. (1969). *Photosynthesis*. Wiley, New York.

Richardson, A.D., Anderson, R.S., Arain, M.A., Barr, A.G., Bohrer, G., Chen, G., Chen, J.M., Ciais, P., Davis, K.J., Desai, A.R., Dietze, M.C., Dragoni, D., Garrity, S.R., Gough, C.M., Grant, R., Hollinger, D.Y., Margolis, H.A., McCaughey, H., Migliavacca, M., Monson, R.K., Munger, J.W., Poulter, B., Raczka, B.M., Ricciuto, D.M., Sahoo, A.K., Schaefer, K., Tian, H., Vargas, R., Verbeeck, H., Xiao, J., Xue, Y. (2012). Terrestrial biosphere models need better representation of vegetation phenology: results from the North American Carbon Program Site Synthesis. *Global Change Biology*, 18, 566–584. doi:*10.1111/j.1365-2486.2011.02562.x*

Sage, R.F. (2004). The evolution of C-4 photosynthesis. *New Phytologist*, 161, 341–370.

Salisbury, F.B., and Ross, C. (1969). *Plant Physiology*. Wadsworth Publishing Company, Belmont.

Schaefer, M.T. (2018). Measurement of above ground biomass. Ch 12 in *Effective Field Calibration and Validation Practices: A practical handbook for calibration and validation satellite and model-derived terrestrial environmental variables for research and management*. Version 1.3. TERN Australia, ISBN 978-0-646-94137-0.

Schenk, T., Seo, S., and Csatho, B. (2001). Accuracy study of airborne laser scanning data with photogrammetry. International Archives of Photogrammetry and Remote Sensing, Volume XXXIV, Part 3/W4. Pp. 113–118 in *Land Surface Mapping and Characterization Using Laser Altimetry*, ISPRS III/3 and III/6 Workshop, Annapolis, MD.

Schmidt, M., Carter, J., Stone, G., and O'Reagain, P. (2016). Integration of Optical and X-Band Radar Data for Pasture Biomass Estimation in an Open Savannah Woodland. *Remote Sensing*, 8, 989. doi:*10.3390/rs8120989*

Schwartz, M.D. (Ed) (2013). *Phenology: An Integrative Environmental Science*. 2nd Edn. Springer Verlag, The Netherlands. 610p. doi.*10.1007/978-94-007-6925-0*

Schwinning, S., and Weiner, J. (1998). Mechanisms determining the degree of size asymmetry in competition among plants. *Oecologia*, 113, 447–455.

Smith, F.C. (1993). Evergreen vs. Deciduous Woody Plants: Which Wins Where. *Maine Naturalist*, 1(4), 205–212.

Straile, D. (2002). North Atlantic Oscillation synchronizes food-web interactions in central European lakes. *Proceedings of the Royal Society of London B Biological Sciences*, 269, 391–395. doi:*10.1098/rspb.2001.1907*

Sullivan, J.A., and Deng, X.W. (2003). From seed to seed: the role of photoreceptors in Arabidopsis development. *Developmental Biology*, 260(2), 289–297. *https://doi.org/10.1016/S0012-1606(03)00212-4*

Tackenberg, O. (2007). A New Method for Non-destructive Measurement of Biomass, Growth Rates, Vertical Biomass Distribution and Dry Matter Content Based on Digital Image Analysis. *Annals of Botany*, 99(4), 777–83.

Taiz, L., Zeiger, E., Moller, I.M., and Murphy, A. (2015). *Plant Physiology and Development*. 6th edn online. Sinauer Associates. *www.plantphys.net*

Tanaka, T., Yamaguchi, J., and Takeda, Y. (1998). Measurement of forest canopy structure with a laser plane range-finding method—development of a measurement system and applications to real forests. *Agricultural and Forest Meteorology*, 91, 149–60.

Tarnopolsky, M., and Seginer, I. (1999). Leaf temperature error from heat conduction along thermocouple wires. *Agricultural and Forest Meteorology*, 93, 185–194.

TERN Australia (2018). *Effective Field Calibration and Validation Practices: A practical handbook for calibration and validation satellite and model-derived terrestrial environmental variables for research and management*. A TERN Landscape Assessment Initiative, NCRIS. ISBN 978-0-646-94137-0. *https://www.tern.org.au/NEW-CalVal-handbook-for-remote-sensing-bgp4370.html*

Thursby, G.B., Chintala, M.M., Stetson, D., Wigand, C., and Champlin, D.M. (2002). A rapid, non-destructive method for estimating aboveground biomass of salt marsh grasses. *Wetlands*, 22, 626–30.

Tomasel, F.G., Paruelo, J.M., Abras, G., Ballarin, V., and Moler, E. (2001). A chromaticity-based technique for estimation of above-ground plant biomass. *Applied Vegetation Science*, 4, 207–212.

Udompetaikul, V., Upadhyaya, S.K., Slaughter, D., Lampinen, B., and Shackel, K. (2011). Plant Water Stress Detection Using Leaf Temperature and Microclimatic Information. *Proceedings of 2011 ASABE Annual International Meeting*. Paper 1111555, 7–10 August, Louisville.

Vermeire, L.T., and Gillen, R.L. (2001). Estimating herbage standing crop with visual obstruction in tallgrass prairie. *Journal of Range Management*, 54, 57–60.

Vitousek, P. (1982). Nutrient Cycling and Nutrient Use Efficiency. *The American Naturalist*, 119(4), 553–572.

Yokozawa, M., and Hara, T. (1995). Foliage Profile, Size Structure and Stem Diameter-Plant Height Relationship in Crowded Plant Populations. *Annals of Botany*, 76, 271–285.

Zehm, A., Nobis, M., and Schwabe, A. (2003). Multiparameter analysis of vertical structure based on digital image processing. *Flora*, 198, 142–160.

Zhang, Q., Li, Q., and Zhang, G. (2012). Rapid determination of leaf water content using VIS/NIR Spectroscopy Analysis with Wavelength Selection. *Journal of Spectroscopy*, 27, 93–105.

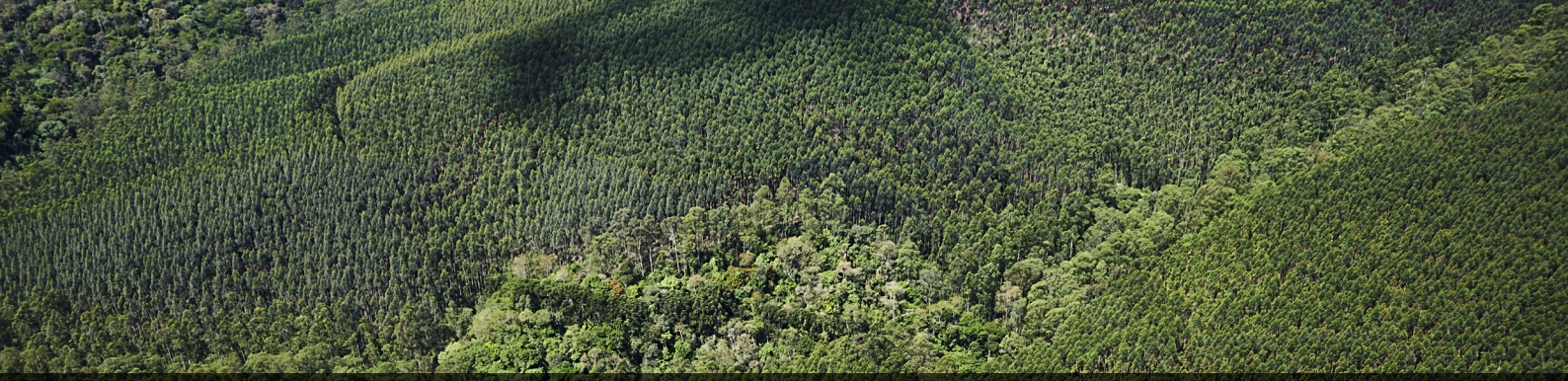

6 Attributes of Plant Communities

Plants tend to grow with friends, and individual species are frequently found in association with a predictable range of friends, through both facilitative and competitive mechanisms. Groups of plants can be characterised by a number of attributes such as their species composition, their spacing, their foliage volume, their canopy texture and colour, and their dynamics (see Section 2.3.1).

Often in vegetation science there is a need to more formally define plant communities into a classification scheme, so that the classification can serve as a surrogate for biodiversity (Margules and Pressey, 2000). Typically, the primary goal is to arrange a set of observations into groups based on various floristic and environmental attributes, many of which are discussed in this section. The groups have several purposes, but a common purpose in this context is to serve as a mapping classification scheme (see Section 2.3.1). The methods for creating the groups in the classification scheme can be directed by expert knowledge, numerical analysis, or some combination of both (De Caceres and Wiser, 2012). Expert knowledge employs *a priori* subjective knowledge to manually devise the groups and allocate observations to those groups. Numerical methods typically employ some form of supervised or unsupervised clustering approach, which group observations by analysing pattern and structure in the community attribute data (usually floristics and/or environmental information; see Volume 2E for details of classification methods).

Various methods have been devised to sample vegetation communities. Such methods are often based on quadrats, predefined areas within which vegetation attributes of a small number of plants are measured to infer traits that are representative of the larger population (see Volume 2D—Section 12). Quadrats are sometimes located along a sampling transect. Detailed guidelines for vegetation surveys in Australia are provided in Hnatiuk *et al.* (2009) and Muir *et al.* (2011).

The following sub-sections describe attributes of plant communities that are relevant to EO analyses:

- formations—combinations and permutations of different plants (see Section 6.1);
- horizontal spacing and pattern—layout of plants (see Section 6.2);
- density and cover—number and spread of plants (see Section 6.3);
- canopy colour and texture—how plant canopies blend (see Section 6.4);
- growth stages and phenology—how plants age and interact with seasonal variations (see Section 6.5); and
- succession—how associations change with time (see Section 6.6).

If we concentrate on any one particular species our impression will be one of flux and hazard, but if we concentrate on total community properties (such as biomass in a given trophic level) our impression will be of pattern and steadiness.
(May, 1974)

Background image: Textural variation within eucalypt forest canopy. **Source:** © Shutterstock image ID 186362276

6.1 Formations

Floristic composition, or association, indicates the variety of botanical species within a particular community. While botanical classification of individual plants involves visual comparison with standardised descriptive keys, which rely on both structural and floristic characteristics (see Section 5.1), structural classification of groups of plants is largely based on their growth form, vertical stratification, and spacing.

Any vegetation grouping can contain multiple growth forms, such as trees and ground covers, which tend to coexist as discrete layers or strata, with the tallest, or upper, stratum often typifying the group (see Figure 5.1). A hierarchical Australian system of classifying vegetation type on the basis of structural and floristic attributes was presented by Hnatiuk *et al*., (2009) and is summarised in Table 6.1. In this system, the broad floristic formation is defined by, and named after, the major species or genera that characterise the dominant stratum. In the nomenclature of NVIS (see Section 2.3.1), an association expands on the broad floristic formation to nominate three dominant or co-dominant species in each stratum (see Table 2.7).

Many vegetation classification systems stratify the vertical distribution of plants into height classes, where vegetation layers, or strata, are defined to differentiate between and within growth forms (see Table 6.2 and Figure 6.1). Such categories are relative to each association rather than corresponding to predefined heights.

Vegetation height is often correlated with biome, being an indication of both climatic extremes and edaphic resources. Since the diverse range of biomes in Australia complicates the task of defining absolute height classes, relative classes, which can be consistent within regional assessment areas, are recommended (NCST, 2009). An Australian implementation of relative height classes is given in Table 6.3. An integrated, structural classification that has been developed using optical and microwave datasets to map biomass across Australia is described in Excursus 6.1.

Figure 6.1 Height strata

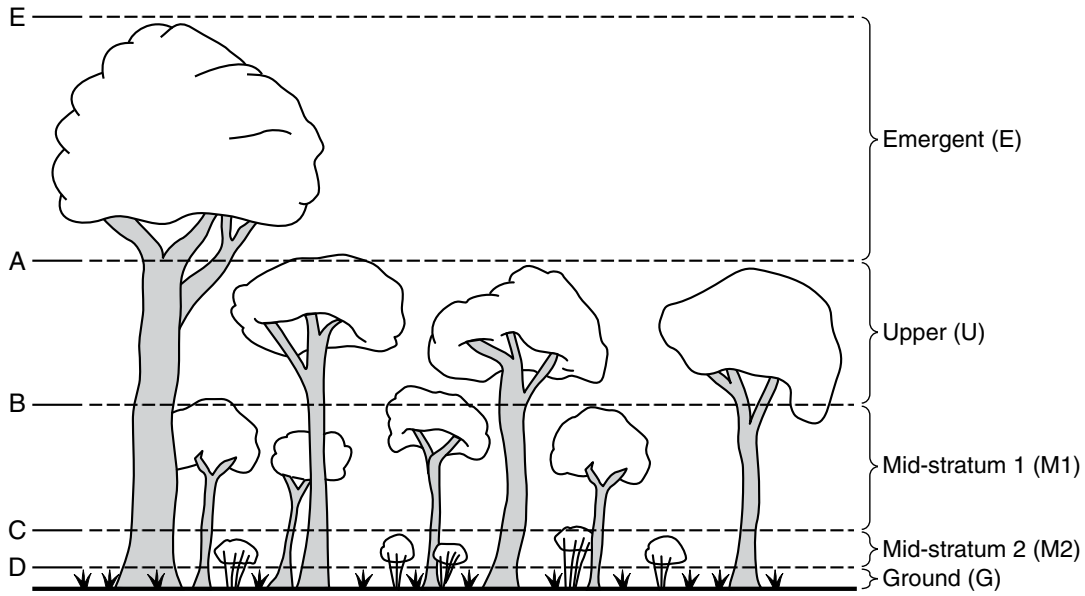

Source: Hnatiuk *et al.* (2009) Figure 8

Table 6.1 Vegetation formations

Vegetation Attributes	Vegetation Category		
	Formation	Structural Formation	Broad Floristic Formation
Life form (woody/non-woody)	✓	✓	✓
Crown separation	✓	✓	✓
Crown type		✓	✓
Growth forms in each stratum		✓	✓
Height of each stratum		✓	✓
Foliage cover of lower stratum		✓	✓
Cover and height of emergents		✓	✓
Characteristic species of dominant stratum			✓
Example	Dense woody plants	Very tall, dense trees	Very tall, dense *Eucalyptus* trees

Source: Hnatiuk *et al.* (2009)

Table 6.2 Height strata

Stratum	Description	Example
Emergent	Tallest plants above canopy, which may be dominant layer in sparse vegetation	E
Upper or Dominant	Vegetation forming canopy layer that has greatest ecological impact is generally the tallest stratum	U
Middle	Vegetation between canopy and ground layer when present	M1
		M2
Ground	Vegetation close to ground and is usually < 2 m (may be the dominant layer, as in grasslands).	G

Adapted from Hnatiuk *et al.* (2009)

Table 6.3 Height classes

Height (m)		Life Form	
Min	Max	Woody	Non-Woody
50	–	Giant	–
35	50	Extremely tall	–
20	35	Very tall	–
10	20	Tall	–
5	10	Medium	Giant
2	5	Low	Extremely tall
1	2	Dwarf	Very tall
0.5	1	Miniature	Tall
0.25	0.5	Micro	Medium
0.05	0.25	Nano	Low
–	0.05	–	Dwarf

Source: Hnatiuk *et al.* (2009)

Excursus 6.1—Vegetation Height and Structure Map

Source: Scarth *et al.* (2019)
National structure map: *http://auscover.org.au/purl/icesat-vegetation-structure*
Biomass library: *http://www.auscover.org.au/purl/biomass-plot-library*
Further information: *https://www.tern.org.au/satellite-eye-on-australias-vegetation/*

A detailed national map of vegetation structure (height and cover) has been developed for Australia based on EO datasets (see Table 6.4). This 30 m resolution structure map of Australian forest and woodland structure was derived from:

- Landsat TM/ETM+ imagery (30 m resolution; dry season 1987–2010) processed to Foliage Projective Cover (FPC);
- ALOS (Advanced Land Observing System) PALSAR (Phased Arrayed L-band Synthetic Aperture Radar) L-band Fine Beam Dual (HH and HV) mosaic product (25 m resolution) for 2010; and
- ICESat (Ice, Cloud and land Elevation satellite) GLAS (Geoscience Laser Altimeter System) L2 GLA14 (Global Land Surface Altimetry), acquired 2003–2009.

Table 6.4 Summary of structural classes

Structural formations used in the national structure map are adapted from NVIS (DEWR, 2007), Specht (1970), and Specht and Specht (1999)—see Section 2.3.1 and Table 2.6.

Lifeform and height of tallest stratum	Foliage Projective Cover (FPC) or Crown Cover (CC) of the tallest plant layer			
	Dense (70–100% FPC; > 80% CC)	Mid-dense (30–70% FPC; 50–80% CC)	Sparse (10–30% FPC; 20–50% CC)	Very Sparse/Isolated (< 10% FPC; 0.25–20% CC)
Trees > 30 m	Tall closed forest	Tall open forest	Tall woodland	Tall open woodland
Trees 10–30 m	Closed forest	Open forest	Woodland	Open woodland
Trees 5–10 m	Low closed forest	Low open forest	Low woodland	Low open woodland
Shrubs 2–8 m	Closed scrub	Open scrub	Tall shrubland	Tall open shrubland
Shrubs 0–2 m	Closed heath	Open heath	Low shrubland	Low open shrubland

Source: Scarth *et al.* (2019)

Figure 6.2 Processing overview

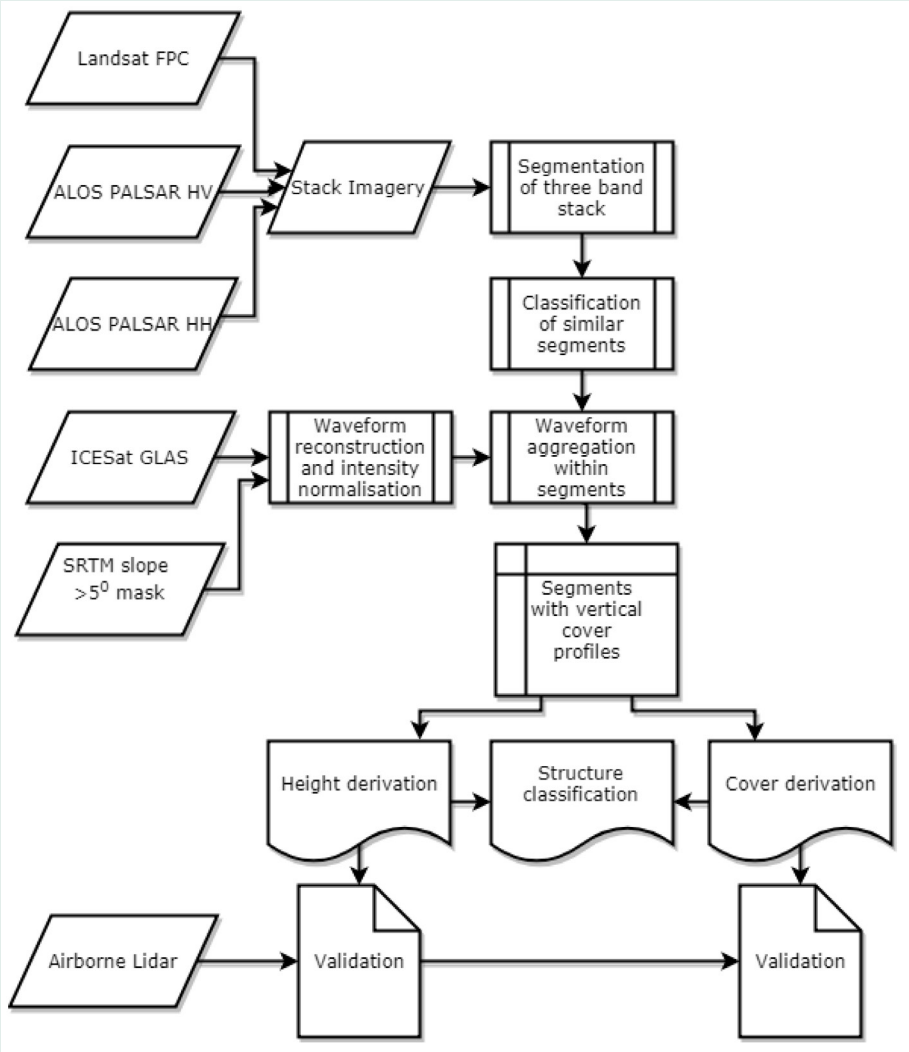

Source: Scarth *et al.* (2019) Figure 3

ALOS PALSAR data were integrated with Landsat-derived FPC data to produce a unique segmentation of the landscape into regions with similar vegetation structure. These regions were classified and associated with vertical plant profiles derived from ICESat GLAS waveforms to characterise vegetation height. Airborne lidar data was used to validate a range of forest structural types. The processing steps are summarised in Figure 6.2, with the resulting map being shown in Figure 6.3.

The Biomass library was constructed by methodically collating tree level data from over 15,000 plots located in all states, comprising over 1 million diameter measurements of individual trees. The biomass of each tree was estimated using a suite of allometric equations (Paul *et al.*, 2016, 2019) and biomass estimates for each plot were scaled to a per hectare metric. Both the structure map and the National Biomass Library are available online from TERN Australia (see Section 6.7).

Figure 6.3 Vegetation height and structure

Vertical plant profiles for the Australian continent, including height, cover, age class, and L-band backscatter characteristics based on the ICESat and Landsat time series and ALOS PALSAR datasets.

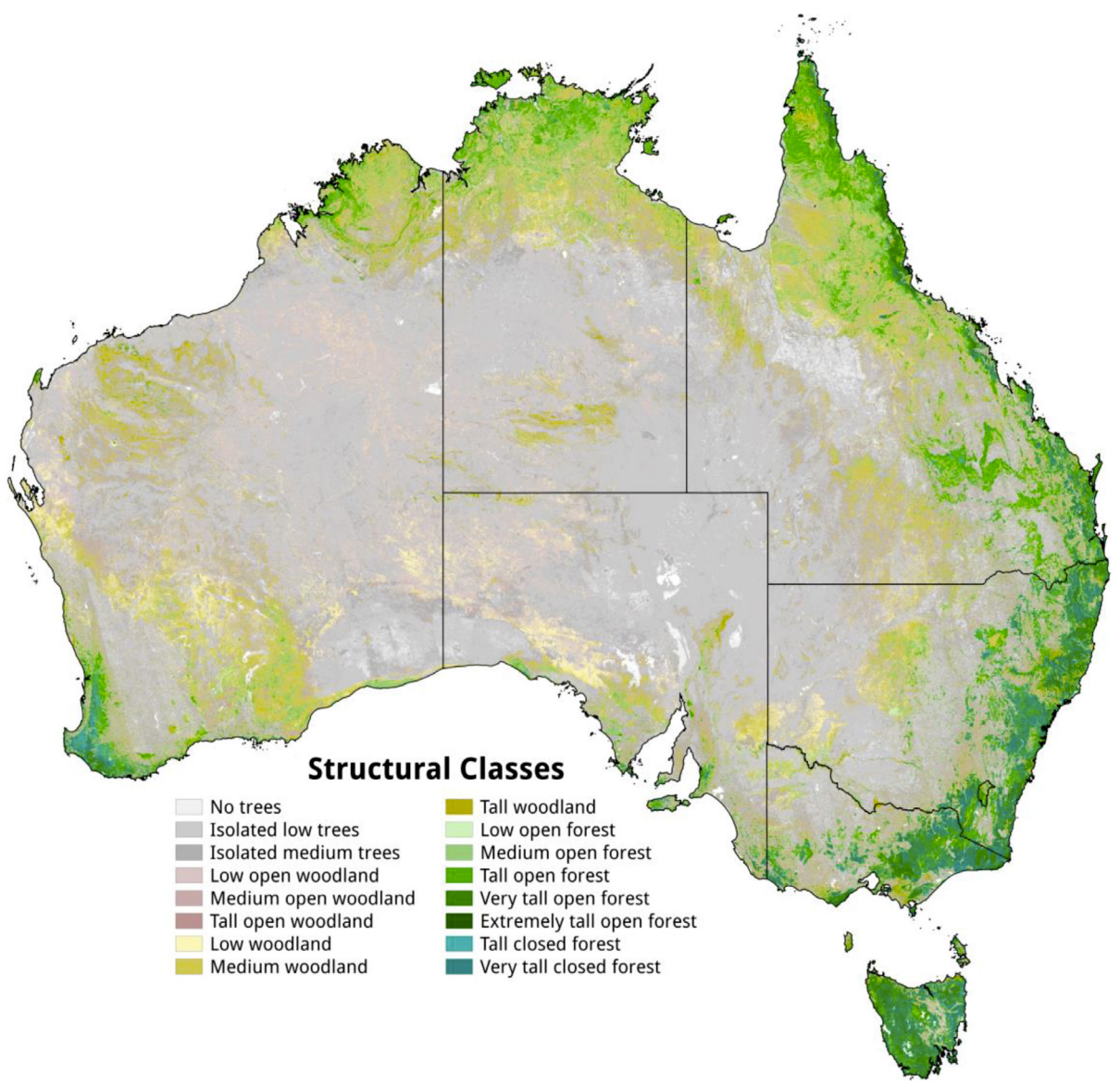

Source: Scarth *et al.* (2019) Figure 11

6.2 Horizontal Spacing and Pattern

Spacing of plants depends on their frequency and arrangement. Frequency indicates the likelihood of locating a particular species at a specific location and is indicative of its abundance. Estimates of species frequency are determined using field sampling of presence/absence counts within quadrats. Since frequency is often related to vegetation pattern and density, it can be misrepresented by quadrat methods when the quadrat size is inappropriate. The horizontal pattern formed by plants can be generalised into three types:

- random—unpredictable spacing, often resulting from wind dispersal of seed;
- regular—uniform distribution, usually resulting from controlled planting by *Homo sapiens*; or
- clumped—common for seedlings growing near a seed plant (see Figure 6.4).

Most natural vegetation associations create random or clumped patterns, such as uneven-aged forests, resulting from a continuous cycle of plant establishment and senescence. After a mayor disturbance however, such as a fire, natural regeneration can be arranged in random clumps of uniform age. By contrast, man-made forests are often planted in a regular pattern at one time, forming an even-aged forest, in which the range of tree ages is generally within 20% of the rotation age. The underlying pattern of plants directly influences the canopy texture (see Section 6.4).

Figure 6.4 Population distribution patterns

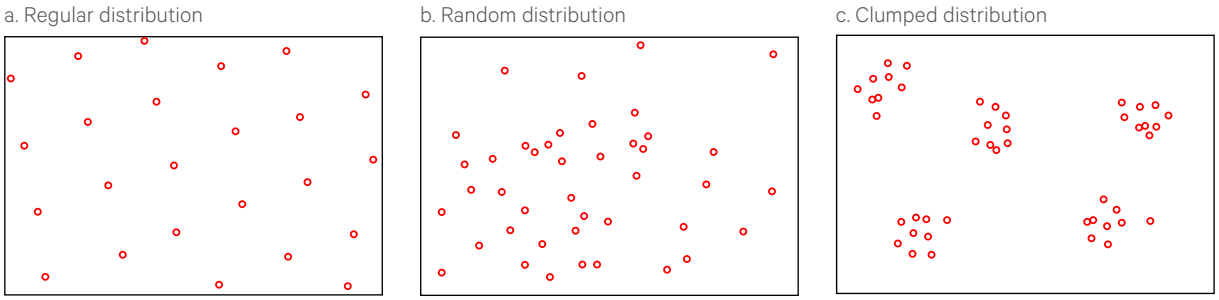

Source: Yerpo, Wikimedia Commons. (Retrieved from *http://en.wikipedia.org/wiki/Species_distribution#mediaviewer/File:Population_distribution.svg*)

6.3 Density and Cover

Vegetation density indicates the number of individual plants per unit area. Cover is the proportion of ground occupied by vegetation. Given the overlapping nature of vegetation, the combined cover for all plants in a given area can exceed 100%. Vegetation cover can be estimated from field sampling, aerial photography, or satellite imagery. Traditional measures of vegetation cover include foliage cover (see Section 6.3.1), cover-abundance (see Section 6.3.2), leaf area index (LAI—see Section 6.3.3), fraction of absorbed photosynthetically active radiation (fAPAR—see Section 6.3.4), basal area (BA—see Section 6.3.5), and fractional cover (see Section 6.3.6).

6.3.1 Foliage cover

Foliage cover, or leaf density, represents the amount of photosynthetic material, or biomass, of green vegetation within a given area. This has been measured in various ways, some of which include both foliage and branches, rather than just foliage. The term foliage cover is often reserved for estimates of foliage (and branch) material in ground layer vegetation (Hnatiuk *et al.*, 2009).

Some traditionally used measures attempt to estimate cover on the basis of vertical projection, that is, the proportion of ground beneath plants that would be shaded when the Sun is directly overhead:

- Foliage Cover %—the percentage of a sample site covered by the vertical projection of foliage (and branches for woody vegetation; Carnahan, 1977)
- Foliage Projective Cover (FPC)—the proportion of ground covered by the vertical projection of foliage only (Specht *et al.*, 1974).

These measures involve estimation of the extent of ground shadowing resulting from overhead foliage and have proved to be variable between estimators. More recent measures of vegetation density have attempted to reduce the subjectivity of field measurements by focusing on crown extent, rather than the foliage density. Within a defined sample area, % crown cover records the percentage of area covered by a vertical projection of the crown and is the recommended measure for plants higher than 1.5 m (Hnatiuk *et al*., 2009). The Crown Separation Ratio (CSR; Walker *et al*., 1988; Penridge and Walker, 1988) is computed as:

$$\text{CSR} = \frac{\text{mean distance between crowns}}{\text{mean crown width}}$$

This is best measured separately for each vegetation stratum and assumes approximately circular crowns. When measured in accordance with guidelines, CSR is directly related to crown cover %. Estimates of foliage density can subsequently be incorporated to convert crown projection estimates to foliage projection estimates. This process typically involves matching the actual tree crowns to photos of crown openness (Hnatiuk *et al*., 2009):

$$\%\ \text{foliage cover} = \%\ \text{crown cover} \times \text{crown type}$$

The term foliage cover is often reserved for estimates of foliage (and branch) volume in ground layer vegetation (Hnatiuk *et al*., 2009). For a measured distance, % foliage cover is the percentage covered by the vertical projection of plant material.

6.3.2 Cover-abundance

Cover-abundance estimates the quantity of individual species in a given sample area. The Braun-Blanquet Cover-Abundance Scale (Mueller-Dombois and Ellenberg, 1974) is commonly used to record vegetation cover-abundance on the basis of either:

- cover estimate—where vegetation covers more than 5% of the sample area; or
- plant count—when vegetation cover is less than 5%.

This method has been shown to be more efficient than density sampling methods, especially for baseline studies such as environmental impact analyses (Wikum and Shanholtzer (1978).

6.3.3 Leaf area index (LAI)

Leaf Area Index (LAI) attempts to quantify the extent of leaf overlap so varies with plant growth. It represents the total area of leaves (one-sided) projecting into a given vertical column and is computed as:

$$\text{LAI} = \frac{\text{total leaf area (one surface)}}{\text{ground area}}$$

This dimensionless parameter is considered to characterise the interface between canopy and atmosphere. Since the area of foliage that can intercept solar radiation essentially drives the microclimates within and beneath canopies, LAI is also indicative of canopy energy exchange processes, water interception and transpiration rates, and stand productivity (Bréda, 2003; see Section 7).

LAI estimates have traditionally required destructive, time-consuming sampling of leaves (see Section 5.1.2). Direct and semi-direct methods of measuring leaf area are reviewed by Bréda (2003). Indirect methods include the use of optical instruments that measure radiation transmission through the canopy, which can be subsequently converted to Plant Area Index (PAI) or Surface Area Index (SAI). Both of these measures implicitly include both foliage and woody elements of the canopy. Where multiple optical instruments are available, the canopy gap fraction ("the fraction of view that is unobstructed by canopy in any particular direction"; Welles and Cohen, 1996) can be computed (Schaefer *et al*., 2018). PAI/LAI estimates can also be derived using terrestrial laser scanning (Jupp *et al*., 2009; Strahler *et al*., 2008; see Excursus 5.1).

LAI is used to model the growth and yield of crops and forests (see Sections 12, 14, and 16). Many methods for deriving LAI assume that leaves are randomly distributed, so do not consider clumping or overlapping arrangements that commonly occur in nature. LAI models also need to consider the impact of leaf size (relative to the canopy extent) and leaf orientation, since these factors vary in different types of vegetation and modify how much radiation is transmitted through the canopy (Hill *et al*., 2006a, 2006b). Various adjustments have been proposed for these factors (such as Chen *et al*., 1997), but many authors recommend use of direct LAI measurements to calibrate any indirect estimates of canopy LAI in Australian ecosystems (Coops *et al*., 2004; Schaefer *et al*., 2018). Further, given the vertical leaf inclination of most *Eucalyptus* species, projective foliage cover has demonstrated closer correlation with some satellite-based LAI products than indirect LAI estimates (Hill *et al*., 2006a).

Given the functional link between LAI and the spectral reflectance of plant canopies, numerous techniques have been developed to derive LAI estimates from EO data (see Section 8.1). Procedures for validating LAI products derived from satellite imagery are detailed in Schaefer *et al*. (2018).

6.3.4 Fraction of absorbed photosynthetically active radiation (fAPAR)

Photosynthetically Active Radiation (PAR) is defined as EMR with wavelengths in the range 400–700 nm and includes both direct and diffuse light. Incident PAR represents the amount of PAR that reaches the top of a vegetation canopy. As detailed in Volume 1A, this varies with geographic location, season and atmospheric conditions. The Intercepted PAR (IPAR) is the amount of PAR reaching layers within the canopy as the light penetrates through the top layer. The amount of light that is actually absorbed by vegetation is called Absorbed PAR (APAR). The fraction of APAR (fAPAR) indicates the proportion of PAR that is absorbed by all vegetation layers within a canopy and is commonly estimated from transmittance measurements using the generalised relationship:

$$\text{fAPAR} = \frac{\text{APAR}}{\text{PAR}}$$

fAPAR includes:

- photosynthetically active vegetation components (PAV)—mostly chloroplasts;
- non-photosynthetically active vegetation components (NPV)—mostly senescent foliage, branches, and stems; and
- non-photosynthetic components in leaves—veins and cell walls (Xiao *et al*., 2004).

Thus, fAPAR is the proportion of PAR absorbed by both photosynthetic (PAV) and non-photosynthetic (NPV) components of vegetation:

$$\text{fAPAR} = \text{fAPAR}_{\text{PAV}} + \text{fAPAR}_{\text{NPV}}$$

It should be noted that the proportion of fAPAR deriving from PAR varies in different ecosystems. For example, in communities with sparse canopies, such as savannas and shrublands, $\text{fAPAR}_{\text{NPV}}$ can increase fAPAR by 10% to 40% (Asner *et al*., 1998). Accordingly, transmittance measurements may need to be taken at different heights within different ecosystems (Restrepo-Coupe *et al*., 2018). fAPAR can be viewed as representing the energy absorption capacity of a vegetation community (Fensholt *et al*., 2004) and is frequently expressed as a function of LAI (Baret and Guyot, 1991; Myneni and Williams, 1994; Ruimy *et al*., 1994, 1999). fAPAR can also be derived using quantum sensors, directional measurements, or three-dimensional models of canopy optics. fAPAR estimates can be impacted by solar zenith angle, diffuse radiation levels, canopy architecture, and variations in soil albedo (Gower *et al*., 1999). Methods for validating fAPAR products derived from EO imagery are reviewed by Baret *et al*. (2013) and Schaefer *et al*. (2018). An example of an EO-based fAPAR map of Australia is shown in Figure 6.5.

Figure 6.5 Fraction of Absorbed Photosynthetically Active Radiation (fAPAR)

fAPAR derived from MODIS/Terra imagery (LPDAAC MOD15A2 mosaic) acquired between 1 and 8 January 2016 (inclusive). This gridded 8-day composite shows fAPAR on a scale from 0 to 1.

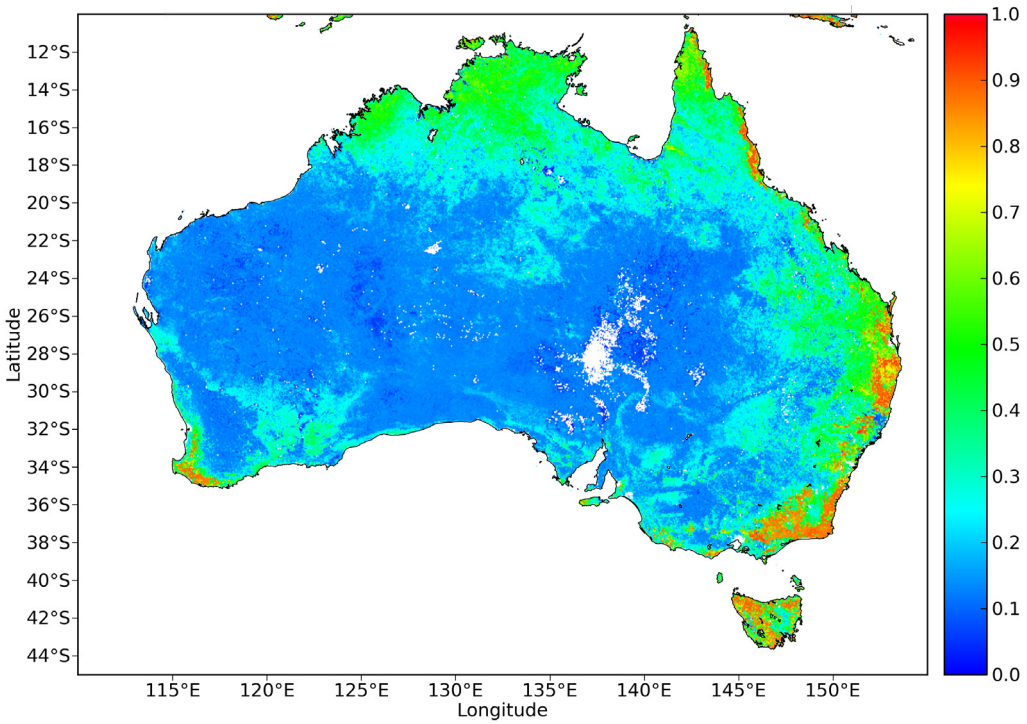

Source: TERN AusCover. (Retrieved from *http://www.auscover.org.au/purl/lpdaac-mosaic-mod15a2-v5*)
AusCover is the remote sensing data products facility of the Terrestrial Ecosystem Research Network (TERN; *http://www.tern.org.au*)

6.3.5 Basal area (BA)

Forest development can be characterised by its canopy, the combined leaves, twigs, and branches of all tree crowns in a stand, or the stand structure, the size and frequency of stems within a given area. Measurement of the latter is readily achievable and directly related to timber production (see Section 16.5). Tree volume is also indicative of carbon stores and woody biomass (see Section 17).

Basal area (BA), or cross-sectional area, indicates the proportion of area occupied by the base of a plant, such as a tree trunk, and is computed as:

$$BA = \frac{\text{sum of trunk areas at breast height}}{\text{ground area}}$$

Basal area has been traditionally computed from manual measurements of individual trees using a calibrated tape measure or caliper at a trunk height of 1.3 m (or 1.4 m in some countries[7]). Estimates of basal area can also be derived using lidar instruments (see Excursus 5.1 and Volume 1A—Section 15.1). When combined with laser altimetry, surface lidar instruments enable accurate canopy structure measurements to be derived for forests (see Excursus 6.1 and Section 16).

6.3.6 Fractional cover

Functionally, all vegetative material can be described as either photosynthetic—green, photosynthesising leaves—or non-photosynthetic—dead plant material (above ground), woody material, and litter (Guerschman *et al.*, 2009). Many sparsely vegetated landscapes, such as savanna and grassland ecosystems, can simplistically be classified in terms of three ground components:

- photosynthetic vegetation;
- non-photosynthetic vegetation; and
- bare ground (soil, gravel, rock).

Fractional cover represents the ground area covered by each of these components as a percentage of a given area. Since the structure and scale of vegetation is closely tied to water and energy balance in these landscapes, estimates of fractional cover are valuable for a range of analyses relating to carbon and nutrient uptake, water and energy cycling, and fire and erosion potential (see Sections 7 and 9.1).

Traditionally, fractional cover estimates have been derived from ground-based measurements "using a variety of qualitative and quantitative approaches centred on plots or transects, where the locations have been chosen to be representative of vegetation communities, ecosystem types or management practices" (Scarth *et al.*, 2018). However, more recently, accurate estimates of fractional cover can be determined from EO imagery, where individual image pixels form the area unit for which vegetation fractions are estimated (see Excursus 8.3).

6.4 Canopy Colour and Texture

Both the colour and texture of a vegetation canopy are indicative of plant type(s), density, age, and condition. The composite 'colour' of a canopy is readily summarised in EO imagery, with each reflectance measurement being integrated over the area of an optical pixel (see Volume 1B—Section 1.2). As detailed in Section 4 above, the canopy reflectance in particular wavelengths can be indicative of the vegetation composition, condition, density, structure, and/or age. For example, when the spectral characteristics of surface features are plotted on a crossplot of red versus NIR reflectance, green vegetation forms a characteristic triangular shape (Kauth and Thomas, 1976; see Section 8.1.1). Bare soil typically plots in a line along the base of the vegetation triangle while vegetation plots above the soil line, with its greenness and cover determining distance from the line (see Figure 6.6).

Monitoring the changes in canopy colour through time can differentiate between vegetation with varying phenological cycles and allow vegetation types to be identified more accurately (see Section 9.2). For example, vegetation that stays green throughout the year is characterised by smaller annual variations in colour than deciduous or annual vegetation (see Section 9.1).

The imaged texture within a canopy is directly dependent on image scale relative to the plant crown diameter (see Volumes 1 and 2). Textural variations within a canopy can be indicative of changes to vegetation condition or structure (see Volume 2C—Section 6.1). Textural characteristics within an EO image can also be exploited to delineate individual tree crowns and estimate biomass (Cabello-Leblic, 2018).

7 Breast height is fixed at 1.3 m in Australia, UK, Canada and continental Europe, and at 1.4 m in the USA, New Zealand, Burma, India, Malaysia and South Africa.

Figure 6.6 Vegetation cover triangle

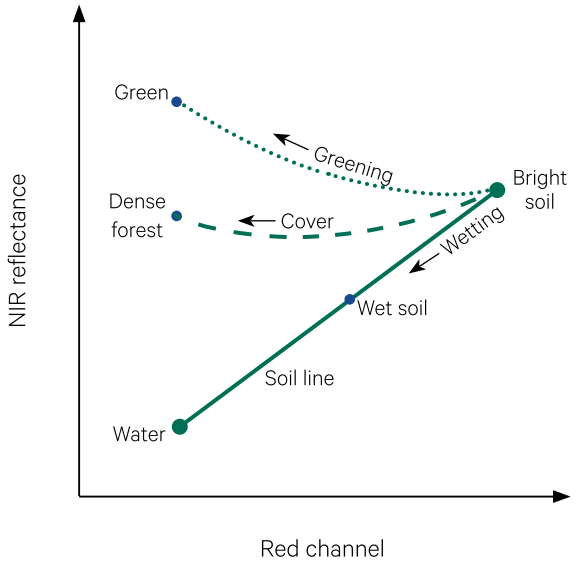

Source: Harrison and Jupp (1990) Figure 92

Figure 6.7 Simulated reflectance for increasing grass cover

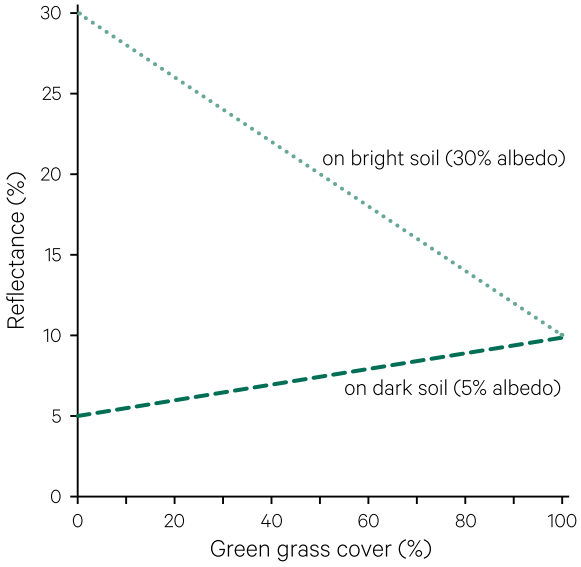

Adapted from: McVicar *et al.* (2002)

When a vegetation canopy is not continuous, the 'colour' measured by a remote sensor will result from a blend of the vegetation colour and the background colour (see Volume 1B—Section 6.6). As such, different densities of vegetation cover will appear as different 'colours' when grown on different coloured soils. One example of the impact of soil colour on the reflectance from a grassy ground cover is provided by McVicar *et al.* (2002) based on work by Roderick *et al.* (2000). Using an unshaded, Lambertian surface, the variations in albedo were modelled as grass cover (with 10% albedo) increased on both light and dark soils. As illustrated in Figure 6.7, while full grass cover produces the same canopy reflectance on both soil colours, the gradations from full cover to bare soil resulted in markedly different reflectances, both in terms of the overall reflectance values for equivalent partial grass coverage and the rate of reflectance change between gradations. In this simulation, a 20% increase in green grass cover raised the overall albedo by 1% on dark soil, but the same increase in grass cover resulted in a 4% decrease in total albedo on bright soil.

While this model simplifies many aspects of imaging a real canopy, it demonstrates the reality of composite reflectance interactions within an EO pixel. The relative reflectance range corresponding to increased grass cover on dark soil is effectively narrower than the corresponding range on bright soil. This situation is particularly relevant to selecting the radiometric resolution required to detect a given gradation of change in canopy density. As detailed in Table 6.5, an 8% variation in grass cover on dark soil would vary the imaged reflectance by 1 digital number in 8-bit data, whereas only 2% variation in grass cover on bright soil would result in the same difference in imaged reflectance values. Again, while these simulated figures do not account for many of the complexities involved with imaging with remote sensors, they rightly indicate the discriminatory advantages of sensors with increased radiometric resolution (see Volume 1B—Section 1).

Table 6.5 Effect of sensor quantisation on radiometric sensitivity

Quantisation	Number of grey levels	Precision (1/level)	Change in green grass cover (%)	
			On dark soil	On bright soil
7 bit	128	0.007813	15.63	3.91
8 bit	256	0.003906	7.812	1.953
10 bit	1024	0.000977	1.954	0.489
12 bit	4096	0.000244	0.488	0.122

Source: McVicar *et al.* (2002)

The transfer of EMR through a vegetative canopy has been simulated by radiative transfer modelling, which uses information about the shape, size, and density of plants to determine how incoming radiation is reflected, absorbed, or transmitted by the canopy (see Volume 1B—Section 5). Analyses of sub-pixel components to derive fractional cover estimates are described in Sections 8.3.

6.5 Growth Stages

Within a group of plants, a growth stage describes the prevalent life cycle development phase. Various growth stages have been defined for different types of plants. For example, the following five stages are commonly used to describe the growth of Australian native vegetation (Hnatiuk *et al*., 2009):

- early regeneration—small juvenile plants of variable density, possibly associated with occasional older, emergent plants;
- advanced regeneration—well-developed immature plants of variable density, generally not reproducing;
- uneven age—reproducing plants of mixed size and age, often forming two or more vertical strata;
- mature—reproducing plants at maximum height with full, healthy crowns; and
- senescent—over-mature plants showing signs of aging.

These stages are typically sampled for the dominant vegetation type and condition at each sample site. For forests, leaf area and twig volume tend to stabilise during early growth stages, so that wood growth is the major component of increased biomass for older forests (see Section 16). Environmental disturbances, such as fire or windthrow, often trigger the demise of an aging generation of plants and assist the establishment of the next generation. For example, the timing of growth stages for a eucalypt forest could be described as:

- disturbance, germination and early growth: 0–5 years;
- saplings and regrowth: 5–100 years;
- mature: 100–250 years; and
- senescent: > 250 years (Jacobs, 1955).

Other factors driving the cyclic nature of vegetation succession are detailed in Section 6.6.

6.6 Succession

Previous sections have introduced the concepts of the life cycle for individual plants (see Section 5.3) and growth stage assessment for groups of plants (see Section 6.5). Like all forms of life, plants age, and their form and interactions with the environment change as they age. Ecological succession considers how plants establish, thrive, and reproduce at particular locations through time and attempts to identify those factors that determine both their survival and their successors.

The term ‘primary succession’ is used to describe the process of succession on pristine, bare earth, possibly resulting from lava flows, whereas ‘secondary succession’ follows a disturbance to a previously vegetated site, as might occur after fire, flood, or landslide. Secondary succession is more common than primary succession, and also more rapid due to the presence of seed and organic matter, taking decades for grasslands or centuries for forests, rather than millennia.

The general mechanism of succession was described by Clements (1916) in terms of six transitional phases:

1. nudation—starting point is a bare site resulting from disturbance or natural history;
2. migration—propagules arrive to enable plant establishment;
3. ecesis—vegetation establishes and grows;
4. competition—between growing and reproducing plants for space, light, and nutrients;
5. reaction—environmental changes resulting from presence of plants; and
6. stabilisation—climax community when plant interactions are in equilibrium with environment.

This process typically involves a wide range of species, some of which are best suited to rapidly colonising new areas with low nutrient levels (pioneer species), followed by a series of transitional species with increasingly more complex structures and requirements (seral species), until finally a stable, but not static, community is formed (climax species). For example, the factors involved with forest succession are illustrated in Figure 6.8.

Figure 6.8 Forest succession

An abstract diagram showing forest succession over time. Increase in biomass, biodiversity and soil thickness are also shown, as well as the fluctuation of different plant communities over the process of succession.

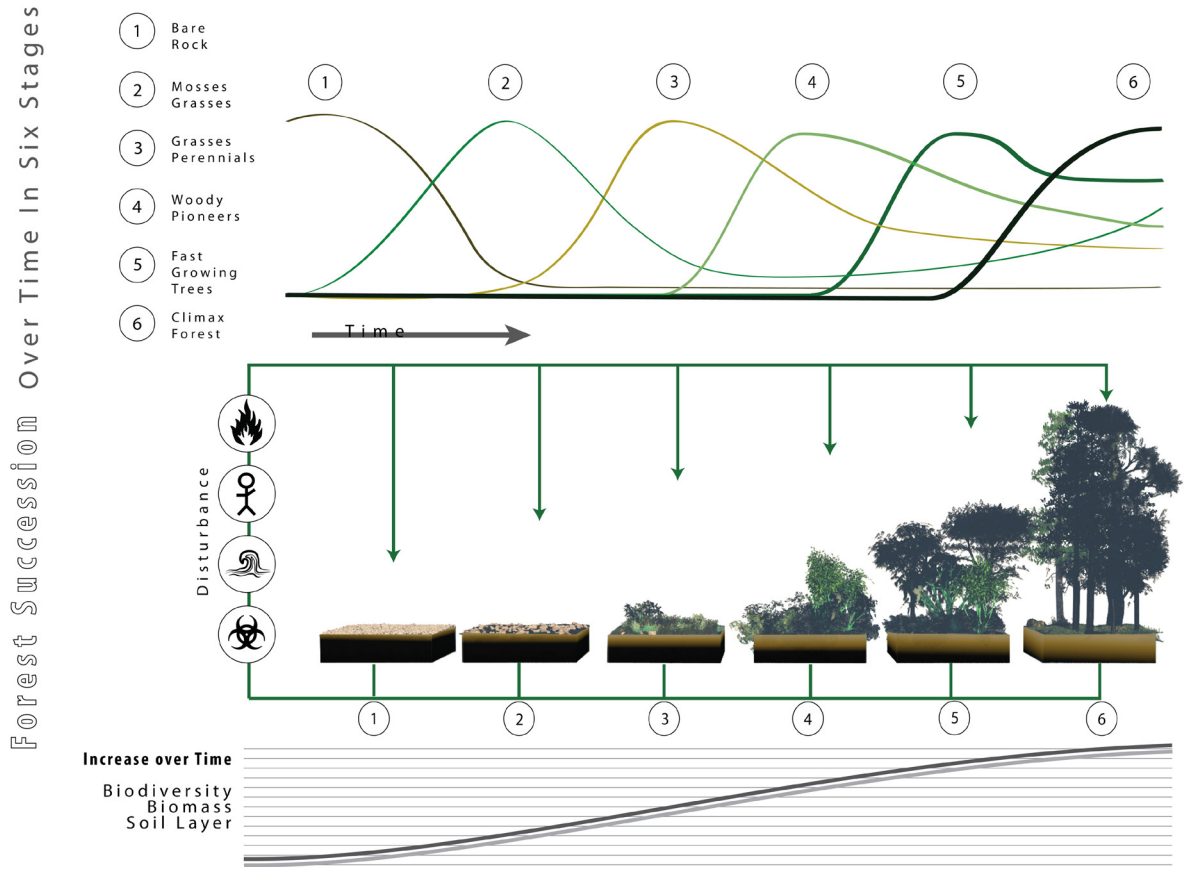

Source: Lucas Martin Frey, Wikimedia Commons. (Retrieved from *http://upload.wikimedia.org/wikipedia/commons/4/41/Forest_succession_depicted_over_time.png*)

Ecological theory implies that the climax community is balanced, independent, and resilient. This phase could theoretically continue indefinitely without external disturbance and is characterised by stability in terms of energy input and output, nutrient uptake and recycling, and species composition (Clements, 1916; Tansley, 1935; Whittaker, 1953). Nature, however, does not always comply with theories so, while succession is continuous in any situation, the neatly defined phases may not always be apparent or spatially coherent at a given location or instance in time (Connell and Slatyer, 1977). A mature forest, for example, can comprise a patchwork of communities at varying stages of succession. In concert with increasing vegetation cover and height through primary succession, richer and deeper soils are slowly formed until climax communities occur on 'mature' soils. The interrelationships between temperature and moisture in the processes of vegetation and soil succession can be seen to underlie many climatic classification systems (see Sections 1 and 2.2.3).

An understanding of succession underlies ecosystem dynamics and is important for assessing and managing any vegetation resource (see Section 7). As the structural complexity of successive stages increases, the capacity of a vegetation community to provide a greater range of habitats and food sources for fauna also increases. The successional stage of a vegetation community can thus be indicative of faunal composition and diversity, and provide valuable information for managing a range of terrestrial resources.

An understanding of ecological succession provides a basis for resolving man's conflict with nature. (Odum, 1969)

6.7 Further Information

Field Guides

NCST (2009)

TERN Australia (2018)

Guerschman *et al*. (2018)

Ecology

Pianka, E.R. (2011). *Evolutionary Ecology*. 7th Edn. Eric R. Pianka.

Miller, G.T.Jr, and Spoolman, S.E. (2009). Essentials of Ecology, 5th edn. Brooks/Cole Cengage Learning. ISBN-13: 978-0-495-55795-1 *https://www.academia.edu/40164243/Essentials_of_Ecology*

Vegetation Height and Structure Map of Australia

National structure map: *http://auscover.org.au/purl/icesat-vegetation-structure*

Biomass library: *http://www.auscover.org.au/purl/biomass-plot-library*

6.8 References

Asner, G.P., Wessman, C.A., and Archer, S. (1998). Scale Dependence of Absorption of Photosynthetically Active Radiation in Terrestrial Ecosystems. *Ecological Applications*, 8, 1003–1021. doi:*10.1890/1051-0761(1998)008[1003:SDOAOP]2.0.CO;2*

Baret, F., and Guyot, G. (1991). Potentials and limits of vegetation indices for LAI and APAR assessment. *Remote Sensing of Environment*, 35, 161–173. *https://doi.org/10.1016/0034-4257(91)90009-U*

Baret, F., Weiss, M., Lacaze, R., Camacho, F., Makhmara, H., Pacholcyzk, P., and Smets, B. (2013). GEOV1: LAI and FAPAR essential climate variables and FCOVER global time series capitalizing over existing products. Part 1: Principles of development and production. *Remote Sensing of Environment*, 137, 299–309.

Bréda, N.J.J. (2003). Ground-based measurements of leaf area index: a review of methods, instruments and current controversies. *Journal of Experimental Botany*, 54 (392), 2403–2417.

Cabello-Leblic, A. (2018). Tree crown delineation. Ch 11 in *Effective Field Calibration and Validation Practices: A practical handbook for calibration and validation satellite and model-derived terrestrial environmental variables for research and management*. A TERN Landscape Assessment Initiative, NCRIS. ISBN 978-0-646-94137-0.

Carnahan, J.A. (1977). 'Natural Vegetation' map with commentary. *Atlas of Australian Resources, Second Series*. Department of Natural Resources, Canberra.

Chen, J.M., Rich, P.M., Gower, S.T., Norman, J.M., and Plummer S. (1997). Leaf area index of boreal forests: theory, techniques and measurements, *Journal of Geophysical Research*, 102(D24), 29429–29443.

Clements, F.E. (1916). *Plant Succession: Analysis of the Development of Vegetation*. Carnegie Institution of Washington Publication Sciences. *http://dx.doi.org/10.5962/bhl.title.56234*

Connell, J.H., and Slatyer, R.O. (1977). Mechanisms of Succession in Natural Communities and Their Role in Community Stability and Organization. *The American Naturalist*, 111(982), 1119–1144.

Coops, N.C., Smith, M.L., Jacobsen, K.L., Martin M., and Ollinger, S. (2004). Estimation of plant and leaf area index using three techniques in a mature eucalypt canopy, *Austral Ecology*, 29, 332–341.

De Caceres, M., and Wiser, S.K. (2012). Towards consistency in vegetation classification. *Journal of Vegetation Science*, 23, 387–393.

Fensholt, R., Sandholt, I., and Rasmussen, M.S. (2004). Evaluation of MODIS LAI, fAPAR and the relation between fAPAR and NDVI in a semi-arid environment using *in situ* measurements. *Remote Sensing of Environment*, 91(3–4), 490–507.

Gower, S.T., Kucharik, C.J., and Norman, J.M. (1999). Direct and Indirect Estimation of Leaf Area Index, fapar and Net Primary Production of Terrestrial Ecosystems, *Remote Sensing of Environment*, 70, 29–51.

Guerschman, J.P., Hill, M.J., Renzullo, L.J., Barrett, D.J., Marks, A.S., and Botha, E.J. (2009). Estimating fractional cover of photosynthetic vegetation, non photosynthetic vegetation and bare soil in the Australian tropical savannah region upscaling Hyperion and MODIS sensors. *Remote Sensing of Environment*, 113, 928–945.

Guerschman, J., Leys, J., Rozas Larraondo, P., Henrikson, M., Paget, M., and Barson, M. (2018). *Monitoring groundcover: an online tool for Australian regions*. CSIRO, Canberra. *https://doi.org/10.25919/5bf84026e556d*

Harrison, B.A., and Jupp, D.L.B. (1990) *Introduction to Image Processing: Part TWO of the microBRIAN Resource Manual*. CSIRO, Melbourne. 256 p.

Hill, M.J., Senarath, U., Lee, A., Zeppel, M., Nightingale, J.M., Williams, R., and McVicar, T.R. (2006a). Assessment of the MODIS LAI product for Australian ecosystems, *Remote Sensing of Environment*, 101, 495–518.

Hill, M.J., Held, A.A., Leuning, R., Coops, N.C., Hughes, D., and Cleugh, H.A. (2006b). MODIS spectral signals at a flux tower site: Relationships with high-resolution data, and CO_2 flux and light use efficiency measurements. *Remote Sensing of Environment*, 103, 351–368.

Hnatiuk R.J., Thackway R., and Walker J. (2009). *Vegetation. In: Australian Soil and Land Survey: Field Handbook* (3rd edn). (Ed: National Committee on Soil and Terrain) pp. 73–125. CSIRO Publishing, Melbourne.

Jacobs, M. (1955). *Growth Habit of the Eucalypts*. CSIRO, Canberra. (Reprinted in 1986 by IFA).

Jupp, D.L.B., Culvenor, D.S., Lovell, J.L., Newnham, G.J., Strahler, A.H., and Woodcock, C.E. (2009). Estimating forest LAI profiles and structural parameters using a ground-based laser called 'Echidna®'. *Tree Physiology*, 29, 171–181.

Kauth, R.J., and Thomas, G.S. (1976). The Tasselled Cap—a graphic description of the spectral-temporal development of agricultural crops as seen by Landsat. *Proceedings of Symposium on Machine Processing of Remotely Sensed Data*. Purdue University, West Lafayette, Indiana, 4B41-4B51. *http://docs.lib.purdue.edu/lars_symp/159*

McVicar, T.R., Davies, P.J., Qinke, Y., and Zhang, G. (2002). An Introduction to Temporal-Geographic Information Systems (TGIS) for Assessing, Monitoring and Modelling Regional Water and Soil Processes. In *Regional Water and Soil Assessment for Managing Sustainable Agriculture in China and Australia* (Eds: T.R. McVicar, Li Rui, J. Walker, R.W. Fitzpatrick, and Liu Changming) ACIAR Monograph No. 84, 205–223.

Margules, C.R., and Pressey, R.L. (2000). Systematic conservation planning. *Nature*, 405, 243–253.

May, R.M. (1974). *Stability and Complexity in Model Ecosystems*. 2nd edn. Princeton University Press, Princeton, New Jersey.

Mueller-Dombois, D., and Ellenberg, H. (1974). *Aims and methods of vegetation ecology*. John Wiley and Sons, New York.

Muir, J., Schmidt, M., Tindall, D., Trevithick, R., Scarth, P., and Stewart, J., (2011). *Guidelines for Field measurement of fractional ground cover: a technical handbook supporting the Australian collaborative land use and management program*. Tech. rep., Queensland Department of Environment and Resource Management for the Australian Bureau of Agricultural and Resource Economics and Sciences, Canberra. *http://data.daff.gov.au/data/warehouse/pe_hbgcm9abll07701/HndbkGrndCovMontring2011_1.0.0_HR.pdf*

Myneni, R.B., and Williams, D.L. (1994). On the relationship between FAPAR and NDVI. *Remote Sensing of Environment*, 49, 200–211. *https://doi.org/10.1016/0034-4257(94)90016-7*

NCST (2009). *Australian Soil and Land Survey Field Handbook*. 3rd edn. National Committee on Soil and Terrain, CSIRO, Canberra. 264 p.

Odum, E.P. (1969). The Strategy of Ecosystem Development. *Science*, 164(3877), 262–270.

Paul, K. I., Roxburgh, S. H., Chave, J., England, J. R., Zerihun, A., Specht, A., Lewis, T., Bennett, L. T., Baker, T. G., Adams, M. A., Huxtable, D., Montagu, K. D., Falster, D. S., Feller, M., Sochacki, S., Ritson, P., Bastin, G., Bartle, J., Wildy, D., Hobbs, T., Larmour, J., Waterworth, R., Stewart, H. T., Jonson, J., Forrester, D. I., Applegate, G., Mendham, D., Bradford, M., O'Grady, A., Green, D., Sudmeyer, R., Rance, S. J., Turner, J., Barton, C., Wenk, E. H., Grove, T., Attiwill, P. M., Pinkard, E., Butler, D., Brooksbank, K., Spencer, B., Snowdon, P., O'Brien, N., Battaglia, M., Cameron, D. M., Hamilton, S., McAuthur, G., and Sinclair, J. (2016). Testing the generality of above-ground biomass allometry across plant functional types at the continent scale. *Global Change Biology*, 22 (6), 2106–2124. doi:*10.1111/gcb.13201*

Paul, K., Larmour, J., Specht, A., Zerihun, A., Ritson, P., Roxburgh, S., Sochacki, S., Lewis, T., Barton, C.V.M., England, J.R., Battaglia, M., O'Grady, A.P., Pinkard, E.A., Applegate, G., Jonson, J., Brooksbank, K., Sudmeyer, R., Wildy, D.T., Montagu, K., Bradford, M.G., Butler, D.W., and Hobbs, T. (2019). Testing the generality of below-ground biomass allometry across plant functional types. *Forest Ecology and Management*, 432, 102–114. doi:*10.1016/j.foreco.2018.08.043*

Penridge, L., and Walker, J. (1988). The crown-gap ratio and crown cover: derivation and simulation study. *Australian Journal of Ecology*, 13, 1090–1120.

Restrepo-Coupe, N., Huete, A., and Davies, K. (2018). Satellite Phenology Validation. Ch 9 in *Effective Field Calibration and Validation Practices: A practical handbook for calibration and validation satellite and model-derived terrestrial environmental variables for research and management*. A TERN Landscape Assessment Initiative, NCRIS. ISBN 978-0-646-94137-0.

Roderick, M.L., Chewings, V., and Smith, R.C.G. (2000). Remote sensing in vegetation and animal studies. In *Field and Laboratory Methods for Grassland and Animal Production Research*. (Eds: L. Mennetje and R.M. Jones) Wallingford UK, CABI, pp. 205–225.

Ruimy, A., Saugier, B., and Dedieu, G. (1994). Methodology for estimation of terrestrial net primary production from remotely sensed data. *Journal of Geophysical Research*, 99, 5263–5283. *https://doi.org/10.1029/93JD03221*

Ruimy, A., Kergoat, L., Bondeau, A., and Potsdam NPP Model Intercomparison Participants. (1999). Comparing global models of terrestrial net primary productivity (NPP): analysis of differences in light absorption and light-use efficiency. *Global Change Biology*, 5 (Suppl. 1), 56–64. doi:*10.1046/j.1365-2486.1999.00007.x*

Scarth, P., Guerschman, J.P., Clarke, K., and Phinn, S. (2018). Validation of Australian Fractional Cover Products form MODIS and Landsat Data. Ch 7 in *Effective Field Calibration and Validation Practices: A practical handbook for calibration and validation satellite and model-derived terrestrial environmental variables for research and management*. A TERN Landscape Assessment Initiative, NCRIS. ISBN: ISBN 978-0-646-94137-0. *https://www.tern.org.au/NEW-CalVal-handbook-for-remote-sensing-bgp4370.html*

Scarth, P., Armston, J., Lucas, R., and Bunting, P. (2019). A Structural Classification of Australian Vegetation Using ICESat/GLAS, ALOS PALSAR, and Landsat Sensor Data. *Remote Sensing*, 11(2), 147. *https://doi.org/10.3390/rs11020147*

Schaefer, M.T., Farmer, E., Soto-Berelov, M., Woodgate, W., and Jones, S. (2018). Overview of ground based techniques for estimating LAI. Ch 6 in *AusCover Good Practice Guidelines: Effective Field Calibration and Validation Practices: A practical handbook for calibration and validation satellite and model-derived terrestrial environmental variables for research and management*. A TERN Landscape Assessment Initiative, NCRIS. ISBN 978-0-646-94137-0.

Specht, R.L., and Specht, A. (1999). *Australian plant communities : dynamics of structure, growth and biodiversity*. Oxford University Press, Melbourne. ISBN 019553705X

Specht, L., Roe, E., and Boughton, V. (eds) (1974). Conservation of major plant communities in Australia and Papua New Guinea. *Australian Journal of Botany Supplement*, 7.

Strahler, A.H., Jupp, D.L.B., Woodcock, C.E., Schaaf, C.B., Yau, T., Zhau, F., Yang, X., Lovell, J., Culvenor, D., Newnham, G., Ni-Miester, W., and Boykin-Morris, W. (2008) Retrieval of forest structural parameters using a ground-based lidar instrument (Echidna®). *Canadian Journal of Remote Sensing*, 34(2), S426–S440.

Tansley, A.G. (1935). The use and abuse of vegetational concepts and terms. *Ecology*, 16, 284–307.

TERN Australia (2018). *Effective Field Calibration and Validation Practices: A practical handbook for calibration and validation satellite and model-derived terrestrial environmental variables for research and management*. A TERN Landscape Assessment Initiative, NCRIS. ISBN 978-0-646-94137-0. *https://www.tern.org.au/NEW-CalVal-handbook-for-remote-sensing-bgp4370.html*

Walker, J., Crapper, P., and Penridge, L. (1988). The crown-gap ratio I and crown cover: the field study. *Australian Journal of Ecology*, 13, 101–108.

Welles, J.M., and Cohen, S. (1996). Canopy structure measurement by gap fraction analysis using commercial instrumentation. *Journal of Experimental Botany*, 47(9), 1335–1342. *https://doi.org/10.1093/jxb/47.9.1335*

Whittaker, R.H. (1953). A consideration of climax theory: the climax as a population and pattern. *Ecological Monographs*, 23(1), 41–78. *https://doi.org/10.2307/1943519*

Wikum, D.A., and Shanholtzer, G.F. (1978). Application of the Braun-Blanquet Cover-Abundance Scale for Vegetation Analysis in Land Development Studies. *Environmental Management*, 2(4), 323–329.

Xiao, X., Zhang, Q., Braswell, B., Urbanski, S., Boles, S., Wofsy, S., Moore III, B., and Ojima, D. (2004). Modeling gross primary production of temperate deciduous broadleaf forest using satellite images and climate data. *Remote Sensing of Environment*, 91, 256–270. doi:*10.1016/j.rse.2004.03.010*

7 Attributes of Ecosystems

The concept of an ecosystem—comprising all biotic and abiotic factors in an environment—is introduced in Section 1.2.3. The distribution of a species and the productivity of an ecosystem both depend on the success or failure of individual plants, while the success or failure of each plant largely results from the influence of the environment on the rates of its vital processes (see Section 5). Vegetation is thus a delicate integrator of environmental conditions and can be viewed as indicative of those conditions (Billings, 1970).

The interactions that exist between an organism and its environment are both complex and interrelated—or 'holocoenotic'. The various environmental factors described in Section 1.1 not only interact with the organism but also among themselves. As such, it is difficult to isolate and change one part of the environment without affecting the other parts; should the normal pattern of one factor be altered, the others will also change until a comparable balance is achieved. Conversely, while vegetation establishment needs certain environmental prerequisites, once this has happened further modification to the environment may then occur as the vegetation exerts its influence on the locality.

Given the gradual changes that often occur between ecosystems, it can be difficult to precisely define their boundaries and extent (Kessell, 1979). Gradual changes in soil moisture, elevation, humidity, and soil fertility typically result in corresponding changes in vegetation height, density, and species composition. For example, a major factor driving woody vegetation change in Australia is soil fertility, with poor soils typically supporting open (dry sclerophyll) forest, better soils supporting tall open (wet sclerophyll) forests, and high fertility soils supporting rainforests (IFA, 1985).

The following sub-sections consider measureable properties of ecosystems in terms of:

- biodiversity (see Section 7.1);
- stability and equilibrium (see Section 7.2);
- function and condition (see Section 7.3);
- productivity (see Section 7.4);
- energy balance (see Section 7.5); and
- water balance (see Section 7.6)

The unique features that define individual ecosystem types are scale-dependent. The four key elements of an ecosystem type may be organised on spatial, temporal and thematic scales. Spatially, ecosystems vary in extent and grain size from water droplets to oceans, with boundaries delimited physically or functionally. Temporally, ecosystems may develop, persist and change over time frames that vary from hours to millennia. They appear stable at some temporal scales, while undergoing trends or fluctuations at others. Thematic scale refers to similarity of features within and between ecosystems, their degree of uniqueness in composition and processes, which may be depicted hierarchically.
(Keith et al., 2013)

Background image: This panoramic view of Corobinnie Hill, northern Eyre Peninsula, SA, features a spread of vegetation types, including shrubs, mallee and wheatfields. **Source:** Matthew Bolton

7.1 Biodiversity

Section 1 above introduced the integrated nature of ecology. The interactions between environmental factors and plant genetics result in a diverse range of combinations and permutations of species within plant associations and communities in nature. The extent of heterogeneity may not always be apparent, with variations still occurring in the chemical composition of foliage when species composition and density appear to be homogeneous. Such variations are particularly relevant to herbivores whose distribution and abundance is directly related to forage quality (Youngentob *et al.*, 2012).

Terrestrial biodiversity tends to be greatest near the equator and decreases towards the polar regions, forming latitudinal gradients (see Section 1.3). While a wide range of indicators of biodiversity have been proposed (see Section 3.4.1), species diversity is a commonly used measure. A greater range of species in a community results in a greater range of resources for consumers. Many environmental factors, such as climatic stability, predation, and competition, contribute to species diversity, and can interact in complex ways (Pianka, 1971; see Figure 7.1).

Species richness (or species density) refers to the number of species present in a given area. The relative importance of individual species, however, is not always based on abundance, and can vary both within and between communities and ecosystems. Species diversity encapsulates the concepts of species density and relative importance and represents the likelihood of predicting the species of a randomly selected individual. In a monoculture, for example, species diversity is low since it would be easy to predict the species for any individual.

Figure 7.1 Biodiversity factors

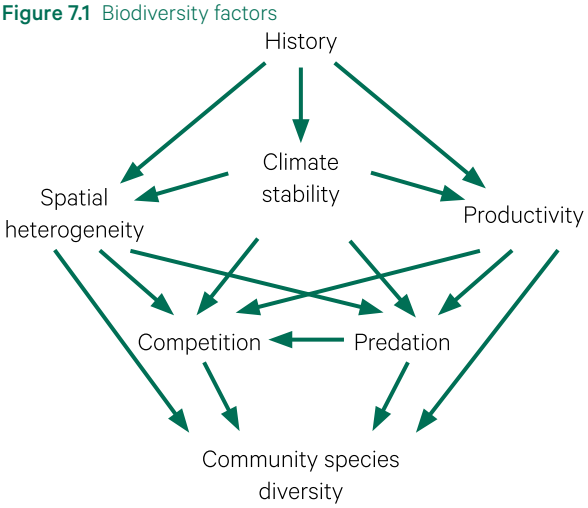

Adapted from: Pianka (1971)

While increased ecosystem diversity has traditionally been considered to coincide with greater ecological stability and resilience (MacArthur, 1955), recent studies have suggested that relatively simple ecosystems are more likely to be stable than complex ones. In some ecosystem models, the likelihood of achieving a stable equilibrium point actually decreased with increases in the number of species, the strength of interaction between species, and the frequency of that interaction (May, 1973). Empirical studies both support and reject this hypothesis. Studies based on vegetation diversity suggest that more complex communities stabilised ecosystem processes and were more resilient after perturbations, such as drought, but did not stabilise population processes, with reduced interannual biomass variability for higher biodiversity (Tilman, 1996; Tilman *et al.*, 1998). In contrast, herbivore populations appeared to be more stable when feeding on a restricted range of species (Watt, 1968). It should be noted that the concept of equilibrium also varies with spatial scale (see Section 7.2). The use of EO datasets to monitor global and Australian biodiversity is detailed in Section 19.

Resilience and transformation are not opposites. They can be complementary. Maintaining resilience at one scale can require transformational changes at other scales. … Resilience includes knowing when an unwanted transformation is inevitable and instead deliberately transforming all or parts of the system such that the new system delivers what is valued and wanted. … It's about learning where not to go rather than perfectly controlling where to go.
(Walker, 2020)

7.2 Stability and Equilibrium

Ecosystems and landscapes constantly change. As part of the natural cycle of our environment, plants grow, water courses change, soil moves and air circulates—the environment keeps changing. Natural disasters, such as fire, flood, drought, and tectonic activity can impose massive and sudden changes on landscapes and ecosystems (see Section 1.1.2.3). Earth's inhabitants, who are all part of the ecosystem, superimpose other changes, such as land clearing, cropping or afforestation, urban developments, mining, dam building, and other engineering works. The sum total of all these changes is a very dynamic planet (see Section 1.3.3).

Landscape disturbances can result from natural and anthropogenic causes (see Section 3.4.1). When changes occur suddenly, both the cause and impact are clearly evident. However, when changes are gradual, the driving factors can be more difficult to identify. One of the challenges for observing landscape dynamics is the lack of a clear baseline which defines 'stability' or 'balance'. Indeed, both the rate and extent of 'normal' landscape changes differ in different ecosystems, with some ecosystems rapidly recovering from major disturbances, and others showing scars for extended periods.

Separating the effects of 'natural' disturbance from anthropogenic changes presents a further challenge in many landscapes (see Section 15). More recently, ecosystem changes have been described by their impact on human populations. This perspective considers ecosystems in terms of the services they deliver and encourages sustainable management of resources in order to maintain those ecosystem services (see Section 20.3).

An ecosystem is a dynamic complex of plant, animal, and microorganism communities and the nonliving environment interacting as a functional unit.
(MEA, 2005)

Coupled with landscape stability is the concept of equilibrium. As introduced in Section 6.6, ecological succession assumes that plant communities progressively establish themselves on a given site until a state of equilibrium is achieved between competing components. This view of the landscape was accepted for most of the twentieth century, with agricultural management regimes aiming to maintain equilibrium by defining appropriate capacities for grazing animals and/or crop rotations. While the linear succession model can be observed to apply to some vegetated landscapes, it has been found wanting in resource-limited environments such as drylands, where plant growth is controlled by abiotic factors (see Section 15).

Excursus 7.1 introduces some equilibrium and non-equilibrium models that have been developed to simulate ecosystem dynamics in grazed landscapes.

An ecosystem functions by continually cycling energy and materials through living organisms that grow, reproduce and then die. This cycling of energy and materials through living organisms has evolved in response to a mix of disturbances (e.g. fires or floods), stresses (e.g. droughts or diseases) and ecological interactions (e.g. competition or predation) over millions of years. Recent changes in the frequency and intensity of these disturbances and stresses raises important issues about the ability of species and ecosystems to survive and adapt.
(DEWHA, 2010)

Excursus 7.1—Modelling Grazed Landscapes

The grazing system in grasslands and rangelands can be represented as the interaction of multiple environmental factors as illustrated in Figure 7.2. The traditional view of ecosystem dynamics assumes an equilibrium state as the endpoint of succession, which is maintained by the interactions between its components (see Section 7.3). This situation applies where plant growth is mostly constant over time, with continuous consumption by herbivores.

However, drylands, which occupy most of the Australian continent, are landscapes with complex environmental interactions, where plant growth rate is strongly controlled by rainfall, which is highly variable in both space and time. In these landscapes the equilibrium theory has proven to be inadequate for predicting the likely outcomes of natural or anthrogenic disturbances (Stringham *et al*., 2003). As an alternative, a non-equilibrium framework has been used to conceptualise vegetation dynamics in terms of multiple successional pathways and steady states, change thresholds, and discontinuous and irreversible transitions (Westoby *et al*., 1989; Stringham *et al*., 2003).

Characteristics of equilibrium and non-equilibrium modelling frameworks are summarised in Table 7.1. In a non-equilibrium system the carrying capacity of the system is too dynamic for close tracking between the climate and populations, since rather than cycles being limit-driven, they are controlled by abiotic factors. Most rangeland ecosystems occupy an intermediate position somewhere between equilibrium and non-equilibrium behaviour.

Figure 7.2 The grazing system

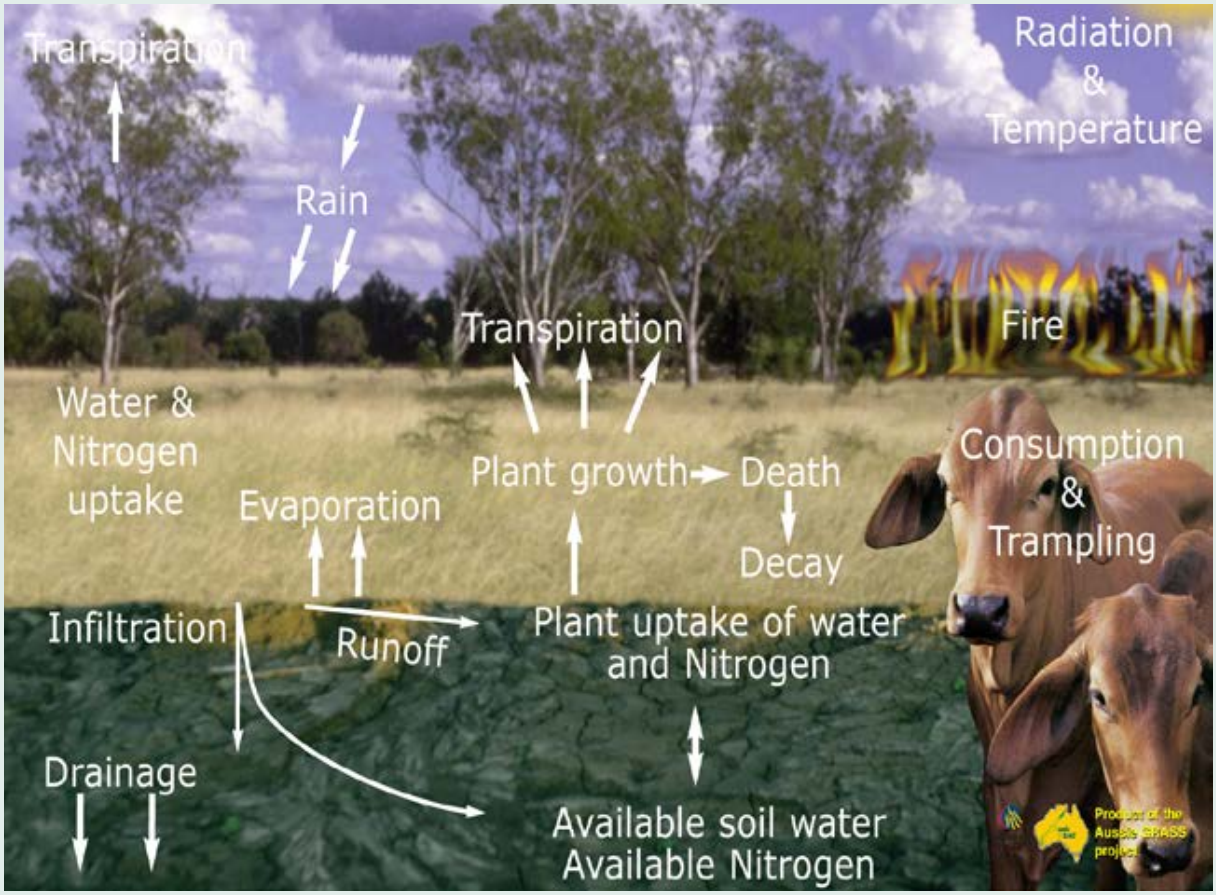

Source: McKeon and Carter (2015) Figure 1.1

For example, over the past century, a series of ecological models have been applied to rangeland environments around the world (see Table 7.2). For most of the twentieth century, "the rangelands were viewed as equilibrium systems potentially disturbed by grazing" (Pickup *et al.*, 1994), with the corollary that equilibrium could be restored by adjusting carrying capacity (Illius and O'Connor, 1999). Range models assume that the species composition of plant communities results from the opposing forces of plant succession and grazing intensity. In this modelling context, grazing is viewed as slowing, stopping, or reversing secondary succession, such that plant communities are produced that differ in species composition from the historical climax plant community, which would represent the single reference (equilibrium) point (Briske *et al.*, 2005, 2017). However, the expansion of woody weeds could not be reversed by the removal of grazing (Westoby *et al.*, 1989) and during prolonged droughts plant production and livestock numbers were rarely balanced. These observations led to the adoption of a non-equilibrium approach for modelling rangelands. Indeed, recent evidence suggests that grazing and other disturbances can disrupt the natural state for decades after grazing is removed (Sims *et al.*, 2019).

Humans interact with nature through the use of simplified and incomplete perceptions of its structure, interrelationships, and dynamics. (Briske et al., 2017)

Table 7.1 Equilibrium versus nonequilibrium systems

Characteristic	Equilibrium system	Nonequilibrium system
Ecological metaphor	'Balance of nature'	'Flux of nature'
Abiotic patterns	Relatively constant	Stochastic/variable
Plant-herbivore interactions	Tight coupling	Weak coupling
	Biotic regulation	Abiotic drivers
Population patterns	Density dependence	Density independence
	Populations track carrying capacity	Dynamic carrying capacity limits population tracking
Community/ ecosystem	Competitive structuring	Competition not expressed
	Internally regulated	External drivers

Adapted from: Briske *et al.* (2017) Table 6.1

By comparison, the State-and-Transition Modelling (STM) approach to managing natural resources considers the complexities of vegetation dynamics under a variable climate with changing stressors, such as grazing and fire (see Table 7.3 for terminology). Although originally introduced as 'management language' rather than ecological theory, STM models are now widely used to understand ecosystem response to disturbances in rangeland environments and can represent all known or anticipated stable states that may occupy a given site (Briske *et al.*, 2017). While STM theory accommodates discontinuous and non-reversible vegetation change and is relevant to many grazed savanna land types, it may be inadequate for the more arid and semi-arid regions experiencing highly variable, often episodic, rainfall with consequent unpredictable vegetation responses under grazing. Moreover, its conceptual nature means that the framework often fails to adequately deal with the spatial realities of paddock heterogeneity and uneven grazing distribution (Ash *et al.*, 1994). Nonetheless, STM models are useful both in terms of organising data and portraying landscape function.

Table 7.2 Rangeland management models

Name	Description	Metric	References
Range model	Envisioned vegetation dynamics to occur along a single axis on which grazing intensity linearly counteracts secondary succession	Range condition rating derived from comparison of species composition with a reference site, which is used to infer production goals and ecological assessments	Dyksterhuis (1949) Joyce (1993)
Non-equilibrium persistent model	Livestock maintain equilibrium with forage in key resource areas but may not do so when forage is abundant in the wet season	Rainfall variability metric defined the non-equilibrium point	Ellis and Swift (1988) Illius and O'Conner (1999)
State-and-Transition model	Organised as a collection of all recognised or anticipated stable states that individual ecological sites may support	Change direction of ecological indicators used to modify state resilience	Westoby *et al.* (1989) Bestelmeyer *et al.* (2017) Stringham *et al.* (2003)

Source: Briske (2017)

Table 7.3 State-and-Transition model terms

Term	Definition
State	A state is a recognisable, resistant, and resilient complex of two components, the soil base and the vegetation structure. The vegetation and soil components are necessarily connected through integrated ecological processes which interact to produce a sustained equilibrium that is expressed by a specific suite of vegetative communities.
Ecological indicators	Characteristics or attributes of phenomena that are being monitored, that is, inventoried over time.
Trend	Overall temporal or spatial trajectory of an indicator, statistically measured in terms of direction, strength, and rate.
Benchmark	A benchmark reference, or standard, is a baseline value of a measurement indicator by which an indicator can be compared and judged.
Disturbance	Discrete event in time, such as drought or fire, that significantly reduces the abundance of a natural resource and can be characterised in terms of the magnitude of its impact.
Transitions	A trajectory of system change away from the current stable state that is triggered by natural events, management actions, or both. The primary difference between the reversible and irreversible property of a transition is defined by the ability or inability of the system to repair itself.
Threshold	Boundary in space and time between any and all states, or along irreversible transitions, such that one or more of the primary ecological processes has been irreversibly changed and must be actively restored before return to a previous state is possible.
Resilience	Capacity of a system to return to a former configuration following a disturbance, that is, how far a system can be displaced from equilibrium before return to equilibrium is precluded. Ecological resilience is the degree, manner and pace of recovery of indicators after a disturbance.
Resistance	Capacity of a system to remain unchanged by a disturbance, that is, it indicates the ability of a system to remain at or near its equilibrium condition by maintaining control of its ecological processes.
Feedback mechanisms	Ecological processes that influence the rate of change among system variables.

Source: Stringham *et al.* (2003); Briske *et al.* (2017); Washington-Allen and Ravi (2012)

A good example of the practical application of STM to rangeland management in Australia, including monitoring, is the Grazing Land Management (GLM) package (DAFF, 2013). GLM provides guidelines to assist northern beef producers in understanding and better managing their grazing practices. 'Grazing land condition' is defined as "the capacity of land to respond to rain and produce useful forage, and is a measure of how well the grazing ecosystem is functioning" (MLA, 2006). One or more defined vegetation and soil characteristics are used to relate land condition to a particular state or condition class (see Table 7.4). These characteristics are expected to remain relatively stable within a range of climatic variations, grazing pressures and other forms of disturbance, such as fire. An increase in grazing pressure for the same set of seasonal conditions (or maintaining the same stocking rate in a drought) may cause the landscape to transition to a more degraded state, depending on its inherent stability and/or resilience, where the latter is characterised by the ability of vegetation to recover when more favourable conditions return.

Resilience-based management, which specifically "acknowledges both the dependence and impact human populations have on natural resources and ecosystem services" (Briske, 2017), is gaining popularity in a variety of natural resource management fields and reflects our philosophical shift from being consumers of natural resources to being their stewards (see Sections 19 and 21.4).

Table 7.4 Grazing land condition classes

The ABCD framework in the Grazing Land Management (GLM) defines four condition classes based on the listed features. 3P: perennial, productive, and palatable).

Class	Features
A	High density and good cover of perennial grasses dominated by 3P species for a particular land type Little bare ground (usually < 30%) Few or no weeds Good soil condition—no erosion and good surface condition; High organic matter Little woody thickening.
B	Some decline in the health and/or density of 3P grasses An increase in other less favoured or weed species Some decline in soil condition Some signs of previous erosion and/or increased bare ground (usually > 30% but < 60%).
C	Moderate to low density of preferred grasses or moderate density of intermediate grasses Mainly annual grasses and forbs Many weeds Some erosion Often poor ground cover (< 60%) Some woody thickening.
D	General lack of any perennial grasses or palatable forbs Severe erosion or scalding, resulting in restricted plant growth; Ground cover mainly comprises weeds and annuals Thickets of woody plants or weeds cover most of the area Restoration to a better condition is reliant on high inputs of time, energy and money and land in this condition will not recover in the short term by excluding grazing.

Source: MLA (2011) Table 1

7.3 Function and Condition

Traditionally, ecosystems have been assessed in terms of their biological composition and structure. Landscapes can also be usefully described, however, in terms of their function, that is, their ecosystem processes, such as the transport, usage, and cycling of resources in space and time (Ludwig and Tongway, 1997).

One conceptual framework for landscape functionality is the Trigger-Transfer-Reserve-Pulse (TTRP) ecosystem model, which defines a sequence of processes that 'maintain' a landscape. In this framework, resource 'losses' from the landscape are offset by resource inputs and feedback mechanisms (see Figure 7.3). An example input, or trigger, would be rainfall, which may become runoff that is either lost or absorbed into the soil as reserve to support future plant growth. That plant growth may then be removed by consumption, recycled back into the reserve, or act as a physical obstruction to modify subsequent transfer processes (Tongway and Hindley, 2004). This whole framework has also been depicted as resting on a fulcrum to emphasise the need for balance between internal feedback processes and resource extraction (Tongway and Ludwig, 2006).

Landscape function describes how well the landscape's biophysical system operates. This can be represented as a continuum of regulated resources, which is an objective assessment, independent of social and economic values. When a landscape loses function, it can be viewed as 'leaking' out of 'boundaries'; conversely, when control over resource loss is increased, landscape function is boosted (Tongway and Hindley, 2004). However, once we start to consider how well a landscape might be suited to a particular purpose or land use, the emphasis has moved from its objective function to its subjective 'condition' (see Figure 7.5). The 'condition' of something can be equated to its 'state of being' or 'health'. Clearly, such relative terms will vary with the purpose of the assessment. For example, a landscape condition that is acceptable for pastoral activities may be less acceptable for carbon sequestration goals and unacceptable for biodiversity conservation. One of the advantages of monitoring ecological condition is to be able to project future condition states based on defined states relating to management practices and/or climatic variations, such as potential trajectories of change for a grazed landscape based on the current land condition and differing future management strategies (Lunt *et al.*, 2007).

Figure 7.3 Ecosystem processes and feedback loops

This conceptual framework for the Trigger-Transfer-Reserve-Pulse (TTRP) ecosystem model represents sequences of ecosystem processes and feedback loops within a landscape.

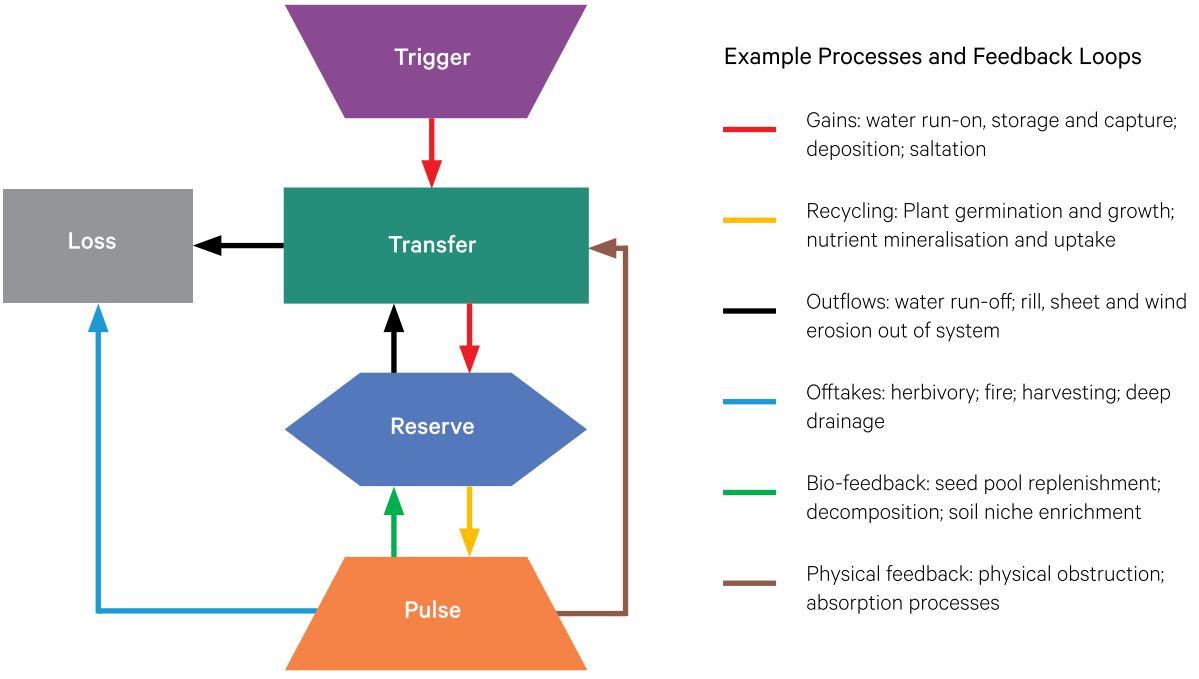

Adapted from: Tongway and Hindley (2004) Figure 5 and Tongway and Ludwig (2006) Figure 1

Figure 7.4 Landscape function examples

On the left of these photographs, where the ground is covered by vegetation and litter, the soil is protected from rain and wind. In contrast on the right, unfenced side, the unprotected soil surface allows sediments to 'leak' from the landscape.

a. Upper Burdekin Catchment, Queensland, 22 May 2003

b. Near boundary of Herbert and Burdekin shires, Queensland, 3 December 2003

Source: John Ludwig, CSIRO

An example of landscape function being lost at a grazing site is shown in Figure 7.4. On the left of these photographs, where grazing animals have been excluded, dense vegetation and litter cover over the soil surface, retain rainwater, and prevent wind erosion. By contrast, on the grazed side of the fencelines, the soil has been bared and shows surface damage from animal movements. Such unprotected soil surfaces allow soil sediments to 'leak' from the landscape. A healthy—or functional—landscape conserves its water and soil resources while a 'leaky'—or dysfunctional—one loses these resources (Tongway and Ludwig, 1997a, 1997b). Since vegetation cover and its spatial patterns strongly impact landscape function, metrics that represent the patchiness of vegetation cover and/or the condition and undulations of the soil surface can then be used as indicators of landscape function both for ecological and hydrological purposes (Wilcox *et al*., 2003; Ludwig *et al*., 2005).

An indicator is a convenient or useful substitute for something that is difficult to measure, such as land condition. In Australian rangelands, for example, useful indicators are related to soil losses via eco-hydrological processes (Ludwig *et al*., 2007), which are directly impacted by management practices (Pickup and Chewings, 1994). Other indicators of land condition from a pastoral perspective include:

- ground cover, and particularly basal cover—that part of the herbage layer rooted in the ground, which protects the soil surface against erosion from overland flow of water in heavy or intense rainfall;
- pasture biomass—particularly available forage;
- herbage composition—including the proportion of palatable, perennial grasses[8];
- woody-layer dynamics—any long term change in tree and shrub density;
- accelerated soil erosion; and the
- presence of weeds.

For example, ground cover is a useful indicator of the state of grazed rangelands because it protects the soil surface against erosion, provides some information about landscape 'leakiness', approximates pasture biomass (available forage) in some vegetation types, infers carbon dynamics (particularly the effectiveness with which organic matter is being returned to the soil through litter), and indicates habitat quality where entirely native species are present, which may be of value for inferring biodiversity condition (Fisher and Kutt, 2006). In this environment, when information is known about the composition and palatability of pasture species and appropriate cover-mass relationships, ground cover estimates can be used to infer pasture biomass (see Sections 14 and 15).

8 Pasture grasses are classified as 2P (perennial and palatable) or 3P (perennial, productive and palatable).

Figure 7.5 Landscape function versus landscape condition

This diagram clarifies the differences between landscape (or ecosystem) functionality, that is its 'state', from its suitability for a particular purpose, that is its 'condition'. While functionality is an objective description, condition is fundamentally based on value judgements, which will vary for different purposes. For example, the land use goals of pastoral productivity, biodiversity, or carbon sequestration may apply different value judgements to a given landscape state and, as a consequence, derive different assessments of its condition.

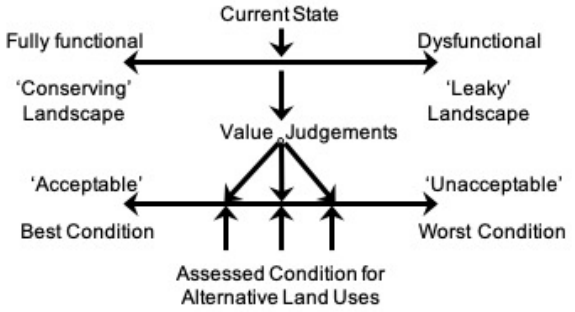

Source: Ludwig *et al.* (1997)

In some environments, landscape function could be envisaged as a continuum between a 'conserving' landscape and a 'leaky' landscape (see Figure 7.5). For example, this 'leakiness' indicator has been used to monitor the health of arid and semi-arid landscapes in Australia (Ludwig *et al.*, 2007; see Section 8.1.6). It also provides an axis along which the potential consequences of alternative land uses can be evaluated (see Sections 8.1.6 and 15). The framework illustrated in Figure 7.5 shows how an indicator of the functional state of a landscape, currently positioned midway along a continuum, may lead, through a 'values prism' (Gibbons and Freudenberger, 2006), to different assessments of its condition, depending on how different stakeholders value this level of functionality relative to their specific land use goals (Ludwig and Bastin, 2008).

For example, in Australian rangelands (see Section 15), environmental stakeholders who are predominantly interested in either pastoral production or biodiversity as land use goals would assess landscape condition using different criteria. In this context, contrasting expressions for indicators that singularly, or in combination, suggest better or poorer land condition are listed in Table 7.5 below. Using appropriate indicators, the question of 'what is the condition of the landscape?' (interpreted as 'how healthy is it?') becomes two questions:

- how functional is it for the intended/desired purpose? and
- how do its relevant indicators compare or interrelate?

Such criteria rely on the selection of appropriate indicators, that is, convenient, quantifiable aspects of land condition. As noted above, one indicator of landscape function is leakiness—its capacity to capture and retain rainwater, soils, and their nutrients on site, rather than lose them to the surrounding landscape(s) (see Figure 7.3 and Figure 7.5). These resources are not only vital for plant and animal growth, but provide food and shelter for the providers of numerous ecosystem 'services', such as pollination (see Section 20.3).

The degree to which the comparative terms in Table 7.5 apply at a particular location can only really be judged by comparison with appropriate reference or benchmark sites. To monitor land condition in grazed landscapes, for example, it may be possible to physically locate useful reference areas, such as water-remote locations, exclosures, or other small paddocks protected from continuous grazing. However, suitable reference areas may not be available where land types are highly preferred for grazing and/or are well watered. It is also necessary to account for any spatial differences in the amount and timing of rainfall when using information from reference areas.

Table 7.5 Examples of land condition indicators

Pastoral assessment		Biodiversity assessment	
Better condition	**Poorer condition**	**Better condition**	**Poorer condition**
More feed for livestock	Less or no feed for livestock	More feed for native fauna	Less or no feed for native fauna
More palatable perennials	Few or no perennials	Wide range of 'desirable' perennials	Few or no 'desirable' perennials
More ground cover and litter	Low ground cover or no litter	Wide range of ground covers and litter	Low ground cover or no litter
Lower utilisation—less grazing pressure	Higher utilisation—more grazing pressure	Plant growth ≥ grazing	Plant growth < grazing
No or few feral herbivores	Presence of feral herbivores	Wide range of herbivores	Small range of herbivores, mostly feral
Appropriate balance between trees and grasses	Too many or too few trees and shrubs	Diversity of trees and shrubs for faunal habitats	Small range of trees and shrubs

Source: Ludwig *et al.* (1997)

7.4 Productivity

The rate at which energy is stored by photosynthesis can be used as an indication of the productivity of an ecosystem, or its rate of biomass production (see Section 5.1.2). This process can be considered as a sequence of four energy flows within the terrestrial carbon cycle (see Excursus 1.2 and Figure 1.4):

- Gross Primary Productivity (GPP)—total amount of energy fixed in an ecosystem in unit time (including energy used in respiration). This equals the biomass produced per unit area in a given time.
- Net Primary Productivity (NPP)—amount of stored organic matter in plant tissue, after respiration, that is necessary for its production. This equals GPP minus autotrophic respiration, that is, the biomass available to consumers.
- Net Ecosystem Productivity (NEP)—amount of stored organic matter that is not consumed by heterotrophs (namely, NPP minus heterotrophic respiration).
- Secondary Productivities (such as Net Biome Productivity, NBP)—equals NEP minus consumption, that is, the energy stored at the consumer level (Odum, 1971).

GPP equates with the carbon removed from the atmosphere by plants, while NPP is defined as the difference between carbon gained by photosynthesis and the carbon lost by respiration (McCallum *et al.*, 2009; see Section 5.2). Since NPP effectively quantifies the conversion of atmospheric carbon (CO_2) into plant biomass, it can be viewed as the first step in carbon accumulation (Running *et al.*, 2004). Alarmingly, the human appropriation of net primary production (HANPP), which quantifies the human impact on the biosphere, is estimated to have doubled from 13% to 25% of global NPP between 1910 and 2005 (Krausman *et al.*, 2013; see Sections 20 and 21.2).

Figure 7.6 GPP over Australia

Mean monthly GPP was derived from MODIS imagery from January 2001 to December 2019 using methods detailed in Donohue et al. (2014).

a. Tree cover

b. Grass cover

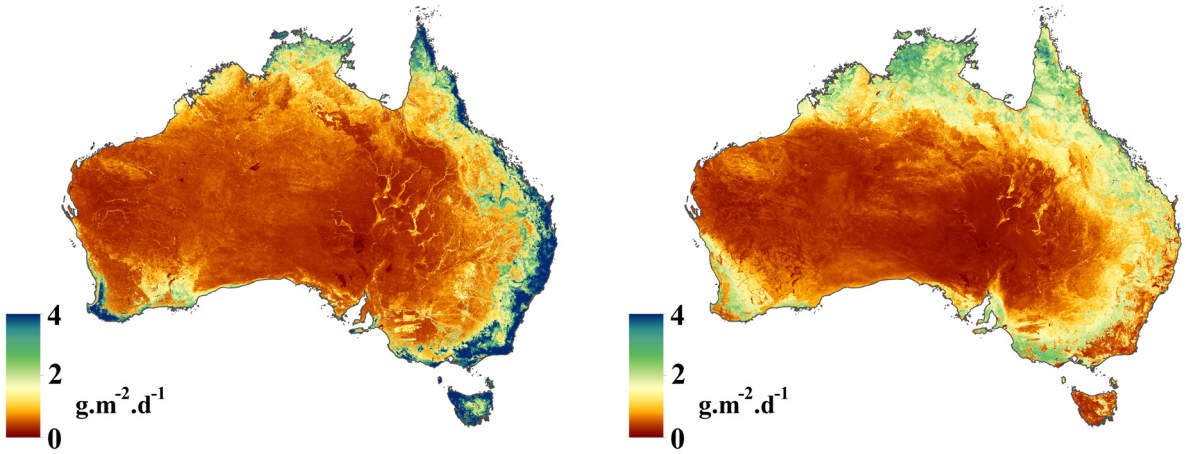

c. GPP time series

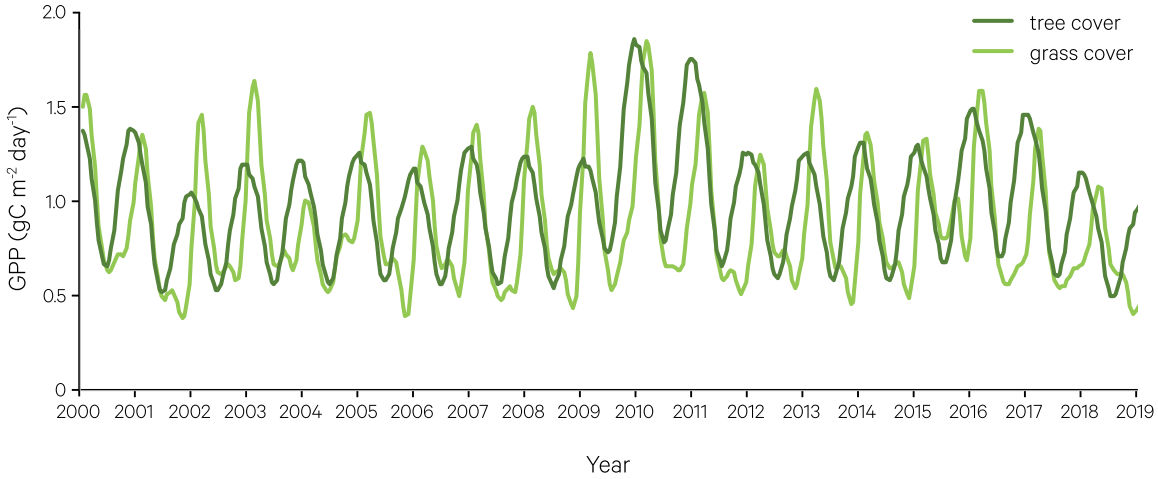

Source: Randall Donohue, CSIRO

As light levels, temperature, water availability, and nutrient supply fluctuate with diurnal and seasonal cycles, GPP also varies (see Figure 7.6). Annual GPP differences between ecosystems largely result from differences in canopy coverage and the duration of photosynthetic activity. Daily measurements (or estimates) of absorbed photosynthetic radiation (APAR; see Section 6.3.4) can be integrated over longer time periods, such as a growing season, to summarise the radiation available to a given plant canopy (Donohue *et al.*, 2014). Estimates of annual APAR effectively integrate diurnal and seasonal variations in solar radiation through changing atmospheric conditions to determine the amount of radiation absorbed by a vegetated canopy and, by inference, quantify the area of leaf cover that absorbs that radiation (see Sections 6.3 and 8.1).

Monteith (1972, 1977) observed the relationship between the rate of vegetative productivity and the rate of canopy light absorption, and proposed a straightforward modelling approach to estimate GPP and NPP from measurements of canopy reflective properties:

$$GPP = PAR \times fAPAR \times (LUE \times carbon_{dry}) \times environmental\ constraints$$

$$NPP = GPP - autotrophic\ respiration$$

where fAPAR is the fraction of absorbed photosynthetically active radiation (see Section 6.3.4). The efficiency with which plants utilise light to store carbon via photosynthesis varies as they grow. This characteristic, called photosynthetic Light Use Efficiency (LUE), can be computed as:

$$LUE = \frac{GPP}{APAR}$$

As such, LUE effectively estimates the amount of carbon fixed via photosynthesis for each unit of APAR. LUE underlies the many production efficiency models (PEM) that have been developed in recent decades. Such models initially assumed that photosynthetic carbon uptake by plants is proportional to the radiation absorbed by canopies, but recent studies have questioned this relationship, with variations being observed between plant functional types (PFT; see Sections 4.1.2 and 4.2.1) and photosynthetic pathways (see Section 5.2.1). LUE has also been observed to vary with species composition, nutrient availability, water stress, temperature, frost, and phenological stage (McCallum *et al.*, 2009), and increase with a greater proportion of diffuse to direct radiation (Gu *et al.*, 2002).

In global estimates of productivity, conversion efficiency parameters are determined for each type of biome and can be varied to account for changes in vegetation type and/or climatic conditions (see Section 17). Conversion efficiency parameters are used to convert estimates of APAR (as units of energy) to NPP (as units of biomass; Running *et al.*, 2004). PEM rely heavily on satellite observations for estimates of LUE, and meteorological data and fAPAR to estimate daily to yearly productivity at a range of spatial scales. For example, the BigFoot modelling approach (Running *et al.*, 1999; Cohen *et al.*, 2003) applies a biogeochemistry model to each cell of coregistered spatial datasets to derive NPP. In this model, the drivers are solar radiation and precipitation/temperature etc, with LAI and land cover being used for model initialisation. Other metrics related to productivity include:

- standing crop—a measure of the total amount of living organic matter, or biomass, in a given area at a given time, generally expressed as calories or g/m^2;
- turnover—the ratio of standing crop to production; and
- maintenance: structure ratio—indicative of turnover or energy flow rate = R/B

where

R is the total community respiration; and
B is the total community biomass.

Sellers (1985, 1987) explored the relationships between canopy reflectance and the leaf processes of photosynthesis and transpiration. This work integrated leaf models to estimate canopy photosynthetic activity and observed a near linear relationship between the ratio of NIR and red reflectances, as measured by remote sensors, and APAR, for high canopy covers. As the canopy cover decreases and the soil surface is visible to the remote sensor, this relationship becomes non-linear, especially for bright soils (see Section 6.4). Given that the canopy biophysical characteristics of photosynthetic capacity and bulk stomatal resistance are similarly related to the passage of PAR through the canopy, these characteristics also share a linear relationship with canopy reflectance in NIR and red wavelengths (see Sections 8.1.4 and 10.2.2).

7.5 Energy Balance

Plants and ecosystems can be viewed as thermodynamic engines whose energy source is the Sun (see Section 1). The First Law of Thermodynamics applies when the input energy equals the output energy, that is, the system is at equilibrium (see Volume 1A—Section 2.10.3). The Second Law of Thermodynamics, which observes that we don't live in a perfect world and that some energy is 'wasted' whenever useful energy is produced, also applies to plants and ecosystems (Monteith, 1972). The energy balance of ecosystems can be modelled to determine their stability in successional terms and their productivity in both ecological and economic terms.

Land surface temperature (LST) is commonly derived using EO datasets (see Volume 1B—Section 7.6). Canopy temperature is sometimes used as a surrogate for transpiration, but its relationship with air temperature and transpiration rate involves complex interactions of atmospheric, soil, and plant properties (see Section 5.2.4). Canopy temperature has also been useful as an indicator of drought resistance since those genotypes that maintain transpiration rates with lower canopy temperatures are more likely to withstand drought conditions (Blum, 2017; see Section 5.2.3). At the canopy or ecosystem level, a combination of instruments is used to estimate thermal energy balance, including:

- radiometers—measure upwelling and downwelling longwave and shortwave radiation (e.g. thermal sensors; see Volume 1B—Sections 7 and 8);
- heat flux sensors—measure heat transfer into the ground (e.g. ground heat flux plates and soil temperature probes); and
- eddy-covariance estimates of latent heat exchanges (evaporative flux) from anemometer and water vapour gas analyser measurements. Measurement of atmospheric factors using flux towers, as coordinated by the global consortium FLUXNET, is described in Excursus 7.2.

A range of models has been proposed to represent the fluxes of energy, water, and carbon between the biosphere, atmosphere, hydrosphere, and geosphere (see Excursus 1.2 and Section 7.6). Such models include Land Surface Models (LSM) that describe the energy balance at the interface between terrestrial surfaces and the atmosphere:

Net radiation =
(downwelling SWIR EMR × (1 – SWIR albedo))
+ downwelling thermal EMR
– upwelling thermal EMR

Over the surface of the globe, these energy components achieve equilibrium, but not at a local scale. Different land surfaces store different amounts of energy in different cycles (diurnal, seasonal, and longer term). The local imbalances in these components drive the Earth's climate.

Section 5.2.4 introduced the terms sensible and latent heat fluxes. The net radiation equation above can also be written in the form:

$$R_n = H + \lambda E + G + F$$

where

R_n is the net radiation;
H is the sensible heat flux derived from the difference between surface and air temperatures, aerodynamic resistance, density of air, and specific heat of air;
λ is the latent heat of vaporisation;
E is evapotranspiration;
G is the soil flux; and
F is the chemical energy flux stored in photosynthesis.

Aerodynamic resistance depends on the wind speed and surface roughness length, which in turn is related to vegetation height since taller vegetation, such as forest trees, allow more exchange of turbulent heat fluxes than shorter vegetation, such as grass (see Section 13). These components are interrelated and changes in one component flow on to other components (Pitman, 2003) and also affect the exchange of materials and gases, such as CO_2.

LSM have progressed from simple models based on uniform surfaces to multi-layer, EO-based models, that include multiple vegetation and soil characteristics, to detailed foliage models that account for cell structure and biochemical processes (see Section 10.2).

Energy is indeed present in all things. Living organisms draw it from their environment, as plants take it from the sun in photosynthesis and animals take chemical energy from their food through digestion and respiration. They accumulate it in their own bodies and use it to power their movements and behaviour. When they die, the energy accumulated in their bodies is released to continue on its way in other forms. The flow of energy on which your body and your brain depend at this very moment is part of the cosmic flux, and the energy within you will flow on after you are dead and gone, taking endless new forms.
(Rupert Sheldrake, 1994)

Excursus 7.2—Flux Towers

Source: Beringer *et al.* (2016); Isaac *et al.* (2017); van Gorsel *et al.* (2018)

Within atmospheric boundary layers, vertical turbulence is measured using the eddy flux technique, also known as eddy covariance or eddy correlation (EC). This statistical technique is used to compute the flux (or flow) of various gases through the atmosphere from continuous micrometeorological measurements at selected locations. Such measurements track the vertical and horizontal movement of air parcels by eddies and are typically taken from mobile or fixed towers known as Flux Towers.

A global network of over 500 flux towers is coordinated by FLUXNET to measure the exchanges of CO_2, water vapour and energy between the biosphere and the atmosphere (FLUXNET, 2018; Williams *et al.*, 2009; Oliphant, 2012). This network provides continuous, long term micrometeorological measurements for monitoring the state of ecosystems globally (see Volume 1A—Section 10.1). In Australia and New Zealand, data from nearly 30 flux towers, managed by a dozen institutions, are collated by TERN Ecosystem Processes (formerly TERN OzFlux and TERN Supersites), as part of FLUXNET (see Figure 7.7). OzFlux was established to provide the Australian and global modelling communities with consistent observations of energy, carbon and water exchange between the atmosphere and the key ecosystems of Australia and New Zealand: tropical rainforest and savanna, schlerophyll forest and woodland, alpine meadow, peatland, semi-arid woodland, savanna, grasslands, croplands, and pastures (Beringer *et al.*, 2016).

The flux towers measure CO_2 flux as well as sensible and latent heat flux. Processed data from the flux tower network is available from a number of places (see Section 7.7) and include Net Ecosystem Exchange (NEE), Gross Primary Productivity (GPP) and Ecosystem Respiration (ER) in addition to evapotranspiration (ET), precipitation, and the components of the surface energy balance (see Figure 7.7b). Using flux measurements in conjunction with models and EO datasets, ecosystem dynamics (productivity, respiration, evapotranspiration, water-use efficiency) can be explored within the context of climate fluctuations, meteorological drivers, phenology, and management activities. Broad science outcomes from analyses of EC data provided by the flux tower network include:

- improved methods for observations and interpretation (Beringer *et al.*, 2016; Isaac *et al.*, 2017; McHugh *et al.*, 2017);
- upscaling of ecosystem scale measurements to regional and larger scales using EO and physical modelling (Haverd *et al.*, 2016; Laubach *et al.*, 2016; Restrepo-Coupe *et al.*, 2016; Trudinger *et al.*, 2016; Whitley *et al.*, 2016); and
- better understanding of the interactions between carbon, water and energy cycles and their responses to changes related to land use, climate, extreme weather, and fire (Bristow *et al.*, 2016a; Hinko-Najera *et al.*, 2017; Hunt *et al.*, 2016; Moore *et al.*, 2016a; van Gorsel *et al.*, 2016; Fest *et al.*, 2017).

By directly quantifying sensible heat and moisture fluxes in and around vegetation canopies, EC moisture flux towers provide reliable measures of Actual Evapotranspiration (AET) over large areas (hundreds to thousands of m^2; Drexler *et al.*, 2004), and are commonly used with catchment water balance data to validate EO-based estimates of AET (Glenn *et al.*, 2011). While the accuracy of EC measurements have been assessed as being 15–30%, which impacts the accuracy of any studies they are used to validate (Allen *et al.*, 2011), they deliver important, ecosystem level information about the factors that impact AET (Glenn *et al.*, 2011) and expand our understanding of ecological, biogeochemical and hydrological processes in terrestrial ecosystems. Nonetheless, uncertainty exists in all methods, and EC towers are currently one of the best means of measuring AET at the ecosystem scale via an *in situ*, non-destructive approach. Beringer *et al.* (2016) identify four key benefits from these flux towers for Australia:

- providing accurate, continuous half-hourly to annual estimates of sinks and sources of greenhouse gases and water from ecosystems for carbon accounting and water management that are particularly important in an arid country like Australia (Hutley *et al.*, 2005; Raupach *et al.*, 2013);
- evaluating the effects of disturbance, topography, biodiversity, stand age, insect/pathogen infestation, and extreme weather on carbon and water fluxes, particularly cyclone, fire, and heat waves in the Australian environment (Beringer *et al.*, 2014; Bowman *et al.*, 2009; van Gorsel *et al.*, 2016; Hutley *et al.*, 2013);
- examining the effects of land management practices, such as harvest, fertilisation, irrigation, tillage, thinning, cultivation, and clearing, especially for agricultural activities (Bristow *et al.*, 2016b; Campbell *et al.*, 2015; Cleverly *et al.*, 2020); and
- producing important ground truth data for parameterizing, validating, and improving satellite EO and global inversion products (Anav *et al.*, 2015; Running *et al.*, 1999; Schimel *et al.*, 2015), particularly for phenology (Ma *et al.*, 2013; Moore *et al.*, 2016b) and water balance.

Figure 7.7 Flux tower distribution and site data

a. Locations of flux tower sites are shown in red for active sites and blue for inactive sites. The thumbnail plots show monthly average air temperature and precipitation at Bureau of Meteorology sites that are representative of the tower locations. The diameter of the symbol marking the tower locations is proportional to the canopy height (see scale at bottom left of map).

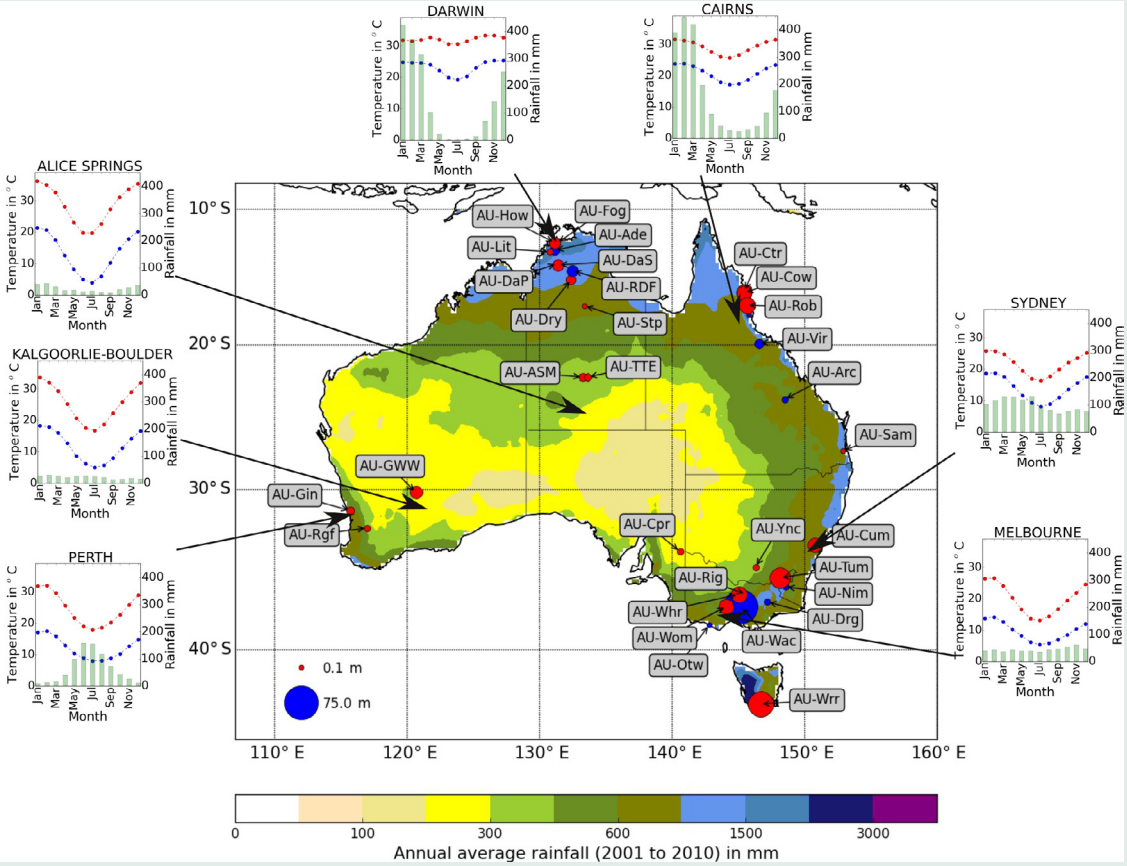

b. Site diagram for an individual flux tower

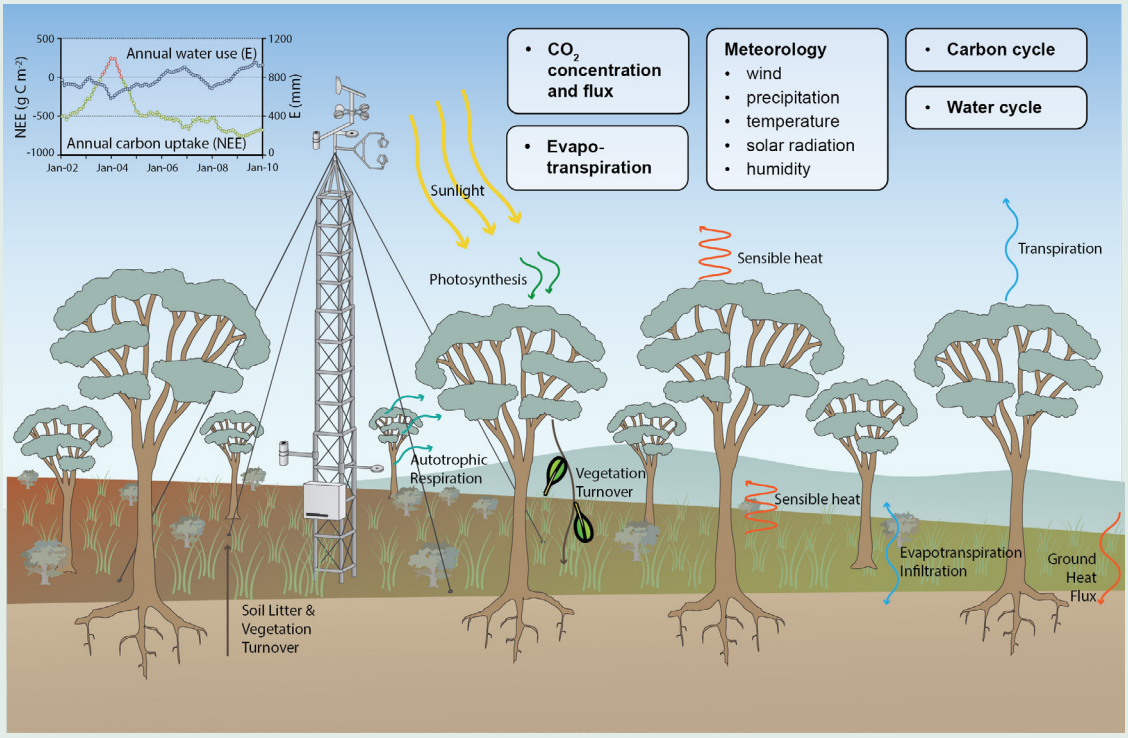

Source: a. Isaac *et al.* (2017) Figure 1; b. Mark Grant, TERN

7.6 Water Balance

Each year more than half a million cubic kilometres of water is moved around the Earth's surface, between the surface and sub-surface storage, and between the surface and the atmosphere (see Volume 3B). This cycling of water is referred to as the hydrological cycle (see Volume 1A—Section 4.2.2). Water balance modelling attempts to understand the interactions of components within the hydrological cycle:

- within atmosphere—solar radiation and moisture transport;
- from atmosphere to surface—various forms of precipitation;
- surface to atmosphere transfers—evaporation from land and water surfaces, and transpiration from plants; and
- surface and sub-surface transfers—runoff, infiltration and percolation into soil layer, deep seepage to groundwater, and groundwater discharge to lakes, streams, and seas.

The Australian climate has highly variable rainfall and runoff, and these components of the hydrological cycle vary widely in both space and time (see Section 2.2). These factors make water balance modelling particularly challenging for the Australian environment (Zhang *et al*., 2002).

Transpiration describes the process of water entering the atmosphere from plants (see Section 5.2.3) while evapotranspiration (ET) collectively refers to the transfer of water vapour to the atmosphere from both vegetated and unvegetated surfaces (see Section 2.2.1). Evapotranspiration is a major determinant of water balance in dry continents such as Australia and varies with the:

- availability of water in the landscape;
- climatic conditions, such as temperature, cloudiness, humidity, and wind speed; and
- rates of transpiration by individual plants.

Evapotranspiration increases with temperature, so is regulated by the same drivers that regulate temperature, namely latitude, altitude, cloud cover, and topography (see Section 5.2.4). Potential ET (PET) defines a theoretical water volume for an ecological system, which represents the water than can be 'extracted' from it for known inputs of solar energy and precipitation. The Actual ET (AET) is often less than the potential when water supply is limited. AET can be viewed as the reciprocal of precipitation, although only 90% of precipitation returns to the atmosphere via evapotranspiration (NWC, 2007). On a regional basis, when PET exceeds precipitation, there is a water deficit; when precipitation exceeds PET, there is a water surplus. During times of water surplus, water may be stored by plants, by soil, or by the water table, for use during times of water deficit.

Water balance modelling "is based on the law of conservation of mass: any change in the water content of a given soil volume during a specified period must equal the difference between the amount of water added to the soil volume and the amount of water withdrawn from it" (Zhang *et al*., 2002). Water balance can be considered at a range of scales, such as the root zone for a small number of plants, for a whole catchment, for a continent or the whole globe. At a catchment scale, the water balance equation can be given as:

$$\Delta S = P - ET - Q - R$$

where all components are spatially averaged for the catchment:

S is the water storage;
P is precipitation;
ET is evapotranspiration;
Q is surface runoff; and
R is recharge (Zhang *et al*., 2002).

Water balance models need to be tailored to specific climates and landscapes and may be integrated with other process models (see Section 7.5). For example, the WAVES model (Dawes and Short, 1993; Zhang *et al*., 1996) simulates the energy, water, carbon, and solute balances of a one-dimensional soil-canopy-atmosphere system (Zhang *et al*., 2002). EO-based water balance models are further discussed in Sections 9.4 and 10.2.3, and Excursus 10.2.

7.7 Further Information

Global NPP Image Composites

https://neo.sci.gsfc.nasa.gov/view.php?datasetId=MOD17A2_M_PSN

TERN Ecosystem Processes

http://www.tern.org.au/OzFlux-pg17729.html

Processed data from the flux tower network is available from *http://data.ozflux.org.au/portal/home.jspx* and *http://dap.ozflux.org.au/thredds/catalog.html* for example, including Net Ecosystem Exchange (NEE), Gross Primary Productivity (GPP), and Ecosystem Respiration (ER) in addition to evapotranspiration (ET), precipitation, and the components of the surface energy balance (see Excursus 7.2).

7.8 References

Allen, R.G., Pereira, L.S., Howell, T.A., Jensen, M.E. (2011). Evapotranspiration information reporting: I. Factors governing measurement accuracy. *Agricultural Water Management*, 98, 899–920.

Anav, A., Friedlingstein, P., Beer, C., Ciais, P., Harper, A., Jones, C., Murray-Tortarolo, G., Papale, D., Parazoo, N. C., Peylin, P., Piao, S., Sitch, S., Viovy, N., Wiltshire, A., and Zhao, M. (2015). Spatiotemporal patterns of terrestrial gross primary production: A review. *Reviews of Geophysics*, 53, 785–818. doi:*10.1002/2015RG000483*,

Ash, A.J., Bellamy, J.A., and Stockwell, T.G.H. (1994). State and transition models for rangelands. 4. Application of state and transition models to rangelands in northern Australia. *Tropical Grasslands*, 28, 223–228.

Beringer, J., Hutley, L.B., Abramson, D., Arndt, S. K., Briggs, P., Bristow, M., Canadell, J.G., Cernusak, L.A., Eamus, D., Evans, B.J., Fest, B., Goergen, K., Grover, S.P., Hacker, J., Haverd, V., Kanniah, K., Livesley, S. J., Lynch, A., Maier, S., Moore, C., Raupach, M., Russell-Smith, J., Scheiter, S., Tapper, N.J., and Uotila, P. (2014). Fire in Australian Savannas: from leaf to landscape. *Global Change Biology*, 11, 6641. doi:*10.1111/gcb.12686*

Beringer, J., Hutley, L.B., McHugh, I., Arndt, S.K., Campbell, D., Cleugh, H.A., Cleverly, J., Resco de Dios, V., Eamus, D., Evans, B., Ewenz, C., Grace, P., Griebel, A., Haverd, V., Hinko-Najera, N., Huete, A., Isaac, P., Kanniah, K., Leuning, R., Liddell, M.J., Macfarlane, C., Meyer, W., Moore, C., Pendall, E., Phillips, A., Phillips, R.L., Prober, S. M., Restrepo-Coupe, N., Rutledge, S., Schroder, I., Silberstein, R., Southall, P., Yee, M.S., Tapper, N.J., van Gorsel, E., Vote, C., Walker, J., and Wardlaw, T. (2016). An introduction to the Australian and New Zealand flux tower network—OzFlux. *Biogeosciences*, 13, 5895–5916. *https://doi.org/10.5194/bg-13-5895-2016*

Bestelmeyer, B.T., Brown, J.R., Havstad, K.M., Alexander, R., Chavez, G., and Herrick, J.E. (2003). Development and use of state-and-transition models for rangelands. *Journal of Range Management*, 56, 114–126.

Bestelmeyer, B.T., Ash, A., Brown, J.R., Densambuu, B., Fernández-Giménez, M., Johanson, J., Levi, M., Lopez, D., Peinetti, R., Rumpff, L., and Shaver, P. (2017). State and Transition Models: Theory, Applications, and Challenges. Ch 9 in *Rangelands Systems* (Ed: Briske, D.D.). Springer Series on Environmental Management. *https://doi.org/10.1007/978-3-319-46709-2_9*

Billings, W.D. (1970). *Plants, Man and the Ecosystem*. 2nd Edn. Wadsworth Publ. Co., Belmont. 160 p. ISBN 0-333-14633-6.

Blum, A. (2017). Osmotic adjustment is a prime drought stress adaptive engine in support of plant production. *Plant, Cell and Environment*, 40, 4–10.

Bowman, D.M.J.S., Balch, J.K., Artaxo, P., Bond, W.J., Carlson, J.M., Cochrane, M.A., D'Antonio, C.M., DeFries, R.S., Doyle, J.C., Harrison, S.P., Johnston, F.H., Keeley, J.E., Krawchuk, M.A., Kull, C.A., Marston, J.B., Moritz, M.A., Prentice, I.C., Roos, C.I., Scott, A.C., Swetnam, T.W., van der Werf, G.R., and Pyne, S.J. (2009). Fire in the Earth System. *Science*, 324, 481–484. doi:*10.1126/science.1163886*

Briske, D.D. (2017) (Ed). *Rangelands Systems*. Springer Series on Environmental Management. *https://doi.org/10.1007/978-3-319-46709-2_9*

Briske, D.D., Fuhlendorf, S.D., and Smeins, F.E. (2005). State-and-transition models, thresholds, and rangeland health: A synthesis of ecological concepts and perspectives. *Rangeland Ecology and Management*, 58, 1–10.

Briske, D.D., Illius, A.W., and Anderies, J.M. (2017). Nonequilibrium Ecology and Resilience Theory. Ch 6 in *Rangelands Systems* (Ed: Briske, D.D.). Springer Series on Environmental Management. doi:*10.1007/978-3-319-46709-2–6*

Bristow, M., Hutley, L.B., Beringer, J., Livesley, S.J., Arndt, S.K., and Edwards, A.C. (2016a). Greenhouse gas emissions from tropical savanna deforestation and conversion to agriculture. *Biogeosciences*, 13, 6285–6303.

Bristow, M., Hutley, L.B., Beringer, J., Livesley, S.J., Edwards, A.C., and Arndt, S.K. (2016b). Quantifying the relative importance of greenhouse gas emissions from current and future savanna land use change across northern Australia. *Biogeosciences*, 13, 6285–6303. *https://doi.org/10.5194/bg-13-6285-2016*.

Campbell, D.I., Wall, A.M., Nieveen, J.P., and Schipper, L.A. (2015). Variations in CO_2 exchange for dairy farms with year-round rotational grazing on drained peatlands. *Agriculture, Ecosystems and Environment*, 202, 68–78. doi:*10.1016/j.agee.2014.12.019*, 2015.

Cleverly, J., Vote, C., Isaac, P., Ewenz, C., Harahap, M., Beringer, J., Campbell, D.I., Daly, E., Eamus, D., He, L., Hunt, J., Grace, P., Hutley, L.B., Laubach, J., McCaskill, M., Rowlings, D., Rutledge Jonker, S., Schipper, L.A., Schroder, I., Teodosio, B., Yu, Q., Ward, P.R., Walker, J.P., Webb, J.A., Grover, S.P.P. (2020). Carbon, water and energy fluxes in agricultural systems of Australia and New Zealand. *Agricultural and Forest Meteorology*, 287, 107934. doi:*10.1016/j.agrformet.2020.107934*.

Cohen, W.B., Turner, D.P., Running, S.W., and Gower, S.T. (2003). Comparisons of land cover and LAI estimates derived from ETM+ and MODIS for four sites in North America: a quality assessment of 2000/2001 provisional MODIS products. *Remote Sensing of Environment*, 88, 233–255.

DAFF (2013). *Grazing BMP self-assessment: Grazing land management, Northern Australian module*. Department of Agriculture, Fisheries and Forestry, Queensland.

Dawes, W.R., and Short, D.L. (1993). *The efficient numerical solution of differential equations for coupled water and solute dynamics: the WAVES model*. Technical Memorandum 93/18, CSIRO Division of Water Resources, Canberra.

DEWHA (2010). *Ecosystem Services: Key Concepts and Applications*. Occasional Paper No 1, Department of the Environment, Water, Heritage and the Arts, Canberra.

Donohue, R.J., Hume, I.H., Roderick, M.L., McVicar, T.R., Beringer, J., Hutley, L.B., Gallant, J.C., Austin, J.M., van Gorsel, E., Cleverly, J.R., Meyer, W.S., and Arndt, S.K. (2014). Evaluation of the remote-sensing-based DIFFUSE model for estimating photosynthesis of vegetation. *Remote Sensing of Environment*, 155, 349–365.

Drexler, J.Z., Snyder, R.L., Spano, D., Paw, K.T.U. (2004). A review of models and micrometeorological methods used to estimate wetland evapotranspiration. *Hydrological Processes*, 18, 2071–2101.

Dyksterhuis, E.J. (1949). Condition and management of rangeland based on quantitative ecology. *Journal of Range Management*, 2, 104–105.

Ellis, J.E., and Swift, D.M. (1988). Stability of African pastoral ecosystems: Alternate paradigms and implications for development. *Journal of Range Management*, 41, 450–459.

Fest, B.J., Hinko-Najera, N., Wardlaw, T., Griffith, D.W.T., Livesley, S.J., and Arndt, S.K. (2017). Soil methane oxidation in both dry and wet temperate eucalypt forests shows a near-identical relationship with soil air-filled porosity. *Biogeosciences*, 14, 467–479. *https://doi.org/10.5194/bg-14-467-2017*

Fisher, A., and Kutt, A. (2006). *Biodiversity and Land Condition in Tropical Savanna Rangelands: Summary Report*. Tropical Savannas CRC, Darwin, NT.

FLUXNET (2018). *FLUXNET* webpage, ORNL DAAC NASA website: *http://fluxnet.ornl.gov/*

Gibbons, P., and Freudenberger, D. (2006). An overview of methods used to assess vegetation condition at the scale of the site. *Ecological Management and Restoration*,7, S10-S17.

Glenn, E., Doody, T.M., Guerschman, J.P., Huete, A.R., King, E.A., McVicar, T.R., van Dijk, A.I.J.M., van Niel, T.G., Yebra, M., and Zhang, Y. (2011). Actual evapotranspiration estimation by ground and remote sensing methods: the Australian experience. *Hydrological Processes*, 25(26), 4103–4116. doi:*10.1002/hyp.8391*

Gu, L., Baldocchi, D., Verma, S.B., Black, T.A., Vesala, T., Falge, E.M., and Dowty, P.R. (2002). Advantages of diffuse radiation for terrestrial ecosystem productivity. *Journal of Geophysical Research*, 107(D6). doi:*10.1029/2001JD001242*.

Haverd, V., Smith, B., Raupach, M., Briggs, P., Nieradzik, L., Beringer, J., Hutley, L., Trudinger, C.M., and Cleverly, J. (2016). Coupling carbon allocation with leaf and root phenology predicts tree–grass partitioning along a savanna rainfall gradient. *Biogeosciences*, 13, 761–779. *https://doi.org/10.5194/bg-13-761-2016*

Hinko-Najera, N., Isaac, P., Beringer, J., van Gorsel, E., Ewenz, C., McHugh, I., Exbrayat, J.-F., Livesley, S.J., and Arndt, S.K. (2017). Net ecosystem carbon exchange of a dry temperate eucalypt forest. *Biogeosciences*, 14, 3781–3800. *https://doi.org/10.5194/bg-14-3781-2017*

Hunt, J.E., Laubach, J., Barthel, M., Fraser, A., and Phillips, R.L. (2016). Carbon budgets for an irrigated intensively grazed dairy pasture and an unirrigated winter-grazed pasture. *Biogeosciences*, 13, 2927–2944. *https://doi.org/10.5194/bg-13-2927-2016*

Hutley, L.B., Leuning, R., Beringer, J., Cleugh, H.A. (2005). The utility of the eddy covariance techniques as a tool in carbon accounting: tropical savanna as a case study. *Australian Journal of Botany*, 53, 663–675.

Hutley, L.B., Evans, B.J., Beringer, J., Cook, G.D., Maier, S.M., and Razon, E. (2013). Impacts of an extreme cyclone event on landscape-scale savanna fire, productivity and greenhouse gas emissions, *Environmental Research Letters*, 8, 045023. doi:*10.1088/1748-9326/8/4/045023*

IFA (1985). *Think Trees, Grow Trees*. Dept. Arts, Heritage and Environment/Institute of Foresters of Australia. AGPS, Canberra.

Illius, A.W., and O'Connor, T.G. (1999). On the Relevance of Nonequilibrium Concepts to Arid and Semiarid Grazing Systems. *Ecological Applications*, 9(3), 798–813.

Isaac, P., Cleverly, J., McHugh, I., van Gorsel, E., Ewenz, C., and Beringer, J. (2017). OzFlux data: network integration from collection to curation. *Biogeosciences*, 14, 2903–2928. *https://doi.org/10.5194/bg-14-2903-2017*

Joyce, L.A. (1993). The life cycle of the range condition concept. *Journal of Range Management*, 46, 132–138.

Keith, D.A., Rodríguez, J.P., Rodríguez-Clark, K.M., Nicholson, E., Aapala, K., Alonso, A., Asmussen, M., Bachman, S., Basset, A., Barrow, E.G., Benson, J.S., Bishop, M.J., Bonifacio, R., Brooks, T.M., Burgman, M.A., Comer, P., Comín, F.A., Essl, F., Faber-Langendoen, D., Fairweather, P.G., Holdaway, R.J., Jennings, M., Kingsford, R.T., Lester, R.E., Nally, R. Mac, McCarthy, M.A., Moat, J., Oliveira-Miranda, M.A., Pisanu, P., Poulin, B., Regan, T.J., Riecken, U., Spalding, M.D., and Zambrano-Martínez, S. (2013). Scientific Foundations for an IUCN Red List of Ecosystems. *PLoS ONE*, 8(5), e62111. doi:*10.1371/journal.pone.0062111*

Kessell, S.R. (1979). *Gradient Modelling: Resource and Fire Management*. Springer-Verlag, New York.

Krausman, F., Erb, K.-H., Gingrich, S., Haberl, H., Bondeau, A., Gaube, V., Lauk, C., Plutzar, C., and Searchinger, T.D. (2013). Global human appropriation of net primary production doubled in the 20th century. *Proceedings of the National Academy of Sciences of the USA*, 110(25), 10324–10329. *https://doi.org/10.1073/pnas.1211349110*

Laubach, J., Barthel, M., Fraser, A., Hunt, J.E., and Griffith, D.W.T. (2016). Combining two complementary micrometeorological methods to measure CH_4 and N_2O fluxes over pasture. *Biogeosciences*, 13, 1309–1327. *https://doi.org/10.5194/bg-13-1309-2016*

Ludwig, J.A., and Bastin, G.N. (2008). Rangeland condition: its meaning and use. A Discussion Paper prepared for the Australian Collaborative Rangelands Information System (ACRIS) Management Committee. ACRIS. *https://www.environment.gov.au/system/files/resources/09f881fe-8119-4719-bfa0-6a2a55e90a1b/files/rangeland-condition-meaning-use.pdf*

Ludwig, J.A., and Tongway, D.J. (1997). A landscape approach to rangeland ecology. Ch 1 in *Landscape Ecology, Function and Management: Principles from Australia's Rangelands*. (Eds. J. Ludwig, D. Tongway, D. Freudenberger, J. Noble, and K. Hodgkinson). pp. 1–12. CSIRO Publishing, Melbourne.

Ludwig, J.A., Tongway, D.J., Freudenberger, D.O., Noble, J.C., and Hodgkinson, K.C. (Eds) (1997). *Landscape Ecology, Function and Management: Principles from Australia's Rangelands*. CSIRO Publishing, Melbourne, Australia.

Ludwig, J.A., Wilcox, B.P., Breshears, D.D., Tongway, D.J., and Imeson, A.C. (2005). Vegetation patches and runoff-erosion as interacting ecohydrological processes in semiarid landscapes. *Ecology*, 86, 288–297.

Ludwig, J.A., Bastin, G.N., Chewings, V.H., Eager, R.W., and Liedloff, A.C. (2007). Leakiness: A new index for monitoring the health of arid and semiarid landscapes using remotely sensed vegetation cover and elevation data. *Ecological Indicators*, 7, 442–454.

Lunt, I., Eldridge, D.J., Morgan, J.W., and Witt, G.B. (2007). Turner Review No. 13: A framework to predict the effects of livestock grazing and grazing exclusion on conservation values in natural ecosystems in Australia. *Australian Journal of Botany*, 55, 401–415. doi:*10.1071/BT06178*

Ma, X., Huete, A., Yu, Q., Coupe, N. R., Davies, K., Broich, M., Ratana, P., Beringer, J., Hutley, L. B., Cleverly, J., Boulain, N., and Eamus, D. (2013). Spatial patterns and temporal dynamics in savanna vegetation phenology across the North Australian Tropical Transect. *Remote Sensing of Environment*, 139, 97–115. doi:*10.1016/j.rse.2013.07.030*

Macarthur, R. (1955). Fluctuations of Animal Populations and a Measure of Community Stability. *Ecology*, 36(3), 533–536.

May, R.M. (1973). *Stability and complexity in model ecosystems*. Princeton University Press, Princeton.

McCallum, I., Wagner, W., Schmullius, C., Shvidenko, A., Obersteiner, M., Fritz, S., and Nilsson, S. (2009) Satellite-based terrestrial production efficiency modelling. *Carbon Balance and Management*, 4, 8. doi:*10.1186/1750-0680-4-8*

McHugh, I.D., Beringer, J., Cunningham, S.C., Baker, P.J., Cavagnaro, T.R., Mac Nally, R., and Thompson, R.M. (2017). Interactions between nocturnal turbulent flux, storage and advection at an "ideal" eucalypt woodland site. *Biogeosciences*, 14, 3027–3050. *https://doi.org/10.5194/bg-14-3027-2017*.

McKeon, G., and Carter, J. (2015). AussieGRASS: An Operational National Pasture Model. Ch 1 in *AussieGRASS Environmental Calculator—Product Descriptions v1.5*. Department of Science, Information Technology and Innovation, Queensland.

MEA (2005). *Ecosystems and Human Well-being: Synthesis*. Millennium Ecosystem Assessment, Island Press, Washington, DC.

MLA (2006). *Grazing Land Management. Sustainable and productive natural resource management*. Meat and Livestock Australia Ltd. ISBN 1 74036 9343

MLA (2011). *Biodiversity Condition Assessment for Grazing Lands*. Meat and Livestock Australia Ltd, North Sydney. ISBN 9781741916393

Monteith, J.L. (1972). Solar Radiation and Productivity in Tropical Ecosystems. *Journal of Applied Ecology*, 9(3), 747–766.

Monteith, J.L. (1977). Climate and the efficiency of crop production in Britain. *Philosophical Transactions of The Royal Society B: Biological Sciences*, 281(980), 294–294. doi:*10.1098/rstb.1977.0140*.

Moore, C.E., Beringer, J., Evans, B., Hutley, L.B., McHugh, I., and Tapper, N.J. (2016a). The contribution of trees and grasses to productivity of an Australian tropical savanna. *Biogeosciences*, 13, 2387–2403. doi:*10.5194/bg-13-2387-2016*

Moore, C.E., Brown, T., Keenan, T.F., Duursma, R.A., van Dijk, A.I.J.M., Beringer, J., Culvenor, D., Evans, B., Huete, A., Hutley, L.B., Maier, S., Restrepo-Coupe, N., Sonnentag, O., Specht, A., Taylor, J.R., van Gorsel, E., and Liddell, M.J. (2016b). Reviews and syntheses: Australian vegetation phenology: new insights from satellite remote sensing and digital repeat photography. *Biogeosciences*, 13, 5085–5102. doi:*10.5194/bg-13-5085-2016*

NWC (2007). *Australian Water Resources 2005*. National Water Commission, Canberra. ISBN: 978-1-921107-48-1

Odum, E.P. (1971). *Fundamentals of Ecology*. 3rd edn. W.B. Saunder Co., Philadelphia.

Oliphant, A.J. (2012). Terrestrial Ecosystem-Atmosphere Exchange of CO_2, Water and Energy from FLUXNET; Review and Meta-Analysis of a Global in-situ Observatory. *Geography Compass*, 6(12), 689–705. doi:*10.1111/gec3.12009*

Pianka, E.R. (1971). Species diversity. In *Topics in the Study of Life: The Bio Source Book*. pp 401-406. Harper and Row, New York.

Pickup, G., and Chewings, V.H. (1994). A grazing gradient approach to land degradation assessment in arid areas from remotely-sensed data. *International Journal of Remote Sensing*, 15, 597–617.

Pickup, G., Bastin, G.N., and Chewings, V.H. (1994). Remote-sensing-based Condition Assessment for Nonequilibrium Rangelands under Large-Scale Commercial Grazing. *Ecological Applications*, 4(3), 497–517.

Pitman, A.J. (2003). The Evolution of, and Revolution in, Land Surface Schemes designed for Climate Models. *International Journal of Climatology*, 23, 479–510.

Raupach, M.R., Haverd, V., and Briggs, P.R. (2013). Sensitivities of the Australian terrestrial water and carbon balances to climate change and variability. *Agriculture and Forest Meteorology*, 182–183, 277–291. doi:*10.1016/j.agrformet.2013.06.017*

Restrepo-Coupe, N., Huete, A., Davies, K., Cleverly, J., Beringer, J., Eamus, D., van Gorsel, E., Hutley, L.B., and Meyer, W.S. (2016). MODIS vegetation products as proxies of photosynthetic potential along a gradient of meteorologically and biologically driven ecosystem productivity. *Biogeosciences*, 13, 5587–5608. doi:*10.5194/bg-13-5587-2016*

Running, S.W., Baldocchi, D.D., Turner, D.P., Gower, S.T., Bakwin, P.S., and Hibbard, K.A. (1999). A global terrestrial monitoring network integrating tower fluxes, flask sampling, ecosystem modeling and EOS satellite data. *Remote Sensing of Environment*, 70, 108–127.

Running, S.W., Nemani, R.R., Heinsch, F.A., Zhao, M., Reeves, M., and Hashimoto, H. (2004). A continuous satellite-derived measure of global terrestrial primary production. *Biosciences*, 54(6), 547–560.

Schimel, D., Pavlick, R., Fisher, J. B., Asner, G. P., Saatchi, S., Townsend, P., Miller, C., Frankenberg, C., Hibbard, K., and Cox, P. (2015). Observing terrestrial ecosystems and the carbon cycle from space. *Global Change Biology*, 21, 1762–1776. doi:*10.1111/gcb.12822*.

Sellers, P.J. (1985). Canopy reflectance, photosynthesis and transpiration. *International Journal of Remote Sensing*, 6(8), 1335–1372.

Sellers, P.J. (1987). Canopy Reflectance, Photosynthesis, and Transpiration. II. The Role of Biophysics in the Linearity of Their Interdependence. *Remote Sensing of Environment*, 21, 143–183.

Sheldrake, R. (1994). *The rebirth of Nature: The Greening of Science and God*. Park Street Press, Rochester, Vermont. 272 p.

Sims, R.J., Lyons, M., and Keith, D.A. (2019). Limited evidence of compositional convergence of restored vegetation with reference states after 20 years of livestock exclusion. *Austral Ecology*, 44(4), 734–746. *https://doi.org/10.1111/aec.12744*

Stringham, T.K., Krueger, W.C., and Shaver, P.L. (2003). State and transition modeling: An ecological process approach. *Journal of Range Management*, 56, 106–113.

Tilman, D. (1996) Biodiversity: Population Versus Ecosystem Stability. *Ecology*, 77(2), 350–363.

Tilman, D., Lehman, C.L., and Bristow, C.E. (1998) Diversity-Stability Relationships: Statistical Inevitability or Ecological Consequence? *The American Naturalist*, 151(3), Notes and Comments.

Tongway, D.J., and Hindley, N. (2004). *Landscape function analysis: procedures for monitoring and assessing landscapes. With special reference to minesites and rangelands*. CSIRO Sustainable Ecosystems, Canberra.

Tongway, D.J., and Ludwig, J.A. (1997a). The nature of landscape dysfunction in rangelands. In *Landscape Ecology, Function and Management: Principles from Australia's Rangelands*. (Eds: Ludwig, J.A., Tongway, D.J., Freudenberger, D.O., Noble, J.C., Hodgkinson, K.C.). CSIRO Publishing, Melbourne.

Tongway, D.J., and Ludwig, J.A. (1997b). The conservation of water and nutrients within landscapes. In *Landscape Ecology, Function and Management: Principles from Australia's Rangelands*. (Eds: Ludwig, J.A., Tongway, D.J., Freudenberger, D.O., Noble, J.C., Hodgkinson, K.C.) CSIRO Publishing, Melbourne.

Tongway, D.J., and Ludwig, J.A. (2006). *Assessment of Landscape Function as an Information Source for Mine Closure*. Mine Closure (Eds: Fourie, A., and Tibbett, M.). Perth. ISBN 0-9756756-6-4 ISBN 0-9756756-6-4

Trudinger, C.M., Haverd, V., Briggs, P.R., and Canadell, J.G. (2016) Interannual variability in Australia's terrestrial carbon cycle constrained by multiple observation types. *Biogeosciences*, 13, 6363–6383. *https://doi.org/10.5194/bg-13-6363-2016*

van Gorsel, E., Wolf, S., Cleverly, J., Isaac, P., Haverd, V., Ewenz, C., Arndt, S., Beringer, J., Resco de Dios, V., Evans, B., Griebel, A., Hutley, L.B., Keenan, T., Kljun, N., Macfarlane, C., Meyer, W.S., McHugh, I., Pendall, E., Prober, S.M., and Silberstein, R. (2016). Carbon uptake and water use in woodlands and forests in southern Australia during an extreme heat wave event in the "Angry Summer" of 2012/2013. *Biogeosciences*, 13, 5947–5964. *https://doi.org/10.5194/bg-13-5947-2016*

van Gorsel, E., Cleverly, J., Beringer, J., Cleugh, H., Eamus, D., Hutley, L. B., Isaac, P., and Prober, S. (2018). Preface: OzFlux: a network for the study of ecosystem carbon and water dynamics across Australia and New Zealand. *Biogeosciences*, 15, 349–352. *https://doi.org/10.5194/bg-15-349-2018*.

Walker, B. (2020). Resilience: what it is and is not. *Ecology and Society*, 25(2), 11. *https://doi.org/10.5751/ES-11647-250211*

Washington-Allen, R.A., and Ravi, S. (2012). Dryland Analysis and Monitoring. In *Encyclopedia of Life Support Systems* (Ed: Squires, V.R.). UNESCO-EOLSS, Oxford.

Watt, K.E.F. (1968). *Energy and Resource Management*. McGraw-Hill, New York.

Westoby, M., Walker, B., and Noy-Meir, I. (1989). Opportunistic management for rangelands not at equilibrium. *Journal of Rangeland Management*, 42(4), 266–274.

Whitley, R., Beringer, J., Hutley, L.B., Abramowitz, G., De Kauwe, M.G., Duursma, R., Evans, B., Haverd, V., Li, L., Ryu, Y., Smith, B., Wang, Y.-P., Williams, M., and Yu, Q. (2016). A model inter-comparison study to examine limiting factors in modelling Australian tropical savannas. *Biogeosciences*, 13, 3245–3265. *https://doi.org/10.5194/bg-13-3245-2016*

Wilcox, B.P., Breshears, D.D., and Allen, C.D. (2003). Ecohydrology of a resource-conserving semiarid woodland: effects of scale and disturbance. *Ecological Monographs*, 73(2), 223–239.

Williams, M., Richardson, A.D., Reichstein, M., Stoy, P.C., Peylin, P., Verbeeck, H., Carvalhais, N., Jung, M., Hollinger, D.Y., Kattge, J., Leuning, R., Luo, Y., Tomelleri, E., Trudinger, C.M., and Wang, Y.-P. (2009). Improving land surface models with FLUXNET data. *Biogeosciences*, 6, 1341–1359. *https://doi.org/10.5194/bg-6-1341-2009*.

Youngentob, K.N., Renzullo, L.J., Held, A.A., Jia, X., Lindenmayer, D.B., and Foley, W.J. (2012). Using imaging spectroscopy to estimate integrated measures of foliage nutritional quality. *Methods in Ecology and Evolution*, 3, 416–426. doi:*10.1111/j.2041-210X.2011.00149.x*

Zhang, L., Dawes, W.R., and Hatton, T.J. (1996). Modelling hydrological processes using a biophysically based model—application of WAVES to FIFE and HAPEX-MOBILHY. *Journal of Hydrology*, 185, 147–169.

Zhang, L., Walker, G.R., and Dawes, W.R. (2002). Water balance modelling: concepts and applications. In *Regional Water and Soil Assessment for Managing Sustainable Agriculture in China and Australia* (Eds: McVicar, T.R., Li Rui, Walker, J., Fitzpatrick, R.W., and Liu Changming). ACIAR Monograph No. 84, pp 31–47.

EO Methods

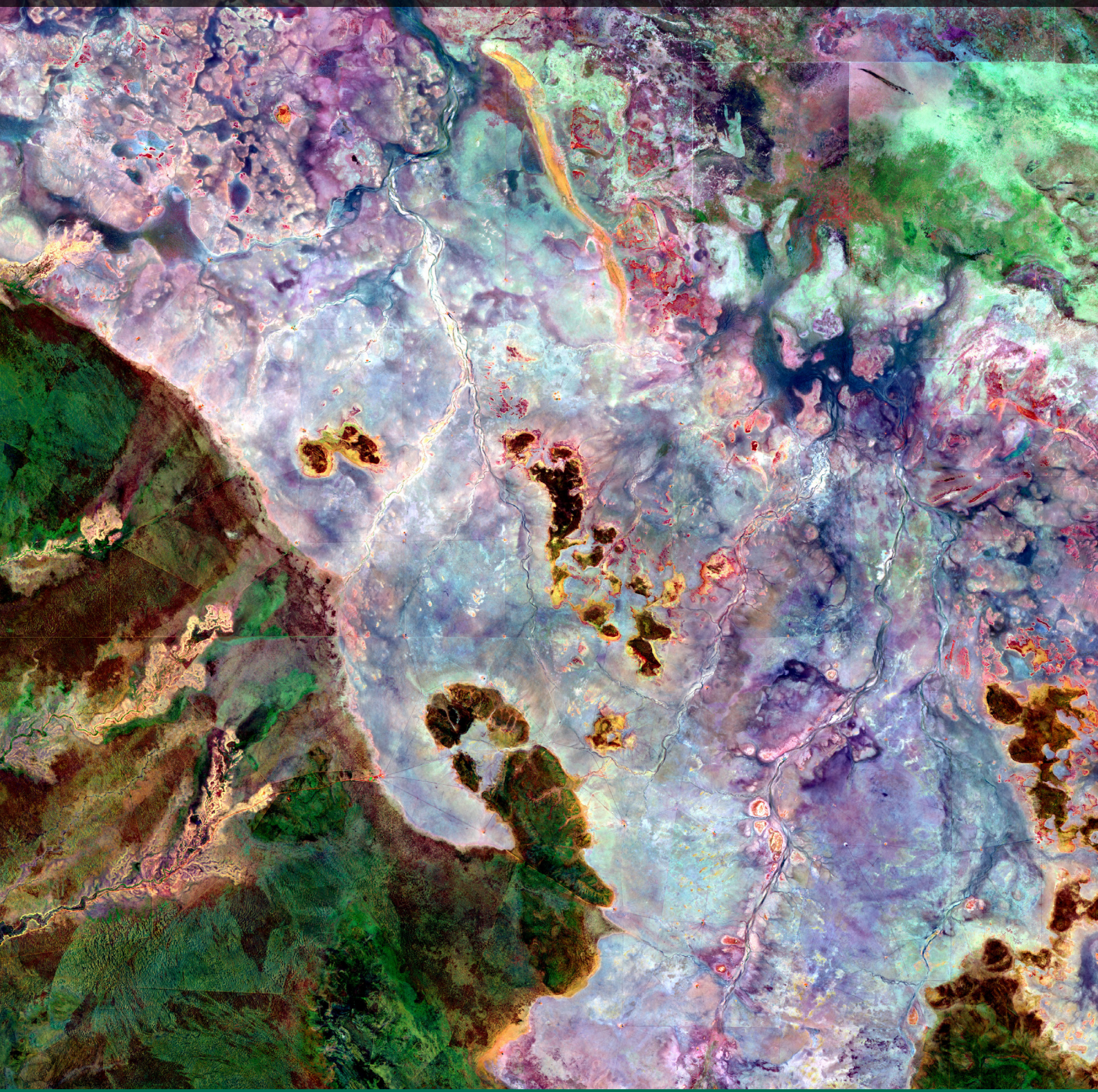

Mapping, monitoring, and modelling of terrestrial landscapes are complementary activities, with shared benefits as summarised in the table below (see also Volume 2D—Section 1.5), where:

- mapping describes the collation of geographic information about a given landscape as a consistent spatial coverage, which implicitly represents a single point in time;
- monitoring describes changes in the landscape relative to a defined baseline; and
- modelling extends current knowledge to predict or infer landscape condition at some future time and/or for a specified set of conditions.

Complementary benefits of mapping, monitoring, and modelling

Relationship	Benefits
Mapping→monitoring	Spatial framework for selecting representative sites; System for spatial extrapolation of monitoring results; and Broad assessment of resource condition.
Monitoring→mapping	Quantifies and defines important resource variables for mapping; and Assesses land suitability over time (including risk assessments for recommended land management).
Modelling→monitoring	Determines whether trends in specific land attributes can be successfully detected with monitoring; and Identifies key components of system behaviour that can be measured in a monitoring program.
Monitoring→modelling	Validates model results; and Provides data for modelling.
Modelling→mapping	Allows spatial and temporal prediction of landscape processes.
Mapping→modelling	Provides data for modelling; and Provides spatial association of input variables.

Source: McKenzie *et al.* (2008a) Table 1.1

Sections 8 to 10 below review EO-based methods that can be used to map, monitor, and model terrestrial vegetation. The image processing procedures that underlie many of these methods are detailed in Volume 2. Applications of EO-based mapping, monitoring, and modelling are introduced in Volume 2D—Section 14. The EO-based methods described in the following three sections are furthered exampled in the context of specific Australian applications areas in Sections 11 to 20.

Contents

8 Mapping 165

9 Monitoring 191

10 Modelling 213

Background image on previous page: Sentinel-2A image acquired on 29 November 2020 over Newcastle Waters, NT, and displayed using SWIR, NIR and green bands as RGB. **Source:** Norman Mueller, Geoscience Australia

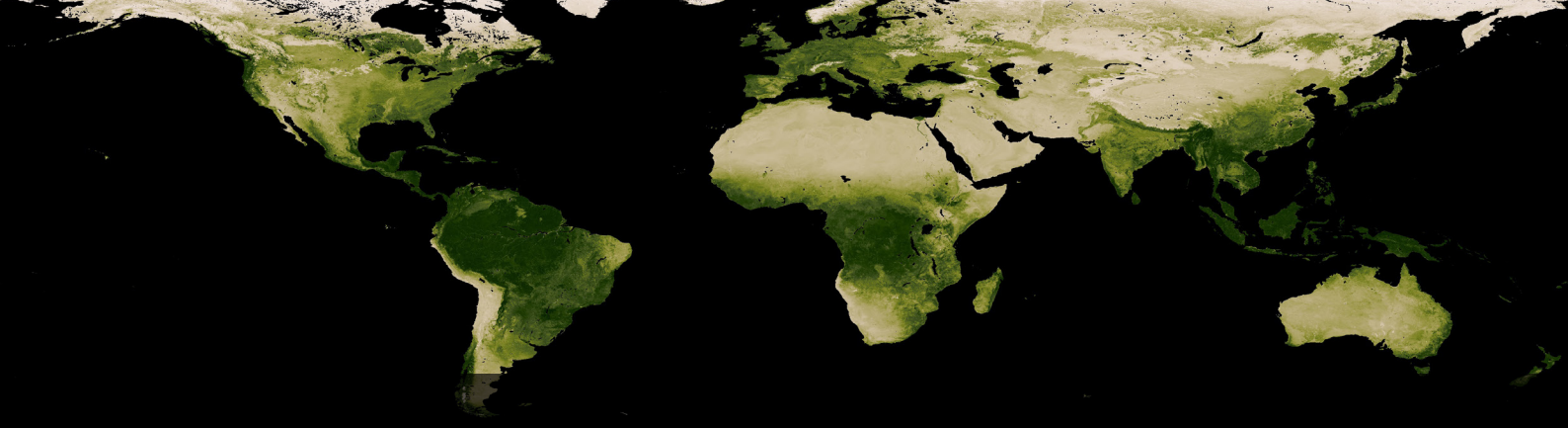

8 Mapping

EO-based mapping relates to identifying and labelling surface features in EO imagery at a single instance in time (see Volume 1). Imagery to be used for mapping of terrestrial vegetation requires accurate geometric and radiometric calibration as detailed in Volumes 2A, 2B, and 2D.

EO images can vary in terms of their spectral, spatial, radiometric, and temporal resolutions and extents (see Table 8.1, and Volumes 1B and 2D). The scale of any EO data source largely determines its suitability to a particular study:

- spatial scale dictates the sizes of features that might be discerned;
- spectral scale indicates the types of features that can be identified;
- temporal scale is particularly relevant to phenological studies (see Section 5.3.2) and longer term changes in land cover or condition; and
- radiometric scale relates to intrinsic data quality and determines the magnitude of surface reflectance differences that can be discerned.

Sensor design constraints do not allow high resolution data to be acquired in all dimensions simultaneously (see Volume 1A—Section 13.3 and Volume 1B—Section 1). While high spatial resolution imagery is valuable for detailed analyses, it supplies data volumes that would be unmanageable for landscape scale analyses. However, as spatial resolution decreases, more pixels will cover multiple ground features so that their spectral values will not be unique to a single surface feature. Such mixtures can also create characteristic patterns and textures that are valuable for land cover inventories (see Section 8.3 and Volume 2E).

Interpretation of EO data for inventory purposes involves a variety of image processing techniques, including:

- spectral indices—combining two or more bands (or channels) into a single plane of data to focus on a particular characteristic (see Section 8.1);
- spectral classification—grouping spectrally similar pixels into classes to represent ground features (see Section 8.2); and
- sub-pixel analyses—determining the proportions of basic ground components within each pixel (see Section 8.3).

Other approaches that analyse EO imagery for mapping purposes include:

- spatial analyses—exploiting the image spatial patterns to delineate objects and gradients, such as tree crown delineation (Ke and Quackenbush, 2011) or Geographic Object-Based Image Analysis (GEOBIA; see Volume 2A—Excursus 10.1); and
- structural analyses—modelling the three-dimensional structure of surface features, such as Geometric-Optical Modelling (see Volume 2X—Excursus 1.1) or Point Cloud Modelling of lidar data (Burt *et al.*, 2018; see Excursus 5.1).

Background image: MODIS/Terra global composite image showing the Normalised Difference Vegetation Index (NDVI) for October 2016 (derived from MOD13C1/MOD13C2 products), with deeper shades of green indicating higher photosynthetic activity. (Note: the vertical extent of this composite image has been clipped and the aspect ratio changed.) **Source:** NASA Earth Observations. (Retrieved from *https://neo.sci.gsfc.nasa.gov/view.php?datasetId=MOD_NDVI_M*)

Table 8.1 Sampling dimensions in EO imagery

Dimension	Characteristic		
	Resolution	Density	Extent
Spectral	Width of each wavelength channel	Number of channels detected by sensor	Range of wavelengths covered by all channels
Spatial	Ground area imaged per optical pixel	Number of pixels and lines in image	Area covered by image
Radiometric	Smallest change in detected energy that would be represented as a different image brightness level	Number of gradations (grey levels) used to represent full range of radiances that could be detected by sensor	Actual range of radiances detected in each channel
Temporal	Time period over which each image is acquired	Frequency of successive image acquisitions	Total time period for which this imagery is available

Adapted from: Emelyanova *et al.* (2012)

8.1 Spectral Indices

A wide range of spectral indices has been proposed to improve image interpretation. These indices highlight the spectral response that is characteristic of particular surface features such as vegetation greenness, water content, or fire footprints (see Volume 2C). They also offer the advantage of reducing the volume of large datasets. Numerous studies have either demonstrated the efficacy of these indices to represent environmental gradients and/or compared spectral indices derived from different sensors (for example Huete, *et al.*, 1997, 2002; Liu, 2004, 2008). Indices based on ratios of image spectral bands offer a robust data compression tool, with the advantages of simplified comparisons between multi-date imagery and possible cross-calibration between different sensor systems (Glenn *et al.*, 2008a).

Some vegetation spectral indices have been shown to have strong positive correlation with the fraction of photosynthetically active radiation (fAPAR) absorbed by a canopy (see Section 6.3.4 and 7.4). Accordingly, these have proven most reliable for mapping vegetative features that are directly related to canopy light absorption, such as vegetation condition and density (see Sections 8.1.1–8.1.3). In addition, when accurate validation data are available, indices have been developed to monitor processes related to fAPAR (such as productivity; see Section 8.1.4), assess water content (see Section 8.1.5), and highlight landscape 'leakiness' (see Section 8.1.6).

Spectral indices have also been used to estimate various attributes related to canopy architecture, such as fractional vegetation cover, leaf area index (LAI), emissivity, and albedo (see Section 6.3). However, unlike features directly related to canopy absorption, the relationships between spectral indices and these attributes are less direct and reliable, and derived results can be misleading (Glenn *et al.*, 2008a).

8.1.1 Greenness

The green colour of vegetation results from absorption of red and blue wavelengths by the chlorophyll pigment for photosynthesis and reflection of green wavelengths (see Section 4.3). However, it is the combined 'colour' resulting from the chlorophyll content of foliage, the area covered by leaves, and the density and structure of the canopy that determines the optical 'greenness' for a given patch of vegetation as measured by a remote sensor.

Greenness indices rely upon highlighting the characteristically high near infrared (NIR) reflectance and low red reflectance of healthy, green foliage (see Figure 5.5). Reflectance values in NIR and red are differenced or ratioed to emphasise those pixels that are likely to contain a high proportion of photosynthetic material (see Volume 2C—Section 11). The simplest greenness index involves ratioing red and NIR reflectances and is commonly referenced as the Simple Ratio (SR; see also Volume 2C—Sections 10 and 11):

$$SR = \frac{NIR}{red}$$

where NIR is near infrared reflectance (ρ_{NIR}) and red is ρ_{red}.

One of the most common indices, the Normalised Difference Vegetation Index (NDVI; see Volume 2C—Section 11), is based on the simple difference of NIR (ρ_{NIR}) and red (ρ_{red}) reflectance, normalised by the equation (Rouse *et al.*, 1973; Tucker, 1979):

$$NDVI = \frac{\rho_{NIR} - \rho_{red}}{\rho_{NIR} + \rho_{red}}$$

Figure 8.1 Normalisation effect in 'Normalised Difference Vegetation Index' (NDVI)

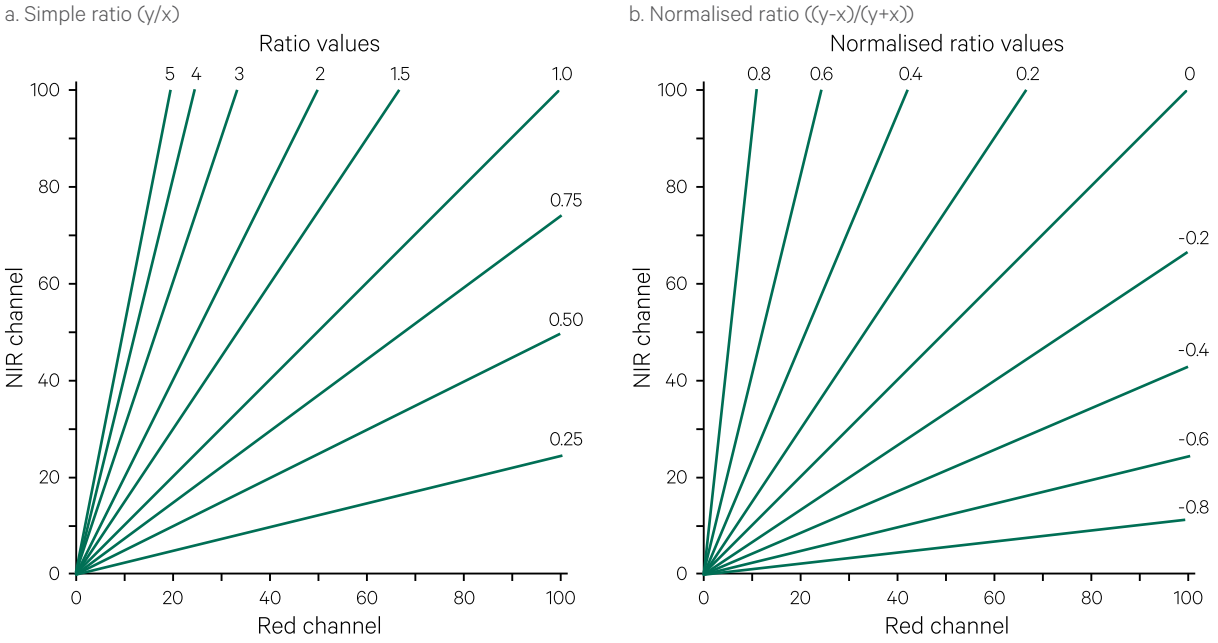

Source: Harrison and Jupp (1990) Figure 94

As illustrated in Figure 8.1, the normalising of NDVI values results in a controlled range of raw ratio values between -1 and 1 and thus greatly simplifies the scaling of output data and comparison of multi-temporal imagery. Since NDVI is functionally equivalent to SR via the equation:

$$NDVI = \frac{SR - 1}{SR + 1}$$

then SR = 1 is equivalent to NDVI = 0, and SR = 4 is the same as NDVI = 0.60, and so on.

NDVI has been related to a range of vegetation characteristics, including cover and condition, which may indicate crop yield in agricultural systems (see Sections 11 to 14). NDVI derived from airborne image spectrometry data has also been used to infer forage quality for herbivores at a landscape scale, with higher NDVI pixels being indicative of more nutritious foliage (Youngentob *et al.*, 2012). Not only can spectral indices be normalised for comparison between multiple images, but they can be differenced between two images to show temporal changes in greenness (see Volume 2D). For example, since fire reduces the amount of green vegetation, greenness indices have been used to map fire footprints, infer burn severity, and monitor recovery (see Sections 9.2.1 and 18). Such indices are also used to determine fire risk by mapping the curing status of grasslands and the fire-prone nature of woody vegetation (Chuvieco *et al.*, 2003; Lasaponara, 2005; see Section 18.3.1.2).

Various studies have observed that NDVI saturates for dense vegetation (Carlson and Ripley, 1997; Huete *et al*, 1985), with NDVI reportedly approaching maximum value for fractional covers as low as 60% (Jiang *et al.*, 2006). Felderhof (2007) observed limitations of NDVI in arid and semi-arid Australia where bare soil and senescent vegetation affect NDVI and restrict its usefulness in mapping spinifex fuel load. Dilley *et al.* (2004) observed an exponential relationship between NDVI computed from AVHRR imagery and grassland curing. Other researchers have observed a linear relationship between EO-based NDVI and grassland curing for selected soil types (Allan *et al.*, 2003).

A variant of NDVI is the green NDVI (GNDVI; Gitelson *et al.*, 1996a), which substitutes the green band for the red band, and is more sensitive to chlorophyll a concentration in foliage and less impacted by atmospheric effects:

$$GNDVI = \frac{\rho_{NIR} - \rho_{green}}{\rho_{NIR} + \rho_{green}}$$

For sugar and horticultural crops, GNDVI has been shown to be better correlated with yield than NDVI (see Section 12).

Transformed Vegetation Index (TVI) is a modified version of NDVI which avoids operating with negative NDVI values and introduces a normal distribution (Deering *et al.*, 1975):

$$TVI = \sqrt{\frac{\rho_{NIR} - \rho_{red}}{\rho_{NIR} + \rho_{red}} + 0.5}$$

Many other variations of NDVI have been proposed, including the Enhanced Vegetation Index (EVI; Huete *et al.*, 1999, 2002; Liu and Huete, 1995; Jiang *et al.*, 2008), which attempts to reduce saturation by accounting for effects due to atmosphere and background, though not necessarily topographic effects (Matsushita *et al.*, 2007):

$$EVI = G \times \left(\frac{\rho_{NIR} - \rho_{red}}{\rho_{NIR} + C_1 \times \rho_{red} + C_2 \times \rho_{blue} + L} \right)$$

where

- ρ_{red} and ρ_{NIR} are corrected values for MODIS bands 1 (red) and 2 (NIR) respectively;
- ρ_{blue} is the corrected value for MODIS band 3 (blue—500 nm);
- G is a gain factor (G=2.5; Huete *et al.*, 1994, 1997);
- L is an adjustment for the canopy background (L=1); and
- C_1 and C_2 are coefficients for aerosol resistance (C_1=6, C_2=7.5).

EVI was designed to reduce interference from atmospheric and vegetated canopy characteristics that can impact NDVI and produce a clearer signal for green vegetation (Huete *et al.*, 2002). Accordingly, EVI is more sensitive to variations in canopy structure (Gao *et al.*, 2000) and thus has been more responsive for land covers with high biomass, such as tropical forests (Huete *et al.*, 2002) and crops (Wardlow *et al.*, 2007). It has also been shown to be a useful indicator of tree richness (Waring *et al.*, 2006). EVI uses data from the 500 nm (blue) band to remove the effects of smoke, aerosols, and thin clouds, and masks out cloud, cloud shadows, marine (as opposed to inland) waters, and aerosols (Huete *et al.*, 2011). A variant of EVI, called EVI2, that is computed using only two spectral bands, has also been proposed for sensors without a blue band (Jiang *et al.*, 2008). Both NDVI and EVI products are routinely and freely available at global and regional scales (see Volume 2D—Excursus 10.1). Their use for phenological studies is discussed in Section 9.3.

Other indices have been proposed to reduce the effects of atmospheric scattering, such as the Atmospherically Resistant Vegetation Index (ARVI; Kaufman and Tanre, 1992), or the soil background, such as the Soil Adjusted Vegetation Index (SAVI; Huete, 1988):

$$ARVI = \frac{\rho_{NIR} - \left(\rho_{red} + \gamma\left(\rho_{blue} - \rho_{red}\right)\right)}{\rho_{NIR} + \left(\rho_{red} + \gamma\left(\rho_{blue} - \rho_{red}\right)\right)}$$

where γ usually ~ 1).

$$SAVI = \left(\frac{\rho_{NIR} - \rho_{red}}{\rho_{NIR} + \rho_{red} + L} \right)\left(1 + L\right)$$

where L is a soil brightness correction factor (where L=0.5). The Optimised Soil Adjusted Vegetation Index (OSAVI; Rondeaux *et al.*, 1996) uses a different value for L to minimise soil effects:

$$OSAVI = \left(\frac{\rho_{800} - \rho_{670}}{\rho_{800} + \rho_{670} + L} \right)\left(1 + L\right)$$

where L=0.16

The Visible Atmospherically Resistant Index (VARI) was found to be minimally sensitive to atmospheric effects (Gitelson *et al.*, 2002):

$$VARI = \left(\frac{\rho_{green} - \rho_{red}}{\rho_{green} + \rho_{red} - \rho_{blue}} \right)$$

Both atmospheric and soil corrections are combined in the Soil and Atmospherically Resistant Vegetation Index (SARVI; Kaufman and Tanre, 1992), in which red reflectance is replaced by a linear combination of both red and blue reflectance. The EVI formulation is based on SARVI and the merging the SAVI with ARVI equations.

An Absolute Greenness index (Gabs) was proposed to distinguish the weather-related variations in NDVI from longer term temporal variability (such as curing) within a selected time period (Eidenshink *et al.*, 1990):

$$Gabs = \left(\frac{\text{observed NDVI} - \text{min NDVI}}{\text{max NDVI}} \right)$$

A normalised NDVI or Relative Greenness index (RG), which ranks the current NDVI of each pixel relative to its minimum and maximum NDVI over a specified period of time, was found to better distinguish the volume of dead fuel from live fuel (Burgan and Hartford, 1993):

$$RG = \left(\frac{\text{observed NDVI} - \text{min NDVI}}{\text{max NDVI} - \text{min NDVI}} \right) \times 100$$

The Fire Potential Index (FPI), based on RG of AVHRR data and fuel modelling, was developed for regional scale fire danger assessment (Burgan *et al*., 1998) and demonstrated strong correlation with actual fire occurrence and predicting fire potential. Fiorucci *et al*. (2007) used a similar methodology, involving SPOT VEGETATION imagery integrated with meteorological forecasts, to improve the accuracy of assessing fire danger.

Another type of vegetation index is based on a linear combination of visible and NIR channels to highlight their differences in terms of transformed dimensions relating to brightness, greenness, and yellowness (see Volume 2C—Section 11.1.3). The vegetation cover triangle (see Figure 6.6) effectively corresponds to one plane in this transformed space. A popular example of this approach is the Kauth-Thomas Greenness (or Tasselled Cap) Transformation, which was developed for Landsat MSS by Kauth and Thomas (1976) and adapted to other sensors by Crist and Cicone (1984), Cicone and Metzler (1984) and Roberts *et al*. (2018). These indices have been most relevant to agricultural applications (see Sections 11 to 14).

A range of composite image products based on greenness indices are now available from EO time series datasets (see Excursus 8.1). Since the spectral bands observed by different sensors often span similar wavelength ranges, the opportunity exists to merge their spectral information. For example, as detailed in Volume 2D—Section 6.2, Emelyanova *et al*. (2012, 2013) demonstrated the blending of Landsat ETM+ and MODIS imagery, thus providing surrogate imagery with MODIS frequency and Landsat spatial resolution. Such techniques, however, may not be appropriate for imagery from all sensors. Composite imagery derived from multiple sensors is introduced in Volume 2D—Section 10.2.

Man must rise above Earth, to the top of the atmosphere and beyond, for only thus will he fully understand the world in which he lives.
(Socrates)

Excursus 8.1—Composite Image Products

Composite EO image products are introduced in Volume 2D—Section 10, including a discussion of compositing methods and their constraints. A number of such products are now routinely available to provide a summary image representing a given time period for a selected spectral index (see Section 8.1.1). While these composite images are useful for large area coverage, and rapid assessment of surface condition, changes and long term monitoring of trends, it is important to consider their provenance and any consequent constraints when interpreting results.

For example, the MOD13Q1 product suite is based on a composite of 250 m resolution imagery over a 16-day period (see Volume 2D), which is corrected for atmospheric effects (see Volume 1B—Section 3.5). The impact of viewing and illumination angles becomes increasingly significant in imagery with larger pixel sizes, such as MODIS, especially for tall vegetation with multiple sources of shadow. The MOD13Q1 product does not currently normalise reflectance values to an observer in zenith position, so its time series potentially comprises imagery acquired with varying viewing geometry.

Gill *et al.* (2009) investigated the use of two VI products within the MOD13Q1 product, namely NDVI and EVI, to assess the impact of variations in viewing geometry on the estimation of tree and grass cover. Their results indicated that MODIS EVI was more sensitive to variations in view angle than NDVI, and hence vegetation structure (as also proposed by Gao *et al*, 2000), and more sensitive to monitoring change in high biomass vegetation (Huete *et al.*, 1994). Variations in EVI were found to be greatest in more complex land covers, such as tropical rainforest, eucalypt woodland, and semi-arid woodland.

Other comparisons between MODIS NDVI and EVI composite images showed that, while both indices agreed with monthly precipitation patterns, there were significant differences between their values, with NDVI generally being higher, especially for shaded backgrounds, and better suited to mapping savanna and deciduous vegetation (Silveira *et al.*, 2007). Foliage Projective Cover (FPC; see Section 2.3.1) is believed to be proportional to evergreen vegetation (Lu *et al.*, 2003) and MODIS NDVI was considered more appropriate to estimate FPC in low biomass vegetation (Gill *et al.*, 2009). In studies of vegetation phenology in Amazonia, vegetation fraction for open tropical forest showed a strong positive correlation with EVI, but not with NDVI (Anderson *et al.*, 2011). Wardlow and Egbert (2010) reported high thematic accuracy from both EVI and NDVI when used to map large area cropping in Kansas. Moura *et al.* (2012) compared EVI derived from both MODIS and MISR imagery for tropical forest sites. Results from these analyses demonstrated significant variability in both intra-annual and interannual trends within MODIS EVI time series datasets, that were not directly related to canopy photosynthetic activity, but were associated with view and illumination effects. EVI was considered to be more sensitive to view angle and view direction than NDVI.

The use of MODIS data for large area crop classifications is reviewed by Wardlow and Egbert (2010). Both MODIS EVI and NDVI showed high correlation with crops in the US Central Great Plains. EVI appeared to be more sensitive to biomass differences during the growing season with NDVI being more sensitive to lower biomass levels during early greening and late senescence.

8.1.2 Hyperspectral indices

In addition to the broad band spectral indices introduced in Section 8.1.1, the narrow bands of hyperspectral data can be used to compute a range of indices that highlight subtle changes in vegetation type, health, and density (Xue and Su, 2017). In particular, reflectance variations in the 'red edge' range (see Section 4.3) are highlighted by many hyperspectral ratios. For example, the Normalised Difference Red Edge index (NDRE), substitutes the red edge band for the red band in the NDVI equation:

$$NDRE = \frac{\rho_{NIR} - \rho_{red\text{-}edge}}{\rho_{NIR} + \rho_{red\text{-}edge}}$$

Since the red edge band can penetrate a leaf more deeply than the red band, it is more sensitive to higher chlorophyll contents. As such, it correlates more closely with crop health than NDVI when a crop is close to harvest. It is also used to map within-crop variability of foliar nitrogen. A derivative of this index is the Canopy Chlorophyll Content Index (CCCI; Barnes *et al.*, 2000), which has strong correlation with foliar nitrogen:

$$CCCI = \frac{NDRE - NDRE_{min}}{NDRE_{max} - NDRE_{min}}$$

Figure 8.2 Within field crop variability

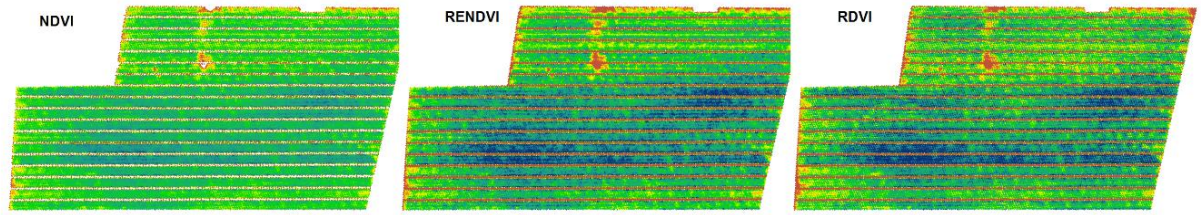

Source: Suarez *et al.* (2018) Figure 18

When combined with the Canopy Nitrogen Index (CNI; originally the nitrogen stress index, NSI; Rodriguez *et al.*, 2006), a much stronger correlation was derived for rainfed wheat (Fitzgerald *et al.*, 2010; Cammarano *et al.*, 2011). CCCI has also been used to differentiate between high and low levels of leaf nitrogen in Victorian pear crops (APAL, 2019).

Another popular hyperspectral index is the Red Edge Normalised Difference Vegetable Index (RENDVI; Gitelson *et al.*, 1996b; Sims and Gamon, 2002):

$$\text{RENDVI} = \frac{\rho_{750} - \rho_{705}}{\rho_{750} + \rho_{705}}$$

Whereas most of the greenness indices described in Section 8.1.1 are based on broad differences in vegetation biomass, RENDVI is more sensitive to differences in pigment concentration. This sensitivity is particularly useful as a crop approaches maturity and its photosynthetic capacity is reduced (Suarez *et al.*, 2018; see Figure 8.2).

Two narrow absorption features at 505 nm and 531 nm have been related to the xanthophyll pigments, violaxanthin, antheraxanthin, and zeaxanthin, and can be used to detect changes in pigment concentration (see Excursus 4.1). The Photochemical Reflectance Index (PRI) compares absorption at 531 nm with a xanthophyll-insensitive reference at 570 nm (Gamon *et al.*, 1992, 1997):

$$\text{PRI} = \frac{\rho_{531} - \rho_{570}}{\rho_{531} + \rho_{570}}$$

PRI measures the light use efficiency (LUE) of foliage (see Sections 7.4 and 8.1.4), thus indicates water stress and CO_2 uptake by plants (see Section 17.4.5).

8.1.3 Vegetation cover and condition

In regions with sparse vegetation, such as much of central Australia, vegetation may not be the dominant component of the landscape (see Figure 2.1). In arid landscapes the soil background is the dominant feature at a range of scales, from the regional view to an field quadrat. For medium scale EO imagery, any given pixel is likely to comprise multiple landscape features, which renders indices based on vegetation greenness less useful in such environments.

Furthermore, the dominant vegetation in many of these environments often comprises mixes of green, dry, and woody material, with little contrast between red and infrared (IR) reflectance.

Accordingly, a range of spectral indices has been proposed for vegetation features other than greenness. One index that was developed to map vegetation—both dry and green—in arid rangelands is called PD54 (Pickup *et al.*, 1993). PD54 was developed for Landsat MSS imagery and is based on green and red reflectance (bands 4 and 5 respectively). This index maps vegetation cover as the scaled perpendicular distance from a predefined soil line and is similar to the perpendicular vegetation index (PVI; Richardson and Wiegand, 1977). More recently, the fractional cover methods introduced in Sections 8.3 and Excursus 8.3 are used in these environments.

Cellulose Absorption Index (CAI) describes the relative depth of the lignocellulose absorption feature at 2100 nm and can be used to quantify crop residues (Daughtry *et al.*, 1996; Daughtry, 2001) and plant litter (Nagler *et al.*, 2003). Daughtry *et al.* (2005) computed CAI as:

$$\text{CAI} = \left(\frac{\rho_{2031} + \rho_{2211}}{2} \right) - \rho_{2101}$$

The Anthocyanin Reflectance Index (ARI; Gitelson *et al.*, 2001) ratios the green and red edge reflectances to indicate the physiological status of vegetation:

$$\text{ARI} = \frac{1}{\rho_{561}} - \frac{1}{\rho_{706}}$$

ARI was subsequently modified (MARI) to include NIR reflectance include consideration of variability in leaf thickness (Gitelson *et al.*, 2006):

$$\text{MARI} = \left(\frac{1}{\rho_{561}} - \frac{1}{\rho_{706}} \right) \times \rho_{780}$$

These indices have been successfully used for non-destructive estimation of anthocyanin content in grapevine leaves (Steele *et al.*, 2009). However, they also require precise spectral bands as acquired by hyperspectral sensors rather than multispectral sensors.

The Land Condition Index (LCI), inspired by CAI, is based on the normalised difference of MODIS bands 6 and 7 (Clarke *et al*., 2011). Since this ratio yields relatively high values for both photosynthetic and non-photosynthetic vegetation but low values for bare soil, it highlights exposed ground. This is particularly useful for "measuring the severity and duration of soil exposure over extensive cropping areas" (Clarke *et al*., 2011). LCI also showed closer correlation with fractional soil cover (see Excursus 8.3) than NDVI. A continental LCI product is available from TERN Australia as MODIS 16-day composites from 2000 to 2011 at 500 m spatial resolution (see Section 8.4).

8.1.4 Plant productivity

The concepts of plant and ecosystem productivity are introduced in Sections 5.1.2 and 7.4. Various metrics can be considered to be indicative of the productivity of vegetation, such as LAI (see Section 6.3.3), fAPAR (see Section 6.3.4), and LUE (see Section 7.4). Such metrics summarise the capacity of groups of plants to produce energy via photosynthesis. That capacity is related to the density of leaf cover, the concentration of chlorophyll in leaves, and a range of other factors determining plant health (see Sections 5.2 and 5.3). Seasonal and phenological variations in fAPAR are informative for identifying ecosystems and monitoring ecosystem health and integrity (see Section 7).

Various greenness indices have been related to APAR, fAPAR, and LAI. It should be noted, however, that LAI is related to canopy light interception but is not linearly related to fAPAR (see Section 6.3.4). NDVI has been used to estimate LAI for uniform canopies of monocultures, such as crops and irrigated pastures, but is not appropriate to derive LAI for more complex and/or mixed canopies (Glenn *et al*., 2008).

In particular, SR and NDVI (see Section 8.1.1) have been used extensively for canopy productivity studies. Since,

$$\text{fAPAR} = \frac{\text{APAR}}{\text{PAR}}$$

Gross Ecosystem Productivity (GEP, which is commonly used interchangeably with GPP) is often modelled from estimates of LUE, fAPAR, and PAR (see Section 6.3):

$$\text{GEP} = \text{LUE} \times \text{fAPAR} \times \text{PAR}$$

A number of indices with sensitivity to non-chlorophyll plant pigments have also been proposed (see Section 4.3). The Photochemical Reflectance Index (PRI; see Section 8.1.2) is sensitive to plant xanthophyll levels, so can be considered to be indicative of the efficiency of PAR usage and also soil moisture and nutrient status (Peñuelas *et al*., 1995, 1997a). This has been related to carbon fluxes and GPP (Gamon *et al*., 1990, 1992; see Section 17), and selectively correlated with LUE (with variations related to differences in vegetation age, type, and leaf persistance; Grace *et al*., 2007). Net Primary Productivity (NPP; see Section 7.4) has also been mapped from NDVI imagery. For example, Raupach *et al*. (2001) used AVHRR NDVI imagery to compute NPP, over Australia based on available data for climate and agricultural inputs (such as irrigation and nutrients). Similar maps were produced to include carbon stored in growing plants (leaf, wood, and root), and growing plants plus litter. These maps show close correlation with the land cover patterns highlighted in vegetation index imagery and captured in land cover classes. More recently, Donohue *et al*. (2014) used the generic DIFFUSE model to estimate GPP for trees, C3 and C4 plants in Australia from MODIS time series datasets (see Figure 7.6), verified against eddy flux tower-derived estimates (see Excursus 7.2).

It should be noted that the relationship between reflectance and LAI is direct, but the relationship between reflectance and productivity, or biomass, in indirect (Hill, 2004). Canopies with different volumes of biomass may result in the same LAI measurement due to variations in canopy structure, density, and composition. Accordingly, biomass estimates from optical EO data perform best for canopies with simpler structures that are dominated by green, actively growing vegetation. This occurs, for example, in grasslands managed for pasture, where growth is initiated by seasonal variations in temperature and/or rainfall, and steadily continues until it reaches maximum greenness (Hill, 2004; see Section 14).

Measurement of above ground biomass to validate EO analyses is detailed in Schaefer (2018). The use of airborne and ground-based lidar (see Excursus 5.1) to derive estimates of forest biomass is described in Section 16 and models for estimating plant productivity in the context of carbon cycling are detailed in Section 17.

8.1.5 Water content

Attributes of foliage water content were introduced in Section 4.2.1. One indicator of moisture content in vegetation is chlorophyll content (see Section 8.1.1), but variations in chlorophyll concentration can also result from other factors, including species differences, phenological status, atmospheric pollution, nutrient deficiency, toxicity, pathology, and radiation stress (Ceccato *et al.*, 2001). Good indicators of plant water content need to be independent of these factors. It should be noted, however, that water stress can induce changes in plant architecture as well as water content, so modelling approaches that incorporate information on plant structure may be more appropriate for some applications (Jacquemoud and Ustin, 2003).

Equivalent Water Thickness (EWT; Green *et al.*, 1991; Gao and Goetz, 1995; see Section 4.2.1) and radiative transfer simulations (Jacquemoud *et al.*, 1996; Zarco-Tejada *et al.*, 2003) have been related to the relative water content of vegetation (Dennison *et al.*, 2003). EO data can also be used to quantify the water content of vegetation by relying on the liquid water absorption features in optical wavelengths (see Section 13). Since NIR and SWIR reflectance is influenced to varying degrees by internal leaf structure, water content, and dry matter content, reflectance data in both these wavelength regions are needed to determine water content (see Section 4.3). Various studies have selected wavelengths in both of these spectral regions to compute ratios and normalised ratios, which have demonstrated good correlation with EWT, with double ratios providing stronger correlations (Colombo *et al.*, 2008). EWT can also be estimated using the Normalised Difference Infrared Index (NDII; Hardinsky *et al.* 1983):

$$\text{NDII} = \frac{\rho_{870} - \rho_{1650}}{\rho_{870} + \rho_{1650}}$$

and the Normalised Difference Water Index (NDWI; Gao, 1996; Serrano *et al.*, 2000; see Volume 3B—Section 11):

$$\text{NDWI} = \frac{\rho_{870} - \rho_{1240}}{\rho_{870} + \rho_{1240}} = \frac{\text{red} - \text{SWIR}}{\text{red} + \text{SWIR}}$$

WI and NDWI derived from AVIRIS imagery have been shown to account for most of the variation in canopy relative water content, though results are dependent on vegetation species (Serrano *et al.*, 2002).
Datt (2012) developed two semi-empirical indices for *Eucalyptus* species, which demonstrated much stronger correlations with EWT and less sensitivity to radiation scatter than other indices:

$$\frac{\rho_{850} - \rho_{2218}}{\rho_{850} + \rho_{1928}}$$

and

$$\frac{\rho_{850} - \rho_{1788}}{\rho_{850} + \rho_{1928}}$$

Other indices that have been proposed to infer vegetation moisture properties from EO imagery include the Normalised Difference Moisture Index (NDMI):

$$\text{NDMI} = \frac{\rho_{\text{NIR}} - \rho_{\text{SWIR}}}{\rho_{\text{NIR}} + \rho_{\text{SWIR}}}$$

and the Moisture Stress Index (MSI), which was originally formulated for Landsat TM bands 5 and 4 (Hunt and Rock, 1989; Ceccato *et al.* 2001):

$$\text{MSI} = \frac{\rho_{1650}}{\rho_{820}}$$

and the Water Index (WI; Peñuelas *et al.*, 1997b):

$$\text{WI} = \frac{\rho_{900}}{\rho_{2218}}$$

Some of the other spectral indices that have been proposed to represent plant water content include:

- Plant Water Index ($\text{PWI} = \frac{\rho_{970}}{\rho_{900}}$; Peñuelas *et al.*, 1997b);
- Relative Depth Index (RDI; Rollin and Milton, 1998);
- Global Vegetation Moisture Index (GVMI; Ceccato *et al.*, 2002a, 2002b);
- Simple Ratio Water Index ($\text{SRWI} = \frac{\rho_{860}}{\rho_{1240}}$; Zarco-Tejada et al., 2003); and
- Canopy Structure Index (CSI; Sims and Gamon, 2003).

The water absorption features that are prominent in EO measurements of vegetation enable an invaluable landscape scale measure of plant water content (see Section 9.4). Colombo *et al.* (2008) obtained more robust estimates of both leaf and canopy EWT from hyperspectral indices than from inversion of leaf and canopy radiative transfer models (see Section 10.2). As discussed in Section 18.3.1.2, various studies have evaluated the capacity of using water content indices derived from EO data to infer fuel moisture for fire risk prediction (Verbesselt *et al.*, 2002, 2007; Chuvieco *et al.*, 2002; Dennison *et al.*, 2003, 2005; Yebra *et al.*, 2008; Caccamo *et al.*, 2011a).
Caccamo *et al.* (2011b) found NDII based on MODIS band 6 offered best results for drought monitoring of high biomass vegetation.

8.1.6 Landscape 'leakiness'

The concept of landscape function, and the tendency of a dysfunctional landscape to 'leak' soil and water resources, was introduced in Section 7.3. An EO-based Leakiness Index (*LI*) that indicates the potential of a landscape to leak, that is not retain, soil sediments was developed by Ludwig *et al.* (2002, 2007):

$$LI = 1 - \left(\frac{L_{max} - L_{calc}}{L_{max} - L_{min}} \right)^{k}$$

where

- *LI* ranges from 0.0 (non-leaky) to 1.0 (totally leaky);
- L_{calc} is determined with reference to EO pixel values and DEM data by modelling surface flows to and from adjacent pixels (using the T-HYDRO model; Ostendorf and Reynolds, 1993), based on the assumption that pixels with greater vegetation cover are more likely to retain water and soil resources, and slow their flow to pixels at lower elevations;
- L_{max} is defined as the value of L_{calc} when all pixel covers are zero;
- L_{min} is the minimum leakiness value (and is typically set to zero for simplicity); and
- *k* defines the shape and steepness of the relationship between *LI* and vegetation cover.

Figure 8.3 Leakiness index

The leakiness index relates vegetation cover to soil loss based on field site measurements.

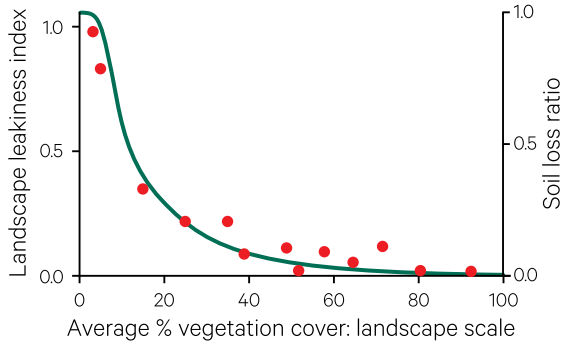

Adapted from: Ludwig *et al.* (2007) Figure 1b

EO-based vegetation cover estimates are calibrated against field site data, with appropriate consideration of scaling differences. Values of *LI* decrease non-linearly with increasing vegetation cover (see Figure 8.3). *LI* has been used to successfully monitor the condition of rangeland sites using EO datasets over several decades (Ludwig et.al., 2007; see Section 15).

8.2 Spectral Classification

Traditionally, one of the most commonly used image processing techniques for analysing EO imagery is classification. Image classification is introduced in Volume 2A—Section 9, while extensive details of this process, and its many variations, are provided in Volume 2E.

Images are classified in a wide range of application areas to identify and delineate 'classes', that is, to separate the image into a set of categories that contain 'similar' pixels. In this context, the definition of 'similar' will depend on the selected input data, the selected processing method, and the intended purpose of the classification. The use of appropriate image data is paramount to a credible classification result. An understanding of the selected classification process is also essential to ensure that the resulting classes capture the intrinsic variation in the image (see Volume 2E).

Probably the most common end-product from classifying an EO image is a map which aims to describe 'land cover' (see Section 3). Such maps typically have a range of categories which differentiate geographic regions using characteristics of their vegetation, soils, and landforms. The successful mapping of such regional differences using EO data requires that the selected categories are differentiated somehow in the data itself and can be extracted cleanly using image classification and segmentation methods (see Volume 2E).

Supervised image classification can be viewed as both an art and a science. Volume 2E mostly addresses issues relating to the science. The art of this area of analysis involves both identifying those characteristics of image data that most effectively distinguish between the required categories, then determining a processing pathway that most efficiently produces a reliable land cover map. A key issue in these two activities is to establish the level of detail with which the categories can be reliably differentiated in the image.

As detailed in Volume 1, EO data records levels of radiation being reflected from, or emitted by, the Earth's surface, such that each pixel value represents some pre-defined type and level of radiation for a given area on the Earth's surface at one instant in time. Accordingly, certain categories may be differentiable in one EO image but not in another. If the characteristics defining the categories exhibit

seasonal variation, this may also be true for two images acquired at different times from the same sensing system. The likelihood of a given category of interest being differentiated by image classification can be most readily determined using the exploratory image analysis tools discussed in Volumes 2A, 2C, and 2E. Time spent becoming familiar with an image is usually reimbursed by uncovering a clear and efficient processing pathway through the subsequent stages of classification. These initial analyses also indicate those image channels that provide the best discrimination, and can assist in the selection of transformations to highlight category differences and/or reduce data volume. As discussed in Volume 2E, the choice of allocation algorithms generally depends on the number of categories required and the processing resources (in terms of both interpreter's time and computing facilities) available for the study.

However, image classification should not be viewed solely as a means for interpolating and extrapolating known categories over a given area. By recording objective and consistent measurements of surface radiation, EO data provide an ideal basis for such analyses. However, the imagery should also be considered as an additional source of information that may highlight patterns or occurrences of surface features which are not discernible by other means or anticipated by the interpreter's classes. By forcing a classification to follow a strictly supervised pathway (which effectively assumes that the interpreter already knows everything there is to know about the study area and is simply assessing how well these features can be mapped from an image), useful additional information that is available from the image may be ignored. The Mosaic Model approach introduced in Volume 2A—Section 9 and recommended in Volume 2E attempts to combine supervised and unsupervised techniques during image classification to derive maximum information from the image.

Various categorisations of land use/land cover for classifying EO data have been proposed. One of the more commonly used systems was proposed by Anderson *et al.* (1976). As detailed in Excursus 3.1, this system describes a four level hierarchy of categories which was developed by USGS (United States Geological Survey). The higher levels are necessarily generalised to apply to a range of environments and describe land cover in terms of geographical, and somewhat academic, labels. Many classifications require a set of labels which are specifically tailored to the application problem being studied, so would correspond to Level III or Level IV in the Anderson system.

The following sub-sections discuss characteristics of EO data and processing algorithms which are relevant to classifying several major land cover categories: vegetation, geology and soils, water, and urban features.

8.2.1 Vegetation

Well-established reflectance characteristics for vegetation provide a good starting point for determining the expected parameters for classes relating to vegetation in EO images. As detailed in Sections 4.3 and 8.1, high NIR and low red reflectance values are reliably used to identify healthy green vegetation (see Figure 4.3). As vegetation condition deteriorates, the NIR reflectance decreases before, and more dramatically than, the green decreases and red increases (see Figure 4.4). The 'red edge', the sharp increase in reflectance between red and NIR wavelengths, also occurs at shorter wavelengths as plant health declines. The latter change is a subtle one though, only detectable by sensors with high spectral resolution (see Section 8.1.2).

These heuristic observations can guide selection of the most appropriate image channels to use for mapping vegetation. Most typically red, NIR, and SWIR channels are considered to provide the best discrimination of vegetation types. In most cases, the red and IR channels usually provide best separation between different land cover types. Various vegetation indices have been proposed to highlight gradients within vegetation in EO images (see Section 8.1). These are most commonly based on red and NIR reflectance channels and generally combine channels using ratios or differences. Drawing on 22 years of published hyperspectral studies, a review of wavebands for vegetation class discrimination found that visible and red edge channels were the most frequently selected, followed by portions of the SWIR, then NIR spectral regions (Hennessy *et al.*, 2020).

Seasonal effects need careful consideration when selecting EO imagery for mapping vegetation (see Volume 1B—Section 1.4 and Volume 2D). For example, known characteristics of crop development may define a stage of growth when the crop will be markedly different from surrounding vegetation (see Sections 5.3.2 and 9.3). This may occur at full greenness for an irrigated crop which is growing near slower-maturing or later-sown crops, or non-irrigated areas, or at the crop's haying stage if it is mixed with later-maturing crops (see Section 12). Similarly, as native grasslands dry off, trends within wooded vegetation often become easier to differentiate (see Section 9.1). For example, in tropical environments, at the end of the wet season all vegetation is so lush that EO measurements cannot easily distinguish between different types. A few months after the start of the dry season however, most vegetation has dried out and a much greater range of vegetation types can be delineated.

A major problem for vegetation mapping in many Australian environments is the extent of bushfires, which result in prominent, dark scars in EO imagery (see Section 18), which can be spectrally similar to the edges of waterbodies. In the wet/dry tropics, image dates need to be carefully selected to allow some 'drying' of vegetation after the wet season, but preferably precede most fires in the dry season. In temperate woodlands and forests, understorey shrubs (such as acacias) may have flowering characteristics which alter their EO reflectance. The greenness of grasses, and possibly lichens and/or mosses, vary more rapidly with moisture availability than woody vegetation, and can also modify imaged values in woodlands and open forest (see Section 9.1). Leaf and bark colour, and the leaf volume of trees themselves, can also change with the seasons, so need to be considered if tree mapping is an important aspect of the classification (see Section 5.3.2). Sun angle becomes significant for forest and woodland vegetation, with higher Sun angles (closer to midday and the summer solstice) resulting in less shadowing of the background in imaged scenes (see Volume 1B—Section 3.5 and Volume 2X—Excursus 1.1).

One example of classifying vegetation type using EO datasets to determine vegetation condition relative to a defined benchmark (see Section 3.2.2) is presented in Excursus 8.2.

8.2.2 Geology and soils

As with vegetation, various factors can alter the 'typical' reflectance for exposed soil or rock surfaces (see Figure 3.2). These factors were introduced in Volume 1B—Section 6.3 and include:

- moisture—wet soils have greater absorption, hence lower reflectance, for all wavelengths;
- organic matter—reflectance of visible to NIR wavelengths can be reduced by up to 60% by organic matter in soils (5% organic matter content results in darker soils, with higher proportions of organic matter resulting in minimal reflectance reductions);
- surface texture and roughness—determined by grain size and structure of aggregated grains. In general, the rougher a soil surface, the more shadowing and darker its appearance. For example, coarse grained sands reflect less strongly than fine grained sands. Strongly structured soils, with high clay content, often form a rougher surface than weaker structured sands which further reduces reflectance; and
- mineral content:
  - ferric iron-bearing oxides and oxyhydrides (or limonites) have an absorption band centred on ultraviolet wavelengths which results in lower reflectance up to about 550 nm, and can have shallow absorption in 850–950 nm. Their relatively high reflectance in yellow/red wavelengths causes the characteristic reddish colours of iron-rich soils;
  - carbonate minerals and silicates containing hydroxyl ions (such as micas and clay minerals) exhibit absorption peaks in the wavelength range 2.1–2.5 μm; and
  - increasing silica content causes the characteristic absorption peak in 8–14 μm range to occur at shorter wavelengths.

Geological analyses often aim to identify linear features and patterns in images so tend to use enhancement techniques rather than classification methods. Filtering techniques can be used to highlight lineaments or directional patterns (see Volume 2C—Section 5). Some enhancements concentrate maximum image information into three channels for visual interpretation such as:

- Hue Saturation Intensity (HSI) transformations; see Volume 2C—Section 8);
- Principal Components Analysis (PCA; see Volume 2C—Section 9); and
- decorrelation stretching (see Volume 2C—Section 9.4).

A range of spectral indices have also been developed to discriminate surface minerals (see Volume 2C—Excursus 10.1), especially for ASTER imagery (Cudahy, 2012).

While multispectral satellite imagery can be used to discriminate and identify surface features related to lithology and soils, applications that are particularly concerned with discriminating geological features often use hyperspectal imagery (Jupp and Datt, 2004) and/or EO sensors that detect energy sources other than EMR, such as radioactivity or magnetism (see Volume 1A—Sections 6 and 7).

An impediment to using EO for geological applications is that the surface layer can often mask underlying geology. Since vegetation cover often conceals the soil surface, a 'software defoliant' was developed by Fraser and Green (1987) for geological analyses, which significantly removed the vegetation component in woodland images (see Volume 2C—Section 9). Alternatively, geobotany attempts to link anomalies in vegetation type and growth patterns to characteristics of soil geochemistry (Goetz *et al.*, 1983), but can be confounded by many climate-related factors such as fire (Simpson, 1990). The spectral response of exposed rock surfaces can also be modified by lichen cover, iron-rich coatings, and deep weathering. For example, past chemical weathering events in Australia are reported to have altered surface materials to depths of hundreds of metres over a large proportion of the continent (Simpson, 1990).

Thermal infrared (TIR) information can also be useful for mapping hydrogeology, geology, and soil type and condition (see Volume 1B—Section 7). In particular, the difference in temperature between daytime and nighttime images indicates the rate at which surface materials heat and cool. This phenomena is referred to as thermal inertia and has been shown to be principally related to moisture content and lithology. Classification of thermal inertia images offer a useful summary of these features. Daytime thermal imagery in conjunction with meteorological data can be used to estimate evapotranspiration (ET), which is a significant parameter in plant growth and the hydrologic cycle (see Sections 5.2.3 and 7.6 respectively).

Excursus 8.2—NSW State Vegetation Type Map (SVTM)

Source: NSW DPIE (2019)
Further information: *https://www.environment.nsw.gov.au/vegetation/state-vegetation-type-map.htm*

The NSW State Vegetation Type Map (SVTM) locates Plant Community Types (PCT) on a consistent base over NSW. This product uses EO image products to extrapolate known landscape characteristics from thousands of survey sites across NSW. Based on the datasets and processes described below, each map unit is finally coded in terms of three hierarchical attributes:

- formations;
- classes; and
- PCT—indicate the species assemblage at local and regional scales.

Vegetation map outputs comprise pre-1750 (before European clearing) PCT coverage and extant PCT coverage. Specific datasets used to create these regional scale maps include:

- high resolution aerial photography (ADS40/80: 50 cm resolution for vegetation classification across eastern and central NSW);
- satellite time series imagery (SPOT-5: 2.5 m resolution, 2005–2013 for vegetation classification across western NSW; Shuttle Radar Topography Mission (SRTM); Landsat TM/ETM+: 25 m resolution, 1989–2008);
- relevant botanical and environmental variables recorded at survey sites (primarily based on pre-existing, full floristic survey data in the Bionet Flora Survey database and augmented by additional surveys to fill data gaps);
- statewide (continuous and categorical) environmental layers covering geology, climate, topography, and water; and
- archival mapping and other historical references, and other compatible regional scale mapping.

The process flow used to create SVTM is consistent with the NVIS methodology (Thackway *et al*., 2008). As summarised in Table 8.2, this process flow follows parallel pathways for analysing the site-based and image datasets. In the fifth stage (Spatial Product Development), these datasets are analysed jointly using the following processes:

- use expert interpretation and GIS technology to assign pre-1750 vegetation photo patterns to all polygons in imagery based on GEOBIA segmentation (see Volume 2A—Excursus 10.1), enviromental layers, and site survey data;
- model the distribution of plant communities within geographical constraints created by vegetation photo patterns and label each polygon as a PCT (unless a non-PCT class, such as rock or water);
- use expert interpretation to review and edit modelling outputs to complete the pre-1750 vegetation coverage; and
- mask out areas which are no longer native vegetation to create an extant vegetation coverage.

The map resulting from this processing sequence is available online (see Section 8.4) and can be accessed in terms of available sub-regions. The SVTM system has been designed to incorporate new data when available, thus maintaining currency of this product.

Table 8.2 SVTM workflow

Site-based data	Spatial data
1. Acquire field data and determine plant type	2. Acquire spatial data
3. Classification and allocation	4. Image processing
5. Spatial product development	
6. Publish maps	

8.2.3 Water

Known reflectance characteristics are again a good starting point for selecting appropriate channels to use for mapping water features. As introduced in Volume 1B—Section 6.4 and detailed in Volume 3B, water has higher reflectance of shorter wavelengths, with reflectance decreasing as wavelength increases up to the NIR region where radiation is totally absorbed (see Figure 3.2). NIR channels are useful to delineate water from land, while the rate of decrease in radiation from blue to IR can be related to water depth. TIR measurements have also been correlated with algal concentrations and thermal pollution. Calibrated EO time series, such as Digital Earth Australia (DEA; see Volume 2D—Section 11.2), have been valuable for delineating persistent and ephermal watercourses in Australia (Mueller *et al*., 2016; see Volume 1A—Excursus 5.1) and mapping tidal variations in shorelines (see Volume 3B). Volume 3B reviews processing techniques and applications for these and other EO applications to surface waters, including water quality.

Snow cover exhibits characteristically high reflectance in visible wavelengths, though some reduction in reflectance occurs with age and impurities (see Volume 1B—Section 6.5). Reflectance is lower for IR wavelengths, especially for older snow and glacier ice, with NIR wavelengths (in the range 1.0–1.3 μm) being sensitive to grain size (Dozier, 1984). Thermal wavelengths can be confusing for mapping snow and generally offer less contrast than visible and IR wavelengths (Salomonson, 1983). Engman and Gurney (1991) recommend the use of visible channels from satellite imagery for identifying and mapping snow, preferably selecting a channel close to IR wavelengths (such as Landsat TM3), since there is greater difference between snow and non-snow at those wavelengths. Snow and cloud can be most easily separated in SWIR bands, with snow having much lower values than cloud (Dozier, 1984).

8.2.4 Urban features

Urban here refers to the man-made environment of buildings and roads with small pockets of vegetation. Being monochromatic, many urban materials such as concrete and asphalt have uniform levels of reflectance across the visible (and NIR) wavelengths. As with bare soil, moisture lowers these reflectances. Shadows can also reduce reflectance levels averaged over several objects and can result in well-defined directional patterns in images featuring buildings.

The extent of spatial intermixing of different surface materials that occurs in urban areas is a major problem when using standard classification algorithms. This problem exists at two levels: firstly the spatial resolution of most EO data is of a size which combines multiple surface components, such as vegetation, roofs, and pavement in a single pixel; secondly the categories of interest often pertain to land uses (such as residential areas) that are defined in terms of spatial patterns rather than distinct spectral values. The increasing spatial resolution of both airborne and spaceborne EO sensors is encouraging greater use for monitoring of water usage, drainage, construction, tree removal, and thermal efficiency in urban areas. EO measurements in the 8–14 μm TIR window highlight urban concentrations since these generally emit more thermal energy than natural features in the environment (see Volume 1B—Section 7). Within urban centres, the SWIR window of 3.5–5.5 μm can identify points of high thermal radiation such as mills, power plants, or fires. Features with differing thermal inertia characteristics, such as roads/paving, vegetation, and water, can also be differentiated by the change between their daytime and nighttime temperatures.

A cloak of loose, soft material, held to the earth's hard surface by gravity,
is all that lies between life and lifelessness.
(Wallace H. Fuller)

8.3 Sub-pixel Analyses

One image feature extraction approach, which was originally applied to multispectral imagery (Adams and Adams, 1985; Smith *et al.*, 1990) and is now widely used for hyperspectral imagery, is variously called mixture analysis, endmember analysis, or spectral unmixing (Keshava and Mustard, 2002; Keshava, 2003). This approach attempts to quantify the proportion of pre-defined ground components within each pixel. Many variants of 'sub-pixel' analysis have been adapted to a wide range of applications (Somers *et al.*, 2011), including mapping the proportion or fraction of vegetation cover, or fractional cover (Guerschman *et al.*, 2009), within each pixel. Sub-pixel analysis is essentially based on a number of assumptions:

- a finite number of ground components can be defined, such as photosynthetic vegetation, non-photosynthetic vegetation, and bare soil, which describe the spectral variation in an EO image;
- each ground component is spectrally distinct and can be represented by their spectral value(s) or 'endmembers';
- a 'pure' image pixel could contain just one type of ground component, in which case its spectral value(s) could be directly associated with that ground component;
- most image pixels are mixed pixels, comprising different areal proportions (or 'fractions') of each ground component; and
- the spectral value(s) of mixed pixels are indicative of the proportions of its ground components.

A block of 'pure' pixels for a given component would therefore appear as a single 'colour' (or set of spectral value/s) with no variance. A block of 'mixed' pixels with the same 'mix' of components would appear to be a similar, but variable, colour. Most image classification methods use image 'colour' (as spectral values) to associate each image pixel with one from a selected set of feature (or ground cover) classes. By contrast, sub-pixel methods rely on image variance to determine the varying proportions of a small number of pre-defined ground components in each pixel. There are a two key issues to consider in this scenario:

- how are the endmembers defined, both in terms of the full set of ground components and their spectral value(s)? and
- how are their proportions determined, that is, the contribution that each component makes towards the pixel spectral value/s (Hapke, 1981, 1984, 1986)?

A number of models have been proposed to describe how the unique spectral value(s) of each ground component is combined into a single set of mixed pixel values for an individual pixel. These models can be grouped into two broad categories based on the way ground component spectral values(s) are combined to produce the value(s) of a given pixel:

- linear mixture models (LMM; also commonly known as Spectral Mixture Analysis: SMA)—assume that the ground components present within a given pixel combine as a simple addition of their spectral values(s) in proportion to the area of the pixel they occupy. LMM are relatively straightforward mathematically but ignore the numerous interactions that can occur between ground components within a pixel and also the variations that can occur within an image, both of which can result in the situation where a given set of ground components could occur in the same proportions in two different pixels yet result in different spectral value(s); or
- non-linear mixture models (NLMM)—recognise that incident light can be scattered both within and between ground components before their combined reflectance is measured by the sensor, so their combination would not be linear (Keshava and Mustard, 2002). NLMM attempt to account for these intra-pixel variations but invariably introduce mathematical complexity for model implementation and greater uncertainly in the modelled results.

LMM can be seen to work when, for a given pixel, the incident light only interacts with one ground component and the components are mixed at a 'macroscopic scale'. An example of this situation would be a checkerboard pattern. In this case, the reflected light from multiple ground components is only mixed at the sensor. Since ground components rarely contribute equally to the measured radiance from a mixed pixel, with some components simply being more reflective than others (see Figure 3.2), the pixel radiance is unlikely to be a simple additive combination of either the mass or cross-sectional area of the proportional radiances of its ground components (see Section 6.4 and Volume 1B—Section 6.6). However, numerous studies have yielded results which indicate that LMM offer an acceptable model for many real world scenarios (Bioucas-Dias *et al.*, 2012) and many algorithms have been developed to implement these models (Zare and Ho, 2014). Variations of LMM include multiple endmember spectral mixture analysis (MESMA), which extends SMA to permit endmembers to vary, in both number and type, for different image pixels (Roberts *et al.*, 1998).

Mathematically, in LMM the pixel signature (r_s) is assumed to be a linear sum of reflectances from each of n endmembers weighted in proportion to its cover (k_j) in the pixel:

$$r_s = \sum_{j=1}^{n} k_j R_j$$

where

the pixel signature, r_s, is the linear sum of the reflectances of each cover type (R_j) weighted by its proportion (k_j) in the pixel;

$k_j \geq 0$ for j=1,n; and

$$\sum_{j=1}^{n} k_j = 1$$

Sub-pixel or endmember analysis seeks to invert this mixing by deriving the proportions (k_j) of each component in the pixel signature. This can feasibly be derived from the EO data provided that, if there are n components (trees, shrubs, grass, etc.), then there are at least (n–1) channels of data that separate the endmembers spectrally. There has been considerable work aimed at deriving endmembers from hyperspectral imagery (Boardman, 1990), spectral libraries and/or spectral measurements in the field (TERN Australia, 2018). Some limitations to this approach include:

- broad-band signatures of ground components (such as the tree and shrub crowns over much of Australia) are not markedly spectrally distinct;
- where spectrally distinct crowns exist, their distinction is confounded by the effects of shadowing within crowns and cast shadow on the background, with bigger plants shading smaller plants. This makes the signature of the endmembers difficult to estimate as the signature depends on the proportions of crowns and shadows present and variations in Sun and look angles; and
- relatively low covers of trees and shrubs, together with shadowing, introduce such high spectral variance into the data relative to the spectral contrasts between endmembers that the numerical methods used in the endmember analysis become highly unstable.

Shadow effects obviously depend primarily on the Sun angle (see Volume 1B—Section 3.5). Although the crown cover is the same, lower Sun angles clearly decrease image brightness. Differences due to shadowing can be taken into account in endmember analysis, provided the endmember values are recalculated for each temporal image and one or more components labelled ‘shade’ are added to the list. However, its successful application still depends on an assumption of linear scaling along cover gradients due to changes in Sun position and sensor view angle. These assumptions in practice are erroneous in structured vegetation (that is, vegetation with discontinuous cover of trees or shrubs), which may limit the application of such methods to general synoptic estimates of change in cover (see Volume 2X—Excursus 1.1).

Sub-pixel analysis is being used to derive a number of standard image products from EO data in Australia, such as fractional cover (see Excursus 8.3) and persistent green vegetation (see Section 9.1).

Excursus 8.3—Fractional Cover

Source: TERN Australia: *http://www.auscover.org.au/dataset_categories/land-cover-dynamics-and-phenology/*
Further information: Guerschman *et al.* (2009, 2015); Muir *et al.* (2011); Stewart *et al.*, (2014); Scarth *et al.* (2018); Guerschman and Hill (2018)

Fractional cover represents the percentages of photosynthetic vegetation (F_{pv}), non-photosynthetic vegetation (F_{npv}), and bare soil (F_{bs}) in a given area (see Section 6.3.6 and Figure 8.4). These proportions are particularly valuable for a range of regional and continental monitoring programs, including estimation of:

- total biomass—for ecosystem studies of carbon and nutrient uptake, surface albedo, and heat exchange between the land surface and the atmosphere (Guerschman *et al.*, 2009, 2015);
- ground cover monitoring—to assess pastures and crops (Muir *et al.*, 2011; Stewart *et al.*, 2014);
- landscape condition—by observing regional soil exposure dynamics (Clarke *et al.*, 2014) and managing stubble to achieve zero tilling;
- compliance monitoring—to detect removal of woody vegetation (see Volume 2D—Excursus 14.3);
- fuel loads that impact fire frequency and intensity (Tindall *et al.*, 2014; He *et al.*, 2019); and
- susceptibility to wind and water erosion (DustWatch, 2019).

Along with standing biomass and growth rate, fractional cover represents one of three vital inputs for assessment of sustainable global rangeland productivity.
(Guerschman and Hill, 2018)

Figure 8.4 Fractional cover index image

a. Example image in true colour

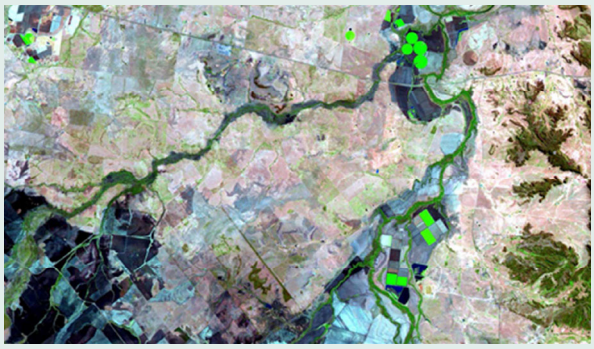

b. The fractional vegetation cover image showing the photosynthetic ('green'), non-photosynthetic ('non-green'), and bare ground fractions. For example, vigorously growing crops in centre pivots at the top right of the image are shown in green, and bare/fallow crops in the lower left are shown in red.

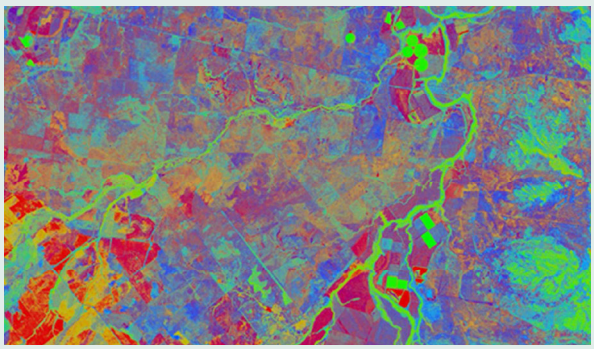

c. Thematic colour key based on three endmembers

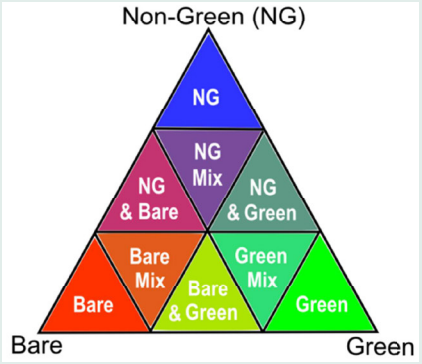

Source: Tindall *et al.* (2014)

Fractional cover methods rely on reflectance spectra at defined sites for calibration and validation (Scarth *et al.*, 2018). These methods are based on the image processing approaches of spectral indices (see Section 8.1) and linear unmixing/spectral mixture analysis (see Section 8.3 and Volume 2E). Australian variants of fractional cover products that are available from TERN Australia (see Section 8.4) include:

- MODIS fractional cover derived from all bands of the MODIS MCD43A4 collection 6 daily product, using a linear unmixing methodology (Guerschman *et al.*, 2015), with calibration and validation from 3022 field observations (Guerschman and Hill, 2018). This 8-day fractional cover product is available in 500 m spatial resolution from 2000 to the present and maintains consistency with previous Australian versions (Guerschman *et al.*, 2009, 2015; Gill *et al.*, 2014). A suite of derivative products is also produced including:
  - monthly fractional cover (aggregated from the 8-day composites using the medoid method);
  - total vegetation cover (photosynthetic + non-photosynthetic); and
  - anomaly of total cover against the time series (difference between total vegetation cover in a given month and the mean total vegetation cover for that month in all years available).

  This product is being upgraded to use MODIS Collection 6.1 products for compatibility with GEOGLAM-RaPP global fractional cover datasets (see Excursus 11.1).
- MODIS 16-day composites based on Relative Spectral Mixture Analysis (RSMA; Okin *et al.*, 2007), Spectral Mixture Analysis Time Series (SMATS; Okin *et al.*, 2013), and Absolute Relative Spectral Mixture Analysis (ARSMA; Clarke *et al.*, 2011) methods, which measure changes in fractional covers relative to a baseline date at 500 m spatial resolution.
- Landsat seasonal fractional cover based on constrained linear spectral unmixing (Scarth *et al.*, 2010; see Section 8.3). This product is available from Digital Earth Australia (DEA; see Volume 2D—Section 11.2) at 25 m spatial resolution from 1986 to the present.

Figure 8.5 Fractional cover endmembers

a. Conceptual approach for locating the endmembers for 'pure' photosynthetic vegetation (f_{PV}), non-photosynthetic vegetation (f_{NPV}), and bare soil (f_{BS}) in a crossplot of NDVI versus CAI. In this example, point (a) represents a ground site halfway between f_{BS} and f_{PV}, while point (b) represents an equal mix of all three components.

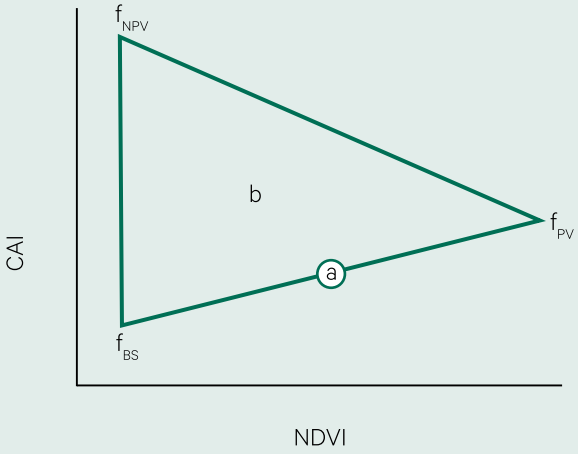

b. MODIS Fractional cover for Australia in April 2015

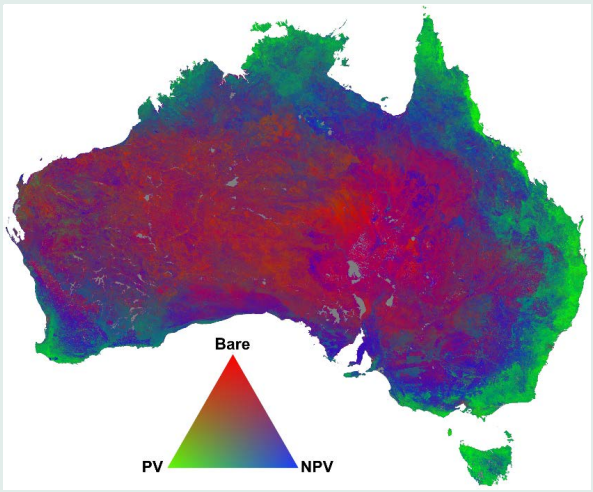

Source: a. Based on Guerschman *et al.* (2009) Figure 2; b. TERN Australia (2018) Figure 7.8

8.4 Further Information

Spectral Indices

Index Database for remote sensing indices: *https://www.indexdatabase.de/*

Fractional Cover Products

TERN Australia (2018): *http://www.auscover.org.au/dataset_categories/vegetation-structural-properties-biomass/*

DEA: *https://docs.dea.ga.gov.au/notebooks/02_DEA_datasets/Introduction_to_Fractional_Cover.html*; *https://d28rz98at9flks.cloudfront.net/79676/Fractional_Cover_FC25_v1_5.PDF*

NSW State Vegetation Type Mapping

SVTM: *https://www.environment.nsw.gov.au/vegetation/state-vegetation-type-map.htm*

8.5 References

Adams, J.B., and Adams, J.D. (1984). Geologic mapping using LANDSAT MSS and TM images: Removing vegetation by modeling spectral mixtures. In *Third Thematic Conference Remote Sensing for Exploration Geology*, ERIM, Colorado Springs, CO, Vol. 2. pp. 615–622.

Allan, G., Johnson, A., Cridland, S., and Fitzgerald, N. (2003). Application of NDVI for predicting fuel curing at landscape scales in northern Australia: can remotely sensed data help schedule fire management operations? *International Journal of Wildland Fire*, 12(4), 299–308.

Anderson, J.R., Hardy, E.E., Roach, J.T., and Witmer, R.E. (1976). *A Land Use and Land Cover Classification System for Use with Remote Sensor Data*. USGS Professional Paper 964. 28p.

Anderson, L.O., Aragão, L.E.O.C., Shimabukuro, Y.E., Almeida, S., and Huete, A. (2011). Fraction images for monitoring intra-annual phenology of different vegetation physiognomies in Amazonia. *International Journal of Remote Sensing*, 32(2), 387–408.

Barnes, E.M., Clarke, T.R., Richards, S.E., Colaizzi, P.D., Haberland, J., Kostrzewski, M., Waller, P., Choi, C., Riley, E., Thompson, T., Lascano, R.J., Li, H., and Moran, M.S. (2000). Coincident detection of crop water stress, nitrogen status and canopy density using ground based multispectral data. In *Proceedings of 5th International Conference on Precision Agriculture*, Bloomington, Minnesota, USA.

Bioucas-Dias, J.M., Plaza, A., Dobigeon, N., Parente, M., Du, Q., Gader, P., and Chanussot, J. (2012). Hyperspectral unmixing overview: Geometrical, statistical, and sparse regression-based approaches. *IEEE Journal of Selected Topics in Applied Earth Observations and Remote Sensing*, 5(2), 354–379.

Boardman, J. (1990). Inversion of high spectral resolution data. *Proceedings of SPIE, 1298, Imaging Spectroscopy and Terrestrial Environment*. Orlando, Florida. pp 222–223.

Burgan, R.E., and Hartford, R.A. (1993). *Monitoring vegetation greenness with satellite data*. USDA, Forest Service, General Technical Report INT-297, Intermountain Research Station, Ogden, UT, 43 pp.

Burgan, R.E., Klaver, R.W., and Klaver, J.M. (1998). Fuel models and fire potential from satellite and surface observations. *International Journal of Wildland Fire*, 8(3), 159–170.

Burt, A., Disney, M., and Calders, K. (2018). Extracting individual trees from lidar point clouds using treeseg. *Methods in Ecology and Evolution*, 10, 438–445. *doi.org/10.1111/2041-210X.13121*

Caccamo, G., Chisholm, L.A., Bradstock, R.A., Puotinen, M.L., and Pippen, B.G. (2011a). Monitoring live fuel moisture content of heathland, shrubland and sclerophyll forest in south-eastern Australia using MODIS data. *International Journal of Wildland Fire*, 21(3), 257–269.

Caccamo, G., Chisholm, L.A., Bradstock, R.A., and Puotinen, M.L. (2011b). Assessing the sensitivity of MODIS to monitor drought in high biomass ecosystems. *Remote Sensing of Environment*, 115, 2626–2639.

Carlson, T., and Ripley, D. (1997). On the relation between NDVI, fractional vegetation cover, and leaf area index. *Remote Sensing of Environment*, 62, 241–252.

Ceccato, P., Flasse, S., Tarantla, S., Jacquemoud, S., and Grégoire, J.-M. (2001). Detecting vegetation leaf water content using reflectance in the optical domain. *Remote Sensing of Environment*, 77, 22–33.

Ceccato, P., Gobron, N., Flasse, S., Pinty, B., and Tarantola, S. (2002a). Designing a spectral index to estimate vegetation water content from remote sensing data: Part 1: Theoretical approach. *Remote Sensing of Environment*, 82(2–3), 188–197. doi:*0.1016/S0034-4257(02)00037-8*

Ceccato, P., Flasse, S., and Grégoire, J.-M. (2002b). Designing a spectral index to estimate vegetation water content from remote sensing data: Part 2: Validation and applications. *Remote Sensing of Environment*, 82(2–3), 198–207. *https://doi.org/10.1016/S0034-4257(02)00036-6*

Chuvieco, E., Riano, D., Aguado, I., and Cocero, D. (2002). Estimation of fuel moisture content from multitemporal analysis of Landsat Thematic Mapper reflectance data: application in fire danger assessment. *International Journal of Remote Sensing*, 23(11), 2145–2162.

Chuvieco, E., Aguado, I., Cocero, D., And, D., and Rian, O. (2003). Design of an empirical index to estimate fuel moisture content from NOAA-AVHRR images in forest fire danger studies. *International Journal of Remote Sensing*, 24, 1621–1637.

Cicone, B.C., and Metzler, M.D. (1984). Comparison of Landsat MSS, Nimbus–7, CZCS, and NOAA–7 AVHRR features for land-use analysis. *Remote Sensing of Environment*, 14, 257–265.

Clarke, K., Lewis, M., Dutkiewicz, A., Forward, G., and Ostendorf, B. (2011). *Spatial and Temporal Monitoring of Soil Erosion Risk with Satellite Imagery*. Land Condition Monitoring Reports #4. University of Adelaide, Report for the South Australian Department for Environment and Natural Resources. Adelaide.

Clarke, K., Lawley, E., Raja Segaran, R., and Lewis, M. (2014). *Spatially-explicit environmental indicators for regional NRM planning for climate change*. The University of Adelaide, Report for Natural Resources SA Arid Lands. Adelaide,

Colombo, R., Meroni, M., Marchesi, A., Busetto, L., Rossini, M., Giardino, C., and Panigada, C. (2008). Estimation of leaf and canopy water content in poplar plantations by means of hyperspectral indices and inverse modeling. *Remote Sensing of Environment*, 112, 1820–1834.

Crist, E.P., and Cicone, R.C. (1984). Application of the Tasselled Cap concept to simulated Thematic Mapper data. *Photogrammetric Engineering and Remote Sensing*, 50, 343–352.

Cudahy, T. (2012). *Satellite ASTER Geoscience Product Notes for Australia*. CSIR0 ePublish No. EP-30-07-12-44. *https://publications.csiro.au/rpr/download?pid=csiro:EP125895&dsid=DS4*

Datt, B. (2012). Visible/near infrared reflectance and chlorophyll content in *Eucalyptus* leaves. *International Journal of Remote Sensing*, 20(14), 2741–2759. doi:*10.1080/014311699211778*

Daughtry, C.S.T. (2001). Discriminating crop residues from soil by short-wave infrared reflectance. *Agronomy Journal*, 93, 125–131.

Daughtry, C.S.T., McMurtrey III, J. E., Chappelle, E. W., Hunter, W. J., and Steiner, J. L. (1996). Measuring crop residue cover using remote sensing techniques. *Theoretical and Applied Climatology*, 54, 17–26.

Daughtry, C.S.T., Hunt, E.R.Jr., Doraiswamy, P.C., and McMurtry, III J.E. (2005). Remote sensing the spatial distribution of crop residues. *Agronomy Journal*, 97, 864–871.

Deering, D. W., Rouse, J. W., Haas, R. H., and Schell, J. A. (1975). Measuring Forage Production of Grazing Units from Landsat MSS Data. *10th International Symposium on Remote Sensing of Environment*, 2, 1169–1178.

Dennison, P.E., Roberts, D.A., Thorgusen, S.R., Regelbrugge, J.C., Weise, D., and Lee, C. (2003). Modelling Seasonal Changes in Live Fuel Moisture and Equivalent Water Thickness using a Cumulative Water Balance Index. *Remote sensing of Environment*, 88(4), 442–452. doi:*10.1016/j.rse.2003.08.015*

Dennison, P.E., Roberts, D.A., Peterson, S.H., and Rechel, J. (2005). Use of Normalized Difference Water Index for monitoring live fuel moisture. *International Journal of Remote Sensing*, 26(10), 1035–1042.

Dilley, A.C., Millie, S., O'Brien, D.M., and Edwards, M. (2004). The relation between Normalized Difference Vegetation Index and vegetation moisture content at three grassland locations in Victoria, Australia. *International Journal of Remote Sensing*, 25(19), 3913–3930. doi:*10.1080/01431160410001698889*

Donohue, R.J., Hume, I.H., Roderick, M.L., McVicar, T.R., Beringer, J., Hutley, L.B., Gallant, J.C., Austin, J.M., van Gorsel, E., Cleverly, J.R., Meyer, W.S., and Arndt, S.K. (2014). Evaluation of the remote-sensing-based DIFFUSE model for estimating photosynthesis of vegetation. *Remote Sensing of Environment*, 155, 349–365.

Dozier, J. (1984). Snow reflectance from Landsat-4 Thematic Mapper. *IEEE Transactions on Geoscience and Remote Sensing*, 22, 323–328.

DustWatch (2019). *Community DustWatch* webpage, NSW Department of Planning, Industry and Environment website: *https://www.environment.nsw.gov.au/topics/land-and-soil/soil-degradation/wind-erosion/community-dustwatch*

Eidenshink J. C., Burgan, R. E., and Haas, R. H. (1990). Monitoring fire fuels condition by using time series composites of Advanced Very High Resolution Radiometer (AVHRR) data. *Proceedings of Resource Technology 90*. Washington, DC, ASPRS, 68–82.

Emelyanova, I.V., McVicar, T.R., Van Niel, T.G., Li, L.T., and van Dijk, A.I.J.M. (2012). *On blending Landsat—MODIS surface reflectances in two landscapes with contrasting spectral, spatial and temporal dynamics*. WIRADA project 3.4: Technical report. Australia: CSIRO Water for a Healthy Country Flagship. *https://doi.org/10.4225/08/5852dc6879ab8*

Emelyanova I.V., McVicar, T.R., Van Niel, T.G., Li, L.T., and van Dijk, A.I.J.M. (2013). Assessing the accuracy of blending Landsat-MODIS surface reflectances in two landscapes with contrasting spatial and temporal dynamics: A framework for algorithm selection. *Remote Sensing of Environment*, 133, 193–209.

Engman, E.T., and Gurney, R.J. (1991). *Remote Sensing in Hydrology*. Chapman and Hall, London. 255 p.

Felderhof, L. (2007). *The Fire Patchiness Paradigm: A Case Study in Northwest Queensland*. Ph. D thesis, James Cook University, Townsville, Queensland, Australia.

Fiorucci, P., Gaetani, F., Lanorte, A., and Lasaponara, R. (2007). Dynamic fire danger mapping from satellite imagery and meteorological forecast data. *Earth Interactions*, 11(7), 1–17. doi:*10.1175/EI199.1*

Fraser, S.J., and Green, A.A. (1987). A software defoliant for geological analysis of band ratios. *International Journal of Remote Sensing*, 8, 525–532.

Gamon, J.A., Field, C.B., Bilger, W., Bjorkman, O., Fredeen, A.L., and Peñuelas, J. (1990). Remote sensing of the xanthophyll cycle and chlorophyll fluorescence in sunflower leaves and canopies. *Oecologia*, 85, 1–7.

Gamon, J.A., Peñuelas, J., Field, C.B. (1992). A narrow-waveband spectral index that tracks diurnal changes in photosynthetic efficiency. *Remote Sensing of Environment*, 41, 35–44.

Gamon, J.A., Serrano, L., and Surfus, J.S. (1997). The photochemical reflectance index: an optical indicator of photosynthetic radiation use efficiency across species, functional types, and nutrient levels. *Oecologia*, 112, 492–501.

Gao, B.C. (1996). NDWI—a normalised difference water index for remote sensing of vegetation liquid water from space. *Remote Sensing of Environment*, 58, 257–266.

Gao, B.C., and Goetz, A.F.H. (1995). Retrieval of equivalent water thickness and information related to biochemical components of vegetation canopies from AVIRIS data. *Remote Sensing of Environment*, 52(3), 155–162. doi:*10.1016/0034-4257(95)00039-4*

Gao, X., Huete, A. R., Ni, W., and Miura, T. (2000). Optical–biophysical relationships of vegetation spectra without background contamination. *Remote Sensing of Environment*, 74, 609–620.

Gallaudet, T.C., and Simpson, J.J. (1991). Automated cloud screening of AVHRR imagery using split-and-merge clustering. *Remote Sensing of Environment*, 38, 77–121.

Gill, T.K., Phinn, S.R., Armston, J.D., and Pailthorpe, B.A. (2009). Estimating tree-cover change in Australia: challenges of using the MODIS vegetation index product. *International Journal of Remote Sensing*, 30(6), 1547–1565.

Gill, T., Heidenreich, S., and Guerschman, J.P. (2014). *MODIS Monthly Fractional Cover: Product Creation and Distribution*. Joint Remote Sensing Research Program Publication Series. *http://www.gpem.uq.edu.au/cser-web/docs/JRSRP_Publication_Series/gillt.2014.modis_monthly_cover.pdf*

Gitelson, A.A., Kaufman, Y.J., and Merzlyak, M.N. (1996a). Use of a green channel in remote sensing of global vegetation from EOS-MODIS. *Remote Sensing of Environment*, 58, 289–298.

Gitelson, A.A., Merzlyak, M.N., and Lichtenthaler, H.K. (1996b). Detection of Red Edge Position and Chlorophyll Content by Reflectance Measurements near 700 nm. *Journal of Plant Physiology*, 148(3–4), 501–508. *https://doi.org/10.1016/S0176-1617(96)80285-9*

Gitelson, A.A., Merzlyak, M.N., Chivkunova, O.B. (2001). Optical properties and nondestructive estimation of anthocyanin content in plant leaves. *Photochemical Photobiology*, 74(1), 38–45.

Gitelson, A.A., Kaufman, Y.J., Stark, R., and Rundquist, D. (2002). Novel algorithms for remote estimation of vegetation fraction. *Remote Sensing of Environment*, 80(1), 76–87.

Gitelson, A.A., Keydan, G.P., and Merzlyak, M.N. (2006). Three-band model for non-invasive estimation of chlorophyll assessment in higher plant leaves. *Journal of Plant Physiology*, 160, 271–282.

Glenn, E.P., Huete, A.R., Nagler, P.L., and Nelson, S.G. (2008a). Relationship between remotely-sensed vegetation indices, canopy attributes and plant physiological processes: what vegetation indices can and cannot tell us about the landscape. *Sensors*, 8, 2136–2160.

Goetz, A.F.N., Rock, B.N., and Rowan, L.C. (1983). Remote sensing for exploration: an overview. *Economic Geology*, 78, 5773–5790.

Grace, J., Nichol, C., Disney, M., Lewis, P., Quaife, T., and Bowyer, P. (2007). Can we measure terrestrial photosynthesis from space directly, using spectral reflectance and fluorescence? *Global Change Biology*, 13, 1484–1497.

Green, R.O., Conel, J.E., Margolis, J.S., Brugge, C.J., and Hoover, G.L. (1991). An inversion algorithm for the retrieval of atmospheric and leaf water absorption from AVIRIS radiance with compensation for atmospheric scattering, *Proceedings of 3rd Annual Airborne Visible/ Infrared Imaging Spectrometer (AVIRIS) Workshop*, Pasadena, California, JPL Publication 91-28, pp. 51–61.

Guerschman, J.P., and Hill, M.J. (2018). Calibration and validation of the Australian fractional cover product for MODIS collection 6. *Remote Sensing Letters*, 9(7), 696–705. doi:*10.1080/2150704X.2018.1465611*

Guerschman, J.P., Hill, M.J., Renzullo, L.J., Barrett, D.J., Marks, A.S., and Botha, E.J. (2009). Estimating fractional cover of photosynthetic vegetation, non photosynthetic vegetation and bare soil in the Australian tropical savannah region upscaling Hyperion and MODIS sensors. *Remote Sensing of Environment*, 113, 928–945.

Guerschman, J. P., Scarth, P. F., McVicar, T. R., Renzullo, L. J., Malthus, T. J., Stewart, J. B., Rickards, J.E., and Trevithick, R. (2015). Assessing the effects of site heterogeneity and soil properties when unmixing photosynthetic vegetation, non-photosynthetic vegetation and bare soil fractions from Landsat and MODIS data. *Remote Sensing of Environment*, 161, 12–26. doi:*10.1016/j.rse.2015.01.021*

Hapke, B.W. (1981). Bidirectional reflectance spectroscopy. 1. Theory. *Journal of Geophysical Research*, 86, 3039–3054.

Hapke, B.W. (1984). Bidirectional reflectance spectroscopy. 3. Correction for macroscopic roughness. *Icarus*, 59, 41–59.

Hapke, B.W. (1986). Bidirectional reflectance spectroscopy. 4. The extinction coefficient and the opposition effect. *Icarus*, 67, 264–280.

Hardisky, M. A., Klemas, V., & Smart, R. M. (1983). The influence of soil salinity, growth form, and leaf moisture on the spectral radiance of Spartina alterniflora canopies. *Photogrammetric Engineering and Remote Sensing*, 49, 77–83.

Harrison, B.A., and Jupp, D.L.B. (1990) *Introduction to Image Processing: Part TWO of the microBRIAN Resource Manual*. CSIRO, Melbourne. 256 p.

He, J., Loboda, T.V., Jenkins, L., and Chen, D. (2019). Mapping fractional cover of major fuel type components across Alaskan tundra. *Remote Sensing of Environment*, 232, 111324. *https://doi.org/10.1016/j.rse.2019.111324*

Hennessy, A., Clarke, K., and Lewis, M. (2020). Hyperspectral classification of plants: A review of waveband selection generalisability. *Remote Sensing*, 12(1), 113.

Hill, M.J. (2004). Grazing agriculture—Managed Pasture, Grassland and Rangeland. In *Manual of Remote Sensing, Volume 4, Remote Sensing for Natural Resource Management and Environmental Monitoring*. (Ed: S.L. Ustin). Wiley International, New York. 768 p.

Huete, A.R. (1988). A soil-adjusted vegetation index (SAVI). *Remote Sensing of Environment*, 25, 295–309.

Huete, A, Jackson, R., and Post, D. (1985). Spectral response of a plant canopy with different soil backgrounds. *Remote Sensing of Environment*, 17, 37–53.

Huete, A., Justice, C., and Liu, H. (1994). Development of vegetation and soil indices for *MODIS–EOS, Remote Sensing of Environment*, 49, 224–234.

Huete, A.R., Liu, H.Q., Batchily, K., and Leeuwen, W. (1997). A comparison of vegetation indices over a global set of TM images for EOS-MODIS. *Remote Sensing of Environment*, 59, 440–451.

Huete, A., Justice, C., and van Leeuwen, W. (1999). *MODIS vegetation index (MOD 13) algorithm theoretical basis document (ATBD) Version 3. 0*. EOS Project Office, NASA Goddard Space Flight Center, Greenbelt, MD.

Huete, A.R., Didan, K., Miura, T., Rodriguez, E.P., Gao, X., and Ferreira, L.G. (2002). Overview of the radiometric and biophysical performance of the MODIS vegetation indices. *Remote Sensing of Environment*, 83, 195–213.

Huete, A., Didan, R., van Leeuwen, W., Miura, T., and Glenn, E. (2011). MODIS Vegetation Indices. Ch 26 in *Land Remote Sensing and Global Environmental Change*, Remote Sensing and Digital Image Processing Volume 11, Springer Science+Business Media, LLC. ISBN 978-1-4419-6748-0.

Hunt, E.R., Jr, and Rock, B.N. (1989). Detection of changes in leaf water content using near- and middle-infrared reflectances. *Remote Sensing of Environment*, 30, 43–54.

Jacquemoud, S., and Ustin, S.L. (2003). Application of radiative transfer models to moisture content estimation and burned land mapping. *Proceedings of 4th International Workshop on Remote Sensing and GIS Applications to Forest Fire Management*. pp 3–12. (Eds: E. Chuvieco, P. Martin and C Justice). 5–7 June, 2003, Ghent, Belgium.

Jacquemoud, S., Ustin, S L., Verdebout, J., Schmuck, G., Andreoli, G., and Hosgood, B. (1996). Estimating leaf biochemistry using the PROSPECT leaf optical properties model. *Remote Sensing of Environment*, 56, 194–202.

Jiang, Z., Huete, A., Chen, J., Chen, Y., Li, J., Yan, G., and Zhang, X. (2006). Analysis of NDVI and scaled difference vegetation index retrievals of vegetation fraction. *Remote Sensing of Environment*, 101, 366–378.

Jiang, Z., Huete, A., Didan, K., and Miura, T. (2008). Development of a two-band enhanced vegetation index without a blue band. *Remote Sensing of Environment*, 112(10), 3833–3845. *https://doi.org/10.1016/j.rse.2008.06.006*

Jupp, D.L.B., and Datt, B. (Eds) (2004). *Evaluation of the EO-1 Hyperion Hyperspectral Instrument and its Applications at Australian Validation Sites 2001–2003*. CSIRO Earth Observation Centre, Canberra.

Kaufman, Y. J., and D. Tanre (1992). Atmospherically resistant vegetation index (ARVI) for EOS-MODIS. *IEEE Transactions on Geoscience and Remote Sensing*, 30(2), 261–270.

Kauth, R.J., and Thomas, G.S. (1976). The Tasselled Cap—a graphic description of the spectral-temporal development of agricultural crops as seen by Landsat. *Proceedings of Symposium on Machine Processing of Remotely Sensed Data*. Purdue University, West Lafayette, Indiana, 4B41–4B51. *http://docs.lib.purdue.edu/lars_symp/159*

Ke, Y., and Quackenbush, L.J.L. (2011). A review of methods for automatic individual tree-crown detection and delineation from passive remote sensing. *International Journal of Remote Sensing*, 32, 4725–4747.

Keshava, N. (2003). A Survey of Spectral Unmixing Algorithms. *Lincoln Laboratory Journal*, 14(1), 55–78.

Keshava, N., and Mustard, J.F. (2002). Spectral Unmixing. *Signal Processing Magazine*, IEEE, 19(1), 44–57. doi:*10.1109/79.974727*

Lasaponara, R., (2005). Inter-comparison of AHVRR-based fire susceptibility indicators for the Mediterranean ecosystems of Southern Italy. *International Journal of Remote Sensing*, 26, 853–870.

Liu, H.Q., and Huete, A.R. (1995). A feedback based modification of the NDVI to minimize canopy background and atmospheric noise. *IEEE Transactions on Geoscience and Remote Sensing*, 33, 457–465.

Liu, G.-R., Liang, C.-K., Kuo, T.-H., Lin, T.-H., and Huang, S.-J. (2004). Comparison of the NDVI, ARVI and AFRI Vegetation Index, along with their relations with the AOD using SPOT-4 Vegetation data. *TAO* 15(1), 15–31.

Liu, J., Miller, J.R., Haboudane, D., Pattey, E., and Hochheim, K. (2008). Crop fraction estimation from casi hyperspectral data using linear spectral unmixing and vegetation indices. *Canadian Journal of Remote Sensing*, 34, S124–S138.

Lu, H., Raupach, M.R., McVicar, T.R., and Barrett, D.J. (2003). Decomposition of vegetation cover into woody and herbaceous components using AVHRR NDVI time series. *Remote Sensing of Environment*, 86, 1–18.

Ludwig, J.A., Eager, R.W., Bastin, G.N., Chewings, V.H., and Liedloff, A.C. (2002). A leakiness index for assessing landscape function using remote sensing. *Landscape Ecology*, 17, 157–171.

Ludwig, J.A., Bastin, G.N., Chewings, V.H., Eager, R.W., and Liedloff, A.C. (2007). Leakiness: A new index for monitoring the health of arid and semiarid landscapes using remotely sensed vegetation cover and elevation data. *Ecological Indicators*, 7, 442–454.

Matsushita, B., Yang, W., Chen,, J., Onda, Y., and Qiu, G. (2007). Sensitivity of the Enhanced Vegetation Index (EVI) and Normalized Difference Vegetation Index (NDVI) to Topographic Effects: A Case Study in High-Density Cypress Forest. *Sensors*, 7, 2636–2651.

Moura, Y.M., Calvão, L.S., dos Santos, J.R., Roberts, D.A., and Breunig, F.M. (2012). Use of MISR/Terra data to study intra- and inter-annual EVI variations in the dry season of tropical forest. *Remote Sensing of Environment*, 127, 260–270.

Muir, J., Schmidt, M., Tindall, D., Trevithick, R., Scarth, P., and Stewart, J., (2011). *Guidelines for Field measurement of fractional ground cover: a technical handbook supporting the Australian collaborative land use and management program*. Techical report, Queensland Department of Environment and Resource Management for the Australian Bureau of Agricultural and Resource Economics and Sciences, Canberra. *http://data.daff.gov.au/data/warehouse/pe_hbgcm9abll07701/HndbkGrndCovMontring2011_1.0.0_HR.pdf*

Mueller, N., Lewis, A., Roberts, D., Ring, S., Melrose, R., Sixsmith, J., Lymburner, L., McIntyre, A., Tan, P., Curnow, S., and Ip, A. (2015). Water observations from space: Mapping surface water from 25 years of Landsat imagery across Australia. *Remote Sensing of Environment*, 174, 341–352. *https://doi.org/10.1016/j.rse.2015.11.003*

Nagler, P.L., Inoue, Y., Glenn, E.P., Russ, A.L., and Daughtry, C.S.T. (2003). Cellulose absorption index (CAI) to quantify mixed soil-plant litter scenes. *Remote Sensing of Environment*, 87, 310–325.

NSW DPIE (2019). *State Vegetation Type Map* webpage, NSW Department of Planning, Industry and Environment website: *https://www.environment.nsw.gov.au/vegetation/state-vegetation-type-map.htm*

Okin, G.S. (2007). Relative spectral mixture analysis—A multitemporal index of total vegetation cover. *Remote Sensing of Environment*, 106(4), 467–479. doi:*10.1016/j.rse.2006.09.018*

Okin, G.S., Clarke, K.D., and Lewis, M.M. (2013). Comparison of methods for estimation of absolute vegetation and soil fractional cover using MODIS Normalized BRDF-Adjusted Reflectance Data. *Remote Sensing of Environment*, 130, 266–279. doi:*10.1016/j.rse.2012.11.021*

Ostendorf, B., and Reynolds, J.F. (1993). Relationships between a terrain-based hydrologic model and patch-scale vegetation patterns in an arctic tundra landscape. *Landscape Ecology*, 8, 229–237.

Peñuelas, J., Filella, I., and Gamon, J.A. (1995) Assessment of photosynthetic radiation-use efficiency with spectral reflectance. *New Phytology*, 131, 291–96.

Peñuelas, J., Llusia, J., Piñol, J., and Filella, I. (1997a). Photochemical reflectance index and leaf photosynthetic radiation-use efficiency assessment in Mediterranean trees. *International Journal of Remote Sensing*, 18, 2863–2868.

Peñuelas, J., Piñol, J., Ogaya, R., and Filella, I. (1997b). Estimation of plant water concentration by the reflectance water Index WI (R900/R970). *International Journal of Remote Sensing*, 18, 2869-2875.

Pickup, G., Chewings, V.H., and Nelson, D.J. (1993). Estimating changes in vegetation cover over time in arid rangelands using Landsat MSS data. *Remote Sensing of Environment*, 43, 243–263. *https://doi.org/10.1016/0034-4257(93)90069-A*

Raupach, M.R., Kirby, J.M., Barrett, D.J., and Briggs, P.R. (2001). *Balances of Water, Carbon, Nitrogen and Phosphorus in Australian Landscapes: (1) Project Description and Results*. CSIRO Land and Water Technical Report 40/01, Canberra.

Richardson, A.J., and Wiegand, C.L. (1977). Distinguishing Vegetation from Soil Background Information. *Photogrammetric Engineering and Remote Sensing*, 43(12), 1541–1552.

Roberts, D., Gardner, M., Church, R., Ustin, S., Scheer, G., and Green, R.O. (1998). Mapping chaparral in the Santa Monica mountains using multiple endmember spectral mixture models. *Remote Sensing of Environment*, 65, 267–279.

Roberts, D., Dunn, B., and Mueller, N. (2018). Open Data Cube Products Using High-Dimensional Statistics of Time Series. *Proceedings of 2018 IGARSS*, 22–27 July, Valencia Spain.

Rollin, E.M., and Milton, E.J. (1998). Processing of high spectral resolution reflectance data for the retrieval of canopy water content information. *Remote Sensing of Environment*, 65, 86–92.

Rondeaux, G, Steven, M., and Baret, F. (1996). Optimisation of Soil-Adjusted Vegetation Indices. *Remote Sensing of Environment*, 55, 95–107

Rouse, J.W., Haas, R.H., Schell, J.A., and Deering, D.W. (1973). Monitoring vegetation systems in the Great Plains with ERTS. *Proceedings of the 3rd ERTS Symposium*, NASA SP-351 I, 309–317.

Salomonson, V.V. (1983). Water Resources Assessment. In *Manual of Remote Sensing*. (Ed: R.N. Colwell). 2nd Edn. American Society of Photogrammetry and Remote Sensing, Falls Church, Virginia.

Scarth, P., Röder, A., and Schmidt, M. (2010). Tracking grazing pressure and climate interaction—the role of Landsat fractional cover in time series analysis. In *Proceedings of the 15th Australasian Remote Sensing and Photogrammetry Conference (ARSPC)*, 13–17 September, Alice Springs, Australia. Alice Springs, NT. doi:*10.6084/m9.figshare.94250*

Scarth, P., Guerschman, J.P., Clarke, K., and Phinn, S. (2018). Validation of Australian Fractional Cover Products form MODIS and Landsat Data. Ch 7 in *Effective Field Calibration and Validation Practices: A practical handbook for calibration and validation satellite and model-derived terrestrial environmental variables for research and management*. A TERN Landscape Assessment Initiative, NCRIS. ISBN: ISBN 978-0-646-94137-0. *https://www.tern.org.au/NEW-CalVal-handbook-for-remote-sensing-bgp4370.html*

Schaefer, M.T. (2018). Measurement of above ground biomass. Ch 12 in *Effective Field Calibration and Validation Practices: A practical handbook for calibration and validation satellite and model-derived terrestrial environmental variables for research and management*. A TERN Landscape Assessment Initiative, NCRIS. ISBN 978-0-646-94137-0.

Serrano, L., Ustin, S.L., Roberts, D.A., Gamon J.A., and Peñuelas, J. (2000). Deriving water content of chaparral vegetation from AVIRIS data. *Remote Sensing of Environment*, 74(3), 570–581.

Serrano, L., Peñuelas, J., and Ustin, S.L. (2002). Remote sensing of nitrogen and lignin in Mediterranean vegetation from AVIRIS data. *Remote Sensing of Environment*, 81, 355–364. doi:*10.1016/S0034-4257(02)00011-1*

Silveira, E.M., de O., Carvalho, L.M.T., Acerbi Jr., F.W., and de Mello, J.M. (2007). The Assessment of Vegetation Seasonal Dynamics using Multitemporal NDVI and EVI images derived from MODIS. *IEEE Workshop on Analysis of Multi-temporal Remote Sensing Images*, 14(2), 177–184. 18–20 July 2007, Belgium.

Simpson, C.J. (1990). Deep weathering, vegetation and fireburn. Significant obstacles for geoscience remote sensing in Australia. *International Journal of Remote Sensing*, 11(11), 2019–2034. DOI:*10.1080/01431169008955158*

Sims, D.A., and Gamon, J.A. (2002). Relationships between leaf pigment content and spectral reflectance across a wide range of species, leaf structures and developmental stages. *Remote Sensing of Environment*, 81, 337–354.

Sims, D.A., and Gamon, J.A. (2003). Estimation of vegetation water content and photosynthetic tissue area from spectral reflectance: A comparison of indices based on liquid water and chlorophyll absorption features. *Remote Sensing of Environment*, 84(4), 526–537. doi:*10.1016/S0034-4257(02)00151-7*

Smith, M.O., Ustin, S.L., Adams, J.B., and Gillespie, A.R. (1990). Vegetation in deserts: I. A regional measure of abundance from multispectral images. *Remote Sensing of Environment*, 31(1), 1–26. *https://doi.org/10.1016/0034-4257(90)90074-V*.

Somers, B., Asner, G.P., Tits, L., and Coppin, P. (2011). End member variability in Spectral Mixture Analysis: A review. *Remote Sensing of Environment*, 115, 1603–1616.

Steele, M.R., Gitelson, A.A., Rundquist, D.C., and Merzlyak, M.N. (2009) Nondestructive estimation of Anthocyanin Content in Grapevine Leaves. *American Journal of Enology and Viticulture*, 60(1), 87–92.

Stewart, J.B., Rickards, J.E., Randall, L.A., McPhee, R.K., and Paplinska, J.Z. (2014). *Ground cover monitoring for Australia: Final report July 2012 to June 2013, ABARES Technical report 14.1*. Australian Bureau of Agricultural and Resource Economics and Sciences, Canberra, May 2014.

Suarez, L.A., McPhee, J., O'Halloran, J., van Sprang, C., and Robson, A. (2018). *Adoption of precision systems technology in vegetation production*. Literature Review for VG16009, Horticulture Innovation Australia, Queensland.

TERN Australia (2018). *Effective Field Calibration and Validation Practices: A practical handbook for calibration and validation satellite and model-derived terrestrial environmental variables for research and management*. A TERN Landscape Assessment Initiative, NCRIS. ISBN: ISBN 978-0-646-94137-0. *https://www.tern.org.au/NEW-CalVal-handbook-for-remote-sensing-bgp4370.html*

Thackway, R., Neldner, J., and Bolton, M. (2008). Vegetation. In: *Australian Soil and Land Survey Handbook Guidelines for Conducting Surveys* (2nd Edition). (Eds: N.J. McKenzie, M.J. Grundy, R. Webster, and A.J. Ringrose-Voase). CSIRO Publishing, Melbourne.

Tindall, D., Trevithick, R., Scarth, P., Collett, L., Goodwin, N., Denham, R., and Flood, N. (2014). *Ground cover and fire in the grazing lands*. RP64G Synthesis Report, Department of Science, Information Technology, Innovation and the Arts. Brisbane.

Tucker, C.J. (1979). Red and photographic infrared linear combinations for monitoring vegetation. *Remote Sensing of Environment*, 8(2), 127–150.

Verbesselt, J., Fleck, S., and Coppin, P. (2002). Estimation of fuel moisture content towards Fire Risk Assessment: A review. In: *Forest Fire Research and Wildland Fire Safety* (Ed: Viegas), Millpress. Rotterdam. ISBN 90-77017-72-0.

Verbesselt, J., Somer, B., Lhermitte, S., Jonckheere, I., van Aardt, J., and Coppin, P. (2007). Monitoring herbaceous fuel moisture content with SPOT VEGETATION time-series for fire risk prediction in savanna ecosystems. *Remote Sensing of Environment*, 108, 357–368.

Wardlow, B.D., and Egbert, S.L. (2010). A comparison of MODIS 250-m EVI and NDVI data for crop mapping: a case study for southwest Kansas. *International Journal of Remote Sensing*, 31(3), 805–830.

Wardlow, B.D., Egbert, S.L., and Kastens, J.H. (2007). Analysis of time-series MODIS 250 m vegetation index data for crop classification in the U.S. Central Great Plains. *Remote Sensing of Environment*, 108, 290–310.

Waring, R.H., Coops, N.C., Fan, W., and Nightingale, J.M. (2006). MODIS enhanced vegetation index predicts tree species richness across forested ecoregions in the contiguous U.S.A. *Remote Sensing of Environment*, 103, 218–226.

Xue, J., and Su, B. (2017). Significant Remote Sensing Vegetation Indices: A Review of Developments and Applications. *Journal of Sensors*, 1–17. doi:*10.1155/2017/1353691*

Yebra, M., Chuvieco, E., and Riano, D. (2008). Estimation of live fuel moisture content from MODIS images for fire risk assessment. *Agricultural and Forest Meteorology*, 148, 523–536.

Youngentob, K.N., Renzullo, L.J., Held, A.A., Jia, X., Lindenmayer, D.B., and Foley, W.J. (2012). Using imaging spectroscopy to estimate integrated measures of foliage nutritional quality. *Methods in Ecology and Evolution*, 3, 416–426. doi:*10.1111/j.2041-210X.2011.00149.x*

Zarco-Tejada, P.J., Rueda, C.A., and Ustin, S. L. (2003). Water content estimation in vegetation with MODIS reflectance data and model inversion methods. *Remote Sensing of Environment*, 85, 109–124.

Zare, A., and Ho, K.C. (2014). Endmember Variability in Hyperspectral Analysis. *IEEE Signal Processing Magazine*, 31(1), 95–104.

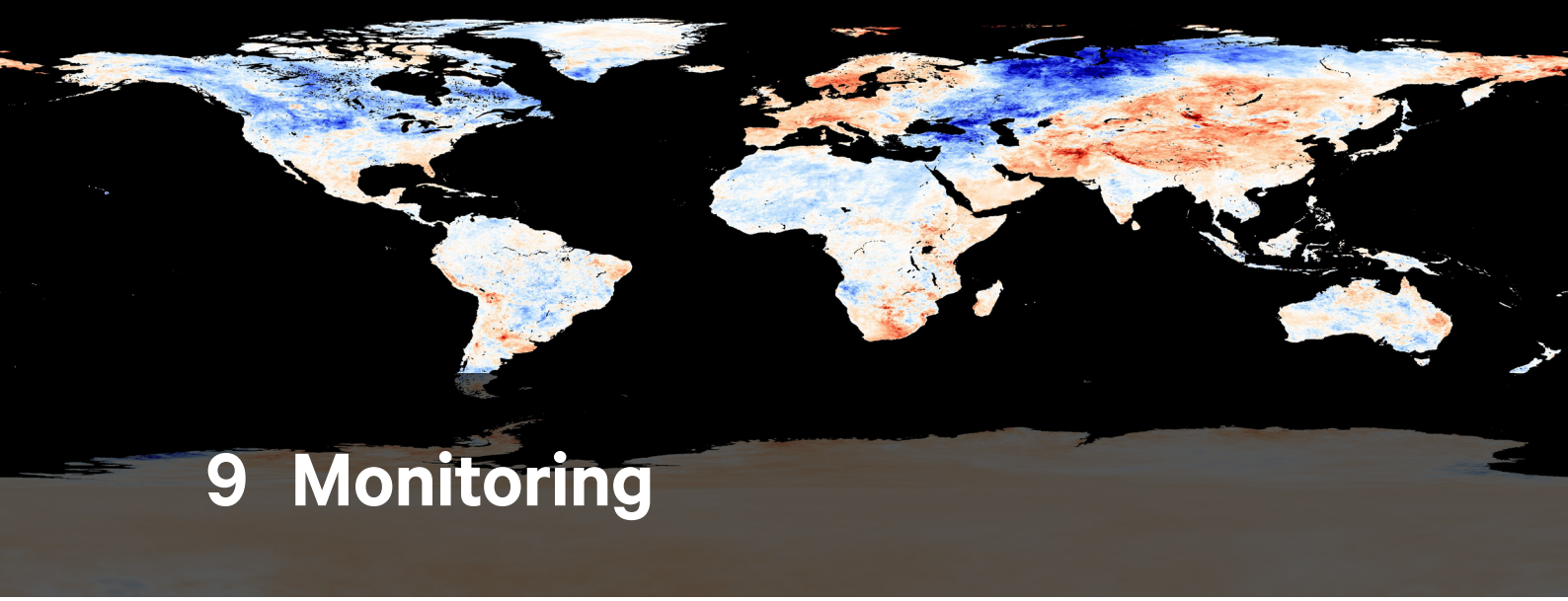

9 Monitoring

One of the great promises of EO was the prospect of using 'objective' measurements to monitor changes in land cover and condition over selected time periods (Singh, 1989). In the context of terrestrial vegetation, various applications of environmental monitoring can be readily listed:

- identifying and quantifying land use changes (see Section 3.4.2);
- measuring the extent and rate of deforestation and afforestation (see Section 16);
- tracking land degradation (see Section 11.4);
- highlighting stress conditions in vegetation (due to biotic and abiotic factors; see Sections 9.5 and 9.6);
- showing the extent of damage from disaster events, such as fire or flood (see Section 18 and Volume 3B); and
- gauging long term changes in vegetative cover due to recurrent drought and other climatic variations (see Sections 3.4.1, 9.2.2, 11.3 and 15).

Of all the questions which can come before this nation, short of the actual preservation of its existence in a great war, there is none which compares in importance with the great central task of leaving this land even a better land for our descendants than it is for us.
(Theodore Roosevelt)

However, in some areas, the application of this technology has hitherto fallen short of its promise. Like most technological solutions, using EO for environmental monitoring presents its own set of problems. While images represent 'objective' measurements of surface energy that can be related to different surface features, the measurements can vary with a number of factors which are independent of changes in those features. For example, the calibration of imaging sensors can vary over time, so that the same physical radiance level in a selected wavelength band could result in (slightly) different recorded values in different overpasses (see Volume 2A—Section 3). Changes in Sun position with diurnal and annual cycles directly affect surface illumination, and hence any remote measurements of reflected energy (see Volume 1B—Section 3). Similarly, scattering by atmospheric particles can modify the surface radiance levels recorded by an airborne or spaceborne sensor (see Volume 1B—Section 4). Short-term surface conditions, such as increased soil moisture after a rainfall event, can also reduce radiance levels. Finally, digital comparison of multiple images generally requires that images are precisely registered geometrically (see Volumes 2B and 2D). This process can introduce spatial errors which could be falsely interpreted as land cover changes.

Background image: MODIS global composite image showing Land Surface Temperature (LST) anomaly for October 2016 (based on science datasets from MOD11C1, MOD11C2, and MOD11C3 products). Colour scale ranging from blue (-12°C) to red (+12°C) indicates the deviation of monthly temperature in October 2016 from the average monthly temperature between 2001–2010. (Note: the vertical extent of this composite image has been clipped and the aspect ratio changed.) **Source:** NASA Earth Observations. (Retrieved from *https://neo.sci.gsfc.nasa.gov/view.php?datasetId=MOD_LSTAD_M*)

'Real' land cover changes still need to be interpreted in an informed way. For example, spectral variation between successive growing seasons for cultivated crops may initially appear to be related to seasonal productivity, but may also be due to cultivation factors (such a planting pattern, or timing of fertiliser application), differences in maturity (due to changes in crop variety or soil condition), or differences in weather or irrigation (such as stress from heat, cold, wind damage, or excessive or insufficient moisture). The multivariate nature of the environment, combined with variable land use practices, suggest that methodologies for accurately monitoring land cover may never be fully automated. Nevertheless, EO does offer relatively inexpensive, regularly acquired, and internally consistent datasets for investigating changes in land cover, use and/or condition, especially when calibrated and validated as Analysis Ready Data (ARD; see Volume 2D—Section 3.2).

In the context of EO, monitoring relies upon the availability of multiple images for a given location. Two or more coincident images are required to detect changes in land cover or condition, and the increasing archive of EO time series imagery offers greater choice of image resolutions and extents than ever before. Image processing methods that are relevant to environmental monitoring using time series datasets are detailed in Volume 2D. As introduced in Volumes 1 and 2, EO imagery enables the creation of global maps showing vegetation greenness. Spectral indices derived from EO datasets (see Section 8.1) have been related to a range of ecological parameters, which attempt to quantify trends in vegetation cover and structure in space and time, including:

- Foliage Projective Cover (FPC)—fraction of ground surface vertically covered by photosynthetically active components of vegetation (that is, excluding stems and branches; see Sections 6.3.1);
- Leaf Area Index (LAI)—ratio of upper green leaf surface area to ground area (see Section 6.3.3, 8.1.1 and 8.1.4);
- fraction of Absorbed Photosynthetically Active Radiation (fAPAR)—proportion of photosynthetically active radiation (400–700 nm) used by plants (see Section 6.3.4 and 8.1.4);
- fractional cover—proportions of photosynthesising vegetation, non-photosynthetic vegetation, and bare soil within a given area (see Section 6.3.6 and Excursus 8.3) and
- Net Primary Productivity (NPP)—the availability of carbon or biomass in a landscape (see Sections 7.2, 8.1.4 and 17).

Table 9.1 Potential reference site measurements

Environmental factor	Attribute	Measurement
Vegetation	Structure	Height, density, layers, spatial configuration
	Species	Abundances, ages
	Litter	Size, volume, distribution
Soil	Type	Texture, mineral content
	Depth	Topsoil and subsoil layers
	Nutrient status	Proportions of major and minor nutrients
Climate	Precipitation	Diurnal, seasonal, annual, and longer term ranges
	Temperature	
	Humidity	
	Aerosols	Density, type

Monitoring landscape condition necessarily relies on reference sites, at which a range of detailed measurements can be made. Examples of relevant quantitative measurements at these sites are listed in Table 9.1. Of particular relevance to Australian terrestrial ecosystem studies is the Terrestrial Ecosystem Research Network (TERN), which is introduced in Volume 2D—Excursus 12.2. Detailed guidelines for measuring vegetation and soil parameters for environmental inventory and monitoring are provided in TERN Australia (2018), McKenzie *et al*. (2008), and NCST (2009). Integration of EO data with other spatial datasets, including site-based data, is introduced in Volume 2D—Sections 12–14.

The following sub-sections consider monitoring applications using EO imagery in the specific contexts of:

- vegetation types—such as annual versus perennial (see Section 9.1);
- change indices—for fire and other disturbances (see Section 9.2);
- phenology—monitoring changes in vegetation growth stage and condition (see Section 9.3);
- evapotranspiration—quantifying regional moisture loss due to evaporation and transpiration (see Section 9.4);
- plant water stress—monitoring water stress in vegetation, particularly to optimise irrigation scheduling (see Section 9.5); and
- plant vigour—nutritional status, pests and diseases (see Section 9.6).

9.1 Vegetation types

Various EO-based methods have been developed to monitor changes in different types of terrestrial vegetation. For many applications, accurate maps of perennial (mostly woody) vegetation are valuable. For example, some operational systems that monitor perennial vegetation in Australia include:

- Statewide Landcover and Trees Study (SLATS) has been used operationally in Queensland since 1995 and in NSW since 2006 (see Volume 2D—Excursus 14.3 for details). The SLATS methodology identifies woody vegetation changes at intervals of 1–2 years using a well-defined processing workflow, and produces annual reports and maps detailing the location and extent of change across each state (Scarth *et al.*, 2008; Danaher *et al.*, 2011). Near real time detection of vegetation change has been recently implemented using EO datasets with higher spatial and temporal resolutions.
- LandMonitor is a collaborative monitoring project in WA that was initially developed in 1988 to map salinity and vegetation in southwest WA from Landsat imagery (Allen and Beetson, 1999). It now delivers state-wide maps of vegetation extent and change in perennial vegetation cover (Landgate, 2019). This EO-based time series is integrated with DEM and other spatial datasets to allow vegetation history and salinity risk to be monitored efficiently (McFarlene and Wallace, 2019).
- A persistent green vegetation product (Gill *et al.*, 2017, 2018) was derived from the photosynthetic vegetation component of the Landsat fractional cover product (see Excursus 8.3) for the decade from 2000 to 2010. This product maps the density and extent of woody vegetation in Australia with an overall accuracy of 82%.

Annual or deciduous vegetation exhibits a larger annual change in photosynthetic activity and canopy reflectance than evergreen vegetation (see Section 5.3.3). Monitoring of vegetation colour throughout the year can help to separate areas of deciduous and evergreen vegetation cover. Using data collected over several years, persistently green vegetation can similarly be differentiated from vegetation that is suspectible to seasonal or weather-related browning in hot weather. Some advantages of mapping persistently green vegetation include highlighting reliable areas of fodder, locating potential groundwater resources, indicating areas with high fire risk, and identifying useful checkpoints for monitoring vegetation dynamics (Johansen *et al.*, 2012). Perennial and annual plants also have significantly different ecohydrological characteristics as summarised in Table 9.2, with some variations due to plant age (McVicar *et al.*, 2010). These characteristics have been shown to influence catchment water balance at sub-catchment scales (Donohue *et al.*, 2010a).

Time series analysis of EO-based vegetation indices has been used to differentiate between vegetation that is persistently green and vegetation that browns off during the annual cycle (Lu *et al.*, 2003, Donohue *et al.*, 2008). For example, Donohue *et al.* (2009) used a calibrated AVHRR Normalised Difference Vegetation Index (NDVI) time series dataset from 1981 to 2006 (Donohue *et al.*, 2008) to analyse fAPAR trends for Australia in terms of

- slowly varying, persistent vegetation—perennial, woody; and
- rapidly varying, recurrent vegetation—annual, herbaceous, and ephemeral (see Figure 9.1).

fAPAR trends were compared with climate records to observe an increase in vegetation cover in Australia of 7.8% from 1981 to 2006, which corresponded to a 7% increase in precipitation during the same time period. In terms of vegetation categories, however, this analysis reported that persistent vegetation increased over 21%, while recurrent vegetation decreased by 7% (see Volume 2D—Excursus 8.1).

Table 9.2 Ecohydrological characteristics of perennial and annual vegetation

Vegetation type	Root depth	Photosynthetic rate	Leaf area change	Water use
Annual/ephermal	Shallow	High	Fast	Alternately high and low
Perennial/non-deciduous	Deep	Low	Slow	Generally constant and moderate

Source: McVicar *et al.* (2010) Table 1

Figure 9.1 Seasonal vegetation trends derived from AVHRR NDVI data 1981–2006

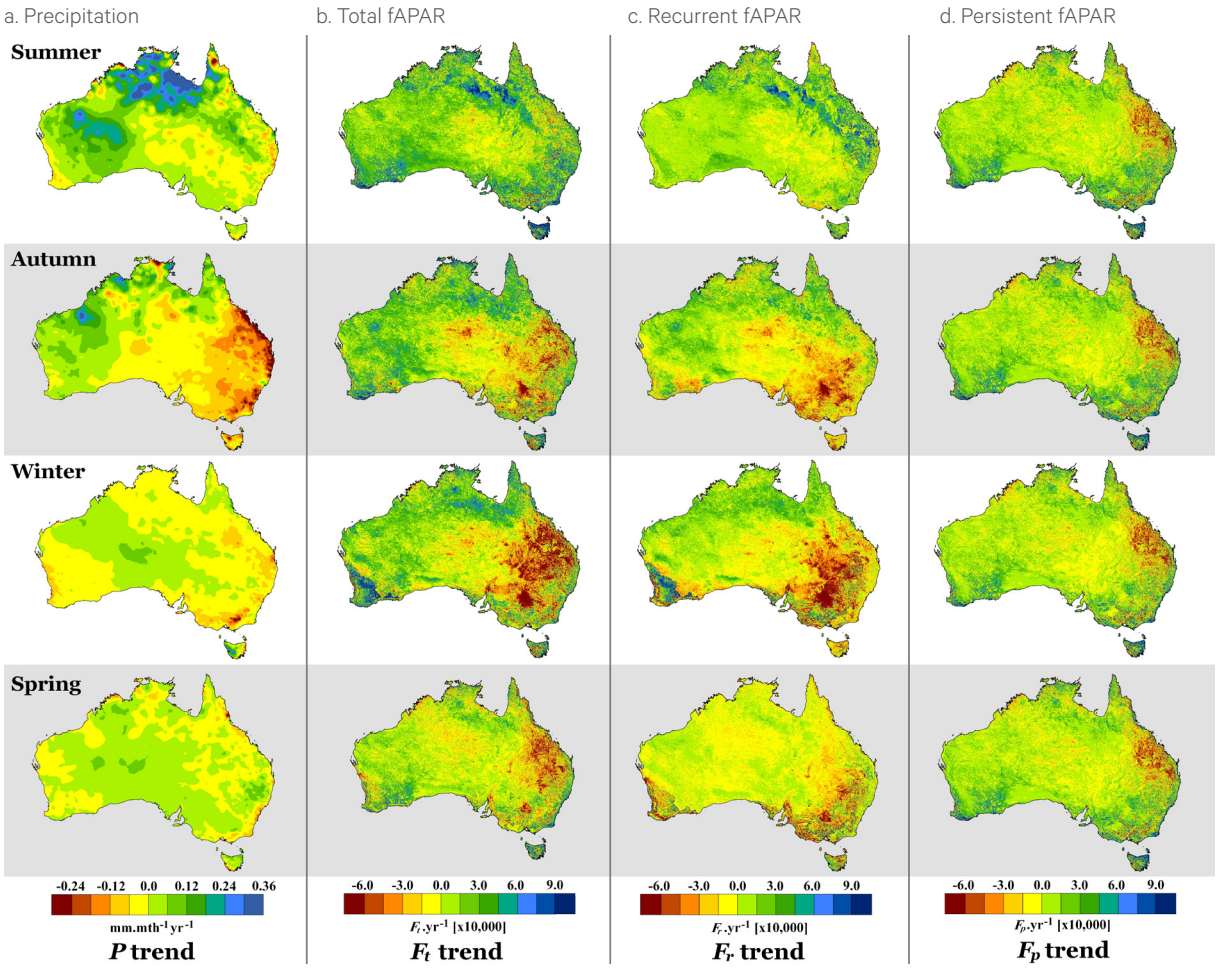

Source: Donohue *et al.* (2009) Figure 5 © Wiley. Used with permission.

9.2 Change Indices

A number of spectral indices have been developed to quantify landscape changes based on a pair of images acquired before and after a change event. As with all monitoring approaches, timing of imagery is important to ensure that the pair capture changes resulting from a specific event (see Volume 2D). For reliable results, these analyses require cloud-free images that are not separately impacted by other environmental conditions such as drought. Below we consider two examples of particular relevance to the Australian environment: fire footprints (see Section 9.2.1) and ecosystem disturbance (see Section 9.2.2).

9.2.1 Fire footprints

A frequent impetus for monitoring land cover change in many parts of Australia is fire. A number of methods for mapping both the extent and severity of fires have been developed, which are discussed in detail in Section 18. Fire indices, however, can saturate in the Australian landscape, resulting in little distinction between areas impacted by high fire severity and those that were completely burnt out (Tony Sparks, *pers. comm.*).

A popular method for mapping fire severity was proposed by Key and Benson (2002, 2006) for Landsat TM/ETM+ imagery based on the Normalised Burn Ratio:

$$NBR = \frac{TM4 - TM7}{TM4 + TM7}$$

Since Landsat TM Band 4 (NIR) is sensitive to changes in vegetation vigour and biomass and Band 7 (SWIR) is sensitive to the visibility and character of soils (Cocke *et al.*, 2005; Key and Benson, 2002), a Normalised Burn Ratio difference image (dNBR), which shows change in NBR due to fire, is then calculated from:

$$dNBR = NBR_{prefire} - NBR_{postfire}$$

Although originally developed for Landsat TM imagery, the ratio has been adapted for use with other EO data with similar spectral channels. Uses and limitations of this method for mapping fire severity are described in Section 18.

Miller and Thode (2007) reported higher accuracy in mapping high fire severity areas using a Relative dNBR index (RdNBR) and suggested that a relative index offers a more consistent basis for comparing fires across space and time:

$$RdNBR = \frac{NBR_{prefire} - NBR_{postfire}}{\sqrt{\left|\frac{NBR_{prefire}}{1000}\right|}}$$

Other indices have been developed for mapping fire footprints, including the Mid-infrared Bi-spectral Index (MIRBI), which was derived from MODIS MIR channels 6 and 7 to detect burned savanna vegetation (Trigg and Flasse, 2001):

$$MIRBI = 10 \times \text{MODIS Band 7} - 9.8 \times \text{MODIS Band 6} + 2$$

As detailed in Section 18, different methods for mapping fire footprints have also been compared in several studies (Trigg and Flasse, 2001; Roman-Cuesta *et al.*, 2005; Holden *et al.*, 2005; Smith *et al.*, 2007).

9.2.2 Ecosystem disturbance

Major disturbances to terrestrial ecosystems, such as fire, floods, storm damage, and insect epidemics, typically destroy large areas of vegetation, resulting in marked changes to the global carbon cycle (see Section 17). Observing the timing, location, extent, and severity of such disturbances is important both to optimise response and recovery efforts, and understand the impact of these events on ecosystem dynamics.

The MODIS Global Disturbance Index (MGDI; Mildrexler *et al.*, 2007, 2009) detects changes in vegetation greenness and land surface temperature (LST) such that:

- greenness, as measured by the MODIS/Terra Enhanced Vegetation Index (EVI; MOD13A1), is expected to decrease after a major disturbance due to reduction in vegetation cover; and
- LST, as measured by MODIS/Aqua LST (MYD11A2), is expected to increase due to reduction in evapotranspiration from less vegetation cover:

$$CCCI = \frac{NDRE - NDRE_{min}}{NDRE_{max} - NDRE_{min}}$$

$$MGDI = (LST_{max}/EVI_{max})/(LST_{mean}/EVI_{mean})$$

where

LST_{max} is the annual maximum of eight-day composite LST;
EVI_{max} is annual maximum of 16-day EVI;
LST_{mean} is the multiyear mean of LST_{max}; and
EVI_{mean} is multiyear mean of EVI_{max}.

MODIS imagery from 2001 to 2013 were analysed to generate an experimental version of this product for Australia (TERN AusCover, 2014). This has been validated using fire events, but could be used to assess any major landscape event and the associated subsequent regeneration (see Section 9.7).

9.3 Phenology

Phenology, the interaction between plant life cycles and seasonal, climatic and other rhythms, is introduced in Section 5.3.2 above. A range of metrics is used to identify and compare phenological stages. As indicated in Table 9.3, these are based on either the dates associated with particular stages of greenness or the magnitude of greenness. Different metrics have been demonstrated to be most effective in assessing different types of vegetation and/or different vegetation characteristics.

Phenological studies have employed three principal tools: *in situ* observations, bioclimatic models, and EO. *In situ* observations, such as field measurements (see Volume 2D—Section 12), automatic sensor networks, and phenocams (Brown *et al.*, 2012, 2016), are essential to validate both bioclimatic models and EO analyses, but are expensive, time-consuming, and invariably introduce inconsistencies over large areas. Most bioclimatic models tend to be specific to selected species and local scales and do not readily extend to larger areas. EO offers the only viable option to scale up *in situ* observations for regional and global coverage (Cleland *et al.*, 2007).

Table 9.3 Significant phenological metrics

Basis	Name of Metric	Application
Greening Dates	Start of growing season (SGS)	Indicate sensitivity of ecosystem productivity to phenology and climate change (Ma *et al.*, 2013; Richardson *et al.*, 2010);
	End of growing season (EGS)	
	Peak period of growing season (PGS)	
Magnitude of Greenness	First derivatives of seasonal greenness profile	Asymmetry between rate of green-up and rate of senescence used to characterise ecosystem type Variations in rates indicative of vegetation health
	Annual integrals of seasonal greenness profile	Variations related to ecosystem productivity
	Amplitude of seasonal greenness profile	Minimum dry season baseline related to persistent green vegetation cover (Donohue *et al.*, 2009) Amplitude (PGS minus baseline) related to recurrent vegetation cover

Source: Restrepo-Coupe *et al.* (2018)

As with other time series datasets, annual, interannual, and longer term patterns need to be differentiated in phenological observations (see Section 5.3.2 and Volume 2D—Section 8 and 9). Changes in phenological metrics between years can result from short-term climatic fluctuations (Elmore *et al.*, 2003) or localised anthropogenic changes (White *et al.*, 2002). Longer-term changes in annual cycles may result from major climate variations or regional anthropogenic influences (Myneni *et al.*, 1997; Potter *et al.*, 2003; Tucker *et al.*, 2001).

EO techniques have proven to be a reliable method of assessing plant phenological status, since vegetation canopy greenness is closely related to the generalised growth stages of emergence, development, maturity, and senescence (or harvest) for most forests, grasslands, and wetlands, as well as most agricultural crops (see Figure 6.6). In particular, time series imagery has enabled new insights into vegetation dynamics and land surface changes (see Section 10 and Volume 2D).

The majority of EO-based phenological studies have analysed changes in vegetation 'greenness' as represented by spectral indices (see Section 8.1). Analyses of historical imagery have allowed models for growing season parameters to be established, and perturbations induced by climatic or anthropogenic factors to be detected (Myneni *et al.*, 1997; Huete *et al.*, 2006). Validation methods for satellite image-based phenology analyses are detailed in Restrepo-Coupe *et al.* (2018). Zeng *et al.* (2020) review vegetation phenological metrics derived from EO time series datasets both in terms of existing methods and emerging techniques.

Most of the large area studies of seasonal vegetation dynamics have been based on the extensive archives of AVHRR, MODIS, or VIIRS imagery, although Landsat imagery has also been used for regional analyses. AVHRR data provides the longest, continuous time series of global imagery, but this dataset has known limitations for detailed vegetation analyses, including problems with radiometric and geometric precision (Goward *et al.*, 1991; Teillet *et al.*, 2000). Comparisons between time series from different sensors yielded similar results in terms of phenological trends between NDVI derived from MODIS and SPOT-Vegetation datasets, but disagreement with NDVI trends from AVHRR GIMMS (Yin *et al.*, 2012).

Since the extent of green plant cover is indicative of phenological stages in annual plants (see Section 6.5), the key transition dates between greening, maturity, senescence, and dormancy can be identified using a greenness index. When the greenness values for each image pixel are plotted against the calendar date, the trend in greenness is clearly visible as increasing during the greening phase, most constant during the maturity phase and decreasing during the senescing phase (see Table 9.4 and Figure 9.2). The dates of these transitions correspond to the inflexion points in an EO-based greenness plot, that is, the dates when the slope of the greenness trend changes (Zhang *et al.*, 2003; see Section 14.3). Changes in meteorological and environmental conditions or plant varieties, however, may vary the precise temporal trajectory of pixel values throughout the growing season from year to year in terms of duration, amplitude, baseline, and start and end dates, (see Volume 2D—Section 9).

While phenological changes in woodlands are less dramatic than in herbaceous plant communities, they can also be observed. For example, a typical annual cycle in NDVI values for pine plantations in southeast NSW shows high winter values correlating with winter rainfall and low summer values corresponding to low rainfall during the summer months (Verbesselt *et al.*, 2009). Since the impacts of variations in tree vigour are maximised in terms of NDVI during the more stressful summer months, they can be summarised by the normalised difference between winter and summer values (Coops *et al.*, 2009), which has been successfully used to map tree mortality these plantations (Verbesselt *et al.*, 2009).

To clearly identify surface features in a thematic classification, the temporal trends associated with each feature type need to be understood, modelled and labelled appropriately. White and Nemani (2006) suggest five principles that should be observed in phenological analyses based on EO:

- results do not apply to individual pixels;
- pixels with similar time patterns should be treated as a group;
- sequences should not be filled, fitted, or smoothed;
- changes in land surface phenology may not correspond to known vegetation events; and
- variability and/or uncertainty measures should be included.

A range of approaches have been used to determine the time of vegetation greening and browning based on EO greenness indices for regional studies of annual plants (see Section 8.1.1) including thresholds for specific levels (White *et al.*, 1997), largest change (Kaduk and Heimann, 1996), backward-looking moving averages (Reed *et al.*, 1994), and empirical equations (Moulin *et al.*, 1997).

Table 9.4 Phenological stages of rice crop

Growth stage		EO greenness
Vegetative	Transplanting	Initial seedling
	Tillering	Increasing greenness for 60–100 days depending on variety
	Stem elongation	
Reproductive	Panicle initiation	
	Booting/heading	
	Flowering	Maximum greenness
Ripening	Milk stage	Decreasing greenness often takes 30 days
	Dough stage	
	Mature	Harvest

Adapted from: Mosleh *et al.* (2015) Figure 1

Figure 9.2 Greenness changes in annual plants

Annual plants typically follow a temporal pattern of increasing greenness during growth then a reduction in greenness after maturity.

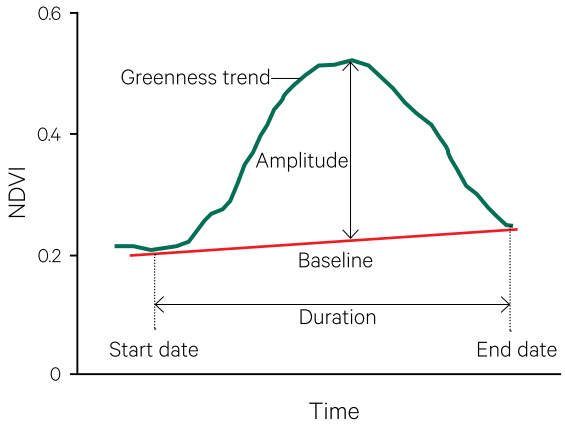

Adapted from: Lhermitte *et al.* (2011) Figure 1

As introduced in Volume 2D—Section 9, various mathematical models can be fitted to EO time series datasets. The following functions have been used to identify phenological transition dates from global imagery archives:

- major changes in curvature for a piecewise logistic function fitted to EVI time series data (Zhang *et al.*, 2003);
- Gaussian forms (Jönsson and Eklundh, 2002, 2004); and
- high order splines (Hermance *et al.*, 2007; Bradley *et al.*, 2007).

Since the phenological status of vegetation impacts energy exchange between the Earth's surface and atmosphere, the relationship between phenology and climate is of prime importance to global monitoring. A Growing Season Index (GSI) was proposed by Jolly *et al.* (2005) to summarise the relative phenological performance of vegetation. At a global scale, this index distinguished major differences in regional phenological controls and could be used both to reconstruct historical variation and forecast future phenological responses to climatic changes. More recent developments include real time monitoring and short term forecasting of phenological changes (White and Nemani, 2006; Zhang *et al.*, 2012), and integration with other models (Nemani *et al.*, 2009). Excursus 9.1 introduces an Australian EO-based product, which monitors phenology.

Figure 9.3 NDVI time series of pine plantation

A 16-day NDVI time series of a pine plantation is decomposed into seasonal, trend, and irregular components. Right hand bars show comparable data ranges. Seasonal amplitude range is around 0.1 NDVI.

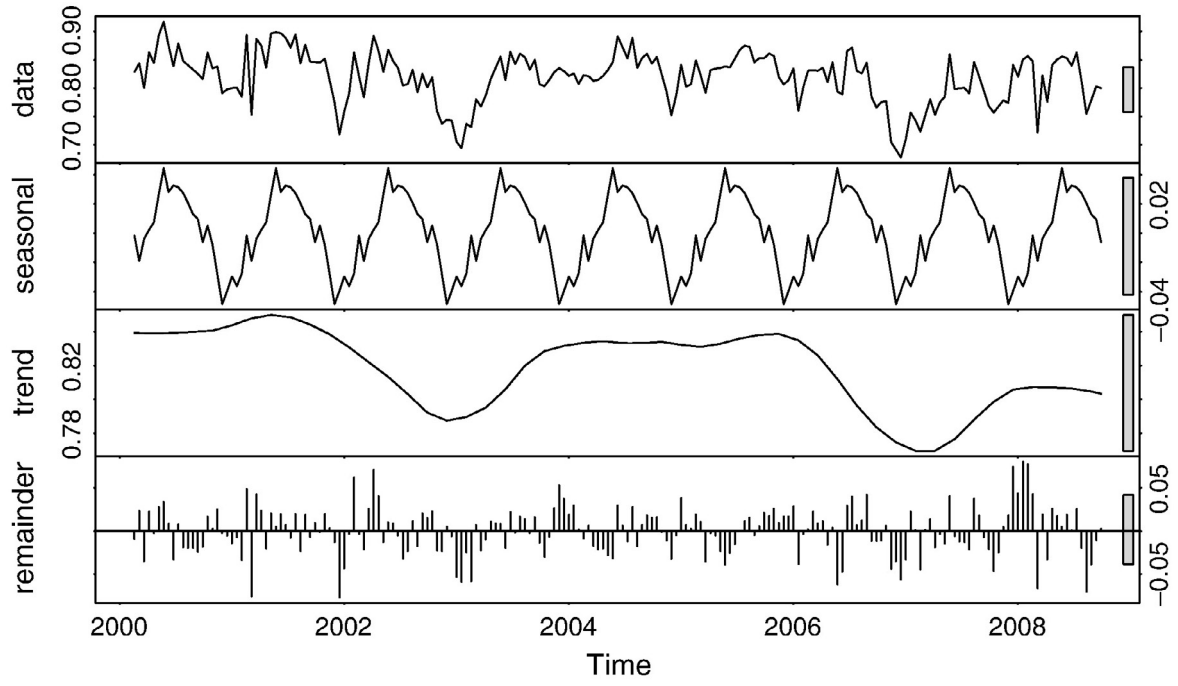

Source: Verbesselt *et al.* (2010) Figure 2

Excursus 9.1—Australian Phenology Product

Source: Qiaoyun Xie, University of Technology Sydney
Further information: Broich *et al.* (2014, 2015); *https://www.tern.org.au/australian-phenology-product/*
Data download: *http://www.auscover.org.au/purl/modis-phenology-uts*

Knowing how different parts of Australia's vegetative land cover are growing and developing with the change of seasons is vital information for environmental scientists, land managers and those in the agricultural and horticultural sectors. The Australian Phenology Product provides detailed information on the seasonal growth and development of Australia's vegetation at continental scale (see Figure 9.2). Potential applications include:

- quantifying ecosystem resilience to climate change;
- estimating bushfire fuel accumulation;
- assessing native vegetation condition;
- monitoring airborne allergens; and
- informing agricultural management decisions and crop yields.

This product has been developed from MODIS Enhanced Vegetation Index (EVI) data and a suite of additional data collected and made available by TERN's facilities. The Version 1 product was released in 2015, providing phenological metrics from 2000 to 2015 at 0.05º spatial resolution using MOD13C1 data as input. MYD13A1 data is now being used to transition the product into the VIIRS era. It quantifies vegetation life cycle dynamics, such as episodes of greening and browning, and analyses how these are influenced by seasonal and interannual variations in climate. Phenological cycles are defined as a period of EVI-measured greening and browning that may occur at any time of the year, extend across the end of a year, skip a year (not occur for one or multiple years) or occur more than once a year. Multiple phenological cycles within a year can occur in the form of double cropping in agricultural areas or be caused by aseasonal rain events in water-limited environments.

Based on per-pixel greenness trajectories measured by MODIS EVI, phenological cycle curves were modelled and their key properties, in the form of phenological curve metrics, were derived including: the first and second minimum point, peak, start and end of cycle; length of cycle, and; the amplitude of the cycle. Integrated EVI under the curve between the start and end of the cycle time for each cycle is calculated as a proxy of productivity (Broich *et al.*, 2015).

When applied to the Version 1 product (0.05° resolution) from 2000 to 2013, results showed high inter- and intra-annual variability in phenological cycles across Australia (Broich *et al.*, 2014). The peak of phenological cycles occurred not only during the austral summer, but also at any time of the year, with their timing varying by more than a month in the interior of the continent. The magnitude of the phenological cycle peak and the integrated greenness were most significantly correlated with monthly SOI within the preceding 12 months. Correlation patterns occurred primarily over northeastern Australia and within the Murray Darling Basin, predominantly over natural land cover and particularly in floodplain and wetland areas. Integrated greenness of the phenological cycles (surrogate of vegetation productivity) in Figure 9.5 showed negative anomalies over most of northern and eastern Australia in 2003 and positive anomalies over most of eastern Australia in 2009–2010, which coincided with the transition from the El Niño-induced decadal droughts to flooding caused by La Niña.

Figure 9.4 Australian Phenology Product

Timing of maximum vegetation index in 2018 at 500 m resolution

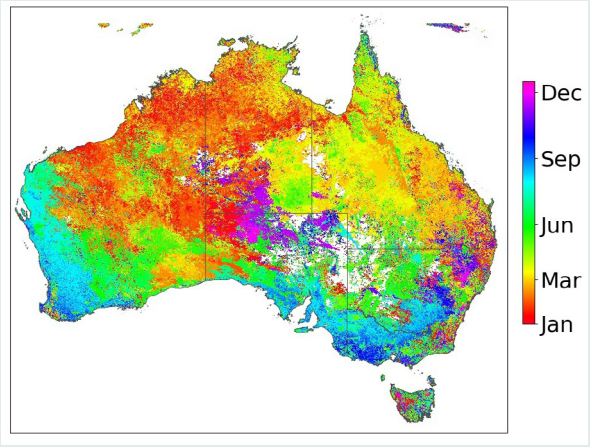

Figure 9.5 Seasonally-integrated EVI from Australian Phenology Product

Seasonally-integrated EVI (the first season) from Australian Phenology Product using MYD13A1 data as input at 500 m resolution for 2003 El Niño dry year case and 2010 La Niña wet year case. White pixels represent areas without detectable vegetation growth.

a. Seasonally-integrated EVI in 2003

b. Seasonally-integrated EVI in 2010

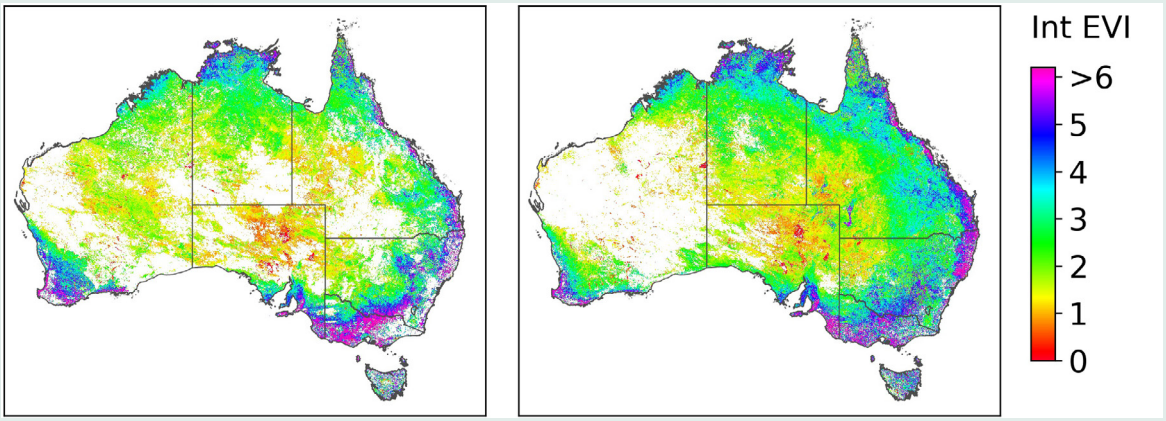

c. Seasonally-integrated EVI in 2003 subtracted by climatology from 2003 to 2018

d. Seasonally-integrated EVI in 2010 subtracted by climatology from 2003 to 2018

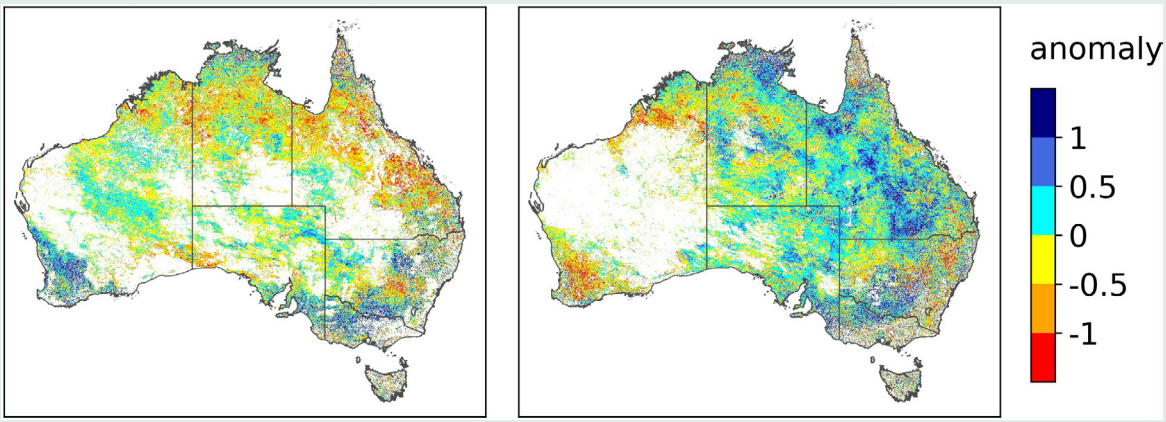

9.4 Evapotranspiration

Evapotranspiration (ET) describes the combined transfer of water vapour to the atmosphere by evaporation and transpiration from the Earth's surface (see Sections 2.2, 5.2.3, and 7.6). Understanding and managing ET is one of the most important biophysical challenges facing natural and man-made ecosystems, and its behaviour can change dramatically with the scale and nature of particular situations. The approaches and solutions to problems relating to ET will rely on increasing use of EO technologies to cope with issues of scale, and will need diverse, customised approaches to tackle problems at farm, district, and continental scales (see Section 13). Accepted methods for estimating large area, actual ET (AET) using ground-based data (Glenn *et al.*, 2011) include:

- EC flux towers (see Excursus 7.2);
- sap flux sensors (see Section 5.2.3); and
- Budyko framework for catchment water balance (Budyko, 1958, 1974; see Excursus 9.2).

EC flux towers are the most commonly used method for validating EO-based studies of ET. Upscaling of data from sap flux sensors to landscape scale analyses is problematic, but such sensors have been useful in focused studies (Doody and Benyon, 2011), woody agricultural crops (Blaike *et al.*, 2001), and when combined with EC methods (Silberstein *et al.*, 2001). The Budyko framework is popular for catchment scale studies (see Excursus 9.2) and has been used in conjunction with estimates of total water storage change derived from GRACE satellite data (Long *et al.*, 2014; see Volume 3B—Excursus 1.1).

In many ecosystems, the proportion of the land surface covered by vegetation is closely related to water balance and landscape dynamics, especially the capability to retain precipitation (see Section 7.6). In savanna ecosystems, which comprise sparse vegetation and bare soil, evapotranspiration controls the water balance. Photosynthetically active vegetation in these landscapes cycles annually between the wet season of moist, green growth, and the dry season of desiccated grasses, dry litter, and groundwater-dependent trees (Guerschman *et al.*, 2009). In this situation, monitoring of photosynthetic vegetation cover provides information about the water cycle as well as ecosystem dynamics (see Section 7).

Excursus 9.2—Budyko Framework

Source: Donohue *et al.* (2007)
Further Information: Budyko (1958, 1974)

Budyko (1958, 1974) describes the partitioning of average precipitation into average evapotranspiration and average run-off based on simple physical relationships now known as the 'Budyko curve'. This curve describes the patterns observed between climate, evapotranspiration, and run-off, and has proven to be a useful model for predicting catchment energy and water balances. The Budyko framework assumes catchments are at steady-state and are driven by the macro-climate. These two conditions depend on the scales of application, such that the framework's reliability is greatest when applied using long term averages (much greater than one year) and to large catchments (> 10,000 km^2).

Budyko described the hydrology of a catchment using a supply-demand framework and a simple bucket model where net drainage is assumed to be negligible. The water balance (see Section 7.6) was defined as:

$$\frac{dS_w}{dt} = P - E - Q$$

where P, E, and Q are catchment-wide estimates of precipitation, evapotranspiration, and run-off fluxes respectively (in kg s^{-1}), and S_w (kg) is the soil water storage. A catchment is in steady-state when changes in S_w are zero. In reality, the water balance is almost continually varying due to fluctuations in P, E, and Q, and steady-state conditions are typically established in analyses by integrating the above equation over a finite time period (τ) that is larger than the timescale of fluctuations in S_w:

$$\int_0^\tau \frac{dS_w}{dt}\,dt = \int_0^\tau P\,dt - \int_0^\tau E\,dt - \int_0^\tau Q\,dt$$

In finite form we have the catchment mass balance:

$$\Delta S_w = \bar{P}\tau - \bar{E}\tau - \bar{Q}\tau$$

or

$$\frac{\Delta S_w}{\tau} = \bar{P} - \bar{E} - \bar{Q}$$

We can convert to the familiar depth units by dividing both sides by the catchment area (A_c, in m^2) and the density of liquid water (ρ_w, as kg m^{-3}):

$$\frac{\Delta S_w}{\rho_w A_c \tau} = \bar{P} - \bar{E} - \bar{Q}$$

The framework can be further extended by noting that soil water depends on the volume of the bucket (V, m^3) and the mass concentration of water in the bucket ($[S_w]$, kg m^{-3}):

$$S_w = V[S_w]$$

An upper limit to $[S_w]$ is set by the pore space within the soil, which is a function of soil texture and structure (Craze and Hamilton, 1991). Soil water can change because of a change in the volume of the bucket or a change in mass concentration within the volume. To the first order we have:

$$\Delta S_w = [S_w]\Delta V + V\Delta[S_w]$$

The volume of the bucket depends on the catchment area and bucket depth (z, m):

$$V = A_c z$$

For a given catchment, the area is fixed and the volume of the bucket can only change because of the change in depth (Δz) so that:

$$\frac{1}{\rho_w}\left([S_w]\frac{\Delta z}{\tau} + z\frac{\Delta[S_w]}{\tau}\right) = \frac{\bar{P} - \bar{E} - \bar{Q}}{\rho_w A_c}$$

Formulating the water balance in this way allows links to be made between vegetation characteristics and the spatial analysis scales, as well as the 'flux components' (Q and E) and the 'steady-state components' of the water balance (see Donohue *et al.*, 2007). Fluxes of both mass and energy are involved in evapotranspiration and this provides a critical link between the water and energy balances (see Section 7.5). The catchment-wide energy balance is given by:

$$\Delta S_e = R_n - \lambda E - H$$

where the change in energy storage (S_e) is the balance between net radiation (R_n) and the fluxes of latent (λE) and sensible (H) heat (all in J s^{-1}) where λ (in J kg^{-1}) is the latent heat of vaporisation. Note that the sign convention used in the above equation assumes that λE and H are positive away from the surface while R_n is positive into the surface. Using the same form as the previous equation gives:

$$[S_e]\frac{\Delta z_e}{\tau} + z_e\frac{\Delta[S_e]}{\tau} = \frac{\bar{R_n} - \lambda\bar{E} - \bar{H}}{A_c}$$

where z_e (m) is the depth to which energy can be stored. Over annual timescales energy storage can usually be omitted from the energy balance.

Evapotranspiration is limited by the supply of either water or energy. At steady-state, when water is limiting ($R_n / \lambda > P$), the maximum possible E is P, at which Q=0. Similarly, the maximum possible E when energy is limiting is R_n / λ at which H=0. Evapotranspiration approaches one of these two limits as water or energy, respectively, become increasingly limiting. This framework of mass and energy balances and supply and demand-limited evapotranspiration is the key component of Budyko's work. The type and degree of limitation is determined by the radiative index of dryness (Φ), which is the ratio of R_n / λ to P. Values of $\Phi < 1$ represent energy-limited environments, and those where $\Phi > 1$ are water-limited. Intermediate environments occur where $\Phi \sim 1$.

Figure 9.6 Budyko's framework and curve

The curve (green line) describes the relationship between the dryness index and the evaporative index. Line A–B defines the energy-limit to evapotranspiration, and line C–D defines the water-limit.

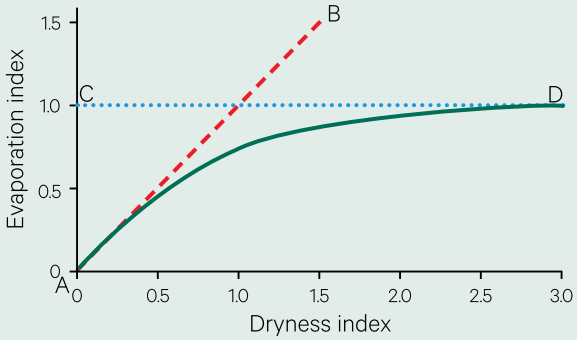

Adapted from: Donohue *et al.* (2007) Figure 1

Catchment scale annual (or longer) evapotranspiration is usually estimated for gauged catchments by assuming that S_w is 0 and hence E is the difference between measured values of P and Q. The need for a simple means of estimating E from ungauged catchments prompted Budyko to develop the 'equation of relationship' that describes the dependency of E on the variables P and R_n / λ:

$$\bar{E} = \left(\frac{\bar{R}_n \bar{P}}{\lambda} \tanh \frac{1}{\Phi} \left(1 - \cosh\Phi + \sinh\Phi \right) \right)^{0.5}$$

This curvilinear relationship, which built on the works of Schreiber (1904) and Ol'dekop (1911), has become known as the Budyko curve (see Figure 9.6).

The assumptions inherent in Budyko's hydrological model are that:

- catchments are at steady-state (that is, $\Delta S_w \approx 0$)—to a large degree, this condition depends on τ; and that
- at large spatial scales (A_c » 1000 km^2), only macro-climatic variables are required to describe catchment water balances.

When applied over long timescales and to large catchments, Budyko's curve reliably predicts catchment water balances. However, when applied to small spatiotemporal scales the inherent assumptions can be violated. In these circumstances, incorporating vegetation into the framework is expected to enhance the framework's predictive capacity (see Donohue *et al.* (2007) for details).

EO-based approaches for predicting ET from vegetated surfaces are reviewed by Glenn *et al.* (2011) and Nouri *et al.* (2013). EO imagery offers the opportunity to monitor the spatiotemporal variability of ET using:

- thermal estimation—the difference between air temperature and thermal infrared (TIR)-derived surface temperature has been used to compute the sensible heat flux (H; see Section 7.5) in the equation:

  $$LE = R_n - G - H$$

  where LE is the latent heat flux associated with AET, R_n is the net radiation, and G is the ground heat flux (Glenn *et al.*, 2011). Using EO or ground-based estimates of the other parameters, LE can be computed as a surrogate for AET. Various models have been proposed on this basis (Li and Lyons, 1999), from simple regression relationships (see Section 13) to sophisticated, surface energy balance models (see Section 10.2.3). While such models have known limitations (Glenn *et al.*, 2007; Kalma *et al.*, 2008), with appropriate processing reasonable agreement has been achieved between modelled and ground-based estimates (McVicar and Jupp, 2002, Mc Vicar *et al.*, 2007); or
- vegetation indices (VI; see Section 8.1)—estimates of LAI or vegetation cover, primarily from AVHRR and MODIS imagery, have been used as inputs to ET models at regional and continental scales (Glenn *et al.*, 2010; see Section 7.6). LAI and canopy conductance can be derived using VI where estimates of maximal stomatal conductance, and the constraints of stomatal conductance, are available from ground measurements of AET, meteorological data, and/or appropriate physiological models, although the bare soil component of AET must be estimated separately (Glenn *et al.*, 2011). The Penman-Monteith equation is then used to calculate AET by using EO-based estimates of canopy conductance (see Section 13.4.2). This approach relies on empirical relationships, which can be impractical to rescale spectrally, temporally, or spatially (Donohue *et al.*, 2010b; Abuzar *et al.*, 2014; see Volume 2D—Section 4.3). However, simplified models of landscape ET derived from empirical relationships are an essential starting point when dealing with the challenges associated with data sparse, rainfed conditions, where rainfall deficits, vegetation type and cover, and evaporative demand interact to determine landscape ET (see Section 7.6).

Alternative conceptual approaches for estimating AET from VI were categorised by Yebra *et al.* (2013) as:

- estimating actual or maximum, leaf level, stomatal conductance;
- using LAI as a surrogate for AET to scale from stomatal to canopy conductance;
- using an empirical relationship to estimate either canopy conductance or surface conductance (including soil evaporation); and
- developing direct empirical equations between the VI and AET measurements.

Some of these approaches rely on spatial and/or temporal scaling from site-specific measurements to regional and continental scale models (see Section 10). Again, uncertainties in ET estimates can result when the scales of underlying datasets are poorly matched (van Niel *et al.*, 2011). Examples of EO-based indices that have been developed to map and monitor evapotranspiration (ET) for

drought assessment include the Drought Severity Index (DSI; Su *et al.*, 2003) and Evaporative Drought Index (EDI; Anderson *et al.*, 2007; Yao *et al.*, 2010; Bayarjargal *et al.*, 2006).

Surface energy balance models that have been proposed to estimate AET include SEBAL (Surface Energy Balance Algorithm for Land, Bastiaanssen *et al.*, 1998; Bastiaanssen, 2000) and METRIC (Mapping Evapotranspiration at High Resolution with Internal Calibration, Allen *et al.*, 2007). In Australia, these models have been successfully used to monitor crop water requirements (see Section 13) and wetland AET (Khan *et al.*, 2009).

King *et al.* (2011) evaluated continental AET products for Australia, and concluded that estimates based on water balance modelling (Raupach *et al.*, 2009, van Dijk, 2010) proved to be most reliable in regions where AET depends on precipitation, but EO-based methods (Guerschman *et al.*, 2009), which accounted for surface and groundwater contributions, were more appropriate in areas where vegetation is dependent on other water sources. EO-based estimates of ET have become essential inputs to national water resources assessment processes in Australia (van Dijk and Renzullo, 2011; see Excursus 10.2).

9.5 Plant Water Stress

As introduced in Sections 4.2.1, 5.2.3, and 5.2.4, plant water stress is signalled by increasing plant temperature and reducing transpiration rates. Since air temperature, relative humidity, wind speed, and incoming irradiance can also impact canopy temperature, a normalised index was developed to account for such factors (Idso *et al.*, 1981). The Crop Water Stress Index (CWSI) was proposed by Jackson (1981, 1988) to map variations in canopy water status using remotely sensed temperature:

$$\text{CWSI} = \frac{\text{canopy temp.} - \text{reference temp.}}{\text{maximum temp.} - \text{reference temp.}}$$

where

reference temperature is measured from comparable, non-stressed vegetation; and

maximum temperature is the upper temperature tolerated without transpiration.

CWSI values range from zero for a fully transpiring plant to one for a non-transpiring plant with leaf temperature 4–6°C above the air temperature. As with similar indices, the validity of the CWSI is critically dependent on the selection of appropriate reference data. Field measurements of leaf thermal properties can be problematic, with variations continually being induced by fluctuations in irradiance and air currents. View angle variations will also result in different temperature measurements (Jones *et al.*, 2002).

CWSI has been widely used for monitoring water stress and scheduling irrigation in a range of cereal and horticultural crops (Alderfasi and Nielsen, 2000; Irmak *et al.*, 2000; Orta *et al.*, 2003; Taghvaeian *et al.*, 2012; Poblete-Echeverria *et al.*, 2017; Alghory and Yazar, 2019). For example, Park *et al.* (2017) acquired high resolution thermal imagery using UAV to map variability of plant water stress in nectarine and peach orchards in Victoria. Stem water potential and stomatal conductance were measured directly on the ground. An adaptive CWSI, derived from crop pixels only (isolated from soil background), showed better agreement with the direct measurements than the conventional CWSI.

At a regional scale, McVicar and Jupp (2002) used the Normalised Difference Temperature Index (NDTI) to monitor moisture availability from integrated meteorological and EO datasets:

$$\text{NDTI} = \frac{T_{max} - T_s}{T_{max} - T_{min}}$$

where

T_s is the observed surface temperature for an EO pixel with a given NDVI value; and

T_{max} and T_{min} are respectively the highest and lowest surface temperatures for pixels with the same NDVI value.

A Resistance Energy Balance Model (REBM) was used to calculate NDTI from meteorological station records, which were then interpolated using EO-based covariates (see Section 10.1.2). These authors considered NDTI as a 'specific time-of-day version of CWSI'.

At global, regional and country levels, the FAO Agricultural Stress Index System (ASIS) monitors agricultural areas that are very likely to experience water stress or drought (Rojas, 2015; FAO, 2020). This system relies on the Agricultural Stress Index (ASI; Rojas *et al.*, 2011), which compares the Vegetation Health Index (VHI) with the seasonal VHI average, where the crop season is defined using a phenological model derived from NDVI. VHI is one of several global products generated by NOAA/NESDIS since 1981 to map vegetation health. Derived from AVHRR and VIIRS imagery, VHI is a global, validated, weekly composite with 4 km spatial resolution based on proxies for the relative moisture and thermal conditions:

$$VHI = a \times VCI + (1 - a) \times TCI$$

where

VCI (Vegetation Condition Index) indicates the moisture condition of vegetation, derived from NDVI time series imagery:

$$VCI_i = 100 \times \frac{NDVI_i - NDVI_{min}}{NDVI_{max} - NDVI_{min}}$$

TCI (Thermal Condition Index) indicates the thermal condition of vegetation, derived from brightness temperature (BT) time series imagery:

$$TCI_i = 100 \times \frac{BT_i - BT_{min}}{BT_{max} - BT_{min}}$$

a is a coefficient that determines the relative contributions of VCI and TCI to the health status of vegetation (NOAA STAR, 2019). Typically a=0.5 unless the contribution of moisture and temperature status to vegetation health is known (Rojas *et al.*, 2011).

In the calculation of VCI and TCI, the NDVI and BT time series are filtered to remove high frequency noise and adjusted for land surface non-homogeneity (Kogan, 1997). VHI, VCI, and TCI are used to define drought conditions (where all indices < 40) as well as the risk of fire and malaria. The VH product suite has been used for early drought detection, assessing drought area coverage, duration, and intensity, and for monitoring drought impacts on vegetation and agricultural crops (NOAA STAR, 2019; see Section 11.2). ASI has been used to historically identify major droughts and their impact on the African continent (Rojas *et al.*, 2011). ASIS has been incorporated into the Global Information and Early Warning System (GIEWS; FAO, 2020; see Section 11.2) to indicate regions that are currently water-stressed and may be facing drought conditions (Fritz *et al.*, 2019).

9.6 Plant Vigour

Characteristics of leaf optical reflectance that change with variations in plant vigour are introduced in Section 4.3. In terms of EO, thermography, chlorophyll fluorescence and hyperspectral imaging have been the most promising approaches to identify and quantify plant diseases (Mahlein *et al.*, 2012).

Approaches used to measure plant biochemistry, and thus plant vigour, based on spectroscopic measurement can be grouped into two categories (Ustin *et al.*, 2004):

- empirical—using linear and non-linear combinations of spectral bands, which highlight canopy characteristics (Hall *et al.*, 1995; Price, 1992b); and
- analytical and semi-analytical—using canopy reflectance (CR) models, based on radiative transfer theory and leaf optical simulation (Meroni *et al.*, 2004), which can be inverted to estimate leaf and canopy parameters (Privette *et al.*, 1996; Bicheron and Leroy, 1999; Jacquemoud *et al.*, 2009).

Some of the most important biochemical compounds involved in carbon, water and nutrient cycling include the light absorbing pigments (principally chlorophylls and carotenoids; see Excursus 4.1) and nitrogen, which are directly related to the photosynthetic capacity in plants (see Section 5.2.1; Gitelson *et al.*, 2006, 2009; Ollinger and Smith, 2005). In particular, leaf chlorophyll content varies with the photosynthetic capacity, productivity, stress, age, and development stage of a plant (Curran *et al.*, 1990; Ustin *et al.*, 1998).

Various plant stress factors modify the proportion of light-absorbing pigments to reduce light absorption, which further decreases leaf chlorophyll content (Zarco-Tejada *et al.*, 2000). As introduced in Section 4.3, leaf absorption of wavelengths in the spectral region from 550 nm to 700 nm (visible red) is closely related to the concentration of chlorophyll pigments (Thomas and Gausman, 1977; Carter and Knapp, 2001; Devlin and Witham, 1983). As chlorophyll concentration increases, the red absorption feature both broadens and deepens, which moves the 'edges'

of that feature (Horler *et al*., 1983). Of greatest significance is the movement of its 'red edge' (that is, EMR wavelengths from around 690 nm to 740 nm) towards longer wavelengths as chlorophyll content increases (Rock *et al*., 1988, Curran *et al*., 1990; Ustin *et al*., 1998). Accordingly, when red reflectance is standardised by a non-absorbing waveband, it is strongly correlated with leaf pigment changes (Curran, 1989; Curran *et al*., 1997), especially leaf chlorophyll concentration (Turrell *et al*., 1961; Thomas and Gausman, 1977; Everitt *et al*., 1985).

Various indices have been designed to capture the position and shape of the 'red edge' (see Section 8.1.2), many of which can be used to track chlorophyll concentration (Horler *et al*., 1983; Curran *et al*., 1991; Miller *et al*., 1991; Filella and Penuelas, 1994; Curran *et al*., 1995; see Section 8.1). Changes in plant vigour, due to nutritional status, pests, and/or diseases, has been monitored using EO datasets for several decades (see Sections 11 to 16).

9.7 Further Information

TERN Auscover products

Ecosystem Disturbance Index: *http://www.auscover.org.au/purl/modis-disturbance-index*

Phenology: *http://www.auscover.org.au/purl/modis-phenology-uts*

National Vegetation Information System

NVIS: *http://www.environment.gov.au/land/native-vegetation/national-vegetation-information-system*

http://www.environment.gov.au/land/native-vegetation/national-vegetation-information-system/data-products

NVIS Technical Working Group (2017) Australian Vegetation Attribute Manual: National Vegetation Information System, Version 7.0. Department of the Environment and Energy, Canberra. Prep by Bolton, M.P., deLacey, C., and Bossard, K.B. (Eds)

https://www.environment.gov.au/land/native-vegetation/national-vegetation-information-system/data-products#mvg51

New South Wales

Statewide Landcover and Trees Study (SLATS): *https://www.environment.nsw.gov.au/topics/animals-and-plants/native-vegetation/reports-and-resources*

NSW Report on Native Vegetation 2014–16: *https://www.environment.nsw.gov.au/vegetation/reports.htm*

NSW Fire Extent and Severity Mapping (annual monitoring and reporting framework): *https://www.environment.nsw.gov.au/topics/animals-and-plants/native-vegetation/landcover-monitoring-and-reporting/fire-extent-and-severity-maps*

DustWatch: *https://www.environment.nsw.gov.au/topics/land-and-soil/soil-degradation/wind-erosion/community-dustwatch*

Queensland

Ground cover monitoring: *https://www.qld.gov.au/environment/land/management/mapping/statewide-monitoring/groundcover*

Ground cover disturbance index: *http://qldspatial.information.qld.gov.au/catalogue/custom/detail.page?fid={E2021208-DBCB-4963-A0F7-D4C7FD3150F2}*

Statewide Landcover and Trees Study (SLATS): *https://www.qld.gov.au/environment/land/management/mapping/statewide-monitoring/slats*

Victoria

Habitat Hectares: *https://www.environment.vic.gov.au/__data/assets/pdf_file/0016/91150/Vegetation-Quality-Assessment-Manual-Version-1.3.pdf*

Spatial data for Victoria: *https://www2.delwp.vic.gov.au/maps?_ga=2.6531511.420315026.1549698228-873342548.1549698228*

Western Australia

LandMonitor: *https://landmonitor.landgate.wa.gov.au/home.php*

9.8 References

Abuzar, M., Sheffield, K., Whitfield, D., O'Connell, M., and McAllister, A. (2014). Comparing Inter-Sensor NDVI for the Analysis of Horticulture Crops in South-Eastern Australia. *American Journal of Remote Sensing*, 2, 1–9. *http://doi.org/10.11648/j.ajrs.20140201.11*

Alderfasi, A.A., and Nielsen, D.C. (2001). Use of crop water stress index for monitoring water status and scheduling irrigation in wheat. *Agricultural Water Management*, 47, 69–75. *https://doi.org/10.1016/S0378-3774(00)00096-2*

Alghory, A., and Yazar, A. (2019). Evaluation of crop water stress index and leaf water potential for deficit irrigation management of sprinkler-irrigated wheat. *Irrigation Science*, 37, 61–77. *https://doi.org/10.1007/s00271-018-0603-y*

Allen, A., and Beetson, B. (1999). The Land Monitor Project; A Multi-agency project of the Western Australian Salinity Action Plan supported by the Natural Heritage Trust. *Proceedings of WALIS Forum 1999*, Perth, WA, March 1999. pp. 74–77. *https://landmonitor.landgate.wa.gov.au/reports/walis_1999.pdf*

Allen R.G., Tasumi, M., and Trezza, R. (2007). Satellite-Based Energy Balance for Mapping Evapotranspiration with Internalized Calibration, METRIC, Model. *Journal of Irrigation and Drainage Engineering*, 133, 380–394.

Anderson, M.C., Norman, J.M., Mecikalski, J.R., Otkin, J.A., and Kustas, W.P. (2007). A climatological study of evapotranspiration and moisture stress across the continental United States based on thermal remote sensing: 2. Surface moisture climatology. *Journal of Geophysical Research*, 112, D1111.

Bastiaanssen, W.G.M. (2000). SEBAL-based sensible and latent heat fluxes in the irrigated Gediz Basin, Turkey. *Journal of Hydrology*, 229, 87–100.

Bastiaanssen, W.G.M., Menenti, M., Feddes, R.A., and Holtslag, A.A.M. (1998). A remote sensing surface energy balance algorithm for land (SEBAL). 1. Formulation. *Journal of Hydrology*, 212–213, 198–212.

Bayarjargal, Y., Karnieli, A., Bayasgalan, M., Khudulmur, S., Gandush, C., and Tucker, C.J. (2006). A comparative study of NOAA–AVHRR derived drought indices using change vector analysis. *Remote Sensing of Environment*, 105, 9–22.

Bicheron, P., and Leroy, M. (1999). A method of biophysical parameter retrieval at global scale by inversion of a vegetation reflectance model. *Remote Sensing of Environment*, 67, 251–266.

Blaikie, S.J., Chacko, E.K., Lu, P., and Muller, W.J. (2001). Productivity and water relations of field-grown cashew: a comparison of sprinkler and drip irrigation. *Australian Journal of Experimental Agriculture*, 41, 663–673.

Bradley, B.A., Jacob, R.W., Hermance, J.F., and Mustard, J.F. (2007). A curve fitting procedure to derive inter-annual phenologies from time series of noisy satellite NDVI data. *Remote Sensing of Environment*, 106(2), 137–145.

Broich, M., Huete, A., Tulbure, M. G., Ma, X., Xin, Q., Paget, M., Restrepo-Coupe, N., Davies, K., Devadas, R., and Held, A. (2014). Land surface phenological response to decadal climate variability across Australia using satellite remote sensing. *Biogeosciences*, 11, 5181–5198. *https://doi.org/10.5194/bg-11-5181-2014*

Broich, M., Huete, A., Paget, M., Ma, X., Tulbure, M., Restrepo Coupe, N., Evans, B., Beringer, J., Devadas, R., Davies, K., and Held, A. (2015). A spatially explicit land surface phenology data product for science, monitoring and natural resources management applications. *Environmental Modelling and Software*, 64, 191–204. *https://doi.org/10.1016/j.envsoft.2014.11.017*

Brown, T.B., Zimmermann, C., Panneton, W., Noah, N., and Borevitz, J. (2012). High-resolution, time-lapse imaging for ecosystem-scale phenotyping in the field. Ch 7 in *High Throughput Phenotyping in Plants: Methods and Protocols, Methods in Molecular Biology*. (Ed: Normanly, J.). Springer-Science, New York. ISBN 978-1-61779-995-2

Brown, T.B., Hultine, K.R., Steltzer, H., Denny, E.G., Denslow, M.W.,Granados, J., Henderson, S., Moore, D., Nagai, S., SanClements, M., Sánchez-Azofeifa, A., Sonneta, O., Tazik, D., and Richardson, A.D. (2016). Using phenocams to monitor our changing Earth: toward a global phenocam network. *Frontiers in Ecology and the Environment*, 14(2), 84–93. doi:*10.1002/fee.1222*

Budyko, M.I. (1958). *The heat balance of the earth's surface*. U.S. Dept. of Commerce, Washington.

Budyko, M.I. (1974). *Climate and life*. Academic, New York.

Carter, G.A., and Knapp, A.K. (2001). Leaf optical properties in higher plants: linking spectral characteristics to stress and chlorophyll concentration. *American Journal of Botany*, 88(4), 677–684. *https://doi.org/10.2307/2657068*

Cleland, E.E., Chuine, I., Menzel, A., Mooney, H.A., and Schwartz, M.D. (2007). Shifting plant phenology in response to global change. *Trends in Ecology and Evolution*, 22(7), 357–365. *https://doi.org/10.1016/j.tree.2007.04.003*

Cocke, A.E., Fulé, P.Z., and Grouse, J.E. (2005). Comparison of burn severity assessments using Differenced Normalised Burn Ratio and ground data. *International Journal of Wildland Fire*, 14, 189–198. doi:*10.1071/WF04010*

Coops, N.C., Waring, R.H., Wulder, M.A., and White, J.C. (2009). Prediction and assessment of bark beetle-induced mortality of lodgepole pine using estimates of stand vigour derived from remotely sensed data. *Remote Sensing of Environment*, 113, 1058–1066.

Craze, B., and Hamilton, G.J. (1991). Soil physical properties. In *Soils - Their Properties and Management*. (Eds: Charman, P.E.V., and Murphy, B.W.) Sydney University Press, South Melbourne. pp 147–164.

Curran, P.J. (1989). Remote sensing of foliar chemistry. *Remote Sensing of Environment*, 30, 271–278.

Curran, P.J., Dungan, J.L., and Gholz, H.L. (1990). Exploring the relationship between reflectance red-edge and chlorophyll content in slash pine. *Tree Physiology*, 7, 33–48.

Curran, P.J., Dungan, J.L., Macler, B.A., and Plummer, S.E. (1991). The effect of a red leaf pigment on the relationship between red edge and chlorophyll concentration. *Remote Sensing of Environment*, 35, 69–76.

Curran, P.J., Windham, W.R., and Gholz, H.L. (1995). Exploring the relationship between reflectance red edge and chlorophyll concentration in slash pine leaves. *Tree Physiology*, 15, 203–206.

Curran, P.J., Kupiec, I.A., and Smith, G.M. (1997). Remote sensing the biochemical composition of a slash pine canopy. *IEEE Transactions on Geoscience and Remote Sensing*, 35, 415–420.

Danaher, T., Scarth, P., Armston, J., Collett, L., Kitchen, J., and Gillingham, S. (2011). Remote Sensing of Tree-Grass Systems: The Eastern Australian Woodlands. In *Ecosystem Function in Savannas: Measurement and Modelling at Landscape to Global Scales*. (Eds: Hill, M.J., and Hanan, N.P.) CRC Press, Boca Raton, pp. 175–194.

Devlin, R.M., and F.H. Witham, F.H. (1983). *Plant physiology*. 4th Edn. Willard Grant Press, Boston, 497 p.

Donohue, R.J., Roderick, M.L., and McVicar, T.R. (2007). On the importance of including vegetation dynamics in Budyko's hydrological model. *Hydrology and Earth System Sciences*, 11, 983–995.

Donohue, R.J., Roderick, M.L., McVicar, T.M. (2008). Deriving consistent long-term vegetation information from AVHRR reflectance data using a cover-triangle based framework. *Remote Sensing of Environment*, 112, 2938–2949.

Donohue, R.J., McVicar, T.R., Roderick, M.L. (2009). Climate-related trends in Australian vegetation cover as inferred from satellite observations, 1981–2006. *Global Change Biology*, 15, 1025–1039.

Donohue, R.J., Roderick, M.L., McVicar, T.R. (2010a). Can dynamic vegetation information improve the accuracy of Budyko's hydrological model? *Journal of Hydrology*, 390, 23–34.

Donohue, R.J., McVicar, T.R., and Roderick, M.L. (2010b). Assessing the ability of potential evaporation formulations to capture the dynamics in evaporative demand within a changing climate. *Journal of Hydrology*, 386, 186–197. *http://doi.org/10.1016/j.jhydrol.2010.03.020*

Doody, T., and Benyon, R. (2011). Quantifying water savings from willow removal in Australian streams. *Journal of Environmental Management*, 92, 926–935.

Elmore, A.J., Mustard, J.F., and Manning, S.J. (2003). Regional patterns of plant community response to changes in water: Owens Valley, California. *Ecological Applications*, 13(2), 443–460.

Everitt, J.H., Richardson, A.J., and Gaussman, H.W. (1985). Leaf reflectance—nitrogen-chlorophyll relations in buffelgrass. *Photogrammetric Engineering and Remote Sensing*, 51, 463–466.

FAO (2020). *Earth Observation* webpage, UN Food and Agriculture Organisation website: *http://www.fao.org/giews/earthobservation/index.jsp?lang=en*

Filella, I., and Peñuelas, J. (1994). The red edge position and shape as indicators of plant chlorophyll content, biomass and hydric status. *International Journal of Remote Sensing*, 15, 1459–1470.

Fritz, S., See, L., Bayas, J.C.L., Waldner, F., Jacques, D., Becker-Reshef, I., Whitcraft, A., Baruth, B., Bonifacio, R., Crutchfield, J., Rembold, F., Rojas, O., Schucknecht, A., Van der Velde, M., Verdin, J., Wu, B., Yan, N., You, L., Gilliams, S., Mücher, S., Tetrault, R., Moorthy, I., and McCallum, I. (2019). A comparison of global agricultural monitoring systems and current gaps. *Agricultural Systems*, 168, 258–272. *https://doi.org/10.1016/j.agsy.2018.05.0*

Gill, T., Johansen, K., Phinn, S., Trevithick, R., Scarth, P., and Armston, J. (2017). A method for mapping Australian woody vegetation cover by linking continental-scale field data and long-term Landsat time series, *International Journal of Remote Sensing*, 38(3), 679–705. Doi: *10.1080/01431161.2016.1266112*

Gill, T., Johansen, K., Scarth, P., Armston, J., Trevithick, R., and Flood, N. (2018). Persistent Green Vegetation Fraction. Ch 8 in *Effective Field Calibration and Validation Practices: A practical handbook for calibration and validation satellite and model-derived terrestrial environmental variables for research and management*. A TERN Landscape Assessment Initiative, NCRIS. ISBN 978-0-646-94137-0.

Gitelson, A.A., Keydan, G.P., and Merzlyak, M.N. (2006). Three-band model for non-invasive estimation of chlorophyll assessment in higher plant leaves. *Journal of Plant Physiology*, 160, 271–282.

Gitelson, A.A., Chivkunova, O.B., and Merzlyak, M.N. (2009). Nondestructive estimation of anthocyanins and chlorophylls in anthocyanic leaves. *American Journal of Botany*, 96(10), 1861–1868.

Glenn, E.P., Huete, A.R., Nagler, P.L., Hirschboeck, K.K., and Brown, P. (2007). Integrating remote sensing and ground methods to estimate evapotranspiration. *Critical Reviews in Plant Sciences*, 26, 139–168.

Glenn, E.P., Nagler, P.L., and Huete, A.R. (2010). Vegetation Index methods for estimating evapotranspiration by remote sensing. *Surveys in Geophysics*, 31(6), 531–555. doi:*10.1007/s10712-010-9102-2*

Glenn, E., Doody, T.M., Guerschman, J.P., Huete, A.R., King, E.A., McVicar, T.R., van Dijk, A.I.J.M., van Niel, T.G., Yebra, M., and Zhang, Y. (2011). Actual evapotranspiration estimation by ground and remote sensing methods: the Australian experience. *Hydrological Processes*, 25(26), 4103–4116. doi:*10.1002/hyp.8391*

Goward, S. N., Markham, B., Dye, D.G., Dulaney, W., and Yang, A.J. (1991). Normalized difference vegetation index measurements from the Advanced Very High Resolution Radiometer. *Remote Sensing of Environment*, 35, 257–277.

Guerschman, J.P., Van Dijk, A.I.J.M., Mattersdorf, G., Beringer, J., Hutley, L.B., Leuning, R., Pipunic, R.C., and Sherman, B.S. (2009). Scaling of potential evapotranspiration with MODIS data reproduces flux observations and catchment water balance observations across Australia. *Journal of Hydrology*, 369, 107–119.

Hall, F. G., Townshend, J. R., and Engman, E. T. (1995). Status of remote sensing algorithms for estimation of land surface state parameters. *Remote Sensing of Environment*, 51, 138–156.

Hermance, J.F., Jacob, R.W., Bradley, B.A., and Mustard, J.F. (2007). Extracting phenological signals from multiyear AVHRR NDVI time series: Framework for applying high-order annual splines with roughness damping. *IEEE Transactions on Geoscience and Remote Sensing*, 45(10), 3264–3276.

Holden, Z.A., Smith, A.M.S., Morgan, P., Rollins, M.G., and Gessler, P.E. (2005). Evaluation of novel thermally enhanced spectral indices for mapping fire perimeters and comparisons with fire atlas data. *International Journal of Remote Sensing*, 26(21), 4801–4808.

Horler, D.N.H., Dockray, M., and Barber, J. (1983). The red edge of plant leaf reflectance. *International Journal of Remote Sensing*, 4(2), 273–288. doi: *10.1080/01431168308948546*

Huete, A.R., Didan, K., Shimabukuro, Y.E., Ratana, P., Saleska, S.R., Hutyra, L.R., Yang, W., Nemani, R.R., and Myneni, R. (2006). Amazon rainforests green-up with sunlight in dry season. *Geophysical Research Letters*, 33(6), L06405. *https://doi.org/10.1029/2005GL025583*.

Idso, S.B., Jackson, R.D., Pinter, P.J., Jr., Reginato, R.J., and Hatfield, J.L. (1981). Normalizing the Stress-Degree-day parameter for environmental variability. *Agricultural Meteorology*, 24, 45–55. *https://dx.doi.org/10.1016/0002-1571(81)90032-7*

Irmak, S., Haman, D.Z., and Bastug, R. (2000). Determination of Crop Water Stress Index for Irrigation Timing and Yield Estimation of Corn. *Agronomy Journal*, 92, 1221–1227.

Jackson, R.D., Idso, S.B., Reginato, R.J., and Printer, P.J. (1981). Canopy temperature as a crop water stress indicator. *Water Resources Research*, 17(4), 1133–1138.

Jackson, R.D., William, P.K., and Choudhury, B.J. (1988). A Reexamination of the Crop Water Stress Index. *Irrigation Science*, 9, 309–317.

Jacquemoud, S. Verhoef, W., Baret, F., Bacour, C., Zarco-Tejada, P.J., Asner, G.P., François, C., and Ustin, S.L. (2009). PROSPECT plus SAIL models: a review of use for vegetation characterization. *Remote Sensing of Environment*, 113, S56–S66.

Johansen, K., Gill, T., Trevithick, R., Armston, J., Scarth, P., Flood, N., and Phinn, S. (2012). Landsat based Persistent Green-Vegetation Fraction for Australia. *Proceeding of 16th Australasian Remote Sensing and Photogrammetry Conference*. Melbourne.

Jolly, W.M., Nemani, R., and Running, S.W. (2005). A generalized, bioclimatic index to predict foliar phenology in response to climate. *Global Change Biology*, 11, 619–632. doi:*10.1111/j.1365-2486.2005.00930.x*

Jones, H.G., Stoll, M., Santos, T., de Sousa, C., Chaves, M.M., and Grant, O.M. (2002). Use of infrared thermography for monitoring stomatal closure in the field: application to grapevine. *Journal of Experimental Botany*, 53(378), 2249–2260. doi:*10.1093/jxb/erf083*

Jönsson, P., and Eklundh, L. (2002). Seasonality extraction by function fitting to time-series of satellite sensor data. *IEEE Transactions on Geoscience and Remote Sensing*, 40(8), 1824–1832.

Jönsson, P., and Eklundh, L. (2004). TIMESAT—a program for analysing time-series of satellite sensor data. *Computers and Geosciences*, 30, 833–845.

Kaduk, J., and Heimann, M. (1996). A prognostic phenology model for global terrestrial carbon cycle models. *Climate Research*, 6, 1–19.

Kalma, J.D., McVicar, T.R., McCabe, M.F. (2008). Estimating land surface evaporation: A review of methods using remotely sensed surface temperature data. *Surveys in Geophysics*, 29, 421–469.

Key, C.H., and Benson, N.C. (2002). *Measuring and remote sensing of burn severity*. USGS Wildland Fire Workshop, 31 October to 3 November 2000. Los Alamos, NM. USGS Open-File Report 02-11.

Key, C.H., and Benson, N.C. (2006). *Landscape Assessment: Sampling and Analysis Methods*. USDA Forest Service, Rocky Mountain Research Station General Tech. Rep. RMRS-GTR-164-CD. Odgen, UT.

Khan, S., Hafeez, M., Abbas, A., and Ahmad, A. (2009). Spatial assessment of water use in an environmentally sensitive wetland. *Ambio*, 38, 157–165.

King, E.A., van Niel, T.G., van Dijk, A.I.J.M., Wang, Z., Paget, M.J., Raupach, T., Guerschman, J., Haverd, V., McVicar, T.R., Miltenberg, I., Raupach, M.R., Renzullo, L.J., and Zhang, Y. (2011). *Actual Evapotranspiration Estimates for Australia Intercomparison and Evaluation*. Water for a Healthy Country National Research Flagship, CSIRO, Canberra.

Kogan, F.N. (1997). Global Drought Watch from Space. *Bulletin of the American Meteorological Society*, 78(4), 621–636.

Landgate (2019). *Landmonitor* webpage, Landgate website: *https://landmonitor.landgate.wa.gov.au/home.php*

Lhermitte, S., Verbesselt, J., Verstraeten, W.W., and Coppin, P. (2011). A comparison of time series similarity measures for classification and change detection of ecosystem dynamics. *Remote Sensing of Environment*, 115, 3129–3152.

Li, F.Q., and Lyons, T.J. (1999). Estimation of regional evapotranspiration through remote sensing. *Journal of Applied Meteorology*, 38, 1644–1654.

Long, D., Longuevergne, L., and Scanlon, B.R. (2014). Uncertainty in evapotranspiration from land surface modelling, remote sensing, and GRACE satellites. *Water Resources Research*, 50(2), 1131–1151. *https://doi.org/10.1002/2013WR014581*

Lu, H., Raupach, M.R., McVicar, T.R., and Barrett, D.J. (2003). Decomposition of vegetation cover into woody and herbaceous components using AVHRR NDVI time series. *Remote Sensing of Environment*, 86, 1–18.

Ma, X., Huete, A., Yu, Q., Coupe, N.R., Davies, K., Broich, M., Ratana, P., Beringer, J., Hutley, L.B., Cleverly, J., Boulain, N., Eamus, D. (2013). Spatial patterns and temporal dynamics in savanna vegetation phenology across the North Australian Tropical Transect. *Remote Sensing of Environment*, 139, 97–115. doi:*10.1016/j.rse.2013.07.030*

Mahlein, A.K., Oerke, E.C., Steiner, U., and Dehne, H.W. (2012). Recent advances in sensing plant diseases for precision crop protection. *European Journal of Plant Pathology*, 133(1), 197–209. doi:*10.1007/s10658-011-9878-z*

McFarlane, D.J., and Wallace, J.F. (2019). *Measuring native vegetation extent and condition using remote sensing technologies—a review and identification of opportunities*. The Western Australian Biodiversity Science Institute, Perth.

McKenzie, N.J., Grundy, M.J., Webster, R., and Ringrose-Voase, A.J. (Eds) (2008). *Guildelines for Surveying Soil and Land Resources*. Australian Soil and Land Survey Handbook Series. CSIRO Publishing, Melbourne.

McVicar, T.R., and Jupp, D.L.B. (2002). Using covariates to spatially interpolate moisture availability in the Murray-Darling Basin: a novel use of remotely sensed data. *Remote Sensing of Environment*, 79, 199–212.

McVicar, T.R., Van Niel, T.G., Li, L.T., Hutchinson, M.F., Mu, X.M., Liu, Z.H. (2007). Spatially Distributing Monthly Reference Evapotranspiration and Pan Evaporation Considering Topographic Influences. *Journal of Hydrology*, 338, 196–220.

McVicar, T.R., Donohue, R.J., O'Grady, A.P., and Li, L. (2010). *The effects of climatic changes on plant physiological and catchment ecohydrological processes in the high-rainfall catchments of the Murray-Darling Basin: A scoping study*. Water for a Healthy Country National Research Flagship, CSIRO. 95 p.

Meroni, M., Colombo, R., and Panigada, C. (2004). Inversion of a radiative transfer model with hyperspectral observations for LAI mapping in popular plantations. *Remote Sensing of Environment*, 92(2), 195–206.

Mildrexler, D.J., Zhao, M., Heinsch, F.A., and Running, S.W. (2007). A New Satellite Based Methodology for Continental Scale Disturbance Detection. *Ecological Applications*, 17, 235–250.

Mildrexler, D.J., Zhao, M., and Running, S.W. (2009). Testing a MODIS Global Disturbance Index across North America. *Remote Sensing of Environment*, 113(10), 2103–2117. doi:*10.1016/j.rse.2009.05.016*

Miller, J.D., and Thode, A.E. (2007) Quantifying burn severity in a heterogeneous landscape with a relative version of the delta Normalised Burn Ratio (dNBR). *Remote Sensing of Environment*, 109, 66–80.

Miller, J.R., Wu, J., Boyer, M.G., Belanger, M., and Hare, E.W. (1991). Seasonal patterns in leaf reflectance red-edge characteristics. *International Journal of Remote Sensing*, 12, 1509–1523.

Mosleh, M.K., Hassan, Q.K., and Chowdhury, E.H. (2015). Application of remote sensors in mapping rice area and forecasting its production: A review. *Sensors*, 15.1, 769–791.

Moulin, S., Kergoat, L., Viovy, N., and Dedieu, G. G. (1997). Global-scale assessment of vegetation phenology using NOAA/AVHRR satellite measurements. *Journal of Climate*, 10, 1154–1170.

Myneni, R.B., Keeling, C.D., Tucker, C.J., Asrar, G., and Nemani, R.R. (1997). Increased plant growth in the northern high latitudes from 1981 to 1991. *Nature*, 386, 698–702.

NCST (2009). *Australian Soil and Land Survey Field Handbook*. 3rd edn. National Committee on Soil and Terrain (Australia). CSIRO Publishing, Melbourne. 246 p.

Nemani, R., Hashimoto, H., Votava, P., Melton, F., Wang, W., Michaelis, A., Mutch, L., Milesi, C., Hiatt, S., and White, M. (2009). Monitoring and forecasting ecosystem dynamics using the Terrestrial Observation and Prediction System (TOPS). *Remote Sensing of Environment*, 113, 1497–1509.

NOAA STAR (2019). STAR—*Global Vegetation Health Products: Background and Explanation* webpage, NOAA Center for Satellite Applications and Research website: *https://www.star.nesdis.noaa.gov/smcd/emb/vci/VH/VH-Syst_10ap30.php*

Nouri, H., Beecham, S., Kazemi, F., Hassanti, A.M., and Anderson, S. (2013). Remote sensing techniques for predicting evapotranspiration from mixed vegetated surfaces. *Hydrology and Earth System Sciences*, 10, 3879–3925.

Ol'dekop, E. M. (1911). On evaporation from the surface of river basins. *Transactions on meteorological observations*, 4. Tartu, Estonia.

Ollinger, S.V., and Smith, M.L. (2005). Net Primary Production and Canopy Nitrogen in a temperate forest landscape: an analysis using imaging spectrometry, modeling and field data. *Ecosystems*, 8, 760–778.

Orta, A.H., Erdem, Y., and Erdem, T. (2003). Crop water stress index for horticulture. *Scientia Horticulturae*, 98(2), 121–120.

Park, S., Ryu, D., Fuentes, S., Chung, H., Hernández-Montes, E., and O'Connell, M. (2017). Adaptive Estimation of Crop Water Stress in Nectarine and Peach Orchards Using High-Resolution Imagery from an Unmanned Aerial Vehicle (UAV). *Remote Sensing*, 9, 828. *https://doi.org/10.3390/rs9080828*

Poblete-Echeverría, C., Espinace, D., Sepúlveda-Reyes, D., Zúñiga, M., and Sanchez, M. (2017). Analysis of crop water stress index (CWSI) for estimating stem water potential in grapevines: comparison between natural reference and baseline approaches. *Acta Horticulturae*, 1150, 189–194. *https://doi.org/10.17660/ActaHortic.2017.1150.27*

Potter, C., Tan, P.N., Steinbach, M., Klooster, S., Kumar, V., Myneni, R., and Genovese, V. (2003). Major disturbance events in terrestrial ecosystems detected using global satellite data sets. *Global Change Biology*, 9(7), 1005–1021.

Price, J.C. (1992b). Estimating Leaf Area Index from Remotely Sensed Data. *Proceedings of IGARSS '92*, Houston. Vol. 1. pp. 1500–1502.

Privette, J.L., Emery, W.J., and Schimel, D.S. (1996). Inversion of a vegetation reflectance model with NOAA AVHRR data. *Remote Sensing of Environment*, 58, 187–200.

Raupach, M.R., Briggs, P.R., Haverd, V., King, E.A., Paget, M.J., and Trudinger, C.M. (2009). *Australian Water Availability Project (AWAP), CSIRO Marine and Atmospheric Research Component: Final Report for Phase 3*. CAWCR Technical Report No. 013, Canberra, Australia. 67 p.

Reed, B.C., Brown, J.F., VanderZee, D., Loveland, T.R., Merchant, J.W., and Ohlen, D.O. (1994) Measuring phenological variability from satellite imagery. *Journal of Vegetation Science*, 5, 703–714.

Restrepo-Coupe, N., Huete, A., and Davies, K. (2018). Satellite Phenology Validation. Ch 9 in *Effective Field Calibration and Validation Practices: A practical handbook for calibration and validation satellite and model-derived terrestrial environmental variables for research and management*. A TERN Landscape Assessment Initiative, NCRIS. ISBN 978-0-646-94137-0.

Richardson, A.D., Black, T.A., Ciais, P., Delbart, N., Friedl, M.A., Gobron, N., Hollinger, D.Y., Kutsch, W.L., Longdoz, B., Luyssaert, S., Migliavacca, M., Montagnani, L., Munger, J.W., Moors, E., Piao, S., Rebmann, C., Reichstein, M., Saigusa, N., Tomelleri, E., Vargas, R., Varlagin, A. (2010). Influence of spring and autumn phenological transitions on forest ecosystem productivity. *Philosophical Transactions of the Royal Society B Biological Sciences*, 365, 3227–3246. doi:*10.1098/rstb.2010.0102*

Rock, B.N., Hoshizaki, T., and Miller, J.R. (1988). Comparison of *in situ* and airborne spectral measurements of the blue shift associated with forest decline. *Remote Sensing of Environment*, 24, 109–127.

Rojas, O. (2015). *Protocol for Country-Level ASIS: Calibration and National Adaptation Process*. Technical report. Food and Agriculture Organization of the United Nations.

Rojas, O., Vrieling, A., Rembold, F. (2011). Assessing drought probability for agricultural areas in Africa with coarse resolution remote sensing imagery. *Remote Sensing of Environment*, 115, 343–352. *http://dx.doi.org/10.1016/j.rse.2010.09.006*.

Roman-Cuesta, R.M., Retana, J., Gracia, M., and Rodriguez, R. (2005) A quantitative comparison of methods for classifying burned areas with LISS-III imagery. *International Journal of Remote Sensing*, 26(9), 1979–2003.

Scarth, P., Gillingham, S., and Muir, J. (2008). Assimilation of spectral information and temporal history into a statewide woody cover change classification. *Proceedings of the 14th Australasian Remote Sensing and Photogrammetry Conference*. Darwin, Australia.

Schreiber, P., (1904). Über die Beziehungen zwischen dem Niederschlag und der Wasserführung der Flüsse in Mitteleuropa. *Meteorologische Zeitschrift*, 21, 1904.

Silberstein, R., Held, A., Hatton, T., Viney, N., and Sivapalan, M. (2001). Energy balance of a natural jarrah (*Eucalyptus marginata*) forest in Western Australia: Measurements during the spring and summer. *Agricultural and Forest Meteorology*, 109, 79–104. doi:*10.1016/S0168-1923(01)00263-5*

Singh, A. (1989). Digital change detection techniques using remotely-sensed data. *International Journal of Remote Sensing*, 10, 989–1003.

Smith, A.M.S., Drake, N.A., Wooster, M.J., Hudak, A.T., Holden, Z.A., and Gibbons, C.J. (2007). Production of Landsat ETM+ reference imagery of burned areas within Southern African savannas: comparison of methods and application to MODIS. *International Journal of Remote Sensing*, 28(12), 2753–2775.

Su, Z., Yacob, A., Wen, J., Roerink, G., He, Y., Gao, B., Boogaard, H., and van Diepen, C. (2003). Assessing relative soil moisture with remote sensing data: Theory, experimental validation, and application to drought monitoring over the North China Plain. *Physics and Chemistry of the Earth* (B), 28(1-3), 89–101.

Taghvaeian, S., Chávez, J.L., and Hansen, N.C. (2012). Infrared Thermometry to Estimate Crop Water Stress Index and Water Use of Irrigated Maize in Northeastern Colorado. *Remote Sensing*, 4, 3619–3637. doi:*10.3390/rs4113619*

Teillet, P.M., Saleous, N.E., Hansen, M.C., Eidenshink, J.C., Justice, C.O., and Townshend, J.R.G. (2000). An evaluation of the global 1-km AVHRR land dataset. *International Journal of Remote Sensing*, 21, 1987–2021.

TERN AusCover (2014). *Ecosystem Disturbance Index* webpage, Terrestrial Ecosystem Research Network website: *http://www.auscover.org.au/purl/modis-disturbance-index*

TERN Australia (2018). *Effective Field Calibration and Validation Practices: A practical handbook for calibration and validation satellite and model-derived terrestrial environmental variables for research and management*. A TERN Landscape Assessment Initiative, NCRIS. ISBN 978-0-646-94137-0. *https://www.tern.org.au/NEW-CalVal-handbook-for-remote-sensing-bgp4370.html*

Thomas, J.R., and Gausman, H.W. (1977). Leaf reflectance vs leaf chlorophyll and carotenoid concentrations for eight crops. *Agronomy Journal*, 69, 799–811.

Trigg, S., and Flasse, S. (2000). Characterizing the spectral-temporal response of burned savannah using *in situ* spectroradiometry and infrared thermometry. *International Journal of Remote Sensing*, 21(16), 3161–3168.

Tucker, C.J., Slayback, D.A., Pinzon, J.E., Los, S.O., Myneni, R.B., and Taylor, M.G. (2001). Higher northern latitude normalized difference vegetation index and growing season trends from 1982 to 1999. *International Journal of Biometeorology*, 45, 184–190.

Turrell, F.M., Weber, J.R., and Austin, S.W. (1961). Chlorophyll content and reflection spectra for citrus leaves. *Botanical Gazette*, 123, 10–16.

Ustin, S.L., Smith, M.O., Jacquemoud, S., Verstraete, M.M., and Govaerts, Y. (1998). Geobotany: vegetation mapping for earth sciences. In: *Manual of Remote Sensing: Remote Sensing for the Earth Sciences. Vol. 3*, 3rd Edn. Ed. A.N. Rencz. John Wiley, New York. pp 189–248.

Ustin, S.L., Jacquemoud, S., Zarco-Tejada, P.J., and Asner, G.P. (2004). Remote sensing of the environment: state of the science and new directions, in Manual of Remote Sensing. *Volume 4: Remote Sensing for Natural Resource Management and Environmental Monitoring* (Ed: S.L. Ustin). John Wiley and Sons. pp. 679–729.

Van Dijk, A.I.J.M. (2010). *AWRA Technical Report 3. Landscape Model (version 0.5) Technical Description*. WIRADA / CSIRO Water for a Healthy Country Flagship, Canberra.

Van Dijk, A.I.J.M., and Renzullo, L.J. (2011). Water resource monitoring systems and the role of satellite observations. *Hydrological and Earth System Sciences*, 15, 39–55.

Van Niel, T.G., McVicar, T.R., Roderick, M.L., Van Dijk, I.J.M., Renzullo, L.J., and Van Gorsel, E. (2011). Correcting for systematic error in satellite-derived latent heat flux due to assumptions in temporal scaling: Assessment from flux tower observations. *Journal of Hydrology*, 409, 140–148. doi:*10.1016/j.jhydrol.2011.08.011*

Verbesselt, J., Robinson, A., Stone, C., and Culvenor, D. (2009). Forecasting tree mortality using change metrics derived from MODIS-satellite data. *Forest Ecology and Management*, 258, 1166–1173.

Verbesselt, J., Hyndman, R., Newnham, G., and Culvenor, D. (2010). Detecting trend and seasonal changes in satellite image time series. *Remote Sensing of Environment*, 114 (1), 106–115.

White, M.A., and Nemani, R.R. (2006). Real-time monitoring and short-term forecasting of land surface phenology. *Remote Sensing of Environment*, 104, 43–49.

White, M.A., Thornton, P.E., and Running, S.W. (1997). A continental phenology model for monitoring vegetation responses to interannual climatic variability. *Global Biogeochemical Cycle*, 11, 217–234.

White, M.A., Nemani, R.R., Thornton, P.E., and Running, S.W. (2002). Satellite evidence of phenological differences between urbanized and rural areas of the eastern United States deciduous broadleaf forest. *Ecosystems*, 5, 260–273.

Yao, Y., Liang S., Qin Q., and Wang, K. (2010). Monitoring drought over the conterminous United States using MODIS and NCEP Reanalysis-2 data. *Journal of Applied Meteorology and Climatology*, 49(8), 1665–1680. doi:*10.1175/2010JAMC2328.1*.

Yebra, M., Van Dijk, A.I.J.M., Leuning, R., Huete, A., and Guerschman, J.P. (2013). Evaluation of optical remote sensing to estimate actual evapotranspiration and canopy conductance. *Remote Sensing of Environment*, 129, 250–261.

Yin, H., Udelhoven, T., Fensholt, R., Pflugmacher, D., and Hoster, P. (2012). How Normalised Difference Vegetation Index (NDVI) Trends from Advanced Very High Resolution Radiometer (AVHRR) and Système Probatoire d'Observation de la Terre VEGETATION (SPOT VGT) Time Series Differ in Agricultural Areas: An Inner Mongolian Case Study. *Remote Sensing*, 4, 3364–3389.

Zarco-Tejada, P.J., Miller, J.R., Mohammed, G.H., and Noland. T.L. (2000). Chlorophyll fluorescence effects on vegetation apparent reflectance. I. Leaf-level measurements and model simulation. *Remote Sensing of Environment*, 74, 582–595.

Zeng, L., Wardlow, B.D., Xiang, D., Hu, S., and Li, D. (2020). A review of vegetation phenological metrics extraction using time-series, T multispectral satellite data. *Remote Sensing of Environment*, 238, 111511. *https://doi.org/10.1016/j.rse.2019.111511*

Zhang, X., Friedl, M.A., Schaaf, C.B., Strahler, A.H., Hodges, J.C.F., Gao, F., Reed, B.C., and Huete, A. (2003). Monitoring vegetation phenology using MODIS. *Remote Sensing of Environment*. 84, 471–475.

Zhang, X., Goldberg, M.D., and Yu, Y. (2012). Prototype for monitoring and forecasting fall foliage coloration in real time from satellite data. *Agricultural and Forest Meteorology*, 158–159, 21–29. doi:*10.1016/j.agrformet.2012.01.013*

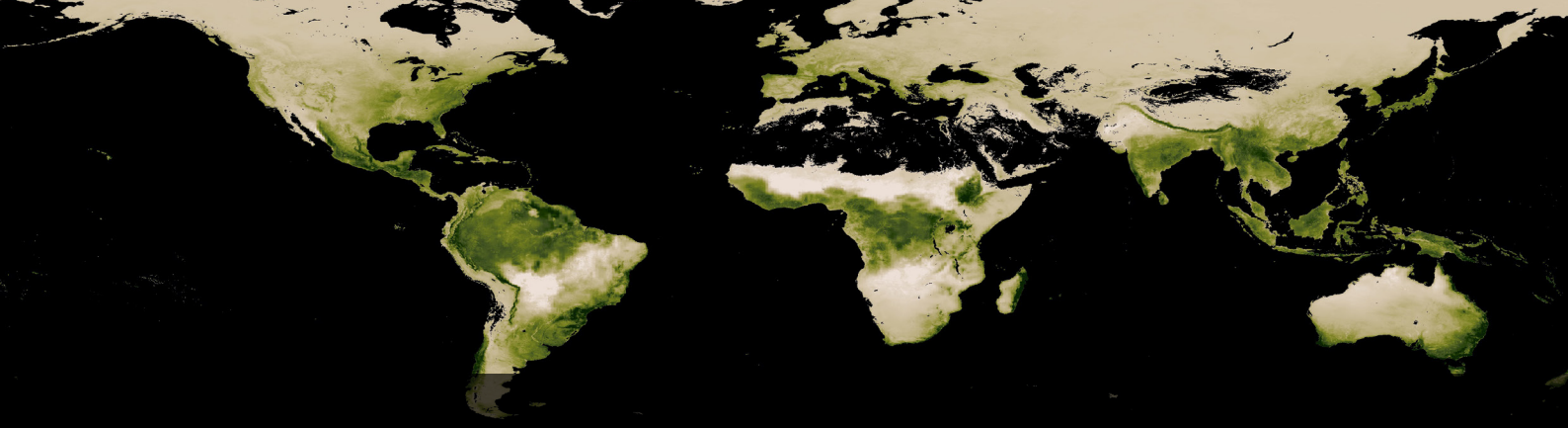

10 Modelling

EO imagery offers a unique perspective for landscape scale analyses with a range of resolutions (see Volumes 1 and 2). For terrestrial vegetation, this perspective allows ecophysiological information relating to photosynthetic activity, biomass, productivity, water content, phenology, soil moisture, and nutrient status to be acquired and analysed consistently and repeatedly over large areas. Modelling based on EO datasets aims to use this perspective to improve our understanding of environmental processes, with the ultimate goal of predicting the future environmental impact of changes in current conditions.

Depending on the underlying questions to be answered, models can be simple or complex (Robins *et al.*, 2003). All models approximate reality, and greater functionality means greater complexity. Understandably, more complex questions require more complex models, which deliver more detailed explanations of the underlying processes and drivers. More complex models also require more data and more processing, as well as a deeper understanding of the resource being modelled.

However, models only estimate parameters—they do not supply absolute answers (Robins *et al.*, 2003). As complexity increases, systematic error, resulting from overly simplified assumptions, decreases, but calibration error, due to poorly fitted parameters, increases (Zhang *et al.*, 2002; see Figure 10.1). As a general rule, a model should only be as complex as it needs to be to achieve its defined goal. The reliability of modelled results can be determined by comparison with historical measurements, field validation (see Volume 2D), or sensitivity analysis, where input parameters and/or assumptions are varied slightly to assess the extent of change in modelled values (Robins *et al.*, 2003).

The most appropriate criteria for evaluating a model will depend on its purpose. For example, a common example of an applied plant productivity model based on EO datasets is a crop yield model, which typically correlates a relevant EO-based statistic (such as vegetation greenness—see Section 8.1.1) with a ground-based measure of crop productivity.

Such models, which are intended to reduce the risks inherent in food supply, need to be reliable, objective, timely, consistent, simple, and cost-effective (see Sections 10.2.2 and 12).

In this section, we will revisit the EO analysis framework, which underlies modelling of terrestrial vegetation (see Section 10.1), then introduce three commonly used scales of EO-based modelling for vegetated landscapes (see Section 10.2). EO datasets are also valuable for terrestrial ecosystem models to define model drivers, validate model results, and quantify uncertainty (Pasetto *et al.*, 2018).

Figure 10.1 Modelling error

As complexity increases, systematic error decreases and calibration error increases.

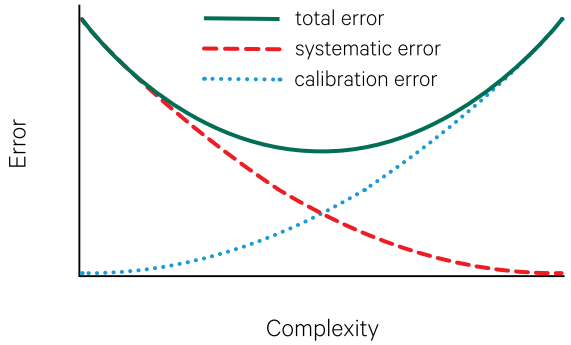

Source: Zhang *et al.* (2002) Figure 5

Background image: MODIS global composite showing Net Primary Productivity (NPP) for November 2016, with deeper shades of green indicating higher productivity to a maximum of 6.5 gC/m^2/day. (Note: the vertical extent of this composite image has been clipped and the aspect ratio changed.)
Source: NASA Earth Observations. (Retrieved from *https://neo.sci.gsfc.nasa.gov/view.php?datasetId=MOD17A2_M_PSN*)

10.1 Modelling Considerations

Modelling allows future conditions to be predicted for a given scenario. It can also be used to predict the impact of potential changes in current conditions, such as resource characteristics, land uses, or management policies. Volume 2A—Section 2.3 introduces three generic modelling approaches that can be used in the context of EO:

- empirical or analytical models—simple relationships, such as regression analysis, between empirical measurements of surface attributes with EO measurements;
- semi-empirical or semi-analytical models—use prior knowledge, including assumptions and generalisations, to tailor an EO model to a specific situation; and
- physics-based models—rely on physical relationship between the surface attributes and the EO measurements. These models are generally more flexible, transferable and computationally intensive.

Figure 10.2 Measurement and analysis of image features

Interpreting imagery from EO sensors is an indirect process, whereby a measurement model is used to transform EO observations to measurements of some measurable property, and a structure model is used to relate those measurements to application-specific attributes. Forward modelling is indicated by red arrows and inverse modelling by blue arrows.

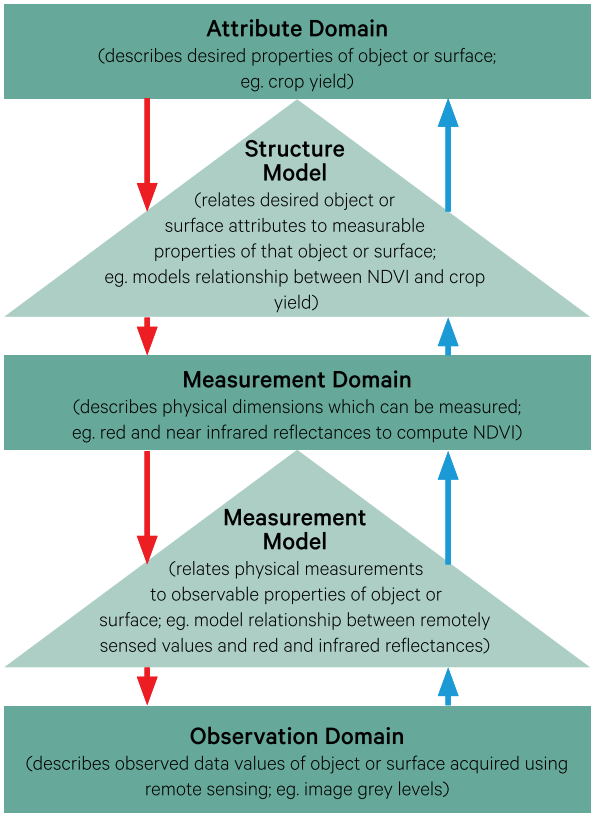

Adapted from: Harrison and Jupp (1989) Figure 33

Some fundamental concepts regarding modelling in the context of EO datasets are introduced in Volumes 2D and 2E. In Section 10.1.1 below we review those concepts that are particularly relevant to modelling of terrestrial vegetation then consider interpolation and extrapolation of data (see Section 10.1.2), appropriate scaling (see Section 10.1.3), and spatial patterns (see Section 10.1.4).

10.1.1 Underlying EO model

As detailed in Volume 1A—Section 1 and Volume 2D—Section 1.1, the relationship between a feature in an EO image and its quantifiable attributes of the Earth's surface is an indirect one. This relationship is illustrated in Figure 10.2 and implicitly involves two modelling stages:

- the measurement model—relates EO-based observations to empirical measurements. Examples of measurements models include image calibration processes that correct for radiometric and geometric distortions in the acquired EO dataset (see Volume 1B—Section 2, Volume 2A—Section 3, Volume 2B, and Volume 2D—Section 3). The measurement model also accounts for distortions in image values resulting from the interaction between the imaging process and the landscape and its component features (see Volume 1B—Section 3 and Volume 2D—Section 1); and
- the structure model—relates calibrated EO-based measurements to attributes of the Earth's surface (see Volumes 2C, 2D and 2E). This section describes approaches to developing structure models using EO datasets for terrestrial vegetation.

The downward and upward arrows in Figure 10.2 distinguish between forward (red) and inverse (blue) models (see Volume 2A—Section 2.3 and Volume 2D—Section 14.3). Forward models infer EO measurements from surface attributes. For example, a forward model for terrestrial vegetation may use measurements of specific plant attribute(s) to model its EO reflectance or emission value(s). Conversely, inverse models infer surface attributes from EO measurements. An example of an inverse model for terrestrial vegetation would be to use EO reflectance or emission value(s) to model specific plant attribute(s).

A model is a tool that helps us predict changes in a particular system before they happen. Models are used for all sorts of purposes: from trying to predict the weather, to trying to predict the stock market. (Robins et al., 2003)

10.1.2 Interpolation and extrapolation

Interpolation estimates new, intermediate data points within a discrete set of known values, whereas extrapolation estimates new data points beyond the range of existing points. Methods for spatial and temporal interpolation of time series datasets were discussed in Volume 2D. Interpolation methods assume strong correlation between the known data points.

Extrapolation assumes some continuity, correspondence, or parallelism between the known and the unknown. Predictive models extrapolate known values in time by assuming that current trends will continue into the future. Spatial extrapolation may be valid where the relationship between a spatially limited dataset and a dataset covering a larger area is known, and this relationship can be used to infer likely values of the limited data into the larger area. In ecology, spatial extrapolation generally follows the framework outlined in Figure 10.3.

When working with sparse spatial datasets, modellers can either interpolate the data before modelling or apply the model to the sparse data then interpolate the modelled results. These approaches are often called 'interpolate then calculate' (IC) and 'calculate then interpolate' (CI) respectively. For very sparse spatial datasets, such as meteorological records, CI has been shown to be more robust (Stein *et al.*, 1991).

Spatially rich (or comprehensive) and temporally stable datasets, such as elevation, can also be used as a covariate when extrapolating sparse datasets. McVicar and Jupp (2002) used AVHRR imagery as a covariate for meteorological records to map moisture availability over the Murray-Darling Basin (MDB). Normalised Difference Temperature Index (NDTI) was derived from temperature data acquired at spatially insolated meteorological stations then extrapolated using covariates derived from AVHRR imagery and interpolated meteorological data (see Section 9.5). Using the EO imagery ensured 'stability' in the interpolated results and avoided direct interpolation, with its inherent problems, from sparse meteorological data (see Volume 2D—Section 13.3).

Figure 10.3 Basic framework for extrapolation in ecology

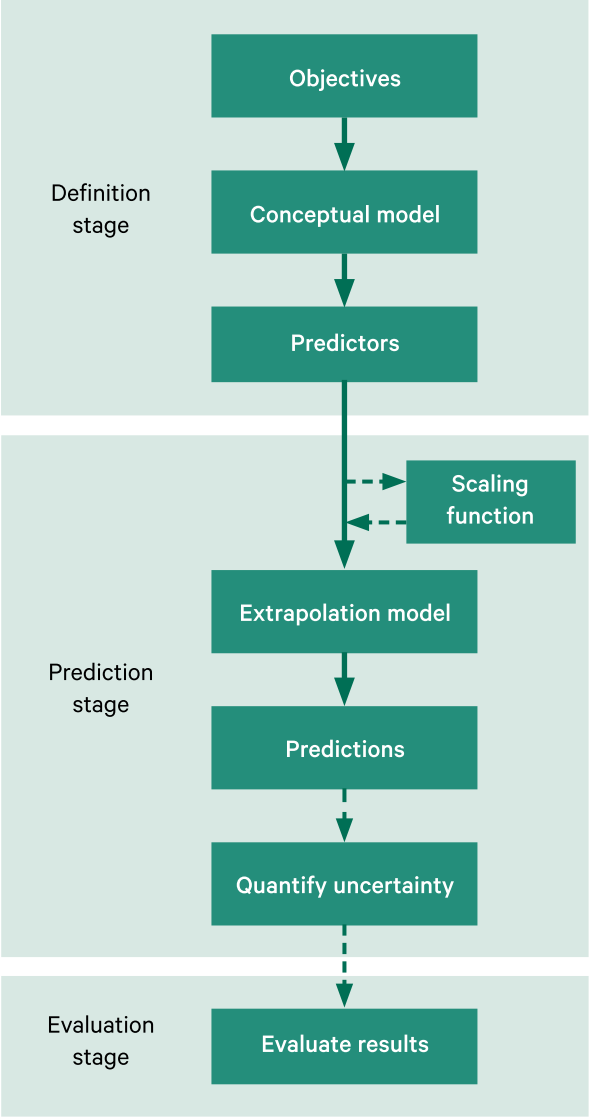

Adapted from: Miller *et al.* (2004) Figure 1

Many environmental variables influence the signals that reach a remote sensor. If we wish to use these remotely sensed signals to estimate environmental variables then we need to ensure that the number of remotely sensed signals is greater than the number of environmental signals that are causing those signals to vary.
(Curran, 2001)

10.1.3 Scaling

An understanding of scale is important for all landscape mapping, monitoring, and modelling activities. Mismatches in the scales of measurement, estimation and prediction for landscape features have long presented challenges to cartographers, geographers, and EO scientists (Gallant *et al.*, 2008) and are particularly relevant to image selection for EO analyses. To address such problems, multi-scale approaches have been proposed for many applications (see Volume 2D—Section 1.4; see Figure 3.1), and EO archives now offer a spatially and temporally extensive range of datasets for terrestrial vegetation studies (see Volume 2D—Section 2). Selection of the most appropriate EO imagery for a given application is considered in Volume 2D—Section 1.2 and the concept of 'intrinsic scale' is discussed in Volume 2D—Section 1.4. In some cases, it may be appropriate to increase the temporal frequency of time series datasets by using image blending methods (Emelyanova *et al.*, 2013; see Volume 2D—Excursus 6.2).

Upscaling and downscaling of EO datasets are described in Volume 2D—Section 4.3. As geographical terms:

- upscaling implies moving up the scale hierarchy, that is, to a larger extent with less detail; and
- downscaling implies moving down the scale hierarchy, that is, to a smaller extent with more detail.

Similarly, with appropriate prerequisites and constraints, terrestrial vegetation models can be developed for a particular spatial scale then upscaled to cover larger areas. For example, a model for the diffusion of CO_2 from the atmosphere to the interior of a single leaf has been aggregated to simulate CO_2 transfer at the scale of vegetated canopies, or even the entire globe (Williams *et al.*, 2004). Such scaling has enabled a range of EO-based models to be incorporated in regional and global vegetation studies (see Section 10.2.3).

Scaling up—extrapolating monitoring from small plots to larger, more representative landscapes—is a significant challenge. Ludwig *et al.* (2007) propose a five-step procedure that is based on scaling to determine when EO analyses require additional data sources to assess landscape health (see Figure 10.4). This procedure defines the focal scale as 'the size of the area over which the core problem occurs', then uses smaller and larger scales to check for cross-scale interactions in landscape patterns and processes.

Figure 10.4 Scaling procedure

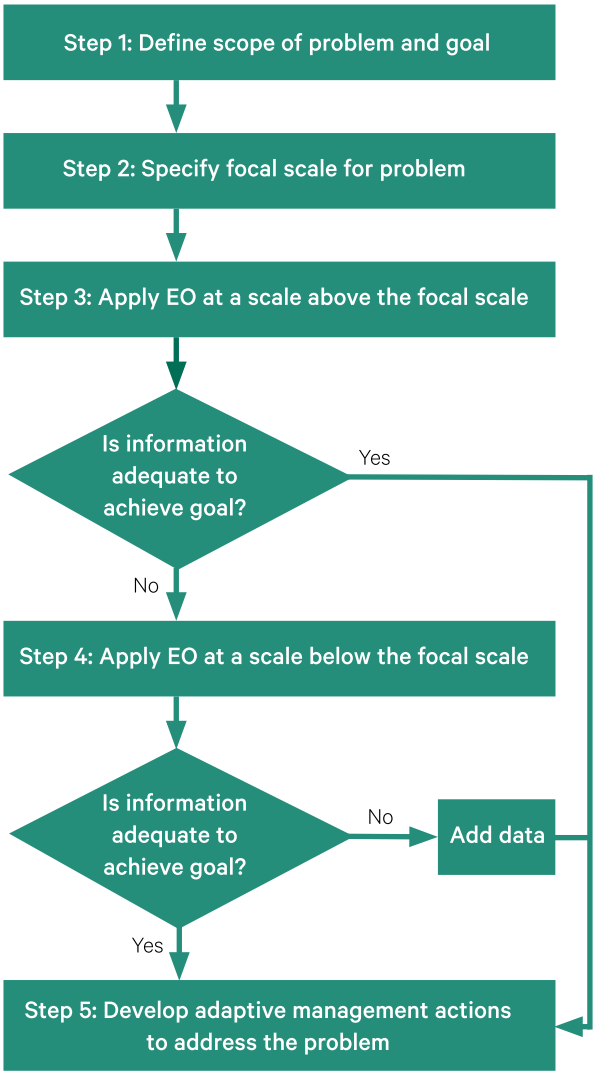

Adapted from: Ludwig *et al.* (2007) Figure 1

Increasing the complexity of a model does not necessarily lead to a more accurate model and it is essential that model complexity matches the availability of data.
(Zhang et al., 2002)

10.1.4 Spatial patterns

From a statistical viewpoint, any given landscape is merely one manifestation of numerous, equally probable, landscapes that may have occurred at a particular location. This perspective enables stochastic models to be developed, which generate potential variations for each actual landscape or ecosystem. For example, if a specific process operates in the landscape, particular patterns are more likely to occur (Fortin *et al*., 2003). In Figure 10.5, three hypothetical landscapes are shown with varying spatial patterns, but the same number of patches and the same edge density. Differentiation between these landscape patterns obviously requires consideration of pattern alignment and scale.

The growing body of geographical data, principally from EO sources, provides the opportunity to examine, identify, and quantify spatial processes within actual landscapes. The increasing archives of time series datasets further enables such processes to be analysed over time (see Volume 2D). A number of statistical tools have been proposed to understand these processes, including multivariate statistics, ordination methods, spatial statistics, geostatistics, and landscape pattern indices (Fortin *et al*., 2003). Spatial pattern analysis essentially attempts to quantify the composition and configuration of landscape components (Remmel and Csillag, 2003). Some specific EO methods to map and monitor landscape patterns are described in Sections 8 and 9.

Figure 10.5 Hypothetical landscape patterns

These simulated landscapes of two components have the same number of patches, contagion, landscape shape index, edge density, and proportion of components, yet display different degrees of spatial autocorrelation.

a. Random—purely random stochastic pattern

b. Noodles—elongated narrow patches

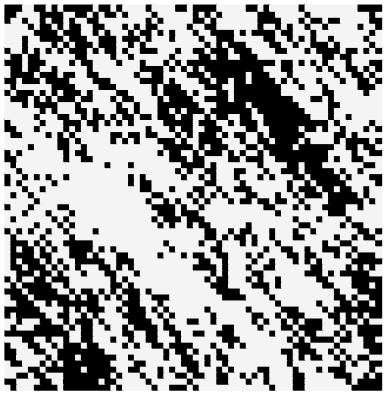

c. Bumpy—larger contiguous patches

Adapted from: Remmel and Csillag (2003) Figure 1

Landscapes are spatially heterogeneous areas characterised by a mosaic of patches that differ in size, shape, contents, and history. When spatial heterogeneity is considered, the explicit treatment of scale becomes necessary and hierarchies emerge. Landscape ecology is the science of studying and improving the relationship between spatial pattern and ecological processes on a multitude of scales and organisational levels. (Wu, 2013)

10.2 EO-based Models for Terrestrial Vegetation

A diverse range of modelling approaches have been proposed for EO datasets. Many models have been developed to determine plant productivity for various applications, including food crops and pasture (see Sections 11 to 15), forestry (see Sections 16), carbon sequestration (see Section 17), and fire management (see Section 18). Others have been developed to estimate crop water requirements (see Section 13), fuel moisture (see Section 18) and biodiversity risk (see Section 19). The following sub-sections introduce selected approaches that are particularly relevant to studies of terrestrial vegetation at three broad spatial scales:

- leaf models (see Section 10.2.1);
- plant productivity models (see Section 10.2.2); and
- global and regional models (see Section 10.2.3).

10.2.1 Leaf models

The structure, composition and functions of plant leaves are introduced in Section 4. Of particular relevance to EO is the interaction between leaves and the ambient EMR (see Section 4.3). The optical properties of leaves are directly related to their biochemical composition (primarily pigments), enabling EO datasets to be used to estimate leaf pigment concentrations for both individual leaves and canopies using either:

- statistical models based on spectral indices, regression relationships, or machine learning (see Section 8); or
- radiative transfer models (see Volume 1B—Section 5) for:
  - leaves, which simulate spectral reflectance and transmittance based on leaf biochemistry, such as the popular PROSPECT model (Jacquemoud and Baret, 1990); and
  - canopies, which (for known optical properties of leaf and soil, vegetation architecture, and acquisition conditions) simulate spectral and bidirectional reflectance (Féret *et al*., 2017), such as SAIL (Scattering by Arbitrary Inclined Leaves; Verhoef, 1984, 1985; derived from the one-dimensional model by Suits, 1972).

A number of physical and mathematical models have been developed to simulate the spectral consequences of variations in leaf biochemical and physical composition. Some of these are detailed in OPTICLEAF (2020) and reviewed by Ustin *et al*. (2004) and Jacquemoud and Ustin (2019). Jacquemoud and Ustin (2014) describe computer simulations models for leaves in terms of six categories (ordered by increasing complexity) as summarised in Table 10.1. Only the radiative transfer models may be iteratively inverted to derive leaf anatomical or biochemical components from spectral data (Jacquemound and Ustin, 2001). For example, the contribution of chlorophyll, water, dry matter, and structure to leaf spectral properties was simulated by Ceccato *et al*. (2001) and Bacour *et al*. (2002) using the PROSPECT model.

As well as furthering our understanding of leaf optical properties, leaf models have been integrated with canopy models. For example, PROSAIL combines the PROSPECT leaf model with the canopy model SAIL (Baret *et al*., 1992; Jacquemoud *et al*., 2009). PROSPECT requires input parameters for leaf structure and biochemical content to simulate directional-hemispherical reflectance and transmittance for the wavelength range 400–2500 nm whereas SAIL models canopy architecture from bidirectional reflectance measurements. This integrated modelling approach allowed the precise relationship between the reflectance from a canopy and its biophysical and biochemical properties to be examined and quantified for specific wavelength ranges. These models are used operationally in precision agriculture to monitor crop growth, allowing fertiliser application to be restricted to areas of lowered productivity (see Section 12.6). In natural vegetation canopies, such models enable mapping of ecosystem functionality, vegetation health, and fuel moisture (Jacquemoud *et al*., 2009). For example, Punalekar *et al*. (2018) used proximal hyperspectral data from Sentinel-2A 10 m imagery with the radiative transfer model PROSAIL to estimate LAI and biomass for dairy farms in southern England, and reported that this approach outperformed NDVI-based estimates.

Ecosystem models that elegantly represent salient ecological processes deliver the capacity to monitor and predict change, estimate risks of ecosystem collapse and explore alternative future management scenarios. Such models can be parameterised, initiated, or validated with remote sensing data. … Remote sensing data therefore has great potential for parameterizing a wide variety of ecosystem models, and is increasingly being used to assess the skill of models at reproducing ecosystem dynamics.
(Murray et al., 2018)

Table 10.1 Leaf models

Model	Models	Example
Plate Model (Allen *et al.*, 1969)	Cumulative hemispherical reflectance/refraction from internal and external surfaces of leaf blades modelled as stacks of absorbing plates	PROSPECT (Jacquemoud and Baret, 1990; Baret and Fourty, 1997; Féret *et al.*, 2008, 2017)
Compact Spherical Particle Model	Radiative transfer model to simulate optical properties of conifer needles based on interaction of light with powders (Melamed,1963)	LIBERTY (Leaf Incorporating Biochemistry Exhibiting Reflectance and Transmittance Yields; Dawson *et al.*, 1998)
N-flux Models	Leaf as slabs of absorbing and diffusing material	Two-flux model (Kubelka and Munk, 1931; Allen and Richardson, 1968; Vargas, 1999; Cordon and Lagorio, 2007);
		Four-flux model (Fukshansky *et al.*, 1991; Martinez von Remisowsky *et al.*, 1992; Richter and Fukshansky, 1996)
Radiative Transfer Equation	Optical Scattering Model based on leaf as turbid homogeneous plate	LEAFMOD (Leaf Experimental Absorptivity Feasibility MODel; Ganapol *et al.*, 1998)
Stochastic Approach	Radiative transfer simulation based on optical properties on leaf tissues simulated by Markov chain	LFMOD1 (Tucker and Garatt, 1977)
		SLOP (Stochastic model for Leaf Optical Properties; Maier *et al.*, 1999)
Ray Tracing Models	Complex Internal Leaf Structure model based on internal leaf structure and optical constants of constituents	RAYTRAN (Govaerts and Verstraete, 1998)

Adapted from categories in Jacquemoud and Ustin (2014)

10.2.2 Plant productivity models

Plant productivity indicates the rate at which plants store energy—and accumulate biomass—via photosynthesis (see Section 7.4). While a wide range of environmental factors can impact the productivity of terrestrial vegetation (see Sections 1.1 and 4 to 7), the major factors influencing plant growth can be grouped in terms of:

- defining factors—determine the potential growth under ideal conditions, but include factors that we cannot directly control such as CO_2, radiation, temperature, and crop characteristics (physiology, phenology, and canopy architecture);
- limiting factors—indicate the attainable growth under controlled conditions. These factors can be controlled to increase production, such as water and nutrients; and
- reducing factors—impact actual growth under real conditions, such that production is reduced if these factors (such as weeds, diseases, pests, and pollutants) are not controlled (Bouman *et al.*, 1996).

Plant productivity models have traditionally attempted to differentiate between these factors on the basis of their impact on plant production and the extent to which they can be 'controlled'. A commonly encountered model to track changes in particular types of terrestrial vegetation is a crop simulation model (CSM). A CSM uses information about physics, plant physiology, and ecology to mimic crop growth and development using a range of parameters (such as weather, soil conditions, and management practices) in order to forecast various crop productivitiy metrics (such as yield, date of maturity for harvest, and fertiliser efficiency). More sophisticated models, tailored to specific crops, can advise on fertiliser and irrigation requirements during crop growth and assess the expected impact of different scenarios on crop yield, such as changes in sowing dates, crop varieties or weather conditions. These models typically rely on historical records and ground measurements but can only practically be tested at a limited number of ground sites. All such modelling predictions are made under the assumption that the crop will not be impacted by unforeseen factors, such as severe frosts or extreme weather events, before harvest.

A well-established CSM that was developed in Australia is the Agricultural Production Systems sIMulator (APSIM) modelling framework (APSIM, 2020; Keating *et al.*, 2003). APSIM comprises plant, soil, animal, and climate models that simulate relevant processes and, where appropriate, their responses to various interactions and external stresses (Holzworth *et al.*, 2014, 2018). EO-based modelling of crop growth is often integrated with CSM to spatially and temporally extrapolate the results from field test sites, thus constraining crop forecasts by current growing conditions (FAO, 2016; see Section 11.2). For example, APSIM is used by agricultural monitoring systems, such as Yield Prophet, a decision support tool which models the growth of major grain crops (BCG, 2017), and Graincast™ (see Excursus 12.1). Another operational cropping system model is WOFOST (World Food STudies; de Wit *et al.*, 2019; see Section 11.6), which is implemented in the European MARS crop yield forecasting system.

Specific EO-based models to estimate plant productivity have been developed for Australian cereal and horticultural crops (see Section 11), including sugar cane (see Volume 1B—Excursus 1.1), peanuts (see Volume 1B—Excursus 9.1), and tree crops (see Section 12.7), as well as pasture growth (see Section 13), forest biomass (see Section 16), and carbon dynamics (see Section 17). For example, the AussieGRASS model combines EO-based water balance and plant growth models to forecast pasture growth (see Excursus 10.1). This type of model is used by governments and industries to manage climatic influences, such as drought, on grazing lands (Nikolova *et al*., 2013).

From modest beginnings in the mid-1900s, agricultural systems models have greatly benefitted from the confluence of growing environmental awareness, increased global multidisciplinary cooperation, and significant improvements in data acquisition and processing technologies (Jones *et al*., 2017). Advanced models now relate biophysical and meteorological processes to economic and ecological outcomes, and dynamically estimate the impacts of various land management scenarios on agricultural resources from local to global scales (FAO, 2017; see Section 11).

10.2.3 Global and regional models

A wide variety of models relying on EO datasets have been developed to monitor terrestrial vegetation at regional and global scales. Large scale monitoring of our planet is closely related to the concept of Earth being an essentially closed system, which comprises four integrated spheres (atmosphere, hydrosphere, geosphere, and biosphere; see Excursus 1.2 and Volume 1A—Section 4.1). These spheres exchange energy and matter via four fundamental cycles (energy, water, earth, and carbon; see Volume 1A—Section 4.2). This global view enables a multidisciplinary approach to understanding Earth systems and their processes in a range of spatial and temporal scales. A sufficient network of *in situ* sensors to monitor these systems and processes is impractical in terms of both cost and time, leaving EO datasets as the only feasible, relevant, and cost-effective source for this information. Examples of global models include Terrestrial Ecosystem Models (TEM) and General Circulation Models (GCM).

TEM primarily track vegetation productivity in terms of Net Primary Productivity (NPP; see Section 7.4). Specific examples of these models, in the context of carbon dynamics, are given in Section 17. Major categories of TEM are:

- Dynamic Global Vegetation Models (DGVM)—process-based models of global biogeochemical fluxes and vegetation dynamics to better understand terrestrial biosphere processes and their interactions with other Earth spheres (Prentice *et al*., 2007; Sitch *et al*., 2008; Boit *et al*., 2019); and
- Production Efficiency Models (PEM)—describe the productivity of vegetation by assuming a linear relationship between canopy photosynthesis and the fraction of absorbed photosynthetically active radiation (fAPAR) to monitor NPP (Monteith, 1972, 1977).

GCM simulate the global climate system by representing physical circulation patterns and processes in and between the atmosphere, ocean, cryosphere, and the land surface. Relevant components of GCM include:

- energy balance models—link climate and biophysical models to describe energy and mass transfers between the Earth's surface and the atmosphere (see Section 7.5). Examples of Land Surface Models (LSM) include soil-vegetation-atmosphere transfer (SVAT) models and surface energy balance (SEB) models; and
- water balance models—describe the movement of water through the water cycle (see Section 7.6). An Australian implementation of EO-based water balance modelling to support regulatory monitoring of water resources is summarised in Excursus 10.2.

These large scale models have a multidisciplinary focus. Their development has only been possible in recent decades with the advent of high speed computing and sophisticated algorithms to manage large datasets. DGVM, for example, integrate research from plant geography, biophysics, vegetation dynamics, plant physiology and biogeochemisty, and anthropogenic activities, to simulate the interactions between ecosystem state variables, ecosystem processes, and driving variables (Prentice *et al*., 2007; see Figure 10.6).

Figure 10.6 Modular structure of Dynamic Global Vegetation Models

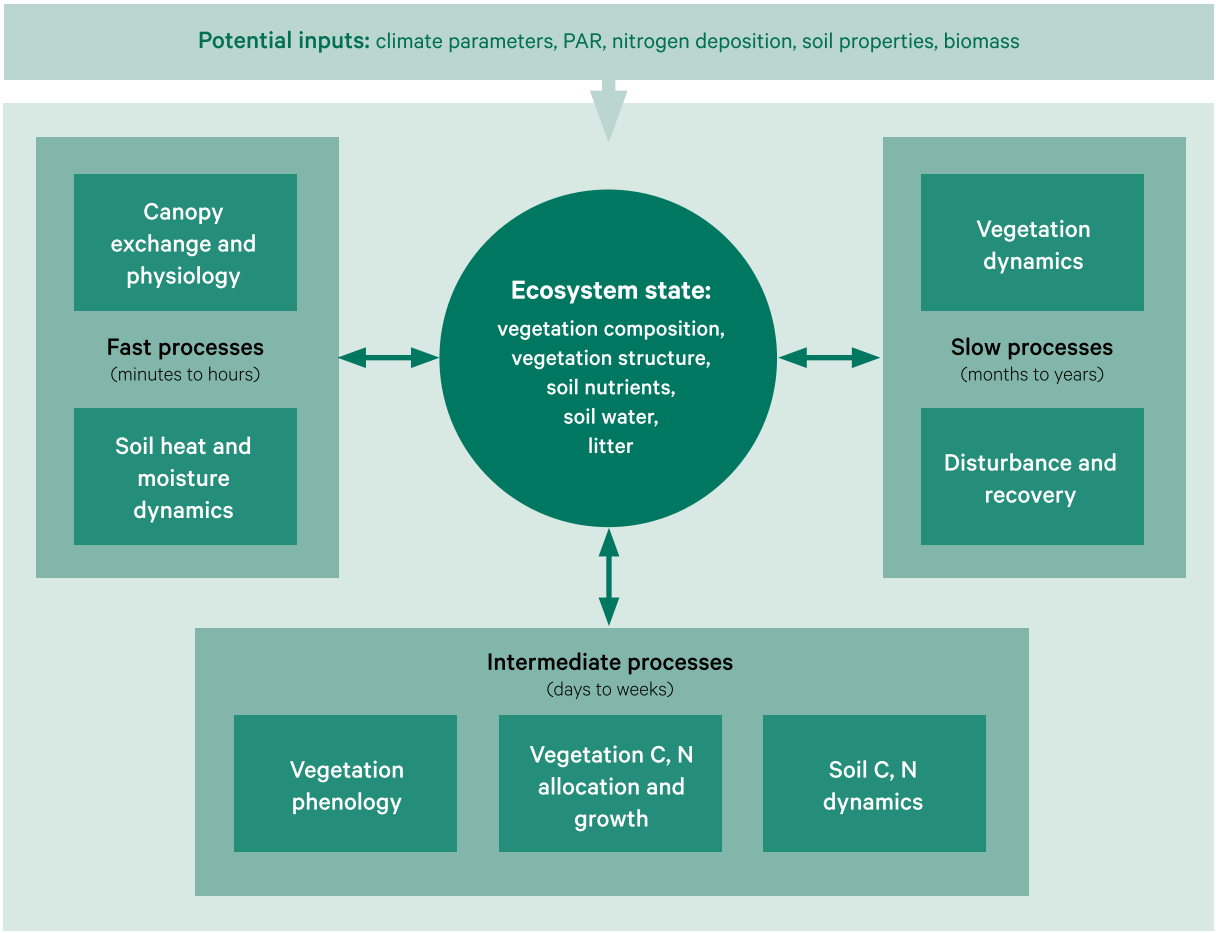

Adapted from: Prentice *et al.* (2007) Figure 15.2

Dynamic Global Vegetation Models (DGVMs) offer the possibility of integrating large amounts of geospatial data to quantify and project a large range of ecological variables important for ecosystem service provisioning under future scenarios.
(Boit et al., 2019)

Excursus 10.1—AussieGRASS

Source: John Carter, Queensland Department of Environment and Science; *https://www.longpaddock.qld.gov.au/aussiegrass/*
Further information: McKeon and Carter (2015); DSITI (2015)

The AussieGRASS model monitors key biophysical processes associated with pasture growth (such as degradation and recovery) at regional scales (for example, local government areas, or bioregions). Its companion system, FORAGE, extends the implementation to property and paddock scale (Zhang and Carter, 2018; see Section 15.4). AussieGRASS provides time series of rainfall and pasture growth information, as well as projections for the season ahead. The projections are useful for forage budgeting, assessing the impacts of drought, and forecasting bushfire risk.

AussieGRASS is an advanced spatial water balance and plant growth model, producing output on a daily timestep across Australia (Carter *et al*., 2000). The model was initially built on the point scale GRASP (GRASS Production) simulation model (Rickert *et al*., 2000), using the SILO climate data base (Jeffrey *et al*., 2001), and calibrated using satellite data, plus over 600,000 field pasture biomass observations (Hassett *et al*., 2000). The AussieGRASS system has been operational on an Australia-wide basis since 1996.

Within the AussieGRASS framework, GRASP is run on a daily timestep (1890–current). The observed climate data are spatially interpolated to construct gridded datasets on a regular 0.05° × 0.05° grid (approximately 5×5 km) across Australia. The spatial framework includes inputs of key climate variables (rainfall, evaporation, temperature, vapour pressure, and solar radiation), soil and pasture types, tree and shrub cover, domestic livestock, and other herbivore numbers. In simulating continental pasture response to climate variability, calibration has relied on EO-based datasets to estimate green vegetation cover, coupled with extensive ground truthing across Australia since 1994 (Hassett *et al*. 2000).

Various forms of validation have been conducted with independent datasets (Carter *et al*., 2003) and inter-model comparisons (McKeon and Carter, 2015). EO-based input datasets include fire scars, tree density, flooded area, and land use maps. Fractional photosynthetic and non-photosynthetic cover (Scarth *et al*., 2010) from the entire Australian Landsat TM archive is used as a primary EO calibration dataset (see Excursus 8.3). This is supplemented with data from radar and gravity satellites for soil moisture, plus EO of chlorophyll fluorescence and atmospheric CO_2.

Many challenges exist with modelling the EO signals due to issues like time and space scaling. These include sensed versus modelled depth of soil water, variations in mass to cover relationships with vegetation structure, obscured cover, and using a single observation at one time in the day versus a modelled daily integral.

AussieGRASS provides a platform for translating seasonal climate outlooks into estimates of future plant growth, including the impacts of total grazing pressure from domestic stock and other herbivores. It is a powerful tool for value-adding to climate information, as it takes into account current condition (e.g. soil moisture, ground cover, nitrogen status, and grass basal cover) to provide a probabilistic view of plant growth for the coming three-month period. AussieGRASS outputs are also being increasingly used for various environmental analyses, such as drought analysis, estimating plant net primary production for soil carbon mapping, providing soil moisture as an initial condition for air pollution models, analysing how stock numbers influence the potential amount of biomass which can be burnt, analysing conditions suitable for dust storms, and estimating the impact of removing tree cover on deep soil water infiltration.

Excursus 10.2—Water Resources Assessment

Further Information: BoM (2008, 2013); Frost *et al.* (2018)

Water is a very precious resource in Australia (see Volume 3B). Current and accurate information about the distribution, storage, availability, and use of water is necessary to manage this resource, especially at regional and continental scales. The Water Act 2007 assigned responsibility to the Bureau of Meteorology (BoM) for regular reporting on the status and usage of Australia's water resources (BoM, 2008). These statutory functions include:

- issuing national water information standards;
- collecting and publishing water information;
- conducting regular national water resources assessments;
- publishing an annual National Water Account;
- providing regular water availability forecasts;
- advising on matters relating to water information; and
- enhancing understanding of Australia's water resources.

These assessments help water resource managers and policy makers understand past and present practices governing water management. In line with the National Water Initiative (NWI), which outlines "a shared commitment by governments to increase the efficiency of Australia's water use, leading to greater certainty for investment and productivity, for rural and urban communities and for the environment" (DAWR, 2018), they also help to formulate future policies and practices. The Australian Water Resource Assessment Modelling System (AWRAMS) has been developed to generate two major information products for this purpose (see Section 10.3):

- the annual National Water Account (NWA: *www.bom.gov.au/water/nwa*)—water accounting for nationally significant urban and rural regions, including information on water stores and flows, water rights, and water use (BoM, 2013; see Section 20.5); and
- Australian Water Resources Assessment (AWRA) reports—daily, monthly and annual estimates of water balance parameters (Hafeez *et al.*, 2015).

The AWRA system is a spatial water resources monitoring system to capture and model the major water flow processes at regional and national scales. It comprises two integrated modules which collectively represent the Australian terrestrial water cycle:

- AWRA-L—models hydrological processes between the atmosphere and the landscape, including groundwater (Van Dijk, 2010; Viney *et al.*, 2015; Frost *et al.*, 2018); and
- AWRA–R—a conceptual hydrological model that simulates processes between the atmosphere and rivers (Dutta *et al.*, 2015).

This operational system includes major water storages and the fluxes in and between component models based on a 0.05° grid. AWRA-L simulates the daily flow of water through each grid cell in the landscape, with the hydrological response of deep-rooted and shallow-rooted vegetation being modelled separately (Frost *et al.*, 2018). Inputs to AWRA-L include *in situ* datasets routinely collected by BoM, estimates from the OzFlux network (see Excursus 7.2), and parameters derived from EO time series imagery (Frost and Wright, 2018—see Figure 2 therein). Ongoing, daily AWRA-L gridded outputs include soil moisture, evapotranspiration, surface runoff, and groundwater recharge/storage/lateral flow. These parameters have also been modelled retrospectively, providing a simulation of the Australian terrestrial water cycle for over a century (Hafeez *et al.*, 2015). AWRAMS has been released for public access, including a community modelling system (AWRA CMS; see Section 10.3).

10.3 Further Information

Modelling Leaf Optical Properties

http://www.photobiology.info/Jacq_Ustin.html

Terrestrial Observation and Prediction System (TOPS)

https://ecocast.arc.nasa.gov/

Water Resource Modelling

Bureau of Meteorology: *http://www.bom.gov.au/water/index.shtml*

Australian Landscape Water Balance: *http://www.bom.gov.au/water/landscape/#/sm/Actual/day/-28.4/130.4/3/Point////2020/8/24/*

AWRA Community Modelling System (AWRA CMS): *https://github.com/awracms/awra_cms*

National Water Account (NWA): *www.bom.gov.au/water/nwa*

10.4 References

Allen, W.A., and Richardson, A.J. (1968). Interaction of light with a plant canopy. *Journal of the Optical Society of America*, 58(8), 1023–1028.

APSIM (2020). *Agricultural Production Systems sIMulator* website: *https://www.apsim.info/apsim-model/*

Bacour, C., Jacquemoud, S., Tourbier, Y., Dechambre, M., and Frangi, J.P. (2002). Design and analysis of numerical experiments to compare four canopy reflectance models. *Remote Sensing of Environment*, 79, 72–83.

Baret, F., Jacquemoud, S., Guyot, G., and Leprieur, C. (1992). Modeled analysis of the biophysical nature of spectral shifts and comparison with information content of broad bands. *Remote Sensing of Environment*, 41, 133–142.

Baret, F., and Fourty, T. (1997). Estimation of leaf water content and specific leaf weight from reflectance and transmittance measurements. *Agronomie*, 17(9-10), 455–464.

BCG (2017). *Yield Prophet* website, Birchip Cropping Group: *https://www.yieldprophet.com.au/yp/Home.aspx*

Boit, A., Sakschewski, B., Boysen, L., Cano-Crespo, A., Clement, J., Alaniz, N.G., Kok, K., Kolb, M., Langerwisch, F., Rammig, A., Sachse, R., van Eupen, M., von Bloh, W., Zemp, D.C., and Thonicke, K. (2019). Using Dynamic Global Vegetation Models (DGVMs) for Projecting Ecosystem Services at Regional Scales. In *Atlas of Ecosystem Services* (Eds: Schröter M., Bonn A., Klotz S., Seppelt R., Baessler C.). Springer, Cham. *https://doi.org/10.1007/978-3-319-96229-0_10*

BoM (2008). *The Water Act 2007 and the Bureau of Meteorology*. Bureau of Meteorology, April 2008. *http://www.bom.gov.au/water/regulations/document/water_act_2007.pdf*

BoM (2013). *The National Water Account. Companion Guide*. Bureau of Meteorology, Melbourne. *http://www.bom.gov.au/water/nwa/document/companion-guide.pdf*

Bouman, B.A.M., van Keulen, H., van Laar, H.H., and Rabbinge, R. (1996). The 'School of de Wit' crop growth simulation models: A pedigree and historical overview. *Agricultural Systems*, 52(2–3), 171–198. *https://doi.org/10.1016/0308-521X(96)00011-X*

Carter, J.O., Hall, W.B., Brook, K.D., McKeon, G.M., Day, K.A., and Paull, C.J. (2000). AussieGRASS: Australian Grassland and Rangeland Assessment by Spatial Simulation. In *Applications of seasonal climate forecasting in agricultural and natural ecosystems—the Australian experience*. (Eds. G. Hammer, N. Nicholls and C. Mitchell), Kluwer Academic Press, Netherlands. pp 229–249.

Carter, J.O., Bruget, D., Hassett, R., Henry, B., Ahrens, D., Brook, K., Day, K., Flood, N., Hall, W., McKeon, G., and Paull, C. (2003). Australian Grassland and Rangeland Assessment by Spatial Simulation (AussieGRASS) In *Science for Drought, Proceedings of the National Drought Forum 2003*. (Eds: Stone, R., and Partridge, I.). Department of Primary Industries, Queensland. pp 152–159.

Ceccato, P., Flasse, S., Tarantla, S., Jacquemoud, S., and Grégoire, J.-M. (2001). Detecting vegetation leaf water content using reflectance in the optical domain. *Remote Sensing of Environment*, 77, 22–33.

Cordon, G.B., and Lagorio, M.G. (2007). Absorption and scattering coefficients: A biophysical-chemistry experiment using reflectance spectroscopy. *Journal of Chemical Education*, 84(7), 1167–1170.

Curran, P.J. (2001). Imaging spectrometry for ecological applications. International *Journal of Applied Earth Observation and Geoinformation*, 3(4), 305–312. doi:*10.1016/S0303-2434(01)85037-6*

DAWR (2018). Department of Agriculture and Water Resources website. *National Water Initiative* webpage: *http://www.agriculture.gov.au/water/policy/nwi*

Dawson, T.P., Curran, P.J., and Plummer, S.E. (1998). LIBERTY—Modeling the Effects of Leaf Biochemical Concentration on Reflectance Spectra. *Remote Sensing of Environment*, 65, 50–60.

De Wit, A., Boogaard, H., Fumagalli, D., Janssen, S., Knapen, R., van Kraalingen, D., Supit, I., van der Wijngaart, van Diepen, K. (2019). 25 years of the WOFOST cropping systems model. *Agricultural Systems*, 168, 154–167. *https://doi.org/10.1016/j.agsy.2018.06.018*

DSITI (2015). *AussieGRASS Environmental Calculator—Product Descriptions v1.5*. Department of Science, Information Technology and Innovation, Queensland. *https://data.longpaddock.qld.gov.au/static/about/publications/pdf/agrass_product_descriptions.pdf*

Dutta, D., Kim, S., Hughes, J., Vaze, J., and Yang, A. (2015). *AWRA-R version 5.0 Technical Report*. CSIRO Land and Water, Canberra. *https://publications.csiro.au/rpr/download?pid=csiro:EP154523&dsid=DS2*

Emelyanova I.V., McVicar, T.R., Van Niel, T.G., Li, L.T., and van Dijk, A.I.J.M. (2013). Assessing the accuracy of blending Landsat-MODIS surface reflectances in two landscapes with contrasting spatial and temporal dynamics: A framework for algorithm selection. *Remote Sensing of Environment*, 133, 193–209.

FAO (2016). *Crop Yield Forecasting: Methodological and Institutional Aspects*. UN Food and Agricultural Organisation, Rome. *http://www.amis-outlook.org/fileadmin/user_upload/amis/docs/resources/AMIS_CYF-Methodological-and-Institutional-Aspects_web.pdf*

FAO (2017). *Review of the Available Remote Sensing Tools, Products, Methodologies and Data to Improve Crop Production Forecasts*. UN Food and Agriculture Organization, Rome. ISBN 978-92-5-109840-0.

Féret, J.B., François, C., Asner, G.P., Gitelson, A.A., Martin, R.E., Bidel, L.P.R., Ustin, S.L., le Maire, G., and Jacquemoud, S. (2008). PROSPECT-4 and 5: Advances in the leaf optical properties model separating photosynthetic pigments. *Remote Sensing of Environment*, 112(6), 3030–3043.

Féret, J.B., Gitelson, A.A., Noble, S.D., and Jacquemoud, S. (2017). *Remote Sensing of Environment*, 193, 204–215. doi:*10.1016/j.rse.2017.03.004*

Fortin, M.-J., Boots, B., Csillag, F., and Remmel, T.K. (2003). On the Role of Spatial Indices in Understanding Landscape Indices in Ecology. *Oikos*, 102(1), 203–212.

Frost, A.J., and Wright, D.P. (2018). *Evaluation of the Australian Landscape Water Balance model: AWRA-L v6*. Bureau of Meteorology. *http://www.bom.gov.au/water/landscape/assets/static/publications/AWRALv6_Model_Evaluation_Report.pdf*

Frost, A.J., Ramchurn, A., and Smith, A. (2018). *The Bureau's Operational AWRA Landscape (AWRA-L v6) Model: Technical description of the Australian Water Resources Assessment Landscape model version 6*. Bureau of Meteorology. *http://www.bom.gov.au/water/landscape/assets/static/publications/AWRALv6_Model_Description_Report.pdf*

Fukshansky, L., Fukshansky-Kazarinova, N., and Martinez v. Remisowsky, A. (1991). Estimation of optical parameters in a living tissue by solving the inverse problem of the multiflux radiative transfer. *Applied Optics*, 30(22), 3145–3153.

Gallant, J.C., McKenzie, N.J., and McBratney, A.B. (2008). Scale. Ch 3 in *Guidelines for Surveying Soil and Land Resources*. Australian Soil and Land Survey Handbook Series. (Eds: McKenzie, N.J., Grundy, M.J., Webster, R., and Ringrose-Voase, A.J.) CSIRO Publishing, Melbourne.

Ganapol, B.D., Johnson, L.F., Hammer, P.D., Hlavka, C.A., and Peterson D.L. (1998). LEAFMOD: a new within-leaf radiative transfer model. *Remote Sensing of Environment*, 63(2), 182–193.

Govaerts, Y., and Verstraete, M.M. (1998). Raytran: a Monte Carlo ray-tracing model to compute light scattering in three-dimensional heterogeneous media. *IEEE Transactions on Geoscience and Remote Sensing*, 36(2), 493–505.

Hafeez, F., Frost, A., Vaze, J., Dutta, D., Smith, A., and Elmahdi, A. (2015). A new integrated continental hydrological simulation system. *Water: Journal of the Australian Water Association*, 42(3), 75–82.

Harrison, B.A., and Jupp, D.L.B. (1989) *Introduction to Remotely Sensed Data: Part ONE of the microBRIAN Resource Manual*. CSIRO, Melbourne. 156 p.

Hassett, R.C., Wood, H.L., Carter, J.O., and Danaher, T.J. (2000). A field method for statewide ground-truthing of a spatial pasture growth model. *Australian Journal of Experimental Agriculture*, 40, 1069–1079.

Holzworth, D.P., Huth, N.I., deVoil, P.G., Zurcher, E.J., Herrmann, N.I., McLean, G., Chenu, K., van Oosterom, E.J., Snow, V., Murphy, C., Moore, A.D., Brown, H., Whish, J.P.M., Verrall, S., Fainges, J., Bell, L.W., Peake, A.S., Poulton, P.L., Hochman, Z., Thorburn, P.J., Gaydon, D.S., Dalgliesh, N.P., Rodriguez, D., Cox, H., Chapman, S., Doherty, A., Teixeira, E., Sharp, J., Cichota, R., Vogeler, I., Li, F.Y., Wang, E., Hammer, G.L., Robertson, M.J., Dimes, J.P., Whitbread, A.M., Hunt, J., van Rees, H., McClelland, T., Carberry, P.S., Hargreaves, J.N.G., MacLeod, N., McDonald, C., Harsdorf, J., Wedgwood, S., Keating, B.A. (2014). APSIM—evolution towards a new generation of agricultural systems simulation. *Environmental Modelling and Software*, 62, 327–350. *https://doi.org/10.1016/j.envsoft.2014.07.009*

Holzworth, D., Huth, N.I., Fainges, J., Brown, H., Zurcher, E. Cichota, R., Verrall, S., Herrmann, N.I., Zheng, B., and Snow. V. (2018). APSIM Next Generation: Overcoming Challenges in Modernising a Farming Systems Model. *Environmental Modelling and Software*, 103, 43–51. *https://doi.org/10.1016/j.envsoft.2018.02.002*

Jacquemoud, S., and Baret, F. (1990). PROSPECT: A Model of Leaf Optical Properties Spectra. *Remote Sensing of Environment*, 34, 75–91.

Jacquemoud, S., and Ustin, S.L. (2001). Leaf Optical Properties: A State of the Art. *Proceedings of 8th International Symposium Physical Measurements and Signatures in Remote Sensing*. pp 223–232. Aussois (France), 8-12 January, 2001. CNES.

Jacquemoud, S., Verhoef, W., Baret, F., Bacour, C., Zarco-Tejada, P.J., Asner, G.P., Francois, C., and Ustin, S.L. (2009). PROSPECT + SAIL Models: a review of use for vegetation characterization. *Remote Sensing of Environment*, 113, S56–S66.

Jacquemoud, S., and Ustin, S.L. (2014). Modeling Leaf Optical Properties. In *Photobiological Sciences Online* (Ed: S.C. Smith). American Society of Photobiology. *http://www.photobiology.info/*

Jacquemoud, S., and Ustin, S. (2019). *Leaf Optical Properties*. Cambridge University Press, Cambridge. doi:*10.1017/9781108686457*

Jeffrey, S.J., Carter, J.O. Moodie, K.B., and Beswick, A.R. (2001). Using spatial interpolation to construct a comprehensive archive of Australian climate data. *Environmental Modelling and Software*, 16/4, 309–330.

Jones, J.W., Antle, J.M., Basso, B., Boote, K.J., Conant, R.T., Foster, I., Godfray, H.C.J., Herrero, M., Howitt, R.E., Janssen, S., Keating, B.A., Munoz-Carpena, R., Porter, C.H., Rosenzweig, C., and Wheeler, T.R. (2017). Brief history of agricultural systems modeling. *Agricultural Systems*, 155, 240–254. *https://doi.org/10.1016/j.agsy.2016.05.014*

Keating, B.A., Carberry, P.S., Hammer, G.L., Probert, M.E., Robertson, M.J., Holzworth, D., Huth, N.I., Hargreaves, J.N., Meinke, H., and Hochman, Z. (2003). An overview of APSIM, a model designed for farming systems simulation. *European Journal of Agronomy*, 18(3–4), 267–288.

Kubelka, P., and Munk, F. (1931). Ein beitrag zur optik der farbanstriche. *Zeitschrift fur Technische Physik*, 12, 593–601.

Ludwig, J.A., Bastin, G.N., Wallace, J.F., and McVicar, T.R. (2007). Assessing landscape health by scaling with remote sensing: when is it not enough? *Landscape Ecology*, 22, 163–169. doi:*10.1007/s10980-006-9038-6*

Maier, S.W., Lüdeker, W., and Günther, K.P. (1999). SLOP: a revised version of the stochastic model for leaf optical properties. *Remote Sensing of Environment*, 68(3), 273–280.

Martinez von Remisowsky, A., McClendon, J.H., and Fukshansky, L. (1992). Estimation of the optical parameters and light gradients in leaves: multi-flux versus two-flux treatement. *Photochemistry and Photobiology*, 55(6), 857–865.

McKeon, G., and Carter, J. (2015). AussieGRASS: An Operational National Pasture Model. Ch 1 in *AussieGRASS Environmental Calculator—Product Descriptions v1.5*. Department of Science, Information Technology and Innovation, Queensland.

McVicar, T.R., and Jupp, D.L.B. (2002). Using covariates to spatially interpolate moisture availability in the Murray-Darling Basin: a novel use of remotely sensed data. *Remote Sensing of Environment*, 79, 199–212.

Melamed, N.T. (1963). Optical properties of powders: Part I. Optical absorption coefficients and the absolute value of the diffuse reflectance. *Journal of Applied Physics*, 34, 560–570. *https://doi.org/10.1063/1.1729309*

Miller, J.R., Turner, M.G., Smithwick, E.A.H., Dent, C.L., and Stanley, E.H. (2004). Spatial Extrapolation: The Science of Predicting Ecological Patterns and Processes. *BioScience*, 54(4), 310–320. *https://doi.org/10.1641/0006-3568(2004)054[0310:SETSOP]2.0.CO;2*

Monteith, J.L. (1972). Solar Radiation and Productivity in Tropical Ecosystems. *Journal of Applied Ecology*, 9(3), 747–766.

Monteith, J.L. (1977). Climate and the efficiency of crop production in Britain. *Philosophical Transactions of The Royal Society B: Biological Sciences*, 281(980), 294–294. doi:*10.1098/rstb.1977.0140*.

Murray, N.J., Keith, D.A., Bland, L.M., Ferrari, R., Lyons, M.B., Lucas, R., Pettorelli, N., Nicholson, E. (2018). The role of satellite remote sensing in structured ecosystem risk assessments. *Science of the Total Environment*, 619–620, 249–257. *https://doi.org/10.1016/j.scitotenv.2017.11.034*

Nikolova, S., Bruce, S., Randall, L., Barrett, G., Ritman, K., and Nicholson, M. (2012). *Using remote sensing data and crop modelling to improve crop production forecasting: a scoping study.* ABARES technical report 12.3. Australian Bureau of Agricultural and Resource Economics and Sciences, Canberra.

OPTICLEAF (2020). *OPTICLEAF The database on leaf optical properties* website: *http://opticleaf.ipgp.fr/index.php?page=home*

Pasetto, D., Arenas-Castro, S., Bustamante, J., Casagrandi, R., Chrysoulakis, N., Cord, A.F., Dittrich, A., Domingo-Marimon, C., El Serafy, G., Karnieli, A., Kordelas, G.A., Manakos, I., Mari, L. Monteiro, A. Palazzi, E., Poursanidis, D., Rinaldo, A., Terzago, S., Ziemba, A., and Ziv, G. (2018). Integration of satellite remote sensing data in ecosystem modelling at local scales: practices and trends. *Methods in Ecology and Evolution*, 9, 1810–1821.

Prentice, I.C., Bondeau, A., Cramer, W., Harrison, S.P., Hickler, T., Lucht, W., Sitch, S., Smith, B., and Sykes, M.T. (2007). Dynamic Global Vegetation Modeling: Quantifying Terrestrial Ecosystem Responses to Large-Scale Environmental Change. In *Terrestrial Ecosystems in a Changing World* (Eds: Canadell, J.G., Pataki, D.E., and Pitelka, L.F.). Springer-Verlag, Heidelberg.

Punalekar, S.M., Verhoef, A., Quaife, T.L., Humphries, D., Bermingham, L., and Reynolds, C.K. (2018). Application of Sentinel-2A data for pasture biomass monitoring using a physically based radiative transfer model. *Remote Sensing of Environment*, 218, 207–220.

Remmel, T.K., and Csillag, F. (2003). When are two landscape pattern indices significantly different? *Journal of Geographic Systems*, 5, 331–351.

Richter, T., and Fukshansky, L. (1996). Optics of a bifacial leaf: 1. A novel combined procedure for deriving the optical parameters. *Photochemistry and Photobiology*, 63(4), 507–516.

Rickert, K.G., Stuth, J.W., and McKeon, G.M. (2000). Modelling pasture and animal production. In *Field and Laboratory Methods for Grassland and animal Production Research*. (Eds: Mannetje, L.T., and Jones, R.M.). CABI publishing, New York. pp 29–66.

Robins, L., Freebairn, D., and Sedger, A. (2003). *Groundwater Models. A Community Guide to Better Understanding*. Murray-Darling Basin Commission, Canberra. ISBN: 1 876830 45 X

Scarth, P., Röder, A., and Schmidt, M. (2010). Tracking grazing pressure and climate interaction the role of Landsat fractional cover in time series analysis. In *Proceedings of Australasian Remote Sensing and Photogrammetry Conference*, Alice Springs, 13–17 September. *figshare.com/articles/Tracking_Grazing_Pressure_and_Climate_Interaction_-_The_Role_of_Landsat_Fractional_Cover_in_Time_Series_Analysis/94250/1*

Sitch, S., Huntingford, C., Gedney, N., Levy, P.E., Lomas, M., Piao, S.L., Betts, R., Ciais, P., Cox, P., Friedlingstein, P., Jones, C.D., Prentice, I.C., and Woodward, F.I. (2008). Evaluation of the terrestrial carbon cycle, future plant geography and climate-carbon cycle feedbacks using five Dynamic Global Vegetation Models (DGVMs). *Global Change Biology*, 14(9), 2015–2039. *https://doi.org/10.1111/j.1365-2486.2008.01626.x*

Stein, A., Staritsky, I.G., Bouma, J., Van Eijsbergen, A.C., and Bgegt, A.K. (1991). Simulation of moisture deficits and areal interpolation by universal cokriging. *Water Resources Research*, 27, 1963–1973.

Suits, G.H. (1972). The calculation of the directional reflectance of a vegetative canopy. *Remote Sensing of Environment*, 2, 117–125.

Tucker, C.J., and Garratt, M.W. (1977). Leaf optical system modeled as a stochastic process. *Applied Optics*, 16(3), 635–642.

Ustin, S.L., Jacquemoud, S., Zarco-Tejada, P.J., and Asner, G.P. (2004). Remote sensing of the environment: state of the science and new directions, in Manual of Remote Sensing. *Volume 4: Remote Sensing for Natural Resource Management and Environmental Monitoring* (Ed: S.L. Ustin). John Wiley and Sons. pp. 679–729.

Van Dijk, A.I.J.M. (2010). *AWRA Technical Report 3. Landscape Model (version 0.5) Technical Description*. WIRADA / CSIRO Water for a Healthy Country Flagship, Canberra.

Vargas, W.E. (1999). Two-flux radiative transfer model under nonisotropic propagating diffuse radiation. *Applied Optics*, 38(7), 1077–1085.

Verhoef, W. (1984). Light scattering by leaf layers with application to canopy reflectance modeling: the SAIL model. *Remote Sensing of Environment*, 16, 125–141.

Verhoef, W. (1985). Earth observation modeling based on layer scattering matrices. *Remote Sensing of Environment*, 17, 165–178.

Viney, N., Vaze, J., Crosbie, R., Wang, B., Dawes, W., and Frost, A. (2015). *AWRA-L v5.0: technical description of model algorithms and inputs*. CSIRO, Australia.

Williams, M., Woodward, F.I., Baldocchi, D.D., and Ellsworth, D. (2004). CO_2 capture from the leaf to the landscape, In *Photosynthetic Adaptation: Chloroplast to Landscape* (Eds: W.K. Smith, T.C. Vogelmann and C. Critchley) Ecological Studies 178, Springer.

Wu, J. (2013). Landscape Ecology. In *Ecological Systems* (Ed: Leemans R.). Springer, New York. *https://doi.org/10.1007/978-1-4614-5755-8_11*

Zhang, B., and Carter, J. (2018) FORAGE—An online system for generating and delivering property-scale decision support information for grazing land and environmental management. *Computers and Electronics in Agriculture*, 150, 302–311.

Zhang, L., Walker, G.R., and Dawes, W.R. (2002). Water balance modelling: concepts and applications. In *Regional Water and Soil Assessment for Managing Sustainable Agriculture in China and Australia* (Eds: McVicar, T.R., Li Rui, Walker, J., Fitzpatrick, R.W., and Liu Changming). ACIAR Monograph No. 84. pp 31–47.

Observing Agriculture

In this context, 'agriculture' describes a land use, an activity, a segment of economics, even a political portfolio. In Australia, both the state and federal political systems have their own unique departments of agriculture. Like many other developed countries, agriculture in Australia often describes the demarcation between urban and rural areas. Agriculture also defines the ancestral origins of most Australians.

The earliest EO sensors enabled scientists to assess, monitor, and measure plant material on a regular basis, with significantly more advanced sensors becoming available over time (see Volume 1A—Sections 12 and 13 and Volume 1B—Section 10). An overview of agriculture in Australia and its ongoing challenges is presented in Section 11. Subsequent sections consider the use of satellite, airborne and proximal EO datasets to observe vegetation in the Australian landscape for specific agricultural applications:

- monitor crop type, condition, extent, and yield (see Section 12);
- model crop water use in irrigated horticulture (see Section 13);
- estimate pasture biomass and growth rates (see Section 14);
- assess condition and distribution of pasture species, including woody perennial vegetation, in rangelands (see Section 15); and
- observe the biomass and condition of both native forests and plantations (see Section 16).

Contents

11 Agriculture Overview 231

12 Crops 249

13 Irrigated Horticulture 263

14 Pastures 281

15 Rangelands 299

16 Forestry 323

Background image on previous page: A Copernicus Sentinel image acquired on 12 August 2019 near Pingrup, WA, is overlaid by paddock boundaries defined by ePaddocks™ (CSIRO, 2020). This application uses artificial intelligence to segment EO imagery into farm and paddock parcels, which can then be analysed to determine crop type and/or yield. **Source:** Franz Waldner, CSIRO (Waldner and Diakogiannis, 2020)

11 Agriculture Overview

The increased scales of operations on modern farms present major challenges for monitoring the water, nutrient, pest, and disease status of various crops to ensure that products are suited to market requirements. EO-based forecasting of crop yield or pasture growth has become an essential part of modern agriculture, which enables efficient marketing and distribution of produce. This involves monitoring pest infestations and fertiliser requirements during growth, determining the best time to harvest crops, then managing its storage and sale. Reliable monitoring and forecasting—with an emphasis on Early Warning Systems (EWS)—are also critically important for shaping food policy and addressing food security concerns around the world (FAO, 2017).

An integrated suite of timely EO technologies is required at a range of scales to meet the management requirements of food and fibre crops in Australia. Recent advances in EO technologies, particularly the advent of Digital Earth Australia (DEA; see Volume 2D), have transitioned this field from a promising research tool to a practical management necessity for many Australian agricultural activities. For example, a collaborative project between Geoscience Australia (GA) and the Australian Bureau of Statistics (ABS) is merging ABS agricultural census/survey data (de-identified) with DEA images to rapidly develop regional maps of crops and land covers. Such maps then form an ideal basis for assessing the impact of natural disasters, determining crop suitability in changing environmental conditions, and estimating crop yield for financial and actuarial applications (ABS, 2020b).

An overview of Australian agricultural activities is presented in Section 11.1. The remainder of this section reviews four pivotal topics for using EO datasets to map, monitor, and model agricultural activities both globally and in Australia, namely, defining essential agricultural variables (see Section 11.2), monitoring managed landscapes (see Section 11.3), understanding land degradation (see Section 11.4) and addressing food security (see Section 11.5). The following five sections describe EO-based methods that are being developed or used operationally for specific Australian agricultural sectors.

For about two million years humans lived by gathering, herding and hunting. Then in the space of a few thousand years a radically different way of life emerged based on a major alteration to natural ecosystems in order to produce crops and provide pasture for animals. This more intensive system of food production was developed separately in three core areas of the world .... and marked the most important transition in human history. Because it was capable of providing much greater quantities of food it made possible the evolution of settled, complex, hierarchical societies and a much faster growth in human population. .... By about 2000 BC all the major crops and animals that make up the contemporary agricultural systems of the world had been domesticated.

....

Agriculture is most definitely not an easier option than gathering and hunting. It requires far more effort in clearing land, sowing, tending and harvesting crops and in looking after domesticated animals. It does not necessarily provide more nutritious food, nor does it offer greater security because it selects and depends on a far smaller range of plants and animals. The one advantage agriculture has over other forms of subsistence is that in return for a greater degree of effort it can provide more food from a smaller area of land.
(Ponting, 1991)

Background image: Landsat-8 OLI image over the mixed agricultural district of Kerang, Victoria, acquired on 2 July 2018. This image is displayed using bands 4, 3, 2 as RGB and clearly differentiates irrigated and non-irrigated crops (see also Volume 2C—Excursus 11.1). **Source:** Norman Mueller, Geoscience Australia

11.1 Agriculture in Australia

The mainland of Australia is the sixth largest continent in the world and has the dubious honour of being the driest, with the majority of its land area receiving less than 500 mm of rainfall per year (see Figure 2.7). Approximately 97% of the Australian population live outside the lower rainfall zone, that is, within 15% of Australia's land area (see Figure 2.15). It can be easily extrapolated from these figures that of the whole continent (a little less than the size of the USA), when areas of dense urban populations (including the advancing peri-urban regions) are excluded, only a very small area remains with access to sustainable water reserves that is suitable for intensive farming. Given Australia's hugely varied rainfall patterns, ranging from summer rainfall in the north to predominantly spring rainfall in the south (see Section 2.2), other factors, such as soil types, determine viable agricultural activities (see Section 2.5.2).

Each of the 89,400 agricultural landholdings in Australia (ABS, 2020a), from any production sector and/or locality, is unique in terms of its size, soil, topography, climate, vegetation cover, economic security, and/or proximity to market. Since the majority of landholdings are privately owned and work from a low economic base, farmers and graziers are often obliged to rely on less expensive processes to improve efficiency and profitability.

Figure 11.1 Agricultural land uses in Australia

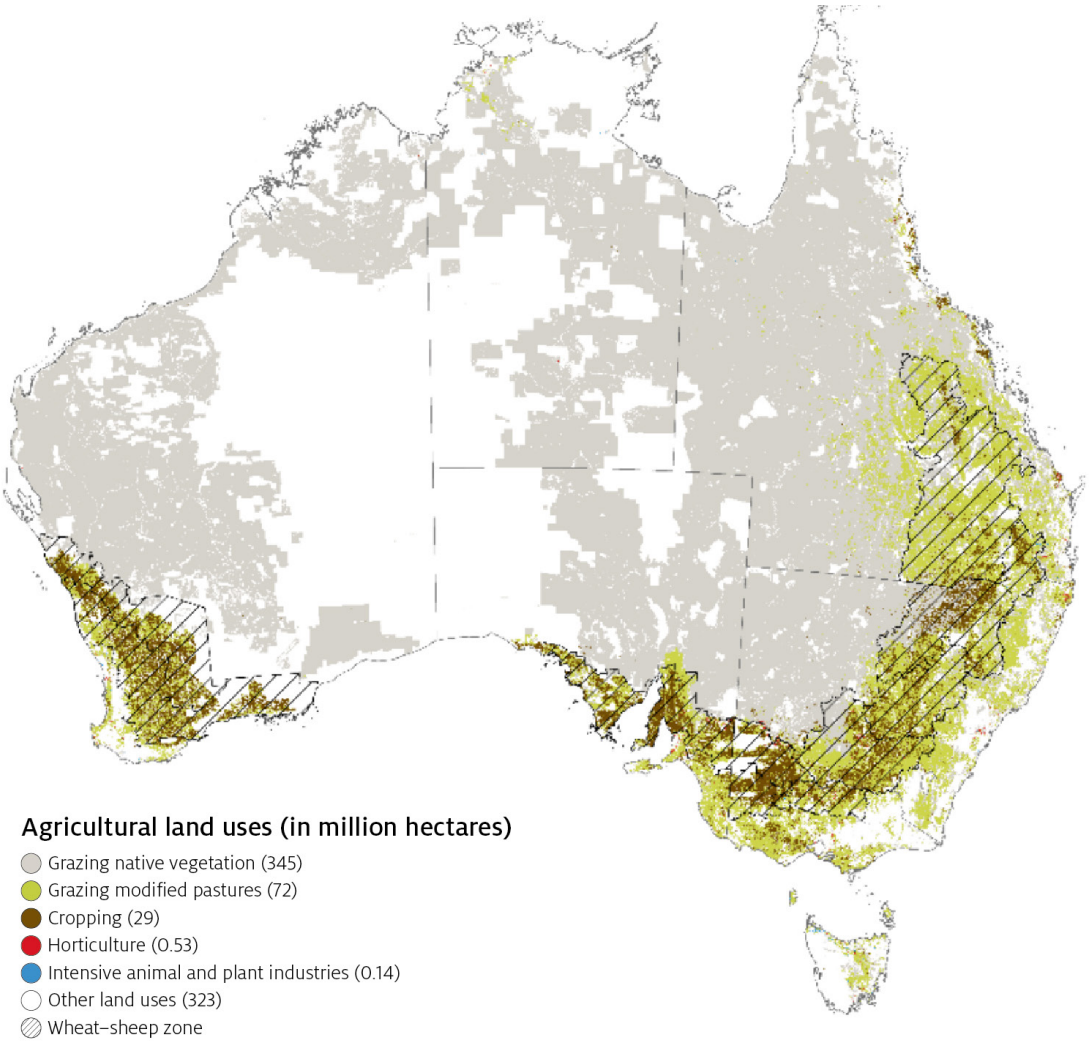

Source: ABARES (2020b). (Retrieved from *https://www.agriculture.gov.au/sites/default/files/images/agricultural-production-zones.png*)

Australian agricultural areas devoted to food production include broad-acre cropping (cereals, legumes, and oil; see Section 12), irrigated horticulture (see Section 13), grasslands (see Section 14), and rangelands (see Section 15). In addition, both native forests and exotic plantations are managed for timber production (see Section 16). Just over half of the 769 million ha of land in Australia is used for agricultural holdings (ABS, 2020c), of which around 87% is grazed (see Figure 11.1). Grazing predominantly occurs on arid and semi-arid native pastures, known as rangelands, with improved pasture only covering around 10% of the grazing area.

The gross value of Australian agricultural production in 2020/21 is estimated as $61 billion with approximately 75% of produce being exported (ABARES, 2020a). Australian agriculture accounts for:

- 59% of water extractions (9,434 gigalitres used by agriculture in 2015/16);
- 11% of goods and services exports in 2018/19; and
- 2.2% of value added (GDP) and 2.6% of employment in 2018/19 (ABARES, 2020b).

In 2019, the Australian Bureau of Statistics (ABS) reported that the Australian population exceeded 25 million and by 2050 this number may have increased by 50%. In addition to the anticipated demand resulting from population growth in neighbouring countries, this population increase may strain the capacity of farmers to meet the projected domestic food requirements (see Section 11.5).

The primary source of agricultural commodity statistics, with a focus on aggregated production, is the five-yearly ABS Agricultural Census, which is sent to 170,000 farms whose agricultural activities have an estimated value exceeding $5,000. In non-census years, the ABS survey 30,000 farms. The Australian Bureau of Agricultural and Resource Economics and Sciences (ABARES) also survey around 70% of farms in the broadacre cropping, grazing and dairy industries each year (~2,000 farms) for detailed information on finances, which is extrapolated to produce regional, state, and national crop production estimates in February, June, September, and December (Nikolova *et al.*, 2012).

Amidst the goodwill towards Australia's productive landscapes, clever farmers and strong agricultural research sector, there is often a lack of recognition that the underlying resource base of soils and biodiversity has been gripped in a cycle of decline for decades.
(Ogilvy, 2020)

11.2 Essential Agricultural Variables

A relatively recent focus in EO considers 'essential variables' (EV), that is, a minimal, streamlined, yet comprehensive set of independent, constraining variables that can be derived from EO datasets, which collectively characterise the state, trend, and future evolution of the integrated Earth System (Masó *et al.*, 2020; see Excursus 1.2) based on its energy and matter cycling (Whitcraft *et al.*, 2019; see Section 10.2.3). EV effectively define a set of common, geo-referenced measurements of physical, chemical, and/or biological attributes that can be acquired on a regular basis to efficiently analyse relevant drivers, pressures, states, impacts, and responses in a range of Earth System disciplines, or 'domains' (Masó *et al.*, 2020).

Figure 11.2 Driving force–pressure–state–impact–response (DPSIR) framework

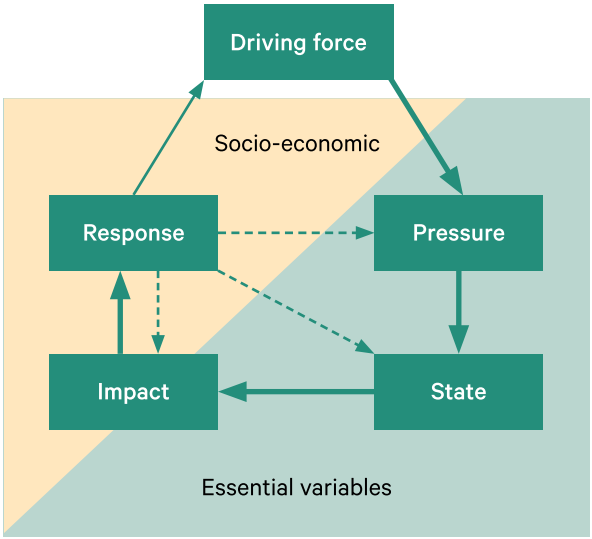

Adapted from: Mace and Baillie (2007) Figure 2 and Masó *et al.* (2020) Figure 3

Figure 11.3 Essential Variables in the context of UN Sustainable Development Goals

SDG: Sustainable Development Goals; EO: Earth Observation

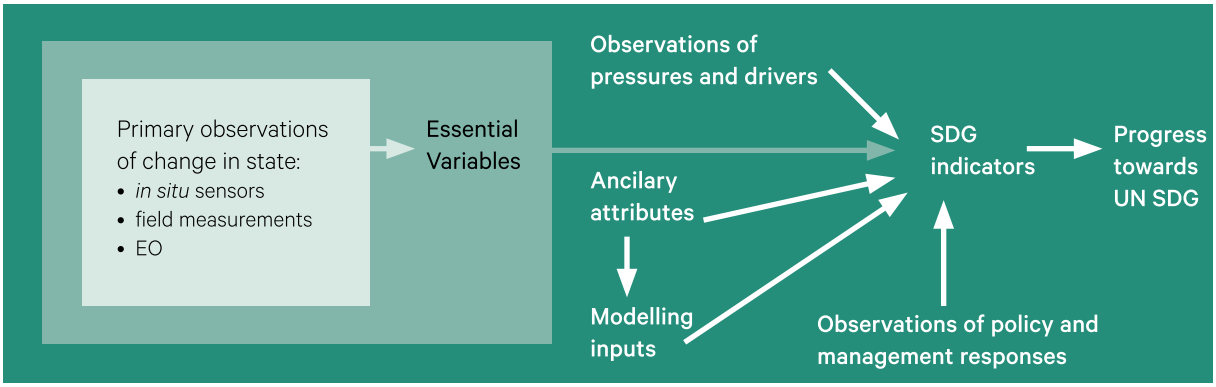

Adapted from: Masó *et al.* (2020) Figure 4

As well as maximising cost-effectiveness, recommended criteria for EV include being relevant to purpose, readily communicated to target audiences, and able to differentiate between measures of pressure, state, and response (Mace and Baillie, 2007). The driving force–pressure–state–impact–response (DPSIR) framework (OECD, 1993) is often used to construct and evaluate sets of indicators (see Figure 11.2). This conceptual framework classifies indicators as measures of pressure, state, impact, or response in social-environmental systems, and offers a convenient tool to analysing the socio-economic impacts of anthropogenic activities on the environment, including causal relationships (Burkhard and Müller, 2008). For example, social changes can be viewed as drivers which apply pressure to the environment, resulting in impacts on people or ecosystems. In response, policies are introduced to relieve pressure and restore the desired state. Since indicator development is inevitably an evolutionary process, this framework highlights potential gaps in current indicator sets, enables the impact of changes in components and their interactions to be assessed, and helps to retain focus on achievable implementation targets (Mace and Baillie, 2007).

Existing EV include Essential Climate Variables (ECV; Bojinski *et al.*, 2014; see Volume 1A—Section 1.5.2), Essential Ocean Variables (EOV; Moltmann *et al.*, 2019; see Volume 3B), and Essential Biodiversity Variables (EBV: Pereira *et al.*, 2013; see Section 19.3). These standardised variables have particular value for global monitoring applications towards the United Nations (UN) Sustainable Development Goals (SDG; see Section 20.4), such as food security (Patias *et al.*, 2019; see Figure 11.3 and Section 11.5).

One of the activities of the Group on Earth Observation (GEO) Global Agricultural Monitoring initiative (GEOGLAM) is to develop a set of globally-relevant Essential Agricultural Variables (EAV) that are relevant to agricultural activities (Whitcraft *et al.*, 2019; GEO, 2019). EAV will help standardise EO-based products for regional and global agricultural monitoring (see Excursus 11.1) and further integrate EO datasets into operational systems designed to reduce land degradation (see Section 11.4), alleviate food insecurity (see Section 11.5), and monitor crop condition and yield (see Section 12).

Resilience describes the capacity of a system to maintain its equilibrium in the face of impacts or pressures that arise from natural or human-made interactions or events. 'Resilience' comes from the Latin word 'resilire', which means to 'leap back' after adversity. A resilient system has the capacity to absorb disturbance and essentially retain the same function, structure and feedbacks. …. Modified ecosystems are generally ecologically simpler and therefore have less resilience to external pressures (eg. variations in climate) than complex ecosystems.
(DEWHA, 2010)

11.3 Monitoring Managed Landscapes

To ensure the health of both soil and vegetation, monitoring is an integral part of the adaptive management of cultivated and grazed natural resources. For example, EO-based systems to monitor pasture productivity and condition have been established for decades in Australia (see Excursus 14.1 and Section 15.4). Similarly, an international, EO-based system, GEOGLAM RaPP (see Excursus 11.1), observes the condition of pastures and rangelands on a global scale to estimate biomass dynamics and productivity (see Sections 13 and 15), and reduce land degradation (see Section 11.4).

The 'condition' of land has been described as a concept in which "specific indicators like vegetation cover, production, or composition .... at a particular location (are compared with) the assumed potential for that attribute within that vegetation type or compared to other locations" (Friedel *et al*., 2000; see also Sections 7.2 and 7.3 above). In the context of rangelands for example, to monitor condition means "to determine to what extent human factors (e.g. grazing management) have caused departure from the assumed potential" (Bastin and Ludwig, 2006).

Land condition is analogous to human health and the rating (or rank) given to an area is often subjective, and can be contentious (see Section 7.3). This uncertainty is increased in the arid rangelands where large fluctuations in the amount and timing of rainfall can produce considerable natural variation in the vegetation attributes used to determine condition. As such, it is often difficult to know which parts of the grazed rangelands are remaining stable, or are improving or deteriorating over time. Since drought is part of the normal climatic variation experienced by the Australian rangelands, land condition can only be assessed in these landscapes in the context of the variation between the episodic drought years and the infrequent years of high rainfall.

Figure 11.4 Seasonal quality matrix

This matrix summarises site level change in condition indicators with respect to rainfall amount. The upper left and lower right 'traffic light' colours focus attention on those groups of sites showing change that is contrary to seasonal expectations.

Seasonal conditions	Decline	No change	Increase
Above average			~
Average		~	
Below average	~		

The term 'seasonal quality' has been used to indicate the relative value of rainfall to vegetation (Bastin *et al*. 2008) and can assist with understanding landscape change. The seasonal quality matrix (see Figure 11.4) focuses attention on unexpected change. Here, site level change based on indicators is interpreted with respect to recent 'seasonal quality'. In this case recent seasonal conditions may be classified as above average, average, or below average, based on rainfall prior to the most recent assessment. A decline in indicator value following above average rainfall, or an increase following below average rainfall, strongly suggest non-rainfall related causes. The former is often associated with enhanced fire activity, while the latter suggests favourable land management practices. The seasonal quality matrix also underpins the development and application of EO-based methods for monitoring land condition in these landscapes (see Section 15).

Landscape Functional Analysis (LFA; Tongway and Hindley, 2004; see Section 7.3 above) was developed to quantify degradation and recovery in drylands. Its conceptual framework is the Trigger-Transfer-Reserve-Pulse (TTRP) model (see Figure 7.3), which describes ecosystem function in terms of the transport, usage, and cycling of scarce natural resources (such as water, topsoil, organic matter, seeds) in space and/or time:

- triggers are climatic drivers, management interventions or disturbances;
- transfers are processes such as wind and water erosion that move nutrients into reserves;
- reserves are zones or patches (above or below ground) where nutrients are stored; and
- pulses are increased floral or faunal productivity resulting from the stored nutrients and available soil moisture.

While traditional approaches assess vegetation characteristics, such as composition and structure, LFA focuses on landscape function to understand the regulation of resource outputs versus inputs and internal feedbacks (Reinhart, 2009). The loss of resources from the landscape, such as by erosion or runoff, indicates its 'leakiness' (see Sections 7.3 and 8.1.6), whereas gains in resources may indicate increased capacity in its 'reserve' zones, possiby due to successful restoration activities, and therefore a more tightly coupled system. The distribution of reserve zones in dryland landscapes is characteristically patchy and discontinuous with different resources occurring at different patch scales in both space and time (Tongway and Hindley, 2004). These concepts are further explored in Section 15.

Excursus 11.1—GEOGLAM RaPP

Source: Guerschman *et al.* (2018)
Further information: *https://www.geo-rapp.org*
Reporting tool: *https://map.geo-rapp.org/*

An integrated system for observing the condition of Earth's pastures and rangelands is being established by the Group on Earth Observation (GEO) Global Agricultural Monitoring initiative (GEOGLAM; see Section 21.3). In particular, the GEOGLAM Rangeland and Pasture Productivity (RaPP) aims to enable the condition of rangelands and pasture lands to be monitored routinely at global, regional, and national scales, with the goal of estimating biomass dynamics and productivity. The Australian component of this system uses MODIS imagery to map fractional cover (FC: photosynthetic vegetation, non-photosythetic vegetation, and bare soil) on a monthly basis at 500 m spatial resolution (see Excursus 8.3). In regions with < 20% trees cover, ground cover can be represented as the sum of photosynthetic and non-photosynthetic vegetation, or the total vegetation cover (see Figure 5.1).

These EO-based products extend the community-based work of Leys *et al.* (2008) in NSW in the development of the DustWatch program, which monitors wind erosion risk (see Section 11.6). Much of Australia's agricultural land has a significant risk of wind erosion (see Section 11.4), which can result in localised loss of soil and nutrients and a reduction in regional air quality (see Figure 11.5). Water erosion on hillslopes is also a risk in some rangeland and cropping regions, with subsequent impact on water quality. One of the primary factors in controlling soil erosion is the retention of a protective cover layer over the soil surface, including vegetation, litter, biological crusts, and stones. To avoid wind erosion, more than half the soil surface needs to be covered (Leys, 1991), while to prevent water erosion, over 70% ground cover is required (Lang, 2005). Thus, higher levels of total vegetation cover can be used to indicate lower soil erosion risk.

A range of spatial datasets are integrated by RaPP (see Table 11.1 and Leys *et al.*, 2020) to provide interactive tools that can be applied to a defined region, including:

- change in ground cover for a defined time interval;
- time series plot of mean ground cover; and
- statistical comparisons of current ground cover with previous conditions and 'normal' state.

These tools assist users to visualise changes in total vegetation cover and distribution through time at a variety of scales over the entire Australian land mass.

The main objective of GEOGLAM is to reinforce the international community's capacity to produce and distribute relevant, timely, and accurate information on agricultural land use and production at national, regional, and global scales, using Earth observation (EO) data, toward enhancing knowledge and improving sustainable decisions related to agriculture and food security. (GEO, 2019)

Table 11.1 RaPP spatial datasets

FC: Fractional Cover; TV: Total Vegetation; GC: Ground Cover; PGC: Persistent Ground Cover; CHIRPS: Climate Hazards Group InfraRed Precipitation with Station data (*https://www.chc.ucsb.edu/data/chirps*); CLUM: Catchment scale Land Use for Australia (see Section 3.3.4 and 3.5);

Data type	Source	Description
EO time series	MODIS Fractional Cover (FC)	Monthly (FC, TV, TV anomalies, TV deciles)
		8-day (FC, TV)
	Seasonal Landsat/Sentinel FC	Landsat (FC, GC, PGC—see Section 9.1)
		Sentinel-2 (FC)
Climate	Rainfall	Totals (CHIRPS), Monthly anomalies
Land use and land cover	CLUM (2017)	See Section 3.3.4
	Land use of Australia	National scale (2010–11)
	Ramsar wetlands	See Volume 3B
	IBRA 7.0 regions and subregions	See Sections 2.4 and 3.3.2
	Collaborative Australian Protected Areas Database (CAPAD)	CAPAD (2018)
	Major vegetation subgroups	NVIS (see Section 2.3.1)
	Vegetation height and structure	See Excursus 6.1
Boundaries	Australian rangelands	See Section 15
	NRM regions 2017	See Section 3.4
	Local Government Areas 2016	Australian Bureau of Statistics
	Census Mesh Blocks 2011	
	State Suburbs (SSC) 2016	
	Census Statistical area level	
	River regions	Bureau of Meteorology

Source: Guerschman *et al.* (2018) Table 2; see also Leys *et al.* (2020)

Land degradation is actually generally a slow process therefore it's the cumulative impact of both rapid and prolonged effects that cause land degradation. Perennial woody vegetation such as trees and shrubs generally change over periods of months, years or decades; except when major disturbance events occur such as fire, cyclones or land clearing. The non-woody ground cover is generally more dynamic and can change over much shorter time periods (e.g. weeks to months), in response to rainfall events and land management practices such as grazing and cropping. It can therefore be a useful indicator of land management, particularly if it is understood in the context of local or regional climate patterns and landscape variability (i.e. soil types and landform pattern).
(Guerschman et al., 2018)

11.4 Land Degradation

At a global scale, land degradation is not a new problem (see Excursus 11.2). In Australia, the majority of agricultural lands have been actively degraded since European settlement and this trend still continues in parts of the country. The challenge now is to learn from history before it is too late (see Section 21).

Wind and water erosion continually relocate soil in Australia, with soil erosion rates due to water exceeding the rate of soil formation by orders of magnitude. Soil erosion on Australian cropping land has been assessed as unsustainable (Bui *et al.*, 2010), delivering excessive volumes of sediments and nutrients to inland and coastal watercourses and waterbodies. Wind erosion removes topsoil, sometimes in sufficient volume to create dust storms (see Volume 1B—Section 4), which present a significant hazard to human health, vegetation, infrastructure, and aviation, and inflict substantial economic costs to the affected communities (Tozer and Leys, 2013; see Figure 11.5). Since bare land is most susceptible to soil loss from both agents, the first step towards controlling this problem involves retaining ground cover on grazing lands and minimising soil disturbance on cropping land (SOE, 2016a). Both local systems such as DustWatch (Leys *et al.*, 2018) and global systems such as GEOGLAM RaPP (see Excursus 11.1) utilise EO datasets to monitor potential and actual erosion. Meteorological datasets and models are also instrumental in understanding dust transport pathways in Australia and developing a dust trajectory climatology (O'Loingsigh *et al.*, 2017).

Despite this erosion potential, an estimated 35% of Australian agricultural land is currently overgrazed and/or over-cultivated (Ogilvy, 2020). While drought—like fire (see Section 18)—is a characteristic of the Australian landscape, when coupled with overgrazing the resulting environmental degradation can be long term (Hendy *et al.*, 2003; see Section 15). For example, McKeon *et al.* (2004) document and analyse eight extended droughts up until the end of the 20th century that occurred in different parts of Australia (see Table 11.2), each of which resulted in significant land degradation.

There is an intimate relationship between the landscape, its geological and climatic history, weathered and transported soil types, groundwater and the hazard posed by salt load within the soil.
(Spies and Woodgate, 2005)

Excursus 11.2—Learning from History

Source: Ponting (1991), Carson (1962)

To be ignorant of what occurred before you were born is to always remain a child. For what is the worth of human life, unless it is woven into the life of our ancestors by records of history.
(Marcus Tullius Cicero)

Ecosystems provide a variety of essential resources for human inhabitants, primarily food, water, clothing, shelter, and energy (see Section 20.3). However, humans are a unique species—they have spread into every ecosystem on Earth, yet repeatedly demonstrate the capacity to destroy the ecosystems that support them. History offers numerous examples of societies that have developed, flourished, specialised, foundered, then collapsed as a result of overexploitation, mismanagement, degradation, and/or pollution of their available natural resources (including other humans). This sequence has played out to different extents and over different time periods—largely depending on the resilience of the natural ecosystem—all around the globe, most notably in Mesopotamia, the Indus Valley, ancient Egypt, the Maya, and Easter Island (Ponting, 1991).

Agricultural practices change natural ecosystems by clearing land, introducing new species, exposing soil to erosion, changing nutrient recycling, and possibly developing irrigation methods (Asner *et al.*, 2004). Agriculture necessitates settled communities and population growth, which generally requires further clearing of forests for construction and fuel. To support these communities, additional mechanisms are then needed to supply water, dispose of wastes and revitalise the soil between crops. This transformation from natural to managed ecosystems has intensified in recent centuries, with the support of technological advances in machinery for clearing and tilling land, and the availability of an increasing array of chemical agents to promote the growth of food plants and animals and discourage pests and disease (Ramankutty *et al.*, 2018). Such agents include artificial fertilisers, insecticides, herbicides, and soil treatments, which deliver short term economic benefits, but their longer term cost—in terms of pollution, species depletions, human health, water quality, and disruptions to the food web—is still being accounted (Carson, 1962).

Environmental degradation is not a new problem for human communities, but it is now becoming more widespread and more urgent on a global basis (see Sections 19 and 20). Recent understanding of the processes of degradation are prompting effective control of this problem in some parts of the world, including Australia (McKeon *et al.*, 2004). For example, since the mid-1900s, soil erosion has declined in many regions due to better land management practices, including control of feral animals, rotational grazing, minimum tilling, regenerative agriculture, and a focus on sustainable development.

EO is playing a key role in optimising the use of agricultural chemicals through precision farming and avoiding over-grazing through programs such as GEOGLAM RaPP (see Excursus 11.1). A range of spatial technologies now provide essential information to farmers and bureaucrats to guide their stewardship of land resources in both tactical and strategic decisions at a range of scales in time and space. EO datasets are also being used to monitor the global status of terrestrial vegetation across a range of application areas (see Section 21). Hopefully, these examples demonstate that we have started to learn from history.

What has been, that will be; what has been done, that will be done. Nothing is new under the sun.
(Book of Ecclesiastes 1:9)

Figure 11.5 Dust storm

This landscape view of the approaching 'Red Dawn' dust storm was taken around 1 pm on 23 September 2009 at Kars Station, 60 km east of Broken Hill, NSW. Red dust that had been collected in central Australia was quickly transported across the continent leading to an estimated loss of 2.54 Mt of soil (Leys *et al.*, 2011). Along the eastern coastline the plume extended in a 3000 km swath, from the Gulf of Carpentaria, Queensland, to Eden, in southeast NSW (see Volume 1B—Figure 4.6b). Red Dawn ultimately shrouded an area spanning 840,000 km^2, significantly reduced air quality (with a total dust load between 12.1 Mt and 17.5 Mt), and resulted in an estimated cost of A$299 million to NSW (Tozer and Leys, 2013).

Source: Fred Hughes, Kars Station

To mitigate the impact of drought in impoverished communities, insurance schemes based on EO analyses have been developed for Africa, such as Index-based Livestock Insurance (IBLI). For example, since 2010, the International Livestock Insurance Institute (ILRI) have offered index-based insurance to protect vulnerable pastoralists from asset losses related to climatic conditions, particularly those located in drought-prone, arid and semi-arid lands in Kenya and Ethiopia (ILRI, 2020). ILRI relies on Early Warning Systems (EWS; see Section 12.3), which use EO and meteorological datasets to predict natural disasters such as drought (CTA, 2018). Based on historical trends, the index approach uses NDVI imagery to highlight years when forage will be inadequate for stock. By allowing farmers to claim assistance through dry seasons they avoid grazing dry soils and thereby increasing erosion, so conserve the natural resources for better growing seasons in the future. This approach also discourages the consumption of seed reserves or breeding stock in lean years, which would ultimately intensify poverty into the future (Barnett and Mahul, 2007).

Table 11.2 Eight extended droughts in Australia

In each case the start of the drought period is defined as the first year with rainfall less than 70% of the mean.

Period	Location	Environmental Impact	Social/Government Consequence
1898/99 to 1902/03	Western NSW	Soil erosion, woody weed infestation, rabbit plagues	Substantial financial losses and financial hardship resulting in the Royal Commission of 1901
1925/26 to 1929/30	South Australia and Western NSW	Substantial loss of perennial vegetation and soil erosion	Government legislation for regulation of carrying capacity and soil conservation
1935/36 to 1940/41	Gascoyne region of Western Australia	Substantial loss of perennial shrubs, soil erosion and animal losses	Royal Commission of 1940
1941/42 to 1944/45	Western NSW	Substantial dust storms and animal losses	Paintings (Russell Drysdale)
1958/59 to 1965/66	Central Australia	Wind and water erosion	Extensive surveys and reassessment of carrying capacity
1964/65 to 1967/68	Western NSW	Large increases in woody weeds	Reduced carrying capacity and income in 1960s
1964/65 to 1967/68	Southwest Queensland	Soil erosion and woody weed infestation	Government-sponsored Southwest Strategy supporting review of recommended carrying capacities and property amalgamation
1984/85 to 1987/88	Northeast Queensland	Soil erosion and loss of 'desirable' perennial grasses	Extensive government-sponsored surveys and dramatic grazier response

Adapted from: McKeon *et al.* (2004) Table 1

Table 11.3 Total economic value of ecosystem services

Value	Type	Examples
Use	Direct	Agricultural produce, fuel, transport
	Indirect	Flood mitigation, pollination, pest control
	Option	Genetic resources with potential future value
Non-use	Existence	Value of existence of other species
	Bequest	Value of functional ecosystem to future generations

Source: DEWHA (2010) Box 4

A significant soil degradation problem in Australia is salinity. Anthropogenic salinity is not a new problem globally however, having occurred in ancient agricultural settlements, such as Mesopotamia, and contributed to the demise of numerous civilisations (Jacobson and Adams, 1958; see Excursus 11.2). Salinity occurs when water tables rise to ground level and bring natural salts to the soil surface. In addition to some naturally saline land, vegetation clearing and inappropriate irrigation have induced salinity problems in several regions of Australia. Salinity reduces water and soil quality and can lead to reduced biodiversity of both plants and invertebrates in low lying agricultural lands (Beresford *et al*., 2001; Clarke *et al*., 2002). In the most recent comprehensive survey (NLWRA, 2001), dryland (non-irrigated) salinity affected 5.7 million ha in Australia, primarily in southwest WA and Victoria, and this is expected to increase to 17 million ha by 2050 (SOE, 2016b). Globally, soil salinity is estimated to impact nearly 1 billion ha, or around 7% of the land surface, especially in arid and semi-arid regions (Ghassemi *et al*., 1995), and at least 20% of irrigated land (Pitman and Läuchli, 2002). A number of EO-based approaches have been proposed to map and monitor salinity using sensors that detect electromagnetic radiation (EMR), electromagnetic induction (EMI), and geophysical attributes (see Volume 1A—Sections 5–9), with an emphasis on data fusion and data integration methods, and adequate ground truthing (Metternicht and Zinck, 2003; Spies and Woodgate, 2005).

Soil acidification is an even more widespread problem than salinity, due to the use of agricultural fertilisers on light soils with low pH, which can lead to unhealthy changes in soil biota, increased leaching of selected nutrients, loss of clay particles, erosion, and reduced Net Primary Productivity and carbon sequestration. Acid soils are more likely to release heavy metals into watercourses and the food chain, and increase siltation and eutrophication of waterbodies (see Volume 3B). NLWRA (2001) estimated that around 50 million ha of Australia's agricultural land and about 23 million ha of subsoil are affected by soil acidity, with most of these areas occurring in WA and NSW (SOE, 2016b).

The concept of ecosystem services, that is, the services that ecosystems deliver to human society, is described in Section 7.3. The total economic value of ecosystem services includes both use and non-use values (see Table 11.3). For example, a study of the relationship between soil condition in Australian agricultural lands, their management practices, and the ecosystem services they provide (Cork *et al*., 2012), concluded that the practices of increasing soil carbon, reducing surface soil acidity, and maintaining ground cover on agricultural soils not only improved financial returns from agricultural activities, but also resulted in fewer dust storms, cleaner water from catchments, less reliance on agricultural chemicals, and an enhanced 'sense of place, mental wellbeing and acquisition of knowledge'.

Monitoring in drylands used primarily for commercial and subsistence livestock operations, typically concentrates on indicators related to plant-herbivore interactions and soil stability in relation to trampling. Most monitoring in drylands concentrates first on vegetation attributes and secondarily on soils attributes where vegetation attributes, such as cover, usually serve as a proxy for soil attributes, such as soil erosion. This is due to an observed negative linear correlation between declining vegetation cover and increased erosion. Assessment requires time series data of the drivers of change, including human and herbivore population and demographics, climate, and fire data.
(Washington-Allen and Ravi, 2012)

11.5 Food Security

Food security is not a new problem. For most of human history, the majority of the world's population has lived on the brink of starvation, with high rates of infant morality, short lifespans, ongoing malnutrition, and the recurrent dangers of famine and disease. Some fortunate societies have only managed to escape this lifestyle in recent centuries, mostly by exploiting the resources of colonies (Ponting, 1991).

Of the Earth's total land surface (13.2×10^9 ha), just over half (7×10^9 ha) is considered arable (Zaman *et al*., 2018). However, as land degradation reduces the area of arable land around the world, less land is available to grow food (see Section 11.4). In the face of growing population pressures—and the need for land for other purposes—we are faced with a situation where more food is required but less land is available to grow it. This situation simply repeats the pattern of demise witnessed in many civilisations throughout human history (see Excursus 11.2).

The UN defines food security as the global situation "when all people, at all times, have physical, social and economic access to sufficient, safe and nutritious food that meets their dietary needs and food preferences for an active and healthy life" (FAO, 2020a). Despite food being a basic human need and right, around 10% of the world's population have inadequate food supplies on a daily basis. At the same time, current estimates indicate that up to 30% of all food produced is lost or wasted. In this context, losses can occur at each stage in the supply chain between the grower and the consumer (FAO, 2020a). Thus food security involves more than just food availability, but also access to, utilisation of, and stability of food supplies:

- availability—food supply and trade, not just quantity but also the quality and diversity of food. Improving availability requires sustainable productive farming systems, well-managed natural resources, and policies to enhance productivity.
- access—economic and physical access to food. Improving access requires better market access for smallholders allowing them to generate more income from cash crops, livestock products, and other enterprises.
- utilisation—how the human body uses the various nutrients in food. Improving utilisation requires improving nutrition and food safety, increasing diversity in diets, reducing post-harvest loss, and adding value to food.
- stability—being food secure at all times. Food insecurity can be transitory due to weather, employment, conflict, and market fluctuations. Social networks can play an important role is supporting people through transitory food insecurity (AIFSRC, 2014).

Australia is currently one of the lucky nations, producing far more food than it consumes, and only importing around 10% of consumed food and beverages (ABARES, 2020c). As such it enjoys the status of being ranked as "the world's equal lowest level of undernourishment" (ABARES, 2020c based on FAO, 2020b). However, 4% of Australians are viewed as food insecure (Lindberg *et al*., 2015), including children (McCrindle, 2017), with an increasing number of diet-related problems becoming apparent in the wider population (Farmar-Bowers *et al*., 2013). Recommendations to improve food security in Australia include:

- improving efficiency in food production, processing, and distribution;
- reducing wastage and minimise costs; and
- encouraging greater productivity in agriculture and food processing (PMSEIC, 2010).

In addition to the land degradation factors described above that are directly related to agricultural activities, land use pressures from a growing population are also actively shrinking the area of land available to agriculture in Australia. Despite only 6% of Australian landscapes being deemed suitable for cultivated crops and pastures, these areas are also considered to be the most appropriate for energy production and other developments. Urban encroachment, mining, conservation, and other land uses have already reduced the area of productive land in Australia by 9% in the last two decades (Ogilvy, 2020). If we continue to degrade the available agricultural resource and allocate productive land for other land uses, food security will become a more urgent problem for our nation.

Wealth and vegetation go together, and that exacerbates environmental injustice. The poor bear the burden of degraded environments.
(Natalie Jeremijenko)

Soil is a non-renewable resource, its preservation is essential for food security and our sustainable future. (FAO)

At a global level, much effort is being expended to increase and monitor food production. FAO (2009) estimated that to feed the world's population by 2050, we will need 70% more food (AIFSRC, 2014). Recommendations to avoid increased inequality, energy usage, and land degradation globally, have included trading safety nets, appropriate environmental policy, and consumer education (Martin and Laborde, 2018). By delivering information on global agricultural production that is timely, objective, and repeatable, EO datasets are contributing to numerous efforts to both improve food security (e.g. Song *et al.*, 2017; see Section 12.3) and reduce disaster risk (see Section 11.4). For example, the Vegetation Health Index (VHI; see Section 9.5) underpins several monitoring systems being used to ensure future food security (Kogan, 2019).

With food security being one of the UN SDGs (see Section 20.4), a number of global, EO-based systems, such as the CropWatch system (Wu *et al.*, 2014), have been developed towards this goal. These systems continually monitor food crops and provide early warning of potential food crises (see Section 12.5). EWS rely on EO datasets to detect signs of looming drought and flood conditions, often in conjunction with financial relief schemes, such as IBLI (see Section 11.4). Such schemes alleviate current hardship, avoid extending food security ramifications into future seasons, and reduce the potential for further land degradation.

One aspect of food security that is often overlooked is the essential ecosystem service of pollination (see Section 20.3 and Table 20.6). Since nearly 90% of wild flowering plants require animal pollination (particularly by wild pollinator species), pollinators not only sustain biodiversity and ecosystem functions that help to stabilise the biosphere (see Volume 1A—Section 4.1.4), but their abundance and diversity also impacts crop yield and/or quality (Kearns *et al.*, 1998; IPBES, 2017). 5–8% of global food production relies on pollination services and around 75% of food crops are directly impacted by animal pollination, with these crops supplying an estimated 35% of the global food stock (Klein *et al.*, 2007; Potts *et al.*, 2016). While recent decades have seen a significant increase in the cultivation of pollinator-dependent crops (Aizen *et al.*, 2009), the yield of these crops has increased at a lower rate than that of other crops and also demonstrated greater variability (based on FAO data for 1961–2008; Garibaldi *et al.*, 2011).

A wide range of studies suggest that the populations of pollinators—both wild and managed—are declining. Potential reasons for this decline include the direct and indirect impacts of both agricultural chemicals and genetically modified crops on pollinators, biodiversity loss (see Section 19), and climatic variability (IPBES, 2017). While EO is currently used to monitor related indicators of pollination, such as crop health and production, regional biodiversity, and remnant habitat extent, it could also be used to gain insight into pollination services (Galbraith *et al.*, 2015), as well as the interactions between pollination and plant health, and their impacts on the spatial and temporal variability of yield in pollinator-dependent crops (Willcox *et al.*, 2018).

On some estimates, there is almost 20% more food available per person now than there was three decades ago, nearly 30% more calories per person per day than necessary, and as much as one third of food produced globally (1.3 billion tonnes) is lost or wasted each year. (Ogilvy et al., 2015)

11.6 Further Information

Global EO-based Agricultural Statistics

GSARS (2017). *Handbook on Remote Sensing for Agricultural Statistics*. Global Strategy to improve Agricultural and Rural Statistics, Rome.

GSARS (2015). *Handbook on Master Sampling Frames for Agricultural Statistics: Frame Development, Sample Design and Estimation*. Global Strategy to Improve Agricultural and Rural Statistics, UN Statistical Commission, Rome. *http://gsars.org/wp-content/uploads/2016/02/MSF-010216-web.pdf*

Erosion in Australia

NSW Community Dustwatch: *https://www.environment.nsw.gov.au/topics/land-and-soil/soil-degradation/wind-erosion/community-dustwatch*

Soils for Life: *https://soilsforlife.org.au/*

Food Security in Australia

Clancy and Lesslie (2013)

Australian Department of Foreign Affairs and Trade: *https://www.dfat.gov.au/aid/topics/investment-priorities/agriculture-fisheries-water/agriculture-food-security/Pages/agriculture-food-security-initiatives*

International Food Sustainability

GEOGLAM Rangeland and Pasture Productivity (RaPP) tool:

Australia: *https://map.geo-rapp.org/#australia*

Global: *https://www.geo-rapp.org*

Information: *https://www.csiro.au/en/Research/LWF/Areas/Landscapes/Earth-observation/RAPP-Map-GEOGLAM*

CropWatch reports: *http://www.cropwatch.com.cn/htm/en/index.shtml*

Crop Monitor: *Cropmonitor.org*

SERVIR: *http://servir.rcmrd.org/*

EO4SD (Earth Observation for Sustainable Development) is a new ESA initiative which aims to achieve a step increase in the uptake of satellite-based environmental information in the IFIs regional and global programs: *https://eo4sd.esa.int/*

World Food Studies—WOFOST: *https://www.wur.nl/en/Research-Results/Research-Institutes/Environmental-Research/Facilities-Products/Software-models-and-databases/WOFOST.htm#:~:text=WOFOST%20(WOrld%20FOod%20STudies)%20is,production%20of%20annual%20field%20crops.&text=In%20the%20Global%20Yield%20Gap,available%20soil%20and%20water%20resources.*

11.7 References

ABARES (2020a). *Agricultural overview: June quarter 2020* (Howden, M., Nelson, R., and Cameron, A.) Department of Agriculture, Water and the Environment website: *https://www.agriculture.gov.au/abares/research-topics/agricultural-outlook/agriculture-overview*

ABARES (2020b). *Snapshot of Australian Agriculture 2020* (Jackson, T., Hatfield-Dodds, S., and Zammit, K. Department of Agriculture, Water and the Environment website: *https://www.agriculture.gov.au/abares/publications/insights/snapshot-of-australian-agriculture-2020*

ABARES (2020c). *Analysis of Australia's food security and the COVID-19 pandemic* webpage, Department of Agriculture, Water and the Environment website: *https://www.agriculture.gov.au/abares/publications/insights/australian-food-security-and-COVID-19#what-is-food-security*

ABS (2020a). *Improving agricultural crop statistics using satellite data, 2020* webpage, Australian Bureau of Statistics website: *https://www.abs.gov.au/ausstats/abs@.nsf/0/13BE1A5F2BDE7E9FCA2585920016C460?Opendocument*

ABS (2020b). *Agricultural Commodities, Australia, 2018–19* webpage, Australian Bureau of Statistics website: *https://www.abs.gov.au/ausstats/abs@.nsf/mf/7121.0*

ABS (2020c). *Land Management and Farming in Australia, 2016–17* webpage, Australian Bureau of Statistics website: *https://www.abs.gov.au/AUSSTATS/abs@.nsf/mf/4627.0*

AIFSRC (2014). *Australian International Food Security Research Centre* website: *https://aifsc.aciar.gov.au/food-security-and-why-it-matters.html*

Aizen, M.A., Garibaldi, L.A., Cunningham, S.A., and Klein, A.M. (2009). How much does agriculture depend on pollinators? Lessons from long-term trends in crop production. *Annals of Botany*, 103, 1579–1588.

Asner, G.P., Elmore, A.J., Olander, L.P., Martin, R.E., and Harris, A.T. (2004). Grazing Systems, Ecosystem Responses, and Global Change. *Annual Review of Environment and Resources*, 29, 261–299.

Barnett, B., and Mahul, O. (2007). Weather Index Insurance for Agriculture and Rural Areas in Lower-Income Countries. *American Journal of Agricultural Economics*, 89(5), 1241–1247. *https://doi.org/10.1111/j.1467-8276.2007.01091.x*

Bastin, G.N., and Ludwig, J.A. (2006). Problems and prospects for mapping vegetation condition in Australia's arid rangelands. *Ecological Management and Restoration*, 7, S71–S74.

Bastin, G., and the ACRIS Management Committee (2008). *Rangelands 2008—Taking the Pulse*. National Land and Water Resources Audit, Canberra. doi:*10.1071/RJ08072*

Beresford, Q., Phillips, H., and Bekle, H. (2001). The salinity crisis in Western Australia: a case of policy paralysis. *Australian Journal of Public Administration*, 60(4), 30–38.

Bojinski, S., Verstraete, M., Peterson, T.C., Richter, C., Simmons, A., and M. Zemp, M. (2014). The Concept of Essential Climate Variables in Support of Climate Research, Applications, and Policy. *Bulletin of the American Meteorological Society*, 95, 1431–1443.

Bui, E.N., Hancock, G.J., Chappell, A., and Gregory, L.J. (2010). *Evaluation of tolerable erosion rates and time to critical topsoil loss in Australia*. CSIRO Sustainable Agriculture Flagship, Canberra.

Burkhard, B., and Müller, F. (2008). Drivers-Pressure-State-Impact-Response. In *Ecological Indicators. Volume 2 of Encyclopedia of Ecology* (Eds: Jorgensen, S.E., and Fath, B.D.). Elsevier. ISBN 978-0-08-045405-4

CAPAD (2018). *Collaborative Australian Protected Area* Database: *https://www.environment.gov.au/land/nrs/science/capad*

Carson, R. (1962). *Silent Spring*. Penguin, Reading, UK.

Clarke, C.J., George, R.J., Bell, R.W., and Hatton, T.J. (2002). Dryland salinity in south-western Australia: its origins, remedies, and future research directions. *Australian Journal of Soil Research*, 40(1), 93–1113.

Clancy, T.F., and Lesslie, R.G. (2013). *A scoping assessment for a national research centre addressing land use and food security issues*. Canberra, ACT: Department of Agriculture, Fisheries and Forestry.

CLUM (2017). *Catchment Scale Land Use of Australia—Update September 2017*. Australian Bureau of Agiculture and Resource Economics and Sciences: *https://data.gov.au/dataset/ds-dga-c128490d-fb8f-49eb-9757-3ca1350b87c8/details*

Cork, S., Eadie, L., Mele, P., Price, R., and Yule, D. (2012). *The relationships between land management practices and soil condition and the quality of ecosystem services delivered from agricultural land in Australia*. Kiri-ganai Research Pty Ltd, Canberra.

CSIRO (2020). *ePaddocks*™ webpage, Commonwealth Scientific and Industrial Research Organisation website: *https://research.csiro.au/digiscape/digiscapes-projects/epaddocks-mapping-every-paddock-across-the-australian-grain-region/*

CTA (2018). *Index-Based Livestock Insurance as an Innovation Tool against Drought Loss*. Technical Centre for Agricultural and Rural Cooperation. ISBN 978-92-9081-636-2

DEWHA (2010). *Ecosystem Services: Key Concepts and Applications*. Occasional Paper No 1, Department of the Environment, Water, Heritage and the Arts, Canberra.

FAO (2009). *How to Feed the World in 2050*. UN Food and Agriculture Organization: *http://www.fao.org/fileadmin/templates/wsfs/docs/expert_paper/How_to_Feed_the_World_in_2050.pdf*

FAO (2017). *Review of the Available Remote Sensing Tools, Products, Methodologies and Data to Improve Crop Production Forecasts*. UN Food and Agriculture Organization, Rome. ISBN 978-92-5-109840-0.

FAO (2020a). *The State of Food Security and Nutrition in the World 2020*. UN Food and Agriculture Organization, Rome. *http://www.fao.org/3/ca9692en/online/ca9692en.html*

FAO (2020b). *Suite of food security indicators: domestic food price volatility (index)/value*. UN Food and Agriculture Organization, Rome. *http://www.fao.org/faostat/en/#data/FS*

Farmar-Bowers, Q., Higgins, V, and Millar, J. (Eds) (2013). *Food Security in Australia*. Springer. 476 p. doi:*10.1007/978-1-4614-4484-8*

Friedel, M.H., Laycock, W.A, and Bastin, G.N. (2000). Assessing rangeland condition and trend. In *Field and Laboratory Methods for Grassland and animal Production Research*. (Eds: Mannetje, L.T., and Jones, R.M.). CABI publishing, New York. pp 29–66.

Galbraith, S.M., Vierling, L., and Bosque-Pérez, N. (2015). Remote sensing and ecosystem services: current status and future opportunities for the study of bees and pollination-related services. *Current Forestry Reports*, 1(4), 261–274. doi:*10.1007/s40725-015-0024-6*

Garibaldi, L.A., Aizen, M.A., Klein, A.M., Cunningham, S.A., and Harder, L.D. (2011). Global growth and stability of agricultural yield decrease with pollinator dependence. *Proceedings of National Academy of Science*, 108, 5909–5914. *https://doi.org/10.1073/pnas.1012431108*

GEO (2019). *Essential Agricultural Variables for GEOGLAM—White Paper.* Group on Earth Observations, Draft, 27 March 2019. *http://earthobservations.org/geoglam_resources/3%20Earth%20Observation%20Data%20Coordination/Draft%20EAV%20White%20Paper.pdf*

Ghassemi, F., Jakeman, A. J., & Nix, H. A. (1995). *Salinisation of land and water resources: human causes, extent, management and case studies*. The Australian National University, Canberra, Australia; CAB International, Wallingford, Oxon, UK.

Guerschman, J., Leys, J., Rozas Larraondo, P., Henrikson, M., Paget, M., and Barson, M. (2018). *Monitoring groundcover: an online tool for Australian regions*. CSIRO, Canberra. *https://doi.org/10.25919/5bf84026e556d*

Hendy, E.J., Gagan, M.K., and Lough, J.M. (2003). Chronological control of coral records using luminescent lines and evidence for non-stationary ENSO teleconnections in northeast Australia. *Holocene*, 13, 187–199.

ILRI (2020). *International Livestock Resarch Institute* website: *https://www.ilri.org/about-us*

IPBES (2017). *Assessment Report on Pollinators, Pollination and Food Production*. Intergovernmental Science-Policy Platform on Biodiversity and Ecosystem Services, Zenodo. *http://doi.org/10.5281/zenodo.3402857*

Jacobson, T., and Adams, R.M. (1958). Salt and silt in ancient Mesopotamian agriculture. *Science*, 128(3334), 1251–1258.

Kearns, C.A., Inouye, D.W., and Waser, N. (1998). Endangered mutualisms: the conservation of plant-pollinator interactions. *Annual Reviews of Ecological Systems*, 29, 83–112. doi:*10.1146/annurev.ecolsys.29.1.83*

Klein, A.M., Vaissiere, B.E., Cane, J.H., Steffan-Dewenter, I., Cunningham, S.A., Kremen, C., and Tscharntke, T. (2007). Importance of pollinators in changing landscapes for world crops. *Proceedings of Royal Society* B, 274, 303–313.

Kogan, F. (2019). *Remote Sensing for Food Security*. Springer International Publishing, Switzerland. ISBN 978-3-319-96255-9

Lang, D. (2005). Maintaining groundcover to reduce erosion and sustain production. *Agfacts P2.1.14*, NSW Department of Primary Industries. *https://www.dpi.nsw.gov.au/__data/assets/pdf_file/0018/162306/groundcover-for-pastures.pdf*

Leys, J.F. (1991). The threshold friction velocities and soil flux rates of selected soils in south-west New South Wales. Australia. *Acta Mechanica*, 2, 103–112.

Leys, J., McTainsh, G., Strong, C., Heidenreich, S., Biesaga, K. (2008). DustWatch: using community networks to improve wind erosion monitoring in Australia. *Earth Surface Processes and Landforms*, 33, 1912–1926. *https://doi.org/10.1002/esp.1733*

Leys, J.F., Heidenreich, S.K., Strong, C.L., McTainsh, G.H., and Quigley, S. (2011). PM10 concentrations and mass transport during 'Red Dawn' Sydney September 2009. *Aeolian Research*, 3, 327–342. doi:*10.1016/j.aeolia.2011.06.003*

Leys, J., Strong, C., Heidenreich, S., and Koen, T. (2018). Where She Blows! A Ten Year Dust Climatology of Western New South Wales Australia. *Geosciences*, 8, 232. doi:*10.3390/geosciences8070232*

Leys, J.F., Howorth, J.E., Guerschman, J.P., Bala, B., and Stewart, J.B. (2020). *Setting targets for National Landcare Program monitoring and reporting vegetation cover for Australia*. NSW Department of Planning, Industry, and Environment.

Lindberg, R., Lawrence, M., Gold, L., Friel, S., and Pegram, O. (2015). Food insecurity in Australia: Implications for general practitioners. *Australian Family Physician*, 44(11), 859–862. *https://www.racgp.org.au/afp/2015/november/food-insecurity-in-australia-implications-for-general-practitioners/#2*

Mace, G.M., and Baillie, J.E.M. (2007). The 2010 Biodiversity Indicators; Challenges for Science and Policy. *Conservation Biology*, 21(6), 1406–1413.

Martin, W., and Laborde, D. (2018). The free flow of goods and food security and nutrition. Ch 3 in *2018 Global food policy report*. pp. 20–29. Washington, DC: International Food Policy Research Institute (IFPRI). *https://doi.org/10.2499/9780896292970_03*

Masó, J., Serral, I., Domingo-Marimon, C., and Zabala, A. (2020). Earth observations for sustainable development goals monitoring based on essential variables and driver-pressure-state-impact-response indicators. *International Journal of Digital Earth*, 13(2), 217–235. *https://doi.org/10.1080/17538947.2019.1576787*

McCrindle (2017). *Foodbank Hunger Report 2017*. *https://2qean3b1jjd1s87812ool5ji-wpengine.netdna-ssl.com/wp-content/uploads/2018/04/Foodbank_HungerReport_McCrindle_Oct2017_Digital.pdf*

McKeon, G.M., Hall, W.B., Henry, B.K., Stone, G.S., and Watson, I.W. (2004). *Pasture Degradation and Recovery in Australia's Rangelands: Learning From History*. Queensland Department of Natural Resources, Mines and Energy, Brisbane.

Metternicht, G.I., and Zinck, J.A. (2003). Review article. Remote sensing of soil salinity: potentials and constraints. *Remote Sensing of Environment*, 85, 1–20.

Moltmann, T., Turton J., Zhang, H.-M., Nolan, G., Gouldman, C., Griesbauer, L., Willis, Z., Piniella, Á.M., Barrell, S., Andersson, E., Gallage, C., Charpentier, E., Belbeoch, M., Poli, P., Rea, A., Burger, E.F., Legler, D.M., Lumpkin, R., Meinig, C., O'Brien, K., Saha, K., Sutton, A., Zhang, D., and Zhang, Y. (2019). A Global Ocean Observing System (GOOS), Delivered Through Enhanced Collaboration Across Regions, Communities, and New Technologies. *Frontiers in Marine Science*, 6, 291. *https://www.frontiersin.org/article/10.3389/fmars.2019.00291*

Nikolova, S., Bruce, S., Randall, L., Barrett, G., Ritman, K., and Nicholson, M. (2012). *Using remote sensing data and crop modelling to improve crop production forecasting: a scoping study*. ABARES technical report 12.3. Australian Bureau of Agricultural and Resource Economics and Sciences, Canberra.

NLWRA (2001). *Australian dryland salinity assessment 2000: extent, impacts, processes, monitoring and management options*. National Land and Water Resources Audit, Canberra.

OECD. (1993). *OECD Core Set of Indicators for Environmental Performance Reviews. A Synthesis Report by the Group on the State of the Environment*. OCDE/GD(93)179. Organisation for Economic Co-operation and Development, Paris. 35 p

Ogilvy, S. (2020). *Toward a methodology for incorporating ecological capital into the accounts of individual entities*. Ph.D. Thesis, ANU. *https://openresearch-repository.anu.edu.au/handle/1885/204830*

Ogilvy, S., Kulkarni, A., and Hurley, S. (2015). *From vicious to virtuous cycles: a sustainable future for Australian agriculture*. CPD discussion paper, August 2015. *https://cpd.org.au/wp-content/uploads/2015/08/Vicious-to-virtuous-cycles-2015.pdf*

O'Loingsigh, T., Chubb, T., Baddock, M., Kelly, T., Tapper, N.J., De Deckker, P., and McTainsh, G. (2017). Sources and pathways of dust during the Australian "Millennium Drought" decade. *Journal of Geophysical Research: Atmospheres*, 122, 1246–1260. doi:*10.1002/2016JD025737*.

Patias, P., Verde, N., Tassopoulou, M., Georgiadis, C., and Kaimaris, D. (2019). Essential variables: describing the context, progress, and opportunities for the remote sensing community. *Proceedings of Society of Photo-Optical Instrumentation Engineers (SPIE) 11174*, Seventh International Conference on Remote Sensing and Geoinformation of the Environment (RSCy2019),111740C (27 June 2019). *https://doi.org/10.1117/12.2533604*

Pereira, H.M., Ferrier, S., Walters, M., Geller, G.N., Jongman, R.H.G., Scholes, R.J., Bruford, M.W., Brummitt, N., Butchart, S.H.M., Cardoso, A.C. (2013). Essential biodiversity variables. *Science*, 339, 277–278.

Pitman, M.G., and Läuchli, A. (2002). *Global Impact of Salinity and Agricultural Ecosystems*. Ch 1 in Salinity: Environments—Plants—Molecules. (Eds: Läuchli, A., and Lüttige, U.). Kluwer Academic Publishers, Netherlands.

PMSEIC (2010). *Australia and Food Security in a Changing World. Can we feed ourselves and help feed the world in the future?* The Prime Minister's Science, Engineering and Innovation Council, Canberra, Australia. *https://www.chiefscientist.gov.au/sites/default/files/FoodSecurity_web.pdf*

Ponting, C. (1991). *A Green History of the World*. Penguin.

Potts, S.G., Imperatriz-Fonseca, V., Ngo, H.T., Zizen, M.A., Biesmeijer, J.C., Breeze, T.D., Dicks, L.V., Garibaldi, L.A., Hill, R., Settele, J., and Vanbergen, A.J. (2016). Review: Safeguarding pollinators and their value to human well-being. *Nature*, 540, 220–229. *https://doi.org/10.1038/nature20588*

Ramankutty, N., Mehrabi, Z., Waha, K., Jarvis, L., Kremen, C., Herrero, M., and Rieseberg, L.H. (2018). Trends in Global Agricultural Land Use: Implications for Environmental Health and Food Security. *Annual Review of Plant Biology*, 69(1), 789–815.

Reinhart, K.O. (2009). Rangeland Communities: Structure, Function and Classification. Ch 6 in *Range and Animal Sciences and Resources Management*. Eolss Publishers, Oxford, UK.

SOE (2016a). *Soil: Formation and erosion*, State of Environment 2016 website: *https://soe.environment.gov.au/theme/land/topic/2016/soil-formation-and-erosion*

SOE (2016b). *Soil: Salinity and acidification* webpage, State of Environment 2016 website: *https://soe.environment.gov.au/theme/land/topic/2016/soil-salinity-and-acidification*

Song, X.-P., Potapov, P.V., Krylov, A., King, L., Di Bella, C.M., Hudson, A., Khan, A., Adusei, B., Stehman, S.V., and Hansen, M.C. (2017). National-scale soybean mapping and area estimation in the United States using medium resolution satellite imagery and field survey. *Remote Sensing of Environment*, 190, 383–395.

Spies, B., and Woodgate, P. (2005). *Salinity Mapping Methods in the Australian Context*. Report prepared for Programs Committee of Natural Resource, Department of Environment, Heritage, Agriculture, Fisheries and Forestry, Canberra. ISBN: 0 642 55128 6

Tongway, D.J., and Hindley, N.L. (2004). *Landscape Function Analysis Manual: Procedures for Monitoring and Assesssing Landscapes with Special Reference to Minesites and Rangelands, Version 3.1*. CD-ROM. CSIRO Sustainable Ecosystems, Canberra.

Tozer, P., and Lees, J. (2013). Dust storms—what do they really cost?. *The Rangelands Journal*, 35, 131–142.

Waldner, F., and Diakogiannis, F. I. (2020). Deep learning on edge: extracting field boundaries from satellite images with a convolutional neural network. *Remote Sensing of Environment*, 245, 111741.

Washington-Allen, R.A., and Ravi, S. (2012). Dryland Analysis and Monitoring. Ch in *Range and Animal Sciences and Resources Management—Volume II*. UNESCO-EOLSS.

Whitcraft, A.K., Becker-Reshef, I., Justice, C.O., Gifford, L., Kavvada, A., and Jarvis, I. (2019). No pixel left behind: Toward integrating Earth Observations for agriculture into the United Nations Sustainable Development Goals framework. *Remote Sensing of Environment*, 235, 111470. *https://doi.org/10.1016/j.rse.2019.111470*

Willcox, B.K., Robson, A.J., Howlett, B.G., and Rader, R. (2018). Toward an integrated approach to crop production and pollination ecology through the application of remote sensing. *PeerJ*, 6:e5806. DOI *10.7717/peerj.5806*

Wu, B., Meng, J., Li, Q., Yan, N., Du, X., and Zhang, M. (2014). Remote sensing-based global crop monitoring: experiences with China's CropWatch system. *International Journal of Digital Earth*, 7(2),113–137. DOI *10.1080/17538947.2013.821185*

Zaman, M., Shahid, S.A., Heng, L. (2018). *Guideline for Salinity Assessment, Mitigation and Adaptation Using Nuclear and Related Techniques*. Springer Open. *https://doi.org/10.1007/978-3-319-96190-3*

12 Crops

Barbara Harrison and Graham Donald

This section focuses on the use of EO datasets to map and monitor food crops, both in Australia and globally. EO technologies now feature in the management of a wide range of Australian crops, including cereals, legumes, vegetables, fruits, nuts, and other seeds.

As introduced in Section 10.2.2, Crop Simulation Models (CSM) simulate the growth, development and yield of crops as a function of soil conditions, weather and management practice (Hoogenboom *et al*., 2004). These models allow observations at specific ground sites to be extrapolated temporally to improve our understanding of the interactions between physiological processes and agronomic activities.

In conjunction with historical yield datasets and meteorological records, CSM can be used to estimate yield for larger areas (see Section 11.2). EO-based datasets are increasingly being integrated with CSM to derive surrogates of crop growth, such as Leaf Area Index (LAI) (see Section 6.3.3). Some of the methods used to achieve this integration are reviewed in FAO (2017).

Forecasting crop production (and crop yield in particular) has been a constant concern since the beginning of the history of agriculture. Forecasting techniques have evolved, as has agriculture itself and the specifications of the forecasts needed. Those who use forecast data are always seeking greater accuracy, granularity, comparability, and timeliness. Those who produce the data or contribute to their production always operate under financial and technical constraints. Obtaining timely knowledge presents a very real challenge.
(FAO, 2016)

12.1 Crops in Australia

Weather and climatic conditions split the Australian continent into two growing regions (northern and southern) and two growing seasons (summer and winter) for crops (see Figure 2.6, Figure 2.10 and Figure 2.11). The northern region, which spans central and southern Queensland and northern NSW, has summer rains, so grows a dryland summer crop (sorghum, sunflowers, maize, mungbeans, soybeans, cotton, and peanuts) in addition to a winter crop (wheat, barley, oats, chickpeas, triticale, faba beans, lupins, field peas, canola, millet/panicum, safflower, and linseed). Southern regions, including central NSW to Victoria, Tasmania, southern SA and southwest WA, have a Mediterranean climate with dry summers and winter rainfall. These areas principally grow winter crops (wheat, barley, oats, triticale, cereal rye, lupins, field peas, canola, chickpeas, faba beans, vetch, lentils, and safflower) and require irrigation for summer crops (rice and maize; Australian Grain, 2019a).

Background image: Canola crop near Kojonup, WA, photographed on 28 February 2013. **Source:** Keith Lightbody, Wikimedia Commons. (Retrieved from *https://commons.wikimedia.org/wiki/File:Canola_crop_near_Kojonup.jpg*)

Recommended Chapter Citation: Harrison, B.A., and Donald, G.E. (2021). Crops. Ch 12 in *Earth Observation: Data, Processing and Applications. Volume 3A—Terrestrial Vegetation*. CRCSI, Melbourne. pp. 249–262.

An area covering 19 million ha was planted to cereal, legume and oil crops in Australia during 2018, which produced a total of 33 million tonnes (Australian Grain, 2019b)[9]. Over half of this area grew wheat, which delivered around 3% of global production. Wheat is a major export crop for Australia, with only about 30% of production being destined for the domestic market (AEGIC, 2020).

The horticultural industry in Australia produces fruit, vegetables, nuts, flowers, turf, and nursery products for both domestic and international markets (DAWR, 2016). Horticulture comprises the second largest rural production industry after wheat (AuSHS, 2019), with the major crops by area being grapes, apples, bananas, and potatoes (Nikolova *et al.*, 2012). The major horticulture growing areas are located in the naturally well-watered and/or irrigated locations of:

- Goulburn Valley of Victoria;
- Murrumbidgee Irrigation Area of New South Wales (NSW);
- Sunraysia district of Victoria and NSW;
- Riverland region of South Australia;
- northern Tasmania;
- southwest Western Australia; and
- coastal strips of both northern NSW and Queensland (DAWR, 2016; see Figure 11.1).

12.2 EO Sensors for Crops

A range of platforms (proximal, airborne and spaceborne; see Volume 1A—Sections 10–12) and sensors (active and passive; see Volume 1A—Sections 13–16 and Volume 1B—Sections 6–8) are being used to observe terrestrial vegetation. The EO datasets acquired by these sensors vary in terms of their spectral, spatial, radiometric, and temporal resolutions, densities and extents (see Volume 1B—Section 1) and fidelity (see Volume 1B—Section 2.1). Some characteristics of EO sensors that are relevant to studies of agricultural crops are summarised in Table 12.1. As with all EO analyses, validation of results using independent datasets is essential (see Volume 2D—Section 12 and Volume 2E). Recommended validation procedures to use with EO datasets are detailed in TERN Australia (2018) and Malthus *et al.* (2013).

The major EO sensors used to map and monitor agricultural crops have traditionally detected optical reflectances. The most commonly used approaches for mapping vegetation biomass fundamentally detect the differences between red and near infrared (NIR) reflectance (see Section 8.1.1). EO-based estimates of ET are also used to monitor irrigation requirements (Abuzar *et al.*, 2019; see Sections 9.4, 9.5 and 13).

Table 12.1 EO sensors relevant to crops

TIR: Thermal infrared: SAR: Synthetic Aperture Radar; DEM: Digital Elevation Model; ET: Evapotranspiration

Type	Sensor	Platform	Relevance	Advantages	Disadvantages
Passive optical	Multispectral radiometer	Satellite or airborne	National or regional land cover mapping	Global, recurrent coverage, low cost;	Low accuracy, coarse scale
	Hyperspectral spectroradiometer	Airborne	Crop mapping, intensive agriculture Plant biochemical functioning and health	High spectral resolution, highlight plant stress	High cost, high data volume
	TIR radiometer	Field, satellite or airborne	Soil/canopy temperature, water stress	Surrogate measure for ET	Resolution depends on platform
Active optical	Lidar	Airborne and terrestrial	Crop structure DEM	Detailed structure for plant canopy and soil surface	High cost, specialised processing
	Active optical sensors	Ground vehicles or RPAS	Crop cover and condition mapping	Convenience, low cost, independent of sunlight	Low availability
Active microwave	SAR	Satellite or airborne	Vegetation structure, soil moisture	All weather, operates at night	Data availability, noisy data, complex processing
Proximal	Passive optical sensors (phenocam, hyperspectral), meteorological sensors (including soil moisture)	Ground, tractor or tower-based (see Excursus 7.2 and Volume 2D—Section 12)	Soil, crop, and atmospheric variability, Phenology	Continuous, long term measurements	High cost and require skilled maintenance
Locational	GPS	Portable devices	Locating field sites	Low cost	Coverage in remote regions or below dense canopies

9 Please note: The 2018 cropping area was below the average of 22 million ha due to a prolonged drought.

SAR sensors detect characteristics of both soil and vegetation (see Volume 1B—Section 8). Satellite-based SAR is used to monitor agricultural and land cover practices at both global and regional scales, assess soil moisture status, and quantify plant biomass (Zhou *et al*., 2016). Multi-temporal datasets of integrated optical and SAR imagery have delivered operational inventories of major crops in Canada for a range of cropping systems (McNairn *et al*., 2008).

Cereal crops in Australia cover thousands of hectares so are often mapped using satellite imagery whereas horticultural crops are grown in smaller areas and generally require imagery acquired by aircraft. The principal satellite sensors that are used for crop mapping and yield estimation are Landsat, MODIS, and Sentinel, all of which are broadband optical sensors with adequate spatial coverage and temporal frequency (see Section 11.2). Accurate monitoring of crop nutrition has been demonstrated using airborne hyperspectral imagery (see Section 9.6 and Volume 1A—Section 14; Pullanagari *et al*., 2016), which is particularly valuable for varying fertiliser applications in precision agriculture (Cilia *et al*., 2014).

Traditional EO-based monitoring of agricultural vegetation observes crop greenness and temperature as indicators of biomass, vigour, and water stress (see Sections 8 and 9 above). More recent approaches focus on nutrient status, principally nitrogen, but also phosphorus and potassium (see Section 5.3.5 and 9.6). Aerial and ground-based gamma radiometry have also been trialled for mapping soil properties (Hall *et al*., 2014; see Volume 1A—Section 6). New proximal sensors, such as soil pH sensors and Electromagnetic Induction (EMI) sensors, are also being deployed to monitor the impact of soil condition on crops. By mapping the apparent electrical conductivity, electromagnetic induction (EMI) sensors (such as EM38) can be used to highlight the spatial variations in clay, salt, and moisture content of soils (Stanley *et al*., 2014; Heil and Schmidhalter, 2017).

A range of active and passive sensors that are being used for precision agriculture are reviewed in Suarez *et al*. (2018). Other digital innovations being embraced by precision agriculture, such as using Variable Rate Technology (VRT) rather than the traditional uniform application of fertilisers, are designed to control the efficient use of inputs for maximised outputs (see Section 12.6). Terrestrial Laser Scanning (TLS) and Airborne Laser Scanning (ALS) have also been successfully trialled for mapping tree structure in avocado, macadamia, and mango orchards in Australia (Wu *et al*., 2020; see Excursus 5.1).

An increasing number of growers are using unmanned aerial vehicles (UAV, commonly called drones; see Volume 1A—Section 11.2), carrying multispectral, hyperspectral, and thermal sensors, to monitor the health, nutrient status, and yield of horticultural crops (see Section 11.5). Since these platforms are typically flown at low altitude for agricultural applications, the acquired sensor measurements are minimally impacted by atmospheric effects. UAV-acquired datasets are also being used to ground truth crop mapping from satellite imagery (Hegarty-Craver *et al*., 2020).

A new area of research for crops is solar induced chlorophyll fluorescence (SIF), which is a direct measure of photosynthetic activity (Mohammed *et al*., 2019; see Section 17.3.2). SIF can be detected using optical sensors (especially hyperspectral). Several satellites can currently be used to do this but there are few bespoke SIF systems planned for future launch.

12.3 Crop Type and Agricultural Land Use

Crop type mapping is valuable for a wide range of crops in Australia. Growers, distributors and consumers all directly benefit from efficiencies derived from knowledge of crop extent, timing, vigour, variability, and yield, while indirect benefits extend to efficient responses to biosecurity threats and natural disasters.

A range of EO methods for mapping land cover have been used to map agricultural land uses and different types of crops (see Section 3). Early mapping of agricultural land cover used the Normalised Difference Vegetation Index (NDVI; see Section 8.1.1; Hill *et al*., 1999) and image classification (Hill *et al*., 2005). More recently, EO time series datasets have enabled more sophisticated analyses, both for mapping crop type, and also for quantifying crop condition and predicting crop yield (see Section 12.4).

The optimum timing of EO image acquisition to differentiate between crops, and separate yield categories for a single crop, varies considerably with both crop and growing region (Van Niel and McVicar, 2003, 2004). Single date analyses can be misleading if the image date is not indicative of the crop peak growth stage. The best relationships between vegetation indices and crop yield for grain crops have been observed when the image is acquired at the mid grain-filling stage (Shanahan *et al*., 2001; Panek and Gozdowski, 2020; see Section 9.3). However, temporal characteristics of crops can vary from year to year, depending on sowing dates and other management practices, and also climatic variations between seasons.

Some recent approaches that have been developed to differentiate agricultural crops using EO datasets in Australia include:

- applying geostatistical concepts to EO time series to differentiate broad crop groups (Pringle *et al.*, 2018);
- applying curve fitting methods to EO time series to characterise the phenology of specific crops, then use these characteristics to discriminate between crops and estimate crop areas (Potgieter *et al.*, 2013);
- deriving climate-driven, crop-specific stress indices to explain the influence of agro-environmental heterogeneity in croplands at finer spatial scales (Chen *et al.*, 2020a);
- monitoring fallow dynamics using biased support vector machines (see Volume 2E) with fractional cover images (see Excursus 8.3; Zhao *et al.*, 2020);
- classifying summer cropping in irrigated areas of the Murray-Darling Basin (MDB; see Section 2.1 and Figure 2.4) using a random forest model (see Volume 2E) with EO-based estimates of vegetation phenology and water use (Peña-Arancibia *et al.*, 2014);
- using balancing methods to more accurately classify rare and infrequent crops (Waldner *et al.*, 2019); and
- refining criteria for using blended datasets (see Volume 2D—Section 6) to increase the density of EO time series datasets for crop identification and yield prediction (Chen *et al.*, 2020b).

12.4 Crop Extent, Condition and Production Forecasts

Two of the most established applications of EO datasets are mapping crop area and forecasting crop yield. As crops mature the spectral characteristics of vegetation vary temporally with phenological changes (see Sections 5.3.2 and 9.3). They also vary both temporally and spatially with changes in ambient environmental conditions (see Volume 1B—Section 1). EO datasets allow these variations to be mapped through time to analyse a single growing season and/or trends across several seasons. The spatial variations in EO imagery, within individual crop fields and districts, can highlight infestations of weeds, diseases in plants and soils, and deficiencies in water or nutrients.

Traditionally, such analyses relied on correlations between EO-based greenness indices and crop yield (see Volume 2C—Section 11 and 8.1.1). One of the spectral indices that is commonly used for crop mapping is NDVI (see Section 8.1.1), which is considered a surrogate for LAI or fAPAR (fraction of Absorbed Photosynthetically Active Radiation; see Section 6.3; FAO, 2017). The most appropriate spectral information and algorithms to correlate with crop yield, however, vary with crop type, season, age, condition, and location, with stressed situations being more challenging (Suarez *et al.*, 2018). When based on spectral indices, the most appropriate index is typically selected as the one with the highest correlation with yield data, then index values for a crop image can be classifed into appropriate categories such as low, medium, and high (see Volume 1B—Excursus 9.1). While originally such methods were applied to broadacre cereal crops, principally wheat and rice (Tucker *et al.*, 1980), more recently higher resolution imagery has enabled this approach to be used with a range of fruit, nut, and vegetable crops (see Section 12.6). Other EO-based approaches to yield mapping include image classification (see Volume 2E), machine learning regression methods (Kamir *et al.*, 2020), semi-empirical models (Chen *et al.*, 2020a), and integrated crop models, which combine relevant spectral indices with predictive models (Schut *et al.*, 2009).

For example, Crop-SI is a semi-empirical model that is used to estimate the yield of wheat, barley, and canola crops in the dryland Australian wheatbelt (Chen *et al.*, 2020a). It combines a radiation use efficiency model with meteorology-driven Stress Indices (SI) at critical crop growth stages (e.g. anthesis and grain-filling; see Table 12.2). These crop-specific SI (e.g. drought, heat, and cold stress) help explain the impact of high spatial agro-environmental heterogeneity, which has lead to substantial improvement in grain yield prediction.

Another example of EO-based yield forecasting in Australia is SugarMaps, a prototype system which provides automated processing and delivery of EO imagery to over 95% of the sugar industry. Products include crop vigour, derived yield, and qualitative foliar nitrogen concentration maps for most Australian growing regions (UNE CASI, 2020).

Timely and reliable crop production forecasts are crucial to making informed food policy decisions and enabling rapid responses to emerging food shortfalls.
(FAO, 2017)

Table 12.2 Crop-SI model

Approach	Input parameters	Derived parameters		Result
Radiation Use Efficiency (RUE)	Top of atmosphere shortwave irradiance	Photosynthetically Active Radiation (PAR)	Carbon fixation	Grain yield estimate
	Ratio of irradiance at sloping surface to that at a horizontal surface			
	Atmospheric transmissivity			
	NDVI	fraction of Absorbed Photosynthetically Active Radiation (fAPAR)		
	Diffuse fraction	RUE		
	Photosynthetic capacity			
Support Vector Machine (SVM) feature selection	Air temperature	Meteorologically-driven Stress Index (SI)		
	Precipitation			

Source: Chen *et al.* (2020) Figure 2

Automated mapping of paddock boundaries helps farmers to monitor productivity and land condition at a relevant scale. A new Digiscape project, ePaddocks™, uses artificial intelligence to interpret high spatial resolution satellite imagery in order to define paddock boundaries (CSIRO, 2020a; Waldner and Diakogiannis, 2020; see page before Section 11). This facility is being applied across the Australian grain region and will be integrated with other EO-based systems to classify land use and identify crop types (see Sections 3 and 12.3). The benefits (to both individual farmers and the wider agricultural sector) of focusing yield forecasts on individual land parcels include land management, harvest logistics, and financial analysis.

For a selected crop in a given season, integrated forecasting systems aim to deliver near real time estimates of crop area, which can be merged with near real time predictions of yield, to determine the likely total production (Nikolova *et al.*, 2012). Traditionally, most estimates of crop yield and production have been derived from climate-driven models, with expert knowledge supplying estimates of planted area and production rates. Such models, however, cannot account for unexpected changes in seasonal conditions during the forecast period, such as natural disasters, and are typically less accurate for winter cropping. In Australia, different crop forecasting methods are used in different regions and jurisdictions, and plans are underway to develop a nationally-consistent approach for all major crops (Nikolova *et al.*, 2012). Increasingly EO-based datasets and biophysical crop growth models are being integrated with agroclimatic models, and crop, soil, and management datasets, to improve the accuracy, frequency, and latency of spatially-explicit, agricultural forecasts at regional, national, and global scales. Ultimately such systems enable mapping of crop type, area, condition and yield, and forecasting of crop production on a regional and global basis (FAO, 2017; see Section 12.5,).

Meteorological datasets are valuable in crop monitoring, not only to track production but also to warn of potentially damaging weather condition. For example, the Australian Tree Crop Map Severe Weather App integrates live weather data with maps of commercial horticulture tree crops (avocado, banana, citrus, macadamia, mango, and olive) to provide early warning of possible storm damage (see Section 12.7).

The type and precision of crop forecasting varies with the purpose and scale of analysis from global predictions to farm-based estimates (see Table 12.3). In recent years, improvements in near real time crop-specific monitoring at regional and national scales, including crop type mapping and vegetation status, have been achieved using high resolution, satellite-derived EO imagery and automated workflows (Inglada *et al.*, 2015; Defourny *et al.*, 2019). These products provide valuable input to global monitoring initatives such as GEOGLAM (see Excursus 11.1).

While many existing crop yield models have not scaled up from field to regional scales with sufficient accuracy, some recent, scalable crop yield models are showing promise in this area (Lobell *et al.*, 2015; Donohue *et al.*, 2018). However, the utility of crop models is determined by both their spatial and temporal scales. Since the primary goal of these models is to reduce risk in all steps along the food supply chain from farm to market, timeliness in delivering results—particularly minimum latency—is essential to all users (FAO, 2016). An Australian system that delivers multi-scale, real time forecasting of yield for cereal crops is introduced in Excursus 12.1.

Table 12.3 Scales of crop forecasting

Ground scale	User	Decision	EO spatial resolution
Field	Farmer	Crop and resource management	Very high
Farm	Producers, suppliers	Business, marketing, supply chain	High
Agroecological zone	Districts, farmer co-ops	Economic optimisation, environmental management	Medium
Regional	State/regional agencies	Land use and economic planning, environmental management	Medium
National	Governments	Food security, disaster relief, strategic planning, trade policy, environmental impact and policy	Low
Global	International agencies, multinational companies	International treaties, protocols, global treaties	Very low

Adapted from: FAO (2016) and Potgieter *et al.* (2013) Figure 1

Excursus 12.1—Graincast

Source: CSIRO (2020b)

Graincast™ uses national weather and soils information to estimate the soil moisture that is available to plants on a daily basis, and the crop yield potential for the current season. This estimate can apply to an individual paddock, a farm, a region, or a nation. Graincast™ provides objective information for farmers and land managers to make better informed management decisions in near real time.

Inputs to Graincast™ include:

- daily rainfall, temperature, and solar radiation data at 5 km resolution from the Bureau of Meteorology (BoM, 2020);
- climate data from SILO (Scientific Information for Land Owners) climate database at 5 km resolution (Queensland Government, 2020); and
- soil data from the Soil and Landscape Grid of Australia (SLGA; Grundy *et al.*, 2015) at 90 m resolution.

These data layers are integrated with cadastre, elevation, and/or EO datasets to generate multiple outputs:

- maps of crop species growing in each paddock derived using adaptive learning algorithms applied to available optical and SAR images from the Landsat-8 and Sentinel-2 satellites;
- estimates of yield potential and 'plant available soil water' for the current season calculated using the APSIM (Agricultural Production Systems sIMulator) crop model (Holzworth *et al.*, 2014, 2018; see Section 10.2.2) based on the SLGA and SILO datasets;
- time series of historical water-limited, potential yield estimates for a particular paddock, to assist with benchmarking, diagnosing yield constraints and setting yield targets; and
- seasonal yield forecasts derived using real time crop models based on NDVI computed from multiple satellite images (Donohue *et al.*, 2018).

Since APSIM needs to estimate the daily dynamics of plant available water (PAW) to simulate crop growth under the current seasonal conditions, Graincast™ can also be used to provide an estimate of PAW in real time, without the need for local knowledge of the actual soil type in each paddock. Such estimates of PAW often provide better estimates of soil water than a single, poorly calibrated, standalone, soil water sensor (Freebairn *et al.*, 2018).

At this stage of development, Graincast™ forecasts are based on known conditions to the date of publication and the probable conditions to harvest based on the previous 30 years. Extreme events, such as severe frosts, heat shocks, floods, and hail storms, can have significant local implications that are not included in the forecasts and may result in lower than forecast yields if they are more widespread than usual. Also, forecasts do not account for large scale outbreaks of pests or diseases which may also result in lower than forecast yields.

12.5 Global Crop Monitoring Systems

The original large scale study of global wheat production, the Large Area Crop Inventory Experiment (LACIE; MacDonald *et al*., 1975; Erickson, 1984), achieved its goals to:

- demonstrate that multispectral, EO from space was economical, timely, and repeatable;
- forecast the global wheat crop area, yield, and production using Landsat-2 MSS imagery and NOAA meteorological data, together with climatological and conventional data sources; and
- validate techniques to deliver timely estimates of crop production (Erickson, 1984).

This pioneering project paved the way for many more precise and accurate EO-based crop models, whose results can be directly interpreted in terms of economic outcomes (see Section 10.2.2). Sophisticated modelling approaches have been developed using EO time series datasets, integrated with meteorological records and soil surveys, to monitor and profile crop productivity through time (FAO, 2016). For example, eight global and regional agricultural monitoring systems, reviewed by Fritz *et al*. (2019), are summarised in Table 12.4. These systems enable early warnings of potential food famines to be coordinated and disseminated efficiently (Atzberger, 2013) by monitoring weather conditions and crop growth, then highlighting anomalies in key indicators such as precipitation, Land Surface Temperature (LST; see Section 7.5), and NDVI (FAO, 2017). In addition to essential input from analysts to vet input data, guide processing, and check results, agricultural monitoring systems now rely on four major sources of information:

- meteorological—e.g. precipitation, temperature, evapotranspiration, solar radiation, relative humidity, wind speed, snow cover, atmospheric pressure (many of these parameters are also derived from EO sensors);
- optical satellite EO—e.g. vegetation indices, soil moisture;
- crop models—e.g. water balance, biophysical; and
- auxillary datasets—e.g. cadastre, elevation, census, climatic/agroecological zones, soils, crop type, crop calendar (Fritz *et al*., 2019; see Figure 2 therein).

Typical model outputs include forecasts of crop condition, intensity, yield, and area impacted by critical anomalies. Not surprisingly, forecasts tend to improve during the growing season. While several of these systems supply regular reports and online maps, they are not validated statistically and significant discrepancies exist between the results of different systems. Many of the global land cover mapping products are used as input to define crop type and these also display major differences with respect to cropland (Fritz *et al*., 2011; Waldner *et al*., 2015). Similarly, many global crop calendars do not account for detailed spatial variations (Fritz *et al*., 2019), and refinements in agricultural system models are needed both in terms of data and methods (Jones *et al*., 2017).

Although EO-based datasets deliver reliable estimates of crop condition and condition anomalies, they do not currently supply the quantitative estimates of crop area or forecasts of crop production required to accurately monitor food security (see Section 11.5). Other areas where these systems could be improved include more consistent calibration and validation protocols, global maps of crop intensity and crop type, additional information on crop management, better access via portable smart devices, and inclusion of crowdsourced and volunteered data (including social media; Fritz *et al*., 2019).

VRT (Variable Rate Technology) is essentially managing variability within paddocks by adjusting major inputs such as fertiliser to their optimum profit level. A synthesis of previous yield maps, imagery and soils data can be used to define zones within paddocks that warrant varying levels of inputs. (Agtrans Research, 2007)

Table 12.4 Global and regional agricultural monitoring systems

CAS-IRSDE: Institute of Remote Sensing and Digital Earth at the Chinese Academy of Sciences; USDA-FAS: United States Department of Agriculture-Foreign Agricultural Service; WFP: World Food Programme; EC-JRC: European Commission Joint Research Centre

System	Coordinator	Start Date	Purpose	Outputs	Reference
Global information and early warning system (GIEWS)	UN FAO	Early 1970s	Global food crop production, consumption and trade	Quarterly reports and *ad hoc* briefs plus monthly bulletins on food price trends	*http://www.fao.org/giews/en/*
			Agricultural Stress Index (ASI) System	Regional hotspot maps of water stressed crops based on ASI every ten days (see Section 9.5)	
Famine early warning systems network (FEWS NET)	USAID	1985	Quantify changes in crop area planted and crop yield	Quarterly outlook reports with monthly updates for selected food insecure countries and alerts on emerging crises	*http://www.fews.net/*
MARS crop yield forecasting system (MCYFS)	EC-JRC	1992	Operational estimates of area, yield and production at pan-European level for EU member states	Monthly bulletins, maps updated three times per month	*https://agri4cast.jrc.ec.europa.eu/*
				Visualisations via JRC MARS Explorer	*http://www.marsop.info/en/web/mars-explorer/home*
CropWatch	CAS-IRSDE	1998	Predictions of crop conditions and production, both within China and globally	Quarterly and annual bulletin with updates for global coverage, regional indicators (VHI, VCI) and detailed national/sub-national estimates	*http://www.cropwatch.com.cn/*
Crop Explorer	USDA-FAS	2001	Global crop conditions and production estimates, for all major commodities, for all foreign countries	Data visualisation products and numerous maps and charts updated every 10 days	*https://www.fas.usda.gov/*
Group on Earth Observations Global Agricultural Monitoring Initiative (GEOGLAM)	GEO	2013	Assessment of crop growing conditions, crop status and agroclimatic conditions that may have an impact on global production of wheat, maize, rice, and soy for Agricultural Market Information System (AMIS)	Monthly reports	*http://www.geoglam.org/index.php/en/*
Seasonal Monitor	WFP	2014	Monitor growing season status and to provide early warning of conditions detrimental to crop and pasture production within WFP regions of interest	Monthly reports	*https://www.wfp.org/content/seasonal-monitor*
				Dataviz visualisation platform	*http://dataviz.vam.wfp.org/*
Anomaly Hot Spots of Agricultural Production (ASAP)	EC-JRC	2017	Identify areas where unfavourable growing conditions for both crops and rangelands may represent a potential food security problem	Early warnings every ten days based on rainfall estimates/NDVI with verified hotspots for potential food security updated monthly	*https://mars.jrc.ec.europa.eu/asap/*

Source: Fritz *et al.* (2019)

12.6 Precision Agriculture

Precision agriculture comprises a range of digital technologies that are designed to monitor variations in the environmental conditions of plant, animal and soil resources in order to optimise their productivity, reduce their environmental impact and enhance food security (Zhang *et al.*, 2002; Mulla, 2013; Bramley and Trengove, 2013). These technologies allow farmers to vary the use of inputs, such as the selection and application of seeds, fertilisers, pesticides, and water, and/or cultivation methods (planting, tillage, harvesting), to match varying soil and crop conditions across a field (Srinivasan, 2006).

Technologies involved with precision agriculture basically rely on EO sensors carried by satellite, airborne (manned and unmanned), and ground platforms. Local platforms, such as low-level aircraft and quad bikes, offer convenience and flexibility for data acquisition in a precision agriculture environment. For example, when equippled with active optical sensors, these two platforms have respectively enabled assessment of plant vigour for cereal crops (Lamb *et al.*, 2009, 2011) and perennial pastures (Trotter *et al.*, 2010).

Examples of location-specfic data that can be acquired by relevant sensors include:

- soil moisture, temperature, albedo, nutrient content, compaction, and elevation;
- animal location, digestion, and fertility;
- plant biomass, moisture status, temperature, and nutritional and physiological status; and
- air temperature, humidity, precipitation, and wind speed and direction.

Analysis of soil, plant and atmospheric datasets enables precise application of irrigation water, fertilisers and chemicals to deter pests and weeds. This information also provides early warning of disease, deficiency conditions, or weed infestations at specific locations (Mahlein *et al*., 2012). Animal tracking devices monitor grazing patterns, and allow graziers to optimise stocking rates and resource usage (see Volume 1A—Excursus 10.1) and implement virtual fencing (Butler *et al*., 2004; CSIRO, 2020c). Automated plant counts derived from drone imagery are also being trialled to monitor non-overlapping vegetable crops, such as brassicas and lettuce (O'Halloran and van Sprang, 2019).

A wide range of agricultural robots with both remote and proximal sensors are now available to plow, fertilise, treat and harvest crops, while automated imaging systems can deliver rapid analyses of the spatial variations in crop and soil condition, and produce georeferenced yield maps. For ease of access in the field, many of these applications have been adapted to control by smartphone or tablet.

Variable Rate Technology (VRT) are also being embraced by the grains industry to tailor crop management to variations in growing conditions within crops (Suarez *et al*., 2018). By adjusting agricultural inputs to suit environmental conditions, precision agriculture not only increases the output of agricultural enterprises, but improves the efficiency of resource use with less pollution (Agtrans Research, 2007). This is particularly important for fertiliser use where excessive applications can leach into waterways. Ideally nutrient supply only matches, but does not exceed, crop requirements to achieve maximum profit (see Figure 12.1). For example, Basso *et al*. (2016) analysed high resolution satellite imagery, which had been transformed using the Canopy Chlorophyll Content Index (CCCI; see Section 8.1.2) and validated using hand-held spectrometers, to map the spatial uptake of nitrogen applications by wheat crops. Thus, VRT, coupled with EO datasets, can both reduce potential environmental problems resulting from excessive use of fertiliser and avoid expenses that do not contribute to crop yield.

Figure 12.1 Crop response to fertiliser application

Additional fertiliser increases crop yield only up to a site-specific threshold. However, before this threshold, there may be a break-even point at which the cost of extra fertiliser exceeds the value of increased crop yield.

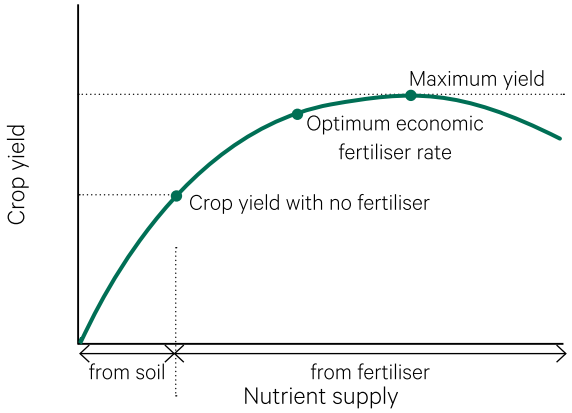

Adapted from: *http://adlib.everysite.co.uk/adlib/defra/content.aspx?id=2RRVTHNXTS.88UF41WXRQOZS*

Selected precision agriculture monitoring datasets have been coupled with crop production models and meteorological records to deliver real time estimates of seasonal yield. In conjunction with a decision support framework, farmers can then assess the seasonal profitability of additional inputs for individual crops. When integrated with Geographic Information Systems (GIS), precision agriculture readily generates 'Paddock to Plate' forecasts to achieve efficient marketing of produce (see Volume 1B—Excursus 9.1).

Precision agriculture allows the performance of a crop and its environmental conditions to be monitored closely throughout is growth cycle and enables harvesting to be timed for maximum yield. This approach also allows growers to focus on crop quality by selective harvesting (Bramley and Trengove, 2013). Especially for horticultural crops, prior knowledge of harvest time allows growers to optimise labour, packaging, and marketing requirements. Some of the agricultural industries in Australia that are adopting precision agriculture include:

- viticulture (Bramley, 2010; Bramley *et al*., 2011; Bramley and Trengove, 2013; Fuentes *et al*., 2014);
- broadacre cropping—Australian wheat growers are optimising crop productivity and profit by using the Yield Prophet application (CSIRO, 2020d);
- sugar (see Volume 1B—Excursus 1.1; Rahman and Robson, 2016a, 2016b, Robson *et al*., 2016a);
- fruit crops (see Volume 1B—Excursus 9.1; APAL, 2019);
- nut crops (Robson *et al*., 2016b, 2017); and
- vegetable production (Suarez *et al*., 2018).

12.7 Further Information

Plant Phenomics

https://www.plantphenomics.org.au/about-us/

Australian Crop Monitoring

Agricultural Production Systems sIMulator (APSIM): *https://www.apsim.info/apsim-model/*

Graincast: *https://research.csiro.au/graincast/*

Queensland Crop Mapping: *https://www.qld.gov.au/environment/land/management/mapping/statewide-monitoring/crops*

International Monitoring Systems

Cropwatch: *http://www.cropwatch.com.cn/htm/en/index.shtml*

EuroGEO: e-shape/eurogeo/h2020/eu-cap

GEOGLAM Rangeland and Pasture Productivity (RaPP) tool:

Australia: *https://map.geo-rapp.org/#australia*

Global: *https://www.geo-rapp.org*

Precision Agriculture

Srinivasan (2006)

CSIRO Precision Agriculture webpage: *https://www.csiro.au/en/Research/AF/Areas/Sustainable-farming-systems/Precision-agriculture*

Society of Precision Agriculture Australia (SPAA): *www.spaa.com.au*

Tree Crops

Australian Tree Crop Map Dashboard: *https://une-2351.maps.arcgis.com/apps/dashboards/8fd2ce70111e40088127867c63b9127e*

Australian Tree Crop Map Severe Weather App: Overlays live weather data with the location and extent of commercial horticulture tree crops in Australia. Mapped commodities include: avocado, banana, citrus, macadamia, mango and olive: *https://une-2351.maps.arcgis.com/apps/webappviewer/index.html?id=03c4d068ada9458da2eeb3e44d6f45ad*

12.8 References

Abuzar, M., Whitfield, D., McAllister, A., and Sheffield, K. (2019). Application of ET-NDVI-relationship approach and soil-water-balance modelling for the monitoring of irrigation performance of treed horticulture crops in a key fruit-growing district of Australia. *International Journal of Remote Sensing*, 40(12), 4724–4742. doi:*10.1080/01431161.2019.1573337*

AEGIC (2020). *Wheat* webpage, Australian Export Grains Innovation Centre website: *https://www.aegic.org.au/publications/australian-grains/wheat/*

Agtrans Research (2007). *An Economic Analysis of the GRDC Investment in Precision Agriculture Variable Rate Technology (VRT)*. Grains Research and Development Corporation Project Code: ATR00002. ISBN 978-1-921779-04-6 *https://grdc.com.au/__data/assets/pdf_file/0021/225084/grdc_impass_precisionagricultureanalysis.pdf*

APAL (2019). *Drones deployed to assess nitrogen needs of pears* webpage, (4 September 2019) Apple and Pear Australia Ltd website: *https://apal.org.au/drones-deployed-to-assess-nitrogen-needs-of-pears/*

AuSHS (2019). *Australian Horticulture* webpage. Australian Society of Horticultural Science website: *http://aushs.org.au/australian-horticulture/*

Australian Grain (2019a). *The Grain Industry*. Australian Grain website: *http://www.ausgrain.com.au/industry.html*

Australian Grain (2019b). *Grain Yearbook 2019*. Australian Grain. Greenmount Press. *http://www.ausgrain.com.au/Back%20Issues/287ybgrn19/287ybgrn19.pdf*

Atzberger, C. (2013). Advances in remote sensing of agriculture: context description, existing operational monitoring systems and major information needs. *Remote Sensing*, 5, 949–981. *http://dx.doi.org/10.3390/rs5020949*

Basso, B., Fiorentino, C., Cammarano, D., and Schulthess, U. (2016). Variable rate nitrogen fertilizer response in wheat using remote sensing. *Precision Agriculture*, 17(2), 168–182. doi:*10.1007/s11119-015-9414-9*

BoM (2020). *Climate Data Online* webpage, Bureau of Meteorology website: *http://www.bom.gov.au/climate/data/*

Bramley, R., and Trengove, S. (2013). Precision agriculture in Australia: Present status and recent developments. *Engenharia Agricola*, 33(3), 575–588.

Bramley, R.G.V. (2010). Precision Viticulture: Managing vineyard variability for improved quality outcomes. In: (Ed: Reynolds, A.G.) *Managing wine quality. Viticulture and wine quality*. Woodhead Publishing, Cambridge. pp. 445–480.

Bramley, R.G.V., Le Moigne, M., Evain, S., Ouzman, J., Florin, L., Fadaili, E.M., Hinze, C.J., and Cerovic, Z.G. (2011). On-the-go sensing of grape berry anthocyanins during commercial harvest: development and prospects. *Australian Journal of Grape and Wine Research*, 17(3), 316–326. doi:*10.1111/j.1755-0238.2011.00158.x*

Butler, Z., Corker, P., Peterson, R., and Rus, D. (2004). Virtual Fences for Controlling Cows. *Proceedings of IEEE International Conference on Robotics and Automation, September 2004*. New Orleans, LA, USA. pp. 4429–4436, Volume 5. doi:*10.1109/ROBOT.2004.1302415*

Chen, Y., Donohue, R.J., McVicar, T.R., Waldner, F., Mata, G., Ota, N., Houshmandfar, A., Dayal, K., Lawes, R.A. (2020a). Nationwide crop yield estimation based on photosynthesis and meteorological stress indices. *Agricultural and Forest Meteorology*, 284, 107872. *https://doi.org/10.1016/j.agrformet.2019.107872*

Chen, Y., McVicar, T.R., Donohue, R.J., Garg, N., Waldner, F., Ota, N., Li, L., and Lawes, R. (2020b). To Blend or Not to Blend? A Framework for Nationwide Landsat–MODIS Data Selection for Crop Yield Prediction. *Remote Sensing*, 12(10), 1653. *https://doi.org/10.3390/rs12101653*

Cilia, C., Panigada, C., Rossini, M., Meroni, M., Busetto, L., Amaducci, S., Boschetti, M., Picchi, V., and Colombo, R. (2014). Nitrogen Status Assessment for Variable Rate Fertilization in Maize through Hyperspectral Imagery. *Remote Sensing*, 6(7), 6549–6565. *https://doi.org/10.3390/rs6076549*

CSIRO (2020a). *ePaddocks*™ webpage, Commonwealth Scientific and Industrial Research Organisation website: *https://research.csiro.au/digiscape/digiscapes-projects/epaddocks-mapping-every-paddock-across-the-australian-grain-region/*

CSIRO (2020b). *Graincast*™ webpage, Commonwealth Scientific and Industrial Research Organisation website: *https://research.csiro.au/graincast/*

CSIRO (2020c). *Virtual fencing* webpage, Commonwealth Scientific and Industrial Research Organisation website: *https://www.csiro.au/en/Research/AF/Areas/Livestock/Virtual-fencing#:~:text=Virtual%20fencing%20is%20an%20animal,need%20for%20an%20actual%20fence*.

CSIRO (2020d). *Yield Prophet*© webpage, Commonwealth Scientific and Industrial Research Organisation website: *https://www.csiro.au/en/Research/AF/Areas/Digital-agriculture/Cropping-pastures/Yield-Prophet*

DAWR (2016). *Horticulture fact sheet*, Department of Agriculture and Water Resources: *http://www.agriculture.gov.au/ag-farm-food/hort-policy/horticulture_fact_sheet*

Defourny, P., Bontemps, S., Bellemans, N., Cara, C., Dedieu, G., Guzzonato, E., Hagolle, O., Inglada, J., Nicola, L., Rabaute, T., Savinaud, M., Udroiu, C., Valero, S., Bégué, A., Dejoux, J.-F., El Harti, A., Ezzahar, J., Kussul, N., Labbassi, K., Lebourgeois, V., Miao, Z., Newby, T., Nyamugama, A., Salh, N., Shelestov, A., Simonneaux, V., Sibiry Traore, P., Traore, S.S., and Koetz, B. (2019). Near real-time agriculture monitoring at national scale at parcel resolution: Performance assessment of the Sen2-Agri automated system in various cropping systems around the world. *Remote Sensing of Environment*, 221, 551–568.

Donohue, R., Lawes, R., Mata, G., Gobbett, D., and Ouzman, J. (2018). Towards a national, remote-sensing-based model for predicting field-scale crop yield: application to three winter crop species. *Field Crops Research*, 227, 79–90. *https://doi.org/10.1016/j.fcr.2018.08.005*

Erickson, J.D. (1984). The LACIE Experiment in Satellite Aided Monitoring of Global Crop Production. Ch 8 in *The Role of Terrestrial Vegetation in the Global Carbon Cycle: Measurement by Remote Sensing*. (Ed: G.M. Woodwell). John Wiley and Sons Ltd.

FAO (2016). *Crop Yield Forecasting: Methodological and Institutional Aspects*. UN Food and Agricultural Organisation, Rome. *http://www.amis-outlook.org/fileadmin/user_upload/amis/docs/resources/AMIS_CYF-Methodological-and-Institutional-Aspects_web.pdf*

FAO (2017). *Review of the Available Remote Sensing Tools, Products, Methodologies and Data to Improve Crop Production Forecasts*. UN Food and Agriculture Organization, Rome. ISBN 978-92-5-109840-0.

Freebairn, D.M., Ghahramani, A., Robinson, J.B., McClymont, D. (2018). A soil water monitoring tool using modelling, on-farm data and mobile technology. *Environmental Modelling and Software*, 104, 55–63. *https://doi.org/10.1016/j.envsoft.2018.03.010*

Fritz, S., See, L., McCallum, I., Schill, C., Obersteiner, M., van der Velde, M., Boettcher, H., Havlík, P., Achard, F., (2011). Highlighting continued uncertainty in global land cover maps for the user community. *Environmental Research Letters*, 6, 044005. *http://dx.doi.org/10.1088/1748-9326/6/4/044005*

Fritz, S., See, L., Bayas, J.C.L., Waldner, F., Jacques, D., Becker-Reshef, I., Whitcraft, A., Baruth, B., Bonifacio, R., Crutchfield, J., Rembold, F., Rojas, O., Schucknecht, A., Van der Velde, M., Verdin, J., Wu, B., Yan, N., You, L., Gilliams, S., Mücher, S., Tetrault, R., Moorthy, I., and McCallum, I. (2019). A comparison of global agricultural monitoring systems and current gaps. *Agricultural Systems*, 168, 258–272. *https://doi.org/10.1016/j.agsy.2018.05.0*

Fuentes, S., Poblete-Echeverría, C., Ortega-Farias, S., Tyerman, S., and de Bei, R. (2014). Automated estimation of leaf area index from grapevine canopies using cover photography, video and computational analysis methods. *Australian Journal of Grape and Wine Research*, 20(3), 465–473.

Grundy, M., Viscarra Rossel, R., Searle, R., Wilson, P., Chen, C., and Gregory, L. (2015). The Soil and Landscape Grid of Australia. *Soil Research*, 53, 835–844.

Hall, D, Galloway, P., Lemon, J., Curtis, B., van Burgel, A., and Kong, K. (2014). *The agronomy jigsaw*. Department of Agriculture and Food, Western Australia. Bulletin 4850. ISSN 1833-7236. *https://www.agric.wa.gov.au/sites/gateway/files/Agronomy%20jigsaw%20bulletin%204850.pdf*

Hegarty-Craver, M., Polly, J., O'Neil, M., Ujeneza, N., Rineer, J., Beach, R.H., Lapidus, D., and Temple, D.S. (2020). Remote Crop Mapping at Scale: Using Satellite Imagery and UAV-Acquired Data as Ground Truth. *Remote Sensing*, 12, 1984. doi:*10.3390/rs12121984*

Heil, K., and Schmidhalter, U. (2017). The Application of EM38: Determination of Soil Parameters, Selection of Soil Sampling Points and Use in Agriculture and Archaeology. *Sensors*, 17(11), 2540. *https://doi.org/10.3390/s17112540*

Hill, M.J., Vickery, P.J., Furnival, E.P., and Donald, G.E. (1999). Pasture land cover in eastern Australia from NOAA-AVHRR NDVI and classified Landsat TM. *Remote Sensing of Environment*, 67, 32–50 doi:*10.1016/S0034-4257(98)00075-3*

Hill, M.J., Ticehurst, C.J., Lee, J.S., Grunes, M.R., Donald, G.E., and Henry, D. (2005). Integration of optical and radar classifications for mapping pasture type in western Australia. *IEEE Transactions on Geoscience and Remote Sensing*, 43, 1665–1681. doi:*10.1109/TGRS.2005.846868*

Holzworth, D.P., Huth, N.I., deVoil, P.G., Zurcher, E.J., Herrmann, N.I., McLean, G., Chenu, K., van Oosterom, E.J., Snow, V., Murphy, C., Moore, A.D., Brown, H., Whish, J.P.M., Verrall, S., Fainges, J., Bell, L.W., Peake, A.S., Poulton, P.L., Hochman, Z., Thorburn, P.J., Gaydon, D.S., Dalgliesh, N.P., Rodriguez, D., Cox, H., Chapman, S., Doherty, A., Teixeira, E., Sharp, J., Cichota, R., Vogeler, I., Li, F.Y., Wang, E., Hammer, G.L., Robertson, M.J., Dimes, J.P., Whitbread, A.M., Hunt, J., van Rees, H., McClelland, T., Carberry, P.S., Hargreaves, J.N.G., MacLeod, N., McDonald, C., Harsdorf, J., Wedgwood, S., Keating, B.A. (2014). APSIM—evolution towards a new generation of agricultural systems simulation. *Environmental Modelling and Software* 62, 327–350. *https://doi.org/10.1016/j.envsoft.2014.07.009*

Holzworth, D., Huth, N.I., Fainges, J., Brown, H., Zurcher, E. Cichota, R., Verrall, S., Herrmann, N.I., Zheng, B., and Snow. V. (2018). APSIM Next Generation: Overcoming Challenges in Modernising a Farming Systems Model. *Environmental Modelling and Software*, 103, 43–51. *https://doi.org/10.1016/j.envsoft.2018.02.002*

Hoogenboom, G.J., White J.W., and Messina, C.D. (2004). From genome to crop: integration through simulation modelling. *Field Crop Research*, 90, 145–163.

Inglada, J., Arias, M., Tardy, B., Hagolle, O., Valero, S., Morin, D., Dedieu, G., Sepulcre, G., Bontemps, S., Defourney, P., and Koetz, B. (2015). Assessment of an Operational System for Crop Type Map Production Using High Temporal and Spatial Resolution Satellite Optical Imagery. *Remote Sensing*, 7, 12356–12379. doi:*10.3390/rs70912356*

Jones, J.W., Antle, J.M., Basso, B., Boote, K.J., Conant, R.T., Foster, I., Godfray, H.C.J., Herrero, M., Howitt, R.E., Janssen, S., Keating, B.A., Munoz-Carpena, R., Porter, C.H., Rosenzweig, C., Wheeler, T.R. (2017). Toward a new generation of agricultural system data, models, and knowledge products: state of agricultural systems science. *Agricultural Systems*, 155, 269–288. *http://dx.doi.org/10.1016/j.agsy.2016.09.021*

Kamir, E., Waldner, F., and Hochman, Z. (2020). Estimating wheat yields in Australia using climate records, satellite image time series and machine learning methods. *ISPRS Journal of Photogrammetry and Remote Sensing*, 160, 124–135. *https://doi.org/10.1016/j.isprsjprs.2019.11.008*

Lamb, D.W., Trotter, M.G., and Schneider, D.A. (2009). Ultra low-level airborne (ULLA) sensing of crop canopy reflectance: A case study using CropCircle™ sensor. *Computers and Electronics in Agriculture*, 69, 86–91.

Lamb, D.W., Schneider, D.A., Trotter, M.G., Schaefer, M.T., and Yule, I.J. (2011). Extended-altitude, aerial mapping of crop NDVI using an active optical sensor: A case study using a Raptor™ sensor over wheat. *Computers and Electronics in Agriculture,* 77, 69–73.

Lobell, D.B., Thau, D., Seifert, C., Engle, E., Little, B. (2015). A scalable satellite-based crop yield mapper. *Remote Sensing of Environment*, 164, 324–333. *https://doi.org/10.1016/j.rse.2015.04.021*

MacDonald, R.B., Hall, F.G., and Erb, R.B. (1975). The Use of LANDSAT Data in a Large Area Crop Inventory Experiment (LACIE). *LARS Symposia*. Paper 46. *http://docs.lib.purdue.edu/lars_symp/46*

Mahlein, A.K., Oerke, E.C., Steiner, U., and Dehne, H.W. (2012). Recent advances in sensing plant diseases for precision crop protection. *European Journal of Plant Pathology*, 133(1), 197–209. doi:*10.1007/s10658-011-9878-z*

Malthus, T.J., Barry, S., Randall, L.A., McVicar, T., Bordas, V.M., Stewart, J.B., Guerschman, J.-P., and Penrose, L. (2013). *Ground cover monitoring for Australia: Sampling strategy and selection of ground control sites*. CSIRO, Australia.

McNairn, H., Champagne, C., Shang, J., Holmstrom, D., and Reichert, G. (2008). Integration of optical and Synthetic Aperture Radar (SAR) imagery for delivering operational annual crop inventories. *ISPRS Journal of Photogrammetry and Remote Sensing*, 64(5), 434–449. *https://doi.org/10.1016/j.isprsjprs.2008.07.006*

Mohammed, G.H., Colombo, R., Middleton, E.M., Rascher, U., van der Tol, C., Nedbal, L., Goulas, Y., Pérez-Priego, O., Damm, A., Meroni, M., Joiner, J., Cogliati, S., Verhoef, W., Malenovský, Z., Gastellu-Etchegorry, J.-P., Miller, J.R., Guanter, L., Moreno, J., Moya, I., Berry, J.A., Frankenberg, C., Zarco-Tejada, P.J. (2019). Remote sensing of solar-induced chlorophyll fluorescence (SIF) in vegetation: 50 years of progress. *Remote sensing of environment*, 231, 111177. *https://doi.org/10.1016/j.rse.2019.04.030*

Mulla, D.J. (2013). Twenty five years of remote sensing in precision agriculture: key advances and remaining knowledge gaps. *Biosystems Engineering*, 114(4), 358–371. doi:*10.1016/j.biosystemseng.2012.08.009*

Nikolova, S., Bruce, S., Randall, L., Barrett, G., Ritman, K., and Nicholson, M. (2012). *Using remote sensing data and crop modelling to improve crop production forecasting: a scoping study*. ABARES technical report 12.3. Australian Bureau of Agricultural and Resource Economics and Sciences, Canberra.

O'Halloran, J., and van Sprang, C. (2019). Automating plant counts using drone imagery. pp 41–42 in *Vegetables Australia* (May/June 2019), AUSVEG Ltd and Horticulture Innovation Australia Ltd 2019. *http://era.daf.qld.gov.au/id/eprint/7131/1/VG16009%20Final%20Literature%20review.pdf*

Panek, E., and Gozdowski, D. (2020). Analysis of relationship between cereal yield and NDVI for selected regions of Central Europe based on MODIS satellite data. *Remote Sensing Applications: Society and Environment*, 17, 100286. *https://doi.org/10.1016/j.rsase.2019.100286*

Peña-Arancibia, J.L., McVicar, T.R., Paydar, Z., Li, L.T., Guerschman, J.P., Donohue, R., Dutta, D., Podger, G., Van Dijk, A., and Chiew, F. (2014). Dynamic identification of summer cropping irrigated areas in a large basin experiencing extreme climatic variability. *Remote Sensing of Environment*, 154, 139–152.

Potgieter, A.B., Lawson, K., and Huete, A.R. (2013). Determining crop acreage estimates for specific winter crops using shape attributes from sequential MODIS imagery. *International Journal of Applied Earth Observation and Geoinformation*, 23(1), 254–263. *https://doi.org/10.1016/j.jag.2012.09.009*

Pringle, M.J., Schmidt, M., and Tindall, D.R. (2018). Multi-decade, multi-sensor time-series modelling—based on geostatistical concepts—to predict broad groups of crops. *Remote Sensing of Environment*, 216, 183–200. *https://doi.org/10.1016/j.rse.2018.06.046*

Pullanagari, R.R., Kereszturi, G., and Yule, I.J. (2016). Mapping of macro and micro nutrients of mixed pastures using airborne AisaFENIX hyperspectral imagery. *ISPRS Journal of Photogrammetry and Remote Sensing*, 117, 1–10. *https://doi.org/10.1016/j.isprsjprs.2016.03.010*

Queensland Government (2020). *SILO: Australian climate data from 1889 to yesterday* webpage, Queensland Government website: *https://www.longpaddock.qld.gov.au/silo/*

Rahman, M.M., and Robson, A.J. (2016a). A Novel Approach for Sugarcane Yield Prediction Using Landsat Time Series Imagery: A Case Study on Bundaberg Region. *Advances in Remote Sensing* 5, 93–102. *http://dx.doi.org/10.4236/ars.2016.52008*

Rahman, M.M., and Robson, A.J. (2016b). Integrating Landsat-8 and Sentinel-2 Time Series Data for Yield Prediction of Sugarcane Crops at the Block Level. *Remote Sensing*, 12(8), 1313. *https://doi.org/10.3390/rs12081313*

Robson, A., Rahman, M.M., Falzon, G., Verma, N.K., Johansen, K.J., Robinson, N., Lakshmanan, P., Salter, B., and Skocaj, D. (2016a). Evaluating Remote Sensing Technologies for Improved Yield Forecasting and for the Measurement of Foliar Nitrogen Concentration in Sugarcane. *Proceedings of the 38th Australian Society of Sugar Cane Technologists*, April, Mackay, Queensland.

Robson, A.J., Rahman, M.M., Muir, J., Saint, A., Simpson, C., and Searle, C. (2016b). Evaluating satellite remote sensing as a method for measuring yield variability in Avocado and Macadamia tree crops, *Proceedings of the Society of Precision Agriculture Australia*, 12 September, Toowoomba, Australia.

Robson, A.J., Rahman, M.M., and Muir, J. (2017). Using Worldview Satellite Imagery to Map Yield in Avocado (*Persea americana*): A Case Study in Bundaberg, Australia. *Remote Sensing*, 9(12), 1223. *https://doi.org/10.3390/rs9121223*

Schut, A.G.T., Stephens, D.J., Stovold, R.G.H., Adams, M., and Craig, R.L. (2009). Improved wheat yield and production forecasting with a moisture stress index, AVHRR and MODIS data. *Crop and Pasture Science*, 60(1), 60–70.

Shanahan, J., Schepers, J.S., Francis, D.D., Varvel, G.E., Wilhelm, W., Tringe, J.M., Schlemmer, M.R., and Major, D.J. (2001). Use of Remote-Sensing Imagery to Estimate Corn Grain Yield. *Agronomy Journal*, 93, 583–589.

Srinivasan, A. (Ed) (2006). *Handbook of Precision Agriculture: Principles and Applications*. The Haworth Press, New York. ISBN-13: 978-1-56022-945-4.

Stanley, J.N., Lamb, D.W., Falzon, G., and Schneider, D.A. (2014). Apparent electrical conductivity (Eca) as a surrogate for neutron probe counts to measure soil moisture content in heavy clay soils (Vertosols). *Soil Research*, 52(4), 373–378.

Suarez, L.A., McPhee, J., O'Halloran, J., van Sprang, C., and Robson, A. (2018). *Adoption of precision systems technology in vegetation production*. Literature Review for VG16009, Horticulture Innovation Australia, Queensland.

TERN Australia (2018). *Effective Field Calibration and Validation Practices: A practical handbook for calibration and validation satellite and model-derived terrestrial environmental variables for research and management*. A TERN Landscape Assessment Initiative, NCRIS. ISBN 978-0-646-94137-0. *https://www.tern.org.au/NEW-CalVal-handbook-for-remote-sensing-bgp4370.html*

Trotter, M.G., Lamb, D.W., and Schneider, D.A. (2010). Evaluating an active optical sensor for quantifying and mapping green herbage mass and growth in a perennial grass pasture. *Crop and Pasture Science*, 61, 389–398.

Tucker, C.J., Holben, B.N., Elgin, J.H. Jr., and McMurtrey, J.E. Jr. III (1980). Remote sensing of total dry matter accumulation in winter wheat. *Remote Sensing of Environment*, 11, 171–189.

UNE CASI (2020). *SugarMaps* webpage, University of New England Computation Analytics Software Informatic website: *https://casi.une.edu.au/#!/projects*

Van Niel, T.G., and McVicar, T.R. (2003). A simple method to improve field-level rice identification: toward operational monitoring with satellite remote sensing. *Australian Journal of Experimental Agriculture*, 43, 379–387.

Van Niel, T.G., and McVicar, T.R. (2004). Determining temporal windows for crop discrimination with remote sensing: a case study in south-eastern Australia. *Computers and Electronics in Agriculture*, 45, 91–108.

Waldner, F., Fritz, S., Di Gregorio, A., Defourny, P. (2015). Mapping priorities to focus cropland mapping activities: fitness assessment of existing global, regional and national cropland maps. *Remote Sensing*, 7, 7959–7986. *http://dx.doi.org/10.3390/rs70607959*

Waldner, F., Chen, Y., Lawes, R., and Hochman, Z. (2019). Needle in a haystack: Mapping rare and infrequent crops using satellite imagery and data balancing methods. *Remote Sensing of Environment*, 233, 11375. *https://doi.org/10.1016/j.rse.2019.111375*

Waldner, F., and Diakogiannis, F. I. (2020). Deep learning on edge: extracting field boundaries from satellite images with a convolutional neural network. *Remote Sensing of Environment*, 245, 111741.

Wu, D., Johansen, K., Phinn, S., and Robson, A. (2020). Suitability of Airborne and Terrestrial Laser Scanning for Mapping Tree Crop Structural Metrics for Improved Orchard Management. *Remote Sensing*, 12, 1647. doi:*10.3390/rs12101647*

Zhang, N., Wang, M., and Wang, N. (2002). Precision agriculture—a worldwide overview. *Computers and Electronics in Agriculture*, 36(2–3),113–132. doi:*10.1016/S0168-1699(02)00096-0*

Zhao, L., Waldner, F., Scarth, P., Mack, B., and Hochman, Z. (2020). Combining fractional cover images with one-class classifiers enables near real-time monitoring of fallows in the northern grains region of Australia. *Remote Sensing*, 12(8), 1337. *https://doi.org/10.3390/rs12081337*

Zhou, Z.-S., Caccetta, P., Sims, N.C., and Held, A. (2016). Multi-band SAR Data for Rangeland Pasture Monitoring. *Proceedings of IEEE IGARSS 2016*. pp. 170–173, July 2016. doi:*10.1109/IGARSS.2016.7729035*

13 Irrigated Horticulture

Des Whitfield, Andrew McAllister, Mohammad Abuzar, and Mark O'Connell

Australian horticulture is introduced in Section 11.1. This section focuses on the use of EO datasets to monitor the water requirements of irrigated fruit, nut, and vine crops in southeastern Australia.

Since most of Australia is too dry for commercial, rainfed fruit production, Australian horticultural enterprises, including those in the Riverland and Mallee areas of South Australia and Victoria, respectively, commonly rely on irrigation to supply more than half of the crop water requirements in the majority of seasons. Discretionary irrigation may be practised in other parts of Australia where rainfall routinely provides > 50 % of crop water requirements.

Water needs of crops vary greatly in time and space. Spatial differences are attributable to variations in crop vegetation status (crop type, age, and growth conditions), and temporal differences are associated with seasonal and daily weather conditions, and rainfall contributions to root zone soil water. Irrigators are consequently required to employ sophisticated real time information and analytical tools to ensure that crops receive the requisite amounts of water. Over-irrigation wastes water and results in irrigation runoff and/or deep drainage losses from the root zone. Over-supply is therefore conducive to nutrient runoff (and/or leaching) and shallow water tables, respectively. Conversely, effects of under-supply are readily seen in reduced rates of crop growth, and lowered yields and product quality. Irrigation should therefore be used to ensure that root zone soil moisture optimally supports the rapid rates of crop growth and water use conducive to high yields of high quality produce, with minimal contributions to nutrient runoff and deep drainage.

Over-allocation of available water resources and over-irrigation are also important at district and regional scales. Over-allocation of resources, where too many irrigators are granted access to a limited resource, leads to district scale water shortages (under-irrigation) in dry years, chronic limits on the availability of environmental water, and elevated water prices where marginal producers and industries are increasingly required to review their participation in irrigated farming.

13.1 Irrigated Horticulture in Southeast Australia

Irrigated fruit and vegetable production on the Murray River in southeast Australia dates back to colonial support for the establishment of irrigation settlements in the region and the arrival of the pioneering Chaffey brothers in the 1890s.

Irrigated horticulture is now expanding rapidly in the southern Murray-Darling Basin (MDB; see Section 2.1). High growth rates are especially evident in the Mallee region of northwest Victoria, where the formative years of irrigation development (1887–1947) accounted for 22,000 ha of crops (principally wine-grapes, dried grapes, and citrus), another 52,000 ha was added during 1947–1997, with a further 48,000 ha added 1998–2017 (Argus, 2015). Small scale family farm units have been superseded by large scale, highly capitalised farming investments. Irrigated almonds continue to expand into non-traditional 'green-field' areas that were previously used for rainfed grains. The relatively new capability of flying fresh produce into Asian markets has supported the recent rapid expansion of table grapes in the Robinvale-Euston districts on the NSW/Victoria border.

Background image: Apricot trees (c.v. Golden May) planted on Tatura Trellis at the Stonefruit Experimental Orchard, SmartFarm Tatura, Victoria, photographed in August 2019. Source: Mark O'Connell

Recommended Chapter Citation: Whitfield, D., McAllister, A., Abuzar, M., and O'Connell, M. (2021). Irrigated Horticulture. Ch 13 in *Earth Observation: Data, Processing and Applications. Volume 3A—Terrestrial Vegetation*. CRCSI, Melbourne. pp. 263–280.

The routine and severe spring-summer rainfall deficiencies experienced in inland southeast Australia impose an absolute dependence on irrigation to meet the high yield and quality standards required of modern, high value, horticulture enterprises. Notwithstanding, irrigation requirements vary annually, depending on annual variations in spring-summer rainfall deficiencies.

Severe summer rainfall deficits experienced in the southern MDB consequently impose an obligate need for irrigation on horticultural producers in the region. Accordingly, the reliable production of profitable high yielding, high quality produce is intrinsically dependent on the external factors that influence the price and availability of water, and, also, the management factors that govern on-farm water use efficiency. Irrigation licensing regimes in the Mallee, for example, operate on fixed annual allocations of supplementary irrigation that range to maxima of 14 ML/ha for almonds grown in Victoria and to 16 ML/ha for almonds in South Australia. Actual seasonal requirements differ from prescribed license volumes, and Victoria makes provision to adjust licensed volumes for extraordinary seasonal demands. Further expansion of the fruit, nut, and vine industries in the southern MDB will occur against a backdrop of increased regional uncertainty in patterns of autumn and winter rainfall, and the associated risk that major storage levels in Lakes Eildon, Dartmouth and Burrinjuck fall short of crop demands in summer. There exists, therefore, a strong need to gauge water use and demand in the fruit, nut, and vine industries of the southern MDB to ensure that irrigators are able to match irrigation amounts to crop demand at field and farm scales and, further, that regional resources are optimally employed to satisfy irrigation, social and environmental demands for water. In addition, there is an over-arching requirement to ensure that irrigation-induced rates of root zone drainage do not exacerbate salinity concerns in the Murray River.

In this Section, we present examples of 'Satellite-based Irrigation Demand Analytics' for fruit, nut, and vine crops grown in the southern MDB, with focus on:

- relationships between crop water use (evapotranspiration, ET; see Sections 2.2 and 9.4) and crop vegetation status (inferred by the satellite-based Normalised Difference Vegetation Index, NDVI; see Section 8.1.1) in major fruit, nut, and vine crops grown in the southern MDB; and the
- potential use of those data in daily irrigation management and in the assessment of the minimum quantities of water that are needed to produce high yields of high quality horticultural products in the region.

13.2 EO Sensors for Irrigated Horticulture

Mapping and monitoring of irrigated horticulture using EO datasets principally depends upon optical sensors to highlight differences between red and near infrared (NIR) reflectance (see Section 8.1.1). Thermal and passive microwave sensors are also relevant to derive land surface temperature (LST; see Section 7.5 and Volume 1B—Sections 7.6 and 8.1.1). Some of the sensor characteristics that are relevant to studies of irrigated horticulture are summarised in Table 13.1. In particular, drones are being increasingly employed to survey horticultural crops (for example, Gonzalez-Dugo *et al*., 2013; see Section 12.2).

Table 13.1 EO sensors relevant to irrigated horticulture

TIR: Thermal infrared; GPS: Global Positioning System; RPAS: Remotely piloted aircraft system; DEM: Digital elevation model; ET: evapotranspiration

Type	Sensor	Platform	Relevance	Advantages	Disadvantages
Passive optical	Multispectral radiometer	Satellite or airborne	National or regional land cover mapping	Global, recurrent coverage, low cost	Low accuracy, coarse scale
	Hyperspectral spectroradiometer	Airborne	Plant biochemical functioning and health	High spectral and spatial resolution highlight plant stress and crop nutrition	High cost, high data volume
	TIR radiometer	Field, satellite, or airborne	Soil/canopy temperature, water stress	Surrogate measure for ET	Resolution depends on platform
Active optical	Lidar	Airborne and terrestrial	Crop structure and identification, DEM	Detailed structure for plant canopy and soil surface	High cost, specialised processing
	Active optical sensors	Ground vehicles or RPAS	Crop cover and condition mapping	Convenience, independent of sunlight	Low availability, specialised hardware
Proximal	Passive optical sensors (phenocam, hyperspectral), meteorological sensors (including soil moisture)	Ground, tractor, or tower-based (see Excursus 7.2 and Volume 2D—Section 12)	Soil, crop, and atmospheric variability Phenology	Continuous, long term measurements	High cost and require skilled maintenance
Locational	GPS	Portable devices	Locating field sites	Low cost	Coverage in remote regions or below dense canopies

13.3 Fundamentals of Irrigation Management

Irrigation systems and their management vary widely between regions, crops, and industries in Australia. System options range from traditional gravity or surface irrigation systems to the modern pressurised irrigation systems where water is delivered to crops through pipes, driplines and sprays. Pressure-based systems reliably and precisely deliver small amounts of water at daily and sub-daily intervals, whereas gravity-based systems are characterised by large infrequent deliveries, and are used to replenish root zone soil water stores at intervals of four or more days.

The quantum of water captured in the root zone after gravity irrigation is directly dependent on the soil water deficit in the root zone at the time of irrigation. Gravity-based irrigators must schedule irrigation events based on competing needs to ensure that root zone soil water deficits are large enough to maximise the retention of water applied to bays and furrows, and small enough to support rapid rates of crop growth. Errors in the timing (scheduling) of irrigation events in relation to soil water deficits, and/or the application of irrigation volumes that are poorly related to soil water deficits and crop requirements, cause unacceptable quantities of surface runoff from fields, and excessive root zone drainage. Inefficiencies are amplified when soil water retention is limited by the soil physical properties.

Pressure-based systems are able to deliver precise quantities of water to the soil, and are consequently conducive to fixed-interval irrigation events (such as daily), allowing irrigators to replenish the precise amounts of water used by crops in the intervening time interval (with appropriate allowance for rainfall). The modern pressurised irrigation systems adopted extensively by horticulture industries in southeast Australia in recent decades are commonly used for fixed-interval irrigation and thereby rely on precise estimates/measurements of the quantum of root zone soil water consumed by crops (ET*; see Section 13.4.1) over periods ≤ 2 days.

The management of root zone soil water deficits is central in considerations of irrigation water management. Soil water deficits determine the optimal timing and amount of applied water in gravity irrigation and, further, the amount of water delivered at fixed time intervals in pressurised systems. Cahn and Johnson (2017) described contemporary approaches to irrigation scheduling in vegetable crops grown in California. They emphasised that the use of soil moisture monitoring had progressed from limits imposed by sensor accuracy and cost to current demands for large scale whole-farm systems where the labour costs required for the installation and removal of sensors over multiple fields outweighed the lower cost of modern sensors. They proposed that technical improvements in weather station networks, satellite and aerial imaging, and digital communication networks allow irrigators to combine satellite and weather data to assist in the progression from small to large scale irrigation farming systems.

Many Australian irrigators continue to rely on soil moisture sensors and, with the possible exception of IrriSAT (Hornbuckle, 2014; Montgomery *et al*., 2015; see Section 13.9), the combined use of satellite and weather data to assist in large scale irrigation management systems is generally regarded as an emerging technology.

Weather-based estimates of irrigation water requirements are widely based on the crop coefficient method, which accounts for both crop and weather effects on water use (Doorenbos and Pruitt, 1974; Allen *et al*., 1998; Jensen and Allen, 2016). The method relies on an initial measure of evaporative demand ('potential' evaporation), which accounts for the effects of weather on crop water use. The most widely used measure of evaporative demand, known as reference crop evapotranspiration (ET_{ref}), is modified by crop-specific factors incorporated into the crop coefficient to estimate crop water use (see Section 13.4).

Estimates of crop water use by the crop coefficient method are combined with rainfall data in soil water balance models to gauge the net effects of crop water use (ET), weather, and rainfall on the consumption of root zone soil water by crops. Soil water models reveal when soil water deficits become unacceptable for crop growth, and thereby predict both timing of irrigation events and the amounts of water required to maintain an optimal root zone soil water status. The management of multiple fields in large scale whole-farm irrigation management systems is achieved by combining field- and crop-specific satellite data (field/crop-specific estimates of crop coefficient) with an estimate of evaporative demand based on weather data sourced from a local automatic weather station or a web-based weather service. As described by Cahn and Johnson (2017), water use estimates based on satellite and weather data are inherently scalable over numerous fields, and thereby provide a practical basis for affordable whole-farm irrigation management systems.

13.4 Irrigation Requirements of Horticultural Crops

Crop water use is synonymous with ET, which describes the quantities of water evaporated by soil and leaf surfaces (evaporation, E, and transpiration, T, respectively; see Sections 7.6 and 9.4). Estimates of Irrigation Water Requirement (IWR) are therefore based on the amount of water required to compensate for ET losses from the root zone. Models of root zone soil water balance provide an explicit soil water accounting mechanism that allow irrigators to maintain a favourable soil water regime using irrigation to ensure that total water deliveries (irrigation + rainfall) are optimally matched to prevailing field-specific values of well-watered rates of ET (ET*).

13.4.1 Weather-based estimates of soil water status in orchards

Weather-based estimates of root zone soil water status are routinely based on soil water balance calculations where changes in soil moisture, are derived from estimates of ET* and rainfall following irrigation. In general terms, irrigation is required to compensate for rainfall deficits, estimated by:

$$\sum\left(ET^{*} - RF_{e}\right)$$

where RF_e is 'effective' rainfall in mm (see Table 13.2 for definitions of major water use terms).

Calculations of the crop-specific values of ET* are routinely based on the assumption that ET* is directly proportional to the weather (evaporative demand) experienced by crops (see Section 13.4.2), as modified by crop characteristics (see Section 13.4.3).

Table 13.2 Definition of major water use terms

Parameter Group	Term	Definition
Evapotranspiration	ET	Generic evapotranspiration
	ET*	Well-watered ET
	ET_{ref}	Reference crop ET
	ET_o	'Short' reference crop ET
	ET_r	'Tall' reference crop ET
	ET_rF	Fractional ET_r
Crop water use coefficients	K_c	Crop water use coefficient
	K_{cb}	Basal crop coefficient
	K_{co}	Coefficient for 'short' crop
	K_{cr}	Coefficient for 'tall' crop
	K_d	Crop density coefficient
Vegetation	FC	Fractional Cover
	VI	Vegetation Index

13.4.2 Reference crop evapotranspiration

Evaporative demand, defined as the maximum or 'potential' rate of ET under the prevailing weather conditions, depends on solar radiation, humidity, temperature, and windspeed (see Section 7.6). The availability of affordable automatic weather stations has provided widespread access to site-specific estimates of evaporative demand, and an associated increase in the adoption of weather-based, soil moisture modelling approaches in irrigation scheduling and control systems.

Prior to FAO56 (Allen *et al.*, 1998), numerous variants of reference crop ET (ET_{ref}) were used to describe 'potential' rates of ET by crops (for example, FAO24; Doorenbos and Pruitt, 1977). The use of different measures of potential evaporation in reports of crop water use severely compromised the transferability of water use findings between researchers and regions. FAO56 contributors defined the 'short' crop version of ET_{ref} (ET_o) as a standardized measure of evaporative demand and proposed standardised procedures for the computation of ET_{ref} based on estimates of ET* that are appropriate to an extensive uniform sward of short green grass. The grass reference was adopted largely due to the preponderance of global lysimeter studies conducted on grass to that time.

The American Society of Civil Engineers (ASCE) Environmental and Water Resources Institute (EWRI) subsequently complemented short crop ET_{ref} with an optional 'tall' crop ET_{ref} (ET_r), based on alfalfa (ASCE-EWRI, 2005) for use in the USA. The alfalfa standard recognised the long history of alfalfa used in agricultural applications in the USA and provided continuity with the established use of short and tall forms of ET_{ref} in USA (ASCE-EWRI, 2005; Jensen and Allen, 2016).

Table 13.3 Values of C_n and C_d coefficients

Values of coefficients, C_n and C_d, appropriate to daily estimates of ET_o and ET_r, in the equation for ET_{ref} (Allen *et al.*, 2006)

Coefficient	C_d	C_n
'short' crop ET_o	0.34	900
'tall' crop ET_r	0.38	1600

Mathematically, both short and tall versions of ET_{ref} were founded on the Penman-Monteith equation, expressed as:

$$ET_{ref} = \frac{0.408\Delta\left(R_n - G\right) + \gamma \frac{C_n}{T+273} u_2 \left(e_s - e_a\right)}{\Delta + \gamma\left(1 + C_d u_2\right)}$$

where

ET_{ref} is reference crop ET (mm/day);
R_n is net radiation at the crop surface (MJ/m^2/day);
G is soil heat flux density (MJ/m^2/day);
C_n is the numerator constant that changes with reference type (tall/short) and calculation time step in ET_{ref} (see Table 13.3);
C_d is the denominator constant that changes with reference type (tall/short) and calculation time step in ET_{ref} (see Table 13.3);
u_2 is wind speed at 2 m (m/s);
e_s is saturation vapour pressure (kPa);
e_a is actual vapour pressure (kPa);
γ is the psychrometric constant (kPA ºC^{-1}); and
T is the mean daily air temperature at 2 m (ºC).

The values of C_n and C_d for short and tall reference crops derive from the definition of vegetation characteristics adopted for the respective crops (vegetation height, leaf area index, stomatal resistance), and their impact on the full form Penman-Monteith equation (see Table 13.3). The short reference crop was defined by FAO56 as an hypothetical crop with an assumed height of 0.12 m, a surface resistance of 70 s/m and an albedo of 0.23, and closely resembled the evaporation from an extensive, actively-growing, adequately-watered, green grass sward of uniform height. The tall crop reference was based on an extensive uniform sward of alfalfa with a height of 0.5 m.

13.4.3 Crop characteristics

ET_o and ET_r provide standardised indices of evaporative demand (ASCE-EWRI, 2005). Crop-specific values of ET* are calculated for 'non-reference' target crops by multiplying measures of ET_{ref} (ET_o, ET_r) by an associated crop coefficient (K_{co}, K_{cr}) as follows:

$$ET^* = K_{co} ET_o = K_{cr} ET_r$$

Crop- and field-specific values of K_{co} and K_{cr} account for all factors that cause crop-specific values of ET* to differ from the reference estimates, ET_o and ET_r, respectively, that apply to extensive crops of uniform height and complete ground cover. Foliage and ground cover vary with both crop age and seasonal or phenological stages of crop growth in deciduous tree, nut, and vine crops. Typical row-based planting configurations mean that fruit, nut, and vine crops rarely achieve full cover. Tabulated values of K_{co} for deciduous crops therefore require adjustments for growth (crop age), and seasonal and cultural differences in foliage cover.

In addition, the nominal values of K_{co} tabulated in FAO56 were described as 'typical' values expected for 'standard sub-humid climatic conditions' (average daytime minimum relative humidity (RH) ≈ 45%; wind speed ≈ 2 m/s), and height-dependent climate corrections were needed in order to apply tabulated values of K_{co} in conditions where average daytime minimum RH < 45% and/or wind speed > 2 m/s. The magnitude of designated climate corrections increased with crop height.

The assignment of tabulated K_{co} values to fruit, nut, and vine crops grown in southeast Australia therefore depends on an adequate accounting for differences in foliage cover due to crop growth/age, seasonal phenological changes, planting configuration, and crop- and height-dependent climate corrections. These and other effects are responsible for a voluminous scientific literature directed to the quantification and understanding of variations in K_{co} attributable to differences in crop characteristics and growth conditions (for example, Guerra *et al*., 2016). Accordingly, the cost and complexity of establishing a comprehensive range of crop coefficients for the range of crop types, and crop cultural and management variants, is prohibitive for the wide array of crop types and configurations grown in horticultural regions in Australia and elsewhere.

13.4.4 Why two reference crops?

Height-dependent climate adjustments are required if the crop coefficient approach based on short crop ET_{ref} (ET_o) is applied to fruit, nut, and vine crops grown in the warm, dry climate experienced in southeast Australia and the southern MDB. However, the greater roughness of the 'tall' crop alfalfa reference means that measures of ET_r approximate peak-season rates of ET* for most tall crops, including orchards, in warm dry climates, and climate/height adjustments are unnecessary when the alternative 'tall' crop ET_{ref} (ET_r) is used with tall crops under warm, dry climatic conditions (Allen and Pereira, 2009).

ET_o and ET_r are both estimated by the equation for ET* above, but differ in their numerator and denominator coefficients (C_n and C_d) used for daily estimates of ET_{ref} (see Table 13.3). ET_r tends to be 20–40% larger than ET_o (Allen and Pereira, 2009). K_c values associated with the alternative ET_o and ET_r reference values must be clearly distinguished as K_{co} and K_{cr}, respectively.

13.5 Satellite-based Estimates of ET

The importance of vegetation status in K_c values has been established by many studies relating K_c values, developed in lysimeter studies, to satellite- and ground-based vegetation indices (VI; see Section 8.1; for example Johnson and Trout, 2012). VI have been overwhelmingly based on the red and NIR bands obtained from EO (such as Heilman *et al.*, 1982; Bausch and Neale, 1987; Neale *et al.*, 1989; Hunsacker *et al.*, 2003). As detailed in Volume 2C—Section 11, and summarised in Section 8.1.1 above, NDVI and other VI are strongly related to the vegetation cover of the soil surface (or Fractional Cover: FC; Johnson and Trout, 2012; see Excursus 8.3). For example, Rajan and Maas (2014) modelled ET* in cotton using satellite-based estimates of FC as a direct surrogate for K_c.

Below we consider satellite-based estimates of ET based on the:

- relationship between the crop water coefficient (K_c) and EO-based VI (see Section 13.5.1);
- relationship between surface temperature (T_s) and VI (see Section 13.5.2); and
- surface energy balance models (see Section 13.5.3).

13.5.1 K_c-VI relationships

Web-based, irrigation scheduling approaches have been developed based on the observed linear relationships between K_c and VI. Global examples include:

- Demeter in Europe(DEMonstration of Earth observation TEchnologies in Routine irrigation advisory services; Belmonte *et al.*, 2005;);
- TOPS-SIMS in USA (Terrestrial Observation and Prediction System Satellite Irrigation Management Support; Cahn and Johnson, 2017; *https://ecocast.arc.nasa.gov/simsi/*); and
- IrriSAT in Australia (Hornbuckle, 2014).

TOPS-SIMS, supported by NASA and USGS, aims to provide contemporary field scale K_c data and real time weather data to support real time, weather-based, irrigation management by combining field-specific values of NDVI and K_c with district ET_o data for the state of California (Cahn and Johnson, 2017). TOP-SIMS uses ET_o data sourced from an extensive network of weather stations (CIMIS) operated by the Californian Department of Water Resources.

Reflectance-based K_c-VI approaches (such as TOPS-SIMS, Irrisat) are founded on relationships linking ET* to a crop coefficient based on FC and/or NDVI. EO-based measures of the T_s /NDVI relationships in irrigated crops, and/or ET/NDVI relationships based on surface energy balance estimates of ET, potentially play an important role in the development of practical irrigation management systems based on readily-acquired, reflectance-based VI (see Section 9.4).

13.5.2 T_s-VI relationships

Remotely sensed values of NDVI are not directly related to vegetation water status or rates of evapotranspiration. Early EO-based studies of vegetation water status and water use (or ET) focused on relationships between surface temperature (T_s) and NDVI on the basis that T_s was inversely related to ET, since evaporative cooling due to ET decreases vegetation temperature and T_s. Remotely sensed T_s/NDVI values were commonly confined within a trapezoidal space described by the approximate limits, $0.1 \leq NDVI \leq 0.9$ (which can be optionally interpreted in terms of FC; $0 \leq FC \leq 1$) and upper and lower 'warm' and 'cool' edges associated with low and high rates of ET, respectively.

The trapezoid/triangle approach proposed by Moran *et al.* (1994, 1996) provided an initial quantitative approach to remotely sensed ET and soil moisture estimation (see Figure 13.1). Weather-dependent rates of ET were ascribed to each of the vertices of the trapezoid (dry, bare soil; water-stressed vegetation; well-watered vegetation; saturated bare soil) based on the Penman-Monteith equation (see first equation in Section 13.4.2). Intermediate pixel scale ET estimates were linearly interpolated based on the proximity of T_s/NDVI values to the warm and cool fronts in the trapezoidal T_s/NDVI distribution (that is, the ratio BC/BA in Figure 13.1).

Figure 13.1 Variation of surface-air temperature differences with vegetation cover

Diagram depicting the trapezoidal distribution of surface-air temperature differences ($T_s - T_a$) relative to values of fractional vegetation cover (FC, SAVI or NDVI) as seen in many vegetation/water stress studies. The 'warm' $T_s - T_a$ front is associated with low rates of ET (ET=0), and the 'cool' front depicts well-watered patches of vegetation and/or wet soils (ET=ET*). Moran *et al.* (1994) estimated the ratio ET/ET* by the ratio BC/BA.

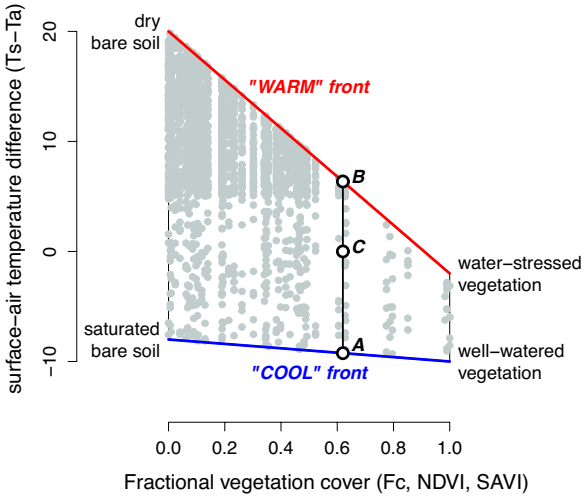

Adapted from: Moran *et al.* (1994, 1996)

13.5.3 Surface energy balance models

Bastiaanssen *et al.* (1998) published the seminal SEBAL model (Surface Energy Balance Algorithm for Land), a satellite-based energy balance approach to estimate land surface ET (see Section 9.4). SEBAL incorporated sub-models to estimate components of the surface energy balance (SEB) equation, expressed as:

$$\left(R_n - G\right) = H + LE$$

where,

R_n is net radiation measured above the vegetation (MJ/m^2/day);
G is soil heat flux (MJ/m^2/day);
H is sensible heat flux (MJ/m^2/day); and
LE is latent heat flux (ET).

LE is estimated as the residual:

$$LE = \left(R_n - G\right) - H$$

Pixel scale estimates of H are derived by identifying 'wet' and 'dry' endmember pixels, where the sensible heat, H, assumed the values:

- H = 0 (LE = R_n) for 'wet' endmembers; and
- H = R_n (LE = 0) for 'dry' endmembers.

Relative to the trapezoid approach, 'dry' and 'wet' endmember pixels in SEBAL analyses corresponded to the vertices associated with 'large T_s + low NDVI' and 'low T_s + large NDVI' respectively in Figure 13.1.

Bastiaanssen and Allen subsequently collaborated to produce the METRIC model (Mapping Evapotranspiration at High Resolution with Internal Calibration), an adaption of SEBAL that was tailored to irrigation applications (Allen *et al.*, 2007). Whilst METRIC also employed wet and dry endmember pixels, the wet pixel in METRIC is associated with:

$$H = R_n - \mathrm{ET}_r$$

rather than the assumption, H=0, used by SEBAL. The use of ET_r to approximate ET at the wet 'anchor' pixel compensated for regional advection effects, and supported the extrapolation of instantaneous satellite-derived values of ET to periods of 24 hours and longer. METRIC can be applied across crop types and growing conditions, and has significant advantages over conventional methods of estimating ET from documented crop calendar curves (see Figure 13.3) in that neither the crop development stages, nor the specific crop type need to be known with METRIC. Allen *et al.* (2011) provide a detailed comparison of the SEBAL and METRIC algorithms.

The energy balance methods employed in SEBAL and METRIC respond to reductions in ET caused by water stress. Values of evaporative fraction (LE/R_n) produced by SEBAL and fractional ET_r ($\mathrm{ET}_r\mathrm{F} = \mathrm{ET}/\mathrm{ET}_r$) from METRIC may be associated with crops that are inadequately supplied with water. Supporting evidence is required before satellite-based SEB estimates of ET can be equated with well-watered values, ET*. $\mathrm{ET}_r\mathrm{F}$ estimates in Section 13.7 (made with the Agriculture Victoria rendition of METRIC) were equated with values of K_{cr} (see first equation, Section 13), based on comparisons with published data for irrigated summer crops grown in USA.

13.6 METRIC Model: Summer Crops

Tasumi *et al.* (2005) applied the METRIC model to irrigated summer crops grown in Idaho, USA. They employed Landsat imagery to study field scale $\mathrm{ET}_r\mathrm{F}$/NDVI relationships. Data were acquired as a series of snapshots at overpass intervals of approximately 16 days during crop growth periods and the resultant $\mathrm{ET}_r\mathrm{F}$/NDVI data were collated in order to develop seasonal $\mathrm{ET}_r\mathrm{F}$/NDVI relationships for the major irrigated summer crops grown in Magic Valley, Idaho, in 2000. Tasumi *et al.* (2005) made the *a priori* assumption that all irrigated crops were adequately supplied with water (that is, K_c = $\mathrm{ET}_r\mathrm{F}$) for the crops in their study.

K_c/NDVI relationships for potato and sugar beets (see Figure 13.2) showed that NDVI values extended over the approximate limits, 0.1 ≤ NDVI ≤ 0.85, encompassing the range of FC, 0 ≤ FC ≤ 1.0 (from bare ground to full canopy cover; see, for example, Bastiaanssen and Ali, 2003). Tasumi *et al.* (2005) reported that the lower observed limit on K_c ($\mathrm{ET}_r\mathrm{F}$) increased approximately linearly with increases in NDVI over the entire range of NDVI, and consequently equated the lower observed limit on K_c with K_{cb} (the basal crop coefficient), which describes the minimum rate of ET of a crop adequately supplied with water (surface evaporation = 0). K_{cb} is defined as the value of $\mathrm{ET}_r\mathrm{F}$ when the soil surface is dry (E ≈ 0), and transpiration is maintained at maximal rates (Allen *et al.*, 1998). The K_{cb} line has important practical implications, as it represents the irrigation trigger point, beyond which a further reduction in root zone soil water leads to the onset of crop water stress.

Figure 13.2 Crop coefficient variations

Variation in crop coefficients, K_c, estimated as fractional 'tall' crop evapotranspiration (ET_rF), versus NDVI for potato and sugar beet crops in the Magic Valley area of Idaho for three Landsat dates during crop development in 2000.

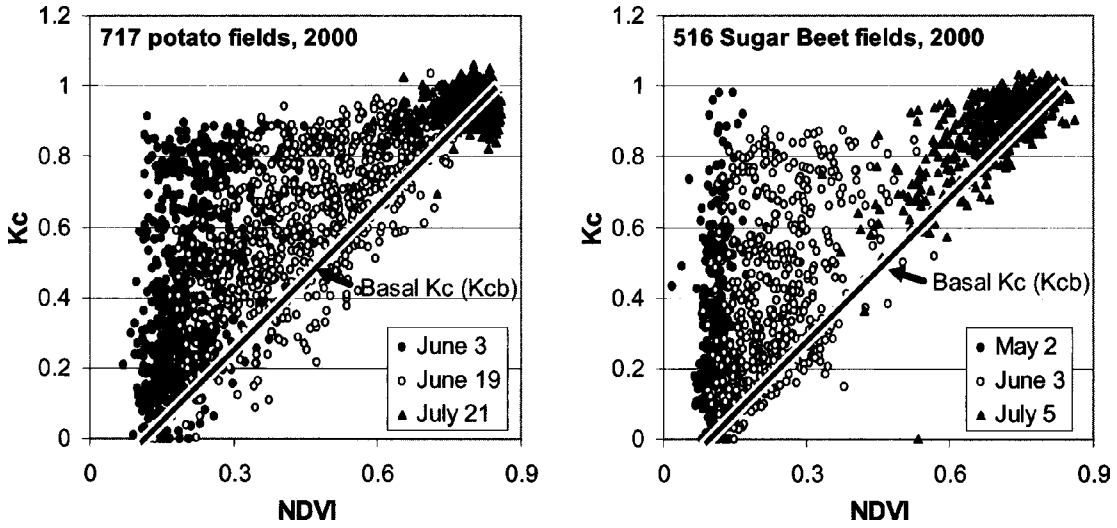

Source: Tasumi *et al.* (2005)

Maximum values of K_c were described by $K_c = ET_rF = 1.0$, over the observed range of NDVI (see Figure 13.2). The limit, $K_c = ET_rF = 1.0$, complied with energy balance limits on the rates of ET observed in lysimeter studies of dry surface, full cover crops ($ET = ET_r$; Allen *et al.*, 2007; Jensen and Allen, 2016). The dry surface limit, $ET_rF = 1.0$, extends to an approximate maximum, $ET_rF \leq 1.20$, in fields where the vegetation and/or soil surface are wet by recent rain or irrigation (Tasumi *et al.*, 2005; Allen *et al.*, 2007). Tasumi *et al.* (2005) attributed the large range in ET_rF at low NDVI ($0 \leq ET_rF \leq 1.0$) to variations in surface soil moisture, caused by rain and/or irrigation events, during periods of low plant cover.

K_c (ET_rF) values were therefore confined to a triangular K_c/NDVI space within K_c and NDVI limits, $K_{cb} \leq K_c \leq 1.0$ and $0.1 \leq NDVI \leq 0.85$, respectively. Rainfall and irrigation-induced increases in ET_rF were progressively diminished by increases in FC during crop growth.

The range of NDVI in the Idaho ET_rF/NDVI data encompassed recently sown crops with a vegetation-free soil surface, and fully grown crops with complete canopy cover, and therefore extended across the potential range of FC seen in annual field crops ($0 \leq FC \leq 1$).

13.7 METRIC Model: Irrigated Horticulture

13.7.1 Introduction

Whilst perennial fruit, nut, and vine crops grown in the southern MDB show little physical resemblance to irrigated annual summer crops (see Section 13.6), the hydrologic responses elucidated by the latter provided a comparative, contextual framework for the study and interpretation of ET/NDVI data in horticultural crops grown in the southern MDB. In contrast to perennial fruit, nut, and vine crops, summer annuals are resown into freshly-prepared seedbeds in spring each year (FC=0) and crops exhibit an extended period of low plant cover during germination, emergence and establishment stages of growth, then subsequent growth and leaf expansion is rapid under favourable conditions, resulting in near complete cover of the soil surface before crops set seed, mature and senesce. Conversely, perennial fruit, nut, and vine crops undergo an establishment period of up to seven years before they reach full production. Once established, deciduous horticultural species also show marked seasonal trends in foliage cover: FC typically increases rapidly in spring, followed by a prolonged period of maximal incomplete cover during fruit/nut growth, and harvest in summer or autumn. Deciduous species lose leaves during cooler months, whereas evergreen species, including citrus, maintain a more or less constant foliage cover and water use capability (K_c) throughout the year (see Sections 4 and 5).

Figure 13.3 Typical crop coefficient curve

Typical crop coefficient curve for Southern Hemisphere deciduous tree crops: seasonal changes in the basal crop coefficient (K_{cb}) are approximated by piecewise linear changes on calendar transition dates t_1, t_2, t_3, and t_4. Peak-season values of K_{cb} (t_2–t_3) vary depending on the crop age, orchard configuration, growth conditions and tree/vine management.

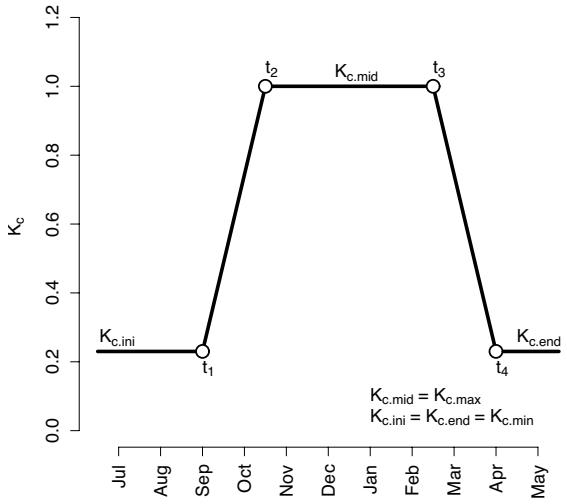

Source: Mohammed Abuzar, Agriculture Victoria

Seasonal water use of temperate deciduous species (and annual summer crops) is therefore characterised by large temporal variations in K_c that closely follow seasonal changes in foliage cover. To account for the impact of variable vegetation cover and background evaporation from soil in orchards and natural landscapes, Allen *et al.* (1998) introduced the basal crop coefficient (K_{cb}), which is principally the transpiration component of ET, with negligible evaporation from soil. As such, it represents the minimum rate of ET for a crop adequately supplied with water.

Crop 'calendars' are used to describe the seasonal progression in K_c values attributable to changes in vegetation cover of deciduous perennial horticultural crops. Calendars for deciduous tree crops in the Southern Hemisphere typically show:

- a small value for the basal crop coefficient, K_{cb}, ($K_{cb\ ini}$) in the early stages of foliage development;
- followed by an increase to a maximum ($K_{cb\ mid}$) associated with the period of peak foliage cover; and
- a subsequent post-harvest decline and return to the minimum values ($K_{cb\ ini}$) seen in winter (see Figure 13.3).

In order to facilitate field operations, vegetation cover of the soil surface is carefully planned and managed in row-based fruit, nut, and vine plantings. Canopy/row configurations may also vary within and between orchards in order to promote yield and quality outcomes. Allen and Pereira (2009) described changes in K_{cb} of orchards as a function of crop height and canopy cover. They employed a density coefficient (K_d) to account for the increase in K_{cb} (and associated increase in K_c)with increased vegetation cover:

$$K_{cb} = K_{cb\ min} + K_d\left(K_{cb\ full} - K_{cb\ min}\right)$$

Changes in K_{cb} in the range $K_{cb\ min}$– K_{cb} full were related to the effects of vegetation cover (FC) and crop height (h) depending on the value of K_d applicable to the target crop. K_d showed a near-linear dependence on FC for low values of FC, and achieved a maximum (K_{cr}=1) at sub-maximal values of FC in tall crops (h > 2m).

The equation above is consistent with the empirical, satellite-based, linear relationship linking K_{cb} to NDVI derived by Tasumi *et al.* (2005; see Figure 13.2), which described a linear increase in K_{cb} of irrigated summer annual crops (h < 2 m) with increasing NDVI over the full range of NDVI (0.1 ≤ NDVI ≤ 0.85; Tasumi *et al.*, 2005: $K_{cb} \approx 1.33 \times (\text{NDVI} - 0.1)$).

Values of $K_{c\ mid}$ (see Figure 13.3) coincide with seasonal maximum values of evaporative demand experienced in the southern MDB, and hence with maximal daily values of IWR. Minimum values of K_{cb}, denoted $K_{c\ ini}$ and $K_{c\ end}$ in Figure 13.3, apply to deciduous fruit, nut, and vine crops during the autumn-winter period. Seasonal changes in K_{cb} of evergreen citrus species are minor, and the values $K_{cb} = K_{c\ mid}$ apply throughout the year.

13.7.2 Model implementation

METRIC analyses (Allen *et al.*, 2007) were conducted to investigate ET_rF/NDVI relationships seen in perennial fruit, nut, and vine crops grown in the southern MDB during the summer period (peak-season irrigation demand), and to explore the potential relevance of the triangular ET_rF/NDVI relationship in those crops. Analyses were undertaken for the period December 2008–February 2010 in the Riverland (RL), Sunraysia/Mallee (SR), and Goulburn-Murray (GM) irrigation districts of SE Australia. These analyses employed Landsat-5 imagery acquired during peak-season irrigation periods (October–April, inclusive). Landsat images were georeferenced to contemporary, field scale, district land use maps (see Table 13.4).

Image-synchronised values of ET_r were computed using district-specific, meteorological data generated by automatic weather stations operated by the Bureau of Meteorology for sites at Loxton (RL), Mildura (SR) and Tatura (GM; see Table 13.5 and Figure 13.4). Values of ET_r were calculated according to standardised ASCE procedures (ASCE EWRI, 2005).

Figure 13.4 Irrigation districts

Map showing the extents of the Riverland, Sunraysia/Mallee and Goulburn-Murray Irrigation Districts in the southern MDB. Representative meteorological data were sourced for the towns of Loxton, Mildura and Tatura, respectively. Inset shows the study region in a continental context.

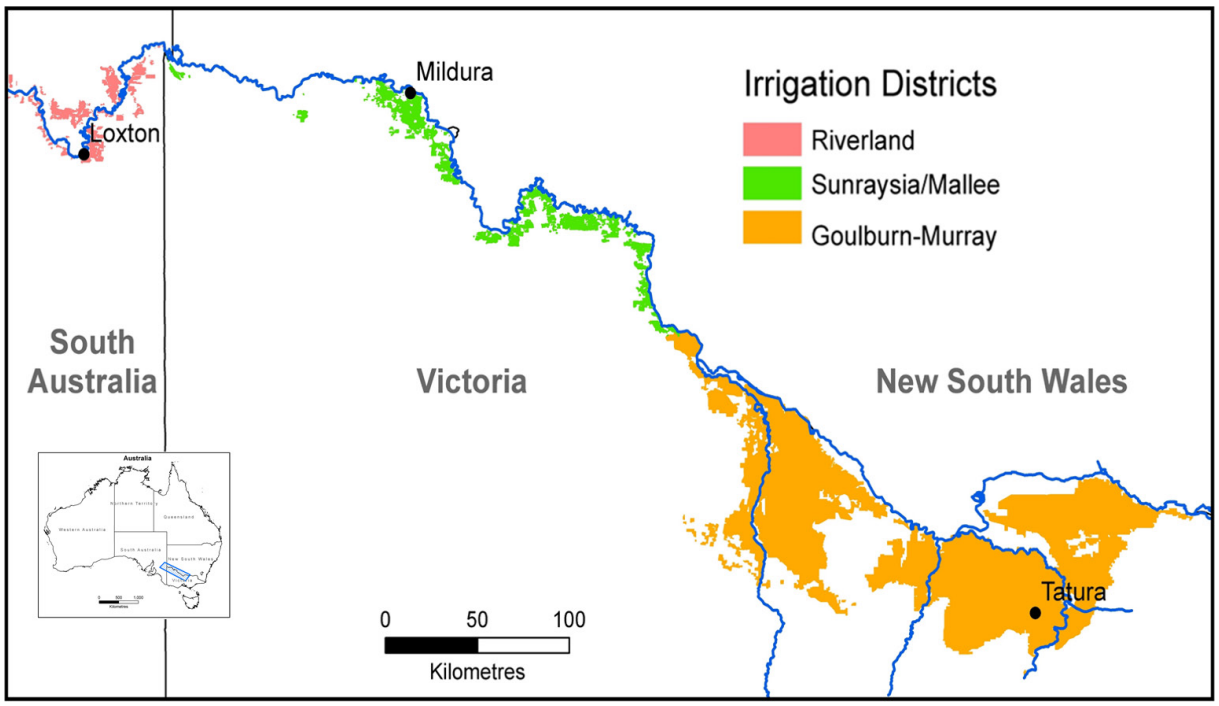

Source: Des Whitfield, Agriculture Victoria

Table 13.4 Landsat-5 images used in analysis

Clear-sky Landsat-5 images were employed in analyses of ET$_r$F/NDVI relationships in irrigated fruit, nut, and vine crops in the southern MDB. District/date indices were formulated according to irrigation district and date of image acquisition (as doy/year, where doy was day of year, e.g. Jan 1 = doy 1, and year was year of century, e.g. 2000).

Irrigation district	District Code	Acquisition Date	Path/ Row	District/ Date index	Source of landuse map
Riverland	RL	2010-02-16	96/84	RL047/10	River Murray Irrigated Crops Data (June 2008) produced by the South Australian MDB Resource Information Centre of the South Australian MDB Natural Resources Management Board (SAMDBNRM, 2010)
Sunraysia/ Mallee	SR	2008-12-20	95/84	SR355/08	SunRise21 (*www.sunrise21.org.au*)
		2009-01-05	95/84	SR005/09	
Goulburn-Murray	GM	2008-11-03	93/85	GM308/08	Shepparton Preserving Co. Ltd
		2009-01-22	93/85	GM022/09	
		2009-02-23	93/85	GM054/09	
		2009-03-27	93/85	GM086/09	
		2009-04-12	93/85	GM102/09	

Field scale values of ET_rF (ET/ET_r) and NDVI were computed for all fruit, nut, and vine crops grown in each district according to the procedures described in Allen *et al.* (2007)[10]. Analytical estimates of momentum roughness length (z_{0m}), effects of elevation, and the assignment of hot and cold pixels were as follows:

- The NDVI-albedo (α) approach (see equation 34b in Allen *et al.*, 2007) was used for estimates of z_{0m}. We used the relationship published by Teixeira *et al.* (2009) for a mixture of agricultural and natural ecosystems seen in the Sao Francisco River basin, Brazil:

$$z_{0m} = \exp\left(0.26\left(\frac{NDVI}{\alpha}\right) - 2.21\right)$$

  The NDVI-albedo (α) approach helps to distinguish z_{0m} of tall and short vegetation types that have similar NDVI but different albedo (Allen *et al.*, 2007; Teixeira *et al.*, 2009), so avoids the need for crop-specific land cover/vegetation height relationships to describe z_{0m}.

- Given the minor variation in elevation across the southern MDB (see Table 13.5), the METRIC model was applied using a constant elevation of 80 m.
- Hot 'anchor' pixels (ET = ET_rF = 0) were identified within low NDVI (NDVI ≤ 0.3) pixels showing high surface temperature (defined as the upper 2% of T_s), located in non-irrigated fields adjacent to irrigated farms. Cold anchor pixels were selected from fields associated with centre-pivot irrigation of tomatoes (in Riverland district), carrots (in Sunraysia) or lucerne (in Goulburn-Murray). Identified cold-pixel crops closely resembled the theoretical alfalfa crop underpinning estimates of ET_r, with candidate pixels being confined to the upper range of irrigation NDVI, and the lower range of irrigation T_s. Crops were assumed to receive regular, adequate irrigation at intervals of 3–4 days, as observed for lucerne (in Goulburn-Murray). Cold-pixel crops were therefore assumed to be free of surface water (or dry) at the times of satellite overpass, and the value of ET_rF appropriate to dry surface foliage, ET_rF = 1.0, was assigned to cold pixels.

Table 13.5 Automatic weather station sites

Site details of automatic weather stations that were used for district METRIC analyses. Station number represents the official designation used by the Bureau of Meteorology, Australia.

District	Site	Station number	Latitude (°S)	Longitude (°E)	Elevation (m asl)
GM	Tatura	81049	36.4378	145.2672	114
SR	Mildura	76031	34.2358	142.0867	51
RL	Loxton	24024	34.4390	140.5978	30

Source: Weatherzone (*www.weatherzone.com.au*)

Paired pixel scale values of ET_rF /NDVI were attributed to irrigated tree and vine crops based on the delineation of fields in land use maps. Field scale values of ET_rF and NDVI were estimated by respective pixel scale means. Crop-specific analyses were restricted to major crops in each district, and included almond, citrus, and grape crops in both Riverland and Sunraysia districts, and pear, peach, apple and apricot crops in the Goulburn-Murray irrigation area.

ET_rF /NDVI analyses targeted peak-season irrigation periods when fully-grown crops typically experience large rainfall deficits (maximum annual values of evaporative demand coupled with low rainfall). Clear-sky weather conditions provided five scenes for the Goulburn-Murray district in season 2008–09 (see Table 13.4), which allowed for a detailed temporal analysis of the major fruit crops grown in the district.

13.7.3 ET_rF /NDVI relationships

Figure 13.5 shows the peak-season NDVI and ET_rF distributions seen in 29 crop/district/date combinations for fruit, nut, and vine crops grown in the southern MDB within the study period. NDVI was predominantly confined to the range 0.1 ≤ NDVI ≤ 0.70, and consequently never achieved the large values (NDVI > 0.80) seen in the Idaho data (see Figure 13.2). Reduced maxima in the fruit, nut, and vine data were attributed to row-based plantings in horticultural crops (FC < 1). The large variability in peak-season NDVI within the range 0.1–0.70 was attributed primarily to differences in crop age and development, and differences in planting patterns, orchard management, and growth conditions.

10 Analyses were conducted using ENVI/IDL software (Harris Geospatial, Broomfield CO, USA).

Figure 13.5 also shows relatively few observations of ET_rF in the range $ET_rF > 1$, which are expected under conditions where ET is enhanced by direct evaporation of liquid water from wet soil/plant surfaces due to recent irrigation and/or rainfall. Irrigation was employed judiciously during the drought period experienced during the study (Goodwin and O'Connell, 2017), and rainfall events were scarce. Nevertheless, almost all ET_rF observations exceeded the NDVI-dependent K_{cb} baseline associated with the reference ET/NDVI triangle (see Figure 13.6 and Figure 13.7), providing strong empirical support for the assumption that crops were adequately supplied with water:

$$ET = ET^*$$

$$K_{cr} = ET_rF\ (= ET/ET_r)$$

Figure 13.5 Quartile representations

Quartile representations of the distribution of peak-season, field scale values of NDVI and ET_rF in fruit, nut, and vine crops in the southern MDB irrigation districts in the period 2008–10 inclusive (see Table 13.4 for district/date codes). Blue lines show the range of observed field scale measures of NDVI and ET_rF, respectively, while solid black bars represent the range of observations in the second and third quartiles. Green dots indicate the median values. Vertical lines demark the values NDVI = 0.1, $ET_rF = 0$ and $ET_rF = 1$.

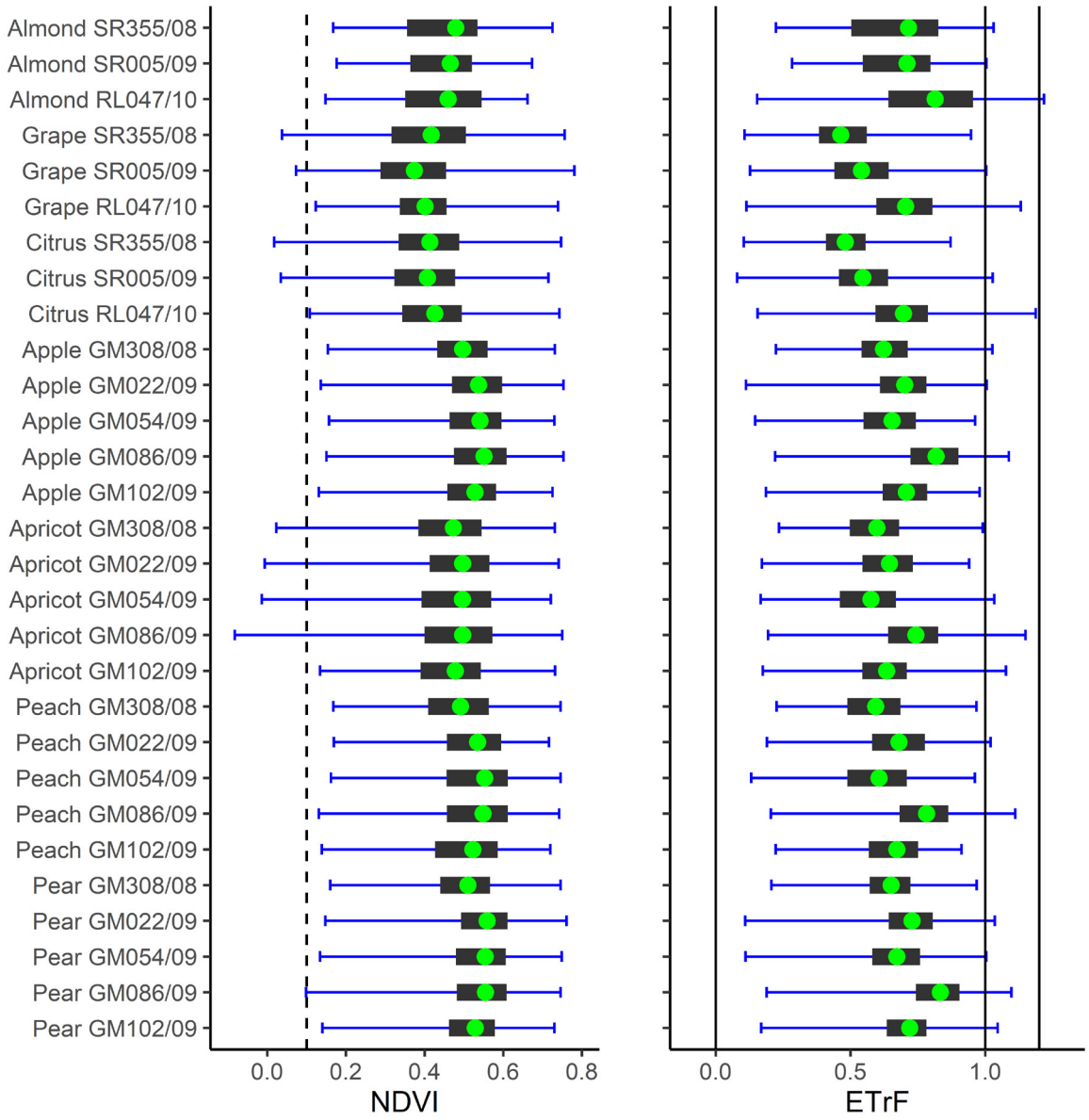

Source: Des Whitfield, Agriculture Victoria

Representative ET_rF/NDVI relationships in Figure 13.6 and Figure 13.7 showed few observations where high rates of ET ($ET_rF > 0.9$) were associated with low NDVI, which is consistent with the scarcity of rainfall events during the study period. ET_rF/NDVI relationships were therefore free of rainfall effects at low NDVI (compared with Figure 13.2 of Tasumi *et al.*, 2005), and ET_rF was consequently significantly related to NDVI ($P < 0.05$) in all 29 crop/district/date combinations available to the study.

Figure 13.6 Relationships for selected crops

Peak-season, field scale ET_rF/NDVI relationships of almond, grape and citrus crops grown in the Sunraysia/Mallee (SR) in 2008/09 irrigation season and Riverland (RL) districts in 2009/10 (see Table 13.4 for district/date codes). Grey triangles represent limits on ET_rF/NDVI values seen in irrigated summer annual crops (Tasumi *et al.*, 2005). White lines represent least squares lines of best fit.

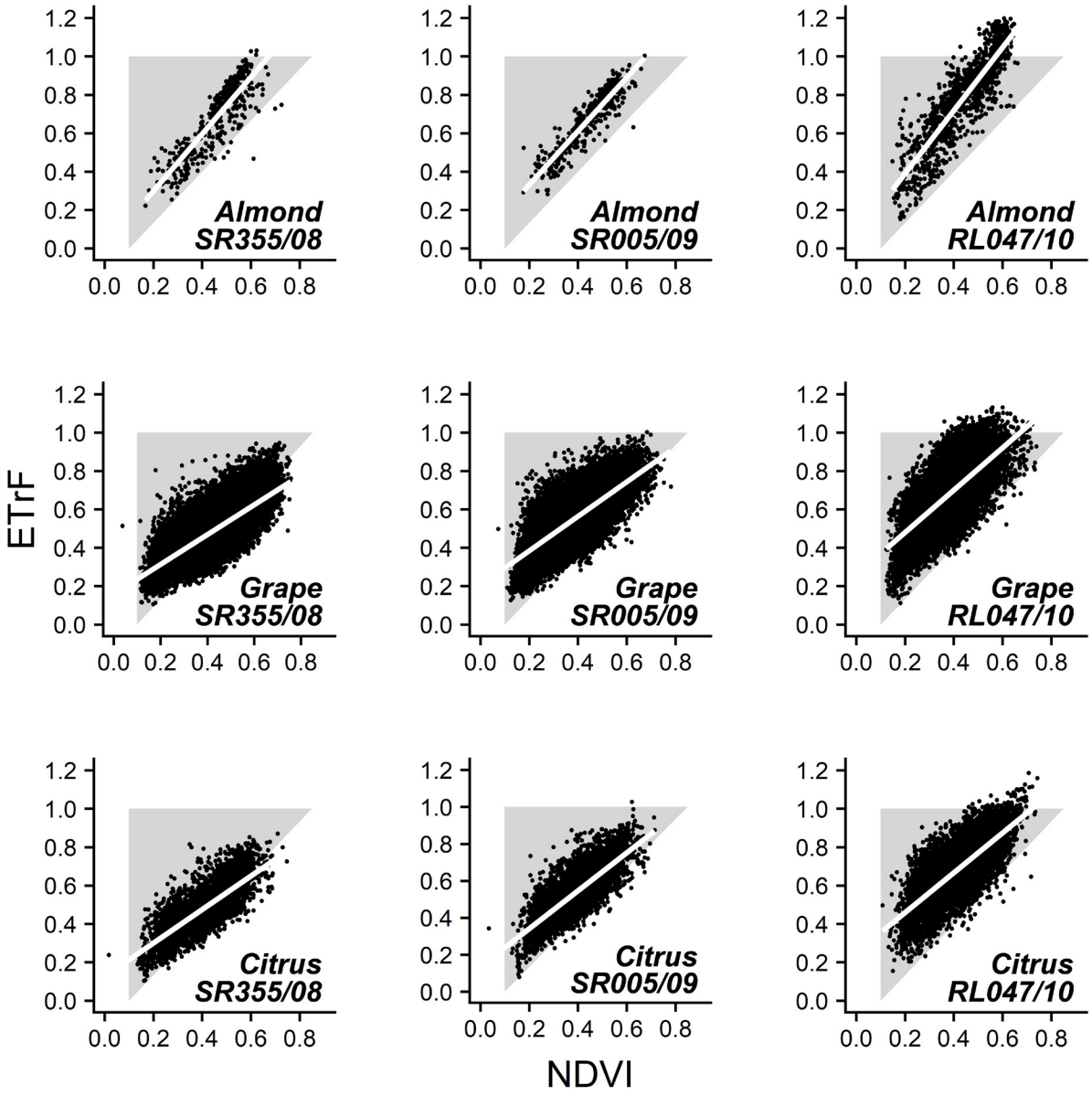

Source: Des Whitfield, Agriculture Victoria

The linear regression relationships shown in Figure 13.6 and Figure 13.7 were appraised by investigating differences in the predicted values of ET_rF at endmember values of NDVI (0.1 and 0.85) defined by the ET_rF/NDVI reference triangle (using the values ET_rF_{min} and ET_rF_{max} respectively), along with appropriate 95% fiducial limits, for each crop/district/date combination.

The analysis paralleled the endmember approach adopted by Allen and Pereira (2009), who described changes in K_{cb} of 'tall' horticultural crops in terms of a density coefficient, K_d, for values of K_{cb} within the range, $K_{cb\ min} - K_{cb\ full}$ (see equation for K_{cb} in Section 13.7.1).

Figure 13.7 Representative ET_rF/NDVI relationships for selected crops

Representative peak-season field scale ET_rF/NDVI relationships seen in pear, peach, and apricot crops grown in Goulburn-Murray Irrigation District in 2008/09 irrigation season (see Table 13.4 for district/date codes). Grey triangles represent limits on ET_rF/NDVI values seen in irrigated summer annual crops (Tasumi *et al.*, 2005). White lines depict least-squares lines of best fit.

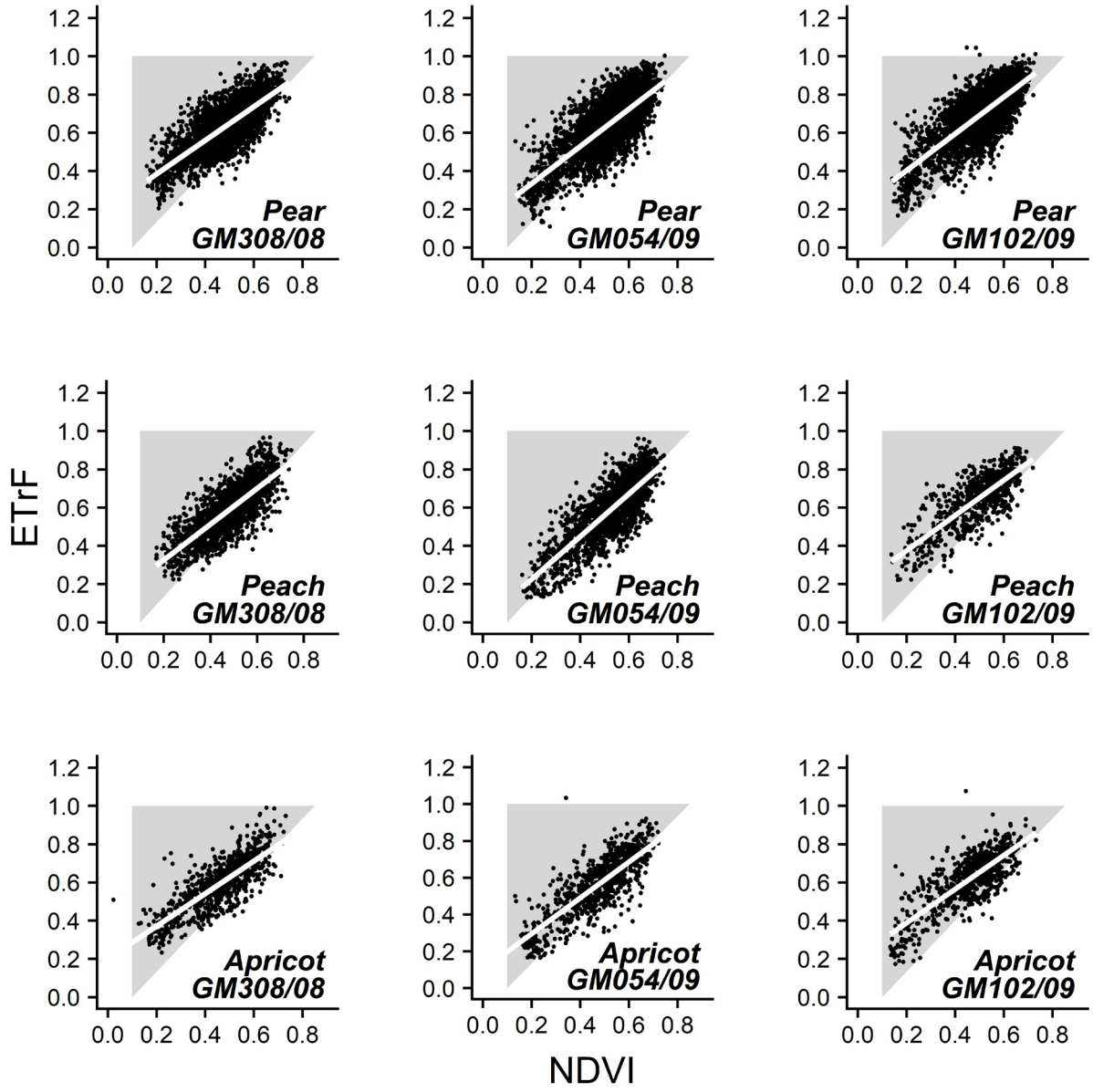

Source: Des Whitfield, Agriculture Victoria

Figure 13.8 shows that regression estimates of ET_rF_{min} were confined to the approximate range $0.1 \leq ET_rF_{min} \leq 0.4$ (fiducial limits $-0.1 \leq ET_rF_{min} \leq 0.6$). The mean value of ET_rF_{min} ($ET_rF_{min} = 0.27$) fell within fiducial limits appropriate to individual crop/district/date combinations.

Figure 13.8 shows that regression estimates of ET_rF_{max} ranged between 0.8 and 1.4 (fiducial limits $0.7 \leq ET_rF_{max} \leq 1.75$). The data clearly demonstrated that the mean value of ET_rF_{max} for almonds exceeded values seen in non-almond crops. The mean value of ET_rF_{max} in non-almond crops was consistent with the estimate $ET_rF_{max} = 1.00$ (see Figure 13.8), whereas the mean value for almonds was $ET_rF_{max} = 1.32$.

Figure 13.8 Endmember regression estimates of ET_rF_{min} and ET_rF_{max}

Predicted values of endmember estimates of ET_rF_{min} (brown) and ET_rF_{max} (green) in crop/district/date combinations (see Table 13.4 for district/date codes) enumerated in the southern MDB in seasons, 2008/09 and 2009/10, and associated fiducial limits (95%). Mean value of the coefficient, ET_rF_{min}, was 0.27 in all fruit, nut, and vine crops (shown as brown vertical line), while mean value of ET_rF_{max} was 1.00 in non-almond crops (shown as green vertical line). ET_rF_{max} assumed the value, $ET_rF_{max} = 1.32$, in almond crops grown in the southern MDB (shown as grey vertical line).

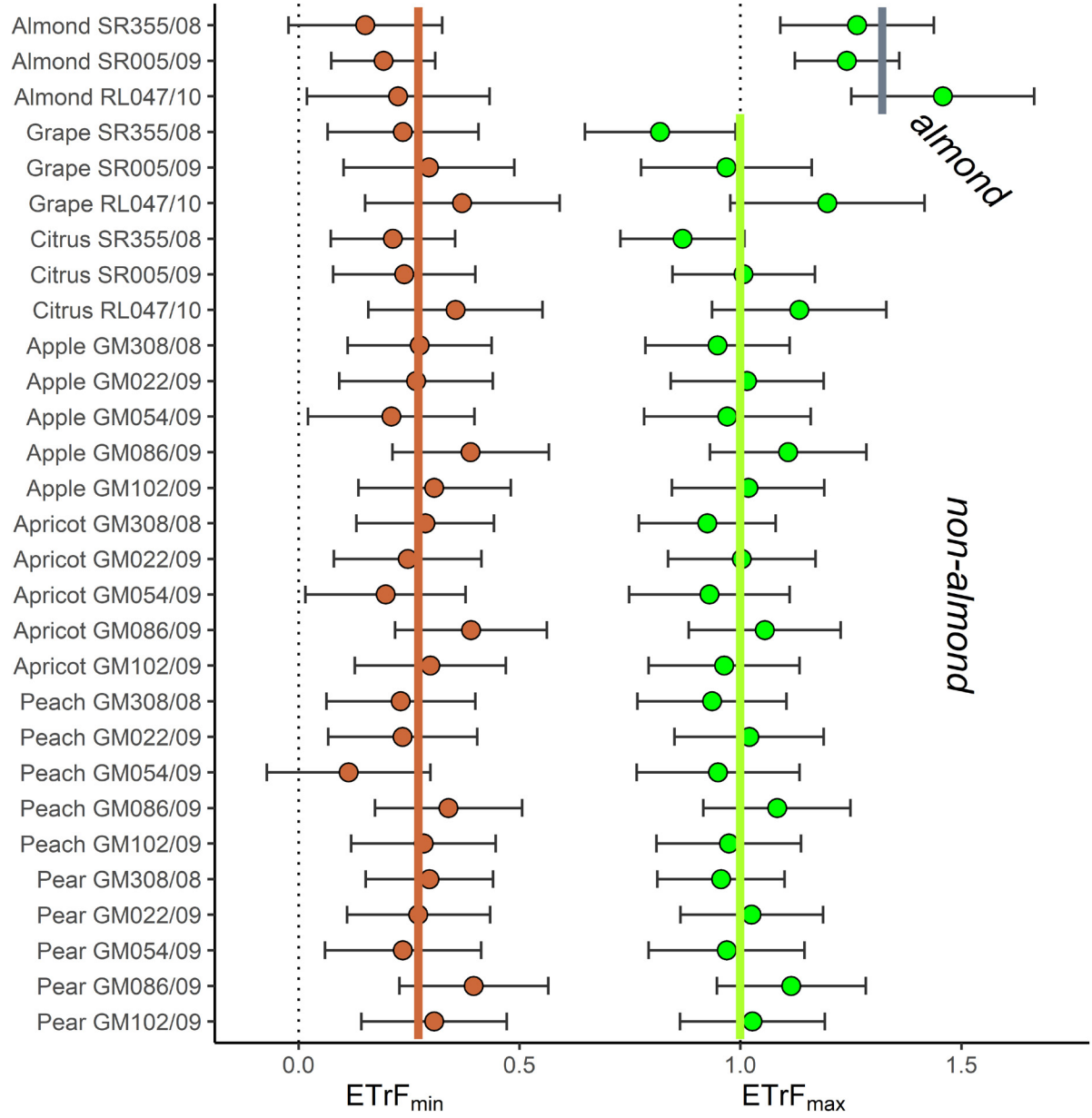

Source: Des Whitfield, Agriculture Victoria

The preceding analysis of satellite-based ET_rF/NDVI relationships for irrigated fruit, nut, and vine crops grown in the southern MDB showed large variations in peak-season values of ET_rF. Derived estimates of ET_rF_{min} and $ETrF_{max}$ were attributed to adequately watered crops on the dual basis that:

- satellite-based ET_rF measures were related exclusively to irrigated fields and crops defined by irrigation land use maps; and
- field scale observations of ET_rF overwhelmingly exceeded values associated with the nominal lower limit (K_{cb}) of the ET_rF /NDVI triangle derived from Tasumi *et al*. (2005).

The severe lack of rainfall experienced by irrigation districts during the drought conditions of this study further suggested that estimates of ET_rF shown in Figure 13.5, Figure 13.6, and Figure 13.7 were closely associated with K_{cb} values expected for adequately watered, fruit, nut, and vine crops.

ET_rF showed strong, statistically-significant, linear relationships with NDVI in all peak-season crop/date/district combinations addressed by this study (see Figure 13.6 and Figure 13.7), providing strong independent support for the use of the K_c-VI to determine IWR of horticultural crops grown in the southern MDB. Endmember analyses of linear K_c/NDVI relationships (see Figure 13.8) showed that complex variations in FC, crop height, and tree/vine planting distributions were described by crop-specific endmember values of ET_rF estimated for the extremes of NDVI, namely NDVI = 0.1 and NDVI = 0.85, according to the ET_rF/NDVI triangle derived from Tasumi *et al*. (2005). Data shown in Figure 13.8 further suggested that linear ET_rF/NDVI relationships applicable to fruit, nut, and vine crops in the range $ET_rF \leq 1$ may be described by:

$$ET_rF = ET_rF_{min} + \frac{(NDVI - 0.1)(ET_rF_{max} - ET_rF_{min})}{0.75}$$

Here, ET_rF_{min} described the lower limit on ET_rF at minimal NDVI (NDVI = 0.1), while ET_rF_{max} described differences in ET_rF seen at maximal NDVI (NDVI = 0.85). ET_rF_{max} varied between species, assuming the values ET_rF_{max} = 1.32 in almond, and ET_rF_{max} = 1.00 in all other species included in the range of fruit, nut, and vine crops. Values of ET_rF afforded by the equation above are limited to the maximum rate of ET attributable to well-watered alfalfa (ET_rF = 1; Allen *et al*., 2007; Allen and Pereira, 2009; Jensen and Allen, 2016).

Derived estimates of ET_rF_{min} and ET_rF_{max} may therefore be combined with weather-based measures of ET_r to estimate rates of ET* for use in real time, field scale irrigation management, or regional and farm scales in order to ensure an optimal balance between water supply and demand in horticultural crops.

13.8 Application to Irrigated Horticultural Crops in Southeast Australia

Seasonal and annual analyses of regional and farm scale irrigation demand may be conducted by undertaking crop water balance analyses based on weather, and the area and peak-season NDVI of constituent crops. This proposed regional approach contrasts with existing methods, which use census and other data to describe crop type and area, usually without regard to differences in the irrigation water requirements associated with crop age or size, and rely on historic water use data and/or the application of a predefined set of K_c values to describe crop water use capability.

Regional water use assessments are important in districts where crop mix and/or crop area are subject to rapid change. Regular assessments allow water managers to stay abreast of changes in the regional supply/consumption differentials that vary with changes in crop mix, crop area, and climate. Variations in crop mix change the K_c values that determine irrigation intensity (water use per ha), and changes in climate (rainfall deficit) also lead to changes in irrigation intensity. The largest changes in irrigation water use/demand are ultimately attributable to changes in the area of irrigated crops.

Irrigation farmers require a clear understanding of crop-specific water requirements in order to gauge irrigation demand of existing and prospective crops, and are challenged by the need to ensure that irrigation practices satisfy the yield and quality targets of crops, with minimal over-irrigation and consequent impact on the deep drainage to underlying water tables. Thus irrigators are primarily concerned with issues of irrigation intensity, and the need to ensure that irrigation applications are closely aligned to the temporal and spatial variations that arise from the range of crops and fields that contribute to on-farm irrigation demand. Methods described in this chapter provide the potential to define and refine crop-dependent, field scale water use targets and are further suited to turnkey regional supply/demand analytics when assessments of district and farm scale irrigation supply and demand are augmented by EO crop mapping techniques.

Seasonal trends in K_c of deciduous crops are important to farm/district scale assessments of irrigation demand. These may be incorporated in analyses of well-established crops by the use of crop calendars for temporal scaling of in-season values of NDVI (see Figure 13.2). Alternatively, multiple satellite images may be used to undertake real time, field-customised irrigation management (such as IrriSAT; Hornbuckle, 2014; see Section 13.9).

In all cases, estimates of ET* are readily incorporated in soil water balance analyses to estimate field- and crop-specific irrigation water requirements. Methods described in Section 13.7 therefore provide a formal, objective basis for the irrigation demand analytics needed to ensure that irrigation demand is appropriately matched to irrigation resources at field, farm and district scales in irrigated fruit, nut, and vine crops of the southern MDB.

13.9 Further Information

Australian Horticulture

Australian Department of Agriculture and Water Resources: Horticulture fact sheet: *http://www.agriculture.gov.au/ag-farm-food/hort-policy/horticulture_fact_sheet*

Australian Society of Horticultural Science (AuSHS):

Australian Horticulture webpage: *http://aushs.org.au/australian-horticulture/ http://aushs.org.au/australian-horticulture/*

Australian Horticulture Statistics Handbook 2017/18: *https://www.horticulture.com.au/growers/help-your-business-grow/research-reports-publications-fact-sheets-and-more/australian-horticulture-statistics-handbook/*

IrriSAT

Hornbuckle (2014)

Montgomery *et al.* (2015)

https://irrisat-cloud.appspot.com/

Evapotranspiration

Allen *et al.* (1998)

ASCE-EWRI (2005)

Jensen and Allen (2016)

13.10 References

Allen, R.G., Pereira, L.S., Raes, D., and Smith, M. (1998). *Crop evapotranspiration: Guidelines for computing crop water requirements*. United Nations FAO Irrigation and Drainage Paper 56. FAO, Rome. ISBN 92-5-104219-5 *http://www.fao.org/3/X0490E/x0490e00.htm#Contents*

Allen, R.G., Pruitt, W.O., Wright, J.L., Howell, T.A., Ventura, F., Snyder, R., Itenfisu, D., Steduto, P., Berengena, J., Yrisarry, J.B., Smith, M., Pereira, L.S., Raes, D., Perrier, A., Alves, I., Walter, I., and Elliott, R. (2006). A recommendation on standardized surface resistance for hourly calculation of reference ET_o by the FAO56 Penman-Monteith method. *Agricultural Water Management*, 81, 1–22.

Allen, R.G., Tasumi, M., and Trezza, R. (2007). Satellite-Based Energy Balance for Mapping Evapotranspiration with Internalized Calibration, METRIC. Model. *Journal of Irrigation and Drainage Engineering*, 133, 380–394.

Allen, R.G., and Pereira, L.S. (2009). Estimating crop coefficients from fraction of ground cover and height. *Irrigation Science*, 28, 17–34.

Allen, R.G., Irmak, A., Trezza, R., Hendrickx, J.M.H., Bastiaanssen, W.H.M., and Kjaersgaard, J. (2011). Satellite-based ET estimation in agriculture using SEBAL and METRIC. *Hydrological Processes*, 25, 4011–4027.

Argus S. (2015). *Summary report: Irrigated crops of the Lower Murray-Darling: 1997 to 2015*. *https://www.sunrisemapping.org.au*

ASCE-EWRI (2005). *The ASCE Standardized Reference Evapotranspiration Equation*. Final Report: Environmental and Water Resources Institute of the American Society of Civil Engineers, Virginia, USA. 70 p.

Bastiaanssen, W.G.M., and Ali, S. (2003). A new crop yield forecasting model based on satellite measurements applied across the Indus Basin, Pakistan. *Agriculture, Ecosystems and Environment*, 94, 321–340.

Bastiaanssen, W.G.M., Menenti, M., Feddes, R.A., and Holtslag, A.A. (1998). A remote sensing surface energy balance algorithm for land (SEBAL). *Journal of Hydrology*, 212–213, 198–212.

Bausch, W.C., and Neale, C.M.U. (1987). Crop coefficients derived from reflected canopy radiation: a concept. *Transactions of the American Society of Agricultural Engineers*, 30, 703–709.

Belmonte, A.C., Jochum, A.M., Garcia, A.C., Rodriguez, A.M., and Fuster, P.L. (2005). Irrigation management from space: Towards user-friendly products. *Irrigation and Drainage Systems*, 19, 337–353.

Cahn, M.D., and Johnson, L.F. (2017). Review: New Approaches to Irrigation Scheduling of Vegetables. *Horticulturae*, 3, 28.

Doorenbos, J., and Pruitt, W.O. (1977). *Crop water requirements*. United Nations FAO Irrigation and Drainage Paper Number 24 (rev). 144 p.

Goodwin, I., and O'Connell, M.G. (2017). Drought water management: an Australian perspective. *Acta Horticulturae*, 1150, 219–232.

Gonzalez-Dugo, V., Zarco-Tejada, P., Nicolas, E., Nortes, P.A., Alarco, J.J., Intrigliolo, D.S., and Fereres, E. (2013). Using high resolution UAV thermal imagery to assess the variability in water status of five fruit tree species within a commercial orchard. *Precision Agriculture*, 14(6), 660–678. doi:*10.1007/s11119-013-9322-9*

Guerra, E., Ventura, F., and Snyder, R. (2016). Crop Coefficients: A Literature Review. *Journal of Irrigation and Drainage Engineering*, 142(3), [06015006]. *https://doi.org/10.1061/(ASCE)IR.1943-4774.0000983*

Heilman, J.L., Heilman, W.E., and Moore, D.G. (1982). Evaluating the crop coefficient using spectral reflectance. *Agronomy Journal*, 74, 967–971.

Hornbuckle, J. (2014). *Vineyard Irrigation—delivering water savings through emerging technology*. Final Report, Grape and Wine Research and Development Corporation Project CSL0901, 90 p.

Hunsaker, D.J., Pinter, P.J., Barnes, E.M., and Kimball, B.A. (2003). Estimating cotton evapotranspiration crop coefficients with a multispectral vegetation index. *Irrigation Science*, 22, 95–104.

Jensen, M.E., and Allen, R.G. (2016). *Evaporation, evapotranspiration, and irrigation water requirements*. American Society of Civil Engineers. *https://doi.org/10.1061/9780784414057*

Johnson, L.F., and Trout, T.J. (2012). Satellite NDVI Assisted Monitoring of Vegetable Crop Evapotranspiration in California's San Joaquin Valley. *Remote Sensing*, 4, 439–455.

Montgomery, J., Hornbuckle, J., Hume, I., and Vleeshouwer, J. (2015). IrriSAT—weather based scheduling and benchmarking technology. *Proceedings of 17th ASA Conference*, Hobart, Australia. *http://www.agronomyaustraliaproceedings.org/images/sampledata/2015_Conference/pdf/agronomy2015final00449.pdf*

Moran, M.S., Clarke, T.R., Inoue, Y., and Vidal, A. (1994). Estimating Crop Water Deficit Using the Relation between Surface-Air Temperature and Spectral Vegetation Index. *Remote Sensing of Environment*, 49, 246–263.

Moran, M.S., Rahman, A.F., Washburne, J.C., Goodrich, D.C., Weltz, M.A., and Kustas, W.P. (1996). Combining the Penman-Monteith equation with measurements of surface temperature and reflectance to estimate evaporation rates of semiarid grassland. *Agricultural and Forest Meteorology*, 80, 87–109.

Neale, C.M.U., Bausch, W.C., and Heermann, D.F. (1989). Development of reflectance based crop coefficients for corn. *Transactions of the American Society of Agricultural Engineers*, 32, 1891–1899.

Pereira, L.S., Perrier, A., Allen, R.G., and Alves, I. (1999). Evapotranspiration: Concepts and Future Trends. *Journal of Irrigation and Drainage Engineering*, 125, 45–51.

Rajan, N., and Maas, S.J. (2014). Spectral crop coefficient approach for estimating daily crop water use. *Advances in Remote Sensing*, 3, 197–207.

SAMDBNRM, (2010). *Regional Plan, Volume 3: Regulatory and Policy Framework*. South Australian MDB Natural Resources Management Board. 74 p.

Tasumi, M., Allen, R.G., Trezza, R., and Wright, J.L. (2005). Satellite-Based Energy Balance to Assess Within-Population Variance of Crop Coefficient Curves. *Journal of Irrigation and Drainage Engineering*, 131, 94–109.

Teixeira, A.H.C., Bastiaanssen, W.G.M., Ahmad, M.D., and Bos, M.G. (2009). Reviewing SEBAL input parameters for assessing evapotranspiration and water productivity for the Low-Middle Sao Francisco River basin, Brazil Part A: Calibration and validation. *Agricultural and Forest Meteorology*, 149, 462–476.

Yang, Y., Roderick, M.L., Zhang, S., McVicar, T.R., and Donohue, R.J. (2018). Hydrologic implications of vegetation response to elevated CO_2 in climate projections. *Nature Climate Change*, 9, 44–48. doi:*10.1038/s41558-018-0361-0*

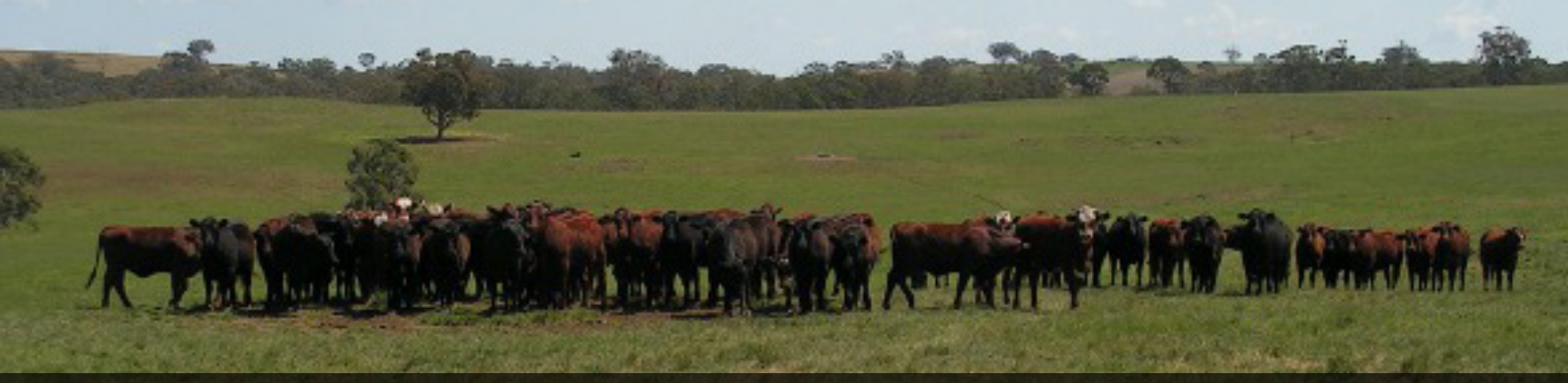

14 Pastures

Graham Donald

This section considers EO methods for extracting information to assist the management of pasture lands in Australia. In this context, the term 'pasture' combines the grassland definitions of Hill (2004):

- human-made pastures and grasslands—largely resulting from clearing of forested lands to grow pasture for dairy, meat, or wool production, as occurs in the coastal and hinterland regions of NSW, Victoria, and WA; and
- highly managed natural grasslands—naturally grassy regions now used to graze livestock, such as the semi-improved pastoral regions of eastern Australia.

To be a successful farmer one must first know the nature of the soil.
(Xenophon)

Section 15 below will consider EO methods that are more appropriate for the semi-arid and arid Australian rangelands, where vegetation density and stocking rates are much lower.

At a global level, grasslands are the most prevalent type of vegetation cover (Latham *et al*., 2014), the second largest terrestrial carbon sink (Derner and Schuman, 2007), and the cheapest source of fodder for livestock (Ali *et al*., 2016). However, the combined impacts of urbanisation, industrial development, overgrazing, intensive management, and climate change have meant that the area of agricultural land, and particularly permanent pasture cover, has declined in recent decades both on a global basis and in Australia (Poore, 2016; see Figure 14.1).

To assist graziers making management decisions, a number of spatial technologies have become available including EO-based information. Some of the attributes of grasslands that can be retrieved from EO datasets include biomass, forage quality, growth rate, land cover, and degradation (Ali *et al*., 2016). These data provide an objective assessment of pasture condition to assist farmers and graziers in resource monitoring and management, and thereby measure the sustainability of agricultural practices over many years. EO-based systems allow graziers and farmers to self-regulate their activities to maintain the health of their pastures, and enable governmental authorities to regulate regional issues such as deforestation and the protection of native grasses.

As with many applications, the major improvements with EO data in agriculture are likely to result from its integration with other spatial services and the 'sense making' processes that will be derived from complex system modelling. In essence, this includes all the information required for balancing the agricultural, economic, and ecological systems in a sustainable management environment that cannot be otherwise achieved without EO technology (see Section 20).

Background image: Cattle grazing in New England region, NSW. **Source:** Graham Donald

Recommended Chapter Citation: Donald, G.E. (2021). Pastures. Ch 14 in *Earth Observation: Data, Processing and Applications. Volume 3A—Terrestrial Vegetation.* CRCSI, Melbourne. pp. 281–298.

Figure 14.1 Area of agricultural land

a. Global

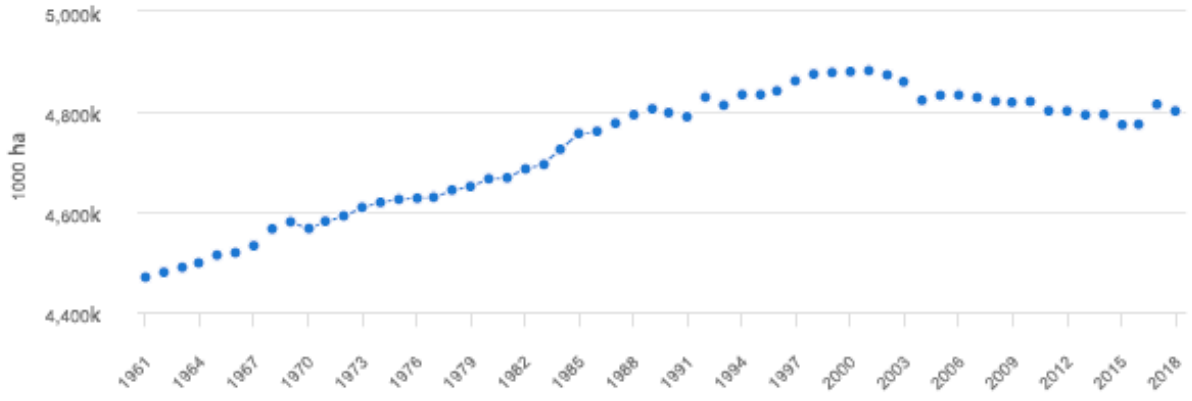

b. In Australia

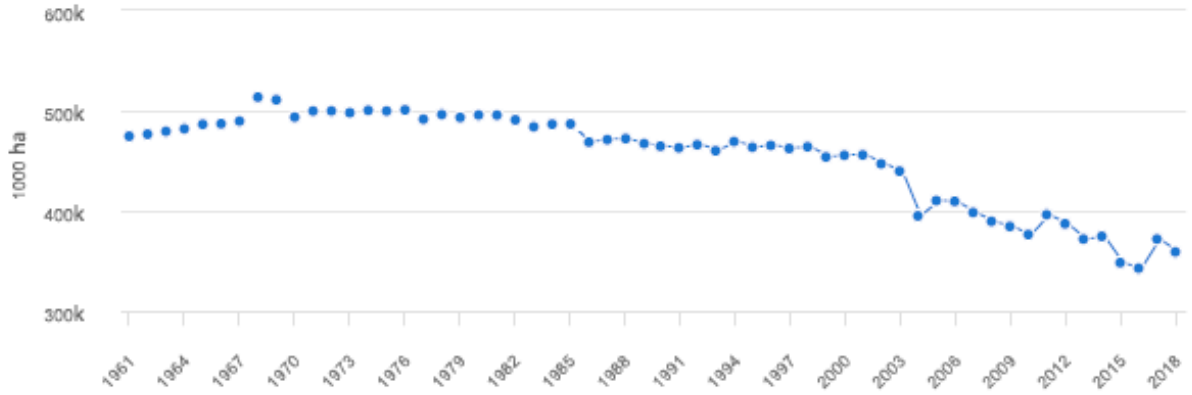

Source: FAOSTAT (2019)

14.1 Pastures in Australia

In Australia, pastoral regions are relatively well-vegetated and enjoy a Mediterranean climate (see Sections 2.2 and 2.4). The coastal belt and hinterlands of Queensland, NSW, and Victoria, plus southeast SA, southwest WA, and Tasmania, receive the highest rainfalls so are best suited to dairy farms, horticulture, and fine wool production (see Figure 11.1). In the drier 'wheat-sheep zone', which covers the slopes and plains of NSW, northern Victoria, southern SA, and parts of southwest WA, larger properties grow grain crops, legumes, and oilseeds, often in rotation with grazing by sheep or cattle (McIvor, 2005).

The main livestock grazed commercially in Australia are sheep and cattle. Sheep are primarily grazed for meat in areas with higher rainfall and grown for wool on drier pastures.

The Australian Bureau of Statistics (ABS) regularly collects agricultural census data, with the major unit for aggregation and reporting being the Statistical Local Area (SLA; see Section 11.1). SLA boundaries are based on subdivisions or groupings of Local Government Areas (LGA) or their equivalent. Data are reported at the end of March for each census year, so statistics actually relate to production in the previous year. ABS agricultural census datasets have been used to validate estimates of pasture development and production derived from EO-based greenness indices, such as NDVI (see Section 8.1.1).

14.2 EO Sensors for Pastures

In the last decades of the twentieth century, various data storage and analysis tools, such as Geographic Information Systems (GIS), were embraced by many areas of land management, including agriculture. These systems integrate spatially-defined grids, raster layers, and cadastral datasets, within a variety of geographic coordinate systems, and enable spatial manipulation, merging, and statistical analyses at the national, regional, station/farm, paddock, or even at a point, scale (see Volume 2D—Section 13). They also provide a means to integrate EO data with other datasets and generate derivative products (see Section 8).

A wide range of EO datasets at varying spectral and spatial scales are now being used to map and monitor agricultural activities (see Table 14.1). Satellite imagery has been used in agriculture since the early 1970s and offers an excellent means to monitor land cover at national, regional, and farm scales (see Sections 3 and 12.3). In particular, outside the intensive agricultural areas, medium resolution satellite imagery (such as acquired by Landsat) has been one of the most productive means of identifying seasonal pasture cycles. In general terms, a relationship exists between the spatial resolution of EO imagery and the reliability/accuracy of the prediction, such that, in most cases, a higher image resolution improves the predictive capability. This assumption is related to the farm/station paddock size and the uniformity of biomass composition (see Section 10.1). With the more recent advent of higher resolution, spaceborne sensors, more detailed information is available allowing the horticulture, viticulture, and intensive farming production sectors to make use of this emerging technology (see Sections 12.6 and 13).

Repeated coverage of seasonal events and cycles has also enabled time series analysis of agricultural activities using multiple, accurately-located, EO datasets (see Sections 9 and 10). Time series of EO-based data offer new opportunities for agricultural applications, including identifying crop types, monitoring land cover, and assessing the productivity of land uses relative to their economic return (see Volume 1B—Section 1.4 and Volume 2D). For example, the Landsat NDVI time series dataset has been used to demonstrate the change and content of vegetation and salinity across the southwest region of WA (Caccetta *et al*., 2000). The power of this vegetation monitoring observation subsequently became a major component in the Land Monitoring Project, extending across Australia (Wallace *et al*., 2006).

Both spaceborne and airborne hyperspectral sensors provide valuable information for agricultural applications. For example, a ground-based hyperspectral sensor study (Edirisinghe *et al*., 2004) demonstrated excellent prediction of *in vitro* digestibility and protein content for field pasture. Remotely piloted aircraft (see Volume 1A—Section 11.2) offer great flexibility for data acquisition over small areas.

Within GIS, optical, thermal, and microwave EO data and derived products have been integrated with many other spatial datasets, such as rainfall, temperature, soil, topography, and cadastre. Many GIS and EO data sources also depend on accessing accurate locational information via Global Positioning System (GPS) and the Global Navigational Satellite System (GNSS; see Volume 1B—Section 10).

Table 14.1 EO sensors relevant to pastures

TIR: thermal infrared; SAR: Synthetic Aperture Radar; DEM: Digital Elevation Model; ET: Evapotranspiration

Type	Sensor	Platform	Relevance	Advantages	Disadvantages
Passive optical	Multispectral radiometer	Satellite or airborne	National or regional land cover mapping	Global coverage, low cost	Low accuracy, coarse scale
	Hyperspectral spectro-radiometer	Airborne	Plant biochemical functioning and health	High spectral resolution, highlight plant stress	High cost, high data volume
	TIR radiometer	Satellite or airborne	Soil temperature	Surrogate measure for ET	Low spatial resolution
Active optical	Lidar	Airborne and terrestrial	DEM	Hydrology	High cost, specialised processing
	Active optical sensors	Ground vehicles or RPAS	Cover and condition mapping	Convenience, low cost, independent of sunlight	Specialised hardware
Passive microwave	Microwave radiometer	Satellite	Soil moisture	High temporal frequency, large spatial coverage, cloud penetration	Low spatial resolution
Active microwave	SAR	Satellite or airborne	Plant biomass	All weather, independent of sunlight	Data availability
Locational	GPS	Portable devices	Tracking livestock	Low cost	Low signal reception in remote areas

Microwave imagery, both passive and active, has the advantages of being largely independent of weather and lighting conditions (see Volume 1B—Section 8). Satellite-based Synthetic Aperture Radar (SAR) can be used for monitoring agricultural and land cover practices at a global and regional scales, assessing soil moisture status, and quantifying plant biomass (Zhou *et al.*, 2016). Airborne SAR (C-, L- and P-band) has been used to predict grassland biomass and the types and heights of grass cover in grass cover monitoring studies (Hill *et al.*, 1996, 1999a, 2005). Since optical EO datasets primarily describe chlorophyll and water content (see Section 4.3), whereas microwave information is more relevant to the structural appearance of pasture, the fusion of optical and radar images can also be valuable (Hill *et al.*, 2005; Schmidt *et al.*, 2016).

14.3 Phenology and Production

Time series modelling is widely used for deriving phenological metrics (see Section 9.3) and monitoring changes in EO-based indices (see Volume 2D). For example, for a grassland pasture region in southwest Australia, Hill and Donald (2003) extracted agricultural production data from long term ABS agricultural census data (see Sections 11.1 and 14.1) for the period 1983–1997, then compared these data with NOAA AVHRR NDVI 15 day composites (calculated using a maximum value method; Holben, 1986; see Excursus 8.1). Bi-weekly images were processed into an NDVI time series from which a number of metrics were derived (see Figure 14.2, Table 14.2 and Table 14.3).

In this example, the period of lag corresponded approximately to the length of the non-growing period, therefore the forward and backward lag periods were set to 13 intervals corresponding to the non-growing period of 6.5 months. For each NDVI pixel, a time series curve was produced and averaged within each SLA. The resulting metrics were then correlated with the agricultural ABS statistics (Hill and Donald, 2003). The area under the curve, or the integrated NDVI value, represents the accumulated amount of vegetation greenness, or net primary production (NPP; Reed *et al.*, 1994; see Section 7.4), which related well to agricultural production within each SLA. These metrics are most appropriate in highly seasonal grasslands systems, such as those regions with Mediterranean climates in southern Australia (Hill, 2004).

Figure 14.2 Basic metrics

The phenology metrics defined in Table 14.2 and Table 14.3 can be derived from attributes of an NDVI profile (line shown with points) and its smoothed curve.

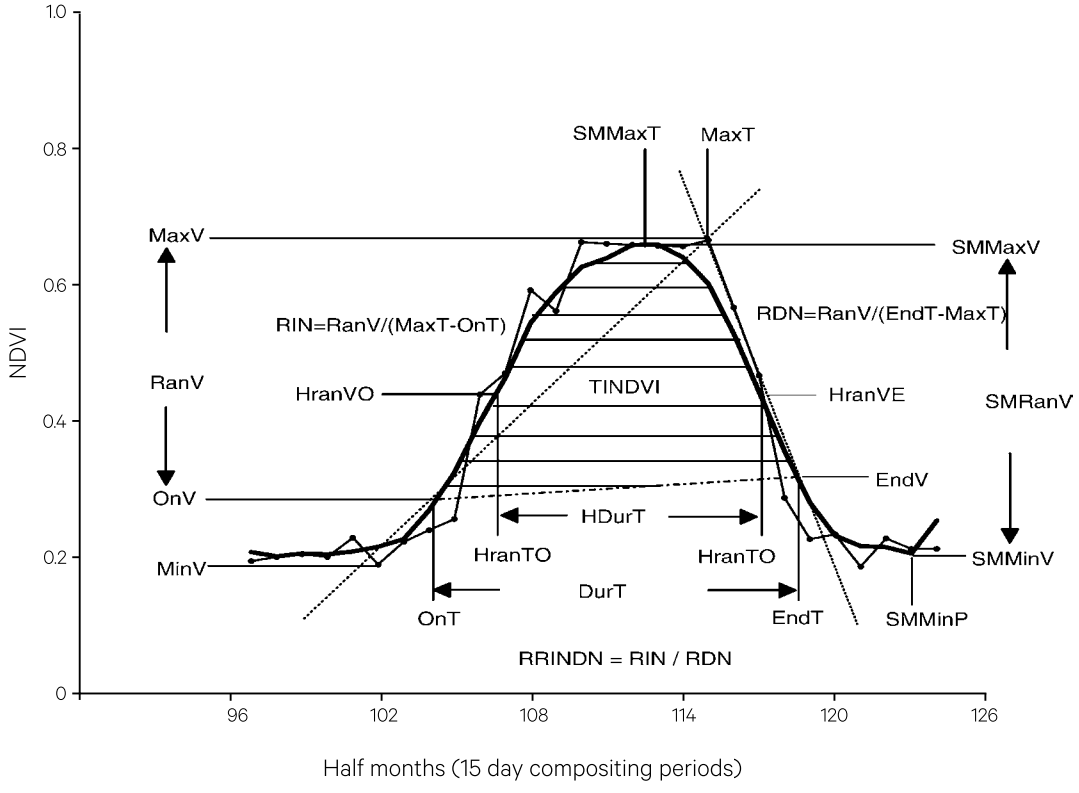

Adapted from: Hill and Donald (2003) from Reed *et al.* (1994)

Table 14.2 Description of NDVI metrics

Abbreviation	Definition	Metric
OnT	Intersection of forward lag and smooth curve	Starting date of NDVI high period
OnV	Value of NDVI at forwards intersection	NDVI at start of high period
EndT	Intersection of backwards lag and smooth curve	End date of NDVI high period
EndV	Value of NDVI at backwards intersection	NDVI at end of high period
MaxT	Time of maximum raw corrected NDVI	Date of maximum NDVI
MaxV	Maximum value of corrected raw NDVI	Maximum NDVI
DurT	Time from forwards to backwards intersections	Length of NDVI high period
RanV	Difference between minimum and maximum value of smooth curve	Amplitude of season
RIN	Slope of line from forwards intersection to raw maximum	Rate of NDVI increase
RDN	Slope of line from raw maximum value to backwards intersection	Rate of NDVI decrease
TINDVI	Integrated area under smooth NDVI curve	"Magnitude" of season
DurNT	Time from backwards to forwards intersection	Length of NDVI low period

Source: Hill and Donald (2003) Table 1

Table 14.3 Supplementary metrics

Abbreviation	Definition	Metric
RRINDN	Rate of increase/rate of decrease	"Quality" of season
HranTO	Time of half range value at onset—equals OnV+(RanV/2) when rising	Start of active growing season
HranVO	Half range value at onset—OnV+(RanV/2)	NDVI at start of active growing season
HranTE	Time of half range value at end—equals EndV+(RanV/2) when falling	End of active growing season
HranVE	Half range value at end—EndV+(RanV/2)	NDVI at end of active growing season
HdurT	Duration of period from HranTO to HranTE	Duration of active growing season
SMMaxT	Time of maximum smooth NDVI curve	Date of peak of season
SMMaxV	Maximum value of smooth NDVI curve	Value at peak of season
SMMinT	Time of minimum smooth NDVI curve	Date of season minimum
SMMinV	Minimum value of smooth NDVI curve	Value of season minimum

Source: Hill and Donald (2003) Table 1

14.4 Pasture Growth Rate

Pasture Growth Rate (PGR) is a biophysical property of grassland vegetation that represents the daily increase in biomass (measured as kg of total dry matter/ha/day). PGR is influenced by climatic factors and management practices (Ali *et al*., 2016), and provides valuable information for graziers to determine the 'feed on offer' (FOO; Edirisinghe *et al*., 2000, 2002) for their livestock in the context of individual paddocks.

NDVI time series datasets, in conjunction with estimates of PAR, moisture, and temperature, can be used to model PGR (Hill *et al*., 2004). Based on a variation of the light use efficiency (LUE) models (Prince, 1991; see Section 7.4), the PGR model requires greater than 60% grass cover to ensure that biomass assumptions are valid. Hill *et al*. (2004) modelled PGR as:

$$PGR = LUE \times APAR$$

where

PGR is in units of g/ha;
LUE is in units of g/MJ; and
APAR is in units of MJ/m^2.

This model has underpinned the successful Australian application called Pastures from Space (PfS; see Volume 1A—Excursus 14.1), an EO-based system that maps PGR (see Excursus 14.1). PfS, and its successor PfS+, were developed by CSIRO using a range of EO datasets and models (Hill *et al*., 2004; Donald *et al*., 2004a; Smith *et al*., 2011; Donald *et al*., 2015, 2016). The PfS/PfS+ were hosted by Landgate (WA) as a near real time tool to map pasture productivity at farm and paddock scales from 2000 to 2018. It is now available for Western Australia via DIPRD (WA, see Section 11.6) to deliver FOO and PGR imagery. PfS/PFS+ is a product of a consortium comprising CSIRO, DPIRD (WA), and LandGate (WA).

These online PGR estimates provide a time series record of the changes in Gross Annual Pasture Production (GAPP) for Australian pastures, thus making it a useful tool for monitoring climatic effects on plant production and the impacts of land use. Biweekly estimates of PGR can be averaged to derive annual figures. Annual PGR and NDVI profiles reveal paddock NPP (or total dry matter, TDM) and provide a means to compare the productivity of paddocks over time and identify analogous years. National maps of PGR also provide an input to the supply chain management process, highlight those areas/regions that have responded favourably to climatic changes, and deliver confidence to those purchasing livestock or supplying urban markets.

A dairy farmer was asked about the benefit of satellite EO models of providing 'feed on offer' (FOO) and pasture growth rate (PGR) to the farm operations. He replied "What we wish to know is how many days grazing is there and to which paddock the cows should go next". At a farm/station scale EO-based models can illustrate those pasture types that are more productive and reliable. The moral here is to keep the message simple to assist farmers with their day-to-day decision-making processes. (Graham Donald)

Excursus 14.1—EO-based Pasture Products

Source: Graham Donald

A number of operational products based on EO datasets are now available to assist farmers and graziers to improve their management techniques and productivity (see Section 14.8). Below we summarise some pioneering Australian systems.

SatMap

One of the first significant EO-based products for pasture management was SatMap (Vickery and Hedges, 1987), which was designed to assist with proposed fertiliser applications. Initially, this farm map defined classes of pasture growth status and provided a fertility index for pastures in the Northern Tablelands of NSW in terms of three levels of pasture ranging from slow (native pastures), medium (semi-improved or degraded), to fast growth (highly improved). In conjunction with the Grassgro DSS (Hill *et al*., 1999b), a component of the GRAZPLAN DSS (Donnelly *et al*., 1997), SatMap data provided a soil fertility scalar to spatially simulate pasture production and weaning weights of lambs.

In a long term grazing trial, a set of improved pastures used for sheep grazing were allocated to high and low stocking rates, then half of these were systematically rotated leaving areas to recover. Landsat images of these areas showed significant differences between treatments as management impacts and seasonal conditions took effect (Donald *et al*., 2013). All Landsat optical bands were processed into clusters and subsequently classified using unsupervised maximum likelihood procedures (using the ISODATA algorithm; see Volume 2E). The resulting classifications showed discrimination across a continuum from sparse, dry pastures to highly improved, green pastures (Vickery *et al*., 1997). Since satellite surveillance objectively reflects the strengths and weaknesses of a farm unit with respect to its soil types, slope, aspect, and pasture composition, such applications inform decisions relating to renovating pasture, maintaining pasture composition, and continuing soil fertility, as well as adjusting stocking rates and grazing management across every paddock for an entire farm.

Pastures from Space

Pastures from Space (PfS) provides near real time information tools at whole-of-farm and within-paddock levels for Australian pastoral businesses. Using EO datasets PfS estimates pasture production during the growing season to derive pasture biomass, or 'feed on offer', FOO (Edirisinghe *et al*., 2000, 2002). When combined with climate and soil data, the model forecasts pasture growth rate, PGR. The technology was initially developed in WA and has since been validated across Australia's southern and Mediterranean agricultural regions, and also New Zealand's dairy pastures (CSIRO, 2019).

In 2000, the introduction of the PGR model (Hill *et al*., 2004) into the southwestern grasslands of WA was met by enthusiasm from farmers (see Volume 1A—Excursus 14.1) and road signs were erected to advertise the local PGR. Prior to this, the WA Department of Agriculture (DAFWA) was in the process of demonstrating to farmers how to manually assess FOO and PGR.

The Australian PGR model (Hill *et al*., 2004) differentiates itself from related models by the fusion of weekly real time BoM continental 5×5 km gridded climate data and weekly composited daily MODIS 250×250 m NDVI information (Holben *et al*., 1986; see Section 14.4), incorporating:

- a light use efficiency index (LUE; Gower *et al*., 1999);
- fAPAR (Goward *et al*., 1994);
- a growth index (Nix, 1981, Fitzpatrick and Nix, 1970);
- weekly local climate data (BoM National Climate Centre); and
- MODIS NDVI imagery (LandGate, GA; see Section 8.1.1).

NDVI provides a practical means for determining fAPAR (Goward *et al*., 1994), which relates to LAI and NPP (see Sections 6.3 and 7.4). This PGR prediction model was calibrated on approximately 50 farms in southwest WA over the years 1995–99, and validated for the next six years (Donald *et al*., 2004a). DAFWA pasture technicians provided 8–10 geolocated point values for PGR and FOO values in each paddock, for a range of pasture types over the growing season (May to October).

Figure 14.3 Examples of Pasture Growth Rate imagery

This example Landsat image was acquired on 26 July 2016 for a farm in southwest WA.

a. Normalised Difference Vegetation Index (NDVI)

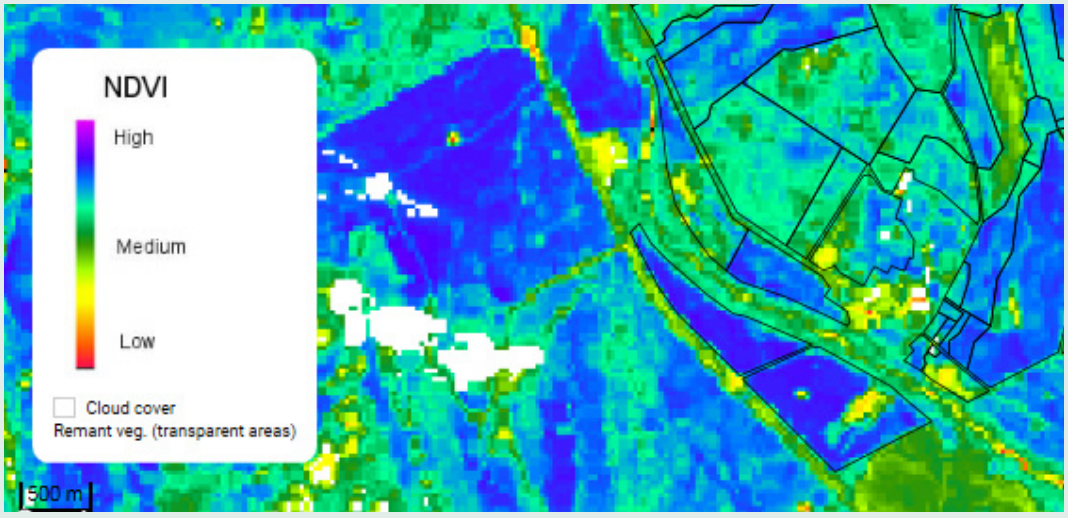

b. Farm Pasture Growth Rate (PGR)

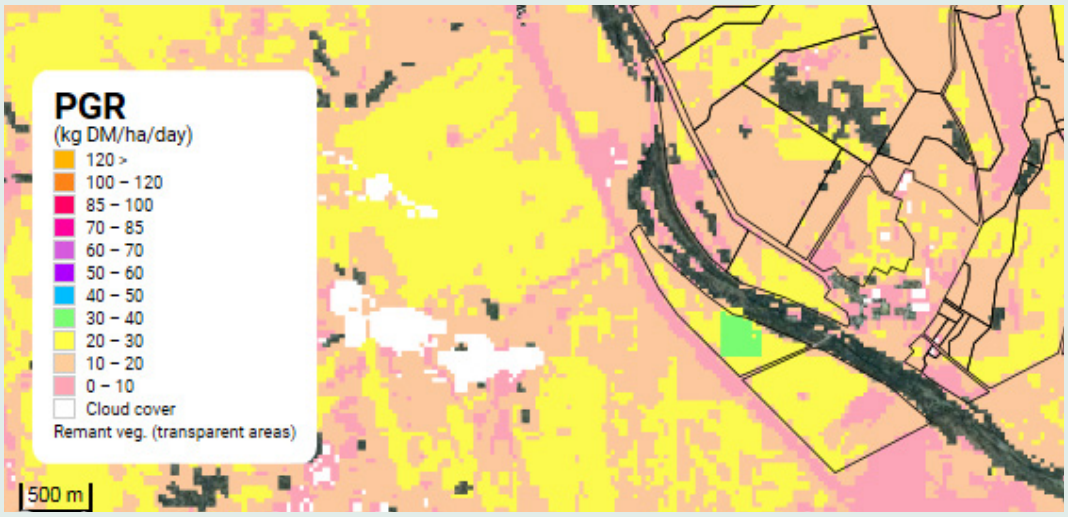

c. Feed On Offer (FOO)

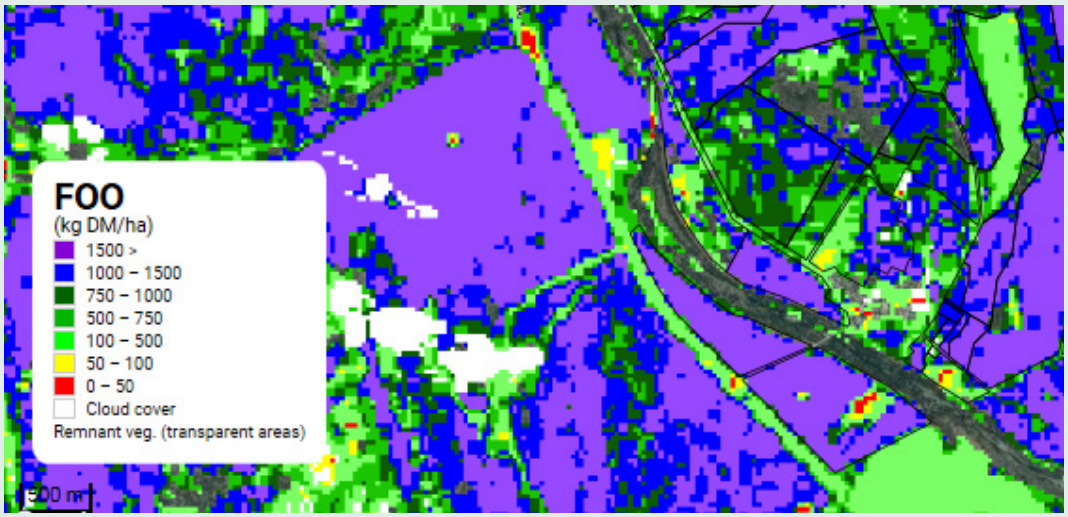

Source: PfS+, *www.landgate.gov.wa.gov.au*

National estimates of FOO, PGR, and NDVI were available online from WA Landgate, as PfS from 1999, and PfS+ from 2016, until 2018 at national, regional, and farm scales (Donald *et al*., 2004b, Donald *et al*., 2010a; see Figure 14.3). Since its inception, this product has enjoyed numerous enhancements:

- Smith *et al*. (2011) derived a MODIS NDVI FOO model suitable for the southern temperate pastures where paddock sizes exceed 100 ha.
- Donald *et al*. (2015, 2016) modified the MODIS (and, where possible, included Landsat) NDVI model to assess total green biomass and total accrued biomass as TDM, which is also referred to as gross annual pasture production (GAPP). This modified model was released as Rangewatch (see below). Weekly PGR, TDM, and GAPP are also available as averages for each paddock.
- When intersected with geo-located farm cadastre information, individual real time paddock PGR and biomass data can be extracted. This process was improved by incorporating a national perennial remnant vegetation cover (Furby, 2002) to exclude scrub and forest from paddock and farm estimates.
- Farmers can also input their own localised rainfall if they believe it differs from the BoM integrated estimate. This is useful as generalised BoM data may not pick up local storms that can impact farm management. A secondary benefit provides farmer interaction, which enhances the experience, encourages adoption, and contributes to overall confidence in the product.

The weekly plot of GAPP over time for each paddock, for each growing season, over many years, reflects the productivity capacity of individual paddocks and provides farmers with a tool to highlight those paddocks that may require additional attention. Paddock data can be filtered into FatStock (a livestock module and Smartphone app), which allows farmers to describe the livestock grazed on the selected paddock and provides information relating to the management of these livestock, such as the suggested stocking rate and grazing days. Spatial maps of these data are very useful for other farm activities, such as highlighting the need for fertilisers, proposed fencing, and potential cereal cropping, which may offer a more financial proposition. Sensitivity of NDVI is limited at high LAI, and therefore at high green biomass levels, however moderate relationships have been obtained between biomass and NDVI for grazed rangeland (see RangeWatch product below).

One example of a farmer's application of PfS+ (Foley, 2017), involved applying climate forecasts and replacing MODIS with Landsat NDVI in the PfS model to provide a spatial representation of PGR and a paddock average FOO (Smith *et al*., 2011). This grazier also used PfS+ to generate the liveweight growth rate of his sheep, which, when combined with climate forecasts, allowed him to adjust the paddock stocking rates to maximise his financial return.

RangeWatch

The Landsat time series datasets provide an opportunity to assess fractional ground cover estimates of bare ground, green vegetation, and non-green vegetation (see Excursus 8.3; Scarth *et al*., 2010, 2015), with the inference that any increase in bare ground over time could suggest either overstocking or climatic extremes in rangelands (see Section 15). Using this approach, the Rangewatch tool was developed from PfS. This was initially developed in the Kimberley region (Donald *et al*., 2015, 2016) and validated on a Pilbara cattle station in the northern rangeland regions of WA. This tool gave graziers assistance to maximise production, self-regulate the sustainability of sensitive rangelands, and assess available biomass suitable for livestock. As spectral bands of the MODIS and Landsat sensors are similar, merged spectral information were used to provide more intensive time series spectral information at the Landsat spatial resolution (Emelyanova *et al*., 2012, 2013; see Volume 2D—Section 6.2). More recent adaptations include a variety of livestock intake requirements and a stocking rate calculator to predict the potential number of grazing days remaining. When combined with livestock tracking, this EO-based information also identified regions on large cattle stations where watering points could be installed.

The imagery from Rangewatch (PfS+) demonstrated the potential benefits of better quality pastures in higher producing regions and suggested where fencing around better quality pastures could improve livestock production (Donald *et al*., 2015). Another rangelands study (Donald *et al*., 2016) showed that pasture utilisation (the amount of edible pasture) was less than 20% and in some cases the amount of ground cover was as low as 15%. PfS+ has also provided WA graziers and WARMS (Western Australian Regional Monitoring System—see Section 15.3.2) the ability to independently assess station management.

14.5 Biomass Monitoring

While vegetation greenness indices are valuable for estimating the biomass of green pasture, in many parts of Australia, especially where perennial pasture species are prevalent, grass still provides valuable fodder after it has turned brown (see Section 15). In these environments biomass estimates based on a cover-to-mass relationship can be derived throughout the annual cycle. As introduced in Excursus 8.3, fractional cover (FC) can determine the proportions of green vegetation, non-green vegetation, and bare soil contained within each pixel. With appropriate time series models, persistent vegetation (such as evergreen trees; see Section 9.1.) can be separated from other green vegetation, allowing the 'non-woody' non-green and green proportions to be used to estimate biomass. A limitation of approaches relying on the cover-to-mass relationship is that this relationship will change depending on the land type and species mix, allowing only local scale or very generalised global estimates to be made.

To improve the cover-to-mass approach requires either time series integration of the cover fractions and/or inclusion of other data, such as additional spectral bands, indices, and ancillary datasets (for example, climatic and land type information). These improvements have been achieved in recent years with the advent of Sentinel-2 data, with valuable spectral information in the red edge region and a revisit time of five days. One promising way to utilise this additional information is to implement a machine learning (ML) approach based on calibration against field data (see Volume 2E). Using this ML approach, biomass estimates can be derived for each new satellite image to provide a dynamic sequence of biomass snapshots to assist decision making on rural properties. In time, these sequences could be quantified in terms of seasonal and longer term trends in biomass and related to climatic and/or environmental drivers.

A variety of *in situ* data allows these models to be rapidly calibrated and validated to account for differing environmental and/or atmospheric conditions. For example, the farm management app *AgriWebb* enables farmers to photograph and record relevant information about the type and quantity of pasture at specific locations for easy integration with EO-based analyses. Open data kit (ODK) based field applications, as used by TERN and several government organisations, have also been used to collect a large amount of publicly available biomass data. The availability of current, accurately-located, *in situ* data means the generic model can be calibrated for spatial and temporal differences in biomass, then validated independently. This 'living laboratory' process allows continual refinement of models, interpretation, and ground data collection to improve both the accuracy and precision of the derived estimates (see Excursus 14.2), which can be directly used to derive carrying capacity by farmers (see Section 15).

Excursus 14.2—Integrated Biomass Estimation

Source: Peter Scarth, cibolabs
Further Information: *https://www.cibolabs.com.au/*

Using a 'living laboratory' model of data science tailored to Australian agriculture, estimates of biomass and food on offer (FOO) are now commercially available to graziers at 10 m resolution every five days. Using predictive models based on field calibration data applied to Sentinel-2 imagery from the ESA archives, these estimates allow graziers to monitor biomass in each paddock and property throughout the year.

Over 2,000 field samples of total standing dry matter (TSDM) across northern and eastern Australia were collected over a two-year period (see Figure 14.4). This dataset aims to capture much of the variability across species and land types in the grazing regions. Coincident Sentinel-2 imagery and the associated Landsat-derived persistent green fraction is used to train a three layer, multilayer perceptron regression model using a 50% dropout, a maximum norm constraint, and a robust loss function to avoid open prediction. A national biomass map resulting from this modelling process is shown in Figure 14.5.

33% of the field site data is used for training, with the remainder reserved for validation. To determine the prediction error, the model is trained 100 times for approximately 16,000 epochs before reaching the termination criterion, and results in a median prediction error of 295±8 kg/ha. (Note that in ML terminology, an epoch indicates the number of passes of the entire training dataset the ML algorithm has completed.) In this example, significant outliers can be attributed to missed cloud or shadow, poor tree or shrub cover estimation, significant rainfall events close to the calibration time, or heavy grazing in the week following the field observation.

The relative simplicity of this model, coupled with the availability of global imagery in cloud optimised formats, means that biomass estimates can be obtained in either batch mode over large areas in a high performing computing environment, or on demand as a cloud computing function. The typical latency between image capture and delivery is under 24 hours. This enables fast interrogation of individual paddocks from global scale imagery, either in the user's browser or through integrations with other farm management software, including detailed statistical summaries over space and time.

Figure 14.4 Biomass calibration/validation sites

These photographs sample more than 2000 field calibration sites across Australia. The locations of these sites are shown as blue dots on the map in Figure 14.5. The sites are used to train a machine learning (ML) model which allows per pixel prediction of Total Standing Dry Matter (TSDM) from Sentinel-2 image data.

Figure 14.5 Sample national biomass map, September 2020

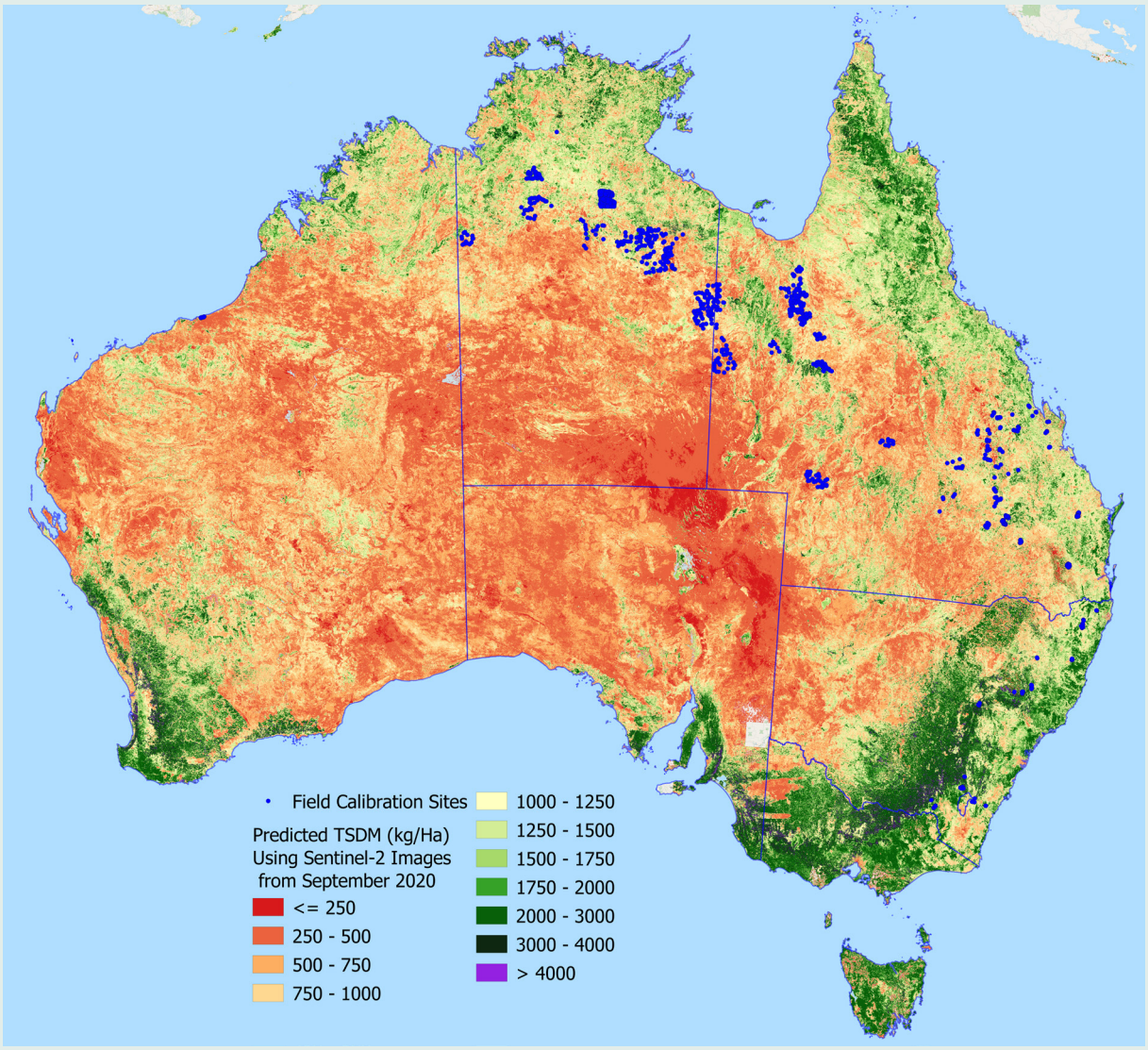

14.6 Precision Grazing

There has been an increase in the number farmers and graziers embracing EO-based, precision agriculture technologies to assist with the growing complexity of farm management decisions (see Section 12.6). For example, farmers in rangelands, grasslands, or intensive grazing environments are implementing GPS tracking of livestock (see Volume 1A—Section 10).

Recent perturbed climate events, coupled with insecurity in the economic sector, have made landholders more aware that they need to improve their understanding of farm management. Farmers have the capacity to monitor the locations and movements of their livestock across the farm, which in turn provides information on grazing behaviour (Trotter *et al*., 2010). For example, satellite-based datasets can provide frequent, up-to-date, biomass assessments of PGR, total biomass and ground cover (see Section 14.4).

Several precision agricultural companies are also developing a range of products for integrated precision agriculture, some of which rely on drones (see Volume 1A—Section 11 and Section 12.6). In combination with GPS tracking, this information provides a powerful tool for managing livestock production in a sustainable manner. In light of these resource and economic factors, farmers have to be more flexible in choosing enterprises from the number of production sectors available.

Biosecurity research (Donald *et al*., 2010b, Miron *et al*., 2007) also showed that livestock movements, both on and off farm, were highly correlated to PGR and biomass estimates. This provided inputs into models pre-empting livestock movements within regions, which is necessary for those needing supply chain movements. Results demonstrated a high correlation between the movement of cattle at farm locations and PGR/biomass within six SLAs in southern Queensland.

Livestock tracking is also critically important in the event of an outbreak of an exotic disease, such as foot and mouth. Early detection and identification of an area around infected stock reduces the spread of the disease (Miron *et al*., 2007). Meat Livestock Australia (MLA), in conjunction with state governments, has introduced a National Livestock Identification Scheme (NLIS) to electronically track the movement of livestock off-farm via radio frequency identification (RFID). This technology will undoubtedly be eventually refined to enable ready integration into a GIS system and thus enable many other uses, including tracking livestock theft.

14.7 Wool Production

The sale of greasy wool is highly dependent on its fibre diameter and tensile strength, with a lesser emphasis on colour, condition, and length. Finer wool has a lower fibre diameter and a higher price by weight.

Throughout the grazing year, pasture nutrition varies with seasons and climatic conditions. Since the fibre diameter profile (FDP) reflects the sheep's nutritional status, the nutritional composition of pasture can impact fibre diameter. A rapid shift in nutrition from poor to high, as can occur at the end of a drought, may cause severe fibre weakening (referred to as 'tender') and reduced yield (Mata and Masters, 2002), which together substantically reduces the value of a fleece. Particularly in the highly prized Saxon merino genotype, where the fleece is valued primarily by its fibre diameter and tensile strength, wool that becomes tender has little or no value.

While wool fibre diameter is not only dependent on nutrition but a number of other factors, including genetics and physical stresses, such as lambing, the yearly variation in the profile of the fibre diameter is mostly attributed to quantity and quality of pasture. The weakest stage of the wool profile occurs at the change of season when there is an increase in available green pasture. Managing these changes of seasonal pasture growth across the major wool producing regions of Australia will help graziers to maintain the fleece staple strength and achieve a more even diameter profile.

The fibre diameter of wool has been associated with the seasonal environmental nutrition of grazing pastures in a number of wool producing regions (Whelan *et al*., 2008). This environmental nutritional profile can be easily observed in NDVI imagery. Whelan *et al*. (2008) predicted the average fibre diameter of the wool clip using NDVI and showed that the NDVI profile could be used to indicate when feed availability should be increased or decreased to avoid weakening of the wool staple. NDVI from strategic wool producing regions may forecast wool production with more certainty than rainfall data and expert opinion (Whelan *et al*., 2007). Thus, combining estimates of sheep numbers with NDVI, FOO, and PGR may provide an ongoing platform to predict the Australian wool supply, and in conjunction with the FDP, its potential economic value.

Using the tools within EO applications such as PfS, farmers can detect changes in PGR across a farm, highlight areas where wool staple strength may be at risk, then decide whether to avoid risking profitability at the next shearing. An example of the efficacy of the PfS+ model with respect to its application in sheep farming was reported by Foley (2017), a wool producer in the southern region of WA, who was able to improve overall wool production by 60%, increase lambing rates, and double pasture production.

14.8 Further Information

Agricultural Statistics

ABARES (2018). Snapshot of Australian Agriculture. *Insights* (1): *https://www.agriculture.gov.au/abares/publications/insights/snapshot-of-australian-agriculture*

UN Food and Agriculture Organisation (FAO): *http://www.fao.org*

EO-based Pasture Models

Pastures from Space:

WA Agriculture and Food: *https://www.agric.wa.gov.au/sheep/understanding-pastures-space-south-west-western-australia*

https://www.csiro.au/en/Research/AF/Areas/Digital-agriculture/Cropping-pastures/Pastures-from-Space

CIBO-Labs—Building Solutions for Agriculture: *https://www.cibolabs.com.au*

FarmMap4D Spatial Hub (formerly NRM Spatial Hub; see Volume 1B—Excursus 10.3): *http://www.farmmap4d.com.au/*

14.9 References

Ali, I., Cawkwell, F., Dwyer, E., Barrett, B., and Green, S. (2016). Satellite remote sensing of grasslands: from observation to management—a review. *Journal of Plant Ecology*, 9(1), 649–671. *https://doi.org/10.1093/jpe/rtw005*

Caccetta, P.A., Allan, A., and Watson, I. (2000). The land monitor project, *Proc. 10th Australian Remote Sensing and Photogrammetry Conference*, Adelaide, Australia.

CSIRO (2019). Pastures from Space webpage, Commonwealth Scientific and Industrial Research Organisation website: *https://www.csiro.au/en/Research/AF/Areas/Digital-agriculture/Cropping-pastures/Pastures-from-Space*

Derner, J.D., and Schuman, G.E. (2007). Carbon sequestration and rangelands: A synthesis of land management and precipitation effects. *Journal of Soil Water Conservation*, 62, 77–85.

Donald, G.E., Edirisinghe, A., Henry, D.A., Mata, G., Gherardi, S.G., Oldham, C.M., Gittins, S.P., and Smith, R.C.G. (2004a). Pastures from Space—Validation of predictions of pasture growth rates. In *Proceedings of Australian Society of Animal Production*, 25, 232.

Donald, G.E., Edirisinghe, A., Craig, R., Henry, D.A., Mata, G., Gherardi, S.G., and Stovold, R. (2004b). Advantages of TERRA MODIS imagery over AVHRR to quantitatively estimate pasture growth rate in south west region of Western Australia. *Proceedings of 12th Australian Remote Sensing and Photogrammetry Conference*, Fremantle, Australia.

Donald, G.E., Edirisinghe, A., Henry, D.A., Gherardi, S.G., Gittins, S., and Mata, G. (2010a). Using MODIS imagery, and climate and soil data to estimate pasture growth rates on properties in the south-west of Western Australia. *Animal Production Science*, 50(6), 611–615

Donald, G.E, Miron, D.J., Dyall, T., and Garner, M.G. (2010b).Temporal and spatial regional cattle farm turn-off patterns in Eastern Australia. *Animal Production Science*, 50(6), 359–362

Donald, G.E., Scott, J.M., and Vickery, P.J. (2013). Satellite derived evidence of whole farmlet and paddock responses to management and climate. *Animal Production Science*, 53, 699–710

Donald, G.E., Mundava, C., Stovold, R., Lamb, D., and Santich, N. (2015). Satellite rangelands monitoring tool for pastoralists. *Australian Rangelands Conference*, 12th April, Alice Springs, NT.

Donald, G.E., Santich, N., Stovold, R., Abbott, S., and Lamb, D. (2016). RANGEWATCH: An NDVI-light use efficiency based method of estimating forage in northern Australia. A case study in the Pilbara region of Western Australia. *Proceedings of 57th Annual Conference of the Grasslands Society Southern Australia*, 31 Aug–1 Sept, Hamilton, Victoria.

Donnelly, J.R., Moore, A.D., and Freer, M. (1997). GRAZPLAN: Decision support systems for Australian grazing enterprises. I. Overview of the GRAZPLAN project, and a description of the MetAccess and LambAlive DSS. *Agricultural Systems*, 54(1), 57–76.

Edirisinghe, A., Hill, M.J., Donald, G.E., Hyder, M., Warren, B., Wheaton, G.A., and Smith, R.C.G. (2000). Estimation of feed on offer and growth rate of pastures using remote Sensing. *Proceedings of 10th Australian Remote Sensing and Photogrammetry Conference*, Adelaide, Australia. Paper No. 112.

Edirisinghe, A., Donald, G.E., Hill, M.J. (2002). Precision management of feed supply through the timely delivery of biomass and growth rate predictions of Western Australian annual pastures. *Proceedings of 29th International Symposium on Remote Sensing of Environment*, Buenos Aires, Argentina.

Edirisinghe, A., Donald, G.E., Henry, D.A., and Hulm, E. (2004). Pastures from Space—Assessing forage quality using remote sensing. *Proceedings of 25th Biennial Australian Society of Animal Production*, 4–8 June, Melbourne.

Emelyanova, I.V., McVicar, T.R., Van Niel, T.G., Li, L.T., and van Dijk, A.I.J.M. (2012). *On blending Landsat-MODIS surface reflectances in two landscapes with contrasting spectral, spatial and temporal dynamics*. WIRADA Project 3.4: Technical report. CSIRO Water for a Healthy Country Flagship, Australia. 72 pp.

Emelyanova I.V., McVicar, T.R., Van Niel, T.G., Li, L.T., and van Dijk, A.I.J.M. (2013). Assessing the accuracy of blending Landsat-MODIS surface reflectances in two landscapes with contrasting spatial and temporal dynamics: A framework for algorithm selection. *Remote Sensing of Environment*, 133, 193–209.

FAOSTAT (2019) FAOSTAT Land Use webpage, UN Food and Agriculture Organisation website: *http://www.fao.org/faostat/en/#data/RL/visualize*

Fitzpatrick, E.A., and Nix, H.A. (1970). The climate factor in Australian grasslands ecology. In *Australian Grasslands*. (Ed: R.M. Moore), pp. 3–26. Canberra, Australian National University Press.

Foley, M. (2017). Top tech and know how to boost profitability. *LandonLine*, May 2017, Fairfax media.

Furby, S. (2002). Land Cover Change. Specification for remote sensing analysis. *National Carbon Accounting System, CSIRO, Technical Report No. 9*, 402 p.

Goward, S.N., Waring, R.H., Dye, D.G., and Yang, J. (1994). Ecological remote sensing at OTTER: Satellite macroscale observations. Ecological Applications 4, 322–343.

Gower, S.T., Kucharik, C.J., and Norman, J.M. (1999). Direct and indirect estimation of leaf area index, fAPAR, and net primary production of terrestrial ecosystems. *Remote Sensing of Environment*, 70, 29–51.

Hill, M.J. (2004). Grazing agriculture—Managed Pasture, Grassland and Rangeland. In *Manual of Remote Sensing, Volume 4, Remote Sensing for Natural Resource Management and Environmental Monitoring*. (Ed: S. L. Ustin) Wiley International, New York. 768 p.

Hill, M.J., Vickery, P.J., Donald, G.E., Furnival, E.P., and Mulcahy, C. (1996). Managing the pastoral landscape: Adding a spatial dimension? *Proceedings of 8th Australian Agronomy Conference*, Toowoomba, QLD. pp 309–312.

Hill, M.J., Donald, G.E., and Vickery, P.J. (1999a). Relating backscatter to biophysical properties of temperate perennial grasslands. *Remote Sensing of Environment* 67, 15–31.

Hill, M.J., Donald, G.E., Vickery, P.J., Moore, A.D., and Donnelly, J.R. (1999b). Combining satellite data with a simulation model to describe spatial variability in pasture growth at a farm scale. *Australian Journal of Experimental Agriculture*, 39, 285–300.

Hill, M.J., and Donald, G.E. (2003). Estimating spatio-temporal patterns of agricultural productivity in fragmented landscapes using AVHRR NDVI time series. *Remote Sensing of Environment*, 84, 367–384. doi:*10.1016/S0034-4257(02)00128-1*

Hill, M.J., Donald, G.E., Hyder, M.W., and Smith, R.C.G. (2004). Estimation of pasture growth rate in the south west of Western Australia from AVHRR NDVI and climate data. *Remote Sensing of Environment*, 93, 528–545. doi:*10.1016/j.rse.2004.08.006*

Hill, M.J., Ticehurst, C.J., Lee, J.S., Grunes, M.R., Donald, G.E., and Henry, D. (2005). Integration of optical and radar classifications for mapping pasture type in western Australia. *IEEE Transactions on Geoscience and Remote Sensing*, 43, 1665–1681. doi:*10.1109/TGRS.2005.846868*

Holben, B.N. (1986). Characteristics of maximum-value composite images from temporal AVHRR data. *International Journal of Remote Sensing*, 11, 1417–1434.

Latham, J., Cumani, R., Rosati, I., and Bloise, M. (2014) *Global Land Cover SHARE (GLC-SHARE): database Beta-Release Version 1.0-2014*. *http://www.fao.org/uploads/media/glc-share-doc.pdf*

Mata, G., and Masters, D. (2002). Management of intake in winter to contol Micron blowout and improve staple strength. *Wool Technology and Sheep Breeding*, 50(3), 471–476.

McIvor, J.G. (2005). Australian Grasslands. Ch 9 in *Grasslands of the World*. (Eds: Suttie, J.M., Reynolds, S.G., and Batello, C.). FAO, Rome. *http://www.fao.org/3/y8344e0g.htm#bm16*

Miron, D.J., Emelyanova, I.V., Donald, G.E., and Garner, G.M. (2007). Agent based model of livestock movements. *International Conference on Complex Systems 2007*, 28 October–2 November, Boston, MA, USA, 2007 *http://necsi.org/events/iccs7/viewpaper.php?id=196*

Nix, H. (1981). Simplified simulation models based on specified minimum data sets: The CROPEVAL concept. Pp. 151–169 in *Application of Remote Sensing to Agricultural Production Forecasting*. (Eds. A Berg and A. Balkema). Rotterdam.

Poore, J. (2016). Call for conservation: Abandoned pasture. *Science*, 351, 6269.

Prince, S. (1991). A model of regional primary production for use with coarse resolution satellite data. *International Journal of Remote Sensing*, 12(6), 1313–1330. doi:*10.1080/01431169108929728*

Reed, B.C., Brown, J.F., VanderZee, D., Loveland, T.R., Merchant, J.W., and Ohlen, D.O. (1994). Measuring phenological variability from satellite imagery. *Journal of Vegetation Science* 5, 703–714. *https://doi.org/10.2307/3235884*

Scarth, P., Roder, A., and Schmidt, M. (2010). Tracking grazing pressure and climate interaction, the role of Landsat fractional cover in time series analysis. *Proc. 15th Australasian Remote Sensing and Photogrammetry Conference*, 13-17 September, Alice Springs, NT.

Scarth, P., Armston, J., Flood, N., Denham, R., Collett, L., Watson, F., Trevithick, B., Muira, J., Goodwin, N., Tindall, D., and Phinn, S. (2015). Operational application of the Landsat time series to address large area land cover understanding, *International Archives of the Photogrammetry, Remote Sensing and Spatial Information Sciences*, Volume XL-3/W3, ISPRS Geospatial Week 2015, 28 September–3 October, La Grande Motte, France.

Schmidt, M., Carter, J., Stone, G., and O'Reagain, P. (2016). Integration of Optical and X-Band Radar Data for Pasture Biomass Estimation in an Open Savannah Woodland. *Remote Sensing*, 8, 989. doi:*10.3390/rs8120989*

Smith, R., Adams, M., Gittins, S., Gherardi, S., Wood, D., Maier, S., Stovold, R., Donald, G., Khokar, S., and Allen, A. (2011). Near real-time Feed on Offer from MODIS for the early season grazing management of Mediterranean annual pastures. *International Journal of Remote Sensing*, 32, 4445–4460.

Trotter, M.G., Lamb, D.W., Donald, G.E., and Schneider, D.A. (2010). Active optical sensors for quantifying and mapping pasture biomass: A case study using red and near infrared waveband combinations from a Crop Circle™ in Tall Fescue (*Festuca arundinacea*) pastures, *Crop Pasture Science*, 61, 389–398.

Vickery, P.J., and Hedges, D.A. (1987). Use of Landsat MSS data to determine the fertiliser status of improved grasslands. *Proceedings of 4th Australasian Remote Sensing Conference* (Ed: D. Bruce). pp.287-96. Floreat, WA.

Vickery, P.J., Hill, M.J., and Donald, G.E. (1997). Landsat derived maps for pasture growth status: association of classification with botanical composition. *Australian Journal of Experimental Agriculture*, 37, 547–562.

Wallace, J., Behn, G., and Furby, S. (2006). Vegetation condition assessment and monitoring from sequences of satellite imagery. *Ecological Management and Restoration* 7(S1), S31–S36. *https://doi.org/10.1111/j.1442-8903.2006.00289.x*

Whelan, M., Cottle, D.J., Gherardi, S., and Clarke, A. (2007). The potential for predicting Australian wool supply using remote sensed data. *International Wool Textile Organisation*, May, Edinburgh.

Whelan, M.B., Genty, K.G., Cottle, D.J., Lamb, D., and Donald, G.E. (2008). The relationship between a satellite derived vegetative index and wool fibre diameter profiles. *World Congress on Animal Production*, 23–28 November, South Africa.

Zhou, Z.-S., Caccetta, P., Sims, N.C., and Held, A. (2016). Multi-band SAR Data for Rangeland Pasture Monitoring. *Proceedings of IEEE IGARSS 2016*, pp. 170–173, July 2016. doi:*10.1109/IGARSS.2016.7729035*

15 Rangelands

Gary Bastin

Arid and semi-arid landscapes, or drylands (aridity index < 0.65), occur in both tropical and temperate latitudes, and cover 41.3% of the land surface of Earth (IUCN, 2019). They are home to a third of the world's population and more than 28% of endangered species globally (IUCN, 2019). They also feature significantly in terms of global biophysical risks identified by the World Economic Forum (WEF, 2018).

Dryland landscapes are predominantly used for grazing and commonly known as 'rangelands'. In Australia, they include (but are not limited to) the ecoregions labelled as deserts and xeric shrublands (see Section 2.4.1), temperate grasslands, savannas and shrublands (see Section 2.4.5), and tropical and subtropical grasslands, savannas, and shrublands (see Section 2.4.6) in Figure 2.14. From Section 2.2 and Table 2.4 it is readily apparent that the majority of the Australian continent is arid or semi-arid and thus considered as rangeland.

Much of the information in the following sections describing the Australian rangelands derives from the Australian Collaborative Rangelands Information System (ACRIS, Bastin *et al*., 2008, 2009; DSEWPC, 2013). From 2002 to 2014 ACRIS operated as a partnership between the Australian Government and the state/territory jurisdictions responsible for rangelands, primarily to collate the available, and often disparate, biophysical, and socio-economic datasets to report change in this environment (see Figure 15.1).

The following sub-sections introduce EO of rangelands in terms of:

- Australian conditions (see Section 15.1);
- relevant sensors (see Section 15.2);
- land condition (see Section 15.3);
- operational systems (see Section 15.4); and
- conserving biodiversity (see Section 15.5).

The rangelands encompass tropical woodlands and savannas in the far north; vast treeless grassy plains (downs country) across the mid-north; hummock grasslands (spinifex), mulga woodlands and shrublands through the mid-latitudes; and saltbush and bluebush shrublands that fringe the agricultural areas and Great Australian Bight in the south. Across this gradient, seasonal rainfall changes from summer-dominant (monsoonal) in the north to winter-dominant in the south. Soils are characteristically infertile. Great climate variability and the dominating influence of short growing seasons distinctly characterise rangeland environments.
(Bastin et al., 2008)

Background image: The Bokhara Plains Station, 35 km north of Brewarrina, NSW, is a case study in Soils for Life. (For details visit: *https://soilsforlife.org.au/bokhara-plains-reaching-the-real-potential-of-the-nsw-rangelands/*). **Source:** Kirsty Yeates

Recommended Chapter Citation: Bastin, G.N. (2021). Rangelands. Ch 15 in *Earth Observation: Data, Processing and Applications. Volume 3A—Terrestrial Vegetation*. CRCSI, Melbourne. pp. 299–322.

Figure 15.1 Framework for ACRIS reporting

ACRIS attempted to integrate available and suitable biophysical, economic and social data to describe and understand changes in Australia's rangelands. Key drivers of change are related to their effects on landscape values and their further impact on socio-economic outcomes. Ideally these outcomes then feed back to the drivers via appropriate learning and adaptive management.

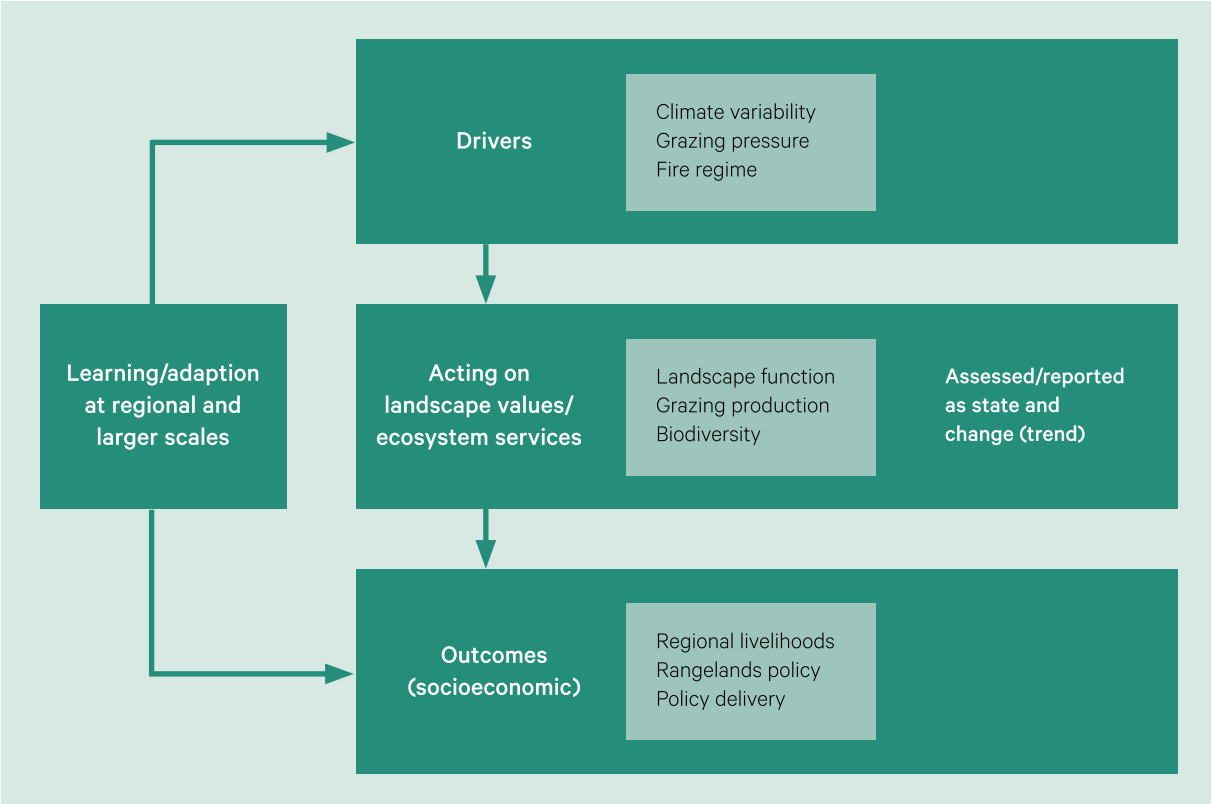

Adapted from: Bastin *et al.* (2009) Figure 1

15.1 Rangelands in Australia

The Australian Rangelands Society defines rangelands as 'all those environments where natural ecological processes predominate and where values and benefits are based primarily on natural resource areas which have not been intensively developed for primary production' (ARS, 2019). In Australia, rangelands occur where regular cropping is (generally) not possible due to insufficient rainfall and/or poor soils. These areas are principally used for grazing by both domestic livestock and wild fauna. They cover 81% of the country (Bastin *et al.*, 2008; see Figure 15.2) and are popularly referred to as 'the outback'. They are also home to numerous indigenous communities, who actively support the health and wellbeing of remote, rangeland communities, and play an important role in the stewardship of indigenous cultural heritage (Foran *et al.*, 2019). Rangelands landscapes include savannas, woodlands, shrublands, grasslands, and wetlands, and span latitudes ranging from monsoonal to temperate (Bastin *et al.*, 2008).

Despite being the least populated region in Australia (see Figure 2.15), the economic value realised from rangelands totals nearly $60 billion annually (ARS, 2019). Most of this revenue is generated from mineral mining, with the remainder mostly being derived from agriculture and tourism. Land uses across Australia's rangelands in the 2001/2002 financial year are summarised in Figure 15.2.

Australia's rangelands are characterised by infertile soils, large climatic variations, and short growing seasons (Bastin *et al.*, 2008). Grazing from domestic stock (principally sheep and cattle, plus some goats), native wildlife (principally kangaroos), and feral animals (rabbits, goats, camels, horses, and donkeys), combined with a highly variable rainfall, frequent fires, and exotic weeds, present unique and complex management challenges for maintaining biodiversity and landscape stability in this region. The task of monitoring vegetation change is further exacerbated by highly variable vegetation patterns and remote locations, where permanent landmarks are, quite literally, few and far between.

There is no such thing as 'pristine' in the Southern Rangelands [of WA]. The landscape is ever changing and evolving, and being shaped by different processes, including those introduced by humans. (Pollock, 2019)

Understanding, monitoring, and managing the rangelands as a whole becomes more tractable when they are stratified into components reflecting their biophysical characteristics. A number of classification systems have been used to categorise biogeographic differences in this region, including NVIS (National Vegetation Information System; see Section 2.4.1) and IBRA (Interim Biogeographic Regionalisation of Australia; see Section 2.5). Characteristics, locations, and extents of major vegetation types and their underlying soils are broadly summarised in terms of 52 IBRA bioregions in Bastin *et al*. (2008). Relevant state-based systems include regional ecosystems in Queensland and land systems in other jurisdictions, while SA developed a seamless mapping system relating land systems to component units of bioregions in the rangelands of that state (see Section 2.3.1).

For EO analyses, however, hierarchical categorisations are most useful to allow further stratification for monitoring and assessment of the rangelands landscape. The IBRA bioregions provide a convenient stratification for dealing with the broadly different environments/landscapes within the rangelands and, with their component units, were the preferred regionalisation for the ACRIS Management Committee (Bastin *et al*., 2008).

Despite decades of grazing, much of the rangelands environment can still be considered as 'natural' (see Figure 3.3 classes I, II and III). Many ecosystems are largely intact but require careful management to maintain biodiversity and, where grazed, their productive value. Potential agents of degradation include the impact of overgrazing by domestic, feral and native herbivores, inappropriate fire regimes, introduced predators, weeds and other invasive biota (DSEWPC, 2013), and poor road design and maintenance in some areas (OAGWA, 2017).

Figure 15.2 Land uses in Australian rangelands

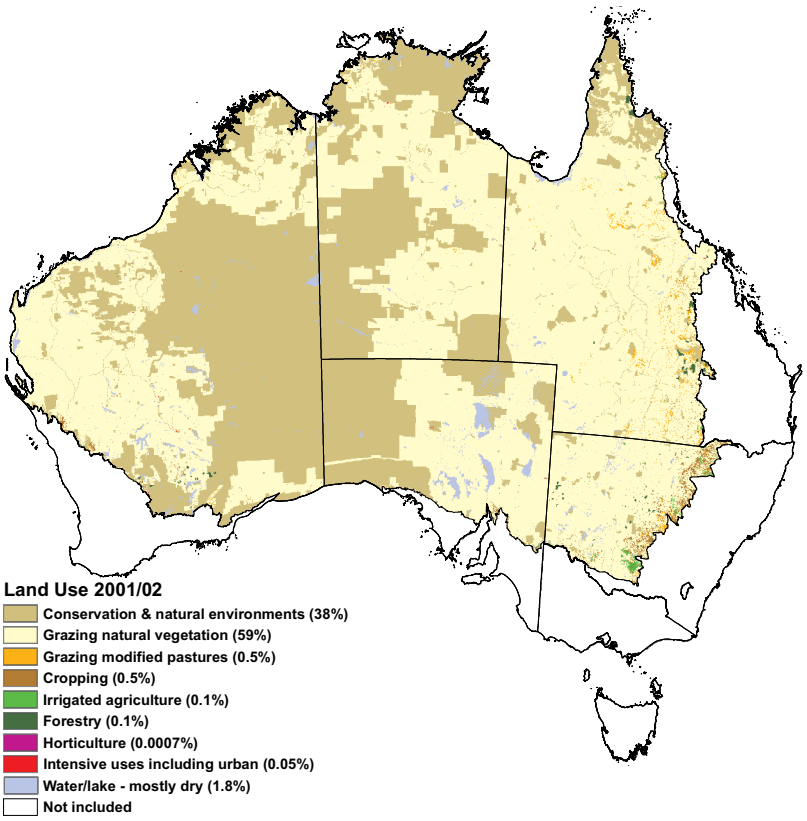

Source: Bastin *et al.* (2008) Figure 3.108 (p130) Updated data can be downloaded from: *http://www.agriculture.gov.au/abares/aclump/land-use/data-download*

15.1.1 Vegetation

Vegetation in rangelands varies from tropical savannas and woodlands in northern Australia to arid environments in central Australia, and semi-arid shrublands in southern regions. Ground-layer species composition can vary greatly in short time periods, particularly in the arid zone. Rangelands encompass a wide variety of vegetation associations, structures and densities, with underlying soils varying from cracking clays to alluvial loam to sand dunes. As in most ecosystems, perennial species act as an environmental anchor, sustaining the landscape by stabilising the soil surface and recycling nutrients.

In rangelands, forage comprises any non-woody plant material. In addition to grasses, many shrub species have leaves that are palatable for stock, and palatable perennial grasses and shrubs sustain livestock into dry times and drought. The ACRIS Management Committee described these palatable perennial species as 'critical stock forage' and examples of the results of jurisdictional monitoring for this key indicator of rangeland condition are given in Bastin *et al*. (2008; see pages 42–51). Although some weed species provide valuable pasture, others are spreading rapidly through cleared areas in savanna regions and into the arid zone (see Section 2.3.2). Biodiversity has also been observed to reduce in many rangeland areas that have been colonised by exotic weeds (see Section 15.5).

While droughts can be extended and devastating (see Section 15.1.2), rangeland vegetation responds quickly to most rainfall events. Especially in central and southern Australia, vegetation growth, and subsequently fuel loads, are directly related to antecedent rain (Bastin *et al*., 2008; Bastin and Allan, 2012).

Recurring periods of higher rainfall can also encourage germination and growth of woody species in the Australian rangelands. This response is not always advantageous for the broader landscape, and has contributed to woody thickening, which may restrict future pasture growth through competition for soil water, nutrients, or light (see Section 15.1.3).

To survive the harsh climatic conditions in arid and semi-arid regions, many plants have adapted to the limited soil nutrients and moisture, and generous exposure to sunlight (see Sections 4.2 and 5.2 above). Such adaptations typically involve:

- reducing water loss by limited transpiration;
- efficient root systems to maximise water uptake;
- controlled or deferred photosynthesis until conditions are favorable;
- conscientous storage and recycling of nutrients; and
- rapid growth and reproduction when circumstances are advantageous (Stafford Smith and McAllister, 2008).

Native vegetation has also adapted to fire—a frequent and harsh environmental broom, particularly in the northern tropical savanna (see Section 18).

While these vegetation communities appear to be robust, having become established in extreme climates, some are fragile, at times balancing between survival and demise. Even where plant communities have adapted to these conditions, they cannot necessarily withstand major changes in their environment (see Section 7). Ecosystems find their own range of stability in managing environmental resources, and significant perturbations can takes years or decades of recovery. Additional environmental pressures, whether from grazing, increased fire frequency, extended drought or excessive water usage, can undermine the stability of rangeland ecosystems (see Section 7.2). Once degraded, vegetation recovery can take many years of above average rainfall and low grazing pressure to enable plant populations and perennial root systems to recoup (McKeon *et al*., 2004; Pollock, 2019), with decades sometimes being required to attain pre-degradation levels of ecosystem 'health' and pasture productivity. One example of this process is illustrated in Figure 15.3.

I love a sunburnt country, a land of sweeping plains,
of ragged mountain ranges, of droughts and flooding rains.
I love her far horizons, I love her jewel-sea,
Her beauty and her terror, the wide brown land for me.
(Dorothea MacKellar, from 'My Country')

Figure 15.3 Vegetation Recovery

This sequence of photos shows the vegetation recovery process at a fixed location in the Victoria River Research Station, 40 km north of Victoria River Downs Homestead and 220 km southwest of Katherine in the Northern Territory.

a. April 1973—extensive areas of bare soil before construction of cattle-proof exclosure

b. June 1978—revegetation with grasses, forbs and the introduced shrub *Calotopis procera* (rubberbush)

c. June 1989—rubberbush has been replaced by native tree and shrub species

d. June 2000—landscape dominated by native perennial black spear grass (*Heteropogon contortus*)

Source: Bastin *et al.* (2008) Figure 2.1

15.1.2 Water

An overriding constraint in most rangelands is water. While major river systems exist around the fringes of the Australian rangelands (see Figure 2.2), rainfall is episodic and ephemeral, and surface water is scarce. Thus, in most of this region, rainfall is the primary driver of landscape change (Bastin *et al.*, 2008). Duration, frequency, volume, and timing of rain are significant for both floral and faunal populations. Droughts—extended periods without rain—have occurred in Australia for millennia (Hendy *et al.*, 2003), but in conjunction with overgrazing can be devastating (see Section 11.4 and Table 11.2).

The Great Artesian Basin (GAB; see Section 2.1 and Figure 2.5), which underlies much of northeastern Australia and extends into central Australia, enables settlement and enterprises in this region. Prior to the first deep bores drilled in the late 19th Century to access the GAB, semi-permanent waterholes and springs along major rivers and mountain ranges, plus a few wells, supplied the only reliable water sources. Now, in addition to surface water in large catchments or drainage basins (such as the Lake Eyre Basin), smaller dams or earthern tanks at paddock scale and localised aquifers accessed by bores or wells provide water for communities, livestock, and limited irrigation (mainly horticulture), but don't promote pasture growth for grazing (Bastin *et al.*, 2008). Tens of thousands of bores, some reticulated using polyphene piping, tanks, and troughs, have now been installed to supply water for stock.

The density and location of these waterpoints is significant for both livestock production and land degradation, as well as biodiversity of native and introduced fauna and flora (James *et al*., 1999). Landsberg *et al*. (1997) estimated that there are few areas in pastoral rangelands that are located more than 10 km from a source of water (Croft *et al*., 2007; see Figure 15.4). There is concern that the artificial supply of water in rangelands has impacted biodiversity by biasing the distribution of native vegetation and further encouraging the spread of some exotic flora and fauna (James *et al*., 1999; DEWHA, 2009), resulting in loss of biodiversity and landscape functionality (Howes and McAlpine, 2008; see Section 15.5).

Figure 15.4 Density of waterpoints

For a typical rangeland region in central Australia, this graph shows the proportion of land area at different distances from a water point (natural and artificial).

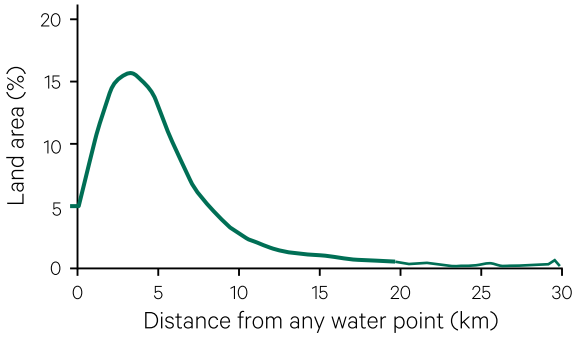

Adapted from: Biograze (2000)

Droughts are inevitable in Australia's rangelands. Yet, despite the physical hardship, the social heartbreak, the animal suffering, the financial and economic consequences, and the environmental damage we know for certain will occur, we appear to be surprised by the next inevitable drought.
(McKeon et al., 2004)

15.1.3 Fire

Fire affects long term changes in vegetation, such that a decreased fire frequency encourages tree growth and an increased fire frequency encourages grass growth. Accordingly, fire has long been used by indigenous land managers to promote pasture (Jurskis, 2015). In some rangeland bioregions, the longterm suppression of fire, either through active management to eliminate or control fire, or the lack of fuel due to grazing, has resulted in an increase in woody biomass in the the semi-arid savannas from both native and exotic shrubs (Burrows *et al*., 1990; Fuhlendorf *et al*., 2008). This change is known as woody thickening and considered undesirable for both grazing and habitat balance. Woody thickening has also been observed in Australia's northern tropical savannas (Murphy *et al*., 2014).

The use of controlled burning to reduce fuel load, and hence the intensity of late season fires, is increasing, particularly in northern rangeland areas (see Section 18). In the savannas of northern Australia, where high (summer monsoonal) rainfall encourages high fuel loads, fire is frequent and extensive. More than half the area of some bioregions can be burnt annually (Bastin *et al*., 2008). The most extensive fires occur in the late dry season, and these are intense in terms of burn severity and largely uncontrolled. Early dry-season burning using controlled fires, particularly on indigenous-held land, are being promoted to mitigate greenhouse gas emissions and reduce the severity of late season fires (Russell-Smith and Sangha, 2018; see Section 18). In arid and semi-arid central Australia, fires are more episodic and linked to prior rainfall, which stimulates plant growth (Bastin *et al*., 2008, Bastin and Allan, 2012). Widespread fire, however, is rare in the chenopod shrublands of the southern rangelands.

15.1.4 Grazing

The spatially dominant land use in Australian rangelands is livestock grazing. Bastin *et al*. (2008) reported that nearly 3.7 million km^2 of native vegetation and 30,000 km^2 of modied pastures were used for this purpose in 2001/2002, while Foran *et al*. (2019) estimated a slightly smaller area (3.4 million km^2) based on figures from ABARES (2017) and URS Australia P/L (2013). Cattle grazing predominates in northern regions, with greater numbers of sheep in southern regions (Foran *et al*., 2019), however, sheep numbers have declined in recent decades, partly due to problems with dingo control (see Section 2.3.3).

Figure 15.5 Impact of artificial waterpoints on native species

While the presence of artificial waterpoints increases the abundance of some native species of fauna and flora, other species can be negatively impacted.

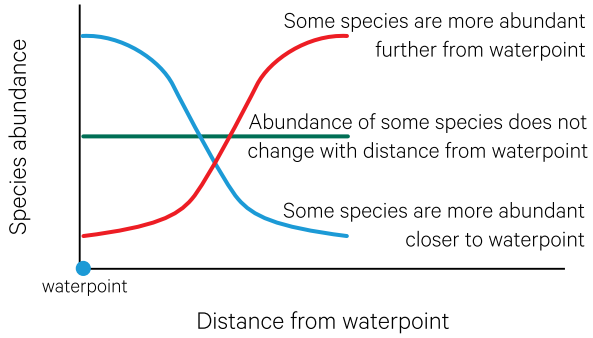

Adapted from: Biograze (2000)

As a general trend, grazing pressure has been observed to decline with distance from water (Andrew and Lange, 1986). The term 'piosphere' describes the impact of grazing on vegetation and soils in a zone centred on an animal attractant, such as water or mineral licks, with impacts being most concentrated closer to the centre of the zone (Lange, 1969; Andrew and Lange, 1986). Accordingly, in large paddocks, the impact of livestock on vegetation and soils is greatest near waterpoints (Pickup *et al.*, 1994), with 'near' equating to ~3 km for sheep and ~5 km for cattle. Within the piosphere, increased soil erosion is likely with reduced vegetation cover and changes in soil chemistry (Washington-Allen *et al.*, 2004). Soil erosion is greatest within 2–3 km from the water source (Howes and McAlpine, 2008).

Historically, excessive grazing pressure has resulted in land degradation, which manifests as degraded soil structure, increased soil erosion, loss of palatable forage, and an increase in unpalatable woody weeds (see Section 11.4). Although most native species of flora and fauna survive in grazed areas of rangelands, the presence of artificial watering points has altered the composition of some species, with their abundance and extent being largely determined by distance from water (Howes and McAlpine, 2008; see Figure 15.5).

The potential response of vegetation to grazing exclusion varies with the initial site productivity (see Table 15.1). Provided landscapes have not crossed a degradation threshold, either a reduction in grazing pressure or a sequence of wetter years can facilitate recovery to an improved state (Ash *et al.*, 2011). In the arid and semi-arid rangelands, recovering the most degraded state by manipulating grazing pressure alone (such as wet season spelling) is more problematic since extensive erosion and/or woody thickening generally results. Erosion control often requires earthworks to manage flows of rainwater and increase on site infiltration to restore the water cycle. Limited grass growth and fuel accumulation precludes the use of fire for thinning woody thickets.

Table 15.1 Potential responses of vegetation to grazing exclusion

Site degradation	Initial site productivity	
	Low	**High**
Low	Native dominance	Native dominance
	Small increase in biomass	Large increase in biomass
	Small change in exotic biomass	Potential increases in large exotic species
	Possible minor increase in small scale richness of low biomass species	Decline in small scale plant richness, especially in low biomass species
High	Native: exotic co-dominance	Exotic dominance
	Small increase in biomass	Large increase in biomass
	Possible minor increase in small scale richness of low biomass species	Decline in small scale richness, especially in low biomass species
	Limited increase in native richness owing to propagule constraints	Negligable increase in native diversity owing to competition and propagule constraints

Source: Lunt *et al.* (2007) Table 1

The worst instances of pasture degradation occur when overgrazing is coupled with drought (McKeon *et al*., 2004; see Section 11.4). Past expectations of carrying capacity, sometimes unwittingly encouraged by government policy, have led to undesired outcomes, in terms of both environmental and social devastation, as landscapes, stock, and communities are impacted by drought (see Table 11.2). For example, until 1992, NT pastoral leases had a minimum stocking covenant and, in some cases, the prescribed number exceeded the inherent carrying capacity of the land types (or land systems) present on the lease. Closer settlement schemes in both Queensland and NSW in the 1900s produced leases which became unviable and were often severely degraded with both climate variability (drought) and changing economic circumstances. Australian literature contains many examples of pastoral families that have faced emotional and financial ruin during severe droughts (e.g., Ker Conway, 1989). With hindsight, it appears these disasters could have been avoided, or at least mitigated, by appropriate management of pastoral resources. For example, the impact of grazing is now considered to be more benign, and difficult to distinguish from the effects of large interannual variability in rainfall.

15.1.5 Socio-economic factors

Human settlement patterns in Australian rangelands are highly variable. Being remote from large urban centres, these communities are often isolated and tend to be distanced from political attention and influence. In Figure 15.6, regions classified as 'remote' by the Australian Bureau of Statistics (ABS) for population census purposes (ABS, 2016) are compared with the accepted boundary of rangelands based on environmental attributes (Bastin *et al*., 2008) and the extent of grazing (ABARES, 2017).

Some of the areas used for pastoral activities in rangelands are owned under freehold title, but much of the area is crown land and leased to pastoralists with specific conditions and restrictions. Pastoral leases now cover 44% of the Australian mainland (Austrade, 2019) and over half the area defined as rangelands (Foran *et al*., 2019). These leases are administrated by state and territory jurisdictions, who have legislative responsibility to regularly assess and monitor the leased land condition.

Figure 15.6 Remote populations in Australia

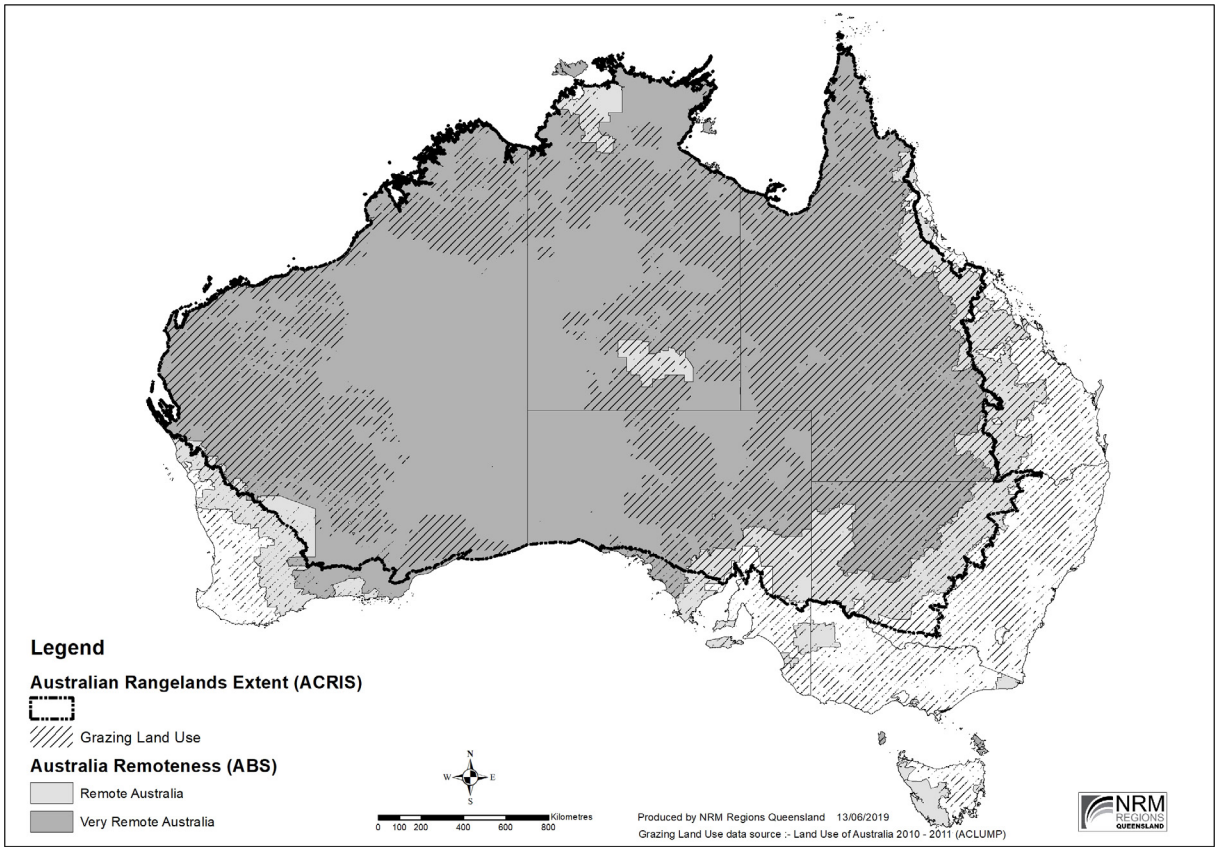

Source: Foran *et al*. (2019) Figure 1

Monitoring of rangelands is undertaken at a range of scales, including:

- paddock and property—as part of enterprise management to determine forage budgeting, appropriate stocking rates, etc; and
- regional, usually agency-based—to fulfill legislative responsibilities for leasehold and Crown lands to ensure that natural resources are suitably managed.

Foran *et al.* (2019) outlined the current challenges facing rangeland communities in Australia and proposed some systemic actions that are needed to address these concerns. A national, integrated approach to rangeland monitoring that maximises the value of EO datasets would help the custodians of this environment to understand and maintain its resilience for the benefit of current and future generations (Sparrow, 2017).

15.2 EO Sensors for Rangelands

As indicated by the examples provided in the following sub-sections, the most commonly used EO sensors for observing rangelands detect passive optical wavelengths to discern differences in the land surface and its vegetative cover (see Table 15.2). The scale of the Australian rangelands necessitates reliance on spaceborne rather than airborne sensors.

The optical reflectance of a hypothetical dryland pixel has been described as a function of:

- geometry—viewing and illumination positions (see Volume 1B—Section 3);
- tissue optics for all vegetative components—living and dead (see Sections 4 and 5 above);
- canopy structure—volume and orientation of vegetative tissue including litter (see Sections 5 and 6 above);
- landscape structure—crown size, canopy cover and height (see Section 7 above); and
- soil optics—mineral content, organic matter, surface roughness, grain size distribution, and cryptobiotic soil crusts (Asner, 1998; see Volume 1B—Section 6.4).

The sparse density and high spatial variability of vegetation in rangelands landscapes pose challenges to EO analyses in terms of selecting the optimal spatial scale for imagery (see also Volume 2D). Several aspects of grassland ecosystems relating to scale are particularly relevant to EO monitoring (Hill, 2004):

- scale of sward variation relative to pixel size—grassland 'texture' can vary from a uniform monoculture to different mixtures of grasses, tussocks, shrubs, and bare soil;
- persistence of spatial patterns—can be examined using spatial and temporal statistics (see Volume 2A—Section 8) and may be informative to land managers;
- temporal variations may be driven by climate/phenology or management practices—both spatial and temporal variations in vegetation are further complicated by the movements and appetites of grazing animals;
- scale and density of ground sampling relative to pixel size—ground 'truth' data need to represent structural and chemical properties, especially for quantitative products, and be sufficiently dense to relate to image pixel size; and
- surveys for ecological, botanical, or production attributes may require different spatial resolutions, revisit frequencies and spectral discrimination capabilities.

The impact of EO image spatial resolution on spatial statistics is introduced in Volume 2A—Section 8.2. In the context of rangelands:

- high resolution (H-resolution) pixels are generally smaller than vegetation entities so depict them against a contrasting background; and
- low resolution (L-resolution) pixels are generally larger than vegetation entities so observe an integrated signal for vegetation and background.

Table 15.2 EO sensors relevant to rangelands

TIR: Thermal infrared; SAR: Synthetic Aperture Radar

Type	Sensor	Platform	Relevance	Advantages	Disadvantages
Passive optical	Multispectral radiometer	Satellite (or airborne)	Mapping vegetation extent, biomass, biodiversity, and productivity Monitoring land degradation	Local to national scale, recurrent coverage with high temporal frequency and extent, low cost;	Cloud contamination
	TIR radiometer	Satellite (or airborne)	Soil/canopy temperature Mapping fire potential, severity, and extent Assessing drought and monitoring regional hydrological changes	Highlight thermal anomalies	Low resolution, low signal to noise ratio
Active microwave	Multi-band SAR	Satellite (or airborne)	Soil characteristics Vegetation structure and biomass Water dynamics	All weather, operates at night	Data availability, noisy data, complex processing

In this sparsely-vegetated landscape, most medium resolution optical sensors image dryland vegetation as L-resolution, with each pixel representing a mixture of different soil types (with varying age, mineralogy, and parent materials) and different vegetation types (with varying growth forms, cluster patterns, and condition, where vegetation condition is defined as the vigour, photosynthetic capacity, or stress of a particular vegetation canopy or cluster; Asner, 2004).

Thus, a given pixel contains multiple landscape components so is well-suited to fractional cover analyses (Scarth *et al*., 2012; see Section 8.3). Since dryland canopies have low leaf area index (LAI; see Section 6.3.3), leaf level variations are not a major component of canopy reflectance in optical wavelengths (Asner, 2004). Accordingly, most variations in EO reflectance in rangeland landscapes can be assumed to result from changes in canopy cover (Guerschman *et al*., 2009). Slow rates of decomposition means that non-photosynthetic material accumulates in these landscapes, which increases spectral reflectance across all optical wavelengths, especially in herbaceous canopies.

In rangeland environments, thermal sensors are also used to monitor fire (see Section 18) and regional hydrology (see Section 7.6 and Excursus 10.2), including drought. Multi-band SAR sensors have also been investigated for mapping the dynamics of above ground biomass in tropical and sub-tropical rangelands (Zhou *et al*., 2016).

15.3 Rangeland Condition

In more arid regions, a useful indicator of habitat condition is the amount of vegetation versus bare soil covering the ground surface, especially relative to what might be expected for a given rangeland climate and soil type (see Section 7.3). The 'intactness' of vegetation cover in this landscape indicates the structural and functional integrity of habitats, which is critical for maintaining plants and animal populations. There are three key considerations when analysing EO data for the purpose of monitoring land condition in rangelands:

- determining an appropriate and suitably robust index of vegetation cover based on the spectral properties or dimensions of the sensor (see Section 8.1 and Volume 2C);
- examining spatial patterns in the derived index, including typical summary statistics for stratified areas, such as land type/system, paddock, or property (see Volumes 2A and 2E); and
- exploring the temporal dynamics of spatially-summarised data (see Volume 2D).

Approaches that are used to monitor the health of grazed rangelands rely on multiple, reliable indicators that individually, and in combination, provide objective and consistent information from which land condition can be assessed (see Section 7.3). These approaches can be differentiated in terms of their reliance on point, population, or pattern sampling (see Figure 15.7). Conventional ground-based techniques for assessing land condition and its change (trend) utilise a limited number of *point*-based assessments at stratified locations within landscapes and paddocks, which acquire repeated measures at fixed sites (see Figure 15.7a). EO-based methods analyse the spectral properties of the *population* of pixels within an area of interest (landscape type, paddock, or region) with varying levels of sophistication (see Figure 15.7b). Grazing gradient methods (Pickup and Chewings, 1994; Pickup *et al*., 1994) search for systematic spatial *patterns* in vegetation cover (see Figure 15.7c) that are explicitly related to grazing, such as the persistence of grazing gradients within paddocks (see Section 15.3.1). Methods such as land cover change analysis (Karfs, 2002) examine patterns of change through time (see Section 15.3.1.2). All three approaches can be used to look for change over time (Pickup *et al*., 1998; Wallace *et al*., 2006).

The ecological sustainability of pastoral lands is not adequately protected by the State's current system of land monitoring and administration. Pastoral lands have been under threat for over 75 years and during that time there has been limited progress to halt the decline in pastoral land condition. Current knowledge of the environmental condition of individual leases is poor. A reduction in the scope of monitoring since 2009 and limited use of remote sensing tools has contributed to a lack of understanding of land condition at the lease level, and restricted visibility of the extent of land condition issues across the pastoral estate. Future sustainability of the pastoral industry and the Crown's land estate relies on being able to make informed decisions on how to address existing issues and prevent new ones. (OAGWA, 2017)

Figure 15.7 Monitoring approaches

Schematic representation of point (ground-based), population (high and low resolution EO-based) and pattern (EO grazing gradients) approaches to monitoring condition and trend, and some of their key characteristics.

a. Point: ground-based monitoring

- small sample area (generally < 5 ha per site), and few sample sites (1–2 per paddock or 1 per water point)
- rapid subjective assessment or quantitative and descriptive information about plant species and soil; typically includes information about vegetation composition
- problems of measurement error and repeatability
- data can be presented in easily understood tables/charts
- data seem readily interpretable (but dependent on the underlying model of landscape change, which may be poorly developed for some ecosystems)
- generally inadequate spatial or temporal sampling for separating grazing impacts from site-specific and seasonal effects

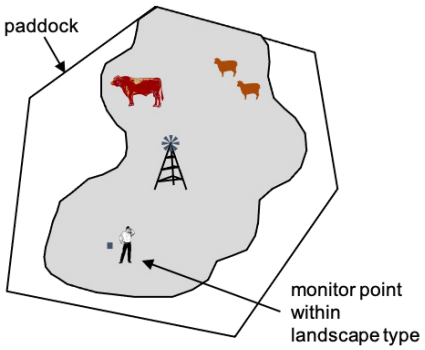

b. Population: satellite data and change over time

- general advantages of satellite data:
  - can analyse total area grazed
  - repeat coverage and selective acquisition
  - historical archive for many sensors
  - range of spatial resolutions
- landscape change expressed through differences in fractional cover over time
- VegMachine and other tools provide tailored, user-friendly software for analysing time series data
- inference based on ancillary data is generally required to separate grazing effects from natural variation

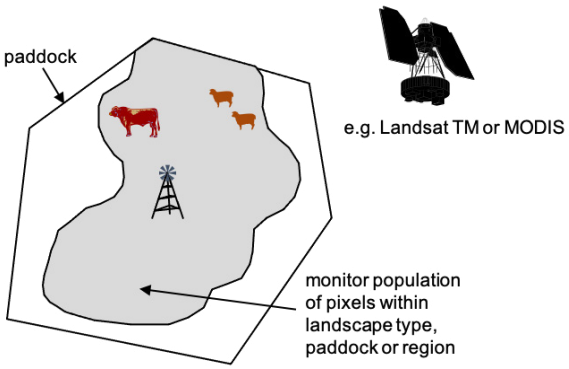

c. Pattern: satellite data and change over space and time—grazing gradient methods

- general advantages as for satellite data above
- search for systematic change in cover related to grazing, reliably identifying grazing effect but requiring larger paddocks
- stratification according to landscape type (e.g. land systems) allows separate grazing effects within large paddocks to be monitored
- uses an explicit definition of land degradation to determine landscape change (ability of vegetation cover to respond to large episodic rainfall events, when received)
- reasonably complex—results not easily understood or accepted by land managers
- broadly applicable to rangelands with < 500 mm annual rainfall

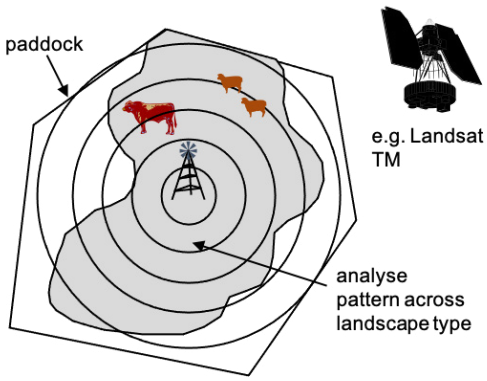

The utility of the pattern approach (see Figure 15.7c) to understanding grazing effects on vegetation cover dynamics is enhanced where the range in rainfall variability is restricted to either above average or below average seasonal conditions (see Figure 11.4). These two constraints correspond, respectively, with ecological analogues of vegetation resilience and persistence (or stability; see Section 7.2).

In the sub-sections below, we consider EO-based approaches that have been developed for monitoring vegetation resilience (see Section 15.3.1), landscape condition and leakiness (see Section 15.3.2), and ground cover persistence (see Section 15.3.3) in the Australian rangelands.

15.3.1 Vegetation resilience

Resilience is "a measure of the persistence of systems and their ability to absorb change and disturbance and still maintain the same relationships between system variables" (Holling 1973). Vegetation resilience, specifically the increase in ground cover after much above average (and often, episodic) rainfall, underpins the grazing gradient methods developed by Pickup *et al.* (1994; see Section 8.1.3).

15.3.1.1 Grazing gradients

As introduced in Section 15.1.4, grazing gradients of vegetation cover develop with increasing distance from stock watering points in large paddocks (> 100 km^2—shown as the red line in Figure 15.8). Water-remote areas provide a guide to the expected (reference) cover at any point in time, such that the extent to which ground cover increases (recovers) after large rainfall events indicates the landscape's capacity to retain its inherent resilience to respond to such events (see Section 7.2). Thus, in Figure 15.8, the horizontal green line shows the expected average level of ground cover in a fully resilient landscape, where all areas at increasing distance from water have similar cover, while the brown curve indicates a permanent effect from grazing with the vegetation cover response closer to water being suppressed, even after substantial rainfall.

Ecosystem resilience is thought to be a product of the diversity of ecosystem functional groups, the diversity of species within those functional groups, and diversity within species and populations (Folke et al. 2004). .... Resilience has been an important quality of the ecology of Australia's biodiversity, as ecosystems have had to develop a range of evolutionary strategies to cope with the naturally high variability of rainfall, poor soils, and the long term drying of the continent. (DEWHA, 2010)

Figure 15.8 Stylised grazing gradient based on remotely sensed ground cover

In the grazing gradient methods, the resilience of vegetation cover near stock watering points indicates condition. In this diagram, the red curve indicates vegetation cover relative to distance from water before rain. After substantial rains, vegetation either recovers at all distances from water, which would indicate a fully resilient landscape (green line), or remains sparse closer to water, which indicates loss of resilience (brown curve).

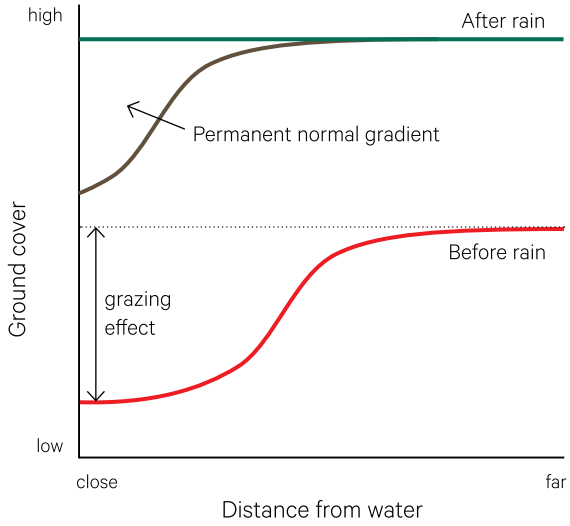

Adapted from: Bastin and Ludwig (2006) Figure 1a

15.3.1.2 Land Cover Change Analysis

Contemporaneous with the application of grazing gradient methods in central Australia (Bastin *et al.*, 1993, 1996, 1998), the 'land cover change analysis' (LCCA) method was developed for monitoring grazing effects in WA and the NT (Wallace *et al.*, 1994). This method had its genesis from the observation that a major indicator of condition in many grazing regions was the loss of perennials and their replacement by seasonally-dependent annuals.

In the shrublands and grasslands of WA, multi-temporal Landsat image sequences were used to produce maps of the differential temporal responses of annuals and perennials (see Volume 2D). For example, areas known to be in poor condition have a negative slope over time (indicating cover loss) and increasing seasonal variance (indicating increased presence of annuals). Other meaningful, pixel level, trend summaries include areas of positive slope (increasing cover) and no change (stable cover over time). This analysis was initially based on limited ground knowledge, but subsequent field validation demonstrated that the maps were useful for interpreting condition (Karfs, 2002; Karfs *et al.*, 2004). Long term cover trends from multi-year image sequences also provided information on shrub invasion and cover dynamics, from which aspects of condition could be inferred (Wallace *et al.*, 2006).

The LCCA method was widely tested in the Kimberley (WA), Victoria River (NT) regions and southwest Queensland (Wallace and Thomas, 1998, Karfs *et al*., 2004), and subsequently developed into 'VegMachine' (Peel *et al*., 2006, Beutel *et al*., 2015). This software package assisted graziers and natural resource management staff to summarise and benchmark vegetation cover change, based on EO data, over long periods at user specified locations. VegMachine is now freely available online (Beutel *et al*., 2015, 2019) and is described in Excursus 15.1.

15.3.2 Landscape condition and leakiness

Mapping land condition in the rangeland environment in Australia is difficult due to the enduring problems of its vast extent coupled with the spatial complexity and temporal variability of arid-zone vegetation. Methods used to map vegetation condition in rangelands need to be (Bastin and Ludwig, 2006):

- robust—rigorous methods are needed to differentiate the impact of management decisions on vegetation from its inherent variability over space and time;
- efficient—effective methods must be suited to large area mapping at low cost; and
- general—the complex interactions between vegetation, climate, fire and grazing in rangelands means that methods need to be adaptable to specific environments.

Given debate about the relevance and suitability of current paradigms for understanding vegetation dynamics in parts of the rangelands (see Briske *et al*., 2003 for a review), some monitoring systems focus on vegetation change over time (see Sections 7.3 and 11.3). This avoids the often fraught process of trying to 'shoe horn' assessments into ill-fitting and often arbitrary condition classes. Causality is a fundamental component of understanding change; in this case, determining the most plausible reasons for observed change, be they related to climatic variations or due to grazing, fire, or other forms of disturbance. For example, the Western Australian Rangeland Monitoring System (WARMS; Watson *et al*., 2007a, 2007b; Novelly *et al*., 2008) is a sophisticated site-based monitoring system for reporting regional scale change in perennial vegetation under grazing. WARMS focuses on change and its most probable causes when interpreting monitoring data.

The concept of landscape function—the capacity of a landscape to capture and retain rainwater, soils and their nutrients after rainstorms (Ludwig *et al*., 2007)—is introduced in Section 7.3 above. The capacity to retain these components depends not just on vegetation cover *per se* but its distribution in the landscape. In Figure 15.9a, the relevant vegetative and surface water components in a rangelands environment are identified. Landscape Function Analysis (LFA) relies on measurement of the sizes of vegetation patches, the inter-patch distances (or fetch), and the soil surface condition of both patches and fetches (Tongway and Hindley, 2004), which in combination demonstrate how rainwater moves through the landscape (see Figure 15.9b). Since its development, this approach has been used for research and land management purposes in a range of landscapes (Eldridge *et al*., 2020).

Figure 15.9 Landscape function

a. A transect to measure simple indicators of land condition in Landscape Functional Analysis (LFA)

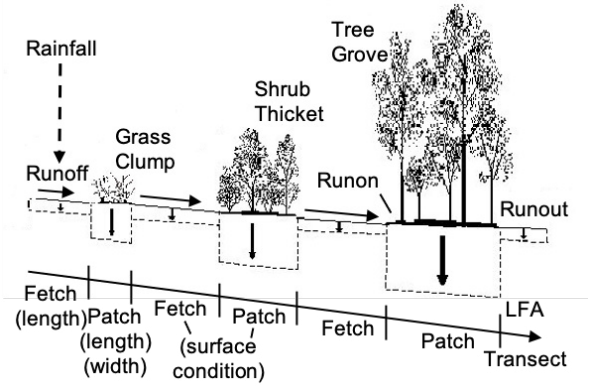

b. The role of vegetation patches as obstructions to surface flows, where a high cover of patches on the upper slopes greatly slows runoff to enhance water retention and a low cover on lower slopes leads to long fetches and loss of water, that is, a 'leaky' landscape.

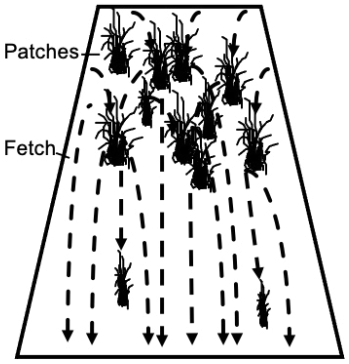

Source: Bastin and Ludwig (2006) Figures 1b and 1c

Figure 15.10 Leakiness index example

a. Leakiness index for rangeland monitoring site compared with mean levels of persistent vegetation cover for five monitoring periods from 1980 to 2002. b. Annual rainfall from 1979 to 2004 in relation to 305 mm average.

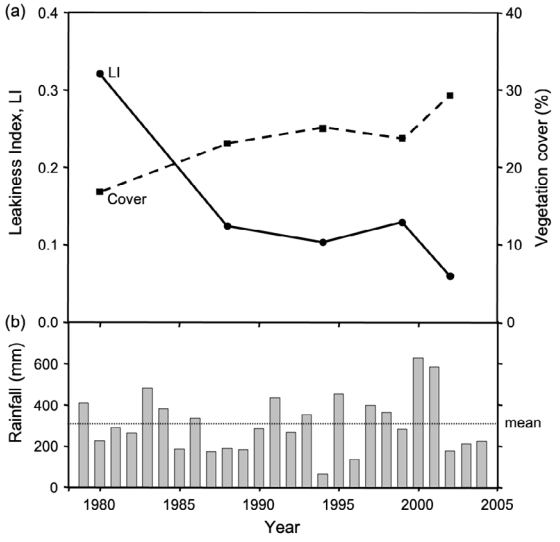

Source: Ludwig *et al.* (2007) Figure 4

The leakiness index (see Section 8.1.6) used EO imagery and DEM data to derive landscape scale values for leakiness (see Figure 15.10). This method has been applied to change in landscape leakiness from 1986 to 2005 for selected sub-catchments of the Fanning River, Queensland (Bastin *et al*, 2007). Leakiness Index (LI) values were calculated with the Leakiness Calculator (version LI4). In this study changes over time in indicated leakiness of sub-catchments dominated by native perennial-tussock grasses were contrasted with those dominated by an introduced stoloniferous mat-forming grass, Indian couch (*Bothriochloa pertusa*). For example, under the Grazing Land Management (GLM) program in Queensland (FutureBeef, 2020), the former pastures tend to be in good condition and the latter in reduced condition. For the same level of average cover, pastures dominated by Indian couch were deemed to be more leaky than the native tussock grasses. Of critical importance, average cover appeared to decline to relatively low values following a run of poor, wet seasons (such as occurred in the mid 1990s) and, at this time, values of the leakiness index reached relatively high values. While this study was supported by limited ground data, the results demonstrate the importance of:

- maintaining minimum acceptable levels of persistent pasture cover (particularly on hillslopes); and
- managing to improve the density and cover of native perennial-tussock grasses in the pasture.

This method has been used for research purposes in different parts of the rangelands overseas and as a connectivity index to link vegetation patterns with erosion risk (Xu *et al*., 2018, 2019). However, there are no known applications of the leakiness index as part of jurisdictional monitoring of rangelands in Australia.

15.3.3 Persistence of ground cover

In drier years, retained ground cover is critical for minimising the risk of wind and water erosion. It is reasonable to infer that most of the cover present in drier (and drought) years comprises perennial species (see Section 9.1)

The Dynamic Reference Cover Method (DRCM) automatically calculates an expected (reference) level of ground cover for each Landsat TM pixel in a nominated dry/drought year (Bastin *et al*., 2012). The difference between the actual and reference cover—the cover deficit—indicates the extent to which an area has been modified by past grazing. Change in cover deficit from one drought period to the next provides an objective and systematic way of determining how ground cover is being managed when its presence is most critical.

Landsat fractional cover (see Excursus 8.3) for repeat dry years between 1988 and 2005 was analysed with DRCM at sub-bioregional scale for approximately 640,000 km^2 of the Queensland rangelands (Bastin *et al*., 2014). All 34 sub-regions analysed had similar or increased levels of seasonally-adjusted ground cover at the end of the analysis period (2003 or 2005). Allowing for possible landscape heterogeneity effects on assessed condition, at the first assessment in 1988 the Einasleigh Uplands bioregion was in a comparatively better state at the end of the period and those analysed parts of the Mulga Lands bioregion in poorer state. Most sub-regions of the Cape York Peninsula, Brigalow Belt North, Desert Uplands, Gulf Plains and Mitchell Grass Downs bioregions, lay between these two end-states. Simulated levels of pasture utilisation based on modelled pasture growth and statistically-based grazing pressure supported the results of this regional assessment of land condition.

It is important to remember that remotely sensed ground cover is but one indicator of the functionality of rangelands under grazing use. Information about other indicators is also required, such as the persistence of palatable perennial forage species, the dynamics of the woody layer, and erosion status. Thus ground-based monitoring is required in addition to EO analyses, but the value of the ground component is increased where it complements information available from EO.

A number of operational systems and products have been developed to use EO datasets for monitoring change in woody vegetation cover, including the Statewide Landcover and Tree Study (SLATS; see Volume 2D—Excursus 14.3) and the Persistent Green Vegetation product (see Section 9.1). The routine monitoring of woody cover dynamics in Australia's arid rangelands is currently limited by the lack of a suitably robust cover index for 'non-green' canopies such as *Acacia* species, however, research is continuing in this area (e.g. Barnetson *et al.*, 2019).

15.4 Operational Systems for Monitoring Rangelands

A range of systems have been developed to monitor Australian rangelands (see Table 15.3). In the absence of a national coordinating body, current details for these programs are difficult to determine, although status reports on pastoral leases are available for some states (such as OAGWA, 2017 and DENR, 2019). These systems have been improved over time and in some states multiple systems are still in use in different regions. For example, FORAGE is an online decision support system developed in Queensland for grazing land managers, which integrates information specific to individual properties including rainfall, pasture growth, seasonal rainfall and pasture growth outlooks, ground cover, Foliage Projective Cover (FPC), soil erodibility, land types, and climate projections (Zhang and Carter, 2018). More generic systems for mapping vegetation and ecosystems at both the state/territory and national level (see Section 2.3.1) complement and support the rangeland-specific systems.

Excursus 15.1 describes an operational, EO-based system that has been specifically developed to monitor the rangeland environment in Australia. The international Group on Earth Observation (GEO) Global Agricultural Monitoring initiative (GEOGLAM; see Section 21.3) is also developing the GEOGLAM Rangeland and Pasture Productivity (RaPP) application to monitor the condition of pastures and rangelands globally (see Excursus 11.1).

Table 15.3 Rangelands in Australia

This table summarises the status of rangelands monitoring in 2008. Current status for most jurisdictions are difficult to update in the absence of a national coordinating body. Reassessment of ground sites varies with jurisdiction between one and 14 years.

State/ Territory	% of state as rangelands	Rangeland tenure	Rangeland population (2016)	Permanent monitoring sites	Monitoring system
NSW	60	Mostly leasehold with small areas freehold	52,670	350 sites monitored annually	Rangeland Assessment Program (RAP) SLATS (see Volume 2D—Excursus 14.3)
NT	98	46% pastoral leases	89,444	2333 pastoral monitoring sites	Integrated monitoring program which relates site-based data to Landsat fractional cover (DENR, 2019)
SA	85	60% pastoral leases 40% conservation or regional reserves	62,797	Baseline monitoring on ~400 sites and resource inventories on each of the 328 pastoral leases	Arid Lands Information System (ALIS) based on Grazing gradient assessment in northern leases Land Condition Index (LCI) in southern leases
Queensland	82	75% freehold and leasehold grazing properties	124,050	~1000 pastoral leases	SLATS (see Volume 2D—Excursus 14.3) AussieGRASS (see Excursus 10.1) FORAGE (Zhang and Carter, 2018) VegMachine (see Excursus 15.1)
WA	87	42% pastoral leases	81,341	1622 sites monitored since 1992 on 435 pastoral leases Grassland sites assessed 3 yearly and shrublands assessed 5 yearly	Western Australian Rangelands Monitoring System (WARMS; see also OAGWA, 2017, Table 3)

Source: Bastin *et al.* (2008); Foran *et al.* (2019); NSW DPI (2019); Austrade (2019); OAGWA (2017)

Excursus 15.1—VegMachine

Source: *https://vegmachine.net*
Further Information: Beutel *et al.* (2019)

VegMachine is a free, online tool that uses time series of satellite imagery and derived products to summarise spatial and temporal changes in land cover on Australia's grazing lands. The software has been refined and used by government agencies, Natural Resource Management (NRM) groups and pastoralists since 2002, with the current national website being launched in 2016 (Beutel *et al*, 2019). Using VegMachine, for selected areas a user can:

- generate comprehensive ground cover monitoring reports;
- measure land cover change or estimate soil erosion rates;
- view satellite image land cover products; and
- better understand the links between management, climate and cover in grazing land.

Figure 15.11 VegMachine comparisons

a. This partial screenshot compares two adjacent sites that are separated by a fence. The North site (red) has had consistently more ground cover and better land condition than the South site (blue) over that period. Red and blue lines respectively show the median seasonal ground cover at each site, and the red band shows the 'range' (actually 20th to 80th percentile) of ground cover values on the North site. The analysis reflects known conditions at the sites since 2003, and also suggests the observed difference extends back to the early 1990s. Since the two sites are in the same land type with a common rainfall history, management is the most likely cause of the observed differences.

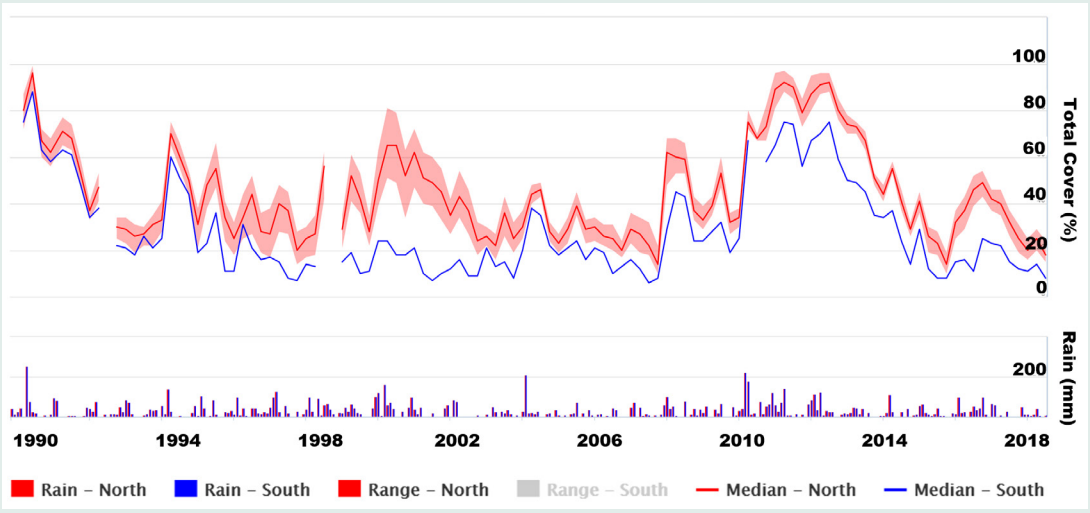

b. This extract from a regional comparison report shows the total ground cover in part of a paddock that has been very heavily grazed from 2005. The pale grey bands show the percentiles of ground cover in the FT05 land type of the surrounding region (5th–20th: lower grey band; 50th: central grey line; 80th–95th: upper grey band). The overlaid time trace shows median ground cover in the same land type within the paddock. The symbols along the time trace classify cover in the paddock relative to the regional cover percentiles (Well below: < 5th; Below: 5th–20th; Similar: 20th–80th; Above: 80th–95th; Well above > 95th). This analysis shows cover in the paddock has declined dramatically since 2005, corresponding to the increased grazing pressure over this period. This trend is evident despite the presence of rainfall-driven fluctuations in regional cover (higher in 2010–2012, and lower in 2004–2007 and 2013–2014).

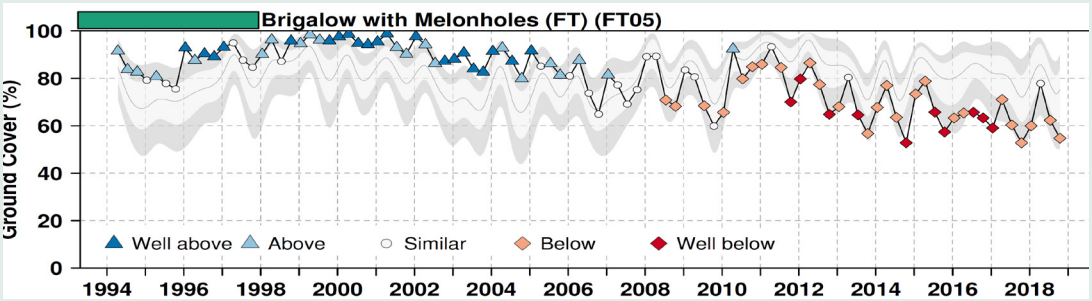

Source: Beutel *et al.* (2019) Figure 2

The current datasets interrogated by VegMachine date from 1990 and include imagery from Landsat TM/ETM+/OLI and Sentinel-2 as the products: seasonal ground cover (see Section 9.2), fractional cover (see Section 8.3), and persistent green cover (see Section 9.1). These datasets can be viewed as images at a range of scales, and ranked in time and space. Spatial comparisons are particularly informative for 'identifying paddocks in need of more attention' (Brinsmead 2017; QRIScloud, 2018; see Figure 15.11). Paddock-by-paddock and land type-by-land type analyses of ground cover change from 1990 to the present allow graziers to clearly see the impact of management decisions and infrastructure changes on their properties.

15.5 Conserving Biodiversity

The major threats to biodiversity in Australia are considered to be habitat fragmentation, climatic changes, land use change, invasive species, grazing pressure, altered fire regimes, and changed hydrology (DEWHA, 2009), all of which are significant landscape factors in rangelands (see Sections 7.1 and 19). While threatened biota occur in greatest abundance in areas with high population and the highest land use pressures, there is evidence that the numbers of small mammals in tropical savannas are declining. All changes in conservation status of threatened species in recent decades have shown declines and virtually every bioregion includes several threatened taxa.

The Australian rangelands comprise 52 IBRA bioregions and 244 subregions (see Section 2.4). In many of these bioregions, grazing by domestic livestock has resulted in significant impacts on soils, landscape processes, and native biota, with ongoing loss of landscape function, particularly within the piosphere (see Section 15.1.4). Lunt *et al*. (2007) identified six site factors that could be used "to predict, interpret and compare the impacts of grazing on natural ecosystems":

- soil and ecosystem processes—positive, negative, or no impact of grazing;
- grazing history—including loss of grazing-sensitive species;
- site productivity—in terms of landscape function;
- plant palatability—of dominant native and exotic species;
- plant recruitment—impact on germination and growth; and
- context in the broader landscape—across different spatial scales.

These characteristics were integrated into a hierarchical decision tree, which concluded that "livestock grazing is likely to be detrimental to biodiversity conservation in many ecological contexts" (Lunt *et al*., 2007; see also Table 15.1).

Although a number of state/territory and federal programs have been undertaken to monitor the condition of rangelands in Australia, these have been disproportionately funded given the extent of the rangeland environment. Monitoring programs include the TERN AusPlots Rangelands program, which uses a standardised approach to sample soil and vegetation characteristics at 442 sites within the rainfall range of 129–1437 mm (White *et al*., 2012; Guerin *et al*., 2017). Many state-based programs are tailored to the information needs of local regions and produce data that are difficult to compare across the continent. Also, pastoral monitoring programs, which focus on pastorally productive country, typically collect different data from environmental monitoring programs that aim to assess biodiversity. Although biological assets are declining in Australia, existing data are insufficient to report on biodiversity trends at a national level (DEWHA, 2009).

Locking up the land purely for conservation is not the solution to our environmental problems [in the WA rangelands]. We must do better than that. I have no doubt that if we do lock it up, ecological processes will take over and the land will heal itself into a stable state. But, eventually, those small conservation areas are certain to fail if we do not change the way that we manage the surrounding land. Even if those small pockets of pristine wilderness did manage to persist, the increasing pressure to produce food from dwindling resources would eventually mean that they were overrun in a last-ditch effort to wring the final bit of productivity from the landscape to feed ourselves.
(Pollock, 2019)

Native vegetation is a cost-effective and powerful surrogate for biodiversity. The distribution of threatened species and communities is closely aligned with areas where native vegetation has been extensively cleared. (DEWHA, 2009)

To understand the impact of grazing on plant biodiversity and composition in Australia—and its consequential impact on fauna—requires a systematic approach to biodiversity monitoring at a landscape scale. Potential frameworks for jurisdictional monitoring of biodiversity in the rangelands were proposed by Eyre *et al.* (2011a) (see Excursus 15.2) and McAlpine *et al.* (2014). To date, however, no rangeland jurisdiction in Australia has implemented this monitoring framework operationally. More studies are required to link habitat condition indicators to those species that are dependent on particular proportions and types of groundcover. Linkages between groundcover and biological diversity have hitherto been based on local sites only. To assess this relationship across our rangelands, broader landscape and regional analyses will be needed (Sparrow, 2017).

Recognising that management improvements for grazing can also benefit biodiversity, tools are being developed to assist rangeland managers to assess land condition in terms of biodiversity. For example, procedures for assessing the biodiversity condition, or BioCondition, of grazing lands in southern Queensland have been defined with support from Meat and Livestock Australia (Eyre *et al.*, 2011b; MLA, 2011, 2012). This complements the Grazing Land Management (GLM) package, which promotes sustainable management by graziers in northern Australia (DPIF, 2006; see Excursus 7.1). BioCondition is designed for rapid assessment of sites and rests on three components:

- a set of site-based and landscape-scaled attributes, which indicate biodiversity (see Table 15.4);
- benchmarks for each attribute derived from reference sites; and a
- rating system for the relative value of attribute to benchmark values.

Similar systems have been developed for other jurisdictions (such as Butler *et al.*, 2020, Table 1; see Section 3.4.1).

Towards avoiding loss of biodiversity, and stressing the importance of maintaining and enhancing landscape heterogeneity, various reviews of biodiversity status that are limited to specific regions have hitherto offered a 'portfolio of partial solutions' (Waters and Hacker, 2008). However, in order to effectively manage rangelands across Australia, consistent and objective monitoring protocols are required in all jurisdictions and at all landscape scales to provide reliable answers to the questions:

- where is change occurring?
- how much change is there?
- what is driving that change? (Sparrow, 2017).

The challenge for future land managers will be to balance the requirements of agricultural production for growing human populations with appropriate safeguards for biodiversity conservation. Given the scale of Australian rangelands, EO datasets need to be a significant part of any monitoring solution.

Table 15.4 BioCondition indicators

Indicator	Attribute
Site-based	Regeneration—recruitment of dominant tree species
	Diversity—native plant species richness for four life forms
	Cover/complexity—tree canopy cover and canopy health (%); tree height (m); shrub layer cover (%); native perennial 'decreaser' grass species basal area; native perennial forb and non-grass cover (%); native annual grasses, forb, and non-grass cover (%); cryptogram cover
	Habitat—large trees and hollows; fallen woody material; litter cover
	Weeds—weed cover
Landscape	Size of patch
	Context
	Connectivity
	Distance to artificial water

Source: MLA (2011) Table 2

...our ability to report change in biodiversity is limited due to inadequate data (Bastin et al., 2008)

Excursus 15.2—Rangelands Biodiversity Monitoring Framework

Source: Eyre *et al.* (2011a, 2011b)

A framework for jurisdictional monitoring of biodiversity in the rangelands was proposed by Eyre *et al.* (2011a). This systematic and scaled approach combines field measurements and EO-based methods to integrate:

- direct measures of biodiversity attributes;
- indirect measures of biodiversity (through indicators or surrogates);
- measures of drivers of biodiversity; and
- measures of response indicators.

As detailed in Section 19, changes in biodiversity drivers exert a pressure on biotic attributes, leading to a change in their state (where biotic attributes measure biodiversity either directly, in terms of abundance or extent of a species, or indirectly, as habitat condition). In this context, biodiversity drivers impact environmental attributes at both the local and landscape scales, and include indicators such as climate variations, management practices, and disturbances (Eyre *et al.*, 2011a). This framework follows the multi-resolution approach of relating EO datasets to ground measurements shown in Figure 3.1 and identifies three spatially hierarchical and complementary components that are integrated through research, analysis and modelling:

- Targeted monitoring—localised, field-based monitoring to address specific management questions based on target species that are known to be indicators of change or have been identified as vulnerable. These programs need to be well-defined, focused in terms of spatial extent and stated goals, and reviewed frequently.
- Surveillance monitoring—broadscale, field-based sampling for a range of species across multiple ecosystems.
- Landscape scale monitoring—regional to national scale information on habitat quality and trends in threats to, or drivers of, biodiversity, using data from systematic ground-based and EO methods with frequent coverage.

Some of the biodiversity driver indicators that would be observed in each layer of this hierarchy include:

- incidence of fire—threatens species habitat or species directly, and varies with ecoregion;
- vegetation clearing and fragmentation—directly threatens habitat for native species, most commonly in tropical savanna environments;
- grazing pressure—threatens habitat and competition for resources, and includes both domestic and feral animals;
- feral predator abundance and distribution—endangers native fauna and domestic stock;
- invasive plant abundance and distribution—threatens habitat quality, competes with native flora, and can change fire regimes;
- climatic data—particularly rainfall and temperature, to provide context for both short and long term variations (Eyre *et al.*, 2011a).

Any biodiversity sampling system also needs to ensure that surveillance sites are stratified by bioregions within jurisdictions (Eyre *et al.*, 2011a).

15.6 Further Information

GEOGLAM Rangeland and Pasture Productivity (RaPP) tool

Australia: *https://map.geo-rapp.org/#australia*

Global: *https://www.geo-rapp.org*

Information: *https://www.csiro.au/en/Research/LWF/Areas/Landscapes/Earth-observation/RAPP-Map-GEOGLAM*

Australian Collaborative Rangelands Information System (ACRIS)

ACRIS: *http://www.environment.gov.au/land/rangelands/acris*

Bastin *et al.* (2008)

Foran *et al.* (2019)

Soils for Life

A not-for-profit charity dedicated to supporting Australian farmers and rural communities in regenerating soils and landscapes to build natural and social capital and transform food systems: *https://soilsforlife.org.au/about/*

FarmMap4D Spatial Hub

Online, subscription tool for mapping, assessing and monitoring property infrastructure, land resources and ground cover: *http://www.farmmap4d.com.au/mapping/*

Northern Territory

DENR (2019). Rangelands Field Monitoring Manual Version 5. Department of Environment and Natural Resources, NT. ISBN 1 920772 93 6

New South Wales

SLATS: *https://www.environment.nsw.gov.au/topics/animals-and-plants/native-vegetation/reports-and-resources*

Queensland

SLATS: *https://www.qld.gov.au/environment/land/management/mapping/statewide-monitoring/slats*

FORAGE: *https://www.longpaddock.qld.gov.au/forage/about/*

Vegmachine: *https://vegmachine.net/*

AussieGRASS: national simulation framework for Australian grasslands and rangelands based on GRASP soil water and pasture growth model: *https://www.longpaddock.qld.gov.au/aussiegrass/*

BioCondition: MLA (2012)

Western Australia

https://www.agric.wa.gov.au/rangelands/assessing-rangeland-condition

OAGWA (2017)

WARMS: Watson *et al.*, 2007a, 2007b; Novelly *et al.*, 2008

Rangelands NRM: *https://rangelandswa.com.au*

TERN AusPlots

Rangelands: *https://www.tern.org.au/AusPlots-Rangelands-pg28320.html*

World Atlas of Desertification (3rd edition)

https://wad.jrc.ec.europa.eu/

15.7 References

Andrew, M.H., and Lange, R.T. (1986). Development of a new piosphere in arid chenopod shrubland grazed by sheep. 2: Changes to the vegetation. *Australian Journal of Ecology*, 11, 411–424.

ABARES (2017). *Landuse by NRM region*. Australian Bureau of Agricultural and Resource Economics and Sciences website: *http://www.Agriculture.gov.au/abares/aclump/land-use/catchment-scale-land-use-reports*

ABS (2016). *Quickstats—data by geography.* Australian Bureau of Statistics website: *http://www.abs.gov.au/websitedbs/D3310114.nsf/Home/Census?OpenDocument&ref=topBar*

ARS (2019). *Australian Rangelands Society* website, landing page. *https://www.austrangesoc.com.au/*

Ash, A.J., Corfield, J.P., McIvor, J.G., and Ksiksi, T.S. (2011). Grazing management in tropical savannas: Utilisation and rest strategies to manipulate rangeland condition. *Rangeland Ecological Management*, 64, 223–239. doi:*10.2111/REM-D-09-00111.1*

Asner, G.P. (1998). Biophysical and biochemical sources of variability in canopy reflectance. *Remote Sensing of Environment*, 64, 234–253.

Asner, G.P. (2004). Biophysical Remote Sensing Signatures of Arid and Semiarid Ecosystems. Ch. 2 in *Manual of Remote Sensing, Volume 4, Remote Sensing for Natural Resource Management and Environmental Monitoring*. (Ed: Ustin, S.L.) Wiley International, New York. 768 p.

Austrade (2019). *Pastoral leases* webpage, Austrade website: *https://www.austrade.gov.au/land-tenure/Land-tenure/pastoral-leases*

Barnetson, J., Phinn, S., and Scarth, P. (2019). Mapping woody vegetation cover across Australia's arid rangelands: utilising a machine-learning classification and low-cost Remotely Piloted Aircraft System. *International Journal of Applied Earth Observation and Geoinformation*, 83, 101909. *https://doi.org/10.1016/j.jag.2019.101909*

Bastin, G., and Allan, G. (2012). After the smoke has cleared: 2011 fire in central Australia. *Range Management Newsletter*, 12/2, 3–6. Australian Rangeland Society, Australia.

Bastin, G.N., and Ludwig, J.A. (2006). Problems and prospects for mapping vegetation condition in Australia's arid rangelands. *Ecological Management and Restoration*, 7, S71–S74.

Bastin, G.N., Pickup, G., Chewings, V.H., and Pearce, G. (1993). Land degradation assessment in central Australia using a grazing gradient method. *The Rangeland Journal*, 15, 190–216. doi:*10.1071/RJ9930190*

Bastin, G.N., Pickup, G., and Stanes, A. (1996). Estimating Landscape Resilience from Satellite Data and its Application to Pastoral Land Management. *The Rangeland Journal*, 18(1), 118–135.

Bastin, G.N., Tynan, R.W., and Chewings, V.H. (1998). Implementing satellite-based grazing gradient methods for rangeland assessment in South Australia. *The Rangeland Journal*, 20, 61–76.

Bastin, G.N., Abbott, B.N., Chewings, V.H., and Wallace, J. (2007). *Metrics of landscape health for sustainable grazing in the Burdekin Dry Tropics, Queensland*. Project report for the Sustainable Grazing Program Great Barrier Reef catchments node Water for a Healthy Country Flagship, CSIRO. doi:*https://doi.org/10.4225/08/59a70b5a5345c*

Bastin, G., and the ACRIS Management Committee (2008). *Rangelands 2008—Taking the Pulse*. National Land and Water Resources Audit, Canberra. *http://www.environment.gov.au/land/publications/acris-rangelands-2008-taking-pulse*

Bastin, G.N., Stafford Smith, D.M., Watson, I.W., and Fisher, A. (2009). The Australian Collaborative Rangelands Information System: preparing for a climate of change. *The Rangeland Journal*, 31, 111–125. doi:*10.1071/RJ08072*

Bastin, G., Scarth, P., Chewings, V., Sparrow, A., Denham, R., Schmidt, M., O'Reagain, P., Shepherd, R., and Abbott, B. (2012). Separating grazing and rainfall effects at regional scale using remote sensing imagery: a dynamic reference-cover method. *Remote Sensing of Environment*, 121, 443–457. doi:*10.1016/j.rse.2012.02.021*

Bastin, G., Denham, R., Scarth, P., Sparrow, A., and Chewings, V. (2014). Remotely-sensed analysis of ground-cover change in Queensland's rangelands, 1988–2005. *The Rangelands Journal*, 36, 191–204. *http://dx.doi.org/10.1071/RJ13127*

Beutel, T., Karfs, R., Wallace, J., Trevithick, R., Scarth, P., and Tindall, D. (2015). VegMachine® in Queensland. In *Innovation in the Rangelands. Proceedings of the 18th Australian Rangeland Society Biennial Conference*. Alice Springs, NT. (Ed: Friedel, M.H.) Australian Rangeland Society, Parkside, SA.

Beutel, T.S., Trevithick, R., Scarth, P., and Tindall, D. (2019). VegMachine.net. online land cover analysis for Australian rangelands. *The Rangeland Journal*, 41, 355–362. *https://doi.org/10.1071/RJ19013*

Biograze (2000) *Biograze: waterpoints and wildlife*. CSIRO, Alice Springs NT.

Brinsmead, N. (2017). Let's get technical. Introducing you to VegMachine®. *Envoy*, 2017, 17.

Briske, D.D., Fuhlendorf, S.D., and Smeins, F.E. (2003). Vegetation dynamics on rangelands: A critique of the current paradigms. *Journal of Applied Ecology*, 40, 601–614.

Burrows, W.H., Carter, J.O., Scanlan, J.C., and Anderson, E.R. (1990). Management of savannas for livestock production in north-east Australia: contrasts across the tree-grass continuum. *Journal of Biogeography*, 17(4/5), 503–512. doi:*10.2307/2845383*

Butler, D., Thackway, R., and Cosier, P. (2020). *Technical Protocol for Constructing Native Vegetation Condition Accounts Version 1.0 - May 2020*. Accounting for Nature Limited, Sydney, Australia. *https://static1.squarespace.com/static/5dc38cde1d028031235ca3cf/t/5fa246b73c71c92e01513cc7/1604470479988/AfN+Native+Vegetation+Technical+Protocol+ACCREDITED.pdf*

Croft, D.B., Montague-Drake, R., and Dowle, M. (2007). Biodiversity and water point closure: is the grazing piosphere a persistent effect? In *Animals of Arid Australia: out on their own?* (Eds: Dickman, C., Lunney, D., and Burgin, S.) Royal Zoological Society of NSW, Mosman. pp143–171.

DENR (2019). *NT Pastoral Land Board Annual Reports*: *https://depws.nt.gov.au/boards-and-committees/pastoral-land-board*

DEWHA (2009). *Assessment of Australia's Terrestrial Biodiversity 2008*. Biodiversity Assessment Working Group of the National Land and Water Resources Audit for the Australian Government, Canberra.

DEWHA (2010). *Ecosystem Services: Key Concepts and Applications*. Occasional Paper No 1, Department of the Environment, Water, Heritage and the Arts, Canberra.

DPIF (2006). *The ABCD pasture condition guide: Mulga and Mitchell Grass*. Department of Primary Industries and Fisheries, Charleville. ISSN 0727-6273

DSEWPC (2013). *The Australian Collaborative Rangelands Information System (ACRIS): Reporting Change in the Rangelands*. Department of Sustainability, Environment, Water, Population and Communities, Canberra. *https://www.environment.gov.au/system/files/resources/46e443c5-673a-4093-948d-d87830cfc2f9/files/acris-reporting-change.pdf*

Eldridge, D.J., Delgado-Baquerizo, M., Quero, J.L., Ochoa, V., Gozalo, B., Escolar, C., García-Gómez, M., Prina, A., Bowker, M.A., Bran, D.E., Castro, I., Cea, A., Derak, M., Espinosa, C.I., Florentino, A., Gaitán, J.J., Gatica, G., Gómez-González, S., Ghiloufi, W., Gutierrez, J.R., Gusmán-Montalván, E., Hernández, R.M., Hughes, F.M., Muiño, W., Monerris, J., Ospina, A., Ramírez, D.A., Ribas-Fernández, Y.A., Romão, R.L., Torres-Díaz, C., Koen, T.B., and Maestre, F.T. (2020). Surface indicators are correlated with soil multifunctionality in global drylands. *Journal of Applied Ecology*, 57(2), 424–435.

Eyre, T.J., Fisher, A., Hunt, L.P., and Kutt, A.S. (2011a). Measure it to better manage it: a biodiversity monitoring framework for the Australian rangelands. *The Rangeland Journal*, 33, 239–253.

Eyre, T.J., Kelly, A.L., Neldner, V.J., Wilson, B.A., Ferguson, D.J., Laidlaw, M., and Franks, A.J. (2011b). *BioCondition: A Condition Assessment Framework for Terrestrial Biodiversity in Queensland. Assessment Methodology Manual*. Department of Environment and Resource Management, Brisbane.

Folke, C., Carpenter, S., Walker, B., Scheffer, M., Elmqvist, T., Gunderson, L., and Holling, C.S. (2004). Regime shifts, resilience, and biodiversity in ecosystem management. *Annual Review of Ecology Evolution and Systematics*, 35, 557–81 doi:*10.1146/annurev.ecolsys.35.021103.105711*

Foran, B., Stafford Smith, M., Burnside, D., Andrew, M., Blesing, D., Forrest, K., and Taylor, J. (2019). Australian rangelands futures: time now for systemic responses to interconnected challenges. *The Rangeland Journal*, 41, 271–292. *https://doi.org/10.1071/RJ18105*

Fuhlendorf, S.D., Archer, S.A., Smeins, F., Engle, D.M., and Taylor, C.A. (2008). The Combined Influence of Grazing, Fire, and Herbaceous Productivity on Tree-Grass Interactions. In *Western North American Juniperus Communities: A Dynamic Vegetation Type*. 196. (Ed: Van Auken, O.W.) Springer, New York, NY. Pp. 219–238.

FutureBeef (2020). *Grazing land management* webpage, FutureBeef website: *https://futurebeef.com.au/knowledge-centre/grazing-land-management/*

Guerin, G.R., Sparrow, B., Tokmakoff, A., Smyth, A., Leitch, E., Baruch, Z., and Lowe, A.J. (2017). Opportunities for Integrated Ecological Analysis across Inland Australia with Standardised Data from Ausplots Rangelands. *PloS ONE*, 12(1), e0170137. *https://doi.org/10.1371/journal.pone.0170137*

Guerschman, J.P., Hill, M.J., Renzullo, L.J., Barrett, D.J., Marks, A.S., and Botha, E.J. (2009). Estimating fractional cover of photosynthetic vegetation, non photosynthetic vegetation and bare soil in the Australian tropical savannah region upscaling Hyperion and MODIS sensors. *Remote Sensing of Environment*, 113, 928–945.

Hendy, E.J., Gagan, M.K., and Lough, J.M. (2003). Chronological control of coral records using luminescent lines and evidence for non-stationary ENSO teleconnections in northeast Australia. *Holocene*, 13, 187–199.

Hill, M.J. (2004). Grazing agriculture–Managed Pasture, Grassland and Rangeland. Ch. 9 in *Manual of Remote Sensing, Volume 4, Remote Sensing for Natural Resource Management and Environmental Monitoring*. (Ed: Ustin, S.L.) Wiley International, New York. 768 p.

Holling, C.S. (1973). Resilience and stability of ecological systems. *Annual Review of Ecology and Systematics*, 4, 1–23.

Howes, A.L., and McAlpine, C.A. (2008). *The impact of artificial watering points on rangeland biodiversity: A review*. DKCRC Working Paper 15, The WaterSmart™ Literature Reviews. Desert Knowledge CRC, Alice Springs.

IUCN (2019). *Global Drylands Initiative* webpage. International Union for Conservation of Nature website: *https://www.iucn.org/theme/ecosystem-management/our-work/global-drylands-initiative*

James, C.D., Landsberg, J., and Morton, S.R. (1999). Provision of watering points in the Australian arid zone: a review of effects on biota. *Journal of Arid Environments*, 41(1), 87–121. *https://doi.org/10.1006/jare.1998.0467*

Jurskis, V. (2015). *Firestick Ecology*. Connor Court Publishing, Ballarat.

Karfs, R. (2002). *Rangeland monitoring in tropical savanna grasslands Northern Territory, Australia: relationships between temporal satellite data and ground data*. Masters Thesis, Research School of Tropical Environment Studies and Geography, James Cook University, Townsville, Queensland.

Karfs, R.A., Daly, C., Beutel, T.S., Peel, L., and Wallace J.F. (2004). VegMachine—Delivering monitoring information to northern Australia's pastoral industry. *Proceedings of 12th Australasian Remote Sensing and Photogrammetry Conference, Fremantle Western Australia*. RSPAA, Perth.

Ker Conway, J. (1989). *The Road from Coorain*. Mandarin, London.

Landsberg, J., James, C.D., Morton, S.R., Hobbs, T.J., Stol, J., Drew, A., and Tongway, H. (1997). *The Effects of Artificial Sources of Water on Rangeland Biodiversity*. Environment Australia and CSIRO, Canberra.

Lange, R.T. (1969). The piosphere, sheep track and dung patterns. *Journal of Range Management*, 22, 396–400. *http://hdl.handle.net/10150/649971*

Ludwig, J.A., Bastin, G.N., Chewings, V.H., Eager, R.W., and Liedloff, A.C. (2007). Leakiness: a new index for monitoring the health of arid and semiarid landscapes using remotely sensed vegetation cover and elevation data. *Ecological Indicators*, 7, 442–454. doi:*10.1016/j.ecolind.2006.05.001*

Lunt, I., Eldridge, D.J., Morgan, J.W., and Witt, G.B. (2007). Turner Review No. 13: A framework to predict the effects of livestock grazing and grazing exclusion on conservation values in natural ecosystems in Australia. *Australian Journal of Botany*, 55, 401–415. doi:*10.1071/BT06178*

McAlpine, C., Thackway, R., and Smith, A. (2014). *Towards an Australian Rangeland Biodiversity Monitoring Framework*. A discussion paper developed from a biodiversity monitoring workshop convened by Australian Collaborative Rangeland Information System (ACRIS) held at the University of Queensland, Brisbane, 30–31 October 2013. University of Queensland, Brisbane. *https://espace.library.uq.edu.au/view/UQ:342912/Acris_Report.pdf*

McKeon, G.M., Hall, W.B., Henry, B.K., Stone, G.S., and Watson, I.W. (2004). *Pasture Degradation and Recovery in Australia's Rangelands: Learning From History*. Queensland Department of Natural Resources, Mines and Energy, Brisbane.

MLA (2011). *Biodiversity Condition Assessment for Grazing Lands*. Meat and Livestock Australia Ltd, North Sydney. ISBN 9781741916393

MLA (2012). *Biodiversity Condition Toolkit for Grazed Lands*. Meat and Livestock Australia Ltd. ISBN 9781741919240

Murphy, B.P., Lehmann, C.E.R., Russell-Smith, J., and Lawes, M.J. (2014). Fire regimes and woody biomass dynamics in Australian savannas. *Journal of Biogeography*, 41(1). doi:*10.1111/jbi.12204*

Novelly, P.E., Watson, I.W., Thomas, P.W.E., and Duckett, N.J. (2008). The Western Australian Rangeland Monitoring System (WARMS)—operating a regional scale monitoring system. *The Rangeland Journal*, 30, 271–281. doi:*10.1071/RJ07047*

NSW DPI (2019). *Rangelands* webpage. NSW Department of Primary Industries website: *https://www.dpi.nsw.gov.au/agriculture/pastures-and-rangelands/rangelands*

OAGWA (2017). *Management of Pastoral Lands in Western Australia*. Report 17: October 2017. Office fo the Auditor General Western Australia, Perth. *https://www.parliament.wa.gov.au/publications/tabledpapers.nsf/displaypaper/4010833a47ac7e4cc25e5b46482581b600166282/$file/833.pdf*

Peel, L.J., Beutel, T.S., Bull, A.L., Karfs, R.A., and Wallace, J. (2006). *NBP.315 VegMachine—Extending Integrated Rangeland Monitoring Information to Industry*. Meat and Livestock Australia, North Sydney, NSW.

Pickup, G., and Chewings, V.H. (1994). A grazing gradient approach to land degradation assessment in arid areas from remotely-sensed data. *International Journal of Remote Sensing*, 15, 597–617.

Pickup, G., Bastin, G.N., and Chewings, V.H. (1994). Remote-sensing-based Condition Assessment for Nonequilibrium Rangelands under Large-Scale Commercial Grazing. *Ecological Applications*, 4(3), 497–517. *https://doi.org/10.2307/1941952*

Pickup, G, Bastin, G.N., and Chewings, V.H. (1998). Identifying trends in land degradation in non-equilibrium rangelands. *Journal of Applied Ecology*, 35, 365–377. *https://doi.org/10.1046/j.1365-2664.1998.00319.x*

Pollock, D. (2019). *The Wooleen Way*. Scribe, Melbourne. ISBN: 9781925849257

QRIScloud (2018). *QRIScloud delivers satellite data to Australian farmers, government and the public*. *https://www.qriscloud.org.au/about-qriscloud/case-studies/item/82-qriscloud-delivers-satellite-data-to-australian-farmers-govt-and-the-public*

Russell-Smith, J., and Sangha, K.K. (2018). Emerging opportunities for developing a diversified land sector economy in Australia's northern savannas. *The Rangeland Journal*, 40, 315–330. *doi.org/10.1071/RJ18005*

Scarth, P., Röder, A., and Schmidt, M. (2012). Tracking Grazing Pressure and Climate Interaction—The Role of Landsat Fractional Cover in Time Series Analysis. *Proceedings of the 15th Australasian Remote Sensing and Photogrammetry Conference (ARSPC)*, 13–17 September, Alice Springs, Australia. *https://doi.org/10.6084/m9.figshare.94250.v1*

Sparrow, B. (2017). Monitoring in the Australian Rangelands: Where we've come from and where we should be headed. *Proceedings of the 19th Australian Rangeland Society Biennial Conference*. Australian Rangeland Society, Parkside, SA.

Stafford Smith, M., and McAllister, R.R.J. (2008). Managing arid zone natural resources in Australia for spatial and temporal variability—an approach from first principles. *The Rangeland Journal*, 30, 15–27.

Tongway, D.J., and Hindley, N.L. (2004). *Landscape Function Analysis Manual: Procedures for Monitoring and Assesssing Landscapes with Special Reference to Minesites and Rangelands, Version 3.1*. CD-ROM. CSIRO Sustainable Ecosystems, Canberra.

URS Australia P/L (2013). *Sustainable Land Use and Economic Development Opportunities in the Western Australian Rangelands*. Unpublished report prepared for the Department of Agriculture and Food, South Perth, WA. *https://d3n8a8pro7vhmx.cloudfront.Net/modernoutback/pages/515/attachments/original/1472028646/Rangeland_Opportunities_Final_Report_URS_2013.pdf?1472028646*

Wallace, J.F., and Thomas, P.W.E. (1998). *Rangeland monitoring in northern Western Australia using sequences of Landsat imagery*. Report to National Landcare Program Project No. 953024. Agriculture Western Australia, unpublished.

Wallace, J.F., Holm, A. Mc.R., Novelly, P.E., and Campbell N.A. (1994). Assessment and monitoring of rangeland vegetation composition using multi-temporal Landsat data. In *Proceedings 7th Australian Remote Sensing Conference*, Melbourne. pp. 1102–1109.

Wallace, J., Behn, G., and Furby, S. (2006). Vegetation condition assessment and monitoring from sequences of satellite imagery. *Ecological Management and Restoration*, 7, S31–S36. *https://doi.org/10.1111/j.1442-8903.2006.00289.x*

Washington-Allen, R.A., Van Niel, T.G., Ramsey, R.D., and West, N.E. (2004). Remote Sensing-Based Piosphere Analysis. *GIScience and Remote Sensing*, 41(2), 136–154, doi:*10.2747/1548-1603.41.2.136*

Waters, C., and Hacker, R. (2008). *Integration of biodiversity and primary production in northern and western New South Wales*. NSW Department of Primary Industries.

Watson, I.W., Thomas, P.W.E., and Fletcher, W.J. (2007a). The first assessment, using a rangeland monitoring system, of change in shrub and tree populations across the arid shrublands of Western Australia. *The Rangeland Journal*, 29, 25–37. doi:*10.1071/RJ07018*

Watson, I.W., Novelly, P., and Thomas, P.W.E. (2007b). Monitoring changes in pastoral rangelands—the Western Australian Rangeland Monitoring System (WARMS). *The Rangeland Journal*, 29, 191–205. doi:*10.1071/RJ07008*

WEF (2018). *The global risks report 2018*. World Economic Forum, Geneva. Switzerland. *https://www.weforum.org/reports/the-global-risks-report-2018*

White, A., Sparrow, B., Leitch, E., Foulkes, J., Flitton, R., Lowe, A.J., and Caddy-Retalic, S. (2012). *AusPlots Rangelands Survey Protocol Manual*. The University of Adelaide Press, Adelaide. ISBN 978-1-922064-38-7

Xu, S., Zhao, Q., Ding, S., Qin, M., Ning, L., and Ji, X. (2018). Improving Soil and Water Conservation of Riparian Vegetation Based on Landscape Leakiness and Optimal Vegetation Pattern. *Sustainability*, 10, 1571.

Xu, S., Zhao, Q., Liu, Y., Ding, S., and Qin, M. (2019). Sensitivity and Applicability of Landscape Leakiness Index in Determining Soil and Water Conservation Function of a Subtropical Riparian Vegetation Buffer Zone. *Environmental Engineering Science*, 36(2), 227–236.

Zhang, B., and Carter, J. (2018). FORAGE—An online system for generating and delivering property-scale decision support information for grazing land and environmental management. *Computers in Electronics in Agriculture*, 150, 302–311. *https://doi.org/10.1016/j.compag.2018.05.010*

Zhou, Z.-S., Caccetta, P., Sims, N.C., and Held, A. (2016). Multi-band SAR Data for Rangeland Pasture Monitoring. *Proceedings of IEEE IGARSS 2016*, pp. 170–173, July 2016. doi:*10.1109/IGARSS.2016.7729035*

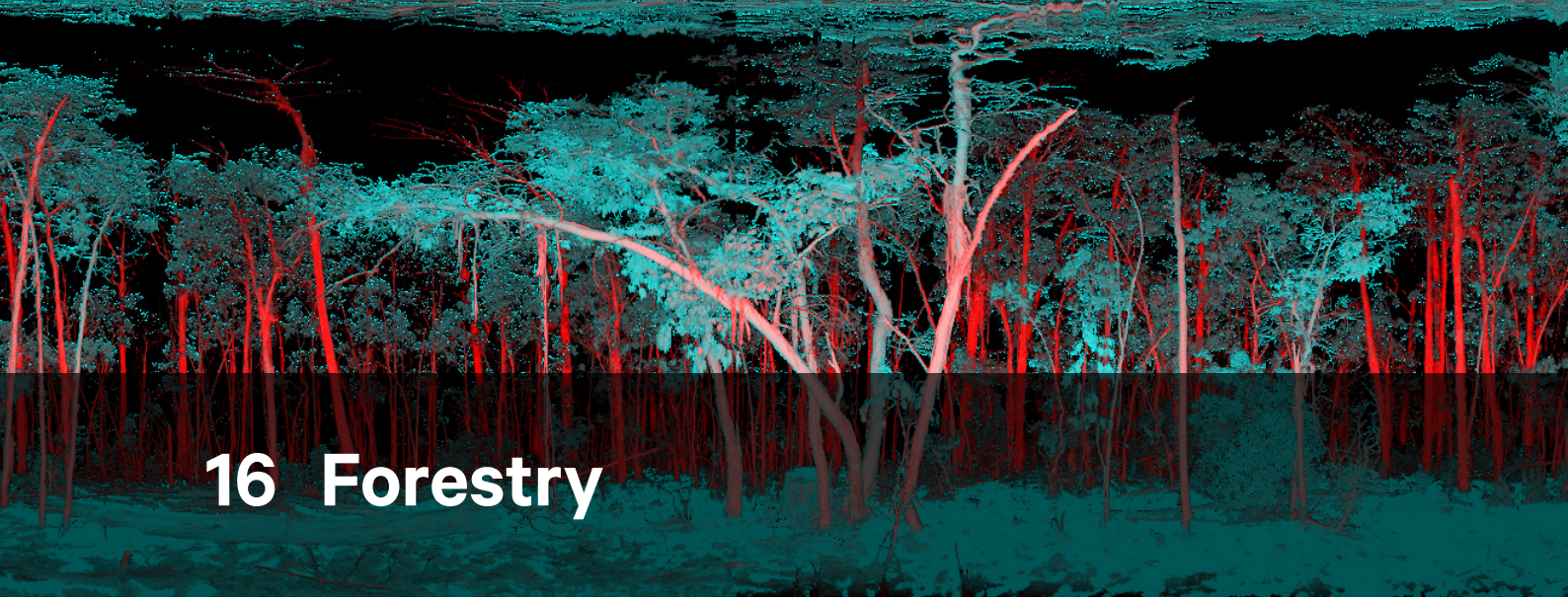

16 Forestry

Nicholas Coops and Barbara Harrison

The need for accurate, timely, and cost-effective forest information has never been more critical (White *et al.*, 2016). Australia's commitment to sustainable forest management and conservation of biodiversity, as well as a renewed focus on biomass and bioenergy, and increasing awareness of climate change scenarios, all require detailed knowledge of the existing forest resource, and a greater understanding of the dynamic processes of forest growth and stand condition.

Forestry has long-established practices for using airborne EO datasets for timber volume estimation and sampling stratification. However, like other forestry communities around the world, the use of EO in Australia has increased in recent decades in response to the need for accurate, and spatially explicit, information on land cover change, forest health assessment, fire severity and burn scar mapping, and carbon sequestration, as well as estimation of areas planted and harvested.

Traditionally, EO imagery acquired by most state-based forest organisations in Australia comprised medium scale, aerial photography (1:10,000–1:25,000), which was manually interpreted to stratify large heterogeneous forests into smaller, more uniform areas deemed suitable for ground sampling (Smith and Woodgate, 1985). The resulting maps enabled relevant metrics of timber volume and/or environmental health to be determined, recorded, and monitored. The advent of readily available, high spatial resolution, digital EO imagery has seen a shift in forestry EO data usage, enabling more automated processing to derive relevant forest attributes.

The wide range of information needs and users, however, resulted in many different EO data sources and approaches being used for different purposes, with no single EO platform or processing stream being suitable to meet all user requirements (Packalen and Maltamo, 2008). In addition, the complexity of the Australian forest environment makes the development of generalised EO procedures to cover such diversity a difficult task. Australian forest canopies are typically more open than their northern hemisphere counterparts, which means many EO-based methods that were derived overseas may not be appropriate. Extensive shadowing, which is common in most images, is caused by complex topography in most forested landscapes (for example, see banner image for Section 1). This undulating foundation is overlaid with a variety of natural and human disturbance regimes leading to an array of structural and floristic patterns (see Section 2.3.1). The high degree of speciation and intra-species variation in the genus *Eucalyptus* further complicates the situation, as does the canopy geometry of that genus, which features generally vertical leaves and a wide variety of leaf forms, with juvenile to old and insect-damaged leaves sometimes being present on a single tree (Lees and Ritman, 1991). As a result, hybrid methods, which use a combination of technologies, are likely to continue, such as airborne lidar for Digital Elevation Model (DEM) development and volume assessment, coupled with more conventional optical imagery for species and health assessment. In the drier and less productive areas, which are essentially unmanaged, combinations of freely available, satellite-based optical and radar datasets offer viable alternatives.

Background image: Terrestrial scan of an open eucalypt forest at Tumbarumba, Australia, acquired using Dual-Wavelength Echidna Lidar (DWEL; Douglas *et al.*, 2015). The image uses a blue–red colour table applied to the normalised difference index (NDI), which is computed from the wavelengths, in nm, as (1064–1548)/(1064+1548). The distinction between woody and non-woody material can clearly be seen in the level of the NDI, irrespective of range from the instrument.
Source: Glenn Newnham, CSIRO (from Newnham *et al.*, 2015, Figure 1)

Recommended Chapter Citation: Coops, N.C., and Harrison, B.A. (2021). Forestry. Ch 16 in *Earth Observation: Data, Processing and Applications. Volume 3A—Terrestrial Vegetation*. CRCSI, Melbourne. pp. 323–350.

Vast expanses of Eucalyptus forests present in springtime an unforgettable picture, the straight, clean trunks rising in a blend of tints that range from delicate cream to ochre, from pearl pink to deepest red, a single giant trunk sometimes displaying all of these colours at once.
(Elizabeth Kenny, from 'And They shall Walk')

EO methods that are relevant to assessment of forest vegetation are introduced in earlier sections of this volume. In this section, we discuss the role EO technology can play in improving our understanding of forests across Australia. To do so we focus on assessment of those components commonly considered when describing forest vegetation and managing the forest resource, namely:

- forest type—zonation of plant communities and species (see Section 16.3);
- forest hydrology—catchment and drainage characteristics (see Section 16.4);
- forest structure—plant height and stratification (see Section 16.5);
- forest functionality—forest health and biosecurity (see Section 16.6);
- forest diversity—ecosystem richness (see Section 16.7); and
- forest disturbance—landscape scale changes (see Section 16.8).

Characteristics of Australian forests are introduced in Sections 2.3.1 and 2.4 and detailed in Section 16.1. EO sensors that are relevant to forest mapping and monitoring are summarised in Section 16.2.

Silviculture is the art and science of controlling the establishment, growth, composition and quality, health, protection and utilisation of stands of trees or forests to meet the diverse needs and values of forest owners and society on a sustainable basis. Silvicultural practice embodies a range of treatments to maintain and enhance the utility of the forest for any defined management purpose.
(IFA Forestry Policy Statement 2.9; IFA, 2008)

16.1 Forestry in Australia

In Australia, a forest is defined as:

> *An area, incorporating all living and non-living components, that is dominated by trees having usually a single stem and a mature or potentially mature stand height exceeding 2 m and with existing or potential crown cover of overstorey strata about equal to or greater than 20%. This includes Australia's diverse native forests and plantations, regardless of age. It is also sufficiently broad to encompass areas of trees that are sometimes described as woodlands.*[11]

Using this definition, Australia contains around 3% of global forests by area (SOFR, 2018). These forests vary significantly in structure and floristic diversity, from dense rainforests, to sparse, multi-stemmed mallee associations, to exotic plantations (see Section 2.3.1).

The area of forest in Australia is monitored by the National Forest Inventory (NFI), which incorporates systematic and validated analyses of multi-temporal Landsat imagery (including data from the National Greenhouse Gas Inventory, formerly known as the National Carbon Accounting System—NCAS) in conjunction with state and territory records and ground surveys. Forests cover 17% of the Australian land mass (134 Mha; SOFR, 2018), the vast majority of which (132 Mha) comprises native hardwood forests, dominated by species from *Eucalyptus* and/or *Acacia*, with relatively small areas of forest being dominated by *Callitris*, *Melaleuca*, and *Casuarina* (see Table 16.1).

11 Forests Australia: *https://www.agriculture.gov.au/abares/forestsaustralia/australias-forests*

Table 16.1 Forest area in Australia

Category	Description	Area ('000 ha)	% Area
Native	*Acacia*	10,813	8.07
	Callitris	2,011	1.50
	Casuarina	1,236	0.92
	Eucalyptus (including species from *Corymbia* and *Angophora)*	101,058	75.40
	Mangrove	854	0.64
	Melaleuca	6,382	4.76
	Rainforest	3,581	2.67
	Other native forest	5,679	4.24
	Total	131,615	98.2
Commercial plantations	Softwood species	1,015	0.77
	Hardwood species	922	0.67
	Unknown or mixed species	11	0.0
	Total	1,949	1.45
Other forests	Non-industrial plantations and various planted forests	474	0.35
Total	All forests	134,037	100

Source: SOFR (2018) Table 1.5

These native forests are largely distributed throughout Tasmania and near the northern, eastern and southern coastal and hinterland regions of continental Australia (see Figure 16.1a). Six tenure categories of native forest are recognised by the NFI (with the proportion by area shown in parentheses below):

- Leasehold forest (35.9%)—Crown land held under leasehold title and generally regarded as privately managed, including land with special conditions for designated Indigenous communities (see Section 2 for definitions of land tenure categories in Australia).
- Private forest (31.2%)—land held under freehold title and private ownership.
- Nature conservation reserve (16.5%)—publicly owned land formally reserved for conservation and recreational purposes including national parks, nature reserves, and state and territory recreation and conservation areas.
- Other Crown land (8.4%)—reserved for purposes including utilities, mining, water catchments, and use by indigenous communities.
- Multiple-use public forest (7.4%)—publicly owned forest on which government agencies manage a range of forest values including wood harvesting, water supply, biodiversity conservation, recreation, and environmental protection.
- Unresolved tenure (0.6%)—areas of unknown tenure (SOFR, 2018).

In Australia, most native forest grows on privately-owned or leasehold land (see Figure 16.1b), which is managed for forestry and/or grazing purposes (see Section 15). In total, around one third of the native forest area (46 Mha) is protected for biodiversity conservation (SOFR, 2018). Many Australian forests also serve an important function as water catchment areas for major cities and towns. Importantly, an estimated 22 million tonnes of carbon were sequestered in Australian forests in 2016 (SOFR, 2018).

Two thirds of the vegetation in the native forest area is commonly described as woodland, with crown cover of 20–50%, while around one quarter is designated open forest (50–80% crown cover), and only 3% as closed forest (see Table 16.2). Native forests are commonly sub-divided by both height and crown cover into nine structural classes as illustrated in Figure 16.2. Around two thirds of native forest are classified as medium height (10–30 m), about 30% as low (2–10 m) and the remainder as tall (> 30 m; SOFR, 2018). Distribution of these structural classes is closely related to moisture availability, past and present land uses, altitude and underlying geology (see Section 2).

Table 16.2 Native forest classes

Type	Crown Cover (%)	Area ('000 ha)	% Area
Woodland	20–50	91,455	69
Open forest	50–80	33,962	26
Closed forest	80–100	3,622	3
Unknown	–	2,576	2
Total	–	131,615	100

Source: SOFR (2018)

The Australian bush owes its peculiarity, more than anything else, to Eucalyptus. No other continental forest or woodland is so dominated by a single genus. Other biomes on Earth have scleromorphs, most have grasses, and few are spared wholly from fire, but none has the combination that exists in Australia and has given the bush its indelible character.
(Pyne, 1992)

Figure 16.1 Australian forests

a. Forest type

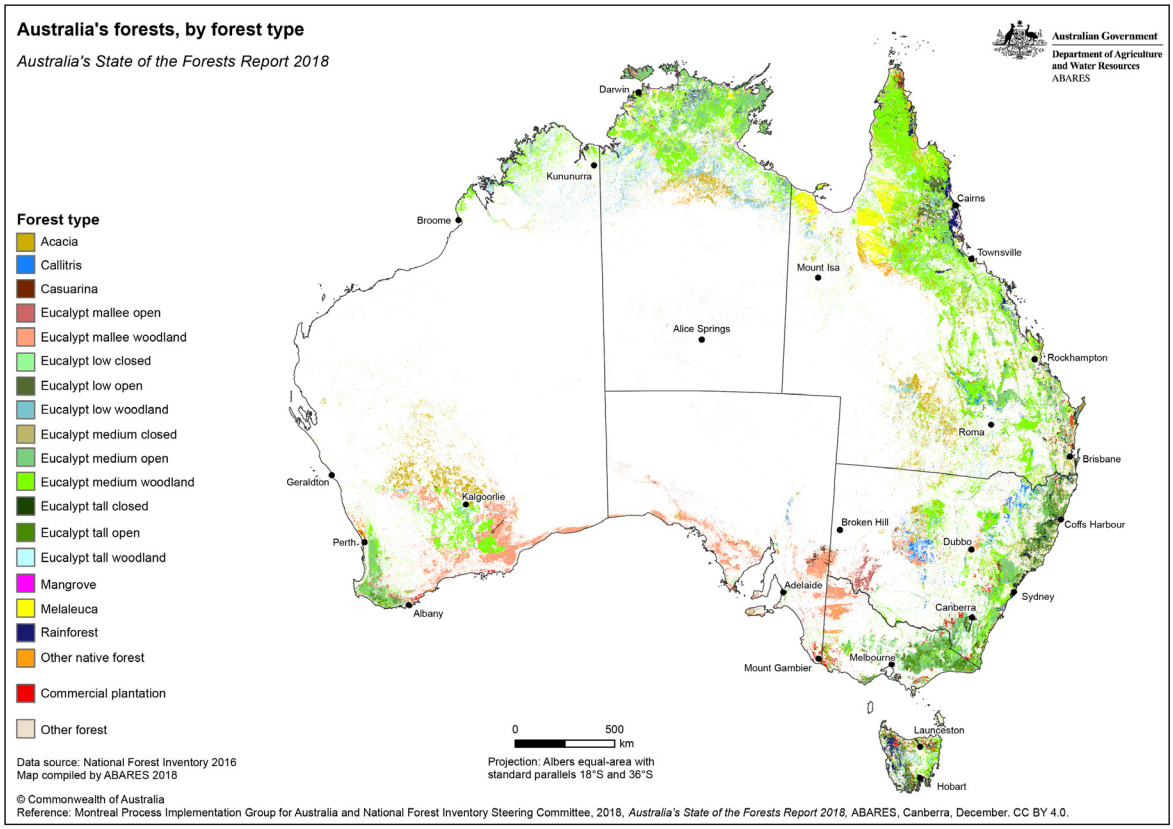

b. Tenure

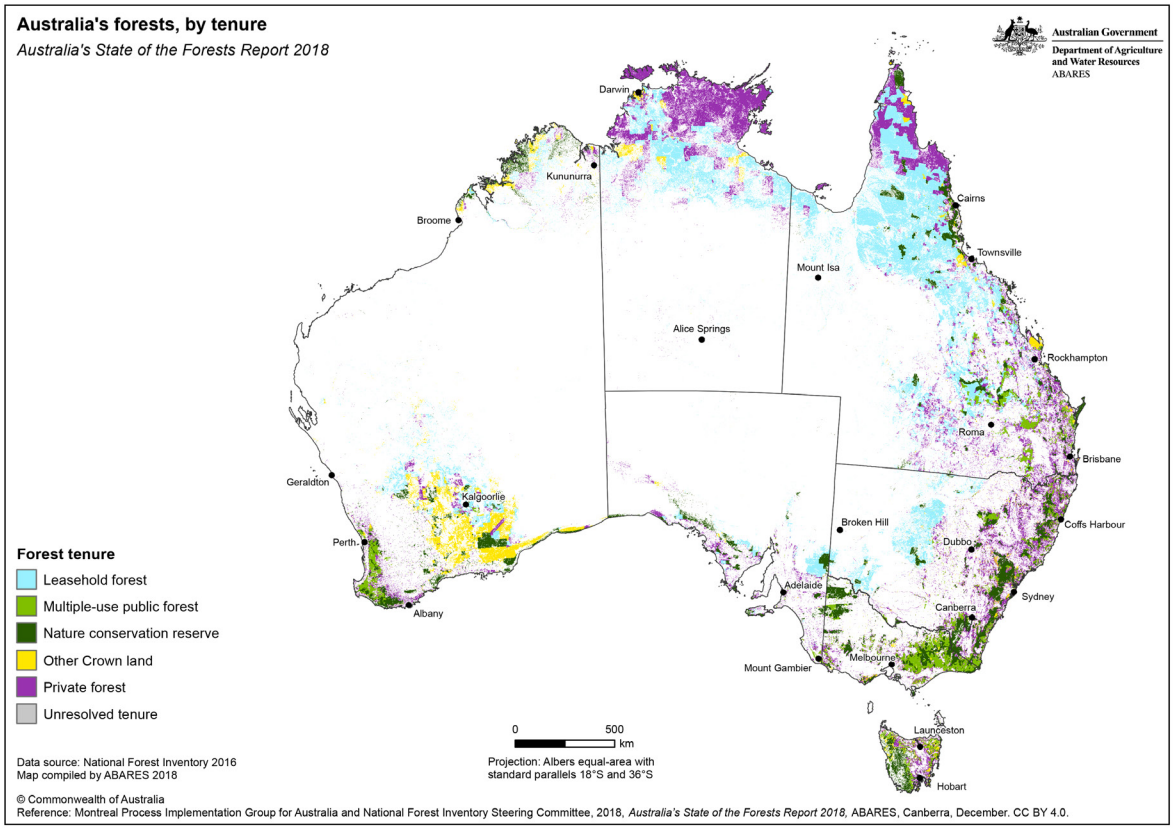

Source: SOFR (2018) Figures 1.1 and 1.4

Figure 16.2 Native forest categories

Native forests are sub-divided by height and crown cover into nine general categories. The percentages below each diagram represent the proportion of each height/crown cover type within Australia's total area of native forests.

Source: SOFR (2018) Figure 1.2

16.2 EO Sensors for Forestry

Since the launch of the Landsat series of satellites in 1972, numerous studies have been undertaken to map forest area, condition, and structure from satellite imagery (Skidmore *et al.*, 1987). The relevance of different EO sensors to forestry applications is summarised in Table 16.3.

Passive optical sensors (including panchromatic, multispectral, and hyperspectral) are introduced in Volume 1A—Section 14 and their data characteristics are considered in Volume 1B—Section 6. While multispectral imagery acquired by satellite sensors has produced valuable global forest maps, their accuracy and spatial resolution are both low (see Section 16.3). Various studies have also combined passive optical datasets with data derived from other EO and GIS sources for a range of forestry applications (e.g. Hayward and Stone, 2011; Stone *et al.*, 2008).

In recent years, standardised time series of passive optical imagery (see Volume 2D) have enabled a greater understanding of the temporal changes in forested lands around the globe. For example, Digital Earth Australia (DEA) has enabled ready access to the Landsat archive for monitoring the Australian landscape (see Volume 2D—Section 11.2). Hyperspectral sensors are relevant to understanding spectral covariates for various subtle variations of forest type and condition, and their datasets have been used to deduce plant species and biochemical status (see Section 16.6).

Light Detection and Ranging (lidar, also known as laser scanning; see Excursus 5.1) is an active form of EO that uses light emissions in the form of pulsed lasers to measure the distance from the sensor to a target (see Volume 1A—Section 15.1). These active optical sensors can be mounted in a variety of spaceborne and airborne platforms and also ground-based instruments (see Volume 1A—Section 10), with Airborne Laser Scanning (ALS) being most commonly used for forestry applications. Both forestry and topographic ALS applications rely on pulses of NIR wavelengths, typically at 1064 nm (Lim *et al.*, 2003). Lidar sensors can provide information relevant to describing the three-dimensional distribution of vegetation canopy components as well as the sub-canopy topography (see Section 16.5).

Table 16.3 EO sensors relevant to forestry

SAR: Synthetic Aperture Radar; DEM: Digital Elevation Model

Type	Sensor	Platform	Relevance	Advantages	Disadvantages
Passive optical	Multispectral radiometer	Satellite or airborne	Broad forest type and condition mapping	Global coverage, low cost	Relatively low spectral and spatial resolution
	Hyperspectral spectro-radiometer	Satellite or airborne	Species mapping Plant biochemical functioning and health	High spectral resolution, highlight plant stress	High data volume, specialised processing
Active optical	Lidar	Satellite, airborne and terrestrial	Forest structure Biomass DEM Fuel load	Detailed structure for trees and stands, forestry hydrology	High cost, specialised processing
Active microwave	SAR	Satellite or airborne	Biomass Forest disturbance	All weather, so useful in tropical regions	More complex processing

The application of lidar technology to forestry, both in Australia and internationally, has been rapid. In Australia, various studies have examined the application of lidar data to plantations (Bennett, 2005; Alam *et al.*, 2012), open woodlands, and tall eucalypt forests (Lovell *et al.*, 2003, Lee *et al.*, 2004, Lucas *et al.*, 2006; Jupp and Lovell, 2007; Fedrigo *et al.*, 2018; Fisher *et al.*, 2020). In North America and Europe, lidar is well recognised as a mature EO technology, routinely being applied to forest management and operations (Næsset, 2002, Reutebuch *et al.*, 2005, Wulder *et al.*, 2008, White *et al.*, 2013). For example, the Area Based Approach (ABA; Næsset 2002) has been used operationally for a decade to process lidar point cloud data into spatial metrics for forest inventory applications (Wulder *et al.*, 2008; White *et al.*, 2013). This approach enables precise prediction of a suite of basic forest inventory variables, such as stem volume, basal area, and height. Lidars carried by unmanned aerial vehicles (UAV) are gaining popularity, and advances in this field will likely result in these sensors being more readily available and applicable to tailored forest management applications (Du Toit *et al.*, 2020). In forestry applications, Terrestrial Laser systems (TLS) complement ALS by providing structural information about tree trunks that can be obscured by the vegetation canopy from an airborne sensor (see Excursus 5.1).

Radar sensors are introduced in Volume 1A—Section 15.2 and detailed in Volume 1B—Section 8. These active microwave sensors also offer the potential to map the structure and biomass of Australian forests, both from spaceborne and airborne platforms, especially in the drier eucalypt forests with lower biomass. The majority of studies investigating the use of radar data for biomass estimation have focused either on coniferous forests in the northern hemisphere, particularly in North America and Eurasia, or tropical regions. However, radar-based methods have also been developed in Australia for the UN REDD+ (Reducing Emissions from Deforestation and Forest Degradation) framework (Mitchell *et al.*, 2017; see Section 17.7.3). Since different radar frequency bands penetrate into multi-layered volumes (such as vegetation canopies) to differing depths, L-band data is often preferred for vegetative studies (see Figure 16.3).

Space-based Synthetic Aperture Radar (SAR) technology is rapidly developing, with the imminent launch of new satellites carrying radars that use longer wavelengths than ever before. For example, at the end of 2020, ESA are launching BIOMASS, a satellite with P-band (~68 cm wavelength) radar which can penetrate the canopy and interact with tree trunks and the ground surface. This will be the first of its kind, as P-band has previously been restricted to airborne platforms.

Figure 16.3 Penetration of radar wavelengths into vegetation layer

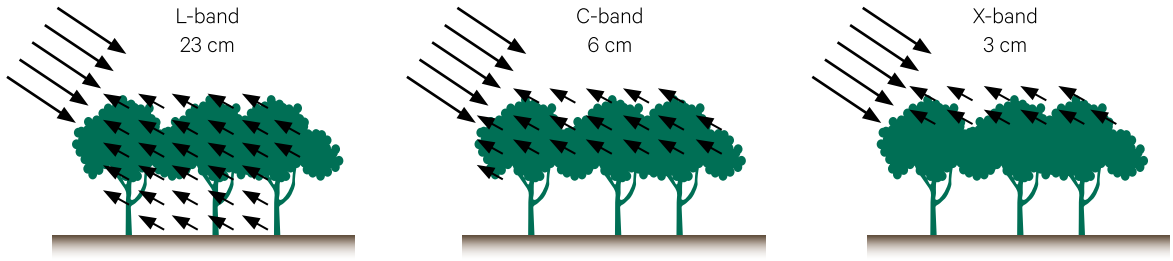

Source: Bruce Forster and Linlin Ge, Course Notes, UNSW

16.3 Forest Type

Conventionally, most processing of digital satellite imagery for mapping forest type has used various image classification procedures (see Volume 2E for details on classification algorithms). Classification accuracy is usually determined using a confusion matrix, which compares the allocation of a number of randomly selected pixels in the image with a known cover class (derived from independent sources such as maps, photographs, or ground data). The overall classification accuracy is then computed as the ratio of the total number of correctly classified pixels to the total number of pixels in each class (see Volume 2E).

Early forest type classifications from multispectral imagery relied on Landsat MSS data and, while spatially comprehensive and revolutionary at the time, generally resulted in low classification accuracy, with only broad forest types (such as coniferous versus broadleaf) being differentiated reliably (for example, see Section 3.3.2). Landsat MSS was also used to estimate rates of forest clearing in Victoria (Woodgate and Black, 1988). The improved spectral, spatial, and radiometric resolutions of Landsat TM/ETM+/OLI, as well as greater temporal resolution in more recent EO satellites such as Sentinel-2, have proved to be superior for classifying forest information. For example:

- SPOT XS and Landsat TM imagery, in conjunction with ancillary datasets, allowed discrimination of species and age classes in native and exotic vegetation (Skidmore and Turner, 1988, Skidmore, 1989);
- a combination of aerial photography and multi-temporal Landsat TM imagery were used to classify and differentiate various forest type associations (including dry eucalypt forest, humid eucalypt forest, and littoral rainforest, Yagüe and Garcia, 2006); and
- the performance of metrics derived from Landsat TM imagery with auxiliary terrain and climatic variables were used to predict forest cover across the state of Victoria, delivering an overall accuracy of 96% for forest/non-forest classification (Mellor *et al.*, 2013).

Hyperspectral imagery and lidar data have also been used to map forest type in Australia. Examples include:

- Lucas *et al.* (2008)—outlined an approach for the use of airborne digital hyperspectral imagery (Compact Airborne Spectrographic Imager: CASI) to discriminate and map mixed-species forests at the tree crown/cluster level for use in biodiversity assessment, which identified dominant genera in the central southeast Queensland study area including *Acacia*, *Eucalyptus*, *Angophora*, and *Callitris*.
- Jafari and Lewis (2012)—utilised Hyperion hyperspectral data to discriminate distinct land cover types in an arid landscape in South Australia using endmember analysis (see Volume 2E and Section 8.3 above).
- Fedrigo *et al.* (2018)—used airborne lidar data as inputs to predict the distribution of rainforest and eucalypt stands that was comparable to existing ecological vegetation classes derived manually. The result was highly accurate (84%), allowing identification of small rainforests that had not previously been identified and demonstrating lidar as a key technology for mapping the structural and spatial complexity of these ecosystems.

16.4 Forest Hydrology

One of the most useful and important products of airborne lidar EO data is the generation of highly accurate and detailed DEM, even under forest canopies (see Excursus 5.1). For forest practitioners, lidar-based DEMs can provide detailed information about the underlying hydrology and water access across the forested landscape. Lidar topographic maps are critical for forest managers for operations and access, terrain stability, and erosion assessment, determination of drainage patterns for catchment protection, and engineering and road constructions (Bater and Coops, 2009; Reutebuch *et al.*, 2005; Wulder *et al.*, 2008).

Knowledge of the surface topography is also useful for forest planning and management decisions, such as selecting tree species for planting or determining an appropriate intensity of management. Murphy *et al.* (2011) utilised a lidar-derived DEM to predict a depth-to-water (DTW) index, which was then used to predict soil drainage, soil type, and a number of additional forest soil properties at Swan Hills, Alberta, Canada. Important indicators of soil moisture content, coarse fragment sand, silt, clay composition, pH, and a range of other nutrients by soil layer type and depth were reliability predicted. Detailed topographic information both identifies and explains those forest ecological processes that are impacted by soil drainage and DTW, including nitrogen loss and forest litter/soil organic matter accumulation from ridge tops to depressions.

As the use of airborne lidar-derived terrain indices is expanding, research is also investigating the application of lidar to the development of predictive landscape ecological site classification modelling, integrating slope, topographic position, water and nutrient availability, as well as vegetation structure more holistically. This is paralleled by the acquisition of new information about the effects of eco-site characteristics on the distribution of wood attributes at different scales (Pokharel *et al.*, 2014).

16.5 Forest Structure

In forest vegetation, a contiguous group of trees within a forest that appears to be uniform in terms of species composition, age, size, structure, density, and/or condition is often referred to as a 'stand'. For silvicultural purposes, a stand is viewed, measured and managed as an integrated unit. Silvicultural practices, such as thinning and harvesting, alter the stand age structure. Accordingly, the distribution of tree diameters (measured by Diameter at Breast Height[12]: DBH) within a stand is closely related to its structure and composition, and indicative of its age and management history (see Section 6). Spatial diversity measures, such as the Stand Variance Index (STVI; Staudhammer and LeMay, 2001), which consider the variance in tree diameter and height within a stand, provide a useful platform to compare the structure of stands.

Desirable forest stand conditions, which meet multiple resource objectives, can generally be expressed in terms of stand structure. A stand structure approach to forest management therefore presents a unifying theme for multiple resource management objectives (O'Hara *et al*., 1996), providing information to:

- enable sound silvicultural practice (Florence, 1996);
- assess suitability of the forest for wildlife;
- estimate fire risk;
- stratify the forest for more efficient ground-based inventories; and
- facilitate point source data, such as growth plots, to be extrapolated to a wider spatial context.

For silvicultural assessment, stand structure is typically represented in terms of mean DBH, tree height, canopy cover, and/or timber volume (see Sections 5 and 6). Estimates of total biomass and/or carbon content in a forest are also relevant to forest ecological studies and carbon accounting (see Sections 7.4 and 17).

The most common method to obtain estimates of volume and growth in forests is by developing relationships between direct measurements of the size and weight of the plants or plant parts and their corresponding EO-based observations (see Section 10). These relationships are developed by dividing a forest stand into different components, such as trees, shrubs, and ground covers, each of which can then be considered separately. Typically, a forest sampling program involves three types of sample measurements:

- non-destructive (such as DBH and height);
- destructive (such as cutting branches and trees, partitioning them into functional groups, such as leaves, main branches, boles, then estimating their dry weight or volumes); and
- various types of litter fall (see Sections 5.1.2 and 6.3).

Empirical methods, such as regression analysis, can then be used to obtain correlations between a comparatively small destructive sample and a significantly larger sample of non-destructive measurements that are representative of the total forest stand. Advances in TLS technologies (see Section 16.2), however, invite new approaches to using structural information in forest biometrics (Newnham *et al*., 2015; see Excursus 5.1).

16.5.1 Stand height and cover

The use of ALS (airborne lidar) data to determine tree height is well established (see Excursus 5.1). This attribute is one of the few physical parameters that can directly be measured by lidar instruments. For example, strong correlations between lidar height and ground-measured height were observed in Blackbutt and River Red Gum forests (r^2=0.95, Turner, 2006). Other studies in Australian conditions have also shown height correlations in the range 89–97% (Bennett, 2005, Tickle *et al*., 2001, Weller *et al*., 2003). Crown cover (see Section 6.3.1) can be computed from ALS data, with lidar-derived estimates showing good correspondence with field data in woodland and open dry eucalypt forest in Queensland (r^2=0.79, Lucas *et al*., 2006). At the same location, Lee and Lucas (2007) found strong relationships between lidar results and field measures of height, (r^2=0.81), tree density (r^2=0.82), crown cover (r^2=0.78), and foliage and branch cover (r^2=0.89).

In addition to predicting stand structural metrics, there has been much focus on estimating forest canopy attributes using EO datasets. Foliage Projective Cover (FPC, see Sections 2.3.1 and Excursus 6.1) is a critical attribute in many vegetation classification schemes (see Section 6.3) and is known to be highly dynamic. It is a required dataset at catchment through to continental scales in Australia and other areas around the world. Across Queensland and NSW, the state governments have mapped FPC using EO imagery to derive maps of land cover and land cover change which support government policies. For example, the Statewide Landcover and Trees Study (SLATS) program has been operationally processing Landsat imagery for several decades (SLATS; see Section 9.1 and Volume 2D—Excursus 14.3).

12 Breast height is fixed at 1.3 m in Australia, UK, Canada and continental Europe, and at 1.4 m in the USA, New Zealand, Burma, India, Malaysia and South Africa.

As part of this program, Armston *et al*. (2009) observed long term trends in woody vegetation in Queensland using Landsat-5 TM and Landsat-7 ETM+ imagery and a combination of modelling approaches. Results indicated that parametric and artificial intelligence models had similar prediction errors (RMSE < 10%), but the latter models had less bias when overstorey FPC was greater than ~60%. All models showed more than 10% bias in plant communities with high herbaceous or understorey FPC.

Two additional biophysical parameters that provide information about the forest canopy and can be accurately estimated using EO approaches are:

- Leaf Area Index (LAI)—a dimensionless unit representing the area of foliage per area of ground (see Section 6.3.3); and
- Fraction of absorbed photosynthetically active radiation (fAPAR)—the fraction of photosynthetically active radiation (PAR) in visible wavelengths that is absorbed by a canopy including overstorey, understorey, and ground cover elements (Gower *et al*., 1999; see Section 6.3.4).

At the global scale, a range of satellite sensors provides estimates for LAI and fAPAR at broad spatial resolution and fine temporal resolution over the Australian continent, including Advanced Very High Resolution Radiometer (AVHRR), Moderate Resolution Imaging Spectroradiometer (MODIS), and the SPOT VEGETATION sensor (see Volume 1A—Sections 12 and 14). A number of studies have assessed the capacity of these global datasets to measure LAI and fAPAR under Australian conditions (Hill *et al*., 2006; Sea *et al*., 2011). For example, Pickett-Heaps *et al*. (2014) investigated the consistency of six fAPAR products (MODIS, MERIS, SeaWIFS, MODIS-TIP, SPOT VEGETATION, and AVHRR) across the Australian continent using multi-year records. Large differences in fAPAR products were observed over much of Australia and these were explained by simple offsets and different sensitivities in fAPAR products to changes in vegetation cover. Relatively high agreement was observed at grassland, shrubland, and agricultural sites, with more significant disagreement occurring at sites classified as forest.

TLS are increasingly being used to measure plot level leaf area and gap fractions within forested landscapes (Zheng and Moskal, 2009; Danson *et al*., 2007) as well as individual tree dimensions, such as stem diameter (with RMSE ranging between 1.5–3.3 cm from field measurements, Hopkinson *et al*. 2004; Tansey *et al*., 2009), plus stem taper (Bienert *et al*., 2007), sweep, and lean (Thies *et al*., 2004). TLS has also been used successfully to estimate standing timber volume, branch size, density and configuration, foliage density, and tree growth (Murphy, 2008; Maas *et al*., 2008, Klemmt *et al*., 2010; Bucksch and Fleck, 2011). Further, TLS enables the estimation of standing timber volume to be based on the full tree profile (rather than simply the traditional approximations of DBH and tree height) and allows bole size and taper to be predicted (Murphy, 2008; Maas *et al*., 2008). For example, an Australian TLS system (Echidna®) has been used to accurately estimate LAI, DBH, and tree density in both native and plantation forests (Jupp *et al*., 2009). Strahler *et al*. (2008) used Echidna® to retrieve a range of forest parameters including mean DBH, stand height, distance to tree, stocking, and foliage area in plantation and native forest stands in NSW. Results indicated that LAI from this TLS system matched favourably with ground-based estimates. Tree stems were clearly delineated, and diameters retrieved very accurately (r^2=0.99), with stand basal area and stocking (a practical index of density) being within 2% of field-measured estimates.

16.5.2 Individual trees

Both the growing availability of high spatial resolution imagery and increasing computing power have enabled greater focus on detecting and measuring individual trees as opposed to obtaining stand level statistics. For analysing individual tree crowns in forests, a general rule is that the image spatial resolution should be much greater than the crown size (that is, more than nine pixels per crown), such that an image spatial resolution ranging between 10 cm and 2 m is preferred (Gougeon and Leckie, 2001). A wide variety of tree crown detection and delineation algorithms have been developed in a range of forest types (Cabello-Leblic, 2018), some especially for Australian conditions (such as Culvenor, 2002; Bunting and Lucas, 2006; Held *et al*., 2001), including wet and dry eucalypt, tropical, deciduous, and mixed species forests. Existing approaches for automated tree crown delineation and tree crown detection can be broadly categorised into four groups (Ke and Quackenbush, 2011):

- local maxima/minima—identifies crown locations based on brightness variations (Pinz, 1991; Walsworth and King, 1999);
- valley following—relies on shading patterns (Gougeon, 1995, 1999);
- region growing—segments the image assuming that treetops are brightest (Culvenor, 2002); and
- watershed segmentation (Serra, 1982; Ticehurst *et al*., 2001).

Culvenor (2002) found region growing was most suited to crown delineation in pre-mature forest canopies where trees have a well-defined crown shape, noting that individual tree crown delineation from spaceborne EO imagery is not a realistic expectation (even via manual image interpretation) in structurally complex forests. Variations in viewing angle and Sun angle inhibited the ability to achieve repeatable results in multi-temporal imagery (see Volume 1B—Section 3). In a mixed species, dry eucalypt forest in Queensland, Bunting and Lucas (2006) found the accuracy of their approach, when compared to field data, to be ~70% (range 48–88%) for either individual trees, or groups of trees from the same species, having DBH greater than 10 cm, with reduced accuracies associated with dense stands containing several canopy layers.

Lidar-derived branching information, such as the number of branches per whorl (Klemmt *et al.*, 2010), can be used to simulate knot morphology (Duchateau *et al.*, 2013) or detailed tree architecture (Runions *et al.*, 2007; Côté *et al.*, 2009, 2011; Van der Zande *et al.*, 2011). In combination with tree models, such as L-systems (Prusinkiewicz and Hanan, 1990) and quantitative structure models (QSM, Calder *et al.*, 2015), individual trees can also be 'reconstructed' accurately (see Figure 16.4).

While many ground-based lidar studies have investigated deriving individual tree structure, the intricate differences between, and complementary features of, TLS and ALS datasets have also been researched (Hilker *et al.*, 2013). The combination of these two perspectives promises to be an effective and efficient tool for measuring the three-dimensional structure of individual trees (Dassot *et al.*, 2011). Given that ground-based measures (such as TLS) focus on the tree trunks whereas airborne data (such as ALS) mainly describe the top of the canopy, there are clear distinctions between TLS and ALS observations. Likewise, TLS data are less suitable for investigating stand structure over larger areas but provide a means for calibrating and validating ALS data, by enabling investigation of changes in the stem density and structure, and branching and understorey characteristics, as a function of overall stand structure. These relationships can then be used to model the relationship between below canopy architecture and the upper canopy light regime (Hilker *et al.*, 2010) and may ultimately allow an indirect retrieval of the complete canopy architecture from ALS measurements across the landscape.

Figure 16.4 TLS-derived tree structure

TLS data was collected for a tree (*Eucalyptus tricarpa*, 21 m tall, in Rushworth forest, Australia) using a RIEGL VZ-400 TLS. The Quantitative Structure Model (QSM) was generated following the procedure described by Calders *et al.* (2015).

a. Point cloud coloured by height

b. QSM

Source: Newnham *et al.* (2015) Figure 3

An alternative approach to scaling up TLS-based attributes for individual trees to forest stands and landscapes has been demonstrated by Côté *et al.* (2012), who built three-dimensional libraries of individual trees and then distributed them across the landscape using L-systems approaches, enabling three-dimensional modelling of entire forest stands (Côté *et al.*, 2012).

16.5.3 Geometric-optical models

Spectral and spatial responses in EO data have also been related to forest variables by numerical models that account for the geometry of the tree structure at the time of the satellite overpass (see Volume 1X—Excursus 1.1). This modelling approach views each pixel as mixtures of four basic components: sunlit canopy, shaded canopy, sunlit background, and shaded background.

Strahler and Li (1981, 1984) modelled conifer trees as widely spaced cones and surmised that the different reflectances of forest pixels result from different mixtures of illuminated/shadowed background and illuminated/shadowed tree crowns within each ground pixel. This geometric-optical model was used to estimate tree density and height in sparse to moderately dense ponderosa pine plantations using Landsat MSS data, with the modelled results being within 10% of the ground-based measurements.

This approach was adapted to Australian forests (Jupp *et al.*, 1986; Walker *et al.*, 1986) and used to demonstrate how geometric-optical models could be interfaced with simple process-based models of vegetation function to predict changes in plant

responses to increasing woody weeds (Jupp and Walker, 1996; see Volume 2X—Excursus 1.1). Scarth and Phinn (2000) applied a similar approach to mixed eucalypt forests in Queensland using Landsat TM imagery and found that modelled estimates of crown cover, canopy size, and tree densities had significant agreement with ground validation, but structural successional stage showed less significant correlation. Others have used the approach to better understand patterns of tree density in EO imagery (Coops and Culvenor, 2000) and predict gap probability profiles (Lovell *et al*., 2012; Haverd *et al*., 2012).

Spectral mixture analysis (see Section 8.3 and Volume 2E) has also been used to determine the proportions of sunlit canopy and background, and shadowed canopy and background, within each EO pixel, with subsequent inversion based on geometric-optical modelling being used to derive stand structural attributes (Coggins *et al*., 2013).

16.5.4 Biomass and fuel load

The importance of assessing forest biomass has been recognised both as an indicator for global climate change and to provide insights into the forest carbon storage (see Section 17; Richards and Brack, 2004). The use of passive optical data to map forest biomass has been well-established through the strong correlations of above ground biomass (AGB) with cover and LAI (see Sections 6.3.3 and 14), as well as with active remote sensing systems such as lidar (see Excursus 5.1). For example, using Landsat time series imagery Nguyen *et al*. (2020) developed a robust approach for monitoring forest biomass dynamics associated with forest disturbance and recovery, which allowed a single date conventional inventory to be extrapolated through time. Lidar has also been used for biomass assessment in regrowth Blackbutt forests on the NSW Central Coast, to estimate AGB components by segmenting canopy height data, which yielded results within 9% of the ground-based estimates (Turner, 2006).

The use of both spaceborne and airborne SAR is still an active area of research in Australia (Watt *et al*., 2012; Richards, 2012). SAR is well-suited to the Australian environment since the majority of Australia's forested area is represented by woodlands, the biomass of which rarely exceeds 100 Mg/ha and is especially low in areas of regeneration (see Section 16.1). C-, L-, and P-band scattering intensity has been shown to saturate at biomass levels of approximately 20–40 Mg/ha, 60–100 Mg/ha, and 150 Mg/ha respectively (see Section 16.2). The biomass of most woodland areas should thus be quantifiable using, as a minimum, single-polarised L-band data, since most of the biomass is below its threshold of saturation (Milne *et al*., 2000). For example, at a long term study site in Queensland, Lucas *et al*. (2006) evaluated the use of multi-frequency, radar data for quantifying the AGB of open eucalypt forests and woodlands. Using NASA JPL AIRSAR (POLSAR) data, empirical relationships between AGB and SAR backscatter confirmed that C-, L-, and P-bands saturated at different levels and revealed both a greater strength in the relationship at higher incidence angles and a larger dynamic range and consistency of relationships at HV polarisations. The study concluded that L-band HV backscatter data acquired at incidence angles approaching or exceeding 45° were best suited to estimating the AGB up to the saturation level of 80–85 Mg/ha (Lucas *et al*., 2006). The availability of P-band SAR data from the BIOMASS mission (see Section 16.2) is expected to provide more information about both tree trunks and the ground surface in forested landscapes.

Another ALS application involves providing spatial layers to forest fuel models, which traditionally have not used significant amounts of EO data due to an inability of spectral data to capture the structural complexity of closed canopies. In the USA, ALS has been used to predict crown bulk density, foliage biomass, and crown volume (Riaño *et al*., 2003). The US Forest Service has also evaluated the capacity of ALS to predict crown bulk density, canopy base height, and crown fuel weight, demonstrating its effectiveness for characterising landscape level, fuel-related variables (Andersen *et al*., 2005). Research under Australian conditions has found that, while it is difficult to distinguish surface and 'near surface' fuels using ALS data (Gould and Cruz, 2012), good correlations could be achieved between lidar-derived understorey attributes and elevated fuel load, fuel cover, and fuel volume (Brown *et al*., 2011). Since understorey vegetation is an important fuel-ladder for crown fires in Australia, mapping of elevated fuel structure is valuable (Turner, 2007).

ALS data has also been used to assess fuels in the wildland-urban interface where wildfires present a significant risk to homes, life, and property. Management of this risk requires current and detailed knowledge of the spatial extent of wildland. ALS has been used to map wildland vegetation based on the combination of a vertically-stratified cover threshold and spatial morphology (Newnham et al., 2012). Results indicated that the proportion of homes destroyed at the wildland-urban interface was greater than previously reported and that there was an exponential decline in the proportion of homes destroyed as a function of distance from wildland (see Section 18).

16.6 Forest Functionality

Plant physiological processes are highly dynamic and can vary over space and time as plants respond to rapidly changing environmental conditions. In the forestry context, plant functionality is closely related to forest health, and EO methods can provide early warning of disease, nutritional imbalance, moisture stress, or increasing predators. Current monitoring programs in Australia are integrating lidar and multispectral data sources to monitor forest biosecurity and manage forest health (NSW DPI, 2015).

Leaf biochemistry is closely related to leaf reflectance characteristics (see Sections 4, 8.1.1, and 9.6), allowing high spatial and spectral resolution imaging techniques to be used to infer information about the chemical composition of a vegetated canopy (Ollinger and Smith, 2005). These relationships only apply to photoactive molecules, such as pigments, and may be obscured by broad leaf water absorption. As detailed in Volume 1A—Section 13, spectrometers measure reflectance in specific, narrow, and often multiple, wavebands allowing imaging spectrometers to be used with ground-based, aerial, or spaceborne platforms for calibration and validation purposes to deliver consistent and contiguous measurements of the Earth's surface.

16.6.1 Plant nutrition

Forest nutrition assessments were amongst the earliest research projects conducted with the hyperspectral scanner, Hyperion, as part of calibration and validation for that instrument in Australia. Coops *et al.* (2003) demonstrated the use of Hyperion image data for mapping nutrient concentrations in *Eucalyptus* and *Pinus* species. These models initially focused on nitrogen but were also shown to be useful for mapping the concentration of additional macronutrients and micronutrients in a southern Australian *P. radiata* estate. Each of these nutrients plays an important role in the physiological functioning of plants and can influence the size and form of plantation trees (see Sections 4.2 and 5.3.5).

In a review of the use of EO technology to map nutrient status and fertiliser requirements in Australian plantations, Sims *et al.* (2013) discussed a number of operational considerations when using EO data. They mapped concentrations of 12 macronutrients and micronutrients in a Queensland exotic pine estate (*P. carribea* and *P. elliotii*) with comprehensive field data collection. They also considered many questions relating to model transferability between species and age classes, including the need for hyperspectral image data, detailed correction approaches, timing of image acquisition, complete sampling of the entire nutrient range in a forest stand, and the impact of stand age and canopy closure.

16.6.2 Plant stress

Factors that impact plant vigour and EO methods to detect stress are described in Sections 9.5 and 9.6. Thus far, the EO approaches that show the most promise for identifying and quantifying plant diseases have been thermography, chlorophyll fluorescence, and hyperspectral imaging (Mahlein *et al.*, 2012).

Various stress factors can induce leaf loss and discolouration (chlorosis and/or redness due to production of anthocyanins; see Excursus 4.1) and reduced leaf and crown sizes in eucalypts (Pook, 1985; Stone and Coops, 2004). Changes in leaf pigment concentrations impact foliar absorption of visible wavelengths, while changes in leaf and crown structure are most obvious in NIR reflectance (Asner, 1998; Gitelson *et al.*, 2002). A range of spectral indices has been developed for vegetation studies that highlight the relative changes in leaf reflectance of red and NIR wavelengths (see Section 8.1 above and Volume 2C). In particular, various vegetation indices have been proposed to identify and monitor stress in different eucalypt species. For example, Datt (1999) developed a series of chlorophyll indices suitable for eucalypt vegetation at both the leaf and stand level. Many of these indices were tested by Coops *et al.* (2002) using CASI-2 imagery, who found that the Datt (1999) indices correlated moderately well with relative leaf chlorophyll content for all dominant eucalypt species in the NSW study area and yielded slightly higher correlation for individual species.

In Australia, forest health has traditionally been surveyed by trained assessors using both ground-based and aerial observations (Carnegie, 2008; Carnegie *et al.*, 2008). Barry *et al.* (2008) used hand-held spectrometers to determine whether spectral analysis methods could detect changes in chlorophyll concentration resulting from stress. Three commercially important species of *Eucalyptus* were observed after defoliation (*E. globulus*) or exposure to cold and nutrient deprivation (*E. pilularis* and *E. grandis*). The resulting leaf loss in both *E. globulus* and *E. pilularis* was strongly correlated with two greenness indices (Modified Chlorophyll Absorption Ratio Index 2: MCARI2 and Modified Triangular Vegetation Index 2: MTVI2) as well as changes in the position and slope of the red edge, while leaf redness induced by stress in *E. grandis* and *E. pilularis* was strongly correlated with the Anthocyanin Reflectance Index (ARI) and the Red-Green Index (RGI; see Section 8.1 above). Stress-related changes in both chlorophyll concentration and leaf loss in *E. pilularis* were more noticeable than in *E. grandis*, possibly due to phenological factors (Stone *et al.*, 2005).

Chisholm (2006) investigated the use of hand-held spectra to assess both chlorophyll and moisture content of *E. camaldulensis* stands subject to a range of moisture stress regimes. Results indicated that moisture stress could be detected using high resolution spectral reflectance data at the leaf level and that the analysis was successful at identifying broad regions of the electromagnetic (EM) spectrum which could be used to discriminate different levels of stress.

In addition to chlorophyll and nitrogen, the past decade has seen advances towards estimation of other plant pigments as indicators of plant stress and light absorption. One of these pigments is xanthophyll, which is produced in a leaf during a process known as photo-protection (see Section 4.2.3). Briefly, while plants can use most of the energy they absorb for photosynthesis, in strong illumination, the photochemical reaction tends to be limited by factors such as temperature, water, or nutrient availability. A change in the concentration of xanthophyll in foliage is indicative of Light Use Efficiency (LUE), which in turn is related to Gross Primary Productivity (GPP; see Section 7.4). Advances in estimation of LUE and GPP from spaceborne sensors have focused on imagery from MODIS or CHRIS-PROBA (Drolet *et al*., 2008, Hilker *et al*., 2009, 2011) in readiness for the European FLEX mission (Mohammed *et al*., 2019), which will measure fluorescence from vegetation, a key attribute for GPP estimation (Coops *et al*., 2011; see Section 17).

16.7 Forest Diversity

In addition to forest structure and function, the diversity of species within forest stands is often a critical piece of information both for forest management and biodiversity assessment. Species diversity, of course, relates to both flora (see Section 16.7.1) and fauna (see Section 16.7.2).

16.7.1 Floral diversity

In Australian conditions, the classification of native forest species is highly challenging (Shang and Chisholm, 2014; Kumar *et al*., 2010). This is largely attributed to similarities in structural and chemical properties between species and the architecture of eucalypt leaves. These leaves are characteristically pendulous, forming a generally open canopy structure, so that the spectral reflectance obtained from EO imagery is strongly affected by the background.

Hyperspectral imagery is often viewed as necessary for discriminating the small spectral differences between species. For example, Lucas *et al*. (2008) produced tree species maps (including *Acacia*, *Angophora*, *Callitris*, and *Eucalyptus*) for central southeast Queensland using hyperspectral imagery acquired by CASI. Classification of the dominant species delivered the most accurate result (76%). The fusion of HyMap (airborne hyperspectral) spectra increased the accuracy for some species, principally due to the additional MIR (middle infrared) spectral wavebands. Shang and Chisholm (2014) assessed the potential of hyperspectral EO data to classify Australian forest species at the leaf, canopy and community levels in eastern NSW and obtained the most accurate classification result at the leaf level (94.7%), which reduced to 84% and 75% at the canopy and community levels respectively.

Rather than attempting to directly detect individual tree species, indirect mapping methods utilise environmental parameters and EO data to predict species distributions or associations with the aid of *a priori* knowledge (Coops *et al*., 2008). Mackey *et al*. (2004) and Berry *et al*. (2007) developed an integrated index to track landscape productivity over the Australian continent using monthly observations of fAPAR during 2003. This index was used to assess how biomass is partitioned and made available as food and other habitat resources for fauna on the premise that, while some animal species reside within a single landscape region, many species are highly mobile, primarily in search of food and habitat. Mobile species often move large distances on a regular (mostly driven by seasonal changes) or irregular (dispersive or nomadic movement reflecting less predictable changes) basis (Gilmore *et al*., 2007). Variations in mean annual, minimum, and seasonal patterns of fAPAR were related to vegetation production and seasonality, which in turn provided insights into species habitat and forage conditions for that year. The integrated index provided useful information about the structure and cover of Australian vegetation and demonstrated that vegetation-related habitat resource availability can readily be tracked through time using EO data and can be quantified in terms of carbon or energy assimilation over ecologically relevant timeframes (Berry *et al*., 2007).

An alternative approach is that of Palmer *et al*. (2002), who proposed the spectral variation hypothesis whereby species richness can be inferred from the variations in the spectral characteristics of an EO image, that is, more unique spectra indicate greater species diversity. A number of studies have tested this approach by comparing field-based, species richness measures to image spectral heterogeneity using both multispectral and hyperspectral imagery (Rocchini *et al*., 2004, 2007; White *et al*., 2010).

Asner and Martin (2009) proposed a 'spectranomics' approach to forest biodiversity monitoring that can be used to link the chemistry, spectroscopy, taxonomy, and ecology of canopies. Initial work has been undertaken examining the leaf spectral and chemical properties of 162 canopy species in tropical forest sites in Queensland. They concluded that, within a site, leaf chemistry varied more strongly among species rather than along a climate gradient and did not aggregate well along genus or family levels, highlighting the spectral and species diversity and complexity in these stands (Asner *et al*., 2009). This work has expanded into the Carnegie Spectranomics Project described by Asner and Martin (2016; see Excursus 16.1).

Excursus 16.1—Carnegie Spectranomics Project

Source: Asner and Martin (2016)

Spectranomics is an approach to conceptually and geographically link plant canopy species and their functional traits to their 'spectral-optical' properties. With the long term goal of advancing EO in the biodiversity science arena, the Carnegie Spectranomics Project has generated tree-of-life, or phylogenetically-based, connections between the spectral properties of plants and their canopy functional traits for more than 13,000 canopy tree and liana specimens in over 3 million tissue samples. This sample represents around 10,000 species, mostly tropical, and focuses on canopy species growing in full sunlight.

Canopy functional traits refer to a constellation of elemental and molecular properties, some of which support growth, such as nitrogen and photosynthetic pigments (which are functionally related), and others that provide defence, like polyphenols and lignin, which have evolved in plant canopy leaves (see Section 4.2). This chemical make-up of plant canopies, and its similarity and uniqueness among species, is called 'chemical phylogeny'. These functional traits mediate leaf processes, whole plant function, and ecosystem dynamics, are often differentially formulated at the species level, and are an essential component of Spectranomics (see Figure 16.5a).

In this context, spectral properties of plant canopies describes the mostly invisible interactions between plant foliage and solar radiation. Between the EM wavelengths from ultraviolet to short wave infrared (350–3500 nm), this interaction is strongly determined by 21 or more chemicals (Asner *et al*., 2011) that underpin plant evolution, and which power the biosphere. Chemometric studies determine how these chemicals relate to reflectance spectra, with methods ranging from traditional spectroscopic assays to new machine learning approaches (Feilhauer *et al*., 2015; Serbin *et al*., 2014; Wold *et al*., 2001; see Figure 16.5b). Spectral properties also provide a tantalising pathway forward to scale up from leaves to landscapes (Ustin *et al*., 2004) and to the planetary level (Jetz *et al*., 2016; see Section 10.2), but only if we can accurately and repeatedly measure and interpret the spectra of plants over increasingly larger portions of Earth (see Figure 16.5c,d).

The Spectranomics database has become increasingly useful for quantitatively testing the relationships between plant phylogeny, canopy traits, and spectral properties at nested biographic scales, whether in tree communities, on mountains, or between continents. It has also transitioned to a forecasting tool to predict what can be remotely mapped and monitored using spectral EO instruments. These insights are feeding back to more focused field studies and improved EO sensor design (Asner *et al*., 2012).

Figure 16.5 Spectranomics Database elements

The essential interactive elements of the Spectranomics Database include phylogenetic, chemical, and spectral information on canopy species.

a. 21 foliar chemical traits are collected, organised and analysed phylogenetically, producing a tree-of-life based on the relatedness of functional trait signatures. This generic phylogeny shows the chemical relatedness of thousands of species in the Spectranomics Database.

b. Chemometric equations are derived to quantitatively relate canopy functional traits (chemicals) to spectral data. Example relationships are shown for foliar lignin, nitrogen (N), and polyphenols. The x-axis indicates spectral wavelength from 400–2500 nm; the y-axes indicate relative importance of the spectrum to each example chemical constituent.

c. An example remotely sensed canopy reflectance spectrum of one species is shown along with indicators of key chemical contributions to the spectrum (Curran, 1989; Kokaly *et al.*, 2009; Ustin *et al.*, 2009).

d. Oblique three-dimensional view of a one hectare portion of lowland Amazonian forest canopy. Different colors indicate different species detected based on chemical traits using airborne imaging spectroscopy.

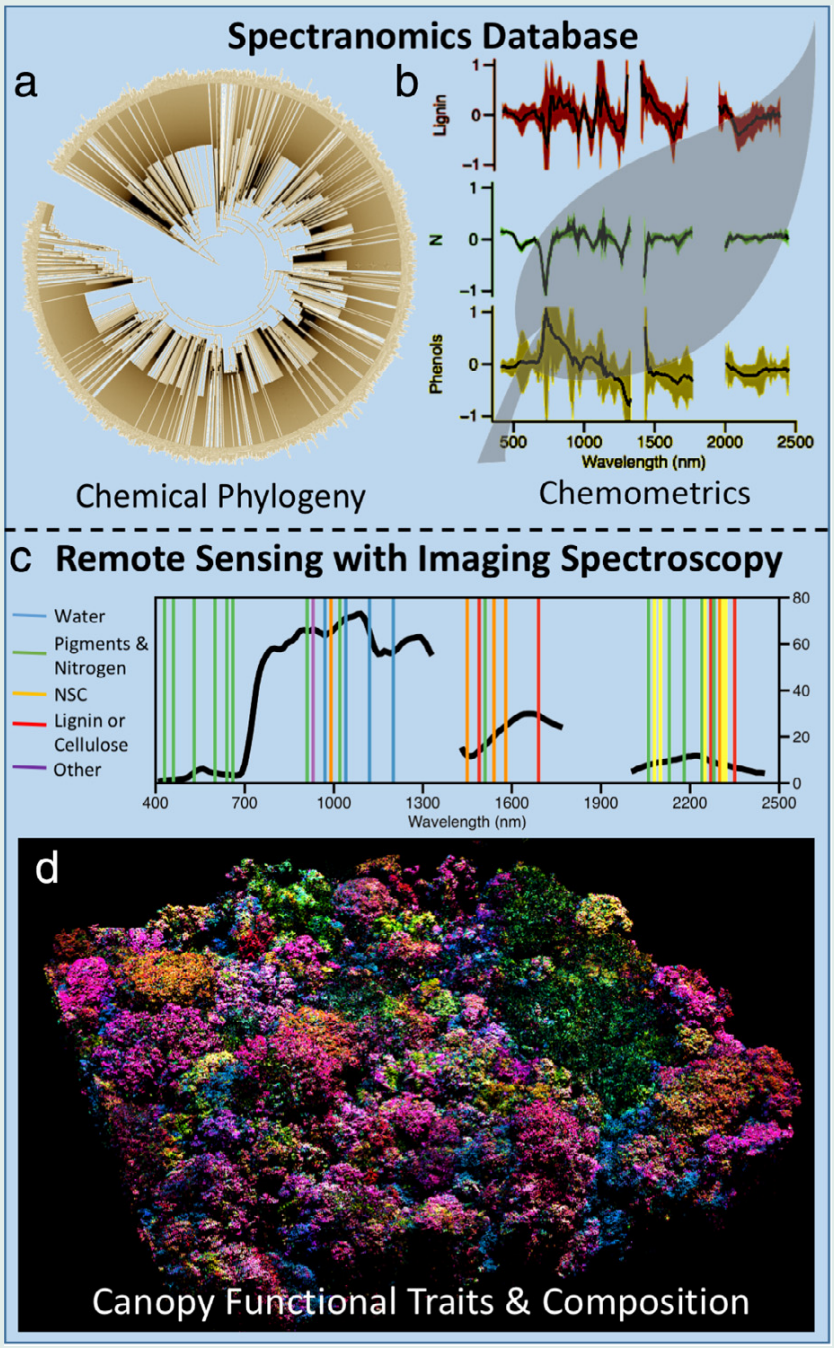

Source: Asner and Martin (2016) Figure 1

16.7.2 Faunal monitoring

In Australian forestry conditions, Coops and Catling (1997) described how airborne video data, if correctly pre-processed, could be used to accurately predict the suitability of the forest for ground-dwelling fauna. They used habitat quality ratings to develop maps of habitat quality across the landscape. It was concluded that these spatial predictions could then be used to stratify the landscape into regions that would predict the distribution and abundance of some faunal groups. These predictions were then verified in the field, with actual species abundances being accurately predicted in over 70% of situations (Catling and Coops, 1999).

Using hyperspectral EO imagery, Youngentob *et al.* (2012) developed relationships between foliage nutritional quality and HyMap imagery acquired with 3.5 m pixels over native eucalypt and plantation forest in NSW. An integrated measure of foliage nutritional quality (available nitrogen) was related to the spectra using continuum removal and derivative analysis. Regression relationships were developed with a range of accuracies (r^2=0.55–0.78). The significant majority of spectral bands selected by the regression analysis related to known foliage pigments and nutrient absorption features. The results indicated the potential of hyperspectral imagery to be used to map variations in foliar constituents across forested landscapes. These types of spatial predictions can then be used to estimate the presence and abundance of folivores (herbivores that specialise in consuming leaves), such as the greater glider.

16.8 Forest Disturbance

Monitoring and quantifying forest disturbance is valuable for a range of forestry activities, including timber harvesting and reforestation. Forest changes can also result from natural disasters such as fire, windthrow, lightning, drought and floods. Other factors that can disturb forests include pollution, predators, and disease, all of which may be introduced by other anthropogenic activities (see Section 9.6). At a landscape scale, such disturbances change forest patterns, and those changes can be delineated in appropriate EO datasets (see Section 9.2).

EO provides an ideal basis to identify forest disturbance, and monitor forest regrowth (Kennedy *et al.*, 2010; Zhu *et al.*, 2012). Approaches which map and monitor landscape disturbance are highly scale-dependent however, both spatially and temporally (see Volume 2D). As such, the landscape patterns and processes that are discernible within any particular image source will be dependent on the target of interest—that is, individual trees or a whole stand—and the spatial, spectral, radiometric, and temporal characteristics of the image data (Turner, 1989; Perera and Euler, 2000; see Volume 1B—Section 1). Disturbances that are non-stand replacing and heterogeneous over the landscape, such as defoliation or partial harvesting, are generally more difficult to detect with EO data than larger and more spatially contiguous, stand-replacing disturbances, such as fire or land clearing (Coops *et al.*, 2006). Hislop *et al.* (2019) utilised Landsat time series data over a 29-year period to map abrupt disturbances in Victorian sclerophyll forests. Using an ensemble approach, they found an overall error rate of 7% and developed annual disturbance maps for 9 million ha of forest for this time period.

16.8.1 Insect damage

At a broad spatial scale, the high radiometric quality and frequent temporal resolution of MODIS can allow non-stand replacing disturbances, such as insect-induced tree mortality, to be detected. Verbesselt *et al.* (2009) used a MODIS time series (250 m; 16-day composite) to assess *Pinus radiata* plantation mortality in southern NSW (see Section 9.3). Results indicated that NDVI images were more effective for assessing tree mortality than the Enhanced Vegetation Index (EVI) or the Normalised Difference Infrared Index (NDII; see Section 8.1).

The more recent development of the Harmonised Landsat-Sentinel Data processing methodology is now allowing sub-weekly, global multispectral observations at 30 m resolution. This resource opens the way for finer scale insect damage assessments in the future (Claverie *et al.*, 2018; see Volume 2D—Section 10.2).

16.8.2 Fire monitoring

EO assessment of fire severity is one of the major success stories in disturbance observation (see Section 18). EO of burn extent has two major advantages over traditional methods of field assessment: cost-effectiveness and global coverage in remote areas. Most commonly, with spectral bands that are sensitive to fire disturbance and being freely available globally, Landsat TM/ETM+/OLI imagery is well-suited to the task of studying fire severity. As detailed in Section 18.5.1, extensive research has demonstrated that fire severity can be assessed using the:

- Normalised Burn Ratio (NBR)—normalised ratio of the NIR and SWIR spectral bands; and the
- Normalised Burn Ratio difference (dNBR; or Differenced NBR)—post-fire NBR is subtracted from a pre-fire NBR (Key and Benson, 2006; see Section 9.2.1).

dNBR has been shown to be particularly useful for forest and ecological research and land management projects as the index accounts for both pre- and post-fire conditions, making the overall approach more transferable across ecosystems (Kasischke *et al*., 2008; Soverel *et al*., 2011).

In Australia, Landsat imagery has been used for several decades to derive a more comprehensive understanding of fire histories (Russell-Smith *et al*., 1997) and seasonality (see Figure 18.1). For example, Goodwin and Collett (2014) developed a new, fully automated approach to classifying burnt areas across Queensland based on different Landsat TM/ETM+ spectral combinations. In their approach time series imagery (rather than just a pair of images pre-and post-fire) is developed and the thermal, reflective and contextual characteristics of landscape patches are assessed through time. The results indicated an overall producer's accuracy of 85% and user's accuracy of 71% (see Volume 2E). Areas frequently misclassified were most often areas of cropping or inundated land, with variations in moisture and ground cover on dark soil. Other approaches to mapping fire severity and extent are detailed in Section 18.5.1.

If there were no Forestry in Australia, beyond mere fire-prevention, the benefits to the country would be incalculable. ... For complete fire-protection three measures are necessary:
1. Watch-towers and a good look-out.
2. Fire-paths.
3. Extra watchers during the fire season.
(David E. Hutchins, from 'A Discussion of Australian Forestry', 1916)

16.8.3 Environmental monitoring

EO datasets have also been used to monitor land use changes for various purposes (see Section 3.4). For example, Furby *et al*. (2008) describe the use of over 5,000 Landsat scenes to map land use changes associated with agriculture and forestry across Australia as part of the NCAS Land Cover Change Project. Dry season Landsat MSS, TM and ETM+ imagery was used to detect land cover change and discriminate between forest and non-forest cover from 1972 onwards. The program was then expanded to map a number of other land cover change attributes such as detection of new hardwood and softwood plantations, forest density classes, and sparse vegetation cover mapping.

The opening up of the complete Landsat archive (Wulder *et al*. 2012) has led to the development of many more monitoring approaches focusing on multi-temporal and pixel-based analyses of EO time series data (Kennedy *et al*., 2010; see Volume 2D). These approaches move beyond scene-based analysis to compositing algorithms which select the best available pixel (BAP) from multiple images acquired within a pre-defined time interval (Roy *et al*., 2010), thus allowing pixel level tracking of forest disturbance through time (Zhu *et al*., 2012). Common to many of these approaches is the derivation of information from spectral changes in Landsat reflectance at a given location over time using what are broadly known as temporal trajectory methods (Hermosilla *et al*., 2016; see Volume 2D—Section 9). For example, Lehmann *et al*. (2013) applied this type of approach to a Landsat time series for continental scale monitoring of disturbances within forested regions of Australia to produce the National Forest Trend (NFT), which identifies within-forest vegetation changes (disturbance and recovery) over time using imagery acquired from 1989 to 2006. By examining the spectral trajectory of a vegetation cover index, this approach can identify processes affecting forests that are of interest to ecologists and forest managers. Trend information along the trajectory, such as the slope curvature, is calculated to highlight areas of forest decline or recovery, which are critical for environmental reporting. Other EO-based monitoring approaches for forest vegetation, such as BFAST (Breaks for Additive Season and Trend) Monitor (Verbesselt *et al*., 2012), are described in Volume 2D.

16.9 Further Information

Australian Forestry

State of the Forests Report (SOFR) 2018: *https://www.agriculture.gov.au/abares/forestsaustralia/sofr/sofr-2018*

Australia's forests at a glance 2019: with data to 2017–18. Australian Bureau of Agricultural and Resource Economics and Sciences, Canberra. *https://doi.org/10.25814/5dc8d577976b8*

Australia's forests webpage, ABARES website: *https://www.agriculture.gov.au/abares/forestsaustralia/australias-forests*

Department of Agriculture: *http://www.agriculture.gov.au/forestry*

Institute of Foresters Australia (IFA)—*http://www.forestry.org.au/*

National Forest Inventory (NFI)—*http://www.agriculture.gov.au/abares/forestsaustralia/australias-national-forest-inventory*

Statewide Landcover and Trees Study (SLATS)

SLATS Queensland: *https://www.qld.gov.au/environment/land/management/mapping/statewide-monitoring/slats*

SLATS NSW: *https://www.environment.nsw.gov.au/topics/animals-and-plants/native-vegetation/reports-and-resources*

16.10 References

Alam, M.M., Strandgard, M.N., Brown, M.W., and Fox, J.C. (2012). Improving the productivity of mechanised harvesting systems using remote sensing. *Australian Forestry*, 75(4), 238–245. doi:*10.1080/00049158.2012.10676408*

Andersen, H.E., McGaughey, R.J., and Reutebuch, S.E. (2005). Estimating forest canopy fuel parameters using lidar data. *Remote Sensing of Environment*, 94, 441–449.

Armston, J.D., Denham, R.J., Danaher, T.J., Scarth, P.F., and Moffiet, T.N. (2009). Prediction and validation of foliage projective cover from Landsat-5 TM and Landsat-7 ETM+ imagery. *Journal of Applied Remote Sensing*, 3(1), 033540. *https://doi.org/10.1117/1.3216031*

Asner, G.P. (1998). Biophysical and biochemical sources of variability in canopy reflectance. *Remote Sensing of Environment*, 64, 234–253.

Asner, G.P., and Martin, R.E. (2009). Airborne spectranomics: mapping canopy chemical and taxonomic diversity in tropical forests. *Frontiers in Ecology and the Environment*, 7, 269–276. *http://dx.doi.org/10.1890/070152*

Asner, G.P., and Martin, R.E. (2016). Spectranomics: Emerging science and conservation opportunities at the interface of biodiversity and remote sensing. *Global Ecology and Conservation*, 8, 212–219. *https://doi.org/10.1016/j.gecco.2016.09.010*

Asner, G.P., Martin, R.E., Ford, A.J., Metcalfe, D.J., and Liddell, M.J. (2009). Leaf chemical and spectral diversity in Australian tropical forests. *Ecological Applications*, 19, 236–253. *http://dx.doi.org/10.1890/08-0023.1*

Asner, G.P., Martin, R.E., Knapp, D.E., Tupayachi, R., Anderson, C., Carranza, L., Martinez, P., Houcheime, M., Sinca, F., Weiss, P. (2011). Spectroscopy of canopy chemicals in humid tropical forests. *Remote Sensing of Environment*, 115, 3587–3598.

Asner, G.P., Knapp, D.E., Boardman, J., Green, R.O., Kennedy-Bowdoin, T., Eastwood, M., Martin, R.E., Anderson, C., Field, C.B. (2012). Carnegie Airborne Observatory-2: Increasing science data dimensionality via high-fidelity multi-sensor fusion. *Remote Sensing of Environment*, 124, 454–465.

AUSLIG (Australian Land and Surveying Information Group) (1990). *Atlas of Australian Resources (3rd Series) Volume 6: Vegetation*. AUSMAP, Department of Administrative Services, Canberra. 64 p.

Barry, K.M., Stone, C., Mohammed, C.L. (2008). Crown-scale evaluation of spectral indices for defoliated and discoloured eucalypts. *International Journal of Remote Sensing*, 29, 47–69.

Bater, C., and Coops, N.C. (2009). Evaluating error associated with lidar-derived DEM interpolation under dense forest canopy. *Computers and Geoscience*, 35, 289–300.

Bennett, L. (2005). *Evaluating the cost effectiveness of various Lidar acquisition specifications on estimates of Dominant Tree Height in Tasmanian Eucalypt Plantations and Single Aged Regrowth*. GIS Project KGA 385, Centre for Spatial Information Science, School of Geography and Environmental Studies, University of Tasmania. 21 p.

Berry, S., Mackey, B., and Brown, T. (2007). Potential applications of remotely sensed vegetation greenness to habitat analysis and the conservation of dispersive fauna. *Pacific Conservation Biology*, 13(2), 120–127.

Bienert, A., Scheller, S., Keane, E., Mohan, F., and Nugent, C. (2007). Tree detection and diameter estimations by analysis of forest terrestrial laserscanner point clouds. *International Archives of Photogrammetry, Remote Sensing and Spatial Information Sciences*, Vol. XXXVI, Part 3/ W52.

Brown, C., Scherl, T., Chylinski, T., and Burns, J. (2011). The use of LiDAR in fuel hazard characterisation and stratification within the Sugarloaf Catchment Area. *AFAC and Bushfire CRC Conference*, Sydney, NSW, 29 August–1 September, 2011.

Bucksch, A., and Fleck, S. (2011). Automated Detection of Branch Dimensions in Woody Skeletons of Fruit Tree Canopies. *Photogrammetric Engineering and Remote Sensing*, 77(3), 229–240.

Bunting, P., and Lucas, R. (2006). The delineation of tree crowns in Australian mixed species forests using hyperspectral Compact Airborne Spectrographic Imager (CASI) data. *Remote Sensing of Environment*, 101, 230–248.

Cabello-Leblic, A. (2018). Tree Crown Delineation. Ch 11 in *Effective Field Calibration and Validation Practices: A practical handbook for calibration and validation satellite and model-derived terrestrial environmental variables for research and management*. A TERN Landscape Assessment Initiative, NCRIS. ISBN 978-0-646-94137-0.

Calders, K., Newnham, G., Burt, A., Murphy, S., Raumonen, P., Herold, M., Culvenor, D., Avitabile, V., Disney, M., Armston, J., and Kaasalainen, M. (2015). Nondestructive estimates of above-ground biomass using terrestrial laser scanning. *Methods in Ecology and Evolution*, 6, 198–208. doi:*10.1111/2041-210X.12301*

Carnegie, A.J. (2008). A decade of forest health surveillance in Australia: an overview. *Australian Forestry*, 71, 161–163.

Carnegie, A., Eldridge, R., and Cante, R. (2008). Forest health surveillance in New South Wales, Australia. *Australian Forestry*, 71, 164–195.

Catling, P.C., and Coops, N.C. (1999). Prediction of the distribution and abundance of small mammals in the eucalypt forests of south-eastern Australia from airborne videography. *Wildlife Research*, 26, 641–650.

Chisholm, L.A. (2006). Detection of moisture stress in *Eucalyptus camaldulensis* using leaf-level spectral reflectance: implications for remote sensing. *International Journal of Geoinformatics*, 2(1), 79–92.

Claverie, M., Ju, J., Masek, J.G., Dungan, J.L., Vermote, E.F., Roger, J.-C., Skakun, S.V., and Justice, C. (2018). The Harmonized Landsat and Sentinel-2 surface reflectance data set. *Remote Sensing of Environment*, 219, 145–161

Coggins, S.B., Coops, N.C., Hilker, T., and Wulder, M.A. (2013). Augmenting forest inventory attributes with geometric optical modelling in support of regional susceptibility assessments to bark beetle infestations. *International Journal of Applied Earth Observation and Geoinformation*, 21, 444–452.

Coops, N.C., and Catling, P.C. (1997). Predicting the complexity of habitat in forests from airborne videography for wildlife management. *International Journal of Remote Sensing*, 18(12), 2677–2686.

Coops, N.C., and Culvenor, D. (2000). Utilizing local variance of simulated high-spatial resolution imagery to predict spatial pattern of forest stands. *Remote Sensing of Environment*, 71(3), 248–260.

Coops, N.C., Stone, C., Culvenor, D.S., Chisholm, L., and Merton, R. (2002). Predicting Chlorophyll Content in Eucalypt Vegetation at the Leaf and Canopy Level using High Spectral Resolution Imagery. *Tree Physiology*, 23, 23–31.

Coops, N.C., Smith, M., Martin, M.E., and Ollinger, S.V. (2003). Prediction of eucalypt foliage nitrogen content from satellite-derived hyperspectral data. *IEEE Transactions on Geoscience and Remote Sensing*, 41, 1338–1346.

Coops N.C., White J.C., and Wulder, M.A. (2006). Identifying and describing forest disturbance and spatial pattern. In: *Understanding forest disturbance and spatial pattern: Remote sensing and GIS approaches*. (Eds: T. Wulder and S.E. Franklin). CRC Press, Taylor and Francis, Boca Raton. Pp 31-61.

Coops, N., Hilker, T., Wulder, M., St-Onge, B., Siggins, A., Newhnam, G., and Trofymow, J.A. (2007). Estimating Canopy Structure of Douglas-fir forest stands from discrete-return LIDAR. *Trees: Structure and Function*, 21(3), 295–310.

Coops, N.C., Wulder, M.A., Duro, D.C., Han, T., and Berry, S. (2008). The development of a Canadian dynamic habitat index using multi-temporal satellite estimates of canopy light absorbance. *Ecological Indicators*, 8, 754–766.

Coops, N.C., Nilker, T., Hall, F.G., Nichol, C.J., Drolet, G.G. (2011). Estimation of Light-use Efficiency of Terrestrial Ecosystem from Space: A Status Report. *Bioscience*, 60(10), 788–797.

Côté, J.-F., Widlowski, J.-L., Fournier, R.A., and Verstraete, M.M. (2009). The structural and radiative consistency of three-dimensional tree reconstruction from terrestrial lidar. *Remote Sensing of Environment*, 113, 1067–1081.

Côté, J.-F., Fournier, R.A., and Egli, R. (2011). An architectural model of trees to estimate forest structural attributes using terrestrial LiDAR. *Environmental Modelling and Software*, 26, 761–777.

Côté, J.-F., Fournier, R.A., Frazer, G.W., and Niemann, K.O. (2012). A fine-scale architectural model of trees to enhance LiDAR-derived measurements of forest canopy structure. *Agricultural and Forest Meteorology*, 166–167, 72–85.

Culvenor, D.S. (2002). TIDA: an algorithm for the delineation of tree crowns in high spatial resolution remotely sensed imagery. *Computers and Geoscience*, 28(1), 33–44.

Curran, P.J. (1989). Remote sensing of foliar chemistry. *Remote Sensing of Environment*, 30, 271–278.

Danson, F.M., Hetherington, D., Morsdorf, F., Koetz, B., and Allgower, B. (2007). Forest canopy gap fraction from terrestrial laser scanning. *IEEE Transactions on Geoscience and Remote Sensing Letters*, 4 (1), 157–160.

Dassot M., Constant T., and Fournier M. (2011). The use of terrestrial LiDAR technology in forest science: application fields, benefits and challenges, *Annals of Forest Science*, 68, 959–974. *http://dx.doi.org/10.1007/s13595-011-0102-2*.

Datt, B. (1999). A new reflectance index for remote sensing of chlorophyll content in higher plants: tests using *Eucalyptus* leaves. *Journal of Plant Physiology*, 154, 30–36.

Douglas, E.S., Martel, J., Li, Z., Howe, G., Hewawasam, K., Marshall, R.A., Schaaf, C.L., Cook, T.A., Newnham, G.J., Strahler, A., and Chakrabarti, S. (2015). Finding leaves in the forest: the dual-wavelength Echidna lidar. *IEEE Geoscience and Remote Sensing Letters*, 12, 776–80.

Drolet, G.G., Middleton, E.M., Huemmrich, K.F., Hall, F.G., Amiro, B.D., Barr, A.G., Black, T.A., McCaughey, J.H., and Margolis, H.A. (2008). Regional mapping of gross light-use efficiency using MODIS spectral indices. *Remote Sensing of Environment*, 112, 3064–3078.

Du Toit, F., Coops, N.C., Tompalski, P., Goodbody, T.R.H., El-Kassaby, Y.A., Stoehr, M., Turner, D., and Lucieer, A. (2020). Characterizing variations in growth characteristics between Douglas-fir with different genetic gain levels using airborne laser scanning. *Trees*, 34, 649–664. *https://doi.org/10.1007/s00468-019-01946-y*

Duchateau, E., Longuetaud, F., Mothe, F., Ung, C., Auty, D., and Achim, A. (2013). Modelling knot morphology as a function of external tree and branch attributes. *Canadian Journal of Forest Research*, 43(3), 266–277.

Fedrigo, M., Newnham, G., Coops, N., Culvenor, D., Bolton, D., and Nitschke, C. (2018). Predicting temperate forest stand types using only structural profiles from discrete return airborne lidar. *ISPRS Journal of Photogrammetry and Remote Sensing*, 136(1) 106–119. *https://doi.org/10.1016/j.isprsjprs.2017.11.018*

Feilhauer, H., Asner, G.P., and Martin, R.E. (2015). Multi-method ensemble selection of spectral bands related to leaf biochemistry. *Remote Sensing of Environment*, 164, 57–65.

Fisher, A., Armston, J., Goodwin, N., and Scarth, P. (2020). Modelling canopy gap probability, foliage projective cover and crown projective cover from airborne lidar metrics in Australian forests and woodlands. *Remote Sensing of Environment*, 237, 111520. *https://doi.org/10.1016/j.rse.2019.111520*

Florence, R.G. (1996). *Ecology and silviculture of eucalypts*. CSIRO Publishing, Melbourne, Australia.

Furby, S.L., Caccetta, P.A., Wu, X., and Chia, J. (2008). Continental Scale Land Cover Change Monitoring in Australia using Landsat Imagery, *Proceedings of Studying, Modeling and Sense Making of Planet Earth*. 1-6 June 2008, Department of Geography, University of the Aegean, Mytilene, Lesvos, Greece.

Gilmore, S., Mackey, B., and Berry, B. (2007). The extent of dispersive movement behaviour in Australian vertebrate animals, possible causes, and some implications for conservation. *Pacific Conservation Biology*, 19, 93–103.

Gitelson, A.A., Kaufman, Y.J., Stark, R., and Rundquist, D. (2002). Novel algorithms for remote estimation of vegetation fraction. *Remote Sensing of Environment*, 80(1), 76-87.

Goodwin, N.R., and Collett, L.J. (2014). Development of an automated method for mapping fire history captured in Landsat TM and ETM time series across Queensland, Australia. *Remote Sensing of Environment*, 148, 206–221. *http://dx.doi.org/10.1016/j.rse.2014.03.021*

Gougeon, F.A. (1995). A crown-following approach to the automatic delineation of individual tree crowns in high spatial resolution aerial images. *Canadian Journal of Remote Sensing*, 21, 274–28.

Gougeon, F.A. (1999). Automated individual tree crown delineation using a valley-following algorithm and rule-based system. *Proceedings of International forum: Automated interpretation of high spatial resolution digital imagery for forestry* (Eds: D.A. Hill and D.G. Leckie) February 10-12, 1998, Victoria, British Columbia. Natural Resources Canada, Canadian Forest Service, Pacific Forestry Centre, Victoria, BC. pp 11–23.

Gougeon, F.A., and Leckie, D.G. (2001). Individual tree crown image analysis—a step towards precision forestry. *First International Precision Forestry Symposium*, Seattle, Washington, 17–20 June 2001.

Gould, J., and Cruz, M. (2012). *Australian Fuel Classification: Stage II*. Ecosystem Sciences and Climate Adaption Flagship. CSIRO, Canberra Australia.

Gower, S.T., Kucharik, C.J., and Norman, J.M. (1999). Direct and Indirect Estimation of Leaf Area Index, fAPAR and Net Primary Production of Terrestrial Ecosystems, *Remote Sensing of Environment*, 70, 29–51.

Haverd, V., Lovell, J.L., Cuntz, M., Jupp, D.L.B., Newnham, G.J., and Sea, W. (2012). The Canopy Semi-analytic P_{gap} And Radiative Transfer (CanSPART) model: Formulation and application. *Agricultural and Forest Meteorology*, 160, 14–35. doi:*10.1016/j.agrformet.2012.01.018*

Haywood, A., and Stone, C. (2011). Semi-automating the stand delineation process in mapping natural eucalypt forests, *Australian Forestry*, 74(1), 13–22. doi:*10.1080/00049158.2011.10676341*

Held, A., Ticehurst, C., Lymburner, L. (2001). Hyperspectral mapping of rainforests and mangroves, in: IGARSS 2001. Scanning the Present and Resolving the Future. *Proceedings of IEEE International Geoscience and Remote Sensing Symposium*. pp. 2787–2789.

Henning, J.G., and Radtke, P.J. (2006). Ground-based laser imaging for assessing three-dimensional forest canopy structure. *Photogrammetric Engineering and Remote Sensing*, 72, 1349–1358.

Hermosilla, T., Wulder, M.A., White, J.C., Coops, N.C., Hobart, G.W., and Campbell, L.B. (2016). Mass data processing of time series Landsat imagery: pixels to data products for forest monitoring. *International Journal of Digital Earth*, 9(11), 1035–1054. doi:*10.1080/17538947.2016.1187673*

Hilker, T., Lyapustin, A., Hall, F.G., Wang, Y.J., Coops, N.C., Drolet, G., and Black, T.A. (2009). An assessment of photosynthetic light use efficiency from space: Modeling the atmospheric and directional impacts on PRI reflectance. *Remote Sensing of Environment*, 113, 2463–2475.

Hilker, T.M., van Leeuwen, M., Coops, N.C., Wulder, M.A., Newnham, G., Culvenor, D.S., Jupp, D.L.B. (2010). Comparing canopy metrics derived from terrestrial and airborne laser scanning in a Douglas-fir dominated forest stand. *Trees: Structure and Function*, 24, 819–832. doi:*10.1007/s00468-010-0452-7*

Hilker,T., Coops, N.C., Hall, F.G., Nichol, C.J., Lyapustin, A., Black, T.A., Wulder, M.A., Leuning, R., Barr, A., Hollinger, D.Y., Munger, B., and Tucker, C.J. (2011). Inferring terrestrial photosynthetic light use efficiency of temperate ecosystems from space. *Journal of Geophysical Research*, 116, G03014.

Hilker, T., Frazer, G.W., Coops, N.C., Wulder, M.A., van Leeuwen, M. Newnham, G.J., Culvenor, D.S., and Stewart, J.D. (2013). Prediction of wood fiber attributes from LiDAR-derived forest canopy indicators. *Forest Science*, 59(2), 231–242. *http://dx.doi.org/10.5849/forsci.11-074*

Hill, M.J., Senarath, U., Lee, A., Zeppel, M., Nightingale, J.M., Williams, R., and McVicar, T.R. (2006). Assessment of the MODIS LAI product for Australian ecosystems, *Remote Sensing of Environment*, 101, 495–518.

Hislop, S., Jones, S., Soto-Berelov, M., Skidmore, A., Haywood, A., and Nguyen, T. (2019). A fusion approach to forest disturbance mapping using time-series ensemble techniques. *Remote Sensing of Environment*, 221, 188–197.

Hopkinson, C., Chasmer, L., Young-Pow, C., and Treitz, P. (2004). Assessing forest metrics with a ground-based scanning lidar. *Canadian Journal of Forest Research*, 34, 573–583. *http://dx.doi.org/10.1139/x03-225*.

Hyyppä, J., Yu, X., Hyyppä, H., Vastaranta, M., Holopainen, M., Kukko, A., Kaartinen, H., Jaakkola, A., Vaaja, M., Koskinen, J., and Alho P. (2012). Advances in forest inventory using airborne laser scanning. *Remote Sensing*, 4, 1190–1207. *http://dx.doi.org/10.3390/rs4051190*.

IFA (2008). *Silviculture in Australia's Native Forests*. Institute of Foresters of Australia Policy Statement 2.9, IFA. *http://www.forestry.org.au/pdf/pdf-public/policies/Statement%202%201%209%20-%20Silviculture%20in%20Native%20Forests%20_Approved%2007-08-08_%20-%20_Web%202%209_.pdf*

Jafari, R., and Lewis, M.M. (2012). Arid land characterisation with EO-1 Hyperion hyperspectral data. *International Journal of Applied Earth Observation and Geoinformation*, 19, 298–307.

Jetz, W., Cavender-Bares, J., Pavlick, R., Schimel, D., Davis, F.W., Asner, G.P., Guralnick, R., Kattge, J., Latimer, A.M., Moorcroft, P. (2016). Monitoring plant functional diversity from space. *Nature Plants*, 2(3), [16024]. *https://doi.org/10.1038/NPLANTS.2016.24*

Jupp, D.L.B., and Lovell, J.L. (2007). Airborne and ground-based lidar systems for forest measurement: background and principles. *CSIRO Marine and Atmospheric Research Paper 17*. 151 p.

Jupp, D.L.B., and Walker, J. (1996). Detecting structural and growth changes in woodlands and forests: the challenge for remote sensing and the role of geometric optical modelling. In: *The Use of Remote Sensing in the Modeling of Forest Productivity at Scales from the Stand to the Globe*. (Eds: Gholz, H.L., Nakane, K., and Shimoda, H.). Kluwer Academic Publishers, Dordrecht.

Jupp, D.L.B., Walker, J., and Penridge, L.K. (1986). Interpretation of vegetation structure in Landsat MSS imagery: a case study in disturbed semi-arid eucalypt woodland. Part 2. Model based analysis. *Journal of Environmental Management*, 23, 35-57.

Jupp, D.L.B., Culvenor, D.S., Lovell, J.L., Newnham, G.J., Strahler, A.H., and Woodcock, C.E. (2009). Estimating forest LAI profiles and structural parameters using a ground-based laser called 'Echidna®'. *Tree Physiology*, 29(2), 171–181.

Kasischke, E.S., Turetsky, M.R., Ottmar, R.D., French, N.H.F., Shetler, G., Hoy, E., and Kane, E.S. (2008). Evaluation of the Composite Burn Index for Assessing Fire Severity in Black Spruce Forests. *International Journal of Wildland Fire*, 17(4), 515–526.

Ke, Y., and Quackenbush, L.J.L. (2011). A review of methods for automatic individual tree-crown detection and delineation from passive remote sensing. *International Journal of Remote Sensing*, 32, 4725–4747.

Kennedy, R.E., Yang, Z., and Cohen, W.B. (2010). Detecting trends in forest disturbance and recovery using yearly Landsat Time Series: 1. LandTrendr—Temporal segmentation algorithms. *Remote Sensing of Environment*, 114, 2897–2910.

Key, C.H., and Benson, N.C. (2006). *Landscape Assessment: Sampling and Analysis Methods*. USDA Forest Service, Rocky Mountain Research Station General Technical Report RMRS-GTR-164-CD. Odgen, UT.

Klemmt, H.-J., Seifert, T., Seifert, S., Kunneke, A., Wessels, B., and Pretzsch, H. (2010). Assessment of branchiness in a *Pinus pinaster* plantation by terrestrial laser scanner data as a link between exterior and interior wood properties. *Proceedings SilviLaser 2010*. 14–17 September, 2010. Freiburg. pp 253–264.

Kokaly, R.F., Asner, G.P., Ollinger, S.V., Martin, M.E., Wessman, C.A. (2009). Characterizing canopy biochemistry from imaging spectroscopy and its application to ecosystem studies. *Remote Sensing of Environment*, 113, S78–S91.

Kumar, L., Skidmore, A.K., and Mutanga, O. (2010). Leaf level experiments to discriminate between *Eucalyptus* species using high spectral resolution reflectance data: use of derivatives, ratios and vegetation indices. *Geocarto International*, 25, 327–344. doi:*10.1080/10106040903505996*

Lee, A., Lucas, R., and Brack, C. (2004). Quantifying vertical forest stand structure using small footprint LiDAR to assess potential stand dynamics. *International Archives of Photogrammetry, Remote Sensing and Spatial Information Science*, XXXVI-8/W2, 213–217.

Lee, A., and Lucas, R.M. (2007). A LiDAR-derived canopy density model for tree stem and crown mapping in Australian woodlands. *Remote Sensing of Environment*, 111, 493–518.

Lees, B.G., and Ritman, K. (1991). Decision-tree and rule-induction approach to integration of remotely sensed and GIS data in mapping vegetation in disturbed or hilly environments. *Environmental Management*, 15, 823–831.

Lehmann, E.A., Wallace, J.F., Caccetta, P.A., Furby, S.L., and Zdunic, K. (2013). Forest cover trends from time series Landsat data for the Australian continent. *International Journal of Applied Earth Observation and Geoinformation*, 21, 453–462.

Lim, K., Treitz, P., Wulder, M., St-Onge, B., and Flood, M. (2003). LiDAR remote sensing of forest structure. *Progress in Physical Geography*, 27, 88–106.

Lovell, J.L., Jupp, D.L.B., Culvenor, D.S., and Coops, N.C. (2003). Using airborne and ground-based ranging LIDAR to measure canopy structure in Australian forests. *Canadian Journal of Remote Sensing*, 29(5), 607–622.

Lovell, J.L., Haverd, V., Jupp, D.L.B., and Newnham, G.J. (2012). The Canopy Semi-analytic P_{gap} And Radiative Transfer (CanSPART) model: Validation using ground based lidar. *Agricultural and Forest Meteorology*, 158–159, 1–12. doi:*10.1016/j.agrformet.2012.01.020*

Lucas, R.M., Cronin, N., Lee, A., Moghaddam, M., Witte, C., and Tickle, P. (2006). Empirical relationships between AIRSAR backscatter and LiDAR-derived forest biomass, Queensland, Australia, *Remote Sensing of Environment*, 100, 407–425

Lucas, R., Bunting, P., Paterson, M., and Chisholm, L. (2008). Classification of Australian forest communities using aerial photography, CASI and HyMap data, *Remote Sensing of Environment*, 112(5), 2088–2103. *http://dx.doi.org/10.1016/j.rse.2007.10.011*.

Maas, H.G., Bienert, A., Scheller, S., and Keane, E. (2008). Automatic forest inventory parameter determination from terrestrial laser scanner data. *International Journal of Remote Sensing*, 29, 1579–1593.

Mackey, B.G., Bryan, J., and Randall, L. (2004). Australia's Dynamic Habitat Template 2003. *Proceedings of MODIS Vegetation Workshop II,* University of Montana.

Mahlein, A.K., Oerke, E.C., Steiner, U., and Dehne, H.W. (2012). Recent advances in sensing plant diseases for precision crop protection. *European Journal of Plant Pathology*, 133(1), 197–209. doi:*10.1007/s10658-011-9878-z*

Markus, T., Neumann, T., Martino, A., Abdalati, W., Brunt, K., Csatho, B., Farrell, S., Fricker, H., Gardner, A., Harding, D., Jasinski, M., Kwok, R., Magruder, D., Lubin, D., Luthcke, S., Morison, J., Nelson, R., Neuenschawander, A., Palm, S., Popescu, S., Shum, CK., Schutz, B.E., Smith, B., Yang, Y., Jasinski, M. (2017). The Ice, Cloud, and land Elevation Satellite-2 (ICESat-2): science requirements, concept, and implementation. *Remote Sensing of Environment*, 190, 260–273. *https://doi.org/10.1016/j.rse.2016.12.029*

Mellor, A., Haywood, A., Stone, C., and Jones, S. (2013). The Performance of Random Forests in an Operational Setting for Large Area Sclerophyll Forest Classification. *Remote Sensing*, 5(6), 2838–2856. *https://doi.org/10.3390/rs5062838*

Milne, T. (2000). Forest and Woodland Biomass and Classification using Airborne and Spaceborne Radar Data. *International Archives of Photogrammetry and Remote Sensing*, Vol. XXXIII, Part B7. Amsterdam 2000.

Mitchell, A.L., Rosenqvist, A., and Mora, B. (2017). Current remote sensing approaches to monitoring forest degradation in support of countries measurement, reporting and verification (MRV) systems for REDD+. *Carbon Balance and Management*, 12(1), 9. *https://doi.org/10.1186/s13021-017-0078-9*

Mohammed, G.H., Colombo, R., Middleton, E.M., Rascher, U., van der Tol, C., Nedbal, L., Goulas, Y., Pérez-Priego, O., Damm, A., Meroni, M., Joiner, J., Cogliati, S., Verhoef, W., Malenovský, Z., Gastellu-Etchegorry, J.-P., Miller, J.R., Guanter, L., Moreno, J., Moya, I., Berry, J.A., Frankenberg, C., Zarco-Tejada, P.J. (2019). Remote sensing of solar-induced chlorophyll fluorescence (SIF) in vegetation: 50 years of progress. *Remote sensing of environment*, 231, 111177. *https://doi.org/10.1016/j.rse.2019.04.030*

Murphy, G. (2008). Determining Stand Value and Log Product Yields Using Terrestrial Lidar and Optimal Bucking: A Case Study. *Journal of Forestry*, 106(6), 317–324.

Murphy, P.N.C., Ogilvie, J., Meng, F.-R., White, B., Bhatti, J.S., and Arp, P.A. (2011). Modelling and mapping topographic variations in forest soils at high resolution: A case study. *Ecological Modelling*, 222(14), 2314–2132.

Næsset, E. (2002). Predicting forest stand characteristics with airborne scanning laser using a practical two-stage procedure and field data. *Remote Sensing of Environment*, 80(1), 88–99.

Newnham, G.J., Siggins, A.S., Blanchi, R.M., Culvenor, D.S., Leonard, J.E., and Mashford, J.S. (2012). Exploiting three dimensional vegetation structure to map wildland extent. *Remote Sensing of Environment*, 123, 155–162.

Newnham, G.J., Armston, J.D., Calders, K., Disney, M.I., Lovell, J.L., Schaaf, C.B., Strahler, A.H., and Danson, F.M. (2015). Terrestrial Laser Scanning for Plot-Scale Forest Measurement. *Current Forestry Reports*, 1, 239–251. doi:*10.1007/s40725-015-0025-5*

Nguyen, T.H., Jones, S.D., Soto-Berelov, M., Haywood, A., and Hislop, S. (2020). Monitoring aboveground forest biomass dynamics over three decades using Landsat time-series and single-date inventory data. *International Journal of Applied Earth Observation and Geoinformation*, 84, 101952. *https://doi.org/10.1016/j.jag.2019.101952*

NSW DPI (2015). *Forest Biosecurity and Resource Assessment*. *http://www.dpi.nsw.gov.au/research/areas/fhr*

O'Hara, K.L., Latham, P.A., Hessburg, P., and Smith, B.G. (1996). A structural classification for inland northwest forest vegetation. *Western Journal of Applied Forestry*, 11(3), 97–102.

Ollinger, S.V., and Smith, M.L. (2005). Net Primary Production and Canopy Nitrogen in a temperate forest landscape: an analysis using imaging spectrometry, modeling and field data. *Ecosystems*, 8, 760–778.

Packalen, P., and Maltamo, M. (2008). Estimating Species-Specific Diameter Distributions and Saw Log Recoveries of Boreal Forests from Airborne Laser Scanning Data and Aerial Photographs: A Distribution-Based Approach. *Canadian Journal of Forest Research*, 38, 1750–1760.

Palmer, M.W., Earls, P.G., Hoagland, B.W., White, P.S., and Wohlgemuth, T. (2002). Quantitative tools for perfecting species lists. *Environmetrics*, 13, 121–137.

Perera, A.H., and Euler, D.L. (2000). Landscape ecology in forest management: An introduction. In: *Ecology of a Managed Terrestrial Landscape: Patterns and Processes of Forest Landscapes in Ontario*. (Eds: A.H. Perera, D.L. Euler and I. D. Thompson). Ontario Ministry of Natural Resources/ UBC Press, Vancouver, BC. pp. 3–11.

Pickett-Heaps, C.A., Canadell, J.G., Briggs, P.R., Gobron, N., Haverd, V., Paget, M.J., Pinty, B., and Raupach, M.R. (2014). Evaluation of six satellite-derived Fraction of Absorbed Photosynthetic Active Radiation (FAPAR) products across the Australian continent. *Remote Sensing of Environment*, 140, 241–256.

Pinz, A.J. (1991). A computer vision system for the recognition of trees in aerial photographs. *NASA, Goddard Space Flight Center, Multisource Data Integration in Remote Sensing* pp. 111–124. (SEE N91-1561507-43).

Pokharel, B., Dech, J.P., Groot, A., and Pitt, D. (2014). Ecosite-based predictive modeling of black spruce (*Picea mariana*) wood quality attributes in boreal Ontario. *Canadian Journal of Forest Research*, 475, 465–475.

Pook, E.W. (1985). Canopy dynamics of *Eucalyptus maculata* Hook. 3. Effects of drought. *Australian Journal of Botany*, 33, 65–79.

Prusinkiewicz, P., and Hanan, J. (1990). Visualization of botanical structures and processes using parametric L-systems. In: *Scientific Visualization and Graphics Simulation* (Ed: D. Thaimann) pp. 183–201. John Wiley and Sons.

Pyne, S.J. (1992). *The Burning Bush: A Fire History of Australia*. Allen and Unwin, Sydney. 520 p. ISBN: 1863731946

Reutebuch, S., Andersen, H., and McGaughey, R. (2005). Light Detection and Ranging (LIDAR): An emerging tool for multiple resource inventory. *Journal of Forestry*, 103(6), 286–292.

Riaño, D., Meier, E., Allgower, B., Chuvieco, E., and Ustin, S.L. (2003). Modeling airborne laser scanning data for the spatial generation of critical forest parameters in fire behavior modeling. *Remote Sensing of Environment*, 86, 177–186.

Richards, J. (2012). *Australia and SAR: A Road Map*. CRCSI, Melbourne.

Richards, G.P., and Brack, C. (2004). A continental biomass stock and stock change estimation approach for Australia. *Australian Forestry*, 67(4), 284–288. doi:*10.1080/00049158.2004.10674948*

Rocchini, D., Chiarucci, A., and Loiselle, S.A. (2004). Testing the spectral variation hypothesis by using satellite multispectral images. *Acta Oecolgica*, 26, 117–120.

Rocchini, D., Ricotta, C., and Chiarucci, A. (2007). Using satellite imagery to assess plant species richness: The role of multispectral systems. *Applied Vegetation Science*, 10, 325–331.

Roy, D.P., Ju, J., Kline, K., Scaramuzza, P.L., Kovalskyy, V., Hansen, M., Loveland, T.R., Vermote, E., and Zhang, C. (2010). Web-enabled Landsat Data (WELD): Landsat ETM+ composited mosaics of the conterminous United States. *Remote Sensing of Environment*, 114, 35–49.

Runions, A., Lane, B., and Prusinkiewicz, P. (2007). Modeling Trees with a Space Colonization Algorithm. *Proceedings of Eurographics Workshop on Natural Phenomena* (Eds: D. Ebert, and S. Mérillou). *http://www.algorithmicbotany.org/papers/colonization.egwnp2007.pdf*

Russell-Smith, J., Ryan, P.G., and Durieu, R. (1997). A Landsat MSS-derived fire history of Kakadu National Park. *Journal of Applied Ecology*, 34, 748–766.

Scarth, P., and Phinn, S. R. (2000). Determining forest structural attributes using an inverted geometric-optical model in mixed eucalypt forests, Southeast Queensland, Australia. *Remote Sensing of Environment*, 71 (2), 141–157. doi:*10.1016/S0034-4257(99)00066-8*

Sea, W.B., Choler, P., Beringer, J., Weinmann, R.A., Hutley, L.B., and Leuning, R. (2011). Documenting improvement in leaf area index estimates from MODIS using hemispherical photos for Australian savannas. *Agricultural and Forest Meteorology*, 151, 1453–1461.

Serbin, S.P., Singh, A., McNeil, B.E., Kingdon, C.C., Townsend, P.A. (2014). Spectroscopic determination of leaf morphological and biochemical traits for northern temperate and boreal tree species. *Ecological Applications*, 24, 1651–1669.

Serra, J. (1982). *Image Analysis and Mathematical Morphology*. Academic Press, London, New York.

Shang, X., and Chisholm, L.A. (2014). Classification of Australian Native Forest Species Using Hyperspectral Remote Sensing and Machine-Learning Classification Algorithms. *IEEE Journal of Selected Topics in Applied Earth Observations and Remote Sensing*, 7(6), 2481–2489.

Sims, N.C., Culvenor, D.S., Newnham, G., Nicholas C. Coops, N.C., and Hopmans, P. (2013). Towards the Operational Use of Satellite Hyperspectral Image Data for Mapping Nutrient Status and Fertilizer Requirements in Australian Plantation Forests. *IEEE Journal of Selected Topics in Applied Earth Observations and Remote Sensing*, 6(2), 320–328.

Skidmore, A.K. (1989). Unsupervised training area selection in forests using a non-parametric distance measure and spatial information. *International Journal of Remote Sensing*, 10, 133–146.

Skidmore, A.K., and Turner, B.J. (1988). Forest mapping accuracies are improved using a supervised nonparametric classifier with SPOT data. *Photogrammetric Engineering and Remote Sensing*, 54, 1415–1421.

Skidmore, A.K., Wood, G.B., and Shepherd, K.R. (1987). Remotely sensed digital data in forestry: a review, Australian Forestry, 50(1), 40–53. doi:*10.1080/00049158.1987.10674493*

Smith, R.B., and Woodgate, P.W. (1985). Appraisal of fire damage and inventory for timber salvage by remote sensing in mountain ash forests in Victoria. *Australian Forestry*, 48, 252–263.

SOFR (2018). Australia's State of the Forests Report 2018. Montreal Process Implementation Group for Australia and National Forest Inventory Steering Committee 2018, ABARES, Canberra. *https://www.agriculture.gov.au/abares/forestsaustralia/sofr/sofr-2018*

Soverel, N.O., Coops, N.C., Perrakis, D.B., Daniels, L., and Gergel, S. (2011). The transferability of a dNBR derived model to predict burn severity across ten wildland fires in Western Canada. *International Journal of Wildland Fire*, 20, 1–14.

Staudhammer, C.L, and LeMay, V.M. (2001). Introduction and evaluation of possible indices of stand structural diversity. *Canadian Journal of Forest Research*, 31(7), 1105–1115.

Stone, C., and Coops, N.C. (2004). Assessment and monitoring of damage from insects in Australian eucalypt forests and commercial plantations. *Australian Journal of Entomology*, 43, 283–292.

Stone, C., Chisholm, L., and McDonald, S. (2005). Effects of leaf age and psyllid damage on the spectral reflectance properties of *Eucalyptus saligna* foliage. *Australian Journal of Botany*, 53, 45–54.

Stone, C., Turner, R.,and Verbesselt, J. (2008). Integrating plantation health surveillance and wood resource inventory systems using remote sensing, *Australian Forestry*, 71(3), 245–253. doi:*10.1080/00049158.2008.10675043*

Strahler, A.H., and Li, X. (1981). An invertible coniferous forest canopy reflectance model. *Proceedings of 15th International Symosium on Remote Sensing of the Environment*, Ann Arbor, Michigan, May, 1981. pp. 1237–1243.

Strahler, A.H., and Li, X. (1984). Spatial/spectral modeling of conifer forest reflectance, *Proc. Third Australasian Remote Sensing Conference*, Queensland, Australia. pp. 88–90.

Strahler, A.H., Jupp, D.L.B., Woodcock, C.E., Schaaf, C.B. Yao, T., Zhao, F., Yang, X., Lovell, J., Culvenor, D., Newnham, G., Ni-Miester, W., and Boykin-Morris, W. (2008). Retrieval of forest structural parameters using a ground-based lidar instrument (Echidna). *Canadian Journal of Remote Sensing*, 34, Supplement 2, S426–S440.

Tansey, K., Selmes, N., Anstee, A., Tate, N.J., and Denniss, A. (2009). Estimating tree and stand variables in a Corsican Pine woodland from terrestrial laser scanner data. *International Journal of Remote Sensing*, 30, 5195–5209.

TERN Australia (2018). *Effective Field Calibration and Validation Practices: A practical handbook for calibration and validation satellite and model-derived terrestrial environmental variables for research and management*. A TERN Landscape Assessment Initiative, NCRIS. ISBN 978-0-646-94137-0. *https://www.tern.org.au/NEW-CalVal-handbook-for-remote-sensing-bgp4370.html*

Thies, M., Pfeifer, N., Winterhalder, D, and Gorte, B.G.H. (2004). Three-dimensional reconstruction of stems for assessment of taper, sweep and lean based on laser scanning of standing trees. *Scandinavian Journal of Forest Research*, 19, 571–581.

Ticehurst, C., Lymburner, L., and Held, A. (2001). Mapping tree crowns using hyperspectral and high spatial resolution imagery. In: *Third International Conference on Geospatial Information in Agriculture and Forestry*. Denver, Colorado.

Tickle, P.K., Witte, C., Lee, A., Lucas, R.M., Jones, K., and Austin, J. (2001), The use of airborne scanning LIDAR and large scale photography within a strategic forest inventory and monitoring framework. *Proceedings of IEEE International Geoscience and Remote Sensing Symposium. IGARSS 2001*, 9–13 July 2001, Sydney, Australia. IEEE Inc. Piscataway, N.J.

Turner, M. (1989). Landscape Ecology: The Effect of Pattern on Process. *Annual Review of Ecology and Systematics*, 20, 171–197.

Turner, R. (2006). *An airborne lidar canopy segmentation approach for estimating above-ground biomass in Coastal Eucalypt forests*. PhD thesis. School of Biological, Earth and Environmental Sciences. UNSW, Sydney.

Turner, R. (2007). An overview of Airborne LIDAR applications in New South Wales state forests. *ANZIF Conference*, Coffs Harbour, June 2007.

Ustin, S.L., Roberts, D.A., Gamon, J.A., Asner, G.P., Green, R.O. (2004). Using imaging spectroscopy to study ecosystem processes and properties. *BioScience*, 54, 523–534.

Ustin, S.L., Gitelson, A.A., Jacquemoud, S., Schaepman, M., Asner, G.P., Gamon, J.A., Zarco-Tejada, P. (2009). Retrieval of foliar information about plant pigment systems from high resolution spectroscopy. *Remote Sensing of Environment*, 113, S67–S77.

Van der Zande, D., Stuckens, J., Verstraeten, W.W., Mereu, S., Muys, B., and Coppin, P. (2011). 3D modeling of light interception in heterogeneous forest canopies using ground-based LiDAR measurements. *International Journal of Applied Earth Observation*, 13, 792–800, doi:*10.1016/j.jag.2011.05.005*.

Verbesselt, J., Robinson, A., Stone, C., and Culvenor, D. (2009). Forecasting tree mortality using change metrics derived from MODIS satellite data. *Forest Ecology and Management*, 258, 1166–1173.

Verbesselt, J., Zeileis, A., and Herold, M. (2012). Near real-time disturbance detection using satellite image time series. *Remote Sensing of Environment*, 123, 98–108. *https://doi.org/10.1016/j.rse.2012.02.022*

Walker, J., Jupp, D.L.B., Penridge, L.K., and Tian, G. (1986). Interpretation of vegetation structure in Landsat MSS imagery: a case study in disturbed semi-arid eucalypt woodlands. Part 1. Field data analysis. *Journal of Enviromental Management*, 23, 19-33.

Wallace, L., Lucieer, A., Watson, C., and Turner, D. (2012a). Development of a UAV-LiDAR System with Application to Forest Inventory. *Remote Sensing*, 4(6), 1519–1543. doi:*10.3390/rs4061519*

Wallace, L., Lucieer, A., and Watson, C.S. (2012b). Assessing the feasibility of UAV-based LiDAR for high resolution forest change detection. *Proceedings of ISPRS Congress*, 25 August–1 September 2012, Melbourne. ISPRS International Archives of the Photogrammetry, Remote Sensing and Spatial Information Sciences XXXIX-B7, pp. 499–504. *http://www.terraluma.net/downloads/Wallace_ISPRS2012.pdf*

Walsworth, N., and King, D. (1999). Image modelling of forest changes associated with acid mine drainage. *Computers and Geoscience*, 25(5), 567–580.

Watt, M., Milne, T., Williams, M., and Mitchell, A. (2012). *Robust Imaging from Space: Satellite SAR (Synthetic Aperture Radar)*. CRCSI. *http://www.crcsi.com.au/library/resource/robust-imaging-from-space*

Weller, D., Denham, R., Witte, C., Mackie, C., and Smith, D. (2003). Assessment and monitoring of foliage projected cover and canopy height across native vegetation in Queensland, Australia, using laser profiler. *Canadian Journal of Remote Sensing*, 29, 578–591.

White, J.C., Gómez, C., Wulder, M.A., and Coops, N.C. (2010). Characterizing temperate forest structural and spectral diversity with Hyperion EO-1 data. *Remote Sensing of Environment*, 114, 1576–1589.

White, J.C., Wulder, M.A., Varhola, A., Vastaranta, M., Coops, N.C., Cook, B.D., Pitt, D., and Woods, M. (2013). *A best practices guide for generating forest inventory attributes from airborne laser scanning data using an area-based approach*. Natural Resources Canada, Canadian Forest Service, Canadian Wood Fibre Centre, Victoria, BC. Information Report FI-X-010.

White, J.C., Coops, N.C., Wulder, M.A., Vastaranta, M., Hilker, T., and Tompalski, P. (2016). Remote Sensing Technologies for Enhancing Forest Inventories: A Review. *Canadian Journal of Remote Sensing*, 42(5), 619–641.

Wold, S., Sjostrom, M., Eriksson, L. (2001). PLS-regression: a basic tool of chemometrics. *Chemometrics and Intelligent Laboratory Systems*, 58, 109–130.

Woodgate, P., and Black, P. (1988). *Forest cover changes in Victoria: 1869–1987*. Dept. of Conservation Forests and Lands, Melbourne.

Wulder, M.A., Bater, C.W., Coops, N.C., Hilker, T., White, J.C. (2008). The role of lidar in sustainable forest management. *The Forestry Chronicle*, 84(6), 807–826.

Wulder, M.A., Masek, J.G., Cohen, W.B., Loveland, T.R., and Woodcock, C.E. (2012). Opening the archive: How free data has enabled the science and monitoring promise of Landsat. *Remote Sensing of Environment*, 122, 2–10.

Yagüe, J., and Garcia, P. (2006). A remote sensing survey of vegetation communities adjacent to Myall Lakes, NSW, Australia. *Global developments in environmental earth observation from space. Proceedings of 25th EARSeL Symposium*. Porto, Portugal, 2005. pp 355–365.

Youngentob, K.N., Renzullo, L.J., Held, A.A., Jia, X., Lindenmayer, D.B., and Foley, W.J. (2012). Using imaging spectroscopy to estimate integrated measures of foliage nutritional quality. *Methods in Ecology and Evolution*, 3, 416–26. doi:*10.1111/j.2041-210X.2011.00149.x*

Zheng, G., and Moskal, L.M. (2009). Retrieving leaf area index (LAI) using remote sensing: Theory, method, and sensors. *Sensors*, 9(4), 2719–2745.

Zhu, Z., Woodcock, C.E., and Olofsson, P. (2012). Continuous monitoring of forest disturbance using all available Landsat imagery. *Remote Sensing of Environment*, 122, 75–91.

Observing Carbon Dynamics

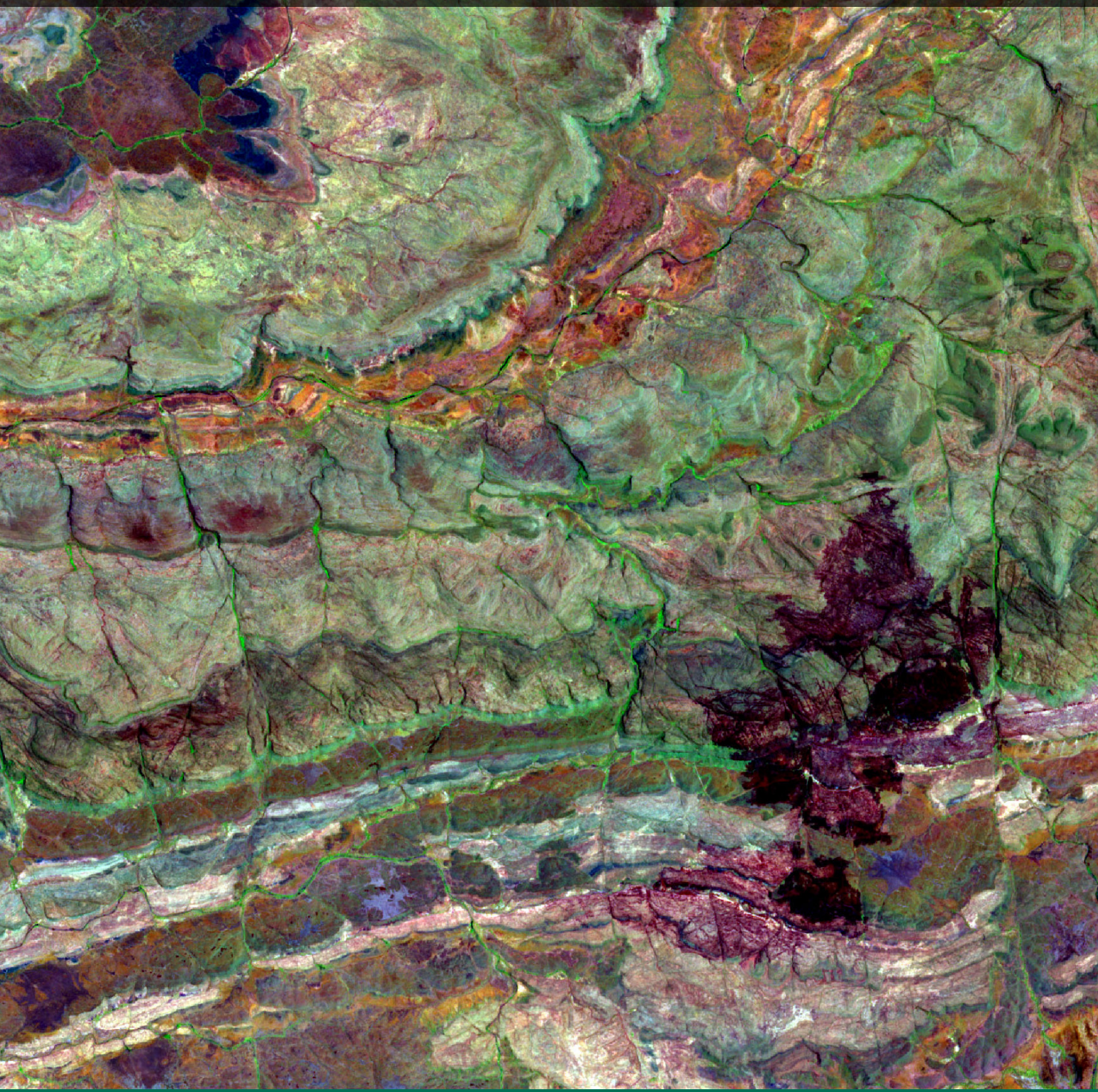

The carbon cycle is introduced in Volume 1A—Section 4.2.4 and Excursus 1.2 above. The following sections consider the use of EO to map and monitor the Australian landscape in two areas that are relevant to carbon studies:

- carbon cycling (see Section 17); and
- fire (see Section 18).

Contents

17 Carbon Cycling 353

18 Fire 389

Background image on previous page: Sentinel-2B image over the Kimberley region, WA, acquired on 13 November 2020 and displayed using bands 11, 8, 3 as RGB. **Source:** Norman Mueller, Geoscience Australia

17 Carbon Cycling

Alfredo Huete

Carbon is the foundation and primary energy source of all life on Earth—from the food that sustains us to the fossil fuels that drives the global economy. Carbon, as an important greenhouse gas, is intertwined with the Earth's climate by helping to regulate the Earth's temperature. Human activities such as the burning of fossil fuels, and land use and land cover modifications, are greatly raising the amounts of carbon dioxide (CO_2) in the atmosphere with associated impacts on global temperatures and climate.

The carbon cycle describes the flow and storage of carbon among the land, ocean, and atmosphere carbon reservoirs (see Figure 17.1, Excursus 1.2 above, and Volume 1A—Section 4.2.4). Most of the carbon is stored in geologic rocks and sediments, including fossil carbon, while the rest is present in the ocean, atmosphere, land, and living organisms. The carbon cycle functions across a wide range of timescales and includes:

- a relatively 'slow' carbon cycle—geologic processes, such as the weathering of rocks, soil formation, sedimentation, and deep ocean storage of carbon; and
- a more active, 'fast' carbon cycle—biologic processes absorb CO_2 from the atmosphere to sustain life and release CO_2 when organisms die, and in the ocean, there are also chemical exchanges of carbon between surface waters and the atmosphere (see Excursus 1.1).

Accurate estimates of carbon pools and fluxes in the biosphere are necessary for quantifying carbon balances across space and time, and at regional to global scales, but are quite challenging to accomplish (Schimel, 1995; Baldocchi *et al*., 2001). The determination of productivity across diverse landscapes is traditionally carried out in various, often inconsistent ways, that include field and plot scale biomass measurements, plant harvests, micrometeorological flux measurements, EO, and empirical and process-based models that may involve field, micrometeorological, and EO data inputs (see Excursus 17.2).

We cannot hope to either understand or to manage the carbon in the atmosphere unless we understand and manage the trees and the soil too.
(Freeman Dyson)

Background image: Major bushfires in southeastern Australia photographed on 18 January 2003 from the International Space Station. Winds direct smoke plumes eastward off the Australian coast, north of Cape Howe, near the NSW/Victoria border. The agricultural valleys of the Murrumbidgee and Murray Rivers give way to the burning, darker bush areas of the mountains, with the extreme eastern coastline of Victoria visible on the right of this image. **Source:** NASA-JSC. (Retrieved from *https://eol.jsc.nasa.gov/Collections/EarthObservatory/articles/Australian_Bushfires.htm*)

Recommended Chapter Citation: Huete, A.R. (2021). Carbon Cycling. Ch 17 in *Earth Observation: Data, Processing and Applications. Volume 3A—Terrestrial Vegetation.* CRCSI, Melbourne. pp. 353–388.

Figure 17.1 The carbon cycle between land, atmosphere, and oceans

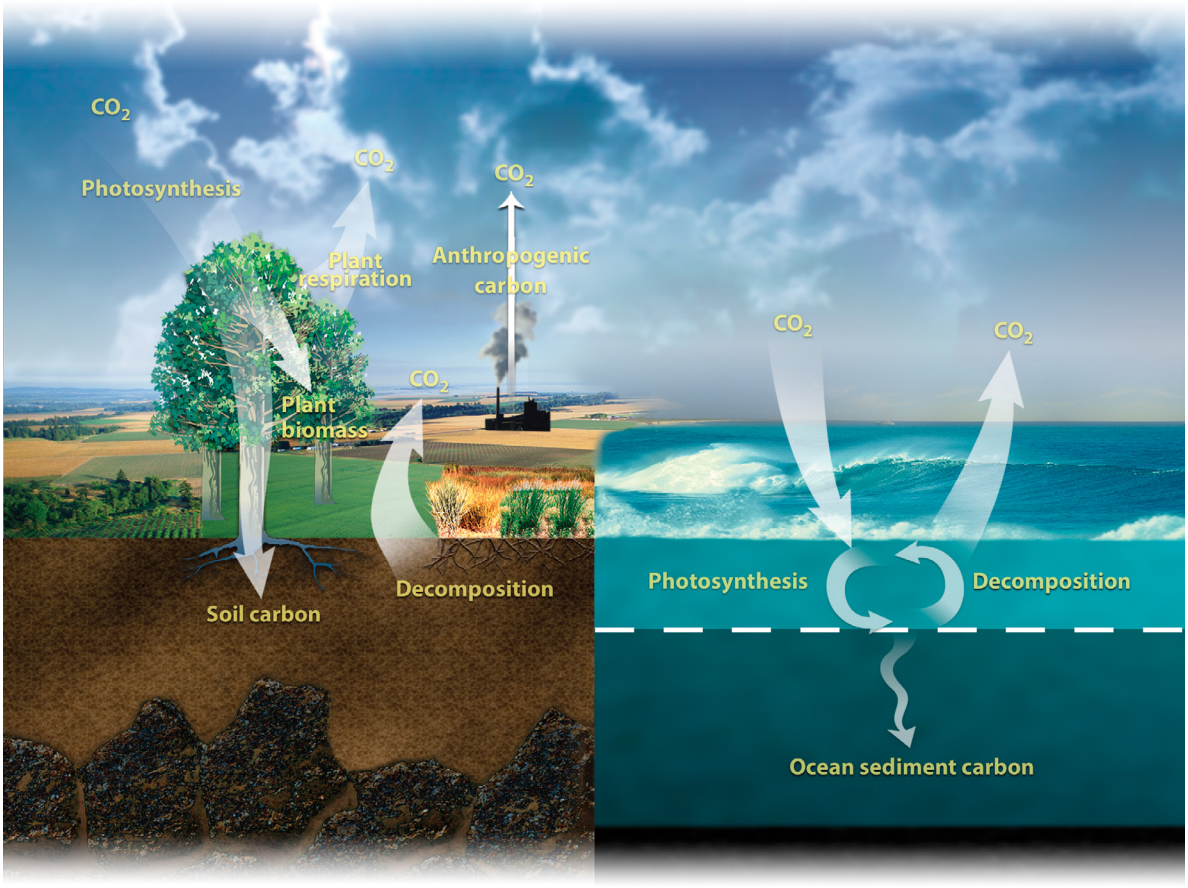

Source: NASA

Carbon is the currency of life. The rapid formation of carbon-rich topsoil is the greatest priority and opportunity of our time.
(Rattan Lal)

Excursus 17.1—The Carbon Cycle

Source: Alfredo Huete, University of Technology, Sydney

The carbon cycle—the flow and storage of carbon among the land, ocean, and atmosphere carbon reservoirs—is introduced in Excursus 1.2 above (see also Volume 1A—Section 4.2.4) and illustrated in Figure 17.1.

Carbon Reservoirs (Pools)

Carbon reservoirs refer to the major storage areas of carbon on the Earth, distributed among land, ocean, and atmosphere (see Figure 17.1). Global quantities of these carbon reservoirs are uncertain. Most of Earth's carbon (estimated at 65,500 Pg, where 1 Pg=1 billion metric tons) is stored in rocks, while the rest is present in the ocean, atmosphere, land surface (vegetation, soil), and fossil fuels, and include:

- atmosphere carbon—as CO_2 and CH_4 carbon gases is estimated at 800 Gt;
- ocean carbon—in the surface ocean (1,000 Gt), deep ocean (37,000 Gt), and reactive sediments (6,000 Gt); and
- terrestrial carbon—as plant biomass (550 Gt), soil (2,300 Gt), and fossil carbon (10,000 Gt).

Slow Carbon Cycle

The slow carbon cycle occurs at geologic timescales (> 1 million years), in which processes of rock weathering, soil formation, and sedimentation of carbonates in oceans move carbon among rocks, soil, ocean, and atmosphere. On average, 0.01–0.10 Pg of carbon move through the slow carbon cycle every year. Carbon moves from the atmosphere to the lithosphere (rocks) as carbonic acid in rainfall. The acid dissolves rocks and initiates the process of chemical weathering, which, along with physical weathering, contributes to soil formation. Chemical weathering releases calcium and other nutrients, which may be transported to the ocean and combine with bicarbonate ions to form calcium carbonate.

In the oceans, calcium carbonate shells from marine organisms, such as corals and plankton produce layers of calcium carbonate that sink to the seafloor, which over time, are cemented together and turn to rock, storing the carbon in limestone, and other carbon-containing rocks. Organic carbon may also be embedded in layers of mud which, under heat and pressure, compress the mud and carbon over millions of years to form sedimentary rock such as shale. In special cases, when dead plant matter builds up faster than it can decay, layers of organic carbon become oil, coal, or natural gas instead of sedimentary rock like shale.

Over time, carbon eventually returns to the atmosphere through volcanoes, At the ocean surface, CO_2 gas dissolves in and ventilates out of the ocean in a steady exchange with the atmosphere. Once in the ocean, the CO_2 gas reacts with water to make the ocean more acidic, and reacts with carbonate from rock weathering to produce bicarbonate ions.

This complex and integrated carbon cycle system maintains a balance among the land-atmosphere-ocean carbon pools that prevents excessive carbon accumulation in the atmosphere or excessive carbon stored in rocks. For example, increases in CO_2 in the atmosphere from volcanic activity, will lead to rising temperatures which will result in more rainfall that increases the weathering of rocks, that will eventually deposit more carbon on the ocean floor. This rebalances the slow carbon cycle through chemical weathering over a period of a few hundred thousand years. This buffering of carbon behaves as a thermostat and helps to maintain the quantity of CO_2 in the atmosphere and keep the Earth's temperature relatively stable. As Earth's climate is intimately tied to atmospheric concentrations of carbon (CO_2 and CH_4), an understanding of the carbon cycle is essential for dealing with current climate change problems, as well as modelling and predicting Earth's future carbon-climate system.

Fast Carbon Cycle

The fast carbon cycle operates at diurnal, annual and decadal timescales, where carbon is exchanged between the land, ocean, and the atmosphere, through the relatively fast processes of photosynthesis and respiration (autotrophic and heterotrophic), fire, and land use and land cover change. Plants, marine biota, soil microbes, and human activities are the main components of the fast carbon cycle and 10–100 Gt of carbon move through this cycle every year through land and ocean uptake of atmosphere CO_2 through photosynthesis, CO_2 diffusion into the ocean, and the release of CO_2 in respiration, decomposition, fire, and air-sea gas exchange.

Photosynthesis

In the process of photosynthesis, plants absorb CO_2 from the atmosphere and use sunlight to combine it with water to form sugar molecules (CH_2O) and oxygen (O_2; see Figure 17.2 and Section 5.2.1). The chemical reaction is:

$$CO_2 + H_2O + \text{light energy} = CH_2O + O_2$$

The organic compounds produced by plants are assimilated for building plant structures (leaves, stems, wood branches, trunks, and roots) and stored in biomass.

The rate of carbon fixation by the biosphere, or total organic carbon produced per unit of time and over a defined area is termed gross primary productivity (GPP; see Section 7.4). GPP is the basis for food, fibre, and wood production, and has important implications for human welfare. It is the largest carbon flux between the terrestrial biosphere and the atmosphere and is a key measure of ecosystem metabolism.

Figure 17.2 Terrestrial photosynthetic carbon cycle

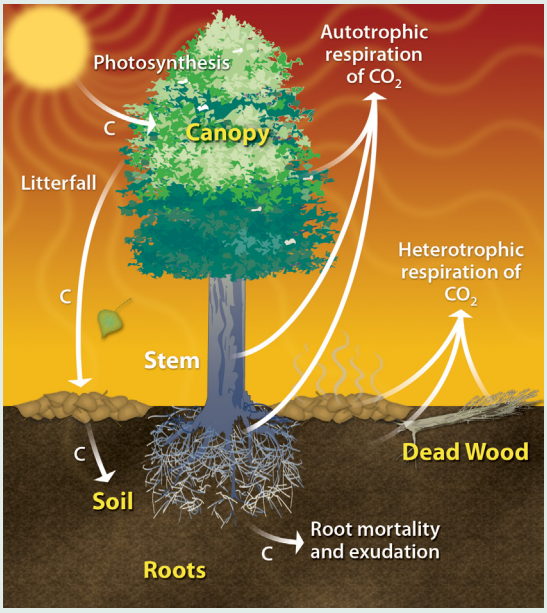

Source: *https://public.ornl.gov/site/gallery/*

Respiration

Part of the carbon fixed in photosynthesis by plants is returned to the atmosphere through the process of respiration (autotrophic respiration; see Section 5.2.2). The energy content of the organic carbon molecules is an excellent source of energy for all living things. Oxygen combines with sugar to release water, CO_2 and energy. The basic chemical reaction is:

$$CH_2O + O_2 = CO_2 + H_2O + \text{energy}$$

There are various mechanisms by which the biosphere-fixed organic carbon molecules return to the atmosphere, but all involve the same chemical reaction. Plants and phytoplankton may break down the sugar to get the energy they need to grow (autotrophic respiration). The plants or phytoplankton may also be consumed by higher organisms, along food chains, and break down the plant sugar to get energy (heterotrophic respiration).

Growing season carbon processes

At seasonal to annual timescales, plants and phytoplankton may die and decay at the end of the growing season, and carbon moves from plants and animals to the atmosphere and soils through microbial decomposition and heterotrophic respiration. Litterfall, plant materials that fall to the ground (leaves, branches, flowers, and fruits), contributes to the buildup of the soil carbon pool. The size of the soil organic carbon pool will be a function of carbon inputs from litterfall, root exudation, and mortality, and the release of carbon during decomposition (Wang *et al.*, 2018; Gray *et al.*, 2015). Fire may also consume plants and stored carbon and release it into the atmosphere (see Section 18).

The fast carbon cycle is tightly coupled between the atmosphere and biosphere, as can be seen by CO_2 fluctuations in the atmosphere with the changing seasons. When the large land masses of the Northern Hemisphere green up during spring and summer, atmospheric CO_2 decreases as carbon is removed from the atmosphere in the process of photosynthesis. This cycle peaks in August, with about 2 ppm of CO_2 drawn out of the atmosphere. In the autumn and winter, many plants senesce and decay with GPP declining while decomposition and heterotrophic respiration increase, thus returning CO_2 back to the atmosphere.

Resource Constraints

Productivity is generally limited by spatially and temporally varying resource constraints (e.g. nutrients, light, water, and temperature; Field *et al.*, 1995; Churkina and Running 1998; Nemani *et al.*, 2003). GPP and microbial respiration will thus be limited by water availability in arid regions and by cold temperatures at very high latitudes and elevations. This results in spatially distributed high biomass, carbon rich ecosystems as well as low biomass areas (e.g. deserts) with low carbon contents over the planet in response to climatic, geologic (nutrient), and topographic variations. The same occurs in the oceans in which primary productivity varies along coastlines and areas of warm and cool ocean currents (see Volume 3B).

Photosynthesis or primary production is essentially an integrator of resource availability, and according to the resource optimisation theory (Field *et al.*, 1995), ecological processes tend to adjust plant characteristics over time periods of weeks or months to match the capacity of the environment to support photosynthesis and maximise growth.

Productivity terms

The net balance between photosynthesis and respiration is defined as net productivity of an area and determines whether an area is source or a sink of CO_2 to the atmosphere (see Section 7.4). Productivity forms the basis of biosphere functioning and carbon, energy, and water budgets. There are various ways to express productivity, including:

- Net primary productivity (NPP), defined as the difference between GPP, or photosynthesis, and autotrophic respiration. Terrestrial net primary productivity (NPP) is the amount of carbon fixed by plants and accumulated as biomass (Cramer *et al.*, 1999).
- Net ecosystem productivity (NEP) is defined as GPP minus ecosystem respiration (ER), which is the sum of autotrophic and heterotrophic respiration. This includes photosynthesis by plants and respiration from soils, and plants, including litter.
- Net biome productivity (NBP) is defined as the overall net ecosystem carbon balance, and includes other processes such as deforestation, harvest, and fire that lead to the loss of, and changes in, carbon.

Figure 17.3 Seasonal variations in photosynthesis (GPP) between hemispheres

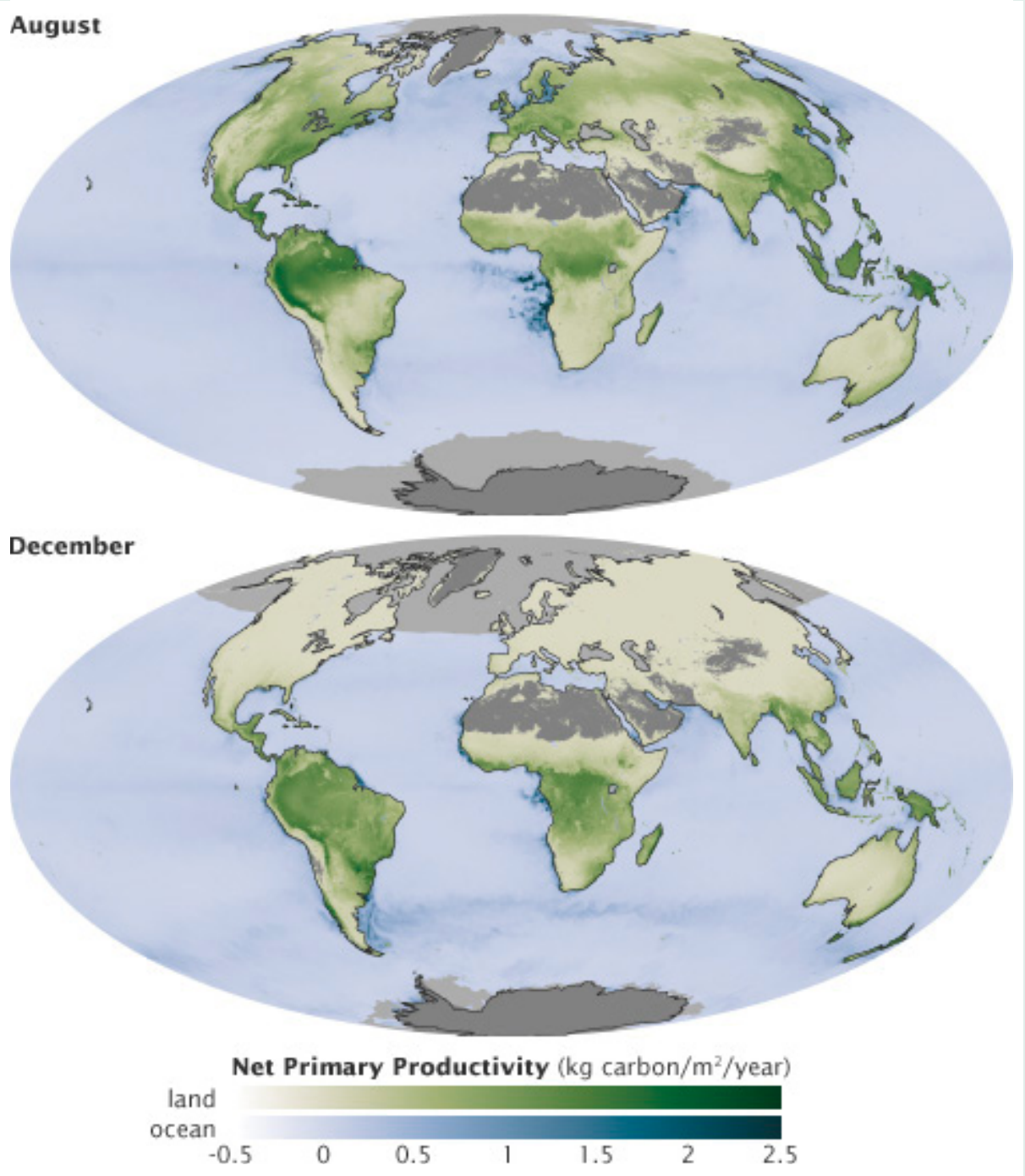

Source: NASA Earth Observatory *https://earthobservatory.nasa.gov/features/CarbonCycle/page3.php*

Excursus 17.2—Measuring Biosphere Productivity

Source: Alfredo Huete, University of Technology, Sydney

In Situ Methods

In situ measures of carbon stocks and productivity involve sampling methods that will vary with biome type, and can include tree inventories, litter traps, grassland forage estimates, destructive sampling, cropland harvests, and market statistics. Field inventory plots and plot networks have been established for carbon monitoring of forests at the national scale (FAO, 2007). The plots enable direct carbon measurements and systematic data collection of forest information over small areas of forest, and although they can be difficult to maintain, they provide valuable *in situ* information on carbon stocks over time (Chambers *et al*., 2009).

Established long term experimental plots further enable cross-site production comparisons. Plot level methods generally measure above ground net primary production (ANPP), from which gross primary production (GPP) can be been estimated by correcting for respiratory losses (Field *et al*., 1995). Agricultural yield statistics combined with maps of cropland areas provide large scale ANPP estimates from local to national level census statistics (Monfreda *et al*., 2008; Guanter *et al*., 2014). These methods are amenable to many uncertainties due to differences in site-based procedures, and in some cases, inconsistent sampling methods over time at a given site (Moran *et al*., 2014). For example, established procedures for biomass clipping of grass sampling plots can vary in timing from either the peak of the growing season or the end of the growing season (see Moran *et al*., 2014).

Eddy covariance flux towers

A global network of over 500 micrometeorological tower sites, known as FLUXNET (see Excursus 7.2), provide continuous measurements of carbon and water flux exchanges between ecosystems and the atmosphere (Baldocchi, 2001). The eddy covariance method is used to directly measure fluxes at a spatial scale of hundreds of metres, by computing the covariance between the vertical velocity and target scalar mixing ratios at each tower site. The carbon gas flux measured is the net amount resulting from autotrophic and soil heterotrophic respiration and photosynthesis, and is termed net ecosystem exchange production (NEE):

$$NEE = GPP + Respiration$$

This yields information on diurnal, daily, and seasonal dynamics plus interannual variations of NEE of CO_2 between the land surface and the atmosphere (Baldocchi *et al*., 2001; Verma *et al*., 2005). GPP is the residual calculated from the direct measurements of NEE and estimates of respiration. This generates valuable *in situ* information for validating EO-based productivity products and for carbon model development and independent evaluation and assessment of their uncertainties.

Earth Observation

Over the last four decades, EO has played an increasingly important role in global (terrestrial and marine) carbon cycle studies. Satellite imaging sensors offer synoptic scale observations of ecosystem states and landscape dynamics, and are seen as invaluable tools to help fill the large spatial gaps and restrictive coverage afforded by *in situ* measurements (experimental plots and eddy covariance flux towers) to better constrain and improve the accuracies of models (see Section 10). EO provides much needed data and information of under-sampled critical regions (e.g. tropical and arctic/boreal environments) and facilitates broadscale patterns of ecosystem functioning. A strategic combination of satellite observations and *in situ* data, can provide the dense sampling in space and time required to characterise the heterogeneity of ecosystem structure and function (Schimel *et al*., 2015).

As illustrated in Figure 17.4, carbon fluxes assessed with EO data include gross primary production (GPP), ecosystem respiration (ER), net primary production (NPP), net ecosystem production (NEP), and net biome production (NBP). The carbon stocks that are quantified by EO include above ground biomass (AGB), litter, and soil organic carbon (SOC).

Figure 17.4 EO of terrestrial carbon cycle studies

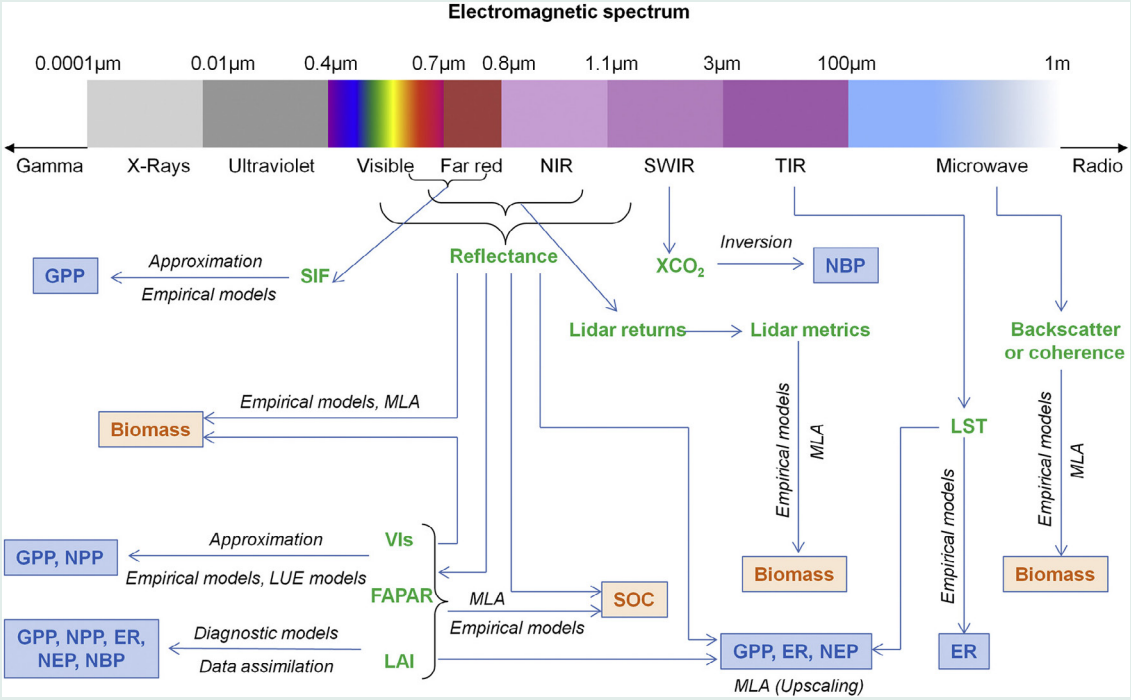

Source: Xiao *et al.* (2019) Figure 2

17.1 Carbon Cycling in Australia

National and regional carbon budgets are important for providing information on spatial and temporal variations in carbon fluxes and stocks in response to climate variability, fire activity, and land use and land cover changes. Haverd *et al.* (2013) performed a comprehensive assessment of the terrestrial carbon budget for Australia over a decadal period from 1990 to 2011. They combined a regional biogeochemical model (BIOS2) and a land surface model (CABLE) constrained by published emissions data and multiple types of observations, including satellite measures of vegetation cover, leaf area index (LAI), and burnt areas from AVHRR and MODIS sensors.

The national carbon budget assessments included the mean, variance, and uncertainty estimates of the following land-atmosphere carbon flux components (Haverd *et al.*, 2013):

- net primary production (NPP) and net ecosystem production (NEP);
- fires and land use change;
- riverine export, dust export, and harvest (wood, crop and livestock); and
- fossil fuel emissions (both territorial and non-territorial).

Their findings demonstrated the Australian terrestrial carbon cycle is characterised by extreme variability in carbon uptake by vegetation, emissions from fires, and land use changes (see Figure 17.5). Overall, Australian ecosystems were absorbing carbon (NEP) by 80 TgC yr^{-1}, with climate variability accounting for 12 TgC yr^{-1} and rising CO_2 levels accounting for 68 TgC yr^{-1}. The relative contributions of the climate and CO_2 forcings (or drivers) varied greatly across bioclimatic regions. In the desert areas of central Australia, CO_2 fertilisation and very high rainfall in 1990–2011 together generated a strong positive NEP response, while in the cool temperate regions the CO_2 fertilisation effect was offset by long term drought (1990–2011) and its negative impact on NEP. The response of NPP to rising CO_2 also varied regionally, being higher for regions where gross primary production (GPP) was strongly influenced by high vapour pressure deficit (VPD).

Moreover, the positive ecosystem gains in NEP (80 TgC yr^{-1}) were partially offset by fire emissions (26 TgC yr^{-1}) and land use change (18 TgC yr^{-1}), resulting in a net biome productivity (NBP) of 36 TgC yr^{-1}. Thus, the aggregate Australian ecosystem net positive NBP offset averaged fossil fuel emissions of 95 TgC yr^{-1}, by 38% (Haverd *et al.*, 2013). The interannual variability (IAV) in the Australian carbon budget was dominated by interannual variability in ecosystem NEP, and exceeded Australia's total fossil fuel carbon emissions. Lateral transport of carbon in rivers accounted for 0.1% of NPP, while net export of carbon by dust was smaller at 0.05%.

Figure 17.5 Australian territorial carbon budget 1990–2011

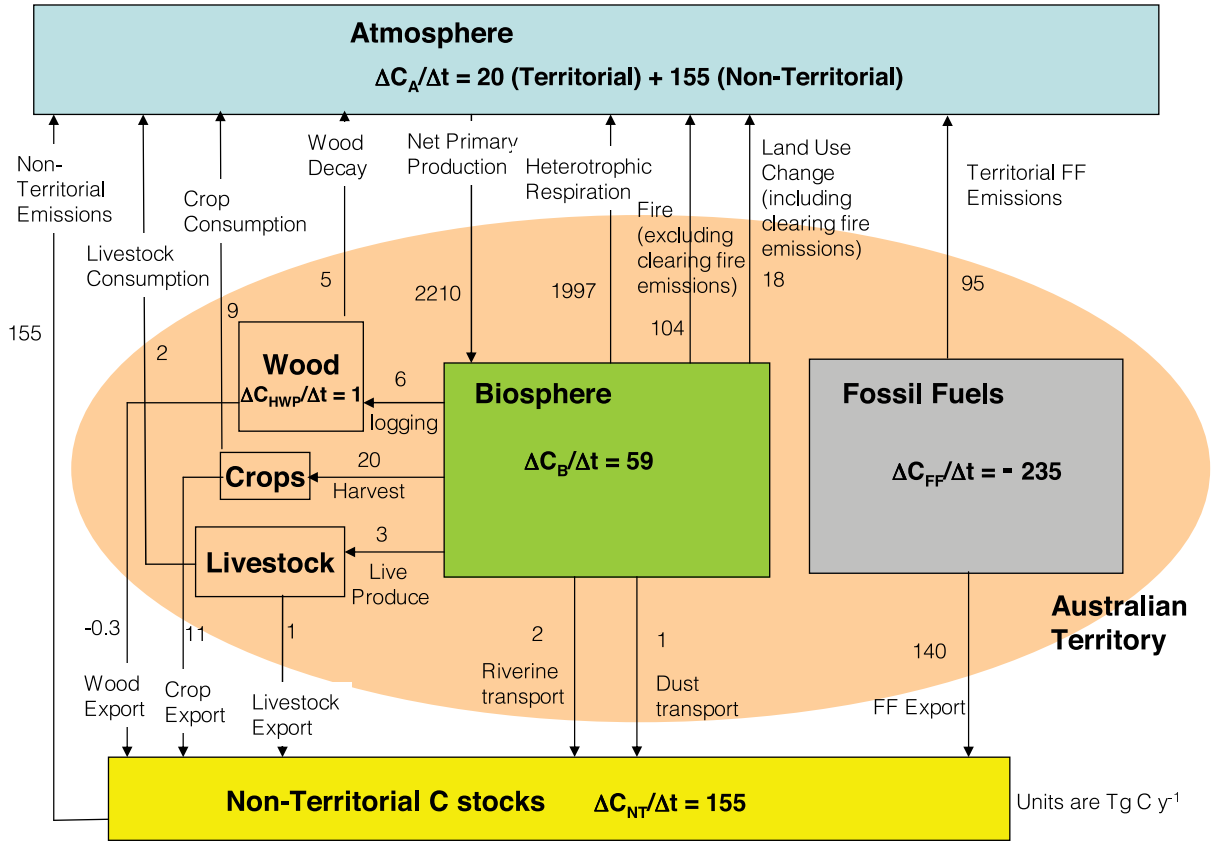

Source: Haverd *et al.* (2013) Figure 1

Australia has also been an active partner in international agreements to track global carbon emissions resulting from forest degradation, including the Reducing Emissions from Deforestation and Forest Degradation in Developing Countries (REDD+) and the UN Global Forest Observations Initiative (GFOI; see Section 17.9). The current EO-based approaches for national measurement, reporting, and verification within the REDD+ framework are reviewed by Mitchell *et al.* (2017).

17.2 EO Sensors for Carbon Cycling

A wide variety of satellite sensors and techniques have been used to quantify carbon fluxes (Running *et al.*, 2004; Xiao *et al.*, 2019) and stocks (Saatchi *et al.*, 2011) at various spatial and temporal scales (see Table 17.1). These include sensors in the optical, thermal, and microwave regions of the electromagnetic (EM) spectrum, and include measures of land and ocean chlorophyll content, leaf area, biomass, solar-induced chlorophyll fluorescence (SIF), canopy height and structure, and atmosphere carbon gases (see Figure 17.4). This combination renders EO a powerful tool for studying vegetation productivity at local, regional, and global scales (Gitelson *et al.*, 2006; Schimel *et al.*, 2015).

Historically, the availability of satellite observations since the 1970s has enabled the assessments of the magnitude, spatial patterns, interannual variability, and long term trends of carbon dynamics at landscape, regional, and global scales. Recent satellites with high resolution spectrometers, which can retrieve concentrations of key atmospheric gases (such as the Orbiting Carbon Observatory-2; OCO-2), are providing valuable insights into global variations in, and sources of, greenhouse gases (see Section 17.6).

Table 17.1 EO sensors relevant to carbon cycling

SAR: Synthetic Aperture Radar

Type	Sensor	Platform	Relevance	Advantages	Disadvantages
Passive optical	Multispectral radiometer	Satellite or airborne	Carbon fluxes and stocks	Long archives, short revisit frequency, global coverage, readily available at a range of spatial scales	Impacted by cloud cover
	Spectrometer	Satellite	Terrestrial chlorophyll fluorescence GPP Drought and heat stress sensitivity	Unique global coverage	Coarse spatial resolution
	Meteorological	Satellite	Atmospheric carbon and energy fluxes	Global coverage	Coarse spatial resolution
Active optical	Lidar	Satellite, airborne, and terrestrial	Forest biomass Fuel load	Detailed structure for trees and stands	High cost, specialised processing
Active microwave	SAR	Satellite or airborne	Biomass Forest disturbance	All weather, available since early 1990s	Medium-coarse resolution
Proximal	Passive optical sensors (phenocam, hyperspectral); meteorological sensors	Ground and tower-based (see Excursus 7.2 and Volume 2D—Section 12)	Ecosystem and atmospheric variability Carbon dynamics Phenology	Continuous, long term measurements	High cost, high data volume, require skilled maintenance

17.3 Biosphere productivity

Vegetation productivity is directly related to the interaction of solar radiation with the plant canopy (see Section 7.4). As plants and phytoplankton grow, the productivity gain resulting from their conversion of CO_2 into biomass through photosynthesis, can be quantified with EO approaches involving vegetation indices (VIs), solar-induced chlorophyll fluorescence (SIF), and light use efficiency (LUE) models. Spectral measures of vegetation growth include vegetation and chlorophyll indices, LAI and fractional vegetation cover (see Section 8). VIs are the most empirical spectral measure of productivity, however, they do not measure photosynthesis fluxes directly. EO complements the detailed information available from *in situ* sensors, such as from flux tower sites (see Excursus 7.2), through broad spatial-temporal coverage and extension, and further enables intercomparisons of vegetation across space and time (see Volume 2D).

Monteith and Unsworth (1990) noted that spectral VIs can legitimately be used to estimate the rate of processes that depend on absorbed light, such as photosynthesis. EO-based estimates of Gross Primary Productivity (GPP) have been implemented at global scales, based on the LUE equation that defines the amount of carbon fixed through photosynthesis as proportional to the solar energy absorbed by green vegetation multiplied by the efficiency with which the absorbed light is used in carbon fixation:

$$GPP = \varepsilon_{par} \times APAR = \varepsilon_{par} \times fAPAR \times PAR$$

where

ε_{par} is the efficiency of conversion of absorbed light into above ground biomass (AGB), or LUE;
PAR is the photosynthetically active radiation;
APAR is the absorbed PAR integrated over a time period; and
fAPAR is the fraction of APAR to the PAR available.

Monteith (1972) suggested that productivity of stress-free annual crops would be linearly related to vegetation absorbed PAR.

Asrar *et al.* (1984) showed the Normalised Difference Vegetation Index (NDVI; see Section 8.1.1) was linearly related with vegetation absorption of light energy, APAR, and thereby related to productivity through the potential capacity of vegetation to absorb light for photosynthesis (see Figure 17.6). The linear relationship between NDVI and fAPAR has been documented through field measurements (Fensholt *et al.*, 2004) and theoretical analyses (Sellers, 1985; Goward and Huemmrich, 1992; Myneni and Williams, 1994), although these relationships were not universal, and appeared to be unique to vegetation type, structure, soil optics. EO products, such as NDVI, were then used to map GPP globally, providing estimates of GPP that approximated eddy covariance (EC) estimates (Schimel *et al.*, 2015).

Figure 17.6 NDVI-APAR relationship

A linear relationship exists between NDVI and vegetation absorption of light energy (APAR) or fraction of APAR across multiple cropland and biome sites in Africa.

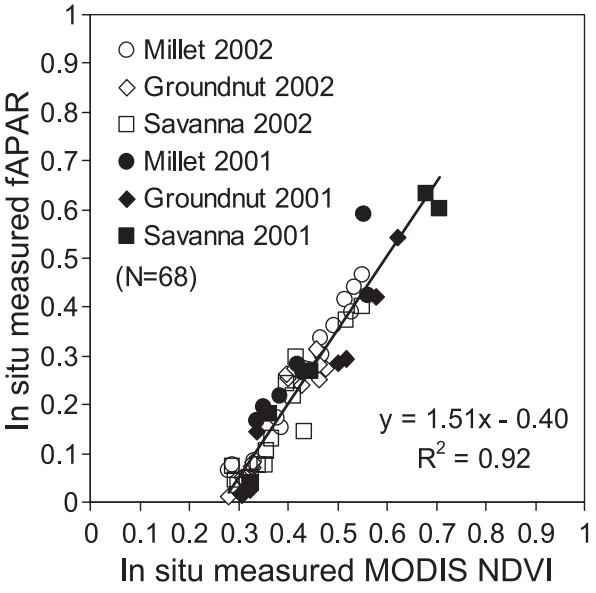

Source: Fensholt *et al.* (2004) Figure 10

17.3.1 Relationships between EO and flux tower GPP estimates

The advent of global, flux tower networks (see Excursus 7.2) has provided the opportunity to validate remotely sensed retrievals of productivity with *in situ* GPP estimates derived from the tower flux measures of net ecosystem exchange (NEE). This has been useful for validating EO spectral measures and carbon models, and to cross-calibrate EO-based methods. With the measurement footprint of flux towers at least partially overlapping the pixel size of daily return satellites (e.g. 250 m for MODIS), EO can simplify the upscaling of ecosystem processes, such as photosynthesis, from the network of flux towers to larger landscape units and to regional scales. Today, the integration of independently derived tower measured carbon fluxes with satellite data is the focus of many investigations across many ecosystems (Glenn *et al.*, 2008).

Several studies have suggested that EO products, such as VIs, are able to estimate GPP with relatively good accuracy, thus potentially simplifying carbon balance models and offering opportunities for region-wide upscaling of carbon fluxes (Glenn *et al.*, 2008). As top-of canopy measurements, flux towers do not require knowledge of LAI or details of canopy architecture to estimate fluxes facilitating their comparisons with satellite spectral index measures that similarly involve community properties resulting from integrative, top-of-canopy radiation interactions.

Rahman *et al.* (2005) initially reported that the Enhanced Vegetation Index (EVI; see Section 8.1.1) provided reasonably accurate estimates of GPP across a wide range of North American ecosystems. The strength of the linear relationships between EVI and tower GPP in temperate forests was greater in seasonally contrasting deciduous forests compared with more aseasonal evergreen forests (Rahman *et al.*, 2005; Sims *et al.*, 2006). Strong correlations between EVI and GPP were reported across Northern Europe (Olofsson *et al.*, 2008), across African tropical savanna ecosystems (Sjostrom *et al.*, 2011), and in dry to humid tropical forest sites in Southeast Asia and the Amazon (Xiao *et al.*, 2005; Huete *et al.*, 2006, 2008). Ma *et al.* (2013) observed good convergences between MODIS EVI and tower GPP across mesic and xeric tropical savannas in northern Australia.

The relationships between EVI and tower GPP are partly a result of fairly good correlations between LUE and EVI that make an independent estimate of LUE less necessary. Sims *et al.* (2006) reported that LUE derived from nine flux towers in North America was well-correlated with EVI (r^2=0.76), while Wu *et al.* (2011) reported moderate correlation between EVI and tower LUE in temperate and boreal forest ecosystems in North America. Further, the 16-day averaging period removes much of the influences of short term fluctuations in solar radiation and other environmental parameters, thereby minimising the need for climatic drivers.

Sims *et al.* (2006) further noted that when data from the winter period of inactive photosynthesis was excluded by use of land surface temperature (LST) observations below 0°, the EVI-tower GPP relationship improved. This demonstrates a limitation of spectrally-based satellite products for GPP estimations, in that spectral measurements record evergreen coniferous forests to remain 'green', even when temperatures inhibit photosynthesis (GPP).

Distinct differences in VI relationships with tower GPP were found between phenology-driven and meteorologically-driven Australian ecosystems. Restrepo-Coupe *et al.* (2016) found that in primarily meteorologically-driven (e.g. PAR, temperature, and/or precipitation) and relatively aseasonal ecosystems, there were no statistically significant relationships between GPP and MODIS vegetation products (LAI, fAPAR, VIs). The poor correlations were observed where meteorology and phenology were asynchronous (e.g. Mediterranean ecosystems). On the other hand, in phenology-driven ecosystems, changes in the vegetation status can be well-represented by VIs, and highly correlated VI-GPP relationships can be found in locations where key meteorological variables and vegetation phenology were synchronous.

The validation of satellite-based productivity products remains challenging due to a variety of spatial and temporal scaling issues. These include the matching of large satellite pixels (~1 km) with field plot scale measurements in both time and space. Li *et al.* (2007) demonstrated limitations associated with disparate footprints between satellite and tower flux measurements and the need for Landsat spatial resolutions for flux footprint matching, particularly in non-forested canopies. However, tower data of fluxes potentially offer much more than simply validating and/or calibrating EO products and models. An understanding of why satellite–flux tower relationships hold, or do not hold, will greatly advance and contribute to our comprehension of the carbon cycle mechanisms and scaling factors at play.

17.3.2 Solar-induced chlorophyll fluorescence (SIF) as proxy for GPP

More recent capabilities to measure solar-induced chlorophyll fluorescence (SIF) from airborne and space-based platforms now provides a more direct approach for estimating GPP (Frankenberg *et al.*, 2011; Joiner *et al.*, 2011). The PAR absorbed by chlorophyll in leaves is used to drive photosynthesis, but some radiation is also dissipated as heat or emitted back into the atmosphere at longer wavelengths (650–850 nm; see Volume 1A—Section 5). This re-emitted red and near infrared (NIR) light from illuminated plants as a by-product of photosynthesis, or SIF, has been found to strongly correlate with GPP (Baker, 2008; Meroni *et al.*, 2009). Chlorophyll fluorescence may be conceptualised as:

$$SIF = \varepsilon_f \times PAR \times fAPAR$$

where ε_f is the fAPAR photons that are re-emitted from the canopy as SIF photons, or yield of fluorescence photons.

SIF data provide information on both the light absorbed and the efficiency with which it is being used for photosynthesis. It is an independent measurement, linked to chlorophyll absorption, providing unique information on photosynthesis relative to VIs. The SIF expression can be combined with the GPP-based LUE equation to yield:

$$GPP = \frac{\varepsilon_{par}}{\varepsilon_f} \times SIF$$

Empirical studies at the leaf and canopy scale indicate that the two LUE terms tend to covary under the conditions of the satellite measurement (Flexas *et al.*, 2002). SIF is seen as one way to increase the effective remotely sensed temporal resolution of vegetation photosynthesis, with near real time capabilities. SIF has been found to be more dynamic than greenness measures, and respond more quickly to environmental stress, through both change in stress-induced LUE and canopy light absorption (Porcar-Castell *et al.*, 2014: Schimel *et al.*, 2015). Vegetation indices, on the other hand, sense long and medium term changes (weeks to months) in canopy chlorophyll, related to canopy stress, phenology, and photosynthetic capacity of the vegetation (Glenn *et al.*, 2008).

As SIF responds to both incoming radiation and fluorescence yield, one may also normalise SIF by PAR (SIF/ PAR) to better relate SIF signals to canopy properties (Shen *et al.*, 2020). Shen *et al.* (2020) also combined SIF and EVI, as measure of SIF per unit greenness. Current sensors with capabilities to measure SIF include, NASA's Orbiting Carbon Observatory-2 (OCO-2) satellite, the Global Ozone Monitoring Instrument (GOME-2), and the more recent TROPOspheric Monitoring Instrument (TROPOMI) on board the Copernicus Sentinel-5.

17.4 Net Primary Productivity

17.4.1 VIs as proxies for ANPP

Vegetation indices (VIs) may be more appropriate measures of net primary productivity, NPP, the balance between GPP and plant autotrophic respiration, that is, VIs measure the vegetation remaining after respiration (R_a):

$$NPP = GPP - R_a$$

At short timescales, plants respond to the dynamics of environmental variables through stomatal closure and other diurnal adjustments that cannot be easily sensed by satellite-derived VIs and other LAI, fAPAR, or fractional cover products (see Section 8).

Variations in GPP and LUE are likely to be significant over shorter, daily time frames when water or temperature stress develops. At moderate to longer (e.g. weekly to monthly) timescales, plants tend to increase leaf foliage under favorable environments as an investment of resources into their photosynthetic apparatus, and reduce leaf foliage under stress when leaves are expensive to produce and maintain. Thus, at longer timescales, there is a convergence of satellite greenness vegetation signals with biologic and structural canopy properties (Glenn *et al.*, 2008).

Several studies have suggested that ecosystem NPP can be captured with an annual VI integral, that integrates growing season production through VI relationships with APAR. Goward *et al.* (1985) found good relationships between above ground NPP (ANPP) and integrated NDVI from AVHRR, over annual growing periods of North American biomes. Wang *et al.* (2004) found that the NDVI integral over the early growing season was strongly correlated to *in situ* forest measurements of diameter increase and tree ring width in the U.S. central Great Plains.

The integrated Enhanced Vegetation Index (iEVI) was also found to be a good proxy of ANPP. Ponce-Campos *et al.* (2013) compiled *in situ* field measures of ANPP over a range of North American and Australian biomes, and found iEVI to be an effective surrogate to estimate ANPP:

$$ANPP = 51.42 \times iEVI \times 1.15$$

where a log–log relation accounted for the uneven distribution of ANPP estimates over time.

The annual integrated VI offers a robust approximation of vegetation productivity, because, in general, VIs provide both a measure of the capacity to absorb light energy, as well as reflect recent environmental stress acting on the canopy, with stress forcings showing up as reductions in VI expressed as either less chlorophyll and/or less foliage (Running *et al.*, 2004).

17.4.2 Ecosystem respiration

Whereas optical EO data acquired in the visible, NIR, and short wave infrared (SWIR) wavelengths are used to determine ecosystem fluxes, GPP, and NPP, ecosystem respiration (ER) is more commonly measured using LST observations from thermal infrared (TIR) wavelengths (Rahman *et al.*, 2005; see Volume 1B—Section 7). ER is a combined measure of autotrophic and heterotrophic respiration and is a large carbon flux from the Earth's surface to the atmosphere.

Since the main controlling factor of microbial activity is air and surface (soil, water) temperature, using remotely sensed measurements of land surface temperature (LST) has the potential to provide information on the spatial and temporal estimates or retrievals of ER. Rahman *et al.* (2005) found a strong correlation between MODIS-derived LST and EC tower-derived ER over North American sites (especially forests), and Schubert *et al.* (2012) found good relationships over peat lands in Sweden. Others have combined LST with either EVI or a water index in order to obtain better estimates of GPP or NEE, which were then used to derive ER. For example, MODIS LST was combined with EVI in a modified Temperature-Greenness (T-G) model (Sims *et al.*, 2008; see Section 17.5.3) to investigate ER in insect-infested forests (Moore *et al.*, 2013). Tang *et al.* (2011) combined MODIS LST with a water index to model ER in a mixed temperate forest. Kimball *et al.* (2009) used LST derived from the Advanced Microwave Scanning Radiometer for EOS (AMSR-E) sensor and found it to be an effective surrogate for soil respiration (heterotrophic respiration and root respiration) across a broad range of boreal forest, grassland, and tundra sites in the boreal and arctic biomes. Methods to constrain ER estimates with other drivers, such as soil moisture, vegetation production, or nutrient limitations will further improve EO-based estimates of ER (Jagermeyr *et al.*, 2014).

17.4.3 Net ecosystem productivity and net biome productivity

Net ecosystem productivity (NEP) and net biome productivity (NBP) both estimate net ecosystem carbon uptake/release. The fluxes contributing to NEP are GPP and autotrophic (R_a) and heterotrophic (R_h) respiration, while NBP is mainly determined by NEP minus the loss of carbon by processes such as fire and harvest:

$$NEP = GPP - R_a - R_h$$

$$NBP = NEP - fire - harvest$$

The recent availability of column CO_2 concentration retrievals from newly launched satellites has made it feasible to quantify NEP and NBP from satellite observations. These satellites use high resolution spectrometers to measure the intensity of sunlight, at different wavelengths, for retrievals of columnar CO_2 and CH_4 concentrations. For example, NASA's OCO-2 (launched in 2014) provides comprehensive, global measurements of CO_2 in the atmosphere, including seasonal fluctuations of the greenhouse gas and their spatial sources and sinks. This enables a better understanding of how ecosystems absorb and release CO_2, both seasonally and across years in response to interannual climate variability. Basu *et al.* (2013) estimated the global distribution of CO_2 fluxes using column CO_2 measurements from the GOSAT instrument. Inversions of satellite CO_2 observations provide useful constraints on terrestrial carbon sinks and sources.

17.4.4 Growing season phenology

Numerous efforts have been made to improve upon the characterisation of the plant growing, or productivity, season at regional scales using satellite-based phenology models (see Section 9.3).

The phenological life cycles of plant species and communities have large effects on their rates of photosynthesis and annual productivity (Tucker *et al.*, 1986) and VIs are able to provide seasonal and annual growing season metrics of plant productivity (see Section 8.1). Phenological factors such as leaf age and life expectancy play important roles in productivity (Wilson *et al.*, 2001) with some vegetation production models explicitly incorporating phenophase periods, such as bud burst to full leaf expansion, and full expansion to dormancy (Xiao *et al.*, 2004). LST satellite data and/or meteorological air temperature data (T_a) are also used to identify biologically inactive seasonal periods, for example, masking cold temperature time intervals from the VI integrals.

Generally, *in situ* measures of productivity are made at discrete times within the growing season and there is a need to synchronise the satellite measurements with scheduled or variable destructive or harvesting sampling dates to reduce *in situ* ANPP-VI uncertainties. Often it is difficult to predict and sample at peak productivity and greenness periods. Continuous VI growing season productivity profiles allow one to better synchronise VI temporal values with actual *in situ* sampling periods. For example, Moran *et al.* (2014) found significant improvements in productivity–iEVI relationships across a range of grassland sites, when the EVI was only partially integrated from the beginning to the peak of the growing season period (rather than the full season). This was due to the synchronisation of time periods to peak biomass periods when grassland ANPP destructive sampling is typically conducted (see Section 5.1.2). In such cases, EO data provides better temporal stability and opportunities to reduce productivity uncertainties.

17.4.5 Photochemical Reflectance Index

The Photochemical Reflectance Index (PRI; Gamon *et al.*, 1997; see Section 8.1.2) derived from tower-based spectral measurements and MODIS data (Middleton *et al.*, 2018) provides a scaled LUE measure based on light absorption processes by carotenoids (see Section 4.3 and Excursus 4.1), which has been shown to be a good proxy for LUE:

$$\mathrm{PRI} = \frac{\rho_{531} - \rho_{570}}{\rho_{531} + \rho_{570}}$$

The potential of PRI as an EO-based proxy for LUE has been demonstrated (Goerner *et al.*, 2009). The spectral variations at 531 nm are associated with dissipation of excess light energy by xanthophyll pigments (a major carotenoid group of yellow pigments; see Section 4.3) in order to protect the photosynthetic leaf apparatus. Carotenoids function in light absorption in plants as well as protecting plants from the harmful effects of high light conditions, hence lower carotenoid/chlorophyll ratios, indicate lower physiological stress. However, the PRI has also been shown to be very sensitive to canopy structure, gap fraction, background, viewing angle, and LAI, which complicates the association between PRI and LUE (Middleton *et al.*, 2018). In addition, although the short term variation in leaf level PRI appears indeed to be controlled by non-photochemical quenching (NPQ), the seasonal variation in leaf level PRI seems to be controlled by the slow changes in pigment pools rather than NPQ. The mechanistic link between the PRI and LUE appears to be highly dependent on scale and remains to be fully elucidated.

17.5 Carbon Models

There are many empirical, diagnostic, and process-based models that have been developed over the past few decades to quantify land and ocean productivity, with many of these methods integrating independently derived carbon flux measurements from satellite data, EC tower fluxes, and field measurements (see Excursus 17.2). Estimates of daily GPP and annual NPP are now routinely produced operationally over the global terrestrial surface at 1 km spatial resolution through production efficiency models (PEM) with near real time satellite data inputs from MODIS (Turner *et al.*, 2006; see Section 10.2.3).

EO–based modelling approaches focus on the fAPAR term (see Section 6.3.4), which is derived through spectral VI relationships (Asrar *et al.*, 1984; Sellers, 1985; Goward and Huemmrich, 1992; see Section 8.1.4). The fundamental basis for these models is the LUE equation that defines the amount of carbon fixed through photosynthesis (GPP), as proportional to the PAR from solar energy that is absorbed by vegetation multiplied by the efficiency with which the absorbed light is used in carbon fixation (see Sections 7.4 and 17.3):

$$\mathrm{GPP} = \varepsilon_{par} \times \mathrm{APAR} = \varepsilon_{par} \times \mathrm{fAPAR} \times \mathrm{PAR}$$

This simple LUE-based productivity equation comprises a large amount of biological complexity, resulting in numerous productivity modelling approaches that tend to emphasise either the fAPAR equation term or LUE (ε). The LUE approach has been one of the most important methods to map GPP and NPP regionally or globally (Potter *et al.*, 1993; Running *et al.*, 2004).

17.5.1 EO-based LUE models

The LUE concept has been widely adopted by the EO community to assess and extrapolate carbon processes through knowledge of two conversion coefficients:

- fAPAR (see Section 6.3.4); and
- LUE or ε (see Section 7.4).

EO data play a significant role in the LUE approach by providing information on vegetation type, growth status, and environmental conditions. fAPAR is readily estimated using remotely sensed 'greenness' measures (see Section 8.1.1), or through satellite MODIS-FPAR products (Zhao *et al.*, 2005). Longer term GLASS-FAPAR products (Xiao *et al.*, 2015) extend the temporal coverage of FAPAR back to 1982 and can potentially lead to long term GPP estimates.

LUE (ε) however is very difficult to measure as it dynamically varies with plant functional type, vegetation phenophase, and different environmental stress conditions (Ruimy *et al.*, 1995; Turner *et al.*, 2004; Sims *et al.*, 2006; Jenkins *et al.*, 2007). As a result, there are scarce measurements of LUE available, particularly at the landscape scale, and potential or maximum LUE values have only been specified for a limited set of biome types, with these values down-regulated by environmental stress scalars derived from meteorological inputs (Zhao *et al.*, 2005; Heinsch *et al.*, 2006).

EO also provides measures of two other inputs of LUE models, namely water stress (Jones *et al.*, 2017) and incident radiation (Zhang *et al.*, 2014), as well as spatially explicit information on land cover type (Friedl *et al.*, 2010) that determines maximum LUE and other model parameters.

17.5.2 Greenness and radiation (G-R) models

The fraction of PAR absorbed by chlorophyll throughout the canopy ($fAPAR_{chl}$) could lead to more accurate cropland GPP estimates than the MODIS-FPAR (Zhang *et al.*, 2014). VIs are commonly used, but chlorophyll indices can also be coupled with measures of light energy, PAR, to provide robust estimates of GPP. Canopy level chlorophyll represents a community property that is most relevant in quantifying the amount of absorbed radiation used for productivity. Gitelson *et al.* (2006) showed that for the same LAI amount, the chlorophyll content during the green-up stage might be more than two times higher than the chlorophyll content in leaves in the reproductive and senescence stages:

$$GPP = VI_{chl} \times PAR_{toc}$$

where

PAR_{toc} is the top-of-canopy measured PAR (MJ m^{-2} day^{-1}); and
VI_{chl} is a chlorophyll-related spectral index.

Peng *et al.* (2013) described two types of chlorophyll spectral indices:

- commonly used VIs, such as EVI and the Wide Dynamic Range Vegetation Index (WDRVI), which indirectly indicate total chlorophyll content through 'greenness' estimates; and
- chlorophyll indices, such as the MERIS Terrestrial Chlorophyll Index (MTCI), which directly represent the leaf chlorophyll content.

The WDRVI equation is:

$$WDRVI = \frac{a \times \rho_{NIR} - \rho_{red}}{a \times \rho_{NIR} + \rho_{red}}$$

where a is a weighing coefficient with value between 0.1 and 0.2 (Gitelson, 2004; Gitelson *et al.*, 2006).

MTCI is the ratio of the difference in reflectance between an NIR and red edge band and the difference in reflectance between red edge and red band as:

$$MTCI = \frac{\rho_{753.75} - \rho_{708.75}}{\rho_{708.75} + \rho_{681.25}}$$

where $\rho_{753.75}$, $\rho_{708.75}$, and $\rho_{681.25}$ are reflectances in the centre wavelengths of the MERIS narrow-band channel settings (Dash and Curran, 2004). In the Greenness and Radiation (G-R) model, both fAPAR and LUE are driven by total chlorophyll content with strong correlations between GPP/PAR and canopy chlorophyll content (Gitelson *et al.*, 2006; Peng *et al.*, 2011).

Ma *et al.* (2014) found significant improvements in the use of G-R models, relative to EVI alone, for predicting tower GPP, demonstrating the importance of this quantity as a critical driver of savanna vegetation productivity (Whitley *et al.*, 2011; Kanniah *et al.*, 2013a). The G-R model has been successfully applied in estimating GPP in natural ecosystems (Sjostrom *et al.*, 2011; Wu *et al.*, 2011, 2014) and croplands, including maize, soybeans, and wheat (Wu *et al.*, 2010; Peng *et al.*, 2011).

Two definitions of LUE become apparent in G-R models, with this term either defined as the ratio of GPP to APAR, or the ratio of GPP to PAR (Gower *et al.*, 1999), with the latter sometimes referred to as ecosystem-LUE or eLUE:

$$\varepsilon = \frac{GPP}{APAR}$$

$$eLUE = \frac{GPP}{PAR} = fAPAR \times \varepsilon$$

An advantage of using chlorophyll-based VIs in G-R models is that the biological drivers of photosynthesis, fAPAR and ε resulting from environmental stress and leaf age phenology, are combined into eLUE, thereby simplifying EO-based productivity estimates.

Other measures of PAR that have been used include 'potential' PAR, or maximal clear-sky PAR ($PAR_{potential}$; Peng *et al.*, 2013; Rossini *et al.*, 2015) and top-of-atmosphere PAR (PAR_{toa}). $PAR_{potential}$ can be calibrated from long term PAR_{toc} measurements or modelled using an atmosphere radiative transfer code (Kotchenova and Vermote, 2007). Gitelson *et al.* (2014) found an improved performance of $PAR_{potential}$ relative to PAR_{toc} noting that decreases in PAR_{toc} during the day do not always imply a decrease in GPP. Further, Kanniah *et al.* (2013) showed that the negative forcings of wet season cloud cover over Australian tropical savannas were partly compensated by enhanced LUE resulting from a greater proportion of diffuse radiation. Ma *et al.* (2014) found that coupling of EVI with PAR_{toa} better predicted GPP than coupling EVI with PAR_{toc} and attributed this to tower sensor-based measurement uncertainties of PAR_{toc} , as well as better approximations of meteorological controls on GPP by PAR_{toa}.

17.5.3 Temperature-Greenness (T-G) model

Although potentially useful in certain cases, the simple VI 'greenness' model—defined as the straightforward relationship between VIs and GPP—exhibits various limitations due to its inability to always recognise between-growth and inactive-growth periods, in which spectral 'greenness' may show little change. These inactive periods are associated with evergreen vegetation in winter months with low temperatures, as well as evergreen vegetation growing in Mediterranean climates in which high temperature, vapor pressure deficit, and soil drought limit growth (Sims *et al.*, 2008; Vickers *et al.*, 2012).

For these reasons, Sims *et al.* (2008) introduced the temperature and greenness (T-G) model, using combined daytime LST and EVI products from MODIS. They found the T-G model substantially improved the correlation between predicted and measured GPP at 11 EC flux tower sites across North American biomes compared with the MODIS GPP product or MODIS EVI alone, while keeping the model based entirely on remotely sensed variables without any ground-based meteorological inputs (Sims *et al.*, 2008). The T-G model may be described as follows:

$$GPP = EVI_{scaled} \times LST_{scaled} \times m$$

$$LST_{scaled} = \min\left[\left(\frac{LST}{30}\right);\left(2.5 - \left(0.05 \times LST\right)\right)\right]$$

$$EVI_{scaled} = EVI - 0.10$$

where

- LST_{scaled} sets GPP to zero when LST is less than zero, and defines the inactive winter period;
- EVI_{scaled} adjusts EVI values to a zero baseline value in which GPP is known to be zero;
- m is a scalar that varies between deciduous and evergreen sites, with units of mol C m^{-2} day^{-1}; and
- LST_{scaled} also accounts for low temperature limitations to photosynthesis when LST is between 0°C and 30°C, and accounts for high temperature and high VPD stress in sites that exceed LST values of 30°C (Sims *et al.*, 2008; see Figure 17.7).

LST is closely related to VPD and thus can provide a measure of drought stress, consistent with the BIOME-BGC model, where temperature and VPD are used as scalars directly modifying LUE (Running *et al.*, 2004). LST is a useful measure of physiological activity of the upper canopy leaves, provided that leaf cover is high enough that LST is not significantly affected by soil surface temperature. Thus, the T-G model has been found less useful in sparsely vegetated ecosystems (e.g. shrublands) where soil surface temperatures significantly influence derived LST values, rendering them less useful as indicators of plant physiology. As an example, Ma *et al.* (2014) found coupling EVI with LST showed no improvements in predicting savanna GPP compared with using EVI alone over the relatively open tropical savannas in northern Australia, with appreciable soil exposure. This may also be due to temperature not being a limiting factor or significant driver of photosynthesis in tropical savannas (Leuning *et al.*, 2005; Cleverly *et al.*, 2013; Kanniah *et al.*, 2013).

Figure 17.7 Combined temperature-greenness model

GPP is enhanced by increasing temperatures up to 30°C. Solid line is scaled LST from the T-G model.

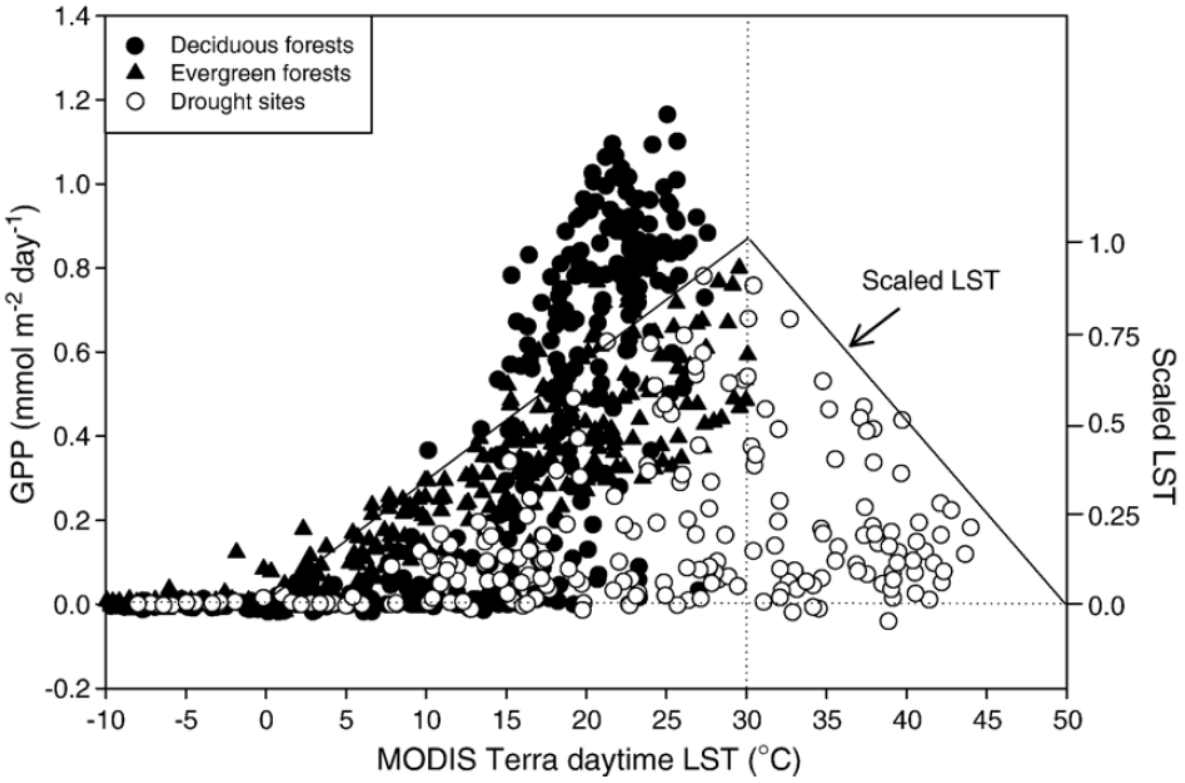

Source: Sims *et al.* (2008) Figure 2

17.5.4 Carbon modelling

Modelling of carbon, water, and energy fluxes between terrestrial surfaces and the atmosphere are increasingly important for hydrological and climate studies. Ecophysiological information relating to photosynthetic activity, biomass, productivity, water content, phenology, soil moisture, and nutrient status may be acquired and analysed consistently and repeatedly over large areas.

The BIOME-BGC (BioGeochemical Cycles) model calculates daily GPP as a function of incoming solar radiation, conversion coefficients, and environmental stresses (Running *et al.*, 2004). This was implemented as the first operational standard satellite product for MODIS (MOD17), providing global estimates of GPP, expressed as follows:

$$GPP = \varepsilon_{max} \times 0.45 \times SW_{rad} \times fAPAR \times f(VPD) \times f(T_{min})$$

where

ε_{max} is the maximum LUE (g C MJ^{-1}) obtained from a biome properties lookup table (BPLUT);

SW_{rad} is shortwave downward solar radiation (MJ^{-1} day^{-1}), of which 45% is assumed to be PAR;

f(VPD) and $f(T_{min})$ are vapor pressure deficit and air temperature reduction scalars for the biome specific ε_{max} values; and

fAPAR is directly input from the MODIS-FPAR (MOD15) product (Running *et al.*, 2004; Zhao *et al.*, 2005).

MODIS-FPAR retrievals are physically-based and use biome specific lookup tables generated using a three-dimensional radiative transfer model (Myneni et al., 2002).

The reduction scalars encompass LUE variability resulting from water stress (high daily VPD) and low temperatures (low daily minimum temperature, T_{min}; Running *et al.*, 2004). The MODIS GPP product is directly linked to EO and weather forecast products and can provide near real time information on productivity and the influence of anomalies such as droughts. A consistent forcing meteorology is based upon the NCEP/NCAR (National Centres for Environmental Prediction/National Centre for Atmospheric Research) Reanalysis II datasets (see Figure 17.8).

Figure 17.8 MODIS NPP product based on BIOME-BGC model

Global mean annual NPP (g C m^{-2} $year^{-1}$) over the period 2000–2015 based on the MODIS GPP/NPP product.

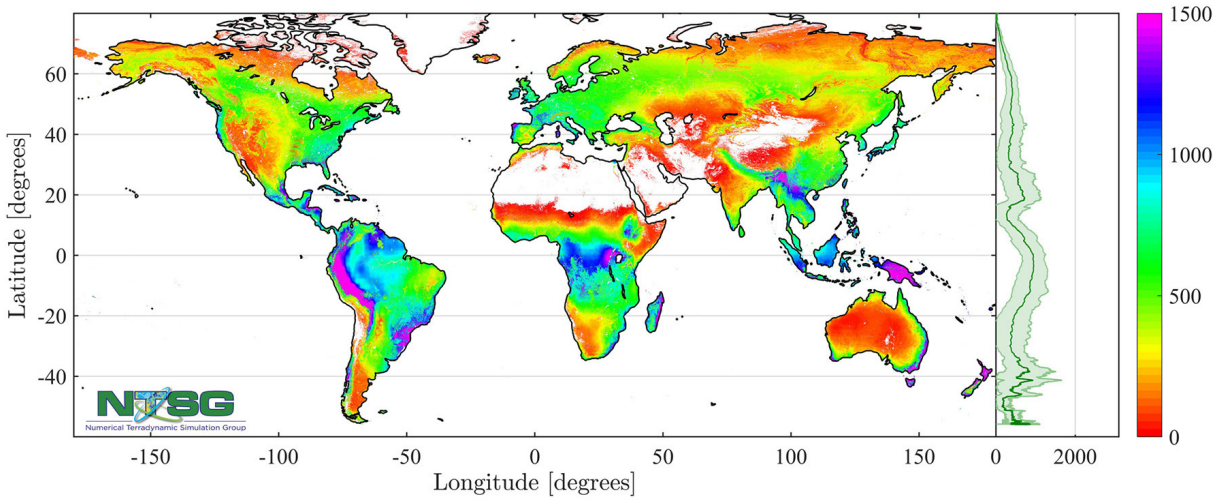

Source: Steven W. Running, NTGS (see *http://www.ntsg.umt.edu/project/modis/default.php*)

Using these satellite products, Zhao and Running (2010) found that global NPP declined slightly by 0.55 Pg C due to drought from 2000 to 2009. Ichii *et al.* (2007) used the BIOME-BGC model to simulate seasonal variations in GPP for different rooting depths, 1–10 m, over Amazon forests, then determine which rooting depths best estimated GPP to be consistent with satellite-based EVI. They were subsequently able to map rooting depths at regional scales and improve the assessments of carbon, water, and energy cycles in tropical forests.

The utility and accuracy of MODIS GPP/NPP products have been validated in various FLUXNET studies (see Excursus 7.2), which have also demonstrated the value of independent tower flux measurements to better understand the satellite-based GPP/NPP products (Leuning *et al.*, 2005; Zhao *et al.*, 2005, 2006; Turner *et al.*, 2006). These studies highlight the capabilities of MODIS GPP to correctly predict observed fluxes at tower sites, but also draw attention to some of the uncertainties associated with use of coarse resolution and interpolated meteorology inputs, uncertainties with the LUT-based values, noise and uncertainties in the satellite fAPAR inputs, and difficulties in constraining the LUE term (Zhao *et al.*, 2005; Heinsch *et al.*, 2006; Yuan *et al.*, 2010). Since meteorological inputs are often not available at sufficiently detailed temporal and spatial scales, they can introduce substantial errors into the carbon exchange estimates.

Turner *et al.* (2006) concluded that although the MODIS NPP/GPP products are generally responsive to spatial–temporal trends associated with climate, land cover, and land use, they tend to overestimate GPP at low productivity sites and underestimate GPP at high productivity sites. Similarly, Sjostrom *et al.* (2011) found that although MODIS GPP described seasonality at 12 African flux tower sites quite well, it tended to underestimate tower GPP at the dry sites in the Sahel region due to uncertainties in the meteorological and fAPAR input data and the underestimation of ε_{max}. Jin *et al.* (2013) reported the MODIS GPP product to substantially underestimate tower GPP during the greening up phase at a woodland savanna site in Botswana, while overestimating tower-GPP during the browning down phase.

Some studies have found that when properly parameterised with site level meteorological measurements, MODIS GPP becomes more closely aligned with flux tower derived GPP (Turner *et al.*, 2003; Kanniah *et al.*, 2009). Kanniah *et al.* (2011), however, found that utilizing site-based meteorology could only improve GPP estimates during the wet season over northern Australian savannas, and suggested the MODIS GPP product has a systematic limitation in the estimation of savanna GPP in arid and semi-arid areas due to the lack of the representation of soil moisture. Sjostrom *et al.* (2011) also found soil moisture information to be quite important for accurate GPP estimates in drier African savannas.

17.5.5 Vegetation Photosynthesis Model (VPM)

Xiao *et al.* (2004) developed a mostly satellite-based vegetation photosynthesis model (VPM) that estimates GPP using satellite inputs of EVI and the land surface water index (LSWI):

$$GPP = \varepsilon \times fAPAR_{chl} \times PAR_{toc}$$

$$\varepsilon = \varepsilon_{max} \times T_{scalar} \times W_{scalar} \times P_{scalar}$$

where

$fAPAR_{chl}$ is estimated as a linear function of EVI;
PAR_{toc} is measured at the site;
T_{scalar}, W_{scalar}, and P_{scalar} are scalars for the effects of temperature, water, and leaf phenology on vegetation, respectively (see Figure 17.9);
T_{scalar} is based on air temperature and uses minimum, maximum, and optimum temperature for photosynthesis at each time step; and
W_{scalar} is based on satellite-derived LSWI that accounts for the effect of water stress on photosynthesis:

$$W_{scalar} = \frac{1+LSWI}{1+LSWI_{max}}$$

$$LSWI = \frac{\rho_{nir} - \rho_{swir}}{\rho_{nir} + \rho_{swir}}$$

where

ρ_{swir} is the reflectance in a broadband SWIR band (e.g., MODIS, 1580–1750 nm); and
$LSWI_{max}$ is the maximum value for the growing season.

P_{scalar} accounts for the effect of leaf age on photosynthesis and is dependent on the growing season life expectancy of the leaves (Wilson *et al.*, 2001). P_{scalar} is calculated over two phenophases as:

$$P_{scalar} = \frac{1 + LSWI}{2}$$

from bud burst to full leaf expansion, and P_{scalar}=1, after full expansion (Xiao *et al.*, 2004).

Figure 17.9 Primarily Satellite-based Vegetation Photosynthesis and Respiration Model (VPRM)

LSWI: Land Surface Water Index; EVI: Enhanced Vegetation Index; Gross Ecosystem Exchange (GEE): light-dependent part of Net Ecosystem Exchange (NEE); Respiration (R): light-independent part of NEE; $FAPAR_{PAV}$: fraction of incident light absorbed by the photosynthetically active vegetation in the canopy; T_{scale}, P_{scale}, and W_{scale}: scalars for temperature, leaf phenology, and canopy water content, respectively; λ, PAR_0, α, and β: four model parameters, one set per vegetation type.

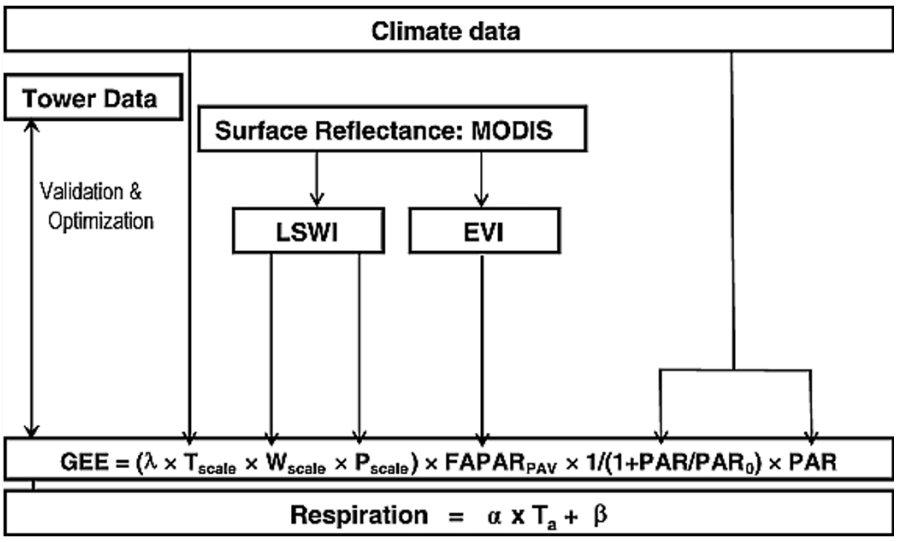

Source: Mahadevan *et al.* (2008)

The VPM model has been applied to both MODIS and SPOT-4 VEGETATION sensor data to produce tower-calibrated estimates of GPP across a wide range of biomes, including evergreen and deciduous forests, grasslands, and shrub sites in temperate North America and in seasonally moist tropical evergreen forests in the Amazon (Xiao *et al.*, 2005; Mahadevan *et al.*, 2008; Jin *et al.*, 2013).

Mahadevan *et al.* (2008) further developed the vegetation photosynthesis and respiration model (VPRM), a satellite-based assimilation scheme that estimates hourly values of NEE using EVI, LSWI, and high-resolution meteorology observations of sunlight and air temperature (see Figure 17.9). NEE represents the difference between uptake (photosynthesis) and loss (respiration) processes that vary over a wide range of timescales. The VPRM model provides fine-grained fields of surface CO_2 fluxes for application in inverse models at continental and smaller scales. This capability is presently limited by the number of vegetation classes for which NEE can be constrained using EC tower flux data.

Another popular LUE model for quantifying GPP or NPP, which has incorporated satellite products, is the Carnegie Ames Stanford Approach (CASA) Biosphere model (Potter *et al.*, 1993). CASA has been widely used to simulate carbon dynamics at regional to global scales using NDVI and EVI inputs.

17.6 Anthropogenic carbon emissions

Human activity is significantly altering the global cycling of carbon through the burning of fossil fuels and land cover modifications (including fires—see Section 18), all of which result in more carbon accumulating in the atmosphere. The burning of fossil carbon fuels from coal, oil, and natural gas currently releases over 8 Gt of carbon annually into the atmosphere, representing the primary source of increased atmospheric CO_2 (see Figure 17.10). Land cover modifications and land use changes currently transfer an additional 1 Gt of carbon into the atmosphere each year. Increases in CO_2 (a greenhouse gas) warms the atmosphere by absorbing TIR energy emitted by the Earth (see Volume 1A—Section 5.2.2) and then re-emitting it in all directions, including towards the Earth's surface, and thereby having a significant impact on the warming of our planet. As a result, average global temperatures have risen 0.8°C since 1880.

Figure 17.10 Global Carbon Budget 2009–2018

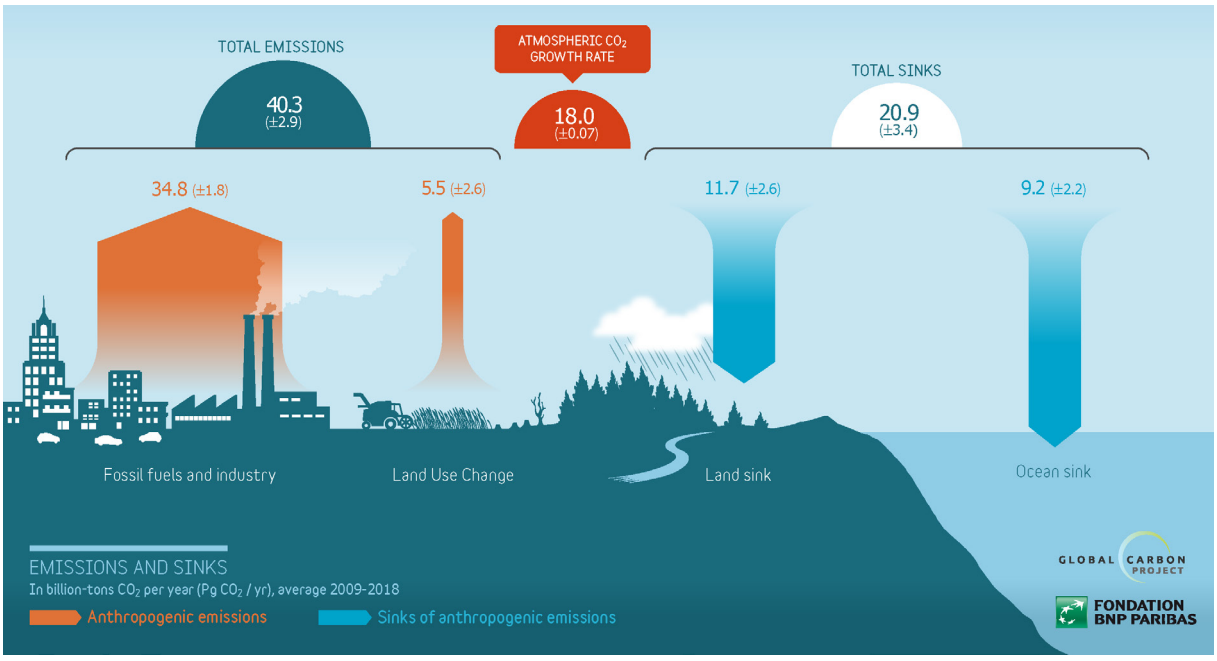

Source: Global Carbon Atlas, *http://www.globalcarbonatlas.org/en/content/global-carbon-budget*

17.6.1 CO_2 emissions

Ground-based CO_2 measurements first began in 1958 by Dr. Charles Keeling at Mauna Loa, Hawaii, and have steadily recorded increasing CO_2 concentrations in the atmosphere over time (see Figure 17.11). An increasing number of ground stations now provide a broader view of carbon in the atmosphere, with models and estimates filling in some details. These show the levels of CO_2 in the atmosphere to have increased from about 280 ppm, at the beginning of the Industrial Revolution, to over 400 ppm at present—a greater than 40% increase—significantly exceeding their envelope over the last several million years (Sellers *et al*., 2018).

Our knowledge of global CO_2 from ground stations is restricted by the inability to collect sufficient measurements over the oceans and remote land areas, and by incomplete reporting by countries and companies that are monitoring this gas. EO technologies for measuring atmospheric column CO_2 and CH_4 concentrations from space have made many recent advances, enabling inversions of carbon fluxes from satellite observations with high accuracy and coverage. Remotely sensed greenhouse gas observations provide a significant potential for improving our understanding of the natural carbon cycle and for the monitoring of anthropogenic emissions.

NASA's OCO–2 satellite was designed to study how carbon sources and sinks are distributed and how they change over time. OCO–2 is able to map and monitor areas that have not been observed much before, such as vast ocean areas, remote tropical forests and high latitude tundra areas. This allows the pinpoint location of CO_2 emitting sources and the estimation of the net ecosystem productivity (NEP). OCO-2 is also used to identify emissions from urban areas, biomass burning, volcanoes, and 'hidden' sources. Other current and planned satellite missions include OCO-3, GeoCARB, GOSAT-2, Sentinel-5P, and CO2M. They will enable large scale and consistent measurements with the same instrument over all land and sea surfaces.

Figure 17.11 Changes in carbon dioxide concentration

Interannual and seasonal time series of monthly average atmospheric CO_2 measurements at Mauna Los Observatory, Hawaii. This is known as the Keeling curve in honour of Dr. Charles Keeling who first started making these monthly measurements in 1958.

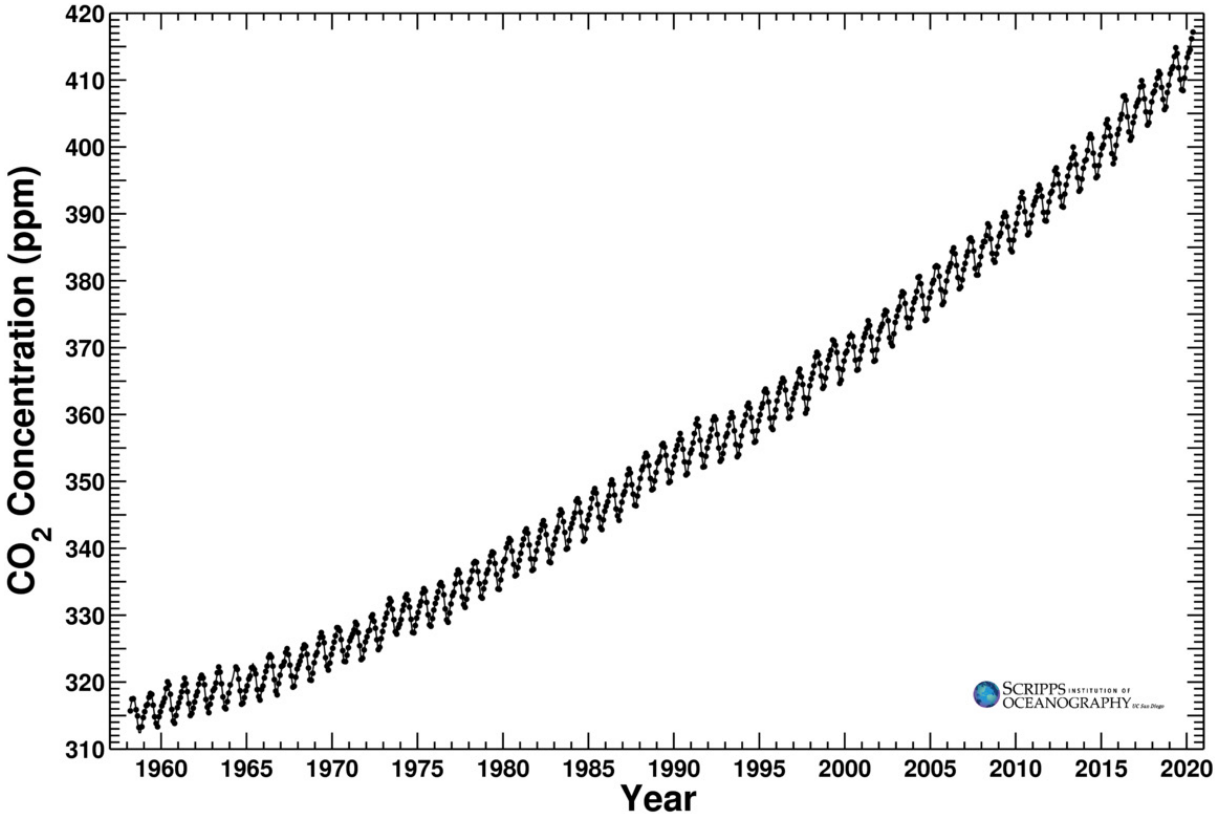

Source: Scripps Institute of Oceanography, *http://scrippsco2.ucsd.edu/data/atmospheric_co2/primary_mlo_co2_record*

17.6.2 Examples of satellite studies of CO_2 emissions and flux inversions

It is a challenge to isolate recent human emissions from natural cycles and long term accumulations, and spatially-temporally attribute specific human CO_2 emissions. Some examples of attempts to do this are mentioned below.

17.6.2.1 El Niño-Southern Oscillation (ENSO)

The El Niño-Southern Oscillation (ENSO) is a recurring climate warming and cooling pattern involving water temperature changes in the Pacific Ocean (see Volume 3B). The oscillation period ranges from two to seven years and is referred to as the ENSO cycle. El Niño and La Niña are the extreme phases of the ENSO cycle, representing the warming and cooling phases of the ocean surface, respectively. Both phases significantly influence the rainfall distribution patterns, and thereby carbon cycle patterns in many parts of the world, including Australia.

EO has been instrumental in understanding how CO_2 fluctuates during ENSO cycles, and what roles the land and ocean play in this process. During the 2015–2016 El Niño, for instance, droughts, heat, and fires in tropical areas caused plants and soil on three continents to contribute to the largest growth of CO_2 on record. During this event, because of little rain and higher than normal temperatures in South America, Africa, and Asia, some plants did not absorb as much CO_2 while others died and decomposed more quickly, releasing the carbon they had absorbed from the air. During this period, an extra 2.5 Gt of CO_2 was released into the air compared to 2011, when conditions were normal. That extra carbon came from tropical areas in South America, Africa, and Asia—where plants all reacted differently. In South America, the growth of plants was stunted by drought, causing them to extract less CO_2 than usual. In Africa, the heat caused dead plants to decompose more quickly, releasing high amounts of CO_2, and in Asia, drought and heat caused forest fires, which also pumped huge quantities of carbon into the air.

17.6.2.2 Volcanoes and cities

The OCO-2 satellite makes such high resolution measurements that researchers can look at CO_2 concentrations over very small areas, such as a city or a volcano. CO_2 is higher in urban areas, where there are more cars and power plant emissions, than in suburban areas. The findings show that the OCO-2 satellite can quickly scan cities for pollution, complementing ground-based measurements.

OCO-2 data can also be used to monitor active volcanoes, such as the Yasur volcano in Vanuatu, which constantly spews out a plume rich in CO_2. These measurements suggest that Yasur is pumping out 41.6 kt of CO_2 a day. By processing OCO-2 data to account for seasonal changes, as well as the background level (already near 400 ppm), one is left with the signal of emissions from motor vehicles, power plants, and other industrial processes.

17.6.3 Land use and land cover modification

Changes in land cover, land use activities and land use management decisions will have corresponding impacts on carbon absorption and the carbon cycle (see Figure 17.10). The activities of deforestation, land degradation, forest logging and forest conversion to pastures and cropland remove large carbon stocks in woody biomass and replace them with vegetation that has lower carbon storage. The woody carbon that has accumulated over many years is then released back into the atmosphere, either through burning or decomposition (Friedlingstein *et al*., 2019).

Increasing agricultural expansion activities will have the greatest impact and incursion onto rangelands to meet an ever expanding human population (see Section 15). Carbon emissions also result from disturbances such as fire and insect outbreaks. Agriculture intensification has increased to grow more food on less land (see Section 11.5). These managed agricultural lands release additional greenhouse gases (GHG), including methane (Sellers *et al*., 2018) whose concentration has risen from 715 ppb in 1750 to 1,774 ppb in 2005.

Whereas deforestation can release large amounts of CO_2 into the atmosphere, forest regrowth acts to remove CO_2. In many areas, abandoned farmland is reverting to forest and drawing carbon out of the atmosphere, and these forests store much more carbon, both in wood and soil, than crops would.

Various EO datasets and approaches have been used to estimate carbon emissions from land use, land cover change, disturbance, and other sources. In particular, time series satellite data from the Landsat satellites, have enabled detailed monitoring of changes in forest cover (Hansen *et al*., 2013; see Section 16), and land cover modifications resulting from urbanisation and expansion of agricultural lands (see Section 3). MODIS sensors also measure fire activities, and map burned areas and the subsequent regeneration of the landscape (see Section 18).

17.6.4 Effects of Carbon Cycle Changes

The changes in the carbon cycle impact each of the carbon reservoirs. About half of the fossil carbon emissions into the atmosphere each year are removed by the fast carbon cycle (see Excursus 17.1), but the remainder stays in the atmosphere. Increased carbon in the atmosphere can alter or induce plant growth, either through CO_2 fertilisation and its warming related increase in biological activity and plant growth (see Section 17.6.4.1) or changes in growing season phenology (see Section 17.6.4.2). Through increased levels of photosynthesis, plants have taken up approximately 25% of the CO_2 that humans have put into the atmosphere. This is termed a land cover sink (see Section 17.6.4.3).

17.6.4.1 Carbon fertilisation

With more atmospheric CO_2 available to convert to plant matter in photosynthesis, plants are able to grow more. This increased growth is referred to as carbon fertilisation and was associated with significant changes in global LAI (Myneni *et al.*, 1997; see Figure 17.12). CO_2 fertilisation increases plant growth until the plant reaches another limiting resource, such as water, nutrients, or light. Donohue *et al.* (2013) demonstrated that even in warm arid regions, with the effects of rainfall variations removed, the fertilisation effect was a significant land surface process that accounted for an 11% increase in green cover in the first decade of this century. The amount of carbon that plants take up varies greatly from year to year, but in general, the world's plants have increased the amount of CO_2 they absorb since 1960.

Figure 17.12 Change in global leaf area across 1982–2015

The change in MODIS-derived leaf area across the globe from 1982 to 2015 is associated with CO_2 fertilisation.

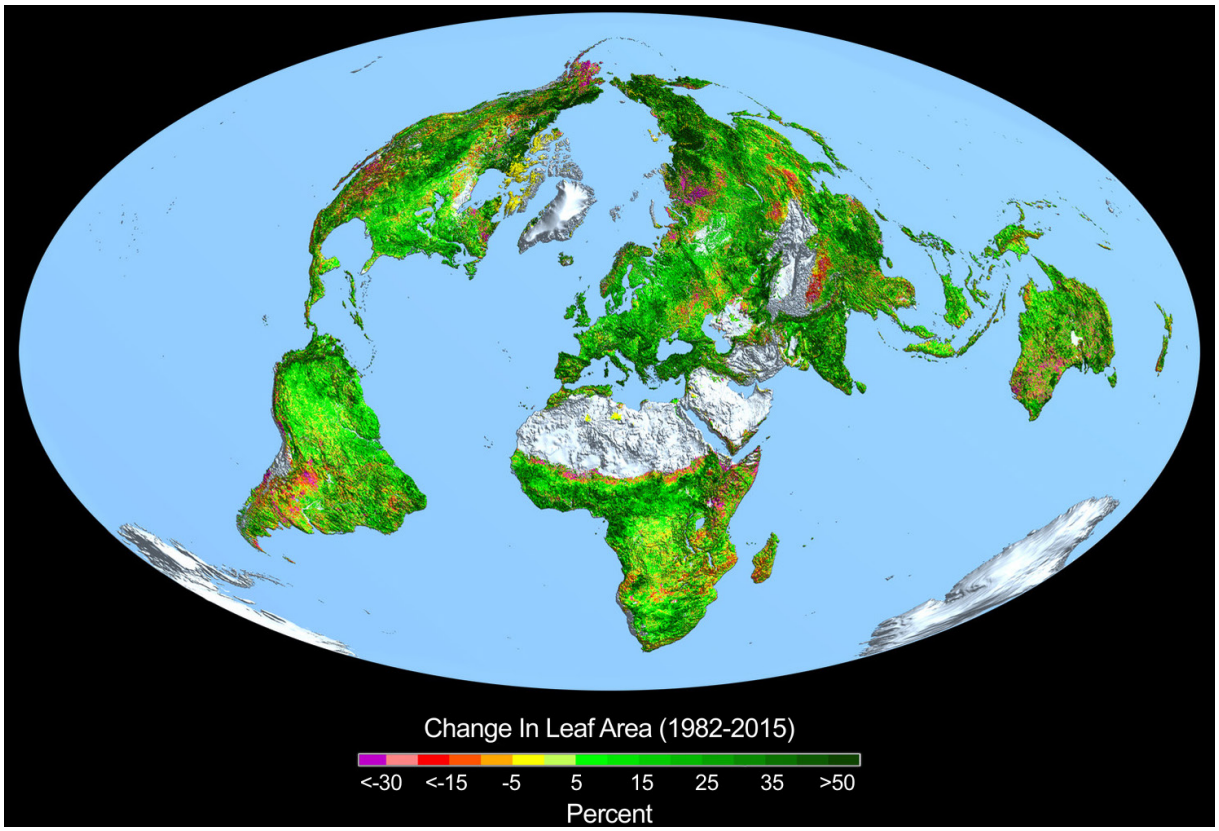

Source: *https://www.nasa.gov/feature/goddard/2016/carbon-dioxide-fertilization-greening-earth/*

17.6.4.2 Climate change and variability impacts on the carbon cycle

Interannual variations in climate (precipitation and temperatures) can also cause significant variations in biosphere-atmosphere carbon cycling. GPP is a critical intersection between the terrestrial biosphere and the Earth's climate. The increases of CO_2 and CH_4 and other greenhouse gases shift the Earth's climate on time and space scales that are important to humans (Sellers *et al.*, 2018).

During ENSO cycles (see Section 17.6.2.1), drought and wet years alter the net uptake and release of CO_2. In dry El Niño years, the vegetation is unable to absorb as much CO_2 due to water limitations. Thus CO_2 levels in the atmosphere will be higher than in more normal years. Further, dry years can increase the frequency and intensity of fire activity resulting in greater CO_2 emissions into the atmosphere. The opposite may occur in wet La Niña years, in which less vegetation is water limited and more CO_2 can be absorbed from the atmosphere through photosynthesis.

17.6.4.3 Australian carbon sink anomaly in 2011

The amount of carbon that plants take up varies greatly from year to year, due to variations in limiting factors that restrict photosynthesis and plant growth. As an example, in an unusual, extremely wet year across Australia in 2011, an exceptionally large land carbon sink anomaly was recorded, of which more than half was attributed to Australia (see Figure 17.13; Ma *et al.*, 2016).

The biggest changes in the land carbon cycle are likely to come because of climate change. Continued global warming can extend the growing seasons and prolong growth, unless water becomes a limiting factor. However, warmer temperatures can also stress plants and, with a longer, warmer growing season, the plants need more water to survive. There is already evidence that plants in the Northern Hemisphere slow their growth in the summer because of warmer temperatures and water shortages (Angert *et al.*, 2005).

EO datasets have been used in a vast number of carbon-climate studies over northern latitudes, Africa, and the Amazon (Tucker *et al.*, 1986; Myneni *et al.*, 1997; Tucker *et al.*, 2001; Zhou *et al.*, 2001; Xiao and Moody, 2005; Saleska *et al.*, 2016). Satellite measurements have helped assess how the global carbon cycle is changing through time. They help us gauge the impact we are having on the carbon cycle by releasing carbon into the atmosphere or finding ways to store it elsewhere. They will show us how our changing climate is altering the carbon cycle, and how the changing carbon cycle is altering our climate. A better understanding of the carbon cycle is essential for improving projections of the Earth's carbon-climate system under future conditions (Schimel *et al.*, 2015).

Figure 17.13 Australian interannual variations in carbon-related indicators

Variations are shown for the continental summation of NEP (Pg C yr^{-1}), continental average of annual integrated EVI, continental average of SIF_n (PAR normalised SIF, mW m^{-2} sr^{-1} nm^{-1}), continental average of Total Water Storage Change (TWSC, cm), and continental total fire carbon emission (Pg C yr^{-1}). NEP is derived from GOSAT atmospheric inversion modeling. The gray shaded area represents the Bayesian uncertainty range of inverted NEP (±1σ).

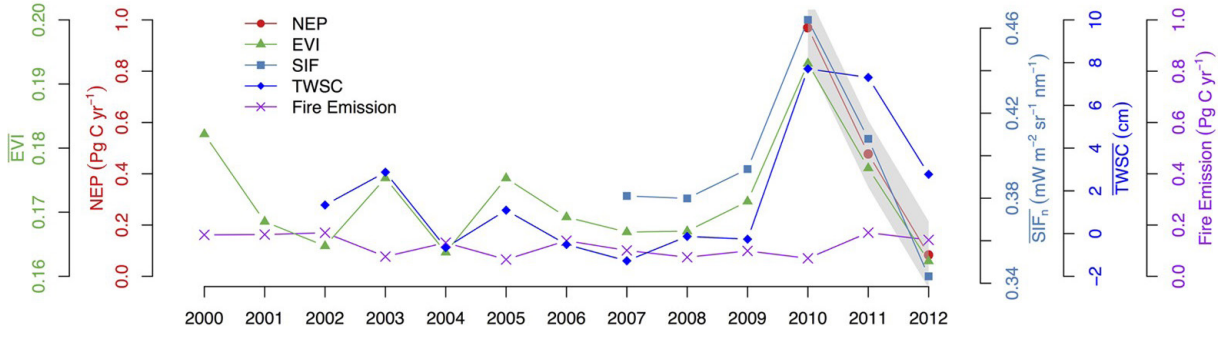

Source: Ma *et al.* (2016) Figure 1b

17.7 Carbon stocks

Measurements of carbon stocks, including vegetation biomass and soil organic carbon, are essential in quantifying the carbon cycle, and various optical, microwave, and lidar observations have been employed to quantify these.

17.7.1 Biomass carbon stock

Above ground biomass (AGB; see Section 5.1.2) can be estimated from passive optical EO methods that are sensitive to vegetation canopy properties (see Sections 12, 14, and 16). Coarse spatial resolution satellite data are frequently used to produce biomass estimates at regional or global scales for forest, grassland, and tundra ecosystems (Chopping *et al.*, 2011; John *et al.*, 2018; Epstein *et al.*, 2012), while medium spatial resolution data, such as from Landsat and Sentinel-2, are more frequently used for biomass estimations at local and regional scales (Turner *et al.*, 2004; Friedl *et al.*, 1994; Shoshany and Karnibad, 2011). Fine spatial resolution data (< 5 m) from high spatial resolution imaging sensors such as QuickBird, Ikonos, and WorldView-2/-3 can be used to calculate local tree biomass (Palace *et al.*, 2008; Fuchs *et al.*, 2009) and grass biomass (Sibanda *et al.*, 2017).

Satellite-derived AGB estimates are based on empirical models, machine learning (ML) methods, and allometric models (see Section 10). The variables derived from passive optical EO data for use in these models may include spectral reflectance, VIs, spatial texture, and vegetation canopy attributes (see Section 8). For example, empirical regression models have been developed by associating VIs to field biomass measurements (Roy and Ravan, 1996; Heiskanen, 2006; Cohen *et al.*, 2003). Spatial texture algorithms can improve biomass estimations by quantifying the spatial characteristics of images, such as contrast, objects, edge features, and heterogeneity (Sarker and Nichol, 2011; see Volume 2C—Section 6). Vegetation canopy attributes include fractional cover, clumping, LAI, and shadow fraction, and are used as proxies of AGB (see Section 6). Other important canopy structural quantities in deriving foliage biomass and total standing biomass in forests are tree height, crown size and area, density, and shadow fraction (Franklin and Hiernaux, 1991; Greenberg *et al.*, 2005; Leboeuf *et al.*, 2007; see Section 16). Spectral unmixing models (Hall *et al.*, 1995) and canopy reflectance models, such as the Li–Strahler geometric-optical model, can retrieve crown size, tree shadow, and density in satellite imagery (Li and Strahler, 1985; see Volumes 1X and 2X).

ML algorithms are increasingly being used in biomass estimation efforts (see Section 14.5). These non-parametric approaches have been used to estimate forest AGB with time series MODIS reflectances and environmental data over large regional areas in California (Baccini *et al.*, 2004), Africa (Baccini *et al.*, 2008), and Russia (Houghton *et al.*, 2007), as well as for AGB estimates over grasslands in Mongolia and Inner Mongolia (John *et al.*, 2018). Similarly, random forests were used to calculate biomass at regional scales using many other types of satellite data (Breiman, 2001; Powell *et al.*, 2010; Karlson *et al.*, 2015). However, both empirical and ML approaches for AGB estimations remain impracticable to directly transfer across biomes, or even different vegetation phenological stages, and saturation is a common problem.

Allometric models are a physically-based approach for the estimation of forest AGB. The simplest and most commonly used allometric models relate tree diameter at breast height (DBH) to AGB as a power function (see Section 16.5). More sophisticated models employ a wider range of forest variable measurements (e.g. canopy crown size, crown depth, tree height, and stem diameter) to derive AGB based on field observations (TerMikaelian and Korzukhin, 1997). Although the tree allometric models are generally species-specific and site-specific, they can be generalised to estimate biomass in mixed species across larger regions (Wirth *et al.*, 2004). For example, general allometric models were derived using linear least squares regression from field measurements of conifer, deciduous and mixed trees (Zhang and Kondragunta, 2006).

17.7.2 Soil organic carbon

EO of soil organic carbon (SOC) builds upon laboratory-based spectral measurements of soils in visible-to-SWIR EM wavelengths that have been conducted since the mid-1990s (Ben-Dor *et al.*, 1999; Rossel *et al.*, 2006). Organic matter influences the shape of a soil spectral signature due to vibrations of O-H and C-H bonds linked to lignin and cellulose and laboratory-based spectral measurements have been shown to accurately estimate soil organic carbon (Ben-Dor *et al.*, 1997; see Volume 1B—Section 6.3). Using a fuzzy clustering method to classify over 1500 soil samples, Shi *et al.* (2014) found that the soil clusters generally decreased in their reflectance with increasing SOC content (soil darkening).

Several studies have successfully mapped SOC content at landscape and regional scales using visible-to-SWIR satellite imagery (Jarmer *et al.*, 2010), the hyperspectral Hyperion sensor (Gomez *et al.*, 2008), and hyperspectral

airborne sensors (Hbirkou *et al*., 2012). Landsat and MODIS data have been used for SOC content mapping, either as spectral bands (Were *et al*., 2015; Grinand *et al*., 2017) or through biophysical variables, such as NDVI and percent vegetation cover (Gray *et al*., 2015; Mishra *et al*., 2010; Somarathna *et al*., 2016). Using such satellite sensors, Wang *et al*. (2018) found large variability in the performance of SOC stock estimations over semi-arid rangelands of eastern Australia. Long term MODIS satellite data can also be used to examine the trends in SOC at regional scales (Chen *et al*., 2019).

Further progress has been made in SOC mapping by incorporating SpectroTransfer Functions (STFs) that link soil properties measured by laboratory analysis with the visible-to-SWIR imagery (Gomez *et al*., 2008; Stevens *et al*., 2010). The STFs can only be applied over exposed bare soils, such as croplands during ploughing periods (Bartholomeus *et al*., 2011), bare soil pixels in arid ecosystems, and exposed soils resulting from ecosystem disturbances (Jarmer *et al*., 2010). Other studies have successfully estimated SOC content using STFs with laboratory (Rossel and Hicks, 2015; Guo *et al*., 2019), field (Cambou *et al*., 2016), and image data (Guo *et al*., 2019). In another STF approach, each variable associated with SOC stocks (soil organic matter, soil bulk density) is separately estimated followed by an equation linking SOC to these variables (Mishra *et al*., 2010).

One can also incorporate environmental data with soil properties determined through visible-to-SWIR laboratory analysis by use of SCORPAN (Soil properties, Climate properties, Organisms, Relief setting, Parent material, Age, and the spatial coordinate, N) ML techniques (McBratney *et al*., 2003). The SCORPAN models are mainly based on random forest and boosted regression trees (Wang *et al*., 2018). As they use environmental variables indirectly linked to SOC content, they potentially have higher mapping coverage than STF models and can be applied over croplands, rangelands, shrublands, and grasslands. Wang *et al*. (2018) showed that the use of seasonal fractional cover data derived from visible-to-SWIR image data in association with environmental predictors (climate, parent material, and relief) improved the performance of SOC stock prediction.

17.7.3 Microwave EO

Microwave EO sensors, including 'passive' radiometers and 'active' scatterometers, have been used in forest estimates of AGB since the early 1990's (see Excursus 6.1 and Section 16.5). Spaceborne SAR can observe under all-weather conditions, and is of particular use for the estimation of forest AGB over areas covered by cloud all year (see Volume 1B—Section 8). Le Toan *et al*. (1992) observed the strong correlation of L- and P-band SAR backscattering coefficients with red pine biomass, and Dobson *et al*. (1992) reported a strong dependency of the backscatter of airborne polarimetric SAR at P-, L-, and C-bands on AGB of conifer forests. Generally, the penetration of microwaves into the forest varies positively with longer wavelengths, such as L-band (23.5 cm) and P-band (70.0 cm; see Section 16). Later studies estimated forest biomass with multi-band and multi-polarisation SAR data (e.g. Ranson and Sun, 2000; Ni *et al*., 2016) and interferometric coherence (Luckman *et al*., 2000). These studies showed that the SAR backscatter increased almost linearly with increasing biomass until it saturates at a biomass level that depends on the radar frequency.

Mitchell *et al*. (2017) conducted a review of methods for assessments of forest degradation and their role in carbon emissions for national reporting within the framework of UN REDD+. Various assessment methods exist employing multi-resolution SAR and/or optical and lidar data. They reviewed two main approaches for monitoring forest degradation, with the first being the detection of changes in canopy cover, and the second involving the quantification of loss (or gain) in AGB. They concluded that improvements in canopy cover change detections were being made through SAR-optical data fusion and the use of very high resolution data, while increased sensitivities to forest structure and biomass were being achieved using repeat SAR with lidar data. They further noted progress in discrimination of forest age and growth stage using data fusion methods and lidar height metrics, and new interferometric SAR and lidar applications in linking changes in forest structure to degradation in tropical forests (Mitchell *et al*., 2017).

Neither the SAR backscattering coefficients nor the interferometric coherence are a direct measurement of forest AGB, but instead they directly measure the canopy spatial structure, characterised by tree density, tree height, and/or tree diameter at breast height (DBH; see Section 16.5). Novel methods for direct measurements of forest spatial structure employ modern SAR methods, such as Polarimetric Interferometric Synthetic Aperture Radar (PolInSAR) and three-dimensional point cloud tomographic SAR (TomoSAR) data (Frey *et al*., 2008), that can directly detect the three-dimensional structure of forest, reduce the biomass saturation problem, and provide improved methods for monitoring forest AGB. Currently, PolInSAR and TomoSAR data are only acquired by airborne sensors, however, their potential advantages in AGB estimations will be fully explored with the upcoming BIOMASS (Europe), NISAR (USA, India), and Tandem-L (Germany) missions, scheduled in 2020–2022 timeframes (Le Toan *et al*., 2011).

17.7.4 Lidar and above ground biomass

Lidar is an active remote sensing technology that offers much potential for terrestrial carbon assessments and for quantifying AGB in forests (Lefsky *et al*. 2005; see Section 16.5), shrublands, and grasslands (Li *et al*., 2017; see Excursus 5.1). Opportunities to fuse temporally dynamic vegetation optical measurements with lidar have promising potential for better assessments of not only standing wood biomass, but also forest disturbance, biomass loss, and carbon accumulation through forest regrowth (Asner *et al*. 2007). Lidar can also serve as a reliable replacement for inventory plots in areas lacking field data.

Terrestrial laser scanning (TLS; see Excursus 5.1) provides very detailed vertical structure data for forests, enabling separation of points from trunk, branch, and leaves (Liang *et al*., 2016; see Volume 1A—Section 10). The quantitative, three-dimensional laser point information provided can be used in structural models (Disney *et al*., 2018) or for development of allometric equations to estimate AGB (Kankare *et al*., 2013). Thus, lidar integration with field inventory plots can provide calibrated lidar estimates of above ground carbon stocks, which can then be scaled up using satellite data on vegetation cover, topography, and rainfall from satellite data to model carbon stocks.

Airborne laser scanners (ALS) are increasingly being used to estimate larger scale forest AGB, through its capability to to quantify height, density, crown width, and crown volume at scales from individual trees to more extensive forest stands (Popescu *et al*., 2018; Tao *et al*., 2014; see Volume 1A—Section 15.1). The larger airborne footprint waveform data has also led to reasonable biomass estimates for a variety of forest types (Drake *et al*., 2002). The Global Observation of Forest Cover and Land Dynamics (GOFC-GOLD) program recommended the use of ALS data for biomass estimation in local efforts in reducing emissions from deforestation and forest degradation (REDD+; GOFC-GOLD, 2016).

Several spaceborne lidar sensors have also been utilised in larger scale canopy structure studies and for estimates of AGB. The Geoscience Laser Altimeter System (GLAS) aboard the ICESat satellite was shown to be able to estimate forest AGB in pan-tropical and temperate forests (Baccini *et al*., 2008; Saatchi *et al*.,2011; Lefsky *et al*., 2005; see Excursus 6.1). New generation lidar instruments are becoming available, such as the Advanced Topographic Laser Altimeter System (ATLAS) and the Global Ecosystem Dynamics Investigation (GEDI). The GEDI system, launched in December 2018, contains a three-laser system flying on the International Space Station (ISS), and the full waveform lidar has a circular footprint of ~25 m (Stavros *et al*., 2017). It is the first spaceborne lidar mission specifically designed to study forests and facilitate the estimation of AGB at large scales. As with the airborne instruments, the retrievable structural height and density metrics can be combined with biomass data from field plots or TLS data to build biomass estimation models (Zhao *et al*., 2009).

17.8 The Future

New space-based observations can strongly complement *in situ* observations in providing required quantitative ecosystem information globally (see Sections 19 and 20). While spaceborne measurements have uncertainty and bias errors of their own, they can help in reducing bias errors associated with relatively sparse *in situ* systems. Given the challenges of long term, *in situ* observations at regional scales, satellite measurements have made increasingly important contributions, complementing the detailed information available *in situ* by providing broad spatial and temporal coverage.

New space-based observations, including fluorescence, hyperspectral, thermal, and lidar are greatly expanding the number of ecosystem properties that can be quantified from space. Many of the key fluxes and stocks shown in Figure 17.1, Figure 17.2 and Figure 17.10, can, or will soon, be estimated using EO instruments and techniques. Combined, they now enable a more thorough coupling of the environmental conditions that plants experience with improved characterisation of their biophysical states, and with better monitoring capabilities to track plant responses to environmental changes. These advances are providing a better understanding of the dynamics of terrestrial productivity and the use of satellite data to drive productivity models of the land surface.

To have comprehensive knowledge of carbon stocks and fluxes everywhere and over time involves the coordination of *in situ* and remote observations. It still remains a challenge to develop such a coherent set of terrestrial ecosystem observations of the carbon cycle, and be able to develop early warning and prediction capabilities of carbon cycle feedbacks. All of these observations will have the common goal of helping us better understand our planet and understand how it is changing to benefit food, health, and economic security.

17.9 Further Information

Additional Reading

Viscarra Rossel, R.A., Webster, R., Bui, E.N., and Baldock, J.A. (2014). Baseline map of organic carbon in Australian soil to support national carbon accounting and monitoring under climate change. *Global Change Biology*, 20(9), 2953–2970. *https://doi.org/10.1111/gcb.12569*

Angelopoulou, T., Tziolas, N., Balafoutis, A., Zalidis, G., and Bochtis, D. (2019). Remote sensing techniques for soil organic carbon estimation: A review. *Remote Sensing*, 11(6), 1–18. *https://doi.org/10.3390/rs11060676*

Global Projects

UN Global Forest Observations Initiative (GFOI): *http://www.fao.org/gfoi*

Reducing Emissions from Deforestation and Forest Degradation in Developing Countries (REDD+): *https://redd.unfccc.int/*

Australia

National Inventory System (NIS; formerly National Carbon Accounting System: NCAS): *https://www.industry.gov.au/data-and-publications/national-inventory-reports*

National Greenhouse Accounts (Land sector estimates): *https://www.industry.gov.au/data-and-publications/land-sector-estimates-may-2017-update*

Climate Change Strategies: *https://www.industry.gov.au/strategies-for-the-future/australias-climate-change-strategies*

National Greenhouse and Energy Reporting: *http://www.cleanenergyregulator.gov.au/NGER/About-the-National-Greenhouse-and-Energy-Reporting-scheme*

International Forest Carbon Initiative: Australia's IFCI supported global efforts to establish a REDD+ mechanism under the UNFCCC. Jointly administered by the Australian Department of Climate Change and Energy Efficiency and AusAID, the Initiative enabled Australia to work closely with developing countries to find practical ways to reduce forest emissions: *https://www.unredd.net/partners/103-international-forest-carbon-initiative-australia-.html*

Roxburg, S., Karunaratne, S., and Paul, K. (2017). *A revised above-ground maximum biomass layer for Australia's national carbon accounting system*. CSIRO Land and Water, Canberra. *https://publications.csiro.au/rpr/download?pid=csiro:EP181854anddsid=DS1*

NASA

The Carbon Cycle: *https://www.earthobservatory.nasa.gov/features/CarbonCycle/page1.php*

A New Space-Based View of Human Made Carbon Dioxide: *https://www.jpl.nasa.gov/news/news.php?feature=6666*

Orbiting Carbon Observatory-2: *https://ocov2.jpl.nasa.gov/*

17.10 References

Angert, A., Biraud, S., Bonfils, C., Henning, C.C., Buermann, W., Pinzon, J., Tucker, C.J., and Fung, I. (2005). Drier summers cancel out the CO_2 uptake enhancement induced by warmer springs. *Proceedings of the National Academy of Science*, 102(31), 10823–10827.

Asner, G.P., Knapp, D.E., Kennedy-Bowdoin, T., Jones, M.O., Martin, R.E., Boardman, J., and Field, C.B. (2007). Carnegie Airborne Observatory: in-flight fusion of hyperspectral imaging and waveform light detection and ranging (wLiDAR) for three-dimensional studies of ecosystems. *Journal of Applied Remote Sensing*, 1, 013536.

Asrar, G., Fuchs, M., Kanemasu, E.T., Hatfield, J.L. (1984). Estimating absorbed photosynthetic radiation and leaf-area index from spectral reflectance in wheat. *Agronomy Journal*, 76, 300–306.

Baccini, A., Friedl, M.A., Woodcock, C.E., and Warbington, R. (2004). Forest biomass estimation over regional scales using multisource data. *Geophysical Research Letters*, 31, L10501.

Baccini, A., Laporte, N., Goetz, S.J., Sun, M., and Dong, H. (2008). A first map of tropical Africa's above-ground biomass derived from satellite imagery. *Environmental Research Letters*, 3, 045011.

Baker, N.R. (2008). Chlorophyll fluorescence: A probe of photosynthesis in vivo. *Annual Review of Plant Biology*, 59, 89–113.

Baldocchi, D., Falge, E., Lianhong, G., Olson, R., Hollinger, D., Running, S., Anthoni, P., Bernhofer, C., Davis, K., Evans, R., Fuentes, J., Goldstein, A., Katul, G., Law, B., Xuhui, L., Malhi, Y., Meyers, T., Munger, W., Oechel, W., and Paw U, K.T. (2001). FLUXNET: A New Tool to Study the Temporal and Spatial Variability of Ecosystem-Scale Carbon Dioxide, Water Vapor, and Energy Flux Densities. *Bulletin of the American Meteorological Society*, 82(11), 2415–2434.

Bartholomeus, H., Kooistra, L., Stevens, A., van Leeuwen, M., van Wesemael, B., Ben-Dor, E., and Tychon, B. (2011). Soil organic carbon mapping of partially vegetated agricultural fields with imaging spectroscopy. *International Journal of Applied Earth Observation and Geoinformation*, 13, 81–88.

Basu, S., Guerlet, S., Butz, A., Houweling, S., Hasekamp, O., Aben, I., Krummel, P., Steele, P., Langenfelds, R., Torn, M., Biraud, S., Stephens, B., Andrews, A., and Worthy, D. (2013). Global CO_2 fluxes estimated from GOSAT retrievals of total column CO_2. *Atmospheric Chemistry and Physics*, 13, 8695–8717.

Ben-Dor, E., Inbar, Y., and Chen, Y. (1997). The reflectance spectra of organic matter in the visible near-infrared and short wave infrared region (400–2500 nm) during a controlled decomposition process. *Remote Sensing of Environment*, 61, 1–15.

Ben-Dor, E., Irons, J.A., and Epema, G.F. (1999). Soil reflectance. In *Manual of Remote Sensing: Remote Sensing for the Earth Sciences*. John Wiley and Sons Inc, New York. pp. 111–189.

Breiman, L. (2001). Random forests. *Machine Learning*, 45, 5–32.

Cambou, A., Cardinael, R., Kouakoua, E., Villeneuve, M., Durand, C., and Barthes, B.G. (2016). Prediction of soil organic carbon stock using visible and near infrared reflectance spectroscopy (VNIRS) in the field. *Geoderma*, 261, 151–159.

Chambers, J.Q., Negrón-Juárez, R.I., Hurtt, G.C., Marra, D.M., and Higuchi, N. (2009). Lack of intermediate-scale disturbance data prevents robust extrapolation of plot-level tree mortality rates for old-growth tropical forests. *Ecology Letters*, 12(12), E22–E5.

Chen, D., Chang, N.J., Xiao, J.F., Zhou, Q.B., and Wu, W.B. (2019). Mapping dynamics of soil organic matter in croplands with MODIS data and machine learning algorithms. *Science of the Total Environment*, 669, 844–855.

Chopping, M., Schaaf, C.B., Zhao, F., Wang, Z.S., Nolin, A.W., Moisen, G.G., Martonchik, J.V., and Bull, M. (2011. Forest structure and aboveground biomass in the southwestern United States from MODIS and MISR. *Remote Sensing of Environment*, 115, 2943–2953.

Churkina, G., and Running, S.W. (1998). Contrasting climatic controls on the estimated productivity of global terrestrial biomes. *Ecosystems*, 1, 2, 206–215.

Cleverly, J., Boulain, N., Villalobos-Vega, R., Grant, N., Faux, R., Wood, C., Cook, P.G., Yu, Q., Leigh, A., and Eamus, D. (2013). Dynamics of component carbon fluxes in a semi-arid *Acacia* woodland, central Australia. *Journal of Geophysical Research: Biogeosciences*, 118, 3, 1168–1185.

Cohen, W.B., Maiersperger, T.K., Gower, S.T., and Turner, D.P. (2003). An improved strategy for regression of biophysical variables and Landsat ETM+ data. *Remote Sensing of Environment*, 84, 561–571.

Cramer, W., Kicklighter, D., Bondeau, A., Iii, B.M., Churkina, G., Nemry, B., Ruimy, A., Schloss, A., Intercomparison, T., and Model, P.O.T.P.N. (1999). Comparing global models of terrestrial net primary productivity (NPP): overview and key results. *Global Change Biology*, 5(S1), 1–15.

Dash, J., and Curran, P.J. (2004). The MERIS terrestrial chlorophyll index. *International Journal of Remote Sensing*, 25, 5403–5413.

Disney, M.I., Vicari, M.B., Burt, A., Calders, K., Lewis, S.L., Raumonen, P., and Wilkes, P. (2018). Weighing trees with lasers: advances, challenges and opportunities. *Interface Focus*, 8, 20170048.

Dobson, M.C., Ulaby, F.T., LeToan, T., Beaudoin, A., Kasischke, E.S., and Christensen, N. (1992). Dependence of radar backscatter on coniferous forest biomass. *IEEE Transactions on Geoscience and Remote Sensing*, 30, 412–415.

Donohue, R.J., Roderick, M.L., McVicar, T.R., and Farquhar, G.D. (2013). Impact of CO_2 fertilization on maximum foliage cover across the globe's warm, arid environments. *Geophysical Research Letters*, 40, 3031–3035.

Drake, J.B., Dubayah, R.O., Clark, D.B., Knox, R.G., Blair, J.B., Hofton, M.A., Chazdon, R.L., Weishampel, J.F., and Prince, S.D. (2002). Estimation of tropical forest structural characteristics using large-footprint lidar. *Remote Sensing of Environment*, 79, 305–319.

Epstein, H.E., Raynolds, M.K., Walker, D.A., Bhatt, U.S., Tucker, C.J., and Pinzon, J.E. (2012). Dynamics of aboveground phytomass of the circumpolar Arctic tundra during the past three decades. *Environmental Research Letters*, 7, 015506.

FAO (2007). *State of the World's Forests*. UN Food and Agriculture Organisation, Rome.

Fensholt, R., Sandholt, I., and Rasmussen, M.S. (2004). Evaluation of MODIS LAI, fAPAR and the relation between fAPAR and NDVI in a semi-arid environment using *in situ* measurements. *Remote Sensing of Environment*, 91(3–4), 490–507.

Field, C.B., Randerson, J.T., and Malmstrom, C.M. (1995). Global net primary production: combining ecology and remote sensing. *Remote Sensing of Environment*, 51, 74–88.

Flexas, J., Escalona, J.M., Evain, S., Gulías, J., Moya, I., Osmond, C.B., and Medrano, H. (2002). Steady-state chlorophyll fluorescence (Fs) measurements as a tool to follow variations of net CO_2 assimilation and stomatal conductance during water-stress in C3 plants. *Physiologia Plantarum*, 114(2), 231–240

Frankenberg, C., Fisher,J.B., Worden,J., Badgley,G., Saatchi, S.S., Lee,J-E.,Toon, G.C., Butz, A., Jung, M., Kuze, A., and Yokota, T. (2011). New global observations of the terrestrial carbon cycle from GOSAT: Patterns of plant fluorescence with gross primary productivity. *Geophysical Research Letters*, 38, L17706.

Franklin, J., and Hiernaux, P.H.Y. (1991). Estimating foliage and woody biomass in Sahelian and Sudanian woodlands using a remote sensing model. *International Journal of Remote Sensing*, 12, 1387–1404.

Frey, O., Morsdorf, F., and Meier, E. (2008). Tomographic imaging of a forested area by airborne multi-baseline P-band SAR. *Sensors*, 8, 5884–5896.

Friedl, M.A., Michaelsen, J., Davis, F.W., Walker, H., and Schimel, D.S. (1994). Estimating grassland biomass and leaf area index using ground and satellite data. *International Journal of Remote Sensing*, 15, 1401–1420.

Friedl, M.A., Sulla-Menashe, D., Tan, B., Schneider, A., Ramankutty, N., Sibley, A., Huang, X.M. (2010). MODIS collection 5 global land cover: algorithm refinements and characterization of new datasets. *Remote Sensing of Environment*, 114, 168–182.

Friedlingstein P., Jones, M.W., O'Sullivan, M., Andrew, R. M., Hauck, J., Peters, G. P., Peters, W., Pongratz, J., Sitch, S., Le Quéré, C., Bakker, D. C. E., Canadell, J. G., Ciais, P., Jackson, R. B., Anthoni, P., Barbero, L., Bastos, A., Bastrikov, V., Becker, M., Bopp, L., Buitenhuis, E., Chandra, N., Chevallier, F., Chini, L. P., Currie, K. I., Feely, R. A., Gehlen, M., Gilfillan, D., Gkritzalis, T., Goll, D. S., Gruber, N., Gutekunst, S., Harris, I., Haverd, V., Houghton, R. A., Hurtt, G., Ilyina, T., Jain, A. K., Joetzjer, E., Kaplan, J. O., Kato, E., Klein Goldewijk, K., Korsbakken, J. I., Landschützer, P., Lauvset, S. K., Lefèvre, N., Lenton, A., Lienert, S., Lombardozzi, D., Marland, G., McGuire, P. C., Melton, J. R., Metzl, N., Munro, D. R., Nabel, J. E. M. S., Nakaoka, S.-I., Neill, C., Omar, A. M., Ono, T., Peregon, A., Pierrot, D., Poulter, B., Rehder, G., Resplandy, L., Robertson, E., Rödenbeck, C., Séférian, R., Schwinger, J., Smith, N., Tans, P. P., Tian, H., Tilbrook, B., Tubiello, F. N., van der Werf, G. R., Wiltshire, A. J., and Zaehle, S. (2019). Global Carbon Budget 2019. *Earth System Sciences and Data*, 11, 1783–1838.

Fuchs, H., Magdon, P., Kleinn, C., and Flessa, H. (2009). Estimating aboveground carbon in a catchment of the Siberian forest tundra: combining satellite imagery and field inventory. *Remote Sensing of Environment*, 113, 518–531.

Gamon, J.A., Serrano, L., and Surfus, J.S. (1997). The photochemical reflectance index: an optical indicator of photosynthetic radiation use efficiency across species, functional types, and nutrient levels. *Oecologia*, 112, 492–501.

Gitelson, A.A. (2004). Wide dynamic range vegetation index for remote quantification of biophysical characteristics of vegetation. *Journal of Plant Physiology*, 161, 165–173.

Gitelson, A.A., Viña, A., Verma, S.B., Rundquist, D.C., Arkebauer, T.J., Keydan, G., Leavitt, B., Ciganda, V., Burba, G.G., and Suyker, A.E. (2006). Relationship between gross primary production and chlorophyll content in crops: Implications for the synoptic monitoring of vegetation productivity. *Journal of Geophysical Research: Atmospheres*, 111(D8), D08S11.

Gitelson, A.A., Peng, Y., Arkebauer, T.J., and Schepers, J. (2014). Relationships between gross primary production, green LAI, and canopy chlorophyll content in maize: Implications for remote sensing of primary production. *Remote Sensing of Environment*, 144, 65–72.

Glenn, E.P., Huete, A.R., Nagler, P.L., and Nelson, S.G. (2008). Relationship between remotely sensed vegetation indices, canopy attributes and plant physiological processes: what vegetation indices can and cannot tell us about the landscape. *Sensors*, 8, 2136–2160.

Goerner, A., Reichstein, M., and Rambal, S. (2009). Tracking seasonal drought effects on ecosystem light use efficiency with satellite-based PRI in a Mediterranean forest. *Remote Sensing of Environment*, 113(5), 1101–1111.

GOFC-GOLD (2016). A sourcebook of methods and procedures for monitoring and reporting anthropogenic greenhouse gas emissions and removals associated with deforestation, gains and losses of carbon stocks in forests remaining forests, and forestation. In *GOFC-GOLD Report Version COP22-1*. GOFC-GOLD Land Cover Project Office, Wageningen University, The Netherlands.

Gomez, C., Rossel, R.A.V., and McBratney, A.B. (2008). Soil organic carbon prediction by hyperspectral remote sensing and field vis-NIR spectroscopy: an Australian case study. *Geoderma*, 146, 403–411.

Goward, S.N., Tucker, C.J., and Dye, D.G. (1985). North American vegetation patterns observed with the NOAA-7 advanced very high resolution radiometer. *Vegetatio*, 64, 3–14.

Goward, S.N., and Huemmrich, K.F. (1992). Vegetation canopy PAR absorptance and the normalized difference vegetation index: an assessment using the SAIL model. *Remote Sensing of Environment*, 39, 119–140.

Gower, S.T., Kucharik, C.J., and Norman, J.M. (1999). Direct and Indirect Estimation of Leaf Area Index, fAPAR, and Net Primary Production of Terrestrial Ecosystems. *Remote Sensing of Environment*, 70(1), 29–51.

Gray, J.M., Bishop, T.F.A., and Wilson, B.R. (2015). Factors controlling soil organic carbon stocks with depth in eastern Australia. *Soil Science Society of America Journal*, 79, 1741–1751.

Greenberg, J.A., Dobrowski, S.Z., and Ustin, S.L. (2005). Shadow allometry: estimating tree structural parameters using hyperspatial image analysis. *Remote Sensing of Environment*, 97, 15–25.

Grinand, C., Le Maire, G., Vieilledent, G., Razakarnanarivo, H., Razafimbelo, T., and Bernoux, M. (2017). Estimating temporal changes in soil carbon stocks at ecoregional scale in Madagascar using remote-sensing. *International Journal of Applied Earth Observation and Geoinformation*, 54, 1–14.

Guo, L., Zhang, H., Shi, T., Chen, Y., Jiang, Q., and Linderman, M. (2019). Prediction of soil organic carbon stock by laboratory spectral data and airborne hyperspectral images. *Geoderma*, 337, 32–41.

Guanter, L., Y. Zhang, M. Jung, J. Joiner, M. Voigt, J. A. Berry, C. Frankenberg, A. Huete, P. Zarco-Tejada, J.-E. Lee, M.S. Moran, G. Ponce-Campos, C. Beer, G. Camps-Valls, N. Buchmann, D. Gianelle, K. Klumpp, A. Cescatti, J.M. Baker, and T.J. Griffis. (2014) Global and time-resolved monitoring of crop photosynthesis with chlorophyll fluorescence. *Proceedings of the National Academy of Sciences*, 111(14), E1327–E1333.

Hall, F.G., Shimabukuro, Y.E., and Huemmrich, K.F. (1995). Remote sensing of forest biophysical structure using mixture decomposition and geometric reflectance models. *Ecological Applications*, 5, 993–1013.

Hansen, M.C., Potapov, P.V., Moore, R., Hancher, M., Turubanova, S.A., Tyukavina, A., Thau, D., Stehman, S.V., Goetz, S.J., Loveland, T.R., Kommareddy, A., Egorov, A., Chini, L., Justice, C.O., and Townshend, J.R.G. (2013). High-resolution global maps of 21st-century forest cover change. *Science*, 342, 850–853.

Haverd, V., Raupach, M., Briggs, P., Canadell, J., Davis, S., Law, R., Meyer, C., Peters, G., Pickett-Heaps, C., Sherman, B. (2013). The Australian terrestrial carbon budget. *Biogeosciences*, 10, 851–869. doi:*10.5194/bg-10-851-2013*

Hbirkou, C., Patzold, S., Mahlein, A.K., and Welp, G. (2012). Airborne hyperspectral imaging of spatial soil organic carbon heterogeneity at the field-scale. *Geoderma*, 175, 21–28.

Heinsch, F.A., Zhao, M.S., Running, S.W., Kimball, J.S., Nemani, R.R., Davis, K.J., Bolstad, P.V., Cook, B.D., Desai, A.R., Ricciuto, D.M., Law, B.E., Oechel, W.C., Kwon, H., Luo, H.Y., Wofsy, S.C., Dunn, A.L., Munger, J.W., Baldocchi, D.D., Xu, L.K., Hollinger, D.Y., Richardson, A.D., Stoy, P.C., Siqueira, M.B.S., Monson, R.K., Burns, S.P., and Flanagan, L.B. (2006). Evaluation of remote sensing based terrestrial productivity from MODIS using regional tower eddy flux network observations. *IEEE Transactions on Geoscience and Remote Sensing*, 44, 1908–1925.

Heiskanen, J. (2006). Estimating aboveground tree biomass and leaf area index in a mountain birch forest using ASTER satellite data. *International Journal of Remote Sensing*, 27, 1135–1158.

Houghton, R.A., Butman, D., Bunn, A.G., Krankina, O.N., Schlesinger, P., and Stone, T.A. (2007). Mapping Russian forest biomass with data from satellites and forest inventories. *Environmental Research Letters*, 2, 045032.

Huete, A.R., Didan, K., Shimabukuro, Y.E., Ratana, P., Saleska, S.R., Hutyra, L.R., Yang, W.Z., Nemani, R.R., and Myneni, R. (2006). Amazon rainforests green-up with sunlight in dry season. *Geophysical Research Letters*, 33, L06405.

Huete, A.R., Restrepo-Coupe, N., Ratana, P., Didan, K., Saleska, S.R., Ichii, K., Panuthai, S., and Gamo, M. (2008). Multiple site tower flux and remote sensing comparisons of tropical forest dynamics in Monsoon Asia. *Agricultural and Forest Meteorology*, 148, 748–760.

Ichii, K., Hashimoto, H., White, M.A., Potters, C., Hutyra, L.R., Huete, A.R., Myneni, R.B., and Nemanis, R.R. (2007). Constraining rooting depths in tropical rainforests using satellite data and ecosystem modeling for accurate simulation of gross primary production seasonality. *Global Change Biology*, 13, 67–77.

Jagermeyr, J., Gerten, D., Lucht, W., Hostert, P., Migliavacca, M., and Nemani, R. (2014). A high-resolution approach to estimating ecosystem respiration at continental scales using operational satellite data. *Global Change Biology*, 20, 1191–1210.

Jarmer, T., Hill, J., Lavee, H., and Sarah, P. (2010). Mapping topsoil organic carbon in nonagricultural semi-arid and arid ecosystems of Israel. *Photogrammetric Engineering and Remote Sensing*, 76, 85–94.

Jenkins, J.P., Richardson, A.D., Braswell, B.H., Ollinger, S.V., Hollinger, D.Y., and Smith, M.L. (2007). Refining light-use efficiency calculations for a deciduous forest canopy using simultaneous tower-based carbon flux and radiometric measurements. *Agricultural and Forest Meteorology*, 143(1–2), 64–79.

Jin, C., Xiao, X., Merbold, L., Arneth, A., Veenendaal, E., and Kutsch, W.L. (2013). Phenology and gross primary production of two dominant savanna woodland ecosystems in Southern Africa. *Remote Sensing of Environment*, 135, 189–201.

John, R., Chen, J.Q., Giannico, V., Park, H., Xiao, J.F., Shirkey, G., Ouyang, Z.T., Shao, C.L., Lafortezza, R., and Qi, J.G. (2018). Grassland canopy cover and aboveground biomass in Mongolia and Inner Mongolia: spatiotemporal estimates and controlling factors. *Remote Sensing of Environment*, 213, 34–48.

Joiner, J., Yoshida, Y., Vasilkov, A.P., Yoshida, Y., Corp, L.A., and Middleton, E.M. (2011). First observations of global and seasonal terrestrial chlorophyll fluorescence from space. *Biogeosciences*, 8, 637–651.

Jones, L.A., Kimball, J.S., Reichle, R.H., Madani, N., Glassy, J., Ardizzone, J.V., Colliander, A., Cleverly, J., Desai, A.R., Eamus, D., Euskirchen, E.S., Hutley, L., Macfarlane, C., and Scott, R.L. (2017). The SMAP level 4 carbon product for monitoring ecosystem land-atmosphere CO_2 exchange. *IEEE Transactions on Geoscience and Remote Sensing*, 55, 6517–6532.

Kankare, V., Holopainen, M., Vastaranta, M., Puttonen, E., Yu, X.W., Hyyppa, J., Vaaja, M., Hyyppa, H., and Alho, P. (2013). Individual tree biomass estimation using terrestrial laser scanning. *ISPRS Journal of Photogrammetry and Remote Sensing*, 75, 64–75.

Kanniah, K.D., Beringer, J., Hutley, L.B., Tapper, N.J., and Zhu, X. (2009). Evaluation of Collections 4 and 5 of the MODIS Gross Primary Productivity product and algorithm improvement at a tropical savanna site in northern Australia. *Remote Sensing of Environment*, 113(9), 1808–1822.

Kanniah, K.D., Beringer, J., and Hutley, L.B. (2011). Environmental controls on the spatial variability of savanna productivity in the Northern Territory, Australia. *Agricultural and Forest Meteorology*, 151(11), 1429–1439.

Kanniah, K.D., Beringer, J., and Hutley, L. (2013). Exploring the link between clouds, radiation, and canopy productivity of tropical savannas. *Agricultural and Forest Meteorology*, 182–183, 304–313.

Karlson, M., Ostwald, M., Reese, H., Sanou, J., Tankoano, B., and Mattsson, E. (2015). Mapping tree canopy cover and aboveground biomass in Sudano-Sahelian woodlands using Landsat-8 and random forest. *Remote Sensing*, 7, 10017–10041.

Kimball, J.S., Jones, L.A., Zhang, K., Heinsch, F.A., McDonald, K.C., and Oechel, W.C. (2009). A satellite approach to estimate land-atmosphere CO_2 exchange for boreal and Arctic biomes using MODIS and AMSR-E. *IEEE Transactions on Geoscience and Remote Sensing*, 47, 569–587.

Kotchenova, S.Y., and Vermote, E.F. (2007). Validation of a vector version of the 6S radiative transfer code for atmospheric correction of satellite data. Part II. Homogeneous Lambertian and anisotropic surfaces. *Applied Optics*, 46(20), 4455–4464.

Le Toan, T., Beaudoin, A., Riom, J., and Guyon, D. (1992). Relating forest biomass to SAR data. *IEEE Transactions on Geoscience and Remote Sensing*, 30, 403–411.

Le Toan, T., Quegan, S., Davidson, M.W.J., Balzter, H., Paillou, P., Papathanassiou, K., Plummer, S., Rocca, F., Saatchi, S., Shugart, H., and Ulander, L. (2011). The BIOMASS mission: mapping global forest biomass to better understand the terrestrial carbon cycle. *Remote Sensing of Environment*, 115, 2850–2860.

Leboeuf, A., Beaudoin, A., Fournier, R.A., Guindon, L., Luther, J.E., and Lambert, M.C. (2007). A shadow fraction method for mapping biomass of northern boreal black spruce forests using Quick Bird imagery. *Remote Sensing of Environment*, 110, 488–500.

Lefsky, M.A., Harding, D.J., Keller, M., Cohen, W.B., Carabajal, C.C., Espirito-Santo, F.D., Hunter, M.O., and de Oliveira, R. (2005). Estimates of forest canopy height and aboveground biomass using ICESat. *Geophysical Research Letters*, 32, L22S02.

Leuning, R., Cleugh, H.A., Zegelin, S.J., and Hughes, D. (2005). Carbon and water fluxes over a temperate *Eucalyptus* forest and a tropical wet/dry savanna in Australia: measurements and comparison with MODIS remote sensing estimates. *Agricultural and Forest Meteorology*, 129(3–4), 151–173.

Li, X.W., and Strahler, A.H. (1985). Geometric-optical modeling of a conifer forest canopy. *IEEE Transactions on Geoscience and Remote Sensing*, 23, 705–721.

Li, A.H., Dhakal, S., Glenn, N.F., Spaete, L.P., Shinneman, D.J., Pilliod, D.S., Arkle, R.S., and McIlroy, S.K. (2017). Lidar aboveground vegetation biomass estimates in shrublands: prediction, uncertainties and application to coarser scales. *Remote Sensing*, 9, 903.

Li, Z., Yu, G., Xiao, X., Li, Y., Zhao, X., Ren, C., Zhang, L., and Fu, Y. (2007). Modeling gross primary production of alpine ecosystems in the Tibetan Plateau using MODIS images and climate data. *Remote Sensing of Environment*, 107(3), 510–519.

Liang, X.L., Kankare, V., Hyyppa, J., Wang, Y.S., Kukko, A., Haggren, H., Yu, X.W., Kaartinen, H., Jaakkola, A., Guan, F.Y., Holopainen, M., and Vastaranta, M. (2016). Terrestrial laser scanning in forest inventories. *ISPRS Journal of Photogrammetry and Remote Sensing*, 115, 63–77.

Luckman, A., Baker, J., and Wegmuller, U. (2000). Repeat-pass interferometric coherence measurements of disturbed tropical forest from JERS and ERS satellites. *Remote Sensing of Environment*, 73, 350–360.

Ma, X., Huete, A., Yu, Q., Coupe, N.R., Davies, K., Broich, M., Ratana, P., Beringer, J., Hutley, L.B., Cleverly, J., Boulain, N., and Eamus, D. (2013). Spatial patterns and temporal dynamics in savanna vegetation phenology across the North Australian Tropical Transect. *Remote Sensing of Environment*, 139, 97–115.

Ma, X., Huete, A., Cleverly, J., Eamus, D., Chevallier, F., Joiner, J., Poulter, B., Zhang, Y., Guanter, L., Meyer, W., Xie, Z., and Ponce-Campos, G. (2016). Drought rapidly diminishes the large net CO_2 uptake in 2011 over semi-arid Australia. *Scientific Reports*, 6, 37747.

Ma, X., Huete, A., Yu, Q., Restrepo-Coupe, N., Beringer, J., Hutley, L.B., Kanniah, K.D., Cleverly, J., and Eamus, D. (2014). Parameterization of an ecosystem light-use-efficiency model for predicting savanna GPP using MODIS EVI. *Remote Sensing of Environment*, 154, 253–271.

Mahadevan, P., Wofsy, S.C., Matross, D.M., Xiao, X., Dunn, A.L., Lin, J.C., Gerbig, C., Munger, J.W., Chow, V.Y., and Gottlieb, E.W. (2008). A satellite-based biosphere parameterization for net ecosystem CO_2 exchange: Vegetation Photosynthesis and Respiration Model (VPRM). *Global Biogeochemical Cycles*, 22, GB2005.

McBratney, A.B., Santos, M.L.M., and Minasny, B. (2003). On digital soil mapping. *Geoderma*, 117, 3–52.

Meroni, M., Rossini, M., Guanter, L., Alonso, L., Rascher, U., Colombo, R., and Moreno, J. (2009). Remote sensing of solar-induced chlorophyll fluorescence: Review of methods and applications. *Remote Sensing of Environment*, 113(10), 2037–2051.

Middleton, E.M., Huemmrich, K.F., Zhang, Q., Campbell, P.I.K.E., and Landis, D.R. (2018). Spectral bio-indicators of photosynthetic efficiency and vegetation stress. Ch 5 in Volume 3: *Biophysical and Biochemical Characterization and Plant Species Studies*, pp. 133–179, of *Hyperspectral Remote Sensing of Vegetation* 2nd edn. (Eds: Thenkabail, P.S., Lyon, J.G., and Huete, A.) Taylor and Francis.

Mishra, U., Lal, R., Liu, D.S., and Van Meirvenne, M. (2010). Predicting the spatial variation of the soil organic carbon pool at a regional scale. *Soil Science Society of America Journal*, 74, 906–914.

Mitchell, A.L., Rosenqvist, A., and Mora, B. (2017). Current remote sensing approaches to monitoring forest degradation in support of countries measurement, reporting and verification (MRV) systems for REDD+. *Carbon Balance and Management*, 12, 9. *https://doi.org/10.1186/s13021-017-0078-9*

Monfreda, C., Ramankutty, N., and Foley, J.A. (2008). Farming the planet: 2. Geographic distribution of crop areas, yields, physiological types, and net primary production in the year 2000. *Global Biogeochemical Cycles*, 22, GB1022. *https://doi.org/10.1029/2007GB002947*

Monteith, J.L. (1972). Solar-radiation and productivity in tropical ecosystems. *Journal of Applied Ecology*, 9, 747–766.

Monteith, J.L., and Unsworth, M.H. (1990). *Principles of Environmental Physics*, 2nd edn. Antony Rowe Ltd., Eastbourne, U.K.

Moore, D.J.P., Trahan, N.A., Wilkes, P., Quaife, T., Stephens, B.B., Elder, K., Desai, A.R., Negron, J., and Monson, R.K., (2013). Persistent reduced ecosystem respiration after insect disturbance in high elevation forests. *Ecological Letters*, 16, 731–737.

Moran, M.S., Ponce-Campos, G.E., Huete, A., McClaran, M.P., Zhang, Y.G., Hamerlynck, E.P., Augustine, D.J., Gunter, S.A., Kitchen, S.G., Peters, D.P.C., Starks, P.J., and Hernandez, M. (2014). Functional response of U.S. grasslands to the early 21st-century drought. *Ecology*, 95, 2121–2133.

Myneni, R.B., and Williams, D.L. (1994). On the relationship between FAPAR and NDVI. *Remote Sensing of Environment*, 49(3), 200–211.

Myneni, R.B., Keeling, C.D., Tucker, C.J., Asrar, G., and Nemani, R.R. (1997). Increased plant growth in the northern high latitudes from 1981 to 1991. *Nature*, 386, 698–702.

Myneni, R.B., Hoffman, S., Knyazikhin, Y., Privette, J.L., Glassy, J., Tian, Y., Wang, Y., Song, X., Zhang, Y., Smith, G.R., Lotsch, A., Friedl, M., Morisette, J.T., Votava, P., Nemani, R.R., and Running, S.W. (2002). Global products of vegetation leaf area and fraction absorbed PAR from year one of MODIS data. *Remote Sensing of Environment*, 83, 214–231.

Nemani, R.R., Keeling, C.D., Hashimoto, H., Jolly, W.M., Piper, S.C., Tucker, C.J., Myneni, R.B., and Running, S.W. (2003). Climate-driven increases in global terrestrial net primary production from 1982 to 1999. *Science*, 300, 1560–1563.

Ni, W., Sun, G., Zhang, Z., and Yu, H. (2016). Retrieval of forest aboveground biomass through the synergy of X-band (TeraSAR-X/TandDEM-X) and L-band (PALSAR-2) InSAR data. In *2016 IEEE International Geoscience and Remote Sensing Symposium (IGARSS)*. pp. 5304–5306.

Olofsson, P., Lagergren, F., Lindroth, A., Lindström, J., Klemedtsson, L., Kutsch, W., and Eklundh, L. (2008). Towards operational remote sensing of forest carbon balance across Northern Europe. *Biogeosciences*, 5(3), 817–832.

Palace, M., Keller, M., Asner, G.P., Hagen, S., and Braswell, B. (2008). Amazon forest structure from IKONOS satellite data and the automated characterization of forest canopy properties. *Biotropica*, 40, 141–150.

Peng, Y., Gitelson, A.A., Keydan, G., Rundquist, D.C., and Moses, W. (2011). Remote estimation of gross primary production in maize and support for a new paradigm based on total crop chlorophyll content', *Remote Sensing of Environment*, 115(4), 978–989.

Peng, Y., Gitelson, A.A., and Sakamoto, T. (2013). Remote estimation of gross primary productivity in crops using MODIS 250m data. *Remote Sensing of Environment*, 128, 186–196.

Ponce-Campos, G.E., Moran, M.S., Huete, A., Zhang, Y.G., Bresloff, C., Huxman, T.E., Eamus, D., Bosch, D.D., Buda, A.R., Gunter, S.A., Scalley, T.H., Kitchen, S.G., McClaran, M.P., McNab, W.H., Montoya, D.S., Morgan, J.A., Peters, D.P.C., Sadler, E.J., Seyfried, M.S., and Starks, P.J. (2013). Ecosystem resilience despite large-scale altered hydroclimatic conditions. *Nature*, 494, 349–352.

Popescu, S.C., Zhou, T., Nelson, R., Neuenschwande, A., Sheridan, R., Narine, L., and Walsh, K.M. (2018). Photon counting LiDAR: an adaptive ground and canopy height retrieval algorithm for ICESat-2 data. *Remote Sensing of Environment*, 208, 154–170.

Porcar-Castell, A., Tyystjarvi, E., Atherton, J., van der Tol, C., Flexas, J., Pfundel, E.E., Moreno, J., Frankenberg, C., and Berry, J.A (2014). Linking chlorophyll a fluorescence to photosynthesis for remote sensing applications: mechanisms and challenges. *Journal of Experimental Botany*, 65, 4065–4095.

Potter, C.S., Randerson, J.T., Field, C.B., Matson, P.A., Vitousek, P.M., Mooney, H.A., and Klooster, S.A. (1993). Terrestrial ecosystem production: a process model based on global satellite and surface data. *Global Biogeochemical Cycles*, 7, 811–841.

Powell, S.L., Cohen, W.B., Healey, S.P., Kennedy, R.E., Moisen, G.G., Pierce, K.B., and Ohmann, J.L. (2010). Quantification of live aboveground forest biomass dynamics with Landsat time-series and field inventory data: a comparison of empirical modeling approaches. *Remote Sensing of Environment*, 114, 1053–1068.

Pyne, S.J. (1992). *The Burning Bush: A Fire History of Australia*. Allen and Unwin, Sydney. 520 p. ISBN: 1863731946

Rahman, A.F., Sims, D.A., Cordova, V.D., and El-Masri, B.Z. (2005). Potential of MODIS EVI and surface temperature for directly estimating per-pixel ecosystem C fluxes. *Geophysical Research Letters*, 32(19), L19404.

Ranson, K.J., and Sun, G. (2000). Effects of environmental conditions on boreal forest classification and biomass estimates with SAR. *IEEE Transactions on Geoscience and Remote Sensing*, 38, 1242–1252.

Restrepo-Coupe, N., Huete, A., Davies, K., Cleverly, J., Beringer, J., Eamus, D., van Gorsel, E., Hutley, L.B., and Meyer, W.S. (2016). MODIS vegetation products as proxies of photosynthetic potential along a gradient of meteorologically and biologically driven ecosystem productivity. *Biogeosciences*, 13, 5587–5608.

Rossel, R.A.V., and Hicks, W.S. (2015). Soil organic carbon and its fractions estimated by visible-near infrared transfer functions. *European Journal of Soil Science*, 66, 438–450.

Rossel, R.A.V., Walvoort, D.J.J., McBratney, A.B., Janik, L.J., and Skjemstad, J.O. (2006). Visible, near infrared, mid infrared or combined diffuse reflectance spectroscopy for simultaneous assessment of various soil properties. *Geoderma*, 131, 59–75.

Rossini, M., Nedbal, L., Guanter, L., Ac, A., Alonso, L., Burkart, A., Cogliati, S., Colombo, R., Damm, A., Drusch, M., Hanus, J., Janoutova, R., Julitta, T., Kokkalis, P., Moreno, J., Novotny, J., Panigada, C., Pinto, F., Schickling, A., Schuttemeyer, D., Zemek, F., and Rascher, U. (2015). Red and far red Sun-induced chlorophyll fluorescence as a measure of plant photosynthesis. *Geophysical Research Letters*, 42, 1632–1639.

Roy, P.S., and Ravan, S.A. (1996). Biomass estimation using satellite remote sensing data—an investigation on possible approaches for natural forest. *Journal of Biosciences*, 21, 535–561.

Ruimy, A., Jarvis, P., Baldocchi, D., and Saugier, B. (1995). CO_2 fluxes over plant canopies and solar radiation: a review. *Advances in Ecological Research*, 26, 1–68.

Running, S.W., Nemani, R.R., Heinsch, F.A., Zhao, M.S., Reeves, M., and Hashimoto, H. (2004). A continuous satellite-derived measure of global terrestrial primary production. *Bioscience*, 54, 547–560.

Saatchi, S.S., Harris, N.L., Brown, S., Lefsky, M., Mitchard, E.T.A., Salas, W., Zutta, B.R., Buermann, W., Lewis, S.L., Hagen, S., Petrova, S., White, L., Silman, M., and Morel, A. (2011). Benchmark map of forest carbon stocks in tropical regions across three continents. *Proceedings of the National Academy of Sciences*, 108, 9899–9904.

Saleska, S.R., Wu, J., Guan, K.Y., Araujo, A.C., Huete, A., Nobre, A.D., and Restrepo-Coupe, N. (2016). Dry-season greening of Amazon forests. *Nature*, 531, E4–E5.

Sarker, L.R., and Nichol, J.E. (2011). Improved forest biomass estimates using ALOS AVNIR-2 texture indices. *Remote Sensing of Environment*, 115, 968–977.

Schimel, D.S. (1995). Terrestrial ecosystems and the carbon cycle. *Global Change Biology*, 1, 77–91.

Schimel, D., Pavlick, R., Fisher, J.B., Asner, G.P., Saatchi, S., Townsend, P., Miller, C., Frankenberg, C., Hibbard, K., and Cox, P. (2015). Observing terrestrial ecosystems and the carbon cycle from space. *Global Change Biology*, 21, 1762–1776.

Schubert, P., Lagergren, F., Aurela, M., Christensen, T., Grelle, A., Heliasz, M., Klemedtsson, L., Lindroth, A., Pilegaard, K., Vesala, T., and Eklundh, L. (2012). Modeling GPP in the Nordic forest landscape with MODIS time series data—Comparison with the MODIS GPP product. *Remote Sensing of Environment*, 126, 136–147.

Sellers, P.J. (1985). Canopy reflectance, photosynthesis and transpiration. *International Journal of Remote Sensing*, 6, 1335–1372.

Sellers, P.J., Schimel, D.S., Moore, B., Liu, J., and Eldering, A. (2018). Observing carbon cycle–climate feedbacks from space. *Proceedings of the National Academy of Sciences*, 115(31) 7860–7868.

Shen, J., Huete, A., Ma, X., Ngoc, N.T., Joiner, J., Beringer, J., Eamus, D., and Yu, Q. (2020). Spatial pattern and seasonal dynamics of the photosynthesis activity across Australian rainfed croplands. *Ecological Indicators*, 108, 104669.

Shi, Z., Wang, Q.L., Peng, J., Ji, W.J., Liu, H.J., Li, X., and Viscarra Rossel, R.A. (2014). Development of a national VNIR soil-spectral library for soil classification and prediction of organic matter concentrations. *Science China Earth Sciences*, 57, 1671–1680.

Shoshany, M., and Karnibad, L. (2011). Mapping shrubland biomass along Mediterranean climatic gradients: the synergy of rainfall-based and NDVI-based models. *International Journal of Remote Sensing*, 32, 9497–9508.

Sibanda, M., Mutanga, O., Rouget, M., and Kumar, L., (2017). Estimating biomass of native grass grown under complex management treatments using WorldView-3 spectral derivatives. *Remote Sensing*, 9(1), 55.

Sims, D.A., Rahman, A.F., Cordova, V.D., El-Masri, B.Z., Baldocchi, D.D., Bolstad, P.V., Flanagan, L.B., Goldstein, A.H., Hollinger, D.Y., Misson, L., Monson, R.K., Oechel, W.C., Schmid, H.P., Wofsy, S.C., and Xu, L. (2008). A new model of gross primary productivity for North American ecosystems based solely on the enhanced vegetation index and land surface temperature from MODIS. *Remote Sensing of Environment*, 112(4), 1633–1646.

Sims, D.A., Rahman, A.F., Cordova, V.D., El-Masri, B.Z., Baldocchi, D.D., Flanagan, L.B., Goldstein, A.H., Hollinger, D.Y., Misson, L., Monson, R.K., Oechel, W.C., Schmid, H.P., Wofsy, S.C., and Xu, L. (2006). On the use of MODIS EVI to assess gross primary productivity of North American ecosystems. *Journal of Geophysical Research: Biogeosciences*, 111(G4), G04015.

Sjostrom, M., Ardo, J., Arneth, A., Boulain, N., Cappelaere, B., Eklundh, L., de Grandcourt, A., Kutsch, W.L., Merbold, L., Nouvellon, Y., Scholes, R.J., Schubert, P., Seaquist, J., and Veenendaal, E.M. (2011). Exploring the potential of MODIS EVI for modeling gross primary production across African ecosystems. *Remote Sensing of Environment*, 115, 1081–1089.

Somarathna, P.D.S.N., Malone, B.P., and Minasny, B. (2016). Mapping soil organic carbon content over New South Wales, Australia using local regression kriging. *Geoderma Regional*, 7, 38–48.

Stavros, E.N., Schimel, D., Pavlick, R., Serbin, S., Swann, A., Duncanson, L., Fisher, J.B., Fassnacht, F., Ustin, S., Dubayah, R., Schweiger, A., and Wennberg, P. (2017). ISS observations offer insights into plant function. *Nature Ecology and Evolution*, 1(7), 194.

Stevens, A., Udelhoven, T., Denis, A., Tychon, B., Lioy, R., Hoffmann, L., and van Wesemael, B. (2010). Measuring soil organic carbon in croplands at regional scale using airborne imaging spectroscopy. *Geoderma*, 158, 32–45.

Tang, X.G., Liu, D.W., Song, K.S., Munger, J.W., Zhang, B., and Wang, Z.M. (2011). A new model of net ecosystem carbon exchange for the deciduous-dominated forest by integrating MODIS and flux data. *Ecological Engineering*, 37, 1567–1571.

Tao, S.L., Guo, Q.H., Li, L., Xue, B.L., Kelly, M., Li, W.K., Xu, G.C., and Su, Y.J. (2014). Airborne Lidar-derived volume metrics for aboveground biomass estimation: a comparative assessment for conifer stands. *Agricultural and Forest Meteorology*, 198, 24–32.

TerMikaelian, M.T., and Korzukhin, M.D. (1997). Biomass equations for sixty-five North American tree species. *Forest Ecology and Management*, 97, 1–24.

Tucker, C.J., Fung, I.Y., Keeling, C.D., and Gammon, R.H. (1986). Relationship between atmospheric CO_2 variations and a satellite-derived vegetation index. *Nature*, 319, 195–199.

Tucker, C.J., Slayback, D.A., Pinzon, J.E., Los, S.O., Myneni, R.B., and Taylor, M.G. (2001). Higher northern latitude normalized difference vegetation index and growing season trends from 1982 to 1999. *International Journal of Biometeorology*, 45, 184–190.

Turner, D.P., Urbanski, S., Bremer, D., Wofsy, S.C., Meyers, T., Gower, S.T., and Gregory, M. (2003). A cross-biome comparison of daily light use efficiency for gross primary production. *Global Change Biology*, 9, 3, 383-395.

Turner, D.P., Ollinger, S.V., and Kimball, J.S. (2004). Integrating remote sensing and ecosystem process models for landscape- to regional-scale analysis of the carbon cycle. *Bioscience*, 54, 573–584.

Turner, D.P., Ritts, W.D., Cohen, W.B., Gower, S.T., Running, S.W., Zhao, M.S., Costa, M.H., Kirschbaum, A.A., Ham, J.M., Saleska, S.R., and Ahl, D.E. (2006). Evaluation of MODIS NPP and GPP products across multiple biomes. *Remote Sensing of Environment*, 102, 282–292.

Vickers, D., Thomas, C.K., Pettijohn, C., Martin, J.G., and Law, B.E. (2012). Five years of carbon fluxes and inherent water-use efficiency at two semi-arid pine forests with different disturbance histories. *Tellus B*, 64.

Wang, J., Rich, P.M., Price, K.P., and Kettle, W.D. (2004). Relations between NDVI and tree productivity in the central Great Plains. *International Journal of Remote Sensing*, 25(16), 3127–3138.

Wang, B., Waters, C., Orgill, S., Gray, J., Cowie, A., Clark, A., and Liu, D.L. (2018). High resolution mapping of soil organic carbon stocks using remote sensing variables in the semi-arid rangelands of eastern Australia. *Science of the Total Environment*, 630, 367–378.

Were, K., Bui, D.T., Dick, O.B., and Singh, B.R. (2015). A comparative assessment of support vector regression, artificial neural networks, and random forests for predicting and mapping soil organic carbon stocks across an Afromontane landscape. *Ecological Indicators*, 52, 394–403.

Whitley, R.J., Macinnis-Ng, C.M.O., Hutley, L.B., Beringer, J., Zeppel, M., Williams, M., Taylor, D., and Eamus, D. (2011). Is productivity of mesic savannas light limited or water limited? Results of a simulation study. *Global Change Biology*, 17(10) 3130–3149.

Wilson, K.B., Baldocchi, D.D., and Hanson, P.J. (2001). Leaf age affects the seasonal pattern of photosynthetic capacityand net ecosystem exchange of carbon in a deciduous forest. *Plant, Cell and Environment*, 24(6), 571–583.

Wirth, C., Schumacher, J., Schulze, E.D. (2004). Generic biomass functions for Norway spruce in Central Europe—a meta-analysis approach toward prediction and uncertainty estimation. *Tree Physiology*, 24, 121–139.

Wu, C., Chen, J.M., and Huang, N. (2011). Predicting gross primary production from the enhanced vegetation index and photosynthetically active radiation: Evaluation and calibration. *Remote Sensing of Environment*, 115(12), 3424–3435.

Wu, C., Gonsamo, A., Zhang, F., and Chen, J.M. (2014). The potential of the greenness and radiation (GR) model to interpret 8-day gross primary production of vegetation. *ISPRS Journal of Photogrammetry and Remote Sensing*, 88, 69–79.

Wu, C., Niu, Z., and Gao, S. (2010). Gross primary production estimation from MODIS data with vegetation index and photosynthetically active radiation in maize. *Journal of Geophysical Research–Atmospheres*, 115, 12.

Xiao, J., and Moody, A. (2005). Geographical distribution of global greening trends and their climatic correlates: 1982-1998. *International Journal of Remote Sensing*, 26, 2371–2390.

Xiao, J., Chevallier, F., Gomez, C., Guanter, L., Hicke, J.A., Huete, A.R., Ichii, K., Ni, W., Pang, Y., Rahman, A.F., Sun, G., Yuan, W., Zhang, L., and Zhang, X. (2019). Remote sensing of the terrestrial carbon cycle: A review of advances over 50 years. *Remote Sensing of Environment*, 233, 111383.

Xiao, X.M., Hollinger, D., Aber, J., Goltz, M., Davidson, E.A., Zhang, Q.Y., and Moore, B. (2004). Satellite-based modeling of gross primary production in an evergreen needleleaf forest. *Remote Sensing of Environment*, 89, 519–534.

Xiao, X., Zhang, Q., Saleska, S., Hutyra, L., De Camargo, P., Wofsy, S., Frolking, S., Boles, S., Keller, M., and Moore Iii, B. (2005). Satellite-based modeling of gross primary production in a seasonally moist tropical evergreen forest. *Remote Sensing of Environment*, 94(1),105–122.

Xiao, Z.Q., Liang, S.L., Sun, R., Wang, J.D., and Jiang, B. (2015). Estimating the fraction of absorbed photosynthetically active radiation from the MODIS data based GLASS leaf area index product. *Remote Sensing of Environment*, 171, 105–117.

Yuan, W., Liu, S., Yu, G., Bonnefond, J.-M., Chen, J., Davis, K., Desai, A.R., Goldstein, A.H., Gianelle, D., Rossi, F., Suyker, A.E., and Verma, S.B. (2010). Global estimates of evapotranspiration and gross primary production based on MODIS and global meteorology data. *Remote Sensing of Environment*, 114(7), 1416–31.

Zhang, X.Y., and Kondragunta, S. (2006). Estimating forest biomass in the USA using generalized allometric models and MODIS land products. *Geophysical Research Letters*, 33, L09402.

Zhang, X.T., Liang, S.L., Zhou, G.Q., Wu, H.R., and Zhao, X. (2014). Generating Global Land Surface Satellite incident shortwave radiation and photosynthetically active radiation products from multiple satellite data. *Remote Sensing of Environment*, 52, 318–332.

Zhao, M.S., Heinsch, F.A., Nemani, R.R., and Running, S.W. (2005). Improvements of the MODIS terrestrial gross and net primary production global data set. *Remote Sensing of Environment*, 95, 164–176.

Zhao, M., Running, S.W., and Nemani, R.R. (2006). Sensitivity of Moderate Resolution Imaging Spectroradiometer (MODIS) terrestrial primary production to the accuracy of meteorological reanalyses. *Journal of Geophysical Research-Biogeosciences*, 111(G1). *https://doi.org/10.1029/2004JG000004*

Zhao, M., and Running, S.W. (2010). Drought-Induced Reduction in Global Terrestrial Net Primary Production from 2000 Through 2009. *Science*, 329(5994), 940–943.

Zhao, K., Popescu, S., and Nelson, R. (2009). Lidar remote sensing of forest biomass: A scale-invariant estimation approach using airborne lasers. *Remote Sensing of Environment*, 113, 182–196.

Zhou, L.M., Tucker, C.J., Kaufmann, R.K., Slayback, D., Shabanov, N.V., and Myneni, R.B. (2001). Variations in northern vegetation activity inferred from satellite data of vegetation index during 1981 to 1999. *Journal of Geophysical Research—*Atmosphere, 106, 20069–20083.

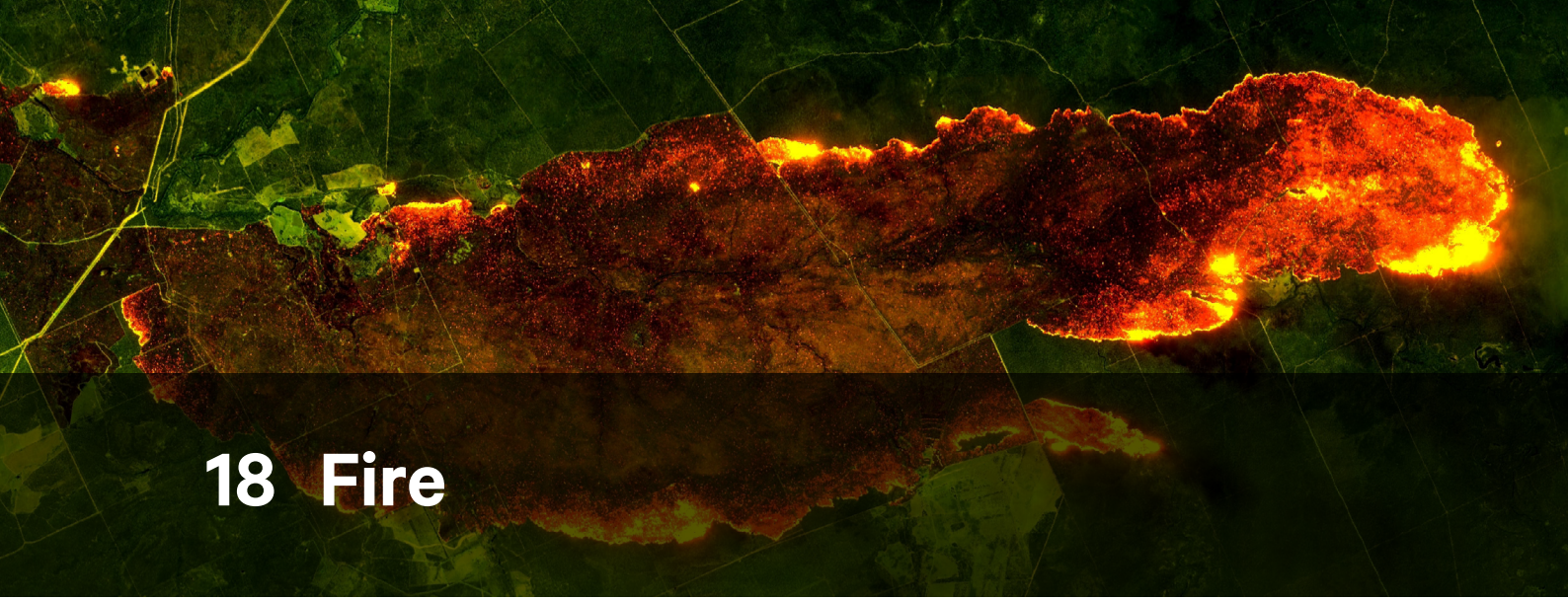

18 Fire

Rebecca Gibson, Marta Yebra, Barbara Harrison, and Ross Bradstock

EO datasets have been used in many studies related to fire prediction, behaviour, occurrence, and impact (Tian *et al.*, 2005; Lentile *et al.*, 2006; Roy *et al.*, 2013; Chu and Guo 2014; Pettorelli *et al.*, 2014; Mueller *et al.*, 2017; Chuvieco *et al.*, 2020). These studies can be summarised into three broad groups:

- predictive fire analyses: examining pre-fire conditions which would affect fire likelihood and consequence (see Section 18.3);
- active fire analyses: identifying fire occurrence and magnitude to most effectively direct suppression and evacuation (see Section 18.4); and
- retrospective fire analyses: examining conditions after a fire event, which may include pre-fire conditions, to understand fire extent, severity, emissions, behaviour, impact, and recovery (see Section 18.5).

The temporal and spatial resolution of satellite and airborne imagery is constantly advancing (see Volume 1) and access to satellite imagery is continually enhanced as data acquisition, storage, and processing become faster, cheaper, and more accessible (see Volume 2). With rapidly advancing technologies, it is an ongoing challenge to successfully transfer the results of academic research into an operational environment (see Section 18.2). While there are still many limitations involved with the operational use of EO data for fire mapping and monitoring, significant advances have been made in this field in recent decades (see Section 18.6).

The Fire (Katie Ford)

When a human is asked about a particular fire,
she comes close:
then it is too hot,
so she turns her face—

and that's when the forest of her bearable life
appears,
always on the other side of the fire. The fire
she's been asked to tell the story of,
she has to turn from it, so the story you hear
is that of pines and twitching leaves
and how her body is like neither—

all the while there is a fire
at her back
which she feels in fine detail,
as if the flame were a dremel
and her back its etching glass.

You will not know all about the fire
simply because you asked.
When she speaks of the forest
this is what she is teaching you,

you who thought you were her master.

Background image: A bushfire at Lancefield, Victoria, on 7 October 2015, was imaged from 20,000 feet altitude. This false colour composite is displayed using thermal infrared (8.5–13 μm) as red, middle infrared (3–5 μm) as green, and visible blue (~0.5 μm) as blue. **Source:** Robert Norman, Air Affairs Australia Pty Ltd

Recommended Chapter Citation: Gibson, R.K., Yebra, M., Harrison, B.A., and Bradstock, R.A. (2021). Fire. Ch 18 in *Earth Observation: Data, Processing and Applications. Volume 3A—Terrestrial Vegetation.* CRCSI, Melbourne. pp. 389–426.

18.1 Fire in Australia

Fire is a major factor in shaping the Australian landscape (Pyne, 1992; Kershaw *et al.*, 2002; Ellis *et al.*, 2004). Fire regimes around Australia differ with the flammability of vegetation, attributes of weather and climate, and characteristics of terrain (see Section 2). The 'seasonality' of fires in Australia has been observed to vary with latitude, with northern regions being considered more likely to burn during winter and spring and southern areas being more susceptible to fire in summer and autumn (Luke and McArthur, 1978). These trends are largely governed by rainfall, which drives fuel accumulation (Bradstock, 2010). An EO-based analysis derived from AVHRR (Advanced Very High Resolution Radiometer) imagery (1997–2005) and rainfall data (1969–2004), which mapped the seasonal distribution of recent Australian fires (Russell-Smith *et al.*, 2007), shows a more complex pattern of fire activity (see Figure 18.1).

As introduced in Section 1.1.2.3, many Australian plants have developed mechanisms to recover and/or benefit from fire. Indigenous use of fire prior to European settlement is believed to have been frequent and widespread (Pyne, 1992; see Section 2.5.1). In recent centuries, however, the frequency and severity of bushfires in Australia has changed due to different settlement patterns, land management practices and climatic variations (Bartlett *et al.*, 2007; Jurskis, 2015), often with disasterous consequences to the landscape, local communities, infrastructure, and wildlife (see Table 18.1). A shift to significantly more hazardous fire regimes may be occurring in Australia (and elsewhere), characterised by increasing fire frequency and intensity associated with dynamic fire propagation, and the development of catastrophic 'fire storms' (Sharples *et al.*, 2016; Pyne, 2020; Oldenborgh *et al.*, 2020). For example, the unprecedented 2019/20 bushfire season burned nearly 19 million ha nationally, destroyed over 3,000 homes, and resulted in 33 deaths (Filkov *et al.*, 2020; CoA, 2020).

Figure 18.1 Fire seasonality in Australia

This map was derived from AVHRR imagery (1997–2005) and classification of rainfall data (1969–2004). The legend table below this map details the main burning period and average proportion of each coloured region that is burned each year.

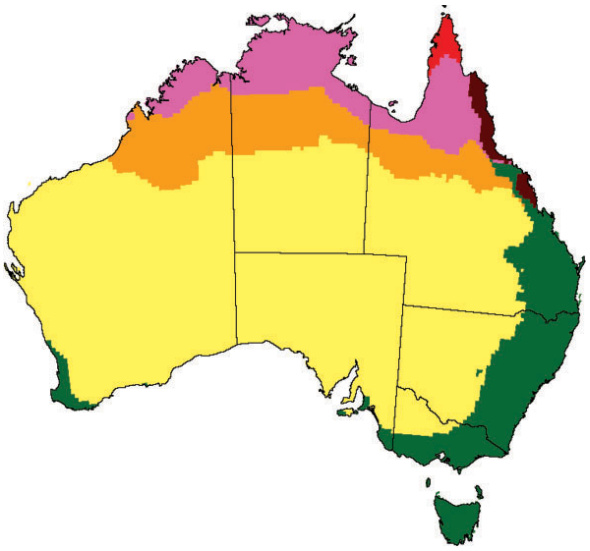

Colour	Main burning period	Mean annual burned area (%)
Pink	May–November	35
Red	July–November	27
Orange	August–November	19
Brown	September–November	5
Yellow	September–December	3
Green	December–March	1

Source: Russell-Smith *et al.* (2007) Figure 8c

Occasional, major fires are a long standing part of our ecological furniture, with their imprint hard-wired into the lifecycles of our biota. If we are to live in these environments we must do so on the understanding that we will not eliminate risk.
(Ross Bradstock)

Table 18.1 Major bushfires in Australia

This sample of fire seasons shows the 'worst' fire years in recent history based on area burned, number of fires, and/or damage to settlements.

Year(s) [name]	State	Area burned (Million ha)	Deaths	Homes/ shops burned	Other losses	Estimated cost at time of fires
1851 [Black Thursday]	Victoria	5	~12	–	25% of state burned; Huge livestock loss	–
1926/27	NSW	>2	8	many	–	> £1 million
1938/39 [including Black Friday]	Victoria	1.52	71	> 700	69 timber mills	–
1944	Victoria	>1	49	500	Huge stock loss	–
1951	Queensland	2.8	–	–	Significant stock loss	£2 million
1951/52	NSW	4.5	11	–	–	£6 million
1957/58	NSW	>2	5	158	Community facilities	–
1960/61	WA	>1.5	–	132	Other buildings	–
1966/67	Tasmania	0.26	64	>1,400	Significant livestock and infrastructure loss	–
1968/69	NT	4.0	–	–	Remote areas	–
	NSW	>2	14	80	81 buildings	–
1969/70	NT	4.5	–	–	Remote areas	–
1974/75	NT	4.5	–	–	Over 100 million ha burned nationally	–
	Queensland	7.3	–	–		–
	NSW	4.5	6	–		–
	SA	16	–	–		–
	WA	29	–	–		–
1983 [Ash Wednesday]	Victoria	0.15	47	1620	> 1,500 other buildings and 32,400 livestock	$138 million
	SA	0.16	28	383	200 other buildings	$38 million
1984/85	NSW	3.5	–	5	Livestock and infrastructure	$40 million
2002	NT	38	–	–	Remote areas	–
2002/03 [Alpine/Canberra]	NSW	1.5	3	86	151 days of severe fire activity	$12 million
	Victoria	1.1	(1)	41	Livestock	
	ACT	>0.16	4	488	Plantations, livestock, Observatory, 100 other structures	> $350 million
2003	WA	15.5	–	–	Remote areas	–
2009 [Black Saturday]	Victoria	>0.4	173	2,029	Community facilities	$1070 million
2019/20 [Black Summer]	NT	6.8	–	5	> 1 billion vertebrate animals; Global impacts of smoke	$40 billion
	Queensland	2.5	–	48		
	NSW	5.6	25	2,475		
	ACT	0.06	–	–		
	Victoria	1.5	5	396		
	Tasmania	0.036	–	2		
	SA	>0.29	3	186		
	WA	2.2	–	1		

Sources: Ellis *et al.* (2004); Filkov *et al.* (2020); ADRKH (2020)

In this fire-prone country, reducing fire risk will be strongly dependent on reducing fire severity, a metric of loss or change in organic matter caused by fire (Keeley, 2009). Major fires typically follow major droughts (as distinct from drier, herbaceous-dominated ecosystems where major fires typically follow major rains), with their impact becoming more devastating when they are adjacent to areas of urban and peri-urban expansion. In recent decades the incidence and severity of megafires, where fire behaviour characteristics exceed all efforts at control, have increased in Australia (Bradstock *et al*., 2012a).

One of the greatest advantages of using EO datasets in fire studies is the ability to look back on the vegetation, soil and other environmental conditions that preceded fire. While the scale of observation is often deficient in field-based fire studies that focus on single events, EO techniques offer the regional, national, and global scales required to adequately inform fire research and management (see Volume 2D).

For many years, EO imagery has been used globally to identify hotspots—pixels with abnormally high temperatures that may highlight fire ignitions. Hotspot imagery is routinely generated in Australia to enable fire response agencies to investigate small fires before they threaten lives and resources (see Section 18.6.2).

EO datasets are also used to map fire severity. The degree of combustion resulting from a fire is a function of its intensity and duration, as evidenced by the condition of the post-fire landscape. Incomplete combustion leaves a carbon residue (char or black ash), while complete (or near-complete) combustion produces a mineral (incombustible) residue (white ash or silica). Accordingly, the fuel consumption of a fire can be inferred from the proportion of white ash per unit area. For example, black ash is produced during the first 20 minutes of savanna fires, after which time the cumulative fire effects produce white ash (Roy and Landmann, 2005; Smith *et al*., 2005).

The volume of white ash has been found to be significantly correlated with surface fuel consumption, thereby indicating fire severity (Hudak, 2013). Increasing availability of hyperspectral and multispectral image capture by remotely piloted aircraft (or drones) provides greater access to the spatial and spectral resolution required to examine the characteristics of ash, an ecologically significant feature related to fire severity (Hamilton *et al*., 2017)

An initial assessment of fire severity provides a valuable overview of fire impact for land management and planning authorities to plan immediate rehabilitation activities. This has particular value in water catchment areas where post-fire rain can potentially accelerate erosion and reduce water quality. Such analyses also allow environmental scientists to foresee impacts on fauna and flora. Rapid response teams are commonly deployed from land management agencies immediately after a fire is contained. For example, the US Forestry Service (USFS) deploys Burned Area Emergency Response (BAER) teams, and in Australia, most jurisdictions have an equivalent systems of Rapid Risk Assessment Team (RRAT) deployments. These teams assess immediate post-fire landscape conditions in order to identify areas with highest need for site stabilisation treatments.

Identifying factors which can precipitate high fire severity, such as high fuel load, low fuel moisture, terrain liability, and meteorological pre-conditions (Bradstock *et al*., 2010; Estes *et al*., 2017), are paramount for predicting fire occurrence and activity (see Section 18.3). Similarly, real time monitoring of high fire intensity during active fires enables mitigation efforts to be directed to areas of greatest need (Keramitsoglou *et al*., 2004; see Section 18.4). Finally, analysis of fire severity patterns of past fires—and determining their drivers—will allow informed management decisions to reduce the severity of future fires (see Section 18.5).

18.2 EO Sensors for Fire

The recent report by the Australian 'Bushfire Earth Observation Taskforce' (ASA, 2020) highlighted the fact that the most appropriate combination of imagery and analysis methods for EO of fire will vary with the specific objectives of inquiry (see Table 18.2). For example, sensors used for detection of active fires will have different spatial, spectral, and temporal resolutions (see Volume 1B—Section 1) compared to sensors for post-fire analysis of fire severity. The many different biogeographic landscapes in Australia may also influence the imagery and analysis methods most appropriate for the type of inquiry. For example, the capacity of passive optical sensors to accurately capture spectral signatures from understorey layers is limited under very dense canopies (see Section 18.3.1.3).

Applications using MODIS (Moderate Resolution Imaging Spectroradiometer) data in Australia demonstrate these scale and landscape considerations. A wide range of global MODIS products for fire mapping have been available for over a decade (see Excursus 8.1 and Volume 2D—Excursus 10.1) including:

- MOD14/MYD14/MCD14—a thermal anomalies product that shows active fires and biomass burning. It is available as daily (day and night) images and composites (based on 8 day or monthly data; see Excursus 18.1); and
- MCD64A1—a monthly 500m resolution burned area product that improves on the original algorithm used for MCD64 (Roy *et al*., 2005; Giglio *et al*., 2009). Padilla *et al*. (2015) found MCD64A1 to be superior to MCD45A1 for mapping burned area.

In the sparsely-populated, open savanna landscapes of northern Australia, the MODIS active fire product (MOD14) is particularly useful for fires with an active flaming area of 100–300 m^2 (Maier *et al*., 2013). While the low spatial resolution of MODIS thermal infrared (TIR) imagery (1 km pixel size) limits its utility in southern regions, where forests are more dense and multi-layered, it can provide a useful cross-check against other fire information sources and helps to locate fires started by lightning in these landscapes (see Sections 18.6 and 18.7).

Similarly, tailored algorithms to estimate fuel moisture content (FMC) from MODIS optical bands with 500 m spatial resolution (Yebra *et al*., 2018) have been used to characterise fuel condition and flammability across Australia (see Figure 18.2a), which is essential for providing a broadscale sense of fuel dryness (see Section 18.3.1.2). However, when applied to a higher spatial resolution version dataset (such as Sentinel-2), local FMC gradients in the landscape can be delineated (see Figure 18.2b). These detailed gradients may act as soft containment lines when planning prescribed burns or prepositioning firefighting resources but would not be identifiable using a coarser spatial resolution image product.

However, the pace of technology development is continually increasing, with rapidly evolving improvements in the spatial, temporal, and spectral resolutions of sensors. For example, while geostationary sensors have traditionally had a temporal resolution of imaging the Earth each 1–2 days (see Volume 1A—Section 12), newer sensors supply more frequent imagery. One example is the Advanced Himawari Imager (AHI) on board Himawari-8, which provides hemispherical imagery every 10 minutes at 2 km spatial resolution. This improved temporal resolution greatly increases the likelihood of detecting new fire hotspots (Wickramasinghe *et al*., 2016; Xu *et al*., 2017), extracting fire rate of spread (Liu *et al*., 2018), and even detecting pre-fire fuel condition, such as FMC, at a sub-daily timescale (Quan *et al*., 2018).

In addition to the EO data available from public good satellites, the International Charter for Space and Major Disasters (ICSMD) supplies EO 'assets' from international space agencies and commercial enterprises to assist emergency managers during the disaster response phase (ICSMD, 2020). This initiative supplies data at no charge and also coordinates the acquisition of appropriate datasets at relevant locations. For example, in November 2019 Geoscience Australia (GA) activated the charter on behalf of Emergency Management Australia Crisis Coordination Centre (CCC) and New South Wales Rural Fire Service (NSW RFS) to access additional EO imagery to help with that catastrophic fire season.

Table 18.2 EO sensors relevant to fire-related studies

TIR: Thermal infrared; SAR: Synthetic Aperture Radar

Type	Sensor	Platform	Relevance	Advantages	Disadvantages
Passive optical	Multispectral radiometer	Satellite or airborne	Fuel moisture content Fuel type and fire severity Weather monitoring	Global coverage, low cost	Cloud contamination
	Hyperspectral spectro-radiometer	Airborne or terrestrial	Fuel moisture content Fuel type and fire severity	High spectral resolution, highlight plant stress	High cost, high data volume, specialised processing
	TIR radiometer	Satellite or airborne	Fire detection and fuel moisture content Weather monitoring	Global coverage, low cost	Coarse scale, cloud contamination, incapacity to detect small fires
Active optical	Lidar	Satellite, airborne, or terrestrial	Fuel structure and load	High accuracy, penetrates cloud, smoke	Data availability, high cost, specialised processing
Active microwave	SAR	Satellite, airborne, or terrestrial	Fuel structure, load, and moisture content Weather monitoring	All weather, so useful in tropical regions, penetrates cloud, smoke	Data availability, specialised processing

Figure 18.2 Fuel Moisture Content estimates

Local fuel moisture content (FMC) estimates derived using MODIS and Sentinel-2 satellite imagery acquired on 21 November 2019 over the Namadgi National Park, ACT. Both maps were produced using the FMC method described in Yebra *et al.* (2018), with FMC (%) values ranging from 17 (red) to 136 (blue). The higher spatial resolution of the Sentinel-2 imagery is able to detect terrain-driven gradients that are not visible in the MODIS product.

a. MODIS

b. Sentinel-2

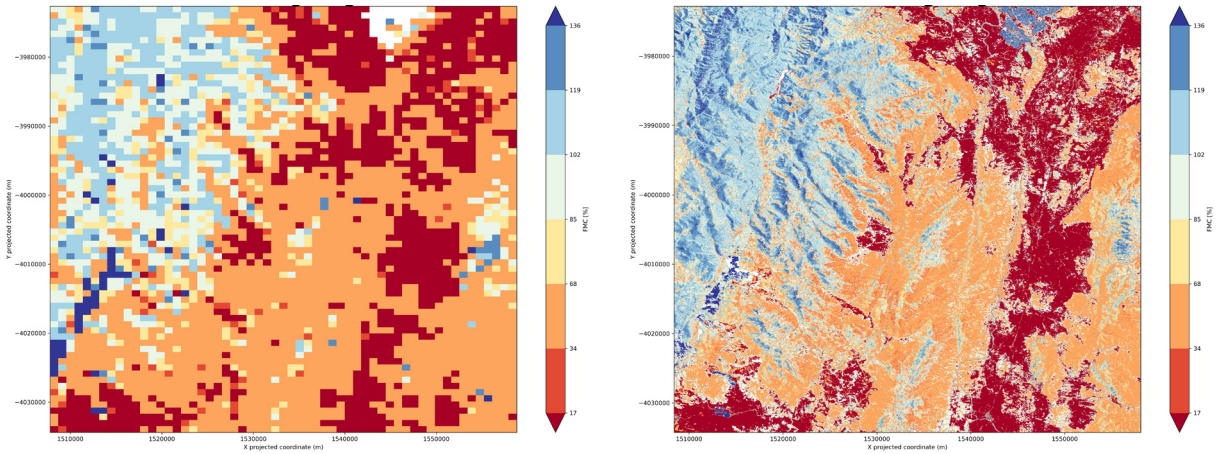

Source: Ivan Kotzur, University of Western Sydney

The use of sensors carried by remotely operated aircraft (commonly known as remotely piloted aircraft (RPA), unmanned aerial vehicles (UAV), or drones, and formally labelled Remotely Piloted Aerial Systems (RPAS); see Volume 1A—Section 11.2) is another rapidly evolving technology with applications in fire management and research. There is significant interest by fire management agencies in Australia in using UAV for monitoring active fires, as pioneered in the USA (Wing *et al.*, 2014). Research has recently been conducted in Australia on the use of UAV in fire severity assessments (McKenna *et al.*, 2017). Many opportunities exist to enhance the use of UAV-mounted sensors for fire management in Australia following international developments, such as mapping fuel structure and moisture assessment (Shin *et al.*, 2018; Polinova *et al.*, 2019). A UAV platform can carry a versatile range of sensors, including multispectral, hyperspectral, thermal, and lidar. The capacity for sub-centimeter spatial resolution and lack of cloud contaminated imagery are significant advantages of UAV. However, further development in radiometric and atmospheric corrections (Tu *et al.*, 2018) is needed to enhance the scientific rigour for EO applications of UAV imagery, particularly for broadscale and multi-temporal applications.

Both multispectral and thermal line scan imagery have been acquired for many fires over several decades around Australia. The data is generally used in fire fighting and suppression operations during a fire event, but it has also been investigated in fire behaviour research (Filkov *et al.*, 2018; Storey *et al.*, 2020a, 2020b). Analysis of this imagery has the potential to provide unique insights into the behaviour and progress of fires in different landscapes and the way fires interact with terrain and weather conditions (Sharples *et al.*, 2012). This understanding will improve fire mitigation efforts for the best possible outcome.

Given the unique biogeographic features of Australia, being able to spectrally characterise land cover changes induced by fire, with high precision, would greatly advance our understanding of Australian ecosystems and their dynamic interaction with fire (see Section 2.4). Hyperspectral imaging provides an opportunity for greater precision due to the narrow bandwidths, compared to the broad spectral bands of multispectral sensors (see Volume 1A—Section 14.3.3). Comparisons of multispectral and hyperspectral data for assessing fire severity using optical wavelengths indicate that fractional cover and burned fraction estimates were significantly better when derived from hyperspectral data (Veraverbeke *et al.*, 2014). However, advanced analysis techniques are required, which may limit the operational capacity. Hyperspectral imagery has not been widely explored for fire extent or severity studies in Australia, however, this sensor type has provided valuable fire-related information in overseas studies (e.g. Kokaly *et al.*, 2007) and warrants further investigation in the Australian fire-prone landscape. A detailed spectral library of Australian land cover components, both pre-fire and post-fire, would significantly improve our understanding of the information provided by EO imagery (see Volume 2D—Section 12.3).

18.3 Predictive Fire Analyses

Predictive analyses are relevant to the pre-fire environment to delineate those areas that are most likely to be vulnerable to fire. The major factors which determine fire behaviour and propagation are:

- fuels (biomass and flammability; see Section 18.3.1);
- weather (see Section 18.3.2); and
- ignitions (see Section 18.3.3).

Climate and terrain have biogeographic influences on these key drivers, which are inevitably interrelated:

- fuel type, structure, volume, and moisture content are dependent on climate and terrain; while
- the interaction between topography and weather creates environmental conditions that are either more or less conducive to fire.

EO data can be used to derive near real time information about fuel load and weather conditions, which can then be readily related to terrain data. Local scale quantitative field measurements, such as fuel type, biomass, and moisture content can be scaled up through models against regional climatic and terrain data (see Section 10 and Volume 2D). Integrated modelling of the factors driving the occurrence of wildfire are used in risk analysis approaches, such as fire danger indices (see Section 18.3.4). These tools allow for efficient management of fire fighting resources and early warning systems to help protect lives and assets.

18.3.1 Fuels

Fuel is the live and dead vegetation that may be consumed by fire. Total biomass and flammability of fuels contribute to the incidence and spread of fire. The specific characteristics of fuel which are relevant to bushfire likelihood include:

- fuel type and structure—size (diameter), horizontal and vertical distribution, and vegetation type (see Section 18.3.1.1);
- fuel moisture content (see Section 18.3.1.2); and
- fuel load (weight per unit area) and density (weight per unit volume; see Section 18.3.1.3).

An understanding of the distribution, volume and flammability of vegetative fuel in the landscape is essential for risk assessment and fuel management. Fuel is the only driver of fire which can be controlled, so fuel reduction is the primary management tool for reducing fire likelihood, although the efficacy of prescribed burning in reducing future fire risk is partial at best, due to the strong influence of fire weather on fire incidence and spread (Bradstock *et al*., 2012b).

18.3.1.1 Fuel type and structure

The type, density, and structure of fuel vary within and between landscapes and biogeographic regions (see Section 2.4). Some vegetation communities are more prone to fire than others, due to the flammability and volume of fuel they produce and accumulate. While the attributes of vegetation communities are highly variable in Australia, in terms of species composition, structure, and function, the mechanisms influencing fire behaviour can be condensed into a small number of categories. Bradstock *et al*. (2012c) reviewed fire regimes and biodiversity for Australian ecosystems in terms of seven major fuel types:

- **Grasslands** dominate the Australian landscape. This fuel type includes annual or perennial grasses, crops and improved pastures, and open forests and woodlands with a grassy understorey. Weather is generally more significant than fuel load in determining fire intensity and extent in grassy fuel systems (Morgan, 1999). However, fuel load may directly influence fire behaviour in grasslands through the spatial continuity of fuel. For example, heavily grazed grasslands may have scattered patches of bare ground (Bradstock *et al*., 2012c). Fire frequency and time-since-fire influence grassland composition and structure (Lund and Morgan, 2002), although the abundance of most grassland species is not adversely affected by fire (McDougall and Kirkpatrick, 1994).
- **Spinifex grasslands** occur on low nutrient soils in arid and semi-arid climates and cover about 25% of Australia. Although spinifex species are taxonomically classified as grasses, the fire behaviour they propagate is sufficiently different to warrant a separate fuel class (Bradstock *et al*., 2012c). Moisture content of spinifex reduces with age, which increases its flammability. Wind speed has been modelled as the major factor in determining fire rate of spread in spinifex grasslands, with fuel quantity and moisture also being significant (Burrows *et al*., 2006). Fire frequency varies from three to 30 years with fires following antecedent rain (Allan and Southgate, 2002)
- **Shrublands** include *Acacias*, chenopod shrublands and heathlands. This fuel type generally occurs on deficient, acid soils in Mediterranean, temperate, and tropical climates. Shrublands have fine, well-aerated fuels with dead foliage persisting in some species. Without the protection of a canopy layer, fuels are directly exposed to wind and Sun so dry quickly even after rain. Inter-fire periods depend on post-fire fuel density and have been reported to vary from 18 months to 8 years (Keith *et al*., 2002). Time-since-fire has been modelled as the main determinant of fire spread, with higher fire severity resulting in longer intervals between fires (Bradstock *et al*., 1998).

- **Mallee-heaths** in semi-arid (200–500 mm), southern Australia, occur in lateritic and aeolian sandplains, dunefields, and flats. These shrublands are characterised by multi-stemmed eucalypts and a Mediterranean climate. Vegetation density, and hence flammability, is affected by soil type, with cover ranging from 20% to 50%. Fuels are often discontinuous and inadequate for fire spread. After sufficient fuel accumulation, large episodic fires can occur in summer initiated by lightning and fanned by changeable winds (Bradstock and Cohn, 2002).
- **Dry sclerophyll forests** dominated by eucalypts cover the Great Dividing Range (GDR) from Queensland to Victoria and into Tasmania. This mountainous landscape features significant variation in topography, with vegetation density increasing in moister areas such as valleys. Leaf litter is the major fire fuel in these forests. Open forests burn more frequently than closed forests due to lower fuel moisture. Research has shown a wide range in fire intensity both within and between fires in these forests (Gill and Catling, 2002). Areas of forest also occur in the Mediterranean climates of southwest WA and southeast SA.
- **Other forests/woodlands:** Prior to European settlement, temperate woodlands covered extensive areas in southeast Australia, predominantly on the drier side of the GDR from Queensland to Victoria and into Tasmania. Much of this fuel type is now used for agriculture and therefore unaccustomed to fire. Similarly, most of the former Mediterranean woodlands in southwest WA have also been cleared for agricultural activities. Mean annual rainfall in these areas varies between 200 mm and 800 mm. Relatively little is known about the floristic composition or fire regimes of these woodlands before European settlement. Litter fuels accumulate more slowly in woodlands than in forests due to both the lower vegetation density and greater termite activity, so fires occur less frequently (Hobbs, 2002).
- **Rainforests** occur in high rainfall areas of nutrient rich, well-drained soils in tropical, sub-tropical, and temperate climates. The absence of fire in some areas is allowing rainforest to expand into wet sclerophyll forest and tropical savannas, and in other areas intense, late dry season fires in tropical savannas are damaging the margins of small patches of rainforest. Recovery of rainforest from fire depends on the frequency and seasonality of fires (Russell-Smith and Stanton, 2002).

Attempts to map multi-layer fuel structure using passive optical datasets have been primarily confounded by the concealing effect of overstorey vegetation. Reasonable fuel structure mapping accuracies have been obtained for grasslands, but dense forest and shrub cover can obscure estimates of the height of surface fuel. Active sensor systems offer the opportunity to measure the three-dimensional structure of vegetation more directly (see Section 16.5). Forest fuel structure has been estimated using various lidar platforms (see Excursus 5.1):

- airborne (or Airborne Laser Scanning, ALS; Hall *et al.*, 2005; Hudak *et al.*, 2008; Chen *et al.*, 2017a), including UAV-based (Wallace *et al.*, 2016); and
- ground-based (or Terrestrial Laser Scanning, TLS; Jupp *et al.*, 2008; Strahler *et al.*, 2008; Chen *et al.*, 2016; Marselis *et al.*, 2016).

Studies using ALS to map Australian forest floristics and structure have produced results comparable to conventional vegetation surveys (Tickle, *et al.*, 2006; Lucas *et al.*, 2008a, Price and Gordon, 2016). While surface and near surface fuels are generally modelled by small footprint lidar with less accuracy compared to elevated fuels (Turner, 2007; see also Section 12), the data may still provide a useful indicator (Price and Gordon, 2016). Recent developments in international research have applied fusion techniques for integrated modelling of forest structure using ALS data with satellite radar and multispectral imagery (Manzanera *et al.*, 2016, Garcia *et al.*, 2018).

18.3.1.2 Fuel moisture content

Fuel moisture is one of the key fire limiting switches that determines the propensity of vegetation to burn (Bradstock, 2010). The moisture content of both live and dead fuels is influenced primarily by temperature, humidity, and soil moisture. EO data has traditionally contributed to the fuel moisture characterisation of live fuel types, while dead fuel types (that is, not photosynthetically active) are generally derived from weather variables. Fuel moisture content (FMC) is inversely related to the flammability of vegetation and fire rate of spread. Traditionally FMC studies have been based on field observation or indirect estimates derived from atmospheric data. EO data offer an internally consistent approach to interpolate available FMC field data over a wide area (Nolan *et al.*, 2016a, 2016b). Alternatively, direct estimates of FMC can be retrieved from EO data based on radiative transfer models (RTM) inversion techniques (Yebra *et al.*, 2013, 2018).

As grasses senesce or become dormant their FMC content gradually decreases and their flammability correspondingly increases. This process is called curing, which is measured as the percentage of grass fuel that is dead. Grasslands that are less than 50% cured are not likely to foster and spread fire, however, when grass is between 70–90% cured, the rate of spread of a fire significantly increases (Cheney and Sullivan, 2008). In Australia, grassland curing is an integral component of the Grassland Fire Danger Index (GFDI; Cheney and Sullivan, 2008). As grasses cure, their spectral reflectance increases in the visible and middle infrared (MIR) wavelengths and decreases in the near infrared (NIR) region (Danson and Bowyer, 2004; see Section 4.3).

Numerous studies have attempted to relate vegetation indices derived from EO data to the curing state of grasslands. The Normalised Differenced Vegetation Index (NDVI) has been used to indicate vegetation greenness in many studies (see Section 8.1.1) and is closely correlated with the moisture content of vegetation. In Australia, Paltridge and Barber (1988) established an inverse exponential relationship between FMC and NDVI derived from AVHRR data. Dilley *et al.* (2004) showed that the relationship between curing and NDVI varied between sites and derived a more accurate relationship between GCI and NDVI. A Relative Greenness approach was then developed using MODIS-derived NDVI (Grassland Curing Index (GCI) algorithm-C; Newnham *et al.*, 2011). This method is used by Landgate to produce Curing Index maps for WA (see Section 18.7). More recently, Martin *et al.* (2015) developed a satellite model for estimating the degree of curing based on EO time series and weekly ground-based observations. Results from these studies are used by the Bureau of Meteorology (BoM) to produce Australia-wide curing maps and a more quantitative curing estimate for computing GFDI[13].

In forested landscapes, NDVI has been correlated with FMC for fire risk prediction in various locations, including in southern Spain (Aguado *et al.*, 2003), the Canadian boreal forests (Oldford *et al.*, 2006), Mediterranean grasslands and shrublands (Chuvieco *et al.*, 2002), and African savannas (Verbesselt *et al.*, 2007). Several studies have reported significant correlations between live fuel moisture and alternative vegetation indices (such as NDVI < NDWI < VARI; see Section 8.1.1; Stow *et al.*, 2006, Hao and Qu 2007, Caccamo *et al.*, 2012; Garcia *et al.*, 2020). However, empirical studies relating FMC to EO-based vegetation indices have reported variable results (Yebra *et al.*, 2008; Casas *et al.*, 2014), which may be due to sensor and site-dependent effects.

As introduced in Section 10 and Volume 1B—Section 5, RTM are based on physical relationships between spectral reflectance and the biophysical (such as water content) and structural (such as leaf area index, LAI) properties of vegetation (see Sections 5 and 6). Therefore RTM are independent of sensor or site conditions and are generally more universal than empirical modelling (Casas *et al.* 2014; Yebra *et al.* 2013). Yebra *et al.* (2018) derived a continental-wide FMC model for Australia using RTM inversion techniques, based on MODIS imagery (see Figure 18.2). This model was evaluated using high quality field data from around Australia and a flammability index, and indicated reasonable skill in fire risk prediction[14]. Ongoing research within the NSW Bushfire Risk Management Research Hub (co-led by the University of Western Sydney and the Australian National University) aims to develop spatially explicit monitoring and forecasting of dead and live fuel moisture in forested landscapes by integrating biophysical and EO modelling.

Emerging alternative approaches to modelling fuel moisture in forested landscapes include the use of radar data. Airborne SAR was used to model live fuel moisture against field data in a semi-arid Australian forest dominated by white cypress pine (Tanase *et al.*, 2014). Sentinel-1 C-band SAR was also used to model fuel moisture against field data in a Juniper, Redberry and Oak forest in central Texas, USA (Wang *et al.*, 2019). Sophisticated integration or radar and optical sensors provide improved accuracies of fuel moisture compared to traditional vegetation indices derived from optical datasets, such as NDVI (Rao *et al.*, 2020). Radar may also provide the opportunity to monitor soil moisture content, which is related to the moisture availability of fine surface fuels (Tanase *et al.*, 2014; Punithraj *et al.*, 2019). The recent and imminent launches of several spaceborne SAR sensors with high temporal revisit times and suitable sensor characteristics provide great opportunities for advancement of current knowledge and operational practices in fuel moisture monitoring for fire risk prediction.

One who neglects or disregards the existence of earth, air, fire, water and vegetation disregards his own existence which is entwined with them. (Mahavira)

13 This data is available from TERN AusCover (see Section 18.7).

14 Both FMC and Flammability estimates for Australia can be accessed via the Australian Flammability Monitoring website (see Section 18.7).

18.3.1.3 Fuel load and density

A range of EO data sources and methods have been used to estimate fuel load (as t/ha; Roff *et al.* 2005, 2006; Chafer *et al.*, 2004; Chafer, 2007). Many surrogates for forest fuel load, such as biomass or LAI, vary with species composition, tree height, and forest structure. As such, reflectance-based methods may be more appropriate when fuel load is estimated indirectly, using fire extent and/or severity derived from EO to infer fire history (time-since-fire), with ancillary vegetation type data and known fuel accumulation curves subsequently being used to model fuel loads (Brandis and Jacobson, 2003; Duff *et al.*, 2013). Recently, the Vegetation Structure Perpendicular Index (VSPI) derived from Landsat data has been used to estimate stand age by fitting post-fire VSPI time series to an exponential decay curve (Massetti *et al.* 2019). Time-since-fire may be a poor predictor of fuel load in some cases, as interactions between fire severity, vegetation type, and landscape productivity influence both the fuels remaining after fire and the rates of fuel re-accumulation (Price and Gordon, 2016). Direct measures of fuel load from active sensors may reduce such modelling uncertainty.

Active sensors such as lidar have has been used to estimate fuel load in Australia and as input into operational hazard mapping (Power, 2006, 2008). The use of active sensors may overcome limitations in estimating fuel load under dense canopies that obstruct the view of understorey layers (see Excursus 5.1 and Section 16.5). For example, predictive models of surface fuel in eucalypt forests in southeastern Australian have been developed using estimates of litter-bed depth derived from TLS, topographical data, and relevant environmental factors including previous fire disturbance (Chen *et al.*, 2017a).

One of the problems with validating EO methods for estimating fuel load is the lack of sufficient and objective field data. Visual assessment methods for estimating fuel load typically involve a qualitative element subject to observer bias, and destructive field sampling is only viable for a small number of sites (see Section 5.1.2). Field assessment methods of fuel load, such as McCarthy *et al.* (1999) and Gould *et al.* (2008), are expensive, time-consuming, complicated and subjective. Furthermore, recent evidence indicates visual assessment overestimated fuel load for very high and extreme fuel hazard categories, compared to destructively sampled surface fuels (McColl-Gausden and Penman, 2017).

Keane *et al.* (2001) discuss other challenges involved with mapping fuel loads, including fuelbed complexity, fuel type diversity, fuel variability, and fuel model generalisations. Multi-scale fuel mapping methods, based on vegetation community, composition, and structure derived from field data, EO and gradient modelling, may help to overcome the limitations of using EO datasets to estimate fuel loads (McColl-Gausden *et al.*, 2019; Jenkins *et al.*, 2020). This methodology was further developed in the LANDFIRE (Landscape Fire and Resource Management Planning Tools) system in the US, which combines fire behaviour and fuel models (Rollins, 2009). Similar systems are operational in Australia, such as FireTools used by NSW National Parks and Wildlife Service, which is used to predict fuel loads and plan prescribed burning. The integrated modelling being developed by the NSW Bushfire Risk Management Research Hub aims to characterise fuels using lidar data, then quantify initial post-fire fuel loads and re-accumulation curves in key fuel types, under varying levels of fire severity (NSW BRMR, 2020).

18.3.2 Weather conditions and topography

A range of weather variables affect fire ignition and propagation, both directly and indirectly, including temperature, relative humidity, precipitation, dew point temperature, solar insolation, wind speed, and wind direction (Rothermel, 1972). The risk of large fires that are difficult to control increases with extreme fire weather, which is the combination of low relative humidity, high temperature, and strong winds. Specific combinations of these conditions exacerbate fire danger in different ways, with wind direction and velocity largely determining the direction and speed of fire spread. Nocturnal temperature inversions can also lead to increased fire behaviour that is unrelated to wind (McRae et al., 2008).

Unstable atmospheric conditions can precipitate extreme fire-atmosphere interactions, such as violent pyrocumulonimbus (pyroCb) storms (Fromm *et al.*, 2010). Pyroconvection can influence widespread flaming and unpredictable fire behavior through strong and erratic changes in surface wind speed and direction, wind shear, mid-level moist instability, latent heating inside the convective cloud, and increased ignition likelihood through lightning (Sharples *et al.*, 2016; Potter, 2012a, 2012b). An increased risk of pyroconvection with future climate change has been identified for southeast Australia during spring and summer, due to decreased vertical atmospheric stability and humidity, combined with more severe, near surface conditions (Dowdy and Pepler, 2018).

Certain interactions between topography and meteorological conditions can escalate fire danger, such as dynamic channelling (Kossmann *et al*., 2001; Sharples *et al*., 2012), where fire is directed by terrain to spread down valleys as well as in the major wind direction (Sharples, 2009). The direction and rate of channelling can be predicted by analysis of slope, aspect, and wind regime (McRae, 2004; Sharples *et al*., 2012). Numerous other complex interactions with slope and wind characteristics have been described with associated effects on fire behaviour, such as:

- atypical lateral fire spread on steep lee-facing slopes, which may be associated with pyroconvective activity (Simpson *et al*., 2016).
- Foehn winds, the warm dry winds down the lee slopes of mountains caused by adiabatic compression, which can increase the intensity and rate of spread of fires (Sharples *et al*., 2010).
- mountain wind waves occur as air movement is deflected over a ridge. Lee slope eddies can draw any nearby fire into the channelling zone and circulate embers downwind (Sharples *et al*., 2009). Terrain can also produce jet-like winds when airflow is accelerated through narrow passes (Stensrud, 1996).
- low level jets may be produced through geostrophic forcing due to horizontal differences in sensible and latent heat fluxes with elevation variation in mountainous regions. The high wind speed and abrupt atmospheric warming and drying increase the potential for fire ignition and propagation (Sharples *et al*., 2009).

Meteorological terrain interactions are often difficult to predict and therefore present significant risk to firefighters. Satellite imagery captures characteristic cloud patterns produced by some of these phenomena. For example, mountain wind waves and 'dry slots' of low humidity air in the upper atmosphere are visible in water vapour imagery. A range of near real time TIR imagery is also available which shows surface temperature and detects thermal belts (see Volume 1B—Section 7). Meteorological events have been observed in conjunction with several extreme fires in Australia (Mills, 2008a, 2008b, Fromm *et al*., 2006, Cruz *et al*., 2012).

The use of EO to detect and predict drivers of the meteorological-terrain conditions that increase fire danger is an active area of research. A better understanding of the interaction between weather and topography on fire intensity and rate of spread will enable suppression agencies to anticipate extreme fire events with more certainty, and to plan and manage resources accordingly.

18.3.3 Ignitions

EO detection of fire ignitions is particularly useful for operational management of active fires, however, predicting ignition risk requires an understanding of the drivers of ignitions. Fire ignition datasets developed from EO products offer spatially consistent, regional scale data to study and model drivers of ignitions. For example, satellite-derived ignition data has been used to model the spatial relationships between anthropogenic land use or disturbance features and ignition for different ecoregions (Fusco *et al*., 2016; Vilar *et al*., 2016). Predicting areas prone to lightning-caused ignitions has also been analysed through coupled modelling of EO-based hotspot ignition data and lightning occurrence (Krawchuk *et al*., 2009).

Line Scanning Systems mounted to aircraft have been used for many years for active firefighting purposes, however, systematic use of this EO data type for fire behaviour analyses has been limited (see Section 18.2). Recently, research has commenced into using line scans in fire behaviour analysis, with recommendations for routine capture of this data source (Filkov *et al*., 2018). Line scans are being used to understand drivers of increased spotting risk (Storey *et al*., 2020a, 2020b). Spotting dynamics are known to dominate fire propagation in catastrophic wildfires. For example, during the 2009 Black Saturday fire in Victoria (Cruz *et al*., 2012; see Table 18.1), prolific short range spotting linked with crown fire propagation in eucalypt forest promoted extremely fast rates of spread. Greater understanding of the circumstances that are conducive to increased spotting risk may enable better forecasting, preparedness, and mitigation.

18.3.4 Risk analysis

Risk assessment includes both the physical probability of fire occurrence (likelihood) and the potential extent of damage (consequence). Analysis of EO data in conjunction with GIS has led to an improved understanding of both fire behaviour and likelihood (Chuvieco *et al*., 2010, 2014). Being able to identify those locations where fire is likely to occur and, if it occurs, whether it is likely to spread, allows incident management authorities to manage suppression resources most effectively.

Fire danger indices have long been used to estimate the likelihood of fire ignition and propagation (Burgan *et al*., 1998). These indices are basically derived from measures of weather, topography and fuel dryness. Satellite EO data has been used to compute inputs for these indices for decades (Verbesselt *et al*., 2002).

Australian fire danger ratings are currently based on two indices:

- Grassland Fire Danger Index (GFDI); and
- Forest Fire Danger Index (FFDI).

Initially developed as analogue meters (McArthur, 1966, 1967), these indices were subsequently expressed as equations by Noble *et al.* (1980). They indicate the likelihood of fire events and the likelihood of fire suppression. Both indices are derived from estimates of average wind velocity, relative humidity, air temperature, and fuel moisture. The latter component should reflect long term fuel moisture, that is, seasonal rather than diurnal variation in moisture content. An estimate of grassland curing is used to represent fuel moisture when computing GFDI, whereas a drought factor is used to compute FFDI. The drought factor is calculated using precipitation data and the Keetch-Byram Drought Index (KBDI; Keetch and Byram, 1968), where KBDI indicates the dryness of soils, deep forest litter, logs, and living vegetation.

Many other indices have been used to assess fire danger. For example, the Haines index (Haines, 1988), which measures lower atmosphere stability and dryness, quantifies the potential for forest fire growth and is used operationally by the USFS. The Continuous Haines Index is modified for more appropriate applications in Australia, due to high values of Haines index occurring very frequently in Australia (Mills and McCaw, 2010). However, a single index is not expected to precisely indicate the multi-faceted dimensions of fire risk.

A new National Fire Danger Rating System prototype was trialled by the NSW RFS over the summer of 2017/18 to better incorporate extreme fire behaviour. The revised system is based on empirical fire behaviour models and fuel type mapping, as well as meteorological data. This system aims to provide greater ability to understand and predict localised fire danger risk with improved scientific accuracy, rather than applying the same fire danger across large areas (Kenny *et al.*, 2019).

Several international systems have combined EO data with weather and/or topographic data to estimate fire danger (Leblon *et al.*, 2007), ignition potential (Chuvieco *et al.*, 2004), and seasonal fire risk (Manzo-Delgado *et al.*, 2009). In particular, the LANDFIRE Project has produced a comprehensive system which integrates a range of geospatial tools to model various landscape attributes across continental USA, including fire regime condition class (Rollins, 2009). Some Australian fire mitigation agencies produce risk maps to show those areas whose topography and fuel load are associated with a higher likelihood of fire (for example, see *https://www.bnhcrc.com.au/hazardnotes/77*). Bushfire threat has also been analysed in terms of proximity to bushland (Chen and McAneney, 2004, 2005) and changing demographics (Lowell *et al.*, 2009).

18.4 Active Fire Analyses

Active fires typically progress through two stages, flaming then smoldering, which are characterised by different temperatures, intensities, and emissions of aerosol particles. EO imagery from both satellite and airborne platforms has been used to map and monitor active fires. Space photography of extreme fire events graphically demonstrates the impact of the smoke plume on the upper atmosphere.

Several polar orbiting satellites are operationally used to map active fires globally (see Section 18.4.1). Recently, the new generation of geostationary sensors, with greater spatial and temporal resolution, have improved the capacity for active fire detection. This data can be combined with meteorological satellite imagery and prediction models, as well as imagery from airborne sensors, for both tactical and strategic fire suppression and to predict the volume and movement of smoke (see Section 18.4.2).

18.4.1 Satellite imagery

EO TIR bands have varying sensitivities to the temperature ranges associated with flaming and smoldering fires (Dozier, 1981; see Volume 1B—Section 7). An EO image pixel may comprise a mixture of areas that are unburned, flaming, and smoldering, which complicates detection of fire pixels using satellite imagery (Justice *et al.*, 2006). Change between an active flaming fire front and a low intensity smouldering fire can occur in a short space of time. As such, the revisit frequency of an EO sensor is an important part of the accurate detection of active fires. Differentiation between current fires and the normal land temperature is another major challenge in active fire detection methods. For this reason, detection of smouldering fires from satellite imagery remains a challenge given their relatively low temperatures and small spatial extent compared to flaming fires. Cloud contamination is a general problem in satellite imagery applications, and can obscure the detection of active fires.

Numerous EO methods have been developed to identify pixels containing active fires (see Excursus 18.1). Most algorithms use MIR and TIR bands (such as AVHRR band 3: 3.8 μm; and band 4: 10.8 μm respectively) with differing sensitivities to flaming and smoldering fires (Giglio and Justice, 2003, Plank et al., 2017). These regions of the electromagnetic spectrum are particularly useful for detecting active

fire because, under normal conditions, the background emission in the TIR range is significantly greater than that in the MIR range. By contrast, when a fire occurs, the emitted radiation becomes more intense at the shorter wavelength in the MIR range (Jones *et al.*, 2017). Other image channels (such as AVHRR band 2, NIR) can also be used to identify and exclude 'bright' non-fire pixels (such as small clouds or bare soil patches), although such masks can also eliminate fire pixels affected by smoke.

Early algorithms compared individual pixels with fixed thresholds. More sophisticated contextual algorithms have been used to determine relative thresholds based on the statistics of neighbouring pixels (Ressl *et al.*, 2009; Plank *et al.*, 2017). Methods using a multi-temporal approach to detecting active fires have also been developed (Koltunov and Ustin, 2007) and some methods use a combination of all three types of algorithms (fixed threshold, contextual, or multi-temporal; Jones *et al.*, 2017). While active fire detection algorithms have been developed for many satellite sensors (Giglio *et al.*, 2000; Calle *et al.*, 2008), MODIS imagery became the preferred image source for detecting hotspots since it offers superior spatial resolution and significantly less saturation of the thermal signal, resulting in fewer false positives (Jones *et al.*, 2017).

An internationally coordinated initiative to produce a globally consistent system that includes fire mapping and monitoring is the Global Observations of Forest Cover and Land Cover Dynamics (GOFC-GOLD; see Section 18.7). The fire mapping and monitoring program within GOFC-GOLD aims to develop a real time, global observation network based on geostationary sensors (GOES, MSG and MTSAT) for large area fire detection. Results reported by Calle *et al.* (2008) demonstrated the feasibility of using MSG SEVIRI data to detect and map forest fires at national and global scales.

18.4.2 Airborne imagery

Various airborne sensors have been integrated with inertial measurement units and differential global positioning units for streamlined geo-referencing. Such systems provide detailed, rectified imagery showing location, intensity, and direction of fire fronts and spot fires and their potential targets. Some airborne sensors that are used for fire mapping and monitoring, either singly or in combination, include:

- multispectral scanners, such as Daedalus 1268 ATM (with 12 bands spanning the visible, NIR, short wave infrared (SWIR) and TIR wavelengths), can be used before, during, and after fires to assess fuel and map fire fronts, perimeters, intensity, and impact (see Figure 18.3);
- TIR digital cameras or radiometers (some with selectable temperature ranges) can image the area, perimeter, temperature, and intensity of active fires;
- forward looking infrared (FLIR) scanners can penetrate smoke to locate hotspots and fire edges in active fires, which can be useful to direct suppression or mopping up operations including:
  - assessing the effort required to black out remote edges using Remote Area Fire Teams (RAFT);
  - in conjunction with visible imagery, indicating whether ground staff can gain access to remote fires; and
  - Helicopter-mounted FLIR, providing Air Attack Supervisors and Air Observers additional vision through smoke to see fire perimeters and landmarks for suppression coordination and mapping;
- hyperspectral scanners can capture fire intensity information during active fires (Dennison and Roberts, 2009);
- digital cameras and video cameras can capture valuable aerial views of active fires; and
- radar and lidar systems can be used to detect smoke plumes during active fire.

A variety of sensor platforms are used during active fire image capture, including helicopters and fixed-wing airplanes. Helicopters are more manouverable and can take off and land in more diverse environments, but have higher operational costs and smaller payload capacity than fixed-wing airplanes (Allison *et al.*, 2016). The use of piloted aircraft can be limited in extreme fire conditions due to safety risks. Recent advances in the technology and affordability of UAV show promise in the operational capture of EO imagery during active fires, with reduced risk to personnel safety when compared to manned aircraft (Yuan *et al.*, 2015, Allison *et al.*, 2016). Many of the same sensor types that can be mounted on manned aircraft are available for UAV platforms, including multispectral, hyperspectral and thermal sensors, digital cameras, and video recorders. While operational deployment of UAV is currently not widely adopted, there is increasing reporting of their use during operational fire management in Australia.

Intelligence system which integrate data from EO (scanners plus video) with GIS and downlink in near real time are used in high fire risk areas (Kontoes *et al.*, 2009a, 2009b). These data sources are not only invaluable to fire managers during operational fire containment, but also provide an objective record of fire activity, which can be used to reconstruct time sequences and further understand fire behaviour. For example, imagery from multispectral and thermal sensors mounted on aircraft have been used to observe the direction and rate of channelling (McRae, 2008; Sharples *et al.*, 2012).

Excursus 18.1—Fire Detection Products

Hotspot imagery, which highlights the locations of active fires, has been available for several decades from a range of satellite sensors. Giglio *et al.* (1999) evaluated three algorithms that had been proposed for large area detection of fire using AVHRR data and presented an enhanced algorithm for global monitoring which demonstrated a high probability of detecting small fires and excluding false positives in a range of landscapes. Landgate (WA) developed a hotspot detection method for Australian conditions (Craig *et al.*, 2002) using AVHRR imagery, which detected most hotspots (Smith *et al.*, 2007b)[15]. More recently, this process has been modified to identify hotspots using MODIS and Digital Earth Australia (DEA) datasets (GA, 2020).

The MODIS Fire and Thermal Anomalies product (MOD14/MYD14) has been available for over a decade (see Section 18.2). The algorithm used for this global product computes brightness temperatures from two 4 μm channels (21 and 22, which saturate at different temperatures) and channel 31 (11 μm). Other channels may be used to exclude 'bright', non-fire pixels (channels 1, 2 and 7) or cloud (channels 1, 2, 7 and 32; Giglio *et al.*, 2003; Justice *et al.*, 2006). Validation of MODIS Fire Products has mostly used higher spatial resolution imagery from sensors such as Landsat and ASTER (Morisette *et al.*, 2005; Schroeder *et al.*, 2008a, 2008b), as well as comparisons with databases maintained by fire management agencies (Benali *et al.*, 2016).

Satellite-based active fire detection systems can show 'false-alarms' (false positives or commission error), due to sunglint, forest clearing, desert boundaries, black soil, or hot rocks (Giglio *et al.*, 2016; GA, 2020). False negatives (omission error) from satellite-based systems may be due to small fires, fires of short duration, persistent cloud cover, thick smoke, or topographic shadow effects (de Klerk, 2008; Hawbaker *et al.*, 2008; Benali *et al.*, 2016; Giglio *et al.*, 2016). Updated algorithms for the MODIS Fire and Thermal Anomalies product (Collection 6) were targeted to address limitations observed with the previous Collection 5 fire product, notably the occurrence of false alarms caused by small forest clearings, and the omission of large fires obscured by thick smoke (Giglio *et al.*, 2016). Ongoing research into the physical properties and processes of fire, and their relation to remotely sensed measurements may help to further reduce these errors in EO of active fires.

Improved fire detection products have recently been developed that build on the well-established MODIS Fire and Thermal Anomalies product. Schroeder *et al.* (2014) describe an algorithm that uses the Visible Infrared Imaging Radiometer Suite (VIIRS), launched in October 2011 aboard the Suomi-National Polar orbiting Partnership (S-NPP) satellite. Initial assessments indicate significant improvements in the mapping capabilities of active fires, compared to the MODIS product, including greater consistency in delineating burned area extent (Schroeder *et al.*, 2014).

Recent advances in geostationary sensors also offer potential improvement in satellite-based active fire detection methods. For example, the Advanced Himawari Imager onboard the Himawari-8 satellite in 2014, provides near real time access to imagery at ten-minute intervals. The high temporal resolution provides an increased volume of data, capturing contextual information to describe background temperature of a landscape in the absense of fire, and increases the opportunity for cloud-free imagery (Hally *et al.*, 2018). Wickramasinghe *et al.* (2016) have developed a multi-spatial resolution approach to the surveillance of active fire lines using data acquired by Himawari-8. In Australia, the DEA Hotspots service routinely delivers hotspot information detected from Himawari-8 imagery (see Section 18.7).

15 A contextual algorithm based on Lee and Tag (1990) and Flasse and Ceccato (1996) used AVHRR bands 3 and 5, as well as latitude and Sun elevation to classify pixels as 'fire' or 'possibly fire'.

Among the ancient elements, fire is the odd one out. Earth, water, air—all are substances. Fire is a reaction. It synthesises its surroundings, takes its character from its context. It burns one way in peat, another in tallgrass prairie, and yet another through lodgepole pine; it behaves differently in mountains than on plains; it burns hot and fast when the air is dry and breezy, and it might not burn at all in fog. It's a shape shifter.
(Pyne, 2015)

Figure 18.3 Aerial imagery of active fire

A bushfire near Myall Park (western Darling Downs, Queensland) on 5 December 2021 was imaged from 25,000 feet. These true and false colour composites demonstrate the valuable fire information provided by the longer infrared wavelengths that is obscured by smoke in visible wavelengths (see also banner image for Section 18 on page 389).

a. True colour composite

b. False colour composite using 2.2 μm (SWIR) as red, 1.6 μm (SWIR) as green, and ~0.5μm (visible blue) as blue.

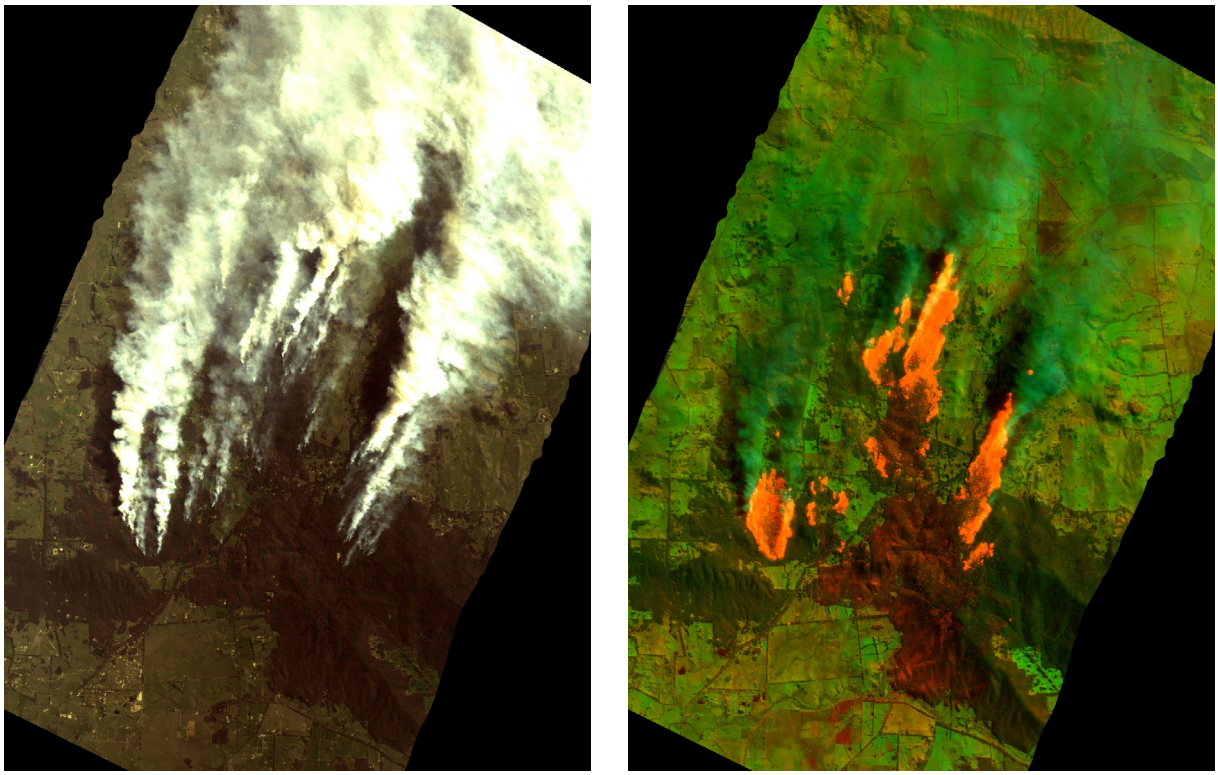

Source: Robert Norman, Air Affairs Australia Pty Ltd

18.5 Retrospective Fire Analyses

A major advantage of using EO in fire studies is the ability to retrospectively view the environmental conditions that preceded a fire. Standardised EO time series datasets offers this unique ability to obtain pre-fire environmental conditions after a fire event has occurred (see Volume 2D). Equivalent retrospective analyses are generally only possible with field studies prior to planned burns, which may not necessarily burn the area that was measured.

EO-based retrospective fire analyses characterise the effects of fire on the landscape, including removal of vegetation and alteration of vegetation structure. These changes may reveal understorey vegetation or soil, and deposition of charcoal and ash. Change detection techniques that capture the difference between pre- and post-fire imagery in relation to reflectance properties of soil, water, and vegetation, are commonly used in EO of fire extent and severity (Miller *et al.*, 2009; Cansler and McKenzie, 2014; see Volume 2D). Pre-processing of EO data is especially pertinent for image differencing techniques (see Volume 2C). For example, Gitas and Devereux (2006) demonstrated a 40% increase in mapping accuracy of forest fires after using topographic correction. Variations in solar angle and atmospheric influences also have demonstrable effects on the spectral separation of burned and unburned vegetation (Trigg *et al.*, 2005; see Volumes 2A and 2X).

Reflectance properties of land cover may be influenced by fire severity, vegetation, topography, and the spectral and spatial resolutions of the EO sensor (see Volume 1B—Section 6). In general, visible and NIR reflectances decrease after fire due to charring and reduced green vegetation (Trigg and Flasse, 2000). In some cases, the presence of white ash and the exposure of highly reflective soils can increase visible and NIR reflectance (Roy and Landmann, 2005; Huang *et al.*, 2016). A post-fire rise in MIR and SWIR reflectances occurs due to greater soil exposure and changes in vegetation moisture content (Poon and Kinoshita, 2018). Ratios of NIR and SWIR bands therefore enhance the contrast

between burned and unburned areas, although the precise relationship between spectral indices and fire severity is poorly understood (Lentile *et al*., 2006). To maximise the value of EO, the underlying processes that control fire effects need to be better understood and linked directly to EO measurements.

There are generally two temporal categories for analysing fire effects (Reinhart, 2001):

- First-order or immediate effects—the direct consequence of fire, such as damage to, and death of, vegetation, fuels consumed, and smoke produced; and
- Second-order or delayed effects—the impact of subsequent weather conditions and time, including dispersion of smoke, erosion, and vegetation recovery, changes in species composition, and other ecological responses.

First order effects are only observable for a short period after the fire, while second order effects may be observable for months or years after the fire. The length of time varies with fire severity, seasonality, and productivity of the landscape. First order effects may become undetectable within days in highly dynamic ecosystems during peak growth periods. Similarly, dissipation of ash and charcoal will modify radiance of burned areas (Roy *et al*., 2002), which may be exacerbated with high post-fire rainfall. Vegetation may start to regrow, with growth rates dependent on primary productivity and environmental factors. Vegetative recovery (second-order effect) has phenological signals that may mask the first-order effects. Field validation may increase confidence that the targeted effects (first or second order) are being captured by the imagery used.

Several authors have noted the lack of standardisation for describing and measuring post-fire effects (Morgan *et al*., 2001; Lentile *et al*., 2006; Keeley, 2009). Many commonly used methods are qualitative, so lack an objective basis to consistently apply them to different times, places, and scales. A standardised Australian system would greatly improve data quality and fire management outcomes for assessing fire impacts.

This section will discuss some of the most useful retrospective analyses of fire in EO, including;

- delineating the extent of a fire and classifying the severity of its impact on vegetation (see Section 18.5.1);
- monitoring environmental recovery after fire (see Section 18.5.2); and
- analysing fire history and fire behaviour to understand underlying patterns and major drivers (see Section 18.5.3).

Operational systems that use EO datasets to map fire extent and severity are introduced in Section 18.6.

18.5.1 Fire extent and severity

Fire extent (variously termed fire scar, burned area, fire footprint, and fire perimeter) delineates burned from unburned ground, whereas fire severity measures the loss or change in organic matter caused by fire (Keeley, 2009). Fire severity differs from fire intensity, which is the energy output of the fire. Fire impacts vary regionally due to differences in climate, vegetation, topography, and biogeography, but are generally more heterogeneous in areas of low and moderate severity compared to high severity (Turner *et al*., 1999). Fire releases carbon stored in living and decaying vegetation so fire severity metrics may also be used to estimate carbon emissions (Chuvieco, 2008; see Section 17).

Fire extent and severity mapping is best suited to a post-fire analysis, as the perimeter and proportions of severity classes continue to change during an active fire (Hudak *et al*., 2007). Traditional measures of fire severity relied on field determination of the depth of burn in vegetation structure, the volume of scorched vegetation, and changes in soil colour and condition. EO data now provides a cheaper and more extensive basis for evaluating fire extent and severity, with arguably greater standardisation and accuracy compared to either manual hand-digitisation in the field or helicopter-based methods (Kolden and Weisberg, 2007). Fire severity classifications derived from EO are useful for many applications, including:

- understanding post-fire fuel loads and re-accumulation in relation to fire severity and fuel type (Eskelson and Monleon, 2018);
- modelling environmental drivers and landscape patterns of fire severity (King *et al*., 2008; Estes *et al*., 2017);
- assessing impacts of fire severity on habitats and ecological processes (Berry *et al*., 2016; Collins *et al*., 2019; Walker *et al*., 2019);
- understanding effects of climate change on fire regimes (Enright *et al*., 2015; Wang *et al*., 2015);
- analysing effectiveness of hazard reduction treatments and predicting severity of subsequent wildfires (Bradstock *et al*., 2010; Price *et al*., 2012);
- identifying high erosion risk sites when combined with slope and aspect information (Salis *et al*., 2019);
- calibrating fire behaviour models and exploring patterns of fire occurrence (Diaz-Delgado *et al*., 2004); and
- predicting ecosystem recovery (Lentile *et al*., 2009).

Fire severity information is also valuable for operational activities, such as salvaging timber and predicting impacts on water quality within water supply catchments. To map fire extent and fire severity both require the delineation of burned from unburned areas, with severity requiring additional

information about the relative scale of impact within the area burned. Fire extent and severity may be mapped manually by aerial reconnaissance or on the ground. Activities undertaken by many operational fire management organisations, such as the NSW RFS and the USFS, routinely capture aerial and ground-based sketch mapping of fire extents. While suited to the objectives at time of capture, such as emergency incident management, there are accuracy and consistency limitations in using such fire history data for other applications. EO offers a cost-effective, standardised, repeatable, landscape scale view, which is particularly advantageous for remote and inaccessible locations. Digital Earth Australia (DEA; see Volume 2D—Section 11.2) has offered an unprecedented opportunity to develop a continental fire history map for Australia (Renzullo *et al*., 2019; see Section 18.7).

Accuracy of fire extent and severity mapping using EO imagery is influenced by temporal, spectral and spatial resolution (see Section 18.2 and Volume 1B—Section 1). Temporally, the data needs to image the effects of fire as soon as possible after combustion, once smoke has sufficiently cleared. The date of the post-fire imagery needs to be late enough that the full extent of the fire has been reached (that is, the fire is extinguished), and early enough that post-fire recovery of vegetation has not commenced. Vegetative recovery rates are not well-quantified at a standardised, regional scale. They are likely to be highly variable between vegetation types and climate regions. However, in forest and woodland communities, moderate resolution satellite imagery is typically used to capture immediate post-fire effects for up to 6–8 weeks post-fire. In some landscapes, fire effects are clearly measurable for some time afterwards, so field measurements can still be usefully conducted at a much later date.

Spectrally, EO data needs to be unaffected by smoke and cloud. While smoke and cloud contamination may inhibit suitable acquisition of post-fire imagery, the recent EO satellite launches have significantly increased the frequency of capture of multispectral imagery. The NIR and SWIR spectral wavelengths are important in detecting fire effects and delineating burned from unburned area. The charring and removal of vegetation results in a post-fire reduction in NIR, while soil exposure and increased radiation absorption by the charred vegetation results in a post-fire rise in SWIR (Pereira *et al*., 1999). Acquisition of SWIR reflectance is generally limited to large satellite-borne sensors, due to the cryogenic cooling systems required, however future developments in technology are likely to eliminate this limitation (Keller, 2019). Radar and other active sensors such as lidar can penetrate cloud and smoke as well as the forest canopy to inform about fire effects in the understorey (see Excursus 5.1 and Volume 1A—Section 15). While active sensors have demonstrated applications in fire extent and severity mapping (Tanase *et al*. 2014; Hu *et al*., 2019), passive optical sensors are more commonly used. Current research is being undertaken on the potential for integrating active and passive sensors for fire extent and severity mapping, as well as monitoring post-fire recovery.

Spatially, EO data must be sensitive to the landscape patterns of burned and unburned ground as well as the scale of fire severity. Many EO analyses of fire extent and severity are conducted at a local scale, using imagery from medium scale sensors (such as Landsat TM and Sentinel-2 MSI). For large fires (> 100 ha), accuracies over 80% are common. The accuracy of estimates from coarse spatial resolution data is affected by the spatial patterns of fires. With coarser resolution sensors (such as MODIS) many small, scattered fires can be easily omitted, leading to an underestimation of total area burned, whereas a predominance of large, compact fires can cause overestimation of burned area (Eva and Lambin, 1998; Silva *et al*., 2005). Higher resolution sensors have the potential for greater precision in mapping fine scale patterns in severity and unburned mosaics within the larger fire extent. Operational products of fire extent and severity are available from a number of international and Australian agencies as detailed in Sections 18.6 and 18.7. Several studies have highlighted deficiencies in these products (Bradley and Millington, 2006) while some have reported consistency with other image-based maps (Boschetti *et al*., 2008). National scale, fire severity mapping programs are not currently operational in Australia, and presents a clear gap in Australia's fire mapping capability.

Regardless of the method used to produce a fire severity classification, some form of validation of results is required before it should be used on an operational basis. High resolution aerial photography that is captured immediately post-fire provides a surrogate for field observation data to independently validate EO-based fire extent and severity mapping products. Although not routinely captured after all fires in most jurisdictions in Australia, land and fire management agencies often commission large or otherwise notable fires to be flown for high resolution aerial photography. Various satellites are also able to capture high resolution imagery suitable for independent validation techniques (see Volume 1A—Section 12). While this data is not freely available, high resolution post-fire imagery can be a worthwhile investment for many applications when compared to the time and cost invested in traditional field validation. High resolution imagery is also suitable for broadscale landscape studies and validation of various EO-modelled fire mapping products (such as Vanderhoof *et al*., 2017, Collins *et al*., 2018, Gibson *et al*., 2020).

18.5.1.1 Normalised Burn Ratio

A commonly used reflectance index in fire extent and severity mapping is the differenced normalised burn ratio (dNBR), which highlights the differences between pre- and post-fire imagery to detect the fire-induced spectral response in the NIR and SWIR wavelengths (Lopez Garcia and Caselles, 1991; Key and Benson, 1999; see Section 9.2.1 for equations). This index has been shown many times to be more effective than NDVI for this application. Initially developed for Landsat TM imagery, the dNBR is also suited to data with similar spectral bandwidths, such as Sentinel-2 MSI. The dNBR is used in national fire extent and severity mapping programs, such as the US Monitoring Trends in Burn Severity (MTBS; Eidenshink *et al*., 2007), and has been shown to produce reasonable accuracy compared to field validation for severity within a single fire, across a range of vegetation communities (for example, approximately 60–70% accuracy; Miller and Thode, 2007; Soverel *et al*., 2010; see Section 18.6.3). Miller and Thode (2007) also produced higher accuracy maps, especially for high fire severity classes in heterogenous landscapes, using dNBR relativised for the pre-fire NBR (the RdNBR; see Section 9.2.1; also Miller *et al*., 2009).

Many studies have compared alternative reflectance indices against the dNBR, which has been widely reported to be more sensitive to fire effects than dNDVI and NDVI (Hudak *et al*. 2007, Escuin *et al*., 2008). Other studies have reported that NBR and its variants were insensitive to some post-fire spectral changes soon after fire occurrence (Roy *et al*., 2006; Lewis *et al*., 2007). Variations in NBR can occur due to changes in seasonal solar elevation and topographic shadowing in high latitudes (Verbyla *et al*. 2008, French *et al*. 2008). Many spectral indices are confounded by dark soil backgrounds, which become indistinguishable from burned areas. In forest communities with understorey/mid-storey structural layers, reflectance indices in general have greater accuracies in quantifying canopy fire effects than sub-canopy fire effects, which is an expected limitation of passive optical EO approaches.

The dNBR, like many other fire severity reflectance indices, have limited accuracy when thresholded into standardised severity classes for comparison between different fires, due to the influence of pre-fire vegetation structure, soil type, and vegetation moisture (Miller and Thode, 2007; Kolden *et al*., 2015). A combination of multiple indices may provide more complete and accurate information than any single index (Miller and Thode, 2007). Indices measuring the relative sub-pixel cover of photosynthetic, non-photosynthetic material, and bare ground (such as fractional cover, or spectral unmixing; see Excursus 8.3) may provide a closer estimate of the quantity of organic matter consumed by fire compared to NBR.

18.5.1.2 Composite Burn Index

The Composite Burn Index (CBI), also referred to as the Geometrically-structured Composite Burn Index (GeoCBI), was specifically developed to validate regional classification schemes of EO-derived fire severity data (Cansler and McKenzie, 2014). It is the most commonly used method to field validate and calibrate fire severity reflectance indices (e.g. Strand *et al*., 2013; McCarley *et al*., 2017). Measurements of surface and vegetation changes are visually estimated and aggregated into a unitless score and the protocol requires a subjective estimate of pre-fire condition by including field plots in adjacent unburned areas. Miller and Thode (2007) also report that some transformation may be required when dNBR or RdNBR is used to model CBI since NBR is sensitive to soil conditions and CBI is primarily a vegetation severity measurement. CBI reaches a maximum value when there is complete vegetation mortality as opposed to dNBR (which varies in value after complete vegetation mortality, resulting in a nonlinear relationship between dNBR to CBI). Furthermore, CBI correlates poorly to biophysical metrics and to the spectral reflectance of the top surface, which is likely due to the combinations of effects that can result in the same CBI score (Hudak *et al*., 2007; Miller and Thode, 2007). Keeley (2009) questioned the validity of using a composite field index (such as CBI) that combines attributes of fire severity and ecosystem response, even if it is correlated with spectral measures.

18.5.1.3 Alternative approaches

Spectral unmixing is increasingly being demonstrated as an effective, if somewhat complicated, method for mapping fire extent and severity in EO (see Section 8.3 and Volume 2E). Spectral unmixing uses a calibrated relationship with high quality, quantitative field data (Scarth *et al*., 2010; Guerschman *et al*., 2015), which may be more directly analogous to traditional field-based assessment (Lentile *et al*., 2006; Morgan *et al*., 2014; Meddens *et al*., 2016). Spectral unmixing methods have been used with hyperspectral imagery to assess fine scale effects of fire on the soil surface (Robichaud *et al*., 2007; Lewis *et al*., 2007). Alencar *et al*. (2011) used a system based on a Monte Carlo mixture modeling approach to define the usual photosynthetic, non-photosynthetic, and bare fractions, plus a fraction called shade/burn (defined as having zero reflectance in all spectral wavelengths) to distinguish the canopy disturbances caused by fire from those caused only by logging. The resulting Burn Scar Index (Alencar *et al*., 2011) produced a classification accuracy of 88.9% for burned area, and 95.15% for unburned area. Gibson *et al*. (2020) compared the performance of multiple indices (including spectral unmixing of Sentinel-2 data and

reflectance-based indices) in a machine learning framework trained on severity class samples derived from high resolution post-fire aerial photograph interpretation and concluded that the addition of fractional cover-based indices was particularly helpful in delineating burned from unburned areas.

RTM inversion shares some similarities with spectral unmixing (see Section 8.3), with the spectral response of target surface types being obtained through an RTM, rather than from sampling the image directly (Yin *et al*., 2019). Pixels are subsequently classified as one of the modelled surfaces based on the similarity to the modelled spectral responses. De Santis *et al*. (2010) developed this approach for the purpose of mapping fire severity by using the PROSPECT leaf RTM coupled to the GeoSail canopy RTM to forward model spectra for 30 different surfaces with different fire severity levels (defined by their GeoCBI index; see Section 18.5.1.2) in coastal California. These spectra formed a Look-Up Table (LUT), and for each pixel, the closest match was defined by the 'spectral angle' between model and observed reflectances (see Volume 2D—Section 7). The approach showed a strong linear relationship with field-observed GeoCBI values.

Recent advances in computing technology, such as readily accessible cloud-based satellite data and processing services, have opened new frontiers to develop more sophisticated techniques with complex datasets and multiple indices. Recent examples in fire extent severity mapping include principal components analysis (PCA; Aitkaci *et al*., 2018, Alexandris *et al*., 2017; see Volumes 2C and 2D), supervised image classification using machine learning (see Volume 2E) and Google Earth engine (Collins *et al*., 2018), and the integration of reflectance and fractional cover indices in a machine learning framework (Gibson *et al*., 2020). Some of these techniques have demonstrated greater sensitivity and predictive power compared to traditional approaches, particularly in complex heterogeneous environments.

18.5.2 Fire recovery

Post-fire recovery is a second-order effect of fire, characterised as a successional process towards either the pre-fire community structure and function or to an alternative stable state (Turner *et al*., 2016). Measuring and monitoring fire severity and subsequent post-fire recovery are essential for understanding the full effects of fire across the landscape. The relationship between fire severity and post-fire recovery rates has long been a focus for ecology and global carbon cycle studies and is becoming a more pressing issue, as the frequency and severity of fire disturbance increases with warmer and drier global climatic conditions (Turner *et al*., 2016, Meng *et al*., 2018).

Post-fire forest recovery is closely connected to fire severity, with strong spatial heterogeneity across the landscape (Bolton *et al*., 2015). The interaction between first-order fire effects (fire extent and severity) and environmental variables, such as rainfall and climate conditions, influence the post-fire recovery trajectory over time, which may be observable for decades after a fire. The rate of ecosystem recovery after fire depends on local and regional weather, the timing and severity of fire, and the type of vegetation affected. In some communities, high severity burns may encourage subsequent weed invasion and erosion, and may destroy seed or vegetative sources. By contrast, in other communities, high severity fires may promote greater rates of resprouting or seedling emergence than lower severity fires. Post-fire vegetation recovery rates may also vary between species within a community and between conspecific individuals (such as age-related variation in resprouting response to fire; Bellingham and Sparrow, 2000). For example, a homogenous area of extreme fire severity (that is, 100% post-fire loss of above ground biomass) may display heterogeneous patterns in the rates of vegetative resprouting in one vegetation community, while another community may display a more even and rapid rate of resprouting or regrowth (for example, a closed forest with a mix of resprouter and obligate seeder plant functional types (see Section 4.2.1) compared to an open grassland). Such variation in recovery from fire can create difficulty in applying and interpreting metrics of fire recovery between different communities. This highlights the importance of local knowledge for interpreting EO fire mapping products.

A wide range of approaches to monitoring post-fire recovery have been explored in the literature, including image classification (see Section 8.2 and Volume 2E), NDVI (Malak and Pausas, 2006), dNBR (Lentile *et al*., 2007), SAR-based recovery index (Minchella *et al*., 2009), char fraction (Smith *et al*., 2007a), and NDVI time series (Hope *et al*., 2007). Spectral unmixing has also been used for multi-temporal cover change mapping (Okin, 2007), as well as the vegetation structure perpendicular index (VSPI; Massetti *et al*., 2019). LandTrendr, based on Landsat SWIR data, has also been tested for recovery monitoring applications. However, it requires a recovery curve pattern assumed *a priori* (Kennedy *et al*., 2010), which may be a limitation for applying the model at a landscape scale without local knowledge.

The limitations of different EO sensors for monitoring post-fire recovery are becoming widely recognised. The key limitation of optical sensors is the difficulty in separating post-fire forest canopy recovery from understorey recovery (Castro *et al*., 2011; Fisher *et al*., 2016). While understorey vegetation (including shrubs, herbaceous, and woody) can

recover quickly after a fire event, the structure and function of understorey vegetation may differ from the pre-fire canopy in terms of lifeform, productivity, and capacity for carbon and water storage (Swanson *et al*., 2011).

Radar sensors can penetrate cloud, haze, and smoke, and are sensitive to forest structure and biomass (see Volume 1A—Section 15.2 and Volume 1B—Section 8). The SAR L-band sensitivity to forest structural parameters allows for differentiation between forest growth and degradation stages, which may be useful for post-fire regrowth monitoring (Joshi *et al*., 2015), although known soil moisture effects need to be carefully accounted for (Chu and Guo, 2014). Discriminating post-fire recovery from ALOS PALSAR data was observed to be difficult during early stages of regrowth due to saturation effects (Tanase *et al*., 2011). Multi-sensor integrated approaches for recovery monitoring are becoming more commonly explored, especially as computing power and processing limitations are further reduced with advancing technology.

18.5.3 Fire history and behaviour

Fire extent and severity mapping compiled over many years gives the opportunity for spatiotemporal patterns of fire incidence, frequency, and severity to be examined (Boer *et al*., 2006, 2008; Tolhurst and McCarthy, 2016; Case and Staver, 2017). Over 40 years of global satellite data are now available to analyse the progression of a wide range of fire events. Various statistics can be derived from such fire history databases, including years burned, years since last burn, extent of burned area, and frequency of fire, which are commonly used by land and fire management agencies to inform prescribed burning plans. Many of these statistics are now available on web-based fire mapping systems (see Section 18.7). Time series analysis techniques are particularly useful in this context to highlight and quantify patterns of change (see Volume 2D—Sections 8 and 9). Time series analyses of fire extent and severity can help to inform the role of fuel treatments and previous wildfire on subsequent fire extent and severity patterns across the landscape (Tolhurst and McCarthy, 2016, Lydersen *et al*., 2017).

Recent advances in fire behaviour studies have integrated analyses of EO data captured prior to, during and immediately after a fire event. For example, meteorological observations during a fire event may be used to help understand the role of pyro-convection in driving atypical and dangerous fire behaviour (pyroCb storms; Fromm *et al*., 2010, McRae *et al*., 2015; see Section 18.3.2). Line scan aerial imagery can help to understand the interaction between wind and terrain on fire behaviour (Sharples *et al*., 2012) and factors influencing patterns of spotfire dynamics (see Section 18.3.3). A strong understanding of the effects of meteorological conditions on fire behaviour allows the forecasting of violent and dangerous fire conditions (see Section 18.3.4). Maps of hotspots and subsequent fire extents may be compared to model fire progression (see Section 18.4). This approach is particularly useful for large, unimpeded fires, as occur in tropical savanna landscapes.

Fire simulation systems, such as Phoenix Rapidfire in Australia (Tolhurst *et al*., 2008), offer a fire behaviour analysis tool that is commonly used for decision support by land and fire managers (Miller *et al*., 2015). Inputs include atmospheric conditions, fuel conditions, topography, and initial fire location, which can be sourced from a range of databases or derived from satellite imagery. However, fire simulation systems generally use rate of spread models generated under moderate conditions (to enable safe control of the experimental fire), and as such may have limited accuracy in predicting the dynamic wildfire behaviours that occur under more extreme fire weather conditions (Filkov *et al*., 2018).

Recent climatic changes have been associated with increased frequency of extreme fire weather and consequently, extreme fire events (Collins, 2014; Stavros *et al*., 2014). These changes are increasing the potential for erratic and extreme fire behavior that puts lives and property at greater risk. Under extreme fire weather conditions, fire behaviour can rapidly change with regard to rate of spread and fire intensity, including unusual or unpredictable phenomena such as plume-dominated spread, vorticity-driven lateral spread, and mass spotting events (Sharples *et al*., 2012). Further research and more sophisticated prediction models of fire behaviour are increasingly more critical to provide early warnings to protect the lives of fire fighters and local communities.

18.6 Operational Systems for Fire Management

EO methods offer a consistent, scientific base from which known measures of fire likelihood can be extrapolated (both fuel ignition and potential). The vast landscapes of the Australian environment make EO the only cost-effective way to achieve the broadscale assessments required for fire management. While EO imagery offers a unique perspective of any landscape, the challenge in Australia is to identify those elements in this perspective which are associated with the potential for fire in our landscape—and its impact.

Hitherto EO has been an underutilised resource for mapping, monitoring, and studying fire in Australia. While most agencies use EO data for some aspects of fire planning and management, the potential benefits of this technology are not being completely realised. Operational use of EO for fire management in Australia is often opportunistic, relying on data, equipment, methods and validation as these become available. Many risk assessment procedures for fire management currently rely upon subjective measures of fuel condition and load, which can vary significantly within and between geographic regions and jurisdictions.

Following the unprecedented bushfire crisis of 2019/20, five recommendations from the NSW Independent Bushfire Inquiry focus on further government investment into EO of fire to improve fire management and emergency response:

- 4—establish a spatial technology acceleration program to maximise the information available from the various EO technologies;
- 18—ensure that there is a single whole-of-government procurement and acquisition program for imagery;
- 22—as part of the spatial technology acceleration program, support deployment of EO and image processing technologies for monitoring and auditing;
- 36—invest in long term ecosystem and land management monitoring, modelling, forecasting, research and evaluation, and harness citizen science, to (among other things) better understanding the influence of different land management practices on landscape flammability; and
- 51—expand the Remotely Piloted Aerial Systems (RPAS) capability of NSW Fire and Rescue.

Recommendations from the Royal Commission into National Natural Disaster Arrangements, 2020, reiterate the need for national coordination and dissemination of relevant spatial information, including EO datasets (CoA, 2020).

Nonetheless, EO datasets are already being used operationally in a number of areas of fire management in Australia. Operational systems implement research that will continue to be enhanced with ongoing development and refinements, including:

- modelling flammability (see Section 18.6.1);
- hotspots to locate active fires (see Section 18.6.2); and
- fire extent and severity following fires (see Section 18.6.3).

18.6.1 Flammability models

The Australian Flammability Monitoring System (AFMS; *http://anuwald.science/afms*) is an experimental, operational, near real time flammability data service developed by the Australian National University (ANU) with funding from the Bushfire and Natural Hazards CRC (BNHCRC) to support fire risk management and fire operation response activities such as hazard reduction burning and pre-positioning firefighting resources and, in the longer term, the new National Fire Danger Rating System (see Table 18.3). The AFMS has been built in consultation with end users to make sure the system is adapted to their needs in terms of, for example, data content and formats. The AFMS provides information on fuel moisture content and flammability across Australia at 500 m resolution. It also displays information on soil moisture content near the surface (0–10 cm) and shallow soils (10–35 cm) as research outcomes from the joint BoM/BNHCRC project entitled 'Improving land dryness measures and forecast'. The AFMS is the only system of this kind at a continental scale and it is in the process of being transitioned to GA to sustain the system into the longer term.

Table 18.3 Current and potential uses of the Australian Flammability Monitoring System

FMC: Fuel Moisture Content

Stage	Purpose	Usage examples
1. Planning	Assist with scheduling plan prescribed burns	Drier FMC in a forest may indicate more potential to scorch the canopy
		Fuel moisture differential can act as soft control lines
		Long term fuel conditions for the Prescribed Burning Decision Support Tool (PB-DST)
		Emissons assessment and smoke dispersion
2. Preparedness	Amend preparedness levels	These relate to Fire Danger Rating in response to lower/higher than average landscape dryness conditions or exceed set defined thresholds
3. Response	Assist in firefighting and resources allocation	FMC as an input in Spinifex grass fire behaviour
		Highlight potential for anomalies in predicted rate of spread: for lower FMC a fire may spread faster than predicted
		Soft control lines based on fuel moisture differential

Source: Marta Yebra, ANU

18.6.2 Hotspot imagery

Web-based GIS systems are commonly used to provide near real time, end user access to active fire products in order to support natural resource management and operational fire management decisions. A range of web-based platforms have been developed, using different satellite systems to derive end user products for different regions of the world (see Section 18.4.1 and Excursus 18.1).

In Australia, AVHRR and MODIS imagery are incorporated into several web-based active fire monitoring systems to deliver hotspot information in near real time (with 0.5–2 hour delay). As detailed in Section 18.7, such systems include Firenorth, NAFI (North Australian Fire Information), and Landgate FireWatch (WA). The revised Sentinel Hotspots system (now called DEA Hotspots) also incorporates information from the AHI sensor on the Himawari-8 satellite using algorithms developed by Landgate to derive active fire products (GA, 2020). In addition, Australian fire information is available from Sentinel Asia and some global fire mapping systems (see Section 18.7).

18.6.3 Fire extent and severity

National scale estimates of fire extent have been derived from a range of imagery, including AVHRR (Otón *et al*., 2019) and MODIS (Roy *et al*., 2002, Roy *et al*., 2005, Chen *et al*., 2017b). One of the global MODIS land products (MCD45A1) is a monthly, 500 m, burned area product (Roy *et al*., 2005), based on an automatic algorithm that uses a "bidirectional reflectance distribution function (BRDF) model-based expectation approach" (Roy *et al*., 2002). Various updates and refinements to the MODIS burned area algorithms have occurred, with the current version (collection 6) providing considerably more sensitivity than the original (Giglio *et al*., 2016). Chuvieco *et al*. (2018) developed an algorithm that uses MODIS red and NIR reflectances and thermal anomalies data, which provides the highest spatial resolution (~250 m) among the existing global burned area datasets.

The Monitoring Trends in Burn Severity (MTBS) project maps the fire extent and severity of all large fires (> 1000 acres in the west; > 500 acres in the east) in the USA using Landsat imagery since 1984 (Eidenshink *et al*., 2007; see Section 18.7). This work is sponsored by the Wildland Fire Leadership Council (WFLC) and conducted by the USGS Centre for Earth Resources Observation and Science (EROS) and USFS Remote Sensing Applications Centre (RSAC). The project uses dNBR and RdNBR to manually delineate fire extents (see Section 18.5.1.1). Analyst input is required to determine appropriate image thresholds of dNBR and/or RdNBR fire severity classes, based on the method proposed by Key and Benson (2006). Fires in a range of landscapes have been cross-calibrated to maintain consistency. Results are used to determine long term fire trends for policy purposes, pre- and post-fire assessment and monitoring, LANDFIRE data inputs (see Section 18.3.4), and academic fire severity research.

In Australia, automated or semi-automated systems are operational for fire extent mapping over the rangelands of northern Australia, with differing approaches being adopted in different jurisdictions. Queensland government produces an annual burned area map based on Goodwin and Collett (2014). The NAFI burned area methodology involves differencing pre- and post-fire MODIS imagery with a subsequent segmentation and classification step including some supervisor input. Landgate (WA) also deliver burned area maps and fire history products (see Section 18.7).

In NSW, the Department of Planning, Industry and Environment (DPIE) in partnership with the NSW RFS, is in the final stages of testing an operational fire extent and severity mapping system (FESM), based on a Sentinel-2 random forest algorithm (Gibson *et al*., 2020). The FESM system was used to support NSW and ACT Government rapid response operations during the bushfire crisis of 2019/20.

In Victoria, the Department of Environment, Land, Water and Planning (DELWP), in partnership with La Trobe University, have implemented a severity mapping system that closely aligns with the severity classification framework used in NSW (Collins *et al*., 2018). This mapping, which uses Landsat and Google Earth Engine, was generated and made publicly available for the Victorian fires following the bushfire crisis of 2019/20.

An automated algorithm for nation-wide burned area and severity mapping using DEA infrastructure (see Volume 2D—Section 11.2) was recently developed and is close to operational. The algorithm includes a sequence of:

- change detection—for individual pixels based on the cosine distance between the observed and geometric median reflectances for preceding years (Roberts *et al*., 2017);
- change characterisation—uses absolute and relative NBR and cosine distance changes to quantify fire severity and duration;
- region growing—helps to improve classification by contracting pixels with below-threshold evidence of burning; and
- attribution—integrates results with DEA Hotspots (see Section 18.7) and any externally-available fire maps to produce a burned area product with pixels identified as: potential (detected change); corroborated (change coinciding with detected fire); or confirmed (change coinciding with externally provided burn information).

Depending on the objective of fire mapping and the jurisdiction in Australia, there may be a trade-off decision regarding the spectral and spatial resolution of different data types for operational programs of mapping fire extent and severity. For local scales, where high resolution post-fire aerial imagery has been captured, hand digitisation of fire extent and severity may be appropriate. This is routinely undertaken by the Victorian government, for example. However, for broader scales, or where high resolution post-fire aerial photography is not routinely captured, satellite sensors using spectral analysis will be more appropriate. The most suitable data source and mapping strategy is also likely to vary between landscapes, climatic zones, and biogeographic regions (Gregoire *et al*., 2003). Edwards *et al*. (2013) proposed that fire severity classification in northern Australia, dominated by open savanna woodlands, would be suited to simply differentiating 'Severe' from 'Not-Severe'. By contrast, in forested ecosystems of southern Australia, fire severity is more accurately categorised with a higher number of classes to discriminate varying levels of scorch, and consumption of canopy and understorey layers (McCarthy *et al*., 2017; Gibson *et al*., 2020). Approaches to mapping fire extent may also require different solutions in landscapes where fire locations are generally unknown, such as vast remote areas of northern Queensland, Western Australia, and the Northern Territory, compared to NSW and Victoria where 95% of fires have their locations identified and mapped by incident management authorities shortly after ignition.

18.7 Further Information

2020 Royal Commission into National Natural Disaster Arrangements

https://naturaldisaster.royalcommission.gov.au/publications/html-report

Geoscience Australia (GA)

Bushfires: *https://www.ga.gov.au/scientific-topics/community-safety/bushfire*

DEA Hotspots is an upgraded version of Sentinel Hotspots originally developed by CSIRO. DEA Hotspots, features a number of contextual layers and interactive functions, including historical fire data, with latency of 17–60 minutes: *https://hotspots.dea.ga.gov.au/*

TERN AusCover

Fire Dynamics and Impact—a range of monthly fire-related maps to track vegetation and landscape changes over time: *http://www.auscover.org.au/dataset_categories/fire-dynamics-impact/*

Seasonal composites of fractional cover based on Landsat-5, -7 and -8 for every calendar season since 1986 are available from: *http://auscover.org.au/purl/landsat-seasonal-fractional-cover*

Landgate (Western Australia)

Landgate provide several satellite online fire products and services:

- My FireWatch—national hotspot map updated every 2–4 hours: *https://myfirewatch.landgate.wa.gov.au/*
- FireWatch Pro—advanced fire information for management agencies: *https://firewatch-pro.landgate.wa.gov.au/home.php*
- Aurora—fire spread predictions and simulations: *https://aurora.landgate.wa.gov.au/home.php*

Other relevant Landgate products derived from EO datasets include maps of lightning detection, greenness/curing and burned area: *www.landgate.wa.gov.au/maps-and-imagery*

North Australia Fire Information (NAFI)

The North Australia Fire Information (NAFI) website was designed to meet the bushfire needs of fire managers in northern Australia. NAFI is a MODIS-based fire scar mapping system hosted by Charles Darwin University, which presents near real time hotspots and regularly updated fire scar maps, and includes data related to fire history: *https://www.firenorth.org.au/nafi3/*

New South Wales

NSW DPIE, in conjunction with NSW RFS, have developed a semi-automated fire extent and severity mapping (FESM) approach using Sentinel-2 imagery: *https://datasets.seed.nsw.gov.au/dataset/fire-extent-and-severity-mapping-fesm*

Australian Fire History

ANU WALD/GA DEA: an automated workflow is being developed to map burned area extent for operational use across Australia, with a focus on woody vegetation (Renzullo *et al.*, 2019): *http://wald.anu.edu.au/challenges/bushfires/burn-mapping/*

Victoria: This dataset represents the spatial extent of fires recorded in Victoria since 1903 primarily on public land, including bushfires and DELWP planned burn information. Since 2006 fire severity data has been included in the Fire History dataset. Country Fire Authority (CFA) data on fires occurring on private land has also been included since 2009: *https://discover.data.vic.gov.au/dataset/fire-history-records-of-fires-primarily-on-public-land*

Australian Flammability Monitoring System (AFMS)

AFMS allows users to visualise and interpret national scale information on live fuel moisture content and its uncertainty, a flammability index, and soil moisture content (both near surface and in shallow soil) as maps or graphs: *http://wenfo.org/afms/*

Sentinel Asia

Sentinel Asia is a cooperative led by the APRSAF (Asia-Pacific Regional Space Agency Forum) to share disaster information in the Asia-Pacific region (Held and Kaku, 2007). This region experiences the largest proportion of natural disasters in the world, many of which are observable in real time using satellite EO: *https://sentinel-asia.org/*

The Global Observations of Forest Cover and Land Cover Dynamics (GOFC-GOLD)

Internationally coordinated initiative to produce a globally consistent system that includes fire mapping and monitoring: *http://gofc-fire.umd.edu/*

MODIS Fire Products

modis.gsfc.nasa.gov/data/dataprod/index.php

Monitoring Trends in Burn Severity (MTBS)

fsgeodata.fs.fed.us/mtbs/

Fire Philosophy Publications

Bradstock, R.A., Gill, A.M., and Williams, R.J. (2012). *Flammable Australia: Fire Regimes, Biodiversity and Ecosystems in a Changing World*. CSIRO, Melbourne. 333pp.

Dyer, R., Jacklyn, P., Partridge, I., Russell-Smith, J., and Williams, D. (Eds). (2002). *Savanna Burning Understanding and Using Fire in Northern Australia*. Tropical Savannas Cooperative Research Centre, Darwin. 136pp.

Jurskis, V. (2015). *Firestick Ecology*. Connor Court Publishing, Ballarat. 335p. ISBN: 9781925138740

Latz, P. (2007). *The Flaming Desert: Arid Australia—a Fire Shaped Landscape*. Alice Springs, NT. 164pp. ISBN: 9780646481753

Pyne, S.J. (1992). *The Burning Bush: A Fire History of Australia*. Allen and Unwin, Sydney. 520pp. ISBN: 1863731946

Pyne, S.J. (2012). *Fire: Nature and Culture*. Reaktion Books, London. 224pp. ISBN: 978 1 78023 046 7.

Pyne, S.J. (2015a). *The Fire Age*. Aeon essay: *https://aeon.co/essays/how-humans-made-fire-and-fire-made-us-human*

Pyne, S.J. (2020). *The Still-Burning Bush*. Scribe Short Books, Melbourne. 144pp. ISBN: 1920769757

Steffensen, V. (2020). *Fire Country, How Indigenous Fire Management Could Help Save Australia*. Explore Australia. 240pp. ISBN: 9781741177268

18.8 References

ADRKH (2020). *Australian Disaster Resilience Knowledge Hub* website: *https://knowledge.aidr.org.au/about/*

Aguado, I., Chuvieco, E., Martin, P., and Salas, J. (2003). Assessment of forest fire danger conditions in southern Spain from NOAA images and meteorological indices. *International Journal of Remote Sensing*, 24(8), 1653–1668.

Aitkaci, M., Gitas, I.Z., Alioua, A., and Khaddaj, T. (2018). Burned area mapping using single-date principal components analysis. In *Recent advances in environmental science from the Euro-Mediterranean and Surrounding Regions. Proceedings of EMCEI-1, Tunisia 2017*. Advances in Science, Technology and Innovation (IEREK Interdisciplinary Series for Sustainable Development) (Eds: A. Kallel, M. Ksibi, B. H. Dhia and N. Khelifi). Springer, Chamonix, Switzerland. *https://doi.org/10.1007/978-3-319-70548-4_507*

Alencar, A., Asner, G.P., Knapp, D., and Zarin, D. (2011). Temporal variabillity of forest fires in eastern Arizonia. *Ecological Applications*, 21(7), 2397–2412.

Alexandris, N., Koutsias, N., and Gupta, S. (2017). Remote sensing of burned areas via PCA, Part 2: SVD-based PCA using MODIS and Landsat data. *Open Geospatial Data, Software and Standards*, 2(21).

Allan, G., and Southgate, R. (2002). Fire regimes in the spinifex landscapes of Australia. In: *Flammable Australia: the Fire Regimes and Biodiversity of a Continent* (Eds: R. Bradstock, J. Williams and A. Gill) pp 145–176. Cambridge University Press, Cambridge

Allison, R.S., Johnston, J.M., Craig, G., and Jennings, S. (2016). Airborne Optical and Thermal Remote Sensing for Wildfire Detection and Monitoring. *Sensors*, 16, 1310.

ASA (2020). *Bushfire earth Observation Taskforce*. Australian Space Agency, Canberra. *https://naturaldisaster.royalcommission.gov.au/system/files/exhibit/IND.0003.0001.0001.pdf*

Bartlett, T. Leonard, M., and Morgan, G. (2007). The mega-fire phenomenon: some Australian perspectives. In: *The 2007 Institute of Foresters of Australia and New Zealand Institute of Forestry Conference: Programme, Abstracts and Papers*. Institute of Foresters of Australia, Canberra.

Bellingham, P.J., and Sparrow, A.D. (2000). Resprouting as a life history strategy in woody plant communities. *Oikos*, 89(2), 409–416.

Benali, A., Russo, A., Sa, A.C.L., Pinto, R.M., Price, O., Koutsias, N., and Pereira, J.M.C. (2016). Determining fire dates and locating ignition points with satellite data. *Remote Sensing*, 8(326), rs8040326.

Berry L.E., Lindenmayer D.B., Dennis T.E., Driscoll D.A., Banks S.C. (2016). Fire severity alters spatio–temporal movements and habitat utilisation by an arboreal marsupial, the mountain brushtail possum (Trichosurus cunninghami). *International Journal of Wildland Fire*, 25, 1291–1302. *https://doi.org/10.1071/WF15204*

Boer, M.M., Norris, J., Sadler, R.J., Grierson, P.F. (2006). Ecologically sustainable management of fire-prone landscapes in southern Australia: A complex systems point of view. *Forest Ecology and Management*, 234S, S155.

Boer, M., Sadler, R., and Grierson, P. (2008). Objective characterisation of fire regimes for science-based management of fire-prone landscapes. *Proceedings of Australasian Fire and Emergency Services Authorities Council conference*, 2008.

Bolton, D.K., Coops, N.C., and Wulder, M.A. (2015). Characterizing residual structure and forest recovery following high-severity fire in the western boreal of Canada using Landsat time-series and airborne LiDAR data. *Remote Sensing of Environment*, 163, 48–60.

Boschetti, L., Roy, D., Barbosa, P., Boca, R., and Justice, C. (2008). A MODIS assessment of the summer 2007 extent burned in Greece. *International Journal of Remote Sensing*, 29(8), 2433–2436.

Bradley, A.V., and Millington, A.C. (2006). Spatial and temporal scale issues in determining biomass burning regimes in Bolivia and Peru. *International Journal of Remote Sensing*, 27(11), 2221–2253.

Bradstock, R.A. (2010). A biogeographic model of fire regimes in Australia: current and future implications. *Global Ecology and Biogeography*, 19, 145–158.

Bradstock, R.A., and Cohn, J. (2002). Fire regimes and biodiversity in semi-arid mallee ecosystems. In *Flammable Australia: The Fire Regimes and Biodiversity of a Continent*. (Eds: R.A. Bradstock, J.E. Williams, and M.A. Gill) Cambridge University Press, Cambridge.

Bradstock, R.A., Bedward, M., Kenny, B.J., and Scott, J. (1998). Spatially explicit simulation of the effect of prescribed burning on fire regimes and plant extinctions in shrublands typical of south-eastern Australia. *Biological Conservation*, 86, 83–95.

Bradstock, R.A., Hammill, K.A., Collins, L., and Price, O. (2010). Effects of weather, fuel and terrain on fire severity in topographically diverse landscapes of south-eastern Australia. *Landscape Ecology*, 25(4), 607–619. doi:*10.1007/s10980-009-9443-8*

Bradstock, R.A., Williams, D.J., and Gill, A.M. (2012a). Future fire regimes of Australian ecosystems: new perspectives on enduring questions of management. Ch 15 in *Flammable Australia: Fire Regimes, Biodiversity and Ecosystems in a Changing World*. CSIRO, Melbourne. pp 307–324.

Bradstock, R.A., Cary, G.J., Davies, I., Lindenmayer, D.B., Price, O.F., and Williams, R.J. (2012b). Wildfires, fuel treatment and risk mitigation in Australian eucalypt forests: Insights from landscape-scale simulation. *Journal of Environmental Management*, 105, 66–75.

Bradstock, R.A., Williams, D.J., and Gill, A.M. (Eds) (2012c). *Flammable Australia: Fire Regimes, Biodiversity and Ecosystems in a Changing World*. CSIRO, Melbourne. 333 p.

Brandis, K., and Jacobson, C. (2003). Estimation of vegetative fuel loads using Landsat TM imagery in New South Wales, Australia. *International Journal of Wildland Fire*, 12, 185–194.

Burgan, R., Klaver, R., and Klaver, J. (1998). Fuel models and fire potential from satellite and surface observations. *International Journal of Wildland Fire*, 8, 159–170.

Burrows, N.D., Burbidge, A.A., Fuller, P.J., and Behn, G. (2006). Evidence of altered fire regimes in the Western Desert region of Australia. *Conservation Science Western Australia*, 5(3), 272–284.

Caccamo, G., Chisholm, L.A., Bradstock, R.A., Puotinen, M.L., and Pippen, B.G. (2012). Monitoring live fuel moisture content of heathland, shrubland and sclerophyll forest in South-Eastern Australia using MODIS data. *International Journal of Wildland Fire*, 21, 257–269.

Calle, A., Gonzalez-Alonso, F., and Merino de Miguel, S. (2008). Validation of active forest fires detected by MSG-SEVIRI by means of MODIS hot spots and AwiFS images. *International Journal of Remote Sensing*, 29(12), 3407–3415.

Cansler, C.A., and McKenzie, D. (2014). Climate, fire size and biophysical setting control fire severity and spatial pattern in the northern Cascade Range, USA. *Ecological Applications*, 24(5), 1037–1056.

Casas, A., Riaño, D., Ustin, S.L., Dennison, P., and Salas, J. (2014). Estimation of water-related biochemical and biophysical vegetation properties using multitemporal airborne hyperspectral data and its comparison to MODIS spectral response. *Remote Sensing of Environment*, 148, 28–41. *http://dx.doi.org/10.1016/j.rse.2014.03.011*

Case, M.F., and Staver, A.C. (2017). Fire prevents woody encroachment only at higher than historical frequencies in a South African savanna. *Journal of Applied Ecology*, 54, 955–962.

Castro, J., Allen, C.D., Molina-Morales, M., Marañón-Jiménez, S., Sánchez-Miranda, Á., and Zamora, R. (2011). Salvage Logging Versus the Use of Burnt Wood as a Nurse Object to Promote Post-Fire Tree Seedling Establishment. *Restoration Ecology*, 19, 537–544. *https://doi.org/10.1111/j.1526-100X.2009.00619.x*

Chafer, C.J., Noonan, M., Macnaught, E. (2004). The post-fire measurement of fire severity and intensity in the Christmas 2001 Sydney wildfires. *International Journal of Wildland Fire*, 13, 227–240.

Chafer, C.J. (2007). Using Satellite Imagery to Estimate Landscape Fuel Loads in a Diverse Eucalypt Environment on the Central Coast of New South Wales, Australia. A report prepared by SCA for the NSW RFS, March 2007.

Chen, K., and McAneney, J. (2004). Quantifying bushfire penetration into urban areas in Australia. *Geophysical Research Letters*, 31, L12212. doi:*10.1029/2004GL020244*

Chen, K., and McAneney, J. (2005). The bushfire threat in urban areas. *Australian Science*, 14–16.

Chen, Y., Zhu, X., Yebra, M., Harris, S., and Tapper, N. (2016). Strata-based forest fuel classification for wild fire hazard assessment using terrestrial LiDAR. *Journal of Applied Remote Sensing*, 10(4), 046025.

Chen, Y., Zhu, X., Yebra, M., Harris, S., and Tapper, N. (2017a). Development of a Predictive Model for Estimating Forest Surface Fuel Load in Australian Eucalypt forests with LiDAR Data. *Environmental Modelling and Software*, 97, 61–71.

Chen, D., Pereira, J.M.C., Masiero, A., and Priotti, F. (2017b). Mapping fire regimes in China using MODIS active fire and burned area data. *Applied Geography*, 85, 14–26.

Cheney, P., and Sullivan, A. (2008). *Grassfires—Fuel, Weather and Fire Behaviour*. Melbourne, CSIRO Publishing, Melbourne.

Chu, T., and Guo, X. (2014). Remote sensing techniques in monitoring post-fire effects and patterns of forest recovery in Boreal forest regions: A review. *Remote Sensing*, 6, 470–520.

Chuvieco, E. (2008). Satellite Observations of Biomass Burning. In *Earth observation of global change: the role of remote sensing in monitoring the global environment*. (Ed: E. Chuvieco). Springer, NY.

Chuvieco, E., Riano, D., Aguado, I., and Cocero, D. (2002). Estimation of fuel moisture content from multitemporal analysis of Landsat Thematic Mapper reflectance data: application in fire danger assessment. *International Journal of Remote Sensing*, 23(11), 2145–2162.

Chuvieco, E., Aguado, L., and Dimitrakopoulos, A.P. (2004). Conversion of fuel moisture content values to ignition potential for integrated fire danger assessment. *Canadian Journal of Forest Research*, 34(11), 2284–2293.

Chuvieco, E., Aguado, I., Yebra, M., Nieto, H. Salas, J., Martín, M.P., Vilar, L., Martínez, J., Martín, S., Ibarra, P., de la Riva, J., Baeza, M.J., Rodríguez, F., Molina, J.R., Herrera, M.A., and Zamora, R, (2010). Development of a framework for fire risk assessment using Remote Sensing and Geographic Information System technologies. *Ecological Modelling*, 221, 46–58.

Chuvieco, E., Aguado, I, Jurdao, S., Pettinari, M.L., Yebra, M., Salas, J., de la Riva B, J., Ibarra, P., Rodrigues, M., Echeverría, M., Azqueta, D. Román, M.V., Bastarrika, A., Martínez, S., Recondo, C., Zapico, E., and Martínez-Vega, J. (2014). Integrating geospatial information into fire risk assessment. *International Journal of Wildland Fire*, 23, 606–619.

Chuvieco, E., Lizundia-Loiola, J., Pettinari, M.L., Ramo, R., Padilla, M., Tansey, K., Mouillot, F., Laurent, P., Storm, T., Heil, A., and Plummer, S. (2018). Generation and analysis of a new global burned area product based on MODIS 250 m reflectance bands and thermal anomalies. *Earth System Science Data*, 10(4), 2015–2031.

Chuvieco, E., Aguado, I., Salas, J., Garcia, M., Yebra, M., and Oliva, P. (2020). Satellite Remote Sensing Contributions to Wildland Fire Science and Management. *Current Forestry Reports*, 6, 81–96. *https://doi.org/10.1007/s40725-020-00116-5*

CoA (2020). *Royal Commission into National Natural Disaster Arrangements Report*. Commonwealth of Australia, Canberra. *https://naturaldisaster.royalcommission.gov.au/*

Collins, B.M. (2014). Fire weather and large fire potential in the northern Sierra Nevada. *Agricultural and Forest Meteorology*, 189–190, 30–35.

Collins, L., Griffioen, P., Newell, G., and Mellor, A. (2018). The utility of Random Forests for wildfire severity mapping. *Remote Sensing of Environment*, 216, 374–384. *https://doi.org/10.1016/j.rse.2018.07.005*

Collins, L., Bennett, A.F., Leonard, S.W.J., and Penman, T.D. (2019). Wildfire refugia in forests: Severe fire weather and drought mute the influence of topography and fuel age. *Global Change Biology*, 25(11). *https://doi.org/10.1111/gcb.14735*

Craig, R., Heath, B., Raisbeck-Brown, N., Steber, M., Marsden, J., and Smith, R. (2002). The distribution, extent and seasonality of large fires in Australia, April 1998-March 2000, as mapped from NOAA-AVHRR imagery. In *Australian Fire Regimes: Contemporary Patterns (April 1998-March 2000) and Changes since European Settlement*. (Eds: Russell-Smith, J., Craig, R., Gill, A.M., Smith, R., and Williams, J.). Australia State of the Environment Second Technical Paper Series (Biodiversity), Department of the Environment and Heritage, Canberra.

Cruz, M.G., Sullivan, A.L., Gould, J.S., Sims, N.C., Bannister, A J., Hollis, J.J., and Hurley, R.J. (2012). Anatomy of a catastrophic wildfire: The Black Saturday Kilmore East fire in Victoria, Australia. *Forest Ecology and Management*, 284, 269–285.

Danson, F.M., and Bowyer, P. (2004). Estimating Live Fuel Moisture Content from Remotely Sensed Reflectance. *Remote Sensing of Environment*, 92, 309–321.

de Klerk, H. (2008). A pragmatic assessment of the usefulness of the MODIS (Terra and Aqua) 1-km active fire (MOD14A2 and MYD14A2) products for mapping fires in the fynbos biome. *International Journal of Wildland Fire*, 17, 166–178. *https://doi.org/10.1071/WF06040*

De Santis, A., Asner, G.P., Vaughan, P.J., and Knapp, D.E. (2010). Mapping burn severity and burning efficiency in California using simulation models and Landsat imagery. *Remote Sensing of Environment*, 114, 1535–1545.

Dennison, P.E., and Roberts, D.A. (2009). Daytime fire detection using airborne hyperspectral data. Remote Sensing of Environment, 113, 1649–1657.

Diaz-Delgado, R., Lloret, F., and Pons, X. (2004). Statistical analysis of fire frequency models for Catalonia (NE Spain, 1975–1998) based on fire scar maps from Landsat MSS data. *International Journal of Wildland Fire*, 13, 89–99.

Dilley, A., Millie, S., O'Brien, D., and Edwards, M. (2004). The relation between normalised difference vegetation index and vegetation moisture content at three locations in Victoria, Australia. *International Journal of Remote Sensing*, 25(19). 3913–3928.

Dowdy, A.J., and Pepler, A. (2018). Pyroconvection risk in Australia: Climatological changes in atmospheric stability and surface fire weather conditions. *Geophysical Research Letters*, 45(4), 2005–2013.

Dozier, J. (1981). A method for satellite identification of surface temperature fields of subpixel resolution. *Remote Sensing of Environment*, 11, 221–229.

Duff, T.J., Bell, T.L., and York, A. (2013). Predicting continuous variation in forest fuel load using biophysical models: a case study in south-eastern Australia. *International Journal of Wildland Fire*, 22, 318–332.

Edwards, A.C., Maier, S.W., Hutley, L.B., Williams, R.J., and Russell-Smith, J. (2013). Spectral analysis of fire severity in north Australia tropical savannas. *Remote Sensing of Environment*, 136, 56–65.

Eidenshink, J., Schwind, B., Brewer, K., Zhu, Z., Quayle, B., and Howard, S. (2007). A project for monitoring trends in burn severity. *Fire Ecology Special Issue*, 3(1), 3–21.

Ellis, S., Kanowski, P., and Whelan, R. (2004). *National Inquiry on Bushfire Mitigation and Management*. Commonwealth of Australia, Canberra.

Enright, N.J., Fontaine, J.B., Bowman, D.M.J.S., Bradstock, R.A., and Williams, R.J. (2015). Interval squeeze: altered fire regimes and demographic responses interact to threaten woody species persistence as climate changes. *Frontiers of Ecology and Environment*, 13(5), 265–272.

Escuin, S., Navarro, R., and Fernandez, P. (2008). Fire severity assessment by using NBR (Normalised Burn Ratio) and NDVI (Normalized Difference Vegetation Index) derived from LANDSAT TM/ETM images. *International Journal of Remote Sensing*, 29(4), 1053–1073.

Eskelson, B.N.I., and Monleon, V.J. (2018). Post-fire surface fuel dynamics in California forests across three burn severity classes. *International Journal of Wildland Fire*, 27, 114–124.

Estes, B.L., Knapp, E.E., Skinner, C.N., Miller, J.D., and Preisler, H.K. (2017). Factors influencing fire severity under moderate burning conditions in the Klamath Mountains, northern California, USA. *Ecosphere*, 8(5), e01794. *https://doi.org/10.1002/ecs2.1794*

Eva, H., and Lambin, E.F. (1998). Remote sensing of biomass burning in tropical regions: sampling issues and multisensor approach. *Remote Sensing of Environment*, 64, 292–315.

Filkov, A.I., Duff and T.J., Penman, T.D. (2018). Improving fire behaviour data obtained from wildfires. *Forests*, 9(2), 81.

Filkov, A.I., Ngo, T., Matthews, S., Telfer, S., and Penman, T.D. (2020). Impact of Australia's catastrophic 2019/20 bushfire season on communities and environment. Retrospective analysis and current trends. *Journal of Safety Science and Resilience*, 1(1), 44–56. *https://doi.org/10.1016/j.jnlssr.2020.06.009*

Fisher, A., Day, M., Gill, T., Roff, A., Danaher, T., and Flood, N. (2016). Large-area, high-resolution tree cover mapping with multi-temporal SPOT-5 imagery, New South Wales, Australia. *Remote Sensing*, 8(6), 515. *https://doi.org/10.3390/rs8060515*

Flasse, S.P., and Ceccato, P. (1996). A contextual algorithm for AVHRR fire detection. *International Journal of Remote Sensing*, 17, 419–424.

French, N.H.J., Kasischke, E.S., Hall, R.J., Murphy, K.A., Verbyla, D.L., Hoy, E.E., and Allen, J.L. (2008). Using Landsat data to assess fire and burn severity in the North American boreal forest region: an overview and summary of results. *International Journal of Wildland Fire*, 17(4), 443–462.

Fromm, M., Tupper, A., Rosenfield, D., Servranckx, R., and McRae, R. (2006). Violent pyroconvective storm devestates Australia's capital and pollutes the stratosphere. *Geophysical Research Letters*, 33(5). *https://doi.org/10.1029/2005GL025161*

Fromm, M., Lindsey, D.T., Servranckx, R., Yue, G., Trickl, T., Sica, R., Doucet, P., and Goudin-Beekmann, S. (2010). The untold story of pyrocumulonimbus. *Bulletin of American Meteorological Society*, 91, 1193–1209.

Fusco, E., Abatzoglou, J.T., Balch, J.K., Finn, J.T., and Bradley, B.A. (2016). Quantifying the human influence on fire ignition across the western USA. *Ecological Applications*, 26(8), 2390–2401.

Garcia, M., Saatchi, S. Ustin, S., and Balzter, H. (2018). Modelling forest canopy height by integrating airborne LiDAR samples with satellite Radar and multispectral imagery. *International Journal of Applied Earth Observation and Geoinformation*, 66, 159–173.

García, M., Riaño, D., Yebra, M., Salas, J., Cardil, A., Monedero, S., Ramirez, J., Martín, M.P., Vilar, L., Gajardo, J., and Ustin, S. (2020). A Live Fuel Moisture Content Product from Landsat TM Satellite Time Series for Implementation in Fire Behavior Models. *Remote Sensing*, 12, 1714. *https://doi.org/10.3390/rs12111714*

GA (2020). *Digital Earth Australia Hotspots Product Description*. D2020-64303. Ecat Reference #70869. Geoscience Australia, Canberra. *hotspots.dea.ga.gov.au/cache/DEA+Hotspots+-+Product+Description+-+Version+1.6_final.pdf*

Gibson, R., Danaher, T., Hehir, W., and Collins, L. (2020). A remote sensing approach to mapping fire severity in south-eastern Australia using sentinel 2 and random forest. *Remote Sensing of Environment*, 240(111702).

Giglio, L., and Justice, C.O. (2003). Effect of wavelength selection on characterisation of fire size and temperature. *International Journal Remote Sensing*, 24(17), 3515–3520.

Giglio, L., Kendall, J.D., and Justice, C.O. (1999). Evaluation of global fire detection algorithms using simulated AVHRR infrared data. *International Journal of Remote Sensing*, 20, 1947–1985.

Giglio, L., Kendall, J.D., and Tucker, C.J. (2000). Remote sensing of fires with TRMM VIRS. *International Journal Remote Sensing*, 21, 203–207.

Giglio, L., Descloitres, J., Justice, C.O., Kaufman, Y.J. (2003). An Enhanced Contextual Fire Detection Algorithm for MODIS. *Remote Sensing of Environment*, 87, 273–282.

Giglio, L., Loboda, T., Roy, D.P., Quayle, B., and Justice, C.O. (2009). An active-fire based burned area mapping algorithm for the MODIS sensor. *Remote Sensing of Environment*, 113, 408–420

Giglio, L., Schroeder, W., and Justice, C.O. (2016). The collection 6 MODIS active fire detection algorithm and fire products. *Remote Sensing of Environment*, 178, 31–41.

Gill, M.A., and Catling, P.C. (2002). Fire regimes and biodiversity of forested landscapes of southern Australia. In *Flammable Australia: The Fire Regimes and Biodiversity of a Continent*. (Eds: R.A. Bradstock, J.E. Williams, and M.A. Gill) Cambridge University Press, Cambridge.

Gitas, I.Z., and Devereux, B.J. (2006). The role of topographic correction in mapping recently burned Mediterranean forest areas from LANDSAT TM images. *International Journal of Remote Sensing*, 27(10), 41–54.

Goodwin, N.R., and Collett, L. (2014). Development of an automated method for mapping fire history captured in Landsat TM and ETM+ time series. *Remote Sensing of Environment*, 148, 206–221.

Gould, J.S., McCaw, W.L., Cheney, N.P., Ellis, P.F., and Matthews, S. (2008). *Field Guide: Fire in Dry Eucalypt Forest. Fuel Assessment and Fire Behaviour Prediction in Dry Eucalypt Forest*. CSIRO Publications, Melbourne. 92 p.

Gregoire, J.-M., Tansey, K., and Silva, J.M.N. (2003). The GBA2000 Initiative: developing a global burnt area database from SPOT-VEGETATION imagery. *International Journal of Remote Sensing*, 24(6), 1369–1376.

Guerschman, J.P., Scarth, P.F., McVicar, T.R., Renzullo, L.J., Malthus, T.J., Stewart, J.B., Rickards, J.E., and Trevithick, R. (2015). Assessing the effects of site heterogeneity and soil properties when unmixing photosynthetic vegetation, non-photosynthetic vegetation and bare soil fractions for Landsat and MODIS data. *Remote Sensing of Environment*, 161, 12–26.

Haines, D.A. (1988). A lower atmospheric severity index for wildland fire. *National Weather Digest*, 13(2), 23–27.

Hall, S.A., Burke, I.C., Box, D.O., Kaufman, M.R., and Stoker, J.M. (2005). Estimating stand structure using discrete-return lidar: an example from low density, fire prone ponderosa pine forest. *Forest Ecology and Management*, 208, 189–209.

Hally, B., Wallace, L., Reinke, K., Jones, S., and Skidmore, A. (2018). Advances in active fire detectionn using a multi-temporal method for next-generation geostationary satellite data. *International Journal of Digital Earth*, 12(9), 1030–1045.

Hamilton, D., Bowerman, M., Colwell, J., Donohoe, G., and Myers, B. (2017). Spectroscopic analysis for mapping wildland fire effects from remotely sensed imagery. *Journal of Unmanned Vehicle Systems*, 5(4), 146–158. doi:*10.1139/juvs-2016-0019*

Hao, X., and Qu, J.J. (2007). Retrieval of real-time live fuel moisture content using MODIS measurements. *Remote Sensing of Environment*, 108, 130–137.

Hawbaker, T.J., Radeloff, V.C., Syphard, A.D., Zhu, Z, and Stewart, S.I. (2008). Detection rates of MODIS active fire products in the United States. *Remote Sensing of Environment*, 112, 2656–2664.

Hobbs, R. (2002). Fire regimes and their effects in Australian temperate woodlands. In *Flammable Australia: The Fire Regimes and Biodiversity of a Continent*. (Eds: R.A. Bradstock, J.E. Williams, and M.A. Gill) Cambridge University Press, Cambridge.

Hope, A., Tague, C., and Clark, R. (2007). Characterizing post-fire vegetation recovery of California chaparral using TM/ETM+ time-series data. *International Journal of Remote Sensing*, 28(6), 1339–1354.

Hu, T., Q. Ma, Y. Su, J. J. Battles, B. M. Collins, S. L. Stephens, M. Kelly and Q. Guo (2019). A simple and integrated approach for fire severity assessment using bi-temporal airborned LiDAR data. *International Journal of Applied Earth Observation and Geoinformation*, 78, 25–38.

Huang, H., Roy, D.P., Boschetti, L., Zhang, H.K., Yan, L., Kumar, S.S., Gomez-Dans, J., and Li, J. (2016). Separability analysis of Sentinel-2a Multi-Spectral Instrument (MSI) data for burned area discrimination. *Remote Sensing*, 8(10), 873. *https://doi.org/10.3390/rs8100873*

Hudak, A.T., Morgan, P., Bobbitt, M.J., Smith, A.M.S., Lewis, S.A., Lentile, L.B., Robichaud, P.R., Clark, J.T., and McKinley, R.A. (2007). The relationship of multispectral satellite imagery to immediate fire effects. *Fire Ecology Special Issue*, 3(1), 64–90.

Hudak, A.T., Crookston, N.L., Evans, J.S., Hall, D.E., and Falkowski, M.J. (2008). Nearest neighbour imputation of species-level, plot-scale forest structure attributes from LiDAR data. *Remote Sensing of Environment*, 112, 2232–2245. [Corrigendum: *Remote Sensing of Environment*, 113, 289–290.]

Hudak, A.T., Ottmar, R.D., Vihnanek, R.E., Brewer, N.W., Smith, A.M.S., and Morgan, P. (2013). The relationship of post-fire white ash cover to surface fuel consumption. *International Journal of Wildland Fire*, 22(6), 780–785. *https://doi.org/10.1071/WF15074*

ICSMD (2020). *International Charter for Space and Major Disasters* website: *https://disasterscharter.org/web/guest/home*

Jenkins, M.E., Bedward, M., Price, O., and Bradstock, R.A. (2020). Modelling bushfire fuel hazard using biophysical parameters. *Forests*, 11(9), 925. *https://doi.org/10.3390/f11090925*

Jones, S., Reinke, K., Mitchell, S., McConachie, F., and Holland, C. (2017). *Advances in the remote sensing of active fires: a review—detection, mapping and monitoring v1.0*. Bushfire and Natural Hazards CRC, Melbourne.

Joshi, N., Mitchard, E.T.A., Woo, N., Torres, J., Moll-Rocek, J., Ehammer, A., Collins, M. Jepsen, M.R., and Fensholt, R. (2015). Mapping dynamics of deforestation and forest degradation in tropical forests using radar satellite data. *Environmental Research Letters*, 10(3), [034014].

Jupp, D.L.B., Culvenor, D.S., Lovell, J.L., Newnham, G.J., Strahler, A.H., and Woodcock, C.E. (2008). Estimating forest LAI profiles and structural parameters using a ground-based laser called Echidna. *Tree Physiology*, 29, 171–181.

Jurskis, V. (2015). *Firestick Ecology*. Connor Court Publishing, Ballarat.

Justice, C., Giglio, L., Boschetti, L., Roy, D., Csiszar, I., Morisette, J., and Kaufman, Y. (2006). *MODIS Fire Products (Version 2.3, 1 October 2006)*. Algorithm Technical Background Document. MODIS Science Team, NASA. *http://modis.gsfc.nasa.gov/data/atbd/atbd_mod14.pdf*

Keane, R.E., Burgan, R., van Wagtendonk, J. (2001). Mapping wildland fuel for fire management across multiple scales: integrating remote sensing, GIS and biophysical modelling. *International Journal of Wildland Fire*, 10, 301–319.

Keeley, J.E. (2009). Fire intensity, fire severity and burn severity: a brief review and suggested usage. *International Journal of Wildland Fire*, 18, 116–126.

Keetch, J.J., and Bryam, G.M. (1968). *A drought index for forest fire control*. U.S.D.A. Forest Service Research Paper SE-38. 32 p.

Keith, D.A., McCaw, W.L., and Whelan, R.J. (2002). Fire regimes in Australian heathlands and their effects on plants and animals. In *Flammable Australia: The Fire Regimes and Biodiversity of a Continent*. (Eds: R.A. Bradstock, J.E. Williams, and M.A. Gill) Cambridge University Press, Cambridge.

Keller, J. (2019). Air force readies shortwave infrared sensors for satellites to reveal materials and lasers on the ground. *Military and Aerospace Electronics*. November 20th, 2019. *https://www.militaryaerospace.com/sensors/article/14072398/shortwave-infrared-sensors-satellites*

Kennedy, R.E., Yang, Z., and Cohen, W.B. (2010). Detecting trends in forest disturbance and recovery using yearly Landsat Time Series: 1. LandTrendr—Temporal segmentation algorithms. *Remote Sensing of Environment*, 114, 2897–2910.

Kenny, B., Matthews, s., Grootemaat, S., and Hollis, J., Sauvage, S., and Fox-Hughes, P. (2019). Australian Fire Danger Rating System Research Prototype: National fuel map. *Proceedings of the 6th International Fire Behavior and Fuels Conference, April 29–May 3, 2019, Sydney, Australia*. Published by the International Association of Wildland Fire, Missoula, Montana, USA.

Keramitsoglou, I., Kiranoudis, C.T., Sarimvels, H., and Sifakis, N. (2004). A multidisciplinary decision support system for forest fire crisis management. *Environmental Management*, 33(2), 212–225.

Kershaw, A.P., Clark, J.S., Gill, A.M., and D'Costa, D.M. (2002). A history of fire in Australia. In *Flammable Australia*. (Eds: R.A. Bradstock, J.E. Williams and A.M. Gill). Cambridge, Cambridge University Press. pp. 3–25.

Key, C.H., and Benson, N.C. (1999). Measuring and remote sensing of burn severity: the CBI and NBR. *Proceedings of Joint Fire Science Conference and Workshop, Vol. 2, June*, (Eds. L.F. Neuenschwander, K.C. Ryan) pp. 284. University of Idaho, Moscow, ID.

Key, C.H., and Benson, N.C. (2006). *Landscape Assessment: Sampling and Analysis Methods*. USDA Forest Service, Rocky Mountain Research Station General Tech. Rep. RMRS-GTR-164-CD. Odgen, UT.

King, K., Marsden-Smedley, J., Cary, G., Allan, G., Bradstock, R., Gill, M. (2008). *Modelling fire dynamics in the West MacDonnell Range area*. Working Paper 20, Desert Knowledge CRC, Alice Springs.

Koltunov, A., and Ustin, S.L. (2007). Early fire detection using non-linear multitemporal prediction of thermal imagery. *Remote Sensing of Environment*, 110(1), 18–28.

Kokaly, R.F., Rockwell, B.W., Haire, S.L., and King, T.V.V. (2007). Characterization of post-fire surface cover, soils and burn severity at the Cerro Grande Fire, New Mexico, using hyperspectral and multispectral remote sensing. *Remote Sensing of Environment*, 106, 305–325.

Kolden, C.A., and Weisberg, P.J. (2007). Assessing accuracy of manually-mapped wildfire perimeters in topographically dissected areas. *Fire Ecology Special Issue*, 3(1), 22–31.

Kolden, C.A., Abatzoglou, J.T., and Smith, A.M.S. (2015). Limitations and utilisation of monitoring trends in burn severity products for assessing wildfire severity in the USA. *International Journal of Wildland Fire*, 24, 1023–1028.

Koltunov, A., and Ustin, S.L. (2007). Early fire detection using non-linear multitemporal prediction of thermal imagery. *Remote Sensing of Environment*, 110, 18–28.

Kontoes, C., Keramitsoglou, I., Sifakis, N., and Konstantinidis, P. (2009a). SITHON: An Airborne Fire Detection System Compliant with Operational Tactical Requirements. *Sensors*, 9, 1204–1220.

Kontoes, C.C., Poilvé, H., Florisch, G., Keramitsoglou, I., and Paralikidis, S. (2009b). A comparative analysis of a fixed thresholding vs. a classification tree approach for operational burn scar detection and mapping. *International Journal of Applied Earth Observation and Geoinformation*, 11(5), 299–316. doi:*10.1016/j.jag.2009.04.001*.

Kossman, R., Sturman, A., Zawar-Reza, P. (2001). Atmospheric influences on bush fire propagation and smoke dispersion over complex terrain. *Proceedings of 2001 Australasian Bushfire Conference, Christchurch*, NZ.

Krawchuk, M.A., Moritz, M.A., Parisien, M.-A., Van Dorn, J., and Hayhoe, K. (2009). Global pyrogeography: the current and future distribution of wildfire. *PloS ONE*, 4(4), e5102.

Leblon, B., Augusto, P., Garcia, F., Oldford, S., Maclean, D.A., Flannigan, M. (2007). Using cumulative NOAA-AVHRR spectral indices for estimating fire danger codes in northern boreal forests. *International Journal of Applied Earth Observation*, 9, 335–342.

Lee, T. F., and Tag, P. M. (1990). Improved detection of hotspots using the AVHRR 3.7 μm channel. *Bulletin of the American Meteorological Society*, 71, 1722–1730.

Lentile, L.B., Holden, Z.A., Smith, A.M.S., Falkowski, M.J., Hudak, A.T., Morgan, P., Lewis, S.A., Gessler, P.E., and Benson, N.C. (2006). Remote sensing techniques to assess active fire characteristics and post-fire effects. *International Journal of Wildland Fire*, 15, 319–345.

Lentile, L.B., Morgan, P., Hudak, A.T., Bobbitt, M.J., Lewis, S.A., Smith, A.M.S., and Robichaud, P.R. (2007). Post-fire burn severity and vegetation response following eight large wildfires across the western United States. *Fire Ecology Special Issue*, 3(1), 91–108.

Lentile, L.B., Smith, A.M.S., Hudak, A.T., Morgan, P., Bobbitt, M.J., Lewis, S.A., and Robichaud, P.R. (2009). Remote sensing for prediction of 1-year post-fire ecosystem condition. *International Journal of Wildland Fire*, 18(5), 594–608.

Lewis, S.A., Lentile, L.B., Hudak, A.T., Robichaud, P.R., Morgan, P., and Bobbitt, M.J. (2007). Mapping ground cover using hyperspectral remote sensing after the 2003 Simi and Old wildfires in southern California. Fire Ecology Special Issue, 3(1), 109–128.

Liu, X., He, B., Quan, X., Yebra, M., Qiu, S., Yin, C., Liao, Z., and Zhang, H. (2018). Near Real-Time Extracting Wildfire Spread Rate from Himawari-8 Satellite Data. *Remote Sensing*, 10(10), 1654. *https://doi.org/10.3390/rs10101654*

López García, M.J., and Caselles, V. (1991). Mapping burns and natural reforestation using thematic mapper data. *Geocarto International*, 1, 31–37. *https://doi.org/10.1080/10106049109354290*

Lowell, K., Shamir, R., Siqueira, A., White, J., O'Connor, A., Butcher, G., Garvey, M., and Niven, M. (2009). Assessing Capabilities of Geospatial Data to Map Built Structures and Evaluate Their Bushfire Threat. *International Journal of Wildland Fire*, 18(8), 1010–1020. *https://doi.org/10.1071/WF08077*

Lucas, R., Bunting, P., Paterson, M., and Chisholm, L. (2008a). Classification of Australian forest communities using aerial photography, CASI and HyMap data. *Remote Sensing of Environment*, 112(5), 2088–2103.

Luke, R., and McArthur, A. (1978). *Bushfires in Australia*. Australian Government Publishing Service, Canberra.

Lund, I.D., and Morgan, J.W. (2002). The role of fire regimes in temperate lowland grasslands of south-eastern Australia. In *Flammable Australia: The Fire Regimes and Biodiversity of a Continent*. (Eds: R.A. Bradstock, J.E. Williams, and M.A. Gill) Cambridge University Press, Cambridge.

Lydersen, J. M., B. M. Collins, M. L. Brooks, J. R. Matchett, K. L. Shive, N. A. Povak, V. R. Kane and D. F. Smith (2017). Evidence of fuels management and fire weather influencing fire severity in an extreme fire event. *Ecological Applications*, 27(7), 2013–2030.

Maier, S.W., Russell-Smith, J., Edwards, A.C., and Yates, C. (2013). Sensitivity of the MODIS fire detection algorithm (MOD14) in the savanna region of the Northern Territory, Australia. *ISPRS Journal of Photogrammetry and Remote Sensing*, 76, 11–16. *https://doi.org/10.1016/j.isprsjprs.2012.11.005*

Malak, D.A., and Pausas, J.G. (2006). Fire regime and post-fire Normalised Difference Vegetation Index changes in the eastern Iberian peninsula (Mediterranean basin). *International Journal of Wildland Fire*, 407–413.

Manzanera, J. A., A. Garcia-Abril, C. Pascual, R. Tejera and S. Martin-Fernandez (2016). Fusion of airborne LiDAR and multispectral sensors reveals synergic capabilities in forest structure characterisation. *GIScience and Remote Sensing*, 53(6), 723–728.

Manzo-Delgado, L., Sanchez-Colon, S., and Alvarez, R. (2009). Assessment of seasonal forest fire risk using NOAA-AVHRR: a case study in central Mexico. *International Journal of Remote Sensing*, 30(19), 4991–5013.

Marselis, S.M., Yebra, M., Jovanovic, T., and van Dijk, A.I.J.M. (2016). Deriving comprehensive forest structure information from mobile laser scanning observations using automated point cloud classification. *Environmental Modelling and Software*, 82, 142–151.

Martin, D., Chen, T., Nichols, D. Bessel, R. Kidnie, S. Alexander, J. (2015). Integrated ground and satellite-based observations to determine the degree of grassland curing. *International Journal of Wildland Fire*, 24(3), 329–339.

Massetti, A., Rüdiger, C., Yebra, M., Hilton, J. (2019). The Vegetation Structure Perpendicular Index (VSPI): a forest condition index for wildfire predictions. *Remote Sensing of Environment*, 224, 167–181. *https://doi.org/10.1016/j.rse.2019.02.004*

McArthur, A.G. (1966). *Weather and Grassland Fire Behaviour*. Australian Forestry and Timber Bureau Leaflet. 100, 23 p.

McArthur, A.G. (1967). *Fire Behaviour in Eucalypt Forests*. Australian Forestry and Timber Bureau Leaflet 107, 25 p.

McCarley, T.R., Kolden, C.A., Vaillant, Andrew N.V., Hudak, A.T., Smith, A.M.S., and Kreitler, J. (2017). Landscape-scale quantification of fire-induced change in canopy cover following mountain pine beetle outbreak and timber harvest. *Forest Ecology and Management*, 391, 164–175, *https://doi.org/10.1016/j.foreco.2017.02.015*

McCarthy, G.J., Tolhurst, K.G., and Chatto, K. (1999). *Overall fuel hazard guide, 3rd edn*. Research report 47, Fire Management Branch, Department of Natural Resources and Environment, Victoria.

McCarthy, G., Moon, K., and Smith. L. (2017). Mapping fire severity and fire extent in forest in Victoria for ecological and fuel outcomes. *Ecological Management and Restoration*, 18, 54–64.

McColl-Gausden, S.C., and Penman, T.D. (2017). Visual assessment of surface fuel loads does not align with destructively sampled surface fuels. *Forests*, 8(11), 408.

McColl-Gausden, S.C., Bennett, L.T., Duff, T.J., Cawson, J.G., and Penman, T.D. (2019). Climatic and edaphic gradients predict variation in wildland fuel hazard in south-eastern Australia. *Ecography*, 43(3), 443–455. *https://doi.org/10.1111/ecog.04714*

McDougall, K., and Kirkpatrick, J.B. (1994). *Conservation of Lowland Native Grasslands in South-Eastern Australia*. World Wide Fund for Nature Australia, Sydney.

McKenna, P., Erskine, P.D., Lechner, A.M., and Phinn, S. (2017). Measuring fire severity using UAV imagery in semi-arid central Queensland, Australia. *International Journal of Remote Sensing*, 38(14), 4244–4264.

McRae, R. (2004). The Breath of the Dragon—Observations of the January 2003 ACT Bushfires. *Proceedings of 2004 Australasian Bushfire Research Conference, Adelaide*.

McRae, R. (2008). *2003 ACT Bushfires Fire Behaviour Post-Analysis*. Unpublished report, ACT ESA, Canberra.

McRae, R., Sharples, J.J., and Weber, R.O. (2008). *High Fire Risk: The Thermal Belt in Australia*. Poster: AFAC/BushfireCRC Conference 2008, Adelaide.

McRae, R.H.D., Sharples, J.J., and Fromm, M. (2015). Linking local wildfire dynamics to pyroCb development, *Natural Hazards and Earth System Science*, 15, 417–428. *https://doi.org/10.5194/nhess-15-417-2015*

Meddens, A. J. H., C. A. Kolden and J. A. Lutz (2016). Detecting unburned areas within wildfire perimeters using Landsat and ancillary data across the northwestern United States. *Remote Sensing of Environment*, 186, 275–285.

Meng, R., Wu, J., Zhao, F., Cook, B.D., Hanavan, R.P., and Serbin, S.P. (2018). Measuring short-term post-fire forest recovery across a burn severity gradient in a mixed pine-oak forest using multi-sensor remote sensing techniques. *Remote Sensing of Environment*, 210, 282–296.

Miller, J.D., and Thode, A.E. (2007). Quantifying burn severity in a heterogenous landscape with a relative version of the delta Normalized Burn Ratio (dNBR). *Remote Sensing of Environment*, 109, 66–80.

Miller, J.D., Knapp, E.E., Key, C.H., Skinner, C.N., Isbell, C.J., Creasy, R.M., and Sherlock, J.W. (2009). Calibration and validation of the relative differenced Normalized Burn Ratio (RdNBR) to three measures of fire severity in the Sierra Nevada and Klamath Mountains, California, USA. *Remote Sensing of Environment*, 113, 645–656.

Miller C., Hilton J., Sullivan A., Prakash M. (2015). SPARK—A Bushfire Spread Prediction Tool. In: *Environmental Software Systems. Infrastructures, Services and Applications*. (Eds: Denzer R., Argent R.M., Schimak G., Hřebíček J.) ISESS 2015. IFIP Advances in Information and Communication Technology, vol 448. Springer, Chamonix.

Mills, G.A. (2008a). Abrupt surface drying and fire weather Part 1: overview and case study of the South Australian fires of 11 Janurary 2005. *Australian Meteorological Magazine*, 57, 299–309.

Mills, G.A. (2008b). Abrupt surface drying and fire weather Part 2: a preliminary synoptic climatology in the forested areas of southern Australia. *Australian Meteorological Magazine*, 57, 311–328.

Mills, G.A., and McCaw, L. (2010). *Atmospheric Stability Environments and Fire Weather in Australia—extending the Haines Index*. CAWCR Technical Report No. 20, Centre for Australian Weather and Climate Research. ISBN: 978-1-921605-56-7

Minchella, A., Frate, F.D., Capogna, F., Anselmi, S., and Manes, F. (2009). Use of multitemporal SAR data for monitoring vegetation recovery of Mediterranean burned areas. *Remote Sensing of Environment*, 113, 588–597.

Morgan, J.W. (1999). Defining grassland fire events and the response of perennial plants to annual fire in temperate grasslands of south-eastern Australia. *Plant Ecology*, 1444, 127–144.

Morgan, P., Hardy, C.C., Swetnam, T.W., Rollins, M.G., and Long, D.G. (2001). Mapping fire regimes across time and space: Understanding coarse and fine-scale fire patterns. *International Journal of Wildland Fire*, 10, 329–342.

Morgan, P., Keane, R.E., Dillon, G.K., Jain, T.B., Hudak, A.T., Karau, E.C., Sikkink, P.G., Holden, Z.A., and Strand, E.K. (2014). Challenges of assessing fire and burn severity using field measures, remote sensing and modelling. *International Journal of Wildland Fire*, 23, 1045–1060.

Morisette, J., Giglio, L., Csiszar, I., and Justice, C.O. (2005). Validation of the MODIS active fire product over Southern Africa with ASTER data. *International Journal of Remote Sensing*, 26, 4239–4264.

Mueller, E.V., Skowronski, N. Clark, N., Gallagher, M., Kremens, R., Thomas, J.C., El Houssami, M., Filkov, A., Hadden, R.M., Mell, W., and Simeoni, A. (2017). Utilization of remote sensing techniques for the quantification of fire behaviour in two pine stands. *Fire Safety Journal*, 91, 845–854.

Newnham, G.J., Verbesselt, J., Grant, I.F., and Anderson, S.A.J. (2011). Relative Greenness Index for assessing curing of grassland fuel. *Remote Sensing of Environment*, 115(6), 1456–1463. *https://doi.org/10.1016/j.rse.2011.02.005*

Noble, I.R., Bary, G.A.V., Gill, A.M. (1980). McArthur's fire-danger meters expressed as equations. *Australian Journal of Ecology*, 5, 201–203.

Nolan, R.H., Boer, M.M., Resco de Dios, V., Caccamo, G., and Bradstock, R.A. (2016a). Large scale, dynamic transformations in fuel moisture drive wildfire activity across southeastern Australia. *Geophysical Research Letters*, 43, 4229–4238.

Nolan, R.H., Resco de Dios, Boer, M.M., Caccamo, G., Goulden, M.L., and Bradstock, R.A. (2016b). Predicting dead fine fuel moisture at regional scales using vapour pressure deficit from MODIS and gridded weather data. *Remote Sensing of Environment*, 174, 100–108.

NSW BRMR (2020). *NSW Bushfire Risk Management Research Hub* website: *https://www.uow.edu.au/science-medicine-health/research/cermb/nsw-bushfire-risk-management-research-hub/*

Okin, G.S. (2007). Relative spectral mixture analysis—A multitemporal index of total vegetation cover. *Remote Sensing of Environment*, 106, 467–479.

Oldford, S., Leblon, B., Maclean, D., and Flannigan, M. (2006). Predicting slow-drying fire weather index fuel moisture codes with NOAA-AVHRR images in Canada's northern boreal forests. *International Journal of Remote Sensing*, 27(18), 3881–3902.

Otón, G., Ramo, R., Lizundia-Loiola, J., and Chuvieco, E. (2019). Global Detection of Long-Term (1982–2017) Burned Area with AVHRR-LTDR Data. *Remote Sensing*, 11, 2079.

Padilla, M., Stehman, S.V., Ramo, R., Corti, D., Hantson, S., Oliva, P., Alonso-Canas, I., Bradley, A.V., Tansey, K., Mota, B., Pereira, J.M., Chuvieco, E. (2015). Comparing the accuracies of remote sensing global burned area products using stratified random sampling and estimation. *Remote Sensing of Environment*, 160, 114–121.

Paltridge, G.W., and Barber, J. (1988). Monitoring grassland dryness and fire potential in Australia with NOAA/AVHRR Data. *Remote Sensing of Environment*, 25(3) 381–394.

Pereira, J.M.C., Sa, A.C.L., Sousa, A.M.O, Silva, J.M.N., Santos, T.N., and Carreiras, J.M.B. (1999). Spectral characterization and discrimination of burnt areas. In *Remote Sensing of Large Wildfires*. (Ed: E. Chuvieco). Springer-Verlag, Berlin.

Pettorelli, N., Laurance, W.F., O'Brien, T.G., Wegmann, M., Nagendra, H., and Turner, W. (2014). Satellite remote sensing for applied ecologists: opportunities and challenges. *Journal of Applied Ecology*, 51, 839–848.

Plank, S., Fuchs, E.-M., and Frey, C. (2017). A Fully Automatic Instantaneous Fire Hotspot Detection Processor Based on AVHRR Imagery—A TIMELINE Thematic Processor. *Remote Sensing*, 9, 30.

Polinova, M., Wittenberg, L., Kutiel, H., and Brook, A. (2019). Reconstructing pre-fire vegetation condition in the wildland urban interface (WUI) using artificial neural network. *Journal of Environmental Management*, 238, 224–234.

Poon, P.K., and Kinoshita, A.M. (2018). Estimating evapotranspiration in a post-fire environment using remote sensing and machine learning. *Remote Sensing*, 10, (1728).

Potter, B.E. (2012a). Atmospheric interactions with wildland fire behaviour—I. Basic surface interactions, verticle profiles and synoptic structures. *International Journal of Wildland Fire*, 21(7), 779–801.

Potter, B.E. (2012b). Atmospheric interactions with wildland fire behaviour—II. Plume and vortex dynamics. *International Journal of Wildland Fire*, 21(7), 802–817.

Power, C. (2006). A Spatial Decision Support System for Mapping Bushfire Hazard Potential using Remotely Sensed Data. *Proceedings of Bushfire Conference 2006*. Brisbane, 6–9 June 2009.

Power, C. (2008). *Fuel Hazard Mapping (Karawatha) Project Report for Brisbane City Council*, Open Space Planning Section.

Price, O.F., and Bradstock, R.A. (2012). The efficacy of fuel treatment in mitigating property loss during wildfires: insights from analysis of the severity of the catastrophic fires in 2009 in Victoria, Australia. *Journal of Environmental Management*, 113, 146–157. *https://doi.org/10.1016/j.jenvman.2012.08.041*

Price, O., and Gordon, C.E. (2016). The potential for LiDAR technology to map fire fuel hazard over large areas of Australian forest. *Journal of Environmental Management*, 181, 663–673.

Punithraj, G., Pruthviraj, U., and Shetty, A. (2019). Surface Soil Moisture Retrieval Using C-Band Synthetic Aperture Radar (SAR) over Yanco Study Site, Australia—A Preliminary Study. In *Applications of Geomatics in Civil Engineering*. (Eds: Ghosh, J.K., and da Silva, I.) Springer Professional. *https://doi.org/10.1007/978-981-13-7067-0_8*

Pyne, S.J. (1992). *The Burning Bush: A Fire History of Australia*. Allen and Unwin, Sydney. 520pp. ISBN: 1863731946

Pyne, S.J. (2015). *The Fire Age*. Aeon essay: *https://aeon.co/essays/how-humans-made-fire-and-fire-made-us-human*

Pyne, S.J. (2020). *The Still-Burning Bush*. Scribe Short Books, Melbourne. 144pp. ISBN: 1920769757

Quan, X., He, B., Yebra, M., Liu, X., Liu, X., Zhung, X., and Cao, H. (2018). Retrieval of Fuel Moisture Content from Himawari-8 Product: Towards Real-Time Wildfire Risk Assessment. *IGARSS 2018 - 2018 IEEE International Geoscience and Remote Sensing Symposium*, Valencia, 2018, pp. 7660–7663. doi:*10.1109/IGARSS.2018.8517602*.

Rao, K., Park Williams, A., Fortin Flefil, J., and Konings, A.G. (2020). SAR-enhanced mapping of live fuel moisture content. *Remote Sensing of Environment*, 245, 111797.

Reinhart, E.D., Keane, R.E., and Brown, J.K. (2001). Modeling fire effects. *International Journal of Wildland Fire*, 10, 373–380.

Renzullo, L.J., Tian, S., van Dijk, A.I.J.M., Rozas Larraondo, P.R., Yebra, M., Yuan, F., and Mueller, N. (2019). Burn extent and severity mapping by spectral anomaly detection in the Landsat data cube. *23rd International Congress on Modelling and Simulation, 1–6 December 2019, Canberra, ACT, Australia*. *https://mssanz.org.au/modsim2019/H7/renzullo.pdf*

Ressl, R., Lopez, G., Cruz, I., Colditz, R.R., Schmidt, M., Ressl, S., and Jimenez, R. (2009). Operational active fire mapping and burnt area identification applicable to Mexican Nature Protection Areas using MODIS and NOAA-AVHRR direct readout data. *Remote Sensing of Environment*, 113, 1113–1126

Roberts, D., Mueller, N., and McIntyre, A. (2017). High-Dimensional Pixel Composites From Earth Observation Time Series. *IEEE Transactions on Geoscience and Remote Sensing*, 55(11), 6254–6264. *https://ieeexplore.ieee.org/stamp/stamp.jsp?arnumber=8004469*

Robichaud, P.R., Lewis, S.A., Laes, D.Y.M., Hudak, A.T., Kokaly, R.F., and Zamudio, J.A. (2007). Postfire soil burn severity mapping with hyperspectral image unmixing. *Remote Sensing of Environment*, 108, 467–480.

Roff, A., Goodwin, N., and Merton, R. (2005). *Assessing Fuel Loads using Remote Sensing*. NSW RFS Technical Report, University of NSW, Sydney.

Roff, A.M., Taylor, G.R., Turner, R., Day, M., Mitchell, A., and Merton, R. (2006). Hyperspectral and Lidar Remote Sensing of Forest Fuel Loads in Jilliby State Conservation Area. *Proceedings of 13th Australian Photogrammetric and Remote Sensing Conference*, Canberra, Australia.

Rollins, M.G. (2009). LANDFIRE: a nationally consistent vegetation, wildland fire, and fuel assessment. *International Journal of Wildland Fire*, 18, 235–249.

Rothermel, R. (1972). *A mathematical model for predicting fire spread in wildland fuels*. Research Paper INT-115. Ogden, Utah, USDA Forest Service.

Roy, D.P., and Landmann, T. (2005). Characterizing the surface heterogeneity of fire effects using multi-temporal reflective wavelength data. *International Journal of Remote Sensing*, 26(19), 4197–4218.

Roy, D.P., Lewis, P., and Justice, C. (2002). Burned area mapping using multi-temporal moderate spatial resolution data—a bi-directional reflectance model-based expectation approach. *Remote Sensing of Environment* 83, 263–286.

Roy, D.P., Lewis, P., and Justice, C.O. (2005). Prototyping a global algorithm for systematic fire-affected area mapping using MODIS time series data. *Remote Sensing of Environment*, 97, 137–162.

Roy, D.P., Boschetti, L., and Trigg, S.N. (2006). Remote sensing of fire severity: assessing the performance of the Normalized Burn Ratio. *IEEE Geoscience and Remote Sensing Letters*, 3(1), 112–116.

Roy, D.P., Boschetti, L., and Smith, A.M.S. (2013). Satellite remote sensing of fires. In *Fire Phenomena and the Earth System: An interdisciplinary guide to fire science*. 1st edn (Ed: C.M. Belcher). John Wiley and Sons, Ltd.

Russell-Smith, J., and Stanton, P. (2002) Fire regimes and fire management of rainforest communities across northern Australia. In *Flammable Australia: The Fire Regimes and Biodiversity of a Continent*. (Eds: R.A. Bradstock, J.E. Williams, and M.A. Gill) Cambridge University Press, Cambridge.

Russell-Smith, J., Yates, C.P., Whitehead, P.J., Smith, R., Craig, R., Allan, G.E., Thackway, R., Frakes, I., Cridland, S., Meyer, M.C.P., and Gill, A.M. (2007). Bushfires 'down under': patterns and implications of contemporary Australian landscape burning. *International Journal of Wildland Fire*, 16, 361–377.

Salis, M., Del Giudice, L., Robichaud, P.R., Ager, A., Canu, A., Duce, P., Pellizzaro, G., Ventura, A., Alcasena-Urdiroz, F., Spano, D., and Arca, B. (2019). Coupling wildfire spread and erosion models to quantify post-fire erosion before and after fuel treatments. *International Journal of Wildland Fire*, 28, 687–703. *https://doi.org/10.1071/WF19034*

Scarth, P., Roder, A., and Schmidt, M. (2010). Tracking grazing pressure and climate interaction—The role of Landsat fractional cover in time series analysis. *Proceedings of the 15th Australasian Remote Sensing and Photogrammetry Conference, Alice Springs*, Australia.

Schroeder, W., Prins, E., Giglio, L., Csiszar, I., Schmidt, C., Morisette, J., and Justice, C.O. (2008a). Validation of GOES and MODIS active fire detection products using ASTER and ETM+ data. *Remote Sensing of Environment*, 112, 2711–2726.

Schroeder, W., Ruminski, M., Csiszar, I., Giglio, L., Prins, E., Schmid, C., and Morisette, J. (2008b). Validation of analyses of an operational fire monitoring product: The Hazard Mapping System. *International Journal of Remote Sensing*, 29(20), 6059–6066.

Schroeder, W., Oliva, P., Giglio, L., and Csiszar, I.A. (2014). The new VIIRS 375m active fire detection data product: Algorithm description and initial assessment. *Remote Sensing of Environment*, 143, 85–96.

Sharples, J.J. (2009). An overview of mountain meteorological effects relevant to fire behaviour and bushfire risk. *International Journal of Wildland Fire*, 18, 737–754.

Sharples, J.J., Mills, G.A., McRae, R.H., and Weber, R.O. (2010). Foehn-like winds and elevated fire danger conditions in southeastern Australia. *Journal of Applied Meteorology and Climatology*, 49, 1067–1095.

Sharples, J.J., McRae, R.H., and Wilkes, S.R. (2012). Wind-terrain effects on the propagation of wildfires in rugged terrain: fire chanelling. *International Journal of Wildland Fire*, 21, 282–296.

Sharples, J.J., Cary, G.J., Fox-Hufghes, P., Mooney, S., Evans, J.P., Fletcher, M.S., Fromm, M., Grierson, P., McRae, R., and Baker, P. (2016). Natural Hazards in Australia: extreme bushfire. *Climatic Change*, 139, 85–99.

Shin, P., Sankey, T., Moore, M.M., and Thode, A.E. (2018). Evaluating unmanned aerial vehicle images for estimating forest canopy fuels in a Ponderosa pine stand. *Remote Sensing*, 10, 1266.

Silva, J.M.N., Sá, A.C.L., and Pereira, J.M.C. (2005). Comparison of burned area estimates derived from SPOT-VEGETATION and Landsat ETM1 data in Africa: Influence of spatial pattern and vegetation type. *Remote Sensing of Environment*, 96, 188–201.

Simpson, C.C., Sharples, J.J., and Evans, J.P. (2016). Sensitivity of atypical lateral fire spread to wind and slope. *Geophysiology Research Letters*, 43, 1744–1751.

Smith, A.M.S., Wooster, M.I., Drake, N.A., Dipotso, F.M., Falkowski, M.J., and Hudak, A.T. (2005). Testing the potential of multi-spectral remote sensing for retrospectively estimating fire severity in African savanna environments. *Remote Sensing of Environment*, 97, 92–115. doi:*10.1015/J.RSE-2005.04.014*.

Smith, A.M.S., Lentile, L.B., Hudak, A.T., and Morgan, P. (2007a). Evaluation of linear spectral unmixing and dNBR for predicting post-fire recovery in North American ponderosa pine forest. *International Journal of Remote Sensing*, 28(22), 5159–5166.

Smith, R., Adams, M., Maier, S., Craig, R., Kristina, A., and Maling, I. (2007b). Estimating the area of stubble burning from the number of active fires detected by satellite. *Remote Sensing of Environment*, 109, 95–106.

Soverel, N.O., Perrakis, D.D.B., and Coops, N.C. (2010). Estimating burn severity from Landsat dNBR and RdNBR indices across western Canada. *Remote Sensing of Environment*, 114, 1896–1909.

Stavros, E.N., Abatzoglou, J.T., McKenzie, D., and Larkin, N.K. (2014). Regional projections of the likelihood of very large wildland fires under a changing climate in the contiguous Western United States. *Climatic Change*, 126, 455–468.

Stensrud, D.J. (1996). Importance of low-level jets to climate: a review. *Journal of Climate*, 9, 1698–1711.

Storey, M.A., Price, O.F., Sharples, J., and Bradstock, R. (2020a). Drivers of long-distance spotting during wildfires in south-eastern Australia. *International Journal of Wildland Fire*, 29(6), 459–472. *https://doi.org/10.1071/WF19124*

Storey, M.A., Price, O.F., Bradstock, R.A., and Sharples, J.J. (2020b). Analysis of variation in distance, number, and distribution of spotting in southeast Australian wildfires. *Fire*, 3(2), 10. *http://dx.doi.org/10.3390/fire3020010*

Stow, D., Niphadkar, M., and Kaiser, J. (2006). *International Journal of Wildland Fire*, 15, 347–360.

Strahler, A.H., Jupp, D.L.B., Woodcock, C.E., Schaaf, C.B., Yao, T., Zhao, F., Yang, X., Lovell, J., Culvenor, D., Newnham, G., Ni-Miester, W., and Boykin-Morris, W. (2008). Retrieval of forest structural parameters using a ground-based lidar instrument (Echnida). *Canadian Journal of Remote Sensing*, 34, S426-40.

Strand, E.K., Bunting, S.C., and Keefe, R.F. (2013). Influence of Wildland Fire Along a Successional Gradient in Sagebrush Steppe and Western Juniper Woodlands. *Rangeland Ecology and Management*, 66(6), 667–679. *https://doi.org/10.2111/REM-D-13-00051.1*

Swanson, M.E., Franklin, J.F., Beschta, R.L., Crisafulli, C.M., DellaSala, D.A., Hutto, R.L., Lindenmayer, D.B., and Swanson, F.J. (2011). The forgotten stage of forest succession: early-successional ecosystems on forest sites. *Frontiers in Ecology and the Environment*, 9, 117–125. *https://doi.org/10.1890/090157*

Tanase, M., de la Riva, J., Santoro, M., Pérez-Cabello, F., and Kasischke, E. (2011). Sensitivity of SAR data to post-fire forest regrowth in Mediterranean and boreal forests. *Remote Sensing of Environment*, 115(8), 2075–2085.

Tanase, M.A., Santoro, M., Aponte, C., and de La Riva, J. (2014). Polarimetric properties of burned forest areas at C- and L-band. *IEEE Journal of Selected Topics in Applied Earth Observations and Remote Sensing*, 7(1), 267–276.

Tian, X., Mcrae, D., Shu, L., Wang, M. (2005). Satellite remote-sensing technologies used in forest fire management. *Journal of Forestry Research*, 16(1), 73–78.

Tickle, P.K., Lee, A., Lucas, R.M., Austin, J., and Witte, C. (2006). Quantifying Australian forest floristics and structure using small footprint LiDAR and large scale aerial photography. *Forest Ecology and Management*, 223, 379–394.

Tolhurst, K.G., and McCarthy, G. (2016). Effect of prescribed burning on wildfire severity: a landscape-scale case study from the 2003 fires in Victoria. *Australian Forestry*, 79(1), 1–14.

Tolhurst, K., Shields, B., and Chong, D. (2008). Phoenix: development and application of a bushfire risk management tool. *The Australian Journal of Emergency Management*, 23, 47–54.

Trigg, S., and Flasse, S. (2000). Characterizing the spectral-temporal response of burned savannah using *in situ* spectroradiometry and infrared thermometry. *International Journal of Remote Sensing*, 21(16), 3161–3168.

Trigg, S.N., Roy, D.P., and Flasse, S.P. (2005). An *in situ* study of the effects of surface anisotrophy on the remote sensing of burned savannah. *International Journal of Remote Sensing*, 26(21), 4869–4876.

Tu, Y., Phinn, S., Johansen, K., and Robson, A. (2018). Assessing radiometric correction approaches for multi-spectral UAS imagery for horticultural applications. *Remote Sensing*, 10, 1684.

Turner, R. (2007). *Assessment of Fuel Loads by Remote Sensing. Sub-report on Airborne Laser Scanner application in the Jilliby Catchment Area*. Final report to NSW RFS 30 March, 2007. Forests New South Wales.

Turner, M.G., Romme, W.H., and Gardner, R.H. (1999). Prefire heterogeneity, fire severity, and early postfire plant reestablishment in subalpine forests of Yellowstone National Park, Wyoming. *International Journal of Wildland Fire*, 9, 21–36.

Turner, M.G., Twhitby, T.G., Tinker, D.B., and Romme, W. (2016). Twenty-four years after the Yellowstone Fires: Are postfire lodgepole pine stands converging in structure and function? *Ecology*, 97(5), 1260–1273.

van Oldenborgh, G.J., Krikken, F., Lewis, S., Leach, N.J., Lehner, F., Saunders, K.R., van Weele, M., Haustein, K., Li, S., Wallom, D., Sparrow, S., Arrighi, J., Singh, R.P., van Aalst, M.K., Philip, S.Y., Vautard, R., and Otto, F.E.L. (2020, in review). Attribution of the Australian bushfire risk to anthropogenic climate change. *Natural Hazards and Earth System Sciences Discussions*. *https://doi.org/10.5194/nhess-2020-69*

Vanderhoof, M.K., Brunner, N., Beal, Y.G., and Hawbaker, T.J. (2017). Evaluation of the U.S. Geological Survey Landsat Burned Area Essential Climate Variable across the conterminous U.S. using commercial high-resolution imagery. *Remote Sensing*, 9(7), 743.

Veraverbeke, S., Stavros, E.N., and Hook, S.J. (2014). Assessing fire severity using imaging spectroscopy data from the Airborne Visible/Infrared Imaging Spectrometer (AVIRIS) and comparison with multispectral capabilities. *Remote Sensing of Environment*, 154, 153–163.

Verbesselt, J., Fleck, S., and Coppin, P. (2002). Estimation of fuel moisture content towards Fire Risk Assessment: A review. In: *Forest Fire Research and Wildland Fire Safety* (Ed: Viegas), Millpress. Rotterdam. ISBN 90-77017-72-0.

Verbesselt, J., Somer, B., Lhermitte, S., Jonckheere, I., van Aardt, J., and Coppin, P. (2007). Monitoring herbaceous fuel moisture content with SPOT VEGETATION time-series for fire risk prediction in savanna ecosystems. *Remote Sensing of Environment*, 108, 357–368.

Verbyla, D.L., Kasischke, E.S., and Hoy, E.E. (2008). Seasonal and topographic effects on estimating fire severity from Landsat TM/ETM+ data. *International Journal of Wildland Fire*, 17, 527–534.

Vilar, L., Camia, A., San-Miguel-Ayanz, J., and Pilar Martín, M. (2016). Modeling temporal changes in human-caused wildfires in Mediterranean Europe based on Land Use-Land Cover interfaces. *Forest Ecology and Management*, 378, 68–78.

Walker, R.B., Coop, J.D., Downing, W.M., Krawchuk, M.A., Malone, S.L., Meigs, G.W. (2019). How Much Forest Persists Through Fire? High-Resolution Mapping of Tree Cover to Characterize the Abundance and Spatial Pattern of Fire Refugia Across Mosaics of Burn Severity. *Forests*, 10, 782. *https://doi.org/10.3390/f10090782*

Wallace, L., Lucieer, A., Malenovsky, Z., Turner, D., and Vopenka, P. (2016). Assessment of forest structure using two UAV techniques: a comparison of airborne laser scanning and structure from motion (SfM) point clouds. *Forests*, 7(3), 62.

Wang, L., Quan, X., He, B., Yebra, M., Xing, M., and Liu, X. (2019). Assessment of the dual polarimetric Sentinel-1A data for forest fuel moisture content estimation. *Remote Sensing*, 11, 1568.

Wang, X., Thompson, D.K., Marshall, G.A., Tymstra, C., Carr, R., and Flannigan, M.D. (2015). Increasing frequency of extreme fire weather in Canada with climate change. *Climatic Change*, 130(4), 573–586.

Wickramasinghe, C., Jones, S., Reinke, K., and Wallace, L. (2016). Development of a multi-spatial resolution approach to the surveillance of active fire lines using Himawari-8. *Remote Sensing*, 8(11), 932.

Wing, M.G., Burnett, J.D., and Sessions, J. (2014). Remote sensing and unmanned aerial system technology for monitoring and quantifying forest fire impacts. *International Journal of Remote Sensing Applications*, 4(1), 18.

Xu, G., and Zhong, X. (2017). Real-time wildfire detection and tracking in Australia using geostationary satellite: Himawari-8. *Remote Sensing Letters*, 8, 1052–1061.

Yebra, M., Chuvieco, E., and Riano, D. (2008). Estimation of live fuel moisture content from MODIS images for fire risk assessment. *Agricultural and Forest Meteorology*, 148, 523–36.

Yebra, M., Chuvieco, E., Danson, M., Dennison, P., Hunt, E.R, Jurdao, S., Riano, D., Zylstra, P. (2013). A global review of remote sensing of live fuel moisture content for fire danger assessment: moving towards operational products. *Remote Sensing of Environment*, 136, 455–468.

Yebra, M., Quan, X., Riano, D., Rozas-Larraondo, P., van Dijk, A., and Cary, G. (2018). A fuel moisture content and flammability monitoring methodology for continental Australia based on optical remote sensing. *Remote Sensing of Environment*, 212, 260–272.

Yin, C., He, B., Yebra, M., Juan, X., Edwards, A.C., Liu, X., Liao, Z., Lui, K. (2019). Burn Severity Estimation in Northern Australia Tropical Savannas Using Radiative Transfer Model and Sentinel-2 Data. *IGARSS 2019 (2019 IEEE International Geoscience and Remote Sensing Symposium) Yokohama, Japan*. pp. 6712–6715. doi:*10.1109/IGARSS.2019.8899857*.

Yuan, C., Zhang, Y., and Lui, Z. (2015). A survey on technologies for automatic forest fire monitoring, detection and fighting using unmanned aerial vehicles and remote sensing techniques. *Canadian Journal of Forest Research*, 45(7), 783–792.

Observing Ecosystems

Section 1 introduces environmental factors that shape and impact ecosystems and their global distribution. Significant attributes of ecosystems are described in Section 7.

Ecological integrity is said to be “the ability of an ecological system to support and maintain a community of organisms that has species composition, diversity, and functional organisation comparable to those of natural habitats within a region” (Parrish *et al*., 2003). In the following two sections we consider ecological integrity in terms of biodiversity (see Section 19) and sustainability (see Section 20).

Contents

19 Biodiversity 429

20 Sustainability 451

Background image on previous page: Landsat-8 OLI image over the Gulf of Carpentaria, NT, acquired on 7 June 2016, displayed uisng bands 6, 5, 3 as RGB.
Source: Norman Mueller, Geoscience Australia

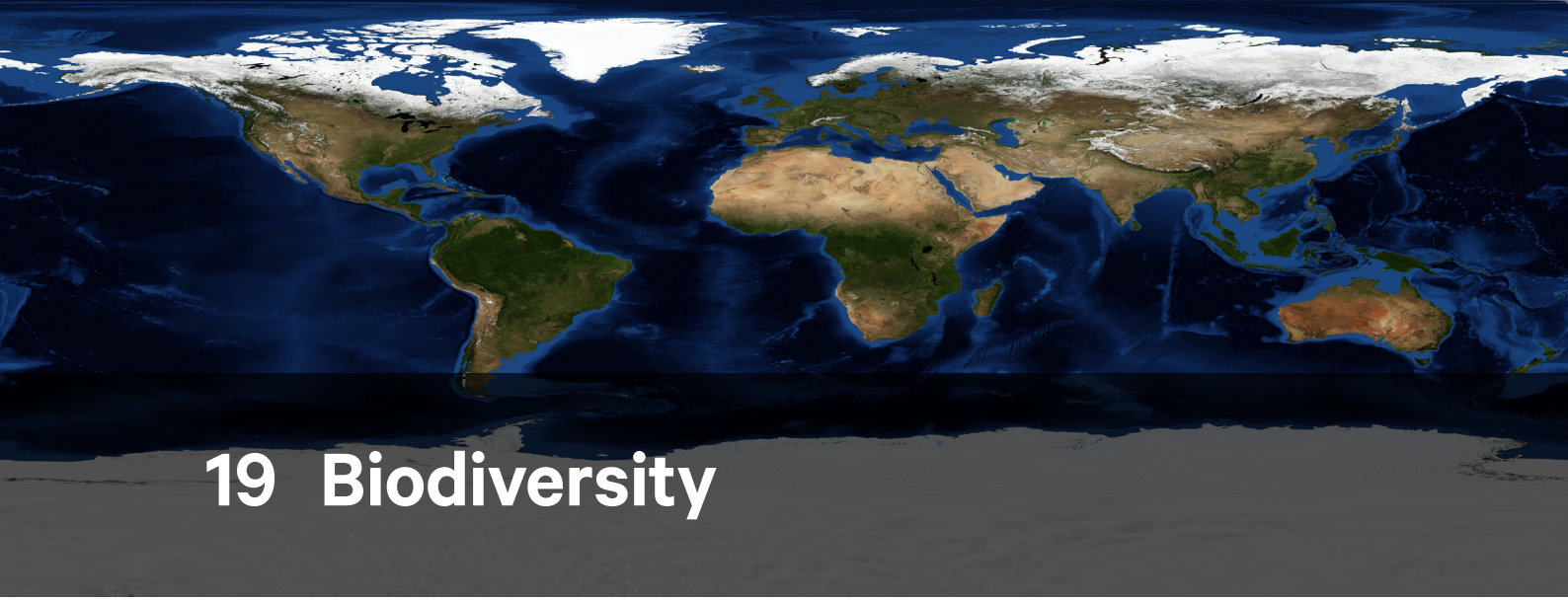

19 Biodiversity

Biodiversity is a relatively recent term, blended from the Greek word '*bios*', meaning life, and the Latin word '*diversitas*', meaning variety or difference. It basically represents the concept of biological diversity and embraces all life forms on Earth (see Sections 1.3.1 and 7.1).

As human populations have expanded, global biodiversity has been observed to decline at both local and global scales (see Section 11.4). Many organisms change their environments to create niches which provide them and their progeny with a competitive advantage over other species in terms of access to, and use of, various resources (Pereira *et al.*, 2012). However, the impact of *Homo sapiens* on global biodiversity vastly exceeds that of other species (see Excursus 11.2). Since the industrial revolution, this impact has accelerated due to massive technological changes and rapid population growth (see Figure 19.1), and has been accompanied by significant pollution of air, water and soil from a wide range of new, toxic materials. The major anthropogenic drivers for biodiversity change (namely, fire, hunting, fishing, agriculture and forest clearing, island invasions, pollution, and anthropogenic climate change) have all been increasing in parallel with population growth over this time period (Pereira *et al.*, 2012). The main threats to biodiversity of mammals, birds and amphibians have been identified (in decreasing order) as:

- habitat changes—urban development, agriculture, mining, transportation;
- overexploitation—fishing, hunting;
- invasive species—introduced exotics;
- climatic variations—temperature and precipitation patterns, sea level rise; and
- pollution—water, air, soil (Pereira *et al.*, 2012; IPBES, 2019).

In response to the global decline in biodiversity, the United Nations Envrionment Programme (UNEP) developed an international legal instrument called the Convention on Biological Diversity (CBD), which was presented at the 1992 UN Conference on Environment and Development (the Rio 'Earth Summit') and ratified at the end of 1993 with the support of 168 world leaders. The objectives of this convention were:

- conservation of biological diversity;
- sustainable use of the components of biological diversity; and
- fair and equitable sharing of the benefits arising out of the utilisation of genetic resources (CBD, 2020a).

To achieve these objectives, a global strategy was designed, which could be translated into national biodiversity policies and procedures (BIP, 2010). The Strategic Plan for Biodiversity 2011–2020 included the Aichi Biodiversity Targets, which defined five strategic goals:

A. Address the underlying causes of biodiversity loss by mainstreaming biodiversity across government and society;
B. Reduce the direct pressures on biodiversity and promote sustainable use;
C. Improve the status of biodiversity by safeguarding ecosystems, species, and genetic diversity;
D. Enhance the benefits to all from biodiversity and ecosystem services; and
E. Enhance implementation through participatory planning, knowledge management, and capacity building (CBD, 2020b).

Background image: Blue Marble Next Generation image with topography and bathymetry for April 2004. (Note: the vertical extent of this composite image has been clipped and the aspect ratio changed.) **Source:** NASA. (Retrieved from *https://visibleearth.nasa.gov/collection/1484/blue-marble*)

Figure 19.1 Human population growth

Human population growth since 10,000 BC to present day shows an exponential rate of increase since the industrial revolution.

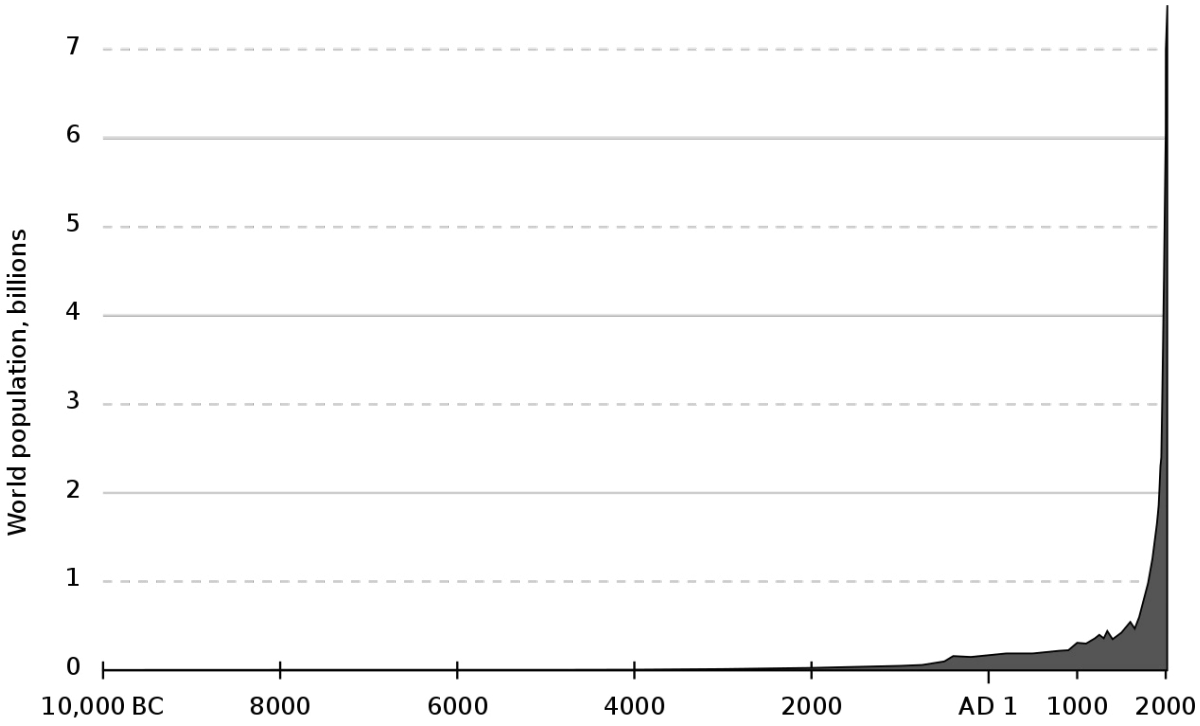

Source: El T, Wikimedia: *https://commons.wikimedia.org/wiki/File:Population_curve.svg*

Within this set of goals, 20 targets (to be achieved by 2020) were outlined based on measurable indicators of progress (CBD, 2020b). Using the CBD framework, National Biodiversity Strategies and Action Plans (NBSAP), which define policies, planning processes, and research agendas to ensure "consideration of the conservation and sustainable use of biological resources into national decision-making", are then developed and implemented by all signature nations. A revised Global Biodiversity Framework is currently being prepared by CBD for post-2020.

The International Union for Conservation of Nature (IUCN) defines six categories for protected areas based on management objectives, which are used as a global standard for defining and recording such regions (IUCN, 2020a):

"Ia Strict Nature Reserve: Category Ia are strictly protected areas set aside to protect biodiversity and also possibly geological/geomorphical features, where human visitation, use and impacts are strictly controlled and limited to ensure protection of the conservation values. Such protected areas can serve as indispensable reference areas for scientific research and monitoring.

Ib Wilderness Area: Category Ib protected areas are usually large unmodified or slightly modified areas, retaining their natural character and influence without permanent or significant human habitation, which are protected and managed so as to preserve their natural condition.

II National Park: Category II protected areas are large natural or near natural areas set aside to protect large-scale ecological processes, along with the complement of species and ecosystems characteristic of the area, which also provide a foundation for environmentally and culturally compatible, spiritual, scientific, educational, recreational, and visitor opportunities.

The human appropriation of Earth's natural resources is not only leading to biodiversity loss but also to large alterations of biodiversity distribution, composition, and abundance.
(Pereira et al., 2012)

III Natural Monument or Feature: Category III protected areas are set aside to protect a specific natural monument, which can be a landform, sea mount, submarine cavern, geological feature such as a cave or even a living feature such as an ancient grove. They are generally quite small protected areas and often have high visitor value.

IV Habitat/Species Management Area: Category IV protected areas aim to protect particular species or habitats and management reflects this priority. Many Category IV protected areas will need regular, active interventions to address the requirements of particular species or to maintain habitats, but this is not a requirement of the category.

V Protected Landscape/ Seascape: A protected area where the interaction of people and nature over time has produced an area of distinct character with significant, ecological, biological, cultural and scenic value: and where safeguarding the integrity of this interaction is vital to protecting and sustaining the area and its associated nature conservation and other values.

VI Protected area with sustainable use of natural resources: Category VI protected areas conserve ecosystems and habitats together with associated cultural values and traditional natural resource management systems. They are generally large, with most of the area in a natural condition, where a proportion is under sustainable natural resource management and where low-level non-industrial use of natural resources compatible with nature conservation is seen as one of the main aims of the area."

Global ecosystem maps are necessary to assess the representation of ecosystems in protected areas. In particular, Sayre *et al.* (2020) derived a global dataset with 250 m spatial resolution to map terrestrial ecosystems by combining climate, landform and vegetation information. Of the 431 identified ecosystems, 278 were described as natural/semi-natural. Using Aichi target 11, which defines adequate representation as 17% of the global ecosystem area being managed for conservation to meet IUCN management categories I–IV (see also Table 3.6), only 19 of the natural/semi-natural ecosystems were adequately represented, 44 were poorly represented (8.5–17% of total area was protected), 206 were very poorly represented (< 8.5%) and 9 were not protected at all. When assessed against IUCN categories 1–VI and including undesignated protected areas, these proportions improved to around one third as adequate, one third as poor and one third as very poor.

In order to monitor biodiversity globally, a set of agreed and appropriate indicators are required "to measure status and trends of biodiversity, sustainable use, threats to biodiversity, ecosystem integrity and ecosystem goods and services, status of knowledge, innovations and practice, and status of resource transfers" (BIP, 2010; see also Section 7.1). Global, EO-based, biodiversity indicators that can be used for standardised monitoring are being developed by the Group for Earth Observations Biodiversity Observation Network (GEOBON; see Section 19.3), which are commonly called 'Essential Biodiversity Variables' (EBV; see Section 11.2).

Standardised criteria for assessing the risk of biodiversity loss (see Section 19.4) are needed to improve the management of biodiversity resources and protect ecosystem services (see Section 20.3). Such criteria have been developed by the IUCN for both species and ecosystems (see Excursus 19.1). Despite the bleak outlook for biodiversity risk around the world, in recent decades biodiversity monitoring has shown that some improvements are being achieved by global, regional and national initiatives to conserve specific habitats, reintroduce threatened species, enforce environmental legislation, and increase public awareness (Pereira *et al.*, 2012).

An overview of Australian biodiversity is presented in Section 19.1 and Australian biodiversity monitoring systems based on EO datasets are described in Section 19.5. Some EO sensors that are appropriate for assessing biodiversity are reviewed in Section 19.2.

An understanding of risks to biodiversity is needed for planning action to slow current rates of decline and secure ecosystem services for future human use.
(Keith et al., 2013)

19.1 Biodiversity in Australia

To date, a diverse range of policies and programs have been implemented by different jurisdictions to manage and conserve biodiversity in Australia (see Section 19.5). The central environmental legislation at a federal level is the Environmental Protection and Biodiversity Conservation Act (EPBC) 1999, which "provides a legal framework to protect and manage nationally and internationally important flora, fauna, ecological communities and heritage places as defined in the EPBC Act as matters of national environmental significance" (DAWE, 2020a).

Biodiversity indicators are used for various environmental reporting exercises, including Australian state and federal State of Environment (SoE) reports. For example, the Victorian SoE 2018 report evaluated that, in that state, 75% of the biodiversity indicators had declined or were not known (SoE, 2018), which is consistent with global trends (IPBES, 2019). Land management practices that have been identified as having the greatest impact on biodiversity in Australia are summarised in Table 19.1.

Natural Resource Management (NRM) is the integrated management of the natural resources that make up Australia's natural landscapes, such as land, water, soil, plants and animals. That is, our land, water and biodiversity assets.
(NRM, 2019)

Table 19.1 Land management practices with ongoing impact on biodiversity in Australia

Land Management Practice	Impacts on biodiversity	Geographic Area
Removing native vegetation Replacing native grasses with improved pasture	Habitat destruction and fragmentation, reduced population sizes, isolation of populations, reduced resilience to other threats, loss of species and diversity, depleted condition and functioning of ecosystems	Ongoing threat to vegetation communities in southeast Queensland and northern NSW, parts of Tasmania and the NT Small scale clearing threatens remnants in all settled areas of Australia
Increasing the intensity of grazing	Habitat depletion and fragmentation, reduced population sizes, isolation of populations, reduced resilience to other threats, loss of species and diversity, depleted condition and functioning of ecosystems	Ongoing pressure across the rangelands, the wheat–sheep zone, and alpine areas, including grazing by livestock, native herbivores, and invasive herbivores
Increasing the intensity of artificial watering points	Habitat destruction, increased competition from invasive species, loss of species and diversity, depleted condition and functioning of ecosystems	Ongoing pressure across much of the rangelands.
Extracting surface and groundwater for irrigation and other uses; Draining wetlands	Depletion of river flows and aquatic habitat, loss of species and diversity, increased vulnerability to invasive species and other threats, depletion of condition, and functioning of aquatic ecosystems	Ongoing threat in all major irrigation areas, especially in the Murray-Darling Basin Groundwater extraction is an ongoing threat to wildlife and natural systems in the Great Artesian basin, southwest Western Australia, and many areas of southern Australia
Converting from livestock to cropping	Habitat destruction and fragmentation, reduced population sizes, isolation of populations, reduced resilience to other threats, loss of species and diversity, depleted condition and functioning of ecosystems, depletion of the condition of aquatic and marine ecosystems	Relatively stable but ongoing threat across the intensive land use wheat–sheep belt of southeastern Australia Ongoing threat to the Great Barrier Reef
Altering natural fire regimes	Depleted composition and structure, reduced resilience to other threats	Australia-wide, but impacts significant in northern savannas and fire-sensitive and fire-dependent communities (e.g. monsoon vine thickets)
Revegetating cleared areas	Increased habitat and reduced fragmentation, increased resilience to other threats	Natural regeneration occurs throughout the country Revegetation programs are primarily implemented in southern Australia Large scale examples aim to link remnants across landscapes.
Reducing the density of livestock	Reduced competition, increased resilience to other threats	Occurs in response to drought throughout grazing lands and in some areas as part of sustainable grazing management programs Newly acquired conservation areas are generally destocked.

Source: DEWHA (2009) Table 5.5

Table 19.2 Biodiversity in Australia's terrestrial vegetation

Key finding	Description
Native vegetation is a key surrogate for biodiversity	Native vegetation is a cost-effective and powerful surrogate for biodiversity. The distribution of threatened species and communities is closely aligned with areas where native vegetation has been extensively cleared.
The extent of native vegetation is known	National mapping of native vegetation has advanced significantly since 2002 with improvements in data and in mapping technologies (e.g. through NVIS). Although important gaps remain (in scale, and in defining some major vegetation groups such as derived native grasslands), we now know the extent of most major vegetation types in the landscape.
Native vegetation has been modified or cleared	Native vegetation has been modified and cleared since European settlement, especially from intensive agricultural and urban areas (particularly in southern and eastern Australia and in southwestern Australia). The losses have been greatest in eucalypt woodlands and have also been significant in eucalypt open forest and mallee woodlands and shrublands. The loss of biota in the cleared and modified areas has been dramatic and continues today (e.g. in woodland birds).
Native vegetation is being lost faster than it is replaced	Broadscale clearing has been reducing since 2002, however nationally, native vegetation is still being cleared and modified faster than it is replaced. A net loss of forest (including native and non-native vegetation) of around 260,000 ha per year occurred between 2000 and 2004 and was primarily attributed to clearing for agriculture and urban development.
We are making progress towards assessing native vegetation condition	Since 2002, there has been progress in the collaboration between national, state, and territory jurisdictions in improving Australia's vegetation information. This includes approaches to modelling, monitoring, and mapping vegetation condition, on both national and more localised scales. Reference-based methodologies are being used in most states for target setting, investment and planning decisions, and reporting.

Source: DEWHA (2009) Table 2

Measures of biodiversity are introduced in Section 7.1. The major indicators for biodiversity assessment in terrestrial ecosystems in Australia are defined as:

- native vegetation extent and distribution;
- changes in native vegetation extent and distribution; and the
- status and trends of native vegetation condition (DEWHA, 2009; see Table 19.2).

Mapping of native vegetation, an effective indicator of biodiversity, has improved in recent decades with systems like NVIS (see Section 2.3.1), although information gaps remain. The available data indicates that native vegetation still grows on 87% of the Australian continent (DEWHA, 2009), however 62% of this area is likely to be modified (Thackway and Lesslie, 2006). Not surprisingly, the greater concentrations of threatened species occur in the eastern, southern and southwestern coastal fringes where population densities are highest.

In order to conserve biodiversity in Australia, a network of conservation parks and reserves has been coordinated by the National Reserve System (NRS) to meet the IUCN principles of 'comprehensiveness, adequacy and representativeness' (CAR):

- comprehensiveness—samples the full range of regional ecosystems recognisable at an appropriate scale within each IBRA bioregion;
- adequacy—at a bioregional scale, consider ecological viability and resilience for each reserve and the reserve system; and
- representativeness—sample regional variability (IBRA sub-region; DEWHA, 2009).

In 2006, 11.6% of the Australian land mass was officially reserved, however, while 49 bioregions satisfied the goals of ≥ 10% representation in reserves, 36 did not (DEWHA, 2009). Although the NRS is a collaborative undertaking between state and federal jurisdictions to provide linked refuges across the landscape, differing priorities and progress towards CAR persist both within and between jurisdictions.

Conservation reserves alone cannot protect the biodiversity of a region. Even if 10% of every ecosystem could be included, which is highly unlikely, in the protected area network, most species would not be included. Any conservation reserve system will fail if the broader land use management practices ignore the conservation of biodiversity in off-reserve areas.
(Tony Brandis, from 'Rescuing the Rangelands')

19.2 EO Sensors for Biodiversity

Passive optical satellite imagery provides the overwhelming majority of EO information to inform biodiversity decision making and legislative instruments, such as mapping and monitoring of land cover, land use, biophysical vegetation properties, and vegetation extent (see Sections 3, 8, and 9). This data source is now available at a range of spatial scales, from pixels spanning centimetres to kilometres, with data archives dating back many decades (see Volume 1A—Section 14). Many of these archives have been calibrated and standardised for ease of use, and reprocessed into a variety of composite image datasets with relevance to biodiversity (see Volume 2D).

Other sources of EO datasets that are relevant to mapping and monitoring biodiversity are summarised in Table 19.3. A growing variety of ground-based sensors are also being utilised to collect *in situ* and near ground data (see Volume 2D—Section 12).

> *Changes in and the loss of biodiversity directly influences the capacity of an ecosystem to produce and supply essential services, and can affect the long term ability of ecological, economic and social systems to adapt and respond to global pressures. (DEWHA, 2010)*

Table 19.3 EO sensors relevant to biodiversity

TIR: Thermal infrared; SAR: Synthetic Aperture Radar; RPAS: Remotely Piloted Aircraft Systems; ET: Evapotranspiration

Type	Sensor	Platform	Relevance	Advantages	Disadvantages
Passive optical	Multispectral radiometer	Predominantly satellite, decreasingly airborne	Local to national scale	Global, recurrent coverage, high temporal frequency and extent, low cost, significant calibration/validation efforts established, many operational processing methods	Some low spatial resolution datasets are not appropriate for detailed studies
	Hyperspectral spectro-radiometer	Predominantly airborne	Species discrimination Plant biochemical functioning and health	High spectral resolution	High cost, high data volume, lower signal to noise ratio, greater processing complexity
	TIR radiometer	Field, satellite or airborne	Soil/canopy temperature	Surrogate measure for ET plus input into EO modelling	Low resolution, low signal to noise ratio
Active optical	Lidar	Predominantly airborne, increasingly terrestrial, emerging satellite	Vegetation structure, volume, and biomass Water balance applications DEM	Highlights detailed structure of plant canopy and soil surface	High cost, specialised processing, longer acquisition times
	Active optical sensor	Ground vehicles or RPAS	Cover and condition mapping Specific property recognition (e.g. disease, optical properties of water)	Convenience, low cost, independent of sunlight	Low availability and limited surface coverage
Passive microwave	Microwave radiometer	Satellite	Soil moisture Climate variables	High temporal frequency, large spatial coverage, cloud penetration	Very low energy targets, very coarse spatial resolution
Active microwave	SAR	Satellite or airborne	Soil characteristics Vegetation structure Water dynamics	All weather, operates at night	Data availability, noisy data, complex processing
Proximal	Passive optical sensor (phenocam, hyperspectral); meteorological	Ground and tower-based (see Excursus 7.2 and Volume 2D—Section 12)	Ecosystem and atmospheric variability Carbon dynamics Phenology	Continuous, long term measurements	High cost, high data volume, require skilled maintenance
Positioning	GPS	Portable devices linked to satellite-based positioning systems	Locating field sites for cal/val	Low cost	Coverage in remote regions or below dense canopies
Citizen Science	Portable, hand-held r	Ground-based	Validation of species occurrence and major phenological events	Low cost, public involvement	Potentially subjective

19.3 Global Biodiversity Indicators

While we are acutely aware of the alarming rate of biodiversity loss worldwide, it is a challenge to quantify the status of global biodiversity change using an approach that is consistent over space and time. There has been considerable debate on the topic of measuring and monitoring biodiversity at a global scale (e.g. EASAC, 2004; Teillard *et al.*, 2016; OECD, 2020). Various sets of global biodiversity indicators have been proposed (BIP, 2019), but many accepted measures, such as the Living Planet Index (LPI; WWF, 1998), have been assessed as failing "to fulfill fundamental scientific requirements" (Böhringer and Jochem, 2007).

One framework that has been proposed to identify and classify appropriate indicators for consistent biodiversity monitoring and evaluation at regional and global scales is the response-pressure-state-benefit framework (Sparks *et al.*, 2011; see Figure 19.2), where the linkages between indicators show the interaction of relevant factors in biodiversity loss (see also Figure 11.2). The function of each indicator is summarised in Table 19.4. This framework underpins the biodiversity monitoring program being implemented in NSW (see Section 19.5).

Major gaps and uncertainties currently exist within the survey data records that are available to monitor global biodiversity (Pereira *et al.*, 2012). There are also significant variations between and within national and regional monitoring programmes. Coupled with insufficient financial resources and a lack of consensus on reliable, scalable biodiversity indicators, these factors have thwarted implementation of an operational 'global system of harmonised observations' (Pereira *et al.*, 2013). However, EO offers considerable potential for both direct and indirect assessment of biodiversity (Gillespie *et al.*, 2008) and conservation planning (Rose *et al.*, 2014) at regional to global scales, particularly with the advent of high spatial resolution, spaceborne sensors.

If you can't measure it, you can't manage it.
(Peter Drucker)

Figure 19.2 Response-pressure-state-benefit (RPSB) framework

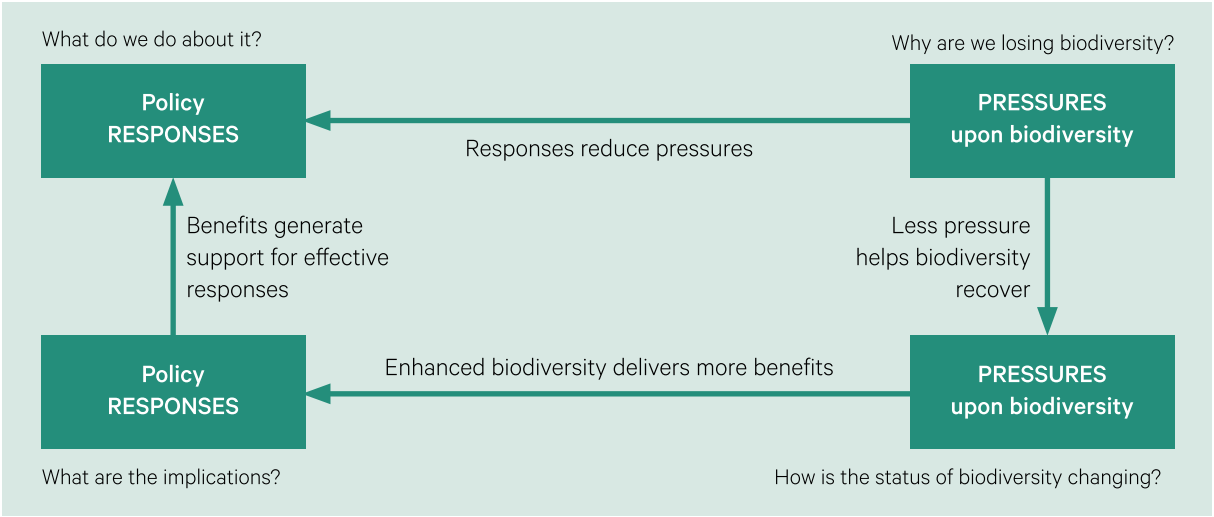

Adapted from: Sparks *et al.* (2011)

Thus it happens in affairs of state, for when the evils that arise have been foreseen (which it is only given to a wise man to see), they can be quickly redressed, but when, through not having been foreseen, they have been permitted to grow in a way that every one can see them, there is no longer a remedy.
(Machiavelli, from 'The Prince', 1513)

Since raw biodiversity data is typically sparse and heterogeneous, using EO data as covariates with appropriate modelling tools allows the available raw data to be sensibly interpolated both spatially and temporally (Jetz *et al.*, 2019; see Volume 2D). Progress towards a globally-accepted, EO-based set of indicators is being achieved by GEOBON. This international initative of GEO (Group for Earth Observations, a voluntary intergovernmental partnership; see Volume 1A—Section 1.5) aims to "improve the acquisition, coordination and delivery of biodiversity observations and related services to users including decision makers and the scientific community" and establish an integrated, global network to observe biodiversity in a timely and consistent fashion at a range of scales. This network will help to assess progress towards the CBD Strategic Plan and Aichi Targets (GEOBON, 2020; Walters and Scholes, 2017).

A major focus for GEOBON is defining a set of EBV that can be measured and modelled globally, preferably by integrating EO datasets with *in situ* observations (Pereira *et al.*, 2013; GEOBON, 2020; Masó *et al.*, 2020; see Section 11.2), where an ideal EBV is defined as:

- "able to capture critical scales and dimensions of biodiversity;
- biological;
- a state variable (in general);
- sensitive to change;
- ecosystem agnostic (to the degree possible); and
- technically feasible, economically viable and sustainable in time" (GEOBON, 2020).

Table 19.4 RPSB indicators

Indicator	Function	Example
Response	Measure implementation of policies or actions aimed to prevent or reduce biodiversity loss	Conservation actions including offsets
Pressure	Measure the extent and intensity of the threats to or causes of biodiversity loss	Certain land uses
State	Measure the current condition and status of biodiversity or ecological integrity	Status of threatened species or condition of suitable habitats
Benefit	Quantify the benefits that humans derive from biodiversity	Ecosystem services

Source: Sparks *et al.* (2011); OEH and CSIRO (2019)

The current set of EBV classes and candidates are listed in Table 19.5. Primary observations from *in situ* monitoring and EO systems are preprocessed and combined into EBVs, which represent an intermediate data layer for harmonisation between sampling protocols and measurement systems (see Figure 11.3). All EBV classes should be included in a biodiversity monitoring program. EBVs inform multiple biodiversity and ecosystem service indicators, such as those needed to assess the Aichi Biodiversity targets. Some indicators require the integration of EBVs with other sources of information such as data on ancillary biodiversity attributes (slowly changing variables), drivers and pressures, management and policy responses, and valuation and demand of ecosystem services. Future projections of drivers and policy responses can be used to develop scenarios for biodiversity and ecosystem services using models calibrated and validated with EBVs (Pereira *et al.*, 2013). Further integration between these EBV and appropriate models and infrastructure will support assessment at a range of scales for both policy and research purposes.

Table 19.5 EBV classes and candidates

EBV class	EBV candidate
Genetic composition	Co-ancestry Allelic diversity Population genetic differentiation Breed and variety diversity
Species populations	Species distribution Population abundance Population structure by age/size class
Species traits	Phenology Morphology Reproduction Physiology Movement
Community composition	Taxonomic diversity Species interactions
Ecosystem function	Net primary productivity Secondary productivity Nutrient retention Disturbance regime
Ecosystem structure	Habitat structure Ecosystem extent and fragmentation Ecosystem composition by functional type

Source: GEOBON (2020)

19.4 Risk Assessment

As introduced above, global biodiversity is declining dramatically, especially since the start of the industrial age. These changes include both loss and alteration of biodiversity, in differing proportions (see Figure 19.3). In Australia, one example of this decline is the current extent of Brigalow communities (*Acacia harpophylla* dominant and co-dominant) which before pastoral settlement covered 10.2 million ha in southeast Queensland (Neldner, 2018)[16]. By 1940, the extent of brigalow had been reduced to less than 8.5 million ha, and by 1970 it covered half this area (Accad and Neldner, 2015). Various social and political factors contributed to the significant decline for this vegetation group, including subsided ringbarking during the Great Depression and mechanical and chemical clearing following World War 2 (Seabrook *et al.*, 2006). Brigalow now covers only 1.3 million ha and is an EPBC-listed Endangered Ecological Community (Neldner *et al.*, 2017).

The IUCN Red List of Ecosystems (RLE) defines criteria for assessing declining ecosystem biodiversity at a global scale (see Excursus 19.1). These criteria satisfy the IUCN design goals of generality, precision, realism and simplicity (Keith *et al.*, 2015) and have been applied to a wide range of ecosystems around the world. RLE has been used to assess ecosystem risk in Australia for a range of ecosystem types (Keith, 2015), including Alpine herbfields (Williams *et al.*, 2015), lowland rainforests (Metcalfe and Lawson, 2015), forests (Burns *et al.*, 2015; Auld and Leishman, 2015), woodlands (Tozer *et al.*, 2015; Wardle *et al.*, 2015), and wetlands (Pisanu *et al.*, 2015). While widespread, these individual case studies do not satisfactorily represent the status of Australian ecosystems. Keith (2015) recommends a comprehensive risk assessment approach comprising:

- a systematic and consistent framework for assessment and scaling with precise differentiation of ecosystems—current typologies for terrestrial vegetation are not consistent with IUCN RLE;
- high to medium resolution spatial data showing ecosystem distribution—EO time series datasets are invaluable here, together with other spatial data (see Volume 2D);
- long term ecological monitoring for assessing and managing ecosystems—such as the TERN Long Term Ecological Research Network (LTERN; see Section 19.6); and
- cross-disciplinary collaboration and cooperation.

Figure 19.3 Biodiversity change in terms of loss and alterations

Loss of biodiversity includes both species extinctions and loss of genetic diversity, while alteration of biodiversity includes changes in species composition and relative abundance, changes in community structure, and changes in species range or extent.

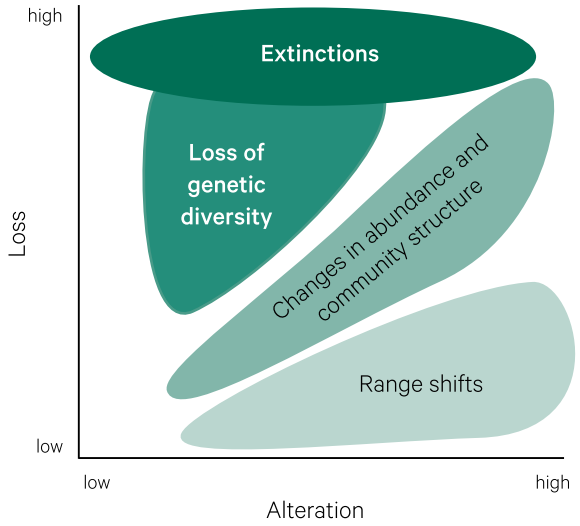

Adapted from: Pereira *et al.* (2012) Figure 1

Many data sources are relevant for ecosystem risk assessment, including those from short and long term monitoring programs, field surveys, and underwater, aerial and satellite sensors. Of these, satellite remote sensing offers the greatest opportunity to evaluate ecosystem change beyond the site level and to scale the risk assessment process to provincial, national and continental jurisdictions.
(Murray et al., 2018a)

16 *http://www.environment.gov.au/cgi-bin/sprat/public/publicshowcommunity.pl?id=28&status=Endangered*

EO datasets are being used increasingly to assess risks to biodiversity, ideally with sufficient spatial and temporal resolutions to represent ecosystem dynamics and detect rapid change. Some of the environmental variables that can be monitored using EO include area loss, biomass change, and disease stress, which can subsequently be used to estimate the spatial extent of biotic and abiotic degradation. EO time series can also be analysed to derive disturbance histories that could further inform forecasts of degradation (Murray *et al.*, 2018a). Appropriate EO data and methods need to be selected for such assessments and repeated as new data become available. For example, Figure 19.4 summarises a framework for using EO datasets to list ecosystems in the RLE:

- evaluate the risk assessment protocol and define assessment unit (01–02);
- develop conceptual ecosystem model and identify indicator variables to monitor with EO (03–06);
- incorporate field data and ecosystem models;
- evaluate ecosystem against risk assessment criteria (07–09);
- summarise and review results (10–12); and
- formally list ecosystem in RLE (13).

An online mapping platform, remap (Remote Ecosystem Assessment and Monitoring Pipeline; Murray *et al.*, 2018b), enables ecosystem status maps to be generated rapidly from freely available EO imagery and other spatial datasets (remap, 2020). This tool is designed for users without specialist knowledge of EO and relies on machine learning algorithms (see Volume 2E) to generate RLE-compatible assessments of ecosystems.

There are risks and costs in a program of action, but they are far less than the long range risks and costs of comfortable inaction.
(John F. Kennedy)

Figure 19.4 EO framework for ecosystem risk assessment

Source: Murray *et al.* (2018a) Figure 2

Excursus 19.1—IUCN Red Lists of Threatened Species and Ecosystems

Source: Keith *et al.* (2013); Rodríguez *et al.* (2015)
Further information: IUCN Red List of Threatened Species: *https://www.iucnredlist.org/*
IUCN Red List of Ecosystems: *https://www.iucn.org/theme/ecosystem-management/our-work/red-list-ecosystems*
IUCN-CEM (2016); Bland *et al.* (2016)
IUCN–CEM Research and development: *https://iucnrle.org/resources/research-development/*

The International Union of Conservation of Nature (IUCN) was established in 1948 to examine the impact of anthropogenic activities on nature. Since its inception it has expanded into a democratic union of 1,400 government and civil organisations around the world, with access to expertise in a wide variety of disciplines related to natural resources. The IUCN has contributed to numerous international conventions, strategies and agreements that address global challenges to conserve nature and achieve sustainable and equitable use of its resources (IUCN, 2020a).

Two of its global achievements are the Red List of Threatened Species and the Red List of Ecosystems.

IUCN Red List of Threatened Species

The IUCN Red List of Threatened Species "provides information about range, population size, habitat and ecology, use and/or trade, threats, and conservation actions that will help inform necessary conservation decisions" (IUCN, 2020b). This list has become the most comprehensive source of information relating to extinction risk status of 116,000 animal, plant, and fungal species globally and is used by a wide range of agencies with interests in land management, education, business, and nature conservation. Its ongoing assessments enable the status of listed species to be monitored and new species to be included with a target of assessing an additional 44,000 species in 2020 (IUCN, 2020b). By 2020, 31,000 species were listed as threatened with extinction (IUCN, 2020c), representing over a quarter of those assessed.

IUCN Red List of Ecosystems (RLE)

In recognition that the ecosystems have changed more rapidly since 1950 due to human impact, a new conservation policy tool was developed by the IUCN to assess the risk of ecosystem collapse. The resulting global standard is called the Red List of Ecosystems Categories and Criteria (RLE) and was accepted by the IUCN in 2014 for application at local, national, regional, and global scales (IUCN-CEM, 2020). All freshwater, marine, terrestrial, and subterranean ecosystem types of the world at a global level are planned for assessment using RLE by 2025, with periodic updates to monitor progress towards international targets, such as the Aichi Targets (CBD, 2010) or Sustainable Development Goals (UN General Assembly, 2012; see Excursus 20.2).

RLE is a generic method that can be used to assess terrestrial, subterranean, inland and marine waters, and transitional environments. RLE determines ecosystem status in three broad divisions of eight categories:

- least concern—not currently facing significant risk of collapse;
- threatened—critically endangered, endangered or vulnerable; or
- collapse—endpoint of ecosystem decline, "when most of the diagnostic components of the characteristic biota are lost from the system, or when functional components (biota that perform key roles in ecosystem organisation) are greatly reduced in abundance and lose the ability to recruit. Chronic changes in nutrient cycling, disturbance regimes, connectivity, or other ecological processes (biotic or abiotic) that sustain the characteristic biota may also signal ecosystem collapse" (Keith *et al.*, 2013; see Figure 19.5a).

In this context, an ecosystem comprises four essential elements:

i. a biotic complex or assemblage of species;
ii. an associated abiotic environment or complex;
iii. the interactions within and between those complexes; and
iv. a physical space in which these operate (Tansley, 1935).

'Ecosystem type' is considered to be synonymous with the terms 'ecological community', 'habitat', and 'vegetation type' (Keith *et al.*, 2013). Nicholson *et al.* (2015) review terms used in ecosystem risk assessment.

Figure 19.5 RLE categories and criteria and categories

a. RLE risk categories

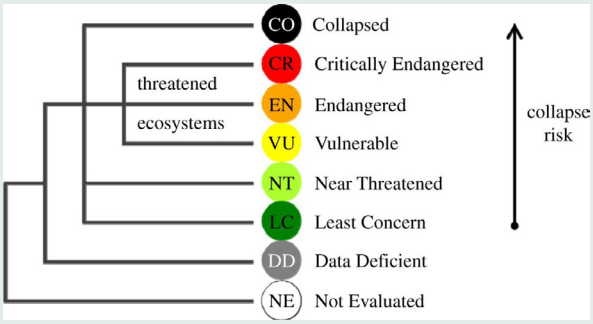

b. Mechanisms of ecosystem collapse and symptoms of collapse risk

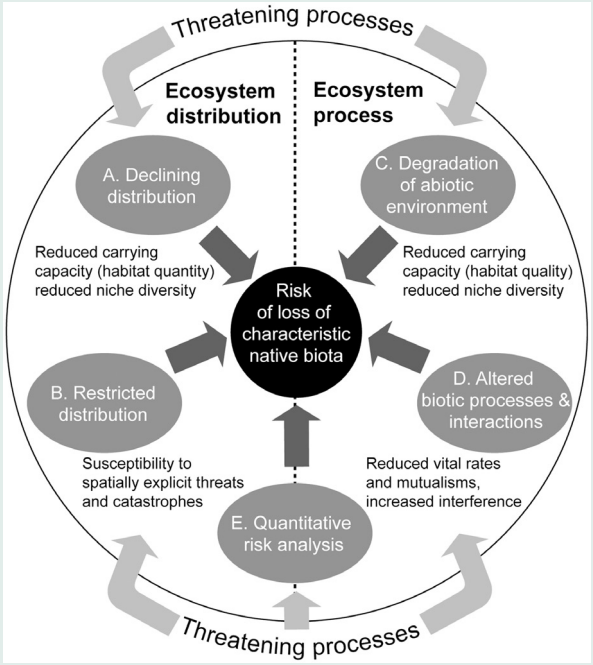

Source: a. Keith *et al.*, (2013) Figure 2; b. Rodríguez *et al.* (2015) Figure 2

The underlying conceptual model identifies four distributional and functional symptoms of ecosystem risk as the basis for assessment criteria:

- Criterion A: rates of decline in ecosystem distribution—identify each ecosystem type that is currently declining in extent or may decline in the near future using at least two measures of its distribution taken at different points in time and calibrated to the timescales of RLE assessments;
- Criterion B: restricted distributions with continuing declines or threats—evaluate the risk of loss of all occurrences of an ecosystem type by considering the interaction between the spatial extent of threats and the spatial distribution of ecosystem occurrences;
- Criterion C: rates of environmental (abiotic) degradation—evaluate the risk of collapse posed by degradation of the abiotic environment by measuring an appropriate abiotic variable; and
- Criterion D: rates of disruption to biotic processes—evaluate the risk of collapse posed by degradation of the biotic environment by measuring an appropriate biotic variable.

Criterion E is a quantitative estimate of the risk of ecosystem collapse, which enables integrated assessment of multiple processes and provides a conceptual anchor for the other criteria (Keith *et al.*, 2013; see Figure 19.5b). This criterion relies on specific process-based ecosystem models to estimate risk of collapse over a 50 or 100 year timeframe. Criteria A, C, and D assess ecosystem decline over three timeframes:

- current—preceding 50 years;
- future—next 50 years; and
- past—relative to the reference years 1750, which is assumed to be the onset of industrial exploitation of the environment (see Figure 19.6b and Section 3.3.1).

The steps followed to apply the RLE are summarised in Figure 19.6c. In 2018, 1,397 ecosystem units in 100 countries had been assessed following the IUCN RLE protocol (Bland *et al.*, 2018). This approach has been used to assess ecosystem risk in Australia for a range of ecosystem types (Keith *et al.*, 2015; see Section 19.4).

Figure 19.6 Application of RLE

AOO: area of occupancy; EOO: extent of occurrence.

a. Sequence for assessment protocol

<table>
<tr><td colspan="5">Describe ecosystem
(characteristic biota, abiota, interactions, location, and spatiotemporal/thematic scale)</td></tr>
<tr><td colspan="2" rowspan="2">Identify approprate measure of distribution
(maps, sightings)</td><td colspan="3">Describe salient mechanisms of ecosystem dynamics and function
(process model)</td></tr>
<tr><td>Identify appropriate measure of distribution
(maps, sightings)</td><td>Identify appropriate measure of biotic interaction</td><td>Model ecosystem dynamics</td></tr>
<tr><td>Assess rate of change
Criterion A</td><td>Assess current extent
Criterion B</td><td>Assess rate of substrate degradation
Criterion C</td><td>Assess rate of disruption of interactions
Criterion D</td><td>Assess risk of collapse
Criterion E</td></tr>
<tr><td>A1: present
A2: future
A3: historic</td><td>B1: EOO
B2: AOO
B3: locations
and for B1 and B2:
i. Continuing decline
ii. Threats (e.g. fragmentation)
iii. Number of locations</td><td>C1: present
C2: future
C3: historic</td><td>D1: present
D2: future
D3: historic</td><td></td></tr>
</table>

b. Timescales for assessment of change under criteria A, C,and D. Historic declines are relative to the reference date of 1750.

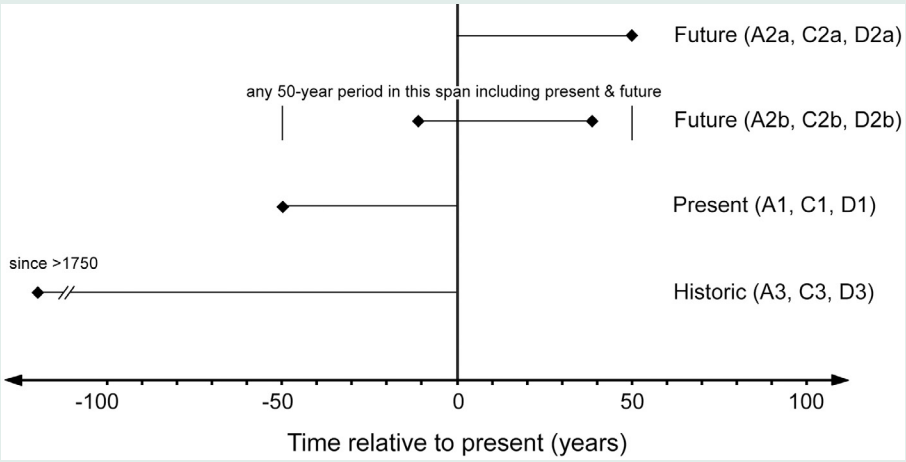

c. Summary of assessment steps.

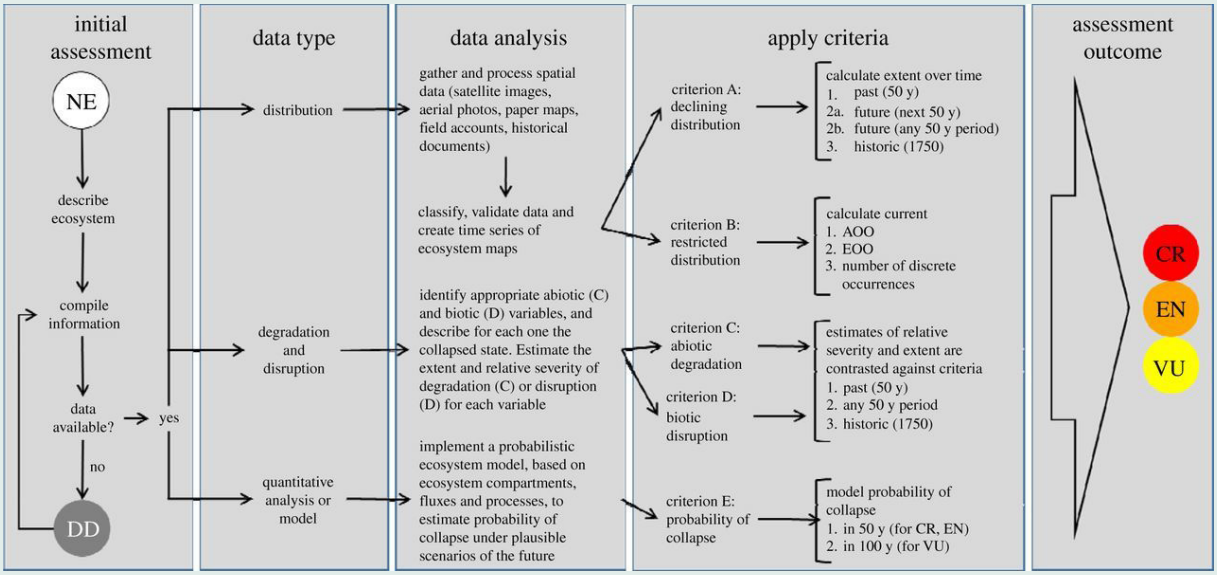

Source: a. Keith *et al.* (2013) Figure 3; b. Keith *et al.* (2013) Figure 4; c. Rodríguez *et al.* (2015) Figure 3

19.5 Australian Biodiversity Monitoring

The two most significant issues impacting biodiversity management at a national level in Australia have been identified as the lack of systematic monitoring, and limitations in resources available to respond to threats (DEWHA, 2010). Inconsistencies occur both within and between jurisdictions in terms of legislation and regulation related to biodiversity. There is also a trend toward increased private land biodiversity conservation (DEWHA, 2009), such as the Australian Wildlife Conservancy (see Section 20.5). Policy tools that could be used to promote natural resource management and biodiversity conservation in Australia are summarised in Table 19.6.

The Australian Biodiversity Conservation Strategy (ABCS) 2010–2030 (CoA, 2014) identified ten national targets based on the CBD Strategic Plan for Biodiversity 2011–2020 template (see Table 19.7). Progress on the Aichi targets from 2014 to 2018 is reviewed in CoA (2020). The Australian national strategy was updated in 2019 as *Australia's Strategy for Nature 2019–2030* (DAWE, 2020b) to coordinate other federal, state, and territory initiatives in this area, in both the public and private sectors. This strategy includes a dedicated website listing relevant projects, Australia's Nature Hub (see Section 19.6), and rests on three priorities:

- connect all Australians with nature;
- care for nature in all its diversity; and
- share and build knowledge (DAWE, 2020b).

In parallel, the Global Strategy for Plant Conservation (GSPC; also managed by CBD) includes 16 global targets for 2020 (CBD, 2020c). ABCS targets 1, 2, 4, 5, 6 and 7 relate to the GSPC.

Table 19.6 Policy tools

Tool	Options	Example
Suasion	Education	Information to landholders
	Promotion of best practice	Extension programs
	Grants	Community assets
Regulation	Restrictions	Land use planning, compliance monitoring
	Taxes	Carbon tax
Market-based	Pricing	EcoTendors, rebates, LGA rates, revolving funds,
	Quantity regulation	Cap and trade schemes, offsets
	Market friction	Environmental labelling, eco certification

Source: DEWHA (2010)

Under the NSW Biodiversity and Conservation Act 2016, state-wide biodiversity is being assessed using a suite of indicators 'to measure different aspects of biodiversity and ecological integrity' as part of the Biodiversity Indicator program (DPIE, 2020a). The NSW Environmental Monitoring and Assessment and Reporting (eMAR) Framework is used with the RPSB framework as the basis for selecting indicators and grouping them into functional themes (Sparks *et al.*, 2011; see Figure 19.2 and Table 19.8). For terrestrial species and ecosystems, biodiversity indicators are mostly derived from EO datasets and environmental models (OEH and CSIRO, 2019) and supported by *in situ* and related data (such as NSW BioNet; see Section 19.6). The first assessment from this program concluded that in 2013 relative to the reference year of 1750:

- 79–91% of the original, within-species, plant genetic diversity still existed;
- the original habitat effectiveness for supporting native species had reduced to one third; and
- half of the species rated as 'threatened' were likely to be extinct in another century without effective management (DPIE, 2020b).

To retain existing biodiversity within the Australian landscape, several state governments have legislated to limit the area of land that can be cleared of native vegetation. Compliance monitoring for such legislation now relies on EO datasets (see Volume 2D—Section 14.2.2). One operational system for detecting changes in woody vegetation is the Statewide Landcover and Trees Study (SLATS; see Section 9.1 and Volume 2D—Excursus 14.3). An EO-based, hierarchical framework for monitoring biodiversity in rangelands is described in Section 15.5 (Eyre *et al.* 2011; see Excursus 15.2), and floral and faunal components of forest diversity are considered in Section 16.7.

Other approaches for assessing vegetation condition compare current vegetation characteristics with a benchmark representing a mature and long undisturbed state. The benchmark that has been adopted for Australia is the estimated condition of vegetation in 1750, prior to European settlement and industrialisation (see Section 3.1.1). One benchmark-based method that assesses 'vegetation quality' using EO datasets is the Victorian model of Vegetation Quality Assessment (VQA; formerly known as Habitat Hectares), which is described in Excursus 19.2.

Table 19.7 Australian Biodiversity Conservation Strategy 2010–2030 Targets

ABCS Target Number	Target for 2015	Maps to Aichi Targets
1	Achieve a 25% increase in the number of Australians and public and private organisations who participate in biodiversity conservation activities	1, 2, 4, 17
2	Achieve a 25% increase in employment and participation of Indigenous peoples in biodiversity conservation	2, 14, 18
3	Achieve a doubling of the value of complementary markets for ecosystem service	3
4	Achieve a national increase of 600,000 km^2 of native habitat managed primarily for biodiversity conservation across terrestrial, aquatic, and marine environments	5, 7, 11
5	1,000 km^2 of fragmented landscapes and aquatic systems are being restored to improve ecological connectivity	5, 7, 11, 14, 15
6	Four collaborative continental scale linkages are established and managed to improve ecological connectivity	5, 11, 14, 15
7	Reduce by at least 10% the impacts of invasive species on threatened species and ecological communities in terrestrial, aquatic, and marine environments	9, 10, 12
8	Nationally agreed science and knowledge priorities for biodiversity conservation are guiding research activities	18, 19
9	All jurisdictions will review relevant legislation, policies and programs to maximise alignment with Australia's Biodiversity Conservation Strategy	2, 4, 17
10	Establish a national long term biodiversity monitoring and reporting system	2, 19

Source: CoA (2014)

Table 19.8 NSW Biodiversity Indicator Program

Tool	Theme	Indicator family
Biodiversity	Expected survival of biodiversity	Listed threatened species and ecological communities
		All known and undiscovered species
	State of biodiversity	All known species
		State of biodiversity including undiscovered species
		Field monitoring of species and ecosystems
Ecological integrity	Ecosystem quality	Habitat condition
		Pressures
	Ecosystem management	Management responses
		Management effectiveness
		Capacity to sustain ecosystem quality
	Ecosystem integrity	Capacity to retain biological diversity
		Capacity to retain ecological functions

Source: OEH and CSIRO (2019)

The Habitat Condition Assessment System (HCAS) is being developed to provide a nationally consistent coverage of biodiversity habitat condition in Australia (Donohue *et al.*, 2013; Harwood *et al.*, 2016), where habitat condition is defined as "the condition of terrestrial areas in terms of their predicted capacity to support the wildlife expected there under natural conditions" (CSIRO, 2019). This system combines EO and environmental datasets with reference site data and spatial ecological modelling to estimate habitat condition at 250 m resolution across terrestrial Australia.

Many of the mechanisms and symptoms of species vulnerability are relevant to ecosystems, because species are integral parts of ecosystems. Yet ecosystems embody processes and higher-order components of biodiversity that are difficult or impossible to account for in species-by-species assessment. Whereas species risk assessment rests on population theory, ecosystem risk assessment must draw from a wider array of inter-related theories that deal with continua, niches, fractal geometry, succession, resilience, ecological integrity, biodiversity-ecosystem function and insurance, as well as population theory. The success of ecosystem risk assessment therefore rests on a robust synthesis of conservation planning and process ecology to translate theoretical foundations into a practical assessment protocol that can be applied to a wide variety of ecosystems by specialist assessors with differing backgrounds and limited data.
(Keith et al., 2013)

Excursus 19.2—Vegetation Quality Assessment

Source: Parkes *et al.* (2003), DELWP (2017)
Further Information: DSE (2004): *https://www.environment.vic.gov.au/__data/assets/pdf_file/0016/91150/Vegetation-Quality-Assessment-Manual-Version-1.3.pdf*

To effectively manage native vegetation, information is needed about the:

- vegetation type;
- previous and current ecological processes that shape that vegetation type;
- function of that vegetation type in the local landscape; and
- effectiveness of that function (Parkes *et al.*, 2003).

The Vegetation Quality Assessment (VQA; formerly Habitat Hectares) method has been used across Victoria for over a decade. VQA determines the condition of current vegetation by comparing the existing vegetation features with those of a defined bioregional benchmark that represents "the *average characteristics* of a mature and apparently long-undisturbed stand of the *same* community type" (Parkes *et al.*, 2003). Design characteristics of this method include consistency, objectivity, simplicity, and efficiency across a wide range of vegetation communities. Results from this method also need to be easily communicated to land owners.

Vegetation mapping in Victoria delineates 28 bioregions—landscape scale categories comparable to ecoregions (see Section 2.4). Vegetation characteristics are represented by Ecological Vegetation Classes (EVC), a hierarchical classification that aggregates floristic communities ("defined by a combination of floristics, life form, position in landscape and an inferred fidelity to a particular environment"; DSE, 2004). For VQA, benchmarks relate to a single EVC in one bioregion. Details of field assessment for this method are provided in DSE (2004).

The final score derived for a site combines assessment of 'site condition' (largely determined by field work) and 'landscape context' (best calculated using GIS) components (see Table 19.9). The final habitat score is the sum of all scores from each site converted from a percent to a decimal, while the final Habitat Hectare score is the product of the decimal habitat score (quality) and the area of vegetation (quantity).

Given the broad categories defined by VQA, this method is not used to quantify change over time. However, the information from 17,000 VQA sites has been extrapolated using EO and other spatial datasets to create a regional scale map showing the condition of native vegetation across Victoria (DSE, 2004; DELWP, 2017).

Table 19.9 VQA scoring

Criteria	Component	Score
Site Condition (derived from field assessment)	Large trees	10
	Tree canopy cover	5
	Understorey	25
	Lack of weeds	15
	Recruitment	10
	Organic litter	5
	Logs	5
Landscape Context (derived from spatial datasets)	Patch size	10
	Neighbourhood	10
	Distance to core area	5
	Total	100

Source: DSE (2004)

Essentially, this method ('habitat hectares') attempts to assess how 'natural' a site is by comparing it to the same vegetation type in the absence of major ecosystem changes that have occurred following European settlement of Australia.
(Parkes et al., 2003)

19.6 Further Information

IUCN Red Lists

IUCN Red List of Threatened Species: *https://www.iucnredlist.org/*

IUCN Red List of Ecosystems: *https://www.iucn.org/theme/ecosystem-management/our-work/red-list-ecosystems*

IUCN-CEM (2016)

IUCN–CEM Research and development: *https://iucnrle.org/resources/research-development/*

Australian Biodiversity Policies and Programs

Review of the EPBC Act: *https://epbcactreview.environment.gov.au/*

National Environmental Science Program: *https://www.environment.gov.au/science/nesp/about*

Biodiversity Information for Australia

Australia's Nature Hub: *https://www.australiasnaturehub.gov.au/*

Department of Agriculture, Water and the Environment: *http://www.environment.gov.au/biodiversity*

Collaborative Australian Protected Area Database: *http://www.environment.gov.au/land/nrs/science/capad*

Common Assessment Method: *https://www.environment.gov.au/biodiversity/threatened/cam*

Australia State of the Environment 2016: *https://soe.environment.gov.au/*

Australia State of the Environment 2016—Biodiversity: *https://soe.environment.gov.au/sites/default/files/soe2016-biodiversity-launch-version2-24feb17.pdf?v=1488792935*

Australian Biological Resources Study: *https://www.environment.gov.au/science/abrs*

Australia's State of the Forest report: *http://www.agriculture.gov.au/abares/forestsaustralia/sofr/sofr-2018*

Atlas of Living Australia: *https://www.ala.org.au/*

Australasian Virtual Herbarium: *https://avh.chah.org.au/*

Terrestrial Ecosystem Research Network (TERN): *https://www.tern.org.au/*

LTERN: *https://www.ltern.org.au/*

Australian Wildlife Conservancy: *https://www.australianwildlife.org/*

Operational Biodiversity Monitoring

New South Wales:

BioNet: *https://www.environment.nsw.gov.au/topics/animals-and-plants/biodiversity/biodiversity-indicator-program*

Victoria:

Habitat Condition Assessment System (HCAS): CSIRO (2019)

https://research.csiro.au/biodiversity-knowledge/projects/hcas/

Global Biodiversity

Intergovernmental Panel on Biodiversity and Ecosystem Services: *https://ipbes.net/*

Aichi Targets: *www.cbd.int/sp/targets*

Sustainable Development Goals: *https://sustainabledevelopment.un.org*

Global Footprint Network: *https://www.footprintnetwork.org/*

Global ecosystems: *https://rmgsc.cr.usgs.gov/outgoing/ecosystems/Global/*

Biodiversity Indicators

European Academies' Science Advisory Council: *https://royalsociety.org/~/media/royal_society_content/policy/publications/2005/9667.pdf*

Nature Serve: *https://www.natureserve.org/biodiversity-science/conservation-topics/biodiversity-indicators#:~:text=Biodiversity%20indicators%20help%20us%20measure,as%20the%20protection%20of%20important*

Ecosystem Assessment

Global Ecosystem and Environment Observation Analysis Research Cooperation (GEOARC): *https://www.earthobservations.org/activity.php?id=144*

ECOPOTENTIAL Project: a large, European-funded H2020 project, focusing on a targeted set of internationally recognised Protected Areas in Europe, European Territories and beyond, and addressing crossscale ecological interactions and landscape-ecosystem dynamics at regional to continental scales, as well as long term and large scale environmental and ecological challenges: *https://www.ecopotential-project.eu/*

EC CORDIS Ecopotential Project: *https://cordis.europa.eu/article/id/254154-earth-observation-data-for-ecosystem-monitoring*

19.7 References

Accad, A., and Neldner, V.J. (2015). *Remnant Regional Ecosystem Vegetation in Queensland, Analysis 1997–2013*. Queensland Department of Science, Information Technology and Innovation, Brisbane.

Auld, T.D., and Leishman, M.R. (2015). Ecosystem risk assessment for Gnarled Mossy Cloud Forest, Lord Howe Island, Australia. *Austral Ecology*, 40, 364–372.

BIP (2010). *Biodiversity indicators and the 2010 Target: Experiences and lessons learnt from the 2010 Biodiversity Indicators Partnership*. Secretariat of the Convention on Biological Diversity, Montréal, Canada. Technical Series No. 53, 196 p.

BIP (2019). *List of global indicators available for review* webpage, Biodiversity Indicators Partnership website: *https://www.bipindicators.net/list-of-global-indicators-available-for-review*

Bland, L.M., Keith, D.A., Miller, R.M., Murray, N.J., and Rodríguez, J.P. (Eds.) (2016). *Guidelines for the application of IUCN Red List of Ecosystems Categories and Criteria, Version 1.0*. IUCN, Switzerland. ISBN: 978-2-8317-1769-2

Bland, L.M., Nicholson, E., Miller, R.M., Andrade, A., Etter, A., Ferrer-Paris, J.R., Kontula, T., Lindgaard, A., Pliscoff, P., Skowno, A., Zager, I., and Keith, D.A. (2018). Impacts of the IUCN Red List of Ecosystems on Conservation Policy and Practice. *Preprints*, 2018120097. doi:*10.20944/preprints201812.0097.v1*

Böhringer, C., and Jochem, P.E.P. (2007). Measuring the immeasurable—A survey of sustainability indices. *Ecological Economics*, 63, 1–8.

Burns, E.L., Lindenmayer, D.B., Stein, J., Blanchard, W., McBurney, L., Blair, D., and Banks, S.C. (2015). Ecosystem assessment of mountain ash forest in the Central Highlands of Victoria, south-eastern Australia. *Austral Ecology*, 40, 386–399.

CBD (2010). The strategic plan for biodiversity 2011–2020 and the Aichi Biodiversity Targets, decision X/2. In *10th Conference of the Parties, Convention on Biological Diversity*. Montreal, Canada. 13 p.

CBD (2020a). The Convention on Biological Diversity website: *https://www.cbd.int/convention/*

CBD (2020b). *Strategic Plan for Biodiversity 2011–2020, including Aichi Biodiversity Targets* webpage, Convention on Biological Diversity website: *https://www.cbd.int/sp/*

CBD (2020c). *Global Strategy for Plant Conservation* webpage, Convention on Biological Diversity website: *https://www.cbd.int/gspc/*

CoA (2014). *Australia's Fifth National Report to the Convention on Biological Diversity*. Commonwealth of Australia, Canberra. *https://www.cbd.int/doc/world/au/au-nr-05-en.pdf*

CoA (2020). *Australia's Sixth National Report to the Convention on Biological Diversity 2014–2018*. Commonwealth of Australia, Canberra. *https://www.cbd.int/doc/nr/nr-06/au-nr-06-en.pdf*

CSIRO (2019). *The Habitat Condition Assessment System (HCAS). Progress update for stakeholders: June 2019*. CSIRO Land and Water: *https://research.csiro.au/biodiversity-knowledge/wp-content/uploads/sites/69/2019/07/BKP-2HCAS-Factsheet-20190627.pdf*

DAWE (2020a). *Environment Protection and Biodiversity Conservation Act 1999 (EPBC Act)* webpage, Department of Agriculture, Water and Environment website: *https://www.environment.gov.au/epbc*

DAWE (2020b). *Australia's Strategy for Nature*. Department of Agriculture, Water and the Environment, Canberra. *https://naturehub.govcms.gov.au/sites/default/files/2019-11/Australia_s_Strategy_for_Nature_%20web.pdf*

DELWP (2017). *Biodiversity information explanatory document*. Victorian Department of Environment, Land, Water and Planning, Melbourne.

DEWHA (2009). *Assessment of Australia's Terrestrial Biodiversity 2008*. Report prepared by the Biodiversity Assessment Working Group of the National Land and Water Resources Audit for the Australian Government, Canberra.

DEWHA (2010). *Ecosystem Services: Key Concepts and Applications*. Occasional Paper No 1, Department of the Environment, Water, Heritage and the Arts, Canberra. ISBN 978-1-76047-341-9

Donohue, R.J., Harwood, T.D., Williams, K.J., Ferrier, S., and McVicar, T.R. (2013). *Estimating habitat condition using time series remote sensing and ecological survey data*. CSIRO Earth Observation and Informatics Transformational Capability Platform Client Report EP1311716, CSIRO, Australia. 44 p. *https://publications.csiro.au/rpr/pub?pid=csiro:EP1311716*

DPIE (2020a). *A Biodiversity Indicator Program for NSW* webpage, NSW Department of Planning, Industry and Environment website: *https://www.environment.nsw.gov.au/topics/animals-and-plants/biodiversity/biodiversity-indicator-program*

DPIE (2020b). *NSW Biodiversity Outlook Report*. Results from the Biodiversity Indicator Program: First assessment. Department of Planning, Industry and Environment, Sydney. 77p. *https://www.environment.nsw.gov.au/-/media/OEH/Corporate-Site/Documents/Animals-and-plants/Biodiversity/Biodiversity-Indicator-Program/biodiversity-outlook-report-first-assessment-200621.pdf*

DSE (2004). *Vegetation Quality Assessment Manual–Guidelines for applying the habitat hectares scoring method. Version 1.3*. Victorian Government Department of Sustainability and Environment, Melbourne.

EASAC (2004). *A users' guide to biodiversity indicators*. European Academies' Science Advisory Council, 29 November 2004. *https://royalsociety.org/~/media/royal_society_content/policy/publications/2005/9667.pdf*

Eyre, T.J., Fisher, A., Hunt, L.P., and Kutt, A.S. (2011). Measure it to better manage it: a biodiversity monitoring framework for the Australian rangelands. *The Rangeland Journal*, 33, 239–253.

GEOBON (2020). *The Groups on Earth Observations Biological Observation Network* website: *https://geobon.org/*

Gillespie, T.W., Foody, G.M., Rocchini, D., Giorgi, A.P., and Saatchi, S. (2008). Measuring and modelling biodiversity from space. *Progress in Physical Geography*, 32(2), 203–221. doi:*10.1177/0309133308093606*.

Harwood, T.D., Donohue, R.J., Williams, K.J., Ferrier, S., McVicar, T.R., Newell, G., and White, M. (2016). Habitat Condition Assessment System: A new way to assess the condition of natural habitats for terrestrial biodiversity across whole regions using remote sensing data. *Methods in Ecology and Evolution*, 7(9), 1050–1059. doi:*10.1111/2041-210X.12579*.

IUCN (2020a). *Protected Area Categories* webpage, International Union for Conservation of Nature website: *https://www.iucn.org/theme/protected-areas/about/protected-area-categories*

IUCN (2020b). *Background and History* webpage for IUCN Red List of Threatened Species. International Union for Conservation of Nature website: *https://www.iucnredlist.org/about/background-history*

IUCN (2020c). *Summary Statistics* webpage for IUCN Red List of Threatened Species. International Union for Conservation of Nature website: *https://www.iucnredlist.org/resources/summary-statistics#Figure%202*

Jetz, W., McGeoch, M.A., Guralnick, R., Ferrier, S., Beck, J., Costello, M.J., Fernandez, M., Geller, G.N., Keil, P., Merow, C., Meyer, C., Muller-Karger, F.E., Pereira, H.M., Regan, E.C., Schmeller, D.S., and Turak, E. (2019). Essential biodiversity variables for mapping and monitoring species populations. *Nature Ecology and Evolution*, 3, 539–551. *https://doi.org/10.1038/s41559-019-0826-1*

Keith (2015). Assessing and managing risks to ecosystem biodiversity. *Austral Ecology*, 40, 337–346.

Keith, D.A., Rodríguez, J.P., Rodríguez-Clark, K.M., Nicholson, E., Aapala, K., Alonso, A., Asmussen, M., Bachman, S., Basset, A., Barrow, E.G., Benson, J.S., Bishop, M.J., Bonifacio, R., Brooks, T.M., Burgman, M.A., Comer, P., Comín, F.A., Essl, F., Faber-Langendoen, D., Fairweather, P.G., Holdaway, R.J., Jennings, M., Kingsford, R.T., Lester, R.E., Nally, R. Mac, McCarthy, M.A., Moat, J., Oliveira-Miranda, M.A., Pisanu, P., Poulin, B., Regan, T.J., Riecken, U., Spalding, M.D., and Zambrano-Martínez, S. (2013). Scientific Foundations for an IUCN Red List of Ecosystems. *PLoS ONE*, 8(5), e62111. doi:*10.1371/journal.pone.0062111*

Keith, D.A., Rodríguez, J.P., Brooks, T.M., Burgman, M.A., Barrow, E.G., Bland, L., Comer, P.J., Franklin, J., Link, J., McCarthy, M.A., Miller, R.M., Murray, N.J., Nel, J., Nicholson, E., Oliveira-Miranda, M.A., Regan, T.J., Rodríguez-Clark, K.M., Rouget, M., and Spalding, M.D. (2015). The IUCN Red List of Ecosystems: Motivations, Challenges, and Applications. *Conservation Letters*, 8, 214–226.

IPBES (2019). *Global assessment report on biodiversity and ecosystem services of the Intergovernmental Science-Policy Platform on Biodiversity and Ecosystem Services*. (Eds: E.S. Brondizio, J. Settele, S. Díaz, and H. T. Ngo). Intergovernmental Panel on Biodiversity and Ecosystem Services secretariat, Bonn, Germany. *https://ipbes.net/global-assessment*

IUCN-CEM (2016). *The IUCN Red List of Ecosystems*. Version 2016-1. *https://iucnrle.org/*

IUCN-CEM (2020). *Global Context* webpage for IUCN Red List of Ecosystem. International Union for Conservation of Nature Commission on Ecosystem Management website: *https://iucnrle.org/about-rle/context/*

Masó, J., Serral, I., Domingo-Marimon, C., and Zabala, A. (2020). Earth observations for sustainable development goals monitoring based on essential variables and driver-pressure-state-impact-response indicators. *International Journal of Digital Earth*, 13(2), 217–235. *https://doi.org/10.1080/17538947.2019.1576787*

Metcalfe, D.J., and Lawson, T.J. (2015). Coastal lowland rainforests of the Wet Tropics bioregion, Queensland, Australia. *Austral Ecology*, 40, 373–385.

Murray, N.J., Keith, D.A., Bland, L.M., Ferrari, R., Lyons, M.B., Lucas, R., Pettorelli, N., Nicholson, E. (2018a). The role of satellite remote sensing in structured ecosystem risk assessments. *Science of the Total Environment*, 619–620, 249–257. *https://doi.org/10.1016/j.scitotenv.2017.11.034*

Murray, N.J., Keith, D.A., Simpson, D., Wilshire, J.H., Lucas, R.M. (2018b), Remap: An online remote sensing application for land cover classification and monitoring. *Methods in Ecology and Evolution*, 1–9. *https://doi.org/10.1111/2041-210X.13043*

Neldner, J. (2018). *The Impacts of Land Use Change on Biodiversity in Australia. Ch 8 in in Land Use in Australia: Past, Present and Future*. (Ed: Thackway, R.). ANU eVIEW, Canberra. ISBN: 9781921934421

Neldner, V.J., Niehus, R.E., Wilson, B.A., McDonald, W.J.F., Ford, A.J., and Accad, A. (2017). *The Vegetation of Queensland. Descriptions of Broad Vegetation Groups. Version 3.0*. Queensland Herbarium, Department of Science, Information Technology and Innovation, Brisbane. *publications.qld.gov.au/dataset/redd/resource/78209e74-c7f2-4589-90c1-c33188359086*

Nicholson, E., Regan, T.J., Auld, T.D., Burns, E.L., Chisholm, L.A., English, V., Harris, S., Harrison, P., Kingsford, R.T., Leishman, M.R., Metcalfe, D.J., Pisanu, P., Watson, C.J., White, M., White, M.D., Williams, R.J., Wilson, B., Keith, D.A. (2015). Towards consistency, rigour and compatibility of risk assessments for ecosystems and ecological communities. *Austral Ecology*, 40, 347–363. *https://doi.org/10.1111/aec.12148*.

NRM (2019). *Biosecurity* webpage, NRM Regions Australia website: *http://nrmregionsaustralia.com.au/biosecurity/*

OECD (2020). *Biodiversity indicators, valuation and assessments* webpage, Organisation for Economic Co-operation and Development website: *http://www.oecd.org/environment/resources/biodiversity-indicators-valuation-and-assessments.htm*

OEH and CSIRO (2019). *Measuring Biodiversity and Ecological Integrity in New South Wales: Method for the Biodiversity Indicator Program*. Office of Environment and Heritage NSW and Commonwealth Scientific and Industrial Research Organisation, NSW Government, Sydney.

Parkes, D., Newell, G., and Cheal, D. (2003). Assessing the quality of native vegetation: The 'habitat hectares' approach. *Ecological Management and Restoration*, 4, S29–S38.

Parrish, J.D., Braun, D.P., and Unnasch, R.S. (2003). Are We Conserving What We Say We Are? Measuring Ecological Integrity within Protected Areas. *BioScience*, 53(9), 851–860. *https://doi.org/10.1641/0006-3568(2003)053[0851:AWCWWS]2.0.CO;2*

Pereira, H.M., Navarro, L.M., and Martins, I.S. (2012). Global Biodiversity Change: The Bad, the Good, and the Unknown. *Annual Review of Environmental Resources*, 37, 25–50. *https://www.annualreviews.org/doi/pdf/10.1146/annurev-environ-042911-093511*

Pisanu P., Kingsford R.T., Wilson B., and Bonifacio R. (2015). Status of connected wetlands of the Lake Eyre Basin, Australia. *Austral Ecology*, 40, 460–71. *https://doi.org/10.1111/aec.12203*

Pope Francis (2015). *Laudato Si': On Care for Our Common Home*. Catholic Truth Society, London.

remap (2020). *remap: Enabling large-scale ecosystem mapping and assessment* website: *https://remap-app.org*

Rodríguez, J.P., Keith, D.A., Rodríguez-Clark, K.M., Murray, N.J., Nicholson, E., Regan, T.J., Miller, R.M., Barrow, E., Bland, L.M., Boe, K., Brooks, T.M., Oliveira-Miranda, M.A., Spalding, M., and Wit, P. (2015). A practical guide to the application of the IUCN Red List of Ecosystems criteria. *Philosophical Transactions* B, 370, 2014003. *http://dx.doi.org/10.1098/rstb.2014.0003*

Rose, R.A., Byler, D., Eastman, J.R., Fleishman, E., Geller, G., Goetz, S., Guild, L., Hamilton, H., Hansen, M., Headley, R., Hewson, J., Horning, N., Kaplin, B.A., Laporte, N., Leidner, A., Leimgruber, P., Morisette, J., Musinsky, J., Pintea, L., Prados, A., Radeloff, V.C., Rowen, M., Saatchi, S., Schill, S., Tabor, K., Turner, W., Vodacek, A., Vogelmann, J., Wegmann, M., Wilkie, D., and Wilson, C. (2014). Ten ways remote sensing can contribute to conservation. *Conservation Biology*, 29(2), 350–359. doi:*10.1111/cobi.12397*.

Sayre, R., Karagulle, D., Frye, C., Boucher, T., Wolff, N.H., Breyer, S., Wright, D., Martin, M., Butler, K., Van Graafeiland, K., Touval, J., Sotomayor, L., McGowan, J., Game, E.T., and Possingham, H. (2020). An assessment of the representation of ecosystems in global protected areas using new maps of World Climate Regions and World Ecosystems. *Global Ecology and Conservation*, 21, e00860. *https://doi.org/10.1016/j.gecco.2019.e00860*

Seabrook, L., McAlpine, C., and Fensham, R. (2006). Cattle, crops and clearing: Regional drivers of landscape change in the Brigalow Belt, Queensland, Australia, 1840–2004. *Landscape and Urban Planning*, 78, 373–385. *doi.org/10.1016/j.landurbplan.2005.11.007*

SoE (2018). *State of the Environment 2018*. Commissioner for Environmental Sustainability Victoria. *https://www.ces.vic.gov.au/reports/state-environment-2018*

Sparks, T.H., Butchart, S.H.M., Balmford, A., Bennun, L., Stanwell-Smith, D., Walpole, M., Bates, N.R., Bomhard, B., Buchanan, G.M., Chenery, A.M., Collen, B., Csirke, J., Diaz, R.J., Dulvy, N.K., Fitzgerald, C., Kapos, V., Mayaux, P., Tierney, M., Waycott, M., Wood, L., and Green, R.E. (2011). Linked indicator sets for addressing biodiversity loss. *Oryx*, 45(03), 411–419. doi:*10.1017/S003060531100024X*.

Tansley, A.G. (1935). The use and abuse of vegetational concepts and terms. *Ecology*, 16, 284–307.

Teillard, F., Anton, A., Dumont, B., Finn, J.A., Henry, B., Souza, D.M., Manzano P., Milà i Canals, L., Phelps, C., Said, M., Vijn, S., White, S. (2016). *A review of indicators and methods to assess biodiversity—Application to livestock production at global scale*. Livestock Environmental Assessment and Performance (LEAP) Partnership. FAO, Rome, Italy.

Thackway, R., and Lesslie, R. (2006). Reporting vegetation condition using the Vegetation Assets, States, and Transitions (VAST) framework. *Ecological Management and Restoration*, 7(1), 53–62.

Tozer, M.G., Leishman, M.R., and Auld, T.D. (2015). Ecosystem risk assessment for Cumberland Plain Woodland, New South Wales, Australia. *Austral Ecology*, 40, 400–410.

UN General Assembly (2012) *The future we want*. Resolution adopted by the United Nations (UN) General Assembly on 27 July 2012 (RES/66/288).

Walters, M., and Scholes, R.J. (2017). *The GEO Handbook on Biodiversity Observation Networks*. Springer, Chamonix.

Wardle, G.M., Greenville, A.C., Frank, A.S.K., Tischler, M., Emery, N.J., and Dickman, C.R. (2015). Ecosystem risk assessment of Georgina gidgee woodlands in central Australia (Qld, NT, SA). *Austral Ecology*, 40, 444–459.

Williams, R.J., Wahren, C.-H., Stott, K.A.J., Camac, J.S., White, M., Burns, E., Harris, S., Nash, M., Morgan, J.W., Venn, S., Papst, W.A., and Hoffmann, A.A. (2015). An IUCN red list ecosystems risk assessment for alpine snow patch herbfields, south-eastern Australia. *Austral Ecology*, 40, 433–443.

WWF (1998). *Living Planet Report 1998*. World Wildlife Fund.

Ecological culture cannot be reduced to a series of urgent and partial responses to the immediate problems of pollution, environmental decay and the depletion of natural resources. There needs to be a distinctive way of looking at things, a way of thinking, policies, an educational resistance to the assault of the technocratic paradigm. Otherwise, even the best ecological initiatives can find themselves caught up in the same globalised logic. To seek only a technical remedy to each environmental problem which comes up is to separate what is in reality interconnected and to mask the true and deepest problem of the global system.
(Pope Francis, 2015)

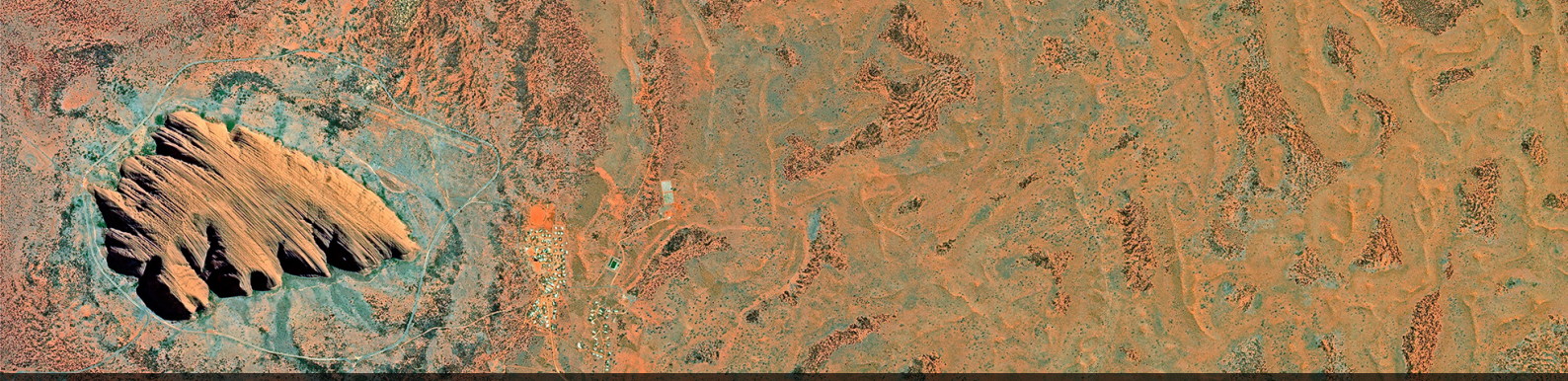

20 Sustainability

Sustainability of natural resources implies a balance between their consumption and production. Various trends in the management of natural resources can be observed in recent decades, with the focus moving from 'productivity' to 'conservation' to 'sustainability' to 'resilience' over time. Each of these focal points requires consideration when managing natural resources and each requires appropriate environmental indicators to objectively assess and monitor changes in the landscape. Whether one focus is given priority over another is largely a philosophical, if not political, decision. For example, attributes of three different natural resource management models are summarised in Table 20.1. While this specific example applies to rangeland environments, the succession of models from left to right reflects the increasing awareness of ecosystem values in land management in recent decades.

Throughout recorded history, societal attitudes to nature have influenced the management of natural resources. An anthropocentric worldview characterises most ancient, medieval, and modern cultural beliefs, as stated by a wide range of authors, including:

- Xenophon—"the gods have provided everything carefully for the benefit of man";
- Aristotle—"Nature .... has made all animals for the sake of man";
- Genesis—"be fruitful and multiply and replenish the earth and subdue it";
- Calvin—God "created all things for man's sake"; and
- Bacon—"the world is made for man, not man for the world".

Development of the scientific method in the seventeenth century was used to justify these beliefs, with the reductionist approach being applied to nature:

- Descartes—"I do not recognise any difference between the machines made by craftsmen and the various bodies that nature alone composes"; and carried into economics
- Carey—"the earth is a great machine, given to man to be fashioned to his purpose".

The Darwinism view of 'survival of the fittest' reinforced the outlook of humans struggling against nature to survive and control it. Freud wrote of the human need of "taking up the attack on nature, thus forcing it to obey human will, under the guise of science".

In addition to an anthropogenic worldview, in recent centuries the notion of 'progress' has emerged, which envisions science and technology continually improving the productivity of nature and increasing human potential. This perspective, however, is in stark contrast with ancient and medieval beliefs, which tended to view history either as an undirected sequence, or as a process of steady decay from a 'golden age' or 'paradise' (Ponting, 1991).

The Australian government's budget for expenditure in 2018–19 was $488.6 billion. The environmental portfolio stands to receive about $1.5 billion—about one third of 1% of what we as Australians spend our money on. Is this an accurate representation of how much we value the environment?
(Pollock, 2019)

Background image: Pansharpened SPOT-6 image over Uluru-Kata Tjuta National Park, NT, acquired on 17 October 2012. **Source:** © Airbus DS 2012

Table 20.1 Comparison of natural resource management models

Attribute	Management model		
	Steady-state	Ecosystem	Resilience-based
Ecological models	Succession-retrogression	State-and-transition rangeland health	Multiple social-ecological systems/ novel ecosystems
Reference condition	Historic climax plant community	Historic climax plant community, including historical range of variation	Landscapes with maximum options for ecosystem services
Role of humans	Use ecosystems	Part of ecosystems	Direct trajectories of ecosystem change
Ecosystem services	Meat and fibre products	Several ecosystem services	Options for diverse ecosystem services
Management goals	Sustain maximum yield of commodities	Sustain multiple uses	Sustain capacity of social-ecological systems to support human wellbeing
Science-management linkages	Top-down from management agencies	Top-down from management agencies	Multi-scaled social learning institutions
Knowledge systems	Management experience and agricultural experiments	Multidisciplinary science and ecological experiments	Collaborative groups, spatially reference, updatable databases

Source: Bestelmeyer and Briske (2012) Table 2

While we are now reaching the limit of our global natural resources, the rate of material extraction continues to accelerate (see Figure 20.1). Clearly it is time to consider more broadly the sustainable role of humankind on Earth and how our resources should be managed into the future. In practical terms at a local scale, better natural resource management decisions are made when managers understand the problem, have the motivation to adopt a changed practice, and have the capacity to implement it (Gordon *et al.*, 2001). Such decisions necessitate the involvement of land custodians and experienced scientists who understand the landscape firsthand, and can objectively track its processes, productivity, and vulnerabilities over time.

Below we consider aspects of sustainability in Australia in Section 20.1 and suitable EO sensors for observing sustainability in Section 20.2. Assessment of ecosystem services is introduced in Section 20.3, the conundrum of sustainable development is reviewed in the context of EO in Section 20.4, then EO-based environmental-economic accounting is described in Section 20.5.

Figure 20.1 Global GDP versus global material extraction 1900 to 2005

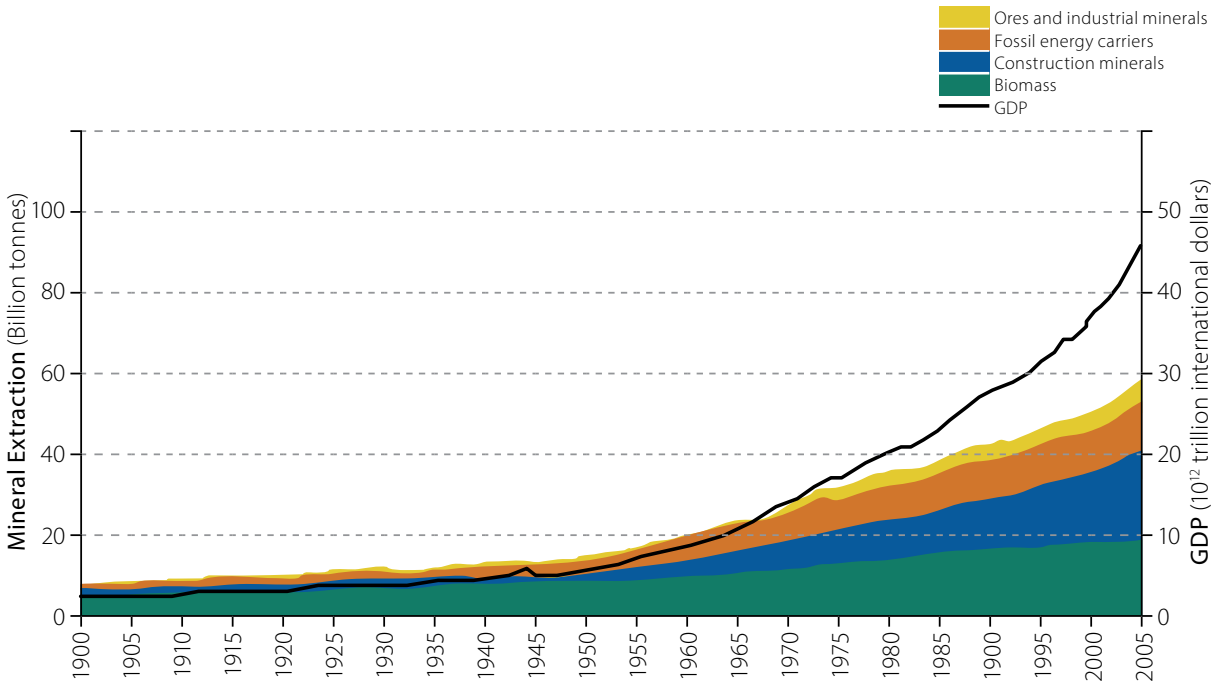

Source: WGCS (2016) Figure 1 (based on Krausmann *et al.*, 2009)

20.1 Sustainability in Australia

We like to think that the terrestrial landscape is both sustainable and resilient, but is that really the case? This section considers how EO is being used to assess sustainability in Australian landscapes.

Australian jurisdictions have generated an impressive array of environmental legislation and policies in recent decades. While there is a growing trend to 'restructure', 'consolidate', and 'streamline' their implementation, especially within politically expedient timeframes, are these changes achieving their intended goals of better management of natural resources?

Logically, in the absence of vested interests and predetermined ideologies, environmental policy is founded objectively on a well-established, scientific understanding of the environment. Such understanding should be derived from data that is appropriate and calibrated, and analysed using methods that are validated, consistent and repeatable (see Volume 2). The driver here is science, which is used to shape and inform policy. Once policy becomes widely accepted however, there is a tendency for policy to drive science, which clearly defeats the assumption of objectivity.

An accounting approach based on relevant economic, environmental, and social datasets, which are consistent through space and time, can be used to derive objective indicators to shape policy. A common base of data, accounts, and indicators will also ensure compatibility between policies and their implementation across jurisdictions and geographic regions. By linking socio-economic and environmental datasets, policy makers can:

- analyse both the impact of economic policies on the environment and the impact of environmental policies on the economy;
- use a quantitative basis for policy design;
- identify socio-economic drivers, pressures, and responses that will impact the environment;
- define environmental regulations and resource management strategies with greater precision; and
- establish integrated indicators for the relationships between the environment and the economy (DEWHA, 2010).

The use of environmental accounting in Australia is introduced in BoM (2013). A global model for environmental-economic accounting has been developed by the System of Environmental Economic Accounting (SEEA; see Figure 20.2 and Excursus 20.4). The SEEA framework is typically applied at national, state, or regional scales, and links through to mainstream accounting systems such as the System of National Accounts (SNA; CoA, 2018). Implementation of systems such as SEEA need to be phased to "build practical understanding and political acceptance" by all concerned (Vardon *et al*., 2016). This system has been used by the Australian Bureau of Statistics (ABS) since 1996 to produce the Australian Environmental Economic Accounts (AEEA; ABS, 2018; see Section 20.5).

Instead of seeing the environment as the foundation of human history, settled societies, especially modern industrial societies, have acted under the illusion that they are somehow independent from the natural world, which they have generally preferred to see as something apart which they can exploit more or less with impunity. Ever since the first great transition which began 10,000 year ago, and particularly in the last two centuries, humans have put increasing pressure on the earth's environment—in defiance of basic ecological principles. They have destroyed climax ecosystems to create agricultural land leading to environmental damage such as widespread soil erosion. Through a combination of hunting and farming they have driven individual animals to extinction and severely reduced the population of others. Either deliberately or accidentally they have introduced new animals and plants and thereby disrupted ecosystems, often with unpredictable results. .... it is clearly far too soon to judge whether modern industrial societies, with their very high rates of energy and resource consumption and high pollution levels, and the rapidly rising human population in the rest of the world are ecologically sustainable. Past human actions have left contemporary societies with an almost insuperably difficult set of problems to solve.
(Ponting, 1991)

Figure 20.2 System of Environmental Economic Accounting

The UN-based System of Environmental Economic Accounting (SEEA) provides "an integrated statistical framework for organizing biophysical data, measuring ecosystem services, tracking changes in ecosystem assets, and linking this information to economic and other human activity" (SEEA, 2020a).

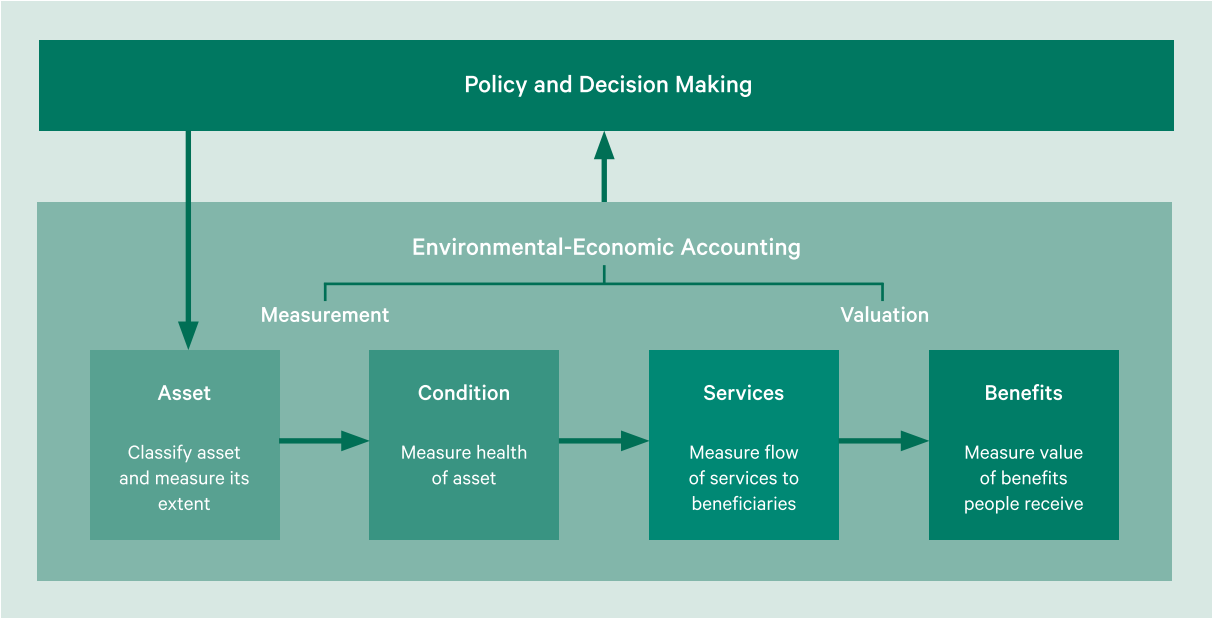

Source: Vardon *et al.* (2018)

20.2 EO Sensors for Sustainability

Various ecosystem properties that are indicative of ecosystem services can be derived from EO datasets, including definition of ecoregions, topography, hydrology, vegetation type and productivity, and changes in land use or climate (Andrew *et al.*, 2015; see Table 20.4). Similarly, assessment of sustainable development criteria increasingly relies on EO-based data (see Section 20.4). Operational systems for environmental accounting and environmental-economic accounting already derive data from EO time series datasets and as this field continues to expand, that reliance will also increase and become more standardised (see Section 20.5). As summarised in Table 19.3, sources of EO datasets that are relevant to assessing sustainability are primarily acquired at a regional to global scale, with *in situ* and higher resolution data being used to calibrate and validate the resulting products.

Table 20.2 EO sensors relevant to sustainability

TIR: Thermal infrared; SAR: Synthetic Aperture Radar

Type	Sensor	Platform	Relevance	Advantages	Disadvantages
Passive optical	Multispectral radiometer	Satellite or airborne	Vegetation cover and extent, biomass, biodiversity, and productivity Land degradation	Globally consistent and contiguous, local to national scale, recurrent coverage with high temporal frequency and extent, low cost	Cloud contamination, limited spectral discrimination
	TIR radiometer	Satellite or airborne	Soil/canopy temperature Fire potential, severity, and extent Drought conditions Regional hydrological changes	Highlight thermal anomalies	Low resolution, low signal to noise ratio
Passive microwave	Microwave radiometer	Satellite	Soil moisture, Climate variables	High temporal frequency. large spatial coverage, cloud penetration	Very low energy targets so very coarse spatial resolution
Active microwave	SAR	Satellite or airborne	Soil characteristics Vegetation structure Water dynamics	All weather, operates at night	Data availability, noisy data, complex processing

20.3 Ecosystem Services

The concept of ecosystem services was developed to encourage an awareness of the societal benefits being derived from ecosystems and the importance of biodiversity conservation (Westman, 1977; Ehrlich and Ehrlich, 1981), with the intention of fostering a stewardship approach towards sustainable resource management by which those essential services would be maintained (Daily, 1997; Costanza *et al*., 1997, 2017). The Millennium Ecosystem Assessment (MEA, 2005) identified global categories for ecosystem services (see Excursus 20.1) that can be used to assess the sustainable use of ecosystems (see Section 20.5).

While ecosystem functions and services are linked with biodiversity (see Section 19), one cannot be used to represent the other for several reasons:

- for many species, functional roles can only be observed at specific spatial and temporal scales;
- ecosystem services are identified and valued relative to social, cultural, and economic factors, which may vary at a local scale; and
- whether changes in ecosystem function or abiotic environments are beneficial to conservation goals or not requires a subjective judgment (Keith *et al*., 2013).

Some of the challenges and opportunities inherent in this approach to ecosystem assessment were defined by Birkhofer *et al*. (2015; see Table 20.3). These authors conclude that "ecosystem service research is challenging for ecologists, but developing a multifaceted understanding of how nature promotes human wellbeing is crucial for the sustainable use of the Earth's resources. Ecosystem service research offers ecologists the unique opportunity to act as promoters for the understanding of how to conserve and sustain benefits gained from nature."

Ecosystem services are impacted by a range of natural and anthropogenic factors. Assessment of ecosystem services is based on relevant indicators selected using criteria that are specific, measurable, achievable, realistic and time-sensitive (Dawson *et al*., 2016). For example, Figure 20.3 depicts ecological processes and functions that generate provisioning, regulating, and habitat services in extensive agriculture from 'ecological capital'. In this context, ecological capital comprises ecosystem assets, including productive assets (production herds that deliver progeny, grasslands and pastures for forage, and soils and soil biota to sustain vegetation) and supporting assets (trees and shrubs that offer shade, shelter, and habitat). Relevant regulating services include avoiding water pollution, maintaining soil productivity and structure, and sequestering carbon. All of these ecosystem services influence both the current and future production of crops and livestock, and the regenerative capacity of the ecological capital (Ogilvy, 2020).

Potential sources of data for ecosystem mapping are summarised in Andrew *et al*. (2015) and Pettorelli *et al*. (2017), including EO datasets (Alcaraz-Segura *et al*., 2014; de Araujo Barbosa *et al*., 2015; Andrew *et al*., 2014; Ramirez-Reyes *et al*., 2019; see Table 20.4). Some of the challenges and opportunities associated with using EO in ecosystem modelling and assessment are considered by Ramirez-Reyes *et al*. (2019) and summarised in Figure 20.4. Methods to quantify uncertainty in EO-based assessments of ecosystem services are also being developed (Stritih *et al*., 2019). An integrated framework for using EO products with socio-cultural and economic datasets to assess ecosystem services was proposed by Cord *et al*. (2017). Integrated resource monitoring systems involving ecosystem services are further discussed in Section 20.5.

Biodiversity and associated ecosystem services can be thought of as natural capital. We also think about social capital, which is a measure of community intangibles such as networks, cultural pursuits, trust, commitment to local wellbeing and shared values, and physical capital, which is the result of past investments in the conversion of components of natural capital through construction and maintenance, such as infrastructure. The set of these types of capital forms the foundations of a nation's wealth. (DEWHA, 2010)

Excursus 20.1—Millennium Ecosystem Assessment

Source: MEA (2005)

The consequences of ecosystem change for human wellbeing have been highlighted in recent years by the UN-funded Millennium Ecosystem Assessment (MEA, 2005), which defines four fundamental 'ecosystem services':

- provisioning services for food, water, fibre, fuel and other commodities;
- supporting services for photosynthesis, primary productivity, oxygen production, soil formation, biodiversity conservation, water and nutrient cycling;
- regulating services for air quality, climate variables, seed dispersal, herbivory, water quality, water flow regulation, carbon sequestration, bioturbation, erosion control, pests and disease prevention, pollination; and
- cultural services for spiritual fulfillment, aesthetic enjoyment, heritage values, recreation, and education.

Changes in drivers that indirectly affect biodiversity, such as population, technology, and lifestyle can lead to changes in drivers directly affecting biodiversity, such as resource consumption. These result in changes to ecosystems and the services they provide thereby affecting human wellbeing. These interactions can take place at local, regional, and global scale and between these scales in short and long time intervals.

The MEA report also presents a scientific basis for sustainable use of ecosystems by assessing:

- What are the current conditions and trends of ecosystems, ecosystem services, and human wellbeing?
- What are plausible future changes in ecosystems and their ecosystem services and the consequent changes in human wellbeing?
- What can be done to enhance wellbeing and conserve ecosystems? What are the strengths and weaknesses of response options that can be considered to realise or avoid specific futures?
- What are the key uncertainties that hinder effective decision making concerning ecosystems?
- What tools and methodologies developed and used in the MEA can strengthen capacity to assess ecosystems, the services they provide, their impacts on human wellbeing, and the strengths and weaknesses of response options?

The four main findings from this assessment were:

- Over the past 50 years, humans have changed ecosystems more rapidly and extensively than in any comparable period of time in human history, largely to meet rapidly growing demands for food, fresh water, timber, fibre, and fuel. This has resulted in a substantial and largely irreversible loss in the diversity of life on Earth.
- The changes that have been made to ecosystems have contributed to substantial net gains in human wellbeing and economic development, but these gains have been achieved at growing costs in the form of the degradation of many ecosystem services, increased risks of nonlinear changes, and the exacerbation of poverty for some groups of people. These problems, unless addressed, will substantially diminish the benefits that future generations obtain from ecosystems.
- The degradation of ecosystem services could grow significantly worse during the first half of this century and is a barrier to achieving the Millennium Development Goals.
- The challenge of reversing the degradation of ecosystems while meeting increasing demands for their services can be partially met under some scenarios that the MEA has considered, but these involve significant changes in policies, institutions, and practices that are not currently underway. Many options exist to conserve or enhance specific ecosystem services in ways that reduce negative trade-offs or that provide positive synergies with other ecosystem services.

Table 20.3 Ecosystem services—challenges and opportunities

Land Management Practice	Impacts on Biodiversity	Geographic Area
Understanding anthropogenically modified systems	Identifying human impact on service-providing units and ecosystem services	Consideration of relationships between biodiversity and ecosystem service provision and management interventions
	Considering matrix effects in modified landscapes	Identifying effects of anthropogenic interventions on service-providing units at different spatial scales
Assessing ecosystem services	Assessing relationships between services and measures usually quantified in ecological studies	Identifying ecological measures that are reliable indicators of ecosystem service provision
	Accounting for dynamics and uncertainties in models of service provision	Evaluation of uncertainty, integration of evolutionary aspects and human impacts into process-based models and socio-economic models
Analysing relationships between ecosystem services	Understanding if relationships between ecosystem services are indirect or direct	Performing studies that model direct and indirect effects, experimental test for relationships and developing mechanistic models
	Solving issues with the visualisation and statistics tesing of relationships between multiple services	Accounting for non-linear relationships when visualising or analysing relationships between services
Considering appropriate spatial and temporal scales	Upscaling from experimental plots to scales relevant for management of most ecosystem services	Coupling research on mechanisms for service provision with conservation-oriented research
	Understanding temporal dynamics of services provision to develop sustainable management and conservation strategies	Utilising existing long term studies and promoting the need for such research projects

Source: Birkhofer *et al.* (2015) Table 1

Figure 20.3 Ecosystem services in extensive agriculture

This conceptual diagram relates the inter- and intra-ecological functions and processes in extensive agriculture that generate ecosystem services. Degradation of the functions and processes within and between elements of ecological capital (or assets) invariably leads to decline in the capacity to capture, store and cycle free inputs from nature. The listed inputs and outputs only sample the larger sets of potential resources and outcomes.

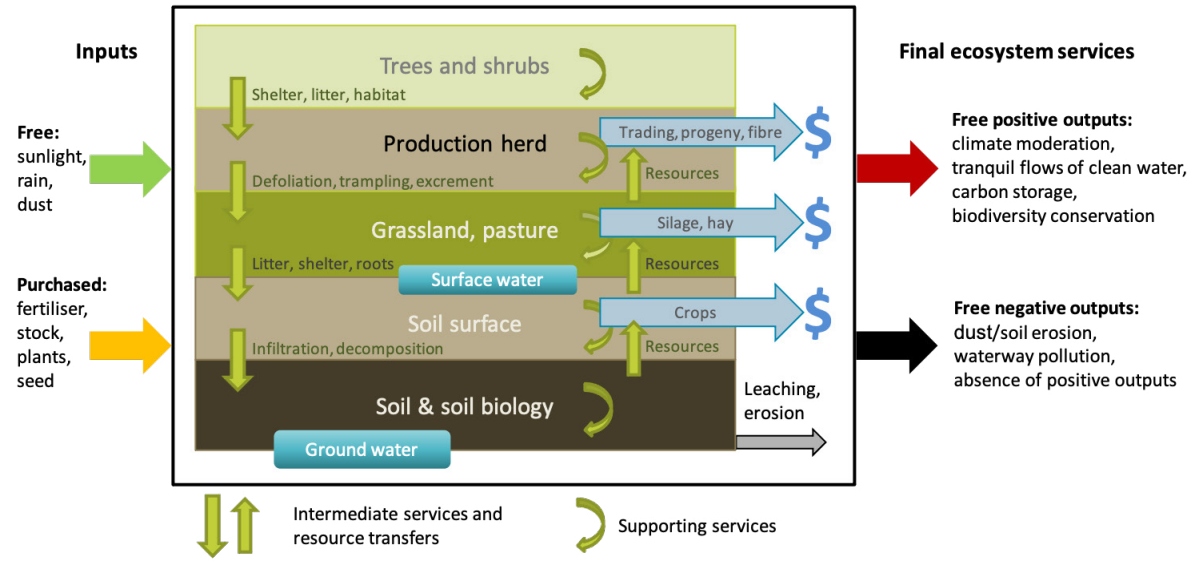

Source: Ogilvy (2020) Figure 2

Table 20.4 EO capabilities relevant to ecosystem services

Abbreviations: NDVI: normalised difference vegetation index; MODIS: moderate resolution imaging spectroradiometer; fAPAR: fraction of absorbed photosynthetically active radiation; NPP: net primary productivity, VI: vegetation index.

Ecosystem service or process	EO product	Potential EO data source
Plant traits	Pigment, dry matter, water, chemical content, leaf area index, leaf angle distribution	Spectral analysis or radiative transfer models
	Roughness, height, vertical structure	Lidar, radar, multiangle
	Life form	Land cover classification
	Phenology	Multi-temporal imagery
Species	Species map,	Chemical or structural uniqueness, hyperspectral imaging, lidar, image texture
	Habitat suitability map	Varied (climate, topography, land cover, productivity, etc)
Biodiversity	Spectral diversity	Range/variability of biochemistry, NDVI or reflectance
	Environmental surrogates	Varied (productivity, topography, land cover, disturbance, etc)
Abundance of functional components	Vegetation fraction, litter fraction	Spectral unmixing, MODIS Continuous Fields
Biomass, carbon storage	Canopy structure	Lidar, radar, multiangle data
Photosynthesis, carbon sequestration	Productivity	fAPAR, photosynthetic efficiency, fluorescence, MODIS NPP
Disturbance	Change in biomass, plant traits, land cover	Multi-temporal imagery
	Fire detection	Thermal anomalies
	Drought monitoring	Water content, surface temperature, evapotranspiration
	Plant stress	Spectral indexes
Soil characteristics	Land form	Digital Elevation Model
	Soil texture, moisture, chemistry	Radar, hyperspectral imaging
Evapotranspiration	Evapotranspiration	Thermal imagery, VIs, climate data
Hydrology variables	Precipitation	Thermal imagery, VIs, climate data
	Soil moisture	Radar, passive microwave radar
	Water, snow/ice extent	Optical, radar, passive microwave, radar altimetry
	Water level, Groundwater	Gravity surveys, subsidence, surface water fluxes
Landscape structure	Landscape metrics	Land cover, quantitative heterogeneity patterns
Ecosystem classification	Ecosystem classification	Varied (productivity, climate, topography, land cover, etc)

Source: Andrew *et al.* (2014) Table 2

Land use policies and planning transform landscapes, affecting the long term mosaics of unmodified, modified, removed and replaced vegetation ecosystems. In turn, land use policies, planning instruments and decisions affect the viability of landscapes to generate publicly acceptable mixes of ecosystem services, including clean air, healthy crops, clean water, and parks and reserves for the protection of nature and recreation.
(Thackway, 2018)

Figure 20.4 EO in ecosystem service assessment

Ecosystem service models have been applied across scales, from local to global, to quantify ecosystem service supply and demand. Technical and conceptual barriers remain to creating models that effectively integrate social and biophysical systems that are comparable and transferable across geographies. EO data may reduce these barriers by providing new ways to measure ecosystem service drivers that are consistent across time and space.

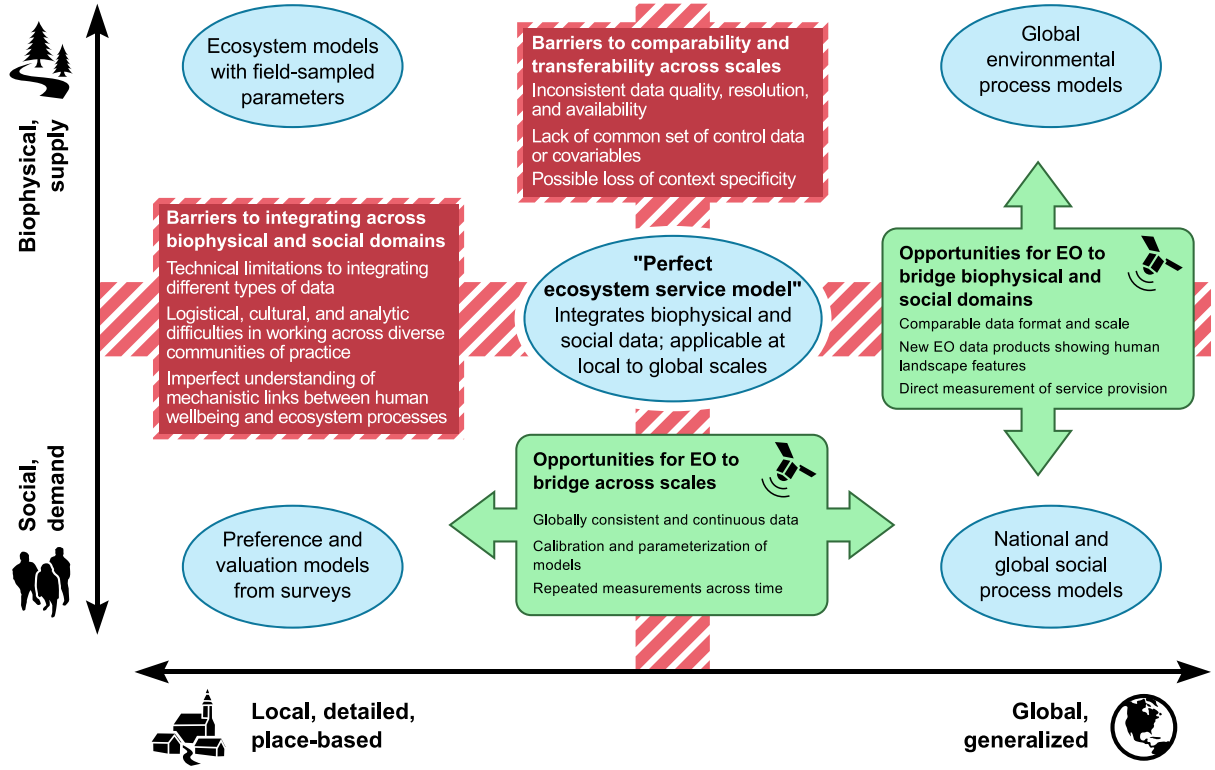

Source: Ramirez-Reyes *et al.* (2019) Figure 1

Ecosystem services have traditionally been valued in terms of market pressures, but some have been directly or indirectly undervalued or ignored in terms of ecosystem biodiversity and resilience (see Sections 7 and 19). In many regions of Australia, this undervaluing has resulted in unsustainable resource usage and environmental degradation (see Sections 11.4 and 15). Some of the major challenges in measuring the variety of ecosystem services in Australia include:

- lack of detailed information about ecosystem processes with most data being derived from models;
- key processes have differing cycle durations and complexity; and
- research is not necessarily transferable across ecosystems—Australia's size and diversity means that ecosystem services differ in terms of speed and sequence in different locations (DEWHA, 2010).

Traditional market measurement systems exist for some, but not all, ecosystem services. Hopefully, as new markets develop for ecosystem services, such as carbon trading (see Section 17), environmental water flows (see Volume 3B), and vegetation offsets (see Volume 2D—Excursus 14.3), their real economic value will become more apparent (see Section 21).

Sustain (from) Latin, sub meaning 'from below' and tenere meaning 'to hold'

20.4 Sustainable Development

The word 'sustainable' is defined by the Merriam-Webster Dictionary as meaning 'of, relating to, or being a method of harvesting or using a resource so that the resource is not depleted or permanently damaged'. The word was originally coined in German from the concept of 'sustained yield' in forestry, that is, a balance between resource consumption and production. More recently, The Brundtland Report (1987) entitled 'Our Common Future', produced by several UN countries, defined 'sustainable development' as satisfying "the needs of the present without compromising the ability of future generations to meet their own needs" and signalled "a new era of economic growth—growth that is forceful and at the same time socially and environmentally sustainable" (Purvis *et al.*, 2018). The elements of sustainable development were defined by Jacobs *et al.* (1987) as the:

- integration of conservation and development;
- satisfaction of basic human needs;
- achievement of equity and social justice;
- provision for social self-determination and cultural diversity; and
- maintenance of ecological integrity.

Of the wide range of models that have been proposed to represent the most critical components of sustainable development and their interrelationships (Brown *et al.*, 1987; Kidd, 1992; Boyer *et al.*, 2016; Purvis *et al.*, 2018), Figure 20.5 shows one of the most popular depictions, in which three interrelated pillars—social, economic, and ecological—jointly impact the environment. The precise definitions of these three interest areas have varied depending whether they are seen as perspectives to consider, or systems to be balanced, integrated, or reconciled (Purvis *et al.*, 2018; see Table 20.5). Accordingly, the relative importance of each pillar is weighted differently by different individuals, with the viability of continued economic growth being highly debatable. Moreover, Kidd (1992) argues that different "strains of thought" have adopted the term 'sustainability' to represent fundamentally different concepts, and some observers consider "the term 'sustainable development', like that of 'sustainable growth', to be an oxymoron (Redclift, 2005; Johnston *et al.* 2007; Brand, 2012)" (Purvis *et al.*, 2018). In the face of limiting resources, however, conflicts over land management and resource distribution inevitably arise and this model enables analysis of competing demands.

Figure 20.5 Three pillars of sustainability

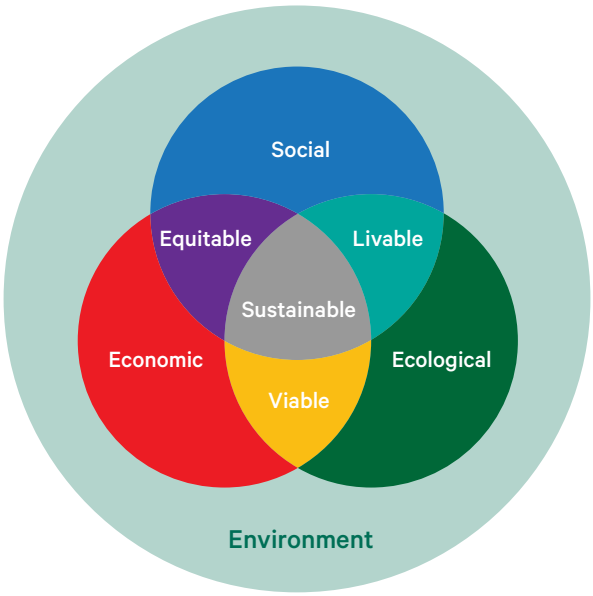

Human history cannot be understood in a vacuum. All human societies have been, and still are, dependent on complex, interrelated physical, chemical and biological processes. These include the energy produced by the sun, the circulation of the elements crucial for life, the geophysical processes that have caused the continental land masses to migrate across the face of the globe and the factors regulating climatic change. These constitute the essential foundations for the way in which the various types of plants and animals (including humans) form complex, interdependent communities. ... Research in a wide variety of disciplines is increasingly making it clear that life on earth and all human societies depend on the maintenance of a number of delicate balances within and between a whole series of complex processes. The findings help us to understand the way in which the environment has influenced the development of human societies and, just as important, the human impact on earth.
(Ponting, 1991)

Table 20.5 Definitions of sustainabililty pillars

Citation	Social	Ecological	Economic	Goal
Brown *et al.* (1987)	Continued satisfaction of basic human needs	Continued productivity and functioning of ecosystems; protection of genetic resources and conservation of biological diversity	Limitations that a sustainable society must place on economic growth	Three distinct but interrelated perspectives
Barbier (1987)	Cultural diversity, institutional sustainability, social justice, participation	Genetic diversity, resilience, biological productivity	Satisfying basic needs (reducing poverty), equity-enhancing, increasing useful goods and services	Maximise the goals across all these systems through an adaptive process of trade-offs
Munasinghe (1993)	Equity and participation	Preserve biological and physical systems	Maximise income whilst maintaining capital stock	Integration of competing "non-comparable" objectives
Elkington (1997)	People	Planet	Profit	Triple bottom line (TBL) accounting method
Custance and Hillier (1998)	Social progress	Protection of the environment	Maintenance of economic growth	Balance between three broad objectives

Source: Purvis *et al.* (2018)

Given the differing, and somewhat ambiguous, perceptions of sustainability, numerous methods have been proposed to implement sustainable development. Hugé *et al.* (2013) grouped these disparate interpretations into three broad 'discourses' on sustainable development (where discourse is defined as "a specific ensemble of ideas, concepts, and categorisations that are produced, reproduced, and transformed in a particular set of practices and through which meaning is given to physical and social realities"; Hajer, 1995):

- integration: pragmatically integrates development and environmental goals—relying on mostly anthropocentric frameworks, such as ecosystem services (see Section 20.3), and involves compromise and political consensus at a jurisdictional level;
- limitations: emphasises imposition of limits on human activities—based on ecological limits to population growth and resource availability, this approach requires strategies to manage resource scarcities and ethical constraints to ensure social justice, and embraces the concepts of resilience (see Sections 7 and 15 and Excursus 21.1), ecological footprints (see Excursus 20.3), and critical environmental capital (see Section 20.3); and
- process of change: this view sees change and uncertainty as an inherent continua in the development cycle, requiring transformation of society so that human lifestyles adapt to resource availability.

One of the key requirements for monitoring sustainable development is the definition of operational indicators "that provide manageable units of information on economic, environmental, and social conditions" (Custance and Hillier, 1998; Böhringer and Jochem, 2007).

The 2030 Agenda for Sustainable Development identified 17 global goals that were explicitly based on the three pillars of sustainability shown in Figure 20.5 (see Excursus 20.2). Progress towards these goals and their 169 targets is monitored using an agreed global indicator framework of 231 unique indicators (UN, 2019, 2020a). The Global Indicator Framework reports on progress towards indicators using available datasets (traditional national accounts, household surveys, and routine administrative data) and new data sources such as geospatial information, citizen science, and Big Data (GEO, 2020a). Geospatial datasets, including EO, are essential to make this process feasible, effective, and ongoing. For example, satellite-based EO data can:

- complement traditional data sources;
- provide spatially and temporally denser information on multiple scales;
- deliver wall-to-wall ecosystem coverage;
- improve frequency or richness of data;
- save money on traditional survey methods;
- provide the only viable option in relation to global indicators; and
- allow consistent and comparable measurements across different countries and regions (GEO, 2017).

Examples of EO-based monitoring programs working towards these sustainable development goals (SDG) are given in Section 21.3. The Global Footprint Network is a freely accessible, online system that monitors sustainability for nations, regions, and the collective world by comparing resource production with consumption. As detailed in Excursus 20.3, it paints a bleak picture for our sustainable future on planet Earth.

Excursus 20.2—Global Sustainable Development Agreements

Source: *https://sustainabledevelopment.un.org*

The 2030 Agenda for Sustainable Development, adopted by all UN Member States in 2015, provides a shared blueprint for peace and prosperity for people and the planet, now and into the future. Based on 17 Sustainable Development Goals (SDGs), this build on decades of work to attain global agreement to end poverty and conserve natural resources. Originating at the Earth Summit in Rio de Janeiro, Brazil, in 1992, where more than 178 countries adopted Agenda 21 (a comprehensive plan of action to build a global partnership for sustainable development to improve human lives and protect the environment), global collaboration moved through various agreements and goals, including the Millennium Development Goals (MDG), and culminated in the UN Conference on Sustainable Development in Rio de Janeiro, Brazil, in June 2012, ("The Future We Want") where a process was launched to develop a set of SDGs to build upon the MDGs.

Several major international agreements were adopted in 2015, including (see Section 20.6 for links):

- Sendai Framework for Disaster Risk Reduction (March 2015);
- Addis Ababa Action Agenda on Financing for Development (July 2015);
- Transforming our world: the 2030 Agenda for Sustainable Development with its 17 SDGs (adopted at the UN Sustainable Development Summit in New York, September 2015); and
- Paris Agreement on Climate Change (December 2015).

The 17 SDGs are:

Goal 1: End poverty in all its forms everywhere.

Goal 2: End hunger, achieve food security and improved nutrition and promote sustainable agriculture.

Goal 3: Ensure healthy lives and promote wellbeing for all at all ages.

Goal 4: Ensure inclusive and equitable quality education and promote lifelong learning opportunities for all.

Goal 5: Achieve gender equality and empower all women and girls.

Goal 6: Ensure availability and sustainable management of water and sanitation for all.

Goal 7: Ensure access to affordable, reliable, sustainable and modern energy for all.

Goal 8: Promote sustained, inclusive, and sustainable economic growth, full and productive employment and decent work for all.

Goal 9: Build resilient infrastructure, promote inclusive and sustainable industrialisation, and foster innovation.

Goal 10: Reduce inequality within and among countries.

Goal 11: Make cities and human settlements inclusive, safe, resilient, and sustainable.

Goal 12: Ensure sustainable consumption and production patterns.

Goal 13: Take urgent action to combat climate change and its impacts.[17]

Goal 14: Conserve and sustainably use the oceans, seas, and marine resources for sustainable development.

Goal 15: Protect, restore, and promote sustainable use of terrestrial ecosystems, sustainably manage forests, combat desertification, and halt and reverse land degradation and halt biodiversity loss.

Goal 16: Promote peaceful and inclusive societies for sustainable development, provide access to justice for all, and build effective, accountable, and inclusive institutions at all levels.

Goal 17: Strengthen the means of implementation and revitalise the global partnership for sustainable development.

In order to make the 2030 Agenda a reality, broad ownership of the SDGs must translate into a strong commitment by all stakeholders to implement the global goals.

If you harvest a crop you are removing nutrients from that ecosystem—
for sustainable production they need to be replaced.
(Rattan Lal)

17 Acknowledging that the United Nations Framework Convention on Climate Change is the primary international, intergovernmental forum for negotiating the global response to climate change.

Excursus 20.3—Global Footprint Network

Source: GFN (2020)

The Global Footprint Network measures the sustainability of populations around the world in terms of two metrics that are standardised to units of global hectares (gha—biologically productive hectare with world average biological productivity for a given year):

- ecological footprint (EF)—their consumption of resources and absorption of waste products; and
- biocapacity (BC)—the productivity of their ecological assets (Borucke *et al.*, 2013).

These metrics are used to generate several national, regional, and global accounts, including:

- ecological deficit—BC < EF, meaning that the population is not self-sufficient so relies on imported goods, liquidation of ecological assets, and/or CO_2 emissions into the atmosphere;
- ecological reserve—BC > EF; and
- 'Earth Overshoot Day'—the number of days in a given year that the biocapacity of Earth can support its population. When counted on from 1 January, this has moved from 29 December in 1970 (when global resource demand was about equal to supply) to 29 July in 2019 (when we are collectively overbudget; Wackernagel *et al.*, 2019; GFN, 2020).

The balance between ecological footprint and biocapacity for Australia is shown in Figure 20.6. While we are still keeping our consumption head above the 'pool' of available resources, the ecological reserve is decreasing with time.

In the Global Footprint Network, usage of the world's productive surface area is represented by six categories (cropland, grazing land, fishing grounds, built-up land, forest area, and carbon demand on land), each of which is tracked to derive the ecological footprint for each population (city, nation, or state). The average area of biologically active surface per person globally is 1.6 gha. The total EF for selected countries in 2016 can be compared in terms of these productive surface area categories or relative to population, which paints a different picture.

One measure of sustainable development compares the UN Human Development Index (HDI, based on average longevity, income, and access to education) for a population with its EF. An HDI over 0.8 is considered 'very high'. In 2016 Australia had an HDI value of 0.94 versus an EF (in units of gha per person) of 6.64—a lucky country indeed!

Figure 20.6 Ecological Footprint and Biocapacity for Australia

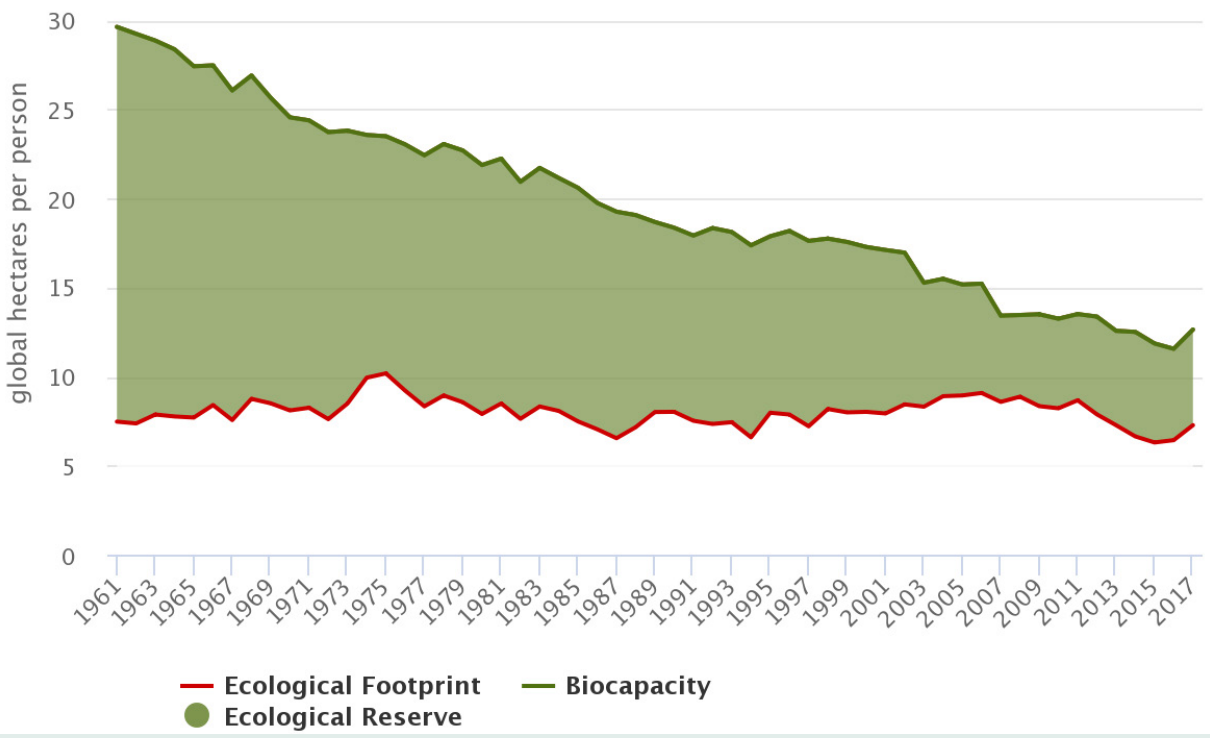

Source: Global Footprint Network, 2021 National Footprint and Biocapacity Accounts: *https://data.footprintnetwork.org/#/countryTrends?cn=10&type=BCpc,EFCpc*

20.5 Environmental-Economic Accounting

When the social science of economics was introduced only a few centuries ago, it represented a shift in social organisation towards market-driven trading of land, labour, and capital, rather than the feudal bartering system that had operated for many centuries in most of the 'civilised' world prior to the industrial revolution. Investments, increased productivity, and individual wealth—namely capitalism—were encouraged, with the expectation that economic gain would benefit society (Smith, 1776). However, classical economics, where the free market achieves balance between supply and demand (through the pursuit of individual self-interest, division of labour, and freedom of trade), and more recent economic theories (including Keynesian and Marxist), where governments regulate demand to ensure full employment, all focus on production, assume resources are infinite, and regard labour as a commodity. They also ignore the social and environmental costs of producing goods, such as air, water, and soil pollution, and the direct and indirect impacts of these 'externalities' on the health and wellbeing of humans and other biota (Ponting, 1991).

In any organisation that manages money, accounting is the process of tracking, analysing, and reporting the movement of finances and assets. The goal is generally to ensure that income is greater than expenditure, while complying with statutory regulations. Accounting has traditionally been limited to measuring and scrutineering the commodites of land, labour, and capital, but in the last few decades there have been attempts to also reckon the environmental costs of production, and the impact of current consumption on future production and sustainability (e.g. Schumacher, 1973; Henderson, 1978).

The concepts and practices of ecosystem and environmental accounting were introduced in Volume 2D—Section 14.2.1. In a general sense, environmental accounting tracks relevant environmental attributes to monitor the condition of natural resources, whereas ecosystem accounting is defined as "a coherent framework for integrating measures of ecosystems and the flows of services from them with measures of economic and other human activity" (SEEA, 2020a). These approaches are complementary, with the latter having a greater focus on ecosystem integrity and "how individual environmental assets interact as part of natural processes within a given spatial area" (SEEA, 2020a).

One example of an Australian environmental accounting system is OzWALD, a model-data fusion system that is heavily reliant on EO datasets (van Dijk *et al.*, 2017; van Dijk and Rahman, 2019). OzWALD ingests a variety of datasets into a water balance model to estimate relevant parameters for vegetation, as well as energy, water, and carbon balance, and generates national annual reviews of the current status of, and relative changes in, the Australian environment (see Volume 2D—Excursus 14.2). Examples of ecosystem accounting measures are given in Table 20.6 (see also Vallecillo *et al.*, 2018). Bio-economic modelling approaches have also been developed in recent decades and used to determine the direct and indirect impacts of agricultural intensification on selected ecosystem services (Flichman and Allen, 2013; Kirchweger *et al.*, 2020; Ogilvy, 2020).

The measure of success is not whether you have a tough problem to deal with,
but whether it's the same problem you had last year.
(John Foster Dulles)

Table 20.6 Examples of ecosystem accounting measures

ABARES: Australian Bureau of Agricultural and Resource Economics; ABS: Australian Bureau of Statistics; BoM: Bureau of Meteorology

Ecosystem service	Example	Accounting
Provisioning	Agricultural commodities	Annual statistics (ABARES, ABS)
	Agricultural fertilisers	Patchy records by government and research agencies
	Fresh water	National Water Accounts (ABS, BoM)
Supporting	Native vegetation extent	National Vegetation Information System (NVIS)
	Soil resources	Australian Soil Resources Information System (ASRIS)
Regulating	Carbon sequestration	National Carbon Accounting System (NCAS)
	Pollination	Bio-economic models
	Water quality	SEEA-Water
Cultural	Recreation	Tourism statistics
	Landscape aesthetics	Real estate value

The Accounting for Nature (AfN) framework develops biophysical accounts for environmental assets (such as vegetation, soils, biota, and waterways, including groundwater) using a common environmental condition index (Econd), based on reference condition benchmarks (WGCS, 2016). Such measures of environmental condition inform management decisions to improve, rather than degrade, natural capital. The AfN framework presents a standardised "system of rules and processes designed to ensure the integrity and transparency of environmental accounts, no matter the environmental asset being measured" (AfN, 2020). It is designed for local/regional scale applications, such as individual farms, which can be aggregated to national scale, and links through to enterprise microeconomic and accounting systems, including the option of independent certification of environmental accounts. AfN complements other systems for standards and compliance with the goal of promoting sustainability at the level of individuals and enterprises (see Section 20.6). It is also compatible with SEEA (see Excursus 20.4).

Environmental-economic accounting aims to understand both the condition of the environment and its relationship with the economy. SEEA, an accepted international standard for environmental-economic accounting, is described in Excursus 20.4.

Since the full costs of any action anywhere in the world must be borne by someone, somewhere, sometime, it is important that our accounting system makes provision for this. We accept however, that ecological processes are so complex and can spread so far in space and time, that this will be exceptionally difficult. Nonetheless, given the truism that a satisfactory accounting system is one which supports and helps perpetuate the social system from which it derives, we must attempt to devise one which is fitted to a society based on a sober assessment of ecological reality and not on the anthropocentric pipe-dream that we can do what we will to all species, not excepting, it seems, future generations of our own. It is worth recalling Prof. Commoner's dictum that since economics is the science of the distribution of resources, all of which are derived from the ecosphere, it is foolish to perpetuate an economic system which destroys it. Ideally (and as befits the etymology of the two words), ecology and economics should not be in conflict: ecology should provide the approach, the framework for an understanding of the interrelationships of social and environmental systems, and economics should provide the means of quantifying those interrelationships in the light of such an understanding, so that decisions on alternative courses of action can be made without undue difficulty.
(Goldsmith and Allen, from A Blueprint for Survival #243, 1972)

Excursus 20.4—System of Environmental Economic Accounting

Source: SEEA (2018, 2020a)

The System of Environmental-Economic Accounting (SEEA) is an international statistical standard that uses a systems approach to bring together economic and environmental information to measure the contribution of the environment to the economy and the impact of the economy on the environment. It uses internationally agreed standard concepts, definitions, classifications, accounting rules and tables for producing internationally comparable statistics and accounts. The SEEA is produced and released under the auspices of the UN, the European Commission (EC), the Food and Agriculture Organisation of the UN (FAO), the Organisation for Economic Co-operation and Development (OECD), International Monetary Fund (IMF), and the World Bank Group (WBG).

The System of National Accounts (SNA) is a measurement framework that has been evolving since the 1950s to embody the pre-eminent approach to the measurement of economic activity, economic wealth, and the general structure of the economy. The SEEA framework follows a similar accounting structure and uses concepts, definitions, and classifications consistent with the SNA in order to facilitate the integration of environmental and economic statistics.

SEEA Central Framework (SEEA CF) focuses on physical quantities of stocks and flows of goods and services, their monetary values, and tracking supply and use (see Figure 20.7). This central framework is very human-centric, for example harvesting of crops considers the value added to produce, then receive, goods and services. Without the human 'user' to receive the goods and services, there is no 'transaction' to link environmental economic accounts to the SNA (UN, 2014). SEEA CF is an accepted statistical standard that facilitates accounts in several thematic areas, including:

- Agriculture, Forests, and Fisheries—integrates information on the environment and the economic activities of these industries that impact and directly depend on the environment and its resources. Integrating information about agriculture, forestry, and fisheries facilitates understanding of the trade-offs and dependencies between these activities and their related environmental factors.
- Air Emissions—provide information on emissions released to the atmosphere by establishments and households as a result of production, consumption, and accumulation processes. The air emissions accounts record the generation of air emissions by resident economic units according to type of gaseous or particulate substance.
- Energy—supports analysis of the role of energy within the economy, the state of energy inputs, and various energy-related transactions of environmental interest. Energy information is typically presented in physical terms, but monetary valuations are also applied to various stocks and flows.
- Environmental Activity—provides information on transactions concerning activity undertaken to preserve, protect, and manage the environment. Understanding environmental activity is critical to understanding whether economic resources are being used effectively to reduce pressures on the environment and maintain the capacity of the environment to deliver benefits.
- Ecosystems—constitutes an integrated statistical framework for organizing biophysical data, measuring ecosystem services, tracking changes in ecosystem assets, and linking this information to economic and other human activity.
- Land—provides information on land use and land cover, and can enable an assessment of the changing shares of different land uses and land covers within a country. Understanding these characteristics and changes is critical to understanding the impacts of urbanisation, the intensity of crop and animal production, afforestation and deforestation, the use of water resources, and other direct and indirect uses of land.
- Material Flow—provides an aggregate overview of material inputs and outputs in terms of inputs from the environment, outputs to the environment, and the physical amounts of imports and exports. Understanding economy-wide material flow is critical to understanding resource use by the economy and eco-efficiency.
- Water—an integrated approach to water monitoring, bringing together a wide range of water related statistics across sectors into one coherent information system. This serves as a conceptual framework and set of accounts which presents hydrological information alongside economic information in a consistent manner.

Figure 20.7 Overview of SEEA Central Framework

Natural inputs from the environment to the economy include mineral, timber, and water resources. Within the economy, industries, households, and governments produce and consume goods and services, or products. Residuals from the economy to the environment include air emissions and return flows of water (see also Figure 20.3).

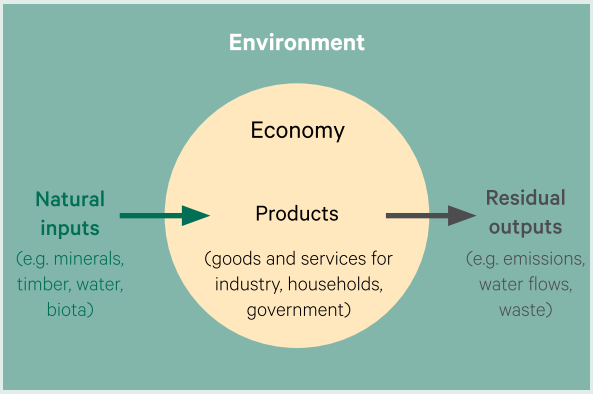

Adapted from: UN (2014)

While SEEA CF considers individual environmental assets and how those assets move between the environment and the economy (see Figure 20.7), SEEA Experimental Ecosystem Accounting (SEEA EA) views the perspective of ecosystems and determines how individual environmental assets interact as part of natural processes within a given spatial area (see Figure 20.8). This framework is still considered 'experimental' but is currently undergoing a large, global revision process, with the aim of becoming a statistical standard. SEEA EA primarily accounts for the non-human elements of environmental-economic accounts. Although it still emphasises the goods and services benefitting humans, it considers ecosystem extent and condition, and the future capacity to produce and provide goods and services. These considerations can relate to land use and management practices, environmental sustainability and degradation, progress towards achieving set targets, or other long term environmental interventions through monitoring and evaluation (CoA, 2018). Currently this framework comprises a set of accounts to quantify ecosystems in terms of:

- ecosystem extent—serves as a common starting point for ecosystem accounting, by organising information on the extent of different ecosystem types within a country in terms of area;
- ecosystem condition—measures the overall quality of an ecosystem asset, and captures, in a set of key indicators, the state or functioning of the ecosystem in relation to both its naturalness and its potential to supply ecosystem services;
- ecosystem services—measures their supply as well as their corresponding users and beneficiaries, classified by broad national accounting categories or other groupings of economic units;
- monetary asset—records the monetary value of opening and closing stocks of all ecosystem assets within an ecosystem accounting area and additions and reduction to those stocks; and
- thematic—covers accounts for land, water, carbon, and biodiversity, which are standalone accounts on topics of importance in their own right for policy and analysis, but also of direct relevance in the compilation of ecosystem accounts.

The global revision process may see improved incorporation of environmental/ecosystem integrity, intrinsic values, biodiversity, and inter- and intra-ecosystem service flows that support environmental/ecosystem functioning into the SEEA EA (SEEA, 2020b).

Thus, an environmental-economic account, such as SEEA, presents information in physical and monetary terms regarding environmental stocks and flows between the environment and the economy as well as economic activity related to the environment. By providing a full picture of its connection to the economy, environmental-economic accounts can help make the case for protecting and conserving biodiversity (see Section 19). Ecosystem accounts used in combination with information on expenditures provide decision makers with a clear picture of the return-on-investment from biodiversity protection. Examples of the kinds of questions that the SEEA can help answer include:

- Who benefits and who is negatively impacted from natural resource use? What are the impacts on the state of the environment and on specific sectors of the economy?
- How does depletion of natural resources affect measures of the real income of a nation? What extracting industries and owners of natural resources are responsible for depletion?
- To what extent is decoupling between resource use and economic growth taking place? Which sectors have the highest water productivity or are most energy intensive?
- How is the wealth of nations, specifically its natural capital, developing over time?
- Are the expenditures on environmental protection effective?
- To what extent is the tax system greening? What economic instruments are in place? And what is the impact of new instruments?

- What is the size of environmental investment in the economy? How many green jobs is the economy generating?
- Are current trends in production and consumption of resources sustainable? Is the amount of waste generated increasing or not; how much of this is being recycled in what economic sectors?
- What is the carbon footprint or water footprint of the nation?
- Which ecosystem services are being generated, who is benefiting from them, and where are they located?

Over 80 countries, including Australia, maintain active environmental-economic accounting programs based on SEEA. This is an ongoing project with updates, extensions, and resources being undertaken in several areas, including biodiversity and SDG (see Sections 19.3 and 20.4 respectively).

Figure 20.8 Environmental accounts versus environmental-economic accounts

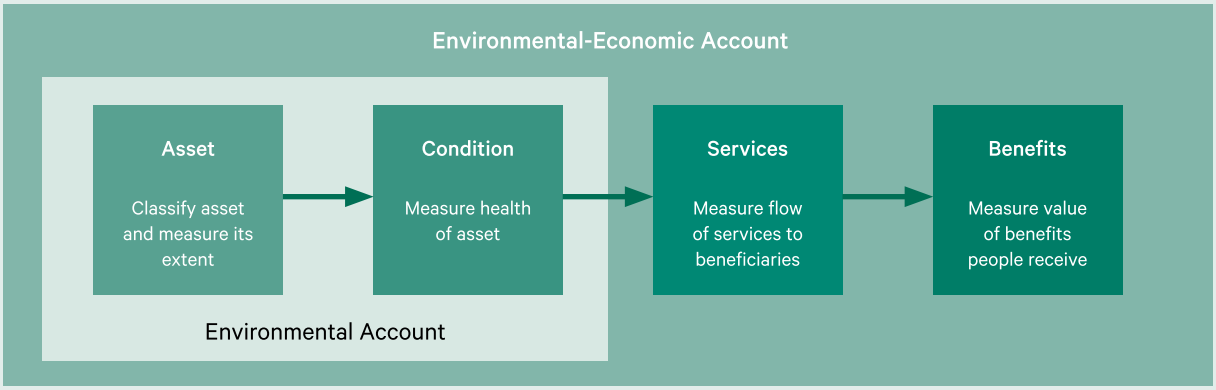

Adapted from: CoA (2018) page 3

Economics has enthroned some of our most unattractive predispositions: material acquisitiveness, competition, gluttony, pride, selfishness, shortsightedness, and just plain greed.
(Henderson, 1978)

In Australia, the SEEA framework is used to generate the Australian Environmental Economic Accounts (AEEA) for the themes of water, energy, waste, and greenhouse gas emissions (ABS, 2019a). Some data used in AEEA is sourced externally, such as the National Carbon Accounting System (NCAS), that reports Australia's national and international greenhouse gas emissions (see Section 17). Other jurisdictions and private organisations have also applied this approach for specific areas of environmental accounting. Examples of Australian environmental economic accounts based on SEEA are listed in Table 20.7, some of which are derived from EO data sources (CoA, 2018).

A national plan entitled 'Environmental Economic Accounting—A Common National Approach: Strategy and Action Plan' (CoA, 2018) has the vision that the "Australian community understands the environment's contribution to our quality of life, and its condition and value are accounted for in decision making for a prosperous and healthy society". The Strategy is hoping to set up a level of consistency across the applications of SEEA within Australia, and is assisting in bringing together expertise and experience towards this purpose from federal, state, and territory government agencies, the private sector and academia (CoA, 2018).

This collaborative effort between the Australian Department of Agriculture, Water and the Environment (DAWE; formerly Department of Environment and Energy), its state and territory counterparts, and the ABS compiles data from various jurisdictions and agencies, with the aim of presenting an integrated perspective at a range of scales within Australia: national, single and multi-state/territory, regional, local, and farm. For example, a recent iteration of the ABS waste accounts (ABS, 2019b) was developed and released under this strategy. Current projects under the Strategy include:

- an experimental national land account (see Section 3.3.4);
- case studies of experimental ecosystem accounts; and
- pilot studies of ocean accounts (see Volume 3B).

ABS and the Bureau of Meteorology (BoM) have also collaborated to produce an integrated water account for the ACT (ABS, 2019c). These pilot accounts use the Australian Water Accounting Standard (AWAS; BoM, 2012) and SEEA frameworks to integrate two complementary Australian environmental-economic accounting approaches, namely the:

- ABS Water Account, Australia (WAA), which defines the:
  - flows of water from the environment to the water supply industry and other economic activities;
  - flows of water from the water supply industry to households and businesses; and the
  - monetary values associated with water supplied and used in the economy; and the
- BoM National Water Account (NWA), which defines the:
  - volume of water in the environment and its availability; and the
  - rights to abstract water and the actual abstraction over time (ABS, 2019c; see Excursus 10.2).

This collaboration produced a range of water accounts for the ACT in terms of water assets and liabilities, water condition and quality, as well as the physical and monetary supply and use of water. Such integrated, quantitative information is valuable for reporting and managing water resources for both the economy and the environment.

Table 20.7 Australian environmental economic accounts based on SEEA

These accounts quantify environmental resources in terms of the available assets and their supply and usage in both the environment and the economy. (ABS: Australian Bureau of Statistics; DEE: Department of Environment and Energy; DELWP Victorian Department of Environment, Land, Water and Planning; BoM: Bureau of Meteorology)

Account name	Agency	Subject	Scale	Measurement units	Frequency
Water Account, Australia	ABS	Water supply and use within the economy	National, state/territory	Megalitres, dollars	Annual
Energy Account, Australia	ABS	Energy supply and use within the economy	National	Petajoules, dollars	Annual
Waste Account, Australia	ABS/DEE	Waste generation by industry and households	National	Megatonnes, dollars	Annual
National Greenhouse Accounts	DEE	Greenhouse gas emissions	National, state/territory, industry	Tonnes of carbon equivalent	Annual
National Water Account	BoM	Availability and usage of water resources in the environment	National, regional	Megalitres	Annual
Natural Capital Finance Alliance	Natural Capital Coalition	Business dependencies on natural capital	Business	Varies	Varies
Land Account	ABS	Land use, land cover, and value	Regional, state/territory	Area (ha), dollars	Experimental
Experimental Ecosystem Accounts for the Great Barrier Reef Region	ABS	Ecosystem goods and services	Regional	Area, dollars	Experimental
Victorian Experimental Ecosystem Accounts	DELWP	Ecosystem extent and services indicator	State, regional	Area per unit time (e.g. ha/year)	Experimental
Integrated Water Accounts for the Canberra region	ABS/BoM	Water assets, supply, usage, and quality for society and environment	Territory	Megalitres, dollars	Pilot

Source: CoA (2018) Tables 1 and 2 and ABS (2019c)

SEEA requires time series data to establish the opening and closing stocks for the accounting period. It also requires the ability to undertake change detection for tracking flows, or reasons for change that can be linked to human use/management or to natural processes and disturbance regimes.

As introduced in Section 3.2, the Earth Observation Data for Ecosystem Monitoring (EODESM; Lucas and Mitchell, 2017; EcoPotential, 2021) constructs land cover categories for different points in time according to the Food and Agriculture Organisation (FAO) Land Cover Classification System (LCCS, Version 2; see Excursus 3.1) and has been advanced to include an evidence-based change framework that integrates the Drivers-Pressures-State-Impacts-Response framework (DPSIR; see Section 11.2) and a globally relevant taxonomy of change (Lucas *et al.*, *in prep*). This combined capability was implemented within Digital Earth Australia (DEA; see Volume 2D—Section 11.2) to generate continental maps of land cover and change dynamics for 2010 and 2015, that were subset for four test areas in eastern Australia (Lucas *et al.*, 2019) and used to support accounting under SEEA as demonstration.

Change detection requires consistency in data over time, not just availability (see Volume 2D). To effectively inform the decision making process, the frequency of the time series dataset is important. Some of the reasons for change will occur at short timescales at finer resolutions, while others are only visible in longer timescales at coarser resolutions. It is a balancing act to determine the range of end user requirements for environmental-economic accounts and match those requirements through to the correct spatial and non-spatial environmental, economic, and socio-cultural data and indicators (Vardon *et al.*, 2016).

As detailed in Sections 11–19 above, EO datasets, being timely, objective, repeatable, and relatively inexpensive, are appropriate for various environmental mapping, monitoring, and modelling studies (see Sections 8–10) in a wide range of applications involving terrestrial vegetation. Many global organisations, such as the UN Global Working Group on Big Data for Official Statistics (UN, 2020b), the Global Strategy to Improve Agricultural and Rural Statistics (GSARS, 2015, 2017), and GEO Earth Observations for Ecosystem Accounting (EO4EA; GEO, 2020b), are exploring the viability of deriving official statistics from a range of spatial data sources including EO, with methodological, legal, security, and privacy ramifications (UN, 2015). EO4EA "envisions a future where EO systems enable environmental transparency and the value of ecosystems is incorporated into conventional economic accounts and decision making, leading to an important shift in the valuation of natural resources and the use of that information for policy and programmatic decision making" (GEO, 2019). Some relevant guiding questions to assess the suitability of using EO data products for these purposes are given in García *et al.* (2016) and Murray *et al.* (2018).

The adoption of agriculture was the most fundamental change in human history. Not only did it produce settled societies for the first time, it also radically changed society itself. Gathering and hunting groups were essentially egalitarian, but sedentary communities, almost from the beginning, resulted in increasing specialisation within society and the emergence of religious, political and military elites and a state with the power to direct the rest of society. At the root of these social changes was a new attitude to the ownership of food. Gathering and hunting groups generally regarded plants and animals not as things 'owned' by individuals but as available to all. Plants and animals are taken from the wild and there are normally strong social conventions on how food must be shared between all members of the group. Agriculture introduced the idea of ownership of food either by individuals or larger organisations. The move to growing crops in fields and the practice of herding and breeding flocks of animals opened the way to viewing resources used and the food produced as 'property' and the far greater degree of time and effort involved compared with gathering and hunting encouraged this trend.
(Ponting, 1991)

20.6 Further Information

Sustainable Development (UN)

Sustainable Development Goals: *https://sustainabledevelopment.un.org*

Sendai Framework for Disaster Risk Reduction 2015–2030: *https://sustainabledevelopment.un.org/frameworks/sendaiframework*

Addis Ababa Action Agenda of the Third International Conference on Financing for Development: *https://sustainabledevelopment.un.org/frameworks/addisababaactionagenda*

Transforming our world: the 2030 Agenda for Sustainable Development: *https://sustainabledevelopment.un.org/post2015/transformingourworld*

United Nations Sustainable Development Summit 2015: *https://sustainabledevelopment.un.org/post2015/summit*

Paris Agreement: *https://sustainabledevelopment.un.org/frameworks/parisagreement*

Division for Sustainable Development Goals: *https://sustainabledevelopment.un.org/about*

High-Level Political Forum on Sustainable Development: *https://sustainabledevelopment.un.org/hlpf*

GEO: Earth Observation for Sustainable Development: *https://eo4sd.esa.int/*

https://www.earthobservations.org/documents/publications/201703_geo_eo_for_2030_agenda.pdf

https://www.earthobservations.org/documents/publications/201704_geo_unggim_4pager.pdf

Ecosystem Services

Intergovernmental Science-Policy Platform on Biodiversity and Ecosystem Services (IPBES): *https://ipbes.net/*

Environmental-Economic/Ecosystem Accounting

UN Framework: System of Environmental-Economic Accounting (SEEA): *https://seea.un.org/*

Earth Observation for Ecosystem Accounting (EO4EA): *https://www.eo4ea.org/*

Wealth Accounting and the Valuation of Ecosystem Services (WAVES): *https://www.wavespartnership.org/*

Australian Environmental-Economic Accounts

ABS: *https://www.abs.gov.au/Environmental-Management*

Australian Environmental Information Systems

NEII (National Environmental Information Infrastructure): *http://neii.gov.au/data-viewer*

Accounting for Nature (AfN) Framework: *https://www.accountingfornature.org/*

OzWALD:

Australia's Environment: *http://wald.anu.science/data_services/data/continuous-and-comprehensive-national-environmental-reporting-australias-environment/*

Australia's Environmental Explorer: *www.ausenv.online*

State of Environment: SOE 2016: *https://www.environment.gov.au/science/soe*

State-based Environmental Monitoring

Statewide Landcover and Trees Study (SLATS, Queensland): *https://www.qld.gov.au/environment/land/management/mapping/statewide-monitoring/slats*

Ground cover monitoring (Queensland): *https://www.qld.gov.au/environment/land/management/mapping/statewide-monitoring/groundcover*

SLATS NSW: *https://www.environment.nsw.gov.au/topics/animals-and-plants/native-vegetation/reports-and-resources*

Habitat Hectares (Victoria): *https://www.environment.vic.gov.au/native-vegetation/native-vegetation/biodiversity-information-and-site-assessment*

Spatial data for Victoria: *https://www2.delwp.vic.gov.au/maps?_ga=2.6531511.420315026.1549698228-873342548.1549698228*

20.7 References

AfN (2020). *Accounting for Nature* website: *https://www.accountingfornature.org/*

ABS (2018). *Australian Environmental-Economic Accounts, 2018*, webpage: *http://www.abs.gov.au/ausstats/abs@.nsf/mf/4655.0*

ABS (2019a). *Australian Environmental-Economic Accounts, 2019*, webpage: *https://www.abs.gov.au/AUSSTATS/abs@.nsf/Lookup/4655.0Explanatory%20Notes12019?OpenDocument*

ABS (2019b). *Waste Account, Australia, Experimental Estimates, 2016–17* webpage: *https://www.abs.gov.au/ausstats/abs@.nsf/mf/4602.0.55.005*

ABS (2019c). *Integrated Water Accounts for the Canberra region, 2013–14 to 2016–17* webpage: *https://www.abs.gov.au/AUSSTATS/abs@.nsf/mf/4610.0.55.010*

Alcaraz-Segura, D., Di Bella, C.M., and Straschnoy, J.V. (Eds) (2014). *Earth Observation of Ecosystem Services*. CRC Press, Boca Raton. ISBN: 978-1-4665-0589-6

Andrew, M.E., Wulder, M.A., and Nelson, T.A. (2014). Potential contributions of remote sensing to ecosystem service assessments. *Progress in Physical Geography*, 38(3), 328–353. doi:*10.1177/0309133314528942*

Andrew, M.E., Wulder, M.A., Nelson, T.A., and Coops, N.C. (2015). Spatial data, analysis approaches, and information needs for spatial ecosystem service assessments: a review. *GIScience and Remote Sensing*, 52(3), 344–373. doi:*10.1080/15481603.2015.1033809*

Barbier, E.B. (1987). The concept of sustainable economic development. *Environmental Conservation*, 14, 101–110. *https://doi.org/10.1017/S0376892900011449*

Bestelmeyer, B.T., and Briske, D.D. (2012). Grand challenges for resilience-based management of rangelands. *Rangeland Ecology and Management*, 65, 654–663.

Birkhofer, K., Diehl, E., Andersson, J., Ekroos, J., Früh-Müller, A., Machnikowski, F., Mader, V.L., Nilsson, L., Sasaki, K., Rundlöf, M., Wolters, V., Smith, H.G. (2015). Ecosystem services—current challenges and opportunities for ecological research. *Frontiers in Ecology and Evolution*, 2, 87. *https://www.frontiersin.org/article/10.3389/fevo.2014.00087*

Böhringer and Jochem (2007). Measuring the immeasurable—A survey of sustainability indices. *Ecological Economics*, 63, 1–8.

BoM (2012). *Australian Water Accounting Standard 1: Preparation and Presentation of General Purpose Water Accounting Reports*. Water Accounting Standards Board, Bureau of Meteorology. ISBN 978-0-642-70629-4 *http://www.bom.gov.au/water/standards/documents/awas1_v1.0.pdf*

BoM (2013). *Guide to environmental accounting in Australia, Environmental Information Programme Publication Series no. 3*, Bureau of Meteorology, Canberra, Australia.

Borucke, M., Moore, D., Cranston, G., Gracey, K., Iha, K., Larson, J., Lazarus, E., Morales, J.C., Wackernagel, M., and Galli, A. (2013). Accounting for demand and supply of the biosphere's regenerative capacity: The National Footprint Accounts' underlying methodology and framework. *Ecological Indicators*, 24, 518–533. *https://doi.org/10.1016/j.ecolind.2012.08.005*

Boyer, R., Peterson, N., Arora, P., Caldwell, K. (2016). Five approaches to social sustainability and an integrated way forward. *Sustainability*, 8, 1–18. *https://doi.org/10.3390/su8090878*

Brand, U. (2012). Green economy—The next oxymoron? *GAIA–Ecological Perspectives on Science and Society*, 21, 5.

Brown, B.J., Hanson, M.E., Liverman, D.M., and Merideth, R.W. (1987). Global sustainability: Toward definition. *Environmental Management*, 11, 713–719. *https://doi.org/10.1007/BF01867238*

CoA (2018). *Environmental Economic Accounting: A Common National Approach Strategy and Action Plan*. Prepared by the Interjurisdictional Environmental-Economic Accounting Steering Committee for the Meeting of Environment Ministers, Commonwealth of Australia. *https://eea.environment.gov.au/about/national-strategy-and-action-plan*

Cord, A.F., Brauman, K.A., Chaplin-Kramer, R., Huth, A., Ziv, G., and Seppelt, R. (2017). Priorities to advance monitoring of ecosystem services using Earth observation. *Trends in Ecology and Evolution*, 32(6), 416–428. ISSN 0169-5347

Costanza, R., dArge, R., de Groot, R., Farber, S., Grasso, M., Hannon, B., Limburg, K., Naeem, S., Oneill, R.V., Paruelo, J., Raskin, R.G., Sutton, P., van den Belt, M. (1997). The value of the world's ecosystem services and natural capital. *Nature*, 387(6630), 253–260.

Costanza, R., de Groot, R., Braat, L., Kubiszewski, I., Fioramonti, L., Sutton, P., Farber, S., and Grasso, M. (2017). Twenty years of ecosystem services: How far have we come and how far do we still need to go? *Ecosystem Sciences*, 28, 1–16. *https://doi.org/10.1016/j.ecoser.2017.09.008*

Custance, J., and Hillier, H. (1998) Statistical issues in developing indicators of sustainable development. *Journal of the Royal Statistical Society*, 161, 281–290.

Daily, G.C. (1997). *Nature's Services: Societal Dependence on Natural Ecosystems*. Island Press, Washington DC.

Dawson, T.P., Cutler, M.E.J., and Brown, C. (2016). The role of remote sensing in the development of SMART indicators for ecosystem services assessment, *Biodiversity*, 17(4), 136–148. doi:*10.1080/14888386.2016.1246384*

de Araujo Barbosa, C.C., Atkinson, P.M., and Dearing, J.A. (2015). Remote sensing of ecosystem services: A systematic review. *Ecological Indicators*, 52, 430–443.

DEWHA (2010). *Ecosystem Services: Key Concepts and Applications*. Occasional Paper No 1, Department of the Environment, Water, Heritage and the Arts, Canberra.

Ehrlich, P., and Ehrlich, A. (1981). *Extinction: The Causes and Consequences of the Disappearance of Species*. Random House, New York.

Elkington, J. (1997). *Cannibals with forks: the triple bottom line of 21st century business*. Capstone, Oxford.

EcoPotential (2021). *EODESM: Earth Observation Data for Ecosystem Monitoring* webpage, EcoPotential website: *http://www.ecopotential-project.eu/products/eodesm.html*

Flichman, G., and Allen, T. (2013). *Bio-Economic Modeling: State-of-the-Art and Key Priorities*. Working Paper, International Food Policy Research Institute, Washington. *http://ebrary.ifpri.org/utils/getfile/collection/p15738coll2/id/129231/filename/129442.pdf*

García, L., Rodríguez, J.D., Wijnen, M., Pakulski, I. (Eds) (2016). *Earth Observation for Water Resources Management: Current Use and Future Opportunities for the Water Sector*. World Bank Group, Washington, D.C. doi:*10.1596/978-1-4648-0475-5*.

GEO (2017). *Earth Observations in support of the 2030 Agenda for Sustainable Development*. JAXA. *https://www.earthobservations.org/documents/publications/201703_geo_eo_for_2030_agenda.pdf*

GEO (2019). *Implementation Plan for the Earth Observation for Ecosystem Accounting (EO4EA) Initiative. 2020–2022 GEO Work Program*. Group on Earth Observation. *http://earthobservations.org/documents/gwp20_22/eo_for_ecosystem_accounting_ip.pdf*

GEO (2020a). *Earth Observations for the Sustainable Development Goals* webpage, Group on Earth Observation website: *https://www.earthobservations.org/geo_sdgs.php*

GEO (2020b). *Earth Observations for Ecosystem Accounting* website, Group on Earth Observations: *https://www.eo4ea.org/*

GFN (2020). *Global Footprint Network* website: *https://www.footprintnetwork.org/*

Goldsmith, E., and Allen, R. (1972). A Blueprint for Survival. *The Ecologist*, 2(1). *https://web.archive.org/web/20090831193545/http://www.theecologist.info/key27.html*

Gordon, J., Vincent, D., Haberkorn, G., MacGregor, C., Stafford-Smith, M., and Breckwoldt, R. (2001). *Indicators within a decision framework: Social, economic and institutional indicators for sustainable management of the rangelands*. National Land and Water Resources Audit, Canberra.

GSARS (2015). *Handbook on Master Sampling Frames for Agricultural Statistics: Frame Development, Sample Design and Estimation*. Global Strategy to Improve Agricultural and Rural Statistics, UN Statistical Commission, Rome. *http://gsars.org/wp-content/uploads/2016/02/MSF-010216-web.pdf*

GSARS (2017). *Handbook on Remote Sensing for Agricultural Statistics*. Global Strategy to Improve Agricultural and Rural Statistics, UN Statistical Commission, Rome. *http://gsars.org/wp-content/uploads/2017/09/GS-REMOTE-SENSING-HANDBOOK-FINAL-04.pdf*

Hajer, M.A. (1995). *The politics of environmental discourse: Ecological modernization and the policy process*. Oxford University Press, Oxford.

Henderson, H. (1978). *Creating Alternative Futures: The End of Economics*. Kumarin Press, West Hartford. *https://sustainable-finance.io/wp-content/uploads/2018/04/Creating-AF.pdf*

Hugé, J., Waas, T., Dahdoub-Guebas, F., Koedam, N., and Blocak, T. (2013). A discourse-analytical perspective on sustainability assessment: interpreting sustainable development in practice. *Sustainability Science*, 8, 187–198. doi:*10.1007/s11625-012-0184-2*

Jacobs, P., Gardner, J., and Munro, D.A. (1987). Sustainable and equitable development: an emerging paradigm. *Conservation with equity: strategies for sustainable development*. (Eds: Jacobs, P., and Munro, D.A.) IUCN, Cambridge. pp 17–29.

Johnston, P., Everard, M., Santillo, D., Robert, K.-H. (2007). Reclaiming the definition of sustainability. *Environmental Science and Pollution Research*, 14, 60–66. *https://doi.org/10.1065/espr2007.01.375*

Jurskis, V. (2015). *Firestick Ecology*. Connor Court Publishing, Ballarat. 335 p. ISBN: 9781925138740

Keith, D.A., Rodríguez, J.P., Rodríguez-Clark, K.M., Nicholson, E., Aapala, K., Alonso, A., Asmussen, M., Bachman, S., Basset, A., Barrow, E.G., Benson, J.S., Bishop, M.J., Bonifacio, R., Brooks, T.M., Burgman, M.A., Comer, P., Comín, F.A., Essl, F., Faber-Langendoen, D., Fairweather, P.G., Holdaway, R.J., Jennings, M., Kingsford, R.T., Lester, R.E., Nally, R. Mac, McCarthy, M.A., Moat, J., Oliveira-Miranda, M.A., Pisanu, P., Poulin, B., Regan, T.J., Riecken, U., Spalding, M.D., and Zambrano-Martínez, S. (2013). Scientific Foundations for an IUCN Red List of Ecosystems. *PLoS ONE*, 8(5), e62111. doi:*10.1371/journal.pone.0062111*

Kidd, C.V. (1992). The evolution of sustainability. *Journal of Agricultural and Environmental Ethics*, 5, 1–26. *https://doi.org/10.1007/BF01965413*

Kirchweger, S., Clough, Y., Kapfer, M., Steffan-Dewenter, I., and Kantelhardt, J. (2020). Do improved pollination services outweigh farm-economic disadvantages of working in small-structured agricultural landscapes? Development and application of a bio-economic model. *Ecological Economics*, 169, 106535. *https://doi.org/10.1016/j.ecolecon.2019.106535*

Krausmann, F., Gingrich, S., Eisenmenger, N., Erb K. H., Haberl, H., and Fischer-Kowalski, M. (2009). Growth in global materials use, GDP and population during the 20th century. *Ecological Economics*, 68(10), 2696–2705.

Lucas, R., and Mitchell, A., (2017). Integrated Land Cover and Change Classifications. In *The Roles of Remote Sensing in Nature Conservation: A Practical Guide and Case Studies*. (Eds: Díaz-Delgado, R., Lucas, R., Hurford, C.). Springer, Cham, Switzerland. pp. 295–308.

Lucas, R., Mueller, N., Siggins, A., Owers, C., Clewley, D., Bunting, P., Kooymans, C., Tissott, B., Lewis, B., Lymburner, L., and Metternicht, G. (2019). Land Cover Mapping using Digital Earth Australia. *Data*, 4, 143. doi:*10.3390/data4040143*

Lucas, R.M., German, S., Metternicht, G., Schmidt, B., Owers, C., Prober, S., Richards, A., Tretreault-Campbell, S., Williams, K., Mueller, N., Tissot, B.., Chua, S., Colwood, A., Hills, T., Gunawardana, D., McIntyre, A., Chognard, S., Hurford, C., Planque, C., Punalekar, S., Clewley, D., Murray, D., Manakos, I., Blonda, P., Sonnerschein, R., Bunting, P., and Horton, C. (*in prep.*). A Globally Relevant Change Taxonomy and Evidence-based Change Classification Framework. *Global Change Biology,* submitted July 2021.

MEA (2005). *Ecosystems and Human Well-being: Synthesis*. Millennium Ecosystem Assessment, Island Press, Washington, DC.

Munasinghe, M. (1993). *Environmental economics and sustainable development*. The World Bank, Washington

Murray, N.J., Keith, D.A., Bland, L.M., Ferrari, R., Lyons, M.B., Lucas, R., Pettorelli, N., Nicholson, E. (2018). The role of satellite remote sensing in structured ecosystem risk assessments. *Science of the Total Environment*, 619–620, 249–257. *https://doi.org/10.1016/j.scitotenv.2017.11.034*

Ogilvy, S. (2020). *Toward a methodology for incorporating ecological capital into the accounts of individual entities*. Ph.D. Thesis, ANU. *https://openresearch-repository.anu.edu.au/handle/1885/204830*

Pettorelli, N., Schulte, Bühne, H., Tulloch, A., Dubois, G., Macinnis-Ng, C., Queirós, A.M., Keith, D.A., Wegmann, M., Schrodt, F., Stellmes, M., Sonnenschein, R., Geller, G.N., Roy, S., Somers, B., Murray, N., Bland, L., Geijzendorffer, I., Kerr, J.T., Broszeit, S., Leitão, P.J., Duncan, C., El Serafy, G., He, K.S., Blanchard, J.L., Lucas, R., Mairota, P., Webb, T.J., Nicholson, E. (2017). Satellite remote sensing of ecosystem functions: opportunities, challenges and way forward. *Remote Sensing in Ecology and Conservation*, 4, 71-93. *https://doi.org/10.1002/rse2.59*.

Pollock, D. (2019). *The Wooleen Way*. Scribe, Melbourne. ISBN: 9781925849257

Ponting, C. (1991). *A Green History of the World*. Penguin.

Purvis, B., Mao, Y., and Robinson, D. (2018). Three pillars of sustainability: in search of conceptual origins. *Sustainability Science*, 14, 681–695. *https://doi.org/10.1007/s11625-018-0627-5*

Ramirez-Reyes, C., Brauman, K.A., Chaplin-Kramer, R., Galford, G.L., Adamo, S.B., Anderson, C.B., Anderson, C., Allington, G.R.H., Bagstad, K.J., Coe, M.T., Cord, A.F., Dee, L.E., Gould, R.K., Jain, M., Kowal, V.A., Muller-Karger, F.E., Norriss, J., Potapov, P., Qiu, J., Rieb, J.T., Robinson, B.E., Samberg, L.H., Singh, N., Szeto, S.H., Voigt, B., Watson, K., and Wright, T.M. (2019). Reimagining the potential of Earth observations for ecosystem service assessments. *Science of the Total Environment*, 665, 1053–1063. doi:*10.1016/j.scitotenv.2019.02.150*.

Redclift, M. (2005). Sustainable Development (1987–2005): An Oxymoron Comes of Age. *Sustainable Development*, 13, 212–227. doi:*10.1002/sd.281*

Schumacher, E.F. (1973). *Small is Beautiful: A Study of Economics as if People Mattered.* *https://web.archive.org/web/20141014171926/http://www.ditext.com/schumacher/small/small.html*

SEEA (2018). *The Role of the System of Environmental-Economic Accounting as a Measurement Framework in Support of the post-2020 Agenda. System of Environmental Economic Accounting, UN Committee of Experts on Environmental-Economic Accounting.* *https://seea.un.org/sites/seea.un.org/files/seea_2020_final.pdf*

SEEA (2020a). *System of Environmental Economic Accounting* webpage: *https://seea.un.org/ecosystem-accounting*

SEEA (2020b). *SEEA EEA Revision: Research Areas* webpage: *https://seea.un.org/content/seea-eea-revision-research-areas*

Smith, A. (1776). *Inquiry into the Nature and Causes of the Wealth of Nations*. Strahan and Cadell, London.

Stritih, A., Bebi, P., and Grêt-Regamey, A. (2019). Quantifying uncertainties in earth observation-based ecosystem service assessments. *Environmental Modelling and Software*, 111, 300–310.

Thackway, R. (Ed.) (2018). *Land Use in Australia: Past, Present and Future*. ANU eVIEW, Canberra. ISBN: 9781921934421

The Brundtland Report (1987). *Report of the World Commission on Environment and Development: Our Common Future*. UN. *https://sustainabledevelopment.un.org/content/documents/5987our-common-future.pdf*

UN (2014). *System of Environmental-Economic Accounting 2012: Experimental Ecosystem Accounting*, European Commission, Organisation for Economic Co-Operation and Development, United Nations and World Bank. eISBN: 978-92-1-056285-0. *https://unstats.un.org/unsd/envaccounting/seearev/eea_final_en.pdf*

UN (2015). *Report of the Global Working Group on Big Data for Official Statistics*. UN Economic and Social Council E/CN.2/2014/4. *https://unstats.un.org/unsd/statcom/doc15/2015-4-BigData-E.pdf*

UN (2019). The *Sustainable Development Goals Report*. UN, Rome. *https://unstats.un.org/sdgs/report/2019/*; *https://unstats.un.org/sdgs/report/2019/The-Sustainable-Development-Goals-Report-2019.pdf*

UN (2020a). *Sustainable Development Goals Indicators* website: *https://unstats.un.org/sdgs/?aspxerrorpath=/sdgs/indicators/Official* (List of all indicators: *https://unstats.un.org/sdgs/indicators/Global%20Indicator%20Framework%20after%202020%20review_Eng.pdf*)

UN (2020b). *Satellite Imagery and Geo-Spatial Data* webpage, BigData UN Global Working Group: *https://unstats.un.org/bigdata/taskteams/satellite/*

Vallecillo, S., La Notte, A., Polce, C., Zulian, G., Alexandris, N., Ferrini, S., and Maes, J. (2018). *Ecosystem services accounting: Part I - Outdoor recreation and crop pollination*. EUR 29024 EN, Publications Office of the European Union, Luxembourg. JRC110321. doi:*10.2760/619793*

van Dijk, A., Summers, D., Renzullo, L., and Yebra, M. (2017). *OzWALD Gridded Environmental Data for Australia. v2*. CSIRO. Data Collection. *https://doi.org/10.4225/08/5a3c52da083b8*

van Dijk, A., and Rahman, J. (2019). *Synthesising multiple observations into annual environmental condition reports: the OzWALD system and Australia's Environment Explorer*. MODSIM2019, Canberra.

Vardon, M., Burnett, P., and Dovers, S. (2016). The accounting push and the policy pull: balancing environment and economic decisions. *Ecological Economics*, 124, 145–152.

Vardon, M., Ovington, J., Juskevics, V., Purcell, J., and Eigenraam, M. (2018). Down Payments on National Environmental Accounts. Ch. 14 in *Land Use in Australia: Past, Present and Future*. (Ed: Thackway, R.). ANU eVIEW, Canberra. ISBN: 9781921934421

Wackernagel, M., Beyers, B., and Rout, K. (2019). *Ecological Footprint: Managing our Biocapacity Budget*. New Society Publishers. ISBN: 9780865719118

Westman, W.E. (1977). How much are nature's services worth? *Science*, 197(4307), 960–964.

WGCS (2016). *Accounting for Nature: A scientific method for constructing environmental asset condition accounts*. Wentworth Group of Concerned Scientists, Sydney. *https://static1.squarespace.com/static/5dc38cde1d028031235ca3cf/t/5ec60133aaeba61a09874858/1590034904424/Wentworth-Group-2016-Accounting-for-Nature.pdf*

Nature is not a place to visit, it is home.
(Gary Snyder)

Observing Our Future

One generation passes and another comes, but the world forever stays.
(Ecclesiastes 1:3)

Contents

21 The Road Ahead 479

Background image on previous page: Sentinel-2A image acquired on 14 October 2020 showing Lake Gordon (northern waterbody) and Lake Pedder (southern waterbody) in southwest Tasmania. Lake Gordon was formed by damming the Gordon River and Lake Pedder was enlarged by damming the Huon and Serpentine Rivers, both for hydroelectric power in the early 1970s. This image is displayed using bands 4, 5, 2 as RGB. Source: Norman Mueller, Geoscience Australia

21 The Road Ahead

A growing range of EO technologies is supplying more data—in more detail and more quickly—over the whole Earth, which, with appropriate analysis, can help us to use our finite resources for the maximum benefit of current and future populations. But exactly how will EO impact the stewardship of Australian terrestrial vegetation into the future? In these final sub-sections, we consider:

- smart technology to help the environment (see Section 21.1);
- an objective outlook on global problems (see Section 21.2);
- the benefits of EO-based solutions to society (Section 21.3); and, in conclusion,
- the attitudinal change required to share a sustainable future (see Section 21.4).

21.1 The Smart Environment

The Internet of Things (IoT) and Integrated 'Smart' Systems were introduced in Volume 1B—Section 10. The IoT is defined as "the network of physical objects that contain embedded technology to communicate and sense or interact with their internal states or the external environment" (Gartner, 2020). The projected development of this technology over time is summarised in Figure 21.1.

Smart systems integrate sensing technologies with cognitive functions. These systems are being implemented in a wide range of industrial, scientific, agricultural, medical, educational, environmental, and infrastructure applications. Advances continue at an accelerated pace for both urban and rural populations with the potential uses of these ubiquitous technologies being literally limited by imagination.

Forecasts from the International Data Corporation (IDC) suggest that the many billions of devices connected to the IoT will generate a staggering 80 ZB of data by 2025 (Futureiot, 2019)[18]. These sensors build on a wide variety of technologies that have become established around the globe, including rapid telecommunications, accurate positioning (see Volume 2B), artificial intelligence (see Volume 2E), high speed computing, and data integration (see Volume 2D). IoT is measuring and remotely controlling 'things' that had not been connected with previous technology, thus reaching more individuals, communities, and locations (WEF, 2020a).

Towns and cities can also be viewed as modified, human-dominated ecosystems that require flows of resource inputs from which energy, water and materials are extracted and used to support human wellbeing and culture, while producing concentrated waste streams that are detoxified and absorbed by nature. Efforts to increase the reuse and recycling of waste materials can be seen as shifting ecosystems into a more cyclic form, closer to the pattern of natural ecosystems.
(DEWHA, 2010)

18 1 ZB (Zettabyte) = a billion TB (Terabytes) = 1,000,000,000,000,000,000,000 bytes

Background image: Sentinel-2B image acquired on 14 February 2019 showing the Diamantina River, Queensland, in full flood, with flood waters cutting Springvale Road, near Diamantina Lakes. This image is displayed using bands 4, 8, 2 (red, NIR and blue) as RGB. **Source:** Norman Mueller, Geoscience Australia

Figure 21.1 The Internet of Things technology roadmap

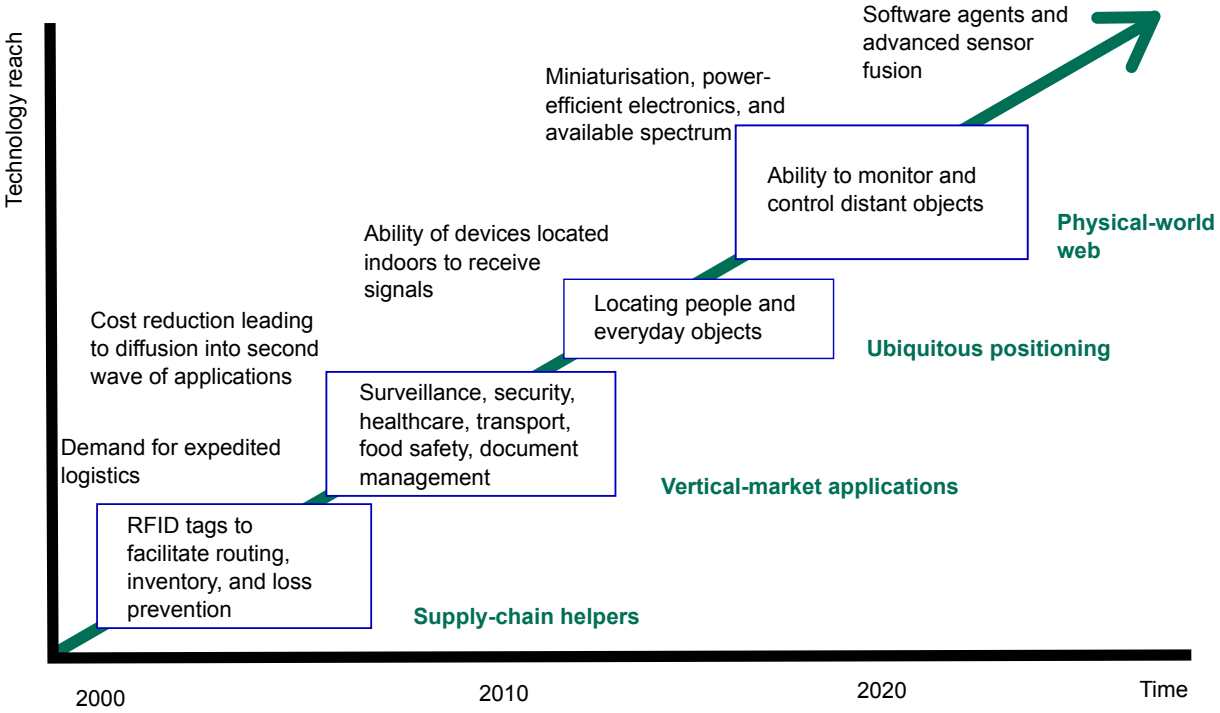

Source: SRI Consulting Business Intelligence/National Intelligence Council, Wikimedia Commons. (Retrieved from *https://commons.wikimedia.org/wiki/File:Internet_of_Things.svg*)

The IoT for Sustainable Development project by the World Economic Forum (WEF) is encouraging the use of IoT for rapid implementation of the UN Sustainable Development Goals (SDG; WEF, 2020b; see Excursus 20.2). This project is analysing over 640 existing IoT system deployments in terms of their social value. The five key peformance indicators for IoT systems are:

- scale of project—what is the impact of this system on individuals, social sectors and geographic region and extent?
- target penetration—how many SDG targets are benefitted by each system?
- influence of targets—what is the potential effectiveness of each system towards each target?
- scalability and replicability—is the system structurally scalable to improve the benefits to target and can the system be replicated to achieve other targets?
- focus on vulnerable groups—does the system significantly focus on vulnerable, underdeveloped, or underserved groups?

Results thus far indicate that 84% of the IoT systems currently being used can benefit SDGs and that three-quarters of these systems focus on just five SDGs (ordered in terms of decreasing target impact—see Excursus 20.2):

- SDG-9—industry, innovation, and infrastructure;
- SDG-11—smart cities and communities;
- SDG-7—affordable and clean energy;
- SDG-3—good health and wellbeing; and
- SDG-12—responsible production and consumption.

Many of these projects monitor resources with direct impact on vulnerable communities, such as water quality, air pollution, or energy usage. 95% of current IoT projects were found to be small to medium scale, so one challenge will be to improve the scalability of these projects in the future. While various forms of technology have directly contributed to environmental degradation, this may be one area where digital technology can help to resolve the global challenges of resource shortages, waste management, and environmental pollution.

Anyone who thinks that you can have infinite growth in a finite environment is either a madman or an economist.
(David Attenborough)

Smart systems simplify data collection and analysis, reduce maintenance costs, and improve performance. Current environmental applications include monitoring the quality and other properties of air, water, and soil in real time (Aitkenhead *et al.*, 2013). For environmental applications, some questions to ponder when deploying smart technologies are:

- Is the observer changing the observed? How would we know?
- Who can access the data? Does access to some data sources need to be limited for security, privacy, or commercial reasons?
- How would the system recover from sabotage, accidents, or malfunctions?
- Many EO and smart sensor applications involve implicit reliance on international goodwill, but how enduring is this?

As detailed in previous sections, calibrated and validated EO datasets have many well-established benefits for the mapping, monitoring, and modelling of terrestrial vegetation, including consistency over space and time, locational accuracy with global coverage, and ready integration with other spatial datasets. Selection of the most appropriate data and processing options for specific applications is described in Volume 2D—Section 2. Recent advances in freely available, web-based access to calibrated time series datasets and Analysis Ready Data (ARD, such as DEA, see Volume 2D—Section 11.2) simplify usage of these enormous archives.

For example, since 2002, the intergovernmental Group on Earth Observations (GEO) has been encouraging member governments to coordinate projects, strategies, and investments in EO for the benefit of both public and private users (GEO, 2020). A key component of its mission is to build the Global Earth Observation System of Systems (GEOSS), a set of coordinated, independent data and processing systems based on EO, that are accessible and interoperable, with identified quality and provenance (GEOSS, 2017). The goal of GEOSS is to deliver the data and information necessary to:

- bring qualitative improvements in our understanding of the Earth system (see Volume 1A—Section 4); and
- enhance the ability to make global policies and decisions that promote the environment and human health, safety, and welfare.

Advanced algorithms for processing massive data volumes are now being tailored for EO data and packaged for non-specialised users, with increasing reliance on web-based workflows (Sudmanns *et al.*, 2019). The 'traditional' approach to producing EO-based information required that the complete dataset be downloaded, analysed locally, then transformed into a map, which is delivered to the end user along a one-way path (see Volume 1B—Section 9.3). This traditional model is progressively being replaced by an online workflow, where the data provider generates ARD in a cloud environment in which EO analysts can access and process them. The end product would also reside within the cloud environment, to be accessed by the end user.

Thus, the distinction between smart technologies and EO-based systems is blurring over time, with both being reliant on the IoT, advanced analytical tools, and accessible, interactive interfaces, including virtual reality and augmented reality (Lymburner *et al.*, 2019). Selected examples of integrated, EO-based systems for managing natural resources include:

- Terrestrial Observation and Prediction System (TOPS)—integrates ecosystem models with satellite and surface weather observations to produce ecosystem nowcasts and forecasts for natural resources management, public health, and disaster management (Nemani *et al.*, 2009; NASA, 2020);
- Digiscape Future Science Platform (CSIRO)—uses EO data with environmental models to improve profitability and environmental outcomes from Australian agriculture (see Section 21.5); and
- Google Earth Engine and associated applications that rely on cloud computing, such as remap—online mapping platform to map and report the status of ecosystems (remap, 2020; see Section 19.4).

Our contemporary culture, primed by population growth and driven by technology, has created problems of environmental degradation that directly affect all of our senses: noise, odours and toxins, which bring physical pain and suffering, and ugliness, barrenness, and homogeneity of experience, which bring emotional and psychological suffering and emptiness. In short, we are jeopardizing our human qualities by pursuing technology as an end rather than a means. Too often we have failed to ask two necessary questions: First, what human purpose will a given technology or development serve? Second, what human and environmental effects will it have?
(U.S. Senate Public Works Committee, 1969)

21.2 An Objective Worldview

Sections 11 to 20 above describe the mapping, monitoring, and modelling of terrestrial vegetation for different applications. Despite advanced technologies such as EO, which can accurately track environmental degradation, the scale of the devastation is not being reduced. A glance at history confirms that this is not a new problem (see Excursus 11.2). However, the extent of problems relating to food security, various forms of pollution, soil fertility and erosion, landscape degradation, deforestation, carbon emissions, biodiversity loss, overpopulation, and excess consumption have grown markedly in the past few decades. For example, the human appropriation of net primary production (HANPP)—human usage of global NPP for food, timber, and fuel—is now estimated as 13–25%, which is double the estimate for a century ago (Krausmann *et al*., 2013). Other estimates such as the Global Footprint Network, which monitors sustainability (see Excursus 20.3), suggest that we are already substantially eating into the environmental capital of future generations.

One of the greatest dangers in environmental management is to allow current decisions to maximise the gains of the current population (or part thereof) to the detriment of future populations. A glance at the legislative control measures introduced to manage the Australian—and other—terrestrial environments provides numerous examples of the underlying principle of human manipulation of well-intended policy. This phenomenon is captured in Goodhart's Law and Campbell's law, that is:

Any observed statistical regularity will tend to collapse once pressure is placed upon it for control purposes.
or
When a measure becomes a target, it ceases to be a good measure.
(Charles Goodhart—Goodhart's Law)

and

The more any quantitative social indicator is used for social decision-making, the more subject it will be to corruption pressures and the more apt it will be to distort and corrupt the social processes it is intended to monitor.
or
Evidence-based policy tends to morph into policy-based evidence.
(Donald T. Campbell—Campbell's law)

The world is now facing significant environmental problems that have been derived from a long term, subjective, and blinkered view of global resources in the face of accelerating population growth (see Sections 19 and 20). At this juncture, it would be prudent to step back and take an objective view of human societies—past and present—and their interactions with their environments (see Excursus 11.2). To avoid further degradation, we need to identify the existing environmental problems and their major drivers, then understand the interconnections between the different drivers and different problems. To achieve an objective view of the world, indicators based on science—untainted by vested interests and ideologies—need to be defined and consistently tracked for each major driver on a global basis. While the technology to support this approach exists, the objectivity of many accepted indicators has already been questioned (Böhringer and Jochem, 2007).

The field of environmental-economic accounting is relatively new but holds promise for considering the environmental impacts of economic activities (see Section 20.5). In most nations—including Australia—the primary metric for the economy is gross domestic product (GDP), which does not account for environmental degradation, natural resource depletion, or loss of biodiversity (Obst, 2017). A key challenge for improving environmental visibility in our national decision making process is to demonstrate how the environment contributes to the prosperity and wellbeing of all Australians. Effective implementation of environmental-economic accounting will require identification of the most critical environmental costs and benefits in the Australian landscape and waterscape, then appropriate legislation to change the accepted accounting practices in all jurisdications. Current projections suggest that the integration of these changes with existing environmental reporting activities will be progressive over several years (see Figure 1 in CoA, 2018).

GEO has promoted the concept of 'essential variables' (EVs), which identify those with a "high impact, high feasibility and relatively low cost of implementation" (GEO, 2019a; see Section 11.2). The first set of EVs to be proposed were the Essential Climate Variables (ECV; see Volume 1A—Section 1.5). More recent examples include Essential Biodiversity Variables (see Section 19.3), Essential Ocean Variables, and Essential Water Variables (see Volume 3B). EVs are currently being used to monitor SDGs (see Excursus 20.2), with plans to develop and review more, particularly those with relevance to Societal Benefit Areas (SBA; see Section 21.3). This emphasis on the benefits of technology to society is a step in the right direction.

21.3 Societal Benefit Areas

While the benefits of EO are many and varied, it is easy to become beguiled by their direct technological advances and economic gains rather than their more indirect benefits to human societies. Both social and environmental systems differ from physical systems in their complexity and response to disturbance. These differences are important when contemplating ways to improve human living standards and ecosystem sustainability—both with and without technologies like EO.

Excursus 21.1 summarises the concept of social-ecological resilience and the attitudinal changes required to restore functional ecosystems and promote genuinely sustainable societies.

In recent years the focus of global EO usage has moved from maximising its economic advantages to promoting its societal benefits, particularly in less affluent regions of the world. For example, GEO (Group on Earth Observation; see Section 21.1) work programmes focus on eight domains that demonstrate the benefits of EO to society (GEO, 2017). These SBA align with several SDG and other international agreements on sustainability (see Excursus 20.2) to advance the use of EO for:

- Biodiversity and Ecosystem Sustainability: strengthens conservation, restoration, and sustainable management of ecosystems by using EO data sources;
- Disaster Resilience: aims to achieve a substantial reduction in losses of life and property from natural disasters through EO-based disaster mapping and better mitigation and response;
- Energy and Mineral Resource Management: since the use of fossil fuel energy accounts for more than two thirds of greenhouse gas emissions, EO-based mapping can help to increase the global share of renewable energy sources, such as solar and wind power;
- Food Security and Sustainable Agriculture: EO, with other agricultural data, contributes to crop monitoring to counter food insecurity (SDG 2);
- Infrastructure and Transportation Management: EO supports planning, monitoring, and management of infrastructure (dams, roads, rail, ports, and pipelines) and transportation (air, land, and sea) to meet and measure SDG 9, build resilient infrastructure, promote sustainable industrialisation, and foster innovation;
- Public Health Surveillance: provides alerts on air quality, weather extremes, water-related illness, vector-borne disease, and assessments of access to health facilities, all derived from EO-related datasets (SDG 3);
- Sustainable Urban Development: promotes equity, welfare, and shared prosperity for all levels of human settlement by using EO to develop and assess urban footprints, foster national urban planning, and show land change over time; and
- Water Resources Management: uses EO technologies to support accessibility to, and sustainable management of, water resources, and sanitation via sound science-based public policies, modelling, and data integration.

Some of the specific flagships and initiatives being undertaken by GEO that have particular relevance to Australian terrestrial vegetation are summarised in Table 21.1. In addition, GEO Community Activities include GEO Citizen Science, GEO Essential Variables, GEO Global Ecosystems, Global Agricultural Drought Monitoring, Global Crop Pest and Disease Habitat Monitoring and Risk Forecasting, Global Ecosystems and Environment Observation Analysis Research Cooperation (GEOARC), and Global Land Cover (GEO, 2019b). With an emphasis on societal benefits, early warning systems are being developed for a range of natural disasters, such as droughts, so that they can be managed to minimise their social, environmental, and economic impacts (e.g. GEOGLAM Crop Monitor or GEOGLAM-RaPP; see Excursus 11.1). This approach encompasses prudent insurance schemes for vulnerable communities, such as Index-Based Livestock Insurance (ILRI, 2020) and crop area yield index Insurance, which not only provide short-term relief but help to conserve soil, seed, and livestock resources for future use (Barnett and Mahul, 2007; Carter *et al*., 2007; see Section 11.4).

Although change is part of the working of complex systems, the speed with which human activity has developed contrasts with the naturally slow pace of biological evolution. Moreover, the goals of this rapid and constant change are not necessarily geared to the common good or to integral and sustainable human development. Change is something desirable, yet it becomes a source of anxiety when it causes harm to the world and to the quality of life of much of humanity.
(Pope Francis, 2015)

Excursus 21.1—Social-ecological Resilience

Source: Walker (2019, 2020)

Humanity has become remarkably adept at understanding how to mitigate countless conventional risks that can be relatively easily isolated and managed with standard risk management approaches. But we are much less competent when it comes to dealing with complex risks in systems characterised by feedback loops, tipping points and opaque cause-and-effect relationships that can make intervention problematic. .... Just as a piece of elastic can lose its capacity to snap back to its original shape, repeated stress can lead systems—organisations, economies, societies, the environment—to lose their capacity to rebound. If we exhaust our capacities to absorb disruption and allow our systems to become brittle enough to break, it is difficult to overstate the damage that might result (WEF, 2018).
(Foran et al., 2019)

In Physics, resilience denotes "the capacity of an elastic body to absorb energy then release that energy as it springs back to its original shape". The Merriam-Webster Dictionary also defines resilience as "an ability to recover from or adjust easily to change". This term is now used in a wide variety of contexts, including psychology, engineering, and agriculture.

Environmental resilience commonly refers to the capacity of the environment to maintain 'equilibrium' when subject to natural or anthropogenic influences and disturbances (DEWHA, 2010), and fundamentally derives from biodiversity at the species and ecosystem levels (Folke *et al.*, 2004). Walker (2019) emphasises that the resilience of any system (person, ecosystem, enterprise, or settlement) is the ability "to absorb disturbance and reorganise so as to keep functioning in the same kind of way—to have the same 'identity'.... In essence it is about learning how to change in order not to be changed".

Resilience can be seen as a combination of the:

- internal dynamics of adaptive change—which can be described in terms of four phases: growth, conservation, collapse, and reorganisation. While the growth and conservation phases are mostly predictable, the phases of collapse and reorganisation are not, especially if a system stays in the conservation phase too long; and
- threshold dynamics in response to disturbances—unpredictable, external changes.

Ecosystems and societies are not physical systems and do not behave like them and their diversity is often maintained by unpredictable variations and chance events. In these systems, the flexibility to respond to change by reorganising actually enhances resilience. Characteristics of resilient societies include anticipation of potential problems, power to respond to problems (which is based on quality and trust in social networks), support systems for social infrastructure that will be safe after failure, and an adaptive approach to the future (Walker, 2019). In societies, individuals, and ecosystems, studies of low resilience often focus on the scale of a specific problem rather than the extended, interconnected environment, which invariably operates at multiple scales with cross-scale interactions.

While humans like to reduce uncertainty, this can lead to unnatural rigidity in lifestyles, societies, and ecosystems, which ultimately undermines their preparedness for, and the likelihood of recovery from, major perturbations. Conversely, resilience to disturbances in any system is increased by the attributes of diversity, access to reserves, rapid response ability, and connectivity. Resilient behaviour in any social-ecological system can be encouraged by wise governance and social norms, and an awareness of the consequences of inflexibility.

Resilience necessarily involves testing boundaries, with the goal of not crossing ones that lead to undesirable outcomes. When this does happen the goal becomes one of crossing back if possible, otherwise reorganising into a new system with a similar function and purpose—all of which sounds a lot like parenting. In short, Walker (2019) advocates that we—as individuals, societies, and globally—should celebrate change, embrace uncertainty, and not shoot for utopia.

Table 21.1 GEO projects

GEO Project	Description	Focus	Approach
GEO-BON (Flagship)	Biodiversity Observation Network	Global Essential Biodiversity Variables (EBV) Reinforce existing or develop new Biodiversity Observation Networks	Provide sustained and interoperable data, information, and knowledge on ecosystem services that derive from diverse communities of living organisms, to contribute to the development of effective conservation actions, mitigation, and adaptation strategies that help ensure the sustainable use of resources
GEOGLAM (Flagship)	Global Agricultural Monitoring	Increase market transparency Improve food security	Produce and disseminate relevant, timely, and actionable information on agricultural conditions and outlooks of production at national, regional, and global scales
GFOI (Flagship)	Global Forest Observations Initiative	Coordinate EO-based forest monitoring activities	Develop methods and guidelines for estimating future carbon stocks to support countries in their effort to build national forest monitoring systems
GEO-DARMA (Initiative)	Data Analysis for Risk Management	Support operational disaster risk reduction activities Raise awareness of EO benefits in all phases of disaster risk management	Establish an inclusive, comprehensive process to address local disaster risk reduction requirements by using EO technologies efficiently
EO4EA (Initiative)	Earth Observations for Ecosystem Accounting	Further the development and use of EO for natural capital accounting, consistent with the set of standards and guidelines put forth by the UN SEEA and specifically the Ecosystem Accounts	Document, pioneer, develop, and test the methods and tools that will allow EO technology to more effectively enable the widespread adoption of ecosystem accounting
EO4SDG (Initiative)	Earth Observations for Sustainable Development Goals	Improve the quality, coverage, and availability of data to support the implementation of the development agenda at all levels	Package reproducible EO integrated methodologies and guidelines, in partnership with its end users, encompassing all relevant EO datasets, available tools and platforms, training material, as well as use cases and national experiences per SDG target and indicator supported EO
GEO Human Planet (Initiative)	Human Planet	Generate the global scale data and knowledge needed to advance our understanding of societal processes and their impact on Earth systems Generate useful indicators to inform policy	Develop a new generation of measurements and information products that provide new scientific evidence and more integrated understanding of the human presence on planet Earth in support of global policy processes with agreed, actionable and goal-driven metrics
GEO-LDN (Initiative)	Land Degradation Neutrality	Enhance national capacities to measure and map degraded lands Identify the most appropriate interventions	Facilitate the provision of space-based information and *in situ* measurements for improved land management and planning
GUOI (Initiative)	Global Urban Observation and Information	Improve urban monitoring and assessment by developing a series of satellite-based essential urban variables and indicators of sustainable cities through international cooperation and collaboration	Generate various data products of global urban areas using EO data, provide EO-based urban data services through various systems and tools, develop new models and algorithms to assess and monitor urban environments, create a better knowledge of cities, and develop essential urban variables and indicators for sustainable cities for SDG 11
GWIS (Initiative)	Global Wildfire Information System	Provide harmonised information on wildfires that could be used at different scales, from national to global	Provide information on fire danger, active fires, burned areas, emissions, as well as reports on wildfire regime and statistics at national, regional, and global level and integrate with existing EO-based fire monitoring products

Source: GEO (2019b)

It is an exciting time that we live in, as we are charged with no less than finding solutions to one of the greatest threats our species has ever faced.
(Pollock, 2019)

21.4 Stewards of Tomorrow

Quite simply, the Earth is our home, the only one we have. We all share the planet and its very finite resources.

Describing environmental concerns in pastoral leases in southwest WA, Pollock (2019) observed that "…. the problem with the Southern Rangelands at its most fundamental is not a landscape problem. It is a human problem—a problem within our culture and our psyche, a problem we must fix within ourselves, for ourselves. Humans have a long history of abusing their resources, but we are getting to the pointy end of the stick now. If we don't develop a new culture around responsible use and restoring the ecological balance, we are going to be in big trouble. Perhaps we already are."

This conclusion is not new. Many philosophers, historians and scientists have expressed this view down the ages, with increasing frequency in the past century (see Table 21.2). Overexploitation of finite resources has seen past civilisations collapse (see Excursus 11.2) and modern civilisation is not immune to this possibility, especially given the widespread, environmental impacts of industrialisation and urbanisation.

Preceding sections indicate that one species in the global ecosystem, *Homo sapiens*, has been pushing past the boundaries of social-ecological resilience (see Excursus 21.1) for quite some time. History supplies many examples of human civilisations engineering their own demise by overusing available resources (Ponting, 1991). The key to sustainability and resilience in any landscape is good stewardship of the environment, which will require a cultural shift in attitude to land, ownership and lifestyle.

Nature favours those organisms which leave the environment in better shape for their progeny to survive. (James Lovelock)

While many technologists prefer to believe that technology will solve all environmental problems, there is little precedent for the view that the very factors that cause problems can finally solve them. But, perhaps, with the right attitude and sufficient goodwill, EO technologies will be an exception.

When we speak of the 'environment', what we really mean is a relationship existing between nature and the society which lives in it. Nature cannot be regarded as something separate from ourselves or as a mere setting in which we live. We are part of nature, included in it and thus in constant interaction with it. Recognising the reasons why a given area is polluted requires a study of the workings of society, its economy, its behaviour patterns, and the ways it grasps reality. Given the scale of change, it is no longer possible to find a specific, discrete answer for each part of the problem. It is essential to seek comprehensive solutions which consider the interactions within natural systems themselves and with social systems. We are faced not with two separate crises, one environmental and the other social, but rather with one complex crisis which is both social and environmental. Strategies for a solution demand an integrated approach to combating poverty, restoring dignity to the excluded, and at the same time protecting nature.
(Pope Francis, 2015)

Table 21.2 Recommended reading

Reference	Focus
Essay on the Principle of Population (Malthus, 1798)	Describes a continuous historical cycle from increasing human population numbers until the available food supply is exceeded, resulting in widespread famine and disease which reduce the population until it is in balance with food production.
The Tragedy of the Commons: (Hardin, 1968)	The population problem has no technical solution; it requires a fundamental extension in morality.
The Limits to Growth (Meadows *et al*., 1970)	Man can create a society in which he can live indefinitely on Earth if he imposes limits on himself and his production of material goods to achieve a state of global equilibrium with population and production in carefully selected balance.
A Blueprint for Survival (Goldsmith and Allen, 1972)	If current trends are allowed to persist, the breakdown of society and the irreversible disruption of the life-support systems on this planet are inevitable—possibly by the end of the century, certainly within the lifetimes of our children.
Small is Beautiful: Economics as if people mattered (Schumacher, 1973)	Advocates that government effort must be concentrated on sustainable development to evolve a more democratic and dignified system of industrial administration, a more humane employment of machinery, and a more intelligent utilisation of the fruits of human ingenuity and effort.
Creating Alternative Futures: The End of Economics (Henderson, 1978)	Explains misleading assumptions in national economics, which distort the goal of human development worldwide, and redefines health, wealth, and progress for humanity's long term survival.
A Green History of the World (Ponting, 1991)	Overviews human history in the context of natural resource management.
Dirt: The Erosion of Civilisation (Montgomery, 2007)	Argues that we are—and have long been—using up Earth's soil. Once bare of protective vegetation and exposed to wind and rain, cultivated soils erode bit by bit, slowly enough to be ignored in a single lifetime but fast enough over centuries to limit the lifespan of civilisations.
Laudato Si' (Pope Francis, 2015)	On care for our common home—reviews current ecological crises and offers guidance for human development to achieve a more coherent commitment to the environment.
Finding Resilience (Walker, 2019)	A current analysis of how ecosystems, societies, and individuals cope with disturbance and adversity.

For the first time in history, the shape of the world that is unfolding expresses collective materialism rather than prescribed religion. In the advanced countries, the individual is evolving his own personal beliefs within his own home. The greatest threat to his existence may not be commercialism, or war, or pollution, or noise, or consumption of capital resources, or even the threat of extinction from without, but rather the blindness that follows sheer lack of appreciation and the consequent destruction of those values in history that together are symbolic of a single great idea.
(Jellicoe and Jellicoe, 1995)

21.5 Further Information

Smart Technologies

UNEP 'Why does technology matter': *https://www.unenvironment.org/explore-topics/technology/why-does-technology-matter*

Smart Cities: SMURBS/ERA-planet: *https://smurbs.eu/the-project/#summary*

IoT Australia (2019). *IoT Facts and Forecasts 18 October 2019*, IoT Australia website: *https://www.iotaustralia.org.au/2019/10/18/iot-facts-and-forecasts/gartner-tips-surveillance-cameras-to-be-top-5g-iot-application-but-not-for-long/*

Digiscape

https://research.csiro.au/digiscape/

21.6 References

Aitkenhead, M., Donnelly, D., Coull. M., and Black, H. (2013). E-SMART: Environmental Sensing for Monitoring and Advising in Real-Time. In *Environmental Software Systems. Fostering Information Sharing*. (Eds: Hřebíček, J., Schimak, G., Kubásek, M., and Rizzoli, A.E.). ISESS 2013. IFIP Advances in Information and Communication Technology, vol 413. Springer, Berlin, Heidelberg. *https://doi.org/10.1007/978-3-642-41151-9_13*

Barnett, B., and Mahul, O. (2007). Weather Index Insurance for Agriculture and Rural Areas in Lower-Income Countries. *American Journal of Agricultural Economics*, 89(5), 1241–1247. *https://doi.org/10.1111/j.1467-8276.2007.01091.x*

Böhringer, C., and Jochem, P.E.P. (2007). Measuring the immeasurable—A survey of sustainability indices. *Ecological Economics*, 63, 1–8.

Carson, R. (1962). *Silent Spring*. Penguin, Reading, UK.

Carter, M.R., Galarza, F., and Boucher, S. (2007). Underwriting Area-based Yield Insurance to Eliminate 'Risk Rationing' and Crowd-in-Credit Supply and Demand. *International Conference on Rural Finance Research*. FAO, Rome.

CoA (2018). *Environmental Economic Accounting: A Common National Approach Strategy and Action Plan*. Prepared by the Interjurisdictional Environmental-Economic Accounting Steering Committee for the Meeting of Environment Ministers, Commonwealth of Australia. *https://eea.environment.gov.au/about/national-strategy-and-action-plan*

DEWHA (2010). *Ecosystem Services: Key Concepts and Applications*. Occasional Paper No 1, Department of the Environment, Water, Heritage and the Arts, Canberra.

Folke, C., Carpenter, S., Walker, B., Scheffer, M., Elmqvist, T., Gunderson, L., and Holling, C.S. (2004). Regime shifts, resilience, and biodiversity in ecosystem management. *Annual Review of Ecology, Evolution and Systematics*, 35, 557–581.

Foran, B., Stafford Smith, M., Burnside, D., Andrew, M., Blesing, D., Forrest, K., and Taylor, J. (2019). Australian rangelands futures: time now for systemic responses to interconnected challenges. *The Rangeland Journal*, 41, 271–292.

Futureiot (2019). *IDC forecasts connected IoT devices to generate 79.4ZB of data in 2025* webpage, Futureiot website: *https://futureiot.tech/idc-forecasts-connected-iot-devices-to-generate-79-4zb-of-data-in-2025/*

Gartner (2020). *Gartner Glossary*: *https://www.gartner.com/en/information-technology/glossary/internet-of-things*

GEO (2017). *Earth Observations in support of the 2030 Agenda for Sustainable Development*. Group of Earth Observations, JAXA. *https://www.earthobservations.org/documents/publications/201703_geo_eo_for_2030_agenda.pdf*

GEO (2019a). *Essential Agricultural Variables for GEOGLAM—White Paper*. Group on Earth Observations, Draft, 27 March 2019. *http://earthobservations.org/geoglam_resources/3%20Earth%20Observation%20Data%20Coordination/Draft%20EAV%20White%20Paper.pdf*

GEO (2019b). *Implementation Plan for the Earth Observation for Ecosystem Accounting (EO4EA) Initiative. 2020–2022 GEO Work Program*. Group on Earth Observation. *http://earthobservations.org/documents/gwp20_22/eo_for_ecosystem_accounting_ip.pdf*

GEO (2020). *GEO at a Glance* webpage, Group on Earth Observations website: *https://www.earthobservations.org/geo_wwd.php*

Goldsmith, E., and Allen, R. (1972). A Blueprint for Survival. *The Ecologist*, 2(1). *https://web.archive.org/web/20090831193545/http://www.theecologist.info/key27.html*

Hardin, G. (1968). The Tragedy of the Commons. *Science*, 162(3849), 1243–1248. *https://science.sciencemag.org/content/sci/162/3859/1243.full.pdf*

Henderson, H. (1978). *Creating Alternative Futures: The End of Economics*. Kumarin Press, West Hartford. *https://sustainable-finance.io/wp-content/uploads/2018/04/Creating-AF.pdf*

ILRI (2020). *International Livestock Research Institute* website: *https://www.ilri.org/about-us*

Jellicoe, G., and Jellicoe, S. (1995). *The Landscape of Man*. 3rd edn. Thames and Hudson, London.

Krausmann, F., Erb, K.-H., Gingrich, S., Haberl, H., Bondeau, A., Gaube, V., Lauk, C., Plutzar, C., and Searchinger, T.D. (2013). Global human appropriation of net primary production doubled in the 20th century. *Proceeding of the National Academy of Science*, 110(25), 10324–10329.

Lymburner, L., Krause, C., Lamaye, A., Newey, V., and Burton C. (2019). *Characterising changes in Australian and African wetlands through time using Landsat*. Virtual Reality Installation at GeoWeek 2019.

Malthus, T. (1798). *An Essay on the Principle of Population*. London. *http://www.esp.org/books/malthus/population/malthus.pdf*

Meadows, D.H., Meadows, D.L., Randers, J., and Berhrens, W.W. (1970). *The Limits to Growth*. Club of Rome. *https://clubofrome.org/publication/the-limits-to-growth/*

Montgomery, D.R. (2007). *Dirt: The Erosion of Civilisations*. University of California Press. 295 p.

NASA (2020). *TOPS: Extending Access to NASA Data and Model Results for Ecosystem* webpage, NASA website: *https://earthdata.nasa.gov/esds/competitive-programs/access/tops*

Nemani, R., Hashimoto, H., Votava, P., Melton, F., Wang, W., Michaelis, A., Mutch, L., Milesi, C., Hiatt, S., and White, M. (2009). Monitoring and forecasting ecosystem dynamics using the Terrestrial Observation and Prediction System (TOPS). *Remote Sensing of Environment*, 113, 1497–1509.

Obst, C. (2017). Australia must make the environment integral to economic decision-making. *The Conversation*, 16 January, 2017. *https://theconversation.com/australia-must-make-the-environment-integral-to-economic-decision-making-69037*

Pollock, D. (2019). *The Wooleen Way*. Scribe, Melbourne. ISBN: 9781925849257

Ponting, C. (1991). *A Green History of the World*. Penguin.

Pope Francis (2015). *Laudato Si': On Care for Our Common Home*. Catholic Truth Society, London.

remap (2020). *remap: Enabling large-scale ecosystem mapping and assessment* website: *https://remap-app.org*

Schumacher, E.F. (1973). *Small is Beautiful: Economics as if People Mattered*. *https://web.archive.org/web/20141014171926/http://www.ditext.com/schumacher/small/small.html*

Sudmanns, M., Tiede, D., Lang, S., Bergstedt, H., Trost, G., Augustin, H., Baraldi, A., and Blaschke, T. (2019). Big Earth data: disruptive changes in Earth observation data management and analysis?, *International Journal of Digital Earth*. doi:*10.1080/17538947.2019.1585976*

Walker, B. (2019). *Finding Resilience*. CSIRO, Melbourne.

Walker, B. (2020). Resilience: what it is and is not. *Ecology and Society*, 25(2), 11. *https://doi.org/10.5751/ES-11647-250211*

WEF (2018). *The global risks report 2018*. World Economic Forum, Geneva, Switzerland. *https://www.weforum.org/reports/the-global-risks-report-2018*

WEF (2020a). *The effect of the Internet of Things on sustainability* webpage, World Economic Forum website: *https://www.weforum.org/agenda/2018/01/effect-technology-sustainability-sdgs-internet-things-iot/*

WEF (2020b). *IoT for Sustainable Development Project* webpage, World Economic Forum website: *http://widgets.weforum.org/iot4d/*

Glossary

Selected terms used in this sub-volume are defined below. Further details for each entry can be found in the sub-volume(s) indicated by parentheses after the term definition.

ABARES—Australian Bureau of Agricultural and Resources Economics and Sciences (3A)

ABS—Australian Bureau of Statistics (3A)

ACRIS—Australian Collaborative Rangelands Information System (3A)

ACT—Australian Capital Territory (3A)

active sensors—lidar and radar sensors that generate their own energy source then detect its 'echo' (1A)

AET—Actual ET (3A)

AGB—Above Ground Biomass (3A)

ALOS—Advanced Land Observing Satellite (1, 3)

ALS—Airborne Laser Scanning (1A, 3A)

ALUM—Australian Land Use and Management classification system (3A)

ANPP—Above ground NPP (3A)

ANU—Australian National University (1, 3)

APAR—Absorbed Photosynthetically Active Radiation (3A)

APSIM—Agricultural Production Systems sIMulator (3A)

ARD—Analysis Ready Data (2D)

ASRIS—Australian Soil Resource Information System (3A)

ASTER—Advanced Spaceborne Thermal Emission and Reflectance Radiometer (1A)

AUSLIG—Australian Surveying and Land Information Group (3A)

AVHRR—Advanced Very High Resolution Radiometer (1A)

AWRA—Australian Water Resources Assessment (3A)

BA—Basal Area (3A)

BC—BioCapacity (3A)

BoM—Bureau of Meteorology

BR—Bowen Ratio (3A)

CAI—Cellulose Absorption Index (3A)

cal/val—calibration and validation (2D, 3A, 3B)

CAM—Crassulacean Acid Metabolism (3A)

CASI—Compact Airborne Spectrographic Imager (3A)

CCCI—Canopy Chlorophyll Content Index (3A)

CLUM—Catchment scale Land Use Management data for Australia (3A)

CSIRO—Commonwealth Scientific and Industrial Research Organisation

CSM—Crop Simulation Model (3A)

CSR—Crown Separation Ratio (3A)

CWSI—Crop Water Stress Index (3A)

DBH—Diameter at Breast Height (3A)

DEA—Digital Earth Australia (2D, 3A, 3B)

DEM—Digital Elevation Model (2D, 3A)

DLCD—Dynamic Land Cover Dataset (3A)

DSS—Decision Support System (3A)

EAV—Essential Agricultural Variables (3A)

EBV—Essential Biodiversity Variables (3A)

ECV—Essential Climate Variables (1A, 3A)

EF—Ecological Footprint (3A)

EMR—ElectroMagnetic Radiation (1A)

ENSO—El Niño-Southern Oscillation (3A)

EO—Earth Observation (1A)

ER—Ecosystem Respiration (3A)

ET—EvapoTranspiration (3A)

EV—Essential Variables (1A, 3A, 3B)

EVI—Enhanced Vegetation Index (2C, 3A)

EWS—Early Warning Systems (3A)

EWT—Equivalent Water Thickness (3A)

FAO—UN Food and Agriculture Organisation (3A)

fAPAR—fraction of Absorbed Photosynthetically Active Radiation (3A)

FC—Fractional Cover (3A)

FMC—Fuel Moisture Content (3A)

FPC—Foliage Projective Cover (3A)

GA—Geoscience Australia (1, 3)

GAB—Great Artesian Basin (3A)

GCM—General Circulation Model (3A, 3B)

GDP—Gross Domestic Product (3A)

GEO—Group on Earth Observation (1A, 3A)

GEOBIA—GEographic Object-Based Image Analysis (2A, 3A, 3B)

GEOBON—GEO Biodiversity Observation Network (3A)

GEOGLAM RaPP—GEO Global Agricultural Monitoring Rangeland and Pasture Productivity (3A)

GEP—Gross Ecosystem Productivity (3A)

GPP—Gross Primary Productivity (3A)

GPS—Global Positioning System (1B, 3A)

HSI—Hue Saturation Intensity (2A, 2C, 2X)

IBLI—Index-Based Livestock Insurance (3A)

IBRA—Interim Biogeographic Regionalisation of Australia (3A)

IGBP—International Geosphere-Biosphere Program (3A)

IMU—Inertial Measurement Unit (3A)

IoT—Internet of Things (1B, 3A)

IR—InfraRed (1A, 1B)

IUCN—International Union of Conservation of Nature (3A)

LAI—Leaf Area Index (3A)

LCCS—Land Cover Classification System (3A)

LDMC—Leaf Dry Matter Content (3A)

LMM—LInear Mixture Model (2E, 3A)

LST—Land Surface Temperature (3A)

LUE—Light Use Efficiency (3A)

MARS—Monitoring Agricultural ResourceS (3A)

MDB—Murray-Darling Basin (3A)

MERIS—MEdium Resolution Imaging Spectrometer (1A)

METRIC—Mapping Evapotranspiration at High Resolution with Internal Calibration (3A)

MIR—Middle InfraRed (1A)

ML—Machine Learning (2E, 3A)

MODIS—Moderate Resolution Imaging Spectroradiometer (1A)

MVG—Major Vegetation Groups (3A)

NBP—Net Biome Productivity (3A)

NBR—Normalised Burn Ratio (3A)

NCAS—National Carbon Accounting System (3A)

NCST—National Committee on Soil and Terrain (2D, 3A)

NDRE—Normalised Difference Red Edge index (3A)

NDTI—Normalised Difference Temperature Index (3A)

NDVI—Normalised Difference Vegetation Index (2C, 3A)

NDWI—Normalised Difference Water Index (3A)

NEE—Net Ecosystem Exchange (3A)

NEP—Net Ecosystem Productivity (3A)

NFI—National Forest Inventory (3A)

NIR—Near InfraRed (1A, 1B)

NLWRA—National Land and Water Resources Audit (3A)

NPP—Net Primary Productivity (3A)

NRM—Natural Resource Management (3A)

NSW—New South Wales (3A)

NT—Northern Territory (3A)

NUE—Nitrogen Use Efficiency (3A)

NVIS—National Vegetation Information System (2D, 3A)

NWA—National Water Account (3A)

OCO-2—Orbiting Carbon Observatory 2 (3A)

PAR—Photosynthetically Active Radiation (3A)

passive sensors—radiometers, spectroradiometers and spectrometers that detect reflected EMR in optical wavelengths and emitted EMR in thermal wavelengths (1A)

PCA—Principal Components Analysis (2C, 2X)

PEM—Production Efficiency Model (3A)

PfS—Pastures from Space (1A, 3A)

PFT—Plant Functional Types (3A)

PGR—Pasture Growth Rate (3A)

PRI—Photochemical Reflectance Index (3A)

REDD—Reducing Emissions from Deforestation and forest Degradation (3A)

red edge—transition from low red reflectance to high NIR reflectance in green leaves (~680–780 nm)

RFS—Rural Fire Service (3A)

RLE—Red List of Ecosystems (3A)

RMSE—Root Mean Square Error (3A)

RN—Reynolds Number (3A)

RTM—Radiative Transfer Model (1B, 3A, 3B)

RUE—Radiation Use Efficiency (3A)

RWC—Relative Water Content (3A)

SA—South Australia (3A)

SAIL—Scattering by Arbitrary Inclined Leaves model (3A)

SAR—Synthetic Aperture Radar (1A, 1B)

SCORPAN—Soil properties, Climate properties, Organisms, Relief setting, Parent material, Age, and the spatial coordinate N (3A)

SDG—Sustainable Development Goals (3A)

SEB—Surface Energy Balance model (3A)

SEBAL—Surface Energy Balance Algorithm for Land (3A)

SEEA—System of Environmental Economic Accounting

SIF—Solar-Induced chlorophyll Fluorescence (3A)

SILO—Scientific Information for Land Owners (3A)

SLA—Specific Leaf Area (3A)

SLATS—Statewide Landcover and Trees Study (2D, 3A)

SLGA—Soil and Landscape Grid of Australia (3A)

SMA—Spectral Mixture Analysis (2E, 3A)

SNA—System of National Accounts (3A)

SOC—Soil Organic Carbon (3A)

SOFR—State Of the Forests Report (3A)

STF—SpectroTransfer Functions (3A)

STM—State-and-Transition Model (3A)

SVAT—Soil-Vegetation-Atmosphere Transfer model (3A)

SVTM—NSW State Vegetation Type Mapping (3A)

SWIR—Short Wave InfraRed (1A)

TEM—Terrestrial Ecosystem Model (3A)

TERN—Terrestrial Ecosystem Research Network (2D, 3A)

TIR—thermal infrared (1A, 1B)

TLS—Terrestrial Laser Scanning (1A, 3A)

UNEP—United Nations Environment Programme (3A)

UAV—Unmanned Aerial Vehicle (1A)

UV—UltraViolet (1A, 1B)

VARI—Visible Atmospherically Resistant Index (3A)

VAST—Vegetation Assets, States and Transitions (3A)

VCI—Vegetation Condition Index (3A)

VHI—Vegetation Health Index (3A)

VI—Vegetation Index (2C, 3A)

VPD—Vapour Pressure Deficit (3A)

VQA—Vegetation Quality Assessment (3A)

VRT—Variable Rate Technologies (3A)

WEF—World Economic Forum (3A)

WA—Western Australia (3A)

Earth Observation:
Data, Processing and Applications

Volume 3B: Applications—Surface Waters

This publication is available in PDF format at *eopublications.au*.
We welcome your comments regarding the readability and usefulness of this report.
To provide feedback, please email *feedback@eopublications.au*.

Publisher:
Australia and New Zealand CRC for Spatial Information

ISBN [ONLINE]:
978-0-6482278-3-0

Copyright:
All material in this publication is licensed under a Creative Commons Attribution 4.0 Australia Licence, save for content supplied by third parties, and logos. Creative Commons Attribution 4.0 Australia Licence is a standard form licence agreement that allows you to copy, distribute, transmit, and adapt this publication provided you attribute the work. The full licence terms are available from *https://creativecommons.org/licenses/by/4.0/legalcode*. A summary of the licence terms is available from *https://creativecommons.org/licenses/by/4.0/*.

Disclaimer:
While every effort has been made to ensure its accuracy, the CRCSI does not offer any express or implied warranties or representations as to the accuracy or completeness of the information contained herein. The CRCSI and its employees and agents accept no liability in negligence for the information (or the use of such information) provided in this report.

Recommended Citation for Volume 3B:
CRCSI (2021). *Earth Observation: Data, Processing and Applications. Volume 3B: Applications—Surface Waters*. (Eds. Harrison, B.A., Anstee, J.M., Dekker, A.G., King, E.A., Griffin, D.A., Mueller, N., Phinn, S.R., Kovacs, E., and Byrne, G.) CRCSI, Melbourne.

The recommended citation for each contributed chapter is given on the first page of the chapter.

Latest Revision:
October 2025

Background image on previous page: Sentinel-2A imagery acquired on 8 June 2020 over the eastern portion of the Wide Bay Burnett region in southeast Queensland. This region includes the cities of Bundaberg in the northeast and Maryborough, west of Fraser Island. In addition to tourism and fishing, this district supports a variety of agricultural production, principally beef, citrus, sugarcane, and forestry.
Source: Norman Mueller, Geoscience Australia

Acknowledgements

Production of this series of texts would not have been possible without the financial support of CSIRO, CRCSI, GA, BNHCRC and FrontierSI, input from members of the editorial panels and direction from members of the various advisory panels.

Volumes 1 and 2 of this series are based on text originally published in Harrison and Jupp (1989, 1990, 1992, and 1993)[1]. Many illustrations and some text from these publications have been reproduced with permission from CSIRO.

The following authors are thanked for their contributed chapters:

- 11. **Extent**: Norman Mueller (Geoscience Australia)
- 12. **Level**: Edward King (CSIRO)
- 13. **Bathymetry**: Kim Picard (Geoscience Australia), Janet Anstee (CSIRO), and Barbara Harrison (CSIRO)
- 14. **Temperature**: Helen Beggs (Bureau of Meteorology)
- 15. **Ice**: Rob Massom (Australian Antarctic Division and Australian Antarctic Program Partnership)
- 16. **Wind and Waves**: Mark Hemer (CSIRO) and Salman Khan (CSIRO)
- 17. **Circulation**: David Griffin (CSIRO)
- 18. **Colour**: Janet Anstee (CSIRO)
- 19. **Quality**: Arnold Dekker (Satdek), Janet Anstee (CSIRO), Barbara Harrison (CSIRO), and Edward King (CSIRO)
- 20. **Ecology**: Janet Anstee (CSIRO), Chris Roelfsema (University of Queensland), Eva Kovacs (University of Queensland), and Stuart Phinn (University of Queensland)
- 21. **Looking Ahead**: Barbara Harrison (CSIRO), Edward King (CSIRO), Arnold Dekker (Satdek), David Hudson (Geoscience Australia), and Stuart Phinn (University of Queensland)

Chapter 13 is published with the permission of the CEO, Geoscience Australia.

Other contributors are gratefully acknowledged:

- excursus authors: Paul Tregoning (Excursus 1.1), Paul Irving (Excursus 2.1 and Excursus 19.4), Edward King (Excursus 2.2 and Excursus 12.1), Rachael Thomas (Excursus 3.1), Mark Baird (Excursus 5.1), Helen Beggs (Excursus 14.1), Madeleine Cahill (Excursus 14.2), Rob Massom (Excursus 15.1), Mark Hemer and Salman Khan (Excursus 16.1), David Griffin (Excursus 17.2), Chari Pattiaratchi (Excursus 17.3), Klaus Joehnk and Tapas Biswas (Excursus 18.1), Janet Anstee (Excursus 19.3 and Excursus 20.2)
- reviewers: Rachael Thomas (Section 3), Marian Wiltshire (Excursus 5.1), Phillip Ford (parts of Section 5), Kim Picard (Sections 6 and 10), Sean Chua (Section 11), David Griffin (Sections 12 and 16), Nick Crosbie (Excursus 19.3),
- illustrations: Elizabeth Fredericks, Carl Davies (CMDphotographics), Edward King, Matt Chamberlain, Tony Sparks, Ron Hoeke, Rachael Thomas, Joanne Ocok, Paul Packard, Vince Bicello, James Dyer, Simon Hunter, Bill Johnson, Carmon Amos, Sharon Bowen, Nathan Drayson, Janet Anstee, Vittorio Brando, Arnold Dekker, Lesley Clementson, Bozena Wojtasiewicz, Bruce Forster, Linlin Ge, Peter Harrison, Kim Picard, Andrew Carroll, Norman Mueller, Benoit Legresy, Helen Beggs, Leon Majewski, Phillip Reid, Christopher Griffin, Madeleine Cahill, Salman Khan, David Griffin, Susan Wijffels, Nearmap, Erin Hester, Yi Qin, Daniel Haines, Paul Irving, Chris Roelfsema

We thank those owners of copyrighted illustrative material for permission to reproduce their work. Credits for individual illustrations are provided below the relevant graphic.

All volumes in this series are covered by the copyright provisions of CC BY 4.0 AU.

1 Harrison, B.A., and Jupp, D.L.B. (1989) Introduction to Remotely Sensed Data: Part ONE of the microBRIAN Resource Manual. CSIRO, Melbourne. 156 p.
Harrison, B.A., and Jupp, D.L.B. (1990) Introduction to Image Processing: Part TWO of the microBRIAN Resource Manual. CSIRO, Melbourne. 256 p.
Harrison, B.A., and Jupp, D.L.B. (1992) Image Rectification and Registration: Part FOUR of the microBRIAN Resource Manual. MPA, Melbourne.
Harrison, B.A., and Jupp, D.L.B. (1993) Image Classification and Analysis: Part THREE of the microBRIAN Resource Manual. MPA, Melbourne.

Table of Contents

Volume 3B: Applications—Surface Waters a

Acknowledgements i

Introduction 1

1 The Blue Planet 3
- **1.1** The Hydrological Cycle 5
- **1.2** Categories of Surface Waters 7
  - **1.2.1** Oceans 7
  - **1.2.2** Coastal waters 9
  - **1.2.3** Inland waters 11
- **1.3** Physical Layers within Waterbodies 11
  - **1.3.1** Water surface 11
  - **1.3.2** Water column 11
  - **1.3.3** Substratum 12
- **1.4** Global Water Circulation 12
  - **1.4.1** Currents 13
  - **1.4.2** Gyres 14
  - **1.4.3** Eddies 15
  - **1.4.4** Langmuir circulation 15
- **1.5** Global Carbon Cycle 16
- **1.6** Further Information 18
- **1.7** References 19

2 Australia's Surface Water Environment 21
- **2.1** Marine Jurisdiction 21
  - **2.1.1** Territorial Sea Baseline 26
  - **2.1.2** Territorial Sea 26
  - **2.1.3** Coastal Waters 26
  - **2.1.4** Contiguous Zone 26
  - **2.1.5** Exclusive Economic Zone 26
  - **2.1.6** Australian Fishing Zone 27
  - **2.1.7** Continental Shelf 27
- **2.2** Marine Geomorphology and Bioregionalisation 27
- **2.3** Regional Water Circulation 29
- **2.4** Australian Marine Environment 34
- **2.5** Antarctica 35
- **2.6** Australia's Inland Water Resources 37
- **2.7** Australian Water Usage 39
- **2.8** Further Information 39
- **2.9** References 40

3 Aquatic Ecosystems 43
3.1 Aquatic Ecosystem Zones 43
3.2 Aquatic Habitats 45
3.3 Aquatic Organisms 54
3.3.1 Microorganisms 55
3.3.2 Algae 56
3.3.3 Plants 59
3.3.4 Animals 60
3.4 Further Information 60
3.5 References 61

Measureable Properties of Surface Waters 65

4 Attributes of Water Surface 67
4.1 Level 67
4.2 Shape 68
4.3 Texture 71
4.4 Surface Tension 74
4.5 Temperature 74
4.6 Floating Layers 74
4.7 Ice cover 75
4.8 Further Information 76
4.9 References 76

5 Attributes of Water Column 77
5.1 Physical 77
5.1.1 Water depth 77
5.1.2 Density and stratification 81
5.1.3 Temperature 82
5.1.4 EMR absorption and transmission 83
5.1.5 Transparency and suspended particles 86
5.2 Chemical 88
5.2.1 Salinity 88
5.2.2 pH 89
5.2.3 Dissolved matter 89
5.3 Biological 93
5.3.1 Microorganisms 93
5.3.2 Macroalgae and macrophytes 94
5.4 Further Information 95
5.5 References 95

6 Attributes of Substratum 99
6.1 Waterbody Depth 99
6.2 Geomorphic Features 99
6.3 Composition 102
6.4 Benthos 103
6.5 Further Information 104
6.6 References 104

7 Attributes of Waterbodies 105
7.1 Observed Colour 105
7.2 Extent and Permanence 105
7.3 Depth and Volume 106
7.4 Carbon Cycling 108
7.5 Dynamics 110
7.6 Further Information 112
7.7 References 112

EO Data and Models 115

8 Optical EO 117
8.1 Optical EO Framework 122
8.1.1 Scattering 124
8.1.2 Fluorescence 125
8.1.3 Water surface effects 125
8.1.4 Radiative transfer theory 128
8.1.5 Atmospheric correction 128
8.2 Optically Active Constituents of Water 129
8.2.1 Pure water 130
8.2.2 Phytoplankton and cyanobacteria pigments 130
8.2.3 Non-algal particles (NAP) 133
8.2.4 Coloured dissolved organic matter (CDOM) 133
8.2.5 Coloured dissolved inorganic matter (CDIM) 134
8.3 Optical Properties of Water 134
8.3.1 Inherent Optical Properties 134
8.3.2 Apparent Optical Properties 135
8.3.3 Optical properties of substratum 137
8.4 Optical EO Models 140
8.4.1 Radiative Transfer Modelling 142
8.4.2 Water column 143
8.4.3 Substratum factors 144
8.4.4 Integrated models 145
8.5 Optical EO sensors 146
8.6 Further Information 150
8.7 References 150

9 Microwave EO 155
9.1 Microwave EO Framework 158
9.1.1 Review of microwave EMR 158
9.1.2 Observing microwave EMR 160
9.2 Passive Microwave 161
9.3 Imaging Radar 162
9.4 SAR Interferometry 164
9.5 Radar Altimetry 165
9.6 Microwave Scatterometry 166
9.7 Further Information 167
9.8 References 167

10 Acoustic EO 169
10.1 Acoustic EO Framework 170
10.2 Echosounders 171
10.2.1 Single beam echosounders 172
10.2.2 Sidescan sonar 172
10.2.3 Multibeam echosounders 173
10.3 Acoustic Surveys and Platforms 175
10.4 Acoustic Data Processing 176
10.5 Further Information 177
10.6 References 177

Observing Surface Water Dimensions 179

11 Extent 181
Norman Mueller
11.1 Extent of Australian Surface Waters 182
11.2 EO Sensors for Water Extent 183
11.3 Delineating Shorelines 186
11.3.1 Passive optical analysis 186
11.3.2 Synthetic Aperture Radar 191
11.4 Monitoring Floods 191
11.4.1 The International Charter for Space and Major Disasters 191
11.4.2 The Copernicus Emergency Management Service 192
11.5 Permanent/Temporary water 193
11.6 Further Information 193
11.7 References 194

12 Level 197
Edward King
12.1 Level of Australian Surface Waters 198
12.2 EO Sensors for Sea Level 199
12.2.1 Radar altimetry 200
12.2.2 EO sensor calibration 203
12.3 Causes of Change in Sea Level 205
12.3.1 Short term change 206
12.3.2 Seasonal to decadal change 207
12.3.3 Longer term change 209
12.4 Measuring Sea Level 210
12.4.1 Paleo indicators 210
12.4.2 Tide gauges 210
12.4.3 Satellite altimetry 213
12.5 Monitoring Sea Level 215
12.5.1 In geological ages 215
12.5.2 In recent centuries 216
12.5.3 In recent decades 216
12.6 Modelling Future Sea Level 217
12.7 Further Information 219
12.8 References 220

13 Bathymetry 223
Kim Picard, Janet Anstee, and Barbara Harrison

13.1 Bathymetry of Australian Surface Waters 225
13.2 EO Sensors for Bathymetry 231
13.3 Seafloor Mapping 231
13.3.1 Satellite radar altimetry 232
13.3.2 Echosounders 233
13.4 Coastal Monitoring 234
13.4.1 Lidar bathymetry 234
13.4.2 Satellite-derived bathymetry (SDB) 235
13.5 Further Information 238
13.6 References 238

Observing Surface Water Energy 243

14 Temperature 245
Helen Beggs

14.1 Temperature of Australian Surface Waters 245
14.2 EO Sensors for Water Temperature 246
14.2.1 Infrared sensors 247
14.2.2 Passive microwave sensors 250
14.3 Sea Surface Temperature 250
14.3.1 Retrieval of satellite SST 252
14.3.2 Validation of satellite SST 253
14.3.3 'GHRSST' satellite SST products 254
14.4 Global Sea Surface Temperature Products 258
14.4.1 Numerical Weather Prediction model input 262
14.4.2 Climate monitoring 262
14.4.3 Feature resolution 262
14.4.4 Coral bleaching nowcasting 263
14.4.5 Verification 263
14.5 Regional SST Products 263
14.5.1 IMOS satellite SST products 266
14.5.2 High resolution SST climatologies and extreme events 271
14.6 Inland Water Temperature 271
14.7 Further Information 273
14.8 References 274

15 Ice 281
Rob Massom

15.1 Ice in Australian Surface Waters 281
15.1.1 Antarctic Ice Sheet 283
15.1.2 Antarctic sea ice 285
15.2 EO Sensors for Ice 289
15.3 EO of the Antarctic Ice Sheet 290
15.3.1 Ice sheet surface morphology and areal change 290
15.3.2 Icebergs 291

15.3.3 Ice surface temperature 292
15.3.4 Surface melt 293
15.3.5 Ice sheet velocity 293
15.3.6 Surface elevation 294
15.3.7 Ice sheet mass balance 296
15.4 EO of Sea Ice 297
15.4.1 Sea ice concentration, extent, and seasonality, and their variability 297
15.4.2 Coastal landfast sea ice (fast ice) distribution 299
15.4.3 Sea ice motion and dynamics 300
15.4.4 Sea ice and snow cover thickness 301
15.5 Outlook: Future Opportunities and Needs 302
15.6 Further Information 303
15.7 References 304

16 Winds and Waves 311
Mark Hemer and Salman Khan
16.1 Winds and Waves in Australian Surface Waters 313
16.2 EO Sensors for Winds 314
16.2.1 ***In situ*** wind measurements 315
16.2.2 Scatterometers 315
16.2.3 Passive microwave radiometers 317
16.2.4 Satellite altimeters 317
16.2.5 Synthetic Aperture Radar 318
16.2.6 GNSS Reflectometry 319
16.3 EO Sensors for Waves 320
16.3.1 ***In situ*** wave measurements 320
16.3.2 Satellite altimeters 321
16.3.3 SAR imagery 322
16.3.4 Emerging platforms 324
16.4 Further Information 324
16.5 References 325

17 Circulation 329
David Griffin
17.1 Circulation of Australian Surface Waters 331
17.2 EO Sensors for Water Circulation 334
17.2.1 Radar altimeters 334
17.2.2 Passive optical 335
17.3 Circulation Patterns 337
17.4 Ocean Fronts 339
17.5 Further Information 340
17.6 References 341

Observing the Waterscape 343

18 Colour 345
Janet Anstee
18.1 Colour of Australian Surface Waters 347

18.2 EO Sensors for Water Colour 348
18.3 Classifications of Water Colour 348
18.3.1 Classifications based on AOP 349
18.3.2 Classifications based on IOP 350
18.3.3 Optical Water Types (OWT) 351
18.4 Transparency 351
18.5 Dissolved Matter 354
18.5.1 CDOM 354
18.5.2 DOC 354
18.6 Chlorophyll Content 357
18.7 Substratum 359
18.8 Further Information 361
18.9 References 361

19 Quality 367
Arnold Dekker, Janet Anstee, Barbara Harrison, and Edward King
19.1 Quality of Australian Surface Waters 368
19.2 EO Sensors for Water Quality 368
19.3 Inland Water Quality 371
19.3.1 Traditional methods 372
19.3.2 EO approaches 372
19.4 Pollution 378
19.4.1 Plastic debris 378
19.4.2 Shipping 379
19.4.3 Oil spills 380
19.5 Algal Blooms 385
19.6 Marine Heatwaves 386
19.7 Salinity 387
19.8 Further Information 388
19.9 References 389

20 Ecology 395
Janet Anstee, Chris Roelfsema, Eva Kovacs, and Stuart Phinn
20.1 Ecology of Australian Surface Waters 397
20.2 EO Sensors for Water Ecology 400
20.3 Coastal Wetlands 403
20.3.1 Seagrass meadows 404
20.3.2 Mangrove forests 405
20.3.3 Saltmarshes 407
20.4 Estuarine Ecosystems 408
20.5 Coastal waters 409
20.6 Coral Reefs 410
20.6.1 Structural characteristics 411
20.6.2 Optical properties 412
20.6.3 EO datasets and applications 412
20.6.4 Mapping biophysical properties 416
20.7 Marine Fauna 421
20.7.1 Fisheries 422

20.7.2 Animal counts 423
20.8 Further Information 424
20.9 References 425

Looking Ahead 437

21 Over the Horizon 439
Barbara Harrison, Edward King, Arnold Dekker, David Hudson, and Stuart Phinn
21.1 The Global Picture 439
21.2 From Data to Information 443
21.3 Smart Management of Surface Water Resources 445
21.4 The Human Factor 445
21.5 Further Information 447
21.6 References 447

Glossary 449

List of Figures

Figure 1.1 Gravity Recovery and Climate Experiment (GRACE) 3

Figure 1.2 Murray-Darling Basin total water storage 4

Figure 1.3 Water mass anomalies 4

Figure 1.4 The global water cycle 5

Figure 1.5 River catchment 6

Figure 1.6 Artesian well 6

Figure 1.7 ETOPO1 global relief model 8

Figure 1.8 Oceans of the world 8

Figure 1.9 Major marine geomorphic features 9

Figure 1.10 Large scale atmospheric circulation 12

Figure 1.11 Major non-tidal currents 14

Figure 1.12 Eddies in waters around Tasmania 15

Figure 1.13 Langmuir circulation 15

Figure 1.14 Ocean carbon pumps 16

Figure 1.15 Biological pump 17

Figure 2.1 Names and limits of oceans and seas around Australia 22

Figure 2.2 Australian Charting Area 23

Figure 2.3 UNCLOS marine zone boundaries 23

Figure 2.4 Australia's Maritime Zones 24

Figure 2.5 Australian Search and Rescue Region 25

Figure 2.6 Seafloor morphology around Australia 28

Figure 2.7 Provincial marine bioregions 28

Figure 2.8 Three-dimensional model of water masses defined by pelagic regionalisation 29

Figure 2.9 Example of global forecast 31

Figure 2.10 BRAN 2020 reanalysis 32

Figure 2.11 Sample ocean temperature 33

Figure 2.12 Littoral forecast example 34

Figure 2.13 Types of ice in polar regions 35

Figure 2.14 Australian Antarctic Territory 36

Figure 2.15 Australia's average annual rainfall 37

Figure 2.16 Australian inland waterbodies 38

Figure 2.17 Major drainage divisions in Australia 38

Figure 3.1 Aquatic zones for marine waters 44
Figure 3.2 Inland floodplain wetland distribution in the MDB 46
Figure 3.3 Mosaics of inland floodplain wetland types 47
Figure 3.4 Longitudinal, lateral and vertical hydrological pathways 48
Figure 3.5 Inundation patterns 49
Figure 3.6 Conceptual models of common inland floodplain wetlands in MDB 50
Figure 3.7 Examples of common inland floodplain wetlands in the MDB 52
Figure 3.8 Simple food chain 54
Figure 3.9 Phytoplankton forms 57
Figure 4.1 Global-mean sea level (GMSL) estimates 67
Figure 4.2 Change in sea surface topography 1993–2019 68
Figure 4.3 Tidal forces due to the Moon 69
Figure 4.4 Spring and neap tides 69
Figure 4.5 Lunar cycle of tides 69
Figure 4.6 Types of tides 70
Figure 4.7 Global distribution of tide cycles 70
Figure 4.8 Tidal range 71
Figure 4.9 Water wave 72
Figure 4.10 Energy spectrum of ocean waves 72
Figure 4.11 Algal bloom 75
Figure 5.1 Argo global array 78
Figure 5.2 Bathymetry of Bass Strait 79
Figure 5.3 Ocean glider transect 80
Figure 5.4 Thermohaline circulation patterns 81
Figure 5.5 Stratification of water column 82
Figure 5.6 Lake stratification 82
Figure 5.7 Electromagnetic spectrum 84
Figure 5.8 Atmospheric opacity 84
Figure 5.9 Reflectance from different water colours 85
Figure 5.10 Light attenuation in water 85
Figure 5.11 Turbidity caused by flocculation 86
Figure 5.12 Secchi disk 87
Figure 5.13 pH scale 89
Figure 5.14 Separation of dissolved and particulate matter 90
Figure 5.15 Deep chlorophyll maximum for northeast Pacific Ocean 93

Figure 6.1 Morphological features 100
Figure 6.2 Global Seafloor Geomorphic Feature map (GSFM) 102
Figure 7.1 Proposed waterbody depth regions for Seabed 2030 107
Figure 7.2 Aquatic carbon in freshwater system 109
Figure 7.3 Earth System Science 111
Figure 8.1 Measurement and analysis of image features 117
Figure 8.2 Polar angles 118
Figure 8.3 Solid angle 118
Figure 8.4 Geometric framework for optical studies 119
Figure 8.5 Radiative transfer process 120
Figure 8.6 Specular reflection 120
Figure 8.7 Radiance definitions 121
Figure 8.8 Cosine law 121
Figure 8.9 Downwelling and upwelling irradiance 121
Figure 8.10 EMR reflectance from water 124
Figure 8.11 Scattering directions 124
Figure 8.12 Internal reflection and refraction 126
Figure 8.13 Sun-sensor geometry of example images 127
Figure 8.14 Impact of sun-sensor geometry on image quality 128
Figure 8.15 Absorption spectrum of pure water 130
Figure 8.16 Effect of salinity on scattering by water 130
Figure 8.17 Absorption spectra of algal pigments 131
Figure 8.18 Water colour variations due to phytoplankton 131
Figure 8.19 Absorption spectra for phytoplankton 132
Figure 8.20 CDOM Absorption spectra 133
Figure 8.21 Simulation of substratum reflectance at different water depths 138
Figure 8.22 Modelled subsurface irradiance reflectance 139
Figure 8.23 Relationship underlying optical EO models 140
Figure 9.1 Blackbody radiation 156
Figure 9.2 Radar wavelengths 157
Figure 9.3 Radar penetration in ice/snow cover 158
Figure 9.4 Electromagnetic wave 159
Figure 9.5 Bragg scattering 163
Figure 9.6 SAR composite images 163
Figure 9.7 InSAR operation 164

Figure 9.8 Operation of radar altimeter 165
Figure 9.9 Global wind power 166
Figure 10.1 Longitudinal or compression waves 169
Figure 10.2 Speed of sound varies with water depth 170
Figure 10.3 Hull-mounted sonar system 171
Figure 10.4 Beam patterns of sonar systems 172
Figure 10.5 Comparison of sonar systems 172
Figure 10.6 Sidescan sonar image of shipwreck 173
Figure 10.7 Multibeam mapping 174
Figure 10.8 Swath overlap for backscatter data 175
Figure 10.9 Relationship between reference ellipsoid, antenna, water line, and chart datum 175
Figure 11.1 Scales of observing ocean changes 181
Figure 11.2 A selection of hydrologic features of Australia from the Geofabric 182
Figure 11.3 Region north of Lake Eyre during flooding 184
Figure 11.4 Sentinel-1a SAR image of Lake Sorrell in Tasmania, acquired on the 7 May 2015 185
Figure 11.5 NIDEM process 187
Figure 11.6 GLOWABO overview 188
Figure 11.7 GLOWABO estimates 189
Figure 11.8 Distribution of lakes by latitude and elevation 190
Figure 11.9 Charter Activation 192
Figure 12.1 Reference frames and measurements for sea level observation 198
Figure 12.2 Variability of Australian tides 199
Figure 12.3 Operation of SWOT 201
Figure 12.4 Simulated SWOT measurements 202
Figure 12.5 SWOT fast sampling swaths 202
Figure 12.6 *In situ* measurement sites 203
Figure 12.7 Example calibration site 204
Figure 12.8 Converting mooring measurements into datum 205
Figure 12.9 Factors affecting sea level at a range of spatial and temporal scales 205
Figure 12.10 Tropic Cyclone Yasi 206
Figure 12.11 Wave setup 207
Figure 12.12 Mean sea level 208
Figure 12.13 Ocean-climate system variability 208
Figure 12.14 Tide gauge records 209
Figure 12.15 PSMSL tide gauge stations 211

Figure 12.16 GLOSS network of tide gauge stations 211
Figure 12.17 TOPEX/Poseidon altimeter coverage 214
Figure 12.18 Ground tracks of several altimeter missions 215
Figure 12.19 The past three centuries of the global sea level record 216
Figure 12.20 The satellite era mean sea level record 216
Figure 12.21 Historical sea level change 217
Figure 12.22 Projected sea level changes around Australia in 2090 218
Figure 13.1 Improvements in GEBCO over time 224
Figure 13.2 Search for MH370 relative to available bathymetric datasets 226
Figure 13.3 Australian Bathymetric and Topographic Grid 227
Figure 13.4 Primary bathymetric units 228
Figure 13.5 Distribution of geomorphic features around Australia's continental margin 229
Figure 13.6 Satellite altimetry versus acoustic datasets 231
Figure 13.7 Example of bathymetric data improvements 232
Figure 13.8 Global map of marine gravity 233
Figure 13.9 AusSeabed bathymetry holdings (by survey) in January 2020 234
Figure 13.10 Lidar bathymetry 235
Figure 14.1 Average SST around Australia 246
Figure 14.2 AVHRR/3 GAC grid resolution and sampling 248
Figure 14.3 Nighttime SST maps 249
Figure 14.4 Near-surface oceanic temperature gradients 251
Figure 14.5 Nighttime SST maps for 13 March 2019 over the Queensland region 256
Figure 14.6 Australian AVHRR ground stations 266
Figure 14.7 Skin SST maps 267
Figure 14.8 SST maps 268
Figure 14.9 IMOS nighttime, 6-day AVHRR L3S SST around Tasmania 269
Figure 14.10 Argo temperature profile and SST 270
Figure 14.11 Daytime SWT map from VIIRS 272
Figure 15.1 Satellite-derived map of the Antarctic Ice Sheet and surrounding sea ice 282
Figure 15.2 Plan view and cross section profiles across Antarctica 283
Figure 15.3 Schematic of an Antarctic ice shelf 284
Figure 15.4 Schematic of an ice sheet and its individual mass balance components 285
Figure 15.5 Extent of Antarctic sea ice in 2015/2016 286
Figure 15.6 Photographs of Antarctic pack ice and fast ice 287
Figure 15.7 Portion of Mosaic of Antarctica (MOA) map 291

Figure 15.8 Warming trend of Antarctica from 1957 through 2006 292
Figure 15.9 Byrd Glacier velocity 294
Figure 15.10 Antarctic ice shelf thickness changes 295
Figure 15.11 DEM of the Antarctic Ice Sheet 296
Figure 15.12 Extent of Arctic versus Antarctic sea ice 298
Figure 15.13 Fast ice coverage and persistence 299
Figure 15.14 Mean monthly (March through November) ice drift for 1982-2015. 300
Figure 16.1 Example wave spectrum 312
Figure 16.2 Significant wave height 313
Figure 16.3 Australian Marine Energy Atlas 314
Figure 16.4 Scatterometer missions 316
Figure 16.5 GNSS-R system 319
Figure 16.6 Australian wave buoy network 320
Figure 16.7 Global buoys for March 2016 321
Figure 16.8 Australasian SAR database 323
Figure 17.1 Mean surface currents around Australia 331
Figure 17.2 Speed of Antarctic Circumpolar Current 335
Figure 17.3 Temperature variations 336
Figure 17.4 Detailed view of temperature variation 336
Figure 17.5 Circulation in EAC 338
Figure 17.6 MODIS Chlorophyll a OC3 29 May 2018 339
Figure 17.7 Frontal systems on Australian northwest shelf 340
Figure 18.1 Characteristic reflectance features of water colour constitutents 345
Figure 18.2 Simulations of waterbody reflectance 346
Figure 18.3 Variations in surface water colour 347
Figure 18.4 Hue angle conversion 348
Figure 18.5 The Forel-Ule colour scale 349
Figure 18.6 Ternary diagrams 350
Figure 18.7 Non-algal particulates 352
Figure 18.8 Simulated EO reflectance for different substrates 353
Figure 18.9 Blackwater plume 355
Figure 18.10 Blackwater event 356
Figure 18.11 MODIS chlorophyll a concentration products 358
Figure 18.12 Epiphytic growth on seagrass blades 359
Figure 18.13 Impact of water depth on substrate spectra 360

Figure 19.1 Great Barrier Reef shown in true colour 370

Figure 19.2 Effect of spatial resolution on Lake Burley Griffin, Canberra 374

Figure 19.3 Cyanobacteria bloom 375

Figure 19.4 *In situ* measurement locations 376

Figure 19.5 HydraSpectra installation 376

Figure 19.6 HydraSpectra reflectance data 377

Figure 19.7 Weathering processes associated with an oil spill 380

Figure 19.8 Duration of oil weathering processes 381

Figure 19.9 Beach profile showing potential oil spill deposits 381

Figure 19.10 AMSA oil spill response process 384

Figure 19.11 MODIS image of algal bloom 386

Figure 19.12 Defining marine heatwaves 387

Figure 19.13 Global salinity image composites 388

Figure 20.1 Great Barrier Reef Marine Park 398

Figure 20.2 Australia's other marine parks 399

Figure 20.3 EO data resolutions for seagrass and mangrove features in coastal environments 401

Figure 20.4 Wetland habitat zones 403

Figure 20.5 Seagrass spatial and organisational scales 404

Figure 20.6 Mangrove features versus image resolution 407

Figure 20.7 Coral diversity 410

Figure 20.8 Coral reef hierarchical scales 411

Figure 20.9 Comparison of spatial resolution and extent for four EO sensors 413

Figure 20.10 Exposure (directional) filtering 414

Figure 20.11 Approaches to reef mapping 417

Figure 20.12 Automated classification of geomorphic zones 418

Figure 20.13 Mapping reef biophysical properties 419

Figure 20.14 eReefs modelling extent 420

Figure 20.15 Pelagic sampling methods 422

Figure 21.1 Spectral characteristics of hyperspectral PACE OCI compared with heritage spaceborne ocean colour sensors 440

Figure 21.2 Pressures and drivers on global ocean biology 443

List of Tables

Table 1.1 Dimensions of oceans 7

Table 1.2 Geomorphological categories of coastal landforms 10

Table 2.1 Australia's maritime zones 24

Table 2.2 Area of Australian Exclusive Economic Zones 26

Table 2.3 Categories of waterbodies in Australia 39

Table 3.1 The plant kingdom 55

Table 3.2 Most common phytoplankton groups 57

Table 3.3 Most frequently occurring algal groups 58

Table 3.4 Classification of macrophytes 59

Table 4.1 Beaufort scale 71

Table 4.2 Categories of waves 73

Table 4.3 WMO Sea State tables for waves and swells 73

Table 5.1 Factors impacting ocean water density 81

Table 5.2 Trophic status categories for freshwater lakes 92

Table 6.1 Generic geomorphic features 100

Table 7.1 Seabed 2030 minimum mapping resolutions 107

Table 7.2 Modelled scenarios for Antarctica and Southern Ocean in 2070 110

Table 8.1 Terminology for EO geometry 119

Table 8.2 Light behaviour in different media 120

Table 8.3 Impact of cosine law on irradiance 121

Table 8.4 Hydrologic optics terms 122

Table 8.5 Inherent optical properties 123

Table 8.6 Apparent Optical Properties 123

Table 8.7 Some fluorescence features in waterbodies 125

Table 8.8 Major photo pigments for phytoplankton taxonomic classes 132

Table 8.9 Commonly used Inherent Optical Properties 135

Table 8.10 Commonly used Apparent Optical Properties 136

Table 8.11 Optical depth 137

Table 8.12 Forward and inverse models 141

Table 8.13 Mathematical inversion models for aquatic ecosystem variables 141

Table 8.14 Optical EO sensors for aquatic mapping 147

Table 8.15 Recommended spectral bands for assessing water quality and characterising benthos 149

Table 8.16 Recommended spectral bands for atmospheric and air-interface correction 150
Table 9.1 Spectral regions observed by EO sensors 155
Table 9.2 Radar bands used for EO 157
Table 9.3 Effects of EMR on matter 159
Table 9.4 Wave-matter interactions relevant to EO 159
Table 9.5 Polarisation options for radar signals 161
Table 10.1 MBES footprint 173
Table 10.2 Examples of sounding accuracy and TPU 176
Table 11.1 EO sensors relevant to water extent 183
Table 12.1 EO sensors relevant to water level 199
Table 12.2 Satellite missions providing data from a radar altimeter instrument 200
Table 12.3 Predicted temperature variations 217
Table 13.1 Surface areas of primary bathymetric units 228
Table 13.2 Geomorphic features of Australian continental margin 230
Table 13.3 EO sensors relevant to bathymetry 231
Table 13.4 Examples of neural network and machine learning models 236
Table 13.5 Examples of semi-analytical models 238
Table 14.1 EO sensors relevant to water temperatures 247
Table 14.2 AVHRR/3 channels 247
Table 14.3 Global, Daily, Multi-Sensor SST analysis products in GHRSST L4 format 258
Table 14.4 GHRSST products 263
Table 15.1 EO sensors relevant to ice 289
Table 16.1 EO sensors relevant to water waves 314
Table 17.1 Water circulation terms 329
Table 17.2 Names and abbreviations of major currents 332
Table 17.3 EO sensors relevant to water circulation 334
Table 18.1 EO sensors relevant to water colour 348
Table 19.1 Suitability of optical EO sensors to map water quality variables 369
Table 19.2 EO sensors relevant to water quality 370
Table 19.3 Size distribution of waterbodies in Australia 373
Table 19.4 National water quality system based on EO 374
Table 19.5 Major EO sensors for oil spill detection 382
Table 19.6 Environmental limitations on oil spill detection 383
Table 20.1 Commonwealth Marine Reserves IUCN protected area management categories 400
Table 20.2 EO sensors relevant to coastal and marine water ecology 401

Table 20.3 Suitability of optical EO sensors for mapping aquatic ecosystem features 402

Table 20.4 Backscatter from mangroves 406

Table 20.5 Four reef differentiation scales 412

Table 21.1 Global monitoring systems 441

Table 21.2 Essential Ocean Variables 442

Table 21.3 Big Earth data challenges 444

Table 21.4 Target variables for pressures and drivers in the aquatic biological environment 446

List of Excurses

Excursus 1.1—Global Freshwater Resources 3

Excursus 1.2—Coriolis Force and Ferrel's Law 13

Excursus 2.1—Australian Maritime Safety Authority (AMSA) 25

Excursus 2.2—Bluelink Ocean Forecasting 30

Excursus 3.1—Inland Floodplain Wetlands 46

Excursus 3.2—Phytoplankton Groups 57

Excursus 4.1—Astronomical Tides 69

Excursus 4.2—Water Waves 72

Excursus 5.1—Ocean Profile Sensors 78

Excursus 7.1—Nippon Foundation-GEBCO Seabed 2030 Project 107

Excursus 7.2—The Global System 111

Excursus 8.1—Optics Review 118

Excursus 9.1—Radar 156

Excursus 11.1—GLOWABO 188

Excursus 12.1—Surface Water and Ocean Topography (SWOT) 201

Excursus 12.2—The National Operations Centre (NOC) Tidal Unit 212

Excursus 13.1—Australian Bathymetric and Topographic Grid 227

Excursus 14.1—Selecting a Satellite SST Product 257

Excursus 14.2—Sea Surface Temperature around Tasmania 269

Excursus 15.1—The Importance of EO for Sea Ice 287

Excursus 16.1—Marine Surface Winds and Waves 312

Excursus 17.1—Major Currents around Australia 332

Excursus 17.2—Example Circulation Study 337

Excursus 17.3—Ocean Fronts 339

Excursus 18.1—Blackwater Events 355

Excursus 19.1—Australian Inland Water Quality 371

Excursus 19.2—Assessing Inland Water Quality using Optical EO 373

Excursus 19.3—Western Treatment Plant, Werribee 375

Excursus 19.4—Operational Oil Spill Response 384

Excursus 20.1—Biodiversity 396

Excursus 20.2—Marine Protected Areas 398

Excursus 20.3—Coral Bleaching 415

Excursus 21.1—Essential Ocean Variables 442

Introduction

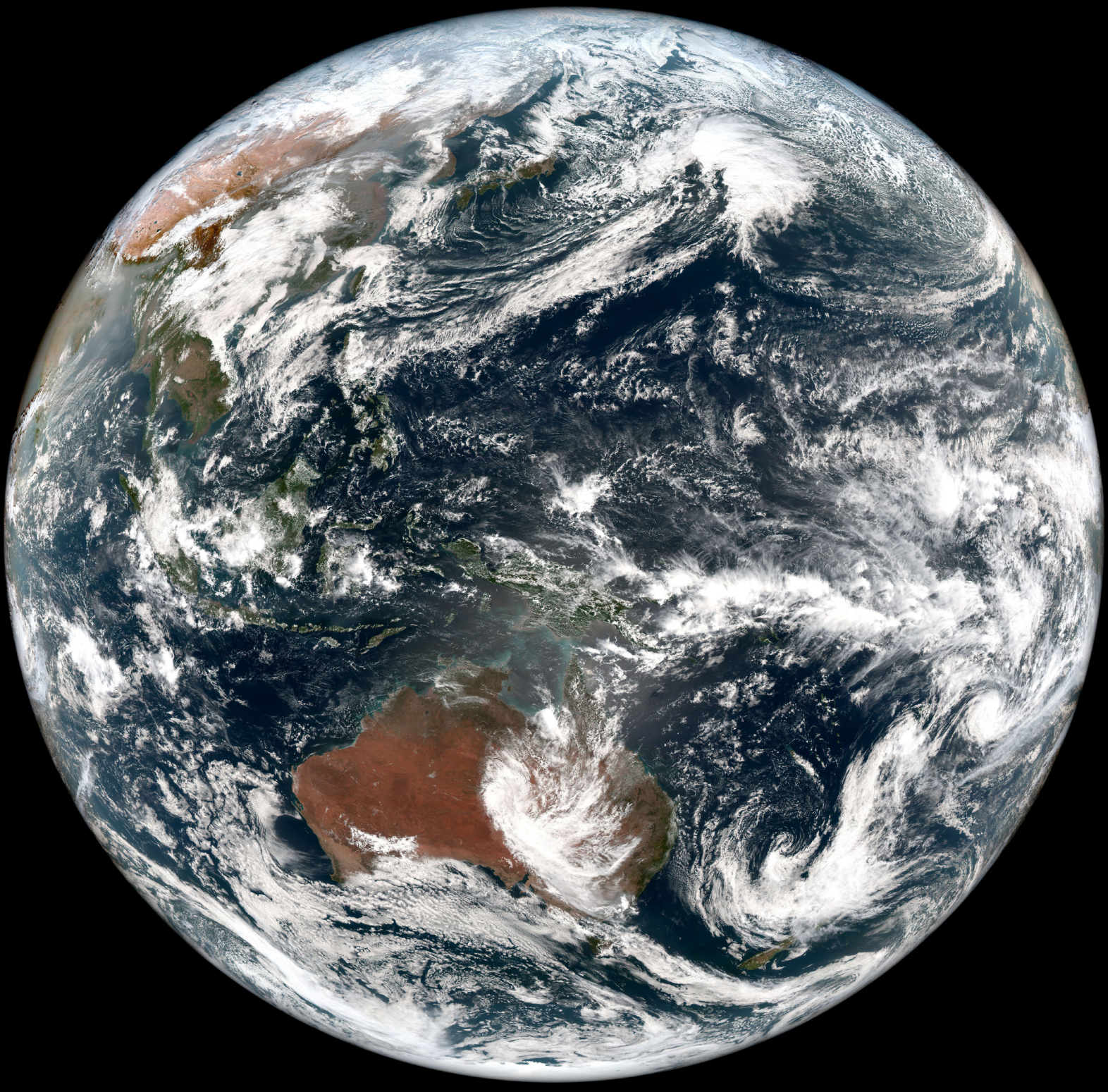

This series of publications, *Earth Observation: Data, Processing and Applications*, comprises three volumes. Volume 1 in this series is presented as three sub-volumes, which together outline the basics of Earth Observation (EO) in terms of energy sources, data acquisition, sampling characteristics, image availability, data interpretation and usage. Volume 2 (six sub-volumes) describes the various options involved with image representation, analysis, transformation, integration and modelling, including details of relevant algorithms, with emphasis on their underlying mathematical and statistical principles. These volumes provide valuable background information for understanding specific applications of EO. They also define terminology used in Volume 3, which currently comprises two sub-volumes: 3A, Terrestrial Vegetation, and 3B, Surface Waters.

Volume 3B details how EO methods are used to map, monitor and model various characteristics of Australia's inland, coastal and marine waters. In this context, surface waters include sea ice, ice sheets and shelves, and icebergs in Antarctica and the Southern Ocean. The introductory sections in this sub-volume describe background topics that are relevant to understanding EO studies of these surface waters:

- water on Earth—the hydrological cycle, categories of surface water, physical layers within waterbodies, global water circulation, and the global carbon cycle (see Section 1);
- surface waters in the Australian environment—legislative and environmental zones, waterbody characteristics, and water distribution and usage (see Section 2); and
- aquatic ecosystems—relevant characteristics of ecological zones, habitats and organisms within the Australian marine environment (see Section 3).

Sections 4 to 7 respectively summarise attributes of the water surface, water column, substratum and waterbodies that are relevant to EO-based studies. Sections 8 to 10 review characteristics of optical, microwave and acoustic EO datasets. Sections 11 to 20 introduce specific application areas where EO datasets are being used to observe Australian surface waters. Section 21 concludes this sub-volume by considering some potential future challenges in this area.

Contents

1 The Blue Planet 3

2 Australia's Surface Water Environment 21

3 Aquatic Ecosystems 43

Background image on previous page: Full disk image captured by Himawari-8 geostationary satellite on 1 January 2016, displayed as natural colour composite. **Source:** © Bureau of Meteorology/JMA

1 The Blue Planet

With over 70% of the Earth's surface being covered by water, our planet can reasonably be called the 'Blue Planet'. The total volume of water of Earth has been estimated as 1,386 million km^3, 96.5% of which occurs in the oceans (Shiklomanov and Rodda, 2003). Of the 2.53% that is freshwater, nearly 69% is frozen in permanent ice and glaciers, and around 30% exists as groundwater. Thus, only a very small proportion of the total water on Earth is available for routine use. Estimates of global freshwater reserves are now being refined and monitored using integrated EO technologies (see Excursus 1.1).

The following subsections provide an overview of global water characteristics:

- water movement around the planet, that is, the hydrological cycle (see Section 1.1);
- categories of surface waters (see Section 1.2)
- physical layers within surface waterbodies (see Section 1.3);
- global circulation of surface waters (see Section 1.4); and
- the global 'blue' carbon cycle (see Section 1.5).

Excursus 1.1—Global Freshwater Resources

Source: Paul Tregoning, Australian National University

Changes in Earth's gravity are caused by mass movements of water, due to:

- ocean circulation and currents;
- the exchange between continents and oceans through the hydrological cycle; and also
- through the current melting of glaciers and ice sheets in polar regions.

Measurements from the Gravity Recovery and Climate Experiment (GRACE) inferred gravity changes over the Earth. The GRACE mission (operational from 2002 to 2017) used microwave ranging to measure the precise change in distance between two spacecraft, which is affected by changes in the Earth's gravitational field (see Figure 1.1). The GRACE Follow-on mission, launched in May 2018, includes a laser ranging system to deliver these measurements with substantially greater accuracy.

Figure 1.1 Gravity Recovery and Climate Experiment (GRACE)

The GRACE mission measured the precise distance between twin satellites accurate to about 1/10 of the thickness of a human hair. Slight changes in the distance between these satellites occur over time as differences in the Earth's gravity field cause the speeds of the satellites to vary as they orbit around Earth.

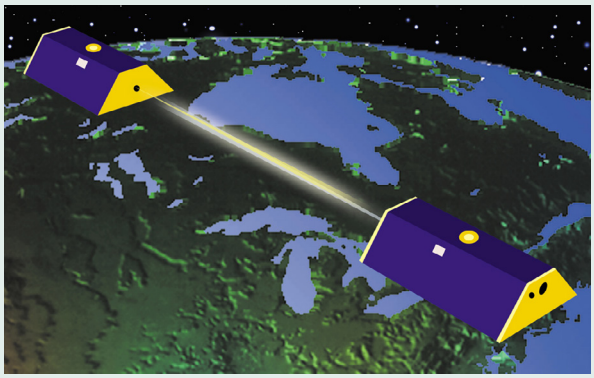

Background image: Portion of the Southern Hemisphere from 'one million miles' (1.6 million km) away, taken by NASA's Earth Polychromatic Imaging Camera (EPIC) on 6 July 2015 from the Deep Space Climate Observatory (DSCOVR). This image uses the red, green and blue channels. **Source:** NASA. Retrieved from *http://www.nasa.gov/press-release/nasa-satellite-camera-provides-epic-view-of-earth*

Figure 1.2 Murray-Darling Basin total water storage

Time series of the changes in total water storage, averaged over the entire Murray-Darling Basin system, from April 2002 to June 2020, showing the annual variations and long term trends of droughts and wet times during this period.

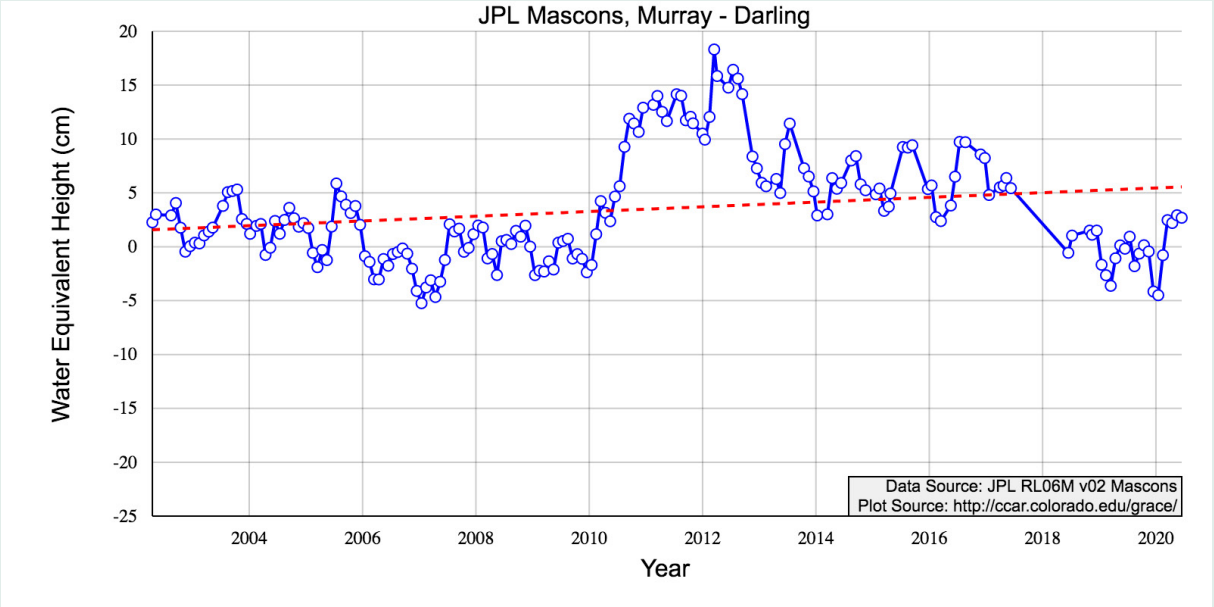

An integrated NASA study that monitored the availability of freshwater in 34 regions globally has been able to distinguish changes due to natural climatic factors from those due to anthropogenic causes (Rodell *et al.,* 2018). This study involved analysis of:

- 14 years of data from GRACE;
- Landsat imagery;
- satellite precipitation data from the Global Precipitation Climatology Project;
- irrigation maps; and
- published reports of agricultural, mining and reservoir operations.

Distinct patterns emerged of wet areas becoming wetter, especially in polar and tropical regions, and dry areas becoming drier, often due to groundwater depletion.

At a national scale, GRACE data provides the potential to estimate changes in total water storage in Australian drainage basins at monthly intervals and to quantify the severity of droughts and floods. For example, water storage in the Murray-Darling Basin was estimated using GRACE and GRACE Follow-On data (see Figure 1.2). These results showed that an average of 5.52 Gt per year of water were lost from surface and subsurface storage during the Millenium Drought (ending in 2009), comprising soil moisture, surface waters (from rivers, dams, reservoirs) and groundwater. The breaking of the drought is clearly visible, with significant water mass increase occurring between 2010 and 2012. Unfortunately, another drought occurred in the subsequent years, as captured by GRACE data (2012–2017) and GRACE Follow-On data (2018–2019).

Similarly, water anomalies (expressed in terms of an equivalent water height, or the height of water as a column or disk required to equal the mass change) were estimated from 30 days of GRACE data during the January 2011 floods in northeastern Australia. In Figure 1.3, the southernmost blue region near Rockhampton indicates the start of flooding, while the blue regions near Cairns and in the Gulf of Carpentaria are related to mass changes caused by wind-driven water movement associated with Tropical Cyclone Yasi.

Figure 1.3 Water mass anomalies

Estimates of water height anomaly (mm) based on 30 days of GRACE data show higher water volumes in northeastern Australia after the January 2011 floods.

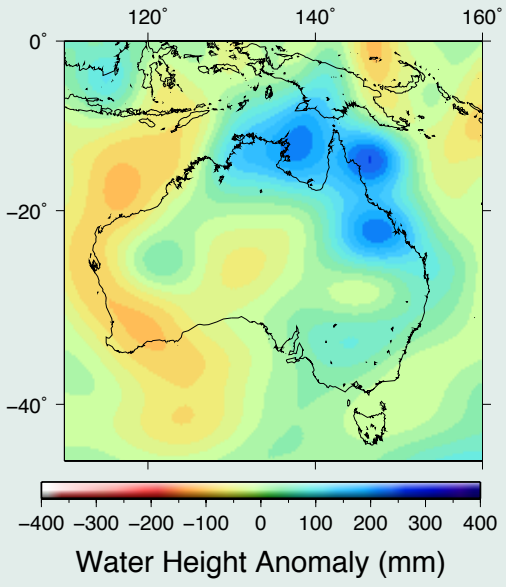

1.1 The Hydrological Cycle

The hydrosphere comprises all the water on the Earth's surface, inside the Earth and in its atmosphere. Water constantly moves:

- between locations on the Earth's surface;
- between the surface and subsurface storage; and
- between the surface and the atmosphere (see Figure 1.4).

Water can exist in the form of liquid water, water vapour, ice, or snow, and may be nearly pure or contain dissolved and/or suspended substances. As surface water is heated by the Sun, it evaporates to become water vapour in the atmosphere. Plants also release water vapour to the atmosphere by transpiration (see Volume 3A). As water vapour rises in the atmosphere, it cools and condenses, forming clouds. Global air currents move clouds until they release their water as precipitation, in the form of rain, hail or snow. This sub-volume focuses on surface waters.

Water on the surface of the Earth is stored in the natural depressions of oceans and lakes, or the man-made storage facilities of reservoirs and dams. Some surface water is frozen, in the form of polar ice caps and their glaciers, in millennial time scales. Other frozen surface water regularly melts with seasonal changes. This includes sea ice that covers a vast, though seasonally-variable, area of the high-latitude Southern Ocean.

Water running on the Earth's surface, or runoff, can come directly from precipitation or melting sources. Rivers obey the laws of gravity and transport water from higher to lower elevations, generally delivering it to larger storage, such as a lake or an ocean. Many changes occur in rivers between its source and the outlet to a larger waterbody. Near the source, river water is generally clear, cold, and low in nutrients, and hence most likely low in phytoplankton. At this point, the river channel is likely to be narrow, shallow, and lined with rock. Further along, the river typically widens and deepens, runs through softer soils, and may include marshes and wetlands. The water in midstream sections of rivers is generally warmer and more turbid than near the source. Higher populations of phytoplankton would live in these waters.

Figure 1.4 The global water cycle

Each year, more than half a million cubic kilometres of water is moved around the Earth's surface, mostly between the oceans and the atmosphere, and some between the surface and subsurface storage.

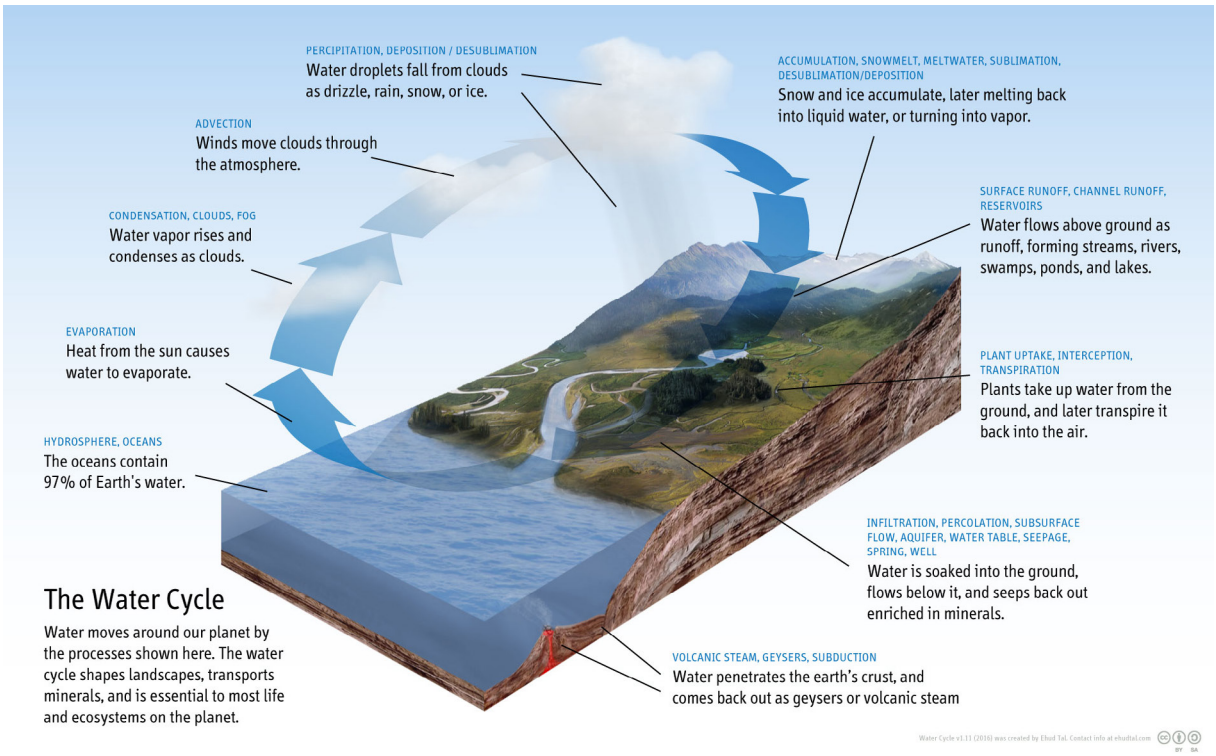

Source: Ehud Tal, Wikimedia. Retrieved from *https://upload.wikimedia.org/wikipedia/commons/b/b1/Diagram_of_the_Water_Cycle.jpg*

Most rivers meet the sea via estuaries or deltas. Estuaries are semi-enclosed waterbodies at the river mouth where river flow and tides mix fresh and saltwater. These areas are typically turbid and nutrient rich, which provides valuable habitat for marine and bird life. Deltas result from settling river sediment, which creates shallower riverbeds. Deltas can occur where one river meets another, a river meets a lake or reservoir, or a river meets an open sea that has weak tidal currents. The formation of deltas gradually slows down the flow of rivers and lengthens its journey through meanders. Inland rivers can also flow into dry salt lakes, as occurs in Central Australia.

The area of land draining into a river is referred to as its catchment or watershed. Characteristics of the catchment area, or drainage basin, determine the size and flow rate of the river, as well as sources of organic and inorganic inputs to flows, which impact water quality (see Figure 1.5). A hierarchical system of catchments often exists such that catchments drain into other catchments.

Figure 1.5 River catchment

This schematic shows two drainage basins divided by a ridge. Individual basins drain into a network of streams and rivers which carry surface flow downhill.

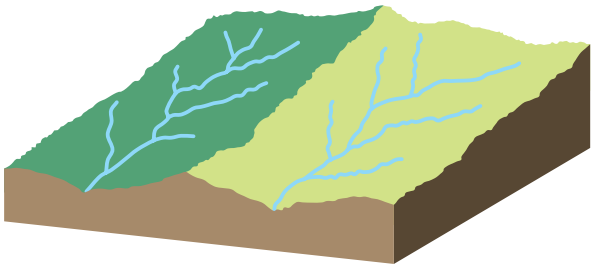

Before flowing towards a drainage channel, precipitation can be intercepted by vegetation, buildings, or small surface depressions within a catchment. Interception of rainfall allows some precipitation to soak into the ground rather than flow away. Water can infiltrate into the soil layer and be stored as soil moisture or percolate through the soil until it reaches the water table. Beneath the Earth's surface, soil and/or rock are typically layered in two distinct zones. The upper zone is aerated, that is, it contains some air. Water in this zone is available to plants. In the lower, rocky zone, air pockets are saturated with water. This saturated zone is called an aquifer. The boundary between these zones is called the water table. The depth of the water table varies with the volume of water that is added to (recharge) and/or removed from (discharge) the aquifer. A spring occurs when groundwater naturally overflows onto the land surface. Groundwater is often extracted from aquifers artificially by installing a well or bore. Unconfined aquifers require a pump to raise groundwater to the surface from a bore. Confined aquifers, however, exist above layers of relatively impermeable rock such that natural internal pressures spontaneously eject the groundwater to (or above) the surface. Such waters are called artesian waters (see Figure 1.6).

Figure 1.6 Artesian well

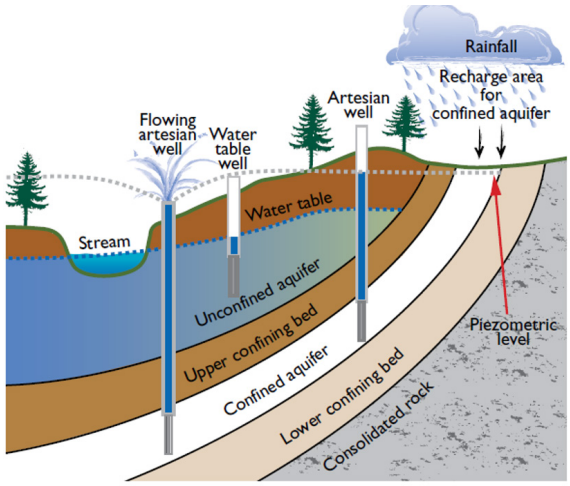

Figure 1. Geological and topographical controls affecting artesian and flowing artesian wells.

Source: UGSG (2018). Retrieved from: *https://www.usgs.gov/media/images/artesian-wells-can-bring-water-land-surface-naturally*

1.2 Categories of Surface Waters

Bodies of water on the Earth's surface can be categorised in several ways. The most basic division of waterbodies (non-frozen) relates to their salt content, with marine waters being salty, and freshwater systems, as the name implies, generally containing low levels of salt. For practical purposes, it is also common to subdivide marine waters into oceans and coastal waters. Accordingly, to discuss surface waters in this text, three broad categories will be used:

- inland: freshwater rivers and lakes located within continental boundaries;
- coastal: shallow marine waters adjacent to continental boundaries; and
- oceans: deeper marine waters bordering coastal waters.

Accepted legislative definitions for marine zones in Australia are introduced in Section 2.1. These zones are located relative to the Territorial Sea Baseline (TSB), a reference boundary that effectively defines a border between land and sea. In most cases, the TSB corresponds to the Lowest Astronomical Tide (LAT; GA, 2021). For administrative purposes, these definitions allow our three water categories to be described more precisely as:

- inland waters: fresh waterbodies located within the TSB;
- coastal waters: marine waters within 3 nautical miles (M) from TSB (where 1 M≈1.8 km); and
- oceans: marine waters more than 3 M from TSB.

Unfortunately, these precise definitions do not always correlate with the physical characteristics of these three water classes, such as their constituents, optical properties, or variations in water depth. For the purposes of the following discussion, these terms will be defined as:

- oceans: deeper marine waters at least 3 M away from the TSB. These large waterbodies are saline and subject to tidal variations (see Section 1.2.1).
- coastal waters: shallower marine waters adjacent to the TSB. These include estuaries, beaches, salt marshes, mudflats, and mangrove swamps, as well as the shallow waters on the fringe of oceans that contain coral reefs and lagoons, seagrass meadows and kelp forests (see Section 1.2.2); and
- inland waters: freshwater rivers and lakes located within the TSB. Most inland waterbodies have low levels of dissolved salt, but some salt lakes can contain higher concentration of salts than seawater. Ponds, dams, and lakes feature standing water while rivers and streams have flowing water (see Section 1.2.3).

1.2.1 Oceans

Our oceans constitute a contiguous saline waterbody that covers around 70% of the Earth's surface. This single mass is sometimes called the 'world ocean'. For convenience it is divided into five major regions, here listed in order of increasing area:

- Arctic;
- Southern;
- Indian;
- Atlantic; and
- Pacific Oceans (see Figure 1.8).

The ETOPO1 is a 1 arc-minute digital representation of Earth's solid surface that integrates land topography and ocean bathymetry using global and regional datasets (Amante and Eakins, 2009; see Figure 1.7). The area and volume of each ocean have been estimated from this model (Eakins and Sharman, 2010; see Table 1.1).

Table 1.1 Dimensions of oceans

Estimates based on ETOPO1 Ice Surface global relief model with error estimates 0.1% for area and 1% for volume.

Ocean	Area (km^2)	Volume (km^3)	Average Depth (m)	Maximum Depth (m)
Arctic	15,558,000	18,750,000	1,205	5,567
Atlantic	85,133,000	310,410,900	3,646	8,486
Indian	70,560,000	264,000,000	3,741	7,906
Pacific	161,760,000	660,000,000	4,080	10,803
Southern	21,960,000	71,800,000	3,270	7,075

Source: Eakins and Sharman (2010).

Figure 1.7 ETOPO1 global relief model

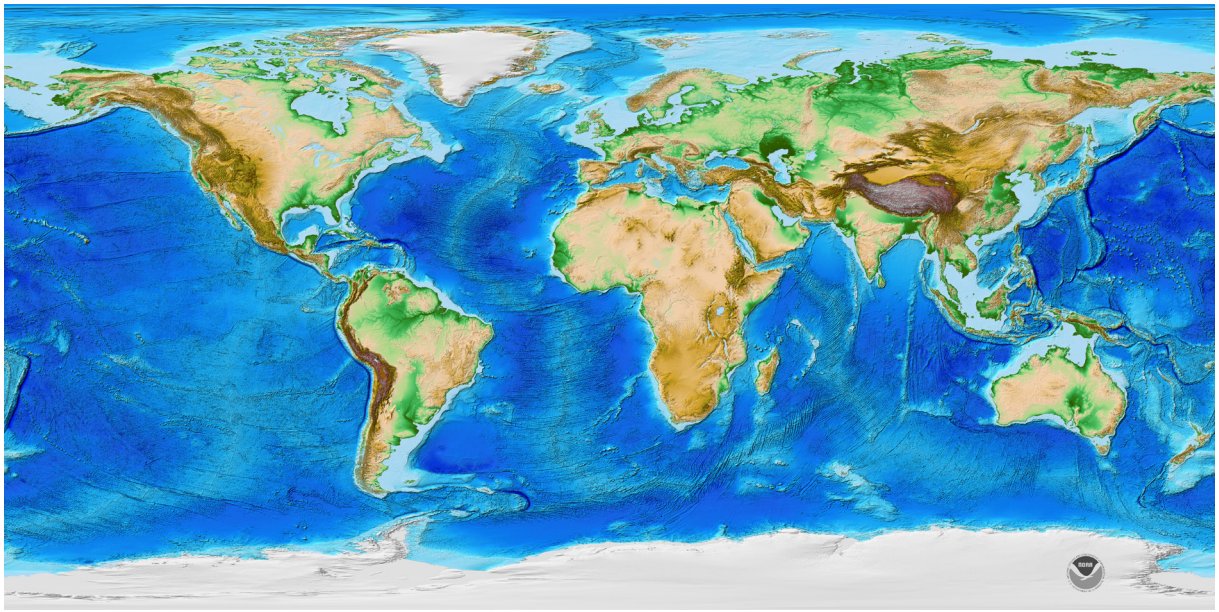

Source: NOAA. Retrieved from: *https://www.ngdc.noaa.gov/mgg/global/global.html*

Figure 1.8 Oceans of the world

Note that the precise boundaries between oceans may vary with jurisdictions. In this map, ocean boundaries were modified from IHO (1953) to include major oceans and marginal seas.

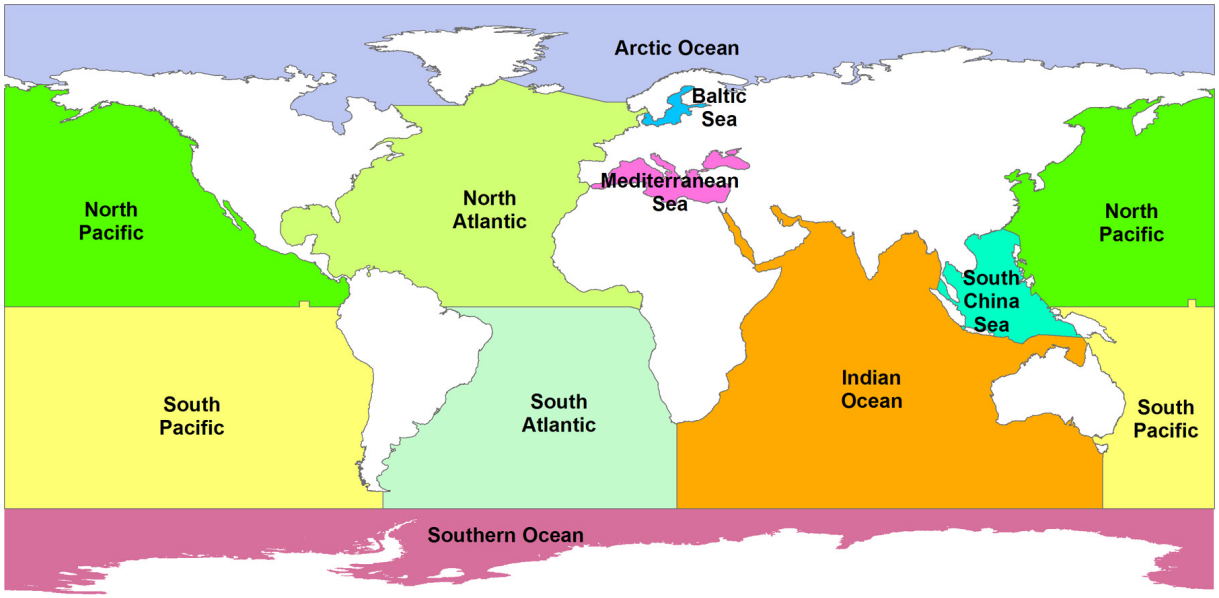

Source: NOAA. Retrieved from: *https://www.ngdc.noaa.gov/mgg/global/etopo1_ocean_volumes.html*

The average depth of the ocean is 3,720 m with the deepest point found in the Mariana Trench (11,033 m). In total, oceans cover around 362 million km^2 and comprise 1.335 million km^3 of water. The topography of the ocean floor is similar to that of land masses, featuring mountains, volcanoes, plateaus and deep trenches. As introduced in Section 2.1, shallow, sloping seas called 'continental shelves' surround most continents. At their edge, the 'continental slope' leads to the deeper parts of the ocean, where volcanoes, abysses, oceanic ridges, abyssal plains, fracture zones, guyots, trenches and seamounts occur (see Figure 1.9). Underwater plains, usually between 3,000 m and 6,000 m depth, called abyssal plains cover over 50% of the Earth's surface. The abyssal rise, which links the abyssal plain and the continental slope, is also called the continental rise.

Figure 1.9 Major marine geomorphic features

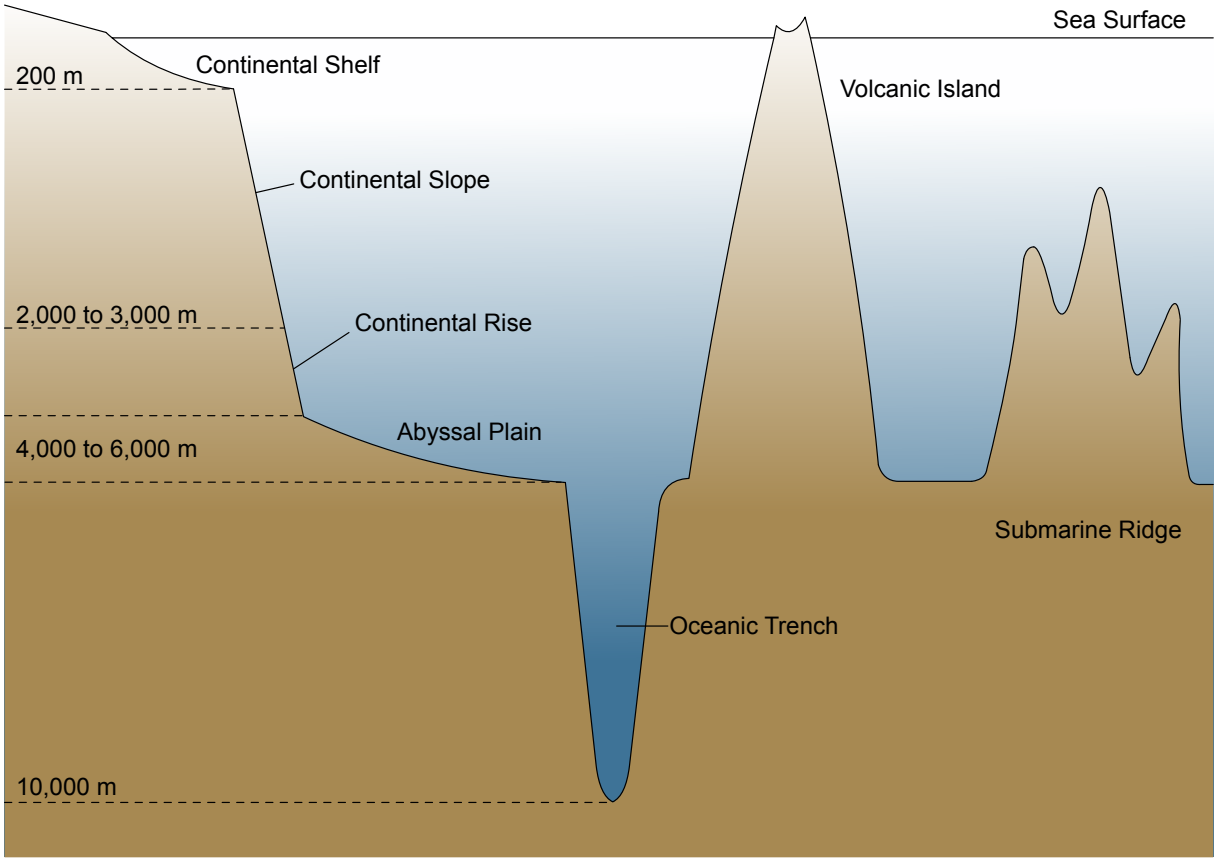

Source: Wikimedia. Retrieved from *https://upload.wikimedia.org/wikipedia/commons/1/13/Oceanic_basin.svg*

Ocean waters provide a significant heat store for our planet and are in constant motion (see Sections 1.4 and 17). They also act as a long term sink for atmospheric carbon dioxide (CO_2). As atmospheric carbon levels increase with deforestation and burning of fossil fuels, the amount of CO_2 being absorbed by the oceans has increased, making these waters more acidic.

Long term climate records indicate the global sea temperatures have risen over the past half century (see Sections 4.5, 5.1.3 and 14), especially in the upper water layers (few hundred metres). This change has prompted movement of marine species from their traditional territories to cooler waters. Since water expands as it warms, sea levels have also been observed to rise 20 cm in the last century leaving 70% of the global shorelines on higher ground (see Sections 4.1 and 12). Moreover, as ocean waters increase in temperature, ice sheets and glaciers melt (see Sections 4.7 and 15), thus adding stored water to the circulating surface waters and further contributing to sea level rise.

Productivity in oceans refers to photosynthetic activity, primarily of phytoplankton, which is the source of the marine food chain (see Section 3.3). Location, season and depth can all affect the productivity of ocean waters (see Section 18.6). Ocean productivity has obvious relevance to several marine industries, including fishing, aquaculture and tourism.

1.2.2 Coastal waters

A coastline marks the dynamic boundary between land and sea. Since this boundary moves with marine tides, the coastal, or littoral, zone is commonly defined as intertidal and subtidal fringes of land, extending from the high tide mark to the continental shelf (see Section 2.1.7). The supralittoral (or supratidal or splash) zone is the narrower, transient area above the spring high tide line that is often splashed by seawater, but is not submerged, and therefore not part of the littoral zone.

Estuaries are the interface region where freshwater from inland rivers and streams mixes with saltwater from the ocean. The biota of estuaries is suited to variations in salt concentrations and temperatures. They also benefit from the nutrient-rich soils transported by rivers, which create one of the most productive ecosystems on Earth. Estuaries provide valuable breeding grounds for many invertebrates, fish, and birds. Estuary habitats in Australia include seagrasses, mangroves, saltmarshes, melaleuca swamps, open waters, muddy and sandy basins, coastal floodplains, intertidal mudflats, coral reefs, sandy shoals and beaches, rocky shores, and macroalgae (Turner *et al*., 2004). The hydrological processes between these habitats include:

- precipitation from atmosphere;
- surface water flows from catchments;
- flow changes due to biota, e.g. burrowing crabs;
- tidal flows and mixing of freshwater and salt waters in estuaries;
- runoff from tides, storms, and floods between wetland pools and estuaries;
- evapotranspiration from vegetation;
- evaporation from waterbodies; and
- surface water exchange with groundwater (OzCoasts, 2018).

Numerous environmental factors, such as climate, topography, tectonic setting, geology, sediments, tidal currents, wave action, river flow and biota, shape estuaries and coastal waterways (Ryan *et al*., 2003). When tectonic and sea level conditions are stable, the geomorphology of coastal waterways is controlled by waves, tides, and rivers to form seven coastal landform classes (see Table 1.2). Two immature categories, embayments and drowned river valleys, evolve into tide-dominated or wave-dominated estuaries, which, with sediment infilling, subsequently become tide-dominated deltas or wave-dominated deltas respectively. The water, nutrient and sediment dynamics of these coastal landform categories are furthered detailed in Ryan *et al*. (2003).

The dynamics and stability of estuaries directly impact the condition of coastal marine waters. Sediment entering coastal waters from estuaries can negatively influence beaches and coral reefs, as well as local industries, for example, fishing, aquaculture, and tourism. Various activities in coastal catchments, such as forestry, agriculture, and urban development, can change the nutrient status or sediment load of coastal rivers, with a direct impact on coastal ecosystems. There is also increasing evidence illustrating the benefit of coastal subtidal and intertidal vegetation as an ecosystem-based defence against climate change impacts and sea level rise (Temmerman *et al.,* 2013).

Coastal environments are productive. In some cases, the standing biomass of the substratum (the material comprising the seabed surface) can be greater than that of the water column (Mazel, 2001). Of particular relevance to coastal studies is the capricious nature of some substratum features in both space and time. Not only can substratum type change abruptly, but the impact of some substratum types on the optical properties of water can also change with water movement (see Section 8.4.3).

Table 1.2 Geomorphological categories of coastal landforms

Coastal Landform	Sediment Trapping	Turbidity	Circulation	Sediment risk to habitat	Dominant Feature
Wave-dominated Estuary	High	Low	Partly mixed	High	Central basin
Coastal Lagoons	Low	Low	Partly mixed	Low	Intertidal flats, barriers and channels
Strandplain					
Tide-dominated estuary	Moderate	High	Well mixed	Moderate	Mangroves, salt marshes and channels
Tidal creek and flat	Low	High	Well mixed	Low	Mangroves and salt marshes
Wave-dominated delta	Low	Low	Partly mixed	Low	Mangroves and channels
Tide-dominated delta	Low	High	Well mixed	Low	Mangroves
Embayments	Low	Low	Partly mixed	Low	Rocky coastal indentation; immature landform enroute to wave- or tide-dominated estuary or delta
Drowned river valleys					

Source: Turner *et al.* (2004) and OzCoasts (2018). Retrieved from: *http://www.ozcoasts.gov.au/conceptual_mods/science_models.jsp*

1.2.3 Inland waters

Inland waters include dams, rivers, lakes, reservoirs, and estuaries, which contain standing or flowing freshwater. They also exist beneath the land surface as groundwater. All water in the biosphere circulates through the oceans and atmosphere over time. As introduced in Section 1.1, less than 1% of the total amount of water in the biosphere exists as inland water. Nonetheless, it supports a diverse range of ecosystems, which are distinctly different from marine and terrestrial ecosystems.

The habitats supported by inland waters can be classified as either lotic (flowing water) or lentic (still water). Five major types of inland waterbodies can be defined, based on the permanency, salt content and circulation of the water:

- lotic—flowing water (rivers, streams or creeks):
  - permanently freshwater;
  - temporarily freshwater; or
  - permanently saline;
- lentic—relatively still waters (lakes, ponds and wetlands)
  - permanent; or
  - temporary.

The distribution of these inland waterbody types varies with climatic region. For example, permanent waters are more common in temperate and tropical climates, while salt lakes characterise arid environments.

The movement of inland waters create drainage systems, which can be categorised as:

- exoheric—open systems that drain into the ocean via lakes, rivers and streams;
- endorheic—closed systems that drain to inland termini (such as temporary or permanent salt lakes), where they evaporate into the atmosphere or percolate into groundwater; or
- arheic—small quantities of unpredictable rainfall that form haphazard drainage patterns.

Lentic waterbodies tend to occur in basins created by volcanoes, glaciers, and tectonic activity, or depressions resulting from water, wind, and chemical erosion, while lotic waters occur in areas of low elevation, which have possibly resulted from water erosion.

Lotic: flowing water (from Latin: lotus meaning washed)
Lentic: still water (from Latin: lentus meaning slow)

1.3 Physical Layers within Waterbodies

All waterbodies can be considered to comprise three fundamental layers, namely the:

- water surface—the boundary between the waterbody and the atmosphere (see Section 1.3.1);
- water column—the layer of water between the water surface and the lithosphere or seabed (see Section 1.3.2); and
- substratum—the topmost layer of consolidated or unconsolidated material of the seabed beneath the waterbody (see Section 1.3.3).

1.3.1 Water surface

The surface of a waterbody is also referred to as the air/water interface as it forms a boundary between the atmosphere and the water column (see Section 4). Different waterbodies have different surface characteristics, depending on biogeography, topography, water flow, atmospheric conditions, chemical and/or biological composition, and temperature (e.g. ice in the form of both glacial ice and sea ice—see Section 15.1).

1.3.2 Water column

The body of water extending from the water surface to the seabed can be viewed as a water column (see Section 5). All solar radiation (both direct and diffuse) is either reflected or refracted by the water surface. Solar and sky radiation intercepted by the surface is refracted into the water column, then transmitted, scattered, or absorbed (see Excursus 8.1). The scattering and absorption characteristics of the water column depend on those of pure water and the specific chemical and biological composition of the waterbody (see Section 8). In the terminology of aquatic zones (see Section 3.1), the pelagic zone corresponds to the water column.

1.3.3 Substratum

Below the water column lies the seabed—the solid base of the waterbody (see Section 6). The substratum layer rests on the seabed (or lithosphere) and may comprise sand, silt, mud, rocks, and live and/or dead coral. Aquatic macroalgae (seaweeds), seagrasses, and benthic microalgae (BMA; also called 'microphytobenthos', Cahoon, 1999), may grow in this layer (Pennesi *et al.,* 2015). Most macroalgae are attached to the substratum whereas seagrasses prefer to grow in an unconsolidated substrate.

Significant changes can occur in substratum features over small intervals of space, depth, and time. The substratum surface can also vary abruptly in depth, slope, composition, and texture. The geomorphology of the substratum influences movement of water in the water column.

Depending on the depth and scattering/absorption properties of the water column above it, this layer may also reflect some of the radiation refracted by the water column from the water surface (see Section 8.3.3). In this case, the colour and texture of the substratum, and those of any vegetation it supports, will form part of the spectral characteristics of the reflected energy.

1.4 Global Water Circulation

The horizontal movement of the surface layers of a waterbody, particularly in oceans, is closely related to atmospheric patterns of surface winds. While the large scale movement of air around our planet varies with small scale weather systems, its global structure can be represented as a series of latitude-based wind bands that form the Hadley, Ferrel and Polar cells in each hemisphere (see Figure 1.10). Fluctuations in wind velocity, however, happen across the full range of time scales, from seconds to years (see Excursus 4.2).

Figure 1.10 Large scale atmospheric circulation

Three latitude-based belts of surface winds encircle each hemisphere: 0°–30° (trade winds or Hadley cell); 30°–60° (westerlies or Ferrel cell); and 60°–90° (polar easterlies or Polar cell), with the lower latitude and subantarctic bands having greatest impact on surface water movement.

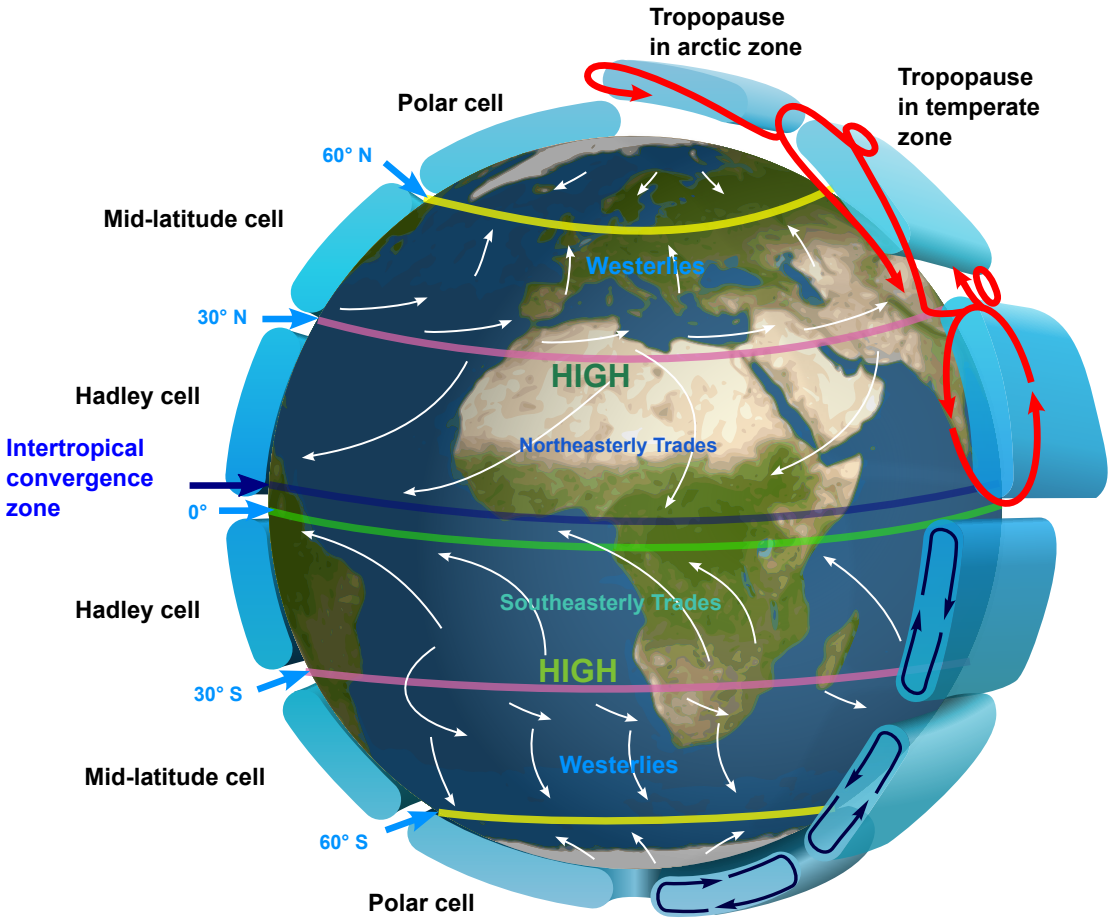

Source: Wikimedia. Retrieved from: *https://commons.wikimedia.org/wiki/File:Earth_Global_Circulation_-_en.svg*

1.4.1 Currents

A current is a continuous, directed movement of water generated by a range of forces. Surface currents are driven by global wind patterns, while slower deep ocean currents result from thermohaline circulation (see Sections 5.1.2). Due to Earth's rotation, both winds and currents are influenced by the Coriolis Effect, which causes them to turn in a clockwise direction in the Northern Hemisphere and an anticlockwise direction in the Southern Hemisphere (see Excursus 1.2). The geomorphology of ocean and coastal features also modifies the location, direction, and velocity of currents. Both atmospheric winds and water circulation help to compensate for differential solar heating of our planet, by drawing surplus heat from equatorial regions to the polar regions (see Volume 1A—Section 4).

Current: A non-periodical, generally horizontal movement of water (or other fluid) due to many causes such as prevalent winds, temperature differential etc., but not to gravitational forces of the Moon and Sun. (Australian Hydrographic Office Glossary)

Excursus 1.2—Coriolis Force and Ferrel's Law

Source: NOAA SciJinks (*https://scijinks.gov/coriolis/*)
Further Information: NOAA National Ocean Service Education: *https://oceanservice.noaa.gov/education/tutorial_currents/04currents1.html*

Coriolis force, first described by Gustave-Gaspard de Coriolis in 1835, is an inertial force that applies upon any object moving relative to a rotating reference frame. It acts in a direction that is perpendicular to the axis of the object and its strength varies with the object's mass and rotation rate. For objects rotating in a clockwise direction, the Coriolis force acts to the left of the object's motion, while for objects rotating in an anticlockwise direction, it acts to the right.

The rotation of Earth on its axis from west to east creates an inertial force which tends to redirect the flow of fluids around it. The impact of this force is described by Ferrel's law:

If a body moves in any direction
on the Earth's surface,
there is a deflecting force arising
from the Earth's rotation,
which deflects it to the right
in the northern hemisphere
and to the left
in the southern hemisphere.
(William Ferrel, 1856)

This pattern of deflection of objects that is caused by the Coriolis force is called the Coriolis Effect. On Earth, the Coriolis force influences the direction of both winds and water currents and has a major influence on storm systems and the trajectories of objects flying long distances (including aeroplanes), the Coriolis Effect results in the latitude-related deflection gradients of:

- no deflection at the equator;
- deflection to the right in the Northern Hemisphere;
- deflection to the left in the Southern Hemisphere; and
- maximum deflecton at the poles (Strahler, 1975).

Figure 1.11 Major non-tidal currents

Red shading indicate warmer currents and blue shading indicate colder currents.

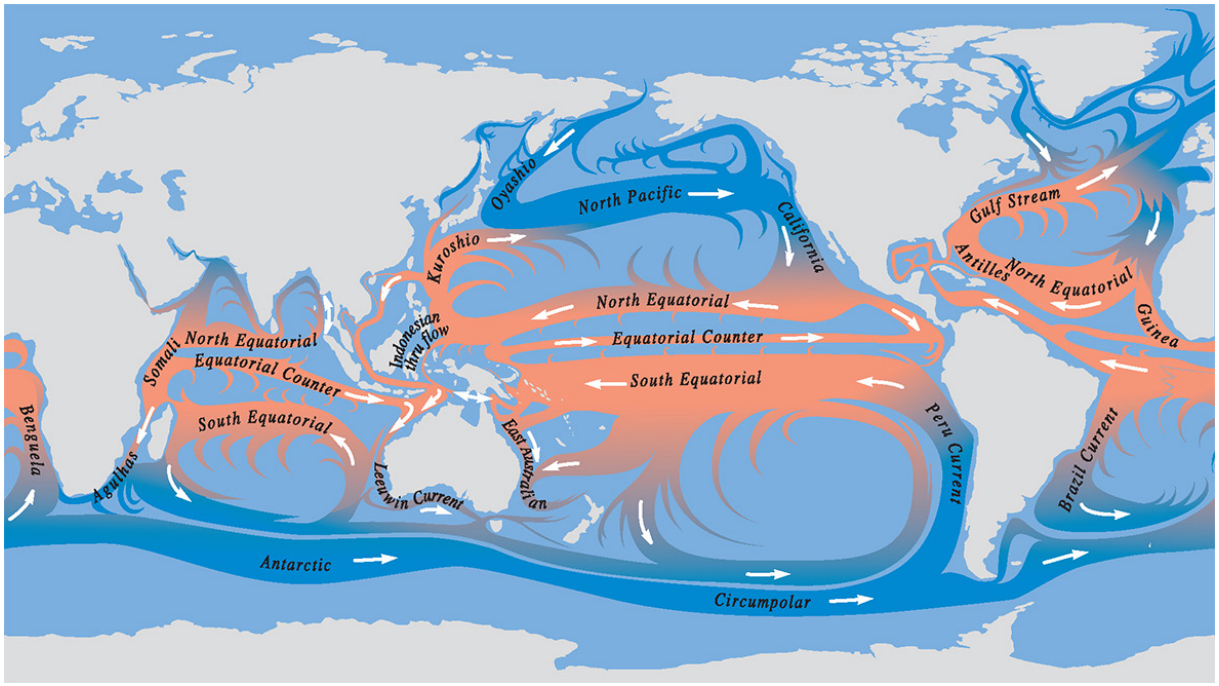

Source: Veron (2000a). Retrieved from: *http://www.coralsoftheworld.org/page/distributions/*

Time-dependent movements of global waters occur at a variety of space and time scales, from the water surface to the deepest layers. Only a small part of this movement can be explained by 'predictable' frequency variations such as tides and inertial motion (Wells, 1986). The horizontal movement of water that is generated by astronomical tides is called a tidal current (see Excursus 4.1).

Thus, the movement of surface water is largely determined by the distribution of surface winds, with seasonal changes in wind distribution modifying surface water circulation (see Sections 16 and 17). Non-tidal currents can be permanent or temporary, depending on variations in local weather conditions. Distribution, circulation and temperature of the major global non-tidal currents are shown in Figure 1.11.

Many aquatic species rely on currents to provide transport, deliver sustenance, and distribute offspring. Upwelling currents move colder nutrient-rich waters fom the ocean floor to the surface, thus supporting a range of life forms in the marine food chain (see Section 3). Downwelling currents push dense, oxygen-rich surface waters to lower depths, which enables deep ocean ventilation. Currents also transport salt and other chemicals around the globe, sculpt shorelines, and impact shipping routes (NOS, 2021a).

1.4.2 Gyres

A large system of rotating ocean currents, largely formed by wind and Coriolis forces, is called a gyre (NOS, 2021b). These permanent systems span thousands of kilometres and form a significant component of global weather patterns. Sea level in the centre of gyres is higher than global mean sea level. As illustrated in Figure 1.11, there are five major ocean gyres:

- North Pacific—clockwise;
- South Pacific—anticlockwise;
- North Atlantic—clockwise;
- South Atlantic—anticlockwise; and
- Indian—anti-clockwise.

Two smaller gyres also exist in the two subpolar regions.

Gyres are bounded by permanent ocean currents, called boundary currents, that travel alongside continental boundaries. Boundary currents are classified into two groups based on their location relative to ocean basins:

- eastern boundary currents—occur along the west coast of continents or the eastern side of ocean basins, and tend to be cooler, slower, wider and shallower, transporting water from higher to lower latitudes. These currents are often enriched by coastal upwelling, so are considered productive. Off the WA coast, however, instead of a 'classical'

equatorward, cold, productive eastern boundary current, the warm Leeuwin Current flows southward with a general absence of upwelling, which fundamentally impacts the ecology of the region. The northward flowing current near WA that is shown in Figure 1.11 is the weaker West Australian Current.

- western boundary currents—occur along the east coast of continents or the western side of ocean basins. They tend to be warmer, faster, narrower, and deeper, transporting water from lower to higher latitudes. The East Australia Current is a western boundary current that flows southward along the east coast of Australia (see Excursus 17.1).

1.4.3 Eddies

Temporary features of contained, swirling water are called eddies (NOS, 2021c). Smaller than gyres, these looping currents can also travel long distances. They may form in currents or mid-ocean, but are most obvious in western boundary currents. Such movement is important for circulating nutrients from deeper waters to the surface. Eddies are visible in EO imagery and provide valuable information on ocean circulation patterns, meteorological conditions, and fishing potential (see Figure 1.12 and Section 17).

Figure 1.12 Eddies in waters around Tasmania

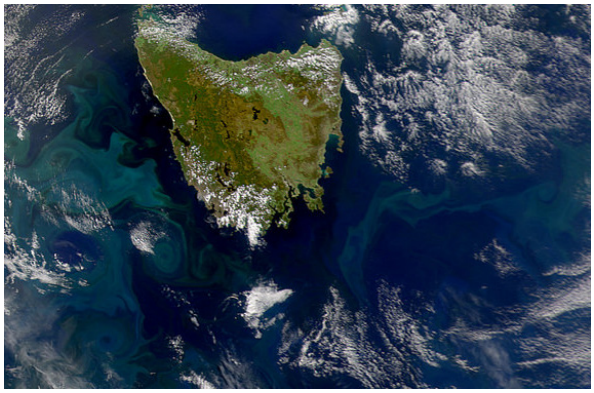

Source: NOAA. Retrieved from: *http://oceanservice.noaa.gov/facts/eddy.html*

1.4.4 Langmuir circulation

Another local water circulation feature that can be observed by its impact on floating material is called Langmuir circulation, which comprises tubes of circulating water, parallel with the surface and mostly aligned with the wind direction. First studied by Irving Langmuir, these cells are visible in many waterbodies, including oceans, seas, lakes and rivers, as lines of floating material (such as seaweed, algae, oil and debris) collected on the water surface (see Figure 1.13a). As each tube in a pair rotates towards the other, water circulates past the surface forcing surface material into a line between the cells (see Figure 1.13b). These cells typically form parallel lines of floating material, or windrows, which typically have a horizontal spacing and depth of 4–6 m but can have much greater separation and depth. They act as a natural 'clean-up' mechanism for a range of buoyant materials, including plastic particles (van Sebille *et al.*, 2020), and attract a variety of wildlife.

Figure 1.13 Langmuir circulation

a. Lines of sargassum can stretch for miles along the water surface in the Sargasso Sea

b. Formation of Langmuir cells

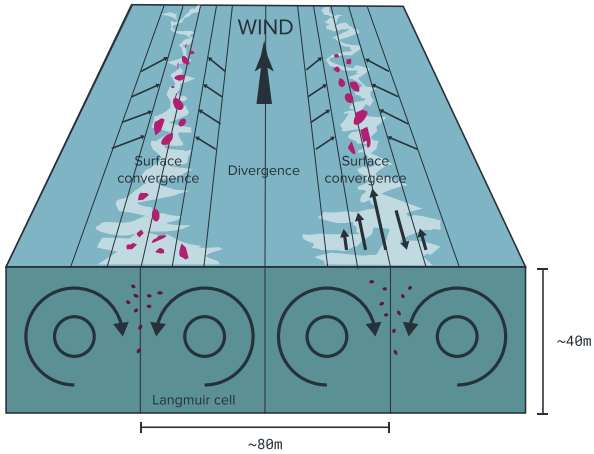

Source: a. NOAA. Retrieved from: *https://commons.wikimedia.org/wiki/File:Lines_of_sargassum_Sargasso_Sea.jpg* b. van Sebille *et al.* (2020) Figure 3

1.5 Global Carbon Cycle

The carbon cycle is introduced in Volume 1—Section 4.2.4 and Volume 3A—Section 17. Surface waters play an important role in the global cycling of carbon, from readily available carbon in the form of atmospheric CO_2 to carbon stored in 'sinks', such as fossil fuels beneath the seafloor. The carbon stored in coastal and marine ecosystems, either in the plants or the sediment below, is called 'blue carbon' (The Blue Carbon Initiative, 2020; see Section 7.4). In conjunction with field studies and modelling, a wide range of EO sensors are being employed to track and interpret current changes in the global carbon cycle and understand its principal driving forces (NASA, 2020; see Sections 7.4 and 7.5).

At a global scale, when atmospheric CO_2 dissolves in surface waters, the level of CO_2 in the atmosphere is lowered; when carbon is released from carbon sinks, such as burning of fossil fuels, it is released back to the atmosphere as CO_2 (see Figure 1.14). Current estimates indicate that around 50 times more carbon is stored in the ocean than in the atmosphere, and nearly half the carbon emissions being released by burning of fossil fuels returning to the ocean via the 'ocean carbon pump' (NASA, 2020). The 'ocean carbon pump' comprises two fundamental transfer mechanisms:

- a biological pump, which moves carbon from the atmosphere to the seabed via aquatic organisms (Volk and Hoffert, 1985; see Section 3.3); and
- a physical pump, which transports water and dissolved inorganic carbon from the surface to the deep sea (see Section 1.4).

While the physical pump is slow and robust, the biological pump is directly impacted by climatic and geographic variables (see Figure 1.15). These carbon pumps relate to coupled physical-biogeochemical processes that are influenced by (change in) ocean properties and structure (stratification), and sea ice. The high-latitude Southern Ocean plays an immensely important role in the ocean uptake (and subsequent storage) of anthropogenic CO_2 and heat from the atmosphere (Rintoul *et al.*, 2019). Marine habitats, such as mangroves, seagrass beds and salt marshes also form effective carbon sinks, but in a shorter time scale than fossil fuels, and with more vulnerability to degraded water quality and environmental conditions (see Section 20).

Figure 1.14 Ocean carbon pumps

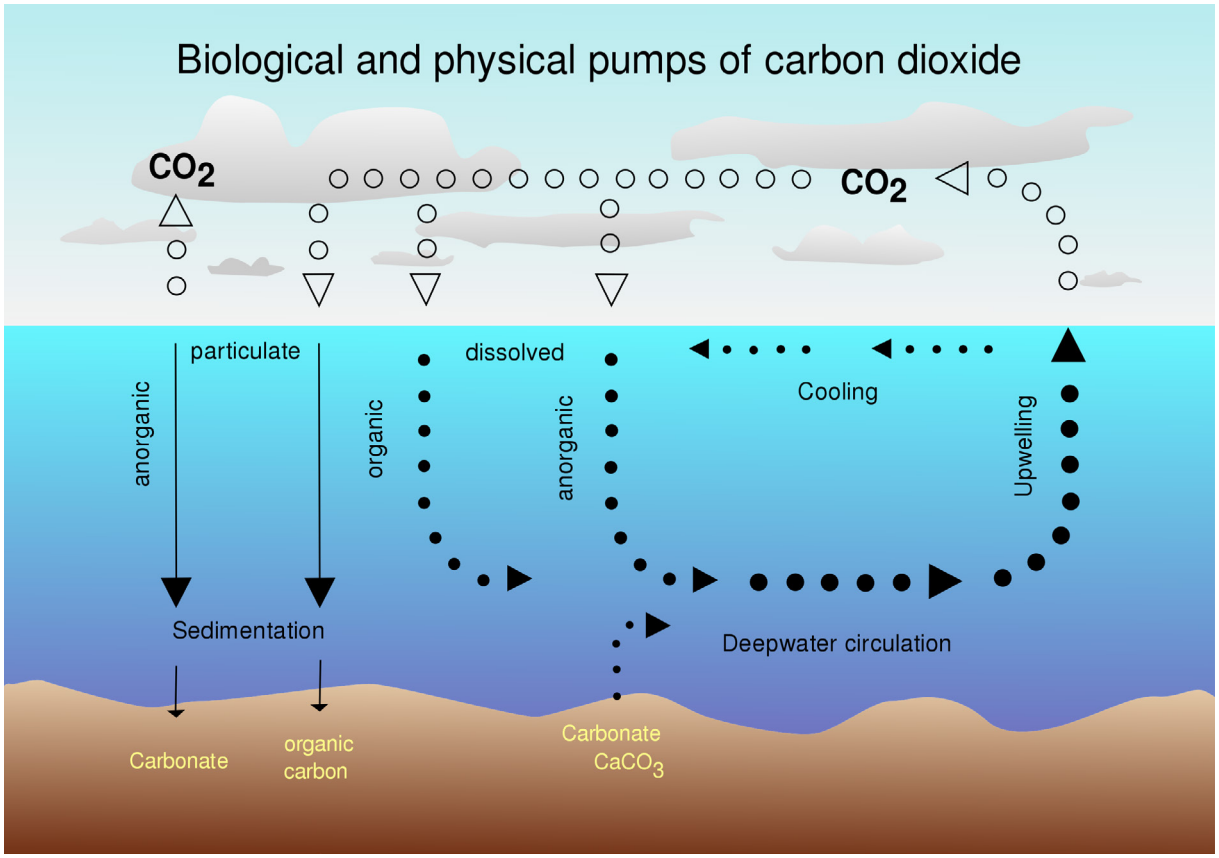

Source: Hannes Grobe and McSush, Wikimedia. Retrieved from: *https://commons.wikimedia.org/wiki/File:CO2_pump_hg.svg*

Figure 1.15 Biological pump

CO_2 is converted into organic matter during photosynthesis by phytoplankton growth in the surface ocean. A small amount of this material reaches the deep sea where it is sequestered from the atmosphere, either as organic carbon, or dissolved CO_2 after bacterial remineralisation. The overall effect is known as the 'biological pump'. The deeper the carbon is transported into the ocean interior, the longer it remains isolated from the atmosphere.

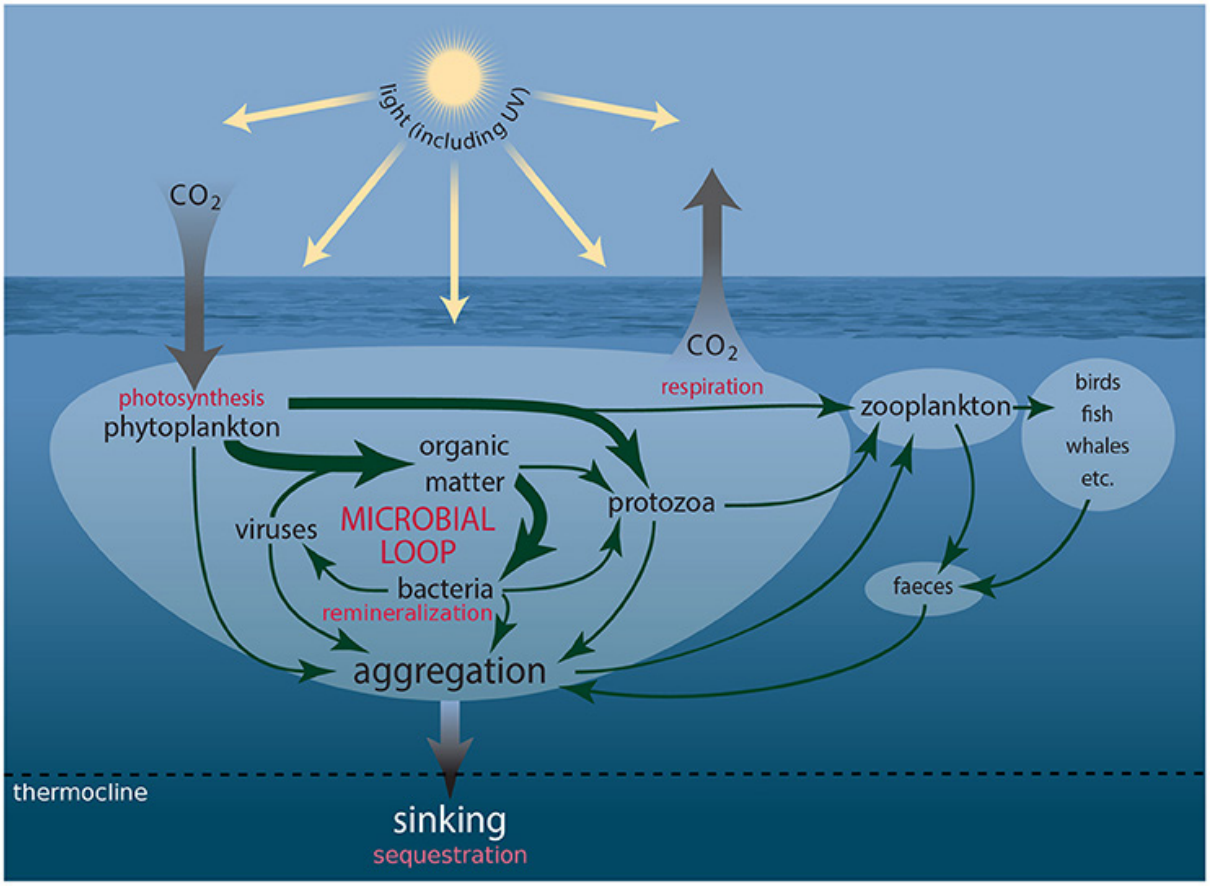

Source: Deppeler and Davidson (2017) Figure 1

Aquatic organisms use carbon for:

- photosynthesis—phytoplankton converts atmospheric and dissolved carbon into organic matter (and also return 0_2 and CO_2 to the atmosphere via respiration); and
- calcification—marine organisms containing calcium (principally coccolithophores, unicellar algae) use dissolved carbon to create calcium carbonate for their structural components. As these organisms decay, their structure decomposes and sinks to form sediments, and ultimately rocks, on the seafloor.

As expanded in Section 7.4, a balance is required between these processes. The concentration of CO_2 in ocean water has been observed to vary with both atmospheric CO_2 concentration and water temperature, with both increasing in recent centuries. Since the ocean absorbs around 30% of the CO_2 that is released into the atmosphere, increased levels of atmospheric CO_2 also increases the amount of CO_2 absorbed by the ocean, making it more acidic. Thus, as the CO_2 concentration of oceans increases, the pH of these waters decreases (see Section 5.2.2), potentially leading to broad scale ocean acidification. At the current rate of 22 million tons per day it is estimated that at least 25% of atmospheric CO_2 is dissolved into the ocean, resulting in these waters now being 30% more acidic than they were 200 years ago.

However, lower pH levels in surface waters, including coastal estuaries and waterways, means that there are more hydrogen ions and fewer carbonate ions for calcifying organisms, such as crustaceans and corals, to use for growing shells and skeletons. As pH levels in these waters continue to fall, these organic structures may even dissolve. Such changes in the ecology of aquatic habitats could have significant implications for the stability of the ocean food web and global carbon cycle (see Sections 3 and 7.4).

One marine geoengineering solution intended to accelerate the growth of phytoplankton, and thus increase the rate of CO_2 transfer from the atmosphere to the oceans, has been ocean fertilisation. This process involves stimulating primary productivity by 'fertilising' ocean waters with nutrients, such as iron, nitrogen or phosphorus. While it is uncertain that the increased phytoplankton growth from ocean fertilisation will actually sequester carbon in the deep sea in the longer term, there is evidence that it may result in undesirable changes to the marine food chain and various marine ecosystems. It may also decrease subsurface oxygen and further increase ocean pH (ACE CRC, 2008, 2016).

1.6 Further Information

The Hydrosphere

https://www.pbslearningmedia.org/resource/buac17-35-sci-ess-waterdistribute/saltwater-and-freshwater-distribution-on-earth/

http://education.nationalgeographic.com/education/activity/our-hydrosphere/?ar_a=1

Tides

NOAA National Ocean Service: Tides and Water Levels: *https://oceanservice.noaa.gov/education/tutorial_tides/*

Currents

CSIRO Australasian currents: *https://www.csiro.au/en/Research/Environment/Oceans-and-coasts/Australasian-ocean-currents*

NOAA National Ocean Service:

Currents: *https://oceanservice.noaa.gov/education/tutorial_currents/welcome.html*

Ocean currents *http://www.noaa.gov/resource-collections/ocean-currents*

NASA: Ocean Motion and Surface Currents: *http://oceanmotion.org/html/introduction-general.htm*

NOAA National Ocean Service: *https://oceanservice.noaa.gov/welcome.html*

Oceana: *http://oceana.org*

Sea Ice

Biogeochemical Exchange Processes at Sea Ice Interfaces (BEPSII): *https://sites.google.com/site/bepsiiwg140/vision*

Nomenclature

IHO-IOC (2018). GEBCO (General Bathymetric Chart of the Oceans) Gazetteer of Undersea Feature Names: *https://www.gebco.net/data_and_products/undersea_feature_names/*

Sea Level Rise

NOAA: *https://oceanservice.noaa.gov/education/sea-level-rise/welcome.html*

CSIRO: *https://research.csiro.au/slrwavescoast/sea-level/*

Australian Water Industry

Australian Water Association: *www.awa.asn.au*

Australian Water Storages

Bureau of Meteorology: *http://www.bom.gov.au/akamai/https-redirect.html#/water-storages/about*

Australian Inland Waters

Topographic Drainage Divisions and River Regions: *http://www.bom.gov.au/water/about/riverBasinAuxNav.shtml*

Australian Coasts

CSIRO: *https://research.csiro.au/slrwavescoast/extremes/causes-extreme-sea-levels/*

OzCoasts: *http://www.ozcoasts.gov.au/*

Australian Oceans

Ross (1995)

Offshore Constitutional Settlement: *https://www.ag.gov.au/Internationalrelations/InternationalLaw/Pages/TheOffshoreConstitutionalSettlement.aspx*

GA: Australian Marine Spatial Information System (AMSIS): *http://www.ga.gov.au/scientific-topics/marine/jurisdiction/amsis*

CAWCR (Collaboration for Australian Weather and Climate Research): *https://www.cawcr.gov.au/publications/*

IMOS:

Australian Ocean Data Network (AODN): *https://portal.aodn.org.au/*

Ocean Current: *http://oceancurrent.imos.org.au*

Bluelink: *https://www.csiro.au/en/Research/OandA/Areas/Oceans-and-climate/Bluelink*

Oceanwatch Australia: *http://www.oceanwatch.org.au*

1.7 References

ACE CRC (2008). *Position Analysis: Ocean Fertilisation*: *Science and Policy Issues*. The Antarctic Climate and Ecosystems Cooperative Research Centre, Hobart. *http://acecrc.org.au/wp-content/uploads/2015/03/2008-ACE-PA-Ocean-Fertilisation.pdf*

ACE CRC (2016). *Position Analysis: Ocean Fertilisation*. The Antarctic Climate and Ecosystems Cooperative Research Centre, Hobart. ISSN: 1835-7911. *http://acecrc.org.au/wp-content/uploads/2016/07/ACE106_Position-Analysis_Ocean-Fert_April-2016_WEB.pdf*

AHS (2017) *Names and Limits of Oceans and Seas around Australia*. Australian Hydrographic Service Fact sheet: *http://www.hydro.gov.au/factsheets/WFS_Names_and_Limits_of_Oceans_and_Seas_Around_Australia.pdf*

Amante, C., and Eakins, B.W. (2009). *ETOPO1 1 Arc-Minute Global Relief Model: Procedures, Data Sources and Analysis*. NOAA Technical Memorandum NESDIS NGDC-24, 19 pp, March 2009. *http://www.ngdc.noaa.gov/mgg/global/relief/ETOPO1/docs/ETOPO1.pdf*

Cahoon, L. (1999). The role of benthic microalgae in neritic ecosystems. *Oceanography and marine biology*, 37, 47–86.

Deppeler, S.L., and Davidson, A.T. (2017). Southern Ocean Phytoplankton in a Changing Climate. *Frontiers in Marine Science*, 4, 40. *https://www.frontiersin.org/article/10.3389/fmars.2017.00040*

Eakins, B.W. and Sharman, G.F. (2010). *Volumes of the World's Oceans from ETOPO1*. NOAA National Geophysical Data Center, Boulder, CO, 2010: *https://www.ngdc.noaa.gov/mgg/global/etopo1_ocean_volumes.html*

IHO (1953). *The Limits of Oceans and Seas*. International Hydrographic Organisation Special Publication 23, 3rd Edition, Monte Carlo. *http://www.iho-ohi.net/*

IHO-IOC (2018). *GEBCO (General Bathymetric Chart of the Oceans) Gazetteer of Undersea Feature Names*. *https://www.gebco.net/data_and_products/undersea_feature_names/*

Mazel, C.H. (2001). Optics of the Seafloor. *Oceanography*, 14(3), 54–63.

NASA (2020). *NASA Science. Carbon Cycle* webpage: *https://science.nasa.gov/earth-science/oceanography/ocean-earth-system/ocean-carbon-cycle*

NOS (2021b). *What is a gyre?* webpage, NOAA National Ocean Service website: *https://oceanservice.noaa.gov/facts/gyre.html*

NOS (2021a). *Currents* webpage, National Ocean Service (NOAA) website: *https://oceanservice.noaa.gov/education/tutorial_currents/welcome.html*

NOS (2021c). *What is an eddy?* webpage, NOAA National Ocean Service website: *http://oceanservice.noaa.gov/facts/eddy.html*

OzCoasts (2018). *OzCoasts Australian Online Coastal Information* website: *https://ozcoasts.org.au/*

Pennesi, C., Rindi, F., Totti, C., and Beolchini, F. (2015). Marine Macrophytes: Biosorbents. In *Springer Handbook of Marine Biotechnology*. (Ed: Kim S.K.) Springer Handbooks. Springer, Berlin, Heidelberg.

Rintoul, S., Bindoff, N., and Hobbs, W. (2019). *Position Analysis: Causes and Consequences of Southern Ocean Change*. The Antarctic Climate and Ecosystems Cooperative Research Centre, Hobart.

Rodell, M., Famiglietti, J.S., Wiese, D.N., Reager, J.T., Beaudoing, H.K., Landerer, F.W., and Lo, M.-H. (2018). Emerging trends in global freshwater availability. *Nature*, 557, 651–659. doi:10.1038/s41586-018-0123-1

Ross, D.A. (1995). *Introduction to Oceanography*. HarperCollins, New York. pp. 236–242.

Ryan, D.A., Heap, A.D., Radke, L., and Heggie, D.T. (2003). *Conceptual models of Australia's estuaries and coastal waterways: applications for coastal resource management*. Geoscience Australia, Record 2003/09, 136 pp.

Shiklomanov, I.A., and Rodda, J.C. (2003). *World Water Resources at the Beginning of the Twenty-First Century*. United Nations Educational, Scientific and Cultural Organization (UNESCO). Cambridge University Press, Cambridge. ISBN 0 521 82085 5 *http://catdir.loc.gov/catdir/samples/cam034/2002031201.pdf*

SOE (2011). *State of Environment Report 2011*. *http://155.187.2.69/soe/2011/report/inland-water/index.html*

SOE (2017). *State of Environment Report 2016*. Australia's water resources: Inland water (2016): *https://soe.environment.gov.au/theme/inland-water/topic/2016/australias-water-resources*

Strahler, A.N. (1975). *Physical Geography*. Wiley, New York.

Symonds, P., Alcock, M., and French, C. (2009). Setting Australia's Limits: Understanding Australia's marine jurisdiction. *AusGeo News* 93, March 2009, Geoscience Australia.

Temmerman, S., Meire, P., Bouma, T.J., Herman, P.M., Ysebaert, T., De Vriend, H.J. (2013). Ecosystem-based coastal defence in the face of global change. *Nature*, 504(7478), 79–83. doi:10.1038/nature12859

The Blue Carbon Initiative (2020). *The Blue Carbon Initiative* website: *https://www.thebluecarboninitiative.org/*

Turner, L., Tracy, D., Tilden, J., and Dennison, W.C. (2004). *Where river meets sea: Exploring Australia's estuaries*. CRC for Coastal Zone Estuary and Waterway Management, Brisbane.

USGS (2018). *United States Geological Survey* website: *https://www.usgs.gov/science/science-explorer/Water*

van Sebille, E., Aliani, S., Law, K.L., Maximenko, N., Alsina, J., Bagaev, A., Bergmann, M., Chapron, B., Chubarenko, I., Cózar, A., Delandmeter, P., Egger, M., Fox-Kemper, B., Garaba, S.P., Goddijn-Murphy, L., Hardesty, B.D., Hoffman, M., Isobe, A., Jongedijk, C., Kaandorp, M., Khatmullina, L., and Koelmans, A.A. (2020). The physical oceanography of the transport of floating marine debris. *Environmental Research Letters*, 15(2), [023003]. *https://doi.org/10.1088/1748-9326/ab6d7d*

Veron, J.E.N. (2000a). *Corals of the World*. Australian Institute of Marine Science, Townsville. Volumes 1–3. 1410 p.

Volk, T., and Hoffert, M.I. (1985). Ocean carbon pumps: Analysis of relative strengths and efficiencies in ocean-driven atmospheric CO_2 changes. In *The Carbon Cycle and Atmospheric CO2: Natural Variations Archean to Present*. pp 99–110. (Eds: Sundquist, E., and Broecker, W.S.). Geophysical Monograph 32, American Geophysical Union, Washington, D.C.

Wells, N. (1986). *The Atmosphere and Ocean. A Physical Introduction*. Taylor and Francis, London.

2 Australia's Surface Water Environment

This section provides an overview of the surface water environment within and surrounding the Australian land masses. The Australian continent and its islands are described in Volume 3A. The following topics are covered below:

- marine jurisdiction, including names of marine territories and entitlements of zones (see Section 2.1);
- geomorphology of marine waters (see Section 2.2);
- circulation of marine waters in the Australasian region (see Section 2.3);
- environmental factors affecting marine waters (see Section 2.4);
- Antarctica (see Section 2.5);
- characteristics of inland waters (see Section 2.6); and
- water storage and consumption (see Section 2.7).

2.1 Marine Jurisdiction

In addition to its land areas, Australia regulates vast marine areas extending from its continental coastline and encircling its many islands (GA, 2021a). The total confirmed area of marine jurisdiction is 13.86 million km^2, nearly twice its continental landmass (Symonds *et al.,* 2009). This makes Australia custodian of around 3.8% of the Earth's oceans, and, with both land and marine jurisdictions combined, around 5.4% of the Earth's surface. For cartographic and hydrographic (rather than legal) purposes, the names and limits of marine waters around Australia are defined by The Australian Hydrographic Service (AHS) as illustrated in Figure 2.1. In addition to its marine jurisdiction zones, Australia has obligations within its charting area (see Figure 2.2) as specified by the:

- International Convention for the Safety of Life at Sea (SOLAS) convention;
- United Nations Convention on the Law of the Sea (UNCLOS); and the
- Australian Navigation Act 2012.

This charting area obligates Australia to provide hydrographic services to the international maritime community, including surveying, charting, and publishing nautical information and International Series (IS) Charts, as specified by the International Hydrographic Organisation (IHO). Australia also supports hydrographic services in Papua New Guinea and the Solomon Islands (AHS, 2017a).

The coastline of Australia is an old one. For long ages there has been none of the major convulsions of the earth's crust that have resulted in the peculiar contours of many other great land-masses. There have been inland seas in past ages but they have dried up and are now part of the land. There have been deep gulfs penetrating far into the interior, but they too have long since gone.
(Charles F. Laseron, 1953)

Background image: Australian land mass surrounded by portion of its marine jurisdiction. **Source:** Blue Marble World topography and bathymetry composition, November 2004, NASA.

Figure 2.1 Names and limits of oceans and seas around Australia

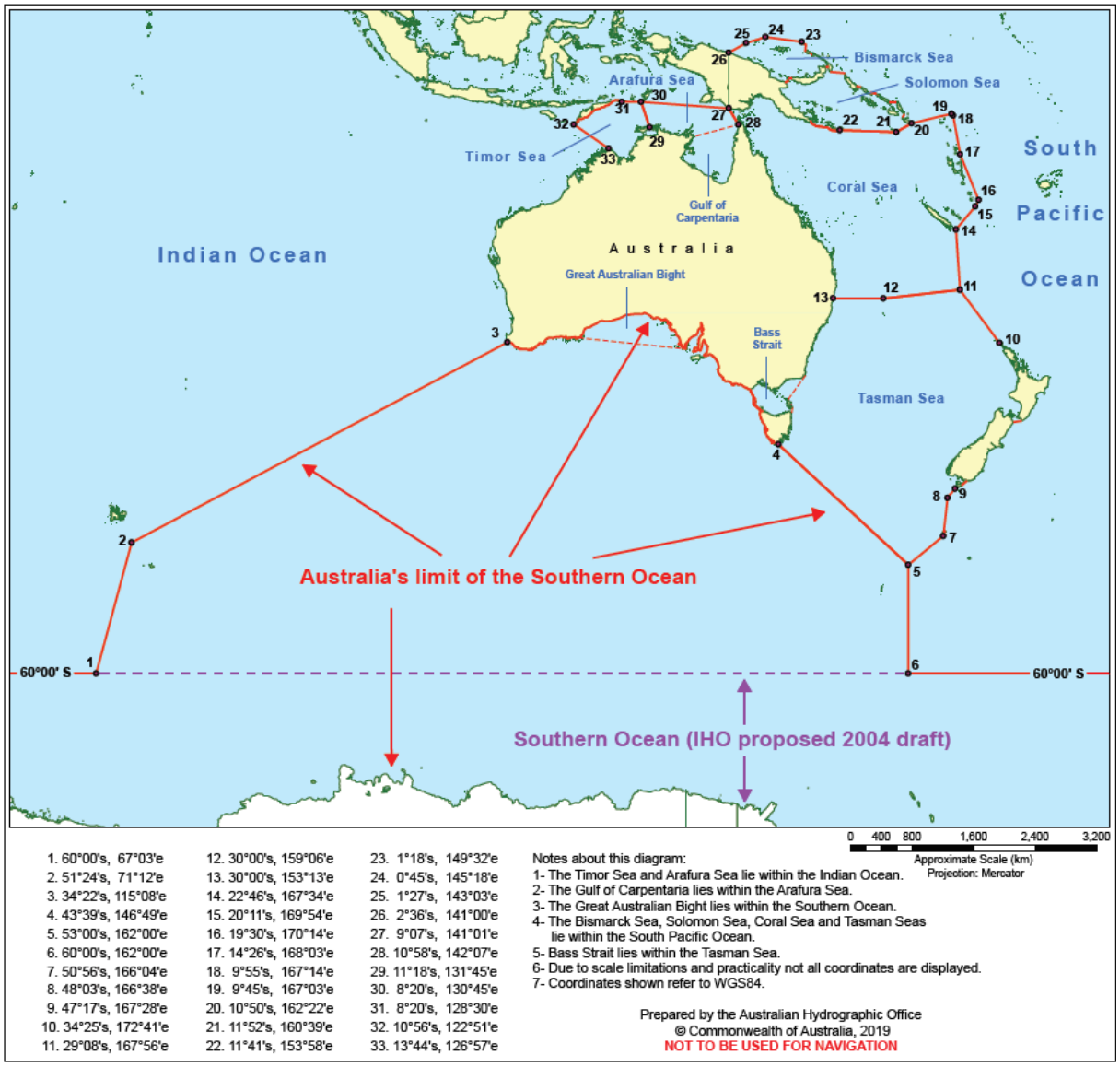

Source: AHS (2017b). Retrieved from: *https://www.hydro.gov.au/factsheets/FS_Hydrographic_Surveying-Limits_of_oceans_and_seas_around_Aus.pdf*

Within Australian waters (3–200 M from the Territorial Sea Baseline, TSB), the Australian Marine Safety Authority (AMSA) is responsible for navigation safety and protection of the marine environment, including surveillance of ship-sourced pollution (see Section 19.4). AMSA also maintains a national search and rescue service for maritime and aviation traffic (see Excursus 2.1).

Figure 2.2 Australian Charting Area

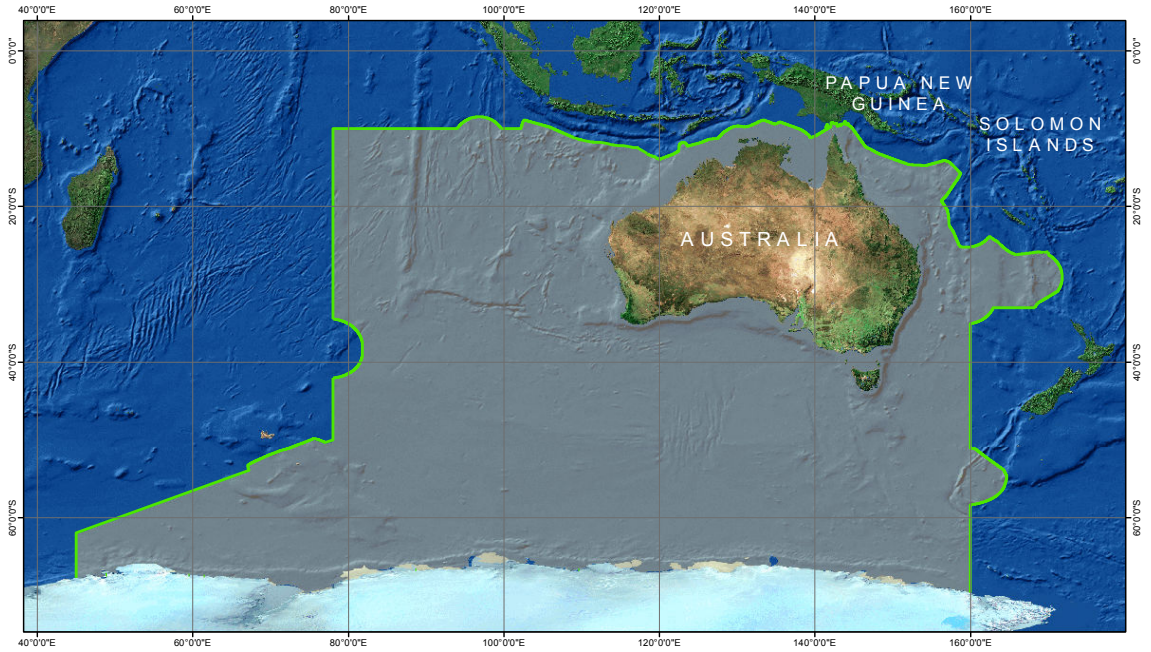

Source: AHS (2017a). Retrieved from: *http://www.hydro.gov.au/business-publications/HydroScheme_2017-2020_WEB_20171103.pdf* page 3

UNCLOS established a legal order to distinguish national and international government of seas and oceans. This convention determines the location of several marine zones, relative to a precisely defined interface between land and sea (UN, 1982). In combination with Australian legislation, six marine zones have been defined around Australian land. The relative extents of these zones, as measured from the official baseline (TSB; see Section 2.1.1), and the rights they bestow to Australia, are summarised in Table 2.1 and illustrated in Figure 2.3. Each zone is described below and the extents of most of these zones are shown in Figure 2.4.

Figure 2.3 UNCLOS marine zone boundaries

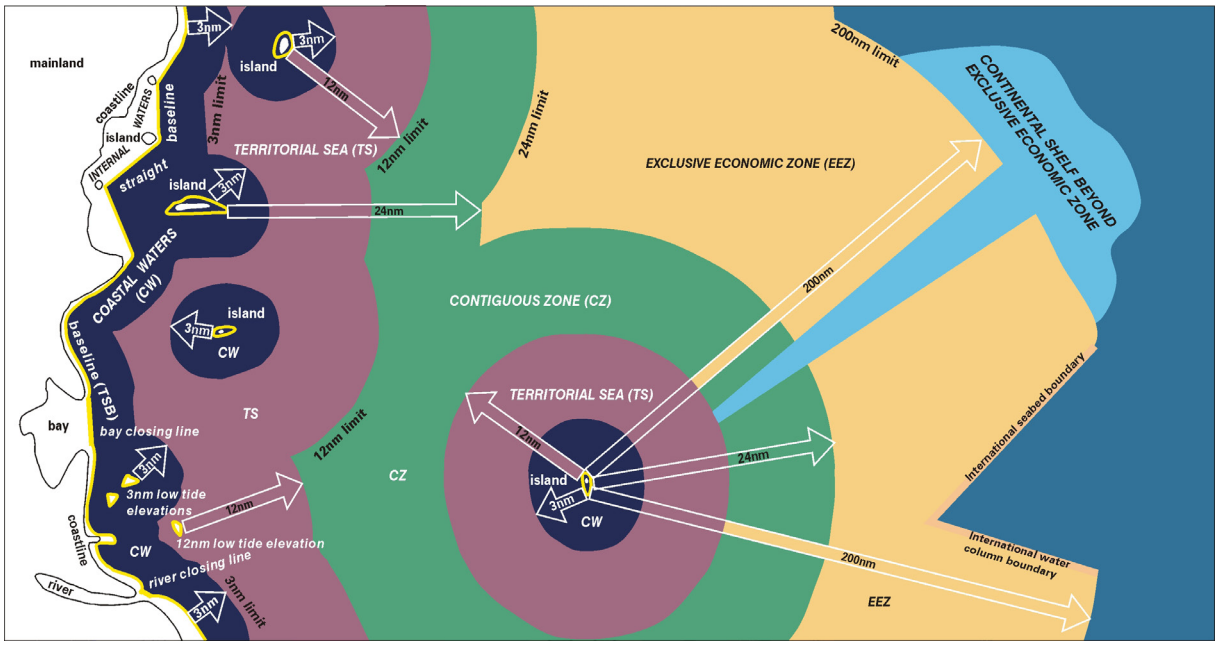

Source: GA (2021a)

Figure 2.4 Australia's Maritime Zones

Refer to Figure 2.3 for colour codes.

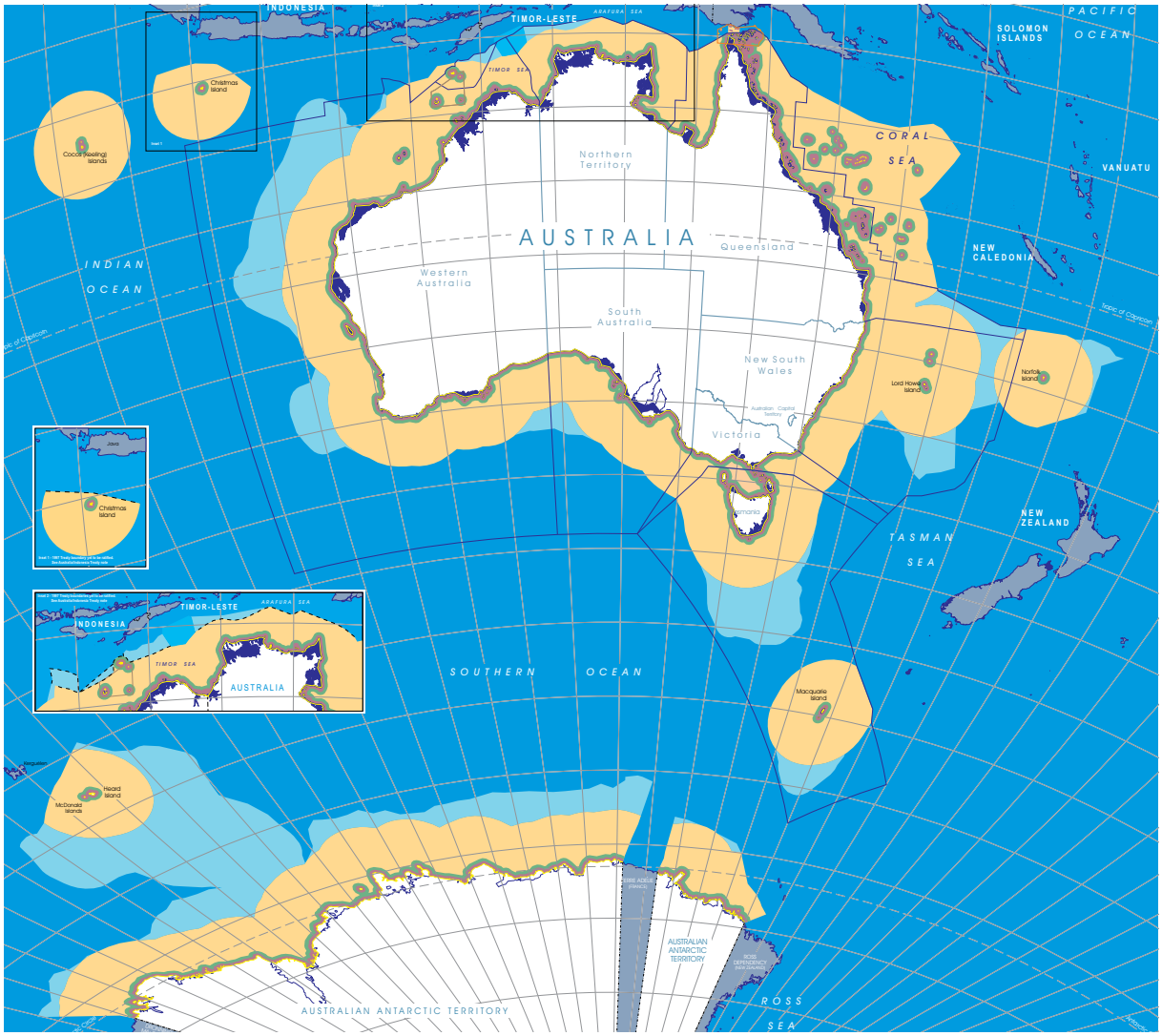

Source: GA (2021a). Note that this map was produced in 2005 (GeoGat 63690) and updated regional maps are available at 1:500,000 from *http://www.ga.gov.au/scientific-topics/marine/jurisdiction/map-series*

Table 2.1 Australia's maritime zones

1 M: 1 nautical mile (≈1,852 m); TSB: Territorial Sea Baseline

From TSB	To						Area (million km²)	Sovereign Rights to		
	Distance from TSB (M)					Nearest EEZ		Air	Water	Seabed and subsoil
	3	12	24	200	350 (max.)					
Coastal Waters							0.15	Full		
Territorial Waters – limit of sovereign territory							0.85			
			Contiguous Zone				n/a	Customs, immigration, quarantine		
			Exclusive Economic Zone				10.19		Economic and conservation activities	
		Australian Fishing Zone							Fishing	
			Continental Shelf (generally only extends to 200 M from TSB)				2.56			Exploration, exploitation
					High Seas		n/a			

Source: Content derived from GA (2021a)

Excursus 2.1—Australian Maritime Safety Authority (AMSA)

Source: Paul Irving, AMSA
Further Information: *https://www.amsa.gov.au/*

AMSA promotes the safety and protection of our marine environment and combats ship-sourced pollution. Often in partnership with individual states and territories, AMSA provides much of the infrastructure for safety of navigation in Australian waters, and maintains a national search and rescue service for the maritime and aviation sectors. Spaceborne and airborne technologies are now a fundamental means of delivering these functions across the nearly 53 million sq. km (around 10% of the Earth's surface) that makes up Australia's search and rescue region. This covers the Australian continent and large areas of the Indian, Pacific and Southern Oceans, as well the Australian Antarctic territories (see Figure 2.5). AMSA's use of satellite technologies extends from communications to Earth Observation.

Inmarsat and Iridium provide Australia's Global Maritime Distress and Safety Services (GMDSS). This allows distress beacons to be detected and information distributed through the Cospas-Sarsat system. AMSA also works with partners, such as NASA and the new Australian SmartSAT CRC to explore possible future enhancements to the distress beacon system, which will provide more sensitivity and potentially two-way communications.

The satellite automatic identification system (S-AIS) provides AMSA with real time information transmitted from ships about their facilities, location, and voyage. This augments shore-based VHF AIS stations, that work best close to land. The S-AIS data is used to monitor ships around Australia, building a dynamic picture for maritime domain awareness. This provides information to undertake oil spill prosecutions, ship-reporting Synthetic Aperture Radar (SAR), and casualty management. Through Airservices Australia, AMSA also receives aviation reporting and provides safety services for aviation search and rescue functions.

AMSA uses satellite-based SAR data from various international service providers to identify illegal maritime oil spills, and to support oil spill response functions (see Excursus 19.4). In particular, AMSA has been collaborating with CSIRO Oceans and Atmosphere, as they develop new capabilities to improve oil spill identification using direct acquisitions from new satellite constellations and the use of artificial intelligence in image analysis.

Figure 2.5 Australian Search and Rescue Region

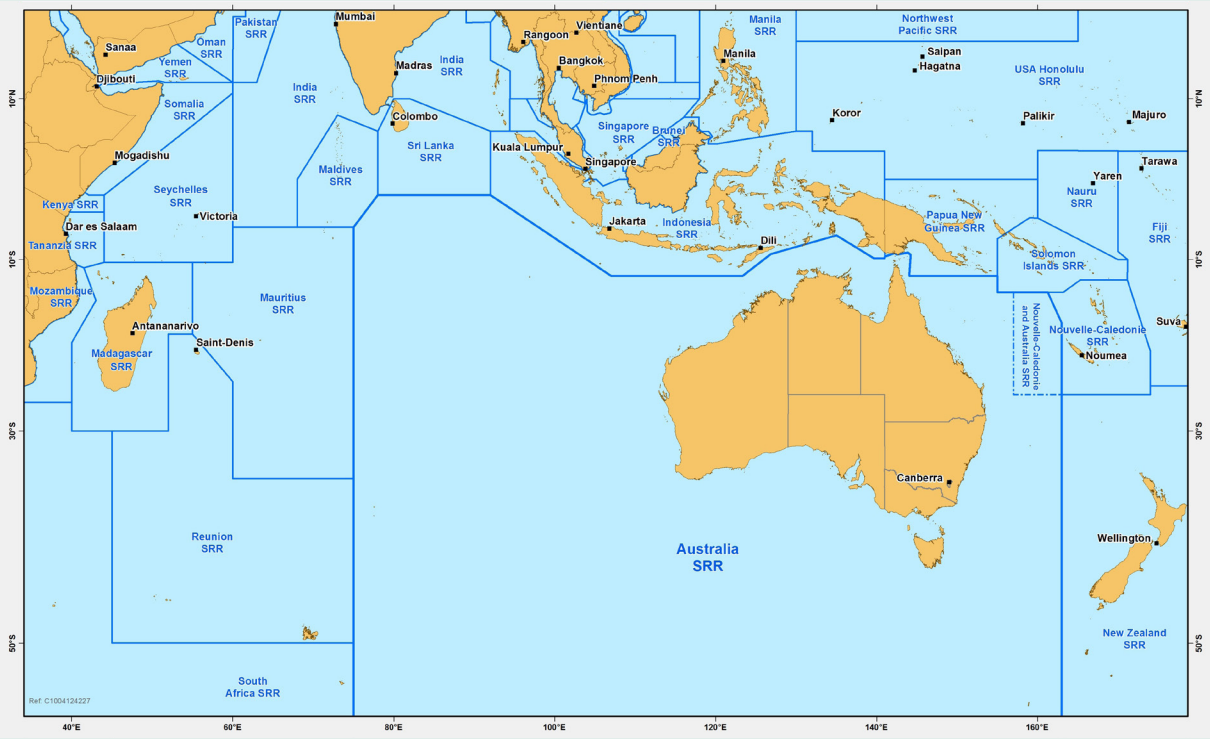

Source: AMSA. Retrieved from *https://www.amsa.gov.au/sites/default/files/2017-05-sar-australia-search-rescue-region.jpg*

2.1.1 Territorial Sea Baseline

The Territorial Sea Baseline (TSB) is defined as the 'low water' along the coastline (GA, 2021a). The Australian TSB is based on the Lowest Astronomical Tide (LAT) and interpolates bays, rivers, islands and, where necessary, deeply indented coastlines. Derivation of the LAT relies on EO, topographic and bathymetric maps, and hydrological charts. The distance between high and low tide can be particularly significant for small islands such as atolls.

2.1.2 Territorial Sea

Each nation implicitly retains sovereignty over adjacent marine areas up to 12 nautical miles (M) from its coastline[2]. Jurisdiction includes the air space above these marine areas, and their seabed and subsoil. The landward boundary of the Territorial Sea is defined by the TSB and its extent is determined by extrapolating from the TSB.

Australia's area of Territorial Sea covers 0.85 million km^2 (including Coastal Waters—see Section 2.1.3). The federal government administers activities within its 0.70 million km^2 of Territorial Sea, including mining, fishing, shipping, navigation and conservation.

2.1.3 Coastal Waters

Within the Territorial Sea, Australian states and territories govern their adjacent coastal waters up to 3 M from the TSB, excluding low tide elevations more than 3 M from the coastline. Their jurisdiction includes the water column and subjacent seafloor, and totals 0.15 million km^2. Within these regions activities such as fishing and exploration are regulated by the relevant state or territory, as permitted in the Offshore Constitutional Settlement (AGD, 1980).

2.1.4 Contiguous Zone

Another marine zone defined by UNCLOS is the Contiguous Zone, which lies directly on the seaward side of the territorial zone, and extends up to 24 M from the TSB. Within this zone, Australia is permitted to prevent and punish infringement of relevant laws, including those relating to customs, immigration, taxes, and health.

Table 2.2 Area of Australian Exclusive Economic Zones

Note: Excluding Antartica EEZ

EEZ	Area (km^2)
Mainland Australia (including Tasmania and minor islands)	6,048,681
Macquarie Island	471,837
Cocos Island	463,371
Norfolk Island	428,618
Heard and McDonald Islands	410,722
Christmas Islands	325,021
Total	8,148,250

Source: Geoscience Australia

2.1.5 Exclusive Economic Zone

Also extending further seaward from the Territorial Sea is the Exclusive Economic Zone (EEZ), whose outer limit is defined by UNCLOS as being within 200 M from the TSB. The boundaries of the Australian EEZ were defined by the Seas and Submerged Land Act (1973) and the Maritime Legislation Amendment Act (1994) and this maritime territory is the third largest in the world (after USA and France). The areas of EEZ for Australia's major land areas are listed in Table 2.1.

Within this zone, Australia has sovereign rights for specific economic activities within the water, seabed and subsoil. These rights allow exploration, exploitation, conservation, and management of both living and non-living natural resources within and below those waters, as well as production of energy and installation of observation facilities for research, protection, and preservation.

Marine waters between defined EEZ are referred to as the High Seas. Subject to regulations of UNCLOS, these waters are shared by all nations for peaceful purposes, including navigation, overflight, submarine cable and pipelines, installation of observation facilities, fishing, and scientific research.

2 1 nautical mile (M) = 1,852 metres. This approximates the mean length of 1 minute of latitude.

2.1.6 Australian Fishing Zone

The federal government of Australia manages fisheries in Commonwealth waters, that is, those marine areas within the Territorial Sea and EEZ, but excluding Coastal Waters and defined 'excepted waters'. The latter occur in the Torres Strait and adjacent to the Australian Antarctic Territory. The Australian Fishing Zone is established via the Fisheries Management Act 1991 and covers 8 milllion km^2.

2.1.7 Continental Shelf

UNCLOS defines the Continental Shelf of a nation as comprising the seabed and subsoil of its submarine areas from the seaward boundary of its Territorial Sea to the outer edge of its continental margin, or up to 200 M from the TSB where the continental margin terminates at less than this distance. In general, the continental shelf cannot extend further than 350 M from the TSB and covers the same area as the EEZ. Within the Continental Shelf, the sovereign nation has exclusive rights to explore and exploit the natural resources of the seabed and subsoil, and/or authorise and regulate these activities by other nations, but must cooperate with other nations with regard to navigation through the waters above the Continental Shelf and infrastructure (such as cables) on the marine floor. In 2008, the Commission on the Limits of the Continental Shelf (established under UNCLOS) extended the area of Australia's Continental Shelf by 2.56 million km^2. This extension was based on the geomorphology of the continental margins surrounding the Australian land mass (Symonds *et al*., 2009).

2.2 Marine Geomorphology and Bioregionalisation

With the launch of Australia's Ocean Policy in 1998, the Australian federal government committed to an integrated, ecosystem-based approach to the planning and management of all ocean uses (CoA, 1998). Although this policy proved to be shortlived, being disbanded in 2005, it gave impetus to a number of valuable investigations into the Australian marine environment (Vince *et al*., 2015). In order to effectively manage maritime areas, an understanding of bathymetry (shape of the seabed) and geomorphic features (type of seabed forms) is fundamental.

The geomorphology of the Australian continental margin has been detailed in Harris *et al*. (2005) and Heap and Harris (2008), including systematic collation of available data sources to enable measurement of the surface area and distribution of geomorphic features within the limits of the EEZ (see Excursus 13.1). Major geomorphological features around Australia are shown with recognised maritime zones in Figure 2.6).

Broadscale mapping of seabed environments into a series of 'seascapes' has uncovered great diversity in Australia's marine jurisdiction, including aspects of the seabed that may be important for conservation and biodiversity management. These seascapes combine aspects of water depth, sediment type, geomorphology, sea-floor temperature, disturbance by tides and waves, slope of the seabed and amount of primary production. These parameters are related in complex ways to the distribution of biodiversity, so areas where there are many seascapes might also be areas with a high diversity of species or ecological communities (SOE, 2011; Whiteway et al., 2007)

Figure 2.6 Seafloor morphology around Australia

Major geomorphological features around the Australian continent are overlaid with maritime zones.

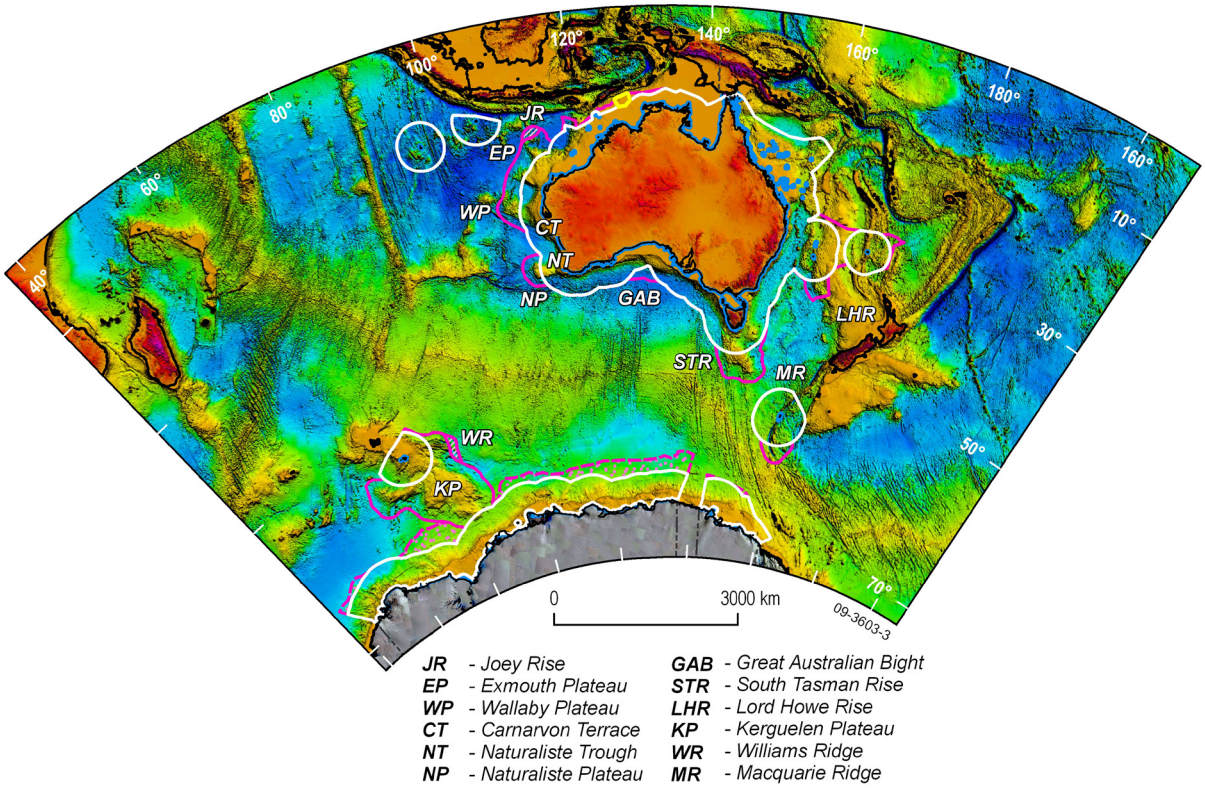

Source: Symonds *et al.* (2009) Figure 3. Retrieved from: *http://www.ga.gov.au/ausgeonews/ausgeonews200903/limits.jsp*

Figure 2.7 Provincial marine bioregions

IMCRA v4.0 defines 41 provincial bioregions in Australia's waters, comprising 24 provinces (with biotic endemism) and 17 transitional zones. These reflect biogeographic patterns in the distribution of demersal (bottom-dwelling) fish.

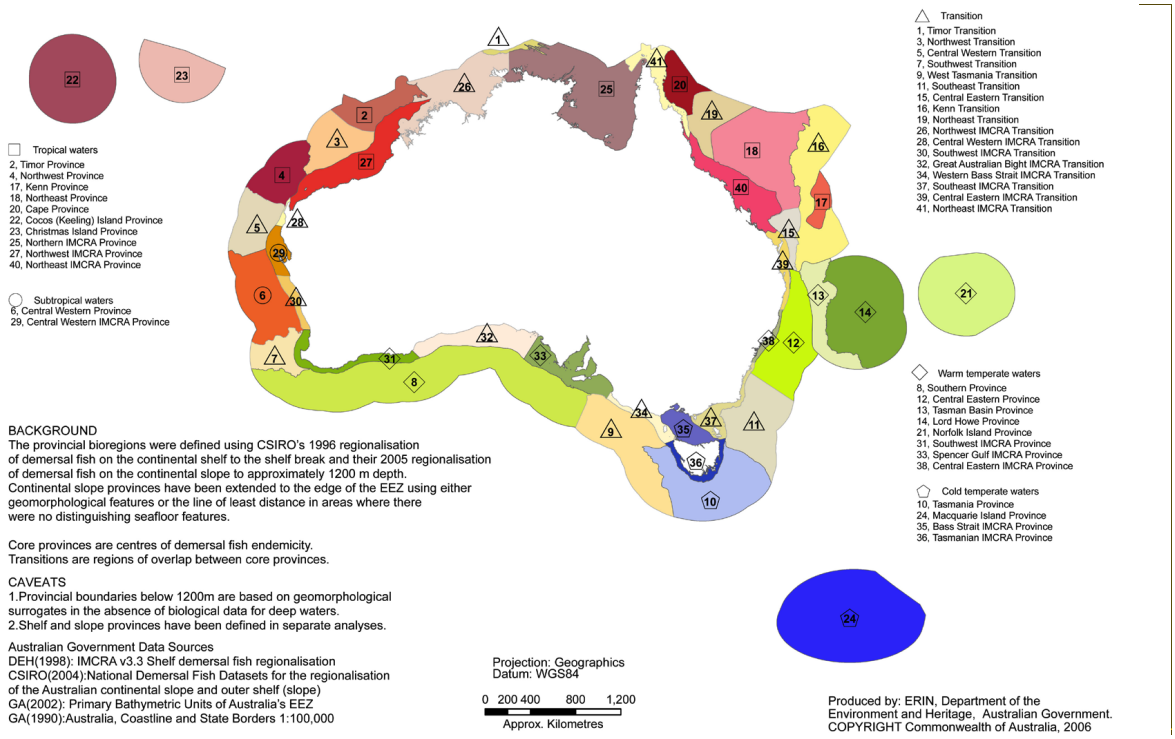

Source: CoA (2006) Map 1.

Figure 2.8 Three-dimensional model of water masses defined by pelagic regionalisation

25 three-dimensional water masses have been defined around Australia based largely on latitudinal oceanographic processes. Water mass 13 (green) is Pacific Central-South subtropical water, which extends to a depth of 250 m. Water mass 10 (light blue) is the southern Subtropical Convergence, which extends down to 800 m depth, and is part of the Southern Ocean.

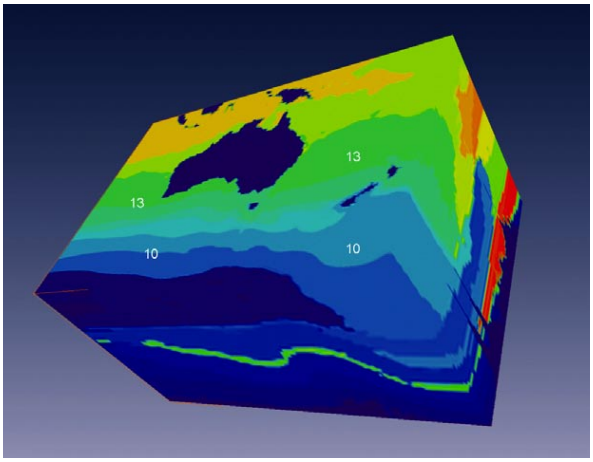

Source: CoA (2006) Figure 1

To simplify the process of regional planning within the Australian EEZ, the Interim Marine and Coastal Regionalisation of Australia (IMCRA v4.0) delineates 'bioregions' (areas that are ecologically similar; see Volume 3A). IMCRA v4.0 combines IMCRA v3.3, which covered inshore waters, and the National Marine Bioregionalisation (NMB; CoA, 2005), which described off-shelf waters. It comprises two regionalisations:

- benthic—based on biogeography of fish, which uses geomorphology as a proxy (Heap *et al*., 2005; Last *et al*., 2005; see Figure 2.7); and
- pelagic—based on three-dimensional oceanographic characteristics of defined waterbodies (Lyne and Hayes, 2005; see Figure 2.8).

2.3 Regional Water Circulation

The Australian continent is bounded by three oceans and four seas (see Figure 2.1). The closest land mass to the south is Antarctica. While the impact of currents varies with the seasons, the most significant ocean and coastal major currents in the Australasian region are the:

- East Australian Current (EAC)—carrying subtropical warmth down the eastern coastline of Australia from Cairns to Tasmania. This western boundary current is driven by the South Pacific Gyre, which in turn, is triggered by seasonal changes in the upper atmosphere over Antarctica. Eddies are frequent and can be recurrent, commonly spanning 200–300 km in diameter (CSIRO, 2018).
- Leeuwin Current (LC)—forming near the North West Shelf of WA coastline and traveling south to Cape Leeuwin, across the southern shelf as the South Australia Current, then down the west coast of Tasmania as the Zeehan Current, this 5,000 km current is the longest coastal current in the world. It forms an unusual eastern boundary current for the Indian Ocean gyre and a northern boundary current for the Southern Ocean.
- Antarctic Circumpolar Current (ACC)—connecting the southern Atlantic, Pacific and Indian Oceans this powerful current flows eastward around Antarctica and is highly significant in the global climate system.
- Indonesian Throughflow (ITF)—flowing westward through the Indonesian Archipelago, this system of currents transports water from the Pacific Ocean to the Indian Ocean, warms the waters carried south by the Leeuwin current, and contributes to monsoonal weather in Asia and Australia. Without the ITF, Australia would have a classical northward flowing eastern boundary current instead of the LC.
- Zeehan Current (ZC)—the final stage of the Leeuwin Current, moving southeastward along the edge of the continental shelf of western Bass Strait and western Tasmania (see Section 16 for details).

The CSIRO Atlas of Regional Seas (CARS) records mean ocean properties and average seasonal properties for Australian waters derived from historical subsurface ocean property measurements (Ridgway *et al*., 2002). This atlas can be used to generate valuable insights into regional water circulation characteristics (see Section 16). Water circulation patterns infer bioenergetics and can be used to model regional water productivity (CoA, 2006; see Section 16). The collaborative Bluelink partnership (see Excursus 2.2) models ocean dynamics to deliver improved operational forecasts for a range of ocean users.

Excursus 2.2—Bluelink Ocean Forecasting

Source: Edward King, CSIRO
Further Information: *https://research.csiro.au/bluelink*; Brassington *et al.* (2007); Schiller *et al.* (2019)

The ocean is an energetic, stratified, saline fluid in which currents, eddies, fronts and other three-dimensional structures form, evolve and dissipate over time in response to forcing at the surface through wind friction, solar radiation (including loss via evaporation), ice formation and melt, and terrestrial freshwater inflow. Knowledge of the surface and near-surface conditions is important information for decision makers for a wide range of maritime industries and Defence operations. Applications include:

- understanding the subsea acoustic environment (e.g. sonar ranges and shadow zones);
- tactical decision making, including:
  - optimum navigation;
  - safe operating conditions;
  - surface and coastal wave environments; and
  - limits of knowledge/uncertainty;
- maritime incident response (e.g. oil spills, people, objects adrift);
- sea level variations for ports and coastal management; and
- planning for coastal infrastructure.

Bluelink is a partnership, established in 2001, between the CSIRO (Australia's national research organisation), the Bureau of Meteorology (BoM, Australia's operational forecasting agency) and the Department of Defence, to deliver operational forecasts of ocean properties globally. Although the original focus was on global forecasts, today they are produced across three scales: globally, regionally, and in the littoral zone. The global forecasts are produced routinely on a daily basis, with the regional and littoral forecasts at higher resolution over smaller areas nested within the global forecast when and as required.

Global forecasts

Global ocean forecasts, like meteorological forecasts, combine knowledge of the physics of ocean hydrodynamics (encoded in an ocean model) with *in situ* and remotely sensed (satellite) observations of the ocean state to capture the existing conditions and evolve them forward over time. The observations are sparse in both time and space, and the model cannot capture the ocean dynamics at all scales, so the model state is always an approximation of the true conditions in the ocean. A mathematical technique called data assimilation is used to continuously update and correct the model with the most recent observations so that forecasts are always based on a combination of best available historical observations and physical knowledge of the ocean.

Three technological developments have been key to making global ocean forecasting practical:

- satellite observations of the global ocean surface, primarily sea surface height from altimetry missions (see Section 12) since 1993, but also sea surface temperature (see Section 14) from even earlier, provide a frequent measurement of the surface boundary conditions. Remotely sensed height and temperature give important information about integrated column density and surface density respectively;
- since the start of the 21st century, the Argo robotic float program (*https://argo.ucsd.edu/*) has provided observations of the subsurface physical oceanography (temperature and salinity) to a depth of 2000 m (see Excursus 5.1). Around the globe, approximately 4,000 floats each report once every 10 days yielding about 400 ocean depth profiles daily; and
- high performance computing has reached a scale and capability in the past 20 years that enables the physical ocean models to be run with grid spacings sufficient to resolve the key mesoscale features of the ocean that are important for maritime operations.

In combination, these developments, together with the incorporation of data assimilation techniques, underpins the production of ocean forecasts.

The Bluelink partnership developed a system to produce global ocean forecasts at sub-mesoscale scales (10s of km), resolving the important structures, at short to medium-range (days to weeks). The BoM now runs the operational forecast model (known as OceanMAPS) daily, covering the globe between latitudes 75°S and 75°N. The model provides temperature, salinity, and current estimates at approximately 50 depths from the surface to the deep ocean, with higher density (more closely spaced layers) in the 500 m closest to the surface. Sea surface height (without tides or the pressure component of storm surge) is also produced. Output for the Australasian region can be explored at the BoM website (see Figure 2.9).

Ongoing development of the model and data assimilation scheme occurs through a range of national and international partnerships. Notably the Cosima partnership (*cosima.org.au*) is incorporating a sea ice capability to the core model that will extend the forecast reach to higher latitudes to make it truly global. CSIRO is responsible for the Bluelink Reanalysis (BRAN), a multi-decadal historical run of the model that uses all of the best available observations (which may not be either available, or fully quality-controlled, at the time that the BoM runs its daily forecast; see Figure 2.10). Thus, BRAN provides a historical record of the global ocean, and is also a testbed for innovations in the model and data assimilation, which enables thorough evaluation before they are incorporated into the forecast system. OceanMAPS and BRAN are both very resource (memory and compute) intensive and run on supercomputers operated by the BoM and the National Computational Infrastructure (NCI) respectively.

Regional forecasts

The second tier of the Bluelink modelling suite is the Relocateable Ocean Atmosphere Model (ROAM), which enables a higher resolution ocean model to be run in a region of interest specified interactively by a forecaster via a web interface. Runs of the ROAM-Ocean model typically provide forecasts with a horizontal spatial resolution of 1–2 km over an area of several hundred km (see Figure 2.11), for between two and four days ahead. Constraining the area of modelling and nesting within the global model makes the computational demand of the higher resolution tractable. The higher resolution model captures the sub-mesoscale physics, including internal tides, fine scale fronts and filaments, recirculations around headlands, coastal sea level, and coastal or open ocean upwellings. The ROAM ocean model is nested within the global model and so incorporates all the benefits of the assimilated observations. The regional modelling suite also includes ROAM-Atmosphere and ROAM-Wave models that can be run in restricted regions to provide higher resolution forecasts of parameters relevant to marine operations.

Figure 2.9 Example of global forecast

An example of Bluelink forecasting for daily average surface temperature and current strength and direction in the Tasman Sea on 28 September 2020.

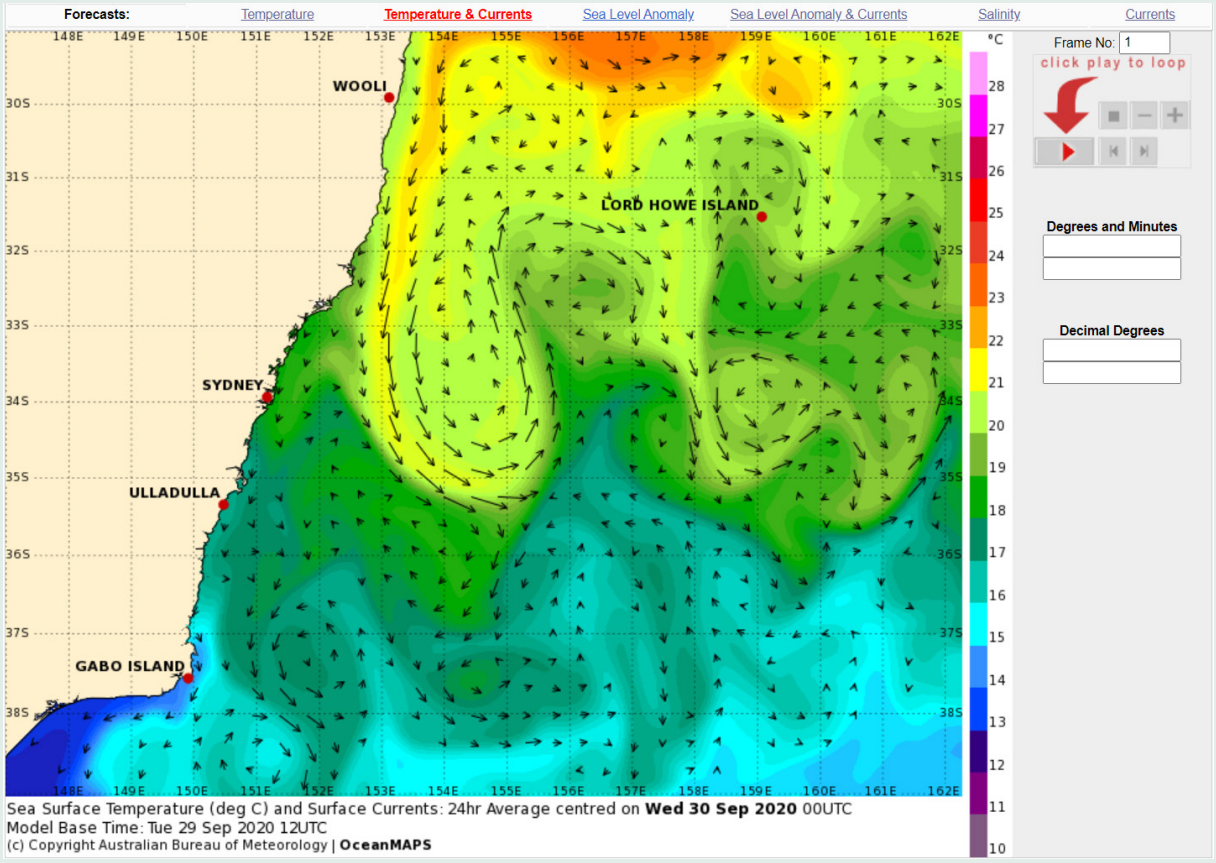

Source: Bureau of Meteorology. Retrieved from *http://www.bom.gov.au/oceanography/forecasts/index.shtml*

Figure 2.10 BRAN 2020 reanalysis

The BRAN 2020 reanalysis captures the evolving historical state of the ocean every day since 1993 until the recent present. The example shown here is surface current speed from mid-2010, with colours ranging through the visible spectrum for low to high current speeds.

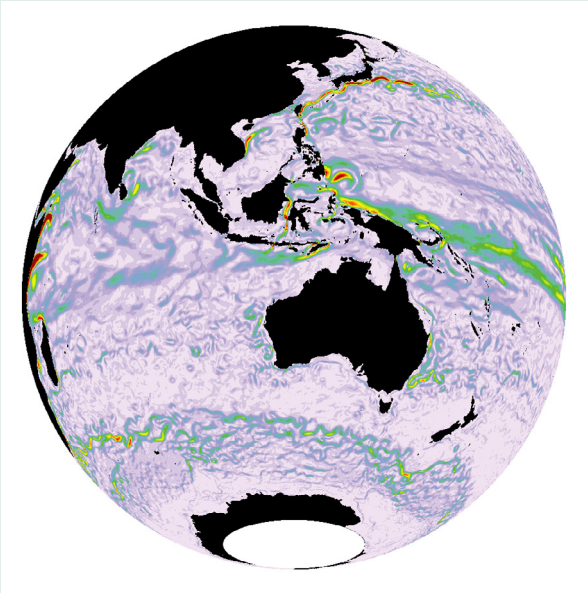

Source: Matt Chamberlain, CSIRO

Litttoral forecasts

Littoral forecasts are an emerging focus for Bluelink and comprise the third tier of the system known as ROAM-Surf. These use the mature Simulating Waves Nearshore (SWAN) spectral wave model, and the fully phase-resolved XBeach model to provide information on conditions to be expected in the littoral zone, where the interaction of the surface waves and currents with the seafloor becomes significant. These forecasts include wave propagation and breaking, currents, rip-currents, and sediment transport right up to the beach face at spatial resolutions down to a few metres (see Figure 2.12). In combination with ROAM Atmosphere, they enable operational decision making and risk control for nearshore activities, such as amphibious landings operations.

Although the Bluelink partnership has been in place for nearly two decades, the forecast system it has developed remains under active development. Some areas of focus are:

- extension to a fully global forecast including sea ice;
- inclusion of biogeochemistry in order to forecast water clarity;
- improvements in littoral forecasts, including techniques for remotely determining near-shore bathymetry; and
- employment of unstructured grids in the ROAM-Ocean models to improve representation in complex bathymetric environments and computational efficiency.

Figure 2.11 Sample ocean temperature

Relocateable Ocean Atmosphere Model (ROAM) forecasts for coastal waters bordering southwest Victoria on 29 July 2020

a. At 0.5 m water depth (temperature range 12.43–15.5°C)

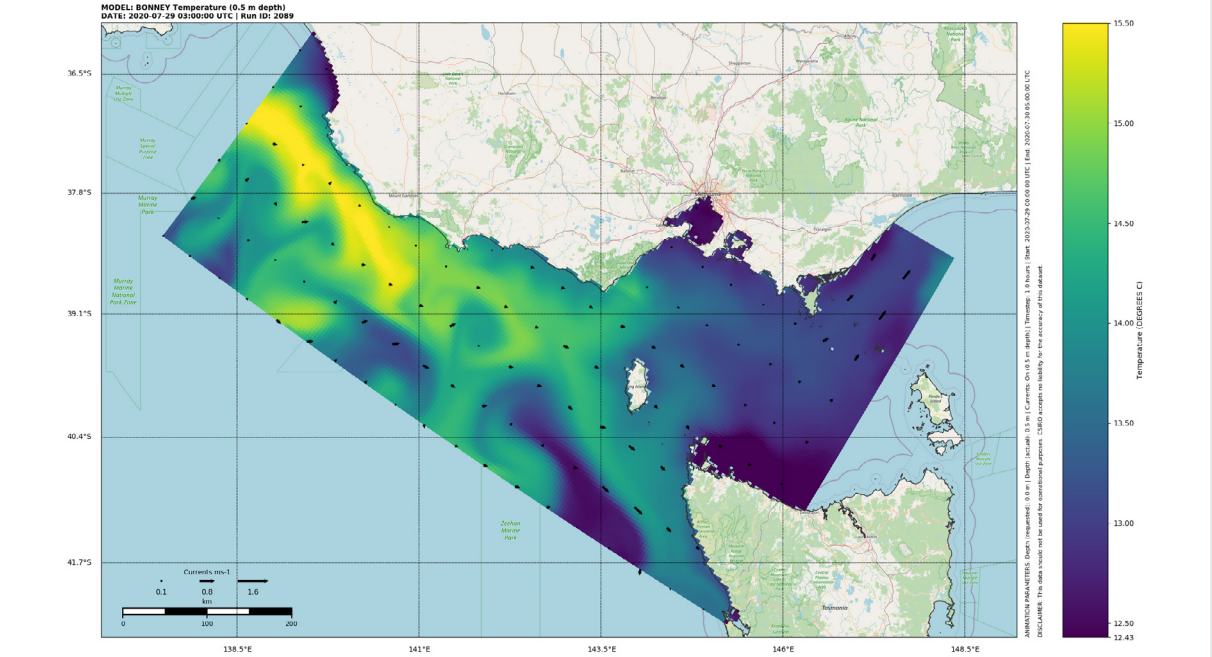

b. At 105 m water depth (temperature range 12.68–15.35°C)

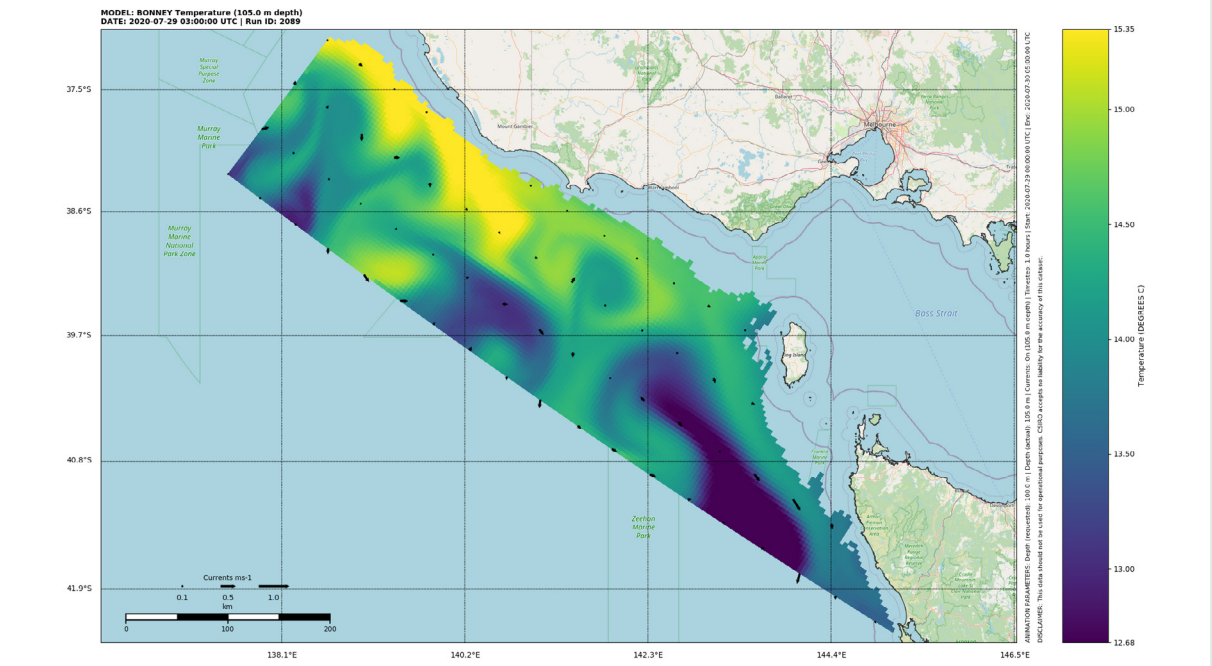

Figure 2.12 Littoral forecast example

Gunnamatta Beach , Mornington Peninsular, Victoria

a. True colour image of beach

b. Forecast currents in the presence of a wave field

c. Underlying bathymetry

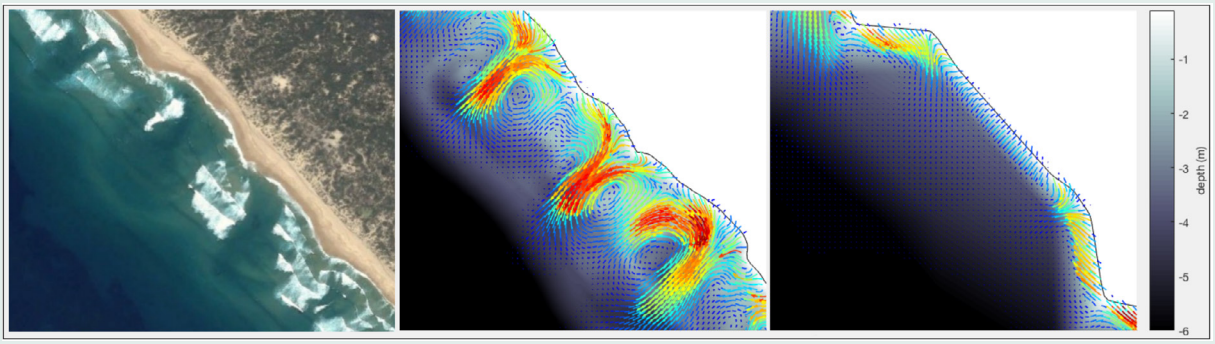

Source: Ron Hoeke, CSIRO

2.4 Australian Marine Environment

Coastal zone mapping and monitoring are increasingly important in Australia given that around half its population live within 7 km of its shores, and up to 85% of Australians live within 50 km of the coast (NMSP, 2015). The coastline of the Australian mainland is estimated to span around 34,000 km and includes more than 1,000 estuaries (GA, 2021b). While the states and territories manage coastal resources, the federal government defines maritime boundaries, monitors shoreline location, assesses environmental condition, coordinates natural disaster mitigation efforts, develops shallow water bathymetric models, and evaluates the potential impact of groundwater extraction on coastal aquifers.

Most Australian coastal waters are considered to contain low levels of nutrients, and are therefore not very productive, due to limited mixing with ocean waters (SOE, 2011). However, seasonal variations in water condition, driven by river outflows and coastal runoff, mean that coastal waters can vary from clear, with low nutrients, to turbid, and more productive. Many marine species tend to be locally endemic, particularly in southern regions, grouping into unique ecosystems in a diverse range of habitats.

As part of the international, decadal project entitled 'Census of Marine Life' (see Section 2.8), and using species counts from four primary databases[3], Butler *et al.* (2010) estimated that Australian marine waters supported more than 33,000 marine species, mostly animals (130 of these species were introduced, and another 58 are listed as threatened), but the total number of macroscopic species could be as high as 250,000. Database records confirmed the existence of:

- 8525 species of molluscs;
- 6,365 species of crustaceans; and
- 5,184 species of fish.

While, the major economic return from Australian marine waters comes from the oil and gas industry (see Section 19.4), coastal fisheries and aquaculture comprise the most profitable renewable industry. Australian oceans do not support the same volumes of fish and related species as occur in waters around other continents in the Southern Hemisphere at comparable latitudes. Areas of upwelling currents, and related higher productivity, do occur, however, in selected locations (see Section 16; SOE, 2011).

3 Australian Faunal Directory, Codes for Australian Aquatic Biota, Online Zoological Collections of Australian Museums, and Australian node of the Ocean Biogeographic Information System (OBIS).

2.5 Antarctica

Antarctica warrants numerous superlatives: the world's largest cold desert; coldest, windiest, driest and highest continent; and largest store of ice (90% of global total) and freshwater (that is, the potentially largest source of sea level rise). It is also home to the world's deepest continental shelf; largest wind-driven currents (circling around it in the circumpolar Southern Ocean); and the oldest and most detailed climate records in continental ice. Moreover, Antarctica is the only continent without a native human population (SOE, 2011).

Continental Antarctica, with its islands and ice shelves, comprises an area of 13.7 million km^2 (AAD, 2018), which is roughly equivalent to that of Australia's marine jurisdiction. The Antarctic continent is further surrounded by sea ice that covers an approximate area of 19 million km^2 at its maximum annual extent each September to October (spring) and melts back to a summer minimum of around 3 million km^2 each February (Parkinson, 2019). As introduced in Section 1.3.1, two dynamic, though distinctly different, forms of ice occur in polar regions (see Figure 2.13):

- ice sheets—over prolonged periods of time, snow accumulates and compacts on land to form extensive sheets of glacial ice. Far from being static, the ice flows under gravity towards the surrounding ocean in the form of glaciers and ice streams. On reaching the ocean and in certain places, the ice continues to advance in the form of floating glacier tongues and ice shelves, which can reach hundreds of metres in thickness. Subsequent breakages (termed 'calvings') from floating ice sheet margins form icebergs.
- sea ice—when ocean water freezes (at ~-1.8°C), it forms floating crystals of ice that subsequently coalesce into buoyant sheets of ice and acquire a snow cover, that is, the ice intercepts and accumulates snowfall that would otherwise have fallen directly into the ocean. Sea ice that is constantly in motion under the influence of winds and ocean currents is referred to as 'pack ice', which is made up of contiguous parcels of ice termed 'floes'. In contrast, sea ice that remains stationary when attached to the coastline, the seafloor, or icebergs grounded on the seafloor is called 'fast ice'. Although generally up to a metre or so thick, sea ice can attain thicknesses in excess of 10 m in places, due to either its great age (thermodynamic growth) or by deformation (dynamic thickening where two pieces of ice collide). In certain key coastal locations, areas of open water surrounded by sea ice can recur seasonally or persist for longer time periods. These are called polynyas, and influence global ocean circulation and biological production.

Figure 2.13 Types of ice in polar regions

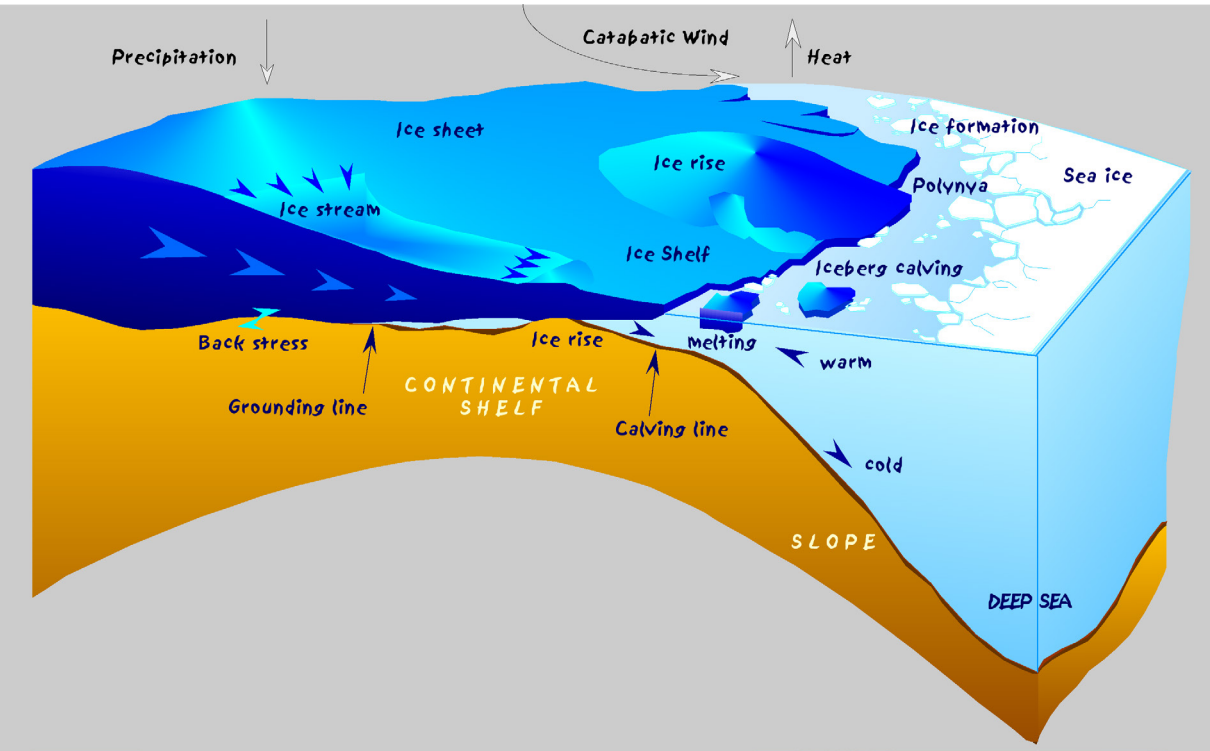

Source: Hannes Grobe, Wikimedia. Retrieved from: *https://commons.wikimedia.org/wiki/File:Antarctic_shelf_ice_hg.png*

In the Arctic, a greater proportion of the sea ice coverage persists into summer than in Antarctica,

where most sea ice melts back each spring-summer—although this situation is changing as the Arctic Ocean loses much of its perennial sea ice cover, which is being replaced by more of a seasonal ice cover (see Section 15). Arctic sea ice also occurs closer to the pole (mostly above 70°N) than Antarctic sea ice, which only extends south of about 70°S in the great embayments of the Ross and Weddell seas.

Significantly, 70% of Earth's available freshwater is stored in the Antarctic Ice Sheet, which, if melted, is sufficient to elevate sea levels by 60 m (SOE, 2011; Fretwell *et al.*, 2013). The Antarctic environment directly impacts global weather patterns and climate, and acts as a sensitive indicator of climate change, with recent observations confirming that polar ice coverage is melting at a faster rate than expected (Scott *et al.*, 2009). EO datasets play a crucial role in monitoring this vast and remote region (see Section 15).

Seven countries, including Australia, claim territory in Antarctica. The Australian Antarctic Territory comprises 42% of Antarctica, covering all land/ice sheet and islands south of 60°S and from longitude 45°E to 138°E, and from 142°E to 160°E (see Figure 2.14). Australia's subantarctic islands (namely, Macquarie, Heard and McDonald Islands) are included on the World Heritage List.

Despite territorial claims, Antarctica is effectively governed by the Antarctic Treaty System, which is jointly signed by 48 member countries to manage the area south of the 60°S parallel as a 'natural reserve, devoted to peace and science' (The Madrid Protocol, 1998). The Convention on the Conservation of Antarctic Marine Living Resources (CCAMLR) regulates fishing in this region, with the stated goal of sustaining relevant ecosystems, rather than industries (CCAMLR, 1984).

Figure 2.14 Australian Antarctic Territory

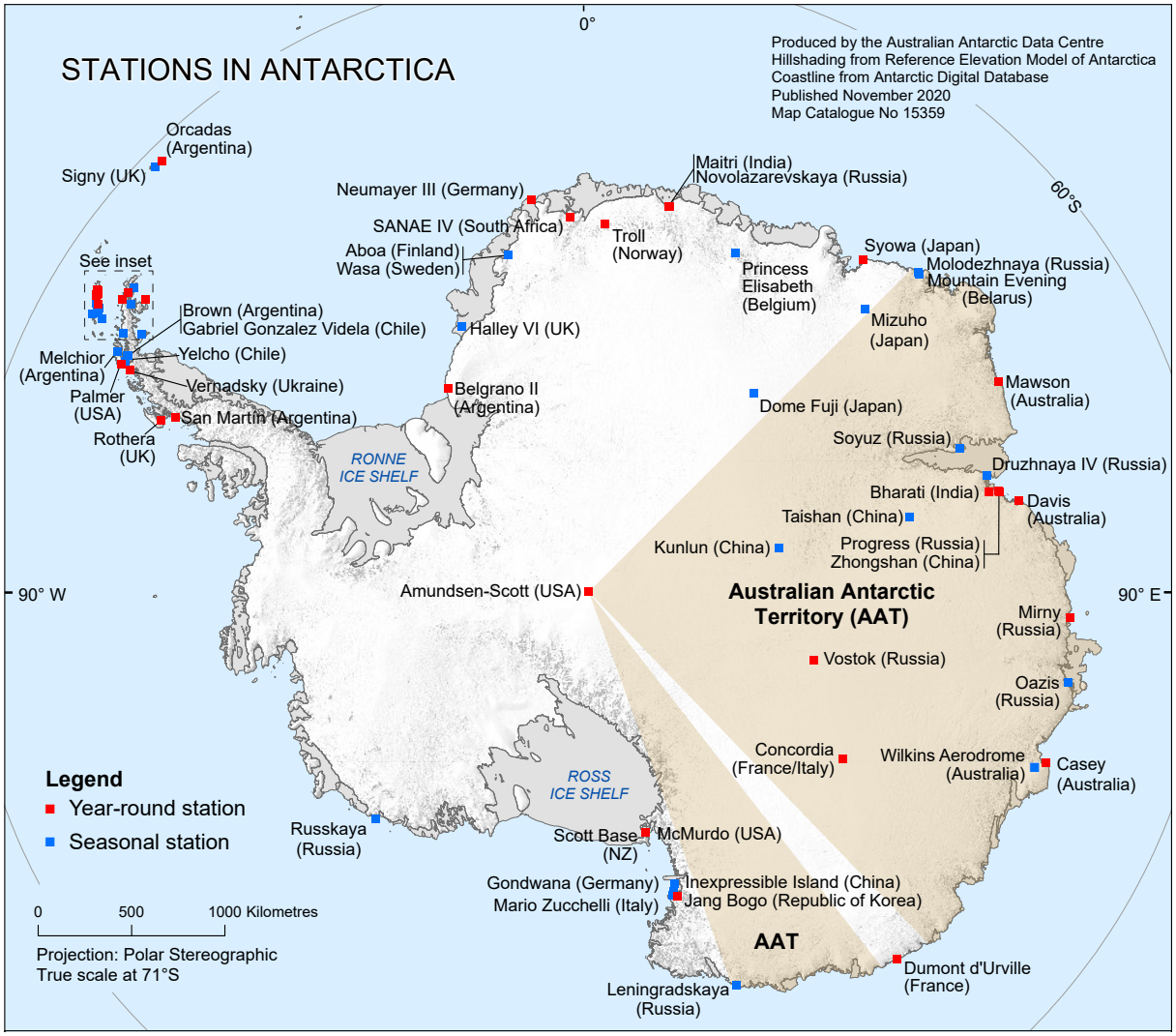

Source: Australian Antarctic Data Centre. Retrieved from *https://data.aad.gov.au/aadc/mapcat/display_map.cfm?map_id=15359*

2.6 Australia's Inland Water Resources

Australia's average annual rainfall is 430 mm, with regional variations ranging from less than 100 mm in inland deserts to over 3,000 mm in the tropical north (see Figure 2.15 and Volume 3A—Section 2). 88% of this rainfall is subsequently lost through evapotranspiration, leaving an estimated 383,000 GL to enter Australia's water environment (SOE, 2017). Although both the timing and volume of rainfall is variable, largely due to the El Niño Southern Oscillation (ENSO), distribution can be described in terms of two broad seasonal regimes:

- monsoonal northern regions, with significant rainfall from October through April only; and
- temperate southern regions, with maximum rainfall from April through November (SOE, 2011).

These rainfall patterns mean that inland surface waterbodies in Australia (see Figure 2.16) have fluctuating flow conditions, and many are dry for much of the time. Even when water is permanently stored, large changes can occur in flow regimes, which impact aquatic ecosystems and other water users. Given their fragiility and importance, many Australian rivers and wetlands are protected under federal or state legislation (EPBC Act, 1999). Additionally, 66 Australian wetlands, covering more than 8.3 million ha, are listed under the Ramsar Convention for Wetlands of International Importance (DAWE, 2021).

Based on surface water flows, 13 drainage divisions have been defined within Australia (see Figure 2.17). Most of these divisions are sufficiently extensive to contain the boundaries of recharge and discharge for their associated aquifers, with the exception of the Great Artesian Basin, which spans three drainage divisions (SOE, 2017; see Volume 3A—Section 2). The number and extent of inland waterbodies in Australia is summarised in Table 2.2.

Figure 2.15 Australia's average annual rainfall

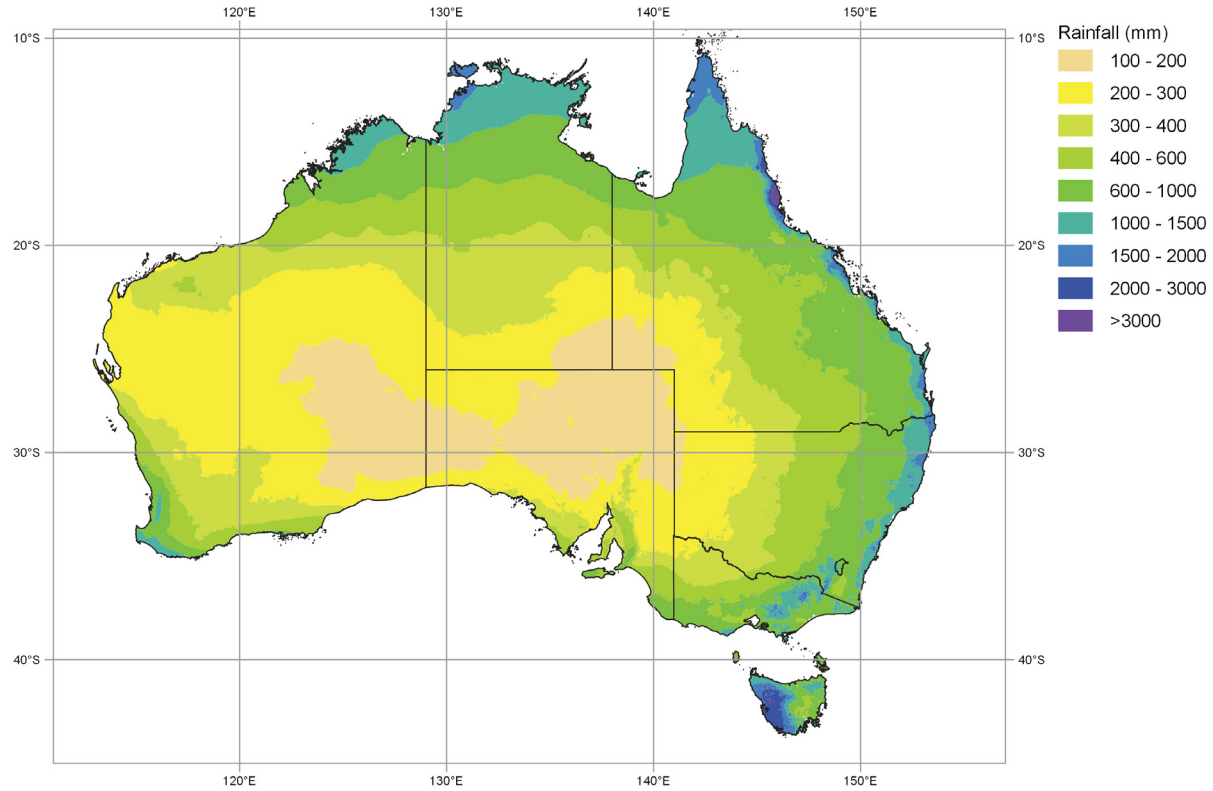

Source: Tony Sparks, Icon Water, using gridded data from BoM (2020a) based on a standard 30-year climatology (1961–1990)

Figure 2.16 Australian inland waterbodies

While this map implies a dense network of rivers and waterbodies in many parts of Australia, most are ephemeral, and the waterbodies shown as blue in central Australia are salt lakes.

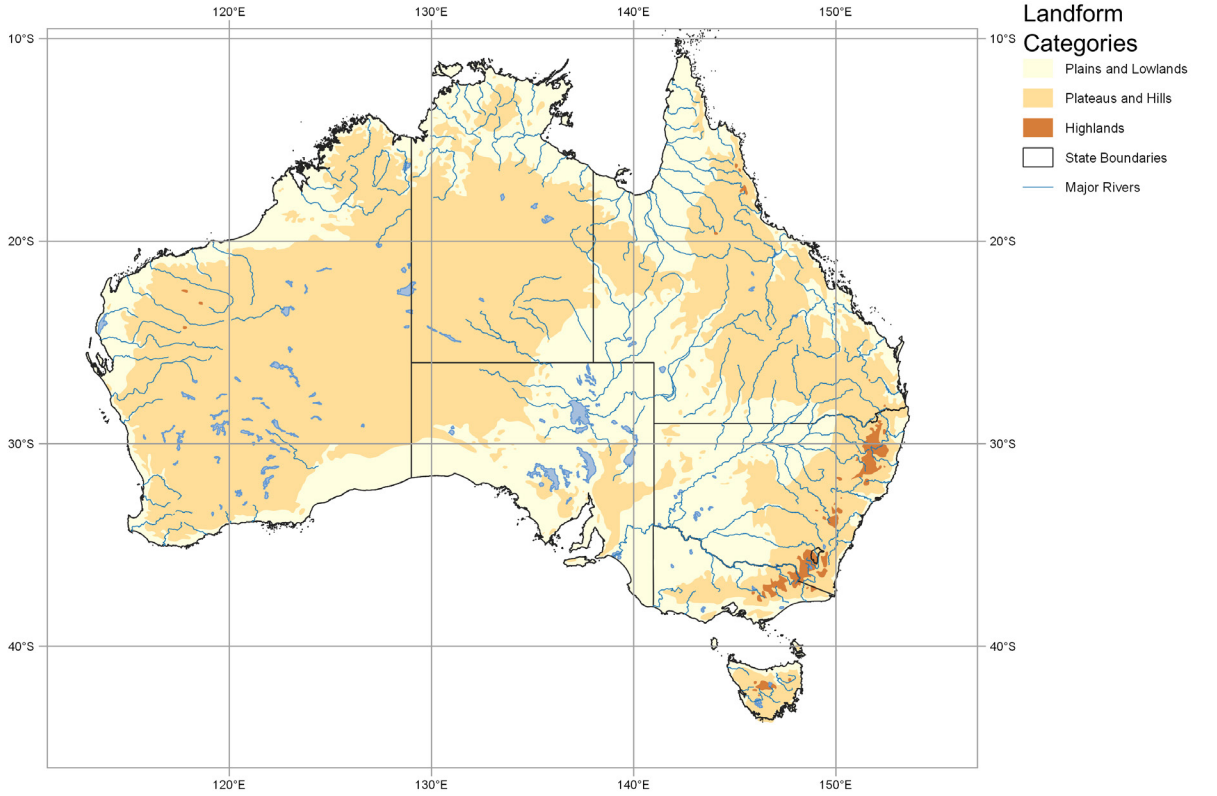

Source: Tony Sparks, Icon Water, using data from GA (2002) for waterbodies

Figure 2.17 Major drainage divisions in Australia

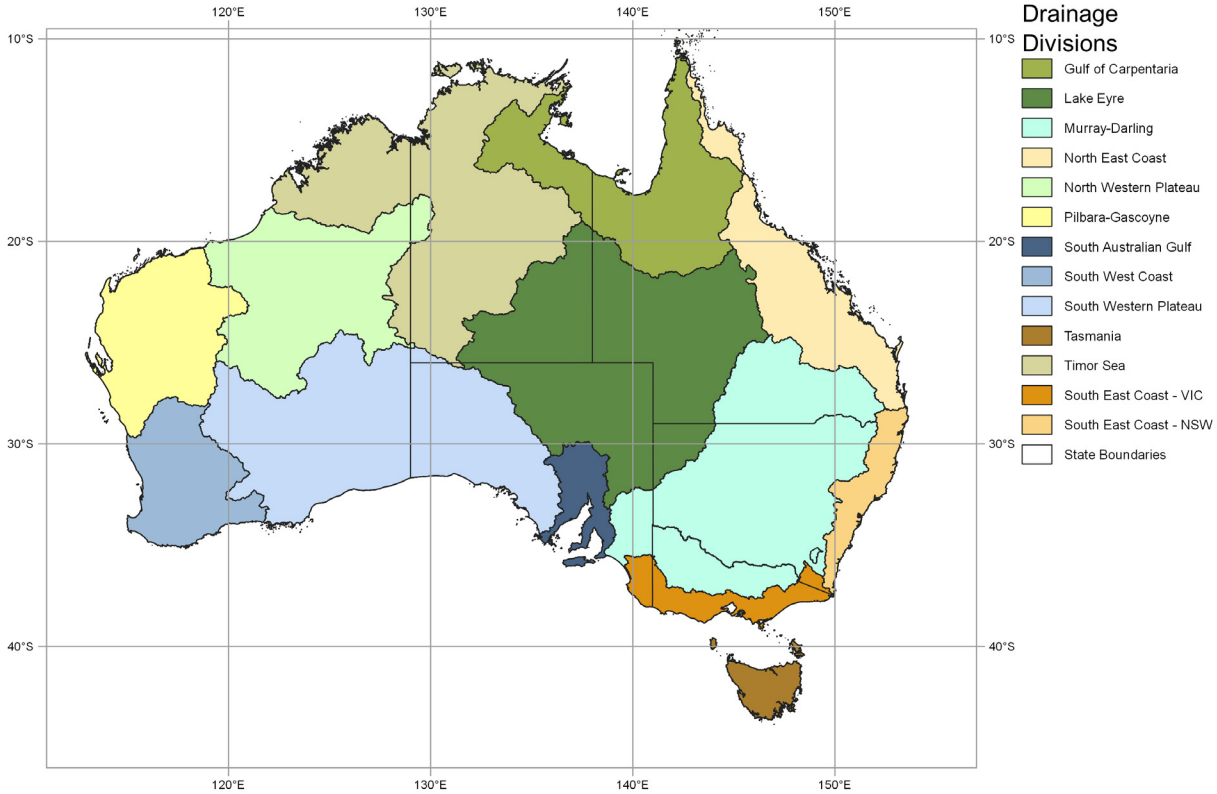

Source: Tony Sparks, Icon Water, using data derived from the Geofabric Hydrology Reporting Catchments product (BoM, 2020b)

Table 2.3 Categories of waterbodies in Australia

Type of Waterbody	Number	Area (km²)	Comment
Lake	108,830	188,085	Over half occur in WA with greater area in NT
Watercourse Area	10,965	40,265	Over half occur in WA with greater area in NT
Land Subject to Inundation	17,458	406,887	Around a quarter occur in each of NT and Qld, with greater area in NT
Swamp	9,342	42,809	Nearly half occur in Qld with greatest area in NT
Town Rural Storage	2,347	16,936	Nearly half occur in Qld with greatest area in NT
Settling Pond	264	441	Highest numbers in WA and Qld with greatest area in WA nd NT
Total	149,000	695,423	Distribution varies widely between states

Source: Dekker and Hestir (2012)

2.7 Australian Water Usage

Understandably, as the driest inhabited continent on Earth, Australia manages the largest area of surface water storage per capita (BoM, 2020c). Our 305 publicly-owned lakes, reservoirs and weirs have a total storage capacity of 80.8 million ML. Water levels in these storages are routinely monitored by relevant authorities and standardised by the BoM for publication (see Section 1.6).

Australia's annual water consumption (domestic and industrial) in 2015–16 was estimated as 16,132 GL (ABS, 2017), with agriculture being the largest single user (consuming 9,604 GL). During this time period, environmental extraction of water was estimated as 75,544 GL, of which 65,238 GL was ultimately discharged back to the environment.

2.8 Further Information

Australian Marine Waters

Australian Hydrographic Service: *http://www.hydro.gov.au*

Australian Marine Spatial Information System (AMSIS)

http://maps.ga.gov.au/interactive-maps/#/theme/amsis

National Marine Science Plan

http://www.marinescience.net.au/fileadmin/user_upload/documents/National_Marine_Science_Plan_2015_Factsheet_20150807.pdf

Seasonal Ocean Water Properties

CSIRO Atlas of Regional Seas (CARS): *http://www.marine.csiro.au/~dunn/cars2009/*

Coastal Change

https://www.coastalrisk.com.au/home

https://coastadapt.com.au/tools/coastadapt-datasets#future-datasets

https://ecat.ga.gov.au/geonetwork/srv/eng/catalog.search#/metadata/104160

Antarctica

Australian Antarctic Commission: *http://www.antarctica.gov.au*

Committee for Environmental Protection: 25 Years of the Protocol on Environmental Protection to the Antarctic Treaty. Secretariat of the Antarctic Treaty, Buenos Aires, 2016. *https://www.ats.aq/documents/atcm39/ww/atcm39_ww007_e.pdf*

2.9 References

ABS (2017). *Water Account, Australia 2015–16*: *http://www.abs.gov.au/ausstats/abs@.nsf/mf/4610.0*

AAD (2018). *Antarctic environment* webpage on Australian Antarctic Division website: *http://www.antarctica.gov.au/about-antarctica/environment*

AGD (1980). *Offshore constitutional settlement. A milestone in cooperative federalism*. Attorney-General's Department. AGPS, Canberra.

AHS (2017a). *Hydroscheme 2017–2020*. Australian Hydrographic Office, Department of Defence. *http://www.hydro.gov.au/business-publications/HydroScheme_2017-2020_WEB_20171103.pdf*

AHS (2017b). *Names and Limits of Oceans and Seas around Australia*. Australian Hydrographic Service Fact sheet: *http://www.hydro.gov.au/factsheets/WFS_Names_and_Limits_of_Oceans_and_Seas_Around_Australia.pdf*

BoM (2020a). *Long-range weather and climate* webpage. Bureau of Meteorology website: *http://www.bom.gov.au/climate/averages/maps.shtml*

BoM (2020b). *Topographic Drainage Basins and River Regions* webpage. Bureau of Meteorology website: *http://www.bom.gov.au/water/about/riverBasinAuxNav.shtml*

BoM (2020c). *Water Information* webpage, Bureau of Meteorology website: *http://www.bom.gov.au/water/dashboards/#/water-storages/summary/state*

Brassington, G.B., Pugh, T. Spillman, C. Schulz, E. Beggs, H. Schiller, A. and Oke, P.R. (2007). BLUElink> Development of operational oceanography and servicing in Australia. Journal of Research and Practice in Information Technology, 39, 151–164.

Butler, A.J., Rees, T., Beesley, P., and Bax, N.J. (2010). Marine biodiversity in the Australian region. *Plos One*, 5(8), e11831.

CCAMLR (1984). *Report of the third meeting of the scientific committee*. Commission for the Conservation of Antarctic Marine Living Resources, Hobart.

CoA (1998). *Australia's Oceans Policy*. Commonwealth of Australia. ISBN 0 642 54580 4. *http://www.environment.gov.au/archive/coasts/oceans-policy/publications/pubs/policyv1.pdf*

CoA (2005). *National Marine Bioregionalisation of Australia. Summary*. Commonwealth of Australia. Department of Environment and Heritage, Canberra, Australia.

CoA (2006). *A Guide to the Integrated Marine and Coastal Regionalisation of Australia Version 4.0*. Commonwealth of Australia. Department of the Environment and Heritage, Canberra, Australia.

CSIRO (2018). *Causes of extreme sea levels* webpage, Commonwealth Scientific and Industrial Research Organisation website: *https://research.csiro.au/slrwavescoast/extremes/causes-extreme-sea-levels/*

DAWE (2021). *Australian Ramsar Wetlands* webpage, Department of Agriculture, Water and the Environment website: *https://www.environment.gov.au/water/wetlands/australian-wetlands-database/australian-ramsar-wetlands*

DE (2013). *Australia's Ramsar Sites*. Department of Environment website: *http://www.environment.gov.au/water/wetlands/publications/factsheet-australias-ramsar-sites*

Dekker, A.G., and Hestir, E.L. (2012). *Evaluating the Feasibility of Systematic Inland Water Quality Monitoring with Satellite Remote Sensing*. Water for a Healthy Country National Research Flagship, CSIRO.

EPBC Act (1999). *Environment Protection and Biodiversity Conservation Act*. Department of Environment and Energy Website: *http://www.environment.gov.au/epbc/about*

Fretwell, P., Pritchard, H.D., Vaughan, D.G., Bamber, J.L., Barrand, N.E., Bell, R., Bianchi, C., Bingham, R.G., Blankenship, D.D., Casassa, G., Catania, G., Callens, D., Conway, H., Cook, A.J., Corr, H.F.J., Damaske, D., Damm, V., Ferraccioli, F., Forsberg, R., Fujita, S., Gim, Y., Gogineni, P., Griggs, J.A., Hindmarsh, R.C.A., Holmlund, P., Holt, J.W., Jacobel, R.W., Jenkins, A., Jokat, W., Jordan, T., King, E.C., Kohler, J., Krabill, W., Riger-Kusk, M., Langley, K.A., Leitchenkov, G., Leuschen, C., Luyendyk, B.P., Matsuoka, K., Mouginot, J., Nitsche, F.O., Nogi, Y., Nost, O.A., Popov, S.V., Rignot, E., Rippin, D.M., Rivera, A., Roberts, J., Ross, N., Siegert, M.J., Smith, A.M., Steinhage, D., Studinger, M., Sun, B., Tinto, B.K., Welch, B.C., Wilson, D., Young, D.A., Xiangbin, C., and Zirizzotti, A. (2013). Bedmap2: improved ice bed, surface and thickness datasets for Antarctica. *Cryosphere*, 7(1), 375–393.

GA (2002). *GEODATA TOPO 10M 2002* webpage, Geoscience Australia website: *https://ecat.ga.gov.au/geonetwork/srv/eng/catalog.search#/metadata/60803*

GA (2021a). *Maritime Boundary Definitions* webpage, Geoscience Australia website: *https://www.ga.gov.au/scientific-topics/marine/jurisdiction/maritime-boundary-definitions#:~:text=The%20term%20Territorial%20Sea%20Baseline,some%20cases%2C%20the%20continental%20shelf*.

GA (2021b). *Australia's Coasts and Estuaries* webpage, Geoscience Australia website: *https://www.ga.gov.au/scientific-topics/marine/coasts-estuaries#:~:text=The%20Australian%20coastline%20extends%20approximately,includes%20more%20than%201000%20estuaries*.

Harris, P., Heap, A., Passlow, V., Shaffi, L., Fellows, M., Porter-Smith, R., Buchanan, C., and Daniell, J. (2005). *Geomorphic Features of the Continental Margin of Australia*. Geoscience Australia, Canberra.

Heap, A.D., and Harris, P.T. (2008). Geomorphology of the Australian margin and adjacent seafloor. *Australian Journal of Earth Sciences*, 55(4), 555–585. doi:10.1080/08120090801888669

Heap, A.D., Harris, P.T., Last, P., Lyne, V., Hinde, A., and Woods, M. (2005). *Draft Benthic Marine Bioregionalisation of Australia's Exclusive Economic Zone*. Geoscience Australia Report to the National Oceans Office. Geoscience Australia, Canberra.

Last, P., Lyne, V., Yearsley, G., Gledhill, D., Gomon, M., Rees, T., and White, W. (2005). *Validation of National Demersal Fish Datasets for the Regionalisation of the Australian Continental Slope and Outer Shelf*. CSIRO Report to the National Oceans Office. CSIRO Marine Research, Hobart.

Lyne, V., and Hayes, D. (2005). *Pelagic Regionalisation: National Marine Bioregionalisation Integration Project*. CSIRO Report to the National Oceans Office. CSIRO Marine Research, Hobart.

NMSP (2015). *National Marine Science Plan 2015–2025*: *http://www.marinescience.net.au/national-marine-science-plan/*

Parkinson, C.L. (2019). A 40-y record reveals gradual Antarctic sea ice increases followed by decreases at rates far exceeding the rates seen in the Arctic. *Proceedings of National Academy of Science*, 116, 14414–14423. *https://doi.org/10.1073/pnas.1906556116*

Ridgway K.R., Dunn, J.R., and Wilkin, J.L. (2002). Ocean interpolation by four-dimensional least squares—Application to the waters around Australia. *Journal of Atmospheric and Oceanic Technology*, 19(9), 1357–1375.

Scott, J.B.T., Gudmundsson, G.H., Smith, A.M., Bingham, R.G., Pritchard, H.D., and Vaughan, D.G. (2009). Increased rate of acceleration on the Pine Island Glacier strongly coupled to changes in gravitational driving stress. *The Cryosphere*, 3, 125–131.

Schiller, A., Brassington, G., Oke, P., Cahill, M., Divakaran, P., Entel, M., Freeman, J., Griffin, D., Herzfeld, M., ; Hoeke, R., Huang, X., Jones, E., King, E., Parker, B., Pitman, T., Rosebrock, U., Sweeney, J., Taylor, A., Thatcher, M., Woodham, R., and Zhong, A. (2019). Bluelink Ocean Forecasting Australia: 15 Years of Operational Ocean Service Delivery with Societal, Economic and Environmental Benefits. *Journal of Operational Oceanography*, 13(1), 1–18. *https://doi.org/10.1080/1755876X.2019.1685834*

SOE (2011). *State of Environment Report 2011*. *http://155.187.2.69/soe/2011/report/inland-water/index.html*

SOE (2017). *State of Environment Report 2016*. Australia's water resources: Inland water (2016): *https://soe.environment.gov.au/theme/inland-water/topic/2016/australias-water-resources*

Symonds, P., Alcock, M., and French, C. (2009). Setting Australia's Limits: Understanding Australia's marine jurisdiction. *AusGeo News* 93, March 2009, Geoscience Australia.

The Madrid Protocol (1998). *The Protocol on Environmental Protection to the Antarctic Treaty*. Secretariat of the Antarctic Treaty. *https://www.ats.aq/e/ep.htm*

UN (1982) *United Nations Convention on the Law of the Sea*. United Nations Treaty Series. *http://www.un.org/depts/los/convention_agreements/convention_overview_convention.htm*

Vince, J., Smith, A.D.M., Sainsbury, K.J., Cresswell, I.D., Smith, D.C., and Haward, M. (2015). Australia's Ocean Policy: Past, present and future. *Marine Policy*, 57, 1–8. *https://doi.org/10.1016/j.marpol.2015.02.014*

Whiteway, T., Heap, A.D., Lucieer, V., Hinde, A., Ruddick, R., Harris, P.T. (2007). *Seascapes of the Australia margin and adjacent seafloor: methodology and results*. Geoscience Australia, Canberra.

3 Aquatic Ecosystems

Ecology is the science that looks at interactions between organisms and their environment. As detailed in Volume 3A, an ecosystem describes the assemblage of organisms living in a particular environment, and their connections in terms of energy and nutrient recycling. Aquatic ecosystems, by definition, exist in aquatic environments—both natural and man-made—including oceans (and sea ice), coastal waters, rivers, wetlands, dams, and lakes.

As with all ecosystems, the specific characteristics of aquatic habitats determine the organisms that live there. Relevant characteristics include food and nutrient availability, water and air temperature, water circulation, shelter, and water depth.

3.1 Aquatic Ecosystem Zones

A number of related, but overlapping, terms are used to describe specific regions of surface water as they relate to aquatic ecosystems. In this context, waterbodies are divided into zones based on: distance from the shore, light penetration, and/or the depth of the substrate (see Figure 3.1).

The **Benthic Zone** is the lowest level of any aquatic ecosystem, extending from the shoreline to deep water. This zone consists of rock, sand, and sediment on the floor of an ocean, sea, lake, or river. As such, the conditions of the benthic zone can vary significantly between shallow coastal waters and deep ocean. It supports a wide range of benthic organisms, or 'benthos', depending on local conditions, such as the amount of light that reaches it, the ambient temperature, and available nutrients.

The **Intertidal Zone** spans between the high and low tide marks and describes the coastal land that is exposed to changing tides. It is impacted by waves at high tide, and Sun and wind at low tide. Benthos living in the intertidal zone, such as barnacles, are adapted to these harsh, cyclic conditions.

The **Neritic Zone** occurs along coastlines between the low tide mark and the continental shelf. Since some sunlight reaches the bottom of this relatively shallow zone, it fosters photosynthetic organisms, such as phytoplankton, benthic microalgae, and macroalgae. Most coral reefs occur in this zone. Organisms such as molluscs, sponges, crustaceans, and worms can live on the seafloor of this zone.

Freshwater ecosystems are a foundation of our social, cultural, spiritual and economic well being.
*(Likens **et al.**, 2009)*

Background image: Phytoplankton—the foundation of the oceanic food chain. **Source:** NOAA MESA Project. Retrieved from *https://commons.wikimedia.org/wiki/File:Phytoplankton_-_the_foundation_of_the_oceanic_food_chain.jpg*

The **Photic Zone** refers to water that is close enough to the surface to admit sufficient light for photosynthesis. In lakes, this region is referred to as the **Limnetic Zone**.

The Photic Zone can be further divided into the **Euphotic**, or sunlit, zone and the **Dysphotic**, or twilight, zone. The lower extent of the Euphotic zone is defined as that water depth where only 1% of the photosynthetically active radiation (PAR) penetrating the water surface is 'visible'. Thus, as little as 1% of light entering the Euphotic zone reaches the Dysphotic Zone. The Euphotic zone includes shallow, coastal waters and the upper part of deeper, ocean waters. In clear water, this zone can extend down to 200 m. The Euphotic zone supports phytoplankton, microscopic algae and cyanobacteria as well as water plants and zooplankton, and the vast majority of marine life. Most photosynthesis on Earth occurs in the Euphotic Zone.

The **Aphotic Zone** (or midnight zone) refers to the darker, deeper waters below 1000 m in which light levels are too low for photosynthesis. This zone is also called **Deep Sea** in oceans and the **Profundal Zone** in lakes. The Aphotic Zone comprises 90% of the total area of oceans on Earth.

The **Oceanic Zone** spans between the continental shelves of different land masses.

The **Pelagic Zone** describes open water in oceans that is both away from the coast and above the seafloor, and includes both photic and aphotic waters.

The **Demersal Zone** includes water near the seabed, but below the pelagic zone.

The **Littoral Zone** extends from the high tide mark to the continental shelf and thus includes the intertidal and neritic zones defined above.

The **Riparian** zone occurs along the edges of rivers or streams and includes the riverbed, banks, and floodplains.

Figure 3.1 Aquatic zones for marine waters

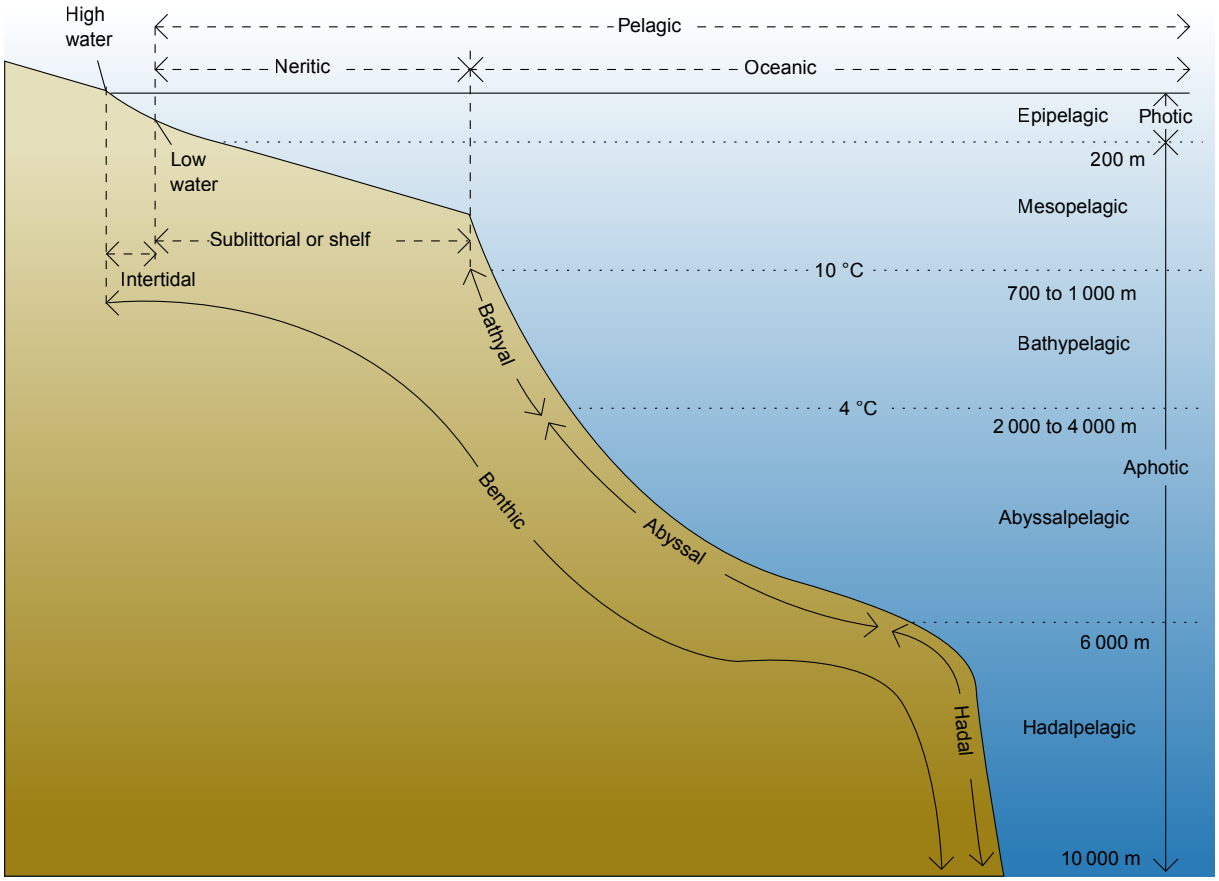

Source: Wikimedia. Retrieved from *https://commons.wikimedia.org/wiki/File:Oceanic_divisions.svg*

3.2 Aquatic Habitats

A range of aquatic habitats exist in surface waters, including:

- seas and oceans—contiguous waterbodies containing saltwater and covering around 70% of the globe. At high latitudes, this includes habitats covered by sea ice;
- coastal waters—aquatic fringes along land masses;
- estuaries—the interface between rivers and open sea, containing a fluctuating mix of freshwater and saltwater as determined by tidal water movement;
- rivers and streams—flowing waterbodies containing freshwater;
- lakes—permanent waterbodies at least 2 m deep and covering more than 0.25 ha. The largest supply of available freshwater on Earth is contained in lakes (Kalff, 2002); and
- inland floodplain wetlands—habitats reliant on variable flow and flooding regimes, including lakes and lagoons, grass-sedge-herb swamps, floodplain shrublands, and eucalypt forests and woodlands (see Excursus 3.1).

All aquatic habitats vary in terms of inflows, outflows, shoreline extent, water depth, geology, geomorphology, climate, and surrounding vegetation. In turn, these characteristics impact the physical, chemical, and biological attributes of the habitat, including resident organisms. To protect coastal and ocean habitats, numerous Marine Protected Areas (MPA) have been defined around Australia in recent decades to ensure that these unique and valuable regions are managed sustainably (see Excursus 20.2). Similarly, RAMSAR wetlands, and other nature reserves containing wetlands, rivers, and lakes, have been established to protect inland aquatic habitats.

While the precise definitions of wetlands and riparian zones can vary, both these terms describe the occurrence of vegetation in the transition zone between surface waterbodies, such as streams, rivers or lakes, and higher ground. The term 'wetlands' refers to areas that are partially or fully inundated on a periodic basis, and includes the soil, flora, and fauna existing in these areas, whereas the riparian zone describes the terrestrial or aquatic vegetation that fringes watercourses. In both cases, the presence of water promotes the growth of plants that are adapted to these environments and these plants impact the ecology of the watercourses. For example, riparian vegetation provides habitat for a wide range of faunal species, stabilises river banks, filters sediment, reduces floodwater velocity, and modulates water temperature (DWER, 2021; WaterNSW, 2021). Both wetlands and riparian zones are sensitive to land management practices that change surface water flows, and actively help to maintain water quality and waterbody health (see Excursus 3.1).

The National Intertidal Subtidal Benthic (NISB) Habitat Classification Scheme (Mount and Bricher, 2008a) defines a common set of identifiers for national reporting of aquatic habitats in Australia. NISB was used to produce nationally consistent Estuarine, Coastal and Marine (ECM) maps for seagrass, mangrove, saltmarsh, rocky reef, coral reef, macroalgae, shorelines (beaches), coastal wetlands, and estuaries (Mount and Bricher, 2008b), which "contribute to vulnerability and risk assessments of coastal ecosystems and human infrastructure" (DAWE, 2015). These maps show detailed habitat extent and distribution at local, state, and regional scales, and more general habitat distribution at regional and national scales.

Clearly, coasts and oceans face pressures from multiple human uses, and conflicts exist between competing human uses and between these uses and imperatives to protect the ocean environment and ecosystems (Vince ***et al.****, 2015).*

Excursus 3.1—Inland Floodplain Wetlands

Source: Rachael Thomas, NSW Department of Planning, Industry and Environment

Introduction

Floodplains are part of the riverine landscape formed as a result of alluvial processes. They are inherently heterogeneous and among the most biologically productive and diverse ecosystems in the world (Thoms *et al.*, 2016; Ward *et al.*, 2002; Tockner and Stanford, 2002). EO-based monitoring approaches for wetlands are considered in Section 20.

The Murray-Darling Basin (MDB) in southeastern Australia is a large (1 million km^2) complex system of rivers that rise in the high rainfall areas of the southeastern dividing ranges and flow westward for long distances (see Figure 2.15, Figure 2.16 and Figure 3.2). These rivers flow across the semi-arid to arid inland regions where rainfall is low (annual < 406 mm) and evaporation is high (exceeding 2000 mm)—and ultimately into the Southern Ocean. The rivers of the MDB exhibit high flow variability, which is primarily determined by the El Niño Southern Oscillation (ENSO) climate phenomenon (Walker *et al.*, 1995; van Dijk *et al.*, 2013).

Large floodplains, or 'floodscapes', are formed on the lowlands of these large alluvial rivers where the valley floor widens in a downstream direction and river flow velocity decreases to form low energy environments (Thoms *et al.*, 2016). Floodplain complexity is characterised by a diverse mosaic of landforms (such as channels, flats and basins), which provide the physical template for wetland habitats (Semeniuk and Semeniuk, 2011; Thoms and Parsons, 2016). The presence of water drives the productivity of floodplain wetlands as floodplains are variably inundated by the lateral overflow of their associated rivers producing a dynamic mosaic of wet and dry habitats. Vegetation communities of the floodplain landscape also reveal a heterogenous mosaic distribution which together with landform and variable inundation patterns begin to characterise inland floodplain wetlands (see Figure 3.3).

Figure 3.2 Inland floodplain wetland distribution in the MDB

Insets show locations of example inland floodplain wetlands: A: 1.Gwydir wetlands, 2. Narran Lakes, 3. Macquarie Marshes, and B: 4. Booligal wetlands, 5. Great Cumbung Swamp, 6. Lower Murrumbidgee (Lowbidgee floodplain), 7. Barmah-Millewa Forest Swamps

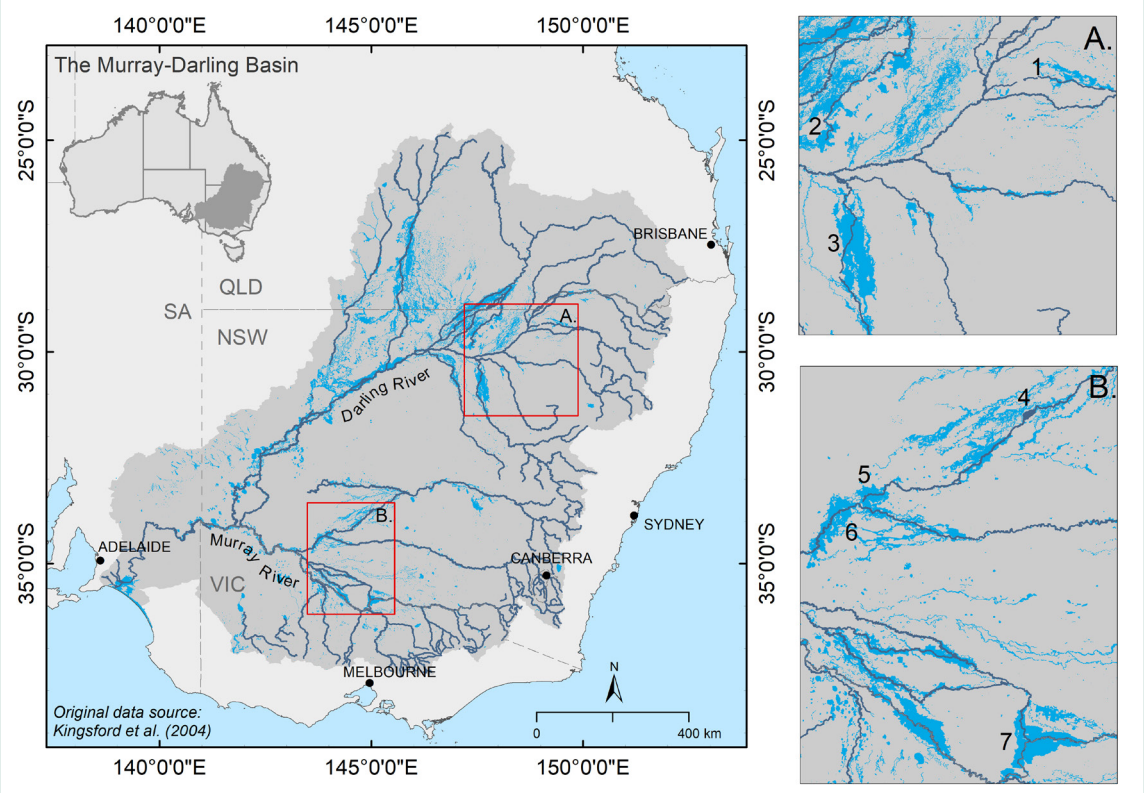

Figure 3.3 Mosaics of inland floodplain wetland types

a. Grassland-sedgeland-herbland swamps with open water lakes and lagoons

1. Common reed grasslands in the Macquarie Marshes

2. Common reed grasslands in the Great Cumbung Swamp at the terminus of the Lachlan River

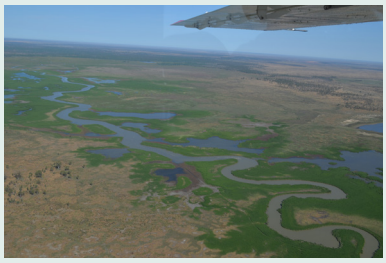

3. Rushlands in and around Moira Lake in Millewa Forest of the Murray River

b. Lignum shrubland swamps with open water lakes and lagoons

1. Narran Lakes system

2. Booligal wetlands

3. Lowbidgee floodplain

c. river red gum forest and woodlands with open water lakes and lagoons

1. Lowbidgee floodplain including Piggery Lake

2. Mid-Murrumbidgee Yarradda Lagoon, an oxbow lagoon amongst river red gum woodlands

3. Macquarie Marshes

Source: Copyright © to photographers: Rachael Thomas (a1, b1); Joanne Ocok (a2); Paul Packard (b2, b3); Vince Bicello (a3);James Dyer (c2); Simon Hunter (c1); Bill Johnson (c3)

High variability of flows drives the ecological 'boom' and 'bust' of these floodplain systems. Flooding of habitats triggers a series of dynamic ecological processes that produces a huge increase in species biodiversity and abundance for which inland floodplain wetlands are recognised (Bunn *et al.*, 2006; Kingsford *et al.*, 1999). Accordingly, many are in protected areas (such as National Parks or Nature Reserves) and some are also recognised as Wetlands of International Importance under the Ramsar Convention for supporting unique wetland habitat, rare and threatened species, and providing important habitat for waterbirds (Pittock *et al.*, 2015; see Section 2.6). Many of the MDB rivers are regulated by large dams and weirs built to support agricultural production and this has altered flows and impacted the ecology of inland floodplain wetlands (Kingsford, 2000; Kingsford *et al.*, 2015). Environmental flows are managed in the MDB to mitigate the impacts of river regulation by restoring flow and flooding regimes for the ecological requirements of the system (Arthington, 2012; Swirepik *et al.*, 2016).

Hydrology

Highly variable river flows, or flow regimes, drive the dynamics of hydrological connectivity in riverine landscapes, influencing the longitudinal (in-channel river flows), lateral (overbank floodplain and wetland inundation) and vertical connectivity (groundwater) pathways that shape and sustain the riverine landscape (Walker *et al*., 1995; see Figure 3.4). Flow regimes connect instream and fringing habitats longitudinally along rivers, and laterally across wetland and low-lying floodplain habitats through the variable nature of hydrological connectivity: from low flows, to small and large freshes, to bankfull and overbank wetland inundating flows.

Ecologically important aspects of the flow regime are characterised by the magnitude (extent), duration, timing and flood frequency (Poff *et al*., 1997). Flow and flooding regimes describe the hydrological variability in relation to the ecological function they support, for example, nutrient cycling, growth, breeding, migration, and dispersal of plants and animals. The most influential driver of inland floodplain wetland ecosystems is variations in flooding regime (lateral connectivity), which produce a dynamic heterogeneous mosaic of wet and dry habitats across the floodplain (Bunn and Arthington, 2002; see Figure 3.5).

Figure 3.4 Longitudinal, lateral and vertical hydrological pathways

Hydrological pathways connect inland floodplain habitats with the variations of the flow regime.

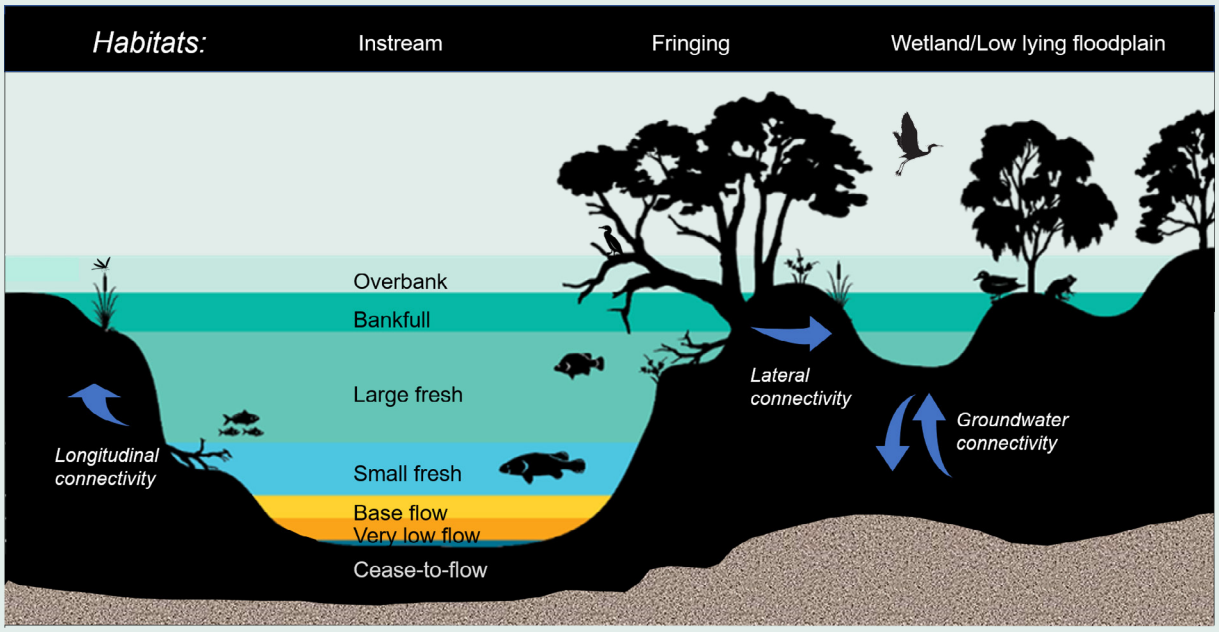

Adapted from: DPIE Long-term Water Plans (DPIE, 2020)

Figure 3.5 Inundation patterns

The distribution of variable inundation patterns during a five year period (2014–2019) across the inland floodplains of the Lower Murrumbidgee (Lowbidgee) and Lower Lachlan is shown below. This is based on annual inundation maps derived from satellite imagery using mapping methods modified from Thomas *et al.* (2015).

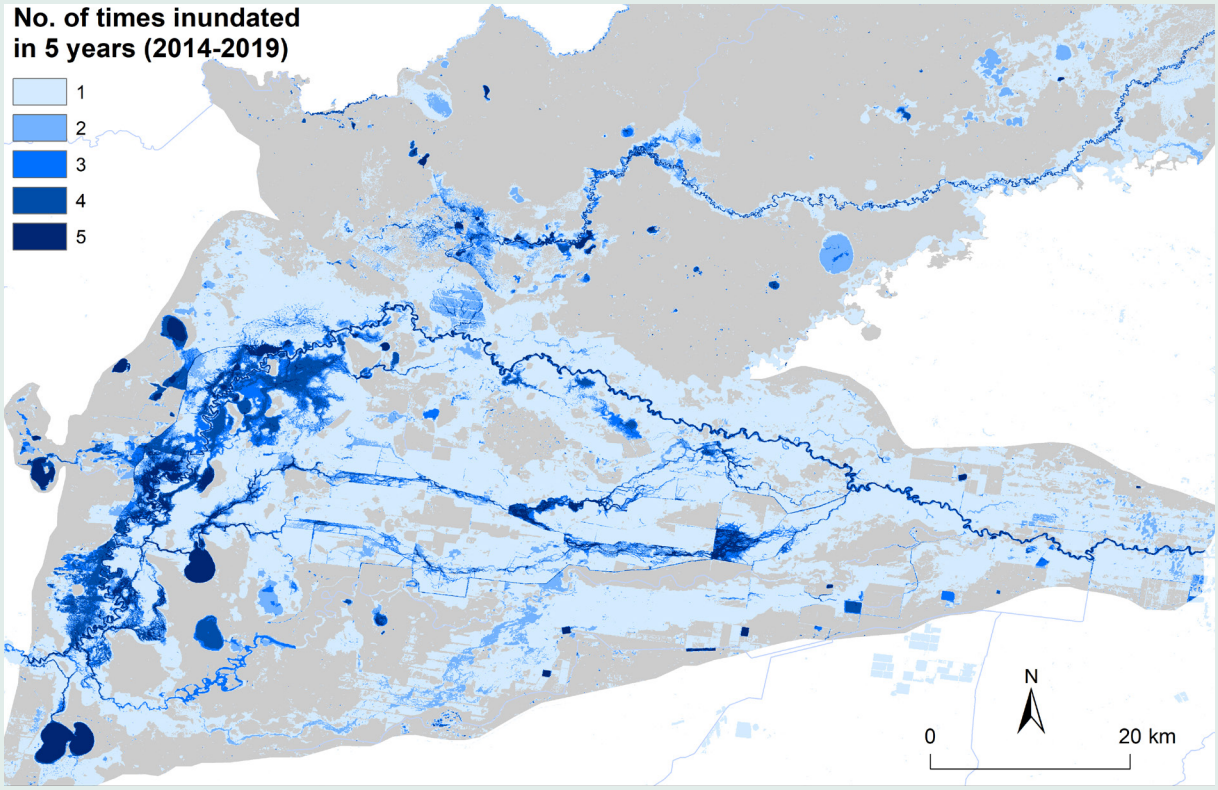

Floodplain wetland types

The components that characterise floodplain wetlands are diverse landforms, the inundation regime, and vegetation cover types (see Figure 3.6). Vegetation in the inland floodplains of the MDB is distributed as a mosaic with low tree diversity and a high diversity of understorey/wetland plant species that transition from dry- to wet-adapted species when inundated (Roberts *et al.*, 2016). Different types of inland floodplain wetland vegetation rely on specific ecological water regimes for their growth, survival, and reproduction.

As detailed below, four common types of inland floodplain wetlands in the MDB (see Figure 3.6) are:

- floodplain lakes and lagoons, which retain areas of open water and include aquatic plant species;
- herbaceous swamps, which include aquatic plants, forbs, grasslands, sedgelands, and rushlands;
- floodplain shrubland swamps; and
- tree swamps (Eucalypt forests and woodlands).

The resulting vegetation mosaic provides many functional fauna habitats for waterbirds, fish, frogs, turtles, and invertebrates.

Figure 3.6 Conceptual models of common inland floodplain wetlands in MDB

a. Floodplain lakes and lagoons (e.g. lagoons of the Mid-Murrumbidgee, Narran Lakes, Macquarie Marshes, Lachlan)

b. Grassland-sedgeland-herbland swamps (e.g Gwydir, Great Cumbung Swamp, Macquarie Marshes)

c. Floodplain shrubland (lignum) swamps (e.g. Lowbidgee floodplain, Narran Lakes system, Booligal wetlands)

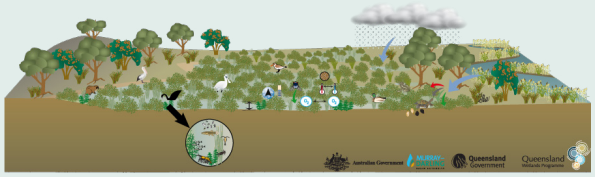

d. Tree swamps (Eucalypt forests and woodlands; e.g. Macquarie Marshes, Lowbidgee, Barmah-Millewa forests)

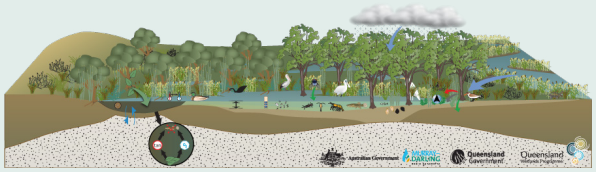

Source: QDES (2013) © WetlandInfo, Department of Environment and Science, Queensland

Lakes and lagoons

Naturally occurring lakes and lagoons on inland floodplains are a basin landform and vary in size (from a few to thousands of hectares), shape (e.g. circular, oxbow), and depth (< 1–5 m deep; see Figure 3.3 and Figure 3.7). Together, the varying connectivity with associated creeks, overland flows, and lake geomorphology influence the flooding regime dynamics of lakes and lagoons. These waterbodies provide a wide variety of habitat types in patches of deep and shallow open water, submerged aquatic vegetation, mudflats along the shoreline, and a vegetated littoral zone of emergent grasses, sedges, shrubs, or trees, which enable diverse and abundant communities of invertebrates, fish, frogs, and waterbirds to shelter, feed and breed. Waterbirds that are commonly found in lakes and lagoons are those that dive for food (e.g. cormorants), or forage on aquatic plants in deep water (e.g. black swans, ducks) or along the shoreline (e.g. shorebirds). The debris from floating and submergent aquatic plants provide breeding habitats for duck species. When flooded, lakes and lagoons provide open water habitat, retaining water in an otherwise dry floodplain landscape after floodwaters have receded in adjacent areas to function as important refugia between flood events.

Grassland-sedgeland-herbland swamps

Inland floodplain wetlands dominated by grassland, sedgelands, or herblands occur on varied landforms, including basins, flats, and channel networks, which influence lateral connectivity, water depth, and subsequent inundation regime dynamics (see Figure 3.3). There is a high diversity of grassland, sedgeland, and herbland plant species found in inland floodplain wetlands, which can be individually widespread across the MDB, but their species assemblage distribution is primarily in response to water availability and the variations in depth, duration, and frequency of flooding (see Figure 3.7). Many of these plant species are functionally related in their response to water regimes: terrestrial (dry, damp), amphibious (tolerator, responder), and submerged (emergent, submerged; Casanova, 2011). After flooding there is an increase in habitat heterogeneity, plant species, cover, and height. Plant communities can be monospecific or heterogenous in their species assemblage composition. They provide the architectural habitat structure for fauna to shelter, take refuge, forage, and breed.

Grassland plant species typically found in inland floodplain wetlands are usually perennial and morphologically diverse:

- tall (1–3 m, such as the common reed, *Phragmites australis*)—can form vast and dense monospecific grassland swamps, most notably in the Macquarie Marshes and the Great Cumbung Swamp (see Figure 3.3). Tall and dense emergent cover in shallow water provides structural habitat for cryptic waterbird species, such as the Australasian bittern, and nesting substrate for coots and grebes. When adjacent to open water lagoons, common reed is an important waterbird breeding habitat for colonial nesters.
- mat-forming—occur on most riverbanks of western MDB rivers, but sometimes they can form extensive grasslands as occur on the Gwydir floodplain and in the Macquarie Marshes (see Figure 3.3).
- tussock—grow as isolated clumps typically in flat, shallow wetlands with turbid waters and are distributed most extensively in the hotter and drier parts of the north and west of the MDB (see Figure 3.3); and

- aquatic—grow in flooded wetlands with long buoyant stems floating on the water surface (Roberts and Marston, 2011).

Sedgelands are a diverse plant group that occurs in the inland floodplain wetlands of the MDB (Roberts and Marston, 2011). They can occur in a range of shallow water and wet-dry habitats and form dense stands of entire wetlands or understories of forests and woodlands. Sedgelands provide important refuge habitat for frogs, foraging grounds for swamp hens and ducks, and breeding habitat for brolgas. For example, Marsh Club-rush (*Bolboschoenus fluviatilis*) is a tall (1–2 m) perennial sedge, which occurs as small patches or as extensive monospecific stands. It is listed in NSW as a critically endangered ecological community with the most significant stand occurring in the inland floodplain wetlands of the Gwydir River (see Figure 3.2). The widespread perennial tall (2–3 m) emergent rush species of Cumbungi (*Typha domingensis* and *T.orientalis*) are widely spread across most inland floodplain wetlands because they grow in the water or on the mudflats of wetlands that have permanent, near-permanent, or seasonal water regimes. Cumbungi typically forms dense mono-specific stands in patches or as a littoral fringe around lakes, lagoons, and in rivers, and provides suitable refuge habitat for a range of cryptic waterbirds, shelter for small fish fish and frogs, and breeding habitat for cryptic waterbirds or colonially nesting waterbirds.

Herblands comprise a diverse and dynamic group of plants that transition from dry- to wet-adapted species when inundated so can be aquatic, amphibious, or terrestrial. Aquatic plants grow while inundated, whereas amphibious plants tolerate wetting and drying and persist during the drying phase as floods recede. Terrestrial plants also develop during the drying phase and then dominate the dry phase. Herblands can occur on the lakebeds or shoreline, in riverbanks or riverbeds, or can be part of the larger vegetation mosaic that includes forests, woodlands, and shrublands.

Shrubland (lignum) swamps

Lignum (*Duma florulenta*), a multi-stemmed shrub, is the most ecologically significant inland floodplain shrub species occurring on the floodplains of most major rivers in the MDB (Roberts and Marston, 2011). Flooding is the main influencer of lignum growth, and flood frequency strongly affects the size and vigour of individual shrubs, which can grow to 3 m in height, diameter and width to form extensive and dense shrublands. Lignum is often associated with other shrub species and is also an important structural component of the understorey of many woodland communities, especially those of river cooba (*Acacia stenophylla*), river red gum (*Eucalyptus camaldulensis*), black box (*E. largiflorens*), and coolibah (*E. coolabah*). During extensive flooding the structure of lignum shrublands is flattened and becomes significant habitat for colonial-nesting waterbirds, by providing a nesting platform that protects them from rising floodwaters whilst near foraging habitat (Brandis *et al*., 2011). During flooding, lignum shrubland swamps also provide important sheltering habitat for fish, frogs, and aquatic invertebrates, whereas during dry periods they provide niche habitat for understorey herbs to grow (Freestone *et al*., 2017).

Eucalypt forests and woodlands

In the riverine systems of the MDB, the most widely distributed tree is the river red gum (*E. camaldulensis*) which forms extensive forest and woodland habitat across the entire Basin (Roberts and Marston, 2011). The other woodland tree species that dominate inland floodplain wetlands are black box (*E. largiflorens*), distributed from the central Basin to southwestern rivers, and coolibah (*E. coolabah*), which is distributed from central to northwest regions. Forests tend to be confined to frequently flooded locations, whereas woodlands are located in more variably flooded regions. River red gum forests and woodlands growing along the riverine habitat of the main rivers and tributaries that connect wetlands provide important corridors for movement of fauna especially waterbirds. They also provide important fish habitat within channels through fallen trees and branches, providing cover from predatory birds and other fish, feeding and breeding locations, and refuge from the current. Tree canopies of river red gums moderate temperature by providing shade over rivers and swamps (see Figure 3.7). River red gum litter provides one of the most important biologically accessible carbon sources to inland floodplain habitats that are influenced by highly variable flow regimes (Francis and Sheldon, 2002). Forest and woodland tree canopies and hollows provide important habitat for roosting and breeding waterbirds. Woodland trees are important habitats for a range of fauna because they provide canopy, hollows, and fallen logs, which are not otherwise available in adjacent shrublands or grasslands (Roberts and Marston, 2011). Understorey composition of river red gum, coolibah, and black box forests and woodlands varies with inundation regimes (e.g. aquatic plant species, sedgelands, grassy-herblands), which provides the ecological character of the tree habitat.

Figure 3.7 Examples of common inland floodplain wetlands in the MDB

a. Inundated lagoon with aquatic vegetation species in the Murrumbidgee River system

b. Inundated sedgeland swamp in the Gwydir wetlands

c. Lignum shrubland swamp in the Lowbidgee floodplain

d. Inundated river red gum forest with an aquatic plant species understorey in the Macquarie Marshes

Copyright © to photographers a. Carmon Amos; b. Joanne Ocock; c. Sharon Bowen; d. Rachael Thomas

Fauna

The mosaic of inland floodplain wetland habitats supports a diversity of fauna, sometimes in high abundance, and often at critical life cycle stages (Roberts and Marsden, 2011). Waterbirds, fish, frogs, and other dependent fauna, including freshwater crabs and mussels, snails, water rats, and snakes, rely on these important habitats, so are often found throughout the inland floodplain wetlands of the MDB.

Waterbirds

Inland floodplain wetlands across the MDB form a large landscape of strategically located diverse habitats to which waterbirds will travel large distances to find temporary wetland resources so they can breed, feed, and take refuge in an otherwise dry landscape (Kingsford *et al.*, 2010). These wetland habitats are critical for supporting a high diversity of waterbirds (> 165 species in the Murray-Darling).

During times of increased water availability (flooding) inland floodplain wetlands (vegetated swamps, floodplains and lakes) support high abundances of waterbirds (e.g. 300,000 waterbirds; Kingsford and Thomas, 1995) and when water is scarce, rivers and lake habitats provide critical refugia (Bino *et al.*, 2015). Waterbird species have similar feeding and habitat preferences and can be grouped on the basis of these ecological requirements (Kingsford *et al.*, 2010; Spencer *et al.*, 2010):

- dabbling and diving ducks—feed on small invertebrates and plant material in shallow water or the littoral zone;
- herbivores—forage on plants in either deep water or at the edge of the wetlands, or in grasslands;
- piscivores—feed on fish in the main body of water of lakes, lagoons, and swamps;
- large wading birds—feed in wetlands with shallow water, grasslands, and sedgelands; while

- small wading birds (shorebirds)—are restricted to the shoreline of a wetland where there are mudflats (Kingsford *et al*., 2010; Spencer *et al*., 2010).

Several waterbird species are listed as threatened through state and Commonwealth legislations (NSW Biodiversity Conservation Act, 2016; Environmental Protection and Biodiversity Conservation Act, 1999) and migratory waterbird species that utilise inland floodplain habitats are listed under international migratory bird agreements (JAMBA, CAMBA and RoKAMBA[4]; OEH, 2012).

Diverse inland floodplain wetland habitats support waterbird nesting habitat preferences for a range of different types of waterbirds. Several inland floodplain wetlands of the MDB are globally significant Ramsar sites for waterbirds that breed in colonies (e.g. Narran Lakes, Macquarie Marshes, Gwydir wetlands, Barmah Forest; see Figure 3.2) and include some of Australia's largest waterbird breeding events ever recorded (e.g. in the Macquarie Marshes; Kingsford and Johnson, 1998). Waterbirds species can also breed in rookeries using the tree canopy of eucalypt trees in or over water, and herbivores will breed in common reeds and cumbungi.

Frogs, fish and other fauna

The variety of inland floodplain habitats supports an equally diverse range of dependent faunal species, including turtles, crustaceans, and frogs.

Frogs are an important part of these ecosystems as they are a food source for waterbirds, fish and reptiles as well as being a predator. They are a diverse faunal group but different species share similarities in their behaviours and habitat preferences (Ocock *et al*., 2016):

- marsh frogs prefer well vegetated wetlands and floodplain creeks where water levels rise when they are seasonally (or intermittently) inundated providing refuge and breeding habitat;
- tree frogs prefer woodland habitat; while
- burrowing frogs also occur in inland floodplain wetlands and are active after periods of high rainfall.

Aquatic vegetation is important for the entire frog life cycle as it provides a substrate for attaching eggs, tadpole feeding, metamorphosis, and shelter from predators (Wassens and Maher, 2011).

The inland floodplain wetland and connected river habitats of the MDB support a native fish community estimated at 46 species (Lintermans, 2007). Native fish communities respond to different conditions and so have different distributions through the MDB system. Some are restricted to the warmer water in the north, or to southern locations with access to the sea, or they vary with altitude. Fish diversity is highest in inland floodplains habitats where there are slow-flowing turbid rivers surrounded by open water lagoons, vegetated swamps, and river red gum forests.

Groups of fish species (known as guilds) have similar life spans, flow responses and habitat preferences (DPIE, 2020). The extent and condition of fish populations in the MDB have been in decline due to river regulation, impediments to fish passage, habitat degradation, and poor water quality, and many native fish species are listed as threatened or vulnerable under State or National legislation (Riches *et al*., 2016). Significant declines occurred after 2007 when there was an extreme reduction in water availability during the Millennium drought.

4 JAMBA: Japan-Australia Migratory Bird Agreement; CAMBA: China-Australia Migratory Bird Agreement; RoKAMBA: Republic of Korea-Australia Migratory Bird Agreement

3.3 Aquatic Organisms

A diverse range of organisms live in water—both freshwater and seawater. Most aquatic organisms require water, energy, carbon, and oxygen, plus the nutrients nitrogen, phosphorus, potassium, iron, sulphur, and selenium. For example, when the availability of nitrogen and phosphorus is limited, aquatic plant growth can become inhibited. The interdependence of organisms within an ecosystem can be represented in terms of a simple food chain, (see Figure 3.8). As detailed in Volume 3A, primary producers synthesise organic matter from raw ingredients via photosynthesis, so include plants and photosynthesing microorganisms. Secondary producers (herbivores, carnivores, and decomposers) assimilate organic material from other organims (living or dead).

Organisms can also be differentiated in terms of their biomass production, that is, the increase in biomass over a given time period. A productive environment accumulates biomass as living plant or animal tissue over time. The marine food chain depends on phytoplankton, which is estimated to be responsible for around 40% of the global photosynthetic activity (Falkowski, 1994). As such, the concentration of phytoplankton is viewed as an indicator of marine ecosystem health, with consequent impact on global climate stability.

Figure 3.8 Simple food chain

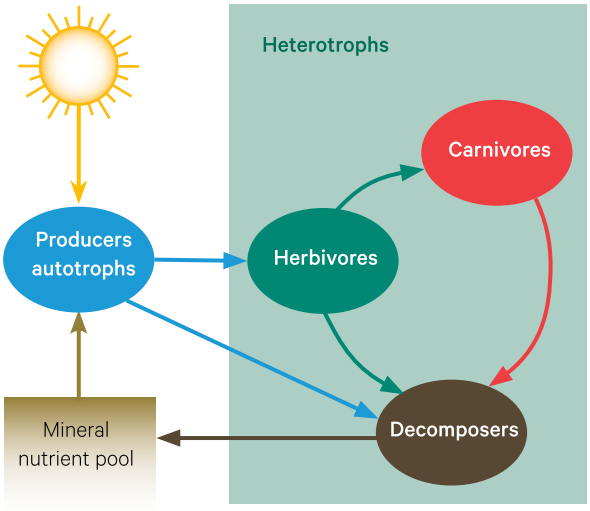

Microphytobenthos, microscopic algae, and cyanobacteria living in intertidal and aquatic sediment, are also important in aquatic ecosystems (see Section 3.3.2.1). While the productivity of phytoplankton is widely recognised, the productive capacity of the seemingly 'unvegetated' habitats that support microphytobenthos has only been investigated in recent decades (MacIntyre *et al.*, 1996). The distribution and concentration of phytoplankton, microphytobenthos, and cyanobacteria are directly related to the temperature, circulation, and nutrient content of the photic zone (see Excursus 3.2).

One approach to classifying living organisms defines three domains based on evolutionary development: Bacteria, Archaea, and Eukaryota. Species in Bacteria and Archaea are collectively known as prokaryotes, which are single-celled organisms with cell size 1–10 μm (such as cyanobacteria), whereas eukaryotes have a more complex and larger (10–100 μm) cell structure. The Plant Kingdom has also been sub-divided on the basis of reproductive characteristics and morphology (see Table 3.1; see also Volume 3A—Excursus 1.1;).

In this sub-volume, aquatic organisms will be considered in terms of four broad groupings:

- microorganisms—an imprecise label for microscopic life forms, including viruses, bacteria, fungi, and protozoa (see Section 3.3.1);
- algae—photosynthesising plant-like organisms (without roots, stems, or leaves), both microscopic and individually visible, that are either attached to the substratum or suspended in the water column (see Section 3.3.2);
- plants—photosynthesising organisms, which may be attached to the substratum or suspended in water (see Section 3.3.3); and
- animals—both vertebrates and invertebrates (see Section 3.3.4).

Aquatic biota that occur in the water column are further discussed in Section 5.3.

Table 3.1 The plant kingdom

Angiosperm class names are based on the Cronquist system. Note that since cyanobacteria is classified as bacteria, it is not included in this table.

Sub-Kingdom	Division	Major sub-groups
Cryptogamae (non-flowering and non-seeding plants; reproduce via spores)	Thallophyta (algae and fungi; non-vascular)	Bacillariophyta (diatoms)
		Charophyta (stoneworts)
		Chlorophyta (green algae, ~8,000 species)
		Chrysophyta (golden brown algae)
		Haptophyta/ Prymnesiophyta (e.g. Coccolithophorids)
		Pyrrophyta/Dinophyta (dinoflagellates, ~200 species)
		Phaephyta (brown algae—kelp)
		Rhodophyta (red algae, ~6,000 species)
		Glaucophyta (rare freshwater algae)
		Tribophyta (yellow-green algae)
	Bryophyta (non-vascular)	Hepaticae (liverworts)
		Anthocerotae (hornworts)
		Musci (mosses)
	Pteidophyta (vascular)	Psilopsida (two small genera of fern-like plants)
		Lycopsida (club mosses; five genera with > 1000 species)
		Equisetopsida (horsetail; one genus)
		Pteridopsida (ferns; ~9,000 species)
Phanerogamae (or Spermatophyta: seeding plants with roots, stems, and leaves)	Gymnospermae (non-flowering; seed not enclosed in fruit)	Cycadophyta (one genus: *Cycadaceae*; < 200 species)
		Ginkgophyta (one genus and species: *Ginkgo biloba*)
		Coniferophyta (two orders: Pinales and Taxale; ~200 species)
		Gnetophyta (three genera; ~ 100 species)
	Angiospermae (flowering plants)	Liliopsida (monocotyledons—one seed leaf; ~60,000 species)
		Magnoliopsida (dicotyledons—two seed leaves; ~200,000 species)

3.3.1 Microorganisms

By definition, individual microorganisms are too small to see with the naked eye, but colonies can become visible. These organisms exist in large quantities in all ecosystems. They play an essential role in aquatic ecosystems via photosynthesis and/or decomposition.

3.3.1.1 Viruses

Viruses are prevalent in surface waters, just as they are in terrestrial environments, with the highest abundance appearing to occur in coastal waters and sediments. They comprise the greatest genetic diversity in the ocean and can migrate between inland and marine waters.

Viruses catalyse the movement of nutrients from a range of organisms (phytoplankton, grazers, carnivores and bacteria) to the 'pools' of dissolved organic matter (DOM) and particulate organic matter (POM). While their importance in aquatic environments has only been recognised in recent decades (Suttle, 2005), they have significant impacts on the composition of planktonic communities (Weinbauer and Rassoulzadegan, 2004), as well as cycling nutrients and energy from living organisms to dissolved forms (Wilhelm and Suttle, 1999). Such cycling is significant for the global carbon cycle (see Section 1.5).

3.3.1.2 Bacteria

Bacteria are abundant in most aquatic environments (both marine and inland waters), and often enter a waterbody in runoff from adjacent land. Bacteria include some of the smallest known organisms and can reproduce very rapidly. They inhabit decaying material and hard surfaces, or suspend in water. Photosynthesising bacteria are predominantly prokaryotic cyanobacteria. While these organisms are commonly called blue-green algae, they are not true plants but belong to the kingdom Monera (see Section 3.3.2.1 and Excursus 3.2). Non-photosynthesising bacteria absorb dissolved organic compounds from their surroundings.

3.3.1.3 Fungi

Fungi can be single-celled organisms or filaments (hyphae). These non-photosynthesing organisms are also abundant in aquatic ecosystems and help to decompose plant material, especially material containing cellulose and lignin, by dissolving the absorbing organic compounds.

3.3.1.4 Protozoa

Protozoa are single-celled organisms that consume bacteria, algae, and other protists (see Volumes 1 and 3A). Some protozoa are parasites and induce disease.

3.3.2 Algae

The non-taxonomic term 'algae' is used to describe a variety of plant-like organisms without vascular tissue to internally transfer water and nutrients (that is, without true roots, stems, or leaves). While not classified as plants botanically, for convenience algae are often included in aquatic plant groupings. These photosynthesising organisms grow in both marine and inland waterbodies and can be considered in terms of two size groups:

- microalgae—diverse group of unicellular aquatic organisms, such as cyanobacteria, that exist in the water column or benthos (see Section 3.3.2.1); and
- macroalgae—eukaryotic organisms with compartmentalised cells and simple plant-like structures, such as kelp (see Section 3.3.2.2).

3.3.2.1 Microalgae

Microscopic algae, such as phytoplankton, can exist as single cells, chains, or colonies (see Section 5.3.1). The structure of these microorganisms allows them to suspend in calm water, or propel through the water column (Biocyclopedia, 2019). Their rapid production mechanisms supply most of the world's oxygen via photosynthesis, and help to absorb nutrients and heavy metals. In excess, however, they can result in algal blooms and deterioration of water quality (Entwisle *et al.*, 1997; see Sections 4.6 and 19.5).

The term microalgae encompasses both phytoplankton and microscopic algae living in the benthos, with the same classes of algae occurring in each group (see Excursus 3.2). The term 'microphytobenthos' encompasses photosynthesising microorganisms that inhabit the surface layers of intertidal, subtidal and submerged sediments, and includes unicellular eukaryotic algae (Baccilariophyceae, Chlorophyceae and Dinophyceae) and prokaryotic Cyanobacteria (MacIntyre *et al.*, 1996). However, depending on water depth, movement and particulate content, the distinction between phytoplankton and microphytobenthos can become unclear (MacIntyre *et al.*, 1996).

Rising ocean temperatures will likely increase stratification of the water column and reduce nutrient input into the photic zone. This will increase the likelihood of nutrient limitation in marine microalgae, leading to changes in the abundance and composition of phytoplankton communities, which in turn will affect global biogeochemical cycles.
Gerecht et al. (2014)

Excursus 3.2—Phytoplankton Groups

The most common groups of phytoplankton are listed in Table 3.2 and some of their diverse forms are illustrated in Figure 3.9. Over 5,000 species of marine phytoplankton have been identified globally (Sournia *et al.*, 1991).

Cyanbacteria, or blue-green algae, have the cell structure of primitive bacteria. They prefer calm, warm nutrient-rich water with high pH, as occurs during drought conditions, and can multiply extremely rapidly in suitable conditions to form a thick, green scum. While some species are sometimes toxic, all can produce contact irritants, and some change the colour and taste of water. As such, they present a threat to livestock and recreational water users.

The largest and most diverse phytoplankton group is diatoms, which are generally coloured brown or yellow. These organisms require silica for their cell wall. Their abundant presence has little impact on the taste or smell of water. They have been estimated to account for up to 20% of the global carbon fixation via photosynthesis, more than the combined contribution from tropical rainforests (Mann, 1999).

Dinoflagellates are capable of independent movement and will alter the taste and odour of water in large numbers. Some species are toxic, as occasionally occur in red tides. Green algae do not usually impact the taste of water unless a large population is present.

Table 3.2 Most common phytoplankton groups

Group	Description			
	Form	Occurrence	Trophic mode	Example
Cyanobacteria	Bacteria	Marine, freshwater, and terrestrial	Autotrophic	Blue-green algal blooms; spirulina
Diatoms	Unicellular or colonial coccoid algae	Marine, freshwater, and terrestrial	Autotrophic and heterotrophic	Ubiquitous in moist habitats; commonly used for environmental assessment
Dinoflagellates	Flagellate protists	Marine and Freshwater	Autotrophic and mixotrophic	*Noctiluca scintillans*, which can cause red tides
Chlorophyta (Green algae)	Unicellular colonial flagellates	Marine and Freshwater	Autotrophic	Chlorella
Coccolithophores	Unicellular eukaryote	Marine waters	Autotrophic	Important primary producers that thrive in warm, nutrient-poor waters

Figure 3.9 Phytoplankton forms

Phytoplankton are extremely diverse, varying from photosynthesizing bacteria (cyanobacteria), to plant-like diatoms, to armor-plated coccolithophores. Note: drawings are not to scale.

a. Cyanobacteria b. Diatom c. Dinoflagellate d. Green algae e. Cocolithophore

Source: Sally Bensusen, NASA. Retrieved from *https://upload.wikimedia.org/wikipedia/commons/archive/8/8a/20190514231026%21Phytoplankton_types.jpg*

Macroalgae ('seaweeds') are an ancient class of large multicellular plants that resemble vascular plants but lack the complex array of tissues used for reproduction and water transport.
OzCoasts (2018)

3.3.2.2 Macroalgae

This term 'macroalgae' collectively applies to algae that are visible to the naked eye (Diaz-Pulido and McCook, 2008). These multi-celled organisms feature a variety of shapes, sizes, and structures, and can occupy a variety of habitats. They extract nutrients from the water column and can be anchored to hard surfaces in the benthos by simple root-like structures called holdfasts (Entwisle *et al.*, 1997).

Macroalgae are traditionally described in terms of their photosynthetic pigments, and include (see Table 3.3):

- green algae (Division Chlorophyta), for example *Ulva lactuca* (sea lettuce);
- brown algae (Class Phaeophyceae in Division Heterokontophyta), including large kelps; and
- red algae (Division Rhodophyta), such as crustose coralline algae (Diaz-Pulido and McCook, 2008).

As indicated in Table 3.3, a range of photosynthetic pigments have been found in algae. These pigments are located as macromolecular complexes within the chloroplast (Jeffrey and Vesk, 1997). For example, the pigments phycoerythrin and phycocyanin are phycobilins, efficient light-trapping molecules that occur in some algal species (see Table 3.3). These pigments are bonded to water-soluble proteins called phycobiliproteins, which transfer the light energy to chlorophyll pigments for photosynthesis. This mechanism allows red algal species to grow at greater water depths than other algae. Red coralline algae, for example, grow at water depths of 268 m, the deepest of any photosynthetic organism (OzCoasts, 2018).

Many species of algae have economic value for their pigments and other components (alginates, agar, and carrageenan), which are extracted for industrial use from the flexible cell wall components. Algae provide food sources for fish, crustaceans, indigenous gourmands, food supplements (such as wakame for human and animal consumption), and fertilisers for terrestrial vegetation (Entwisle *et al.*, 1997). They are also cultivated for use in aquaculture and aquariums.

Table 3.3 Most frequently occurring algal groups

Life Form	Plants			Bacteria
Common Name	Red Algae	Green Algae	Brown Algae	Blue-Green Algae
Botanical Division	Rhodophyta	Chlorophyta	Heterokontophyta; (Class Phaeophyceaae)	Cyanophyta
Distribution	Marine habitats	Marine, freshwater and terrestrial habitats	Predominantly marine habitats	Almost every marine, freshwater, and terrestrial habitats
Diversity (Approximate # species)	5,000–5,500 globally; 1,300 in Australia	8,000 globally; 2,000 in Australia	1,500–2,000 globally; 350 in Australia	2,698 described species; over 6,000 estimated[5]
Appearance	Small and inconspicuous; diverse reddish forms growing in limited beds	Grass-green, sometimes with greyish hue	Most conspicuous; large and brown	Small and inconspicuous, unless present as algal bloom in marine or freshwater; predominantly greenish-blue, but may appear as other colours
Chlorophyll pigments	Chlorophyll a	Chlorophyll a Chlorophyll b	Chlorophyll a Chlorophyll c	Mostly Chlorophyll a; some genera have Chlorophyll b instead
Masking/accessory pigments	Phycoerythrin	Carotenoids and Xanthophylls	Fucoxanthan	Phycocyanin; Phycoerythrin
Extracts	Agar; Carrageenan	None	Alginates	Potential for biofuel

Source for most entries: Huisman (2000)

5 Nabout *et al.* (2013)

Macrophyte (from) Greek: makro meaning 'large' and phuton meaning 'plant'

3.3.3 Plants

Non-algal aquatic plants include angiosperms (flowering plants), pteridophytes (ferns), and bryophytes (mosses, hornworts and liverworts; see Table 3.1 and Volume 3A). Since all plant life forms require light for photosynthesis, the distribution of aquatic vegetation is restricted to either the upper water layers of a waterbody where light can penetrate (the photic zone—see Section 3.1) or, in shallow waters, the seafloor. The major types of aquatic plant life are commonly differentiated by their attachment to the substratum or to other plants or animals (Huisman, 2000; see Section 5.3.2).

Large aquatic plants (visible to the naked eye), or 'vascular plants in which specialised cells transport water and minerals from true roots' (Bowden *et al.,* 2017), are commonly termed macrophytes. These plants need to grow in standing water, where the water level is at or above the soil surface, or near a waterlogged environment. Being supported by water, they typically develop much less structural tissue than terrestrial plants, but contain additional air spaces to increase buoyancy. Macrophytes are traditionally described in terms of their growth habit (see Table 3.4). The form of some macrophytes can change between these categories during the seasonal cycle and/or the life cycle. Submerged plants and macroalgae are collectively known as submerged aquatic vegetation (SAV).

Commonly encountered examples of macrophytes include mangroves, seagrasses, lilies, rushes, and reeds. For example, seagrasses are vascular plants growing in coastal and inland waters that derive nutrients from the benthos via roots. While seagrass flowers are inconspicuous, seagrasses are true flowering plants (Division Magnoliophyta). They are considered to be closely related to terrestrial plants, having vascular tissue and green foliage resembling grass or leaves. Around 60 species are known worldwide, with about half of those occurring in Australia (see Section 20.3.1). While the distribution of tropical seagrasses is typically sparse, in other locations seagrasses can form dense, extensive beds in shallow coastal waters, which are important for stabilising sediments and furnishing nurseries for juvenile fish and invertebrates (Huisman, 2000).

Bryophytes lack true roots and xylem tissue. They tend to occur in faster and shallower streams than macrophytes, with harder substrates. These plants require less light than macrophytes and have been used as biomonitors for water quality (Gecheva and Yurukova, 2014).

Aquatic vegetation is vulnerable to seasonal water level changes and heavy rains. While they provide valuable habitat and food for animals and microorganisms, invasive growth can threaten ecosystem health, and reduce accessibility and the aesthetic appearance of the waterbody (Bowden *et al.,* 2017).

Table 3.4 Classification of macrophytes

Classification	Example	Characteristic of plant
Emergent (rooted)	mangroves, rushes, reeds, seagrass, cumbungi, sedges, cattails	normally erect and standing above the water surface, but some species tolerate submergence; all produce aerial reproductive organs
Floating leaved (rooted)	waterliliy, alligator weed, nardoo	permanently submerged and produce floating leaves that differ in morphology from submerged leaves in still and slow-flowing water; produce floating or aerial reproductive organs
Submerged (rooted)	mosses, bladderwort, ribbonweed, sea tassel,arrowhead, water plantain	permanently submerged; produce floating, aerial, or submerged reproductive organs
Free-floating (not rooted)	duckweed, azolla, liverwort, salvinia	not attached to the substrate; produce floating, aerial, or very rarely submerged reproductive organs

Source: Bowden *et al.* (2017) Table 13.1; Aquatic Technologies: *https://aquatictechnologies.com.au/Free+Floating+Aquatic+Weeds+Australia*

3.3.4 Animals

Aquatic animal life forms are diverse, abundant, and exist at all water depths. Aquatic animals can be grouped into three broad categories:

- benthos—those animals that live on the seafloor. As well as microscopic organisms collectively called 'microphytobenthos', benthos include immobile sponges and corals, creeping crabs and snails, burrowing worms, crustaceans and bivalves, plus barnacles and sea squirts;
- nekton—swimming animals including fish, serpents, seals, dolphins, and whales; and
- plankton—minute animals called zooplankton, most of which do not have the ability to move themselves around so tend to drift and float with water movement.

3.4 Further Information

Marine Parks

Parks Australia: *https://parksaustralia.gov.au/marine/parks/*

Australian Marine Parks Science Atlas: *https://atlas.parksaustralia.gov.au/amps*

Marine Life

Phytoplankton: *https://earthobservatory.nasa.gov/Features/Phytoplankton*

Aquatic plants and algae: *https://manoa.hawaii.edu/exploringourfluidearth/biological/aquatic-plants-and-algae/what-are-aquatic-plants-and-algae*

Algae, Phytoplankton and Chlorophyll: *https://www.fondriest.com/environmental-measurements/parameters/water-quality/algae-phytoplankton-chlorophyll/*

Macroalgae: *https://thefishsite.com/articles/macroalgae-the-facts*

Aquatic Macrophytes: *https://environment.des.qld.gov.au/__data/assets/pdf_file/0027/90783/biological-assessment-background-to-aquatic-macrophytes-collecting-data-along-a-belt-transect.pdf*

Exploring our Fluid Earth: *https://manoa.hawaii.edu/exploringourfluidearth/*

Sea Ice Ecosystems: Thomas (2017)

Marine Food Webs

NZ Science Learning Hub: *https://www.sciencelearn.org.nz/resources/143-marine-food-webs*

Marine Habitats

National Intertidal Subtidal Benthic (NISB) Habitat Classification Scheme:

Mount and Bircher (2008a, 200b);

https://www.environment.gov.au/fed/catalog/search/resource/details.page?uuid=5c6b3f45-dfce-4859-9af3-08d175e24881

Blue Habitats: *http://www.bluehabitats.org*

Regional Aquatics Monitoring Program (RAMP): *http://www.ramp-alberta.org/RAMP.aspx*

Wetlands

https://wetlandinfo.des.qld.gov.au/wetlands/ecology/aquatic-ecosystems-natural/

https://www.environment.nsw.gov.au/topics/water/water-for-the-environment

Systems for Marine Biota

Census of Marine Life: *http://www.coml.org/*

This international projection records the diversity, distribution and abundance of life in the ocean, and spawned OBIS (see below).

Global Oean Observing System for Marine Life: *https://www.goosocean.org/*

Ocean Biogeographic Information System (OBIS): *http://www.iobis.org/about/*

OBIS is a global open-access data and information clearing-house on marine biodiversity for science, conservation and sustainable development.

Online Zoological Collections of Australian Museums (OZCAM): *https://www.ozcam.org.au/*

Australia's Marine Biodiversity Hub: *http://www.marinehub.org/index.php/site/home/*

CSIRO Atlas of Regional Seas (CARS)/Oceanographic database (CSIRO Marine and Atmospheric Research)

Australian Biological Resources Study (ABRS): Numbers of Living Species in Australia and the World (Chapman, 2006, 2009)

The Codes for Australian Aquatic Biota database maintained by CSIRO Marine and Atmospheric Research (*www.cmar.csiro.au/caab*)

The Australian Faunal Directory: *https://biodiversity.org.au/afd/home*

NIMPIS (National Introduced Marine Pest Information System—part of the National System for the Prevention and Management of Marine Pest Incursions (Sliwa *et al.*, 2009)

3.5 References

Arthington, A.H. (2012). *Environmental flows: saving rivers in the third millennium*. Vol 4. University of California Press, Berkley.

Bino, G., Kingsford, R.T., and Porter, J. (2015). Prioritizing Wetlands for Waterbirds in a Boom and Bust System: Waterbird Refugia and Breeding in the Murray-Darling Basin. *PLoS ONE*, 10(7), e0132682. doi:10.1371/journal.pone.0132682

Biocyclopedia (2019). *How Algae Move* webpage: *https://biocyclopedia.com/index/algae/anatomy/how_algae_move.php*

Bowden, W.B., Glime, J.M., and Riis, T. (2017). Macrophytes and Bryophytes. Ch 13 in *Methods in Stream Ecology (Vol. 1)* 3rd *edn*. Elsevier Inc. pp. 243–271. *http://dx.doi.org/10.1016/B978-0-12-416558-8.00013-5*

Brandis, K.J., Kingsford, R.T., Ren, S., and Ramp, D. (2011). Crisis Water Management and Ibis Breeding at Narran Lakes in Arid Australia. *Environmental Management*, 48, 489–498.

Bunn, S.E., and Arthington, A.H. (2002). Basic principles and ecological consequences of altered flow regimes for aquatic biodiversity. *Environmental Management*, 30, 492–507.

Bunn, S.E., Thoms, M.C., Hamilton, S.K., and Capon, S.J. (2006). Flow variability in dryland rivers: boom, bust and the bits in between. *River Research and Applications*, 22, 179–186.

Casanova, M.T. (2011). Using water plant functional groups to investigate environmental water requirements. *Freshwater Biology*, 56, 2637–2652.

Chapman, A.D. (2006). Numbers of living species in Australia and the world. *Australian Biological Resources Study*. Canberra. 60 p.

Chapman, A.D. (2009). *Numbers of living species in Australia and the world*. 2nd edn. Australian Biological Resources Study, Canberra. 80 p. *http://www.environment.gov.au/biodiversity/abrs/publications/other/species-numbers/2009/index.html*.

DAWE (2015). *National Intertidal Subtidal Benthic (NISB) Habitat Classification Scheme* webpage, Department of Agriculture, Water and the Environment website: *https://www.environment.gov.au/fed/catalog/search/resource/details.page?uuid=5c6b3f45-dfce-4859-9af3-08d175e24881*

Diaz-Pulido, G., and McCook, L.J. (2008). Macroalgae (Seaweeds). In *The State of the Reef Report. Environmental Status of the Great Barrier Reef*. (Ed: Chin, A.). Great Barrier Reef Marine Park Authority, Townsville. ISBN: 1 876945 34 6 *http://www.gbrmpa.gov.au/__data/assets/pdf_file/0019/3970/SORR_Macroalgae.pdf*

DPIE (2020). *Long-term Water Plans for nine river catchments in NSW* webpage, NSW Government Department of Planning, Industry and Environment website: *https://www.environment.nsw.gov.au/topics/water/water-for-the-environment/planning-and-reporting/long-term-water-plans*

DWER (2021). *Aquatic and riparian vegetation* webpage, WA Department of Water and Environmental Regulation website: *https://www.water.wa.gov.au/water-topics/waterways/values-of-our-waterways/aquatic-and-riparian-vegetation*

Entwisle, T.J., Sonneman, J.A., and Lewis, S.H. (1997). *Freshwater algae in Australia. A guide to conspicuous genera*. Sainty and Associates, Sydney. ISBN 0646314084.

Falkowski, P.G. (1994). The role of phytoplankton photosynthesis in global biogeochemical cycles. *Photosynthesis Research*, 39(3), 235–258. doi:10.1007/BF00014586

Francis, C., and Sheldon, F. (2002). River Red Gum (*Eucalyptus camaldulensis* Dehnh.) organic matter as a carbon source in the Lower Darling River, Australia. *Hydrobiologia*, 481, 113–124.

Freestone, F. L., Brown, P., Campbell, C.J., Wood, D.B., Nielsen, D.L., and Henderson, M.W. (2017). Return of the lignum dead: Resilience of an arid floodplain shrub to drought. *Journal of Arid Environments*, 138, 9–17.

Gecheva, G., and Yurukova, L. (2014). Water pollutant monitoring with aquatic bryophytes: a review *Environmental Chemistry Letters*, 12, 49–61.

Gerecht, A.C., Šupraha, L., Edvardsen, B., Probert, I., and Henderiks, J. (2014). High temperature decreases the PIC / POC ratio and increases phosphorus requirements in Coccolithus pelagicus (Haptophyta). *Biogeosciences*, 11, 3531–3545. *https://doi.org/10.5194/bg-11-3531-2014*

Huisman, J. (2000). *Marine Plants of Australia*. University of Western Australia Press/Australian Biological Resources Study.

Jeffrey, S.W., and Vesk, M. (1997). Introduction to marine phytoplankton and their pigment signatures. Ch 2 in *Phytoplankton pigments in oceanography: guidelines to modern methods*. (Eds: Jeffrey, S.W., Mantoura, R.F.C., and Wright, S.W.) UNESCO, Paris.

Kalff, J. (2002). *Limnology: inland water ecosystems*. Prentice Hall, New Jersey.

Kingsford, R. (2000). Ecological impacts of dams, water diversions and river management on floodplain wetlands in Australia. *Austral Ecology*, 25, 109–127.

Kingsford, R., and Thomas, R. (1995). The Macquarie Marshes in Arid Australia and Their Waterbirds: A 50- Year History of Decline. *Environmental Management*, 19, 867–878.

Kingsford, R.T., and Johnson, W.J. (1998). The impact of water diversions on colonially nesting waterbirds in the Macquarie Marshes in arid Australia. *Colonial Waterbirds*, 21, 159–170.

Kingsford, R.T., Curtin, A.L., and Porter, J.L. (1999). Water flows on Cooper Creek in arid Australia determine 'boom' and 'bust' periods for waterbirds. *Biological Conservation*, 88, 231–248.

Kingsford, R.T., Roshier, D.A., and Porter, J.L. (2010). Australian waterbirds - time and space travellers in dynamic desert landscapes. *Marine and Freshwater Research*, 61, 875–884.

Kingsford, R.T., MacNally, R., King, A., Walker, K.F., Bino, G., Thompson, R., Wassens, S., and Humphries, P. (2015). A commentary on 'Long-term ecological trends of flow-dependent ecosystems in a major regulated river basin', by Matthew J. Colloff, Peter Caley, Neil Saintilan, Carmel A. Pollino and Neville D. Crossman. *Marine and Freshwater Research*, 66, 970–980.

Likens, G.E., Walker, K.F., Davies, P.E., Brookes, J., Olley, J., Young, W.J., Thoms, M.C., Lake, P. S., Gawne, B., Davis, J., Arthington, A.H., Thompson, R., and Oliver, L. (2009). Ecosystem science: toward a new paradigm for managing Australia's inland aquatic ecosystems. *Marine and Freshwater Research*, 60, 271–279. *https://doi.org/10.1071/MF08188*

Lintermans, M. (2007). *Fishes of the Murray-Darling Basin: An introductory guide*. MDBC Publication No. 10/07. MDBA, Canberra.

MacIntyre, H L., Geider, R.J., and Miller, D.C. (1996). Microphytobenthos: the ecological role of the Secret Garden of unvegetated, shallow-water marine habitats. 1. Distribution, abundance and primary production. *Estuaries*, 19(2A), 186–201.

Mann, D.G. (1999). The species concept in diatoms. *Phycologia*, 38, 437–495.

Mount, R.E., and Bricher, P.J. (2008a). *Estuarine, Coastal and Marine (ECM) National Habitat Map Series User Guide Version 1 February 2008*. Spatial Science Group, School of Geography and Environmental Studies, University of Tasmania. Report to the Department of Climate Change and the National Land and Water Resources Audit, Canberra, ACT.

Mount, R.E., and Bricher, P.J. (2008b). *Estuarine, Coastal and Marine (ECM) National Habitat Map Series Project Report February 2008*. Spatial Science Group, School of Geography and Environmental Studies, University of Tasmania. Report to the Department of Climate Change and the National Land and Water Resources Audit, Canberra, ACT.

Nabout, J.C., da Silva Rocha, B., Carneiro, F.M., and Sant'Anna, C.L. (2013). How many species of Cyanobacteria are there? Using a discovery curve to predict the species number. B*iodiversity and Conservation*, 22, 2907–2918. *https://doi.org/10.1007/s10531-013-0561-x*

OEH (2012). *Macquarie Marshes Ramsar Site—Ecological character description Macquarie Marshes Nature Reserve and U-block components*. Office of Environment and Heritage, Sydney.

Ocock, J., Kingsford, R.T., Penman, T.D., and Rowley, J.J.L. (2016). Amphibian abundance and detection trends during a large flood in a semi-arid floodplain wetland. *Herpetological Conservation and Biology*, 11, 408–425

OzCoasts (2018). *OzCoasts Australian Online Coastal Information* website: *https://ozcoasts.org.au/*

Pittock, J., Finlayson, M., Arthington, A. H., Roux, D., Matthews, J. H., Biggs, H., Harrison, I., Blom, E., Flitcroft, R., Froend, R., Hermoso, V., Junk, W., Kumar, R., Linke, S., Nel, J., Nunes da Cunha, C., Pattnaik, A., Pollard, S., Rast, W., Thieme, M., Turak, E., Turpie, J., van Niekerk, L., Willems, D., and Viers, J. (2015) Managing freshwater, river, wetland and estuarine protected areas. In *Protected Area Governance and Management*. (Eds: G. L. Worboys, M. Lockwood, A. Kothari, S. Feary and I. Pulsford) pp. 569–608. ANU Press, Canberra.

Poff, N., Allan, J., Bain, M., Karr, J., Prestegaard, K., Richter, B., Sparks, R., and Stromberg, J. (1997). The natural flow regime. *BioScience*, 47, 769–784.

QDES (2013). *Wetland (aquatic ecosystem) types* webpage, Wetland Info website, Queensland Department of Environment and Science: *https://wetlandinfo.des.qld.gov.au/wetlands/ecology/aquatic-ecosystems-natural/*

Riches, M., Gilligan, D., Danaher, K., and Pursey, J. (2016). *Fish communities and threatened species distributions of NSW*. NSW Department of Primary Industries, Tamworth. *https://www.dpi.nsw.gov.au/__data/assets/pdf_file/0007/669589/fish-communities-and-threatened-species-distributions-of-nsw.pdf*

Roberts, J., and Marston, F. (2011). *Water regime for wetland and floodplain plants. A source book for the Murray-Darling Basin*. National Water Commission, Canberra.

Roberts, J., Colloff, M., and Doody, T. (2016). Riverine vegetation of inland south-eastern Australia. In *Vegetation of Australian Riverine Landscapes. Biology, ecology and management*. (Eds: Capon, S., James, C., and Reid, M.) CSIRO Publishing. Clayton South, Australia

Semeniuk, C.A., and Semeniuk, V. (2011). A comprehensive classification of inland wetlands of Western Australia using the geomorphic-hydrologic approach. *Journal of the Royal Society of Western Australia*, 94, 449–464

Sliwa, C., Migus, S., McEnnulty, F., and Hayes, K.R. (2009). Marine bioinvasions in Australia. Ch 25 in *Biological invasions in marine systems*. (Eds: Rilov, G., Crooks, J.A.) Ecological Studies 204. Berlin, Heidelberg: Springer-Verlag. pp 425–437.

Sournia, A., Chrdtiennot-Dinet, M.-J., and Ricard, M. (1991). Marine phytoplankton: how many species in the world ocean? *Journal of Plankton Research*, 13, 1093–1099.

Spencer, J.A., Heagney, E.C., and Porter, J.L. (2010). *Final report on the Gwydir waterbird and fish habitat study. NSW Wetland Recovery Program*. Rivers and Wetlands Unit, Department of Environment, Climate Change and Water NSW.

Suttle, C.A. (2005). Viruses in the sea. *Nature*, 437, 356–361.

Swirepik, J.L., Burns, I.C., Dyer, F.J., Neave, I.A., O'Brien, M.G., Pryde, G.M., and Thompson, R.M. (2016). Establishing Environmental Water Requirements for the Murray–Darling Basin, Australia's Largest Developed River System. *River Research and Applications*, 32, 1153–1165.

Thomas, D.N. (Ed.) (2017). *Sea Ice*, 3rd edn. Wiley-Blackwell, New York (USA) and Oxford (UK). ISBN: 978-1-118-77838-8 664 pp.

Thomas, R.F., Kingsford, R.T., Lu, Y., Cox, S.J., Sims, N.C., and Hunter, S.J. (2015). Mapping inundation in the heterogeneous floodplain wetlands of the Macquarie Marshes, using Landsat Thematic Mapper. *Journal of Hydrology*, 524, 194–213.

Thoms, M., and Parsons, M. (2016). The physical template of Australia's floodplain landscapes. In *Vegetation of Australian Riverine Landscapes. Biology, ecology and management*. (Eds: Capon, S., James, C., and Reid, M.) CSIRO Publishing, Clayton South, Australia.

Thoms, M., Parsons, M., and Southwell, M. (2016). The physical template of Australia's rivers. In *Vegetation of Australian Riverine Landscapes. Biology, ecology and management*. (Eds: Capon, S., James, C., and Reid, M.) CSIRO Publishing, Clayton South, Australia.

Tockner, K., and Stanford, J.A. (2002). Riverine flood plains: present state and future trends. *Environmental Conservation*, 29(3), 308–330.

van Dijk, A.I.J.M., Beck, H.E., Crosbie, R.S., de Jeu, R.A.M., Liu, Y.Y. Podger, G.M., Timbal, B., and Viney, N.R. (2013). The Millennium Drought in southeast Australia (2001–2009): Natural and human causes and implications for water resources, ecosystems, economy, and society. *Water Resources Research*, 49, 1040–1057.

Vince, J., Smith, A.D.M., Sainsbury, K.J., Cresswell, I.D., Smith, D.C., and Haward, M. (2015). Australia's Ocean Policy: Past, present and future. *Marine Policy*, 57, 1–8. *https://doi.org/10.1016/j.marpol.2015.02.014*

Walker, K.F., Sheldon, F., and Puckridge, J.T. (1995). An ecological perspective on large dryland rivers. *Regulated Rivers: Research and Management*, 11, 85–104.

Ward, J.V., Tockner, K., Arscott, D.B., and Claret, C. (2002). Riverine landscape diversity. *Freshwater Biology*, 47, 517–539.

Wassens, S., and Maher, M. (2011). River regulation influences the composition and distribution of inland frog communities. *River Research and Applications*, 27(2), 238–246

WaterNSW (2021). *Riparian Zones* webpage, Water NSW website: *https://www.waternsw.com.au/water-quality/catchment/living/managing-land/riparian*

Weinbauer, M.G., and Rassoulzadegan, F. (2004). Are viruses driving microbial diversification and diversity? *Environmental Microbiol*ogy, 6, 1–11.

Wilhelm, S.W., and Suttle, C.A. (1999). Viruses and nutrient cycles in the sea. *Bioscience*, 49, 781–788.

Measureable Properties of Surface Waters

The three major categories of waterbodies (inland, coastal, and ocean) share a number of measurable properties (see Section 1.2), such as the waterbody size, surface, water column, substratum, or history. For example, some properties of the water column that can be measured in relative or precise terms include depth, temperature, transparency, and composition (chemical and/or biological). In addition to these properties of the water itself, waterbodies can vary in terms of their substratum characteristics, emergent vegetation, and the dynamics of the water surface.

The following sections introduce the variations that can occur in, and the measurement methods used for, these generic characteristics of waterbodies:

- water surface attributes—level, shape, texture, surface tension, surface temperature, floating layers, and ice cover (see Section 4);
- water column attributes—physical, chemical and biological (see Section 5);
- water substratum attributes—waterbody depth, geomorphology, composition, and benthos (see Section 6); and
- waterbody attributes—observed colour, extent and permanence, waterbody depth, carbon cycling, and dynamics (see Section 7).

Contents

4 Attributes of Water Surface 67

5 Attributes of Water Column 77

6 Attributes of Substratum 99

7 Attributes of Waterbodies 105

Background image on previous page: Sentinel-2 true colour composite image acquired on 10 February 2019 showing muddy floodwaters from the Burdekin River entering the Coral Sea, off the northern Queensland coast, potentially impacting the Great Barrier Reef. **Source:** ESA (CC-BY-SA 3.0). Retrieved from *http://www.esa.int/ESA_Multimedia/Images/2019/04/Queensland_floods*

4 Attributes of Water Surface

The most visible feature of a waterbody—from land, air, or space—is its surface layer. If the water surface is essentially transparent, features of the water column may also be visible and, for shallow waterbodies, it may also be possible to discern attributes of the substratum.

Characteristics of the water surface can both inform and belie characteristics of the waterbody. The interaction between incident radiation and the water surface is particularly important for EO of surface waters that are not covered by ice. Unlike the reflectance from terrestrial surfaces, the radiation reflected from a water surface is generally considered as 'noise', with the useful information originating below the surface. In some studies, waves or currents 'visible' on or below the water surface are used to infer water dynamics or locate floating objects (see Sections 1.4, 4.3, and 16). Typically, however, direct solar reflectance from the water surface, such as sunglint, is best avoided for optical EO of surface waters, which can be achieved by selecting imagery with appropriate illumination and sensor geometry (see Volume 1B—Section 3.5 and 2A—Section 3.2.1).

Water surfaces can vary in terms of:

- level (see Section 4.1);
- shape (see Section 4.2);
- texture (see Section 4.3);
- surface tension (see Section 4.4);
- temperature (see Section 4.5);
- floating layers (see Section 4.6); and
- ice cover (see Section 4.7).

4.1 Level

Sea level varies both in space and time, due to a range of factors including tides, waves, storm surges, and tectonic activity. Other sources of sea level variation include extraction of groundwater, seepage into aquifers, construction of reservoirs that reduce surface runoff, changes in water temperature, and melting of glaciers and ice sheets (see Sections 12.3 and 15). Sea level is also known to cycle with the seasons (see Section 12.3.2).

Traditionally the tidal datum called mean sea level (MSL) was defined as "the arithmetic mean of hourly heights of the sea at the tidal station observed over a period of time (preferably 19 years)" (AHO, 2020). Historically MSL was used as a standard geodetic reference point, from which other elevations and water depths were measured. Since space-based geodetic methods have become available (see Volume 1A—Section 3.3), the topography of our planet—including sea surface topography—has been measured and monitored more accurately and consistently, both spatially and temporally.

Figure 4.1 Global-mean sea level (GMSL) estimates

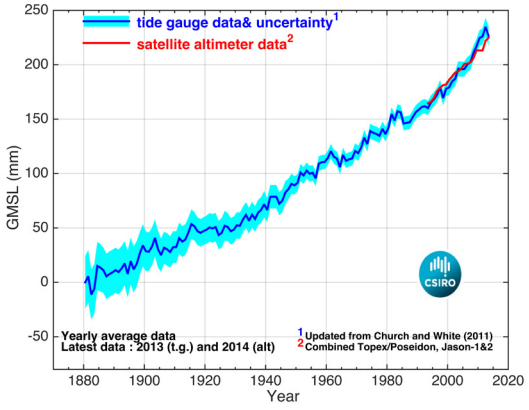

Source: Church and White (2011). Retrieved from: *https://research.csiro.au/slrwavescoast/sea-level/measurements-and-data/sea-level-data/*

Background image: An artifical inlet called the Dawesville channel, WA, links the rough water of Indian Ocean (left) to the smooth surface of the Peel-Harvey estuary (right). The difference between these water surfaces is varying Fresnel reflectance (see Section 8.1.3) of sunglint and skyglint due to ocean swell. This pseudo true colour composite image was acquired on 23 December 2014. Source: Planet Labs Inc. (CC-BY-SA 4.0). Retrieved from *https://www.planet.com/gallery/#!/post/dawesville-channel*

Figure 4.2 Change in sea surface topography 1993–2019

Colour spectrum ranges from sea surface height changes of -10 mm/yr (blue) to 10 mm/yr (red).

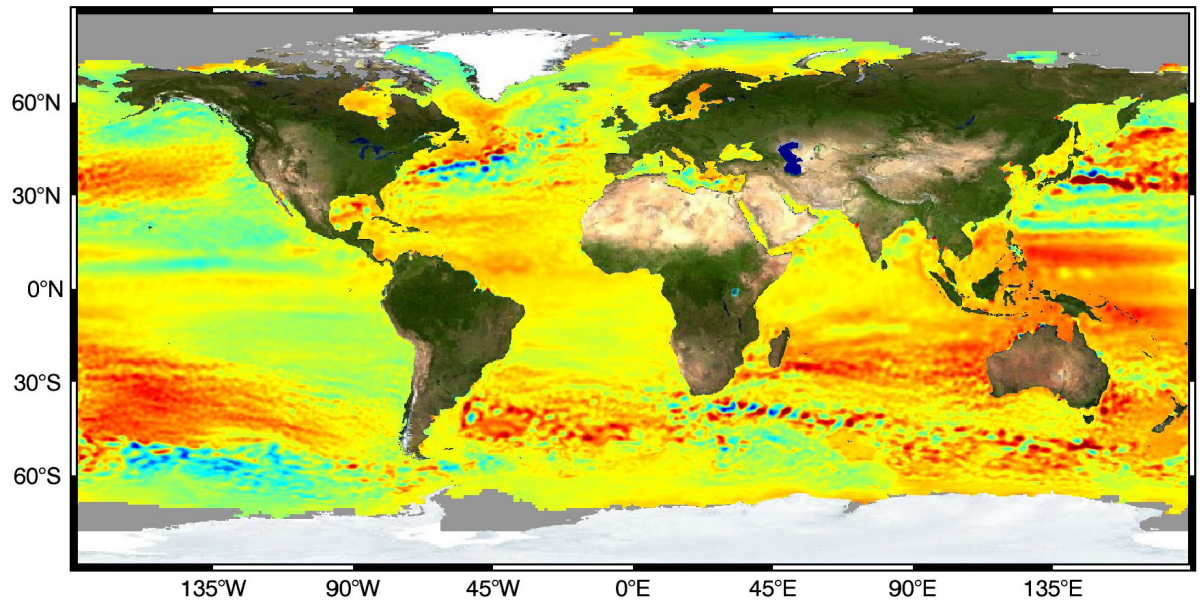

Source: NASA. Retrieved from: *https://sealevel.nasa.gov/internal_resources/185*

Traditional estimates of changes in sea level with respect to a defined datum have relied on long term averages of tide gauge measurements (see Section 12.4.2) and, in some cases, the midpoint between the mean high and low tide marks was used as a surrogate. These estimates were necessarily localised and sparse, therefore difficult to interpolate over large areas, or track with certainty through time.

The global perspective of EO sensors now allows variations in the sea surface topography to be analysed for the whole planet and compared over time. In particular, as described in Sections 9.5 and 12, satellite altimetry provides valuable data for estimating the average height of the entire ocean surface, or global-mean sea level (GMSL; see Figure 4.1).

Analyses of sea level records indicate that GMSL has been rising globally for several centuries, and predictions suggest that this trend is likely to continue and possibly accelerate (see Sections 12.5 and 12.6). For example, between 1880 and 2014, GMSL increased by 230 mm (Church and White, 2011; see Figure 4.1). The natural consequences of this trend include flooding of low-lying land and a reduction in land area, most significantly on islands (Nicholls and Lowe, 2006). In the last few decades, satellite altimetry has enabled global monitoring of sea surface height, or mean dynamic topography (see Figure 4.2). The use of EO datasets acquired by microwave sensors to map and monitor sea level is further discussed in Section 12.

4.2 Shape

Being a fluid, the shape of a water surface can vary considerably with forces within, on, above, or below the water column. There are several types of movement that can change the surface shape of natural waterbodies, including:

- tides—underlying surface rhythms for marine waters resulting from the gravitational forces of the Moon and the Sun, combined with the rotation of the Earth, that cause sea level to rise and fall (see Excursus 4.1);
- waves—generated either by water molecules on the surface being dragged along by air molecules in atmospheric winds, or by seismic activity (see Excursus 4.2);
- ripples, or capillary waves, result from some external body or pressure impacting the surface (these are quickly corrected by surface tension when the external influence is removed; see Excursus 4.2);
- internal waves—subsurface movement between layers in the water column with differing densities;
- flow—the effect of gravity on water encouraging downhill movement in rivers and streams; and
- wake—trail of recirculating water that has been impacted by a moving or stationary body.

The shape of a water surface is rarely static and can strongly influence its texture and observed colour. Resonances within partially or fully bounded waterbodies can result in oscillating standing waves called seiches. These oscillations literally cause the water to 'sway back and forth' between shores creating short term variations in water levels that can last for days, gradually diminishing back to equilibrium. Seiches typically result from atmospheric disturbances, but can also be related to seismic activity (USGS, 2018).

Excursus 4.1—Astronomical Tides

Further Information: NOAA: *https://oceanservice.noaa.gov/education/tutorial_tides/*

Ocean tides are the response of Earth's waters to the gravitational forces exerted by the Moon and the Sun. Although the Sun is 27 times larger than the Moon, it is significantly further away from Earth, which reduces its tide-generating force to 46% of the Moon's (NOAA, 2018). Since proximity matters to gravitational forces, when the Moon is closer to one side of the Earth, its pull has more impact on water on that side of the planet, creating a surface 'bulge'. On the opposite side of Earth, however, inertia creates a counter-bulge (Ross, 1995). Elsewhere, the Moon's gravitational force is balanced by inertial forces (see Figure 4.3). These tidal bulges follow the position of the Moon relative to the equator, allowing highest tides to occur at different latitudes.

During the lunar cycle, the gravitational forces of our Moon and the Sun either work together to create spring tides (at new moon or full moon) or against each other to form neap tides (at first and third quarter moons; see Figure 4.4). The balance of these forces changes gradually between two spring tides and two neap tides within each lunar cycle (see Figure 4.5).

Figure 4.3 Tidal forces due to the Moon

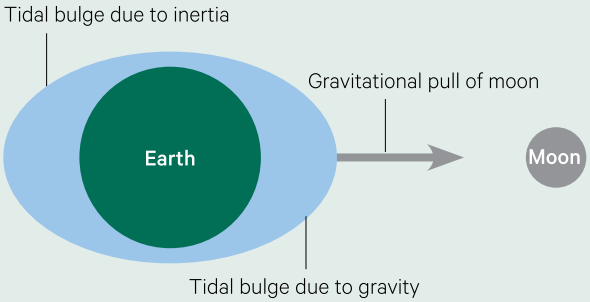

Figure 4.4 Spring and neap tides

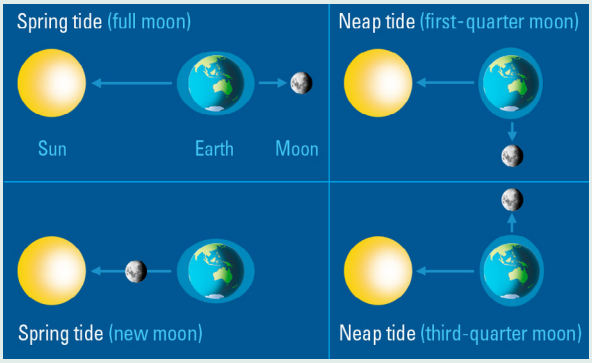

Source: COSPPar (2014)

Figure 4.5 Lunar cycle of tides

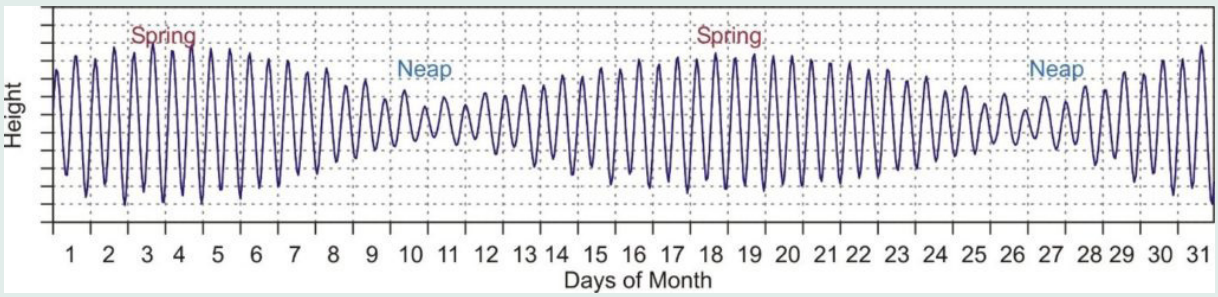

Source: CSIRO. Retrieved from: *https://research.csiro.au/slrwavescoast/extremes/causes-extreme-sea-levels/*

Tide: 1. The periodic rise and fall of the water of oceans, seas, bays, etc., caused mainly by the gravitational interactions between the Earth, Moon and Sun. (Australian Hydrographic Office Glossary)
2. A tide is a distortion in the shape of one body induced by the gravitational pull of another nearby object. (Morrison and Owen, 1996)

Figure 4.6 Types of tides

a. Semidiurnal

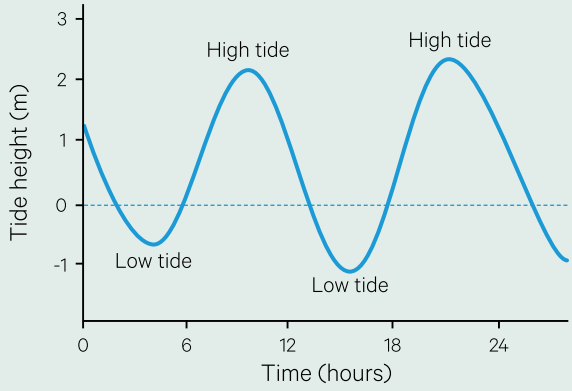

b. Mixed semidiurnal

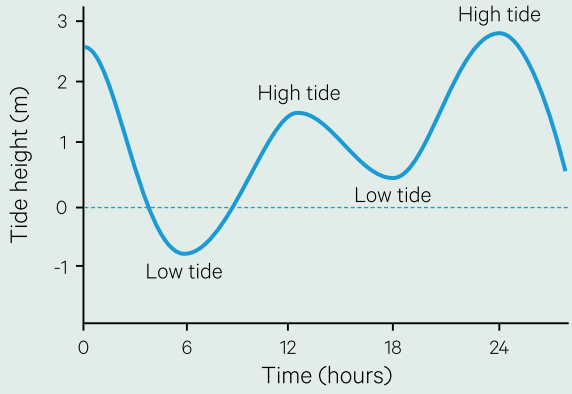

c. Diurnal

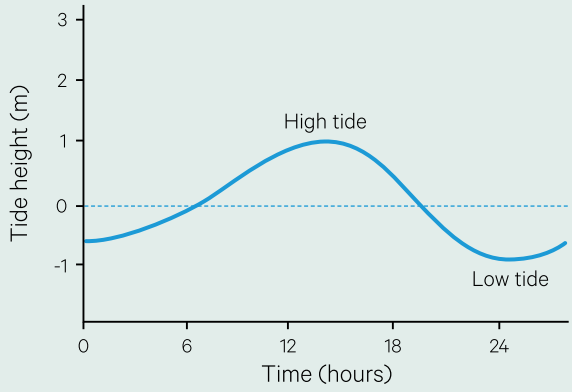

Without any topography on the Earth's surface, all locations across the globe would experience two equivalent high and low tides each lunar day. Instead, larger continents obstruct the flow of tidal bulges from west to east with Earth's rotation, resulting in complex patterns of tidal movement within each ocean basin. Accordingly, depending on the proximity of a shoreline to open ocean waters, three basic tidal patterns may be observed at a given location during each lunar day (see Figure 4.7):

- semidiurnal—the most common pattern of two high tides and two low tides of similar height;
- mixed semidiurnal—two pairs of high and low tides with different heights; or
- diurnal—only one high tide and one low tide (see Figure 4.6).

The global distribution of these three tidal patterns is illustrated in Figure 4.7.

The term tidal range is used to define the difference between high and low tide heights (see Figure 4.8), which can vary from a few centimetres in deep ocean to several metres in coastal areas (CSIRO, 2018). Tide height can also be modified by the shape and geomorphology of coastlines, bays and estuaries, tidal rivers, and local weather patterns. Since the boundary between sea and land varies with the tides, the line corresponding to the lowest astronomical tide (LAT; or, more colloquially, low tide mark) is used to define the shoreline.

Figure 4.7 Global distribution of tide cycles

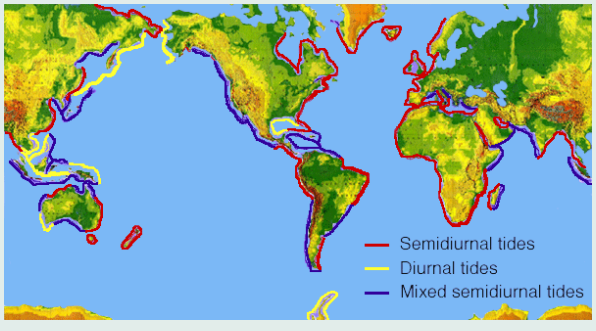

Source: NOAA (see Section 4.8)

Figure 4.8 Tidal range

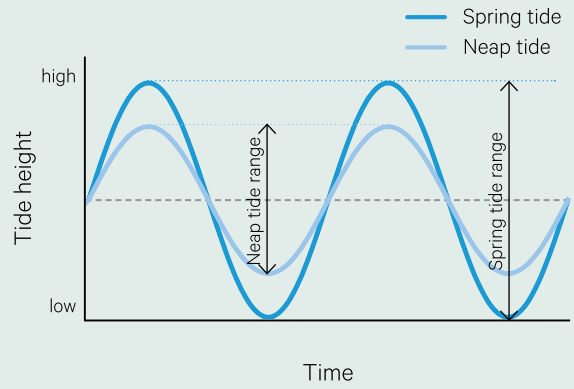

Tidal currents and tidal height are both manifestations of tides. A tidal current is said to flow (or flood), as it moves towards the high tide mark, and ebb, as it recedes to the low tide mark. Tidal currents are most noticeable when water has to flow through restrictions, as occur at the edge of the continental shelf or in passageways into bays.

Attributes of Australian tides are monitored by the National Operations Centre (NOC) Tidal Unit (see Excursus 12.2).

4.3 Texture

Water texture changes the way light is reflected from the surface. This can result in sunglint when the angle at which sunlight is reflected from the water surface is the same as the angle used to view the surface (see banner image for Section 4). Sunglint causes the water surface to appear as a mirror (bright silver, see Section 7.1). Skyglint is also reflected from the surface, but as it is mostly diffuse downwelling irradiance, the resulting surface reflectance is also diffuse. It is still affected by the angles of the water surface (due to swell, waves, and wavelets) to the incident irradiance field (as illustrated in the Section 4 banner image of the Peel-Harvey inlet on page 67.

Table 4.1 Beaufort scale

Beaufort number	Descriptive term	Wind speed (km/hr)	Description on sea	Description land
0	Calm	0	Sea surface like a mirror	Smoke rises vertically
1	Light winds	1–5	Small wavelets, ripples formed but do not break; glassy appearance maintained	Wind felt on face: leaves rustle; ordinary vanes moved by wind
2		6–11		
3		12-19		
4	Moderate winds	20–29	Small waves, becoming longer; fairly frequent white horses	Raises dust and loose paper; small branches are moved
5	Fresh winds	30–39	Moderate waves, taking a more pronounced form: many white horse are formed—chance of spray	Small trees in leaf begin to sway; crested wavelets form on inland waters
6	Strong winds	40–50	Large waves begin to form; the white foam crests are more extensive with probably some spray	Large branches in motion; whistling heard in telephone wires; umbrellas used with difficulty.
7	Near gale	51–62	Sea heaps up and white foam from breaking waves begins to be blown in streaks along direction of wind.	Whole trees in motion; inconvenience felt when walking against wind.
8	Gale	63–75	Moderately high waves of greater length; edges of crests begin to break into spindrift; foam is blown in well-marked streaks along the direction of the wind.	Twigs break off trees; progress generally impeded.
9	Strong gale	76–87	High waves; dense streaks of foam; crests of waves begin to topple, tumble and roll over; spray may affect visibility.	Slight structural damage occurs, roofing dislodged; larger branches break off.
10	Storm	88–102	Very high waves with long overhanging crests; the resulting foam in great patches is blown in dense white streaks; the surface of the sea takes on a white appearance; the tumbling of the sea becomes heavy with visibility affected.	Seldom experienced inland; trees uprooted; considerable structural damage.
11	Violent storm	103–117	Exceptionally high waves; small and medium sized ships occasionally lost from view behind waves; the sea is completely covered with long white patches of foam; the edges of wave crests are blown into froth.	Very rarely experienced - widespread damage
12	Hurricane	>118	The air is filled with foam and spray. Sea completely white with driving spray; visibility very seriously affected	Very rarely experienced - widespread damage

Source: BoM (2018b); MetOffice (2018)

The texture or roughness on the surface of a waterbody can be created by waves (see Excursus 4.2), currents, and tides (see Excursus 4.1), as well as the movement of water vehicles and recreational water users. As waves travel, refract, and break, both their texture and observed colour changes. The spatial scale of surface texture will vary with many factors, including wave height and velocity, water composition, and temperature and atmospheric influences.

Traditionally, mariners used observations of water surface roughness to estimate wind speed. Various qualitative scales were devised for this purpose until the Beaufort scale was adopted as the official, if somewhat subjective, gauge in the early 1800s. Modern versions of this scale indicate wind speed for 12 categories of surface texture (see Table 4.1). By contrast, the Douglas scale that was adopted by WMO describes wave height (see Table 4.3). More recently, however, WMO advocates the use of instruments such as wave buoys and anemometers to directly quantify wind characteristics (WMO, 2018). EO technologies that can be used to map and monitor wave activity are detailed in Section 16.

Excursus 4.2—Water Waves

Wave: 1. A periodic disturbance which moves through or over the surface of the medium (eg. water) with speed dependent upon the properties of the medium. It is characterised by frequency, length, and amplitude. 2. A ridge-like deformation, or undulation of a liquid or solid surface. (Australian Hydrographic Office Glossary)

Wind blowing over a water surface creates waves. While the wave moves horizontally, the water in the wave does not move with the wave—it just oscillates in a vertical, circular pattern. A wave 'breaks' when its base is unable to support its top, as frequently occurs in shallow water along shorelines, or when two waves collide.

Figure 4.9 Water wave

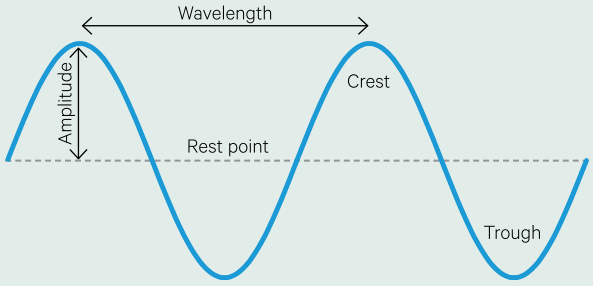

Figure 4.10 Energy spectrum of ocean waves

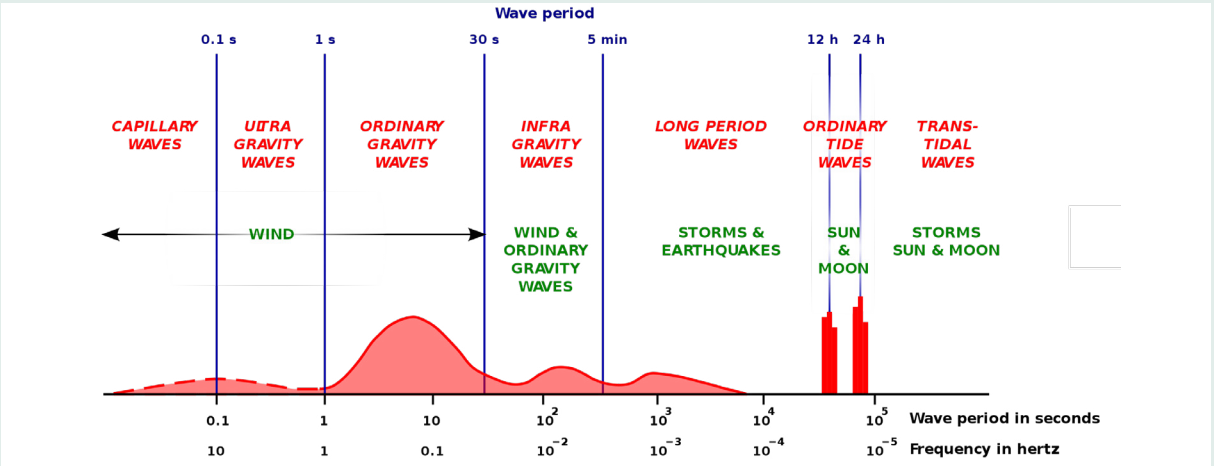

Adapted from: Munk (1950) Figure 1. Retrieved from *https://commons.wikimedia.org/wiki/File:Munk_ICCE_1950_Fig1.svg*

Table 4.2 Categories of waves

Name	Wave length (m)	Wave period (sec)	Wave phase velocity (m/sec)	Description
Capillary wave	< 0.0173	0.1	> 0.023	Ripples generated by gusts and dissipated by gravity and surface tension in less than 30 seconds by viscosity.
Wind wave	1.6–39	1–5	1.6–7.8	Generated by friction from surface winds and restored by gravity. Wave motion rapidly reduces with water depth.
Swell	156–624	10–20	15.6–31.2	Generated by turbulent surface winds and restored by gravity. Wave motion rapidly reduces with water depth.
Tsunami	200,000	1,000	200	Seismic waves have lower velocity but greater amplitude in shallow, coastal water. (Note: These figures apply to deep ocean water.)

Source: Wells (1986) Chapter 8

Wave height, the vertical distance from the wave crest to wave trough (twice the amplitude), varies with wind speed, duration, and fetch (or the distance it blows). While the wavelength is the horizontal distance between two successive crests or troughs (see Figure 4.9), the wave period is the time taken to travel one wavelength. The number of complete wave cycles in a given time unit is the wave frequency. A wave's energy or velocity is the product of its wavelength and frequency. These characteristics can be used to generate an energy spectrum for surface waves in the ocean (see Figure 4.10).

Wave characteristics are also used to classify various forms of water waves (see Table 4.2). Regular waves with longer periods are called swell waves, and result from distant weather systems (BOM, 2018a). Another type of water wave is a 'seiche', which is a standing wave that occurs in a confined space, such as an enclosed waterbody (see Section 4.2).

The term 'sea state' is used in oceanography to describe the condition of the surface of a waterbody. Sea state is determined qualitatively by observations of the surface conditions or quantified by measurements such as wave height and period. Wind waves and swell waves both contribute to sea state (BOM, 2018a). The combined effects of 'wind sea' (ten categories based on wave average height; see Table 4.3a) and swell (eight categories based on wave length, period and height; see Table 4.3b) were coded into the Douglas Scale, and adopted by the WMO.

Table 4.3 WMO Sea State tables for waves and swells

a. Ten categories based on wave height

Code	Description	Wave height (m)	Effect
0	Calm (glassy)	0	No waves breaking on beach
1	Calm (rippled)	0–0.1	No waves breaking on beach
2	Smooth	0.1–0.5	Slight waves breaking on beach
3	Slight	0.5–1.25	Waves rock buoys and small craft
4	Moderate	1.25–2.5	Sea becoming furrowed
5	Rough	2.5–4.0	Sea deeply furrowed
6	Very rough	4.0–6.0	Sea much disturbed with rollers having steep fronts
7	High	6.0–9.0	Sea much disturbed with rollers having steep fronts (damage to foreshore)
8	Very high	9.0–14.0	Towering seas
9	Phenomenal	> 14	Precipitous seas (experienced only in cyclones)

b. Eight categories based on wavelength, period and height

Description	Wave length (m)	Wave Period (sec)	Wave Height (m)
Low swell of short or average length	0–200	< 11	0–2
Long, low swell	> 200	>11	0–2
Short swell of moderate height	0–100	< 8	2–4
Average swell of moderate height	100–200	8–11	2–4
Long swell of moderate height	> 200	> 11	2–4
Short heavy swell	0–100	< 8	> 4
Average length heavy swell	100–200	8–11	> 4
Long heavy swell	> 200	> 11	> 4

Source: BoM (2018a)

4.4 Surface Tension

The intermolecular forces that hold a surface together are called surface tension. Such forces vary for different materials in different environments. The surface tension of water at 20°C is 72.8 mN/m. This is higher than most liquids and varies inversely with temperature.

The surface layer or skin of waterbodies, also known as the air-water interface, results from surface tension. This characteristic allows objects to float on the surface of fluids even when they are denser than the fluid itself. It also determines the shape of water droplets.

Pollutants, such as oil slicks and detergents, change the surface tension of water and impact its movement patterns and optical properties. Since capillary waves depend on surface tension, they are most impacted by surface films of oil and similar organic matter, and their absence can be indicative of these types of pollutants (see Section 19.4).

4.5 Temperature

Water temperature typically decreases with water depth (see Section 5.1.2). Near the water surface however, the water 'skin' experiences a miniscule region of slightly increased temperature (Donlon *et al.,* 2002; see Figure 14.4). The diurnal difference in skin temperature can vary between 0.6 K and 2.8 K (Zeng *et al.,* 1999; Heron *et al*., 2013).

Different wavelengths of electromagnetic radiation (EMR) penetrate the water surface to different water depths (see Section 5.1.4 and Volume 1B—Section 7). Thermal infrared (TIR) wavelengths only penetrate the upper 10 μm of the ocean (Sea Surface Temperature skin: SST skin), or the 'skin layer' (see Sections 5.1.3 and 14), whereas microwave sensors penetrate the upper 1 mm of the water column (SST subskin; see Section 9). Thus EO-based measurements from TIR sensors relate to the SST skin temperature, while measurements from microwave sensors represent the temperature at the lower boundary of the skin layer. Below the skin layer, temperatures vary with water column depth, and *in situ* measurements are required (and need to be recorded with the depth of acquisition; Heron *et al.,* 2013). Sea surface temperature is monitored operationally at regional and global scales using a range of EO datasets (see Section 14).

4.6 Floating Layers

The surface of a waterbody can support various types of material that float, such as algal blooms, seaweeds, sea ice, pollution, and flotsam (see Figure 1.13a). One growing source of floating matter in marine waterbodies globally is plastic debris (see Section 19.4.1). Floating layers can change the optical properties of the water surface (see Section 8.1.3) and may be indicative of local water circulation patterns (see Section 16).

The term 'algal bloom' describes a rapid increase in algae populations in freshwater or marine waters and are distinguished by discolouration of the water surface (see Section 19.5). Algal blooms occur as natural ecological responses to variations in ambient light, temperature, and nutrient levels in aquatic environments, and are most common in warm, calm, and stratified conditions in estuaries, and in coastal waters with high nutrient loads (OzCoasts, 2020).

These transient features manifest with differing speeds, extents, and intensities, depending on latitude, season, distance from shore, and the rate of grazing by zooplankton. They generally appear as coloured 'scum' on the surface of waterbodies (see Figure 4.11) but are not always visible. Some, but not all, algal blooms are harmful to other aquatic species and/or humans (see Section 19.5).

Figure 4.11 Algal bloom

An algal bloom was photographed on 10 February 2021 in the Murrray River, near its junction with the Darling River. This bloom in the foreground appears milky due to photo bleaching as it dies, in contrast with the clear water in the distance.

Source: Nathan Drayson, CSIRO

4.7 Ice cover

In polar regions, both landmasses and waterbodies may be covered with ice (and snow). Two main categories of surface ice can be defined in polar regions. These are:

- glacier ice, which accumulates (from snowfall and subsequent compaction) over a land mass and occurs in the extensive ice sheets in Antarctica and Greenland, the coastal margins of which can extend across the ocean in the form of floating glacier tongues and ice shelves; and
- sea ice, which is frozen seawater and occurs in the high-latitude waters of the Arctic region and the Southern Ocean around Antarctica (see Section 2.5. Note that sea ice also occurs in winter in certain lower-latitude regions, such as the Bohai Sea, Sea of Okhotsk, and the Baltic Sea).

While their ice-covered surfaces may appear to be similar, the formation and nature of ice in the Arctic region (around the North Pole) and the Antarctic region (around the South Pole) are quite different due to their different geographical settings and related formation and melt processes (for details see Massom, 2009). Antarctica is a frozen continent surrounded by a highly dynamic and stormy ocean, whereas the Arctic comprises a frozen ocean basin largely surrounded by land (NASA Earth Observatory, 2016).

Due to their high reflectance and strong insulative properties, the polar ice and snow masses substantially modify the surface radiation balance of ocean surface properties and the interaction of the ocean and its surface with the atmosphere. Moreover, the presence of a snow and ice surface significantly limits the input of solar radiation to heat the upper ocean, while sea ice formation and melt processes also modify the characteristics of the underlying ocean through injection of brine and freshwater respectively, and contribute in places to global ocean (thermohaline) circulation (see Section 5.1.2). As detailed in Section 15, EO has a crucially important role to play in the measurement and monitoring of polar snow and ice masses, which are vulnerable to climate change.

4.8 Further Information

Tides

NOAA: *https://oceanservice.noaa.gov/education/tutorial_tides/*

4.9 References

AHO (2020). *Tidal Glossary* webpage, Australian Hydrographic Office website: https://www.hydro.gov.au/prodserv/data/tides/tidal-glossary.htm

BOM (2018a). *Waves* webpage, Bureau of Meteorology website: *http://www.bom.gov.au/marine/knowledge-centre/reference/waves.shtml*

BOM (2018b). *Beaufort Wind Scale*, Bureau of Meteorology website glossary. *http://www.bom.gov.au/lam/glossary/beaufort.shtml*

Church, J.A. and White, N.J. (2011), Sea-level rise from the late 19th to the early 21st century. *Surveys in Geophysics*, 32, 585–602. doi:10.1007/s10712-011-9119-1.

COSPPar (2014). *Tides and extreme tide events* factsheet. Climate and Oceans Support Program in the Pacific, Commonwealth of Australia. *http://cosppac.bom.gov.au/assets/pdf/COSPPac-PSLM-Tide-Fact-Sheet.pdf*

CSIRO (2018). *Why Does Sea Level Change?* webpage, Sea Level Rise website: *https://www.cmar.csiro.au/sealevel/sl_drives_seas_dec.html*

Donlon, C.J., Minnett, P.J., Gentemann, C.L., Nightingale, T.J., Barton, I.J., Ward, B., Murry, M.J. (2002). Toward improved validation of satellite sea surface skin temperature measurements for climate research. *Journal of Climate,* 15(4), 353–369.

Heron, S.F., Heron, M.L., and Pichel, W.G. (2013). Thermal and Radar Overview. Ch 11 in *Coral Reef Remote Sensing*. (Eds: Goodman, J.A., Purkis, S.J., and Phinn, S.R.). Springer, Dordrecht. ISBN 978-90-481-9291-5.

MetOffice (2018). *Beaufort wind force scale* webpage, UK Meteorological Office website: *https://www.metoffice.gov.uk/guide/weather/marine/beaufort-scale*

Massom, R.A. (2009). Principal Uses of Remote Sensing in Sea-Ice Field Research. In *Handbook on Field Techniques in Sea-Ice Research* (Eds: H. Eicken *et al.,*). University of Alaska Press, Fairbanks, USA, pp. 405–466.

Morrison, D. and Owen, T. (1996). *The Planetary System*. Addison-Wesley. 570 p.

Munk, W.H. (1950). Origin and generation of waves. *Proceedings* 1st *International Conference on Coastal Engineering, Long Beach, California*. ASCE. pp. 1–4.

NASA Earth Observatory (2016). *Sea Ice* webpage, NASA Earth Observatory website: *https://earthobservatory.nasa.gov/features/SeaIce*

Nicholls, R.J. and Lowe, J.A. (2006). Climate stabilisation and impacts of sea level rise. In Avoiding Dangerous Climate Change (eds. H.J. Schellnhuber, W. Cramer, N. Nakicenovic, T.M.L. Wigley, and G. Yohe). Cambridge University Press, Cambridge. and Nicholls, R.J. and Tol, R.S.J. (2006). Impacts and responses to sealevel rise: a global analysis of the SRES scenarios over the twenty-first century. *Philosophical Transactions of the Royal Society, London A*, 364, 1073–1095.

NOAA (2018). *Tides and Water Levels* webpage, National Ocean Service website: https://oceanservice.noaa.gov/education/tutorial_tides/tides02_cause.html

OzCoasts (2020). *OzCoasts Australian Online Coastal Information (Geoscience Australia) website*: *http://www.ozcoasts.gov.au/index.jsp*

Ross, D.A. (1995). *Introduction to Oceanography*. HarperCollins, New York. pp. 236–242.

Wells, N. (1986). *The Atmosphere and Ocean. A Physical Introduction*. Taylor and Francis, London.

USGS (2018). *Seismic Seiches* webpage, United States Geological Survey website: *https://earthquake.usgs.gov/learn/topics/seiche.php*

WMO (2018). *Frequently Asked Questions* webpage, World Meteorological Organisation website. Marine Meteorology and Oceanography Programme: *http://www.wmo.int/pages/prog/amp/mmop/faq.html*

Zeng, X., Zhao, M., Dickinson, R.E., and He, Y. (1999). A multiyear hourly sea surface skin temperature data set derived from the TOGA TAO bulk temperature and wind speed over the tropical Pacific. *Journal of Geophysical Research,* 104, 1525–1536.

5 Attributes of Water Column

Water columns in surface waters can vary widely in terms of their physical (see Section 5.1), chemical (see Section 5.2), and biological (see Section 5.3) composition, both within and between waterbodies.

5.1 Physical

Physical characteristics of the water column that are relevant to EO studies include water depth (see Section 5.1.1), density and stratification (see Section 5.1.2), temperature (see Section 5.1.3), interactions with electromagnetic radiation (EMR; see Section 5.1.4), and transparency (see Section 5.1.5).

5.1.1 Water depth

When referencing waterbodies, depth can have two different meanings:

- the vertical distance between the water surface and the substrate—this is measured by bathymetric methods (see Section 13) and is referred to therein as the waterbody depth; and
- the vertical distance from the water surface within the waterbody—this is referenced therein as the water depth.

Bathymetry systematically measures waterbody depth to map the topography of submerged surfaces. Such measurements originally relied on sounding lines from ships or platforms, and now use various EO technologies, carried by ships, aircraft, or satellites, including:

- multispectral and hyperspectral sensors—infer waterbody depth in relatively shallow coastal and inland waters using light absorption properties (see Section 13.4.2, plus Volume 1);
- airborne bathymetric lidar—most cost-effective for surveying waterbody depth in small, relatively shallow areas with clear waters (see Section 13.4.1);
- satellite altimetry—sea surface mapping from satellite altimetry can be used to infer seafloor topography (see Section 13.3.1); and
- echosounders—single and multi-beam acoustic sensors for mapping waterbody depths in deep water (see Section 10.2).

Some measurable changes occur in the properties of water with increasing distance from the water surface. A region of water depth that involves rapid change in some property is referred to as a cline, such as temperature (thermocline), salinity (halocline), or density (pycnocline). Salinity and temperature gradients are further discussed in Sections 5.1.2 and 5.1.3). An array of autonomous *in situ* floating sensors routinely measure temperature, salinity, and other characteristics from the water surface to 2,000 m deep. This global operation of sensors is introduced in Excursus 5.1.

Background image: This photo shows the journey of Sun and skylight through the atmosphere, the air-water interface, and the water column to the benthos. Note the changes in colour and intensity from the sky to the bottom of the river. **Source**: Mel-nik, ©iStock photo ID 519368058

Excursus 5.1—Ocean Profile Sensors

Source: Mark Baird, CSIRO
Further information: Integrated Marine Observing System (IMOS) website: *https://imos.org.au/facilities/argofloats;* Volume 2D—Excursus 12.3; *http://biogeochemical-argo.org/*

Autonomous Underwater Vehicles (AUV), untethered and unmanned robotic platforms equipped with a range of sensors, are used to perform planned aquatic surveys (Monk *et al*., 2018). AUV either cruise along defined tracks at 2 m/sec or hover at precise locations and travel slowly (Huvenne *et al*., 2018) to acquire information about the water surface, water column, or substrate.

Every ten days nearly 4,000 profiling floats within the Argo network measure temperature and salinity around the globe, from the water surface down to water depths of 2000 m (see Figure 5.1). These autonomous sensors are cheap, reusable, and remotely-controlled, and can be equipped with a range of sensors to deliver ocean profile data in all weather conditions. Since 2003 these high resolution, hydrographic profiles have been instrumental in providing new information about the broad structure of our oceans. A new global network of biogeochemical sensors on Argo profiling floats is currently being developed by an international consortium called Biogeochemical-Argo to monitor a range of parameters related to nutrient and carbon cycling (see Section 1.5).

The operational cycle of an Argo float for one profile involves:

- deployment by ship or aircraft;
- slow descent to 2000 m takes 6 hours at 10 cm/s;
- float drifts with ocean currents for 9 days;
- oil is pumped from internal reservoir to inflate the external bladder causing the float to rise;
- water temperature and salinity profile is recorded during ascent; and
- at surface, for up to 12 hours, data is transmitted to satellite.

The bladder oil is then pumped back to an internal reservoir for the float to begin a new profile and uploaded data is sent to weather and climate forecasting centres around the world. In addition to profiling data, the movement of floats provides information about the direction and velocity of currents.

Observations from these floats have provided independent confirmation of global warming of ocean waters as deep as 2000 m. The greatest change was observed at latitudes below 20°S, attributed to the fact that oceans comprise a larger proportion of surface area in the Southern Hemisphere.

Figure 5.1 Argo global array

A growing array of Argo profiling floats deliver *in situ* measurements of ocean waters around the globe.

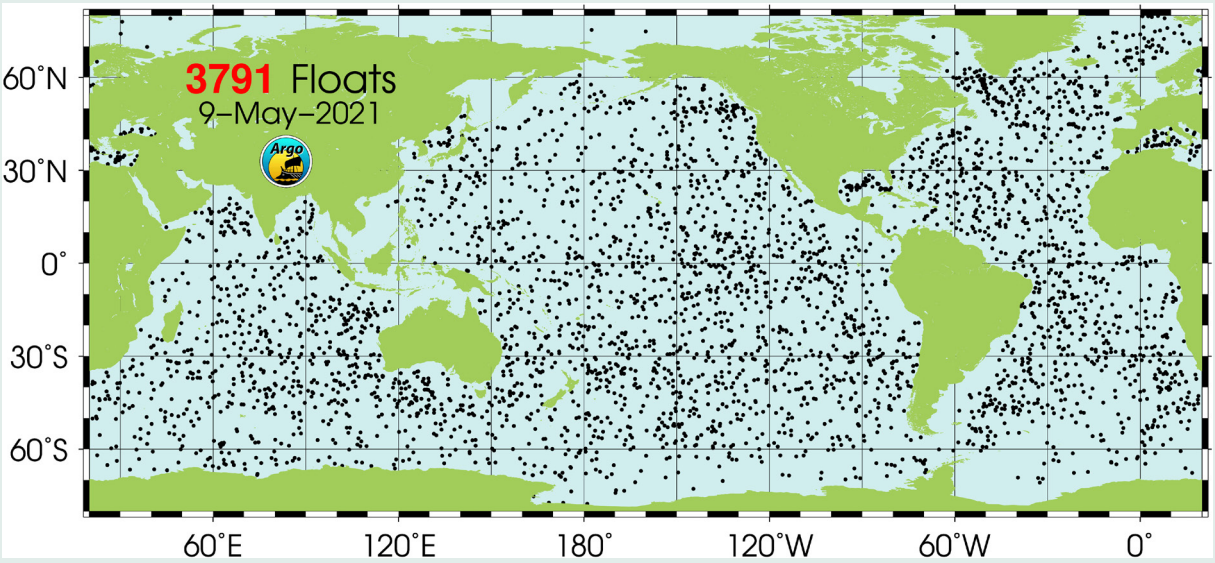

Source: Scripps Institution of Oceanography, University of California San Diego. Retrieved from: *https://argo.ucsd.edu/about/status/*

Figure 5.2 Bathymetry of Bass Strait

The colour spectrum shows depth of water in the Bass Strait, from red (0 m) to blue (100 m).

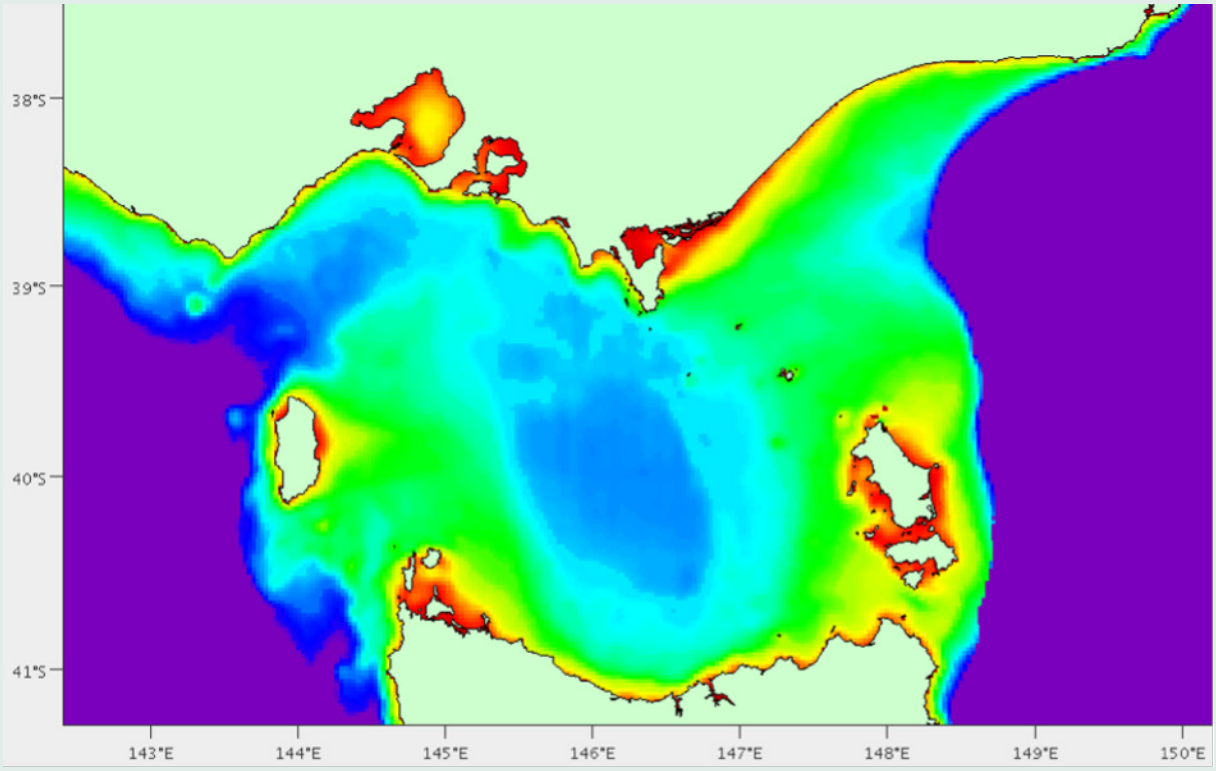

The Ocean Gliders facililty within IMOS (Integrated Marine Observing System—see Volume 2D) operates a fleet of underwater ocean gliders that undertake measurements from shelf and boundary currents in Australian waters. This unprecedented insight into ocean temperature and salinity is freely available online from IMOS. For example, in early 2018 the IMOS Ocean Glider Facility launched the third annual glider travelling from east to west across Bass Strait, the channel of water between the Australian mainland and Tasmania (Baird, 2018). The glider transect indicated the presence of a dense cold pool in the deepest part of Bass Strait, which is shown as a blue region in Figure 5.2. The centre of Bass Strait is deeper than its surrounds and would have formed a large freshwater lake when Bass Strait was exposed over 15,000 years ago. Nowadays the deepest part of Bass Strait is 80 m deep with the deepest outlet to the north at 70 m. Thus the ancient lake continues to act as a place where dense water can collect.

During winter, strong winds and surface cooling create a well-mixed, dense water mass in Bass Strait, which gradually becomes denser than the water in the Tasman Sea to the east because the cooling is confined to the depth of the strait. Once the density difference becomes large enough in the winter, the cold dense pool exits Bass Strait as a bottom density current at the northeastern side.

The cold, dense pool of water detected by the glider is low in oxygen, most likely a remnant of the previous winter (see Figure 5.3). This bottom layer at 70–80 m water depth was the portion of Bass Strait water that could not exit in the previous winter because of the 70 m deep ridge across the eastern edge of Bass Strait. High chlorophyll a levels indicate a bloom has occurred in the deep water where both nutrients and some light are present. The oxygen maximum just above the interface shows the bloom is growing. But once winter comes, they will be mixed to the surface and then flow northward out of Bass Strait. Only the unlucky ones will get trapped for another summer—perhaps to be seen by the next Bass Strait glider.

Figure 5.3 Ocean glider transect

a. Temperature (°C)

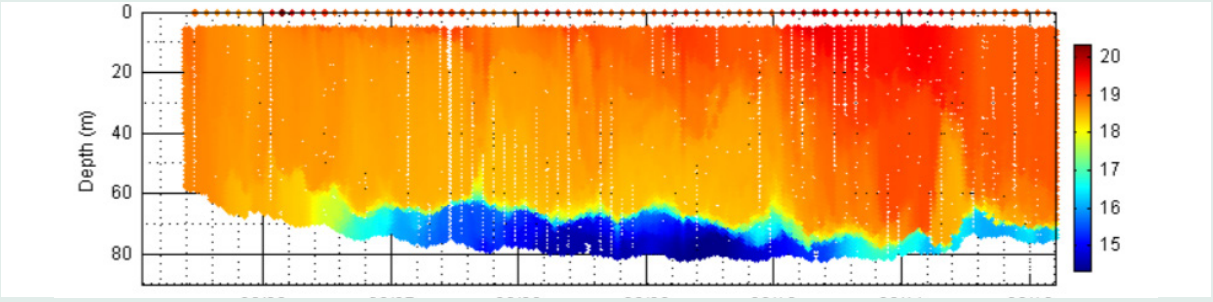

b. Density (kg/m^3)

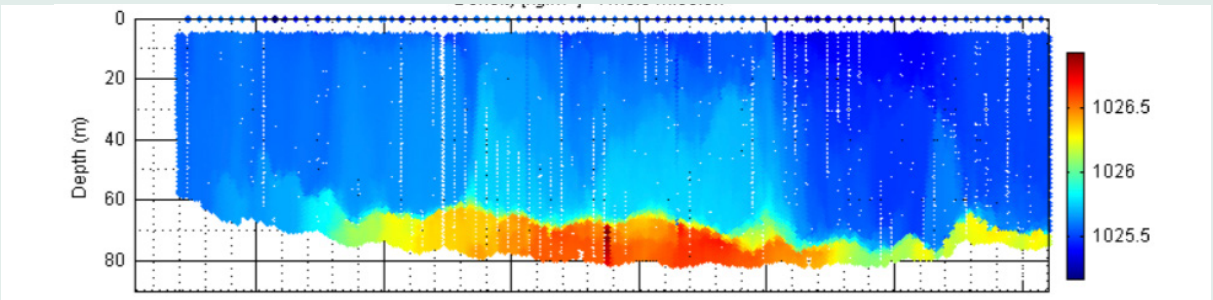

c. Chlorophyll a (µm/L)

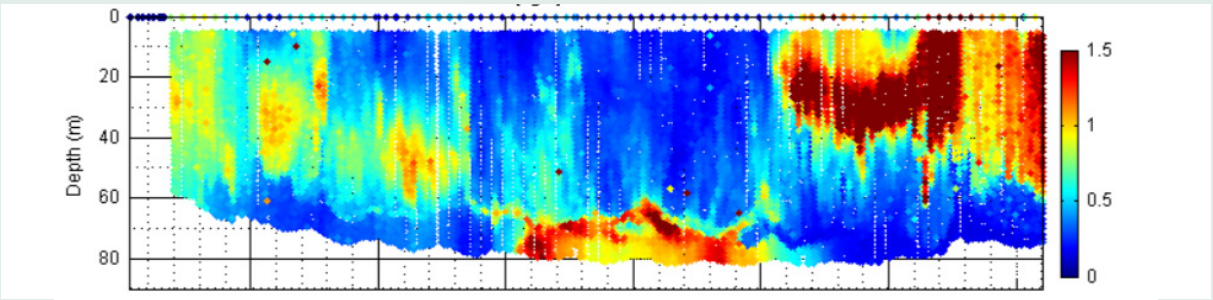

d. Oxygen (mg/L)

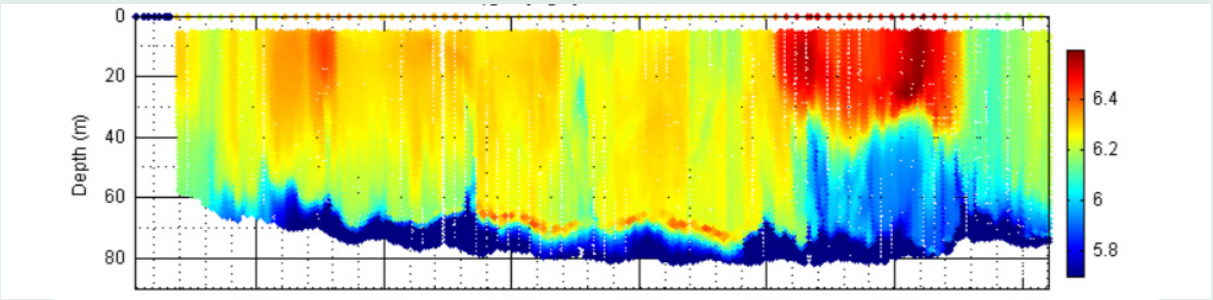

e. b700 (light scattering coefficient at 700 nm; *m-1.sr*$^{-1}$)

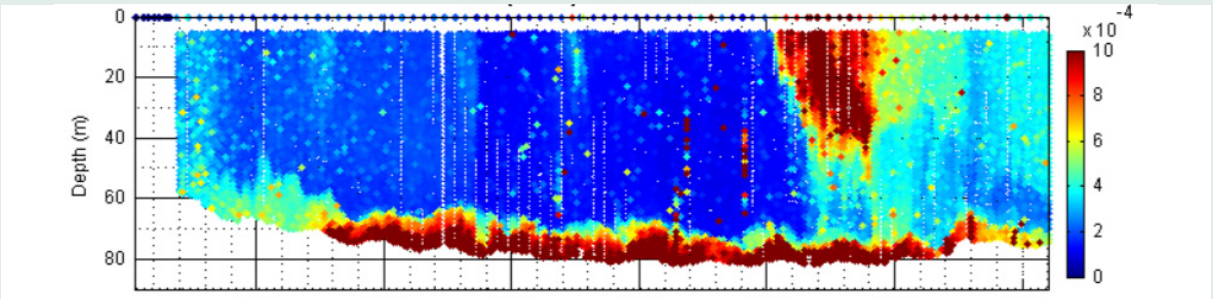

5.1.2 Density and stratification

Density is defined as the mass of a substance per unit volume. At 4°C pure water has the approximate density of 1 g/ml. However, water density increases with increasing salinity or pressure, and with decreasing temperature (see Table 5.1). Since denser water tends to sink and less dense water tends to rise, water density enables water circulation in waterbodies (see Section 16).

In oceans, cold, dense water masses tend to sink at high latitudes, which draws warmer water from low latitudes towards the poles. This density-driven, or 'thermohaline', cycle results in global ocean circulation patterns, which redistribute heat, salt, and nutrients, and carry carbon from the surface ocean and atmosphere to the deep ocean (see Figure 5.4).

While temperature generally decreases with increasing water depth, the characteristics of salinity, density, and pressure all tend to increase. In some waterbodies, density transitions can result in stratification of the water column into three layers of water (see Figure 5.5):

- surface layer—relatively shallow, well-lit, moving, and least dense;
- transition layer—rapid temperature loss with increasing water depth; and
- deep zone—cold, dark, calm water, with highest density.

The transition zone effectively inhibits mixing of the circulating, surface ocean waters (about 20% by volume) with the cold, deeper waters (about 80% by volume). In both lakes and oceans, however, stratification can occur at water depths of 1 m.

A similar stratification of the water column can be observed in lakes (see Figure 5.6). In temperate climates lake water warms and cools with the seasonal change, which results in vertical cycling of water within the lake. Many Australian lakes are monomictic, where only one seasonal period of circulation occurs in winter (MacKinnon and Herbert, 1996) and during other times, there is thermal stratification with an obvious epilimnion (see Figure 5.6).

Figure 5.4 Thermohaline circulation patterns

These diagrams show the slow, large scale circulation pattern of ocean waters, one cycle of which takes nearly a millenium.

a. Warm, northward-moving waters in the North Altantic cool and sink into the deep ocean then resurface to warm in the Southern, Indian and North Pacific oceans. Surface currents then carry the warm water back through the Pacific, Indian, and South Atlantic oceans into the North Altantic.

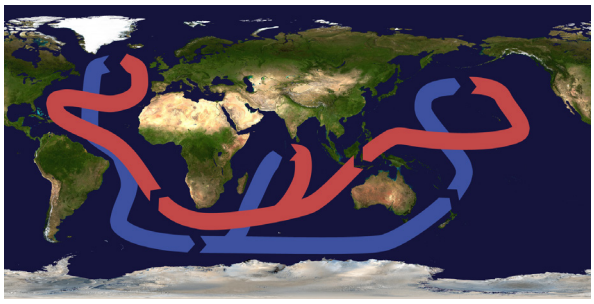

b. Near polar perspective of thermohaline 'conveyor belt' which circulates ocean waters around the globe. This azimuthal equidistant projection (see Volume 2B) views the world ocean as a single unit.

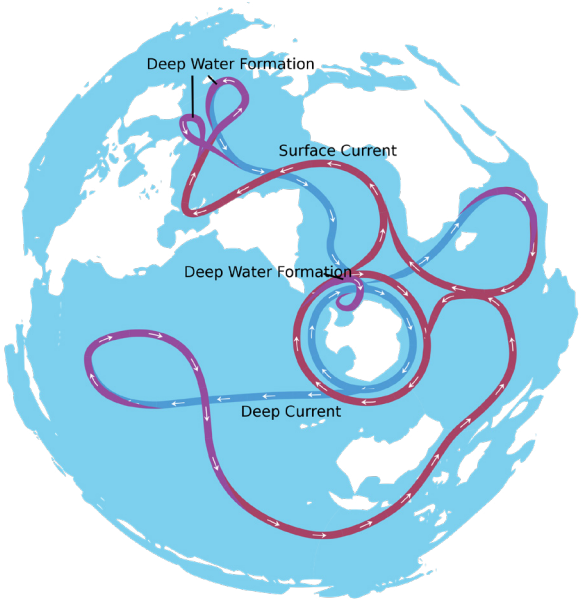

Source: Wikimedia. a. Retrieved from: *https://upload.wikimedia.org/wikipedia/commons/b/b0/Thermohaline_circulation.png* b. *https://upload.wikimedia.org/wikipedia/commons/thumb/a/a6/Conveyor_belt.svg/1991px-Conveyor_belt.svg.png*

Table 5.1 Factors impacting ocean water density

Both temperature and salinity impact water density in oceans.

Climate	Density factors
Wet (low evaporation + high rainfall)	—> Lower salinity —> density decreases —> water rises
Dry (high evaporation + low rainfall)	—> higher salinity —> density increases —> water sinks
	High salinity + low temperature —> greater density increases —> water sinks more
Polar (less heat from sun)	—> temperature decreases —> density increases —> water sinks
Tropical (more heat from sun)	—> temperature increases —> density decreases —> water rises

Figure 5.5 Stratification of water column

Changes in temperature and salinity with increasing water depth result in changes to water density, which create three vertical layers within the water column:
1. A surface layer of lowest density, which is relatively shallow, well-lit and moving;
2. A transition layer, in which temperature decreases rapidly with increasing water depth; and
3. A lower layer of cold, stable, dark water, which has the highest density.

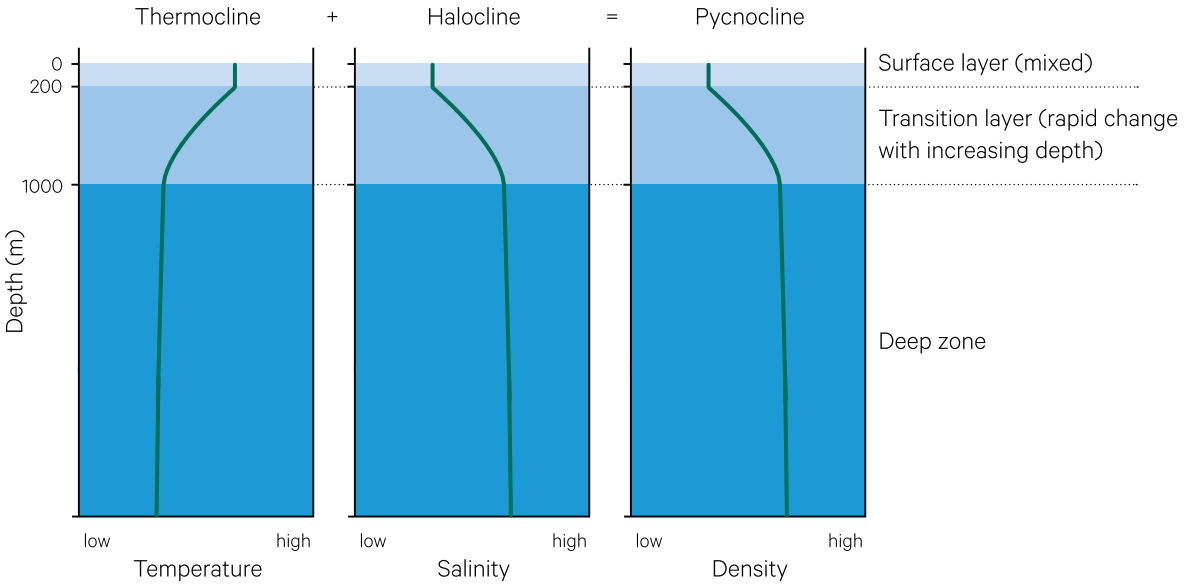

Figure 5.6 Lake stratification

In freshwater systems, temperature and density determine the separation of lakes into three layers:
I. Epilimnion—the top, warmer layer of the lake;
II. Metalimnion (or thermocline)—the middle layer that forms a thermal barrier between the upper and lower layers; and
III. Hypolimnion—the lower, cooler layer.
The scales associate each layer with their corresponding temperatures (right) and water depths (left). The top arrow indicates wind movement over the water surface, which initiates turnover in the epilimnion and hypolimnion.

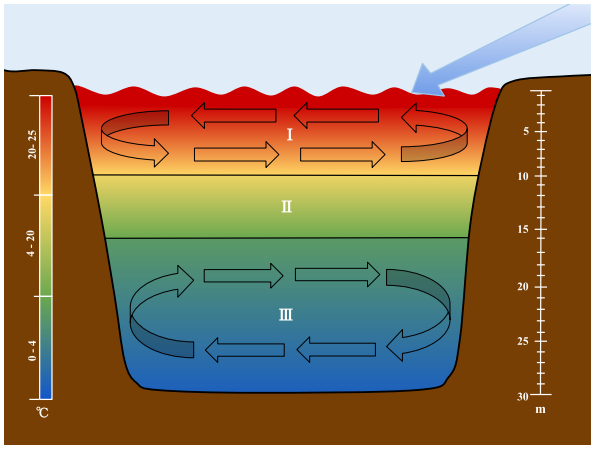

Source: Mbrookings19, Wikimedia. Retrieved from *https://commons.wikimedia.org/wiki/File:Lake_Stratification_(11).svg*

5.1.3 Temperature

The temperature of water in a waterbody will vary with season, latitude, altitude, aspect, exposure, colour, and depth. Some of these factors, principally waterbody colour and depth, can also lead to variations in temperature within a waterbody (see Figure 5.5). The natural range of temperatures across all waterbodies varies from less than 0°C in polar areas, where water freezes into ice, to over 100°C in geothermal features, where water boils and condenses into steam (Te Ara, 2018). Water colour can impact temperature when solar energy is absorbed by darker, shallower waters, making them warmer than the equivalent depth in clear water. Similarly, solar energy penetrates to greater depths in clear water, distributing the heat across a larger depth range.

At sea level, pure water freezes at 0°C and boils at 100°C. Impurities, including salt, in water will slightly increase its boiling point and lower its freezing point. This has obvious implications for thermal analyses of water pollution and wastewater. At higher altitudes, with lower atmospheric pressure, both the freezing and boiling temperatures of water will be lowered.

Unless covered by ice, waterbodies are warmed by solar radiation and cooled by evaporation and surface winds, and shallow water is generally warmer than deep water due to absorption of solar energy. The resistance of a material to changes in temperature is described as its thermal inertia. This property controls diurnal and seasonal temperature variations of surface materials. Large waterbodies have high thermal inertia—they warm and cool slowly relative to their surroundings.

While 75% of ocean waters have temperatures in the range -1 to 6°C, the thermal properties of the ocean surface are very variable, ranging from sub-zero temperatures in extreme polar regions to over 34°C in tropical waters (BOM, 2018). This variation is largely driven by turbulence (Minnett and Kaiser-Weiss, 2012). Large waterbodies in non-polar regions develop a transition zone, or thermocline, in which the temperature of the water changes rapidly relative to the waters above or below (see Figure 5.5). The water depth, thickness and persistence of thermoclines varies with season, latitude, and turbulence. A thermocline in a waterbody tends to inhibit mixing of warmer, more turbulent surface waters and deeper, cooler, and calmer waters. Accordingly, only surface waters, comprising around 2% of all ocean water, tend to change in temperature with external heating. Upwelling fronts, where the thermocline breaks through the water surface, can also create vertical stratification of water temperature (Tomczak, 1998).

The temperature of water in rivers has been observed to be more closely related to the local air temperature than the upstream water temperature. The waters of the Murray River, for example, annually vary between 6–28°C at the headwaters, 7–30°C in the middle reaches and 9–30°C in South Australia (Shafron *et al.*, 1990). Reservoirs, however, introduce thermal stratification of stored water during summer in the same way that oceans develop thermoclines. In the Hume Reservoir, for example, the temperature of water discharged from outlets located below the reservoir's thermocline may be more than 5°C cooler than the surface water during spring and summer, with the temperature varying with water storage levels (Sherman, 2005). When this cooler, denser, deep water is released, it has been observed to reduce the temperature of river water downstream. Such sudden cooling has been termed 'cold water pollution' since it is likely to have adverse effects on water biota, particularly during spring when many species of native fish are spawning. Similarly, the release of wastewater, from industrial, agricultural, and/or domestic activities, can change the temperature of river water.

'Unnatural' changes in temperature within a waterbody can significantly impact a wide range of resident organisms, including native fish species. An increase in temperature of only 1°C lasting one month, for example, can initiate coral bleaching (see Excursus 20.3).

The temperature of a water surface can be measured by *in situ* sensors or remote thermal infrared (TIR) sensors. These sensors only measure the surface temperature of a waterbody, which is impacted by both Sun and wind (see Section 14). In Australian waters the lowest Sea Surface Temperatures (SST) typically occur in early spring while the highest temperatures occur in autumn. Changes in SST indicate water movement, which may be helpful to locate pelagic fish species (see Section 20.7.1). The temporal distribution of temperature measurements in inland waterbodies provides valuable insight into its thermal cycle (Lindell *et al.*, 1999; see Volume 1B—Section 7).

5.1.4 EMR absorption and transmission

Electromagnetic radiation (EMR) can be viewed as a continuous energy spectrum ranging from very short, high energy waves to longer waves with much lower energy, all of which travel at the speed of light (3×10^8 m/s through a vacuum; see Figure 5.7). Commonly accepted ranges for EMR spectral regions are:

- ultraviolet (UV): 0.1–0.38 μm;
- visible: 0.38–0.7 μm;
- infrared (IR): 0.7–1,000 μm; and
- microwave: >1 mm–1 m.

Infrared wavelengths are often subdivided into the regions:

- near infrared (NIR): 0.7–1.3 μm;
- short wave infrared (SWIR): 1.3–3 μm;
- middle infrared (MIR) or mid-wavelength (or medium wave) infrared (MWIR): 3–8 μm;
- thermal infrared (TIR) or long wavelength infrared (LWIR): 8–15 μm; and
- far infrared (FIR): 15–1,000 μm.

Figure 5.7 Electromagnetic spectrum

Names are assigned to regions of the spectrum for convenience – there are no clearly defined divisions. Cosmic rays are high energy, charged particles that travel at close to the speed of light. They are not EMR but included for comparison. Note: scales are logarithmic.

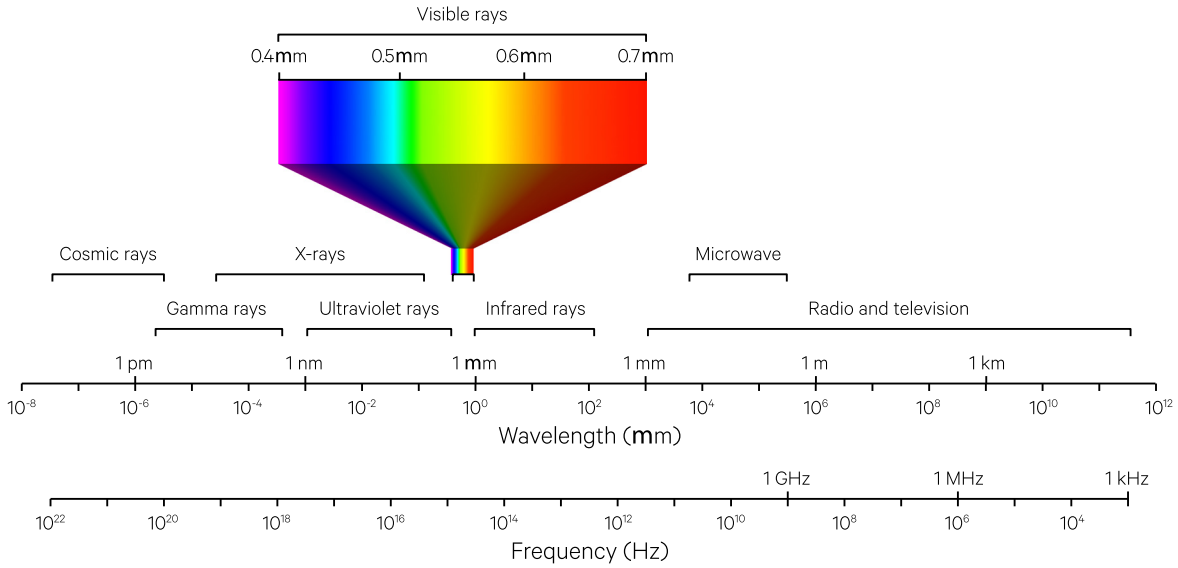

Adapted from: Harrison and Jupp (1989) Figure 2

Most EMR originates from the sun, particularly for shorter wavelengths. Some regions of the EMR spectrum are absorbed by atmospheric gases before they reach the surface of Earth (see Figure 5.8). The gradual reduction in intensity of EMR as it travels through a medium is called attenuation (see Volume 1B—Sections 4 and 5).

EMR radiation is attenuated by pure water and its constituent materials (due to absorption and backscattering), such that the intensity of energy in all wavelengths decreases exponentially with increasing water depth. Less than 1% of total EMR energy intercepted at the surface of a very clear and transparent waterbody will be detected at water depths greater than 100 m. In clear water, the Beer-Lambert Law (see Volume 1A—Section 2.9) can be used to estimate the intensity of light likely to reach a given water depth. For example, the EMR spectra corresponding to four typical Australian water colours are shown in Figure 5.9). The absorption of light by pure water also varies slightly with temperature (Pegau and Zaneveld, 1993).

Figure 5.8 Atmospheric opacity

Some wavelength regions of the EM spectrum are absorbed by atmospheric gases so cannot be used for EO of surface features on Earth. Note: Scale is logarithmic.

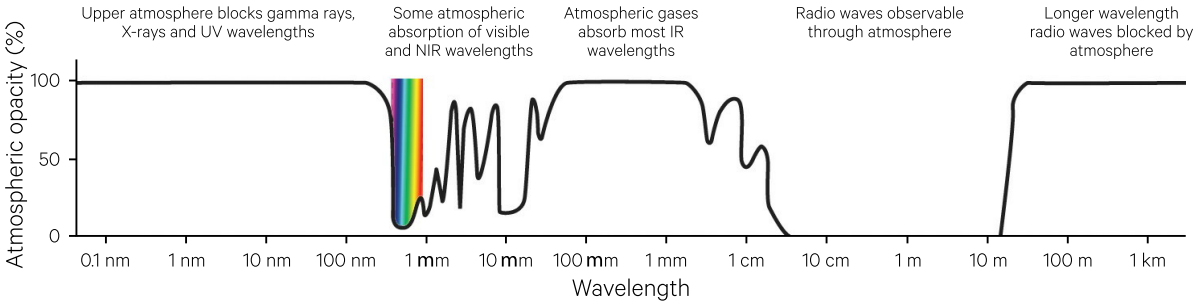

Adapted from: Wikimedia Commons at *https://commons.wikimedia.org/wiki/File:Atmospheric_electromagnetic_opacity.svg* (original source: NASA)

The extent of EMR attenuation in the visible and NIR range varies with wavelength, with shorter wavelengths reaching greater water depths before being absorbed or scattered (see Figure 5.10). In clear, calm, oligotrophic ocean water:

- blue wavelengths are mostly absorbed at a water depth around 60 m;
- green wavelengths are mostly absorbed at a water depth around 30 m;
- yellow wavelengths are mostly absorbed at a water depth around 20 m;
- orange wavelengths are mostly absorbed at a water depth around 10 m;
- red wavelengths are mostly absorbed at a water depth around 5 m; and
- near infrared wavelengths are mostly absorbed at a water depth around 0.5 m.

Optical properties of water as they relate to EO are reviewed in Excursus 8.1 and further detailed in Section 8.3

Figure 5.9 Reflectance from different water colours

Variations in water colour result in varying spectral characteristics for waterbodies. This graph shows the spectra resulting from four different water colours.

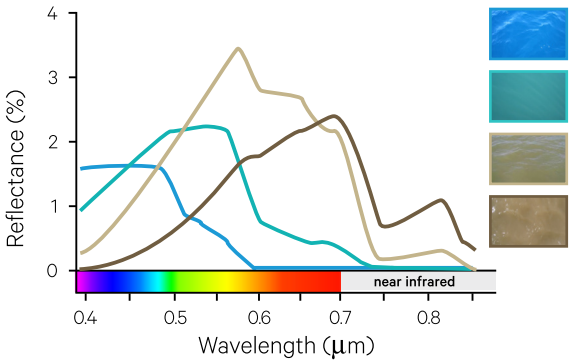

Source: Vittorio Brando, ISAC-CNR

Figure 5.10 Light attenuation in water

The amount of downwelling light in the water column after attenuation by pure water is shown as a function of water depth from 1–20 m, presuming the white substrate reflects 100% of all wavelengths. Light attenuation increases with water depth and with wavelength due to increased molecular pure water absorption. The y-axis shows the amount of light at each water depth as a fraction of the surface downwelling irradiance.

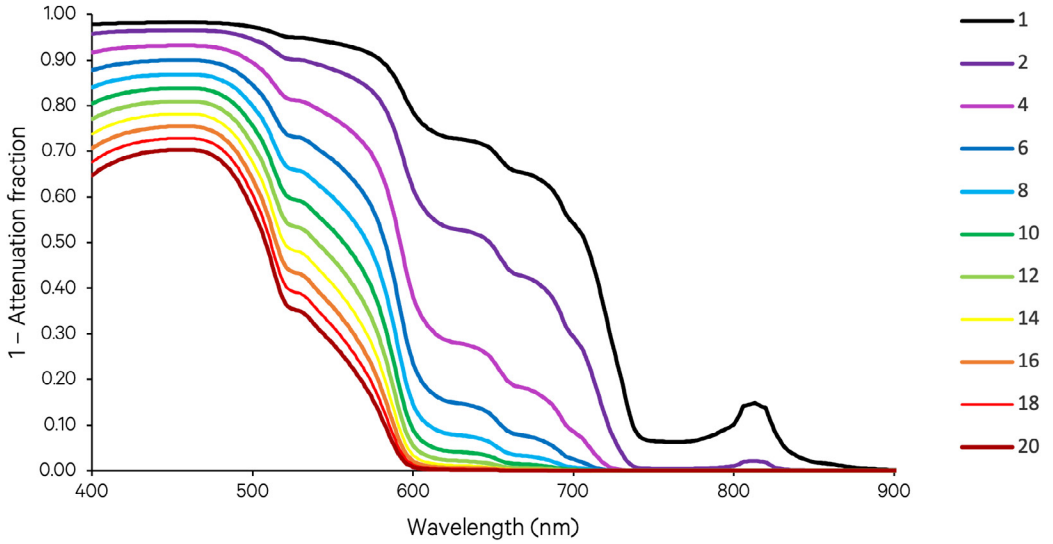

Source: Arnold Dekker, SatDek

5.1.5 Transparency and suspended particles

The relative clarity of water is commonly described in terms of turbidity or transparency. The term turbidity is often used in an attempt to quantify the concentration of suspended sediments in water at a particular time. In this context, sediments may include any particulate matter of mineral or organic origins, such as clay or silt, or detritus and biomass from phytoplankton, macrophytes, or zooplankton. Coloured dissolved organic matter also influences transparency and vertical attenuation of light and thus need to be accounted for in the total light attenuation budget.

Turbidity levels are related to both water flow and available sediment and particle size. Water circulation encourages loose sediments to become suspended, and the extent of turbidity will depend on both the level of agitation within the waterbody and the buoyancy of loose particles. As such, the turbidity of water in a waterbody varies with the surrounding and underlying soil type, the erodibility of the soil, adjacent land activities, the geology and geography of its catchment area, and recent weather conditions. Runoff laden with nitrogen and phosphorus from fertilised soils, for example, (depending on other growth limiting factors such as light and temperature) encourages the growth of phytoplankton and macrophytes, which ultimately (through their breakdown products) increases the concentration of detritus. Weather conditions, such as wind- and wave-based resuspension of bottom sediments in shallow lakes, can also initiate water movement so that settled sediments become resuspended.

Turbidity in inland and coastal waters is strongly driven by runoff and river flow, so can increase dramatically during flooding. Conversely, by controlling flow rate, reservoirs on rivers act as sediment traps. A local maximum turbidity tends to occur where fresh and saltwater meet and tidal movements interact with river flow. At this interface, water mixing encourages fine particles to clump together, or flocculate, resulting in turbidity (see Figure 5.11). An example of this is visible in the image of floodwaters on the page before Section 4.

Most rivers transition from clear, fast-flowing highland headwaters running through gravel streambeds to slower, muddy-bottomed lowland sections with inflowing tributaries. In particular, rivers that travel through fine clay soils, such as the Darling River in western NSW, are more likely to be turbid, unless their flow rate is slow enough to allow suspended particles to settle out of the water (Shafron *et al.*, 1990).

Figure 5.11 Turbidity caused by flocculation

The interface between freshwater and saltwater encourages flocculation of fine particles. Maximum turbidity tends to occur in this region. Light attenuation in the water column is increased by turbidity. A Secchi depth is related to turbidity and measures the water transparency.

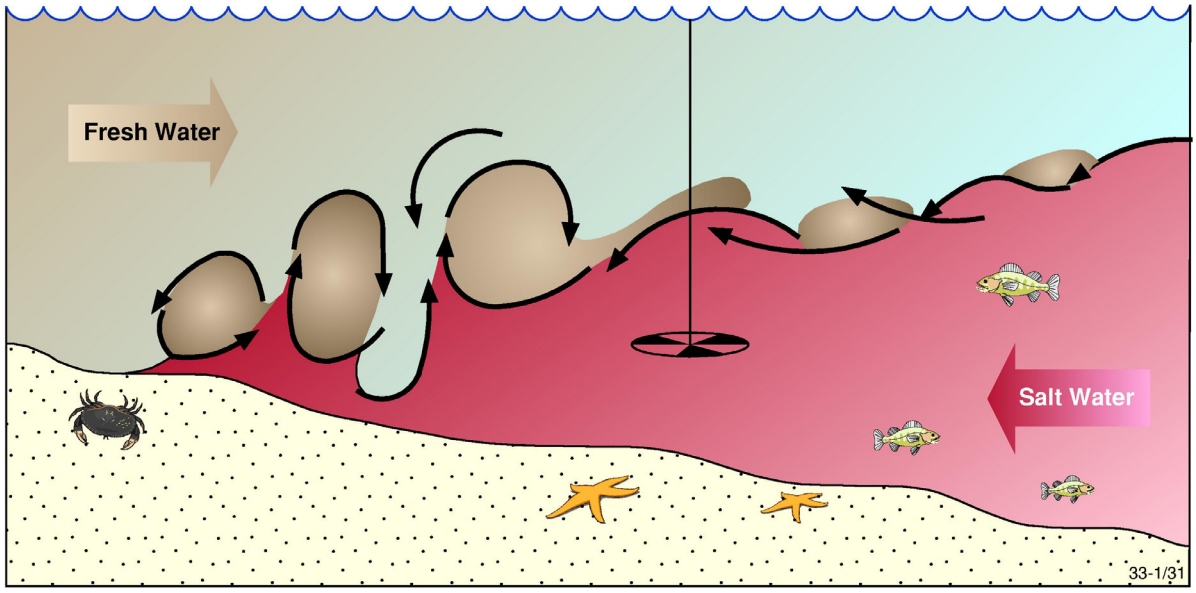

Source: OzCoasts (2018)

High levels of suspended sediment can impact aquatic biota, either directly by smothering benthic organisms, or indirectly by reducing light levels and photosynthetic activity. Elevated turbidity also affects water consumers and can disable water filtration apparatus. When fine clays are prevalent in riverbeds, as tends to occur in tropical regions, the river water is frequently turbid. Abnormally high levels of turbidity, however, can be transported into coastal marine areas in river plumes, and negatively impact fragile ecosystems such as coral reefs (see Section 20.6). The fine clay and colloidal particles of these sediments also carry nutrients as ions and organic molecules. This mechanism has been estimated to account for 40% of the nitrogen and 60–80% of the phosphorus leaving the Great Barrier Reef (GBR) catchment (Furnas, 2003).

Once turbid river waters reach the sea, their flow rate slows down and larger sediments are deposited. Saline marine waters encourage sediments to flocculate and settle. Over time, this transportation of sediment changes the geomorphology of coastlines (Furnas, 2003; see also Sections 1.1 and 1.2.2 above).

Figure 5.12 Secchi disk

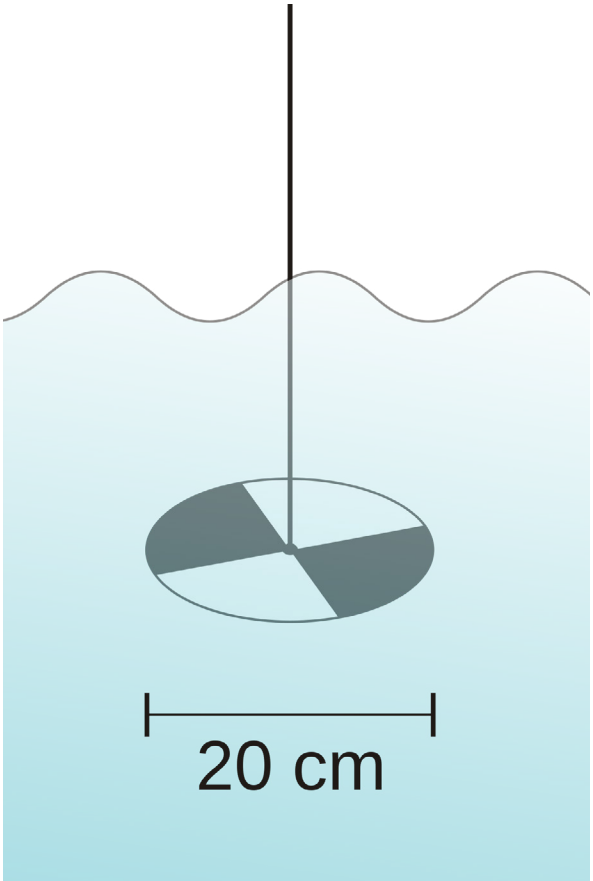

Source: Mysid, Wikimedia. Retrieved from *https://commons.wikimedia.org/wiki/File:Secchi_disks.svg*

Blackwater events (see Excursus 18.1) can occur in waterbodies due to very high concentrations of dissolved organic carbon (DOC) and black particulates, which generally results from leaf litter decomposition (often from *Eucalyptus* species) and/or the presence of dark minerals. Significant quantities of ash can also enter waterbodies after fire, creating a range of water colours and impacting water quality.

The suspended sediment load of water samples is directly measured in terms of the Total Suspended Matter (TSM; also called Total Suspended Solids: TSS or Suspended Sediment Concentration: SSC), that is, the mass of suspended particles per unit volume of water that does not pass through a filter (Blackburn and Dekker, 2006). In this context, the nominal pore size for sediment filters is generally in the range 0.45–0.7 μm for optical purposes. Traditional measurement methods derive the dry weight of sediment from water samples at specific point locations.

TSM can be viewed as a collective term for the sum of phytoplankton, detritus, and mineral matter. The various suspended sediment particles that manifest as turbidity change the optical properties of the water. Turbid waters have a brighter reflectance across all wavelengths than clear waters (except when the mineral detritus is black, as can occur with particulate matter from fires or of volcanic origin), and this characteristic can be used to map the concentration of suspended sediment. Indirect optical measures of turbidity are based on the impact of turbidity on the interaction between light and water. Some of the methods that are used to quantify water transparency based on its optical behaviour include (Dekker and Hestir, 2012):

- visual measurements of water clarity or transparency—have traditionally relied upon the Secchi disk (see Volume 1B—Section 6.4). The black and white disk is lowered to the water depth at which the black and white segmentation can no longer be discriminated (the Secchi depth; see Figure 5.12). The limit of light penetration (K_d) is generally 2 to 3 times the Secchi depth;
- spectrophotometers—used for laboratory analyses of water samples to determine concentrations of non-algal particulates (NAP) and TSM;
- submersible laser scattering instruments (such as LISST-100)—measure *in situ* particle size distribution and optical transmission, as well as water pressure and temperature;
- submersible backscatterometers—measure *in situ* optical backscattering, with some instruments measuring multiple wavelengths (e.g. BB-9);
- submersible hyperspectral light absorption and beam attenuation meters—allow detailed *in situ* spectral measurements (e.g. AC-S); and
- *in situ* spectroradiometers—can measure above-water or in-water light reflectance

Various studies have demonstrated a strong relationship between TSM and optical measurements of turbidity (Brando *et al.,* 2006; Webster *et al.,* 2006). Similar correlations have been established between scattering in green, red or NIR wavelengths and TSM concentrations. These correlations have proved valuable for mapping turbidity in waterbodies (see Section 18.1).

The large variation in the concentration of suspended sediments, phytoplankton, and coloured dissolved organic matter (CDOM) in many inland, estuarine, and coastal waters results in a highly variable light climate (see Section 5.2.3). Optical models play a key role in understanding and quantifying the effect of water composition on optical variables obtained from either *in situ* or EO measurements (see Section 19). Further information on EO of inland waters is provided by Greb *et al.* (2018).

5.2 Chemical

The chemical composition of the water column can impact EO measurements in terms of salinity (see Section 5.2.1), pH (see Section 5.2.2), and both organic and inorganic dissolved matter (see Section 5.2.3).

5.2.1 Salinity

Salts in water lower its specific heat and freezing point and raise its boiling point. Seawater freezes at ~2°C. Salts are expelled from sea ice as it freezes, which increases the salinity and density of surrounding waters. Water can also become more saline via evaporation, whereas the addition of precipitation, runoff, and melting ice all reduce the salinity of a waterbody.

Seawater, on average, contains 3.5% salts, dissolved gases, organic substances, and suspended matter. The most common mineral constituents of sea salt are sodium, chloride, sulphate, magnesium, calcium, and potassium. Salt content affects other properties of water, such as absorption and scattering of light (see Section 8.2.5). The salinity of estuaries fluctuates with tidal penetration and typically decreases with distance inland from the coast. Many coastal lakes and lagoons, for example, are intermittently open and closed to the ocean (and termed ICOLL: Intermittently Open and Closed Lakes and Lagoons; NSW NPI, 2015). In Western Australia, some ICOLLs have salinity levels that are twice the concentration of seawater. Thus, salinity is an important indicator of circulation between marine and freshwater sources.

Dissolved salt concentration in river systems is primarily due to dryland salinity and typically involves chlorides, bicarbonates, and sulphates, of sodium, calcium, magnesium, and potassium. River salinity can often be traced to the combined impacts of reduced flow (due to river regulation or drought) and clearing of catchment vegetation. Where the groundwater, geology, and soils within a catchment area are naturally saline, its rivers and lakes are likely to have a naturally high salt concentration. Another mechanism for introducing salt to inland waterbodies can be seen with salt lakes. Lake Eyre in arid central Australia, for example, is 13 m below mean sea level at its deepest point and, as its water evaporates, a salt crust remains on the dried lake surface.

Salinity is measured in terms of electrical conductivity, which varies with the number of dissolved ions per volume and the mobility of the ions (which, in turn, varies with temperature and pressure). *In situ* sensors measure electrical conductivity as an indicator of Total Dissolved Salts (TDS). Officially, salinity is defined as the ratio of the electrical conductivity of a sample at 15°C and 1 atmosphere pressure to that of a standard solution with 32.4356 g of potassium chloride per kg of water (UNESCO, 1981a, 1981b). As such, salinity measurements do not have units. The standard salinity of seawater is 35 and 75% of ocean waters on Earth have salinity in the range 34 to 35. During the dry season, the salinity of tropical waters can increase to 36, but major flooding and heavy rain can reduce it to 33 (Furnas, 2003) or less (Schroeder *et al.*, 2012).

Saline waters affect the taste, hardness and corrosiveness of domestic water and can reduce plant growth. Both marine and freshwater aquatic organisms generally achieve optimal function within a relatively narrow salinity range, so would be adversely impacted by large or rapid variations. A global network of autonomous Argo floats have been collecting information on salinity and temperature profiles in ocean waters for over a decade (see Excursus 5.1).

5.2.2 pH

The acidity (low pH) or alkalinity (high pH) of natural waters varies with soil type, geology, vegetation, algal content, land use, and climatic conditions. pH indicates the activity of hydrogen ions expressed as moles per litre on a logarithmic scale from 0 to 14 (where 7.0 is considered neutral; see Figure 5.13). The pH of most natural freshwater systems varies in the range 6.5–9.0. The pH of seawater approximates 8.2.

Changes in pH are resisted by most natural waters by the interactions of other minerals with hydroxyl ions. The pH of waterbodies can change with environmental conditions including increased atmospheric CO^2 concentrations, salinity, temperature, photosynthetic activity, decomposition, soil disturbance, and industrial, agricultural, and domestic pollutants. Prolonged drought, for example, can expose acid sulphate soils in waterbodies and lead to the formation of sulphuric acids, which lowers the pH of the water after rain. Organic matter leaching into waterbodies can also raise their pH, while conversely land clearing and pollution can result in lowered pH levels.

Nutrients and pollutants are more soluble in acidic water. Accordingly, the higher nutrient levels of waterbodies with acidic water encourage plant and algal growth, which in turn deoxygenates the water column. While some diurnal pH variation does occur in most waterbodies, aquatic organisms have mostly adapted to thrive within relatively narrow pH ranges, so rapid changes in acidity or alkalinity can adversely impact ecological balance.

pH of waterbodies is measured directly using *in situ* sensors. While pH cannot be directly measured using EO sensors, EO imagery can help to identify conditions resulting from acidic water. For example, while algal blooms initially increase water pH, the ensuing anaerobic conditions can cause water pH levels to decline (Dekker and Hestir, 2012).

The salinity of any water body is the result of an equilibrium between the environmental ionic inputs and removals. (Smyth and Elliot, 2016)

Figure 5.13 pH scale

The ph of example solutions is indicated beside this scale.

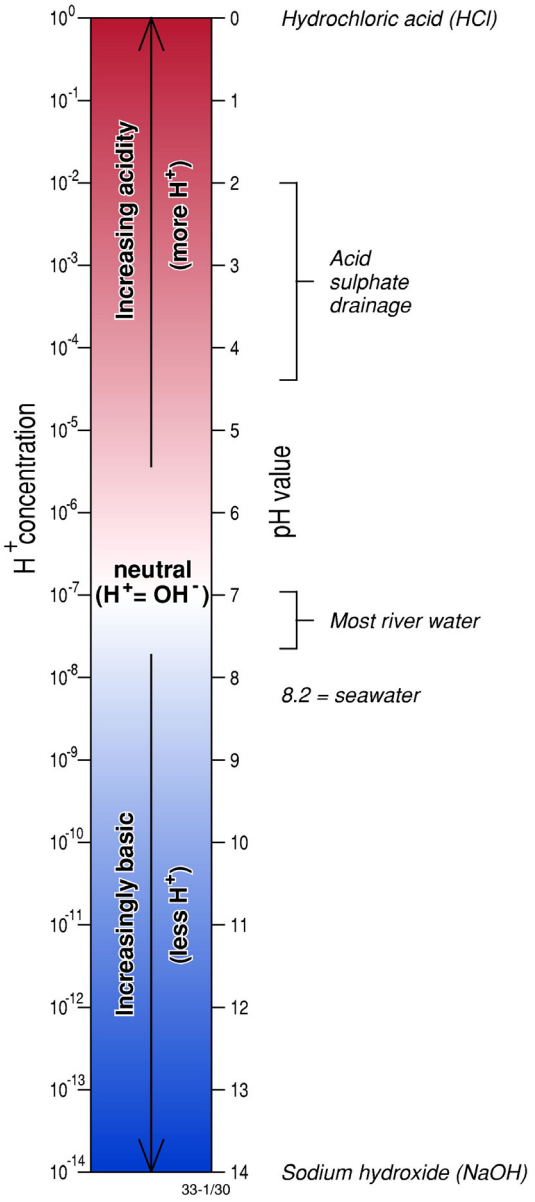

Source: *http://www.ozcoasts.gov.au/indicators/ph_coastal_waterways.jsp*

5.2.3 Dissolved matter

Dissolved materials have been traditionally separated from particulate matter by filtering water samples through glass fibre or membrane filters (see Figure 5.14). Dissolved matter in waterbodies originates from either organic (see Section 5.2.3.1) or inorganic (see Section 5.2.3.2) substances.

Figure 5.14 Separation of dissolved and particulate matter

The continuum of sizes and separation methods for organic matter in seawater are shown. Note scale is logarithmic.

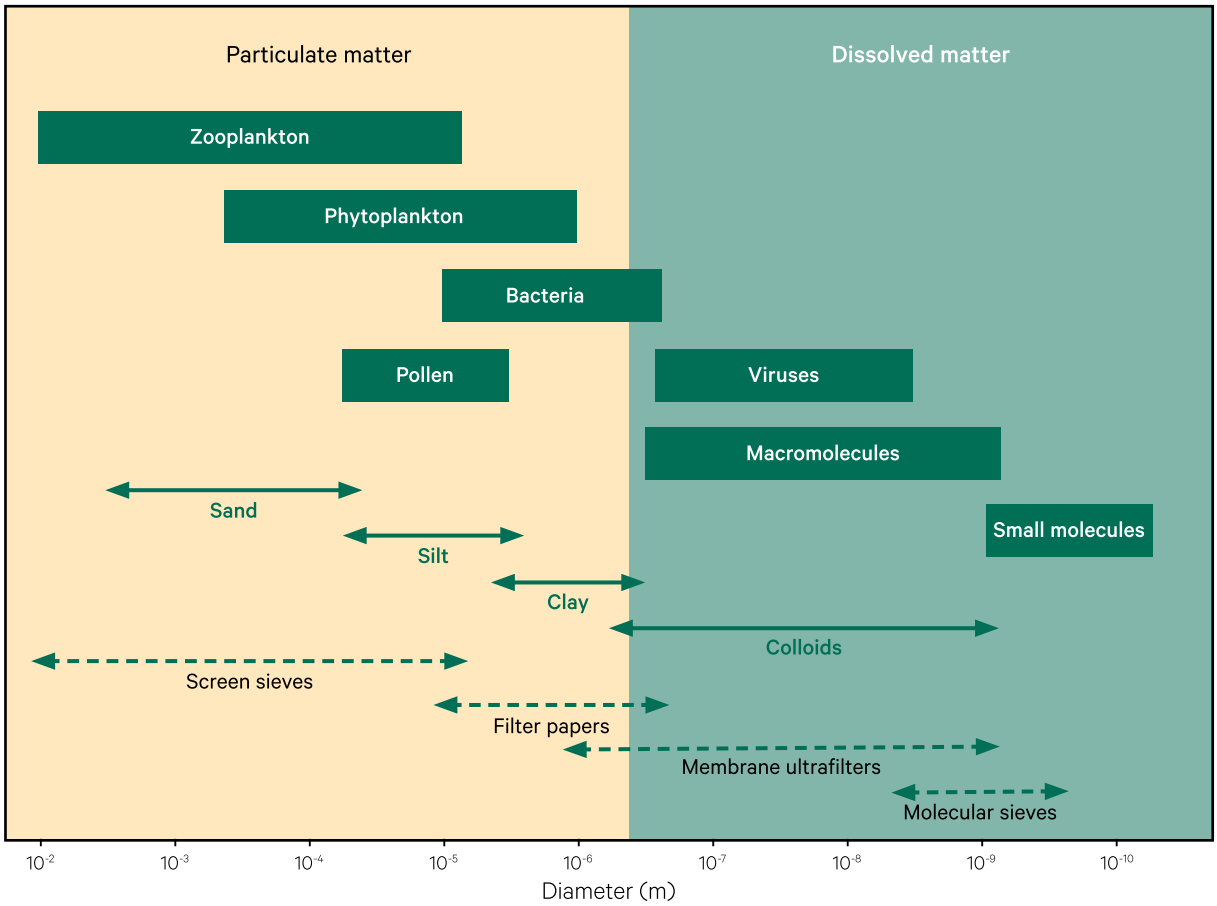

Adapted from: Hedges (2002)

DOM concentration, composition, and chemistry are highly variable and depend on the sources of organic matter (allochthonous versus autochthonous); on the temperature, ionic strength, pH, major cation composition of the water; on the surface chemistry of sediment sorbents that act as solubility controls; and on the presence of photolytic and microbiological degradation processes.
Leenheer and Croué (2003)

5.2.3.1 Organic

Various organic substances, such as tannins from decaying tree bark and leaves or decomposing algae or macrophytes, dissolve in natural waters. Such substances (whether dissolved or colloidal) have become known as yellow substances (Bricauld *et al.*, 1981), Gelbstoff (Carder *et al.*, 1989), gilvin (Kirk, 1976), aquatic humus (Lindell *et al.*, 1999), or Coloured (or Chromophoric) Dissolved Organic Matter (CDOM).

While their colour varies with the parent material, which can derive from both aquatic and terrestrial origin, they can result in water colours from green to yellow to brown as concentration increases. Greater concentrations of CDOM occur in inland and coastal waters than in ocean waters. Origins of the dissolved organic matter can be either:

- autochthonous—found at the site; or
- allochthonous—found elsewhere.

The term 'dissolved' is meant to indicate all water and CDOM passing through a filter size of either 0.47 micron (μm) or 0.20 μm, the latter being preferred as it is half of the wavelength of the deepest blue visible light. Chemical methods can be used to determine the concentration of dissolved organic matter (DOM) in discrete water samples.

The presence of CDOM exponentially increases absorption of light with decreasing wavelengths (Pozdnyakov and Grassl (2003). The resulting colour can be measured using spectrophotometric readings. Often the spectral absorption of filtered water samples at 380 nm or 440 nm is provided if a single number is required (Lindell *et al*., 1999).

Since carbon approximates half the DOM by weight, the concentration of DOM is generally expressed in terms of unit grams of carbon per unit volume. As such, the terms DOM and Dissolved Organic Carbon (DOC) are sometimes used interchangeably (Pozdnyakov and Grassl, 2003). DOC comprises 'a complex mixture of aromatic and aliphatic hydrocarbon structures that have attached functional groups', with the majority being humic substances (HS; Leenheer and Croué, 2003). HS derive from the non-bioconsumable residue of plant or animal matter and have relatively high molecular weights (Sachse *et al.,* 2005). HS decrease the transparency of water, especially in the blue and blue-green wavelengths (see Section 18.5), and thus reduce the depth of the euphotic zone. Accordingly, CDOM tends to limit photosynthesis (and hence phytoplankton production), slightly increases water acidity, and binds toxic metals and organic contaminants. The marine DOC also has a central role in the global carbon cycle, as it is the largest stores of carbon in the ocean and is the intermediatory pathway for carbon to be transferred into the food webs (Seritti, *et al.,* 2003).

5.2.3.2 Inorganic

Various minerals, such as phosphorus, nitrogen, and silica, are nutrients for aquatic plants. In excess, however, they encourage the growth of undesirable algae and bacteria. Increased nutrient levels in waterbodies have been observed to coincide with increased growth of ephemeral macroalgae, phytoplankton and epiphytes, and decreased growth of perennial macrophytes (Hardison *et al*., 2013).

Wastewater from urban, industrial, and irrigation activities can contribute large quantities of nutrients to inland and coastal waters. The limited measurements available for waterways within largely pristine catchments indicate lower nutrient levels than for those rivers and streams impacted by land clearing and agriculture within the GBR catchment area (Furnas, 2003). Nutrient levels in waterbodies can also be increased after fire, due to extensive loss of vegetation and greater catchment erosion, or when water volume is reduced by drought conditions. Flushing of waterways by tides or freshwater flows both dilutes and transports nutrients. In the coastal rivers near the GBR, both the average nutrient concentrations and the relative abundances of individual nutrients vary both between and within rivers (Furnas, 2003), although the differences between rivers is generally less than the temporal variation within individual rivers.

Phosphorus can enter waterbodies from urban areas and agricultural land. It is considered a 'conservative' pollutant as it stays in the river water and does not leach into groundwater. Nitrogen, however, is not a conservative pollutant, and can infiltrate groundwater storages. Calcium and magnesium ions 'harden' water, that is, they increase surface tension and limit the efficacy of surfactants, such as cleaning products.

The oceanographic community's perception of DOM [Dissolved Organic Matter] has evolved from an emphasis on a dilute and largely separate pool of remarkably old and static substances to the current view of a dynamic assemblage of organic molecules that interact with each other, trace metals, and living organisms over a broad continuum of space and time scales. The sparingly reactive components of this molecular continuum that persist and change on time scales sampled by conventional oceanographic surveys represent a small molecular outcrop of a churning mass of molecules through which much of the total primary production of the ocean cycles.
Hedges (2002)

Table 5.2 Trophic status categories for freshwater lakes

Trophic Status	Nutrient Level	Productivity	Water Clarity	Dissolved Oxygen	Possible Causal Agents
Oligotrophic	Low	Low	High	High	Acid rain
Mesotrophic	Medium	Medium	Medium	Medium	Balanced conditions
Eutrophic	High	High	Low	Low	Fertiliser or faecal contamination
Hypertrophic	Super-saturated	Extremely high	Extremely low	Lacking	Excessive nutrients or low flow

Eutrophication describes the condition of a waterbody enriched by nutrients, which can result in excessive primary production[6], reduced secondary production[7], and lead to long term loss in species diversity. The natural process of eutrophication occurs slowly, due to long term weathering and leaching of nutrients from soils and vegetation. By increasing the volume of phytoplankton and aquatic plants, this enrichment results in more productive waters. Eutrophication can also occur rapidly, resulting from anthropogenic activities, such as forest clearing and agricultural practices, or following the addition of polluted wastewater. Relevant pollutants in wastewater may include polyphosphates from detergents, or fertiliser residues from irrigation. Rapid eutrophication encourages accelerated growth of phytoplankton, some types of which have a detrimental impact on water quality. Exhaustion of individual nutrients can also disrupt the balance of nutrients, leaving some in excess quantities.

Of the many parameters that have been used to classify lake habitats, trophic status is currently the most widely used. Several indices have been proposed to express the trophic status of lake water based on varying levels of dissolved oxygen, total phosphorus, total nitrogen, chlorophyll a, transparency, and/or organic matter in sediments. Table 5.2 summarises the relationships between nutrient levels and other water characteristics for four trophic status categories.

The classic method for assigning lake trophic level is that of Carlson (1977), which combines quantitative measurements of chlorophyll, total phosphorus, and the Secchi disk (see Section 5.1.5) into a single index. This is intuitively attractive as the chlorophyll content provides a measure of the standing crop of phytoplankton, while the total phosphorus defines the upper limit of biomass production (since most lake systems in the Northern Hemisphere are phosphorus limited). In the case where nitrogen is the limiting nutrient, as typically occurs in Australian inland waters, cyanobacteria often become the dominant phytoplankton class through their ability to fix nitrogen from the atmosphere. The deep, or subsurface, chlorophyll maximum (chl max) describes a layer of high chlorophyll in stratified marine and freshwater that may coincide with primary productivity and phytoplankton abundance (Moeller *et al.*, 2019).

Dissolved oxygen concentration is also a general indicator of lake trophic status. Photosynthesis fixes inorganic carbon from the water column and produces oxygen. The interpretation of dissolved oxygen measurement is complicated by the dynamics of photosynthesis during daytime illumination (when the oxygen concentration rises) and the respiration of the phytoplankton and sediments during the night (which consume oxygen and produce carbon dioxide). Ideally the 24-hour integral of the dissolved oxygen concentration and the day/night difference in dissolved oxygen offer the most representative measures of trophic status and of classifying trophic status. Positive dissolved oxygen integral indicates autotrophy while a negative dissolved oxygen integral indicates heterotrophy (Pace and Prairie, 2005).

Nutrient concentration is thus an important limiting factor in the production of phytoplankton quite apart from its significance for understanding the global biogeochemical cycling to which EO methods can contribute. The principal nutrients required by phytoplankton are the biologically available forms of nitrogen, phosphorus, and silicon, plus many other trace nutrients. Water composition is determined by chemical analysis of water samples collected from the waterbody. A strong distinction is made between the nutrient content of the filtered sample, which is assumed to be readily available for phytoplankton growth, and the total nutrient concentrations, which lumps together all the different chemical forms of nitrogen and phosphorus, and includes phosphorus containing minerals, some of which do not sustain phytoplankton growth, and the nitrogen and phosphorus that are already incorporated into phytoplankton. When using EO datasets, consideration must be given to the interplay between mixing dynamics, the optical depth of the water column in relation to the mixing depth, and the capability to support phytoplankton growth, especially in lakes (Wetzel, 2001).

6 Primary production refers to chemical energy directly produced by living organisms from 'new' organic materials, primarily via photosynthesis (see Volume 3A).
7 Secondary production refers to biomass generated by heterotrophic organisms by consuming matter created by primary producers (see Volume 3A).

5.3 Biological

The diversity of biological life forms in surface waters is immense. In this section we review the most relevant characteristics of aquatic biota in terms of:

- microorganisms (microalgae and other microbiota; see Section 5.3.1); and
- macroalgae and macrophytes (see Section 5.3.2).

5.3.1 Microorganisms

5.3.1.1 Phytoplankton and other microalgae

Despite the literal meaning of the term 'phytoplankton' (wandering plants), this collective noun is commonly used to encompass a diverse assemblage of microscopic organisms—bacteria, protists, or single-celled plants—that live in a wide range of aquatic environments (see Section 3.3.1). Myriad species of phytoplankton have adapted to specific water conditions, and can rapidly respond to changes in water clarity, nutrient content, salinity, and temperature (see Sections 5.1 and 5.2). Within the commonly accepted usage of the term, most—but not all—organisms included in the 'phytoplankton community' do photosynthesise (Ian Jameson[8], *pers. comm.*). Phytoplankton species can be differentiated into three groups in terms of the mechanism by which they obtain carbon:

- 'autotrophic'—obtain all their carbon via photosynthesis;
- 'mixotrophic'—consume other organisms as well as photosynthesising; and
- 'heterotrophic'—only derive carbon from other organisms (or zooplankton).

The most common groups of phytoplankton are introduced in Excursus 3.2. Phytoplankton perform a critical role in the aquatic food chain, providing the food supply for a wide range of aquatic animals, such as zooplankton, molluscs and crustaceans (see Figure 3.8). Both marine and freshwater phytoplankton oxygenate water (see Figure 1.15). Most species included in the phytoplankton community are denser than water, so require some water movement to stay suspended, but some species can move independently (see Section 3.3.2.1). Their growth is accelerated by light, heat, water, and nutrients, and decreased by turbidity and cool conditions. Deep outflows from water reservoirs generally do not transfer phytoplankton unless water levels are low, but they can seed the outflowing waters with spores, thus enabling blooms downstream if growing conditions are suitable. In the right conditions, rapid eutrophication can lead to visible algal blooms (see Section 19.5).

The circulating, surface waters, also called the mixed layer, define the region of greatest photosynthetic activity (see Figure 5.15). Phytoplankton can either fix CO_2 from the atmosphere or obtain it in its dissolved form in water (Hülse *et al.*, 2017). The most productive waters have been observed to be those with shallow mixed layers, either due to a shallow water column or a shallow mixed layer above the thermocline (Kirk, 1994). In seawaters, the mixed layer is typically 20–100 m deep, with the depth varying seasonally in temperate and polar latitudes. In ocean waters where the density gradient is stable, a deep chlorophyll layer also occurs, commonly 10 m thick, near the base of the euphotic zone. Its occurrence is possibly related to nutrient availability (Kirk, 1994).

Phyto—plant
plankton—wandering

A number of laboratory-based analyses can be used to estimate phytoplankton concentration in water samples (Dekker and Hestir, 2012):

- high performance liquid chromatography (HPLC)—accurately measures concentrations of chlorophyll, cyano-phycocyanin, cyano-phycoerythrin, and all other phytoplankton pigments;
- spectrophotometers—accurately identify chlorophyll based on spectral characteristics, with lowered accuracy for cyano-phycocyanin; and
- microscopic cell identification and counting methods—render exact counts for available samples but are time consuming and require expert taxonomic knowledge.

Figure 5.15 Deep chlorophyll maximum for northeast Pacific Ocean

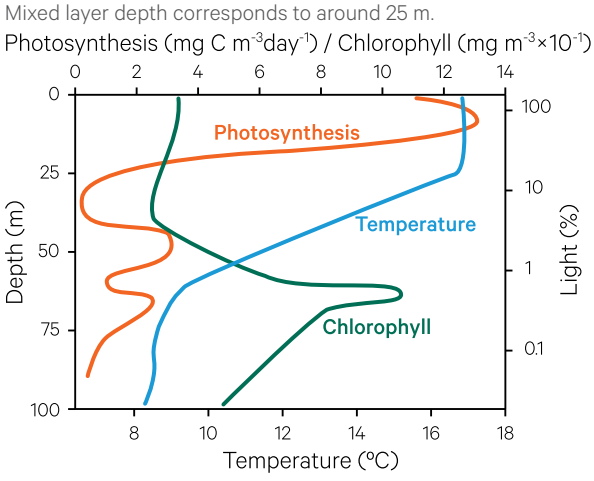

Adapted from: Kirk (1994) Figure 11.1

8 Curator, Australian National Algae Culture Collection, CSIRO, 2014.

The concentration of pigments in natural waters can also be estimated *in situ* using fluorometers to measure fluorescence of chlorophyll and accessory pigments. Fluorometers transmit a light beam of a specific wavelength known to induce chlorophyll fluorescence (such as 443 nm for chlorophyll a) and measure the wavelength of the emitted return (between 650–700 nm, centred on 683 nm, for chlorophyll a.) The algal concentration can be inferred from these measurements (Xing *et al*., 2007). *In situ* optical measurements using submerged hyperspectral light absorption and beam attenuation meters and in-water or above-water spectroradiometers are increasingly popular for inferring phytoplankton concentration from the spectral characteristics of its major pigments (chlorophyll, cyano-phycocyanin, and cyano-phycoerythrin). Similar methods based on EO data have been developed to map phytoplankton based on its chlorophyll concentration (see Section 18.6).

5.3.1.2 Other microbiota

Pathogens, such as viruses, parasites, protozoa, and bacteria from human or animal origins, can be introduced into waterbodies either directly or from wastewater or runoff, and many occur naturally. These are typically identified by indicator species, such as *Escherichia coli* (*E. coli*). Since bacteria in water are generally associated with particulate matter, their concentration is determination in terms of 'clump' count, rather than individual organisms. Microbiological analyses involve incubation trials based on different regimes of medium, temperature, and time. Different groups of organisms can be identified based on their incubation characteristics under different regimes.

Environmental DNA (eDNA) methods are based on molecular analysis of the DNA present in environmental samples (such as sediment, water, faeces, etc), and offers an opportunity to identify the diversity and abundance of organisms using non-invasive sampling techniques (Stewart, 2019). For example, these techniques have been used to determine fish diets in freshwater environments to ultimately derive ecosystem food webs (Rees *et al*., 2019), and derive the composition and spatial patterns of wetland plant communities (Shackleton *et al*., 2019). Similarly, eDNA is relevant to assessing the bacterial and viral composition of natural waters.

5.3.2 Macroalgae and macrophytes

Macroalgae (algae that are visible to the naked eye) are introduced in Section 3.3.2.2. These organisms are important to the ecology of shallow coastal waterways and coral reefs, and are typically found growing attached to hard substrates such as rocks, shells, and coral skeletons (Diaz-Pulido and McCook, 2008; OzCoasts, 2018).

In Australia, macroalgae are valued for their intrinsic biodiversity, providing food and refuge for juvenile fish, crabs, and a wide range of herbivores. Macroalgae thrive in nutrient-rich waters to such an extent that the occurrence of particular types of macroalgae can be indicative of the nutrient status of water. Macroalgal blooms impact the natural environment directly, by reducing light available to macrophytes, or indirectly, where the presence of decomposing mats of macroalgae drastically lower the dissolved oxygen content of the water column, resulting in massive fish kills (Valeila *et al*., 1997; OzCoasts, 2018).

Large aquatic plants or macrophytes (see Section 3.3.2) are also important as primary producers (Pennesi *et al*., 2015) and have been called 'ecological engineers' (Jones *et al*., 1994), that is, organisms that directly or indirectly change the physical state in biotic or abiotic matter and consequently impact the availability of resources to other organisms. All macrophytes offer a diversity of habitats and shelter for aquatic organisms. Rooted macrophytes also help to stabilise the substratum, and by reducing the movement of water, they also increase sedimentation of suspended particles in waterbodies (Bowden *et al*., 2017).

A significant function of macrophytes is their direct uptake of dissolved nutrients (principally nitrogen and phosphorus) from water, and their indirect nutrient cycling via the denitrifying bacteria they support. Accordingly, some macrophytes are being used for biological filtration in sewerage treatment systems.

The condition of macrophyte and macroalgal communities is directly related to the water quality of their environment. Suspended sediments and/or growth of algae will reduce light levels and, in excess levels, can kill submerged vegetation. While such plants live in 'extreme' conditions, others do not re-colonise readily, so need to be managed with care. Anthropogenic disturbance presents the greatest threat to the sustainability of aquatic ecosystems (Wilcox, 1995; Short and Wyllie-Echeveria, 1996; Meinesz, 1999).

Aquatic carbon, particularly DOC, benefit plants by attenuating UVB radiation, binding heavy metals, and generating CO_2, but high concentrations can also retard growth. Humic substances (see Section 5.2.3.1) colour the water, thus reducing light transmission, and contain chemicals that disrupt biochemical processes in aquatic organisms, including photosynthesis of macrophytes (Steinberg *et al.,* 2008).

Recent studies have shown that the concentration of aquatic carbon is increasing in freshwater ecosystems, especially DOC, possibly due to climate change (Reitsema *et al.,* 2018). Changes have also been observed in the composition of DOM (with links to DOC), particularly near urban areas, which render it less susceptible to photodegradation (Williams *et al.,* 2016). Other potential changes related to climate variations, which are likely to impact aquatic organisms, include rising sea level, elevated water temperature, coastal erosion, and increased flow of water carrying anthropogenic sources of POC and DOC (IPCC, 2014).

Ground-based surveys of aquatic vegetation composition are usually in the form of quadrant surveys of very limited spatial scale, and have traditionally involved destructive sampling of biomass at selected locations. Mapping based on EO data has the obvious advantages of being non-destructive, faster, spatially-coherent and consistent, and more cost-effective (Mumby *et al*., 1997; Clark *et al*., 1997). The use of EO to map aquatic vegetation is considered in Section 20.

5.4 Further Information

Kirk (1976, 1994, 2010)

Tomczak (1998)

IMOS State and Trends of Australia's Ocean Report: 1. Physical and Chemical Environment: *https://www.imosoceanreport.org.au/time-series/environment/*

Oceans: *https://www.sciencelearn.org.nz/topics/oceans*

5.5 References

Baird, M. (2018). *Bass Strait Glider Reveals the Ancient Bassian Lake* . IMOS Marine Matters, 29. *https://imos.org.au/fileadmin/user_upload/shared/IMOS_General/documents/newsletters/IMOS_Marine_Matters_Issue_29_WEB.pdf*

Blackburn, D., and Dekker, A.G. (2006). *Remote Sensing study of marine and coastal features and interpretation of changes in relation to natural and anthropogenic processes*. Adelaide Coastal Waters Study Technical Report 6. Prepared for ACWS Steering Committee, Sept 2006. David Blackburn Env. P/L and CSIRO LW.

BOM (2018*). Bureau of Meteorology* website: *http://www.bom.gov.au/*

Bowden, W.B., Glime, J.M., and Riis, T. (2017). Macrophytes and Bryophytes. Ch 13 in *Methods in Stream Ecology* (Vol. 1) 3rd edn. Elsevier Inc. pp. 243–271. *http://dx.doi.org/10.1016/B978-0-12-416558-8.00013-5*

Brando, V., Dekker, A., Marks, A., Qin, Y and Oubelkheir, K. (2006). *Chlorophyll and suspended sediment assessment in a macrotidal tropical estuary adjacent to the Great Barrier Reef: spatial and temporal assessment using remote sensing*. Cooperative Research Centre for Coastal Zone, Estuary & Waterway Management Technical Report 74.

Bricaud, A., Morel, A., and Prieur, L. (1981). Absorption by dissolved organic matter of the sea (yellow substance) in the UV and visible domains, *Limnology and Oceanography*, 26, 43–53.

Carder, K.L., Steward, R.G., Harvey, G.R., and Ortner, P.B. (1989). Marine humic and fulvic acids: Their effects on remote sensing of ocean chlorophyll. *Limnology and Oceanography*, 34(1), 68–81.

Carlson, R.E. (1977) A trophic state index for lakes. *Limnology and Oceanography*, 22(2), 361–369.

Clark, C.D., Ripley, H.T., Green, E.P., Edwards, A.J., and Mumby, P.J. (1997). Mapping and measurement of tropical coastal environments with hyperspectral and high spatial resolution data. *International Journal of Remote Sensing*, 18, 237–242.

Dekker, A.G., and Hestir, E. L. (2012). *Evaluating the Feasibility of Systematic Inland Water Quality Monitoring with Satellite Remote Sensing*. Water for a Healthy Country National Research Flagship, CSIRO.

Diaz-Pulido, G., and McCook, L.J. (2008). Macroalgae (Seaweeds). In *The State of the Reef Report. Environmental Status of the Great Barrier Reef*. (Ed: Chin, A.). Great Barrier Reef Marine Park Authority, Townsville. ISBN: 1 876945 34 6 *http://www.gbrmpa.gov.au/__data/assets/pdf_file/0019/3970/SORR_Macroalgae.pdf*

Furnas, M. (2003). *Catchments and Corals. Terrestrial Runoff to the Great Barrier Reef*. AIMS, Townsville. 334pp.

Greb, S., Dekker, A.G., and Binding, C. (Eds) (2018). *Earth Observations in Support of Global Water Quality Monitoring. IOCCG Report Series, No. 17,* International Ocean Colour Coordinating Group, Dartmouth, Canada.

Hardison, A., Canuel, E., Anderson, I., Tobias, C., Veuger, B., and Waters, M. (2013). Microphytobenthos and benthic macroalgae determine sediment organic matter composition in shallow photic sediments. *Biogeosciences Discussions*, 10, 2791–2834. doi:10.5194/bgd-10-2791-2013.

Harrison, B.A., and Jupp, D.L.B. (1989) *Introduction to Remotely Sensed Data: Part ONE of the microBRIAN Resource Manual*. CSIRO, Melbourne. 156 p.

Hedges, J.I. (2002). Why Dissolved Organics Matter. Ch. 1 in *Biogeochemistry of marine organic matter*. (Eds: D. Hansell and C. Carlson). Academic Press, San Diego. ISBN: 0-12-323841-2

Hülse, D., Arndt, S., Wilson, J.D.;,Munhoven, G., and Ridgwell, A. (2017). Understanding the causes and consequences of past marine carbon cycling variability through models. *Earth Science Review*, 171, 349–382.

Huvenne, V.A.I., Robert, K., Marsh, L., Lo Iacono, C., Le Bas, T., Wynn, R.B. (2018). ROVs and AUVs. In *Submarine Geomorphology* (Eds: A. Micallef, S. Krastel, and A. Savini) Springer Geology. Springer, Switzerland. ISBN: 978-3-319-57851-4

IPCC (2014). Climate Change 2014: *Impacts, Adaptation, and Vulnerability. Part A: Global and Sectoral Aspects. Contribution of Working Group II to the Fifth Assessment Report of the Intergovernmental Panel on Climate Change* (Eds: Field, C.B., Barros, V.R., Dokken, D.J., Mach, K.J., Mastrandrea, M.D., Bilir, T.E., Chatterjee, M., Ebi, K.L., Estrada, Y.O., Genova, R.C., Girma, B., Kissel, E.S., Levy, A.N., MacCracken, S., Mastrandrea, P.R., and White, L.L.). Cambridge University Press, Cambridge, United Kingdom and New York, NY, USA, 1132 p.

Jones, C.G., Lawton, J.H., and Shachak, M. (1994). Organisms as ecosystem engineers. *Oikos,* 69, 373–386.

Kirk, J.T.O. (1976). *Light and Photosynthesis in Aquatic Ecosystems*. Cambridge University Press, Cambridge. 414 p.

Kirk, J.T.O. (1994). *Light and Photosynthesis in Aquatic Ecosystems*, 2nd Edn. Cambridge University Press, Cambridge. 509 p.

Kirk, J.T.O. (2010) *Light and Photosynthesis in Aquatic Ecosystems*, 3rd Edn. Cambridge University Press, Cambridge. 662 p.

Leenheer, J. A., and Croué, J. (2003). Characterizing dissolved aquatic organic matter. *Environmental Science and Technology*, 37, 18A–26A. doi:10.1021/es032333c

Lindell, T., Pierson, D., Premazzi, G., and Ziliolli, E. (1999). (Eds) *Manual for monitoring European lakes using remote sensing techniques*. Office for official publications of European Communities, Luxembourg. 161 p.

MacKinnon, M.R., and Herbert. B.W. (1996). Temperature, Dissolved Oxygen and Stratification in a Tropical Reservoir, Lake Tinaroo, Northern Queensland, Australia. *Marine Freshwater Research*, 47, 937–949.

Meinesz, A. (1999). *Killer algae: the true tale of a biological invasion*. University of Chicago Press, Chicago. 360 p.

Minnett, P., and Kaiser-Weiss, A. (2012). *Near-surface oceanic temperature gradients*. GHRSST Discussion document, version 12, Jan 2012. *https://www.ghrsst.org/wp-content/uploads/2021/04/SSTDefinitionsDiscussion.pdf*

Moeller, H.V., Laufkötter, C., Sweeney, E.M., and Johnson, M.D. (2019). Light-dependent grazing can drive formation and deepening of deep chlorophyll maxima. *Nature Communications*, 10, 1978. *https://doi.org/10.1038/s41467-019-09591-2*

Monk J, Barrett N, Bridge T, Carroll A, Friedman A, Ierodiaconou D, Jordan A, Kendrick G, and Lucieer V. (2018). Marine sampling field manual for autonomous underwater vehicles (AUVs). In *Field Manuals for Marine Sampling to Monitor Australian Waters*. (Eds: Przeslawski, R., Foster, S.). National Environmental Science Programme (NESP). pp. 65–81.

Mumby, P.J., Green, E.P., Edwards, A.J., and Clark, C.D. (1997). Measurement of seagrass standing crop using satellite and digital airborne remote sensing. *Marine Ecology Progress Series*, 159, 51–60.

NSW NPI (2015). *Management of coastal lakes and lagoons in NSW* webpage, NSW Department of Primary Industries website: *https://www.dpi.nsw.gov.au/fishing/habitat/aquatic-habitats/wetland/coastal-wetlands/management-of-coastal-lakes-and-lagoons-in-nsw*

OzCoasts (2018). *OzCoasts Australian Online Coastal Information (Geoscience Australia) website*: *http://www.ozcoasts.gov.au/index.jsp*

Pace, M.L., and Prairie, Y.T. (2005). Respiration in Lakes. Ch 7 in *Respiration in Aquatic Ecosystems* (Eds: P.A. del Giorgio and P.J. le B. Williams) Oxford University Press, Oxford. pp 103–121.

Pegau, W.S., and Zaneveld, J.R.V. (1993). Temperature-dependent absorption of water in the red and near-infrared portions of the spectrum. *Limnology and Oceanography*, 38 (1), 188–192.

Pennesi, C., Rindi, F., Totti, C., and Beolchini, F. (2015). Marine Macrophytes: Biosorbents. In: *Springer Handbook of Marine Biotechnology*. (Ed: Kim, S.K.) Springer Handbooks. Springer, Berlin, Heidelberg.

Pozdnyakov D.V., and Grassl, H. (2003). *Colour of inland and coastal waters: A methodology for its interpretation*. Springer-Praxis, Chichester.

Rees, G.N., Shackleton, M.E., Watson, G.O., Dwyer, G.K., and Stoffels, R.J. (2019). Metabarcoding demonstrates dietary niche partitioning in two coexisting blackfish species. *Marine and Freshwater Research*, 71, 512–517. *https://doi.org/10.1071/MF18491*

Reitsema, R.E., Meire, P., and Schoelynck, J. (2018). The Future of Freshwater Macrophytes in a Changing World: Dissolved Organic Carbon Quantity and Quality and Its Interactions With Macrophytes. *Frontiers in Plant Science*, 9, 629. doi:10.3389/fpls.2018.00629

Sachse, A., Henrion, R., Gelbrecht, J., and Steinberg, C. E. W. (2005). Classification of dissolved organic carbon (DOC) in river systems: Influence of catchment characteristics and autochthonous processes. *Organic Geochemistry*, 36, 923–935. doi:10.1016/j.orggeochem.2004.12.008

Schroeder, T, Devlin, M.J., Brando, V.E., Dekker, A.G., Brodie, J.E., Clementson, L.A., and McKinna, L. (2012). Inter-annual variability of wet season freshwater plume extent into the Great Barrier Reef lagoon based on satellite coastal ocean colour observations. *Marine Pollution Bulletin*, 65, 210–223. doi:10.1016/j.marpolbul.2012.02.022

Seritti A., Manca B.B., Santinelli C., Murru E., Boldrin A., and Nannicini L. (2003). Relationships between dissolved organic carbon (DOC) and water mass structures in the Ionian Sea (winter 1999). *Journal of Geophysical Research*, 108(C9), 8112. doi:10.1029/2002JC001345

Shackleton, M.E., Rees, G.N., Watson, G., Campbell, C., and Nielsen, D. (2019). Environmental DNA reveals landscape mosaic of wetland plant communities. *Global Ecology and Conversation*, 19, e00689. *https://doi.org/10.1016/j.gecco.2019.e00689*

Shafron, M., Croome, R., and Rolls, J. (1990). Water Quality. Ch 9 in *The Murray* (Eds: Mackay, N., and Eastburn, D.). Murray Daring Basin Commission, Canberra.

Sherman, B., (2005). *Hume Reservoir Thermal Monitoring and Modelling*. Final Report for State Water as agent for MDBC. CSIRO Land and Water Client Report, April 2005.

Short, F.T., and Wyllie-Echeveria, S. (1996). Natural and human-induced disturbance of seagrasses. *Environmental Conservation*, 23 (1), 17–27. doi:10.1017/S0376892900038212

Smyth, K., and Elliot, M. (2016). Effects of changing salinity on the ecology of the marine environment. In *Stressors in the Marine Environment* (Eds: Solan, M. and Whitely, N.M.). Oxford University Press, Oxford. doi:10.1093/acprof:oso/9780198718826.003.0009

Steinberg, C.E.W., Meinelt, T., Timofeyev, M.A., Bittner, M., and Menzel, R. (2008). Humic substances (review series). Part 2: Interactions with Organisms. *Environmental Science and Pollution Research*, 15, 128–135. doi:10.1065/espr2007.07.434

Stewart, K.A. (2019). Understanding the efects of biotic and abiotic factors on sources of aquatic environmental DNA. *Biodiversity and Conservation*, 28, 983–1001. *https://doi.org/10.1007/s10531-019-01709-8*

Te Ara (2018). *Unique geothermal fields* webpage, The Encyclopedia of New Zealand website: *https://teara.govt.nz/en/hot-springs-mud-pools-and-geysers/page-1*

Tomczak, M. (1998). *Shelf and Coastal Oceanography* website: *https://incois.gov.in/Tutor/ShelfCoast/index.html*

UNESCO (1981a). The Practical Salinity Scale 1978 and the International Equation of State of Seawater 1980. *UNESCO Technical Papers in Marine Science 36*. 25 p.

UNESCO (1981b). Background papers and supporting data on the Practical Salinity Scale 1978. *UNESCO Technical Papers in Marine Science 37*. 144 p.

Valeila, I., McClelland, J., Hauxwell, J., Behr, P.J., Hersh, D., and Foreman, K. (1997). Macroalgal blooms in shallow estuaries: Controls and ecophysiological and ecosystem consequences. *Limnology and Oceanography*, 42(5–2), 1105–1118.

Webster, I.T., Atkinson, I., Bostock, H., Brooke, B., Douglas, G., Ford, P., Hancock, G., Herzfeld, M., Leeming, R., Lemckert, C., Margvelashvili, N., Noble, B., Oubelkheir, K., Radke, L., Revill, A., Robson, B., Ryan, D., Schacht, C., Smith, C., Smith, J., Vicente-Beckett, V., and Wild-Allen, K. (2006). *The Fitzroy Contaminants Project. A Study of the Nutrient and Fine-Sediment Dynamics of the Fitzroy Estuary and Keppel Bay.* Cooperative Research Centre for Coastal Zone, Estuary and Waterway Management Technical Report #42, Coastal CRC, Queensland. ISBN 1 921017 56 2

Wetzel, R.G. (2001). *Limnology.* 3rd Edn. Academic Press. ISBN 9780127447605

Wilcox, D.A. (1995). Wetland and aquatic macrophytes as indicators of anthropogenic hydrologic disturbance. *Natural Areas Journal,* 15(3), 240–248.

Williams, C.J., Frost, P.C., Morales-Williams, A.M., Larson, J.H., Richardson, W.B., Chiandet, A.S., and Xenopoulos, M.A. (2016). Human activities cause distinct dissolved organic matter composition across freshwater ecosystems. *Global Change Biology,* 22, 613–626. doi:10.1111/gcb.13094

Xing, X.-G., Zhao, D-Z., Liu, Y.-G., Yang, J._H., Xiu, P., and Wang, L. (2007). An overview of remote sensing of chlorophyll fluorescence. *Ocean Science Journal*, 42(1), 49–59.

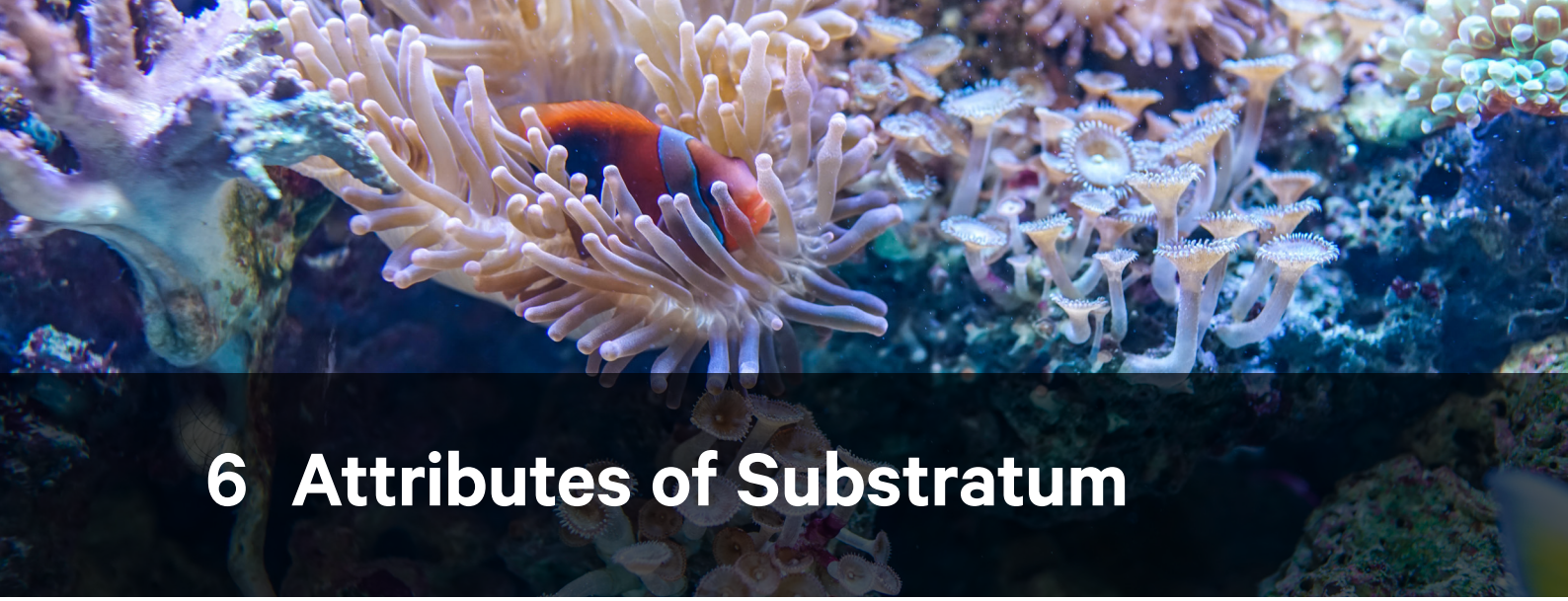

6 Attributes of Substratum

The solid surface that underlies a waterbody is called the seabed or seafloor. The generic term substratum describes an underlying layer or substance beneath the ground surface. In an aquatic environment, the substratum layer rests on the seabed (or lithosphere) and may comprise a variety of materials such as sand, silt, mud, rocks, and coral (see Section 1.3.3). It forms the interface between the seabed and the water column and hosts a range of aquatic organisms, by providing both food and habitat (see Section 3).

Variations in the substratum can be described in terms of four interrelated attributes:

- waterbody depth (see Section 6.1);
- geomorphic features (see Section 6.2);
- composition (see Section 6.3); and
- benthos (see Section 6.4).

6.1 Waterbody Depth

Bathymetry measures the vertical distance from the water surface to the substrate in a waterbody (see Section 13). As introduced in Section 5, the depth of a waterbody impacts several physical, chemical, and biological attributes of the water column. Both light penetration and temperature decrease with increasing water depth in waterbodies (see Section 8). In oceans, light levels below 200 m are insufficient for photosynthesis, but this may decrease to 1 m water depth in very turbid waterbodies (see Section 5.1.5).

The depth of the substratum directly impacts the type of organisms, both plants and animals, which can exist there. Accordingly, classification of benthic animals is based on two primary depth regions:

- shallower littoral region—with more light and warmth, supporting primary producing organisms; and the
- deep region—with virtually no light, containing colder waters, accommodating organisms that do not rely on sight, comprising the bathyal, abyssal, and hadal zones (see Section 6.4).

However, it is not only the depth of the substratum but its shape that is ecologically significant (see Section 6.2). Water movement also tends to be reduced at greater water depths, which in turn impacts the materials that comprise the substratum (see Section 6.3).

6.2 Geomorphic Features

Marine geomorphology is the study of landforms, their processes, form and sediments at the seabed. Geomorphology is scale dependent, and significant for a range of marine activities, such as:

- designing and monitoring Marine Protected Areas (MPA; see Excursus 20.2);
- understanding benthic ecosystems and seafloor geology (see Sections 2.2, 3 and 20); and
- assessing living and non-living seabed resources, including those with economic value, such as seabed mining (Harris and Baker, 2012; Harris *et al.*, 2014).

The major geomorphic zones (continental shelf, the continental slope, the continental rise, and the abyssal plain) are continental in scale (see Figure 1.9). In bathymetric terms these broad zones are also called Primary Bathymetric Units (see Excursus 13.1). For most practical purposes, the continental zones are subdivided into distinct geomorphic features, which are regional and local in scale (Geo-Seas, 2012). Dove et al. (2020) defined 40 geomorphic features based on a two-part classification of morphology (bathymetric highs and lows, plus surfaces and lineaments; see Figure 6.1), and geomorphology. Definitions of these generic features are listed in Table 6.1.

Background image: Coral substrate. **Source:** Michelle Raponi, Pixabay. Retrieved from *https://pixabay.com/photos/underwater-coral-reef-fish-ocean-3250644/*

Figure 6.1 Morphological features

a. Bathymetric highs

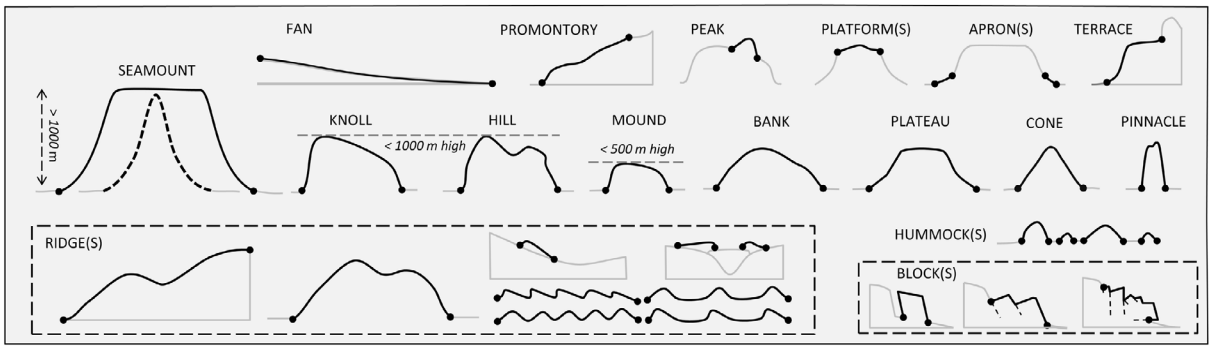

b. Bathymetric lows

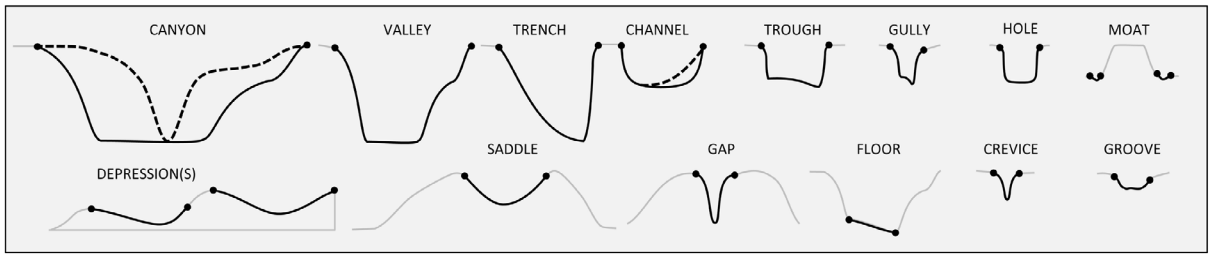

c. Planar surfaces, inclined planes and surfaces

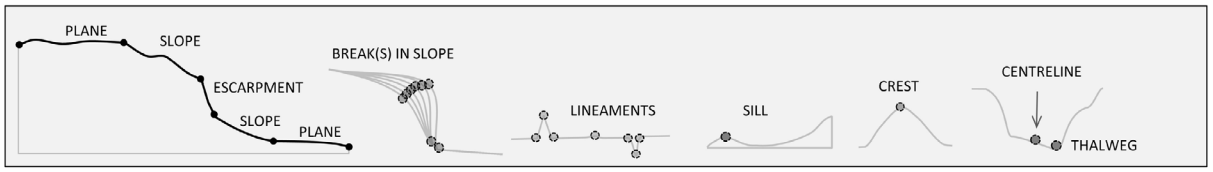

Source: Dove *et al.* (2020) Figure 3

Table 6.1 Generic geomorphic features

Term	Definition
APRON	A gently-dipping surface, occurring at the base of a bathymetric high, that is elevated relative to the adjacent seafloor.
BANK	An elevation of the seafloor, often found in water depths less than 200 m (adapted from IHO, 2019). *BANKS are lower elevation than SEAMOUNTS, and tend to occur in shallower water.*
BLOCK	A discrete, usually angular mass comprising at least two relatively flat surfaces.
BREAK IN SLOPE	A marked and/or abrupt change in slope. *BREAK IN SLOPE can be used to define the limit of other features (e.g. SHELF, PLATFORM, ESCARPMENT).*
CANYON	A typically elongated, steep-sided bathymetric low that generally deepens down-slope (modified from IHO, 2019). *CANYONS tend to be higher gradient and more complex features than CHANNELS and are larger and more sinuous than GULLIES. VALLEYS tend to have a more limited depth range than CANYONS.*
CENTRELINE	A line that represents the mid-line long axis of a feature. Contrast CENTRELINE with THALWEG and CREST, which define the lines of lowest and highest elevation, respectively, along an elongate feature.
CHANNEL	A general term for an elongated bathymetric low (adapted from IHO, 2019). *CHANNELS tend to have flatter and lower gradient FLOORS than GULLIES and CANYONS, and usually have more variable cross-sections than TROUGHS.*
CONE	A topographic high of generally conical shape, which may have a truncated peak. *CONES have more pointed peaks and are more symmetrical than KNOLLS.*
CREST	A line of highest elevation along a bathymetric high, the lateral position of which can vary longitudinally. *CRESTS contrast with CENTRELINES, which define mid-line axes along elongated features.*
CREVICE	An elongated narrow opening (adapted from Goudie, 2014). *Unlike CANYONS, CREVICES do not necessarily deepen downslope, and unlike TROUGHS, they are not flat bottomed.*

Term	Definition
DEPRESSION	A general term for a closed-contoured bathymetric low. *DEPRESSIONS vary in scale from small local features to larger basins. They generally have lower gradient sides than HOLES.*
ESCARPMENT	A steep slope, separating areas of relatively lower slope (modified from IHO, 2019).
FAN	An elevated feature which expands (and typically descends) from a locus to a commonly curved outer margin.
FLOOR	A relatively broad and lower gradient feature within a bathymetric low, flanked by higher and steeper gradient features.
GAP	A narrow break in an elevated feature (modified from IHO, 2019). *GAPS are generally narrower than SADDLES.*
GROOVE	An elongated, narrow and relatively shallow bathymetric low which commonly occurs in parallel or sub-parallel groups. *Unlike GAPS, GROOVES are elongated features, and often occur in groups. GROOVES tend to have higher length/width ratios than CREVICES*
GULLY	A steep-sided, low sinuosity, relatively high-gradient channel. *GULLIES are typically smaller than CANYONS.*
HILL	A distinct elevation generally of irregular shape, less than 1000 m above the surrounding relief as measured from the deepest isobath that surrounds most of the feature (IHO, 2019). *HILLS have more irregular profiles than KNOLLS, and their length generally exceeds their height (contrast with PEAKS). They are also smaller than SEAMOUNT, and larger than individual HUMMOCKS.*
HOLE	A sub-circular (in planform) bathymetric low with steep walls and a generally flat FLOOR (modified from IHO, 2019). HOLES generally have steeper sides than DEPRESSIONS.
HUMMOCK	A small KNOLL or MOUND, which commonly occurs in groups. HUMMOCKS are generally smaller than KNOLLS and HILLS
KNOLL	A distinct elevation with a smooth, commonly rounded profile, <1000 m above the surrounding relief (modified from IHO, 2019). *KNOLLS have more regular profiles than HILLS, and their width generally exceeds their height (contrast with PEAKS). They are also smaller than SEAMOUNTS, and larger than individual HUMMOCKS.*
LINEAMENT	A linear to curvilinear topographic feature of positive, negative or indeterminate relief. May be discontinuous with variable relief (positive to negative) along its length.
MOAT	An annular or partially annular bathymetric low typically located at the base of isolated elevation (modified from IHO).
MOUND	A distinct elevation with a variable, sometimes rounded profile which is generally less than 500 m above the surrounding seafloor (modified from IHO, 2019).
PEAK	A prominent, commonly pointed elevation rising from a larger feature (modified from IHO, 2019)
PINNACLE	A spire-shaped pillar, either isolated or rising from a larger feature (IHO, 2019).
PLANE	A flat, or sub-horizontal surface.
PLATEAU	A generally closed-contoured, relatively flat-topped bathymetric high with one or more relatively steep sides (modified from IHO, 2019).
PLATFORM	A generally broad, planar surface that is at least partially elevated, and lower gradient, than the surrounding areas (adapted from Goudie, 2014).
PROMONTORY	A protrusion extending from a bathymetric high into deeper water (adapted from IHO, 2019).
RIDGE	An elongated elevation of varying complexity, size and gradient (length > width) (modified from IHO, 2019).
SADDLE	A broad pass in an elevated feature (modified from IHO, 2019). *SADDLES are generally broader (relative to their height) than GAP*
SEAMOUNT	A prominent feature rising more than 1000 m above the surrounding relief (modified from IHO, 2019). *SEAMOUNTS are larger than KNOLLS and HILLS (<1000 m) and may incorporate PEAKS (and other features).*
SILL	A relatively shallow elevated feature between (or adjacent to) bathymetric lows (e.g. DEPRESSIONS) (modified from IHO, 2019).
SLOPE	An inclined surface.
TERRACE	A generally elongated and planar feature consisting of an upper planar surface, and relatively steeper descending slope. The planar surface is bounded on one side by a steeper ascending slope (modified from IHO, 2019). A TERRACE is not closed-contoured like a PLATEAU, and its lower-gradient surface can be mapped as a PLATFORM.
THALWEG	A line of lowest elevation along an elongate bathymetric low, the lateral position of which can vary longitudinally. *THALWEGS contrast with CENTRELINES, which define mid-line axes along bathymetric lows.*
TRENCH	A long, deep, asymmetrical bathymetric low with relatively steep sides (adapted from IHO, 2019). Unlike TROUGHS, TRENCHS are typically asymmetric in cross-section.
TROUGH	An elongate bathymetric low, generally wide and flat bottomed with symmetrical and sub-parallel sides (modified from IHO, 2019). Unlike DEPRESSIONS, TROUGHS are not necessarily closed-contoured, and unlike VALLEYS, they do not always deepen down-slope. Unlike TRENCHS, TROUGHS are typically symmetrical in cross-section
VALLEY	An elongated bathymetric low, typically occurring between prominent bathymetric highs, which generally widens and deepens down-slope (modified from IHO). *VALLEYS have more limited depth ranges than CANYONS.*

Source: Dove *et al.* (2020)

Figure 6.2 Global Seafloor Geomorphic Feature map (GSFM)

This is the first digital, global map showing the distribution of seafloor geomorphic features.

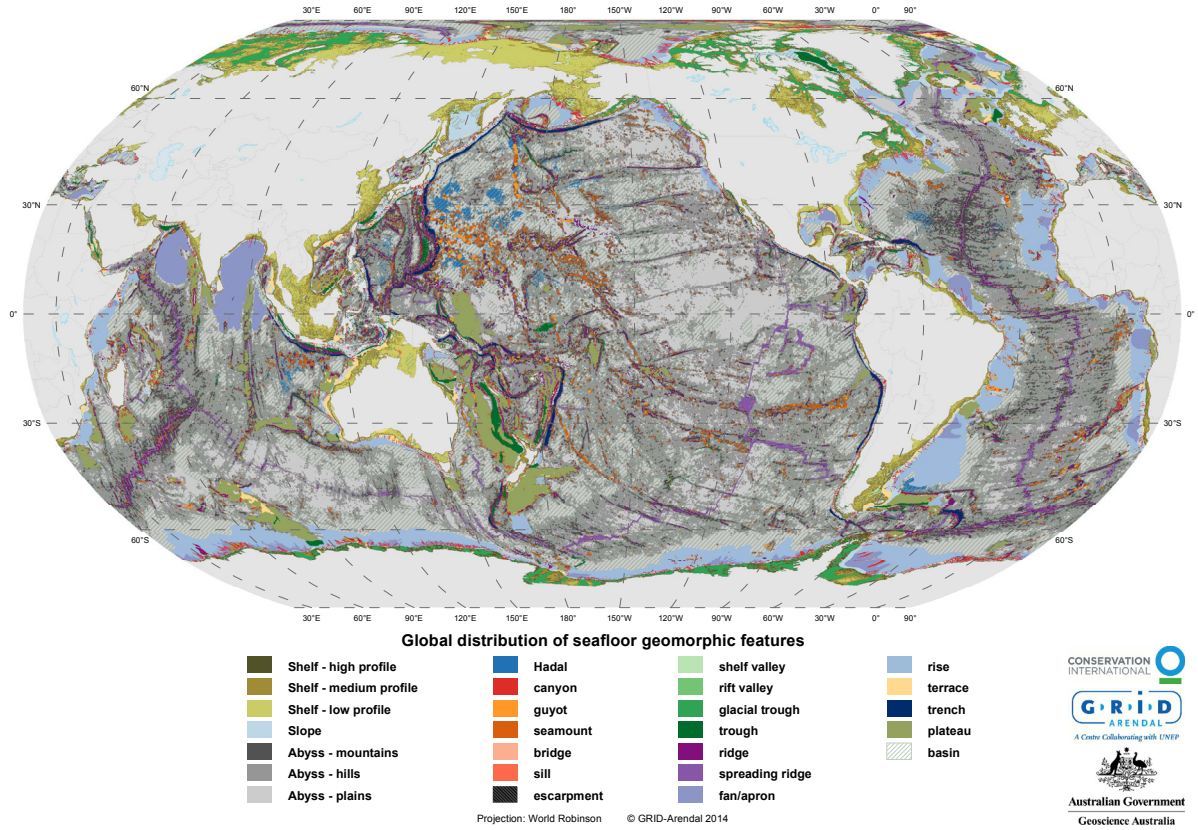

Source: Conservation International, GRID-Arsenal and Geoscience Australia. Retrieved from: *http://www.bluehabitats.org*

A classification of 29 geomorphic feature categories was used to produce the first digital Global Seafloor Geomorphic Feature map (GSFM; Harris *et al.*, 2014; see Figure 6.2). Based on Shuttle Radar Topography Mapping (SRTM30_PLUS) data and other datasets, this product has enabled global and regional estimates of physiographic characteristics, such as area, abundance, and size, for a range of geomorphic features, and comparisons of selected characteristics in different geographic regions.

6.3 Composition

The substratum may comprise rock, reefal material, sand, and/or sediment that have settled out of the water column. These components can occur in varying combinations, depending on local geology and water movement. Loose materials offer a medium for microbial and plant growth, and a wide range of habitats for animal life (see Section 3). The packing density of substrate materials is related to grain size, which regulates the flow of water and determines the availability of dissolved oxygen to benthic fauna. The quality of the benthic environment is essentially determined by the organic content of sediments and the size and shape of their particles.

Four types of seafloor substrates are recognised to support specific benthic organisms:

- sandy soft (psammon)—occurring along exposed shorelines, these loose sands and gravels are regularly moved by waves, facilitating circulation of oxygen and nutrients for corals, nematodes, echinodermata, and sponges;
- muddy soft (pelos)—offer more stable and anoxic conditions that are endured by bivalves and annelids, which can siphon oxygen and nutrients from the water column;
- hard—support stationary fauna with tentacles and mobile crinoidea;
- secondary hard—unconsolidated organic and inorganic materials accumulate on the ocean floor and coalesce to support annelid tube worms.

In Australia, Geoscience Australia (GA) is responsible for the national marine samples database (MARS), which quantifies and catalogues seabed sediment samples from Australian marine waters (Passlow *et al.*, 2005). MARS includes quantitative analyses of > 40,000 sediment samples, as well as subsample records of grain size, mud, sand, gravel, and/or carbonate concentrations (see Section 5.4). Sediment cores are analysed in terms of mineralogy, age, geochemical properties, bulk density, p-wave velocity, porosity, and magnetic susceptibility. Relationships between sediment properties and geomorphic features have contributed to the development of the national benthic bioregionalisation (CoA, 2005).

6.4 Benthos

Depending on waterbody depth and composition, the substratum may support a variety of plant and animal life, including microphytobenthos, seagrass, macroalgae, and corals. In favourable conditions, a rich community of organisms coexist on and in the substratum. Most of the sand and mud dwelling organisms live on detritus from decomposed plant material. In some environments, the patterns of benthic marine biodiversity are clearly related to abiotic attributes, such as latitude, waterbody depth, current velocity, and substrate type (Roff *et al.*, 2003; Post *et al.*, 2006), allowing relevant attributes to be used as surrogates of biodiversity (McArthur *et al.*, 2010). The Australian standardised nomenclature for benthic habitat classification is given in Butler *et al.* (2017).

The diverse group of benthic organisms is commonly divided into overlapping categories based on size:

- microbenthos—microscopic organisms, such as microphytobenthos (less than 0.1 mm);
- meiobenthos—tiny, motile fauna living in aquatic sediments (0.1–1.0 mm);
- macrobenthos—visible invertebrates and macroalgae living on or in submerged sediments (greater than 1.0 mm);

or location:

- endobenthos—smaller organisms living in sandy or muddy sediments; and
- epibenthos—larger organisms living on the seabed and comprising around 80% of all benthic fauna.

Ocean benthic biome definitions are based on the water column depth above the substratum (see Figure 3.1). Their substrata support varying aquatic organisms:

- sublittoral zone—substratum of the continental shelf with sufficient light penetration to allow photosynthesis, which supports a rich diversity of plant and animal life;
- bathyal zone—substratum of the continental slope, which supports fewer organisms;
- abyssal zone—substratum of the deep ocean, which supports hardy organisms that can survive on detritus sifted from sediments; and
- hadal zone—substratum of hydrothermal vents in deep ocean trenches, which only supports invertebrates such as tubeworms and clams that live in microscopic Archaea.

The National Marine Bioregionalisation (NMB) defines a benthic bioregionalisation of Australia's EEZ as well as a pelagic regionalisation of water column structure (CoA, 2005; see Section 2.2).

...spatial changes in seabed biota are strongly related to mud and gravel content, seabed disturbance from waves and currents, water depth, and geomorphology.
(Heap, 2006)

6.5 Further Information

Benthic bioregionalisation for Australian EEZ: CoA (2005)

Bentho-Pelagic Processes: Alfred Wegener Institute: *https://www.awi.de/en/science/biosciences/bentho-pelagic-processes.html*

Geo-Seas: *http://www.geo-seas.eu/; http://www.geo-seas.eu/documents/geoseas/html_page/Geo-Seas_D10_5_B.pdf*

Keene *et al.* (2008)

Marine Sediments Database (MARS): GA (2018), Passlow *et al.* (2005); *https://ecat.ga.gov.au/geonetwork/srv/eng/catalog.search?node=srv#/metadata/69869*

6.6 References

Butler, C., Lucieer, V., Walsh, P., Flukes, E., and Johnson, C. (2017). *Seamap Australia [Version 1.0] the development of a national benthic marine classification scheme for the Australian continental shelf*. Seamap Australia, University of Tasmania. ISBN: 978-1-925646-61-0

CoA (2005). *National Marine Bioregionalisation of Australia. Summary*. Department of Environment and Heritage, Canberra, Australia.

Dove, D., Nanson, R., Bjarnadóttir, L.R., Guinan, J., Gafeira, J., Post, A., Dolan, M.F.J., Stewart, H., Arosio, R., and Scott, G. (2020). *A two-part seabed geomorphology classification scheme: (v.2)*. Open Report Prepared by the MIM-GA Geomorphology Working Group. doi:10.5281/ZENODO.4075248

GA (2018) *Marine Sediments (MARS) Database* webpage, Geoscience Australia website: *https://ecat.ga.gov.au/geonetwork/srv/eng/catalog.search?node=srv#/metadata/a05f7892-eef2-7506-e044-00144fdd4fa6*

Geo-Seas (2012). *Pan-European infrastructure for management of marine and ocean geological and geophysical data. Deliverable 10.5: Standards for seabed habitat mapping (Part B: Terrain)*. *http://www.geo-seas.eu/documents/geoseas/html_page/Geo-Seas_D10_5_B.pdf*

Goudie, A. (2014). *Alphabetical glossary of geomorphology, version 1.0*. Electronic edition of the International Association of Geomorphologists (IAG). 2014. 84 p.

Harris, P.T., and Baker, E.K. (Eds.) (2012). *Seafloor Geomorphology as Benthic Habitat: GeoHab Atlas of Seafloor Geomorphic Features And Benthic Habitats*. Elsevier, Amsterdam, p. 947.

Harris, P.T., Macmillian-Lawler, M., Rupp, J., and Baker, E.K. (2014). Geomorphology of the oceans. *Marine Geology*, 352, 4–24.

Heap, A. (2006). Classifying Australia's seascapes for marine conservation. *AusGeo News 84*, March 2006. Geoscience Australia.

IHO (2019) *Standardization of Undersea Feature Names: Guidelines Proposal form Terminology*. (Edition 4.2.0 October, 2019). Monaco, International Hydrographic Bureau, IHO Publication B–6.

Keene, J., Baker, C., Tran, M. and Potter, A. (2008). *Geomorphology and Sedimentology of the East Marine Region of Australia*. Geoscience Australia, Record 2008/10. Geoscience Australia, Canberra. 262 p.

McArthur, M.A., Brooke, B.P., Przeslawski, R., Ryan, D.A., Lucieer, V.I., Nichol, S., McCallum, A.W., Mellin, C., Cresswell, I.D., Radke, L.C. (2010). On the use of abiotic surrogates to describe marine benthic biodiversity. *Estuarine, Coastal and Shelf Science*, 88, 21–32.

Passlow, V., Rogis, J., Hancock, A., Hemer, M., Glenn, K and Habib, A. (2005). *Final Report, National Marine Sediments Database and Seafloor Characteristics Project*. Geoscience Australia, Record 2005/08.

Post, A.L., Wassenberg, T.J., Passlow, V. (2006). Physical surrogates for macrofaunal distributions and abundance in a tropical gulf. *Marine and Freshwater Research*, 57, 469e483.

Roff, J.C., Taylor, M.E., and Laughren, J. (2003). Geophysical approaches to the classification, delineation and monitoring of marine habitats and their communities. *Aquatic Conservation: Marine and Freshwater Ecosystems*, 13(1), 77–90. doi:10.1002/aqc.525

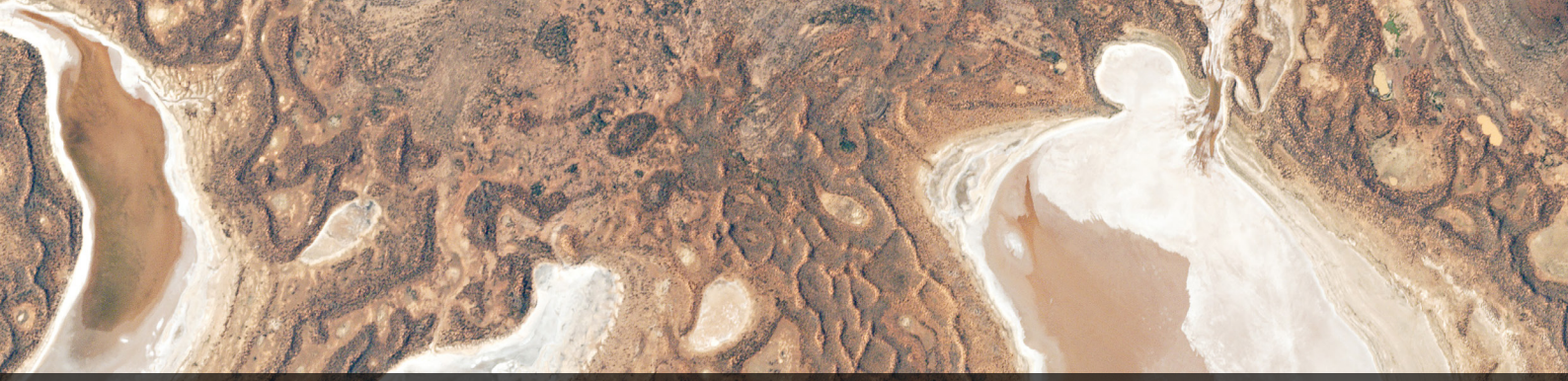

7 Attributes of Waterbodies

Waterbodies can be described in terms of a number of attributes, including:

- observed colour (see Section 7.1);
- extent and permanence (see Section 7.2);
- depth and volume (see Section 7.3);
- carbon cycling (see Section 7.4); and
- dynamics (see Section 7.5).

7.1 Observed Colour

The colour of a waterbody, when observed from above its surface, critically depends on illumination and viewing conditions (see Sections 5.1.4 and 8). It can also vary with changes in:

- the shape, texture, and surface tension of the surface (see Sections 4.2, 4.3, and 4.4 respectively);
- the presence of floating matter (see Section 4.6) and ice cover (see Section 4.7);
- the colour of the water column (see Section 5); and/or
- the colour of the underlying water column and/or substratum (see Section 6).

Oil slicks and other pollutants can dampen wave action and increase reflectance of some wavelengths (see Section 19.4.3). Ocean surface waves create 'whitecaps' as they break, which change the observed water colour (Estep and Arnone, 1994). Algal blooms floating on the water surface can also dramatically change the apparent water colour (see Section 19.5).

Water surface roughness, or texture, changes the way light is reflected from the surface and can result in sunglint and skyglint (see Section 4.3). Skyglint is caused by diffuse blue skylight, or in cloudy conditions diffuse white to grey light, being reflected from the water surface, and only comprises a small proportion of diffuse upwelling radiation (see Section 8.1.3).

7.2 Extent and Permanence

Current knowledge about surface water extent is valuable for a wide range of applications, including:

- updating cartographic boundaries;
- monitoring floodwaters;
- assessing aquatic habitats;
- delineating wetland dynamics;
- determining minimum flow requirements of rivers; and
- modelling hydrology for water resource management.

Surface water is readily discernible from both bare and vegetated land by using near infrared (NIR) reflectance (see Section 5.1.4), since while NIR wavelengths are absorbed by pure water, they are strongly reflected by dry land surfaces and vegetation (see Volume 3A). In highly turbid waters the NIR reflectance may increase slightly (see Section 5.1.5).

Background image: The northeastern portion of Lake Carnegie, a large ephemeral lake in central WA, is imaged by the Flock-1 satellite on 26 January 2016.
Source: Planet Labs Inc. (CC-BY-SA 4.0). Retrieved from *https://www.planet.com/gallery/#!/post/lake-carnegie*

Most difficulties with delineating land-water boundaries in EO imagery are related to floating plants, algal scum, or overhanging riparian vegetation. The interface between land and water, however, generally involves varying water depth and colour, which may make the boundaries of waterbodies more difficult to delineate using optical imagery. Other forms of EO data, including TIR and radar imagery, can also be used to delineate surface water extent (see Section 11).

Many Australian waterbodies are ephemeral, and their permanence has been characterised by analysis of EO image time series (see Volume 1A—Excursus 5.1). EO methods for monitoring the permanence of waterbodies are described in Section 11.5.

7.3 Depth and Volume

The depth of a waterbody invariably changes across its extent. As well as obvious differences between shallow borders and deep, central areas, the topography of submerged zones can vary significantly due to features such as coral reefs, and underwater ridges and trenches (see Sections 2.2 and 6.2). Seafloor shape impacts water movement (see Section 16) and the distribution of marine biota (see Section 20).

The volume of water in a waterbody is a function of the depth of the water column (see Section 5.1.1), the extent of the water surface (see Section 11) and the depth profile(s) of the waterbody (see Section 12). The depth and extent of the water column, however, can change over time with precipitation, runoff, outflow, and evaporation. The depth profile of a waterbody also varies over time with the processes of sedimentation, erosion and dredging.

Depth measurements in water are called soundings. Originally measured using sounding lines from ships, a range of EO technologies can now be used to measure water depth in both shallow and deep waters (see Section 10). Such measurements at individual points can be processed into map or image form to create bathymetric charts. The Nippon Foundation-GEBCO Seabed 2030 project is coordinating and extending bathymetric datasets around the globe to create a public map of seafloor topography by 2030 (see Excursus 7.1).

Depth sounding instruments include lidar (based on laser) and sonar (based on sound; see Sections 10 and 13.3.2). Lidar is deemed more cost-effective than multi-beam acoustic surveys for coverages of less than 100 km^2 and water depths less than 50 m, although the cost of lidar surveys varies significantly with sampling density (Purkis and Brock, 2013; see Section 13.4.1). Shallow seafloor topographic maps have also been derived from synthetic aperture radar (SAR) imagery, although the processing requires imagery to be acquired under favourable conditions involving tidal flow and requires depth soundings for calibration (see Section 13.3.1).

Light attenuation in pure water increases with increasing water depth (see Figure 5.10). This relationship allows multispectral and hyperspectral imagery to be used to estimate water depth in optically shallow waters (that is, where there is a measurable amount of light being reflected from the benthos through the water column and through the air-water interface; Brando *et al.,* 2009). Such methods rely on the varying attenuation properties of different wavelengths of light through water (see Section 5.1.4). In shallow waters, changes in substrate colour also impact optical properties (see Section 8.4.3). While these estimates are not the same as depth sounding, and rarely achieve the same accuracy or maximum depth that may be obtained using depth sounding techniques, they are spatially comprehensive. Stereophotogrammetric methods using high resolution imagery with multi-angle sensors have been used in conjunction with multispectral and hyperspectral methods to determine water depth (Collings *et al*., 2018; see Section 13.4.2).

Excursus 7.1—Nippon Foundation-GEBCO Seabed 2030 Project

Source: GEBCO (2017)
Further Information: Mayer *et al.* (2018)

Seabed 2030, a collaborative project between the Nippon Foundation and the General Bathymetric Chart of the Oceans (GEBCO), intends to collate all current bathymetric data to create a 'definitive', publicly-available map of the world ocean floor by 2030. Launched in 2017 at the UN Ocean Conference, this project seeks to map the extensive areas of seafloor topography that are currently unmapped—these are estimated to be up to 80% of the global seafloor (Mayer *et al.*, 2018). It builds on more than 100 years of GEBCO's history of global seafloor mapping and coordinates inputs from academic, public and industry sources (Wölfl *et al.*, 2019). The expected mapping resolutions of this project are summarised in Table 7.1 and shown in Figure 7.1. Australia is contributing to this global effort through its national seabed mapping coordination program, AusSeabed (see Section 10.4).

Table 7.1 Seabed 2030 minimum mapping resolutions

Waterbody depth range (m)	Grid cell size (m)	% world ocean
0–1500	100 x 100	13.7
1500–3000	200 x 200	11
3000–5750	400 x 400	72.6
5750–11,000	800 x 800	2.7

Source: Mayer *et al.* (2018) Table 2

Figure 7.1 Proposed waterbody depth regions for Seabed 2030

Depth regions based on 2°×2° deep water multibeam installed on surface vessels, calculated at 60° from nadir (see Table 7.1).

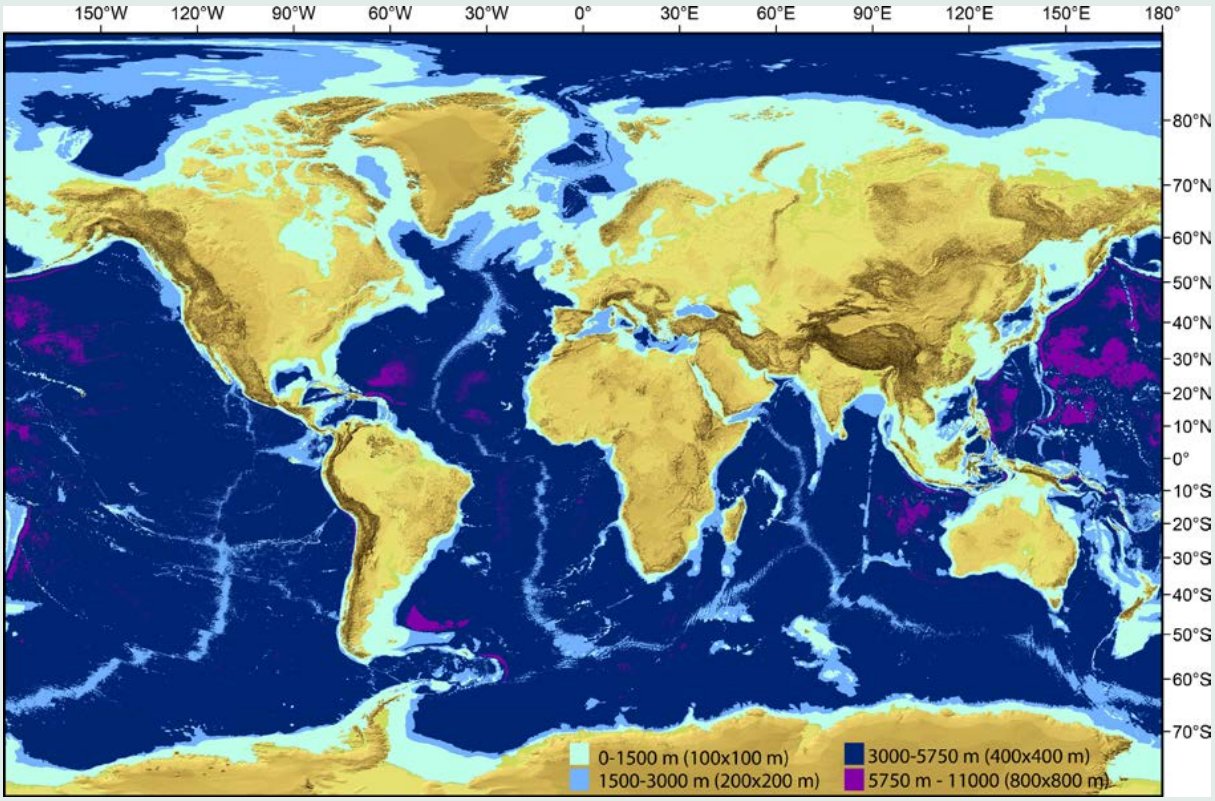

Source: Mayer *et al.* (2018) Figure 7

7.4 Carbon Cycling

The role of waterbodies in the global carbon cycle is briefly introduced in Section 1.5. The most comprehensive measure of carbon in an aqueous system is called Total Carbon (TC). The sources of carbon compounds in water are generally differentiated by their genesis in the aquatic carbon cycle:

- Total Organic Carbon (TOC)—amount of carbon detected in organic compounds, which originate from primary producers (see Volume 3A). In an aquatic environment, this is derived from photosynthesis via decaying plant life, bacterial growth, biological processes, or chemical activity:
  - Dissolved Organic Carbon (DOC)—an aquatic equivalent of soil humus, and that portion of the TOC remaining after filtering through a pore size of 0.2 µm (Laanen *et al.*, 2011; see Section 5.2.3.1); and
  - Particulate Organic Carbon (POC)—particulate matter resulting from photosynthetic processes.
- Total Inorganic Carbon (TIC)—dissolved CO_2 and carbonic acid salts derived from calcification and geological processes:
  - Dissolved Inorganic Carbon (DIC)—dissolved carbon resulting from calcification processes, mostly in the form of carbonates and bicarbonates, with a tiny proportion of carbonic acid (see Section 5.2.3.2); and
  - Particulate Inorganic Carbon (PIC)—particulate matter resulting from calcification processes, mostly comprising carbonates (see Section 1.5).

The actual proportions of these different forms, and their interactions, vary between waterbodies depending on local geography and biogeochemistry. A simplified view of these interactions within a freshwater system, and between that system and the surrounding environment, is illustrated in Figure 7.2. In higher latitudes, carbon cycling involves a complex interplay of oceanic and terrestrial systems, including seasonal sea ice (Capelle *et al.*, 2020). Carbon is transferred into and out of the freshwater system via several mechanisms:

- runoff from land—carbon in the form of DIC, DOC and POC can enter the waterbody from terrestrial ecosystems. From there it may continue in the water cycle and be carried to the ocean, enter the food web by being consumed by organisms, be emitted into the atmosphere as CO_2, or sink to the substratum as sediment.
- atmospheric CO_2—enters the aquatic system via photosynthesis and is returned to the atmosphere via respiration. Dissolved CO_2 can also become carbonic acid for use by marine organisms in calcification.
- sediments—both organic and inorganic forms of carbon can sink from the water into the sediments of the substratum where it may be stored for millenia. Natural processes, such as tectonic activity, and human interventions, such as deep sea mining, can remove this stored carbon from the aquatic system.

Aquatic organisms are an important link between organic and inorganic forms of carbon. DOC comprises around 90% of TOC in most inland waterbodies, with concentrations in the range 0.1–332 mg/l (Sobek *et al.*, 2007). While flocculation, the process of clumping small particles together, may transform DOC into POC (see Figure 5.11), POC can also gradually degrade to become DOC. The water pH tends to determine the balance between inorganic carbon forms (Stumm and Morgan, 1996).

Carbon is transported continuously by rivers as particulate and dissolved organic carbon (POC, DOC) and as dissolved inorganic carbon (DIC) that functions in weathering reactions. Of the global carbon fluxes to the oceans from the continents, about 18% moves in riverine transport as POC, 37% as DOC, and 45% as DIC. Proportions of DIC, POC, and DOC in the rivers of the world are variable; differences emanate from lithology, which controls DIC levels, and differences in relief that control the DOC/POC ratios. DIC is very low in many tropical rivers of humid regions, and there DOC is the dominating form of exported carbon. Within the pelagic zone of lakes and reservoirs, however, the ratio of DOC/POC is ca. 10:1.
Wetzel (2001)

Figure 7.2 Aquatic carbon in freshwater system

C: carbon; P: photosynthesis; R: respiration; DIC: dissolved inorganic carbon; DOC: Dissolved organic carbon; PIC: particulate inorganic carbon; POC: particulate organic carbon

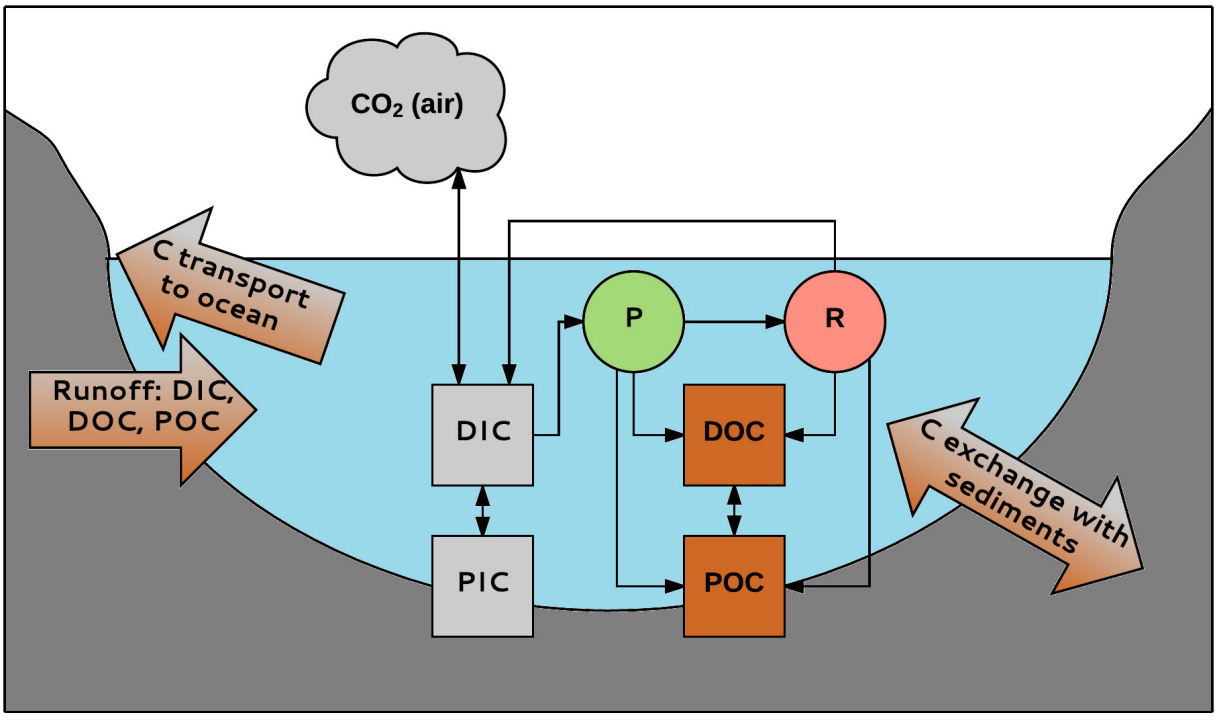

Source: Reitsema *et al.* (2018) Box 1

POC constitutes one of the major causes of surface water pollution, with the proportion of riverine POC increasing with the flow rate and size of the river. The ratio of PIC to POC production is an indicator of the ratio of calcification to photosynthesis in selected marine organisms, such as coccolithophores (calcifying algae such as *Emiliania huxleyi*). Since these organisms convert carbon into POC via photosynthesis, and remove carbon from water via calcification to form PIC, the PIC/POC ratio indicates whether they function as a source (high ratio) or sink (low ratio) of atmospheric CO_2 (Gerecht *et al.*, 2014). Changes in this ratio have been correlated with several environmental factors such as:

- higher CO_2 levels decreased the ratio of PIC/POC in *E. huxleyi* (Zondervan *et al.*, 2001; 2002);
- higher water temperatures decreased the ratio of PIC/POC in *E. huxleyi* (Gerecht *et al.*, 2014); and
- deficiencies in zinc and cobalt both increased the ratio of PIC/POC in *E. huxleyi* (Boye *et al.*, 2017).

Such results raise significant concerns about the future impact of increasing atmospheric CO_2 levels and surface water temperatures on aquatic environments, and the implications of ocean acidification on ocean chemistry (IPCC, 2014; see Section 1.5). Several algorithms have been developed to estimate surface concentrations of PIC (Balch *et al.*, 2005; Gordon *et al.*, 2001) and POC (Duforet-Gaurier *et al.*, 2010; Gardner *et al.*, 2006; Stramski *et al.*, 2008) for EO datasets and, when calibrated using ship-based observations, these levels can be mapped and monitored at global and regional scales (Swirgon and Stramska, 2015). EO-based algorithms have been developed to monitor other indicators of the ocean carbon cycle including primary productivity (Antoine *et al.*, 1996; Behrenfeld and Falkowski, 1997) and coloured dissolved and detrital organic materials (Maritorena *et al.*, 2002; Siegel *et al.*, 2002). These methods are further discussed in Sections 8 and 18.

7.5 Dynamics

Like all environmental features, waterbodies are not static, but change with diurnal, seasonal and longer term cycles. An important part of understanding dynamics in any natural feature is to separate the cyclic from longer term changes. Some of the features of waterbodies that change in human time frames include water extent, level, depth, temperature, ice cover, and movement, as well as their physical, chemical, and biological composition, which impact water colour, quality and ecology (see Sections 11 to 20 respectively). While seasonal meteorological cycles involving precipitation and evaporation determine the 'standard' characteristics of waterbodies, such as their extent, volume, and quality, extreme meteorological events (e.g. storms and floods) can radically modify these characteristics.

Water moves locally, regionally, and globally by various mechanisms, including transient currents, thermohaline circulation, and wind-driven circulation (see Section 17). In polar regions, the formation, presence, and subsequent melting of dynamic sea ice is a major feature that transforms the surface (and deeper) waters of the high-latitude oceans (including the Southern Ocean). Unlike the ice that forms on waterbodies in lower latitudes, coverage of sea ice is either annual or perennial depending on the location (see Section 15).

The environmental drivers of marine life differ with many factors, including an organism's position in the food web (see Section 3.2). For example, in the Southern Ocean, Boyd *et al.* (2019) identified different sets of drivers for the following trophic levels:

- phytoplankton at the base of the food web is driven by temperature, sunlight, pH, CO_2, nutrients, and trace elements;
- benthic organisms in the middle of the food web are driven by pH, CO_2, temperature, and oxygen; and
- pelagic organisms at the top of the food web are driven by CO_2, temperature, and pH (see Sections 3 and 5).

The response of particular biota to different drivers also varies with habitat, but changes in these drivers are likely to modify the distribution and prevalence of individual species. Global phenomena, such as ocean acidification, have implications not just for individual species (Collins *et al.*, 2014), but also for the aquatic food web, the carbon cycle, and global weather patterns (see Section 1.5).

Table 7.2 Modelled scenarios for Antarctica and Southern Ocean in 2070

For the two modelled scenarios of high and low CO_2 emissions, changes in eleven characteristics were predicted relative to a 1986–2005 reference period.

Data	Characteristic	Modelled scenario for 2070	
		Low emissions	High emissions
Atmosphere/ocean/ice differences (IPCC, 2013; DeConto and Pollard, 2016; Hauri *et al.*, 2016)	Global air temperature	+0.9°C	+2.9°C
	Antarctic contribution to sea level	6 cm	27 cm
	Antarctic air temperature	+0.9°C	+3.0°C
	Southern Ocean temperature	+0.7°C	+1.9°C
	Summer (February) sea ice extent	12% loss	43% loss
	Ice shelf volume	8% reduction	23% reduction
Ecosystem states and pressures (IPCC, 2013; Aronson *et al.*, 2015; Atkinson *et al.*, 2004; Chown *et al.*, 2012a, 2012b; Duffy *et al.*, 2017; Dodds *et al.*, 2017; Gutt *et al.*, 2015; Hauri *et al.*, 2016)	Ocean acidification/reduced calcification	Surface waters saturated	Surface waters corrosive to aragonite shells of pteropods
	Biological invaders	Double reference level	Ten times reference level
	Ecosystem structure	Penguins and krill	Crustaceans and salps
	Human presence	3 times reference level	8 times reference level
	Resource use	Small increase	Signficant increase

Source: Rintoul *et al.* (2018) Figure 2

By providing a series of consistent observations from a synoptic viewpoint, EO imagery offer a unique opportunity to monitor the timing and extent of environmental change. Long term change detection generally requires images that were acquired in the same season since some water features, such as macroalgae, change seasonally in terms of distribution and abundance. EO time series data in Analysis Ready format, such as Digital Earth Australia (DEA) imagery (see Volume 2D—Excursus 11.2), provides useful for modelling exercises (either as input or validation) for forecasting or predicting future conditions (see Volume 2D—Section 14), such as coral bleaching (see Excursus 20.3).

In conjunction with EO imagery, the Integrated Marine Observing System (IMOS) operates a variety of equipment in Australia's coastal and ocean waters to research the dynamic nature of these regions (see Excursus 5.1 above and Volume 2D—Excursus 12.3). Sophisticated systems such as eReefs have also been developed to integrate EO datasets with other environmental data to monitor regional biogeochemical cycles (see Volume 2D—Excursus 14.4). At a global scale, Earth System Science (ESS; see Excursus 7.2) offers an appropriately-scaled platform on which historical and current datasets can be analysed and integrated to model future environmental conditions on our dynamic planet.

One example of using global modelling to assess likely trajectories for future conditions in the Southern Ocean is given in Rintoul *et al.* (2018). This analysis considers two opposing scenarios of continued high CO_2 emissions versus a future with reduced emissions over the period from 2020 to 2070. The impacts of these scenarios are summarised in terms of eleven characteristics, relative to a 1986–2005 reference period (see Table 7.2). Further modelling indicated that continuing high CO_2 emissions until 2300 could result in nutrients being trapped in the Southern Ocean, which would reduce nutrient export to lower latitudes, decrease primary productivity by 24%, and potentially result in a 20% reduction in fishery yields (LaufKötter *et al.*, 2018; Moore *et al.*, 2018; Rintoul *et al.*, 2019). Such analyses demonstrate how current governance and lifestyle choices determine future environmental conditions, even in remote locations (Boyd *et al.*, 2019).

Excursus 7.2—The Global System

Earth System Science (ESS), a multidisciplinary approach to understanding the structure and function of Earth as an integrated system (Steffen *et al.*, 2020; see Volume 1A—Section 4.1 and Volume 3A—Excursus 1.2), describes events on Earth in terms of their interactions with four integrated spheres (see Figure 7.3):

- atmosphere—gaseous, protective layer around the Earth;
- hydrosphere—all surface waters, groundwater and atmospheric water in any state (see Section 1);
- geosphere—solid components of Earth on land and under water; and
- biosphere—all forms of life on Earth.

ESS analyses the dynamic geochemical processes and interactions occurring between these spheres to better understand the Earth—its past, present and future—at global to local scales. Of particular relevance to surface waters is the hydrological cycle, which circulates water—and energy—between these four spheres (see Section 1.1).

Figure 7.3 Earth System Science

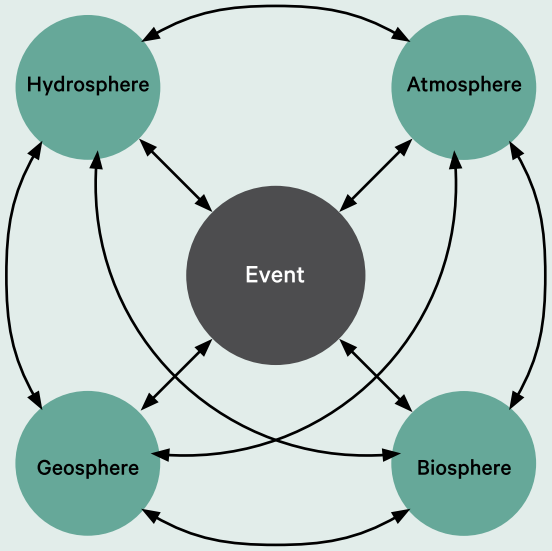

To monitor changes within the integrated ESS framework requires consistent observations of unambiguous and agreed variables that minimally describe major states and trends. These criteria have become known as 'essential variables' (EV) and have been embraced by a wide range of international bodies to develop interchangeable data repositories to monitor our planet (see Volume 3A). Given the global scale of analysis, EO datasets are at the core of this approach. Examples of EV include:

- essential climate variables (ECV; see Volume 1A—Section 1.5.2);
- essential agricultural variables (EAV; see Volume 3A—Section 11.3);
- essential biodiversity variables (EBV; see Volume 3A—Section 19.3);
- essential water variables (EWV; GEOGLOWS, 2016); and
- essential ocean variables (EOV; see Excursus 21.1).

EOV describe the physics and biogeochemistry of the ocean system and its biological and ecological components (NASA Earthdata, 2020). Global monitoring of ocean properties based on EOV is further discussed in Section 21 in the context of marine biodiversity.

7.6 Further Information

General Bathymetric Chart of the Oceans (GEBCO): *https://www.gebco.net/*

Geomorphology: Dove *et al.* (2020)

7.7 References

Antoine, D., Andre, J.M., and Morel, A. (1996). Oceanic primary production: 2. Estimation at global scale from satellite (Coastal Zone Color Scanner) chlorophyll. *Global Biogeochemical Cycles*, 10(1), 56–69.

Aronson, R.B., Smith, K.E., Vos, S.C., McClintock, J.B., Amsler, M.O., Moksnes, P.O., Ellis, D.S., Kaeli, J.W., Singh, H., Bailey, J.W., Schiferl, J.C., van Woesik, R., Martin, M.A., Steffel, B.V., Deal, M.E., Lazarus, S.M., Havenhand, J.N., Swalethorp, R., Kjellerup, S. and Thatje, S. (2015) No barrier to emergence of bathyal king crabs on the Antarctic shelf. *Proceedings of the National Academy of Sciences*, 112 (42), 12997–13002. doi:10.1073/pnas.1513962112

Atkinson, A., Siegel, V., Pakhomov, E. A., and Rothery, P. (2004)Long-term decline in krill stock and increase in salps within the Southern Ocean. *Nature,* 432, 100–103.

Balch, W.M., Gordon, H.R., Bowler, B.C., Drapeau, D.T., and Booth, E.S. (2005). Calcium Carbonate Measurements in the Surface Global Ocean based on MODIS Data. *Journal of Geophysical Research,* 110, C07001. doi:10.1029/2004JC002560

Behrenfeld, M.J., and Falkowski, P.G. (1997). Photosynthetic rates derived from satellite-based chlorophyll concentration. *Limnology and Oceanography*, 42 (1), 1–20.

Boye, M., Adjou, M.A., Dulaquais, G., and Tréguer, P. (2017). Trace metal limitations (Co, Zn) increase PIC/POC ratio in cocolithophore *Emiliania huxleyi*. *Marine Chemistry*, 192, 22–31. doi.org/10.1016/j.marchem.2017.03.006

Boyd P.W., Kawaguchi, S. Strzepek, R. Meiners, K. Hallegraeff, G. McMinn, A., Swadling, K., and Reilly, D. (2019). *Report Card: Potential Tipping Points for life in the Southern Ocean*. Antarctic Climate and Ecosystems Cooperative Research Centre, Hobart, Australia. *http://dx.doi.org/10.25959/100.00031768*

Brando, V.E., Anstee, J.M., Wettle, M., Dekker, A.G., Phinn, S.R., and Roelfsema, C. (2009). A physics based retrieval and quality assessment of bathymetry from suboptimal hyperspectral data. *Remote Sensing of Environment*, 113, 755–770. doi:10.1016/j.rse.2008.12.003.

Capelle, D.W., Kuzyk, Z.Z.A., Papkyriakou, T., Guéguen, C., Miller, L.A., and Macdonald, R.W. (2020). Effect of terrestrial organic matter on ocean acidification and CO2 flux in an T Arctic shelf sea. *Progress in Oceanography*, 185, 102319. *https://doi.org/10.1016/j.pocean.2020.102319*

Chown, S.L., Lee, J.E., Hughes, K.A., Barnes, J., Barrett, P.J., Bergstrom, D.M., Convey, P., Cowan, D.A., Crosbie, K., Dyer, G., Frenot, Y., Grant, S.M., Herr, D., Kennicutt, M.C., Lamers, M., Murray, A., Possingham, H.P., Reid, K., Riddle, M.J., Ryan, P.G., Sanson, L., Shaw, J.D., Sparrow, M.D., Summerhayes, C.,Terauds, A., and Wall, D.H. (2012a). Challenges to the future conservation of the Antarctic. *Science*, 337(6091). 158–159. *https://doi.org/10.1126/science.1222821*

Chown, S.L., Huiskes, A.H., Gremmen, N.J., Lee, J.E., Terauds, A., Crosbie, K., Frenot, Y., Hughes, K.A., Imura, S., Kiefer, K., Lebouvier, M., Raymond, B., Tsujimoto, M., Ware, C., Van de Vijver, B., and Bergstrom, D.M. (2012b). Continent-wide risk assessment for the establishment of nonindigenous species in Antarctica. *Proceedings of the National Academy of Sciences*, 109(13), 4938–4943. doi:10.1073/pnas.1119787109

Collings, S., Botha, E.J., Anstee, J., and Campbell, N. (2018). Depth of Satellite Images: Depth Retrieval Using a Stereo and Radiative Transfer-based Hybrid Method. (2018). *Remote Sensing*, 8, 1247. *https://doi.org/10.3390/rs10081247*

Collins, S., Rost, B. and T.A. Rynearson. (2014). Evolutionary potential of marine phytoplankton under ocean acidification. *Evolutionary Applications*, 7, 140–155.

DeConto, R.M., and Pollard, D. (2016). Contribution of Antarctica to past and future sea-level rise. *Nature*, 531, 591–597.

Dodds, K., Hemmings, A.D., and Roberts, P. (2017). *Handbook on the Politics of Antarctica*. Edward Elgar, Cheltenham.

Dove, D., Nanson, R., Bjarnadóttir, L.R., Guinan, J., Gafeira, J., Post, A., Dolan, M.F.J., Stewart, H., Arosio, R., and Scott, G. (2020). *A two-part seabed geomorphology classification scheme: (v.2)*. Open Report Prepared by the MIM-GA Geomorphology Working Group. doi:10.5281/ZENODO.4075248

Duffy, G.A., Coetzee, B.W.T., Latombe, G., Akerman, A.H., McGeoch, M.A., and Chown, S.L. (2017). Barriers to globally invasive species are weakening across the Antarctic. *Diversity and Distributions*, 23, 982–996. *https://doi.org/10.1111/ddi.12593*

Duforet-Gaurier, L., Loisel, H., Dessailly, D., Nordkvist, K., Alvain., S. (2010). Estimates of particulate organic carbon over the euphotic depth from in situ measurements, Application to satellite data over the global ocean. *Deep Sea Research I*, 57 (3), 351–367.

Estep, L., and Arnone, R.A. (1994). Effect of whitecaps on determination of chlorophyll concentration from satellite data. *Remote Sensing of Environment,* 50, 328–334.

Gardner, W.D., Mishonov, A.V., and Richardson., M.J. (2006). Global POC concentrations from *in-situ* and satellite data. *Deep-Sea Research II*, 53, 718–740.

GEBCO (2017). *Seabed 2030: Roadmap for Future Ocean Floor Mapping*. The Nippon Foundation/GEBCO (General Bathymetric Chart of the Oceans), June 2017. *https://www.gebco.net/documents/seabed_2030_roadmap_v10_low.pdf*

GEOGLOWS (2016). *Working Group 3: Essential Water Variables and Observations* webpage, GEO Global Water Sustainability website: *https://www.geoglows.org/pages/workinggroup3*

Gerecht, A.C., Šupraha, L., Edvardsen, B., Probert, I., and Henderiks, J. (2014). High temperature decreases the PIC / POC ratio and increases phosphorus requirements in *Coccolithus pelagicus* (Haptophyta), *Biogeosciences*, 11, 3531–3545. *https://doi.org/10.5194/bg-11-3531-2014*

Gordon, H.R., Boynton, G.C., Balch, W.M., Groom, S.B., Harbour, D.S., and Smyth, T.J. (2001). Retrieval of coccolithophore calcite concentration from SeaWiFS imagery. *Geochemical Research Letters*, 28(8), 1587–1590.

Gutt, J., Bertler, N., Bracegirdle, T.J., Buschmann, A., Comiso, J., Hosie, G., Isla, E., Schloss, I.R., Smith, C.R., Tournadre, J., and Xavier, J.C. (2015). The Southern Ocean ecosystem under multiple climate change stresses—an integrated circumpolar assessment. *Global Change Biology*, 21(4), 1434–1453. doi:10.1111/gcb.12794

Hauri, C., Friedrich, T., and Timmermann, A. (2016). Abrupt onset and prolongation of aragonite undersaturation events in the Southern Ocean. *Nature Climate Change*, 6, 172–176.

IPCC (2013). *The Physical Science Basis. Contribution of Working Group I to the Fifth Assessment Report of the Intergovernmental Panel on Climate Change*. (Eds: Stocker, T.F. *et al.*) Cambridge University Press, Cambridge.

IPCC (2014). *Climate Change 2014: Impacts, Adaptation, and Vulnerability. Part A: Global and Sectoral Aspects. Contribution of Working Group II to the Fifth Assessment Report of the Intergovernmental Panel on Climate Change* (Eds: Field, C.B., Barros, V.R., Dokken, D.J. , Mach, K.J., Mastrandrea, M.D., Bilir, T.E., Chatterjee, M., Ebi, K.L., Estrada, Y.O., Genova, R.C., Girma, B., Kissel, E.S., Levy, A.N., MacCracken, S., Mastrandrea, P.R., and White, L.L.). Cambridge University Press, Cambridge, United Kingdom and New York, NY, USA, 1132 p.

Laanen, M.L., Peters, S.W.M., Dekker, A.G., and van der Woerd, H.J. (2011). Assessment of the scattering by sub-micron particles in inland waters. *Journal of the European Optical Society,* 6, 11046.

Laufko¨tter, C., and Gruber, N. (2018). Will marine productivity wane? *Science*, 359, 1103–1104.

Maritorena, S., Siegel, D.A., and Peterson. A.R. (2002). Optimal tuning of a semi-analytical model for global applications. *Applied Optics*, 41, 2705–2714.

Mayer, L., Jakobsson, M., Allen, G., Dorschel, B., Falconer, R., Ferrini, V., Lamarche, G., Snaith, H., and Weatherall, P. (2018). The Nippon Foundation—GEBCO Seabed 2030 Project: The Quest to See the World's Oceans Completely Mapped by 2030. *Geosciences*, 8, 63. *http://www.mdpi.com/2076-3263/8/2/63*

Moore, J.K., Fu, W., Primeau, F., Britten, G.L., Lindsay, K., Long, M., Doney, S.C., Mahowald, N., Hoffman, F., and Randerson, J.T. (2018). Sustained climate warming drives declining marine biological productivity, *Science*, 359(6380), 1139–1143.

NASA Earthdata (2020). *Essential Variables* webpage, NASA Earthdata website: *https://earthdata.nasa.gov/learn/essential-variables*

Purkis, S.J., and Brock, J.C. (2013). Lidar Overview. Ch 5 in *Coral Reef Remote Sensing*. (Eds: Goodman, J.A., Purkis, S.J., and Phinn, S.R.). Springer, Dordrecht. ISBN 978-90-481-9291-5.

Reitsema, R.E., Meire, P., and Schoelynck, J. (2018). The Future of Freshwater Macrophytes in a Changing World: Dissolved Organic Carbon Quantity and Quality and Its Interactions With Macrophytes. *Frontiers in Plant Science*, 9, 629. doi:10.3389/fpls.2018.00629

Rintoul, S.R., Chown, S.L., DeConto, R.M., England, M.H., Fricker, H.A., Mason-Delmotte, V., Naish, T.R., Siegert, M.J., and Xavier, J.C. (2018). Choosing the future of Antarctica. *Nature*, 558, 233–241. *https://doi.org/10.1038/s41586-018-0173-4*

Siegel, D.A., Maritorena, S., Nelson, N.B., Hansell, D.A., and Lorenzi-Kayser, M. (2002). Global distribution and dynamics of colored dissolved and detrital organic materials. *Journal of Geophysical Research*, 107, 3228. doi:10.1029/2001JC000965

Sobek, S., Tranvik, L.J., Prairie, Y.T., Kortelainen, P., and Cole, J.J. (2007). Patterns and regulation of dissolved organic carbon: an analysis of 7,500 widely distributed lakes. *Limnology and Oceanography,* 52, 1208–1219. *https://doi.org/10.4319/lo.2007.52.3.1208*

Steffen, W., Richardson, K., Rockström, J., Schellnhuber, H.J., Dube, O.P., Dutreuil, S., Lenton, T.M., and Lubchenco, J. (2020). The emergence and evolution of Earth System Science. *Nature Reviews Earth and Environment*, 1, 54–63. *https://doi.org/10.1038/s43017-019-0005-6*

Stramski, D., Reynolds, R. A., Babin, M., Kaczmarek, S., Lewis, M. R., Röttgers, R., Sciandra, A., Stramska, M., Twardowski, M. S., Franz, B. A., and Claustre, H. (2008). Relationships between the surface concentration of particulate organic carbon and optical properties in the eastern South Pacific and eastern Atlantic Oceans. *Biogeosciences*, 5, 171–201. *doi.org/10.5194/bg-5-171-2008*.

Stumm, W., and Morgan, J.J. (1996). *Aquatic Chemistry: Chemical Equilibria and Rates in Natural Waters. Environmental Science and Technology.* John Wiley and Sons Inc., New York.

Swirgon, M., and Stramska, M. (2015). Comparison of in situ and satellite ocean colour determinations of particulate organic carbon concentration in the global ocean. *Oceanologia*, 57, 25–31. *doi.org/10.1016/j.oceano.2014.09.002*

Wetzel, R.G. (2001). The Inorganic Carbon Complex. Ch 11 in *Limnology* 3rd Edn. (Ed: Wetzel, R.G.). Academic Press. pp 187–204. ISBN: 9780127447605

Wölfl, A.-C., Snaith, H., Amirebrahimi, S., Devey, C.W., Dorschel, B., Ferrini, V., Huvenne, V.A.I., Jakobsson, M., Jencks, J., Johnston, G., Lamarche, G., Mayer. L., Millar, D., Pedersen, T.H., Picard, K., Reitz, A., Schmitt, T., Visbeck, M., Weatherall, P., and Wigley, R. (2019). Seafloor Mapping—The Challenge of a Truly Global Ocean Bathymetry. *Frontiers in Marine Science*, 6, 283. doi:10.3389/fmars.2019.00283

Zondervan, I., Zeebe, R.E., Rost, B., and Riebesell, U. (2001). Decreasing marine biogenic calcification: A negative feedback on rising atmospheric pCO_2. *Global Biogeochemical Cycles*, 15(2), 507–516. doi.org/10.1029/2000GB001321

Zondervan, I., Rost, B., and Riebesell, U. (2002). Effect of CO_2 concentration on the PIC/POC ratio in the coccolithophore *Emiliania huxleyi* grown under light-limiting conditions and different daylengths. *Journal of Experimental Marine Biology and Ecology*, 272, 55–70.

EO Data and Models

Various EO technologies are appropriate for mapping and monitoring different aspects of surface waters, including:

- multispectral and hyperspectral sensors—water extent (see Section 11), depth (see Section 13.4.2), concentrations of optically active constituents in coastal and inland waters (see Sections 18 and 19), and occurrence of aquatic biota (see Section 20);
- thermal infrared sensors—accurate sea surface temperature and charts of coastal currents (see Sections 14, 15, and 16);
- microwave radiometers—ocean salinity and soil moisture (see Section 19);
- radar sensors—sea surface height, seafloor mapping, coastal currents, and ocean waves, (see Sections 12, 13.3.1, 16, and 17);
- lidar sensors—bathymetry, water column profiling, and fisheries (see Section 13.4.1); and
- sonar sensors—bathymetry and submerged geomorphology (see Sections 10 and 13.3.2).

Modes of EO data acquisition are introduced in Volume 1A—Sections 14 to 16. In the following three sections we focus of those properties of water that can be measured and modelled using EO sensors in the context of Australian surface waters. Specifically, these sections address:

- optical EO (see Section 8);
- microwave EO (see Section 9);
- acoustic EO (see Section 10).

Contents

8 Optical EO 117

9 Microwave EO 155

10 Acoustic EO 169

Background image on previous page: These tidal channels through the Great Barrier Reef system, Queensland, were imaged on 8 July 2016. **Source:** Planet Labs Inc. (CC-BY-SA 4.0). Retrieved from *https://www.planet.com/gallery/#!/post/reef-20160708*

8 Optical EO

An indirect relationship exists between features in an EO dataset and quantifiable attributes of the Earth's surface (see Figure 8.1). EO data processing operates on the 'data space', or observation domain, and relies on implicit assumptions within defined measurement and structure models that relate the data back to selected parameters of the surface, or the attribute domain (see Volume 2D—Section 1). This indirect relationship is particularly relevant to aquatic applications of EO and applies to all EO data sources (see Volume 1A—Section 1).

Optical wavelengths comprise the ultraviolet (UV), visible, near infrared (NIR), and short wave infrared (SWIR) regions of the electromagnetic spectrum (see Section 5.1.4). The behaviour of these 'reflective' wavelengths can be described in terms of geometric or ray optics (see Volume 1A—Section 2.8), since they are shorter than the lenses and sensors that detect them. Within the optical wavelength range, atmospheric absorption reduces solar transmission of some wavelength intervals (see Figure 5.8).

This section summarises some fundamental principles of using optical EO to observe surface waters. The basic principles of optics and lenses are introduced in Volume 1A—Section 2, some of which are reviewed in Excursus 8.1, and the underlying framework of optical EO is considered in Section 8.1. In subsequent subsections we describe:

- optically active constituents of water (see Section 8.2);
- optical properties of water (see Section 8.3);
- optical EO models (see Section 8.4); and
- optical EO sensors (see Section 8.5).

Figure 8.1 Measurement and analysis of image features

Interpreting imagery from EO sensors is an indirect process, whereby a measurement model is used to transform EO observations to measurements of some measurable property, and a structure model is used to relate those measurements to application-specific attributes.

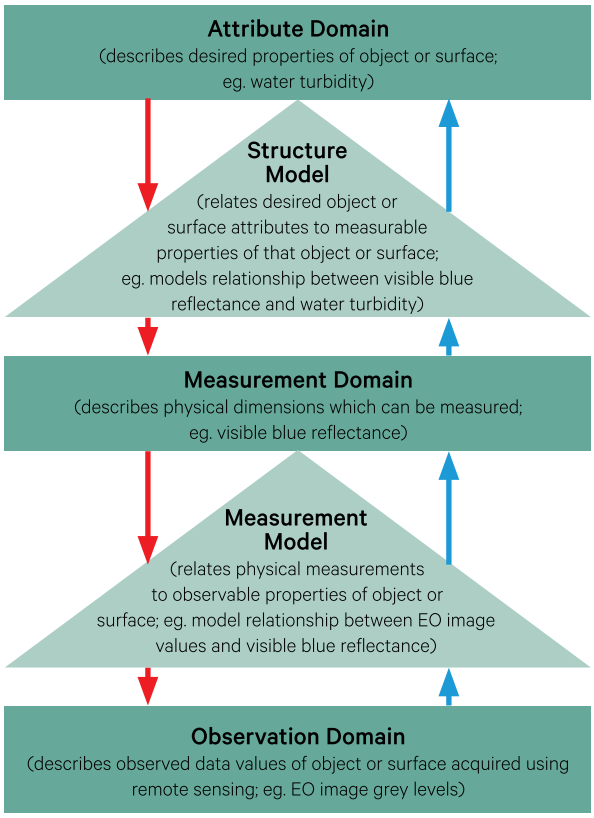

Adapted from: Harrison and Jupp (1989) Figure 33

Background image: Optical image of Sydney Harbour acquired by Flock-1 satellites on 29 November 2015. **Source:** Planet Labs Inc. (CC BY SA 4.0). Retrieved from *https://medium.com/planet-stories/imaging-australian-flooding-from-space-b6f30b025e2d*

Excursus 8.1—Optics Review

Optics is the scientific study of light properties—how light interacts with matter and how it can be detected and measured by instruments. In the context of EO, optical wavelengths generally refer to those wavelengths whose behaviours are best described by ray optics (see Volume 1A—Section 2.8), namely ultraviolet (UV), visible, and infrared (IR: near, short wave, and thermal; see Section 5.1.4). An understanding of optics and optical laws underpins all optical EO studies and is relevant to an expanding range of engineering applications.

Geometric concepts

Some basic geometric concepts referenced in optics include:

- polar angle:
  - in two dimensions (on a plane), this angular measure is the counterclockwise angle between the X-axis and a point in the X-Y plane (see Figure 8.2a); and
  - in three dimensions (on a sphere), the polar angle is measured from the Z-axis (see Figure 8.2b); and
- solid angle (ω *or* Ω)—three-dimensional angle defined by a cone extracted from a sphere, derived from the surface area of the cone (A) and the radius of the sphere (R) (see Figure 8.3)

The terms used to define the position of celestial bodies, or airborne and spaceborne sensors, relative to locations on the Earth's surface are summarised in Table 8.1 and Figure 8.4a. The angles derived from these positions are used in EO to define the geometry between the illumination source, the target, and the viewing sensor (see Figure 8.4b). As illustrated in Figure 8.4c, the spherical coordinate system, locations are referenced in terms of the polar zenith and azimuth angles and denoted (θ, ϕ). The position of a light source is determined using the zenith and azimuth angles for light streaming downwards. Conversely, the nadir and azimuth angles are used to determine the position of a light source from which light streams upwards.

Figure 8.2 Polar angles

a. Polar angle in a plane

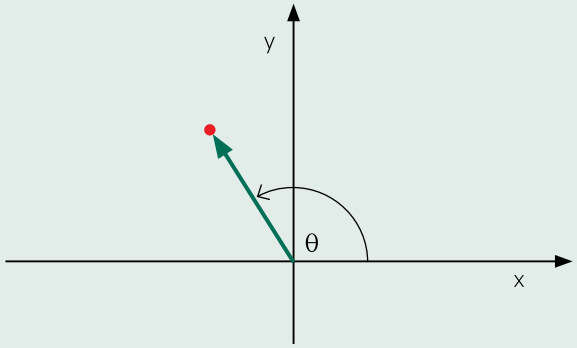

b. Polar angle in spherical coordinates

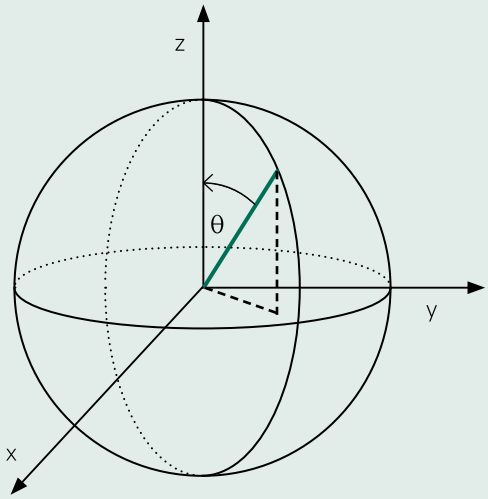

Figure 8.3 Solid angle

Solid angle $\Omega = A/R^2$ steradians, where A is the area on the surface of a sphere of radius R that is intersected by a cone originating from the centre of the sphere

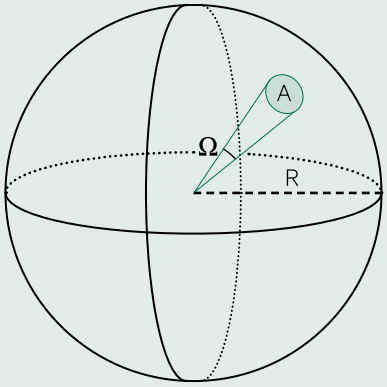

Figure 8.4 Geometric framework for optical studies

a. Defining positions

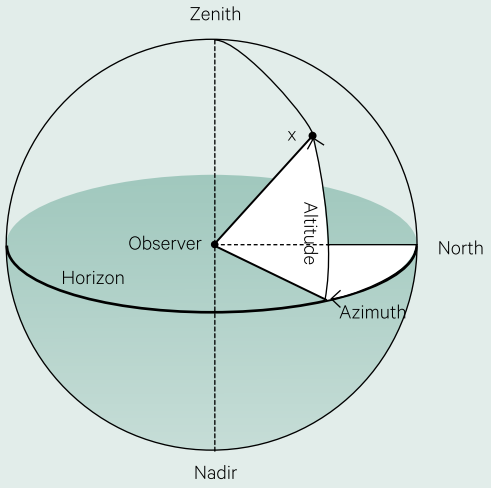

b. Defining angles

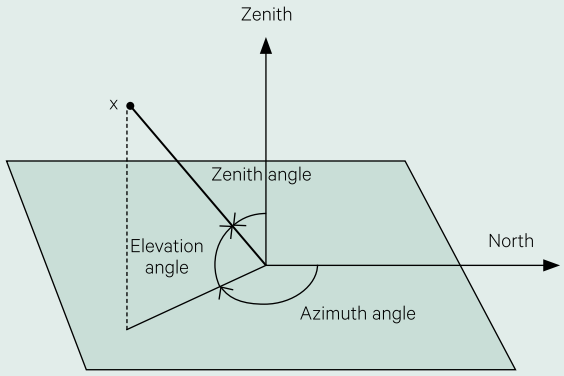

c. The basic geometry of a passive EO sensor viewing reflected solar radiation from an illuminated target surface is shown below.

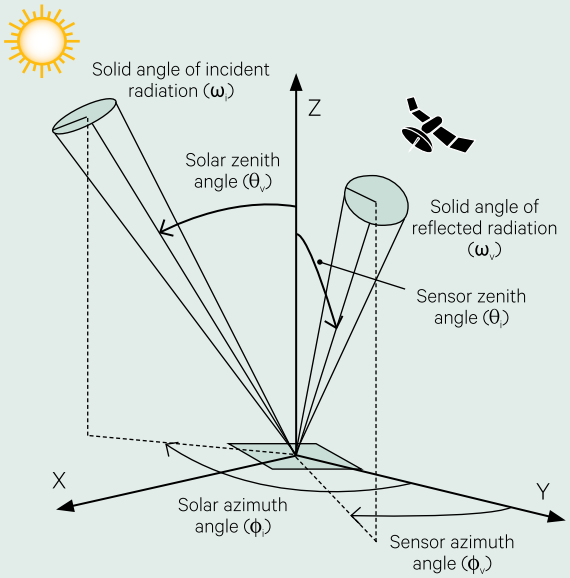

Table 8.1 Terminology for EO geometry

Position	Definition	Symbol
Zenith	Point directly above observer	*Z*
Nadir	Point directly below observer	*N*
Zenith angle	Angle between zenith and body measured on vertical plane through zenith, observer, and body	*z* or θ
Elevation or altitude	Angle between horizon and body measured on vertical plane through observer	*h* or α
Azimuth	Angle between reference direction (usually North) and horizontal projection of body measured clockwise from reference direction (usually North)	*a* or ϕ

Electromagnetic radiation

Visible light energy is loosely defined as that subset of electromagnetic radiation (EMR) with wavelengths in the range 380–700 nm. As introduced in Volume 1A—Section 5, EMR comprises streams of photons moving at the speed of light (c). While the speed of light is defined as 3×10^8 m/sec through a vacuum, it actually varies through different media (see Table 8.2). Under water, the spectral distribution of solar radiation also changes significantly with water depth (Kirk, 2010; see Figure 5.10).

Each photon has a wavelength (λ) and frequency (ν), which are related by:

$$c = \lambda \nu$$

Photon energy (ε) varies with its frequency, so that high frequency (short wavelength) photons contains more energy than lower frequency (longer wavelength) photons (see Volume 1A—Section 2.5).

Matter absorbs or transmits incoming, or incident, EMR depending on whether or not that energy excites physical processes in the matter's atoms and molecules. The nature of excitation varies with the wavelength or frequency of the energy and the molecular composition of the matter being irradiated. Thus, EM energy is selectively absorbed by materials depending on how different frequencies of EMR interact with the molecules, atoms, and nuclei of the material (see Volume 1A—Section 2.2). When the frequency of the incident EM energy does not match the energy levels required for absorption, that energy is transmitted through or scattered by the object. Thus, the transparency of an object (allowing transmission of incident radiation through the object) and its opacity (resulting in reflectance of incident radiation) are determined by the physical and chemical structure of the object, relative to the wavelength of the radiation.

Table 8.2 Light behaviour in different media

Medium	Refractive Index	Velocity of Light (m/sec)
Vacuum	1.0	~3 x 10^8 (=299,792,458)
Air	1.00028	~3 x 10^8 (=299,702,547)
Natural Waters	1.33	~2.25 x 10^8 (=225,407,863)

Source for refractive index data: Kirk (1994)

Figure 8.5 Radiative transfer process

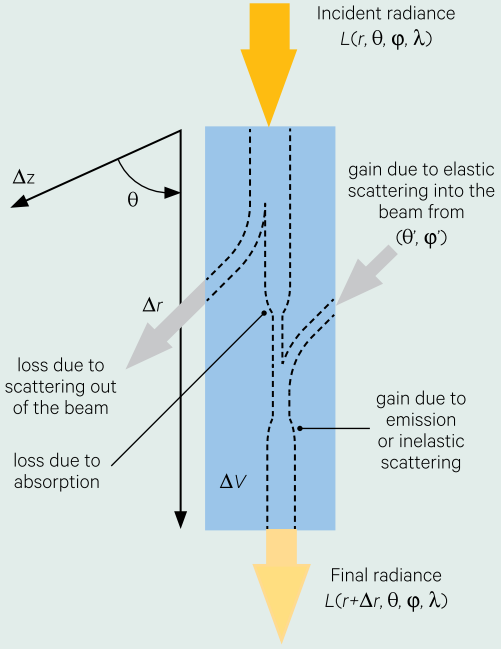

Figure 8.6 Specular reflection

The extent to which a surface obeys the law of reflection depends on its surface texture relative to the wavelength of incident radiation. In specular reflection from a smooth surface the angle of incidence (θ_1) equals the angle of reflection (θ_2).

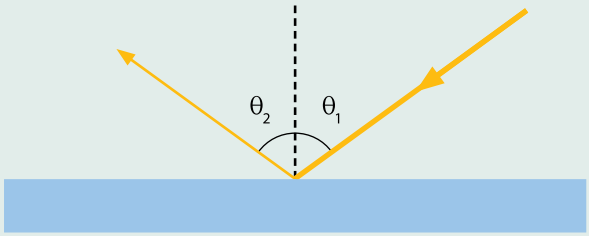

Source: Harrison and Jupp (1989) Figure 7

Radiative Transfer (RT) describes the transfer of energy as photons through a medium and the interactions of photons with surface materials. Thus, RT models account for the impact of absorption, emission, and scattering on energy propagation through a medium. Figure 8.5 illustrates the processes that can affect a single beam travelling a distance Δr through a medium.

In terms of EO, the interaction of incoming radiation with surface features depends on both the spectral reflectance properties of the surface materials and the surface smoothness relative to the radiation wavelength (see Volume 1A—Section 2.5). A relatively 'smooth' surface, which reflects energy without any scattering (that is, where the angle of incidence equals the angle of reflection), is called a 'specular' or 'mirror' reflector. 'Diffuse' or 'Lambertian' reflectance occurs when the surface is rough relative to the wavelength(s) of the incoming radiation and causes the energy to be reflected equally in all directions (see Figure 8.6). While calm water can act as a specular reflector, most of the Earth's surface materials are diffuse reflectors in the visible wavelengths (especially at the spatial resolution of most EO imagery) but may display specular reflectance properties in the microwave wavelengths. Surface orientation relative to both the energy source and sensing device also affects the amount of radiation detected by the sensor. Other aspects of the interaction of EMR with the Earth's surface are discussed in Volume 1B—Sections 4 to 6.

Measuring EMR

The energy associated with EMR can be measured in a number of ways:

- radiant flux (Φ)—number of photons per second (*J/sec* or *W*); this measures the rate of radiant energy flow;
- radiant intensity (*I*)—radiant flux per unit solid angle in a specified direction (*W/sr*);
- radiance (*L*)—radiant intensity per unit area on a plane perpendicular to the flow direction ($W/m^2/sr$; see Figure 8.7). This can be defined in terms of:
  - field radiance—radiant intensity intercepted by a point in space, or a point on a surface; and
  - surface radiance—radiant intensity emitted from a point on a surface; and
- irradiance (*E*)—radiant flux per unit area that is incident on a surface from any direction in a hemisphere (W/m^2).

Figure 8.7 Radiance definitions

The radiance (*L*) from a source area *A* is measured in terms of the radiant flux within a specified solid angle in a given direction.

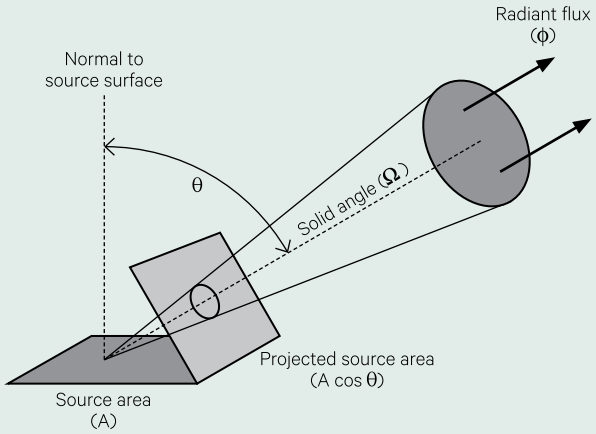

Adapted from: Elachi and van Zyl (2006) Figure 2-10

Table 8.3 Impact of cosine law on irradiance

Zenith angle (°)	Irradiance (%)
0	100
30	87
60	50
85	9

Data source: *http://www.intl-lighttech.com/support/basic-light-measurement-principles-chapter-6-light-measurement-tutorial*

Figure 8.8 Cosine law

For equal aperture observations (area *dA*), the observed solid angle reduces from dΩ at the normal to $d\Omega\cos(\theta)$ for θ° off-normal.

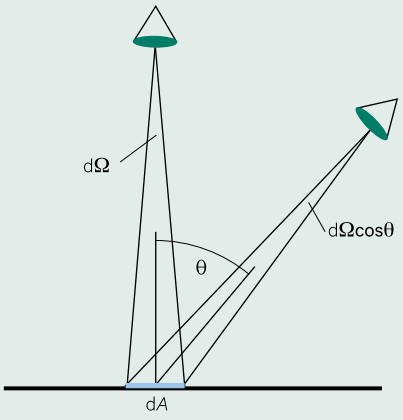

By Lambert's cosine law, the irradiance (*E*) is proportional to the cosine of the zenith angle (θ) for the light source (see Table 8.3):

$$E_\theta = E\cos\theta$$

The same relationship applies to the light scattered (or emitted) from a diffuse (or Lambertian) surface. Thus maximum energy is intercepted, scattered, or emitted when the light stream is perpendicular to a surface. The number of photons per second emitted into equal angle wedges bounded by a circle is proportional to the area of each wedge, with the maximum rate into the wedge that is directed along the normal. When the light stream is directed to or from an off-normal direction, the number of photons is proportionally reduced by the cosine of the angle of the light stream away from the normal (see Figure 8.8). This has obvious implications for the energy detected by a sensor in normal and off-normal positions.

Irradiance onto a horizontal plane can be considered in terms of the upper and lower hemispheres of a sphere:

- downward irradiance (E_d)—downwelling light stream intercepted by the upper surface (see Figure 8.9a); and
- upward irradiance (E_u)—upwelling light stream intercepted by the lower surface (see Figure 8.9b).

Figure 8.9 Downwelling and upwelling irradiance

a. Downwelling irradiance: $E_d = \pi \times L_d$

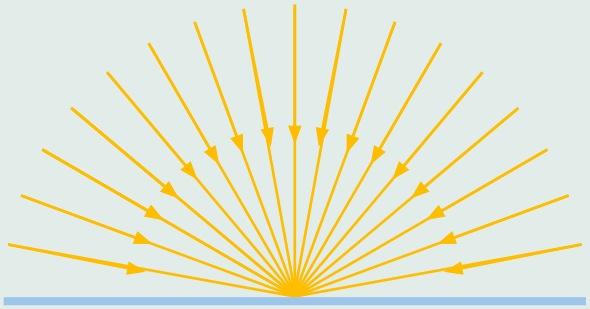

b. Upwelling irradiance: $E_u = \pi \times L_u$

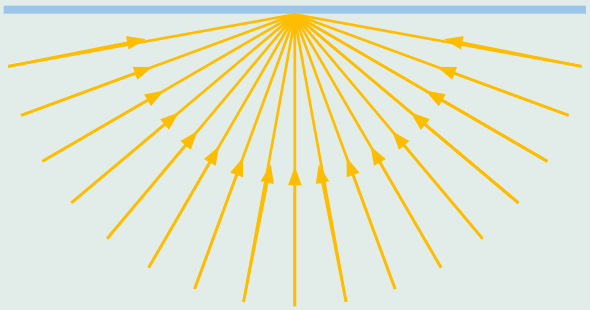

The total upward irradiance at a point on the lower surface is computed by integrating over all solid angles in the lower hemisphere with respect to the Cosine Law; likewise the total downward irradiance is determined by integration over the upper hemisphere. Scalar irradiance, however, integrates equally over all spherical directions about a point, so is always greater than the sum of E_d and E_u (Zimmerman and Dekker, 2006).

Upwelling radiance (L_u) effectively determines the appearance of waterbodies. It is significant for hydrological EO and important in primary productivity and radiative transfer (Ma *et al.*, 2011). Optical properties of waterbodies are further discussed in terms of inherent and apparent optical properties in Sections 8.3.1 and 8.3.2 respectively.

8.1 Optical EO Framework

The topics of water models and EO of waterbodies are introduced in Volume 1B—Section 5.2 and Volume 1B—Section 6.4 respectively. Hydrological optics are detailed in Jerlov (1976), Preisendorfer (1976), Kirk (2010), Mobley (1994), and Mobley (2020). These seminal texts endorse the symbols and definitions for relevant terms summarised in Table 8.4, Table 8.5, and Table 8.6.

Aquatic ecosystem applications of EO rely upon an understanding of the interactions between electromagnetic radiation (EMR) and the atmosphere, the water surface, the water column and, if visible, the substratum. Thus, as illustrated in Figure 8.10, the reflected EMR signal from a waterbody that is detected by the 'viewing cone' of an EO sensor (see Figure 8.4) is impacted by scattering and absorption within the atmosphere and within the water, and reflection and refraction from the water surface (or air/water interface) and possibly from the floor of the waterbody, or substratum.

Table 8.4 Hydrologic optics terms

Description and definition of the spectral radiometric variables. Ξ is the unit sphere (the set of all directions $\boldsymbol{s}$ with solid angle $d\boldsymbol{\Omega}$). μ is the cosine of the zenith angle of the horizontal plane. ∂ is the partial derivative. While all terms are wavelength-dependent, the notation (λ) has been omitted for simplicity. W: watts; m: metre; nm: nanometre; sr: steradian

a. Quantities

Type	Optical Term	Definition	Symbol/equation	Dimensions
Fundamental Quantities	Azimuth angle	see Table 8.1	ϕ	Degrees or radians
	Zenith polar angle	see Table 8.1	θ	Degrees or radians
	Solid angle	see Figure 8.3	ω (or $\boldsymbol{\Omega}$)	sr
	Cosine of polar angle	see Figure 8.8	$\mu \equiv \cos\theta$	n/a
	Water depth	Vertical distance from the water surface within the water column (see Section 5.1.1)	Z	m
Radiometric Quantities	Irradiance	Radiant flux per unit area that is incident on a surface from any direction in a hemisphere	E	W m^{-2} nm^{-1}
	Scalar irradiance	Integral of the radiance distribution at a point over all directions about that point, which measures the radiant intensity at the point	$E_0 = \int_{\Xi} L(\mathbf{s}) d\Omega$	W m^{-2} nm^{-1}
	Downwelling irradiance	See Figure 8.9a	$E_d = \int_{\Xi_d} \mu L(\mathbf{s}) d\Omega$	W m^{-2} nm^{-1}
	Upwelling irradiance	See Figure 8.9b	$E_u = \int_{\Xi_u} \lvert\mu\rvert L(\mathbf{s}) d\Omega$	W m^{-2} nm^{-1}
	Radiance	Radiant intensity per unit area on a plane perpendicular to the flow direction	$L \equiv \frac{\partial^4 Q}{\partial t \partial \boldsymbol{\Omega} \partial A \partial \lambda}$	W m^{-2} sr^{-1} nm^{-1}
	Upwelling radiance	Radiance directed from the downward hemisphere (see Figure 8.9b)	L_u	W m^{-2} sr^{-1} nm^{-1}
	Water-leaving radiance	Radiance that exits the water column at the air-water interface	L_w	W m^{-2} sr^{-1} nm^{-1}

Adapted from: Kirk (1994); Zimmerman and Dekker (2006); Ogashawara (2015)

Absorption occurs when the energy of photons is converted to another wavelength due to interaction with matter. As illustrated in Figure 8.10, an EO sensor detects the backscattered photons that survive the water surface, the water column, the substratum (if visible), and the atmosphere. In most cases, the goal of using EO methods is to reconstruct those constituents that affect (through absorption, backscattering, or fluorescence) the backscattered signal.

Table 8.5 Inherent optical properties

Definitions of Inherent optical properties (IOP) are relative to an infinitesimally thin layer of medium being orthogonally illuminated by a beam of monochromatic light (Kirk, 1994).

Optical Term	Definition	Symbol/equation	Dimensions
Absorptance	Fraction of incident radiation that is absorbed by the medium	A	n/a
Scatterance	Fraction of incident radiation that is scattered by the medium	B	n/a
Transmittance	Fraction of incident radiation that is transmitted by the medium	T	n/a
Attenuance	Fraction of radiant flux that is lost from the incident beam by absorption and scattering combined	C	n/a
Optical density	Measure of transmittance of radiation through an optical medium	D	n/a
Absorption coefficient	Fraction of incident flux that is absorbed divided by the thickness of the layer	a	m^{-1}
Scattering coefficient	Fraction of incident flux that is scattered divided by the thickness of the layer	b	m^{-1}
Attenuation coefficient	Fraction of incident flux that is absorbed and scattered, divided by the thickness of the layer	$c=a+b$	m^{-1}
Volume scattering function	Radiant intensity in a given direction from a volume element illuminated by a p	$\beta(\theta)$	$m^{-1} sr^{-1}$
Scattering phase function	Compares the shape of the angular distribution of scattering in different media with the absolute amount of scattering	$P(\theta)=\frac{\beta(\theta)}{b}$	sr^{-1}

Adapted from: Kirk (1994); Zimmerman and Dekker (2006); Ogashawara (2015)

Table 8.6 Apparent Optical Properties

Optical Term	Definition	Symbol/equation	Dimensions
Irradiance reflectance	Hemispherical measure of irradiance from the water surface	$R \equiv \frac{E_u}{E_d}$	n/a
Subsurface irradiance reflectance	Hemispherical irradiance reflectance just below the water surface (0−)	$R(\lambda,0-)=\frac{E_u(\lambda,0-)}{E_d(\lambda,0-)}$	n/a
Remote sensing reflectance	Reflectance detected within the viewing 'cone' of EO sensor (see Figure 8.4c)	$R_{rs}(\mathbf{s})=\frac{L_u(\mathbf{s})}{E_d}$	sr^{-1}
Subsurface remote sensing reflectance	Reflectance detected within the viewing 'cone' of EO sensor just below the water surface (0−)	$r_{rs}(\lambda,\theta,\varphi,0-)=\frac{L_u(\lambda,\theta,\varphi,0-)}{E_d(\lambda,0-)}$	sr^{-1}
Coefficient of downwelling attenuation	Accounts for rate of change in radiant flux with increasing water depth as light beam travels down through the water column	$K_d \equiv -\frac{1}{E_d}\frac{dE_d}{dz}$	m^{-1}
Coefficient of upwelling attenuation	Accounts for rate of change in radiant flux with decreasing water depth as light beam travels up through the water column	$K_u \equiv -\frac{1}{E_u}\frac{dE_u}{dz}$	m^{-1}
Average cosine of downwelling irradiance	Average value, in an infinitesimally small volume element at that point in the field, of the cosine of the zenith angle of all downwelling photons in the volume element	$\overline{\mu}_d \equiv \frac{E_d}{E_{0d}}$	n/a
Average cosine of upwelling irradiance	Average value of the cosine of the nadir angle of all upwelling photons at a particular point	$\overline{\mu}_u \equiv \frac{E_u}{E_{0u}}$	n/a

Adapted from: Kirk (1994); Zimmerman and Dekker (2006); Ogashawara (2015)

Figure 8.10 EMR reflectance from water

For aquatic targets, four sources can contribute to the radiance detected by a remote sensor, namely the atmosphere, the interface between air and water (the surface), constituents of the water column and, in optically shallow waters, the substrate.

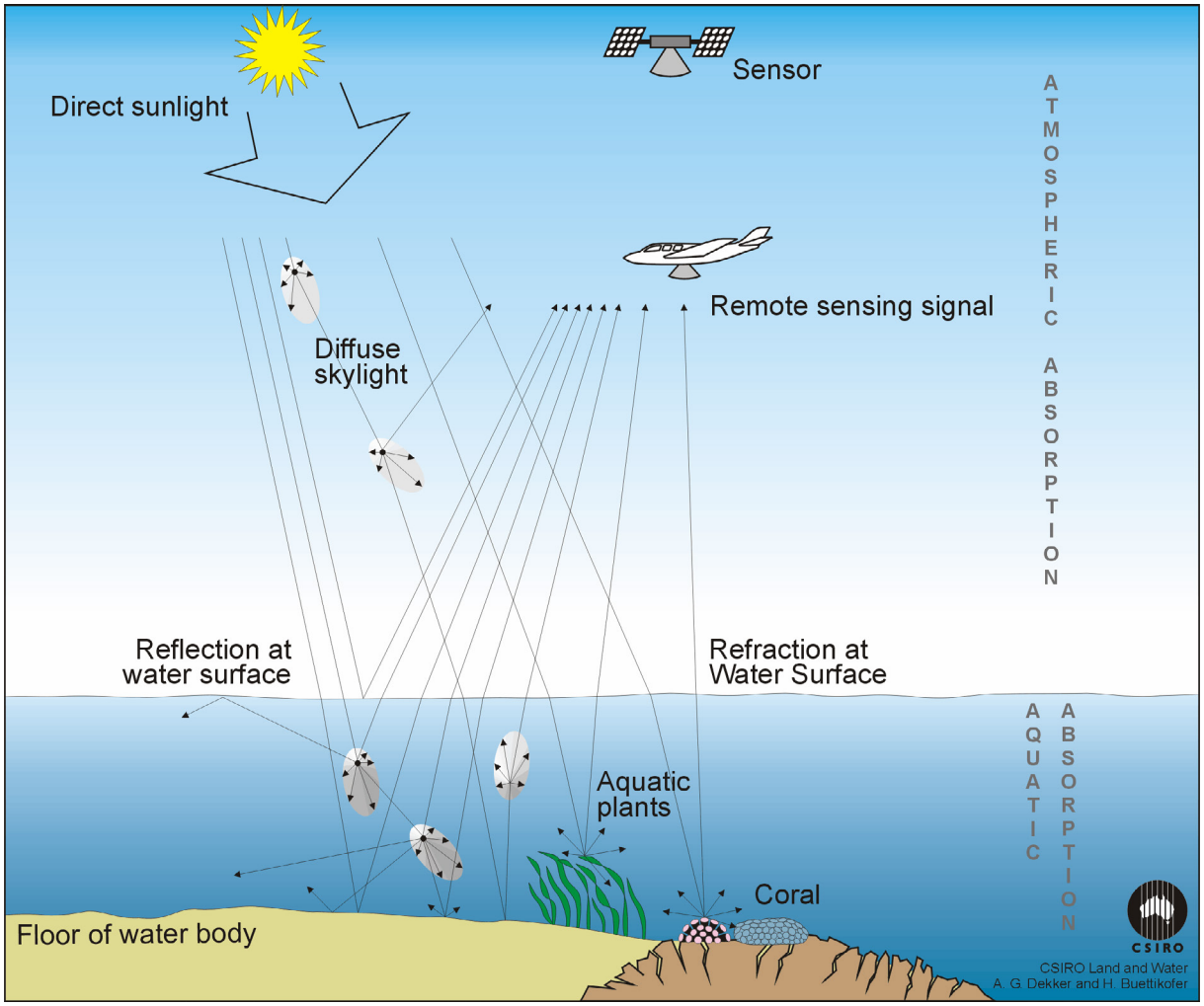

Source: Arnold Dekker, CSIRO

8.1.1 Scattering

Scattering is caused by photons that change direction and/or energy due to interaction with matter (see Volume 1B—Sections 3 and 4). Four fundamental scattering directions can be identified for incident light being intercepted by a waterbody. As depicted in Figure 8.11, forward and backward scattering directions describe the scattering processes with respect to the angle of the incident light, while upward and downward scattering describe the fractions of incident light that are scattered relative to the surface normal (that is, the water surface). Downwelling radiance comprises both direct sunlight and diffuse skylight (or scattered sunlight) at all altitudes within the atmosphere, and specifically just above the water surface.

Figure 8.11 Scattering directions

Forward and backward scattering are defined relative to the direction of the incident beam. Downward and upward scattering are defined relative to a horizontal surface. The upwelling light detected by EO may be derived from light scattered in both forward and backward directions, although the backward scattering will dominate.

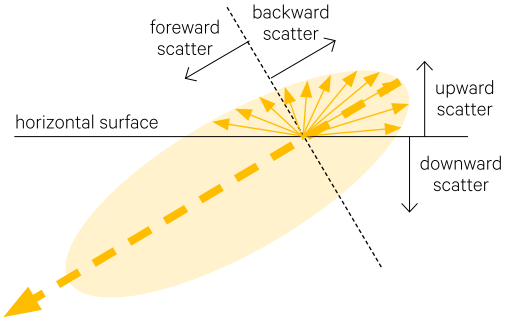

Source: Zimmerman and Dekker (2006) Figure 4

Scattering can be either an elastic process, when the scattered photon has the same wavelength and polarisation as the incident photon, or an inelastic process, when the wavelength and/or polarisation of the scattered photon differ from the incident photon. In natural waters Raman scattering mostly results in the scattered photons having lower energy and thus longer wavelength. Scattering of sunlight off air molecules is called Rayleigh scattering, and results in the blue colour of the sky (see Volume 1B—Section 4.2.1). Mie scattering predominates where there are large air particles (larger than the wavelength of light; see Volume 1B—Section 4.2.2). Rayleigh and Mie scattering are elastic so the scattered photon's energy does not change. In natural waters, two types of inelastic scattering of relevance are Raman scattering and fluorescence (see Section 8.1.2. Raman scattering is virtually instantaneous and does not change incident polarisation. In natural waters, it is essentially due to the interaction of photons with water molecules, and is considered a relatively constant factor that slightly influences underwater light between 550 nm and 650 nm in very clear water.

8.1.2 Fluorescence

Fluorescence is an absorption-emission process that is relatively slow and results in unpolarised photons. In natural waters, dissolved organic matter and photosynthetic pigments (in phytoplankton, seagrasses, macrophytes, and symbiotic algae) contain fluorescent substances. Typically 1–5% of photons absorbed by chlorophyll via photosynthesis are emitted as fluorescence in a 25 nm band centred at 685 nm (Falkowski and Raven, 2007). Fluorescence effects are observed in features associated with both the water column and the substratum (see Table 8.7). Fluorescence imaging (such as the Fluorescence Image Laser line Scan: FILLS; Jaffe *et al*., 2001) can be used to distinguish between a wide variety of substratum features, including hard corals and zoanthids, soft corals, macroalgae, red algae and cyanobacteria, vase sponges, sand, shadow, and non-fluorescent features.

Table 8.7 Some fluorescence features in waterbodies

Example Feature	Description	Fluorescence
Chlorophyll	Photosynthetic pigment in organisms within water column and substratum	Red
Phycoerythrin	Photosynthetic accessory pigment in red algae and cyanobacteria within water column and substratum	Orange
Corals	Substratum fauna	–
Anemones		–
Some sponges		–
Carbonate sediment	Organic matter in calcium carbonate matrix	–
CDOM	Coloured Dissolved Organic Matter	Ultraviolet

Source for data: Mazel (2001); Para *et al.* (2010)

8.1.3 Water surface effects

Waterbody surfaces exhibit swell, waves, and capillary waves with heights or amplitude ranging from a few centimetres to tens of metres. Although their overall distribution can be predicted in a stochastic way, the inherently chaotic nature of these surface effects complicates their removal from surface reflectance. Oil slicks can dampen wave action and increase reflectance of some wavelengths. Ocean surface waves create 'whitecaps', that is bubbles and streaks on their breaking crests, which also change the observed water colour (Estep and Arnone, 1994). Air bubbles, which tend to occur in association with waves, increase reflectance in different wavelengths (Pozdnyakov and Grassl, 2003). These are easier to measure in oceans, but also occur in other natural waters.

At the surface of a waterbody, or the 'air-water interface', two processes can occur:

- downwelling irradiance may be reflected due to the specular or Fresnel reflectance of the water surface; or
- light is refracted (due to a density difference between air and water) and passes into the water column.

Thus, downwelling irradiance above the water surface is either reflected from the surface back into the atmosphere or refracted across the air-water interface into the water. 1–15% of the downwelling irradiance from the atmosphere is reflected from the surface of waterbodies, with most waterbodies reflecting 2–6%. For a flat water surface, these Fresnel reflectance and refraction values can easily be computed. When the situation is more complex, such as a rough water surface with swell, waves, and fractal wavelets, these values can still be computed, or derived through observations (Dekker *et al.*, 2006).

Snell's law describes the change in the angle of light and other waves as they pass through a boundary between two media, such as air and water (see Volume 1A—Section 2.5.2):

$$\frac{\sin\theta_{air}}{\sin\theta_{water}} = \frac{n_{water}}{n_{air}}$$

where

θ is the angle of incidence; and
n is the refractive index.

This equation is used to calculate refraction and reflection of incident light beams at the water surface. The refractive index is a function of the wavelength of the light, as well as the salinity, temperature, and pressure of the water (Parrish, 2020). For seawater the refractive index is generally 1.338 (Plass and Kattawar, 1972) to 1.34 (Mobley, 2020), while freshwater is generally slightly lower at 1.333.

Given the refractive index of seawater, irradiance intercepting a flat seawater surface from the atmosphere at all angles (potentially spanning 180°) only passes into the water column within a compressed cone (spanning a maximum of 97.6°). Conversely, any upwelling light that intercepts the surface at angles outside this cone will not penetrate the surface but becomes reflected internally within the water (see Figure 8.12). Surface roughness tends to slightly widen the solid angle of this cone.

In most studies of surface water, the surface reflected component is an unwanted signal in EO imagery whereas the surface refracted component becomes involved in cascades of absorption and scattering. The light-interaction-with-water processes involving refraction, refractive indices, internal reflection, sea roughness, sunglint, and wind-induced optics have been successfully explained and modelled by optical oceanographers for several decades. When remotely sensing natural waterbodies from satellite and/or aircraft altitudes, numerous techniques have been proposed to remove the impact of surface waves on downwelling solar and sky radiation (Cox and Munk, 1954). Wave energy issues that are a function of local climatic conditions, however, still present difficulties in rigorously detailing how radiation is transferred through the air-water interface.

The extent of water surface reflection observed by a remote (airborne) sensor largely depends on Sun position. Image acquisition by airborne and 'agile' satellite borne sensors (such as Quickbird or WorldView-2/3 which are 'pointable' in space), therefore, would ideally consider the solar zenith angles and azimuths from which (given the field of view of the scanner) it is least likely to image sunglint from a water surface (Botha *et al.*, 2016). In general:

- solar zenith angles between 30° and 60° are optimal over water targets; and
- flight paths should be flown at 0° or 180° headings with respect to the solar azimuth (that is either directly towards or away from the Sun; Mustard *et al.*, 2001; Dekker *et al.*, 2003).

Figure 8.12 Internal reflection and refraction

The direction of travel of light beams from inside a water body (such as substratum reflectance, Raman fluorescence, or backscattering in the water column) determines whether, at the water surface, they are internally reflected back into the waterbody or refracted into the atmosphere.

a. Internal radiance intercepting the water surface outside the 97.6° refraction cone will be internally reflected into the waterbody.

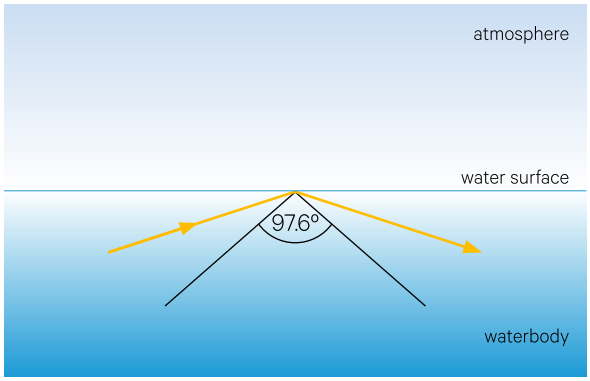

b. Internal radiance intercepting the water surface inside the 97.6° cone will be refracted into the atmosphere.

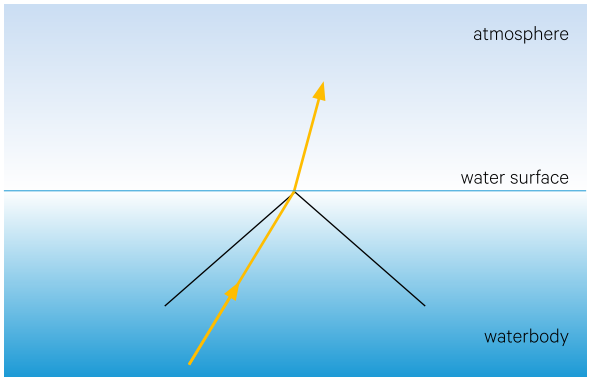

At high latitudes this will mean acquiring imagery in a short period of time around noon in summer to achieve a maximal amount of irradiance. At mid-latitudes the flight time will be dependent on the season since the maximum solar zenith angles increase from summer to winter. Accordingly, the mid-latitude flight time envelope decreases from approximately six to eight hours surrounding noon in summer to two hours surrounding noon in winter. At low latitudes the requirement to fly between 30° and 60° solar zenith angles means that solar noon must also be avoided to prevent sunspot effects (direct reflectance from horizontal water surfaces into the field of view). In this case, there are only two suitable image acquisition periods: one in the morning and one in the afternoon. These considerations are also relevant to ordering high spatial resolution satellite imagery since the new generation of satellite sensors offer selectable viewing angles (that is, in addition to nadir imaging). Off-nadir viewing is advantageous if sunglint and skyglint can be avoided but detrimental if these effects are enhanced.

Image processing methods exist to 'deglint' water surfaces in EO imagery (see Volume 2). While the deglinting process decreases the radiometric resolution of the image data, it may not increase the spectral separation between different substrata (Hedley, 2013). Shipborne, above-water EO sensors face particular challenges with respect to surface-reflected glint (Garaba and Zielinski, 2013) with no current correction methods offering a universal panacea.

One example of the impact of water surface effects in EO imagery is given by Botha et al. (2016), who compare two high spatial resolution EO images that were acquired one minute apart over an optically shallow coastal ecosystem in Tasmania. While the viewing and illumination geometries of the first image were optimal, resulting in minimal sunglint, the second image was acquired with significant sunglint and atmospheric scattering (see Figure 8.13 and Figure 8.14). When satellite-based bathymetry (see Section 13.4.2) was applied to both images, accurate results were obtained from the first image, but water depths were underestimated from the second image.

Figure 8.13 Sun-sensor geometry of example images

Two WorldView-2 images were acquired one minute apart over a shallow coastal lagoon in Tasmania, Australia (42.8211°S, 147.5508°E) on 22 October 2011. The position of the Sun, relative to the target, was constant, while the position of the sensor, relative to the target, changed. The resulting images are shown in Figure 8.14.

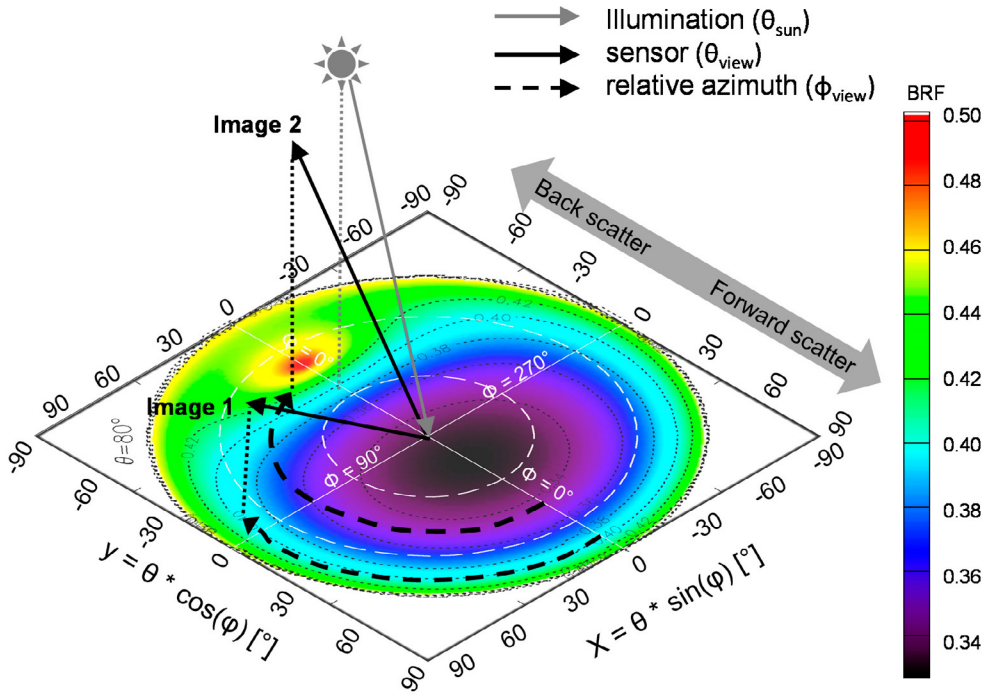

Source: Botha *et al.* (2016) Figure 1

Figure 8.14 Impact of sun-sensor geometry on image quality

These images were acquired using the sun-sensor geometry shown in Figure 8.13, during an outgoing tide with a gentle (16 km/h) southeasterly breeze. Gray mask: exposed land area; 1: location of the *in situ* depth observations (red dots) collected on 22 August 2013; 2: location of the least glint-affected image segment, selected for atmospheric correction inter-comparison; 3: location of an area of water (as homogenous and optically deep as possible) that was selected for the NEΔrsE (Environmental Noise Equivalent Remote Sensing Reflectance Difference) computation.

a. Image 1 (ϕ_{view} = 106°, θ_{view} = 77°) showed minimal sunglint and resulted in accurate water depth estimates.

b. Image 2 (ϕ_{view} = 175°, θ_{view} = 57°) showed significant sunglint and atmospheric path scattering and underestimated water depths.

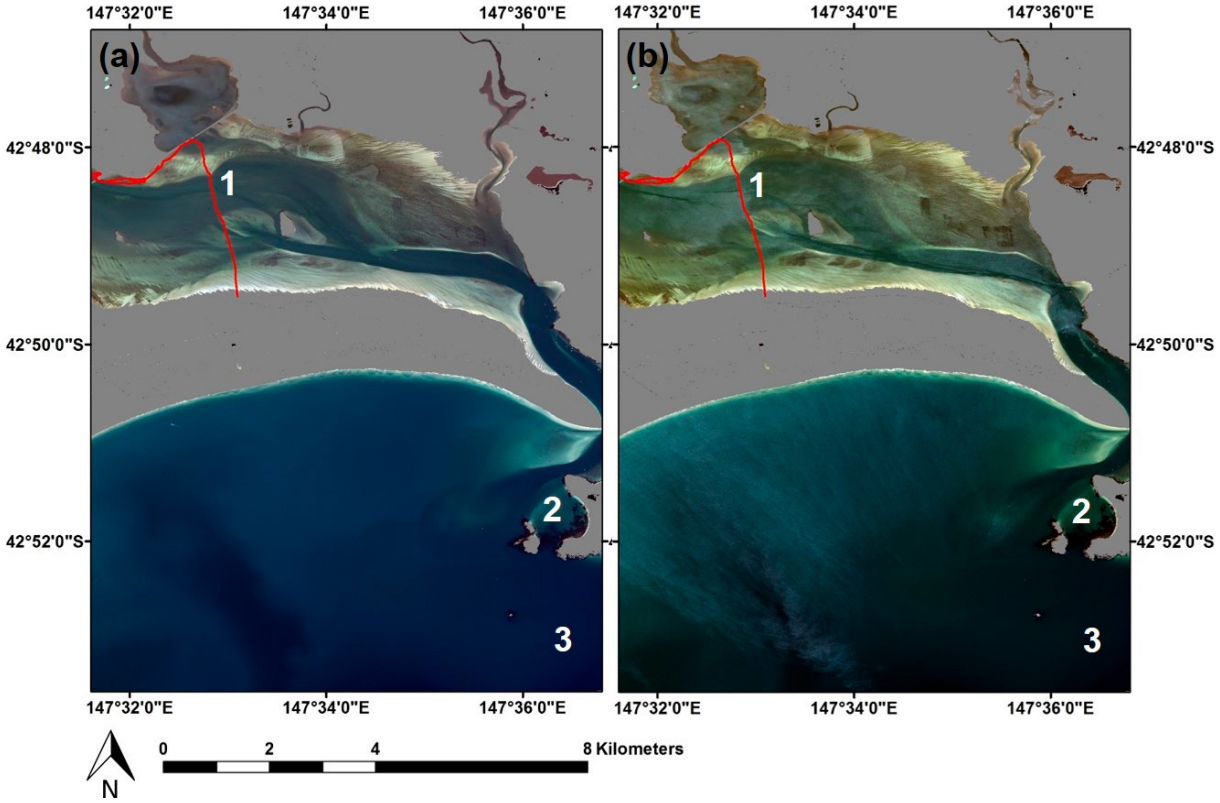

Source: Botha *et al.* (2016) Figure 2

8.1.4 Radiative transfer theory

Scattering and absorption of light occurs as it passes through any medium. In the atmosphere, aerosols, gases, and water absorb or scatter light. Within a natural water column, the absorption and scattering of light depends on water depth, substratum type (if visible), and/or water constituents, (namely pure water, photosynthetic pigments, particulate matter, coloured dissolved organic matter (CDOM), and coloured dissolved inorganic matter (CDIM); see Section 8.1.3). Each of these constituents absorbs and scatters light in a spectral (that is, wavelength-dependent) manner. The light reaching a seagrass canopy, for example, is modified by the interaction of the downwelling irradiance with these water constituents and thus influences the quality of the light available for photosynthesis (see Zimmerman, 2006). The upwelling radiance, then, includes direct and diffuse sunlight that has been reflected by the water surface and/or scattered back through the water surface by the water column after penetrating the surface and interacting with water or benthic components.

As introduced in Volume 1B—Section 5, radiative transfer describes how radiant energy, such as light, is changed by any medium it passes through. Radiative Transfer theory approximates the loss of radiant energy of a beam due to absorption and scattering along a defined path, and any energy gain resulting from scattering into the path (see Figure 8.5). Radiative Transfer models for optical EO imagery of water are detailed in Section 8.4.1.

8.1.5 Atmospheric correction

While the atmospheric correction physics of optical EO data over waters is essentially the same as for terrestrial targets, a few practical differences need to be considered. On land, the signal reflected from the surface contains useful information about the surface, whereas for any waterbody, the signal coming from within the water is the desired signal. Moses *et al.* (2017) provide a useful overview of this process for inland waters.

In most studies of water properties, the signal reflected from the water surface is considered to be noise and comprises the reflected component of diffuse skylight and the direct sunlight impinging on the water surface (see Section 8.1.3). While methods for atmospheric correction of oceans are quite mature, the task is more complex for coastal and inland waters due to highly varying aerosol levels, adjacency effects, elevation issues, less predictable sunglint and skyglint, and local effects with finer spatial resolution data.

Although many atmospheric correction software packages are available, or are included in generic EO processing software, they only function over land targets. For atmospheric correction over waterbodies, various models have attempted to extract the unwanted atmospheric signal from water-leaving radiances. These models range from overly simplistic in attributing all the atmospheric return to a single NIR wavelength band (often incorrectly assuming the water reflectance to be zero) to diligently generating 'generic' atmospheres by practical combinations of air temperature, solar azimuth, terrain elevation, aerosol density, day of year, atmospheric composition, wind speed, and other atmospheric parameters such as visibility and meteorological range (Pahlevan *et al.*, 2021). Artificial neural networks have delivered promising results for atmospheric correction over the GBR (Goyens *et al.,* 2013; Singh *et al.*, 2019).

8.2 Optically Active Constituents of Water

All particulate matter (algae, dead organic matter, and mineral particles) scatters light, with the extent and type of scattering depending on the sizes and refractive indices of particles (see Section 8.1.1). When light is absorbed, however, it can no longer be elastically scattered, but may be emitted as fluorescence (inelastic scattering).

A variety of components that are present in natural waters collectively determine the optical properties of a waterbody. Historically, the terminology used to describe these components has differed between oceanographers studying marine waters and limnologists studying inland lakes. Further, the range of optical components, and their relative complexity, varies for different types of surface waters. Accordingly, the current terminology to describe the optical components of natural waterbodies can appear somewhat confusing. For example, limnological terms that may be encountered in research literature include:

- seston—total particulate matter including terrigeneous sediments, plankton, detritus, volcanic ash, chemical process particulates, and anthropogenic particles (Dekker, 1993; Lindell *et al.*, 1999); this is equivalent to Total Suspended Matter (TSM) and includes pigments and algal biomass; or
- tripton—all particulate matter except phytoplankton pigments, also called detritus; this is equivalent to non-algal particulates (NAP); or
- gilvin, gelbstoff, yellow substance—is equivalent to chromophoric (or coloured) dissolved organic matter (CDOM).

Being photosynthetic agents, pigments absorb light very effectively. While the pigments in algae comprise only 1/3000 of the total algal mass, they absorb significantly more light than the cell material, or biomass. Algal biomass, however, scatters light. For example, the phytoplankton *Coccolithophores* is characterised by significant scattering by its cell structure, which is masked in live organisms by pigments. In dead organisms, however, while pigments decay, the cell structure remains optically significant.

To distinguish between the optical impacts of pigments and particulate matter in natural waterbodies, water samples are filtered in order to extract photosynthetic pigments from the particulate matter using organic solvents and, more specifically, the phytoplankton. Accordingly, the term 'particulate matter' is commonly considered to collectively describe inorganic matter, detritus, plus the algal cell material remaining after pigments have been extracted by filtering. For reasons best understood by ocean colour scientists, this group is also referenced as 'non-algal' particles (NAP), although a better term would be 'non-algal pigmented' particles.

In the following text, optical components will be considered in terms of five discrete groups:

- pure water—optically pure (see Section 8.2.1);
- photosynthetic pigments—from phytoplankton and cyanobacteria (see Section 8.2.2);
- particulate matter—'non-algal' particles (NAP; see Section 8.2.3);
- coloured dissolved organic matter (CDOM)—from hydrocarbon compounds (see Section 8.2.4); and
- coloured dissolved inorganic matter (CDIM)—from mineral compounds (see Section 8.2.5).

8.2.1 Pure water

Molecules of pure liquid water scatter blue wavelengths with rapidly decreased scattering for longer wavelengths. Conversely, pure water absorption of blue wavelengths is very low, but this increases significantly towards NIR wavelengths (see Figure 8.15). Since the least absorption, and some scattering, occurs with blue wavelengths, pure liquid water appears to be coloured blue.

Figure 8.15 Absorption spectrum of pure water

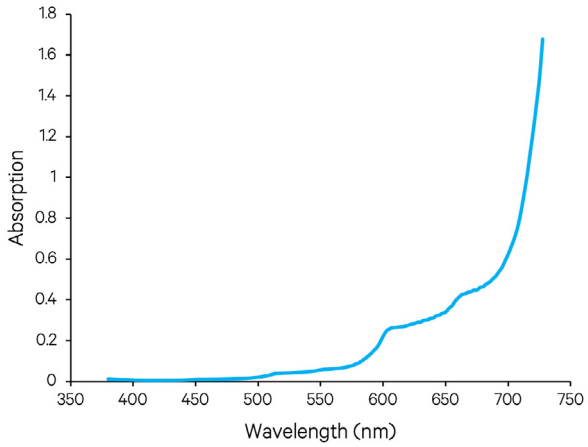

Source: Janet Anstee, CSIRO, using data from Pope and Fry (1997)

Figure 8.16 Effect of salinity on scattering by water

Data from Morel (1968) and Zhang *et al.* (2009) for spectral scattering of water at 20°C. Pure water (shown as solid line) is compared with natural seawater (salinity=3.85%; shown as dashed line). The scattering was measured at five wavelengths, 366 nm, 405 nm, 436 nm, 546 nm and 578 nm (dots), and the scattering is represented with the volume scattering function at 90°, β(90).

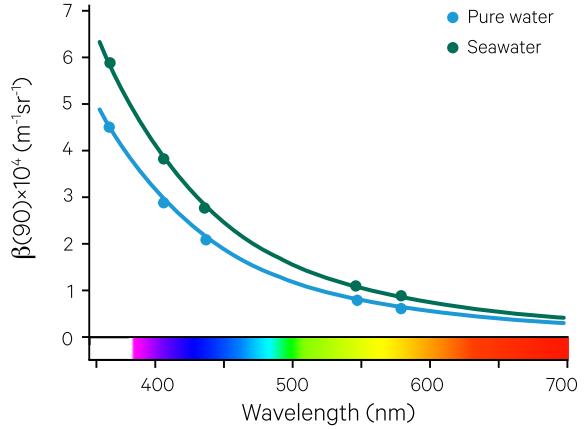

Adapted from: Mobley (2020) *https://www.oceanopticsbook.info/view/optical-constituents-of-the-ocean/water*

Natural waters are rarely pure however, and reflectance characteristics can vary slightly with temperature and salinity. Seawater, for example, is 96.5% pure water, with 3.5% salts, plus dissolved and/or suspended substances. The influence of salinity on scattering is evident in Figure 8.16, with a 30% increase in scattering between the freshwater and seawater samples. Zhang *et al.* (2009) report that while the contribution of salinity to the total scattering is minor (less than 10%) in visible wavelengths for very clear ocean waters, it accounts for up to 80% of the total backscattering. By comparison, in the waters of a clear alpine lake a major contribution to the total backscattering (30–60%) comes from the water itself.

8.2.2 Phytoplankton and cyanobacteria pigments

As introduced in Section 3.3.1, plankton comprise tiny, floating zooplankton (animals) and phytoplankton (plants), some of which are independently mobile. Phytoplankton includes more than 10,000 species, which manifest as a wide range of sizes, shapes, and colours, and occur in inland, coastal, and ocean waters. The composition and concentration of phytoplankton pigments can impact water colour, with the main pigment groups being:

- chlorophylls—which appear as the colour green, due to strongest absorption of blue and red wavelengths;
- carotenoids—which appear to be coloured yellow to red, due to strongest absorption in broad region of blue-green wavelengths; and
- phycobilins—which appear to be predominantly coloured blue, blue-green, and red, due to strongest absorption of yellow to orange wavelengths.

Absorption spectra for these pigments are illustrated in Figure 8.17. To obtain the pigments, the particulate matter, including phytoplankton, that is present after filtering over a 0.45–0.70 μm filter, is flushed with an organic solvent such as ethanol, acetone, or methanol. The filtrate then contains the pure pigments. For cyanobacterial pigments that are water soluble, the cells first need to be destroyed through grinding and heating before the pigments can be flushed out using water.

Figure 8.17 Absorption spectra of algal pigments

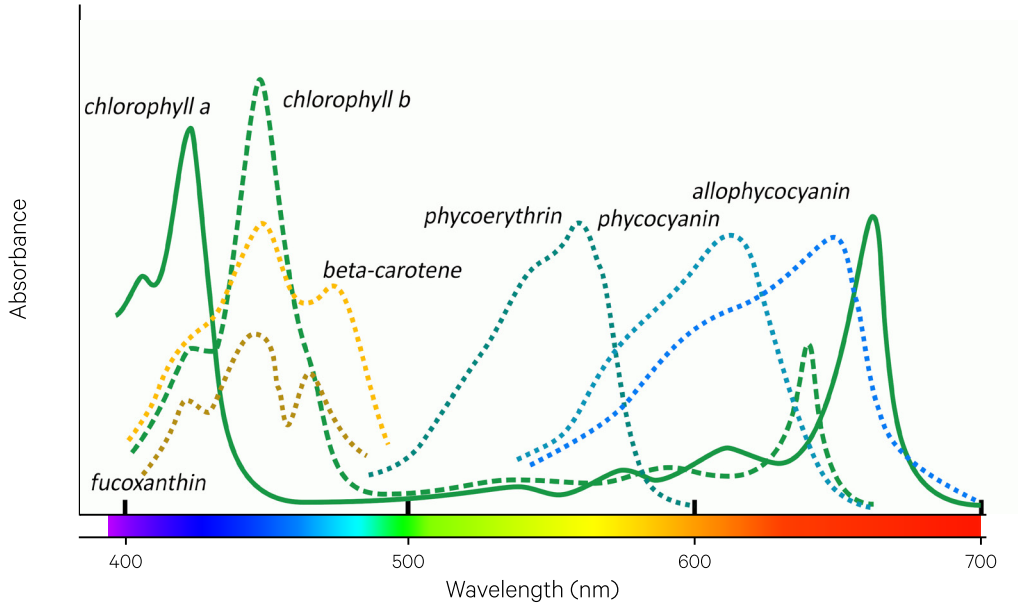

Adapted from: Goodwin and Mercer (1990) by Qiaoyun Xie, University of Technology Sydney. (Original retrieved from *http://biologywiki.apps01.yorku.ca/index.php?title=File:Pigment_spectra.png*)

The most abundant pigment in phytoplankton is chlorophyll a, which has two (*in situ* and *in vivo*) absorption peaks at 438 nm and 676 nm respectively. Cell components and cell walls of phytoplankton also absorb and scatter light. Characteristically, phytoplankton absorption is virtually zero at 720 nm and greater wavelengths. The cyanophycocyanin pigment characterising cyanobacteria (blue-green algae) has a distinctive absorption feature near 620 nm (Simis *et al.*, 2005). Variations in phytoplankton pigments are detailed in Kirk (1994, 2010). Pigments can also be characterised by their fluorescence wavelengths.

Some of the variations in water colour that can result from different species of phytoplankton are shown in Figure 8.18. The absorption spectra for these species are illustrated in Figure 8.17. Two spectra are given for diatoms to indicate the spectral difference resulting from high and low light levels. The major optically active pigments for phytoplankton taxonomic classes are listed in Table 8.8.

Estimates of phytoplankton concentration, derived from bio-optical data, are considered to be indicative of marine primary productivity. Various models have been proposed to relate phytoplankton light absorption to chlorophyll concentration (Bricaud *et al.*, 1995; Brando *et al.*, 2009, 2012; Blondeau-Patissier *et al.*, 2009). These models derive summary parameters, such as the phytoplankton coefficient, which synthesise the absolute cell concentration, composition of the phytoplankton community, and inter-species variations in pigment composition. The total phytoplankton spectrum is obtained as the sum of individual spectra (Mobley, 2020).

Figure 8.18 Water colour variations due to phytoplankton

Phytoplankton species, left to right: diatom, cryptophyte, chorophyte, cyanophyte, premnesiophyte, and dinoflagelate

Source: Mobley (2020) Figure 3. Retrieved from *http://www.oceanopticsbook.info/view/absorption/absorption_by_oceanic_constituents*

Table 8.8 Major photo pigments for phytoplankton taxonomic classes

Diagnostic pigments	Taxonomic association	Typical cell size (μm)	Phytoplankton class
Fucoxanthin	Diatoms	> 20	Microphytoplankton
Peridinin	Dinoflagellates	> 20	Microphytoplankton
Alloxanthin	Cryptophytes	2–2	Nanophytoplankton
Lutein + chlorophyll b	Chlorophytes	< 2	Picophytoplankton
Zeaxanthin and Lutein	Cyanobacteria	< 2	Picoplankton
Chlorophyll b	Prochlorophytes and flagellates	< 2	Picoplankton
Echinenone	Cyanobacteria	< 2	Picoplankton

Source: Joehnk *et al.* (2018)

Figure 8.19 Absorption spectra for phytoplankton

CS-337: *Dolichospermum circinale* (Burrinjuck Dam, Australia)
CS-567: *Microcystis aeruginosa* (Gippsland Lakes, Australia)
CS-1034: *Chrysosporum ovalisporum* (Brisbane, Australia)
CS-505: *Raphidiopsis raciborskii* (Palm Island, Qld, Australia)
CS-588: *Nodularia spumigena* (Gippsland Lakes, Australia)
CS-328: *Arthrospira maxima* (Lake Chad, Africa)
CS-205: *Synechococcus sp.* (Menai Strait, UK)
CS-94: *Synechococcus sp.* (Queenscliff, NSW, Australia)
CS-197: *Synechococcus sp.* (Sargasso Sea)
CS-601: *Synechococcus sp.* (Ace Lake, Antarctica)

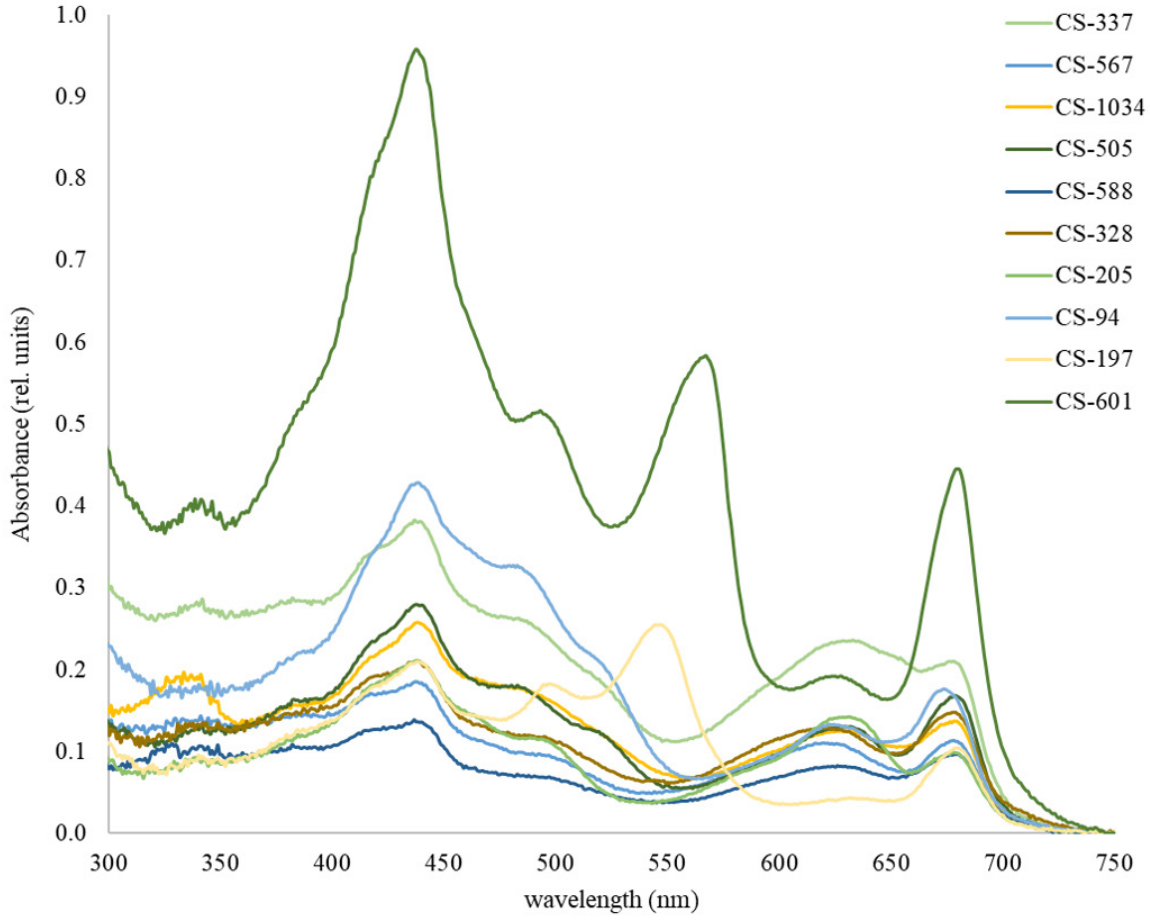

Source: Clementson *et al.* (2021)

8.2.3 Non-algal particles (NAP)

Non-algal particles (NAP) are defined as particulate matter that cannot be extracted by methanol/ethanol/acetone (Kishino *et al.*, 1985). By default, once pigments have been extracted from water samples, NAP is the remaining matter that does not pass through a (0.45–) 0.7 mm filter. This residue can include:

- suspended particulate organic matter (SPOM)—organic particles from bacteria, zooplankton, phytoplankton, including detrital organic matter; and
- suspended particulate inorganic matter (SPIM)—suspended inorganic particles.

All NAP constituents (except iron minerals) mainly absorb UV to blue wavelengths, with absorption reducing exponentially to red to NIR wavelengths (Babin *et al.*, 2003). The proportion of constituents varies with water location, with higher non-organic particle concentrations occurring near rivers and benthic boundary layers. Highest concentrations of NAP occur in inland and coastal waters.

At wavelengths where suspended (undissolved) particles, including algae, in water scatter more radiation than they absorb, the backscattering coefficient will be more than the absorption coefficient, with a consequent increase in the radiance detected by an EO sensor (Kirk, 1994). As such, turbid waters appear brighter in optical wavelengths than clear waters. This characteristic allows EO imagery to be used to map the concentration of NAP in water (see Sections 18.1 and 19). The precise optical properties of suspended sediments vary with their sizes, colours, and concentrations (see Section 5.1.4).

8.2.4 Coloured dissolved organic matter (CDOM)

Rivers and inland waters often contain tannins and other dissolved organic materials that colour their water (Shank *et al.*, 2010). Being dissolved (defined as material passing through a 0.2 μm pore filter[9]; Bricaud *et al.*, 1981), CDOM does not scatter light. Constituents include organic substances, which absorb UV to blue wavelengths with exponential decay towards red wavelengths.

Waters containing high concentrations of CDOM are typically coloured yellow to brown (see Section 5.2.3.1). Highest concentrations occur in inland and coastal waters, and the discharge from inland waters provides a substantial pool of CDOM to coastal waterways. Sources of CDOM in subtropical and tropical coastal waters are primarily derived from leaching or degradation of seagrasses (Otis *et al.*, 2004) or mangrove leaf litter (Maie *et al.*, 2006).

The typical absorption spectrum for CDOM decreases exponentially with wavelength from UV through the visible spectrum (Twardowski *et al.*, 2004). As illustrated in Figure 8.20, the actual slope of the absorption spectrum for each water sample is determined by its CDOM concentration. CDOM absorption spectra are commonly modelled as an exponential decay function of wavelength (Jerlov, 1976):

$$a_{CDOM}(\lambda) = a_{CDOM}(\lambda_0)e^{-S(\lambda_0-\lambda)}$$

where

$a_{CDOM}(\lambda)$ is the absorption coefficient of wavelength λ;
λ_0 is the reference wavelength (often 440 nm); and
S is the slope of the spectrum within a given wavelength interval (nm^{-1}).

To determine the exponential function for specific CDOM sites, the actual absorptions of filtered samples are measured using a spectrophotometer, typically over the wavelengths 250–800 nm. The CDOM spectral slope is then derived by fitting an exponential curve to the measured absorptions from 300–600 nm (Mannino *et al.*, 2008).

Figure 8.20 CDOM Absorption spectra

Stylised absorption spectra for 0.2 μm filtered water samples indicate the spectral slope changes that occur with decreasing CDOM concentration.

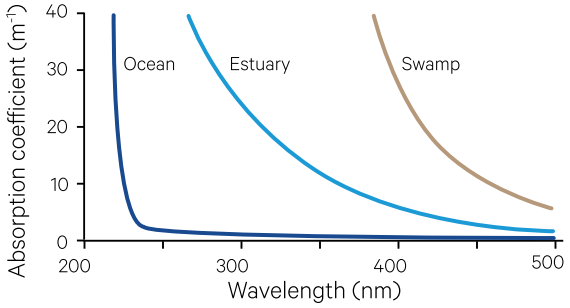

Adapted from: Helms *et al.* (2008) Figure 1a

9 A problem identified by Laanen *et al.* (2011) is that particulate matter is filtered out over 0.7 mm filters (to avoid the filter from clogging up too soon) whereas CDOM is filtered over 0.22 mm filters. This means the 0.22–0.7 mm particulate material is unaccounted for in lab-based bio-optics measurements.

Analysis of over 500 oceanographic field campaigns over a 30 year period in the Global Ocean Carbon Algorithm Database (GOCAD) indicates that the CDOM absorption and spectral slope values are linked to atmospheric and oceanographic processes such as the El Niño Southern Oscillation (ENSO; Aurin *et al*, 2018). For example, exposure of CDOM to sunlight has been shown to increase the spectral absorption slope through photo-bleaching of the CDOM (Del Vecchio and Blough, 2002). In recent studies, it was found that riverine CDOM absorption slopes became very similar to marine CDOM after five days of sunlight exposure (Martin *et al.*, 2018).

8.2.5 Coloured dissolved inorganic matter (CDIM)

The optical absorption characteristics of minerals depends on their colour, which can vary from white to grey, occasionally yellow, brown, or red (and occasionally black in the case of volcanic material). Dissolved inorganic salts have highest absorption in UV wavelengths due to electronic transition bands (see Volume 1—Section 6.3). Scattering by dissolved inorganic salts and/or iron compounds is generally more significant for ocean waters than for freshwater in inland waterbodies.

8.3 Optical Properties of Water

The optical properties of water may be described as either Inherent Optical Properties (IOP; see Table 8.5 and Section 8.3.1) or Apparent Optical Properties (AOP; see Table 8.6 and Section 8.3.2). IOP and AOP are connected via radiative transfer theory (see Section 8.4.1 and Volume 1B—Section 5). Optical properties of the substratum are considered in Section 8.3.3. Systems that classify water colour using IOP and AOP are introduced in Section 18.3.

8.3.1 Inherent Optical Properties

Inherent Optical Properties (IOP) describe the absorption and (back)scattering characteristics of a water sample, including dissolved and suspended components, but not the geometry or magnitude of incoming radiation. As the name implies, IOP describe properties that are *inherent* to the optical behaviour of the water, regardless of lighting conditions. Accordingly, the IOP of a water sample may be measured anywhere, in the field or laboratory, and should yield the same results, assuming no measurement errors are made.

As illustrated in Figure 8.5, when a beam of light enters a volume of water, its energy changes in three ways:

- some is absorbed by the water—absorptance (*A*): proportion of incident light that is absorbed within the volume;
- some is transmitted through the water—transmittance (*T*): proportion of incident light that passes through the volume without interaction; and
- some is scattered out of the beam—scatterance (*B*): proportion of incident light that is scattered out of the beam in all directions.

These three options are represented as fractional components of the incident light beam, such that:

$$A + B + T = 1$$

In pure water, most incident energy is transmitted, rather than scattered or absorbed. Scattering by particles in natural waters, however, extends the path length of light, and thus increases the probability of absorption. It also propagates photons back towards the light source, which is known as backscattering. The precise direction of backscattering depends on the properties of the water.

IOP are defined by illuminating a small volume (thickness Δr) by a narrow, collimated beam of monochromatic light (with spectral radiant power Φ_i). Within the volume, portions of this light are either absorbed (Φ_a), scattered (at angle Ψ within a cone of solid angle $\Delta\Omega$), or transmitted (Φ_t). For a given volume of water, they can be defined as given in Table 8.9.

Shallow waters are generally associated with coasts, currents, and terrigenous inputs, and the optical properties of the water column and the seafloor can vary rapidly in time as well as in space.
(Mazel, 2001)

Table 8.9 Commonly used Inherent Optical Properties

Property	SI units	Symbol	Description
Absorption coefficient	m^{-1}	a	Absorptance per unit distance in the volume, which indicates the distance that a beam of light can penetrate into the volume before it is absorbed. When normalised, this effectively describes the probability of a photon being absorbed by the medium.
Scattering coefficient	m^{-1}	b	Scatterance per unit distance in the volume, which indicates the distance that a beam of light can penetrate into the volume before it is scattered. When normalised this effectively describes the probability of a photon being scattered by the medium.
Backscattering coefficient	m^{-1}	b_b	Indicates the attenuation due to backscattering (90–180° from light source) and computed from the volume scattering function. When normalised this effectively describes the probability of a photon being backscattered.
Forward scattering coefficient	m^{-1}	b_f	Indicates the attenuation due to forward scattering (0–90° from light source) and computed from the volume scattering function. When normalised this effectively describes the probability of a photon being scattered in a forward direction.
Beam attenuation coefficient (or extinction coefficient)	m^{-1}	c	Indicates the distance that a beam of light can penetrate into the volume before it is attenuated (absorbed or scattered). When normalised this effectively describes the probability of a photon being attenuated by the medium.
Volume scattering coefficient	$m^{-1}sr^{-1}$	β	Characterises the intensity of scattering for a given angle. When normalised this effectively describes the probability of a photon being scattered in a particular direction within the medium.
Scattering phase function (or phase function)	sr^{-1}	$\tilde{\beta}$	Indicates the angular distribution of light intensity scattered by a particle at a given wavelength
Single-scattering albedo	n/a	$\tilde{\omega}$ or ω_0	Ratio of the scattering coefficient to the extinction coefficient. This affects radiative transfer and is generally a function of wavelength.

Adapted from: Mobley (2020); AMS (2019)

The two main optical processes in the water column are absorption and elastic scattering (see Section 8.1.1). Absorption is measured in terms of IOP as the absorption coefficient and elastic scattering is quantified by the volume scattering function (see Table 8.4; Dekker *et al.*, 2001). Other IOP can be derived from these primary properties.

The IOP of water vary with its particulate and dissolved materials in terms of:

- composition—type of particulate and dissolved matter;
- morphology—sizes and shapes of particles; and
- concentration—number of particles per unit volume, or particle size distribution.

The magnitude of IOP vary considerably for different water sources, and may be up to several orders of magnitude higher in turbid coastal waters than open ocean water (Mobley, 2020).

8.3.2 Apparent Optical Properties

Since traditionally IOP have not been easy to measure *in situ*, a range of other informative parameters were developed to describe waterbodies (Mobley, 2020). These parameters are known as Apparent Optical Properties (AOP) and provide valuable information about water constituents of waterbodies—their nature and concentrations—from measurements that can be made in the ambient lighting conditions (see Table 8.10). These properties are closer to those measured by EO sensors and can vary if the water is measured at different locations, times, depths, and weather conditions. For example, EO reflectance is an AOP.

As the name implies, AOP are properties that describe how the water *appears* under specific lighting conditions. AOP are relatively stable and are generally consistent with water depth so offer a conduit to describing the optical behaviour of waterbodies. AOP are derived from the relevant IOP and the angular distribution of the ambient lighting conditions. The latter is defined in terms of the geometry of directional radiance vectors, which represents the geometry and magnitude of incident radiation. While IOP are derived from the behaviour of a collimated beam of photons, the AOP are based on the ambient directional radiance, that is, photons heading in a particular range of directions (such as downwards). As such, these parameters are also called diffuse AOP.

Table 8.10 Commonly used Apparent Optical Properties

Remote sensing reflectance (R_{rs}) is a function of wavelength only. K_{PAR} is a function of water depth only. All other AOP are functions of both waterdepth and wavelength.

a. Diffuse attenuation coefficents (K functions)

Property	SI units	Symbol	Definition	Description
Radiance in any direction L	m^{-1}	$K(\theta,\phi)$	$\frac{-d\ln L(\theta,\phi)}{dz}$	EMR energy in all directions
Upwelling radiance L_u	m^{-1}	K_{Lu}	$\frac{-d\ln L_u}{dz}$	Radiance directed upwards
Downwelling irradiance E_d	m^{-1}	K_d	$\frac{-d\ln E_d}{dz}$	Normalised or logarithmic depth derivative of E_d, which indicates the water depth at which downwelling radiation is attenuated.
Upwelling irradiance E_u	m^{-1}	K_u	$\frac{-d\ln E_d}{dz}$	Normalised or logarithmic depth derivative of E_u, which indicates the water depth at which upwelling radiation is attenuated.
Scalar irradiance E_o	m^{-1}	K_o	$\frac{-d\ln E_o}{dz}$	Total number of photons per unit time and area reaching a point from all equally-weighted directions
Photosynthetically active radiation (PAR)	m^{-1}	K_{PAR}	$\frac{-d\ln PAR}{dz}$	EMR in the range 400–700 nm which activates photosynthesis

b. Reflectances

Property	SI units	Symbol	Definition	Description
Irradiance reflectance	n/a	R	$\frac{E_u}{E_d}$	Ratio of upwelling to downwelling plane irradiances, which is more stable than the irradiance measurements alone
Remote sensing reflectance	sr^{-1}	R_{rs}	$\frac{L_w\ (\text{in air})}{E_d\ (\text{in air})}$	Ratio of water-leaving radiance to downwelling irradiance, which is more closely related to EO measurements than R
Subsurface remote sensing reflectance	sr^{-1}	r_{rs}	$\frac{L_u\ (\text{in water})}{E_d\ (\text{in water})}$	Ratio of upwelling radiance (L_u) to downwelling irradiance, just below the water surface

c. Mean cosines

Property	SI units	Symbol	Definition	Description
Of the radiance distribution	n/a	$\overline{\mu}$	$\frac{\left(E_d - E_u\right)}{E_o}$	Summarises range of angular variations in view angle for measured radiance (for given illumination and atmospheric conditions)
Of the downwelling radiance	n/a	$\overline{\mu}_d$	$\frac{E_d}{E_{0d}}$	Uses the Cosine Law to convert the downwelling irradiance E_d (which is intercepted by a surface perpendicular to the incident radiation) to the irradiance that would be intercepted by a horizontal plane, such as the water surface
Of the upwelling radiance	n/a	$\overline{\mu}_u$	$\frac{E_u}{E_{0u}}$	Uses the Cosine Law to convert the upwelling irradiance E_u (which is intercepted by a surface perpendicular to the incident radiation) to the irradiance that would be intercepted by a horizontal plane, such as the water surface

Adapted from: Mobley (2020)

The water-leaving radiance (L_w) is light that has penetrated the water surface, been modified by absorption and scattering, then scattered back to, and through, the surface, such that it may be detected by a sensor located just above the water. Surface radiance (L_r) represents downwelling sunlight and skyglint that is reflected by the water surface, rather than passing through it into the water column. In the case of optically shallow waters, light transmitted to the substratum may be backscattered as well, contributing to the upwelling radiance or irradiance. As illustrated in Figure 8.10, the radiance measured by a sensor positioned above the water surface (L_u) will detect both L_w and L_r and also light scattered and reflected by atmospheric components (L_a). The measured upwelling radiance, however, varies with different illumination positions and intensities, atmospheric composition, and sensor positions. For given illumination and atmospheric conditions, the range of upwelling radiances resulting from angular variations in view angle can be summarised by the upwelling radiance distribution.

Within a sunlit and skylit waterbody, the decrease in irradiance with increasing water depth is approximately exponential for both downwelling and upwelling irradiance. This relationship is conventionally described by the Beer-Lambert equation (see Volume 1A—Section 2.9.2), such that the downwelling plane irradiance at a particular water depth is a function of the:

- downwelling irradiance just below the water surface ($E_d(0)$);
- diffuse attenuation coefficient for downwelling irradiance (K_d); and the
- depth of the overlying water column (z):

$$E_d(z) = E_d(0)^{-K_d z}$$

The diffuse attenuation coefficient of downwelling radiation (K_d) is easily approximated from vertical profiles of spectral irradiance (Zimmerman and Dekker, 2006). Both $E_d(0)$ and K_d are sensitive to changes in water composition (Dekker *et al.*, 2001).

The optical water depth (ζ) is defined as:

$$\zeta = K_d z$$

Table 8.11 Optical depth

Optical depth	Downwelling irradiance (%)	Position in Euphotic Zone
0	100	Upper limit
2.3	10	Mid-point
4.6	1	Lower limit

Data source: Kirk (1994) p 22

The optical depth describes the optical 'penetrability' of a water column rather than the physical attenuation length (τ), or the physical water depth. Optical depth allows the optical nature of different waters to be compared numerically. For example, the same optical depth value will correspond to a much shallower physical depth in coloured, turbid waters, than in clear waters (Kirk, 2010). Being related to the limits of the Euphotic zone, optical depth is particularly relevant to studies of primary productivity (see Table 8.11).

AOP can be measured using *in situ* optical sensors, above-surface spectroradiometers carried on appropriate platforms, and airborne and spaceborne multispectral and hyperspectral scanners (see Section 18).

8.3.3 Optical properties of substratum

In optically shallow water, the substratum may be 'visible' in upwelling radiance due to both the elastic and the inelastic processes (see Section 8.1). As detailed in Section 6, substratum features can vary abruptly and dramatically in terms of space, time, and waterbody depth (Mazel, 2001). The impact of such changes on the optical properties of water can also be dramatic, and the small size of many features requires high spatial resolution measurements. In photosynthetic organisms, pigmentation can also change rapidly in response to illumination variations (Mazel, 2001). This dynamic, three-dimensional tapestry of substratum features presents unique challenges for EO of optically shallow water.

By definition, AOPs, that is the light leaving the substratum at a particular time (see Section 8.3.2), vary with illumination. On the waterbody substratum (or seafloor), lighting conditions change with the:

- time of day;
- season;
- latitude;
- IOPs of water column above;
- tides influencing the height of water column;
- shading by neighbouring features;
- wave focusing;
- shifting of flexible features (such as macrophytes and soft corals) with water movement; and
- fluorescence of organisms and carbonate sediments (Mazel, 2001).

The optical properties of the water play a strong role in determining what biology you will find on the bottom, and the biology of the seafloor plays a dominant role in determining how light interacts with the ocean floor. (Mazel, 2001)

In optically shallow waters, the optical properties of substratum features can modify the shape, symmetry, and/or magnitude of the upwelling radiance distribution (see Section 6; Voss *et al.*, 2003). While traditional EO mapping of substratum features have matched on-site surveys to image values, thus restricting their use to specific sites, more recent research has focused on modelling approaches that encapsulate the optical properties of the three-dimensional nature of the substratum as well as the overlaying water column (Hedley, 2008, 2018).

When reflectance from the substratum contributes to the EO signal, the water is optically shallow, and estimates of bathymetry, water constituents, and substratum type can be derived. Physics-based models have allowed the EO reflectance of specific substratum to be simulated for different water depths (see Figure 8.21). These results highlight the need for high signal-to-noise ratios in EO data to map shallow water features, especially as water depth increases. Understanding the attenuation of reflectance due to depth in different water types is critical for retrieval of substratum information.

Figure 8.21 Simulation of substratum reflectance at different water depths

Subsurface irradiance reflectance is modelled for a 10% reflecting substrate (*R* (0, *H*), where 0.10=10% reflectance) through a water column of varying depths (*H*) with 1 μg/l chlorophyll concentration and 2.1 mg/l TSM. Absorption by CDOM at 440 nm is assumed to be 0.2/m. *R* (inf) is an optically deep water column reflectance at surface and K_d for this water type is shown on the second y-axis. For example, with substratum and a water column height of 0.5 m the cyan (top) line shows that the *R* (0, *H*) at the water surface will vary from 0.65 (or 6.5%) at 400 nm to 9.3% at 550 nm, then decrease due to pure water absorption with increasing wavelength. At 6 m water depth the reflectance at the surface of a 10% reflecting substratum is almost invisible as more than 99% of the signal comes from the waterbody.

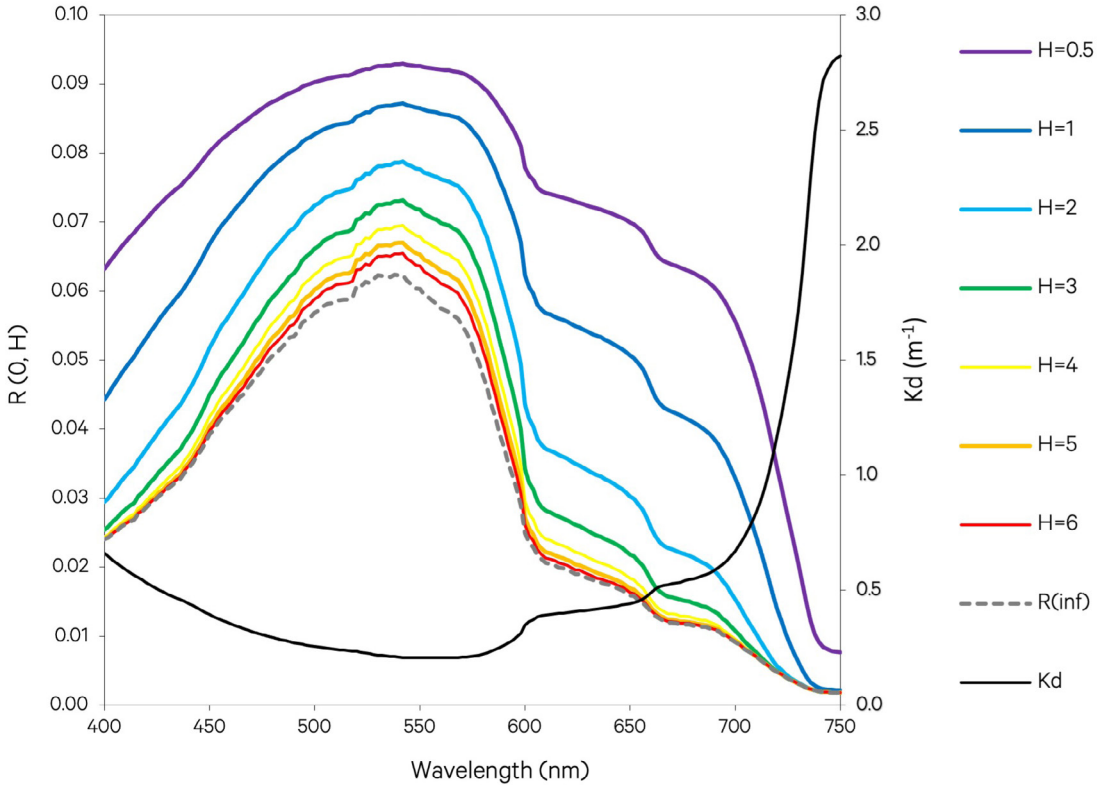

Source: Dekker *et al.* (2001) Figure 14

Figure 8.22 Modelled subsurface irradiance reflectance

Subsurface irradiance reflectance is modelled through varying water columns by a range of sensors.

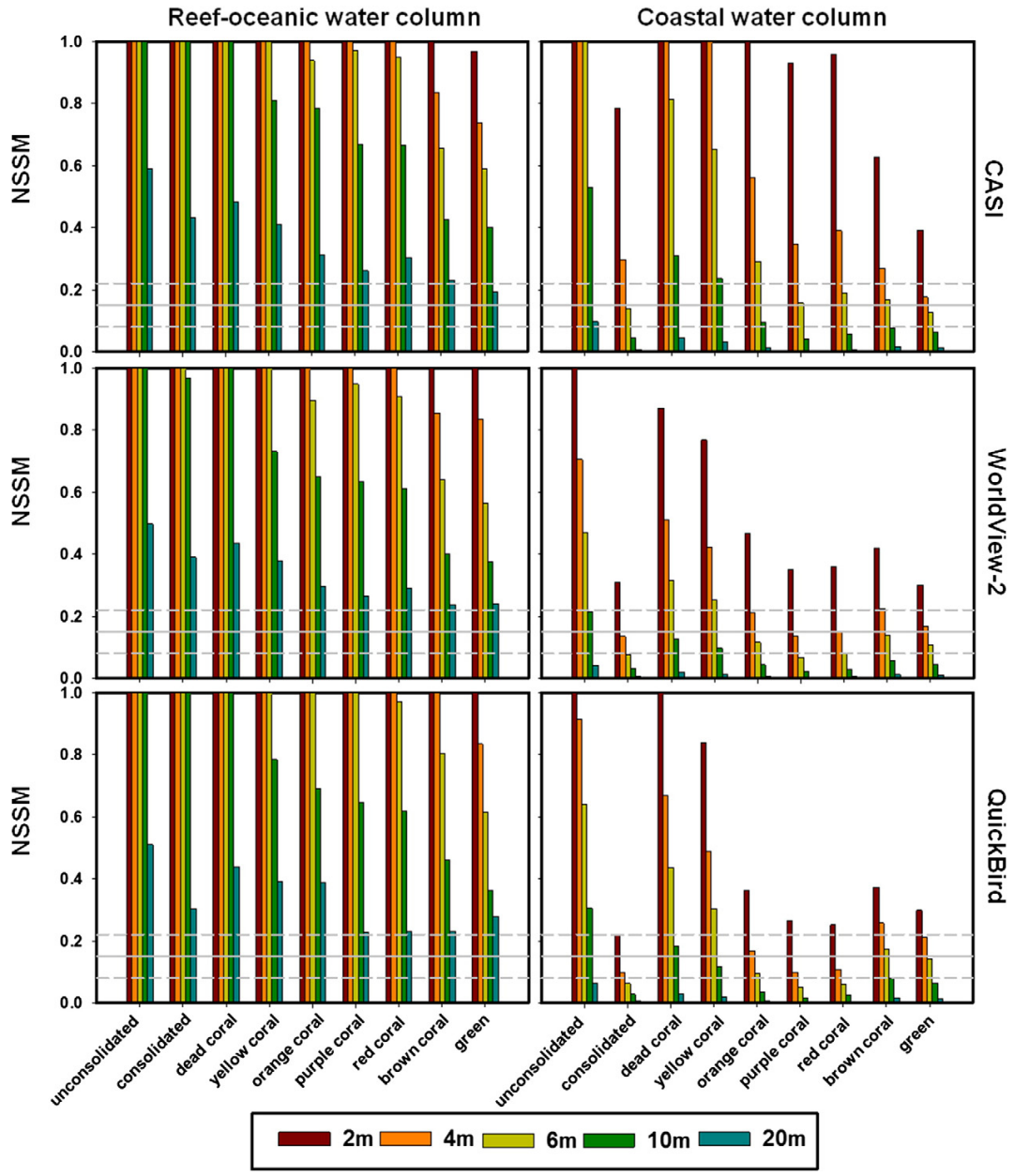

Source: Botha *et al.* (2013) Figure 10

The ability to detect a spectral signal from the substratum is dependent on the spectral optical depth of the water column, the brightness and spectral contrast of the substratum, and the sensor design (Dekker *et al.*, 2001). In Botha *et al.* (2013), a simulation method of assessing the spectral separability of various substrates was developed for three EO sensors (an airborne hyperspectral scanner: CASI: and two spaceborne multispectral sensors: WorldView and QuickBird) with different spectral resolutions and densities, but comparable spatial resolutions. This comparison was based on a measure of spectral difference (nSSM; Botha *et al.*, 2013), which combines the spectral angle and a normalized Euclidean distance between the spectra, to quantify both the spectral detectability and separability. The difference was assessed firstly between the substrate and the optically deep water column, then secondly between a pair of different substrates with different brightnesses and colours at varying water depths and optical water types (see Figure 8.22). Of the three sensors, the best substrate separability for shallow water depths over most substrate types in coastal waters was achieved from CASI, which, as a slower airborne sensor, delivered the highest spectral resolution with highest radiometric resolution.

8.4 Optical EO Models

The goal of optical EO models is to define and exploit the relationship between EO measurements (or a model thereof) and the optical properties of a waterbody. In the context of Figure 8.1 above, this model operates between the measurement domain and the attribute domain. For waterbodies, the relationship allows one of these domains to be computed from the other either as a forward or an inverse model (see Figure 8.23 and Table 8.12):

- forward model—computes likely EO measurements from known water properties; and
- inverse model—computes likely waterbody properties from available EO measurements.

In this context, water properties may include water column characteristics, substratum features, or waterbody depth.

Forward models can only be based on semi-analytical, or analytical (RTF-based) models. In the case of optically shallow waters, forward models require simulation of the entire 'EMR transfer chain' from substratum and substratum vegetation cover, up through the water column (including light absorption, volume scattering, inelastic scattering (fluorescence), and transmission), through the air-water interface, and then through the atmosphere (including adjacency effect) to the EO sensor (see Figure 8.10). Semi-analytical inversion methods in general comprise equations that approximate the radiative transfer function method (see Sections 8.1.1 and 8.1.4) with some relationships between IOP and OAC (optically active constituents) estimated statistically (this is the semi-part of 'semi-analytical').

Figure 8.23 Relationship underlying optical EO models

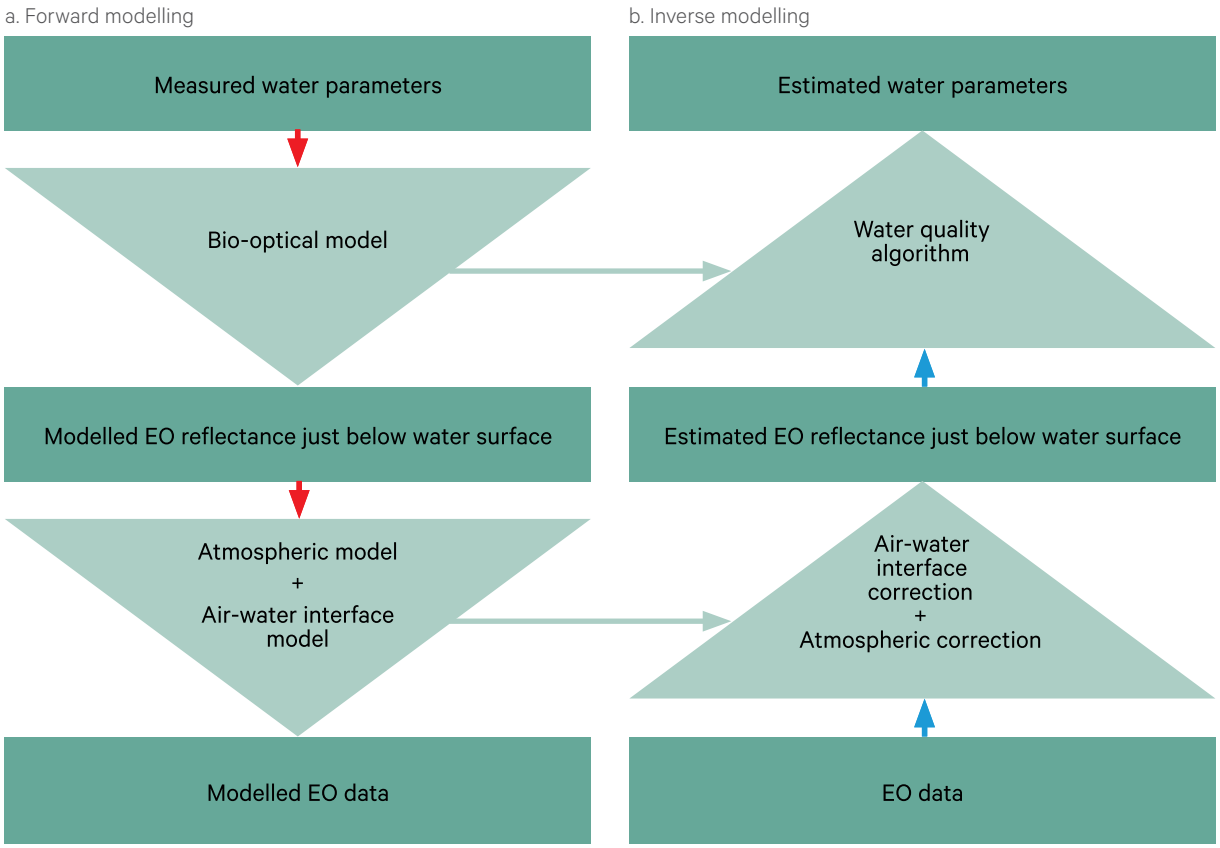

Table 8.12 Forward and inverse models

Model	Possible Inputs	Possible Outputs
Forward	AOP, IOP, concentrations, water depth, substratum (and cover), reflectance library	Just above water or TOA reflectances
Inverse	Just above water reflectances or TOA (EO or *in situ* measurements)	AOP, IOP, concentrations, water depth, substratum (and cover)

Table 8.13 Mathematical inversion models for aquatic ecosystem variables

R: irradiance reflectance; nL_w: near water-leaving radiance; see Table 8.4 for definitions

Inversion Model Type	Empirical	Semi-empirical	Semi-analytical (mostly physics-based)	AI methods
Description	Assume simple stochastic relationship between waterbody properties and EO measurements; uses few spectral bands	Use *a priori* spectral knowledge to determine relationship between water properties and EO measurements; Focuses on bands with relevant spectral information	Use physical laws to model relationship between waterbody/ substratum properties and EO measurements using all spectral bands	Expert at calculating non-linear relationships between waterbody properties and EO measurements using all spectral bands
Essential Inputs	Just above water reflectances or nL_w (EO or *in situ* measurements). A statistically relevant amount and range of variables to be retrieved (OAC, IOP, AOP, transparency, turbidity, etc.) for each image	Just above water reflectances or nL_w (EO or *in situ* measurements); A statistically relevant amount and range of variables to be retrieved (OAC, IOP, AOP, transparency, turbidity, etc.) for each image	Just above water reflectances or nL_w (EO or *in situ* measurements). Relationships between representative IOPS, AOPS with OAC through SIOP and substratum (including cover). Spectral reflectance library	Can be trained empirically, semi-empirically or using semi-analytical or RTFbased models
Preferred Inputs	OAC, IOP, AOP, algal pigments, transparency, turbidity, water depth, substrate optical properties	OAC, IOP, AOP, algal pigments, transparency, turbidity, etc., water depth, substrate optical properties, spectral band selection based on knowledge of absorbing, backscattering and fluorescence effects	SIOP (for all OAC). Substrate spectral reflectance properties	OAC, IOP, AOP, algal pigments, transparency, turbidity, water depth, substrate optical properties
Outputs	For each correlation one of: OAC, IOP, AOP, algal pigments, transparency, turbidity, water depth, substratum type and cover types etc	For each correlation one of OAC, IOP, AOP, algal pigments, transparency, turbidity, water depth, substratum type and cover types etc	Possible in one inversion: OAC, IOP, AOP, algal pigments, transparency, turbidity, water depth, substratum type and cover types etc	Possible in one inversion: OAC, IOP, AOP, algal pigments, transparency, turbidity, water depth, substratum type and cover types etc
Example	Single bands, band ratios, multiple band combinations, simple correlations	Single bands, band ratios, multiple band combinations; causal correlations	Spectral inversion algorithms (iterative inversion, direct inversion, e.g. matrix inversions)	Often requires complex non-linear multiple band combinations
Advantages	Easy to compute for specific waterbody and time provided *in situ* data available; sensitivity can only be estimated for each single waterbody where *in situ* data available	Easy to compute; More accurate than empirical models and faster than semi-analytical inversion methods; Sensitivity and error analysis, intermediate between empirical and semi-analytical methods.	Transferable, flexible, repeatable, most accurate, model based sensitivity can be calculated, model based error analysis estimation built in.	Representative when properly paramaterised, uses all statistically significant spectral bands; Can provide some estimates of sensitivity and error analysis
Disadvantages	Likely to fail when extrapolated temporally or applied to other waters; only makes use of limited amount of spectral data; some empirical relationships may not be causal; band ratios may amplify errors in *R* or nL_w	More transferable than empirical methods but less transferable than semi-analytical methods due to *a priori* spectral knowledge; if properly done relationship is causal	Computationally intensive, requires parameterisation from appropriate input data	Design of AI methods is a 'dark art'; many permutations may be chosen. Once parameterised with representative data very robust. Needs retraining for new water type
Most appropriate for	Optically simple water eg. Chlorophyll concentration in oceans; TSM, also water depth in optically shallow water with homogeneous substratum types and substratum cover	Optically simple and complex waters, e.g. chlorophyll, TSM, CDOM, K_d, also water depth in optically shallow water with homogeneous substratum types and substratum cover	Time series analyses of all water types and optically shallow waters, e.g. coral reef, coastal and inland waterbodies	All water types and optically shallow waters, e.g. coral reef, coastal and inland waterbodies

Inversion models or methods (which are also referred to as algorithms) are designed to estimate waterbody properties (such as OAC, algal species, bathymetry, substratum cover type, and condition) from an EO data source. There are many ways to invert an EO signal (inverse modelling), including:

- empirical models—use simple stochastic relationships, such as regression curves, between input (EO) and output data (see Volume 2A);
- semi-empirical models—use *a priori* spectral band location knowledge (e.g. focusing on the spectral bands adjacent to and in the middle of chlorophyll light absorption bands) to determine a stochastic relationship between input and output data (see Volume 2C);
- semi-analytical models—use knowledge about physical relationships such as IOP, concentration-specific IOP (SIOP) and AOP with the OAC and bathymetry and substratum data, coupled with some statistical approaches for parameterisation (see Volume 2C and Section 18 below);
- machine learning algorithms—use inversion methods such as Artificial Neural Networks (ANN), Maximum Likelihood (ML), or Declarative Machine Learning (DML; see Volume 2E); and
- Object based Image Analysis (OBIA)—mainly used to derive substratum and substratum cover type information over optically shallow waters (see Volume 2A—Section 10).

Note that radiative transfer models cannot be directly inverted so would need one of the above methods for inversion (in which case OBIA is not applicable).

Typically, simpler models are less flexible and transferable than complex and computationally intensive models (see Table 8.13). Sophisticated optical models (such as bio-optical models, Dekker *et al*., 2001; Dekker et al., 2011) now exist which describe the main light processes in both clear and turbid waters, with and without bottom visibility, taking into account highly variable optical conditions in the water column and the substrate, as well as a complex geometry of the incident light field and the viewing angles of an EO sensor.

Semi-analytical models invert the forward bio-optical model, either directly or via iterative methods, to estimate water constituent concentrations and physical properties such as algal pigment concentrations, CDOM, Secchi Disk transparency, vertical attenuation of light, or TSM, and to map substratum type and cover (see Section 18). Radiative transfer models, however, cannot be inverted directly to estimate the same variables. Since OBIA relies on expert knowldege applied to spectral, spatial and textural image information, it is mainly used for mapping substratum type and cover (such as seagrass, macroalgae, corals) in optically shallow waters.

The following subsections describe aspects of optical forward and inverse modelling that are relevant to:

- radiative transfer models (see Section 8.4.1);
- the water column (see Section 8.4.2);
- substratum factors (see Section 8.4.3); and
- integrated models (see Section 8.4.4).

8.4.1 Radiative Transfer Modelling

The Radiative Transfer Equation (RTE) describes the behaviour of radiance passing through a medium, in this case water. Regarding radiance as a beam of photons, six basic interactions between the photons and the medium can occur which modify the beam:

- absorption of beam by medium—photon loss due to conversion to non-radiant energy;
- elastic scattering of beam by medium—photon loss due to scattering the same wavelength in other directions;
- inelastic scattering of beam by medium—photo loss due to scattering in other directions with different wavelength;
- emission of medium—gain of photons by conversion of non-radiant energy into radiant energy;
- elastic scattering of medium—gain of photons by scattering of same wavelength from other directions; and
- inelastic scattering of medium—gain of photons by scattering in other directions with different wavelength.

The optical medium of natural waters has been modelled as a continuous material comprising randomly arranged, single-scattering elements separated by large distances relative to the wavelength of light (Mobley, 1994). Such models have allowed exact solutions to the RTE to be developed (Zimmerman and Dekker, 2006). Relevant model equations and assumptions are detailed in Mobley (2020). Generic methods have been proposed to simplify inversion of RTE models (Hedley *et al*., 2009).

Submerged plant canopies, however, such as seagrass meadows, represent a dense packaging of optically active material. Radiative transfer models for such canopies must rely on more empirical relationships between leaf optical properties and light attenuation by the bulk canopy as well as the water column (see Zimmerman, 2003, 2006; Hedley *et al*., 2017).

Commonly used numerical models include HYDROLIGHT (Mobley and Sundman, 2000) and MOMO (Matrix Operator Method: Fell and Fischer, 2001; Hollstein *et al*., 2010; Hollstein and Fisher, 2012). Such models allow several options for understanding and exploring the optical properties of natural waters, including:

- generating estimates for irradiance at different levels in the water column as a function of selected optical constituents, which can be used to model primary productivity and thermodynamics;
- simulating in-water light fields for different water types from IOP values to determine optimal wavelength bands for EO instruments;
- estimating EO signals that would result from assumed IOP under a range of simulated environmental conditions;
- isolating and removing unwanted parts of EO signals, such as sky radiance;
- varying IOP and boundary conditions to determine the most significant drivers and interrelationships between optical constituents, waterbody features, and environmental conditions;
- simulating optical signatures to develop EO algorithms and evaluate algorithm sensitivity; and
- retrospectively modelling historical water conditions (Mobley, 2020).

Dekker *et al.* (2011) compare five physics-based inversion methods to a semi-empirical method for estimating bathymetry, water column composition, and benthic cover type for a coral reef in the Bahamas and the optically complex Moreton Bay in Australia. The significantly better results from the physics-based inversion methods are particularly pertinent for simple to complex optically shallow waters.

In optically shallow waters, however, best results are obtained from such models when representative SIOPs and spectral reflectances are available. Accurate maps of heterogeneous benthic and substrate features to water depths of 20–25 m have been produced with these approaches (Kutser *et al.*, 2006; Dekker *et al.*, 2011).

8.4.2 Water column

Water column optical inversion models rely directly or indirectly on the optical properties of water introduced in Section 8.3. There is a wide range of forward optical models available for water, from models based on simple analytical solutions developed for specific waters or conditions (see Section 8.4.2.1), to generic radiative transfer models (see Section 8.4.2.4).

Optical properties of the water column that may be estimated from an optical EO signal include:

- suspended matter;
- turbidity;
- vertical attenuation coefficients of downwelling and upwelling light;
- transparency;
- coloured dissolved organic matter (CDOM);
- chlorophyll a content;
- phycobiliprotein pigments (mainly from cyanobacteria); and
- algal blooms, such as red tides and blue-green algal blooms.

If the water column is sufficiently transparent, and the substrate is within the water depth where a sufficient amount of light reaches the bottom and is reflected back out of the water, maps may also be made of seagrasses, macroalgae, sand and sandbanks, coral reefs, and other bottom features (Dekker *et al.*, 2001, 2011; see Section 19).

8.4.2.1 Empirical models

Empirical models assume stochastic relationships between the optical properties of a waterbody and their EO radiance or reflectance measurements. These models typically rely on regression relationships between input and output data, which are implemented using band ratios or simple correlations. This method requires a statistically relevant amount and range for each variable to be retrieved (such as OAC, IOP, AOP, transparency, turbidity) from each image.

Empirical models are easily and rapidly computed for large images, which is a significant advantage given the volume of image data. However, they lack sensitivity to the variations in water composition that can occur in many surface waters, both between waterbodies and over time. As such, empirical relationships are not readily transferable. Moreover, as reflectance or radiance from waterbodies is typically low, slight errors, in for example atmospheric correction, can lead to large errors in an estimated water quality or water substratum variable. When many variables are being retrieved from EO data with only a few broad spectral bands, there will be significant confusion as to what is causing the correlation. These models are most appropriate for studies of optically simple waters and are commonly used to map chlorophyll concentration in oceans. Empirical algorithms for estimating various attributes of inland and transitional waters using EO datasets are reviewed by Matthews (2011).

In optically shallow waters, empirical approaches require *in situ* water depth measurements for parameterisation. These empirical methods work best by assuming homogeneous substrates (and cover types) to water depths of 5–10 m and can be applied to both multispectral and hyperspectral data.

8.4.2.2 Semi-empirical models

Semi-empirical models use *a priori* spectral knowledge to determine the causal relationship between water properties and EO measurements and focus on spectral bands with relevant spectral information. By using *a priori* spectral knowledge to select EO bands for inversion, semi-empirical models are less likely to deliver spurious results than empirical models. This method has more general applicability between similar waterbodies when a statistically relevant amount and range of each variable is to be retrieved from a representative range of waterbodies.

Semi-empirical inversion models also make use of single bands, band ratios, and multiple band combinations and, if done properly, all correlations are causal. As with empirical methods, when many variables are derived from EO data with a few broad spectral bands, there will be significant confusion as to what is causing the correlation. Advantages of these models include:

- the algorithms are easier to compute and more accurate than empirical models;
- they are faster than semi-analytical inversion methods; and
- sensitivity and error analysis is midway between empirical and semi-analytical methods.

8.4.2.3 Semi-analytical models

Mathematical inversion of analytical models often requires some approximations based on modelling or on *in situ* parameterisation, therefore these approaches are often called semi-analytical. Semi-analytical models may involve construction of a forward model for above-water spectral reflectance with several input parameters such as:

- IOPs and AOPs;
- concentrations of water column constituents, such as algal pigments, CDOM and non-algal pigmented particulate and suspended matter, which allow calculation of the SIOP;
- physical descriptive measures of water condition, such as Secchi disk transparency, light attenuation and turbidity;
- water depth; and
- substrate type, which determines the bottom spectral reflectance.

These models are used for both forward and inverse modelling. Such models are more computationally intensive than empirical or semi-empirical models, but faster than physics-based, radiative transfer models (for forward modelling). For complex waters, semi-analytical inversion approaches are preferred over (semi-) empirical algorithms that have become standard in operational applications of EO. These semi-analytical inversion approaches are particularly appropriate for mapping complex optically deep waters and optically shallow waters.

8.4.2.4 Radiative transfer models

Radiative transfer models can be based on Monte Carlo simulation, or simulating the interaction of photons with the atmosphere and the waterbody. The resulting set of modelled photon interactions have allowed mathematical relationships to be established between:

- AOP and IOP of the water column;
- bulk (or composite) IOP and SIOP of the water column;
- radiative transfer from a waterbody to/from the atmosphere; and
- IOP of the water column and the upwelling radiation to the combined concentration of organic and inorganic matter (Bukata, 2005).

In the context of water EO, the RTE (see Section 8.4.1) shows how spectral radiance changes with the optical properties of water. For example, the two-flow model for a homogeneous medium described by Dekker *et al.* (2001) considers three primary changes in downwelling irradiance with increasing water depth:

- decreases with water depth due to absorption of downwelling radiance;
- decreases due to backscattering of downwelling radiance into upwelling radiance; and
- increases due to scattering of upwelling radiance into downwelling radiance.

8.4.3 Substratum factors

In all physics-based EO applications where the substratum is mapped through a water column, an estimate of the water column depth is implicitly or explicitly involved, and vice versa when water depth is mapped there is an implicit assumption about the substratum (and cover) reflectance. In optically shallow waters a measurable signal will be detected from the substratum, or vegetation growing in it, through the water column and through the air-water interface. Water is considered to be optically deep if there is no measurable influence of the benthos on the EO reflectance (Dekker *et al.*, 2001; see Section 18.3.1).

Because of the water column, a given substrate reflectance will be observed to have different reflectance at the water surface for different water depths. Mathematical inversion methods for mapping optically deep and optically shallow waters are summarised in Table 8.13, including their strengths and weaknesses, namely:

- empirical models—use simple stochastic relationships, such as regression curves, between input (EO) and output data (see Volume 2A). In general, these methods cannot deal with variable water column composition, whilst needing a large amount of (difficult to obtain) *in situ* data of substratum type and cover. These methods also require or assume regions of homogenous benthos at varying water depths within the image.
- semi-empirical models—use *a priori* spectral band location knowledge (e.g. focusing on specific spectral bands adjacent to, and in the middle of, pigment bands for substratum cover types, such as seagrasses, macroalgae, or live corals) to determine a stochastic relationship between input and output data (see Volume 2C). As with empirical methods these methods, in general, cannot deal with variable water column composition, and require a large amount of (difficult to obtain) *in situ* data for substratum type and cover.
- semi-analytical models—use knowledge about physical relationships such as IOP, concentration-specific IOP (SIOP), and AOP with the data for OAC, bathymetry and substratum factors, coupled with some statistical approaches for parameterisation (see Volume 2C and Section 18 below). Dekker *et al*. (2011) did a thorough analysis of one empirical and for semi-analytical inversion methods and found the semi-analytical methods were the best performing, and able to deal with both heterogeneous substratum types and varying water column composition.
- machine learning algorithms—use inversion methods such as artificial neural networks (ANN), maximum likelihood (ML), or declarative machine learning (DML). Some of these methods are described in Volume 2E.
- Object based Image Analysis (OBIA)—mostly used for mapping substratum and substratum cover types in optically shallow waters (see Volume 2A—Section 10). The Allen Coral Atlas mapping project (see *https://allencoralatlas.org/*) is using OBIA applied to Sentinel-2 images of all global coral reefs to create a global map of main coral reef features at 10 m spatial resolution. This map does not go down to species level.

The bathymetry and the water column optical properties are thus important to EO in aquatic environments, particularly for seagrass, coral reef, and macroalgal mapping (Dekker *et al*., 2001), since optimal results will be obtained from EO data if the substratum signal (such as from a seagrass canopy) is derived by compensating for the attenuating influence of the water column. Whether a benthic feature, such as seagrass, macroalgae, or coral, can actually be discriminated depends on the spectral optical depth of the water column (and the atmosphere between the sensor and the water surface), the brightness and density of the vegetation, and the spectral contrast between it and the substratum, as well as the spectral, spatial, and radiometric sensitivity of the EO sensor (see Section 20).

EO of optically shallow aquatic environments (seagrass, sand, macroalgae, muds, and coral reefs) requires sensors with a greater signal-to-noise ratio than those required for terrestrial environments (see Section 17.2 below). Coupled with this factor is the number of quantisation levels with which the sensor can record, or its radiometric resolution (see Volume 1B—Section 1.3). This must be high enough to allow a range of brightness levels over which a classification can be performed and sensitive enough to be able to detect the lower water depth of the seagrass beds (Dekker *et al*., 2001).

8.4.4 Integrated models

Other in-water hydrological models that can rely on EO datasets include:

- biogeochemical models—relate primary productivity to water characteristics such as light availability for photosynthesis, temperature, and nutrients. A good biogeochemical model has a good bio-optical model embedded in it; and
- hydrodynamic models—relate circulation within and between waterbodies to water characteristics such as temperature (gradients and stratification), flows, density, salinity, suspended sediment concentration, and bottom roughness and composition. These models can be one-, two- or three-dimensional.

These two types of models can be used in tandem; for example, the hydrodynamic model can be used to parameterise the biogeochemical model for several essential inputs, and results from the biogeochemical model can be used to provide parameters for hydrodynamic models. For example, a combined hydrodynamic and biogeochemical model is essential to model algal growth, and predicting potentially harmful algal blooms. An Australian EO-based, integrated model for surface waters is the eReefs system described in Volume 2D—Excursus 14.4.

8.5 Optical EO sensors

As introduced in Volume 1A—Section 13, the design and management of each EO sensor involves trade-offs between spectral, spatial, radiometric, and temporal resolutions, densities, and extents (see also Volume 1B—Section 1). In the context of complex aquatic ecosystems, essential features of an EO sensor, in order of priority, are defined by CEOS (2018) as:

- spatial resolution—determines the minimum area that can be discriminated so has particular relevance to mapping small waterbodies (although highly detailed imagery will also complicate global mapping studies);
- spectral resolution—spectral wavelengths detected by a sensor determine the aquatic ecosystem variables that can be discerned, both in terms of their amount and accuracy, so specific spectral regions need to be detected. As an example for phytoplankton pigment assessment, two spectral bands are recommended, centred on the wavelengths:
  - 620–624 nm—based on the *in vivo* absorption maximum of cyanophycocyanin for estimating the concentration of cyanobacterial (blue-green) algae; and
  - 676 nm—based on the *in vivo* red absorption maximum of chlorophyll a to determine the overall abundance of algae.

  In order to quantify these absorption features it is also necessary to have two spectral bands adjacent to (but not influenced by) each of these absorption features;
- radiometric resolution—determines the lowest level of radiance detected, and is particularly important for satellite-borne aquatic sensors since the signal leaving a waterbody represents a small proportion of the total signal measured by the sensor (see Volume 1B—Sections 5.2 and 6.4). Landscapes surrounding coastal and inland waterbodies typically exhibit a wide range of radiances, which can be problematic for detecting small differences in dark features; and
- temporal resolution—determines detection of changes, which can vary from hourly (e.g. algal blooms and floods) to days (e.g. pollution events) to weeks (e.g. coral bleaching events) to seasonal or annual (such as floral succession cycles).

A range of archival and current EO sensors provide imagery that is variably suited to mapping water quality, aquatic flora and corals, and shallow water bathymetry (see Table 8.14). In this context, mapped variables for water quality (freshwater, coastal and ocean) include chlorophyll a pigment, cyanophycocyanin, TSM, CDOM, vertical attenuation coefficient for diffuse downwelling irradiance (K_d), and turbidity and/or Secchi Disk transparency (see Sections 18 and 19), and aquatic flora include emergent, floating-leaved and submersed macrophytes, macroalgae, seagrasses, and corals (see Section 20).

A recent development in aquatic EO involves the use of permanent installations of autonomous, near-surface spectroradiometers that effectively emulate an EO signal as measured by an airborne or satellite sensor (albeit atmospherically corrected EO measurements). These above-water *in situ* spectroradiometers:

- provide validation or input to atmospheric correction of satellite images;
- allow application of the same algorithms that are used for EO imagery in combination with their *in situ* sampling programs;
- enable continuous measurements of a waterbody (under daylight conditions);
- can be mounted on any type of superstructure (bridge, tower, buoy, etc); and
- do not suffer from biofouling (but do need cleaning and protecting).

Table 8.14 Optical EO sensors for aquatic mapping

This list provides technical details for various multispectral and hyperspectral sensors carried on previous, current, and future EO missions with spectral bands in the wavelength range 340–1000 nm. Details relate to water mapping applications only. *Names of commercial sensors are italicised.*

Sensor	Dates of Operation	Number of water bands	Spatial resolution (m)	Revisit Frequency	Aquatic mapping suitability		
					Water quality	Flora and corals	Shallow water bathymetry
Hyperion	2000–2017	60	30	16 days (by pointing)	high	high	high
CHRIS-PROBA	2001+	18 or 63	18 or 36	7 days (by pointing)	high	high	high
MERIS	2002–2012	15	260 x 300 coastal; 1150 oceans	2 days (programmable)	high	high	high
HICO	2009–2014	100	90	3–5 days (orbit ±51°)	high	high	high
Sentinel-3	2016+	21	300	daily (with two satellites)	high	high	high
GLIMR	2027	140	300	60 minutes	high	high	high
PRISMA	2019+	66	20	7/25 (by pointing)	high	high	high
EnMap	2021+	90	30	4 days (programmable)	high	high	high
SBG (formerly HysplRI)	?2025+	60	30–45	2–16 days	high	high	high
PACE	2022+	110	1000	daily	high	high	high
ISS HISUI	2019+	60	20 x 30	3–5 days (orbit ±51°)	high	high	high
ISS DESIS	2018+	235	30	3–5 days (orbit ±51°)	high	high	high
OCM-2	2009+	15	300	2–3 days	high	medium	medium
Suomi-VIIRS	2012+	7	740	Daily	mostly high	medium	medium
SGLI	2018+	11	250	2 days	mostly high	medium	medium
GOCI	2010+	8	500	Hourly	mostly high	medium	medium
GOCI-II	2020+	12	250–1000	Hourly	mostly high	medium	medium
Worldview-2	2009+	8	2	1–60 days (programmable)	medium to high	high	medium
Worldview-3	2014+	8	1.24		medium to high	high	medium
IKONOS, QuickBird, SPOT-5/-6 GeoEye etc.	1999+	3–4	2–4	2–3/60 days (programmable)	potential to high	medium	medium
RapidEye	2005+	5	6.5	Daily	potential to high	medium	medium
Sentinel-2	2014	4	10, 20, 60	5 days (with two satellites)	medium to high	medium	medium
Aqua/Terra MODIS	2000+	9	1000	Daily	medium to high	medium	medium
	2000+	2	250, 500		mostly medium	potential	potential
Landsat-4 to -7 MSS	1984–2017	4	30	16 days	medium	medium	medium
Landsat-8 OLI	2013+	5	30	16 days	medium	medium	medium
Himawari-8/-9	2014+	4	500–2000	10 minutes	mostly medium	potential	potential
GOES-R	2017+	4	500–2000	10 minutes	mostly medium	potential	potential
GISAT-1/-2 MSS	2021+	6	42	5–30 minutes	mostly medium	potential	potential
GISAT-1/-2 Hyperspectral	2021+	158	318	5–30 minutes	mostly medium	potential	potential
MSG SEVIRI	2002+	2	1000	96 per day	mostly medium	potential	unsuitable

Adapted from: CEOS (2018) Table 2.7

Ideally a dedicated sensor that was designed for complex aquatic environments would have higher combined spatial and spectral resolutions than are available from current and planned ocean colour sensors (see Table 8.14). It would also include bands that provide information about the biochemistry of inland, estuarine, deltaic, and near-coastal waters, and differentiate macrophytes, macroalgae, seagrasses, and coral reefs (CEOS, 2018). In particular, a comprehensive EO system for observing aquatic ecosystems should:

- estimate algal pigment concentrations of chlorophyll a and cyanobacteria (especially phycoerythrin and phycocyanin) plus accessory pigments, and detect other wavelengths relevant for research into phytoplankton functional types;
- detect algal fluorescence (especially chlorophyll a fluorescence at 684 nm);
- measure suspended matter, possibly split up into organic and mineral matter;
- measure CDOM, and discriminate terrestrial from marine CDOM;
- measure spectral light absorption and backscattering of OAC (see Section 8.2); and
- measure water transparency indicators, such as Secchi disk transparency, vertical attenuation of light and turbidity (see Section 5.1.4);

and in optically shallow waters:

- estimate water column depth (bathymetry); and
- estimate substratum type and cover as well as plants floating at, or just above, the water surface.

For residual sunglint correction (if sunglint mitigation measures are insufficient), and for estimating the atmospheric composition, appropriate spectral bands are required to measure O_3, NO_2, water vapour, and aerosols, as well as NIR and/or SWIR bands for sunglint correction. Thus, for non-oceanic aquatic ecosystems, an appropriate satellite-borne sensor would include (CEOS, 2018):

- approximately 26 bands in the spectral range 380–780 nm for detecting aquatic ecosystem variables (see Table 8.15);
- 15 bands between 360–380 nm and 780–1400 nm to enable removal of atmospheric and air-water interface effects (see Table 8.16);
- spectral resolution: 5 nm (ideal) to 8 nm to achieve an adequate signal-to-noise ratio and Full Width Half Maximum (FWHM; see Volume 1A—Section 13);
- spatial resolution: approximately 17–33 m (which would enable mapping of waterbodies larger than 0.2 ha); and
- radiometric sensitivity: noise-equivalent radiance difference (NEΔL) 0.005 $mWm^{-2}\,sr^{-1}\,nm^{-1}$ (ideal) to 0.010 $mWm^{-2}\,sr^{-1}\,nm^{-1}$;
- radiometric extent: 400 $mWm^{-2}\,sr^{-1}\,nm^{-1}$ in blue wavelengths and 200 $mWm^{-2}\,sr^{-1}\,nm^{-1}$ in red wavelengths for bright targets such as sand; and
- at least one global image every 16 days from Low Earth Orbiting (LEO) satellite (but ideally 1–5 day revisit frequency), preferably in conjunction with Geostationary Earth Orbiting (GEO) satellite imagery at high temporal frequency (see Volume 1A—Section 12).

Table 8.15 Recommended spectral bands for assessing water quality and characterising benthos

FWHM: Full width half maximum (see Volume 1A—Section 13.4); CPC: Cyanophycocyanin; CPE: Cyanophycoerythrin; CDOM: Coloured dissolved organic matter; NAP: non algal pigmented particulate matter; Chl: chlorophyll; PFT: phytoplankton functional type; HAB: harmful algal blooms; FLH: fluorescence line height. NAP, blue and red chlorophyll absorption maxima and related reference bands and HABs detection are ubiquitous in literature. NAP scatters and absorbs light decreasing with increasing wavelength and thus does not need a specific band, although three bands without too much algal pigment or CDOM absorption are useful. The blue chlorophyll absorption band is centered around 438–443 nm *in vivo* and the red chlorophyll band around 676 nm *in vivo*. HABs need Chlorophyll, CPE, and CPC. See Table 8.16 for NAP relevant bands beyond the O_2 absorption feature at 761 nm.

Band number	Waveband centre (mm)	FWHM (mm)	Application
1	+/-380	15	CDOM; NAP; PFT; Mycosporin-like amino acids
2	+/-412	5–8	CDOM; PFT
3	+/-425	5–8	CDOM ; NAP; Blue Chl a absorption reference band; PFT
4	+/-440	5–8	CDOM; Blue Chl a absorption maximum; PFT
5	467	5–8	Band for separating Pheaocystis from diatoms; Blue Chl a absorption band reference band; Accessory pigments
6	+/-475	5–8	Accessory pigments; Blue Chl a absorption band reference band; PFT, NAP
7	+/-490	5–8	Blue Chl band-ratio algorithm; PFT, Accessory pigments
8	+/-510	5–8	Blue Chl band-ratio algorithm; NAP
9	+/-532	5–8	PFT and Carotenoids; NAP
10	+/-542	5–8	NAP
11	555	5–8	NAP; Cyanophycoerythrin reference band; PFT
12	565	5–8	CPE *in vivo* absorption maximum and possibly fluorescence
13	+/-583	5–8	CPE and CPC reference band; Chlorophylls a, b and c ; CPE fluorescence
14	+/-594	5–8	PFT
15	+/-615	5–8	CPC *in vivo* absorption maximum—avoiding Chlorophyll c
16	624	5–8	CPC *in vivo* absorption maximum; suspended sediment, PFT; Chlorophyll c
17	631	5–8	PFT
18	+/-640	5–8	NAP, CPC reference band
19	649	5–8	Chl b *in vivo* absorption maximum
20	665	5–8	FLH baseline
21	676	5–8	Red Chl a *in vivo* absorption maximum
22	683	5	Chlorophyll fluorescence (FLH) band
23	+/-700	5–8	HABs; NAP turbid water; reference band for 2 or 3 band Chl a algorithms
24	+/-710	5–8	FLH baseline; HABs detection; NAP in highly turbid water; reference band for 2 or 3 band Chl a algorithms
25	+/-748	15	NAP in highly turbid water; FLH baseline band
26	+/- 775	15	NAP in highly turbid CDOM rich water
27	+/- 810	15	NAP in highly turbid CDOM rich water

Adapted from: CEOS (2018) Table 2.2

Table 8.16 Recommended spectral bands for atmospheric and air-interface correction

Recommended minimum set of spectral bands for extracting information from EO reflectance spectra of optically deep and shallow waters. * indicates bands covered in Table 8.15. FWHM: Full Width Half Maximum

Waveband centre (mm)	FWHM (mm)	Applications	Band number
+/- 360	8	To constrain the SWIR-based aerosol model over turbid waters	1
+/- 368	8	To constrain the SWIR-based aerosol model over turbid waters	2
+/- 412	8	NO_2	*
+/- 520	8	Aerosol retrieval	3
+/- 575	8	Chappuis band for O_3 absorption	4
+/- 605	8	Chappuis band for O_3 absorption	5
+/- 620	8	Aerosol retrieval	*
+/- 709	8	Aerosol retrieval	*
+/- 740	8	Sunglint removal	*
+/- 761	3	Sunglint removal	6
+/- 775	16	Aerosol retrieval; water vapour reference band	7
+/- 820	16	Water vapour absorption	8
+/- 865	16	Aerosol retrieval; water vapour reference band; sunglint removal	9
+/- 940	16	Water vapour absorption	10
+/-1020	16	water vapour reference band	11
+/-1050	16	water vapour reference band	12
+/-1130	16	Water vapour absorption	13
+/-1135	16	Water vapour reference band	14
+/-1380	16	Cirrus clouds	15

Adapted from: CEOS (2018) Table 2.5

8.6 Further Information

Mobley (2020)

CEOS (2018)

GEBCO: *https://www.gebco.net*

CATDS Ocean Salinity Expert Centre: *http://www.salinityremotesensing.ifremer.fr/home*

8.7 References

AMS (2019). *Meteorology Glossary of American Meteorological Society*: *http://glossary.ametsoc.org/wiki/Main_Page*

Aurin, D., Mannino, A., and Lary, D.J. (2018). Remote Sensing of CDOM, CDOM Spectral Slope, and Dissolved Organic Carbon in the Global Ocean. *Applied Sciences*, 8, 2687. doi:10.3390/app8122687

Babin, M., Stramski, D., Ferrari, G.M., Claustre, H., Bricaud, A., Obolensky, G., and Hoepffner, N. (2003). Variations in the light absorption coefficients of phytoplankton, non-algal particles, and dissolved organic matter in coastal waters around Europe. *Journal of Geophysical Research*, 108(C7), 3211. doi:10.1029/2001JC000882

Blondeau-Patissier, D., Brando, V.E., Oubelkheir, K., Dekker, A.G., Clementson, L.A., Daniel, P. (2009). Bio-optical variability of the absorption and scattering properties of the Queensland inshore and reef waters, Australia. *Journal of Geophysical Research,* 114, C05003.

Botha, E.J., Brando, V.E., Anstee, J.M., Dekker, A.G. and Sagar, S. (2013). Increased spectral resolution enhances coral detection under varying water conditions. *Remote Sensing of Environment,* 131, 247–261.

Botha, E.J., Brando, V.E., and Dekker, A.G. (2016). Effects of Per-Pixel Variability on Uncertainties in Bathymetric Retrievals from High-Resolution Satellite Images. *Remote Sensing*, 8, 459. *https://doi.org/10.3390/rs8060459*

Brando, V.E., Anstee, J.M., Wettle, M., Dekker, A.G., Phinn, S.R., and Roelfsema, C. (2009). A physics based retrieval and quality assessment of bathymetry from suboptimal hyperspectral data. *Remote Sensing of Environment*, 113, 755–770. doi:10.1016/j.rse.2008.12.003.

Brando, V.E., Dekker, A.G., Park, Y.J., and Schroeder, T. (2012). Adaptive semianalytical inversion of ocean color radiometry in optically complex waters. *Applied Optics*, 51, 2808–2833.

Bricaud, A., Babin, M., Morel, A., and Claustre, H. (1995). Variability in the chlorophyll-specific absorption coefficients of natural phytoplankton: Analysis and parameterization. *Journal of Geophysical Research*, 100(C7), 13321–13332.

Bricaud, A., Morel, A., and Prieur, L. (1981). Absorption by dissolved organic matter of the sea (yellow substance) in the UV and visible domains. *Limnology and Oceanography*, 26, 43–53.

Bukata R.P. (2005). *Satellite Monitoring of Inland and Coastal Water Quality*. CRC press, Boka Raton, Florida, USA, 246 p.

CEOS (2018). *Feasibility Study for an Aquatic Ecosystem Earth Observing System*. (Eds: Dekker, A.G., and Pinnel, N.) CSIRO, Canberra.

Clementson, L., Wojtasiewicz, B., and Gunasekera, R. (2021). *Cyanobacterial cultures—absorption spectra, phycocyanin and phycoerythrin concentration for selected cultures*. v1. CSIRO. Data Collection. *https://doi.org/10.25919/9k2k-9n84*

Cox, C., and Munk, W., (1954). Measurement of the Roughness of the Sea Surface from Photographs of the Sun's Glitter. *Journal of the Optical Society of America,* 44, 838–850.

Dekker, A.G. (1993). *Detection of optical water quality parameters for eutrophic waters by high resolution remote sensing*. Ph.D. Thesis. *Earth and Life Sciences*. Vrije Universiteit, Amsterdam. 240 p.

Dekker, A.G., Brando, V.E., Anstee, J.M., Pinnel, N., Kutser, T., Hoogen-boom, J., Peters, S.W.M., Pasterkamp, R., Vos, R.J., Olbert, C., and Malthus, T.J. (2001). Imaging spectrometry of water. Ch 11 in *Imaging Spectrometry: Basic Principles and Prospective Applications*. (Eds: F.D. van der Meer and S.M. de Jong), pp 307–359. Kluwer Academic Publishers, Dordrecht, The Netherlands.

Dekker, A., Byrne, G., Brando, V., and Anstee, J. (2003). *Hyperspectral mapping of intertidal rock platform vegetation as a tool for adaptive management*. CSIRO Land and Water, Canberra, Australia.

Dekker, A.G., Brando, V.E., Anstee, J.M., Fyfe, S., Malthus, T.J.M., and Karpouzli, E.V. (2006). Remote sensing of seagrass ecosystems: use of spaceborne and airborne sensors. Ch. 15 in *Seagrass Biology, Ecology and Conservation*. (Eds: Larkum, A., Orth, R., Duarte, C.). Springer Verlag, Germany, p 347–359.

Dekker, A.G., Phinn, R., Anstee, J., Bissett, P., Brando, V.E., Casey, B., Fearns, P., Hedley, J., Klonowski, W., Lee, Z.P., Lynch, M., Lyons, M., Mobley, C., and Roelfsema, C., (2011). Intercomparison of shallow water bathymetry, hydro-optics, and benthos mapping techniques in Australian and Caribbean coastal environments. *Limnology Oceanography Methods* 9, 396–425.

Del Vecchio, R., and Blough, V. (2002). Photobleaching of chromophoric dissolved organic matter in natural waters: Kinetics and modeling. *Marine Chemistry*, 78, 231–253.

Elachi, C., and van Zyl, J. (2006). *Introduction to the Physics and Techniques of Remote Sensing*, Second Edn. Wiley Interscience, New Jersey.

Estep, L., and Arnone, R.A. (1994). Effect of whitecaps on determination of chlorophyll concentration from satellite data. *Remote Sensing of Environment,* 50, 328–334.

Falkowski, P.G., and Raven, J.A. (2007). *Aquatic photosynthesis*. 2nd edn, Princeton University Press, Princeton, New Jersey.

Fell, F., and J. Fischer. (2001). Numerical simulation of the light field in the atmosphere-ocean system using the matrix-operator method. *Journal of Quantitative Spectroscopy and Radiative Transfer,* 69, 351–388. *doi.org/10.1016/S0022-4073(00)00089-3*

Garaba, S.P., and Zielinski, O. (2013). Methods of reducing surface reflected glint for shipborne above-water remote sensing. *Journal of the European Optical Society—Rapid Publication,* 8, 13058. *http://dx.doi.org/10.2971/jeos.2013.13058*

Goodwin, T.W., and Mercer, E.I. (1990). *Introduction to Plant Biochemistry*. Pergamon Press.

Goyens, C., Jamet, C., and Schroeder, T. (2013). Evaluation of four atmospheric correction algorithms for MODIS-Aqua images over contrasted coastal waters. *Remote Sensing of Environment,* 131, 63–75.

Harrison, B.A., and Jupp, D.L.B. (1989) *Introduction to Remotely Sensed Data: Part ONE of the microBRIAN Resource Manual*. CSIRO, Melbourne. 156 p.

Hedley, J.D. (2008). A three-dimensional radiative transfer model for shallow water environments. *Optics Express*, 16(26), 21887–21021.

Hedley, J.D. (2013). Hyperspectral Applications. Ch 4 in *Coral Reef Remote Sensing*. (Eds: Goodman, J.A., Purkis, S.J., and Phinn, S.R.). Springer, Dordrecht. ISBN 978-90-481-9291-5.

Hedley, J.D. (2018). Influence of Three-Dimensional Coral Structures on Hyperspectral Benthic Reflectance and Water-leaving Reflectance. *Applied Sciences*, 8(12), 2688. doi:10.3390/app8122688

Hedley, J.D., Roelfsema, C., and Phinn, S.R. (2009). Efficient radiative transfer model inversion for remote sensing applications. *Remote Sensing of Environment,* 113, 2527–2532.

Hedley, J.D., Russell, B.J., Randolph, K., Pérez-Castro, M.A., Vasquez-Elizondo, R.M., Enriquez, S., and Dierssen, H.M. (2017). Remote Sensing of Seagrass Leaf Area Index and Species: The Capability of a Model Inversion Method Assessed by Sensitivity Analysis and Hyperspectral Data of Florida Bay. *Frontiers in Marine Science*, 4, 362. doi:10.3389/fmars.2017.00362

Helms, J.R., Stubbins, A., Ritchie, J.D., Minor, E.C., Kieber, D., and Mopper, K. (2008). Absorption spectral slopes and slope ratios as indicators of molecular weight, source, and photobleaching of chromophoric dissolved organic matter. *Limnology and Oceanography*, 53(3), 955–969.

Hollstein, A., and Fischer, J. (2012). Radiative transfer solutions for coupled atmosphere ocean systems using the matrix operator technique, *Journal of Quantitative Spectroscopy and Radiative Transfer*, 113, 536–548. *https://doi.org/10.1016/j.jqsrt.2012.01.010*.

Hollstein, A., von Bismarck, J., Fischer, J., and Preusker, R. (2010). *Description of the Vector Radiative Transfer Model MOMO. ESA support to science project water radiance document* (contract AO 1-5859/08/NL/CT). *Brockmann-consult.de: http://www.brockmann-consult.de/beam-wiki/download/attachments/17563679/momo_model_description.pdf*

Jaffe, J.S., Moore, K.D., McLean, J., and Strand, M.P. (2001). Underwater Optical Imaging: Status and Prospects. *Oceanography,* 14(3), 64–75.

Jerlov, N.G. (1976). *Marine Optics*. Elsevier, New York. 231 p.

Joehnk, K.D., Anstee, J., Ford, P., Botha, H., and Sherman, B. (2018). *Lake Hume blue-green algal risk minimisation*. Report prepared for the Murray-Darling Basin Authority by CSIRO Land and Water, Australia.

Kirk, J.T.O. (1994). *Light and Photosynthesis in Aquatic Ecosystems*, 2nd Edn. Cambridge University Press, Cambridge. 509 p.

Kirk, J.T.O. (2010). *Light and Photosynthesis in Aquatic Ecosystems*, 3rd Edn. Cambridge University Press, Cambridge. 662 p.

Kishino, M., Takahashi, M., Okami, N. and Ichimura, S. (1985). Estimation of the spectral absorption coefficients of phytoplankton in the sea. *Bulletin of Marine Science*, 37(2), 634–642.

Kutser, T., Miller, I., and Jupp, D.L.B. (2006). Mapping coral reef benthic substrates using hyperspectral space-borne images and spectral libraries. *Estuarine, Coastal and Shelf Science,* 70, 449–460.

Laanen, M.L., Peters, S.W.M., Dekker, A.G., and van der Woerd, H.J. (2011). Assessment of the scattering by sub-micron particles in inland waters. *Journal of the European Optical Society,* 6, 11046.

Lindell, T., Pierson, D., Premazzi, G., and Ziliolli, E. (1999). (Eds) *Manual for monitoring European lakes using remote sensing techniques*. Office for official publications of European Communities, Luxembourg. 161 p.

Ma, R., Jiang, G., Duan, H., Bracchini, L., and Loiselle, S. (2011). Effective upwelling irradiance depths in turbid waters: a spectral analysis of origins and fate. *Optics Express,* 19(8), 7128.

Maie, N., Boyer, J.N., Yang, C., and Jaffé, R. (2006). Spatial, geomorphological, and seasonal variability of CDOM in estuaries of the Florida Coastal Everglades, *Hydrobiologia, 569*(1), 135–150.

Mannino, A., Russ, M.E., and Hooker, S.B. (2008), Algorithm development and validation for satellite-derived distributions of DOC and CDOM in the U.S. Middle Atlantic Bight, *Journal of Geophysical Research*, 113, C07051. doi:10.1029/2007JC004493.

Martin, P., Cherukuru, N., Tan, A.S.Y., Sanwlani, N., Mujahid, A., and Müller, M. (2018). Distribution and cycling of terrigenous dissolved organic carbon in peatland-draining rivers and coastal waters of Sarawak, Borneo. *Biogeosciences*, 15, 6847–6865

Matthews, M.W. (2011). A current review of empirical procedures of remote sensing in inland and near-coastal transitional waters. *International Journal of Remote Sensing*, 32(21), 6855–6899. doi:10.1080/01431161.2010.512947

Mazel, C.H. (2001). Optics of the Seafloor. *Oceanography*, 14(3), 54–63.

Mobley, C.D. (1994). *Light and water; Radiative transfer in natural waters*. Academic Press, London, 592 p.

Mobley, C. (2020). *Ocean Optics Web Book*. *http://www.oceanopticsbook.info/view/introduction/overview*

Mobley, C., and Sundman, L.K., (2000). *Hydrolight 4.1 Technical Documentation*, 4.1 edn. Sequoia Scientific Inc., Redmond.

Moses, W.J., Sterckx, S., Montes, M.J., De Keukelaere, L., and Knaeps, E. (2017). Atmospheric Correction for Inland Waters. Ch 3 in *Bio-optical Modeling and Remote Sensing of Inland Waters* (Eds: D.R. Mishra, I. Ogashawara, and A.A. Gitelson), pp 69–100. Elsevier. *https://doi.org/10.1016/B978-0-12-804644-9.00003-3*

Morel, A. (1968). Note au sujet des constantes de diffusion de la lumière pour l'eau et l'eau de mer optiquement pures. *Cahiers Oceanographiques,* 20, 157–162.

Mustard, J., Staid, M., and Fripp, W. (2001). A semianalytical approach to the calibration of AVIRIS data to reflectance over water application in a temperate estuary. *Remote Sensing of Environment*, 75, 335–349.

Ogashawara, I. (2015). Terminology and classification of bio-optical algorithms. *Remote Sensing Letters*, 6(8), 613–617. doi:10.1080/2150704X.2015.1066523

Otis, D.B., Carder, K.L. English, D.C., and Ivey, J.E. (2004). CDOM transport from the Bahamas Banks. *Coral Reefs*, 23(1), 152–160.

Pahlevan, N., Mangin, A., Balasubramanian, S.V., Smith, B., Alikas, K., Arai, K., Barbosa, C., Bélanger, S., Binding, C., Bresciani, M., Giardino, C., Hunter, P., Simis, S., Spyrakos, E., and Tyler, A. (2021). ACIX-Aqua: A global assessment of atmospheric correction methods for Landsat-8 and Sentinel-2 over lakes, rivers, and coastal waters. *Remote Sensing of Environment*, 258, 112366. *https://doi.org/10.1016/j.rse.2021.112366*

Para, J., Coble, P. G., Charriere, B., Tedetti, M., Fontana, C., and Semper, R. (2010). Fluorescence and absorption properties of chromophoric dissolved organic matter CDOM in coastal surface waters of the northwestern Mediterranean Sea, influence of the Rhone River. *Biogeosciences,* 7, 4083–4103.

Parrish, C. (2020). *Index of Refraction of Seawater and Freshwater as a Function of Wavelength and Temperature* webpage, Oregon State University website: *http://research.engr.oregonstate.edu/parrish/index-refraction-seawater-and-freshwater-function-wavelength-and-temperature*

Plass, G.N., and Kattawar, G. (1972). Degree and Direction of Polarization of Multiple Scattered Light 2: Earth's Atmosphere with Aerosols. *Applied Optics*, 11, 2866–2879. doi:10.1364/AO.11.002866.

Pope, R.M., and Fry, E.S. (1997). Absorption spectrum (380–700 nm) of pure water. II. Integrating cavity measurements. *Applied Optics*, 36(33), 8710–8723. *https://doi.org/10.1364/AO.36.008710*

Pozdnyakov, D.V., and Grassl, H. (2003). *Colour of inland and coastal waters: A methodology for its interpretation*. Springer-Praxis, Chichester.

Preisendorfer, R.W. (1976). *Hydrologic optics*. NOAA Tech. Memo. ERL RMEL-67. 90 p.

Shank, G.C., Lee, R., Vähätalo, A., Zepp, R.G., and Bartels, E. (2010). Production of chromophoric dissolved organic matter from mangrove leaf litter and floating Sargassum colonies. *Marine Chemistry*, 119(1–4), 172–181.

Simis, S.G.H., Peters, S.W.M., and Gons, H.J. (2005). Remote sensing of the cyanobacterial pigment phycocyanin in turbid inland water. *Limnology and Oceanography,* 50, 237–245.

Singh, R.K., Shanmugam, P., He, X., and Schroeder, T. (2019). UV-NIR approach with non-zero water-leaving radiance approximation for atmospheric correction of satellite imagery in inland and coastal zones. *Optics Express*, 27(16), 28. *https://doi.org/10.1364/OE.27.0A1118*

Twardowski, M.S., Boss, E., Sullivan, J.M., and Donaghay, P.L. (2004). Modeling the spectral shape of absorbing chromophoric dissolved organic matter. *Marine Chemistry,* 89, 69–88.

Voss, K.J., Mobely, C.D., Sundman, L.K., Ivey, J.E., and Mazel, C.H. (2003). The spectral upwelling radiance distribution in optically shallow waters. *Limnology and Oceanography,* 48 (1), 364–373.

Zhang, X., Lianbo, H., and He, M-X. (2009). Scattering by pure seawater: Effect of salinity. *Optics Express,* 17, 5698–5710.

Zimmerman, R.C. (2003). A biooptical model of irradience distribution and photosynthesis in seagrass canopies. *Limnology and Oceanography,* 48 (1), 568–585.

Zimmerman, R.C. (2006). Light and photosynthesis in seagrass meadows. Ch 13 in *Seagrasses: biology, ecology and conservation*. (Eds: Larkum, A.W.D., Orth, R.J., and Duarte, C.M.) Springer, Dordrecht. pp. 303–321.

Zimmerman, R.C., and Dekker, A.G. (2006). Aquatic optics: basic concepts for understanding how light affects seagrasses and makes them measurable from space. Ch 12 in *Seagrasses: biology, ecology and conservation*. (Eds: Larkum, A.W.D., Orth, R.J., and Duarte, C.M.) Springer, Dordrecht. pp. 295–301.

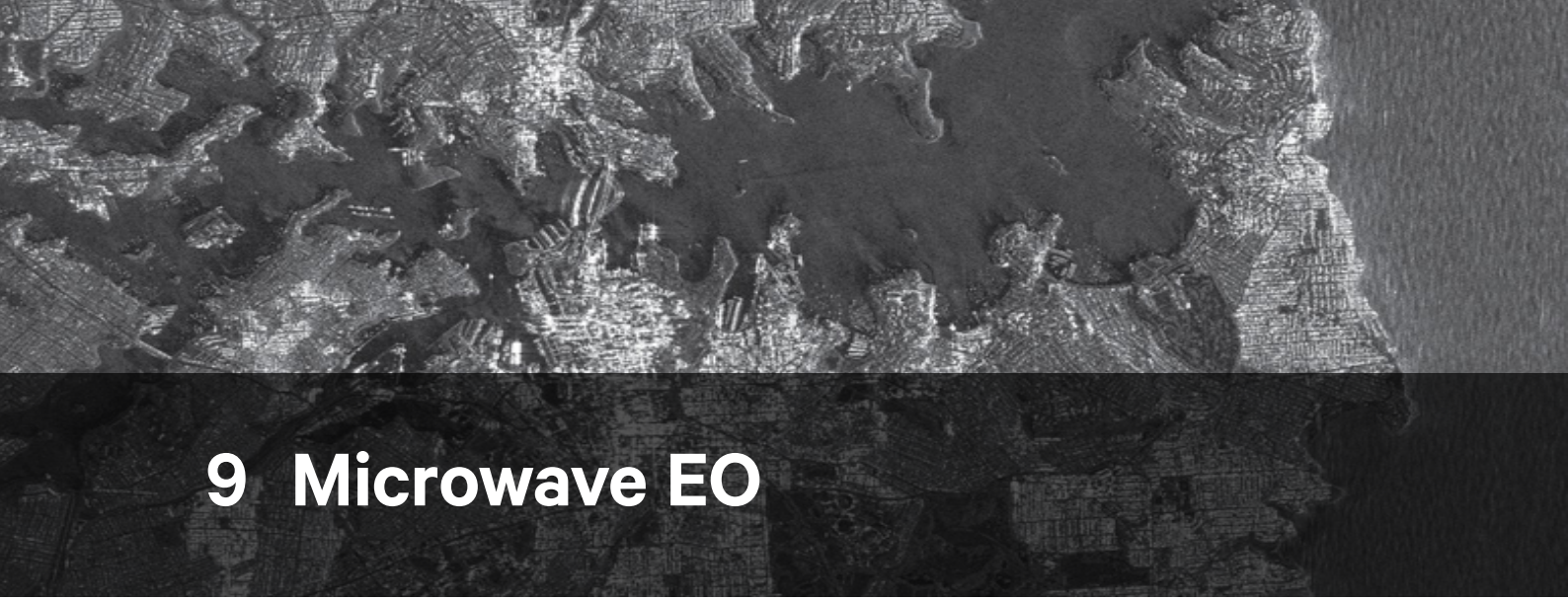

9 Microwave EO

Microwave EO is introduced in Volume 1A—Sections 5 and Volume 1B—Section 9. This form of EO offers advantages over optical datasets for some applications, but can also be complementary when used in conjunction with other EO data sources (Richards, 2009, 2012).

As introduced in Section 5.1.4, electromagnetic radiation (EMR) spans a wide range of wavelengths, with microwave radiation being the region with wavelengths between 1 mm and 1 m (see Figure 5.7). Microwave sensors (described in Volume 1A—Sections 13, 14.5, 15.2 and 16) are commonly classified as either:

- passive—detect energy that originates from an independent source and is scattered or reflected by a target; or
- active—radiate a particular form of energy towards a target object or surface and then detect the amount of that energy which is scattered or reflected by it (see Excursus 8.1).

Passive sensors record the microwave energy that is emitted by all materials on Earth with temperatures above 0K (absolute zero—see Volume 1B—Section 8.1). While microwaves are minimally attenuated by atmospheric conditions and can penetrate solids, the emitted energy in this part of the electromagnetic spectrum is low for the average temperature of the Earth's surface (see Figure 9.1).

Microwaves can be generated electronically using an antenna. Active sensors have the advantage of operating independently of solar illumination and most weather conditions. Active microwave EO is based on radar, an acronym for Radio Detection And Ranging (see Excursus 9.1). Both active and passive microwave sensors may also be categorised as imaging or non-imaging (see Table 9.1).

Table 9.1 Spectral regions observed by EO sensors

Note that, in practice, atmospheric windows restrict these ranges for observing Earth's features (see Volume 1A—Table 5.4).

Spectral region	Wavelength	EO sensor			
		Passive		Active	
		Imaging	Non-imaging	Imaging	Non-imaging
Visible	0.38 to 0.7 μm	Passive radiometers Passive spectroradiometers Passive imaging spectrometers		Lidar	Lidar distance only
Near Infrared	0.7 to 1.1 μm				
Short wave Infrared (SWIR)	1.1 to 3.0 μm		Polarimeters		
Middle Infrared (MIR)	3.0 to 8.0 μm	Passive radiometers Polarimeters			
Thermal Infrared (TIR)	8.0 to 15.0 μm		TIR thermometers		
Microwave	1 mm to 1 m	Microwave radiometers Microwave spectrometers		Radar	Polarimeters Scatterometers
Radio	> 10 cm	Passive radiometers	Sounders	Imaging radar	Altimeters Sounders

Background image: Synthetic Aperture Radar image (S-band) of Sydney Harbour acquired at night by NovaSAR-1 in 2018 with 6 m resolution. **Source:** SSTL. Retrieved from *https://www.sstl.co.uk/media-hub/images/novasar-1*

In this section we will review the microwave EO framework (see Section 9.1) and detail some specific microwave sensors that are used to observe surface waters, namely:

- passive microwave radiometer—detects emissions of thermal radiation in the wavelength range 1–300 mm (see Section 9.2);
- imaging radar—represents systematically acquired lines of radar returns as an image grid (see Section 9.3);
- Synthetic Aperture Radar (SAR) interferometer—exploits the phase difference between two images acquired for the same scene using two separated antennae (see Section 9.4);
- radar altimeter—measures range or distance from the sensor to specific features (see Section 9.5); and
- microwave scatterometer—measures surface texture (see Section 9.6).

Figure 9.1 Blackbody radiation

The wavelength of peak radiant exitance for a blackbody decreases as its temperature increases (Note: Scales are logarithmic)

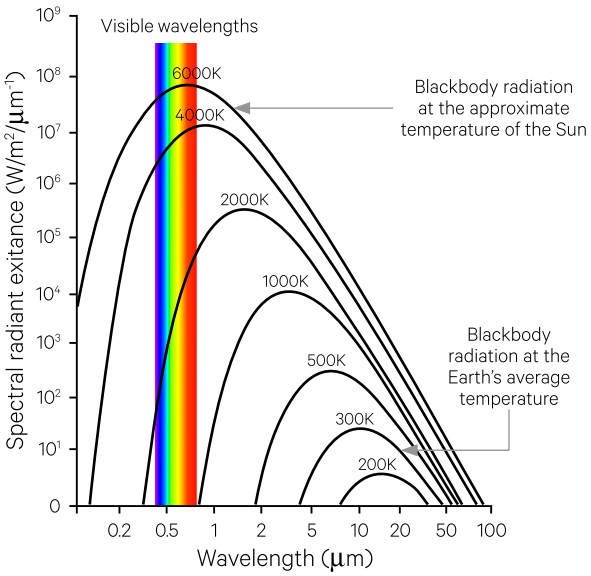

Adapted from: NASA/USGS Astrogeology Science Center Radiance Calculator at *http://astrogeology.usgs.gov/tools/thermal-radiance-calculator/*

Excursus 9.1—Radar

Further information: Volume 1B—Section 8

As introduced in Volume 1A—Section 15.2 and Volume 1B—Section 8, radar sensors use actively transmitted radio waves to detect objects and determine their position or 'range'. The principle of operation for these devices is to direct pulses of microwave energy at an object then record the timing of the echo.

Radar images are acquired in a completely different way to centrally-projected images derived in the optical wavelength regions. Radar EO uses microwave EMR, emitted by a rectangular antenna, carried on an aircraft or spacecraft platform, to irradiate the Earth's surface and measure the amount of returning radiation reflected from surfaces (called backscatter) within the resolution elements of the system. The radiation is transmitted in a fan-shaped beam as a series of pulses of very short length. The time taken for each pulse (travelling at the 'speed of light') to be reflected and returned to the antenna determines the distance of that portion of the Earth's surface from the antenna. The radar equation describes the performance of a radar system, and relates the received return power at the antenna to the target parameters and the parameters of the radar:

$$P_R = \frac{P_\tau G_\tau}{4\pi R^2} \sigma \frac{A_R G_R}{4\pi R^2}$$

where

P_R is the received power (W);
P_τ is the transmitted power (W);
G_τ is the gain of the transmitting antenna in the direction of the target;
σ is the radar cross-section or effective backscatter area of the target (m^2);
A_R is the antenna area (m^2);
G_R is the gain of the receiving antenna in the direction of the antenna; and
R is the range (m).

Radar signals may be transmitted at a range of wavelengths/frequencies. The standard wavelengths used and their standard radar frequency letter codes are given in Table 9.2. In general, atmospheric precipitation has minimal effect on radar signals with frequency < 10 GHz, which provides a distinct advantage over passive and active optical sensors for EO when cloud cover is present. Slight attenuation occurs at wavelengths less than 30 mm under clear

atmospheric conditions, with attenuation increasing as wavelength decreases. Heavy precipitation will cause a strong radar echo at wavelengths of 10 mm or less (this principle being used in both ground and aircraft mounted weather detection radar systems).

The radar bands X-, C- and L- are most commonly used for EO (see Figure 9.2). Since penetration depth of a radar signal increases with increasing wavelength, L-band penetrates deeper than C-band, which penetrates deeper than X-band (see Figure 9.3). The interaction between these wavelengths and features on the Earth's surface is partly a function of the scale of the surface 'texture' and its dielectric properties (electrical reflectivity and conductivity; see Volume 1B—Section 8 for details). Scattered signal amplitude and polarisation provides information about scattering properties and structure. Phase measurements of the return pulse are used in interferometry to reconstruct 3D topography.

Table 9.2 Radar bands used for EO

Band code	Wavelength (mm=10^3 μm)	Frequency (GHz=10^9 Hz)	Example of use
K	7.5–25.0	40.0–12.0	Early airborne systems
X	25.0–37.5	8.0–12.0	Military reconnaissance, terrain mapping, surveillance
C	37.5–75.0	4.0–8.0	Sea-ice surveillance (limited penetration of solids or vegetation)
S	75.0–150.0	2.0–4.00	Medium-range meteorological applications, such as rainfall measurement, airport surveillance
L	150.0–300.0	1.0–2.0	Ice sheet monitoring, glacier dynamics, penetrates vegetation
P	300.0–1000.0	0.3–1.0	Experimental—penetrates vegetation, sea ice, soil, glaciers

Figure 9.2 Radar wavelengths

The radar wavelengths that are commonly used for EO are shown at actual size (on an A4 page).

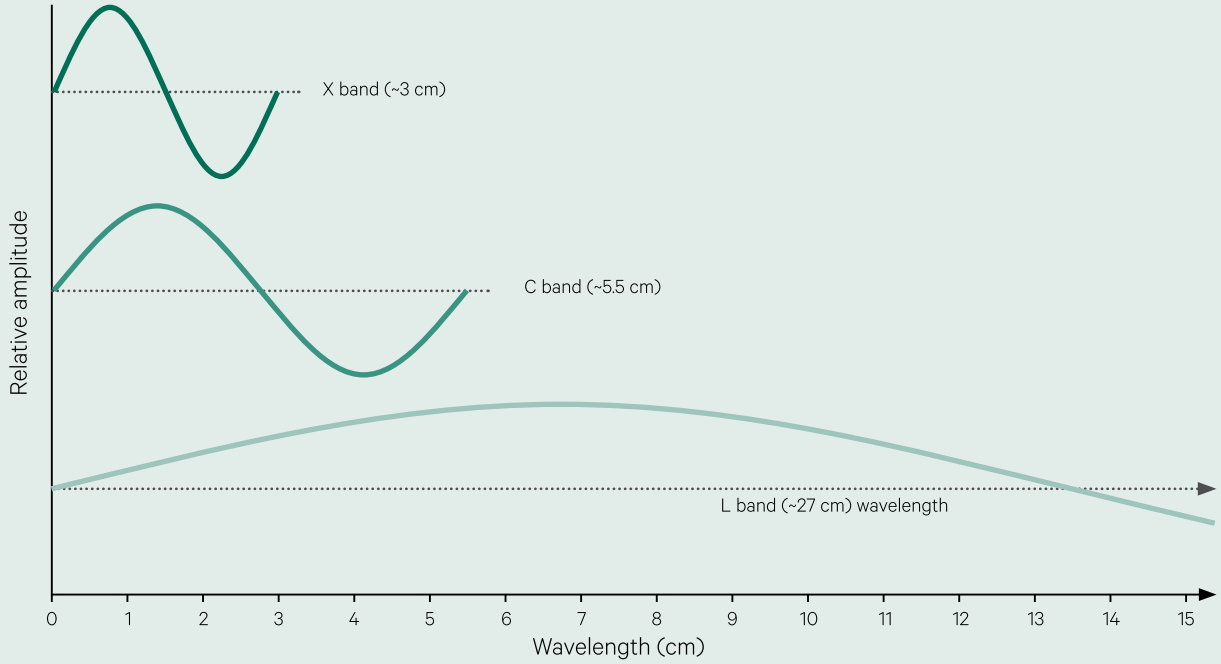

Figure 9.3 Radar penetration in ice/snow cover

While subsurface penetration is possible in the longer L- and C-band radar, it is unlikely from the shorter X-band.

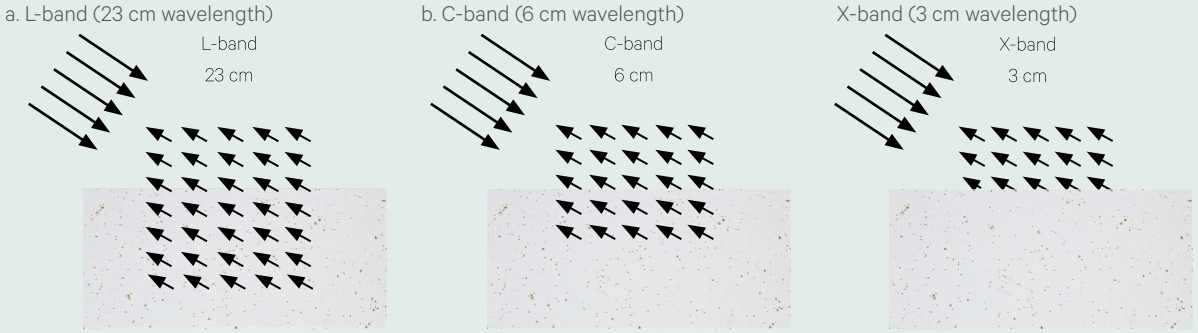

Source: Bruce Forster and Linlin Ge, Course Notes, UNSW

9.1 Microwave EO Framework

The basic physics of EMR is introduced in Volume 1, and in this section we will summarise foundational information that is most relevant to microwave EO. A detailed description of microwave EO can be found in Volume 1B—Section 8.

9.1.1 Review of microwave EMR

EMR is described as having dual natures, comprising both waves and elementary particles, called photons. Newtonian physics views EMR as a wave, which can experience interference and diffraction when propagated through space (see Volume 1A—Section 2.5.2). The quantum view of a beam of EMR, however, is that the energy is not strictly continuous, but packaged into discrete units called photons. In this model, the EMR beam is considered as a stream of photons travelling at 3×10^8 m s^{-1} (the speed of light), where the number of photons per unit area is proportional to the power of the beam (Maged, 2020).

While all EMR waves travel at the same speed, the energy they carry varies with both the wavelength/frequency of radiation and its intensity. Microwaves span the wavelength range 1 mm to 1 m and, like optical wavelengths, can be reflected, transmitted, or absorbed by all forms of matter (see Volume 1A—Section 2). Optical wavelengths are smaller than the lenses and sensors that detect them so can be modelled using geometric or ray optics (see Section 8). Unlike optical wavelengths, however, microwave interactions with matter are best described in terms of the Maxwell equations.

Maxwell viewed EMR as transverse waves combining both magnetic and electric force fields (see Figure 9.4 and Volume 1A—Section 2.4), in which a changing electric field induces a magnetic field and conversely a changing magnetic field induces a changing electric field. Maxwell's equations are a set of partial differential equations that interrelate the symbiotic magnetic and electrical fields, and the electrodynamic properties of matter (electric permittivity, magnetic permeability, and electric conductivity; Ulloa *et al.*, 2019). These equations allow the direction and magnitude of one of these fields to be derived from knowledge of the direction and magnitude of the other (Suits, 1983).

The physical mechanisms whereby different wavelengths of EMR interact with, and impact the structure of, matter are summarised in Table 9.3. The precise atomic and molecular interactions vary both with increasing wave energy and the structure of any matter the wave encounters. Resonant effects, such as rotations, vibrations, or displacements of electrons, atoms, and/or molecules primarily result from higher energy waves (gamma rays to MIR), with the actual impact of a wave depending on its energy level(s). Non-resonant effects, such as conduction and scattering, predominantly result from lower energy waves (TIR and microwave).

The quantum energy of microwave photons is in the range of energies that separate the quantum states of molecular rotation and torsion[10] (see Volume 1B—Section 3 for more detail). At a macro-level, these interactions exhibit as rotational processes, thermal emission, scattering, and conduction. Microwave EO sensors essentially quantify the results of these types of interactions, such that chemical and physical properties of surface and atmospheric features are then inferred from this information (see Figure 8.1). Examples of information that can be derived from observations of these wave-matter interactions are given in Table 9.4.

10 Other interactions can lower the energy of excited electrons in atoms and molecules: fluorescence happens when matter instantaneously emits a photon with lower energy and longer wavelength, while phosphorescence occurs when matter can retain the energy of excitation for a period of time then emit that energy gradually.

Figure 9.4 Electromagnetic wave

An EM wave comprises two sinusoidal waves: an electric wave and a magnetic wave. Each component wave is simultaneously oscillating in planes mutually perpendicular to each other, and also to the direction of travel through space. Wavelength (λ) is measured as the distance between successive wave peaks or troughs. Frequency (ν) is measured as the number of cycles per second passing a fixed point.

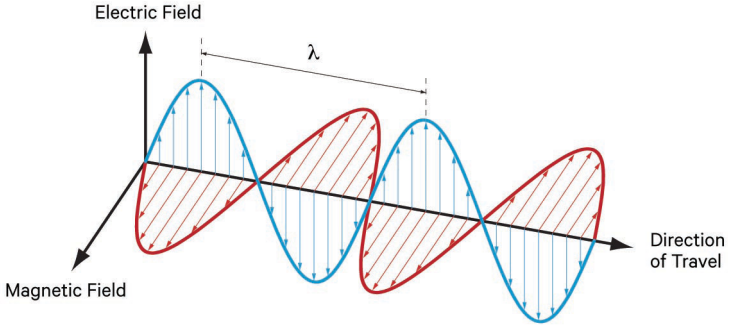

Table 9.3 Effects of EMR on matter

EM Spectral Region	Structural Interactions	Possible Effects
Gamma rays and X-rays	atomic and electronic forces	photoelectric effect, Compton effect, pair production effect
Ultraviolet	electronic excitation and transfer mechanisms	fluorescence, ionisation
Visible and NIR	electronic energy transitions molecular vibrations	molecular vibration, ionic vibration, crystal field effects, charge transfer, electronic conduction
MIR and TIR	molecular vibrations molecular rotations	Si-O stretching vibration, vibrational excitation of atmospheric gases
Microwave	molecular rotations	dielectric heating—primarily by water, oxygen rotational bands

Source: Elachi and van Zyl (2006)

Table 9.4 Wave-matter interactions relevant to EO

EMR Spectral Region	Major Process(es) of Interaction	Information Derived from EO
Gamma rays X-rays	atomic	radioactive material mapping
Ultraviolet	electronic	atmospheric H and He detection
Visible and NIR	electronic molecular vibrations	surface chemical composition
MIR	molecular vibrations and rotations	surface and atmospheric chemical composition
TIR	molecular vibrations and rotations thermal emission	surface constituents surface heat capacity surface and atmospheric temperature
Microwave	molecular rotations thermal emission scattering conduction	surface physical properties surface temperature atmospheric constituents atmospheric precipitation
Radio frequencies	scattering conduction ionospheric effect	surface physical properties subsurface sounding ionospheric sounding

Adapted from: Elachi and van Zyl (2006) Table 2-2

9.1.2 Observing microwave EMR

As introduced in Volume 1A—Section 13, EMR can be observed in terms of:

- amplitude—maximum oscillation of wave from midpoint and proportional to the energy carried;
- energy—as wavelength (the distance travelled in one full wave cycle) or frequency (the number of cycles per unit time), with shorter wavelength at higher frequency carrying more energy;
- polarisation—orientation of electric field of EMR relative to reference vector; and
- coherence—extent to which two waves oscillate in phase; for EM waves, this characteristic describes a relationship in time.

Microwave EO is detailed in Volume 1B—Section 8. Below we review those aspects of EMR observation that are particularly relevant when using microwave datasets for surface water applications.

9.1.2.1 Amplitude

The amplitude, or strength, of the detected microwave signal (either natural emissions for passive sensors, or the echoes of transmitted signals in active sensors) varies with different target materials and their orientations. This is commonly referred to as backscatter. The amount and nature of backscattered EMR can provide information about the size, shape, configuration, and electrical properties of the surfaces and objects irradiated. For example, backscatter is very high when the incoming radiation is at right angles to the object.

The major factors influencing an object's radar return signal intensity are considered to be relief, surface roughness, and electrical properties (see Volume 1B—Section 8.2). Materials differ in terms of their electrical reflectivity and conductivity. One measure of these characteristics is called the 'complex dielectric constant'. For most dry natural materials, the magnitude of this constant has relatively low values (3–8) in the microwave region of the EM spectrum, while water has a value of approximately 80.

The scale of roughness necessary for diffuse reflection decreases with decreasing wavelength and there is a weaker dependence for scattering on the angle of incidence. With decreasing wavelength, the volume scattering component of the backscatter will become more important and, at any given wavelength, the relative contribution of volume scattering increases with increasing angle of incidence (due to the increased slant depth) and will cause the return signal to be depolarised (see Section 9.1.2.3).

9.1.2.2 Energy

The energy carried by EMR is characterised by its wavelength or frequency. As summarised in Table 9.3 and Table 9.4, microwaves interact with matter at the molecular level (see also Volume 1A—Section 15.2 and Volume 1B—Section 8). At these longer wavelengths, the dual electric/magnetic nature of EM waves and their interaction with matter can be modelled by Maxwell's equations (Suits, 1983).

Microwave sensors detect EMR in the wavelength range from 1 mm to 1 m, with different sensors detecting particular wavelengths in this range for specific applications (see Table 9.2). Since this region of the EM spectrum is largely unaffected by the atmosphere, most microwave sensors can operate in all weather conditions.

9.1.2.3 Polarisation

Polarisation, a unique feature of transverse waves, describes the plane in which they oscillate, that is, the orientation of the electric field (or its electric vector) relative to a reference plane. Transverse waves, such as EMR, can be polarised to restrict their vibrations to a single plane relative to the direction of propagation. Microwaves and radio waves are polarised by orienting the antenna to transmit and receive specific wave planes (see Volume 1B—Section 8).

Transmitted signals for imaging radar can be polarised in two orthogonal modes: horizontal (H) and vertical (V), which are typically transmitted separately. These orientations are defined relative to the plane of incidence of EMR, that is, the plane defined by the vertical and the direction of propagation. Horizontal (or plane) polarisation applies when the energy is perpendicular to the wave's plane of incidence. Vertical polarisation, then, is perpendicular to the horizontal polarisation, that is, the electric vector is aligned with both the plane of incidence and the direction of travel.

Interaction with features on the Earth's surface can change the polarisation of the scattered signal, so radar antennae are often designed to receive the H and V signals simultaneously. As a result, polarimetric radar detection systems can measure backscatter amplitude and phase in up to four specific polarisation modes (see Table 9.5). More recently, circular polarisation (the tip of the electric field vector is rotating in a circle as it propagates) is also used, where a circularly polarised wave is transmitted and H and V signals are received. This allows any configuration of transmit and receive to be derived (see Volume 1B—Section 8).

Table 9.5 Polarisation options for radar signals

Transmitted	Received	Code	Type
H	H	HH	Co-polarised
H	V	HV	Cross-polarised
V	H	VH	Cross-polarised
V	V	VV	Co-polarised

Radar system measurements are typically single-polarised (HH or VV or HV or VH), dual-polarised (HH and HV, VV and VH, or HH and VV), or quadrature (quad-) polarised (HH, VV, HV, and VH). A quad-polarised (that is, polarimetric) radar and some dual-polarised systems also measure the signal phase difference between the modes, as well as the signal magnitude, since this is important in polarimetric analysis. Differences in the structure (for example, orientation or shape) of surface features modify the polarisation of reflected microwave energy in varying degrees, with the polarisation mode affecting the scattering intensity 'echo' and thus how the objects appear in the resulting imagery.

9.1.2.4 Coherence

Coherence of a transmitted signal relates to its purity. Two waves with a systematic relationship between their amplitudes are called coherent, that is, they oscillate in phase. In terms of EMR, which comprises two three-dimensional vectors, definition of the underlying physics of coherence is complex, but this characteristic can be simply viewed as their relationship in time. Conversely, waves are 'incoherent' when their amplitudes are randomly related, that is, their waves oscillate out of phase. For example, lasers generate coherent radiation, while sunlight, candles, and incandescent light globes generate incoherent radiation. Since SAR generates coherent radiation, two registered radar images can be differenced to show interference and infer change (see Section 9.4).

9.1.2.5 The Doppler Effect

The Doppler Effect is observed whenever the wave source is moving relative to the observer such that a change in frequency is perceived. For example, when an observer is approaching an energy source, the wave frequency will be observed to be higher than when the observer is moving away. This perception is in fact due to the relative motion of the observer rather than an actual change in the frequency of the wave. This effect can be observed with sound and light waves and is particularly of interest to astronomy for determining the radial velocity of stars and galaxies relative to Earth. Several radar sensors (including traffic speed cameras) are based on the Doppler Effect.

The Doppler effect is used by SAR to effectively increase the length of the physical antenna. By using the flight path of the radar platform, return signals are processed according to their Doppler shifts (that is, a change in wave frequency as a function of the relative velocities of transmitter and receiver). This processing requires that both amplitude and phase information be recorded from objects throughout the time period in which they are within the beam of the moving antenna.

The theoretical increase in the antennae length (the synthetic aperture) allows the computer-processed cross-range or azimuth resolution to be equal to half the real aperture for the whole of the range (near range to far range). Weighted averaging of multiple returns using the platform motion and Doppler shift effects allows the signal that would have been obtained by a longer antenna to be reconstructed. The consequently larger synthetic aperture results in higher spatial resolution imagery that is constant in the along-track (azimuth) and across-track (range) directions (see Volume 1B—Section 8 for details).

9.2 Passive Microwave

Passive microwave radiometers operate in microwave wavelengths from 1 to 300 mm, which are shorter than radar. They rely on detecting the emissions of thermal radiation in the microwave region, which is commonly converted to brightness temperature (see Volume 1B—Section 8.1.1).

In the microwave portion of the spectrum, the two most important properties determining emission levels are the physical temperature (T) of the object and its radiating efficiency or emissivity (ε). Emissivity is the ratio of emitted radiation at a particular wavelength of a real surface to the equivalent radiation from a blackbody at the same temperature and wavelength (see Volume 1A—Section 2.11). In the microwave region, surface materials can have large variations in emissivity. For example, land surfaces can have emissivity of the order of 0.9 while water is of the order of 0.5, although emissivity differences will be less at shorter wavelengths (higher frequencies). Thus, the difference in brightness temperature between land and water at the same kinetic temperature will be largely due to the large difference in their emissivities. It should be noted that ice or snow surfaces and clouds and rain can modify these results (Ferraro *et al.*, 1998).

The intensity of passive microwave radiation emitted by an object depends on its temperature and incident radiation, plus its emittance, reflectance, and transmittance properties. The emitted energy is related to the temperature and moisture content of the emitting object or surface. Surface roughness can also increase the measured radiation from an object or surface because rough texture (such as with ocean waves) increases the surface area of emission per unit area viewed (see Section 16.2.3).

The range of wavelengths detected by microwave radiometers corresponds to the very low energy end of the Earth's energy spectrum (see Volume 1A—Section 5). While all objects emit microwave energy, the amounts are generally very small, so the bandwidth and the spatial resolution of the sensor must be large to allow acquisition of sufficient measurable radiation. A passive microwave sensor detects this naturally emitted microwave energy within the angular field of view of its antenna, which increases with wavelength. Because passive microwave sensors are detecting low energy levels, their imagery has relatively low signal to noise ratio, and the longer wavelengths tend to result in lower spatial resolution. Interpretation of passive microwave imagery is consequently more complex (Ulaby and Long, 2014).

Applications of passive microwave imagery EO include meteorology, hydrology, and oceanography. Oceanographic applications include mapping currents and surface winds (see Sections 16 and 17) and detecting marine pollutants such as oil slicks (see Section 19). There are also detectable differences in microwave emission intensity between water and sea ice (see Section 15), the differentiation of which is important for climatic studies. Other applications include determination of precipitation rates, sea surface temperature (even in cloudy conditions) for global climate studies (see Section 14), and characteristics (including age estimates) for ice and snow cover (see Sections 15.3.4 and 15.4). Non-imaging passive microwave radiometers are used to infer ocean surface wind speed, and atmospheric water content and temperature.

9.3 Imaging Radar

Radar remote sensing is detailed in Volume 1B—Section 8.2 and reviewed in Excursus 9.1 above. The spatial resolution of an imaging radar sensor is determined by its pulse length and beam width. Two types of radar-based systems are commonly used for microwave imaging on aircraft and satellite platforms:

- Side-Looking Airborne Radar (SLAR) or Real Aperture Radar (RAR)—older systems with limited coverage and shorter wavelengths that record amplitude as a function of time; and
- Synthetic Aperture Radar (SAR)—records both amplitude and phase to generate imagery with higher spatial resolution and fewer geometric distortions (see Volume 1A—Section 15.2).

The side-looking nature of imaging radar devices records relief characteristics with higher returns from sensor-facing slopes, and lower or no returns from away-facing slopes or radar shadow areas, in much the same way as an off-nadir Sun position differentially illuminates a landscape with varying relief. Surfaces with local relief variations that are greater than the wavelength of the radar signal will scatter the signal in all directions (diffuse reflectors) and thus return a small, but measurable, portion of the signal to the sensor (see Volume 1A—Section 15). Smooth surfaces, with surface roughness much less than the wavelength of the radar signal, tend to reflect most of the energy away from the sensor (specular reflectors) thus producing a low return signal. While the actual response depends on surface orientation relative to the sensor, more surfaces tend to be specular reflectors for microwave wavelengths than in the optical wavelengths (see Figure 8.6).

Of relevance to surface waters is a scattering mechanism called Bragg Scattering or Bragg Resonance. It has been used to describe scattering from the ocean in terms of resonance with tiny capillary and short gravity waves, even when these waves have a height measured in tenths of a millimetre and ride on waves that are metres high. The short Bragg-scale waves are formed in response to wind stress. If the sea surface is rippled by a light breeze with no long waves present, the radar backscatter is due to the component of the wave spectrum that resonates with the radar wavelength. The Bragg equation defines the ocean wavelengths for Bragg scattering to occur, as a function of radar wavelength (λ_r) and incidence angle (θ; see Figure 9.5):

$$\lambda_s = \frac{\lambda_r}{2\sin\theta}$$

SAR imagery can be acquired as:

- stripmap—the standard acquisition mode with fixed beam direction and no scanning as recorded by SLAR;
- scan—involves moving the antenna in a scan pattern, and is used to capture larger areas with lower spatial resolution; and
- spotlight—used to capture data over small target areas at high spatial resolution, and involves pointing the beam as the platform moves so that the target is in the beam for longer, thus making the synthetic aperture larger.

The roughness of the ocean surface, defined at the scale of a few centimetres, can be detected in SAR imagery, allowing phenomena such as wind, waves, surfactants (e.g. oil), upwelling, boundaries, and bathymetry to be observed (Heron *et al*., 2013). Scattering due to ocean roughness and Bragg scattering are more apparent in VV polarised images (see Figure 9.6). SAR imagery is also used to detect shipping activities (Brusch *et al*., 2011) and track fisheries (Richards, 2012). Different wavelengths and polarisations can be used to monitor a range of surface water features, such as floods and river discharges (see Section 11.4), ice formations (see Section 15), wave heights (Romeiser *et al*., 2004; see Section 16.3.3), and pollution (see Section 19).

Figure 9.5 Bragg scattering

Bragg scattering relationship for an ocean wavelength of λ_s and incoming radiation of λ_r wavelength

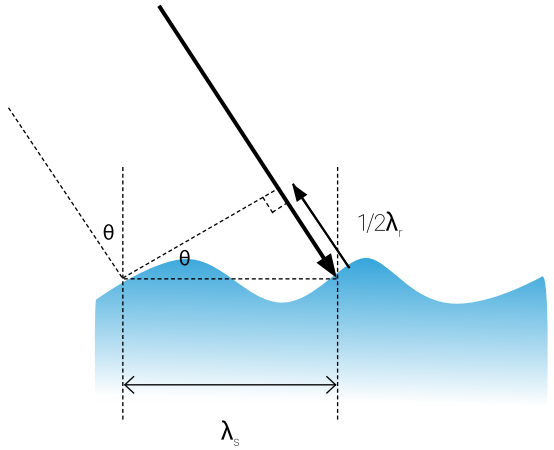

Source: Bruce Forster and Linlin Ge, Course Notes, UNSW

Figure 9.6 SAR composite images

a. Ocean surface roughness for Coastal Panay, Philippines, is highlighted using POLSAR (fully polarised) AIRSAR VV images of increasing wavelength to form a colour composite (C-band as red, L-band as green and P-band as blue)

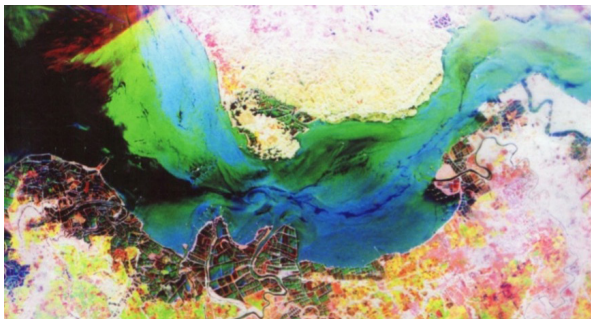

b. Shuttle SIR-C/X SAR (C-band HH, L-band HV and L-band HH displayed as red, green, blue respectively) for sea ice in Antarctica covering an area 45×18 km. Colours indicate ice thickness, which is related to ice growth stages:

- darker lines of open water and smooth ice (< 0.7 cm thick). Blue lines indicate open water in new fractures while bright red lines indicate new ice growth < 0.5 m thick.
- undeformed floes as blue-grey (~0.7 m thick)
- red-tinged deformed ice pieces (< 2 m thick)

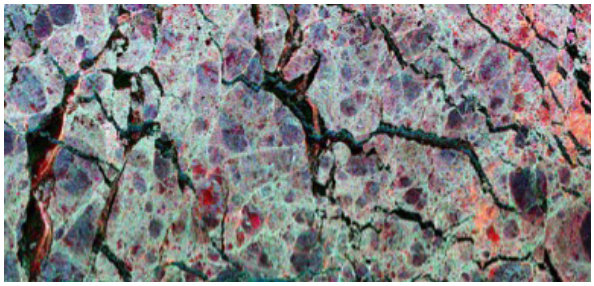

Source: a. NASA JPL; b. CCRS.

9.4 SAR Interferometry

In airborne or spaceborne SAR, radiation is actively transmitted to illuminate the surface, then the backscattered radiation is collected (see Section 9.3). An image of the scene is produced after processing the return signals. Each picture element (pixel) comprises both amplitude and phase information. A conventional SAR image displays the amplitude or power (the square of the amplitude) information.

Interferometric SAR (InSAR), however, exploits the phase information as well as the amplitude. In this technique two images are acquired for the same scene using two separated antennae. After registering the two images and resampling one image to overlay the other, the phases corresponding to each pixel are calculated and differenced, resulting in a phase difference image called an interferogram, which highlights differences in elevation of the imaged surface and changes in position of imaged targets on that surface (see Figure 9.7).

The two antennae may be on the same platform (single-pass InSAR) or the same antenna may be flown twice over the same scene areas (repeat-pass InSAR; see Volume 1B—Section 8.2.7). Along-track interferometry (ATI) uses two antennae, separated in the along-track direction, which detect the same backscattered signals from the Earth's surface, albeit with a very small time lag (Romeiser, 2013). These two datasets are processed to produce two SAR images, the difference of which highlights phase changes and can be used to infer surface velocities (Goldstein and Zebker, 1987).

Figure 9.7 InSAR operation

In this illustration, two SAR images of the same area are acquired at different times. If the surface moves between the two acquisitions a phase shift is recorded. An interferogram maps this phase shift spatially.

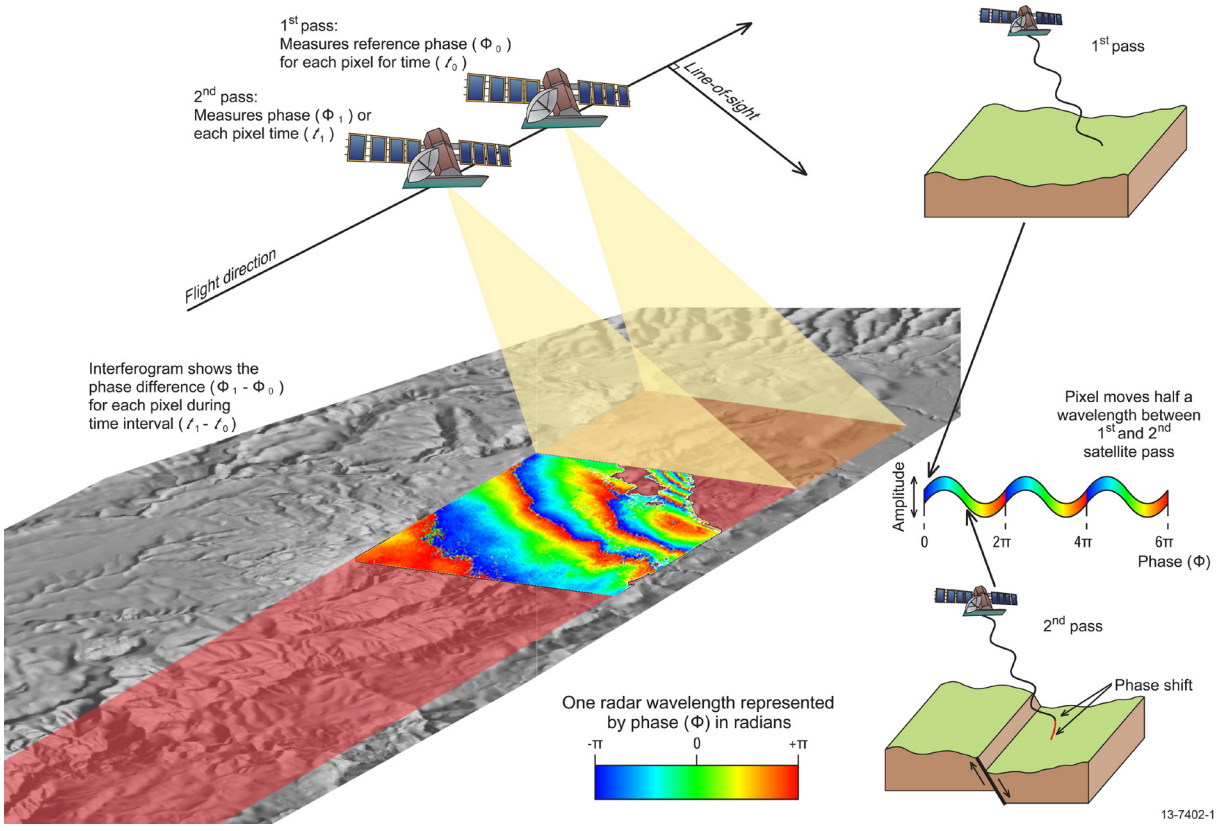

Source: Geoscience Australia. Retrieved from *https://www.ga.gov.au/scientific-topics/positioning-navigation/geodesy/geodetic-techniques/interferometric-synthetic-aperture-radar*

Repeat-pass InSAR allows for differential radar interferometry before and after an event. The phase difference between the two dates is related to the height change and measurements of the order of a few millimetres can be detected. If the antennae are separated parallel to the line of flight in the azimuth (along-track) direction, the motion of the sea surface and the radial velocity of the ground moving target can be measured, whereas if the antennae are separated perpendicular to the line of flight in the range (across-track) direction, altitude information can be derived.

InSAR is being used to measure wave motion (Romeiser, 2013), track ocean currents with greater accuracy than imaging SAR (Romeiser *et al.*, 2004), and monitor the movement of sea ice and ice sheets (see Section 15). It may also prove useful for coastal bathymetric applications (Romeiser, 2013).

9.5 Radar Altimetry

This non-imaging radar detects the microwave backscattering of a surface using a narrow pulse with near normal incidence. Since the basic design of radar devices is to measure distance, by directing the pulse onto the Earth's surface from directly overhead (nadir), the distance being measured is the altitude of the platform above the surface (see Figure 9.8). This relies on accurate knowledge of the platform position with respect to a reference ellipsoid, provided via positioning satellites and ground-based locating systems (see Volume 1A—Section 3).

Figure 9.8 Operation of radar altimeter

Radar altimeters measure the distance between the satellite and the sea surface. The distance between the satellite and the reference ellipsoid is derived by a combination of global positioning satellites, optical laser ranging from ground sites, and radio Doppler ranging from ground sites. Variations in sea surface height, are caused by the combined effect of the geoid and ocean circulation (or dynamic topography).

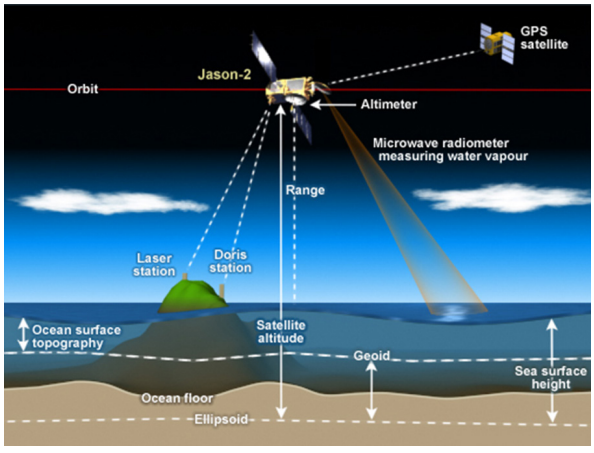

Source: NASA. Retrieved from *https://sealevel.jpl.nasa.gov/missions/technology/*

Conventional radar altimeters have measured distance from the Earth's surface along the satellite's ground track to generate one-dimensional profiles, which can be interpolated to create a two-dimensional map of surface height. While each profile has relatively high resolution along-track, there are significant gaps between tracks for a single altimeter. Datasets from at least two radar altimeters orbiting simultaneously have been merged to produce two-dimensional, global maps of surface height with moderate spatial resolution (Ducet *et al.*, 2000).

Radar altimeters have been carried on several satellites, starting with Skylab in 1973, and more recently the ERS, Jason, and Cryosat platforms (see Volume 1A—Section 16.1.2). The planned SWOT (Surface Water and Ocean Topography) mission will use radar interferometry (see Section 9.4) to enable wide swath sampling, yielding higher spatial resolution data and denser coverage (Fu and Ubelmann, 2014; see Excursus 12.1).

Routine observation of sea surface topography using satellite radar altimetry has been critical for monitoring sea level changes (see Section 12) and global climatic variations (Hwang *et al.*, 2004). Radar altimeters are also used to determine significant wave height and wind speed, and improve tide models (see Section 16). These applications have produced otherwise unattainable data describing the marine geoid, and the related sea floor topography (Vignudelli *et al.*, 2011; see Section 13.3.1). Other marine applications include identifying types of ice masses, monitoring sea/ice boundaries and modelling ice sheet elevation (Helm *et al.*, 2014; see Section 15). Locally, radar altimetry datasets have also been used to detect oil spills (see Section 19), and infer water circulation patterns (see Excursus 2.2 and Section 17).

9.6 Microwave Scatterometry

This non-imaging device measures the microwave scattering or reflective properties of surfaces and is specifically designed to measure backscattering. This requires that the sensor detect more detailed spectral information than acquired by imaging radar but with reduced spatial resolution and areal coverage. The surface is scanned in two or more directions, usually by multiple sensors using either a series of radar pulses or a continuous signal. The intensity, phase, and polarisation of the backscatter beam can be used to observe changes in the surface of waterbodies.

The primary application of microwave scatterometers is to measure wind vectors (that is, speed and direction) over the ocean surface (Barale *et al.*, 2010). This is based on the principle of ocean 'roughness' being caused by wind and resulting in a characteristic surface pattern that may be identified by its scattering properties (see Section 16.2.2). A mathematical model uses the reflectivity data with other sensor characteristics to determine wind speed and direction over the surface. Although radar scatterometers are non-imaging, their data may be used to construct global wind maps when collected over a sufficiently large area.

Spaceborne microwave scatterometers have been carried on several satellite missions, using varying viewing geometries (see Volume 1A—Section 16.1.2.3). Maps of near-surface wind speed and direction are being derived from global scatterometry datasets on a daily basis (Young *et al.*, 2020). These wind vectors provide essential inputs to marine weather and global climate models and are also used with other EO datasets to track severe storm activity and map seasonal trends (see Figure 9.9). Other scatterometry applications of relevance to surface waters include mapping the extent and condition of ice and snow (see Section 15.1).

Figure 9.9 Global wind power

QuikScat data showing wind power density over the global oceans for two seasons.

a. Summer in the Northern Hemisphere

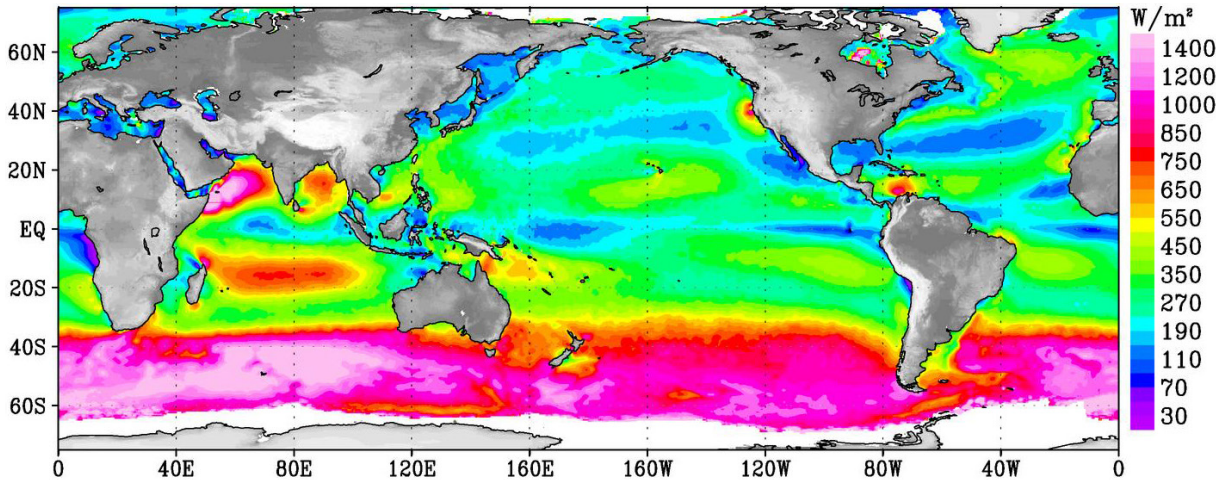

b. Winter in the Northern Hemisphere

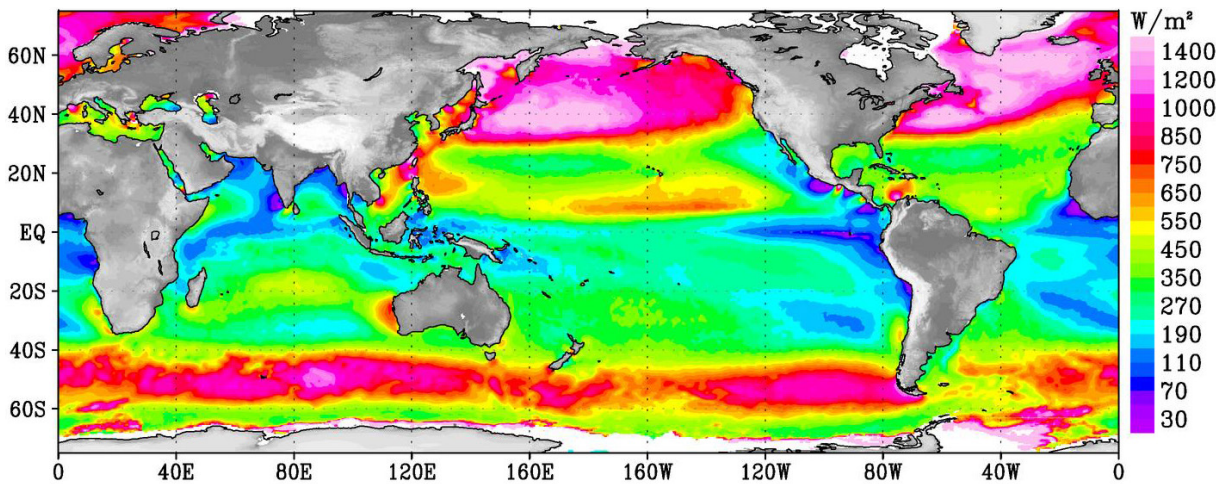

Source: NASA. Retrieved from *https://winds.jpl.nasa.gov/gallery/quikscatdata/?ImageID=10*

9.7 Further Information

Richards (2009)

Ulaby and Long (2014)

ESA Earth Online: *https://earth.esa.int/eogateway*

ESA Radar Altimetry Tutorial and Toolbox: *http://www.altimetry.info/*

9.8 References

Barale, V., Gower, J.F.R., and Alberotanza, L. (2010). *Oceanography from Space: Revisited* (374 p). *http://dx.doi.org/10.1007/978-90-481-8681-5*

Brusch, S. Lehner, S., Fritz, T., Soccorsi, M., Soloview, A., and van Shie, B. (2011). Ship surveillance with TerraSAR-X. *IEEE Transactions on Geoscience and Remote Sensing*, 49(3), 1092–1103.

Ducet, N., Le Traon, P.Y., and Reverdin, G. (2000). Global high-resolution mapping of ocean circulation from the combination of TOPEX/Poseidon and ERS-1 and -2. *Journal of Geophysical Research*, 105(C8), 19477–19498.

Elachi, C., and van Zyl, J. (2006). *Introduction to the Physics and Techniques of Remote Sensing*, Second Edn. Wiley Interscience, New Jersey.

Ferraro, R.R., Smith, E.A., Berg, W., and Huffman, G.J. (1998). A Screening Methodology for Passive Microwave Precipitation Retrieval Algorithms. *Journal of Atmospheric Sciences*, 55(9), 1583–1600. *https://doi.org/10.1175/1520-0469(1998)055<1583:ASMFPM>2.0.CO;2*

Fu, L.-L., and Ubelmann, C. (2014). On the transition from profile altimeter to swath altimeter for observing global ocean surface topography. *Journal of Atmospheric and Oceanic Technology,* 31(2), 560–568.

Goldstein, R.M., and Zebker, H.A. (1987). Interferometric radar measurement of ocean surface currents. *Nature*, 328, 707–709.

Helm, V., Humbert, A., and Miller, H. (2014). Elevation and elevation change of Greenland and Antarctica derived from CryoSat-2. *Cryosphere*, 8(4), 1539–1559. *http://dx.doi.org/10.5194/tc-8-1539-2014*

Heron, S.F., Heron, M.L., and Pichel, W.G. (2013). Thermal and Radar Overview. Ch 11 in *Coral Reef Remote Sensing*. (Eds: Goodman, J.A., Purkis, S.J., and Phinn, S.R.). Springer, Dordrecht. ISBN 978-90-481-9291-5.

Hwang, C., Shum, C., and Li., J. (2004). *Satellite Altimetry for Geodesy, Geophysics and Oceanography*. Proceedings of: International Workshop on Satellite Altimetry. Berlin Heidelberg: Springer-Verlag.

Maged, M. (2020). *Automatic Detection Algorithms of Oil Spill in Radar Images*. CRC Press, Boca Raton, FL.

Richards, J. (2009). *Remote Sensing with Imaging Radar*. Springer, Heidelberg.

Richards, J. (2012). *Australia and SAR: A Road Map*. CRCSI, Melbourne.

Romeiser, R. (2013). The future of SAR-based oceanography: High-resolution current measurements by along-track interferometry. *Oceanography*, 26(2), 92–99. *https://doi.org/10.5670/oceanog.2013.37*.

Romeiser, R., Ufermann, S., and Kern, S. (2004). Status report on the remote sensing of current features by spacebourne synthetic aperture radar. Proceedings of *Second Workshop on Coastal and Marine Applications of SAR*. March 2003, European Space Agency, pp. 105–124 .

Suits, G.H. (1983). The Nature of Electromagnetic Radiation. Ch 2 in *Manual of Remote Sensing* (Ed: R.N. Colwell), pp. 27–60. ASPRS, Falls Church, Virginia.

Ulaby, F.T., and Long, D.G. (2014). *Microwave, Radar and Radiometric Remote Sensing*. The University of Michigan Press.

Ulloa, R.Z., Santiago, M.G.H., and Rueda, V.L.V. (2019). The interaction of microwaves with materials of different properties. Ch. 6 in *Electromagnetic Fields and Waves* (Ed: Yeap, K.H., and Hirasawa, K.). IntechOpen Ltd. doi:10.5772/intechopen.83675

Vignudelli, S., Kostianoy, A. G., Cipollini, P., and Benveniste, J. (2011*). Coastal Altimetry*. Springer-Verlag, Berlin Heidelberg.

Young, I.R., Kirezci, E., and Ribal, A. (2020). The global wind resource observed by scatterometer. *Remote Sensing*, 12, 2920. doi:10.3390/RS12182920

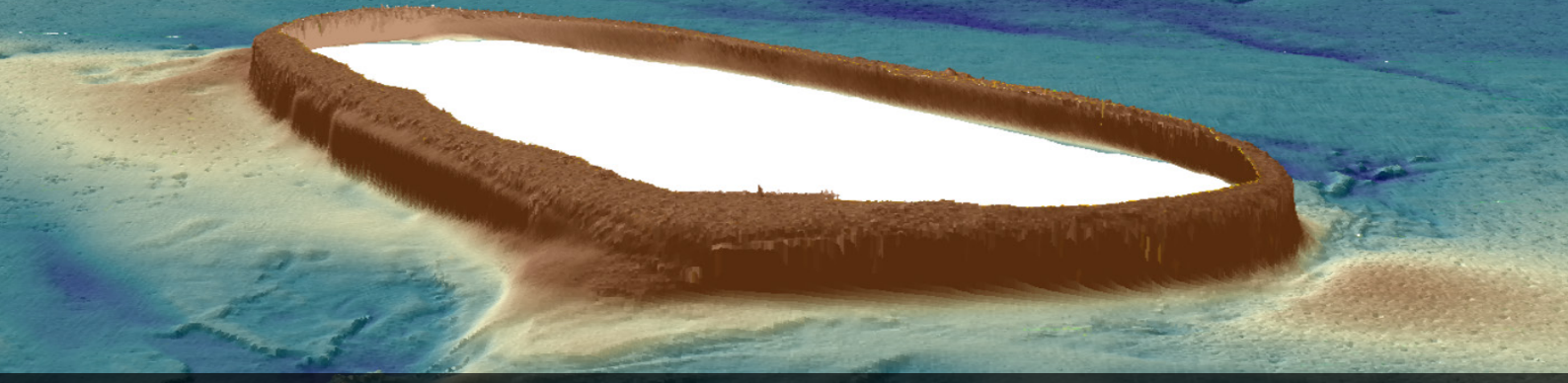

10 Acoustic EO

Since most of the Earth surface is underwater (see Section 1), extensive areas of the globe are not readily visible to optical sensors (see Section 8). In regions of deeper water, acoustic methods (based on detecting sound waves) can provide valuable information about the submerged surface, including the bathymetry, substrate, and benthos.

Vibrational waves, such as sound waves, are introduced in Volume 1A—Section 9. Vibrational waves are disturbances that transfer energy through different media. Sound is a form of energy that is propagated as longitudinal or compression waves where the particles move in the same plane as the wave (see Figure 10.1).

In a spherical wave, such as a sound wave, energy propagates equally in all directions. As such, the power (P) emitted by the source is distributed evenly over a spherical surface (area = $4\pi r^2$) and, assuming that there is no absorption in the medium, the intensity of the wave is given by the formulae:

$$intensity = \frac{P}{4\pi r^2}$$

Thus, the intensity of a sound wave (measured as W/m^2) decreases with the square of the distance from the source, since the same amount of energy is being spread over an increasingly larger area. Like other waves, sound waves undergo reflection, refraction, and diffraction (see Section 8.1 and Volume 1A—Section 2.5.2). The reflection of sound waves off surfaces can produce reverberations and echoes. Diffraction occurs when the wavelength of a sound wave is larger than an object it encounters. However, if the wavelength is smaller than the object it tends to reflect off the object rather than diffract around it.

Unlike electromagnetic radiation (EMR), which travels at a constant speed through a medium, and for which frequency and wavelength definitions can be used interchangeably, the speed of sound waves varies considerably with the elastic properties of the medium through which the waves are travelling. In seawater, the speed of sound is a function of water density and compressibility, both of which are dependent on temperature, pressure, and salinity (see Figure 10.2):

- in deep ocean below 1500 m, the speed of sound is governed by pressure, so increases with water depth;
- in upper ocean waters at equatorial and temperate latitudes, there is greater variation in temperature and some variation in salinity, so the speed of sound is more variable, but tends to decrease with temperature; and
- minimum velocity occurs at the thermocline (see Section 5.1.3; Wells, 1986).

Figure 10.1 Longitudinal or compression waves

In a longitudinal wave, energy moves particles of the medium in the direction of wave propagation. This is comparable to pushing a slinky toy at one end, which causes the coils to compress and dilate as the energy moves to the other end.

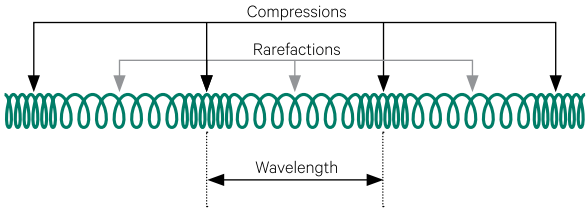

Background image: Multibeam sonar model of Money Shoal, located off the coast of the Northern Territory. This data comes from a marine survey funded by the Marine Biodiversity Hub where Geoscience Australia and the Australian Institute of Marine Science collaborated to map the ocean floor to better understand the biodiversity of the Arafura Marine Park. On this bathymetry image, we see the rich edge of the shoal itself. The top is very rugose highlighting the numerous coral reefs growing on it. This image also shows fields of pockmarks, and a small seafloor crater often created by expulsion of fluid from the subsurface, at the foot of the shoal on either end. The middle of the shoal could not be mapped by ship due to its very shallow nature. Satellite-Derived Bathymetry was later used to complete the mapping of the shoal. **Source:** Geoscience Australia

In ocean water the speed of sound is minimised at water depths in the range 750–1000 m. This zone of minimum speed is known as the Deep Sound Channel (DSC; formerly Sound Fixing and Ranging channel: SOFAR), and enables the guided propagation of undistorted sound for distances up to thousands of kilometres. This channel is commonly used for ocean acoustic tomography and submarine surveillance (DOSITS, 2021).

Light doesn't penetrate beneath the surface of the water, so ocean creatures like whales and dolphins and even 800 species of fish communicate by sound. And a North Atlantic right whale can transmit across hundreds of miles.
(Rose George)

Figure 10.2 Speed of sound varies with water depth

In seawater, the speed of sound is mostly governed by temperature and pressure. From the surface to 1000 m water depth, the effect of temperature dominates. At water depths greater than 1000 m, the effect of pressure is more dominant.

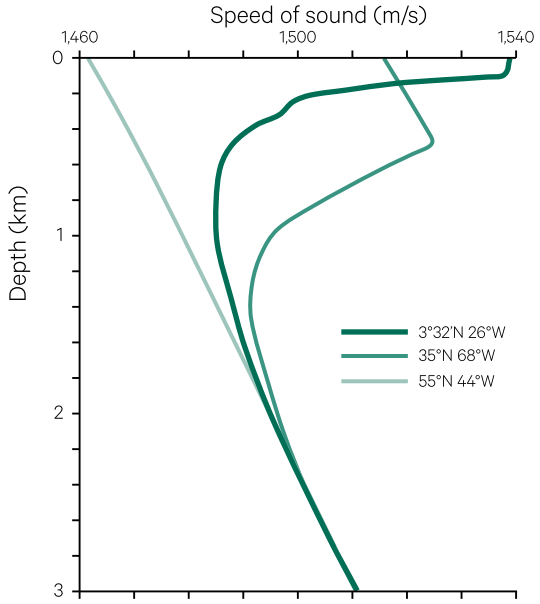

Adapted from: Wells (1986) Figure 2.4

10.1 Acoustic EO Framework

Since sound waves are strongly reflected by the water surface, both active and passive acoustic sensors need to be in contact with the water (Churnside, 2013). Echosounding involves the use of active sonar (SOund NAvigation and Radar) sensors, which transmit short sound pulses (or 'pings') towards the seafloor and measure various characteristics of its echo (reflected sound), including time and strength. While the time between sending the signal and receiving its acoustic return provides a measurement of waterbody depth, or bathymetry data, the strength of the returning signal provides a measurement of seafloor reflectivity. Bathymetric measurements based on sonar echoes have been used to map seafloor topography since the early 1920s (Dierssen and Theberge, 2014).

The proportion of acoustic energy reflected back from the seabed is determined by the impedance contrast (or 'hardness') and the apparent roughness (relative to the acoustic wavelength) of the reflecting surface. In practical terms, the intensity or strength of the return signal, or backscatter intensity, is related to:

- the heterogenity of the seabed material—sizes of sediment grains, bioturbation, and geological layering; and
- the surface roughness—such as seabed substrate, microtopography, and landforms (Lamarche and Lurton, 2018).

In general, since softer materials absorb some of the sound energy, backscatter intensity increases with surface roughness or hardness. Thus, backscatter information can be used to determine bottom type and differentiate between different types of seafloor, such as hard rock or soft sediment, and, by association, benthic habitat and biodiversity (Lamarche *et al*., 2016).

While sonar-based bathymetric measurements relying on timing of echoes are relatively simple in terms of acoustic physics, backscatter measurements involve consideration of more complex acoustic and geophysical processes in both the water and the seabed (Lamarche and Lurton, 2018). Seabed backscatter is defined as the amount of acoustic energy being received by the sonar after a complex interaction with the seabed. This is measured as the surface scattering coefficient, a dimensionless quantity that accounts for the intensity (power) ratio of the incident and scattered waves, determined per unit area at a reference distance of 1 m. When expressed in decibels (dB), this quantity is commonly called the backscatter strength (Lurton, 2010). The intensity of the backscatter received by the sonar depends on the transmitted source level, transmission loss (absorption in the water column and geometrical spreading), and target strength.

Figure 10.3 Hull-mounted sonar system

The sonar system mounted on the hull of a vessel sends out sound waves that bounce off the seafloor and return to the ship.

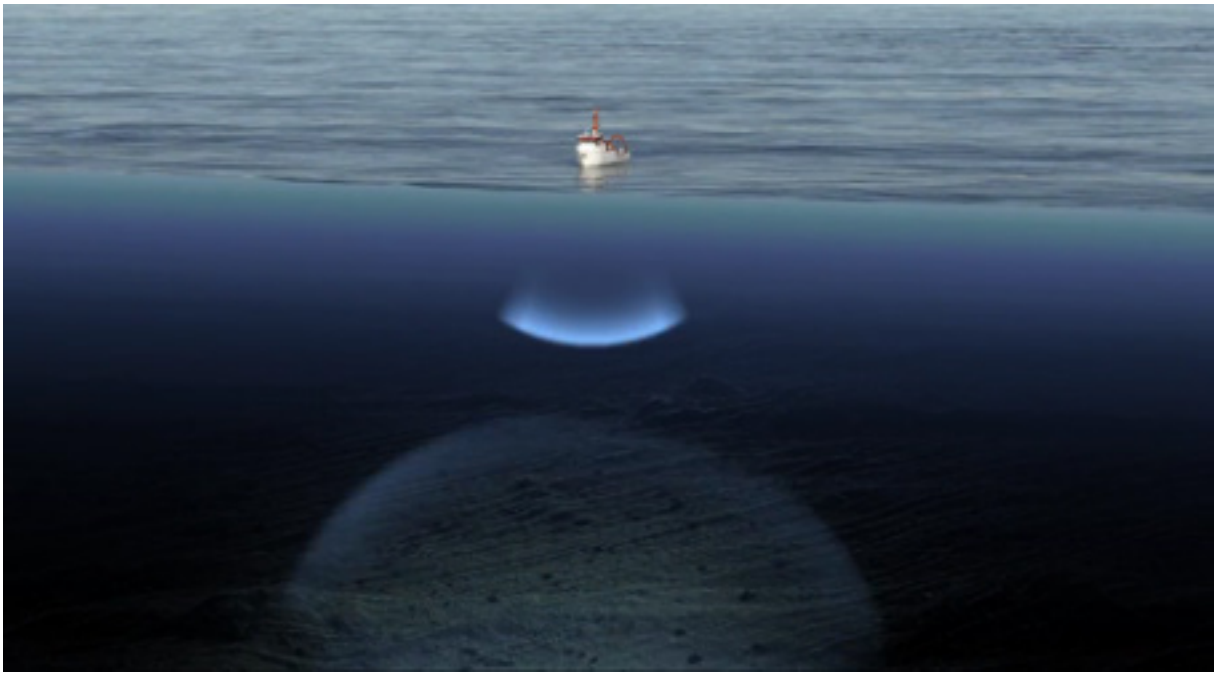

Source: Geoscience Australia

Echosounders use different sound frequencies depending on the application they are used for, the water depth being targeted, and data resolution required. For example:

- measurement of water depth employs frequencies ranging from around 12 kHz to 400 kHz;
- detection of sediment layers below the seafloor uses lower frequencies (generally < 3.5 kHz); and
- identification of pelagic organisms uses higher frequencies (200 kHz; DOSITS, 2021).

Considering that frequency is positively correlated with energy dissipation, higher frequencies (> 200 kHz) are used to map the seafloor in shallow water (< 400 m), and lower frequencies (< 30 kHz) are generally used for deep water (> 2000 m). Frequency also influences data resolution, as does water depth. While frequency mainly controls vertical resolution (for example, better definition of subsurface sediment layers or more precise seafloor depth detection), water depth controls horizontal resolution. In the case of multibeam echosounders (MBES), this is due to the geometry of the sonar beam (a cone) and the sonar swath, which grows with water depth, so is reflected by a wider footprint at the seafloor (see Figure 10.3).

10.2 Echosounders

Echosounders can be grouped in terms of:

- profiling sensors—single beam echosounders that record individual waterbody depth transects or profile lines (see Section 10.2.1); and
- swath sounding systems—use an array of transducers to measure waterbody depth for a strip of the seafloor that is perpendicular to the platform's motion, then combines a sequence of profile lines into a swath:
  - interferometric (also known as bathymetric sidescan; see Section 10.2.2); and
  - beamforming (multibeam echosounders; see Section 10.2.3).

The scanning operations of these three acoustic sensors are illustrated in Figure 10.4. Their ability to detect objects is contrasted with their operating cost in Figure 10.5. Some echosounders operate as dual beam by emitting high frequency and low frequency pulses simultaneously.

Figure 10.4 Beam patterns of sonar systems

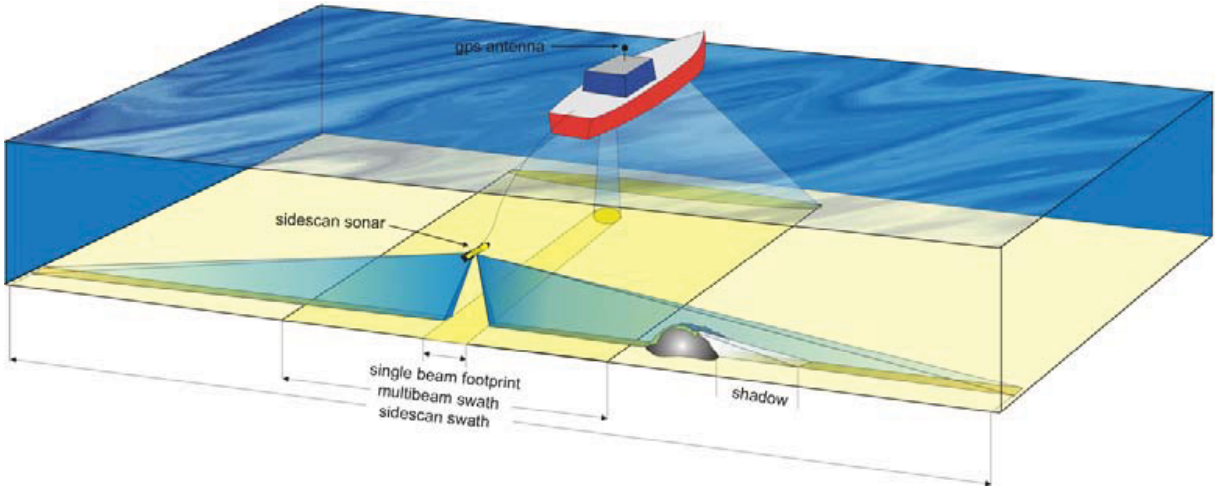

Source: Penrose *et al.* (2005) Figure 4.1

Figure 10.5 Comparison of sonar systems

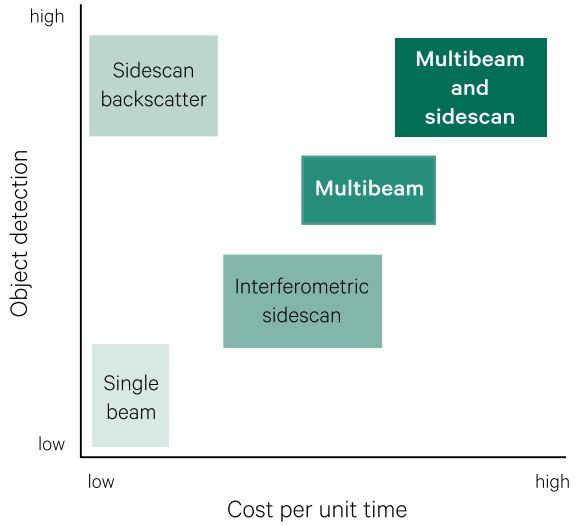

Adapted from: Penrose *et al.* (2005) Figure 8.1

10.2.1 Single beam echosounders

Depth sounders or single beam echosounders (SBES) measure the travel time of a short, directional sonar pulse to determine waterbody depth below the survey vessel (see Figure 10.4). As the vessel moves along the water surface, repeated sonar signals are transmitted and received to record a line of waterbody depths below it.

Profiling SBES emit a narrow, conically-shaped beam to generate a single quantitative measurement for each pulse. Imaging SBES use a fan-shaped acoustic beam to scan large areas of the seafloor, mostly for visual interpretation. This traditional form of sonar has been used for more than five decades, but has known limitations in terms of accuracy and repeatibility. Vessel movement make it difficult to ensure a precise beam orientation and spatial coverage is limited.

SBES have also been adapted to image and characterise the subsurface. They are known as sub-bottom profiling systems. Acoustic energy is reflected at the boundary of materials with differing densities, or acoustic impedance. Since the strength of the reflection varies with the impedance contrast of the materials, different acoustic returns are generated from each boundary, the first boundary being the seafloor. These systems produce an acoustic pulse with set frequency, power, and duration, then record the signals reflected both from the substrate and any underlying sedimentary layers. Although the sonar penetration depth and vertical resolution of sub-bottom profilers can vary with substrate hardness, presence of gas deposits, waterbody depth, and sensor design, these systems can deliver valuable information about benthic habitats (Penrose *et al.*, 2005).

10.2.2 Sidescan sonar

Sidescan sonar (SSS) are imaging SBES that emit one broad beam across a wide angle perpendicular to the path of the platform, and record the intensity or strength of the return signal (also known as backscatter; see Section 10.1 and Figure 10.4). The intensity of consecutive cross-track slices can then be mosaicked to form an image. Traditional SSS do not directly measure waterbody depth, but this can be inferred from the image for specific objects. These images are primarily used for visual detection and recognition of objects (Monahan, 2008). In decreasing importance, the return intensity in sidescan sonars is impacted by sonar frequency, geometry between transducer and target, surface texture, and surface composition and density (Penrose *et al.*, 2005).

Figure 10.6 Sidescan sonar image of shipwreck

This 19th century merchant vessel (labelled IOS-002) was one of two shipwrecks located on the seafloor of the Indian Ocean during the search for MH370 in December 2015. The vessel was identified as an iron, two-decked sailing ship, with overall length ~75 m and weight 1000–1500 tons, which was probably being used to carry coal from the UK to Australasia (Anderson, 2018).

a. Key features

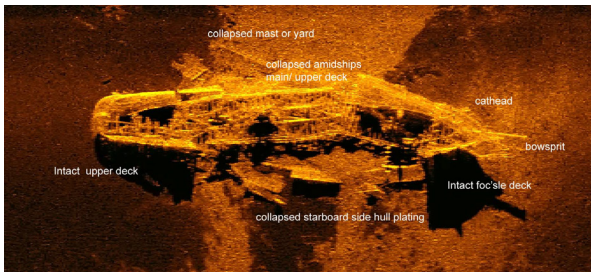

b. Dimensions

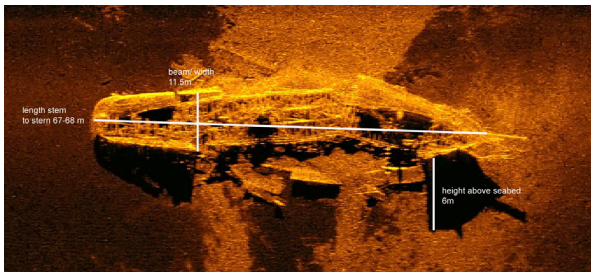

Source: Anderson (2018) Figures 31 and 36. Image source: Fugro/ATSB/WA Museum.

Sidescan systems provide high resolution data with rapid coverage. As a result, they are used for discriminating small features, although their side-looking perspective detects shadows behind objects that protrude from the seafloor (see Figure 10.6). These sidescan datasets can be used to:

- delineate naturally occurring and man-made seafloor features (reefs, sand waves, rocky outcrops, submarine infrastructures, wrecks, pipelines);
- assess environmental issues for marine geology resource management, including the location of ore and aggregate deposits;
- target areas of development suitability (such as the feasibility of undersea cable placement), where identification of seafloor type and geohazards may have considerable impact on the development;
- establish baseline data to support environmental monitoring and habitat mapping;
- detect mines; and
- estimate size of shipwrecks.

Interferometric sidescan sonar (ISSS; also known as Phase Differencing Bathymetric Sonar: PDBS, or bathymetric sidescan) exploit the interference patterns from SSS to model the angle of the echo's return path (Sewada *et al.*, 2018). These systems comprise two (or more) parallel arrays of transducers (or staves), separated by a prescribed distance. By assuming that the arrays receive identical echoes from a given target, the measured time delay (or the phase lag of the two echoes) can be used to determine the incident angle of the acoustic return (Nishimura, 1997). These measurements are then modelled to derive the three-dimensional positions of the sounding points (Kolough, 1984). Compared with MBES, ISSS enable greater coverage of the seafloor, but with reduced accuracy.

10.2.3 Multibeam echosounders

Multibeam echosounders (MBES; also known as multibeam sonar systems) are viewed as the most advanced type of acoustic sensor for observing the seafloor. With high spatial resolution and accuracy, MBES concurrently generate:

- a bathymetry map—indicating seafloor depth and complexity; and
- a backscatter image—indicating surface hardness.

These products can be analysed together to derive an accurate seafloor classification. Generally, the MBES transducer is mounted rigidly to the hull of the survey vessel and its position can be calculated very accurately. However, on a small embarcation, the MBES can be mounted on poles which hang on the side of the ship or at the bow. Other parts of the multibeam system include auxilliary sensors to ensure accurate positioning, motion sensing, and sound speed measurement.

Table 10.1 MBES footprint

The beam footprint for MBES at nadir (m) are given below for selected pairs of beam width and water depth. The MBES footprint increases in outer (off-nadir) beams.

Water depth (m)	Beam width (degrees)					
	0.5	0.7	1	2	3	4
10	0.09	0.12	0.17	0.35	0.52	0.70
25	0.22	0.31	0.44	0.87	1.31	1.74
50	0.44	0.61	0.87	1.74	2.62	3.49
75	0.65	0.92	1.31	2.62	3.92	5.23
100	0.87	1.22	1.75	3.49	5.23	6.97
250	2.18	3.03	4.36	8.72	13.08	
500	4.36	6.11	8.73	17.45		
1000	8.73	12.22	17.45			
1500	13.09	18.33				
2500	21.82					

Source: Picard *et al.* (2020) Table 7

MBES use an array of sonar projectors or transducers pointing in different directions on either side of the platform. Each transducer ensonifies at slightly different times so that all echoes are returned simultaneously as a single strong pulse. Beamforming (a signal processing technique) is then used to derive individual bearings. This results in a beam pattern known as swath that is:

- wide in the across-track direction, which means it covers the area immediately under the vessel and on either side of the vessel; and
- narrow along-track, which means it does not cover the area in front or behind the vessel (see Figure 10.4 and Figure 10.7).

Since the beam footprint is a function of beam width and depth, water depth dictates acoustic data resolution and survey efficiency for MBES (see Table 10.1).

MBES systems generally offer two types of seabed backscatter data, namely:

- 'one-per-beam' backscatter (either beam average or maximum intensity); and
- 'time series' backscatter, similar to sidescan technology (Lamarche and Lurton, 2018).

Recent MBES can also record water column backscatter, resulting from the sonar time series for each beam. Water column data can be used for direct mapping of fish and marine mammals (see Figure 20.15), the mapping of plumes and vents, the location of mid-water targets, and a wide range of physical oceanographic processes (Picard *et al.*, 2020).

Figure 10.7 Multibeam mapping

In this image we see a combination of outputs from multibeam mapping, that is, depth overlaid by backscatter information. In general, red indicates a 'harder' seabed and blue softer. This softness can be witness to the third element of information shown, namely a sub-bottom profile, which provides a cross-section of the seabed subsurface. In this case, the dark layers between the bedforms represent the 'soft' or muddy material accumulated between the hardened and relict bedforms.

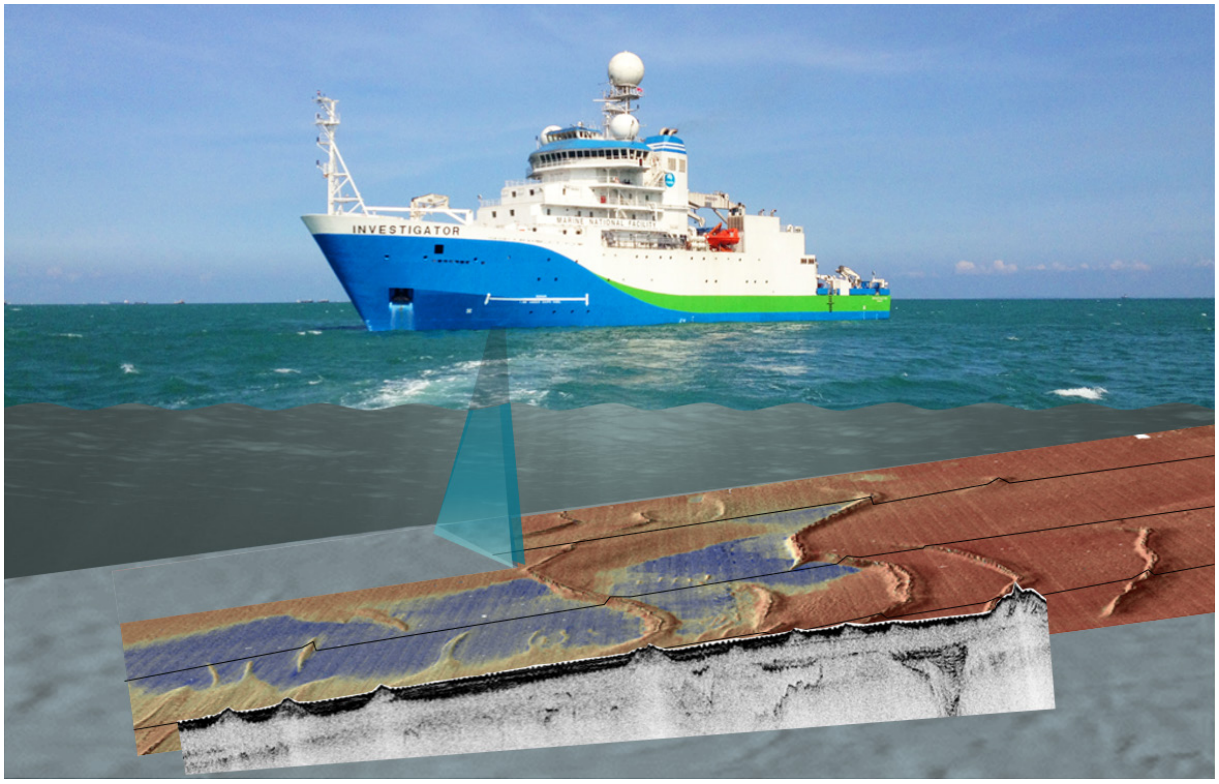

Source: Kim Picard, GA

10.3 Acoustic Surveys and Platforms

Whether the purpose of a marine survey is to identify, delineate, or map biogenic, anthropogenic, or geological features, or produce a navigation chart, survey planning is essential for maximising the value of each survey and delivering consistent datasets that can be integrated and shared quantitatively. Standard procedures for calibration, acquisition, processing, validation, and reporting have been (or are being) developed for MBES nationally and globally (Lamarche and Lurton, 2018; Picard *et al.*, 2020) and other aspects of marine survey (IHO, 2019; Przeslawski and Foster, 2018).

Specific planning tools that are available for MBES surveys in Australia are detailed in Picard *et al.* (2020), including access to national bathymetric holdings as listed in Section 10.5. Picard *et al.* (2020) distinguish between:

- baseline, or exploratory, surveys—which map the distribution of defined marine feature(s) at a particular scale and acquire information needed for more focused surveys; versus
- monitorings surveys—which acquire higher resolution data for specific features at relevant revisit intervals, with greater positional accuracy.

Figure 10.8 Swath overlap for backscatter data

Backscatter data quality is greatest for intermediate incidence angles (shown as unshaded regions below) and reduced near the edges of a swath and near the centre of the swath (shown as shaded regions).

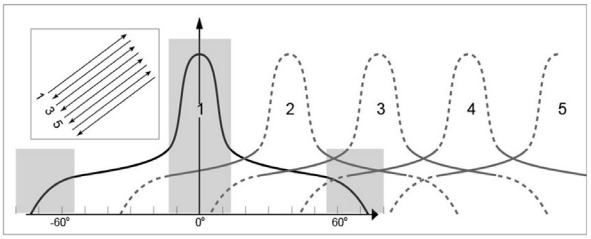

Source: Lamarche and Lurton (2018) Figure 4

Figure 10.9 Relationship between reference ellipsoid, antenna, water line, and chart datum

The most common datums used for seafloor mapping surveys are the ellipsoidal or tidal datum. WL: Water line; RTK: Real Time Kinematic (fixed or float solution); RTG: Real Time GIPSY (real time PPP); PPK: Post Processed Kinematic (fixed or float solution); PPP: Precise Point Positioning; SEP: separation model for datum-to-ellipsoid relationship

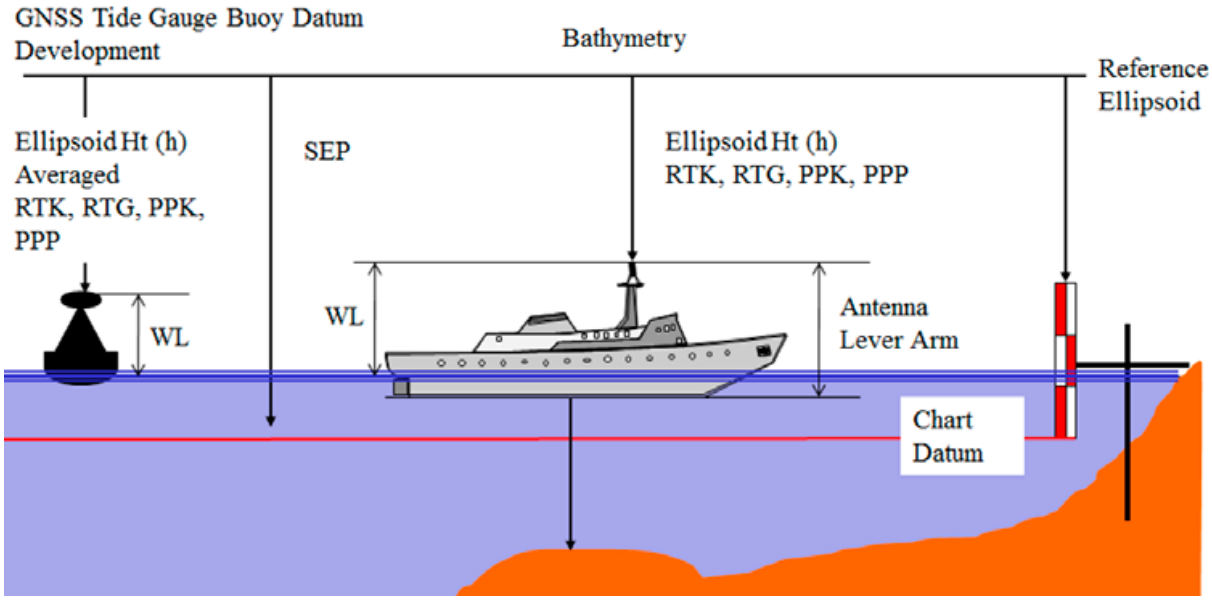

Source: Mills and Dodd (2014) Figure 2

All acoustic surveys require careful planning to ensure that survey lines provide optimal coverage of the seabed for a given area or sampling frame (Foster *et al*., 2018). Ideally, survey planning ensures that each survey line is parallel to the seabed contour direction, spaced appropriately to accommodate waterbody depth and swath width, and overlaps adjacent lines by at least 30% (Picard *et al*., 2020). Overlapping survey lines increase confidence in the data's accuracy and help address any gaps in the data caused by factors such as bad weather. Since the quality of backscatter data is lower near the edges of swaths, and also in the centre due to specular reflection (see Figure 10.8), to avoid using this data requires considerable overlap of swaths (Lamarche and Lurton, 2018). Crosslines or checklines running perpendicular to the main survey lines are also recommended to determine the quality of soundings before survey lines are acquired.

Sonar systems can be towed by a vessel in a 'towfish' container, or mounted on the hull of a manned vessel or on the body of an Autonomous Underwater Vehicle (AUV; see Excursus 5.1). A towed sensor has the advantage of accessing greater waterbody depths but the disadvantage of being more susceptible to rough sea conditions. For mounted systems, the attitude of the platform (in terms of pitch, roll, and yaw—see Volume 2B—Section 2) needs to be carefully tracked to avoid distortions in the resulting acoustic data. The positional instability of most platforms used for underwater sensing necessitates accurate referencing to official ellipsoidal or tidal datums (see Figure 10.9 and Volume 1A—Section 3).

10.4 Acoustic Data Processing

The quality of acoustic data is impacted by various ambient factors during acquisition. For example, platform speed directly impacts sounding density and echo quality, and water column aeration (determined by sea state and survey direction and speed relative to wave action) diminishes the quality and strength of the echo. Longer acoustic pulses increase signal penetration through the water column but reduce vertical resolution (Picard *et al*., 2020).

Specific calibration procedures for MBES are provided by Picard *et al*. (2020) and for seafloor backscatter by Lamarche and Lurton (2018). When processing multibeam bathymetry data, corrections need to be made to allow for factors such as water salinity, sea temperature, and ocean depth, as these affect how quickly sonar signals travel through the water. To calibrate acoustic readings relative to the characteristics of the water column, requires sound velocity profiling (SVP). This measures the speed of sound in water at different vertical levels in the water column for defined frequencies at specific locations in a sampling frame (Lucieer *et al*., 2018). SVP accounts for variations in the temperature and salinity profile of a water column and impacts both the accuracy and uncertainty of each sounding position, horizontally and vertically, especially nearer the edges of each swath (Picard *et al*., 2020).

Thus, all acoustic soundings require processing before they can be used in the form of a raster dataset. Processing includes a set of corrections from all auxillary systems, including ship motion, navigation, sound velocity, and vertical datum. Once these corrections have been applied, it is possible to apply filters to remove outliers and, for bathymetry data, to proceed to creating a surface or digital elevation model (DEM).

Table 10.2 Examples of sounding accuracy and TPU

In this example, TPU (total propagated uncertainty) is computed to 1σ using the Combined Uncertainty Bathymetric Estimator (CUBE).

Depth band (m)	0–5	5–20	20–50	50–100	100–200
Position accuracy					
IHO Standard	5.25	5.50	6.00	6.50	7.25
TPU Estimate	0.27	0.27	0.30	0.34	0.42
Depth accuracy					
IHO Standard	0.38	0.39	0.44	0.50	0.63
TPU Estimate	0.27	0.27	0.28	0.31	0.35

Source: Picard *et al*. (2020) Table 10

The horizontal spatial resolution of acoustic data is determined by the distance between pings along the survey track (which in turn is a function of the platform travel speed and the pulse repetition frequency, PRF; Lucieer *et al.*, 2018). The total propagated uncertainty (TPU) quantifies the survey quality by considering all potential sources of horizontal and vertical error for each measurement (Hare *et al.*, 1995). Sounding measurements, their metadata, and sonar calibration data, are used to estimate TPU, which enables outliers to be identified and removed, and an overall uncertainty surface to be generated for the survey (Lucieer *et al.*, 2018). Examples of IHO accuracy standards and TPU are given in Table 10.2.

10.5 Further Information

International Hydrographic Organisation (IHO)

https://iho.int

AusSeabed

http://www.ausseabed.gov.au/

Visualisations of Seafloor Terrain

Geoscience Australia produces 3D animations and other visualisation products, allowing viewers to 'fly through' the seafloor terrain:

Bathymetry of the Australian Margin: *https://www.ga.gov.au/about/projects/marine/northern-australia-bathymetry*

Bathymetry of Casey Station, Australian Antarctic Region: *https://www.youtube.com/watch?v=ywr6vAC7x1Y*

Bathymetry of Gifford Guyot (2019); *https://atlas.parksaustralia.gov.au/amps?featureId=AMP_TE_GIF*

Bathymetry of the MH370 Search Area: *https://www.youtube.com/watch?v=EDCYGOpNhLI*

Bathymetry of the Western Margins Of Western Australia: *https://www.youtube.com/watch?v=9-3dl8prWRc*

Sonar

DOSITS (2021)

General Bathymetric Chart of the Oceans (GEBCO)

https://www.gebco.net

Archive of seafloor charts: *https://www.gebco.net/data_and_products/historical_gebco_charts/*

International Association of Oil and Gas Producers (IOGP)

Seabed Survey Data Model: *https://www.iogp.org/Geomatics/*

MBES

https://www.hydro-international.com/content/article/state-of-the-art-in-multibeam-echosounders

NOAA

Introduction to Sonar and Multibeam Mapping: *https://oceanexplorer.noaa.gov/okeanos/edu/collection/media/hdwe-MMBkgnd.pdf*

Office of Coast Survey Hydrographic Survey Equipment: *https://nauticalcharts.noaa.gov/learn/hydrographic-survey-equipment.html*

10.6 References

Anderson, R. (2018). *Maritime archaeological analysis of two historic shipwrecks located during the MH370 aircraft search*. Report No. 322, Department of Maritime Archaeology Western Australian Museum.

Churnside, J.H. (2013). Review of profiling oceanographic lidar. *Optical Engineering*, 53(5), 051405. *https://doi.org/10.1117/1.OE.53.5.051405*

Dierssen, H.M., and Theberge, A.E. (2014). Bathymetry: History of Seafloor Mapping. In *Encyclopedia of Natural Resources*, Taylor and Francis. doi:10.1081/E-ENRW-120047531

DOSITS (2021). *Discovery of Sound in the Sea* website, University of Rhode Island: *https://dosits.org/*

Foster, S.D., Monk, J., Lawrence, E., Hayes, K.R., Hosack, G.R., and Przeslawski, R. (2018). Statistical considerations for monitoring and sampling. In *Field Manuals for Marine Sampling to Monitor Australian Waters*, (Eds: Przeslawski, R., Foster, S.). National Environmental Science Programme (NESP). pp 23–41.

Hare, R.M. (1995). Depth and position error budgets for multi-beam echosounding. International Hydrographic Review, 72(1), 35.

IHO (2019). *IHO Standards for Hydrographic Surveys*. 6th edn. International Hydrographic Organisation, Monaco. *https://iho.int/uploads/user/pubs/Drafts/S-44_Edition_6_draft_1_7_1.pdf*

Kolough, D. (1984). Interferometric Side-Scan Sonar A Topographic Sea-Floor Mapping System. International *Hydrographic Review*, 56(2), 35–49.

Lamarche, G., Orpin, A., Mitchell, J., and Pallentin, A. (2016). Benthic habitat mapping. Ch 5 in *Biological sampling in the deep sea*. (Eds: Clark, M.R., Consalvey, M., Rowden, A.A.). Wiley-Blackwell, Hoboken. pp 80–102.

Lamarche G., and Lurton X. (2018). Recommendations for improved and coherent acquisition and processing of backscatter data from seafloor-mapping sonars. *Marine Geophysical Research*, 39, 5–22. doi:10.1007/s11001-017-9315-6. *https://link.springer.com/article/10.1007/s11001-017-9315-6*

Lucieer, V., Picard, K., Siwabessy, J., Jordan, A., Tran, M., and Monk, J. (2018). Seafloor mapping field manual for multibeam sonar. In *Field Manuals for Marine Sampling to Monitor Australian Waters* (Eds: Przeslawski, R., and Foster, S.). National Environmental Science Programme (NESP). pp 42–64.

Lurton, X. (2010). *An introduction to underwater acoustics. Principles and applications*. 2nd edn. Springer Praxis Books, Oxford. ISBN 978 3 540 78480 7

Mills, J., and Dodd, D. (2014). *Ellipsoidally Referenced Surveying for Hydrography*, FIG. Publication No. 62, FIG Commission 4. *http://www.fig.net/resources/publications/figpub/pub62/figpub62.asp*

Monahan, D. (2008). Bathymetry. In *Encyclopedia of Ocean Sciences* 2nd edn (Eds: J.H. Steele, S. Thorpe, and K. Turekian). Elsevier. pp 297–304.

Nishimura, C.E. (1997). *Fundamentals of Acoustic Backscatter Imagery*. Naval Research Laboratory, NRL/FR/7420–97-9848, Washington. *https://apps.dtic.mil/dtic/tr/fulltext/u2/a333800.pdf*

Penrose, J.D., Siwabessy, P.J.W., Gavrilov, A., Parnum, I., Hamilton, L.J., Bickers, A., Brooke, B., Ryan, D.A., and Kennedy, P. (2005). *Acoustic Techniques for Seabed Classification*. Technical Report 32, CRC for Coastal Zone Estuary and Waterway Management.

Picard, K., Leplastrier, A., Austine, K., Bergersen, N., Cullen, R., Dando, N., Donohue, D., Edwards, S., Ingleton, T., Jordan, A., Lucieer, V., Parnum, I., Siwabessy, J., Spinoccia, M., Talbot-Smith, R., Waterson, C., Barrett, N., Beaman, R., Bergersen, D., Boyd, M., Brace, B., Brooke, B., Cantrill, O., Case, M., Dunne, S., Fellows, M., Harris, U., Ierodiaconou, D., Johnstone, E., Kennedy, P., Leplastrier, A., Lewis, A., Lytton, S., Mackay, K., McLennan, S., Mitchell, C., Nichol, S., Post, A., Price, A., Przeslawski, R., Pugsley, L., Quadros, N., Smith, J., Stewart, W., Sullivan J., Tran, M., and Whiteway, T. (2020). *Australian Multibeam Guidelines 2020*. Version 2.0. Record 2018/19. Geoscience Australia, Canberra. *http://dx.doi.org/10.11636/Record.2018.019*

Przeslawski, R., and Foster, S. (Eds). (2018). *Field Manuals for Marine Sampling to Monitor Australian Waters, Version 1*. Report to the National Environmental Science Programme, Marine Biodiversity Hub. 212 p. *http://dx.doi.org/10.11636/9781925297669*

Sewada, J.S., Ioana, C., Geen, M., and Jerome Mars, J. (2018). Wideband signals for Phase Differencing Sonar Systems. *OCEANS'18 MTS/IEEE*, May 2018, Kobe, Japan. Hal-01982962

Wells, N. (1986). *The Atmosphere and Ocean. A Physical Introduction*. Taylor and Francis, London.

Observing Surface Water Dimensions

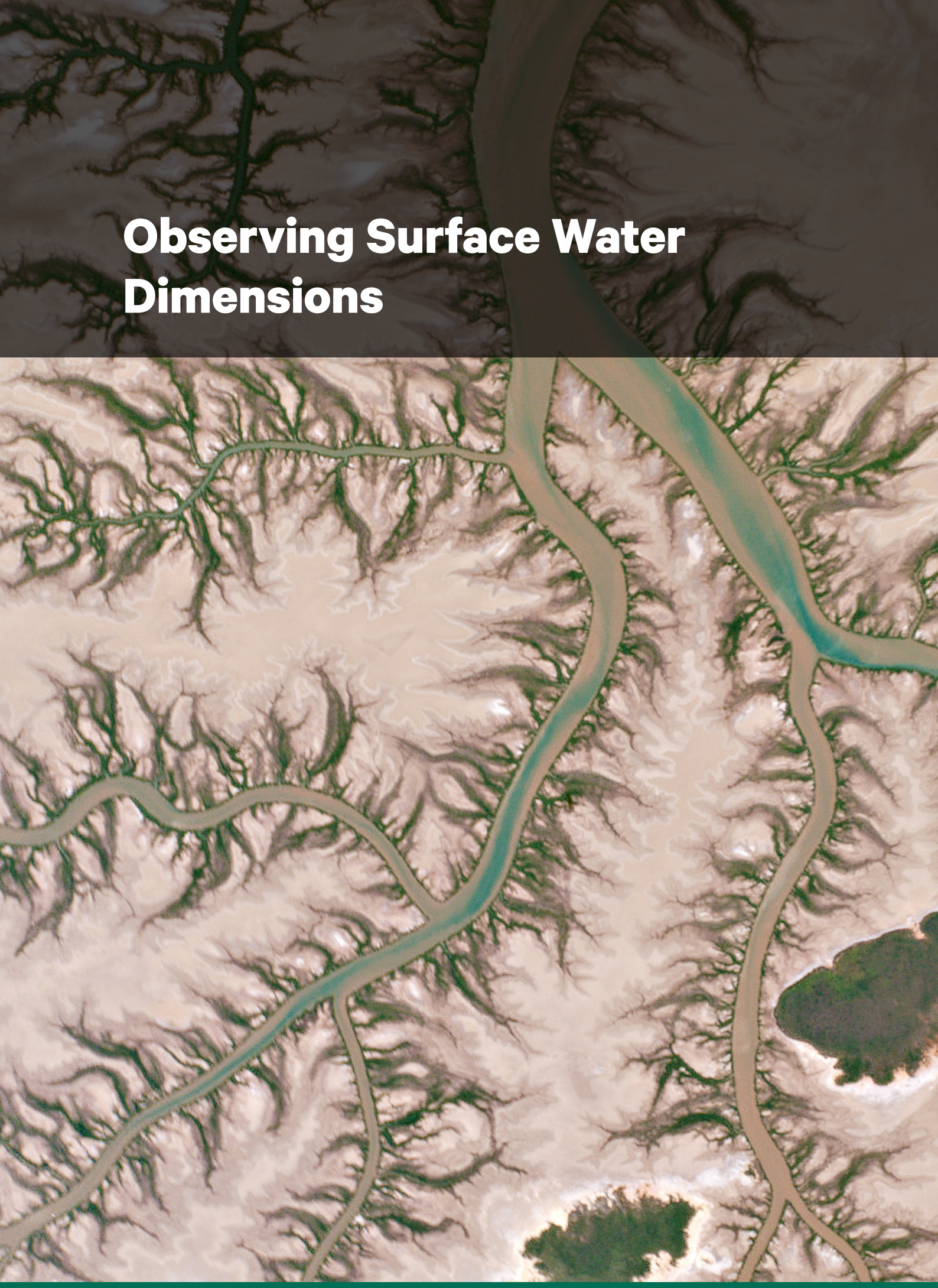

The following three sections detail EO-based analyses that can be used to map and monitor the dimensions of surface waters:

- extent—presents ways to use EO data to map and monitor water extent, including delineating shorelines, monitoring floods, and differentiating permanent and ephemeral waterbodies (see Section 11);
- level—describes EO approaches to measuring and monitoring sea level (see Section 12); and
- bathymetry—discusses EO approaches to mapping waterbody depth and geomorphology in coastal and ocean regions (see Section 13).

Contents

11 Extent 181

12 Level 197

13 Bathymetry 223

Background image on previous page: This image of mangroves bordering tidal flats near the Keep River inlet, Queensland, was acquired on 15 March 2015. **Source:** Planet Labs Inc. (CC BY SA 4.0). Retrieved from *https://www.planet.com/gallery/#!/post/keep-river-mangroves*

11 Extent

Norman Mueller

One of the most readily discernable changes in a waterbody is its extent, which is closely tied to the prevailing meteorological conditions (see Section 7.2). The extent of inland waterbodies impacts nearby human residents and other biota, with both expansion during floods and contraction during drought conditions resulting in changes in water availability and amenity. In coastal areas, floods and storms can dramatically disrupt settlements, services, and aquatic ecosystems.

A number of scales come into play when observing changes in the extent of global surface waters. As illustrated in Figure 11.1, localised water disturbances, such as wind waves, occur at one extreme of spatial and temporal scales, and changes to sea level occur at the other extreme. Nonetheless, EO datasets have proved to be invaluable for monitoring these changes, and differentiating cyclic patterns from longer term variations.

After an overview of the coverage and topographic characteristics of Australian waters (see Section 11.1) and a summary of suitable EO sensors for delineating water extent (see Section 11.2), the use of EO datasets are described in terms of:

- delineating shorelines (see Section 11.3);
- mapping and monitoring floods (see Section 11.4); and
- differentiating permanent and temporary inland waterbodies (see Section 11.5).

Figure 11.1 Scales of observing ocean changes

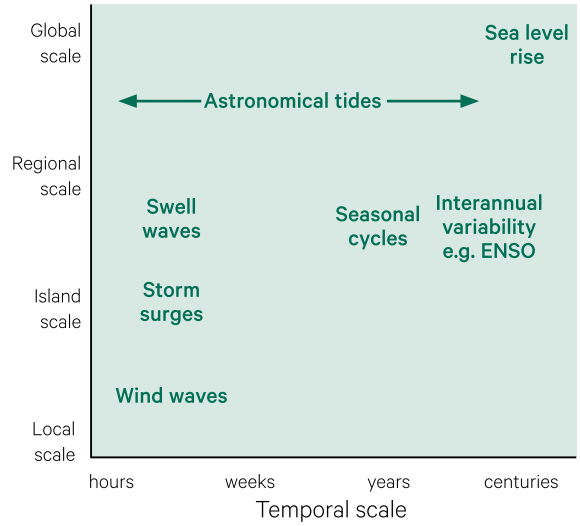

Adapted from: CSIRO (2018)

Background image: Astronaut photograph of flooding in Brisbane, Queensland, taken from the International Space Station on 13 January 2011, when around 20,000 homes were inundated. Brown, sediment-laden floodwaters contrast with rooftops and vegetation, with low-lying suburbs in the northwest being significantly impacted. Source: NASA Earth Observatory ISS026-E-17421. Retrieved from *https://earthobservatory.nasa.gov/images/48625/flooding-in-brisbane-suburbs*

Recommended Chapter Citation: Mueller, N. (2021). Extent. Ch 11 in *Earth Observation: Data, Processing and Applications. Volume 3B—Surface Waters.* CRCSI, Melbourne. pp. 181–195. ISBN 978-0-6482278-5-4

11.1 Extent of Australian Surface Waters

The extent of Australia's vast marine jurisdiction is detailed in Section 2.1. Its inland waterbodies, however, are limited in terms of their abundance, capacity, and permanence.

Australia is the driest continent in the world (see Volume 3A), apart from Antarctica (see Section 2.5). Approximately 35% of the continent is desert, and 70% of the mainland receives less than 500 mm of rainfall per year (GA, 2019). Approximately 12% of rainfall reaches Australia's rivers. By comparison, in Europe 39% of rainfall reaches rivers, and in North America 52% reaches rivers (Parliament of Australia, 2013). Inland surface water is relatively scarce, and Australia is dominated by ephemeral waterbodies, fed by monsoonal summers in the north, and winter rainfall in the south. In contrast to Europe, Australian rivers frequently lack defined channels, are often formed by 'chains of ponds', can cease to flow for long periods, and can experience severe flooding (Finlayson, 2010). As a result, mapping the extent of Australia's surface water from EO can be challenging.

In Australia, the Bureau of Meteorology (BoM) maintains inland water information, providing information on dam levels, river flows, and many other features of the water balance (see *http://www.bom.gov.au/water/*). One aspect of this information is the topographic mapping of Australia's surface water networks, consolidated into the Australian Hydrological Geospatial Fabric (or Geofabric; Atkinson *et al.*, 2008; see Volume 2D—Excursus 13.2). The Geofabric provides information on the location and shape of hydrologic features such as rivers, lakes, wetlands, and catchments, and is a valuable resource when attempting to analyse EO data for water features. Figure 11.2 shows a collection of Australia's water resources as provided by the Geofabric. However, while the Geofabric provides the official distribution of hydrologic features of Australia, it does not provide information on their varying extent resulting from changes in rainfall or water usage. EO datasets provide a valuable addition to surface water data in this regard.

Figure 11.2 A selection of hydrologic features of Australia from the Geofabric

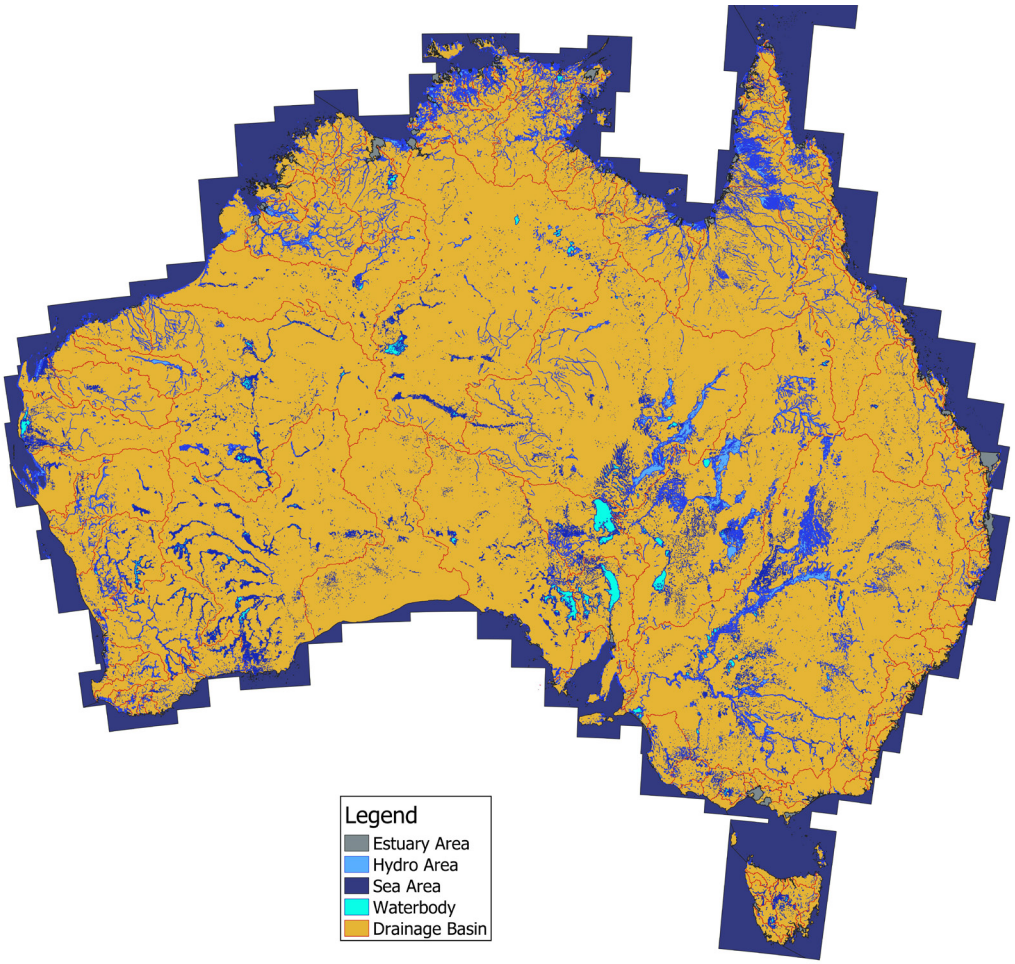

Source: BoM (2019). Map data retrieved from *http://www.bom.gov.au/water/geofabric/download.shtml*

11.2 EO Sensors for Water Extent

Many sensors are able to provide information on water extent. Each type of sensor has advantages and disadvantages and, for each type, many methods have been developed to provide the required output, over the required area, in the required time frame. A range of EO sensors is introduced in Volume 1A—Sections 14 to 16. Interpretation of optical and microwave imagery is considered in Volume 1B—Sections 6 to 8. Both active and passive sensors are used to detect electromagnetic radiation (EMR; see Section 8 and 9), with the most commonly used EO sensors being passive optical and active microwave, with one complementing the other. Table 11.1 describes the general categories of EO sensors which can be used to delineate the extent of surface waters.

The analysis of surface water extent from passive optical sensor data exploits the physical property that water absorbs longer wavelength light far more than shorter wavelength light (see Sections 5.1.4 and 8). This can be observed as the loss of colour in greater water depths when SCUBA diving (everything tends to look more and more bluish, with red wavelengths being absorbed). Similarly, in the analysis of water extent, the shorter wavelengths of blue and green light are reflected far more strongly than the longer near infrared (NIR) and shortwave infrared (SWIR) wavelengths. SWIR is almost totally absorbed by water, with little or no reflection. Hence clear surface water appears extremely dark or black in the shortwave region of the EM spectrum. However as water turbidity increases, reflectance increases as well, which can cause errors in water extent analyses (see Section 18).

A major issue with passive optical data is the occurrence of clouds, which prevent optical sensors from observing the ground beneath them. Clouds also cast shadows, which reduce the reflectance of light from the ground. As a result cloud shadows (and terrain shadows) can be easily mistaken for water. In general the analysis of passive optical imagery for surface water requires good cloud and shadow masking to avoid misclassification errors (see Volume 2). As surface water is associated with rainfall, and hence cloudy conditions, this is a significant disadvantage for the analysis of surface water using passive optical sensors. An example of the response of a passive optical sensor to a land area that includes a variety of water turbidity conditions and mixtures of water, soil and vegetation is demonstrated in Figure 11.3.

Most tribal groups on the coast 18,000 years ago must have slowly lost their entire territory [...] a succession of retreats must have occurred. The slow exodus of refugees, the sorting out of peoples and the struggle for territories probably led to many deaths as well as new alliances.
(Geoffrey Blainey[11])

Table 11.1 EO sensors relevant to water extent

TIR: Thermal infrared; SAR: Synthetic Aperture Radar

Type	Sensor	Platform	Relevance	Advantages	Disadvantages
Passive optical	Multispectral radiometer	Satellite or airborne	Nature, extent, and change in water extent and turbidity	Availability of regularly acquired imagery over very large acquisition areas, spectral discrimination of environmental features, time series	Clouds, high resolution can be expensive, few spectral bands provide little information on quality
	Hyperspectral radiometer	Satellite or airborne	Nature, extent, and change in water extent and turbidity	Multiple spectral measurement bands, best for optical water quality measurement	Clouds, cost, data complexity
	TIR radiometer	Satellite or airborne	Water temperature and extent	Possible to detect water at night	Clouds, low resolution
Active microwave	SAR	Satellite or airborne	Nature, extent, and drift of water and ice; Floods	Cloud penetrating, able to acquire at night	Generally high cost, specialised processing

11 Blainey, G. (1975). *Triumph of the Nomads: A History of Aboriginal Australia.* Macmillan, Melbourne. 285 p.

Figure 11.3 Region north of Lake Eyre during flooding

These images were acquired by Landsat-5 over a region north of Lake Eyre on 28 March 2011 during a flood.

a. True colour image, with the red, green and blue data channels displayed as RGB. This demonstrates a variety of water colours, due to turbidity and salinity, and the difficulty in clearly discriminating the water area from emergent vegetation in the right side of the image.

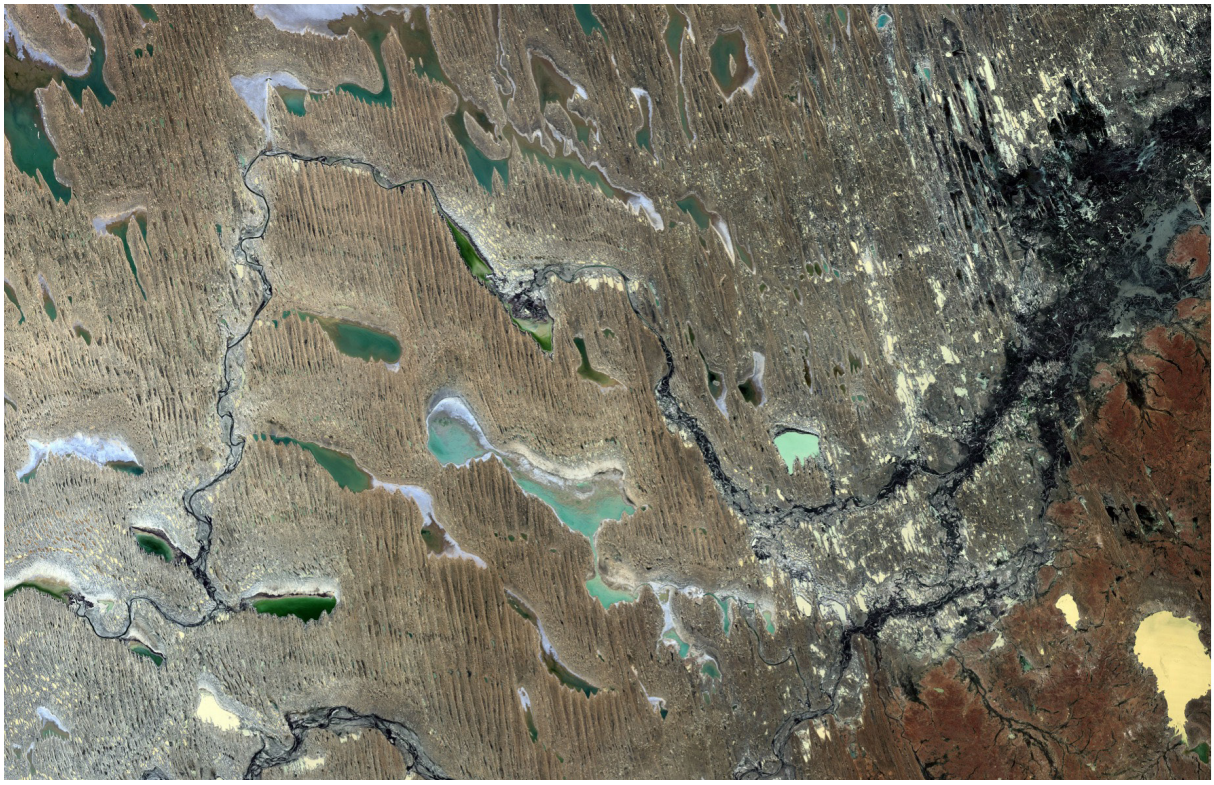

b. The same image shown in false colour, with SWIR, NIR and green displayed as RGB. This strongly highlights water in shades of blue and vegetation in shades of green, enabling easier visual delineation of water extent. The variation in the blue colouring is due to turbidity.

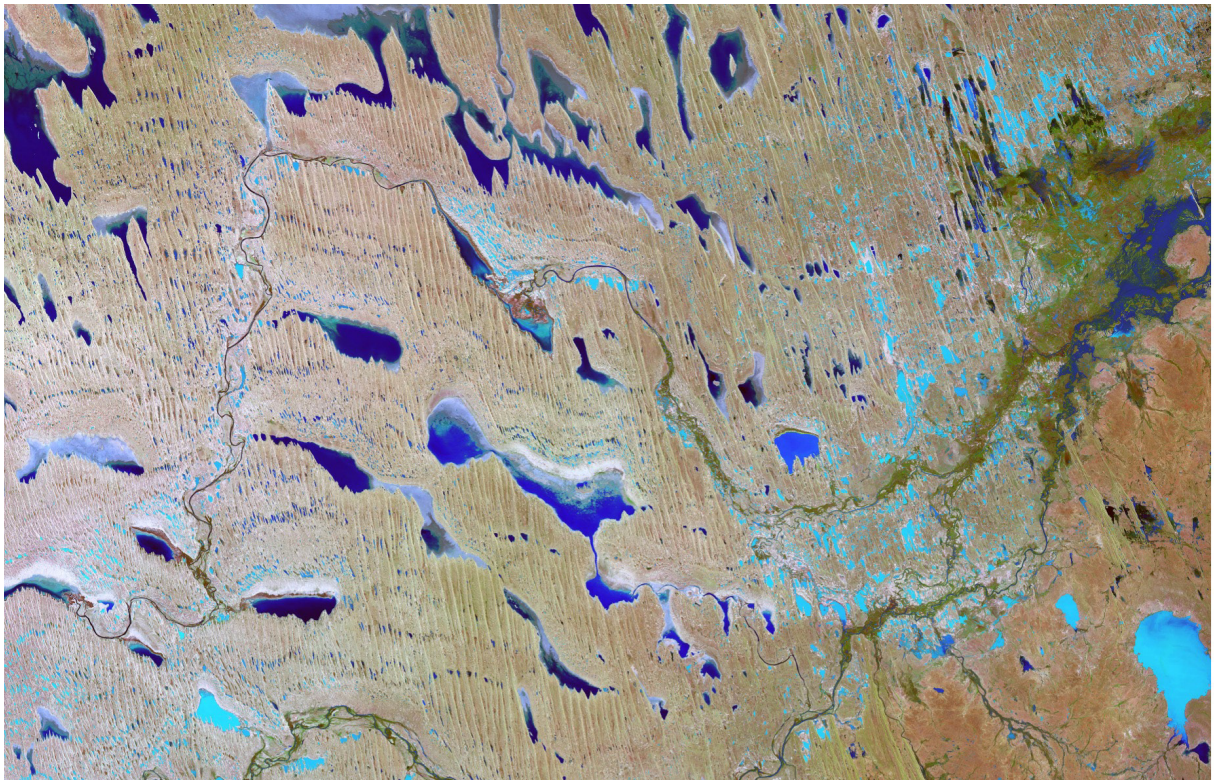

Figure 11.4 Sentinel-1a SAR image of Lake Sorrell in Tasmania, acquired on the 7 May 2015

The waterbody shows a high degree of variation across its area due to wind-induced wave action. Given this variation in backscatter, a simple threshold approach to determining water extent would either underestimate the water in the lake or generate many false positives elsewhere in the image.

Active microwave sensors have the advantage that the wavelengths used are generally able to penetrate clouds, and hence overcome the cloud and shadow challenges that occur with passive optical sensors (see Section 9). In active microwave sensing, a signal is sent to the ground at an angle to the side of the platform (see Volume 1A—Section 15.2 and Volume 1B—Section 8). The signal then interacts with targets on the ground before a portion of the signal is reflected back to the sensor, with the reflected portion depending on the relative size of the ground targets compared to the wavelength of the signal. Where the target is smaller than the wavelength, little or no signal is reflected back to the sensor and most scatters away, while where the target is larger than the wavelength, much of the signal is reflected back to the sensor. Accordingly, targets that have little surface 'roughness', such as surface water, return little information to the sensor so will appear as dark shades in an EO image, while 'rough' targets will appear brighter. However variations can occur where surface water:

- is adjacent to flat, smooth terrain; or
- contains objects such as large rocks, vegetation, debris; or
- wind creates waves on the water surface, subsequently altering the roughness.

As a result, surface water can be misclassified as dry terrain and vice versa, depending on the mixture of targets in an area. The use of multiple images in a time series, and techniques such as coherence (see Section 9.1.2.4), can help in such cases. An example of the response of an active microwave sensor (in this case Synthetic Aperture Radar, SAR) to the variety of features in and adjacent to water is shown in Figure 11.4.

11.3 Delineating Shorelines

The basic issue in determining water extent is that every pixel along a shoreline contains a mixture of terrestrial and water features, and the resulting EO measurement, represented as an image pixel, will be dominated by the feature with the most signal. In open water each pixel comprises a mixture of pure water, turbidity factors, wave action, algae content, etc. At the shoreline, however, these water factors are mixed with vegetation, soil, infrastructure, plus the potential that the sensor might not be able to get a clear observation of the surface due to the other factors blocking its view. For instance, a tall building or dense forest canopy could easily obscure a nearby waterbody from the viewing position of the sensor (see Volume 1B—Section 3). The delineated shoreline is thus the best solution found when determining what the pixel mostly represents from the mixture of features within it. Mapping surface water extent from satellite imagery continues to be a challenge, with many new methods being published each year. The DEA Coastlines product defines shorelines annually since 1988, and their rates of change, for the entire Australian coastline (Bishop-Taylor *et al.*, 2019a).

11.3.1 Passive optical analysis

The absorption of SWIR and NIR wavelengths by water allows some basic water extents to be created from optical imagery with appropriate spectral bands. The approach of a simple threshold applied to a single band is very limited as misclassification can occur with dark, non-water features such as dense, dark forests, dark soil, and mud. In addition, water quality has a large impact on NIR reflection, especially if algae is present in the water (see Section 19).

Better results can be obtained by exploiting the broader spectral response of water, through the use of ratios and normalised difference indices (see Volume 2C—Section 10). Typically these concentrate on comparing an IR band with a visible band, such as NIR and visible green. However these methods generally require fine tuning of thresholds that then do not transfer well between images, and require a lot of manual refinement to provide repeatable results. Of the various forms available for the Normalised Difference Water Index (NDWI) the most popular ones were proposed by McFeeters (1996) and Gao (1996) respectively:

$$\frac{\rho_{green} - \rho_{NIR}}{\rho_{green} + \rho_{NIR}}$$

$$\frac{\rho_{NIR} - \rho_{SWIR}}{\rho_{NIR} + \rho_{SWIR}}$$

A further development substituted the longer SWIR band for the NIR band to create the Modified Normalised Difference Water Index (MNDWI; Xu, 2006):

$$\frac{\rho_{SWIR} - \rho_{green}}{\rho_{SWIR} + \rho_{green}}$$

The applicability of each normalised difference index depends on the situation, and many further developments have been made to create indices that are more robust to other features in imagery such as urban structures and vegetation. In general however the McFeeters (1996) NDWI tends to be useful in coastal applications, while the Xu (2006) MNDWI is more robust to variations in water quality and tends to be useful in freshwater applications. The Gao (1996) NDWI was originally intended as a vegetation water content index, so is used less frequently in open water. For example the European Commission (EC) Joint Research Centre (JRC) employed the Gao (1996) NDWI for broad regional area understanding of vegetation stress (JRC, 2011).

More advanced indices have also been developed. For example an in-depth review of seven index methods was conducted by Fisher *et al.* (2016). The result of this study is a set of high accuracy water indices that are more useful for analyses across multiple images and locations.

Some very large scale surface water products derived from passive optical data have been developed by combining multiple bands and indices using machine learning to create algorithms that are more robust, and applicable across mutliple scenes and time series. The Water Observations from Space (WOfS; Mueller *et al.*, 2016) algorithm used spectral bands and normalised difference indices in a single decision tree produced using machine learning to create a 30-year, continent-wide, surface water product that is automatically updated for each new Landsat image across Australia (see Volume 1A—Excursus 5.1). The resulting data provides an ongoing measure of water extent for Australia. Tulbure *et al.* (2016) employed a random forest machine learning algorithm to examine the 30-year dynamics of surface water in the Murray-Darling Basin from Landsat imagery. The result provides a very high accuracy understanding of surface water for the basin.

Figure 11.5 NIDEM process

The National Intertidal Digital Elevation Model (NIDEM) uses three decades of Landsat imagery to extract and interpolate shoreline contours.

a. 10% intervals of the tidal range mapped from DEA Landsat imagery (colour spectrum from blue to red shows inundated pixels at increasing high tide)

b. Waterline contours extracted and assigned median tidal heights for each 10% interval

c. Interpolated elevation relative to mean sea level from < 2.5 m (blue) to > 1.5 m (yellow)

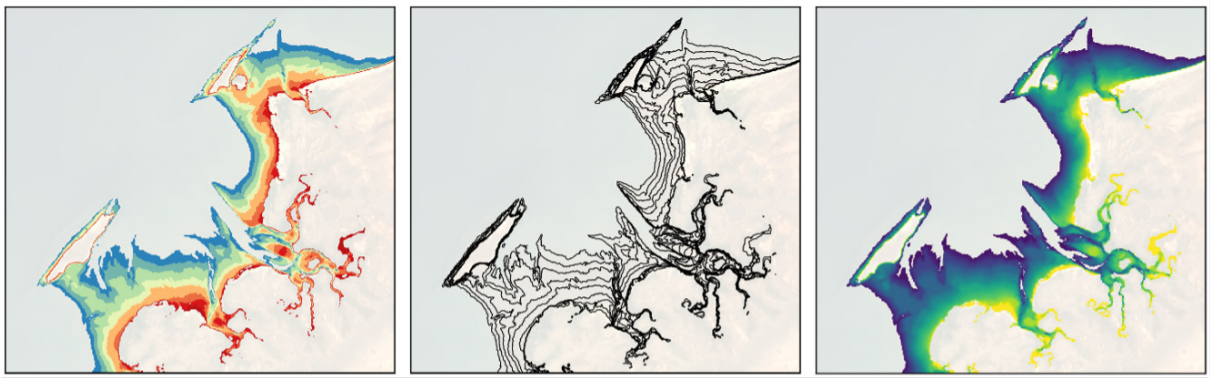

Source: Bishop-Taylor *et al.* (2019b) Figure 17

The National Intertidal Digital Elevation Model (NIDEM; an enhanced version of the Intertidal Extents Model, ITEM)—see Volume 2A—Excursus 2.1), uses EO time series imagery from the Digital Earth Australia (DEA) platform (see Volume 2D—Section 11.2) to map Australia's intertidal zone at continental scale. The intertidal zone is highly significant for migratory shorebirds and marine biodiversity but extremely difficult to map and survey at ground level. As illustrated in Figure 11.5, NIDEM allows changes in our shorelines to be monitored and modelled (Bishop-Taylor *et al.*, 2019b).

At the global scale, Pekel *et al.* (2016) employed expert systems, visual analytics, and evidential reasoning to build a surface water product for the world based on Landsat data from 1984 to 2015. The broad applicability of this product has led to its adoption by the United Nations as an underpinning dataset for understanding surface water change in relation to droughts and population increase, and as a key dataset in measuring surface water change against the Sustainable Development Goals (UN, 2019a; see Volume 3A—Section 20). Excursus 11.1 presents one of the global methods by Verpooter *et al.* (2014) in detail.

These methods for determining surface water extent from optical imagery, all share Landsat as their source data, primarily due to its regular coverage of the globe over the last few decades. Into the future the recent successful launches of the Copernicus satellites in the Sentinel-1 and Sentinel-2 series, will provide similar capacity but at higher spatial and temporal resolution, and also from their SAR sensor, which will be advantageous in cloudy conditions or at night.

Excursus 11.1—GLOWABO

Source: Verpooter *et al.* (2014)
Further Information: Verpooter *et al.* (2012)

A GLObal WaterBodies database (GLOWABO) was compiled from high resolution satellite imagery to enable assessment of global limnological conditions, and quantify the contribution of lakes to global biogeochemical processes (Verpooter *et al.*, 2014). GLOWABO was generated using an automated method for extracting lakes from satellite imagery called GWEM (GeoCover™ Waterbodies Extraction Method; Verpoorter *et al.*, 2012). This method used a global set of regional Landsat GeoCover mosaics comprising 882 nearly cloud-free, pan-sharpened tiles with 14.25 m spatial resolution. These mosaic tiles were created from 8,500 Landsat ETM+ scenes acquired between 1997 and 2003 using ETM bands 2 (green), 4 (NIR), and 7 (SWIR). Elevation data was based on Shuttle Radar Topography Mission digital elevation model (SRTM-DEM) database 4.1 (Jarvis *et al.*, 2008) for all lakes between 60°N and 56°S (excluding the Capsian Sea).

Figure 11.6 GLOWABO overview

Inputs are shown as grey boxes and outputs as white boxes.

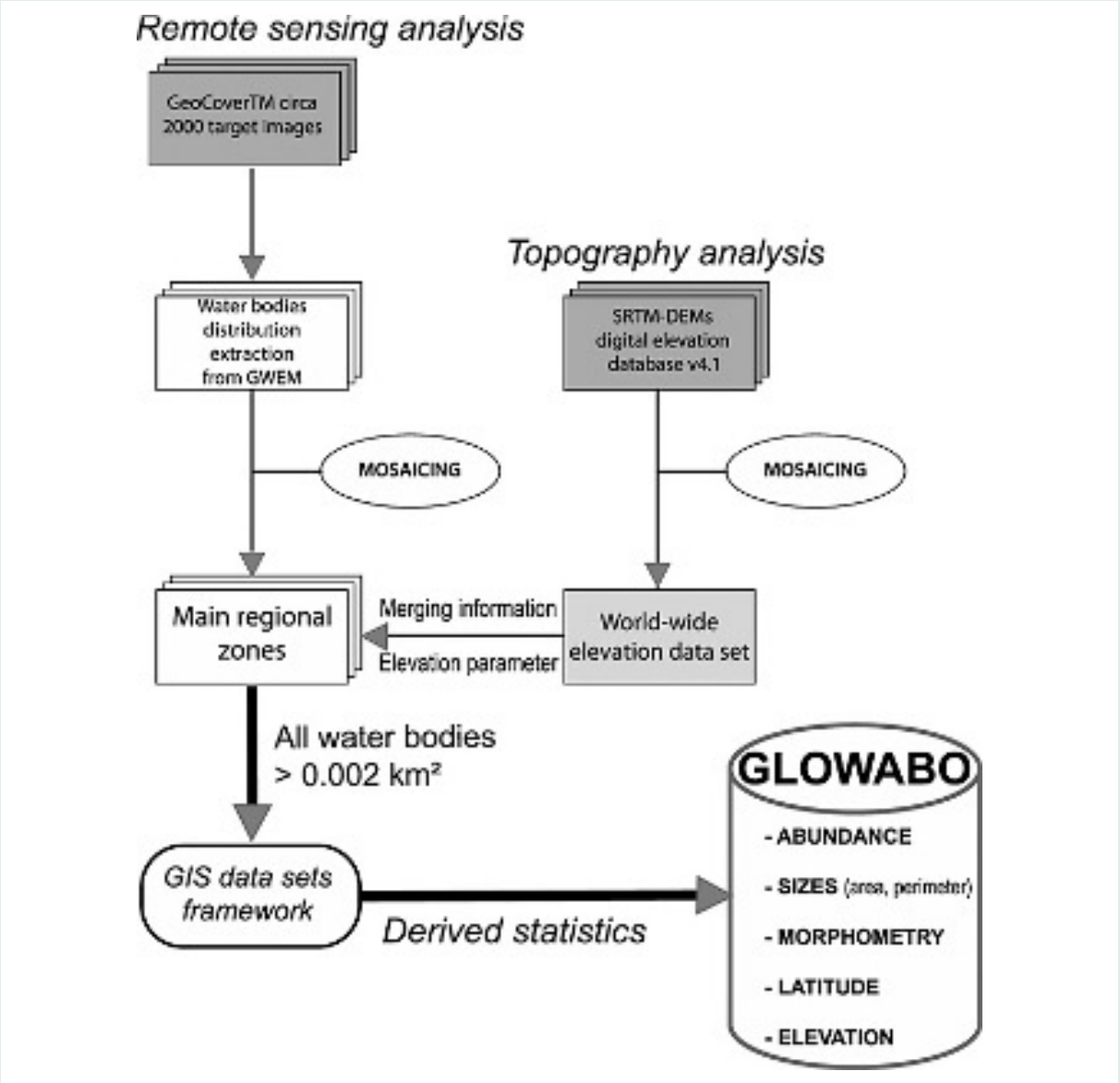

Source: Verpoorter *et al.* (2014) Figure 1

Lake measurements extracted using this method included count, area, perimeter, geographic distribution, elevation, and shape (indicated by shoreline development index: SDI; see Figure 11.6). This inventory concluded that:

- around 117 million lakes of size greater than 0.002 km^2 exist globally compared with a previous estimate of 163 milllion (Downing *et al.*, 2006);
- these lakes cover 3.7% of the non-glaciated land area;
- previous estimates based on map compilations (such as the Global Lake and Wetland Database: GLWD; Lehner and Döll, 2004) underrepresented small lakes, and statistical extrapolations based on size-abundance relationships (such as Downing *et al.*, 2006) overestimated them (see Figure 11.7);
- the greatest abundance, area, and perimeter of waterbodies exist between 45°N and 75°N (see Figure 11.8); and
- 85% of lakes, 50% of lake area and 50% of total lake area occur at elevations below 500 m (see Figure 11.8).

These results are significant for global and regional analyses of hydrologic and biogeochemical processes, including emission of carbon dioxide and methane, sediment burial of carbon and other elements, and primary production (Wetzel, 1992). As high resolution time series datasets become available, it will also be feasible to globally monitor the dynamics of lake abundance, size and distribution.

Figure 11.7 GLOWABO estimates

a. Abundance
b. Total area—global areal extent of lakes is dominated by medium and large lakes
c. Total perimeter
d. Shape (mean SDI)—smaller lakes tend to be rounder.

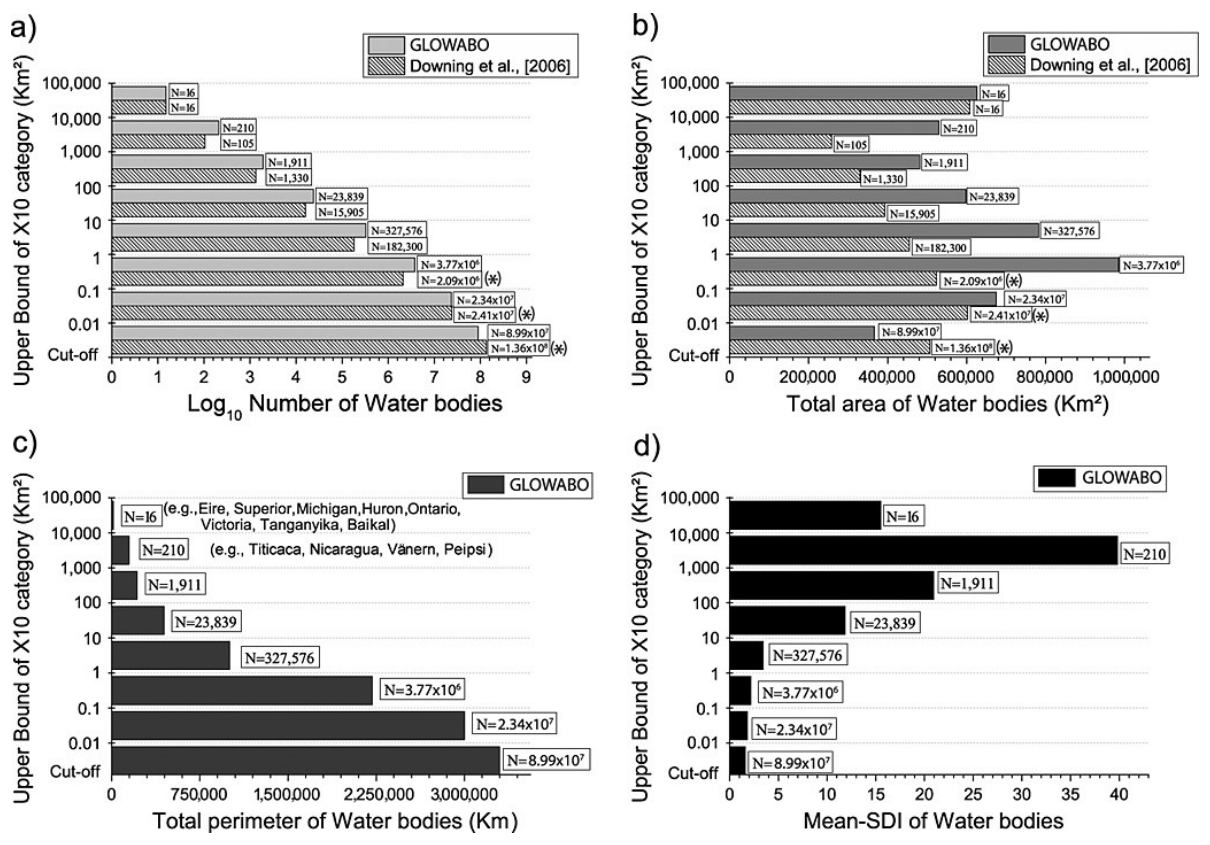

Source: Verpoorter *et al.* (2014) Figure 2

Figure 11.8 Distribution of lakes by latitude and elevation

a. Abundance relative to latitude
b. % cumulative abundance relative to elevation
c. Total area relative to latitude
d. % cumulative area relative to elevation
e. Total perimeter relative to latitude
f. % total perimeter relative to elevation

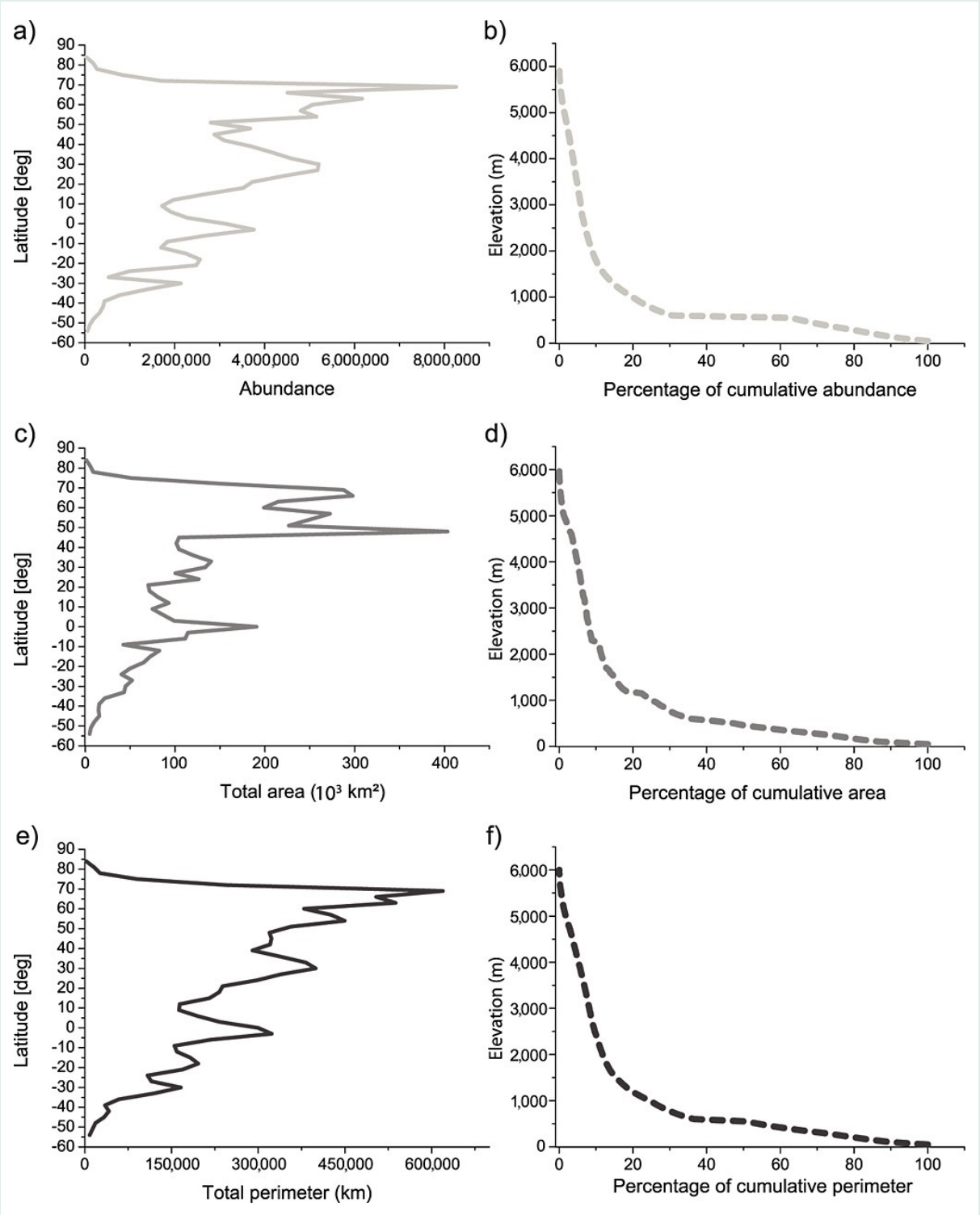

Source: Verpoorter *et al.* (2014) Figure 3

11.3.2 Synthetic Aperture Radar

As described in Section 11.2, the analysis of SAR data presents many advantages and disadvantages for mapping surface water extent. To date, few SAR analysis methods have provided consistent regional and temporal outputs, with most methods being suitable for one general location at a time. However, the growing time series of SAR imagery is presenting new opportunities for estimating water extent in lakes (Vickers *et al*., 2019).

The most basic method for determining water extent from SAR follows a similar concept to passive optical (see Section 11.3.1), employing a threshold on the backscatter to separate the darker, smoother water areas from the brighter, rougher terrestrial areas. However such thresholding normally requires manual tuning by the analyst. A further complication arises from the fact that SAR data is acquired at an angle to the side of the sensor platform, meaning that there will be brightness variation across the track of the SAR image from the changing incident angle of the microwave radiation.

One method to automate the measurement of water extent from SAR for flood mapping has been developed by Twele *et al*. (2016) using high speed analysis of Sentinel-1 SAR. The method employs an automated histogram splitting system to determine a suitable backscatter threshold to find areas that have the highest likelihood of being water. In addition, elevation data is used to constrain a 'growing' algorithm, which broadens areas with high likelihood of being water into adjacent areas so long as the elevation is constrained. This helps to minimise false positives in areas where the backscatter is impacted by non-water features, such as occurs with flooded vegetation and buildings.

11.4 Monitoring Floods

While *in situ* mapping of the extent of a flood can be quite dangerous, as areas impacted by floods are often waterlogged and being quickly eroded, the ability to delineate the area of impact can help determine safe zones for people and livestock, and identify infrastructure and environment at risk of damage. The method for measuring flood extent from EO data is essentially the same as for the more usual water extent mapping, however, responding to any form of natural disaster with EO requires as short a period as possible from image capture to extent provision. Accordingly, it is common to use less accurate methods in order to create a product that is both useful and delivered quickly. In addition, the emergency service agencies that use flood extent datasets often do not have the facilities to analyse imagery themselves, so these datasets are usually simplified for rapid integration into GIS, rather than for extensive scientific use. Typically a flood extent analyst will:

- apply simple thresholding on a NDWI or SAR backscatter channel to produce a base product;
- manually edit the output to remove false classifications due to clouds and shadows, and add areas that the base analysis missed; then
- extract a simplified vector polygon (or set of polygons) from the analysis before either direct delivery to the end user or incorporation into a map product in GIS software.

Some more automated methods have also been developed for flood response. In Australia the Landgate Floodmap service (Landgate, 2019) provides national coverage of flooding in Australia using high frequency, moderate resolution imagery such as from the MODIS satellites Terra and Aqua. The frequent national coverage of these satellites, and their low latency from data acquisition to availability, permits flood information to be produced quickly and regularly (for example, see Volume 1B—Excursus 7.1).

Internationally the Dartmouth Flood Observatory (DFO, 2019) has provided a world-wide flood mapping service since 1993. Using a combination of moderate resolution optical and SAR imagery, this system automatically produces flood extent maps for major flood events around the world.

11.4.1 The International Charter for Space and Major Disasters

The International Charter for Space and Major Disasters (ICSMD) is an international agreement amongst satellite imagery providers to supply their data in times of natural disaster for the purpose of providing assistance with the disaster response (ICSMD, 2020). A wide range of EO imagery providers have volunteered to supply data, whether public good or commercial, at no charge for disaster response.

Figure 11.9 Charter Activation

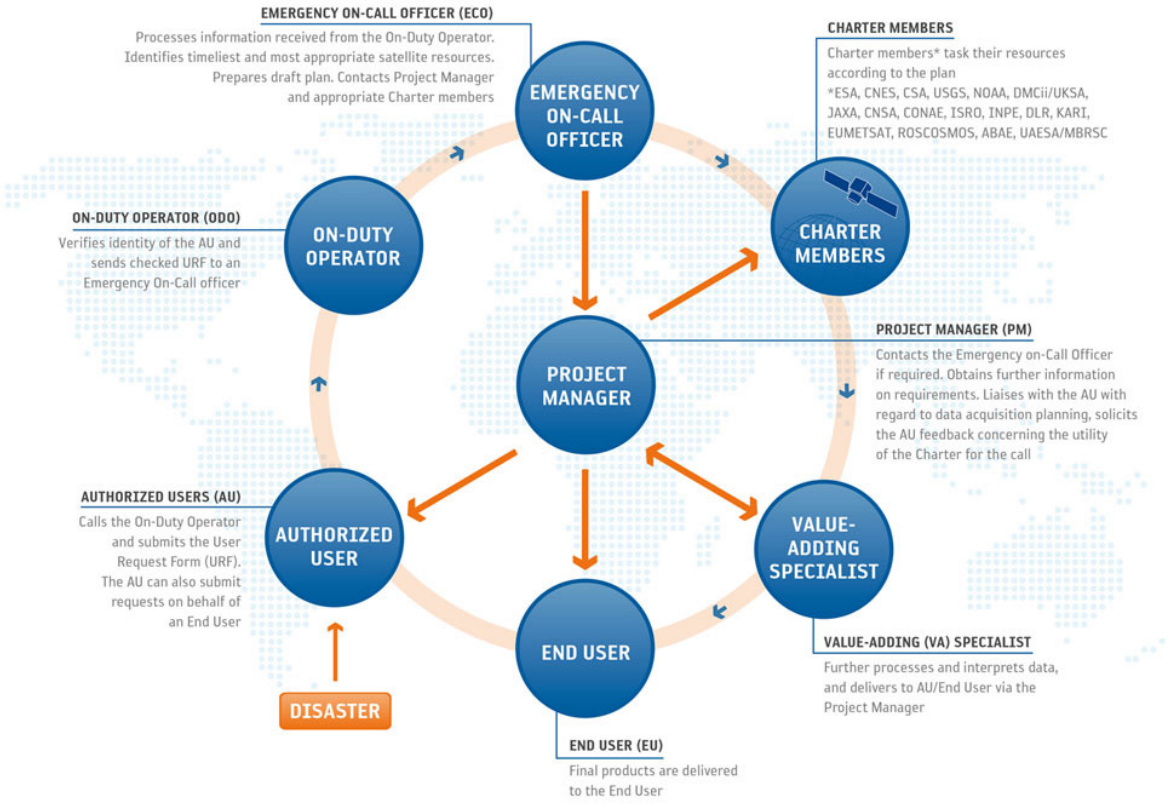

Source: ICSMD (2020)

This data is coordinated through a nominated Project Manager and delivered to a Value Added Provider, who creates extent and impact products for delivery to the end user (see Figure 11.9). Many types of data become available in this way, including very high resolution optical and SAR products.

One example of the use of this Charter for flood mapping in Australia occurred in October 2016 (Disasters Charter, 2016), when the New South Wales State Emergency Service (NSW SES) requested assistance following a long period of heavy rain throughout central NSW. The success of this response to the flooding was due to excellent organisation on the part of NSW SES in understanding the predicted movement of peak flood through the river systems, allowing image capture to be organised to coincide with the peak as closely as possible. Many hundred of images were supplied and analysed, using methods from manual image thresholding, to automated machine learning, to provide regular, ongoing disaster response information to NSW SES.

11.4.2 The Copernicus Emergency Management Service

The Copernicus Emergency Management Service (CEMS) is another facility for the provision of EO data for disaster response. Unlike the Charter, CEMS sources data through the Copernicus programme of the European Commission (EC), then acts as its own Value Added Provider to create mapping products, which it provides directly to the end user. The advantage of this arrangement is that data need not be downloaded from one part of the Earth to another, speeding up map delivery substantially. In addition, CEMS is a dedicated emergency management service responding frequently to disasters around the world, and so has developed considerable skills for providing highly useful disaster response products very quickly. During the 2016 floods in NSW, CEMS was used as a Value Added Provider for the Charter, helping to provide mapping information to the NSW SES (EC, 2019) from both CEMS and the Charter in a coordinated effort.

11.5 Permanent/Temporary water

The UN FAO has defined water seasonality in its Land Cover Classification System (LCCS; UN, 2019b; see Volume 3A—Section 3) according to the number of months per year that surface water is present at a location. Where water exists for over three months the waterbody is considered (semi-) permanent, and where it exists for less than three months the body is considered temporary or seasonal.

From the repeat observations of a waterbody in an EO time series dataset, water perenniality or hydroperiod can be computed from the time series of extracted water extents. This is especially useful for remote waterbodies where *in situ* mapping would have only observed a waterbody in one state of fill, and thus unable to provide information on its permanence. The Water Observations from Space (WOfS) product was originally designed to provide information on areas at risk of flooding, by examining the frequency of water observed in any location and deriving the percentage of time that water was classified as present in the location (see Volume 1A—Excursus 5.1). This subsequently led to the water perenniality information being incorporated into the BoM Geofabric dataset for all of Australia. However since WOfS is derived from passive optical sensors in the Landsat series of satellites, clouds often impact the image, and the time series of water observation is often interrupted. Hence the outputs of WOfS miss waterbodies that are obscured by clouds, and do not provide absolute certainty of the perenniality, or of how continuously water actually has existed in any waterbody. One potential future solution to this problem is to supplement the optical analysis with SAR-derived water extents that can fill in these data gaps.

11.6 Further Information

International Charter for Space and Major Disasters (ICSMD)

https://disasterscharter.org/web/guest/home

Bureau of Meteorology

Information on dam levels, river flows, and many other features of the water balance: *http://www.bom.gov.au/water/*

Water Observations from Space (WOfS)/ DEA Water Observations

https://cmi.ga.gov.au/data-products/dea/613/dea-water-observations-landsat

Floodmap

https://floodmap.landgate.wa.gov.au/

DEA Coastlines

https://cmi.ga.gov.au/data-products/dea/581/dea-coastlines

European Union Science Hub

Monitoring our Blue Planet: First SDG indicator platform launched by Google, the JRC and UN Environment: *https://ec.europa.eu/jrc/en/science-update/monitoring-our-blue-planet-first-sdg-indicator-platform-launched-google-jrc-and-un-environment*

Dartmouth Flood Observatory

https://floodobservatory.colorado.edu/

11.7 References

Atkinson, R., Power, R., Lemon, D., O'Hagan, R., Dovey, D., and Kinny, D., (2008). *The Australian hydrological geospatial fabric—Development methodology and conceptual architecture*. Water for a Healthy Country, CSIRO.

Bishop-Taylor, R., Sagar, S., Lymburner, L., Alam, I., and Sixsmith, J. (2019a). Sub-pixel waterline extraction: Characterising accuracy and sensitivity to indices and spectra. *Remote Sensing*, 11(24), 2984. *https://www.mdpi.com/2072-4292/11/24/2984*

Bishop-Taylor, R., Sagar, S., Lymburner, L., and Beaman, R.J. (2019b). Between the tides: Modelling the elevation of Australia's exposed intertidal zone at continental scale. *Estuarine, Coastal and Shelf Science*, 23, 115–128. *https://doi.org/10.1016/j.ecss.2019.03.006*

Blainey, G. (1975). *Triumph of the Nomads: A History of Aboriginal Australia*. Macmillan, Melbourne. 285 p

BoM (2019). *Australian Hydrological Geospatial Fabric (Geofabric)* website: *http://www.bom.gov.au/water/geofabric/index.shtml*

CSIRO (2018). *Causes of extreme sea levels* webpage, Commonwealth Scientific and Industrial Research Organisation website: *https://research.csiro.au/slrwavescoast/extremes/causes-extreme-sea-levels/*

DFO (2019). *Dartmouth Flood Observatory* website: *http://floodobservatory.colorado.edu/*

Disasters Charter (2016). *Flood in Australia* webpage, International Charter Space and Major Disasters website: *https://disasterscharter.org/web/guest/activations/-/article/flood-in-austral-2*

Downing, J.A., Prairie, Y.T., Cole, J.J., Duarte, C.M., Tranvik, L.J., Striegl, R.G., McDowell, W.H., Kortelainen, P., Caraco, N.F., Melack, J.M., and Middelburg, J.J. (2006). The global abundance and size distribution of lakes, ponds, and impoundments, *Limnology and Oceanography*, 51, 2388–2397. doi:10.4319/lo.2006.51.5.2388

EC (2019). *Copernicus Emergency Management Service*. *https://emergency.copernicus.eu/*

Finlayson, B. (2010). Rivers in Australia. *Frontiers of Earth Science in China*, 4(4), 375–385. *https://doi.org/10.1007/s11707-010-0129-y*

Fisher, A., Flood, N., and Danaher, T. (2016). Comparing Landsat Water Index Methods for Automated Water Classification in Eastern Australia. *Remote Sensing of Environment*, 175, 167–182. doi:10.1016/j.rse.2015.12.055

Gao, B.C., (1996). NDWI—A normalized difference water index for remote sensing of vegetation liquid water from space. *Remote Sensing of Environment*, 58(3), 257–266.

GA (2019). *Deserts* webpage on Geoscience Australia website: *http://www.ga.gov.au/scientific-topics/national-location-information/landforms/deserts*

ICSMD (2020). *International Charter for Space and Major Disasters* website: *https://disasterscharter.org/web/guest/home*

Jarvis, A., Reuter, H.I., Nelson, A., and Guevara, E. (2008). *Hole-filled seamless SRTM data V4*. International Centre for Tropical Agriculture (CIAT). *http://srtm.csi.cgiar.org*

JRC (2011). *NDWI: Normalised Difference Water Index* Product Fact Sheet, European Union Joint Research Centre. *https://edo.jrc.ec.europa.eu/documents/factsheets/factsheet_ndwi.pdf*

Landgate (2019). *Floodmap* webpage, Landgate website: *https://floodmap.landgate.wa.gov.au/*

Lehner, B., and Döll, P. (2004). Development and validation of a global database of lakes, reservoirs and wetlands, *Journal of Hydrology*, 296, 1–22. doi:10.1016/j.jhydrol.2004.03.028

McFeeters, S.K., (1996). The use of the Normalized Difference Water Index (NDWI) in the delineation of open water features. *International Journal of Remote Sensing*, 17(7), 1425–1432. doi:10.1080/01431169608948714

Mueller, N., Lewis, A., Roberts, D., Ring, S., Melrose, R., Sixsmith, J., Lymburner, L., McIntyre, A., Tan, P., Curnow, S., and Ip, A. (2016). Water observations from space: Mapping surface water from 25 years of Landsat imagery across Australia. *Remote Sensing of Environment*, 174, 341–352. *https://doi.org/10.1016/j.rse.2015.11.003*.

Parliament of Australia (2013). *Water* webpage APH website: *https://www.aph.gov.au/About_Parliament/Parliamentary_Departments/Parliamentary_Library/pubs/BriefingBook44p/Water*

Pekel, J.F., Cottam, A., Gorelick, N., and Belward, A.S. (2016). High-resolution mapping of global surface water and its long term changes. *Nature*, 540, 418–422. doi:10.1038/nature20584

Tulbure, M.G., Broich, M., Stehman, S.V., and Kommareddy, A. (2016). Surface water extent dynamics from three decades of seasonally continuous Landsat time series at subcontinental scale in a semi-arid region. *Remote Sensing of Environment*, 178, 142–157. doi:10.1016/j.rse.2016.02.034

Twele, A., Cao, W., Plank, S., and Martinis, S., (2016). Sentinel-1-based flood mapping: a fully automated processing chain. *International Journal of Remote Sensing*, 37(13), 2990–3004. doi:10.1080/01431161.2016.1192304

UN (2019a). The Sustainable Development Goals Report. UN, Rome. *https://unstats.un.org/sdgs/report/2019/*; *https://unstats.un.org/sdgs/report/2019/The-Sustainable-Development-Goals-Report-2019.pd*f

UN (2019b). *Land Cover Classification System v2*, UN Food and Agriculture Organisation. *http://www.fao.org/3/y7220e/y7220e06.htm*

Verpoorter, C., Kutser, T., and Tranvik, L. (2012). Automated mapping of water bodies using Landsat multispectral data. *Limnological and Oceanographic Methods*, 10, 1037–1050. doi:10.4319/lom.2012.10.1037

Verpooter, C., Kutser, T., Seekell, D.A., and Tranvik, L.J. (2014). A global inventory of lakes based on high-resolution satellite imagery. *Geophysical Research Letters*, 41, 6396–6402. doi:10.1002/2014GL060641

Vickers, H., Malnes, E., and Høgda, K.-A. (2019). Long-Term Water Surface Area Monitoring and Derived Water Level Using Synthetic Aperture Radar (SAR) at Altevatn, a Medium-Sized Arctic Lake. *Remote Sensing*, 11, 2780. *https://doi.org/10.3390/rs11232780*

Wetzel, R.W. (1992). Gradient-dominated ecosystems—Sources and regulatory functions of dissolved organic matter in freshwater ecosystems, *Hydrobiologia,* 229, 181–198. doi:10.1007/BF00007000

Xu, H., (2006) Modification of normalised difference water index (NDWI) to enhance open water features in remotely sensed imagery. *International Journal of Remote Sensing*, 27(14), 3025–3033. doi:10.1080/01431160600589179

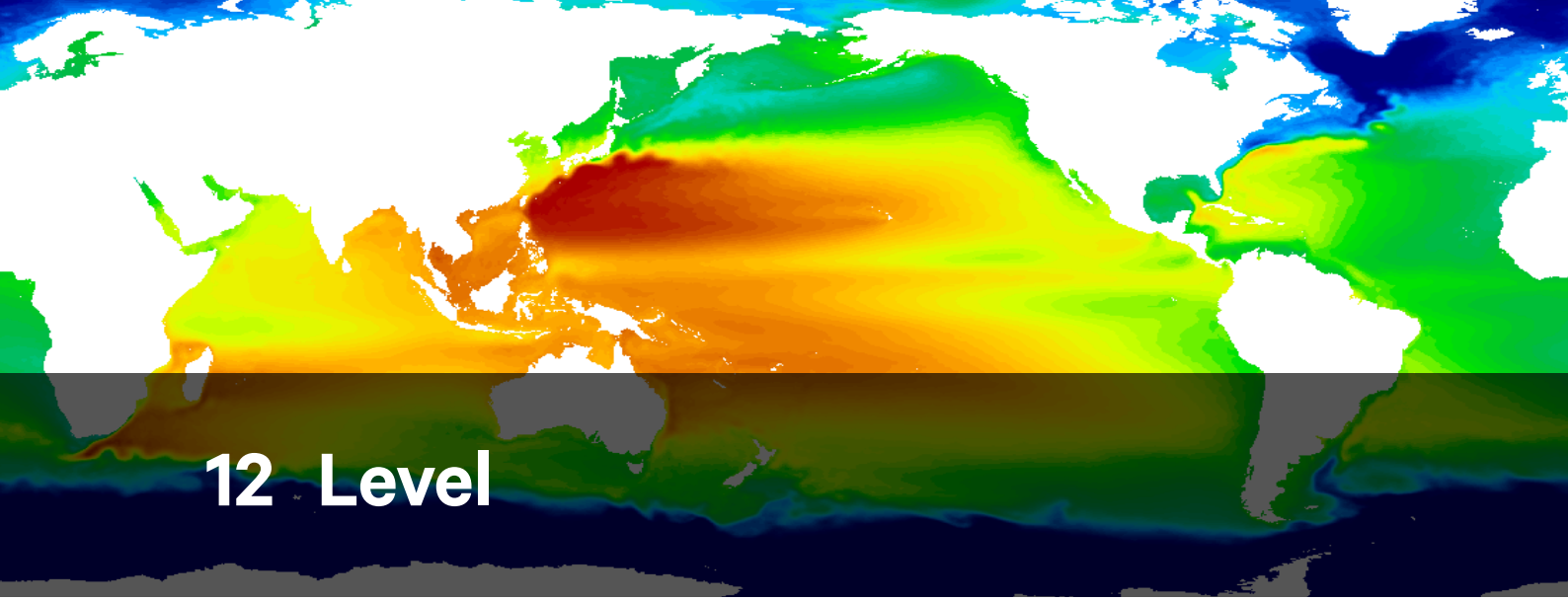

12 Level

Edward King

The level (or height) of the sea surface is a familiar concept to anyone with experience of the coast (see Sections 4.1 and 7.2). It is societally relevant on a day-to-day basis, if not hour by hour, to recreation, port operations, shipping, and other commercial uses of the coastal ocean, such as fishing, aquaculture, and energy generation. Accurate information about the long term change in sea level and the frequency of extreme events is also vitally important to the design and placement of coastal infrastructure, including roads and buildings. For example, a new bridge with a 100 year lifetime and a minimum specified clearance for shipping needs to be constructed to accommodate future sea level rise.

Although sea level is a straightforward concept in an everyday sense, it is important to be clear about how it is measured and with respect to which reference frame (see Volume 1A—Excursus 3.2). The sea surface closely follows the geoid which is determined in turn by the mass distribution in the crust. Measurements made relative to the crust (at tide gauge stations) or to a version of the geoid (followed by a satellite) are made comparable by transfer to a reference ellipsoid. The normal practice in surveying is to refer all measurements to an idealised geocentric reference ellipsoid, aligned with the axis of Earth's rotation (see Volume 2B—Section 1). The sea surface height then is the distance between this reference ellipsoid and the sea surface (see Figure 12.1). All measurements include the astronomical tides but this periodic feature may be removed from consideration over time scales of more than a day.

In a static world the sea surface would lie on an equipotential of the Earth's gravity field, the Geoid (see Volume 1A—Section 3.3). The geoid is an irregular surface, varying by hundreds of metres, depending on the geology, topography (including subsurface ocean trenches and seamounts), and even the presence of water, either in the ocean or as ice (see Volume 1A—Section 8). The presence of various dynamic forcings—including wind, heating and cooling, currents, and changes in salinity—perturb the sea surface away from the geoid giving rise to a dynamic topography of the sea surface, by amounts typically in the range ±1.5 m. Ocean tides also displace the sea surface by several metres. Although they are not spatially uniform they are regular and predictable, so it is usual to consider them separately from dynamic topography.

Tide gauge stations measure the sea surface height relative to the local land surface (see Section 12.4.2). For comparison with other observations, including from other stations, the position of the station relative to the ellipsoid must be accounted for. Over longer periods this position must be monitored as, for example, the foundations of the station could subside, or the local crust can move relative to the ellipsoid due to continental drift and isostatic adjustment (see Volume 1A—Section 3.2).

In the subsections below, we firstly describe sea level variations in Australian waters (see Section 12.1). Next we describe EO sensors that acquire data relevant to monitoring sea level (see Section 12.2), then consider the causes of short and long term changes in sea level (see Section 12.3). Various methods that are used to measure sea level are reviewed in Section 12.4, monitoring approaches used to quantify past sea level changes are discussed in Section 12.5, and projections of future sea level change are presented in Section 12.6.

Background image: The Mean Dynamic Topography MDT-CNES-CLS18 is an estimate of the mean over the 1993–2012 period of sea surface height above the geoid (bias subtracted 0.47 m), with height ranging through the colour spectrum from -1 m (blue) to 1 m (red). Source: AVISO/CNES. Plot derived from data located at *https://www.aviso.altimetry.fr/en/data/products/auxiliary-products/mdt.html*

Recommended Chapter Citation: King, E.A. (2021). Level. Ch 12 in *Earth Observation: Data, Processing and Applications. Volume 3B—Surface Waters.* CRCSI, Melbourne. pp. 197–221. ISBN 978-0-6482278-5-4

Figure 12.1 Reference frames and measurements for sea level observation

The sea surface closely follows the geoid, which is determined in turn by the mass distribution in the Earth's crust. Measurements that are made relative to the crust (at tide gauge stations) or to a version of the geoid (followed by a satellite) are made comparable by transfer to a reference ellipsoid. All measurements include the astronomical tides but this periodic feature is removed for consideration over timescales of more than a day.

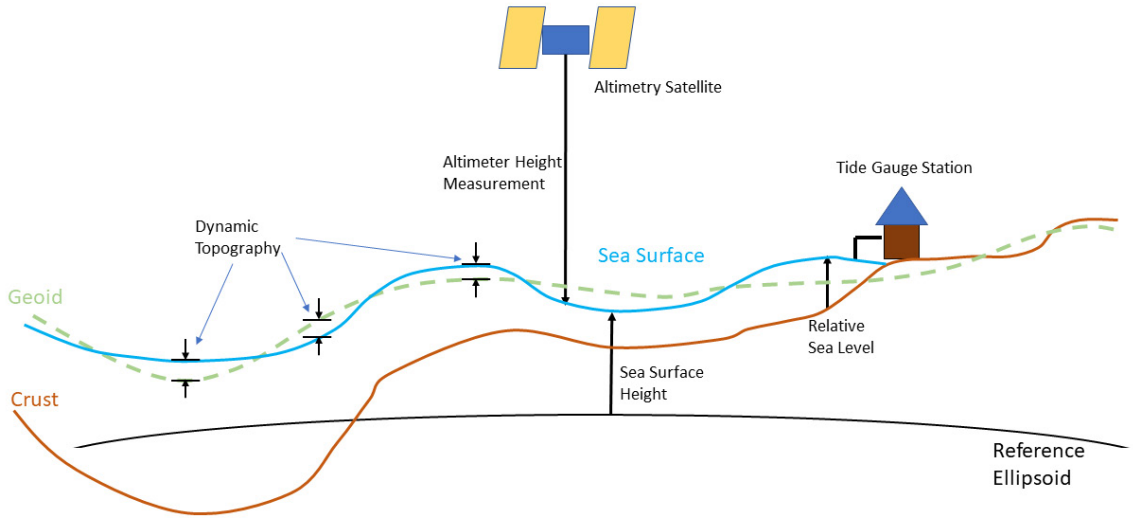

Source: Edward King, CSIRO

12.1 Level of Australian Surface Waters

The factors affecting the sea level on Earth range from local through regional to global, and even solar system scales. These factors include atmospheric forcing (pressure and wind) and their interactions with the seabed and coasts, ocean temperature and salinity (freshwater inflow and evaporation), tectonic plate movement, ice melt, and tidal forces. The time scales of these forcings vary from sub-daily for tides and weather through seasonal to decadal for climate, and even longer for geodetic changes.

The Australian coast experiences the impacts of all of these factors across a range of spatial scales and time frames. Tides range from almost zero in some locations to 6 m or 7 m in parts of the north and northwest. Tropical cyclones can raise storm surges of 5 m or more, and suitably exposed parts of the coast experience enhanced sea levels through wave action. Warm and cold eddies in the East Australian Current result in undulations of the sea surface in the range of 1 m. Changes in global climate will result in long term change to Australian sea levels—a mean increase of around 1 m by 2100 is entirely plausible from current projections (see Section 12.6), and significantly greater change is possible over subsequent centuries. Changes in the ocean circulation and distribution of the mass of water on the Earth's surface (as polar ice melts) mean that these changes in sea level will not necessarily be uniformly distributed around Australia.

As introduced in Excursus 4.1, Earth's tides arise from the response of the oceans to the gravitational attraction of astronomical bodies, primarily the Moon and the Sun. The combinations of lunar and solar gravitational attraction, coupled with regional and local coastline and bathymetry, give rise to a range of different daily tidal height patterns: diurnal, with one high and low per day; semidiurnal, with two equal high and two equal low tides per day; and mixed semidiurnal, with two differing high and two differing low tides per day (Figure 4.6 and Figure 4.7). For further details see, for example, Townsend, 2012, Chapter 6.

The tides are dramatically modified by interaction with the seabed on the continental shelves and near the coast, particularly in embayments and straits that constrain tidal flows. The resulting patterns in sea level can be complex and are often unique to individual locations. The variability of tide height and the types of tide around Australia is shown in Figure 12.2. Despite the complex patterns, once the local characteristics are determined through observation, tides are essentially periodic and predictable because they arise from the known motions of astronomical bodies.

Figure 12.2 Variability of Australian tides

a. Highest astronomical tide (HAT) on a logarithmic colour scale

b. Tide type indicated by the ratio of principal diurnal constituents to the semidiurnal constituents.

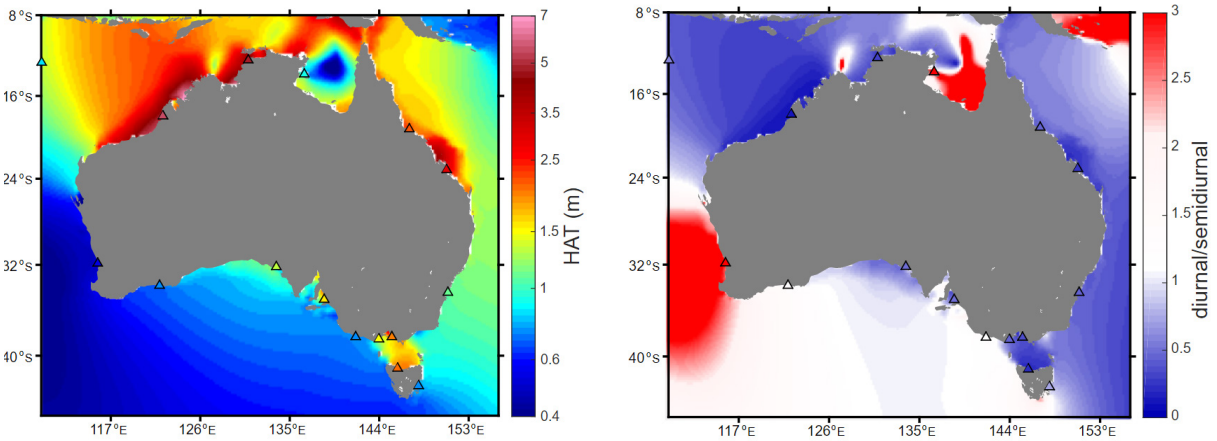

Source: McInnes *et al.* (2016) Figure 2b and 2c

12.2 EO Sensors for Sea Level

The interconnectedness of the oceans means that global scale forcing is relevant even locally, so global observations of sea level are necessary to build a holistic understanding that can explain and, importantly, predict changes into the future. Spaceborne radar altimeters provide such a global observation system.

Multiple radar altimetry instruments have provided a continuous record of global sea level since 1993 with unprecedented precision (see Section 12.2.1). This comprehensive and accurate record has led to the detection, and subsequent characterisation, of many physical phenomena. The improved understanding of the response of the ocean and cryosphere to global climate change, the processes of mesoscale oceanography, and even tides, has been nothing less than a revolution driven by this branch of Earth Observation (EO). Even as it becomes a tool for routine monitoring of sea level, with further improvements in accuracy and coverage and the advent of imaging altimeters such as the imminent SWOT mission (launch due in 2022; see Excursus 12.1), the discovery phase of the satellite altimetry era is far from over.

Gravity measuring satellites, such as the pair that make up the GRACE mission (see Excursus 1.1), also provide important information on the distribution of water between the ocean, the cryosphere, and terrestrial storages (see Table 12.1).

Table 12.1 EO sensors relevant to water level

Type	Sensor	Platform	Relevance	Advantages	Disadvantages
Active microwave	Radar altimeter	Satellite	Sea level change (tidal and non-tidal), Surface wind speed, Topography of ice sheets	All weather, highly precise	Not an imaging system, so measurements are only along infrequently repeated tracks (10–30 days)
Gravity	GRACE mission (see Excursus 1.1)	Satellite	Monitoring changes in distribution of water between the ocean, the cryosphere, and terrestrial storages	Global coverage	Low spatial resolution

12.2.1 Radar altimetry

The satellite altimeter operates by measuring the travel time of a transmitted radio pulse reflected from the sea surface (see Section 9.5 and Figure 12.1). Several adjustments are made to account for delays due to atmospheric and ionospheric effects, also for spreading of the return pulse resulting from reflection over a finite area of the sea surface. Satellite orbits are generally elliptical but are also perturbed by the Earth's gravity field, so the satellite altitude above the reference ellipsoid is not constant. Precision orbit determination, via a range of techniques, is required to translate the measurement into a sea surface height relative to the reference ellipsoid. Determination and monitoring of the geoid (relative to the reference ellipsoid) is, in turn, necessary to derive the dynamic topography (see Volume 1A—Section 3.3). Satellite altimetry is therefore a sophisticated measurement technique, which demands constant attention to detail. This emphasises the immense value of being able to measure the sea surface height globally and repeatedly, capturing not only the dynamic topography at a range of spatial and temporal scales, but also the change in the mean state over the longer term.

Radar altimetry from space has been trialled since the Skylab mission in 1973, and on various other missions through the 1970s and 1980s, including the European ERS missions (1991 and 1995) and the US Navy Geosat and Geosat Follow-On (GFO) satellites. The first high quality altimeter for oceanography was flown on TOPEX/Poseidon, launched in 1992. Since then, there has been a series of missions that have delivered a continuous time series of sea level measurements (see Table 12.2). Of particular note are the series comprising TOPEX/Poseidon, Jason-1/-2/-3 and Sentinel-6, that focused on providing a consistent record of sea surface height from essentially the same orbit over nearly three decades (see Section 12.7).

Table 12.2 Satellite missions providing data from a radar altimeter instrument

Mission	Operational dates	Orbital altitude (km)	Revisit frequency (days)	Goals
Geosat	1985/03–1990/01	800	First 18 months: non-repeating, then 17	Determination of marine geoid
ERS-1	1991/07-2000/03	785	Variously 3, 168 and 35	Atmosphere and ocean observations (multiple payloads)
TOPEX/Poseidon	1992/09-2005/10	1336	9.9	Sea surface height
ERS-2	1995/04–2011/07	785	35	Atmosphere and ocean observations (multiple payloads)
GFO	1998/02–2008/11	800	17	Real time ocean topography
Jason-1	2001/12–2013/06	1336	9.9	Sea surface height
Envisat	2002/03–2012/04	782–799	30–35	Atmosphere and ocean observations (multiple payloads)
OSTM/Jason-2	2008/06–2019/10	1336	9.9	Sea surface height
Cryosat-2	2010/04–present	717	369	Polar ice and sea surface height
Saral	2013/02–present	800	35 day until 2016/07 then non-repeating	Sea surface height
Jason-3	2016/01–present	1336	9.9	Sea surface height
Sentinel-3A	2016/02–present	814	27	Operational monitoring of environment (multiple payloads)
Sentinel-3B	2018/04–present	814	27	Operational monitoring of environment (multiple payloads)
Sentinel-6	2020/11–present	1336	10	Sea surface height

Excursus 12.1—Surface Water and Ocean Topography (SWOT)

Source: Edward King
Further Information: *https://swot.jpl.nasa.gov/*

The Surface Water and Ocean Topography (SWOT) satellite mission is a joint project between NASA and CNES space agencies to fly a new experimental altimetry instrument in 2022. This mission aims to "make the first global survey of Earth's surface water, observe the fine details of the ocean's surface topography, and measure how waterbodies change over time" (NASA, 2021).

The sensor utilises SAR interferometry (see Section 9.4) to produce a map of sea surface height across a swath approximately 120 km in width (see Figure 12.3). SWOT represents a radical step forward from traditional, nadir-sampling altimeters, to more readily provide two-dimensional maps of sea surface topography that characterise significant mesoscale ocean features at a scale that has not previously been possible (see Figure 12.4). The high spatial resolution will also permit altimetry measurements much closer to the coast.

Figure 12.3 Operation of SWOT

The SWOT instrument uses SAR interferometry to map ocean topography and terrestrial surface water topography in two dimensions with a cross-track dimension of 120 km. This total swath is divided into two parallel swaths that each span 50 km in width, with red lines below showing the transmission paths of radar pulses and blue lines showing the reception paths of the radar echoes. Between these two swaths a conventional altimeter tracks the nadir path, which also provides valuable data for calibration and validation.

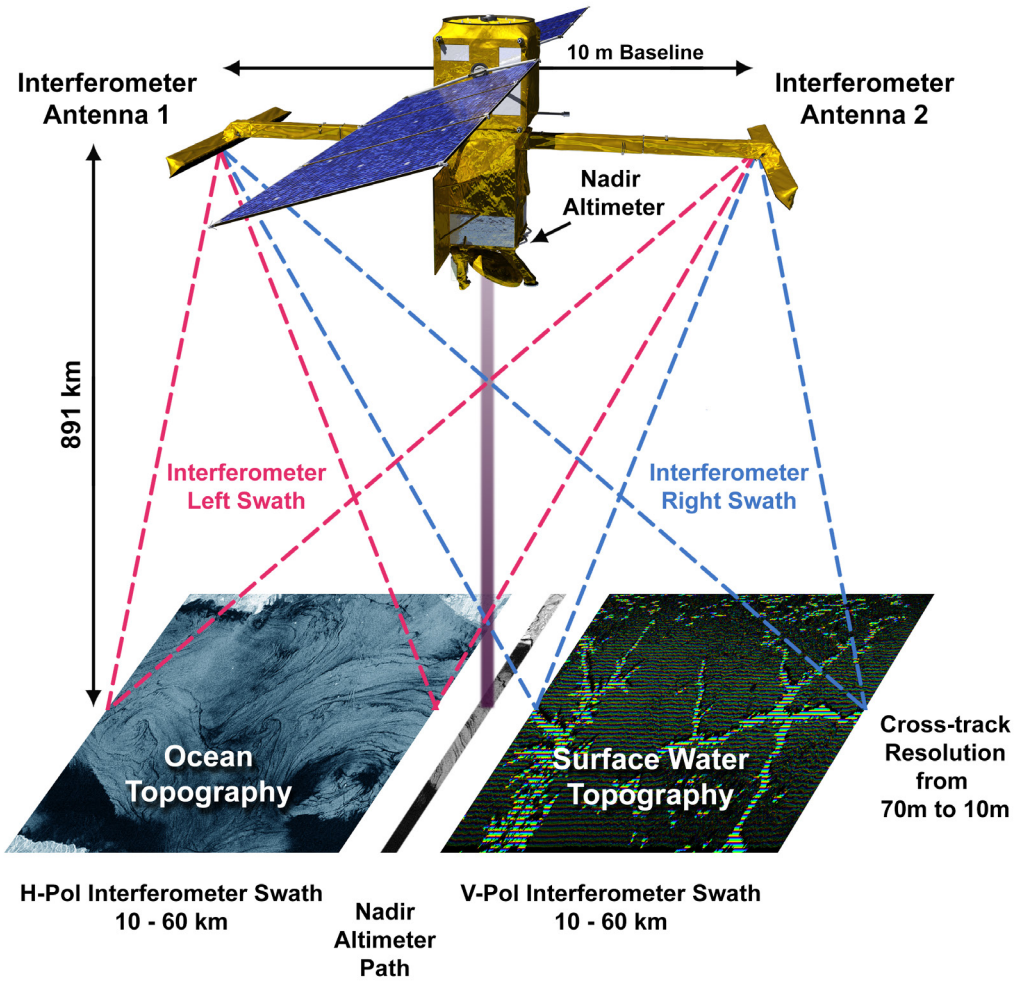

Source: NASA. Retrieved from: *https://swot.jpl.nasa.gov/resources/104/diagram-of-swot-data-collection*

The first six months of the SWOT mission will consist of a fast sampling period (one-day repeat) with reduced global spatial coverage (see Figure 12.5). During this phase of the mission, the satellite will overfly the Bass Strait calibration site daily, but neither of the other two calibration sites located in the Northern Hemisphere. A substantial field campaign is under development, with the support of the Integrated Marine Observing System (IMOS) and international partners, to gather high spatial resolution *in situ* observations (using GPS/GNSS buoys) during this period when the critical instrument characterisation and performance assessment work will be undertaken.

The fast sampling phase of this new instrument offers an unprecedented opportunity for ocean and coastal observing. Plans for several other campaigns and observations during the fast sampling phase are well advanced, including at other instrumented sites around Australia and in the Southern Ocean. After six months, the mission orbit will change to a science orbit with a 21-day repeat that will offer near-global surface coverage over the remainder of the planned three-year primary spacecraft mission.

Figure 12.4 Simulated SWOT measurements

This simulation shows the density of measurements that SWOT will enable, relative to data products previously generated from conventional, nadir-sampling satellite altimeters. Note that the small, white diamonds in Figure 12.4d are gaps between the swath observations.

a. Sea Surface Height (SSH) 'Truth' based on ocean circulation model

b. Jason-1/-2 sampling along ground tracks over one 10-day repeat cycle

c. 2D interpolation of Jason-1/-2 ground tracks

d. Simulated SSH sampled by SWOT swaths over 22-day repeat cycle

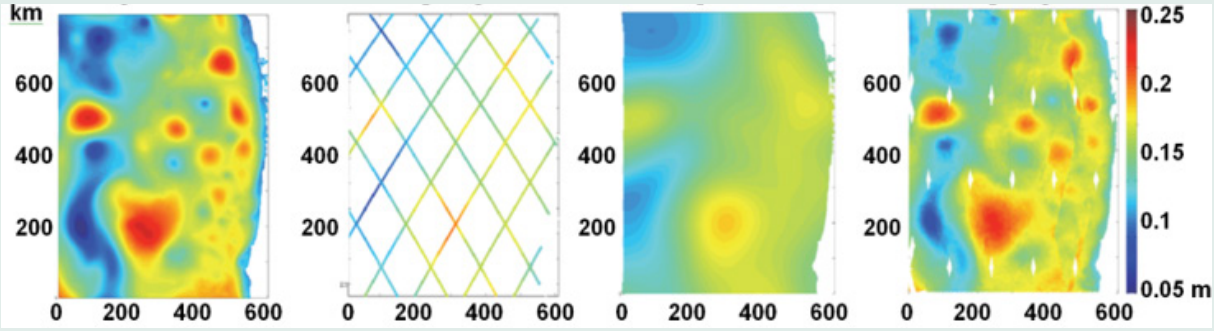

Source: Fu and Ubelman (2014)

Figure 12.5 SWOT fast sampling swaths

The location of the SWOT swaths (yellow) during the fast sampling mission phase is shown relative to the Bass Strait altimetry calibration site and the ground tracks of three conventional, nadir-sampling altimeters.

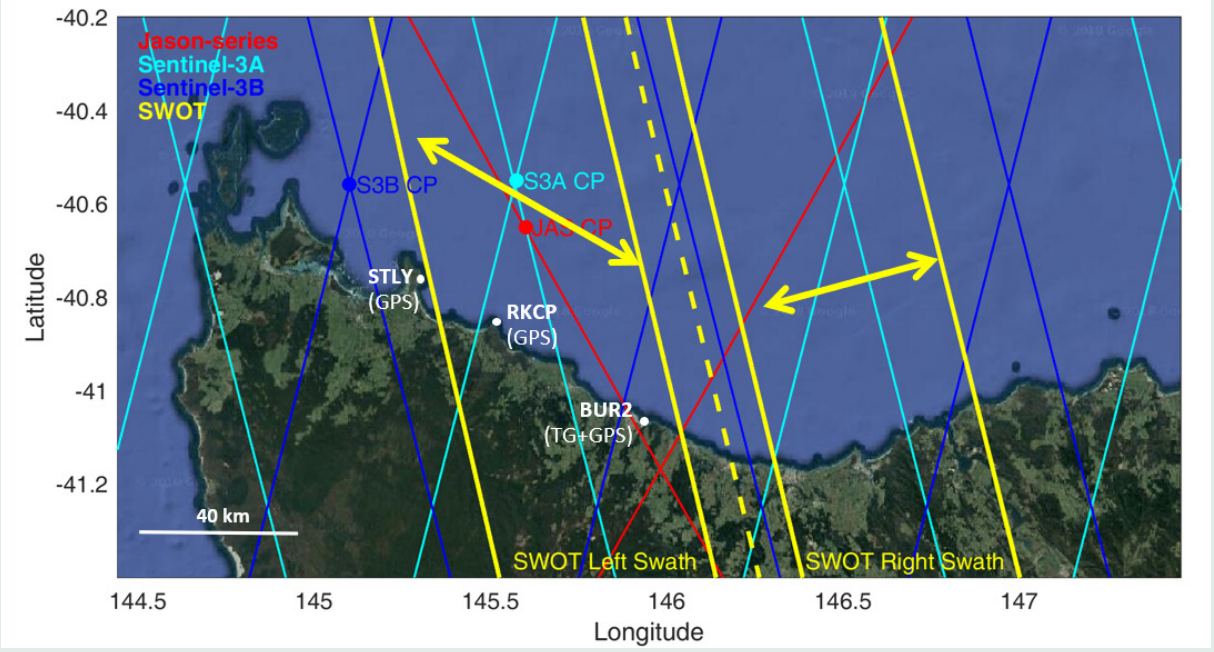

Source: Watson (2018)

12.2.2 EO sensor calibration

The astonishing accuracy achieved by satellite altimeters is realised not only by excellent instrumentation engineering and precise orbit determination in space (see Section 12.4.3), but also through careful and thorough calibration and validation (cal/val) efforts at the Earth's surface (see Volume 2D). The aim of the *in situ* measurement program is to enable sea level data to be compared directly with observations from satellite altimeter instruments, so that the space-based observations are not only accurate and precise, but also that they can be tied to global reference frames. A series of continuous measurements and short campaigns is necessary to deliver this result.

Australia has played a critical role throughout the modern precision altimetry era via a series of moorings and buoy deployments in Bass Strait (see Figure 12.6). These deployments, which are one of only three such altimetry cal/val sites globally, and the only one in the Southern Hemisphere, have been operated since 1992 by CSIRO, the University of Tasmania and partners and, since 2007, with the support of IMOS (see Volume 2D—Excursus 12.3).

Figure 12.6 *In situ* measurement sites

Mooring deployment sites off northwest Tasmania showing the ground tracks of TOPEX and Jason series missions in red and the Sentinel-3A and -3B ground tracks in pink and blue respectively.

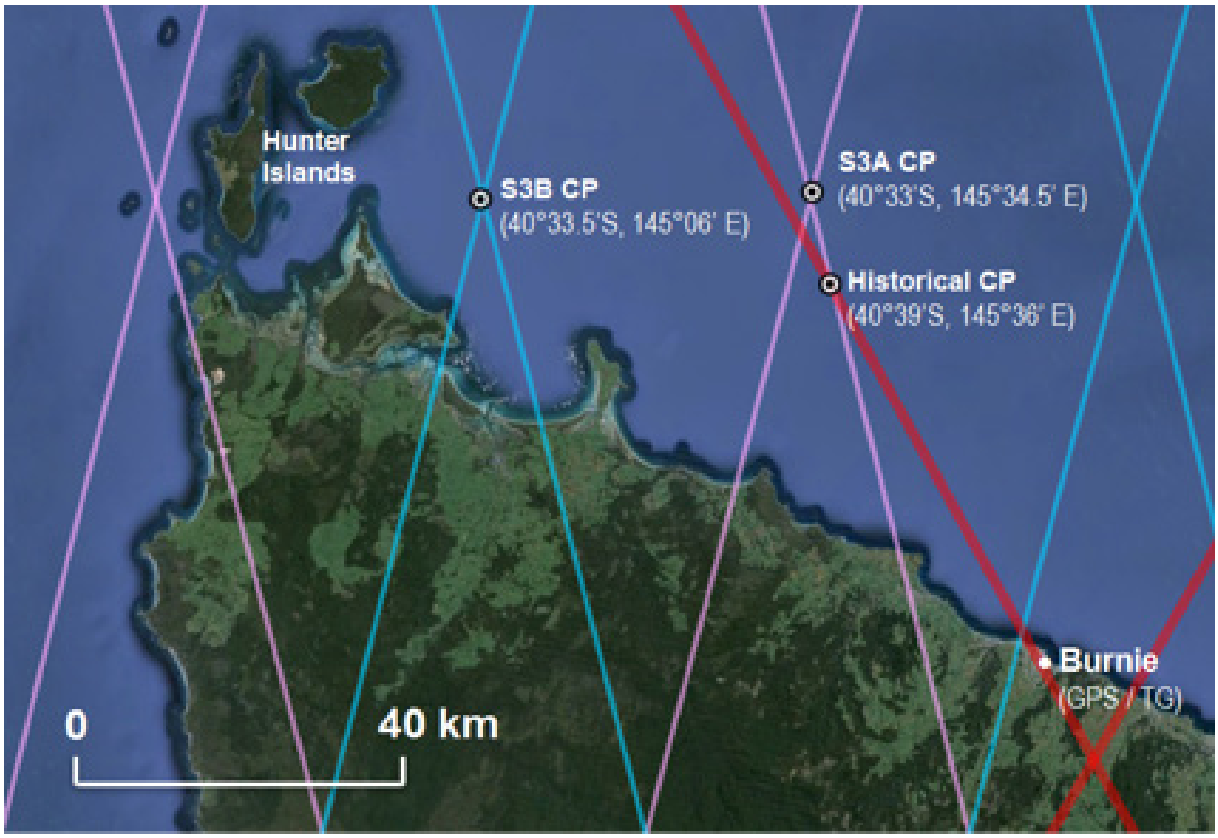

The Bass Strait site was originally located on a descending track of the TOPEX/Poseidon mission, sufficiently far from the coast that the altimeter signal would not be affected by land, but close to the tide gauge located at Burnie port. The water depth is approximately 50 m at this site. This particular ground track also passes close to the satellite laser ranging station at Orroral Valley in the ACT (White *et al.*, 1994). The position and the number of moorings has evolved over the past decade to support the Sentinel-3A and -3B altimeter missions that (because they are flown on satellites with other instruments and missions) have different orbits to the TOPEX/Jason series.

The primary instrumentation used at the calibration site is a high precision pressure sensor at the base of each mooring. Several temperature and salinity instruments are distributed through the water column (see Excursus 5.1). Together, this combination permits an assessment of the water column density, and in turn, measurement of the height of the water column. This represents a measurement of sea level relative to the base of the mooring, where the pressure sensor is located. When the sites are serviced (approximately every six months) collocated GPS buoys are deployed to enable the mooring observations to be tied to the terrestrial reference frame (see Figure 12.7). The coastal tide gauge at Burnie, collocated with a GPS receiver, is transformed (via several corrections) to provide a continuous connection between the mooring and the reference frame in between the periodic GPS buoy deployments (see Figure 12.8). The outcome of this process is the delivery of a record of 'absolute bias' for the satellite altimeter for each overpass, something that has been achieved at this site throughout the modern satellite altimetry era. The absolute bias is a comparison of the satellite altimeter signal with an independent measurement of sea surface height. Monitoring the absolute bias enables estimation of various contributors to the altimeter measurement, such as atmospheric delays and uncertainties in various instrument characteristics, to be understood, and ultimately leads to an improved altimeter data record.

Figure 12.7 Example calibration site

Geometry of the Bass Strait calibration site and associated instrumentation

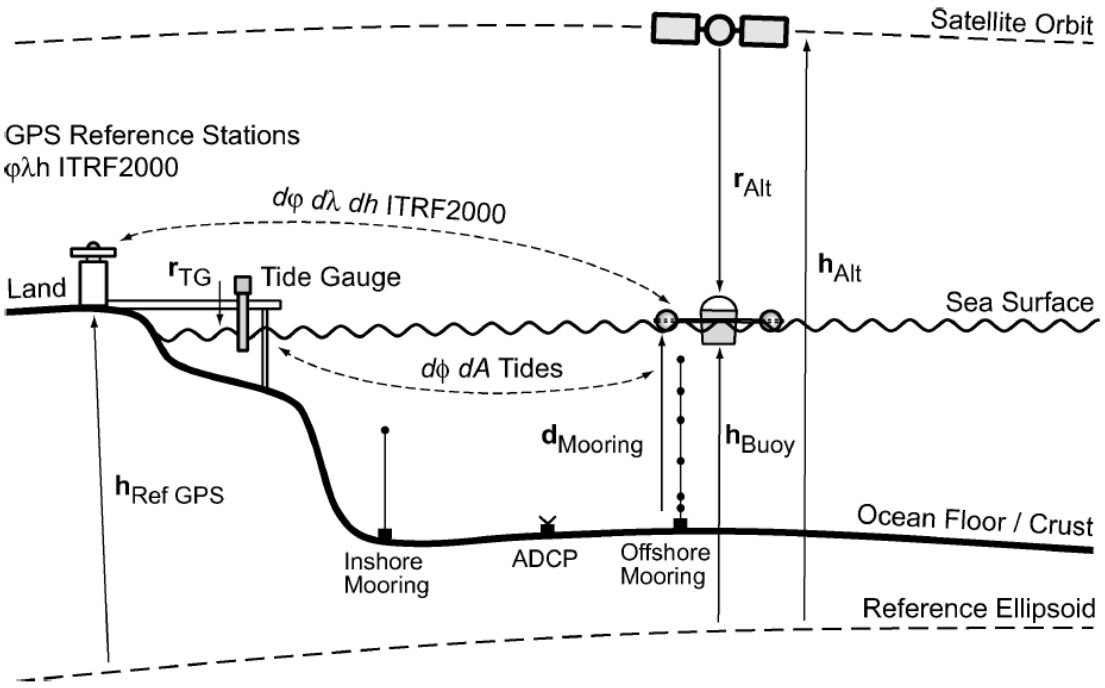

Source: Watson *et al.* (2004)

Figure 12.8 Converting mooring measurements into datum

Process whereby the tide gauge observations, mooring deployments and periodic GPS buoy deployments are combined to transform the mooring measurements into the datum. RSL: relative sea level, VLM: vertical land motion, TG: tide gauge, ITRF2008: GPS reference frame.

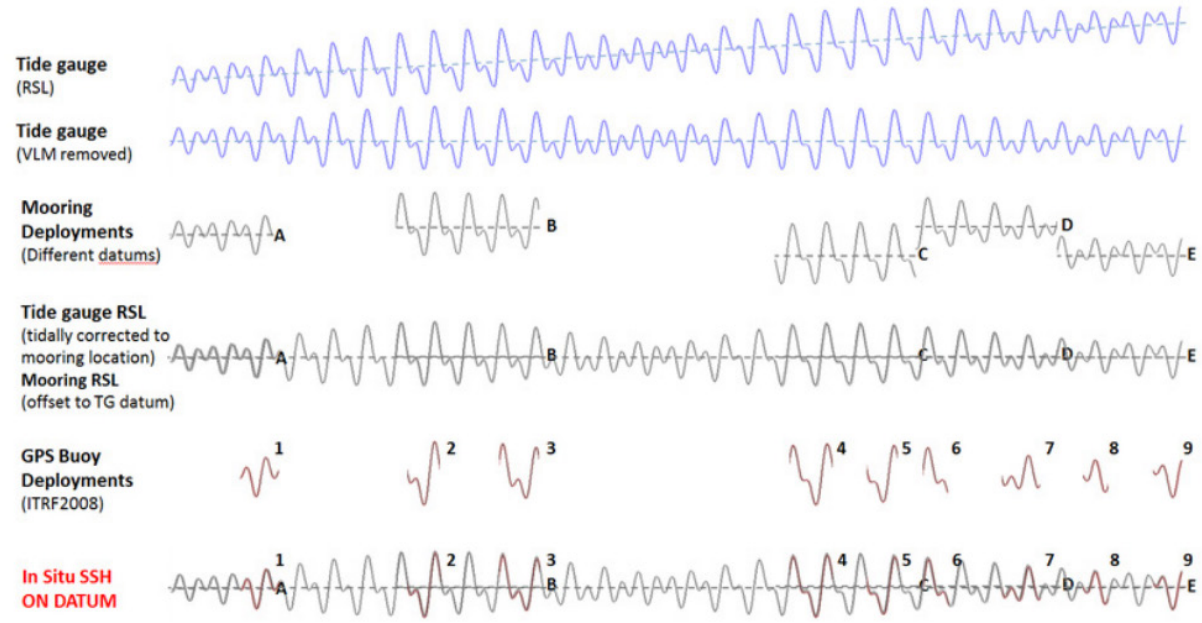

Source: Watson *et al.* (2018)

12.3 Causes of Change in Sea Level

Sea level varies as the volume of water in the oceans of the world changes. This can occur as water is exchanged with other reservoirs including the atmosphere, the cryosphere, and terrestrial storages (see Figure 12.9). Another important cause of volume change—either contraction or expansion—is variation in overall density of the ocean as it stores (or releases) heat. Other changes in sea level arise from localised forcing by the atmosphere, temperature and salinity variation, basin scale circulation, and tides. Relative sea level (measured with respect to land) can change slowly as land is uplifted or subsides over decadal to century time scales, and also abruptly in response to earthquakes.

Figure 12.9 Factors affecting sea level at a range of spatial and temporal scales

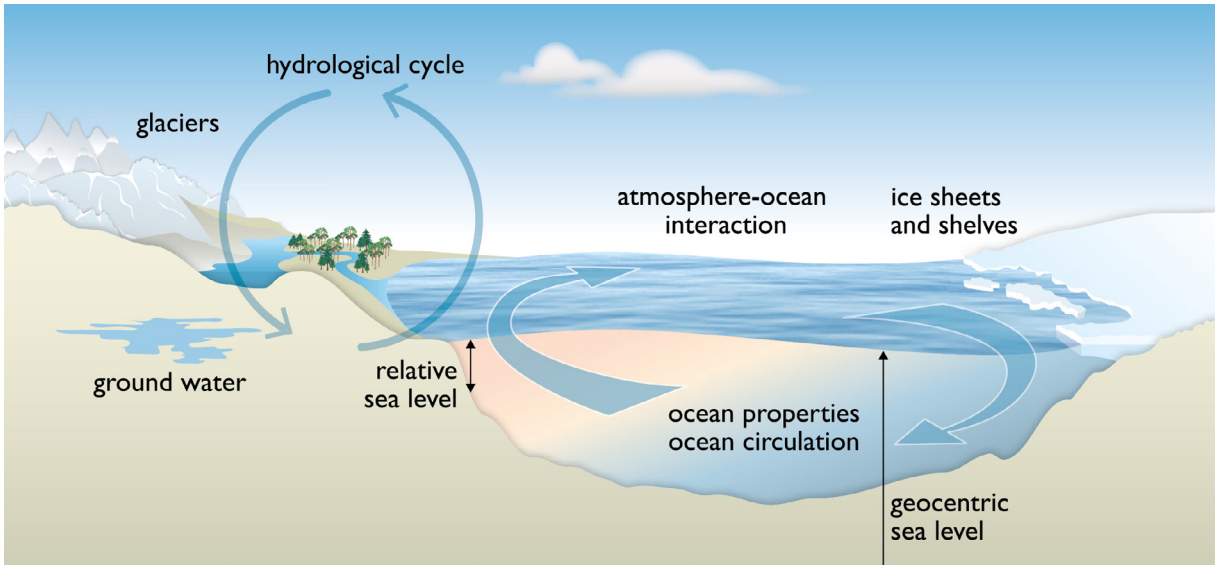

Source: IPCC AR5 Report

12.3.1 Short term change

Over periods of hours to days, sea level change is driven primarily by tides, the atmosphere (pressure and wind), and sometimes by geological events such as earthquakes or landslides that involve displacement of the crust resulting in tsunamis. Tides arise predictably from the motions of astronomical bodies (primarily the Moon and Sun) relative to the Earth (see Excursus 4.1 and Section 12.1) .

The sea surface responds to the mass of the atmosphere overlying it. High pressure weather systems depress the sea surface whereas lows permit it to increase. This effect, known as the inverse barometer, is about 1 cm of sea level rise for every 1 hPa decrease in atmospheric pressure. Intense low pressure systems, such as tropical lows and cyclones, can result in sea level increases of the order of 1 m. In the open ocean this is of little consequence but nearer to the coast it can be very significant. In areas without a steep coastal interface (such as modest cliffs) a storm surge coinciding with high tide can easily overtop coastal infrastructure and defences leading to substantial damage from both the force of the water as well as localised flooding inland.

Powerful storms also bring strong winds that induce localised surface currents in shallow water. When directed towards the shoreline this wind stress results in a piling up of water along the coast, known as wind setup, that adds to the storm surge. When this occurs within semi-enclosed embayments that constrain the along-coast flow of the water, the effect can be further amplified. An extreme example of this occurred in northern Queensland when the very powerful Tropical Cyclone Yasi crossed the coast just north of the town of Cardwell. The clockwise rotation of the cyclone, together with the motion of the whole system towards the southwest, led to the strongest onshore winds occurring immediately to the south of the cyclone track (see Figure 12.10). The recorded storm surge was 5 m above the predicted tide, which was falling at the time. Nevertheless the surge amounted to a 2.3 m excess over the highest astronomical tide and caused significant damage.

Away from the equator, when the wind stress is parallel to the coast, the impact of the Coriolis force on the induced currents is important (see Excursus 1.2). The deflection of ocean water towards or away from the coast (depending on current direction and hemisphere) results in a reduction or increase in relative water level at the coast, known as current setup (or setdown).

Figure 12.10 Tropic Cyclone Yasi

In 2011 one of the largest tropical cyclones, TC Yasi, crossed the Queensland coast just north of Cardwell resulting in damage to buildings and the Bruce Highway at the water front.

a. Location of cyclone

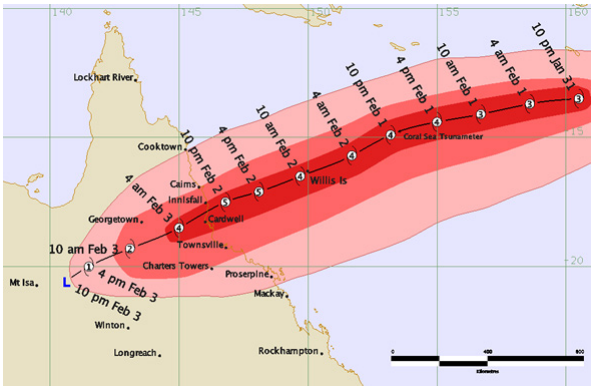

b. Waterfront damage

Source: a. Bureau of Meteorology. Retrieved from: *http://www.bom.gov.au/cyclone/history/yasi.shtml*; b. Paul Crock, AFP. Retrieved from: *http://desdemonadespair.net/2011/02/photo-gallery-aftermath-of-cyclone-yasi.html*

Surface waves, whether part of a local storm or arriving as swell from distant storms, also impact coastal sea levels (see Excursus 4.2 and Section 16). Waves steepen and eventually break as they reach shallow water. When the water close to the coast is deep (for example, isolated islands in the open ocean), the energy carried within waves is delivered directly to the shore. In contrast, when coastal waters are shallower (see Figure 12.11), such as in broad continental shelves or fringing reef systems, the wave energy is dissipated further offshore. As the waves break offshore, their energy can be transferred into shoreward momentum of the water at the break, which then increases the sea level closer to the shore. This process, analogous to wind setup but driven by wave energy, is called wave setup. The specific geometry of the actual shoreline (steep or shallow gradient) combines with the incoming waves to determine the reach of the sea inland. This phenomenon is known as wave runup and is superimposed on the underlying sea level (that would be experienced in the absence of waves, for example, due to tide).

Figure 12.11 Wave setup

Wave setup occurs when the energy of waves breaking offshore translates into increased sea levels inshore. Wave runup is the additional sea surface height resulting from individual waves reaching and running up the shore itself.

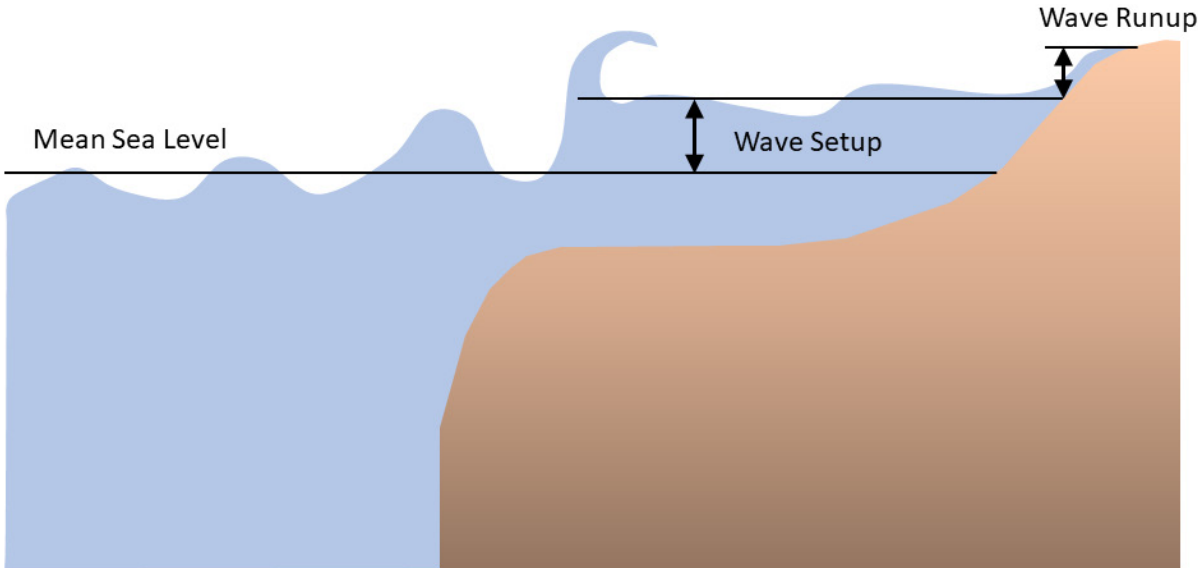

Tsunamis are a special and sometimes extreme case of surface waves impacting sea levels. Some subsea earthquakes result in rapid displacement of the seafloor imparting an impulse into the ocean, which propagates as a long wavelength wave. In the open (deep) ocean, tsunami travel at ~700 km/hr and may be observed as a small vertical displacement (~0.5–1 m). (For example, see the serendipitous satellite altimeter observations of the 2004 Indian Ocean tsunami; Gower, 2005; *https://www.eumetsat.int/satellite-observations-indian-ocean-tsunami*). When the tsunami reaches shallow water it slows to 10–20 km/hr and the crest height increases significantly, up to 10–15 m. In the case of the 2011 Japanese earthquake, flatter areas of the coast were flooded many kilometres inland when the wave overtopped the shoreline. Large tsunamis are immensely destructive—the 2004 Indian Ocean and 2011 Japanese events resulted in estimates of 230,000 and 15,000 deaths respectively. Although tsunamis are usually isolated events, the sea level rise and subsequent return of the water to the sea can last for several hours.

12.3.2 Seasonal to decadal change

The inclination of the Earth's rotational axis to the plane of the orbit around the Sun leads to differential heating in the Northern and Southern Hemispheres over the course of one orbit (see Volume 1A—Section 3.1). This gives rise to the pronounced seasonal weather and climate changes experienced each year. A more subtle impact is on global sea levels. The additional summer heat is absorbed by the ocean in one hemisphere whilst the winter ocean in the opposite hemisphere loses the heat gained in the previous summer. The warmer water is less dense and so occupies a greater volume per unit mass causing a rise in sea level. Consequently the volumes of the Southern and Northern oceans increase and decrease cyclically with opposite phase (see Figure 12.12). However, the effect on sea level is not the same in both hemispheres, with amplitudes of approximately 20 mm in the Southern Hemisphere and 30 mm in the Northern. In the northern winter, the greater land mass results in greater storage of water as ice and snow. This reservoir is released back to the Northern Hemisphere oceans in spring and summer, enhancing the seasonal change in sea levels. As a result, the average sea level across the global ocean contains a small residual seasonal component of 5–10 mm amplitude. Seasonal changes in the atmosphere also result in smaller seasonal changes in sea levels. These include the mean position of the paths of weather features such as low and high pressure systems (affecting sea level via the inverse barometer), and the cyclic strengthening and weakening in surface winds that drive ocean surface currents. These currents transport warm and cold water, so affect ocean density and, in turn, sea level.

Figure 12.12 Mean sea level

Mean sea level in the Northern and Southern Hemispheres over the period 1993–2012 from TOPEX/Poseidon, Jason-1, Jason-2 and Jason-3 satellite altimeter data. The Northern Hemisphere signal is enhanced by the greater storage of water on land as snow and ice during winter. This disparity is visible in the total global sea level as a small residual seasonal variation.

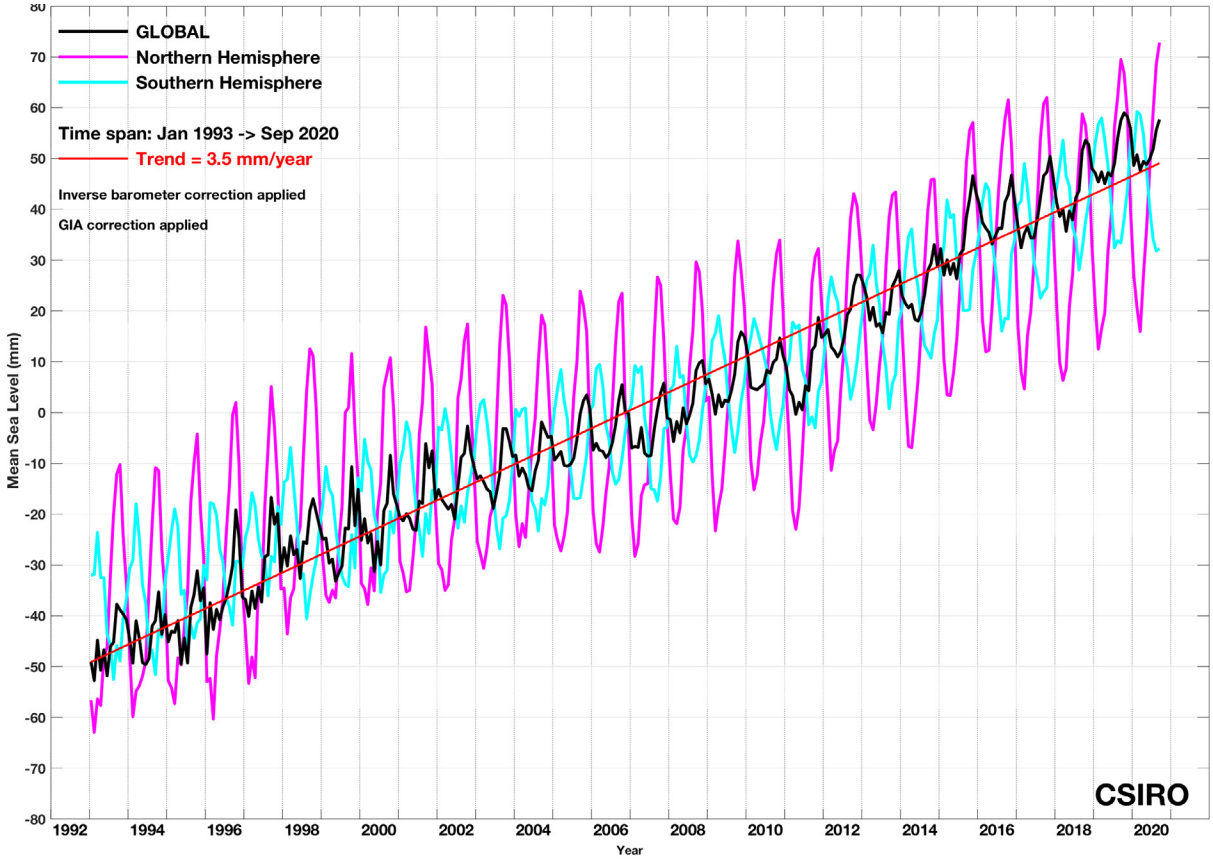

Source: Benoit Legresy, CSIRO

Figure 12.13 Ocean-climate system variability

Examples of sea surface temperature anomalies around Australia

a. Location of the western Pacific warm pool

b. Increased sea surface temperature anomalies (°C) across Northern Australia following a strong La Nina event (May 2010–April 2011)

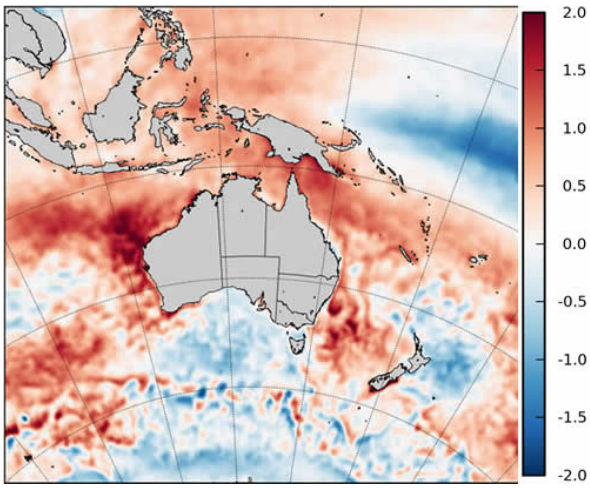

Source: Bureau of Meteorology. Retrieved from a. *http://www.bom.gov.au/climate/enso/history/ln-2010-12/ENSO-what.shtml*; b. *http://www.bom.gov.au/climate/enso/history/ln-2010-12/SST-records.shtml)*

Figure 12.14 Tide gauge records

Monthly (light blue) tide gauge records over 55 years from Fremantle (southwest Western Australia), Kwajalein Atoll (Western Pacific), and San Francisco (Eastern Pacific). The same records with the annual seasonal signal removed are shown in dark blue.

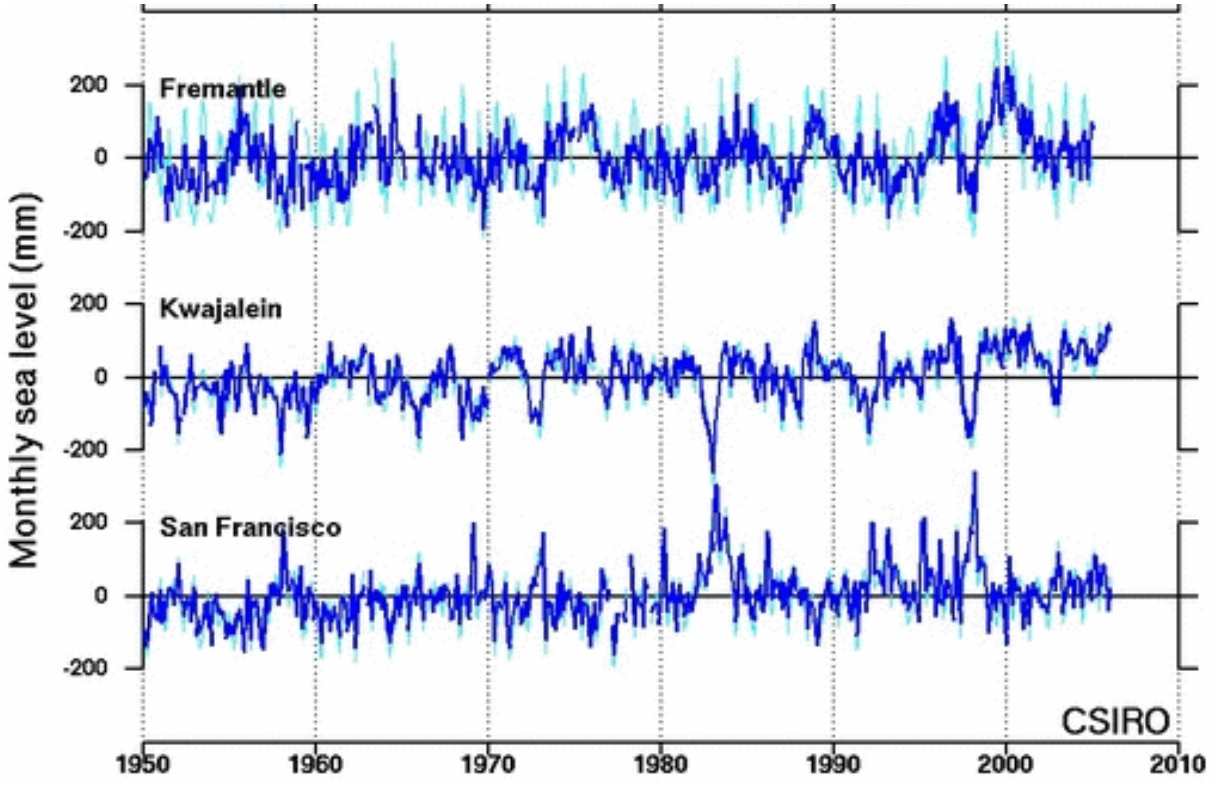

Over periods of years and up to a decade, variability in the ocean-climate system can be detected as sea level change at regional to ocean scales. For example, the El Niño/La Niña oscillation involves changes in the warm pool of surface water in the Western Pacific Ocean over periods of several years (see Figure 12.13a). The size of the pool is strongly affected by the strength of the easterly trade winds in the equatorial Pacific. During strong events there can be sustained changes in ocean surface temperature (see Figure 12.13b) and relative sea level between the Eastern and Western Pacific of the order of 20–30 mm. The tide gauge records shown in Figure 12.14 illustrate this with the strong opposite signals in the San Francisco and Kwajalein records at the time of strong El Niño events in 1983 and 1997. Similar effects can be traced to other long term climate variations such as the Indian Ocean Dipole and Pacific Decadal Oscillation.

12.3.3 Longer term change

Several processes affect global sea levels over much longer periods, from years to decades to centuries. As indicated in Figure 12.9, exchange of water between the ocean, the cryosphere, and the terrestrial hydrosphere is an important factor. Over the longer term, change in the overall heat content of the ocean changes the water density, which is observable as a change in sea level. Change in ocean density due to variation in salinity can also make a very small contribution.

The ocean absorbs 93% of the additional heat trapped in the Earth System by the increased concentrations of greenhouse gases in the atmosphere. The resulting expansion of oceanic water contributes to 1–1.4 mm per year of rise in global sea level. This single factor accounts for a third of global sea level rise observed over the past several decades.

The cryosphere comprises the ice-covered regions of the globe, namely the polar regions (including floating sea ice and terrestrial ice sheets) and the non-polar glaciers (at any latitude but with sufficient altitude for persistent ice; see Section 15). With the Earth in thermal equilibrium, the net quantity of ice stored in the cryosphere is constant over the longer term. The warming of the atmosphere however is leading to erosion of the cryosphere via melting. The contribution of non-polar glacier melt to global sea level rise over the past 40–50 years is 0.6–0.7 mm per year. Direct melting of the Greenland and Antarctic ice sheets has contributed around 0.7 mm per year to global sea level rise in recent decades. Wherever the polar ice is in contact with the ocean, the warmer ocean is also contributing to the melt. Ocean transport of heat from the tropics to the Antarctic ice

sheet, much of which is grounded below sea level, is expected to be an important factor controlling the rate of future sea level rise. The volumes of water stored within the cryosphere are immense, with non-polar glaciers, Greenland, and Antarctica equating to approximately 60 cm, 6 m, and 60 m of potential sea level rise respectively. It is interesting to note that as ice sheets melt and the water runs into the ocean, the decreased mass loading locally allows the underlying crust to rise. This leads to the paradoxical result that, for example, loss of the Antarctic ice sheet will increase relative sea levels less in Antarctica than in locations remote from the source of the additional water.

Other (non-frozen) terrestrial reservoirs exchange water with the oceans via runoff, evaporation, and precipitation (see Section 1.1). Primarily these reservoirs are surface water (rivers, lakes, dam impoundments) and groundwater. Periods of increased dam building in the middle of the 20th century are detectable as a small decease in the rate of Global-Mean Sea Level (GMSL) rise (see Section 4.1). More recently, increased usage of groundwater aquifers for irrigation and other freshwater needs, ultimately delivers terrestrial water to the ocean via runoff (or evaporation and precipitation), contributing to an increase in sea level rise. More information, including a thorough analysis of the quantitative factors involved in these processes, can be found in the Sea Level Change chapter of the IPCFC 5th Assessment report (Church *et al.*, 2013).

12.4 Measuring Sea Level

Contemporary sea level is observed via two primary methods: tide gauges and satellite altimetry. Below we consider two traditional methods used to measure sea level, paleo indicators (see Section 12.4.1) and tide gauges (see Section 12.4.2), then describe the relatively recent option of satellite altimetry (see Section 12.4.3).

12.4.1 Paleo indicators

Before the tide gauge era, knowledge of historical sea levels was derived from paleo indicators, which are markers of past sea levels captured in the natural and human-built environment. Natural markers include geomorphological features such as raised beaches, notches cut by waves, and also fossilised sea life. Of particular value is the record of plants that are known only to exist within a narrow vertical range of the upper limit of the tidal influence in coastal (salt) marshes. The human record comprises buildings originally created at sea level that are now either submerged or elevated, or traces of the impacts of sea action or sea life on historical buildings.

All of these markers are of relative sea level and so apply only locally. This is because they are confounded by uplift and subsidence of the crust over the passage of time. Nevertheless they provide evidence of past sea level change and place some constraints on its likely magnitude.

12.4.2 Tide gauges

Tide gauges are intended to provide a means of observing local short term changes in relative sea level arising from the astronomical tides (see Excursus 4.1), relevant to port operations and other maritime activities. Originally they involved manual recording of high and low tide and their time of occurrence in written form. Progressive automation and improvements in instrumentation have increased the density of the records across the whole of the tide cycle.

Over the longer term, they also provide a record of the sea level range relative to a local reference point. The challenge in using tide gauge records to infer long term sea level change arises in tracking the vertical motion of the reference point relative to a geocentric reference ellipsoid. This motion can arise over a range of time scales from a variety of causes, which can be either gradual or discrete:

- gradual subsidence of either the structure or land upon which the gauge is mounted;
- differences in mounting point as instrumentation is changed or upgraded;
- rapid movement resulting from earthquakes; or
- rising and falling of the crust as part of slow continental motion.

Improvements in instrumentation over decades, or even centuries, of observation also increase the precision of the observations over time, leading to greater relative uncertainty for the earlier part of long-lived tide gauge stations.

Since 1933 the Permanent Service for MSL (PSMSL, *www.psmsl.org*) has been compiling global tide gauge observations and attempting to account for the various effects enumerated above. Although the longest records are concentrated in the Northern Hemisphere, particularly in Europe (see Figure 12.15), the PSMSL dataset provides a high quality record over the most recent few centuries.

Figure 12.15 PSMSL tide gauge stations

Tide gauge stations within the Permanent Service for MSL dataset. 291 gauges have 50+ year records (shown as white dots) and 74 gauges have 100+ year records (shown as red). The longest records are overwhelmingly in the Northern Hemisphere.

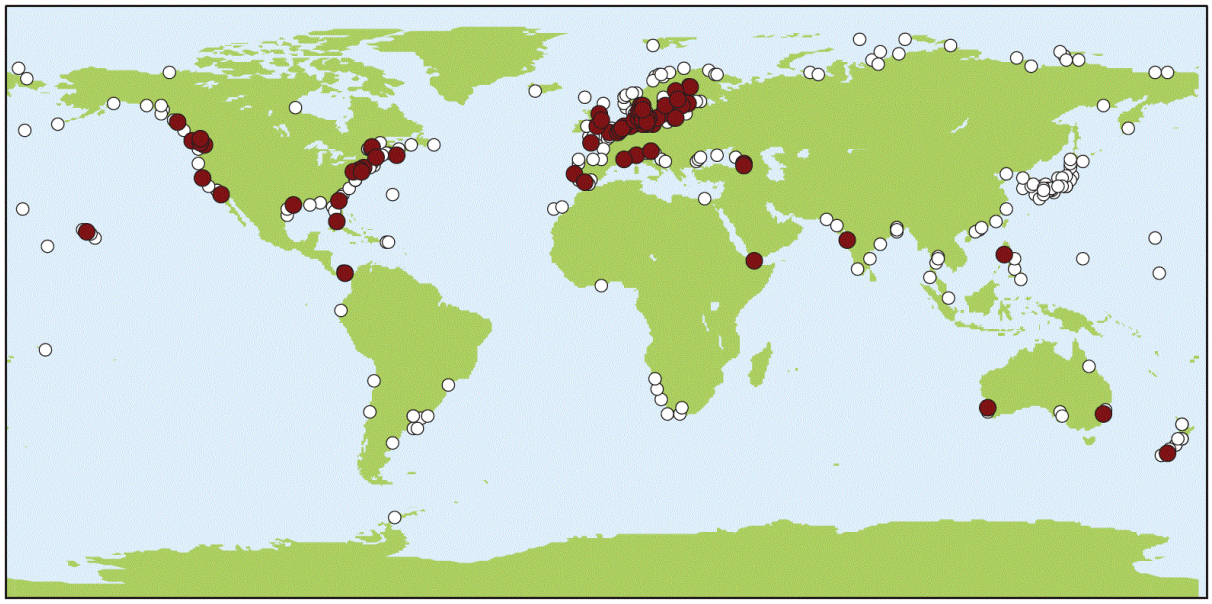

Source: Tamisea *et al.* (2013).

To improve monitoring of sea level over what PSMSL achieved, in 1985 the International Oceanographic Commission (IOC), within the United Nations Educational, Scientific and Cultural Organisation (UNESCO) founded the Global Sea Level Observing System (GLOSS, *https://www.gloss-sealevel.org/*) as a component of the Global Ocean Observing System (GOOS). The GLOSS system provides a means of coordinating tide gauge networks, and standardising quality control. The GLOSS Core Network (GCN; see Figure 12.16) is a set of about 300 stations distributed more uniformly globally. Many are on islands to maximise observations of the open ocean, rather than in coastal and marginal seas where local shelf bathymetry and topographic effects are more pronounced.

Figure 12.16 GLOSS network of tide gauge stations

The 224 active gauges are shown as green dots and 70 inactive gauges are shown as white.

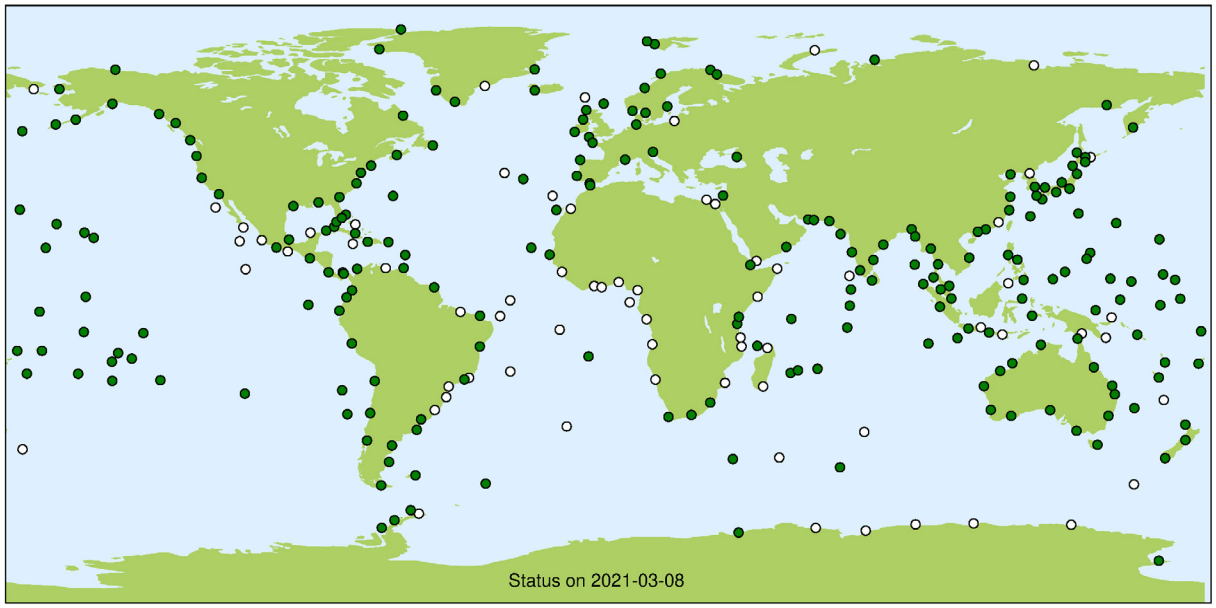

Source: GLOSS. Retrieved from *https://www.gloss-sealevel.org/operational-status*

Modern tide gauge stations record automatically at relatively high frequency (on the order of minutes), so are able to capture observations of short term phenomena such as storm surges and tsunamis. It is worth noting that some modern tide gauges now measure subsurface pressure. This differs from sea level because it includes atmospheric pressure (the inverse barometer effect), which needs to be taken into account to retrieve a measurement of the actual sea surface height measurement. In Australia, the National Tidal Centre at the Bureau of Meteorology (see Excursus 12.2) is the national repository for tide gauge data, including most high frequency observations.

Excursus 12.2—The National Operations Centre (NOC) Tidal Unit

Source: Bureau of Meteorology
Further Information: *http://www.bom.gov.au/oceanography/projects/ntc/ntc.shtml*; *http://www.bom.gov.au/oceanography/projects/abslmp/abslmp.shtml*

The National Operations Centre (NOC) Tidal Unit at the Bureau of Meteorology is the primary source of tide tables, tidal streams, and tidal constituents provided to the Australian Hydrographic Service (AHS). The Tidal Unit also manages the national data archive for sea levels and tides. This unit manages the Australian Baseline Sea Level Monitoring Project (ABSLMP), which is designed to monitor sea level around the coastline of Australia (see Section 12.7). The ultimate goal is to identify long period sea level changes, with particular emphasis on the enhanced greenhouse effect on sea level.

As part of ABSLMP, the Bureau of Meteorology maintains an array of SEAFRAME (SEA-Level Fine Resolution Acoustic Measuring Equipment) stations, which measure sea level very accurately, and record meteorological parameters (water temperature, air temperature, barometric pressure, wind direction, wind gust and wind speed). The array consists of fourteen standard stations distributed around the Australian coast (Darwin, Milner Bay, Thursday Island, Cape Ferguson, Rosslyn Bay, Port Kembla, Burnie, Portland, Port Stanvac, Thevenard, Esperance, Hillarys, and Broome) and on Cocos Keeling Islands, plus two supplementary stations (Lorne and Stony Point). The vertical stability of the gauges is surveyed by State organisations, while Geoscience Australia (GA) maintain earth monitoring installations for geodetic observations at each location, including Global Navigation Satellite System (GNSS) to determine accurate vertical height of the tide gauges. Survey data is archived by GA, with all data being available online.

The Pacific Sea Level and Geodetic Monitoring (PSLGM) project (a continuation of the 20-year South Pacific Sea Level and Climate Monitoring Project, SPSLCMP, which operates under the Climate and Oceans Support Program in the Pacific, COSPPac) provides sea level and meteorological information for 14 countries (Cook Islands, Federated States of Micronesia, Fiji, Kiribati, Marshall Islands, Nauru, Niue, Palau, Papua New Guinea, Samoa, Solomon Islands, Tonga, Tuvalu and Vanuatu), and tide predictions for 17 locations in the Pacific region. Only one of the participating countries (Palau) does not host a permanent tide gauge facility, which provides information on sea levels and tides. This network includes earth monitoring stations for geodetic observations, maintained and implemented by GA. PSLGM provides information about the processes, scale and implications of sea level rise and variability of extreme events on South Pacific communities, and makes sea level data more readily available and usable to support management of coastal infrastructure and industries. It is an important resource for those involved in disaster mitigation and adaptation planning, coastal development, and the shipping, fishing and tourism industries.

12.4.3 Satellite altimetry

The prospect of using spaceborne instrumentation to measure sea level represents a step change, both in spatial coverage and, in the open ocean away from tide gauge stations, in temporal coverage. To determine the range or distance to the sea surface, altimeters use radar, which measures the time a transmitted radio pulse takes to reflect from the ocean surface and return to the spacecraft (see Sections 9.5 and 12.2.1).

The earliest satellite altimeters were flown experimentally during the 1970s, initially on Skylab, Geos-3 and then the short-lived Seasat mission in 1978. Eventually the launch of the joint US/French TOPEX/Poseidon mission in late 1992, initiated the modern era of continuous, high quality, satellite altimetry. This mission has been followed by Jason-1/-2/-3, and in 2021, by the Sentinel-6 missions. Several other satellite altimetry missions have been flown that have complemented this core time series (see Table 12.2). The SWOT mission planned for 2022/23 will carry a novel experimental imaging altimeter (see Excursus 12.1).

12.4.3.1 Instrument operation

Four essential components are required to achieve highly accurate, sea level measurements from a satellite altimeter:

- radar instrumentation that permits a high precision measurement;
- capacity to account for natural factors that affect the observation;
- ability to track the satellite altitude relative to the geocentre with centimetre accuracy; and
- sufficient knowledge of the surface conditions to separate short term and local effects from the underlying persistent sea level.

Several factors affect the choice of radio frequency used for an altimeter. Higher frequencies allow a narrower beam width for a given transmission antenna size (a critical factor for satellite platforms), and permit enough bandwidth to deliver a sharp enough pulse to resolve the distance measurement with precision. As the antenna beamwidth increases, the area illuminated on the sea surface increases and the spatial resolution of the instrument is degraded. An additional constraint is the sensitivity of the signal to perturbation in the atmosphere and ionosphere. Although the atmosphere is transparent at the frequency used, it attenuates and delays the radar pulse depending on its composition and density. The most commonly used frequency is Ku Band (13.6 GHz, 2.2 cm wavelength; see Table 9.2 and Volume 1B—Section 8). Modern altimeters operate a second system at S or C band (3–5 GHz) where there is greater sensitivity to ionospheric delays, enabling a dynamic quantification and correction of the effect.

In addition to the active radar altimeter, a passive microwave radiometer (see Section 9.2) is also usually part of the instrument suite carried on sea surface altimetry missions. The microwave radiometer is used to estimate the water vapour content of the atmosphere along the pulse path, enabling corrections to be applied to the altimeter measurement since water vapour delays the pulse.

A non-smooth sea surface is not uniformly reflective, with wave troughs providing a stronger return than crests. The 'shape' of the returned altimeter pulse allows wind speed and wave height to be estimated, which enables correction of the trough/crest effect. For this reason it is not enough to simply measure the time of return of the leading edge of the pulse—it must also be sampled with sufficient frequency to determine its shape.

Since a satellite altimeter is making a range measurement from a moving platform, any uncertainty in the position of the platform impacts the ultimate value of the range measurement. The task of minimising that uncertainty has given rise to precision orbit determination—a suite of techniques to model and track the satellite path in orbit (see Volume 1A—Excursus 3.2 for a review of Space Geodesy). The satellite tracking system typically has three components based on overlapping, but complementary, methods:

- Satellite global positioning systems (GPS) are used in the same way as GPS receivers on the Earth's surface, by ranging to a constellation of reference satellites that are transmitting positional information (see Volume 1B—Section 10.3). GPS currently provides a three-dimensional positional accuracy of ~3 cm.
- Satellite Laser Ranging (SLR) is a technique in which ground-based lasers reflect from corner reflectors mounted on the satellite (see Volume 1A—Section 16.1.2.1). The light travel time measures the range to the satellite from the laser. The International Laser Ranging Service (ILRS) currently comprises around 40 laser ranging stations around the world to undertake these measurements (ILRS, 2021), yielding a three-dimensional positional accuracy of around 3 cm.
- The French system with the acronym DORIS (Doppler Orbitography and Radiopositioning Integrated by Satellite) consists of about 60 fixed beacons located worldwide (IDS, 2021). A DORIS receiver on the spacecraft detects the doppler shift in these signals (arising from the satellite motion) enabling a precise orbit determination.

All these measurement systems are used to refine knowledge of the satellite orbital model, which itself uses a highly accurate gravity model to describe the motion of the satellite. The gravity model is, like the geoid, a spatially varying field that reflects changes in the distribution and density of the mass of the Earth, although it is smoother than the geoid because of the altitude at which satellites orbit (see Volume 1A—Excursus 3.1). The quality of the gravity model is a limiting factor in the precision of orbit determination. Modern gravity models now incorporate the force exerted by the increased or decreased water from the ocean tides on the satellite (see Excursus 1.1). Although satellite altimeters typically orbit at altitudes of 800–1300 km, there is a non-negligible atmospheric drag effect that needs to be accounted for, as well as a small perturbing force from the solar wind.

Finally, in addition to the range corrections due to the wet and dry path delays, sea state bias, etc, two 'corrections' are often applied to mitigate the problem that altimeter observations are sparse in time (with 10 or more days between revisits), so high frequency variability of the sea surface is badly undersampled. The first 'correction' is to use a tidal model to remove the instantaneous effect of the ocean tides, which creates a 'tideless' sea level. Secondly the local atmospheric pressure is used to correct for the inverse barometer effect, where the sea surface is locally depressed by increasing atmospheric pressure.

Applying these corrections dealiases the data, but it also changes the way the data is subsequently used. One would not, for example, assimilate the 'fully corrected' altimeter data into an ocean model that simulates coastal inundation.

12.4.3.2 Spatial coverage

The spatial coverage achieved by satellite altimeters depends primarily on the orbit in which they are placed. Each radar pulse illuminates a footprint along the ground track yielding a one-dimensional measurement track across the ocean surface. To derive a two-dimensional coverage, the orbit is arranged so that the ground tracks interleave and cross over many revolutions, ultimately repeating, usually with a 10 day revisit frequency. The spacecraft orbital inclination is usually a compromise to achieve sufficient inclination to cover the majority of the global ocean. To reach the entire ocean surface would require an orbit inclination of 90° (since the North Pole is oceanic), but such an orbit would dramatically decrease the coverage at lower latitudes. The TOPEX/Poseidon orbit was chosen so that it would encompass Drake Passage between South America and Antarctica, but not the polar oceans at latitudes greater than ±66° (see Figure 12.17). In contrast, the Cryosat spacecraft series, which uses a specialised altimeter to measure polar ice caps, is in an orbit that passes within 2° of the Earth's poles.

Figure 12.17 TOPEX/Poseidon altimeter coverage

This map shows the ground tracks of a complete 10 day cycle of the TOPEX/Poseidon altimeter mission.

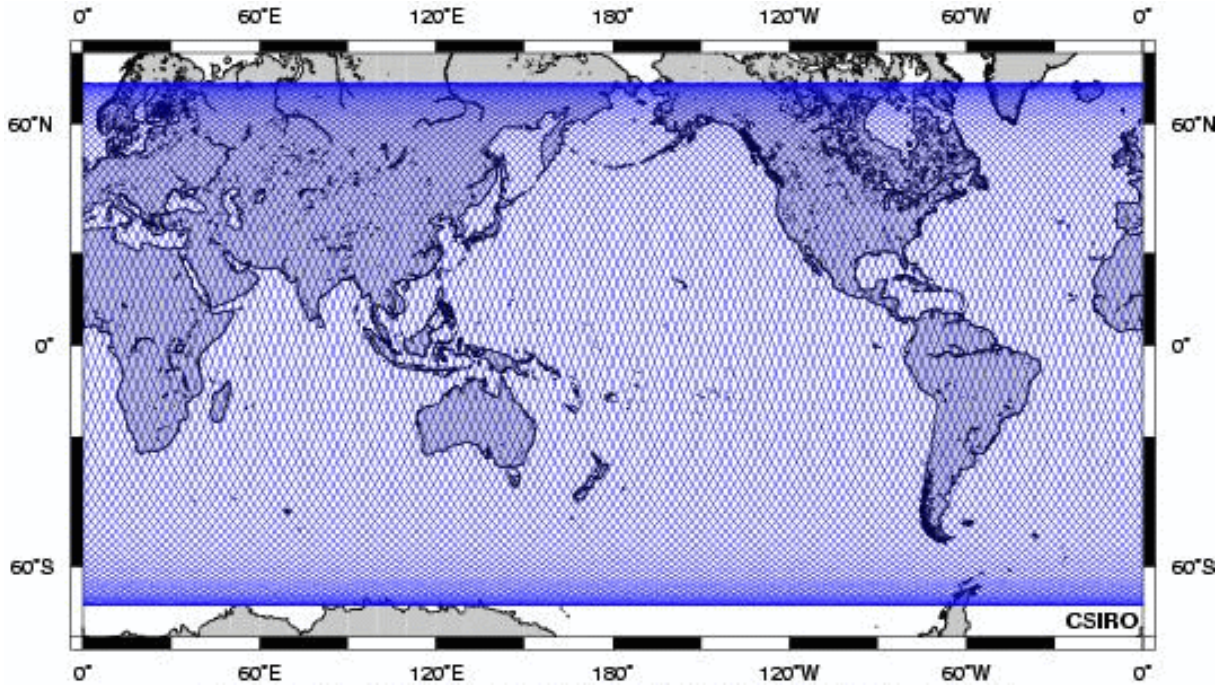

Source: CSIRO

Figure 12.18 Ground tracks of several altimeter missions

Ground tracks of several altimeter missions in southeast Australia are shown: TOPEX/Poseidon and Jason-1 (blue), GEOSAT and GFO (red), and ERS-1/-2 and Envisat (green), with repeat periods of 10, 17 and 35 days respectively.

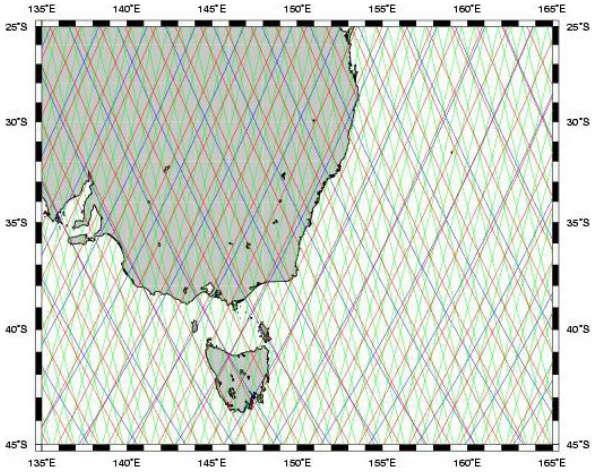

Source: CSIRO

As illustrated in Figure 12.18, one-dimensional ground tracks never provide complete coverage of the ocean surface. For TOPEX/Poseidon, and the follow-on Jason series, the maximum distance between ground tracks is around 300 km at the equator. Other missions, such as ERS and Envisat-1/-2, reduce this to about 100 km at the equator, but do so at the expense of a much longer revisit cycle (35 compared with 10 days).

12.4.3.3 Tide observations

Historically, most observations of tides have come from tide gauge stations at the coast, or on relatively few isolated islands. Knowledge of tide in the open ocean came almost entirely from hydrodynamic modelling, which was subject to spatially varying uncertainty arising from non-uniform distribution of tide gauge stations and a lack of knowledge about the parameterisation of friction effects. The advent of routine satellite altimetry in 1992 provided the first spatially comprehensive and regular measurements of the tide in the open ocean basins. Although the repeat observation time for any location is typically much longer than the tidal cycle, the predictability of the tidal signal (together with careful choice of satellite orbit) enables its separation from the other oceanographic features affecting the sea level measurement. This in turn has improved our understanding of tidal processes and their modelling. An important result of satellite altimetry therefore has been the reduction in tide estimation errors globally from around 10 cm to the level of 1 cm (see Section 5.3, Cazenave and Fu, 2001; Stammer *et al*., 2014).

12.5 Monitoring Sea Level

The accuracy of sea level monitoring has varied with the advent of modern technologies such as satellite altimetry. Below we review the available trend data from three time spans: geological ages (see Section 12.5.1), recent centuries (see Section 12.5.2), and recent decades (see Section 12.5.3).

12.5.1 In geological ages

Over periods of thousands to tens of thousands of years, our knowledge of sea level comes mostly from geomorphological and fossil evidence (see Section 12.4.1). This knowledge is not only direct but relies also on indicators of the state of the Earth's climate from which the mass balance between the cryosphere and hydrosphere (including the oceans) can be inferred. For example, multiple lines of evidence have established that the Earth underwent a period of substantial glaciation (or ice age) between 115,000 and 11,700 years ago. It is estimated that the release of water from ice at the end of that glaciation led to a rise of global MSL of around 100–120 m.

Similarly there is evidence that during periods in the preceeding 1–3 million years the Earth's temperature was 2–3.5°C higher than during the immediate pre-industrial climate. Accordingly, it is likely that sea levels were substantially higher at times than they are now. The sea level known from the geological record will likely always contain significant inaccuracies since, as a relative sea level indicator, it has been subject to glacial isostatic adjustment and other crustal motion.

Since the rise at the end of the last glaciation, indicators suggest a stabilisation of global sea levels. In particular, in the 2,000 years up until ~1800, where the evidence also includes human-built structures, there is little indication of change. More details about the reconstruction of the pre-industrial sea level record can be found in Church *et al*. (2013).

12.5.2 In recent centuries

Since around 1700, sea level has been observed and recorded more accurately and consistently (see Figure 12.19). Until the recent advent of routine satellite altimeter measurements, this record comes mainly from tide gauge stations (see Section 12.4.2). Although the uncertainty is greater in the earlier part of the record where fewer stations were operating, it is clear that global sea level began to rise around 1800 and has been increasing steadily since then.

Figure 12.19 The past three centuries of the global sea level record

The dark blue, green, and orange lines show different tide gauge reconstructions. Light blue is the altimeter record, and the purple points are from salt marsh evidence.

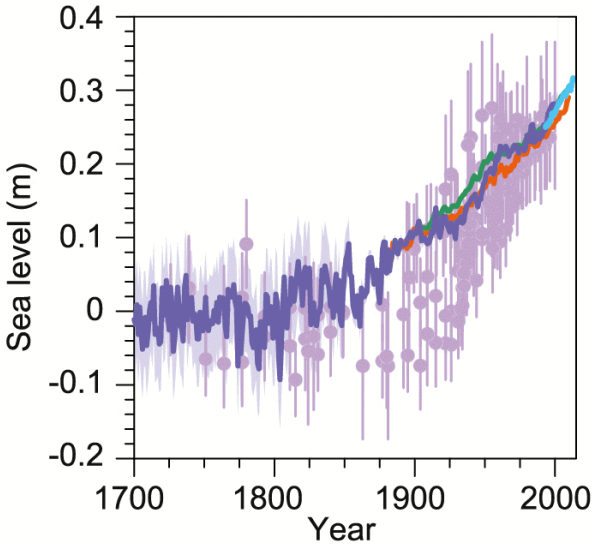

Source: Church *et al.* (2013) Figure 13.3e

12.5.3 In recent decades

Since 1993, a dense, continuous, spatially extensive and precise record of global sea level has become available from the series of satellite altimeter missions (TOPEX/Poseidon and Jason-1/-2/-3; see Figure 12.20). The robust general trend is an increase of 3.3±0.4 mm/year. There is also evidence for an acceleration in that rise of nearly 0.1 mm/yr/yr (Watson *et al.*, 2015). As the record extends over coming decades (and as the accuracy of altimetry techniques continue to improve), the reality of this acceleration will become more certain.

Figure 12.20 The satellite era mean sea level record

Global-Mean Sea Level (GMSL) from TOPEX/Poseidon, Jason-1, Jason-2, and Jason-3 satellite altimeter data

a. Mean sea level record including seasonal signals

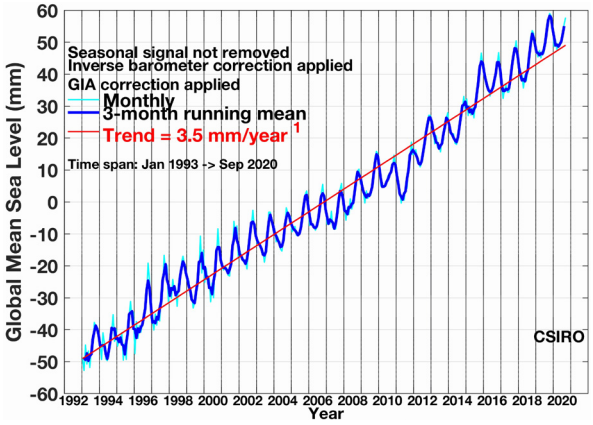

b. Mean sea level record excluding seasonal signals

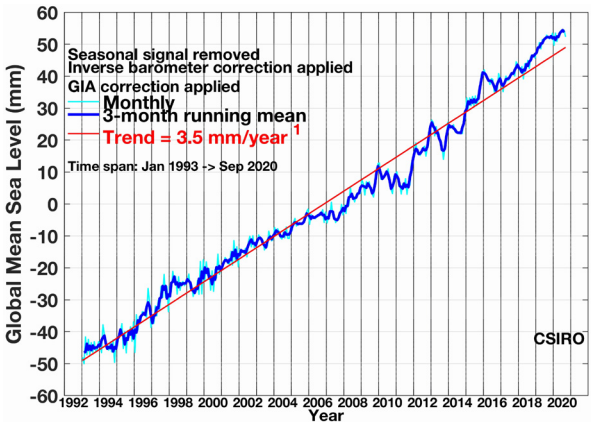

Source: Benoit Legressy, CSIRO. Retrieved from *https://research.csiro.au/slrwavescoast/sea-level/sea-level-changes/*

12.6 Modelling Future Sea Level

Sea level is a function of the volume occupied by ocean waters, which in turn is dependent upon their mass and density (see Section 5.1.2). The state of global climate is therefore a strong mediator of sea level since:

- additional heat trapped within the atmosphere results in ice loss from the cryosphere, increasing the mass of water in the ocean; and
- heat absorbed by the oceans decreases their density, which, for a given mass of water, must increase the volume.

A guide to likely future sea levels can therefore be found in the results of modern climate models, such as those included in the World Climate Research Program Coupled Model Intercomparison Project (WCRP CMIP; *https://www.wcrp-climate.org/wgcm-cmip*). Since a warming climate may also cause increased human reliance on groundwater aquifers for agriculture and other freshwater needs, which ultimately releases more terrestrial water into the ocean, these models need to take account of forcing arising from societal responses.

A significant part of the global effort to understand climate and its evolution occurs within the framework of the Intergovernmental Panel on Climate Change (IPCC), which produces major reports based on the evolving science evidence, typically every 5–8 years. The fifth assessment report (5AR) was completed in 2014 (IPCC, 2014) and the sixth is planned for 2022. An important component of the science underpinning these reports is a comparison of global climate model runs that explore future climates under a range of different greenhouse gas emission scenarios. These scenarios, called Representative Concentration Pathways (RCPs), represent plausible carbon emission trajectories given possible human choices. These are identified by their approximate total radiative forcing in year 2100 relative to 1750, that is, RCP2.6 indicates 2.6 W/m^2. The RCP range from business as usual (rapidly increasing emissions, RCP8.5) through a variety of mitigation approaches including those that reach net-zero emissions at differing rates (see Table 12.3). The agreed emission scenarios serve not only to ease comparison of the performance of the climate models but, since they reflect the consequences of possible interventions, also enable a standardised approach to assessment of the economic and sociological impacts of the choices to be made. IPCC (2013; see Box SPM.1) provides more information on these RCPs.

Table 12.3 Predicted temperature variations

Mean atmospheric temperature changes expected from climate model responses to four of the scenarios in the IPCC AR5 report. Note that temperatures have already increased by nearly 1°C from pre-industrial era when atmospheric CO_2 concentrations were about 270 ppm. Temperature increase is for 2081–2100 relative to 1986–2005.

AR5 Scenario	Atmospheric CO_2 equivalent in 2100 (ppm)	Temperature Increase (°C)
RCP8.5	> 1370	3.7 (2.6–4.8)
RCP6.0	850	2.2 (1.4–3.1)
RCP4.5	650	1.8 (1.1–2.6)
RCP2.6	490	1.0 (0.3–1.7)

Source for data: IPCC (2013) Table SPM.2

Projections of future sea levels are informed by modelling using the various RCP scenarios. While climate models differ in detail as to how they incorporate various physical processes, the IPCC future sea level assessment is based on consideration of models that include the three major causes of sea level change: thermal expansion, transfer of water from the cryosphere to the ocean, and transfer from terrestrial stores to the ocean. Over the past several decades, both our understanding of the processes involved, and (by observational measurement) knowledge of the parameters relevant to each, have improved. Consequently the uncertainty surrounding likely future sea levels has been steadily reduced (see Figure 12.21).

Figure 12.21 Historical sea level change

Historical global mean sea level change (colours as in Figure 12.19) extended with IPCC projections from modelling using the RCP8.5 (red) and RCP2.6 (blue) scenarios with uncertainties indicated by the shaded areas.

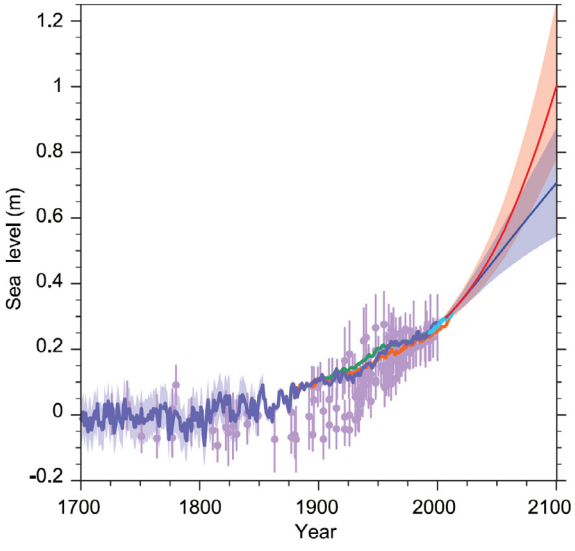

Source: Stocker *et al.* (2013) Figure TFE.2

Figure 12.22 Projected sea level changes around Australia in 2090

Distribution of sea level changes around Australia in 2090 (relative to 1986–2005) arising from the four different IPCC AR5 scenarios (see Table 12.3). The shading indicates the change and the solid lines the uncertainties.

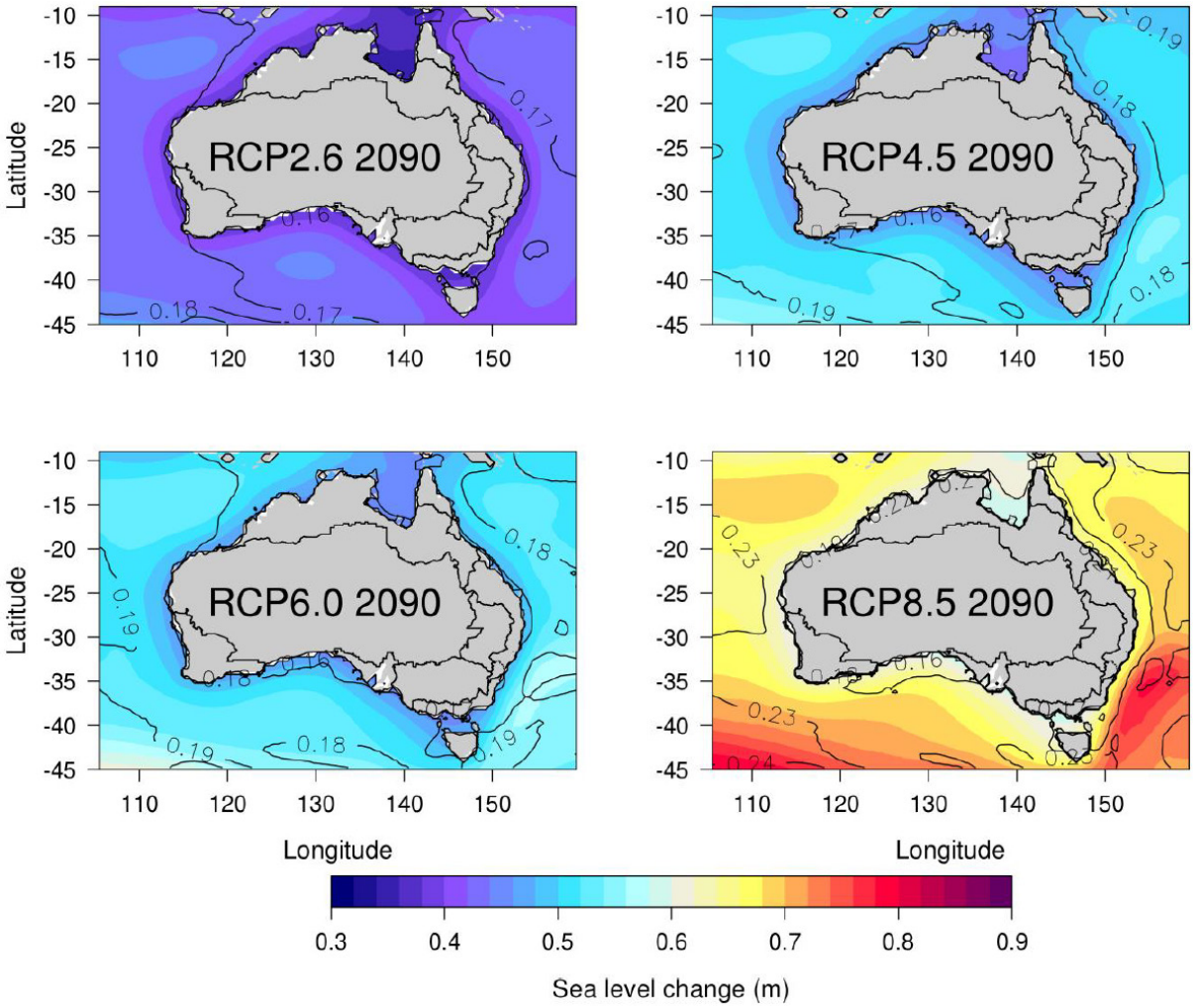

Source: McInnes *et al.* (2015) Figure 3

The IPCC projections indicate global MSL change by the end of this century of somewhere in the range of 0.5–1.2 m, depending on which emission scenario turns out to be the most realistic. It is important to recognise however that not only is sea level change not spatially uniform, it is the change in relative sea level (measured with respect to local land) that determines the impacts. Two factors are particularly significant in this respect: changes in land elevation and changes in the Earth's gravity field. Long term changes in the elevation of continents as they respond to the loss of ice in the last ice age (Glacial Isostatic Adjustment) will continue, and will also affect Greenland and Antarctica further in the future as more ice is lost. Tilting of continents as a consequence of continental motion will result in opposite effects on relative sea level on opposite sides. Subsidence of land, for example due to increased groundwater extraction, can also increase local relative sea level change. The gravitational field change arises as large amounts of ice are lost from the polar ice caps. The ice sheets are massive in their own right and exert a gravitational pull on the surrounding oceans. As the ice melts, this mass becomes mobile and migrates away from the polar regions and results in a reduction of sea level locally as the ocean responds. The relative sea level rise resulting from the loss of ice sheets is therefore greater further away from the poles.

Taking these factors into account, it is possible to use future global MSL changes to develop regional projections. An example product is shown in Figure 12.22 (from McInnes *et al.*, 2015) for the 21st century. Under all scenarios Australian sea levels are expected to increase. The rate of increase varies with the selected RCP scenario, ranging from 4 mm/year

for RCP2.6 to 12 mm/year by the end of the century for RCP8.5. Extreme sea level events, such as storm surges and wave runup, lead to the most significant impacts of sea level rise via coastal flooding and dissipation of wave energy. For current infrastructure and buildings, existing at fixed heights above the (present) highest tide level, the frequency of such events are expected to increase. These quantitative projections of regional sea level change can be used to estimate the additional height that needs to be incorporated into new infrastructure to keep the frequency of such events from increasing. Such projections indicate that further measures will need to be taken to protect existing Australian coastal infrastructure.

12.7 Further Information

An excellent introductory tutorial to satellite altimetry provided by the European and French Space Agencies can be found on the web at *http://www.altimetry.info/*. A definitive reference is Cazenave and Fu (2001).

Bureau of Meteorology

Australian baseline sea level monitoring project:

http://www.bom.gov.au/oceanography/projects/abslmp/abslmp.shtml

Pacific Sea Level Monitoring Project: *http://www.bom.gov.au/pacific/projects/pslm/index.shtml*

ICSM Permanent Committee on Tides and Mean Sea Level

https://www.icsm.gov.au/what-we-do/permanent-committee-tides-and-mean-sea-level

Accuracy of Tidal Predictions: *https://icsm.gov.au/sites/default/files/2017-05/Port_Tidal_Predictions-V0.4.pdf*

Global Sea Level

Sea Level, Waves and Coastal Extremes: *https://research.csiro.au/slrwavescoast/sea-level/*

Global Sea Level Observing System (GLOSS):

https://www.bodc.ac.uk/resources/inventories/gloss_handbook/

Permanent Service for Mean Sea Level: *http://www.psmsl.org*

Measuring sea level rise

AdaptNSW: *https://climatechange.environment.nsw.gov.au/Impacts-of-climate-change/Coasts-and-sea-level-rise/Measurement-of-sea-level-rise*

Useful websites

CSIRO sea level site: *https://research.csiro.au/slrwavescoast/sea-level/*

NASA/JPL Ocean Surface Topography: *https://sealevel.jpl.nasa.gov/*

CNES AVISO satellite altimetry: *https://www.aviso.altimetry.fr/en/home.html*

University of Colorado: *https://sealevel.colorado.edu/*

NOAA National Ocean Service: *https://oceanservice.noaa.gov/education/sea-level-rise/welcome.html*

ESA/CNES radar altimetry tutorial and toolbox: *http://www.altimetry.info/*

Broadview Radar Altimetry Toolbox: *https://earth.esa.int/web/guest/software-tools/content/-/article/basic-radar-altimetry-toolbox-brat-5040*

Several portals and agency sites provide access to data from radar altimetry missions, including

IMOS Gridded sea level anomaly combines altimetry with tide gauges: *http://oceancurrent.imos.org.au/*

AVISO: *https://www.aviso.altimetry.fr/en/data.html*

NASA: *https://sealevel.jpl.nasa.gov/data/get-data/*

CSIRO: *https://research.csiro.au/slrwavescoast/sea-level/measurements-and-data/sea-level-data/*

Historical and current satellite altimeter missions

https://www.aviso.altimetry.fr/en/missions.html

https://podaac.jpl.nasa.gov/Altimetric_Data_Information/Missions

https://sealevel.jpl.nasa.gov/missions/overview-and-partners/

12.8 References

Church, J.A., Clark, P.U., Cazenave, A., Gregory, J.M., Jevrejeva, S., Levermann, A., Merrifield, M.A., Milne, G.A., Nerem, R.S., Nunn, P.D., Payne, A.J., Pfeffer, W.T., Stammer, D., and Unnikrishnan, A.S. (2013). Sea Level Change. pp 1137–1216, In: *Climate Change 2013: The Physical Science Basis*. Contribution of Working Group I to the Fifth Assessment Report of the Intergovernmental Panel on Climate Change. (Eds: T.F. Stocker, D. Qin, G.-K. Plattner, M. Tignor, S.K. Allen, J. Boschung, A. Nauels, Y. Xia, V. Bex and P.M. Midgley). Cambridge University Press, Cambridge, New York, USA. *doi:10.1017/CBO9781107415324.026* (Available from *https://www.ipcc.ch/report/ar5/wg1/*)

Cazenave, A., and Fu, L.-L. (2001). *Satellite Altimetry and Earth Sciences: A Handbook of Techniques and Applications*. International Geophysics Series, Volume 69. Academic Press.

Fu, L.-L., and Ubelmann, C. (2014). On the transition from profile altimeter to swath altimeter for observing global ocean surface topography. *Journal of Atmospheric and Oceanic Technology,* 31(2), 560–568.

Gower, J. (2005). Jason-1 detects the 26 December 2004 tsunami. *EOS*, 86 (4), 37–38.

IDS (2021). *International DORIS Service* website: *https://ids-doris.org/*

ILRS (2021). *International Laser Ranging Service* website: *https://ilrs.gsfc.nasa.gov/*

IPCC (2013). Summary for Policymakers. In: *Climate Change 2013: The Physical Science Basis*. Contribution of Working Group I to the Fifth Assessment Report of the Intergovernmental Panel on Climate Change (Eds: Stocker, T.F., D. Qin, G.-K. Plattner, M. Tignor, S.K. Allen, J. Boschung, A. Nauels, Y. Xia, V. Bex and P.M. Midgley). Cambridge University Press, Cambridge, New York, USA. *https://www.ipcc.ch/site/assets/uploads/2018/02/WG1AR5_SPM_FINAL.pdf*

IPCC (2014). Climate Change 2014: Synthesis Report. Contribution of Working Groups I, II and III to the Fifth Assessment Report of the Intergovernmental Panel on Climate Change (Eds: R.K. Pachauri and L.A. Meyer). IPCC, Geneva, Switzerland. 151 p.

McInnes, K.L., Church, J., Monselesan, D., Hunter, J.R., O'Grady, J.G., Haigh, I.D., and Zhang, X. (2015). Information for Australian impact and adaptation planning in response to sea-level rise. *Australian Meteorological and Oceanographic Journal*, 65(1), 127–149.

McInnes, K.L., White, C.J., Haigh, I.D., Hemer, M.A., Hoeke, R.K., Holbrook, N.J., Kiem, A.S., Oliver, E.C.J., Ranasinghe, R., Walsh, K.J.E., Westra, S., and Cox, R. (2016). Natural hazards in Australia: sea level and coastal extremes. *Climatic Change*, 139(1), 69–83.

NASA (2021). *SWOT Mission Overview* webpage, Surface Water and Ocean Technology website: *https://swot.jpl.nasa.gov/mission/overview/*

Stammer, D., Ray, R.D., Andersen, O.B., Arbic, B.K., Bosch, W., Carrère, L., Cheng, Y., Chinn, D.S., Dushaw, B.D., Egbert, G.D., Erofeeva, S.Y., Fok, H.S., Green, J.A.M., Griffiths, S., King, M.A., Lapin, V., Lemoine, F.G., Luthcke, S.B., Lyard, F., Morison, J., Müller, M., Padman, L., Richman, J.G., Shriver, J.F., Shum, C.K., Taguchi, E., and Yi, Y. (2014). Accuracy assessment of global barotropic ocean tide models. *Reviews of Geophysics*, 52(3), 243–282.

Stocker, T.F., D. Qin, G.-K. Plattner, L.V. Alexander, S.K. Allen, N.L. Bindoff, F.-M. Bréon, J.A. Church, U. Cubasch, S. Emori, P. Forster, P. Friedlingstein, N. Gillett, J.M. Gregory, D.L. Hartmann, E. Jansen, B. Kirtman, R. Knutti, K. Krishna Kumar, P. Lemke, J. Marotzke, V. Masson-Delmotte, G.A. Meehl, I.I. Mokhov, S. Piao, V. Ramaswamy, D. Randall, M. Rhein, M. Rojas, C. Sabine, D. Shindell, L.D. Talley, D.G. Vaughan and S.-P. Xie. (2013). Technical Summary. In: *Climate Change 2013: The Physical Science Basis*. Contribution of Working Group I to the Fifth Assessment Report of the Intergovernmental Panel on Climate Change. (Eds: Stocker, T.F., D. Qin, G.-K. Plattner, M. Tignor, S.K. Allen, J. Boschung, A. Nauels, Y. Xia, V. Bex and P.M. Midgley). Cambridge University Press, Cambridge, New York, USA. (Available from *https://www.ipcc.ch/site/assets/uploads/2018/02/WG1AR5_TS_FINAL.pdf*)

Tamisiea, M.E., Hughes, C.W., Williams, S.D.P., and Bingley, R.M. (2014). Sea level: measuring the bounding surfaces of the ocean. *Philosophical Transactions of the Royal Society A: Mathematical, Physical and Engineering Sciences*, 372(2025), 20130336. *https://doi.org/10.1098/rsta.2013.0336*

Townsend, D.W. (2012). *Oceanography and marine biology: an introduction to marine science*. Sinauer Associates, Sunderland.

Watson, C., White, N., Coleman, R., Church, J., Morgan, P., and Govind, R. (2004). TOPEX/poseidon and Jason-1: absolute calibration in Bass Strait, Australia. *Marine Geodesy,* 27(1–2), 107–131.

Watson, C.S., White, N.J., Church, J.A., King, M.A., Burgette, R.J., and Legresy, B. (2015). Unabated global mean sea-level rise over the satellite altimeter era. *Nature Climate Change*, 5(6), 565–568.

Watson, C.S., Legresy, B., King, M., Beardsley, J., and Deane, A. (2018). A Review of the Altimeter Validation Facility in Bass Strait, Australia. Oral presentation. *FRM4ALT International Review Workshop*. April 23–26. International Review Workshop on Satellite Altimetry Cal/Val activities and applications. Crete, Greece.

White, N.J., Coleman, R., Church, J.A., Morgan, and P.J., Walker, S.J. (1994). A southern hemisphere verification for the TOPEX/POSEIDON satellite altimeter mission. *Journal of Geophysical Research: Oceans*, 99(C12), 24505–24516.

13 Bathymetry

Kim Picard, Janet Anstee, and Barbara Harrison

Bathymetry is the study or measurement of the depth of water from the surface to the seabed, the solid surface that underlies a waterbody, with depth being measured as the vertical distance from a given vertical datum (see Figure 10.9). Thus, in waterbodies, bathymetry corresponds to mapping topography on land. Bathymetric data is used for a range of marine activities, such as to determine Australia's extended continental shelf, highlight shipping hazards, monitor undersea engineering structures, identify potential deep sea fishing sites, and model tsunami.

Traditionally waterbody depth was measured by sample 'soundings' at selected locations, that is, the length of a lead line that was lowered from a ship until it reached the seabed. For the past century a variety of EO-based methods have been used to estimate waterbody depth. Some of the advances in seafloor mapping since 1903 are illustrated in Figure 13.1.

The initial subsections below provide an overview of waterbody depth mapping around Australia (see Section 13.1) and the EO sensors that can provide useful information for bathymetric studies (see Section 13.2). Subsequent sections consider approaches to EO-based bathymetry that are relevant to Australian surface waters:

- seafloor mapping using acoustic and radar datasets (see Section 13.3); and
- coastal monitoring derived from lidar and satellite imagery (see Section 13.4).

The sea does not belong to despots. Upon its surface men can still exercise unjust laws, fight, tear one another to pieces, and be carried away with terrestrial horrors. But at thirty feet below its level, their reign ceases, their influence is quenched, and their power disappears.
(Jules Verne)

Background image: Adele Island, off the northern WA (Kimberley) coast, was photographed from the International Space Station on 11 June 2015. This pristine cay, which spans just under 3 km in length and 1.6 km in width, is surrounded by extensive sandbanks and coral reefs. It is an important breeding sanctuary for migratory birds, a feeding and breeding ground for humpback whales, and home to rare rollolith habitat. Source: NASA Earth Observatory ISS044-E-903. Retrieved from *https://visibleearth.nasa.gov/images/86331/adele-island*

Recommended Chapter Citation: Picard, K., Anstee, J.M., and Harrison, B.A. (2021). Bathymetry. Ch 13 in *Earth Observation: Data, Processing and Applications. Volume 3B—Surface Waters.* CRCSI, Melbourne. pp. 223–241. ISBN 978-0-6482278-5-4

This chapter is published with the permission of the CEO, Geoscience Australia.

Figure 13.1 Improvements in GEBCO over time

These charts show mapping of the Mid-Atlantic Ridge in the General Bathymetric Chart of the Oceans (GEBCO) since 1903.

1st edition: 1903
(18,000 soundings)

2nd edition: 1912–1930
(> 30,000 soundings)

3rd edition; 1932–1966

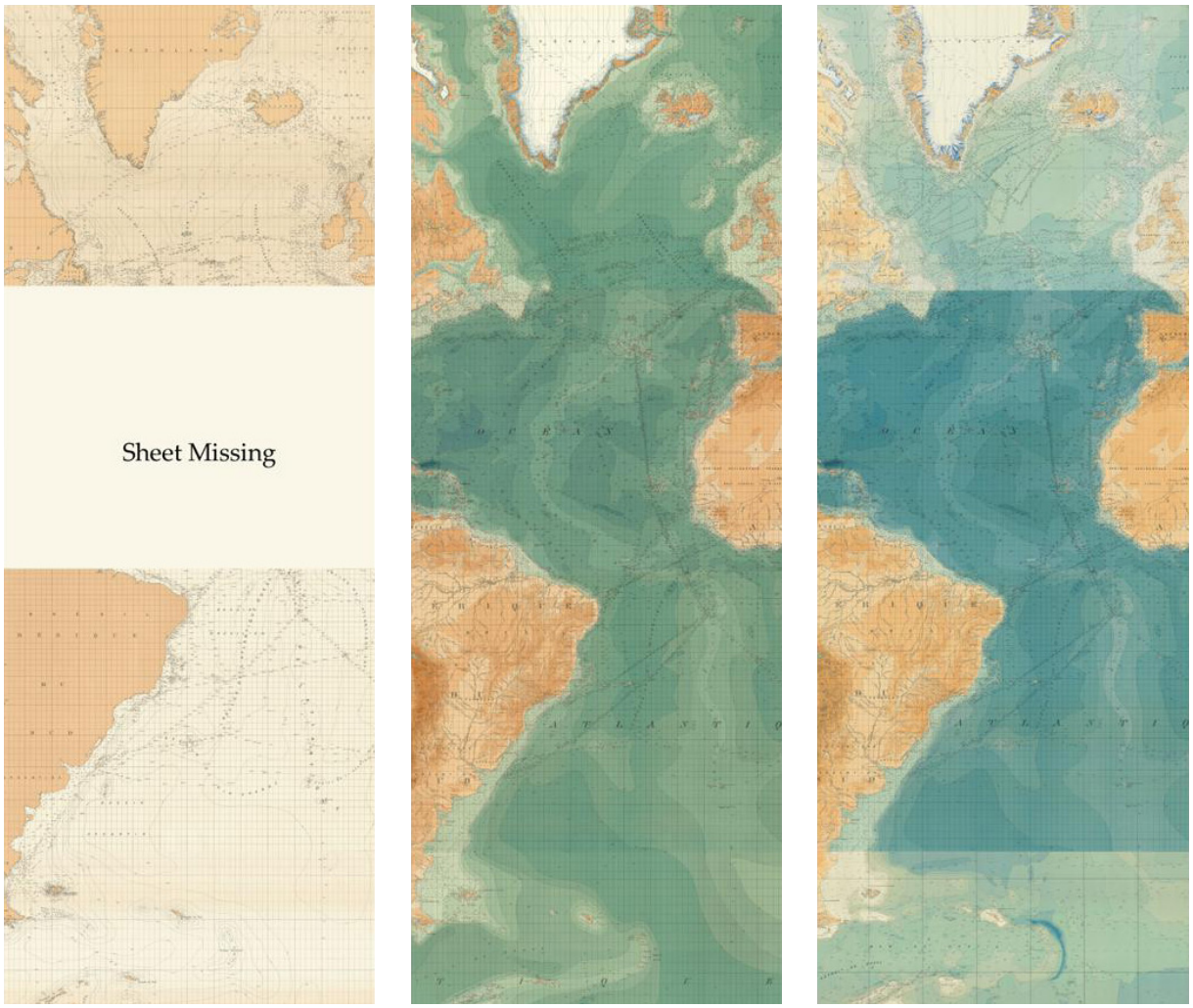

4th edition: 1958+
(based on echosounders supplying signficantly more bathymetric data)

5th edition: 1972–1984
(using many more soundings)

GEBCO–2014 Grid
(part of global terrain model at 30 arc-second intervals)

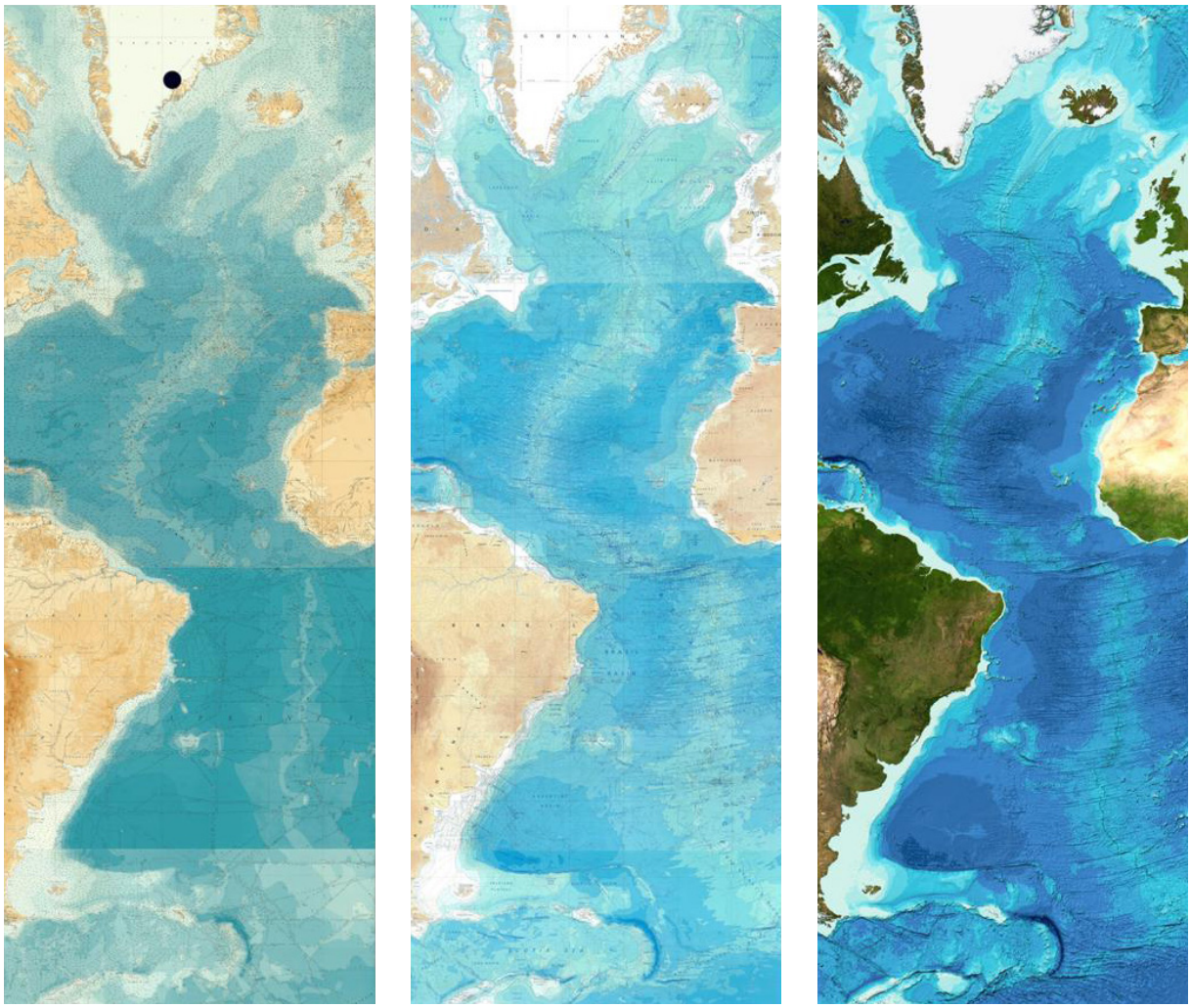

Source: Wölfl *et al.* (2019) Figure 6 (courtesy of Anthony Pharaoh, IHO)

13.1 Bathymetry of Australian Surface Waters

Mapping the shape and composition of the seabed both supports safe navigation and provides data and information for managing Australia's marine estate in a range of scientific applications, including:

- delineating and securing maritime boundaries (see Section 2.1);
- ensuring the safety of life at sea (see Excursus 2.1);
- search and rescue operations (see Figure 13.2);
- monitoring marine conditions (see Excursus 2.2) and flood events (see Section 11.4);
- mapping coastal and nearshore sediments (see Section 6.3);
- understanding geomorphology (see Section 6.2) and geohazards, especially in coastal waters (see Section 20.5);
- conserving marine ecosystems and cultural heritage (see Australasian Underwater Cultural Heritage Database (AUCHD) in Section 13.5);
- assessing alternative energy opportunities (such as offshore wind and wave energy locations; see Section 16.1);
- modelling regional hydrodynamics and global ocean circulation (see Section 17);
- planning aquaculture and monitoring fisheries (see Section 20.7.1);
- deploying and maintaining seafloor installations, such as telecommunication infrastructure; and
- managing oil and gas subsea assets.

Figure 13.2 Search for MH370 relative to available bathymetric datasets

With the disappearance of flight MH370 travelling from Kuala Lumpur to Beijing on 8 March 2014, the lack of high resolution bathymetry hampered the search of parts of the fuselage. In this diagram black lines indicate the available shipborne, single beam echo sounding data, red lines show available multibeam bathymetry, and the green bounding shape highlights the projected search area.

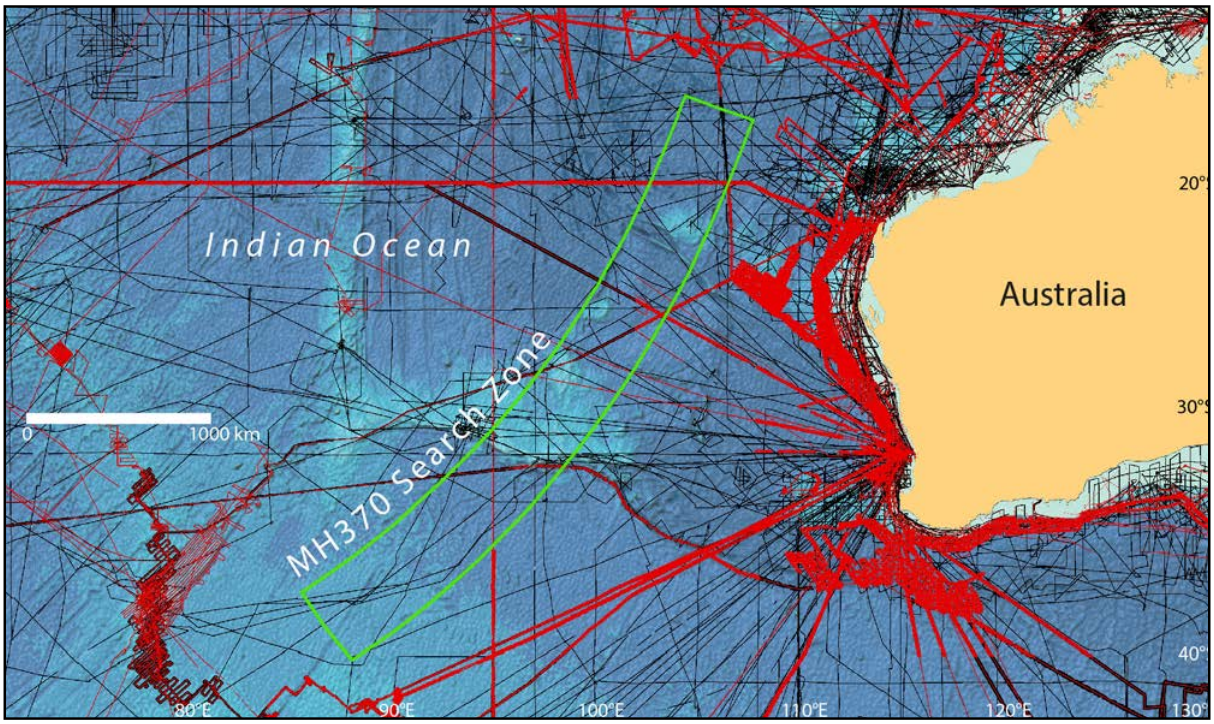

Source: GEBCO (2017) Figure 3-2

The Australian Bathymetric and Topographic Grid provides coverage of (most of) our marine jurisdiction at 250 m horizontal resolution (GA, 2018). The initial bathymetric grid (Harris *et al.*, 2005) enabled the surface area of the seabed and the distribution of defined geomorphic features around the continental margin of Australia to be mapped systematically for the first time, and this was updated with newer datasets in 2009 (see Excursus 13.1 for details). More recently, at a regional level, a few large, high resolution bathymetry models have been compiled, namely the Great Barrier Reef and Coral Sea, the Northern Australia, and the Torres Strait models (Beaman, 2017, 2018, 2020). However, when detailed bathymetric data is needed for operational activities, such as navigating underwater vehicles involved in search and rescue operations in deep ocean areas, the existing resolution and extent of bathymetric data in this region has been found wanting (see Figure 13.2).

In Australia, much of the focus for seabed mapping has involved varying levels of coverage and resolution for the continental shelf and slope waters, resulting in coverage from the upper reaches of estuaries to the abyssal plain for selected locations. This focus derives from the drivers for mapping, vessel and gear availability, and a combination of targeted and opportunistic data collection. Although a significant increase in survey coverage has occurred this century, by 2018 less than 25% of the seafloor in Australia's maritime jurisdiction had been mapped at high resolution (Picard *et al.*, 2018).

While the availability of national bathymetric data varies with the policies of different jurisdictions (Wölfl *et al.*, 2019), national and international efforts are underway to integrate all publicly available data into accessible repositories such as AusSeabed (see Sections 13.3.2 and 13.5) and the General Bathymetric Chart of the Oceans (GEBCO; see Excursus 7.1).

Excursus 13.1—Australian Bathymetric and Topographic Grid

Source: GA (2018): *https://ecat.ga.gov.au/geonetwork/srv/eng/catalog.search?node=srv#/metadata/a05f7892-fae9-7506-e044-00144fdd4fa6*
Further Information: Heap and Harris (2008); Harris *et al.* (2005)

The Australian Bathymetric and Topographic Grid is a consistent, bathymetric data grid, with 250 m resolution, which was created from a range of available datasets (Harris *et al.*, 2005; see Figure 13.3). This grid was produced "specifically to provide regional and local broad scale context for scientific and industry projects, and public education" and "is not suitable for use as an aid to navigation, or to replace any products produced by the Australian Hydrographic Service" (GA, 2018).

The major geomorphic zones, or Primary Bathymetric Units (see Section 6.2), within Australia's marine jurisdiction are the continental shelf, the continental slope, the continental rise, and the abyssal plain (see Figure 13.4 and Table 13.1). These broad categories have been subdivided into bioregions for the National Marine Bioregionalisation (NMB; Keene *et al.*, 2008).

Figure 13.3 Australian Bathymetric and Topographic Grid

Bathymetry is shaded from shallow (white) to deep (blue) for the Australian margin, adjacent seafloor and offshore islands. The subregions indicated are detailed in Heap and Harris (2008).

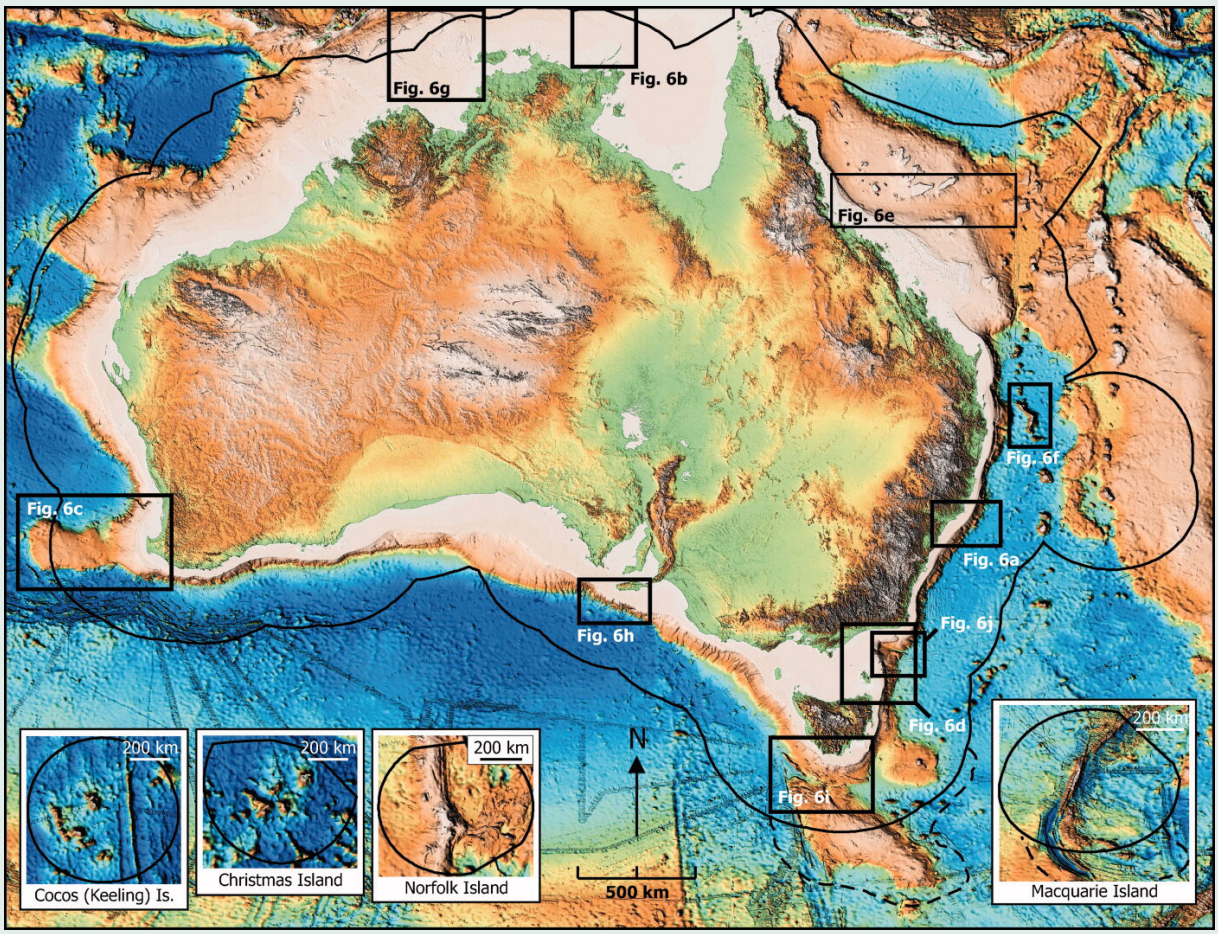

Source: Heap and Harris (2008) Figure 4

Table 13.1 Surface areas of primary bathymetric units

Number	Name	Area (km²)	Area (%)	Distribution
1	Shelf	1,962,030	21.92	Most extensive in northern Australia and connects to Papua New Guinea.
2	Slope	4,011,010	44.8	Continuous around Australian mainland, except in northern Australia.
3	Rise	97,070	1.08	Most well developed in west margin and absent in east margin.
4	Abyssal Plain	2.882,700	32.20	Absent in north and Norfolk Island margins, and most extensive in east and south.
	Total	**8,575,581**	**100**	

Source: Heap and Harris (2008) Table 2

Figure 13.4 Primary bathymetric units

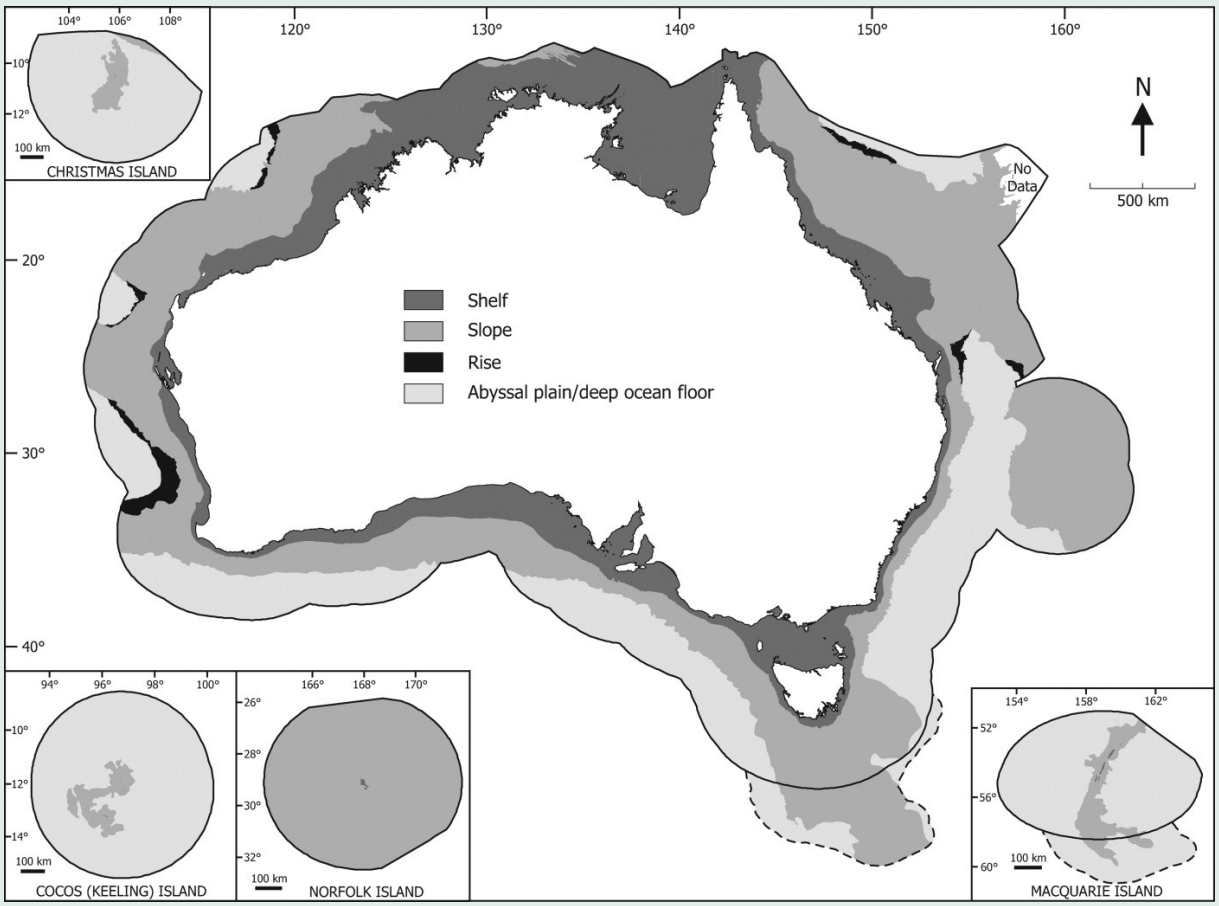

Source: Heap and Harris (2008) Figure 7 (see also: *https://www.environment.gov.au/system/files/resources/36cff669-6183-4ba0-8eab-be8529e78028/files/aspd-bio-2.pdf*)

Drainage maps derived from the Australian Bathymetric and Topographic Grid were also used to identify 21 regional geomorphic features (Heap and Harris, 2008; see Table 13.2). As illustrated in Figure 13.5, the distribution of all features varies regionally. The variety and distribution of these geomorphic features underlie the unique marine environment surrounding Australia. These results have improved our understanding of Australia's continental shelf and slope bathymetry, which is essential for developing regional marine plans and managing our ocean resource, and provided better access to more integrated marine datasets.

Figure 13.5 Distribution of geomorphic features around Australia's continental margin

6,702 individual geomorphic features, covering more than 3.9 million km^2, were identified, leaving 57% of the Australian margin and adjacent seafloor unmapped.

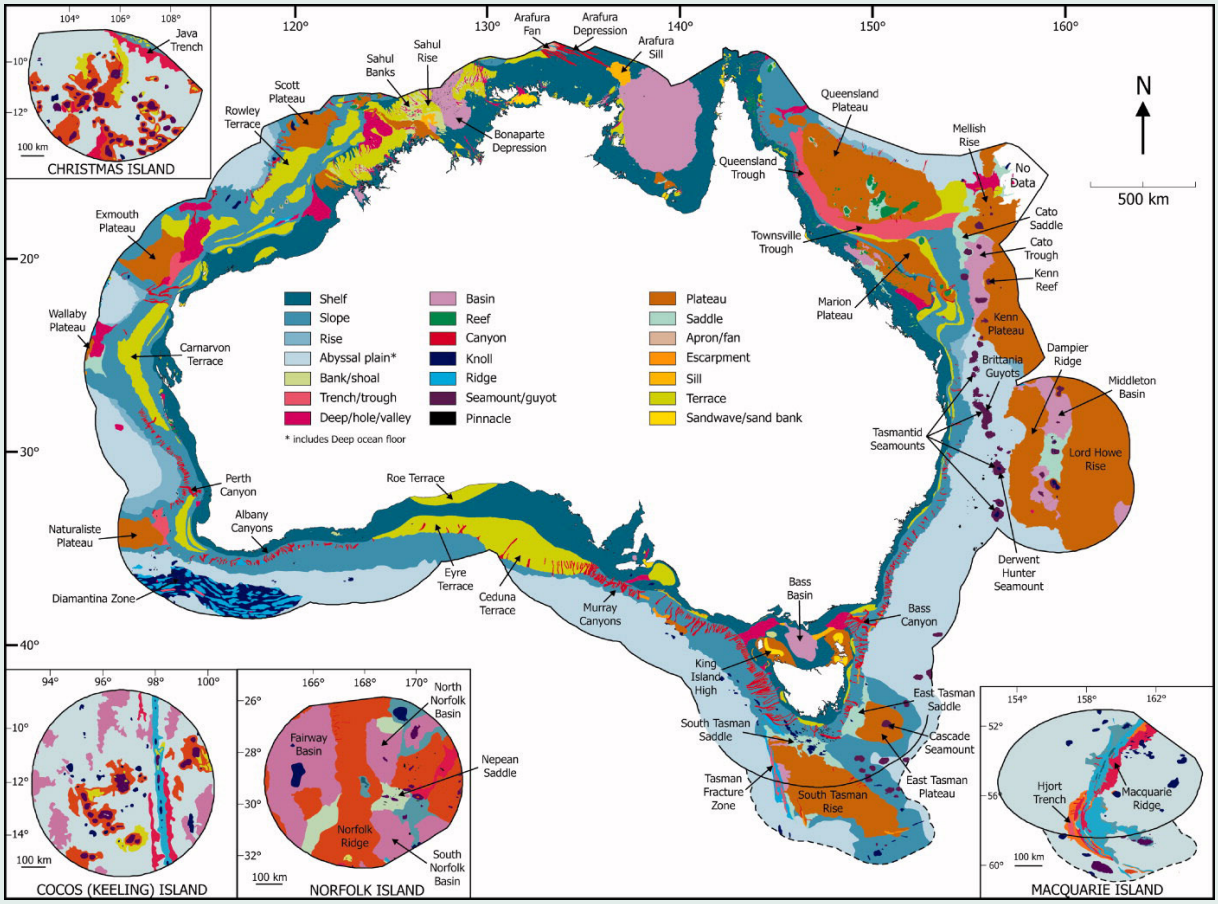

Source: Heap and Harris (2008) Figure 8

Table 13.2 Geomorphic features of Australian continental margin

This set of 21 features was used by Harris *et al.* (2005) to define geomorphic features around the continental margin of Australia, and also to define the global seafloor geomorphic categories shown in Figure 6.2. Features numbered 1 to 20 were derived from IHO (2001) and feature 21 was from Ashley *et al.* (1990).

Number	Name	Definition
1	Shelf	Zone adjacent to a continent (or around an island) and extending from the low water line to a depth at which there is usually a marked increase of slope towards oceanic depths
2	Slope	Slope seaward from the shelf edge to the upper edge of a continental rise or the point where there is a general reduction in slope
3	Rise	Gentle slope rising from the oceanic depths towards the foot of a continental slope
4	Abyssal Plain	Extensive, flat, gently sloping or nearly level region at abyssal depths
5	Bank	Elevation over which the depth of water is relatively shallow but normally sufficient for safe surface navigation
	Shoal	Offshore hazard to surface navigation that is composed of unconsolidated material
6	Deep	In oceanography, an obsolete term which was generally restricted to water depths greater than 6,000 m
	Hole	Local depression, often steep sided, of the seafloor
	Valley	Relatively shallow, wide depression, the bottom of which usually has a continuous gradient. This term is generally not used for features that have canyon-like characteristics for a significant portion of their extent.
7	Trench	Long narrow, characteristically very deep and asymmetrical depression of the seafloor, with relatively steep sides
	Trough	Long depression of the seafloor characteristically flat bottomed and steep sided and normally shallower than a trench
8	Basin	Depression, characteristically in the deep seafloor, more or less equidimensional in plan and of variable extent
9	Reef	Rock lying at or near the sea surface that may constitute a hazard to surface navigation
10	Canyon	A relatively narrow, deep depression with steep sides, the bottom of which generally has a continuous slope, developed characteristically on some continental slopes
11	Knoll	Relatively small isolated elevation of a rounded shape
	Abyssal Hills	Tract, on occasion extensive, of low (100-500 m) elevations on the deep seafloor
	Hill	Small isolated elevation
	Mountains	Large and complex grouping of ridges and seamounts
	Peak	Prominent elevation either pointed or of a very limited extent across the summit
12	Ridge	(a) Long, narrow elevation with steep sides (b) Long, narrow elevation often separating ocean basins (c) Linked major mid-oceanic mountain systems of global extent
13	Seamount	Large isolated elevation, greater than 1000 m in relief above the seafloor, characteristically of conical form
	Guyot	Seamount having a comparatively smooth flat top
14	Pinnacle	High tower or spire-shaped pillar of rock or coral, alone or cresting a summit, which may extend above the surface of the water. It may or may not be a hazard to surface navigation.
15	Plateau	Flat or nearly flat area of considerable extent, dropping off abruptly on one or more sides
16	Saddle	Broad pass, resembling in shape a riding saddle, in a ridge or between contiguous seamounts
17	Apron	Gently dipping featureless surface, underlain primarily by sediment, at the base of any steeper slope
	Fan	Relatively smooth, fan-like, depositional feature normally sloping away from the outer termination of a canyon or canyon system
18	Escarpment	Elongated and comparatively steep slope separating or gently sloping areas
19	Sill	Seafloor barrier of relatively shallow depth restricting water movement between basins
20	Terrace	Relatively flat horizontal or gently inclined surface, sometimes long and narrow, which is bounded by a steeper ascending slope on one side and by a steeper descending slope on the opposite side.
21	Sand Wave	Wave-like bed form made of sand on the seafloor
	Sandbank	Submerged bank of sand in a sea or river that may be exposed at low tide

Source: Harris *et al.* (2005) Tables 2.3 and Heap and Harris (2008) Table 3

13.2 EO Sensors for Bathymetry

The major data sources, platforms, and instruments used for EO are introduced in Volume 1A. Bathymetric and seabed mapping is undertaken using a variety of sensors carried by a range of platforms, including ships, autonomous underwater vehicles (see Excursus 5.1), autonomous surface vehicles, deep-tow equipment, satellites, and fixed wing aircraft (see Table 13.3). The acquired data are used to create products such as bathymetric maps that reveal the topography of the seabed.

Satellite-based radar altimetry provides useful information for regional and global coverage of ocean bathymetry (see Section 13.3.1). Bathymetric maps with higher spatial resolution and accuracy are produced using acoustic data acquired by echosounders (see Sections 10.2.3 and 13.3.2). For coastal bathymetric applications, lidar (see Section 13.4.1) and satellite-based bathymetric methods (see Section 13.4.2) are suitable. Optical sensors that can be used for shallow water bathymetry are listed in Table 8.14.

Table 13.3 EO sensors relevant to bathymetry

Type	Sensor	Platform	Relevance	Advantages	Disadvantages
Passive optical	Multispectral radiometer	Satellite or airborne	Coastal bathymetry	Low cost, large area coverage	Lower vertical accuracy than sonar with direct measurements
Active optical	Bathymetric lidar	Airborne	Coastal bathymetry	High spatial resolution	Small coverage, high cost
Active microwave	Radar altimeter	Satellite	Regional seafloor bathymetry	Global coverage	Low spatial resolution
Sonar	Single beam echosounders	Shipborne	Local seafloor bathymetry	Detailed transects	Small coverage, high cost
	Multibeam echosounders	Shipborne	Detailed seafloor bathymetry	Detailed swath	Small coverage, high cost

13.3 Seafloor Mapping

Generally, very little is known about the seafloor. Although our oceans cover over two-thirds of our planet, only 5% of the global ocean floor has been mapped (Wölfl *et al.*, 2019) and less than 25% of Australia's marine jurisdiction has been mapped in high resolution (see Section 13.1). Existing maps of the seafloor are often low resolution, having been derived from satellite-acquired datasets, and only provide a general indication of waterbody depth.

Bathymetric data for oceans can be collected by:

- satellite altimeters—which use radar instrumentation to measure the height of the ocean surface (see Section 13.3.1); and
- echosounders—which transmit and receive sound waves to determine waterbody depth (see Section 13.3.2).

For the same location, Figure 13.6 and Figure 13.7 compare the spatial resolution of seafloor data acquired by these two sensors.

Figure 13.6 Satellite altimetry versus acoustic datasets

a. Image of seafloor acquired by satellite altimetry

b. Multibeam acoustic data overlaid on satellite image

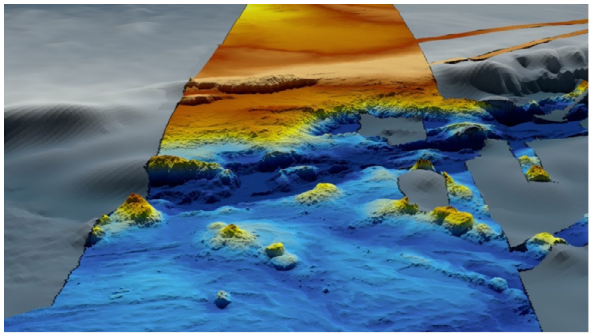

Source: Geoscience Australia

Figure 13.7 Example of bathymetric data improvements

After the disappearance of Malaysia Airlines flight MH370 in 2014, underwater search operations required detailed bathymetric data to be acquired using MBES in the southeast Indian Ocean. The images below compare the level of detail available for Diamantina trench before and after the search. Between these datasets, waterbody depth values differed by more than 100 m in 38% of grid cells, with the maximum difference being 1900 m (Picard *et al.*, 2018).

a. Bathymetric map derived from marine gravity information estimated from satellite altimetry and combined with sonar soundings (Smith and Sandwell, 1997; sourced from SRTM15–PLUS model, Olson *et al.*, 2016).

b. Bathymetric map derived from ship-based MBES data, gridded at 110 m horizontal resolution

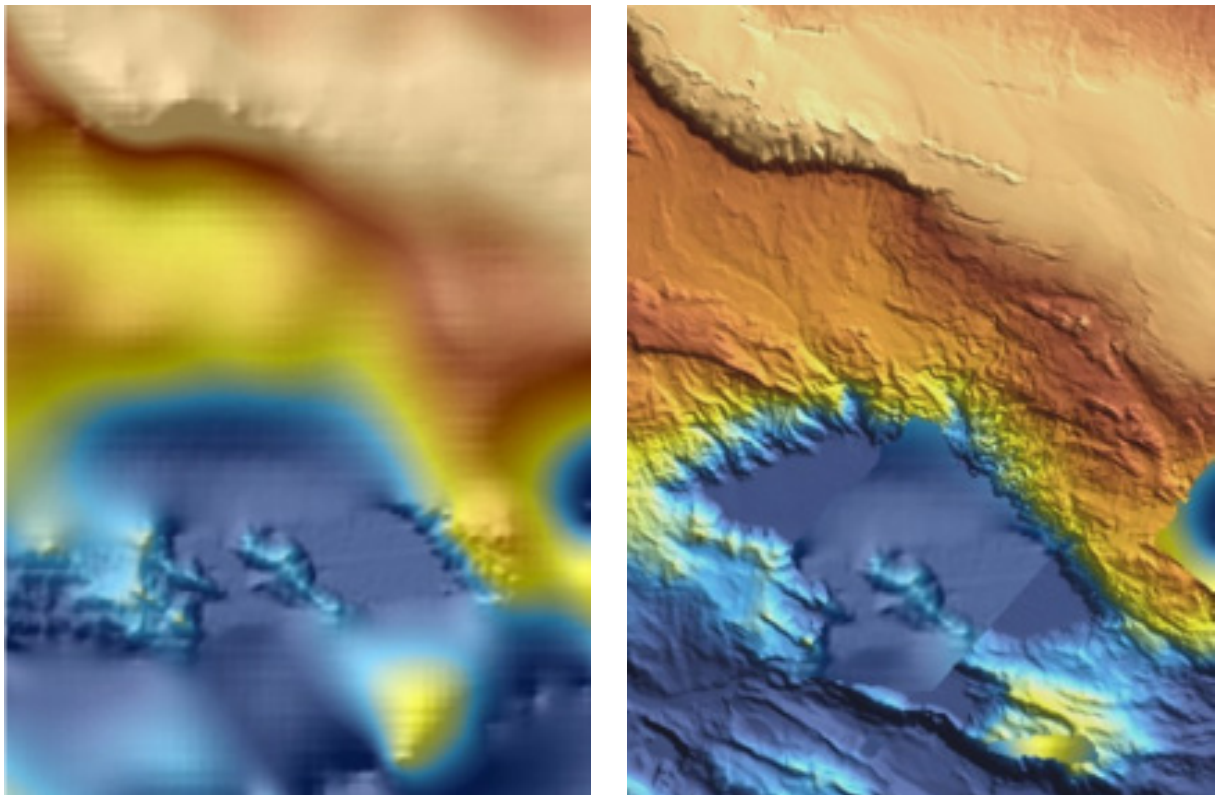

Source: Australian Government (2017)

13.3.1 Satellite radar altimetry

Satellite-borne, radar-based sensors called radar altimeters can be used to measure the height of the ocean surface (see Section 9.5 above and Volume 1A—Section 16). As discussed in Section 12, satellite altimetry measurements can be used to locate seafloor areas that are elevated. Basically, where hills or mountains exist on the seafloor, the gravitational pull around those areas is greater, making the sea surface bulge (Sandwell and Smith, 1997). Low resolution maps of general geomorphic features over a large area can be reliably produced from such datasets.

These datasets have been used to produce regional and global maps of both sea surface and seafloor topography. The first global map showing the topography of ocean basins was developed by Smith and Sandwell (1977) using gravity data from Geosat and satellite altimetry data from ERS-1 with available depth soundings. This revolutionary map provided new insights into the shape of our planet and the boundaries of tectonic plates. The original map has been updated using more recent EO datasets to improve accuracy (Sandwell *et al.*, 2014; see Figure 13.8). Satellite-derived gravity models have become a primary tool for investigating remote ocean basins, mapping tectonic structures, and understanding regional tectonic processes (Sandwell *et al.*, 2014).

Radar altimetry data is also instrumental for monitoring sea level (see Section 12), mapping significant wave heights (see Section 16), and modelling water circulation patterns (see Section 17).

Figure 13.8 Global map of marine gravity

Global Marine Gravity Version 23.1. Colour spectrum shows gravity anomaly from -200 (blue) to 250 (red) mGal.

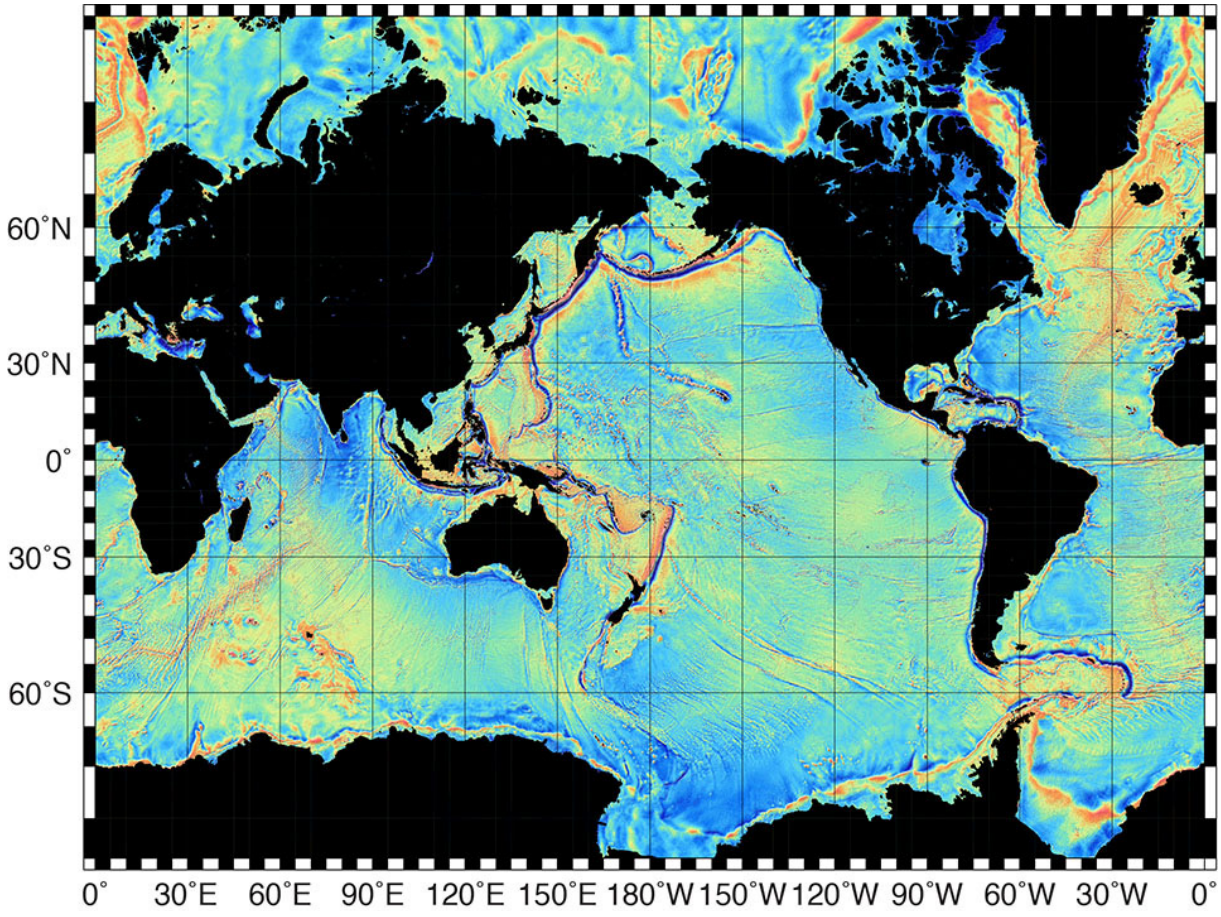

Source: Sandwell *et al.* (2014). Scripps Instituion of Oceanography, 2 October 2014.

13.3.2 Echosounders

Acoustic sensors, which detect sound waves, are introduced in Volume 1A—Section 9.1 and Section 10 above. Bathymetric data is acquired by both research and commercial surveys from two types of acoustic sensor (see Figure 10.4):

- single beam echosounders (SBES)—which produce a single line of waterbody depth points directly under the sensing platform. These measurements are usually acquired from a moving vessel to identify general seafloor patterns and/or schools of fish (see Section 10.2.1); or
- multibeam echosounders (MBES)—which capture swaths of data by acquiring multiple depth points. These datasets are very high resolution, providing data down to better than 1 m accuracy (see Section 10.2.3). With the capability of covering 100% of the seafloor, MBES are becoming the industry standard for hydrographic and geological applications.

Different acoustic frequencies are used to map different waterbody depths, with higher frequencies being used for shallow water and lower frequencies for deep water (see Section 10.1). Higher frequency, shallow water systems provide greater spatial resolution than lower frequency deep water systems (Picard *et al.*, 2020).

The Australian Hydrographic Office (AHO) retains a copy of every bathymetric survey acquired in Australian waters to be used for charting and navigation purposes. Geoscience Australia (GA) uses datasets acquired both internally and by other agencies and companies to produce a range of products to meet government and scientific needs, including:

- maps of individual surveys;
- a 50 m multibeam dataset of Australia, with a backscatter mosaic and a set of angular backscatter response curves; and
- the Australian Bathymetry and Topography Grid (see Excursus 13.1).

Figure 13.9 AusSeabed bathymetry holdings (by survey) in January 2020

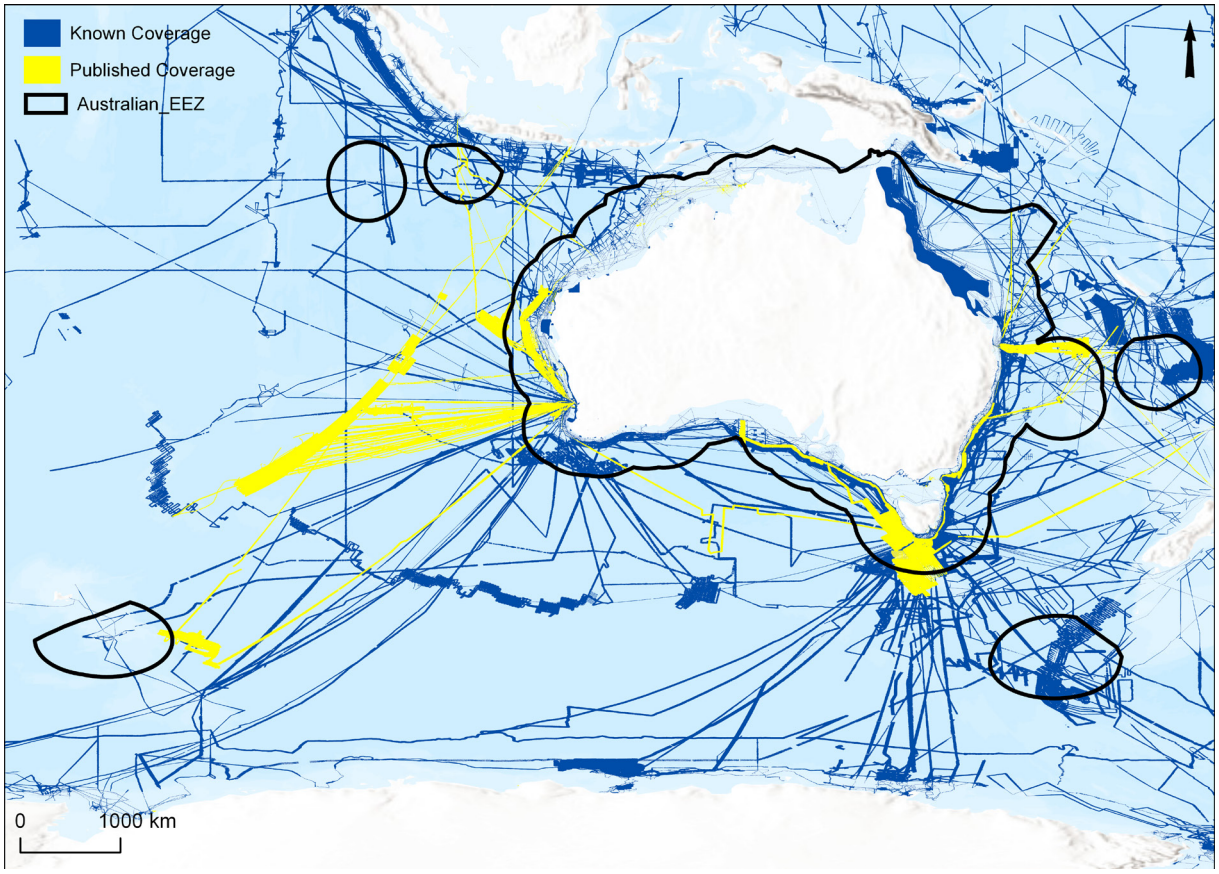

Source: Geoscience Australia

The nationally coordinated program, AusSeabed, is improving the coordination of Australian seabed mapping activities, including collating existing seabed datasets and making them openly accessible, as well as the development of best practice guidelines. The AusSeabed data holdings in January 2020 are illustrated in Figure 13.9. This work contributes to global projects, such as the GEBCO-Nippon Foundation Seabed 2030 project (see Excursus 7.1).

Non-bathymetric applications of acoustic datasets for marine and coastal environments include:

- identification, classification and mapping of benthic habitats (Penrose *et al.*, 2005; see Section 3);
- biomass assessment of pelagic fisheries (see Section 20); and
- engineering and defence investigations of seabed to detect buried munitions, or assess the feasibility of burying cables and pipelines (Austine and Pyne, 2017).

13.4 Coastal Monitoring

While shipborne sensors are appropriate for mapping the seabed in deeper waters, they are not the most appropriate and efficient way to map very shallow waters near land. Bathymetric maps for the narrow coastal margin of the seafloor are best derived from:

- airborne bathymetric lidar systems—which yield datasets with high spatial and vertical resolutions for localised areas (see Section 13.4.1); and
- imagery acquired by spaceborne, optical sensors—which can be used to infer waterbody depth over larger regions (see Section 13.4.2).

13.4.1 Lidar bathymetry

Lidar (LIght Detection And Ranging) instruments can acquire bathymetric data over shallow waters (< 50 m water depth; Volume 1A—Section 15.1). Bathymetric lidar instruments are generally carried by aircraft and traditionally use a 532 nm laser (blue-green). This wavelength offers the most efficient solution in terms of the engineering and physical constraints in lidar instrument design. Lidar can also be used as *in situ* sensors (see Volume 3A—Excursus 5.1). However, the power of lidar must be constrained to comply with eye safety regulations, which limits its potential in some

situations. More recently, oceanographic lidar systems comprise multiple wavelengths. Chen *et al*. (2019) recommend the wavelength range 420–510 nm as optimal for open ocean and 520–580 nm for coastal waters. For 80% of the global ocean a 490 nm laser was shown to be most informative single wavelength (Chen *et al*., 2019).

As with all forms of EMR, some of the laser energy is refracted, backscattered, or absorbed by the water surface, the water column, and the substratum. These factors reduce the lidar signal returned by the substratum and limit the maximum waterbody depth that can be detected. The intense laser signal generated by lidar can penetrate to greater water depths than passive sunlight, and can reach 60 m in clear, coral waters (Purkis and Brock, 2013). The maximum depth penetration of a lidar system depends on its *kd* factor:

$$kd = k \times d$$

where

k is the attenuation coefficient of the water; and
d is the water depth.

Since high water clarity allows maximum light penetration, lidar acquisition is best timed during periods of minimum turbidity. Bathymetric lidar instruments frequently also carry a near infrared laser to measure the distance to the water surface. The waterbody depth is then determined from the time difference (in picoseconds) between the surface return and the substratum return (see Figure 13.10). It should be noted that the speed of light differs through air and water, so a dual wavelength lidar offers greater ranging accuracy. Lidar systems designed to capture submerged topography, rather than measure water depth, require more accurate aircraft positioning information.

Figure 13.10 Lidar bathymetry

Water depth can be computed from the travel time difference (*t*) between pulse returns from the water surface and the bottom. Depth = *ct*/2, where *c* is velocity of laser light pulse.

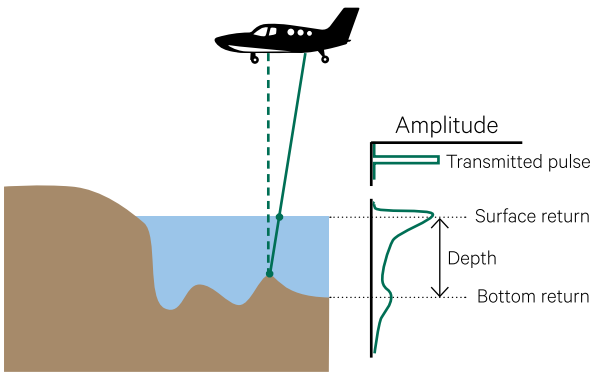

Adapted from: Purkis and Brock (2013) Figure 5.1

Like multibeam sonar, lidar sensors generate a 'point cloud' of data. The raw bathymetric lidar dataset comprises discrete sounding measurements, which can subsequently be processed into contour maps, triangulated area networks (TIN), or raster images (see Volume 2D—Section 13). Dark substrates typically give poor lidar returns, so dense meadows of seagrass and algae growing on the seafloor can create problems for this technology. Cloud cover is also a problem for lidar, but most airborne missions can be timed to avoid cloudy conditions.

Profiling oceanographic lidar systems deliver quantitative profiles for optical properties (beam and diffuse attenuation, absorption, volume scattering at 180°, and total backscattering) of the water column to depths of 20–30 m in productive coastal waters and 100 m in open ocean (Churnside, 2013).

Applications of bathymetric and profiling lidar include charting for navigational use, fisheries surveys, studies of coral reef ecosystems and geomorphology, and monitoring of coastal engineering and environmental change (Purkis and Brock, 2013). In particular, lidar is very appropriate for accurate seafloor mapping around coral reefs and flood vulnerability mapping in coastal terrain (Brock and Purkis, 2009).

13.4.2 Satellite-derived bathymetry (SDB)

As introduced in Section 13.3.2, bathymetric measurements have traditionally been derived from data acquired by shipborne echosounders. These vessels are usually subject to the underkeel clearance, which generally precludes their use in shallow water environments. Lidar systems are also used to acquire bathymetric data and are usually deployed on aircraft (see Section 13.4.1). However, the high cost of both deployment methods has led hydrographic organisations to evaluate and, in some cases, to integrate satellite-derived bathymetry (SDB) into operational products (for example, Canadian and UK Hydrographic Offices, Chénier *et al*., 2018a).

The use of SDB is largely driven by the existing gaps in hydrographic surveys (Chénier *et al*., 2018b), but the acceptance of this method is complicated given the need for adherence to minimum standard requirements for hydrographic surveys as defined by the International Hydrographic Organisation (IHO). The recently modified S-44 includes a specification matrix to allow some flexibility for the inclusion of non-traditional bathymetric data sources such as SDB products (IHO, 2020).

Methods were developed to use passive optical sensors to estimate and monitor bathymetry in coastal waters and were particularly useful for the high spatiotemporal assessment of coastal erosion, sea level changes, wave height modelling, and habitat monitoring (Poursanidis *et al.*, 2019; Traganos *et al.*, 2018). For these purposes, SDB methods have the advantage of large area coverage at lower cost and are ideally suited to monitoring dynamic shorelines, particularly in remote locations (Poppenga *et al.*, 2018). However, deriving bathymetry in shallow waters is complex, as these environments are subject to varying conditions for a range of factors including water depth, substrate, and water type, sunglint, surf zones, and anthropogenic impacts.

SDB methods have been based on either empirical or physics-based methods, although method category names vary with different authors (for example, Casal *et al.* (2020) describes them as either empirical, empirically-tuned physics-based, or physics-based inversion models whereas Traganos *et al.* (2018) refer to analytical, semi-analytical, or empirical methods).

A semi-empirical model such as the spectral band ratio technique (see Volume 2C—Section 10), also known as the natural logarithm method (Dierssen *et al.*, 2003; Stumpf *et al.*, 2003; IHO-IOC, 2016) have been applied in relatively clear waters for the retrieval of water column depth. These methods rely on the near exponential variation in light absorption of pure water as water depth increases (see Sections 5.1.1 and 8.2.1). Accordingly, since the bottom radiance of a longer wavelength band (such as visible green) will decay faster than that of a shorter wavelength band (such as visible blue), the ratio of the two bands will maintain a near constant value in a uniformly mixed water column. The logarithm of the band ratio is then taken to represent water depth changes as a linear gradient.

Empirically-tuned physics-based models adjust for the water column properties and variable light conditions through a regression with the satellite data and *in situ* depth data such as lidar or MBES (Casal *et al.*, 2020). The spatiotemporal application of this model to other locations and times, can be limited by water constituents and substratum changes, which will impact the performance of the model.

Non-linear empirical methods, such as neural networks require sufficient training data from *in situ* observations (or forward bio-optical modelling) to link EO reflectances to the full range of possible water column properties.

Machine Learning (ML) methods have also demonstrated improved performance over traditional empirical algorithms, but this approach has generally been implemented in relatively clear waters with few cases of turbid water. Table 13.4 lists recent models that have demonstrated potential for bathymetric retrievals. ML methods are well suited for large scale time series and, although demanding in time to train and stabilise, they may provide potential for operational deployment.

Table 13.4 Examples of neural network and machine learning models

Name	Description	Reference
BathyNET	BathyNet: A Deep Neural Network for Water Depth Mapping from Multispectral Aerial Images using a U-Net Convolution Neural Network (CNN)	Mandlburger *et al.* (2021)
SVR	Support Vector Regression	Agrafiotis *et al.* (2019)
SVM Non linear SVM	Support Vector Machine Non linear Support Vector Machine	Eugenio *et al.* (2015) Misra *et al.* (2018)
ANN RNN DNN	Artificial Neural Network Recurrent Neural Network Deep Neural Network	Makboul *et al.* (2017) Dickens and Armstrong (2019)
GLM	Lyzenga generalised model	Hassan and Nadaoka (2017)
BAG	Ensemble regression tree-fitting algorithm using bagging	Hassan *et al.* (2017)
LSB	Ensemble regression tree fitting algorithm of least squares boosting	Hassan *et al.* (2016)
RF	Random Forest algorithm	Sagawa *et al.* (2019)
MARS	Multi-adaptive Regression Spline	Hassan and Nadaoka (2017)

Adapted from: Ashphaq *et al.* (2021)

To address the issue of changing substratum and water column properties, radiative transfer equations were used to model the optical properties and concentrations of constituents in the water column, the substratum type, and the water depth from the measured bio-optical properties of the water. Lee *et al.*, (1999, 2001) developed a semi-analytical model for EO that expresses the subsurface remote-sensing reflectance r_{rs} as a function of a set of environmental variables, that is, measureable water properties which can be estimated from EO data (see Section 8.3). When the modelled remote sensing reflectance $r_{rs}^{modelled}$ is compared to the measured satellite remote sensing reflectance r_{rs}^{input}, the set of environmental variables that minimises the difference between the model and input reflectance provides the solution.

In Wettle and Brando (2006), Brando *et al.* (2009), and Dekker *et al.* (2011), the Lee *et al.* (2001) algorithm was enhanced and evolved into SAMBUCA, a semi-analytical model for bathymetry unmixing and concentration assessment. SAMBUCA was now able to retrieve simultaneous outputs of:

- the water's optically active constituent concentrations (chlorophyll a, coloured dissolved organic matter (CDOM), and non-algal particulate);
- the percentage substratum cover type (either as homogeneous or mixtures of two different types); water column depth; and
- metrics to assess the reliability of the retrieval.

Inversion methods have been applied to a range of multispectral and hyperspectral imagery, from both airborne and spaceborne sensors (Brando *et al.*, 2009; Hedley *et al.*, 2009; Botha *et al.*, 2013). All input imagery to these models require atmospheric correction (and possibly sunglint and skyglint corrections; Kay *et al.*, 2009) correction to ensure the r_{rs} is radiometrically corrected (see Sections 7.1 and 8.1.3) as inversion model retrievals can be underestimated from glint-affected images (Botha *et al.*, 2013).

A range of semi-analytical models have been developed for substrate and water column retrievals as shown in Table 13.5. In Dekker *et al.* (2011), a number of these models were compared, along with an empirical Lyzenga model. The HOPE, BRUCE and SAMBUCA models match spectra using a non-linear search to retrieve the best match of water column properties, waterbody depth, and substrate type. Several of the models have lookup tables (LUT), which are produced by numerical solutions of the radiative transfer model (RTM), to build large databases of reflectance spectra that correspond to a range of bio-optical conditions. The CRISTAL model's database is used to find a matched spectral reflectance to r_{rs}^{input}, then the database can provide the water column properties, waterbody depth, and substrate type. The ALLUT model uses an adaptive LUT method for IOP parameterisation of the model, which merges both methods.

It was found that the semi-analytical models performed better than the empirical model and they obtained an increased accuracy of retrievals with improved optical characterisation of the study site. An accurate characterisation or parameterisation provides boundary conditions for the retrieval of the environmental variables. The results of the models in Dekker *et al.*, 2011, were produced in relatively clear waters and such results would be less reliable from waters with higher levels of phytoplankton or CDOM (Botha *et al.*, 2013). Fearns *et al.* (2011) used a physics-based inversion method (which explicitly deals with water column constituents and benthic material estimation) with airborne HyMap imagery to retrieve bathymetry over coral reef environments.

Similarly, Collings *et al.* (2018) used World View-2 satellite imagery of a coastal region near Perth, with water depths of 2–20 m, to compare the classical stereo photogrammetric approach to bathymetric mapping with an RTM method (Semi-Analytical Model for Unmixing and Concentration Assessment: SAMBUCA; Botha *et al.*, 2016). When validated against lidar bathymetry and towed video data, the modelling approach gave the most accurate results over sand substrates, while stereo algorithms were most effective when different depth features were well-contrasted. A hybrid method that stratified the study area by substrate type allowed the most appropriate bathymetric algorithm to be used.

Table 13.5 Examples of semi-analytical models

A common architecture for all Sentinel Toolboxes is being jointly developed by Brockmann Consult, SkyWatch, and C-S called the Sentinel Application Platform (SNAP). ESA: European Space Agency; SANP:

NAME	Description	Reference
HOPE	Hyperspectral Optimization Process Exemplar	Lee *et al.* (1999)
SAMBUCA	Semi-Analytical Model for Unmixing and Concentration Assessment	Brando *et al.* (2009)
BRUCE	Bottom Reflectance Un-mixing Computation of the Environment model	Klonowski *et al.* (2007)
SWAM	Shallow WAter inversion Model—ESA's SANP toolbox (*https://step.esa.int/main/toolboxes/snap/*)	Hedley *et al.* (2018)
SWIM	Shallow Water Inversion Model	McKinna *et al.* (2015)
CRISTAL	Comprehensive Reflectance Inversion based on Spectrum matching and Table Lookup)	Mobley and Bissett (2011)
ALLUT	Adaptive Linearized Lookup Trees	Hedley *et al.* (2009)
SMLUT	Spectrum Matching and Look Up Table inversion method	Mobley *et al.* (2005)
BOMBER	Bio-Optical Model Based tool for Estimating water quality and bottom properties from Remote sensing images	Giardino *et al.* (2012)

Adapted from: Ashphaq *et al.* (2021)

13.5 Further Information

Bathymetry

Geoscience Australia: *http://www.ga.gov.au/scientific-topics/marine/survey-techniques/bathymetry*

International Hydrographic Organisation (IHO) Data Centre for Digital Bathymetry (DCDB): *https://www.ngdc.noaa.gov/iho/*

EOMAP: Satellite Derived Bathymetry: *http://www.eomap.com/services/bathymetry/*

Bathymetric data repositories

General Bathymetric Chart of the Oceans (GEBCO): *https://www.gebco.net*

Archive of seafloor charts: *https://www.gebco.net/data_and_products/historical_gebco_charts/*

AusSeabed: *http://www.ausseabed.gov.au*

Seamap Australia

Australian seabed habitat classification scheme and spatial database: *https://seamapaustralia.org*

Australasian Underwater Cultural Heritage Database

https://www.environment.gov.au/heritage/underwater-heritage/auchd

Marine Gravity

Sandwell and Smith (1997)

Exploring Ocean Tectonics from Space: *https://topex.ucsd.edu/grav_outreach/index.html#grav_map*

13.6 References

Agrafiotis, P., Skarlatos, D., Georgopoulos, A., and Karantzalos, K. (2019). Shallow water bathymetry mapping from uav imagery based on machine learning. *International Archives Photogrammetry, Remote Sensing and Spatial Information Sciences*, XLII-2/W10, 9–6. *https://doi.org/10.5194/isprs-archives-XLII-2-W10-9-2019*

Ashley, G.M., Boothroyd, J.C., Bridge, J.S., Clifton, H.E., Dalrymple, R.W., Elliott, T., Flemming, B.W., Harms, J.C., Harris, P.T., Hunter, R.E., Kreisa, R.D., Lancaster, N., Middleton, G.V., Paola, C., Rubin, D.M., Smith, J.D., Southard, J.B., Terwindt, J.H.I., and Twitchell, D.C. (1990). Classification of large-scale subaqueous bedforms: a new look at an old problem. *Journal of Sedimentary Petrology*, 60, 160–172.

Ashphaq, M., Srivastava, P.K., and Mitra, D. (2021). Review of near-shore satellite derived bathymetry: classification and account of five decades of coastal bathymetry research. *Journal of Ocean Engineering and Science*. *https://doi.org/10.1016/j.joes.2021.02.006*

Austine K., and Pyne, A. (2017). Subsea Cable Route Surveying—Planning challenges. *Hydro International*. *https://www.hydro-international.com/content/article/subsea-cable-route-surveying*

Australian Government (2017). *The Data Behind the Search for MH370*. Available at: *https://geoscience-au.maps.arcgis.com/apps/Cascade/index.html?appid=038a72439bfa4d28b3dde81cc6ff3214*

Beaman, R.J. (2017). *High-resolution depth model for the Great Barrier Reef—30 m*. Geoscience Australia, Canberra.

Beaman, R. (2018). *High-resolution depth model for Northern Australia—30 m*. Geoscience Australia, Canberra.

Beaman, R. (2020). *High-resolution depth model for the Great Barrier Reef and Coral Sea—100 m*. Geoscience Australia, Canberra. *https://ecat.ga.gov.au/geonetwork/srv/eng/catalog.search#/metadata/133163*

Botha, E.J., Brando, V.E., Anstee, J.M., Dekker, A.G., and Sagar, S. (2013). Increased spectral resolution enhances coral detection under varying water conditions. *Remote Sensing of Environment*, 131, 247–261.

Botha, E.J., Brando, V., and Dekker, A.J. (2016). Effects of per-pixel variability on uncertainties in bathymetric retrievals from high-resolution satellite images. *Remote Sensing*, 8, 459. *https://doi.org/10.3390/rs8060459*

Brando, V.E., Anstee, J.M., Wettle, M., Dekker, A.G., Phinn, S.R., and Roelfsema, C. (2009). A physics based retrieval and quality assessment of bathymetry from suboptimal hyperspectral data. *Remote Sensing of Environment*, 113, 755–770. doi:10.1016/j.rse.2008.12.003.

Brock, J.C., and Purkis, S.J. (2009). The emerging role of LiDAR remote sensing in coastal research and resource management. *Journal of Coastal Research*, 53, 1–5.

Casal, G., Hedley, J.D., Monteys, X., Harris, P., Cahalane, C., and McCarthy, T. (2020). Satellite-derived bathymetry in optically complex waters using a model inversion approach and Sentinel-2 data, *Estuarine, Coastal and Shelf Science*, 241, 106814. *https://doi.org/10.1016/j.ecss.2020.106814*.

Chen, S., Xue, C., Zhang, T., Hu, L., Chen, G., and Tang, J. (2019). Analysis of the Optimal Wavelength for Oceanographic Lidar at the Global Scale Based on the Inherent Optical Properties of Water. *Remote Sensing*, 11, 2705. doi:10.3390/rs11222705

Chénier, R., Faucher, M.-A., Ahola, R., Shelat, Y., and Sagram, M. (2018a). Bathymetric Photogrammetry to Update CHS Charts: Comparing Conventional 3D Manual and Automatic Approaches. *ISPRS International Journal Geo-Information*, 7(10), 395. *https://doi.org/10.3390/ijgi7100395*

Chénier, R., Faucher, M.-A., and Ahola, R. (2018b). Satellite-derived bathymetry for improving Canadian Hydrographic Service charts. *ISPRS International Journal Geo-Information*, 7, 306. *https://www.mdpi.com/2220-9964/7/8/306*.

Churnside, J.H. (2013). Review of profiling oceanographic lidar. *Optical Engineering*, 53(5), 051405. *https://doi.org/10.1117/1.OE.53.5.051405*

Collings, S., Botha, E.J., Anstee, J., and Campbell, N. (2018). Depth of Satellite Images: Depth Retrieval Using a Stereo and Radiative Transfer-based Hybrid Method. (2018). *Remote Sensing*, 8, 1247. *https://doi.org/10.3390/rs10081247*

Dekker, AG.., Phinn, SR.., Anstee, J., Bissett, P., Brando, V.E., Casey, B., Fearns, P., Hedley, J., Klonowski, W., Lee, Z.P., Lynch, M., Lyons, M., Mobley, C., and Roelfsema, C. (2011). Intercomparison of shallow water bathymetry, hydrooptics, and benthos mapping techniques in Australian and Caribbean coastal environments. *Limnology and Oceanography Methods*, 9, 396–425.

Dickens, K., and Armstrong, A. (2019). Application of machine learning in satellite derived bathymetry and coastline detection. SMU Data Science Review, 2(1). *https://scholar.smu.edu/datasciencereview/vol2/iss1/4*

Dierssen, H.M., Zimmerman, R.C., Leathers, R.A., Downes, T.V., and Davis, C.O. (2003). Ocean color remote sensing of seagrass and bathymetry in the Bahamas Banks by high resolution airborne imagery. *Limnology and Oceanography*, 48(1), 444–455.

Eugenio, F., Marcello, J., and Martin, J. (2015). High-Resolution Maps of Bathymetry and Benthic Habitats in Shallow-Water Environments Using Multispectral Remote Sensing Imagery. *IEEE Transactions on Geoscience and Remote Sensing*, 53(7), 3539–3549. *https://doi.org/10.1109/TGRS.2014.2377300*

Fearns, P.R.C., Klonowski, W., Babcock, R.C., England, P., and Phillips, J. (2011). Shallow water substrate mapping using hyperspectral remote sensing. *Continental Shelf Research* 31, 1249–1259.

GA (2018). *Australian Bathymetry and Topography Grid* webpage, Geoscience Australia website: *https://ecat.ga.gov.au/geonetwork/srv/eng/catalog.search?node=srv#/metadata/a05f7892-fae9-7506-e044-00144fdd4fa6*

GEBCO (2017). *Seabed 2030: Roadmap for Future Ocean Floor Mapping*. The Nippon Foundation/GEBCO (General Bathymetric Chart of the Oceans), June 2017. *https://www.gebco.net/documents/seabed_2030_roadmap_v10_low.pdf*

Giardino, C., Candiani, G., Bresciani, M., Lee, Z., Gagliano, S., and Pepe, M. (2012). BOMBER: A tool for estimating water quality and bottom properties from remote sensing images. *Computers and Geosciences*, 45, 313–318. *https://doi.org/10.1016/j.cageo.2011.11.022*

Harris, P., Heap, A., Passlow, V., Shaffi, L., Fellows, M., Porter-Smith, R., Buchanan, C., and Daniell, J. (2005). *Geomorphic Features of the Continental Margin of Australia*. Geoscience Australia, Canberra.

Hassan, M., Negm, A., Zahran, M., and Saavedra, O. (2016). Bathymetry Determination from High Resolution Satellite Imagery Using Ensemble Learning Algorithms in Shallow Lakes: Case Study El-Burullus Lake. *International Journal of Environmental Science and Development*, 7(4), 295–301. *https://doi.org/10.7763/IJESD.2016.V7.787*

Hassan, M., Salah, M., Nadaoka, K., and Zahran, M. (2017). Assessment of proposed approaches for bathymetry calculations using multispectral satellite images in shallow coastal / lake areas : a comparison of five models. *Arabian Journal of Geosciences*, 10, 42. *https://doi.org/10.1007/s12517-016-2803-1*

Heap, A.D., and Harris, P.T. (2008). Geomorphology of the Australian Margin and Adjacent Seafloor. *Australian Journal of Earth Sciences*, 55(4), 555–585. *http://dx.doi.org/10.1080/08120090801888669*

Hedley, J.D., Roelfsema, C., and Phinn, S.R. (2009). Efficient radiative transfer model inversion for remote sensing applications. *Remote Sensing of Environment,* 113(11), 2527–2532.

Hedley, J.D., Roelfsema, C., Brando, V., Giardino, G., Kutser, T., Phinn, S., Mumby, P.J., Barrilero, O., Laporte, J., and Koetz, B. (2018). Coral reef applications of Sentinel-2: Coverage, characteristics, bathymetry and benthic mapping with comparison to Landsat 8. *Remote Sensing of Environment*, 216, 598–614. *https://doi.org/10.1016/j.rse.2018.07.014*

Hussein, H.M., and Nadaoka, K. (2017). Assessment of machine learning approaches for bathymetry mapping in shallow water environments using multispectral satellite images. *International Journal of GeoInformatics*, 13(2). *https://doi.org/10.52939/ijg.v13i2.1030*

IHO (2001). *Standardization of Undersea Feature Names: Guidelines Proposal form Terminology*. International Hydrographic Organisation and International Oceanographic Commission, Monaco. 40 p.

IHO (2020). *International Hydrographic Organization Standards for Hydrographic Surveys*. International Hydrographic Organisation. *https://iho.int/uploads/user/pubs/standards/s-44/S-44_Edition_6.0.0_EN.pdf*

IHO-IOC (2016). *The IHO-IOC GEBCO cook book*. IHO Publication B–11 (Monaco), IOC Manuals and Guides 63 (France). International Hydrographic Organization, Intergovernmental Oceanographic Commission. *https://www.gebco.net/data_and_products/gebco_cook_book/*

Kay, S., Hedley, J.D., and Lavender, S. (2009). Sun Glint Correction of High and Low Spatial Resolution Images of Aquatic Scenes: a Review of Methods for Visible and Near-Infrared Wavelengths. *Remote Sensing*, 1(4), 697–730. *https://doi.org/10.3390/rs1040697*

Keene, J., Baker, C., Tran, M., and Potter, A. (2008). *Geomorphology and Sedimentology of the East Marine Region of Australia*. Geoscience Australia, Record 2008/10. Geoscience Australia, Canberra. 262 p.

Klonowski, W.M., Fearns, P.R.C.S., and Lynch, M.J. (2007). Retrieving key benthic cover types andbathymetry from hyperspectral imagery. *Journal Applied Remote Sensing*, 1(1), 011505. *https:/doi.org/10.1117/1.2816113*

Lee, Z.P., Carder, K.L., Mobley, C.D., Steward, R.G., and Patch, J.F. (1999). Hyperspectral remote sensing for shallow waters: II. deriving bottom depths and water properties by optimization. *Applied Optics*, 38, 3831–3843, *https://doi.org/10.1364/AO.38.003831*

Lee, L. Kendall, C., Chen, R.F., and Peacock, T.G. (2001). Properties of the water column and bottom derived from Airborne Visible Imaging Spectrometer (AVIRIS) data. J*ournal of Geophysical Research*, 106, 11639–11651.

Lyzenga, D., Malinas, N., and Tanis, F. (2006). Multispectral bathymetry using a simple physically based algorithm. *IEEE Transactions on Geoscience and Remote Sensing,* 44, 2251–2259.

McKinna, L., Fearns, P., Weeks, Werdell, P.J., S., Reichstetter, M., Franz, B., Shea, D.M., and Feldman, G. (2015). A semianalytical ocean color inversion algorithm with explicit water column depth and substrate reflectance parameterization. *Journal of Geophysical Research: Oceans*, 120(3), 1741–1770. *https://doi.org/10.1002/2014JC010224*

Makboul, O., Negm, A., Mesbah, S., and Mohasseb, M. (2017). Performance Assessment of ANN in Estimating Remotely Sensed Extracted Bathymetry. Case Study: Eastern Harbor of Alexandria. *Procedia Engineering*, 181, 912–919. *https://doi.org/10.1016/j.proeng.2017.02.486*

Mandlburger, G., Kölle, M., Nübel, H., and Soergel, U. (2021). BathyNet: A Deep Neural Network for Water Depth Mapping from Multispectral Aerial Images. *PFG—Journal of Photogrammetry, Remote Sensing and Geoinformation Science*, 89, 71–89. *https://doi.org/10.1007/s41064-021-00142-3*

Misra, A., Vojinovic, Z., Ramakrishnan, B., Luijendijk, A., and Ranasinghe, R. (2018). Shallow water bathymetry mapping using Support Vector Machine (SVM) technique and multispectral imagery. *International Journal of Remote Sensing*, 39(13), 4431–4450. *https://doi.org/10.1080/01431161.2017.1421796*

Mobley, C.D., and Bissett, W.P. (2011). *CRISTAL user's guide and technical documentation*. Sequoia Scientific, Inc. 97 p. *https://www.iisd.org/publications/cristal-users-manual-version-5-community-based-risk-screening-tool-adaptation-and*

Mobley, C.D., Sundman, L.K., Davis, C.O., Bowles, J.H., Downes, T.V., Leathers, R.A., Montes, M.J., Bissett, W.P., Kohler, D.D.R., Reid, R.P., Louchard, E.M., and Gleason, A. (2005). Interpretation of hyperspectral remote-sensing imagery by spectrum matching and look-up tables. *Applied Optics*, 44, 3576–3592. *https://doi.org/10.1364/AO.44.003576*

Olson, C.J., Becker, J.J., and Sandwell, D.T. (2016). *SRTM15_PLUS: Data Fusion of Shuttle Radar Topography Mission (SRTM) Land Topography with Measured and Estimated Seafloor Topography (NCEI Accession 0150537)*. Version 1.1. Asheville: NOAA National Centers for Environmental Information.

Penrose, J.D., Siwabessy, P.J.W., Gavrilov, A., Parnum, I., Hamilton, L.J., Bickers, A., Brooke, B., Ryan, D.A., and Kennedy, P. (2005). *Acoustic Techniques for Seabed Classification*. Technical Report 32, CRC for Coastal Zone Estuary and Waterway Management.

Picard, K., Brooke, B.P., Harris, P.T., Siwabessy, P.J.W., Coffin, M.F., Tran, M., Spinoccia, M., Weales, J., Macmillan-Lawler, M., and Sullivan, J. (2018). Malaysia Airlines flight MH370 search data reveal geomorphology and seafloor processes in the remote southeast Indian Ocean. *Marine Geology*, 395, 301–319. *https://doi.org/10.1016/j.margeo.2017.10.014*

Picard, K., Leplastrier, A., Austine, K., Bergersen, N., Cullen, R., Dando, N., Donohue, D., Edwards, S., Ingleton, T., Jordan, A., Lucieer, V., Parnum, I., Siwabessy, J., Spinoccia, M., Talbot-Smith, R., Waterson, C., Barrett, N., Beaman, R., Bergersen, D., Boyd, M., Brace, B., Brooke, B., Cantrill, O., Case, M., Dunne, S., Fellows, M., Harris, U., Ierodiaconou, D., Johnstone, E., Kennedy, P., Leplastrier, A., Lewis, A., Lytton, S., Mackay, K., McLennan, S., Mitchell, C., Nichol, S., Post, A., Price, A., Przeslawski, R., Pugsley, L., Quadros, N., Smith, J., Stewart, W., Sullivan J., Tran, M., and Whiteway, T. (2020). *Australian Multibeam Guidelines 2020*. Version 2.0. Record 2018/19. Geoscience Australia, Canberra. *http://dx.doi.org/10.11636/Record.2018.019*

Poppenga, S.K., Palaseanu-Lovejoy, M., Gesch, D.B., Danielson, J.J., and Tyler, D.J. (2018). *Evaluating the potential for near-shore bathymetry on the Majuro Atoll, Republic of the Marshall Islands, using Landsat 8 and WorldView-3 imagery*. U.S. Geological Survey Scientific Investigations Report 2018–5024. 14 p. *https://doi.org/10.3133/sir20185024*.

Poursanidis, D., Dimosthenis T., Nektarios C., and Peter R. (2019). Cubesats Allow High Spatiotemporal Estimates of Satellite-Derived Bathymetry. *Remote Sensing*, 11(11), 1299. *https://doi.org/10.3390/rs11111299*

Purkis, S.J., and Brock, J.C. (2013). Lidar Overview. Ch 5 in *Coral Reef Remote Sensing*. (Eds: Goodman, J.A., Purkis, S.J., and Phinn, S.R.). Springer, Dordrecht. ISBN 978-90-481-9291-5.

Sagawa, T., Yamashita, Y., Okumura, T., and Yamanokuchi, T. (2019). Satellite Derived Bathymetry Using Machine Learning and Multi-Temporal Satellite Images. *Remote Sensing*, 11(10), 1155. *https://doi.org/10.3390/rs11101155*

Sandwell, D.T., and Smith, W.H.F. (1997). *Exploring the Ocean Basins with Satellite Altimeter Data* webpage: *https://topex.ucsd.edu/marine_grav/explore_grav.html*

Sandwell, D.T., Müller, R.D., Smith, W.H.F., Garcia, E., and Francis, R. (2014). New global marine gravity model from CryoSat-2 and Jason-1 reveals buried tectonic structure. *Science*, 346(6205), 65-67. doi:10.1126/science.1258213

Smith, W.H.F., and Sandwell, D.T. (1997). Global seafloor topography from satellite altimetry and ship depth soundings. *Science*, 277, 1957–1962.

Stumpf, R.P., Holderied, K., and Sinclair, M. (2003). Determination of water depth with high-resolution satellite imagery over variable bottom types. *Limnology and Oceanography,* 48, 547–556.

Traganos, D., Poursanidis, D., Aggarwal, B., Chrysoulakis, N., and Reinartz, P. (2018). Estimating Satellite-Derived Bathymetry (SDB) with the Google Earth Engine and Sentinel-2. *Remote Sensing*; 10(6), 859. *https://doi.org/10.3390/rs10060859*

Wettle, M., and Brando, V.E. (2006). *SAMBUCA—Semi-analytical model for Bathymetry, un-mixing and concentration assessment*. CSIRO Land and Water, Canberra. *https://doi.org/10.4225/08/5866a187b7a3c*

Wölfl, A.-C., Snaith, H., Amirebrahimi, S., Devey, C.W., Dorschel, B., Ferrini, V., Huvenne, V.A.I., Jakobsson, M., Jencks, J., Johnston, G., Lamarche, G., Mayer, L., Millar, D., Pedersen, T.H., Picard, K., Reitz, A., Schmit,t T., Visbeck, M., Weatherall, P., and Wigley, R. (2019). Seafloor Mapping—The Challenge of a Truly Global Ocean Bathymetry. *Frontiers in Marine Science*, 6, 283. *https://doi.org/10.3389/fmars.2019.00283*

Observing Surface Water Energy

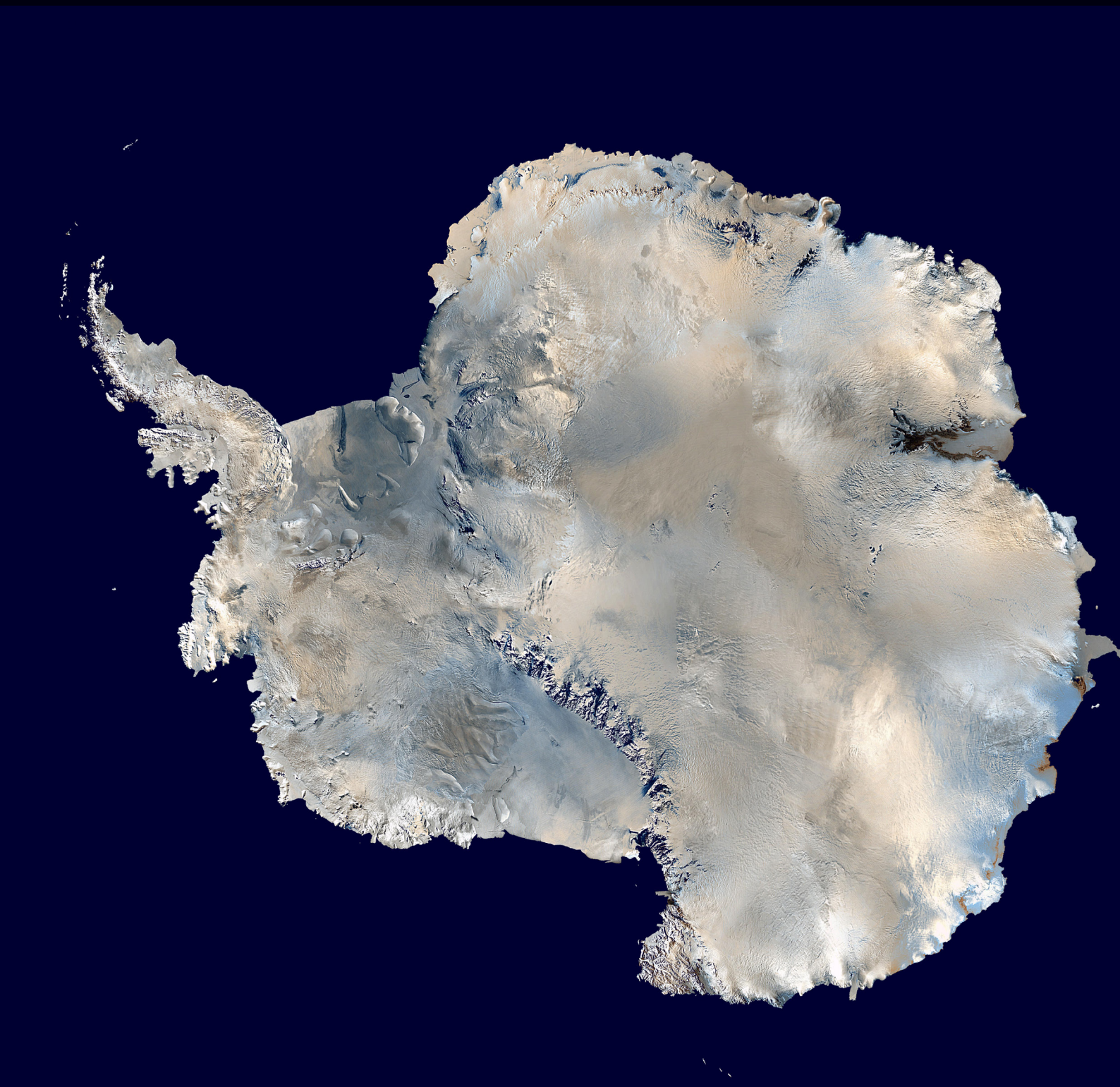

The following four sections detail EO-based analyses that can be used to map and monitor the energy in surface waters:

- temperature—details EO methods and datasets used to estimate sea surface temperature and inland water temperature, and detect sea ice (see Section 14);
- ice—considers EO methods to map and monitor both sea ice and ice sheets (see Section 15);
- wind and waves—describe EO methods for mapping and monitoring marine surface waves (see Section 16); and
- circulation—introduces EO techniques that can be used to monitor ocean circulation patterns (see Section 17).

Contents

14 Temperature 245

15 Ice 281

16 Winds and Waves 311

17 Circulation 329

Background image on previous page: An orthographic projection of Antarctica from NASA's Blue Marble dataset (1 km resolution global satellite composite) derived from MODIS and AVHRR imagery. **Source:** Davepape, Wikimedia Commons. Retrieved from *https://en.wikipedia.org/wiki/File:Antarctica_6400px_from_Blue_Marble.jpg*

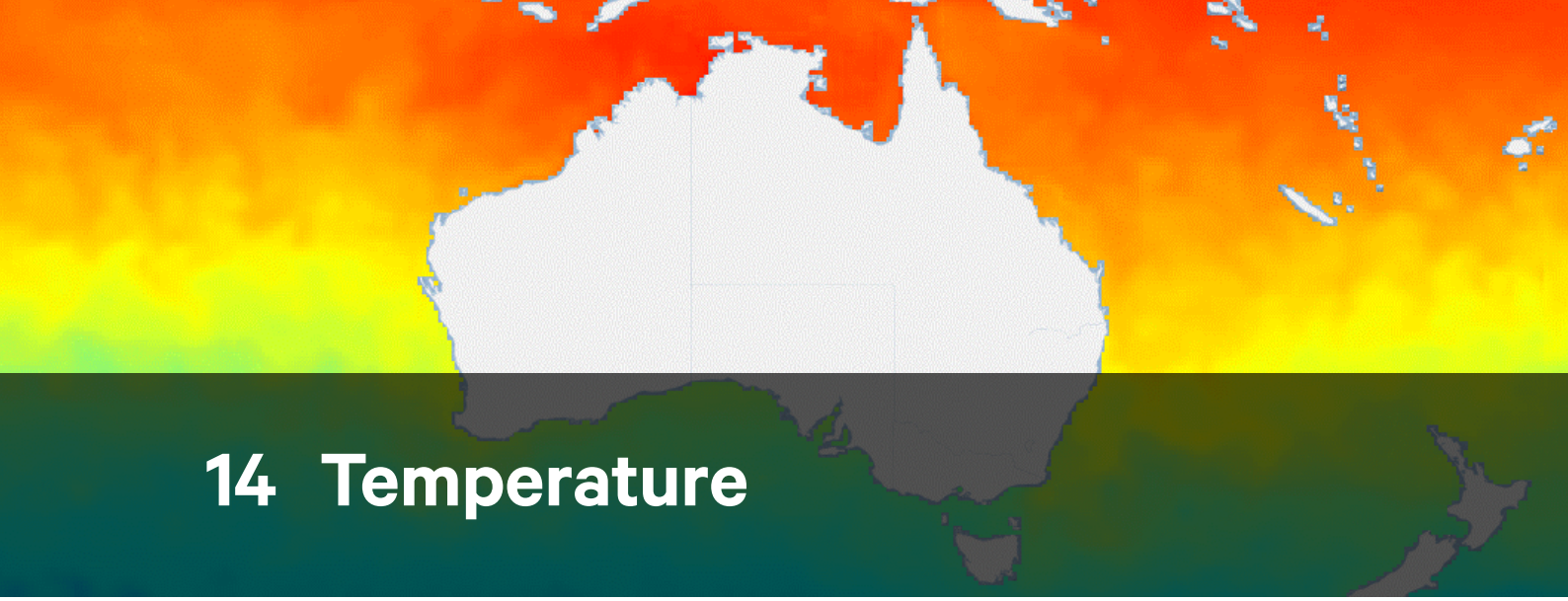

14 Temperature

Helen Beggs

Sea surface temperature (SST) is a vital parameter across a range of marine and climate sciences. Because SST strongly modulates air-sea fluxes it is an essential parameter in weather prediction and atmospheric model simulations. It is also of great importance to the biodiversity and biogeochemistry of the oceans, and marine ecosystem dynamics (Wijffels *et al.,* 2018; see Sections 3, 5, 19, 20, and 21). SST measurements benefit a wide spectrum of operational applications, including ocean, weather, climate and seasonal monitoring/forecasting, military defence operations, validation of atmospheric models, sea turtle tracking, evaluation of coral bleaching, tourism, and commercial fisheries management (Beggs, 2010; O'Carroll *et al.,* 2019; Merchant *et al.,* 2019a). To measure SST, scientists deploy temperature sensors on satellites, drifting and moored buoys, ships, Argo floats, gliders, marine mammals (for example, seals), and ocean reference stations (Merchant *et al.,* 2019a). *In situ* measurements from drifting buoys, moorings, Argo floats, and ships are commonly used to calibrate and validate the satellite-derived SST data (see Section 12.2.2).

In the following sections we introduce temperature variations in Australian surface waters (see Section 14.1) then consider Earth Observation (EO) sensors that are used to map and monitor the temperature of the water surface (see Section 14.2). Methods for retrieving and validating SST from EO imagery are detailed in Section 14.3. Sections 14.4 and 14.5 introduce global and regional satellite products respectively and some sample applications, while Section 14.6 describes the use of EO datasets for observing water temperature of inland waterbodies.

14.1 Temperature of Australian Surface Waters

As discussed in Section 1.2 above, the oceans around Australia cover the extremes of the Tropical Warm Pool to the north of Australia, containing the largest area of warmest surface SSTs on the globe, to the Southern Ocean and the 'Roaring Forties' to the south. Indicative water temperatures surrounding the Australian land mass are shown in Figure 14.1, as derived from remotely sensed SST (Wijffels *et al.,* 2018; Griffin *et al.,* 2017).

Background image: Sea surface temperature image for 2 November 2020. Source: Helen Beggs, Bureau of Meteorology, Melbourne.

Recommended Chapter Citation: Beggs, H. (2021). Temperature. Ch 14 in *Earth Observation: Data, Processing and Applications. Volume 3B—Surface Waters.* CRCSI, Melbourne. pp. 245–279. ISBN 978-0-6482278-5-4.

Figure 14.1 Average SST around Australia

This map from the Atlas of Australian Regional Seas (SSTAARS—see Section 14.7) shows mean sea surface temperature (SST) from 1992 to 2016, as derived from AVHRR imagery.

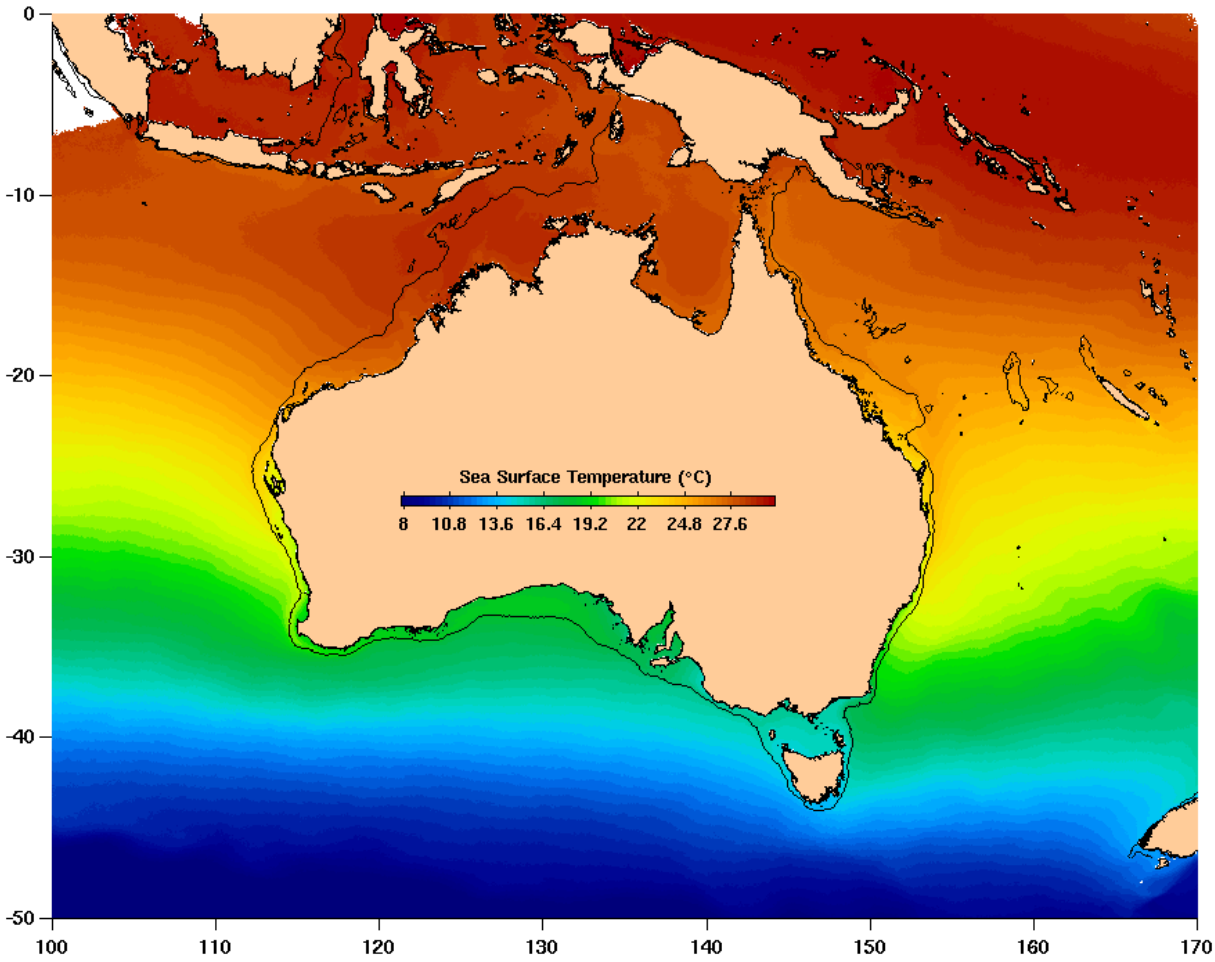

Source: IMOS OceanCurrent (2018). Retrieved from *http://oceancurrent.imos.org.au/monthlymeans.php?link=/30d_MEAN/CLIM_OFAM3_SSTAARS/SST30d/00.gif*

14.2 EO Sensors for Water Temperature

As introduced in Volume 1A—Sections 5.2.2, the thermal radiation of the Earth's surface can be sensed remotely by detecting emissions in the wavelength ranges of:

- middle infrared (MIR: 3–8 μm);
- thermal infrared (TIR: 8–15 μm; see Volume 1A—Section 14.4, and Volume 1B—Section 7); and/or
- microwave (MW: 1–300 mm; see Volume 1A—Section 14.5, and Volume 1B—Section 8.1).

The MIR region is predominantly used for sensing emissions from very hot objects, such as fires and other man-made and natural thermal features on the Earth's surface. Since the TIR radiation range coincides with the peak energy emission of Earth, it is used for monitoring surface water temperature (SWT) and land surface temperature (LST). Passive microwave (PMW) sensors, however, detect emissions of thermal radiation in the microwave region at the very low energy end of the Earth's energy spectrum (see Figure 9.1).

EO sensors used for measuring SWT over the Australian region are listed in Table 14.1, and their essential details are summarised below. For a complete list of satellite sensors that have provided SWTs along with further details, refer to Minnett *et al.* (2019). In the text below, we collectively refer to MIR and TIR sensors as infrared (IR) sensors. Since SST specifically refers to the surface temperature of marine waters, the term SWT is used in this chapter when referring to the surface temperature of both inland and marine waterbodies.

Table 14.1 EO sensors relevant to water temperatures

TIR: Thermal infrared

Type	Sensor	Platform	Spatial Resolution (nadir)	Relevance	Advantages	Disadvantages
Passive optical	TIR wide swath (e.g. AVHRR, MODIS, VIIRS, SGLI)	Polar orbiting satellite (e.g. NOAA-6 to NOAA19, METOPA/B/C, Aqua, Terra, Suomi-NPP, NOAA-20, GCOMC)	0.25–4 km (large off-nadir angles reduce resolution)	SST, Inland water temperatures	Available from 1981, high spatial resolution, good accuracy, good global coverage	Fails over cloud and in presence of atmospheric aerosol, AVHRR on NOAA-6 to NOAA-19 satellites experienced significant orbital drift
	TIR dual-view radiometer (e.g. ATSR-1/2, AATSR, SLSTR)	Polar orbiting satellite (e.g. ERS1/2, Envisat, Sentinel-3a/b)	1–2 km (large off-nadir angles reduce resolution)	SST	Most accurate high resolution satellite SST data source, useful for bias-correcting other satellite SST	Only available from 1991, sparser spatial coverage due to narrower swaths, fails over cloud
	TIR Earth Disc Radiometer (e.g. JAMI, AHI)	Geostationary satellite (e.g. MTSAT-1R, MTSAT-2, Himawari-8/9)	2–10 km (large off-nadir angles reduce resolution)	SST, Inland water temperatures	Frequent update (60 min or 10 min) resolves sub-daily features	Limited field of view with no data at high latitudes, coarser spatial resolution than infrared sensors from polar orbiters, fails over cloud and in presence of atmospheric aerosol
Passive microwave	Microwave radiometer (e.g. AMSR-E, AMSR2, TMI, GMI)	Polar orbiting satellite (e.g. Aqua, GCOM-W, TRMM, GPM)	25–50 km	SST, Snow, Ice	Able to measure SST under non-precipitating cloud and therefore better spatial coverage than infrared	Affected by rain, no useable SST within ~50 km of land

Source for data: Minnett *et al.* (2019)

14.2.1 Infrared sensors

The first instrument to measure SWT from space was the High Resolution Infrared Radiometer (HRIR) in 1964 onboard NASA's sun-synchronous Nimbus-1 satellite (launched in 1964). Since HRIR only had a single infrared (IR) channel (3.5–4.1 μm), it could be used for describing variations in SST in clear-sky regions, but not for quantitative measurements (Allison and Kennedy, 1967).

Accurate EO of SWT became possible with the launch of the multi-channel Advanced Very High Resolution Radiometer (AVHRR) passive IR sensor, which was first carried by the Television Infrared Observation Satellite (TIROS-N) in 1978. The six channels acquired by AVHRR/3 (first carried on NOAA-15 in 1998) are listed in Table 14.2.

Table 14.2 AVHRR/3 channels

The first AVHRR sensor acquired only four channels and AVHRR/2 acquired five channels. Spatial resolution at nadir for all bands in AVHRR/3 is 1.09 km.

Channel number	Wavelength range (μm)	Typical use
1	0.58–0.68	Daytime cloud and surface mapping
2	0.725–1.00	Land-water boundaries
3A	1.58–1.64	Snow and ice detection
3B	3.55–3.93	Night cloud mapping, SST
4	10.30–11.30	Night cloud mapping, SST
5	11.50–12.50	SST

Source: NOAA: *https://www.ospo.noaa.gov/Operations/POES/NOAA19/avhrr.html*

AVHRR sensors have been deployed continuously on the National Oceanic and Atmospheric Administration (NOAA) series of Polar Operational Environmental Satellites (POES), starting with NOAA-6 in 1981 and ending with the launch of NOAA-19 in 2009. NOAA-18 and NOAA-19 are the last in the series of POES satellites to carry AVHRR sensors. Orbital decay of NOAA-18 from 2013, and NOAA-19 from November 2017, has affected the calibration, and therefore accuracy, of AVHRR SST products during some months[12]. Operational AVHRR sensors are also carried on the European Space Agency (ESA) MetOp series of polar orbiters, MetOp-A, -B and –C, starting with the launch of MetOp-A on 19 October 2006. Unlike the POES satellites (whose equatorial crossing times drifted significantly over the lifespan of each satellite since there was no onboard fuel to correct their orbits[13]), the MetOp satellites are sustained in stable 'morning orbits' with equatorial crossing times of 9:30 am and 9:30 pm. However, there will be no AVHRR sensors deployed on future missions, as the Second Generation MetOp satellites (MetOp-SG) will carry different IR sensors. Therefore, after the AVHRR sensor on MetOp-C ceases to operate (expected lifespan out to 2024), there will be no further source of operational AVHRR SWT, ending nearly half a century of continuous global measurements by this remarkably reliable sensor. Courtesy of the AVHRR series of sensors, SSTs provide the longest time series of satellite-derived ocean parameters (Minnett *et al.,* 2019).

With a swath width of ~2700 km, the AVHRRs on POES allowed global daily sampling and produced three types of data:

- Global Area Coverage (GAC) data relies on raw data from these sensors being stored on the satellite and transmitted every few hours to receiving stations on the ground at reduced spatial resolution. The raw data is processed onboard the satellite by subsampling one scan line in three, and averaging every four of five adjacent pixels along each scan line (see Figure 14.2 and Volume 2B).
- Local Area Coverage (LAC) data is recorded onboard at original resolution (1.1 km at nadir) for part of the orbit, then transmitted to a ground station when the satellite is within range.
- High Resolution Picture Transmission (HRPT) data uses real time, direct download to satellite ground stations.

Figure 14.2 AVHRR/3 GAC grid resolution and sampling

Simulated Earth surface footprints for AVHRR/3 showing the relationship between full resolution data (Local Area Coverage, LAC, in blue) and reduced resolution Global Area Coverage (GAC, black outlines).

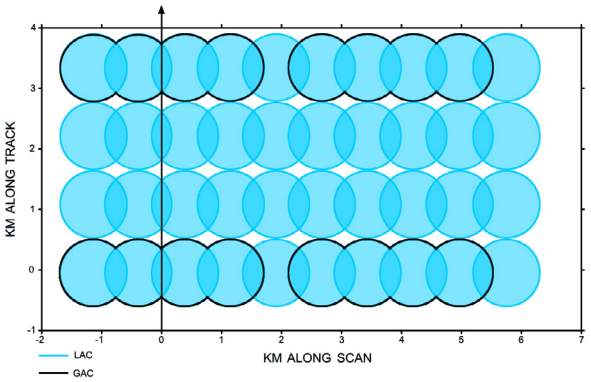

Source: Eumetsat (2011) Figure 4-1

SWTs derived from GAC data have a spatial resolution of ~4 km at nadir (directly below the satellite) which expands to coarser resolution at the edges of swaths (see Figure 14.3a). HRPT data deliver higher resolution SWT measurements at 1.1 km × 1.1 km resolution at nadir, expanding to 2.3 km × 6.2 km resolution at swath edges, although the spatial coverage is limited to the reception limits of the ground station (Griffin *et al.,* 2017). Another daily AVHRR data type, Full Resolution Area Coverage (FRAC), became available following the launch of MetOp-A in 2006. FRAC provides full global coverage with 1.1 km nadir resolution and swath widths of around 2900 km (Eumetsat, 2011; see Figure 14.3b).

In 2018 NOAA officially replaced the AVHRR sensor program with the Visible Infrared Imaging Radiometer Suite (VIIRS) sensor program, after a long trial beginning with the first VIIRS sensor launched in 2011 onboard the Suomi National Polar orbiting Partnership (NPP) platform, maintained in a stable 'afternoon orbit' with equatorial crossing times of 1:20 am and 1:20 pm. The first of the NOAA Joint Polar Satellite Series (JPSS), NOAA-20 (launched 18 November 2017), carries a VIIRS rather than an AVHRR sensor to measure SWT. The VIIRS sensor provides higher spatial resolution SWT, 0.75 km at nadir expanding out to 1.5 km at swath edge, wider swath width (3060 km), better spatial coverage, and lower noise than the AVHRR (see Figure 14.3c). Importantly, VIIRS delivers higher spectral resolution, density, and extent than the AVHRR sensors (see Volume 1B—Section 1), including 22 channels designed to detect cloud and aerosol properties, ocean colour, ice, and fire, as well as LST and SWT (NASA Earthdata, 2019). The NPP and NOAA-20 also have better orbital stability than the POES satellites.

12 See *http://imos.org.au/facilities/srs/sstproducts/sstdata0/sstdata-validation/*

13 See *https://www.star.nesdis.noaa.gov/smcd/emb/vci/VH/vh_avhrr_ect.php*

Figure 14.3 Nighttime SST maps

These maps were produced by mapping data from four operational NOAA level 2 (L2P) products on 11 March 2019. GAC: Global Area Coverage; FRAC: Full Resolution Area Coverage; VIIRS: Visible Infrared Imaging Radiometer Suite; AHI: Advanced Himawari Imager

a. 4 km NOAA-19 GAC AVHRR

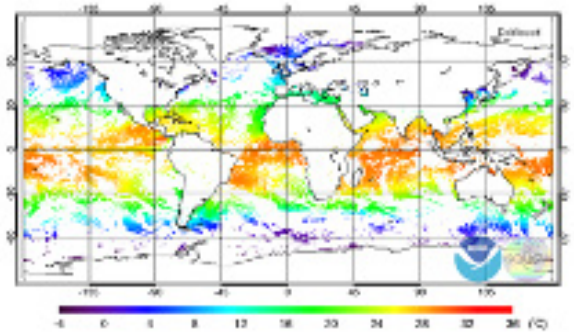

b. 1.1 km MetOp-B FRAC AVHRR

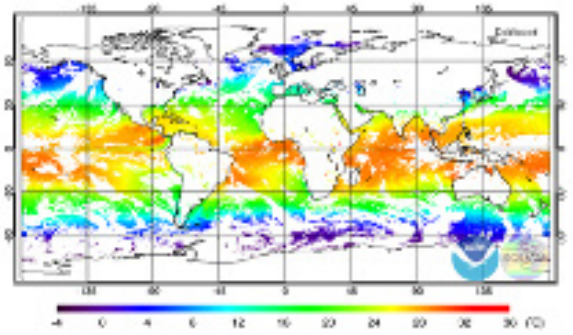

c. 0.75 km NOAA-20 VIIRS

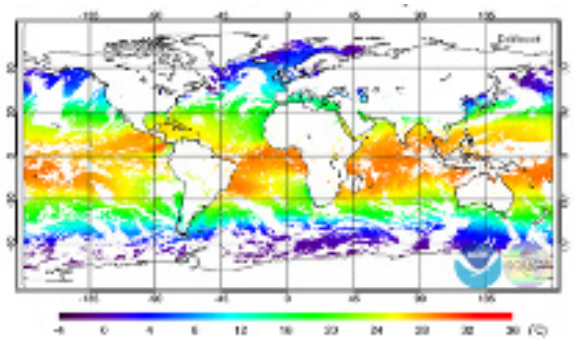

d. 10 minute, 2 km Himawari-8 AHI brightness temperatures

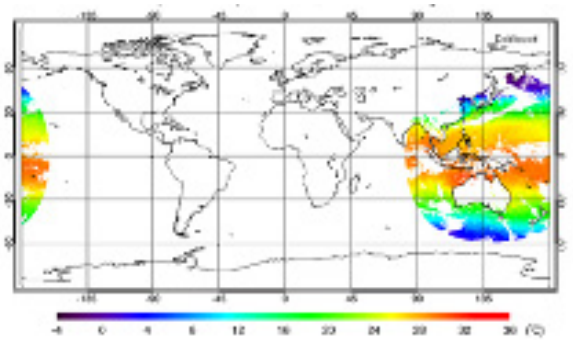

Data are from the NOAA SST Quality Monitor (SQUAM; Dash *et al.*, 2010). Retrieved from *https://www.star.nesdis.noaa.gov/sod/sst/squam*, accessed 16 March 2019.

Recent polar orbiting satellites, such as Suomi NPP, and the JPSS and MetOp series, have had the capability to store the highest resolution IR sensor radiance data onboard, with download to reception stations across the globe every few hours, thus allowing global, daily coverage of around 1 km resolution SWT over cloud-free regions (Figure 14.3b and Figure 14.3c). Even higher spatial resolution SWT (0.25 km at nadir) has been available since 2018 from the Second-generation Global Imager (SGLI) onboard the Japanese Global Change Observation Mission Climate (GCOM-C) polar orbiter (*https://suzaku.eorc.jaxa.jp/GCOM_C/index.html*). The SGLI has a swath width of 1,400 km for SWT, with GCOM-C equatorial crossing times of 10:30 am and 10:30 pm.

Near-global coverage of 1 km resolution SWT was earlier supplied by the Moderate Resolution Imaging Spectroradiometer (MODIS) onboard Terra (launched 18 December 1999) and Aqua (launched 4 May 2002) but, with a swath width of 2330 km (less than AVHRR or VIIRS), the gaps between swaths from one day are filled in on the next.

Although much narrower in swath (~500 km) than the other IR sensors that measure SWT, the dual-view capability of the Along-Track Scanning Radiometer (ATSR) series of IR sensors (ATSR-1, ATSR-2 and AATSR) flown on polar orbiters ERS-1, ERS-2, and EnviSat, from 1991 to 2012, allowed for the accurate determination of atmospheric corrections (such as atmospheric aerosol contamination), which are critical for climate data records (Merchant *et al.,* 2012; Berry *et al.,* 2018). The current generation of dual-view radiometers, the Sea and Land Surface Temperature Radiometer (SLSTR; Donlon *et al.,* 2012; Smith *et al.,* 2014) flying on Sentinel-3a (launched on 4 November 2015) and Sentinel 3b (launched 25 April 2018) has wider swaths than AATSR. All the (A)ATSR and SLSTR sensors flew or fly in morning orbits at around 10 am and 10 pm local equatorial crossing times.

IR sensors on geostationary satellites (from the Himawari series of satellites by the Japanese Meteorological Agency, JMA) have also provided accurate SSTs at high temporal resolution over the Australian region since 2006. While Himawari-6 (also known as MTSAT-1R; Zhang *et al.,* 2016a, 2018) and Himawari-7 (also known as MTSAT-2) provided hourly, 4 km SST observations, the currently operational Himawari-8 (Kurihara *et al.,* 2016; Ditri *et al.,* 2018; Kramar *et al.,* 2016; Griffin and Majewski, 2016; Griffin, 2018) delivers 10 minute, 2 km observations, which, when composited over a number of hours, enables infilling of data gaps due to transient cloud (see Figure 14.3d; Beggs *et al.,* 2018a).

14.2.2 Passive microwave sensors

Unlike IR sensors, passive microwave (PMW) sensors on polar orbiting satellites have the advantage that they can sense SWTs through cloud, but these sensors are impacted by radio frequency interference both from ground-based sources and from geostationary and communication satellites (Gentemann and Hilburn, 2015). PMW SST retrievals also need to be filtered for heavy rain, strong winds, sea ice, sunglint, as well as near land or sea ice, as these retrievals have contributions from emissions that enter through the antenna sidelobes. Due to the microwave frequencies used to measure SST, and limitations of the size of antenna deployable by satellite, PMW sensors are also limited to measuring SST at surface resolutions of several tens of kilometres.

PMW SSTs were retrieved from the Tropical Rainfall Measuring Mission (TRMM) Microwave Imager (TMI) from December 1997 to 2015, although the low inclination orbit only observed up to 40° latitude. The Japanese Advanced Microwave Scanning Radiometer for EOS[14] (AMSR-E) was flown on NASA's Aqua polar orbiter, with spatial resolution of SST retrievals of 74 km × 43 km, 1445 km swath width, and equatorial crossing time of 1:30 am and 1:30 pm (Kawanishi *et al.,* 2003). The AMSR-E was decommissioned in October 2011, when the mechanism to rotate the antenna failed after nine years of valuable global measurements. In the years that followed the failure of AMSR-E, the only source of global PMW SST data was from the WindSat microwave radiometer on the Coriolis polar orbiter (January 2003 to present), with equatorial crossing time of 6 am and 6 pm, and lower accuracy compared with AMSR-E. Fortunately, the second generation Advanced Microwave Scanning Radiometer (AMSR-2) was launched on 17 May 2012, on the Japanese Global Change Observation Mission—Water (GCOM-W; Kachi *et al.,* 2017). As a follow-on to the successful TRMM mission, the Global Precipitation Measurement (GPM) mission was launched on 27 February 2014, with the GPM Microwave Imager (GMI). The GMI's 10.65 GHz channels, have sensitivity to SST variations, but only for warm water, SST > ~13ºC, as at colder temperatures the sensitivity decreases and the noise level increases (Gentemann *et al.,* 2010).

14.3 Sea Surface Temperature

SST is not a single variable but is considered by many to be the temperature within the mixed layer (approximately the upper 10 m) of the ocean. Air-sea fluxes of heat, moisture, and momentum, as well as ocean turbulence, means the temperature variation through the 'mixed layer' can be complex and variable (Minnett *et al.,* 2019). This complexity needs to be considered when comparing or combining measurements of SST from different satellites and *in situ* sensors (Minnett *et al.,* 2019). In order to facilitate these activities, a set of definitions of SST were developed by the international Group for High Resolution SST (GHRSST: *http://www.ghrsst.org*; Donlon *et al.,* 2007), and are now used in all GHRSST-format SST products (GHRSST Science Team, 2012). Figure 14.4 summarises the definition of SST in the upper 10 m of the ocean and provides a framework to understand the differences between complementary SST measurements.

The five different SST definitions are (from Minnett and Kaiser-Weiss, 2012):

- **interface temperature** (SSTint)—the temperature at the air-sea interface on molecular scales (cannot be directly measured);
- **skin sea surface temperature** (SSTskin)—the temperature measured by an IR radiometer typically operating at wavelengths 3.7–12 μm, which represents the temperature within the conductive diffusion-dominated sub-layer at a water depth of ~10–20 μm;
- **subskin sea surface temperature** (SSTsubskin)—the temperature at the base of the conductive laminar sub-layer of the ocean surface, which can be well approximated to the measurement of the surface temperature by a microwave radiometer operating in the 6–11 GHz frequency range (approximately 1 mm water depth);
- **surface temperature at depth** (SSTdepth)—all measurements of water temperature beneath SSTsubskin; and
- **foundation temperature** (SSTfnd)—the temperature free of diurnal temperature variability, that is, the temperature at the first time of the day when the heat gain from the solar radiation absorption exceeds the heat loss at the sea surface (approximately 10 m water depth under calm conditions).

Figure 14.4 Near-surface oceanic temperature gradients

In this schematic, the numbers on the axes are for guidance only and do not represent rigorously derived scales.

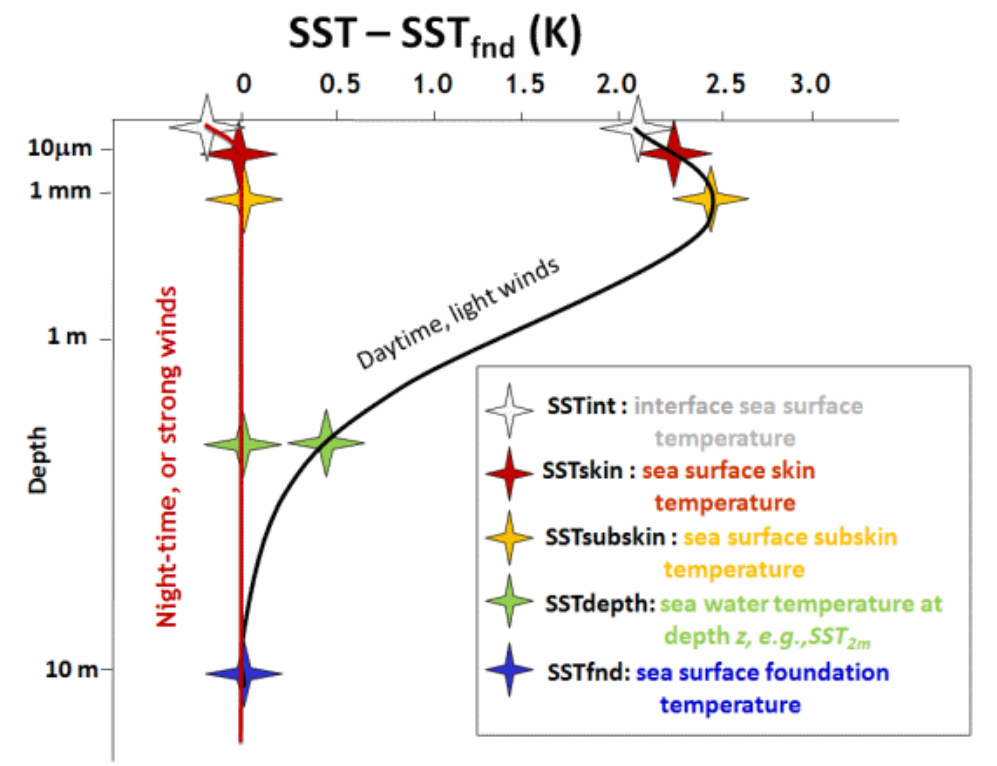

Source: Minnett and Kaiser-Weiss (2012)

In most locations and conditions, the ocean surface is warmer than the atmosphere in contact with it, resulting in heat flow from the ocean to the atmosphere (Minnett *et al.,* 2019). The upward flow of heat in the water is accomplished in the top hundred micrometers or so of the water (Wong and Minnett, 2018) by molecular conduction as the air-sea density difference and near-surface viscous layer of the water suppress the turbulent heat transfer (Soloviev and Lukas, 2014). This results in a vertical temperature gradient in the water, just below the interface, leading to decreasing temperature closer to the interface, which is referred to as the 'thermal skin layer' or 'cool skin layer' (see Figure 14.4). The average daytime ocean cool skin amplitude has been measured as ~0.14K[15] and ~0.20K during night, both under well-mixed conditions (surface wind speeds exceeding 6 ms^{-1}; Zhang *et al.,* 2019), with much larger values being seen at very low wind speeds (Donlon *et al.,* 2002; Minnett *et al.,* 2011). Therefore, for applications requiring accuracy to several tenths of a Kelvin (K) the variable thermal skin effect should be taken into account, and retrievals of IR SST should be considered as SSTskin.

At 10 m water depth, between 50% and 90% of sunlight impinging on the surface has typically been absorbed above that depth level, and the temperature at 10 m water depth is relatively stable with respect to direct heating from the daily solar heating cycle (Merchant *et al.,* 2019a). For this reason, the SST at around 10 m water depth is conceptualised as a foundation temperature above which large sub-daily variability is superimposed, particularly under conditions of low to moderate wind speeds and high insolation (Soloviev and Lukas, 1997). This means that the water depth of the foundation temperature at a given location changes from day to day, but not within the day (Merchant *et al.,* 2019a). The 10 m SST is not directly measurable by EO, although a satellite-derived SST observed around local dawn can be used to estimate the foundation SST, because near-surface temperature stratification that develops during daytime is usually eroded by dawn by surface heat loss and wind-driven mixing. Satellite SSTs observed under well-mixed, moderate (for example, 7–12 ms^{-1}) wind conditions are also considered to be reasonable estimates of foundation temperature (Merchant *et al.,* 2019a).

15 The Kelvin (K) temperature scale defines absolute zero and is related to the Celsius temperature scale as 0K = -273.15°C.

During the daytime, and in the absence of sufficiently strong winds to drive vertical mixing of heat, diurnal warming causes a relatively shallow warm layer to be formed (see Figure 14.4). Driven by solar heating, diurnal variability of SST occurs under moderately low wind speeds in all ocean basins and has been observed using both *in situ* and satellite SST observations (Minnett *et al.,* 2019 and references therein). In the Australian region, diurnal warming of several Kelvin has been observed in the Tropical Warm Pool (Zhang *et al.,* 2016a; Zhang *et al.,* 2016b). The abundance of SST retrievals from space and improvements in understanding of the diurnal cycle allowed for numerical simulations to reproduce the diurnal variability of the upper ocean layer. A selection of these models has been inter-compared in various regions, including the Tropical Warm Pool, using hourly-resolution, geostationary satellite SST data (Karagali and Hoyer, 2013; Zhang *et al.,* 2018).

For more comprehensive overviews of SST the reader is referred to Minnett *et al.* (2019) and Merchant *et al.* (2019a). In the following subsections we consider methods to:

- retrieve SST from satellite imagery (see Section 14.3.1);
- validate the derived SST (see Section 14.3.2); and
- refine SST products and coverage (see Section 14.3.3).

Some pointers for selecting the most appropriate SST product for a particular application are provided in Excursus 14.1.

14.3.1 Retrieval of satellite SST

Satellite radiometers collect accurate radiance measurements, from which brightness temperature (T_B) at the top of the atmosphere can be derived. These T_B values are related to, but not the same as, the SST, because of the absorption, emission, and scattering of radiation from the intervening atmosphere, and because the sea surface does not act as an ideal emitter (that is, its emissivity is not 100%; Minnett *et al.,* 2019). The dominant effect (near nadir) in the infrared region is the atmospheric influence; in microwave wavelengths, it is the variability of surface emissivity around relatively low values over the ocean. For more detail, refer to the review by Merchant and Embury (2014).

The first step in deriving accurate SST from a satellite sensor is to navigate the uncalibrated (level 0) data. In the case of the Integrated Marine Observing System (IMOS; see Volume 2D—Excursus 12.3) HRPT AVHRR data from POES satellites, a high precision, CSIRO-developed, satellite orbit model is implemented to automatically geolocate pixels without the need for per scene ground control points (Wijffels *et al.,* 2018).

The next step is to convert the level 0 data from the satellite to T_B values (level 1), by applying a factory calibration. This step is then followed by identification of those pixels that have been affected by:

- land and cloud, in the case of IR retrievals; or
- precipitation or radio frequency interference, in the case of MW retrievals.

Aspects of SST retrieval from infrared (see Section 14.3.1.1) and microwave (see Section 14.3.1.2) sensors are considered separately below. For additional details around satellite SST geolocation, cloud/land masking, and retrievals please refer to Minnett *et al.* (2019) and Merchant *et al.* (2019a).

14.3.1.1 Infrared temperature retrievals

Cloud and land masking is crucial for satellite-based IR temperature retrievals of surface water. Clouds are opaque to TIR radiation, and even a slightly cloud-contaminated signal (subpixel-sized clouds) can result in a considerably colder measurement of the temperature. Also, for land-contaminated pixels, the signal can be biased, as the LST sometimes differs by several degrees from the SWT. Therefore, strict cloud and land masking are necessary to eliminate affected pixels (Lieberherr and Wunderle, 2018).

Historically, identification of clouds in IR measurements from satellites has been driven mainly by binary tests in a decision tree based on T_B uniformity, T_B minima, and comparisons with low resolution gap-free reference fields (Kilpatrick *et al.,* 2015). The accuracy of these tests often decreases near ocean thermal fronts, at cloud edges, in the presence of small cirrus clouds, and low-level, uniform stratus clouds when cloud temperature can be close to that of the sea surface (Minnett *et al.,* 2019). This reliance on stringent uniformity thresholds often results in the misidentification of strong thermal fronts as clouds. An alternative, probabilistic approach to cloud identification in IR imagery based on Bayes' Theorem was developed by Merchant *et al.* (2005). Joint probability distributions of T_B values in two IR channels were derived in clear-sky conditions by radiative transfer simulations, and in cloudy conditions by visual inspection of satellite imagery. Radiative transfer simulations, with weather prediction model output to give the atmospheric state, are used to give an expectation of clear-sky T_B values, which are compared with probability distributions of cloudy measurements. The measured T_B values are then assigned a probability of having been influenced by clouds. This approach has been widely used for several satellite missions including for the (A)ATSR series (Merchant *et al.,* 2012), NOAA GOES satellites (Maturi *et al.,* 2008), OSI-SAF MetOp series and JMA's Himawari-8 satellite (Kurihara *et al.,* 2016).

As the IR radiation from the sea surface propagates through the atmosphere, some is absorbed or scattered out of the path of the radiometer, attenuating the signal. The T_B measured through a clear atmosphere at satellite altitude are cooler than SST. This atmospheric effect (along with surface emissivity effects) must be compensated for to obtain accurate SST (Merchant *et al.,* 2019a). The IR spectral intervals where the atmosphere is relatively transparent are situated between wavelengths 3.5–4.1 μm and 8–12 μm (see Volume 1B—Section 4). The main gas that contributes to the signal attenuation is water vapor, which is very variable in space and time. Other molecules that contribute to the atmospheric effect are quite well-mixed, so cause a relatively constant effect that is simpler to correct. Taking measurements at different spectral intervals in the windows where the water vapor attenuation is different means the measurements contain information about both the surface and the atmospheric state (Merchant *et al.,* 2019a). The spectral intervals being sensed are defined by the designed characteristics of the radiometer, and are usually referred to as 'bands' or 'channels' (see Volume 1A—Section 14). By assuming adequate linearity, a simple SST algorithm takes the form:

$$SST_{ij} = a_0 + a_i T_i + a_j T_j$$

where a_0, a_i and a_j are coefficients that need to be determined by:

- regression analysis of coincident satellite and *in situ* measurements (Kilpatrick *et al.,* 2001);
- regression analysis of offline simulations using radiative transfer modelling (Llewellyn-Jones *et al.,* 1984); or
- 'on-the-fly' using numerical weather prediction (NWP) fields and fast radiative transfer to give a dynamic linearisation point closer to the observed state (Merchant *et al.,* 2008).

The simple algorithm (equation above) has been applied to AVHRR data, where *I* is channel 4 and *j* is channel 5 (see Table 14.2), to retrieve multi-channel SST (MCSST). To correct some of the limitations of the linearity, the simple algorithm has been modified in various forms (such as the Non-Linear SST: NLSST; Walton *et al.,* 1998), to include a reference SST (or first-guess temperature) and a term that includes the satellite zenith angle.

14.3.1.2 Passive microwave temperature retrievals

Two different retrieval algorithms (from JAXA and NASA respectively) are routinely used to produce official JAXA/NASA SSTs from the PMW sensors, AMSR-E and AMSR-2 (Merchant *et al.,* 2019a). The NASA group has also produced SSTs from WindSAT.

The JAXA algorithm produces SST using the 6 GHz channel (Shibata, 2006), whereas the NASA algorithm (adopted by the US-based company Remote Sensing Systems) determines SST and wind speed at the same time using a radiative transfer based two-step algorithm (Wentz and Meissner, 2007). For both products, data that are affected by rain, strong winds, sun glitter, land or sea ice contamination, and radio frequency interference from ground-based sources, geostationary satellites and communication satellites are excluded, but each group has developed their own exclusion criteria (Merchant *et al.,* 2019a).

Both products are widely used in the operational ocean and atmospheric modelling communities, as well as for scientific research and applications. In Australia, AMSR-E and WindSAT SSTs produced by Remote Sensing Systems (see *http://www.remss.com*) were routinely used in operational SST analyses and ocean general circulation models by the Australian Bureau of Meteorology (BoM; Beggs *et al.,* 2011; Andreu-Burillo *et al.,* 2010) and by CSIRO in the Bluelink ocean Reanalysis model (BRAN; Oke *et al.,* 2013; see Excursus 2.2). In recent years, more accurate SST retrievals from AMSR-2, produced by JAXA, have been used for the BoM SST analyses and ocean models (see *http://www.bom.gov.au/oceanography/forecasts*).

14.3.2 Validation of satellite SST

Validation of satellite-derived SSTs is essential to provide confidence in both the derived SST and its associated uncertainty. The traditional approach is to compare the satellite SST to *in situ* surface-based SST measurements by generating a set of coincidences or 'Matchup Data Base' (MDB) within defined spatial and temporal limits (Merchant *et al.,* 2019a). Statistical methods are then applied to the MDB, from which the mean difference and standard deviation are usually calculated. There are five main types of *in situ* measurements available for satellite SST validation:

- drifting buoys;
- Global Tropical Moored Buoy Array (GTMBA);
- SSTdepth sensors on ships;
- Argo floats (see Excursus 5.1); and
- shipborne radiometers.

SST measurements from the first four platform types are routinely available in near real time from the NOAA/NESDIS In Situ Quality Monitor (iQUAM: *https://www.star.nesdis.noaa.gov/socd/sst/iquam/*).

Networks of drifting buoys provide the most prevalent type of *in situ* measurement for SST (Lumpkin *et al.,* 2016), and these have delivered good coverage from the early 2000's across most regions. Near-global coverage can be obtained using measurements from Argo floats (Roemmich *et al.,* 2009), although the temporal sampling is much lower than from drifting buoys (every nine days rather than hourly). The GTMBA (McPhaden *et al.,* 2010) has the advantage of being in open ocean locations and having consistent long term calibrated records at many locations. Measurements from engine room intakes or hull-mounted sensors from Volunteer Observing Ships (Beggs *et al.,* 2011), although not global in nature, are an important source of data for satellite SST validation due to their availability back to the start of the satellite SST era. Hull-mounted temperature sensors, if properly located and insulated from atmospheric effects, have been demonstrated to provide SST observations of similar accuracy to drifting buoys (Beggs *et al.,* 2011). Finally, we have shipborne radiometers (Donlon *et al.,* 2014), which are the only *in situ* data source to provide a temperature at the same water depth (SSTskin) as is detected by IR sensors on satellites.

There are several online systems that provide near real time validation plots of various satellite SST products, with links listed in Section 14.7.

14.3.3 'GHRSST' satellite SST products

Based on the GHRSST (Group for High Resolution SST; Donlon *et al.,* 2007) definitions for SST products (GHRSST Science Team, 2012), numerous global, spatially-mapped SST products are now available for research and operational applications (Beggs, 2010; Donlon *et al.,* 2009). The following labels are used to differentiate four standard levels of product processing:

- Level 1 (L1)—geolocated T_B from individual sensors;
- Level 2 (L2)—geolocated SSTs from individual satellite sensors over a single swath (orbit), granule (section of orbit), or scene (geostationary satellites only);
- Level 3 (L3)—'composite' SST products (see Volume 2D) created by averaging (but not interpolating) L2 data over space and time onto a grid of prescribed latitudes and longitudes (composite products may be produced from a single sensor or multiple sensors over a single orbit to several days); and
- Level 4 (L4)—gap-free SST 'analyses' created by interpolating multiple observation sources onto a pre-defined grid.

Among the ocean surface parameters monitored from satellites, SST is unique in terms of the large volume of concurrent observations, their spatial coverage, and the number of relevant EO sensors and platforms (Minnett *et al.,* 2019). This characteristic allows L3 composites and L4 analyses to achieve more complete spatial coverage than their constituent L2 inputs. In 2000, the Global Ocean Data Assimilation Experiment (GODAE) High Resolution SST Pilot Project (GHRSST-PP; Donlon *et al.,* 2007) was initiated to develop and demonstrate a system that could deliver high resolution, global coverage SST data products operationally in near real time according to GODAE specifications. Various space, meteorological, and oceanographic agencies contributing to GHRSST-PP (now called the Group for High Resolution SST: GHRSST; see *http://www.ghrsst.org*) provide two major types of near real time SST products in prescribed formats (GHRSST Science Team, 2012): L2 preprocessed (L2P) and L4 analysis products.

GHRSST-L2P products are baseline measurement datasets. SST data generated from different sensors are made available to users in a common, self-describing format (netCDF) together with ancillary information to assist with their interpretation and use by data assimilation systems (Donlon *et al.,* 2009). For every L2 input data file, GHRSST produces a matching L2P product that contains identical SST values in the same geographical layout as those in the source L2 product. On a pixel-by-pixel basis, each SST retrieval is augmented with estimates of the bias error and standard deviation error typically derived from statistical databases of *in situ* and satellite data. Other ancillary fields for each pixel are land/lake/river/ice mask, surface wind speed, aerosol optical depth, sea ice concentration, time of measurement, difference from previous reference SST analysis field, and quality control flags, including a quality level flag. A full description of all GHRSST file formats (L2P, L3U, L3C, L3S, and L4) can be found in GHRSST Science Team (2012). The 'Sensor Specific Error Statistics' (SSES) standard deviation errors (given as 'sses_standard_deviation' values in GHRSST files) associated with the highest quality SST observations (denoted by a 'quality_level' value of 5) are typically in the range 0.3°C to 0.5°C for the various satellite IR SST GHRSST-L2P products currently available. One of the particular strengths of the GHRSST L2P, L3U, L3C, and L3S formats is that users can trade off between spatial coverage and accuracy, depending on the requirements of their application, by selecting either a quality_level or sses_standard_deviation threshold. For more information see Beggs (2010).

The design of the GHRSST L2P format was mainly driven by the requirements of the new 'foundation' SST analyses for the 'best' cloud-free SST with sufficient auxiliary data to enable conversion of SST

observations within or immediately below the cool skin to foundation SST (Donlon *et al.,* 2007). The L2P format has proven to be sufficiently universal that GHRSST L2P files from a range of IR and PMW sensors are now used in many operational systems for near real time SST analyses, ocean forecasting, and seasonal prediction (Beggs, 2010). The L2P products provide SST observations at the highest available spatial resolution at the time and location of observation, and are therefore considered most appropriate for input into numerical models. The consistent formats for GHRSST products facilitate addition of new data streams into operational systems.

Although L2P products provide the most timely geolocated SST values, they come with the downside of high data file sizes and computation overheads, which may be a barrier to some users and applications. GHRSST L2P products can be composited on a regular grid (Griffin *et al.,* 2017) to produce L3 products using:

- a single sensor and single swath/scene (L3U);
- single sensor, multiple swaths/scenes (L3C); and
- multiple sensors (L3S).

These composites are popular for various near-coastal applications including fisheries management, protection of endangered species, environmental monitoring and weather forecasting (Beggs, 2010; see *https://coastwatch.noaa.gov/cw/about-coastwatch.html*). For example:

- various L3U products are used in real time maps of SST to advise recreational and commercial fishers (see *https://support.fishtrack.com/hc/en-us/articles/4402098299163-Transitioning-to-our-App*);
- hourly or daily L3C composites of multiple 10-minute, 2 km resolution scenes from Himawari-8 L2P SST can be used to monitor coastal upwelling or diurnal warming (Huang *et al.,* 2018; Beggs *et al.,* 2018a); and
- multi-sensor L3S products (Beggs *et al.,* 2019; see Section 14.4.4) are used to nowcast coral bleaching over the Great Barrier Reef (see *http://www.bom.gov.au/environment/activities/reeftemp/reeftemp.shtml*).

To illustrate the relative spatial coverage and ability of these products to resolve ocean features, examples of SSTs from L3U, L3C, L3S, and L4 products over the seas around Queensland are shown in Figure 14.5.

L3 SST products, unless composited over a very long time period, will contain some grid locations that lack data values. Several applications require a 'gap-free' L4 SST field. L4 analyses of satellite L2 and L3, and *in situ* SST, are produced operationally at various oceanographic and meteorological agencies around the world using the method of optimal interpolation (OI). In OI (or 'statistical' interpolation) systems, voids in observations are generally filled using a weighted combination of the previous analysis and climatology ('background field') and neighbouring observations (Reynolds *et al.,* 2007; Beggs *et al.,* 2011; Brasnett and Surcell Colan, 2016; Maturi *et al.,* 2017). By nature of the statistical interpolation of observations and background field, an L4 SST analysis generally exhibits smoother ocean features than an L3 non-interpolated SST product, composited over one to several days (Beggs *et al.,* 2018b; see Figure 14.5). Several of these SST analyses provide sea surface boundary forcing in atmospheric and ocean models and are used as a constraint to observations in modelling of the upper ocean circulation (Beggs, 2010; O'Carroll *et al.,* 2019; Merchant *et al.,* 2019a). Accurate SST fields are essential in computing different climate variables, such as heat transfer in ocean-atmosphere coupled systems and surface partial pressure of CO_2 (Vinogradova *et al.,* 2009).

Combination of data from IR and PMW sensors from polar orbiting satellites, and IR sensors on geostationary satellites, often with *in situ* measurements from drifting buoys and ships, now results in high-quality, daily SST L4 analyses with high spatial resolution, ranging from 0.25° (NCEI OISST v2.0; Banzon *et al.,* 2016; Reynolds *et al.,* 2007) down to 0.01° (JPL MUR; Chin *et al.,* 2017). Section 14.4 goes into further details regarding global L4 analysis products.

There are now many real time and reprocessed L2, L3, and L4 global satellite SST products provided in GHRSST format, produced by several agencies, available via the GHRSST Data Assembly Centres (see *https://www.ghrsst.org/ghrsst-data-services/services/*). A list of GHRSST products archived by the NOAA National Oceanographic Data Centre can be found at *https://www.nodc.noaa.gov/SatelliteData/ghrsst/accessdata.html*, although this is by no means comprehensive, as additional GHRSST products are freely disseminated by other agencies, such as the Copernicus Marine Environment Monitoring Service (CMEMS: *http://marine.copernicus.eu/services-portfolio/access-to-products/*), the Japan Aerospace Exploration Agency (JAXA: *https://suzaku.eorc.jaxa.jp/GHRSST/*), and the Australian Ocean Data Network (AODN: *http://portal.aodn.org.au*).

More than 100 real time and reprocessed GHRSST L2P/L3 products have been produced from most environmental satellites equipped with SST sensors. In addition, there are more than 30 near real time daily, global (1–25 km resolution) and regional (1–10 km resolution), GHRSST L4 analyses and reanalyses. A selection of those particularly suitable for Australian applications are presented in Section 14.5, including a summary of various features, and their pros and cons.

Figure 14.5 Nighttime SST maps for 13 March 2019 over the Queensland region

These maps were produced from imagery acquired by different EO sensors and processed using different methods. All products, except Geo-Polar Blended, are on the same 0.02° x 0.02° rectangular grid. ACSPO: Advanced Clear Sky Processor for Oceans

a. 2 km NOAA ACSPO NPP VIIRS L3U

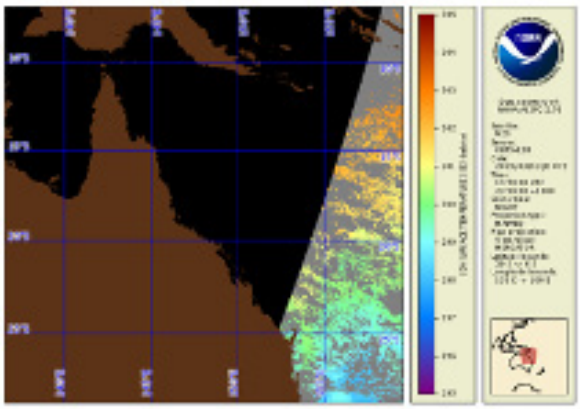

b. 2 km ACSPO NOAA-20 VIIRS L3U

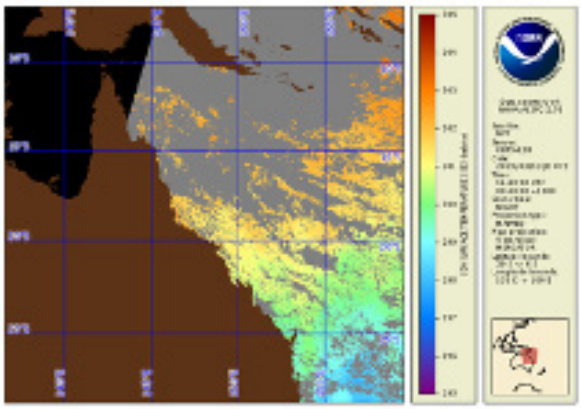

c. 2 km ACSPO METOP-B FRAC AVHRR L3U

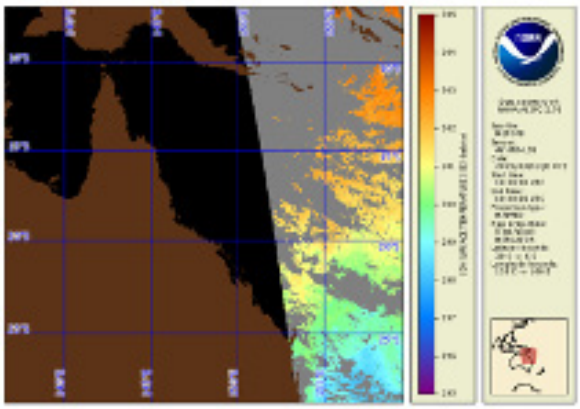

d. 2 km 1-hour Himawari-8 AHI L3C (produced by compositing 2 km 10-min Himawari-8 AHI L3U)

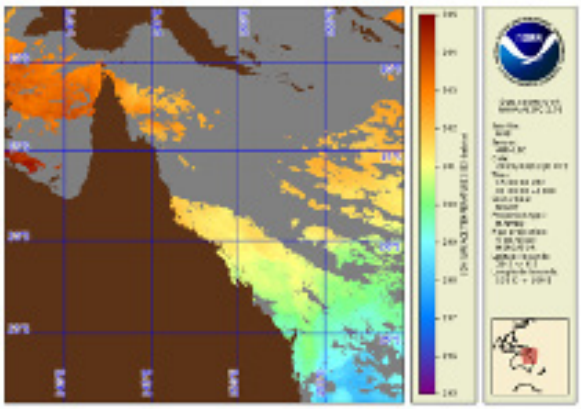

e. 2 km IMOS Multi-sensor L3S (produced by compositing ACSPO NPP VIIRS L3U, ACSPO NOAA-20 VIIRS L3U, 1 km OSI-SAF METOP-B FRAC AVHRR L2P and 2 km IMOS NOAA-18 HRPT AVHRR L2P)

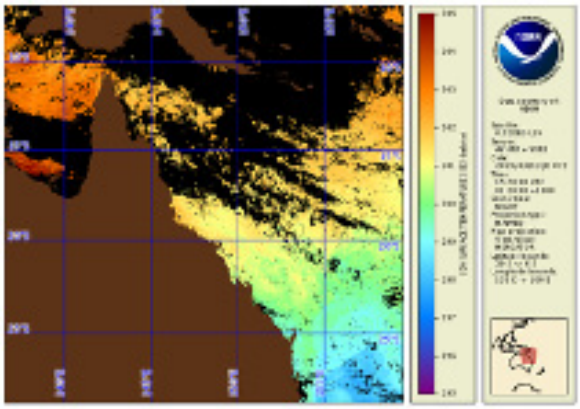

f. 5 km daily Geo-Polar Blended L4 (produced by optimally interpolating nighttime SST from NPP VIIRS L2P, MetOp-B FRAC AVHRR L2P, Himawari-8 AHI L3U over the region)

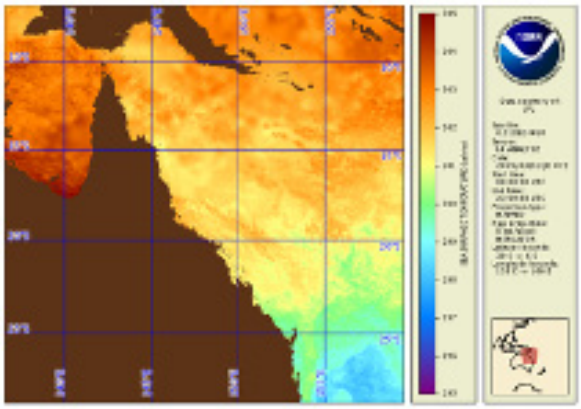

Data are from the NOAA/NESDIS ACSPO Regional Monitor for SST (ARMS) v2.1. Retrieved from: *https://www.star.nesdis.noaa.gov/sod/sst/arms*, accessed 23 March 2019.

Excursus 14.1—Selecting a Satellite SST Product

Source: Helen Beggs, Bureau of Meteorology (Melbourne)
Further Information: *https://www.ghrsst.org/ghrsst-data-services/products/*; see also Beggs (2010), Dash *et al.* (2012), Fiedler *et al.* (2019a), Beggs *et al.* (2018b), Rayner *et al.* (2019b), and Yang *et al.* (2021)

To select from an increasingly wide array of SST products, users need to consider which of the following parameters are most important for the application and analyses being undertaken:

- depth—skin, subskin, or foundation?
- time—are the dataset duration, local time of measurement, and latency suitable?
- temporal resolution—what is the characteristic time period of the process you wish to measure?
- spatial resolution—what is required for the feature/process of interest?
- spatial coverage—L3S composite versus L4 gap-free?
- do you need microwave data to measure SST under cloud, for example during or after a tropical cyclone?
- quality level (cloud contamination)—what is the minimum acceptable level?
- geolocation accuracy—native projection (L2P) or gridded (L3 or L4)?
- SST accuracy and stability—with respect to what reference?
- stability of sensor and orbit—what deviation is acceptable?

Using satellite SST records to produce coherent climate data records is complicated by the changes that can occur over time in the sensors, satellite orbit, and calibrations (O'Carroll *et al.*, 2019). Different methods have been used to stabilise the SST time series, which may impact subsequent analyses of the resulting datasets. For example:

- The long term satellite SST data record known as 'Pathfinder' (Casey *et al.*, 2010) utilises empirical regression algorithms (Kilpatrick *et al.*, 2001) tuned to drifting buoys to provide a self-consistent approach across the series of AVHRR sensors on the POES satellites from NOAA-7 onwards. Pathfinder is constructed from a single AVHRR sensor at a single time, and the tuning to *in situ* data is primarily to account for the many instrumental issues observed in the series, including errors in calibration (O'Carroll *et al.*, 2019).
- The ATSR Reprocessing for Climate (ARC) Project (Merchant *et al.*, 2012) utilised the ATSR series of sensors, which were designed to provide SST suitable for climate studies. ARC differs from Pathfinder in that it maintains independence from *in situ* measurements, has performed careful harmonisation of the T_B from successive sensors, and employs a physics-based retrieval of SSTskin using a Radiative Transfer Model (RTM; Merchant *et al.*, 2012; 2019b). This allows independent validation of the dataset using *in situ* measurements.
- The ESA SST Climate Change Initiative (CCI) Project Phase II (Merchant *et al.*, 2019b; Rayner *et al.*, 2019a) uses the ATSRs to reduce T_B errors in the AVHRR sensors and in the derived SST values, providing a stabilised dataset of both ATSR and AVHRR for the period they coexist (1991 to 2012), and extends backwards and forwards from the ATSR period using consistent, physically-based retrievals for all AVHRR sensors (O'Carroll *et al.*, 2019).

14.4 Global Sea Surface Temperature Products

A selection of global daily L4 SST analyses, available for periods exceeding 10 years, are listed in Table 14.3 along with their advantages and disadvantages. The OSTIA (Operational Sea Surface Temperature and Sea Ice Analysis), CMC (Canadian Meteorological Centre), GAMSSA (Global Australian Multi-Sensor SST Analysis), MUR (Multi-Scale Ultra High Resolution), and MGDSST (Merged Satellite and In-situ Data Global Daily Sea Surface Temperature) L4 products are referred to as foundation SSTs. These analysis schemes minimise the use of retrievals affected by diurnal variability by employing one or more of the following strategies:

- using only nighttime satellite data;
- using additional daytime data with wind speed above 6 ms^{-1} ; and
- excluding L2 SSTs flagged by the producer as having high diurnal variability (Dash *et al.,* 2012).

Some analyses, such as OSTIA (Donlon *et al.,* 2012; Roberts-Jones *et al.,* 2012), use a combination of an accurate satellite SST reference dataset (in 2018 ACSPO NPP VIIRS L3U) and *in situ* SST data to correct for biases in the other satellite SST data streams. Others use a combination of drifting buoy and ship SST observations to correct for regional and seasonal biases (for example MGDSST, CMC, NCEI[16] 'Reynolds' AVHRR-only OISST[17] v2.0). However, issues remain with the calibration and bias-correction of the IR and PMW SST data streams, particularly at high latitudes north of 50°N and south of 50°S (Reynolds *et al.,* 2009; Dash *et al.,* 2012) where available *in situ* SST observations are still relatively sparse. In addition, some analysis biases have occurred over regions where drifting buoy observations, used for bias-correction of satellite SST data, became sparse due to a format change in data uploaded to the Global Telecommunications System on 2 November 2016, as occurred for the NCEI 'Reynolds' near real time, daily, AVHRR-only OISST v2.0 SST analyses (Liu *et al.*, 2019). The OISST issue was resolved on 16 March 2020 with the operational release of an updated version (v2.1) of the AVHRR-only OISST SST analysis (*https://www.ncdc.noaa.gov/oisst/optimum-interpolation-sea-surface-temperature-oisst-v21*), which now ingests all drifting buoy, mooring, ship, and Argo float SST data available from the Global Telecommunications System (GTS), and has been reprocessed back to 1 January 2016.

Table 14.3 Global, Daily, Multi-Sensor SST analysis products in GHRSST L4 format

Analysis and Citation	Date Period	Spatial resolution; depth	SST and sea ice data inputs	Advantages	Disadvantages	Data Access
CMC0.2deg (Brasnett, 2012; Brasnett, 2008)	1991–2017	0.2°; foundation	Drifting buoys, ships (ICOADS to 2006, GTS thereafter) AQUA/AMSR-E, Coriolis/WindSat, TRMM/TMI, MetOp-A/AVHRR, NOAA-16/AVHRR, NOAA-17/AVHRR, NOAA-18/AVHRR, NOAA-19/AVHRR, ERS-1/ATSR-1, ERS-2/ATSR-2, ENVISAT/AATSR, CMC ice	Highly accurate compared to Argo; good temporal and spatial homogeneity; good feature resolution; includes microwave data	Only from 1991	*https://podaac.jpl.nasa.gov/dataset/CMC0.2deg-CMC-L4-GLOB-v2.0*
CMC0.1deg (Brasnett and Surcell, 2016; Brasnett, 2008)	2016–present	0.1°; foundation	Drifting buoys, moorings, ships (GTS) MetOp-A/AVHRR, MetOp-B/AVHRR, NOAA-18/AVHRR, NOAA-19/AVHRR, NPP/VIIRS, GCOM-W/AMSR-2, CMC ice	Highly accurate compared to Argo; good feature resolution; includes microwave data	Only from 2016, but may be combined with CMC0.2deg to extend record	*https://podaac.jpl.nasa.gov/dataset/CMC0.1deg-CMC-L4-GLOB-v3.0*

16 National Centers for Environmental Information (NOAA)
17 Optimum Interpolation Sea Surface Temperature

Analysis and Citation	Date Period	Spatial resolution; depth	SST and sea ice data inputs	Advantages	Disadvantages	Data Access
ESA SST CCI analysis v2.1 (Rayner *et al.*, 2019a; 2019b; Merchant *et al.*, 2019b)	1981–2016	0.05°; 0.2 m	NOAA-7/AVHRR, NOAA-9/AVHRR, NOAA-11 to 19/AVHRR MetOp-A/AVHRR, ERS-1/ATSR-1, ERS-2/ATSR-2, ENVISAT/AATSR, OSI-SAF ice	Consistently recalibrated and reprocessed (A)ATSR and AVHRR data; second lowest standard deviation wrt Argo (after CMC0.2deg); better feature resolution than other long term analyses (incl. CMC); derived climatology highly consistent with TAO-TRITON moorings in western Pacific and agrees well with near-coral logger temperatures at water depths 3–6 m in Florida Keys and Belize (Rayner ***et al.***, 2019)	Cooler than Argo SST by 0.05–0.1K; a few tenths of degree bias in global mean during Oct 1982 to Sep 1983	*https://cds.climate.copernicus.eu/cdsapp#!/dataset/satellite-sea-surface-temperature?tab=form*
Copernicus Climate Change Service (C3S) v2.0 (Merchant *et al.*, 2019b)	2017 to 28 days behind present	0.05°; 0.2 m	Sentinel-3A/SLSTR, MetOp-A/AVHRR, OSI-SAF ice	Same analysis code as ESA SST CCI v2.1 analysis and designed to extend this analysis up to near real time	Validation not yet publicly available	*https://cds.climate.copernicus.eu/cdsapp#!/dataset/satellite-sea-surface-temperature?tab=form*
CMEMS OSTIA reprocessed analysis (Good et al., 2020)	1981 to six months behind present)	0.05°; foundation	Drifting buoys, moorings, ships (ICOADS), ESA SST CCI v2.1 AVHRR and A(A)TSR data, MetOp-B/AVHRR, OSI-SAF Sentinel-3A/SLSTR, Sentinel-3B/SLSTR, AQUA/AMSR-E, GCOM-W/AMSR2, NPP/VIIRS, NOAA-20/VIIRS, MSG1/SEVIRI, MSG2/SEVIRI, MSG4/SEVIRI, GOES-13/ABI, OSI-SAF ice	Good standard deviation of differences to Argo, includes microwave data; very good feature resolution	Disadvantages not yet identified	*https://resources.marine.copernicus.eu/product-detail/SST_GLO_SST_L4_REP_OBSERVATIONS_010_011/INFORMATION*
UK Met Office OSTIA analysis (Donlon *et al.*, 2012)	2006–present	0.05°; foundation	Drifting buoys, moorings (GTS), JCOM-W/AMSR-2 MetOp-B/AVHRR, NPP/VIIRS, NOAA-20/VIIRS, MSG4/SEVIRI, GOES-13/ABI, OSI-SAF ice	Good standard deviation of differences to Argo, includes microwave data; very good feature resolution after 12 March 2019	Reduced temporal homogeneity, reduced feature sensitivity prior to 12 March 2019. Only extends back to 2006, but may be combined with OSTIA reprocessed analysis to extend record	*https://resources.marine.copernicus.eu/product-detail/SST_GLO_SST_L4_NRT_OBSERVATIONS_010_001/INFORMATION*

Analysis and Citation	Date Period	Spatial resolution; depth	SST and sea ice data inputs	Advantages	Disadvantages	Data Access
JMA MGDSST (Guan and Kawamura 2004; Kurihara *et al.*, 2006)	1982–present	0.25°; foundation	Drifting buoys, moorings, ships (GTS), AQUA/AMSR-E, Coriolis/WindSat, GCOM-W/AMSR-2 Pathfinder V5.0/V5.1 (1982-2006), NOAA-17/AVHRR, NOAA-18/AVHRR, NOAA-19/AVHRR, MetOp-A/AVHRR, MetOp-B/AVHRR, JMA ice	Moderate mean and standard deviations of differences to Argo; moderate temporal and spatial homogeneity; moderate feature sensitivity; includes microwave data	Agrees less closely to Argo than GAMSSA, CMC, CCI v2.1 or OSTIA	*http://www.data.jma.go.jp/gmd/goos/data/pub/JMA-product/mgd_sst_glb_D/*
NOAA AVHRR-only Daily OISST v2.0 and v2.1 (Huang *et al.*, 2021; Banzon *et al.*, 2016; Reynolds *et al.*, 2007)	1981–present	0.25°; ~0.2 m	Drifting buoys, moorings, ships, Argo (GTS), Pathfinder V5.0/V5.1 AVHRR (1981-2005), NOAA-16/AVHRR, NOAA-17/AVHRR NOAA-18/AVHRR, NOAA-19/AVHRR, METOP-A/AVHRR, METOP-B/AVHRR, GSFC NASA NSIDC ice (1981–2004), NCEP ice (2005 to present)	Extends back to 1981 and widely used; moderate feature resolution	Largest mean differences and standard deviations compared with Argo; Reduced spatial homogeneity; Uses all day and night data, so may be affected by diurnal warming; accuracy of OISST v2.0 degraded after 2 November 2016 (Liu et al., 2019), so replaced by OISST v2.1 for 1 Jan 2016 to present.	1981–2015: *https://podaac.jpl.nasa.gov/dataset/AVHRR_OI-NCEI-L4-GLOB-v2.0* 2016-present: *https://podaac.jpl.nasa.gov/dataset/AVHRR_OI-NCEI-L4-GLOB-v2.1*
BoM GAMSSA (Beggs *et al.*, 2020; Zhong and Beggs, 2008)	2008–present	0.25°; foundation	Drifting buoys, moorings, ships (GTS), AQUA/AMSR-E, Coriolis/WindSat, GCOM-W/AMSR-2 NOAA-17/AVHRR, NOAA-18/AVHRR, NOAA-19/AVHRR, MetOp-A/AVHRR, MetOp-B/AVHRR, NPP/VIIRS, NOAA-20/VIIRS, ENVISAT/AATSR, NCEP ice	Moderately accurate compared with Argo; smaller standard deviations than other 0.25° analyses (OISST v2.0 and MGDSST); moderate feature sensitivity. Includes microwave data	Only extends back to 2008	*http://thredds.aodn.org.au/thredds/catalog/IMOS/SRS/SST/ghrsst/L4/GAMSSA/catalog.html*

Analysis and Citation	Date Period	Spatial resolution; depth	SST and sea ice data inputs	Advantages	Disadvantages	Data Access
JPL MUR v4.1 (Chin ***et al.***, 2017)	2002–present	0.01°; foundation	Drifting buoys, Moorings, Ships, Argo (iQuam), AQUA/AMSR-E, GCOM-W/AMSR-2, Coriolis/WindSat, DMSP/SSM/I NOAA-16 to 19/AVHRR, MetOp-A/AVHRR, AQUA/MODIS, TERRA/MODIS, OSI-SAF ice	Moderate standard deviation of differences to Argo; good feature sensitivity	Higher standard deviation to Argo than OSTIA, Geo-Polar Blend or CMC L4	*https://podaac.jpl.nasa.gov/dataset/MUR-JPL-L4-GLOB-v4.1*
NOAA Geo-Polar Blended Night (Maturi ***et al.***, 2017)	2002–present	0.05°; foundation	NOAA-16,17,18,19/AVHRR, MetOp-A,B/AVHRR, NPP/VIIRS, GOES-10,11,12,13,15/Imager, GOES-16/ABI, MTSAT-1R,2/JAMI, Himawari-8,9/AHI, Meteosat-8/SEVIRI, Meteosat-11/SEVIRI,	Good standard deviation of differences to Argo; good feature sensitivity; from 2017 closest agreement with Argo (NOAA/NESDIS/STAR, 2019)	Only extends back to 2002, but may be combined with ESA SST CCI analysis v2.1 to extend record	*https://coastwatch.noaa.gov/cw/satellite-data-products/sea-surface-temperature/sea-surface-temperature-near-real-time-geopolar-blended.html*
Met Office GMPE Median from long term analyses (ESA SST CCI GMPE) (Fiedler ***et al.***, 2019a)	1991–2010	0.25°; no specific depth	1991–2007 (6 products), 2008–2010 (4 products)	Validated in Fiedler *et al.* (2019a); small mean difference and standard deviation of difference to Argo; good spatial homogeneity; moderate temporal homogeneity and feature resolution	Source potentially varies from grid box to grid box	*https://catalogue.ceda.ac.uk/uuid/e0659b01259145c8bfb0de6eb12c2690*
Met Office GMPE Median from near real time analyses (Martin ***et al.***, 2012)	2009–present	0.25°; no specific depth	OSTIA (Met Office, UK), RTG_SST_HR (NCEP, USA), K10 (NAVOCEANO, USA), MGDSST (JMA, Japan), RSS MW (Remote Sensing Systems, USA), RSS MW+IR (Remote Sensing Systems, USA), FNMOC (USA), NOAA AVHRR OI.v2 (NOAA/NCEI, USA), CMC (Canada Meteorological Centre), ODYSSEA (Ifremer, France), GAMSSA (BoM, Australia)	Small mean difference and good standard deviation of differences to Argo, similar to CMC, OSTIA and Geo-Polar Blend	Source potentially varies from grid box to grid box	*https://resources.marine.copernicus.eu/product-detail/SST_GLO_SST_L4_NRT_OBSERVATIONS_010_005/INFORMATION*

Source for data: Fiedler *et al.* (2019a), Martin *et al.* (2012), Dash *et al.* (2012), Rayner *et al.* (2019a), NOAA/NESDIS/STAR (2019) and Met Office (2019)

The NOAA SST Quality Monitor (SQUAM) system (Dash *et al.,* 2012; NOAA/NESDIS/STAR, 2019) provides a tool that reveals differences between several of the operational analyses listed in Table 14.3. Maps, histograms, and time series plots for all combinations of 'L4 minus L4' and 'L4 minus Argo SST', for all available dates, are made available for users at *https://www.star.nesdis.noaa.gov/socd/sst/squam/analysis/l4*. In addition, validation plots of the near real time daily SST analyses in Table 14.3 against independent (not ingested) Argo SST (5 m water depth) observations are available at *https://ghrsst-pp.metoffice.gov.uk/ostia-website/gmpe-argo-stats.html*. Validations of the SST reanalyses listed in Table 14.3 are presented in Fiedler *et al.* (2019a) and Rayner *et al.* (2019a). A comprehensive intercomparison of several of these long term SST analyses (including ESA SST CCI v2.1, CMEMS OSTIA reprocessed, JMA MGDSST, NOAA Daily OISST v2.1 and JPL MUR) has recently assessed their suitability for climate applications (Yang *et al.*, 2021).

None of these L4 analysis products were designed, or able, to suit every possible SST application. When selecting an L4 SST analysis it should be borne in mind that grid resolution does not correspond to feature resolution or 'sensitivity' (see Volume 2D). An analysis may be smoother than the output grid resolution depending on the choice of background error covariance and correlation length scale (Dash *et al.,* 2012). Such a product may be perfectly adequate for its intended application (such as for NWP systems where 'noisy' features cause instabilities in the model) but inadequate for another application (such as monitoring of SST frontal dynamics). Coarse resolution input data cannot resolve fine mesoscale features, and an analysis dominated by, for example, PMW SST at ~50 km resolution, cannot be expected to deliver high resolution output. Thus high resolution SST features within each L4 product are dynamic and are visible only when sufficient SST data are available for input—persistent lack of data results in the analysis system reverting to a smooth background climatological value, until new data are again ingested. An example of this can be seen in the 0.01° JPL MUR SST analysis over the Queensland region (see Figure 14.5f), in which, over the southern Queensland coast there are clear conditions and highly resolved ocean features, whereas to the northeast region there is cloud and less resolved features. The challenge for all analysis systems is to maximize the signal-to-noise ratio for a given output grid resolution while maintaining the highest feature resolution possible through the careful choice of analysis design for a given application (Dash *et al.,* 2012; Banzon *et al.,* 2016).

The following subsections discuss specific applications of selected global SST products.

14.4.1 Numerical Weather Prediction model input

Several of the global L4 products listed in Table 14.3 were specifically designed to be used as the boundary condition for NWP models (CMC, OSTIA, MGDSST and GAMSSA). As such, these provide relatively smooth foundation SST fields with minimum daily bias and standard deviation when compared with independent reliable *in situ* data, such as Argo SST.

14.4.2 Climate monitoring

Other climate products (such as ESA SST CCI v2.1, OSTIA reanalysis, and OISST v2.0) were developed to provide reanalyses of the most accurate and available IR SST observations over long time scales, with maximum stability and minimum bias and standard deviation to independent in situ observations. These have not necessarily been designed for coastal applications or for feature sensitivity, and their accuracy largely depends on both the accuracy of the input satellite SST datasets (GAC AVHRR, and for CCI v2.1 also (A)ATSR SSTs) and their bias correction schemes.

CCI v2.1 and OSTIA reprocessed analyses are the only SST products of this group which use AVHRR data that have been consistently recalibrated from raw counts to T_B (Merchant *et al.*, 2019b), which is particularly important for the earlier AVHRR sensors from the 1980s and 1990s (Jon Mittaz, Uni. Reading, *pers. comm.*). The SST CCI v2.1 analysis has been found to compare well with SST from offshore moorings, but less well with coastal moorings (Rayner *et al.*, 2019a), possibly due to the 4 km resolution GAC AVHRR input data and the existence of higher SST variability close to coasts.

14.4.3 Feature resolution

JPL's 1 km SST analysis on the other hand ingests 1 km resolution MODIS IR SST data, and is designed to resolve small scale ocean features in cloud-free regions where MODIS data are available. It has been demonstrated to be useful for studies of coastal upwelling and fisheries off the Peruvian coast (Vazquez-Cuervo *et al.*, 2013), although not necessarily in all Australian near-coastal upwelling regions (see Section 14.5).

14.4.4 Coral bleaching nowcasting

The 0.05° resolution NOAA Geo-Polar Blended L4 analysis (Maturi *et al.*, 2017; see Figure 14.5f) was developed mainly to provide accurate and high resolution daily SSTs for the NOAA Coral Reef Watch program to derive near real time coral bleaching indices (see *https://coralreefwatch.noaa.gov/*; see Excursus 20.3), although it is also suitable for providing a boundary condition to high resolution NWP models. From 1 January 2017, the Geo-Polar Blended foundation SST analyses exhibit one of the closest global agreement with independent Argo SST (5 m) observations of any of the analyses listed in Table 14.3 (NOAA/NESDIS/STAR, 2019).

14.4.5 Verification

The near real time GHRSST Multi-Product Ensemble (GMPE: Martin *et al.*, 2012) and GMPE reanalyses (Fiedler *et al.*, 2019a; Rayner *et al.*, 2019a) are formed from a median of several daily, high resolution, L4 SST analyses to provide a verification source for other satellite-derived SST products. The near real time GMPE L4 is routinely used to monitor a number of global L4 analyses at *https://ghrsst-pp.metoffice.gov.uk/ostia-website/gmpe-monitoring.html* and *https://www.star.nesdis.noaa.gov/socd/sst/squam/analysis/l4*, and has proven to be invaluable for identifying issues with operational L2P, L3U, and L4 products (for example, Martin *et al.*, 2012; Dash *et al.*, 2012; Liu *et al.*, 2019).

14.5 Regional SST Products

There have been several high resolution, satellite-derived, SST products developed specifically for the Australian region and Australian applications by the BoM and CSIRO. These products are listed in Table 14.4, along with their advantages, disadvantages, and example applications. For comparison, the popular NOAA Pathfinder AVHRR L3C product is also listed. The most widely used of the Australian SST products are described below.

Table 14.4 GHRSST products

GHRSST GDS2 format L2, L3, and L4 products, and climatology, covering the Australian region (70°E to 190°E, 70°S to 20°N), are specifically developed for Australian applications. For comparison, the global NOAA Pathfinder version 5.3 AVHRR L3C product is also included.

Product and Citation	Date Period	Spatial resolution; Temporal resolution; depth	SST data inputs	Advantages and Applications	Disadvantages	Data Access
IMOS AVHRR L2P (Griffin *et al.*, 2017)	1992–present	1.1 km at nadir to ~4 km at swath edges; twice daily; skin	IMOS NOAA-9 to NOAA-19 HRPT AVHRR T_B	Timeliness, well-navigated, consistently calibrated, and bias-corrected using regional buoy SSTs; routinely validated (BoM, 2019); used for ingestion into SST analyses and IMOS OceanCurrent 4-hourly SST composite maps	Formed from IR data so gaps in cloudy regions	Contact *ghrsst@bom.gov.aul* for access
IMOS AVHRR L3U (Griffin *et al.*, 2017)	1992–present	0.02°; twice-daily; skin	IMOS NOAA-9 to NOAA-19 HRPT AVHRR L2P, OSI-SAF MetOp-A/FRAC AVHRR L2P, OSI-SAF MetOp-B/FRAC AVHRR L2P, ACSPO NPP VIIRS L3U, ACSPO NOAA-20 VIIRS L3U	Timeliness, consistently calibrated, and bias-corrected using regional buoy SSTs; routinely validated (BoM, 2019); regular grid; used in RT IMOS OceanCurrent maps and fisheries applications (e.g. *www.fishtrack.com*)	Formed from IR data so gaps in cloudy regions	*http://thredds.aodn.org.au/thredds/catalog/IMOS/SRS/SST/ghrsst/L3U/catalog.html*
IMOS AVHRR L3C (Griffin *et al.*, 2017)	1992–present	0.02°; daily; skin	IMOS NOAA-9 to NOAA-19 HRPT AVHRR L3U	Better spatial coverage than the single swath L3U SSTs; routinely validated (BoM, 2019); used in diurnal variation research (Zhang ***et al.***, 2016b)	Formed from IR data so gaps in cloudy regions	*http://thredds.aodn.org.au/thredds/catalog/IMOS/SRS/SST/ghrsst/L3C-1d/catalog.html*

Product and Citation	Date Period	Spatial resolution; Temporal resolution; depth	SST data inputs	Advantages and Applications	Disadvantages	Data Access
IMOS AVHRR L3S (Griffin *et al.*, 2017; Wijffels *et al.*, 2018)	1992–present	0.02°; 1/3/6 days and 1 month; skin	IMOS NOAA-9 to NOAA-19 HRPT AVHRR L3C	High spatial resolution (2 km) and long time series; Routinely validated (BoM, 2019); used in IMOS OceanCurrent, validation of ocean models, and marine heat wave and biological research	Based on HRPT AVHRR only, so limited in spatial coverage; CAPS-based cloud identification means cloud clearing differs south of 20°S (Wijffels *et al.*, 2018).	*http://thredds.aodn.org.au/thredds/catalog/IMOS/SRS/SST/ghrsst/catalog.html* in the L3S-1d, L3S-3d, L3S-6d and L3S-1m sub-directories
IMOS VIIRS L3U (Griffin *et al.*, 2017)	2012–present	0.02°; twice-daily; skin	ACSPO NPP VIIRS L3U, ACSPO NOAA-20 VIIRS L3U	Greater spatial coverage due to global ACSPO VIIRS L3U coverage. Improved VIIRS SST cloud identification and 0.75–1.5 km pixel resolution. Improved accuracy compared with POES AVHRR SSTs. Routinely validated (BoM, 2019)	Formed from IR data so gaps in cloudy regions	*http://thredds.aodn.org.au/thredds/catalog/IMOS/SRS/SST/ghrsst/L3U/catalog.html*
IMOS VIIRS L3C (Griffin *et al.*, 2017)	2012–present	0.02°; twice-daily; skin	IMOS NPP VIIRS L3U, IMOS NOAA-20 VIIRS L3U	Multiple granules composited, so greater spatial coverage than single granule VIIRS L3U (BoM, 2019).	Formed from IR data so gaps in cloudy regions	*http://thredds.aodn.org.au/thredds/catalog/IMOS/SRS/SST/ghrsst/L3C/catalog.html*
IMOS METOP-AVHRR L3U	2012–present	0.02°; twice-daily; skin	OSI-SAF MetOp-A/FRAC AVHRR L2P, OSI-SAF MetOp-B/FRAC AVHRR L2P	Greater spatial coverage than POES HRPT AVHRR due to global METOP FRAC AVHRR coverage and Bayesian cloud identification; improved accuracy compared with POES AVHRR SSTs. Routinely validated (BoM, 2019)	Formed from IR data so gaps in cloudy regions	Contact *ghrsst@bom.gov.au* Will be supplied to *http://thredds.aodn.org.au/thredds/catalog/IMOS/SRS/SST/ghrsst/L3U/catalog.html*
IMOS METOP-AVHRR L3C	2012–present	0.02°; twice-daily; skin	IMOS MetOp-A,B FRAC AVHRR L3U	Mutliple swaths composited, so greater spatial coverage than METOP AVHRR L3U. Routinely validated (BoM, 2019).	Formed from IR data so gaps in cloudy regions	Contact *ghrsst@bom.gov.au* Will be supplied to *http://thredds.aodn.org.au/thredds/catalog/IMOS/SRS/SST/ghrsst/L3C/catalog.html*
IMOS Multi-sensor L3S (Griffin *et al.*, 2017; Beggs *et al.*, 2019)	2012–present	0.02°; 1/3/6 days and 1 month; skin	IMOS NOAA-15 to 19 HRPT AVHRR L3C, IMOS MetOp-A/FRAC AVHRR L3C, IMOS MetOp-B/FRAC AVHRR L3C, IMOS NPP VIIRS L3C, IMOS NOAA-20 VIIRS L3C	Better spatial coverage and accuracy compared with IMOS AVHRR-only L3S or VIIRS L3C; routinely validated (BoM, 2019); used in IMOS OceanCurrent and coastal upwelling research (Beggs *et al.*, 2018a).	Formed from IR data so gaps in cloudy regions	*http://thredds.aodn.org.au/thredds/catalog/IMOS/SRS/SST/ghrsst/catalog.html* in the L3SM-1d, L3SM-3d, L3SM-6d and L3SM-1m sub-directories
IMOS MTSAT-1R L3U v2 (Zhang *et al.*, 2018)	2006–2010	0.05°; hourly; skin	IMOS MTSAT-1R/JAMI L2P v2	Moderately accurate compared with buoys; used for diurnal variation research	Day/night biases in some regions	*http://rs-data1-mel.csiro.au/thredds/catalog/imos-srs/sst/ghrsst/L3U/mtsat1r/catalog.html*
IMOS MTSAT-1R L3U v3 (Zhang *et al.*, 2016a, 2018)	Jan–Apr 2010	0.05°; hourly; skin	IMOS MTSAT-1R/JAMI L2P v3	Highly accurate over the Tropical Warm Pool compared with buoys; low day/night bias over Tropical Warm Pool makes it ideal for diurnal variation studies (Zhang *et al.*, 2016, 2018)	Only available for four months	*http://dapds00.nci.org.au/thredds/catalog/rr5/satellite/GHRSST/MTSAT-1R/catalog.html*

Product and Citation	Date Period	Spatial resolution; Temporal resolution; depth	SST data inputs	Advantages and Applications	Disadvantages	Data Access
BoM Himawari-8 L2P (Griffin and Majewski, 2016; Griffin, 2018)	Mar 2016–present	2 km at nadir; 10 min; skin	JMA Himawari-8/AHI L1	High temporal resolution; used as input into CSIRO's 4-hourly SST composites for IMOS OceanCurrent.	Some residual cloud contamination	Contact *ghrsst@bom.gov.au*
IMOS Himawari-8 L3C (Beggs *et al.*, 2018a)	Oct 2017–present	0.02°; hourly and daily; skin	BoM Himawari-8/AHI L2P	Routinely validated (BoM, 2019); greater spatial coverage and less cloud contamination than the 10-min Himwari-8 L2P data; useful for studies of coastal upwelling and diurnal warming	Some residual cloud contamination	Contact *ghrsst@bom.gov.au*
BoM RAMSSA L4 (Beggs *et al.*, 2011)	2006–present	(1/12)°; daily; foundation	Drifting buoys, moorings, ships, Argo, XBT, CTD (GTS), REMSS AQUA/AMSR-E L2P, REMSS Coriolis/WindSat L3C, JAXA GCOM-W/AMSR-2 L2P, IMOS NOAA-17 to 19/HRPT AVHRR L2P, NAVO NOAA-17 to 19/GAC AVHRR L2P, NAVO MetOp-A and B/GAC AVHRR L2P, EUMETSAT ENVISAT/AATSR L2P, ACSPO NPP/VIIRS L3U, ACSPO NOAA-20/VIIRS L3U, NCEP ice	Includes microwave so measures SST under cloud; gap-free, daily spatial coverage; moderately accurate compared with independent buoys; used for boundary condition of NWP models, and SST anomaly maps	Only from 2006; lower feature resolution and less accurate than IMOS Multi-sensor L3S	*http://thredds.aodn.org.au/thredds/catalog/IMOS/SRS/SST/ghrsst/L4/RAMSSA/catalog.html*
SSTAARS Climatology (Wijffels *et al.*, 2018)	1992–2016	0.02°; daily; 0.2 m	IMOS night-only 1-day AVHRR L3S SST	Resolves small-scale ocean features in coastal regions; stable and accurate compared with independent *in situ* SST (Wijffels *et al.*, 2018); used in IMOS OceanCurrent for SST anomalies and percentiles	Based on IR only, so fewer observations contributed to climatology in cloudy regions	*http://thredds.aodn.org.au/thredds/catalog/CSIRO/Climatology/SSTAARS/2017/AODN-product/catalog.html*
NOAA Pathfinder AVHRR L3C (Casey *et al.*, 2010)	1981–1983 months behind present	0.04°; twice-daily; skin	NOAA Pathfinder NOAA-7 to 19/GAC AVHRR L2P	Available back to 1981; resolves small-scale ocean features in coastal regions; used for long term SST analyses and ocean models	Less spatial coverage compared with IMOS AVHRR L3C due to narrower swath processed; only one satellite processed at a time unlike IMOS L3C; no error estimates (SSES), unlike IMOS L3C; not routinely validated; not available in real time	*https://data.nodc.noaa.gov/cgi-bin/iso?id=gov.noaa.nodc:AVHRR_Pathfinder-NCEI-L3C-v5.3*

Source for data: Griffin *et al.* (2017), Wijffels *et al.* (2018), Beggs *et al.* (2018b), *http://imos.org.au/facilities/srs/sstproducts/sstdata0/*

14.5.1 IMOS satellite SST products

Starting in the mid-1980's, direct broadcast satellite imagery has been acquired at ground stations located in Australia and Antarctica on a daily basis (see Figure 14.6). Building on the archives and processing expertise of CSIRO and the BoM, the IMOS has made these data available as a consistently processed, calibrated, and formatted archive of SST products for the Australasian region (IMOS, 2018). The collection comprises all HRPT overpasses recorded in the Australian and Antarctic region (see Figure 14.6) from AVHRR onboard all operational POES satellites (NOAA-9 to -19) from January 1992 to the present, 'stitched', and geolocated (King, 2003), and stored with full resolution (1.1 km at nadir).

Figure 14.6 Australian AVHRR ground stations

Location and approximate range of Australian ground stations that receive direct broadcast HRPT AVHRR data from NOAA polar orbiting satellites.

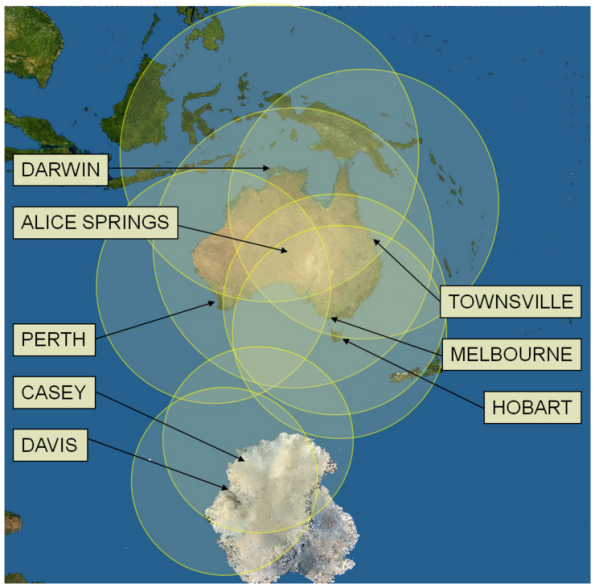

Source: Leon Majewski, Bureau of Meteorology, Melbourne

SST values are derived by regressing the AVHRR T_B to SST observations from drifting and tropical moored buoys in the Australasian region (Griffin *et al*., 2017). The system smoothly and automatically corrects for bias changes in each AVHRR sensor using a running one-year calibration window, adjusted monthly. The data are formatted and flagged according to the GHRSST Data Specification (GDS) 2.0 revision 5 (r5) format specification (GHRSST Science Team, 2012), including time-varying error estimates and quality-level flags for each SST value, calculated using matchups with drifting buoy SST data and proximity to cloud, respectively. The records form a unique 27-year dataset that supplies quality-assured SST values, both at native resolution (L2) and 2 km composites (L3) to within 2 km of coasts (Wijffels *et al*., 2018; see Section 14.3.3 for SST product processing levels and abbreviations). All AVHRR L2P swath data are gridded using a method that weights the pixels by quality level, SSES, and overlap area (Griffin *et al*., 2017), to generate 0.02°×0.02° L3U composites over two domains:

- Australia (70°E to 190°E, 70°S to 20°N); and the
- Southern Ocean (2.5°E to 202.5°E, 77.5°S to 27.5°S).

The highest quality gridded swath SST estimates from multiple passes of the same satellite over the same day for either daytime or nighttime data are averaged to form single sensor L3C composites, then L3S composites formed by combining data from multiple sensors over a fixed time period, such as 1 day, 3 days, 6 days, and 1 month. In order to obtain the most accurate IMOS AVHRR L3U, L3C, or L3S SST estimates at any given grid location, users should choose the highest quality level (5), then subtract the corresponding sses_bias value at that location (Griffin *et al*., 2017; IMOS, 2018). For more details on the IMOS GHRSST products, see IMOS (2018) and references therein.

The VIIRS sensor on NPP and NOAA-20 has now superseded the AVHRR on POES satellites (see Section 14.2.1). To facilitate use of the wider swath and higher resolution VIIRS data (0.75 km compared with 1.1 km for FRAC AVHRR), NOAA produce real time VIIRS L3U SST on the IMOS 0.02° × 0.02° grid (NOAA CoastWatch, 2018). The BoM have composited the NOAA VIIRS L3U data, following the method in Griffin *et al*. (2017), to produce daily day/night L3C composites of VIIRS data on the IMOS grid and domains. The NPP and NOAA-20 VIIRS L3U data are composited, based on quality and uncertainty estimates, with AVHRR SST data from operational POES and MetOp satellites to construct the IMOS 'Multi-sensor L3S' product suite (Griffin *et al*., 2017). This has resulted in improvements to overall quality, accuracy, and coverage of IMOS L3S composites over the IMOS Australian domain (Beggs *et al*., 2019). Figure 14.7 demonstrates the difference in spatial coverage between the AVHRR-only L3S and Multi-sensor L3S. To best use these IMOS L3C and Multi-sensor L3S products, it is recommended that users select data with quality level 4 or higher and subtract sses_bias (Pallavi Govekar, BoM, *pers. comm*. and BoM, 2019).

The IMOS AVHRR and Multi-sensor L3S SSTs are available from the AODN (*http://portal.aodn.org.au*) and SST maps are available for multiple Australian coastal regions from IMOS OceanCurrent (see *http://oceancurrent.imos.org.au*). See Excursus 14.2 for an example of IMOS AVHRR-only L3S SSTs being used in IMOS OceanCurrent. Maps of IMOS Multi-sensor L3S SSTs are also available over some Australian regions from the NOAA ARMS website (see *https://www.star.nesdis.noaa.gov/sod/sst/arms*).

Coastal applications can benefit from the 2 km resolution of the IMOS AVHRR and Multi-sensor L3S products, in contrast to the coarser (4 km), globally-available L3 products (such as NOAA Pathfinder L3C) and statistically-interpolated L4 SST products, which may be unable to provide the required detail. In cloud-free conditions, IMOS Multi-sensor L3S SST products may more accurately reflect near-coastal SST processes, such as coastal upwelling or SST anomalies around reefs, than high resolution, statistically-interpolated, foundation SST analyses such as 1 km resolution JPL MUR L4 (see Figure 14.8 and Beggs *et al*., 2018a) or 5 km NOAA Geo-Polar Blended L4 (see Figure 14.5).

Due to their superior spatial coverage in near-coastal regions, since 21 November 2018 the IMOS multi-sensor, 1-day, nighttime, L3S SSTs have been ingested into the BoM's ReefTemp NextGen coral bleaching nowcasting system (Garde *et al*., 2014; see *http://www.bom.gov.au/environment/activities/reeftemp/reeftemp.shtml*), replacing the IMOS AVHRR-only, 1-day, nighttime, L3S SSTs (Beggs *et al*., 2019). Diurnal warming can also be measured using day-only and night-only IMOS L3C SST products (Zhang *et al*., 2016b), 5 km hourly IMOS MTSAT-1R L3U (Zhang *et al*., 2016a; 2018), or 2 km hourly IMOS Himawari-8 L3C (see Table 14.3; Beggs *et al*., 2018a). For more details on applications of IMOS satellite SST products see Beggs *et al*. (2018b).

Figure 14.7 Skin SST maps

2 km resolution SSTskin maps with quality level 4 and 5 from IMOS data for 10 June 2018 over the IMOS Australian domain (70°E–190°E, 70°S–20°N). For this date, the AVHRR-only L3S was formed using data from NOAA-18 and NOAA-19, and the Multi-sensor L3S included additional data from NPP.

a. AVHRR-only, 1-day, night-only, L3S files

b. Multi-sensor, 1-day, night-only, L3S files

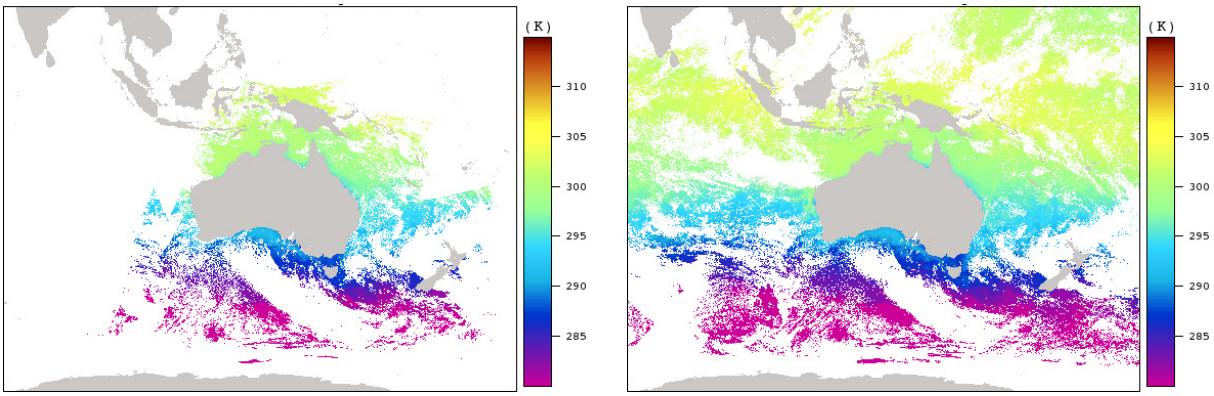

Source: Christopher Griffin, Bureau of Meteorology, Melbourne

Figure 14.8 SST maps

Maps of SSTs at ~0.2 m water depth for 8 March 2018 over the Bonney Coast, southern Australia, from different EO sensors. Temperature is given in °C. The signature of the cold upwelling is well defined in the L3S product but somewhat less defined in the L4 analysis.

a. 2 km IMOS VIIRS 1-day night-only L3C

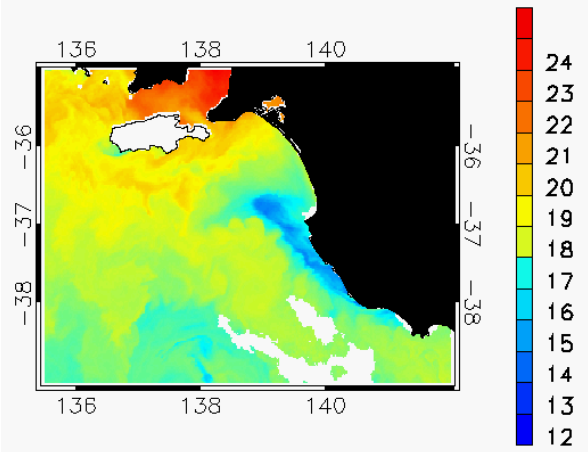

b. 2 km IMOS Himawari-8 1-day night-only L3C

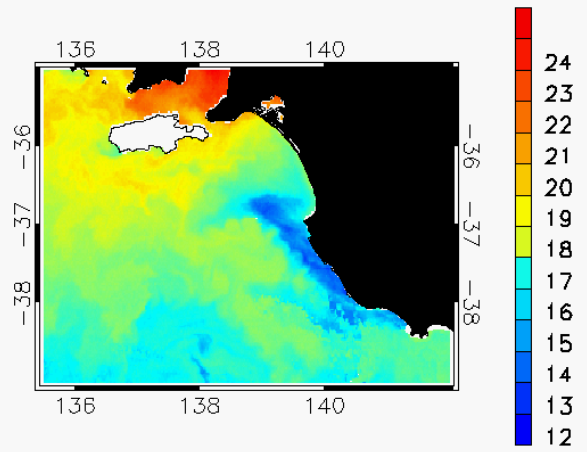

c. 2 km IMOS Multi-sensor 1-day night-only L3S (formed from NOAA-18 and NOAA-19 HRPT AVHRR and NPP VIIRS data)

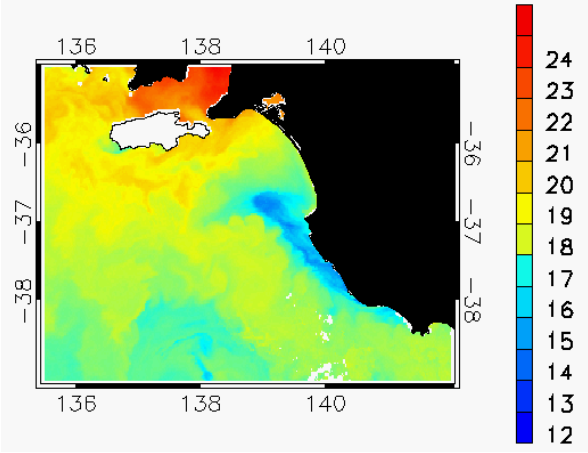

d. 1 km JPL MUR L4 (formed from AMSR-2, MODIS, and GAC AVHRR data).

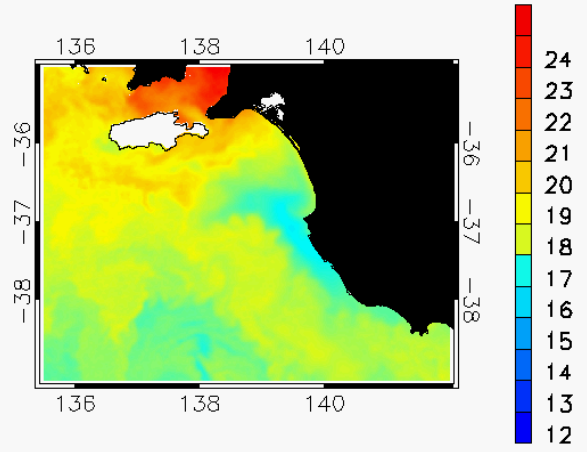

Source: Helen Beggs, Bureau of Meteorology, Melbourne

Excursus 14.2—Sea Surface Temperature around Tasmania

Source: Madeleine Cahill, IMOS OceanCurrent
Further Information: OceanCurrent website:
http://oceancurrent.imos.org.au/news.php
http://oceancurrent.imos.org.au/daily.php?link=DR_SST_daily/pctiles/Tas/20171124.gif

In 2017, SST around Tasmania were above the 90th percentile at the end of November, particularly to the west and south. Temperatures were hottest off the northeast coast, associated with a weak Eastern Australian Current (EAC) eddy, but more unusual were the high temperatures off the west coast (see Figure 14.9) that also peaked at over 18°C, which was more than 3–4°C above the November mean. The blocking high in the Tasman Sea that directed northeasterly winds over Tasmania and brought a record six days of temperatures over 26°C also created the conditions for a week or more of cloudless skies. Cloud-free conditions allow maximum solar heating, particularly at this time of year when UV radiation is reaching its peak. SST indicates that off the west coast temperatures increased by up to 4°C over three weeks.

Figure 14.9 IMOS nighttime, 6-day AVHRR L3S SST around Tasmania

This nighttime, 6-day AVHRR L3S SST image around Tasmania was acquired on 24 November 2017. The coincident locations of Argo floats are shown as magenta circles.

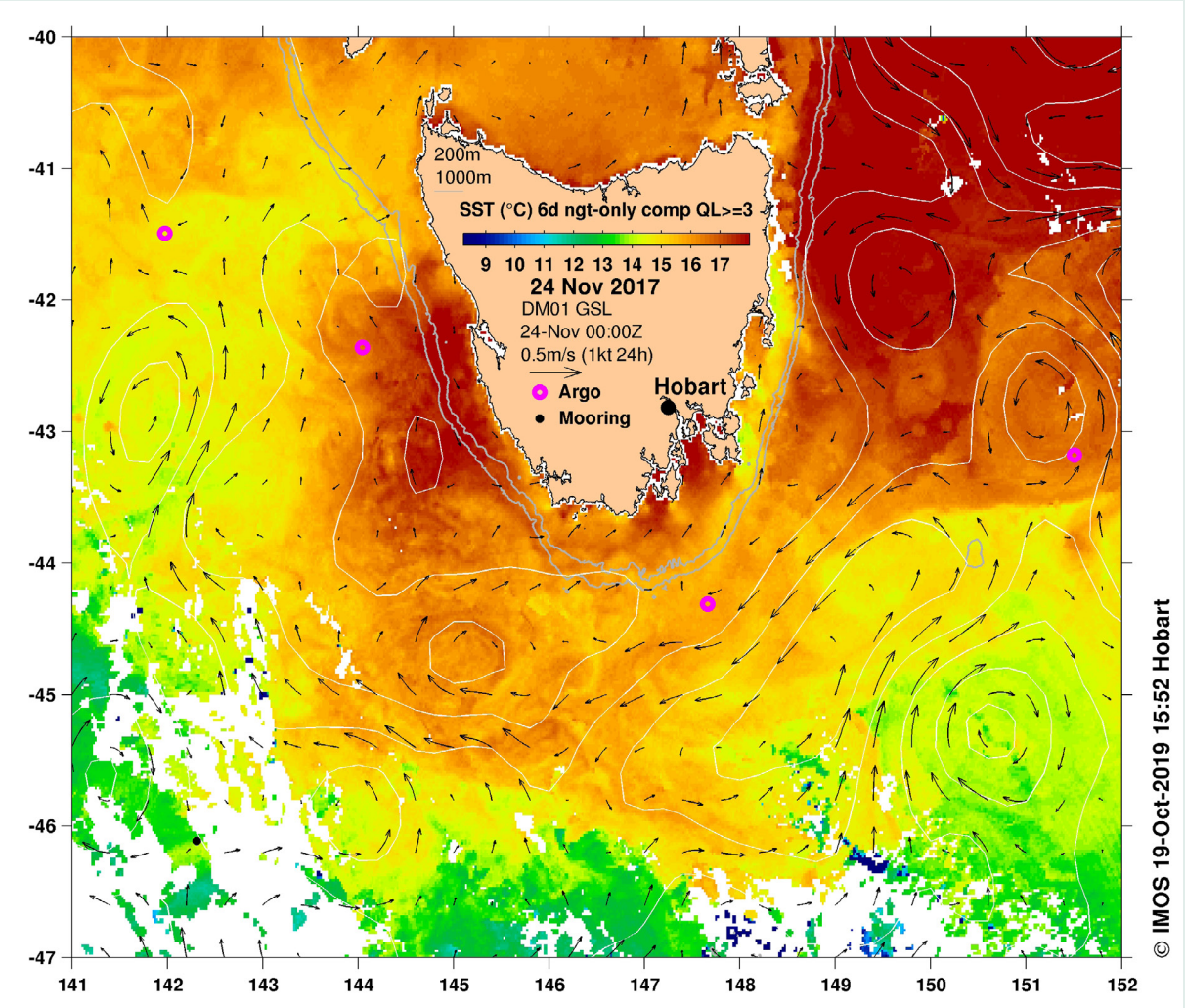

Satellite SST, however, is a measure of only a very thin surface layer (or surface skin) and when winds are very weak there is not much vertical mixing and the SST may only represent a shallow surface layer. Without modelling it is impossible to know how deep this surface layer extends. The unusual weather conditions meant that not only was the sky around Tasmania cloud-free, but the west coast, in the lee of the wind, was almost becalmed as well. The 'hot spot' off the west coast suggests that in this region the heating may only be shallow. The consequence of shallow heating is not only that the extreme temperatures only affect animals and plants near the surface but also that the temperatures will be short-lived and quickly reversed with the next windy day.

Argo floats (shown as magenta circles in Figure 14.9) can provide a window to what is happening beneath the surface. A float off the west coast shelf profiled the water column every ten days through November 2017. The development of a warm mixed-layer throughout the month can be seen in the Argo temperature profiles for that float during November and early December (see Figure 14.10). The closest satellite SST for each profile is also plotted to indicate any discrepancy between the surface and water below. In early November the water was well-mixed down to 60 m and the Argo temperature at 5 m was very close to the mixed layer temperature. For all days that the float profiled, the satellite SST was always within 0.7°C of the temperature at 10 m. After the weather changed, the surface heat was mixed down to 40 m reducing the surface temperature significantly but resulting in an increase of at least 2°C in the mixed layer since the beginning of November.

Based on the SST anomalies, the west coast surface waters were 3–4°C above average for at least 10 days during November. From the Argo profile on November 24, it is clear the low wind speeds allowed the temperatures to be surface intensified at the peak of the event. Unlike the three other profiles, there was no strong thermocline and temperatures at 20 m were about 1°C cooler than at 10 m. So, it is most likely subsurface temperatures, at 10–20 m, would not have reached the 4°C anomaly. In any case, with a 2°C increase in temperature of the top 40 m, the event created a strong injection of heat into surface waters around Tasmania. Unlike the west coast, water temperatures on the east coast, away from sheltered regions, were unaffected by the heating because the atypical northeasterly winds drove an upwelling event that kept the shelf waters cool despite the warm EAC water just offshore.

Figure 14.10 Argo temperature profile and SST

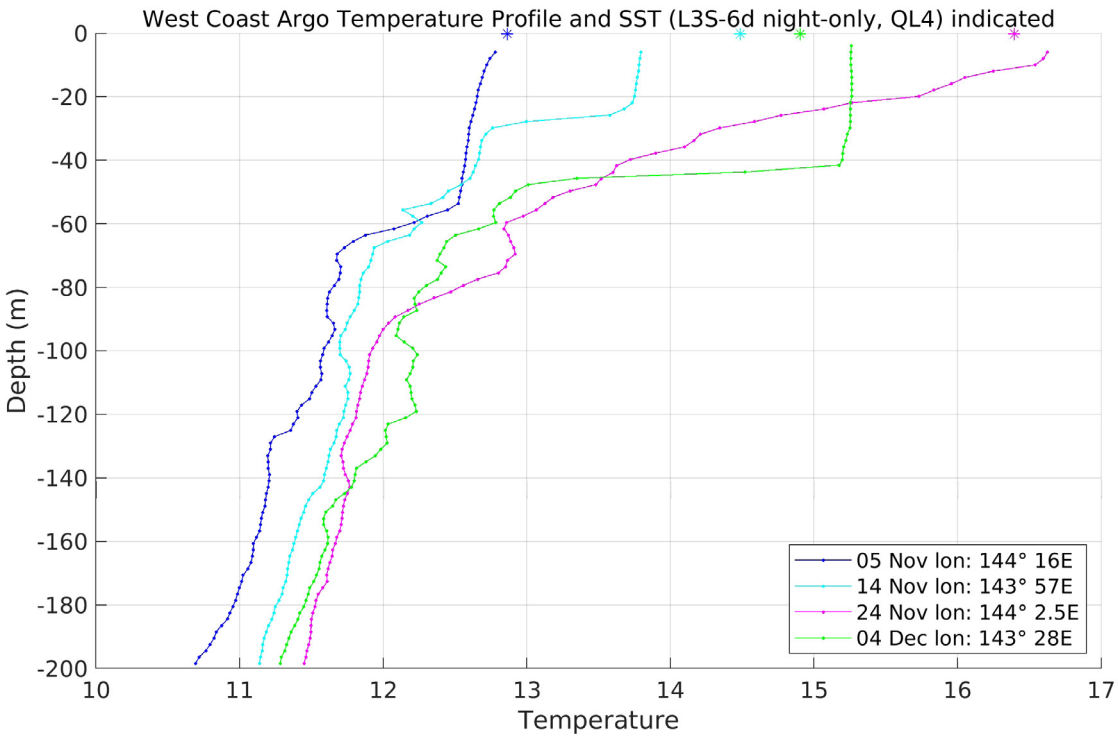

14.5.2 High resolution SST climatologies and extreme events

Quantifying ocean 'extreme' events from SST observations, such as marine heatwaves and cold upwelling, requires a consistent and accurate SST reference, ideally at the same spatial and temporal resolution as the observations and over a period sufficiently long to represent 'typical' ocean conditions. Over the Australian region four high resolution SST climatologies have been compared (Hu *et al.*, 2019) and the following two found to agree most closely over the same time period (1992–2016) and to be most suitable for the study of coastal extreme events.

- The SST Atlas of Australian Regional Seas (SSTAARS: Wijffels *et al.*, 2018; see Figure 14.1 and Table 14.4) was derived from de-biased IMOS 1-day nighttime AVHRR L3S SSTs for the period 1992 to 2016. The SSTAARS 'Atlas' provides the following variables (referenced to middle year, 2005) for each 0.02° × 0.02° pixel:
  - a daily (seasonal fitted) climatological SST (0.2 m);
  - mean SST(0.2 m);
  - decadal trend;
  - monthly seasonal harmonics; and
  - percentiles (all available from the AODN; see *http://portal.aodn.org.au*).
- The SSTAARS Atlas reveals in detail regional oceanographic phenomena, including tidally-driven entrainment cooling over shelves and reef flats, wind-driven upwelling, shelf winter fronts, cold river plumes, and standing mesoscale features in the major offshore currents (Wijffels *et al.*, 2018). SSTAARS daily climatological SSTs are used in conjunction with either IMOS AVHRR L3S or Multi-sensor L3S SSTs to produce maps of SST anomalies and percentiles in IMOS OceanCurrent, which are useful for real time detection of anomalous events (see Excursus 14.2).
- A global, daily, 0.05° resolution, gap-free SST climatology formed from the ESA SST CCI version 2.1 reanalyses for 1981 to 2016 (Merchant *et al.*, 2019b; Rayner *et al.*, 2019a; see Table 14.3) is also highly suitable for use as a high resolution reference for marine heatwave studies over the Australian region, although the feature resolution of the optimally-interpolated SST CCI analysis v2.1 will be significantly coarser than that of the 0.02° composite-based SSTAARS climatology (Hu *et al.*, 2019).

14.6 Inland Water Temperature

Lake surface water temperature (LSWT) is an important parameter with which to assess aquatic ecosystems and the response of various lake characteristics to climate change. Inland waters are warming at highly variable rates that often differ from regional air temperature trends (White *et al.*, 2018). This variable warming is partially attributable to the geographical and morphological characteristics of each individual lake. In very large lakes, significant intra-lake variability in long term warming trends have been observed (White *et al.*, 2018).

Some of the challenges for EO of water temperatures over inland seas, lakes, and the ocean coastal zones include:

- greater atmospheric water vapour, temperature, and aerosol variability than over most of the ocean;
- avoiding land contamination of satellite footprint;
- water surface contaminants; and
- turbidity in interaction with cloud detection (O'Carroll *et al.*, 2019).

Regarding the latter, products are prone to over-masking during the spring-summer warming phase, and to screening of cold, clear water, leading to systematic observation bias (O'Carroll *et al.*, 2019). Problems in satellite-based lake temperature products arise where processing methodologies for cloud detection and temperature retrieval that are optimised for the open ocean (where the atmosphere is usually close to equilibrium with the water surface) are applied. However, inland water-specific methodologies are promising for application of satellite-derived lake temperatures (MacCallum and Merchant, 2012; Crosman *et al.*, 2017; Woolway and Merchant, 2018).

Satellite data for the period 1985 to 2009 was used to measure the surface temperatures of 167 large lakes worldwide (with dimensions of at least 10×10 km pure water area; Schneider and Hook, 2010). Lakes studied were located in North and South America, Europe, Asia, and Africa, but the study excluded Australia, New Guinea, Indonesia, or New Zealand, possibly due to the lack of suitably large lakes. LSWT retrievals derived from 1 km ATSR and 4 km GAC AVHRR Pathfinder version 5 BTs were used. They reported an average warming rate of 0.45°C per decade, with some lakes warming as much as 1°C per decade. The warming trend was global, and the greatest increases were in the mid- to high-latitudes of the Northern Hemisphere (Schneider and Hook, 2010).

To assess climate change and lake dynamics using consistent LSWT data, Lieberherr and Wunderle (2018) used the 1.1 km resolution HRPT AVHRR archive of the University of Bern. To derive such a dataset, challenges such as orbit drift correction, non-water pixel detection, and homogenisation had to be solved. The result was a dataset covering over 35 years of spatial LSWT data for 26 European lakes (Lieberherr and Wunderle, 2018). White *et al.* (2018) had to surmount similar challenges in order to assemble a 0.018° resolution LSWT dataset covering the Laurentian Great Lakes (USA/Canada border), derived from HRPT AVHRR T_B (1986–2016). They subtracted an empirically-determined, mean diurnal cycle to mitigate effects of varying observation times. Adjustments in the georegistration of the images were made to reduce the impact of AVHRR navigational errors on earlier platforms (White *et al.*, 2018). The Australian HRPT archive of well-navigated T_B covering the period 1992 to 2019 (King, 2003; Griffin *et al.*, 2017) offers a similar opportunity to monitor long term trends in Australian inland surface waters, although derivation of LSWT would require sufficient *in situ* LSWT data for either regression or validation.

The IMOS Multi-sensor L3S products (Table 14.4) provide surface water temperatures over most large Australian inland waterbodies. In addition, LSWT data over Australian lakes are available from NOAA (NOAA CoastWatch, 2018) in NPP/NOAA-20 VIIRS L2P/L3U (see Figure 14.11), Aqua/Terra MODIS L2P/L3U, Himawari-8 L3U/L3C SST products, and JPL MUR L4 SST products (see *https://podaac.jpl.nasa.gov*), although the accuracy of the SST values for inland waters would need to be verified using *in situ* water temperature observations. Various federal, state, and municipal environmental and water authorities measure water temperatures in reservoirs, lakes, and rivers. These, and additional targeted temperature datasets, may provide sufficient *in situ* observations to determine the suitability of available satellite-derived SST products for estimates of LSWT in Australia.

Figure 14.11 Daytime SWT map from VIIRS

Daytime surface water temperatures from NPP VIIRS L2P SST files, processed by NOAA/NESDIS/STAR, for 11 December 2018.

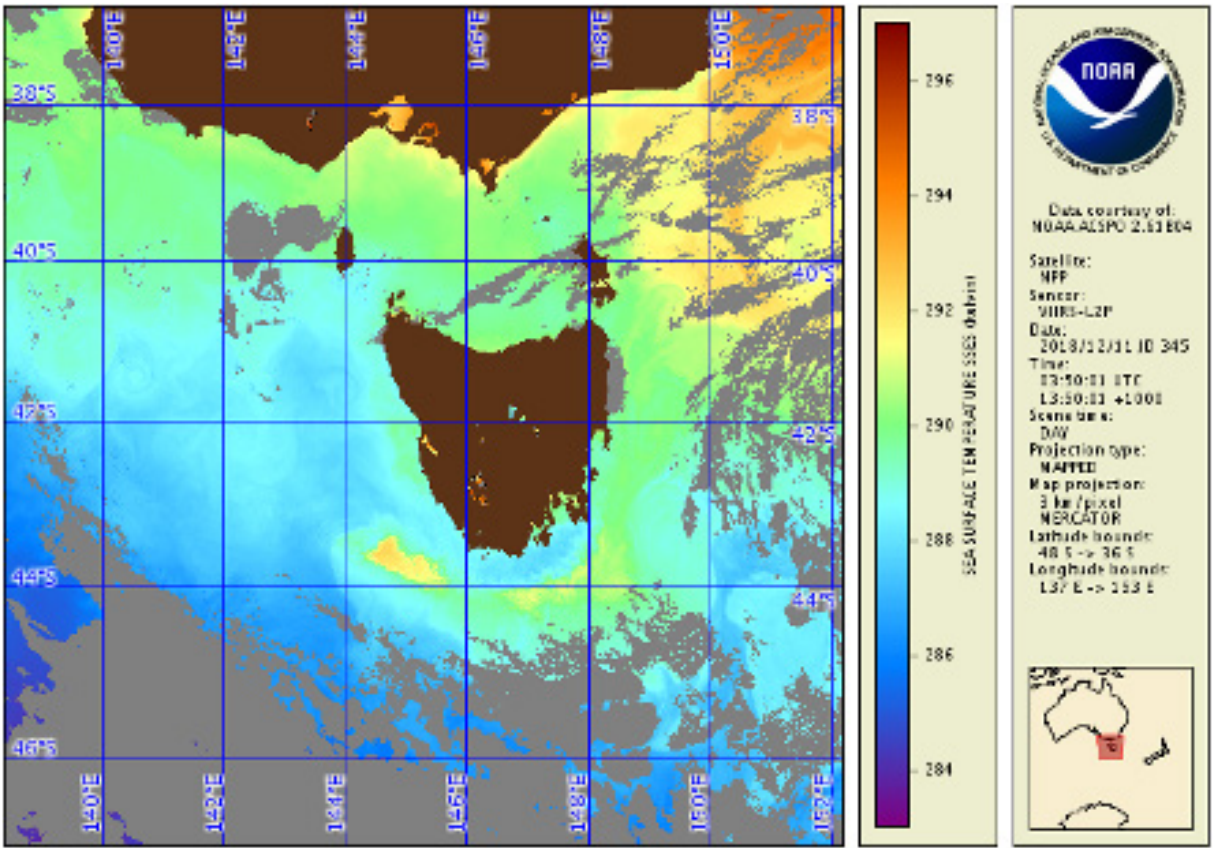

Source: NOAA/NESDIS ACSPO Regional Monitor for SST website (*https://www.star.nesdis.noaa.gov/sod/sst/arms*). Retrieved from: *https://www.star.nesdis.noaa.gov/sod/sst/arms/?datatype=none&data_lev=L2P&satt=VIIRS_NPP&daynight=day&variable=sst&date=2018-12-11&region-selected=TM&curr_slide=0&last_slide=1&masked=true&sses=true&front=false&cmp=false&polar_slide=0*

14.7 Further Information

AODN SST Information

https://help.aodn.org.au/satellite-sst-data/

Australian Institute of Marine Science

AIMS contributions to ocean remote sensing: *https://www.aims.gov.au/docs/research/research-highlights/imos*

Bureau of Meteorology

SST Analyses: *http://www.bom.gov.au/marine/sst.shtml*

SST Short-term Forecasts: *http://www.bom.gov.au/oceanography/forecasts/*

SST Seasonal Forecasts: *http://www.bom.gov.au/oceanography/oceantemp/sst-outlook-map.shtml*

Coral Bleaching Nowcasts: *http://www.bom.gov.au/environment/activities/reeftemp/reeftemp.shtml*

Integrated Marine Observing System (IMOS)

SST Webpage: *http://imos.org.au/facilities/srs/sstproducts/*

SST Product Details: *http://imos.org.au/facilities/srs/sstproducts/sstdata0/*

SST Maps in OceanCurrent: *http://oceancurrent.imos.org.au/*

SST Atlas of Australian Regional Seas (SSTAARS): *https://researchdata.ands.org.au/sst-atlas-australian-climatology-fit/1307263*

SST Data Access:

L3C, L3S: *http://portal.aodn.org.au*

L3U, L3C, L3S, L4: *http://thredds.aodn.org.au/thredds/catalog/IMOS/SRS/SST/ghrsst/catalog.html*

CEOS SST videos

http://ceos.org/home-2/satellite-oceanography-user-workshop-videos-available/

ESA SST Climate Change Initiative

http://esa-sst-cci.org

GHRSST

http://www.ghrsst.org

NASA

Sea Surface Temperature: *https://earthobservatory.nasa.gov/global-maps/MYD28M*

State of the Ocean Web Tool: *https://podaac-tools.jpl.nasa.gov/soto*

Access to Satellite-derived Ocean Products (including SST) from the Physical Oceanography Distributed Active Archive Center (PO.DAAC): *https://podaac.jpl.nasa.gov/*

MUR SST Analysis: *https://podaac.jpl.nasa.gov/dataset/MUR-JPL-L4-GLOB-v4.1?search=MUR&provider=POCLOUD*

NOAA

OceanView online visualisation tool: *https://www.star.nesdis.noaa.gov/socd/ov/*

Validation of SST products in near real time

BoM IMOS L2P/L3U/L3C/L3S: *http://imos.org.au/facilities/srs/sstproducts/sstdata0/sstdata-validation*

EUMETSAT L2P: *http://metis.eumetsat.int/sst*

JAXA AMSR-2 L2P: *https://suzaku.eorc.jaxa.jp/cgi-bin/gcomw/validation/gcomw_validation_ssti1.cgi*

NOAA/NESDIS SQUAM L2P/L3U/L4: *http://www.star.nesdis.noaa.gov/sod/sst/squam*

NOAA/NESDIS iQUAM: *https://www.star.nesdis.noaa.gov/socd/sst/iquam/*

UK Met Office: *https://ghrsst-pp.metoffice.gov.uk/ostia-website/gmpe-argo-stats.html*

14.8 References

Allison, L.J., and Kennedy, J.S. (1967). *An Evaluation of Sea Surface Temperature as measured by the Nimbus I High Resolution Infrared Radiometer.* NASA Technical Note, NASA TN D-4078, 26 p., Washington DC, USA: NASA. *https://ntrs.nasa.gov/archive/nasa/casi.ntrs.nasa.gov/19680000754.pdf*

Andreu-Burillo, I., Brassington, G., Oke, P., and Beggs, H. (2010). Including a new data stream in BLUElink Ocean Data Assimilation System. *Australian Meteorological and Oceanographic Journal,* 59, 77–86.

Banzon, V., Smith, T.M., Chin, T.M., Liu, C, and Hankins, W. (2016). A long-term record of blended satellite and in situ sea-surface temperature for climate monitoring, modeling and environmental studies, *Earth System Science Data*, 8, 165–176. *www.earth-syst-sci-data.net/8/165/2016/ doi:10.5194/essd-8-165-2016*

Beggs, H. (2010). Use of TIR from Space in Operational Systems, In: *Oceanography from Space Revisited*. (Eds: V. Barale, J.F.R. Gower and L. Alberotanza). Springer Science+Business Media B.V. pp. 249–271. doi:10.1007/978-90-481-8681-5. *https://www.researchgate.net/publication/259823623_Use_of_TIR_from_Space_in_Operational_Systems*

Beggs, H., Zhong, A., Warren, G., Alves, O., Brassington, G., and Pugh, T. (2011). RAMSSA—An Operational, High-Resolution, Multi-Sensor Sea Surface Temperature Analysis over the Australian Region, *Australian Meteorological and Oceanographic Journal*, 61, 1–22. *http://www.bom.gov.au/jshess/papers.php?year=2011*

Beggs H., Verein, R., Paltoglou, G., Kippo, H., and Underwood, M. (2012). Enhancing ship of opportunity sea surface temperature observations in the Australian region. *Journal of Operational Oceanography*, 5, 59–73.

Beggs, H., Griffin, C., Brassington, G., and Govekar, P. (2018a). *Measuring coastal upwelling using IMOS Himawari-8 and Multi-Sensor SST*. Presented at ACOMO 2018 Workshop, Canberra, Australia, 9–11 October, 2018. *http://imos.org.au/fileadmin/user_upload/shared/SRS/SST/Beggs_ACOMO_Poster_Coastal_Upwelling_20181004.pdf*

Beggs, H., Griffin, C., Govekar, P., Majewski, L., Qi, L., and Zhong, A. (2018b). *Which IMOS GHRST product should I use?* Presented at the IMOS Data Workshop, Adelaide, Australia, 6 July 2018. *http://imos.org.au/fileadmin/user_upload/shared/SRS/SST/IMOS_Data_Workshop-SST-Beggs_08Jul2018.pdf*

Beggs, H., Griffin, C., and Govekar, P. (2019). *New IMOS multi-sensor sea surface temperature composites provide better coverage and accuracy*. IMOS web article, 21 February 2018. *http://imos.org.au/fileadmin/user_upload/shared/SRS/SST/Beggs_2019_IMOS_Multi-sensor_L3S_article_21Feb2018.pdf*

Beggs, H., Qi, L., Govekar, P., and Griffin, C. (2020). Ingesting VIIRS SST into the Bureau of Meteorology's Operational SST Analyses, In *Proceedings of the 2*1st *GHRSST Science Team Meeting, Virtual Meeting hosted by EUMETSAT*, 1–4 June 2020. P. 104–110. *https://www.ghrsst.org/meetings/21st-ghrsst-international-science-team-meeting-g-xxi/*

Berry, D., Corlett, G., Embury, O., and Merchant, C. (2018). Stability assessment of the (A)ATSR Sea Surface Temperature Climate Dataset from the European Space Agency Climate Change Initiative. Remote Sensing, 10, 126.

BoM (2019). *Near real-time fv01 SST Validation* (Webpage for IMOS GHRSST L2P, L3U, L3C and L3S products from POES HRPT AVHRR, NPP VIIRS and Himawari-8 AHI). BOM/IMOS. *http://opendap.bom.gov.au:8080/thredds/fileServer/abom_imos_ghrsst_archive-1/staticweb/sst-nrt-batch/index01.html*

Brasnett, B. (2008). The impact of satellite retrievals in a global sea-surface-temperature analysis. *Quarterly Journal of the Royal Meteorological Society*, 134, 1745–1760. doi:10.1002/qj.319

Brasnett, B. (2012). *A 20-year Reanalysis of Sea Surface Temperature*. Report, CMC. Available on request from the author at *bruce.brasnett@gmail.com*

Brasnett, B., and Surcel Colan, D. (2016). Assimilating Retrievals of Sea Surface Temperature from VIIRS and AMSR2. *Journal of Atmospheric and Oceanic Technology*. *https://doi.org/10.1175/JTECH-D-15-0093.1*

Casey, K.S., Brandon, T.B., Cornillon, P., and Evans, R. (2010). The Past, Present and Future of the AVHRR Pathfinder SST Program. In *Oceanography from Space: Revisited* (Eds: V. Barale, J.F.R. Gower, and L. Alberotanza). Springer. doi:10.1007/978-90-481-8681-5_16. *https://www.nodc.noaa.gov/SatelliteData/pathfinder4km/OFS_21_Cas_09Dec2009.pdf*

Chin, T.M., Vazquez-Cuervo, J., and Armstron, E.M. (2017). A multi-scale high-resolution analysis of global sea surface temperature. *Remote Sensing of Environment*, 200, 154–169. *https://doi.org/10.1016/j.rse.2017.07.029*

Crosman, E., Vazquez-Cuervo, J., and Chin, T.M. (2017). Evaluation of the Multi-Scale Ultra-High Resolution (MUR) Analysis of Lake Surface Temperature. *Remote Sensing*, 9, 723. doi:10.3390/rs9070723.

Dash, P., Ignatov, A., Kihai, Y., and Sapper, J. (2010). The SST Quality Monitor (SQUAM). Journal of Atmospheric and Oceanic Tech*nology*, 27, 1899–1917. doi:10.1175/2010JTECHO756.1

Dash, P., Ignatov, A., Martin, M., Donlon, C., Brasnett, B., Reynolds, R., Banzon, V., Beggs, H., May, D., McKenzie, B., Cayula, J-F., Chao, Y., Grumbine, R., Maturi, E., Harris, A., Mittaz, J., Sapper, J., Chin, T., Vazquez, J., Armstrong, E., Gentemann, C., Cummings, J., Piolle, J-F., Autret, E., Roberts-Jones, J., Ishizaki, S., Hoyer, J., and Poulter, D. (2012). Group for High Resolultion SST (GHRSST) Analysis Fields Inter-Comparisons Part 2. Near real-time web-based Level 4 SST Quality Monitor (L4-SQUAM). *Deep Sea Research II*, 77–80, 31–43.

Ditri, A.L., Minnett, P.J., Liu, Y., Kilpatrick, K., and Kumar, A. (2018). The Accuracies of Himawari-8 and MTSAT-2 Sea-Surface Temperatures in the Tropical Western Pacific Ocean. *Remote Sensing*, 10(2), 212. doi:10.3390/rs10020212

Donlon, C.J., Minnett, P.J., Gentemann, C.L., Nightingale, T.J., Barton, I.J., Ward, B., and Murray, M.J. (2002). Toward improved validation of satellite sea surface skin temperature measurements for climate research. *Journal of Climate*, 15(4), 353–369.

Donlon, C., Robinson, I., Casey, K., Vasquez, J., Armstrong, E., Gentemann, C., May, D., LeBorgne, P., Piolle, J., Barton, I., Beggs, H., Poulter, D. J. S., Merchant, C., Bingham, A., Heinz, S., Harris, A., Wick, G., Emery, B., Stuart-Menteth, A., Minnett, P., Evans, B., Llewellyn-Jones, D., Mutlow, C., Reynolds, R., Kawamura, H., and Rayner, N. (2007). The Global Ocean Data Assimilation Project (GODAE) High Resolution Sea Surface Temperature Pilot Project (GHRSST-PP). *Bulletin of American Meterological Society*, 88, 1197–1213.

Donlon, C., Casey, K., Robinson, I., Gentemann, C., Reynolds, R., Barton, I., Arino, O., Stark, J., Rayner, N., Le Borgne, P., Poulter, D., Vazquez-Cuervo, J., Armstrong, E., Beggs, H., Llewellyn-Jones, D., Minnett, P., Merchant, C., and Evans, R. (2009). The GODAE High-Resolution Sea Surface Temperature Pilot Project. *Oceanography*, 22, 34–45.

Donlon, C.J., Martin, M., Stark, J., Roberts-Jones, J., Fiedler, E., and Wimmer, W. (2012). The Operational Sea Surface Temperature and Sea Ice Analysis (OSTIA) system. *Remote Sensing of Environment*, 116, 140–158. *https://doi.org/10.1016/j.rse.2010.10.017*

Donlon, C.J., Minnett, P.J., Jessup, A., Barton, I., Emery, W., Hook, S., Wimmer, W., Nightingale, T.J., and Zappa, C. (2014). Chapter 3.2—Ship-borne Thermal Infrared Radiometer Systems, *Experimental Methods in the Physical Sciences Vol. 47* (Eds: G. Zibordi, C.J. Donlon, and A.C. Parr). pp 305–404, Academic Press. *http://doi.org/10.1016/B978-0-12-417011-7.00011-8*

Eumetsat (2011). *AVHRR Level 1b Product Guide*. Doc. No. EUM/OPS-EPS/MAN/04/0029 v3A. EUMETSAT, Germany. *https://www-cdn.eumetsat.int/files/2020-04/pdf_avhrr_l1b_product_guide.pdf*

Fiedler, E.K., McLaren, A., Banzon, V., Brasmett, B., Ishizaki, S., Kennedy, J., Rayner, N., Roberts-Jones, J., Corlett, G., Merchant, C.J., and Donlon, C. (2019a). Intercomparison of long-term sea surface temperature analyses using the GHRSST Multi-Product Ensemble (GMPE) system. *Remote Sensing of Environment*, 222, 18–33. *https://doi.org/10.1016/j.rse.2018.12.015*

Fiedler, E.K., Mao, C., Good, S.A., Waters, J., and Martin, M.J. (2019b). Improvements to feature resolution in the OSTIA sea surface temperature analysis using the NEMOVAR assimilation scheme. *Quarterly Journal of the Royal Meteorological Society*, 145(725), 3609–3625. *https://doi.org/10.1002/qj.3644*

Garde, L.A., Spillman, C.M., Heron, S., and Beeden, R. (2014). ReefTemp Next Generation: A New Operational System for Monitoring Reef Thermal Stress. *Journal of Operational Oceanography*, 7, 21–33

Gentemann, C.L., Meissner, T., and Wentz F.J. (2010). Accuracy of Satellite Sea Surface Temperatures at 7 and 11 GHz. *IEEE Transactions on Geoscience and Remote Sensing*, 48, 1009–1018. doi:10.1109/TGRS.2009.2030322

Gentemann, C.L., and Hilburn, K.A. (2015). In situ validation of sea surface temperatures form the GCOM-W1 AMSR2 RSS calibrated brightness temperatures. *Journal of Geophysical Research: Oceans*, 120, 3567–3585. doi:10.1002/2014JC010574

GHRSST Science Team (2012). *The Recommended GHRSST Data Specification (GDS) 2.0*, document revision 5, available from the GHRSST International Project Office, 2012, pp 123. *https://www.ghrsst.org/wp-content/uploads/2016/10/GDS20r5.pdf*

Good, S., Fiedler, E., Mao, C., Martin, M.J., Maycock, A., Reid, R., Roberts-Jones, J., Searle, T., Waters, J., While, J., and Worsfold, M. (2020). The Current Configuration of the OSTIA System for Operational Production of Foundation Sea Surface Temperature and Ice Concentration Analyses. *Remote Sensing*, 12, 720. doi:10.3390/rs12040720

Griffin, C., and Majewski, L. (2016). *GHRSST Himawari-8 SST at Australian Bureau of Meteorology*. Presented at the 17th GHRSST Science Team Meeting, Washington DC, USA, 6–19 June 2016. *http://imos.org.au/facilities/srs/sstproducts/sstdata0/sstdata-references/*

Griffin, C., Beggs, H., and Majewski, L. (2017). *GHRSST compliant AVHRR SST products over the Australian region*, Version 1, Technical Report, Bureau of Meteorology, Melbourne, Australia, 151 p. *http://imos.org.au/fileadmin/user_upload/shared/SRS/SST/GHRSST-DOC-basic-v1.0r1.pdf*

Griffin, C. (2018). *BoM Himawari-8 AHI Cloud/SST/SSES Algorithms*. Presented at NOAA-BoM SST Workshop, College Park, MD, USA, 3–6 April 2018. *http://imos.org.au/facilities/srs/sstproducts/sstdata0/sstdata-references*

Guan, L., and Kawamura, H. (2004). Merging satellite infrared and microwave SSTs: Methodology and evaluation of the new SST. *Journal of Oceanography*, 60(5), 905.

Hu, Y., Beggs, H., and Wang, X.H. (2019). Inter-comparison of high-resolution SST climatology data sets over the Australian region. In: *SST-CCI-Phase-II SST CCI Climate Assessment Report Issue 1*. European Space Agency. 153 pp. *http://www.esa-sst-cci.org/PUG/pdf/SST_CCI-CAR-UKMO-201_Issue_1-signed.pdf*

Huang, Z., Leplastrier, A., Xie, S., and Feng, M. (2018). *Using Himawari-8 geostationary satellite data for the investigation of highly dynamic oceanographic phenomena*, Presented at the ACOMO 2018 Workshop, Canberra, Australia, 9-11 October 2018. *http://imos.org.au/fileadmin/user_upload/shared/IMOS%20General/ACOMO/ACOMO_2018/Powerpoints/Tuesday/Zhi-Huang.pdf*

Huang, B., Liu, C., Banzon, V., Freeman, E., Graham, G., Hankins, W., Smith, T., and Zhang, H.-M. (2021). Improvements of the Daily Optimum Interpolation Sea Surface Temperature (DOISST) Version 2.1. *Journal of Climate*, 34, 2923–2939. *https://doi.org/10.1175/JCLI-D-20-0166.1*

IMOS (2018). *IMOS Satellite Remote Sensing SST Data* webpage: *http://imos.org.au/facilities/srs/sstproducts/sstdata0/*

IMOS OceanCurrent (2018). *IMOS OceanCurrent Surface Currents and Temperature* website: *http://oceancurrent.imos.org.au*

Kachi, M., Maeda, T., Tsutsui, H., Ono, N., Kasahara, M., and Mokuno, M. (2017). Five years observations of global water cycle by GCOM-W/AMSR2. In: *Proceedings of 2017 IEEE International Geoscience and Remote Sensing Symposium (IGARSS)*, 5641–5643. doi:10.1109/IGARSS.2017.812885

Karagali, I., and Hoyer, J.L. (2013). Observations and modelling of the diurnal SST cycle in the North and Baltic Seas. *Journal of Geophysical Research: Oceans*, 118, 4488–4503. doi:10.1002/jgrc.20320

Kawanishi, T., Sezai, T., Ito, Y., Imaoka, K., Takeshima, T., Ishido, Y., Shibata, A., Miura, M., Inahata, H., and Spencer, R.W. (2003). The Advanced Microwave Scanning Radiometer for the Earth Observing System (AMSR-E), NASA's contribution to the EOS for global energy and water cycle studies. *IEEE Transactions on Geoscience and Remote Sensing*, 41(2), 184–194. doi:10.1109/TGRS.2002.808331

Kilpatrick, K.A., Podesta, G.P., and Evans, R.H. (2001). Overview of the NOAA/NASA Pathfinder algorithm for Sea Surface Temperature and associated Matchup Database. *Journal of Geophysical Research*, 106, 9179–9198

Kilpatrick, K.A., Podesta, G., Walsh, S., Williams, E., Halliwell, V., Halliwell, V., Szczodrak, M., Brown, O.B., Minnett, P.J., and Evans, R. (2015). A decade of sea surface temperature from MODIS. *Remote Sensing of Environment*, 165, 27–41. *http://dx.doi.org/10.1016/j.rse.2015.04.023*

King, E. A. (2003). *The Australian AVHRR Data Set at CSIRO/EOC: Origins, Processes, Holdings and Prospects, CSIRO Earth Observation Centre Report 2003/04*. CSIRO, Canberra. *http://www.eoc.csiro.au/tech_reps/2003/tr2003_04.pdf*

Kramar, M., Ignatov, A., Petrenko, B., Kihai, Y., and Dash, P. (2016). Near Real Time SST retrievals from Himawari-8 data with ACSPO at NOAA. *Proceedings of SPIE 9827*, Ocean Sensing and Monitoring VIII, 98270L. doi:10.1117/12.2229771

Kurihara, Y., Sakurai, T., and Kuragano, T. (2006). Global daily sea surface temperature analysis using data from satellite microwave radiometer, satellite infrared radiometer and in-situ observations. *Weather Service Bulletin*, 73, Special issue, s1–s18 (in Japanese).

Kurihara, Y., Murakami, H., and Kachi, M. (2016). Sea surface temperature from the new Japanese geostationary meteorological Himawari-8 satellite. *Geophysical Research Letters*, 43, 1234–1240. doi:10.1002/2015GL067159

Lieberherr, G., and Wunderle, S. (2018). Lake Surface Water Temperature Derived from 35 Years of AVHRR Sensor Data for European Lakes. Remote Sensing, 10, 990. *https://doi.org/10.3390/rs10070990*

Liu, C., Freeman, E., Kent, E.C., Huang, B., Zhang, H.M., Berry, D.I., Worley, S.J., Ouellet, M., Gaboury, I., Ji, Z., and Banzon, V.F. (2019). *ICOADS Drifting Buoy Data Recovery from BUFR and Its Impact on OISST and ERSST*. Presented at American Meteorological Society 99th Annual Meeting, Phoenix, USA, 6–10 January, 2019. *https://ams.confex.com/ams/2019Annual/webprogram/Paper352621.html*

Llewellyn-Jones, D.T., Minnett, P.J., Saunders, R.W., and Zavody, A.M. (1984). Satellite multichannel infrared measurements of sea surface temperature of the N.E. Atlantic Ocean using AVHRR/2. *Quarterly Journal of the Royal Meteorological Society*, 110, 613–631.

Lumpkin, R., Centurioni, L., and Perez, R. (2016). Fulfilling observing system implementation requirements with the Global Drifter Array. Journal of Atmospheric and Oceanic Tech*nology*, 33, 685–695.

MacCallum, S.N., and Merchant, C.J. (2012). Surface water temperature observations of large lakes by optimal estimation. *Canadian Journal of Remote Sensing*, 38. 25–45. *https://doi.org/10.5589/m12-010*.

Martin M., Dash, P., Ignatov, A., Banzon, V., Beggs, H., Brasnett, B., Cayula, J-F., Cummings, J., Donlon, C., Gentemann, C., Grumbine, R., Ishizaki, S., Maturi, E., Reynolds, R., and Roberts_Jones, J. (2012). Group for High Resolution SST (GHRSST) Analysis Fields Intercomparisons: Part 1. A GHRSST Multi-Product Ensemble (GMPE). *Deep Sea Research II*, 77–80, 21–30. *http://dx.doi.org/10.1016/j.dsr2.2012.04.013*

Maturi, E., Harris, A., Merchant, C., Mittaz, J., Potash, B., Meng, W., and Sapper, J. (2008). NOAA's sea surface temperature products from operational geostationary satellites. *Bulletin of the American Meteorological Society*, 89, 1877–1888.

Maturi, E., Harris, A., Mittaz, J., Sapper, J., Wick, G., Zhu, X., Dash, P., and Koner, P. (2017). A New High-Resolution Sea Surface Temperature Blended Analysis. *Bulletin of the American Meteorological Society*, 98(5), 1015–1026. *https://doi.org/10.1175/bams-d-15-00002.1*

McPhaden, M.J., Ando, K., Bourles, B., Freitag, H.P., Lumpkin, R., Masumoto, Y., Murty, V.S.N., Nobre, P., Ravichandran, M., Vialard, J., Vousden, D., and Yu, W. (2010). The global tropical moored buoy array. *Proceedings of OceanObs '09*. *http://www.oceanobs09.net/proceedings/cwp/McPhaden-OceanObs09.cwp.61.pdf*

Merchant, C.J., and Embury, O. (2014). Ch 4.3—Simulation and inversion of satellite thermal measurements. In: Optical radiometry for ocean climate measurements. Experimental methods in the physical sciences, 47 (47). (Eds: Zibordi, G., Donlon, C.J., and Parr, A.C.). Academic Press, pp 489–526. ISBN 9780124170117. *https://doi.org/10.1016/B978-0-12-417011-7.00015-5*

Merchant, C.J., Harris, A.R., Maturi, E., and MacCallum, S. (2005). Probabilistic physically based cloud screening of satellite infrared imagery for operational sea surface temperature retrieval. *Quarterly Journal of the Royal Meteorological Society*, 131, 2735–2755. doi:10.1256/qj.05.15

Merchant, C.J., Le Borgne, P., Marsouin, A., and Roquet, H. (2008). Optimal estimation of sea surface temperature from split-window observations. *Remote Sensing of Environment*, 112, 2469–2484. ISSN 0034-4257 *https://doi.org/10.1016/j.rse.2007.11.011*.

Merchant, C.J., Embury, O., Rayner, N.A., Berry, D.I., Corlett, G.K., Lean, K., Veal, K.L., Kent, E.C., Llewellyn-Jones, D.T., Remedios, J.J., and Saunders, R. (2012). A 20 year independent record of sea surface temperature for climate from Along-Track Scanning Radiometers. *Journal of Geophysical Research*, 117, C12013. doi:10.1029/2012JC008400

Merchant, C.J., Minnett, P.J., Beggs, H., Corlett, G., Gentemann, C., Harris, A.R., Hoyer, J., and Maturi, E.. (2019a). Global Sea Surface Temperature, In: *Taking the Temperature of the Earth. Steps towards integrated understanding of variability and change* (Eds: Glynn Hulley and Darren Ghent). P. 5–55. Elsevier. *https://doi.org/10.1016/B978-0-12-814458-9.00002-2*

Merchant, C.J., Embury, O., Bulgin, C.E., Block, T., Corlett, G., Fiedler, E., Good, S.A., Mittaz, J., Rayner, N.A., Berry, D., Eastwood, S., Taylor, M., Tsushima, Y., Waterfall, A., Wilson, R., and Donlon, C. (2019b). Satellite-based time-series of sea-surface temperature since 1981 for climate applications. *Scientific Data*, 6(223): 1–18. doi:10.1038/s41597-019-0236-x

Met Office (2019). *Validation of GMPE analyses using Argo* webpage, National Centre for Ocean Forecasting. *https://ghrsst-pp.metoffice.gov.uk/ostia-website/gmpe-argo-stats.html*

Minnett, P.J., Smith, M., and Ward, B. (2011). Measurements of the oceanic thermal skin effect. *Deep Sea Research II*, 58, 861–868.

Minnett, P.J., and Kaiser-Weiss, A.K. (2012). *Near-Surface Oceanic Temperature Gradients*. Discussion Document, Group for High Resolution Sea-Surface Temperature. 7 p. *https://www.ghrsst.org/wp-content/uploads/2021/04/SSTDefinitionsDiscussion.pdf*

Minnett, P.J., Alvera-Azcárate, A., Chin, T.M., Corlett, G.K., Gentemann, C.L., Karagali, I., Li, X., Marsouin, A., Marullo, S., Maturi, E., Santoleri, R., Saux Picart, S., Steele, M., and Vazquez-Cuervo, J. (2019). Half a century of satellite remote sensing of sea-surface temperature. *Remote Sensing of Environment*, 233, 111366. *https://doi.org/10.1016/j.rse.2019.111366*.

NASA Earthdata (2019). *Suomi NPP Visible Infrared Imaging Radiometer Suite (VIIRS)* webpage: *https://ladsweb.modaps.eosdis.nasa.gov/missions-and-measurements/viirs/*

NOAA CoastWatch (2018). *ACSPO Global SST from VIIRS* webpage: *https://coastwatch.noaa.gov/cw/satellite-data-products/sea-surface-temperature/acspo-viirs.html*

NOAA/NESDIS/STAR (2019). *SST Quality Monitor v2.1*. *https://www.star.nesdis.noaa.gov/sod/sst/squam*

O'Carroll, A.G., Armstrong, E.M., Beggs, H., Bouali, M., Casey, K.S., Corlett, G.K., Dash, P., Donlon, C.J., Gentemann, C.L., Hoyer, J.L., Ignatov, A., Kabobah, K., Kachi, M., Kurihara, Y., Karagali, I., Maturi, E., Merchant, C.J., Minnett, P., Pennybacker, M. Ramakrishnan, B., Ramsankaran, R., Santoleri, R., Sunder, S., Saux Picart, S., Vazquez-Cuervo, J., and Wimmer, W. (2019). Observational needs of sea surface temperature. *Frontiers in Marine Science*, 6, 420. *https://doi.org/10.3389/fmars.2019.00420*

Oke, P., Sakov, P., Cahill, M. L., Dunn, J. R., Fiedler, R., Griffin, D. A., Mansbridge, J.V., Ridway, K.R., and Schiller, A. (2013). Towards a dynamically balanced eddy-resolving reanalysis: BRAN3. *Ocean Modelling*, 67, 52–70. *https://doi.org/10.1016/j.ocemod.2013.03.008*

Rayner, N., Tsushima, Y., Atkinson, C., Good, S., Roberts, M., Martin, G., Ackerley, D., Titchner, H., Mao, C., Xavier, P., Comer, R., Hu, Y., Beggs, H., Wang, X.H., Margaritis, G., Renshaw, R., Lamas, L., Esteves, R., Almeida, S., de Azevedo, E., Correia, C., Reis, F., and Willén, U. (2019a). *SST-CCI-Phase-II SST CCI Climate Assessment Report Issue 1*. European Space Agency, 153 p. *https://climate.esa.int/media/documents/SST_cci_CAR_v1.pdf*

Rayner, N., Good, S., Block, T., P. Evadzi, P., and Embury, O. (2019b). *SST-CCI-Phase-II SST CCI Product User Guide Issue 2*, European Space Agency, 115 p. *https://climate.esa.int/media/documents/SST_cci_PUG_v2.pdf*

Reynolds, R.W., Smith, T.M., Liu, C., Chelton, D.B., Casey K.S., and Schlax, M.G. (2007). Daily High-resolution Blended Analyses for sea surface temperature. *Journal of Climate*, 20, 5473–5496.

Roberts-Jones, J., Fiedler, E.K., and Martin, M. (2012). Daily, global, high-resolution SST and sea-ice reanalysis for 1985-2007 using the OSTIA system. *Journal of Climate*, 25, 6215–6232

Roemmich, D., Johnson, G.C., Riser, S., Davis, R., Gilson, J., Owens, W.B., Garzoli, S.L., Schmid, C., and Ignaszewski, M. (2009). The Argo Program: observing the global ocean with profiling floats, *Oceanography*, 22, 34–43.

Schneider, P., and Hook, S.J. (2010). Space observations of inland water bodies show rapid surface warming since 1985. *Geophysical Research Letters*, 37 (22), L22405. doi:10.1029/2010GL045059

Shibata, A. (2006). Features of ocean microwave emission changed by wind at 6 GHz. *Journal of Oceanography*, 62, 321–330. doi:10.1007/s10872-006-0057-3.

Smith, D.L., Nightingale, T.J., Middleton, K., Edeson, R., Cox, C.V., Mutlow, C.T., Maddison, B.J., and Coppo, P. (2014). Calibration approach and plan for the sea and land surface temperature radiometer. *Journal of Applied Remote Sensing*, 8(1), 084980. doi:10.1117/1.JRS.8.084980

Soloviev, A., and Lukas, R. (1997). Observation of large diurnal warming events in the near-surface layer of the western equatorial Pacific warm pool. *Deep Sea Research I*, 44, 1055–1076.

Soloviev, A.V., and Lukas, R. (2014). *The near-surface layer of the ocean: Structure, Dynamics and Applications*. 2nd edn. Springer, New York.

Vazquez-Cuervo J., Dewitte B., Chin T.M., Armstrong E.M., Purca S., Alburqueque E. (2013). An analysis of SST gradients off the Peruvian Coast: The impact of going to higher resolution. *Remote Sensing of Environment*, 131, 76–84.

Vinogradova, N.T., Zaccheo, T.S., Alcala, C.M., and Vandemark, D. (2009). Operational high-resolution sea surface temperature product in the Gulf of Maine. *Journal of Operational Oceanography*, 2, 57–66.

Walton, C.C., Pichel, W.G., Sapper, J.F., and May, D.A. (1998). The development and operational application of nonlinear algorithms for the measurement of sea surface temperatures with the NOAA polar-orbiting environmental satellites. *Journal of Geophysical Research*, 103, 27999–28012.

Wentz, F.J., and Meissner, T. (2007). *AMSR-E Ocean Algorithms*, 051707 Report, 6 p. Remote Sensing Systems, Santa Rosa, CA, USA.

White, C.H., Heidinger, A.K., Ackerman, S.A., and McIntyre, P.B. (2018). A Long-Term Fine-Resolution Record of AVHRR Surface Temperatures for the Laurentian Great Lakes. *Remote Sensing*, 10, 1210. *https://doi.org/10.3390/rs10081210*

Wijffels, S.E., Beggs, H., Griffin, C., Middleton, J.F., Cahill, M., King, E., Jones, E., Feng, M., Benthuysen, J.A., Steinberg, C.R., and Sutton, P. (2018). A fine spatial scale sea surface temperature atlas of the Australian regional seas (SSTAARS): seasonal variability and trends around Australasia and New Zealand revisited. *Journal of Marine Systems*, 187, 156–196. *https://doi.org/10.1016/j.jmarsys.2018.07.005*

Wong, E.W., and Minnett, P.J. (2018). The response of the ocean thermal skin layer to variations in incident infrared radiation. *Journal of Geophysical Research: Oceans*, 123, 19. doi:10.1002/2017JC013351

Woolway, R.I., and Merchant, C.J. (2018). Intralake heterogeneity of thermal responses to climate change: a study of large northern hemisphere lakes. *Journal of Geophysical Research: Atmospheres*, 123, 3087–3098. *https://doi.org/10.1002/2017JD027661*

Yang, C., Leonelli, F.E., Marullo, S., Artale, V., Beggs, H., Nardelli, B.B., Chin, T.M., De Toma, V., Good, S., Huang, B., Merchant, C.J., Sakurai, T., Santoleri, R., Vazquez-Cuervo, J., Zhang, H.-M., and Pisano, A. (2021). Sea Surface Temperature intercomparison in the framework of the Copernicus Climate Change Service (C3S). *Journal of Climate*, 33(13), 5257–5283. *https://doi.org/10.1175/JCLI-D-20-0793.1*

Zhang, H., Beggs, H., Majewski, L., Wang, X.H., and Kiss, A.E. (2016a). Investigating Sea Surface Temperature Diurnal Variation over the Tropical Warm Pool Using MTSAT-1R Data. *Remote Sensing of Environment*, 183, 1–12. *http://www.sciencedirect.com/science/article/pii/S003442571630195X*

Zhang, H., Beggs, H., Wang, X.H., Kiss, A.E., and Griffin, C. (2016b). Seasonal patterns of SST diurnal variation over the Tropical Warm Pool region, *Journal of Geophysical Research: Oceans*, 121. doi:10.1002/2016JC012210. *http://onlinelibrary.wiley.com/doi/10.1002/2016JC012210/epdf*

Zhang H., Beggs, H., Wang, X.H., Rodriguez, J., Thorpe, A.L., Brunke, M., Majewski, L., Kiss, A.E., and Gentemann, C. (2018). Comparison of SST Diurnal Variation Models over the Tropical Warm Pool, *Journal of Geophysical Research: Oceans*, 123. *http://dx.doi.org/10.1029/2017JC013517*

Zhang, H., Babanin, A.V., Ignatov, A., and Beggs, H. (2019). *On the differences between daytime and nighttime ocean cool skin signals under well mixed conditions. GHRSST poster, University of Melbourne.* *http://adf5c324e923ecfe4e0a-6a79b2e2bae065313f2de67bbbf078a3.r67.cf1.rackcdn.com/GHRSST%20XX%20-%202019%20Frascati%20-%20Italy/59-Zang_haifeng_GHRSST.pdf*

Zhong, A., and Beggs, H. (2008). *Analysis and Prediction Operations Bulletin No. 77—Operational Implementation of Global Australian Multi-Sensor Sea Surface Temperature Analysis*, Web Document, 2 October 2008. *http://www.bom.gov.au/australia/charts/bulletins/apob77.pdf*

15 Ice

Rob Massom

It is estimated that at least 10% of the Earth's surface is covered in glacial ice, 90% of which is in Antarctica (USGS, 2021). As part of the water cycle, ice caps, glaciers, and permanent snow store 1.7% of the total volume of water on Earth (see Section 1.1).

The following sub-sections describe ice in Australian surface waters (see Section 15.1), relevant EO sensors for mapping and monitoring ice (see Section 15.2), EO of the Antarctic Ice Sheet (see Section 15.3), EO of sea ice (see Section 15.4), and future opportunities and needs in this area (see Section 15.5).

15.1 Ice in Australian Surface Waters

Although geographically isolated by the circumpolar Southern Ocean, Antarctica is connected to the rest of the world through oceanic and atmospheric circulations, and plays a pivotal role in the global climate system (see Section 2.5). Ubiquitous features are a vast ice sheet surrounded by a seasonally-variable cover of sea ice, which together extend over an area of up to ~33 million km^2—or 6% of the Earth's surface—in winter (see Figure 15.1). By virtue of their physical setting and properties, these two immense snow and ice masses interact strongly not only with each other but also with the high-latitude ocean and atmosphere, to significantly modify and affect the ocean-atmosphere system and the processes therein. In this way, Antarctic ice-ocean-atmosphere interactions and processes affect both regional weather and patterns of oceanic and atmospheric variability across the wider Southern Hemisphere and beyond (see Section 1.4). At the same time, the Antarctic cryosphere is not only a highly sensitive indicator of climate change, which is amplified in polar regions, but it also plays an active role in modulating such change. Sea ice also forms an important habitat for a plethora of organisms, from microscopic algae through krill to whales (Thomas, 2017), and either aids or hinders marine operations and other human activities around the continent.

The fundamental role of the Antarctic cryosphere in the Earth system, and its sensitivity to change in the ocean and atmosphere, implies that warming in the region will have wide-ranging consequences for climate, sea level rise, ecosystems, and human activities (including shipping operations). As such, developing improved understanding of the nature, drivers, and impacts of Antarctic sea ice and ice sheet change is a high priority in climate research, leading towards more accurate model prediction of the future trajectory and effects of cryospheric change (Kennicutt *et al.*, 2014). The challenge is great, given the vast scale, remoteness, dynamism, complexity and inhospitable nature of the Antarctic environment, which is also shrouded in darkness for part of the year and extensively cloud covered. Earth Observation from Space (EOS) has a crucially important role to play here, in concert with autonomous sensors and remote sensing systems, process studies, and *in situ* observations (Lubin and Massom, 2006; Massom and Lubin, 2006). The latter provide important additional information that cannot be obtained by EO alone, and are also a crucial means of calibrating and validating key satellite-derived quantities. Timely sea ice and iceberg information is also required in near real time from EO in support of safe shipping and operational activities around Antarctica (COMNAP, 2015; WMO, 2021).

Background image: RS53617 Jade Iceberg near Macey Island. The top of this iceberg is estimated to be around 30 m above ground level. **Source:** © Peter Layt, Australian Antarctic Division.

Recommended Chapter Citation: Massom, R.A. (2021). Ice. Ch 15 in *Earth Observation: Data, Processing and Applications. Volume 3B—Surface Waters.* CRCSI, Melbourne. pp. 281–310. ISBN 978-0-6482278-5-4.

Figure 15.1 Satellite-derived map of the Antarctic Ice Sheet and surrounding sea ice

Grounded ice sheet and ice shelf motion are derived from multiple satellite interferometric Synthetic Aperture Radar (SAR) images (Rignot *et al.,* 2011) acquired between 2007 and 2009. Ice sheet motion flow lines are superimposed on the MODIS mosaic of Antarctica (Haran *et al.,* 2014). Sea ice motion is the mean of daily gridded Polar Pathfinder radiometry (Tschudi *et al.,* 2016) obtained during winter maximum sea ice extent (September) of each year for the period 1990 to 2016. The motion vectors are superimposed on a map of mean sea ice concentration and extent derived from passive microwave brightness temperatures (Fetterer *et al.,* 2017) for the Septembers of 1990 to 2016. Also shown are the average minimum extent of sea ice recorded between 1990 to 2016 (blue dashed boundaries), the grounded ice sheet and the floating ice shelves (black boundaries), and the bathymetry of the surrounding ocean (Ryan *et al.,* 2009).

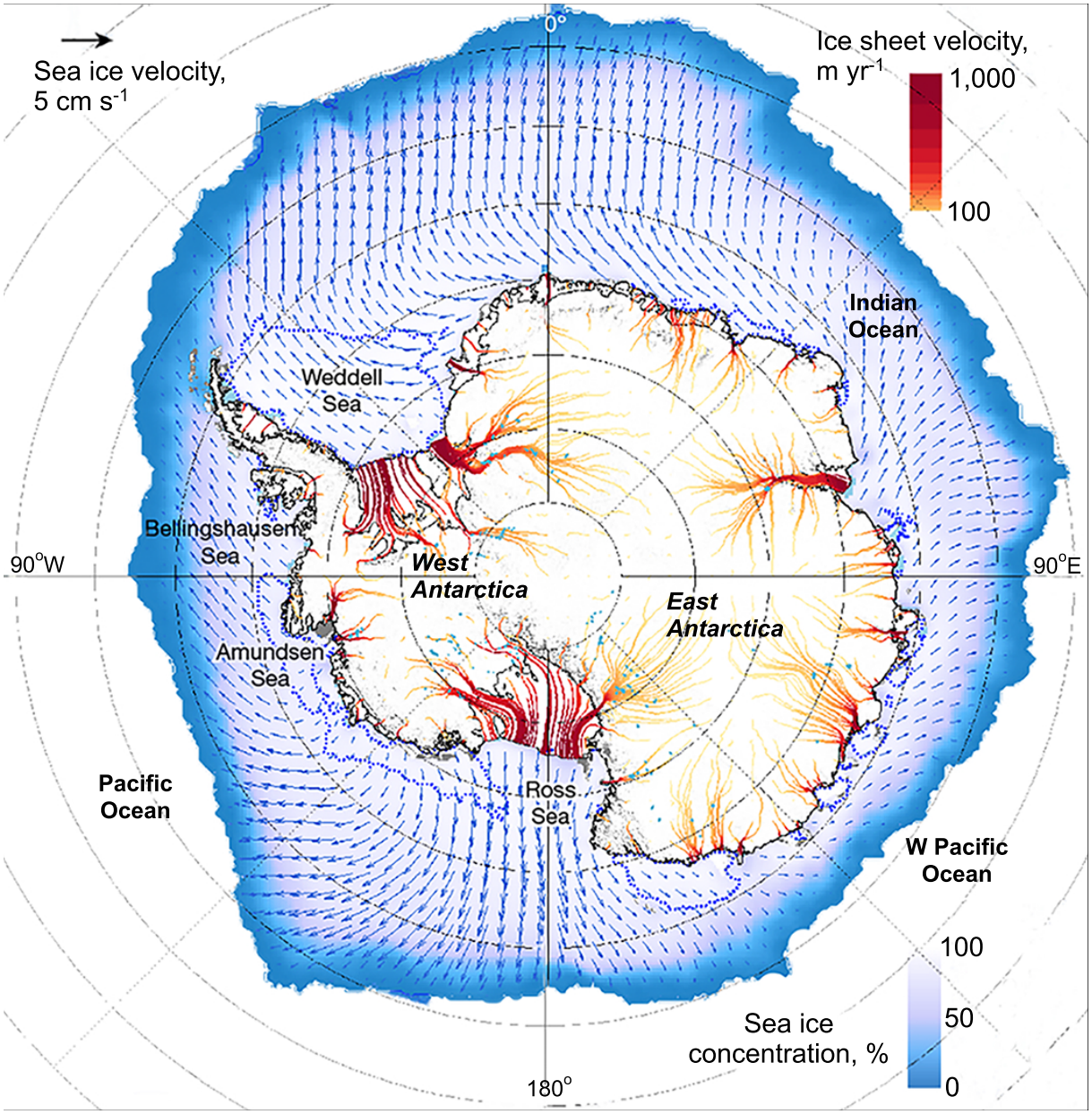

Adapted from Shepherd *et al.* (2018). Figure 1

In the following subsection, we provide a brief description of aspects of the Antarctic Ice Sheet and its surrounding sea ice cover that are relevant to, and measurable by, EO. The importance of EO for mapping and monitoring sea ice is highlighted in Excursus 15.1. Detailed information on the geographical setting of Antarctica and high-latitude Southern Ocean, including seafloor bathymetry and large scale ocean current patterns and fronts, is provided by Post *et al.* (2014). For further information on sea ice, see ACE CRC (2014), Thomas (2017) and Weeks (2010), and see ACE CRC (2017) for ice sheet issues. Annual assessments of change/variability in Antarctic sea ice coverage and duration are provided in annual NOAA BAMS State of the Climate Reports (*https://www.ncei.noaa.gov/bams-state-of-climate*). For further information on the relationship of sea ice and oceanography in the Southern Ocean, see Meredith and Brandon (2016).

15.1.1 Antarctic Ice Sheet

Formed from the accumulation and compaction of snowfall over many thousands of years, the Antarctic Ice Sheet covers nearly 14 million km^2 (or > 99%) of the Antarctic continent; this is twice the size of Australia. Of this, the Australian Antarctic Territory comprises the sector between 45°E and 160°E (excluding 136°E–142°E). The ice sheet is more than 4 km thick in places (mean thickness 2.16 km, maximum thickness 4.776 km) and has an average elevation of 2.5 km. Crucially, it holds ~70% of the Earth's freshwater and more than 90% (approximately 26.9 million km^3) of its ice (Fretwell *et al.*, 2013). If melted, this is enough water to raise mean global sea level by nearly 60 m.

The ice sheet is in fact made up of three major components: the East and West Antarctic ice sheets and the Antarctic Peninsula. The distinct differences between the East Antarctic Ice Sheet (EAIS) and the West Antarctic Ice Sheet (WAIS) are depicted in Figure 15.2. The EAIS contains about nine times the ice volume of the WAIS, and is significantly thicker and higher. Moreover, the WAIS largely sits on bedrock up to 2,500 m below sea level in places, and is termed a marine ice sheet. Ice sheet regions that sit resting on bedrock below sea level are thought to be less stable than those that are grounded above sea level, and are therefore more susceptible to climate change. Dynamic instability in the ice sheet response to global warming is potentially the largest unknown in projecting future sea level rise (SLR; Kennicutt *et al.*, 2014).

Gravity-driven discharge of ice from the inland ice sheet across the boundary between the grounded and freely-floating parts of the ice sheet (termed the grounding line) and into the Southern Ocean occurs mainly via about 30 major glaciers and ice streams, which each drain extensive catchment regions (Zwally *et al.*, 2012). The rate of ice discharge is determined not only by the ice thickness, surface slope, temperature, basal topography and conditions (Cuffey and Patterson, 2010), but is also affected by the presence of floating glacier tongues and ice shelves that abut 74% (or 39,670 km) of the grounded ice sheet boundary (Bindschadler *et al.*, 2011). As floating seaward extensions of fast-flowing outlet glaciers and ice streams, ice shelves play a crucially important role in buttressing (restraining) the dynamic discharge of grounded ice mass into the ocean—to moderate the ice sheet contribution to SLR (see Figure 15.3).

Figure 15.2 Plan view and cross section profiles across Antarctica

These cross sections show the differences between the West Antarctic Ice Sheet (WAIS) and the East Antarctic Ice Sheet (EAIS).

a. Plan view of the continent from A to B

b. Cross section through the continent from A to B

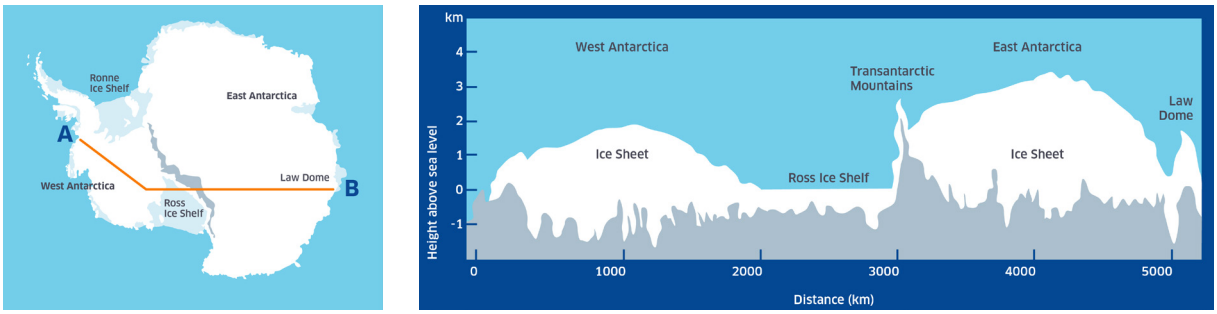

Source: British Antarctic Survey

Figure 15.3 Schematic of an Antarctic ice shelf

The mass budget for an ice shelf is the sum of (i) gains (inputs) from glacier flow across the grounding line and snow accumulation and (ii) losses/outputs by iceberg production and net basal and surface melting.

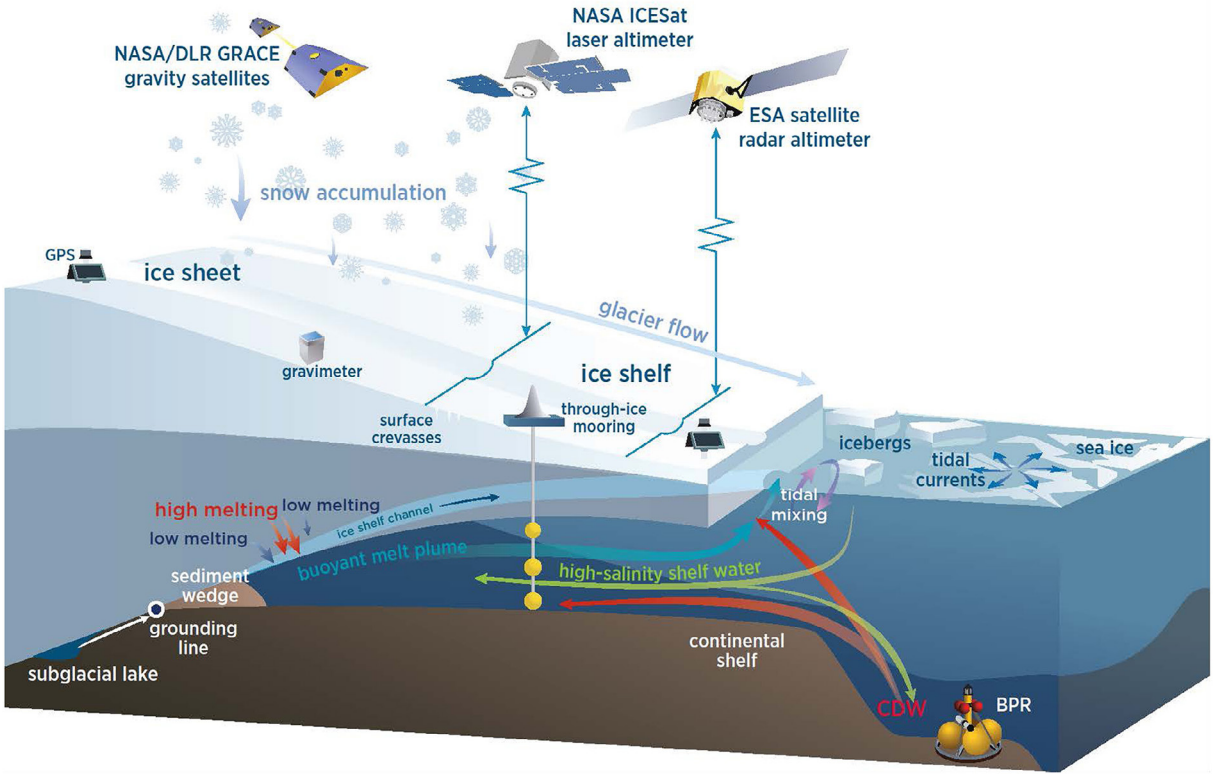

Source: Padman *et al.* (2018) Figure 3

Given their direct contact with the (warming) atmosphere and ocean, ice shelves are the most vulnerable part of the ice sheet system (ACE CRC, 2017), with EOS showing recent extensive thinning due to basal melting by a warming ocean[18] and (in certain regions) abrupt melt-related, large scale disintegration (see Section 15.3.1). The thinning, weakening, or loss of ice shelves diminishes/removes their buttressing capacity, leading to increased flow of grounded ice into the ocean to contribute to SLR. Clearly this is of great concern, and monitoring the rate of dynamic ice discharge and the 'health' of Antarctic ice shelves—and how, where, and why/whether they are changing—is a high priority in EO. Moreover, increased freshwater input to the Southern Ocean from glacial and iceberg melt has potentially important consequences for ocean stratification properties and circulation, as well as marine ecosystems (Kennicutt *et al.*, 2014).

EOS has a crucial role to play in the measurement and monitoring of the *mass balance* of the ice sheet (Bamber and Payne, 2004), and determination of:

- where, how and why this is changing; and
- its contribution to SLR (in concert with modelling and *in situ* observation).

Ice sheet mass balance describes the relationship between:

- total mass gain by snow accumulation; and
- mass loss by a combination of ablation (evaporation), surface melting, basal melting (largely through contact with the ocean), ice discharge, and iceberg calving (Figure 15.4).

The acquisition of regular and reliable repeat measurements of key ice sheet features and properties—and understanding the processes driving observed change—is critical to improving ice sheet models used for the prediction of future ice loss and subsequent SLR (ACE CRC, 2017).

18 Melting of an ice shelf base occurs when water in contact with it is warmer than the freezing point. The freezing point of seawater decreases with water depth, from about -1.9°C at the surface of the ocean to about -4°C at a water depth of 2500 m. As a result, water that is relatively warm, e.g. -0.5°C, will result in strong basal melting of an ice shelf.

Figure 15.4 Schematic of an ice sheet and its individual mass balance components

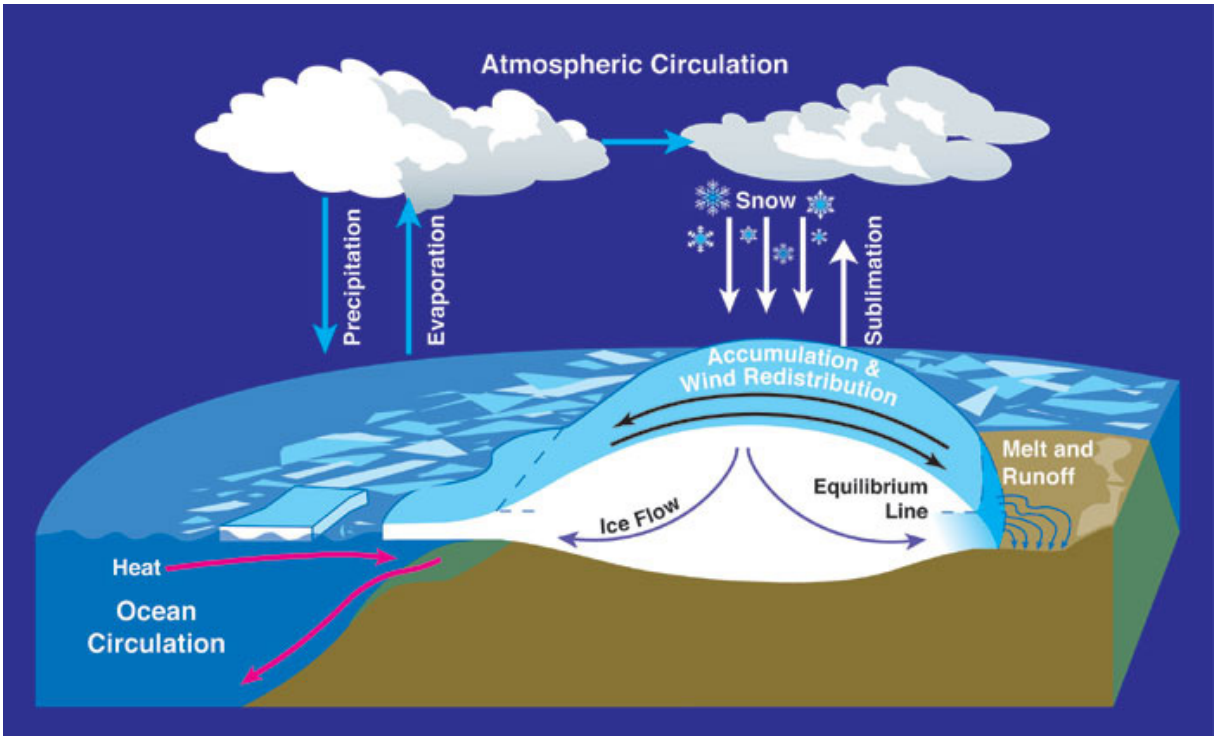

Source: Abdalati (2006) Figure 1. Retrieved from *https://upload.wikimedia.org/wikipedia/commons/a/a2/Mass_balance_atmospheric_circulation.png*

15.1.2 Antarctic sea ice

In contrast to the ice sheet, its floating margins and icebergs, sea ice is frozen seawater that forms when the ocean cools to the point of freezing (approximately -1.8°C for water with a salinity of 34 psu). From a summer minimum of 3–4 million km^2 (in February), Antarctic sea ice coverage expands to about 19–20 million km^2 at its maximum annual extent in September (about 1.5 times the size of the Antarctic continent itself; see Figure 15.5). This annual advance-retreat cycle—in response to large scale climatological patterns of atmospheric and oceanic temperature and circulation—entails one the greatest seasonal changes on Earth. Crucially, it also substantially modifies the surface properties of the high-latitude Southern Ocean, and its interaction with the overlying atmosphere (see Excursus 15.1 below). At its winter maximum, the latitudinal width of the sea ice zone varies substantially around the continent, from only a few hundred kilometres (such as off East Antarctica at 120°E to 135°E) to ~2200 km in the Weddell Sea sector (where it occupies a deep poleward embayment).

Broadly speaking, sea ice is made up of two main components: 1) ***pack ice***, and 2) the less extensive coastal ***landfast*** or ***fast ice*** (see Figure 15.6). Pack ice comprises a heterogeneous agglomeration of different contiguous pieces of ice (termed ***floes***) of varying age, thickness, and size (sub-metre to kilometre scale) that are constantly moving (up to tens of kilometres a day) in response to winds and ocean currents. Most Antarctic pack ice is seasonal and therefore less than one year old—so-called ***first-year ice***. This type of ice has a thickness range of 0.3–2.0 m (typically), although greater thicknesses (of ~10 m) can occur by ice deformation where ice floes collide (Massom *et al.*, 2006). Perennial sea ice (ice that survives one or more summer melt seasons) is generally thicker than typical first-year ice, but is largely confined to southernmost parts of the Weddell, Amundsen, and eastern Ross seas (see Figure 15.5). The remainder that forms and melts back each year is termed the ***seasonal sea ice zone.***

Figure 15.5 Extent of Antarctic sea ice in 2015/2016

Each year, and on average, Antarctic sea ice coverage peaks in September–October, and attains a minimum in February, when it melts completely back to the continent in places.

a. 2015 maximum (October 6)

b. 2016 minimum (19 February)

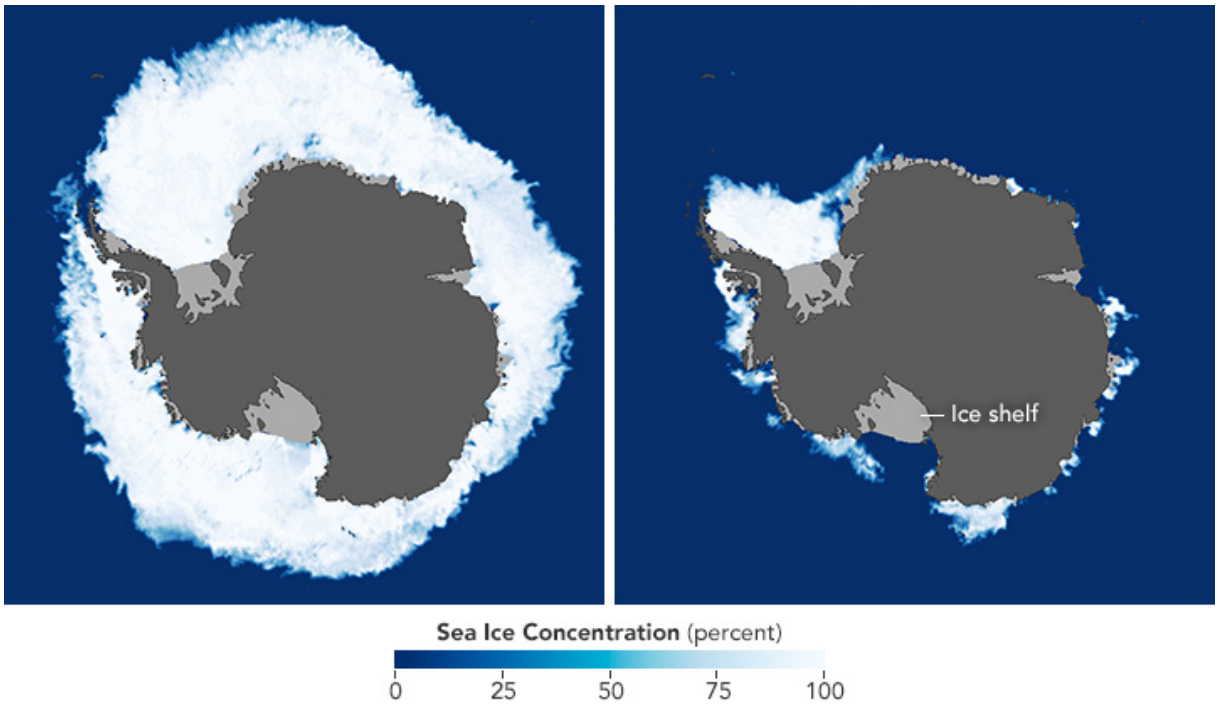

Source: NASA Earth Observatory, based on AMSR2 data supplied by GCOM-W1/JAXA. Retrieved from: *https://earthobservatory.nasa.gov/features/SeaIce/page1.php*

In contrast to pack ice, fast ice is highly-consolidated and stationary sea ice, which is confined to coastal margins, where it is either held in place by myriad grounded icebergs (in waters shallower than about 450 m) and/or by coastal promontories, or occurs in sheltered embayments (Giles *et al.,* 2008a). There, it forms a relatively narrow band from a few kilometres to about 250 km wide in places (Fraser *et al.,* 2012), but plays a key ecological role (Massom *et al.,* 2009) as well as stabilizing ice shelf margins to which it is attached (Massom *et al.,* 2018). Depending on the geographical setting, Antarctic fast ice can be either annual or perennial, and can attain great ages (decades) and thicknesses (of > 10 m) in certain sheltered locations (Massom *et al.,* 2010).

The areal extent of sea ice coverage, its thickness distribution, and patterns of annual advance, retreat, and duration (and their variability) are the product of a complex interplay of both thermodynamic and dynamic processes—the former involving freeze and melt, and the latter involving movement and deformation of the ice driven by winds and ocean currents and interaction with the ice sheet margins and icebergs. At any given time, this complex interplay of processes and the frequent passage of storms creates a highly heterogeneous mixture of ice of different types, ages, and thicknesses. On larger scales, however, the Antarctic sea ice zone is characterised by distinctive large scale components (Massom and Stammerjohn, 2010). The outer part of the pack, called the ***marginal ice zone*** or MIZ, comes into direct contact with the open, high-energy Southern Ocean and is strongly affected by ocean waves that not only generate new ice formation but also break up existing floes. To the south, the more stable mid-pack ice zone (protected by the MIZ) is generally characterised by larger floes and thicker snow cover, but is still affected by a constant passage of storms. Closer to the continent itself, sea ice conditions are strongly affected by interaction with ice sheet margins and grounded icebergs; this is also the realm of fast ice attached to the coast. In the coastal zone, recurrent polynyas (persistent areas of open water bounded by sea ice) play a crucial role as sea ice 'factories' in the freezing season and areas of enhanced melt and biological activity in spring-summer (Barber and Massom, 2007). Polynyas form in the lee of blocking features, such as coastal promontories, and are also maintained by strong katabatic winds cascading seawards from the ice sheet interior.

Figure 15.6 Photographs of Antarctic pack ice and fast ice

Fast ice formation is often associated with grounded icebergs, as shown here.

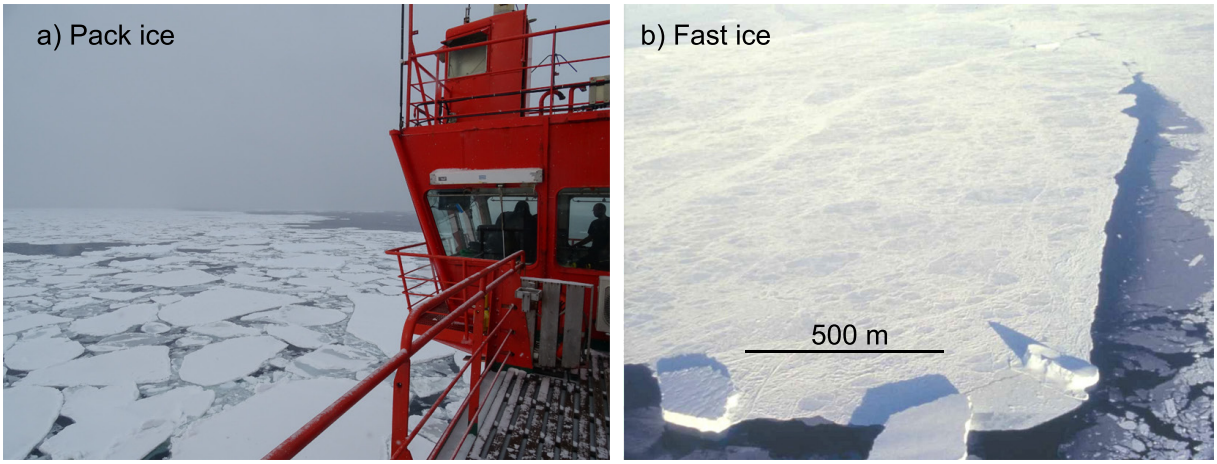

At the microscale and unlike the freshwater ice sheet, sea ice comprises a heterogeneous matrix of ice with small inclusions (pockets/cells) of brine (Petrich and Eicken, 2017), the characteristics of which are constantly modified by the interaction of physical, chemical, and biological processes that vary over space and time. The ice crystals themselves are either long and thin (***columnar ice*** that grows downwards under calm conditions) or more granular (***frazil ice*** that forms under turbulent conditions); a mix of both is typical for Antarctic sea ice. Sea ice older than a few days also accumulates a snow cover, which acts as an insulative and high-albedo blanket to substantially modify the temperature, thermodynamic growth, and properties of the underlying sea ice (Sturm and Massom, 2017). Snow also strongly modifies the amount and spectral properties of light available for phytoplankton growth within and under the ice (Wongpan *et al*., 2018). Moreover, snow makes an important (though poorly quantified) direct contribution to the overall mass balance of the Antarctic sea ice cover by depressing relatively thin sea ice below sea level. This leads to extensive surface flooding to create slush, which subsequently freezes (depending on season) to form *snow ice* (Massom *et al*., 2001a). The introduction of seawater onto the ice further affects its EO signature, particularly at microwave wavelengths. The wetness, crystal structure, and density of the snow cover change/vary in space and time, to also modify sea ice as an EO target (both in terms of optical and microwave properties), and the retrieval of sea ice thickness estimates from altimeter data (see Section 15.4.4).

Sea ice type is classified (named) and categorised depending on its thickness (related to age/stage of development), and based on established international protocol (see *http://aspect.antarctica.gov.au/home/glossary-and-image-library* for a glossary and image library of sea ice types and terms). Excursus 15.1 summarises the key role of various types of EO for measuring and monitoring Antarctic sea ice.

Excursus 15.1—The Importance of EO for Sea Ice

Source: Rob Massom, Australian Antarctic Division/Australian Antarctic Program Partnership
Further Information: Notz and Bitz (2016); Weeks (2010)

Measuring and monitoring Antarctic sea ice and its snow cover—and determining the nature, drivers and effects of change—are crucially important for a number of reasons, and are key steps towards improved (model) prediction of the likely trajectory and impacts of sea ice change in a future warming world (see Notz and Bitz, 2016, for further information). Sea ice forms a pivotal component of the global climate system and strongly modifies ocean-atmosphere interaction over vast areas of the Southern Ocean (as well as in the Arctic). It significantly increases the ocean-surface albedo—to reduce the amount of incoming solar radiation absorbed at the ocean surface—and also insulates the polar ocean from heat loss to the atmosphere during winter (by up to two orders of magnitude; see

Weeks, 2010, for further information) and heat gain during summer. At the same time, sea ice forms a physical barrier to the atmosphere-ocean exchange of wind energy and climate gases such as water vapour and CO_2. Also, brine (dense salty water) rejected downwards by growing sea ice modifies the ocean density structure, and in places induces deep vertical convection and dense cold Antarctic Bottom Water formation that contributes to global ocean thermohaline (overturning) circulation (see Sections 1.4, 5.1.2, and 16). In this way, the influence of Antarctic sea ice reaches the tropics and the Northern Hemisphere as well as the ocean abyss (Bindoff *et al.,* 2000). Due to its intimate association with the ocean and atmosphere, sea ice is not only a sensitive indicator but also a modulator of climate change and variability—the latter by virtue of its key role within the coupled sea ice/ocean/atmosphere system and due to the ice-albedo feedback mechanism.

Sea ice also dominates the seasonal chemical dynamics of the high-latitude Southern Ocean (Vancoppenolle *et al.*, 2013), and plays a crucial role in marine ecosystem structure and function as a key habitat and food source for a wide range of biota, including krill (Massom and Stammerjohn, 2010; Thomas, 2017). Such is the high biological productivity of the Antarctic seasonal sea ice zone that it also plays an important role in the carbon cycle (see Section 1.5). When the ice melts in spring-summer, it injects a pulse of fresher water that stratifies and stabilises the upper ocean and drives intense blooms of algae following their release from the ice. Such blooms are measured by satellite ocean colour sensors (see Sections 8.5 and 18). From a human perspective, sea ice strongly affects safe shipping, tourism, and other operations in high-latitude Southern Ocean waters, including access to resupply of Australian Antarctic bases, and EOS has a key role in informing such operations in a timely fashion.

In general, the influence of sea ice and the magnitude of its effects depend on a number of fundamentally important characteristics (quantities/variables) that can be measured and monitored from space, and their interrelationships and spatiotemporal characteristics. These are:

- **Concentration**—the percentage coverage of sea ice versus ice-free ocean within a given surface area.
- **Extent**—defined as the total area covered by some amount of ice (including open water between floes).
- **Area**—the part of a given area covered by ice alone (that is, the product of ice extent and concentration).
- **Seasonality**—the timings of annual sea ice advance and retreat for a given Antarctic 'sea ice year' (February to February), and the resultant duration of coverage.
- **Thickness distribution**—the fraction of surface area covered by different ice thickness categories.
- **Thickness and properties of snow cover**—sea ice older than a few days typically accumulates a snow cover. This significantly modifies the physical and chemical properties of the underlying ice, and also affects its growth and melt rates, and its climatic and ecological roles (see Sturm and Massom (2017) for further information). Unfortunately, large scale mapping of snow thickness is not currently possible by satellite, although it can be derived from airborne snow radar (for example, the NASA Ice Bridge Project (Kurtz *et al.,* 2012; see Section 15.6). Issues related to snow in the sea ice system, including the lack of accurate information on precipitation, are outlined by Webster *et al.* (2018).
- **Drift** (movement over space and time), and **dynamics** (including deformation)—principal forces acting on the ice are wind (ice moves at 2% of the wind speed when drifting freely and to the left of the wind direction in the Southern Hemisphere; see Figure 1.10), ocean currents (see Section 17), Coriolis force (see Excursus 1.2), and internal ice stress (involving floe-floe collisions and interaction of the sea ice with the ice sheet margins and icebergs; see Section 1). Divergence of the ice motion field creates ephemeral linear openings (*leads*) that rapidly freeze over in winter, while convergence causes the existing ice to deform and thicken. Around Antarctica, these patterns are cyclical on typical scales of 1–3 days with the constant passage of storms, and dynamic thickening predominates once sea ice grows thermodynamically to ~0.5 m (Worby *et al.,* 1998). Sea ice drift also transports sea ice from regions of formation to regions of melt, to significantly affect the ocean freshwater budget and ocean stratification.

15.2 EO Sensors for Ice

Important EO sensors relevant to ice sheet and sea ice measurement and monitoring (either individually or in combination) are listed in Table 15.1. These include visible through near infrared (NIR) to thermal infrared (TIR) radiometers, Synthetic Aperture Radar (SAR), passive microwave radiometers, radar scatterometers, radar and laser altimeters, and gravity sensors (see Sections 8.5 and 9, also Volume 1A—Sections 14 to 16, and Excursus 1.1). For more information, see Lubin and Massom (2006) and Massom and Lubin (2006).

Table 15.1 EO sensors relevant to ice

TIR: Thermal infrared; SAR: Synthetic Aperture Radar

Type	Sensor	Platform	Relevance	Advantages	Disadvantages
Passive optical	Panchromatic, Multispectral, and Hyperspectral radiometers	Satellite or airborne	Mapping/monitoring of ice sheet margin, glacier surface, iceberg calving events, surface melt, snow surface grain size, Ice sheet surface velocity, Estimating thin sea ice thickness (e.g. coastal polynyas), Sea ice floe size distribution (from high spatial resolution datasets), Sea ice extent (both pack ice and fast ice), Surface albedo, Ocean colour (primary production adjacent to/within the sea ice zone), Iceberg distribution (high resolution)	Time series datasets	Does not penetrate cloud, requires sunlight, sensors with high spatial resolution have limited coverage
	TIR radiometer	Satellite or airborne	Mapping of ice surface 'skin' temperature, and adjacent SST, Detection of thin sea ice and estimation of its thickness, Sea ice extent	Does not require sunlight	Does not penetrate cloud
Active optical	Laser altimeter	Airborne or satellite	Measuring and mapping ice sheet topography, surface roughness and elevation, and monitoring elevation change, Measuring and monitoring sea ice thickness (ice plus snow) and ice surface roughness (also scanning laser), Mapping of ice sheet surface velocity and subsurface structure	Does not require sunlight, higher spatial resolution and accuracy (potentially) than radar altimetry	Does not penetrate cloud
Passive microwave	Passive microwave radiometer	Satellite	Large scale detecting, mapping, and monitoring surface melt on ice sheets, Monitoring extent, concentration, and drift of sea ice, Mapping of polynyas (and estimation of sea-ice production rates—see Tamura *et al.*, 2016)	All weather, long time series, daily circum-Antarctic coverage	Low spatial resolution
Active microwave	SAR	Satellite	High resolution mapping of subsurface structure of ice sheet and glaciers, and surface melt on ice sheets, Grounding line detection and monitoring (SAR interferometry), Detection and tracking of icebergs, Crevasse detection and sea ice surface roughness, Measuring surface velocity of glaciers and ice streams, Sea ice velocity and dynamics, Waves in sea ice, Sea ice type classification	All weather, penetrates snow cover, does not require sunlight, high spatial resolution, reasonably long time series	Relatively poor coverage (relatively narrow swath width), data coverage and availability
	Radar altimeter	Satellite	Measuring and mapping ice sheet surface topography and elevation (change), Monitoring sea ice thickness	All weather, does not require sunlight, time series datasets	Generally less accurate than laser altimetry in steeper ice sheet margins, penetrates the surface
	Scatterometer	Satellite	Large scale mapping of sea ice, snow accumulation, and surface melt on ice sheets, Sea ice velocity, Large scale sea ice type classification, Detection and tracking of large icebergs	More detailed spectral data than imaging radar	Lower spatial resolution than imaging radar
Gravity	GRACE mission	Satellite	Monitoring changes in mass balance of ice sheets	Global coverage	Low spatial resolution

Repeat coverage (ideally regular and systematic) by polar orbiting satellites is invaluable for measuring key ice sheet and sea ice parameters over vast remote regions and in detecting and monitoring change/variability. Important environmental factors affecting the use of optical sensors for EO of the polar ice environment are persistent cloud cover year-round and polar darkness in winter. TIR sensors can 'penetrate' polar darkness but not cloud. Active and passive microwave sensors are crucially important tools for penetrating both polar cloud and darkness. The choice of sensor/combination of sensors for a given application depends on the requisite spatial and temporal (as well as spectral and radiometric) resolutions, amongst other things, taking into account inherent tradeoffs that exist between the various satellite sensor classes (see Volume 1). Airborne, under-ice, and on-ice sensors (see Excursus 5.1) provide important high resolution measurements in key areas of interest, and are also crucial to the calibration and validation of satellite data products. They acquire important measurements at scales intermediate between detailed *in situ* (surface) observations and satellite EO (Newman *et al*., 2019).

Below, we provide a brief summary of the main principles, techniques, and applications of EO relating to first the ice sheet and icebergs (see Section 15.3), then sea ice (see Section 15.4). For more detailed information, refer to Lubin and Massom (2006), Massom and Lubin (2006), Massom (2006; 2009), and Spreen and Kern (2016).

15.3 EO of the Antarctic Ice Sheet

Satellite (in tandem with airborne) EO is crucial for observing, studying, and monitoring ice sheet physical properties and dynamical behaviour, and for extending key *in situ* observations in space and time. Underwater observations (see Excursus 5.1) are also crucial, for example, for determining ocean and ice conditions, properties, and interactive processes under floating ice sheet margins such as ice shelves. Here, we provide a brief assessment of fundamental ice sheet quantities measured by EO.

15.3.1 Ice sheet surface morphology and areal change

Since the 1970s, high resolution imaging using visible through TIR wavelengths acquired by spaceborne sensors (for example, Landsat, SPOT, and ASTER) has been extensively used for fine (decametre) scale mapping and monitoring of the ice sheet margin and glacier surface morphology and features such as surface crevasse patterns (Swithinbank, 1988). Important subtle features not detectable on the ground can be distinguished in such imagery when suitably processed and enhanced. Operating at a resolution of hundreds of metres to kilometre scale, modern wider swath, moderate resolution multispectral radiometers (for example, MODIS and VIIRS) offer more extensive coverage at high radiometric resolution, to reveal an immense amount of surface detail in aid of glaciological research. This includes crevasse propagation over time. Such imagery, when cloud-free, has been composited to produce digital image maps of both the entire ice sheet surface and ice shelves and their surface properties, such as snow surface grain size (Scambos *et al.,* 2007). These again provide a wealth of glaciological information as shown in Figure 15.7 (here at 150 m resolution). 'Mosaic of Antarctica' (MOA) maps and vector datasets with the corresponding coastlines, ice sheet grounding lines, and islands are available from the US National Snow and Ice Data Center (NSIDC; see Section 15.6).

The coastal ice sheet margins of Antarctica are highly dynamic and changeable due to glacier advance and retreat via the calving of icebergs from glacier fronts and ice shelves. Such changes are revealed in time series of cloud-free, moderate resolution NOAA AVHRR and MODIS images of Antarctic ice shelves, which are also available from NSIDC (see Section 15.6). This imagery is readily (routinely) available in near real time, enabling scientists to detect major iceberg calving events as and when they occur. Notable discoveries include the extraordinary rapid disintegration of the Larsen B Ice Shelf in early 2002 to form a plume of thousands of icebergs[19]. So far, ice shelf retreat and collapse has been restricted to the Antarctic Peninsula, where significant regional warming has occurred.

19 For animation, see *https://earthobservatory.nasa.gov/world-of-change/LarsenB*

Satellite SAR is a particularly powerful tool in polar research and operations. It complements optical and TIR sensors by providing high resolution observations of microwave radar backscatter unaffected by cloud and darkness (see Section 9.3 and Volume 1A—Section 15). Selected SAR wavelengths can penetrate metres into the upper snow/firn layer (when dry), to provide additional information on crevasse patterns and upper ice sheet and glacier structure (see Figure 9.3). Multiple, wide swath SAR images acquired during the 1997 RADARSAT-1 Antarctic Mapping Project (RAMP) have been compiled into a high resolution radar mosaic of the southern continent (see Section 15.6). This dataset, which clearly shows the ice sheet drainage basins and other key morphological features, has been used to map the floating ice sheet margin and detect, determine, and monitor changes therein in comparison with earlier and subsequent datasets. The RAMP map is highly complementary to the MOA maps in that it provides key information on subsurface features (given the greater penetration of the radar signal). The MOA map, on the other hand, represents surface features.

Figure 15.7 Portion of Mosaic of Antarctica (MOA) map

Part of the MOA map showing patterns of deformation and crevassing as the ice sheet flows around the stationary Steershead Ice Rise near Siple Dome in the Ross Sea Embayment.

Source: Haran *et al.* (2014). Retrieved from: *https://earthobservatory.nasa.gov/features/MOA*

15.3.2 Icebergs

Satellite EO using high to medium resolution visible to TIR imagery and/or SAR imagery is crucial to the detection of iceberg calving events and the subsequent tracking of the icebergs that calve from the many floating glacier tongues and ice shelves around Antarctica. These icebergs vary in size from tens of metres to many kilometres across, depending on the source. They are encountered all around Antarctica, where they either drift away from their calving sites in ocean currents, or become grounded on banks in waters shallower than ~450 m. Large groups of small grounded icebergs occur in certain near-coastal locations, where they strongly affect sea ice conditions up to 200–300 km offshore (Massom *et al.*, 2001b; for example see Figure 15.6b). Either individually or *en masse*, icebergs can also have an important localised to regional effects on:

- ocean properties and circulation (for example, through input of fresh meltwater);
- sea ice dynamics and the formation of coastal fast ice; and
- biological activity, including primary production (by enhancing stratification and nutrient levels in the upper ocean), while disrupting benthic communities by scouring the seafloor.

The calving and grounding of vast icebergs (tens of kilometres in size) can also have serious negative impacts on ocean primary production, the breeding success of penguins, and human access to bases, by diminishing the size of open water areas in the form of recurrent coastal polynyas (e.g. Arrigo *et al.*, 2002). Drifting icebergs can also be a major hazard to shipping, and can occur far north of the sea ice edge.

While icebergs have been studied using visible and TIR imagery, their systematic detection and tracking for both research and operational purposes necessitates use of active satellite microwave sensors. EO of the many thousands of smaller icebergs (< 1–10 km) requires high resolution SAR imagery. Typically and under cold (freezing) conditions, and by virtue of their relatively high backscatter, icebergs show up as distinctly-shaped, bright objects against an ocean or sea ice background. The breakup of icebergs at low latitudes has also been investigated using satellite laser altimeter (ICESat) data (Scambos *et al.*, 2005).

Larger (vast) icebergs are detectable and trackable in time series datasets of appropriately-processed, operational radar scatterometer data (Budge and Long, 2018). Information on the location of large Antarctic icebergs is given at the:

- US Antarctic Iceberg Tracking Database (*www.scp.byu.edu/data/iceberg*); and at the
- US Navy/NOAA National Ice Center (*https://usicecenter.gov/Products/AntarcIcebergs*).

Regarding ice sheet mass balance, it has been estimated from EO that iceberg calving at present accounts for about half of the ice lost from the Antarctic Ice Sheet each year (Depoorter *et al.*, 2013). This amount (proportion) may change in future.

15.3.3 Ice surface temperature

Satellite TIR imaging is the primary tool for monitoring change in ice surface ('skin') temperature (Ts) over large remote regions (see Figure 15.8)—provided cloud cover is not inhibitive and/or can be accurately detected and masked (see Section 14). Cloud masking in EO imagery is typically achieved using multispectral techniques based on differentiating the optical and thermal properties of clouds from a snow/ice background. This is crucial as cloud cover can significantly reduce areal coverage of the surface in daily images. For this reason, large scale maps of Ts are typically composites of cloud-free areas using multiple images acquired over several weeks to months (see Volume 2D). Details of the standard Ts algorithms for the current VIIRS sensor are given in Key *et al.* (2013).

Figure 15.8 Warming trend of Antarctica from 1957 through 2006

Map showing the continent-wide warming trend of Antarctica from 1957 through 2006 (temperature change per decade in °C), based on analysis of cloud-free satellite TIR imagery and weather station data. The underlying (ice sheet) surface colour is based on the Landsat Image Mosaic of Antarctica (LIMA) dataset (*lima.usgs.gov*), while the topography is from a Radarsat-1 SAR-based digital elevation model (*https://nsidc.org/data/NSIDC-0103/versions/2/print*). Sea ice extent in the Southern Ocean surrounding the continent is based on data from the Advanced Microwave Scanning Radiometer for EOS (AMSR-E) acquired on 14 May, 2008 (late austral autumn).

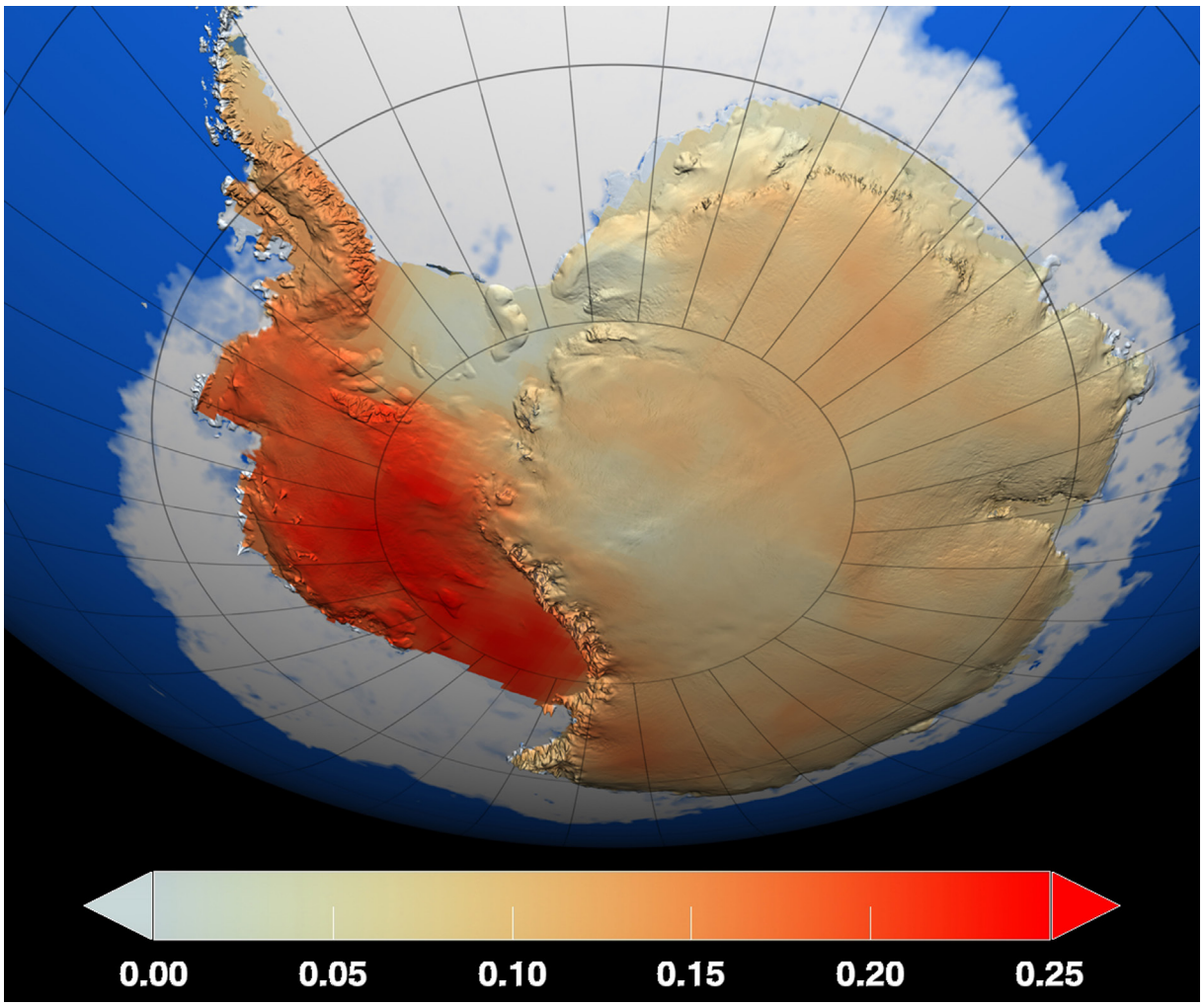

Adapted from: Steig *et al.* (2009). Retrieved from *https://earthobservatory.nasa.gov/images/36736/antarctic-warming-trends*

15.3.4 Surface melt

Closely related to ice sheet surface temperature is surface melt. Melting not only reduces the ice sheet mass, but may in certain areas accelerate ice flow (by meltwater percolating downwards to lubricate the ice sheet base). Pressure from percolating surface meltwater can also enlarge crevasses by a process known as hydrofracture, to reduce ice shelf mechanical integrity (Scambos *et al.,* 2003). Extensive surface ponding was detected and mapped on the Larsen B Ice Shelf prior to its disintegration in 2002 using 250 m resolution MODIS optical imagery. In other regions, meltwater flows across ice shelf surfaces in river systems which drain into the sea (Bell *et al.,* 2017), to locally affect ocean properties (the magnitude of this effect is currently not known). Ocean freshening from increased ice sheet melt may also lead to enhanced sea ice formation, by increasing stratification of the upper ocean and decreasing upward heat entrainment (Bintanja *et al.,* 2013). For these reasons, it is important to not only detect but also monitor surface melt, to determine whether it is changing. Estimation of the magnitude of melt requires coincident surface observations.

Satellite passive microwave radiometry is the primary tool for detecting, mapping, and monitoring the areal extent of large scale (ice sheet-wide) surface melt, its timings of onset and cessation, and its resultant duration (Liu *et al.,* 2006). This is based on the changes in the surface microwave emission characteristics that are observed in microwave brightness temperature observations when snow melts. These date back to 1979 with SMMR then SSM/I. By this method, surface melt patterns can be observed on a daily basis. Annual assessments of Antarctica-wide seasonal melt extent, timings of melt onset and cessation, and resultant duration are provided in annual NOAA BAMS State of the Climate Reports (*https://www.ncei.noaa.gov/bams-state-of-climate*).

Higher resolution, active microwave detection and mapping of surface melt at large scale is also possible using satellite SAR (for example, Luckman *et al.,* 2014) and spaceborne radar scatterometry (for example, the SeaWinds scatterometer flown on QuikSCAT at 5 km resolution (1999–2009) and the MetOp ASCAT at 4.45 km resolution. Such techniques have, for example, revealed change in surface melt duration on Larsen C Ice Shelf (Bevan *et al.,* 2018).

15.3.5 Ice sheet velocity

Two main methods are used to measure the surface velocity of Antarctica's glaciers and ice streams. The first involves the tracking (by maximum cross-correlation) of surface features in repeat-pass and high resolution optical imagery (e.g. Scambos *et al.,* 1992) and SAR imagery (e.g. Giles *et al.,* 2009). The NASA-funded Global Land Ice Velocity Extraction from Landsat (GoLIVE) project provides near real time ice velocity data derived from Landsat-8 panchromatic imagery (*https://nsidc.org/support/how/golive-map-application-user-guide*; see Figure 15.9; Fahnestock *et al.,* 2016). Similarly, the Centre for Polar Observation and Modelling Data Portal (*http://www.cpom.ucl.ac.uk/csopr/iv/index.html*) provides frequently updated maps of ice surface velocity in near real time derived from Sentinel-1 SAR imagery, for two key West Antarctic outlet glaciers that are undergoing loss (Pine Island and Thwaites).

The second technique, namely SAR interferometry or InSAR (see Section 9.4 and Volume 1B—Section 8), is particularly powerful in that it can measure ice velocity and strain rate (velocity gradient) to centimetre accuracy (Goldstein *et al.,* 1993; Rignot *et al.,* 2011). This is based on detecting the phase difference between two (or more) different SAR scenes of the same area but from slightly different viewing angles or orbital positions, and acquired at different times (see Massom and Lubin, 2006; see Figure 9.7). Figure 15.1 depicts a map of InSAR-derived mean annual velocity of the Antarctic Ice Sheet and ice shelves, and clearly shows the approximately 30 principal flow units involved in draining grounded ice across the grounding line and into the ocean (Shepherd *et al.,* 2018).

Taken together, these two methods (feature tracking and InSAR) have not only revolutionised our understanding and quantification of patterns of discharge and their change in key individual glaciers/ice streams. They have also led to systematic repeat surveys of Antarctica-wide ice velocity, revealing that the rate of ice discharge has generally increased over the satellite era (for example, Rignot *et al.,* 2008). Satellite velocity observations show that there was a marked speed-up in grounded ice via tributary glaciers immediately following the rapid disintegration of the Larsen B Ice Shelf in 2002, related to removal of the ice shelf buttressing effect (Rignot *et al.,* 2004; Scambos *et al.,* 2004). While ice shelf disintegration/areal loss (or thinning) does not directly contribute to SLR, as the ice area affected is already floating, there is a strong indirect effect.

Figure 15.9 Byrd Glacier velocity

Image showing the Landsat-derived velocity of the relatively fast moving Byrd Glacier (~2.4 m per day, orange and red) and the slower and narrower Mulock Glacier (pale blue), which exit the Transantarctic Mountains and flow into the Ross Ice Shelf.

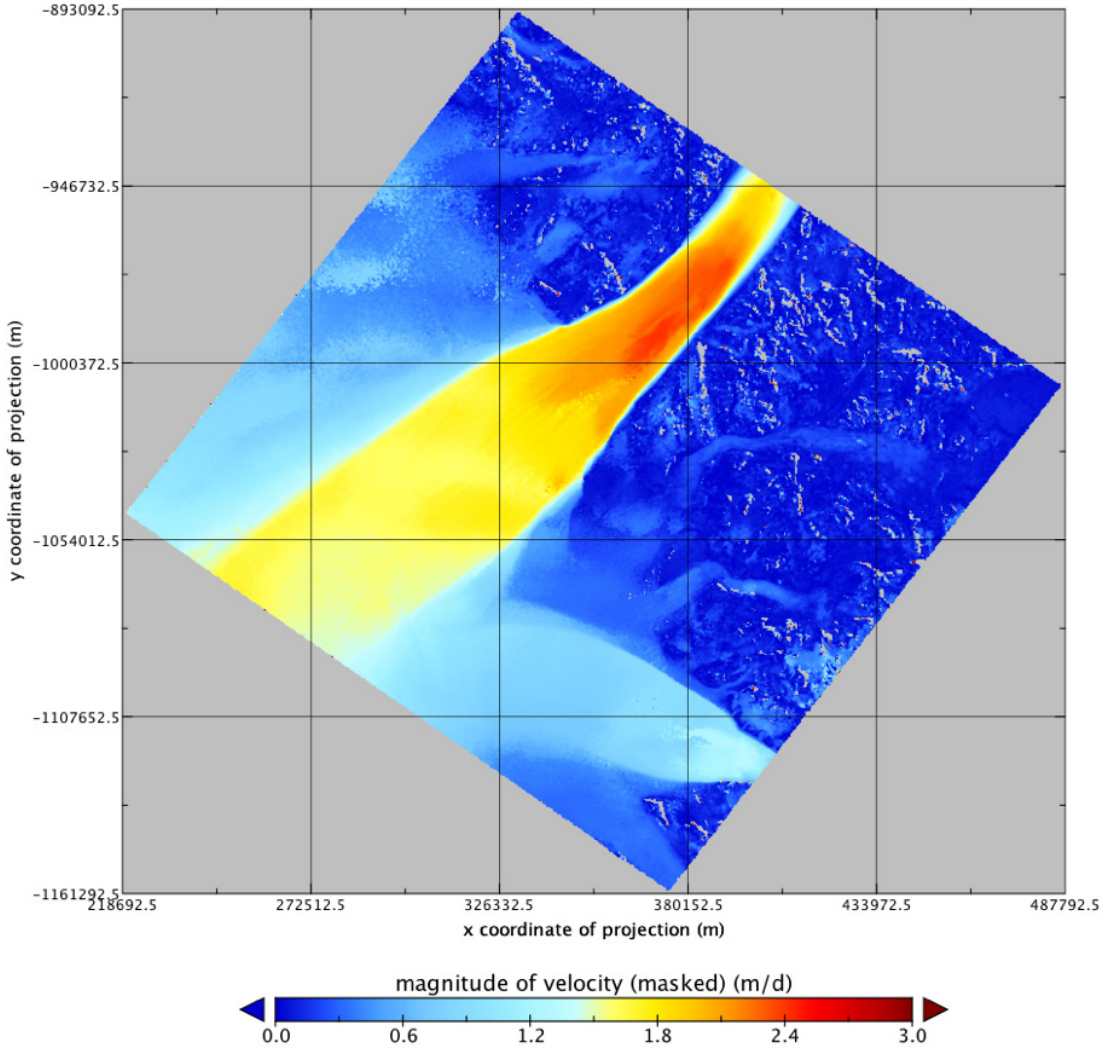

Source: NASA/GoLIVE. Retrieved from *https://nsidc.org/data/nsidc-0710/versions/1/documentation*

15.3.6 Surface elevation

Spaceborne altimeters (both radar and laser) measure surface elevation at high resolution by transmitting a signal toward the surface and accurately measuring the time interval of its return (see Section 9.5), and are a powerful tool for ice sheet observation (see Rémy and Parouty, 2009, for a review; see also Volume 1A—Section 16). Since their advent in 1992, modern radar altimeters (for example, on ERS, Envisat, CryoSat-2 and Sentinel-3 missions) have been important day/night and all-weather tools for the routine measurement of ice sheet elevation and its change over time (to within tens of centimetres), resolving both detailed patterns in individual catchment areas and large scale, Antarctica-wide change (for example, Pritchard *et al.,* 2009; Gourmelen *et al.,* 2017). Such information is crucial to the assessment of change in ice sheet volume and to help monitor Antarctica's contribution to SLR (see Section 15.3.7).

The multi-decadal records have shown that while the surface elevation of most of Antarctica has changed little over the past 25 years, this is not the case in many coastal sectors. There, the altimeter record has revealed receding surface height thinning (at rates of up to metres per year) on some of Antarctica's fastest-flowing glaciers, notably the Pine Island (a major contributor to recent SLR) and Thwaites glaciers in the west (McMillan *et al.,* 2014) and Totten Glacier in the east. This has been attributed to ice shelf thinning (as shown in Figure 15.10) due to basal melt by a warming ocean and associated increases in ice velocity. Of major concern is the possibility of rapid inland retreat of the grounding line in such regions, leading to increased ice sheet instability (see Joughin *et al.,* 2014; Alley *et al.,* 2015).

Figure 15.10 Antarctic ice shelf thickness changes

Change in Antarctic ice shelf thickness from 1994 to 2012 based on analysis of satellite radar altimeter data. For a description of the ice shelves annotated here, please refer to Paolo *et al.* (2015).

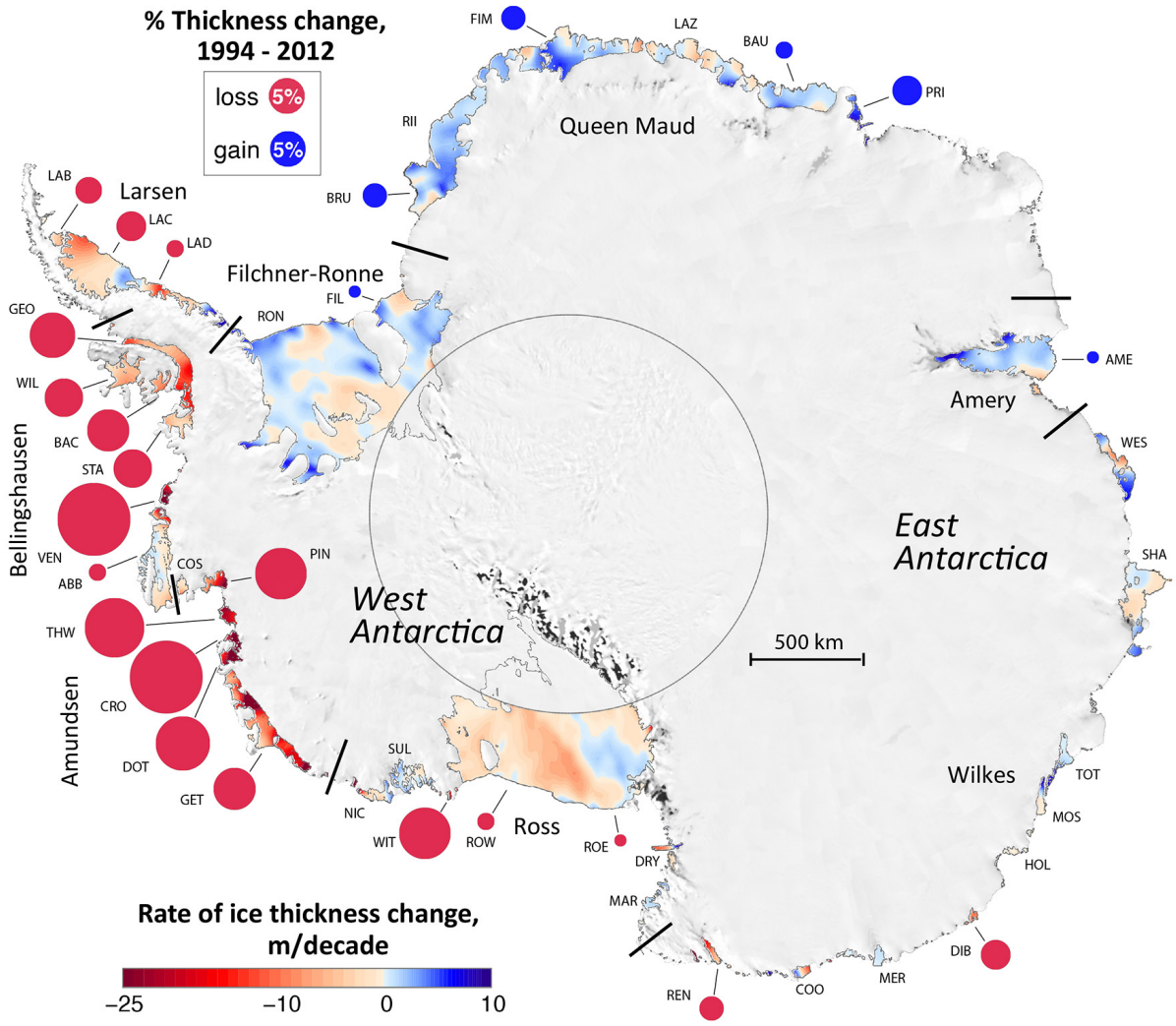

Adapted from Paolo *et al.* (2015) Figure 1

Spaceborne altimeters have revolutionized our understanding of the shape and topographic detail of the Antarctic Ice Sheet, with which to constrain ice dynamics, mass balance estimates (see Section 15.3.7), and models of the ice sheet that are crucial to predicting its likely response to future climatic conditions and contribution to SLR. As an example, a new digital elevation model (DEM) map of Antarctica based on CryoSat-2 altimeter data (Slater *et al.*, 2017) provides the most detailed and accurate three-dimensional view of the full continent to date (see Figure 15.11). Comparison with precise airborne survey data from NASA's Operation IceBridge shows that the new DEM depicts ice elevation to within 9.5 m on average. The model is freely available from the Centre for Polar Observation and Modelling (CPOM) Data Portal (see Section 15.6). Satellite altimetry is also used to map Antarctic sub-glacial lakes and monitor their activity (Siegfried and Fricker, 2018).

Latterly, spaceborne lidar instruments on ICESat (2003–2009) and ICESat-2 (2018+) have provided a more precise means of measuring and monitoring patterns of ice sheet elevation change than radar altimeters (e.g. Smith *et al.*, 2020). This is based upon the relatively small surface illumination area of lasers, which operates better over steeper, craggy Antarctic coastal regions (Markus *et al.*, 2017). The laser return signal also emanates from the surface, whereas radar altimeters can penetrate some depth into the ice sheet surface, depending on both wavelength/frequency and snow/ice conditions (see Figure 9.3). This factor needs to be accounted for in radar-derived estimates of surface elevation change/variability. Being based on an optical instrument, the main disadvantage of laser altimeters is their inability to penetrate cloud cover.

Figure 15.11 DEM of the Antarctic Ice Sheet

This state-of-the-art DEM of the Antarctic Ice Sheet was derived from six years of CryoSat-2 radar altimeter data, with a sampling of the ice sheet surface every kilometre. Gaps that CryoSat could not survey, mostly due to the rugged terrain, are filled in by sophisticated interpolation techniques.

Source: CPOM. Retrieved from: *http://www.cpom.ucl.ac.uk/csopr/icesheets2/dems.php?ais_subject=dem&user_type=normal*

15.3.7 Ice sheet mass balance

Taken together, accurate and sustained EO measurements of changes in ice sheet speed (notably the discharge rate of grounded ice) and surface elevation are (together with ice sheet weight) crucial to the estimation and monitoring of ice sheet mass balance—and therefore the ice sheet stability and contribution to SLR.

There are three main methods for measuring and monitoring ice sheet mass changes, all of which are heavily reliant on EO (ACE CRC, 2018; NSIDC, 2019a). These are the:

- **Volume (elevation) change or geodetic method**—scale monitoring of change in ice surface elevation over time by satellite altimeters (using data available since the early 1990s) has enabled quantitative estimation of the growth or reduction of overall ice volume (e.g. Smith *et al.*, 2020).
- **Mass budget technique**—compares estimates of snow accumulation (input) with ice losses (output) via seaward discharge across flux gates at the ice sheet margins and close to grounding lines from measured ice outflow velocity and thickness change/melt. Major advances in the mapping of glacier ice flow using repeat Landsat optical images (Gardner *et al.,* 2018) and InSAR methods (Mouginot *et al.,* 2014) have greatly facilitated this approach, which still however requires independent information on snow accumulation (currently not well constrained) and an accurate cross-section of each outflowing glacier across its grounding line.
- **Gravimetric approach**—direct 'weighing' of the ice sheet using satellite measurements of gravitational pull as the sensors pass over the ice, that is, detecting changes in the Earth's gravity field over the ice sheet relating to change in ice mass over time due to either accumulation or loss. Key to this was the launch of NASA's Gravity Recovery and Climate Experiment (GRACE) mission in 2003 (see Excursus 5.1). This provided a new means of resolving where the Antarctic Ice Sheet has lost mass, pointing the finger mainly at West Antarctica (Velicogna and Wahr, 2006; Rignot *et al.,* 2011).

Although different, the three methods are complementary and in fact produce similar results at the continental scale—enabling synthesis of the multiple EO-based estimates of ice sheet mass balance. This has revealed that, from 1992 to 2017, Antarctica lost > 2,700 billion tonnes of ice—equivalent to a SLR of 7.6±3.9 mm—with about half of this loss coming since 2012 and mainly from the Antarctic Peninsula and Amundsen Sea sectors (IMBIE Team, 2018). The accelerating mass loss is considered to be largely a response to the thinning of ice shelves due to their contact with warming ocean waters (Pritchard *et al.,* 2012) and, in the case of the Peninsula, rapid wholesale disintegrations of the Larsen A and B ice shelves.

15.4 EO of Sea Ice

Compared to the ice sheet, sea ice represents a more complex, dynamic, and challenging target for EO. It can, however, be readily detected and measured from space by virtue of its distinctive optical and microwave properties compared to open ocean. These are the:

- high reflectance[20] (brightness) of sea ice and snow at optical wavelengths compared to open ocean;
- thermal contrast at TIR wavelengths—the ice/snow surface is generally colder than the non ice-covered ocean, which has a surface temperature approximating -1.8°C during freezing seasons;
- contrast in the passive microwave emissivities[21] of sea ice and ice-free (open) ocean, depending on wavelength/frequency and polarisation[22]; and
- contrast in the microwave (radar) backscatter of sea ice versus open ocean—with sea ice generally being a brighter target, and backscatter depending on the ice thickness, age, and degree of deformation/roughness.

Fundamentally important characteristics of sea ice that can be measured from space are its ***areal extent and seasonality***, ***concentration***, ***motion*** and ***dynamics/deformation***, ***temperature***, ***albedo***, and (potentially) ***thickness*** (also ***snow cover thickness***; see Excursus 15.1). Regular, repeated and sustained basin-scale observations of these parameters are required to:

- understand the large scale dynamic and thermodynamic evolution of the ice cover on seasonal and interannual scales, and change and variability therein;
- detect long term trends in sea ice coverage and properties, including thickness and volume; and
- support safe shipping operations in the high-latitude Southern Ocean.

Taken together, sea ice concentration, thickness distribution and motion are required to determine its mass balance. In the following subsections, we give brief information on key sea ice variables that can be measured and monitored by EO. Massom (2009) and Lubin and Massom (2006) provide further information on error sources, and also on the:

- basic concepts and principles around EO of sea ice;
- applications, strengths, and weaknesses of the different sensor classes for polar ocean research and monitoring; and
- key tradeoffs between them.

Massom (2009) also highlights and discusses key differences between Antarctic and Arctic sea ice as EO targets. This requires different algorithms for extracting key variables from EOS data for each polar region.

15.4.1 Sea ice concentration, extent, and seasonality, and their variability

Spaceborne, wide swath, optical sensors operating at moderate spatial resolution (0.25–1 km; such as MODIS and VIIRS) provide observations of albedo, temperature, and radiative fluxes, and have also been used to derive estimates of thin-ice thickness in coastal polynyas, as well as the interaction of sea ice with ice sheet margins and icebergs. They can also provide information on extent, concentration, and type, based upon the:

- contrasting temperature and albedo of sea ice versus open ocean; and the
- variation of albedo with ice thickness (until the ice becomes snow-covered).

20 Reflectance is the ratio of the intensity of radiation reflected by a target surface to that of the radiation incident upon it.

21 *Emissivity* is the ratio of radiation naturally emitted by a natural surface to that emitted by a *blackbody* (perfect radiator) at the same kinetic temperature.

22 Polarisation describes the direction of orientation in which the electrical field vector of electromagnetic radiation vibrates, and is a key consideration in active and passive microwave EO of sea ice (Long, 2008).

However, persistent cloud cover is an issue (as is polar darkness for optical EO), and cloud masking can be challenging over snow and ice surfaces given their similar optical and thermal properties. For this reason and although it plays a key role in support of shipping and operations due to its ready availability, satellite optical and TIR EO is not the primary source of ice concentration information for monitoring and research purposes. This is more the realm of active and passive microwave EO, which are (largely) unaffected by atmospheric conditions and darkness (see Section 9 and Volume 1A—Section 14).

Satellite-borne, passive microwave sensors (e.g. SMMR, SSM/I, AMSR-E, SSMIS) have provided the most reliable and consistent near real time information on the concentration and extent of the entire Antarctic sea ice cover on a daily/near-daily basis since 1978 and at mapped spatial resolutions ranging from 6.25 km to 25 km. This is based upon the strong frequency-dependent contrast in the microwave emissivities of sea ice and open ocean. Extent is generally defined as the integral sum of all observations with ice concentrations > 15%, while area is the product of ice concentration and extent. A range of sea ice data (including mapped brightness temperatures and derived sea ice concentration) is available from the Scientific Data Search facility managed by the NSIDC (NSIDC, 2019b).

The time series of passive microwave data has been crucial to monitoring change and variability in global sea ice coverage and seasonality (see Figure 15.12). In stark contrast to the Arctic, where sea ice has spiralled since the 1970s, overall Antarctic coverage has paradoxically displayed a slightly increasing trend over the same period (Turner and Comiso, 2017)—of about 1.0±0.5% per decade for 1979–2018 (Parkinson, 2019). In fact, the slight net increase masks strong and contrasting regional contributions, notably a decrease in the Amundsen-Bellingshausen seas sector of –2.5±1.2% per decade for 1979–2018 and increases of up to +2.3±1.2% per decade in other sectors (Parkinson, 2019). Overall and regional trends also show a marked seasonal dependence (Holland, 2014). Moreover, recent years have seen extreme variability, with record maxima in three successive winters (2012, 2013, and 2014; Reid and Massom, 2015) being followed by a record summer minimum in 2017, with below-average overall (net) extent continuing until early 2020 (Reid *et al.*, 2021).

Figure 15.12 Extent of Arctic versus Antarctic sea ice

Plot of the overall extents of Arctic (red) and Antarctic (blue) sea ice for the period January 1979 to December 2019, with the thick lines showing 12-month running means and thin lines showing monthly anomalies. Total area is estimated from satellite image pixels with sea ice concentration of at least 15%. Antarctic sea ice reached a record high in 2014 before decreasing dramatically. The Arctic Ocean's coverage of summertime sea ice has shrunk by about 13% per decade.

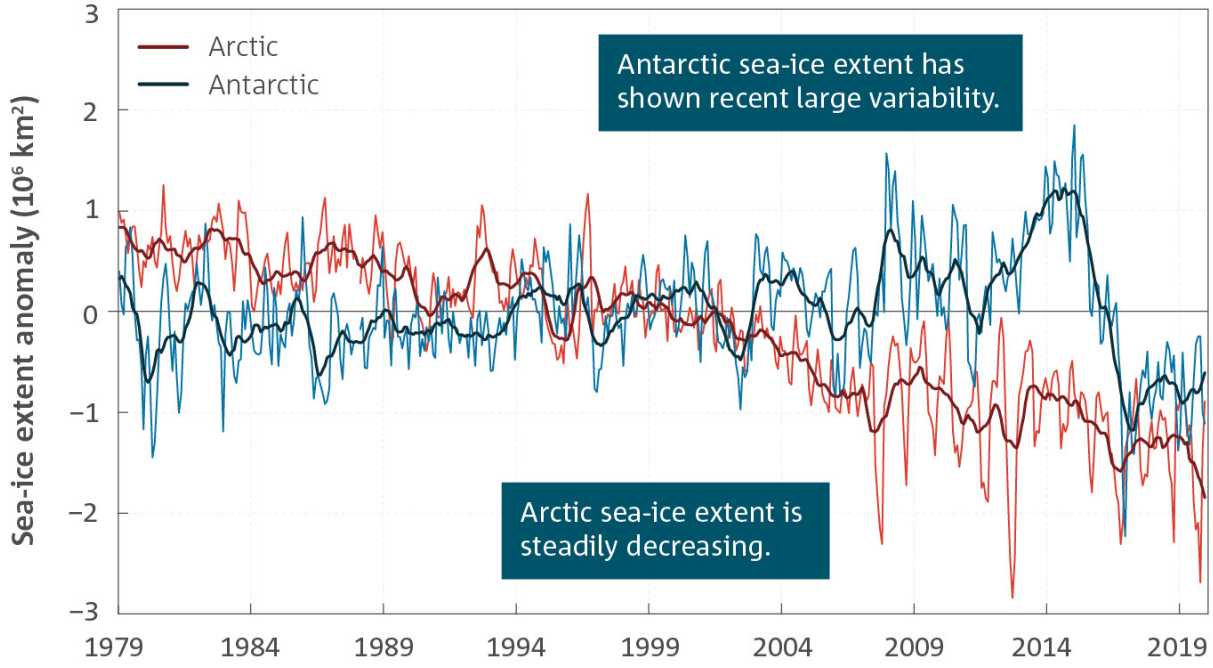

Source: BoM (2021). Retrieved from *http://www.bom.gov.au/state-of-the-climate/cryosphere.shtml*

This time series has also revealed strong regional trends in the seasonality (timings of annual advance and retreat and resultant duration) of sea ice coverage around Antarctica (Stammerjohn *et al.*, 2012) that largely reflect the sea ice concentration and extent patterns (Turner *et al.*, 2015). Duration is defined here as the length of time, during each annual Antarctic sea ice cycle (February to February), that a pixel contains sea ice with a concentration of ≥ 15%. West of the Antarctic Peninsula and in the northwestern Weddell Sea, for the period 1979/80 to 2016/17, annual sea ice duration decreased by about 3 months due to a 2-month-later advance and an approximately 1-month-earlier retreat (Stammerjohn and Maksym, 2016). These changes have had impacts on the marine ecosystem, notably on phytoplankton and penguin communities (Massom and Stammerjohn, 2010), and have also been implicated in the timing and nature of breakup events of the Larsen A and B and Wilkins ice shelves (Massom *et al.*, 2018). In contrast and in the western Ross Sea, the annual sea ice season has lengthened substantially—by about three months over 1979/80 to 2016/17 (Stammerjohn *et al.*, 2012). Patterns of change in sea ice advance, retreat, and duration elsewhere are complex, for example, across East Antarctica (Massom *et al.*, 2013).

Although a number of mechanisms have been proposed to explain these changing and/or varying patterns of Antarctic sea ice coverage around Antarctica—including changes in winds, ocean variability, and freshwater input from precipitation and ice shelf melt—considerable uncertainty remains (Hobbs *et al.*, 2016). Indeed, understanding the nature of sea ice change and variability, and the relevant drivers and impacts, is a high priority in climate research (see NAS, 2017).

Systematic, consistent observations of the marine cryosphere are critical for the operational community, whose primary task is to reduce shipping hazards related to iceberg and sea ice tracking. Operational ice services make extensive use of satellite passive microwave ice concentration data (from the DMSP SSM/I and EOS Aqua AMSR-E), ice extent and type data from optical-TIR imagery (e.g. VIIRS and EOS MODIS), SAR, and radar scatterometer data.

Satellite-based annual assessments of Antarctic sea ice concentration, extent, and seasonality are provided in annual NOAA BAMS State of the Climate Reports (*https://www.ncei.noaa.gov/bams-state-of-climate*).

15.4.2 Coastal landfast sea ice (fast ice) distribution

The mapping and monitoring of fast ice from space represents more of a challenge, given that it forms a relatively narrow zone immediately adjacent to the Antarctic coast. This issue has been successfully addressed through use of wide swath MODIS optical imagery, to produce time series maps of fast ice across East Antarctica (from 20°E to 160°E) at 2 km resolution (Fraser *et al.*, 2012; see Figure 15.13). Cloud cover is removed by first applying NASA's standard cloud masking algorithm, then compositing 20 days of imagery to fill in resultant data gaps. In this way, a time series of 20-day composites has been produced for 2000–2009. These show an upturn in coastal fast ice overall, although the shortness of the time series negates trend analysis. Recent extension of the fast ice extent time series to include circumpolar imagery from 2000 to 2018 (Fraser *et al.*, 2020) indicates a marginally significant decrease in overall (circum-Antarctic) fast ice extent of approximately –2.0±1.8% per decade.

Another technique uses maximum cross-correlation of satellite SAR image pairs separated by 1–3 days to provide more detailed maps (at higher spatial and temporal resolution) to detect and map coastal fast ice (Li *et al.*, 2018), by virtue of its stationary nature compared to pack ice. By this method, sea ice that is not moving is classified as fast ice. Coarser resolution mapping is obtained from passive microwave data based on a relationship between horizontally and vertically polarised AMSR-E brightness temperatures at 89 GHz (Nihashi and Ohshima, 2015).

Figure 15.13 Fast ice coverage and persistence

MODIS-derived map of coastal fast ice coverage and persistence in East Antarctica averaged over an 8.8 year period (March 2000 to December 2008), at a spatial resolution of 2 km.

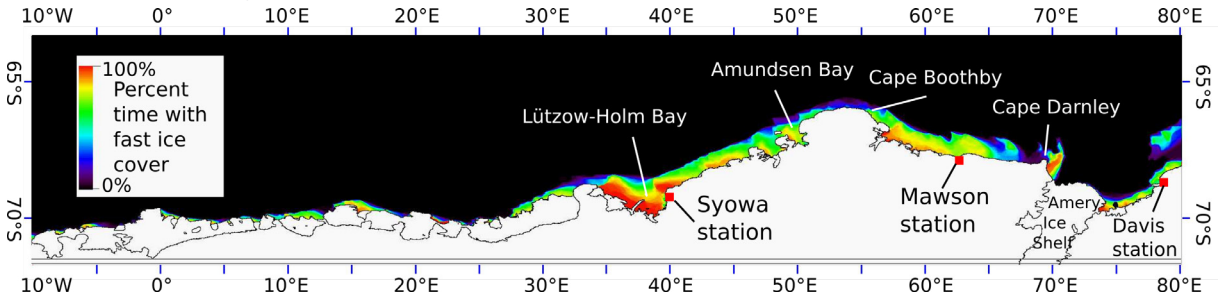

Source: Fraser *et al.* (2012) Figure 2a

15.4.3 Sea ice motion and dynamics

Identifying and understanding the changes in Antarctic sea ice drift over short to broad time scales is of considerable importance, given the contribution of ice dynamics to ice concentration and extent, seasonality (duration) of coverage, ice deformation and thickening, enhanced ice production and heat loss in open water, and therefore the climate system. Moreover, deformation processes related to differential ice motion significantly impact safe and efficient shipping operations around Antarctica.

Tracking of sea ice motion and dynamics is achieved both at low resolution (using visible–TIR radiometers, passive microwave radiometers, and radar scatterometers) and at high resolution (using SAR imagery), the latter typically in smaller regions of interest. In all cases, the technique is based upon identification and tracking of persistent features/floes within the sea ice field in time sequences of overlapping/repeat images, generally through maximum cross-correlation.

Figure 15.14 Mean monthly (March through November) ice drift for 1982-2015.

Contours are isobars (interval: 4 hPa) from ERA-Interim sea level pressure fields. Drift estimates are shown on a 200 km grid to reduce density of vectors within each plot; every other vector is displayed. Red crosses show the centres of three atmospheric lows in the monthly mean fields. Colour spectrum for motion ranges from 0 km/day (blue) to 10 km/day (red).

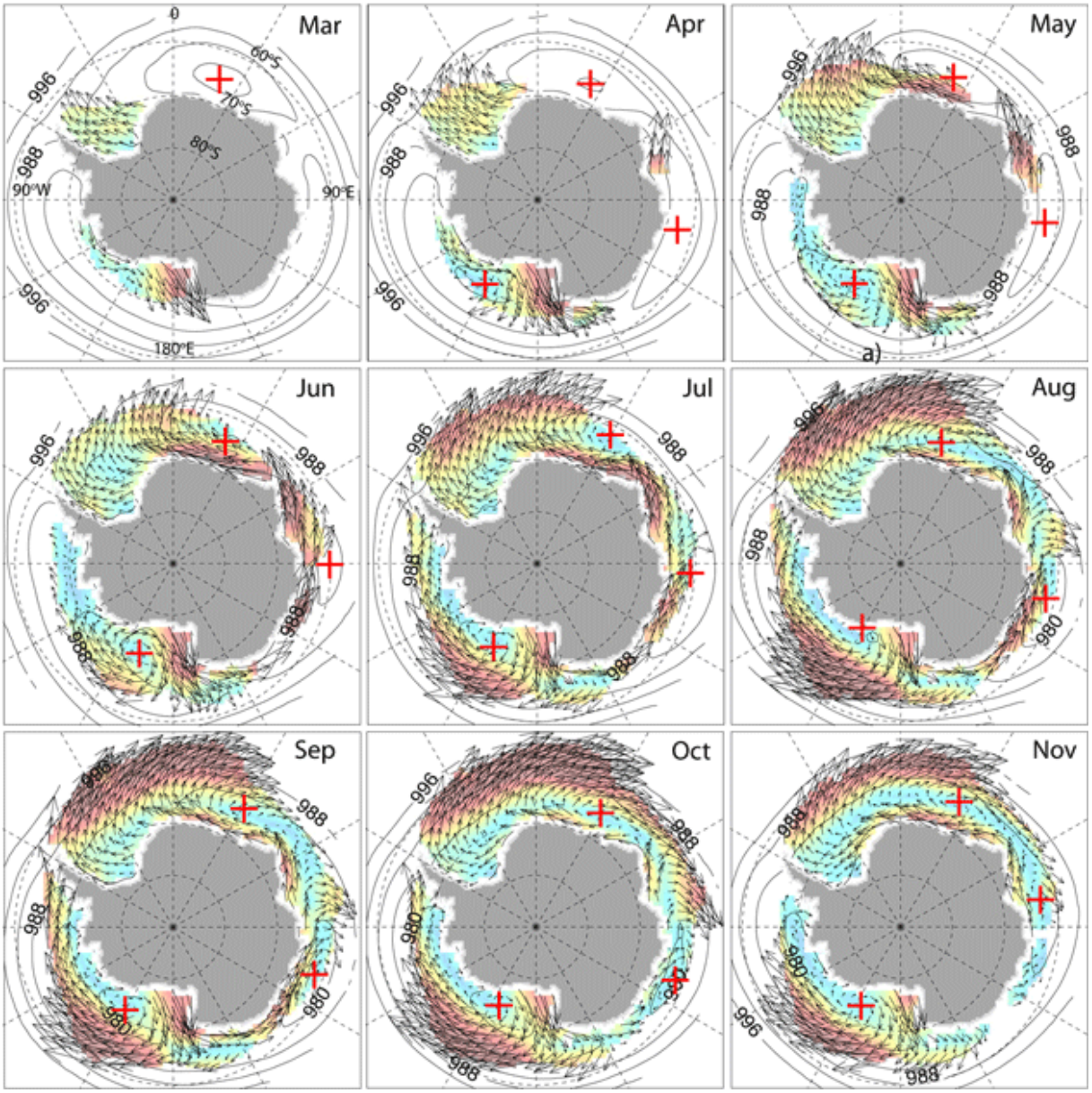

Source: Kwok *et al.* (2017) Figure 226-3243-1. Used with permission.

Moderate resolution, ice drift fields derived from satellite passive microwave brightness temperature data (37 GHz and 85 GHz/91 GHz, the latter since 2009) have enabled assessment of large scale drift patterns in Antarctic sea ice over recent decades (Kwok *et al.,* 2017). Although the coarse resolution of the data used leads to uncertainties of several kilometres for individual displacement vectors, this dataset is long and offers complete circumpolar coverage on a daily/near-daily basis by the SMMR, SSM/I and AMSR-E instruments (uninterrupted by cloud and darkness). The climatological pattern of mean sea ice drift around Antarctica is shown in Figure 15.1. It depicts a strong outer zonal band of eastward drifting sea ice at maximum annual extent within the Antarctic Circumpolar Current that is maintained by strong circumpolar westerly winds, and large scale gyres in the Ross and Weddell seas. Around the coastal margin, sea ice drifts predominantly westwards under the influence of strong prevailing easterly winds and within the Antarctic Coastal Current.

The time series of satellite passive microwave data has given great insight into patterns of sea ice drift and their variability and change in response to changing wind forcing. Indeed, it has revealed substantial regional change in patterns of sea ice drift around Antarctica in recent decades (see Figure 15.14). Notably, sea ice drift speed has decreased in the western Weddell Sea in recent decades, in contrast to the eastern Weddell and Ross seas where it has increased (Holland and Kwok, 2012; Kwok *et al.,* 2017). These large and statistically significant changes have been linked to observed changes in surface wind speed and direction associated with change in large scale modes of climate variability, such as the Southern Annular Mode, and a persistent low pressure anomaly in the Amundsen Sea known as the Amundsen Sea Low (Turner *et al.*, 2016).

Improved sea ice motion products are required, and these are potentially obtainable from the merging of results from passive microwave radiometry, radar scatterometry, and drifting ice buoys, for optimal spatial coverage. While the coarser resolution time series are best suited to analyses of large scale sea ice drift patterns, more detailed characterisation of daily and sub-daily ice motion requires use of high resolution SAR and satellite-interrogated buoy data. This, in turn, requires more frequent and extensive (regular and systematic) SAR coverage of the Antarctic sea ice zone.

15.4.4 Sea ice and snow cover thickness

Satellite EO using laser (lidar) and radar altimeters dating back to 1991 (ERS-1), such as those onboard ICESat-1 and -2 and CryoSat-2 respectively, is crucial to the routine large scale estimation and monitoring of Antarctic sea ice thickness and volume. This is based on the accurate measurement of the elevation above sea level of either the:

- ice surface (for radar altimeters); or
- ice plus snow surface (for laser altimeters).

Derivation of ice thickness from these datasets is based on the hydrostatic relationship (Archimedes Principle) between the above- and below-sea level proportions of the ice cover, requiring accurate knowledge of the snow thickness, and the densities of both ice and snow. The following equations are used to determine sea ice thickness (h_i; Kwok, 2010):

$$h_i = \left(\frac{\rho_w}{\rho_w - \rho_i}\right)\boldsymbol{h_f} - \left(\frac{\rho_w - \rho_s}{\rho_w - \rho_i}\right)h_{fs} \quad \text{(lidar)}$$

$$h_i = \left(\frac{\rho_w}{\rho_w - \rho_i}\right)\boldsymbol{h_{fi}} + \left(\frac{\rho_s}{\rho_w - \rho_i}\right)h_{fs} \quad \text{(radar)}$$

where ρ_i, ρ_s, and ρ_w are the densities of sea ice, snow, and seawater respectively. The key observables from laser altimeter/lidar and radar altimeter differ (and are highlighted in bold in the equations above). For laser, h_f is the total freeboard of both ice and snow (where present) above local sea level, that is, assuming that the laser does not penetrate the snow (see Volume 1A—Section 15.1). For radar altimetry, on the other hand, the measured return is assumed to be from the ice surface (see Section 9.5 and Volume 1A—Section 16). Due to the penetration of the radar wave into the snow volume, its return is assumed to be from the sea ice surface and the measured variable h_{fi} is the freeboard of the ice only.

Although promising results have emerged from satellite altimetry, a number of challenges remain that need to be addressed in order to obtain accurate retrievals of circum-Antarctic sea ice thickness. Lack of information on snow depth and density and their variability/evolution introduces considerable uncertainty into estimates of total ice thickness derived from freeboard observations by satellite altimeters. This underlines the need for dedicated validation experiments, using both airborne and autonomous underwater vehicles (AUV; see Excursus 5.1). Such field campaigns are required to identify and quantify errors associated with the conversion of sea ice freeboard to ice thickness. A further obstacle is the complex relationship between ice elevation and thickness around Antarctica (compared to the Arctic). The presence of significant

areas of seawater flooding at the ice surface affects the density of the overlying snow that is used to compute ice thickness from snow elevation, and also the penetration of the signal for radar altimetry. For radar altimetry, the assumption that the return emanates from the snow-ice interface is not always valid (Giles *et al.,* 2008b). An additional critical gap is large scale information about snow depth on sea ice (Webster *et al.*, 2018).

As a result of these factors, our current knowledge of Antarctic sea ice thickness and snow cover thickness is currently limited to compilations of:

- various *in situ* and near-surface remote sensing observations (Worby *et al.,* 2008; Kwok and Maksym, 2014) that are characterised by large spatiotemporal gaps and may be biased towards thinner ice (Maksym *et al.,* 2012); and
- satellite altimeter data that are limited to certain sectors or short time periods (such as Kurtz and Markus, 2012).

As a result, there is inadequate information to determine whether large scale sea ice thickness and volume are changing around Antarctica (Fox-Kemper *et al.*, *in press*), although large scale estimates of Antarctic sea ice and snow cover thickness are emerging (e.g. Kacimi and Kwok, 2020). By contrast and in the Arctic, a combination of extensive satellite altimeter and submarine sonar data has shown a substantial thinning of the ice cover there, which is consistent with the loss of perennial ice (Kwok and Rothrock, 2009).

15.5 Outlook: Future Opportunities and Needs

Major advances in EO have, in recent decades, led to quantum leaps in our understanding of the Antarctic cryosphere, and change and variability therein. Certain key challenges and opportunities remain, however, notably around ensuring continuation of key sensor time series, and adequate data acquisition across the Antarctic Ice Sheet and sea ice cover (Pope *et al.*, 2017).

Of pressing concern is that the Antarctic Ice Sheet is losing ice mass and contributing to global SLR at an accelerating rate (IMBIE Team, 2018). This highlights the critical need to identify and accurately quantify the nature and drivers of the recent change, including ice shelf thinning, weakening, and collapse. This is in turn crucial to reducing current large uncertainties in model predictions of the likely future fate of the ice sheet and its contribution to SLR in response to climate change. An important factor is the need for satellite observations with improved temporal and spatial sampling to more fully understand the processes driving contemporary patterns of ice sheet imbalance (Shepherd *et al.,* 2018).

The accurate synoptic-scale measurement and monitoring of Antarctic sea ice thickness (and overall volume) and snow cover from space also remains a challenge, yet a high priority. New improved estimates may be possible using dual-frequency radar altimeter sensors and by combining coincident measurements from laser and radar altimeters (Kacimi and Kwok, 2020). There is also a pressing need for coordinated and sustained near-surface observations of the sea ice system—as proposed by the Southern Ocean Observing System (SOOS; Newman *et al.*, 2019). These other data sources include sea ice and snow cover measurements from ships (using electromagnetic induction technology) and snow thickness estimates from airborne snow-thickness radars, such as the NASA IceBridge Mission (NASA, 2019; see Section 15.6). Autonomous airborne and underwater vehicles and sensors (see Excursus 5.1) also have a key role to play, not least in the calibration and validation of satellite-derived thickness estimates, and in bridging the scale gap between detailed *in situ* observations (on the floe scale) and large scale satellite measurements (Newman *et al.*, 2019).

By the same token, our understanding of the coupled atmospheric and oceanic drivers of observed sea ice and Southern Ocean change and variability, and the complex interactions and feedbacks involved, remains incomplete (Hobbs *et al.,* 2016; NAS, 2017). This in turn severely limits our ability to confidently and accurately predict the trajectory of future sea ice change and its impacts. Addressing this critical gap involves EO in conjunction with dedicated surface experiments (including process studies) and model improvements. Also crucial is improved information on snow precipitation rates, properties, and thickness as they affect sea ice formation and melt, and how these may be changing (Webster *et al.,* 2018).

As a final comment, field research observations themselves are crucial for satellite validation purposes in general (and to provide information on key parameters that cannot be measured from space). This requires a standardised methodology to ensure consistent acquisition of data in forms that are optimal for the calibration and validation of satellite data algorithms, specific to the geophysical quantities in question.

15.6 Further Information

Antarctica

General information:

https://www.antarctica.gov.au/about-antarctica/ice-and-atmosphere/ice-sheet/

https://www.antarctica.gov.au/about-antarctica/ice-and-atmosphere/sea-ice/

https://www.ga.gov.au/scientific-topics/marine/antarctica

Antarctic Climate and Ecosystems CRC: *https://stors.tas.gov.au/802018*

SOE (2017) *State of Environment Report 2016.* Antarctic Environment: *https://soe.environment.gov.au/theme/antarctic-environment*

Annual assessments of change and variability in the Antarctic ice sheet, sea ice, Southern Ocean and atmosphere, including seasonal changes in melt extent and timing, are given in annual NOAA BAMS State of the Climate Reports: *https://www.ncei.noaa.gov/bams-state-of-climate*

Maps and Images:

Mosaic of Antarctica (MOA) maps and vector datasets with the corresponding coastlines, ice sheet grounding lines and islands are available at: *https://nsidc.org/data/NSIDC-0730/versions/1*

Landsat Image Mosaic of Antarctica (LIMA) dataset: *lima.usgs.gov*

Time series of NOAA AVHRR and MODIS images of Antarctic ice shelves are available at: *https://nsidc.org/data/iceshelves_images/*

Multiple, wide swath SAR imagery acquired during the 1997 RADARSAT-1 Antarctic Mapping Project (RAMP) have been compiled into a high resolution radar mosaic of the southern continent: *https://nsidc.org/data/NSIDC-0103/versions/2/print*

A new DEM model is freely available from the Centre for Polar Observation and Modelling Data Portal (CPOM) at: *http://www.cpom.ucl.ac.uk/csopr/icesheets2/dems.php?ais_subject=dem&user_type=*

Ice sheets

ACE CRC (2017)

NSIDC (2019a)

US Antarctic Iceberg Tracking Database: *www.scp.byu.edu/data/iceberg*

US Navy/NOAA National Ice Center: *https://usicecenter.gov/Products/AntarcIcebergs*

Global Land Ice Velocity Extraction from Landsat (GoLIVE) project provides near real time, ice velocity data derived from Landsat-8 panchromatic imagery: *https://nsidc.org/data/nsidc-0710/versions/1/documentation*

Centre for Polar Observation and Modelling Data Portal provides frequently-updated maps of ice-surface velocity in near real time derived from Sentinel-1 SAR imagery: *http://www.cpom.ucl.ac.uk/csopr/iv/index.html*

Sea Ice

Thomas (2017)

Weeks (2010)

Sea ice type is classified (named) and categorised depending on its thickness (related to age/stage of development), and based on established international protocol. For a glossary and image library of sea ice terms, see: *http://aspect.antarctica.gov.au/home/glossary-and-image-library*

A range of sea ice data (including brightness temperatures and derived sea ice concentration) are available from the Scientific Data Search service of the US National Snow and Ice Data Center (NSIDC): *https://nsidc.org/data/search/#keywords=sea+ice/sortKeys=score,,desc/facetFilters=%257B%257D/pageNumber=1/itemsPerPage=25*

Alfred-Wegener-Institut (AWI): *https://www.awi.de/en/focus/sea-ice.html*

NASA Earth Observatory: *https://earthobservatory.nasa.gov/Features/SeaIce/page1.php* *https://earthobservatory.nasa.gov/Features/SeaIce/page4.php*

National Snow and Ice Data Centre (NSIDC): *https://nsidc.org/cryosphere/seaice/characteristics/polynyas.html*

Polar ice and snow cover

NASA Ice Bridge Project—the largest airborne survey of Earth's polar ice to date: *https://nsidc.org/data/IDCSI2/versions/1*
https://www.nasa.gov/mission_pages/icebridge/index.html

Sea Ice Ecology

Thomas (2017)

Shipping

COMNAP (2015)

WMO (2021)

European Space Agency (ESA)

Cryosat mission: *https://www.esa.int/Applications/Observing_the_Earth/CryoSat/ESA_s_ice_mission*

Integrated Marine Observing System (IMOS)

IMOS Ocean Current: *http://oceancurrent.imos.org.au/*

Bluelink (see Excursus 2.2)

https://www.csiro.au/en/research/natural-environment/oceans/Bluelink

CSIRO (2017)

Southern Ocean Observing System (SOOS)

This international initiative of the Scientific Committee on Antarctic Research (SCAR) and the Scientific Committee on Oceanic Research (SCOR) facilitates the collection and delivery of essential observations on dynamics and change of Southern Ocean systems: *http://www.soos.aq/*

Newman *et al.* (2019)

15.7 References

Abdalati, W. (2006). Recent changes in high-latitude glaciers, ice caps and ice sheets. *Weather*, 61(4), 95–101.

ACE CRC (2014). *Position Analysis: Antarctic Sea Ice and Climate Change 2014*. Antarctic Climate and Ecosystems Cooperative Research Centre, Hobart. *https://wwwace.aappartnership.org.au/publication/antarctic-sea-ice-and-climate-change/*

ACE CRC (2017). *Position Analysis: The Antarctic Ice Sheet and Sea Level*. Antarctic Climate and Ecosystems Cooperative Research Centre, Hobart. *https://wwwace.aappartnership.org.au/publication/the-antarctic-ice-sheet-sea-level/*

Alley, R.B., Anandakrishnan, S., Christianson, S., Horgan, H.J., Muto, A., Parizek, B.R., Pollard, D., and Walker, R.T. (2015). Oceanic forcing of ice-sheet retreat: West Antarctica and more. *Annual Review of Earth and Planetary Sciences*, 43(1), 207–231.

Arrigo, K.R., van Dijken, G.L., Ainley, D.G., Fahnestock, M.A., and Markus,T. (2002). Ecological impact of a large Antarctic iceberg. *Geophysical Research Letters*, 29(7). *https://doi.org/10.1029/2001GL014160*

Bamber, J., and Payne, A. (Eds). (2004). Mass balance of the cryosphere. In *Observations and Modeling of Contemporary and Future Changes*. Cambridge University Press, Cambridge, UK.

Barber, D.G., and Massom, R.A. (2007). The role of sea ice in Arctic and Antarctic polynyas. pp. 1–54 in *Polynyas: Windows to the World, Elsevier Oceanography Series, 74*. (Eds: W.O. Smith and D.G. Barber). Elsevier, Amsterdam.

Bell, R.E., Chu, W., Kingslake, J., Das, I.,Tedesco, M., Tinto, K.J., Zappa, C.J., Frezzotti, M., Boghosian, A. and Lee, W.S. (2017). Antarctic ice shelf potentially stabilized by export of meltwater in surface river. *Nature*, 544(7650), 344–348. *https://doi.org/10.1038/nature22048*

Bevan, S.L., Luckman, A.J., Kuipers Munneke, P., Hubbard, B., Kulessa, B., and Ashmore, D.W. (2018). Decline in surface melt duration on Larsen C Ice Shelf revealed by the advanced scatterometer (ASCAT). *Earth and Space Science*, 5, 578–591. *https://doi.org/10.1029/2018EA000421*

Bindoff, N.L., Rintoul, S.R., and Massom, R. (2000). Polynyas and Bottom Water formation In Adélie Land, Antarctica, *Papers and Proceedings of the Royal Society of Tasmania*, 133(3), 51–56.

Bindschadler, R., Choi, H., Wichlacz, A., Bingham, R., Bohlander, J., Brunt, K., Corr, H., Drews, R., Fricker, H., Hall, M., Hindmarsh, R., Kohler, J., Padman, L., Rack, W., Rotschky, G., Urbini, S., Vornberger, P., and Young, N. (2011). Getting around Antarctica: new high-resolution mappings of the grounded and freely-floating boundaries of the Antarctic ice sheet created for the International Polar Year. *The Cryosphere*, 5, 569–588. *https://doi.org/10.5194/tc-5-569-2011*

Bintanja, R., van Oldenborgh, G., Drijfhout, S., Wouters, B., and Katsman, C.A. (2013). Important role for ocean warming and increased ice-shelf melt in Antarctic sea-ice expansion. *Nature Geoscience*, 6, 376–379. *https://doi.org/10.1038/ngeo1767*

BoM (2021). *State of the Climate 2020*. Bureau of Meteorology, Melbourne. *http://www.bom.gov.au/state-of-the-climate/cryosphere.shtml*

Budge, J.S., and Long, D.G. (2018). A comprehensive database for Antarctic iceberg tracking using scatterometer data. *IEEE Journal of Selected Topics in Applied Earth Observations and Remote Sensing*, 11(2), 434–442. doi:10.1109/JSTARS.2017.2784186

COMNAP (2015). *The COMNAP Sea Ice Challenges Workshop, Hobart, Tasmania. 12–13 May 2015. Workshop Report*, Council of Managers of National Antarctic Programs. *https://www.comnap.aq/symposiums-workshops-reports*

Cuffey, K. and W.S.B. Patterson. (2010). *The Physics of Glaciers*. Academic Press.

Depoorter, M.A., Bamber, J.L., Griggs, J.A., Lenaerts, J.T., Ligtenberg, S.R., van den Broeke, M.R., and Moholdt, G. (2013). Calving fluxes and basal melt rates of Antarctic ice shelves. *Nature,* 502(7469), 89–92.

Fahnestock, M., Scambos, T., Moon, T., Gardner, A., Haran, T., and Klinger, M. (2016). Rapid large-area mapping of ice flow using Landsat 8. *Remote Sensing of Environment*, 185, 84–94, doi.org/10.1016/j.rse.2015.11.023

Fetterer, F., Knowles, K., Meier, W., Savoie, M. and Windnagel, A.K. (2017). *Sea Ice Index*. Version 2 (NSIDC, Boulder, Colorado, USA.

Fox-Kemper, B., Hewitt, H.T., Xiao, C., Aðalgeirsdóttir, G., Drijfhout, S.S., Edwards, T.L., Golledge, N.R., Hemer, M., Kopp, R.E., Krinner, G., Mix, A., Notz, D., Nowicki, S., Nurhati, I.S., Ruiz, L., Sallée, J.-B., Slangen, A.B.A, and Yu, Y. (*in press*). 2021: Ocean, Cryosphere and Sea Level Change. In *Climate Change 2021: The Physical Science Basis. Contribution of Working Group I to the Sixth Assessment Report of the Intergovernmental Panel on Climate Change*. (Eds: MassonDelmotte, V., Zhai, P., Pirani, A., Connors, S.L., Péan, C., Berger, S., Caud, N., Chen, Y., Goldfarb, L., Gomis, M.I., Huang, M., Leitzell, K., Lonnoy, E., Matthews, J.B.R., Maycock, T.K., Waterfield, T., Yelekçi, O., Yu, R., and Zhou, B.). Cambridge University Press.

Fraser, A.D., Massom, R.A., Michael, K.J., Galton-Fenzi, B.K., and Lieser, J.L. (2012). East Antarctic landfast sea-ice distribution and variability, 2000–2008. *Journal of Climate*, 25, 1137–1156.

Fraser, A.D., Massom, R.A., Ohshima, K.I., Willmes, S., Kappes, P.J., Cartwright, J., and Porter-Smith, R. (2020). High-resolution mapping of circum-Antarctic landfast sea ice distribution, 2000–2018. *Earth System Science Data*, 12, 2987–2999. *https://doi.org/10.5194/essd-12-2987-2020*

Fretwell, P., Pritchard, H.D., Vaughan, D.G., Bamber, J.L., Barrand, N.E., Bell, R., Bianchi, C., Bingham, R.G., Blankenship, D.D., Casassa, G., Catania, G., Callens, D., Conway, H., Cook, A.J., Corr, H.F.J., Damaske, D., Damm, V., Ferraccioli, F., Forsberg, R., Fujita, S., Gim, Y., Gogineni, P., Griggs, J.A., Hindmarsh, R.C. A., Holmlund, P., Holt, J.W., Jacobel, R.W., Jenkins, A., Jokat, W., Jordan, T., King, E.C., Kohler, J., Krabill, W., Riger-Kusk, M., Langley, K.A., Leitchenkov, G., Leuschen, C., Luyendyk, B.P., Matsuoka, K., Mouginot, J., Nitsche, F.O., Nogi, Y., Nost, O.A., Popov, S.V., Rignot, E., Rippin, D.M., Rivera, A., Roberts, J., Ross, N., Siegert, M.J., Smith, A.M., Steinhage, D., Studinger, M., Sun, B., Tinto, B.K., Welch, B.C., Wilson, D., Young, D.A., Xiangbin, C., and Zirizzotti, A. (2013). Bedmap2: improved ice bed, surface and thickness datasets for Antarctica. *The Cryosphere*, 7, 375–393. *https://doi.org/10.5194/tc-7-375-2013*

Gardner, A.S., Moholdt, G., Scambos, T., Fahnstock, M., Ligtenberg, S., van den Broeke, M., and Nilsson, J. (2018). Increased West Antarctic and unchanged East Antarctic ice discharge over the last 7 years. *The Cryosphere*, 12, 521–547. *https://doi.org/10.5194/tc-12-521-2018*

Giles, A.B., Massom, R.A., and Lytle, V.I. (2008a). Fast ice distribution in East Antarctica during 1997 and 1999 determined using Radarsat data. *Journal of Geophysical Research*, 113, C02S14. *https://doi.org/10.1029/2007JC004139*

Giles, K.A., Laxon, S.W., and Worby, A.P. (2008b). Antarctic sea ice elevation from satellite radar altimetry. *Geophysical Research Letters*, 35, L03503. *https://doi.org/10.1029/2007GL031572*

Giles, A.B., Massom, R.A., and Warner, R.C. (2009). A method for sub-pixel scale feature-tracking using Radarsat images applied to the Mertz Glacier Tongue, East Antarctica. *Remote Sensing of Environment,* 113, 1691–1699.

Goldstein, R.M., Engelhardt, H., Kamb, B., and Frolich, R.M. (1993). Satellite radar interferometry for monitoring ice sheet motion: Application to an Antarctic ice stream. *Science*, 262(5139), 1525–1530. *https://www.science.org/doi/10.1126/science.262.5139.1525*

Gourmelen, N., Escorihuela, M.J., Shepherd, A., Foresta, L., Muir, A., Garcia-Mondejar, A., Roca, M., Baker, S.G., and Drinkwater, M.R. (2017). CryoSat-2 swath interferometric altimetry for mapping ice elevation and elevation change. *Advances in Space Research*, 62(6), 1226–1242. *https://doi.org/10.1016/j.asr.2017.11.014*

Haran, T., J. Bohlander, T. Scambos, T. Painter, and M. Fahnestock. (2014). *MODIS Mosaic of Antarctica 2008–2009 (MOA2009) Image Map*. National Snow and Ice Data Center, Boulder, Colorado USA. *http://dx.doi.org/10.7265/N5KP8037*

Hobbs W., Massom, R., Stammerjohn, S., Reid, P., Williams, G., and Meier, W. (2016). A Review of recent changes in Southern Ocean sea ice, their drivers and forcings. *Global and Planetary Change*, 143, 228–250. *https://doi.org/10.1016/j.gloplacha.2016.06.008*

Holland, P.R. (2014). The seasonality of Antarctic sea ice trends. *Geophysical Research Letters*, 41(12), 4230–4237. *https://doi.org/10.1002/2014GL060172*

Holland, P.R., and Kwok, R. (2012). Wind-driven trends in Antarctic sea-ice drift. *Nature Geoscience*, 5, 872–875.

IMBIE Team (2018). Mass balance of the Antarctic Ice Sheet from 1992 to 2017. *Nature,* 558, 219–222.

Joughin, I., Smith, B.E., and Medley, B. (2014). Marine ice sheet collapse potentially under way for the Thwaites Glacier Basin, West Antarctica. *Science*, 344(6185), 735–738. *https://doi.org/10.1126/science.1249055*

Kacimi, S., and Kwok, R. (2020). The Antarctic sea ice cover from ICESat-2 and CryoSat-2: freeboard, snow depth and ice thickness. *The Cryosphere*, 14, 4453–4474.

Kennicutt, M., Chown, S.L., Cassano, J., Liggett, D., Massom, R., Peck, L., Rintoul, S., Storey, J., Vaughan, D., Wilson, T., and Sutherland, W.J. (2014). Six priorities for Antarctic science. *Nature*, 512, 23–25. *https://doi.org/10.1038/512023a*

Key, J. R., Mahoney, R., Liu, Y., Romanov, P., Tschudi, M., Appel, I., Maslanik, J., Baldwin, D., Wang, X., and Meade, P. (2013). Snow and ice products from Suomi NPP VIIRS, *Journal of Geophysical Research: Atmospheres*, 118, 12816–12830. *https://doi.org/10.1002/2013JD020459*

Kurtz, N. T., and Markus, T. (2012). Satellite observations of Antarctic sea ice thickness and volume, *Journal of Geophysical Research*, 117, C08025. doi:10.1029/2012JC008141

Kurtz, N., Studinger, M., Harbeck, J., Onana, V., and Farrell, S. (2012, updated 2015). *IceBridge Sea Ice Freeboard, Snow Depth, and Thickness, Version 1*. NASA National Snow and Ice Data Center Distributed Active Archive Center, Boulder, Colorado USA. *https://doi.org/10.5067/7XJ9HRV50O57*

Kwok, R. (2010). Satellite remote sensing of sea-ice thickness and kinematics: A review. *Journal of Glaciology*, 56(200), 1129–1140. *https://doi.org/10.3189/002214311796406167*

Kwok, R., and Maksym, T. (2014). Snow depth of the Weddell and Bellingshausen sea ice covers from IceBridge surveys in 2010 and 2011: An examination. *Journal of Geophysical Research: Oceans*, 119, 4141–4167. *https://doi.org/10.1002/2014JC009943*

Kwok, R., and Rothrock, D.A. (2009). Decline in Arctic sea ice thickness from submarine and ICESat records: 1958–2008, *Geophysical Research Letters*, 36, L15501. doi:10.1029/2009GL039035

Kwok, R., Pang, S.S., and Kacimi, S. (2017). Sea ice drift in the Southern Ocean: regional patterns, variability, and trends. *Elementa: Science of the Anthropocene*, 5, 32. *http://doi.org/10.1525/elementa.226*

Li, X., Ouyang, L., Hui, F., Cheng, X., Shokr, M., and Heil, P. (2018). An Improved Automated Method to Detect Landfast Ice Edge off Zhongshan Station Using SAR Imagery. *IEEE Journal of Selected Topics in Applied Earth Observations and Remote Sensing*, 11, 4737–4746.

Liu, H., Wang, L., and Jezek, K. (2006). Spatio-temporal variations of snow melt zones in Antarctic Ice Sheet derived from satellite SMMR and SSM/I data (1978–2004), *Journal of Geophysical Research*, 111, 1–20, F01003. *https://doi.org/10.1029/2005JF000318*

Long, D.G. (2008). Microwave sensors—Active and passive. In: *Manual of Remote Sensing, Volume 3: Remote Sensing for the Earth Sciences*. (Eds: R.A. Ryerson and A.N. Rencz). John Wiley and Sons, Hoboken, New Jersey, USA.

Lubin, D., and Massom, R.A. (2006). *Polar Remote Sensing. Volume 1: Atmosphere and Polar Oceans*. Praxis/Springer, Chichester, UK, and Berlin, Germany. 756 p.

Luckman, A., Elvidge, A., Jansen, D., Kulessa, B., Kuipers Munneke, P., King, J., and Barrand, N. (2014). Surface melt and ponding on Larsen C Ice Shelf and the impact of föhn winds. *Antarctic Science*, 26(6), 625–635. *https://doi.org/10.1017/S0954102014000339*

McMillan, M., Shepherd, A., Sundal, A., Briggs, K., Muir, A., Ridout, A., Hogg, A., and Wingham, D. (2014). Increased ice losses from Antarctica detected by CryoSat-2. *Geophysical Research Letters,* 41, 3899–3905. *https://doi.org/10.1002/2014GL060111*

Maksym, T., Stammerjohn, S.E., Ackley, S., and Massom, R. (2012). Antarctic sea ice—A polar opposite? *Oceanography*, 25(3), 140–151. *http://dx.doi.org/10.5670/oceanog.2012.88*

Markus, T., Neumann, T., Martino, A., Abdalati, W., Brunt, K., Csatho, B., Farrell, S., Fricker, H., Gardner, A., Harding, D., Jasinski, M., Kwok, R., Magruder, L., Lubin, D., Luthcke, S., Morison, J., Nelson, R., Neuenschwander, A, Palm, S, Popescu, S, Shum., C, K., Schutz, B. E., Smith, B., Yang, Y. K., Zwally, J., (2017). The Ice, Cloud, and land Elevation Satellite-2 (ICESat-2): Science requirements, concept, and implementation. *Remote Sensing of Environment*, 190, 260–273. *https://doi.org/10.1016/j.rse.2016.12.029*

Massom, R.A. (2006). Remote Sensing. In *Encyclopedia of Antarctica Volume 2* (Ed: B. Riffenburgh). Routledge, New York, pp. 790–796.

Massom, R.A. (2009). Principal Uses of Remote Sensing in Sea-Ice Field Research. In *Handbook on Field Techniques in Sea-Ice Research* (Eds: H. Eicken *et al.*,). University of Alaska Press, Fairbanks, USA, pp. 405–466.

Massom, R.A., and Lubin, D. (2006). *Polar Remote Sensing. Volume 2: Ice Sheets*. Praxis/Springer, Chichester, UK, and Berlin, Germany. 426 p.

Massom, R.A. and Stammerjohn, S.E. (2010). Antarctic sea ice change and variability—Physical and ecological implications. *Polar Science*, 4, 149–186.

Massom, R.A., H. Eicken, C. Haas, M.O. Jeffries, M.R. Drinkwater, M. Sturm, A.P. Worby, X. Wu, V.I. Lytle, S. Ushio, K. Morris, P.A. Reid, S. Warren, and I. Allison. (2001a). Snow on Antarctic sea ice. *Reviews of Geophysics*, 39(3), 413–445.

Massom, R.A., Hill, K., Lytle, V.I., Worby, A., and Allison, I. (2001b). Effects of regional fast-ice and iceberg distributions on the behaviour of the Mertz Glacier Polynya, East Antarctica. *Annals of Glaciology*, 33, 391–398.

Massom, R.A., Stammerjohn, S.E., Smith, R.C., Pook, M.J., Iannuzzi, R.A., Adams, N., Martinson, D.G., Vernet, M., Fraser, W.R., Quetin, L.B., Ross, R.M., Massom, Y., and Krouse, H.R. (2006). Extreme anomalous atmospheric circulation in the West Antarctic Peninsula region in austral spring and summer 2001/2, and its profound impact on sea ice and biota. *Journal of Climate*, 19, 3544–3571.

Massom, R.A., Hill, K., Barbraud, C., Adams, N., Ancel, A., Emmerson L., and Pook, M.J. (2009). Fast ice distribution in Adélie Land, East Antarctica: Interannual variability and implications for emperor penguins (*Aptenodytes forsteri*). *Marine Ecology Progress Series*, 374, 243–257.

Massom, R.A., Giles, A.B., Fricker, H.A., Warner, R.C., Legresy, B., Hyland, G., Young, N., and Fraser, A.D. (2010). Examining the interaction between multi-year landfast sea ice and the Mertz Glacier Tongue, East Antarctica: Another factor in ice sheet stability? Journal of Geophysical Research, 115, C12027. *https://doi.org/10.1029/2009JC006083*

Massom, R.A., Reid, P., Stammerjohn, S., Raymond, B., Fraser A., and Ushio, S. (2013). Change and variability in East Antarctic sea ice seasonality, 1979/80–2009/10. *PloS ONE*, 8(5), e64756. *https://doi.org/10.1371/journal.pone.0064756*

Massom, R.A., Scambos, T.A., Bennetts, L.G., Reid, P., Squire, V.A., and Stammerjohn, S.E. (2018). Antarctic ice shelf disintegration triggered by sea ice loss and ocean swell. *Nature,* 558, 383–389.

Meredith, M.P., and Brandon, M.A. (2016). Oceanography and Sea ice In the Southern Ocean. In *Sea Ice*, 3rd edn (Ed: D.N. Thomas). Wiley-Blackwell, New York (USA) and Oxford (UK), pp. 216–238.

Mouginot, J., Rignot, E., and Scheuchl, B. (2014). Sustained increase in ice discharge from the Amundsen Sea Embayment, West Antarctica, from 1973 to 2013. *Geophysical Research Letters*, 41, 1576–1584. *https://doi.org/10.1002/2013GL059069*

NAS (2017). *Antarctic Sea Ice Variability in the Southern Ocean-Climate System: Proc. Of a Workshop*. The National Academies Press, National Academies of Sciences, Engineering, and Medicine, Washington, DC. doi:10.17226/24696. *https://www.nap.edu/catalog/24696/antarctic-sea-ice-variability-in-the-southern-ocean-climate-system*

NASA (2019). *IceBridge Mission* webpage, National Aeronautical and Space Agency: *https://www.nasa.gov/mission_pages/icebridge/index.html*

Newman, L., Heil, P., Trebilco, R., Katsumata, K., Constable, A., van Wijk, E., Assmann, K., Beja, J., Bricher, P., Coleman, R., Costa, D., Diggs, S., Farneti, R., Fawcett, S., Gille, S.T., Hendry, K.R., Henley, S., Hofmann, E., Maksym, T., Mazloff, M., Meijers, A., Meredith, M.M., Moreau, S., Ozsoy, B., Robertson, R., Schloss, I., Schofield, O., Shi, J., Sikes, E., Smith, I.J., Swart, S., Wahlin, A., Williams, G., Williams, M.J.M., Herraiz-Borreguero, L., Kern, S., Lieser, J., Massom, R.A., Melbourne-Thomas, J., Miloslavich, P., and Spreen, G. (2019). Delivering sustained, coordinated and integrated observations of the Southern Ocean for global impact. *Frontiers in Marine Science*, 6. *https://doi.org/10.3389/fmars.2019.00433*

Nihashi, S., and Ohshima, K.I. (2015). Circumpolar mapping of Antarctic coastal polynyas and landfast sea ice: Relationship and variability. *Journal of Climate*, 28, 3650–3670. *https://doi.org/10.1175/JCLI-D-14-00369.1*

Notz, D., and Bitz, C.M. (2016). Sea Ice in Earth System Models. In *Sea Ice*, 3rd edn (Ed: D.N. Thomas). Wiley-Blackwell, New York (USA) and Oxford (UK), pp. 239–260.

NSIDC (2019a). National Snow and Ice Data Center, *SOTC (State of the Cryosphere): Ice Sheets* webpage: *https://nsidc.org/cryosphere/sotc/ice_sheets.html*

NSIDC (2019b). National Snow and Ice Data Center. *Scientific Data Search* webpage: *https://nsidc.org/data/search/#keywords=sea+ice/sortKeys=score,,desc/facetFilters=%257B%257D/pageNumber=1/itemsPerPage=25*

Padman, L., Siegfried, M.R., and Fricker, H.A. (2018). Ocean tide influences on the Antarctic and Greenland Ice Sheets. *Reviews of Geophysics*, 56 (1), 142–184. *doi.org/10.1002/2016RG000546*

Paolo, F.S., Fricker, H.A., and Padman, L. (2015). Volume loss from Antarctic ice shelves is accelerating. *Science*, 348(6232), 327–331.

Parkinson, C.L. (2019). A 40-y record reveals gradual Antarctic sea ice increases followed by decreases at rates far exceeding the rates seen in the Arctic. *Proceedings of National Academy of Science*, 116, 14414–14423. *https://doi.org/10.1073/pnas.1906556116*.

Petrich, S. and Eicken, H. (2017). Overview of Sea Ice Growth and Properties. In *Sea Ice* 3rd edn (Ed: D.N. Thomas). Wiley, doi.org/10.1002/9781118778371.ch1

Pope, A., Wagner, P., Johnson, R., Shutler, J.D., Baeseman, J., and Newman. L. (2017). Community review of Southern Ocean satellite data needs. *Antarctic Science*, 29(2), 97–138. doi:10.1017/S0954102016000390

Post, A.L., Meijers, A.J.S., Fraser, A.D., Meiners, K.M., Ayers, J., Bindoff, N.L., Griffiths, H.J., Van de Putte, A.P., O'Brien, P.E., Swadling, K.M., and Raymond, B. (2014). Environmental Setting. Part 4 In *Biogeographic Atlas of the Southern Ocean*. (Eds: Broyer, C., Koubbi, P., Griffiths, H.J., Raymond, B., Udekem d'Acoz, C. d', Van de Putte, A.P., Danis, B., David, B., Grant, S., Gutt, J., Held, C., Hosie, G., Huettmann, F., Post, A., Ropert-Coudert, Y.) Scientific Committee on Antarctic Research, Cambridge, UK. 510 p. ISBN 978-0-948277-28-3

Pritchard, H.D., Arthern, R.J., Vaughan, D.G. and Edwards, L.A. (2009). Extensive dynamic thinning on the margins of the Greenland and Antarctic ice sheets. Nature, 461, 971–975.

Pritchard, H., Ligtenberg, S., Fricker, H., Vaughan, D.G., van den Broeke, M.R., and Padman, L. (2012). Antarctic ice-sheet loss driven by basal melting of ice shelves. *Nature*, 484, 502–505.

Reid P., and Massom R.A. (2015). Successive Antarctic sea ice extent records during 2012, 2013 and 2014. In: State of the Climate in 2014. *Bulletin of the American Meteorological Society*, 96 (7), S163–S164.

Reid, P., Stammerjohn, S., Massom, R.A., Barreira, S., Scambos, T., and Lieser, J.L. (2021). Sea ice extent, concentration, and seasonality [in *State of the Climate in 2020*]. *Bulletin of American Meteorology Society*, 102(8), S336–S338.

Rémy, F. and Parouty, S. (2009). Antarctice Ice Sheet and radar altimetry: A review. *Remote Sensing*, 1(4), 1212–1239. doi:10.3390/rs1041212. *https://www.mdpi.com/2072-4292/1/4/1212/htm*

Rignot, E., Casassa, G., Gogineni, P., Krabill, W., Rivera, A., and Thomas, R. (2004), Accelerated ice discharge from the Antarctic Peninsula following the collapse of Larsen B ice shelf. *Geophysical Research Letters*, 31, L18401. doi:10.1029/2004GL020697

Rignot, E,, Bamber, J.L., van den Broeke, M.R., Davis, C., Li, Y., van de Berg, W.J., and van Meijgaard, E. (2008). Recent Antarctic ice mass loss from radar interferometry and regional climate modelling. *Nature Geoscience*, 1, 106–110.

Rignot, E., Mouginot, J., and Scheuchl, B. (2011). Ice flow of the Antarctic Ice Sheet. *Science*, 333, 1427–1430.

Ryan, W.B.F., Carbotte, S.M., Coplan, J.O., O'Hara, S., Melkonian, A., Arko, R., Weissel, R.A., Ferrini, V., Goodwillie, A., Nitsche, F., Bonczkowski, J., and Zemsky, R. (2009). Global multi-resolution topography synthesis. Geochemistry, *Geophysics, Geosystems*, 10(3). *https://doi.org/10.1029/2008GC002332*

Scambos, T.A., Dutkiewicz, M.J., Wilson, J.C., and Bindschadler, R.A. (1992). Application of image cross-correlation to the measurement of glacier velocity using satellite image data. *Remote sensing of environment*, 42(3), 177–186.

Scambos, T., Hulbe, C., and Fahnestock, M. (2003). Climate-induced ice shelf disintegration in the Antarctic Peninsula. *Antarctic Research Series,* 79, 79–92. *https://doi.org/10.1029/AR079p0079*

Scambos, T.A., Bohlander, J.A., Shuman, C.A., and Skvarca, P. (2004). Glacier acceleration and thinning after ice shelf collapse in the Larsen B embayment, Antarctica. *Geophysical Research Letters*, 31, L18402. *https://doi.org/10.1029/2004GL020670*

Scambos, T., Sergienko, O., Sargent, A., MacAyeal, D., and Fastook, J. (2005). ICESat profiles of tabular iceberg margins and iceberg breakup at low latitudes. *Geophysical Research Letters*, 32(23). *https://doi.org/10.1029/2005GL023802*

Scambos, T., Haran, T., Fahnestock, M., Painter, T., and Bohlander, J. (2007). MODIS-based Mosaic of Antarctica (MOA) Data Sets: Continent-wide Surface Morphology and Snow Grain Size. *Remote Sensing of Environment* 111(2), 242–257. *http://dx.doi.org/10.1016/j.rse.2006.12.020*

Shepherd, A., Fricker, H.A., and Farrell, S.L. (2018). Trends and connections across the Antarctic cryosphere. *Nature*, 558, 223–232.

Siegfried, M.R., and Fricker, H. (2018). Thirteen years of subglacial lake activity in Antarctica from multi-mission satellite altimetry. *Annals of Glaciology,* 59(76pt1), 42–55. *https://doi.org/10.1017/aog.2017.36*

Slater, T., Shepherd, A., McMillan, M., Muir, A., Gilbert, L., Hogg, A.E., Konrad, H., and Parrinello, T. (2017). A new Digital Elevation Model of Antarctica derived from CryoSat-2 altimetry, *The Cryosphere*, 12(4), 1551–1562. *https://doi.org/10.5194/tc-12-1551-2018*

Smith, B., Fricker, H.A., Gardner, A.S., Medley, B., Nilsson, J., Paolo, F.S., Holschuh, N., Adusumilli, S., Brunt, K., Csatho, B., Harbeck, K., Markus, T., Neumann, T., Siegfried, M.R., and Zwally, H.J. (2020). Pervasive ice sheet mass loss reflects competing ocean and atmosphere processes. *Science*, 368(6496), 1239. *https://doi.org/10.1126/science.aaz5845*

Spreen, G. and Kern, S. (2016). Methods of satellite remote sensing of sea ice. In *Sea Ice*, 3rd edn (Ed: D.N. Thomas). Wiley-Blackwell, New York (USA) and Oxford (UK), pp. 239–260.

Stammerjohn, S., and Maksym, T. (2016). Gaining (and losing) Antarctic sea ice: variability, trends and mechanisms. In *Sea Ice* (Ed: D.N. Thomas). John Wiley and Sons, Ltd. pp. 261–289.

Stammerjohn, S., Massom, R., Rind, D., and Martinson, D. (2012). Regions of rapid sea ice change: An inter-hemispheric seasonal comparison. *Geophysical Research Letters*, 39, L06501. *https://doi.org/10.1029/2012GL050874*

Steig, E., Schneider, D., Rutherford, S., Mann, M., Comiso, J., and Shindell, D. (2009). Warming of the Antarctic ice-sheet surface since the 1957 International Geophysical Year. *Nature*, 457, 459–463. *https://doi.org/10.1038/nature07669*

Sturm, M., and Massom, R.A. (2017). Snow in the Sea Ice System: Friend or Foe? In *Sea Ice*. 3rd edn (Ed: D. Thomas). Wiley-Blackwell, New York (USA) and Oxford (UK), pp. 65–109.

Swithinbank, C.W.M. (1988). Antarctica. In *Satellite Image Atlas of Glaciers of the World*. (Eds: R.S. Williams, Jr and J.G. Ferrigno). United States Geological Survey, Washington DC, USA. B1–B278.

Tamura, T., Ohshima, K. I., Fraser, A. D., and Williams, G. D. (2016). Sea ice production variability in Antarctic coastal polynyas. *Journal of Geophysical Research: Oceans*, 121, 2967–2979. doi:10.1002/2015JC011537

Thomas, D.N. (Ed.) (2017). *Sea Ice*, 3rd edn. Wiley-Blackwell, New York (USA) and Oxford (UK). ISBN: 978-1-118-77838-8. 664 p.

Tschudi, M., Fowler, C.W., Maslanik, J.A., Stewart, J.S., and Meier, W. (2016). *EASE-Grid Sea Ice Age*. Version 3. NASA NSIDC Distributed Active Archive Center, Boulder, Colorado, USA,.

Turner, J., and Comiso, J. (2017). Solve Antarctica's sea-ice puzzle. *Comment in Nature*, 547, 19–21. *https://doi.org/10.1038/547275a*

Turner, J., Hosking, J.S., Bracegirdle, T.J., Marshall, G.J., and Phillips, T. (2015). Recent changes in Antarctic Sea ice. *Philosophical Transactions of the Royal Society of London A: Mathematical, Physical and Engineering Sciences*, 373(2045), 20140163. *https://doi.org/10.1098/rsta.2014.0163*

Turner, J., Hosking, J.S., Marshall, G.J., Phillips, and T., Bracegirdle, T.J. (2016). Antarctic sea ice increase consistent with intrinsic variability of the Amundsen Sea Low. *Climate Dynamics*, 46, 2391–2402. *https://doi.org/10.1007/s00382-015-2708-9*.

USGS (2021). *Ice, Snow, and Glaciers and the Water Cycle* webpage, United States Geological Survey website: *https://www.usgs.gov/special-topic/water-science-school/science/ice-snow-and-glaciers-and-water-cycle?qt-science_center_objects=0#qt-science_center_objects*

Vancoppenolle, M., Meiners, K.M., Michel, C., Bopp, L., Brabant, F., Carnat, G., Delille, B., Lannuzel, D., Madec, G., Moreau, S., Tison, J.-L., and van der Merwe, P. (2013). Role of sea ice in global biogeochemical cycles: emerging views and challenges. *Quaternary Science Reviews*, 79, 207–230.

Velicogna, I., and Wahr, J. (2006). Measurements of time-variable gravity show mass loss in Antarctica. *Science,* 311, 1754–1756.

Webster, M., Gerland, S., Holland, M., Hunke, E., Kwok, R., Lecomte, O., Massom, R., Perovich, D., and Sturm, M. (2018). Snow in the changing sea-ice systems. *Nature Climate Change*, 8, 946–953.

Weeks, W.F. (2010). *On Sea Ice*. University of Alaska Press, Fairbanks, Alaska, USA. 664 p.

WMO (2021). *Sea-ice Information Services in the World* (WMO-No. 574). World Meteorological Organisation, Geneva, Switzerland. *https://library.wmo.int/index.php?lvl=notice_display&id=7542#.YbFJlL1ByUk*

Wongpan, P., Meiners, K.M., Langhorne, P.J., Heil, P., Smith, I.J., Leonard, G.H., Massom, R.A., Clementson, L.A. and Haskell, T.G. (2018). Estimation of Antarctic land-fast sea ice algal biomass and snow thickness from under-ice radiance spectra in two contrasting areas. *Journal of Geophysical Research—Oceans*, 123(3), 1907–1923.

Worby, A.P., Massom, R. A., Allison, I., Lytle, V. I., and Heil, P. (1998). East Antarctic sea ice: A review of its structure, properties and drift. In *Antarctic Sea Ice Physical Processes, Interactions and Variability*, Antarctic Research Series, 74 (Ed: M.O. Jeffries). pp. 41–68. AGU, Washington D.C.

Worby A., Markus, T., Steer, A., Lytle, V., and Massom, R. (2008). Evaluation of AMSR-E snow depth product over East Antarctic sea ice using in situ measurements and aerial photography. *Journal of Geophysical Research*, 113, C05S94. *https://doi.org/10.1029/2007JC004181*

Zwally, H.J., Giovinetto, M.B., Beckley, M.A., and Saba, J.L. (2012). *Antarctic and Greenland drainage systems* webpage. NASA GSFC Cryospheric Sciences Laboratory, Greenbelt, Maryland, USA. *http://icesat4.gsfc.nasa.gov/cryo_data/ant_grn_drainage_systems.php*

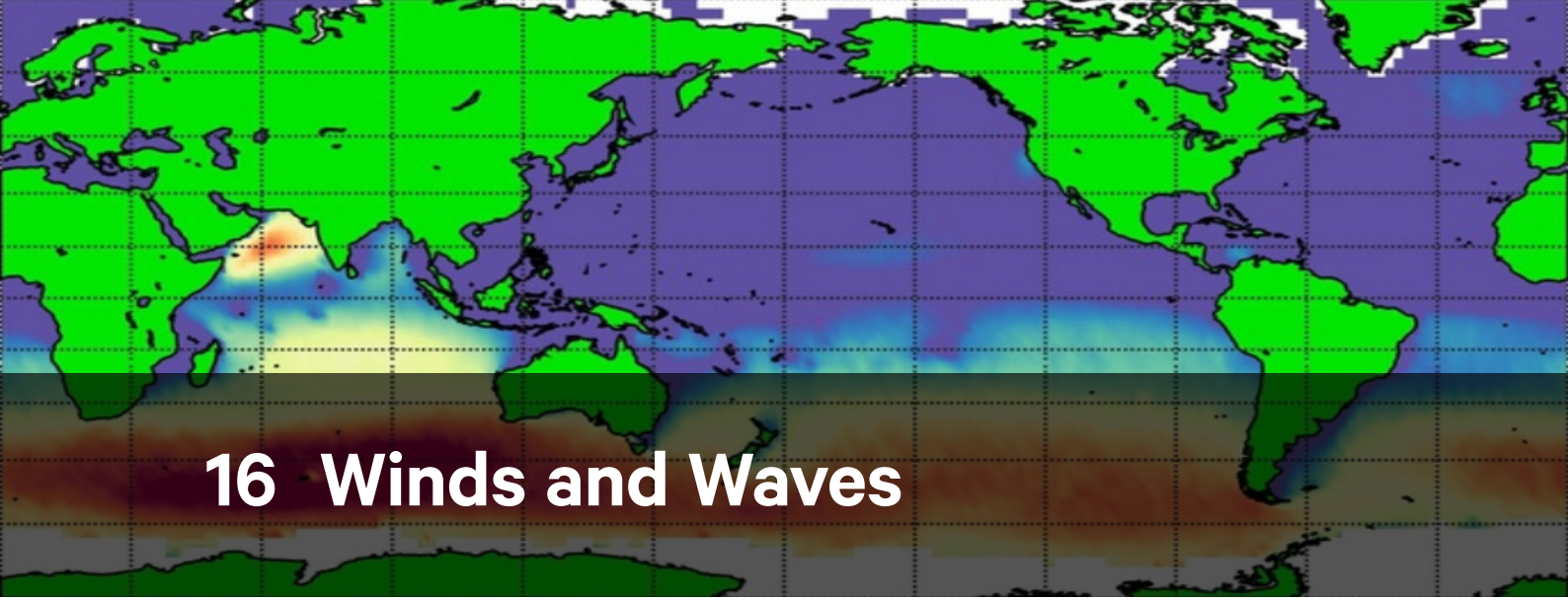

16 Winds and Waves

Mark Hemer and Salman Khan

The marine atmospheric boundary layer is the location of exchanges between the atmosphere and ocean. This exchange occurs in the form of fluxes of energy, momentum, heat, freshwater, gases, and other tracers, and is strongly modulated by interactions between surface winds (on the atmospheric side) and surface waves (on the oceanic side) across the interface (see Excursus 16.1).

Further to these Earth system interactions (see Excursus 7.2), several other marine and coastal sectors need information about marine surface winds and waves. These include sectors requiring near real time data, such as safety at sea and at the coast (see Excursus 2.1), and those requiring long time series data to aid planning and design requirements for marine and coastal Infrastructure. Thus, marine surface winds and waves represent marine data in high demand.

Few *in situ* marine wind datasets exist in the Australian region, and observations are strongly dependent on Earth Observation (EO) data, retrieved from several sensors and platforms. In the Australian region, a loosely coordinated network of *in situ* wave buoys are deployed around the Australian coast, which provide valuable near real time data (see Section 16.3.1). *In situ* buoy data also provide a basis for ground truthing of surface waves measured from satellite platforms, which in turn provide valuable spatial representation of wave fields for broad application.

In the following two sub-sections, we introduce marine winds and waves in Australian surface waters (see Section 16.1), and those EO sensors that are appropriate for observing them (see Sections 16.2 and 16.3).

Background image: Mean monthly global significant wave height for July (southern winter) derived from 33 years of satellite altimeter data (1985–2018). The colours represent wave heights from 2 m (blue) to nearly 5 m (red). This image shows the large wind waves of the Southern Ocean that propagate into the Indian and Pacific oceans as swell. Source: IMOS. Retrieved from *https://imos.org.au/news/newsitem/altimeter-wind-and-wave-database-on-aodn/*

Recommended Chapter Citation: Hemer, M.A., and Khan, S.S. (2021). Waves Ch 16 in *Earth Observation: Data, Processing and Applications. Volume 3B—Surface Waters*. CRCSI, Melbourne. pp. 311–328. ISBN 978-0-6482278-5-4.

Excursus 16.1—Marine Surface Winds and Waves

Surface marine winds are turbulent in nature, with high frequency variability between gusts and relative lulls. Winds are typically represented by average wind speed and direction over a 10-minute period, at some reference level (typically 10 m above sea level). Gusts during the 10-minute period are typically 40% greater than the average wind speed.

The surface wave field at any location can be described by a frequency-directional spectrum (see Excursus 4.2). This spectrum includes peaks of energy representing the:

- high frequency (short wavelength) 'wind-sea'—the waves generated locally by the surface winds present at the site; and
- lower frequency (longer wavelength) 'swell'—the waves that have travelled to the site, having been generated by a distant storm (see Figure 16.1).

Multiple swell peaks may exist, if waves are received from different generating systems at the same time. The complexity of such wave fields is typically summarised via several integrated parameters. The parameters include:

- Significant Wave Height (SWH or HS), to represent the energy of the wave field, and is defined as the average wave height, from trough to crest, of the highest one-third of the waves in the field (see Figure 16.2). Significant wave height can be equivalently defined as four times the square root of the zeroth-order moment (area) of the wave spectrum (H_m0).
- Mean and/or peak wave period are often used to represent the period, frequency, or length of waves. The mean wave period I is the mean of all wave periods in a time series representing the sea state, and the peak wave period (T_p), represents the period/frequency at which the spectral peak in energy occurs.
- Directional characteristics of the wave field are represented by the mean or peak wave direction. The mean wave direction (q_m) is the average of all wave directions in the wave spectrum, and peak wave direction (θ_p) is the direction at which the spectral peak in the directional energy spectrum occurs.

Figure 16.1 Example wave spectrum

This schematic shows one- and two-dimensional wave spectra at the circled location near the coast of Holland, where a long wave swell from the northern North Sea meets a local breeze crossing the southern North Sea. These two forces interact to generate a swell of relatively uniform frequency and direction, and a wind-sea with broader frequency and direction.

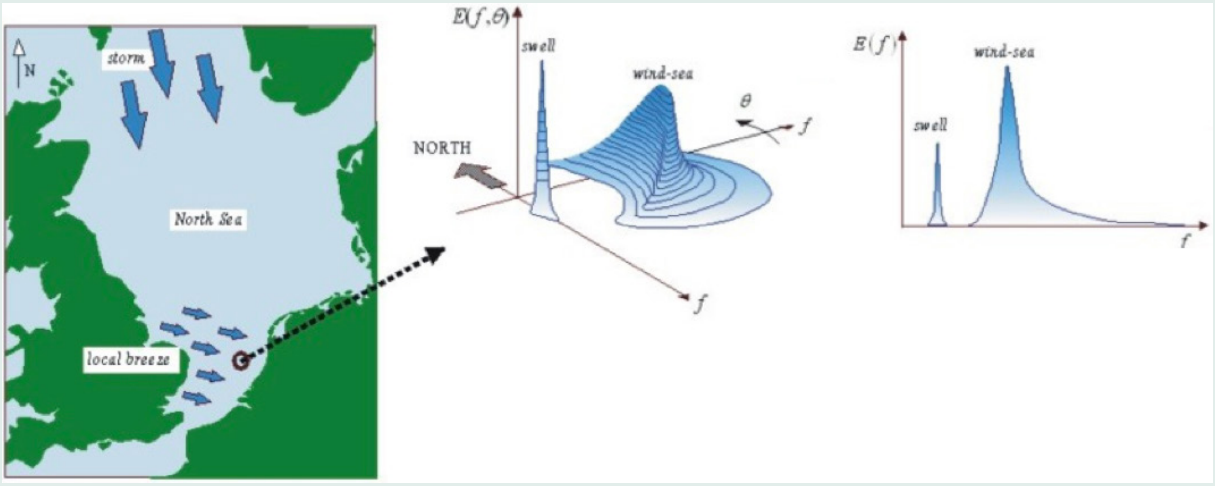

Source: ECMWF (2021) (Adapted from: Holthuijsen, 2007, Figure 3.13)

Figure 16.2 Significant wave height

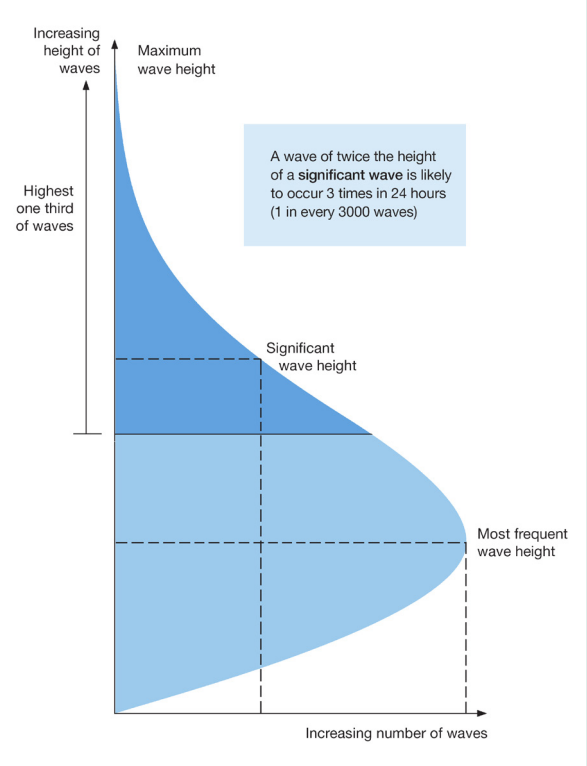

Source: BoM (2021)

For multi-modal seas, neither mean nor peak wave parameters adequately describe the wave field. In these instances, the wave spectrum may be 'partitioned', with integrated parameters defined for individual (wind-sea and swell) peaks in the spectrum.

16.1 Winds and Waves in Australian Surface Waters

The wide latitudinal variation covered by Australia's marine jurisdiction spans a broad range of extremes in marine surface winds and waves (see Section 2.1). Surface marine winds range from the strong extratropical winds of the 'Roaring Forties' (and Furious Fifties) south of the continent, through to the tropical belt, with strong seasonal trade wind/monsoon variability, and tropical cyclone (TC) systems. In the mid-latitudes, intense low pressure systems on the east coast (East Coast Lows and Tasman Lows) can drive severe wind and wave hazards along Australia's most populated coasts.

The strong winds of the Southern Ocean generate swell that propagates northwards and dominates the wave field observed on Australia's southern and western coasts (see banner image at start of Section 16). Waves along Australia's east coast are more variable, often with multiple spectral peaks received from a range of generating systems to the south (Southern Ocean and Tasman Sea) and north (Coral Sea). The waves across the north are typically much lower, except during TC events.

Australia's long, southern-facing coastline gives rise to arguably the largest wave energy resource of any country in the world (Hemer *et al.*, 2018). Wind-waves offer advantages as a source of renewable energy given their predictability and consistency, relative to wind and solar, and are being studied for viable energy generation. The Australian Marine Energy Atlas builds on more than 35 years of wind, wave, and tide data to highlight areas with highest potential for energy deployment (see Figure 16.3). Satellite-measured surface marine winds and waves have provided an invaluable validation dataset to assess the spatiotemporal variability of these resources across the Australian region.

Figure 16.3 Australian Marine Energy Atlas

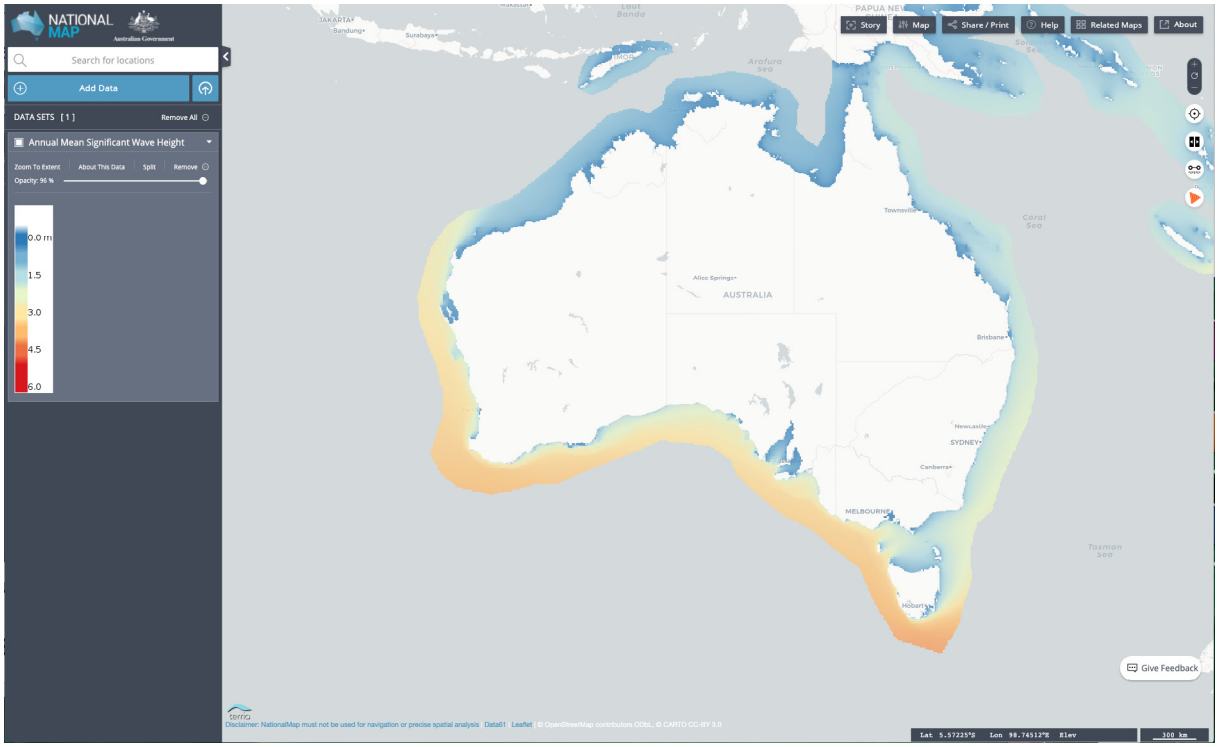

Source: NationalMap. Retrieved from: *https://nationalmap.gov.au/#share=s-daInLA798vii3unPUIMipsuweqi*

16.2 EO Sensors for Winds

A wide variety of EO sensors has been used to map and monitor marine winds (see Table 16.1). Six of these technologies are described in the sub-sections below.

Table 16.1 EO sensors relevant to water waves

SAR: Synthetic Aperture Radar

Type	Sensor	Platform	Relevance	Advantages	Disadvantages
Passive optical	Multispectral radiometer	Satellite	Wave texture, Sunglint	Global coverage, low cost	Low accuracy, coarse scale
Passive microwave	Microwave radiometer	Satellite	Ocean roughness, Surface wind stress	Frequent, global coverage	Impacted by rain
Active microwave	SAR	Satellite or airborne	Surface waves in oceans, wave forecasting, Resolution of directional swell wave spectra	All weather, so useful in tropical regions	High cost, specialised processing, spectral representation limited to long wavelength swell
	Radar altimeter	Satellite	Significant wave height, Surface wind speed,	All weather, so useful in tropical regions	Limited representation of wave field, low frequency sampling
	Scatterometer	Satellite	Surface wind speed and direction,	Frequent, global coverage	Impacted by rain and extreme winds
	Surface Waves Investigation and Monitoring (SWIM) wave scatterometer	CFOSAT	Significant wave height, Directional wave spectrum	Resolution of directional wave spectrum	Single platform (experimental)

16.2.1 *In situ* wind measurements

Few *in situ* marine wind measurements exist in the Australian region, or indeed the Southern Hemisphere. The standard method of marine wind observations is from surface buoys, deployed for weather, navigational, and industrial applications. In Australia, surface marine wind data are predominantly industry owned and operated, and associated with the oil and gas sector (on the North West Shelf, and eastern Bass Strait). In very recent times, industry data also encompasses observations collected for the Star of the South Offshore Wind Project, proposed off the coast of east Gippsland, Victoria. *In situ* surface marine wind observations for which data is openly available is limited to a single meteorological buoy, deployed as part of the Integrated Marine Observing System (IMOS) Southern Ocean Flux Station (SOFS) mooring, in the Sub-Antarctic Zone (46.7°S, 142°E) approximately 350 nautical miles (M) southwest of Tasmania. The SOFS mooring was first deployed in March 2010, and a non-continuous data record spans through to the most recent deployment in April 2021.

This lack of regional *in situ* data has driven high dependency on remotely sensed marine surface winds in studies validating Numerical Weather Prediction (NWP) models for marine surface wind prediction (e.g. Schulz *et al*., 2007). In some such studies, coastal *in situ* observations have been used for this purpose (e.g. Bender, 1996; Alves *et al*., 2002) but these are typically confounded by land effects, and poorly represent the marine winds (Schulz *et al*., 2007). To adequately calibrate and assess the quality of satellite remotely sensed winds, high quality *in situ* buoy data with broad geographic distribution, and of sufficient length, is required. The most used buoy dataset is the US National Data Buoy Centre (NDBC; NDBC, 2009) and is typically considered suitable for the process. The European Centre for Medium Range Weather Forecasts (ECMWF) also manage a buoy database, sourced from several agencies, which has been also used for this purpose (Young *et al*., 2017).

While *in situ* wind measurements for calibration of satellite data are required at a standard reference height of 10 m above sea level, wind anemometers on buoys record measurements at a variety of different heights. These measurements are then translated to 10 m reference height assuming the logarithmic (neutral) boundary layer wind profile (Young *et al*., 2017, 2020; Ribal and Young, 2020). Neutral boundary layer assumptions are made because simultaneous measurements of boundary layer stability (sea surface temperature, air temperature, humidity, etc.) are seldom available. This assumption naturally introduces a calibration error, especially at geographical locations with large stability effects (Young and Donelan, 2018), which should ideally be taken into account (Jang *et al*., 2019). However, when the calibrations are carried out across many different buoys (and locations) and over many years, a broad range of stability conditions is encountered. Hence, on a global scale, it is commonly assumed that such stability effects are averaged out in the calibration (Young *et al*., 2020).

16.2.2 Scatterometers

Satellite scatterometers are active microwave radars with the primary goal of measuring near-surface wind speed and direction over the ocean (see Section 9.6). Scatterometers operate in a side-looking geometry (never observing directly below the satellite) and illuminate the ocean surface at incidence angles typically in the range 20–70°. The electromagnetic wavelength at which these instruments operate varies from 2 cm (Ku-band: NSCAT, QuikSCAT, OSCAT-1, RapidScat, ScatSat) to 5 cm (C-band: ERS, ASCAT). At these viewing geometries and wavelengths, the microwaves are resonant (to the first order) to ocean surface roughness produced by capillary waves, which are the first wave ripples formed due to wind stress on the ocean surface (Wright, 1966). This resonance (often referred to as Bragg scattering) modulates the fraction of energy scattered back towards the radar, and has been experimentally found to be a function of surface wind speed and direction for fixed viewing geometry and instrument properties (Jones and Schroeder, 1978; Stoffelen and Anderson, 1997).

At a given wind direction (relative to the radar look geometry), the backscattered energy increases with wind speed before saturating at a certain level. However, at a given wind speed the backscatter is modulated by the relative wind direction: it has minima at cross-wind directions and maxima at upwind and downwind directions (upwind direction gives slightly stronger backscatter than downwind). Because a single backscatter value can be attributed to a number of wind speed and direction pairs, scatterometers view the ocean surface from several angles to eliminate unlikely wind direction solutions (Stoffelen and Portabella, 2006). Ideally, the solution corresponds to the true wind direction. However, noise in the observations, mostly at low wind speeds and weak backscatter, can affect the quality of fit and thereby result in incorrect directions to be selected. The next best fit is typically in approximately the opposite direction, while the next two minima are in directions roughly perpendicular to the true wind direction.

Figure 16.4 Scatterometer missions

Operating, approved, and planned scatterometer missions, promising an unprecedented amount of ocean observations in the future.

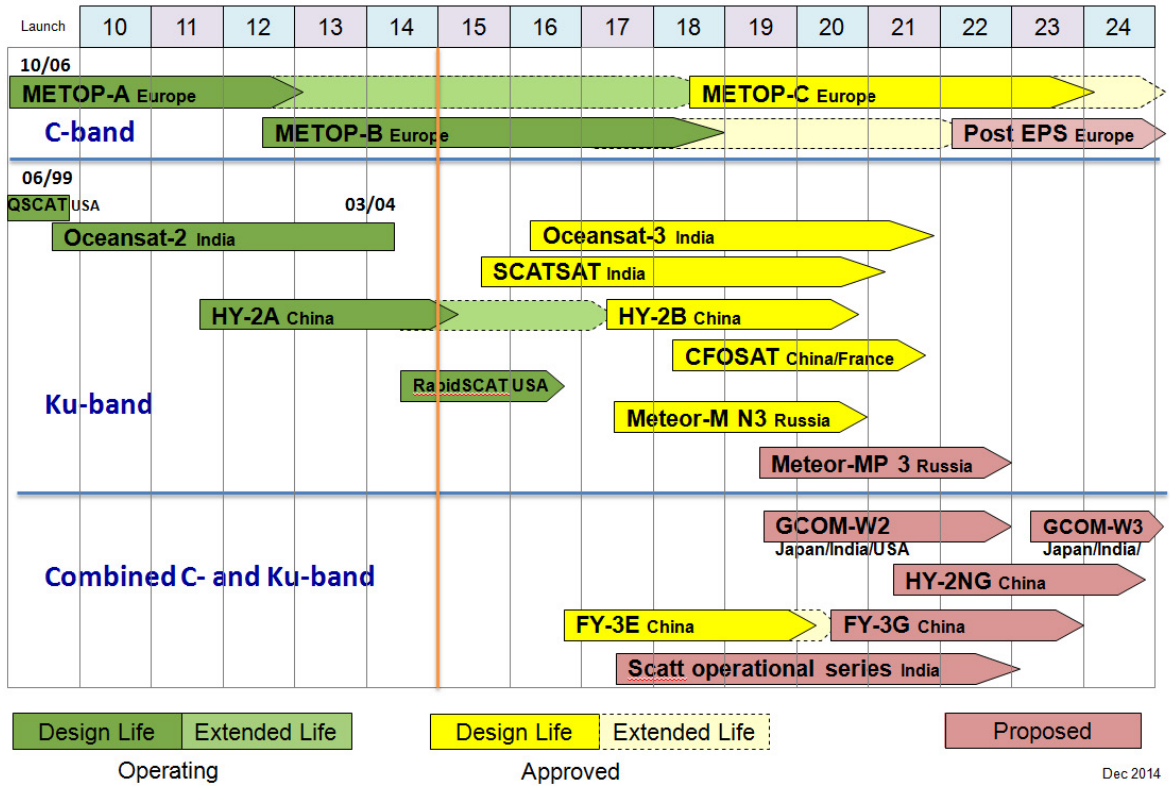

Source: CEOS (2014)

Scatterometers are wide swath instruments (~500–1800 km) with a spatial resolution of 12.5–50 km and rapid global coverage. They are the instrument of choice for global open ocean surface wind vector measurement but become less effective closer to the coast due to contamination of the large scatterometer footprint by land, islands, and other man-made structures. Scatterometer signals are also affected by rain (more in Ku-band than in C-band) and for this reason scatterometer measurements of extreme winds in TC, especially in Ku-band, must be interpreted with caution as a significant portion of the wind field in the storm is generally affected by heavy rain. Moreover, co-polarised (co-pol) scatterometers (HH/VV) lose sensitivity to high winds and start to saturate above wind speeds of ~35 m/s (the strength of Category-1 hurricanes), which makes accurate wind estimates in intense storms difficult. Scatterometers have been widely used for wind data assimilation in NWP models. QuickSCAT (1999–2009), MetOp-A (2007 onwards), MetOp-B (2012 onwards), and ScatSat have all been assimilated in NWP models at various agencies.

Many datasets acquired by satellite scatterometers are available in the public domain:

- QuikSCAT, MetOp-A, OceanSat-2, MetOp-B, and RapidScat data are available from PO.DAAC (*https://podaac.jpl.nasa.gov/*); and
- ERS-1 and ERS-2 data are available from EUMETSAT (*http://archive.eumetsat.int*) and ESA (*https://earth.esa.int*), respectively.

Recently, a multi-mission, calibrated, inter-scatterometer, cross-validated database of scatterometers winds spanning six missions over 27 years (1992–2018) has been developed by the University of Melbourne (Ribal and Young, 2020) and made publicly available through Australia's IMOS ocean data portal, the Australian Ocean Data Network (AODN). These existing databases, and the future prospects with many planned scatterometer missions (see Figure 16.4) will vastly increase the amount of ocean surface wind observations, and represent a revolution in ocean observing.

16.2.3 Passive microwave radiometers

Microwave radiometers are passive instruments that sense the ocean surface brightness temperature, which is related to the emissivity and reflective properties of the ocean surface, explained by the electromagnetic theory of radiative transfer (Ulaby *et al*., 1981; see Sections 9.2 and 14.3.1). The ocean brightness temperature is a function of the ocean roughness (including white capping, wave breaking, and foam) and therefore surface wind stress. Surface wind speed can thus be derived from ocean brightness temperatures typically assuming a neutral boundary layer and a constant value of the drag coefficient. If the radiometer is also fully polarimetric, that is, complete information about the electromagnetic polarisation state (four Stoke's parameters) is available, then the wind direction relative to radiometer look direction can also be derived (Yueh *et al*., 1999). At low wind speed (< ~8 m/s) the directional signal can be noisy, leading to large uncertainties in the wind direction (> ~30°; Bourassa *et al*., 2019).

Radiometers have a wide swath of approximately 1,000–1,400 km and a resolution of about 25–40 km. Because of their wide swath they are typically able to cover most of the Earth within a day or two. However, most traditional radiometers operate in high frequency bands such as X- and K- (SSM/I and SSMIS series, AMSR-2, AMSRE, AMSRJ, GMI, TMI, WindSat), and so are sensitive to rain (Meissner and Wentz, 2012) and also signal saturation at wind speed above ~33 m/s. Resulting daily radiometer measurements have large gaps because of rain, so radiometer-derived winds have been often referred to as fair-weather biased. Traditional radiometers are therefore not very suitable for mapping extreme winds in TC because a large portion of the wind field is also accompanied by heavy rainfall. This limitation is often utilised to derive rain rates (Meissner and Wentz, 2009), which are also delivered as standard products in addition to wind speed by different agencies (e.g. Naval Research Laboratory and Remote Sensing Systems). In some cases, the diversity of frequency bands, coupled with sophisticated geophysical retrieval algorithm design, can be employed to derive all-weather wind speeds as was done for WindSat (Meissner and Wentz, 2009). Alternatively, L-band radiometers, such as the Soil Moisture and Ocean Salinity (SMOS; Cotton *et al*., 2018) and the Soil Moisture Active Passive (SMAP; Meissner *et al*., 2017; see Section 19.7), are virtually unaffected by rain and their signal remains sensitive to wind speed as high as ~70 m/s (strength of Category-5 hurricanes) making them a suitable instrument for monitoring and tracking TC. However, they have lower sensitivity to wind speeds less than 15 m/s and their performance in this regime is worse than scatterometers.

Future missions include:

- NASA JPL's Compact Ocean Wind Vector Radiometer (COWVR) to be mounted on the International Space Station (~2023). It is similar to WindSat, but is more cost-effective and demonstrates new technology for future polarimetric microwave radiometers.
- Weather System Follow-on Microwave (WSF-M) mission is also a continuation of SSMIS and WindSat with similar accuracies to WindSat. The first of the two planned sensors will launch in 2023.
- ESA's Copernicus Imaging Microwave radiometer (CIMR; Donlon, 2019; Meijer, 2019) will have receiving channels in L-, C-, X-, Ku-, and Ka-bands, and a spatial resolution of 5–15 km (55 km at L-band) over a swath of 1920 km. This will be a follow-up of the SMOS and SMAP missions and also provide continuity of AMSR/2 low frequency channels. The prospective launch is 2025 and it is expected to have all-weather ocean wind measurement capability.

16.2.4 Satellite altimeters

The primary goal of satellite radar altimetry is the measurement of the distance between the satellite and the sea surface directly beneath the satellite, which after performing a series of corrections and averaging can be converted into sea surface height anomaly (surface currents) and also the mean sea level with respect to a reference ellipsoid (see Sections 9.5 and 12.2.1). However, opportunistic by-products of significant wave height (see Excursus 16.1) and scalar wind speed can also be derived from radar altimeter measurements.

Satellite altimeters have provided global coverage of wind speed and wave heights for more than three decades onboard polar orbiting satellites (Ribal and Young, 2019). The narrow nadir beam has a cross-track footprint width of ~10 km with typically 1 Hz (relatively high resolution) along-track sampling (every ~7 km). The ground-track separation of up to 400 km can produce considerable gaps in observation for an altimeter, but recently the presence of many altimeters has improved the density of coverage.

Although the instrument of choice for measuring global sea surface wind is a scatterometer, scalar wind speed can also be related to the Normalised Radar Cross Section (NRCS) of the sea surface at normal incidence. Several studies have formalised this relationship and some ground breaking studies were the works of Brown *et al*. (1981), Chelton and McCabe (1985), Chelton and Wentz (1986), Witter and Chelton, (1991), and Abdalla (2012).

The main idea behind deriving altimeter sea surface wind speed is the regression between satellite NRCS and reference wind measurements typically from *in situ* buoys or a NWP model. Generally, wind speed is inversely proportional to the radar backscatter (in dB) at normal incidence: it is the strongest when the sea surface is smooth (lull) and reduces as wind stress roughens the surface. However, overall this relationship is non-linear and only becomes linear as NRCS increases up to a certain threshold (NRCS ~11 dB; Abdalla, 2012; Ribal and Young, 2019), beyond which the relationship is non-linear. A piecewise function has been shown to fit this relationship to a reasonable degree of accuracy for Ku- and Ka-band (only SARAL/Altika) altimeters (Abdalla, 2012; Ribal and Young, 2019), while high wind speeds (> 18 m/s) can be modelled by alternative formulations such as that proposed in Young (1993) and Quilfen *et al.* (2011). There is evidence of the dependence of altimeter wind speed on wave heights in addition to NRCS, but this case is not considered here. Another consideration is the error present in both the altimeter NRCS and reference wind measurements. The NRCS calibration can change over time due to degradation of instrument, satellite drift, etc., while *in situ* measurements have their own errors and NWP models are a simplified version of the real world.

There have been various efforts towards consolidating altimeter databases such as Globwave (*http://cersat.ifremer.fr/about-us/projects/item/102-globwave*), Radar Altimeter Data System (RADS, *http://rads.tudelft.nl*), AVISO (*https://www.aviso.altimetry.fr*), National Satellite Ocean Application Service (NSOAS, *http://www.nsoas.org.cn/*) and National Oceanic and Atmospheric Administration (NOAA) Radar Altimeter Database System (*https://www.star.nesdis.noaa.gov/socd/lsa/RADS.php*). However none of these databases archive all altimeters since 1985. Recently, the University of Melbourne in partnership with IMOS has created a unique database that captures both wind speed and wave height information derived from 13 satellite altimeters, acquired over 33 years. Another initiative is the ESA sea state Climate Change Initiative (CCI) project archive that spans from 1991 to 2018 and captures ten altimeters (Dodet *et al.*, 2020). Such data have been used for many applications, including offshore infrastructure design, calibration/validation of numerical models, climatology, and investigation of long term trends in oceanographic wind speed and wave height (Challenor *et al.*, 1990; Young, 1999; Alves and Young, 2003; Zieger *et al.*, 2009; Young *et al.*, 2011; Young and Ribal, 2019).

16.2.5 Synthetic Aperture Radar

Synthetic Aperture Radar (SAR) is a type of active, side-looking, microwave radar that can take high resolution images of the Earth's surface during day or night and in most weather conditions (see Section 9.3). SAR achieves its high resolution by synthetically increasing the size of the antenna in the satellite orbit direction (azimuth direction) during post-processing, which significantly increases the azimuth spatial resolution. This process utilises the delay-doppler signal, combining many illuminations of a target as it passes through the radar's footprint. The range resolution of a SAR, however, is not improved by the synthetic aperture processing, and in that sense, is similar to a real aperture radar (see Volume 1A—Section 15.2).

Satellite SAR sensors have a wide range of marine applications, including sea ice monitoring and concentration, and deriving surface waves and winds. These datasets can reveal a variety of oceanographic and atmospheric phenomena such as internal waves, oceanographic and atmospheric fronts, atmospheric boundary layer vortices, bathymetric features, rain, and wave-current interactions (Monaldo and Beal, 2004; Brown *et al.*, 1981; Fu and Holt, 1982; Kudryavtsev *et al.*, 2014; Alpers *et al.*, 2016). In this subsection, we will focus on surface winds derived from SAR.

SAR instruments are sensitive to surface wind in a similar way to a scatterometer (Monaldo and Beal, 2004; Jones and Schroeder, 1978). However, unlike a scatterometer, SAR does not look at the same ocean surface from three or more aspect angles, making it necessary to constrain the solution space and invert the correct wind direction. The wind vector inversion from SAR is therefore considered an under-determined problem: one observation of NRCS but two parameters of wind speed and direction to invert. Unless wind direction can be deduced directly from the SAR image as a by-product of other phenomena such as wind streaks, wind rows, or roll vortices (Gerling, 1986), or from doppler information contained in the SAR signal (Mouche *et al.*, 2012), it must be given to the inversion algorithm from an external source such as an NWP model (Portabella *et al.*, 2002) or another matching observation (e.g. *in situ*, scatterometer, radiometer) at a comparable spatial scale. NWP input has the distinct advantage of being available at all locations and times (up to a certain distance and time difference). SAR wind speed and direction retrievals through the scatterometry approach (Portabella *et al.*, 2002) results in ocean wind vector measurements with root mean squared errors of < 2 m/s for wind speed and < 20° for wind direction (Bôas *et al.*, 2019).

Scatterometer and SAR satellite global coverages and spatial resolutions are distinctly different. Scatterometers have a much wider swath compared to SAR satellites and continuously acquire wind speed and direction data over global oceans. SAR satellites primarily map the continents and only some of the SAR satellites (ENVISAT, ERS-1/2, Sentinel-1 A/B, GF-3) have systematically sampled (although not continuously) surface waves in open ocean. Although winds can also be derived from these global records, they are discontinuously sampled every ~100 km or so. Offshore footprints of continental coverage from SAR can be processed to high resolution (as high as tens of metres) wind speed and direction maps. Usually more averaging is done to reduce the effects of speckle noise and also other small scale marine boundary layer phenomena that can manifest in SAR wind retrievals. Nevertheless, these coastal maps can potentially be extremely useful because scatterometer coverage in coastal areas is subject to land contamination due to the much larger footprint and spatial resolution (~12.5–50 km) of a real aperture scatterometer.

C-band SAR platforms are particularly suited for monitoring the ocean surface under a TC because of their high resolution and a reasonably wide swath (up to ~400 km for Sentinel-1). This unique combination makes it possible to characterise the inner core of the storm such as, the eye-wall and radius of maximum wind speed, and rain band locations, as well as more accurate measurements in coastal areas. A shortcoming is the relatively longer repeat cycle time, smaller number of satellite platforms, narrower swath compared to scatterometers, and the planning needed to task existing SAR satellites (with competing priorities) over TC within a few days of their development.

Just like their co-pol scatterometer counterparts, C-band co-pol SAR measurements of TC also lose sensitivity to high winds and saturate above 35 m/s wind speeds. This limitation has been addressed with the proposed dual-pol (co-pol and x-pol) SAR measurements (such as Radarsat-2 and Sentinel-1), where the x-pol component (HV or VH) remains sensitive to high wind speeds as high as 60 m/s (Mouche *et al.*, 2017). These results have attracted a broader audience. For example, EUMETSAT and ESA are now planning to add a cross-polarised channel to the next generation of operational scatterometer missions (that is, the next Polar System Second Generation) dedicated to the ocean surface wind measurement at medium resolution (Stoffelen *et al.*, 2017; Bôas *et al.*, 2019).

Routine coastal images over Europe and North America from Radarsat-2, Envisat, and Sentinel-1 SAR have enabled the development of high resolution coastal SAR winds databases such as the NOAA SAR winds operational data archive (NOAA Office of Satellite and Product Operations) and wind Atlas for Europe (Hasager *et al.*, 2015), yielding practical applications.

16.2.6 GNSS Reflectometry

Global Navigation Satellite System–Reflectometry (GNSS-R) exploits signals of opportunity from Global Navigation Satellite System (GNSS) constellations (see Volume 1B—Section 10.3), using a bistatic radar method (that is, transmitter and receiver in different locations; see Figure 16.5). This contrasts with monostatic methods like a scatterometer (where the transmitter and receiver are co-located on the same satellite). There are many navigation satellite systems in operation, the most common of which is the global positioning system (GPS). The GNSS-R method sees the navigation signals from these systems forward scattered off the Earth's surface in the bistatic specular direction. Dedicated GNSS-R receivers on land, on airborne platforms, or on separate satellites, detect and cross-correlate the reflected signals with direct signals from the same GNSS transmitter, to provide geophysical information about the reflecting surface (Bôas *et al.*, 2019).

Figure 16.5 GNSS-R system

The receiver satellite in Low Earth Orbit (LEO) obtains a direct signal from the GNSS satellite in its zenith antenna and a reflected one from the Earth's surface in its nadir antenna.

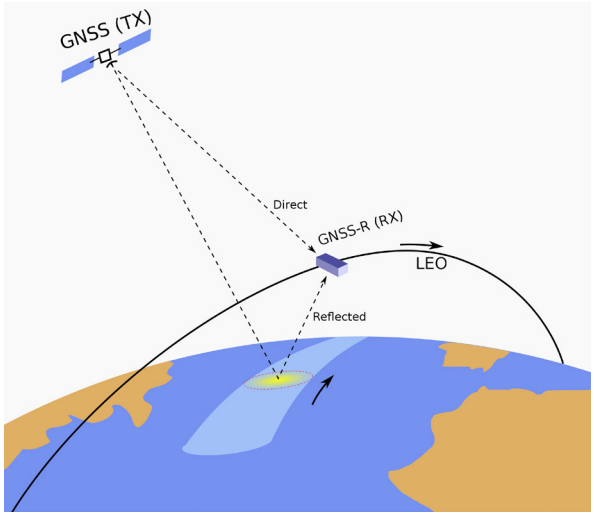

Source: Carlos Molina, Wikimedia Commons. Retrieved from *https://commons.wikimedia.org/wiki/File:GNSS-R_system_diagram.svg*

One of the earliest applications of GNSS-R was observing ocean winds (and waves; e.g. Garrison *et al.*, 1998). There are significant opportunities to exploit this technique, as the passive nature of the receiving hardware enables low power, low mass, and low cost instruments on small satellites, or low payloads on other platforms. However, GNSS-R remains an emerging method for surface marine wind observation. Significant progress has been made internationally in recent years through the UK TechDemoSat-1 (Foti *et al.*, 2017) and the NASA Cyclone Global Navigation Satellite System (CYGNSS) missions (Ruf *et al.*, 2016). Through both missions, retrieval performances are quoted to have RMSEs less than 2 m/s, for wind speeds in the 3–20 m/s range, and able to resolve fine scale structure near the walls of hurricane/cyclone systems (Foti *et al.*, 2017). However, no application of GNSS-R for surface marine wind detection in the Australian region is currently known.

16.3 EO Sensors for Waves

16.3.1 *In situ* wave measurements

The predominant observation platform for *in situ* wave measurements around Australia are moored buoys in the coastal margin (see Section 16.2.1). A semi-coordinated monitoring network of wave measuring buoys is operated by several government agencies from several states, the Commonwealth Bureau of Meteorology, AIMS, IMOS, and in recent years, some university groups (Greenslade *et al.*, 2018; see Figure 16.6). These buoys are almost exclusively located in waters shallower than 100 m water depth, in relatively close (~10 km) proximity to the coast.

While these public facilities provide critical data, their applicability for validation of EO wave data is limited, as the satellite signal is typically contaminated by the coast at these buoy sites. Satellite data processing techniques are being progressively developed to improve the near-shore application, increasing the utility of these observations. It has only been in the past couple of years (since 2018) that this whole network has been made up of directional buoys. Previously, some buoys were not able to collect directional information.

Figure 16.6 Australian wave buoy network

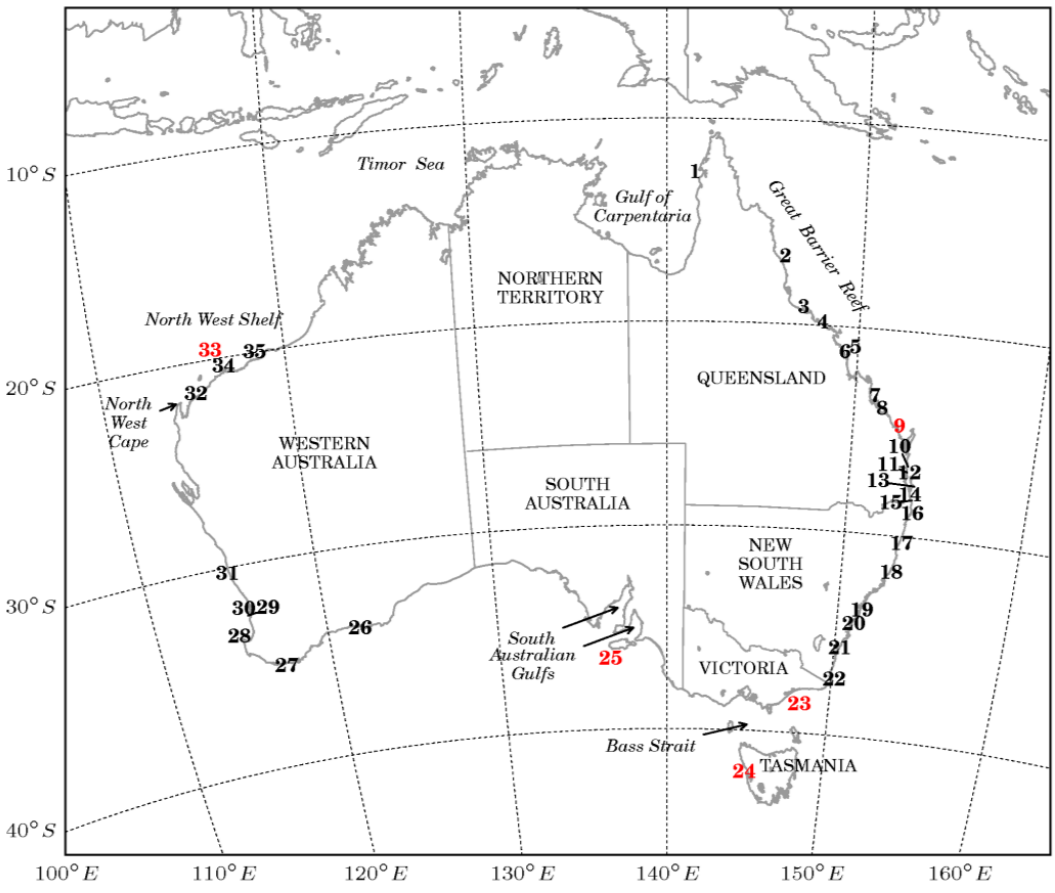

Source: Greenslade *et al.* (2018)

Figure 16.7 Global buoys for March 2016

Global map of *in situ* sensors coordinated by the Data Buoy Cooperation Panel (WMO-IOC) for March 2016. Yellow diamonds: tsunameters (52); red squares: coastal/national marine buoys (310); green triangles: tropical marine buoys (97); black triangles: fixed platforms (103); blue circles: drifting buoys (1,523)

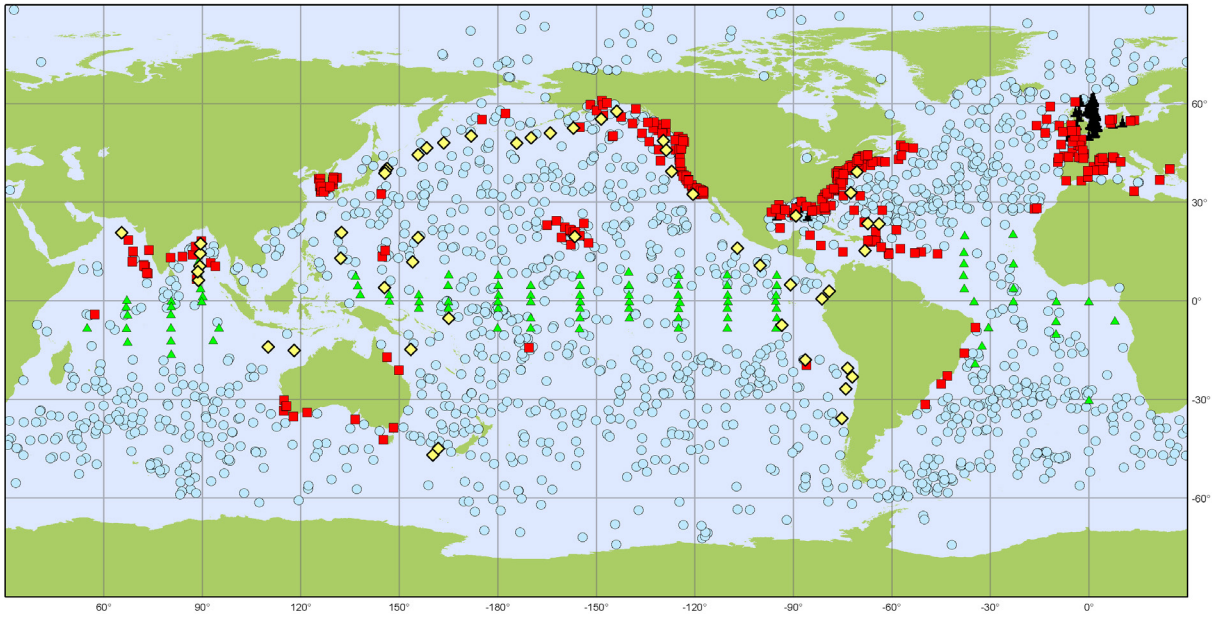

Source: WMO-IOC Data Buoy Cooperation Panel. Retrieved from *https://www.ocean-ops.org/dbcp/network/dbcpmaps.html*

Further to the public sector observation programs, Australia's marine and coastal industries and associated service providers operate a large network of wave observing platforms. These are predominantly moored buoys, but include point measurement benthic moorings (such as Acoustic Doppler Current Profiler, ADCP, and Acoustic Doppler Velocimeter, ADV).

Deep-water wave measurements that are collected sufficiently far offshore to avoid land contamination are also available. These are typically operated by either the US NDBC or Western European nations, with valuable databases coordinated previously via the Joint Technical Commission for Oceanography and Marine Meteorology (JCOMM), and now the UN World Meteorological Organisation (WMO; see Figure 16.7). There are significant global gaps in the spatial distribution of *in situ* measurements, indicating both the value of global satellite derived wave data streams, and also the challenge of verification in some unique wave regimes (such as the Southern Ocean). Ardhuin *et al.* (2019) discuss a range of challenges associated with existing *in situ* wave measurements from moored buoys, recognising that buoys with different physical attributes respond differently, and challenge the notion that moored buoys present a valid 'ground truth'.

In recent years, cost reductions in wave buoy technology has led to the emergence of non-moored, drifting buoy measurements. This blossoming pool of data provides a dataset which is currently untapped for deep-water wave verification of EO products, but introduces further variance in the range of buoy data used as a reference.

16.3.2 Satellite altimeters

EO satellites provide an advantage over *in situ* measurements, by providing a global perspective, which is capable of sampling extreme conditions. Routine sea state measurements from satellite commenced with GEOSAT altimeter measurements in 1985, and an almost continuous record exists since then for altimeter-derived wave conditions. Satellite measurements of wave conditions quickly demonstrated their benefits for resolving global wave conditions, being robust, and sampling through extreme conditions (Young, 1993, 1999; Ardhuin *et al.*, 2019). The limited sampling of satellites however does mean that particular synoptic scale events (such as storms and cyclones) can be easily missed. This limitation is less of an issue when multiple missions are simultaneously operational. The most robust satellite-based measurement of sea state is the significant wave height derived from satellite altimeter wave forms, as a by-product of sea surface height measurements (see Excursus 16.1).

The main oceanographic objective of satellite radar altimetry is to measure the distance between the satellite and the sea surface, by measuring the time for an emitted pulse to reflect off the sea surface at nadir and return to the satellite (see Sections 9.5 and 16.2.4). Echoes reflected back from the wavy surface are registered in time and assembled as radar power signals called waveforms. These waveforms depict the distribution of wave amplitude in the field of view, with a peaked waveform corresponding to low sea state conditions, and a broad waveform corresponding to high sea state conditions. Waveforms are typically averaged, and formed at a rate of 20 Hz. This provides a relatively noisy product, and in order to smooth this noise, HS values are typically averaged to provide a 1 Hz product, which averages data to an approximately 7 km along-track resolution. Although measurements are assigned a longitude/latitude location, the footprint spans over 10 km in diameter, and the resultant HS value is a weighted average over this area.

Altimeters are capable of measuring high extremes, but have difficulty resolving low wave heights below 1 m (Bôas *et al*., 2019). In addition to wave height, altimeters provide a measure of backscatter strength. With calibration, this variable has been used to provide estimates of the mean square slope of the sea surface (Nouguier *et al*., 2016) and wave period (Gommenginger *et al*., 2003).

16.3.3 SAR imagery

Ocean surface waves are one of the features easily visible in SAR images because of the high resolution of SAR compared to the scale of the observed surface waves, and also because the radar signal backscattered toward the radar (due to ocean surface roughness at the scale of capillary waves) is modulated by waves at longer scales (see Section 16.2.5). In fact, longer ocean waves become visible in SAR images because they modulate ocean surface backscatter at Bragg wavelengths. Swells are therefore often well resolved by SAR and are consistent with *in situ* buoy observations (Collard *et al*., 2009) and wave models (Khan *et al*., 2021).

The synthetic aperture post-processing with which a SAR attains a high resolution in azimuth direction (up to a few metres) works well for stationary surfaces (stationary relative to the synthetic aperture integration time of ~0.5 sec) such as land. But, for a moving ocean surface, due to orbital motion of the high frequency surface waves, a similarly high spatial resolution cannot be achieved. This degradation can be up to the order of a couple of hundred metres in the azimuth direction depending on the radar parameters and observation geometry, and varies based on the relative angle between satellite flight direction and wave propagation direction. Generally speaking, SAR cannot image waves shorter than this cut-off wavelength.

SAR can measure directional swell spectra, resolve swell systems, and their associated wave heights, directionalities, and periods, that satellite altimeters are unable to determine. Together these satellite wave data (altimeter and SAR) provide fundamental knowledge of the generation and propagation of waves. Precision of SAR-derived wave spectra is low in environmental conditions with strong distortions from azimuth cut-off effects such as near storms (Ardhuin *et al*., 2019). In the far field, however, emitted swells are well captured by SAR. Nevertheless, SAR-derived swell spectra have been useful in improving the performance of global wave models (Aouf *et al*., 2006; Stopa *et al*., 2016), understanding the propagation of swell systems (Ardhuin *et al*., 2009) and cross-seas (Li, 2016), and are potentially an invaluable source of ocean surface wave measurements for the scientific community.

Interested readers are directed to a variety of studies aimed at deriving wave spectra from SAR imagery (Engen and Johnsen, 1995; Johnsen *et al*., 2003), and empirical methods to directly measure HS from SAR images using CWAVE method and its variations (Schulz-Stellenfleth *et al*., 2007; Li, 2016; Stopa and Mouche, 2017) and to estimate other sea state parameters such as wave energy and wave period (Schulz-Stellenfleth *et al*., 2007; Stopa and Mouche, 2017; Li and Huang, 2020), although precision is reduced compared to HS.

SEASAT (operational in 1978) carried both SAR and altimeter sensors and demonstrated global wave measurements for the first time. At present, the continuity of historical C-band SAR satellites (ERS-1, ERS-2, and ENVISAT, 1991–2012), which measured ocean surface waves globally in the wave mode, is ensured by European Copernicus Sentinel-1A and B, and Chinese GaoFen-3 SAR satellites (2014 onward). Sentinel-1 satellites are carrying forward the flagship of ERS-1 and -2 and ENVISAT SAR global wave mode measurements, and have a nominal lifetime of ~7 years. Future continuity is ensured by follow-on Sentinel-1C and -1D platforms (tentative launch after 2022).

In the Australian context, CSIRO in partnership with IMOS has recently created an Australasian SAR wave spectra database (Khan *et al*., 2021) from Sentinel-1 A and B observations since the start of the respective missions (see Figure 16.8). The aim of this database is to provide an observational source of wave spectra data, which is accurate and easy to use to support research and the scientific community, and to foster uptake of satellite-derived surface wave data.

Figure 16.8 Australasian SAR database

a. Sentinel-1A observations in 2.5°×2.5° bins, acquired between November 2015 and November 2019

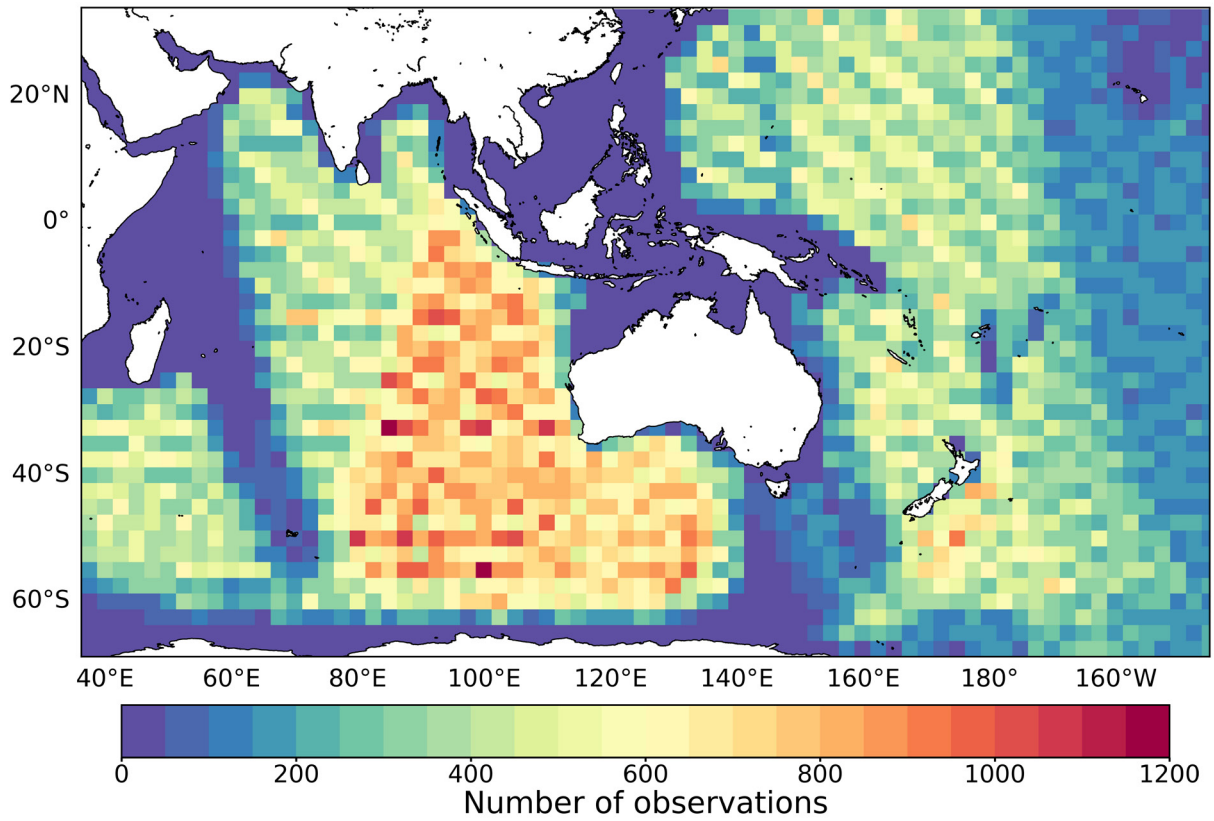

b: Sample directional ocean wave spectra at specific times on 11 September 2018. Radial distances indicate wave period and colour contours show power spectral density, a measure of energy from a particular direction.

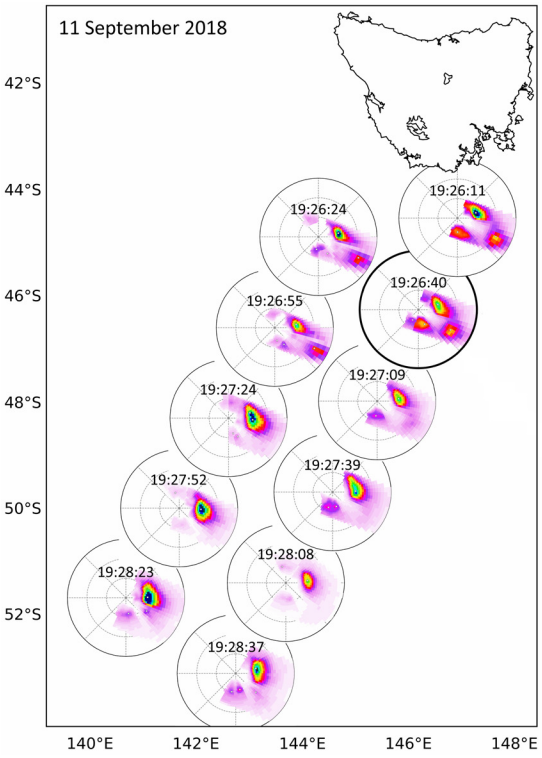

c. Enlarged wave spectrum at 19:26:40

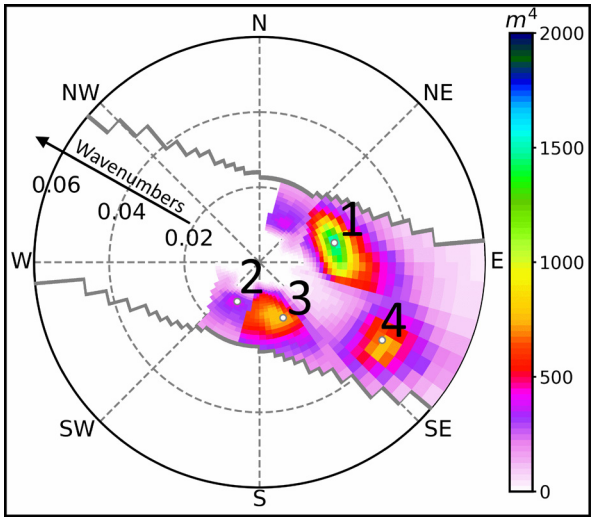

Source: Salman Khan, CSIRO

In other advancements, wave spectra derived from Sentinel-2 satellites have shown high fidelity (Kudryavtsev *et al.*, 2017), while recent airborne demonstrations by Yurovskaya *et al.* (2018) show that daylight sea state monitoring with drones is already feasible. Such efforts are opening new possibilities to combine different emerging satellite measurements (including SAR and altimeter measurements), and possibly provide validation opportunities for ocean surface processes (Ardhuin *et al.*, 2019).

16.3.4 Emerging platforms

A recent addition, and the first purpose-driven satellite platform launched to measure surface wind waves from space, is the 'wave spectrometer' Surface Waves Investigation and Monitoring (SWIM) instrument onboard the Chinese-French Oceanographic Satellite (CFOSAT; Hauser et al., 2017). CFOSAT was launched in 2018, and is now providing routine level-2 wave spectra data, with a wavelength range of 70–500 m (Hauser *et al.*, 2021). The SWIM instrument is a rotating six-beam radar at small incidence angles operating at 13.575 GHz. The SWIM instrument does not suffer from the same so-called 'azimuth cutoff' problem, being able to resolve a more complete representation of the wave spectrum. Another advantage of the CFOSAT is the availability of a wind scatterometer onboard the same platform, enabling a valuable joint datastream for wind-wave investigations.

Optical imagery has been demonstrated as having value for retrieval of directional wave spectra. Kudryavtsev *et al.* (2017) use the Sentinel-2 Multi-Spectral Instrument (MSI) measurements to demonstrate detection of ocean surface wave spectra by exploiting sunglint (see Sections 4.3 and 8.1.3). Results demonstrate high agreement with *in situ* buoy measurements, but are limited in that they cannot offer full global monitoring due to observation constraints (cloud cover and Sun position; see Volume 1B—Sections 3 and 4), but are unique in their ability to resolve coastal areas covered by Landsat and Sentinel-2 satellites (Bôas *et al.*, 2019).

16.4 Further Information

Waves

Australian Marine Energy Atlas: Hemer *et al.* (2018); accessible via National Map

Marine Science Australia: *https://www.ausmarinescience.com/marine-science-basics/waves/*

WaveFoRCE: *http://waveforce.online/*

Integrated Marine Observing System (IMOS)

Wave Buoys: *https://imos.org.au/facilities/nationalmooringnetwork/wave-buoys*

Surface Waves: *https://imos.org.au/facilities/srs/surface-waves*

Australian Ocean Data Network (AODN): *https://imos.org.au/facilities/aodn*

Ocean Current: *http://oceancurrent.imos.org.au/*

https://imos.org.au/news/newsitem/altimeter-wind-and-wave-database-on-aodn

Bluelink

https://www.csiro.au/en/Research/OandA/Areas/Oceans-and-climate/Bluelink

CSIRO

CSIRO (2017)

Ocean waves: *https://research.csiro.au/slrwavescoast/waves/*

ESA

Seastate CCI: *https://climate.esa.int/en/projects/sea-state/*

eoPortal: *https://earth.esa.int/web/eoportal/home*

CFOSat: *https://earth.esa.int/web/eoportal/satellite-missions/c-missions/cfosat*

NOAA

NOAA National Data Buoy Centre(NDBC): *https://www.ndbc.noaa.gov/*

16.5 References

Abdalla, S. (2012). Ku-Band Radar Altimeter Surface Wind Speed Algorithm. *Marine Geodesy*, 35, 276–298. doi:10.1080/01490419.2012.718676

Alpers, W., Zhang, B., Mouche, A., Zeng, K., and Chan, P.W. (2016). Rain footprints on C-band synthetic aperture radar images of the ocean—Revisited. *Remote Sensing of Environment*, 187, 169–185. doi:10.1016/j.rse.2016.10.015

Alves, J.H.G.M., Greenslade, D.J.M., and Banner, M.L. (2002). Impact of a saturation-dependent dissipation source function on operational hindcasts of wind-waves in the Australian region. *Journal of Atmospheric and Ocean Science*, 8, 239–267. doi:10.1080/10236730290026540

Alves, J.H.G.M., and Young, I.R. (2003). On estimating extreme wave heights using combined Geosat, Topex/Poseidon and ERS-1 altimeter data. *Applied Ocean Research*, 25, 167–186. doi:10.1016/j.apor.2004.01.002.

Aouf, L., Lefèvre, J.M., and Hauser, D. (2006). Assimilation of directional wave spectra in the wave model WAM: An impact study from synthetic observations in preparation for the SWIMSAT Satellite mission. *Journal of Atmospheric and Oceanic Technology*, 23, 448–463. doi:10.1175/JTECH1861.1

Ardhuin, F., Chapron, B., and Collard, F. (2009). Observation of swell dissipation across oceans. *Geophysical Research Letters*, 36, L06607. doi:10.1029/2008GL037030

Ardhuin, F., Stopa, J.E., Chapron, B., Collard, F., Husson, R., Jensen, R.E., Johannessen, J., Mouche, A., Passaro, M., Quartly, G.D., Swail, V., and Young, I. (2019). Observing sea states. *Frontiers in Marine Science*, 6, 124. doi:10.3389/fmars.2019.00124

Bender, L.C. (1996). Modification of the physics and numerics in a third-generation ocean wave model. *Journal of Atmospheric and Oceanic Technology*, 13, 726–750. doi:10.1175/1520-0426(1996)013<0726:MOTPAN>2.0.CO;2

Bôas, A.B.V., Ardhuin, F., Ayet, A., Bourassa, M.A., Brandt, P., Chapron, B., Cornuelle, B.D., Farrar, J.T., Fewings, M.R., Fox-Kemper, B., Gille, S.T., Gommenginger, C., Heimbach, P., Hell, M.C., Li, Q., Mazloff, M.R., Merrifield, S.T., Mouche, A., Rio, M.H., Rodriguez, E., Shutler, J.D., Subramanian, A.C., Terrill, E.J., Tsamados, M., Ubelmann, C., and van Sebille, E. (2019). Integrated observations of global surface winds, currents, and waves: Requirements and challenges for the next decade. *Frontiers in Marine Science*, 6, 425. doi:10.3389/fmars.2019.00425

BoM (2021). *Ruling the waves: How a simple wave height concept can help you judge the size of the sea* webpage, Bureau of Meteorology website: *http://media.bom.gov.au/social/blog/870/ruling-the-waves-how-a-simple-wave-height-concept-can-help-you-judge-the-size-of-the-sea/*

Bourassa, M.A., Meissner, T., Cerovecki, I., Chang, P., Dong, X., De Chiara, G., *et al.* (2019). Remotely sensed winds and wind stresses for marine forecasting and ocean modeling. *Frontiers in Marine Science*, 6, 443. doi:10.3389/fmars.2019.00443

Brown, G. ., Stanley, H.R., and Roy, N.A. (1981). The Wind-Speed Measurement Capability of Spaceborne Radar Altimeters. *IEEE Journal of Oceanic Engineering*, 6, 59–63. doi:10.1109/JOE.1981.1145484

CEOS (2014). *Ocean Surface Vector Wind* webpage, Committee on Earth Observation Satellites website: *https://ceos.org/ourwork/virtual-constellations/osvw/*

Challenor, P.G., Foale, S., and Webb, D.J. (1990). Seasonal changes in the global wave climate measured by the geosat altimeter. *International Journal of Remote Sensing*, 11, 2205–2213. doi:10.1080/01431169008955170

Chelton, D.B., and McCabe, P.J. (1985). A review of satellite altimeter measurement of sea surface wind speed: with a proposed new algorithm. *Journal of Geophysical Research*, 90, 4707–4720. doi:10.1029/JC090iC03p04707

Chelton, D.B., and Wentz, F.J. (1986). Further development of an improved altimeter wind speed algorithm. *Journal of Geophysical Research*, 91, 14250. doi:10.1029/jc091ic12p14250

Collard, F., Ardhuin, F., and Chapron, B. (2009). Monitoring and analysis of ocean swell fields from space: New methods for routine observations. *Journal of Geophysical Research*: *Oceans*, 114, 7023. doi:10.1029/2008JC005215

Cotton, J., Francis, P., Heming, J., Forsythe, M., Reul, N., and Donlon, C. (2018). Assimilation of SMOS L-band wind speeds: impact on Met Office global NWP and tropical cyclone predictions. *Quarterly Journal of the Royal Meteorological Society*, 144, 614–629. doi:10.1002/qj.3237

Dodet, G., Piolle, J.F., Quilfen, Y., Abdalla, S., Accensi, M., Ardhuin, F., et al. (2020). The Sea State CCI dataset v1: Towards a sea state climate data record based on satellite observations. *Earth System Science Data*, 12, 1929–1951. doi:10.5194/essd-12-1929-2020

Donlon, C. (2019). *Copernicus Imaging Microwave Radiometer (CIMR) Mission Requirements Document*. ESA. *https://cimr.eu/sites/cimr.met.no/files/documents/CIMR-MRD-v2.0-20190305-ISSUED_0.pdf*

ECMWF (2021). *The ECMWF Integrated Forecasting System* website: *https://confluence.ecmwf.int/display/FUG/2.2+Ocean+Wave+Model+-+ECWAM*

Engen, G., and Johnsen, H. (1995). SAR-Ocean Wave Inversion Using Image Cross Spectra. *IEEE Transactions on Geoscience and Remote Sensing*, 33, 1047–1056. doi:10.1109/36.406690

Foti, G., Gommenginger, C., and Srokosz, M. (2017). First Spaceborne GNSS-Reflectometry Observations of Hurricanes From the UK TechDemoSat-1 Mission. *Geophysical Research Letters*, 44, 12358–12366. doi:10.1002/2017GL076166

Fu, L.-L., and Holt, B. (1982). *Seasat Views Oceans and Sea Ice With Synthetic-Aperture Radar*. JPL Publication 81-120, NASA. *https://earth.esa.int/documents/10174/1020083/Seasat_views_Oceans_Sea_Ice_with_SAR.pdf*

Garrison, J.L., Katzberg, S.J., and Hill, M.I. (1998). Effect of sea roughness on bistatically scattered range coded signals from the Global Positioning System. *Geophysical Research Letters*, 25(13), 2257–2260. doi:10.1029/98GL51615

Gerling, T.W. (1986). Structure of the surface wind field from the Seasat SAR. *Journal of Geophysical Research*, 91, 2308–2320. doi:10.1029/JC091iC02p02308

Gommenginger, C. P., Srokosz, M.A., Challenor, P.G., and Cotton, P.D. (2003). Measuring ocean wave period with satellite altimeters: A simple empirical model. *Geophysical Research Letters*, 30(22), 02150. doi:10.1029/2003GL017743

Greenslade, D.J.M., Zanca, A., Zieger, S., and Hemer, M.A. (2018). Optimising the Australian wave observation network. *Journal of Southern Hemisphere Earth System Science*, 68, 184–200. doi:10.22499/3.6801.010

Hasager, C.B., Mouche, A., Badger, M., Bingöl, F., Karagali, I., Driesenaar, T., Stoffelen, A., Peña, A., and Longépé, N. (2015). Offshore wind climatology based on synergetic use of Envisat ASAR, ASCAT and QuikSCAT. *Remote Sensing of Environment*, 156, 247–263. doi:10.1016/j.rse.2014.09.030

Hauser, D., Tison, C., Amiot, T., Delaye, L., Corcoral, N., and Castillan, P. (2017). SWIM: The First Spaceborne Wave Scatterometer. *IEEE Transactions on Geoscience and Remote Sensing*, 55, 3000–3014. doi:10.1109/TGRS.2017.2658672

Hauser, D., Tourain, C., Hermozo, L., Alraddawi, D., Aouf, L., Chapron, B., *et al*. (2021). New Observations from the SWIM Radar On-Board CFOSAT: Instrument Validation and Ocean Wave Measurement Assessment. *IEEE Transactions on Geoscience and Remote Sensing*, 59, 5–26. doi:10.1109/TGRS.2020.2994372

Hemer, M.A., Pitman, T., McInnes, K., and Rosebrock, U. (2018) *The Australian Wave Energy Atlas Project Overview and Final Report*. CSIRO Oceans and Atmosphere, Australia. 24 p. *https://arena.gov.au/assets/2014/02/Wave-Atlas-Final-Report.pdf*

Holthuijsen, L.H. (2007). *Waves in oceanic and coastal waters*. Cambridge University Press. doi:10.1017/CBO9780511618536

Jang, J.C., Park, K.A., Mouche, A.A., Chapron, B., and Lee, J.H. (2019). Validation of Sea Surface Wind from Sentinel-1A/B SAR Data in the Coastal Regions of the Korean Peninsula. *IEEE Journal of Selected Topics in Applied Earth Observation Remote Sensing*, 12, 2513–2529. doi:10.1109/JSTARS.2019.2911127

Johnsen, H., Engen, G., Collard, F., Kerbaol, V., and Chapron, B. (2003). *Envisat ASAR Wave Mode Products —Quality Assessment and Algorithm Upgrade*.

Jones, W.L., and Schroeder, L.C. (1978). Radar backscatter from the ocean: Dependence on surface friction velocity. *Boundary-Layer Meteorology*, 13, 133–149. doi:10.1007/BF00913867

Khan, S.S., Echevarria, E.R., and Hemer, M.A. (2021). Ocean Swell Comparisons Between Sentinel-1 and WAVEWATCH III Around Australia. *Journal of Geophysical Research*: *Oceans*, 126, e2020JC016265. doi:10.1029/2020JC016265

Kudryavtsev, V., Kozlov, I., Chapron, B., and Johannessen, J.A. (2014). Quad-polarization SAR features of ocean currents. *Journal of Geophysical Research*: *Oceans*, 119, 6046–6065. doi:10.1002/2014JC010173

Kudryavtsev, V., Yurovskaya, M., Chapron, B., Collard, F., and Donlon, C. (2017). Sun glitter imagery of ocean surface waves. Part 1: Directional spectrum retrieval and validation. *Journal of Geophysical Research*: *Oceans*, 122, 1369–1383. doi:10.1002/2016JC012425

Li, X.M. (2016). A new insight from space into swell propagation and crossing in the global oceans. *Geophysical Research Letters*, 43, 5202–5209. doi:10.1002/2016GL068702

Li, X.M., and Huang, B.Q. (2020). A global sea state dataset from spaceborne synthetic aperture radar wave mode data. *Science Data*, 7, 1–12. doi:10.1038/s41597-020-00601-3

Meijer, Y. (2019). *Copernicus CO_2 Monitoring Mission Requirements Document*. ESA. *ftp://193.17.11.194/pub/EPS/out/lang/TriOpSys/ReferenceDocs/Copernicus%20CO2%20mission%20-%20MRD%20-%20v2.0%20-%20v20190927_final.pdf*

Meissner, T., and Wentz, F.J. (2009). Wind-vector retrievals under rain with passive satellite microwave radiometers. *IEEE Transactions on Geoscience and Remote Sensing*, 47, 3065–3083. *https://ieeexplore.ieee.org/document/5196732*

Meissner, T., and Wentz, F. (2012). The emissivity of the ocean surface between 6–90 GHz over a large range of wind speeds and Earth incidence angles. *IEEE Transactions on Geoscience and Remote Sensing*, 50, 3004–3026. *https://ieeexplore.ieee.org/document/6145646*

Meissner, T., Ricciardulli, L., and Wentz, F.J. (2017). Capability of the SMAP mission to measure ocean surface winds in storms. *Bulletin of American Meteorological Society*, 98, 1660–1677. *https://doi.org/10.1175/BAMS-D-16-0052.1*

Monaldo, F. M., and Beal, R. (2004). Wind Speed and Direction. Ch 13 in *Synthetic Aperture Radar Marine User's Manual* (Eds: Jackson, C.R., and Apel, J.R.). NOAA, Washington. pp. 305–320. *http://www.sarusersmanual.com/*

Mouche, A.A., Collard, F., Chapron, B., Dagestad, K.F., Guitton, G., Johannessen, J.A., Kerbaol, V., and Hansen, M.W. (2012). On the use of doppler shift for sea surface wind retrieval from SAR. *IEEE Transactions on Geoscience and Remote Sensing*, 50, 2901–2909. doi:10.1109/TGRS.2011.2174998

Mouche, A.A., Chapron, B., Zhang, B., and Husson, R. (2017). Combined Co- and Cross-Polarized SAR Measurements under Extreme Wind Conditions. *IEEE Transactions on Geoscience and Remote Sensing*, 55, 6746–6755. doi:10.1109/TGRS.2017.2732508

NDBC (2009). *Handbook of Automated Data Quality Control Checks and Procedures*. National Data Buoy Center, National Oceanic and Atmospheric Administration. *https://www.ndbc.noaa.gov/NDBCHandbookofAutomatedDataQualityControl2009.pdf*

Nouguier, F., Mouche, A., Rascle, N., Chapron, B., and Vandemark, D. (2016). Analysis of Dual-Frequency Ocean Backscatter Measurements at Ku-and Ka-Bands Using Near-Nadir Incidence GPM Radar Data. *IEEE Transactions on Geoscience and Remote Sensing*, 13, 1310–1314. doi:10.1109/LGRS.2016.2583198

Portabella, M., Stoffelen, A., and Johannessen, J.A. (2002). Toward an optimal inversion method for synthetic aperture radar wind retrieval. *Journal of Geophysical Research*: *Oceans*, 107, 1–1. doi:10.1029/2001jc000925

Quilfen, Y., Vandemark, D., Chapron, B., Feng, H., and Sienkiewicz, J. (2011). Estimating gale to hurricane force winds using the satellite altimeter. *Journal of Atmospheric and Oceanic Technology*, 28, 453–458. doi:10.1175/JTECH-D-10-05000.1

Ribal, A., and Young, I.R. (2019). 33 years of globally calibrated wave height and wind speed data based on altimeter observations. *Science Data* 6, 1–15. doi:10.1038/s41597-019-0083-9

Ribal, A., and Young, I.R. (2020). Calibration and cross validation of global ocean wind speed based on scatterometer observations. *Journal of Atmospheric and Oceanic Technology*, 37, 279–297. doi:10.1175/JTECH-D-19-0119.1

Ruf, C.S., Atlas, R., Chang, P.S., Clarizia, M.P., Garrison, J.L., Gleason, S., *et al*. (2016). New ocean winds satellite mission to probe hurricanes and tropical convection. *Bulletin of the American Meteorological Society*, 97, 385–395. doi:10.1175/BAMS-D-14-00218.1

Schulz, E.W., Kepert, J.D., and Greenslade, D.J.M. (2007). An assessment of marine surface winds from the Australian Bureau of Meteorology numerical weather prediction systems. *Weather Forecast*, 22, 613–636. doi:10.1175/WAF996.1

Schulz-Stellenfleth, J., König, T., and Lehner, S. (2007). An empirical approach for the retrieval of integral ocean wave parameters from synthetic aperture radar data. *Journal of Geophysical Research*: *Oceans*, 112, 3019. doi:10.1029/2006JC003970

Stoffelen, A., and Anderson, D. (1997). Scatterometer data interpretation: Estimation and validation of the transfer function CMOD4. *Journal of Geophysical Research*: *Oceans*, 102, 5767–5780. doi:10.1029/96JC02860

Stoffelen, A., and Portabella, M. (2006). On bayesian scatterometer wind inversion. *IEEE Transactions on Geoscience and Remote Sensing*, 44, 1523–1533. doi:10.1109/TGRS.2005.862502

Stoffelen, A., Aaboe, S., Calvet, J.C., Cotton, J., De Chiara, G., Saldaña, J.F., *et al*. (2017). Scientific Developments and the EPS-SG Scatterometer. *IEEE Journal of Selected Topics in Applied Earth Observation Remote Sensing*, 10, 2086–2097. doi:10.1109/JSTARS.2017.2696424

Stopa, J.E., and Mouche, A. (2017). Significant wave heights from Sentinel-1 SAR: Validation and applications. *Journal of Geophysical Research*: *Oceans*, 122, 1827–1848. doi:10.1002/2016JC012364

Stopa, J.E., Ardhuin, F., Babanin, A., and Zieger, S. (2016). Comparison and validation of physical wave parameterizations in spectral wave models. *Ocean Modelling*, 103, 2–17. doi:10.1016/j.ocemod.2015.09.003

Ulaby, F.T., Moore, R.K., and Fung, A.K. (1981). *Microwave remote sensing: Active and passive. Volume 1 – Microwave remote sensing fundamentals and radiometry*. *https://ntrs.nasa.gov/citations/19820039342*

Witter, D.L., and Chelton, D.B. (1991). A Geosat altimeter wind speed algorithm and a method for altimeter wind speed algorithm development. *Journal of Geophysical Research*, 96, 8853–8860. doi:10.1029/91JC00414

Wright, J.W. (1966). Backscattering from Capillary Waves with Application to Sea Clutter. *IEEE Transactions on Antennas Propagation*, 14, 749–754. doi:10.1109/TAP.1966.1138799

Young, I.R. (1993). An estimate of the Geosat altimeter wind speed algorithm at high wind speeds. *Journal of Geophysical Research*, 98, 20275–20285. doi:10.1029/93jc02117

Young, I.R. (1999). Seasonal variability of the global ocean wind and wave climate. *International Journal of Climatology*, 950, 931–950.

Young, I.R., and Donelan, M.A. (2018). On the determination of global ocean wind and wave climate from satellite observations. *Remote Sensing of Environment*, 215, 228–241. doi:10.1016/j.rse.2018.06.006.

Young, I.R., and Ribal, A. (2019). Multiplatform evaluation of global trends in wind speed and wave height. *Science*, 364, 548–552. doi:10.1126/science.aav9527

Young, I.R., Zieger, S., and Babanin, A.V. (2011). Global trends in wind speed and wave height. *Science*, 332, 451–5. doi:10.1126/science.1197219

Young, I.R., Sanina, E., and Babanin, A.V. (2017). Calibration and cross validation of a global wind and wave database of altimeter, radiometer, and scatterometer measurements. *Journal of Atmospheric and Oceanic Technology*, 34, 1285–1306. doi:10.1175/JTECH-D-16-0145.1.

Young, I.R., Kirezci, E., and Ribal, A. (2020). The global wind resource observed by scatterometer. *Remote Sensing*, 12, 2920. doi:10.3390/RS12182920

Yueh, S.H., Wilson, W.J., Dinardo, S.J., and Li, F.K. (1999). Polarimetric microwave brightness signatures of ocean wind directions. *IEEE Transactions on Geoscience and Remote Sensing*, 37, 949–959. doi:10.1109/36.752213

Yurovskaya, M., Rascle, N., Kudryavtsev, V., Chapron, B., Marié, L., and Molemaker, J. (2018). Wave spectrum retrieval from airborne sunglitter images. *Remote Sensing of Environment*, 217, 61–71. doi:10.1016/j.rse.2018.07.026

Zieger, S., Vinoth, J., and Young, I.R. (2009). Joint Calibration of Multiplatform Altimeter Measurements of Wind Speed and Wave Height over the Past 20 Years. *Journal of Atmospheric and Oceanic Technology*, 26, 2549–2564. doi:10.1175/2009JTECHA1303.1

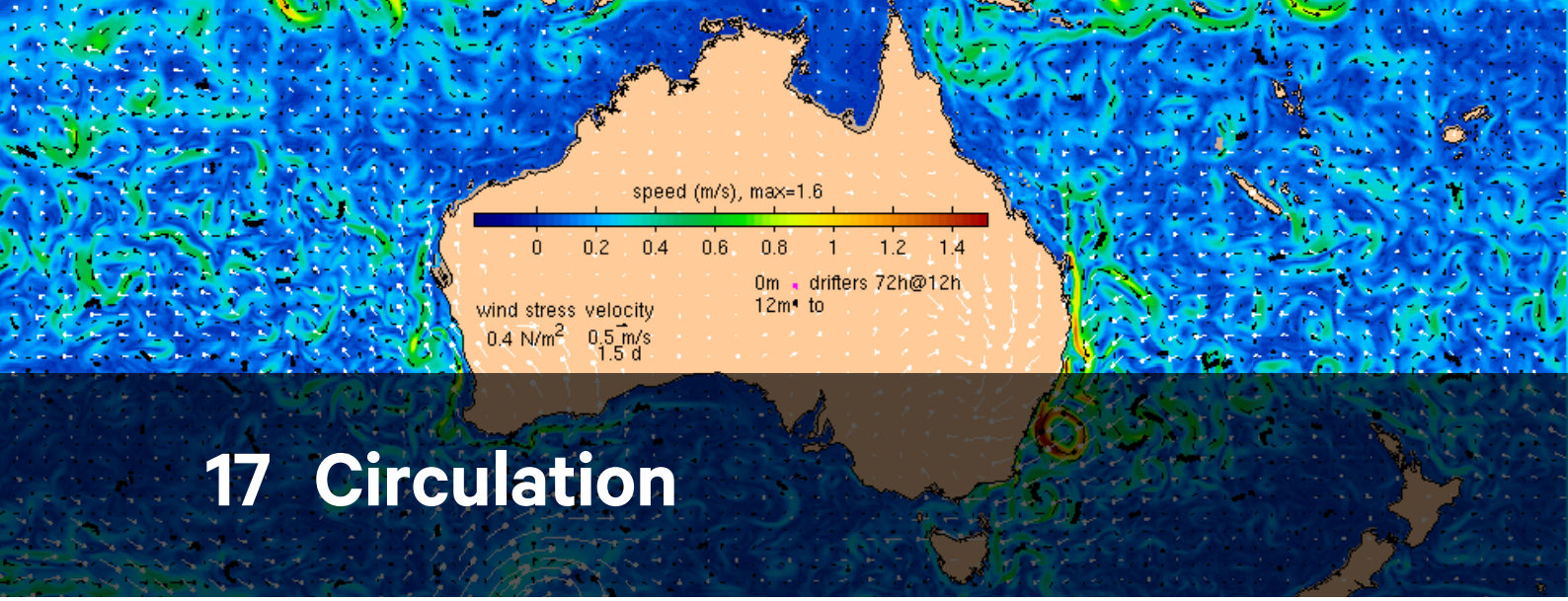

17 Circulation

David Griffin

Circulation of near-surface water (defined here as the water either within a few metres of the surface of the ocean, or within the mixed layer) occurs at a range of spatial and temporal scales. Global water circulation is driven by wind and fluxes across the ocean's surface of heat (solar input, evaporative cooling, etc) and freshwater (due to rain or evaporation). Characteristics of these drivers, in combination with the 'topography' of the seafloor, determine the size, shape, speed, and direction of ocean currents. Our current understanding of the global circulation of near-surface water is introduced in Section 1.4 and regional circulation patterns in the Australian region are described in Section 2.3. Terminology used to describe water circulation is summarised in Table 17.1.

The movement of ocean waters around the globe distributes heat and nutrients, regulates weather patterns, and stabilises climatic variations. Given the vast extent of the global ocean and its relative remoteness, it is challenging to map and monitor horizontal and vertical water circulation patterns.

This is one area where the synoptic perspective of EO datasets that have been acquired over several decades have provided insights into both regional and global patterns of water movement, particularly when teamed with automated *in situ* measurements (see Excursus 5.1).

Table 17.1 Water circulation terms

Term	Definition
Convergent	A front is described as convergent when it has two water masses approaching each other, requiring subduction (sinking) of one of these at the surface.
Current	A non-periodic, generally horizontal movement of water due to many causes such as prevalent winds, temperature differential, etc.
Divergent	A divergent front has water diverging at the surface.
Downwelling	The movement of surface waters downward generally occurs when surface waters converge or encounter the coast.
Eddy	A rotating body of water formed where currents or tidal streams pass obstructions. Others form along the edge of a current or stream, or between two adjacent flows (see Section 1.4.3). Larger eddies can be formed by baroclinic instability or barotropic instability, analogously to how weather systems are formed in the atmosphere.
Front	Regions of strong horizontal gradients in water properties (temperature, density, salinity etc).
Geostrophic flow	Balance between Coriolis force (see Excursus 1.2) and pressure gradient associated with elevation of sea level or horizontal gradient of density.
Gyre	Large system of ocean currents resulting from global wind patterns and the Earth's rotation (see Section 1.4.2)
Upwelling	An upward flow of cold, subsurface water, usually a result of divergence. Upwelling regions are typically rich in nutrients and occur near coastlines when the wind drives water away from the coast (which happens when the wind blows with the coast on the right in the Southern Hemisphere) or in the deep ocean when the curl of the wind stress is cyclonic.

Background image: This Australia-wide view of surface circulation on 23 March 2021 shows the daily average speed (see colour bar) and direction (black arrows) of water movement. White vectors show daily average wind stress. **Source:** David Griffin, CSIRO, from OceanMAPS (see Excursus 2.2).

Recommended Chapter Citation: Griffin, D.A. (2021). Circulation. Ch 17 in *Earth Observation: Data, Processing and Applications. Volume 3B—Surface Waters.* CRCSI, Melbourne. pp. 329–342. ISBN 978-0-6482278-5-4.

The 'global conveyor belt' circulates ocean waters slowly by moving warmer surface waters from the equator to the poles and returning denser polar waters to the equator at depth (see Figure 5.4). Density differences between layers in the water column result from differences in temperature and salinity (see Section 5.1.2). Colder, saltier water is denser than warmer, fresher water at any particular depth. Upwelling delivers colder and nutrient-rich water to the surface, while downwelling returns warmer water with lower density to the depths. The resultant gradients of ocean temperature and salinity are in approximate balance with the Coriolis force acting on the velocities (see Figure 5.4). This slow circulation is known as the thermohaline circulation.

Wind-driven gyres also exist at the scale of ocean basins. Their asymmetry—with greater intensity on the western side of the ocean basin—is due to the Earth's rotation. For example, the East Australian Current (EAC) is one of the great western boundary currents of the world (see Section 17.1). Thus, in broad terms, surface waters are circulated globally, regionally, and locally by two mechanisms:

- slower, density-driven, vertical mixing or 'thermohaline' circulation (see Section 5.1.2); and
- faster, wind-driven, surface movements, such as currents or eddies.

A boundary current is a permanent water circulation feature that flows along the coastline of a landmass (see Section 1.4). The dynamics of boundary currents are determined by features of the ocean basin and its adjacent coastline:

- western boundary currents, which flow around the western edge of an ocean basin (eastern side of landmass) towards the poles, are typically narrow, deep, and fast, and often dissipate energy by shedding eddies; and
- eastern boundary currents occur on the eastern side of ocean basins (western coastlines), generally flow towards the equator, are shallower, slower and wider, and frequently involve coastal upwelling.

The boundary between two distinct water (or air) masses is called a front. This means that significant differences exist in their properties, such as temperature or salinity, within a small distance. As masses move towards or away from each other, they generate convergent or divergent fronts respectively. In surface waters, convergent fronts are characterised by downwelling, whereas divergent fronts generate upwelling. Frontal dynamics can complicate the circulation of surface waters, particularly in coastal regions.

The volume of water that is moved by large scale water circulation mechanisms is measured as the volumetric flow rate and commonly expressed using the non-SI unit Sverdup (Sv; Agrawal, 2018). 1 Sv equals the volume transport of 1 million cubic metres (1 km × 1 km × 1 m) per second.

Below we describe the major water circulation patterns around the Australian land mass in terms of seasonal to interannual variability (see Section 17.1 and Excursus 17.1) and then discuss those EO sensors that are relevant to mapping and monitoring these patterns (see Section 17.2). Subsequent subsections introduce EO methods used to observe circulation patterns (see Section 17.3) and ocean fronts (see Section 17.4).

Oceanography is the study of the composition and motion of the water column and the processes which are responsible for that motion. The principal oceanographic processes influencing Australia's continental shelf waters include waves and tides as well as wind-driven and other oceanic currents. (GA, 2021)

17.1 Circulation of Australian Surface Waters

The island continent of Australia is surrounded by surface and subsurface boundary currents that flow along the continental shelf and slope (see Figure 17.1 and Section 2.3). The unique feature of the water circulation around Australia is that along both the east and west coasts, boundary currents transport warm water southward via the East Australian (EAC) and Leeuwin Currents (LC), respectively (Wijeratne *et al*., 2018). These boundary currents are enhanced through inflows from the south Pacific and south Indian Ocean basins (see Figure 2.1).

Major surface boundary currents around Australia include the Indonesian Throughflow, Holloway, Leeuwin, South Australian, Flinders, Zeehan, East Australian and Hiri currents (see Excursus 17.1). Australia's boundary currents are an important conduit for the poleward heat and mass transport and interocean water exchange in the tropics (Indonesian Throughflow; Sprintall *et al*., 2009) and the subtropics (Tasman Outflow; Hu *et al*., 2015; van Sebille *et al*., 2012).

Figure 17.1 Mean surface currents around Australia

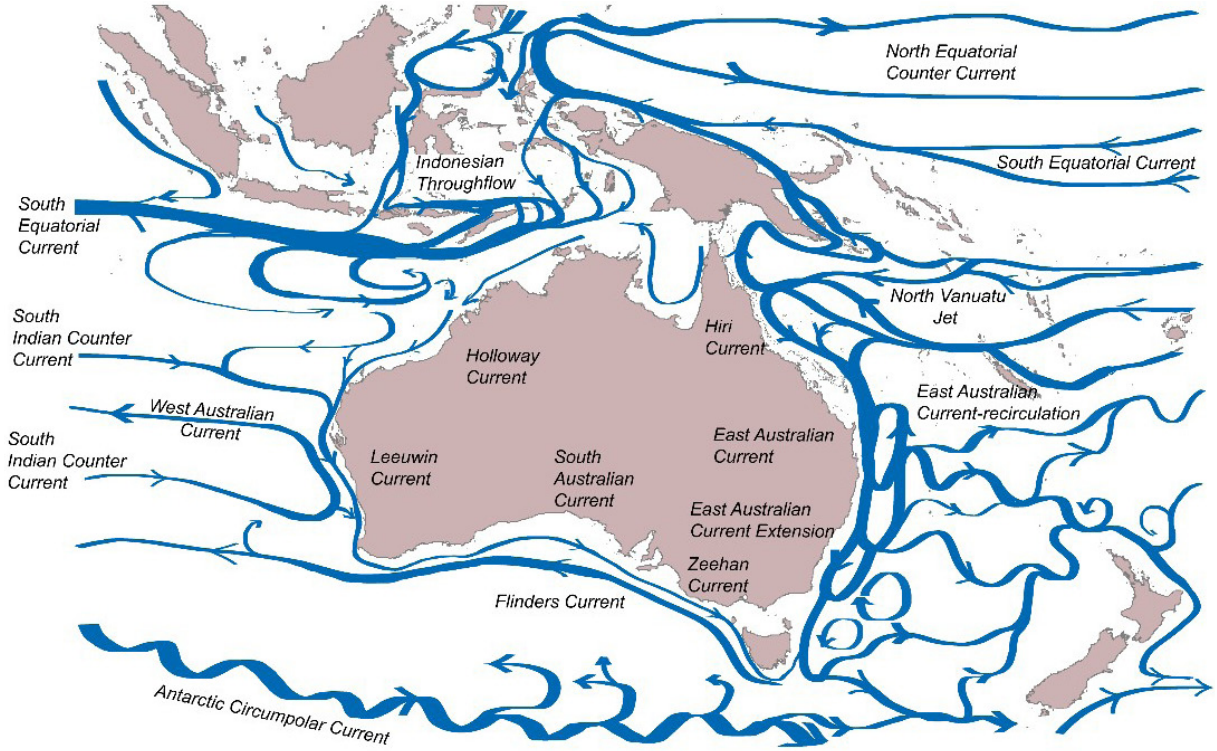

Source: Pattiaratchi and Siji (2018) Figure 1

Excursus 17.1—Major Currents around Australia

Source: Wijeratne *et al.* (2018)

As illustrated in Figure 17.1, there are several currents that transport surface waters around Australia. The names and abbreviations of those discussed in this excursus are summarised in Table 17.2.

Table 17.2 Names and abbreviations of major currents

Name	Abbreviation
Antarctic Circumpolar Current	ACC
East Australian Current	EAC
Flinders Current	FC
Indonesian Throughflow	ITF
Hiri Current	HC
Holloway Current	HLC
Leeuwin Current	LC
North Vanuatu Jet	NVJ
North Caledonia Jet	NCJ
South Australian Current	SAC
South Equatorial Current	SEC
South Indian Counter Current	SICC
West Australian Current	WAC
Zeehan Current	ZC

Indonesian Throughflow

The Indonesian Throughflow (ITF) provides a tropical connection between the Pacific and Indian Oceans and contributes to the South Equatorial Current (SEC), the major westward flow across the Indian Ocean to the eastern Indian Ocean. ITF transports 16.4 Sv (or 10^6 m^3s^{-1}) of water into the Indian Ocean. The ITF is at a maximum during the southeast monsoon (June to August) and its interannual variability is associated with El Niño-Southern Oscillation (ENSO) events with stronger flows during La Niña events (Wijeratne *et al.*, 2018).

Holloway Current

A portion of the ITF flows onto the northwestern Australian continental shelf/slope through the Holloway Current (HLC; Bahmanpour *et al.*, 2016; Wijeratne *et al.*, 2018). The HLC flows to the southwest along the shelf edge of the North West Shelf and contributes to the Leeuwin Current (LC). The HLC extends to depths of 100–200 m and is generally located close to the shelf break. The HLC transport increases towards the southwest with the mean transport of 1.4 Sv at North West Cape. The HLC flows all year round but is subject to seasonal and interannual variability with a maximum in late autumn (April–May) and a minimum in summer (January–February). HLC responds to ENSO events and is stronger during the La Niña and weaker during El Niño events.

South Indian Counter Current

The South Indian Counter Current (SICC) originates in the western Indian Ocean to the south of Madagascar and flows eastward as three branches (southern: sSICC, central: cSICC, and northern: nSICC; Palastanga *et al.*, 2007; Menezes *et al.*, 2014; Wijeratne *et al.*, 2018). While the nSICC is relatively weak, the cSICC (1.4 Sv) and sSICC (6.8 Sv) contribute inflow to the LC at 23°S and 31°S respectively. The combined eastward transport of the cSICC and sSICC is ~8.2 Sv across 100°E with the majority (> 80%) of transport through the sSICC.

West Australian Current

The traditional view of subtropical gyre circulation of the southern Indian Ocean defines the West Australian Current (WAC) as the major eastern boundary current analogue to other ocean basins. However, the presence of the LC modifies this circulation, and the location of the WAC is between the cSICC and sSICC where ~80% of the sSICC flow moves northwards and then offshore.

Leeuwin Current

The Leeuwin Current (LC) is the unique poleward eastern boundary current along the west and south coasts of Australia (Smith *et al.*, 1991; Pattiaratchi and Woo, 2009; Ridgway and Godfrey, 2015). The LC starts at North West Cape, flows along the shelf break (~200 m) to the southern tip of Tasmania, and is described as the longest boundary current in the world (Ridgway and Condie, 2004). The LC follows the curvature of the coastline and turns eastward at Cape Leeuwin and extends along the southern continental shelf/slope as the South Australian Current (SAC). The LC/SAC becomes the Zeehan Current (ZC) and flows around southern Tasmania (Baines *et al.*, 1983; Cresswell, 2000). The southward LC transport increases from north to south with 1.4 Sv through North West Cape to 4.12 Sv at 32.8°S with the increase in transport due to the inflow from sSICC. The maximum LC transport along the western coast

occurs in May–June, with a minimum in October. The transport increases from November to January with a secondary minimum in February. The LC is strongest along the southwest corner of Australia as it flows past Cape Leeuwin into the Southern Ocean. The LC along the south coast has a maximum in June–July, around one month later than along the west coast.

South Australian Current

The South Australian Current (SAC) is the continuation of the LC to the east and has a mean transport of ~1.31 Sv at 136.5°E. The maximum transport occurs in August–September (that is, 4–5 months after the peak of HLC and 2–3 months after the peak in LC along the west coast). The SAC transport is also related to ENSO events with higher transport during La Niña events (Oke *et al*., 2018). The SAC becomes the Zeehan Current (ZC) to the east and is mainly confined to the continental shelf and the upper slope along the west coast of Tasmania with transport 1.9 Sv. The ZC is strongest in September.

Flinders Current

Along the southern coast, offshore of the LC, the Flinders Current (FC) is the dominant flow, extending from the surface to more than 1000 m, flowing westward from Tasmania and past Cape Leeuwin into the Indian Ocean. Along the southern continental slope, the FC is an undercurrent beneath the eastward flowing LC, SAC, and ZC, and a surface current further offshore. The FC gradually intensifies along its pathway from Tasmania to Cape Leeuwin with 6.9 Sv at 122°E increasing to 7.2 Sv at 116.5°E.

South Equatorial, Hiri and East Australian Currents

In the Pacific Ocean, the westward flowing South Equatorial Current (SEC) impinges on the eastern continental shelf slope of Australia (see Figure 16.1). The northern branches of the SEC (North Vanuatu Jet: NVJ, and North Caledonia Jet: NCJ) bifurcate at ~15°S to initiate the Hiri Current (HC), a clockwise circulation that flows into the Gulf of Papua and the southward flowing East Australian Current (EAC) along the Australian coast (Godfrey *et al*., 1980). The HC and EAC have different seasonal cycles—the EAC is at a maximum in December–January whilst the HC peaks in June–July. This indicates that the northern branches of SEC inflow (NVJ and NCJ) contribute more to southward (northward) transport during summer (winter).

NVJ and NCJ contribute a significant component (~11.8 Sv) of the southward EAC transport between 15–22°S. Southward transport of the EAC increased from 11.5 Sv at 20°S to 17.2 Sv at 27°S. To achieve the estimated transport at 27°S of 17.2 Sv, an inflow of ~5.7 Sv is required via the South Caledonia Jet (SCJ). Simulations from ozROMS (a shelf-scale, three-dimensional hydrodynamic model; Wijeratne *et al*., 2018) indicated that inflow from SCJ was mostly confined to the subsurface and transported ~6.4 Sv, in good agreement with the estimate of ~8 Sv by Kessler and Cravatte (2013). Thus SEC inflow to the EAC can be attributed as 65% via NVJ and NCJ and 35% via SCJ.

The EAC recirculation is defined as the northwards flow located further offshore of the main EAC southwards flow (Zilberman *et al*., 2014). The main EAC flow separates from the Australian coast at latitudes 30–34°S and flows eastward as the Tasman Front (TF; Bowen *et al*., 2005; Cetina-Heredia *et al*., 2014, Oke *et al*. 2019). The EAC extension reaches southern Tasmania and flows westward into the eastern Indian Ocean as the Tasman Outflow (TO) or Tasman Leakage (Ridgway and Dunn, 2007; van Sebille *et al*., 2012).

Antarctic Circumpolar Current

The Antarctic Circumpolar Current (ACC) surrounds Antarctica and connects the Indian, Pacific, and Atlantic Oceans. It is the strongest current in the global ocean, transporting 182 Sv from west to east. This current results from strong westerly winds across the Southern Ocean and the significant change in temperature from the equator to the poles. The major fronts in this region are the subantarctic front (SF) and the polar front (PF).

17.2 EO Sensors for Water Circulation

Various EO sensors and their data sources are introduced in Volume 1A, and interpretation of optical, thermal, and microwave imagery is considered in Volume 1B. There is no sensor presently flying that measures water circulation directly, but there are several which, in combination, tell us much about the ocean circulation. These are summarised in Table 17.3.

Table 17.3 EO sensors relevant to water circulation

TIR: Thermal infrared; SAR: Synthetic Aperture Radar

Type	Sensor	Platform	Relevance	Advantages	Disadvantages
Passive optical	Multispectral radiometer	Satellite or airborne	Eddies/currents in coastal zone, Wave texture	Global coverage, low cost	Low accuracy, coarse scale
	Hyperspectral radiometer	Airborne	Eddies/currents in coastal zone	High spectral resolution	High cost, high data volume
	TIR radiometer	Satellite or airborne	Surface water circulation	Possible to detect water movement at night	Clouds, low resolution
Active microwave	SAR	Satellite or airborne	Surface features e.g. ocean fronts, Eddies wakes—detect and track ships	All weather, so useful in tropical regions	High cost, specialised processing
	Radar altimeter	Satellite	Sea level change (tidal and non-tidal), Surface wind speed, Topography of ice sheets	All weather, highly precise	Not an imaging system, so measurements are only along infrequently repeated tracks (10–30 days)
	Scatterometer	Satellite	Surface topography/currents surface wind speed and direction, Sea ice, Snow accumulation	Frequent, global coverage	Impacted by rain and extreme winds
Gravity	Accelerometers	Satellite	Water depth, Mean circulation	Unique global coverage	Relatively coarse resolution

17.2.1 Radar altimeters

The type of mission that comes closest to providing a direct measure of ocean circulation—namely the variations of sea surface height associated with that circulation—is the radar altimeter (see Sections 9.5, 12.2.1 and 16.2.4). As depicted in Figure 12.1, the altimeter measures the distance from the satellite to the surface of the ocean at nadir by measuring the time it takes for an emitted pulse to be returned. Key to its success as a sensor is that it does this with centimetre accuracy at a range of ~1000 km, and that the position of the satellite is also determined with similar precision (using a suite of semi-redundant systems: DORIS, GPS, and laser ranging). As the satellite orbits the Earth it is thus able to acquire a network of lines along which the sea surface height (SSH), relative to a reference ellipsoid, is precisely measured (see Section 12.4.3).

However, oceanographers need to know the sea surface height relative to the geoid, not the reference ellipsoid. This quantity is usually called the dynamic topography (DT) because it is the signal associated with ocean circulation. An estimate of the geoid relative to the reference ellipsoid has been determined from the gravity measurements of the GRACE and GOCE missions, (see Excursus 1.1 and Volume 1A—Section 3.3 and Volume 1A—Figure 8.4), which enables the DT to be estimated (see Figure 12.1). The surface velocity field (V or geostrophic velocity) can be determined in a straightforward manner from the DT (to first order) by geostrophy:

$$V = \frac{\nabla \eta}{f}$$

where f is the Coriolis parameter and η is either the DT at a particular time, or its time-mean, known as the mean dynamic topography (MDT). There is, however, a problem. The geoid is not yet known to the same accuracy as the SSH, so the DT and consequently estimates of V derived from it have relatively large errors at mesoscale resolution. Thus, a map like Figure 17.1 cannot yet be made directly from an EO-based estimate of the MDT. A workaround solution exploits the fact that the time-mean of the SSH (the so-called mean sea surface or MSS) is a very accurate measure of the geoid plus the MDT. By subtracting this from SSH we get an accurate estimate of the

sea surface height anomaly (SSHA), or the departure of DT from the mean. This is why altimetry is often described as a technique for measuring the changes (from daily to seasonally and interannually, or the trend) of sea level, rather than sea level in an absolute sense. To complete this workaround solution, an independent estimate of the MDT can be added to the altimetric SSHA to produce estimates of the DT. For this purpose in the IMOS Gridded Sea Level (GSL) product, we use the MDT of the Bluelink global model (see Excursus 2.2).

Archives of satellite imagery are valuable for mapping the speed of surface water movement. For example, in Figure 17.2 the speed of the ACC was modelled using 23 years ocean height observations derived from satellite altimetry.

Figure 17.2 Speed of Antarctic Circumpolar Current

23 years of satellite altimetry data from the European Copernicus Marine Services were used to map the speed of the ACC.

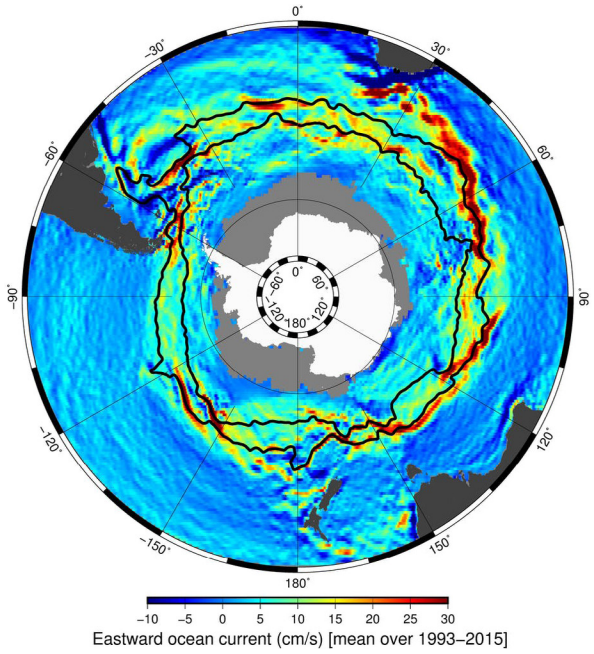

Source: European Copernicus Marine Services. Retrieved from *https://theconversation.com/explainer-how-the-antarctic-circumpolar-current-helps-keep-antarctica-frozen-106164*

17.2.2 Passive optical

While not providing a direct measure of ocean circulation, passive optical imagery of the ocean (see Section 8) does complement altimetry by yielding stunning images (during periods of clear skies) of the complexities of the flow, as well as the impact of both vertical and horizontal advection (bringing cold water to the surface, or warm tropical waters poleward, respectively). Much can be inferred about the water circulation by analysing the differences (over time or space) in EO optical imagery—but none of these analyses are as straightforward as the radar altimetry equation given in Section 17.2.1. Feature tracking can sometimes be used to infer the advection velocities from sequences of optical images (Bowen *et al.*, 2002).

The main weakness of optical imagery is the impact of clouds. Perhaps the least-impacted application of optical imagery is the determination, from many years of images, of the annual cycle of temperature (see Section 14). But what does this tell us about circulation? This is best explained with reference to an example from the Sea Surface Temperature Atlas of the Australian Regional Seas (SSTAARS, Wijffels *et al.*, 2018). To produce SSTAARS, the annual harmonics of a 25-year (1992–2016) record of daily, high resolution (~2 km), gridded SST observations (see Section 14.5.2 and Wijffels *et al.*, 2018) were analysed (see Figure 17.3). The analysis was done independently for each pixel, yielding a highly detailed map for the whole Australasian region, that revealed fresh insights into many features of the seasonal cycle of Australia's regional circulation. Since a consortium of Australian agencies have downloaded and curated the Large Area Coverage (LAC) data directly from the relevant satellites for several decades, Australia is one of the few countries where this analysis is possible.

If there were no ocean circulation, the amplitude of the annual cycle of sea surface temperature (SST) would be a lot more spatially uniform than the observed amplitude (see Figure 17.3a). Figure 17.4, for example, shows how the amplitude of the annual cycle of temperature is greatly reduced along the path of the LC (see Table 17.2), which brings warm water south in winter. Wijffels *et al.* (2018) provide and discuss more detailed images of temperature variations around the Australasian region.

Figure 17.3 Temperature variations

Pixel-wise estimates of (a) the annual harmonic amplitude (°C) and (b) month of the peak temperature. Panels (c) and (d) are as for (a) and (b), but for the semiannual harmonic. Note the change in scale between (a) and (c). Phase is shown in months where '1' relates to January 1 in (a) and January 1/July 1 in (d). As an example, in regions where phase=3 in (b), annual temperatures reach their maximum in March. Grey contours mark the 50 m and 200 m isobaths.

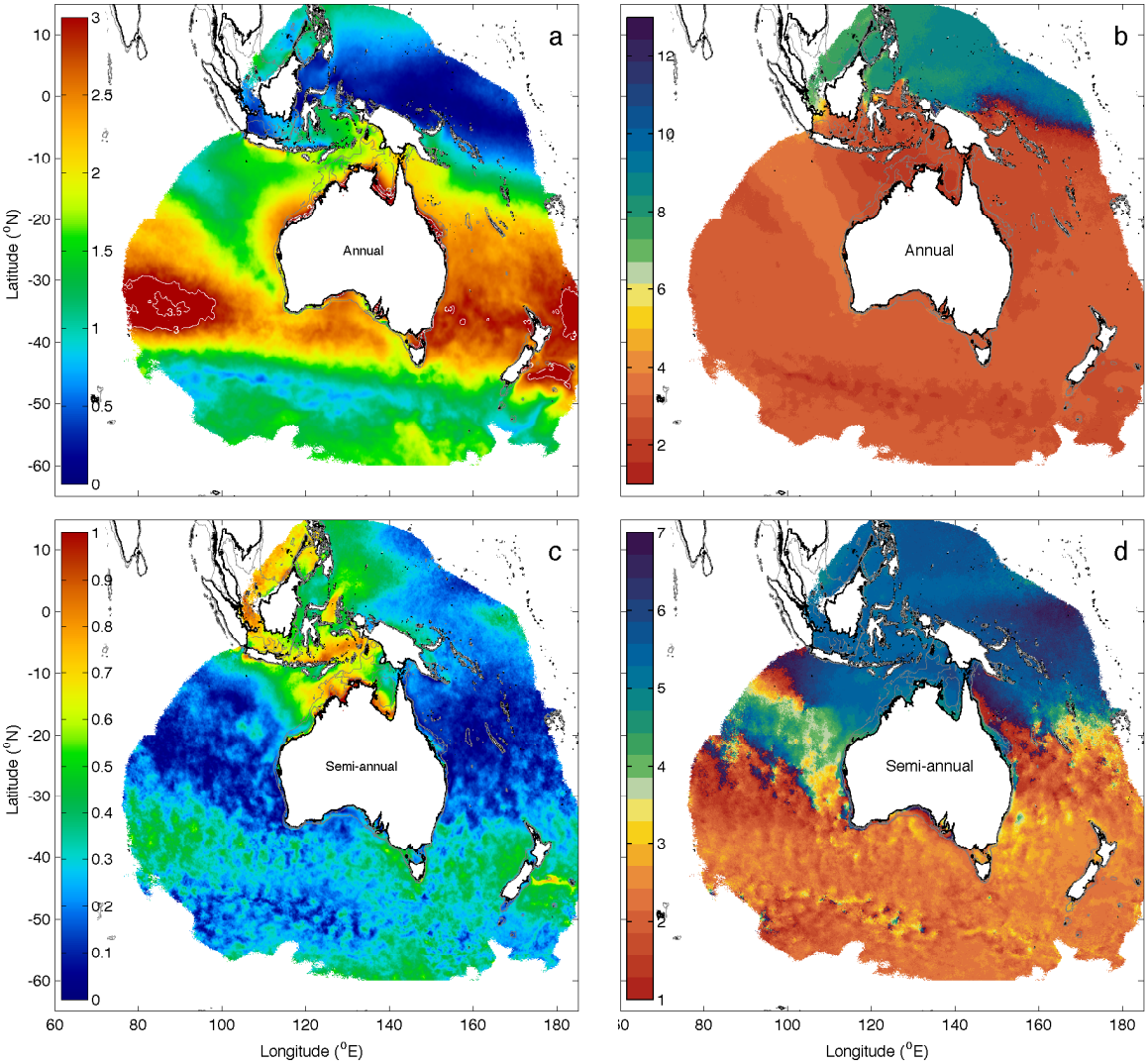

Source: Susan Wijffels, Woods Hole Oceanographic Institution

Figure 17.4 Detailed view of temperature variation

Image shown in Figure 17.3a, with a reduced geographic and temperature range to show more detail.

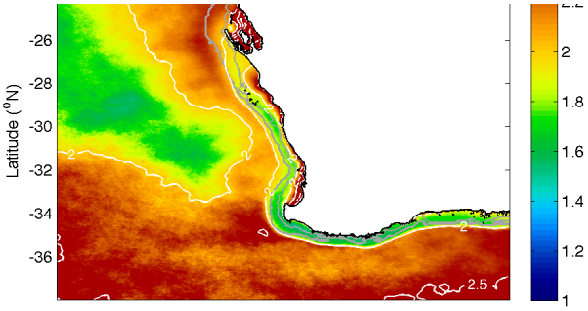

Source: Susan Wijffels, Woods Hole Oceanographic Institution

17.3 Circulation Patterns

The first images of the ocean acquired by the early thermal imaging sensors revealed something about the ocean that oceanographers and mariners had hitherto only glimpsed from the tracks of becalmed ships or drifting bottles—that the circulation of the ocean is incredibly complex and ever-changing. This conclusion relies on the fact that the temperature of the water is, to an extent, a marker of where it is from, and explains why optical images of the surface properties of the ocean often look like a liquid that has been stirred. At high resolution, the stirring is being done by small eddies (see Section 1.4.3). At larger scales the stirring is generated by currents such as the LC or EAC (see Table 17.2 and Excursus 17.1).

In the EAC for example, eddies are very common and can extend 200–300 km in diameter (see Section 2.3). Excursus 17.2 demonstrates how satellite altimetry and passive optical imagery can be used in combination to follow the changing circulation in this dynamic region for a month in Autumn 2021.

Ever since surface current maps were first produced in the nineteenth century the variability of ocean currents has also been recognized.
(Wells, 1986)

Excursus 17.2—Example Circulation Study

Source: David Griffin, CSIRO
Further Information: *http://oceancurrent.imos.org.au/news.php*

The complexity and variability of ocean circulation are particularly intense off the eastern Australian coast near Sydney. Here the EAC interacts with eddies or forms new ones (Oke *et al.*, 2019), which can aid or frustrate sailors. This example follows the movement of a series of eddies in this region during early Autumn 2021 using a combination of radar altimetry and passive optical imagery (SST and ocean colour).

Figure 17.5 shows a sequence of four images at ~10 day intervals, which correspond to occurrences of clear skies. Figure 17.5a shows that on 4 March 2021 the EAC flowed (as it often does, see Schaeffer *et al.*, 2017, Archer *et al.*, 2017) as a narrow (~25 km) jet of warm water that followed the continental margin southwards. It passed Sydney before leaving the shelf near 34.5°S to flow over and around 'warm-core A', a ~300 km diameter anticyclonic eddy. This process of flowing over and around an existing eddy was described as 'flooding' by Baird *et al.* (2011). Warm-core A was flanked by two cyclonic eddies, cold-core A to the northeast, centred near 33.5°S, 155°E, and cold-core B mostly off-image to the south near 36°S, 154.5E°. Like most cold-core eddies, these are less conspicuous in the SST imagery than the warm-core eddies, but are equally conspicuous in the sea level anomaly field. The geostrophic estimate of velocity associated with cold-core A is in good agreement with the trajectory of a satellite-tracked surface drifter. North and east of cold-core A lies warm-core B, a large ridge continuing off-image to the north while also being partially attached (see the saddle point in the sea level field near 34°S, 158°E) to warm-core C in the south, centered at 35.5°S 158°E. Cold-core C at far southeast, centred near 35°S, 160°E, completes the inventory of meso-scale features in this 6°×11° patch of ocean.

Figure 17.5b (13 March) shows that in some places there has been little change, but much in others. The centre of warm-core A has barely moved, but a slight change of shape takes the EAC closer to Jervis Bay (about 200 km south of Sydney) before peeling offshore. In contrast, cold-core A has all but disappeared, its place taken by warm-core B merging with warm-core C. Cold-core B has come more into view, having moved north, while cold-core C is essentially unchanged.

In Figure 17.5c (24 March) two new features are visible:

- cold water along much of the coast, probably the result of strong upwelling-favourable winds that blew in the days prior to the image, associated with the record-breaking storms that resulted in widespread flooding; and
- a frontal eddy (Schaeffer *et al.*, 2017) inshore of the EAC at 31°S, 200 km south of where it was 20 days earlier (see *http://oceancurrent.imos.org.au/product.php?product=oceancolour&region=Bris-Syd&date=20210304040000&rtype=DR*). The other features are all still visible, having evolved, including northwest motion of cold-core B, a precursor of what is shown in the next image.

Figure 17.5d (3 April) shows that a critical stage of the EAC eddy-shedding process has been reached. Warm-core A is becoming mostly isolated from the EAC as cold-core B continues to move farther to the northwest. Much of the EAC is evidently flowing east near 33.5°S into and around warm-cores B and C (which seem to be separating again) instead of warm-core A. To further complicate the situation over the upper continental slope near 32.5°S, the frontal eddy has continued its southward motion, and is now centred near 32.2°S, about 1° north of the incipient point of EAC separation.

Figure 17.5 Circulation in EAC

This sequence of four images showed water circulation in the EAC from 4 March to 3 April 2021. Colour: sea surface temperature (4 hour composite using all available thermal imagery). White contours: sea level isoheights at 0.1 m intervals. Black vectors: geostrophic velocity calculated from the height field (see key for scale). Other symbols are defined in the legends.

a. 4 March 2021

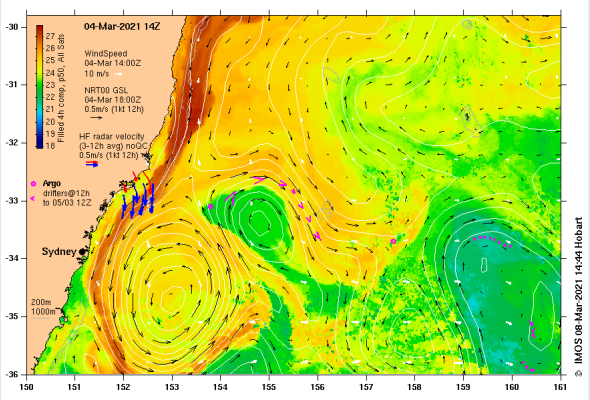

b. 13 March 2021

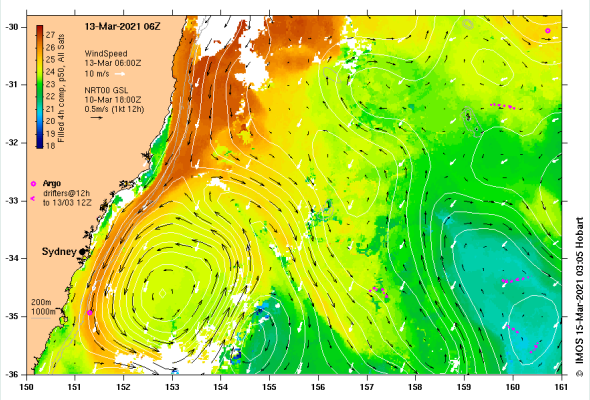

c. 24 March 2021

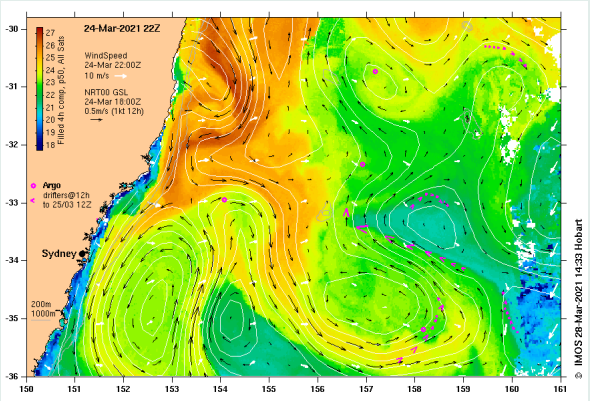

d. 3 April 2021

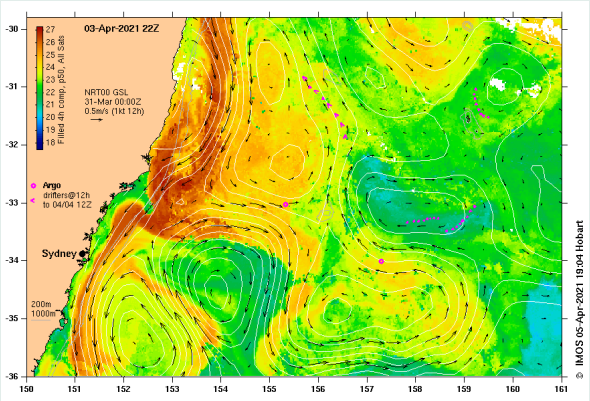

17.4 Ocean Fronts

Fronts are regions where large property changes occur within a small distance. Ocean fronts are defined as regions of large horizontal gradients in water properties (such as temperature and/or salinity). The frontal zone is a region of rapid property change at the surface, and the frontal axis is the location of the largest horizontal property gradient. To avoid strong gradients, both fluids and gases tend to eliminate fronts by turbulent mixing. Since the scale of both ocean and atmospheric fronts depends on the scale of their driving processes, they essentially represent a balance between two or more forces. Accordingly, ocean fronts are associated with convergent flow and vigorous water movement, with greater mixing across larger gradients (Tomczak, 1996).

Ocean fronts are commonly areas of nutrient concentration, thus high primary productivity, with larger fronts serving as fish feeding grounds (see Section 20.7.1). These regions also accumulate floating material, oil, and other forms of pollution. Excursus 17.3 demonstrates the use of EO imagery to monitor the formation and movement of ocean fronts.

Associations between marine vertebrates and oceanographic fronts vary spatially, temporally and between taxa, influenced by both the biophysical properties of fronts and taxon-specific foraging ecology (Hunt et al. 1999). Despite this variability, there now exists a considerable body of evidence indicating that persistent mesoscale frontal zones are ecologically significant across the oceans (e.g. Polovina et al. 2001; Bost et al. 2009).
(Scales et al., 2014)

Excursus 17.3—Ocean Fronts

Source: Chari Pattiaratchi, University of Western Australia
Further Information: *http://oceancurrent.imos.org.au/news.php*

Ocean fronts, defined as regions of large horizontal gradients in water properties (temperature, salinity etc), are areas of high productivity globally. Satellite imagery from the northwest shelf indicates the existence of two types of fronts extending over 1000 km from North West Cape to Cape Leveque. The nearshore band of high chlorophyll (see Figure 17.6) is associated with a very cold band of water at the coast that usually develops every May, persists throughout winter, and is evident in the SSTAARS climatology (see Section 14.5.2). Water in shallow coastal regions become more saline over summer due to evaporation and, with winter cooling, the water becomes much denser than water further offshore. This cool, dense water then flows offshore along the bottom as a dense, shelf water cascade, which has been observed by ocean glider deployments in the region and other regions of Australia.

Figure 17.6 MODIS Chlorophyll a OC3 29 May 2018

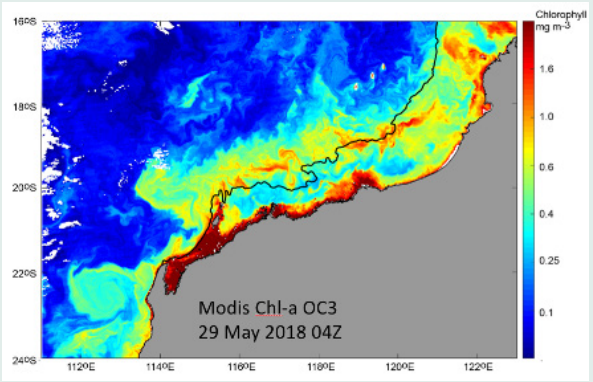

On continental shelves, fronts can also develop just through the reduction of tidal currents with depth, without the influx of different water masses. Simpson and Hunter (1974) showed that a front could develop where mixing due to tidal currents was no longer strong enough to overcome stratification. Many studies undertaken globally have shown that the ratio of the water depth (h) to the cubed value of the nearbed current speed (U) is a good indicator of the location of tidal fronts, in particular where:

$$\log\left(\frac{h}{|U^3|}\right) = 2.7$$

The band of higher chlorophyll found further offshore, suggesting the presence of a second front, lies in close proximity to the predicted Simpson and Hunter tidal front location (indicated by black line in Figure 17.6).

Coastal currents transporting different water masses can also contribute to the existence of fronts and the frontal location could also be related to the location of the Holloway Current that flows towards the southwest. The offshore chlorophyll maximum, although much weaker than in the nearshore front, has affected about 1000 km of the mid-shelf region (see Figure 17.7b). Recent work by Thums *et al.* (2017) demonstrated that flatback turtles (*Natator depressus*) followed the location of the predicted Simpson and Hunter tidal front when migrating along the Kimberley Coast.

Figure 17.7 Frontal systems on Australian northwest shelf

a. Temperature 28 May 2018

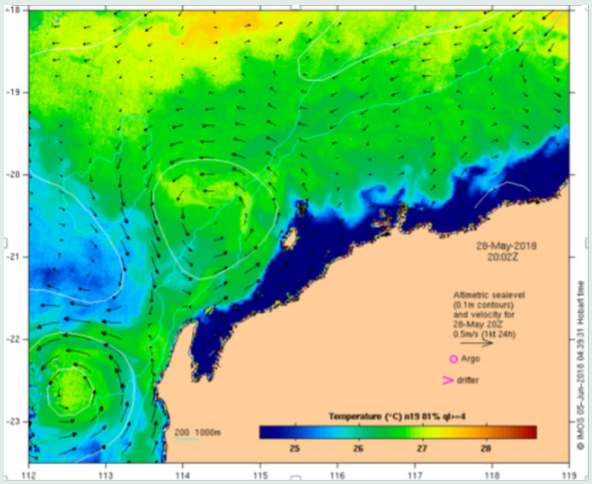

b. MODIS chlorophyll a product 29 May 2018

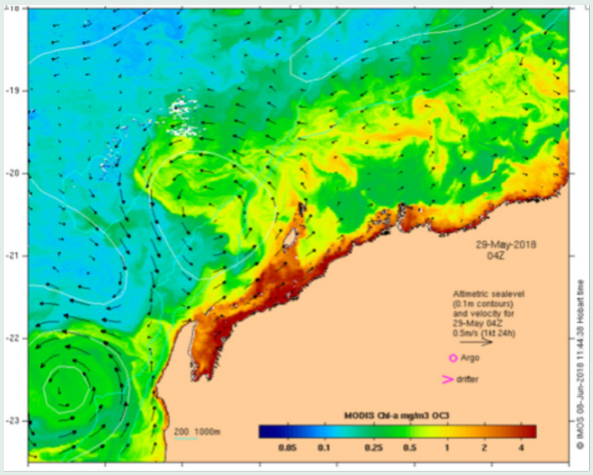

17.5 Further Information

Pattiaratchi, C., Wijeratne, S., and Proctor, R. (2019). A current affair: the movement of ocean waters around Australia. The Conversation. *https://theconversation.com/a-current-affair-the-movement-of-ocean- waters-around-australia-96779*

Pattiaratchi, C.B., and Siji, P. (2020). Variability in ocean currents around Australia. In *State and Trends of Australia's Ocean Report*. (Eds: Richardson, A.J., Eriksen, R., Moltmann, T., Hodgson-Johnston, I., and Wallis, J.R.) Integrated Marine Observing System. *www.imosoceanreport.org.au*

IMOS Ocean Current: *http://oceancurrent.imos.org.au/*

Ocean Current Illustrations:
Diagrams: *https://research.csiro.au/ncmi-idc/information/ocean-circulation/ocean-current-diagrams/*
Animations: *https://research.csiro.au/ncmi-idc/information/ocean-circulation/ocean-current-animations/*

Bluelink:*https://www.csiro.au/en/Research/OandA/Areas/Oceans-and-climate/Bluelink*

Marine Science Australia: *https://www.ausmarinescience.com/marine-science-basics/ocean-currents/*

17.6 References

Agrawal, D.C. (2018). The Sverdrup: The Non-SI Unit of Large-Scale Volume Transport Over the Globe. *The Physics Teacher*, 56, 377. *https://doi.org/10.1119/1.5051151*

Archer, M.R., Roughan, M., Keating, S.R., and Schaeffer, A. (2017). On the variability of the East Australian Current: Jet structure, meandering, and influence on shelf circulation. *Journal of Geophysical Research: Oceans*, 122, 8464–8481. *https://doi.org/10.1002/2017JC013097*.

Bahmanpour, M.H., Pattiaratchi, C., Wijeratne, S., Steinberg, C., and D'adamo, N. (2016). Multi-year observation of the Holloway current along the shelf edge of north-western Australia. *Journal of Coastal Research*, 75, 517–521.

Baird, M.E., Suthers, I.M., Griffin, D.A., Hollings, B., Pattiaratchi, C., Everett, J.D., Roughan, M., Oubelkheir, K., and Doblin, M. (2011). The effect of surface flooding on the physical-biogeochemical dynamics of a warm-core eddy off southeast Australia. *Deep-Sea Research Part II: Topical Studies in Oceanography*, 58, 592–605. doi:10.1016/j.dsr2.2010.10.002

Baines, P.G., Edwards, R.J., and Fandry, C.B. (1983). Observations of a new baroclinic current along the western continental slope of Bass Strait. *Australian Journal of Marine and Freshwater Research*, 34, 155–157.

Bost, C.A., Cotté, C., Bailleul, F., Cherel, Y., Charrassin, J.B., Guinet, C., Ainley, D.G., and Weimerskirch, H. (2009). The importance of oceanographic fronts to marine birds and mammals of the southern oceans. *Journal of Marine Systems*, 78, 363–376.

Bowen, M.M., Emery, W.J., Wilkin, J.L., Tildesley, P.C., Barton, I.J., and Knewtson, R. (2002). Extracting Multiyear Surface Currents from Sequential Thermal Imagery Using the Maximum Cross-Correlation Technique, *Journal of Atmospheric and Oceanic Technology*, 19(10), 1665-1676.

Bowen, M.M., Wilkin, J.L., and Emery, W.J. (2005). Variability and forcing of the East Australian Current. *Journal of Geophysical Research*, 110, C03019. *https://doi.org/10.1029/2004JC002533*

Cetina-Heredia, P., Roughan, M., van Sebille, E., and Coleman, M. (2014). Long-term trends in the East Australian Current separation latitude and eddy driven transport. *Journal of Geophysical Research: Oceans*, 119, 4351–4366. *https://doi.org/10.1002/2014JC010071*

Cresswell, G. (2000). Currents of the continental shelf and upper slope of Tasmania. *Papers and Proceedings of the Royal Society of Tasmania*, 133, 21–30.

GA (2021). *Oceanography* webpage, Geoscience Australia website: https://www.ga.gov.au/scientific-topics/disciplines/oceanography

Godfrey, J.S., Cresswell, G.R., Golding, T.J., and Pearce, A.F. (1980). The separation of the East Australian Current. *Journal of Physical Oceanography*, 10, 430–440.

Hu, D., Wu, L, Cai, W., Gupta, A.S., Ganachaud, A., Qiu, B., Gordon, A.L., Lin, X., Chen, Z., Hu, S., Wang, G., Wang, Q., Sprintall, J., Qu, T., Kashino, Y., Wang, F., and Kessler, W.S. (2015). Pacific western boundary currents and their roles in climate. *Nature*, 522, 299–308. *https://doi.org/10.1038/nature14504*.

Hunt, G. Jr, Mehlum, F., Russell, R., Irons, D., Decker, M., and Becker, P. (1999). Physical processes, prey abundance, and the foraging ecology of seabirds. *Proceedings of 2*2nd *International Ornithological Congress* (Eds N.J. Adams, and R. Slotow), pp. 2040–2056. BirdLife South Africa, Durban, Johannesburg.

Kessler, W.S., and Cravatte, S. (2013). Mean circulation of the Coral Sea. *Journal of Geophysical Research: Oceans*, 118(12), 6385–6410.

Menezes, V.V., Phillips, H.E., Schiller,A., Bindoff, N.L., Domingues, C.M., and Vianna, M.L. (2014). South Indian Countercurrent and associated fronts. *Journal of Geophysical Research: Oceans*, 119, 6763–6791. *https://doi.org/10.1002/2014JC010076*

Oke, P.R., Griffin, D.A., Rykova, T., and De Oliveira, H.B. (2018). Ocean Circulation in the Great Australian Bight in an eddy-resolving ocean reanalysis: the eddy field, seasonal and interannual variability. *Deep Sea Research*, 157–158, 11–26. doi:10.1016/j.dsr2.2018.09.012

Oke, P., Roughan, M., Cetina-Heredia, P.,Pilo, G.,Ridgway, K., Rykova, T., Archer, M.R., Coleman, R.C., Kerry, C.G., Rocha, C., Schaeffer, A., and Vitarelli, E. (2019). Revisiting the circulation of the East Australian Current: its path, separation, and eddy field. *Progress in Oceanography*, 176, 102139. *https://doi.org/10.1016/j.pocean.2019.102139*

Palastanga, V., van Leeuwen, P., Schouten, M., and de Ruijter, W. (2007). Flow structure and variability in the subtropical Indian Ocean: Instability of the South Indian Ocean Countercurrent. *Journal of Geophysical Research*, 112, C01001. *https://doi.org/10.1029/2005JC003395*

Pattiaratchi, C.B, and Siji, P. (2020). Variability in ocean currents around Australia. In *State and Trends of Australia's Ocean Report* (Eds: Richardson, A.J., Eriksen, R., Moltmann, T., Hodgson-Johnston, I., Wallis, J.R.). doi: 10.26198/5e16a2ae49e76

Pattiaratchi, C., and Woo, M. (2009). The mean state of the Leeuwin Current system between North West Cape and Cape Leeuwin. *Journal Royal Society Western Australia*, 92, 221–241.

Polovina, J.J., Howell, E., Kobayashi, D., and Seki, M.P. (2001). The transition zone chlorophyll front, a dynamic global feature defining migration and forage habitat for marine resources. *Progress in Oceanography*, 49, 469–483.

Ridgway, K.R., and Condie, S.A. (2004). The 5500-km-long boundary flow off western and southern Australia. *Journal of Geophysical Research*, 109, C04017. *https://doi.org/10.1029/2003JC001921*

Ridgway, K.R., and Dunn, J.R. (2007). Observational evidence for a Southern Hemisphere oceanic supergyre. *Geophysical Research Letters*, 34, L13612. *https://doi.org/10.1029/2007GL030392*

Ridgway, K.R., and Godfrey, J.S. (2015). The source of the Leeuwin Current seasonality. *Journal of Geophysical Research: Oceans*, 120, 6843–6864. *https://doi.org/10.1002/2015JC011049*

Scales, K.L., Miller, P.I., Hawkes, L.A., Ingram, S.N., Sims, D.W., and Votier, S.C. (2014). On the Front Line: frontal zones as priority at-sea conservation areas for mobile marine vertebrates. *Journal of Applied Ecology*, 51, 1575–1583. doi:10.1111/1365-2664.12330

Schaeffer, A., Gramoulle, A., Roughan, M., and Mantovanelli, A. (2017), Characterizing frontal eddies along the East Australian Current from HF radar observations. *Journal of Geophysical Research: Oceans*, 122, 3964–3980. doi:10.1002/2016JC012171.

Simpson, J.H., and Hunter, J.R. (1974). Fronts in the Irish Sea. *Nature*, 250, 404–406.

Smith, R. L., Huyer, A., Godfrey, J.S., and Church, J. (1991). The Leeuwin current off western Australia, 1986– 1987. *Journal Physical Oceanography*, 21, 323–345.

Sprintall, J., and Revelard, A. (2014). The Indonesian throughflow response to Indo-Pacific climate variability. *Journal of Geophysical Research: Oceans*, 119, 1161–1175. *https://doi.org/10.1002/2013JC009533*

Sprintall, J., Wijffels, S. E., Molcard, R., and Jaya, I. (2009). Direct estimates of the Indonesian throughflow entering the Indian Ocean: 2004–2006. *Journal of Geophysical Research*, 114, C07001. *https://doi.org/10.1029/2008JC005257*

Tomczak, M. (1996). *Fronts in shallow seas and estuaries*. *https://www.mt-oceanography.info/ShelfCoast/notes/chapter09.html*

Thums, M., Waayers, D., Zhi, H., Pattiaratchi, C.B., Bernus, J., and Meekan, M.G. (2017). Environmental predictors of foraging and transit behaviour in flatback turtles (*Natator depressus*). *Endangered Species Research*, 32, 333–349.

van Sebille, E., England, M.H., Zika, J.D., and Sloyan, B.M. (2012). Tasman leakage in a fine resolution ocean model. *Geophysical Research Letters*, 39, L06601. *https://doi.org/10.1029/2012GL051004*

Wells, N. (1986). *The Atmosphere and Ocean. A Physical Introduction*. Taylor and Francis, London.

Wijeratne, S., Pattiaratchi, C., and Proctor, R. (2018). Estimates of Surface and Subsurface Boundary Current Transport Around Australia. *Advancing Earth and Space Science*, 123, 3444–3466. *https://doi.org/10.1029/2017JC013221*

Wijffels, S.E., Beggs, H., Griffin, C., Middleton, J.F., Cahill, M., King, E., Jones, E., Feng, M., Benthuysen, J.A., Steinberg, C.R., and Sutton, P. (2018). A fine spatial scale sea surface temperature atlas of the Australian regional seas (SSTAARS): seasonal variability and trends around Australasia and New Zealand revisited. *Journal of Marine Systems*, 187, 156–196. *https://doi.org/10.1016/j.jmarsys.2018.07.005*

Zilberman, N.V., Roemmich, D.H., and Gille, S.T. (2014). Meridional volume transport in the South Pacific: Mean and SAM-related variability. *Journal of Geophysical Research: Oceans*, 119, 2658–2678. *https://doi.org/10.1002/2013JC009688*

Observing the Waterscape

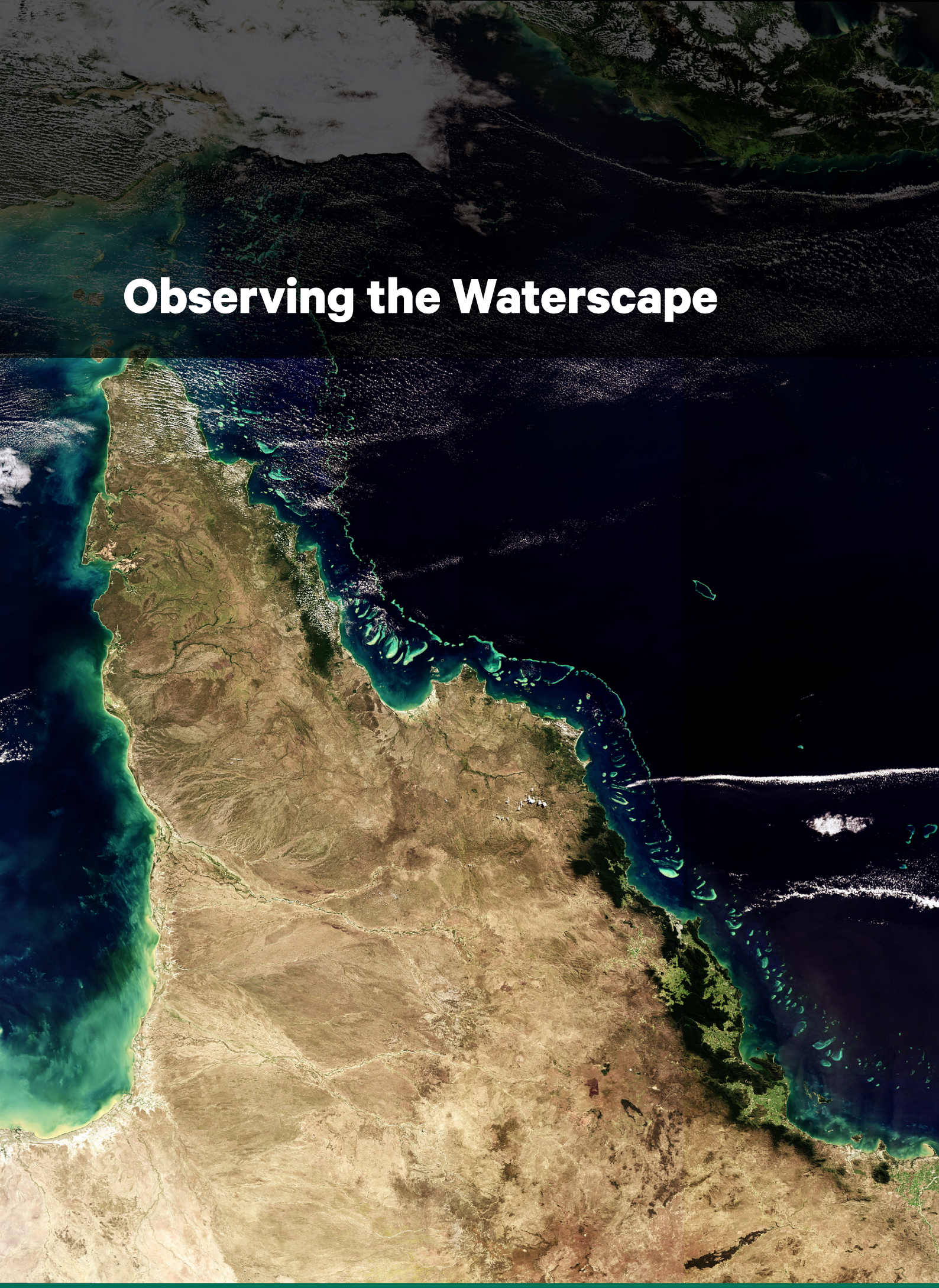

The following three sections describe specific uses of EO data in a range of applications related to the biogeochemical environment of surface waters in Australia. These applications rely on a variety of EO and other data sources, image processing approaches, and scientific models and, while not exhaustive, they represent the diversity of uses for which EO data is relevant in the Australian surface water environment.

The following three sections detail EO-based analyses of water:

- colour—describes use of optical EO imagery to map and model characteristics of water that are related to its perceived colour, and methods that can be used to determine substratum colour (see Section 18); and
- quality—presents EO data and approaches for determining water quality in marine and inland waters (see Section 19).
- ecology—introduces EO methods for mapping and monitoring coastal and marine aquatic environments, (see Section 20).

Contents

18 Colour 345

19 Quality 367

20 Ecology 395

Background image on previous page: Envisat MERIS image of Great Barrier Reef, Queensland, acquired on 18 May 2008. **Source:** © ESA. Retrieved from *https://www.esa.int/ESA_Multimedia/Images/2009/04/The_Great_Barrier_Reef_Australia*

18 Colour

Janet Anstee

Observing water colour is an ancient method for assessing water quality. The surface colour of ocean waters is now considered to be an Essential Climate Variable for biological activity, and can be used to provide information to track long term climate change in aquatic systems (GCOS, 2018).

The colour of waterbodies can be reliably detected using optical EO (see Section 8), and researchers have demonstrated that optical water colour parameters derived from EO datasets can infer water quality (see Section 19). Changes in water colour can be similarly monitored using optical EO datasets by comparing multi-temporal images (see Volume 2D).

Figure 18.1 Characteristic reflectance features of water colour constitutents

Coloured water reflectance components are shown for chlorophyll-rich water. Spectral features are exaggerated in this graph to highlight individual components. Note that the actual reflectance also varies with the density of particles in the water (see Figure 18.2). Note: CDOM = Coloured Dissolved Organic Matter.

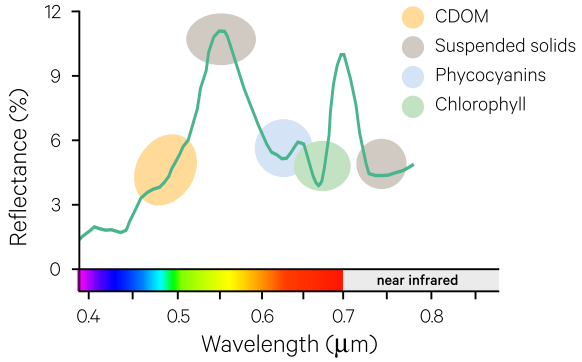

Source: Erin Hester, North Carolina State University

The optical constituents of water (introduced in Section 8) that result in its colour are:

- pure water—optically pure (see Section 8.2.1);
- photosynthetic pigments—phytoplankton and cyanobacteria (see Section 8.2.2);
- particulate matter—'non-algal' particles (NAP), both organic and inorganic (see Section 8.2.3):
- coloured dissolved organic matter (CDOM)—from hydrocarbon compounds (see Section 8.2.4); and
- coloured dissolved inorganic matter (CDIM)—from mineral compounds (see Section 8.2.5).

Where the water colour is clearly attributable to the interactions between pure water and one of the other optical constituents, EO data can be used to reliably map and monitor the concentration of that constituent. This situation occurs for the 'optically simple' waters that characterise deep oceans. In these 'Case 1' waters (as defined in Section 8.3.1) the water colour varies with the concentration of phytoplankton and its breakdown products (see Sections 18.5 and 18.6). As such, simple relationships can be established between phytoplankton concentration and the optical reflectance recorded by EO sensors (see Sections 5.2.3.1 and 8.2.2). However, in complex waters multiple optically active constituents occur resulting in characteristic reflectance features for the four water colour constituents shown in Figure 18.1. These are 'case 2' waters (see Section 8.3.1).

Background image: Algal bloom in Westlake Park, Melbourne, during March 2014. **Source:** © Nearmap

Recommended Chapter Citation: Anstee, J.M. (2021). Colour. Ch 18 in *Earth Observation: Data, Processing and Applications. Volume 3B—Surface Waters.* CRCSI, Melbourne. pp. 345–365. ISBN 978-0-6482278-5-4

In most inland and coastal waters, however, water colour derives from the interactions between multiple optical constituents. These 'Case 2' waters are 'optically complex' and require more sophisticated models based on optical physics to unravel their components (see Section 18.6). In particular, algae can confuse simple mapping techniques as it both contains the pigment of chlorophyll and forms part of suspended matter (Dekker *et al*., 2001).

Optically complex waters involve non-covarying concentrations of several optical constituents (see Section 18.1). Concentrations of these constituents can change rapidly, in both time and space, based on climatic, seismic, and/or anthropogenic 'events', and seasonal, lunar, and diurnal cycles. Optically complex waters can be both:

- optically deep (see Section 18.3.1)—the EO signal only derives from the water surface and the water column (plus atmospheric scattering); and
- optically shallow (see Sections 18.3.1 and 18.3.2)—the reflectance from the substratum is also measurable by an EO sensor.

Modelling approaches to the radiative transfer process are introduced in Section 8.4.2.4. When the optical properties of a natural waterbody are known (or can be reasonably assumed), bio-optical models can simulate the optical impact of varying concentrations of different optical constituents and identify those constituents that make greatest contribution to water colour variations (see Figure 18.2).

Figure 18.2 Simulations of waterbody reflectance

The Bio-opti model was used to generate reflectance spectra assuming a nadir view of a waterbody with depth 10.5 m over a sand substrate. Concentrations of three water column constitutents have been varied, with lowest concentration shown as violet through to the highest concentration as red. These simulations show the impact of these changed concentrations on reflectance spectra.

a. Chlorophyll a (CHLA) 0.001–50 μg/l (with CDOM 0.25 m^{-1}, NAP 22.266 mg/l)

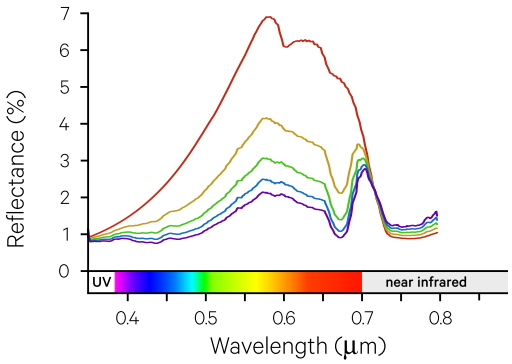

b. Coloured dissolved organic matter (CDOM) 0.001–5 m^{-1} (with CHLA 0.001 μg/l, NAP 22.266 mg/l)

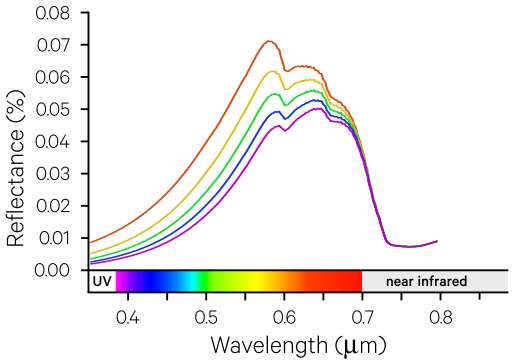

c. Non-organic particles (NAP) 0.001–100 mg/l (with CHLA 0.001 μg/l, CDOM 0.25 m^{-1})

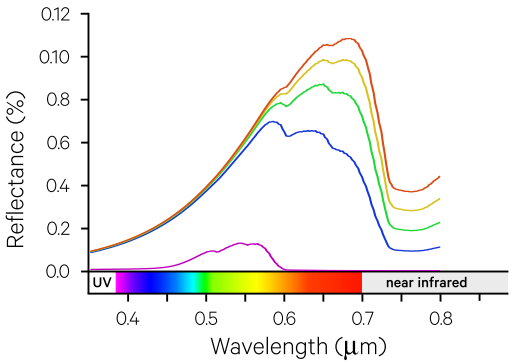

Source: Yi Qin, CSIRO

18.1 Colour of Australian Surface Waters

The near pristine marine waters around parts of Australia justify the poetic description of 'jewel-sea'. However, as introduced in Section 7.1, the colour of a waterbody varies with its organic and inorganic content (which can result from both natural and anthropogenic sources), its depth, and its substratum. While clear water is viewed as 'natural', it may not be 'typical' for some aquatic environments. For example, the water in smaller Australian inland waterbodies is frequently stained brown by tannins leached from the foliage and/or bark of local flora and from soil carbon.

Water colour indicates the type and quantity of the optically active constituents in the water column. Algae, suspended sediment, and dissolved organic material can influence the absorption and/or the scattering of the water. These constituents fluctuate in natural waters due to the inflow of rivers and creeks, or inputs of nutrients, pollution, and sediments; additionally currents and wind can cause mixing and resuspension. For example, in Figure 18.3, water colour ranges from blue to aqua to green in coastal waters, and from green to yellow to brown in inland waters, with the colour varying depending on what is in the water:

- phytoplankton generally makes the water green;
- non-algal particulates, such as sand, silt, or mud make the water vary from caramel to grey to brown; and
- dissolved organic matter makes the water yellow to orange to dark brown or almost black (like black tea).

I love her far horizons,
I love her jewel-sea,
(Dorothea Mackellar, 'My Country')

Figure 18.3 Variations in surface water colour

In the photos below, the water colour ranges from aqua and green to yellow and brown. The colours vary depending on what is within the water: Phytoplankton generally makes the water green, non-algal particulates, such as sand, silt, or mud, make the water caramel, grey, to brown in colour, while dissolved organic matter makes the water yellowish (like black tea)

a. NSW coastal waters

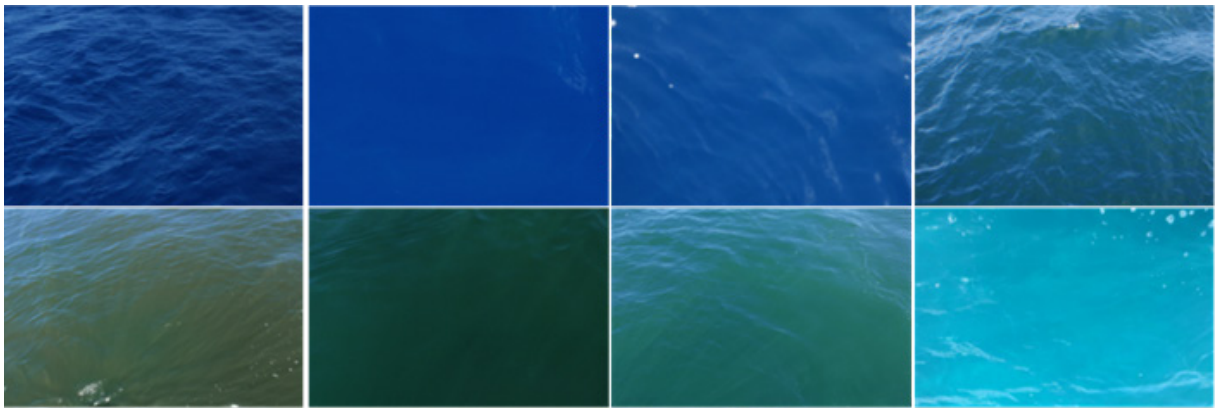

b. Australian Inland waters

Source: Janet Anstee, CSIRO

An innovative approach to monitoring water colour in Australian surface waters is called 'EyeonWater' (see Volume 2D—Excursus 12.4). This project is part of a global effort to equip citizen scientists with simple tools to accurately record water colour information using the Forel-Ule scale (see Section 18.3). It will also increase the spatial and temporal density of water colour observations in Australia, which will enable scientists to validate local water quality products derived from EO imagery. The scientific challenge is to quantify the link between water colour (from the Forel-Ule colour scale) and the concentrations of algae, sediment, and dissolved organic material in the water. Through a series of experiments (such as van der Woerd and Wernand, 2018, Busch *et al.*, 2016), the citizen science measurements of water colour can be linked to concentrations of constituents (algae, sediments, and organic matter), by converting the satellite image spectrum into three chromaticity coordinates, which are then compressed into a single Hue angle and finally a Forel-Ule value (see Figure 18.4). This means the citizen science data ultimately could be used to validate time series of satellite-derived water colour products.

Figure 18.4 Hue angle conversion

A chromaticity diagram showing the relationship between the Forel-Ule scale and the image hue colour angle (α). The outer ring shows the dominant wavelength (in nm) associated with the Forel-Ule scale.

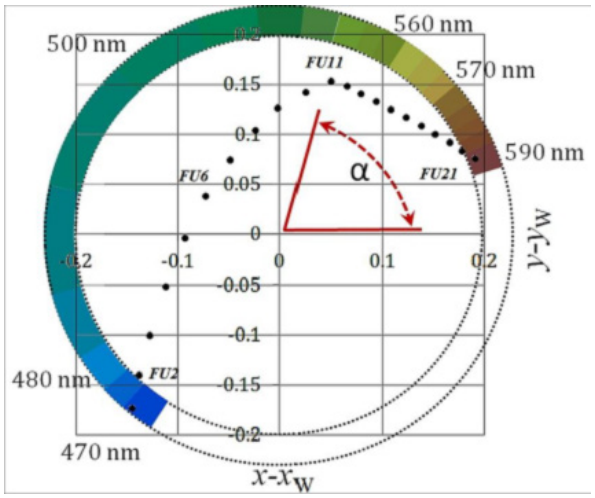

Source: van der Woerd and Wernand (2015)

18.2 EO Sensors for Water Colour

Characteristics of EO sensors are introduced in Volume 1A. The colours of surface waters are mapped and monitored using passive optical sensors carried on a variety of platforms—spaceborne, airborne, shipborne, and onshore (see Table 18.1). Specific features of optical EO sensors that are desirable for mapping water colour are detailed in Section 8.5.

Table 18.1 EO sensors relevant to water colour

Type	Sensor	Platform	Relevance	Advantages	Disadvantages
Passive optical	Smartphone	Handheld	Water colour	Portable, flexible timing	Not accurately calibrated, small area coverage
	Multispectral radiometer	Satellite	Water colour	Large area, regular coverage	Lower spectral resolution
		Airborne or shipborne	Inland and coastal applications of water colour	Higher spatial resolution	More expensive, smaller area coverage
	Hyperspectral radiometer	Satellite, airborne or shipborne	Inland and coastal water colour	High spectral and temporal resolution	Large data volumes, lower spatial resolution

18.3 Classifications of Water Colour

The colour of water is a complex optical feature (Dekker *et al.*, 2001). Variations in water colour are largely related to water absorption characteristics, whereas variations in intensity of colour are more closely related to backscattering properties (see Section 8.1.1). As introduced in Section 8.3, the optical characteristics of water can be described in terms of their inherent (see Table 8.5 and Table 8.9) or apparent (see Table 8.6 and Table 8.10) properties, where:

- inherent optical properties (IOP) are independent of lighting conditions (see Section 8.3.1); and
- apparent optical properties (AOP) are relative to ambient lighting conditions (see Section 8.3.2).

Figure 18.5 The Forel-Ule colour scale

This colour scale differentiates 21 different water colours.

Source: Wernand (2011)

Various schemes have been proposed to classify water colour. Mobley (2020) lists three methods that are commonly used:

- visual matching of a sample to the Forel-Ule Scale—this colour comparator scale was originally developed by Forel (1890) and extended by Ule (1892) and has been used extensively to classify water colour in rivers, lakes and oceans (Wernand and van der Woerd, 2010, van der Woerd and Wernand, 2018; see Figure 18.5);
- analysis of AOP—to differentiate between waters whose colour is dominated by chlorophyll and those whose colour is dominated by inorganic particles (see Section 18.3.1); and
- analysis of IOP—to determine relative absorption of phytoplankton, non-algal particles, and CDOM (see Section 18.3.2).

The content or constituents of the water can be inferred from the natural water colour to assess water quality issues and monitor long term variations (see also Volume 1B—Section 6.4). For example, the Forel-Ule colour scale has been in use since the late 19th century for the assessment and classification of water quality in oceanography and limnology (Novoa *et al.,* 2014, 2015). This scale defines 21 colours, spanning from indigo blue, through blue-green and yellow to chocolate brown (see Figure 18.5). Since one of the most obvious characteristics of water to the human eye is water colour, to use this scale an observer simply visually compares its sample colours with the colour of the water surface.

This approach offers considerable advantages for assessing historical trends in water colour and chlorophyll concentration at a global scale (Wernand, 2011). For example, global records of Forel-Ule water colour from 1889 to 2000 have been archived (Wernand *et al.,* 2013) and are available for temporal comparison with current conditions. The global project, EyeonWater, collates ongoing observations on water colour based on the Forel-Ule scale.

18.3.1 Classifications based on AOP

Use of AOP spectra (see Section 8.3.2) to classify waterbodies was introduced by Jerlov (1968) and developed by Morel and Prier (1977) to describe two types of oceanographic waters:

- Case 1 waters—chlorophyll concentration is higher than inorganic particle concentration; and
- Case 2 waters—inorganic particle concentration is higher than chlorophyll concentration.

More recently, these meanings have changed to:

- Case 1 waters—where phytoplankton and its breakdown products are the dominant factors in colour; and
- Case 2 waters—where colour is determined by phytoplankton, its breakdown products and many other factors, including CDOM (from terrestrial and *in situ* sources), NAP, CDIM, and, where visible, substratum reflectance.

Dekker *et al.* (2001) differentiate between 'optically shallow' and 'optically deep' waters:

- optically shallow waters—where the substrate signal is detectable through the water column by an EO sensor; and
- optically deep waters—where the substrate signal is not detectable through the water column.

Optically shallow waters are more complex to map and model than optically deep waters. Optically shallow waters typically include coastal (estuarine and coral) and inland waterbodies, as well as shallow, ocean water where the substratum is 'visible' to a sensor above the water surface. Examples of optically shallow waters include submerged macrophytes and sandy bottoms in lakes, seagrass and macro-algae meadows in estuarine and coastal environments, and coral reefs in tropical ocean environments. Maritorena *et al.* (1994) summarise and describe the physics of an optically shallow waterbody where part of the reflectance at the surface is composed of a bottom signal and part results from the water column. Semi-analytical models adequately explain the optical properties of optically shallow waters (see Section 8.4.2.3).

By contrast, in optically deep waters, where the substratum is obscured by the water column, the water colour is only determined by the water surface and the water column. Such waters are either too highly attenuating (turbid) or too deep to allow the substratum to be visible at or above the water surface. Optically deep waters include large inland lakes and reservoirs, coastal and ocean waters, whose vast dimensions are suited to coverage by satellite imagery, but also include shallow inland and coastal waters with high sediment or algal concentrations. The optical properties of oceans are determined by phytoplankton and its breakdown products whereas the other waters may have high concentrations of TSM and CDOM. In oceans as 'optically relatively simple' waters, only a limited number of spectral bands in the blue-green wavelengths suffice to infer chlorophyll concentrations with adequate precision for most oceanographic biological purposes (Dekker *et al.*, 2001). The colour of 'optically complex' waters is determined by optical components other than pure water, phytoplankton, and its breakdown products, and may include a composite of:

- phytoplankton and cyanobacteria pigments;
- particulate matter (NAP) from dead particulate organic matter and particulate inorganic matter;
- CDOM from terrestrial or aquatic origin;
- CDIM; and
- if visible, bottom reflectance influences.

The relatively simple band ratio (empirical) algorithms applicable to clear ocean waters are inappropriate for most inland and coastal waters. They are also inappropriate for some algal bloom situations in ocean waters. For example, to identify the optical properties of cyanobacteria algal blooms using EO would require additional spectral bands detecting green, yellow, and orange wavelengths (see Section 8.5).

18.3.2 Classifications based on IOP

IOP analyses can be represented by ternary diagrams, where the central point indicates equal absorption by the three components (phytoplankton, NAP, and CDOM) and each apex corresponds to water containing a single component (see Figure 18.6).

The variation between water sources visible in Figure 18.6b (Blondeau-Patissier *et al.*, 2009) for reefal waters was similar to that found between Mediterranean, North Sea, and Baltic waters by Babin *et al.* (2003). These two publications clearly illustrate that assuming chlorophyll to be the only optically active substance, and relying on algorithms focusing solely on chlorophyll, will not work in these waters.

Figure 18.6 Ternary diagrams

CDOM: Colour dissolved organic matter; NAP: Non-algal particles

a. Absorption properties for CDOM, chlorophyll and NAP derived from 11 Australian coastal and inland study site clusters.

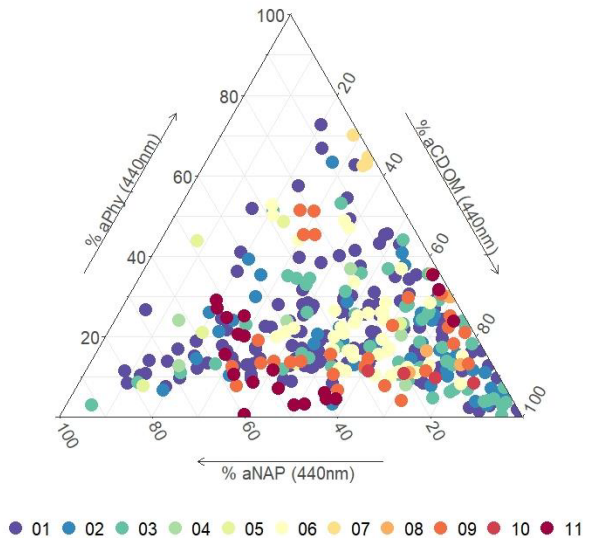

b. Ternary plot for waters flowing into the Great Barrier Reef Lagoon (Fitzroy River), the lagoon waters, and ocean reef waters, showing the variation between these sources.

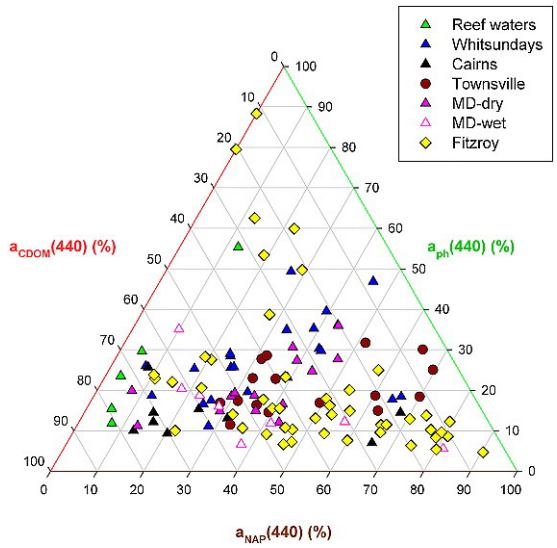

Source: a. Botha *et al.* (2020) Figure 6; b. Blondeau-Patissier *et al.* (2009)

18.3.3 Optical Water Types (OWT)

A recently developed method for characterising optically complex waters is based on classification of Optical Water Type (OWT; Moore *et al.,* 2009, 2014; Vantrepotte *et al.,* 2012). This surge in interest in OWT results from the challenge of trying to develop a single algorithm that applies to multiple types of water, such as from inland to estuarine to coastal to ocean. By initially defining a set of OWT, a locally trained algorithm can then be developed for each water type.

A range of classification methods have been proposed to establish OWT, mostly incorporating some form of cluster analysis to group IOP data based upon differences in the magnitude and shape of reflectance spectra (Spyrakos *et al.,* 2018). For example, rather than discriminating between Case I and Case II waters, Moore *et al.* (2009, 2014) suggested statistically analyzing a range of IOP and AOP, then focusing on the 'shape' of water-leaving reflectance to determine a set of OWT.

OWT can provide information about the concentration of optically significant constituents in each class, proposing a better mechanism for the understanding of biogeochemical and biological variables. OWT classification data has been used to:

- facilitate the empirical retrieval of water column constituents (e.g. McKee and Cunningham, 2006; Melin *et al.,* 2011; Spyrakos *et al.,* 2011);
- train neural networks (e.g. Dzwonkowski and Yan, 2005; Spyrakos *et al.,* 2011);
- parameterize bio optical models, as suggested by Lubac and Loisel (2007) and McKee and Cunningham (2006); and
- understand the role of physical oceanographic processes in complex waters (Cherukuru *et al.,* 2016).

18.4 Transparency

Water transparency is a measure of the clarity of water, and can be estimated by the use of a Secchi disk (a 30 cm white, or black and white, disk), which is lowered into the water column and eventually disappears from view at the secchi depth (see Figure 5.12). The Secchi depth is a measure of the transparency or clarity of the water (Preisendorfer, 1986) or visibility in the vertical direction (Duntley, 1952). Secchi depths have been measured in the world's oceans for over 200 years, enabling large datasets for water transparency to be collated (Wernand, 2011). Measurements of transparency are relevant for the spatiotemporal understanding of water properties, particularly in relation to light availability and fluxes of phytoplankton and suspended sediments. A number of studies have estimated Secchi depth from EO datasets (Phinn *et al.,* 2005; Doron *et al.,* 2011).

Sediments carried by water movement over terrestrial surfaces or shallow substrates can become suspended to create turbid water conditions (see Section 5.1.4). Sources of sediment include river erosion and storm runoff. A healthy aquatic ecosystem will include some turbidity but excessive levels of sediment degrade most aquatic environments, including coral reefs (Pollock *et al.,* 2014). When sediment settles on benthos, it can block light required by aquatic plants for photosynthesis (Fabricius, 2005) and inhibit feeding of organisms. Suspended sediments also attract and transport contaminants, such as nutrients and pesticides, with consequent impact on water quality (see Section 19). As such, sediment load may indicate pollution potential (Ongley, 1996; FAO, 2000). Over time, settling sediments change the hydraulic characteristics of river channels and reduce the storage capacity of reservoirs.

A large turbidity gradient occurs in the first 20 km from many coastlines. Since turbidity results from sediments held in suspension, turbid conditions are maintained by water movement, with sediments settling down out of the water when it is still. Measurements of turbidity can also vary temporally in intertidal and coastal waters, with the concentration of suspended particles potentially changing from near zero to over 100 g/m^3 within one tidal period (Dekker *et al.,* 2001).

Turbid river plumes are often clearly visible as they travel into coastal waters. The concentration of suspended sediments in tropical river plumes, for example, can vary from a few g/l to a few mg/l (Furnas, 2003). The sediment layer, however, may only span a few metres of water in depth, effectively overlaying clearer waters. While highly visible, such plumes pose less danger to nearshore reefal systems than the lower and more concentrated sediment circulated by wind-driven waves (Furnas, 2003).

The presence of sediments increases water reflectance across all optical wavelengths (see Figure 18.7). The actual shape of the spectral reflectance distribution of suspended sediments varies with properties of the sediment particles, namely their:

- absorption and backscattering properties,
- refractive index;
- mineral composition;
- particle size(s); and
- concentration.

Figure 18.7 Non-algal particulates

Effect of increasing NAP concentrations from 0.001 mg/L to 100 mg/L on spectral reflectance just under the water surface (R(0-)), as modelled by Bio-opti for fixed chlorophyll (1.27 μg/L) and CDOM absorption at 440 nm = 0.199 m^{-1}.

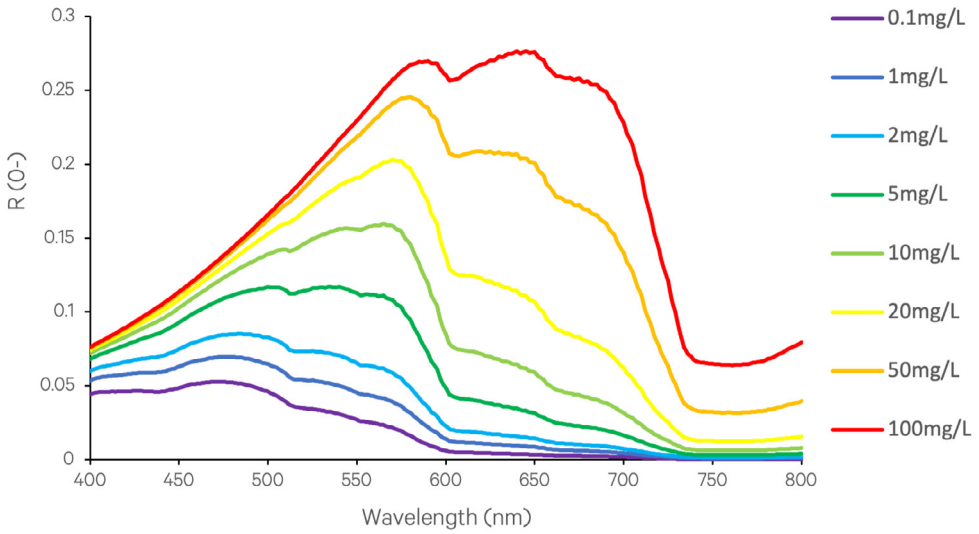

Source: Janet Anstee, CSIRO

There are many different types (e.g. clays, silts, sands) and colours (e.g. white, yellow, red, brown, black) of sediment with different chemical and optical properties (Novo *et al.*, 1989). It should be noted that the observed colour of dry sediment particles changes, in terms of hue, saturation, and intensity, when mixed with water, and also changes with different concentrations of sediment and other water constituents. As the concentration of red loam in clear water increases, for example, the water colour generally changes from yellow to orange then red, whereas in water containing algae with the red loam, the water colour changes from green at low sediment concentrations to orange at high concentrations (Han, 1997). Natural waters, however, generally contain a mixture of different types of sediment.

The particle size of suspended matter in water can also vary markedly between different locations and at different times. Spectral separability and detectably from EO data will be diminished with fewer, less relevant spectral bands (see Figure 18.8, and Sections 8.5 and 18.2).

As illustrated in Figure 18.7, an increased concentration of suspended particles in water tends to strengthen the peak reflectance. This relationship has allowed EO imagery to be used to derive measures of turbidity, often expressed in terms of Total Suspended Solids (TSS) or Suspended Sediment Concentration (SSC; Alfoldi and Munday, 1978; Ritchie and Schiebe, 1986; Curran *et al.*, 1987). As detailed in Volume 2C, processing methods have included:

- correlations with calibration data, using linear (Ritchie *et al.*, 1976;) or logarithmic (Munday and Alfoldi, 1979; Lathrop and Lillesand, 1989) relationships with individual bands;
- correlations with calibration data using linear relationships with combinations of multiple bands (Chen *et al.*, 1992);
- Principal Component Analysis (Blondeau-Patissier *et al.*, 2014); and
- semi-analytical inversion models (see Section 8.4).

EO-based studies of different waterbodies have generally concluded that the strongest relationship between high sediment concentration and water reflectance is observed in the longer optical wavelength bands, principally red and near infrared (Ritchie and Cooper, 1988, 1991; Schiebe *et al.*, 1992).

Figure 18.8 Simulated EO reflectance for different substrates

In Botha *et al.* (2013), EO reflectance spectra were modelled for three different substrate types at 6 m water depth (Y: yellow coral, B: brown coral and OD: optically deep water column), then resampled to the equivalent spectral bands of the imaging spectrometer CASI and the multispectral sensors, Worldview-2, and QuickBird EO, to demonstrate the effect of spectral resolution and water column constituents on the normalised spectral separability metric (nSSM) of the two substratum types from an optically deep water column and from each other. nSSM has higher values for better separation, and accounts for shape and albedo differences between the two spectra.

a. Reef-oceanic water column (Case 1 water)

b. Coastal water column (Case 2 water)

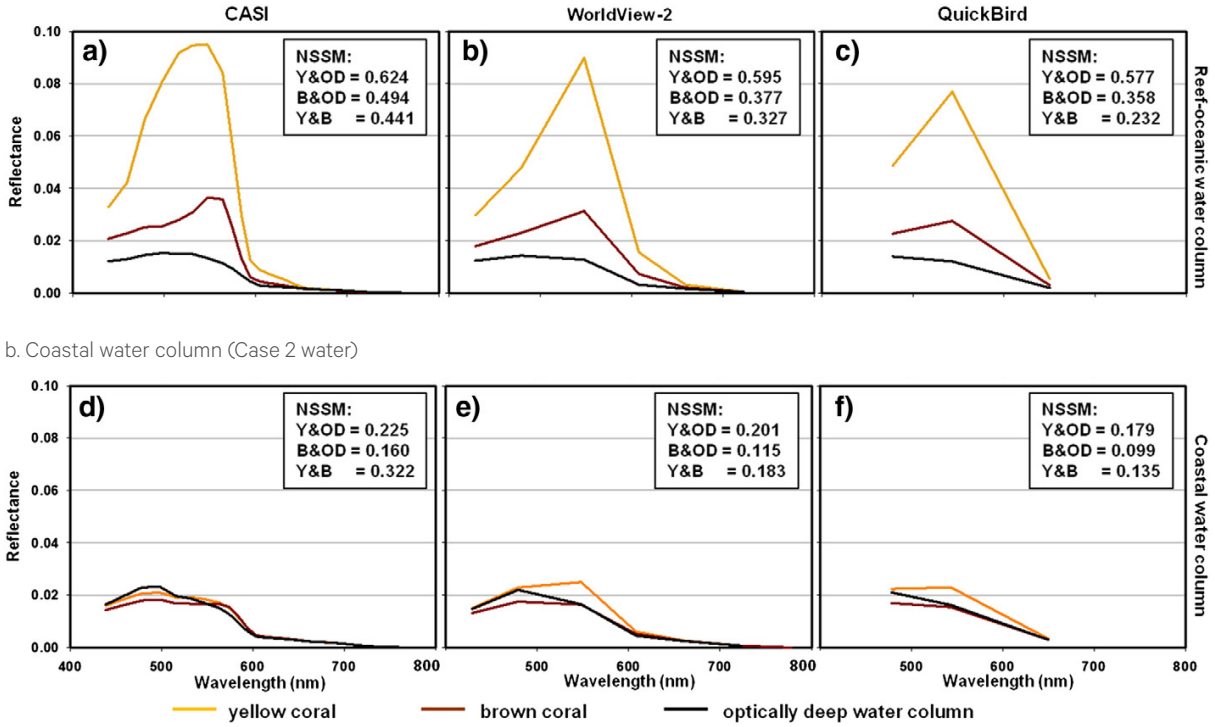

Source: Botha *et al.* (2013) Figure 8

Various studies have focused on spectral characteristics of different types of sediments and observed that:

- turbidity and reflectance are linearly related for bentonite clay and black cotton soil, and have a curvilinear relationship for kaoline and gray soil (Bhargava and Mariam, 1990);
- have a constant relationship for oxisoil sediment (log-linear 450–700 nm and linear 700–1050 nm; Chen *et al.*, 1991)
- finer sediments raise reflectance faster than coarser sediments for equivalent concentrations (Bhargava and Mariam, 1991; Han and Rundquist, 1996);
- the same concentration of red loam soil resulted in higher reflectance in visible wavelengths (400–700 nm) in clear water than in algae-laden water (Han, 1997);
- algae in water had minimum spectral impact on the relationship between turbidity and reflectance for near infrared (NIR) wavelengths in the range 700–900 nm (Han, 1997); and
- the increase in spectral reflectance with increasing concentration of sediment is reduced when sediment load exceeds 600 mg/l (Lodhi *et al.*, 1998).

Optical measurements of known concentrations of sediment using spectroradiometers have allowed precise relationships between SSC and reflectance to be derived for specific types of sediment (Han, 1997). Such measurements have also been integrated over spectral regions corresponding to EO image bands to calibrate SSC image products (Lodhi *et al.*, 1998).

Since the scattering characteristics of suspended particles are closely related to their size, a universal algorithm to map and model suspended sediments, may be unlikely according to Kirk (1994, 2010). However as particle size affects the slope of the backscattering spectrum it may be possible to estimate particle size from a hyperspectral remote sensing signal, in which case a global suspended matter concentration algorithm may be possible.

In waters with stable levels of other optical constituents, forward optical models have indicated that suspended sediment is the principal contributing factor to changes in radiance in the wavelength range 630–690 nm (Tian *et al.,* 2014). However, in most natural waters, as the concentration of one optical constituent varies, the concentrations of other optical constituents also vary. In many instances, this complexity of factors necessitates more sophisticated modelling approaches to extract the concentrations of individual constituents.

When modelling the particulate backscattering spectrum as a power law function of wavelength, the magnitude and shape of backscattering can be estimated. The slope of the particulate backscattering has been shown to be related to chlorophyll (and thus algal biomass) concentration (Twardowski *et al.,* 2001) and particle size distribution (Reynolds *et al.,* 2001, Kostadinov *et al.,* 2009, Slade and Boss, 2015).

Physics-based models can also be used to understand and parameterise changes in spectral IOP of natural waters with varying concentrations of suspended sediment. For example, Dekker *et al.* (1999) developed a reflectance simulation model to estimate the full range of TSM concentrations that could occur in a dynamic tidal estuary in Kalimantan (Indonesia), then derived algorithms to analytically determine the TSM. Lymburner *et al.* (2016) used bio-optical modelling to develop sensor-specific TSM retrieval algorithms for three different Landsat sensors (TM, ETM+, OLI) over a range of Australian inland waterbodies. While the increased radiometric resolution of Landsat-8 OLI reduced image noise and spectral heterogeneity (Pahlevan *et al.,* 2014), TSM retrievals from all three sensors were comparable and highly correlated with coincident field measurements. These results enabled analysis of the Landsat time series to retrospectively characterise multi-decadal TSM dynamics.

18.5 Dissolved Matter

In the following subsections we will discuss EO methods to determine the concentrations of dissolved matter in surface waters, in the form of CDOM (see Section 18.5.1) and dissolved organic carbon (DOC; see Section 18.5.2).

18.5.1 CDOM

Since CDOM-rich water are typically dark, with little light reflected back to the EO sensor, it is difficult to find reliable methods to estimate CDOM from EO data (Brezonik *et al.,* 2015). A method proposed by Hoge and Lyon (1996), then adapted by Brando *et al.* (2012), retrieved CDOM using a matrix inversion method, which effectively decouples CDOM from the other light absorbing constituents. This approach is strongly driven by an understanding of the relationship between IOP and the water-leaving radiative signal (Tyler *et al.,* 2016; Matthews, 2011). Water quality information is found by inverting the EO signal, given the relationship between the subsurface remote sensing reflectance and coefficients of two IOP (absorption and backscattering; Gordon *et al.*, 1988).

Decreasing sea surface salinity has been previously used to determine freshwater discharge (Molleri *et al.,* 2010). CDOM has been found to be inversely correlated with salinity when compared with *in situ* data. In marine waters, CDOM is generally derived from phytoplankton decay, but in coastal waters, CDOM is predominately from anthropogenic sources transported by rivers and runoff. In Schroeder *et al.* (2012), CDOM was used as a surrogate for freshwater extent rather than backscattering or TSM since it was considered to be more reliable for mapping freshwater plumes, particularly where the particulate material in the freshwater plumes would drop out due to sedimentation.

18.5.2 DOC

Determining DOC in aquatic systems is required for modelling in the global carbon cycle (see Sections 1.5 and 7.4). In coastal environments, 80–90% of the total carbon is represented by DOC (Cao *et al.*, 2018) and EO data has been used to estimate DOC in these regions (Schwarz, 2005; ChunHock *et al.*, 2020).

The ratio between DOC and CDOM absorption at 412 nm allows for the potential to assess DOC distribution in ocean waters (Vantrepotte *et al.,* 2015). The CDOM spectral slope in UV wavelengths ($S_{275–295}$) has demonstrated its potential as a tracer of specific CDOM absorption (e.g. Cao *et al.*, 2018), but as UV reflectance is susceptible to errors in atmospheric correction, this approach has been found to overestimate DOC. While the approach has some limitations in its global applications, particularly for turbid waters, it has potential in less turbid waters.

Nearly all terrestrial ecosystems rest, physically and functionally, on an organic-rich soil foundation. Dissolved organic matter (DOM) is the soil of the sea—a large, biochemically resistant reservoir of organic matter providing a substrate for life, and a source for nutrient regeneration, ion exchange capacity, light and heat absorption, and so on.
Ducklow (2002)

The spectral features of river water are functions of its hydrological, biological, and chemical characteristics (see Section 5). CDOM, DOM, and chlorophyll a can be readily detected by *in situ* and EO optical measurements, and numerical relationships can be developed to relate these measurements to DOC (ChunHock *et al*., 2020), and even primary productivity (Robinson *et al*., 2017). In EO algorithms, CDOM has been used as a proxy for DOC in coastal waters by exploiting the relationship between the optically active CDOM and DOC concentrations at specific wavelengths (Ferrari *et al*., 1996).

For EO algorithms, the accurate retrieval of CDOM is required to derive DOC (Vantrepotte *et al*., 2015). Both empirical (Mannino *et al*., 2008) and semi-analytical (Loisel *et al*., 2014) algorithms have been used to retrieve CDOM accurately and from this, the DOC content is calculated. To derive the full spatiotemporal variability of coastal waters requires the *in situ* parameterisation data to be representative of the seasonal and salinity gradients of the region (Vantrepotte *et al*., 2015), especially where mixing between the freshwater and marine waters occur (Harvey *et al*., 2015).

Excursus 18.1—Blackwater Events

Source: Klaus Joehnk and Tapas Biswas, CSIRO
Further information: Vantrepotte *et al*. (2015); MDBA (2020); King *et al*. (2012)

Blackwater events are natural phenomena where a large increase in the carbon content of a waterbody tints the water colour black (see Figure 18.9). These events typically occur in lowland rivers. The extraction of organic material from dried leaves is a process similar to brewing a cup of tea, where clear water turns brown. The more leaf litter is added, the more decomposed it is, and the longer it is left to brew, the stronger and darker the water becomes. The leaching of organic matter is also strongly dependent on the water temperature.

Figure 18.9 Blackwater plume

Drone image of a blackwater plume entering Lake Victoria, South Australia, in November 2016.

Source: SA Water and Daniel Haines

This phenomenon often occurs in the Australian Murray-Darling Basin, one of the largest river basins in the world, after long drought periods when flooding rains lead to large scale inundation of floodplains. During dry years under non-flood conditions, organic matter (such as leaf litter, grass, or bark) accumulates on the floodplains. Whenever a floodplain that has accumulated a large volume of organic material is inundated, dissolved organic carbon (DOC) is leached, which makes the water appear black, hence the name blackwater.

Although carbon itself is an essential part of a thriving aquatic ecosystem, blackwater events go hand in hand with a decrease in dissolved oxygen (DO), eventually drawing oxygen down to hypoxic conditions leading to fish kills. Adding organic matter under higher temperatures increases microbial decomposition of the organic material, which consumes DO from the water. Whenever this process of consumption is higher than oxygen production (for example, due to photosynthetic algae in the water or re-aeration across the air-water boundary), DO levels drop. As the re-aeration of the stagnant or slowly flowing water on the floodplain is hindered, the water gradually turns black (high carbon content) leading to depleted levels of DO. In the worst case, when DO levels fall below 2 mg/l, fish and invertebrates start to suffocate and eventually die, giving rise to hypoxic blackwater, which finds its way slowly back to the river channel further downstream. While these events are often associated with negative impacts such as fish kills, decreased tourism activity, and additional water treatment costs, they also benefit the the overall ecosystem by delivering carbon into the river, to fuel aquatic food webs and increase river productivity, including fish populations.

Figure 18.10 Blackwater event

Large scale blackwater event around Lake Victoria on 28 November 2016 as seen from Sentinel-2 (right) compared with the natural flow regime on 7 August 2016 (left). The blackwater plume flowing into Lake Victoria shows the different colours of carbon-enriched and natural waters.

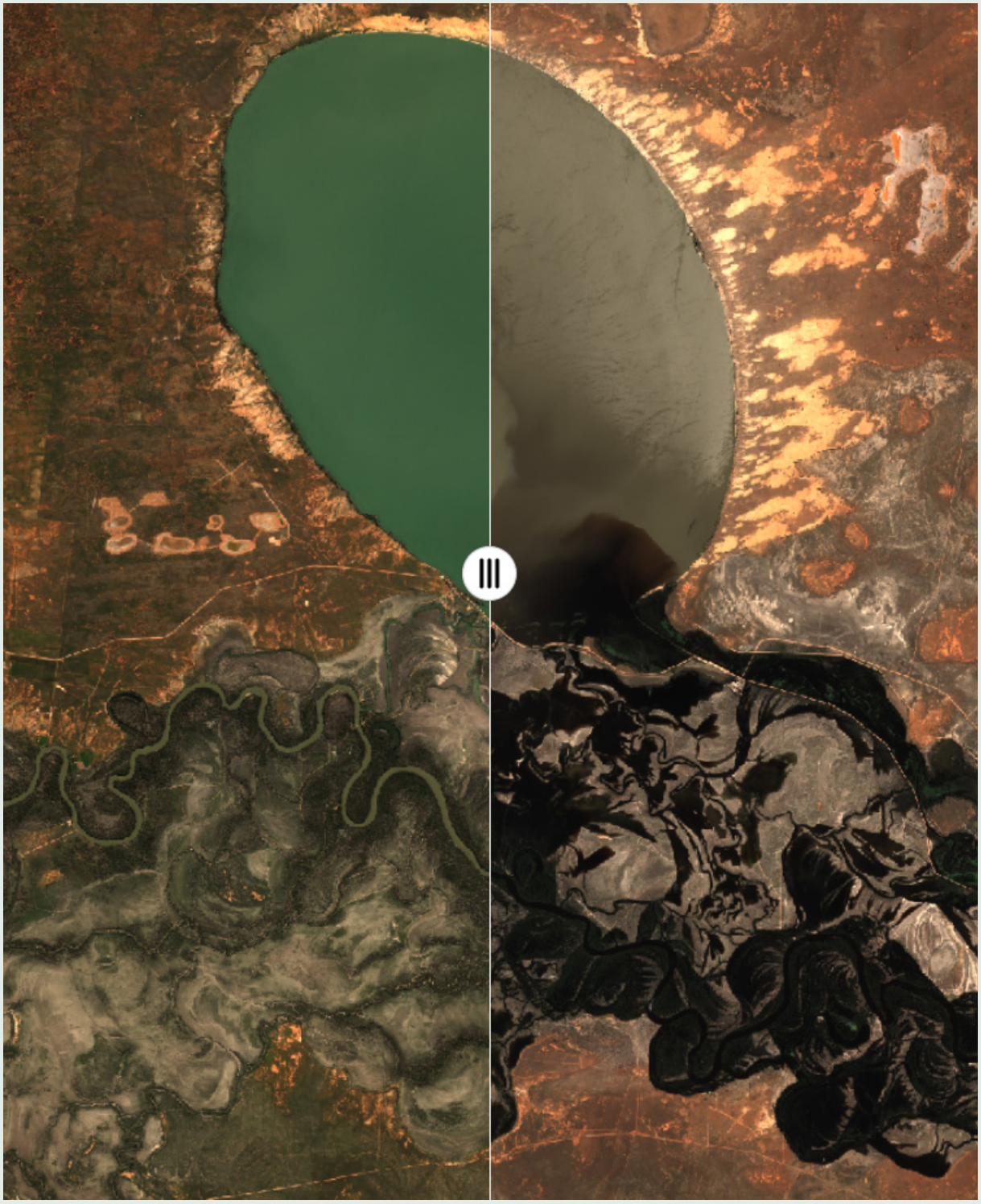

Over decades, river regulation in Australia has reduced the frequency of smaller overbank flows during winter and spring, which would steadily wash out carbon from the floodplains. Without these flows there is now a higher chance of litter accumulation, potentially resulting in more intense blackwater events. Under the Murray-Darling Basin Plan, state governments must take blackwater risks into account when planning water resource usage, by identifying potential causes of poor water quality and establishing cost-effective ways to achieve water quality objectives. It is thus necessary to develop options of adapted flow management with the aim of reducing leaf litter accumulation as much as possible to minimise future hypoxic events.

Since blackwater events can affect extensive areas of floodplains and river reaches over hundreds of kilometres, EO imagery provides the opportunity to track these events and provide early warning to undertake regulatory measures (see Figure 18.10). In combination with hydrodynamic modelling, EO can be used to estimate the risk of blackwater conditions as floodwaters progress. Due to their distinctive colour blackwater events are clearly visible from space, but flooding events also coincide with wet periods and a high chance of cloud cover which may obscure ground features.

Additionally, over recent decades, wildfires have increased in frequency and ferocity across Australia, the US, and other countries around the globe, which can result in similar negative effects on water quality as occur with lowland river blackwater events. For example, large plumes of blackwater generated by wildfire were observed during the devastating fires in southeast Australia in 2019/2020. Depending on burn severity in river catchments, rainfall after wildfires can wash out large quantities of ash and charred organic material, which then make their way into streams, reservoirs, and estuaries. This high carbon content tints the water black resulting in negative effects, such as fish kills caused by hypoxic water and smothering of gills.

18.6 Chlorophyll Content

EO of water colour was initially developed for the oceans, as it provides the only feasible method for assessing these vast areas for water quality. Typically, the optical properties of ocean waters are only affected by phytoplankton and its breakdown products. These waters are relatively simple in terms of their optical properties and are commonly referred to as Case 1 waters (see Section 18.3). A few bands in blue/green wavelengths are sufficient to determine chlorophyll concentrations with a precision that is adequate for most oceanographic-biological purposes (Dekker *et al*., 2001).

Chlorophyll a concentration products derived from satelite imagery are often based on ratios of relevant wavelengths. For example, the NASA chlorophyll a algorithm for MODIS (500 m) imagery computes:

$$\frac{\rho_{488}}{\rho_{555}}$$

(in mg/m^3) as illustrated in Figure 18.11a (NASA Earthdata, 2019). This algorithm assumes that the only optically active constituent affecting image reflectance is chlorophyll. While true for most oceanic waters, this assumption may not be true for coastal and inland waters, and near land this algorithm can deliver misleading results. Extensive fieldwork is generally needed in coastal waters to account for local variations in the optical properties of water (see Figure 18.11b). To avoid the impact of cloud, composite imagery is often used to map seasonal and longer term changes in chlorophyll content (see Volume 2D).

In coastal and inland waters, the retrieval of chlorophyll a is often challenging due to the complexity of the optical properties in these waters compared with clear ocean waters. The ocean colour algorithms that are based on chlorophyll a dominating the blue light absorption fail in the coastal and inland waters where there are high concentrations of sediment and CDOM (Gilerson *et al*., 2021).

Physics-based models (such as the MOMO radiative transfer model) have been used to model concentrations of chlorophyll a and suspended matter from multispectral imagery (CASI airborne imagery with six visible bands) over inland waters (Dekker *et al*., 2001; see Volume 1B—Excursus 6.3). Some of the complexities in mapping optically deep waters include:

- the spectral characteristics of CDOM, the organic fraction of NAP, and chlorophyll overlap in blue wavelengths, so it is not easy to determine which part of the absorption is due to CDOM;
- microalgae can move vertically in the water column, which means the observed surface concentration may underestimate the total volume of biomass;
- the optically active constituents of algal pigments, NAP, and CDOM, may not necessarily co-vary;
- surface effects such as waves or sunglint can increase the observed EO reflectance; and
- inland waters often are impacted by atmospheric adjacency effects from riparian vegetation, bright sands, or other highly reflective terrain features.

Figure 18.11 MODIS chlorophyll a concentration products

Major storms occurred in the Hunter region, north of Sydney, on 21–22 April 2015. On 25 April, the floodwaters appear as a yellow-orange ribbon near the centre of the images below. These MODIS chlorophyll a products highlight the interaction between floodwater from the Hunter River and both the low chlorophyll waters of the East Australian Current (coloured blue) and the more chlorophyll-rich waters of the Tasman Sea (coloured green). Note that these chlorophyll concentration images may confuse high CDOM levels from the land with high levels of aquatic chlorophyll.

a. Monthly NASA product based on 4 km grid using NASA chlorophyll a algorithm (see Volume 1B—Excursus 6.2) for 25 April 2015 at 04Z

b. The same image processed at 1 km and integrated with other datasets by IMOS OceanCurrent. Contours (at 0.1 m interval) show altimetric sea level and arrows indicate geostrophic current velocity for 25 April 2015.

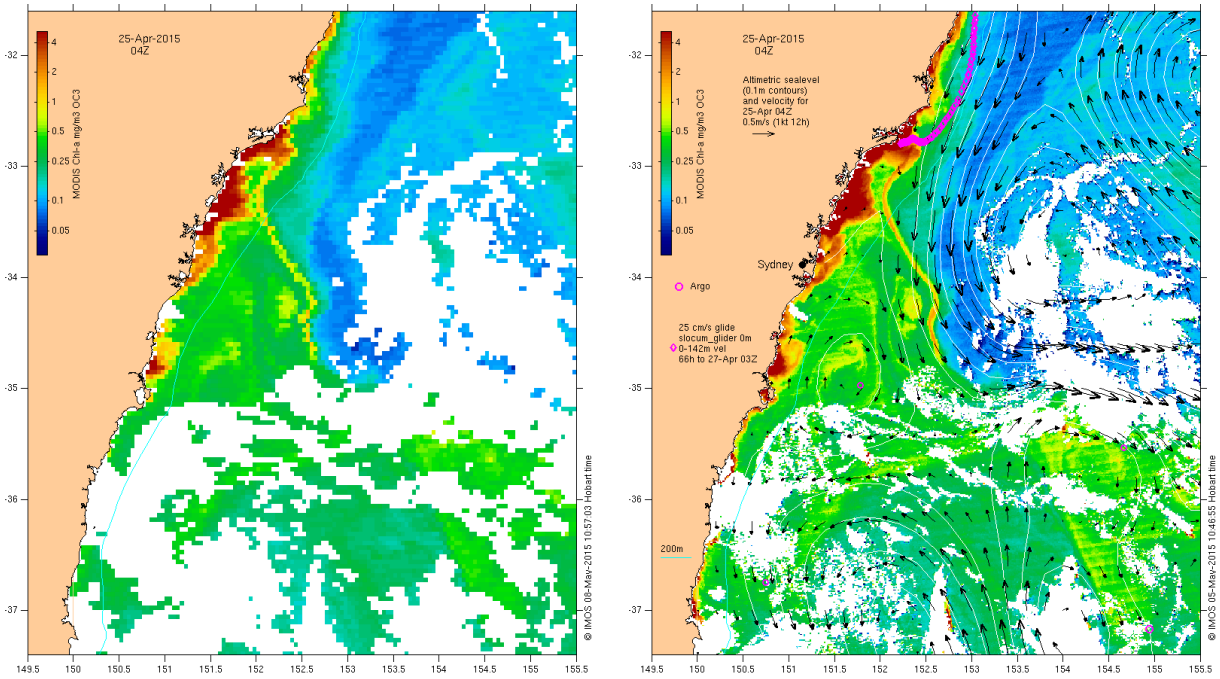

Source: Edward King, CSIRO © IMOS, based on NASA imagery

18.7 Substratum

The optical properties of substrata can change rapidly in both space and time (Mazel, 2001). For example, while seagrass blades stand vertically in calm water, in moving water the blades bend sideways, thus increasing the area of substratum they appear to cover. Epiphytic growth on seagrass blades can also expand rapidly to significantly restrict the amount of photosynthetically active radiation reaching the blades, with consequent reduction in plant productivity (see Figure 18.12).

As introduced in Sections 6 and 8 above, the reflectance from a waterbody is determined by its water depth, water colour, and substratum colour. The interactions between these factors are important in the interpretation of EO imagery in aquatic environments. Different 'above-water' reflectance values can result from a given substratum at different water depths (see Figure 18.13), or from a given substratum beneath different water colours. As such, EO analyses of substratum extent, and/or the vegetation it supports, require corrections for water depth (see Section 8.4.3).

Figure 18.12 Epiphytic growth on seagrass blades

Source: James St John, Wikimedia. Retrieved from: *https://commons.wikimedia.org/wiki/File:Syringodium_filiforme_(manatee_grass)_%26_Thalassia_testudinum_(turtle_grass)_(southeastern_Graham%27s_Harbour,_San_Salvador_Island,_Bahamas)_2_(15860252588).jpg*

Figure 18.13 Impact of water depth on substrate spectra

Reflectance spectra of a range of substrate materials are shown for different water depths. Reflected radiation across all wavelengths is signficantly diminished for all substrates as water depth increases, with the greatest impact occurring in the infrared region.

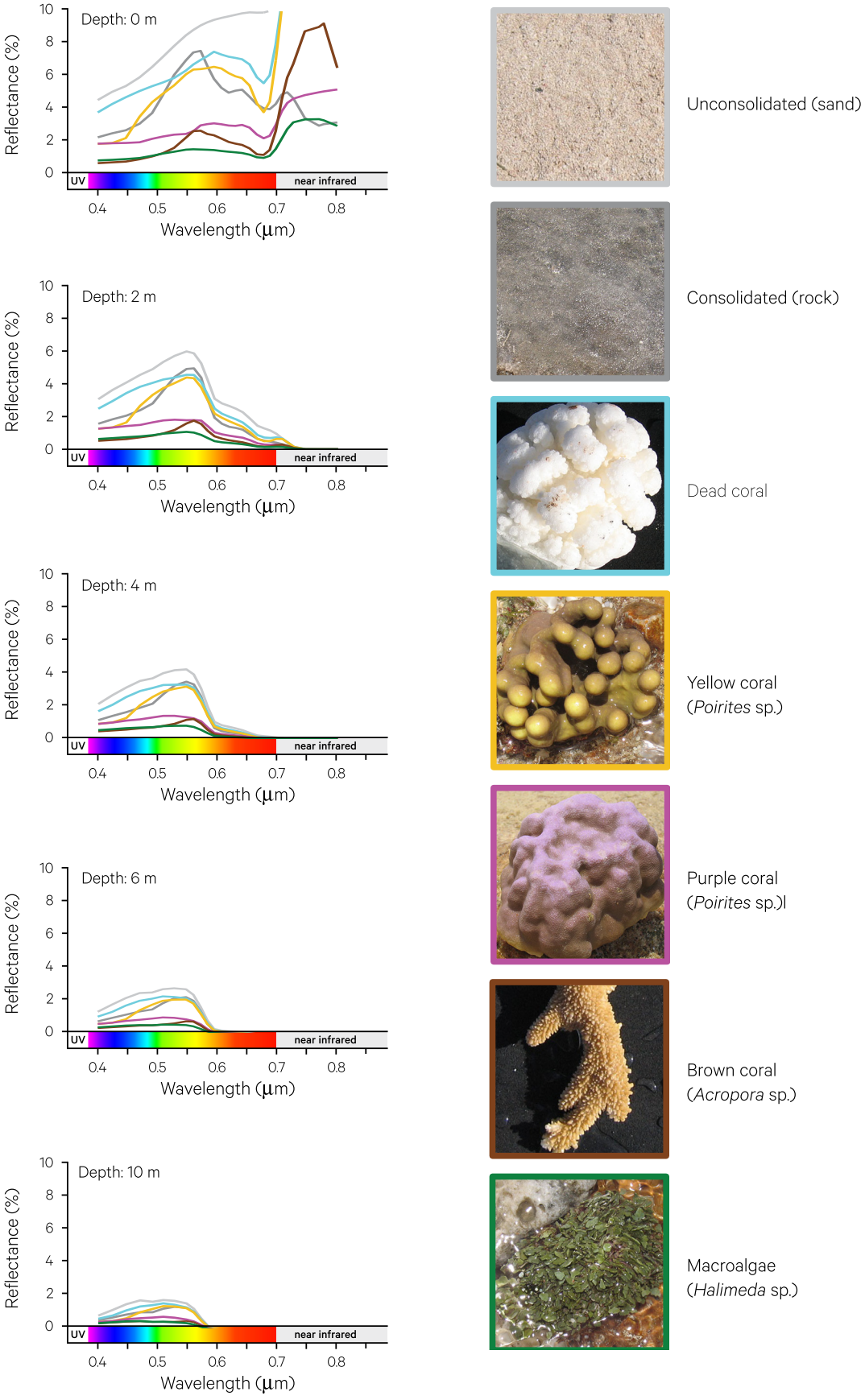

Adapted from: Botha *et al.* (2013)

18.8 Further Information

NASA

NASA Ocean Colour: *https://oceancolor.gsfc.nasa.gov*

NASA Aeronet-Ocean Colour: *https://data.nasa.gov/Earth-Science/AERONET-OCEAN-COLOR/jhyg-mp9e/data?no_mobile=true*

European Union (EU)

Citizens' Observatory for Coast and Ocean Optical Monitoring (Citclops 2012–2015): *http://www.citclops.eu*

EyeOnWater: *https://www.eyeonwater.org*

Australia

CSIRO Australian-waters EO Phytoplankton-type Products Data Base: *http://aesop.csiro.au/*

OzCoasts: *https://ozcoasts.org.au*

EyeOnWater Australia: *https://research.csiro.au/eyeonwater/*

Western Australian Marine Science Institution: *https://www.wamsi.org.au*

18.9 References

Alfoldi, T.T., and Munday, J.C. (1978). Water quality analysis by digital chromaticity mapping of Landsat data. *Canadian Journal of Remote Sensing,* 4(2), 108–126. doi:10.1080/07038992.1978.10854974

Babin, M., Stramski, D.,Ferrari, G.M., Claustre, H., Bricaud, A., Obolensky, G., and Hoepffner, N. (2003). Variations in the light absorption coefficients of phytoplankton, nonalgal particles, and dissolved organic matter in coastal waters around Europe, *Journal of Geophysical Research*, 108(C7), 3211. doi:10.1029/2001JC000882

Bhargava, D.S., and Mariam, D.W. (1990). Spectral Reflectance Relationships to Turbidity Generated by Different Clay Materials. *Photogrammetric Engineering and Remote Sensing*, 56(2), 225–229.

Bhargava, D.S., and Mariam, D.W. (1991). Effects of suspended particle size and concentration on reflectance measurements. *Photogrammetric Engineering and Remote Sensing*, 57(5), 519–529.

Blondeau-Patissier, D., Brando, V.E., Oubelkheir, K., Dekker, A.G., Clementson, L.A., Daniel, P. (2009). Bio-optical variability of the absorption and scattering properties of the Queensland inshore and reef waters, Australia. *Journal of Geophysical Research,* 114, C05003.

Blondeau-Patissier, D., Gower, J.F.R., Dekker, A.G., Phinn, S.R., and Brando, V.E. (2014). A review of ocean color remote sensing methods and statistical techniques for the detection, mapping and analysis of phytoplankton blooms in coastal and open oceans. *Progress in Oceanography*, 123, 123–144. *https://doi.org/10.1016/j.pocean.2013.12.008*.

Botha, E.J., Brando, V.E., Anstee, J.M., Dekker, A.G., and Sagar, S. (2013). Increased spectral resolution enhances coral detection under varying water conditions. *Remote Sensing of Environment,* 131, 247–261.

Botha, E.J., Anstee, J.M., Sagar, S., Lehmann, E., and Medeiros, T.A.G. (2020). Classification of Australian Waterbodies across a Wide Range of Optical Water Types. *Remote Sensing*, 12, 3018. doi:10.3390/rs12183018

Brando, V.E., Dekker, A.G., Park, Y.J., and Schroeder, T. (2012). Adaptive semianalytical inversion of ocean color radiometry in optically complex waters. *Applied Optics*, 51, 2808–2833.

Brezonik, P.L., Olmanson, L.G., Finlay, J.C., and Bauer, M.E. (2015). Factors affecting the measurement of CDOM by remote sensing of optically complex inland waters. *Remote Sensing of Environment*, 157, 199–215. doi:10.1016/j.rse.2014.04.033

Busch, J.A., Bardaji, R., Ceccaroni, L., Freidrichs, a., Piera, J., Simon, C., Thijsse, P., Wernand, M., van der Woerd, H.J., and Zielinski, O. (2016). Citizen Bio-Optical Observations from Coast- and Ocean and Their Compatibility with Ocean Colour Satellite Measurements. *Remote Sensing*, 8, 879. doi:10.3390/rs8110879

Cao, F., Tzortziou, M., Hu, C., Mannino, A., Fichot, C.G., Del Vecchio, R., Najjar, R.G., and Novak, M. (2018). Remote sensing retrievals of colored dissolved organic matter and dissolved organic carbon dynamics in North American estuaries and their margins, *Remote Sensing of Environment*, 205, 151–165. *https://doi.org/10.1016/j.rse.2017.11.014*

Chen, Z., Hanson, J.D., and Curran, P.J. (1991). The form of the relationship between suspended sediment concentration and spectral reflectance: its implications for the use of Daedalus 1268 data. *International Journal of Remote Sensing,* 12(1), 215–222.

Chen, Z., Curran, P., and Hansom, J. (1992). Derivative reflectance spectroscopy to estimate suspended sediment concentration. *Remote Sensing of Environment*, 40, 67–77. doi:10.1016/0034-4257(92)90127-6.

Cherukuru, N., Davies, P.L., Brando, V.E., Brando, V.E., Anstee, J.M., Baird, M.E., Clementson, L.A., and Doblin, M.A. (2016). Physical oceanographic processes influence bio-optical properties in the Tasman Sea. *Journal of Sea Research*, 110, 1–7. doi:10.1016/j.seares.2016.01.008

ChunHock, S., Cherukuru, N., Mujahid, A., Martin, P., Sanwlani, N., Warneke, T., Rixen, T., Notholt, J., and Müller, M. (2020). A New Remote Sensing Method to Estimate River to Ocean DOC Flux in Peatland Dominated Sarawak Coastal Regions, Borneo. *Remote Sensing*, 12, 3380. *https://doi.org/10.3390/rs12203380*

Curran, P. J., Hansom, J. D., Plummer, S. E., and Pedley, M. I. (1987). Multispectral remote sensing of nearshore suspended sediments: a pilot study. *International Journal of Remote Sensing* 8, 103–112.

Dekker, A.G., Peters, S.W.M., Rijkeboer, M., and Berghuis, H. (1999). Analytical processing of multitemporal SPOT and Landsat images for estuarine management in Kalimantan Indonesia. *18th EARSeL Symposium on Operational Remote Sensing for Sustainable Development* (Eds: G.J.A. Nieuwenhuis, R. Vaughan, and M. Molenaar) pp 315–324. A.A.Balkema, Rotterdam, The Netherlands.

Dekker, A.G., Brando, V.E., Anstee, J.M., Pinnel, N., Kutser, T., Hoogen-boom, J., Peters, S.W.M., Pasterkamp, R., Vos, R.J., Olbert, C., and Malthus, T.J. (2001). Imaging spectrometry of water. Ch 11 in *Imaging Spectrometry: Basic Principles and Prospective Applications*. (Eds: F.D. van der Meer and S.M. de Jong), pp 307–359. Kluwer Academic Publishers, Dordrecht, The Netherlands.

Doron, M., Babin, M., Hembise, O., Mangin, A., and Garnesson, P. (2011). Ocean transparency from space: Validation of algorithms estimating Secchi depth using MERIS, MODIS and SeaWiFS data. *Remote Sensing of Environment*, 115, 2986–3001.

Ducklow, H.W. (2002). Foreword in *Biogeochemistry of marine organic matter*. (Eds: D. Hansell and C. Carlson). Academic Press, San Diego. ISBN: 0-12-323841-2

Duntley, S.Q.(1952). *The Visibility of Submerged Objects*. Visibility Laboratory, Scripps Institution of Oceanography, University of California, San Diego. *https://escholarship.org/uc/item/2mz4d121*

Dzwonkowski, B., and Yan, X.H. (2005). Development and application of a neural network based ocean colour algorithm in coastal waters. *International Journal of Remote Sensing*, 26, 1175–1200.

Fabricius, K. (2005). Effects of terrestrial runoff on the ecology of corals and coral reefs: review and synthesis. *Marine Pollution Bulletin*, 50, 125–146. doi:10.1016/j.marpolbul.2004.11.028

FAO (2000). *Water Quality Management and Control of Water Pollution. Proceedings of a Regional Workshop, Bangkok, Thailand, 26–30 October 1999*. Food and Agriculture Organisation, Rome. *http://www.fao.org/3/a-bl035e.pdf*

Ferrari, G.M., Dowell, M.D., Grossi, S., and Targa, C. (1996). Relationship between the optical properties of chromophoric dissolved organic matter and total concentration of dissolved organic carbon in the southern Baltic Sea region. *Marine Chemistry*, 55, 299–316.

Forel, A. (1890) Une nouvelle forme de la gamme de couleur pour l'étude de l'eau des lacs. *Archives des Sciences Physiques et Naturelles/Société de Physique et d'Histoire Naturelle de Genève*, 6, 25.

Furnas, M. (2003). *Catchments and Corals. Terrestrial Runoff to the Great Barrier Reef*. AIMS, Townsville. 334p.

GCOS (2018). Global Climate Observing System: *https://gcos.wmo.int/en/home*

Gilerson, A., Malinowski, M., Herrera, E., Tomlinson, M., Stumpf, R., and Ondrusek, M. (2021). Estimation of chlorophyll-a concentration in complex coastal waters from satellite imagery. *Proceedings of SPIE 11752, Ocean Sensing and Monitoring XIII, 117520B* (12 April 2021). *https://doi.org/10.1117/12.2588004*

Gordon, H.R., O.B. Brown, R. Evans, J. Brown, R.C. Smith, K.S. Baker, and D.C. Clark (1988) A semianalytical model of ocean colour. *Journal of Geophysical Research*, 93(D9), 10909–10924.

Han, L. (1997). Spectral reflectance with varying suspended sediment concentrations in clear and algae-laden waters. *Photogrammetric Engineering and Remote Sensing,* 63(6), 701–705.

Han, L., and Rundquist, D.C. (1996). Spectra characterization of suspended sediments generated from two texture classes of clay soil. *International Journal of Remote Sensing,* 17, 543–649.

Harvey, E.T., Kratzer, S., and Andersson, A. (2015). Relationships between colored dissolved organic matter and dissolved organic carbon in different coastal gradients of the Baltic Sea. *AMBIO*, 44, 392–401. *https://doi.org/10.1007/s13280-015-0658-4*

Hoge, F.E., and Lyon, P.E. (1996). Satellite retrieval of inherent optical properties by linear matrix inversion of oceanic radiance models—an analysis of model and radiance measurement errors. *Journal of Geophysical Research-Oceans*, 101, 16631–16648.

Jerlov, N.G. (1968). *Optical Oceanography*, Elsevier Oceanography Series 5.

Joehnk, K., Sengupta, A., Biswas, T.K., Mosley, L., and Rees, G. (2020). *Assessment and mitigation options of blackwater risk in the River Murray system*. CSIRO Land and Water, Canberra. 60 p. *https://www.mdba.gov.au/publications/independent-reports/assessment-mitigation-options-blackwater-risk-river-murray-system*

King, A.J., Tonkin, Z, and Lieshcke, J. (2012). Short-term effects of a prolonged blackwater event on aquatic fauna in the Murray River, Australia: considerations for future events. *Marine and Freshwater Research*, 63(7), 576–586. *https://doi.org/10.1071/MF11275*

Kirk, J.T.O. (1994). *Light and Photosynthesis in Aquatic Ecosystems*, 2nd Edn. Cambridge University Press, Cambridge. 509 pp.

Kirk, J.T.O. (2010). *Light and Photosynthesis in Aquatic Ecosystems*, 3rd Edn. Cambridge University Press, Cambridge. 662 pp.

Kostadinov, T.S., Siegel, D.A., and Maritorena, S. (2009). Retrieval of the particle size distribution from satellite ocean color observations. *Journal of Geophys. Research*, 114: C09015. doi:10.1029/2009JC005303

Lathrop, R.G., and Lillesand, T.M. (1989). Monitoring water quality and river plume transport in Green Bay, Lake Michigan with SPOT-1 imagery. *Photogrammetric Engineering and Remote Sensing*, 55(3), 349–354.

Lodhi, M.A., Rundquist, D.C., Han, L., and Kuzila, M.S. (1998). Estimation of suspended sediment concentration in water using integrated surface reflectance. *Geocarto International,* 13(2), 11–15. doi:10.1080/10106049809354637

Loisel, H., Vantrepotte, V., Dessailly, D., and Mériaux, X. (2014). Assessment of the colored dissolved organic matter in coastal waters from ocean color remote sensing. *Optics Express*, 22(11), 13109–13124.

Lubac, B., and Loisel, H. (2007). Variability and classification of remote sensing reflectance spectra in the eastern English Channel and southern North Sea. *Remote Sensing of Environment*, 110, 45–58.

Lymburner, L., Botha, H., Hestir, E., Anstee, J., Sagar, S., Dekker, A., and Malthus, T. (2016). Landsat 8: Providing continuity and increased precision for measuring multi-decadal time series of total suspended matter. *Remote Sensing of Environment*, 185, 108–118. doi:10.1016/j.rse.2016.04.011

Mannino, A., Russ, M.E., and S.B. Hooker (2008). Algorithm development and validation for satellite-derived distributions of DOC and CDOM in the U.S. Middle Atlantic Bight. *Journal of Geophysical Research*, 113, C07051. doi:10.1029/2007JC004493.

Maritorena, S., Morel, A., and Gentili, B. (1994). Diffuse reflectance of oceanic shallow waters: Influence of water depth and bottom albedo. *Limnology and Oceanography,* 39(7), 1689–1703.

Matthews, M.W. (2011). A current review of empirical procedures of remote sensing in inland and near-coastal transitional waters. *International Journal of Remote Sens*ing, 32, 6855–6899.

Mazel, C.H. (2001). Optics of the Seafloor. *Oceanography,* 14(3), 54–63.

McKee, D., and Cunningham, A. (2006). Identification and characterisation of two optical water types in the Irish Sea from in situ inherent optical properties and seawater constituents. *Estuarine, Coastal and Shelf Science*, 68, 305–316.

MDBA (2020). *Blackwater* webpage, Murray-Darling Basin Authority website: *https://www.mdba.gov.au/issues-murray-darling-basin/blackwater*

Melin, F., Vantrepotte, V., Clerici, M., D'Alimonte, D., Zibordi, G., Berthon, J.F., and Canuti, E. (2011). Multi-sensor satellite time series of optical properties and chlorophyll-a concentration in the Adriatic Sea. *Progress in Oceanography*, 91, 229–244.

Mobley, C. (2020). *Ocean Optics Web Book*. *http://www.oceanopticsbook.info/view/introduction/overview*

Molleri, G.S.F., de M. Novo, E.M.L., and Kampel, M. (2010). Space-time variability of the Amazon River plume based on satellite ocean color. *Continental Shelf Research,* 30, 342–352.

Moore, T.S., Campbell, J.W., and Dowell, M.D. (2009). A class-based approach for characterizing the uncertainty of the MODIS chlorophyll product. *Remote Sensing of Environment*, 113, 2424–2430.

Moore, T.S., Dowell, M.D., Bradt, S., and Ruiz Verdud, A. (2014). An optical water type framework for selecting and blending retrievals from bio-optical algorithms in lakes and coastal waters. *Remote Sensing of Environment*, 143, 97–111. doi:10.1016/j.rse.2013.11.021

Morel, A., and Prieur, L. (1977). Analysis of variations in ocean color. *Limnology and Oceanography*, 22(4), 709–722.

Munday, J., and Alfoldi, T.T. (1979). Landsat test of diffuse reflectance models for aquatic suspended solids measurement. *Remote Sensing of Environment,* 8(2), 169–183.

NASA Earthdata (2019). *OceanColour Web*: *https://oceancolor.gsfc.nasa.gov/atbd/chlor_a/#sec_2*

Novo, E., Hansom, J., and Curran, P. (1989). The effect of sediment type on the relationship between reflectance and suspended sediment concentration. *International Journal of Remote Sensing,* 10, 1283–1289. doi:10.1080/01431168908903967.

Novoa, S., Wernand, M.R., and van der Woerd, H.J. (2014). The modern Forel-Ule scale: A 'Do-It-Yourself' colour comparator scale for water monitoring. *Journal of European Optical Society—Rapid Publications*, 9, 14025.

Novoa, S., Wernand, M.R., and van der Woerd, H.J. (2015). WACODI: A generic algorithm to derive the intrinsic color of natural waters from digital images. *Limnology and Oceanography Methods*, 13, 697–711.

Ongley, E.D. (1996). *Control of Water Pollution from Agriculture*. FAO Irrigation and Drainage Paper 55. FAO, Rome.

Pahlevan, N., Lee, Z., Wei, J., Schaaf, C.B., Schott, J. R., and Berk, A. (2014). On-orbit radiometric characterization of OLI (Landsat-8) for applications in aquatic remote sensing. *Remote Sensing of Environment*, 154, 272–284.

Phinn, S.R., Dekker, A.G., Brando, V.E., and Roelfsema, C.M. (2005). Mapping water quality and substrate cover in optically complex coastal and reef waters: an integrated approach. *Marine Pollution Bulletin*, 51(1–4), 459–469.

Pollock, F.J., Lamb, J.B., Field, S.N., Heron, S.F., Schaffelke, B., Shedrawi, G., Bourne, D.G., and Willis, B.L. (2016). Correction: Sediment and Turbidity Associated with Offshore Dredging Increase Coral Disease Prevalence on Nearby Reefs. *PLOS ONE*, 11(11), e0165541.

Preisendorfer, R.W. (1986). Secchi disk science: Visual optics of natural waters. *Limnology and Oceanography*, 31(5), 909–926.

Reynolds, R. A., Stramski, D., and Mitchell, B.G. (2001). A chlorophyll-dependent semianalytical reflectance model derived from field measurements of absorption and backscattering coefficients within the Southern Ocean. *Journal of Geophysical Research*, 106, 7125–7138. doi:10.1029/1999JC000311.

Ritchie, J.C., and Cooper, C.M. (1988). Comparison of Measured Suspended Sediment Concentrations with Suspended Sediment Concentrations Estimated from Landsat MSS Data. *International Journal of Remote Sensing,* 9(3), 379–387.

Ritchie, J.C., and Cooper, C.M. (1991). An algorithm for estimating surface suspended sediment concentrations with Landsat MSS digital data. *Journal of the American Water Resources Association* 27, 373–379. doi:10.1111/j.1752-1688.1991.tb01436.x

Ritchie, J.C., and Schiebe, F.R. (1986). Monitoring suspended sediments with remote sensing techniques. In *Hydrological Applications of Space Technology*, 233–243. IAHS Publ. No. 160.

Ritchie, J.C., Schiebe, F.R., and McHenry, J.R. (1976). Remote sensing of suspended sediments in surface waters. *Photogrammetric Engineering and Remote Sensing,* 42, 1539–1545.

Robinson, C.M., Cherukuru, N., Hardman-Mountford, N.J., Everett, J.D., McLaughlin, M.J., Davies, K.P., Van Dongen-Vogels, V., Ralph, P.J., and Doblin, M.A. (2017). Phytoplankton absorption predicts patterns in primary productivity in Australian coastal shelf waters. *Estuarine, Coastal and Shelf Science*, 192, 1–16. *https://doi.org/10.1016/j.ecss.2017.04.012*

Schiebe, F.R., Harrington, J.A., and Ritchie, J.C. (1992). Remote Sensing of Suspended Sediments: the Lake Chicot, Arkansas Project. *International Journal of Remote Sensing,* 13, 1478–1509.

Schroeder, T, Devlin, M.J., Brando, V.E., Dekker, A.G., Brodie, J.E., Clementson, L.A., and McKinna, L. (2012). Inter-annual variability of wet season freshwater plume extent into the Great Barrier Reef lagoon based on satellite coastal ocean colour observations. *Marine Pollution Bulletin*, 65, 210–223. doi:10.1016/j.marpolbul.2012.02.022

Schwarz, J.N. (2005). Derivation of dissolved organic carbon concentrations from SeaWiFS data. *International Journal of Remote Sensing*, 26(2), 283–293. doi:10.1080/01431160410001723691

Slade, W.H., and Boss, E. (2015). Spectral attenuation and backscattering as indicators of average particle size. *Applied Optics*, 54, 7264–7277. doi:10.1364/AO.54.007264

Spyrakos, E., Vilas, L.G., Palenzuela, J.M.T., and Barton, E.D. (2011). Remote sensing chlorophyll a of optically complex waters (rias Baixas, NW Spain): Application of a regionally specific chlorophyll a algorithm for MERIS full resolution data during an upwelling cycle. *Remote Sensing of Environment*, 115, 2471–2485.

Spyrakos, E., O'Donnell, R., Hunter, P.D., Miller, C., Scott, M., Simis, S.G.H., Neil, C., Barbosa, C.C.F., Binding, C.E., Bradt, S., Bresciani, M., Dall'Olmo, G., Giardino, C., Gitelson, A.A., Kutser, T., Li, L., Matsushita, B., Martinez-Vicente, V., Matthews, M.W., Ogashawara, I., Ruiz-Verdu, A., Schalles, J.F., Tebbs, E., Zhang, Y., and Tyler, A.N. (2018). Optical types of inland and coastal waters. *Limnology and Oceanography*, 63, 846–870.

Tian, L., Wai, O.W.H., Chen, X., Liu, Y., Feng, L., Li, J., and Huang, J. (2014). Assessment of Total Suspended Sediment Distribution under Varying Tidal Conditions in Deep Bay: Initial Results from HJ-1A/1B Satellite CCD Images. *Remote Sensing*, 6(10), 9911–9929. doi:10.3390/rs6109911

Twardowski, M.S., E. Boss, J.B. Macdonald, W.S. Pegau, A.H. Barnard, and J.R. Zaneveld (2001). A model for estimating bulk refractive index from the optical backscattering ratio and the implications for understanding particle composition in case I and case II waters. *Journal of Geophysical Research*, 106, 14129–14142.

Tyler, A.N., Hunter, P.D., Spyrakos, E., Groom, S., Constantinescu, A.M., and Kitchen, J. (2016). Developments in earth observation for the assessment and monitoring of inland, transitional, coastal and shelf-sea waters. *Science of The Total Environment*, 572, 1307–1321.

Ule, W. (1892). *Die bestimmung der Wasserfarbe in den Seen*. Kleinere Mittheilungen. Dr. A. Petermanns Mittheilungen aus Justus Perthes geographischer Anstalt, Gotha: Justus Perthes. pp 70–71.

Van der Woerd, H.J., and Wernand, M.R. (2015). True colour classification of natural waters with medium-spectral resolution satellites: SeaWiFS, MODIS, MERIS and OLCI. *Sensors*, 15, 25663–25680.

Van der Woerd, H.J., and Wernand, M.R. (2018). Hue-Angle Product for Low to Medium Spatial Resolution Optical Satellite Sensors. *Remote Sensing*, 10, 180.

Vantrepotte, V., Loisel, H., Dessailly, D., and Meriaux, X. (2012). Optical classification of contrasted coastal waters. *Remote Sensing of Environment*, 123, 306–323.

Vantrepotte, V., Danhiez, F.-P., Loisel, H., Ouillon, S., Mériaux, X., Cauvin, A., and Dessailly, D. (2015). CDOM-DOC relationship in contrasted coastal waters: implication for DOC retrieval from ocean color remote sensing observation. *Optics Express*, 23, 33–54. *https://doi.org/10.1364/OE.23.000033*

Wernand, M.R. (2011). *Poseidons paintbox, Historical archives of ocean colour in global-change perspective*. Utrecht University, p. 240.

Wernand, M.R., and van der Woerd, H.J. (2010). Spectral analysis of the Forel-Ule Ocean colour comparator scale. *Journal of the European Optical Society—Rapid Publications*, 5, 10014s. doi:10.2971/jeos.2010.10014s.

Wernand, M.R., van der Woerd, and H.J., Gieskes, W.W.C., (2013). Trends in ocean colour and chlorophyll concentration from 1889 to 2000, worldwide. *PloS One*, 8, e63766.

19 Quality

Arnold Dekker, Janet Anstee, Barbara Harrison, and Edward King

Water quality is a subjective descriptor of water that is related to its physical, chemical, and/or biological attributes. It attempts to measure the suitability of water for specific requirements, such as human consumption, agricultural use, recreation, fishing, or ecological sustainability. Attributes of water that are relevant to water quality for most uses of water include:

- physical—temperature, transparency, suspended sediment, and turbidity (see Section 5.1);
- chemical—salinity, pH, nutrients and other chemicals, possibly including various contaminants such as industrial byproducts, pesticides, herbicides, and radioactive substances (see Section 5.2);
- biological—phytoplankton, dissolved organic matter, and microbiota (see Section 5.3).

Inland, coastal, and marine water quality are all impacted by a range of meteorological conditions, including precipitation, evaporation, and temperature. The water quality of inland waterbodies is also a function of runoff within their catchments, which is impacted by the geography surrounding lakes, dams, and rivers, and any disruptive land use practices therein, such as urban development (with consequent production of domestic sewage and industrial pollution). Coastal water quality is also affected by freshwater runoff, particularly after flood events (see Section 11.4). As such, it is directly impacted by both management practices in coastal catchments and aquatic activities in the coastal zone, whereas marine water quality is driven by a range of anthropogenic marine and atmospheric activities, including potential pollution from shipping and infrastructure development, and increased CO_2 levels leading to ocean acidification and temperature rises.

The whole aquatic system can be impacted by pollution. Sources of pollution can be natural, as occur following extreme weather events or tectonic activity, or derived from human activities related to agriculture, industry, mining, or urbanisation. The growing number of new contaminants, such as plastics, cosmetic products and therapeutics, raises particular concerns in terms of their bioavailability, bioaccumulation, and toxicity to aquatic organisms (Galloway and Lewis, 2016; SOE, 2016a). Human litter, which enters coastal waters from populated areas, can be carried long distances by wind and water circulation (Reisser *et al*., 2013; Critchell *et al*., 2015). The vast majority of this type of litter is plastic debris (Rochman *et al*., 2016) and microplastics (Browne, 2015; see Section 19.4.1). Other potential sources of marine pollution include shipping (see Section 19.4.1) and oil spills (see Section 19.4.3).

Pollution, also called environmental pollution, the addition of any substance (solid, liquid, or gas) or any form of energy (such as heat, sound, or radioactivity) to the environment at a rate faster than it can be dispersed, diluted, decomposed, recycled, or stored in some harmless form.
(Encyclopedia Britannica)

Background image: Copernicus satellite image of part of the Phytoplankton Monitoring Network administered by the Murray-Darling Basin Authority. This image is rotated counterclockwise, spanning from Lake Victoria on the left to the Murray River on the right. **Source:** National Environmental Information Infrastructure

Recommended Chapter Citation: Dekker, A.G., Anstee, J.M., Harrison, B.A., and King, E.A. (2021). Quality. Ch 19 in *Earth Observation: Data, Processing and Applications. Volume 3B—Surface Waters.* CRCSI, Melbourne. pp. 367–394. ISBN 978-0-6482278-5-4

19.1 Quality of Australian Surface Waters

The quality of marine, coastal, and inland waters directly impacts the productivity, functioning, and resilience of aquatic ecosystems. Deliberate loading, dumping, and incineration of waste in Australia's marine jurisdiction is regulated by the federal government as part of the International Maritime Organisation's agreement known as the London protocol (IMO, 2020), as are the creation and operation of artificial reefs, dredging operations, and burials at sea (DAWE, 2020).

Many Australian estuaries are considered to be experiencing moderate to strong pollution pressure (SOE, 2016a). The diversion of water for irrigation and regulation also changes the natural flow regimes of inland waterbodies, especially within the Murray-Darling Basin (CSIRO, 2008). The major concerns in terms of coastal and marine water quality in northern Australia, including the Great Barrier Reef (GBR) region, are from:

- levels of sediment, nutrients, and contaminants that originate from agricultural, industrial, or urban land; and
- rising water temperatures and higher acidity levels due to climate variations (AIMS, 2019).

For example, excess nutrient levels in aquatic environments can lead to eutrophication, algal blooms (see Section 19.5), increased turbidity, low-oxygen dead zones, fish kills, disruption in natural microbial processes and biogeochemical cycling and, in tropical areas, crown-of-thorns outbreaks, coral bleaching, and coral disease (Chislock *et al*., 2013). Warmer waters also affect the growth and reproduction of many marine organisms (SOE, 2016a; see Section 19.6 and Excursus 20.3). Global collaborations such as GloboLakes (see Section 19.8) are using EO time series datasets to monitor the response of lakes to environmental changes, including climate, at a range of scales.

Common contaminants found in coastal rivers and estuaries include excess metals, nutrients and organic matter, and industrial chemicals, pesticides, herbicides, terrigenous sediments and debris. SOE (2016a)

19.2 EO Sensors for Water Quality

Various EO data sources and their sensors are introduced in Volume 1A, and interpretation of EO imagery is considered in Volume 1B. As detailed in Section 18, EO methods exist to derive concentrations of chlorophyll, non-algal particles (NAP—or suspended sediments) and coloured dissolved organic matter (CDOM) from optical EO imagery. For example, a range of waterbody features, including a flood plume, are visible in the pseudo true colour composite image shown in Figure 19.1.

While most EO sensors are primarily designed for observing land or ocean, several sensors have been used to map inland and coastal water quality, benthic habitats, or bathymetry (see Table 8.14). The specific water quality variables that can be identified from these datasets are detailed in Table 19.1.

CEOS (2018) recommend detailed specifications for the ideal spaceborne optical sensor for EO of non-oceanic, aquatic environments and the parameters for preferred spectral, spatial, radiometric, and temporal characteristics for mapping water quality (Section 8.5). Minimum spectral requirements include bands that detect cyanophycocyanin (centred on the *in vivo* absorption maximum, 620–624 nm) to estimate blue-green algae concentration and chlorophyll a (centred on *in vivo* red absorption maximum, 676 nm). Additionally, numerous other bands (with appropriate spectral and spatial resolution, and radiometric characteristics) are needed in the range 380–780 nm for detecting aquatic ecosystem variables (see Table 8.15), and in the ranges 360–380 nm and 780–1400 nm for correction of atmospheric and air-water interface effects (see Table 8.16).

To adequately track the continuous variations that occur in complex aquatic ecosystems, such as inland and coastal waterbodies, EO sensors need rapid temporal sampling to monitor changes at appropriate spectral and spatial scales to represent the underlying ecosystem processes. Frequent coverage is important if imagery is to be used to monitor the dynamic nature of aquatic systems, with events such as algal blooms and flooding changing on an hourly basis.

Table 19.1 Suitability of optical EO sensors to map water quality variables

This list includes multispectral and hyperspectral sensors carried on previous, current, and future EO missions with spectral bands in the wavelength range 340–1000 nm. Names of commercial sensors are italicised. TSM: Total Suspended Matter; CDOM: Coloured Dissolved Organic Matter

Sensor	Water-quality variables (freshwater, coastal, and ocean)					
	Chlorophyll a	Cyanophycocyanin	TSM	CDOM	Kd	Turbidity and/or Secchi Disk transparency
Hyperion	high	high	high	high	high	high
CHRIS-PROBA	high	high	high	high	high	high
MERIS	high	high	high	high	high	high
HICO	high	high	high	high	high	high
Sentinel-3 OCLI	high	high	high	high	high	high
GLIMR	high	high	high	high	high	high
PRISMA	high	high	high	high	high	high
EnMap	high	high	high	high	high	high
SBG (formerly HyspIRI)	high	high	high	high	high	high
PACE	high	high	high	high	high	high
ISS HISUI	high	high	high	high	high	high
ISS DESIS	high	high	high	high	high	high
OCM-2	high	high	high	high	high	high
Suomi-VIIRS	medium	potential	high	high	high	high
SGLI	medium	Not suitable	high	high	high	high
GOCI	high	potential	high	medium	high	high
GOCI-II	high	potential	high	medium	high	high
WORLDVIEW-2	medium	medium	high	medium	high	high
WORLDVIEW-3	medium	medium	high	medium	high	high
IKONOS, QuickBird, SPOT-5/-6, GeoEye, Planet, etc.	potential	Surface bloom	high	potential	high	high
RapidEye	potential	Surface bloom	high	potential	high	high
SENTINEL-2	medium	Surface bloom	high	medium	high	high
Aqua/Terra MODIS (1 km)	medium	potential	high	high	high	high
Aqua/Terra MODIS (500 m)	Not suitable	Not suitable	potential	medium	medium	medium
Aqua/Terra MODIS (250 m)						
LANDSAT-4 to -7	potential	Surface bloom	potential	medium	medium	medium
LANDSAT-8/-9	potential	Surface bloom	high	potential	high	high
Himawari-8/-9	potential	Not suitable	high	potential	potential	high
GOES-R	potential	Not suitable	high	potential	potential	high
GISAT-1/-2	potential	potential	high	potential	potential	medium
MSG SEVIRI	potential	Not suitable	medium	Not suitable	potential	medium

Adapted from: CEOS (2018) Table 2.7

Figure 19.1 Great Barrier Reef shown in true colour

Water features, including a flood plume, are clearly visible in this MODIS optical image acquired on 28 February 2008. This image is a composite of 500 m and 1 km bands, produced by CSIRO using data courtesy of NASA.

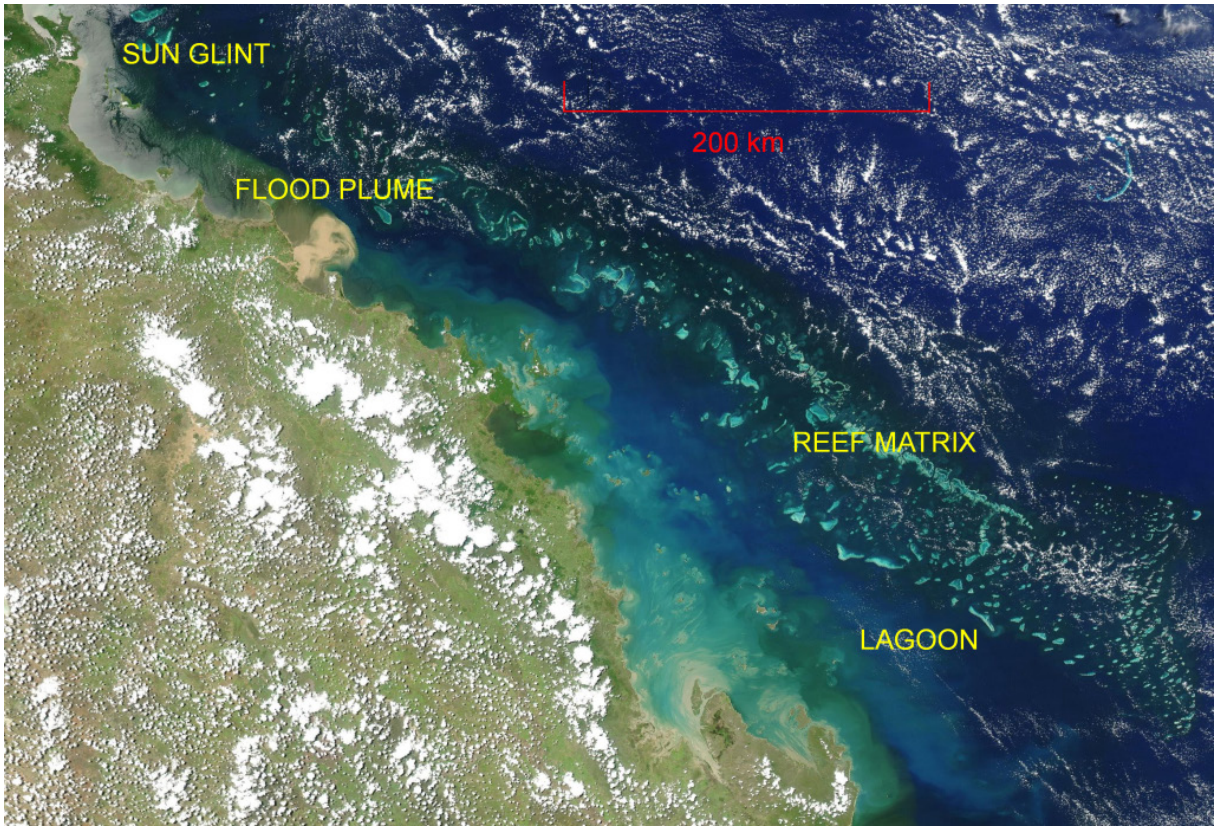

Source: eReefs. Retrieved from: *https://research.csiro.au/ereefs/remote-sensing/how-it-works/*

Unmanned Aerial Vehicles (UAV) or drones are rapidly developing as viable alternatives to satellites and manned aircraft for monitoring various Earth resources (see Volume 1A—Section 11.2). These flexible platforms have the ability to acquire high frequency data for validating water colour observations, as well as spatially-explicit modelling of suspended sediments and chlorophyll content. Data quality and uncertainty associated with radiometric calibration of the sensor system is paramount when assessing water quality. When instruments carried by drones are well-calibrated, however, the acquired multispectral and hyperspectral images can be used to test the performance (precision and optimal range) of empirical and semi-empirical models for the retrieval of chlorophyll a (Matthews, 2011), or used for semi-analytical inversion methods (see Section 8.4).

Table 19.2 EO sensors relevant to water quality

TIR: Thermal infrared; SAR: Synthetic Aperture Radar

Type	Sensor	Platform	Relevance	Advantages	Disadvantages
Passive optical	Multispectral radiometer	Satellite or airborne	Inland water quality, Marine and coastal pollution, Algal blooms	Indicate sediments and coastal erosion, global coverage, range of spatial resolutions available, low cost	Impacted by cloud cover
	Hyperspectral radiometer	Satellite or airborne	Inland water quality, Marine and coastal pollution, Algal blooms	High spectral resolution	Higher cost for airborne data, large data volume, impacted by cloud cover
	TIR radiometer	Satellite	Marine heatwaves	Global coverage, long time series	Low spatial resolution, impacted by cloud cover
Passive microwave	L-band radiometer (ocean brightness temperature)	Satellite	Marine salinity	All weather so useful in tropical regions	Data availability
Active microwave	SAR	Satellite or airborne	Marine and coastal pollution, Ship detection	All weather and at night	High cost, specialised processing

19.3 Inland Water Quality

Comprehensive information about the water quality of inland waterbodies is lacking in many countries, including Australia (SOE, 2011). Strict controls generally exist for waterbodies supplying drinking water, which result in relatively standard taste, odour, and appearance. However, the quality of waterbodies used for agricultural and recreational purposes tends to be monitored less carefully despite the condition of these waterbodies being significant to environmental health, with uncontrolled degradation in water quality impacting both aquatic ecosystems and the bordering terrestrial ecosystems (see Excursus 19.1).

Most attributes of water quality are dynamic and can vary rapidly in both space and time. An understanding of the dynamics of these attributes is essential to managing inland water resources. There are two primary temporal considerations for inland water quality monitoring:

- sampling designed to represent the dynamics of water quality and the range of conditions that can occur over diurnal, seasonal, and annual cycles; and
- sampling designed to develop a time series dataset (see Volume 2D). Time series are essential for assessing the condition and trends of inland water quality as they relate to the effect of water quality management and climatic variations.

Excursus 19.1—Australian Inland Water Quality

Source: Dekker and Hestir (2012)

In 2011, the National Water Quality Assessment (SOE, 2011) surveyed the water quality status of Australian inland drainage regions and their river basins. Compliance with Australian water quality guidelines for discrete point-based samples were summarised in terms of turbidity, salinity (measured as electrical conductivity), pH, total nitrogen, total phosphorus, cyanobacteria, and microbial quality (faecal coliforms, enterococci, and *E. coli*). At that time, most of these variables were routinely measured in less that half the river basins in Australia, with considerable variation in data consistency, especially for cyanbacteria and microbial quality.

Significant differences were observed between the frequency and type of water quality sampling undertaken in the densely populated parts of Australia compared with more remote locations. In some regions, the ephemeral nature of waterbodies may account for infrequent or inconsistent records. Both poor coordination between agencies, and a lack of consistency in the methods and actual water quality variables measured, have made assessing long term trends difficult.

Many Australian inland waters are exposed to cycles of long periods of relatively low flow or drought conditions, interspersed with intense periods of rainfall, leading to flash floods in high relief terrain or extended and extensive floods in flat terrain. Floods cause large fluxes of suspended sediment, dissolved organic material, salt, nutrients, and contaminants, which can lead to changes in the environmental state in aquatic ecosystems. In the wet tropics higher flows occur throughout the year.

Under stable or drought conditions, salinity and seasonal microbial activity need regular monitoring. More frequent sampling is required when algal blooms are likely to affect water quality. However, during intense rainfall and resulting streamflow events it is most important to estimate changes in the material content of water, such as suspended sediment and organic matter. At such times, algal-related measurements are less relevant, since water turbulence and the resuspension and dissolution of soil materials prevents algal growth. The monitoring of rapid changes in water quality during extreme events is a challenge for any monitoring method, but is necessary to understand the effects of extreme flow events on aquatic ecosystems.

19.3.1 Traditional methods

Traditional monitoring of water quality involves systematic collection and analysis of water samples to provide information and knowledge about a body of water. Such monitoring can be conducted by a wide range of organisations, including government agencies, private utilities, agricultural and industrial water providers, and mining companies, for both privately-owned and public waters. Three basic types of water quality measurement methods are suitable for water quality monitoring:

- *in situ* discrete water sampling for field and laboratory analysis;
- *in situ* continuously deployed, automated physicochemical and bio-optical instruments and samplers; and
- EO-based methods from just above the water surface, through to satellite observations.

While *in situ* sampling, conducted manually or automatically, encompasses a wide range of analyses, and yields precise and replicable results, collection of water samples involves logistical difficulties, particularly given the density of coverage required. Adequate sampling strategies should include vertical profiles to determine variations with water depth, transect measurements to determine spatial variations, and repeated sampling over time to determine temporal changes (Lindell *et al.*, 1999). Further, it is often difficult to accurately georeference the locations of point measurements, and to coordinate the collection of samples to coincide with major changes in water quality. The processing time required for analysis of samples adds another layer of complexity when comparing results. The cost of *in situ* sampling is very high, especially relative the coverage achieved. At present, no legislative standards exist in Australia to define preferred methods for water quality monitoring that could deliver comparable results for different waterbodies.

19.3.2 EO approaches

In recent decades both multispectral and hyperspectral imagery acquired by satellites and aircraft have been used to monitor inland water quality (Durand *et al.*, 1999; Dekker and Hester, 2012; Odermatt *et al.*, 2012; IOCCG, 2018). In particular, the technological advances in sensor design with higher spectral and spatial resolution and selected spectral bands have allowed image data to be tailored to specific situations (see CEOS, 2018, and Section 8.5). These advances have also enabled development of calibrated spectral libraries and models for specific water quality parameters.

As detailed in Section 18, EO datasets can be used to assess surface water concentrations of:

- chlorophyll—an indicator of phytoplankton biomass, trophic and nutrient status and the most widely used index of water quality and nutrient status globally (see Section 18.6).
- cyanophycocyanin (CPC) and cyanophycoerythrin (CPE)—indicators of cyanobacterial biomass, which is common in harmful and toxic algal blooms (see Sections 8.2.2 and 19.5).
- coloured dissolved organic matter (CDOM)—the optically measureable component of dissolved organic matter in the water column sometimes used as an indicator of organic matter and aquatic carbon (see Sections 8.2.4 and 18.5.1).
- total suspended matter (TSM) and non-algal particulate matter (NAP)—important for assessing the quality of drinking water and controlling the light environment of aquatic environments (see Section 18.4).

Additionally, the following conditions can also be estimated from optical imagery:

- vertical light attenuation (Kd—Secchi disk transparency) and turbidity—measurements of the underwater light field that are important for assessing the degree of light limitation, rates of primary production, species composition, and other ecosystem responses (see Section 8).
- emergent and submerged macrophytes—down to the depth of visibility, these are important indicators of wetland and aquatic ecosystem health and function (see Section 20).
- bathymetry—if the substratum of a waterbody reflects a measureable amount of light through the water column to above the surface, then the waterbody depth can be estimated (see Section 13.4.2).

The importance of appropriate spatial resolution data to map inland water quality is discussed in Excursus 19.2. Since many EO sensors routinely offer spatially and temporally comprehensive coverage of all waterbodies at low (or no) cost, the combined information from directly measurable optical properties can be used to derive information about eutrophication, environmental flows, carbon, and primary productivity. Non-optical properties, such as nitrogen, phosphate, dissolved oxygen, and organic and inorganic micro-pollutants can be estimated through inference, proxy relationships, or data assimilation with EO optical properties. However, these relationships are stochastic, may not be causal, and may have a limited validity range (Dekker and Hester, 2012).

Multispectral sensors that include a blue spectral band can be used to detect TSM, Secchi disk transparency, turbidity, and CDOM. While algal pigments may be detectable from multispectral datasets, accuracy will be low, especially when these pigments are present at low concentrations, since broad spectral bands cannot discriminate the narrow pigment spectral absorption features of algal pigments from other absorbing and backscattering materials in the water column. As detailed in Volume 1, the highest spectral resolution for optical EO is offered by hyperspectral sensors or 'imaging spectrometers', where the entire visible and nearby NIR spectrum are measured in narrow (5–20 nm) contiguous bands (see Volume 1A—Section 13 and CEOS, 2018). Specifically designed aquatic sensors with more spectral bands, that are both narrower and suitably positioned, would yield more accurate measurements of chlorophyll than multispectral sensors, and enable phytoplankton pigment types, such as the cyanobacterial pigments to be detected (CEOS, 2018; see Section 8.5). Finer spectral resolution may also enable estimation of the particle size distribution, and fractions of organic and mineral particulate matter.

Two main types of forward optical models are available to map water quality, namely generic radiative transfer models (such as HYDROLIGHT; Mobley and Sundman, 2000) and semi-analytical models (see Section 8.4). These forward models are able to predict the light composition leaving a waterbody based on the water column constituents and, if visible, the benthic reflectance. When the substratum is visible, the SAMBUCA (Semi-analytical Method for Benthic Unmixing and water Column Concentration Assessment; Brando *et al.*, 2009; Dekker *et al.*, 2011) has been applied to inland waterbodies, estuarine waters, coastal tidal lagoons, coastal waters, and coral reefs. An example of applying these models is given in Excursus 19.3.

Excursus 19.2—Assessing Inland Water Quality using Optical EO

Source: Dekker and Hestir (2012)

In order for an EO sensor to effectively measure a waterbody, that body of water must be at least three to four times the size of a pixel to ensure that the pixel comprises 'pure' water, and does not contain any significant signal component from surrounding land and/or vegetation. Thus, to resolve a lake using imagery with 30 m pixel resolution, a minimum of 9 (3×3) 'pure' water pixels, but preferably 16 (4×4) pixels is required. This ground area equates to a waterbody that is at least 120 m wide. Table 19.3 summarises the number of waterbodies in Australia that could be assessed using two commonly available sources of EO imagery with long term archives:

- Landsat (30 m pixel resolution), which would require a waterbody to be at least 120 m wide (> 0.01 km^2); and
- MODIS (250 m pixel resolution) or MERIS (300 m pixel resolution), which would require a waterbody to be at least 1000 m wide (> 1 km^2).

Since 2014, Sentinel-2 imagery has also been available with 10 m pixel resolution.

The effect of changing spatial resolution when discerning waterbodies is illustrated in Figure 19.2. Image spatial resolution has consequences for imaging small waterbodies, such as small or medium width river systems. In these situations high spatial resolution imagery (with pixel sizes of 2–10 m) may be the only option, possibly leading to significant data acquisition costs.

Table 19.3 Size distribution of waterbodies in Australia

Note: These categories are not exclusive, so numbers for medium category includes all large waterbodies.

Category	Size	Number	% of Total	Total Surface Area
Small	< 0.01 km^2	86,000	68	475,423
Medium	> 0.01 km^2	63,000	32	220,000
Large	> 1 km^2	2,300	11	77,500

Source: Dekker and Hestir (2012)

Figure 19.2 Effect of spatial resolution on Lake Burley Griffin, Canberra

a. 2 m pixel (typical commercial spatial resolution such as QuickBird or WorldView-2)

b. 10 m pixel (typical of Sentinel-2)

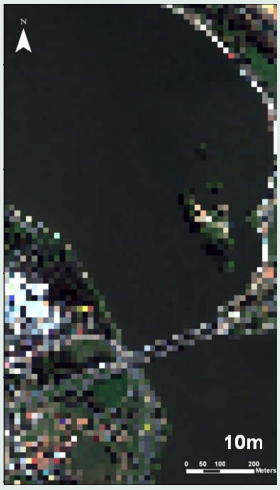

c. 30 m pixel (Landsat)

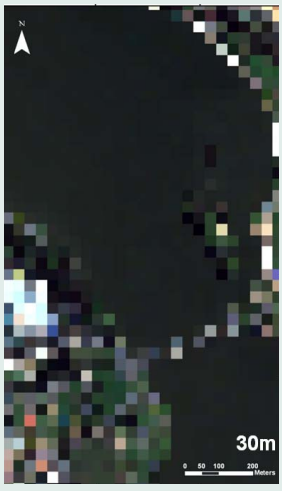

d. 300 m pixel (MERIS)

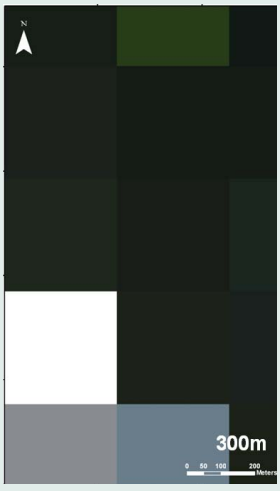

Source: Dekker and Hestir (2012) Figure 3-2

Effective water quality reporting requires a systematic approach that measures the same water quality variables at regular intervals across a wide geographic range. To achieve robust results from optical EO of water quality in Australia, robust methods are required for:

- atmospheric, sunglint and skyglint corrections as appropriate to environmental conditions;
- characterisation of the optical variability of inland waterbodies. This requires collection of a representative spectral library of inland water bio-optical properties to parameterise and validate physics-based inversion algorithms; and
- investigation of scaling effects of *in situ* water quality data versus derived water quality information from EO datasets. This includes investigating the possibility of translating *in situ* algal cell counts to EO-based chlorophyll concentrations, and reconciling point-based measurements with pixel-based measurements.

Dekker and Hestir (2012) recommended a national operational water quality monitoring system based on EO, as summarised in Table 19.4.

Table 19.4 National water quality system based on EO

Water Quality Information	Water Quality Variable
Primary production and eutrophication status	Chlorophyll
	Cyanophycocyanin
	Cyanophycoerythrin
	Surface algal blooms
Aquatic carbon content, carbon fluxes	Coloured dissolved organic matter
Erosion, re-suspension and deposition	Total suspended matter (= sum of chlorophyll – non-algal particles)
Light climate information related to the combined effects of algae, coloured dissolved organic matter and suspended matter	Vertical attenuation of light
	Transparency
	Turbidity
Ecological condition	Emergent macrophytes
	Submerged macrophytes

Source: Dekker and Hestir (2012) Table 5-1

Excursus 19.3—Western Treatment Plant, Werribee

Source: Janet Anstee (CSIRO); Hydraspectra: Tim Malthus and Stephen Gensemer (CSIRO)
Further Information: Joehnk *et al.* (2018); *https://www.melbournewater.com.au/community-and-education/about-our-water/sewerage/western-treatment-plant*; *https://utilitymagazine.com.au/drone-technology-takes-off-at-melbourne-water/*

The Western Treatment Plant (WTP) was established in 1897 to manage human waste from Melbourne's growing suburbs. A network of pipes, sewers, and drains transport sewage 32 km from the city near Port Phillip Bay. The Plant now comprises a network of lagoons, wetlands, and intertidal and shoreline areas that support a diversity of birdlife, including migratory waterfowl from the Northern Hemisphere. In 1982 the facility was declared a Ramsar-listed wetland, and is an important site as it covers 110 km^2, with many shallow lagoons, 1.5–3 m deep.

The Plant operates operates by treating the sewage in Activated Sludge and Nutrient Reduction Plants, and allowing it to flow through anaerobic and aerated aerobic lagoons (a series of ponds). Over a period of about a month, the lagoon bacteria decompose the organic content then solids are settled out of the wastewater in clarifiers. In the process of treating around half of Melbourne's sewage from about 5 million people, a large volume of water is recycled, biogas is generated to run the Plant, and biosolids are available for fertiliser.

Cyanobacteria blooms are a yearly occurrence in WTP's treatment lagoons (see Figure 19.3) where they occasionally interrupt the supply of class A recycled water, which is provided to surrounding market gardens, and reduce the efficiency of lagoon treatment processes. Melbourne Water sought to investigate the potential of EO to resolve the spatial pattern of cyanobacteria blooms and other microalgae and its capacity to detect/quantify surface concentrations. An understanding of bloom spatial patterns at the WTP will facilitate the development of bloom forecasting models (Joehnk *et al.*, 2018) that allow operational and asset management controls (such as desludging targets) to be optimized to avoid and manage nuisance blooms.

Figure 19.3 Cyanobacteria bloom

Sentinel-2A image acquired on 7 March 2018 showing active algal blooms (green) at WTP.

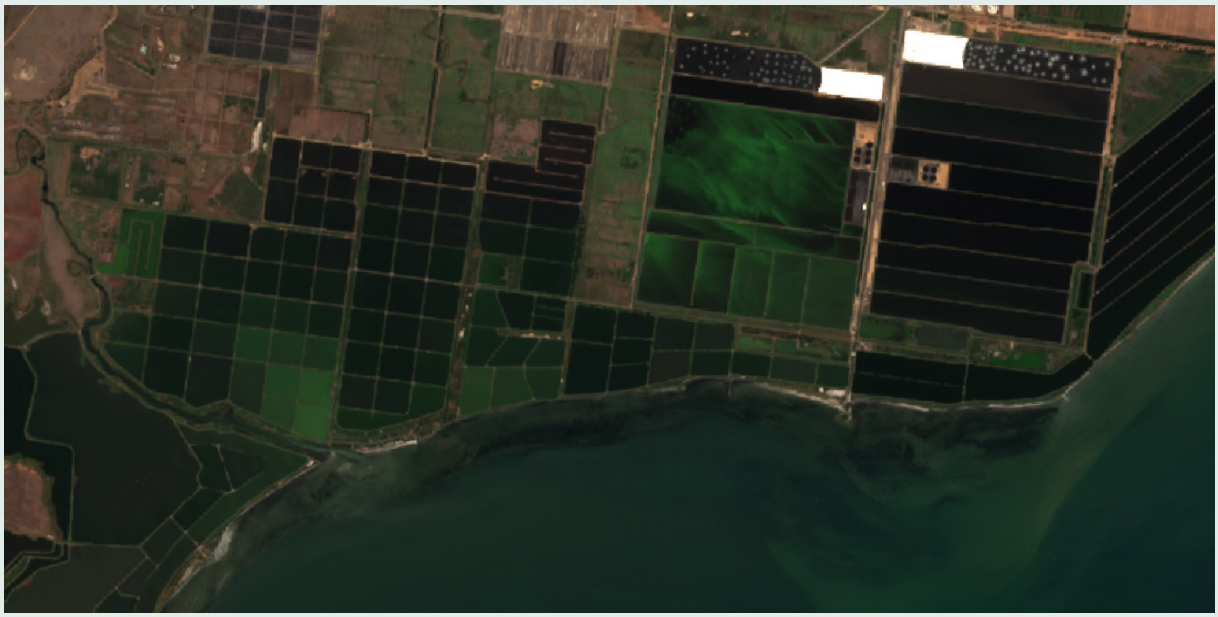

Figure 19.4 *In situ* measurement locations

The field site locations visited during field sampling on 14–15 February 2018.

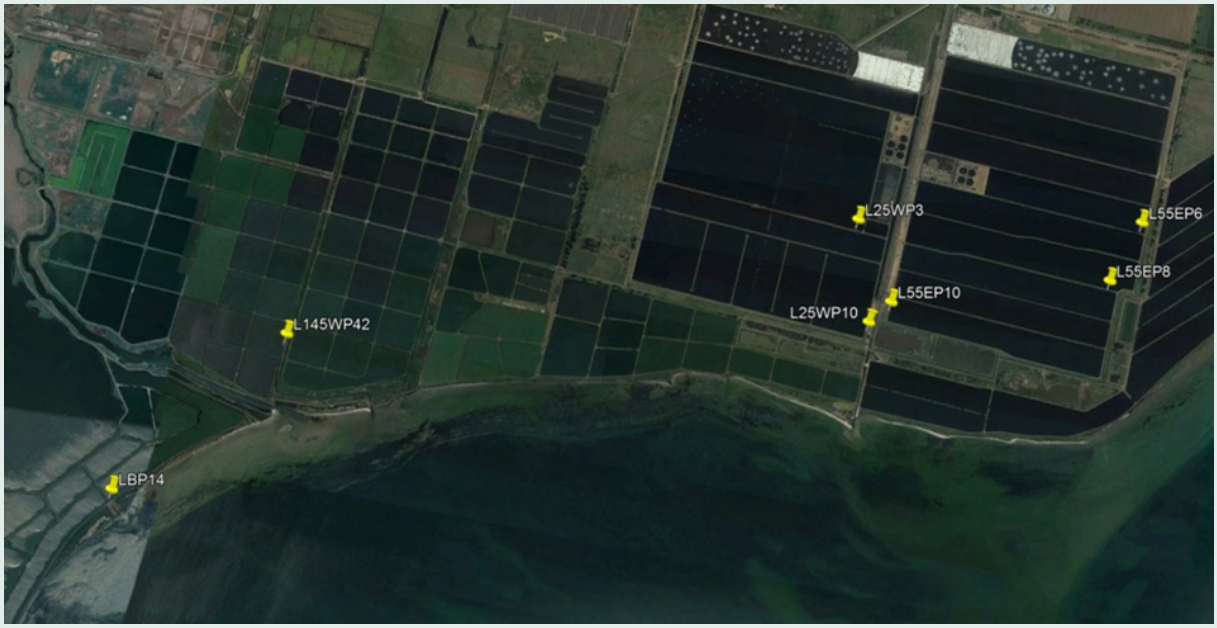

Figure 19.5 HydraSpectra installation

WTP pond L25WP3 on 14 February 2018

Monitoring cyanobacteria blooms remotely requires sensors with high resolution, spectrally, spatially, and temporally, to capture their very dynamic features. While passive optical EO satellite observations often lack the spectral and temporal resolutions required for operational monitoring, and are blocked during periods of cloud cover, these datasets can be complemented by near-surface hyperspectral sensors providing high-frequency images of the water surface. In the case of the WTP, the near-surface sensors can be used to detect scum formation and quantify local cyanobacterial abundance (Malthus *et al.*, 2016). By acquiring EO data, near-surface sensors, together with regular water samples analysis (cell counts, laboratory pigment analysis; Simis *et al.*, 2007), a synoptic overview can be acquired with high frequency monitoring of blooms in problematic areas. The dense data stream will also allow for future data driven, machine learning forecasts.

Initially, a full time series of Digital Earth Australia Landsat data (1987–2016) was used to implement the adaptive linear matrix inversion model (aLMI, Brando *et al.*, 2012) at a selected location to retrieve chlorophyll a as a proxy for cyanobacteria biomass. The aLMI was unable to retrieve data from a number of images in the time series, either due to poor pixel quality (from contamination due to clouds, aerosols, etc) or because the parameterisation inadequately characterised the conditions in the WTP. For the data that was retrieved, the satellite derived data for nearly 30 years were compared with the Melbourne Water *in situ* measurements taken at L55E and L55EP3 (see Figure 19.4).

The database used to parameterise the aLMI model initially was based on an extensive set of inland bio-optical properties collected from NSW and QLD inland reservoirs, dams, rivers, and lakes. This database was amended to include the additional data acquired at the WTP in February 2018. The inclusion of the WTP field data in the parameterisation, generally increased the retrieved value of chlorophyll compared to the previous parameterisation. As the Sentinel-2 imagery is now available on the DEA, its improved capability for chlorophyll a detection, would generate higher temporal frequency of retrievals than Landsat data and be better suited for monitoring the cyanobacteria blooms.

Figure 19.6 HydraSpectra reflectance data

This data was collected at pond L25WP3 in the WTP on 3 March 2018.

a. Hemispherical photograph of water conditions at 11:15 am

b. Normalised reflectance at 11:15 and 17:45

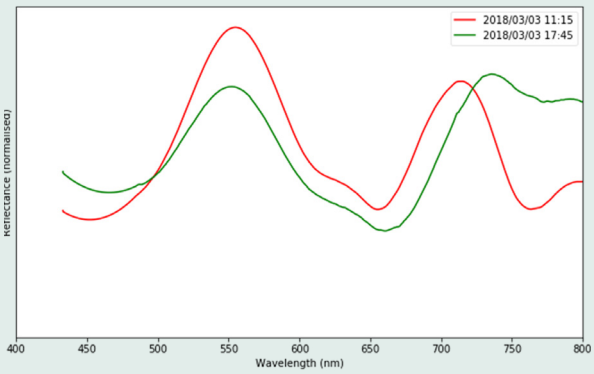

c. Reflectance colourmap summarising the data obtained over the entire day (with decreasing wavelength from left to right). The red circle indicates a surface scum with high reflectance in near infrared wavelengths.

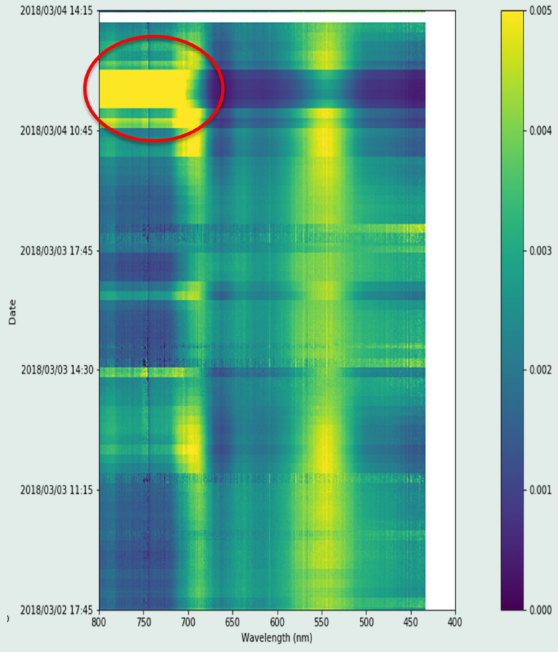

To assess the potential of a near-surface hyperspectral camera, a single sensor was installed at pond L25WP3 of Melbourne Water's WTP (see Figure 19.5). At installation, the sensor head is oriented at 135° relative to magnetic north to minimises the influence of surface sunglint on the measured water surface reflectance. The system was set up to sample every 15 minutes from 6 am to 6 pm, daily. Data were uploaded once per hour to the FTP server via the Telstra 4G network.

Every 15 minutes, the HydraSpectra delivers a hemispherical photograph of the water surface and sky conditions (see , a normalised spectral plot, a colourmap of surface reflectance. Figure 19.6 shows these results for 3 March 2018, when a *Microcystis* bloom appeared at 11.15 am and disappeared at 12.45 pm due to upcoming wind action mixing the water column. In the colourmap (see Figure 19.6c), the bloom's surface scum is detected by near infrared wavelengths and highlighted by a red circle.

The colourmap (see Figure 19.6c) shows bright green reflectance features in the wavelength range 540–560 nm and a high reflectance feature between 680–710 nm, corresponding to a chlorophyll a reflectance peak near 700 nm. There is also a dark feature corresponding to the phycocyanin absorption between 610–630 nm and a very dark absorption feature between 670–680 nm, correlating with chlorophyll a.

Using the near-surface sensing with satellite derived data provides a better understanding of the bloom spatial patterns. The integration of this information with hydrodynamic modelling is the coming challenge but would greatly enhance the prediction of cyanobacteria blooms.

19.4 Pollution

Pollution of aquatic systems is increasing significantly around the globe, and poses a major threat to both water quality and biodiversity. Growing numbers of marine vessels and infrastructure developments increase the opportunities for marine pollution.

Marine pollution impacts different organisms in different ways. Pollutants can bioaccumulate when an organism is unable to excrete them as quickly as they are ingested, then be transferred to other organisms at higher levels in the food chain (see Section 3.3)

The oil and gas industry has been described as the 'economic backbone' of the the marine sector in Australia (SOE, 2011), with significant reserves being extracted from the sea each year, particularly in northwestern waters (ATC, 2013; Wood Mackenzie, 2020). However, the potential for marine pollution is real in the associated activities of exploration surveys and drilling, development of submarine infrastructure, production operation, and decommissioning. In addition to influencing water quality, these activities can impact the marine environment by disturbing the seabed, introducing underwater noise, adding artificial light, and changing air quality. While the actual impacts of these activities are generally localised, their long term effects are unknown (SOE, 2016b).

EO-based methods are being used to monitor marine areas for different forms of potential pollution, including:

- plastic debris (see Section 19.4.1);
- shipping (see Section 19.4.2); and
- oil spills (see Section 19.4.3).

19.4.1 Plastic debris

Over 300 million tons of plastic are manufactured around the world each year, of which 8 million tons move into the global ocean (IUCN, 2020). Eriksen *et al.* (2014) estimated that 250,000 tons (over 5 trillion pieces) of plastic were floating in coastal and marine waters, mostly originating from land (Jambeck *et al.*, 2015), but more recent estimates for the total volume of marine plastic debris are significantly higher (Agamuthu *et al.*, 2019). Plastics are considered to be the major form of marine debris, amounting to 50–90% of all debris in different regions (Agamuthu *et al.*, 2019).

This growing problem has varied ecological impacts on marine biota and water quality (Rochman *et al.*, 2016). The dynamics of marine plastic litter has been tracked, both globally (van Sebille *et al.*, 2012, 2015) and around Australia (Reisser *et al.*, 2013), to determine its origins, transport pathways, and accumulation zones. Most marine debris finally rests on the ocean floor to disturb, and potentially contaminate, benthic habitats (Maximenko *et al.*, 2019).

Marine debris (or marine litter) is defined as any persistent, manufactured or processed solid material discarded, disposed of or abandoned in the marine and coastal environment (UNEP, 2020).

EO is one option to monitor this problem. A range of approaches have been trialled (Mace, 2012), including identifying spectral features for plastics using airborne hyperspectral imagery (Garaba *et al.*, 2018; Garaba and Dierssen, 2018), and developing a reflectance model that accounts for colour, transparency, reflectivity, and shape of debris (Goddijn-Murphy *et al.*, 2018) that could help to the design appropriate EO sensors (see Section 8.5). Sensor calibration also requires *in situ* data for the various type of debris, especially given that the optical characteristics of floating plastics are likely to change over time (see Section 8.3). Surface wind movements may also hide floating material, so image acquisition is best done in low wind conditions (Goddijn-Murphy *et al.*, 2018).

An Integrated Marine Debris Observing System (IMDOS) has been proposed that will use EO and *in situ* datasets to monitor the risks from marine debris (Maximenko *et al.*, 2019). This global system is envisaged to involve a range of optical and SAR sensors, on a variety of platforms, in conjunction with a network of *in situ* observations for calibration and validation.

19.4.2 Shipping

Tens of thousands of maritime vessels transport over 10,000 million tons of goods around the world each year, with maritime trade (measured in terms of weight per unit distance) doubling during the two decades since 2000 (UNCLAD, 2019). Marine safety and traffic surveillance, as well as tracking illegal fishing activities and oil discharges, increasingly rely on EO-based ship detection methods (see Excursus 2.1).

Australia imports and exports a very high proportion of goods by ship and has been assessed as one of the top shipping nations globally based on cargo volume and distance travelled (Gilbert *et al.*, 2003). Through sensitive environments, such as the GBR, approved shipping lanes have been defined to minimise the risk of environmental damage, either by direct contact with underwater features, such as reefs, or via oil spills (see Section 19.4.3).

In coastal and marine waters, a range of vessels have been detected using EO datasets from both optical and SAR sensors (Crisp, 2004; Kanjir *et al.*, 2018; Bereta *et al.*, 2020), with SAR being most commonly used for ship detection (see Section 9). Since ships comprise many metal components, and typically include sharp edges, they reflect radar signals more strongly than the water surface (see Volume 1B—Section 8). While they appear as bright, geometric shapes on a darker surface when sea conditions are calm, in windy and choppy conditions the characteristic speckle of radar images is enhanced, which reduces the contrast between ships and water, and potentially leads to false detections, especially for small vessels (Sagar *et al.*, 2020).

Accuracy of vessel detection using optical imagery varies with the characteristics of individual sensors and weather conditions, and ship detection algorithms have been developed with varying success (Kanjir *et al.*, 2018). Imagery acquired by nighttime optical sensors has also been used to identify shipborne nightlights (Elvidge *et al.*, 2015; Straka *et al.*, 2015).

The position, course, and speed of all Commonwealth-endorsed fishing vessels are monitored by the Australian Fisheries Management Authority (AFMA) via International Maritime Satellite (INMARSAT) communications (AFMA, 2020). This system allows AFMA to track illegal fishing and unauthorised entry to Marine Protected Areas (see Excursus 20.2). The Global Fishing Watch, a public, online map of global fishing activity (*globalfishingwatch.org*), has been modified to create an Australian risk report tool to alert marine managers when suspicious vessels are nearby (*https://research.csiro.au/iuu/*; CSIRO, 2017, 2018).

Ninety nine per cent of Australia's trade by volume is carried by sea.
(Scott Morrison, 2019)

19.4.3 Oil spills

Oil is regularly released into the global ocean from a range of sources. Natural seepages from the ocean floor account for nearly half the oil entering the ocean (NOAA, 2020a) and transitting vessels are permitted to release some oil for cleaning purposes (Espedal and Johannessen, 2000). However, large oil spills—whether resulting from drilling platforms, illegal discharges from ships, or accidents—can have major impacts on marine and coastal environments. Oil spills primarily comprise complex mixtures of hydrocarbons, from crude oil to refined products, which have varying chemical and physical characteristics. With exposure to air, light, and microbes, these characteristics change over time as the component chemicals variously evaporate, dissolve, settle, disperse, and/or degrade (Hook *et al.*, 2016; see Figure 19.7). The time required for these processes, however, varies significantly (see Figure 19.8).

Figure 19.7 Weathering processes associated with an oil spill

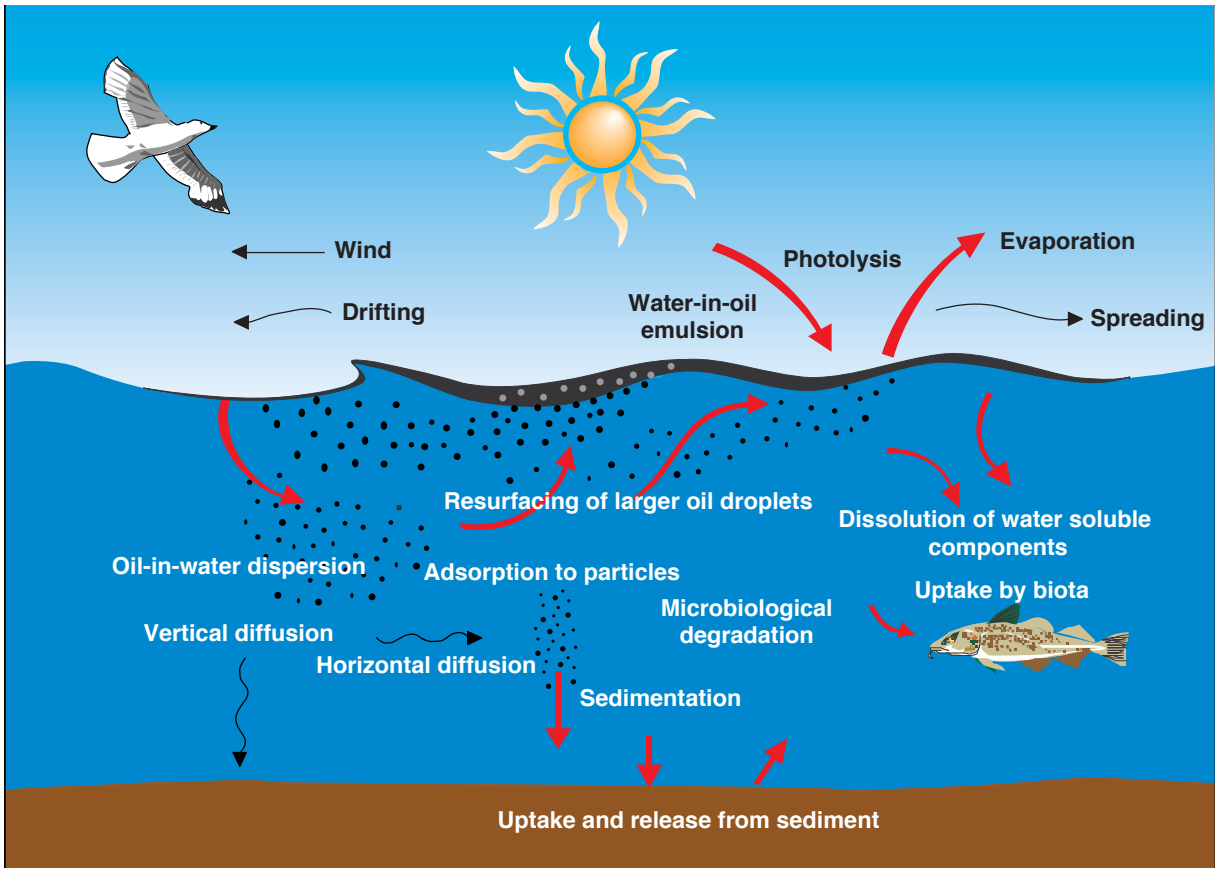

Source: SINTEF (2011) Figure 3.4

Oil spills affect marine life through the direct toxicity of oil, by the smothering effects of the oil on plants and animals, and by coating beaches and rocky shore habitats. The toxicity and physical properties of oil change over time. Chemicals used to disperse oil and increase the rate of breakdown can themselves be toxic to marine life.
(Parliament of Australia, 2018)

Figure 19.8 Duration of oil weathering processes

The relative time scales of different oil weathering processes in the marine environment are compared. The bar thickness indicates relative importance of each process through time, starting from the time of the initial oil spill.

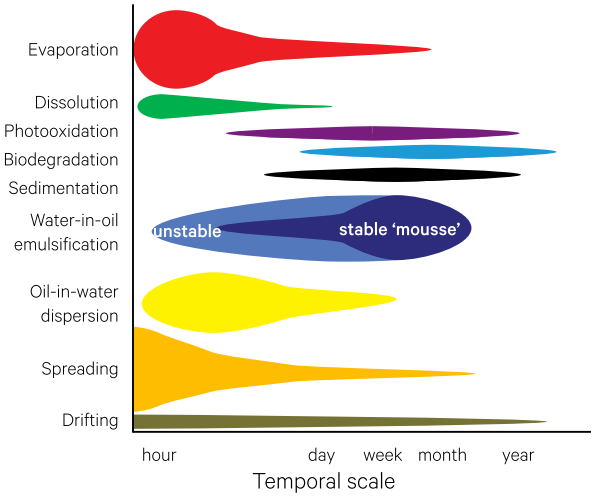

Adapted from: SINTEF (2021) Figure 3.5

Oil spills have differing degrees of toxicity in the marine environment, with refined products generally being considered more toxic (RSC, 2015). Toxicity has been reported to both increase and decrease with time for different organisms in different environments. Oils spills present a particular danger to shorelines, where oil may become concentrated along the high water mark (Hook *et al*., 2016; see Figure 19.9). In terms of marine organisms, oil spills can:

- destroy the insulating ability of furred mammals;
- remove water repellency of bird feathers;
- poison organisms through ingestion;
- reduce the growth in adult fish, including enlarged livers, changes in cardiac and respiration rates, fin erosion, reproduction impairment, and lowered survival of their eggs and larvae (NOAA, 2020b);
- increase photosensitivity; and
- bioaccumulate both in individual organisms and the global food web (RSC, 2015; Hook *et al*., 2016).

As long as there is a global reliance on petroleum products, oil spills will continue to occur.
(Espedal and Johannessen, 2000)

Figure 19.9 Beach profile showing potential oil spill deposits

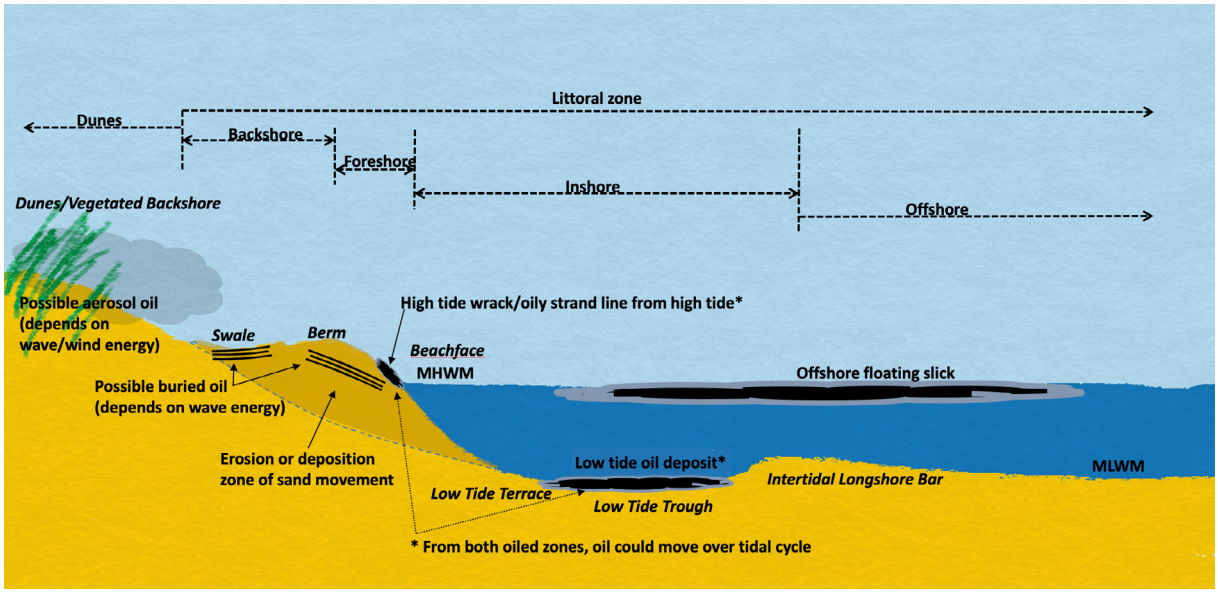

Source: Paul Irving, AMSA

In particular, the GBR is viewed as a 'high risk' area for oil spills from shipping traffic (Sagar *et al*., 2020). In this context, 'risk' implies both a higher likelihood and more significant consequences. Accordingly, to prevent incidents leading to spills the Australian Marine Safety Authority (AMSA: see Excursus 2.1), the Great Barrier Reef Marine Park Authority (GBRMPA), and the Queensland government have implemented a vessel traffic system, coupled with aerial and satellite observation programs to spot oil on the water. For example, in March 2009, a major oil spill near Cape Moreton coincided with tropical cyclone Hamish and resulted in oil being spread along 80 km of the southeast Queensland coastline (DERM, 2009). Similarly, in April 2010, oil from a merchant vessel that ran aground severely damaged Douglas Shoal and created the longest (3 km) known reef scar in the GBR and a 4 km long oil slick, while multiple small, illegal discharges in July 2015 caused numerous fuel oil slicks and coastal strandings between Townsville and Hinchinbrook Island (AMSA, 2020a).

In Australian waters, AMSA and its state and territory partners under the National Plan for Maritime Environmental Emergencies (AMSA, 2019) are responsible for monitoring—and often responding to—oil spills. AMSA (and its partners through AMSA) operationally relies on a variety of EO data sources to both detect an oil spill event, plan an appropriate response, and assess its overall environmental impact(s) (see Excursus 19.4).

EO datasets can be used to detect oil spills when there is a discernible difference between the reflectance or emission from a 'clean' water surface versus that from water covered by an oil slick. A range of EO sensors can be used for this purpose, although almost all are susceptible to detecting 'false positives'—surface features with the appearance of an oil slick—due to ambient biological, oceanographic, bathymetric, atmospheric, or anthropogenic factors (see Table 19.5). Since each type of sensor detects different EMR wavelengths using different sensing mechanisms, it has different advantages and limitations for this application, all of which can vary with environmental conditions (Table 19.6). Accordingly, integrated systems, which utilise data from multiple EO sensors, have been developed for oil spill response (Hook *et al*., 2016). Spaceborne EO datasets are typically most relevant to offshore oil spills, with aerial surveillance being more appropriate for onshore spills (IOGP, 2016).

Table 19.5 Major EO sensors for oil spill detection

Sensing Mechanism	EO sensor	Operation	Major false positives	Limitations
Passive	UV sensors	Detects sunlight reflected from oil slick, especially thin oil sheens	Wind slicks, sunglints, biogenic matter	Darkness, unclear atmospheric conditions, submerged oil (see Table 19.6)
	Optical sensors	Detects sunlight reflected from oil slick; IR sensors can estimate relative oil thickness	River outflows, algae, sediment, organic matter, shoreline and oceanic fronts, weed and kelp beds	Darkness (especially for visible and NIR wavelengths), unclear atmospheric conditions, submerged oil (see Table 19.6)
	TIR sensors	Detects thermal emissions as differences in surface temperature	Upwellings, water inflows, fronts, man-made heat sources	Unclear atmospheric conditions, submerged oil, low spatial resolution (see Table 19.6)
	Hyperspectral sensor	Identify detailed spectral characteristics of oil slick to determine oil type and thickness	Sunglint, white wave caps, shallow water features	Darkness, unclear atmospheric conditions, submerged oil (see Table 19.6)
Active	Laser fluorosensor	Detects irradiated UV wavelengths from oil slick with high sensitivity; Can also estimate oil slick thickness when combined with water Raman signal	Unknown at present (Fingas and Brown, 2018)	Limited spatial extent, darkness, unclear atmospheric conditions (see Table 19.6)
	SAR	Since oil slicks dampen sea capillary waves, their radar returns are different from those of a 'clean' water surface	Low wind areas sheltered by land, rain cells, organic films, wind fronts, algal blooms, current shear zones, mineral oils, turbulent ship wakes, freshwater plumes	High and low wind speeds, submerged oil (see Table 19.6)

Source: Hook *et al.* (2016) Table 6.2 and IOGP (2016) Table 14

Table 19.6 Environmental limitations on oil spill detection

Environmental conditions	EO sensor wavelengths		
	Optical	TIR	Microwave
Lighting	Sunlight required	Not required	Not required
Cloud/Rain/Fog	Does not penetrate	Does not penetrate	Can penetrate
Sea surface	Imagery impacted by very rough seas	Imagery impacted by very rough seas	Imagery most useful when wind speed 3–12 m/s
Ice	Limited if oil is in or under ice	Limited if oil is in or under ice	Best when ice concentration <30% in open water

Source: IOGP (2016) Table 15

Both optical and SAR imagery are used to detect the locations of oil spills and track the extent of their dispersals (Topouzelis, 2008), including illegal discharges from ships (Brekke and Solberg, 2005), and those originating from offshore oil and gas platforms (Liu *et al.*, 2018). Other EO sensors that are relevant to oil spill response include UV/IR sensors, which can estimate the relative thickness of oil slicks, and laser fluorosensors, which are most selective for separating oil slicks from other features (Fingas and Brown, 2014, 2018), can identify the 'type' of oil involved, and estimate its thickness (Hook *et al.*, 2016).

In optical wavelengths, the reflectance characteristics of an oil spill vary with its chemical composition (Lacava *et al.*, 2017; Wettle *et al.*, 2009). While oil spills cannot be differentiated from seawater using visible wavelengths, sunglint in optical imagery (see Section 8.1.3) may expose smooth oil slicks on the water surface (Sun and Hu, 2016; Hu *et al.*, 2018). Since recent discharges of surface oil are typically warmer than surrounding waters, TIR sensors have also been used to highlight temperature differences (Casciello *et al.*, 2011; Grimaldi *et al.*, 2011; Zhou *et al.*, 2017).

SAR imagery, however, has the advantages of being largely independent of lighting and weather conditions (see Section 9.3). Since a surface oil slick has a dampening effect on sea surface roughness, it appears as an area of low backscattering in SAR imagery (Li *et al.*, 2018; see Volume 1B—Section 8), although the actual appearance depends on the type of oil. High frequency radar (X-band) is more sensitive to small variations in surface geometry than lower frequency bands, but can include more speckle noise (Alpers *et al.*, 2017), and VV-polarised SAR is generally considered most appropriate for marine applications (Li *et al.*, 2018).

Oil spill detection using SAR imagery is complicated by the need to differentiate between oil slicks and false positives, or 'look-alikes', such as natural biofilms, algal slicks, grease, sea ice, low wind speed areas, wind shadows, rain cells, or internal waves (Gens, 2008; Alpers *et al.*, 2017). However, the backscatter and visibility of both oil spills and look-alikes are changed to different extents by wind, such that moderate wind speeds can enhance these differences in their appearance (Solberg *et al.*, 1999; Brekke and Solberg, 2005). In some Australian waters, wind shadows, reef shadows, and upwellings are quite common and can contribute to an increased number of false positives when using SAR-based oil spill detection algorithms. The use of SAR sensors is also limited in very calm or rough seas, or when ice is present (see Table 19.6).

SAR imagery has also been used to detect natural hydrocarbon seepage slicks in Australia's offshore environments, especially where surface oil slicks form (Williams and Lawrence, 2002). Additionally, a range of acoustic datasets (see Section 10) have been used to identify sampling sites to determine natural hydrocarbon seepages (Logan *et al.*, 2008).

Excursus 19.4—Operational Oil Spill Response

Source: Paul Irving, AMSA
Further Information: Hook *et al.* (2016) Chapter 6

When an oil spill is reported in Australian waters, the Australian Marine and Safety Authority (AMSA: see Excursus 2.1) conducts an initial risk assessment to determine the most appropriate response. Since the goal of any oil spill response is to minimise the ecological and socioeconomic damage, it is essential that the response process offers 'net environmental benefits' (NEB; Davies and Hope, 2015), where NEB is defined as the "gains in value of environmental services or other ecological properties minus the value of adverse environmental effects caused by those actions" (Efroymson *et al.*, 2004). This assessment requires detailed information about the current situation and its likely ramifications (Hook *et al.*, 2016). In the past decade, AMSA and its National Plan partners (see AMSA, 2019) have responded to 41 significant oil spills in Australian waters. Although around double this number of potential oil spills were reported during this time period, many of those reports were not substantiated, or the spills dissipated naturally without warranting intervention.

Figure 19.10 AMSA oil spill response process

This overview of the AMSA response phase monitoring process shows how it can validate existing knowledge, inform situational awareness, and assess and evalutate operational success.

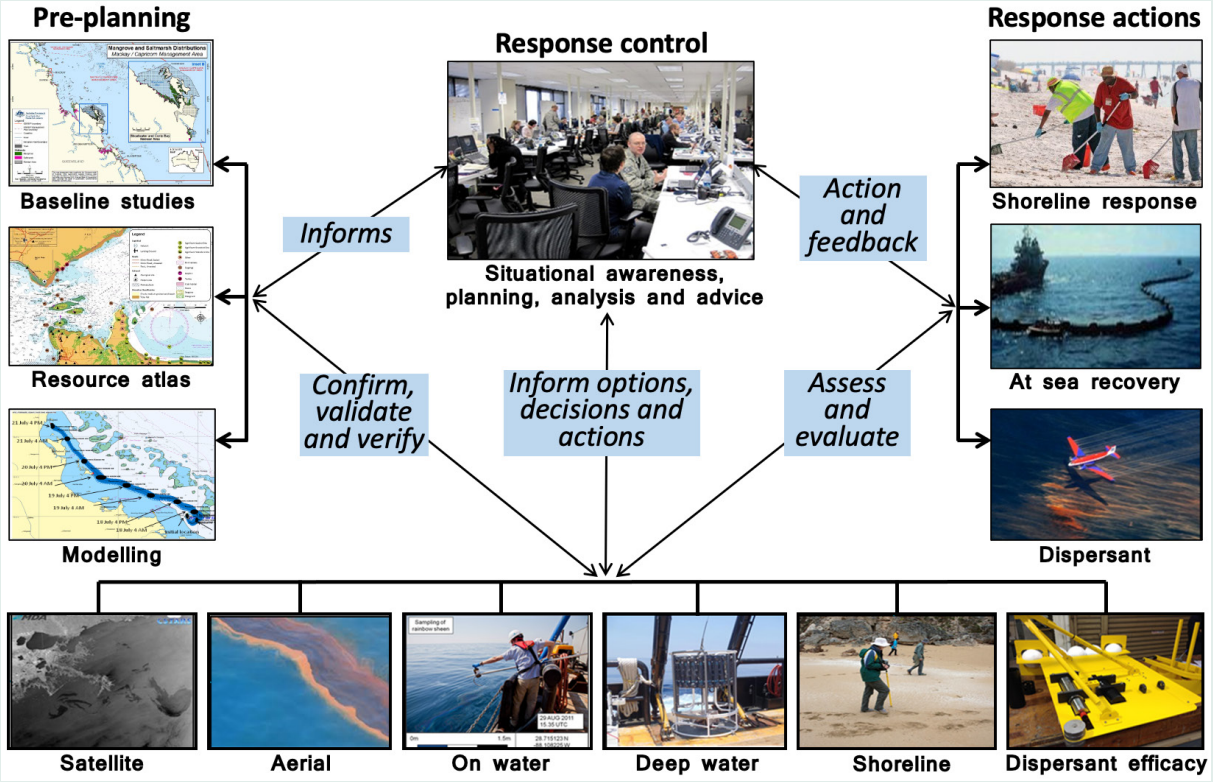

Source: Paul Irving, AMSA

Once it has been determined that a response is appropriate, the response phase needs to be monitored (see Figure 19.10), which requires ongoing detailed information about the current status of the oil spill (Hook *et al.*, 2016). Where available, this information is derived from *in situ* reports, aerial and vessel-based surveillance, oil spill trajectory modelling, and a range of geospatial datasets, including EO. As in any emergency situation, high data quality and rapid processing are needed to ensure that the monitoring information is both current and reliable. With large, frequent coverage and proven data quality, spaceborne EO data has proven to be valuable for locating the extent of the oil slick, mapping its trajectory and ambient conditions, and possibly estimating its thickness. Several operational systems now rely on EO datasets to:

- locate oil slicks that need to be treated with dispersant;
- provide evidence that the dispersant has been applied successfully; and
- dispatch resources to impacted shorelines to remove the stranded oil quickly before it is remobilised by the tide to other sites (Hook *et al.*, 2016).

AMSA have used SAR data for maritime monitoring and marine surveillance since 2013, including detecting oil spills. When looking for spills to initiate a response, or looking for evidence of a spill to initiate a follow-up or prosecution action, AMSA uses a range of remotely sensed evidence, including optical images. Although most incidents have a clear culprit, occasionally a mystery spill occurs, where the culprit needs to be identified. A example of this process is the Pacific Quest oil spill in the Whitsunday Islands in 2002, which used a range of evidence to achieve a conviction. Samples of the spilled oil taken from water were fingerprint-matched to a sample taken from one of six vessels intercepted at their next port of call (Auckland). Satellite location tracking information was used to identify the suspect vessels, and an incidental SPOT image was able to assist by placing the culprit vessel exactly within the footprint of the slick visible to the SPOT sensors (AMSA, 2020b).

19.5 Algal Blooms

An algal or phytoplankton bloom is a temporary biological event involving the rapid growth of microalgae as the natural response to variations in environmental conditions (see Sections 3.3.2.1, 4.6 and 5.3.1.1). As detailed in Sections 8.2.2 and 18.6, algal blooms change the reflectance of surface waters (see Figure 4.11) and this change can be reliably observed using EO (Klemas, 2012; see Figure 19.11).

EO-based methods that have been used to detect phytoplankton blooms in optical imagery include:

- image classification (see Volume 2E);
- band differences and ratios (see Volume 2C);
- semi-analytical inversion models based on forward bio-optical models (see Section 8.4); and
- neural networks (Blondeau-Patissier *et al.*, 2014).

While band ratios and indices are appropriate for mapping algal blooms in ocean waters, more sophisticated modelling approaches are required in the more complex coastal and inland waters. The availability of hyperspectral datasets is expected to improve current methods (Blondeau-Patissier *et al.*, 2014).

Many inversion algorithms have been developed to map specific taxa, however the more sophisticated spectral inversion algorithms derive better results (Bracher *et al.*, 2017). Monitoring of seasonal, annual, and decadal cycles of phytoplankton growth generally requires the integration of EO datasets and appropriate statistical models (Platt *et al.*, 2009; Song *et al.*, 2010) and/or satellite data climatologies (Park *et al.*, 2010; Miller *et al.*, 2006). An example of monitoring algal blooms using an EO time series dataset is described in Blondeau-Patissier *et al.* (2018).

Figure 19.11 MODIS image of algal bloom

An algal bloom stretched along 750 km of the Pilbara coast, northeast WA, in the wake of Cyclone Veronica. Thls image was acquired by MODIS/Aqua on 29 March 2019.

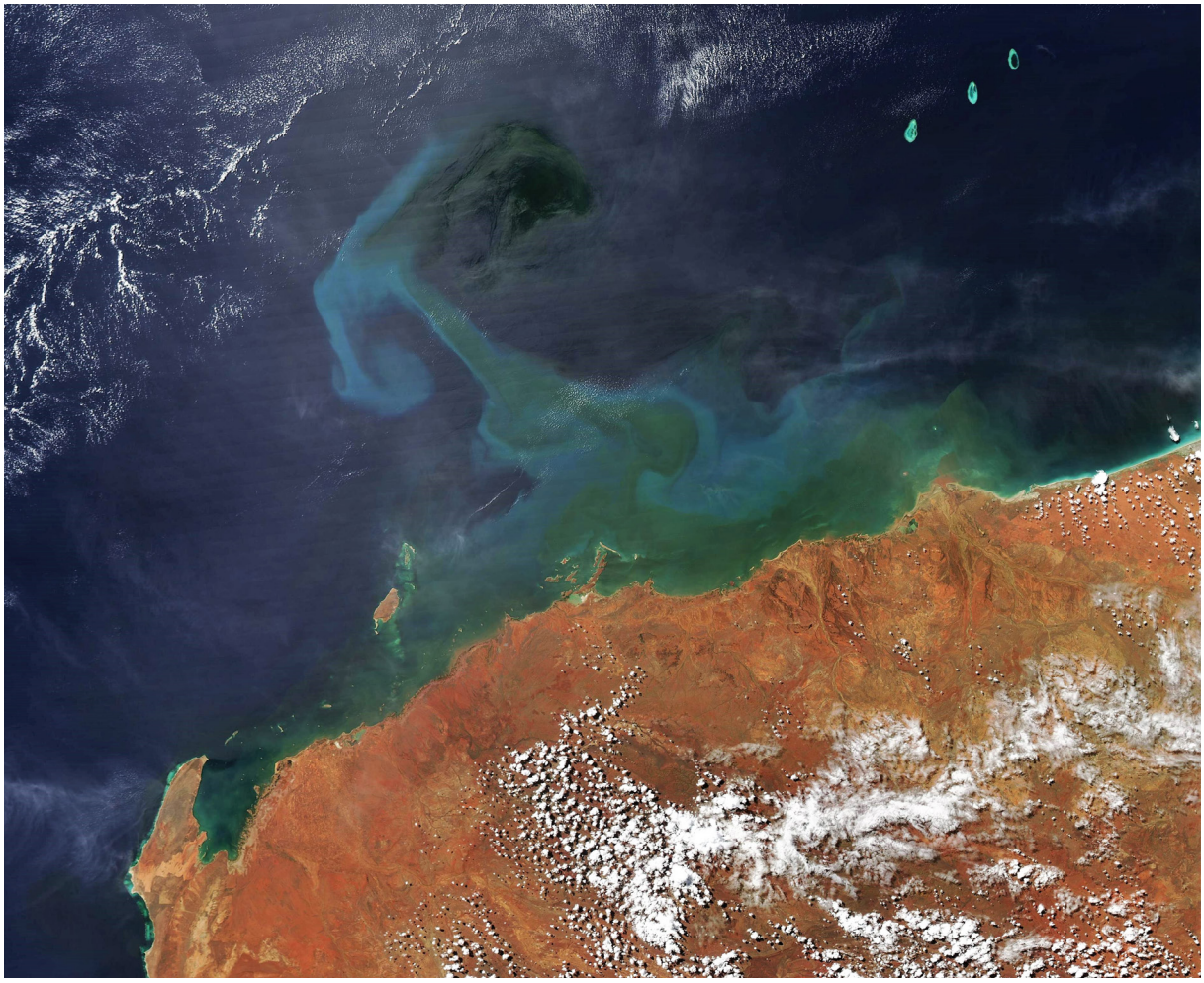

Source: NASA Worldview

19.6 Marine Heatwaves

Just as heatwaves—extended periods of excessively hot weather—happen in the atmosphere, they can occur in the ocean (MHIWG, 2020). Marine heatwaves (MHW) are extreme events, defined as "anomalously warm water events that may last many months and extend over thousands of square kilometres" (Hobday *et al*., 2018). A MHW is defined when the difference between actual water temperature is significantly greater than the expected water temperatures for a given location and season over more than five consecutive days (see Figure 19.12). MHW can occur in any season and have a significant impact on coastal and marine ecosystems, with widespread biological, economic, and political consequences (Mills, 2013; Hobday *et al*., 2016, 2018; Pearce and Feng, 2013; Wernberg *et al*., 2013). In recent years, climatic changes have resulted in a greater frequency of MHW (MHIWG, 2020). One well known consequence of MHW is coral bleaching (Heron *et al*., 2016; McClanahan, 2017; see Excursus 20.3). MHW also impact the distribution of marine species and have resulted in mass mortalities (Sagar *et al*., 2020).

As detailed in Section 14, near real time EO-based estimates of SST are used operationally to monitor the marine environment (see Excursus 14.2), including MHW (Pearce and Feng, 2013; Bond *et al.*, 2015; Di Lorenzo and Mantua, 2016). SST time series datasets are being used to analyse the frequency, duration, extent, and intensity of MHW, as well as their spatial and temporal variability, and seasonal character (Sagar *et al.*, 2020).

Figure 19.12 Defining marine heatwaves

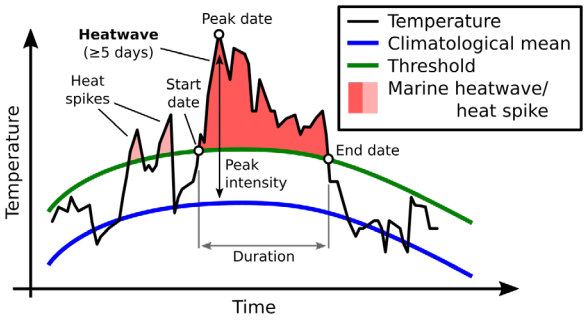

Source: MHIWG (2021)

19.7 Salinity

Salinity, the dissolved salt content of water, is introduced in Section 5.2.1. Ocean surface salinity varies spatially and temporally, so is indicative of the role of ocean waters in the hydrological cycle (see Section 1.1). With over 85% of global evaporation and over 75% of global precipitation occurring over the ocean, information about changes in ocean surface salinity resulting from these processes, can contribute new information about how Earth's freshwater circulates globally, both within the ocean and between the ocean and atmosphere. Since salinity and temperature determines seawater density (s0ee Figure 5.4 and Section 5.2.1), which drives layering and mixing of ocean waters and the formation of water masses (see Section 17), ocean surface salinity data can also provide valuable information about ocean currents and ocean circulation (NASA, 2017).

Salinity largely determines the distribution of marine and estuarine species, often working in combination with other environmental variables (Smyth and Elliott, 2016). While open oceans are relatively stable and similar in terms of most constituents, including total salinity (with the global ocean only varying between 33‰[23] and 37‰; Srokosz and Banks, 2019), coastal waters are impacted by tides, river flows, evaporation, and anthrogenic factors (Wolanski and Elliott, 2015), which varies their salinity levels in daily, tidal, lunar, and seasonal cycles.

Salinity acts synergistically and antagonistically with other environmental stressors in affecting ecology. Factors such as nutrient availability, temperature, pH, and dissolved oxygen have all been shown potentially to interact to produce a dynamic and changing environment where one factor can exacerbate or negate to some extent the detrimental effects of another. Human activities and anthropogenic effluents can modify local salinity regimes and their effects depend on the assimilative capacity of both the area and the species.
(Smyth and Elliot, 2016)

23 ‰: parts per thousand

Figure 19.13 Global salinity image composites

The daily composite SMOS SSS data (0.5° resolution) were obtained from the Ocean Salinity Expertise Center (CECOS) of the CNES-IFREMER Centre Aval de Traitement des Données SMOS (CATDS), at IFREMER, Plouzane (France). The Aquarius data (1° resolution) were furnished through the NASA/CONAE Aquarius/SAC-D Project.

a. Single day sea surface salinity data acquired from SMOS on 15 December 2014.

b. 7 day composite image from Aquarius acquired 10–16 December 2014.

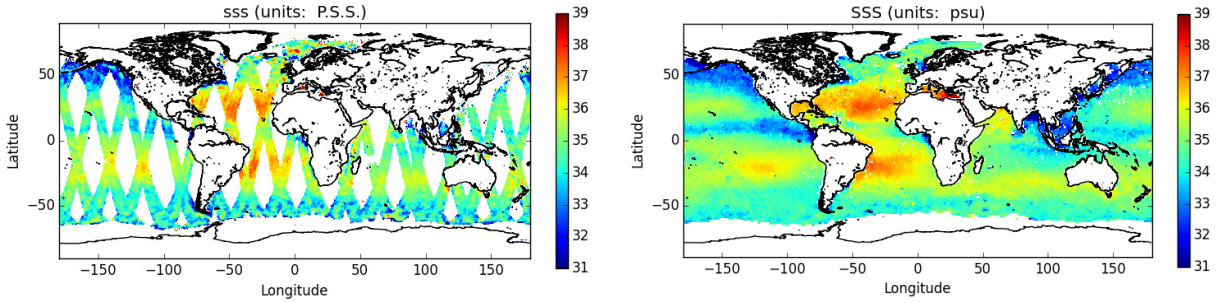

Source: Edward King, CSIRO

As salinity levels of surface waters in oceans change, their dielectric properties at microwave frequencies change slightly (Srokosz and Banks, 2019). On this basis, estimates of sea surface salinity can be derived from carefully calibrated and corrected measurements of 1.4 GHz radiation (L-band) emitted from the ocean surface. These observations are acquired at low spatial resolution (10–100 km) and weekly frequency, but are more difficult in colder waters at high latitudes. Salinity data has been acquired from three satellite missions:

- Soil Moisture and Ocean Salinity (SMOS)—an ESA satellite operating since 2010 (Kerr *et al.*, 2010; Mecklenburg *et al.*, 2016);
- Aquarius—a NASA sensor onboard the Argentine SAC-D spacecraft, which operated from 2011 to mid-2015 (Le Vine *et al.*, 2018); and
- Soil Moisture Active Passive (SMAP)—a NASA mission launched in 2015 to replace Aquarius (Meissner *et al.*, 2019).

These sensors use different techniques to form images but all rely on an accurate measurement of SST (see Section 14) and an estimate of surface wind strength (since surface roughness plays a crucial role in the retrieval algorithm; see Section 16). Products from these missions continue to mature as processing algorithms incorporate advances in instrument understanding, but they are clearly delivering an unprecedented global view of a key ocean variable (see Figure 19.13). Future satellite missions are planned to maintain the continuity of global salinity data.

19.8 Further Information

Inland Water Quality

Dekker and Hestir (2012)

CEOS (2018)

IOCCG: *https://ioccg.org/group/water-quality/*

Water Quality Australia: *https://www.waterquality.gov.au/introduction*

Globolakes (Global Observatory of Lake Responses to Environmental Change)

http://www.globolakes.ac.uk/index.html

Marine Biodiversity Hub

https://www.nespmarine.edu.au/

Marine Heat Wave

http://www.marineheatwaves.org/

NOAA Marine Heatwave Watch: *https://coralreefwatch.noaa.gov/product/marine_heatwave/*

NOAA: *https://research.noaa.gov/article/ArtMID/587/ArticleID/2559/So-what-are-marine-heat-waves*

Maritime Traffic

UNCLAD (2019)

https://www.marinetraffic.com/en/p/company

Australian Marine Water Quality

BOM eReefs Marine Water Quality: *http://www.bom.gov.au/metadata/catalogue/19115/ANZCW0503900427*

IMOS State and Trends of Australia's Ocean Report: 3. Quality: *https://www.imosoceanreport.org.au/time-series/water-quality/*

Department of Environment and Energy (2018). Threat Abatement Plan for the impacts of marine debris on the vertebrate wildlife of Australia's coasts and oceans:

http://www.environment.gov.au/system/files/resources/e3318495-2389-4ffc-b734-164cdd67fe19/files/tap-marine-debris-2018.pdf

Water Quality Guidelines

The Australian and New Zealand Guidelines for Fresh and Marine Water Quality provide authoritative guidance on the management of water quality for natural and semi-natural water resources in Australia and New Zealand. The 2018 revision of the Water Quality Guidelines is presented as an online platform, to improve usability and facilitate updates as new information becomes available:

https://www.waterquality.gov.au/anz-guidelines

GEO AquaWatch

This Group on Earth Observations (GEO) initiative aims to develop and build the global capacity and utility of EO-derived water quality data, products, and information to support water resources management and decision making. In the short term, AquaWatch will develop baseline global water quality monitoring products, and regional and local end-to-end prototype demonstrations:

https://www.geoaquawatch.org

https://earthobservations.org/geoss_wp.php

19.9 References

Agamuthu, P., Mehran, S.B., Norkhairah, A., and Norkhairah, A. (2019). Marine debris: A review of impacts and global initiatives. *Waste Management and Research*, 37(10), 987–1002. *https://doi.org/10.1177/0734242X19845041*

Alpers, W., Holt, B., and Zeng, K. (2017). Oil spill detection by imaging radars: Challenges and pitfalls. *Remote Sensing of Environment*, 201, 133–147.

AFMA (2020). *Satellite Monitoring of fishing boats* webpage, Australian Fisheries Management Authority website: *https://www.afma.gov.au/monitoring-enforcement/satellite-monitoring-fishing-boats*

AIMS (2019). *Water Quality* webpage, Australian Institute of Marine Science website: *https://www.aims.gov.au/water-quality*

AMSA (2019). *National Plan for Maritime Environmental Emergencies*. Australian Maritime Safety Authority. *https://www.amsa.gov.au/marine-environment/national-plan-maritime-environmental-emergencies https://www.amsa.gov.au/sites/default/files/amsa-496-national-plan.pdf*

AMSA (2020a). *Incidents and exercises* webpage, Australian Maritime Safety Authority website: *https://www.amsa.gov.au/marine-environment/incidents-and-exercises*

AMSA (2020b). *Pacific Quest, 25 December 2002* webpage, Australian Maritime Safety Authority website: *https://www.amsa.gov.au/marine-environment/incidents-and-exercises/pacific-quest-25-december-2002*

ATC (2013). *Oil and Gas* webpage, Australian Trade Commission website: *https://www.austrade.gov.au/oil-and-gas/*

Bereta, K., Zissis, D., and Grasso, R. (2020). Automatic Maritime Object Detection Using Satellite Imagery. *IEEE Oceans 2020*. *https://zenodo.org/record/4074827#.X4PMEZMzbUI*

Blondeau-Patissier, D., Gower, J.F., Dekker, A.G., Phinn, S.R., and Brando, V.E. (2014). A review of ocean color remote sensing methods and statistical techniques for the detection, mapping and analysis of phytoplankton blooms in coastal and open oceans. *Progress in Oceanography*, 123, 123–144.

Blondeau-Patissier, D., Brando, V.E., Lønborg, C., Leahy, S.M., and Dekker, A.G. (2018). Phenology of Trichodesmium spp. Blooms in the Great Barrier Reef lagoon, Australia, from the ESA-MERIS 10-year mission. *PLOS ONE*, 13, e0208010. *https://doi.org/10.1371/journal.pone.0208010*

Bond, N.A., Cronin, M.F., Freeland, H., and Mantua, N. (2015). Causes and impacts of the 2014 warm anomaly in the NE Pacific. *Geophysical Research Letters*, 42, 3414–3420.

Bracher, A., Bouman, H.A., Brewin, R.J.W., Bricaud, A., Brotas, V., Ciotti, A.M., Clementson, L., Devred, E., Di Cicco, A., Dutkiewicz, S., Hardman-Mountford, N.J., Hickman, A.E., Hieronymi, M., Hirata, T., Losa, S.N., Mouw, C.B., Organelli, E., Raitsos, D.E., Uitz, J., Vogt, M., and Wolanin, A. (2017). Obtaining Phytoplankton Diversity from Ocean Color: A Scientific Roadmap for Future Development. *Frontiers in Marine Science*, 4. *https://doi.org/10.3389/fmars.2017.00055*

Brando, V.E., Anstee, J.M., Wettle, M., Dekker, A.G., Phinn, S.R., and Roelfsema, C. (2009). A physics based retrieval and quality assessment of bathymetry from suboptimal hyperspectral data. *Remote Sensing of Environment*, 113, 755–770. doi:10.1016/j.rse.2008.12.003.

Brando, V.E., Dekker, A.G., Park, Y.J., and Schroeder, T. (2012). Adaptive semianalytical inversion of ocean color radiometry in optically complex waters. *Applied Optics*, 51, 2808–2833.

Brekke, C., and Solberg, A.H. (2005). Oil spill detection by satellite remote sensing. *Remote Sensing of Environment*, 95, 1–13.

Browne, M.A. (2015). Sources and pathways of microplastic to habitats. In *Marine Anthropogenic Litter* (Eds: Bergmann, M., Gutow, L., and Klages, M.). Springer International Publishing, Switzerland. pp 229–244.

Casciello, D., Lacava, T., Pergola, N., and Tramutoli, V. (2011). Robust Satellite Techniques for oil spill detection and monitoring using AVHRR thermal infrared bands. *International Journal of Remote Sensing*, 32, 4107–4129.

CEOS (2018). *Feasibility Study for an Aquatic Ecosystem Earth Observing System*. (Eds: Dekker, A.G., and Pinnel, N.) CSIRO, Canberra.

Chislock, M.F., Doster, E., Zitomer, R.A., and Wilson, A.E. (2013). Eutrophication: causes, consequences, and controls in aquatic ecosystems. *Nature Education Knowledge*, 4(4), 10.

Crisp, D.J. (2004). *The state-of-the-art in ship detection in synthetic aperture radar imagery*. Defence Science And Technology Organisation Salisbury (Australia) Info Sciences Lab.

Critchell, K., Grech, A., Schlaefer, J., Andutta, F.P., Lambrechts, J., Wolanski, E., and Hamann, M. (2015). Modelling the fate of marine debris along a complex shoreline: lessons from the Great Barrier Reef. *Estuarine, Coastal and Shelf Science*, 167, 414–426.

CSIRO (2008). *Water availability in the Murray–Darling Basin*. A report to the Australian Government from the CSIRO Murray–Darling Basin Sustainable Yields Project, CSIRO, Australia.

CSIRO (2017). *Protecting the world's fisheries. Identifying offending operators and their vessels*. *https://research.csiro.au/iuu/publications/*

CSIRO (2018). *Protecting the world's fisheries. Big data, analytics, and technology to identify offending operators and their vessels*. *https://research.csiro.au/iuu/publications/*.

Davies, A.J., and Hope, M.J. (2015). Bayesian inference-based environmental decision support systems for oil spill response strategy selection. *Marine Pollution Bulletin*, 96, 87–102. doi:10.1016/j.marpolbul.2015.05.041

DAWE (2020). *Sea dumping* webpage, Department of Agriculture, Water and the Environment website: *https://www.environment.gov.au/marine/marine-pollution/sea-dumping*

Dekker, A.G., and Hestir, E.L. (2012). *Evaluating the Feasibility of Systematic Inland Water Quality Monitoring with Satellite Remote Sensing*. Water for a Healthy Country National Research Flagship, CSIRO.

Dekker, AG.., Phinn, SR.., Anstee, J., Bissett, P., Brando, V.E., Casey, B., Fearns, P., Hedley, J., Klonowski, W., Lee, Z.P., Lynch, M., Lyons, M., Mobley, C., and Roelfsema, C. (2011). Intercomparison of shallow water bathymetry, hydrooptics, and benthos mapping techniques in Australian and Caribbean coastal environments. *Limnology and Oceanography Methods*, 9, 396–425.

DERM (2009). *Effect of the March 2009 oil spill on Moreton Bay Ramsar site*. Queensland Department of Environment and Resource Management, Brisbane. *http://www.environment.gov.au/water/topics/wetlands/database/pubs/41-art-3-2-impact-of-march-2009-oil-spill.pdf*

Di Lorenzo, E., and Mantua, N. (2016). Multi-year persistence of the 2014/15 North Pacific marine heatwave. *Nature Climate Change*, 6, 1042–1047. *https://doi.org/10.1038/nclimate3082*

Durand, D., Pozdnyakov, D.V., Sandven, S., Cauneau, F., Wald, L., Jacob, A., Kloster, K., and Miles, M. (1999). *Characterisation of inland and coastal waters with space sensors: final report*. Technical report No. 164, pp. 1–180. Nansen Environmental and Remote Sensing Centre, Bergen.

Efroymson, R.A., Nicolette, J.P., and Suter, G.W. (2004). A framework for Net Environmental Benefit Analysis for remediation or restoration of contaminated sites. *Environmental Management*, 34, 315–331. doi:10.1007/s00267-004-0089-7

Elvidge, C.D., Zhizhin, M., Baugh, K., and Hsu, F.-C. (2015). Automatic boat identification system for VIIRS low light imaging data. *Remote Sensing*, 7, 3020-3036.

Eriksen, M., Lebreton, L.C., Carson, H.S., Thiel, M., Moore, C.J., Borerro, J.C., Galgani, F., Ryan, P.G., and Reisser, J. (2014). Plastic pollution in the world's oceans: more than 5 trillion plastic pieces weighing over 250,000 tons. *PloS ONE*, 9(12), e111913. doi:10.1371/journal.pone.0111913

Espedal, H.A., and Johannessen, O.M. (2000). Cover: Detection of oil spills near offshore installations using synthetic aperture radar (SAR). *International Journal of Remote Sensing*, 21(11), 2141–2144. *http://dx.doi.org/10.1080/014311600500294 68*

Fingas, M., and Brown, C. (2014). Review of oil spill remote sensing. *Marine Pollution Bulletin*, 83, 9–23. doi:10.1016/j.marpolbul.2014.03.059

Fingas, M., and Brown, C.E. (2018). A Review of Oil Spill Remote Sensing. *Sensors*, 18(1), 91. doi:10.3390/s18010091

Galloway, T.S., and Lewis, C.N. (2016). Marine microplastics spell big problems for future generations. *Proceedings of the National Academy of Sciences of the United States of America*, 113(9), 2331–2333.

Garaba, S.P., and Dierssen, H.M. (2018). An airborne remote sensing case study of synthetic hydrocarbon detection using short wave infrared absorption features identified from marine-harvested macro- and microplastics. *Remote Sensing of Environment*, 205, 224–235.

Garaba, S.P., Aitken, J., Slat, B., Dierssen, H.M., Lebreton, L., Zielinski, O., and Reisser, J. (2018). Sensing Ocean Plastics with an Airborne Hyperspectral Shortwave Infrared Imager. *Environmental Science and Technology*, 52, 11699–11707.

Gens, R. (2008). Oceanographic applications of SAR remote sensing. *GIScience and Remote Sensing*, 45, 275–305.

Gilbert, T, Baxter, T., and Spence, A. (2003). The Australian Oil Spill Response Atlas Project. *Proceedings of International Oil Spill Conference, April 2003*. doi:10.7901/2169-3358-2003-1-851

Goddijn-Murphy, L., Peters, S., van Sebille, E., James, N.A., and Gibb, S. (2018). Concept for a hyperspectral remote sensing algorithm for floating marine macro plastics. *Marine Pollution Bulletin*, 126, 255–262. *https://doi.org/10.1016/j.marpolbul.2017.11.011*

Grimaldi, C., Casciello, D., Coviello, I., Lacava, T., Pergola, N., and Tramutoli, V. (2011). An improved RST approach for timely alert and Near Real Time monitoring of oil spill disasters by using AVHRR data. *Natural Hazards and Earth System Sciences*, 11, 1281–1291.

Heron, S.F., Jmaynard, J.A., Van Hooidonk, R., and Eakin, C.M. (2016). Warming trends and bleaching stress of the world's coral reefs 1985–2012. *Scientific reports*, 6, 38402.

Hobday, A.J., Alexander, L.V., Perkins, S.E., Smale, D.A., Straub, S.C., Oliver, E.C.J., Benthuysen, J., Burrows, M.T., Donat, M.G., Feng, M., Holbrook, N.J., Moore, P.J., Scannell, H.A., Gupta, A.S., and Wernberg, T. (2016). A hierarchical approach to defining marine heatwaves. *Progress in Oceanography*, 141, 227–238. *https://doi.org/10.1016/j.pocean.2015.12.014*

Hobday, A.J., Oliver, E.C.J., Sen Gupta, A., Benthuysen, J., Burrows, M.T., Donat, M.G., Holbrook, N.J., Moore, P.J., Thomsen, M.S., Wernberg, T., and Smale, D.A. (2018). Categorizing and naming marine heatwaves. *Oceanography*, 31, 162–173. *https://doi.org/10.5670/oceanog.2018.205*

Hook, S., Batley, G., Holloway, M., Irving, P., and Ross, A. (2016). *Oil Spill Monitoring Handbook*. CSIRO, Clayton South. *https://publications.csiro.au/rpr/download?pid=csiro:EP158596&dsid=DS2*

Hu, C., Feng, L., Holmes, J., Swayze, G. A., Leifer, I., Melton, C., Garcia, O., Macdonald, I., Hess, M., Muller-Karger, F., Graettinger, G., and Green, R. (2018). Remote sensing estimation of surface oil volume during the 2010 Deepwater Horizon oil blowout in the Gulf of Mexico: Scaling up AVIRIS observations with MODIS measurements. *Journal of Applied Remote Sensing*, 12(2), 26008.

IMO (2020). *Convention on the Prevention of Marine Pollution by Dumping of Wastes and Other Matter* webpage, International Maritime Organisation website: *http://www.imo.org/en/OurWork/Environment/LCLP/Pages/default.aspx*

IOCCG (2018). *International Ocean Colour Coordinating Group* website: *https://ioccg.org/*

IOGP (2016). *Satellite remote sensing of oil spills at sea*. IOGP Report 549. International Association of Oil and Gas Producers, London. *https://www.iogp.org/bookstore/product/satellite-remote-sensing-of-oil-spills-at-sea/*

IUCN (2020). *Marine plastics* webpage, Internation Union for Conservation of Nature website: *https://www.iucn.org/resources/issues-briefs/marine-plastics*

Jambeck, J. R., Geyer, R., Wilcox, C., Siegler, T.R., Perryman, M., Andrady, A., Narayan, R., and Law, K.L. (2015). Plastic waste inputs from land into the ocean. *Science*, 347, 768–771.

Joehnk, K.D., Anstee, J., Ford, P., and Robson, B. (2018). *Development of bloom remote sensing capability and cyanobacteria forecasting model for Western Treatment Plant's largest treatment lagoon systems*. Report prepared for Melbourne Water Corporation by CSIRO Land and Water, Australia.

Kanjir, U., Greidanus, H., and Ostir, K. (2018). Vessel detection and classification from spaceborne optical images: A literature survey. *Remote Sensing of Environment*, 207, 1–26.

Kerr, Y., Waldteufel, P., and Wigneron, J.P., Delwart, S., Cabot, F., Boutin, J., Escorihuela, M.-J., Font, J., Reul, N., Gruhier, C., Enach Juglea, S., Drinkwater, M.R., Hahne, A., Martin-Neira, M., Mecklenberg, S. (2010). The SMOS mission: new tool for monitoring key elements of the global water cycle. *Proceedings of the IEEE*, 98, 666–687.

Klemas, V. (2012). Remote Sensing of Algal Blooms: An Overview with Case Studies. *Journal of Coastal Research*, 28, 34–43.

Lacava, T., Ciancia, E., Coviello, I., Di Polito, C.,. Grimaldi, C.S., Pergola, N., Satriano, V., Temimi, M., Zhao, J., and Tramutoli, V. (2017). A MODIS-based Robust Satellite Technique (RST) for timely detection of oil spilled areas. *Remote Sensing*, 9, 128.

Le Vine, D.M., Dinnat, E.P., Meissner, T., Wentz, F.J., Kao, H.-Y., Lagerloef, G., and Lee, T. (2018). Status of Aquarius and Salinity Continuity. *Remote Sensing*, 10, 1585. doi:10.3390/rs10101585

Li, X., Nunziata, F., and Garcia, O. (2018). Oil Spill Detection from Single- and Multipolarization SAR Imagery. *Comprehensive Remote Sensing*, 8, 231–248. *https://doi.org/10.1016/B978-0-12-409548-9.10407-5*

Lindell, T., Pierson, D., Premazzi, G., and Ziliolli, E. (Eds) (1999). *Manual for monitoring European lakes using remote sensing techniques*. Office for official publications of European Communities, Luxembourg. 161pp.

Liu, Y., Hu, C., Sun, C., Zhan, W., Sun, S., Xu, B., and Dong, Y. (2018). Assessment of offshore oil/gas platform status in the northern Gulf of Mexico using multi-source satellite time-series images. *Remote Sensing of Environment*, 208, 63–81.

Logan, G., Jones, A., Ryan, G., Wettle, M., Thankappan, M., Grosjean, E., Rollet, N., and Kennard, J. (2008). *Review of Australian Offshore Natural Hydrocarbon Seepage Studies*. Geoscience Australia Record: 2008/17.

McClanahan, T. (2017). Changes in coral sensitivity to thermal anomalies. *Marine ecology progress series*, 570, 71–85.

Mace, T.H. (2012). At-sea detection of marine debris: Overview of technologies, processes, issues, and options. *Marine Pollution Bulletin*, 65, 23–27.

Malthus, T.J., Botha, E., and Anstee, J. (2016). *Early warning system for harmful algal blooms. Report on Workpackage 2—Rapid Bloom Identification: Satellite sensing*. CSIRO Land and Water, Australia.

Matthews, M.W. (2011). A current review of empirical procedures of remote sensing in inland and near-coastal transitional waters. *International Journal of Remote Sensing*, 32(21), 6855–6899. doi:10.1080/01431161.2010.512947

Maximenko, N., Corradi, P., Law, K.L., van Sebille, E., Garaba, S.P., Lampitt, R.S., Galgani, F., Martinez-Vicente, V., Goddijn-Murphy, L., Veiga, J.M., Thompson, R.C., Maes, C., Moller, D., Löscher, C.R., Addamo, A.M., Lamson, M., Centurioni, L.R., Posth, N., Lumpkin, R., Vinci, M., Martins, A.M., Pieper, C.D., Isobe, A., Hanke, G., Edwards, M., Chubarenko, I.P., Rodriguez, E., Aliani, S., Arias, M., Asner, G.P., Brosich, A., Carlton, J.T., Chao, Y., Cook, A.-M., Cundy, A., Galloway, T.S., Giorgetti, A., Goni, G.J., Guichoux, Y., Hardesty, B.D., Holdsworth, N., Lebreton, L., Leslie, H.A., MacadamSomer, I., Mace, T., Manuel, M., Marsh, R., Martinez, E., Mayor, D., Le Moigne, M., Jack, M.E.M., Mowlem, M.C., Obbard, R.W., Pabortsava, K., Robberson, B., Rotaru, A.-E., Spedicato, M.T., Thiel, M., Turra, A., and Wilcox, C., (2019). Toward the Integrated Marine Debris Observing System. *Frontiers in Marine Science*, 6, 447. *https://doi.org/10.3389/fmars.2019.00447*

Mecklenburg, S., Drusch, M., and Kaleschke, L., Rodriguez-Fernandez, N., Reul, N., Kerr, Y., Font, J., Martin-Neira, M., Oliva, R., Daganzo-Eusebio, E., Grant, J.P., Sabia, R., Macelloni, G., Rautiainen, K., Fauster, J., de Rosnay, P., Munoz-Sabater, J., Verhoest, J., Levens, H., Delwart, S., Crapolicchio, R., de la Fuent, A., and Kornberg, M. (2016). ESA's soil moisture and ocean salinity mission: from science to operational applications. *Remote Sensing of Environment*, 180, 3–18.

Meissner, T., Wentz, F.J., Manaster, A., and Lindsley, R. (2019). *Remote Sensing Systems SMAP Ocean Surface Salinities [Level 2C, Level 3 Running 8-day, Level 3 Monthly], Version 4.0 validated release*. Remote Sensing Systems, Santa Rosa, CA, USA. *www.remss.com/missions/smap. doi:10.5067/SMP40-2SOCS,10.5067/SMP40-3SPCS, 10.5067/SMP40-3SMCS*

MHIWG (2020). *Marine Heatwaves Explained* webpage, Marine Heatwave International Working Group website: *http://www.marineheatwaves.org/all-about-mhws.html*

Miller, P.I., Shutler, J.D., Moore, G.F., and Groom, S.B. (2006). SeaWiFS discrimination of harmful algal bloom evolution. *International Journal of Remote Sensing*, 27, 2287–2301.

Mills, K.E., Apershing, A.J., Brown, C.J., Chen, Y., Chiang, F.-S., Holland, D.S., Lehuta, S., Nye, J.A., Sun, J.C., Thomas, A.C., and Wahle, R.A. (2013). Fisheries Management in a Changing Climate—Lessons from the 2012 Ocean Heat Wave in the Northwest Atlantic. *Oceanography*, 26, 191–195.

Mobley, C., and Sundman, L.K., (2000). *Hydrolight 4.1 Technical Documentation*, 4.1 ed. Sequoia Scientific Inc., Redmond.

Morrison, S. (2019). *National Statement to the United Nations General Assembly*, 25 September 2019, New York. *https://www.pm.gov.au/media/national-statement-united-nations-general-assembly*

NASA (2017). *Aquarius Mission Overview* webpage: *https://www.nasa.gov/mission_pages/aquarius/overview/index.html*

NOAA (2020a). *What is an oil seep?* National Ocean Service, National Oceanic and Atmospheric Administration website: *https://oceanservice.noaa.gov/facts/oilseep.html*

NOAA (2020b). *How does oil impact marine life?* National Ocean Office, National Oceanic and Atmospheric Administration website: *https://oceanservice.noaa.gov/facts/oilimpacts.html*

Odermatt, D., Gitelson, A., Brando, V. E., and Schaepman, M. (2012). Review of constituent retrieval in optically deep and complex waters from satellite imagery. *Remote Sensing of Environment*, 118, 116–126. doi:/10.1016/j.rse.2011.11.013

Parliament of Australia (2018). *Marine Oil Pollution* webpage: *https://www.aph.gov.au/About_Parliament/Parliamentary_Departments/Parliamentary_Library/pubs/BriefingBook43p/marineoilpollution*

Park, Y.J., Ruddick, K., and Lacroix, G. (2010). Detection of algal blooms in European waters based on satellite chlorophyll data from MERIS and MODIS. *International Journal of Remote Sensing*, 31, 6567–6583.

Pearce, A.F., and Feng, M. (2013). The rise and fall of the "marine heat wave" off Western Australia during the summer of 2010/2011. *Journal of Marine Systems*, 111, 139–156.

Platt, T., White, G.N., Zhai, L., Sathyendranath, S., and Roy, S. (2009). The phenology of phytoplankton blooms: ecosystem indicators from remote sensing. *Ecological Modelling*, 220, 3057–3069.

Reisser, J., Shaw, J., Wilcox, C., Hardesty, B.D., Proietti, M., Thums, M., and Pattiaratchi, C. (2013). Marine Plastic Pollution in Waters around Australia: Characteristics, Concentrations, and Pathways. *PloS ONE*, 8(11), e80466. *https://doi.org/10.1371/journal.pone.0080466*

Rochman, C.M., Browne, M.A. Underwood, A., Van Franeker, J.A., Thompson, R.C., and Amaral-Zettler, L.A. (2016). The ecological impacts of marine debris: unraveling the demonstrated evidence from what is perceived. *Ecology*, 97, 302–312.

RSC (2015). *The Behaviour and Environmental Impacts of Crude Oil Released into Aqueous Environments*. Royal Society of Canada, Ottawa, Ontario, Canada. *https://rsc-src.ca/en/behaviour-and-environmental-impacts-crude-oil-released-into-aqueous-environments*

Sagar, S., Falkner, I., Dekker, A., Huang, Z., Blondeau-Patissier, D., Phillips, C., and Przeslawski, R. (2020). *Earth Observation for monitoring of Australian Marine Parks and other off-shore Marine Protected Areas*. Report to the National Environmental Science Program, Marine Biodiversity Hub. Geoscience Australia.

Simis, S.G.H., Ruiz-Verdú, A., Domínguez-Gómez, J.A., Peña-Martinez, R., Peters, S.W.M., and Gons, H.J. (2007). Influence of phytoplankton pigment composition on remote sensing of cyanobacterial biomass. *Remote Sensing of Environment*, 106(4), 414–427.

SINTEF (2011). *Weathering Properties of Bream Crude Oil Related to Oil Spill Response*. SINTEF, Trondheim, Norway.

Smyth, K., and Elliot, M. (2016). Effects of changing salinity on the ecology of the marine environment. In *Stressors in the Marine Environment* (Eds: Solan, M. and Whitely, N.M.). Oxford University Press. doi:10.1093/acprof:oso/9780198718826.003.0009

SOE (2011). *State of Environment Report 2011*. *http://155.187.2.69/soe/2011/report/inland-water/index.html*

SOE (2016a). *Coastal waters* webpage, State of Environment Report 2016: *https://soe.environment.gov.au/theme/coasts/topic/2016/coastal-waters*

SOE (2016b). *Marine oil and gas exploration and production* webpage, State of Environment Report 2016: *https://soe.environment.gov.au/theme/marine-environment/topic/2016/marine-oil-and-gas-exploration-and-production*

Solberg, A.H.S., Storvik, G., Solberg, R., and Volden, E. (1999). Automatic detection of oil spills in ERS SAR images. *IEEE Transactions on Geoscience and Remote Sensing*, 37, 1916–1924.

Song, H., Ji, R., Stock, C., and Wang, Z. (2010). Phenology of phytoplankton blooms in the Nova Scotian shelf-Gulf of Maine region: remote sensing and modeling analysis. *Journal of Plankton Research*, 32, 1485–1499.

Srokosz, M., and Banks, C. (2019). Salinity from space. *Weather*, 74(1), 3–8. doi:10.1002/wea.3161

Straka, W.C., Seaman, C.J., Baugh, K., Cole, K., Stevens, E., and Miller, S.D. (2015). Utilization of the Suomi national polar-orbiting partnership (NPP) visible infrared imaging radiometer suite (VIIRS) day/night band for arctic ship tracking and fisheries management. *Remote Sensing*, 7, 971–989.

Sun, S., and Hu, C. (2016). Sun glint requirement for the remote detection of surface oil films. *Geophysical Research Letters*, 43, 309–316.

Topouzelis, K.N. (2008). Oil Spill Detection by SAR Images: Dark Formation Detection, Feature Extraction and Classification Algorithms. *Sensors*, 8, 6642–6659.

UNCLAD (2019). *Review of Marine Transport 2019*. United Nations Conference on Trade and Development, New York. ISBN 978-92-1-112958-8 *https://unctad.org/system/files/official-document/rmt2019_en.pdf*

UNEP (2020). *Marine Litter* webpage, United Nations Environment Programme website: *https://www.unep.org/explore-topics/oceans-seas/what-we-do/working-regional-seas/marine-litter*

van Sebille, E., England, M.H., and Froyland, G. (2012). Origin, dynamics and evolution of ocean garbage patches from observed surface drifters. *Environmental Research Letters*, 7, 044040.

van Sebille, E., Wilcox, C., Lebreton, L., Maximenko, N., Hardesty, B.D., Van Franeker, J.A., Eriksen, M., Siegel, D., Galgani, F.,and Law, K.L. (2015). A global inventory of small floating plastic debris. *Environmental Research Letters*, 10, 124006.

Wernberg, T., Smale, D.A., Tuya, F., Thomsen, M.S., Langlois, T.J., de Bettignies, T., Bennett, S., and Rousseaux, C.S., (2013). An extreme climatic event alters marine ecosystem structure in a global biodiversity hotspot. *Nature Climate Change*, 3, 78–82.

Wettle, M., Daniel, P.J., Logan, G.A., and Thankappan, M. (2009). Assessing the effect of hydrocarbon oil type and thickness on a remote sensing signal: A sensitivity study based on the optical properties of two different oil types and the HYMAP and Quickbird sensors. *Remote Sensing of Environment*, 113, 2000–2010.

Williams, A., and Lawrence, G. (2002). The role of satellite seep detection in exploring the South Atlantic's ultradeep water, in Surface exploration case histories: Applications of geochemistry, magnetics, and remote sensing. In *AAPG Studies in Geology No. 48 and SEG Geophysical References Series No. 11*, (Eds: Schumacher, D. and LeSchack, L.A.), pp 327–344.

Wolanksi, E., and Elliott, M. (2015). *Estuarine Ecohydrology: An Introduction*, 2nd edn. Elsevier Science, Amsterdam.

Wood Mackenzie (2020). *Australia Oil and Gas Industry Outlook Report*. *https://appea.com.au/wp-content/uploads/2020/06/Australia-Oil-and-Gas-Industry-Outlook-Report.pdf*

Zhou, Y., Jiang, L., Lu, Y.C., Zhan, W.F., Mao, Z.H., Qian, W.X., and Liu, Y.X. (2017). Thermal Infrared Contrast Between Different Types of Oil Slicks on Top of Water Bodies. *IEEE Geoscience and Remote Sensing Letters*, 14, 1042–1045.

20 Ecology

Janet Anstee, Chris Roelfsema, Eva Kovacs, and Stuart Phinn

Ecology is the study of the relationships between living organisms, including humans, and their physical environment; it seeks to understand the vital connections between plants and animals and the world around them. (The Ecological Society of America)

Ecology comprises a range of studies that observe:

- the distribution and abundance of organisms;
- the interactions between organisms; and
- the relationship between individual organisms and their abiotic environment

Aspects of the ecology of aquatic systems are introduced previously in Section 3. As well as marine activities, surface water ecosystems are directly impacted by changes in terrestrial activities and atmospheric variations, including climatic conditions. Given the extent of surface waters on Earth, maintaining their ecological health and balance is paramount for the health of this planet. One measure of this in any environment is its biodiversity (see Excursus 20.1 and Volume 3A—Section 18).

Microscopic phytoplankton organisms are the primary producers in aquatic environments, providing and regulating marine ecosystem services (Tweddle *et al.*, 2018). These organisms generate around half the organic matter on our planet and around half of its atmospheric oxygen (see Section 3.3.2.1), and also function as a CO_2 sink (see Section 1.5). Phytoplankton is the root of the marine food web (see Sections 3 and 5.3), and used as an indicator of marine productivity (IOCCG, 2014). Productivity can also be inferred from geomorphological features (see Section 6.2), with some seafloor features, such as seamounts and submarine canyons which attract pelagic predators for feeding or breeding, being consistent indicators of biodiversity and biomass (Dower *et al.*, 1992; Pollard *et al.*, 2009; Lemos *et al.*, 2018). Other marine features, such as fronts, currents, and upwellings (see Section 17), are more variable in terms of their association with marine biology (Hyrenback *et al.*, 2000).

Phytoplankton community composition, determined by biogeochemical functional groups, has changed over the past century (Dutkiewicz *et al.*, 2019) and phenological studies of phytoplankton taxa indicate that climate variations are impacting a wide range of marine pelagic communities (Edwards and Richardson, 2004). Since deep sea ecosystems depend on production exported from the surface, they are particularly sensitive to environmental change and anthropogenic disturbance, especially the majority of ecosystems that comprise soft sediments (Ashford *et al.*, 2018). Long term phytoplankton monitoring programs (such as Ajani *et al.*, 2016) complement EO time series in establishing trends in phytoplankton diversity and biomass (McClain, 2009), although a longer time series is required to confirm the relationship between phytoplankton trends and climate variations (Henson *et al.*, 2017).

Background image: Suomi-NPP/VIIRS composite acquired on 18 November 2018 showing algal blooms around Tasmania. Source: Ocean Colour Web. Retrieved from *https://oceancolor.gsfc.nasa.gov/gallery/609/?_ga=2.25122042.1316022944.1614576103-2035282742.1614576103*

Recommended Chapter Citation: Anstee, J.M., Roelfsema, C.M., Kovacs, E., and Phinn, S.R. (2021). Ecology. Ch 20 in *Earth Observation: Data, Processing and Applications. Volume 3B—Surface Waters.* CRCSI, Melbourne. pp. 395–436. ISBN 978-0-6482278-5-4

The Millenium Ecosystem Assessment (MEA) was introduced in Volume 3A—Excursus 18.1. The findings of this assessent for coastal and marine ecosystems are summarised in UNEP (2006). Climatic variations, ocean acidification, and commercial pressures are all actively changing ocean habitats, even in the remote Southern Ocean (Constable *et al.*, 2017; Boyd *et al.*, 2019). However, given that the third of the global population living in coastal areas occupy only 4% of the world's land area (UNEP, 2006), the impact of human activities on coastal waters, and their associated intertidal and benthic ecosystems, is paramount. While they are highly productive, their ecosystems are also the most vulnerable to the anthropogenic impacts of:

- degradation—habitat modification and loss leading to biodiversity reduction, and pollution and sedimentation from agricultural, industrial, and urban activities; and
- overexploitation—resulting from unsustainable usage of both biotic and abiotic resources.

Not surprisingly, the consequences of these activities are most severe for island communities. In the cycle of life, degradation and pollution of ecosystems inevitably impact human health and wellbeing, and ultimately become societal problems for both current and future generations all around the globe (see Section 21.4).

This section initially considers surface water ecology in Australia (see Section 20.1) and appropriate EO sensors for water ecology (see Section 20.2), then discusses EO applications to aquatic ecology in terms of:

- wetlands (including seagrass, mangrove, and saltmarsh; see Section 20.3);
- estuarine ecosystems (see Section 20.4);
- coastal waters (see Section 20.5);
- coral reefs (see Section 20.6); and
- marine fauna (see Section 20.7).

Excursus 20.1—Biodiversity

Source: OzCoasts website: *https://ozcoasts.org.au/indicators/coastal-issues/declining_biodiversity/*

The concept of biodiversity refers to the variety of life on three different levels:

- genetic—amount of genetic variability between individuals of a given species;
- species—number of different species (e.g. the species richness) and the 'evenness' (or equitability) with which the different species are distributed; and
- ecosystem—variety of different ecosystems.

In Australia, a comprehensive suite of indicators (pressures on biodiversity, condition of biodiversity, and responses to pressures on biodiversity) were developed as part of the biodiversity theme for the national State of the Environment reporting (*http://www.environment.gov.au/science/soe*). For example, changes in the following biophysical parameters may indicate that a coastal waterway has lost, or is at risk of losing, biodiversity:

- reduced areas of seagrasses, mangroves, salt marshes, intertidal mudflat/sand flats, beaches, and dunes, as well as coral reefs;
- increased frequency of fish kills, algal blooms, or anoxic and hypoxic events;
- reduced diversity of benthic invertebrates, intertidal invertebrates, or fish assemblages;
- water column pH values < 6 or > ~9;
- water column turbidity, chlorophyll a, toxicant or heavy metal levels in excess of ANZECC[24]/ ARMCANZ[25] trigger values;
- sediment heavy metal or toxicant levels in excess of ANZECC/ARMCANZ trigger values;
- widely fluctuating diurnal ranges of pH or dissolved oxygen;
- widely fluctuating seasonal ranges of pH, dissolved oxygen, and salinity; and
- denitrification efficiencies lower then 57%, benthic carbon dioxide fluxes in excess of 12 mmol m^{-2} d^{-1} or sediment ratios of total organic carbon to total sulphur < 5.

24 ANZECC: Australian and New Zealand Environment and Conservation Council
25 ARMCANZ: Agriculture and Resource Management Council of Australia and New Zealand

The oceans cover 70% of the planet's surface area, and marine and coastal environments contain diverse habitats that support an abundance of marine life. Life in our seas produces a third of the oxygen that we breathe, offers a valuable source of protein and moderates global climatic change..
(Convention on Biological Diversity)

20.1 Ecology of Australian Surface Waters

Australia's expansive marine resource is the third largest in the world (see Section 2) and houses a diverse range of mammals, reptiles, fish, invertebrates, flora, and microorganisms, many of which are unique and iconic. Australia is home for this planet's largest coral reef ecosystem, The Great Barrier Reef, which spans 2900 km in length and includes about 3000 individual reefs (see Section 20.6).

Our marine environment is also signficant in terms of global biodiversity, forming part of a migratory network for many marine species. However, it is estimated that less that 25% of the seafloor of our marine estate has been explored (see Section 13.1), with much less than that being described at the habitat level (NMSC, 2015). Marine protected areas (MPA) are important for conserving marine biodiversity, both in coastal and offshore regions (see Excursus 20.2).

While more limited in extent, Australia's inland waters are also critical for a wide variety of biota. Floodplains, for example, are ecosystems with high diversity and productivity which require careful management, particularly in dry landscapes such as Australia (see Excursus 3.1).

In Australia, excluding small offshore islands, the coastline spans around 34,000 km, and includes over 1,000 estuaries (GA, 2020a). Since over half of the growing Australian population lives within seven kilometres of the coast, there are increasing pressures on coastal ecosystems (see Volume 3A—Section 2.5.3). Although the coastal region has major economic, social, and ecological importance, it suffers increasing degradation from a range of anthropogenic activities (Wolanski *et al*., 2008). Degradation can be both direct, such as eutrophication or pollution, or indirect, such as ecosystem decline, and pressures resulting from urbanisation, agriculture, and industry are visibly impacting the biodiversity of coastal waters (see Excursus 20.1).

The term 'coastal zone' generally describes the interface between land and sea, and thus comprises both the portion of land impacted by marine processes, such as tides and waves, and the part of the sea that is impacted by terrestrial processes, such as runoff and erosion. The precise extent of the area denoted as 'coast' and coastal zone varies between jurisdictions and can be justifiably adapted to objectives of policies and management (Harvey and Caton, 2010). For example, while the federal government uses the definition of "the boundaries of the coastal zone extend as far inland and as far seaward as necessary to achieve the policy objectives, with a primary focus on the land/sea interface" (Commonwealth of Australia, 1992), state governments define the term differently, or not all (Harvey and Caton, 2010). Geographically, Australian coasts have been characterised into four regional categories differentiated by humidity (humid and arid) and climate (tropical and warm temperate), such that each category can be described in terms of unique geological, hydrological, meteorological, and biological attributes (see Table 2.2 in Harvey and Caton, 2010).

The coast of Australia displays enormous variety, from tropical rainforest with fringing reefs in the Daintree of North Queensland to the arid sands at Coffin Bay in South Australia; from the hot arid cliffs of the Kimberley coast of northwest Western Australia to the cool, wet, cliffed coast of Western Tasmania; from the alluvial flats and mangroves of the gulf of Carpentaria (Northern Territory) to the saline samphire flats of the Gulf St Vincent (South Australia).
Harvey and Caton (2010)

Excursus 20.2—Marine Protected Areas

Source: Janet Anstee, CSIRO
Further Information: Sagar *et al.* (2020)
Australian Marine Parks Science Atlas: *https://atlas.parksaustralia.gov.au/amps*
Australian Marine Science Program: *https://parksaustralia.gov.au/marine/science/*

Marine parks and aquatic reserves have been established around the world to conserve marine habitats and the various life forms they foster. A network of Marine Protected Areas (MPA) have been declared in both Commonwealth and state/territorial waters to conserve marine biological diversity on a bioregional, ecosystem, habitat, community, and species level (AMP, 2020). This network is designed to be:

- comprehensive—sample the full range of Australia's ecosystems;
- adequate—of appropriate size and configuration to ensure the conservation of marine biodiversity and integrity of ecological processes; and
- representative—reflect the marine life and habitats of the area they are chosen to represent (NHT, undated).

The MPA network was designed using scientific information from:

- detailed surveys of species and habitat at different waterbody depths, only available for a very limited area of Commonwealth waters;
- surrogate information for bathymetry, geomorphology, oceanographic variables, bathomes, Ramsar wetlands, and world heritage areas; and
- models that predict the likely distribution and ecological importance of natural values, such as biota, key ecological features, bioregions, and biologically important areas—based on key ecological features and other biologically significant areas (Sagar *et al.*, 2020).

Using these datasets, 41 bioregions were defined through the Integrated Marine and Coastal Regionalisation of Australia (IMCRA 4.0), with each bioregion representing a large expanse of ocean of broadly similar characteristics (see Section 2.2).

Australia's oldest and most famous marine park is the Great Barrier Reef Marine Park (GBRMP), which spans 14° of latitude (2,300 km) along the Queensland coast and covers 344,400 km^2 of coastal waters (see Figure 20.1). This Park has been managed by the Great Barrier Reef Marine Park Authority (GBRMPA) since 1975 and was declared a world heritage area in 1981. The Great Barrier Reef (GBR) is the longest barrier reef in the world and comprises around 10% of the world's coral reef ecosystems.

In addition to the GBRMP, 3.3 million km^2 of Australia's Commonwealth waters (over 5.5 km from the coast) are protected in a total of 60 marine parks (see Figure 20.2). This constitutes 37% of Australia's oceans and represents the second largest network of marine parks in the world (Parks Australia, 2021). The four IUCN categories that are used to define marine parks shown are listed in Table 20.1. These parks are managed according to six regional management plans, which are shown as different colours in Figure 20.2a: Coral Sea marine park (yellow); temperate (green); southeast (blue); southwest (purple); northwest (magenta); and north (red). Numerous marine parks and aquatic reserves are also managed by state jurisdictions to conserve marine biodiversity in coastal waters. These areas are zoned and managed to ensure that their intrinsic value and sustainability are protected for future generations.

Figure 20.1 Great Barrier Reef Marine Park

Source: Wikimedia Commons. Retrieved from: *https://commons.wikimedia.org/wiki/File:Great_Barrier_Reef_Marine_Park_locator_map.svg*

Figure 20.2 Australia's other marine parks

a. Geographic zones

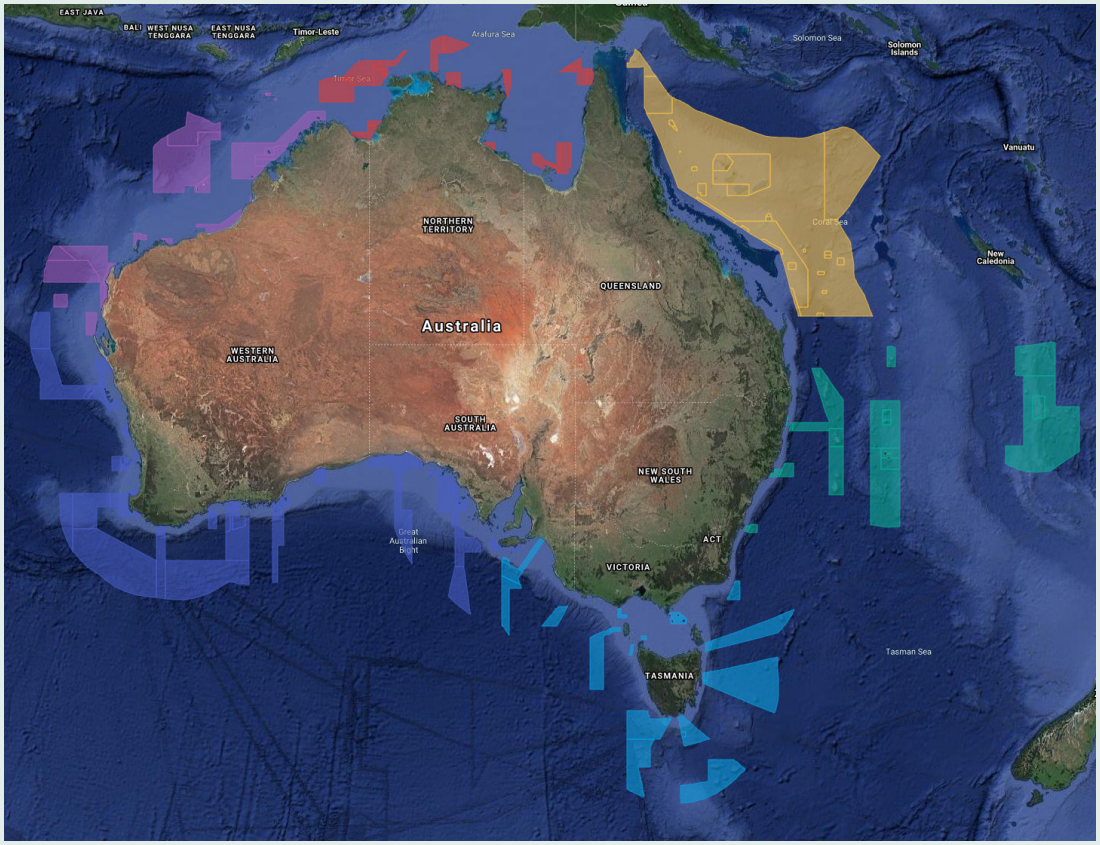

b. Functional zones

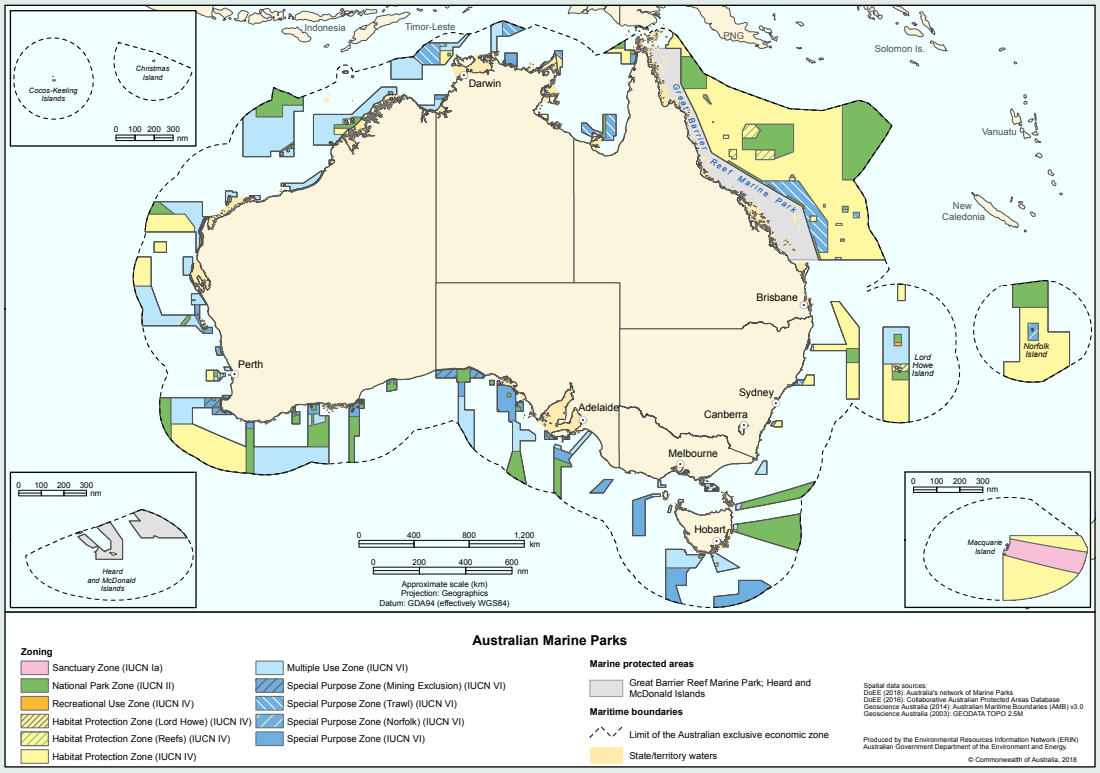

Source: Parks Australia. Retrieved from a. *https://parksaustralia.gov.au/marine/*; b. *https://parksaustralia.gov.au/marine/pub/maps/National-Full-zoning-incl-SE.pdf*

Table 20.1 Commonwealth Marine Reserves IUCN protected area management categories

IUCN category	IUCN number	Management objective
Strict nature reserve	Ia	Managed primarily for scientific research or environmental monitoring
National park	II	Protected and managed to preserve its natural condition
Habitat/species management area	IV	Managed primarily, including (if necessary) through active intervention, to ensure the maintenance of habitats or to meet the requirements of specific needs
Managed resource protected area	VI	Managed to ensure long term protection and maintenance of biological diversity with a sustainable flow of natural products and services to meet community needs

Source: *http://www.environment.gov.au/topics/marine/marine-reserves/overview/legal-framework*

Australian Marine Parks Science Atlas (see Section 20.8), a platform to promote research within these parks, uses spaceborne EO as one of the primary planning and monitoring tools that is being used to produce a range of maps for each park, including the recent rate of ocean surface warming and ocean productivity hotspots, and inter- and intra-seasonal variations in surface water temperatures and chlorophyll a concentrations. Such maps also provide valuable input to conservation planning software (Tulloch *et al*., 2021).

EO is also used to assess and monitor environmental pressures, such as anthropogenic activities (boating, diving, snorkelling, recreational fishing), marine pollution (such as plastic debris and discharge of oils), illegal commercial fishing (FAO, 2018; Kurekin *et al.,* 2019), and impacts of climate change (such as changes in sea temperature, sea level, currents, phytoplankton composition, and/or benthic communities). Monitoring efforts based on EO datasets also guide management programs and actions for marine parks.

A marine protected area is defined as an area of sea (which may include land, the seabed and subsoil under the sea) established by law for the protection and maintenance of biological diversity and of natural and cultural resources.
(NHT, undated)

20.2 EO Sensors for Water Ecology

EO datasets are used in mapping coastal and estuarine habitats, monitoring coastal ecosystem services, assessing coastal ecosystem risk, and tracking ecological parameters in marine areas (Kachelriess, 2014; Ouellette and Getinet *et al*., 2016; Hedley *et al*., 2016a). Important environmental variables that describe key ecosystem properties in the open ocean can be quantified using various EO datasets, including sea level anomalies (see Section 12), sea surface temperature (SST; see Section 14), water circulation (see Section 16), and chlorophyll a (see Section 18.6). The high spatial and temporal resolutions of EO-based datasets now enable natural events that impact water quality, such as plankton blooms (see Section 19.5) and marine heat waves (see Section 19.6), to be mapped, monitored, and modelled (see Volume 2D—Section 14). Anthropogenic pressures that impact marine biodiversity and ecosystem sustainability, such as marine pollution and illegal fishing, can also be targetted (and in some cases quantified) using EO datasets (see Sections 19.4 and 20.7 respectively).

A range of EO sensors is introduced in Volume 1A, and interpretation of optical and microwave imagery is considered in Volume 1B. The types of EO sensors and platforms that can be used to map and monitor aspects of water ecology are summarised in Table 20.2.

Table 20.2 EO sensors relevant to coastal and marine water ecology

TIR: Thermal infrared; SAR: Synthetic Aperture Radar; UAV: Unmanned aerial vehicle;

Type	Sensor	Platform	Relevance	Advantages	Disadvantages
Passive optical	Multispectral radiometer	Satellite or airborne	Coastal ecology Coral reefs Marine ecology	Global coverage, low cost	Lower spatial resolution in early sensors
	Hyperspectral radiometer	airborne	Coastal ecology Coral reefs	High spectral resolution	High cost, high data volume
	TIR radiometer	Satellite or airborne	Coastal and marine habitats Coral bleaching	Global coverage, low cost	Low spatial resolution
Active optical	Lidar	airborne	Bathymetry Shoreline topography Reef morphology	High spatial resolution	Low coverage
Active microwave	SAR	Satellite or airborne	Mangrove mapping Oil/chemical spills Surface wind and wave fields Sea ice	All weather	High cost, specialised processing
Acoustic	Multibeam Echosounder	UAV or shipborne	Benthic habitats Bathymetry	Waterbody depth coverage	Low coverage

CEOS (2018) recommend detailed specifications for the ideal satellite-borne optical sensor for EO of non-oceanic, aquatic environments. Parameters for the preferred spectral, spatial, radiometric, and temporal characteristics for mapping aquatic ecosystems are summarised in Section 8.5. Optical EO sensors that can map macrophytes, macroalgae, seagrasses, and corals are listed in Table 20.3 (see Table 8.14 for technical details of these sensors). For example, the spatial and temporal resolutions required to map and monitor seagrass and mangrove features in coastal environments is illustrated in Figure 20.3. Various EO datasets and techniques are also being used to classify the pelagic ocean into biomes, provinces, and seascapes to enable effective monitoring, management, and conservation of marine estates (Gohin *et al.*, 2008; Hardman-Mountford *et al.*, 2008; Kavanaugh *et al.*, 2016).

Figure 20.3 EO data resolutions for seagrass and mangrove features in coastal environments

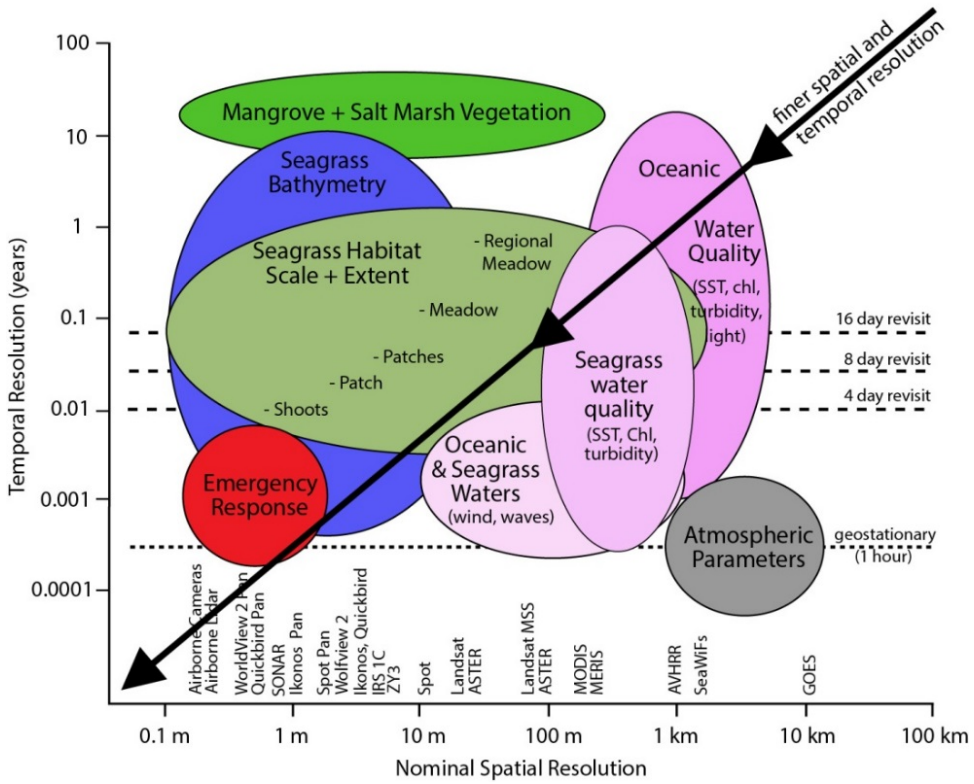

Source: Hedley *et al.* (2016b) Figure 1

While bathymetry derived from multibeam echosounders (MBES) measures ocean depth (see Section 13.3.2), the backscatter intensity can be used as a proxy to understand characteristics of the seafloor, including seafloor hardness and surficial sediment characteristics (see Section 10). These measurements can be used to characterise the environment (or habitat) where marine fauna live, including establishing baseline data to support environmental monitoring and explaining spatial patterns of seafloor biology and biodiversity at continuous scales. Multibeam bathymetry data can be classified by geomorphological analysis to determine the extents of particular habitat types, such as seagrass beds, rocky reef, and sand plains (Lucieer *et al.*, 2018). The biological function of geomorphological features, and their three-dimensional structure into water depths well beyond the reach of EO sensors, has also been explored using satellite-based tracking devices on marine animals (Priede, 2014).

Various configurations of towed underwater camera systems have been used for over a century to obtain images of the seafloor (Bicknell *et al.*, 2016). These platforms are deployed on a cable from a surface vessel and generally use forward-looking oblique and/or downward-looking cameras (Bowden and Jones, 2016, Durden *et al.*, 2016). Towed underwater cameras provide an important non-invasive sampling alternative where extractive methods are either unnecessary or unsuitable, such as in sensitive deep sea habitats (Althaus *et al.*, 2009, Williams *et al.*, 2015, Sherlock *et al.*, 2016), or for repeated sampling in marine reserves (Lawrence *et al.*, 2015). Towed platforms offer cost-effective permanent data capture along transects (up to several kilometres in length) and can traverse highly heterogeneous seafloor topography (Shortis *et al.*, 2007). The quality of imagery acquired by towed systems varies with sea conditions and water clarity, which both vary widely with location, season, and tidal influence. Below 30 m water depth, image quality is also impacted by lighting and camera specifications. A consistent altitude above the seabed is also required to maintain optimal image quality (Carroll *et al.*, 2018).

Table 20.3 Suitability of optical EO sensors for mapping aquatic ecosystem features

This list includes multispectral and hyperspectral sensors carried on previous, current, and future EO missions with spectral bands in the wavelength range 340–1000 nm. Names of commercial sensors are italicised. Note that it focuses on spectral characteristics of sensors rather than spatial resolution and extent, and temporal resolution.

Sensor	Aquatic vegetation type		
	Emergent	Floating-leaved	Submersed
Hyperion	high	high	high
CHRIS-PROBA	high	high	high
MERIS	high	high	high
HICO	high	high	high
Sentinel-3	high	high	high
GLIMR	high	high	high
PRISMA	high	high	high
EnMap	high	high	high
SBG (formerly HyspIRI)	high	high	high
PACE	high	high	high
ISS HISUI	high	high	high
IAA DESIS	high	high	high
OCM-2	medium	medium	medium
Suomi-VIIRS	medium	medium	medium
SGLI	medium	medium	medium
GOCI	medium	medium	medium
GOCI-II	medium	medium	medium
WORLDVIEW-2/-3	high	high	high
IKONOS, QuickBird, SPOT-5,- 6, GeoEye etc.	medium	medium	medium
RapidEye	medium	medium	medium
SENTINEL-2	medium	medium	medium
Aqua/Terra MODIS (1 km)	medium	medium	medium
Aqua/Terra MODIS (500 m)	Not suitable	potential	potential
Aqua/Terra MODIS (250 m)	potential	potential	potential
LANDSAT-4 to -7	medium	potential	potential
LANDSAT-8	medium	medium	medium
Himawari-8/-9	potential	potential	potential
GOES-R	potential	potential	potential
GISAT-1/-2	potential	potential	potential
MSG SEVIRI	potential	potential	potential

Adapted from: CEOS (2018) Table 2.7

20.3 Coastal Wetlands

Wetlands describe areas where water covers the soil continuously or for selected periods of time, which can be naturally occurring or man-made. Examples of wetlands include swamps, marshes, billabongs, lakes, lagoons, saltmarshes, mudflats, mangroves, bogs, fens, and peatlands (see Excursus 3.1). Globally, 54% of wetlands are permanently covered with water and 46% are seasonally inundated (RAMSAR, 2018). These ecosystems include some of the most carbon-rich on Earth and sequester substantially more carbon than forests (Mcleod *et al*., 2011).

RAMSAR (2018) estimate up to 87% of global wetlands have been lost since 1700 and around 35% of wetlands have disappeared since 1970, with the rate of loss increasing this century. These coastal habitats are being degraded by a range of anthropogenic activities, including land reclamation, shoreline infrastructure, rerouting of river systems, domestic grazing, vehicular and pedestrian traffic, rubbish and pollution, and weed invasion (DAWE, 2020). Accordingly, marine species that depend on these habitats are also declining, with 81% of inland wetland species and 36% of coastal and marine species being impacted, 25% of which are at risk of extinction. This decline then reduces water quality and availability, food security, and carbon sequestration.

Aquatic vegetation is introduced in Sections 3.3.2 and 6.4. Wetland vegetation traps and stabilises sediments to reduce the impact of waves, tides, and floods on shorelines and rivers (DAWE, 2020). It also filters the transfer of organic matter and nutrients from runoff to maintain water quality (Pennesi *et al*., 2015). Wetlands support a rich array of biodiversity, including providing nurseries for fish and other marine organisms, and feeding and housing birds (especially migratory), mammals, and reptiles (Turner *et al*., 2004). Over two thirds of global fish consumption depends on coastal wetlands (DAWE, 2020).

The vegetation in coastal wetlands, such as melaleuca swamps, varies in density and height. These tend to occur in low-lying ground near estuaries and can include trees and understorey sedges, grasses, and aquatic herbs. Seagrasses, mangroves, and saltmarshes are synergistic, intertidal communities comprising plants that have adapted to saline and waterlogged conditions on the foreshores of coastal lakes and estuaries (see Figure 20.4). The extent of these ecosystems has significantly reduced in Australia since European settlement, and climate change and sea level rise are expected to further modify their distribution and abundance (DAWE, 2020).

Ecological character is the combination of the ecosystem components, processes and benefits/services that characterise the wetland at a given point in time.
(RAMSAR, 2005)

Figure 20.4 Wetland habitat zones

HAT=Highest Astronomical Tide

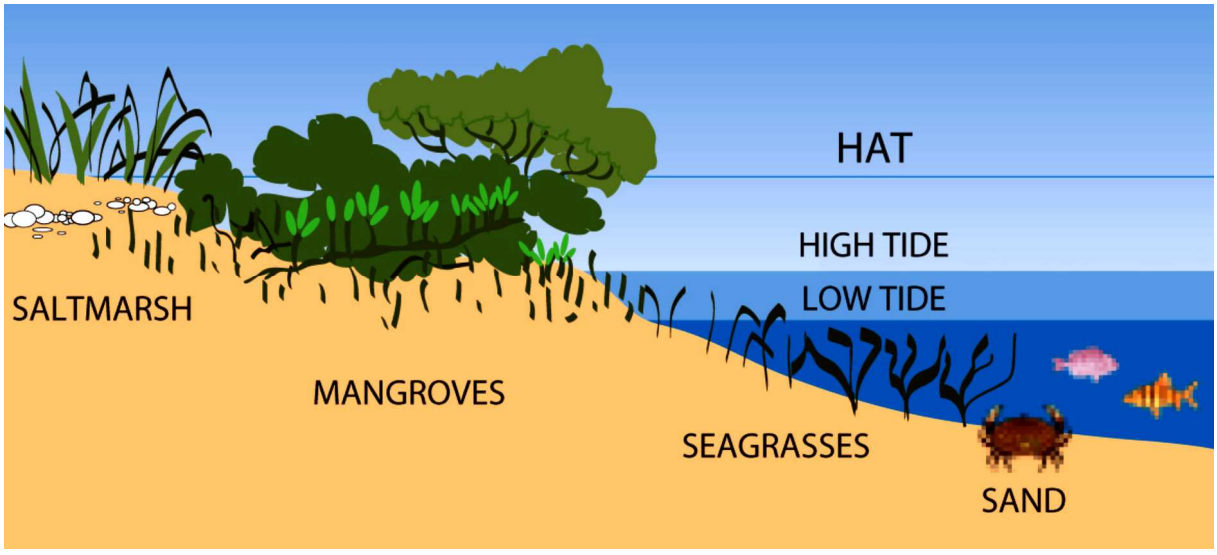

Source: Daly (2013)

Healthy, functioning natural wetlands are critical to human livelihoods and sustainable development. (RAMSAR, 2018)

EO of aquatic vegetation offers advantages over traditional ground-based surveys but presents some challenges. EO of terrestrial plants makes significant use of the red edge (that is, the difference between their characteristically strong absorption of red wavelengths and strong near infrared (NIR) reflectance—see Volume 3A). However, aquatic plants cannot be recognized by this feature since, in water columns deeper than 1–2 m, wavelengths beyond 680 nm are significantly attenuated by pure water (Kirk, 1994, 2010). Below we will describe EO methods to map and monitor seagrass (see Section 20.3.1), mangroves (see Section 20.3.2), and saltmarshes (see Section 20.3.3). Navarro *et al.* (2021) and Ricart *et al.* (2020) demonstrate the utility of EO for quantitative monitoring of these environments in Australia. An example of wetland monitoring using EO is given in Excursus 19.3.

20.3.1 Seagrass meadows

Australia's coastline nurtures the most abundant and diverse range of seagrasses in the world (Turner *et al.*, 2004; Larkum *et al.*, 2018; Phinn *et al.*, 2018). Seagrasses are productive flowering plants that grow in the soft sediments underlying estuaries and coastal waters (see Figure 20.4). By reducing erosion and water movement, seagrasses help to stabilise the seafloor and improve water clarity. They support benthos and algae and offer breeding grounds for many species of fish. In clear waters, seagrasses can grow at water depths greater than 60 m, but growth may be restricted in intertidal waters where turbidity levels are high. Waters with high levels of nutrients and suspended organic matter also tend to restrict growth (Furnas, 2003), making these plants a good indicator of water quality.

Figure 20.5 Seagrass spatial and organisational scales

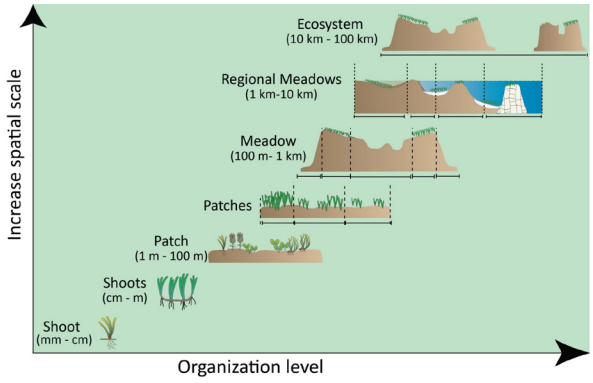

Source: Phinn *et al.* (2018) Figure 15.2

The seagrasses are covered by a water column, which attenuates the light that reaches, interacts with, and is reflected from the benthos. In coastal waters, spectral scattering and absorption by phytoplankton, suspended organic and inorganic matter, and dissolved organic substances further restricts the light passing to the benthos (Dekker *et al.*, 2001). Zimmerman (2006) discusses the effects of higher concentrations of optically active materials in the water column on seagrass photosynthesis. Where light penetrates the water column and can be reflected back to the sensor, spectral discrimination between aquatic plant species concentrates on pigment-related spectral features within the visible wavelengths (Fyfe, 2003). Absolute reflectance from submerged species is generally low (< 10%), often lower than the reflectance from a deep water column and, from a visual perspective, seagrass areas generally appear darker than non-vegetated areas, partly due to shading within the canopy (Zimmerman, 2006).

Seagrasses can be observed at a range of spatial scales (see Figure 20.5). They may grow with sparse cover and can be spectrally confused with other benthic features such as areas of macroalgae, detritus, and corals (Mumby *et al.*, 1997a, 1997b). Textural characteristics and associated physical attributes of the environment (for example, it will not grow on a wall or in a high energy zone) could help differentiate seagrasses from other bottom features. While coral is found on hard substrates (see Section 20.6), seagrass tends to grow in unconsolidated substrates of shallow banks or coral reefs. The small size and/or linear shape and patchy nature of many seagrass meadows means that in many cases moderate to high spatial resolution is also required to accurately determine their distribution and abundance.

The spatial extent of seagrass meadows can either increase or decrease rapidly in response to human impacts or natural dynamics. For meadows such changes may occur within a timeframe of weeks to months, whereas spatial changes in corals be much slower. When assessing the dynamics of seagrass meadows, it is important to understand potential human impacts. This understanding is particularly relevant to the timing of EO data that is being acquired to detect changes in seagrass meadows. For example, monitoring seasonal changes in the extent and density of certain seagrass species would require repeated temporal coverage.

Some of the methods that have been used to map seagrass distribution include:

- Principal Components Analysis (PCA; Bajjouk *et al.*, 1998);
- spectral angle mapping (SAM; Dunk and Lewis, 1999; Alberotanza *et al.*, 1999);
- minimum distance classification (Malthus and George, 1997);
- classification with reference to simulated spectral libraries (Louchard *et al.*, 2000);
- radiative transfer modelling (Dekker *et al.,* 2011);
- semi-automated OBIA (Lyons *et al.,* 2012; Roelfsema *et al.,* 2014; Kovacs *et al.,* 2018).

Details of these techniques are provided in Volume 2. Dekker *et al.* (2001) consider a radiative transfer model or semi-analytical model as essential in accounting for water attenuation and multiple backscatter from a reflective substratum (see Section 8.4). Spectral libraries, either generated from *in situ* spectral measurements or simulated by a two-flow model, are needed to reliably differentiate between different types of substrate materials (see Volume 2D—Section 12.3). Airborne hyperspectral imagery has also enabled separation of some algal and seagrass species (Dunk and Lewis, 1999), with green, red, and brown algae being discriminated using visible wavelengths, and brown vegetation, seagrasses, and floating seaweed being separated using infrared wavelengths (Bajjock *et al.*, 1996). Lyons *et al.* (2012) demonstrated long term mapping of seagrass cover and extent using a moderate resolution sensor independently of *in situ* data, via an object-based image analysis (OBIA) approach (see Volume 2A—Section 10). Where species morphologies/colours were distinct, an OBIA methodology that incorporated *in situ* field data and ecological rules (including waves, water depth, and consolidation) has been used to generate maps that distinguish areas of different seagrass species (Roelfsema *et al.,* 2014; Roelfsema *et al.,* 2015; Kovacs *et al.,* 2018). Roelfsema *et al.* (2014) utilised a semi-automated mapping approach that incorporated field data and high resolution imagery to temporally map seagrass cover, species, and biomass. Further, utilising this semi-automated method, Kovacs *et al.* (2018) compared seagrass cover and species map outputs from moderate and high resolution sensors and concluded that all sensors tested were suitable for mapping seagrass in clear shallow waters, but the higher resolution sensors provided more detail and were considered more representative. Recent developments for global mapping of seagrass meadows include the development of machine learning (ML) approaches within the Google Earth Engine using Sentinel-2 imagery (Traganos *et al.,* 2018).

Regardless of which seagrass mapping approach is used however, baseline field data is required for calibration and validation. For approaches based on radiative transfer modelling, this training data comprises a spectral library based on field measurements, and for empirical approaches, the composition of seagrass meadows needs to be directly determined in the field. For validation of either approach, the composition of seagrass meadows in the field is required as reference data for accuracy assessment (Roelfsema *et al.,* 2015).

20.3.2 Mangrove forests

Mangroves are described as woody plants (see Section 3.3.2), which tend to grow at the fringe of the intertidal shallows, so are exposed to both fresh and salty water (DAWE, 2020). They are the most prolific wetland vegetation group globally yet are also one of the most vulnerable ecosystems (Kuenza *et al.*, 2011). Most mangrove forests grow in tropical and subtropical regions (Giri *et al.*, 2011).

Different mangrove species tend to grow in zones parallel to the shoreline, with zones being demarcated by tide levels and soil salinity, oxygen, and nutrients (Stewart and Fairfull, 2008; see Figure 20.4). Mangroves offer erosion protection and act as a sediment trap for runoff. They also house and/or feed a wide range of both terrestrial and marine species (Turner *et al.*, 2004), including migratory birds, and nurture about 75% of coastal fishery catches (MangroveWatch, 2021; IUCN, 2017). Their characteristic growth form with aerial structural roots and exposed breathing roots (pneumatophores) enables them to withstand tidal inundation and oxygen-depleted soil.

Over 90 species of mangroves in 20 families have been identified globally. Mangroves cover around 11,500 km^2 of Australia's coastal region, with greatest concentrations in the north and east (DAWE, 2020). Australia's mangroves comprise 7% of global mangrove coverage, with 41 species, from 19 families, growing along ~22% of the intertidal zone of our tropical, subtropical, and protected temperate coastal rivers, estuaries, and bays (Stewart and Fairfull, 2008).

EO datasets have been used to map mangrove forests for many decades, involving a range of sensors (Kuenzer *et al.*, 2011; Wang *et al.*, 2019). Mangrove communities can be differentiated on the basis of the texture and reflectance properties of their canopy and foliage, particularly in NIR wavelengths (Ramsey and Jensen, 1996), although soil type and intertidal influences can impact spectral characteristics in sparser vegetation (Meza Diaz and Blackburn, 2003). Mangrove backscatter in SAR imagery is somewhat more complicated as summarised in Table 20.4.

Table 20.4 Backscatter from mangroves

Characteristics of the backscatter signal depend on mangrove structural components, biomass, and forest stand.

Frequency	Description	Polarisation		
		VV	HH	HV
C-band	Penetration into the upper part of the canopy, few metres within the crown; Interaction with leaves and small branches; Increase in backscatter is indicative of changing forest structures; Sensitive to crown characteristics (number, density, size, and leaf orientation) and canopy structure (architecture and heterogeneity); Above-ground biomass saturation in SAR response at 50 t DM ha^{-1}	High sensitivity to increasing biomass; Highest correlation with canopy parameters; Highest correlation for tree height and diameter	High sensitivity to increasing biomass; Related to variations in the canopy structure; Highest correlations for tree height and diameter	Significant relationship with LAI (greater at larger incidence angle); High correlation between backscatter coefficient and mean stem height (larger coefficient at smaller incidence angle); High coefficients for determination of mean DBH, tree height, and basal area
L-band	Deeper canopy penetration, involving scattering from trunks and ground surface; Volume scattering predominates by interaction with multiple branches of various sizes; Increase in backscatter is indicative of changing forest structures; Double-bounce scattering between trunks and ground; Sensitive for biomass; Above-ground biomass saturation in SAR response at 100 t DM ha^{-1}	Soil-vegetation interaction and direct backscattering from soil surface; Domination of volume scattering with increasing biomass	Soil-vegetation interaction and direct backscatter from soil; Domination of volume scattering with increasing biomass; Mapping of flooding in forests with high specular backscatter signal of flooded surfaces; Double-bounce trunk-ground term is enhanced by the presence of water; the smaller the incidence angle, the more dominant this term; Canopy volume scattering dominates for stands under non-flooded ground	High correlation with forest parameters (zonation, basal area, height, biomass level, growth stages); Best correlation for biomass; Backscatter coefficient of biomass is greater at smaller incidence angles
P-band	Penetration reaches underlying soil and water surface; Double-bounce effects; High sensitivity to forest parameters; Above-ground biomass saturation in SAR response at 150 t DM ha^{-1}	High interaction with soil surface; Intensity is dependent on soil moisture and roughness, as well as length and sizes of trunks; No correlation with total biomass	High correlation with total biomass	High correlation, with total biomass showing the largest sensitivity; Best correlation for biomass

Source: Kuenza *et al.* (2011) Table 1

The global distribution and extent of mangroves were mapped by Giri *et al.* (2011), using Landsat imagery and hybrid classification methods. New global inventories are also being derived from multisource EO data, such as lidar and passive optical, and the Google Earth Engine (Yancho *et al.*, 2020).

Classification of satellite-acquired optical imagery has been used for mapping mangrove habitat at regional/national scales, with higher spatial resolution sensors being more appropriate for local scales (Kuenza *et al.*, 2011). The spatial and temporal scales in EO imagery that are required to map mangrove features are summarised in Figure 20.6. Kamal *et al.* (2015) used multi-resolution optical datasets (satellite-acquired) with lidar imagery to derive a hierarchical, object-based classification system for mangrove formation/zonation, canopy structure, and species community. Recent studies have found structural attributes of regenerating mangroves can be characterised from multi-polarised, satellite SAR imagery (Cougo *et al.*, 2015). Lidar datasets have also been used to map mangrove canopy height (Purkis and Brock, 2013).

Until recently, most EO-based mangrove mapping for Australia has been part of global studies (such as the Global Mangrove Watch: Lucas *et al.*, 2014; Thomas *et al.*, 2017; Bunting *et al.*, 2018). 30 years of mangrove dynamics along the entire Australian coastline has now been mapped at 25 m resolution using Digital Earth Australia, a calibrated Landsat archive (see Volume 2D—Section 11.2), with lidar surveys being used to parameterise the canopy cover estimates (Lymburner *et al.*, 2020). These maps allow changes in the extent and density of Australian mangroves to be quantified.

Figure 20.6 Mangrove features versus image resolution

A conceptual temporal and spatial hierarchical organisation of mangroves features identifiable from EO images is shown with the required image pixel resolution for mapping these features.

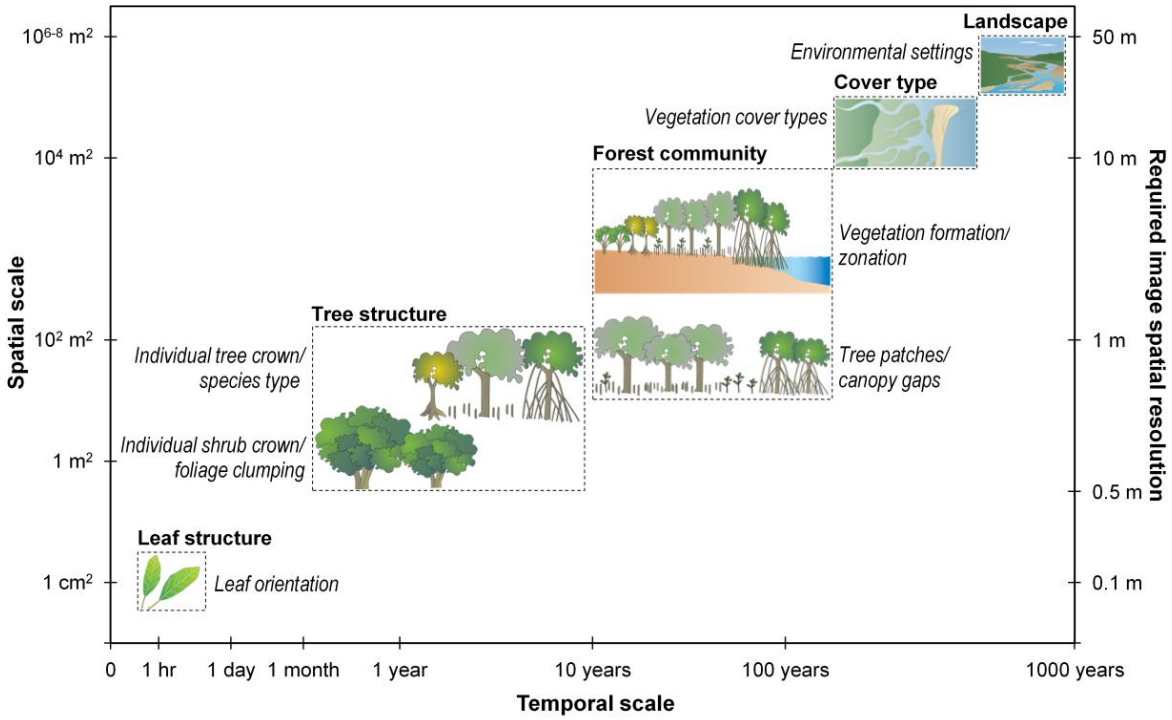

Source: Kamal *et al.* (2015) Figure 1. Symbols are courtesy of the Integration and Application Network, University of Maryland Center for Environmental Science—*ian.umces.edu/symbols/*

20.3.3 Saltmarshes

Saltmarshes, or tidal marshes, grow in the high tide zone on sheltered foreshores with soft substrates (see Figure 20.4), and comprise vegetation such as sedges, rushes, reeds, grasses, succulent herbs, and shrubs, interspersed with bare patches and/or salt pans. Coastal saltmarshes can occur as narrow fringes on steeper slopes with little species variation, to larger expanses on flatter ground with many species, or extend inland along estuary foreshores. Biodiversity tends to increase in elevated areas that are inundated less frequently. Saltmarshes offer refuges for juvenile fish and migratory wading birds, and provide habitat for birds, bats, mammals, insects, and invertebrates (Daly, 2013).

Many saltmarsh areas in Australia have been resumed for agriculture or urban expansion in the last 200 years. Saltmarshes now extend over 13,500 km^2, mostly along the northern and eastern coastlines, with their distribution being largely determined by elevation, salinity, and inundation frequency (Daly, 2013). This represents around one third of the world's saltmarsh coverage and has been estimated to be storing 212 million tonnes of organic carbon in the first 1 m depth (Macreadie *et al.*, 2017). Landward sites with greatest influence from fluvial flows have been observed to have twice the organic carbon volume as marine sites.

The term 'saltmarsh' is used to describe individual plants, groups of plants and the general estuarine habitat dominated by these plants.
(Daly, 2013)

EO-based multispectral and hyperspectral datasets have been used to identify and map wetland vegetation (Haynes, 2016), and estimate selected biochemical and biophysical parameters, such as water content, biomass, and leaf area index (Adam *et al*., 2010). Airborne hyperspectral imagery has been used to discriminate between different saltmarsh vegetation communities (Silvestri *et al*., 2003). Since saltmarsh vegetation species are reliably correlated with elevation, saltmarsh vegetation maps derived from EO using spectral unmixing methods (see Volume 2E) have been used to infer foreshore elevation with accuracies comparable to laser altimetry. Time series datasets have also been used to study their dynamics at a regional scale (Laengner *et al*., 2019), with global studies now focusing on the carbon budgets of these ecosystems (Alongi, 2020). Lidar data is valuable to define high resolution topography, although it exhibits greater vertical uncertainty in saltmarsh than in other environments (Rogers *et al*., 2016), and has been used for identifying saltmarsh shorelines (Farris *et al*., 2019), monitoring erosion and accretion (Fernandez-Nunez *et al*., 2017), and parameterising tidal creek morphology (Chirol *et al*., 2018). Lidar datasets have been used to estimate the spread of invasive plants (Paynter *et al*., 2019), and integrated with hyperspectral imagery to improve habit classification (Hladik *et al*., 2013) and monitor carbon stores (Kulawardhana *et al*., 2014). SAR data have also been used to map shoreline topography, detect structural changes, and monitor recovery (Ramsey *et al*., 1997, 2009, 2014).

20.4 Estuarine Ecosystems

An estuary is the mouth of a river where freshwater mixes with seawater to create brackish water, creating a transition zone, or ecotone (see Volume 3A), between the river and the sea. These aquatic features are partially enclosed, but still subject to both waves and tides from the sea and fluvial flows from the river. Like their adjoining wetlands, they house unique communities of plants and animals, serve as nurseries for birds, fish and other organisms, and filter runoff. These productive ecosystems are also delicate and being degraded by ongoing erosion, eutrophication, pollution, and excessive harvesting (SOE, 2018). The biodiversity of estuaries can be impacted by a variety of environmental factors including estuary size, supply and retention of nutrients, complexity of water circulation, variety and extent of substrate sediment types, the range of available habitats, and tidal range (OzCoasts, 2020).

Estuaries experience constant change due to tidal and fluvial movement, which result in significant variations in water salinity, temperature, pH, and transparency. Accordingly, their ecosystems are highly variable in both space and time. While estuaries comprise a very small proportion of the world's marine waters, they are highly productive. Since turbidity often limits the growth of phytoplankton in these waters (Monbet, 1992), microphytobenthos (see Section 3.3.2.1) significantly contribute to both primary production (Underwood and Kromkamp, 1999) and chlorophyll a biomass (De Jong and de Jonge, 1995).

Transient biofilms are produced by microphytobenthos at the sediment surface, which help to stabilise intertidal mudflats. Since these patchy substratum features vary in colour with photosynthetic pigments, they can be characterised by reflectance spectra (Paterson *et al*., 1998), and detected by both airborne and spaceborne EO sensors (Méléder *et al*., 2003).

Macroscale distribution of microphytobenthos has been mapped in numerous studies using high resolution imagery (eg. Méléder *et al*., 2003). More recently, image time series have been used to map intrannual (Brito *et al*., 2013) and interannual (Benyoucef *et al*., 2014) variations of microphytobenthos biofilms in European estuaries. Such information furthers our understanding of estuarine ecosystem dynamics, allows separation of short and long term changes, and contributes to the identification of key environmental drivers in this environment.

Biodiversity levels in estuaries are a sensitive measure of their health and balance. Their proximity to human settlements make them particularly vulnerable to the impacts of vegetation clearing in adjacent catchments, urban runoff and the influx of stormwater and wastewater. Each of these flows may contain excessive nutrient loadings that may trigger changes in the distribution and structure of estuarine communities, usually by reducing their complexity.
(OzCoasts website)

20.5 Coastal waters

Coastal waters only represent 15% of the global ocean, but concentrate 90% of commercial fisheries, contribute to 25% of global biological productivity, and represent 80% of the marine biodiversity, while being associated with an intensive tourism-related economy.
(Doxaran et al., 2019)

The Australian national marine boundary definition of coastal waters is "a belt of water between the limits of the Australian States and the Northern Territory and a line 3 M seaward of the territorial sea baseline (TSB)" (GA, 2020b; see Section 2.1.3). However, for optical EO applications, coastal waters are commonly defined as marine areas adjacent to land with water depths less than 30 m (Oullette and Getinet, 2016). This depth represents the limit of solar light penetration through the water column that can be reflected by the substratum and detected by an EO sensor (see Section 8).

Coastal waters are estimated to constitute 8–10% of surface waters, and only 0.5% of their volume (Hoepffner and Zibordi, 2009). Since these waters are the closest to population centres, they are the most directly impacted by anthropogenic activities. In Australia and globally they are being degraded by nutrient and sediment pollution, catchment disturbance, marine debris, water abstraction, dredging, fishing, aquaculture, marine infrastructure, shipping, invasive biota, disease, algal and jellyfish blooms, hypoxic (low oxygen) events, and rising sea temperatures (SOE, 2018; NSW EPA, 2017).

EO datasets provide a reliable basis for observing coastal waters over time. In conjunction with field measurements, the use of unmanned aerial vehicles (UAV) and autonomous underwater vehicles (AUV; see Excursus 5.1) are gaining increasing popularity for monitoring this environment, with both offering high spatial resolution data to verify satellite-acquired observations. Various EO sensors are being used to quantify a range of hydromorphological, physical, chemical, and biological properties of coastal waters (Doxaran *et al.*, 2019), including:

- erosion/storm damage on shorelines and beaches (see Section 11.3);
- extent of flooding (see Section 11.4);
- water temperature (see Section 14);
- productivity (see Sections 18.6; Auricht *et al.*, 2017); and
- water quality (see Section 19).

The acquisition of optical imagery by UAV has also been shown to be a cost-effective alternative to manned aerial surveys of marine mammals, such as humpback whales (Hodgson *et al.*, 2017).

The coastal zone of Australia is a dynamic meeting area of earth (lithosphere) and atmospheric forces (atmosphere), of oceans and rivers (hydrosphere), and of terrestrial and marine life (biosphere). Changes, over a variety of time scales, are a characteristic of all coasts, and are an important driver of coastal management.
(Harvey and Caton, 2010)

20.6 Coral Reefs

...travellers tell us of the vast dimensions of the Pyramids and other great ruins, but how utterly insignificant are the greatest of these, when compared to these mountains of stone accumulated by the agency of various minute and tender animals
(Charles Darwin)

Coral reefs have been called the rainforests of the seas (Oceana, 2021). These structures are both complex and massive—and can survive for thousands of years (see Figure 20.7). Colonies of tiny, stony, coral polyps, mostly 1–3 mm diameter, secrete calcium carbonate, which slowly aggregates into a wide variety of forms and colours. Most corals co-exist with symbiotic algae (zooxanthellae), which photosynthesise and play a critical role in coral health. Highly consolidated reefs occur in clear, saline waters of the euphotic zone where temperatures remain above 18°C for most of the year. As such, their distribution is limited to tropical and subtropical waters. Coral growth can be limited by multiple factors, including sediments, eutrophication, pollution, temperature extremes, wave exposure, low light levels, and predators. Since water depth influences light penetration, temperature, and exposure, it provides a clear indicator for the potential presence of coral. Similarly wave energy partly determines the growth of certain types of coral types. For example, branching corals are often found in the protected areas of the reef, whereas massive and encrusting corals are more present on the exposed areas. Waves can therefore provide an indicator for coral types.

EO can accurately map unconsolidated, bright carbonate sand and, by exclusion, consolidated substrates can also be delineated (see Section 18.7). Since corals generally grow on consolidated substrates, EO mapping reliably predicts coral habitat (see Section 20.6.3).

At least two thirds of the world's coral reefs may collapse ecologically within the lifetime of our grandchildren unless we implement effective management of these ecosystems as an urgent priority.
(Joint Statement from IOC/UNEP/IUCN)

Figure 20.7 Coral diversity

A variety of corals form an outcrop on Flynn Reef, part of the Great Barrier Reef near Cairns, Queensland, Australia, on 24 July 2010.

Source: Toby Hudson (CC-BY-SA 3.0). Retrieved from Wikimedia: *https://commons.wikimedia.org/wiki/File:Coral_Outcrop_Flynn_Reef.jpg*

20.6.1 Structural characteristics

The hierarchical levels at which coral reefs are studied varies from individual polyps to whole reef systems (see Figure 20.8). A four level hierarchy differentiates reefs by the sizes of features present, namely reef/non-reef, reef type, reef geomorphic zone, and reef benthic composition (see Table 20.5). A global implementation of this system for use with EO has been released by Kennedy *et al.* (2021).

Individual coral reefs can be classified into five basic types:

- platform reefs—carbonate structures that have grown on submerged rock;
- fringing reefs—directly border shorelines and islands, and do not have a lagoon;
- barrier reefs—separated from shorelines by a lagoon;
- atoll reefs—barrier or fringing reef surrounding a submerged volcanic island; and
- ribbon reefs—a form of barrier reefs that is long and narrow.

Geomorphic zones within each reef are similar for different reef types. Typically reef topography includes several distinct geomorphologic zones, which are predominantly characterised by their depth and level of consolidation:

- Reef slope (sheltered and exposed) spans from the low tide mark to deep water, and includes alternating spurs and channels, or 'buttresses', of variable length (up to 300 m) and width (up to several metres). This zone stabilises the structure of the reef, reduces the impact of waves, and drains debris away from the reef. In contrast to the sheltered side, the exposed part of the slope is vulnerable to the impact of prevailing winds and swell. The shallow reef slopes are the most common area for dense hard coral beds.
- Reef Rim is above the low tide mark and this area includes the *Reef Crest*, which is the highest point within a reef system apart from cays (coral islands).
- Outer Reef Flat is generally sheltered by the reef rim, and therefore less exposed to the prevailing winds and sea. It is predominantly consolidated, with sandy areas in between. It may vary from tens to thousands of metres in width, and from centimetres to metres in depth.
- Inner Reef Flat is generally sheltered by a neighbouring higher outer reef flat or reef rim, and therefore less exposed to the prevailing winds and sea. It is predominantly sandy, with some consolidated areas in between, and comprises similar material to the outer reef flat, with comparable extent and depth.
- Lagoon is generally surrounded by the reef flat and/or reef rim, and is protected from wind and waves. Composition is mostly sand with individual patch reefs or coral bommies (outcrops) in between. Depth can vary from several metres to tens of metres.

The rugosity, or topographic roughness, of a reef can vary with many factors and is indicative of habitat complexity and rigour. As in other coastal waters, water depth over these features varies with the tides, so accurate hydrological charts are essential for navigation in reefal waters.

The benthic habitat type of a reef is determined by the composition and abundance of the different benthic and substrate cover types that exist within the reef system. The main benthic cover types include hard and soft coral, macroalgae, turf algae, crustose coralline algae, benthic microalgae, and seagrass. The most common substrate types include rock, rubble, sand, mud, and silt, the mineral composition of which depends on the reef origin.

Hard coral is commonly divided into different morphologies, such as branching, massive, plate, free living, foliose, or sub-massive. Hard and soft coral species vary in morphologies and colour, with soft corals having eight tentacles and hard corals having more or less than this number. Identification of individual species is mostly determined or verified by gene extraction.

Figure 20.8 Coral reef hierarchical scales

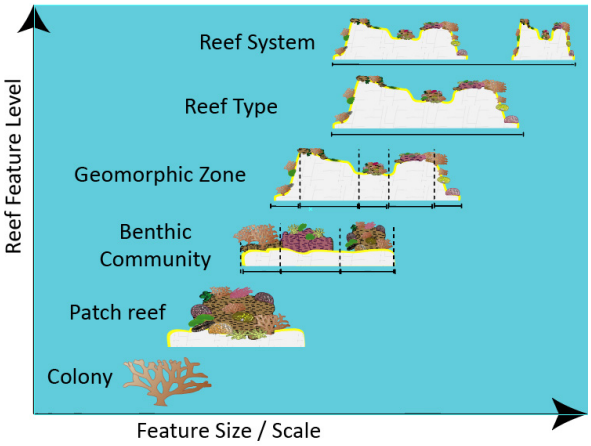

Source: Karen Joyce, James Cook University, and Chris Roelfsema, University of Queensland

Table 20.5 Four reef differentiation scales

Feature level	Linear extent (m)	Scale	Minimum mapping unit (ha)	Feature size (m)
Reef System or Region	1,000s–10,000s	< 1:1,000,000	n/a	n/a
Reef Type	100s–1,000s	1:500,000–1,000,000	25	400
Geomorphic Zone	10s–100s	1:100,000–500,000	5-25	75
Benthic Habitat Type	1s–10s	1:25,000–100,000	0.5–5	25

Source: Roelfsema *et al.* (2013).

20.6.2 Optical properties

Reflectance spectra of different living hard corals vary in both shape and value, with dominant features being in the wavelengths between 550 nm and 700 nm (Kutser *et al.*, 2003; Hochberg *et al.*, 2003; Leiper *et al.*, 2012). Most hard coral species exhibit peak reflectance around 610 nm and secondary peaks around 580 nm and 650 nm. Soft corals have similar reflectance characteristics with a minimum in ultraviolet (UV) wavelengths (Kutser *et al.*, 2000; 2001). Dead coral skeletons initially become overgrown with turf algae then macroalgae (usually red and green), with peak reflectance occurring around 600–605 nm and 650 nm. Given the small spectral differences between corals and algae, it is difficult to differentiate between different organisms using optical data alone. Most reefal rock is 'long dead' coral, which may support turf algae or crustose coraline algae, and since the latter provides an ideal surface to promote coral larvae settlements, its identification is important in coral surveys.

As with other shallow water applications, the existence of the water column above the feature of interest presents a further challenge for EO, since a given benthic type displays different observed reflectances at the water surface for differing water depths and water composition (such as chlorophyll and suspended matter; Botha *et al.*, 2013; see Section 6.1). The relevant light attenuation (absorption plus scattering) characteristics of the water column are:

- intensity decreases exponentially with increasing water depth (see Sections 5.1.1 and 8);
- absorption of all NIR wavelengths (> 700 nm), so NIR reflectance can be used to delineate shorelines (see Sections 7.2 and 11.3) as it only penetrates water for several centimetres;
- absorption of visible wavelengths increases with increasing wavelength, such that red wavelengths are absorbed at shallower depths than blue wavelengths (see Figure 5.10). The visible reflectances in EO imagery are the most useful for mapping benthic features, such as coral reefs.

The inherent spatial heterogeneity of coral reefs occurs at all scales. Typical reefal substrates, such as corals, macroalgae, rubble, and sand, may exhibit significantly different spectral and functional characteristics, yet can occur in a variety of mixtures within a square metre (see Figure 18.13). This spatial variation within individual image pixels is a problem for many EO image classification approaches (see Volume 2E). In this context, spatial analysis tools such as OBIA are more appropriate (see Section 20.6.3).

Reefal waters are typically clear due to low concentrations of phytoplankton and sediments, with most attenuation being due to changes in water depth (see Figure 18.13). However, the air-water interface and surface roughness can both significantly influence the spectral signal entering and leaving the water column (see Sections 4.3 and 8.1.3). Lidar can be combined with other sources of EO data, such as hyperspectral or high spatial resolution multispectral imagery, to enhance mapping of coral reefs.

20.6.3 EO datasets and applications

Some of the properties of coral reefs and their aquatic environments that have been mapped using EO data include reef type, extent, geomorphic zonation, benthic habitat type (composition, abundance, sedimentology), shape (bathymetry, rugosity), water quality (chlorophyll concentration, sedimentation; see Section 19), biochemistry (primary production and calcification), sea surface temperature (see Section 14), bleaching (see Excursus 20.3), and exposure to prevailing winds (see Volume 2C— Sections 6.2 and 6.3).

Mapping coral reef features, either by discriminating benthic features or estimating biophysical properties (such as depth and pigment concentration) requires EO data with appropriate spectral and spatial dimensions (see Volume 1B—Section 1). A greater number of benthic and substrate cover types can be mapped from EO imagery as the number of spectral bands is increased and pixel size decreased (see Figure 20.9). This corresponds to the progression in Table 20.5 from mapping reef/non-reef, to mapping geomorphic zones and reef biotope zones, to mapping benthic communities.

Figure 20.9 Comparison of spatial resolution and extent for four EO sensors

The different spatial dimensions of EO image sources (Quickbird, Landsat ETM+, Aqua/MODIS, and AVHRR) are compared using Heron Island reef, in the southern GBR, Queensland. Images (a–d) show the effects of progressively larger pixel sizes for a reef section spanning 1.5 km, while images (e–g) show variations in image extent, ranging from coverage of a single reef to the entire GBR.

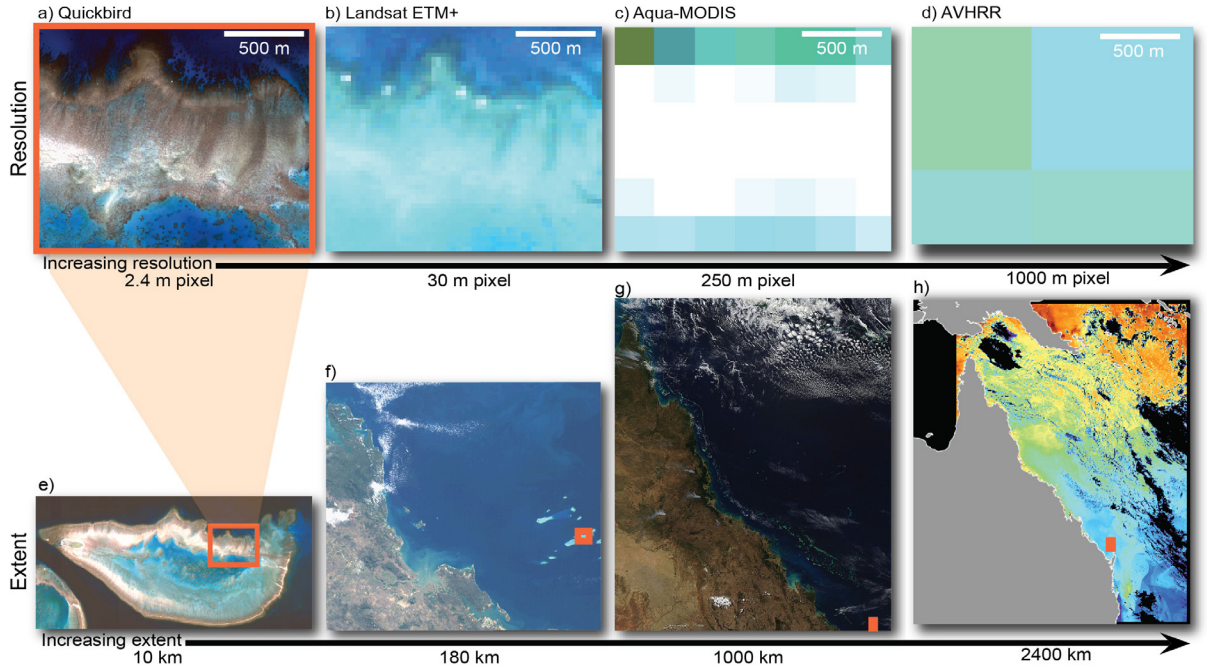

Source: Hedley *et al.* (2016b) Figure 2

Similarly, when mapping coral reef biophysical properties (whether in the water column, benthos, or substrate), more detailed and more precise estimations of biophysical properties can be derived by using an increased number of relevant spectral bands (see Section 8.5). Research on hydro-optics in waterbodies and photosystems in corals has established those wavelength regions that are absorbed by specific chemicals and processes. Accordingly, reflectance signatures resolving these features can be used in algorithms to estimate or map them for each pixel. Large numbers of spectral bands with narrow bandwidths also permits specific absorption features or inflection points (produced by photosynthetic or non-photosynthetic pigments) to be resolved (Hochberg and Atkinson, 2000, 2008; Hedley and Mumby, 2002; Hochberg *et al.*, 2003, 2004; Mumby *et al.*, 2004, Hedley *et al.*, 2012).

The most appropriate, simplest, and historically relevant dataset for reefal studies has been aerial photography, which typically covers from local to regional scales (several km^2 to 100s of km^2), with records stretching back as far as the 1930s (Hernandez-Cruz *et al.*, 2006). Multispectral spaceborne systems cover larger areas than aerial photography (10^4–10^6 km^2) and offer significant repeat capacity at spatial resolutions adequate to the reef feature types and levels being mapped. Hyperspectral sensors (both spaceborne and airborne), with additional spectral bands, much narrower bandwidths, and greater ability to identify specific targets, are particularly relevant to reefal studies (Karpouzli *et al.*, 2004; Garcia *et al.*, 2018, Kobryn *et al.*, 2013). Lidar data has proved useful for bathymetric studies (see Section 13.4.1) and reef geomorphological analysis.

The first instance of using multispectral data for coral reef mapping involved Landsat MSS coverage of the GBR in the 1980s (Smith *et al.*, 1975; Jupp *et al.*, 1985), to estimate bathymetry and reef geomorphologic zones. In the 1990s, a systematic classification scheme of benthic features was developed (Mumby and Harborne, 1999), which has continued to be popular for habitat mapping of coral reefs. Low spatial resolution sensors, such as AVHRR and MODIS, are also relevant to reefal studies for observing regional scale, biological variables such as chlorophyll concentration.

Coral reef structure is closely related to exposure to ocean swells (Andréfouët *et al.*, 2001). Spatial variations in the distribution of plant and animal species are usually strongly influenced by the prevailing wind and wave energy regimes in the littoral and sublittoral zones (see Section 20.6.1). Bathymetric datasets can be processed to show the degree of exposure of shallow water features to wave climate

or sunlight. As detailed in Volume 2C—Sections 6.2 and 6.3, the 'exposure' transformation is similar to relief shading with the 'Sun position' effectively on the horizon. Where detailed bathymetry is not available, EO imagery showing visible blue or green wavelengths can be used as a surrogate for water depth. For example, in Figure 20.10 comparable exposure images have been derived from both Landsat MSS imagery (green band) and a sparse grid of water depth samples. Such transformations have proved useful for mapping subsurface morphology, enabling vulnerable areas to be highlighted for early management intervention.

Thermal sensors are also valuable for mapping conditions conducive to coral bleaching (Abram *et al.*, 2003; Maina *et al.*, 2008; see Excursus 20.3). Since bleached corals reflect electromagnetic radiation (EMR) more strongly than healthy corals at all wavelengths (Holden and LeDrew, 1998, 1999; Yamano and Tamura, 2004), their occurrence is likely to be detectable using multispectral EO. The clear and calm waters that typify reefal environments, and the exposure of reefal system at high tide, allow their shorelines to be delineated clearly using NIR bands (see Section 11.3). The varying shorelines of the intertidal region can be regarded as contours, and also used to map topography (Yamano, 2007).

Figure 20.10 Exposure (directional) filtering

Comparable images have been derived for John Brewer Reef, Queensland, by directional filtering of Landsat MSS imagery and measured depth data. Bright areas indicate a higher local slope and aspect to the selected wind direction, and in the prevailing wind direction these areas indicate greater exposure. Darker areas infer sheltered positions relative to that direction. The resulting images highlight reef morphology and show exposure to the prevailing wind direction (southeast).

a. Transect samples of measured water depth formed a sparse grid of points when registered with Landsat MSS imagery. (Note: null pixels are shown as black.) This sparse dataset was interpolated to create a continuous depth image before exposure (directional) filtering.

Measured depth data | Interpolated depth data | Exposure on interpolated depths

b A Landsat MSS4 (green band) image for John Brewer Reef was despiked and smoothed before directional filtering to show exposure to the prevailing wind direction. The exposure image derived from EO data offers an economical approximation to sourcing measured depth data.

Landsat MSS4 image | Preprocessed MSS4 image | Exposure on preprocessed MSS4

Source: Harrison and Jupp (1990) Plate 6

Excursus 20.3—Coral Bleaching

Further information:

https://coralreefwatch.noaa.gov/satellite/index.php
http://www.bom.gov.au/environment/activities/reeftemp/about.shtml
https://www.aims.gov.au/docs/research/climate-change/coral-bleaching/coral-bleaching.html

Coral reefs around the world are being increasingly threatened by coral bleaching. This phenomenon occurs when corals are stressed by changes in environmental conditions, such as temperature, light, or nutrients. They react by expelling the symbiotic algae that live in their tissues, then turn completely white. The symbiotic algae, colloquially called zooxanthellae, are photosynthetic and provide their host coral with food in return for protection. Their presence gives the corals a distinctive brown hue, and the fluorescent pigments produced by the host add the vibrant colours that characterise living corals.

Acute or prolonged stressful environmental conditions cause a breakdown in this symbiotic relationship, first revealing the fluorescent pigments, and then leaving the white calcium carbonate skeleton visible through the coral tissue. Bleached corals can no longer gain energy from photosynthesis, and if bleaching persists for an extended period, corals will starve and die. For those that survive, bleaching can deplete the corals' energy resource to the extent that corals do not reproduce for one or two years. The threat to corals increases as the bleaching events become more frequent because they have no time to recover.

Mass coral bleaching is caused by unusually high water temperatures that stress corals. Continuous monitoring of sea surface temperature at global scales provides researchers and stakeholders with tools to understand and better manage the complex interactions leading to coral bleaching. When bleaching conditions occur, these tools can be used to trigger bleaching response plans and support appropriate management decisions.

Bleaching has been observed on the GBR since 1982, with severe bleaching events occurring in the summers of 1998, 2002, and 2006. Coral mortality appears to increase with the intensity of the bleaching event, which is determined by how much and for how long temperatures remain above the maximum mean summer temperatures.

The NOAA Coral Reef Watch Program (*https://coralreefwatch.noaa.gov*) provides current reef environmental conditions to quickly identify areas at risk for coral bleaching (Strong *et al.*, 2006, 2011). This program uses EO datasets with modelled and *in situ* data to develop and operate a decision support system to monitor stress factors in coral reef ecosystems. The Version 3.1 products use global, daily sea surface temperature (SST; see Section 14.4.4) at 5 km resolution to highlight anomalies and bleaching hotspots through time (Liu *et al.*, 2017). These products offer managers of coral reef systems an opportunity to determine location of heat stress, and incorporate that information into their management strategies of marine jurisdictions.

In Australia, a similar methodology has been used to develop the ReefTemp Next Generation tool (*http://www.bom.gov.au/environment/activities/reeftemp/reeftemp.shtml*; Garde *et al.*, 2013, 2014). This near real time operational tool provides information on coral bleaching risk for the GBR region, using higher resolution (~2 km), daily (with gaps), 14-day composite (near gap-free) nighttime SST data from selected IMOS SST data sources (see Section 14.5.1). Because these SST data have been calibrated to the Australian region, these products are more accurate than their global counterpart.

With the current high spatial and temporal resolution satelites we have the opportunity to assess the presence of coral bleaching. For example, the Allen Coral Atlas monitoring system (see Section 20.8) is using Sentinel-2 time series imagery, acquired while Degree Heating Weeks (DHW) provided by NOAA Coral Watch are low, to create a baseline reflectance image (Hedley *et al.*, 2018). As other time series datasets become available, they can be assessed and compared with this baseline.

20.6.4 Mapping biophysical properties

Geomorphic zonation classes are differentiated by a combination of pixel colour, texture of groups of pixels, water depth, wave action, and neighbourhood relationships (Mumby *et al*., 1997a; Andréfouet *et al*., 2006; Hamylton, 2017; Roelfsema *et al*., 2018, 2020; Andrefouét and Bionaz, 2021). Similarly, to delineate benthic zones the attributes of water depth, consolidation, slope, and waves are most appropriate.

Traditionally, reef classification relied on expert knowledge and detailed field observations to group natural features into relevant, but often inconsistent, classes (see Figure 20.11). Automated classification methods have been developed to both avoid inconsistency of labels and definitions, and assist reef managers to better understand the underlying biophysical attributes (Kennedy *et al*., 2021). Global mapping of geomorphic zones relies on integrating a variety of *in situ* data with high resolution EO datasets using compute-intensive techniques such as ML and OBIA (Lyons *et al*., 2020). For example, the Allen Coral Atlas global reef mapping project called *Reef Cover* combines EO data and geo-ecological information to map coral reefs at a variety of spatial scales (Kennedy *et al*., 2021; see Figure 20.12).

Production of maps quantifying biophysical properties or processes on coral reefs and their surrounding environments can only be done from fully 'corrected'[26] images (see Volume 2), acquired from spaceborne or airborne platforms (see Volume 1A). Several approaches are commonly used to deliver maps of coral reef biophysical properties:

- Unmixing techniques are used to estimate the relative area of each pixel occupied by a set of coral reef benthic cover types (e.g. coral, sand, algae). As detailed in Volumes 2E and 3A, these techniques assume the image pixel is larger than the features to be mapped and are applied to images which have had the influence of the water column removed (Hedley and Mumby, 2003; Hedley *et al*., 2004; Goodman and Ustin, 2007; Lesser and Mobley, 2007). The mathematical solutions required for these techniques become more accurate as the number of uncorrelated input variables (spectral bands in this case) increases; hence hyperspectral image data are used predominantly in this approach (Hedley, 2013).
- Inversion techniques use empirical or analytical mathematical solutions to extract biophysical information from image pixels, including water depth, concentrations of organic and inorganic material in the water column, and benthic/substrate reflectance signatures (see Section 8.4).

Benthic habitats are mostly categorized either using a hierarchy of geomorphological classes or a set of ecological classes (Mumby and Harborne, 1999; Andréfouët, 2011; Kennedy *et al*., 2021). Classification results are enhanced when relevant spectral libraries are available for referencing. Classification approaches may involve spectral and/or textural information as detailed in Volume 2E, and other spatial and neighbourhood relationships (see Volume 2A—Section 10).

Inversion methods can deliver a range of products relating to the model inputs, including bathymetry, benthic type, and concentration of water constituents (Hedley, 2013). Secondary outputs can further be derived from these initial results. Thus, these models allow derivation of bottom reflectance, spectral absorption coefficients for the water column, or relative light conditions in the benthos.

Moderate resolution imagery, in conjunction with benthic field data and other biophysical properties (including water depth, slope, and wave exposure), was used with semi-automated OBIA and ecogeomorphological rules to generate maps of geomorphic zonation and dominant benthic cover (reef top). These input datasets were then used to create an ecological model that predicted dominant coral type (reef slope) for the shallow offshore reefs of the Capricorn Bunker Group in the southern GBR (Roelfsema *et al*., 2018; see Figure 20.13) and central GBR (Roelfsema *et al*., 2020).

The ecological and geomorphological characteristics of geomorphic zones and benthic classes (Kennedy *et al*., 2021) could be used to form ecogeomorphological rules to differentiate them. Examples include:

- colour and texture of groups of pixels (objects)—for example, inner reef flat has less texture, with predominantly sand cover and mostly homogenous colour, whereas the outer reef flat has more texture due to a mixture of sand, rock, coral, and algae;
- biophysical attributes such as depth, slope, consolidation, and waves—for example, reef crest is shallow, horizontal, consolidated, with high wave energy, whereas back reef slope, is deep, sloping, partly consolidated, with low wave energy; and
- spatial neighbourhood attributes based on adjacency and enclosing between classes—for example, reef crest is adjacent to outer reef and slope, and could not be enclosed by slope.

As a result of these rules, contextual editing was applied to machine learning based classifications of high and moderate resolutions satellite imagery for mapping of large extent reef systems, such as the full extent of the GBR, and reef systems globally (Roelfsema *et al*., 2021, Lyons *et al*., 2020).

26 Corrections in this context include both geometric and radiometric corrections as detailed in Volume 2.

Figure 20.11 Approaches to reef mapping

Reef classification has traditionally relied on human interpretation of field data at a local scale. By integrating decades of local scientific knowledge (1) with global EO imagery (2), automated methods, such as Reef Cover, can define consistent classes across of range of spatial scales (3).

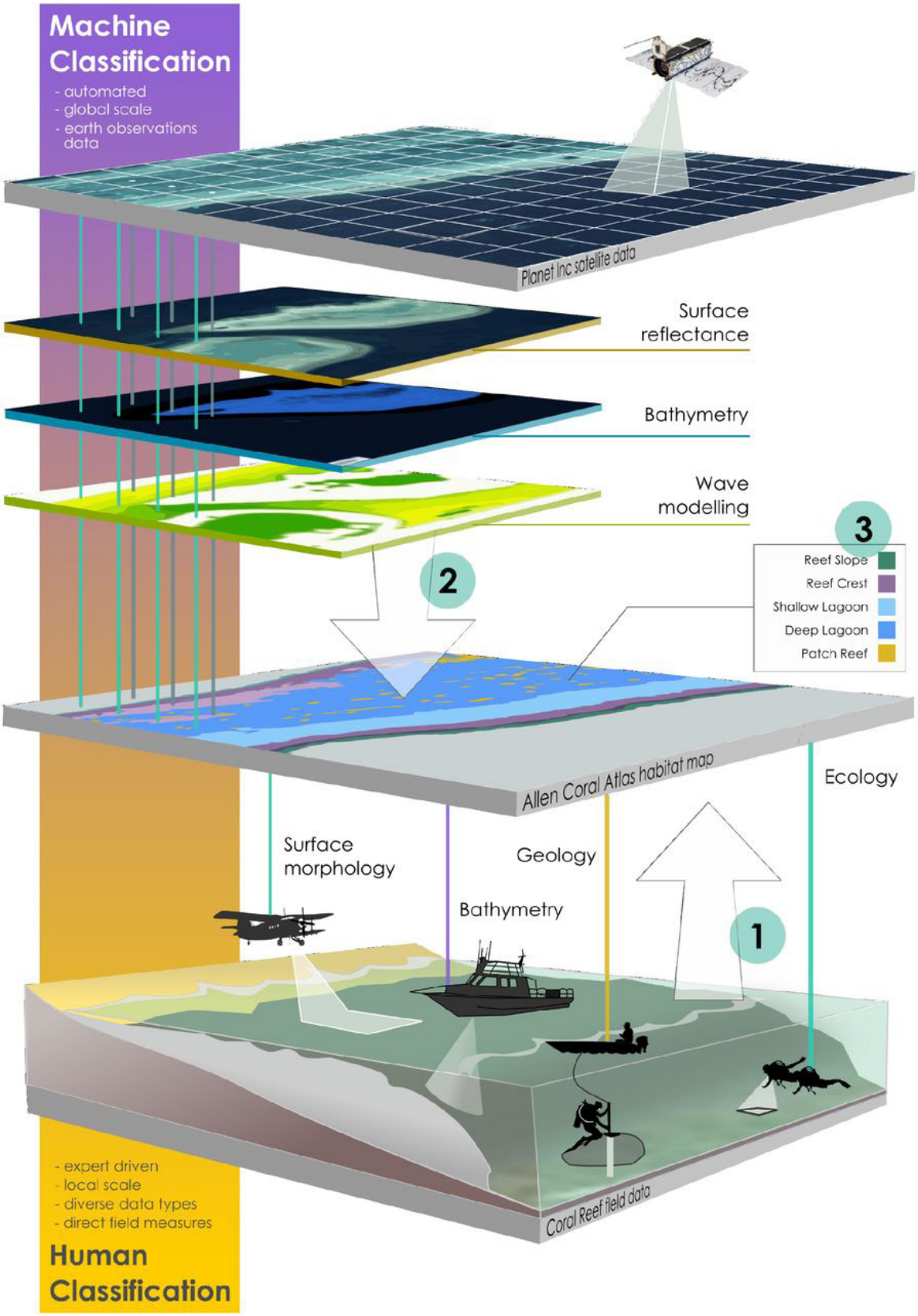

Source: Kennedy *et al.* (2021) Figure 1

Figure 20.12 Automated classification of geomorphic zones

Three fundamental characteristics, water depth, slope angle and exposure to waves, can be used to define the underlaying geomorphic structural features of reefs.

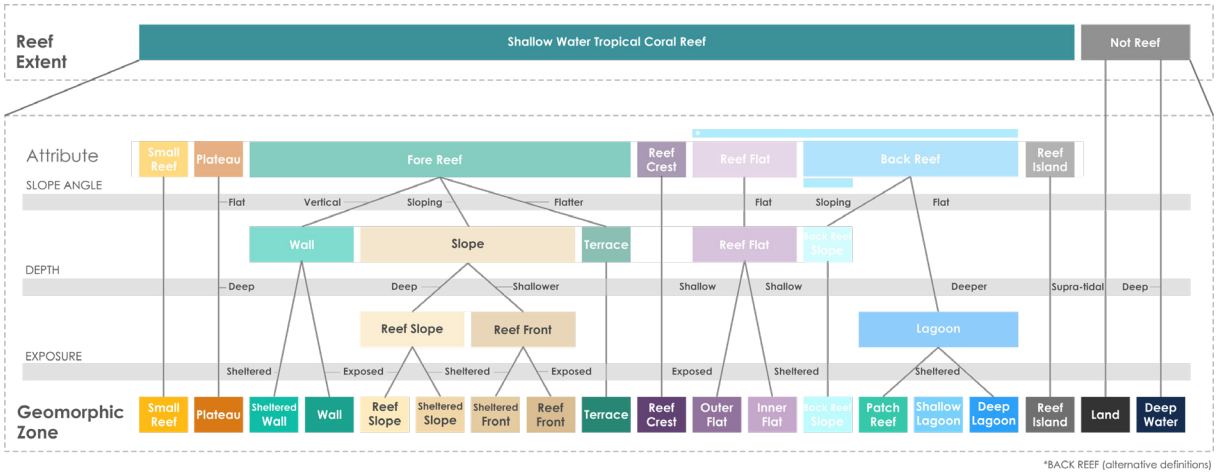

Source: Kennedy *et al.* (2021) Figure 2

Monitoring of coral health is also being conducted using fluorescence imaging lidar instruments (Sasano *et al.*, 2012). Most live corals that build reef structures contain fluorescent proteins, which, when excited by UV radiation, fluoresce in blue-green wavelengths (Alieva *et al.*, 2008). Excitation using radiation at 365±5 nm has been shown to produce a fluorescence peak between 450 nm and 550 nm from live coral, but not from dead coral, sand, or marine vegetation. Imaging lidar systems have been deployed on boats to monitor coral health in conjunction with diving patrols and satellite EO (Sasano *et al.*, 2012).

Ongoing research into EO of coral reefs follows three fundamental paths of development:

- Techniques that compensate for water column and atmosphere effects in the EO signal (Lyzenga, 1978, 1985; Gordon and Clark, 1980; Bierwirth *et al.*, 1993; Gordon, 1997; Lee *et al.*, 1999; Louchard *et al.*, 2003; Gao *et al.*, 2009; Dekker *et al.*, 2011). For coral reefs, an important implication from this research is that for passive sensors to be useful, the substratum must be visibly observable in the imagery. Optically deep areas, or areas with high turbidity, cannot be mapped using passive techniques alone, so require active systems (see Sections 8 and 18).
- Higher level products that provide insight into reef status or function (Atkinson and Grigg, 1984; Mumby *et al.*, 1997a; Hochberg and Atkinson, 2000, 2008; Roelfsema *et al.*, 2002; Lesser and Mobley, 2007; Palandro *et al.*, 2008; Purkis *et al.*, 2008). A number of these products are currently used routinely to monitor reef condition.
- Techniques that integrate satellite-based OBIA approaches and physical coral reef attributes (such as depth, slope and waves) with ecogeomorphological properties (Roelfsema *et al.*, 2018, 2020; Lyons *et al.*, 2020).

Products derived from EO data are increasingly being used to monitor changes in reef composition over time. Pressures such as sedimentation, sea level rise, increased storm frequency, ocean acidification, and temperature changes threaten the longevity of coral reefs (Wilkinson, 2008). Managers need to be able to monitor changes using timely and reliable methods (Cochran, 2013), such as analysis of the growing time series of imagery from airborne and satellite borne sensors (Goodman *et al.*, 2013). To ensure high levels of accuracy from such analyses, it is essential that *in situ* data is available for historical imagery. It is also advisable to select imagery acquired during similar diurnal and seasonal conditions (see Volume 2D). For example, while the spectral characteristics of macroalgae are similar to those of corals making these two features difficult to distinguish, the distribution and abundance of macroalgae can change seasonally in contrast to the slower development of coral. An EO-based ecological statistical model was also used to predict coral type along reef slope on the GBR (Roelfsema *et al.*, 2018, 2020).

The eReefs platform integrates a suite of process models that simulate hydrodynamic state, sediment transport, water quality, carbon chemistry, and basal ecology (Baird *et al.*, 2021), which enables hindcasting, nowcasting, and forecasting for the GBR lagoon and reef matrix (see Volume 2D—Excursus 14.4). This platform uses EO datasets and *in situ* monitoring to assess risks and management options based on past, current, and projected environmental conditions (see Figure 20.14).

Figure 20.13 Mapping reef biophysical properties

These mapping results for the shallow offshore reefs of the Capricorn Bunker Group in the southern GBR were derived using OBIA of Landsat-8 OLI imagery (acquired on 10 April 2017) in conjunction with ecological modelling of data for field-based benthic composition, reef impact, and wave exposure.

a. Geomorphic zonation

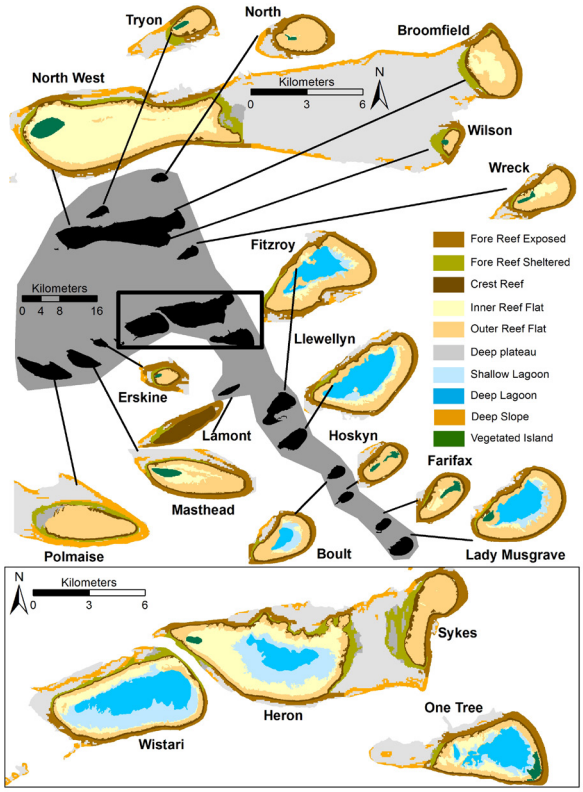

b. Dominant benthic cover, reef top

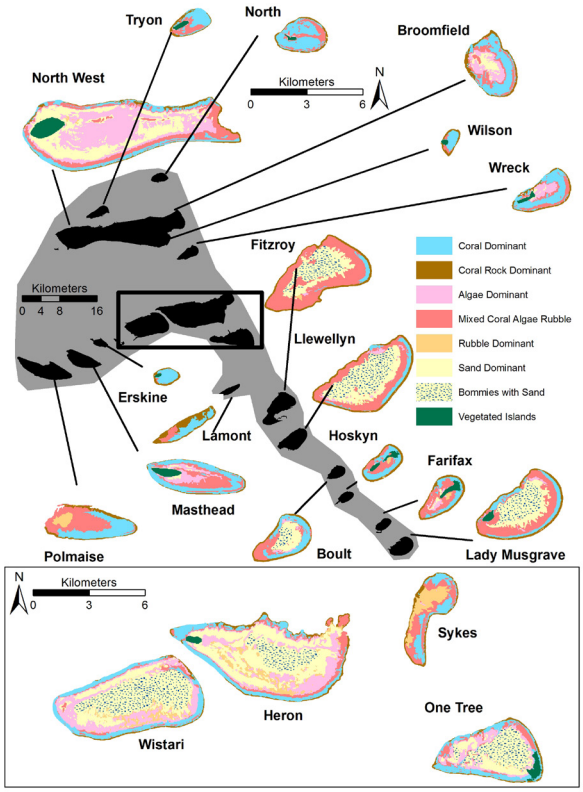

c. Predicted dominant coral type, reef slope

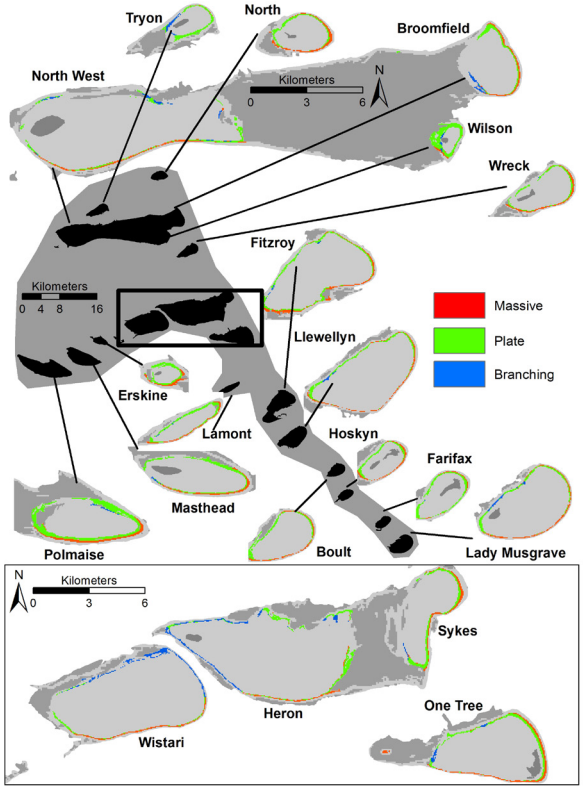

d. Water depth

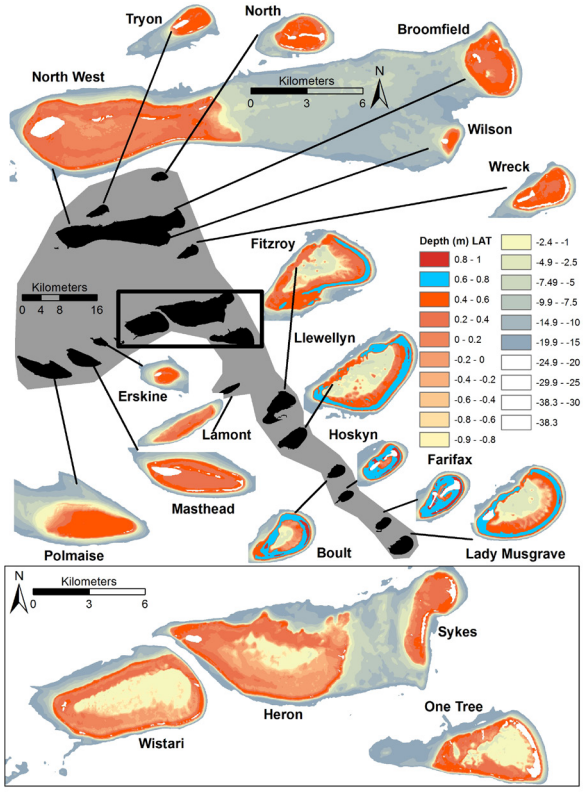

Source: Chris Roelfsema, University of Queensland

Figure 20.14 eReefs modelling extent

eReefs uses a range of EO-based and *in situ* monitoring datasets to model environmental parameters over the GBR region at 1 km or 4 km resolution.

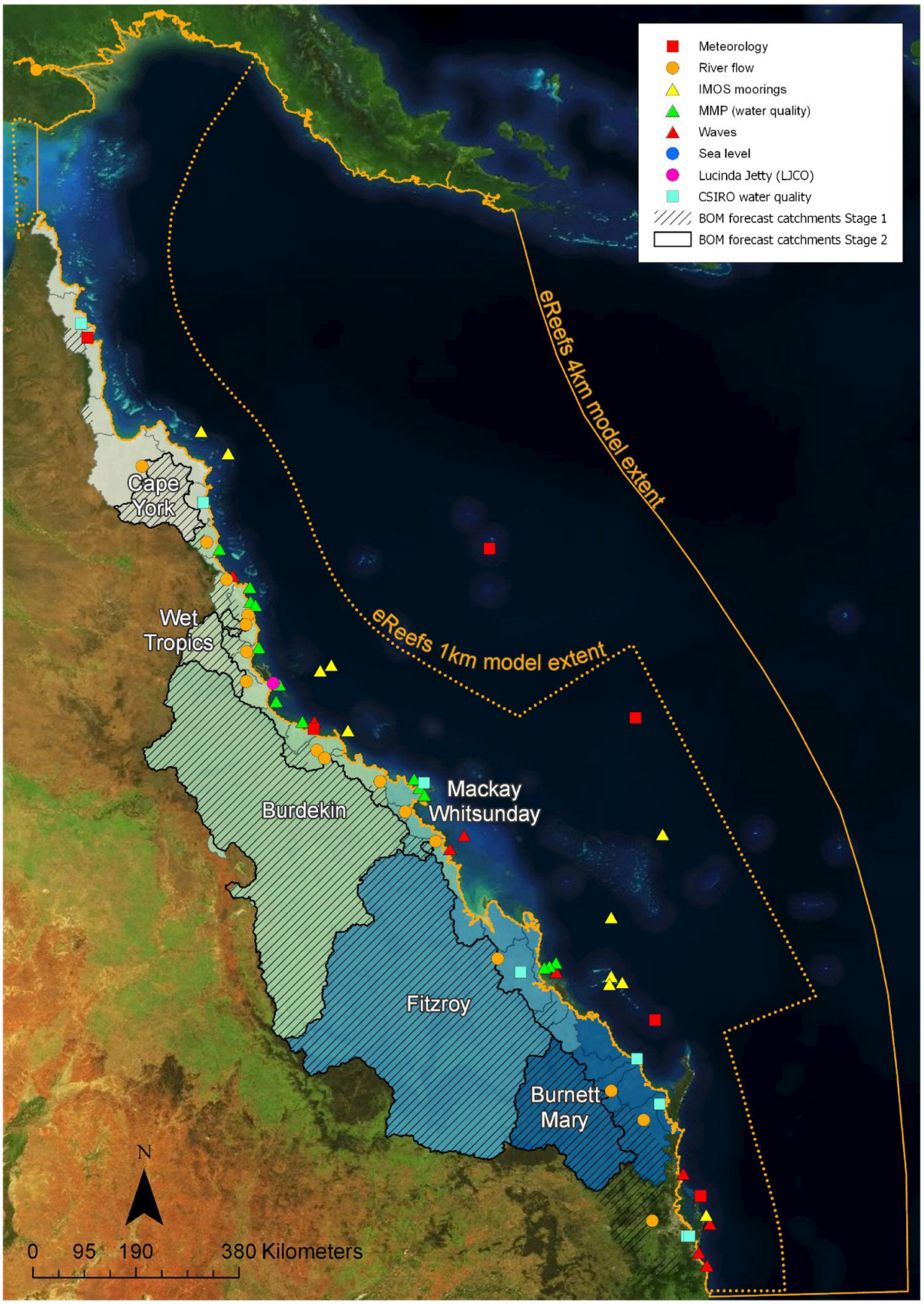

Source: Steven *et al.* (2019)

In future, it is likely that multispectral and hyperspectral imagery can be used to derive reef properties such as the amount of live coral, algae and sediment cover, structural forms of coral cover, benthic microalgae biomass, and coral and algae light absorption efficiency. These properties provide key links for studies assessing coral productivity, coral reef biochemistry, carbon fluxes, and nutrient dynamics on reefs.

20.7 Marine Fauna

The broad concept of biodiversity is detailed in Volume 3A—Section 18. In recent years both overexploitation and climate variations have modified marine ecosystems (Hazen *et al*., 2018). These factors resulted in variability in fish recruitment and changes in species dominance. This situation has ultimately encouraged an ecosystem-oriented approach to managing fisheries globally (Cury *et al*., 2008), namely "a comprehensive, integrated management of human activities, based on the best available scientific knowledge about the ecosystem and its dynamics, in order to identify and take action on influences which are critical to the health of the marine ecosystem, thereby achieving sustainable use of ecosystem goods and services and maintenance of ecosystem integrity" (IOCCG, 2009).

Since the spatial and temporal variability of phytoplankton directly impacts the distribution of higher order marine organisms (Tweddle *et al*., 2018), marine assessments of biodiversity have focused on monitoring fish populations and the distribution and abundance of specific species (Reynolds *et al*., 2017). Below we consider the role of EO in two aspects of observing marine biodiversity: fishery stock assessment (see Section 20.7.1), and large marine animal counts (see Section 20.7.2). Global monitoring programs for marine biodiversity are considered in Section 21.1.

The assessment of coastal and marine biodiversity using remote sensing is largely based on the correlation of traits of organisms and of species' natural 'tolerance windows' with the habitats in which they live, and then tracking with remote sensing how these habitats change over time.
(Canonico et al., 2019)

20.7.1 Fisheries

Pelagic sampling methods, including catch data, tagging, and baited stereo-videography, are reviewed by Bouchet *et al.* (2018) in terms of their suitability for monitoring within MPA (see Excursus 20.2). Different sampling methods span different spatial and temporal scales, in terms of both data resolutions and extents (see Figure 20.15). Such methods can be integrated with EO-based environmental data to assess fisheries stocks, determine environmental variables driving the distribution of specific species, and/or model species distribution (Enever *et al.*, 2017; Harrison *et al.*, 2017).

A range of EO datasets has been used to monitor different aspects of fisheries, which are also relevant for managing marine habitats (IOCCG, 2009; Chassot *et al.*, 2011; Klemas, 2013; Kacev and Lewison, 2016). These include:

- ocean colour—EO-based chlorophyll a estimates (see Section 18.6) can be used to infer phytoplankton biomass or net primary production (NPP). Thus, algal biomass can be linked with the health of pelagic ecosystems and larval fish survival (Platt *et al.*, 2003);
- sea surface temperature (SST)—is correlated with species diversity for many organisms in coastal and open ocean environments (Tittensor *et al.*, 2010; see Section 14), with thermal fronts being associated with high concentrations of fish and fish food (Bakun, 2006; Reese *et al.*, 2011); and
- water circulation—since locations of some fish (and other migratory) species is associated with circulation features (Scales *et al.*, 2014; see Section 17), these can be used to model species distributions (Rajkumar and Shanmugam, 2018).

For example, Platt and Sathyendranath (2008) identified a number of phytoplankton characteristics using EO-derived ocean colour, including the annual production and loss rates, spatial variance in biomass, initiation, duration, and timing and intensity of the maximum intensity of algal blooms. Since these characteristics are particularly relevant to pelagic ecology, EO time series datasets have been used to analyse ecosystem fluctuations and their interactions with valued fish stocks (Platt *et al.*, 2003). Climatological records are also valuable for validating phenological studies and differentiating anomalies from seasonal variations (Payne *et al.*, 2017). Hobday *et al.* (2010, 2011) highlighted pelagic habitats in Australia's southern and eastern ocean territory to predict the abundance of southern bluefin tuna using EO-based datasets. These forecasts now operationally model habitat preferences and ecological niches to enable sustainable management in two aquatic zones (Payne *et al.*, 2017):

- Great Australian Bight (Eveson *et al.*, 2015; *http://www.cmar.csiro.au/gab-forecasts/*); and
- Southeast Australia (Hobday *et al.*, 2011; *https://www.afma.gov.au/fisheries-services/sbt-zones*).

Figure 20.15 Pelagic sampling methods

Varying temporal and spatial scales of pelagic sampling methods used in marine monitoring are compared.

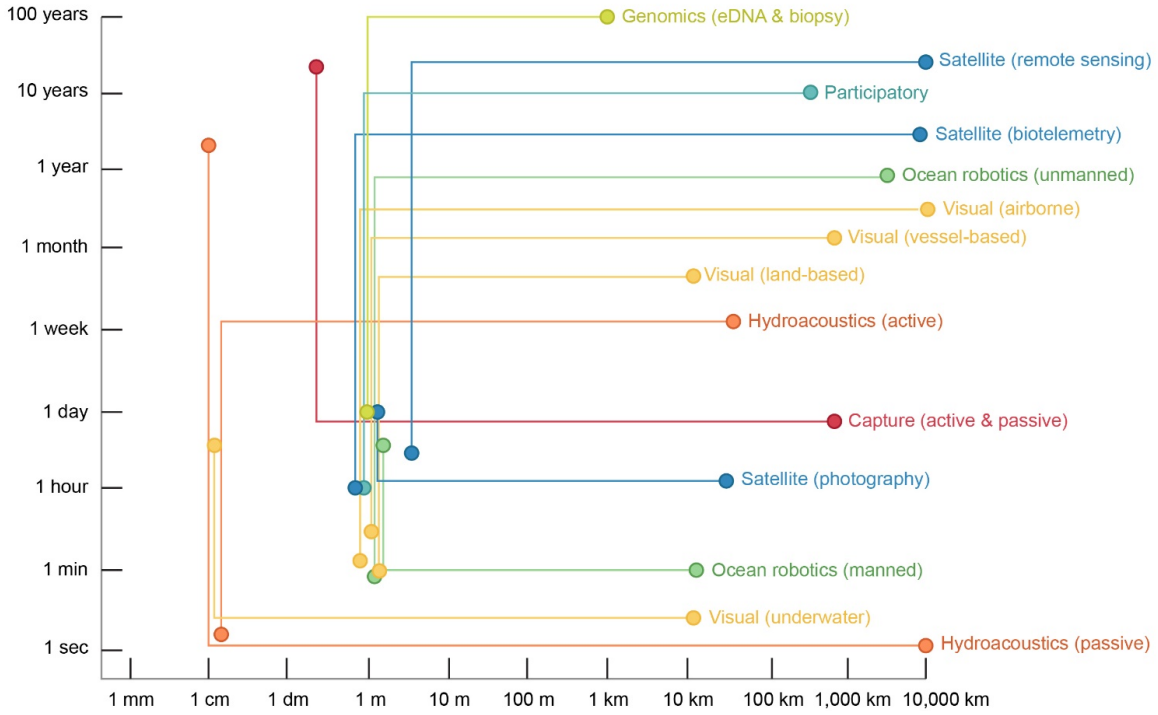

Source: Bouchet *et al.* (2018) Figure 2.3

Fish provide 20% of the world's protein and are the main source of protein for over a billion people. The extraction and cultivation of fish directly provides around 41 million jobs (FAO, 2007), and indirectly employs 162 million people (UNEP, 2006).
(IOCCG, 2009)

20.7.2 Animal counts

While large marine animals, such as penguins (Fretwell *et al.* 2009, 2012; Lynch *et al.*, 2012) and seals (LaRue *et al.*, 2011; McMahon *et al.*, 2014), have been counted using high resolution satellite imagery, automated processing methods enable frequent counts and simplify the use of time series datasets for trend detection. For example, Fretwell *et al.* (2014) used a simple threshold in the panchromatic and coastal (far blue) bands to count whales. However, such methods only observe animals on or near the ocean surface.

The movement of individual aquatic fauna can be tracked by telemetry, which involves attaching an electronic device to an organism that automatically logs or transmits selected data to a receiver. Relevant data for aquatic organisms would include:

- location—horizontal and vertical;
- water parameters—such as depth, temperature, or salinity; and/or
- physiological attributes—such as digestion, metabolic rate, or respiration.

In recent decades, such telemetric methods have delivered new insights into the dynamics of a range of marine species, including their dietary preferences, migration patterns, habitat characteristics, and interactions between predators and prey. Acoustic telemetry allows smaller tags to be deployed than are required for satellite telemetry so can be used on smaller creatures, but the latter can transmit data in shorter time intervals so deliver more continuous time series (Hussey *et al.*, 2015). Acoustic telemetry also requires detectors to be located within a kilometre from a transmitter so are mostly limited to coastal and freshwater studies. Telemetric datasets are being integrated with oceanographic and isotopic datasets to characterise foraging patterns of selected species (Lowther *et al.*, 2013). More recently, biologging devices, which quantify the fine scale, three-dimensional movements and physiological status of organisms, as well as their environmental context (Lennox *et al.*, 2017), are providing more detailed insights into their foraging behaviour (Andrzejaczek *et al.*, 2019) and other interactions with the marine environment (Lennox *et al.*, 2019).

The distribution of selected species has also been modelled using habitat mapping approaches. Forecasting products to assist in operational monitoring of protected species have been developed using tracking data in combination with EO-based environmental variables (including SST, chlorophyll a concentration, altimetry, wind data, and/or bathymetry; Payne *et al.*, 2017). Bycatch data—marine creatures caught unintentionally during commercial fishing activity—also provide valuable information for habitat mapping. Examples of operational EO-based nowcast and forecast ecological systems include:

- TurtleWatch (*http://www.pifsc.noaa.gov/eod/turtlewatch.php*)—developed by NOAA to identify loggerhead turtle habitats north of the Hawaiian islands, then alert fishermen to areas where they might entangle loggerheads (Howell *et al.*, 2008, 2015); and
- WhaleWatch (*https://www.westcoast.fisheries.noaa.gov/whalewatch/*)—funded by NASA and publicly available from NOAA, provides near real time information on the locations of blue whales along the US west coast with the goal of preventing ship strikes and other threats (Hazen *et al.*, 2017).

A similar project to predict the distribution of the endangered North Atlantic right whale (*Eubalaena glacialis*) is being undertaken by modelling the abundance and timing of its main prey, *Calanus finmarchicus* (IOCCG, 2009). More recently, species distribution models, which use daily EO datasets to track oceanographic conditions in conjunction with satellite telemetry and fisheries observer data, have also been developed to reduce bycatch and thus support a sustainable fishing industry (Hazen *et al.*, 2018).

The abundance and distribution of marine megafauna in coastal waters are being tracked by satellite tags using either GPS transmitters (Marsh *et al.*, 1990; Tomkiewicz *et al.*, 2010; Gredzens *et al.*, 2014) or acoustic tracking systems (Zeh *et al.*, 2015; Dwyer *et al.*, 2015). Bayliss and Hutton (2017) observed a strong correlation between dugong abundance and the extent of seagrass that was mapped using Landsat imagery. Such datasets are being used to identify hotspots in order to sustainably manage indigenous harvesting, and better understand the dynamics of both dugong populations and seagrass habitat.

20.8 Further Information

Biodiversity

Global Ocean Observing System (GOOS): *https://www.goosocean.org/*

Marine Biodiversity Observation Network (MBON): *https://marinebon.org/*

Ocean Biogeographic Information System (OBIS): *https://obis.org/*

GeoHab: Marine Geological and Biological Habitat Mapping: *http://geohab.org*

Butler *et al.* (2010, 2017)

Atlas of Living Australia: *https://www.ala.org.au*

Marine Biodiversity Hub: Research for understanding and managing Australia's marine biodiversity: *https://www.nespmarine.edu.au*

Western Australian Marine Science Institution (WAMSI): *https://www.wamsi.org.au*

eAtlas (Australia's Tropical Lands and Seas): *http://e-atlas.org.au/*

Global Aquatic Ecosystem Assessment

ChloroGIN: *http://www.chlorogin.org/*

Blue Carbon

The Blue Carbon Initiative: *https://www.thebluecarboninitiative.org/*

Intergovernmental Oceanographic Commission: *http://www.unesco.org/new/en/natural-sciences/ioc-oceans/sections-and-programmes/ocean-sciences/ocean-carbon/coastal-blue-carbon/*

Marine Parks

Parks Australia: *https://parksaustralia.gov.au/marine/parks/*

Australian Marine Parks Science Atlas: *https://atlas.parksaustralia.gov.au/amps*

Wetlands

Directory of Important Wetlands in Australia: *https://www.awe.gov.au/water/wetlands/australian-wetlands-database/directory-important-wetlands*

Australian Wetlands Database: *https://www.awe.gov.au/water/wetlands/australian-wetlands-database*

Mangroves

Stewart and Fairfull (2008)

IUCN (2017)

MangroveWatch: *http://mangrovewatch.org.au/?option=com_content&view=section&layout=blog&id=18&Itemid=300032*

Australian Coastal and Marine Territory

Australian Marine Spatial Information System (AMSIS): *http://www.ga.gov.au/scientific-topics/marine/jurisdiction/amsis*

GA (2020)

IMOS State and Trends of Australia's Ocean Report: 2. Biological Productivity: *https://www.imosoceanreport.org.au/time-series/productivity/*

IMOS State and Trends of Australia's Ocean Report: 4. Marine Animals: *https://www.imosoceanreport.org.au/time-series/animals/*

OzCoasts: *https://ozcoasts.org.au*

Fisheries

https://globalfishingwatch.org

Benthic Habitat Classification

National standardised nomenclature for benthic habitat classification is documented by Seamap Australia (Butler *et al.*, 2017): ISBN: 978-1-925646-61-0, *https://vocabs.ardc.edu.au/viewById/129*

CATAMI: Classification Scheme is enabling aggregation, annotation and automated processing of underwater imagery from across Australia (Althaus *et al.*, 2015)

Kennedy *et al.* (2021)

Coral reefs

Corals of the world: *http://www.coralsoftheworld.org/page/home/*

Goodman *et al.* (2013)

Remote Sensing Toolkit: *https://www.rsrc.org.au/rstoolkit*

NASA JPL CORAL mIssion: *https://airbornescience.jpl.nasa.gov/campaign/coral*

NOAA Coral Reef Watch: *https://coralreefwatch.noaa.gov/satellite/publications.php*

Allen Coral Atlas: *https://allencoralatlas.org/atlas/*

Coral Watch—citizen science on the reef: *https://coralwatch.org*

OzCoasts (2020). *Algal blooms* webpage, Australian Online Coastal Information website: *https://ozcoasts.org.au/indicators/coastal-issues/freq_algal_blooms/*

ReefTemp Next Generation: *http://www.bom.gov.au/environment/activities/reeftemp/reeftemp.shtml*,

eReefs: *https://research.csiro.au/ereefs/remote-sensing/*

20.9 References

Abram, N.J., Gagan, M.K., McCulloch, M.T., Chappell, J., and Hantoro, S. (2003). Coral reef death during the 1997 Indian Ocean Dipole linked to Indonesian wildfires. *Science*, 301, 952–955.

Adam, E., Mutanga, O., and Rugege, D. (2010). Multispectral and hyperspectral remote sensing for identification and mapping of wetland vegetation: a review. *Wetlands Ecology and Management*, 18, 281–296. *https://doi.org/10.1007/s11273-009-9169-z*

Ajani, P., Hallegraeff, G., Allen, D., Coughlan, A., Richardson, A., Armand, L., Ingleton, T., and Murray, S. (2016). Establishing baselines: a review of eighty years of phytoplankton diversity and biomass in south-eastern Australia. *Oceanography and Marine Biology: An Annual Review*, 54, 387–412.

Alberotanza, L., Brando, V.E., Ravagnan, G., and Zandonella, A. (1999). Hyperspectral aerial images. A valuable tool for submerged vegetation recognition in the Orbetello Lagoons, Italy. *International Journal of Remote Sensing*, 20, 523–533

Alieva, N.O., Konzen, K.A., Field, S.F., Meleshkevitch, E.A., Hunt, M.E., Beltran-Ramirez, V., Miller, D.J., Wiedenmann, J., Salih, A., and Matz, M.V. (2008). Diversity and evolution of coral fluorescent Proteins. *PloS ONE* 3, e2680

Allen Coral Atlas (2021). *Science & Methods* webpage, Allen Coral Atlas website: *https://allencoralatlas.org/methods/*

Alongi, D.M. (2020). Carbon balance in salt marsh and mangrove ecosystems: A global synthesis. *Journal of Marine Science and Engineering*, 8(10), 767. *https://doi.org/10.3390/jmse8100767*

Althaus, F., Williams, A., Schlacher, T., Kloser, R., Green, M., Barker, B., Bax, N., Brodie, P., and Schlacher-Hoenlinger, M. (2009). Impacts of bottom trawling on deep-coral ecosystems of seamounts are long-lasting. *Marine Ecology Progress Series*, 397, 279–294.

Althaus, F., Hill, N., Ferrari, R., Edwards, L., Przeslawski, R., Schönberg, C.H.L., Stuart-Smith, R., Barrett, N., Edgar, G., Colquhoun, J., Tran, M., Jordan, A., Rees, T., Gowlett-Holmes, K. (2015). A Standardised Vocabulary for Identifying Benthic Biota and Substrata from Underwater Imagery: The CATAMI Classification Scheme. *PloS ONE*, 10(10), e0141039. *https://doi.org/10.1371/journal.pone.0141039*

AMP (2020). *Australian Marine Parks* website: *https://parksaustralia.gov.au/marine/science/science-under-the-surface/*

Andréfouët, S. (2011). Reef typology. In: *Encyclopedia of modern coral reefs—structure form and process* (Ed: Hopley, D.). Springer, Dordrecht

Andréfouët, S., Claereboudt, M., Matsakis, P., Pagès, J., and Dufour, P. (2001). Typology of atolls rims in Tuamotu archipelago (French Polynesia) at landscape scale using SPOT-HRV images. *International Journal of Remote Sensing*, 22, 98–1004.

Andréfouët, S., Muller-Karger, F.E., Robinson, J.A., Kranenburg, C.J., Torres-Pulliza, D., Spraggins, S.A., and Murch, B. (2006). Global assessment of modern coral reef extent and diversity for regional science and management applications: a view from space. In *Proceedings of the 10th International Coral Reef Symposium* (Vol. 2, pp. 1732–1745). ICRS.

Andréfouët, S., and Bionaz, O. (2021). Lessons from a global remote sensing mapping project. A review of the impact of the Millennium Coral Reef Mapping Project for science and management. *Science of the Total Environment*, 776, 145987.

Andrzejaczek, S., Gleiss, A.C., Lear, K.O., Pattiaratchi, C.B., Chapple, T.K., and Meekan, M.G. (2019). Biologging Tags Reveal Links Between Fine-Scale Horizontal and Vertical Movement Behaviors in Tiger Sharks (*Galeocerdo cuvier*). *Frontiers in Marine Science*, 14. *https://doi.org/10.3389/fmars.2019.00229*

Ashford, O.S., A.J. Kenny, C.R.B. Froján, M.B. Bonsall, T. Horton, A. Brandt, G.J. Bird, S. Gerken, and A.D. Rogers. (2018). Phylogenetic and functional evidence suggests that deep-ocean ecosystems are highly sensitive to environmental change and direct human disturbance. *Proceedings of the Royal Society B*, 285, 20180923.

Atkinson, M.J., and Grigg, R.W (1984). Model of coral reef ecosystem. II. Gross and net benthic primary production at French Frigate Shoals, Hawaii. *Coral Reefs*, 3, 13–22

Auricht, H.C.C., Clarke, K.D., Lewis, M.M., and Mosley, L.M. (2017). Have droughts and increased water extraction from the Murray River (Australia) reduced coastal ocean productivity? *Marine and Freshwater Research*, 69(3), 343–356. *https://doi.org/10.1071/MF17226*

Baird, M.E., Mongin, M., Skerratt, J., Margvelashvili, N., Tickell, S., Steven, A.D.L., Robillot, C., Ellis, R., Waters, D., Kaniewska, P., and Brodie, J. (2021). Impact of catchment loads of nutrients and sediments on marine water quality on the Great Barrier Reef: An application of the eReefs marine modelling system. *Marine Pollution Bulletin*, 167, 112297.

Bajjouk, T., Guillaumont, B., and Populus, J. (1996). Application of airborne imaging spectrometry system data to intertidal seaweed classification and mapping. *Hydrobiologia,* 326, 463–471. *https://doi.org/10.1007/BF00047847*

Bajjouk, T., Populus, J., and Guillaumont, B. (1998). Quantification of subpixel cover fractions using principal component analysis and a linear programming method: application to the coastal zone of Roscoff (France). *Remote Sensing of Environment*, 64(2), 153–165.

Bakun, A. (2006). Fronts and eddies as key structures in the habitat of marine fish larvae: Opportunity, adaptive response and competitive advantage. *Scientia Marina*, 70, 105–122.

Bayliss, P., and Hutton, M. (2017). *Integrating Indigenous knowledge and survey techniques to develop a baseline for dugong (Dugong dugon) management in the Kimberley*. Final Report of project 1.2.5 of the Kimberley Marine Research Program Node of the Western Australian Marine Science Institution, WAMSI, Perth, Western Australia, 98 p.

Benyoucef, I., Blandin, E., Lerouxel, A., Jesus, B., Rosa, P., Méléder, V., Launeau, P., Barillé, L. (2014). Microphytobenthos internanual variations in a north-European estuary (Loire estuary, France) detected by visible-infrared multispectral remote sensing. *Estuarine, Coastal and Shelf Science,* 136, 43–52.

Bicknell, A.W.J., B.J. Godley, E.V. Sheehan, S.C. Votier, and M.J. Witt. (2016). Camera technology for monitoring marine biodiversity and human impact. *Frontiers in Ecology and the Environment*, 14, 424–432.

Bierwirth, P.N., Lee, T.J., and Burne, R.V. (1993). Shallow sea-floor reflectance and water depth derived by unmixing multispectral imagery. *Photogrammetric Eng Remote Sensing*. 59, 331–338.

Bouchet, P., Phillips, C., Huang, Z., Meeuwig, J., Foster, S., and Przeslawski, R. (2018). *Comparative assessment of pelagic sampling methods used in marine monitoring*. Report to the National Environmental Science Programme, Marine Biodiversity Hub. 149 p. *https://www.nespmarine.edu.au/system/files/Bouchet%20et%20al%20Comparative%20assessment%20of%20pelgic%20sampling%20methods_Milestone%2015%20RPv3.pdf*

Bowden, D.A., and Jones, D.O.B. (2016). Towed cameras. In *Biological Sampling in the Deep Sea*. (Eds: M.R. Clark, M. Consalvey, and A. Rowden) pp. 260–284. John Wiley and Sons.

Boyd P.W., Kawaguchi, S. Strzepek, R. Meiners, K. Hallegraeff, G. McMinn, A., Swadling, K., and Reilly, D. (2019). *Report Card: Potential Tipping Points for life in the Southern Ocean*. Antarctic Climate and Ecosystems Cooperative Research Centre, Hobart, Australia. *http://dx.doi.org/10.25959/100.00031768*

Brito, A., Benyoucef, I., Jesus, B. Brotas, V., Gernez, P. , Mendes, C., Launeau, P., Dias, M., and Barillé, L. (2013). Seasonality of microphytobenthos revealed by remote-sensing in a South European estuary. *Continental Shelf Research,* 66, 83–91. 10.1016/j.csr.2013.07.004

Bunting, P., Rosenqvist, A., Lucas, R., Rebelo, L.-M., Hilarides, L., Thomas, N., Hardy, A., Itoh, T., Shimada, M., Finlayson, M. (2018). The global mangrove watch—a new 2010 global baseline of mangrove extent. *Remote Sensing*, 10 (10), 1669 doi:10.3390/rs10101669

Butler, A.J., Rees, T., Beesley, P., and Bax, N.J. (2010). Marine biodiversity in the Australian region. *Plos One*, 5(8), e11831.

Butler, C., Lucieer, V., Walsh, P., Flukes, E., and Johnson, C. (2017). *Seamap Australia [Version 1.0] the development of a national benthic marine classification scheme for the Australian continental shelf*. Seamap Australia, University of Tasmania. ISBN: 978-1-925646-61-0

Canonico, G., Buttigieg, P.L., Montes, E., Muller-Karger, F.E., Stepien, C., Wright, D., Benson, A., Helmuth, B., Costello, M., Sousa-Pinto, I., Saeedi, H., Newton, J., Appeltans, W., Bednaršek, N., Bodrossy, L., Best, B.D., Brandt, A., Goodwin, K.D., Iken, K., Marques, A.C., Miloslavich, P., Ostrowski, M., Turner, W., Achterberg, E.P., Barry, T., Defeo, O., Bigatti, G., Henry, L.-A., Ramiro-Sánchez, B., Durán, P., Morato, T., Roberts, J.M., García-Alegre, A., Cuadrado, M.S., and Murton, B. (2019). Global Observational Needs and Resources for Marine Biodiversity. *Frontiers in Marine Science*, 6, 367. doi: 10.3389/fmars.2019.00367

Carroll, A., Althaus, F., Beaman, R., Friedman, A., Ierodiaconou, D., Ingleton, T., Jordan, A., Linklater, M., Monk, J., Post, A., Przeslawski, R., Smith, J., Stowar, M., Tran, M., Tyndall, A. (2018). Marine sampling field manual for towed underwater camera systems. In *Field Manuals for Marine Sampling to Monitor Australian Waters* (Eds: Przeslawski, R., Foster, S.). National Environmental Science Programme (NESP). pp. 131–152.

CEOS (2018). *Feasibility Study for an Aquatic Ecosystem Earth Observing System*. (Eds: Dekker, A.G., and Pinnel, N.) CSIRO, Canberra.

Chassot, E., S. Bonhommeau, G. Reygondeau, K. Nieto, J.J. Polovina, M. Huret, N.K. Dulvy, and H. Demarcq. (2011). Satellite remote sensing for an ecosystem approach to fisheries management. *ICES Journal of Marine Science*, 68, 651–666.

Chirol, C., Haigh, I.D., Pontee, N., Thompson, C.E., and Gallop, S.L. (2018). Parametrizing tidal creek morphology in mature saltmarshes using semi-automated extraction from lidar. *Remote Sensing of Environment*, 209, 291–311. *https://doi.org/10.1016/j.rse.2017.11.012*

Cochran, S.A. (2013). Photography Applications. Ch 2 in *Coral Reef Remote Sensing*. (Eds: Goodman, J.A., Purkis, S.J., and Phinn, S.R.). Springer, Dordrecht. ISBN 978-90-481-9291-5

Commonwealth of Australia (1992). *National Strategy for Ecologically Sustainable Development*. AGPS, Canberra.

Constable, A.J., Melbourne-Thomas, J., Trebilco, R., Press, A.J., and Haward, M. (2017). *Position Analysis: Managing Change in Southern Ocean Ecosystems*. Antarctic Climate and Ecosystems Cooperative Research Centre, Hobart, Australia. 39 p. *http://acecrc.org.au/wp-content/uploads/2017/10/2017-ACECRC-Position-Analysis-Southern-Ocean-Ecosystems.pdf*

Cougo, M.F., Souza-Filho, P.W.M., Silva, A.Q., Fernandes, M.E.B., dos Santos, J.R., Abrew, M.R.S., Nascimento, W.R., and Simard, M. (2015). Radarsat-2 Backscattering for the Modeling of Biophysical Parameters of Regenerating Mangrove Forests. *Remote Sensing*, 7(12), 17097–17112. *https://doi.org/10.3390/rs71215873*

Cury, P.M., Y.-J. Shin, B. Planque, J.M. Durant, J.-M. Fromentin, S. Kramer-Schadt, N.C. Stenseth, M. Travers, and V. Grimm. (2008). Ecosystem oceanography for global change in fisheries. *Trends in ecology and evolution*, 23, 338–346.

Daly, T. (2013). *Coastal saltmarsh*. Primefact 1256. NSW Department of Primary Industry, Sydney. *http://www.dpi.nsw.gov.au/__data/assets/pdf_file/0007/459628/Coastal-Saltmarsh-Primefact.pdf*

DAWE (2020). *Wetlands* webpage, Department of Agriculture, Water and the Environment website: *https://www.environment.gov.au/wetlands*

De Jong, D.J., and de Jonge, V.N. (1995). Dynamics and distribution of microphytobenthic chlorophyll-a in the Western Scheldt estuary (SW Netherlands). *Hydrobiologia,* 311, 21–30.

Dekker, A.G., Brando, V.E., Anstee, J.M., Pinnel, N., Kutser, T., Hoogen-boom, J., Peters, S.W.M., Pasterkamp, R., Vos, R.J., Olbert, C., and Malthus, T.J. (2001). Imaging spectrometry of water. Ch 11 in *Imaging Spectrometry: Basic Principles and Prospective Applications*. (Eds: F.D. van der Meer and S.M. de Jong), pp 307–359. Kluwer Academic Publishers, Dordrecht, The Netherlands.

Dekker, A.G., Phinn, S.R., Anstee, J., Bissett, P., Brando, V.E., Casey, B., Fearns, P., Hedley, J., Klonowski, W., Lee, Z.P., Lynch, M., Lyons, M., Mobley, C., and Roelfsema, C. (2011). Inter-comparison of shallow water bathymetry, hydrooptics, and benthos mapping techniques in Australian and Caribbean coastal environments. *Limnology and Oceanography Methods*, 9, 396–425

Dower, J., Freeland, H., and Juniper, K. (1992). A Strong Biological Response to Oceanic Flow past Cobb Seamount. *Deep-Sea Research Part A-Oceanographic Research Papers*, 39, 1139–1145.

Doxaran, D., Bustamante, J., Dogliotti, A.I., Malthus, T.J., and Senechal, N. (2019). Editorial for the Special Issue "Remote Sensing in Coastal Zone Monitoring and Management—How Can Remote Sensing Challenge the Broad Spectrum of Temporal and Spatial Scales in Coastal Zone Dynamic?" *Remote Sensing*, 11, 1028. doi:10.3390/rs11091028

Dunk, I., and Lewis. M.R. (1999). Seagrass and shallow water feature discrimination using Hymap Imagery. *10*th *Australian Remote Sensing and Photogrammetry Conference*. University of Adelaide., Australia.

Durden, J., T. Schoening, F. Althaus, A. Friedmann, R. Garcia, A. G. Glover, J. Greinert, N. J. Stout, D. O. Jones, and A. Jordt. (2016). Perspectives in visual imaging for marine biology and ecology: from acquisition to understanding. *Oceanography and Marine Biology: An Annual Review*, 54, 1–72. CRC Press, Boca Raton, US. doi:10.1201/9781315368597

Dutkiewicz, S., Hickman, A. E., Jahn, O., Henson, S., Beaulieu C., and Monier, E. (2019). Ocean colour signature of climate change. *Nature Communications*, 10, 578.

Dwyer, R.G., Brooking, C., Brimblecombe, W., Campbell, H.A., Hunter, J., Watts, M., Franklin, C.E. (2015). An open Web based system for the analysis and sharing of animal tracking data. *Animal Biotelemetry*, 3(1), 1–11. doi:10.1186/s40317-014-0021-8.

Edwards, M., and Richardson, A.J. (2004). The impact of climate change on the phenology of the plankton community and trophic mismatch. *Nature*, 430, 881–884.

Enever, R., Lewin, S., Reese, A., and Hooper, T. (2017). Mapping fishing effort: Combining fishermen's knowledge with satellite monitoring data in English waters. *Fisheries Research*, 189, 67–76.

Eveson, J.P., Hobday, A.J., Hartog, J.R., Spillman, C.M., and Rough, K.M. (2015). Seasonal forecasting of tuna habitat in the Great Australian Bight. *Fisheries Research*, 170, 39–49.

FAO (2007). *The State of the World's Fisheries and Aquaculture 2006*. FAO Fisheries and Aquaculture Department, Food and Agriculture Organisation of the United Nations, Rome, 2007. 180 p.

FAO (2018). *Technical guidelines on methodologies and indicators for the estimation of the magnitude and impact of illegal, unreported and unregulated (IUU) fishing. Volume 2—Guiding Principles and Approaches*. Version 1 draft. UN Food and Agriculture Organisation, Rome.

Farris, A.S., Defner, Z., and Ganju, N.K. (2019). Identifying salt marsh shorelines from remotely sensed elevation data and imagery. *Remote Sensing*, 11, 1795. doi:10.3390/rs11151795

Fernandez-Nunez, M., Burningham, H., and Ojeda Zujar, J. (2017). Improving accuracy of LiDAR-derived digital terrain models for saltmarsh management. *Journal of Coastal Conservation*, 21, 209–222. *https://doi.org/10.1007/s11852-016-0492-2*

Fretwell, P.T., and Trathan, P.N. (2009). Penguins from space: faecal stains reveal the location of emperor penguin colonies. *Global Ecology and Biogeography*, 18, 543–552.

Fretwell, P.T., LaRue, M.A., Morin, P., Kooyman, G.L., Wienecke, B., Ratcliffe, N., Fox, A.J., Fleming, A.H., Porter, C., and Trathan, P.N. (2012). An emperor penguin population estimate: the first global, synoptic survey of a species from space. *PloS One*, 7, e33751.

Fretwell, P.T., Staniland, I.J., and Forcada, J. (2014). Whales from space: counting southern right whales by satellite. *PloS One*, 9, e88655.

Furnas, M. (2003). *Catchments and Corals. Terrestrial Runoff to the Great Barrier Reef*. AIMS, Townsville. 334pp.

Fyfe, S.K. (2003). Spatial and temporal variation in spectral reflectance: Are seagrass species spectrally distinct? *Limnology and Oceanography*, 48, 464–479.

GA (2020a). *Australia's Coasts and Estuaries* webpage, Geoscience Australia website: *https://www.ga.gov.au/scientific-topics/marine/coasts-estuaries*

GA (2020b). *Oceans and Seas* webpage, Geoscience Australia website: *http://www.ga.gov.au/scientific-topics/national-location-information/dimensions/oceans-and-seas*

Gao, B.C., Montes, M.J., Davis, C.O., and Goetz, A.F.H. (2009). Atmospheric correction algorithms for hyperspectral remote sensing data of land and ocean. *Remote Sensing of Environment*, 113, S17–S24

Garcia, R.A., Lee, Z., and Hochberg, E.J. (2018). Hyperspectral Shallow-Water Remote Sensing with an Enhanced Benthic Classifier. *Remote Sensing*, 10, 147. doi:10.3390/rs10010147

Garde, L.A., Spillman, C.M., Majewski, L., Griffin, C., Kruger, G., and Beggs, H. (2013), *ReefTemp Next Generation*. Centre for Australian Weather and Climate Research (CAWCR) Technical Report, No 063. 44 p.

Garde, L.A., Spillman, C.M., Heron, S.F., and Beeden, R.J. (2014). Reef Temp Next Generation: A new operational system for monitoring reef thermal stress. *Journal of Operational Oceanography*, 7, 21–33.

Giri, C.. Ochieng, E., Tieszen, L.L., Zhu, Z., Singh, A., Loveland, T., Masek, J., and Duke, N. (2011). Status and distribution of mangrove forests of the world using earth observation satellite data. *Global Ecology and Biogeography*, 20, 154–159. doi:10.1111/j.1466-8238.2010.00584.x

Gohin, F., B. Saulquin, H. Oger-Jeanneret, L. Lozac'h, L. Lampert, A. Lefebvre, P. Riou, and F. Bruchon. (2008). Towards a better assessment of the ecological status of coastal waters using satellite-derived chlorophyll-a concentrations. *Remote Sensing of Environment*, 112, 3329–3340.

Goodman, J., and Ustin, S.L. (2007) Classification of benthic composition in a coral reef environment using spectral unmixing. *Journal of Applied Remote Sensing*, 1(1), 011501.

Goodman, J.A., Purkis, S.J., and Phinn, S.R. (2013). *Coral Reef Remote Sensing: A guide for mapping, monitoring and management*. Springer, Dordrecht. doi:10.1007/978-90-481-9292-2

Gordon, H.R. (1997) Atmospheric correction of ocean color imagery in the Earth observing system era. *Journal of Geophysical Research: Atmosphere*, 102, 17081–17106.

Gordon, H.R., and Clark, D.K. (1980). Atmospheric effects in the remote sensing of phytoplankton pigments. *Boundary-Layer Meteorology*, 18, 299–313.

Gredzens, C., Marsh, H., Fuentes, M.M.P.B., Limpus, C.J., Shimada, T., and Hamann, M. (2014). Satellite Tracking of Sympatric Marine Megafauna Can Inform the Biological Basis for Species Co-Management. *PloS ONE*, 9(6), E98944. *https://doi.org/10.1371/journal.pone.0098944*

Hamylton, S.M. (2017). Mapping coral reef environments: A review of historical methods, recent advances and future opportunities. *Progress in Physical Geography*, 41(6), 803–833.

Hardman-Mountford, N. J., Hirata, T., Richardson, K.A., and Aiken, J. (2008). An objective methodology for the classification of ecological pattern into biomes and provinces for the pelagic ocean. *Remote Sensing of Environment*, 112, 3341–3352.

Harrison, B.A., and Jupp, D.L.B. (1990). *Introduction to Image Processing: Part TWO of the microBRIAN Resource Manual*. CSIRO, Melbourne. 256pp.

Harrison, D.P., Hinton, M.G., Kohin, S., Armstrong, E.M., Snyder, S., O'Brien, F., and Kiefer, D.K. (2017). The pelagic habitat analysis module for ecosystem-based fisheries science and management. *Fisheries Oceanography*, 26, 316–335.

Harvey, N., and Caton, B. (2010). *Coastal Management in Australia*. University of Adelaide Press, Adelaide.

Haynes, T.A. (2016). *Scottish saltmarsh survey national report*. Scottish Natural Heritage Commissioned Report No. 786. ISBN 978-0-9807230-3-8

Hazen, E.L., Palacios, D.M., Forney, K.A., Howell, E.A., Becker, E., Hoover, A.L., Irvine, L., DeAngelis, M., Bograd, S.J., Mate, B.R., and Bailey, H. (2017). WhaleWatch: a dynamic management tool for predicting blue whale density in the California Current. *Journal of Applied Ecology*, 54, 1415–1428.

Hazen, E.L., Scales, K.L., Maxwell, S.M., Briscoe, D.K., Welch, H., Bograd, S.J., Bailey, H., Benson, S.R., Eguchi, T., Dewar, H., Kohin, S., Costa, D.P., Crowder, L.B., and Lewison, R.L. (2018). A dynamic ocean management tool to reduce bycatch and support sustainable fisheries. *Science Advances*, 4(5). *https://doi.org/10.1126/sciadv.aar300*

Hedley, J. (2013). Hyperspectral Applications. Ch 4 in *Coral Reef Remote Sensing*. (Eds: Goodman, J.A., Purkis, S.J., and Phinn, S.R.). Springer, Dordrecht. ISBN 978-90-481-9291-5.

Hedley, J.D., and Mumby, P.J. (2002). Biological and remote sensing perspectives of pigmentation in coral reef organisms. *Advances in Marine Biology*, 43, 277–317.

Hedley, J.D., and Mumby, P.J. (2003). A remote sensing method for resolving depth and subpixel composition of aquatic benthos. *Limnology and Oceanography*, 48, 480–488

Hedley, J.D., Mumby, P.J. Joyce, K.E., and Phinn S.R. (2004). Spectral unmixing of coral reef benthos under ideal conditions. *Coral Reefs*, 23, 60–73.

Hedley, J.D., Roelfsema, C.M., Phinn, S.R., and Mumby, P.J. (2012). Environmental and Sensor Limitations in Optical Remote Sensing of Coral Reefs: Implications for Monitoring and Sensor Design. *Remote Sensing*, 4, 271–302. doi:10.3390/rs4010271

Hedley, J.D., Chollet-Ordaz, I., Harborne, A.R., Roelfsema, C., Skirving, E., Strong, A., Christensen, T., Eakin, Dwight, M., Ticzon, V., Bejarano, S., and Mumby, P.J. (2016a). Current Operational Remote Sensing Technologies For Coral Reef Monitoring And Management: A Review. *Remote Sensing*, 8, 118. doi:10.3390/rs8020118

Hedley, J.D., Roelfsema, C.M., Chollett, I., Harborne, A.R., Heron, S.F., Weeks, S.J., Skirving, W.J., Strong, A.E., Eakin, C.M., Christensen, T.R.L., Ticzon, V., Bejarano, S., and Mumby, P.J. (2016b). Remote Sensing of Coral Reefs for Monitoring and Management: A Review. *Remote Sensing*, 8, 118.

Hedley, J.D., Roelfsema, C., Brando, V., Giardino, G., Kutser, T., Phinn, S., Mumby, P.J., Barrilero, O., Laporte, J., and Koetz, B. (2018). Coral reef applications of Sentinel-2: Coverage, characteristics, bathymetry and benthic mapping with comparison to Landsat 8. *Remote Sensing of Environment*, 216, 598–614. *https://doi.org/10.1016/j.rse.2018.07.014*

Henson, S.A., Cole, H.S., Hopkins, J., Martin, A.P., and Yool, A. (2017). Detection of climate change-driven trends in phytoplankton phenology. Global Change Biology, 24(1), e101–e111. *https://doi.org/10.1111/gcb.13886*

Hernández-Cruz, L.R., Purkis, S.J., and Riegl, B.M. (2006). Documenting decadal spatial changes in seagrass and Acropora palmata cover by aerial photography analysis in Vieques, Puerto Rico: 1937–2000. *Bulletin of Marine Science*, 79(2), 401–404.

Hladik, C., Schalles, J., and Alber, M. (2013). Salt marsh elevation and habitat mapping using hyperspectral and LIDAR data. *Remote Sensing of Environment*, 139, 318–330.

Hobday A.J., Hartog, J.R., Timmiss, T., and Fielding, J. (2010). Dynamic spatial zoning to manage southern bluefin tuna (*Thunnus maccoyii*) capture in a multi-species longline fishery. *Fisheries Oceanography*, 19, 243–253.

Hobday, A., Young, J., Moeseneder, C., and Dambacher, J. (2011). Defining dynamic pelagic habitats in oceanic waters off eastern Australia. *Deep Sea Research Part II: Topical Studies in Oceanography*, 58, 734–745.

Hochberg, E.J., and Atkinson, M.J. (2000). Spectral discrimination of coral reef benthic communities. *Coral Reefs*, 19, 164–171

Hochberg, E.J., and Atkinson, M.J. (2008). Coral reef benthic productivity based on optical absorptance and light-use efficiency. *Coral Reefs*, 27, 49–59.

Hochberg, E.J., Atkinson, M.J., and Andrefouet, S. (2003) Spectral reflectance of coral reef bottom-types worldwide and implications for coral reef remote sensing. *Remote Sensing of Environment*, 85, 159–173.

Hochberg, E.J., Atkinson, M.J., Apprill, A., and Andréfouët, S. (2004). Spectral reflectance of coral. *Coral Reefs*, 23, 84–95.

Hodgson, A., Peel, D., and Kelly, N. (2017). Unmanned aerial vehicles for surveying marine fauna: assessing detection probability. *Ecological Applications*, 27(4), 1253–1267. *https://doi.org/10.1002/eap.1519*

Hoepffner, N., and Zibordi, G. (2009). Remote sensing of Coastal Waters. In *Encyclopedia of Ocean Sciences* (2nd edn), pp. 732–741. Academic Press.

Holden, H., and LeDrew, E. (1998). Spectral discrimination of healthy and non-healthy corals based on cluster analysis, principal components analysis, and derivative spectroscopy. *Remote Sensing of Environment*, 65, 217–224.

Holden, H., and LeDrew, E. (1999). Hyperspectral identification of coral reef features. *International Journal of Remote Sensing*, 13, 2545–2563.

Howell, E.A., Kobayashi, D.R., Parker, D.M., Balazs, G.H., and Polovina, J.J. (2008). TurtleWatch: a tool to aid in the bycatch reduction of loggerhead turtles Caretta caretta in the Hawaii-based pelagic longline fishery. *Endangered Species Research*, 5, 267–278. doi: 10.3354/esr00096

Howell, E.A., Hoover, A., Benson, S.R., Bailey, H., Polovina, J.J., Seminoff, J.A., and Dutton, P.H. (2015). Enhancing the TurtleWatch product for leatherback sea turtles, a dynamic habitat model for ecosystem-based management. *Fisheries Oceanography*, 24(1), 57–68. *https://doi.org/10.1111/fog.12092*

Hussey, N.E., Kessel, S.T., Aarestrup, K., Cooke, S.J., Cowley, P.D., Fisk, A.T., Harcourt, R.G., Holland, K.N., Iverson, S.J., Kocik, J.F., Mills Flemming, J.E., and Whoriskey, F.G. (2015). Aquatic animal telemetry: A panoramic window into the underwater world. *Science*, 348(6240), 1255642. doi:10.1126/science.1255642

Hyrenback, D., Forney, K.A., and Dayton, P. (2000). Marine Protected Areas and ocean basin management. Aquatic Conservation Marine and Freshwater Ecosystems, 10(6), 437–458.

IOCCG (2009). *Remote Sensing in Fisheries and Aquaculture*. (Eds: Forget, M.-H., Stuart, V. and Platt, T.). Reports of the International Ocean-Colour Coordinating Group, No. 8. IOCCG, Dartmouth, Canada. *http://ioccg.org/wp-content/uploads/2015/10/ioccg-report-08.pdf*

IOCCG (2014). *Phytoplankton functional types from space*, Reports of the International Ocean Color Coordinating Group, No. 15,. IOCCG, Dartmouth, NS.

IUCN (2017). *Mangroves: nurseries for the world's seafood supply* webpage, International Union for Conservation of Nature website: *https://www.iucn.org/news/forests/201708/mangroves-nurseries-world%E2%80%99s-seafood-supply*

Jupp, D.L.B., Mayo, K.K., Kuchler, D.A., Claasen, D.V.R., Kenchington, R.A., and Guerin, P.R. (1985). Remote sensing for planning and managing the Great Barrier Reef of Australia. *Photogrammetria,* 40, 21–42.

Kacev, D., and Lewison, R.L. (2016). Satellite remote sensing in support of fisheries management in global oceans. In *Earth Science Satellite Applications*, pp. 207–222. (Ed: Hossain, F.), Springer Remote Sensing/Photogrammetry. Springer. 284 p.

Kachelriess, D., Wegmann, M., Gollock, M., and Pettorelli, N. (2014). The application of remote sensing for marine protected area management. *Ecological Indicators*, 36, 169–177.

Kamal, M., Phinn, S., and Johansen, K. (2015). Object-Based Approach for Multi-Scale Mangrove Composition Mapping Using Multi-Resolution Image Datasets. *Remote Sensing*, 7, 4753–4783. doi:10.3390/rs70404753

Karpouzli, E., Malthus, T.J., and Place, C.J. (2004). Hyperspectral discrimination of coral reef benthic communities in the western Caribbean. *Coral Reefs*, 23, 141–151. doi:10.1007/s00338-003-0363-9

Kavanaugh, M.T., Oliver, M.J., Chavez, F.P., Letelier, R.M., Muller-Karger, F.E., and Doney, S.C. (2016). Seascapes as a new vernacular for pelagic ocean monitoring, management and conservation. *ICES Journal of Marine Science*, 73, 1839–1850.

Kennedy, E.V., Roelfsema, C.M., Lyons, M.B., Kovacs, E.M., Borrego-Acevedo, R., Roe, M., Phinn, S.R., Larsen, K., Murray, N.J., Yuwono, D., and Wolff, J. (2021). Reef Cover, a coral reef classification for global habitat mapping from remote sensing. *Scientific Data*, 8, 196. *https://doi.org/10.1038/s41597-021-00958-z*

Kirk, J.T.O. (1994). *Light and Photosynthesis in Aquatic Ecosystems*, 2nd Edn. Cambridge University Press, Cambridge. 509 p.

Kirk, J.T.O. (2010). *Light and Photosynthesis in Aquatic Ecosystems*, 3rd Edn. Cambridge University Press, Cambridge. 662 p.

Klemas, V. (2013). Fisheries applications of remote sensing: An overview. *Fisheries Research*, 148, 124–136.

Kobryn, H.T., Wouters, K., Beckley, L.E., and Heege, T. (2013). Ningaloo Reef: Shallow Marine Habitats Mapped Using a Hyperspectral Sensor. *PLOS One*, 8(7), e70105. doi:10.1371/journal.pone.0070105

Kovacs, E., Roelfsema, C., Lyons, M., Zhao, S., and Phinn, S. (2018). Seagrass habitat mapping: how do Landsat 8 OLI, Sentinel-2, ZY-3A, and Worldview-3 perform? *Remote Sensing Letters*, 9(7), 686–695. *https://doi.org/10.1080/2150704X.2018.1468101*

Kuenzer, C., Bluemel, A., Gebhardt, S., Vo Quoc, T., and Dech, S. (2011). Remote sensing of mangrove ecosystems: a review. *Remote Sensing*, 3, 878–928. doi:10.3390/rs3050878

Kulawardhana, R.W., Popescu, S.C., and Feagin, R.A. (2014). Fusion of lidar and multispectral data to quantify salt marsh carbon stocks. *Remote Sensing of Environment*, 154, 345–357.

Kurekin, A.A., Loveday, B.R., Clements, O., Quartly, G.D., Miller, P.I., Wiafe, G., and Adu Agyekum, K. (2019). Operational Monitoring of Illegal Fishing in Ghana through Exploitation of Satellite Earth Observation and AIS Data. *Remote Sensing*, 11, 293.

Kutser, T., Parslow, J., Clementson, L., Skirving, W., Done, T., Wakeford, M., and Miller, I. (2000). Hyperspectral detection of coral reef bottom types. *Ocean Optics XV*. Monaco.

Kutser, T., Herlevi, A., Kallio, K., and Arst, H. (2001). A hyperspectral model for interpretation of passive optical remote sensing data from turbid lakes. *The Science of the Total Environment*, 268(1–3), 47–58.

Kutser, T., Dekker, A.G., and Skirving, W. (2003). Modeling spectral discrimination of Great Barrier Reef benthic communities by remote sensing instruments. *Limnology and Oceanography*, 48, 497–510.

Laengner, M.L., Siteur, K., and van der Wal, D. (2019). Trends in the Seaward Extent of Saltmarshes across Europe from Long-Term Satellite Data. *Remote Sensing*, 11, 1653. doi:10.3390/rs11141653

LaRue, M.A., Rotella, J.J., Garrott, R.A., Siniff, D.B., Ainley, D.G., Stauffer, G.E., Porter, C.C., and Morin, P.J. (2011). Satellite imagery can be used to detect variation in abundance of Weddell seals (*Leptonychotes weddellii*) in Erebus Bay, Antarctica. *Polar Biology*, 34, 1727.

Larkum, A.W., Kendrick, G.A. and Ralph, P.J. (Eds.) (2018). *Seagrasses of Australia: structure, ecology and conservation*. Springer.

Lawrence, E., Hayes, K., Lucieer, V., Nichol, S., Dambacher, J., and Hill, N. (2015). Mapping Habitats and Developing Baselines in Offshore Marine Reserves with Little Prior Knowledge: A Critical Evaluation of a New Approach. *PloS ONE*, 10, e0141051.

Lee, Z., Carder, K.L., Mobley, C.D., Steward, R.G., and Patch, J.S. (1999). Hyperspectral remote sensing for shallow waters. 2. Deriving bottom depths and water properties by optimization. *Applied Optics*, 38, 3831–3843

Leiper, I., Phinn, S., and Dekker, A.G. (2012). Spectral reflectance of coral reef benthos and substrate assemblages on Heron Reef, Australia. *International Journal of Remote Sensing*, 33(12), 3946–3965. doi: 10.1080/01431161.2011.637675

Lemos, A.T., Ghisolfi, R.D.R., and Mazzini, P.L.F. (2018). Annual phytoplankton blooming using satellite-derived chlorophyll-a data around the Vitoria-Trindade Chain, Southeastern Brazil. *Deep-Sea Research Part I-Oceanographic Research Papers*, 136, 62–71.

Lennox, R.J., Aarestrup K., Cooke S.J., Cowley P.D., Deng Z.D., and Fisk A.T. (2017). Envisioning the future of aquatic animal tracking: Technology, science, and application. *BioScience*, 67(10), 884–896.

Lennox, R.J., Engler-Palma, C., Kowarski, K., Filous, A., Whitlock, R., Cooke, S.J., and Auger-Méthé, M. (2019). Optimizing marine spatial plans with animal tracking data. *Canadian Journal of Fisheries and Aquatic Science*, 76(3), 497–509. *https://doi.org/10.1139/cjfas-2017-0495*

Lesser, M.P., and Mobley, C.D. (2007). Bathymetry, water optical properties, and benthic classification of coral reefs using hyperspectral remote sensing imagery. *Coral Reefs*, 26(4), 819–829.

Liu, G., Skirving, W.J., Geiger, E.F., De La Cour, J.L., Marsh, B.L., Heron, S.F., Tirak, K.V., Strong, A.E., and Eakin, C.M. (2017). NOAA Coral Reef Watch's 5km Satellite Coral Bleaching Heat Stress Monitoring Product Suite Version 3 and Four-Month Outlook Version 4. *Reef Encounter*, 32(1), 39–45.

Louchard, E.M., Reid, P., Stephens, C., Davis, C.O., Leathers, R.A., and Downes, V. (2003). Optical remote sensing of habitats and bathymetry in coastal environments at Lee Stocking Island, Bahamas. A comparative spectral classification approach. *Limnology and Oceanography*, 48, 511–521.

Louchard, E.M., Reid, R.P., and Stephens, C.F. (2000). Classification of sediment types and estimation of water depth using spectral libraries. *Ocean Optics XV*. Monaco.

Lowther, A.D., Harcourt, R.G., Page, B., and Goldsworthy, S.D. (2013). Steady as He Goes: At-Sea Movement of Adult Male Australian Sea Lions in a Dynamic Marine Environment. *PloS ONE*, 8(9), e74348. doi:10.1371/journal.pone.0074348

Lucas, R., Rebelo, L.-M., Fatoyinbo, L., Rosenqvist, A., Itoh, T., Shimada, M., Simard, M., Souza-Filho, P.W., Thomas, N., Trettin, C., Accad, A., Carreiras, J., and Hilarides, L. (2014). Contribution of L-band SAR to systematic global mangrove monitoring. *Marine and Freshwater Research*, 65, 589–603. doi:10.1071/MF13177

Lucieer, V., Picard, K., Siwabessy, J., Jordan, A., Tran, M., and Monk, J. (2018). Seafloor mapping field manual for multibeam sonar. In *Field Manuals for Marine Sampling to Monitor Australian Waters* (Eds: Przeslawski, R., and Foster, S.), pp 42–64. National Environmental Science Programme (NESP).

Lymburner, L., Bunting, P., Lucas, R., Scarth, P., Alam, I., Phillips, C., Ticehurst, C., and Held, A. (2020). Mapping the multi-decadal mangrove dynamics of the Australian coastline. *Remote Sensing of Environment*, 238, 111185. *https://doi.org/10.1016/j.rse.2019.05.004*

Lynch, H.J., White, R., Black, A.D., and Naveen, R. (2012). Detection, differentiation, and abundance estimation of penguin species by high-resolution satellite imagery. *Polar Biology*, 35, 963–968.

Lyons, M.B., Phinn, S.R., and Roelfsema, C.M. (2012). Long term land cover and seagrass mapping using Landsat and object-based image analysis from 1972 to 2010 in the coastal environment of South East Queensland, Australia. *ISPRS Journal of Photogrammetry and Remote Sensing*, 71, 34–46. doi: 10.1016/j.isprsjprs.2012.05.002

Lyons, M., Roelfsema, C.M., Kennedy, E.V., Kovacs, E.M., Borrego-Acevedo, R., Markey, K., Roe, M., Yuwono, D.M., Harris, D.L., Phinn, S.R., Asner, G., Li, J., Knapp, D.E., Fabina, N.S., Larsen, K., Traganos, D., and Murray, N.J. (2020). Mapping the world's coral reefs using a global multiscale earth observation framework. *Frontiers in Ecology and the Environment*, 6(4), 557–568. *https://doi.org/10.1002/rse2.157*

Lyzenga, D.R. (1978) Passive remote sensing techniques for mapping water depth and bottom features. *Applied Optics*, 17, 379–383.

Lyzenga, D.R. (1985), Shallow-water bathymetry using combined lidar and passive multispectral scanner data. *International Journal of Remote Sensing*, 6, 115–125.

Macreadie, P., Ollivier, Q., Kelleway, J., Kelleway, J.J., Serrano, O., Carnell, P.E., Ewers Lewis, C.J., Atwood, T.B., Sanderman, J., Baldock, J., Connolly, R.M., Duarte, C.M., Lavery, P.S., Steven, A., and Lovelock, C.E. (2017). Carbon sequestration by Australian tidal marshes. *Scientific Reports*, 7, 44071. *https://doi.org/10.1038/srep44071*

Maina, J., Venus, V., McClanahan, T.R., and Ateweberhan, M. (2008). Modelling susceptibility of coral reefs to environmental stress using remote sensing data and GIS models. *Ecological Modeling*, 212, 180–199.

Malthus, T.J., and George, D.G. (1997). Airborne remote sensing of macrophytes in Cefni Reservoir, Anglesey, UK. Aquatic Botany, 58, 317–332

MangroveWatch (2021). *Mangrove Watch* website: *http://mangrovewatch.org.au/*

Marsh, H., and Rathbun, G.B. (1990). Development and Application of Conventional and Satellite Radio Tracking Techniques for Studying Dugong Movements and Habitat Use. *Australian Wildlife Research* 17, 83–100.

McClain, C.R. (2009). A decade of satellite ocean color observations. *Annual Review of Marine Science*, 1, 19-42.

Mcleod, E., Chmura, G.L., Bouillon, S., Salm, R., Björk, M., Duarte, C.M., Lovelock, C.E., Schlesinger, W.H., and Silliman, B.R. (2011). A blueprint for blue carbon: toward an improved understanding of the role of vegetated coastal habitats in sequestering CO_2. *Frontiers in Ecology and the Environment*, 9, 552–560. doi:10.1890/110004

McMahon, C.R., Howe, H., van den Hoff, J., Alderman, R., Brolsma, H., and Hindell, M.A. (2014). Satellites, the all-seeing eyes in the sky: counting elephant seals from space. *PloS One*, 9, e92613.

Méléder, V., Barille, L., Launeau, P., Carrere, V., and Rince, Y. (2003). Spectrometric constraint in analysis of benthic diatom biomass using monospecific cultures 10.1016/j.rse.2003.08.009. *Remote Sensing of Environment*, 88(4), 386–400.

Meza Diaz, B., and Blackburn, G.A. (2003). Remote sensing of mangrove biophysical properties: Evidence from a laboratory simulation of the possible effects of background variation on spectral vegetation indices. *International Journal of Remote Sensing*, 24, 53–73.

Monbet, Y. (1992). Control of Phytoplankton Biomass in Estuaries: A comparative analysis of microtidal and macrotidal estuaries. *Estuaries,* 15(4), 563–571.

Mumby, P.J., and Harborne, A.R. (1999). Development of a systematic classification scheme of marine habitats to facilitate regional management and mapping of Caribbean coral reefs. *Biological Conservation*, 88, 155–163.

Mumby, P.J., Green, E.P., Edwards, A.J., and Clark, C.D. (1997a). Coral reef habitat-mapping: how much detail can remote sensing provide? *Marine Biology*, 130, 193–202.

Mumby, P.J., Green, E.P., Edwards, A.J., and Clark, C.D. (1997b). Measurement of seagrass standing crop using satellite and digital airborne remote sensing. *Marine Ecology Progress Series*, 159, 51–60.

Mumby, P.J., Edwards, A.J., Arias-Gonzalez, J.E., Lindeman, K.C., Blackwell, P.G., Gall, A., Gorczynska, M.I., Harborne, A.R., Pescod, C.L., Renken, H., Wabnitz, C.C.C., and Llewellyn, G. (2004). Mangroves enhance the biomass of coral reef fish communities in the Caribbean. *Nature*, 427, 533–536.

Navarro, A., Young, M., Macreadie, P.I., Nicholson, E., and Ierodiaconou, D. (2021). Mangrove and Saltmarsh Distribution Mapping and Land Cover Change Assessment for South-Eastern Australia from 1991 to 2015. *Remote Sensing*, 13(8), 1450. *https://doi.org/10.3390/rs13081450*

NHT (undated). *Australia's Marine Protected Areas: Protecting our coasts and oceans*. Brochure published by National Heritage Trust: *https://parksaustralia.gov.au/marine/pub/scientific-publications/archive/nrsmpa-protect.pdf*

NMSC (2015). *National Marine Science Plan 2015–2025: Driving the development of Australia's blue economy. National Marine Science Committee*. ISBN 978-1-925012-02-6. *https://www.marinescience.net.au/wp-content/uploads/2018/06/National-Marine-Science-Plan.pdf*

NSW EPA (2017). *Coastal, estuarine and marine ecosystems, State of the Environment 2015* webpage, NSW Environmental Protection Agency website: *https://www.epa.nsw.gov.au/about-us/publications-and-reports/state-of-the-environment/state-of-the-environment-2015/20-coastal-estuarine-marine-ecosystems*

Oceana (2021). *Marine science and Ecosystems Coral Reef* webpage, Oceana website: *https://oceana.org/marine-life/marine-science-and-ecosystems/coral-reef*

Ouellette, W., and Getinet, W. (2016). Remote sensing for Marine Spatial Planning and Integrated Coastal Areas Management: Achievements, challenges, opportunities and future prospects. *Remote Sensing Applications: Society and Environment*, 4, 138–157.

OzCoasts (2020). *Changes in biodiversity* webpage, Australian Online Coastal Information website: *https://ozcoasts.org.au/indicators/coastal-issues/declining_biodiversity/*

Palandro, D.A., Andréfouët, S., Hu, C., Hallock, P., Muller-Karger, F.E., Dustan, P., Callahan, M.K., Kranenburg, C., and Beaver, C.R. (2008). Quantification of two decades of shallow-water coral reef habitat decline in the Florida Keys National Marine Sanctuary using Landsat data (1984–2002). *Remote Sensing of Environment*, 112, 3388–3399

Parks Australia (2021). *Australian Marine Parks* webpage, Parks Australia website: *https://parksaustralia.gov.au/marine/parks/*

Paterson, D.M., Doerffer, R., Kromkamp, J., Morgan, G., and Gieske, W., (1998). Assessing the biological and physical dynamics of intertidal sediment ecosystems: a remote sensing approach. In *Proceedings of Third European Marine Science and Technology Conference (MAST Conference)*, Lisbon, 23–27 May 1998 (Eds: Barthel *et al.*), Project Synopses vol. I, pp. 377–390.

Payne, M.R., Hobday, A.J., MacKenzie, B.R., Tommasi, D., Dempsey, D.P., Fässler, S.M., Haynie, A.C., Ji, R., Liu, G., and Lynch, P.D. (2017). Lessons from the first generation of marine ecological forecast products. *Frontiers in Marine Science*, 4, 289.

Paynter, I., Schaaf, C., Bowen, J.L., Deegan, L., Peri, F., and Cook, B. (2019). Characterizing a New England Saltmarsh with NASA G-LiHT Airborne Lidar. *Remote Sensing*, 11(5), 509. *https://doi.org/10.3390/rs11050509*

Pennesi, C., Rindi, F., Totti, C., and Beolchini, F. (2015). Marine Macrophytes: Biosorbents. In: *Springer Handbook of Marine Biotechnology*. (Ed: Kim, S.K.) Springer Handbooks. Springer, Berlin, Heidelberg.

Phinn, S., Roelfsema, C., Kovacs, E., Canto, R., Lyons, M., Saunders, M., and Maxwell, P. (2018). Mapping, Monitoring and Modelling Seagrass Using Remote Sensing. Ch 15 in *Seagrasses of Australia* (Ed: Larkum, A.W.D. *et al.*) Springer International Publishing. https://doi.org/10.1007/978-3-319-71354-0_15

Platt, T., and Sathyendranath, S. (2008). Ecological indicators for the pelagic zone of the ocean from remote sensing. *Remote Sensing of Environment*, 112, 3426–3436.

Platt, T., Fuentes-Yaco, C., and Frank, K.T. (2003). Marine ecology: spring algal bloom and larval fish survival. *Nature*, 423, 398.

Pollard, R.T., I. Salter, R.J. Sanders, M.I. Lucas, C.M. Moore, R.A. Mills, P.J. Statham, J.T. Allen, A.R. Baker, D.C. E. Bakker, M.A. Charette, S. Fielding, G.R. Fones, M. French, A.E. Hickman, R.J. Holland, J.A. Hughes, T.D. Jickells, R.S. Lampitt, P.J. Morris, F.H. Nédélec, M. Nielsdóttir, H. Planquette, E.E. Popova, A.J. Poulton, J.F. Read, S. Seeyave, T. Smith, M. Stinchcombe, S. Taylor, S. Thomalla, H.J. Venables, R. Williamson, and M.V. Zubkov. (2009). Southern Ocean deep-water carbon export enhanced by natural iron fertilization. *Nature*, 457, 577.

Priede, I.G. (2014). Biogeography of the Oceans: a Review of Development of Knowledge of Currents, Fronts and Regional Boundaries from Sailing Ships in the Sixteenth Century to Satellite Remote Sensing. *Pure and Applied Geophysics*, 171, 1013–1027.

Purkis, S.J., and Brock, J.C. (2013). Lidar Overview. Ch 5 in *Coral Reef Remote Sensing*. (Eds: Goodman, J.A., Purkis, S.J., and Phinn, S.R.). Springer, Dordrecht. ISBN 978-90-481-9291-5.

Purkis, S.J., Graham, N.A.J., and Riegl, B.M. (2008). Predictability of reef fish diversity and abundance using remote sensing data in Diego Garcia (Chagos Archipelago). *Coral Reefs*, 27(1), 167–178.

Rajkumar, K.S.P., and Shanmugam, R.S. (2018). Satellite derived extraction of spatiotemporal variability of upwelling and its influence on marine fishery resources. *Journal of Marine Science and Technology—Taiwan*, 26, 92–101.

RAMSAR (2005). *A Conceptual Framework for the wise use of wetlands and the maintenance of their ecological character*. Resolution IX.1 Annex A, Item 15. *https://www.ramsar.org/sites/default/files/documents/pdf/res/key_res_ix_01_annexa_e.pdf*

RAMSAR (2018). *The Global Wetland Outlook—Status and Trends 2018*. The RAMSAR Convention Secretariat, Switzerland. *https://www.global-wetland-outlook.ramsar.org*

Ramsey, E.W., III, and Jensen, J.R. (1996). Remote sensing of mangrove wetlands: Relating canopy spectra to site-specific data. *Photogrammetric Engineering and Remote Sensing*, 62, 939–948.

Ramsey, E.W., III., Nelson, G.A., Laine, S.C., Kirkman, R.G., and Topham, W. (1997). Generation of coastal marsh topography with radar and ground-based measurements. *Journal of Coastal Research*, 13(4), 1335–1341.

Ramsey, E., Rangoonwala, A., Middleton, B., and Lu, Z. (2009). Satellite optical and radar data used to track wetland forest impact and short-term recovery from Hurricane Katrina. *Wetlands*, 29, 66.

Ramsey, E., III., Rangoonwala, A., Chi, Z., Jones, C.E., and Bannister, T. (2014). Marsh dieback, loss, and recovery mapped with satellite optical, airborne polarimetric radar, and field data. *Remote Sensing Environment*, 152, 364–374.

Reese, D.C., O'Malley, R.T., Brodeur, R., and Churnside, J.H. (2011). Epipelagic fish distributions in relation to thermal fronts in a coastal upwelling system using high-resolution remote-sensing techniques. *ICES Journal of Marine Science*, 68(9), 1865–1874. doi:10.1093/icesjms/fsr107

Reynolds, S.D., Norman, B.M., Beger, M., Franklin, C.E., and Dwyer, R.G. (2017). Movement, distribution and marine reserve use by an endangered migratory giant. *Diversity and Distributions*, 23, 1268–1279.

Ricart, A.M., York, P.H., Bryant, C.V., Rasheed, M.A., Ierodiaconou, D., and Macreadie, P.I. (2020). High variability of Blue Carbon storage in seagrass meadows at the estuary scale. *Scientific Reports*, 10(1), 5865. doi:10.1038/s41598-020-62639-y

Roelfsema, C.M., Dennison, W.C., and Phinn, S.R. (2002). Spatial distribution of benthic microalgae on coral reefs determined by remote sensing. *Coral Reefs*, 21(3), 264–274.

Roelfsema, C., Phinn, S., Jupiter, S., Comley, J., and Albert, S. (2013). Mapping coral reefs at reef to reef-system scales, 10s–1000s km^2, using object-based image analysis. *International Journal of Remote Sensing*, 34(18), 6367–6388. doi:10.1080/01431161.2013.800660

Roelfsema, C., Lyons, M., Kovacs, E.M., Maxwell, P., Saunders, M.I., Samper-Villarreal, J., and Phinn, S. (2014). Multi-temporal mapping of seagrass cover, species and biomass: A semi-automated object based image analysis approach. *Remote Sensing of Environment*, 150, 172–186. *https://doi.org/10.1016/j.rse.2014.05.001*

Roelfsema, C., Lyons, M., Dunbabin, M., Kovacs, E.M., and Phinn, S. (2015). Integrating Field Survey Data with Satellite Image Data to Improve Shallow Water Seagrass Maps: The Role of AUV and Snorkeller Surveys? *Remote Sensing Letters*, 6(2), 135–144. doi:10.1080/2150704x.2015.1013643

Roelfsema, C., Kovacs, E., Ortiz, J.C., Wolff, N.H., Callaghan, D., Wettle, M., Ronan, M., Hamylton, S.M., Mumby, P.J., and Phinn, S. (2018). Coral reef habitat mapping: A combination of object-based image analysis and ecological modelling. *Remote Sensing of Environment*, 208, 27–41. *https://doi.org/10.1016/j.rse.2018.02.005*

Roelfsema, C., Lyons, M., Kovacs, E., Kennedy, E., Markey, K., Borrego, R., Tudman, P., Roe, M., Gonzalez-Rivero, M., Callaghan, D., Murray, N., and Phinn, S. (2020). Habitat maps to enhance monitoring and management of the Great Barrier Reef. *Coral Reefs*, 39, 1039–1054. *https://doi.org/10.1007/s00338-020-01929-3*

Roelfsema, C.M., Lyons, M.B., Castro-Sanguino, C., Kovacs, E.M., Callaghan, D., Wettle, M., Markey, K., Borrego-Acevedo, R., Tudman, P., Roe, M., Kennedy, E.V., Gonzalez-Rivero, M., Murray, N., and Phinn, S.R. (2021). How Much Shallow Coral Habitat Is There on the Great Barrier Reef? *Remote Sensing*, 13, 4343. *https://doi.org/10.3390/rs13214343*

Rogers, J., Parrish, C.E., Ward, L.G., and Burdick, D.M. (2016). Assessment of elevation uncertainty in salt marsh environments using discrete-return and full-waveform lidar. *Journal of Coastal Research*, SI 76, 107–122. doi:10.2112/SI76-010

Sagar, S., Falkner, I., Dekker, A., Huang, Z., Blondeau-Patissier, D., Phillips, C., Przeslawski, R. (2020). *Earth Observation for monitoring of Australian Marine Parks and other off-shore Marine Protected Areas*. Report to the National Environmental Science Program, Marine Biodiversity Hub. Geoscience Australia.

Sasano, M., Yamanouchi, H., Matsumoto, A., Kiriya, N., Hitomi, K., and Tamura, K. (2012). Development of boat-based fluorescence imaging lidar for coral monitoring. *Proceedings of 12th International Coral Reef Symposium*, 9–13 July 2012, Cairns, Australia.

Scales, K.L., Miller, P.I., Hawkes, L.A., Ingram, S.N., Sims, D.W., and Votier, S.C. (2014). On the Front Line: frontal zones as priority at-sea conservation areas for mobile marine vertebrates. *Journal of Applied Ecology*, 51, 1575–1583.

Sherlock, M., Marouchos, A., Williams, A., and Tyndall, A. (2016). A vessel towed platform for deepwater high resolution benthic imaging. pp 1–6 in *OCEANS 2016-Shanghai*. IEEE, Shanghi. doi:10.1109/OCEANSAP.2016.7485396.

Shortis, M., Seager, J., Williams, A., Barker, B., and Sherlock, M. (2007). A towed body stereo-video system for deep water benthic habitat surveys. *Proceedings of Eighth Conference on Optical 3-D Measurement Techniques*, Volume II (Eds: A. Grun and H. Kahmen), pp 150–157. ETH Zurich, Switzerland. ISBN 3- 906467-67-8

Silvestri, S., Marani, M., and Marani, A. (2003). Hyperspectral remote sensing of salt marsh vegetation, morphology and soil topography. *Physics and Chemistry of the Earth (Parts A/B/C)*, 28 (1–3), 15–25. *https://www.sciencedirect.com/science/article/pii/S1474706503000044*

Smith, E.V., Rogers, R.H., and Reed, L.E. (1975). Automated mapping and inventory of Great Barrier Reef zonation with Landsat data. In *IEEE Ocean '75*, 1, 775–780.

SOE (2018). *Coastal waters* webpage. State of Environment website: *https://soe.environment.gov.au/theme/coasts/topic/2016/coastal-waters*

Steven, A.D.L., Baird, M.E., Brinkman, R., Car, N.J., Cox, S.J., Herzfeld, M., Hodge, J., Jones, E., King, E., Margvelashvili, N., Robillot, C., Robson, B., Schroeder, T., Skerratt, J., Tickell, S., Tuteja, N., Wild-Allen, K., Yu, J. (2019). eReefs: An operational information system for managing the Great Barrier Reef. *Journal of Operational Oceanography*, 12, 1–17. *https://doi.org/10.1080/1755876X.2019.1650589*

Stewart, M., and Fairfull, S. (2008). *Mangroves*. Primefact 746. NSW Department of Primary Industry, Sydney. *http://www.dpi.nsw.gov.au/__data/assets/pdf_file/0020/236234/mangroves.pdf*

Strong, A.E., Arzayus, F., Skirving, W., and Heron, S.F. (2006). Identifying coral bleaching remotely via Coral Reef Watch—improved integration and implications for climate change. Ch 9 in *Coral Reefs and Climate Change: Science and Management* (Eds: J.T. Phinney, O. Hoegh-Guldberg, J. Kleypas, W. Skirving, and A.E. Strong). American Geophysical Union.

Strong, A.E., Liu, G., Skirving, W., and Eakin, C.M. (2011). NOAA's Coral Reef Watch program from satellite observations. *Annals of GIS*, 17(2), 83–92. *https://doi.org/10.1080/19475683.2011.576266*

Thomas, N., Lucas, R., Bunting, P., Hardy, A., Rosenqvist, A., and Simard, M. (2017). Distribution and drivers of global mangrove forest change, 1996–2010. *Plos One*, 12, e0179302. doi:10.1371/journal.pone.0179302

Tittensor, D.P., Mora, C., Jetz, W., Lotze, H.K., Ricard, D., Berghe, E.V., and Worm, B. (2010). Global patterns and predictors of marine biodiversity across taxa. *Nature*, 466, 1098.

Tomkiewicz, S.M., Fuller, M.R., Kie, J.G., and Bates, K.K. (2010). Global positioning system and associated technologies in animal behaviour and ecological research. *Philosophical Transactions of the Royal Society B,* 365, 2163–2176. doi:10.1098/rstb.2010.0090

Traganos, D., Aggarwal, B., Poursanidis, D., Topouzelis, K., Chrysoulakis, N., and Reinartz, P. (2018). Towards Global-Scale Seagrass Mapping and Monitoring Using Sentinel-2 on Google Earth Engine: The Case Study of the Aegean and Ionian Seas. *Remote Sensing*, 10(8), 1227. *https://doi.org/10.3390/rs10081227*

Tulloch, V.J., Atkinson, S., Possingham, H.P., Peterson, N., Linke, S., Allan, J.R., Kaiye, A., Keako, M., Sabi, J., Suruman, B., and Adams, V.M. (2021). Minimizing cross-realm threats from land-use change: A national-scale conservation framework connecting land, freshwater and marine systems. *Biological Conservation*, 254, 108954.

Turner, L., Tracy, D., Tilden, J., and Dennison, W.C. (2004). *Where river meets sea: Exploring Australia's estuaries*. CRC for Coastal Zone Estuary and Waterway Management, Brisbane.

Tweddle, J. F., Gubbins, M., and Scott, B.E. (2018). Should phytoplankton be a key consideration for marine management? *Marine Policy*, 97, 1–9.

Underwood, G., and Kromkamp, J., (1999). Primary production by phytoplankton and microphytobenthos in estuaries. *Advances in Ecological Research*, 29, 93–153.

UNEP (2006). *Marine and Coastal Ecosystems and Human Well-being: A synthesis report based on the findings of the Millenium Ecosystem Assessment*. United Nations Environmental Programme. 76 p.

Wang, L., Jia, M., Yin, D., and Tian, J. (2019). A review of remote sensing of mangrove forests: 1956–2018. *Remote Sensing of Environment*, 231, 111223. *https://doi.org/10.1016/j.rse.2019.111223*

Wilkinson, C. (2008). *Status of coral reefs of the world*. GCRMN, Townsville.

Williams, A., Althaus, F., and Schlacher, T.A. (2015). Towed camera imagery and benthic sled catches provide different views of seamount benthic diversity. *Limnology and Oceanography: Methods*, 13, 62–73.

Wolanksi, E., Newton, A., Rabalais, N., and Legrand, C. (2008). Coastal Zone Management. In *Encyclopedia of Ecology*, pp. 630–637. Elsevier.

Yamano, H. (2007). The use of multi-temporal satellite images to estimate intertidal reef-flat topography. *Journal of Spatial Science*, 52, 73–79.

Yamano, H., and Tamura, M. (2004). Detection limits of coral reef bleaching by satellite remote sensing: simulation and data analysis. *Remote Sensing of Environment*, 90, 86–103.

Yancho, J.M.M., Jones, T.G., Gandhi, S.R., Ferster, C., Lin, A., and Glass, L. (2020). The Google Earth Engine Mangrove Mapping Methodology (GEEMMM). *Remote Sensing*, 12, 3758.

Zeh, D.R., Heupel, M.R., Limpus, C.J., Hamann, M., Fuentes, M.M.P.B., Babcock, R.C., Pillans, R.D., Townsend, K.A., and Marsh, H. (2015). Is acoustic tracking appropriate for air-breathing marine animals? Dugongs as a case study. *Journal of Experimental Marine Biology and Ecology*, 464, 1–10.

Zimmerman, R.C. (2006). Light and photosynthesis in seagrass meadows. Ch 13 in *Seagrasses: biology, ecology and conservation*. (Eds: Larkum, A.W.D., Orth, R.J., and Duarte, C.M.). Springer, Dordrecht. pp. 303–321.

Looking Ahead

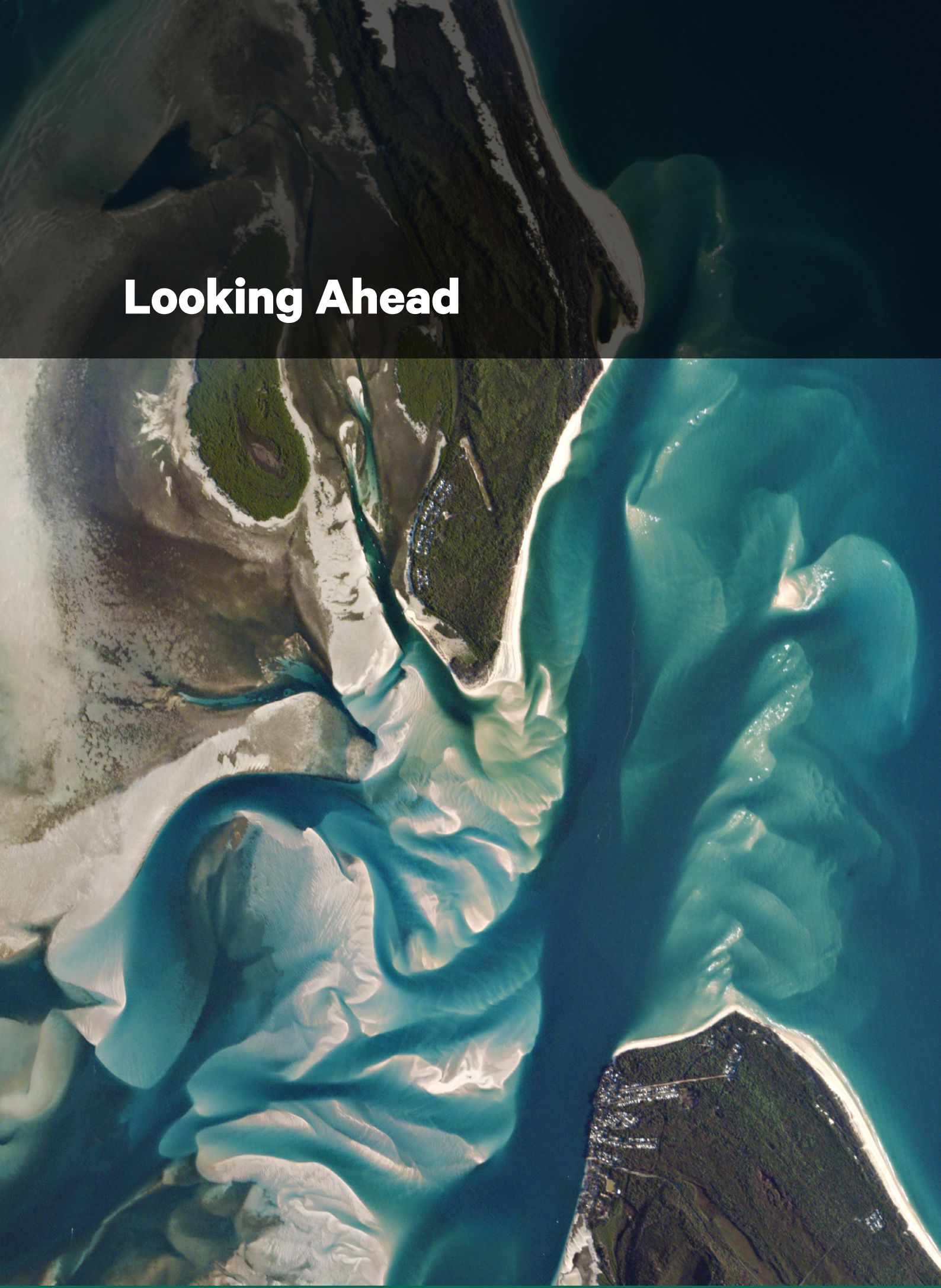

We conclude this sub-volume by looking ahead to new technologies and new methods for integrating EO and other datasets in surface water environments, and review the expanded range of aquatic challenges they can address.

Contents

21 Over the Horizon 439

22 Glossary 449

Background image on previous page: South Passage between Moreton and North Stradbroke Islands, Great Barrier Reef, Queensland, acquired on 1 October 2015. **Source:** Planet Labs Inc. (CC BY SA 4.0). Retrieved from *https://www.planet.com/gallery/#!/post/amity-point*

21 Over the Horizon

Barbara Harrison, Edward King, Arnold Dekker, David Hudson, and Stuart Phinn

Despite covering most of the globe and for the most part being remote from human settlements, our surface waters are increasingly being threatened by anthropogenic activities. Trends in human population growth and their impact on terrestrial vegetation are detailed in Volume 3A—Section 19. The major threats to terrestrial biodiversity—namely habitat changes, overexploitation, invasive species, climatic variations and pollution (see Volume 3A—Section 18)—also apply to aquatic environments, whether inland, coastal, or marine. In order to leave our planet in reasonable shape for future generations, a greater emphasis needs to be placed on sustainability—a balance between consumption and production—in all environments, including surface waters (see Volume 3A—Section 19). In this context, the following subsections consider:

- global coverage of current EO sensors in terms of temporal frequency and spatial extent, and the increased spectral resolution and density of future sensors (see Section 21.1);
- processing advances to interpret and integrate large datasets more rapidly (see Section 21.2);
- smart solutions for using EO resources to manage our water resources more sustainably (see Section 21.3); and
- human impacts on the aquatic environment (see Section 21.4).

I would feel more optimistic about a bright future for man if he spent less time proving he can outwit Nature and more time tasting her sweetness and respecting her seniority.
(E.B. White)

21.1 The Global Picture

Broadscale coverage observation of the ocean by satellite has typically been provided at 1–2 km resolution at roughly daily frequency. Geostationary satellites have generated imagery at hourly frequency, but by dint of their much larger orbit, at even lower spatial resolution. This is now changing as a series of polar orbiting, optical sensors with ~300 m resolution are operational, and geostationary sensor technology advances. In the latter case, 10 minute full-disk imagery at 500 m spatial resolution in the optical spectrum, and 2 km in the infrared, are becoming routine (e.g. Schmit *et al.,* 2005; Da, 2015). These innovations will deliver more useful data for coastal and inland waters where high spatial resolution is needed. The benefits of increased observation frequency are two-fold:

- improved coverage through (moving) broken cloud; and
- an ability to probe aquatic processes at sub-daily (even sub-hourly) time scales.

Background image: City Beach, Perth, photographed in February 2017. **Source:** Akbys, Wikimedia Commons. Retrieved from: *https://commons.wikimedia.org/wiki/File:City_Beach,_Perth,_Australia_(February_2017)_(33389330432).jpg*

Recommended Chapter Citation: Harrison, B.A., King, E.A., Dekker, A.G., Hudson, D., and Phinn, S.R. (2021). Over the Horizon. Ch 21 in *Earth Observation: Data, Processing and Applications. Volume 3B—Surface Waters.* CRCSI, Melbourne. pp. 439–448. ISBN 978-0-6482278-5-4.

Measurements of the status and trends of key indicators for the ocean and marine life are required to inform policy and management in the context of growing human uses of marine resources, coastal development, and climate change.
(Muller-Karger, 2020)

In addition to these large satellites, nanosatellites—miniature satellites carrying multispectral sensors that are often networked into constellations—offer rapid revisit capability at high spatial resolution (see Volume 1A—Section 1.3.3 and Volume 1B—Section 10.6.2). This increased frequency of coverage with good spatial detail is particularly useful for monitoring aquatic events that change rapidly, such as floods (see Section 11.4) and oil spills (see Section 19.4.3).

As well as improvements in spatial and temporal resolution, new types and combinations of satellite sensors are yielding different insights. In particular, the joint US/Argentinian Aquarius (Le Vine *et al.*, 2007) and the European SMOS (Font *et al.*, 2004) missions have delivered, for the first time, near-global maps of sea surface salinity, representing a quantum leap in our understanding of this key physical ocean variable (see Section 19.7). The SWOT mission (see Excursus 12.1) will provide an experimental imaging altimeter while the (currently unfunded) SKIM mission proposed a similar instrument to SWIM that was flown on CFOSAT, but with Doppler capability to retrieve ocean surface currents for the first time. Both of these missions, utilising novel sensor technology, have the capacity and potential to revolutionise sub-mesoscale oceanography. There is a trend also to fly multiple instruments on satellites in close formation (for example, the A-Train, Stephens *et al.*, 2002) so that multi-faceted and complementary observations are made of both aquatic environments and the atmosphere.

Figure 21.1 Spectral characteristics of hyperspectral PACE OCI compared with heritage spaceborne ocean colour sensors

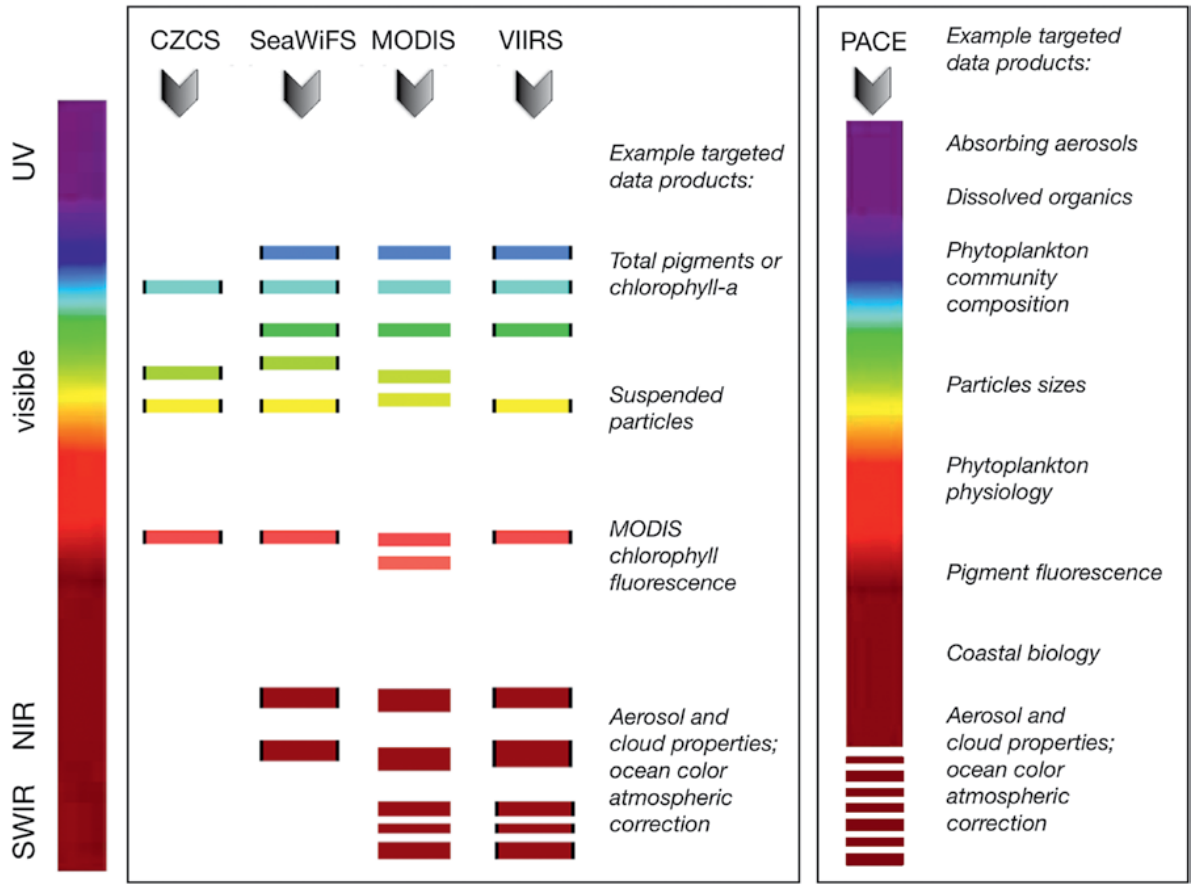

Source: Werdell *et al.* (2019) Figure 2

Protecting our oceans is also one of the world's more pressing environmental challenges.
(Scott Morrison, 2019)

Knowledge of the atmosphere is key to correcting and adjusting the satellite surface imagery, but also these atmospheric processes have direct impact on the sea surface. Contemporaneous observations of different aspects of the ocean surface (for example colour, temperature, salinity, wind stress, and surface height) provide a progressively richer view of the process complexities. Within the next decade, imaging altimeters providing broad rather than narrow-track sea surface height (Guijarro *et al.*, 2003), and hyperspectral optical sensors that enable a far more nuanced interpretation of coastal-ocean biology and sediment transport in coastal regions, will continue to transform our understanding of coastal waters and oceans.

In particular, the PACE mission, which is due for launch in 2023, carries the Ocean Colour Instrument (OCI) and two multi-angle polarimeters (Werdell *et al.*, 2019). OCI has a spatial resolution of 1 km and a temporal frequency of 1–2 days, but most importantly provides full hyperspectral resolution from ultraviolet (UV) to shortwave infrared (SWIR) wavelengths, thus enabling more detailed analyses than were possible with earlier sensors (see Figure 21.1). Together these sensors will improve our understanding of water colour in large inland water bodies, estuaries, coasts and oceans, and also of atmospheric parameters (Sagar *et al.*, 2020; Cawse-Nicholson *et al.*, 2021).

For global studies, a set of common, agreed variables is necessary to enable disparate *in situ* datasets to be exchanged and integrated. Essential Ocean Variables (EOV) have been defined in recent years to this end (Miloslavich *et al.*, 2018; see Excursus 7.2 and Excursus 21.1) and are also linked to components of the UN Sustainable Development Goals (SDG; see Volume 3A—Section 20). EOV are closely related to Essential Biodiversity Variables (EBV; see Volume 3A—Section 19.3) with both being indicative of the status of ecosystem components and ecosystem health (GOOS, 2021). These essential variables define a baseline against which anthropogenic pressures and fundamental environmental changes in the global marine environment can be quantified (see Section 21.4). Given the breadth, depth, and interconnectedness of the world ocean, a global approach is the only feasible way to understand and monitor its complexity and share the cost of acquiring this essential data (Canonico *et al.*, 2019).

Table 21.1 Global monitoring systems

System	Goal	Website
Global Ocean Observing System (GOOS)	Sustained collaborative system of ocean observations, encompassing *in situ* networks, satellite systems, governments, UN agencies, and individual scientists	*https://www.goosocean.org/*
Marine Biodiversity Observation Network (MBON)	Global community of practice within GEO BON (Group on Earth Observations Biodiversity Observation Network) for the sustained collection, curation, and analysis of marine biodiversity data	*https://marinebon.org/*
Ocean Biogeographic Information System (OBIS)	Global open access data and information clearing-house on marine biodiversity for science, conservation, and sustainable development	*https://obis.org/*
Ocean Best Practices System (OBPS)	Global, sustained system comprising technological solutions and community approaches to enhance management of methods as well as support the development of ocean best practices	*https://www.oceanbestpractices.org/*
GEO AquaWatch	Develop and build the global capacity and utility of Earth Observation-derived water quality data, products and information to support water resources management and decision making.	*https://www.geoaquawatch.org/*
GEO Blue Planet (see Greb *et al.*, 2018)	Advance and exploit synergies among the many observational programs devoted to ocean and coastal waters Improve engagement with a variety of users for enhancing the timeliness, quality, and range of services delivered Raise awareness of the societal benefits of ocean observations at the public and policy levels	*https://geoblueplanet.org/*
GeoGLOWS	Provide relevant, actionable water information to promote the use of EO in the decision-making process while promoting the strengthening of observational networks.	*https://www.geoglows.org/*
Integrated Marine Biosphere Research (IMBeR)	Global research project focusing on ocean sustainability in the context of global change	*http://imber.info/*

For freshwater environments, Essential Climate Variables (ECV) have been defined for lakes, and Essential Water Variables (EWV) are in the process of being defined. For coasts there are many related activities around CEOS-Coasts and GEO Blue Planet. A signification development is the adoption of the UN Sustainable Development Goals (SDG) for oceans, inland waters, and wetlands (SDG 14, 6, and 15 respectively), that will require a global effort in monitoring and assessing progress against these SDG goals (see Volume 3A—Section 20.4). The recent global adoption of SEEA (System of Economic Environmental Accounting; see Volume 3A—Section 20.5) will also require systematic monitoring and assessment of our natural resources and thus will be another driver for operational EO applications.

In addition to biodiversity data repositories such as the Global Biodiversity Information Facility (GBIF), a number of global, EO-based systems specifically monitor surface waters with a focus on biodiversity (see Table 21.1). These global monitoring programs are providing the foundation of baseline observations that will be essential to guide efforts and measure progress in conserving biodiversity and improving sustainability in the inland, coastal, and marine environments (see Section 21.4).

Excursus 21.1—Essential Ocean Variables

Source: GOOS: *https://www.goosocean.org/index.php?option=com_content&view=article&id=170&Itemid=114*
Further Information: Lindstrom *et al*., (2012); Muller-Karger *et al*. (2018); Moltmann *et al*. (2019)

Given the vast extent and remoteness of the ocean, *in situ* observations can be both costly and dangerous to acquire. To maximise the value of any data collected, a framework of Essential Ocean Variables (EOV; see Excursus 7.2) has been designed by the Global Ocean Observing System (GOOS; in collaboration with many other global monitoring consortia—see Section 7.5 above) based on the criteria of being:

- relevant—to the GOOS themes of climate, operational ocean services, and ocean health;
- feasible—using established, scientifically understood methods; and
- cost-effective—generates and archives affordable data, primarily by using coordinated, established observing systems and historical datasets.

EOV describe the key physical, biogeochemical, and biological attributes of oceans (see Table 21.2) and are closely related to Essential Biodiversity Variables (EBV; see Volume 3A—Section 18; Muller-Karger *et al*., 2018). Development of EOV was based on the drivers-pressures-state-impact-response (DPSIR) model (Volume 3A—Section 11.3). A review of 24 international conventions or agreements, that were deemed to be relevant to global ocean biology, identified key anthropogenic pressures and societal drivers in the marine environment (see Figure 21.2).

Table 21.2 Essential Ocean Variables

Physics	Biogeochemistry	Biology and Ecosystems	Cross-disciplinary
Sea state	Oxygen	Phytoplankton biomass and diversity	Ocean colour
Ocean surface stress	Nutrients	Zooplankton biomass and diversity	Ocean Sound
Sea ice	Inorganic carbon	Fish abundance and distribution	
Sea surface height	Transient tracers	Marine turtles, birds, mammals abundance and distribution	
Sea surface temperature	Particulate matter	Hard coral cover and composition	
Subsurface temperature	Nitrous oxide	Seagrass cover and composition	
Surface currents	Stable carbon isotopes	Macroalgal canopy cover and composition	
Subsurface currents	Dissolved organic carbon	Mangrove cover and composition	
Sea surface salinity		Microbe biomass and diversity (emerging)	
Subsurface salinity		Invertebrate abundance and distribution (emerging)	
Ocean surface heat flux			

Source: GOOS (2021)

Figure 21.2 Pressures and drivers on global ocean biology

The length of lines between drivers indicates similarity and horizontal bars represent pressures.

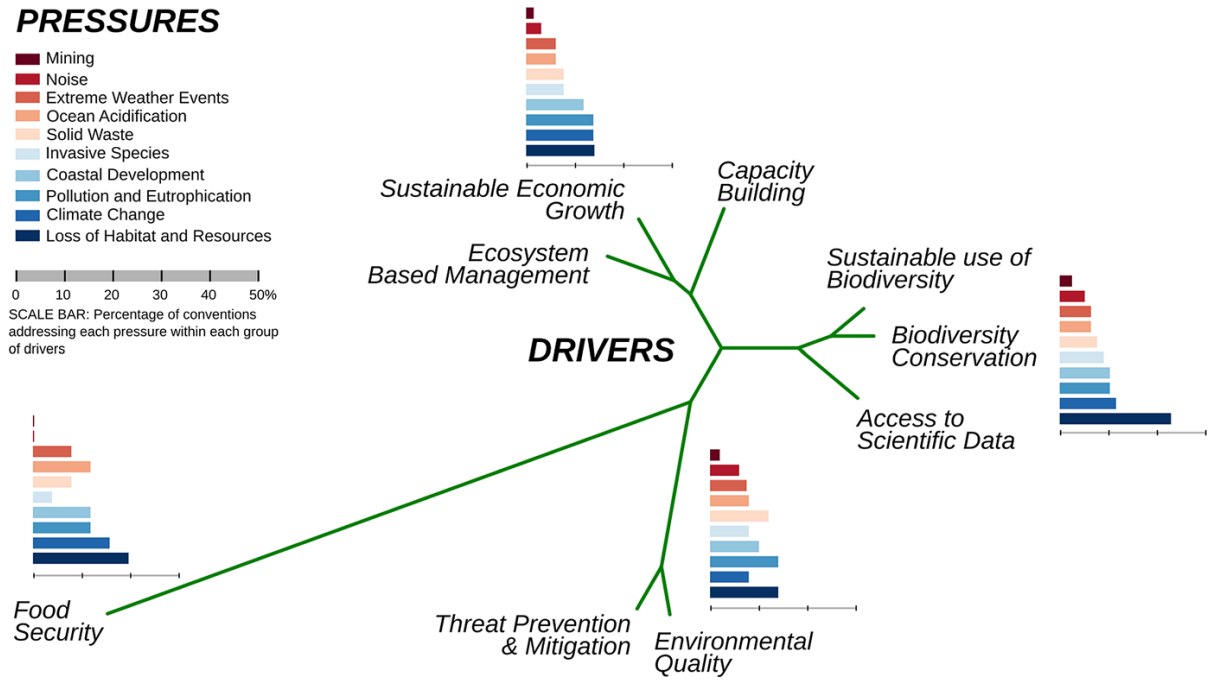

Source: Miloslavich *et al.* (2018) Figure 2

21.2 From Data to Information

In this sub-volume we have presented the state of the art in optical, thermal, microwave, and acoustic EO as they relate to surface waters. However, the many potential synergies between the information from different EO sensors have not yet been realised. As with most technologies, each dataset needs to reach a level of maturity—be sufficiently reliable and understood—before it can be routinely integrated with other datasets (see Volume 2D).

EO has, since its inception, been hamstrung by the ability to produce data volumes that exceed analysis capacity. Without a doubt, the rapid commodification of computing (globally) in the past two decades is reversing this trend by making it possible to handle more observations efficiently and without compromise through averaging or approximation (see Volume 2D). The more detailed knowledge and simultaneous observations of the atmosphere permit a thorough and accurate accounting for its effect in imagery, leading to higher quality biogeophysical products. Enhanced computing capacity also enables more complex retrieval algorithms to use more data to be better able to account for the complexity present within the imaged scene.

Another variation on this theme is sensor-sensor fusion, where similar sensors on different platforms with different revisit times, spatial or spectral resolution are combined (see Volume 2D). For example combining high frequency but low spatial resolution observations from geostationary satellites with the lower frequency higher spatial resolution from low earth orbit, could yield a product that is more useful than either of its constituents. Similar approaches could be used with multispectral and hyperspectral instruments. The recent development of high-altitude drones (so-called pseudo-satellites) that are solar powered and can linger on station at stratospheric altitudes (~20 km) for months at a time offer the prospect of a powerful opportunity to use sensor-sensor fusion to bridge across scales between traditional satellite observations and ground (or near-ground) measurements. All these would benefit from the dramatic improvements in data management and computing capacity that is emerging today.

Lastly, the use of EO data in a model-data fusion (or data assimilating) paradigm, in which theoretical behaviour is dynamically constrained by data, is already having a dramatic impact on understanding of all aspects of terrestrial, freshwater, coastal, and ocean processes. This impact is now extending from physical oceanography into improved biological modelling in the eReefs system (see Section 20.6.4 and Volume 2D—Excursus 14.4), including assessing how changes in catchment management practices impact the waters of the Great Barrier Reef. Improved processing and data handling capacity offers, by far, the greatest prospect for yielding the full potential of satellite data to the study of surface waters on Earth.

While EO datasets have always been huge, rapid developments, from autonomous *in situ* sensors and data collection based on citizen science (see Volume 2D—Section 12), to sensors somewhere in the atmosphere, to sophisticated satellites (singles and swarms), will create an even greater data deluge that will need to be harnessed into meaningful information. Smart data analytics will become core, and it is likely that a paradigm shift in the conversion of data into information will be required (Sudmanns *et al*., 2019). Extremely large datasets have become known as 'big data', where big generally implies five 'v' attributes:

- volume—extremely high;
- variety—wide range of forms;
- velocity—high speed processing required;
- veracity—data uncertainty needs to be addressed; and
- value—goal of data analysis (Sudmanns *et al*., 2019).

EO is one example of 'big Earth data', which Sudmanns *et al*. (2019) define in terms of four characteristics:

- "non-repeatability—observations of physical objects and processes are unique in space and time and generally cannot be repeated;
- uncertainty—big data involves different approaches to observation and recording, as well as indirect observation and sampling;
- multidimensionality—a wide range of data sources and complex analysis methods including cross-scale modelling lead to a wide range of dimensionality and often multidimensionality; and
- computational complexity—combining the first three issues results in a high degree of computational complexity in data analysis."

Some of the challenges involved in maximising the value of this data source for a given area of interest are summarised in Table 21.3. Sudmanns *et al*. (2019) propose that new norms, standards, and guidelines will be required to store, process, and access these massive EO datasets, and integrated web-based workflows will be required to 'bring the user to the data, not the data to the user'. Visualisation is also a key challenge with all types of big data, to ensure they realise their potential.

We are currently on a path to removing the existing bottlenecks in instrumentation, sensors, communication, and computer processing power. A key development during the decade 2010–20 has been the realisation of Analysis Ready Data (ARD) applications, which are opening up archives comprising myriad images into accessible data from which quantitative information can be extracted (see Volume 2D—Sections 3.2 and 11). The next step will be to provide 'Interpretation Ready Data' to end users so they can make informed decisions for managing and taking care of our aquatic ecosystems, resulting in the final end product of decision ready data.

Table 21.3 Big Earth data challenges

Technological challenges	Technological, computational challenges of distributed, highly scalable systems
	Multiple data sources require consistency of definitions of phenomena and measurement parameters
	Data curation and stewardship
Methodological challenges	Provision of Analysis Ready Data (ARD)
	Uncertainty analysis and characterisation
	Model/data validation and quality assurance
Social challenges	Complex interrelated systems and processes at the energy-water-food-climate nexus
	Lack of data regarding some human-centred aspects and 'soft' parameters
	Multiple scales across spatial and temporal processes

Source: Sudmanns *et al*. (2019) Figure 2

21.3 Smart Management of Surface Water Resources

Water underpins all life on Earth. The requirement for spatially and temporally comprehensive information on our ocean, coral reef, coastal, and inland water ecosystems will only increase. Easily accessible, trusted, quantitative, validated information products from EO will enable human society to understand and manage these ecosystems more sustainably. Adaptive management requires:

- long term data trends;
- near real time monitoring of extreme events; as well as
- predictive capability.

These three requirements have consequences for information acquired from EO sensors:

- long term data trends require careful calibration and intercalibration of generations of sensors;
- near real time monitoring requires very fast processing pipelines to get data to decision makers with minimal delays; and
- predictions require combinations of *in situ* and EO-based information with biogeochemical and hydrodynamic models.

Volume 1B—Section 10 and Volume 3A—Section 20 summarise various aspects of the 'smart' environment that directly impact our understanding of planet Earth, including:

- the rapidly maturing Internet of Things (IoT)—a global network of devices, people, processes, and data (see Volume 1B—Section 10.2 and Volume 3A—Section 20.1), including aquatic sensors (see Excursus 5.1);
- the importance of locational accuracy—both in terms of positioning devices, integrated location-based services, and the National Positioning Infrastructure (see Volume 1B—Section 10.3 and Volume 2B), which is particularly critical in remote inland, coastal, coral reef, and marine environments;
- increasing data volumes from a wide range of sources—including EO platforms and sensors, open datasets, and crowdsourced/citizen science contributions (see Volume 1A—Section 1.3.1, Volume 1B—Sections 10.4 and 10.6, and Volume 2D—Section 12); and
- the growth of integrated 'smart' systems—such as ARD and virtual worlds (see Volume 1B—Sections 10.5 and Volume 2D—Sections 3.2 and 11).

In the context of Surface Waters applications of EO, each of these technological aspects of the smart paradigm have already contributed to a greater appreciation of the complexity and fragility of the aquatic environment. Within the smart environment framework, the emphasis in EO is likely to shift from raw data processing and algorithms to how we intelligently harmonise all data streams in a mutually synergistic manner (most likely through sophisticated data assimilation methods) to provide accessible, easily comprehensible, timely, management-relevant information in such a way that it is conducive to good decision-making and will benefit our aquatic environments globally.

21.4 The Human Factor

As detailed in the preceding sections, spaceborne EO methods, together with *in situ* and airborne data, are already making our lives—and those of our fauna and flora—better globally. Some of the current benefits that society now derives from EO of surface waters include:

- mass balance applications for estimating regional and global freshwater availability (see Excursus 1.1);
- monitoring coastal zone integrity, flooding, and potential erosion factors (see Section 11);
- accurate monitoring of sea level and the impact of sea level changes to settlement safety, estuarine health, and storm potential (see Section 12);
- detailed bathymetric mapping for surveillance, search and rescue, and pollution control (see Section 13);
- mapping and monitoring sea surface temperature for ocean, weather, climate, and ecological forecasting and modelling (see Section 14);
- mapping and monitoring conditions in Antarctica and the Southern Ocean for intelligent conservation and climate change impacts (see Section 15);
- monitoring and modelling ocean and coastal water circulation, including waves, to prepare for storms (e.g. Waveforce) and utilise natural energy potential (see Sections 16 and 17);
- monitoring and modelling water quality (both marine and inland) to ensure water security for both social and environmental benefits (see Sections 18 and 19); and
- managing inland, coastal, and marine ecology to ensure sustainable use of resources and protect biodiversity from various sources of pollution and other anthropogenic pressures (see Section 20).

Table 21.4 Target variables for pressures and drivers in the aquatic biological environment

Factor		Target variables
Drivers	Scientific knowledge and data access	Patterns of biodiversity (location of biodiversity hotspots and their relationship to the location of high levels of ecosystem services), primary productivity (photosynthetic activity), harmful algal blooms, zooplankton biomass, fish abundance (catch/captures), levels of bycatch, discards, and waste, population size and trends of threatened species, geographic range and habitat needs of threatened species, key life-history parameters of selected indicator species (leading to detect changes), changes in breeding and nursery areas, reproduction and survival (under eutrophication conditions), noise, species structure of highly productive sea areas
	Sustainable use of biodiversity and resources	Condition of depleted fishing stocks, population size and trends of threatened species, geographic range and habitat needs of threatened species
	Conservation of biodiversity and ecosystems	Trends in abundance, distribution and extinction risks of species, cover condition, representativeness, effectiveness of protected areas, trends in genetic diversity, trends in extent condition and vulnerability of ecosystems (for example to degradation by pollutants, bycatch, invasive species), biomes, habitats (e.g. coral reefs), control of harmful invasive species (e.g. in ballast waters), condition of migratory species and corridors, and areas critical for sensitive life stages (e.g. for Arctic species)
	Improve management: use of integrated ecosystem approach	Assessments on biodiversity and ecosystem services
	Development through sustainable economic growth	Fisheries, economic benefits, access to marine resources and markets
	Capacity building	Taxonomy (biodiversity), technology, implementation of effective conservation and management of straddling and highly migratory fish stocks, develop research capacity, strengthen national data systems, strengthen statistical capacities, improve data accessibility, quality and synthesis
	Threat prevention and impact mitigation	Integrated assessments, sustainability of long term socioeconomic benefits, assessment of transportation corridors
	Environmental quality and health	Oil pollution, chemical pollution, sewage, garbage and debris, air pollution, control of harmful antifouling systems, harmful algal blooms, nutrient enrichment and eutrophication, acidification, biotoxins, pathology, emerging diseases, health indices, sound (noise), marine renewable energy developments
	Food security	Abundance and quality of fisheries stocks, control of harmful algal blooms
Pressures	Loss of resources: habitats/biodiversity (including overfishing)	Species presence/absence and distribution (from microbes to marine mammals), status of populations (e.g. abundance of commercially important, migratory, and "iconic" species), fisheries production, captures and by-catch, extent (cover) of living benthic habitats (coral reefs, seagrasses, mangroves)
	Climate change	Primary productivity, harmful algal blooms, coral bleaching (extent)
	Pollution / eutrophication	Phytoplankton diversity and biomass, presence of toxic, waterborne pathogens, harmful algal blooms
	Coastal development	Extent (cover) of living benthic habitats (coral reefs, seagrasses, mangroves)
	Invasive species	Range (presence) and abundance of invasive species
	Solid wastes	Volume and/or weight marine debris
	Ocean acidification	Calcareous phytoplankton abundance, coral skeletal density
	Extreme weather events	Extent (cover) of living benthic habitats (coral reefs, seagrasses, mangroves) susceptible to storms, hurricanes, extreme rainfall and sedimentation
	Noise	Movement of marine mammals (cetaceans)
	Mining	Diversity of deep sea benthic species

Source: Miloslavich *et al.* (2018) Tables S4 and S5

At some level in monitoring and marine ecology more generally, we have to turn the argument around so that we are monitoring recovery and restoration, or even resilience in the face of increasing threats—as well as the many ongoing declines. Monitoring is but a small and necessary cost to sustain or increase the value of the benefits we get from nature.
(Nicholas Bax)

Many of these benefits use the word 'sustainable'. The concept of sustainability is discussed in detail in Volume 3A—Section 20, including international agreements and initiatives designed to achieve this end, the most relevant of which are the UN SDG. At a global scale, EO offers the only practical approach to monitoring sustainability in both terrestrial and aquatic environments.

To ensure a sustainable future, however, perhaps the fundamental question relating to any application of EO becomes "how can EO be used to both reduce pressures on the environment and improve benefits to society?". The major societal pressures and drivers that have been identified in the marine environment are illustrated in Figure 21.2 and their target variables are defined in Table 21.4. These drivers and pressures are now being tracked using EOV (see Excursus 21.1) within a number of global marine monitoring programs (see Table 21.1). Similar activities are now taking place in coastal and inland water ecosystems globally.

Other examples of a sustainable focus in EO applications are the various activities coordinated by the Group on Earth Observation (GEO; see Volume 3A—Section 20.1), including its Societal Benefit Areas (SBA; see Volume 3A—Section 20.3). In particular, the GEO Blue Planet initiative aims to link coastal and ocean information with society, which has direct implications for transportation, maritime safety, water quality, marine biodiversity, sustainable resource usage, and disaster management, and for inland waters GEO AquaWatch is developing a global EO-based monitoring and modelling system (Greb *et al.*, 2018). EO products are already addressing the global problem of water security, both in terms of monitoring water quality (see Section 19) and the extreme conditions of floods and droughts (Chawla *et al.*, 2020).

In future, we hope that advances in EO data acquisition, integration, and delivery will provide the rich information that humans will use to understand the choices that they can make to protect and enhance the societal benefits, and improve the sustainable use of all aquatic resources.

21.5 Further Information

Essential Ocean Variables

GOOS: *https://www.goosocean.org/index.php?option=com_content&view=article&id=170&Itemid=114*

CSIRO (2017)

21.6 References

Canonico, G., Buttigieg, P.L., Montes, E., Muller-Karger, F.E., Stepien, C., Wright, D., Benson, A., Helmuth. B., Costello, M., Sousa-Pinto, I., Saeedi, H., Newton, J., Appeltans, W., Bednaršek, N., Bodrossy, L., Best, B.D., Brandt, A., Goodwin, K.D., Iken, K., Marques, A.C., Miloslavich, P., Ostrowski, M., Turner, W., Achterberg, E.P., Barry, T., Defeo, O., Bigatti, G., Henry,. L.-A., Ramiro-Sánchez, B., Durán, P., Morato, T., Roberts, J.M., García-Alegre, A., Cuadrado, M.S., and Murton, B. (2019). Global Observational Needs and Resources for Marine Biodiversity. *Frontiers in Marine Science*, 6, 367. doi:10.3389/fmars.2019.00367

Cawse-Nicholson, K., Townsend, P.A., Schimel, D., Assiri, A.M., Blake, P.L., Buongiorno, M.F., Campbell, P., Carmon, N., Casey, K.A., Correa-Pabón, R.E., and Dahlin, K.M. (2021). NASA's surface biology and geology designated observable: A perspective on surface imaging algorithms. *Remote Sensing of Environment*, 257, 112349. *https://doi.org/10.1016/j.rse.2021.112349*

Chawla, I., Karthikeyan, L., and Mishra, A.K. (2020). A review of remote sensing applications for water security: Quantity, quality, and extremes. *Journal of Hydrology*, 585, 124826.

CSIRO (2017). *Oceans: Science and Solutions for Australia*. (Ed: Mapstone, B.D.). CSIRO, Melbourne. *https://bluepeteraustralia.files.wordpress.com/2017/12/oceans-csiro-research.pdf*

Da, C. (2015). Preliminary assessment of the Advanced Himawari Imager (AHI) measurement onboard Himawari-8 geostationary satellite. *Remote Sensing Letters*, 6(8), 637–646. doi:10.1080/2150704X.2015.1066522

Font J., Lagerloef, G.S.E., Le Vine, D.M., Camps, A., and Zanifé, O.-Z. (2004). The Determination of Surface Salinity With the European SMOS Space Mission. *IEEE Transactions on Geoscience and Remote Sensing*, 42(10), 2196–2205.

GOOS (2021). *Essential Ocean Variables* webpage, The Global Ocean Observing System website: *https://www.goosocean.org/index.php?option=com_content&view=article&id=170&Itemid=114*

Greb, S., Dekker, A.G., and Binding, C. (Eds) (2018). *Earth Observations in Support of Global Water Quality Monitoring*. IOCCG Report Series, No. 17, International Ocean Colour Coordinating Group, Dartmouth, Canada.

Guijarro, J., Santoleri, R.. Nardelli, B.B., Borgarelli, L., Croci, R., Venturini, R., Alberti, G., Caramagno, A., and Pirondini, F. (2003). Innovative radar altimeter concepts, *Proceedings of IGARSS '03, IEEE International*, 2, 1080–1082.

Le Vine, D.M., Lagerloef, G.S.E., Colomb, F.R., Yueh, S.H., and Pellerano, F.A. (2007). Aquarius: An instrument to monitor sea surface salinity from Space. *IEEE Transactions on Geoscience and Remote Sensing*, 45(7), 2040–2050.

Lindstrom, E., Gunn, J., Fischer, A., McCurdy, A., and Glover, L.K. (2012). *A Framework for Ocean Observing*. By the Task Team for an Integrated Framework for Sustained Ocean Observing, UNESCO IOC/INF-1284 revision. doi:10.5270/OceanObs09-FOO

Miloslavich, P., Bax, N., Simmons, S. E., Klein, E., Appeltans, W., Aburto-Oropeza, O., Garcia, M.A., Batten, S.D., Benedetti-Cecchi, L., Checkley, *D.M.Jr.*, Chiba, S., Duffy, J.E., Dunn, D.C., Fischer, A., Gunn, J., Kudela, R., Marsac, F., Muller-Karger, F.E., Obura, D., and Shin, Y.-J. (2018). Essential Ocean Variables for sustained observations of marine biodiversity and ecosystems. *Global Change Biology*, 24, 2416–2433. doi:10.1111/gcb.14108

Moltmann T., Turton, J., Zhang, H.-M., Nolan, G., Gouldman, C., Griesbauer, L., Willis, Z., Piniella, Á.M., Barrell, S., Andersson, E., Gallage, C., Charpentier, E., Belbeoch, M., Poli, P.l, Rea, A., Burger, E.F., Legler, D.M., Lumpkin, R., Meinig, C., O'Brien, K., Saha, K., Sutton, A., Zhang, D., and Zhang, Y. (2019). Global Ocean Observing System (GOOS), Delivered Through Enhanced Collaboration Across Regions, Communities, and New Technologies. *Frontiers in Marine Science*, 6, 291. doi:10.3389/fmars.2019.00291

Morrison, S. (2019). *National Statement to the United Nations General Assembly*, 25 September 2019, New York. *https://www.pm.gov.au/media/national-statement-united-nations-general-assembly*

Muller-Karger, F.E., Miloslavich, P., Bax, N.J., Simmons, S., Costello, M.J., Sousa, P.I., Canonico, G., Turner, W., Gill, M., Montes, E., Best, B.D., Pearlman, J., Halpin, P., Dunn, D., Benson, A., Martin, C.S., Weatherdon, L.V., Appeltans, W., Provoost, P., Klein, E., Kelble, C.R., Miller, R.J., Chavez, F.P., Iken, K., Chiba, S., Obura, D., Navarro, L.M., Pereira, H.M., Allain, V., Batten, S., Benedetti-Checchi, L., Duffy, J. E., Kudela, R.M., Rebelo, L.-M., Shin, Y., and Geller, Gary. (2018). Advancing Marine Biological Observations and Data Requirements of the Complementary Essential Ocean Variables (EOVs) and Essential Biodiversity Variables (EBVs) Frameworks. *Frontiers in Marine Science*, 5, 211. doi:10.3389/fmars.2018.00211

Sagar, S., Falkner, I., Dekker, A., Huang, Z., Blondeau-Patissier, D., Phillips, C., Przeslawski, R. (2020). *Earth Observation for monitoring of Australian Marine Parks and other off-shore Marine Protected Areas*. Report to the National Environmental Science Program, Marine Biodiversity Hub. Geoscience Australia.

Schmit, T.J., Gunshor, M.M., Menzel, W.P., Gurka, J.J., Li, J., and Bachmeier, A.S. (2005). Introducing the next-generation advanced baseline imager on GOES-R. *Bulletin of American Meteorological Society*, 86, 1079–1096. *http://dx.doi.org/10.1175/BAMS-86-8-1079*

Stephens, G.L., Vane, D.G., Boain, R.J., Mace, G.G., Sassen, K., Wang, Z., Illingworth, A.J., O'Connor, E.J., Rossow, W.B., Durden, S.L., Miller, S.D., Austin, R.T., Benedetti, A., Mitrescu, C., and The CloudSat Science Team (2002). The Cloudsat Mission and the A-Train. *Bulletin of American Meteorological Society*, 83, 1771–1790. *http://dx.doi.org/10.1175/BAMS-83-12-1771*

Sudmanns, M., Tiede, D., Lang, S., Bergstedt, H., Trost, G., Augustin, H., Baraldi, A., and Blaschke, T. (2019). Big Earth data: disruptive changes in Earth observation data management and analysis? *International Journal of Digital Earth*, 13(7), 832–850. *https://doi.org/10.1080/17538947.2019.1585976*

Werdell, P.J., Behrenfeld, M.J., Bontempi, P.S., Boss, E., Cairns, B., Davis, G.T., Franz, B.A., Gliese, U.B., Gorman, E.T., Hasekamp, O., Knobelspiesse, K.D., Mannino, A., Martins, J.V., McClain, C.R., Meister, G., and Remer, L.A. (2019). The Plankton, Aerosol, Cloud, Ocean Ecosystem Mission: Status, Science, Advances. *Bulletin of the American Meteorological Society*, 100(9), 1775–1794.

Glossary

Sources include glossaries from Australian Hydrographic Office, International Hydrographic Office, and Geoscience Australia.

Term	Definition
AAPP	Australian Antarctic Program Partnership
AAT	Australian Antarctic Territory
AATSR	Advanced Along-Track Scanning Radiometer
ABSLMP	Australian Baseline Sea Level Monitoring Project
ACSPO	Advanced Clear Sky Processor for Oceans
AHI	Advanced Himawari Imager
AHO	Australian Hydrographic Office
AMSA	Australian Marine Safety Authority
AMSR-E	Advanced Microwave Scanning Radiometer for EOS
AMSR2	Advanced Microwave Scanning Radiometer 2
AODN	Australian Ocean Data Network
AOP	Apparent Optical Properties
Aphotic Zone	The Aphotic Zone (or midnight zone) refers to the darker, deeper waters below 1000 m in which light levels are too low for photosynthesis. This zone is also called Deep Sea in oceans and the Profundal Zone in lakes. The Aphotic Zone comprises 90% of the total area of oceans on Earth.
Aquifer	Saturated, subterranean zone below the Water Table. Groundwater is often extracted from aquifers artificially by installing a well or bore. Unconfined aquifers require a pump to raise groundwater to the surface from a bore. Confined aquifers, however, exist above layers of relatively impermeable rock such that natural internal pressures spontaneously eject the groundwater to (or above) the surface. Such waters are called artesian waters.
Artesian Waters	Confine aquifer from which groundwater is spontaneously released to the surface.
ATSB	Australian Transport Safety Bureau
AVHRR	Advanced Very High Resolution Radiometer
Benthic Zone	The lowest level of any aquatic ecosystem which extends from the shoreline to deep water. This zone consists of rock, sand and sediment on the floor of an ocean, sea, lake or river. As such, the conditions of the benthic zone can vary significantly between shallow coastal waters and deep ocean. It supports a wide range of benthic organisms, or 'benthos', depending on local conditions such as the amount of light that reaches it, the ambient temperature and available nutrients.
Benthos	Plants and animals that live on the seafloor. These include immobile sponges and corals, creeping crabs and snails, burrowing worms, crustaceans and bivalves, as well as barnacles, seaweeds, and sea squirts.
BRAN	Bluelink Reanalysis
BoM	Bureau of Meteorology
CARS	CSIRO Atlas of Regional Seas
CASI	Compact Airborne Spectrographic Imager
Catchment	The area of land draining into a river is referred to as its catchment or watershed.
CCI	Climate Change Initiative
CDIM	Coloured dissolved inorganic matter
CDOM	Coloured dissolved organic matter
CMC	Canadian Meteorological Centre
CMEMS	Copernicus Marine Environment Monitoring Service
Coastal Waters	Shallower marine waters within 3M of the Territorial Sea Baseline (TSB). These include estuaries, beaches, salt marshes, mudflats and mangrove swamps, as well as the shallow waters on the fringe of oceans, which contain coral reefs and lagoons, seagrass meadows, and kelp forests.
CoM	Commonwealth of Australia
Confidence Level	Probability that the true value of a measurement will lie within the specified uncertainty from the measured value.

Term	Definition
Contiguous Zone	Belt of water extending 24M from TSB within which Australia may exercise control related to customs, immigration, pollution, and quarantine.
Coriolis force	A composite centrifugal force, due to rotation of the Earth, acting on objects (including air and water) moving in relation to the Earth. It causes deflection of such moving objects to the left in the Southern Hemisphere, and to the right in the Northern Hemisphere.
Correction	Compensation applied to data to adjust for an estimated systematic effect.
CSIRO	Commonwealth Scientific and Industrial Research Organisation
Current	A non-periodical, generally horizontal movement of water (or other fluid) due to many causes such as prevalent winds, temperature differential etc., but not to gravitational forces of the Moon and Sun (see tidal stream)
Cryosphere	The frozen water part of the Earth system, comprising sea ice, ice caps and ice sheets, glaciers, snow cover, icebergs, lake and river ice, and frozen ground.
C3S	Copernicus Climate Change Service
Datum	1. Any numerical or geometrical quantity which may serve as a reference or base for other quantities. In marine applications, a base elevation or plane used as a reference from which to reckon heights or depths, plural: datums. 2. A single piece of information, plural: data.
Deep Sea	Aphotic Zone in Oceans.
Delta	A Delta result from settling river sediment and can occur where one river meets another, a river meets a lake or reservoir, or a river meets an open sea that has weak tidal currents. The formation of deltas gradually slows down flow of rivers.
Demersal Zone	The Demersal Zone includes water near the seabed, but below the pelagic zone.
DIC	Dissolved inorganic carbon
DOC	Dissolved organic carbon
Dysphotic Zone	Lower division of Photic Zone which receives only 1% of the photosynthetically active radiation (PAR) that is intercepted by the water surface.
Ebb (or Ebb Stream)	The horizontal movement of water associated with falling tide, usually setting seaward or in the direction opposite to tide progression. Also known as ebb current or outgoing stream.
Eddy	A circular movement of water, usually formed where currents or tidal streams pass obstructions, along the edge of a current or stream, or between two adjacent flows.
EMR	Electromagnetic radiation
ENSO	El Niño-Southern Oscillation
EO	Earth Observation
EOS	Earth Observation from Space
EOV	Essential Ocean Variable
Error	Difference between a measured value and the correct or true value. Errors can be categorised as systematic or random errors.
Estuary	An estuary is a semi-enclosed waterbody at the river mouth where river flow and tides mix fresh and salt water. These areas are typically turbid and provide a valuable habitat for marine and bird life.
Euphotic Zone	Upper division of Photic Zone, this zone extends from the water surface to that water depth at which only 1% of surface photosynthetically active radiation (PAR) is detected. It includes shallow, coastal waters and the upper part of deeper, ocean waters down to 200 m (in clear water). The Euphotic zone supports phytoplankton, microscopic algae and cyanobacteria as well as water plants and zooplankton, and the vast majority of marine life. It is estimated that 70% of the all photosynthesis on Earth occurs in the Euphotic Zone.
Exclusive Economic Zone (EEZ)	Area within 200 M of TSB, in which Australia has sovereign rights over waters, seabed and subsoil.
Feature	Any object, whether natural or manmade, which is distinct from the surrounding area.
Feature Detection	Ability of a system to detect features of a defined size.
Flow	1. The motion characteristic of a fluid. 2. Combination of tidal stream and current, also known in US as total current.
Freshwater	Inland waterbodies contain no (or low) salt levels.
FWHM	Full Width Half Maximum
GA	Geoscience Australia
GAMSSA	Global Australian Multi-Sensor SST Analysis
GCOM-C	Copernicus Climate Change Service - Climate

Term	Definition
GCOM-W	Copernicus Climate Change Service - Water
GEBCO	General Bathymetric Chart of the Oceans
GEO	Geostationary Earth Orbiting
Geoid	An equipotential surface (i.e. Having the same potential gravity at each point) that would be assumed by the sea level in the absence of tides, currents, water density variations and atmospheric effects. It is the surface of reference for astronomical observations and geodetic levelling.
Geostrophic current	A steady flow where the Coriolis force balances exactly the horizontal pressure gradient.
GFO	Geosat Follow-On
GHRSST	Group for High Resolution SST
GLOSS	Global Sea Level Observing System
GMPE	GHRSST Multi-Product Ensemble
GNSS	Global Navigation Satellite Systems
GOOS	Global Ocean Observing System
GRACE	Gravity Recovery and Climate Experiment
HAB	Harmful algal bloom
HAT	Highest Astronomical Tide
HS	Significant wave height
Hydrosphere	The hydrosphere comprises all the water on the Earth's surface, inside the Earth and in its atmosphere.
Hydrographic survey	A survey of a body of water to determine several classes of data pertaining to it, such as depth, configuration and nature of the bottom, direction and force of the currents, heights and times of tides, location of fixed objects for navigation purposes, etc. These data form the basis for a navigational chart.
ICSMD	International Charter for Space and Major Disasters
IHO	International Hydrographic Office
IMCRA	Interim Marine and Coastal Regionalisation of Australia
IMOS	Integrated Marine Observing System
Inland Waters	Freshwater rivers and lakes located within the Territorial Sea Baseline (TSB). These generally have low levels of dissolved salt. Ponds, dams and lakes feature standing water while rivers and streams have flowing water.
Intertidal Zone	Spanning from the high to low tide marks, this zone describes the coastal land that is exposed to changing tides, and thus impacted by waves at high tide, and Sun and wind at low tide.
IOC	International Oceanographic Commission
IOP	Inherent Optical Properties
IPCC	Intergovernmental Panel on Climate Change
JAXA	Japan Aerospace Exploration Agency
JMA	Japan Meteorological Agency
LAT	Lowest Astronomical Tide
LEO	Low Earth Orbiting
Limnetic Zone	In lakes, that water which is close enough to the surface to admit sufficient light for photosynthesis.
Littoral Zone	The Littoral Zone extends from the high tide mark to the continental shelf and thus includes the intertidal and neritic zones defined above.
LST	Land Surface Temperature
Marine Waters	Salty waterbodies external to land masses.
MBON	Marine Biodiversity Observation Network
Mean Sea Level (MSL)	A tidal datum; the arithmetic mean of hourly heights of the sea at the tidal station observed over a period of time (preferably 19 years).
Metadata	Data describing a dataset and its usage.
MGDSST	Merged Satellite and *in situ* Data Global Daily Sea Surface Temperature
ML	Machine learning
MPA	Marine Protected Areas
MUR	Multi-Scale Ultra High Resolution

Term	Definition
NAP	Non-algal particles
Nautical Mile (M)	Unit of distance equalling 1,852 m, which approximates 1 minute of latitude.
NDBC	National Data Buoy Centre
Nekton	Swimming animals including fish, serpents, and whales.
Neritic Zone	This occurs along coastlines between the low tide mark and the continental shelf. Since some sunlight reaches the bottom of this relatively shallow zone, it fosters photosynthetic organisms, such as phytoplankton and seaweeds. Most coral reefs occur in this zone. Organisms such as mollusks, sponges, crustaceans, and worms can live on the seafloor of this zone.
NMB	National Marine Bioregionalisation
NOAA	National Oceanic and Atmospheric Administration
OAC	Optically active constituents
OBIA	Object based Image Analysis
OBIS	Ocean Biogeographic Information System
OBPS	Ocean Best Practices System
Ocean	Deeper marine waters at least 3 M away from the Territorial Sea Baseline (TSB). These large waterbodies are saline and subject to tidal variations.
Oceanic Zone	The water spanning between continental shelves of different land masses.
OISST	Optimum Interpolation Sea Surface Temperature
OSTIA	Operational Sea Surface Temperature and Sea Ice Analysis
Pelagic Zone	The Pelagic Zone describes open water in oceans that is both away from the coast and above the seafloor, and includes both photic and aphotic waters.
Photic Zone	This zone refers to water that is close enough to the surface to admit sufficient light for photosynthesis. In lakes, this region is referred to as the Limnetic Zone. The Photic Zone can be further divided into the Euphotic, or sunlit, zone and the Dysphotic, or twilight, zone (see Figure 2.9).
Phytoplankton	Microscopic marine plants.
Plankton	Minute animals called zooplankton and microscopic plants called phytoplankton, most of which do not have the ability to move themselves around so tend to drift and float with water movement.
Profundal Zone	Aphotic Zone in lakes
RAMSSA	Regional Australian Multi-Sensor SST Analysis
Riparian Zone	The Riparian zone occurs along the edges of rivers or streams and includes the river bed, banks and floodplains.
RTE	Radiative Transfer Equation
SAR	Synthetic Aperture Radar
SDB	Satellite Derived Bathymetry
Seabed/seafloor	The solid surface that underlies a waterbody.
SEAFRAME	SEA-Level Fine Resolution Acoustic Measuring Equipment
SIOP	Concentration-specific IOP
SLR	Sea level rise
SGLI	Second-Generation Global Imager
SLSTR	Sea and Land Surface Temperature Radiometer
SPIM	Suspended particulate inorganic matter
SPOM	Suspended particulate organic matter
Spring	A spring occurs when groundwater naturally overflows onto the land surface.
SST	Sea Surface Temperature
SSTAARS	Sea Surface Temperature Atlas of the Australian Regional Seas
SSTdepth	Surface sea surface temperature at depth: all measurements of water temperature beneath SSTsubskin.
SSTfnd	Foundation sea surface temperature: the temperature free of diurnal temperature variability, that is, the temperature at the first time of the day when the heat gain from the solar radiation absorption exceeds the heat loss at the sea surface (approximately 10 m water depth under calm conditions).

Term	Definition
SSTint	Interface sea surface temperature: the temperature at the air-sea interface on molecular scales (cannot be directly measured).
SSTskin	Skin sea surface temperature: the temperature measured by an IR radiometer typically operating at wavelengths 3.7–12 μm, which represents the temperature within the conductive diffusion-dominated sublayer at a water depth of ~10–20 μm.
SSTsubskin	Subskin sea surface temperature: the temperature at the base of the conductive laminar sublayer of the ocean surface, which can be well approximated to the measurement of the surface temperature by a microwave radiometer operating in the 6–11 GHz frequency range (approximately 1 mm water depth).
Substratum	This layer rests on the seabed (or lithosphere) and may comprise sand, silt, mud, rocks, and live and/or dead coral.
Systematic Error	Component of measurement error that remains constant or varies in a predictable manner.
Territorial Sea	Belt of Australian water less or equal to 12 M from the Territorial Sea Baseline (TSB), over which Australia has sovereign rights to the water, seabed and subsoil, plus the airspace above.
Territorial Sea Baseline (TSB)	Reference boundary delimiting land and sea, which is used to define Australia's Maritime Zones.
Thermocline	A layer in a body of water in which the temperature decreases with depth at an appreciably greater rate than above and below, also such a gradient of temperature. Also called discontinuity or thermal layer.
Total Horizontal Uncertainty (THU)	Component of total propagated uncertainty (TPU) calculated in the horizontal dimension. THU is a two-dimensional quantity with all contributing horizontal measurement uncertainties included.
Total Propagated Uncertainty (TPU)	Three-dimensional uncertainty with all contributing measurement uncertainties included.
Total Vertical Uncertainty (TVU)	Component of total propagated uncertainty (TPU) calculated in the vertical dimension. TVU is a one-dimensional quantity with all contributing vertical measurement uncertainties included.
TSM	Total suspended matter
Tsunami	A wave generated by seismic activity. Also called seismic sea wave, or, inaccurately, a tidal wave. Barely discernible in the open ocean, their amplitude may increase to several metres in the shallow coastal regions. Most common in the Pacific.
UN	United Nations
Uncertainty	Estimate characterising the range of values within which the true value of a measurement is expected to lie as defined within a particular confidence level. It is expressed as a positive value.
UNCLOS	United Nations Convention on the Law of the Sea
Underkeel Clearance	Distance between the lowest point of the ship's hull and the seabed, riverbed, etc.
UNESCO	United Nations Educational, Scientific and Cultural Organisation
Upwelling	An upward flow of subsurface water, usually a result of divergence, offshore currents, winds, and wind drift transport.
VIIRS	Visible Infrared Imaging Radiometer Suite
Watershed	The area of land draining into a river is referred to as its catchment or watershed.
Water Table	Upper boundary of aquifer.
Wave	1. A periodic disturbance which moves through or over the surface of the medium (eg. water) with speed dependent upon the properties of the medium. It is characterised by frequency, length, and amplitude. 2. A ridge-like deformation, or undulation of a liquid or solid surface.
WST	Water Surface Temperature
WMO	World Meteorological Organisation (UN)
Zooplankton	Minute marine animals.

crc·si

CSIRO

Australian Government
Geoscience Australia

bushfire&natural
HAZARDSCRC

FRONTIER SI